ENGINEERING MECHANICS 2012

18th INTERNATIONAL CONFERENCE

MAY 14-17, 2012, SVRATKA, CZECH REPUBLIC

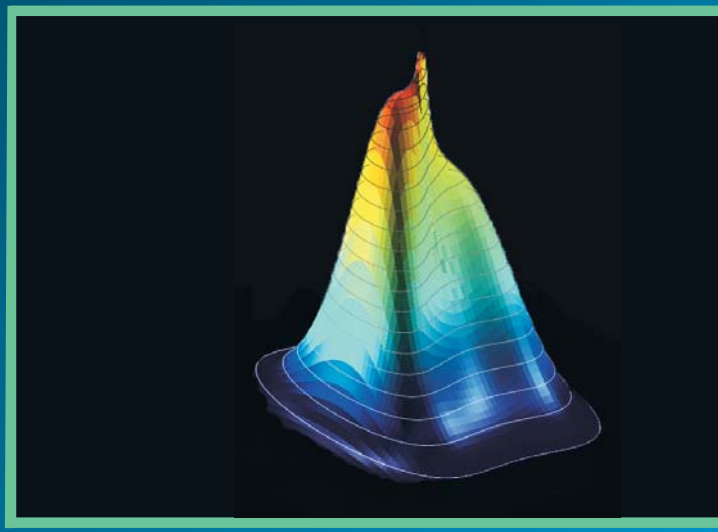

CONFERENCE PROCEEDINGS

Editors: Jiří NÁPRSTEK and Cyril FISCHER

ENGINEERING MECHANICS 2012

18th INTERNATIONAL CONFERENCE
MAY 14-17, 2012, SVRATKA, CZECH REPUBLIC

CONFERENCE PROCEEDINGS

Editors: Jiří Náprstek and Cyril Fischer

Association for Engineering Mechanics

Institute of Theoretical and Applied Mechanics,
Academy of Sciences of the Czech Republic, v.v.i.

Institute of Solid Mechanics, Mechatronics and Biomechanics,
Faculty of Mechanical Engineering, Brno University of Technology

Institute of Thermomechanics,
Academy of Sciences of the Czech Republic, v.v.i.

ŽĎAS, a.s., Žďár nad Sázavou

IFTOMM Member Committee of the Czech Republic

Czech Society for Mechanics

All papers were reviewed by members of the international scientific committee.

The complete set of EM2012 Conference Proceedings consists of two parts:

- **BOOK OF EXTENDED ABSTRACTS**
- **CD ROM (full text of papers and extended abstracts)**

First edition, 2012

Cover figure: Probability density function of a Duffing type SDOF system under multiplicative random excitation. R. Král, J. Náprstek

ISBN 978-80-86246-39-0 (printed, Book of Extended Abstracts)
ISBN 978-80-86246-40-6 (electronic, CD ROM)
ISSN 1805-8248 (printed)
ISSN 1805-8256 (electronic, CD ROM)

The Conference is hosted by the hotel ŽĎAS at Svratka

Honorary committee:

Miroslav Šabart, MSc — **Managing Director of the ŽĎAS, a.s.**

František Mládek — **Mayor of Svratka**

Scientific committee:

Jiří Náprstek, DSc (chairman)
ITAM ASCR, Prague

Prof. Ján Benčat, PhD.
University of Žilina, SK

Prof. Radim Čajka, PhD.
VSB - Technical University of Ostrava, CZ

Assoc. Prof. Vladimír Čech, PhD.
OPROX, a.s., Brno, CZ

Prof. Miloš Drdácký, Dsc.
ITAM AS CR, Prague, CZ

Assoc. Prof. Karel Frydrýšek, PhD.
VSB - Technical University of Ostrava, CZ

Vladimír Fuis, PhD.
Institute of Thermomechanics AS CR, Brno, CZ

Prof. Ardeshir Guran, PhD.
Institute of Structronics, Ottawa, Canada

Jaromír Horáček, Dsc.
Institute of Thermomechanics AS CR, Prague, CZ

Assoc. Prof. Lidia Ilieva-Mitutsova, PhD.
Bulgarian Academy of Sciences, Sofia, BG

Prof. Přemysl Janíček, Dsc.
Brno University of Technology, CZ

Prof. Zbyněk Jaňour, Dsc.
Institute of Thermomechanics AS CR, Prague, CZ

Prof. Miroslav Jícha, PhD.
Brno University of Technology, CZ

Prof. Milan Jirásek, DSc.
Czech Technical University in Prague, CZ

Prof. Zdeněk Kala, PhD.
Brno University of Technology, CZ

Prof. Zdeněk Knésl, PhD.
Institute of Physics of Materials AS CR, Brno, CZ

Prof. Alena Kohoutková, PhD.
Czech Technical University in Prague, CZ

Prof. Ctirad Kratochvíl, Dsc.
Institute of Thermomechanics AS CR, Brno, CZ

Prof. Anne-Maria Laukkanen, PhD.
University of Tampere; FI

Prof. Eduard Malenovský, Dsc.
Brno University of Technology, CZ

Prof. František Maršík, Dsc.
Institute of Thermomechanics AS CR, Prague, CZ

Prof. Arkadiusz Mężyk
Silesian University of Technology, Gliwice, PL

Jiří Minster, DSc.
ITAM AS CR, Prague, CZ

Prof. Bořek Patzák,PhD.
Czech Technical University in Prague, CZ

Prof. Kazimierz Peszynski, PhD.
Univ. of Technol. and Life Science, Bydgoszcz, PL

Prof. Jindřich Petruška, PhD.
Brno University of Technology, CZ

Assoc. Prof. Stanislav Pospíšil, PhD.
ITAM AS CR, Prague, CZ

Prof. Jaromír Příhoda, PhD.
Institute of Thermomechanics AS CR, Prague, CZ

Ladislav Půst, DSc.
Institute of Thermomechanics AS CR, Prague, CZ

Prof. Ján Sládek, Dsc.
ICA, SAS, Bratislava, SK

Prof. Vladimír Sládek, Dsc.
ICA, SAS, Bratislava, SK

Prof. Pavel Šafařík, PhD.
Institute of Thermomechanics AS CR, Prague, CZ

Prof. Michal Šejnoha, Dsc.
Czech Technical University in Prague, CZ

Prof. Alexander Tesár, Dsc.
ICA, SAS, Bratislava, SK

Prof. Václav Tesař, PhD.
Institute of Thermomechanics AS CR, Prague, CZ

Prof. Tomasz Topoliński
Univ. of Technol. and Life Science, Bydgoszcz, PL

Prof. Michael Valášek, DrSc
Czech Technical University in Prague, CZ

Prof. Pavel Vlasák, Dsc.
Institute of Thermomechanics AS CR, Prague, CZ

Prof. Jaroslav Zapoměl, Dsc.
Institute of Thermomechanics AS CR, Ostrava, CZ

Prof. Vladimír Zeman, Dsc.
University of West Bohemis in Pilsen, CZ

Prof. Milan Žmindák, PhD.
University of Žilina, SK

Main Headings

List of sections:

KEY - Keynote Lectures
BIO - Biomechanics
CME - Computational Mechanics
DYN - Dynamics
FLU - Fluid Mechanics
FRA - Fracture Mechanics
HIS - Historical structures
KIN - Kinematics
MCT - Mechatronics
REL - Reliability
SOL - Mechanics of Solids
TER - Thermodynamics

Table of contents

(alphabetic order according to the name of the first author)

KEYNOTE LECTURES

PAPERS

Table of contents

(grouped by sections)

KEY – Keynote Lectures

BIO – Biomechanics

CME – Computational Mechanics

DYN – Dynamics

FLU – Fluid Mechanics

FRA – Fracture Mechanics

HIS – Historical Structures

KIN – Kinematics

MCT – Mechatronics

REL – Reliability

SOL – Mechanics of Solids

TER – Thermodynamics

KEYNOTE LECTURES

18th International Conference
ENGINEERING MECHANICS 2012
Svratka, Czech Republic, May 14 – 17, 2012

pp. 3–4
Paper #36

APPLICATION OF CHAOTIC DYNAMICS IN NATURAL AND TECHNICAL SCIENCES

C. Kratochvíl*, P. Švéda, M. Hortel, A. Škuderová, M. Houfek**

Abstract: *During the entire 20th century there was a gradual transformation of scientific research, which has produced in science and technology especially in the extraordinary interest in complex dynamic systems. They are non-linear systems, operating environments and the irreversible complexity in their name means they have complex structures, relations and interactions (often of different physical nature). It turned out that an inherent attribute of these complex systems and chaos (deterministic and stochastic). The article will focus on some aspects of the manifestations of chaos, its spread, as well as identification, suppression and control. We will mention also other important phenomena - the possible emergence of a new order out of chaos.*

Keywords: ***Dynamical systems, bifurcation, chaotic attractors.***

1. Introduction

Our objects of interest are dynamic systems, describing changes in their status over time. There is a vector situated in the state space, describing system's state in arbitrary point on timeline. Dynamical systems describe the system of nonlinear differential equations. Changes in the system are determined by the solution of these equations and their waveforms are displayed as trajectories in state space.

The emergence of chaos in these systems can lead to extreme amplification of certain disorders. Systems also function as a filter, some disturbances intensify, suppress others. These failure processes are initially linear, but with increasing time nonlinearities are manifested precisely which systems to bring unstable chaotic state due to their sensitivity to character disorders, sensitivity to changes in initial conditions, or even change some system parameters. The result is the unpredictability of their future behavior. However, this orderability and identifiability can then emerge a new order, following the signs of chaos and conflict of chaos and order. And that is becoming one of the major themes of chaos in the current study of scientific knowledge not only in technology and natural sciences but also in other fields (economics, philosophy, etc.).

2. Open dynamical systems

According to Prigogine (1998) isolated the dynamical systems (in which no exchange of energy with the surroundings) usually evolve to chaos, i.e. towards disorder. Their future is only in the direction of entropy increase to its maximum. The increase in entropy becomes "indicator for the development of systems" in a figurative sense "arrow of time" - unless we admit, "... that time here is forgetting the initial conditions, growth and development of the uniformity towards disorder" (Heczko 2003). Current systems are systems to exchange energy, matter and information with others. They are open systems that evolve from simple to complex, from less organized structures to structures more structured. In other words, from the systems' structures "indistinguishable" to so-called "better organized". A certain level of complexity of the system is also subject to certain internal irreversibility of the processes inside the system and raises the volatility and instability. And the volatility and instability may be a source of new order and new order, and can create a "new order from chaos" *(Ordo ab Chaos)*.

* Prof. Ing. Ctirad Kratochvíl, DrSc., Ing. Martin Houfek, Ph.D., Mgr. Petr Švéda: Institute of Solid Mechanics, Mechatronics and Biomechanics, Department of Mechatronics, Faculty of Mechanical Engineering, Brno University of Technology; Technická 2896/2, 616 69 Brno; CZ, e-mail kratochvil@fme.vutbr.cz

** Ing. Milan Hortel, DrSc., Ing. Alena Škuderová, Ph.D.: Department D3 - Dynamics and Vibrations, Institute of Thermomechanics AS CR, v. v. i.; Dolejškova 1402/5, 182 00 Praha 8; CZ

It is in this context to define the term deterministic chaos, which is self-conceived team deterministic nonlinear open systems, where due to extreme sensitivity to initial conditions, failure (or some system parameters) leads to unpredictable behavior and the possible emergence of chaos (locally unstable and globally stable). Chaos often plays a creative role; as a result synergic effect leads to a certain self-regulation of systems. The result is that the structurally distributed energy entirely concentrated on certain symptoms - strange or chaotic tractors, representing the final states of the system.

3. The chaos is characterized by

- The chaotic structure is characterized by alternating states of irregular instability and dissipativity. These irregularities are the essence of the transition of different types of generators of chaos;

- Images show typical Poincare "infinitely" structured point set, consisting of clusters of points with relatively smooth transitions;

- In view of the phase plane (or in the state space), we see tractors strange (strange attractors), which are globally bounded but locally unstable display of complex non-periodic oscillations;

- Tin phase plane is often encountered with the distribution of state trajectories around more centers (usually two), symmetrically spaced around the origin;

- Frequency spectra of chaotic signals represent a significant set of isolated frequencies, among which are "dense areas" of local noise.

4. Conclusions

Here we mention "only" about some aspects of chaos. The paper will discuss the other factors, characterizing chaos: in particular the role of bifurcations that characterize extremely unstable states of open systems. Bifurcation can occur both due to external (accidental?) Effect and increase the influence of disorder in the system. We will mention the classification of chaos, his identity, get acquainted with the important class of chaotic attractors derived from Chu electronic circuits and we will reflect on ways to limit and control the chaos.

Questions unpredictable behavior of chaotic systems and the possibility of a new order will also be the subject of our discussion. Recall "just finding" a startling workers dealing with chaos. Chaotic systems can be put into an unstable state of external intervention, but it subsides after the systems "self" will return to its original condition. If cease interference occurs for systems to "break the original set of rules" and "restructuring". For the system will apply the new rules, although built on the basis of the original, but adapted to new circumstances. What does this mean? Chaotic systems are capable of spontaneous and independent of any outside influence self-organization!

The history of human knowledge continues to move toward discovering new patterns. However, each new law and the notion that it occurs, has a limited scope and duration. There is no reason to believe that the current instruments - differential equations - are still the best tool. I answer the question whether our world is deterministic or random chaotic is in fact uncertain. The answer is "only" that the world exists, evolves, and we observe it, and we are part of it. Our ideas about it - models can be deterministic or chaotic - but they are only approximate models (Pokorný, 2008).

References

Heczko, S. (2003) Teorie chaosu a chování otevřených systémů. *Marathon,* 4. Available on-line http://www.valencik.cz/marathon/03/mar030400.htm

Pokorný, P. (2008) Deterministický chaos-plod počítačové fyziky, *Čs. čas. pro fyziku*, 58.

Prigogine, I. (1998) *Modern Thermodynamics*, J. Willey and Sons, Chicester.

18th International Conference
ENGINEERING MECHANICS 2012
Svratka, Czech Republic, May 14 – 17, 2012

pp. 5–21
Paper #97

TWO-SCALE MODELLING OF STRONGLY HETEROGENEOUS CONTINUA USING THE HOMOGENIZATION APPROACH

E. Rohan* **R. Cimrman**** **V. Lukeš*****

Abstract: *The notion of strong heterogeneity is considered in the sense of material scaling: the idea is to study mathematical models where the coefficients of the partial differential equations associated with one of the material phases depend on the characteristic size ε of the microstructure. This modeling ansatz is justified to represent high contrasts in material properties of different components; it was applied to study wave propagation in two-phase elastic composites with "weak" inclusions, where elasticity is scaled by ε^2, or to describe poroelastic behaviour in double-porous media, where permeability of the second porosity is proportional ε^2. Perforated structures can be handled using similar mathematical tools. For homogenization of thin structures the scaling is related to the thickness, which leads to reduced spatial dimension of the problem. This paper summarizes some models developed using the homogenization approach; namely applications in modelling elastic waves, acoustic transmission and fluid flow in porous media are discussed.*

Keywords: ***homogenization, composites, wave propagation, porous media, perfusion***

1. Introduction

In the context of material modeling, the notion of homogenization is related usually to some approximate treatment of heterogeneous continua designed as mixtures of different constituents. The differences concern just values of the material parameters, or they are more substantial – for instance mixtures of fluid and solid components are considered. In the mechanical community, the homogenization is often understood in the sense of various averaging techniques based on definition of the RVE, the reference volume element. The RVE (small enough, but also sufficiently large) is subject to special loadings and the structural responses allow to compute the effective parameters characterizing the material behaviour. Apart of this averaging technique, there is the Eshelby theory which can describe behaviour of composites with elliptic inclusions which do not affect each other, being sparsely distributed at long distances.

The homogenization we have in mind is based on the asymptotic analysis of partial differential equations describing the continuum behaviour, whereby the small parameter describing the "microstructure size" influences space variation of the equation coefficients. We focus on problems characterized by strong heterogeneities — *large contrasts* in material coefficients; it is shown how the large contrast pronounced by its relationship with the scale may lead to "limit behaviour" which is qualitatively completely different from the one characterizing the original constituents.

Nowadays there exist several methods which allow one to obtain a model of homogenized continuum, i.e. by studying asymptotic behaviour of partial differential equations (PDEs) which governs a given problem characterized by the scale ε. The **periodic unfolding** which has been introduced and employed within the homogenization community recently, Cioranescu et al. (2008a), is relatively easy to use for linear, or quasi-linear problems. It presents a powerful tool for homogenization of locally periodic media even for those who have merely a little training in functional analysis.

Challenges and limitations. The asymptotic analysis of heterogeneous media provides a modeling tool which enables to retain important features of the structure (or microstructure) while reducing complexity of the problem in its primary setting. Periodically distributed structural details inducing some

* Prof. Dr. Ing. Eduard Rohan: Faculty of Applied Sciences, University of West Bohemia in Pilsen, Univerzitní 22, 306 14 Plzeň; CZ, e-mail: rohan@kme.zcu.cz
** Ing. Robert Cimrman, Ph.D.: New Technologies Research Centre, University of West Bohemia in Pilsen, Univerzitní 22, 306 14 Plzeň; CZ, e-mail: cimrman3@ntc.zcu.cz
*** Ing. Vladimír Lukeš, Ph.D.: Faculty of Applied Sciences, University of West Bohemia in Pilsen, Univerzitní 22, 306 14 Plzeň; CZ, e-mail: lukes@kme.zcu.cz

fluctuations of the physical fields can be condensed into the homogenized coefficients of the limit macroscopic (i.e. homogenized) model. Its numerical discretization leads to a computationally tractable problem which can be solved much cheaper than the original problem discretized with enormously large numbers of degrees of freedom, such that a huge computational power would be required to obtain a solution. Obviously, the benefits of "simplified" models obtained by homogenization is even more challenging when inverse problems are treated, like optimal design of the material structure.

However, the homogenized models describe the asymptotic behaviour, so that the limit behaviour is just an approximation of the reality which corresponds to a given scale $\varepsilon_0 > 0$. Apparently, the approximation becomes more accurate with decreasing ε_0, i.e. when the macroscopic structure involves more and more repeating microstructural periods.

Once the global response is known, having solved the macroscopic problem, the detail fluctuating response at the microscopic level can be computed for a given macroscopic position x. This procedure is often called the *microscopic response recovery* and is based on the *corrector functions*. They are obtained by combining the macroscopic solution at x with the local *corrector basis functions*. Thus, also the gradients of the quantity of interest can be obtained, like strains, stresses, or seepage velocities in porous media.

Models with scale-dependent parameters, like models of large contrast composites as an example, may amplify some special effects when passing to the limit with $\varepsilon \to 0$. For instance, limit model of the high contrast elasticity medium exhibits the dispersive behaviour, although the standard composites lead to a nondispersive medium which, in the limit, is characterized by the homogenized elasticity and by the mean-value of the density. In contrast, the ε^2-scaling of the elasticity coefficients in one of the composite constituents results in a frequency-dependent homogenized mass coefficients, hence the wave dispersion is obtained even in the limit $\varepsilon \to 0$.

It is worth to note that the standard homogenized model of composites preserve the homogeneous medium when all the constituents are identical, i.e. homogenization of a homogeneous material results in the same material. This is not possible, in principle, for a heterogeneous medium with scale-dependent parameters which, providing a strong heterogeneity, does not allow to obtain any standard homogeneous medium in the limit.

The main issues discussed in the paper are the following:

- **Homogenization applied in wave propagation problems**. Only solid composite materials are considered here, although an extension for fluid saturated media has been addressed by Mielke and Rohan (2012). The main focus is in the phononic materials ("band-gap materials"), characterized by large heterogeneity in the elasticity coefficients, and in the acoustic transmission on perforated interfaces immersed in the acoustic fluid. Extensions to electromagnetic waves and piezoelectric composites were treated also Leugering et al. (2010).
- **Homogenization of fluid-saturated porous materials** (FSPM) with *double porosity*. It is shown how different topologies of the microstructure with respect to double porosity lead to qualitatively different models. An extension for large-deforming media was proposed, which is based on linearized subproblems. Finally, homogenization of the *fluid perfusion in layered double-porous medium* is described. These topics have applications in modeling the tissue perfusion and in modeling bone poroelasticity.

2. Wave propagation and dispersion in heterogeneous media

In the context of the homogenization method, waves in solid composites and solid-fluid mixtures have been discussed e.g. in Sanchez-Palencia (1980). The classical treatment of elastic waves leads to vanishing wave dispersion in the limit $\varepsilon \to 0$, however, the approach reported by Ávila et al. (2008); Rohan et al. (2009); Rohan and Miara (2009, 2011) allows to retain the dispersion properties even in the limit; this is possible due to the *strong heterogeneity* – large contrast in the elasticity coefficients and the special scaling ansatz of these coefficients. Besides the elastic composites, some other topics related to wave propagation were considered, namely those related to piezo-materials and acoustic waves on a perforated interface.

Combinations of all these topics are natural and challenging in the view of modeling smart systems transmitting waves:

- *Piezo-phononic materials* form a quite natural extension of the purely elastic phononic materials, they provide even more flexibility in designing smart devices, due to possible interplay between the electric field and deformations. The homogenization issues were discussed in Rohan and Miara (2006b, 2009); Cimrman and Rohan (2010).
- It is desirable to extend the acoustic transmission conditions for *compliant perforated plates*, when the plate elasticity cannot be neglected. Moreover, the surface acoustic waves propagating along the interface may interfere with the plate structure – the plate can be constructed as a phononic, or piezo-phononic material, so that band gaps of the plate can influence qualitatively the acoustic transmission in the surrounding medium.
- For homogenization of the electromagnetic waves, analogical methods and modeling approaches are applied, as those introduced in the study of elastic waves. Moreover, in combination with piezoelectric materials, coupling between acoustic and electromagnetic waves is a relevant issue.

2.1. Phononic materials

The *phononic materials (crystals)* are multi-phasic (bi-phasic) elastic media with periodic structure and with large contrasts in elasticity of the phases. Often they are called the *phononic band-gap materials* due to their essential property to suppress propagation of elastic waves in certain frequency ranges. The phononic crystals are used in modern technologies to generate frequency filters, beam splitters, sound or vibration protection devices (for noise reduction), or they may serve as waveguides. Similar phenomena in the propagation of the electromagnetic field were studied even before in the context of the *photonic crystals*.

The method of homogenization provides a useful modeling tool which allows for prediction of the band gap distribution for stationary or long guided waves. The "standard computational approach" based on a full heterogeneous model requires to evaluate the whole Brillouin zone for the dispersion diagram reconstruction; as the consequence, it leads to a killing computational complexity. On the other hand, the homogenized model captures the essential features of the phononic material and may serve a good approximation of the band-gap prediction, while keeping the computational complexity at a very low level. As an advantage, the homogenized model can be employed in inverse problems like optimal design of phononic structures.

Periodic strongly heterogeneous material We consider an open bounded domain $\Omega \subset \mathbb{R}^3$ and the reference (unit) cell $Y =]0,1[^3$ with an embedded inclusion $\overline{Y_2} \subset Y$, whereby the matrix part is $Y_1 = Y \setminus \overline{Y_2}$. Let us note, that Y may be defined more generally as a parallelepiped. Using the reference cell we generate the decomposition of Ω into the union of inclusions and the matrix. Inclusions have the size $\sim \varepsilon$,

$$\Omega_2^\varepsilon = inter \bigcup_{k\in\mathbb{K}^\varepsilon} \varepsilon(\overline{Y_2}+k)\ , \text{ where } \mathbb{K}^\varepsilon = \{k\in\mathbb{Z}|\ \varepsilon(k+\overline{Y_2})\subset\Omega\}\ , \tag{1}$$

whereas the perforated matrix is $\Omega_1^\varepsilon = \Omega \setminus \overline{\Omega_2^\varepsilon}$.

We assume that inclusions are occupied by a "very soft material" in the sense that the coefficients of *the elasticity tensor in the inclusions* are significantly smaller than those of the matrix compartment, however *the material density* is comparable in both the compartments. Such structures exhibit remarkable band gaps; this was proved by both experiments and modeling. Here, as an important feature of the modeling based on asymptotic analysis, the ε^2 scaling of elasticity coefficients in the inclusions appears; the following ansatz is considered:

$$\rho^\varepsilon(x) = \begin{cases} \rho^1 & \text{in } \Omega_1^\varepsilon, \\ \rho^2 & \text{in } \Omega_2^\varepsilon, \end{cases} \qquad c_{ijkl}^\varepsilon(x) = \begin{cases} c_{ijkl}^1 & \text{in } \Omega_1^\varepsilon, \\ \varepsilon^2 c_{ijkl}^2 & \text{in } \Omega_2^\varepsilon. \end{cases} \tag{2}$$

In analogy, the PZ phononic materials can be treated.

Modeling the stationary waves We consider stationary wave propagation in the medium introduced above. Although the problem can be treated for a general case of boundary conditions, for simplicity we restrict the model to the description of clamped structures loaded by volume forces. We assume harmonic single-frequency volume forces $\boldsymbol{F}(x,t) = \boldsymbol{f}(x)e^{i\omega t}$, where $\boldsymbol{f} = (f_i), i = 1,2,3$ is its local amplitude and ω is the frequency. Correspondingly, a dispersive displacement field with the local magnitude $\boldsymbol{u}^\varepsilon$ has the form $\boldsymbol{U}^\varepsilon(x,\omega,t) = \boldsymbol{u}^\varepsilon(x,\omega)e^{i\omega t}$. This allows us to study the steady periodic response of the medium, as characterized by displacement field $\boldsymbol{u}^\varepsilon$ which satisfies the following boundary value problem:

$$\begin{aligned} -\omega^2\rho^\varepsilon\boldsymbol{u}^\varepsilon - \mathrm{div}\boldsymbol{\sigma}^\varepsilon = \rho^\varepsilon\boldsymbol{f} \quad \text{in } \Omega, \\ \boldsymbol{u}^\varepsilon = 0 \quad \text{on } \partial\Omega, \end{aligned} \tag{3}$$

where the stress tensor $\boldsymbol{\sigma}^\varepsilon = (\sigma_{ij}^\varepsilon)$ is expressed in terms of the linearized strain tensor $\boldsymbol{e}^\varepsilon = (e_{ij}^\varepsilon)$ by the Hooke's law $\sigma_{ij}^\varepsilon = c_{ijkl}^\varepsilon e_{kl}(\boldsymbol{u}^\varepsilon)$.

Homogenized model Due to the *strong heterogeneity* in the elastic coefficients, the homogenized model exhibits dispersive behaviour; this phenomenon cannot be observed when standard two-scale homogenization procedure is applied to a medium without scale-dependent material parameters. In Ávila et al. (2008) the unfolding operator method of homogenization (Cioranescu et al., 2008a) was applied with the strong heterogeneity ansatz (2) and in Rohan and Miara (2006b) the analogous result was obtained for the piezoelectric material with the strong heterogeneity scaling.

The resulting limit equations, as derived in Ávila et al. (2008), describe the structure behaviour at the "macroscopic"scale. They involve the homogenized coefficients which depend on the characteristic responses at the "microscopic" scale.

The frequency–dependent homogenized mass involved in the macroscopic momentum equation is expressed in terms of eigenelements $(\lambda^r, \boldsymbol{\varphi}^r) \in \mathbb{R}\times\mathbf{H}_0^1(Y_2), r = 1,2,\ldots$ of the elastic spectral problem which is imposed in inclusion Y_2 with $\boldsymbol{\varphi}^r = 0$ on ∂Y_2:

$$\int_{Y_2} c_{ijkl}^2 e_{kl}^y(\boldsymbol{\varphi}^r)\, e_{ij}^y(\boldsymbol{v}) = \lambda^r \int_{Y_2} \rho^2\boldsymbol{\varphi}^r\cdot\boldsymbol{v} \quad \forall \boldsymbol{v}\in\mathbf{H}_0^1(Y_2)\ , \quad \int_{Y_2}\rho^2\boldsymbol{\varphi}^r\cdot\boldsymbol{\varphi}^s = \delta_{rs}\ . \tag{4}$$

To simplify the notation we introduce the *eigenmomentum* $\boldsymbol{m}^r = (m_i^r)$,

$$\boldsymbol{m}^r = \int_{Y_2}\rho^2\boldsymbol{\varphi}^r. \tag{5}$$

The effective mass of the homogenized medium is represented by mass tensor $\boldsymbol{M}^* = (M_{ij}^*)$, which is evaluated as

$$M_{ij}^*(\omega^2) = \frac{1}{|Y|}\int_Y \rho\delta_{ij} - \frac{1}{|Y|}\sum_{r\geq 1}\frac{\omega^2}{\omega^2-\lambda^r} m_i^r m_j^r\ ; \tag{6}$$

The elasticity coefficients are computed just using the same formula as for the perforated matrix domain, thus being independent of the material in inclusions:

$$C_{ijkl}^* = \frac{1}{|Y|}\int_{Y_1} c_{pqrs}e_{rs}^y(\boldsymbol{w}^{kl}+\boldsymbol{\Pi}^{kl})e_{pq}(\boldsymbol{w}^{ij}+\boldsymbol{\Pi}^{ij})\ , \tag{7}$$

where $\boldsymbol{\Pi}^{kl} = (\Pi_i^{kl}) = (y_l\delta_{ik})$ and $\boldsymbol{w}^{kl}\in\mathbf{H}_\#^1(Y_1)$ are the corrector functions satisfying

$$\int_{Y_1} c_{pqrs}e_{rs}^y(\boldsymbol{w}^{kl}+\boldsymbol{\Pi}^{kl})e_{pq}^y(\boldsymbol{v}) = 0 \quad \forall\boldsymbol{v}\in\mathbf{H}_\#^1(Y_1)\ . \tag{8}$$

Above $\mathbf{H}_\#^1(Y_1)$ is the restriction of $\mathbf{H}^1(Y_1)$ to the Y-periodic functions (periodicity w.r.t. the homologous points on the opposit edges of ∂Y).

The *homogenized equation* of the "macromodel", here presented in its differential form, describes the macroscopic displacement field $\boldsymbol{u}$:

$$\omega^2 M^*_{ij}(\omega) u_j + \frac{\partial}{\partial x_j} C^*_{ijkl} e_{kl}(\boldsymbol{u}) = M^*_{ij}(\omega) f_j \ , \tag{9}$$

where M^*_{ij} at the r.h.s. loading term appears due to the volume forces in (3) proportional to the density.

Using this equation, the dispersion of guided waves can be studied, see Rohan et al. (2009). Heterogeneous structures with finite scale of heterogeneities exhibit the frequency *band gaps* for certain frequency bands. In the *homogeneized medium*, waves can be propagated provided the mass tensor $\boldsymbol{M}^*(\omega)$ is positive definite, or positive semidefinite; this effect is explained below.

We can derive a homogenized model analogous to (9) also for the *piezoelectric phononic* (piezophononic) materials with "soft inclusions", i.e. the scaling (2) is adopted also for parameters of dielectricity, d_{ij}, and piezoelectric coupling, g_{kij}. In this case, however, the spectral problem analogous to (4) comprises an additional constraint arising from electric charge conservation, see Rohan and Miara (2006b); Cimrman and Rohan (2010) for details.

Band gap prediction As the main advantage of the homogenized model (9), by analyzing the dependence $\omega \to \boldsymbol{M}^*(\omega)$ one can determine distribution of the band gaps; it was proved in Ávila et al. (2008), *cf.* Rohan et al. (2009) that there exist frequency intervals G^k, $k = 1, 2, \ldots$ such that for $\omega \in G^k \subset]\lambda^k, \lambda^{k+1}[$ at least one eigenvalue of tensor $M^*_{ij}(\omega)$ is negative. Those intervals where all eigenvalues γ_M of M^*_{ij} are negative are called *strong*, or *full* band gaps. In the latter case the negative sign of the mass changes the hyperbolic type of the wave equation to the elliptic one, therefore, no waves can propagate. In the "weak" bad gap situation only waves with certain polarization can propagate, as explained below.

The band gaps can be classified w.r.t. the waves polarization which is determined in terms of the eigenvectors of $M^*_{ij}(\omega)$. Given a frequency ω, there are three cases to be distinguished according to the signs of eigenvalues $\gamma^r_M(\omega)$, $r = 1, 2, 3$ (in 3D), determining the "positivity, or negativity" of the mass:

1. **propagation zone** – All eigenvalues of $M^*_{ij}(\omega)$ are positive: then homogenized model (9) admits wave propagation without any restriction of the wave polarization;

2. **strong band gap** – All eigenvalues of $M^*_{ij}(\omega)$ are negative: then homogenized model (9) does *not* admit any wave propagation;

3. **weak band gap** – Tensor $M^*_{ij}(\omega)$ is indefinite, i.e. there is at least one negative and one positive eigenvalue: then propagation is possible only for waves polarized in a manifold determined by eigenvectors associated with positive eigenvalues. In this case the notion of wave propagation has a local character, since the "desired wave polarization" may depend locally on the position in Ω.

In Fig. 1 we introduce a graphical illustration of the band gaps analyzed for an L-shaped inclusions. If inclusions (considered in 2D) are symmetric w.r.t. more than 1 axis of symmetry, than only strong band gaps exist. More details on the band gap properties and their relationship to the dispersion of guided waves were discussed in Rohan et al. (2009).

Piezo-electric (PZ) materials. Homogenization of a standard PZ heterogeneous medium leads to the effective constitutive law of the standard form, whereby the effective material parameters are computed for a specific microstructure. However, in Rohan and Miara (2006a) we show that combination of two standard PZ materials can lead to a new material with unusual and interesting properties (new non-zero entry in the coupling tensor) — this is the key for designing the so-called metamaterials, *cf.* Rohan and Miara (2009); Leugering et al. (2010). The PZ materials with large contrasts (respected by scaling in analogy with (2)) in all PZ coefficients were considered in homogenization of *phononic materials*, see Rohan and Miara (2006b); Cimrman and Rohan (2010). It is worth noting that for HZ the above mentioned statements on the structural symmetry do not hold because of the material anisotropy; typically only the weak band gaps exist (Cimrman and Rohan, 2010).

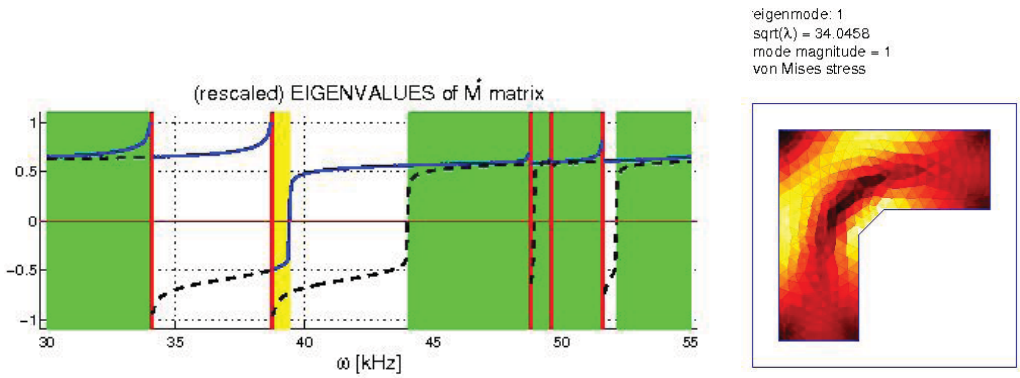

Fig. 1: Left: weak band gaps (white) and strong band gaps (yellow) computed for an elastic composite with L-shaped inclusions, the green bands are propagation zones (the solid and dashed curves describe eigenvalues of $\mathbf{M}^*(\omega)$*); Right: the first eigenmode of the L-shaped clamped elastic inclusion.*

2.2. Acoustic wave transmission on perforated interfaces

Homogenization can be employed to develop approximate models of various transmission and transport phenomena on thin interfaces characterized by a "microstructure" (Cioranescu et al., 2008b). In Rohan and Lukeš (2010b) the homogenization is applied to approximate the acoustic transmission between two halfspaces separated by an interface formed as a solid (rigid) plate perforated periodically by holes of arbitrary shapes, so that the two halfspaces are connected. We consider the acoustic medium occupying domain Ω^G which is subdivided by perforated plane Γ_0 in two disjoint subdomains Ω^+ and Ω^-, so that $\Omega^G = \Omega^+ \cup \Omega^- \cup \Gamma_0$. Denoting by p the acoustic pressure field in $\Omega^+ \cup \Omega^-$, in a case of no convection flow, the acoustic waves in Ω^G are described by the following equations (ω is the frequency of the incident wave related to wave number k through the speed of sound propagation $c = \omega/k$),

$$\begin{aligned} c^2\nabla^2 p + \omega^2 p = 0 \quad &\text{in } \Omega^- \cup \Omega^+ \,, \\ + \text{ boundary conditions} \quad &\text{on } \partial\Omega^G \,, \end{aligned} \tag{10}$$

supplemented by transmission conditions on interface Γ_0. In Rohan and Lukeš (2010b) such conditions were obtained by the two-scale homogenization of a layer with an immersed sieve-like obstacle. In Figure 2 we illustrate such a layer $\Omega_\delta = \Gamma_0 \times]-\delta/2, \delta/2[\subset \mathbb{R}^3$ embedded in $\Omega^G = \Omega^+_\delta \cup \Omega^+_\delta \cup \Omega_\delta \cup \Gamma^\pm_\delta$. The acoustic medium occupies domain $\Omega^\varepsilon_\delta = \Omega_\delta \setminus \overline{S^\varepsilon_\delta}$, where S^ε_δ is the solid *rigid* obstacle which in a simple layout has a form of the periodically perforated slab. However, the aim of the study by Rohan and Lukeš (2010b) was to obtain transmission conditions which describe quite general shape of periodic perforations.

To derive the transmission conditions, the acoustic waves in the layer were subject to asymptotic analysis w.r.t. size of the perforation ε which is related to the thickness $\delta = h\varepsilon$, where $h > 0$ is fixed. The acoustic potential $p^{\varepsilon\delta}$ satisfies the Helmholtz equation in $\Omega^\varepsilon_\delta$

$$\begin{aligned} c^2\nabla^2 p^{\varepsilon\delta} + \omega^2 p^{\varepsilon\delta} = 0 \quad &\text{in } \Omega^\varepsilon_\delta \,, \\ c^2 \frac{\partial p^{\varepsilon\delta}}{\partial n^\delta} = -\mathrm{i}\omega g^{\varepsilon\delta\pm} \quad &\text{on } \Gamma^\pm_\delta \,, \\ \frac{\partial p^{\varepsilon\delta}}{\partial n^\delta} = 0 \quad &\text{on } \partial S^\varepsilon_\delta \cup \partial\Omega^\infty_\delta \,, \end{aligned} \tag{11}$$

where by n^δ we denote the normal vector outward to Ω_δ. Assuming convergence of the interface fluxes (velocities) $g^{\varepsilon\delta} \to g^0$ (in a sence), by homogenization $\varepsilon \to 0$, convergence of $p^{\varepsilon\delta} \to p^0$ is obtained and (11) transforms into the following equations involving homogenized coefficients A, B, F and the layer

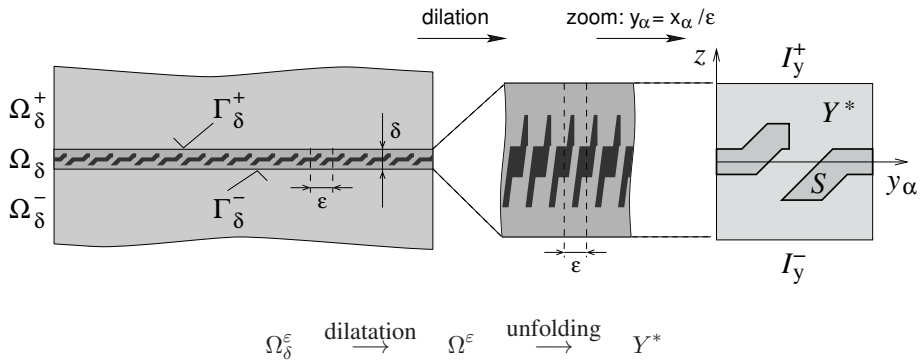

Fig. 2: Left: global problem imposed in entire domain Ω^G before homogenization of the layer Ω_δ. Right: representative cell of the periodic structure. The dark patterns represent the obstacles in the fluid.

porosity f^*,

$$
\begin{aligned}
-\partial_\alpha(A_{\alpha\beta}\partial_\beta p^0) + \omega^2 f^* p^0 - \mathrm{i}\omega\partial_\alpha(B_\alpha g^0) = 0 \quad &\text{on } \Gamma_0\ , \\
-\mathrm{i}\omega h B_\beta \partial_\beta p^0 + \omega^2 F g^0 = -\mathrm{i}\omega\frac{1}{\varepsilon_0}[p]_-^+ \quad &\text{on } \Gamma_0\ , \\
A_{\alpha\beta}\partial_\beta p^0 = 0 \quad &\text{on } \partial\Gamma_0\ ,
\end{aligned}
\tag{12}
$$

where $[p]_-^+/\varepsilon_0$ is the jump of p relative to the "real" layer thickness $h\varepsilon_0 > 0$ and is evaluated on Γ_0 by the acoustic potential field p in Ω^G. To compute A, B, F, microscopic problems have to be solved in the reference microscopic cell $Y^* = Y \setminus \overline{S}$, where domain S represents the obstacle generating the perforation, see Fig. 2 (right).

For the "global problem" (10), the transmission conditions are presented in an implicit form by equations (12): they couple $[p]_-^+$ with normal derivatives $\partial p/\partial n^+ = -\partial p/\partial n^- = -\mathrm{i}\omega g^0$, whereby p^0 describing the "in-layer" wave serves as an internal variable of the model. Out of resonances, p^0 vanishes when $(B_\beta) = 0$, see Fig. 3, Amic $\#1$.

To illustrate influence of the perforation design on the global acoustic response in domain Ω^G, in Fig. 3 the transmission losses for a waveguide fitted with two different perforations on Γ_0 is depicted.

3. Fluid saturated porous media (FSPM) with dual porosity

The models of *fluid saturated porous media* (FSPM) which we have in mind are relevant to the scale where individual fluid-filled pores are not distinguishable, so that at any point of the bulk material both the solid and fluid phases are present, being distributed according to the volume fractions, cf. Coussy (2004); de Boer (2000). The phenomenological description was developed by M. Biot (Biot, 1955); his model is considered here as a basis for modeling media with large contrasts in the hydraulic permeability coefficients, thus, presenting the *strong heterogeneity*. Such a modeling option is related to the notion of the double porosity (Auriault and Boutin, 1992; Arbogast et al., 1990) which introduces yet another scale with even smaller characteristic size than the one characterizing the "microscopic level".

Two important phenomena can be noticed when homogenizing the FSPM:

- In high contrast media, in general, the topology of the microstructure decomposition influences qualitatively the homogenization result.
- When evolutionary models are homogenized, the fading memory effect of the homogenized constitutive laws arise from the fluid microflow governed by the Darcy law.

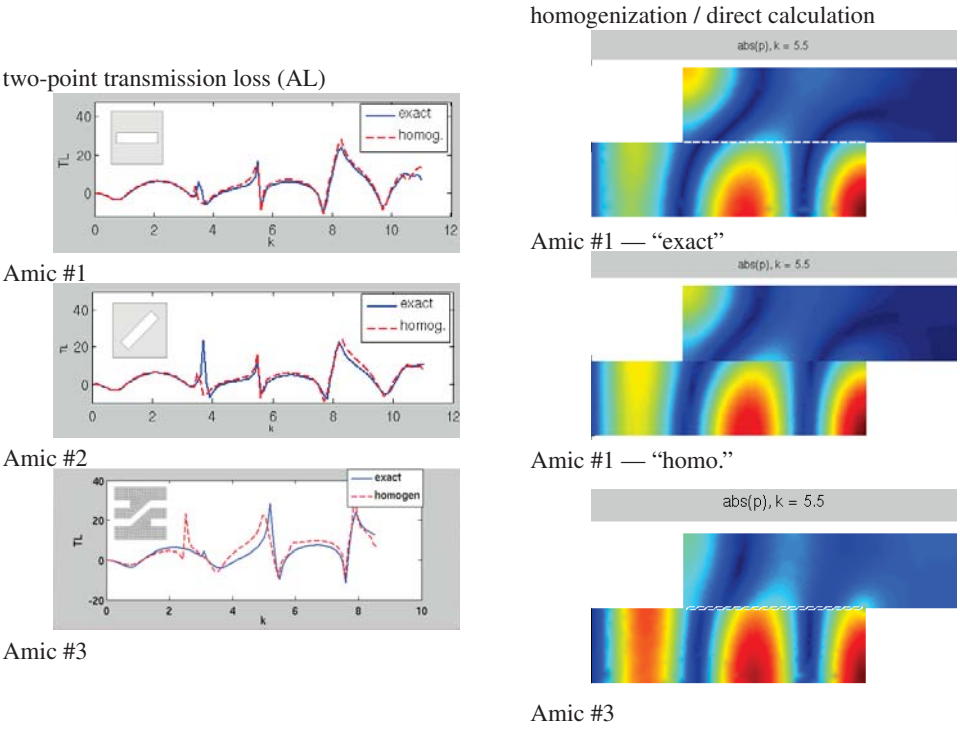

Fig. 3: Left: Transmission losses for three perforation types, #1,#2#3; comparison of solutions obtained for the homogenized transmission conditions (dashed line) with the corresponding direct approximation of the perforated domains (solid line). Right: Spatial distribution of the acoustic potential in the macroscopic domain.

3.1. Biot model and double porosity

The Biot model involves three essential constitutive laws: 1) the relationship between the drained solid skeleton "macroscopic" deformation $\boldsymbol{e}(t,x)$, the fluid pressure in pores $p(t,x)$ and the total stress $\boldsymbol{\sigma}(t,x)$, 2) the relationship between the variation of the fluid content, skeleton (macroscopic) deformation, and the fluid pressure, 3) the Darcy law relating the seepage velocity, $\boldsymbol{w}(t,x)$, with "dynamic fluid pressure", i.e. the static part $p(t,x)$ and the fluid inertia part. In the DISSERTATION , only quasistatic problems are studied so that the following form of the equations is relevant:

$$\begin{aligned} -\nabla\cdot(\boldsymbol{D}\boldsymbol{e}(\boldsymbol{u})) + \nabla\cdot(\boldsymbol{\alpha}p) &= \boldsymbol{f}\ , \\ \boldsymbol{K}^{-1}\boldsymbol{w} + \nabla p &= 0\ , \\ \boldsymbol{\alpha} : \boldsymbol{e}(\dot{\boldsymbol{u}}) + \nabla\cdot\boldsymbol{w} + \frac{1}{\mu}\dot{p} &= 0\ , \end{aligned} \tag{13}$$

where $\boldsymbol{D}$ is the elasticity tensor associated to the drained skeleton, $\boldsymbol{K}$ is the hydraulic permeability (specific to a given fluid), α is the poroelastic stress coefficient and μ is the Biot modulus which depends on compressibility of the solid skeleton and fluid. Obviously, the three field formulation can be reduced to the two field formulation by eliminating $\boldsymbol{w}$. Further reduction of the model is possible when both the phases are incompressible, i.e. when $1/\mu \to 0$ and $\boldsymbol{\alpha} \to \boldsymbol{I}$.

Double porosity and permeability scaling The double porous media are frequent in nature. Besides various fissured rocks, the dual porosity is presented by the canalicular network of the so-called matrix constituting the structure of cortical bone tissue, see Fig. 5, Rohan et al. (2012).

In the *dual porosity*, the permeability coefficient is proportional to ε^2, where ε is the dimensionless scale parameter. In Fig. 4, the *dual porosity* is represented by an array of"horizontal" channels of the

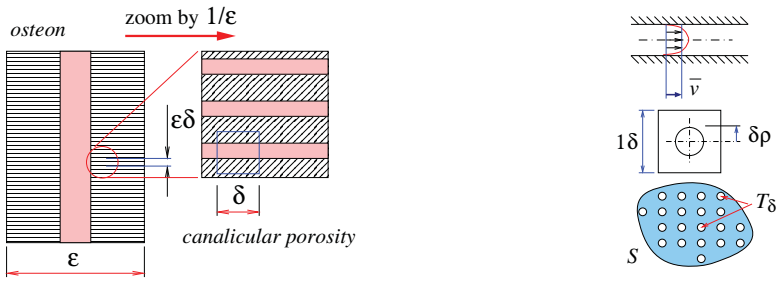

Fig. 4: Left: schematic illustration of the osteon double porous structure. Right: a scheme explaining the permeability δ^2-dependence due to the velocity profile in an array of canals. The total perfused area S is perforated by canals with total cross-section T_δ (bottom), each canal has the cross-section $\pi\rho^2\delta^2$; the square periodic cell is shown (middle) as well as the velocity profile in one canal. (top).

canalicular porosity. It can be shown, Rohan et al. (2012) that if the ratio between the macro-, meso- and micro- scales is the same, i.e. $\delta \sim \varepsilon$, the scale dependent permeability is $\sim \varepsilon^2$, so that the seepage in the dual porosity is given by $\boldsymbol{w}^\varepsilon = -\varepsilon^2 \boldsymbol{K}_\nu \nabla p$, where $\boldsymbol{K}_\nu$ is disproportional to the fluid viscosity.

3.2. Homogenization of FSPM with application in biomechanics

The theory of FSPM has been developed in adherence to applications in civil engineering, oil industry, mining and rock mechanics. Also the tissue biomechanics presents a new challenging field of applications, due to large complexity of processes and interactions undergoing in living tissues.

In contrast with soils, rocks and materials used in civil engineering, the biological materials exhibit much larger organization of their structure. To illustrate the difference, one can consider seepage and consolidation in moist soils, on one hand, and the sophisticated system of heart muscle perfusion, on the other hand. In both these cases, the material contains the solid and liquid phases, however, the structure of pores is very different.

There are several problems in the tissue biomechanics were homogenization with the dual porosity ansatz can be employed as a convenient modelling tool.

- The *smooth muscle tissue* model (Rohan, 2006b) is based on the large deforming FSPM with locally periodic structure. The representative cell contains the fluid-filled inclusion representing the muscle cell. The cytoskeleton is approximated very roughly as a truss with prestretch corresponding to the cell contraction. The extracellular space (the matrix) represents the dual porosity, whereby fluid can flow between the matrix and the cell due permeability of the cell surface. Although from the physiological point of view this model is naive, it contains some important features and can serve as a basis for further model improvements and investigations of the mechanical interactions related to various regimes of tissue contraction.

- The *compact bone* poroelasticity model (Rohan et al., 2012; Rohan and Cimrman, 2011) describes interactions between deformation of the bone tissue and induced flow in the double-porous structure consisting of the Havers-Volkmann channels (the primary porosity) and the canaliculi (the dual porosity). This model is being developed to understand how the flow in the canaliculi populated by mechano-sensitive bone cells depends on the macroscopic load, since this phenomenon influences significantly the bone tissue growth and remodeling.

- The model describing *blood perfusion in deforming tissue* (Rohan, 2006a; Rohan and Cimrman, 2010; Rohan and Lukeš, 2010a) is relevant to the lower levels of the "perfusion tree". The two systems of channels characterize the arterial and venous sectors which exchange the fluid (bood) through the matrix representing the dual porosity. The model has been extended for the large deformation using the linearization based on the updated Lagrangian formulation.

- The model of *blood perfusion in "layered tissues"* (Rohan, 2010) is an attempt to cope with branching organization of the perfusion tree. The tissue periodicity is confined to two directions

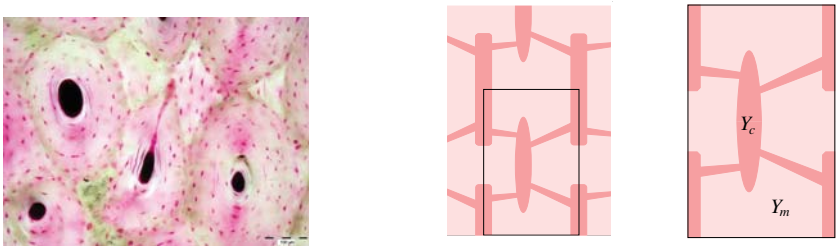

Fig. 5: **Left:** *a micrograph of the osteon porosity arranged in cylindrical geometry. The Haversian canals form the center of each osteon bounded by the cement line. The osteon matrix is penetrated by canalicular porous network arranged almost radially with respect to the osteon axis. (The color image provided by courtesy of Zbyněk Tonar.)* **Right:** *microstructure decomposition w.r.t. the dual porosity: dark pink: Ω_c, light pink: Ω_m, and the representative periodic cell Y decomposition.*

associated with the layer mean-surface, whereas there is no periodicity in the transversal direction. Thus, the tissue volume in 3D can be decomposed into several layers and the homogenization provides several 2D coupled problems, one per each layer.

Two compartment topology of the microstructure The two compartment topology of the microstructure is convenient for modeling bone tissue. Its structure is formed by Haversian and Volkmann channels (the primary porosity) and by porous matrix perforated by canaliculi (the dual porosity).

For finite scale $\varepsilon > 0$ domain $\Omega \subset \mathbb{R}^3$ is decomposed into two principal nonoverlapping parts, the channels Ω_c^ε and the matrix Ω_m^ε, so that $\Omega = \Omega_m^\varepsilon \cup \Omega_c^\varepsilon \cup \Gamma_{mc}^\varepsilon$, $\Gamma_{mc}^\varepsilon = \overline{\Omega_m^\varepsilon} \cap \overline{\Omega_c^\varepsilon}$ is the channel-matrix interface. Domain Ω is generated as a periodic lattice using a representative periodic cell $Y = Y_c \cup Y_m \cup \Gamma$, see Fig. 5 (right), where Y_c generating Ω_c^ε represent the channels of the primary porosity separated from the matrix $Y_m = Y \setminus \overline{Y_c}$ by interface Γ.

The model of the homogenized bone tissue is obtained using the Biot model (13). Following the double-porosity ansatz, the permeability $\boldsymbol{K}^\varepsilon$ is scaled by ε^2 in the dual porosity represented by Y_m, namely using the unfolding operator $\mathcal{T}_\varepsilon(\boldsymbol{K}^\varepsilon(x)) = \varepsilon^2 \chi_m(y)\boldsymbol{K}^m(y) + \chi_c(y)\boldsymbol{K}^c(y)$ with $y \in Y$, $x \in \Omega$, where χ_d, $d = m, c$ is the characteristic function of domain Y_d.

The homogenized equations involve stationary and non-stationary homogenized coefficients which serve as convolution kernels and, thus, are responsible for the fading memory effects. These effects are induced by microflows in the dual porosity, due to the fluid-structure interaction at the microscopic level.

In order to compute the homogenized coefficients, microscopic problems must be solved, so that the characteristic responses of the computational cell Y are obtained, see Fig. 6.

All details upon derivation of the homogenized equations can be found in Rohan et al. (2012). The macroscopic problem can be presented in the weak form: for a.a. $t \in]0, T[$ find couple $(\boldsymbol{u}(t,\cdot), p(t,\cdot)) \in V \times H^1(\Omega)$ ($V \subset \mathbf{H}^1(\Omega)$ is determined by kinematic boundary conditions) with initial condition

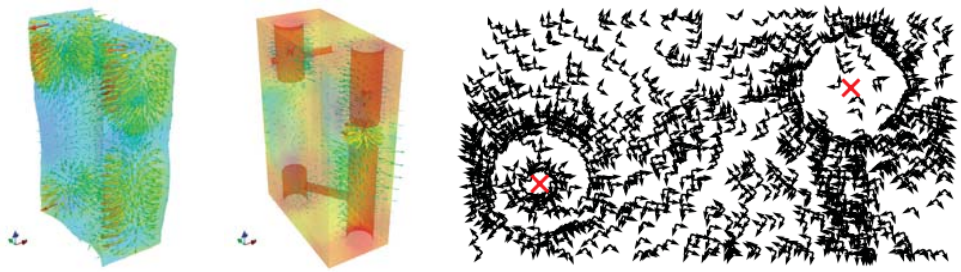

Fig. 6: Characteristic response in the reference cell Y – illustration of corrector basis functions (left) and anisotropy of the permeability in the dual porosity (right).

$p(0,\cdot) = 0$, such that

$$\int_\Omega \mathcal{E}_{ijkl} e_{kl}(\boldsymbol{u}) e_{ij}(\boldsymbol{v}) + \int_\Omega \int_0^t \mathcal{H}_{ijkl}(t-\tau) e_{kl}(\frac{\mathrm{d}}{\mathrm{d}\,\tau}\boldsymbol{u}(\tau))\, d\tau\, e_{ij}(\boldsymbol{v})$$
$$- \int_\Omega (\mathcal{B}_{ij} + \mathcal{P}_{ij}(0))\, p\, e_{ij}(\boldsymbol{v}) - \int_\Omega \int_0^t \frac{\mathrm{d}}{\mathrm{d}\,t}\mathcal{P}_{ij}(t-\tau) p(\tau)\, d\tau\, e_{ij}(\boldsymbol{v}) = \int_{\partial_\sigma\Omega} \boldsymbol{g}\cdot\boldsymbol{v}\, d\Gamma\ , \tag{14}$$

$$\int_\Omega (\mathcal{B}_{ij} + \mathcal{P}_{ij}(0))\, e_{ij}(\frac{\mathrm{d}}{\mathrm{d}\,t}\boldsymbol{u})\, q + \int_\Omega \int_0^t \frac{\mathrm{d}}{\mathrm{d}\,t}\mathcal{P}_{ij}(t-\tau) e_{ij}(\frac{\mathrm{d}}{\mathrm{d}\,\tau}\boldsymbol{u}(\tau))\, d\tau\, q$$
$$+ \int_\Omega \mathcal{C}_{ij}\partial_j p \partial_i q + \int_\Omega q\mathcal{M}\frac{\mathrm{d}}{\mathrm{d}\,t}p + \int_\Omega q \int_0^t \mathcal{N}(t-\tau)\frac{\mathrm{d}}{\mathrm{d}\,\tau}p(\tau)\, d\tau = 0\ ,$$

for all $\boldsymbol{v} \in V_0$ and $q \in H^1(\Omega)$.

Model (14) was implemented numerically, details on the FE discretization and evaluation of the convolution integrals can be found in Rohan and Cimrman (2011).

Three compartment topology In perfused tissues the three compartments correspond to two systems of channels (the arterial and venous sectors) separated by the matrix representing the tissue penetrated by capillaries which form the dual porosity.

In analogy with the two-compartment model, for finite scale $\varepsilon > 0$ domain $\Omega \subset \mathbb{R}^3$ is decomposed into three principal nonoverlapping parts, the channels $\Omega^\varepsilon_\alpha$, $\alpha = 1, 2$ and the matrix Ω^ε_3, so that $\Omega = \bigcup_{i=1,2,3} \Omega^\varepsilon_i \cup \Gamma^\varepsilon_{23} \cup \Gamma^\varepsilon_{13}$, where $\Gamma^\varepsilon_{\alpha 3}$ are the channel-matrix interfaces. The reference cell Y is decomposed accordingly: the channels are represented by Y_1 and Y_2 which are mutually disjoint, i.e. $Y_1 \cap Y_2 = \emptyset$, being separated by $Y_3 = Y \setminus \bigcup_{\alpha=1,2} \overline{Y_\alpha}$. Obviously, domain Ω^ε_3 is connected.

The homogenization procedure (Rohan, 2006a; Rohan and Cimrman, 2010) is applied to the Biot model (13) with the incompressibility constraints, which yields $\boldsymbol{\alpha} = 0$ and $1/\mu = 0$. By virtue of the double-porosity ansatz, the permeability $\boldsymbol{K}^\varepsilon$ is scaled by ε^2 in the dual porosity represented by Y_3, so that using the unfolding operator $\mathcal{T}_\varepsilon\left(K^\varepsilon_{ij}(x)\right) = \varepsilon^2\chi_3(y)K^3_{ij}(y) + \sum_{\alpha=1,2}\chi_\alpha(y)K^\alpha_{ij}(y)$, $y \in Y$, $x \in \Omega$.

As the result of the homogenization, a two-scale system of equations is obtained. Using the Laplace transformation, the two-scale problem is decoupled: *the local microscopic problems* are solved in reference cell Y to obtain the characteristic responses. Consequently, the homogenized coefficients involved in the macroscopic problem can be evaluated using corrector basis functions, see Rohan and Cimrman (2010): quantities.

- $\mathcal{E}_{ijkl}$ is the elasticity tensor. It expresses the overall elasticity (stiffness) of the dried porous skeleton represented by domain Y, thus, including both the porosities.
- $\mathcal{H}_{ijkl}(t)$ is the viscosity tensor related to the macroscopic creep and relaxation phenomena; it expresses the microflow (perfusion) in the dual porosity Y_3.

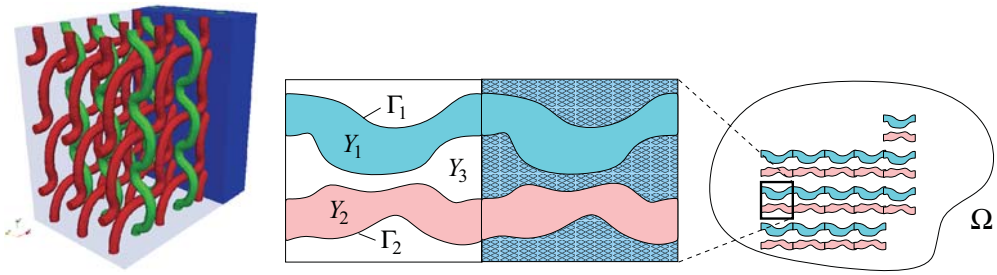

Fig. 7: Left: a three-compartment periodic structure, Right: the scheme of the microstructure decomposition.

- $\mathcal{R}^1_{ij}(t)$ and $\bar{\mathcal{P}}^1_{ij}$ are the poroelastic coefficients which reflect two phenomena: the elasticity of the dried skeleton in Y and permeability of the dual porosity.
- $\tilde{\mathcal{G}}_+(t)$ and $\mathcal{G}^*$ are the perfusion coefficients which control the amount of the fluid exchange between sectors Y_1 and Y_2.
- $\mathcal{C}^\alpha_{ij}$ is the homogenized permeability of the primary porosity in Y_α.

The macroscopic perfusion model describes parallel flows through the two channel systems in deforming medium. The macroscopic displacement field, $\boldsymbol{u}^0(t,\cdot) \in \boldsymbol{V} \subset \mathbf{H}^1(\Omega)$, and the two macroscopic pressures, $p_1(t,\cdot), p_2(t,\cdot) \in H^1_0(\Omega)$ satisfy the equilibrium equation (compare with the two-compartment model (14))

$$\begin{aligned}
&\int_\Omega \left[\mathcal{E}_{ijkl} e^x_{kl}(\boldsymbol{u}^0(t,\cdot)) + \int_0^t \mathcal{H}_{ijkl}(t-\tau)\,\frac{\mathrm{d}}{\mathrm{d}\,\tau} e^x_{kl}(\boldsymbol{u}(\tau,\cdot))\,d\tau\right] e^x_{ij}(\boldsymbol{v}) \\
&- \int_\Omega e^x_{ij}(\boldsymbol{v}) \int_0^t \tilde{\mathcal{R}}^1_{ij}(t-\tau)[p_1(\tau,\cdot) - p_2(\tau,\cdot)]\,d\tau \\
&- \sum_{\alpha=1,2} \int_\Omega \left[\frac{|Y_\alpha|}{|Y|}\delta_{ij} + \bar{\mathcal{P}}^\alpha_{ij}\right] p_\alpha(t,\cdot)\, e^x_{ij}(\boldsymbol{v}) = \int_{\partial_\sigma\Omega} \boldsymbol{g}\cdot\boldsymbol{v}\,dS \quad \forall \boldsymbol{v} \in \boldsymbol{V}_0\ ,
\end{aligned} \tag{15}$$

and the two balance-of-mass equations for $\alpha, \beta = 1, 2,\ \beta \neq \alpha$

$$\begin{aligned}
&\int_\Omega \mathcal{C}^\alpha_{ij}\,\partial^x_j p_\alpha(t,\cdot)\,\partial^x_i q + \int_\Omega q\,\mathcal{G}^* \frac{\mathrm{d}}{\mathrm{d}\,t}\left(p_\alpha(t,\cdot) - p_\beta(t,\cdot)\right) \\
&+ \int_\Omega q \int_0^t \tilde{\mathcal{G}}_+(t-\tau)\frac{\mathrm{d}}{\mathrm{d}\,\tau}\left(p_\alpha(\tau,\cdot) - p_\beta(\tau,\cdot)\right)\,d\tau \\
&+ \int_\Omega q \int_0^t \tilde{\mathcal{R}}^\alpha_{ij}(t-\tau)\frac{\mathrm{d}}{\mathrm{d}\,\tau} e^x_{ij}(\boldsymbol{u}^0(\tau,\cdot))\,d\tau \\
&+ \int_\Omega q \left[\frac{|Y_\alpha|}{|Y|}\delta_{ij} + \bar{\mathcal{P}}^\alpha_{ij}\right] \frac{\mathrm{d}}{\mathrm{d}\,t} e^x_{ij}(\boldsymbol{u}^0(t,\cdot)) = 0\ , \quad \forall q \in H^1_0(\Omega)\ ,
\end{aligned} \tag{16}$$

which govern the fluid flows in the two channels and its redistribution between them. The terms involving the pressure difference $p_\alpha - p_\beta$ reveal the amount of perfused fluid; while coefficient $\mathcal{G}^*$ is related to transition effects, the perfusion in a steady state is determined by the convolution term involving $\tilde{\mathcal{G}}_+(t-\tau)$, since $\tilde{\mathcal{G}}_+(+\infty) > 0$.

The three-compartment two-scale model was implemented in the **SfePy** FE code (Cimrman and et al., 2011). As an example, in Fig. 8 the pressure and perfusion velocities are displayed for a deforming block of tissue with microstructure similar to that of Fig. 7, right.

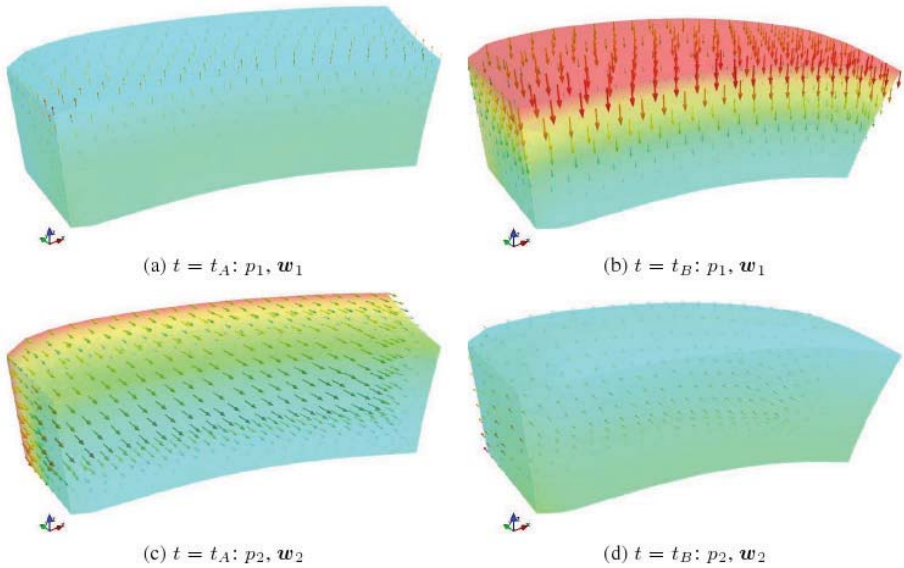

Fig. 8: Deformed perfused block: macroscopic pressures p_1 and p_2 displayed by color map at time $t_A = 60$ s, (a), (c) and $t_B = 80$ s, (b), (d), the associated perfusion velocities are indicated by arrows. Deformation enlarged for visualization. (Computed by R. Cimrman, 2009)

3.3. Homogenization of perfusion in thin layers

Homogenization can be adapted also for structures where the periodicity is restricted to directions within a given plane, as pointed out in Section 2.2..

In paper Rohan (2010) we derived a homogenized model of the Darcy flow in a thin porous non-deformable layer comprising 3 compartments. The reference periodic cell is composed of the matrix representing the dual porosity and of two mutually disconnected channels representing the primary porosity. The resulting model describes macroscopic redistribution of the fluid in the plane to which the thin layer is reduced. Due to the 3D-to-2D reduction and the two-scale decomposition it leads to computationally feasible problem which is now implemented in our in-house developed code *Sfepy*, Cimrman and et al. (2011).

One of the promising applications of the model is the blood perfusion in the brain tissue, see Fig. 9 (left). Although a detailed morphological study is not completed yet, the following assumptions, however simplifying, seem to be relevant:

- change of the microstructure with the depth in the tissue (the radial direction), as indicated by two layers,
- repeated patterns of the microstructure with respect to the tangential direction, so that the periodic "artificial" lattice can be introduced.

Difficulties in modeling the blood perfusion are inherited form the structure of the vascular system which forms vascular trees. An "ideal perfusion tree" can be decomposed into several levels (hierarchies) which can be associated with layers (generated by curved "mean" surfaces); in each of them the vascular network can be approximated by a (locally) periodic structures, where the "plane periodicity" is related to the tangent planes of the generating surface. This simplified view of the real complex system give rise to the idea of decomposing a 3D volume into N layers with a given periodic structure, see Fig. 9 (right), so that the homogenization procedure can be applied.

Problem formulation Homogenization of the Darcy flow in a heterogeneous layer with double porosity was described in Rohan (2010). In Fig. 9 (right) the layer is depicted schematically: Layer $\Omega^\delta =$

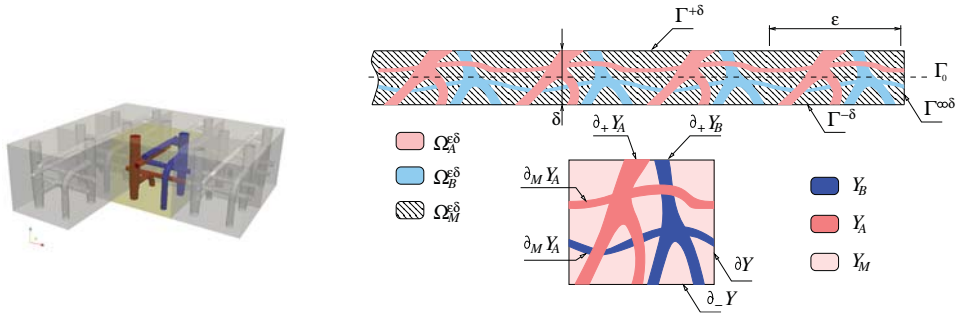

Fig. 9: Left: Representative periodic cell of the layer containing two systems channels. Right: The three compartment heterogeneous layer and the domain and boundary decomposition of the reference periodic cell Y.

$\Gamma_0 \times]-\delta/2, +\delta/2[$ has thickness $\delta > 0$, whereby $\Gamma_0 \subset \mathbb{R}^2$ forms the mean surface. On the "upper" and "lower" boundaries $\Gamma^{\delta+}$ and $\Gamma^{\delta-}$, the fluid exchange with the outer space is controlled by Neumann conditions defined in terms of fluxes $g^{\varepsilon\pm} \in L^2(\Gamma^{\pm})$. Domain Ω^{δ} consists of three disjoint sectors, the matrix $\Omega_M^{\varepsilon\delta}$ and the two channels $\Omega_A^{\varepsilon\delta}$, $\Omega_B^{\varepsilon\delta}$, which are generated as periodic lattices (with period ε). The double porosity in the matrix $\Omega_M^{\varepsilon\delta}$ is introduced using the standard scaling ansatz for the permeability, as described in preceding sections.

In order to obtain a limit (homogenized) problem, the perfusion fluxes $g^{\pm\varepsilon}$ must be scaled properly with respect to ε: we assume that the fluxes through the matrix interface $\Gamma_M^{\pm\varepsilon}$ are of the order ε, whereas fluxes of the channel inlets and outlets are of the order 1. Moreover, local net sources of channels A and B must be specified. For this we introduce $G_D^{\varepsilon}(x')$, $x' \in \Gamma_0$, with $D = A, B$, to describe the fluid volume increase per one period ε in the channel compartment D, and assume $G_D^{\varepsilon} \sim \varepsilon$, i.e. the local source produced in the channel A, or B due to external inlets/outlets is proportional to the thickness $\delta = h\varepsilon$ of the layer.

3.4. Macroscopic equation for single layer

The homogenized problem for pressures p^A and p^B, associated with the channels A and B, describes 2D parallel flows, in homogenized layer $\Gamma_0 \subset \mathbb{R}^2$. Each channel system forms a connected domain (so, we assume at least a small co-lateralization of vessels in the perfusion tree). Two coupled "macroscopic" equations (one for A and one for B) involve the homogenized coefficients: permeabilities $(\mathcal{K}_{\alpha\beta})^{A,B}$ of the channels, the transmission $\mathcal{G}$ and drainage $(\mathcal{S}_{\alpha})^{A,B,k}$ (for channel branches $k \in J_D$) coefficients. They govern the fluid redistribution between the two channel systems A and B: for A we have the following equation which is coupled with the similar equation for channel B (i.e. the role of indices A and B is exchanged):

$$-\frac{\partial}{\partial x_\alpha}\left[\mathcal{K}_{\alpha\beta}^{A}\frac{\partial}{\partial x_\beta}p^A + \sum_{k\in J_A}\mathcal{S}_{\alpha}^{A,k}\tilde{g}_A^k\right] + \mathcal{G}\left(p^A - p^B\right) = c_{hA}\bar{G}_A - \mathcal{F}^{A+}\hat{g}^{+} - \mathcal{F}^{A-}\hat{g}^{-}\ ,$$

where $\mathcal{F}^{A+/-}$, c_{hA} are constants (the summation w.r.t. repeated indices α, β applies). Fluxes $\hat{g}^{+/-}, \bar{G}_D$ and $\tilde{g}_D^k$, $k \in J_D$, $D = A, B$ are given, such that the solvability conditions hold. The term $\mathcal{G}\left(p^A - p^B\right)$, evaluated at point $x \in \Gamma_0$, expresses the amount of fluid (blood) perfused through the matrix (the dual porosity) between sectors A and B. The details are reported in Rohan (2010).

3.5. Model of N-coupled layers

We consider N layers; in each the perfusion is described by the homogenized model involving macroscopic pressures. Flows between the layers are respected by coupling conditions. In the simplest case, we assume perfect-matching microscopic cells of two attached layers, so that, at the microscopic level, the pressures at the "channel junctions" must equal and the fluxes must be opposite. Analogous conditions

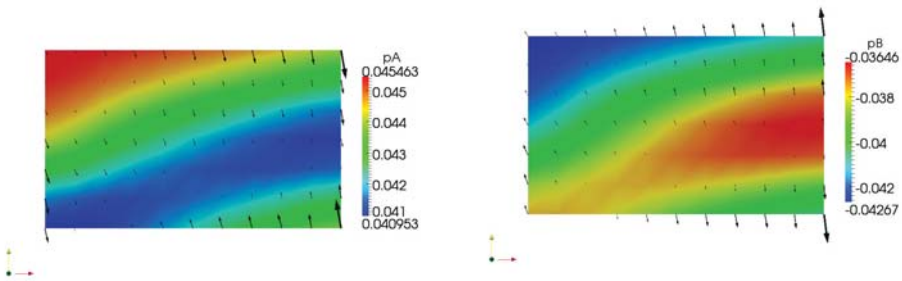

p^A, flux $\quad -\mathcal{K}^A \cdot \nabla p^A$ $\qquad$ p^B, flux $\quad -\mathcal{K}^B \cdot \nabla p^B$

Fig. 10: Solutions of the macroscopic problem: macroscopic pressures and fluxes in Γ_0.

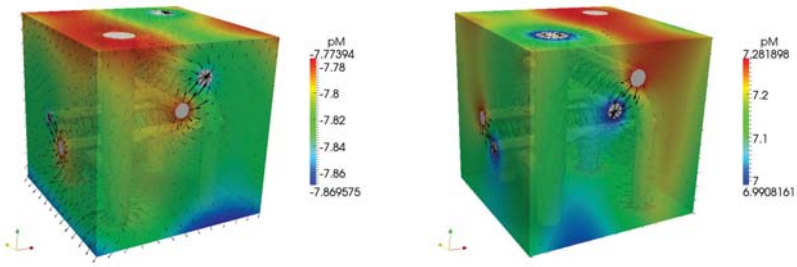

element 1 $\qquad$ element 200

Fig. 11: Perfusion reconstruction at the microscopic level — pressure $p_M(x', \cdot)$ *and perfusion velocities* $\boldsymbol{w}_M(x', \cdot)$ *in matrix, as evaluated at two different macroscopic points (elements).*

express coupling for the pressures and fluxes at the interface in the dual porosity. This approach allows us to approximate the hierarchical structure of the perfusion tree: in each layer the periodic microstructure can be different.

Numerical illustration The homogenized single layer model is implemented in code **SfePy** , material coefficients involved in (3.4.) are evaluated for the microstructure of the 3D periodic cell including two channels, see Fig. 9, left. The macroscopic problem is solved for given external fluxes: two "macroscopic" pressures p^A, p^B in Γ_0 are illustrated in Fig. 10, whereby the local amount of the perfused fluid is given by $\mathcal{G}(p^A - p^B)$. Once the macroscopic pressures are computed, at any point of Γ_0, the fluid pressures and perfusion fluxes can be reconstructed at the microscopic level, see an illustration in Fig. 11.

4. Conclusion

The purpose of the paper was to show various applications of the modelling approach based on homogenization of locally periodic structures with strong heterogeneities. The upscaling procedure consists in asymptotic analysis of partial differential equations (PDE) with oscillating coefficients. The strong heterogeneities are represented by scale-dependent coefficients, like elasticity in modelling the phononic materials, or permeability in modelling fluid saturated double porous media. From the mathematical point of view, sequencies of problems parameterized by the heterogeneity scale ε are considered and their limit solutions for $\varepsilon \to 0$ are to be computed. In linear problems, as considered here, the limit model de-

scribing behaviour of the homogenized medium is represented by macroscopic equations which involve constant material coefficients; these can be computed independently of the macroscopic response using characteristic local (microscopic) responses – solutions of autonomous PDEs defined at microscopic level.

The homogenization approach provides computationally efficient schemes for the multi-scale modeling. Once the macroscopic response is obtained, the "microscopic" responses can be reconstructed using the characteristic local responses. There is a remarkable difference with respect to the standard homogenization in using such schemes: while in a standard case the homogenization result is really independent of the heterogeneity scale, in the "large contrast" case the real material coefficients are defined for a given scale $\varepsilon_0 > 0$. This means that the limit model must be interpreted by an extrapolation for the scale $\varepsilon > 0$; for this so-called corrector result is used.

There are many important issues closely related to the topic discussed in this paper. An extension of the homogenization approach for nonlinear problems is cumbersome; apart of the nonlinear techniques based on the Γ-convergence we proposed a linearization approach based on an incremental formulation and an updating scheme for locally periodic microstructures. Another issue of interest is presented by the multi-level (i.e. reiterated) homogenization which allows for modelling heterogeneities at different scales.

Acknowledgments

The research is supported by projects GACR 106/09/0740 and GACR P101/12/2315 of the Czech Scientific Foundation and in a part by the European Regional Development Fund (ERDF), project "NTIS - New Technologies for Information Society", European Centre of Excellence, CZ.1.05/1.1.00/02.0090.

References

Arbogast, T., Douglas, J., and Hornung, U. (1990). Derivation of the double porosity model of single phase flow via homogenization theory. *SIAM J. Math. Anal.*, 21:823–836.

Auriault, J.-L. and Boutin, C. (1992). Deformable porous media with double porosity. quasi statics. i. coupling effects. *Transp. Porous Media*, 7(1):63–82.

Ávila, A., Griso, G., Miara, B., and Rohan, E. (2008). Multiscale modeling of elastic waves: Theoretical justification and numerical simulation of band gaps. *Multiscale Modeling & Simulation, SIAM*, 7:1–21.

Biot, M. A. (1955). Theory of elasticity and consolidation for a porous anisotropic solid. *J. Appl. Phys.*, 26(2):182–185.

Cimrman, R. and et al. (2011). SfePy home page. http://sfepy.org. Software, finite element code and applications.

Cimrman, R. and Rohan, E. (2010). On acoustic band gaps in homogenized piezoelectric phononic materials. *Appl. Comp. Mech.*, 4:89–100.

Cioranescu, D., Damlamian, A., and Griso, G. (2008a). The periodic unfolding method in homogenization. *SIAM Journal on Mathematical Analysis*, 40(4):1585–1620.

Cioranescu, D., Damlamian, A., Griso, G., and Onofrei, D. (2008b). The periodic unfolding method for perforated domains and neumann sieve models. *J. Math. Pures Appl.*, 89:248–277.

Coussy, O. (2004). *Poromechanics*. John Wiley & Sons.

de Boer, R. (2000). *Theory of Porous Media*. Springer, Berlin.

Leugering, G., Rohan, E., and Seifrt, F. (2010). Modeling of metamaterials in wave propagation. In *Wave Propagation in Periodic Media Analysis, Numerical Techniques and practical Applications*. Matthias Ehrhardt (ed.), E-Book Series Progress in Computational Physics,.

Mielke, A. and Rohan, E. (2012). Homogenization of elastic waves in fluid-saturated porous media using the biot model. *Submitted*.

Rohan, E. (2006a). Homogenization approach to the multi-compartment model of perfusion. *PAMM*, 6:79–82.

Rohan, E. (2006b). Modelling large deformation induced microflow in soft biological tissues. *Theor. and Comp. Fluid Dynamics*, 20:251–276.

Rohan, E. (2010). Homogenization of the darcy flow in a double-porous layer. *SIAM, MMS*. Submitted.

Rohan, E. and Cimrman, R. (2010). Two-scale modelling of tissue perfusion problem using homogenization of dual prous media. *Int. Jour. for Multiscale Comput. Engrg.*, 8:81–102.

Rohan, E. and Cimrman, R. (2011). Multiscale FE simulation of diffusion-deformation processes in homogenized dual-porous media. *Math. Comp. Simul.* In Press.

Rohan, E. and Lukeš, V. (2010a). Homogenization of perfusion in large-deforming medium using the updated lagrangian formulation. In *Proceedings of the ECT 2010 conference*. Coburg-Sax Publ.

Rohan, E. and Lukeš, V. (2010b). Homogenization of the acoustic transmission through perforated layer. *J. of Comput. and Appl. Math.*, 6:1876–1885.

Rohan, E. and Miara, B. (2006a). Homogenization and shape sensitivity of microstructures for design of piezoelectric bio-materials. *Mechanics of Advanced Materials and Structures*, 13:473–485.

Rohan, E. and Miara, B. (2006b). Sensitivity analysis of acoustic wave propagation in strongly heterogeneous piezoelectric composite. In *Topics on Mathematics for Smart Systems*, pages 139–207. World Sci. Publishing Company.

Rohan, E. and Miara, B. (2009). Shape sensitivity analysis for material optimization of homogenized piezophononic materials. In *8th World Congress on Structural and Multidisciplinary Optimization*. ECCOMAS.

Rohan, E. and Miara, B. (2011). Band gaps and vibration of strongly heterogeneous reissner-mindlin elastic plates. *Comptes Rendus Mathematique*, 349:777–781.

Rohan, E., Miara, B., and Seifrt, F. (2009). Numerical simulation of acoustic band gaps in homogenized elastic composites. *International Journal of Engineering Science*, 47:573–594.

Rohan, E., Naili, S., Cimrman, R., and Lemaire, T. (2012). Multiscale modelling of a fluid saturated medium with double porosity: Relevance to the compact bone. *Jour. Mech. Phys. Solids*, 60:857–881.

Sanchez-Palencia, E. (1980). *Non-homogeneous media and vibration theory*. Number 127 in Lecture Notes in Physics. Springer, Berlin.

PAPERS

18th International Conference
ENGINEERING MECHANICS 2012
Svratka, Czech Republic, May 14 – 17, 2012

pp. 25–32
Paper #147

COMPARISON OF TWO POSSIBLE APPROACHES TO INVERSE LAPLACE TRANSFORM APPLIED TO WAVE PROBLEMS

V. Adámek [*], **F. Valeš** [**], **J. Červ** [***]

Abstract: *This paper concerns the investigation of non-stationary wave phenomena in a thin elastic disc under radial impact by means of analytical methods. When the method of integral transforms is used for solving the system of PDEs describing a wave problem solved, one has to overcome the problem of inverse transform. This work focuses on two possible approaches to the inverse Laplace transform. Using the existing analytical solution of the problem, the classic method making use of the residue theorem and the method based on the numerical inverse Laplace transform are compared. Advantages and disadvantages of both approaches, mainly from computational point of view, are discussed and demonstrated.*

Keywords: ***thin disc, radial impact, non-stationary wave problem, analytical solution, inverse Laplace transform.***

1. Introduction

The utilization of analytical methods by the investigation of stationary and non-stationary wave problems in solids brings one significant benefit - the possibility of detailed insight into physical phenomena occurred. This main advantage of this approach can be then used for further analyses related for instance to dispersion and attenuation behaviour, to conditions under which specific types of waves can propagate etc. Consequently, the results of such analyses can be utilized for solving of forward or inverse problems of real components, equipments and structures. On the other hand, it is clear that the application of analytical methods is considerably limited by geometry and material properties of solids studied and by initial and boundary conditions assumed.

The application of Fourier method (separation of variables) in combination with appropriate integral transform represents a classic method for solving the system of PDEs describing a wave problem solved (Graff (1975)). In such cases, the inverse integral transform is one of the primary tasks of the process of analytical solution evaluation. Laplace transform represents one of the most used transform in time domain. There exist two possible approaches to its inversion, analytical and numerical. The first mentioned methods are based on the exact evaluation of Bromwich integral defining the inverse Laplace transform (ILT). This is usually done by the help of Cauchy's residue theorem (see Achenbach (1975)). The use of residue theorem is quite limited, usually to problems of elastic solids, e.g. the existence of branch points in problems of viscoelastic solids makes the inverse process much more complicated. On the other hand, the second mentioned methods making use of the numerical evaluation of Bromwich integral are more general and can be applied to more complicated problems. There exist more than one hundred algorithms for numerical inverse Laplace transform (NILT), from simple ones (see Duffy (2004)) to more sophisticated procedures which usually include sequence accelerators to improve the convergence of numerical process (see Cohen (2007)). The main disadvantage of NILT methods lies in the fact that they distort exact analytical solution. The utilization of modern Computer Algebra Systems (CASs), like Maple, Mathematica etc., which enable to perform difficult symbolic manipulations and multi-precision computations, is one of the possibilities how to overcome this problem.

[*] Ing. Vítězslav Adámek, Ph.D.: Faculty of Applied Sciences, University of West Bohemia, Univerzitní 22; 306 14, Pilsen; CZ, e-mail: vadamek@kme.zcu.cz
[**] Ing. František Valeš, CSc.: Institute of Thermomechanics, Czech Academy of Sciences, Veleslavínova 11; 301 14, Pilsen; CZ, e-mail: vales@it.cas.cz
[***] doc. Ing. Jan Červ, CSc.: Institute of Thermomechanics, Czech Academy of Sciences, Dolejškova 1402/5; 182 00, Prague 8; CZ, e-mail: cerv@it.cas.cz

The main aim of this work is to show the possibility of application of selected NILT algorithm to a specific wave problem without the lost of analytical results accuracy and to demonstrate its robustness and efficiency. In particular, the problem of an elastic thin disc under radial impact is chosen for this purpose. The exact analytical solution, which can be found in Brepta and Červ (1978), is derived in detail in Červ (1974). The exact analytical formulae for displacement components and other mechanical quantities are derived by the help of residue theorem in the last-mentioned work.

2. Analytical solution of chosen wave problem

In this section we will formulate the wave problem used for the testing of analytical and numerical approach to ILT at first. Then a brief description of technique used in Červ (1974) for the derivation of analytical solution will be given and resulting formulae for displacement components transforms will be presented.

2.1. Problem formulation, governing equations

Let us assume a thin elastic disc of constant thickness, of finite radius r_1 and of homogeneous isotropic material properties described by Young modulus E and Poisson's ratio ν. This disc is loaded in radial direction by a uniformly distributed pressure of amplitude σ_0 acting on a part of its rim defined by the angle $2\alpha_0$ (see Fig. 1). The time history of applied load is described by Heaviside function in time so it invokes non-stationary wave phenomena in the disc studied. Introducing the polar coordinates r and φ as depicted in Fig. 1 and taking into account previous description, the external load can be expressed as

$$\sigma_r(r,\varphi,t)|_{r=r_1} = \begin{cases} \sigma_0 H(t) & \text{for } \varphi \in \langle -\alpha_0, \alpha_0 \rangle, \\ 0 & \text{otherwise.} \end{cases} \tag{1}$$

The hyperbolic system of PDEs representing equations of motion of the disc can be derived from momentum conservation formulated for a disc element and using appropriate constitutive and strain-displacement relations. It consists of two coupled PDEs for unknown functions of radial $u_r(r,\varphi,t)$ and circumferential $u_\varphi(r,\varphi,t)$ displacement components (see Červ (1974)). Introducing the well known relation between shear modulus G and parameters E and ν which holds under the assumption of material isotropy, it is useful to rewrite the original system of equations to a system for new unknown functions of dilatation $\Delta_d(r,\varphi,t)$ and rotation $\omega_z(r,\varphi,t)$ of the form

$$\frac{\partial^2 u_r}{\partial t^2} = {c_3}^2 \frac{\partial \Delta_d}{\partial r} - \frac{2{c_2}^2}{r}\frac{\partial \omega_z}{\partial \varphi}, \quad \frac{\partial^2 u_\varphi}{\partial t^2} = \frac{{c_3}^2}{r}\frac{\partial \Delta_d}{\partial \varphi} + 2{c_2}^2 \frac{\partial \omega_z}{\partial r}, \tag{2}$$

where $\Delta_d(r,\varphi,t)$ and $\omega_z(r,\varphi,t)$ are defined by formulae

$$\Delta_d = \frac{\partial u_r}{\partial r} + \frac{1}{r}\left(u_r + \frac{\partial u_\varphi}{\partial \varphi}\right), \quad \omega_z = \frac{1}{2}\left[\frac{\partial u_\varphi}{\partial r} + \frac{1}{r}\left(u_\varphi - \frac{\partial u_r}{\partial \varphi}\right)\right]. \tag{3}$$

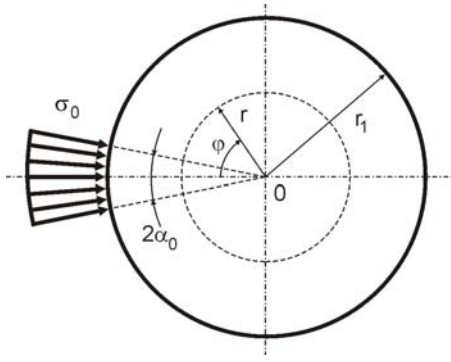

Fig. 1: The geometry of solved problem

Constants c_2 and c_3 correspond to the velocity of equivoluminal (shear) waves and to the velocity of dilatational waves in two-dimensional continuum, respectively (see Červ (1974)).

To complete the problem formulation, initial and boundary conditions have to be defined. For simplicity, the zero initial conditions for both displacement components and their time derivatives are considered. With respect to previous problem description, boundary conditions for stress components can be expressed as

$$\tau_{r\varphi}|_{r=r_1} = 0 \quad \text{and} \quad \sigma_r|_{r=r_1} = -\frac{2\alpha_0\sigma_0}{\pi}\left(\frac{1}{2} + \sum_{n=1}^{\infty}\frac{\sin(n\alpha_0)\cos(n\varphi)}{n\alpha_0}\right)H(t)\,, \tag{4}$$

when the expansion of (1) to the Fourier cosine series is used.

2.2. Derivation of final formulae for integral transforms of displacement components

The system (2) will be now solved by the application of Laplace transform in time domain following by Fourier method in spatial domain. When the Laplace transform is applied to (2), taking into account zero initial conditions, we obtain a system of PDEs for Laplace transforms of original time dependent functions, which can be converted to the system of uncoupled Bessel's type equations for the Laplace transforms of dilatation $\bar{\Delta}_d(r,\varphi,p)$ and rotation $\bar{\omega}_z(r,\varphi,p)$

$$\frac{\partial^2\bar{\Delta}_d}{\partial r^2} + \frac{1}{r}\frac{\partial\bar{\Delta}_d}{\partial r} - \frac{p^2}{c_3^2}\bar{\Delta}_d + \frac{1}{r^2}\frac{\partial^2\bar{\Delta}_d}{\partial\varphi^2} = 0\,, \quad \frac{\partial^2\bar{\omega}_z}{\partial r^2} + \frac{1}{r}\frac{\partial\bar{\omega}_z}{\partial r} - \frac{p^2}{c_2^2}\bar{\omega}_z + \frac{1}{r^2}\frac{\partial^2\bar{\omega}_z}{\partial\varphi^2} = 0\,, \tag{5}$$

where $p \in \mathcal{C}$. The solution of system (5) can be then found using the separation of spatial variables r and φ and resulting relations for $\bar{\Delta}_d(r,\varphi,p)$ and $\bar{\omega}_z(r,\varphi,p)$ can be derived (for more details see Červ (1974)). Introducing these formulae into (3) we obtain required relations for integral transforms of radial $\bar{u}_r(r,\varphi,p)$ and circumferential $\bar{u}_\varphi(r,\varphi,p)$ displacement components in the form

$$\begin{aligned}
\bar{u}_r(r,\varphi,p) = &-\frac{c_3^2}{p^2}J_1\!\left(\frac{ip}{c_3}r\right)\left(\frac{ip}{c_3}\right)P_0(p) - \frac{1}{p^2}\sum_{n=1}^{\infty}\Bigg\{{c_3}^2\left[\frac{n}{r}J_n\!\left(\frac{ip}{c_3}r\right) - \right.\\
&\left. - \left(\frac{ip}{c_3}\right)J_{n-1}\!\left(\frac{ip}{c_3}r\right)\right]P_n(p) + 2\,c_2^2\,\frac{n}{r}J_n\!\left(\frac{ip}{c_2}r\right)Q_n(p)\Bigg\}\cos(n\varphi)\,,\\
\bar{u}_\varphi(r,\varphi,p) = &-\frac{1}{p^2}\sum_{n=1}^{\infty}\Bigg\{2\,c_2^2\left[\frac{n}{r}J_n\!\left(\frac{ip}{c_2}r\right) - \left(\frac{ip}{c_2}\right)J_{n-1}\!\left(\frac{ip}{c_2}r\right)\right]Q_n(p) +\\
&+ c_3^2\,\frac{n}{r}J_n\!\left(\frac{ip}{c_3}r\right)P_n(p)\Bigg\}\sin(n\varphi)\,,
\end{aligned} \tag{6}$$

in which the symbol J_n denotes Bessel function of the first kind and n-th order.

The complex functions $P_n(p)$ $(n = 0, 1, 2, \ldots)$ and $Q_n(p)$ $(n = 1, 2, \ldots)$ are unknown for now and they can be derived by the help of boundary conditions (4). Rewriting these conditions using constitutive and strain-displacement equations in term of displacement components and introducing (6) into their Laplace transforms, we obtain a system of algebraic equations for $P_n(p)$ and $Q_n(p)$. The final formulae of these functions, which are derived in detail in Červ (1974), are quite complicated and can be found in compact form in Brepta and Červ (1978). Subsequently, Laplace transforms of other mechanical quantities (e.g. velocity components, stress components etc.) can be derived on the basis of (6) with relative ease (see Brepta and Červ (1978)).

3. Inverse Laplace transform

This section deals with the basic description of two confronted approaches to ILT applied to the wave problem formulated above. The results of radial velocity transform inversion back to time domain are presented, analysed and discussed. This quantity is suitable for the purpose of this work because it is able to register steep fronts of waves propagated in the disc such that appropriate accuracy analysis of methods being compared can be made.

3.1. Analytical approach to ILT

The analytical ILT procedure is based on the Cauchy's residue theorem (see Achenbach (1975)) which can be written for $p \in \mathcal{C}$ in the form

$$\oint f(p)dp = 2\pi i \sum_{a_i \in A} \operatorname*{Res}_{p=a_i} f(p), \tag{7}$$

i.e. the value of a contour integral of an arbitrary analytic (holomorphic) function $f(p)$ for any enclosed contour is equal to the sum of residues in poles $a_i \in A$, where A is the set of poles contained inside the contour. It can be proved that both integral transforms (6) and other mechanical quantities transforms are holomorphic in complex plane except of their isolated singular points (poles) and hence the application of (7) is possible. To do so, we have to apply the Cauchy's integral theorem at first (Achenbach (1975)) to make the Bromwich-Wagner integration path of the integral defining ILT enclosed.

Using mentioned technique one can derive final exact analytical formula for required radial velocity $v_r(r, \varphi, t)$. Due to the complexity of this relation (see Červ (1974)) it is not possible to present it in this work and we confine only to some remarks regarding this solution. The first note is related to singular points of transforms (6). As shown in the last-mentioned work, these points are simple poles, i.e. complex functions (6) have no essential singularities. These poles can be found as the roots of appropriate frequency equation and for different wavenumber values they represent points of dispersion curves. This means that the use of analytical approach to ILT requires the determination of dispersion curves at first which causes added demands on CPU time. Additionally, it should be mentioned here that the accuracy of dispersion curves determination significantly influences the accuracy of analytical results obtained. The number of terms which are summed during the evaluation process is another important factor which affects the correctness of analytical results. The analytical formula for $v_r(r, \varphi, t)$, as well as the formulae of others quantities, contains two infinite sums: the first one follows from the application of Fourier method (see relations (6)) and the second one represents the summation over an infinite number of singular points (dispersion curves) following from (7). For subsequent usage in the following text, let us denote corresponding summation indices by n and s in sequence.

In spite of the presence of mentioned "numerical factors", the knowledge of actual formula in time domain, which follows from this ILT approach, enable us to determine the physical meaning of each term of derived analytical solution which can be then used for other analyses. In this case, the function $v_r(r, \varphi, t)$ consists of two parts: the first one represents the long-term (stationary) effect of inertial forces following from constant acceleration of all disc particles and the second one expresses the transient wave component of solution (see Červ (1974)).

The evaluation of analytical formula for $v_r(r, \varphi, t)$ has been done using the above mentioned procedure for following material and geometric parameters: $r_1 = 0.05\mathrm{m}$, $\rho = 7800\mathrm{kg\,m^{-3}}$, $\nu = 0.3$ and $E = 2.07 \cdot 10^{11}\mathrm{Pa}$. The disc response to radial load specified by $\sigma_0 = 1\mathrm{Pa}$ and $\alpha_0 = \pi/60$ have been studied in time interval $t \in \langle 0, 50\rangle\,\mu\mathrm{s}$ with constant step $\Delta t = 0.05\mu\mathrm{s}$ at the disc rim and for $\varphi \in \{0, \pi/2, \pi\}$. Dimensionless plots of v_r time histories in selected points are depicted in Fig. 2. These results were obtained by computations performed in the system Maple using 17 significant digits. Fig. 2(a) presents the results in all three selected points for $n = 180$ and $s = 100$. It can be deduced from these curves, mainly from the oscillating character of v_r in the vicinity of steep fronts, that the values of n and s are too low for the solution to be able to represent the disc response correctly. This follows not only from the comparison of curves from Fig. 2(a) and Fig. 4(b) corresponding to $\varphi = \pi$ but also from Fig. 2(b) in which the results for $\varphi = \frac{\pi}{2}$ and for different values of n and s are presented. It is clear from this figure that results for $n = 360$, $s = 200$ and $n = 500$, $s = 300$ are nearly identical. But this conclusion can not be made in case of $\varphi = \pi$ as was verified by additional computations. Finally, one should mention that increasing number of significant digits used does not lead to higher accuracy of analytical results, but causes significant increase of total CPU time, as proved by computations carried out with 34 significant digits.

3.2. Numerical approach to ILT

Numerical approach to ILT consists in the numerical evaluation of Bromwich integral. As stated in Abate and Valkó (2004), algorithms for numerical inverse Laplace transform (NILT) can be usually divided

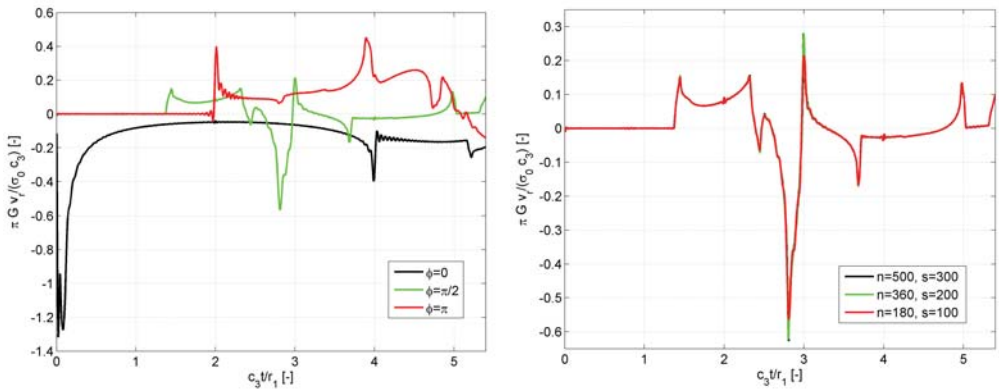

Fig. 2: Results obtained by analytical approach to ILT, dimensionless time plots of v_r: (a) results for $n = 180$, $s = 100$ in three different points at the disc rim, (b) the influence of n and s for $\varphi = \frac{\pi}{2}$

into following four categories considering the methods which are based on: algorithms making use of Fourier series or deformation of Bromwich-Wagner contour and algorithms based on Gaver functionals or Laguerre functions. Many of them include the problem of infinite series, usually with low rate of convergence. In such cases, the methods are combined with a suitable sequence accelerator. A great overview of different NILT algorithms and accelerators is given in Cohen (2007).

Based on our previous experiences acquired by the analytical solution of analogous wave problem of a viscoelastic disc (see Adámek and Valeš (2011a), Adámek and Valeš (2011b)), the combination of FFT-based algorithm and non-linear Wynn's epsilon accelerator (ε-algorithm) was used. This method was adopted mainly from Brančík (1999) where it is used for NILT by the study of wave phenomena in electric circuits. The basic idea of this method consists in a discrete formula of Bromwich integral (see Brančík (1999)) such that the functional value of f in a discrete time kT ($k = 0, 1, \ldots, N-1$), where T is a sampling period in time domain, can be approximated by relation

$$f(kT) \approx f^k = C^k \left\{ 2\mathrm{Re}\left[\sum_{n=0}^{\infty} F_n E_n^k \right] - F_0 \right\}, \tag{8}$$

where

$$C^k = \frac{\Omega}{2\pi} e^{ckT}, \quad F_n = F(c - in\Omega), \quad E_n^k = e^{-ikTn\Omega}, \quad \Omega = \frac{2\pi}{NT} \quad \text{and} \quad c \approx \alpha - \frac{\Omega}{2\pi} \log E_r, \tag{9}$$

in which E_r denotes the desired relative error and α is an exponential order of the real function $f(t)$ (for more details see Brančík (1999) or Cohen (2007)).

Considering relations (8) and (9), the NILT procedure can be divided into two basic steps: in the first one, the functional values of the transform F in specific complex points are calculated; the second step involves the calculation of f^k including the infinite summation using chosen ε-algorithm. First numerical computations performed have shown that the first phase of NILT procedure is sensitive to cumulative numerical errors, therefore it must be carried out precisely to avoid the lost of "analytical" results accuracy. The system Maple, which enables to perform symbolic operations and multi-precision computations, has been used for this purpose. The second step of NILT process, which has not so high precision demands, has been implemented into the Matlab environment, in which the multi-dimensional array operations are much more faster compared to Maple. Using the combination of two mentioned systems, we obtain quite effective and stable tool for NILT of required formulae.

All numerical computations have been done for parameters stated in the section 3.1.. Performed computations have shown that the accuracy of evaluation process depends mainly on the number of digits used during the first phase of evaluation procedure mentioned above, namely on the number of

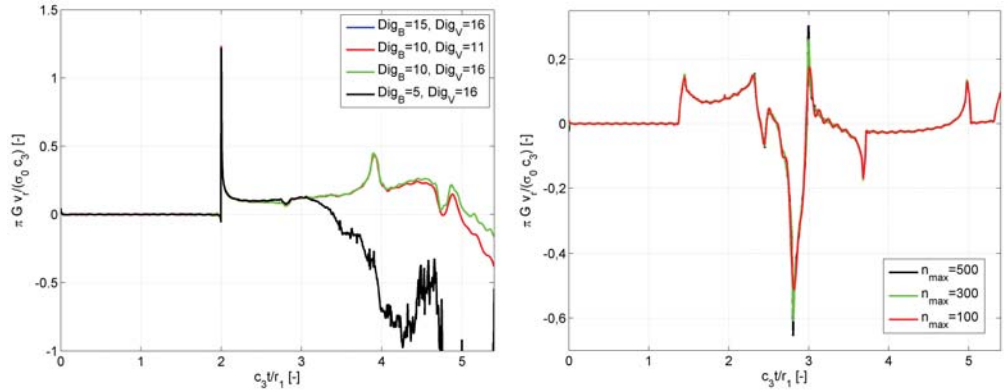

(a) (b)

Fig. 3: Results obtained by NILT, dimensionless time plots of v_r: (a) the influence of number of digits used during computations for $\varphi = \pi$, (b) the influence of n_{max} for $\varphi = \frac{\pi}{2}$

digits Dig_B used for the computation of Bessel function values and number of digits Dig_V used for following operations needed for the determination of functional values of radial velocity transform V_r. The second significant factor, which is obvious from (6), is represented by the number of terms n_{max} which are summed in the infinite sum. The influence of mentioned factors is clear from Fig. 3 in which dimensionless time plots of v_r for different values of φ are presented. The detailed analyses have shown that if $Dig_B < 10$ and $Dig_V < 16$, the results for longer times are of pure accuracy (see Fig. 3(a)). In particular, when $Dig_V < 16$ and $Dig_B \geq 10$ the functional values of V_r for $n \geq 75$ are due to a large number of operations calculated incorrectly (their imaginary or real parts tend to infinity). On the other hand when $Dig_B < 10$ the increasing value of Dig_V can not compensate the errors of Bessel function values. If we use $Dig_B = 10$ and $Dig_V = 16$ or $Dig_B = 15$ and $Dig_V = 16$, we obtain nearly identical results (the green curve coincides with the blue one, see Fig. 3(a)). Further increasing of Dig_B and Dig_V does not bring significantly better results and leads to slow increasing of CPU time. Based on these results, further computations have been done using $Dig_B = 15$ and $Dig_V = 16$.

The dependence of "analytical" results on the second main factor n_{max} is obvious for $\varphi = \frac{\pi}{2}$ from Fig. 3(b). It can be said that the low number of summed terms leads to the solution oscillation and to the reduction of dominant peaks in the disc response. This is caused by the fact that low value of n_{max} act as a "frequency filter". But contrary to previous factor, it does not cause the distortion for long times, so the time shape of v_r for different values of n_{max} is preserved in the whole time interval studied. Finally, one should mention that analogously to the method presented in the section 3.1., the right number of terms which could be summed to obtain results of required accuracy depends on the position of points in which the responses are studied, both in radial and tangential direction.

4. Results comparison and discussion

In this section, we present the comparison of "analytical" results achieved by means of both methods described. Fig. 4 confronts the most accurate results obtained using the analytical ILT approach (curves *RES*), i.e. for $n = 500$ and $s = 300$, with those resulted from the application of chosen NILT algorithm (curves *NILT*) and of a comparable accuracy, i.e. for $n_{max} = 500$ and $n_{max} = 300$. It is evident that the dimensionless time plots of v_r are in good agreement both for $\varphi = \frac{\pi}{2}$ and for $\varphi = \pi$ in the whole time interval of interest. The main discrepancies occur in times corresponding to dominant peaks of v_r, as obvious from detailed views in Fig. 4(a) and from Fig. 4(b). The curves representing results of NILT coincide in the last mentioned figure. Additionally, the results of NILT are probably of higher accuracy, which is indicated by slightly oscillating character of curve *RES* in the vicinity of dominant peak, see the detail in Fig. 4(b).

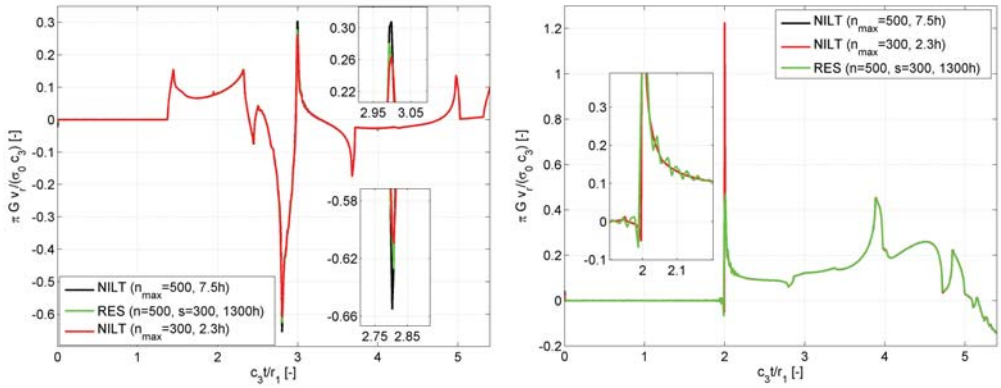

(a) (b)

Fig. 4: Comparison of results obtained by analytical ILT and by NILT: (a) $\varphi = \frac{\pi}{2}$, (b) $\varphi = \pi$

Based on these results, we can make the first conclusion, such that the "analytical" results of comparable quality can be achieved by both approaches. But analogous conclusion can not be made in the case of total CPU time required by each method. These times in hours are stated in the legends of both figures in Fig. 4. Their values correspond to the computations performed on one 2.66 GHz processor. NILT approach requires only several hours depending on the value of n_{max} whereas the method based on the residue theorem needs non-comparably longer time to obtain results of the same accuracy. This extreme difference is mainly caused by the necessity of dispersion curves computation and by doing the double summation without the usage of a suitable sequence accelerator. Moreover, the total CPU time of NILT method could be significantly reduced if the process of Bessel functions evaluation, which consumes more than 95 % of computational time, is speed up by the help of well-known recurrent formulae for Bessel functions. But taking into account the increase of cumulative numerical errors, this improvement can be used only when the number of terms n_{max}, which have to be summed to achieved results of required accuracy, is approximately up to 35. This is applicable only in special cases when the response is investigated near the disc center, i.e. for small values of r.

If we should summarize advantages and disadvantages of both approaches tested, we can say that the analytical method making use of residue theorem, contrary to the NILT based method, gives us the insight into the physical meaning of each term of the analytical solution in time domain. But its numerical implementation is much more time demanding compared to the obtaining results of the same accuracy by the help of NILT procedure. Another significant advantage of the second mentioned method lies in the possibility of its application to the larger set of problems. Since this approach requires the knowledge of the solution in transform domain only, which can be derived easier than that in time domain, it can be used for more complicated wave problems, from geometrical, material and boundary/initial conditions point of view. But this method should be used cautiously because, as stated e.g. in Abate and Valkó (2004), there does not exist any universal NILT algorithm suitable for arbitrary problem so the verification of correctness and accuracy of obtained results by another method is important.

5. Conclusion

This work concerned the comparison of two different approaches to the matter of inverse Laplace transform in the solving process of a chosen non-stationary wave problem. It is demonstrated on the problem of a radial impact on an elastic disc that the results of required accuracy can be obtained not only by the help of an analytical method making use of residue theorem but also by strictly numerical procedure based on the combination of FFT algorithm and Wynn's epsilon algorithm. Presented results clearly show that the numerical approach to ILT does not cause the lost of analytical solution accuracy and that it is much more efficient than the analytical one. Furthermore, it can be applied to other more com-

plicated wave problems, as proved by several works of authors dealing with the non-stationary wave problems of elastic and viscoelastic beams and discs.

Acknowledgments

This work has been supported by the grant GA CR P101/12/2315.

References

Abate, J., Valkó, P. P. (2004), Multi-precision Laplace transform inversion. *International Journal for Numerical Methods in Engineering*, Vol 60, pp 979-993.

Adámek V., Valeš F. (2011), Analytical solution of in-plane response of a thin viscoelastic disc under impact load. *Springer Proceedings in Physics 139: Vibration Problems ICOVP2011*, Vol 139, pp 715-721.

Adámek V., Valeš F. (2011), Transient stress waves in a thin viscoelastic disc under radial impact. In: *Proc. 10th International Conference on the Mathematical and Numerical Aspects of Waves*. The Pacific Institute for the Mathematical Sciences, Burnaby BC, CD ROM, pp 149-152.

Achenbach, J.D. (1975), *Wave Propagation in Elastic Solids*, North Holland, Amsterdam.

Brančík L. (1999), Programs for fast numerical inversion of Laplace transforms in Matlab language environment. In: *Proc. MATLAB Conference 1999*. Prague, pp 27-39.

Brepta R., Červ J. (1978), Thin elastic disc loaded by a sudden radial force. *Acta Technica, CSAV*, Vol 23, No 3, pp 286-305.

Cohen, A.M. (2007), *Numerical Methods for Laplace Transform Inversion*, Springer, New York.

Červ J. (1974), Impact radial force acting on a thin elastic disc. *Report ÚT ČSAV Z 442/74*, Prague. (in Czech)

Duffy, D.G. (2004), *Transform Methods for Solving Partial Differential Equations*, Chapman & Hall/CRC, Boca Raton.

Graff, K.F. (1975), *Wave motion in elastic solids*, Clarendon Press, Oxford.

18th International Conference
ENGINEERING MECHANICS 2012
Svratka, Czech Republic, May 14 – 17, 2012

pp. 33–34
Paper #347

THE BOUNDARY BETWEEN LINEARITY AND NONLINEARITY OF THE DYNAMICS OF GEAR DRIVES

O. Ahmedov*,V. Zeman, M.Byrtus

Abstract: *The vibration of the gear pair of the locomotive wheelset drive gearbox excited by kinematic transmission errors is presented. The mathematical model of the wheelset drive is used for determination of constant gear mesh regions by means of the operational parameters – locomotive speed and longitudinal creepage of both wheels. Using the conditions of constant gear mesh, the areas of constant and interrupted gear mesh are determined. The method is applied to a particular gear drive of the locomotive SKODA 109E.*

Keywords: ***Gear drive, constant gear mesh conditions, constant gear mesh map.***

1. Introduction

Gear drives are often high speed drive systems with front helical gears. Dynamic properties of gear drives are usually significantly affected by manufacturing tolerances and elevation gear modifications (Byrtus & Zeman, 2011). Because of the presence of gear kinematic deviations, they can be assumed as the dominant high-frequency excitation source. The computational model simulates kinematic deviations as a fictitious wedge inserted between the side mashing considering ideal involute teeth (Fig. 1).

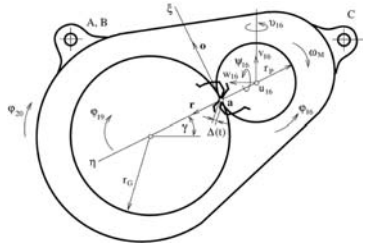

Fig. 1: Scheme of gear mesh

2. Mathematical model of the individual wheelset drive

The individual wheelset drive of the locomotive SKODA 109 E was modelled in (Zeman, Hlaváč & Byrtus, 2010)) and provided the spatial oscillations of its components. The mathematical model of the wheelset drive can be written as

$$\boldsymbol{M}\ddot{\boldsymbol{q}}(t) + \left(\boldsymbol{B} + \boldsymbol{B}_{RM} + \boldsymbol{B}(s_0, v)\right)\dot{\boldsymbol{q}}(t) + \boldsymbol{K}\boldsymbol{q}(t) = \boldsymbol{f}^G(t) + \boldsymbol{f}_0 \tag{1}$$

where $\boldsymbol{M}, \boldsymbol{B}, \boldsymbol{K}$ are mass, damping and stiffness matrices, $\boldsymbol{B}_{RM}, \boldsymbol{B}(s_0, v)$ are rotor damping matrix and matrix of the adhesion properties in contact of wheels and rails. The vector of internal kinematic excitation generated in gear meshing can be expressed in form $\boldsymbol{f}^G(t) = \left(k_z \Delta_z(t) + b_z\, \dot{\Delta}_z(t)\right)\boldsymbol{c}_z$, where $\boldsymbol{c}_z$ is the global vector of geometrical parameters of the gearing. The function $\Delta_z(t)$, defining kinematic transmission error of gearing can be expessed by Fourier series

$$\Delta_z(t) = \sum_{k=1}^{K} (\Delta_{z,k}^C cosk\omega_z t + \Delta_{z,k}^S sink\omega_z t)$$

* Ing. Olimjon Ahmedov, Prof. Ing. Vladimír Zeman, DrSc, Ing. Miroslav Byrtus, Ph.D.: Department of Mechanics, University of West Bohemia, Univerzitní 22 ; 30614 Plsen; CZ, e-mail: ahmedov@kme.zcu.cz, zemanv@kme.zcu.cz, mbyrtus@kme.zcu.cz

where meshing frequency $\omega_z = \frac{\pi n}{30} z$ is function of operation speed n [rpm] and z denotes the gear teeth number.

2.1. Constant gear mesh conditions

The practice is very important to determine conditions for stable working side shot teeth. Solution (1) can be found in the shape of the sum of static and oscillating component $\boldsymbol{q}(t) = \boldsymbol{q}_{st} + \boldsymbol{q}_{dyn}(t)$, where vector $\boldsymbol{q}_{st} = \boldsymbol{K}^{-1}\boldsymbol{f}_0$. From the equations of motion (1) for oscillating component of motion we get

$$\boldsymbol{M}\ddot{\boldsymbol{q}}_{dyn}(t) + \big(\boldsymbol{B} + \boldsymbol{B}_{RM} + \boldsymbol{B}(s_0, v)\big)\dot{\boldsymbol{q}}_{dyn}(t) + \boldsymbol{K}\boldsymbol{q}_{dyn}(t) = [k_z\Delta_z(t) + b_z\,\dot{\Delta}_z(t)]\boldsymbol{c}_z \qquad (3)$$

The constant gear mesh conditions by gearing deformation steady state is

$$\min_{t\in<0,10T_z>} d_z(t) = \min_{t\in<0,10T_z>}\left\{\boldsymbol{c}_z^T[\boldsymbol{q}_{st} + \boldsymbol{q}_{dyn}] + \Delta_z(t)\right\} > 0$$

For an illustration, Fig. 2 includes map of constant gear mesh of the gear drive SKODA 109E. Fig. 2 shows splitting of the operational area into two regions. The gray colored one corresponds to area of uninterrupted gear coupling contact and the white one corresponds to the area of gear mesh contact interruption, i.e. the gray colored area corresponds to area where the linear model holds and the white area corresponds to the area where the model is nonlinear.

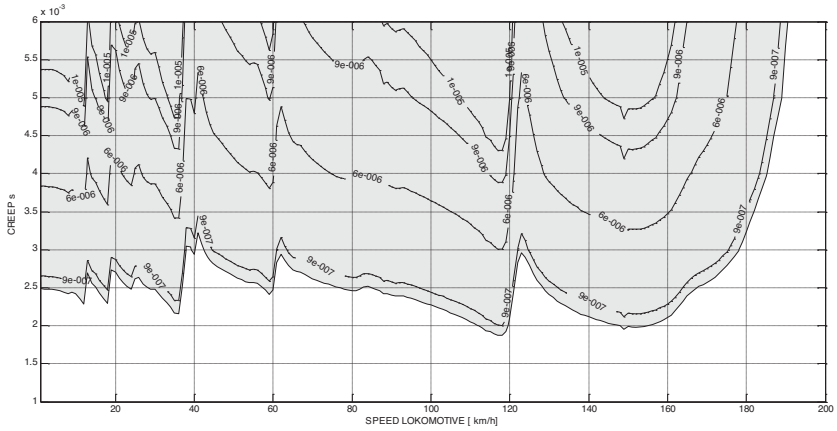

Fig. 2: Map of constant gear mesh of the gear drive SKODA 109E

3. Conclusions

The paper provides a method for modeling vibration gear drives and allows investigation of the region of constant gear mesh in dependence on the operating parameters – speed of locomotive and creep of between wheel and rail. Using the map of constant gear mesh, one can clearly determine when the nonlinearities in gear coupling employ.

Acknowledgements

The authors thank the student grant SGS-2010-046 at the University of West Bohemia and the project MSMT 1M0519- Research Centre of Rail Vehicles for financial support.

References

Byrtus, M., Zeman, V. (2011) On modeling and vibration of gear drives influenced by nonlinear couplings, *Mechanism and Machine theory*, Vol.46 (2011), No. 3, 375–397

Zeman, V., Hlaváč, Z., Byrtus, M. (2010) *Dynamic load of the vehicle bogie components of the electric locomotive 109E caused by short-circuit traction motor moment*. Research report No. VZ č. F10-01/2010, VCKV, ZČU Plzeň

Hajžman. M, Byrtus. M, Zeman V. (2010) Development of the Basic Dynamical Model of a Squirrel Cage Motor. *Engineering Mechanics*, Vol.17, No.3/4, p.225-235

18th International Conference
ENGINEERING MECHANICS 2012
Svratka, Czech Republic, May 14 – 17, 2012

pp. 35–46
Paper #69

TRANSMISSIBILITY OF SUSPENDED SEAT LOADED WITH PASSIVE MASS AND WITH HUMAN DRIVER - DISCUSSION

M. Apetaur[*], B. Janeček, J. Šklíba [**]

Abstract: *Person sitting on a suspended seat, which is excited by floor motion (f.e. truck cab floor), plays a passive as well as an active role in influencing own vibratory motion. Transmissibility of the floor vibration to a person, occupying a suspended seat, differs therefore vastly from transmissibility of the floor vibration to a passive seat load. Identification of these human reactions could be important, as it could alter vibratory comfort criteria as well as demands on active control of suspended seats. Some hints for further research, which could lead to the identification of force reactions of a person sitting on a suspended seat excited by vibratory floor motion, are discussed.*

Keywords: ***Suspended vehicle seat, vibration transmissibility, human reactions***

1. Introduction

Air-suspended seat with active control, intended for use in trucks, was developed at TU Liberec some years ago (Fig.1). Stages of this development were presented in several papers, e.g. (Kupka et al., 2007; Kupka et al., 2006; Janeček et al., 2005).

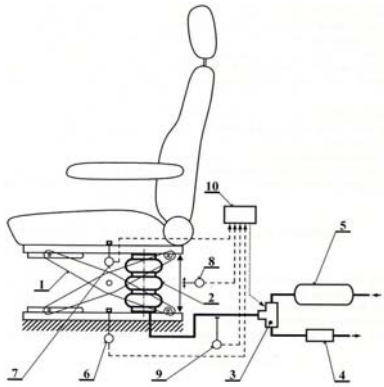

Figure 1. Basic arrangement of the active seat TUL (Apetaur et al., 2009)

Basic philosophy of its control was relatively simple. Important truck cabfloor vertical motion has meaningful frequency content between approx. 0.5 Hz to approx. 12 Hz. It can have (under very hard off-the-road conditions) maximum strokes up to +/-12 cm. The aim of the active seat control was to obtain optimum isolation of the loaded seat from cabfloor vibration. Transmissibility of floor vertical motion to the seat, which would be near to 1 for floor motions with frequency around 1 Hz and which would rapidly fall to lowest achievable values for higher frequencies, was therefore demanded. Excitations with frequencies under 0.5 Hz and over 10 Hz were considered as unimportant.

Seat transmissibility is in the paper defined as frequency dependence of the ratio of seat cushion amplitudes under the load resp. driver to amplitudes of cabfloor vertical motion under the seat.

[*] Prof. Ing. Milan Apetaur, DrSc.: Univerzita J.E. Purkyně, Na okraji 1001, 400 01 Ústí nad Labem, e-mail: apetaur@volny.cz

[**] Doc. Ing. Bedřich Janeček, CSc., Prof. Ing. Jan Šklíba CSc.: Technická univerzita v Liberci, Studentská 2, 46117 Liberec, e-mail: bedrich.janecek@tul.cz, jan.skliba@tul.cz

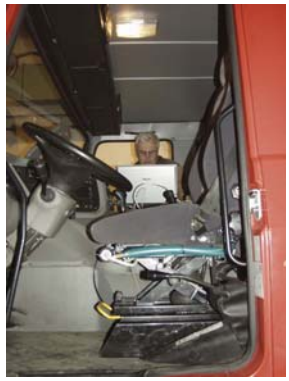

Figure 2. Active seat with a dummy in laboratory and in the truck

Seat transmissibility was tested in the laboratory with passive load, formed both by simple mass and by 3DOF dummy (Fig.2), and excellent fullfilment of this demand was achieved, especially at the latest seat development stage (Fig.3b).

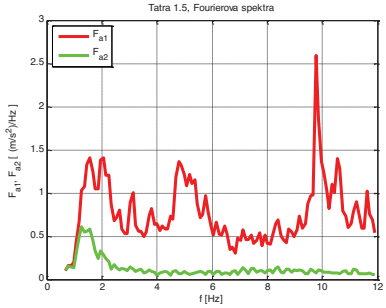

a)

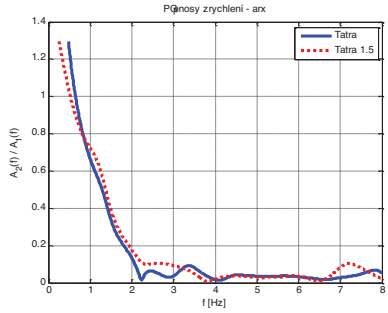

b)

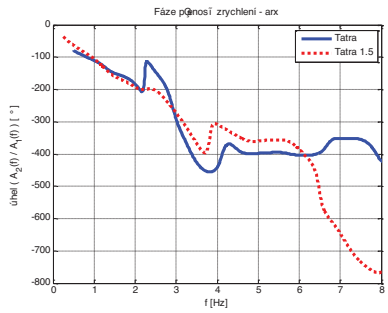

c)

Figure 3. Transmissibility of the active seat TUL (latest development stage) obtained in laboratory with very intensive quasistochastic floor inputs „TATRA 1“ and „TATRA 1.5“ (with maximum total floor stroke of approx. 20 cm): a) Fourier spectrum of the input acceleration „TATRA 1½“and of the resulting seat acceleration, b) amplitude transmissibility, c) phase transmissibility

This result can be compared to the transmissibility of a passive seat from a renown producer, similarly excited (Fig.4).

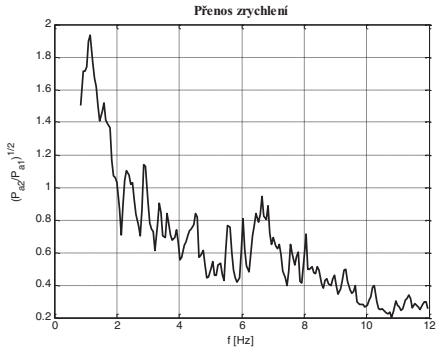

Fig.4 Transmissibility of a a certain production passive seat (low damper adjustment) obtained in laboratory with „TATRA ½" floor input

(Remark: Laboratory tests were carried out with different excitational processes. Laboratory results shown in this paper are mostly achieved on s.c. "TATRA" quasistochatic process, imitating vertical cabfloormovement of loaded TATRA 815 truck running on the "buližnik" test track, differently scaled. (1/2, 2/3, 1, 1.5).)

Figure 5. Test tracks on TATRA proving ground, vehicle is riding on the "belgická" test track, "buližnik" track in front of the figure (Apetaur et al., 2009)

Active seat, occupied by driver, was then tested in a TATRA truck (Fig.2) on different test tracks (Fig.5) and roads. Transmissibilities completely different from those measured in the laboratory were however obtained (Fig.6) *(Apetaur et al., 2009)*.

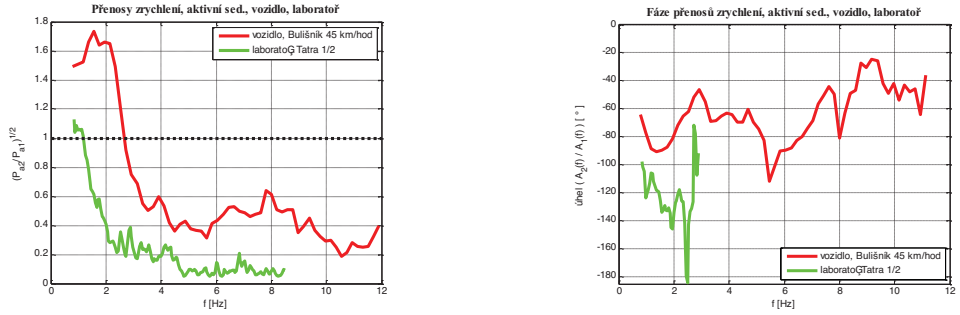

a) b)

Figure 6. Comparison of the transmissibilities of active seat TUL (intermediate development stage) passively loaded in laboratory (green) with signal TATRA ½ and with driver on the test track "buližnik" (red) (Fourier spectrum of both vertical excitations is similar): a) amplitude transmissibilities, b) phase transmissibilities

Same behavior was however observed with a passive seat, tested previously to the tests carried out with active seat TUL, so that very strong influence of the driver on his own motions on any, active or passive, suspended seat has to be accepted as a real phenomenon, as already discussed by the authors in a previous paper (Apetaur et al., 2009).

Person, sitting on a suspended seat, can evidently alter consciously or unconsciously his/her (predominantly) vertical position relatively to the floor. This is possible on non-suspended seats to very small extent only because of the limited elasticity of the seat cushion. Activity of the person, which is sitting on a suspended seat, leads to profound change of the seat+person dynamic system in comparison to seat+passive load dynamic system. The fact, that the person sitting on a suspended seat can influence his/her motion, is of course known, but its extent and effects on the total seat/person vibration transmissibility are surprising.

On-the-road comparison of the driver´s comfort, when sitting on a certain passive seat and on the developped active seat TUL, showed relatively small differences between their measured transmissibilities (Apetaur et al., 2009), though laboratory results with passive load and similar excitation showed far better isolation behavior of the active seat. As transmissibility and weighted acceleration evaluation are so far the only characteristics used for comparison of different seat designs, mentioned on-the-road results led unfortunately to loss of interest from the side of the industrial investor in the continuation of the project and practically to the abandonment of further development of the active seat at TUL.

Two questions arise evidently:

- if a person influences very substantially its motions on the suspended seat, it must use for it some muscular as well as mental energy; is it then correct to judge his/her vibratory comfort on a suspended seat by measuring its vertical acceleration only, as it is commonly done today (ČSN 14253, 2006; ČSN ISO 2631-1, 1999)?
- optimization of the transmissibility of a suspended seat loaded with passive load alone evidently does not express real development tasks on the dynamics of controlled suspended seats in transport vehicles; is it possible to state the demands on dynamic property of a suspended seat respecting the actual driver´s/passenger´s reactions?

Identification of person´s reactions, when sitting on a suspended seat, would be needed to answer both of these questions.

Under the term "identification" is meant:

- determination of the physical nature of human force reactions, which influence seat vertical motion;

- discovery of the relevant kinematic inputs (cab and body motions) causing these force reactions;
- mathematical description of the relations between the kinematic inputs and resulting force reactions of the person.

Simultaneously following important questions have to be answered:

- how individual are these reactions ?
- are they same for different floor motions, described f.e. by their PSDs?
- how do they depend on the properties of the seat vibratory system?

There is practically no knowledge about any of these items, as experimental as well as theoretical research in this field does not exist.

A very elementary attempt was made to get an impression about the possibility of modelling person´ s reactions when sitting on a suspended seat subjected to floor vibration. It is based on results of few available tests, which were not directed to the solution of this problem. This attempt could be therefore directed only to the identification problem in a narrow sense, i.e. to the question whether it seems to be possible to find out relevant kinematic inputs causing such force reactions (of so far unknown nature) of a certain person sitting on a certain seat in a certain truck, which produce vibration transmissibilities similar to those stated in tests.

It must be enhanced, that results shown further must be therefore considered only as an illustration of necessary steps, which could lead to better understanding of this problem.

2. General remarks on the behavior of a person sitting on a suspended seat. Approach to the identification problem

Fig.6 shows comparison of the results gained with the active seat in the laboratory (passive load) and on the testing ground (seat loaded by driver). Difference is significant.

There can be posed an objection, that excitation of the seat with passive load in laboratory and excitation of the seat with driver in the vehicle are different. Whereas the excitation in laboratory is strictly vertical, cab of a riding truck exerts movements in all six DOF, so that the driver in reality does not react on vertical acceleration only. This is to some extent true, but results gained on relatively smooth roads, where cab movements are predominantly vertical**,** show seat/driver system transmissibilities similar to those gained on severe test-tracks and very different from seat/passive load transmissibility (see Fig.10, curves “1” and “4”).

It can be therefore taken as granted, that vertical cabfloor movements form the deciding excitation of the seat/driver system for most driving conditions, even on relatively rough test tracks. Fore-and-aft and tilting motions of the cab should be however taken in further tests into account as potential excitational sources on difficult tracks as well.

Relatively well documented active-seat/driver transmissibilities (measurements TUL) unfortunately cannot be taken as a base for the driver´s effort interpretation, as the controlled seat itself forms a highly non-linear time-dependent dynamic system.

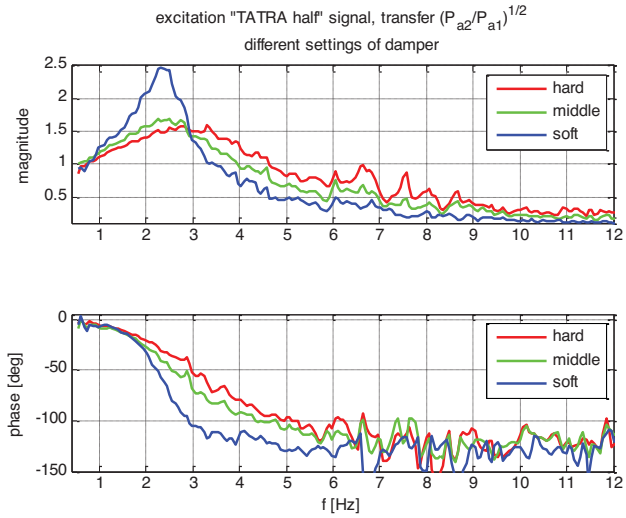

Figure 7. Amplitude and phase transmissibility of a certain passive seat with passive load, „hard", „middle",„soft" damper adjustment, laboratory measurements, quasistochastic " TATRA ½" input; (some difference in natural frequency, seen on the figure, between "soft","middle" and "hard" damper adjustments is caused by the damper properties, as the damper exerts some "stiffness" property, especially in "hard" adjustment)

Following discussion is therefore directed to persons sitting on passively suspended seats. Dynamic behavior of these seats, loaded with passive mass, is very near to that of a linear 1DOF model in practically all so far measured cases (Apetaur et al., 2009). Seat suspension non-linearearities (air spring characteristics, damper characteristics, friction) seem to play a secondary role only. An example is shown on Figure 7.

Measurements, on which following discussion is based, were conducted by another laboratory with a certain passive seat (natural frequency approx. 1.25 Hz for (seat+passive load) mass equal to approx. 80 kg), which could not be tested by us, so that complete data were not available (see Apetaur et al., 2009).

The only possibility for a person, sitting on a suspended seat, to change his/her vibrational behavior is by exerting some time-changing force acting on the seat structure in vertical direction.

It can be produced in different ways.

First, and most probable, is force originated by the sitting person in the contact of its body with the cab, by driver by legs (but he must be able to operate the pedals) and by arms (but he must be able to operate the steering wheel), by passenger by legs only (Remark: in extreme off-road circumstances he can stabilize himself by holding some appropriate handle in the cab; this is often the case.). Reactions of the driver and of the passenger to the floor vibration will be therefore most probably different.

Second possible force origin is dynamic, by near-vertical motion of "free" body parts. Especially motions of head and of upper arms with shoulders can be effective in producing near-vertical forces even without causing notable relative motion of the back to the backrest.

Mentioned forces can have either purely passive, inertial, origin, or can be caused or initiated by subconscious muscular actions of the person.

Motions of body´s chest and internal organs seem to play a secondary role only. Results gained in seat laboratory tests with 3DOF dummy (Fig.2), which imitates passive vibrational properties of a human body, and with simple passive mass, showed very similar transmissibilities.

Basic computations, as well as measurements (Fig.8), have further shown, that flexibility of the seat cushion does not play any substantial role on the seat transmissibility.

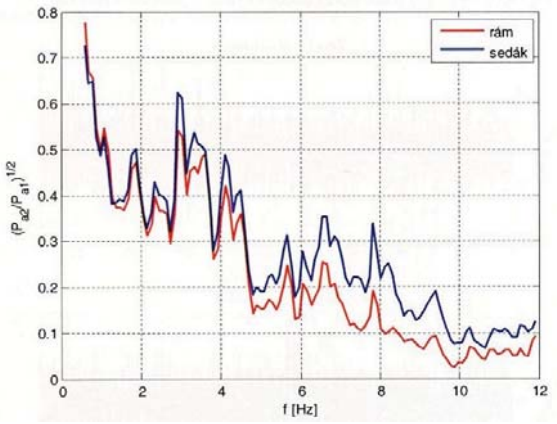

Figure 8. Comparison of the transmissibility from the cabfloor to seat structure ("rám", red) and to seat cushion ("sedák", blue) – active seat TUL (intermediate development stage), laboratory measurement with a dummy, "TATRA ½" input

Simple dynamic model was therefore taken as basis for a very crude "identification" (in narrow sense) attempt.

It was assumed, that the torso of the person, who sits on the seat, is a passive mass joined with movable seat structure mass, linearilly suspended on the cab floor.

The dynamic equilibrium equation of the seat+body dynamic system under these simplifying assumptions is

$$m.(d^2x/dt^2) + b.(dx/dt - dz/dt) + k.(x-z) = F \quad (1),$$

where x(t) is the vertical seat/body motion, z(t) floor vertical motion, F(t) force influence exerted by person sitting on the seat, acting in vertical direction, m (kg) total mass of (seat+body), k (N/m) stiffness of seat spring, b (Ns/m) damping coefficient of seat damping. This equation describes a linear 1DOF system, whose properties need not to be discussed.

Force reaction F(t), influencing motion of the sitting person, must be excited by some input signals $v_i(t)$ perceived by him/her. It can assumed, that these signals induce individual force processes $F_i(t)$, so that the actual reaction force F(t) is composed as their sum

$$F(t) = \Sigma F_i(t) \quad (2a).$$

It is so far unclear, which inputs $v_i(t)$ are causing actual force reactions $F_i(t)$. Evidently all kinematic parameters of cab and seat motions can be taken into account, i.e.:

- stroke, velocity, acceleration, jerk of the floor motion z(t),
- stroke, velocity, acceleration, jerk of the relative seat to floor motion (x(t)-z(t));
- stroke, velocity, acceleration, jerk of the seat motion x(t).

Determination of most important inputs and of their influence will be evidently one of the crucial problems in future proper investigations. It can be expected, that relations between $v_i(t)$ and related force components $F_i(t)$ can be quite complicated.

"Identification" of the human reactions is here understood in a very narrow sense as finding most relevant inputs v_i which excite reaction forces F_i, and laws describing their mutual $F_i(v_i)$ relations. Actual origins of the reaction forces F_i are not discussed, as experimental data are not available.

Proper identification will be evidently complicated by its subjective nature. Results gained by experiments with one driver performing only one drive on a specific track with one damper adjustment are further used. The driver had a perfect knowledge of the test tracks and of the truck, i.e. he was

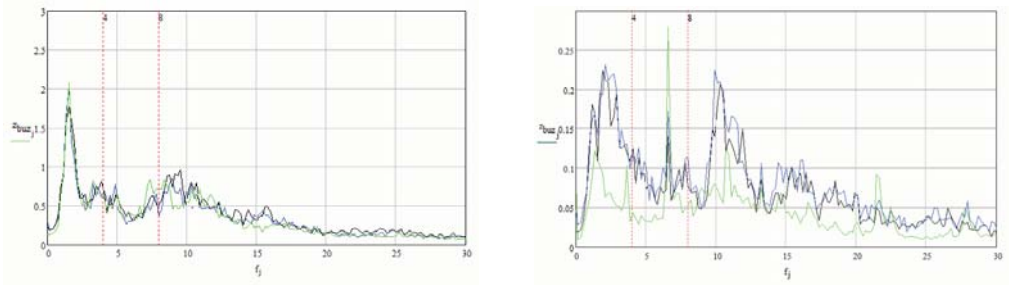

a) b)

Figure 9. Fourier spectrum of the vertical cabfloor motion: a) on "pavé" test track, b) on good public road "silnice"

perfectly aware what vibratory conditions he has to expect, he was prepared to sustain vibrational exposition with a level known to him in advance.

Vehicle rides on three surfaces were taken as basis for further discussion:

- ride on a good public road „silnice" (Fig.9b), vehicle speed 80 km/h, length 1000 m,
- ride on test track „belgická", imitating very bad road, vehicle speed 15 km/h, length 400 m,
- ride on test track „pavé", imitating extremely bad road (Fig.9a), vehicle speed 25 km/h, length 400 m.

Intensity of the vibration of the cabfloor on these tracks can be very roughly scaled:

- "silnice" 1 : "belgická" 2.5 : "pavé" 8, at frequency around 1.5 Hz,
- "silnice" 1 : "belgická" 2 : "pavé" 4, at frequency around 10 Hz,

i.e. intensity of vibrations of the cabfloor on these tracks was vastly different.

Transmissibilities cabfloor/seat, gained by original investigations (partially described in Apetaur et al., 2009), are used in further discussion.

Following observations can be made:

- Floor motion spectra have two distinctive peaks at frequencies approx. 1.5-2 Hz and approx. 10 Hz, corresponding to the natural frequencies of the vehicle suspension and one less pronounced at approx. 6.5 Hz, corresponding to cab suspension; excitation at frequencies below 1 Hz is relatively low, which of course influences accuracy of the determination of the transmissibility at theses frequencies; shown transmissibility values for frequencies under 0.5 Hz should not be taken into account.
- transmissibility at frequencies over 5 Hz is near to 0.5 and is very slightly dependent on the excitation intensity (track properties) as well as on the seat damper adjustment ;
- resonance of the seat+(passive load) dynamic system (at approx. 1.25 Hz) is practically always suppressed;
- transmissibility for frequencies 0.5 to approx. 1.5 Hz is extremely high on all rough tracks.

Measured seat transmissibilities, gained on mentioned three very different tracks, were approximately simplified as indicated on Fig.10. Transmissibilities, gained on other test tracks, lie in the hatched area.

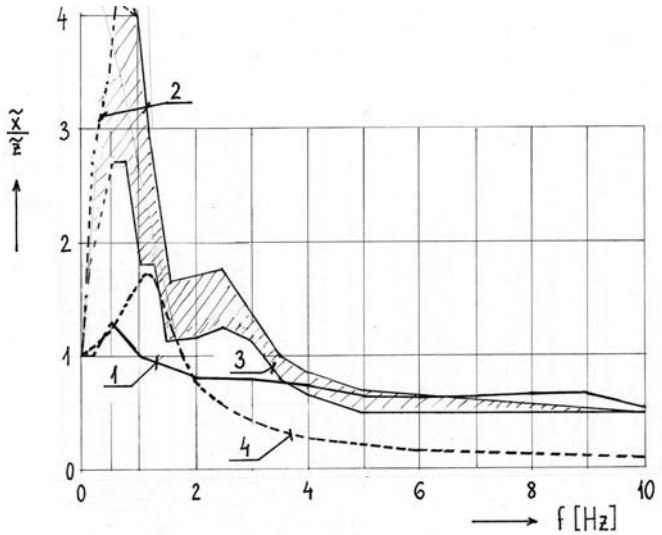

Figure 10. Simplified transmissibilities of seat/driver system measured in on-the-road experiments: "1" silnice=road, 80 km/h;"2" belgická test track, 15 km/h; "3" pavé test track, 25 km/h; "4"(dashed) expected transmissibility of seat/passive load system, medium damping

These simplified transmissibilities were formed as medium ones for "medium" damping of the measured passive seat. Expected amplitude transmissibility of the passive seat, used in the measurements, loaded with passive load is shown on the figure as well. Difference, between the "passive load" transmissibility and the "driver load" transmissibilities, is evident.

Equation (1), with constants m=80 kg, b=480 Ns/m, k=4960 N/m, was used as base for the identification attempt. Forces $F_i(t)$ were arbitrarily supposed to be described by linear second order differential equations with inputs $v_i(t)$. Because of the linearity of the model, its transmissibility could be computed by using harmonic input z(t).

The task was to achieve transmissibilities of this model similar to those shown on Fig.10.

This was done purely empirically, trial and error style, by changing inputs, control laws and constants. Following relations were found at the end:

$$F(t) = F_1(t) + F_2(t) + F_3(t) + F_4(t) \qquad (2b),$$

with individual forces $F_i(t)$ computed as:

$$(dF_1/dt) = -1.F_1 - \beta.(dz/dt);$$

$$(d^2F_2/dt^2) = -60.\,(dF_2/dt) - 4000.F_2 + 128000.(d^2z/dt^2);$$

$$(d^2f_3/dt^2) = -8.(df_3/dt) - 300.f_3 + 200.(d^2x/dt^2);$$

$$F_3=(df_3/dt);$$

$$(d^2F_4/dt^2) = -6.(dF_4/dt) - 62.F_4 - 2400.(\,6.(dx/dt-dz/dt) - 62.(x-z)) \qquad (3).$$

These equations could be used for all three excitational conditions. It is interesting to note, that even for such extremely different excitational conditions only constant β, which directs the transmissibility at low excitational frequencies, had to be changed to get reasonable results. It was stated as:

„road" β=4800; „pavé" β=10400; „belgická" β=16000.

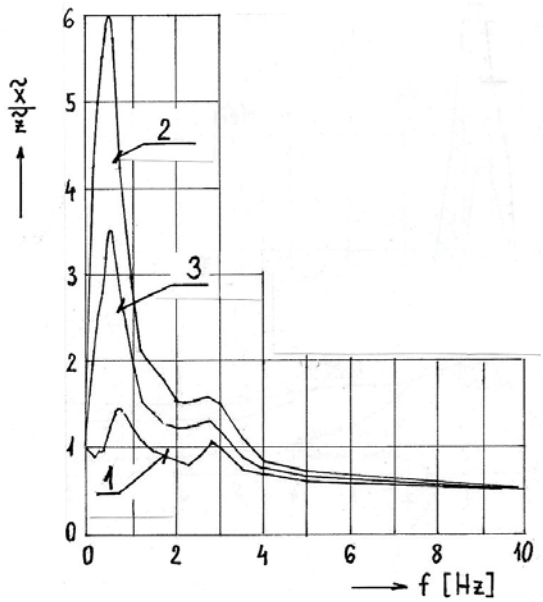

Figure 11. Transmissibilities gained by seat+driver model (Eqs.1,2b,3): "1" silnice=road, 80 km/h;"2" belgická test track,15 km/h; "3" pavé test track,25 km/h

Amplitude transmissibilities gained by this seat/driver model are shown on Fig.11. Computed transmissibilities correspond fairly well with measured ones (Fig.10).

Some initial supposals about the nature of the driver´s reactions were to some extent confirmed by the model:

- reaction (force F_2) of the driver to relatively higher frequency floor excitation (over 5 Hz) seems to be caused by floor acceleration (d^2z/dt^2); its description is qualitatively and quantitatively same on all roads;
- driver tries to diminish relative floor to seat movements in the frequency range 1 to 3 Hz (force F_4), seemingly as reaction to relative body to cabfloor movement (x–z) and its velocity (dx/dt-dz/dt) ; force F_4 seems to suppress pronouncedly resonance effect of the original passive mass dynamic system; its description is qualitatively and quantitatively same on all roads;
- some destabilizing effect (force F_3), caused probably by phase delayed body reactions, can be clearly seen around 2 to 4 Hz; its description is qualitatively and quantitatively same on all roads; force F_3 seems to be dependent on body jerk (d^3x/dt^3).

But:

- origin of the force F_1, which substantially increases transmissibility in the range 0.5 to 4 Hz, is difficult to explain; its stated first order dependence on the floor velocity (dz/dt) is surprising; its description is qualitatively same but quantitatively different (constant β) on different roads; necessary change of constant β cannot be so far explained (excitation intensity in vertical direction is highest on „pavé 3" track, lowest on „silnice 1" track).

(Remark: discussed transmissibilities in the very low frequency range under 1 Hz must be considered very carefully, as cabfloor vibration intensity with frequencies under 1 Hz is in all tests, which were carried out, very low (see Figs. 3 and 9) and the time of observation (around 50 s) of individual rides is for their evaluation relatively short; values shown can be therefore relatively inaccurate.)

The fact, that transmissibilities of the seat+driver system stated for very different input intensities, could be successfully mathematically modelled by linear differential equations with change of one constant (namely β) only, was unexpected and is certainly surprising.

It must be enhanced that shown equations cannot be considered as meaningful solution of the identification problem as:

- experimentally stated transmissibilities were gained from measurements with one subject (driver) performing one drive on a certain track only;
- approximation of the actual transmissibilities on Fig.10 was very crudely done from insufficient data;
- very crude models of the seat system and of the human body were used;
- validity of Eqs.1, 2, 3 was not checked by:
  - phase relations comparison, as no experimental data were available;
  - computation of total correcting force F(t) , which would show, whether the driver is physically able to generate it;
- origin of the individual correcting forces in Eq.3 is unknown; hence validity of their shown differential description is doubtful.

Most probably, other scenarios are possible as well.

The authors see actual value of the shown "identification" attempt in providing some starting points for further research. Its sole positive result can be seen in the fact, that it seems to be possible to find some general mathematical model of force reactions, which correct vibratory motion of a person sitting on a suspended seat which is excited by floor motion.

However, without further research, including relatively costly and time consuming experiments as well as sophisticated identification of their results, there is no chance to enlarge the very limited knowledge presented here.

3.Conclusions

Person, sitting on a suspended seat, influences radically his/her own vibratory motion by exerting time-dependent forces of so far not cleared origin. This is valid for very different floor vibration levels, reaching from very low to extreme ones. Identification of the processes, which cause such muscular and mental involvement of the sitting person in directing his/her vibration, would lead:

- very possibly to the change of vibratory comfort evaluation of persons sitting on suspended seats, as some further conditions, f.e. evaluation of forces between legs and arms and vehicle cab or evaluation of relative motions of different body parts (head to spine, etc.), evidently should be added to the usual method of weighted acceleration evaluation (ČSN 14253, 2006; ČSN ISO 2631-1, 1999);
- to the gain of information for further development work regarding actual demands on active seat control, important for improving driver/passenger/operator vibrational comfort in vehicles and heavy machinery.

Proper identification would demand to distinguish physical nature of the forces, exerted by the sitting person, determination of kinematic inputs, which provoke them, and mathematical description of their relations.

Attempt to identificate reactions of driver sitting on a suspended seat, discussed in the paper, was done in a narrower sense. It had the purpose to find out, whether a mathematical description of the driver´s reactions to kinematic inputs, formed by floor and body motions, seems to be possible at all. Its result is encouraging, though many questions are left open.

Some observations, gained from the identification attempt discussed, about roles of individual kinematic inputs on the origin of human reaction forces are however interesting, though experimentally unconfirmed.

The authors consider the possibility of empirical description of force reactions of a person sitting on a suspended seat, their "identification" in a narrow sense, as realistic.

Proper identification of human reactions, which would lead to its practical exploitation, is however a much more complicated task, demanding laboratory measurements with a group of individuals and their statistical evaluation. Laboratory means as well as theoretical background are at disposal at TUL (see Apetaur et al., 2009) and other laboratories, though evidently new identification algorithm would have to be created because of the multitude of possible inputs.

No interest to support work in this exciting field, dealing with man/machinery interaction, was however found so far.

References

Kupka L., Janeček B., Šklíba J. (2007) Laboratory Verification of the Active Vibration Isolation of the Driver Seat. In: *Recent Advances in Mechatronics – sborník mezinárodní konference Mechatronics Varšava 2007*. Berlin – Heidelberg – New York: Springer, s. 453–457.

Kupka L., Šklíba J., Janeček B., Apetaur M., Kozderka J. (2006) Experimental Research of the Active Vibration Isolation System of the Driver Seat. In: *Sborník národní konference s mezinárodní účastí Engineering Mechanics Svratka 2006.* Praha: ÚTAM AV ČR.

Janeček B., Kupka L., Šklíba J., Apetaur M., Martonka, R. (2005) On the Problem of the Active Control of the Driver Seat. In: *Sborník mezinárodní konference Mechatronics, Robotics and Biomechanics 2005* [CD–ROM]. Brno,.

Apetaur, M., Barbora, J., Buchta, J., Janeček, B., Kupka, L., Marek, M., Šklíba, J. (2009) Testing of Active Controlled Driver´s Seat. In: *Sborník národní konference s mezinárodní účastí Engineering Mechanics Svratka 2009.* Praha: ÚTAM AV ČR.

Standard ČSN 14253 (2006) *Měření a výpočet expozice celkovým vibracím na pracovním místě s ohledem na zdraví*. Praktický návod. Český normalizační institut.

Standard ČSN ISO 2631-1 (1999) *Vibrace a rázy – Hodnocení expozice člověka celkovým vibracím*. Český normalizační institut.

18th International Conference
ENGINEERING MECHANICS 2012
Svratka, Czech Republic, May 14 – 17, 2012

pp. 47–57
Paper #51

THE STUDY OF POLYMERIC HOLLOW FIBER HEAT EXCHANGERS

I. Astrouski*, M. Raudensky**

Abstract: *The polymeric hollow fiber heat exchanger (PHFHE) is a modern type of apparatus which uses polymeric fibers, with a small diameter around 1 mm, for separation of the heat transfer mediums. The main goal of this work is to study different factors which affect heat transfer in polymeric hollow fibers (diameters, length and material of fibers, liquids temperatures and velocities) and to obtain conclusions concerning hollow fiber application. The values of external, internal as well as overall heat transfer coefficient, heat transfer rate, number of transfer units (NTUs), efficiency and pressure drops were obtained for both water-water and water-air applications. The special performed Delphi-based software was prepared to accelerate the computation process.*

Keywords: ***Polymeric hollow fibers, heat exchanger, heat transfer.***

1. Introduction

The first attempts to use polymers as a material for heat exchange equipment started over 40 years ago because of some benefits in comparing them with conventional metals (Whitley, 1957). Polymers as common are less expensive and easier to shape, form and machine than metals. Moreover, the energy required to produce a unit mass of plastics is about 2 times lower than that of common metals, making them environmentally attractive. The smoothness of the polymer surface begets low friction, hence a drop in pressure as well as to good fouling characteristics. Long-term fouling data of polymer heat exchangers is not available, but 76 h test with hard water was performed by Githehens (1965). Polymers have excellent chemical resistance and moreover, their hydrophobic surface promotes dropwise instead of filmwise condensation and, consequently, much higher heat transfer coefficients (Bigg et al., 1989).

In accordance with Malik (2005) most of the commercially available polymer heat exchangers are being used in a corrosive environment or in low temperature applications (ice storage or solar heating of domestic hot water and swimming pools). In particular, plastic heat exchangers were also used for heat recovery in greenhouses (Rousse et al., 2000), in superfluid Stirling refrigerators or 3He-4He dilution refrigerators (Patel & Brisson, 2000). Lately, an interest in the application of polymeric materials in solar water heating systems has also emerged (Tsilingiris, 2000). Also a lot of different fields of plastic heat exchangers application (in the desalination industry, heat recovery, cooling and cryogenic industry, humidification, solar energy industry, microelectronics and computer industry) were quoted by Zaheed (2004).

On the other hand, polymer materials thermal conductivity is low, usually between 0.1 and 0.4 W/m·K which is 100-300 times lower than that of metals and considerably limits the use of polymers for heat exchanges equipment because of big magnitude of wall thermal resistance (Zarkadas & Sirkar, 2004). In order to overcome this deficiency two approaches exist. The first one is to increase thermal conductivity of material. Excellent review of current state of the art of polymers utilizing was performed by T'Joen et al. (2008). In this review the material properties of polymers and polymer matrix composites were examined. It was shown that these materials do hold promise for use in the construction of heat exchangers, but that a considerable amount of research is still required into material properties and life-time behavior. The status of worldwide research in the thermal

* Ing. Ilya Astrouski, ** prof. Ing. Miroslav Raudenský, CSc.: Heat Transfer and Fluid Flow Laboratory, Faculty of Mechanical Engineering, Brno University of Technology, Technicka 2896/2; 616 69, Brno; CZ, e-mail: astrouski@lptap.fme.vutbr.cz

conductivity of carbon nanotubes (CNT) and their polymer composites was done by Han & Fina (2011) as well as Guarded Hot Plate Method of increasing the through-thickness thermal conductivity of CNT composites was described by Han & Chung (2011). The investigation of finned-tube heat exchangers produced from pure and modified polypropylene was performed by Chen (2008). For the heat exchangers designed in that paper, when the plastic thermal conductivity can reach over 15 W/m·K, it can achieve more than 95% of the titanium heat exchanger performance and 84% of the aluminum or copper heat exchanger performance with the same dimension. Using of increased conductivity polypropylene was investigated by Qin et al. (2012). Heat-conducting medium was developed by melt-mixing polypropylene with graphite particles (PP-g-MA). The overall heat transfer coefficient of graphite modified polypropylene hollow fiber heat exchangers reached 1228.7 W/(m^2K) and the overall conductance per unit volume $1.1 \cdot 10^6$ W/(m^3K).

The second approach to decrease wall thermal resistance is to use thin walls between heat transfer mediums. The study of different construction thin wall polymeric heat exchangers was done by Scheffler (2008). Cross-flow plate heat exchangers made of crosscorrugated films of poly(ether ether ketone) (PEEK) were used to study air-air and water-water flow configurations by Zaheed (2004). The heat transfer and the hydrodynamic response of microcapillary films (MCFs) within round and elliptical channels (diameter 30 up to 500 μm) were investigated by Hornung et al. (2005). MCFs are a class of novel, extrusion-processed, polymer films containing an array of continuous, parallel, capillaries that run along the film's length. These studies were added by Hallmark et al. (2005).

Polymeric hollow-fiber based heat exchangers (PHFHEs) are also a type of thin-wall polymer heat exchangers, which were firstly proposed by Zarkadas & Sirkar (2004) as a useful alternative for lower temperature applications. The small devices containing a few hollow PP-based fibers with the liquids in parallel flow at temperatures up to 74°C were studied. The overall heat transfer coefficients of these devices were 647-1314 W/m^2K for the water-water application. As more, proposed heat exchangers had very low values of the height of transfer, large numbers of transfer units (NTUs) for so comparably short devices, high values of heat exchanger effectiveness and overall conductance/volume rate. However, a number of important questions remained unanswered. Part of them were answered by Song et al. (2010) which study a lot of different PHFHEs with emphasis of application for thermal desalination processes and Qin et al. (2012) which study PHFHEs constructed from the modified thermal conductivity polymers.

2. Theoretical consideration

As usual polymeric hollow fibers and films have internal diameters around 0.05 – 2 mm and can be classified as the so-called microdevices (Herwig, 2001). The development of micro-mechanics during the last decades stimulated a great interest in heat transfer studies in micro-channels. A lot of theoretical and experimental investigations devoted to this problem were performed. There is no convincing explanation of the difference between experimental and theoretical results for laminar flow, and between experimental and semi-empirical results for turbulent flow (Yarin et al., 2009). On the one hand, several researchers argue that some new effects exist in micro-channels, e.g., Tso & Mahulikar (2000), Gad-el-Hak (2003). On the other hand, the phenomenon can be related to the discrepancy between the actual conditions of a given experiment and theoretical or numerical solution obtained in the frame of conventional theory (Herwig 2001; Herwig & Hausner 2003).

Thus, there are some additional factors which possible can influence the heat transfer in microchannels can be determined in comparing with conventional theory: dissipation effects which determined by Eckert number (or Brickman number in accordance with Tso & Mahulikar (2000)), axial conduction which determined by Peclet number, conjugate effects and variable properties effects (Herwig, 2001). However, in accordance with Song et al. (2010) and Zarkadas & Sirkar (2005), the axial heat conduction, flow work and viscous dissipation are negligible for laminar flow in polymeric hollow fibers. Two different methods of determining the temperature profile inside the polymeric hollow fiber heat exchanger or the inside, outside and wall heat transfer coefficients were proposed. These methods are a simplified correlation suggested by Hickman and a rigorous solution of the extended Graetz problem by Hsu (Zarkadas & Sirkar, 2004). The simple relationship to calculate internal mean Nusselt number of thermal developing region was proposed by Zarkadas & Sirkar (2005) based on Hickman's one and incremental heat transfer number calculated by Hsu's approach.

2.1. Calculation of fiber heat transfer performance

Firstly, the physical properties of the air and water were calculated based on inlet temperatures of liquids. The formulas obtained from ThermalSpreadsheets were used for determine the specific heat, dynamic viscosity, kinematic viscosity, thermal conductivity and density of air:

$$Cp = 1.22295 \cdot 10^{-10}\, T^4 - 5.35621 \cdot 10^{-7}\, T^3 + \\ + 8.27169 \cdot 10^4 T^2 - 0.295423 \cdot T + 1032.1 \quad (1)$$

$$\mu = 5.41836 \cdot 10^{-15} T^3 + 2.52496 \cdot 10^{-11} T^2 + 5.87333 \cdot 10^{-8} T + 2.80339 \cdot 10^{-6} \quad (2)$$

$$\nu = -1.14681 \cdot 10^{-14} T^3 + 8.87916 \cdot 10^{-11} T^2 + \\ + 4.55037 \cdot 10^{-8} T + 5.43395 \cdot 10^{-6} \quad (3)$$

$$k = \frac{0.0316 - 0.0243}{100} \cdot t + 0.0243 \quad (4)$$

$$\rho = 353.179/T \quad (5)$$

where t and T are temperatures on a scale of Celsius and Kelvin respectively. The results of calculations in adequate range were compared and matched with data from Incropera & DeWitt (1996) so these formulas were chosen for use. The required physical properties of water were taken from the NIST Chemistry WebBook. The Prandtl and Reynolds numbers were calculated as followed:

$$Pr = \frac{c_p \cdot \mu}{\lambda} \quad (6)$$

$$Re = \frac{u \cdot D}{\nu} \quad (7)$$

where c_p, ν and μ, λ are specific heat, kinematic and dynamic viscosities, thermal conductivity respectively.

The outside and inside diameters of fibers D_o and D_i, the outside bulk flow velocity u_o and average inside velocity u_i were used respectively for calculation of outside (around the fibers) and inside (lumen) Reynolds numbers. Average inside velocity was calculated as followed:

$$u_i = \frac{Q_{s,t}}{0.25\pi \cdot N \cdot D_i^2} \quad (8)$$

where $Q_{s,t}$ and N are volumetric flow rate through the tube (fiber) side and number of fibers respectively. The outside Nusselt number was calculated in according with Hilbert formula for single circular tube in cross-flow (Incropera & DeWitt, 1996):

$$Nu_o = C \cdot Re^m \cdot Pr^{0.3333} \quad (9)$$

where C and m are constants were determined in accordance with respective value of Reynolds number (Incropera & DeWitt, 1996). The outside convective heat transfer coefficient was calculated as:

$$h_o = \frac{Nu_o \cdot k_o}{D_o} \quad (10)$$

where k_o is thermal conductivity (W/m·K) of external liquid (water or air with the relevant temperature).

The inside Nusselt number was calculated in accordance with asymptotic solution for thermal developing region proposed by Hickman (Song et al., 2010):

$$\frac{1}{U_w} = \frac{D_i}{D_o \cdot h_o} + \frac{D_i}{2k_w} \cdot ln\left(\frac{D_o}{D_i}\right) \quad (11)$$

$$Nu_w = \frac{U_w D_i}{k_i} \quad (12)$$

$$Nu_{T3} = \frac{(48/11) + Nu_w}{1 + (59/220) Nu_w} \quad (13)$$

where are $k_w = 0.18$ W/m·K is thermal conductivity of isotactic polypropylene which quoted by Mark (1999) in the 0.12 – 0.22 range. Equation (13) yields Nu_{T3} values that fall between 3.66 and 4.364. The lower limit of this Nusselt number range is the limiting Nusselt number corresponding to the

constant wall temperature boundary condition ($Nu_w = \infty$) and the upper limit is the limiting Nusselt number corresponding to the constant heat flux boundary condition ($Nu_w = 0$) (Song et al., 2010). This simplified formula doesn't take into account the influence of developing flow region, but have enough good accuracy for relatively long ducts (hollow fibers of small diameters, for example). Thus, the internal heat transfer coefficient was calculated based on internal Nusselt as:

$$h_i = \frac{Nu_{T3} \cdot k_i}{D_i} \tag{14}$$

where k_i is tube liquid thermal conductivity. Linear thermal resistance and linear overall heat transfer coefficient were calculated as followed:

$$R_l = \frac{1}{D_o \cdot h_o} + \frac{\ln(D_o/D_i)}{2k_w} + \frac{1}{D_i \cdot h_i} \tag{15}$$

$$h_l = \frac{1}{R_l} \tag{16}$$

Furthermore, to estimate the influence of local thermal resistances on overall one the inside, wall and outside local to overall resistance ratios (R_i/R_l, R_w/R_l and R_o/R_l) were calculated:

$$R_i/R_l = \frac{1}{D_o \cdot h_o}/R_l \cdot 100\% \tag{17}$$

$$R_w/R_l = \frac{\ln(D_o/D_i)}{2k_w}/R_l \cdot 100\% \tag{18}$$

$$R_o/R_l = \frac{1}{D_i \cdot h_i}/R_l \cdot 100\% \tag{19}$$

Overall heat transfer coefficient was calculated based on heat transfer area of outside surface of fibers as:

$$U_{ov} = \frac{h_l}{D_o} \tag{20}$$

To obtain a thermal performance characteristics and predictions of outlet liquid temperatures the effectiveness-NTU method was used. Both outside C_o and inside C_i heat capacity rates of liquids were calculated as:

$$C = C_p \cdot \rho \cdot Q_f \tag{21}$$

where C_p, ρ, Q_f are isobaric specific heat, density and volumetric flow rate respectively, and heat capacity ratio:

$$C_r = \frac{C_{min}}{C_{max}} \tag{22}$$

where $C_{min} = \text{minimum}(C_o, C_i)$ and $C_{max} = \text{maximum}(C_o, C_i)$. The number of transfer units (NTU) was obtained by the following relationships:

$$NTU = \frac{h_{ov} \cdot A}{C_{min}} \tag{23}$$

where A is a heat transfer area of outside surface of fibers and calculated based on external surface of fibers:

$$A = \pi \cdot D_o \cdot l \cdot N \tag{24}$$

Because tube liquid flows through a large amount of small diameter fibers we must assume that tube liquid is unmixed. On the other hand the outside liquid flows without separation and so should be considered mixed. If the outside flow heat capacity rate value C_o was bigger than inside one C_i then effectiveness was calculated as (Incropera & DeWitt, 1996):

$$\varepsilon = \left(\frac{1}{C_r}\right)(1 - exp\{-C_r[1 - exp(-NTU)]\}) \tag{25}$$

And vice versa, for bigger inside unmixed flow heat capacity rate value C_i effectiveness was calculated as:

$$\varepsilon = 1 - exp(-C_r^{-1}\{1 - exp[-C_r(NTU)]\}) \tag{26}$$

The maximum possible and actual heat transfer rate were obtained by

$$Q_{max} = C_{min} \cdot (T_{t1} - T_{s1}) \tag{27}$$

$$Q = \varepsilon \cdot Q_{max} \tag{28}$$

Thus outlet temperatures for inside and outside liquids were calculated as:

$$T_{i2} = T_{i1} + \frac{Q}{C_t} \tag{29}$$

$$T_{o2} = T_{o1} + \frac{Q}{C_s} \tag{30}$$

Excellent review of laminar fluid flow in micro-channels was done by Hestroni et al. (2004). They quoted that in case of hydraulic diameters 50-254 μm and Re < 500 and in case of hydraulic diameters 620-1067 μm and Re = 500..2600 Poiseuille number is independent from Reynolds number and equal to 64 for the laminar flow in circular channels. This statement was extended based on investigations of Maynes & Webb (2002) for all range of calculation. Thus the conventional Poiseuille number was used to obtain a prediction of pressure drops in tube side (fibers). Pressure drop of tube side liquid was calculated as

$$\Delta p_{it} = \frac{128 \cdot \mu_{av} \cdot l \cdot Q_{f,t}}{\pi \cdot D_i^4 \cdot N} \tag{31}$$

where $Q_{f,t}$ is a volumetric flow rate through the tube side (fibers), l is length of fibers, D_i is internal diameter and N is number of fibers. Because of strong dependence of dynamic viscosity of water from temperature the average value of viscosity along the fiber μ_{av} was used. This value was obtained as mean of ten local dynamic viscosity values calculated for local temperatures of sub-regions. The local temperatures of sub-regions were obtained based on the assumption of linear distribution of temperatures along the channel and predetermined inlet and outlet temperatures. This assumption is rough for heat transfer calculation (Herwig & Hauser, 2003) but sufficiently accurate for calculation of local dynamic viscosity.

3. Results and discussion

As was previously mentioned the calculating program was performed to calculate heat transfer values and pressure drop of hollow fiber in cross-flow. The work window of calculating program is presented in Figure 1. The input data include external and internal diameter, length of fibers and height of cross-section in which they are located, total number of fibers, material of fibers wall, types and temperatures of liquids inside and outside of fibers, volumetric flow rate for inside liquid and bulk velocity around the fibers for outside one.

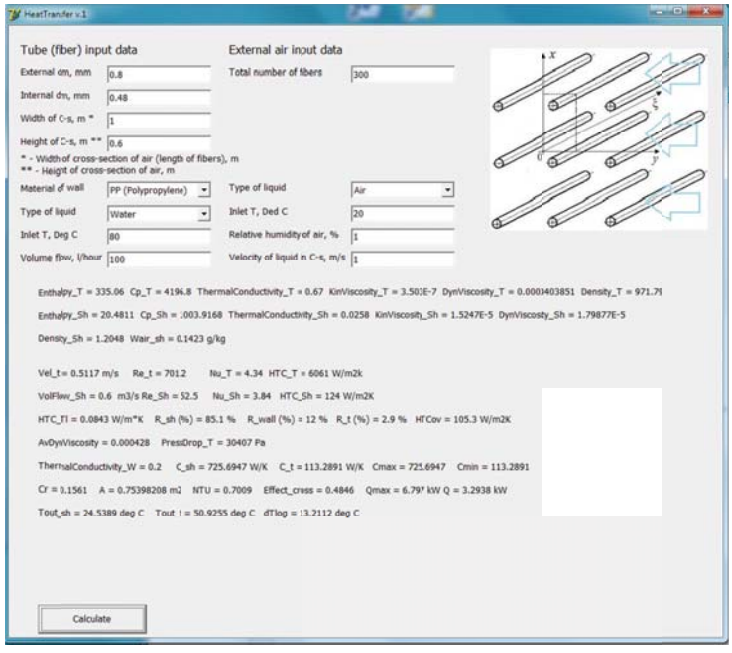

Fig. 1: Work window of calculating program

The output data include the physical properties of liquids, inside tube velocity and outside volumetric flow rate, Reynolds numbers, Nusselt numbers and heat transfer coefficients for both inside and outside, linear heat transfer coefficient, overall heat transfer coefficient, local to overall resistance ratios and pressure drop in tube (fiber) side. The NTU-analysis section has the following output date: heat capacity rates of both flow, heat capacity ratio, heat transfer area based on external surface of fibers, NTU, effectiveness, actual rate of heat transfer, inside and outside liquid output temperatures. The algorithm of calculation and formulas used were described before in Calculation subsection. Program was used to determine different factors magnitude of the influence on heat transfer by varying input parameters. Moreover a number of different fibers comparisons were performed.

3.1 Influence of liquid velocity around the fibers

Overall heat transfer coefficient (HTC_Ov, W/m^{2}K), linear heat transfer coefficient (HTC_l, W/m·K) and heat transfer rate (Q, kW) graphs are presented in the Figure 2 and 3 for both water-water and water-air applications. The multiply coefficients (for example 1/10, 100, 1000 etc.) were used to present different magnitude values in same graphs here and further during the article. To determine outside liquid velocity degree of influence on this parameters it was varied in the range 0.005 – 2 m/s and 0.005 – 20 m/s respectively for outside water and air. Please take note that the kinks in the graphs exist because of utilizing non-linear scale on horizontal axis which contains values of external liquid velocities. Other input conditions were constant and presented in captions of figures. It can be seen that velocity of cross-flow water around the fibers has no strict influence on heat transfer performance and even at very low water velocities (0.005 m/s, for example) values of heat transfer coefficient is not inapplicable small (see Figure 2). This conclusion isn't true for water-air application (see Figure 3) because of external wall-air thermal resistance has the main influence on the overall heat transfer rate and has a strong dependence from velocity of air.

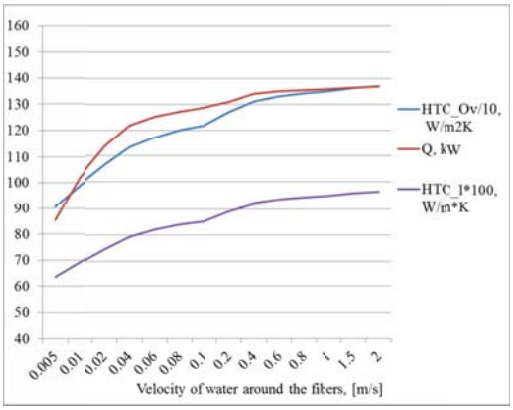

Fig. 2: Influence of external water velocity. 5400 polypropylene fibers with length 0.6 m and external/internal diameters 0.7/0.56 mm are in water cross-flow. Velocity of water inside is 1 m/s, external/internal inlet temperatures of water are 20°/50° C.

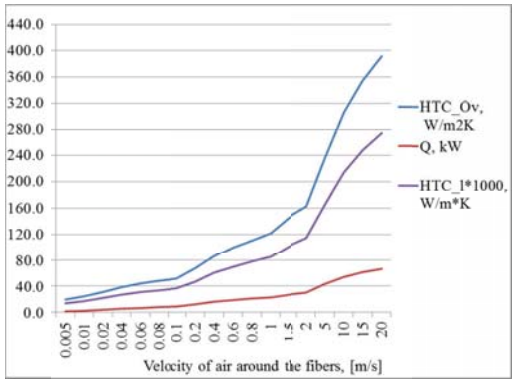

Fig. 3: Influence of external air velocity. 5400 polypropylene fibers with length 0.6 m and external/internal diameters 0.7/0.56 mm are in air cross-flow. Velocity of water inside is 1 m/s, external/internal inlet temperatures of air are 20°/50° C.

3.2 Comparison of different diameter of fibers (for constant external surface and constant mass of fibers)

An amount of fibers which needed to create a 1 m^2 of heat transfer area was calculated. The external diameter of fibers was varied in the range 0.1 – 2.0 mm and other conditions were the constant. Please take note that the internal diameter of fibers was 80% of external one in all calculations described in this article because it was providing the constant value of wall thermal resistance $\ln(D_o/D_i)/2k_w$ during all calculations except of different conductivity cases. Overall heat transfer coefficient (HTC_Ov), linear heat transfer coefficient (HTC_l), heat transfer rate (Q), pressure drop and number of fibers graphs are presented in Figure 4. The working conditions are described in the caption of

figure. It can be seen from graphs that linear heat transfer coefficient has very small dependence on diameter and the same length of different diameter fibers has around the same heat transfer possibility. Big difference in overall heat transfer coefficient is based on big difference in external surface of different diameter fibers. Other side 1 m^2 of heat transfer surface which created by small fibers has bigger heat transfer possibility then the surface created from bigger ones. Thus, it can be concluded that the main advantage of small fibers is a possibility to use more fibers with bigger total length. However, the pressure drops also is much bigger for small fibers and it is important factor which bordered the using of relatively small fibers. Please take note that the kinks in the graphs exist because of utilizing non-linear scale on horizontal axis which contains values of external diameters.

The same conclusions as previous can be done based on comparison of different fibers which can be produced from 1 kg of material. As before the external diameter of fibers and number of fibers was varied and other conditions were the constant and described in the Figure 5 caption. Graphs of the overall heat transfer coefficient (HTC_Ov), linear heat transfer coefficient (HTC_l) and pressure drop is very similar as in previous case but the number of fibers (and total heat transfer rate Q) is different. As well as it is evident that using of smaller fibers gives a possibility to use less of material for construction of heat exchange equipment.

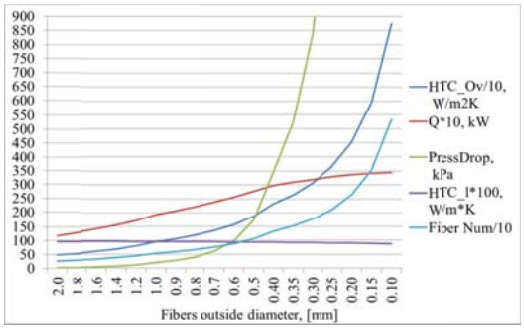

Fig. 4: Comparison of polypropylene fibers with different diameters and constant total external surface. Water-water cross-flow with volumetric flow rate in tube side 1000 l/h, external flow velocity 1 m/s, external/internal inlet temperatures of water are 20°/50° C.

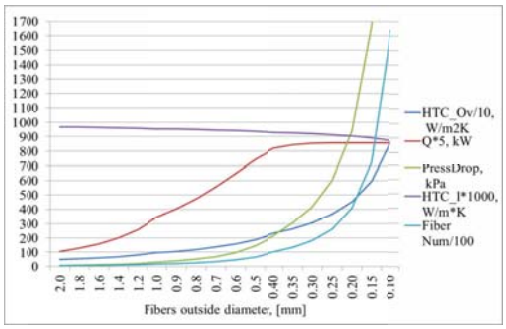

Fig. 5: Comparison of polypropylene fibers with different diameters and constant mass of material. Water-water cross-flow with volumetric flow rate in tube side 5000 l/h, external flow velocity 1 m/s, external/internal inlet temperatures of water are 20°/50° C.

3.3 Influence of wall material thermal conductivity

To study the influence of wall material thermal conductivity two types of fiber materials were studied. The first one was isotactic polypropylene with thermal conductivity k = 0.18 W/m·K (Mark, 1999) and the second was arbitrary material with conductivity 2 W/m·K (around the 11 times higher). The graphs of local to overall thermal resistance ratios and linear heat transfer coefficient are presented in Figures 6 and 7 for both materials (polypropylene and material with conductivity 2 W/m·K). *R_o/R_l, R_w /R_l* and *R_i/R_l* are, respectively, outside, wall and inside to overall linear thermal resistance ratios which were calculated in accordance with formulas (17) – (19). The constant test conditions were followed: fibers in water-water cross-flow, volumetric flow rate inside is 5000 l/hour, velocity around the fibers is 0.05 m/s, external/internal inlet temperatures of water are 20°/ 50° C. The external diameter was varied in 2.0 – 0.4 mm range. It can be seen that the wall thermal resistance plays the main role in the overall one (around the 55 %) in polypropylene application case. This conclusion can be generalized to a lot of other polymers, which have similar thermal conductivity values. The opposite situation takes a place in the case of 2 W/m·K conductivity material (see Figure 7). The wall resistance in this case has a minimal influence on overall one and heat transfer performance can be increased by intensification internal and external convection. Moreover it can be seen that by increasing (from 0.18 to 2 W/m·K) material conductivity eleven times the linear heat transfer coefficient doubles.

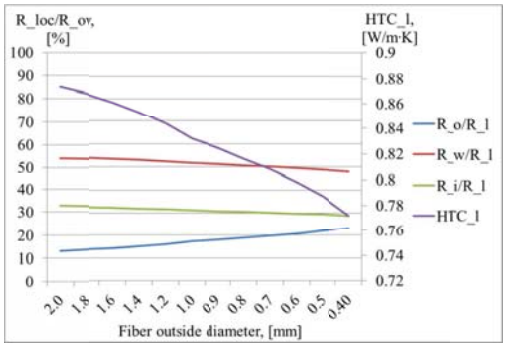

Fig. 6: Local to overall resistance ratios and linear heat transfer coefficient graphs (polypropylene fibers)

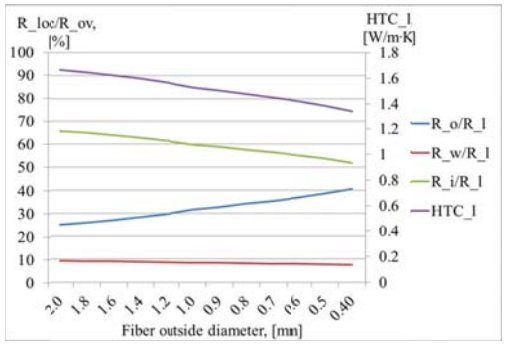

Fig. 7: Local to overall resistance ratios and linear heat transfer coefficient graphs (fibers from increased conductivity material)

3.4 Comparison of different fibers for water-air and water-water application

The main goal of this section is to compare three diameters of fibers for water-to-air heat exchanger design. The standard performance and working conditions of heat exchanger were chosen for comparison: summary heat transfer rate of fibers should be 29 kW, pressure drops is less the 20 kPa, velocity of air around the fibers 2 m/s, inlet temperatures of water/air are 90°/30° C, material of fibers is isotactic polypropylene with density 0.9 g/cm^3 and thermal conductivity 0.18 W/m·K (Mark, 1999). The number of fibers needed, their diameters, length and inside volumetric flow rate were varied such a way that pressure drop, total heat transfer rate and tube volumetric flow rate were similar to required. The results obtained are partly presented in the Table 1. There are the following columns in the table: external diameter *Dex*, a length of fibers *L*, volumetric flow rate trough single fiber *Qfi*, velocity of liquid in fiber *Vi*, inside, outside, linear and overall heat transfer coefficients (*HTCi*, *HTCo*, *HTCl* and *HTC*), efficiency *E*, total heat transfer area *A*, heat transfer rate of single fiber *Q*, inside outlet temperature *Toi*, pressure drops in tube side *dP*, number of fibers *N*, total volumetric flow rate *Qf*, total mass of fibers *M*. They were combined into three groups in accordance with efficiency values: the first one is around 0.15, the second – 0.34, the third – 0.54. It is evident that the smaller values of efficiencies were obtained for lower tube volumetric flow rates and correspond to smaller temperature difference of tube water. The comparison of linear heat transfer coefficients, heat transfer rate, number and mass of fibers for two values of efficiency (0.15 and 0.54 respectively) is presented in Figures 8 and 9. It shows that the linear heat transfer coefficient (and thus thermal performance) is slightly better for bigger fibers (with 0.8 mm outside diameter). The heat transfer rate is several times higher for these fibers based on its larger length and so less fiber needed to obtain required heat transfer capacity. We can see also that bigger fibers are longer for the same pressure drop limit and permit to pump bigger amount of heat transfer medium (they have relatively smaller pressure drops). Other side the small fibers (with 0.4 mm outside diameter) have bigger values of overall heat transfer coefficients and smaller values of total surface needed. As more by utilizing of small fibers the same heat transfer rate can be released in smaller volume (Song et al., 2010). Thus created on the basis of smaller fibers heat exchangers should have a tendency to be more compact and lighter.

Tab. 1: Summary of calculation results for water-air application

Dex, mm	*L,m*	*Qfi, l/h*	*Vi, m/s*	*HTCi, W/m^{2}K*	*HTCo, W/m^{2}K*	*HTCl, W/m·K*	*HTC, W/m^{2}K*	*E*	*A,m^2*	*Q,W*	*Toi,°C*	*dP, kPa*	*N*	*Qf, l/h*	*M, kg*
0.8	0.60	1.20	1.04	4572	171	0.121	151	0.149	3.61	12.1	81.1	15.3	2397	2876	0.234
0.6	0.40	0.74	1.14	6101	199	0.107	179	0.144	3.02	7.2	81.1	19.9	4028	2981	0.148
0.4	0.20	0.29	1.00	9160	247	0.090	228	0.155	2.44	3	80.7	19.8	9667	2803	0.079
0.8	1.05	0.82	0.71	4572	171	0.121	151	0.339	4.07	18.8	69.7	19.9	1543	1265	0.264
0.6	0.65	0.42	0.64	6101	199	0.107	179	0.359	3.49	10.2	68.4	20.1	2843	1194	0.169
0.4	0.30	0.18	0.62	9160	247	0.090	228	0.334	2.67	4.1	70	19.9	7073	1273	0.086
0.8	1.40	0.56	0.48	4572	171	0.121	151	0.553	4.87	21	56.8	20.1	1381	773	0.315
0.6	0.80	0.31	0.48	6101	199	0.107	179	0.524	3.98	11	58.6	19.8	2636	817	0.193
0.4	0.40	0.12	0.41	9160	247	0.090	228	0.556	3.24	4.5	56.6	19.7	6444	773	0.105

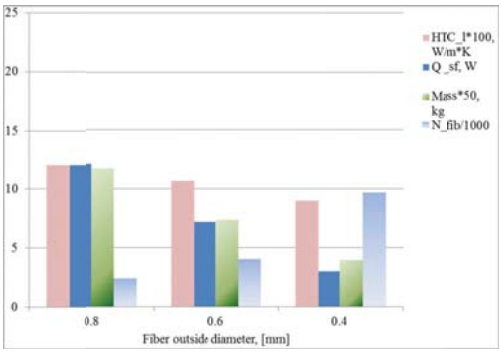

Fig. 8: Three diameters of fibers comparison for $E \approx 0.15$ (Dex_1= 0.8 mm L_1=0.6 m, Dex_2=0.6 mm L_2=0.4 m, Dex_3 = 0.4 mm L_3=0.2 m)

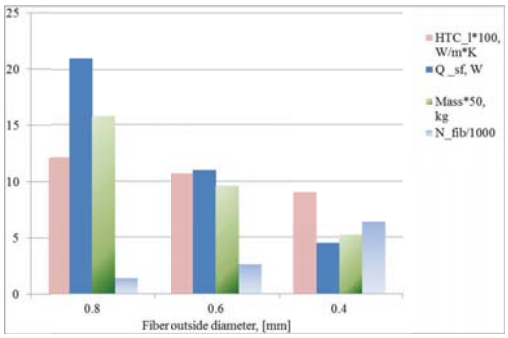

Fig. 9: Three diameters of fibers comparison for $E \approx 0.53$ (Dex_1= 0.8 mm L_1=1.4 m, Dex_2=0.6 mm L_2=0.8 m, Dex_3 = 0.4 mm L_3=0.4 m)

The same work was done for water-water application. Performance and working conditions were following: summary heat transfer rate of fibers should be 29 kW, pressure drops was less than 60 kPa, velocity of water around the fibers was 0.05 m/s, inlet temperatures of inside/outside water were 4°/30° C, material of fibers was isotactic polypropylene. The results obtained are presented in Table 2. They were grouped in accordance with efficiency values: the first was 0.65, the second – 0.95, the third – 0.99. The comparison of linear heat transfer coefficients, heat transfer rate, number and mass of fibers for two values of efficiency (0.65 and 0.99 respectively) is presented in Figures 10 and 11. Around the same conclusions as for water-air application can be done for water-water application: the linear heat transfer coefficient is similar for 0.8, 0.6 and 0.4 mm outside diameters fibers, the bigger heat transfer rate value allows to use less of fibers but it's based on large length of fibers, fibers with larger diameter permit to pump more liquid through tube side (have smaller relative pressure drops), the smaller fibers have bigger values of heat flux and contribute to improving the compactness.

Tab. 2: Summary of calculation results for water-air application

Dex, mm	*L,m*	*Qfi, l/h*	*Vi, m/s*	*HTCi, W/m²K*	*HTCo, W/m²K*	*HTCl, W/m·K*	*HTC, W/m²K*	*E*	*A,m²*	*Q,W*	*Toi,°C*	*dP, kPa*	*N*	*Qf, l/h*	*M, kg*
0.8	0.60	1.19	1.03	3674	5701	0.791	989	0.6570	1.84	23.7	21.1	60.0	1224	1456	0.120
0.6	0.35	0.650	1.00	4906	6617	0.771	1286	0.6710	1.43	13.3	21.4	60.10	2180	1417	0.070
0.4	0.15	0.300	1.04	7371	8491	0.747	1868	0.6330	0.95	5.8	20.4	60.90	5000	1500	0.031
0.8	1.05	0.74	0.64	3674	5701	0.791	989	0.9500	3.58	21.4	28.7	59.7	1355	1003	0.232
0.6	0.6	0.410	0.63	4906	6617	0.771	1286	0.9510	2.77	11.8	28.7	59.80	2458	1008	0.135
0.4	0.25	0.195	0.67	7371	8491	0.747	1868	0.9230	1.66	5.5	28	60.40	5273	1028	0.054
0.8	1.35	0.59	0.51	3674	5701	0.791	989	0.992	5.53	17.8	29.8	60.5	1629	961	0.359
0.6	0.75	0.33	0.51	4906	6617	0.771	1286	0.9900	4.13	9.9	29.8	59.5	2929	967	0.201
0.4	0.35	0.140	0.48	7371	8491	0.747	1868	0.9920	3.05	4.2	29.8	59.50	6905	967	0.098

4. Conclusions

As it shown in Introduction section polymer heat exchangers have a lot advantages and problems concerned with its application are slowly addressing in different studies of polymers. Thus we can assume significant improvement of polymer heat exchanger performance and their wider application in different fields. We have studied theoretically some factors affected heat transfer of polymeric hollow fibers with respect to cross-flow water-water and water-air application. Performed conclusions and comparisons show tendencies which have place in polymer fibers heat transfer and can help to choose adequate fibers and flow conditions.

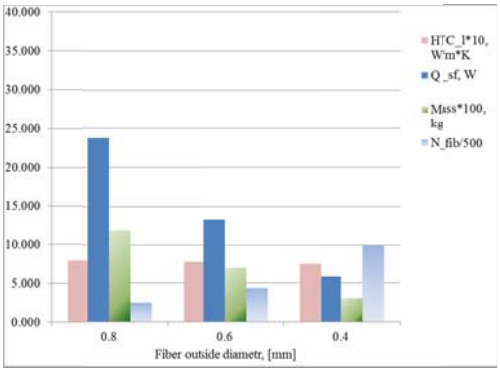

Fig. 10: Three diameters of fibers comparison for E ≈ 0.65 (Dex_1= 0.8 mm L_1=0.6 m, Dex_2=0.6 mm L_2=0.35 m, Dex_3 = 0.4 mm L_3=0.15 m)

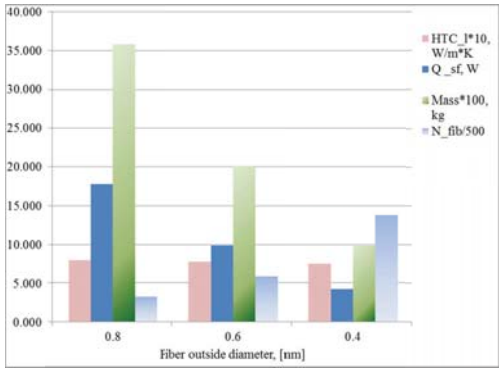

Fig. 11: Three diameters of fibers comparison for E ≈ 0.99 (Dex_1= 0.8 mm L_1=1.35 m, Dex_2=0.6 mm L_2=0.75 m, Dex_3 = 0.4 mm L_3=0.35 m)

Acknowledgements

The paper presented has been supported by the internal grant of the Brno University of Technology No. FSI-S-11-20.

References

Bigg, D. M.; Stichford, G. H.; Talbert, S. G. (1989) Application of polymeric materials for condensing heat exchangers. *Polym. Eng. Sci.*, 29 (16), 1111.

Chen, L., Li Z., Gu Z. Y. (2009) Experimental investigation of plastic finned-tube heat exchangers, with emphasis on material thermal conductivity. *Exp. Therm. Fluid Sci.* 33, pp. 922–928.

Gad-el-Hak M. (2003) Comments on critical view on new results in micro-fluid mechanics. *Int. J Heat Mass Transfer* 46: pp. 3941–3945

Githens R. E., Minor R. W., Tomsic V. J. Flexible tube heat exchangers. *Chem. Eng. Prog*. 1965, 61 (7), 55.4.

Hallmark B., Gadala-Maria F., Mackley M.R. (2005) The melt processing of polymer microcapillary film (MCF) *J. Non-Newton Fluid Mech.* pp. 83–98

Hallmark B., Mackley M.R., Gadala-Maria F. (2005) Hollow microcapillary arrays in thin plastic films *Adv. Eng.Mater.* 7 545–7

Han S. & Chung D.D.L. (2011) Increasing the through-thickness thermal conductivity of carbon fiber polymer–matrix composite by curing pressure increase and filler incorporation. *Composites Science and Technology*, pp.1944-1952

Han Zhidong & Fina Alberto (2011) Thermal conductivity of carbon nanotubes and their polymer nanocomposites: A review. *Prog. Polym. Sci.* pp. 914-944

Herwig H. (2001) Flow and Heat Transfer in Micro Systems: Is Everything Different or Just Smaller? *ZAMM - Journal of Applied Mathematics and Mechanics* 1–10.

Herwig H. & Hausner O. (2003) Critical view on new results in micro-fluid mechanics: an example. *Int. J Heat Mass Transfer* 46: pp. 935–937

Hetsroni G., Mosyak A., Pogrebnyak E., Yarin L.P. (2005) Fluidflow in micro-channels, *Int. J. Heat Mass Transfer* 48 pp. 1982–1998.

Hornung, C. H., Hallmark B., Hesketh, R. P., Mackley M.R. (2006) The fluid flow and heat transfer performance of thermoplastic microcapillary films. *J. Micromech. Microeng.* 16, pp. 434–447.

Incropera, F. P. & DeWitt D. P. (1996) Fundamentals of Heat and Mass Transfer, 4th ed., Wiley, New York

Malik T. & Bullard C. W. (2005) Suitability of Polymer Heat Exchangers for Air Conditioning Applications, *Air Conditioning and Refrigeration Center, University of Illinois.*

Maynes D. & Webb A.R. (2002) Velocity profile characterization in sub-diameter tubes using molecular tagging velocimetry, *Exp. Fluids* 32 3–15.

NIST Chemistry WebBook. Thermophysical Properties of Fluid Systems. Availiabale from http://webbook.nist.gov/chemistry/fluid/ 26 January 2012.

Patel, A. B. & Brisson J. G. (2000) Design, construction and performance of plastic heat exchangers for sub-Kelvin use. *Cryogenics.* 40, 91.

Mark James (1999) Polymer Data Handbook. Oxford University Press, Inc.

Qin Yuchun, Li Baoan, Wang Shichang (2012) Experimental Investigation of a Novel Polymeric Heat Exchanger Using Modified Polypropylene Hollow Fibers. *Ind. Eng. Chem. Res.* 51, pp. 882–890

Rousse D. R., Martin D. Y., Theriault R., Levillee F., Boily, R. (2000) Heat recovery in greenhouses: A practical solution. *Appl. Therm. Eng.* 20, 687.

Scheffler T.B. & Leao A.J. (2008) Fabrication of polymer film heat transfer elements for energy efficient Multi-Effect Distillation. *Desalination,* pp. 696-710

Song Liming, Li Baoan, Zarkadas Dimitrios, Christian Saskia, Sirkar Kamalesh K. (2010) Polymeric Hollow-Fiber Heat Exchangers for Thermal Desalination Processes. *Ind. Eng. Chem. Res.*, 49 (23), pp. 11961–11977

ThermalSpreadSheets. Equations for the Thermophysical Properties of Air. Availiabale from http://thermalspreadsheets.com/?p=1 26 January 2012.

T'Joen C., Park Y., Wang Q., Sommers A., Han X., Jacobi A. (2009) A Review on Polymer Heat Exchangers for HVAC&R Applications, *International Journal of Refrigeration*, 32(5), pp. 763-779

Tsilingiris P.T. (2000) Heat transfer analysis of low thermal conductivity solar energy absorbers. *Appl. Thermal Eng.* 20 (14) 1297.

Tso, C.P. & Mahulikar, S.P. (2000) Experimental verification of the role of Brinkman number in microchannels using local parameters. *International Journal of Heat and Mass Transfer* 43, pp. 1837–1849.

Whitley, D. M. (1957) Plastic heat exchangers gain in severe service. *Chem. Eng.* 64 (9), 308.

Yarin L.P., Mosyak A., Hetsroni G. (2009) Fluid Flow, Heat Transfer and Boiling in Micro-Channels Berlin: Springer

Zaheed L. & Jachuck R.J.J. (2004) Review of polymer compact heat exchangers, with special emphasis on a polymer film unit. *Appl. Therm. Eng.* 24, pp. 2323–2358.

Zarkadas D. M. & Sirkar K. K. (2005) Incremental heat transfer number for laminar flow in circular tubes with the boundary condition of the third kind and simple design formula for shell and tube laminar flow heat exchangers with constant external resistance. *Int. J. Transp. Phenom.* 7 (4), pp. 297–306.

Zarkadas, D. M. & Sirkar K. K. (2004) Polymeric hollow fiber heat exchangers: An alternative for lower temperature applications. *Ind. Eng. Chem. Res*. 43, pp. 8093–8106.

18th International Conference
ENGINEERING MECHANICS 2012
Svratka, Czech Republic, May 14 – 17, 2012

pp. 59–60
Paper #50

MOTION CAPTURING CONTROL FOR PARALLEL KINEMATICS ROBOT

J. Augste, T. Novotný *

Abstract: *This paper deals with using motion capturing technology for control of parallel kinematic robot. As a motion capturing system is used Microsoft Kinect device. Filtering and recognizing algorithms are applied to the output data from this device to capture inaccuracies and gestures that are used for position control. This evaluation system uses cluster computing device connected to the machine. The possibilities to communicate with the machine control unit and to use more tracking devices are discussed.*

Keywords: ***Motion capturing, parallel kinematics, programmable logic controller***

1. Introduction

Nowadays the remotely controlled devices are still frequently used. However the control devices (for example joystick) in many complex applications such as robotic hand control in hazardous environment are very inappropriate. One of the greatest reasons is a significant difference in kinematic structure of controlled and control devices.

Very intuitive option to scan the motion is use of a camera system and image processing. And these two things are implemented in one device Microsoft Kinect. Thanks to its low acquisition cost and its comfort programming interface (SDK) the Microsoft Kinect is the most advantageous choice for experiment realization. The Microsoft Kinect was used to control the parallel kinematics delta robot. This article deals with possibilities of communication between these two devices then it describes its flaws and the principle of robot control system reaction on operator gesture performance.

2.1. Background

The motion capturing technology (tracking of humanoid structure) is very well established. However the data processing and output reaction is not so stable. Because of the gesture recognition initiation and termination as well as unwanted motion recognition is really difficult to ensure.

There are two essential events in motion capturing technology. The first one is poses and the other one is gestures. The experiment requires a combination of both related to a time variable. The time utilization allows creating a system whose feedback is fast and stable. The motion processing device must reduce incoming commands quantity to a robot control system to a minimum level in order to not burden the computational power.

3. Materials and Methods

CNC controlling of robot with parallel kinematics is secured by programmable logic controller from Beckhoff. It allows the rotation calculation of each electric asynchronous motor using inverse kinematics. Input and output signals of the PLC are done via TCP / IP using the programming language C #. Class library reference TwinCAT.Ads.dll. NET contains all the necessary procedures and functions controlling the robot. The second used library is Microsoft.Kinect.dll that includes communication with the video output from the camera, image processing and motion evaluation.

* Ing. Jan Augste, Ing. Tomáš Novotný, ING-PAED IGIP: Institute of Production Machines, Systems and Robotics, Faculty of Mechanical Engineering, Brno University of Technology, Technická 2896/2; 616 69, Brno; CZ, emails: y101686@stud.fme.vutbr.cz, novotny.t@fme.vutbr.cz

Two approaches using the kinematic motion capturing control were created.

The first one is the direct control of the robot. The controlling session is started by operator pose - left hand over head. By moving the right hand the robot is guided to a specific position. The algorithms are used to filter unwanted movements such as shaking, so that the result has been a continuous movement. The procedure is performed using the TCP / IP communication.

In the second case the trajectory is entered first - after making the appropriate gestures of the operator. Then the trajectory is processed by inverse kinematics and sent to the robot that performs it.

Fig. 1: Complexion of the design system

4. Results

Both designed approaches differ in several parameters. One of them is an occasion for a specific application in industry.

The first solution is orientated on control in hazardous environment. Its disadvantage is quite big load on a communication which results in long system reaction on non-linear changes.

The second solution is very perspective for a robot programming. The great disadvantage is in absence of feedback, however there could be haptic feedback or simulation established in the future.

5. Conclusion

Although the motion capturing technology is known for a long time and intensively used in game and movie industry, its utilization in the field of automatic control and programming is not currently widespread.

This text deals with the two possibilities of motion capturing control for parallel kinematics robots. This ways has different utilization so their advantages and disadvantages are incomparable.

It is promised in next version of TwinCAT to enable real-time control using C++ so the next step of the research is to create a real-time control.

References

Webb J., Ashley J. Beginning Kinect Programming with the Microsoft Kinect SDK. Apress (2012). ISBN 978-1430241041.

18th International Conference
ENGINEERING MECHANICS 2012
Svratka, Czech Republic, May 14 – 17, 2012

pp. 61–86
Paper #233

STRUCTURES WITH UGLI IMPERFECTIONS

I. Baláž*, Y. Koleková**

Abstract: *Derivation of the basic formulae for determination of the flexural buckling resistance of frames with members with non-uniform cross-sections and/or non-uniform axial compression forces. Similar formulae given in EN 1993-1-1 (2005) are limited to frames with uniform cross-sections and compression forces. Detailed description of the procedure of iterative calculation (Baláž, I., 2008). Graphical interpretation of the method proposed by the authors and numerical examples for members with uniform cross-sections and uniform axial compression forces.*

Keywords: ***stability, metal structures, flexural buckling resistance, imperfections in the form of first buckling mode.***

1. Introduction

The proposed procedure was the first time published in Baláž, I. (2008) and was verified by calculating of several numerical examples. The procedure is based on Chladný`s method. Derivation of the basic formulae used in this paper differ from the ones published by Chladný in publication Baláž, I. et al. (2007, 2010). The way of calculation proposed by Baláž, I. (2008) was used also in PhD thesis written by Kováč, M. (2010).

Prof. Chladný developed his method with the aim to derive a formula for the lateral forces acting on U-frames of open truss bridges in Chladný, E. (1958) and in Chladný, E. (1974). He showed there the importance of the curvature of the initial imperfection. The results were used in Czechoslovak Bridge Standard ČSN 73 6205 (1984), cl. 39. See also Chladný, E. (1998).

In 2000 proposed Prof. Chladný his method in more generalized form for Eurocode 3, and it was the first time accepted in draft prEN 1993-1-1 (5 June 2002). His contribution is acknowledged in publication (Sedlacek, G. et al., 2004). See there item [52]. Chladný derived the formula for $e_{0,d}$ and is the author of the method given in EN 1993-1-1 (2005), 5.3.2(11). He later generalized it also for non-uniform cross-sections and non-uniform compression forces. This generalization is used in STN EN 1993-1-1/NA (2007) and in EN 1999-1-1 (2007), 5.3.2(11). Chladný applied his method in the design of bridges in practice, e.g. in design of basket handle arch type Apollo bridge in Bratislava, Pentele bridge in Dunaújváros and in investigations of continuous truss bridges. He further modified his method to be convenient for basket handle arch type bridges in the National Annex STN EN 1993-2/NA (2009). Chladný described details of his method and published numerical examples in Baláž, I. – Ároch, R. – Chladný, E. – Kmeť, S. – Vičan, J. (2007, 2010).

2. Flexural buckling resistance of frames with non-uniform members and non-uniform compression normal forces

Flexural buckling resistance of the frame, which consists of members with variable cross-sections, with any boundary conditions, supports and/or variable foundation and under variable axial forces may be verified by the following condition

* Prof. Ing. Ivan Baláž, PhD.: Department of Metal and Timber Structures, Fakulty of Civil Engineering, Slovak University of Technology, Radlinského 11; 813 68, Bratislava; SK, e-mail: ivan.baláž@stuba.sk

** Assoc. Prof. Ing. Yvona Koleková, PhD.: Department of Structural Mechanics, Faculty of Civil Engineering, Slovak University of Technology, Radlinského 11; 813 68, Bratislava; SK, e-mail: yvona.kolekova@stuba.sk

$$\left|\frac{N_{\mathrm{Ed}}(x)}{N_{\mathrm{Rd}}(x)}+\frac{M^{\mathrm{II}}_{\mathrm{Ed,ugli}}(x)}{M_{\mathrm{Rd}}(x)}\right|_{\max}\le 1 \tag{1}$$

where

$N_{\mathrm{Ed}}(x)$ is the axial force distribution, positive if compression, which is effect of the actions. The design values of the axial forces may be calculated by the 1st order theory,

$M^{\mathrm{II}}_{\mathrm{Ed,ugli}}(x)$ is the bending moment distribution, which is the result of axial forces acting in members of frame having "unique global and local initial imperfection" („ugli" imperfection). The design values of this bending moment shall be calculated by the 2nd order theory. The „ugli" imperfection is an equivalent geometrical imperfection, which purpose is to cover in numerical model all imperfections (geometrical and structural) of real structure.

$N_{\mathrm{Rd}}(x)$ is the distribution of the axial force resistance depending on the cross-section class,

$M_{\mathrm{Rd}}(x)$ is the distribution of the bending moment resistance depending on the cross-section class.

The characteristics relating to critical cross-section, which is the cross-section relevant for assessment of flexural buckling resistance of the frame, are below denoted by index „ m ". The most onerous condition (1) occurring in critical cross-section „ m ", may be then rewritten in the form

$$\frac{N_{\mathrm{Ed,m}}}{N_{\mathrm{Rd,m}}}+\frac{M^{\mathrm{II}}_{\mathrm{Ed,ugli,m}}}{M_{\mathrm{Rd,m}}}\le 1 \tag{2}$$

The "ugli" imperfection is defined as follows

$$\eta_{\mathrm{ugli}}(x)=\eta_{0,\mathrm{ugli,m}}\eta_{\mathrm{cr}}(x) \tag{3}$$

where

$\eta_{\mathrm{cr}}(x)$ is the first elastic critical buckling mode, with the amplitude $|\eta_{\mathrm{cr}}(x)|_{\max}=1$.

$\eta_{0,\mathrm{ugli,m}}$ is the amplitude of „ugli" imperfection depending on characteristics of critical cross-section „ m ". Index „ 0 " will in this paper indicate that a value is amplitude of a deflection. The amplitude of „ugli" imperfection may be determined from the condition requiring the following: the critical member of the frame, when under compression axial force, should have the same flexural buckling resistance as its "generalized equivalent member" („gem"). The „gem" is the member simply supported on its ends, having the same cross-section properties (EI_{m}, A_{m}) and axial force ($N_{\mathrm{Ed,m}}$) as the critical member of the frame in its critical cross-section „ m ", and having such buckling length L_{cr}, that its elastic critical axial force is the same as the elastic critical axial force $N_{\mathrm{cr,m}}$ of the critical member of the frame in its critical cross-section „ m ".

The „ugli" imperfection amplitude depending on the characteristics of the critical cross-section „ m " is then defined by

$$\eta_{0,\mathrm{ugli,m}}=\frac{N_{\mathrm{cr,m}}e_{0,\mathrm{d,m}}}{EI_{\mathrm{m}}\left|\eta''_{\mathrm{cr,m}}\right|}=\alpha_{\mathrm{cr}}\frac{N_{\mathrm{Ed,m}}e_{0,\mathrm{d,m}}}{\left|M_{\eta\mathrm{cr,m}}\right|} \tag{4}$$

$$e_{0,d,m} = e_{0,k,m} \frac{1 - \frac{\chi_m \bar{\lambda}_m^2}{\gamma_{M1}}}{1 - \chi_m \bar{\lambda}_m^2} \tag{5}$$

$$e_{0,k,m} = \alpha_m \left(\bar{\lambda}_m - 0.2\right) \frac{M_{Rk,m}}{N_{Rk,m}}, \quad \text{for } \bar{\lambda}_m > 0.2 \tag{6}$$

where

$\left|M_{\eta cr,m}\right|$ is the absolute value of the fictitious bending moment at the critical cross-section „m“, due to $\eta_{cr}(x)$,

$N_{Ed,m}$ is the design value of compression axial force at the critical cross-section „m“, positive if compression,

$M_{Rk,m}$ is the characteristic value of bending moment resistance of the critical cross-section „m“,

$N_{Rk,m}$ is the characteristic value of axial force resistance of the critical-cross section „m“,

$e_{0,d,m}$, $e_{0,k,m}$ are the design (index „d“) and characteristic (index „k“) values of amplitude of “local initial” („li“) imperfection of the “gem” depending on the characteristics of the critical cross-section „m“. It can be easily shown, that „li“ imperfection is used when analysis of individual member is done,

α_m is the imperfection factor for the critical cross-section „m“ and the relevant buckling curve, see Table 6.1 and Table 6.2 in EN 1995-1-1 (2005),

γ_{M1} is the partial factor, which should be applied to the various characteristic values of resistance of members to instability,

$$\bar{\lambda}_m = \sqrt{\frac{N_{Rk,m}}{N_{cr,m}}} \tag{7}$$

is the relative slenderness of the structure, relating to the critical-cross section „m“,

χ_m is the reduction factor depending on the relevant imperfection factor α_m and the relative slenderness $\bar{\lambda}_m$, see 6.3.1 in EN 1995-1-1 (2005),

$N_{cr}(x)$ is the distribution of elastic critical force,

α_{cr} is the minimum force amplifier for the values of the axial force configuration $N_{Ed}(x)$ in members to reach the values of elastic critical force configuration $N_{cr}(x)$. For the given frame, α_{cr} is constant. The ratio $\alpha_{cr} = N_{cr}(x) / N_{Ed}(x)$ gives for all cross-sections „x“ the same numerical value.

The location of the critical cross-section „m“ is generally not known, because it depends on the location of maximum of the sum of two functions in the left side of the condition (1). The value of the second term of the sum in (1) depends on the characteristics of the critical cross-section „m“. The location of the maximum of the first function in (1): $N_{Ed}(x) / N_{Rd}(x)$ usually does not coincide with the location of maximum of the second function in (2): $M^{II}_{Ed,ugli}(x) / M_{Rd}(x)$, which is given by the

location of the maximum of the function $|\eta''_{\mathrm{cr}}(\mathrm{x})/I(x)|_{\max}$. Generally it is therefore necessary to use iterative calculation.

In the special case, when $N_{\mathrm{Ed}}(x)/N_{\mathrm{Rd}}(x)$ is constant, the location of critical cross-section „m“ is determined by the location of $\left|M^{\mathrm{II}}_{\mathrm{Ed,ugli}}(x)/M_{\mathrm{Rd}}(x)\right|_{\max}$ or $|\eta''_{\mathrm{cr}}(\mathrm{x})/I(x)|_{\max}$ and when also $EI(x)$ is constant, by the location of $|\eta''_{cr}(\mathrm{x})|_{\max}$.

Distribution of bending moment $M^{\mathrm{II}}_{\mathrm{Ed,ugli}}(x)$, which is the effect of axial forces acting in members of frame having the „ugli“ imperfection $\eta_{\mathrm{ugli}}(x)=\eta_{0,\mathrm{ugli,m}}\eta_{\mathrm{cr}}(x)$, may be calculated in the following way:

1) The first eigen-value α_{cr} and the first buckling mode $\eta_{\mathrm{cr}}(x)$ and its derivates $\eta'_{\mathrm{cr}}(x)$ and $\eta''_{\mathrm{cr}}(x)$ are obtained by numerical methods using a computer program.

2) The „ugli“ imperfection amplitude $\eta_{0,\mathrm{ugli,m}}$ depending on the characteristics of the critical cross-section „m“ is calculated for the estimated location of the critical cross-section „m“

$$\eta_{0,\mathrm{ugli,m}}=\alpha_{\mathrm{cr}}\frac{N_{\mathrm{Ed,m}}e_{0,\mathrm{d,m}}}{\left|M_{\eta\mathrm{cr,m}}\right|} \tag{8}$$

3) The distribution of the “ugli” imperfection is then

$$\eta_{\mathrm{ugli}}(x)=\eta_{0,\mathrm{ugli,m}}\eta_{\mathrm{cr}}(x) \tag{9}$$

4) The amplitude $\eta_{0,\mathrm{m}}$ of the additive deflection $\eta(x)$, which is the result of axial forces acting in the members of frame with „ugli“ imperfection, may be calculated as

$$\eta_{0,\mathrm{m}}=\frac{\eta_{0,\mathrm{ugli,m}}}{\alpha_{\mathrm{cr}}-1} \tag{10}$$

5) The distribution of the additive deflection $\eta(x)$ is then

$$\eta(x)=\eta_{0,\mathrm{m}}\eta_{\mathrm{cr}}(x)=\frac{\eta_{0,\mathrm{ugli,m}}}{\alpha_{\mathrm{cr}}-1}\eta_{\mathrm{cr}}(x) \tag{11}$$

6) The distribution of the bending moment $M^{\mathrm{II}}_{\mathrm{Ed,ugli}}(x)$ due to „ugli“ imperfection having shape of $\eta_{\mathrm{cr}}(x)$, may be calculated from the formula

$$M^{\mathrm{II}}_{\mathrm{Ed,ugli}}(x)=-EI(x)\eta''(x)=-EI(x)\frac{\eta_{0,\mathrm{ugli,m}}}{\alpha_{\mathrm{cr}}-1}\eta''_{\mathrm{cr}}(x)=kN_{\mathrm{Ed,m}}e_{0,\mathrm{d,m}}\frac{-EI(x)\eta''_{\mathrm{cr}}(x)}{\left|M_{\eta\mathrm{cr,m}}\right|} \tag{12}$$

where

k is the well known ratio of the bending moment calculated according to the 2nd order theory to the bending moment calculated according to the 1st order theory, which is in the case of using elastic critical buckling mode $\eta_{\mathrm{cr}}(x)$ constant value for the whole frame

$$k=\frac{\alpha_{\mathrm{cr}}}{\alpha_{\mathrm{cr}}-1}=\frac{1}{1-\dfrac{1}{\alpha_{\mathrm{cr}}}} \tag{13}$$

It may be also written

$$M_{\mathrm{Ed,ugli}}^{\mathrm{II}}(x) = kN_{\mathrm{Ed,m}}e_{0,\mathrm{d,m}}\frac{-EI(x)\eta''_{\mathrm{cr}}(x)}{EI_{\mathrm{m}}\left|\eta''_{\mathrm{cr,m}}\right|} = kN_{\mathrm{Ed,m}}e_{0,\mathrm{d,m}}\frac{-EI(x)\eta''_{\mathrm{C,cr}}(x)}{EI_{\mathrm{m}}\left|\eta''_{\mathrm{C,cr,m}}\right|} =$$
$$= kN_{\mathrm{Ed,m}}e_{0,\mathrm{d,m}}\frac{M_{\eta\mathrm{cr}}(x)}{\left|M_{\eta\mathrm{cr,m}}\right|} = M_{0,\mathrm{Ed,ugli,m}}^{\mathrm{II}}\frac{M_{\mathrm{C}\eta\mathrm{cr}}(x)}{\left|M_{\mathrm{C}\eta\mathrm{cr,m}}\right|} \tag{14}$$

where

$$\eta_{\mathrm{C,cr}}(x) = C_0\eta_{\mathrm{cr}}(\mathrm{x}) \tag{15}$$

is the first elastic critical buckling mode with amplitude C_0, which may have any numerical value, and

$$M_{0,\mathrm{Ed,ugli,m}}^{\mathrm{II}} = kN_{\mathrm{Ed,m}}e_{0,\mathrm{d,m}} \tag{16}$$

From (14) it may be seen that, the first elastic critical buckling mode $\eta_{\mathrm{C,cr}}(x)$ with any value of the amplitude C_0 may be used, and not only $\eta_{\mathrm{cr}}(\mathrm{x})$ having $C_0 = 1$, when computing ratio of bending moments

$$M_{\eta\mathrm{cr}}(x)/\left|M_{\eta\mathrm{cr,m}}\right|. \tag{17}$$

7) After the distribution of the function on the left side of the condition (1) is known, the condition (2) may be evaluated and checked, if the location of maximum of this function will coincide with estimated location of the critical cross-section „m“ from the first iteration. If the answer is no, the procedure shall be repeated in an iterative way.

8) If the answer is yes, the condition (2) may be evaluated and the frame verified.

3. Numerical examples

Example 1: Given input values: uniform member with cross-section HE 260 B (ARBED), steel grade S 355, partial safety factor $\gamma_{\mathrm{M1}} = 1.1$, member length $L = 4.6\,\mathrm{m}$, action: axial normal force N_{Ed} equals to the resistance, which means that for N_{Ed} utilization grade $U = 1$. Two cases are investigated:

a) flexural buckling about major axis *y-y* (buckling curve “b”, $\alpha = 0.34$),

b) flexural buckling about minor axis *z-z* (buckling curve “c”, $\alpha = 0.49$).

Boundary conditions are the same in both planes: left end is fixed, right end is simple supported.´

a) Flexural buckling about major axis *y-y* (Figure 1-4)

HE 260 B S 355 $f_y = 355\cdot MPa$ $\gamma_{M1} = 1.1$ $f_{y.d} = 322.727\cdot MPa$

$h = 0.26\,m$ $b = 0.26\,m$ buckling curve "b" $\alpha := 0.34$

$A = 11.84 \times 10^3\cdot mm^2$ $I_y = 149.2 \times 10^6\cdot mm^4$ $W_{el.y} = 1.148 \times 10^6\cdot mm^3$

$N_{Rk} = 4.203\cdot MN$ $N_{Rd} = 3.821\cdot MN$ $M_{y.Rk} = 407.54\cdot kN\cdot m$

$N_{Ed} = 3.576\cdot MN$ $N_{cr} = 29.897\cdot MN$ $L_{cr} = 3.216\,m$

$\beta = 0.699$ $\varepsilon := \frac{\pi}{\beta}$ $\alpha_{cr} := \frac{N_{cr}}{N_{Ed}} = 8.36$ $k := \frac{1}{1 - \frac{1}{\alpha_{cr}}} = 1.136$

$\lambda_m := \sqrt{\frac{N_{Rk}}{N_{cr}}} = 0.375$ $\phi := 0.5\cdot\left[1 + \alpha\cdot\left(\lambda_m - 0.2\right) + \lambda_m^{\,2}\right] = 0.6$

$\chi := \frac{1}{\phi + \sqrt{\phi^2 - \lambda_m^{\,2}}} = 0.936$ $e_{o.k} := \alpha\cdot\left(\lambda_m - 0.2\right)\cdot\frac{M_{Rk}}{N_{Rk}} = 5.768\cdot mm$

$e_{o.d} := e_{o.k}\cdot\frac{1 - \frac{\chi\cdot\lambda_m^{\,2}}{\gamma_{M1}}}{1 - \chi\cdot\lambda_m^{\,2}} = 5.847\cdot mm$ $\frac{L}{e_{o.d}} = 786.727$

$$\eta_{cr}(x) := \frac{\left[\left(1 - \cos\left(\frac{\varepsilon\cdot x}{L}\right)\right)\cdot\varepsilon + \sin\left(\frac{\varepsilon\cdot x}{L}\right) - \frac{\varepsilon\cdot x}{L}\right]}{C} \qquad C = 6.283$$

$$\eta 2_{cr}(x) := \frac{\cos\left(\varepsilon\cdot\frac{x}{L}\right)\cdot\frac{\varepsilon^3}{L^2} - \sin\left(\varepsilon\cdot\frac{x}{L}\right)\cdot\frac{\varepsilon^2}{L^2}}{C} \qquad x_m = 2.992\,m$$

$\eta(x) := \frac{\eta_{o.ugli.m}}{\alpha_{cr} - 1}\cdot\eta_{cr}(x)$ $\eta_{o.ugli.m} := \frac{\alpha_{cr}\cdot e_{o.d}\cdot N_{Ed}}{E\cdot I\cdot\left|-\eta 2_{cr}(x_m)\right|} = 7.981\cdot mm$

$M_{II}(x) := -E\cdot I\cdot\eta 2(x)$

$M_{II}(x_m) = 23.751\cdot kN\cdot m$ $k\cdot N_{Ed}\cdot e_{o.d} = 23.751\cdot kN\cdot m$

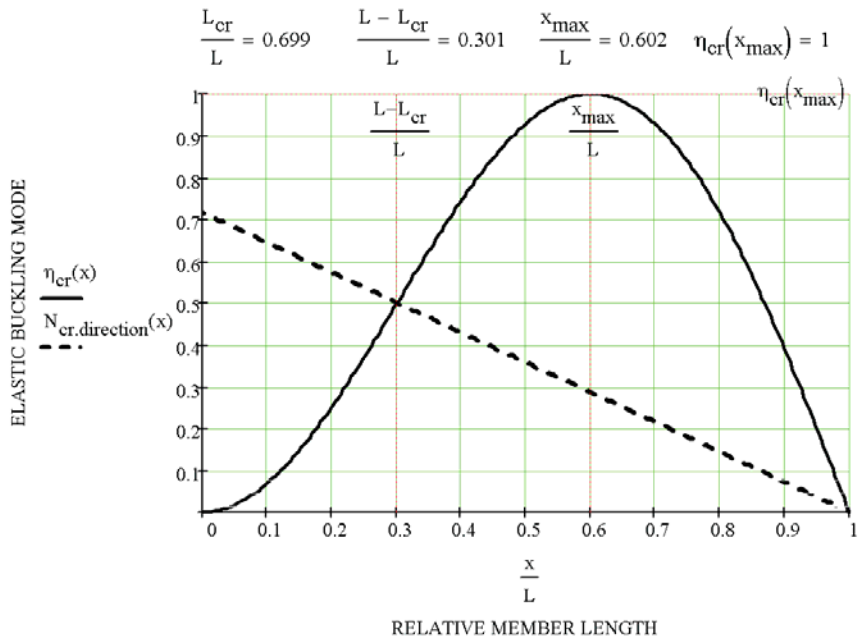

Fig. 1: The first elastic buckling mode $\eta_{cr}(x)$ valid for both cases: a) buckling about y-y and b) buckling about z-z

$x_{max} = 2.768\,m$ $x_m = 2.992\,m$ $L - 0.5 \cdot L_{cr} = 2.992\,m$

$\eta_{o.ugli.m} = 7.981 \cdot mm$ $\eta_{ugli.xm} := \eta_{ugli}(x_m) = 7.842 \cdot mm$

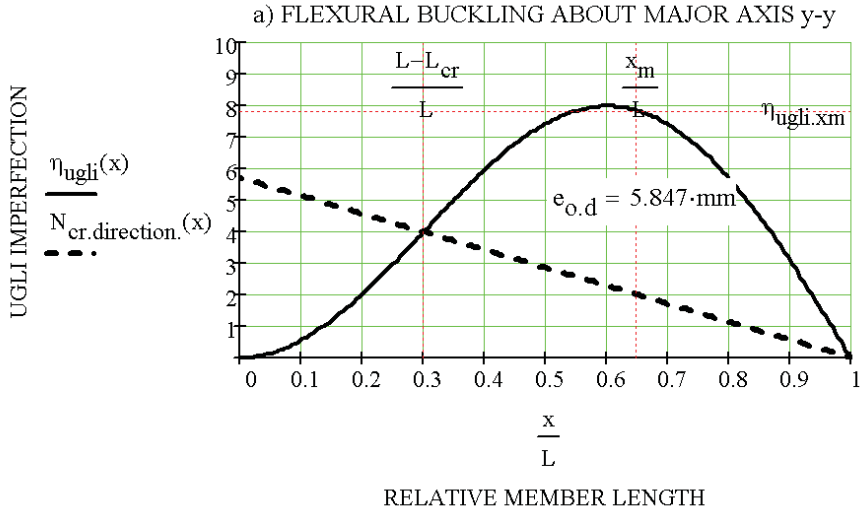

Fig. 2: Uniform global and local initial ("ugli") imperfection valid for buckling about y-y

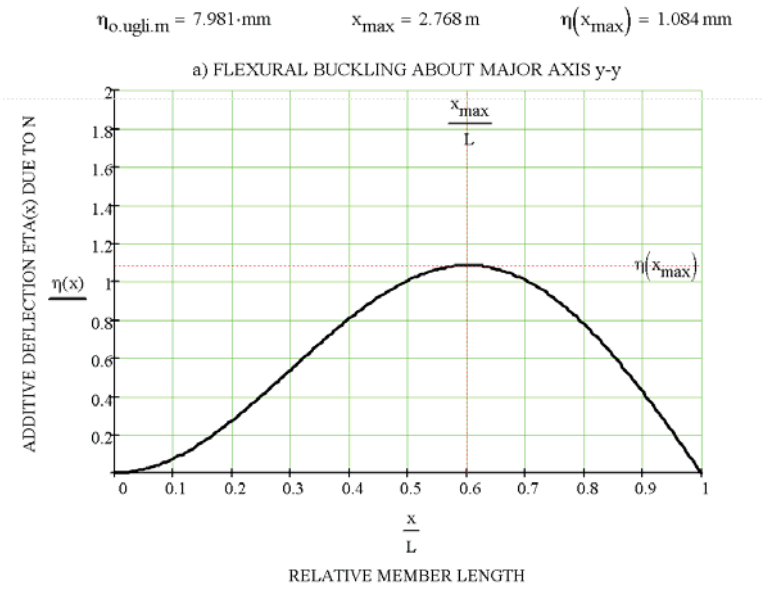

Fig. 3: Additive deflection η(x) due to N_{Ed} for flexural buckling about major axis y-y

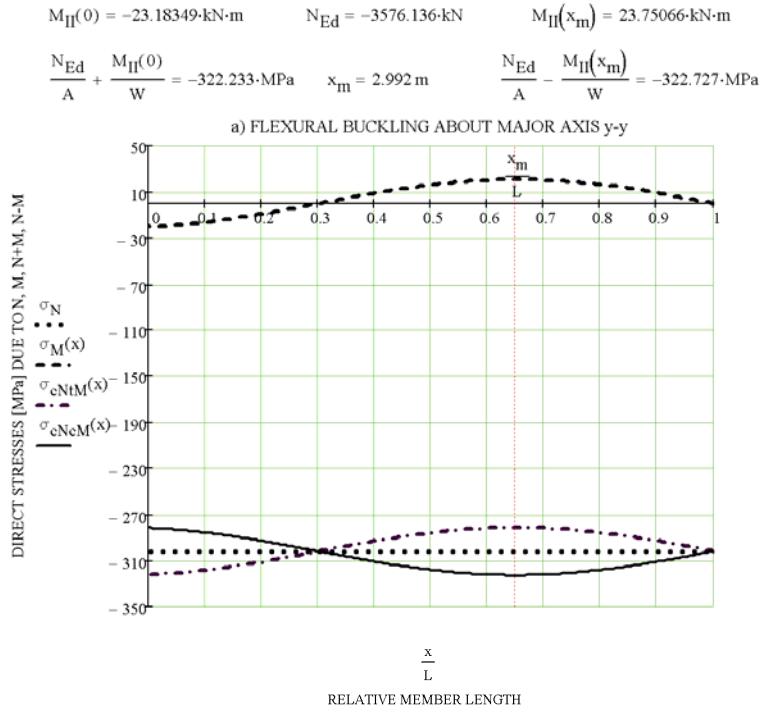

Fig. 4: Direct stresses for flexural buckling about major axis y-y

$$U_1 := \frac{N_{Ed}}{N_{Rd}} + \frac{M_{II}(x_m)}{M_{Rd}} \quad U_1 = 1 \quad \chi = 0.936 \quad f_{y.d} = 322.727 \cdot MP \quad U_2 := \frac{N_{Ed}}{\chi \cdot A \cdot f_{y.d}} \quad U_2 = 1$$

b) Flexural buckling about minor axis z-z

HE 260 B S 355 $f_y = 355\cdot MPa$ $\gamma_{M1} = 1.1$ $f_{y.d} = 322.727\cdot MPa$

$h = 0.26\,m$ $b = 0.26\,m$ buckling curve "c" $\alpha := 0.49$

$A = 11.84 \times 10^3\cdot mm^2$ $I_z = 51.35 \times 10^6\cdot mm^4$ $W_{el.z} = 395 \times 10^3\cdot mm^3$

$N_{Rk} = 4.203\cdot MN$ $N_{Rd} = 3.821\cdot MN$ $M_{z.Rk} = 140.225\cdot kN\cdot m$

$N_{Ed} = 2.911\cdot MN$ $N_{cr} = 10.29\cdot MN$ $L_{cr} = 3.216\,m$

$\beta = 0.699$ $\varepsilon := \frac{\pi}{\beta}$ $\alpha_{cr} := \frac{N_{cr}}{N_{Ed}} = 3.534$ $k := \frac{1}{1 - \frac{1}{\alpha_{cr}}} = 1.395$

$\lambda_m := \sqrt{\frac{N_{Rk}}{N_{cr}}} = 0.639$ $\phi := 0.5\cdot\left[1 + \alpha\cdot\left(\lambda_m - 0.2\right) + \lambda_m^{\,2}\right] = 0.812$

$\chi := \frac{1}{\phi + \sqrt{\phi^2 - \lambda_m^{\,2}}} = 0.762$ $e_{o.k} := \alpha\cdot\left(\lambda_m - 0.2\right)\cdot\frac{M_{Rk}}{N_{Rk}} = 7.179\cdot mm$

$e_{o.d} := e_{o.k}\cdot\frac{1 - \frac{\chi\cdot\lambda_m^{\,2}}{\gamma_{M1}}}{1 - \chi\cdot\lambda_m^{\,2}} = 7.473\cdot mm$ $\frac{L}{e_{o.d}} = 615.508$

$$\eta_{cr}(x) := \frac{\left[\left(1 - \cos\left(\frac{\varepsilon\cdot x}{L}\right)\right)\cdot\varepsilon + \sin\left(\frac{\varepsilon\cdot x}{L}\right) - \frac{\varepsilon\cdot x}{L}\right]}{C} \qquad C = 6.283$$

$$\eta 2_{cr}(x) := \frac{\cos\left(\varepsilon\cdot\frac{x}{L}\right)\cdot\frac{\varepsilon^3}{L^2} - \sin\left(\varepsilon\cdot\frac{x}{L}\right)\cdot\frac{\varepsilon^2}{L^2}}{C} \qquad x_m = 2.992\,m$$

$\eta(x) := \frac{\eta_{o.ugli.m}}{\alpha_{cr} - 1}\cdot\eta_{cr}(x)$ $\eta_{o.ugli.m} := \frac{\alpha_{cr}\cdot e_{o.d}\cdot N_{Ed}}{E\cdot I\cdot\left|-\eta 2_{cr}\left(x_m\right)\right|} = 10.201\cdot mm$

$M_{II}(x) := -E\cdot I\cdot\eta 2(x)$

$M_{II}\left(x_m\right) = 30.346\cdot kN\cdot m$ $k\cdot N_{Ed}\cdot e_{o.d} = 30.346\cdot kN\cdot m$

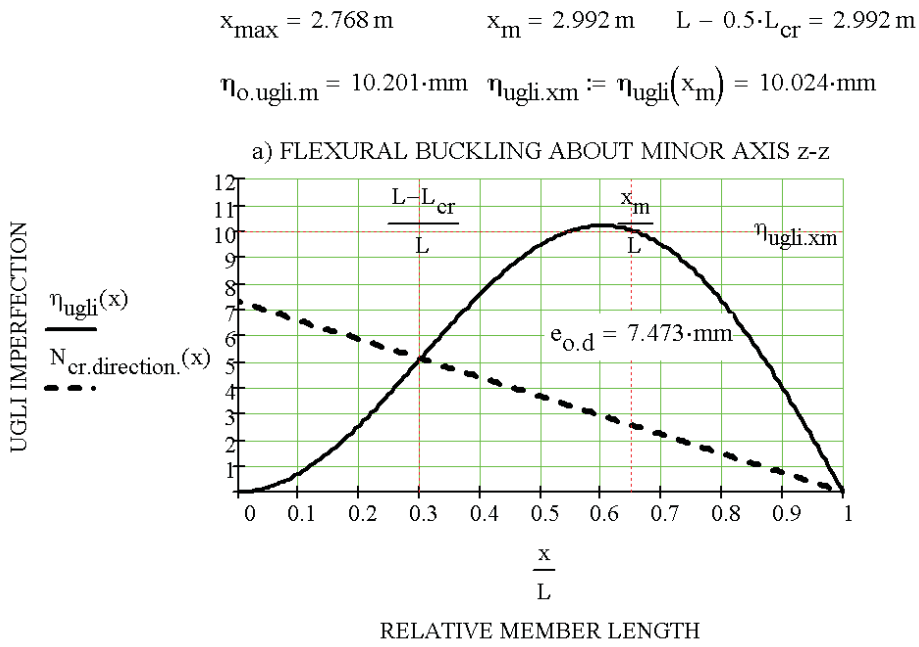

Fig. 5: Uniform global and local initial ("ugli") imperfection valid for buckling about z-z

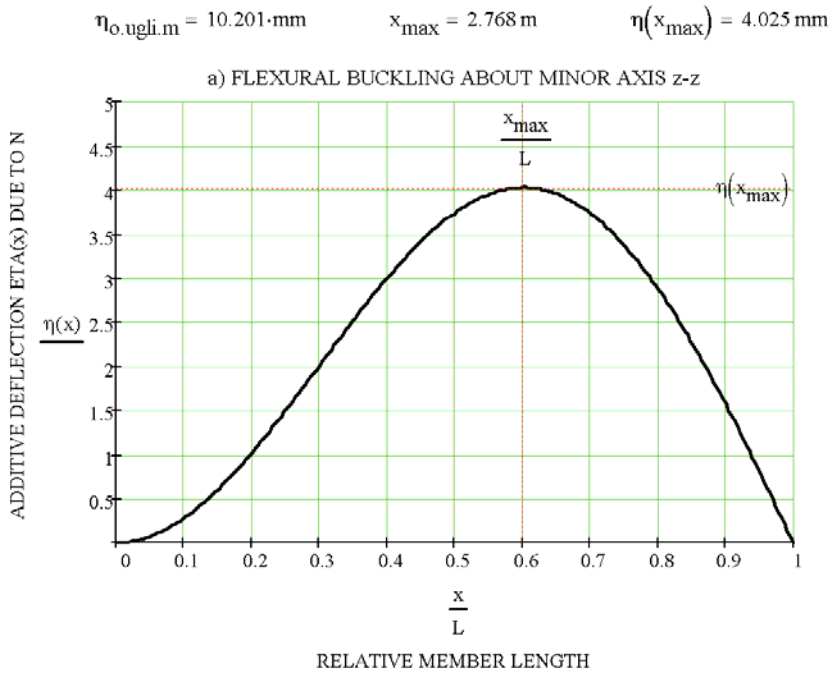

Fig. 6: Additive deflection η(x) due to N for flexural buckling about minor axis z-z

$M_{II}(0) = -29.62084 \cdot kN \cdot m$ $N_{Ed} = -2911.494 \cdot kN$ $M_{II}(x_m) = 30.3455 \cdot kN \cdot m$

$\frac{N_{Ed}}{A} + \frac{M_{II}(0)}{W} = -320.893 \cdot MPa$ $x_m = 2.992\,m$ $\frac{N_{Ed}}{A} - \frac{M_{II}(x_m)}{W} = -322.727 \cdot MPa$

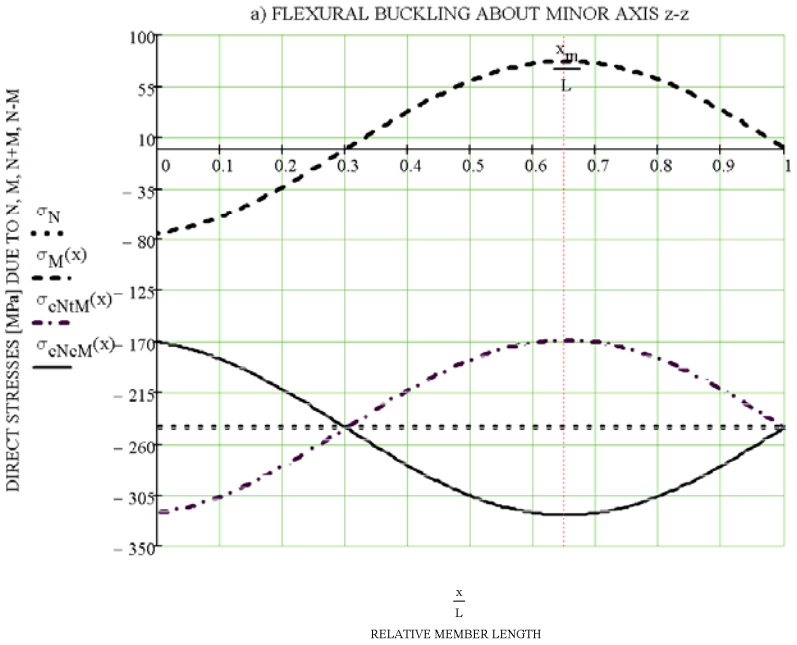

Fig. 7: Direct stresses for flexural buckling about minor axis z-z

$U_1 := \frac{N_{Ed}}{N_{Rd}} + \frac{M_{II}(x_m)}{M_{Rd}}$ $U_1 = 1$ $\chi = 0.762$ $f_{y.d} = 322.727 \cdot MPa$ $U_2 := \frac{N_{Ed}}{\chi \cdot A \cdot f_{y.d}}$ $U_2 = 1$

Example 2: Input data see in Lindner, J. – Heyde, S. (2009) in Fig. 42. Fig. 43 and results on page 305-306 in Lindner, J. – Heyde, S. (2009) are incorrect. Correct values may be obtained very easy by proposed procedure as follows:

$A = 11.84 \times 10^3\,mm^2$ $W_{pl.y} = 1.283 \times 10^6\,mm^3$ $f_y = 355\,MPa$ $\gamma_{M1} = 1$

$N_{Rk} = 4.2032 \cdot MN$ $M_{pl.y.Rk} = 455.465\,kN \cdot m$ $N_{Ed} = 620\,kN$ $\alpha_{cr} = 4.441$

$\alpha = 0.34$ $\beta = 2.30385$ $\lambda_p = 1.23555$ $\chi = 0.459$

$k := \frac{1}{1 - \frac{1}{\alpha_{cr}}} = 1.291$

$e_{o.d} := \alpha \cdot (\lambda_p - 0.2) \cdot \frac{M_{el.y.Rk}}{N_{Rk}} \cdot \frac{1 - \frac{\chi \cdot \lambda_p^2}{\gamma_{M1}}}{1 - \chi \cdot \lambda_p^2} = 34.138\,mm$

$\eta_{o.ugli.m} := e_{o.d} = 34.138\,mm$ $M_{II.Ed.imp} := k \cdot N_{Ed} \cdot e_{o.d} = 27.31674\,kN \cdot m$

Comparison with results obtained by computer program IQ 100:

$EI\eta_{II.cr} = 2.7537 \cdot MN$ $\eta_{o.ugli.m} := \frac{e_{o.d} \cdot N_{cr}}{EI\eta_{II.cr}} = 34.134\,mm$ $M_{II.Ed.imp} := 27.314 \cdot kN \cdot m$

Example 3: Verification of in plane stability of steel large span arches using three different methods given in Eurocodes EN 1993-1-1 (2005), EN 1993-2 (2006), EN 1999-1-1 (2007): a) by equivalent column method and by global analysis taking into account the second order effects and relevant imperfections b) according to 5.3.2(11) in EN 1993-1-1 (2005) and 5.3.2(11) in EN 1999-1-1 (2007) and c) according to Tab.D.8 in EN 1993-2 (2006). The internal forces were calculated by IQ 100 (Rubin, H. – Aminbaghai, M. – Weier, H., (2004)) using 1st and 2nd order analysis with and without imperfections. Details of calculation and distributions of internal forces for hingeless arch are presented here (see Fig. 11-14). Comparisons of all results including ones valid for the same but two-hinged arch are given in Table 1. Details of calculation and internal forces distributions for two-hinged arch are not presented here.

Characteristics of given structure: steel parabolic arch with span $L = 320\,\mathrm{m}$, rise/span ratio $\frac{f}{L} = \frac{40\,\mathrm{m}}{320\,\mathrm{m}} = 0.125$. The shape of arch $\frac{y}{L}\left(\frac{f}{L}, \frac{x}{L}\right)$ and relative half length of the arch $\frac{s}{L}\left(\frac{f}{L}\right)$, which are defined by expressions

$$\frac{y(x)}{L} = 4\frac{f}{L}\frac{x}{L}\left(1 - \frac{x}{L}\right) \text{ and } \frac{s}{L} = \frac{1}{4}\left[\sqrt{\left(4\frac{f}{L}\right)^2 + 1} + \frac{L}{4f}\ln\left[4\frac{f}{L} + \sqrt{\left(4\frac{f}{L}\right)^2 + 1}\right]\right] = 0.52, \text{ respectively.}$$

Material properties: Young modulus $E = 210\,\mathrm{GPa}$, steel grade $S355$, $f_y = 335\,\mathrm{MPa}$ $(t > 40\,\mathrm{mm})$, $\gamma_{\mathrm{M1}} = 1.1$. Properties of uniform cross-section: area $A = 0.381\,\mathrm{m}^2$, in plane second moment of area $I = 1.714\,\mathrm{m}^4$, height of the cross-section $h = 5\mathrm{m}$, in plane elastic section modulus $W = 0.686\,\mathrm{m}^3$, in plane radius of inertia $i = 2.121\,\mathrm{m}$. Class 3 cross-section; buckling curve „c“. Boundary conditions of hingeless arch:

a) in plane: translation fixed and rotation fixed on both ends,

b) the arch is laterally supported and no lost of stability out of plane may occur.

Design values of actions:

a) Permanent action uniform along the length of arch span $g_d = 0.13\,\mathrm{MN/m}$,

b) Variable action along the left half of arch $q_d = 0.02\,MN/m$ (real value would be greater).

c) In plane imperfection according to table D.8 in EN 1993-2 (2006): the shape of two asymmetric waves with design value of amplitude $e_o = \pm L/400 = \pm 320\,\mathrm{m}/400 = \pm 0.8\,\mathrm{m}$ (hingeless arch, buckling curve „c“ in table D.8). Mean value of uniform action along the length of arch span $q_{\mathrm{m,d}} = g_d + 0.5q_{\mathrm{d}} = 0.13 + 0.5 * 0.02 = 0.14\,\mathrm{MN/m}$.

Influence of shortening of arch centre line due to normal force for hingeless arch $\nu = \frac{45}{4}\left(\frac{i}{f}\right)^2 = \frac{45}{4}\left(\frac{2.121}{40}\right)^2 = 0.032$

Horizontal component of thrust $H = \frac{q_{\mathrm{m.d}}L^2}{8f}\frac{1}{1+\nu} = \frac{0.14 * 320^2}{8 * 40}\frac{1}{1 + 0.032} = 43.426\,\mathrm{MN}$.

Replacement of initial imperfections according to table D.8 by equivalent action $q_{\mathrm{equ.eo}} = \pm\frac{8He_{\mathrm{o}}}{(0.5L)^2} = \pm\frac{8 * 43.426 * 0.8}{(0.5 * 320)^2} \pm 0.0109\,\mathrm{MN/m}$.

d) Combination of design values of actions:

for 1st and 2nd order analysis without imperfections (results see in Fig. 11 and Fig. 13 respectively):

in left half of arch span length $q_{\mathrm{l.d}} = g_{\mathrm{d}} + q_{\mathrm{d}} = 0.13 + 0.02 = 0.15\,\mathrm{MN/m}$,

in right half of arch span length $q_{r.d} = g_d = 0.13\,\text{MN/m}$,

for 1st and 2nd order analysis with imperfections (results see in Fig. 12 and Fig. 14 respectively)

in left half of arch span $q_{l.d} = g_d + q_d + q_{equ.eo} = (0.13 + 0.02 + 0.0109)\,\text{MN/m} \approx 0.16\,\text{MN/m}$

in right half of arch span length $q_{r.d} = g_d - q_{equ.eo} = (0.13 - 0.0109)\,\text{MN/m} \approx 0.12\,\text{MN/m}$.

Internal forces

Parabolic arch was replaced by structure having form of polygon. Arch span was divided into 100 equal parts. Uniform loading q was replaced by point loads Q. Structure, values of point loads, reactions, deformations, distributions and values of internal forces N, M, V for hingeless arch may be found in Fig. 11-14.

Values in Fig. 11 and 12 were calculated by 1st order analysis without and with imperfections respectively, and values in Fig. 13 and 14 by 2nd order analysis without and with imperfections respectively. Computer program IQ 100 (Rubin, H. et al., 2004) was used to obtain results. In all calculations the influence of normal force deformations was taken into account.

Verification of arch stability

Characteristic and design values of cross-section resistances

$N_{Rk} = Af_y = 0.381\,\text{m}^2 335\,\text{MPa} = 127.619\,\text{MN}$, $\quad M_{Rk} = Wf_y = 0.686\,\text{m}^3 335\,\text{MPa} = 229.714\,\text{MNm}$

$N_{Rd} = Af_y / \gamma_{M1} = 0.381\,\text{m}^2 335\,\text{MPa}/1.1 = 116\,\text{MN}$,

$M_{Rd} = Wf_y / \gamma_{M1} = 0.686\,\text{m}^3 335\,\text{MPa}/1.1 = 208.8\,\text{MNm}$.

a) Stability verification by using equivalent column method for hingeless arch

Internal forces (Fig. 11):

$N_{Ed,I,q}(a) = -49.2122\,\text{MN}$, $M_{Ed,I,q}(a) = 66.7498\,\text{MNm}$.

Buckling length factor calculated using academic Dinnik`s values for critical loading (Dinnik, A. N., 1939)

$$q_{cr}\left(\frac{f}{L}=0.1\right) = K_{cr}\left(\frac{f}{L}=0.1\right)\frac{EI}{L^3} = 60.7\frac{EI}{L^3}, \quad q_{cr}\left(\frac{f}{L}=0.2\right) = K_{cr}\left(\frac{f}{L}=0.2\right)\frac{EI}{L^3} = 101\frac{EI}{L^3},$$

$$\beta_H\left(\frac{f}{L}=0.1\right) = \pi\sqrt{\frac{8f/L}{K_{cr}\left(\frac{f}{L}=0.1\right)}} = \pi\sqrt{\frac{8*0.1}{60.7}} = 0.361,$$

$$\beta_H\left(\frac{f}{L}=0.2\right) = \pi\sqrt{\frac{8f/L}{K_{cr}\left(\frac{f}{L}=0.2\right)}} = \pi\sqrt{\frac{8*0.2}{101}} = 0.395,$$

$$\beta_{N(a)}\left(\frac{f}{L}=0.1\right) = \beta_H\left(\frac{f}{L}=0.1\right)\frac{\sqrt{\cos\left[\arctan(4f/L)\right]}}{s/L(f/L=0.1)} = 0.361\frac{\sqrt{\cos\left[\arctan(4*0.1)\right]}}{0.513} = 0.678,$$

$$\beta_{N(a)}\left(\frac{f}{L}=0.2\right) = \beta_H\left(\frac{f}{L}=0.2\right)\frac{\sqrt{\cos\left[\arctan(4f/L)\right]}}{s/L(f/L=0.2)} = 0.395\frac{\sqrt{\cos\left[\arctan(4*0.2)\right]}}{0.549} = 0.636,$$

$$\beta_{N(a)}\left(\frac{f}{L}=0.125\right) = \beta_{N(a)}\left(\frac{f}{L}=0.1\right) - \frac{0.125-0.1}{0.2-0.1}\left[\beta_{N(a)}\left(\frac{f}{L}=0.1\right) - \beta_{N(a)}\left(\frac{f}{L}=0.2\right)\right] = 0.667$$

In plane buckling length factor according to table D.4 in EN 1993-2 (2006) $\beta = 0.67$.

In plane critical buckling force $N_{\mathrm{cr}} = \dfrac{\pi^2 EI}{(\beta s)^2} = \dfrac{\pi^2 210000 * 1.714}{(0.67 * 0.52 * 320)^2} = 285.729\,\mathrm{MN}$,

More exact value was taken into account $N_{\mathrm{cr}} = \alpha_{\mathrm{cr}} N_{\mathrm{Ed,I,q}}(a) = 5.8982 * 49.2122 = 290.257\,\mathrm{MN}$,

where $\alpha_{cr} = 5.8982$ is minimum force amplifier, which was calculated by IQ 100 (Rubin, H. et al., 2004).

Relative slenderness $\bar{\lambda} = \sqrt{\dfrac{N_{\mathrm{Rk}}}{N_{\mathrm{cr}}}} = \sqrt{\dfrac{127.619}{290.257}} = 0.663$.

Measure of imperfection $\alpha = 0.49$ (buckling curve „c“).

Factor $\Phi = 0.5\left[1 + \alpha(\bar{\lambda} - 0.2) + \bar{\lambda}^2\right] = 0.5\left[1 + 0.49(0.663 - 0.2) + 0.663^2\right] = 0.833$.

Reduction factor $\chi = \dfrac{1}{\Phi + \sqrt{\Phi^2 - \bar{\lambda}^2}} = \dfrac{1}{0.833 + \sqrt{0.833^2 - 0.663^2}} = 0.747$.

In plane buckling resistance $N_{\mathrm{b,Rd}} = \chi A \dfrac{f_y}{\gamma_{\mathrm{M1}}} = 0.747 * 0.381 \dfrac{335}{1.1} = 86.711\,\mathrm{MN}$.

Equivalent uniform moment factor for sway buckling mode obtained by using method 2 from Annex B in EN 1993-1-1 (2005). $C_{m,y} = 0.9$ and interaction factor is as follows

$$k_{\mathrm{yy}} = C_{\mathrm{m,y}}\left(1 + 0.6\bar{\lambda}\frac{\left|N_{\mathrm{Ed,I,q}}(a)\right|}{N_{\mathrm{b,Rd}}}\right) = 0.9\left(1 + 0.6 * 0.663\frac{\left|-49.2122\right|}{86.711}\right) = 1.103.$$

Utilization grade

$$U_{\mathrm{I}} = \frac{N_{\mathrm{Ed,I,q}}(a)}{N_{\mathrm{b,Rd}}} + \frac{k_{\mathrm{yy}} M_{\mathrm{Ed,I,q}}(a)}{M_{\mathrm{Rd}}} = \frac{\left|-49.2122\right|}{86.411} + \frac{\left|-1.103 * 66.7498\right|}{208.8} = 0.568 + 0.353 = 0.920 < 1.0.$$

b) Verification of strength by using 2nd order analysis with imperfections according to table D.8 EN 1993-2 (2006) for hingeless arch

Internal forces (Fig. 14):

$N_{\mathrm{Ed,II,q,eo}}(a) = -50.0777\,\mathrm{MN}$, $M_{\mathrm{Ed,II,q,eo}}(a) = 103.621\,\mathrm{MNm}$,

Utilization grade

$$U_{\mathrm{II}} = \frac{N_{\mathrm{Ed,II,q,eo}}(a)}{N_{\mathrm{Rd}}} + \frac{M_{\mathrm{Ed,II,q,eo}}(a)}{M_{\mathrm{Rd}}} = \frac{\left|-50.0777\right|}{116} + \frac{\left|-103.621\right|}{208.8} = 0.432 + 0.496 = 0.928 < 1.0.$$

c) Verification of strength by using 2nd order analysis with imperfections having shape of 1st buckling mode according to clause 5.3.2(11) in EN 1993-1-1 (2005) and EN 1999-1-1 (2007) for hingeless arch

The total maximum normal stress $(\sigma_{\mathrm{N}} + \sigma_{\mathrm{M}})$ acts in support *a*, therefore critical point *m* is located in support *a.* In critical point *m* we have (index *m* is omitted in the following quantities):

Internal forces (Fig. 13)

$N_{\mathrm{Ed,II,q}}(a) = -49.6309\,\mathrm{MN}$, $M_{\mathrm{Ed,II,q}}(a) = 67.9147\,\mathrm{MNm}$,

Minimum force amplifier for hingeless arch $\alpha_{\mathrm{cr}} = 5.8982$ was calculated by IQ 100 (Fig. 8).

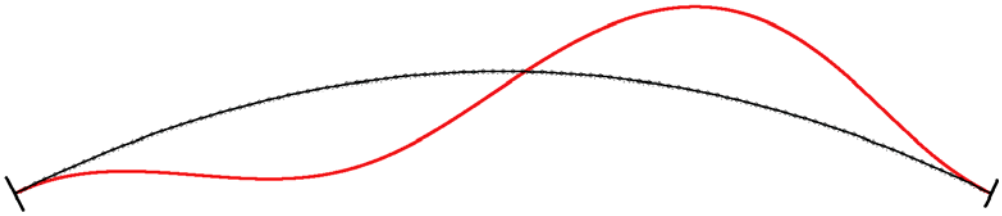

Fig. 8: First buckling mode $\eta_{\mathrm{cr,max}}(29-30)=1$, $\eta_{\mathrm{cr}}(70-71)=-0.999267$. *Minimum force amplifier for the axial force configuration* N_{Ed} *to reach the elastic critical buckling force* $\alpha_{\mathrm{cr}}=5.8982$.

In plane critical force $N_{\mathrm{cr}}=\alpha_{\mathrm{cr}}N_{\mathrm{Ed,II,q}}(a)=5.8982*49.6309=292.733\,\mathrm{MN}$.

Relative slenderness $\bar{\lambda}=\sqrt{\frac{N_{\mathrm{Rk}}}{N_{\mathrm{cr}}}}=\sqrt{\frac{127.619}{292.733}}=0.66$.

Measure of imperfection $\alpha=0.49$ (buckling curve „c“).

Factor $\Phi=0.5\left[1+\alpha(\bar{\lambda}-0.2)+\bar{\lambda}^2\right]=0.5\left[1+0.49(0.68-0.2)+0.68^2\right]=0.831$.

Reduction factor $\chi=\frac{1}{\Phi+\sqrt{\Phi^2-\bar{\lambda}^2}}=\frac{1}{0.831+\sqrt{0.831^2-0.66^2}}=0.749$.

Characteristic value of imperfection amplitude

$$e_{\mathrm{o,k}}=\alpha\left(\bar{\lambda}-0.2\right)\frac{M_{\mathrm{Rk}}}{N_{\mathrm{Rk}}}=0.49(0.66-0.2)\frac{229.714}{127.619}=0.406\,\mathrm{m}.$$

Design value of imperfection amplitude

$$e_{\mathrm{o,d}}=e_{\mathrm{o,k}}\frac{1-\frac{\chi\bar{\lambda}^2}{\gamma_{\mathrm{M1}}}}{1-\chi\bar{\lambda}^2}=0.406\frac{1-\frac{0.749*0.66^2}{1.1}}{0.749*0.66^2}=0.424\,\mathrm{m}$$

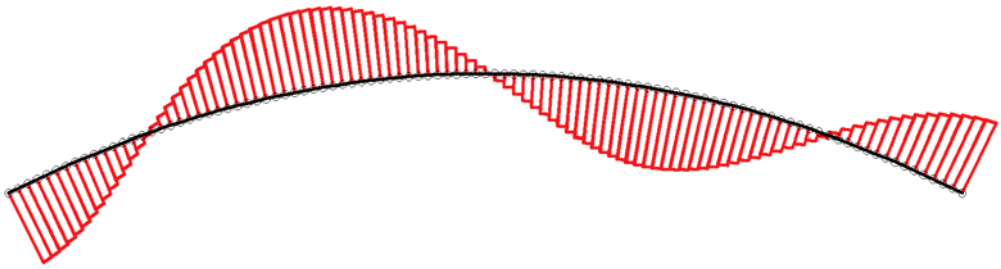

Fig. 9: Bending moment due to $\eta_{\mathrm{cr}}(x)$ ($\left|\eta_{\mathrm{cr}}(x)\right|_{\max}=1$). *In the critical section m (located in left support a) the value* $\left|M^{\mathrm{II}}_{\eta\mathrm{cr,m}}\right|=EI\left|\eta_{\mathrm{cr,m}}''\right|=196.071\,\mathrm{kNm}$. *It was calculated by IQ 100 (Rubin, H. et al., 2004).*

Amplitude of unique global and local initial (“ugli”) imperfection depending on quantities in critical point *m*

$$\eta_{\mathrm{ugli,m}} = \frac{e_{\mathrm{o,d}} N_{\mathrm{cr}}}{\left| EI\eta''_{\mathrm{cr,m}} \right|} = \frac{0.424 * 292.733}{196.071} = 632.815$$

Unique global and local initial ("ugli") imperfection

$$\eta_{\mathrm{init}}(x) \equiv \eta_{\mathrm{ugli}}(x) = \eta_{\mathrm{ugli,m}} \eta_{\mathrm{cr}}(x) = 632.815 \eta_{\mathrm{cr}}(x)$$

Deflection of the structure calculated using 2nd order analysis for the structure with imperfection

$$\eta^{\mathrm{II}}(x) = \frac{1}{\alpha_{\mathrm{cr}} - 1} \eta_{\mathrm{ugli}}(x) = \frac{1}{\alpha_{\mathrm{cr}} - 1} \eta_{\mathrm{ugli,m}} \eta_{cr}(x) = \frac{1}{5.8982 - 1} 632.815 \eta_{\mathrm{cr}}(x) = 129.193 \eta_{\mathrm{cr}}(x) .$$

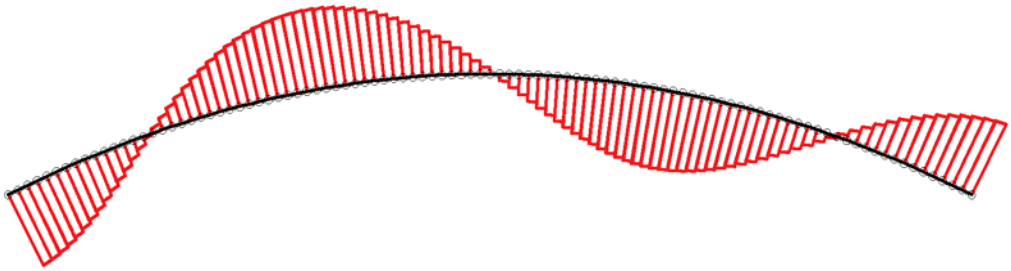

Fig. 10: Bending moment [MNm] *in the structure due to* $\eta_{\mathrm{init}}(x) \equiv \eta_{\mathrm{ugli}}(x)$ *with allowing for 2nd order effects* $M^{\mathrm{II}}_{\eta\mathrm{init,m}} \equiv$ *M(a) = - 25.3311, M(32) = 25.5385, M(68) = - 25.5267, M(b) = 25.2534 (note opposite signs to signs in moment line distribution).*

Bending moment in the structure due to $\eta_{\mathrm{init}}(x) \equiv \eta_{\mathrm{ugli}}(x)$ with allowing for 2nd order effects may be calculated from the formula

$$M^{\mathrm{II}}_{\eta\mathrm{init,m}} = \frac{\eta_{\mathrm{ugli,m}}}{\alpha_{\mathrm{cr}} - 1} \left| M^{\mathrm{II}}_{\eta\mathrm{cr,m}} \right| = \frac{632.815}{5.8982 - 1} 196.071\,\mathrm{kNm} = 129.193 * 196.071\,\mathrm{kNm} = 25.3311\,\mathrm{MNm} .$$

Utilization grade

$$U_{\mathrm{II}} = \frac{N_{\mathrm{Ed,II,q}}(a)}{N_{\mathrm{Rd}}} + \frac{M_{\mathrm{Ed,II,q}}(a)}{M_{\mathrm{Rd}}} + \frac{M^{\mathrm{II}}_{\eta\mathrm{init,m}}}{M_{\mathrm{Rd}}} = \frac{\left|-49.6309\right|}{116} + \frac{\left|-67.9147\right|}{208.8} + \frac{\left|-25.3311\right|}{208.8} =$$

$$= 0.428 + 0.325 + 0.121 = 0.874 < 1.0$$

The similar calculation as for hingeless arch, which is presented in details, was done also for the same but two-hinged arch. Numerical results of stability verification of hingeless and two-hinged arches obtained by using three different Eurocode methods are given in Table 1. Comparisons show good agreement of utilityzation grades. It is necessary to mention that safety margin of method given in 5.3.2(11) is a little bit greater comparing with safety margin of equivalent member method and that the closer we are to utilitization grade $U = 1$ the lesser is difference between safety margins. Method proposed by Chladný for 5.3.2(11) in EN 1993-1-1 (2005) and for 5.3.2(11) in EN 1999-1-1 (2007) uses characteristic value of imperfection amplitude $e_{\mathrm{o,k}}$. The value $e_{\mathrm{o,k}}$, should be based on statistical evaluations of measurements on real structures. In example presented here the value $e_{\mathrm{o,k}}$ is taken according to EN 1993-1-1 (2005), because such evaluations are not available.

Tab. 1: Results of analysis of steel large span parabolic hingeless arch and the same but two-hinged arch using three different procedures of Eurocodes EN 1993-1-1 (2005), EN 1999-1-1 (2007)

	1st order analysis		**2nd order analysis**		
	according to 5.2.2(3)c) in EN 1993-1-1(2005) without imperfections (they are hidden in χ). Method 2, Annex B	with imperfections according to Tab.D.8 in EN 1993-2 $e_o = L/400 = 800\,\text{mm}$	without imperfections	according to 5.2.2(3)a) in EN 1993-1-1 (2005) with imperfections according to 5.3.2(11) in EN 1993-1-1(2005) EN 1999-1-1(2007) $\eta_{ugli,m}$	according to 5.2.2(3)a) in EN 1993-1-1 (2005) with imperfections according to Tab.D.8 in EN1993-2(2006) $e_o = L/400 = 800\,\text{mm}$
HINGELESS ARCH ($\alpha_{cr} = 5.8982$, $\eta_{ugli,m} = 632.8\,\text{mm} \approx L/506$, $e_o = L/400 == 800\,\text{mm}$)					
H [MN]	43.4493		43.906		
$N(a)$	- 49.2122	- 49.6467	- 49.6309		- 50.0777
$M(a) \equiv \equiv M_{min}$ [MNm]	- 66.7498	- 98.0327	- 67.9147		- 103.621
			- 67.9147	$M_{min=}$ - 67.9147 - - 25.3311= = - 93.2458	
M_{max} [MNm]	$M(37)$ = = 31.4032	$M(34)$ = = 48.714	$M(36-37) = 35.6816$		$M(34)$ = = 56.9085
				$M^{II}_{\eta init}(32)$ = = 25.5385, $M_{max} < 61.22$ = = (35.68+25.54)	
Utilitiz. grade	**in left half of arch 0.920**			**in point m ≡ a 0.874**	**in point a 0.928**
TWO-HINGED ARCH ($\alpha_{cr} = 2.7187$, $\eta_{ugli,m} = 742.1\,\text{mm} \approx L/431$, $e_o = L/400 == 800\,\text{mm}$)					
H [MN]	44.5596		44.926		
$N(a)$	- 50.1205	- 50.4683	-50.4376		- 50.7848
N [MN]	$N(27)$ = = - 45.7754	$N(26)$ = = - 45.8839	$N(25)$ = - 46.3515		$N(25)$ = = - 46.359
M_{max} [MNm]	$M(27)$ = = 39.3754	$M(26)$ = = 71.297	$M(25) = 58.2369$		$M(25)$ = = 109.323
				$M^{II}_{\eta init}(25)$ = = 57.80, M(25) = = 58.24+57.80 = = 116.04	
Utilitiz. grade	**in left half of arch 1.019**			**in point (25) ≈ m 0.955**	**in point (25) 0.923**

11a) Point loads: 240 kN + 49 x 480 kN + 448 kN + 49 x 416 kN + 208 kN,

reactions [MN, MNm]: H = 43.4493, V_a = 23.3955, V_b = 21.4045, M_a = 66.7498, M_b = 4.18383

11b) Maximum deformations [m]:

vertical deflection v(40) = 0.40449, (horizontal deflection u(30) = 0.059595)

11c) Bending moments [MNm]:

M(a) = - 66.7498, M(25) = 21.4133, M(37) = 31.4032, M(83) = - 13.0495, M(b) = - 4.18383

11d) Shear force [MN]: maximum value V(a) = 1.47707

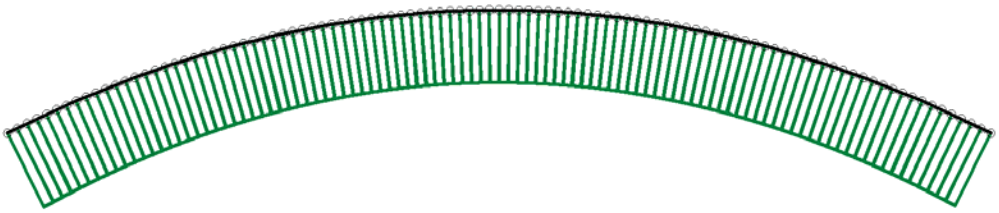

11e) Normal force [MN]: N(a) = - 49.2122, N(.25) = - 44.9711, N(50.) = - 43.4528, N(b) = - 48.3431

Fig. 11: Hingeless parabolic arch. Span L = 320 m, rise 40 m, rigidities EA = 80 000 MN, EI = 360 000 MNm^2. 1st order analysis without imperfections. Shortening due to normal force is taken into account. Vertical loads q_{left} = 0.15 MN/m in left side of arch and q_{right} = 0.13 MN/m in right side of arch were replaced by vertical point loads in 101 points.

12a) Point loads: 256 kN + 49 x 512 kN + 448 kN + 49 x 384 kN + 192 kN,

reactions [MN, MNm]: H = 43.4493, V_a = 24.391, V_b = 20.409, M_a = 98.0327, M_b = - 27.0991

12b) Maximum deformations [m]:

vertical deflection v(35-36) = 0.48801, (horizontal deflection u(29-30) = 0.097073)

12c) Bending moments [MNm]:

M(a) = - 98.0327, M(25) = 37.7718, M(34) = 48.714, M(74) = - 27.7523, M(b) = 27.0091

.

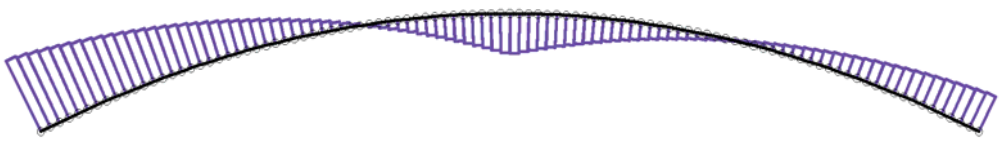

12d) Shear force [MN]: maximum value V(a) = 2.35493

12e) Normal force [MN]: N(a) = - 49.6467, N(.25) = - 45.0293, N(50.) = - 43.4547, N(b) = - 47.9085

Fig. 12: Hingeless parabolic arch. Span L = 320 m, rise 40 m, rigidities EA = 80 000 MN, EI = 360 000 MNm^2. 1st order analysis with imperfections. Buckling curve „c“. Shortening due to normal force is taken into account. Vertical loads q_{left} = 0.16 MN/m in left side of arch and q_{right} =0.12 MN/m in right side of arch were replaced by vertical point loads in 101 points.

13a) Point loads: 240 kN + 49 x 480 kN + 448 kN + 49 x 416 kN + 208 kN,

reactions [MN, MNm]: H = 43.9052, V_a = 23.4183, V_b = 21.3817, M_a = 67.9147, M_b = - 3.4664

13b) Maximum deformations [m]:

vertical deflection v(39) = 0.4295, (horizontal deflection u(30) = 0.06689)

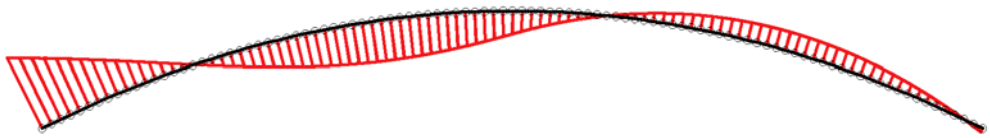

13c) Bending moments [MNm]:

M(a) = - 67.9147, M(25) = 23.9468, M(36-37) = 35.6816, M(79) = - 16.5234, M(b) = 3.4664

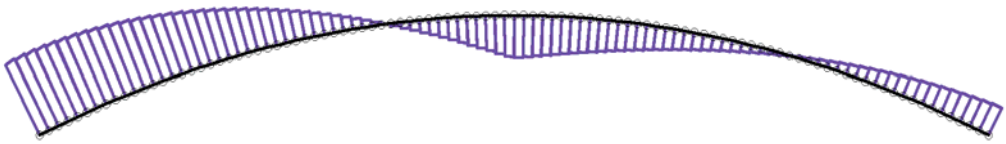

13d) Shear force [MN]: maximum value V(.1) = 1.3276

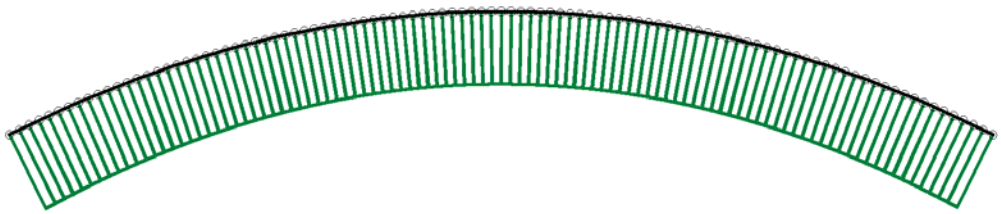

13e) Normal force [MN]: N(a) = - 49.6309, N(.25) = - 45.4245, N(50.) = - 43.9086, N(b) = - 48.7416

Fig. 13: Hingeless parabolic arch. Span L = 320 m, rise 40 m, EA = 80 000 MN, EI = 360 000 MNm^2. 2nd order analysis without imperfections. Shortening due to normal force is taken into account. Vertical loads q_{left} = 0.15 MN/m in left side of arch and q_{right} = 0.13 MN/m in right side of arch were replaced by vertical point loads in 101 points.

14a) Point loads: 256 kN + 49 x 512 kN + 448 kN + 49 x 384 kN + 192 kN,

reactions [MN, MNm]: H = 43.9075, V_a = 24.4384, V_b = 20.3616, M_a = 103.621, M_b = - 39.1536

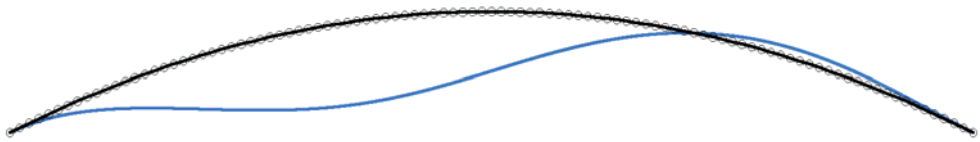

14b) Maximum deformations [m]:

vertical deflection v(35) = 0.5307, (horizontal deflection u(29-30) = 0.111524)

14c) Bending moments [MNm]:

M(a) = - 103.621, M(25) = 43.7785, M(34) = 56.9085, M(73) = - 35.8893, M(b) = 39.1536

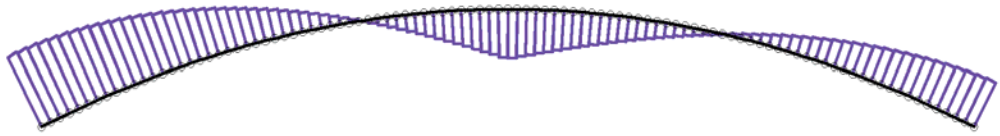

14d) Shear force [MN]: maximum value V(a) = 2.19176

14e) Normal force [MN]: N(a) = - 50.0777, N(.25) = - 45.4846, N(50.) = - 43.9137, N(b) = - 48.2988

Fig. 14: Hingeless parabolic arch. Span L = 320 m, rise 40 m, rigidities EA = 80 000 MN, EI = 360 000 MNm^2. 2nd order analysis with imperfections. Buckling curve „c“. Shortening due to normal force is taken into account. Vertical loads q_{left} = 0.16 MN/m in left side of arch and q_{right} = 0.12 MN/m in right side of arch were replaced by vertical point loads in 101 points.

Example 4: The analysis of two-hinged arch with geometrical and loading parameters of Žďákov bridge was published in Baláž, I. – Koleková, Y. (2011 b).

Example 5: Show how it is easy to find location "m" and to calculate the value of maximum bending moment due to equivalent uniform global and local initial imperfection $\eta_{\text{init}}(x) \equiv \eta_{\text{ugli}}(x)$ acting in the structure in the point "m". The authors developed graphical interpretation of the method valid for members or frames with uniform cross-section and/or with uniform normal force distribution. The graphical interpretation of the method is shown in Fig. 15-17 for 14 structures. The steps of the graphical method:

- draw the first buckling mode,
- identify the buckling length L_{cr}. Keep in the mind that the elastic critical force N_{cr} is transmitted in the direction of the line, which connects two neighbouring inflexion points,
- find the location of the point "m", where the maximum normal stress acts. This stress consists from the normal stress due to uniform normal force and from the normal stress due to maximum bending moment due to equivalent "ugli" imperfection $\eta_{\text{init}}(x) \equiv \eta_{\text{ugli}}(x)$. The point "m" is located: (i) in the middle of the buckling length L_{cr} (see 6 cases in Fig. 15 and 2 non-sway frames in Fig.16 and 2 in Fig.17), or (ii) in the cross-section of the sway frames, where the part of the sinus wave defining buckling length has the maximum displacement (see 2 sway frames in Fig.16 and 2 in Fig.17).
- the value of amplitude $e_{0,\text{d}}$ is defined by the formula derived by Chladný. This formula is today in EN 1993-1-1, (2005), 5.3.2(11), formula (5.10) and in EN 1999-1-1, (2007), 5.3.2(11), formula (5.7). Not convenient symbol e_0 instead of $e_{0,\text{d}}$ is used in Eurocodes. The amplitude $e_{0,\text{d}}$ is located in the point "m".
- calculate factors

$$\alpha_{cr} = \frac{N_{cr}}{N_{Ed}}, \quad k = \frac{1}{1 - \dfrac{1}{\alpha_{cr}}} = \frac{\alpha_{cr-1}}{\alpha_{cr}} \tag{18}$$

- calculate bending moment due to equivalent "ugli" imperfection $\eta_{\text{init}}(x) \equiv \eta_{\text{ugli}}(x)$ from simple formula (16, 19) by hand

$$M^{\text{II}}_{0,\text{Ed,ugli,m}} = kN_{\text{Ed,m}}e_{0,\text{d,m}} \tag{19}$$

Examples 6, 7, 8: relating to the structures with the non-uniform cross-sections and/or the non-uniform normal force distribution were published by Chladný in (Baláž, I. et al., 2007, 2010) and by Kováč in Kováč, M. (2010).

4. Conclusions

New very promissing and useful method for design and verification of stability and flexural buckling resistance of metal members and frames with equivalent uniform global and local initial imperfections is presented. The original method was developed by Chladný and today is used in Eurocodes EN 1993-1-1 (2005) and EN 1999-1-1 (2007). It may be used also for frames with non-uniform cross-sections and/or non-uniform axial force distribution. In the paper new way of derivation of basic formulae of the method and clear step by step description of its application based on this derivation are presented. The original graphical interpretation of the method developed by authors is valid for frames with uniform cross-sections under uniform axial compression forces and enables to obtain very easy the maximum value of bending moment due to equivalent "ugli" imperfection. Several numerical examples show in details application of this method, which may be further developed and used also for lateral torsional buckling of beams.

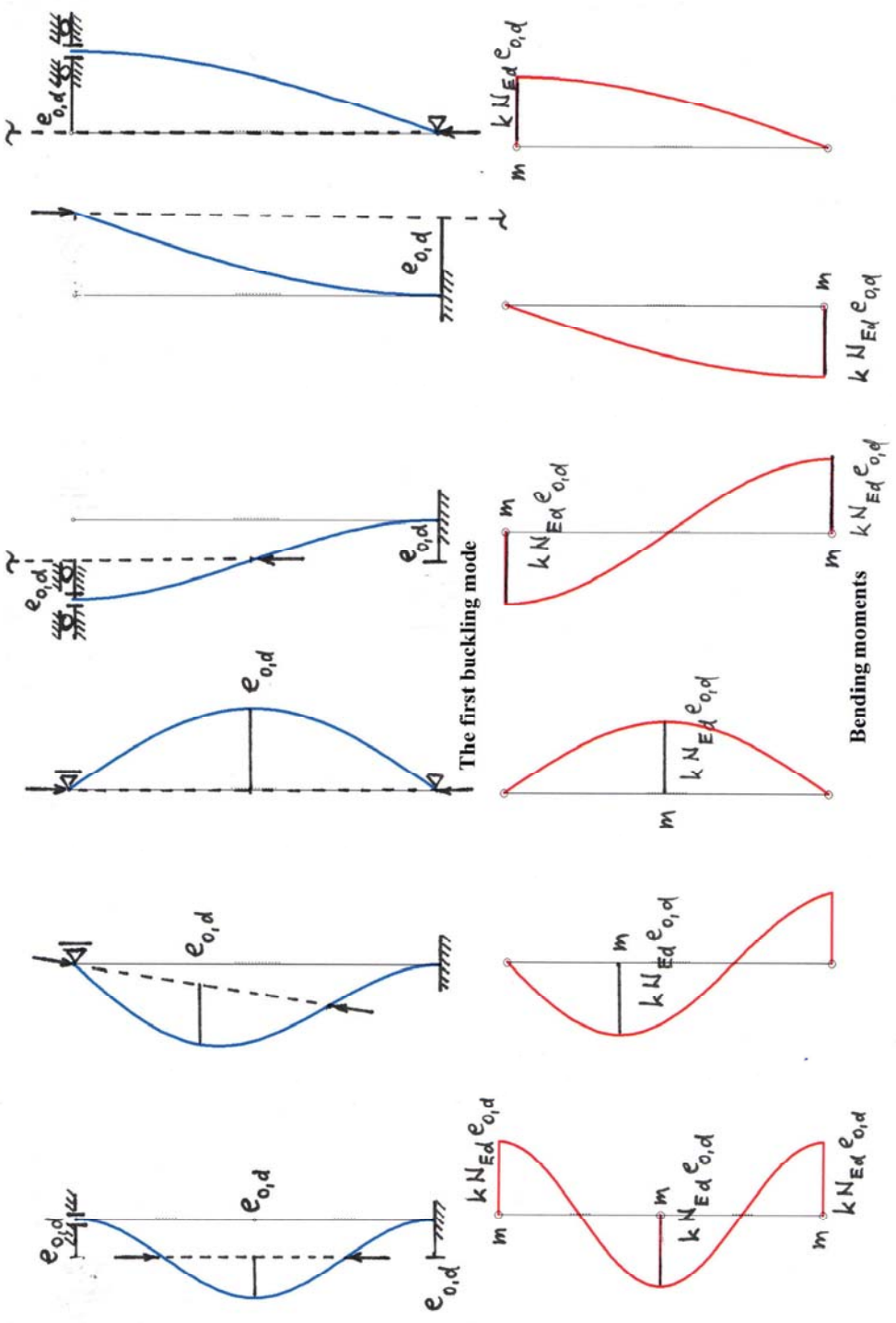

Fig. 15: Bending moments due to equivalent "ugli" imperfections

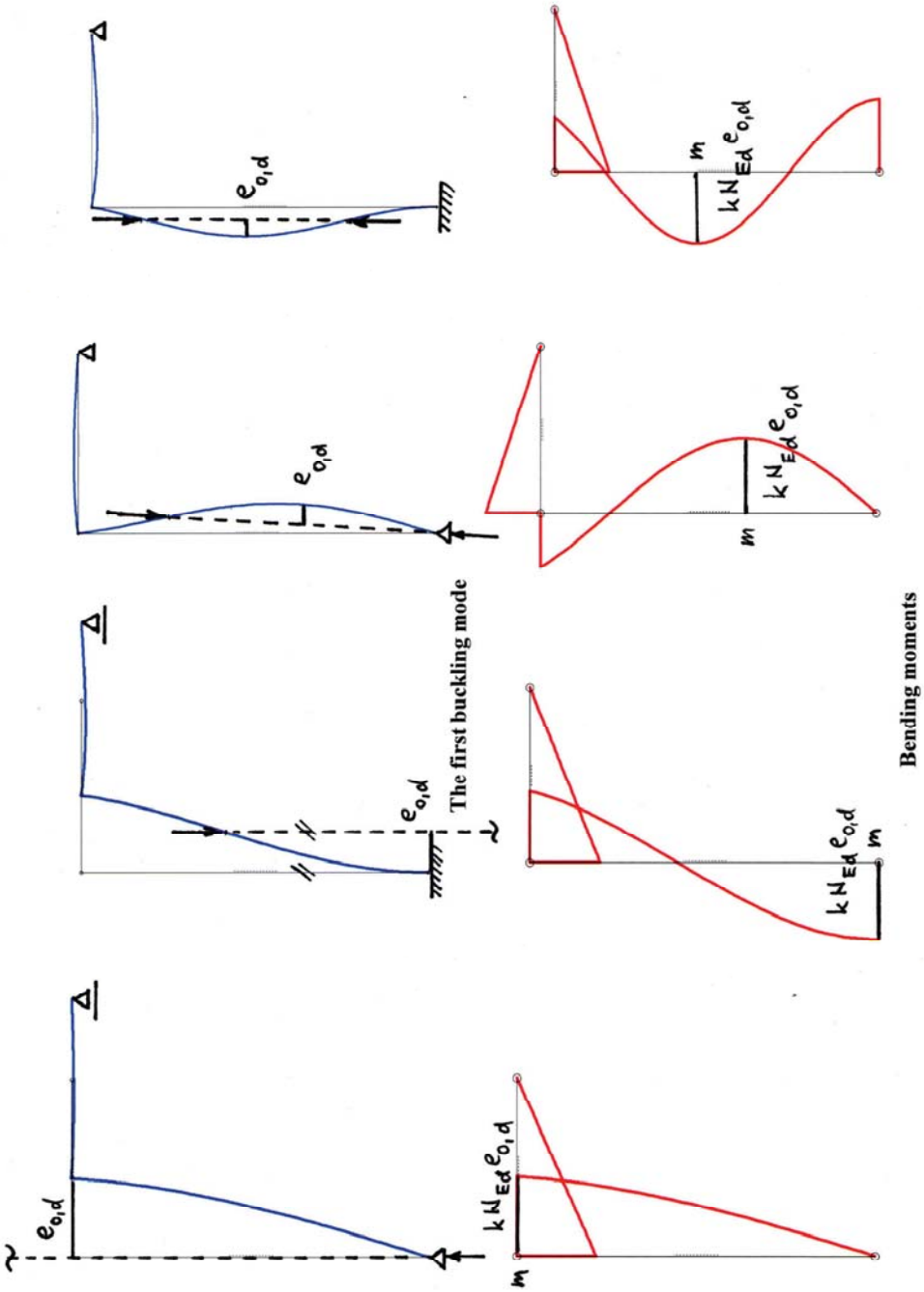

Fig. 16: Bending moments due to equivalent "ugli" imperfections

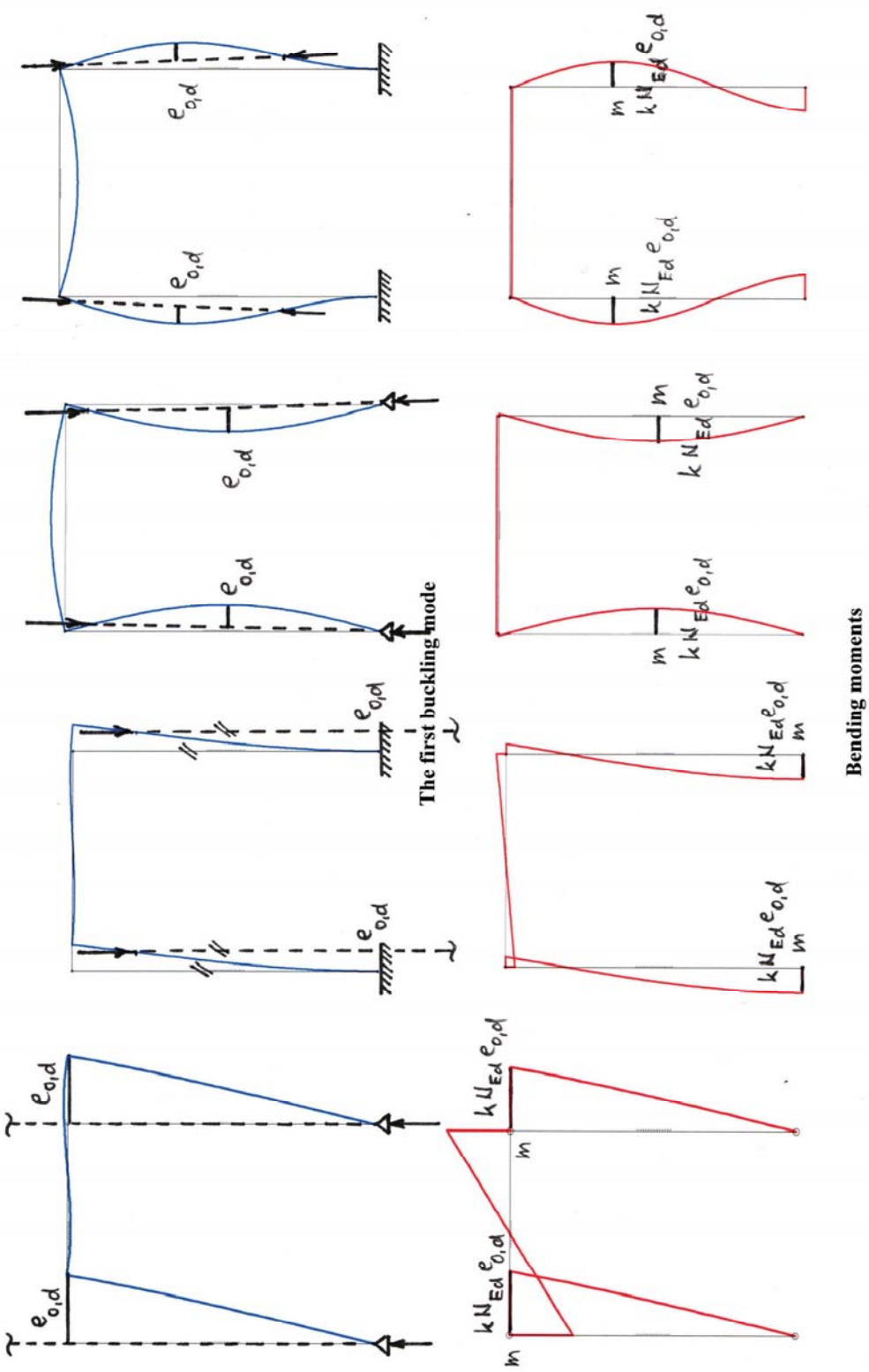

Fig. 17: Bending moments due to equivalent "ugli" imperfections

Acknowledgement

The authors acknowledge support by the Slovak Scientific Grant Agency under the contract No. 1/1101/12.

References

Baláž, I. (2008) Determination of the flexural buckling resistance of frames with members with non-uniform cross-section and non-uniform axial compression forces, in: *Zborník z XXXIV. aktívu pracovníkov odboru OK so zahraničnou účasťou „Teoretické a konštrukčné problémy oceľových a drevených konštrukcií a mostov".* Pezinok , pp.17-22.

Baláž, I. (2009) Resistance of metal frames with UGLI imperfections, in: *Zborník XII. Mezinárodní vědecké konference u příležitosti 110. výročí založení FAST VUT v Brně*, Sekce: Inženýrske konstrukce, pp.11-14.

Baláž, I., Koleková, Y. (2010 a) Flexural buckling resistance of frames with unique global and local initial imperfections, in: *Sborník příspěvků: Mezinárodní konference Modelování v mechanice.* VŠB-TU. Ostrava, Fakulta stavební, Katedra mechaniky, pp.35-36.

Baláž, I., Koleková, Y. (2010 b) Flexural buckling resistance of frames with unique global and local initial imperfections, in: *Sborník příspěvků na CD: Mezinárodní konference Modelování v mechanice.* VŠB-TU Ostrava, Fakulta stavební, Katedra mechaniky, pp.1-6.

Baláž, I., Koleková, Y. (2010 c) Metal frames with non-uniform members and/or non-uniform normal forces with imprefections in the form of elastic buckling mode. ENGINEERING RESEARCH. In: *Aniversary volume honoring Amália and Miklós Iványi.* Pollack Mihaly Faculty of Engineering. University of Pécs, pp. B:3-B:15.

Baláž, I., Koleková, Y. (2010 d) Flexural buckling resistance of metal frames with imperfection in the form of elastic buckling mode, in: *Zborník 36. aktívu pracovníkov odboru oceľových konštrukcií. Oceľové, drevené a kompozitné konštrukcie a mosty.* Hotel Boboty, Terchová – Vrátna. ŽU v Žiline, SSOK, pp.25-32.

Baláž, I., Koleková, Y. (2011 a) Verification of in plane stability of steel arches, in: *Zborník konferencie CONECO "Príprava, navrhovanie a realizácia inžinierskych stavieb".* Bratislava, pp.1-12.

Baláž, I., Koleková, Y. (2011 b) In plane stability of two-hinged arches, in: *Proc. of 6th European Conference on Steel and Composite Structures, Eurosteel 2011*. Budapest, Vol. C, pp.1869-1874.

Baláž, I., Ároch, R., Chladný, E., Kmeť, S., Vičan, J.: (2007, 2010) *Design of Steel Structures According to Eurocodes STN EN 1993-1-1:2006 a STN EN 1993-1-8:2007*. Slovak Chamber of Civil Engineers (SKSI) Bratislava, 1st Edition 2007, 2nd Edition 2010. (In Slovak).

ČSN 73 6205 (1984) *Design of steel bridge structures*. Prague.

Dinnik, A. N. (1939) *Prodoľnyj izgib (teorija i priloženija).* GONTI.

EN 1993-1-1 (2005) *Eurocode 3: Design of Steel Structures. Part 1-1: General Rules and Rules for Buildings* CEN Brussels.

EN 1993-2 (2006) *Eurocode 3: Design of Steel Structures. Part 2: Steel Bridges*. CEN Brussels.

EN 1999-1-1 (2007) *Eurocode 9: Design of Aluminium Structures. Part 1-1: General Structural Rules*. CEN Brussels.

Chladný,E. (1958) *Nosnosť tlačených pásov otvorených mostov (Buckling resistance of compressed chords of open truss bridges)* PhD thesis, SVŠT (Slovak Technical University of technology) Bratislava.

Chladný, E. (1974) *Vzper pružne podopretých tlačených prútov (Buckling of elastically supported compressed members)* Habilitation thesis, SVŠT Bratislava 1974.

Chladný, E. (1998) Nachweise der Querrahmen von Fachwerktrogbrücken mit offenem Querrschnitt nach EC 3-2 und STN 73 6205. In: Entwurf, Bau und Unterhaltung von Brücken im Donauraum. Bauingenieur Sonderpublikation, Springer-VDI- Verlag, Düsseldorf.

Kováč, M. (2010) *Buckling resistance of metal members and frame structures. Application of new Eurocode methods.* (In Slovak). PhD thesis. Faculty of Civil Engineering. Slovak University of Technology in Bratislava. Supervisor: I. Baláž.

Lindner, J., Heyde, S. (2009) *Schlanke Stabtragwerke.* Stahlbau Kalender, pp.305-306.

Rubin, H., Aminbaghai, M., Weier, H. (2004) *Computer program IQ 100*. TU Wien. Vollversion Okt. 2004. Wolters Kluwer Deutschland GmbH, Werner Verlag.

Sedlacek, G., Eisel, H., Hensen, W., Kühn, B., Paschen, M. (2004) *Leitfaden zum Fachbericht DIN 103. Stahlbrücken.* Ausgabe März 2003. Ernst & Sohn, A Wiley.

STN EN 1993-1-1/NA (2007) *Design of steel structures. Part 1-1: General rules and rules for buildings*. Slovak National Annex. SÚTN Bratislava.

STN EN 1993-2/NA (2009) *Design of steel structures. Part 2: Steel Bridges*. Slovak National Annex. SÚTN Bratislava.

18th International Conference
ENGINEERING MECHANICS 2012
Svratka, Czech Republic, May 14 – 17, 2012

pp. 87–95
Paper #320

NATURAL ASHLARS OF HISTORICAL MONUMENT – MODERN METHODS OF DATA PROCESSING AND STORAGE

M. Bednarik[*], K. Kovářová[**], R. Holzer[*], M. Laho[***]

Abstract: *The aim of the introduced contribution is to present the methodology for the research and maintenance of facing ashlars of historical structures. The natural building stone of historic monuments is subjected to various types of deterioration and damages mostly due to weathering processes. If the stone has to be completely changed during the reconstruction, it should be preferentially replaced by variety of the same lithological composition, the same or similar appearance and with the sufficient durability. It is methodologically necessary to generate the ashlars façade plan based on digital photographic procedure in the real scale before the restoration. The aim of this paper is to bring a modern look for the processing, visualization and storage of information obtained in mapping facades of historic buildings. The data processing and their storage in GIS were implemented on the façade of St. Martin's Cathedral in Bratislava. There are also described the basic processes of stone deterioration in this article.*

Keywords: ***Natural ashlars, data processing, GIS, databases, spatial and non-spatial data.***

1. Introduction

The natural building stones in historical monuments ashlars undergo to weathering processes and therefore they are damaged. If the stone has to be completely changed during the reconstruction, it should be preferentially replaced by variety of the same lithological composition, the same or similar appearance and with sufficient durability. Nowadays, it is practically impossible to use the resources of original material, therefore is necessary to find new source of a suitable replacement material. The use of the alternative stone must not change the visual character (color, texture) of monument or ornamental façade elements. From that point of view, the deteriorated façade has to be detailed and well researched and mapped.

The aim of this paper is to bring a modern look for the processing, visualization and storage of information obtained in mapping facades of historic buildings. Processing and visualization of spatial data is processed within Geographic Information Systems (GIS), where used are not only the tools for vectorization (digitalization) of analog data and visualization modulus, but also advanced tools of map algebra. Map algebra is implemented directly in a GIS environment and provides basic and advanced analytical operations with raster and vector data model. Non-spatial data - data stored in the attribute table when processed in the GIS environment and database systems are information about different types of façade damages and their causes, physical and mechanical properties of individual lithological types represented in the object as well as the proposed replacement of whole building blocks. This paper presents the direct examples of the above mentioned approaches of processing of spatial, as well as non-spatial data.

[*] Doc., RNDr. Martin Bednarik, PhD.: Department of Engineering Geology, Comenius University in Bratislava; Mlynská dolina; 842 15, Bratislava; SK, e-mail: mbednarik@fns.uniba.sk

[**] Mgr. Kateřina Kovářová, MBA.: Department of Geotechnics, Czech Technical University in Prague; Thákurova 7; 166 29, Prague; CZ, e-mail: katerina.kovarova@fsv.cvut.cz

[*] Doc. RNDr. Rudolf Holzer, CSc.: Department of Engineering Geology, Comenius University in Bratislava, Mlynská dolina; 842 15, Bratislava 4; SK, e-mail: holzer@fns.uniba.sk

[***]RNDr. Marek Laho, PhD.: National Highway Company; Mlynské Nivy 45; 821 09, Bratislava; SK, e-mail: Marek.Laho@ndsas.sk

To be able to provide the required and quality information about building material (physical-mechanical properties, detailed lithology analysis, rate and cause of deterioration, etc.) is sometimes necessary to take samples during the process of façade photo documentation. The use of indirect nondestructive methods of properties assessment is useful, if sampling is impossible.

2. Facades damages and their causes

First, in the process of mapping façade, is necessary to know the cause of damage of building stone ashlars and to determine the main weathering processe that is responsible for the decay.

The weathering of stone ashlars is natural process during which physical and chemical processes take place (Winkler, 1997). The weathering processes cause physical disintegration and chemical changes having the effect on changes of rock structure and its physical properties. The weathering forms are macroscopically (also microscopically) observable phenomena on the stone surface. The cause of the stone decay is obvious in some cases and therefore the identification of concrete weathering process is possible (Smith *et al.*, 1992). The durability of stones is influenced by certain factors. Warke (1996) distinguishes the factors between those factors, which influenced the stone before its placement into the building structure (e.g. way of extraction, processing of surface), and such factors, which modify the stone after the placement into building structure (e.g. internal environment, surroundings materials, cleaning and conservation).

The degree of damage depends on the stone petrography and stone genetic classification. The characteristic component of stone internal structure is its pore space, which is significantly modified during weathering processes. On the other hand, the properties of pores, such as e.g. their shape, interconnection and size distribution also influence the stone durability and consequently the degree of damage. The presence of intergranular spaces influences the porosity, presence and transport of the liquid phase inside the rock.

Physical weathering

Physical weathering is a set of processes during witch stone is negatively influenced as the effect of physical forces (Ollier, 1969). Neither chemical nor mineralogical composition is affected during these processes, but the grain cohesion may be broken and thus the technical properties may be exacerbated (Winkler, 1997). Physical weathering also causes the changes of internal structure. Among the agents causing the physical weathering belongs e.g. temperature changes (frost, insolation), salt crystallization pressure, mechanical influence of organisms.

Influence of water presence

The presence of water in stone is one of the most significant weathering agents, especially during winter. The freezing water in pores can cause large pressures and can lead to the degradation and disintegration of stone grains. Presence of water in the pore system affects the cohesion of grains if their state changes. The action of frost can cause swelling and shrinking of stone surface (Winkler, 1997; Thomachot & Jeannette, 2002). When water freezes, it increases in volume of approximately 9% (Johannesson, 2010). This can cause large pressure and consequently changes in the pore structure. Hardness of frozen water crystals is 1.5 degrees of Mohs scale at 0°C and 6 degrees at -60°C. The total porosity and pore radius increase depending on the number of freeze/thaw cycles (Winkler, 1997).

Sedimentary rocks often contain clay minerals and therefore they may be sensitive by wetting. The presence of water can cause the swelling of expansive clay minerals. The outward forces of the expansion produce tensile stresses in the stone structure (Bortz & Wonneberger, 1997).

The process of hydration, contribute to the degradation as well. The volume of phase increases during the hydration due to the sorption of water and thus more pressure is exerted on the surrounding area. Hydration and dehydration processes take place in response to changes in temperature and relative humidity.

Influence of salts presence

Crystallization of salts in pores can exacerbate the process of degradation. The origin of salt crystals forming from the solution in the pore space can cause large pressure. According to Goodman (1989) the growth of salt crystals depending on temperature causes pressure of several tens to hundreds of MPa, which exceeds the tensile strength of most rocks. Besides crystallization pressures of forming salts, the process of their hydration, contribute to the degradation as well.

On the other hand, not every salt action results in stone deterioration. The production of surface efflorescence is often impressive and highly visible, but generally causes only little damage. Previously fractured material can be actually bound together by various salts (Doehne, 2002). Besides the influence on the process of physical weathering, crystallization of salts may be accompanied by chemical processes and action of organisms (Goudie & Viles, 1997).

The relationship between the action of salt crystallization and frost action was pointed out by e.g. Williams and Robinson (2001). The authors extended the range of salts, which intensify the frost action, and also shown that the degree of stone damage depends on the combination of salts involved.

Chemical weathering

Chemical weathering is a very complicated process during which the interaction among minerals and present solutions causes mineralogical changes and may lead to the degradation of stone. Factors controlling chemical weathering are following (Ollier, 1969; Winkler 1997): i) concentration of hydrogen ions in system (pH); ii) its ionic potential; iii) and its oxidation/reduction potential. The chemical weathering processes especially are dissolution, oxidation and reduction, carbonatization, hydration and hydrolysis.

Chemical weathering is influenced by the presence of water and dissolved chemicals and gases. Temperature, humidity, presence of organic acids and dissolved carbon dioxide are particularly most relevant to the extent of damage caused by chemical weathering (Winkler, 1997).

3. Processing of ashlars facade plan and data storage results

Preparation of input data and assumptions of technical processing issues

The main instruments, except of external graphics modulus for processing, vectorization, analysis and visualization are Geographic Information Systems environment (GIS) and database systems.

There are many definitions that describe the Geographic Information System. Concise definition is according to Maguire (1991), which describes the GIS as an organized set of computer hardware, software and geographic data for the efficient acquisition, storage, editing, management, analyzing and displaying all forms of geographic information. For façade plan processing the vector data model was applied. Vector representation of conceptual models of reality is based on the object; position the explicit modeling of space. Object reality is represented by geometric types (elements) composed of points, lines and polygons. Vector data are stored in computer memory using the coordinates of points and topological relations (Hofierka, 2003).

The basic requirement placed on the facade plans is their positional accuracy. Important problem is the heterogeneity of different sources (http://sk.wikipedia.org/wiki). Positional accuracy varies and results from the scale, method and precision of data scanning, as well as other factors. Therefore, it needs accurate and correct mutual superposition of all inputs. When processing the façade plans a commercial product by ESRI (Environmental Systems Research Institute) - ArcGIS 9.1, working under the Microsoft Windows had been used.

Database System (often RDBMS or DBMS) is a software system for efficient storage, modification and selection of large amounts of persistent data. At present, almost all used database systems are based on relational data model. The performance and capabilities they provide, we can roughly be divided into "high end" (Oracle Database, Microsoft SQL Server, IBM DB / 2) and "low-end" (MySQL, MiniSQL, ...) and systems between (PostgreSQL, ...). Besides these there are also so called desktop relational database systems, which unlike "full" systems do not provide a high level or even advanced features such as transaction processing, authorization, and robustness, multi-user

access but on the other hand, are much cheaper (Microsoft Access, dBASE, Microsoft FoxPro, Firebird, Interbase, ...). Microsoft Access database in package Microsoft Office 2003 was used for our targets as the database system.

GIS based processing

Based on detailed photo documentation of historic building within frame of field research, the subsequent generation of facade plans using GIS is very useful. The output of this stage is a detailed and accurate plan of the facade, which has incorporated elements of architectural characteristics, lithological composition of individual building blocks and their properties (including those laid down in the laboratory research) and determination of weathering forms.

The first step is facade mapping and identification of individual ashlars of the object using existing paper plans. Those results are usually scanned to digital raster form (.tiff) and georeferenced in GIS environment (Fig. 1). Usually we use large-scale cylindrical scanner with high resolution. Paper plans often do not correspond to the actual state, so during the mapping phase these should be updated.

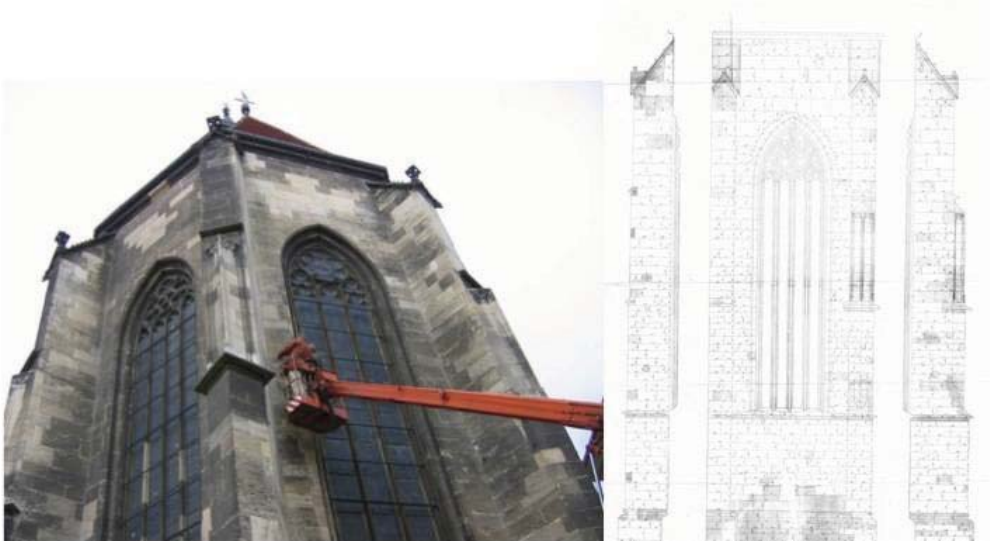

Fig. 1: Left - mapping and identification of individual building blocks, right - an example of existing paper facade plan (Vician et al., 1957).

The second step is using of photogrammetric approach, to create photo documentation of the object façade, predominantly for bottom part of the objects, which is the most affected by chemical, mechanical weathering as well as by human activities. These records should be rectify, georeferenced and digitize using vectorization tools within GIS environment (Fig. 2). Using polygon entities per each building block, the vectorization had been completed.

The third step after the vectorization is visualization of the vectorized parts of facade plans. The visualization is based on non-spatial information stored in attribute table directly connected with individual layers (Fig. 3). We can use the non-spatial data for providing of various analyses using map algebra, e.g. how many and which blocks are damaged due to concrete type of weathering, how many and which ashlars of same lithological type should be replaced, percentually which lithological type is predominantly used on the object and many others.

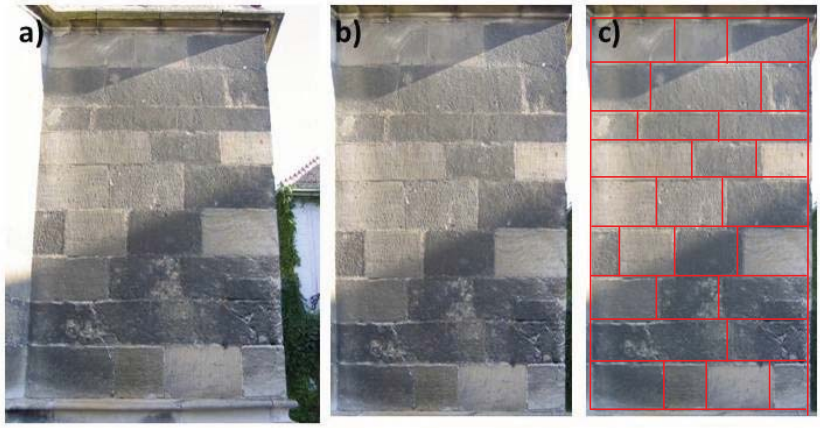

Fig. 2: Using of photogrametry approach: a) photodocumentation, b) rectification, c) vectorization (Laho et al., 2010).

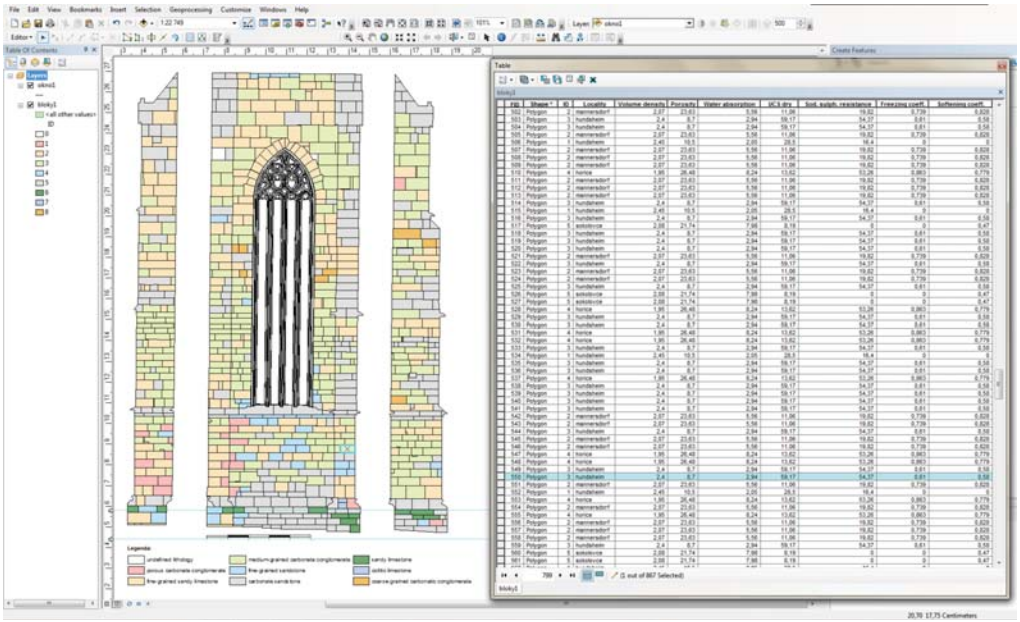

Fig. 3: Processing of part of St. Martin Cathedrale in Bratislava in ArcGIS: left - the visualization represented lithological types; right - the information stored in the attribute table.

Database processing

The modern trend of processing information electronically enables to store a large set of data in a relational database in accordance with modern standards of information technology. Such a process of storage and arrangement of data provides an efficient operation, completion and retrieval of interactive relations.

The methodology used for the database was assembled from generally valid rules for the creation of information structures and for the type and extent of data input assembled in documentation records. The relational database generates an information unit and a tool assembled in documentation records which enables their efficient presentation and processing as specified by the requests of the user. An example of database scheme is presented in Fig. 4. Microsoft Access database in package

Microsoft Office 2003 was used as the database system (Fig. 5). This solution belongs to the cheaper desktop relational database systems.

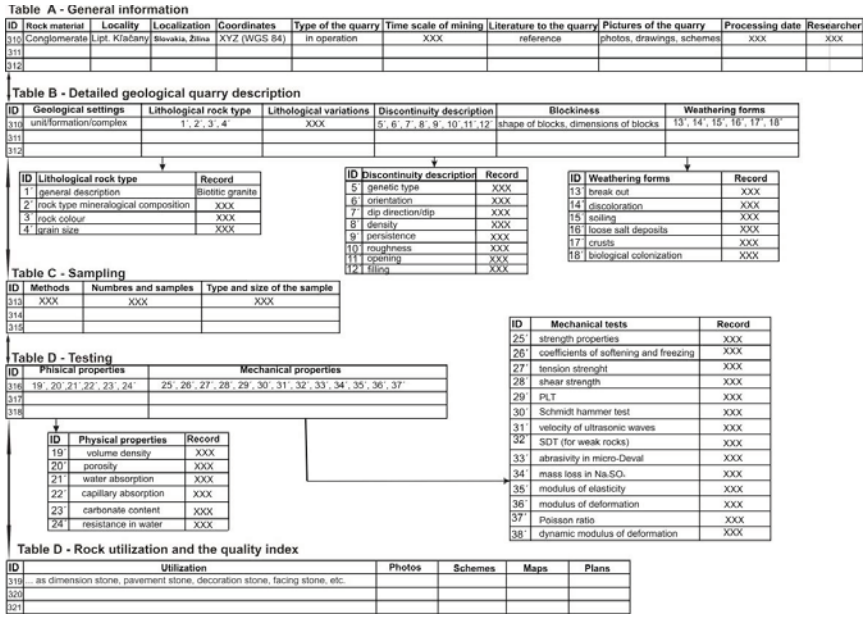

Table A - General information

ID	Rock material	Locality	Localization	Coordinates	Type of the quarry	Time scale of mining	Literature to the quarry	Pictures of the quarry	Processing date	Researcher
310	Conglomerate	Lipt. Kľačany	Slovakia, Žilina	XYZ (WGS 84)	in operation	XXX	reference	photos, drawings, schemes	XXX	XXX
311										
312										

Table B - Detailed geological quarry description

ID	Geological settings	Lithological rock type	Lithological variations	Discontinuity description	Blockiness	Weathering forms
310	unit/formation/complex	1`, 2`, 3`, 4`	XXX	5`, 6`, 7`, 8`, 9`, 10`,11`,12`	shape of blocks, dimensions of blocks	13`, 14`, 15`, 16`, 17`, 18`
311						
312						

ID	Lithological rock type	Record
1`	general description	Biotitic granite
2`	rock type mineralogical composition	XXX
3`	rock colour	XXX
4`	grain size	XXX

ID	Discontinuity description	Record
5`	genetic type	XXX
6`	orientation	XXX
7`	dip direction/dip	XXX
8`	density	XXX
9`	persistence	XXX
10`	roughness	XXX
11`	opening	XXX
12`	filling	XXX

ID	Weathering forms	Record
13`	break out	XXX
14`	discoloration	XXX
15`	soiling	XXX
16`	loose salt deposits	XXX
17`	crusts	XXX
18`	biological colonization	XXX

Table C - Sampling

ID	Methods	Numbres and samples	Type and size of the sample
313	XXX	XXX	XXX
314			
315			

Table D - Testing

ID	Phisical properties	Mechanical properties
316	19`,20`,21`,22`, 23`, 24`	25`, 26`, 27`, 28`, 29`, 30`, 31`, 32`, 33`, 34`, 35`, 36`, 37`
317		
318		

ID	Physical properties	Record
19`	volume density	XXX
20`	porosity	XXX
21	water absorption	XXX
22`	capillary absorption	XXX
23`	carbonate content	XXX
24`	resistance in water	XXX

ID	Mechanical tests	Record
25`	strength properties	XXX
26`	coefficients of softening and freezing	XXX
27`	tension strenght	XXX
28`	shear strength	XXX
29`	PLT	XXX
30`	Schmidt hammer test	XXX
31`	velocity of ultrasonic waves	XXX
32`	SDT (for weak rocks)	XXX
33`	abrasivity in micro-Deval	XXX
34`	mass loss in Na.SO.	XXX
35`	modulus of elasticity	XXX
36`	modulus of deformation	XXX
37`	Poisson ratio	XXX
38`	dynamic modulus of deformation	XXX

Table D - Rock utilization and the quality index

ID	Utilization	Photos	Schemes	Maps	Plans
319	... as dimension stone, pavement stone, decoration stone, facing stone, etc.				
320					
321					

Fig. 4: Database system scheme for data storage (Holzer et al., 2009).

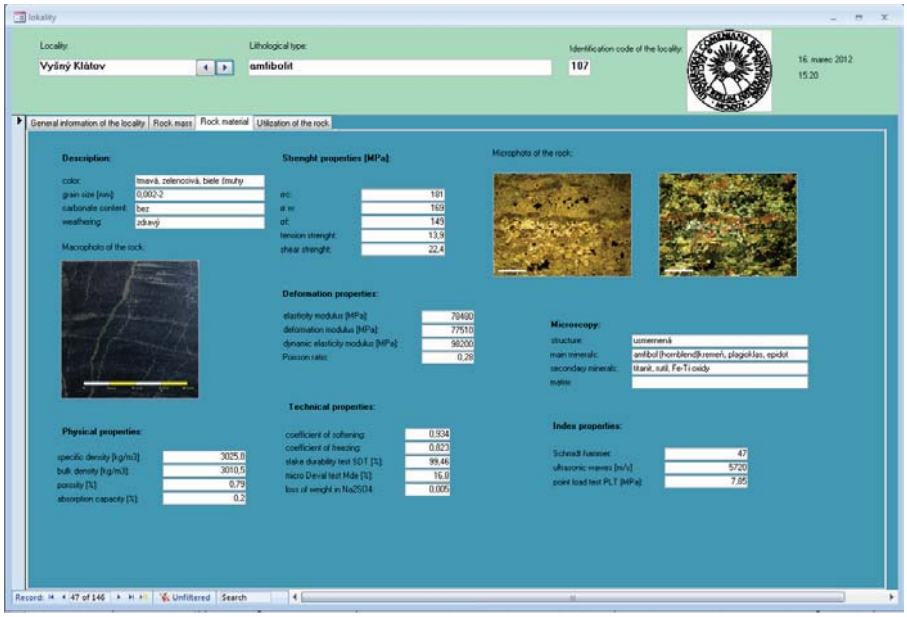

Fig. 5: An example of "user friendly" database using Microsoft Access environment (Holzer et al., 2009).

Spatial and Non-spatial data

Spatial data are bound predominantly to GIS environment. Those data can be presented it two data models. First is vector data model, where all objects are described by point, line or polygon entity and second is raster data model characterized by size of basic cell. Here-in, polygon entity of individual blocks as a vector had been applied to create façade planes.

Non-spatial data can be bound both within GIS environment in the form of attribute tables as well as in database systems. Those data presents huge amount of information from field and laboratory research. For our purposes non-spatial data which are needed for appropriate ashlars replacement can have following structure (modified according to Holzer et al., 2009)):

(1) Position of the object consisting of the object name and district and county name according to the territorial divisions.

(2) The geographical co-ordinates of the JTSK system provide subsequent processing of information for the application of the GIS environment.

(3) The documentation date represents useful information with regard to the history of research.

(4) Façade damages and their causes (see the chapter 2).

(5) Descriptive characteristics of the rock material contain the set of basic data on the character and state of rocks described according the rules of the standard STN EN ISO 14689-1. It concerns:

– Colour of the rock material which predominantly characterizes the weathering degree of the rock;

– Grain size of the rock which is the basic structural characteristic of the rock material. It is described semi-quantitatively according the standard;

– Carbonate content in the rock material which could influence its properties in contact with water. According to the standard three possible states are distinguished: rock without carbonates, carbonate rock and highly carbonate rock;

– Weathering characterizes changes of the rock material, caused by external factors. According to the Technical standard criteria four degrees of rock material weathering are distinguished: fresh – discoloured – disintegrated – decomposed;

– Resistance in water that is one of the most important properties, especially for rocks containing clayey minerals. The water resistance is expressed based on the rock state after a 24 hours submerge in water according to the scale: rock material stable –partly stable – non stable.

(6) Physical properties express the physical state of rock material. They are detected by laboratory tests or by calculation. Within physical properties a Specific rock density (ρ_s in $kg.m^{-3}$, determined according to standard STN EN 1936), Bulk density of dry rock (ρ_d; $kg.m^{-3}$; STN EN 1936), Porosity (n; determined according to formula $n = (\rho_s - \rho_d)/\rho_s$. 100 (%)), Absorption capacity (N; %; STN EN 13755) and Absorption capacity by capillarity (C_f; $g.m^{-2}.s^{0,5}$; STN EN 1925) can be presented.

(7) Deformation properties of rock material express behaviour of rock during its loading and unloading. Deformation properties of rock material are detected by laboratory tests or by calculation. Within deformation properties Modulus of rock elasticity (E; MPa; determined according to standard STN EN 14580), Deformation modulus (E_{def}; MPa; STN EN 14580), Dynamic modulus of rock elasticity (E_{dyn}; MPa; which is calculated from the measured velocity of ultrasonic waves and value of bulk density of rock) and Poisson ratio (υ; non-dimensional; STN EN 14580) can be presented.

(8) Strength properties - express the highest resistance of rock material to actuating strength. Regarding to anisotropy of some types of rocks the orientation of strength in axis x (y) or z is expressed in the corresponding rows. Within strength properties the uniaxial compressive strength on dry samples (σ_{c1}; MPa; STN EN 1926), on saturated samples (σ_{c2}; MPa; samples immersed in water for 48 hours) and on freezing samples (σ_{c3}; MPa; samples after 25 cycles of freezing and thawing) can be presented.

(9) Index properties include mechanical properties of rock material, determined by simple and quick tests. The results of these tests have usually good correlation with conventional strength tests of rock material. Point strength of rock (or Schreiner strength; σ_{vtl}; MPa), Rebound hardness by Schmidt hammer (R; non-dimensional), Velocity of ultrasonic waves spread (v; $m.s^{-1}$) and Point Load Test ($I_{s(50)}$; MPa).

(10) Technical properties of rocks characterize rock material as a material used for various purposes, but foremost in engineering practice. Selection of properties was limited by the possibilities of laboratory testing. Resistance against water expressed by coefficient of softening ($k_1 = \sigma_{c2}/\sigma_{c1}$; non-dimensional), resistance against frost expressed by a coefficient of freezing ($k_2 = \sigma_{c3}/\sigma_{c1}$; non-dimensional), Slake Durability Test (I_d; %), Abrasiveness of rock expressed by coefficient of abrasiveness micro-Deval (M_{DE}; non-dimensional; STN EN 1097-1) and resistance against salt crystallisation ΔM; %; STN EN 12370).

(11) Resources of rock – original or for potential replacement.

(12) Photography of location which contains a general view on location and a more detailed view on the documented part.

(13) Microscopic snap (created at parallel and crossed Nicol prism) with a description of the mineral content and fabric of rock material.

(14) Photography of the glazed surface of the rock sample.

4. Conclusions

The use of the modern approach of façade research and mapping enables to generate a quality façade plan using GIS. This plan provides rich variety of information, especially at the time of reconstruction planning. There are included all the important and useful information about the ashlars material and ornamental façade elements, such as lithological composition, rate of deterioration, weathering forms and as well as the proposal which blocks should by replaced. The modern trend of information electronic processing enables storage of a large set of non-spatial data in a relational database in accordance with modern standards of information technology. At the end, we have the "user friendly" database, which contains all the necessary information.

Acknowledgement

This article was supported as a part of the project: "A comprehensive methodology for the selection and processing of a stone intended for replacements and repairs of the ashlar masonry of historic buildings" (Project No. DF12P01OVV020, supported by the Ministry of Culture of the Czech Republic).

References

Bortz, S. & Wonneberger, B. (1997). Laboratory evaluation of building stone weathering, in: *Degradation of natural building stone. Geotechnical Special Publications 72* (J.F.Labuz ed), ASCE, Reston, pp.85-104.

Doehne, E. (2002) Salt Weathering: A Selective Review, in: *Natural Stone Weathering Phenomena Conservation Strategies and Case Studies. Special Pulications Vol. 205* (S.Siegesmund, T.Weiss & A.Vollbrecht eds), Geological Society, London, pp.51-64.

Goodman, R. (1989) *Introduction to rock mechanics (2nd edition)*. John Wiley & Sons, New York.

Goudie, A. & Viles, H. (1997) *Salt weathering hazards.* John Wiley & Sons, Chichester.

Hofierka, J. (2003) *Geografické informačné systémy a diaľkový prieskum Zeme*. Vysokoškolské učebné texty, Prešovská Univerzita, Fakulta humanitných a prírodných vied, ISBN 80-8068-219-4.

Holzer, R., Laho, M., Wagner, P. & Bednarik, M. (2009) Inžinierskogeologický atlas hornín Slovenska, 1. vyd., Bratislava, Štátny geologický ústav DionýzaŠtúra, pp. 532.

Johannesson, B. (2010) Dimensional and ice content changes of hardened concrete at different freezing and thawing temperatures. *Cement & Concrete Composites*, 32, pp.73-83.

Kovářová, K., Bednarik, M., Holzer, R. & Laho, M. (2011) Methodology of selection of replacement building stone for the purpose of reconstruction of historical monuments, in: *Human, building and landscape planning 5* (Z.Kramářová, A.Mansfeldová & I.Vorel eds), Faculty of Civil Engineering CTU, Prague, pp.166-176.

Laho, M., Bednarik, M. & Holzer, R. (2010) Nové trendy v dokumentácii a tvorbe databázy stavebných blokov presbytéria Konkatedrály sv. Martina v Bratislave, in: *Geotechnika Roč. 13*, č. 3-4, pp. 14-19.

Maguire, D.J., (1991) An overview and definition of GIS. in: *GIS – principles and applications* (Maguire, DJ., Goodchild, M.F., Rhind, D.W. eds.), Essex: Longman Scientific and Technical, pp. 9 – 20.

Ollier, C. (1969) *Weathering.* Oliver & Boyd, Edinburgh.

Smith, B.J., Whalley, B. & Magee (1993) Assessment of building stone decay: a geomorphological approach, in: *Stone cleaning and the nature, soiling and decay mechanism of stone* (R.G.M.Webster ed), Donhead Publishin Ltd., London, pp.249-257.

Thomachot, C. & Jeannette, D. (2005) Evolution of the petrophysical properties of two types of Alsatian sandstone subjected to simulated freeze-thaw conditions, in: *Natural Stone Weathering Phenomena Conservation Strategies and Case Studies. Special Pulications Vol. 205* (S.Siegesmund, T.Weiss & A.Vollbrecht eds), Geological Society, London, pp.19-32.

Vician, E., Ďurkovič & Svetko (1957) Stavebné, reštauračné práce a úpravy okolia Bratislavského dómu. Archív Pamiatkového ústavu Bratislava.

Warke, P. (1996) Inheritance effects in building stone decay, in: *Processes of Urban Stone Decay* (B.J.Smith & P.A.Warke eds), Donhead Publishin Ltd., London, pp.32-43.

Williams, R. & Robinson, D. (2001) Experimental frost weathering of sandstones by various combinations of salts. *Earth Surface Processes and Landforms*, 26, pp.811-818.

Winkler, E. (1997) *Stone in Architecture. Properties, Durability (3rd edition)*. Springer-Verlag, Berlin.

STN EN ISO 14689-1: Geotechnický prieskum a skúšky. Pomenovanie a klasifikácia skalných hornín. Časť 1: Pomenovanie a opis, 2003.

STN EN 1097-1: Skúšky na stanovenie mechanických a fyzikálnych vlastností kameniva. Časť 1: Stanovenie odolnosti voči obrusovaniu (mikro-Deval), 1998.

STN EN 1926: Skúšky prírodného kameňa. Stanovenie pevnosti v tlaku.2002.

STN EN 1936: Skúšky prírodného kameňa. Stanovenie skutočnej a zdanlivej objemovej hmotnosti a celkovej a otvorenej pórovitosti, 2002.

STN EN 12370: Skúšky prírodného kameňa. Stanovenie odolnosti proti kryštalizácii solí, 2002.

STN-EN 13755: Skúšky prírodného kameňa. Stanovenie nasiakavosti pri atmosferickom tlaku, 2003.

STN EN 14580: Skúšky prírodného kameňa. Stanovenie statického modulu pružnosti, 2005.

STN EN 1925: Skúšky prírodného kameňa. Stanovenie súčiniteľa nasiakavosti kapilaritou, 2002.

18th International Conference
ENGINEERING MECHANICS 2012
Svratka, Czech Republic, May 14 – 17, 2012

pp. 97–101
Paper #131

FLOW VISUALIZATION IN CONTROL VALVE WITH PROFILING CONE

L. Bednář[*], L. Tajč[**], M. Miczan[***], L. A. Feldberg[****]

Abstract: *The results from aerodynamic research on the model control valve with profiling cone of steam turbine KODA are presented. Experimental work was realized in the research laboratory CKTI Sankt Petersburg. Pressure pulsations under cone in a big range of operational parameters were measured. Measurements were realized by means of optical interferometry.*

Keywords: ***valve, profiling cone, visualization.***

1. Introduction

The result of the requirements to build turbines operated under constantly increasing admission pressures and higher unit ratings is the necessity to steer the momentary power of the turbine via control valves with relief. As of now, ŠKODA POWER a. s. does not yet offer these valve types in its product portfolio. After the rather limited success of the application of licence to a relief valve for the 1000 MW turbine, the topics of operational reliability and shape of the control valve cone have received systematic attention. Individual variants of the potential valve designs are subject to thorough testing at various laboratory stands. Among the highly useful benefit is the possibility to visualise the flow inside the valves that is realised by CKTI in St. Petersburg under the supervision of ŠKODA POWER (Feldberg 2005). Calculations of flow inside the valves are useful as well (Matas 2004).

Numerous experiments have indicated that designs using a single central relief port are not suitable. New publications (Zarjankin & Simonov 2005) recommend that the cone use a perforated wall. In the valve for the 1000 MW turbine, the perforated ring – damper assisted in the suppression of extreme pressure pulsation during startup at high pressure loss with elevated local values of Mach numbers. A disadvantage of the damper is that it is present also at rated operating conditions. This disadvantage could be removed by controlled steam discharge through the perforated wall of the cone.

The CKTI laboratory has carried out tests to verify the shaped valve cone with relief holes. The needs of the visualisation process required that a desk model of the valve cone be prepared, including the holes. Visualisations were realised using the shadowing method in a Töpler machine and using a Mach – Zehnder interferometer. Pressure pulses are evaluated according to the change in the local optical signal. The relative change of specific gravity is proportional to the relative change of light intensity:

$$\frac{\Delta\rho}{\rho} = \frac{\lambda}{\pi L K \rho} \cdot \frac{\Delta J}{J_0}, \tag{1}$$

ΔJ, J_0 change of intensity in the interference image and its basic value,

[*] Ing. Lukáš BEDNÁŘ: ŠKODA POWER a. s., R&D/EV, Tylova 1/57; 328 00 Plzeň; CZ, e-mail: lukas.bednar@doosan.com

[**] Ing. Ladislav TAJČ, CSc.: ŠKODA POWER a. s., R&D/EVP, Tylova 1/57, 328 00 Plzeň, e-mail: ladislav.tajc@doosan.com

[***] Ing. Martin MICZÁN: ŠKODA POWER a. s., R&D/EVP, Tylova 1/57; 328 00 Plzeň; CZ, e-mail: martin.miczan@doosan.com

[****] Ing. Lev Avramovič FELDBERG, NPO CKTI; Atamanskaya str. 3/6, 191167 St. Petersburg; Russia; e-mail: l_feldberg@mail.ru

$\Delta\rho$, ρ change of specific gravity and specific gravity of steam,

λ, K wavelength of light and constant $k = 22.7 \cdot 10^{-5}$ m^3/kg,

L width of work section.

The following equation governs pressure pulsation:

$$\frac{\Delta p}{p} = \frac{T}{R} \cdot \frac{\Delta \rho}{\rho}, \tag{2}$$

T temperature,

R gas constant.

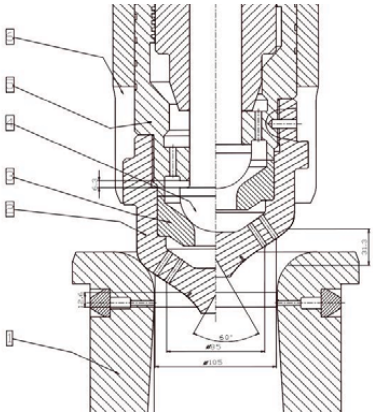

Figure 1: Actual rendering of a cone in a relief valve

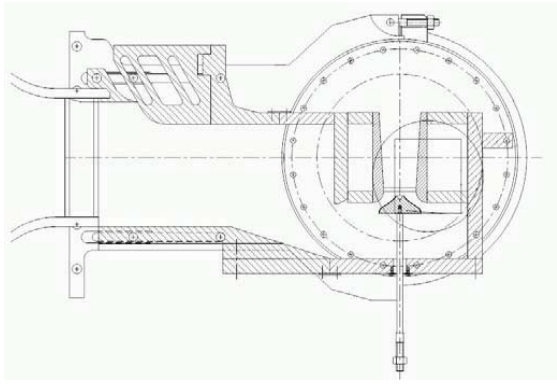

Figure 2: Model of a valve featuring a shaped cone and relief port

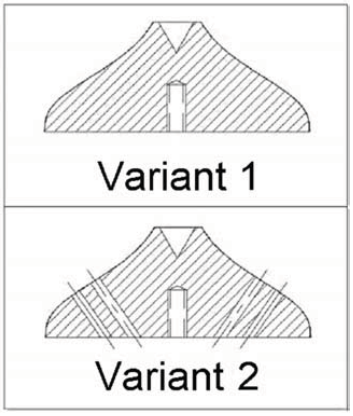

Figure 3 Tested variants of the cone

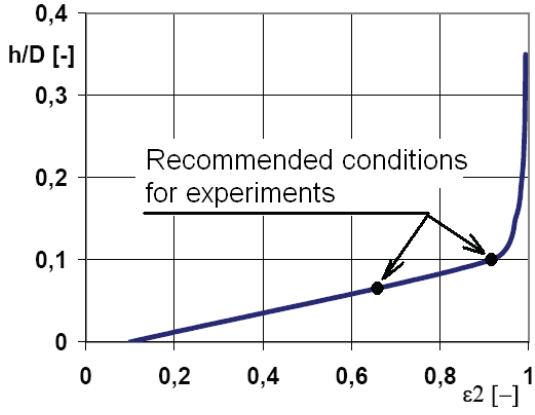

Figure 4: Operational characteristics of the valve, MEI

2. Design of Experiment and Valve Model

The design of the valve assumed for verification by experiment is shown in Figure 1. The cone profile has been prepared using information from the MEI (Moscow Power Engineering Institute). The model for visualisation of flow requires the transition and 3D realisation of the part of interest into a 2D system. For that reason, the number of holes in the model was reduced to preserve the proportional flow area relevant to the neck area. The model of the cone has been simplified against the original

part – see Figure 2. Pressure above the cone is assumed equal to that at the valve intake port. The tested variants are shown in Figure 3. While the first variant shows the cone without perforation, the second models two rows of relief holes. The wind tunnel at CKTI allows the modelling of pressure situations in the valve ranging from $p_2/p_0 = 0.27 \div 0.97$, which corresponds to relative cone lift $h/D_0 = 0.05$ and $p_2/p_0 = 0.66$ as well as $h/D_0 = 0.1$ with $p_2/p_0 = 0.92$.

3. Flow Visualisation

Visualisation of flow using the shadow method has been realised for a wide variety of operating modes. Figure 5 provides an overview of three pressure ratios and lift for variant 1 (cone without perforation). Low lift and low pressure ratio delivers irregular distribution of flow fields. At one side of the cone, separated flow occurs while at the other side of the cone, flow attraction to the cone prevails.

As the lift and pressure ratio increases, the flow fields become balanced and the flow adheres to the cone constantly. The entire area under the cone becomes filled at a lift $h/D_0 = 0.11$ and pressure ratio $p_2/p_0 = 0.87$.

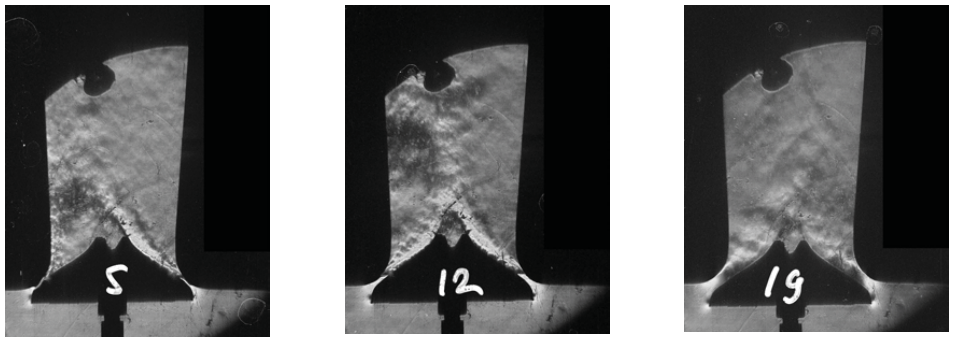

Var.1.: h/D_0=0.02, p_2/p_0=0.35 *Var.1.: h/D_0=0.06, P_2/P_0=0.41* *Var.1.: h/D_0=0.11, P_2/P_0=0.87*

Figure 5: Visualisation of flow under the cone without perforation

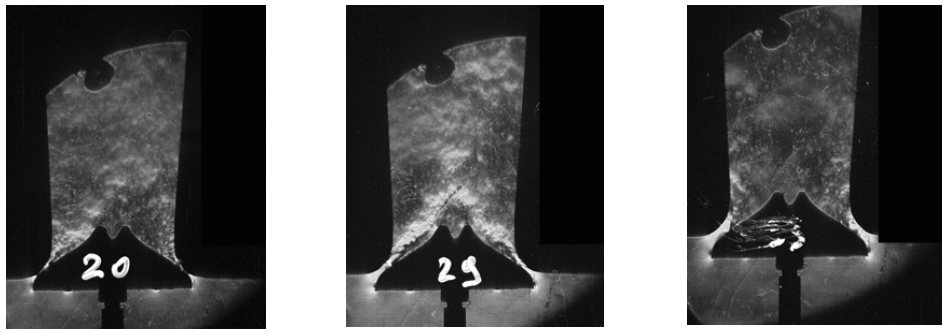

Var.2.: h/D_0=0.01, P_2/P_0=0.35 *Var.2.: h/D_0=0.06, P_2/P_0=0.41* *Var.2.: h/D_0=0.09, P_2/P_0=0.75*

Figure 6: Visualisation of flow under the cone with perforation

The effects of the relief holes can also be inferred from a series of images of flow fields in Figure 6. Relief holes promote stabilisation of flow fields in separating the flow from the cone. The flow lines from the holes possess an ejection effect that leads to partial intake of steam from the environment. A certain asymmetry in specific gravity distribution shows at $h/D = 0.06$ and $p_2/p_0 = 0.41$. However, symmetrical distribution of pressure remains preserved on the cone surface.

4. Measuring of Pressure Pulses

Interferometric measuring enables the assessment of velocity fields, Mach numbers, and changes in pressure pulsation in the location of interest. Locations of pressure pulsation measurement are shown in Figure 7. Assumed are measuring locations in the valve axis under the cone as well as locations across the diffuser neck. Distribution of Mach numbers for cones with and without relief, respectively, is shown in Figure 8. They are compared at identical valve lift $h/D_0 = 0.02$ and pressure ratio $p_2/p_0 = 0.92$. The maximum velocities occur on the surface of the diffuser seat. In cones without relief, a considerable loss of velocity occurs in the central section of the diffuser. Relief holes assist in balancing the velocity in the central section of the diffuser channel. The higher velocities in the seat area assist in limiting the potential separation of flow from the diffuser wall, which promotes the efficiency of the diffuser.

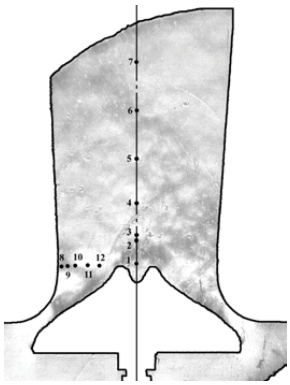

Figure 7: Locations for measuring pressure pulsation

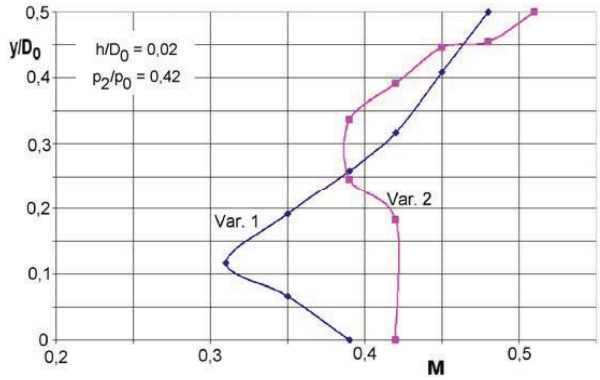

Figure 8: Distribution of Mach numbers in the neck of the diffuser for two variants of cone design

A comparative study of the frequency spectra at light intensity acquired via the shadow and interference methods show higher sensitivity when the interference method is used. The higher sensitivity shows especially in the low frequency range. The interference method looks at changes in specific gravity while the shadow method records changes in the gravity gradient. A comparison of the light intensity spectra in response to frequency taken in location 3 under the cone is shown in Figure 9. Individual peaks of discrete frequencies correspond to the inherent frequencies of the system. Light intensity records taken in the axis under the cone (locations 0 ÷ 7) are shown in Figure 10. Thus a wide band of vibration with the values made visible at inherent frequencies is confirmed. Pulsation in the valve inlet chamber (location 0) are a digit place lower than in the area under the cone. The distribution of the integral value of pulsation intensity in relation to the value in location 1 is shown in Figure 11. As the distance progresses, pulsation intensity becomes up to 3.5 times stronger. Maximum values occur where the flow of media from both sides of the cone coalesce. In the analysed model, the distance was 30 mm from the bottom of the cone.

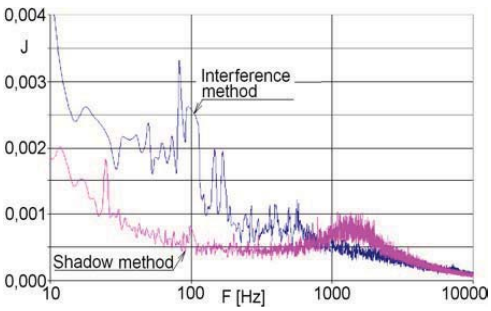

Figure 9: Measuring of pulsation using various optical methods

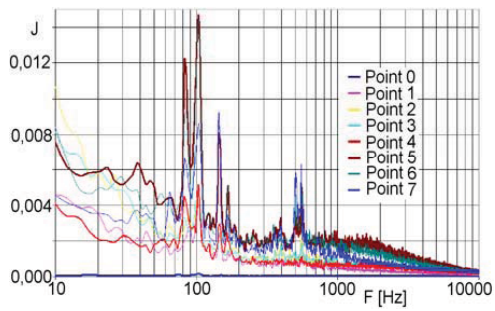

Figure 10: Pulsation spectra in the axis under a cone without relief

Attention was also given to the effect of cone perforation to the intensity of pulsation in the flow. Figure 12 brings a comparison of the pulsation spectra in the neck of the diffuser used in cones with and without perforation, respectively. Perforation clearly assists in damping the pressure pulsation. In the frequency range 90 ÷ 100 Hz, the damping ratio is 10 ÷ 15; in the frequency range 100 ÷ 1000 Hz, the damping ratio is 5 ÷ 10, and in the frequency range 1000 ÷ 10000 Hz the damping ratio is 3 ÷ 5. The assessment of pressure pulsation intensity shows that it is present in various sections of the flow field in the range from 2 to 10%.

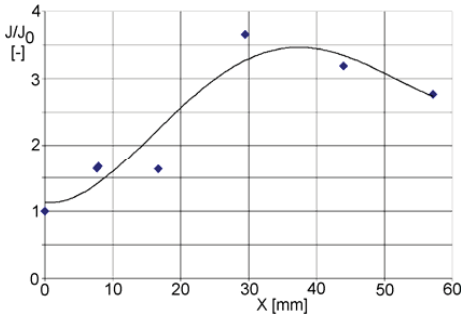

Figure 11: Distribution of pulsation intensity along the channel axis

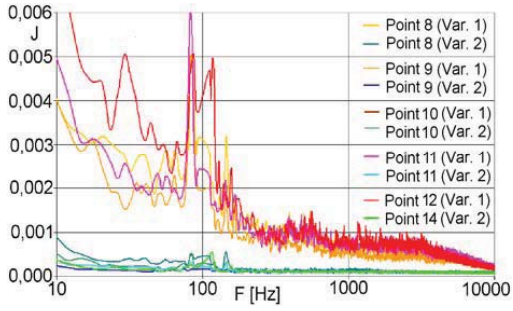

Figure 12: Pulsation spectra in the diffuser neck at cones with and without relief, respectively

5. Conclusions

Flow under the cone of the control valve having the shape as suggested by the MEI may, under certain pressure conditions and at low lift, be unstable with differential flow arrangement on the opposite sides of the cone.

Cone perforation assists in stabilising the flow in the diffuser and under the cone. It also provides symmetrical flow field in the surroundings of the cone. The velocities become balanced in the neck of the diffuser. Flow separation from the cone is evident.

Pressure pulsation ranging from 2 to 10% is present in a non-relief cone.

Maximum pulsation occurs in the area under the cone where the flow from both sides of the cone amalgamates.

Cone perforation assists in damping the pressure pulsation. Damping ratio amounts to 10 to 15 in the low frequency range.

References

Фелдберг Л. А. (2005) Исследование аэродинамических характеристик разгруженного регулирующего клапана на оптическом стенде, *счет ЦКТИ*.

Matas R. (2004) Numerical simulation of flow in shape modifications of control valves in steam turbines for supercritical steam parameters, *Research report NTC Pilsen*.

Зарянкин А. Е. & Симонов Б. М. (2005) Регулирующие и стопорно-регулирующие клапаны паровых турбин, *Издательство МЭИ*.

18th International Conference
ENGINEERING MECHANICS 2012
Svratka, Czech Republic, May 14 – 17, 2012

pp. 103–108
Paper #27

EFFECT OF PATCH REPAIR ON FATIGUE BEHAVIOR

M. Benachour[*], N. Benachour[**], F.Z. SERIARI[***], M. Benguediab[****]

Abstract: *In this paper, effect of patch repair on fatigue crack growth was investigated. In additional loading parameters associated with patch repair was studied in order to shown theirs influence on fatigue life and fatigue crack growth rate.*

Keywords: ***Composite patch repair, aluminum alloy, fatigue crack, stress ratio.***

1. Introduction

During navigation, aircrafts are subject to cyclic loading when damage was created in theses structures. In these situation fatigue problems become an important topic in the maintenance of damaged aircraft structures. Efficient repair technique, called composite patch repair, was used to reinforce the damaged (cracked) structures and extend the service life of aging aircraft. This technique offers significant advantages over traditional repair methods (riveting, fastening, welding). Repair of cracked components by an adhesively bonded composite patch has gained acceptance in aerospace structures (Baker et al., 2002). Beneficial effects of bonded repair can be summarized as: (1) reduction of the stress field near the crack, (2) leads to retardation or complete arrest of the crack growth, (3) provides a high structural efficiency and extends the life of cracked structural components at an economical cost. Investigation into the crack growth behavior of the bonded patch repaired structures has been the primary focus of the majority of previous studies (Sabelkin et al., 2006).

In experimental fatigue investigation conducted by Sabelkin et al. (2006) performed on 2024 T3 aluminum alloy and patched Boron/epoxy composite patch material, fatigue results shown that bonded composite patch repair increase fatigue life about fivefold in the case of stiffened panels while it increased about ten fold in the case of un-stiffened panels. In other work of Sabelkin et al. (2007), experimental and analytical investigation was conducted on 7075 T6 aluminum alloy panel repaired with one sided adhesively bonded composite patch. In this study, crack growth rate was primarily dominated by stress intensity factor of the repaired panel near the bonded patch and the bonded patch repair of a cracked panel provides a considerable increase in the residual strength as well as fatigue life. In review paper established by Jones et al. (2004) revealed that for composite repairs to through cracks in thin sheets the growth of small to medium length cracks, that have low to mid range ΔK's, follows the law proposed by Frost & Dugdale (1958) and Frost et al. (1974). Whenever to the precedent conclusion is valid and bending effects are negligible then the effect of the patch is primarily due to the reduction of the net section stress. In the investigation of Hosseini-Toudeshky (2006), it is experimentally and numerically shown that the crack growths non-uniformly from its initial position along the thickness of a single-side repaired panel and the crack-front shape are an important parameter influencing the stress intensity factor and crack propagation rate. In study conducted by Ong & Shen (1992), various factors affecting the repair of 2.5 mm thick 2024-T3

[*] Dr. Mustapha BENACHOUR, MC_A : IS2M Laboratory, Mechanical Engineering Department, Faculty of Technology, University of Tlemcen, BP 230; 13000, Tlemcen; Algeria (DZ), e-mail: mbenachour_99@yahoo.fr

[**] Ms. Nadjia BENACHOUR, MA_A : IS2M Laboratory, Department of Physics, Faculty of Sciences, University of Tlemcen, BP 230; 13000, Tlemcen; Algeria (DZ), e-mail: nbenachour2005@yahoo.fr

[***] Ms. F.Z. SERIARI, PhD : IS2M Laboratory, Mechanical Engineering Department, Faculty of Technologie, University of Tlemcen, BP 230; 13000, Tlemcen; Algeria (DZ). e-mail: bmf_12002@yahoo.fr

[****] Pr. Mohamed BENGUEDIAB, LMPM Laboratory, Mechanical Engineering Department, Faculty of Technology, University of Sidi Bel Abbes; 22000, Tlemcen; Algeria (DZ), e-mail: benguediab_m@yahoo.fr

aluminium plates have been investigated, especially patch materials. Effect of patch materials on FCG was studied namely boron/epoxy patch and graphite/epoxy patch. Modified walker equation was used to calculate fatigue crack growth. Results show that both boron/epoxy and graphite/epoxy composite patches attain sufficiently high fatigue lives to meet the damage tolerance requirement.

Fatigue behavior of patched aluminum alloys 2024 T3 and 7075 T6 was investigated by Duquesnay et al. (2005). Under constant amplitude loading, effect of stress ratio, R (R=-1, 0, 0.5), on stress life behavior was highlight. At same cycles of failure ($\approx 10^5$ cycles), an increasing in maximum shear stress was shown in increasing of stress ratio for the both aluminum alloys. In the same study, it was shown that patched bare 2024 T3 aluminum alloy present a good resistance comparatively to the unpatched bare. In recent work (Pastor et al., 2009), lifetime extension of the reinforced specimens is significant assuming the same load level for patched and unpatched specimens.

2. Fatigue crack growth behavior

2.1. Material and stress intensity factor for unpatched and patched specimen

Materials used in this study are 2024 T351 and 7050-T74 aluminum alloys obtained on rolled plates in L-T orientation. Basic mechanical properties for this material are presented in Table 1 (see Afgrow database). Mechanical properties of composite patch (Graphite/Epoxy) are indicated in Table 2. Simulation of fatigue crack growth in mode I used thin middle tensile plate specimen M(T) subjected to uniform tensile cyclic load. Geometrical parameters of tested specimens are indicated in Fig. 1.

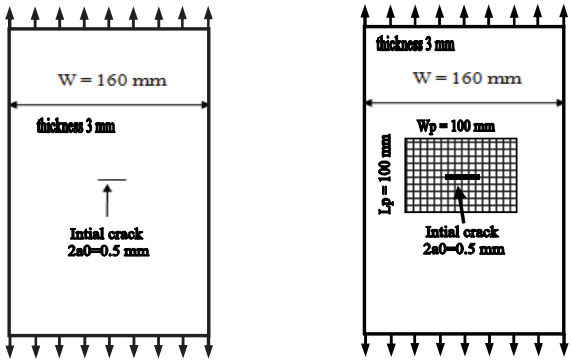

Fig. 1: M(T) specimen detail a) Unpatched specimen b) Patched specimen

Table 1. Mechanical properties of 2024 T351 Al-Alloy

E (GPa)	$\sigma_{0.2}$ (MPa)	K_{IC} (MPa.m$^{1/2}$)	K_C (MPa.m$^{1/2}$)	ν
73.08	372.32	37.36	74.72	0.3

Table 2. Mechanical properties of Graphite Epoxy

E_L (GPa)	E_T (GPa)	G_{XY} (GPa)	ν
172.37	10.342	4.826	0.3

The stress intensity factor for the studied specimen implemented in AFGROW code depends on several parameters is written bellow:

$$\Delta K = \sigma\sqrt{\pi a}.\beta(a/w) \tag{1}$$

Function β is the geometry correction factor, proposed by Newman (1976), is expressed below :

$$\beta = \left[1 - 0.025\ \lambda^2 + 0.06\ \lambda^4\right]\left[\sec\left(\pi a/w\right)\right]^{0.5} \qquad (2)$$

where λ=2a/w and a/w ≤ 0.5

In patched specimen function β was modified and depend on presence of composite patch and width of the patch and numbers of plies (Wp = 100 mm, 8 plies). Variation of recalculated function β is given on Fig. 2.

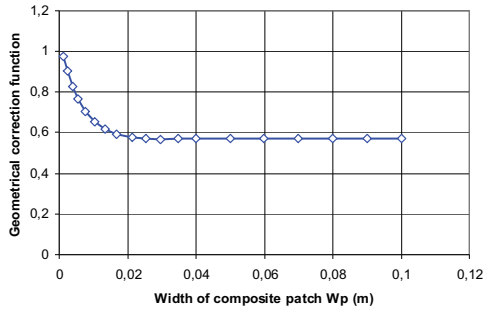

Fig. 2: Geometrical correction function β for patched M(T)specimen

2.2 Fatigue crack growth model

AFGROW code developed by NASA (Harter, 2006) is used for simulation of fatigue crack growth. In NASGRO model used in this study, is expressed bellow:

$$\frac{da}{dN} = C\left[\left(\frac{1-f}{1-R}\right)\Delta K\right]^n \frac{\left(1-\frac{\Delta K_{th}}{\Delta K}\right)^p}{\left(1-\frac{K_{max}}{K_{crit}}\right)^q} \qquad (3)$$

f presents the contribution of crack closure and the parameters C, n, p, q were determined experimentally and ΔK_{th} is the crack propagation threshold value of the stress–intensity factor range. In constant amplitude loading, function f was determined by Newman (1984). Parameters of NASGRO model for the studied materials are presented in Table 3.

Table 3. Parameters of crack growth model for 2024 T351

σ_{max}/σ_0	C	n	p	q
0.3	$1{,}7073e^{-10}$	3.353	0. 5	1

3. Results & discussions

Patched and unaptched M(T) specimen in L-T orientation are subjected to a constant cyclic loading (σ_a=100 MPa) under variation of stress ratio. The K_{max} criterion was adopted for the limit of crack growth. Fig. 3 and Fig.4 showed respectively the effect of stress ratio on fatigue life for unpatched and patched specimen. For two configuration specimens, stress ratio presents the same effects. It is noticed that an increasing in stress ratio increase the fatigue life. It is found that fatigue life of repaired specimen using eight (08) plies of composite patch is affected highly at high stress ratio (i.e R = 0.5) comparatively to the low stress ratio. In all stress ratios, Fatigue life ratio patched/unpatched M(T) specimen is about twice (2) for crack length greater than 10 mm. In experimental fatigue life results (Seo & Lee, 2002) performed on CCT specimen at R =0.1, fatigue life ratio is about 3.5.

The fatigue crack growth rates for different stress ratio in unpatched specimens are shown on Fig. 5. Curves illustrate a general increase in da/dN with R. An important effect of R has been observed clearly for this material at high ΔK stress intensity factor. Also the same effect was shown in patched specimen. It is noticed that at same stress ratio, FCGRs for patched and unpatched specimen have the same slope and threshold stress intensity factor was influenced by patch repair (Fig. 6). Result shown that patched M(T) specimen crack at 5.6 MPa(m)$^{1/2}$ but for unpatched case, M(T) specimen crack at 2.8 MPa(m)$^{1/2}$ at zero stress ratio. For positive stress ratio, cracks grow at the same stress intensity.

Fig. 7 shows the comparison of predicted fatigue crack growth between patched specimen repaired by Graphite/Epoxy and unpatched specimen. It was showing clearly that patch repair retard crack growth. Aslo, it was noticed that after 10 mm of crack length, the difference in crack growth for the botch configuration specimen (Fig. 1) remains almost constant and between initial and 10 mm crack length, da/dN present a nonlinear variation.

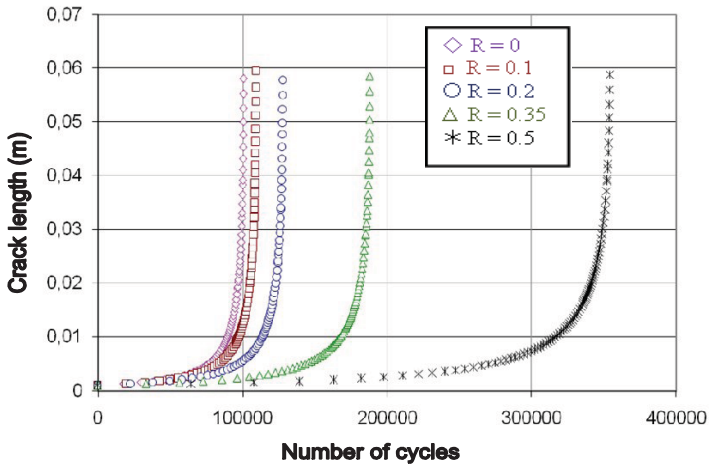

Fig. 3: Effect of stress ratio on fatigue life for unpatched M(T) specimen

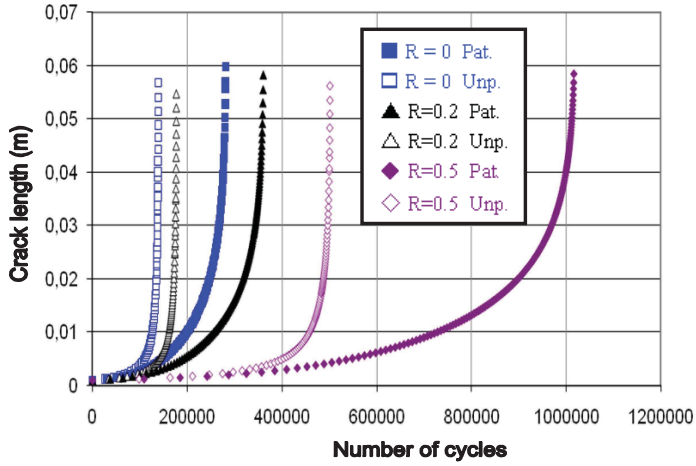

Fig. 4: Comparison and effect of stress ratio "R" on fatigue life for patched "Pat."and unpatched "Unp" M(T) specimen

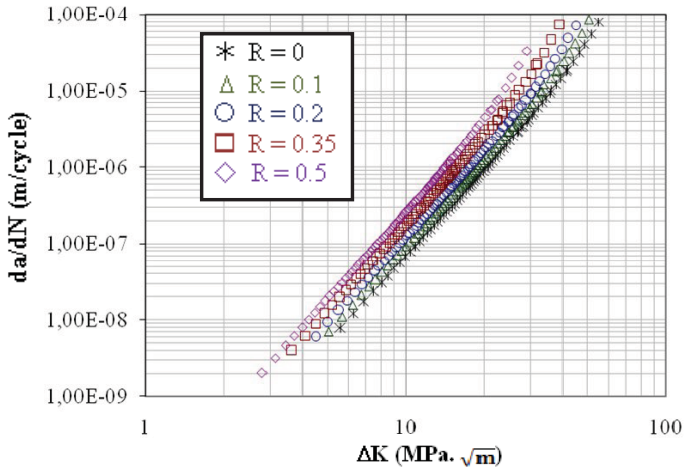

Fig. 5: Effect of stress ratio on FCGRs for unpatched M(T) specimen

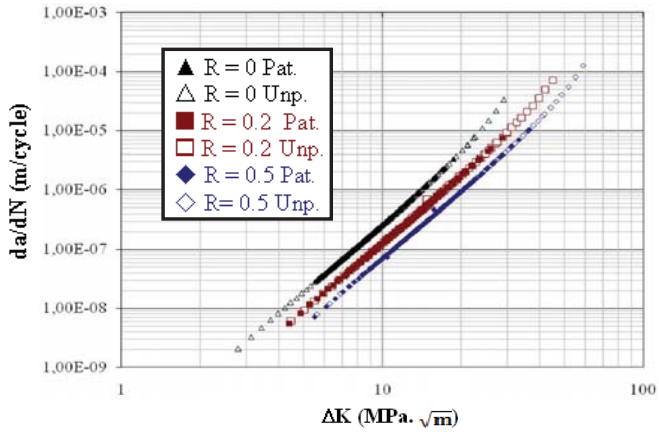

Fig. 6: Effect of stress ratio "R" on FCGRs for patched "Pat." And unpatched "Unp"M(T) specimen

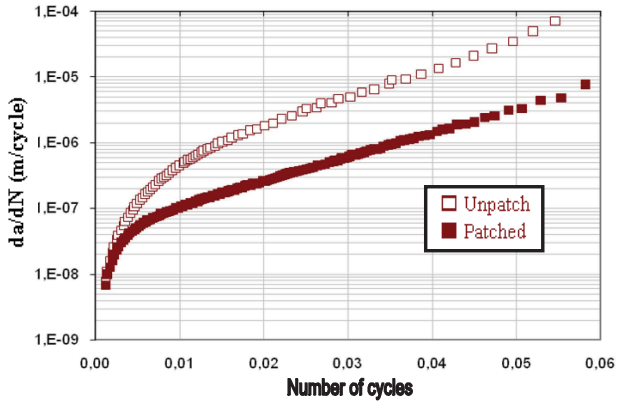

Fig. 7: Effect of patched and unpatched specimen on FCGRs performed on 2024 T351 Al-alloy M(T) specimen

4. Conclusions

Fatigue crack growth behavior of cracked plate with bonded composite patch repair was investigated through empirical study with numerical integration. This study involved fatigue behavior of 3 mm thin specimens with center crack M(T) unrepaired and repaired with four directional graphite/epoxy patch. Conclusions drawn from this study are cited below:

- Fatigue life for repaired and unrepaired specimen was affected by stress ratio.
- In repaired specimen fatigue life was affected highly at high stress.
- Fatigue crack growth rate (FCGR) increased by increasing in stress ratio.
- At the same stress ratio, patch repair affect threshold stress intensity factor and initial crack growth.
- Fatigue crack growth rate was compared for repaired and unrepaired specimen and shown beneficial effects of composite patch to extend the service life of damaged structures.

Acknowledgement

IS2M Laboratory was acknowledging for funding all study of team members.

References

Baker, A.A., Rose, L.R.F., Jones, R. (2002) *Advances in the bonded composite repair of metallic aircraft structure*. Elsevier, Amsterdam.

Duquesnay, D.L., Underhill, P.R., Britt, H.J. (2005) Fatigue failure od adhesively patched 2024 T3- and 7075-T6 clad and bare aluminium alloys. *Fatigue Fract. Engng Mater. Struct.*, 28, pp 381-389.

Frost, N.E., Dugdale, D.S. (1958) The propagation of fatigue cracks in test specimens, *Journal Mechanics and Physics of Solids*, 6, pp 92-110.

Frost, N.E., Marsh, K.J., Pook, L.P. (1974) *Metal Fatigue*, Clarendon Press, Oxford.

Hosseini-Toudeshky, H. (2006) Effects of composite patches on fatigue crack propagation of single-side repaired aluminum panels. *Composite Structures*, 76, pp 243-251.

Harter, J.A. (2006) *AFGROW users guide and technical manual: AFGROW for Windows 2K/XP*. Version 4.0011.14, Air Force Research Laboratory.

Jones, R., Barter, S.A., Molent, L., Pitt, S. (2004) Crack patching: an experimental evaluation of fatigue crack growth, *Journal of Composite Structures*, 67, 2, pp 229-238.

Newman, J.C. (1976) *Predicting failures of specimens with either surface cracks or corner crack at holes*. TN D-8244, NASA Langley Research Center, SA.

Newman, J.C. (1984) A crack opening stress equation for fatigue crack growth". International Journal of Fracture, 24, 3, R131-135.

Ong C.L., Shen, S.B. (1992) The reinforcing effect of composite patch repairs on metallic aircraft structures". *International Journal of Adhesion & Adhesives*, 12, 1, pp 19-26.

Pastor, M.L., Balandraud, X., Robert, J.L., Grédiac, M. (2009) Lifetime prediction of aluminium structures reinforced with composite patches". International Journal of Fatigue, 31, pp 850-858.

Sabelkin, V., Mall, S., Avram, J.B. (2006) Fatigue crack growth analysis of stiffened cracked panel repaired with bonded composite patch. *Engineering Fracture Mechanics*, 73, pp 1553-1567.

Sabelkin, V., Mall, S., Hansen, M.A., Vandawaker, R.M., Derriso, M. (2007) Investigation into cracked aluminum plate repaired with bonded composite patch. *Composite Structures*, 79, pp 55-66

Seo Dae-Cheol, Lee Jung-Ju (2002) Fatigue crack growth behavior of cracked aluminum plate repaired with composite patch". *Composite Structures*, 57, pp. 323-330.

18th International Conference
ENGINEERING MECHANICS 2012
Svratka, Czech Republic, May 14 – 17, 2012

pp. 109–116
Paper #141

SHORT-SPAN RAILWAY COMPOSITE BRIDGES:TEST AND RATING

J. Benčat*

Abstract: *This paper presents an overview of the in–service performance assessments of a steel–concrete composite (SCC) short–span railway bridge superstructure. A field load testing and visual inspections for the assessments of the SCC bridge durability under an actual service environment were conducted. The test result indicates that the SCC bridge superstructure has no structural problems and is structurally performing well in–service as expected. The results may provide a baseline data for future field SCC bridge load bearing capacity assessments and also serve as part of a long–term performance of SCC bridge superstructure.*

Keywords: *Dynamics of bridges, load bearing capacity assessments, bridges static and dynamic loading test, railway steel–concrete composite bridges, DLF, spectral analysis.*

1. Introduction

To investigate its in–service performance, field load testing was conducted under an actual service environment. Field load testing is an attractive tool for re–evaluating the capacity rating of bridges. For the first time, the capacity rating for an SCC railway bridge under in–service environment is calculated and discussed with various existing methods for the rating factors such as allowable stress and DLF (Baťa, et al.1994; Benčat, 2003). As the SCC railway bridge superstructure was instrumented, the real load test was conducted (Benčat, 2007) under similar loading and weather conditions as during initial field loading tests in the 2002 (Benčat, 2003). This was done to ensure the structure's integrity before opening it to the public, to establish base line conditions for a future in–service field load test program, and to compare actual performance with theoretical calculations. After the initial field load test, the follow–up field load test was conducted to ensure that the SCC railway bridge structure was behaving satisfactorily and to check out any signs of degradation. The SCC bridge superstructure was tested using conventional tractile locomotion E 662.2. The results of this test were later used to evaluate bridge in–service bearing capacity.

2. The bridge case – study

The short–span railway bridge on *ŽSR* (*Slovak Republic Railways*) line *Žilina – Čadca* (Fig. 1) was built in 2002. The bridge load bearing structure is created by one span two concrete plates reinforced by rolled **I** sections. Each line direction is supported by two single span plates which are shifted one another with distance 2,425 m. Length of the span is 13 m and width of structure is 9,8 m. Thicknesses of the plates are 0,82m and they are increased on the border to shape **II** – Fig. 2. The soil conditions for foundations of the two abutments are very similar on both riversides the resistant substratum (gravel and sandy gravel). The bridge uppers structure creates continuous track with gravel bed (Bencat, 2002, 2007).

Foundations of the supports are reinforced concrete blocks on the same substratum as the both abutments. For both dilated bridge parts supports are reinforced concrete gravity abutments. Fig. 2 shows the bearing structure cross–section and Fig. 3 depictures schematic plan view of the bridge plates.

* Prof. Ing. Ján Benčat, CSc.: Structure Mechanics Dept., CEF,University of Žilina, University Street 8215/1; 010 26, Žilina; SK, e-mail: jan.bencat@gmail.com

Fig. 1: View of the short–span bridge on ŽSR line Žilina – Čadca

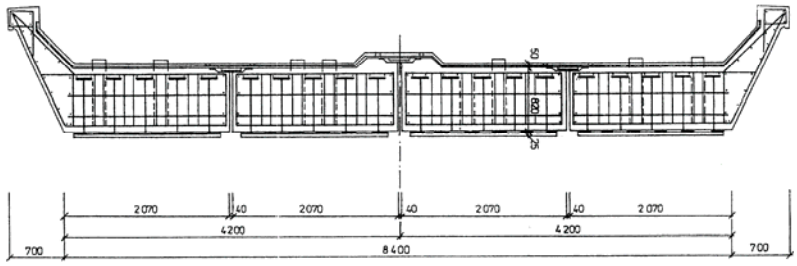

Fig. 2: Cross – section of the load bearing structure

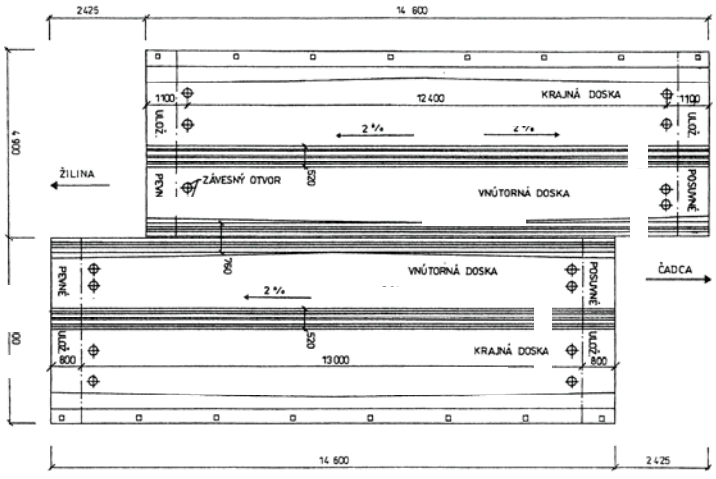

Fig. 3: Schematic plan view of the load bearing structure

3 Finite Element Model Analysis

3.1 Natural frequencies

Bridge static and dynamic numerical analysis was performed using the *IDA NEXIS software*. The 3D global model incorporated all primary and secondary load – carrying members in the bridge were excluded at this stage. Computing system enable to create slab – beam stiff connection. FE model of bridge structure was composed from two main plate using 2D elements stiff connected on beam elements with **I** shape cross section (reinforcement) respecting bridge load bearing structure geometry. Also supports were modelled respecting bridge bearings positions – one side stiff joints and other side slip joints (SUDOP Košice, 2001; The Steel Construction Inst., 20014; Slovak Standard 73 6203).

For the static and dynamic FEM computations the bridge superstructure (continuous track with gravel bed) is considered as a continuous distributed mass and locomotive type E 669.2 is considered as a singular mass. The simplified FE model consists of 1758 joints, 1904 beam elements and 1503 shell elements. Rendered computational model layout is presented on Fig. 4.

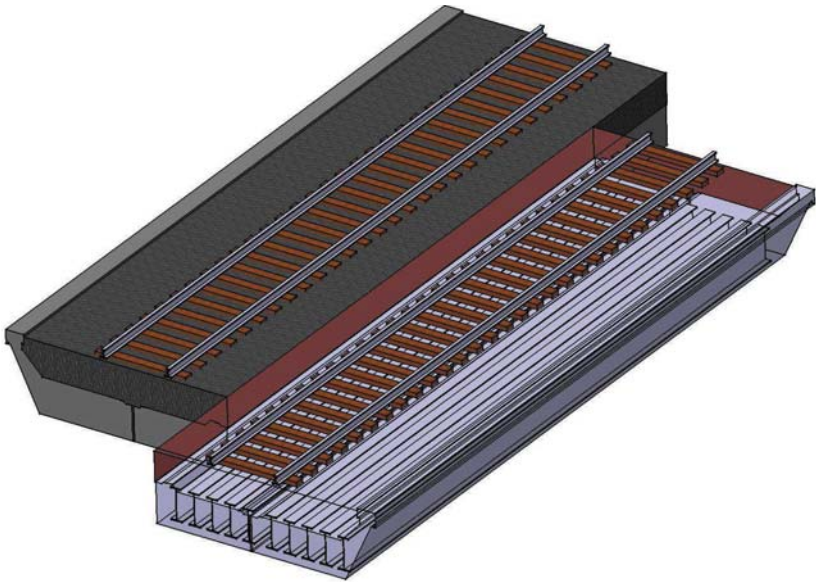

Fig. 4: Global FEM model layout

Using FE model of the bridge structure the first twenty natural frequencies and modes of natural bridge vibration were calculated to compare to their experimental values from the *Dynamic Loading Test* (DLT) measurements. As an example, some of them are shown in the Fig. 5. Comparison of the calculated and experimental natural frequencies values is explained in Tab. 2.

3.1. Bridge deflections calculation for SLT and DLT

The maximum static vertical deflections values in the middle of the spans, positions of measured points, load positions and the effectiveness of the testing loads (Locomotive type E 699.2 of 100 t mass) according to Slovak Standard 73 6203 for the Static Loading Test (SLT) were taking into account and also calculated via IDA Nexis software package. Results from the calculation of static deflections were also used for DLT testing load effectiveness. Fig. 6 shows an example of computed static deflection of bridge due to testing load. Comparison between FEM computed and measured static deflections in the years 2002 and 2007 is in Tab. 1.

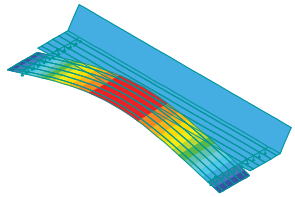

Natural mode 1

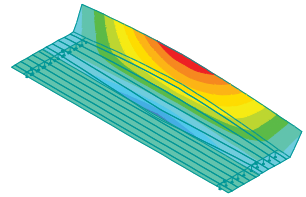

Natural mode 6

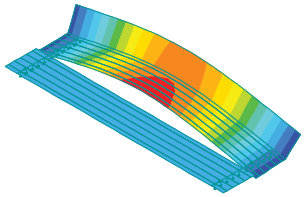

Natural mode 2

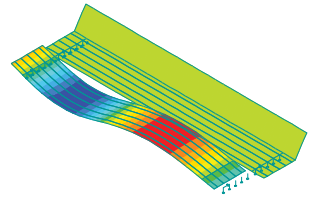

Natural mode 7

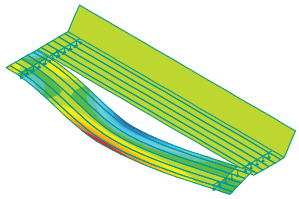

Natural mode 3

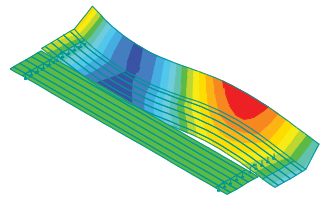

Natural mode 8

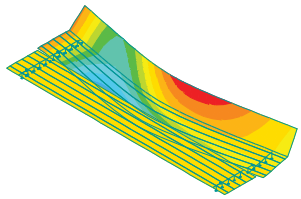

Natural mode 4

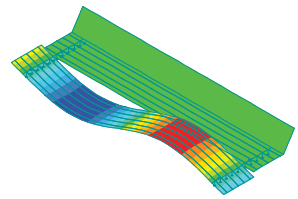

Natural mode 9

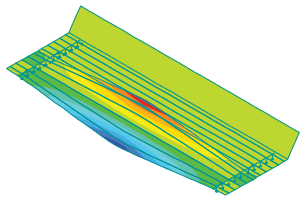

Natural mode 5

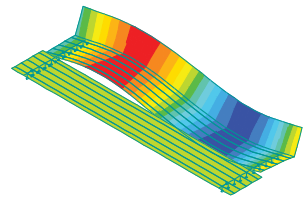

Natural mode 10

Fig. 5: Calculated modes of the bridge natural vibration

4. Dynamic Loading Test

To investigate bridge in–service performance for the two years, field load testing and visual inspections were conducted under an actual service environment in September 2007. Field load testing is an attractive tool for re–evaluating the capacity rating of bridges. Before the *bridge dynamic loading test* performance the *static loading test* was carried out using load locomotive type E699.2 with weight of 100 000 kg. The deflections values in the middle of the tested span were measured using LVTD inductive sensors *Bosh*.

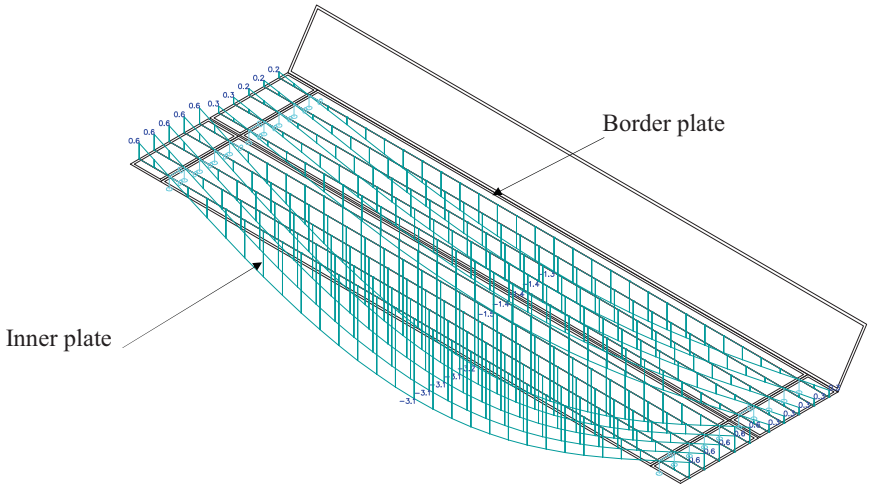

Fig. 6: Calculated deflection of bridge structure due to locomotive E 699.2

Tab. 1: FEM calculated and experimental static deflection values comparison

BRIDGE STATIC DEFLECTIONS	MAXIMAL VERTICAL DEFLECTION - MIDDLE SPAN (mm)							
	Track 1: Čadca–Žilina (2002)		Track 2: Žilina–Čadca (2002)		Track 1: Čadca–Žilina (2007)		Track 2: Žilina–Čadca (2007)	
	Border	Inner	Border	Inner	Border	Inner	Border	Inner
FEM (w_{CAL})	3,158	3,158	3,158	3,158	3,158	3,158	3,158	3,158
Measured el.(w_E)	1,84	1,86	1,88	1,82	1,71	1,70	1,78	1,79
Permanent (w_R)	0,05	0,05	0,00	0,05	0,05	0,05	0,05	0,05
w_E / w_{CAL} (α_1, β)	0,58	0,59	0,60	0,58	0,54	0,54	0,56	1,62
w_R / w_{TOT} (α_2)	0,03	0,03	0,00	0,03	0,03	0,03	0,03	0,03

For static strains analysis *Kistler* 9232A (piezoelectric gauges instrumented on steel part of the plate – **I** sectional bars) and M 502 (string strain gages built in to concrete part of the plate for SLT) were installed on concrete and steel members surfaces.

The dynamic response of the bridge was also induced by passing load locomotive type E 699.2 in the both directions with various speeds. The operating dynamic loading test (DLT) started with a load speed of v = 12 km/h (crawling) which increased up to the maximum achievable speed v = 72 km/h.

A computer – based measurement system (CBMS) was used to record the dynamic response of the bridge excitations induced by testing locomotive over DLT period. The investigated vibration acceleration, deflection and stress amplitudes were recorded at selected points with maximum calculated deflection in the middle of the span – Fig. 7. Output signals from the accelerometers (*Brüel–Kjaer*, BK4500), strains (*Kistler 9232A* – steel, *M 502* – concrete) and deflection sensors (*BOSCH*) were preamplified and recorded on two PC facilities with A/D converters software packages *DAS 16* and *DISYS*. The experimental analysis has been carried out in the *Laboratory of the Department of Structural Mechanics, University of Žilina.* Natural frequencies were obtained using

spectral analysis (Bendat & Piersol, 1993) of the recorded bridge response dynamic components of the structure vibration, which are considered ergodic and stationary. The frequency response spectra have also been obtained by using two – channel real time analyzer BK–2032 in the frequency range 0 ÷10 Hz. Output signal in the form of *Fourier frequency spectrum* (power spectrum) was also recorded by computer and printed by laser printer and x – y plotter. Spectral analysis was performed via *National Instruments* software package *NI LabVIE*. Vibration energy redistribution was observed via stress measuring on steel and concrete surfaces. One of the most important parameter – the *Dynamic Load Factor* (DLF) were evaluated using stress and deflection time histories measured during DLT.

There are presented below (Fig. 9) first of all the values of *dynamic load factor* – δ_{OBS} of the bridge (right bridge, line *Žilina – Čadca*), as an illustrative results example. The bridge vibration forcing was assumed by the run of the locomotive moving with various velocities in the tested parts of the bridge. The function δ_{OBS} against speed of the locomotive motion is plotted in Fig. 9. As an example, Fig. 8 also shows a part of the experimental analysis procedure results of the dynamic components structure vibration from the bridge DLT. Fig. 8 also shows: (a) *deflection time history* – $w(t)$ due to in–service slow train, (b) *stress time history* – $\sigma(t)$, (c) *acceleration time history* – $a(t)$, (d) *stress time history* – $\sigma(t)$ due to locomotive and (e) corresponding *power spectrum* – $S_D(f)$.

Fig. 7: Accelerometers with amplifiers – a part of CBMS

Tab. 2: Calculated and measured natural frequencies

Natural mode	NATURAL FREQUENCY $f_{(j)}$ [Hz]				
	FEM RESULTS	EXPERIMENTAL VALUES (DLT - 2002)		EXPERIMENTAL VALUES (DLT - 2007)	
		Track 1	Track 2	Track 1	Track 2
1	1,918	1,950	1,945	1,995	1,986
2	2,785	2,795	2,790	2,803	2,816
3	5,910	6,054	6,102	6,121	6,152
4	7,534	7,356	7,326	7,359	7,336
5	13,090	12,859	12,891	12,889	12,901
6	13,677	13,206	13,873	13,287	13,804

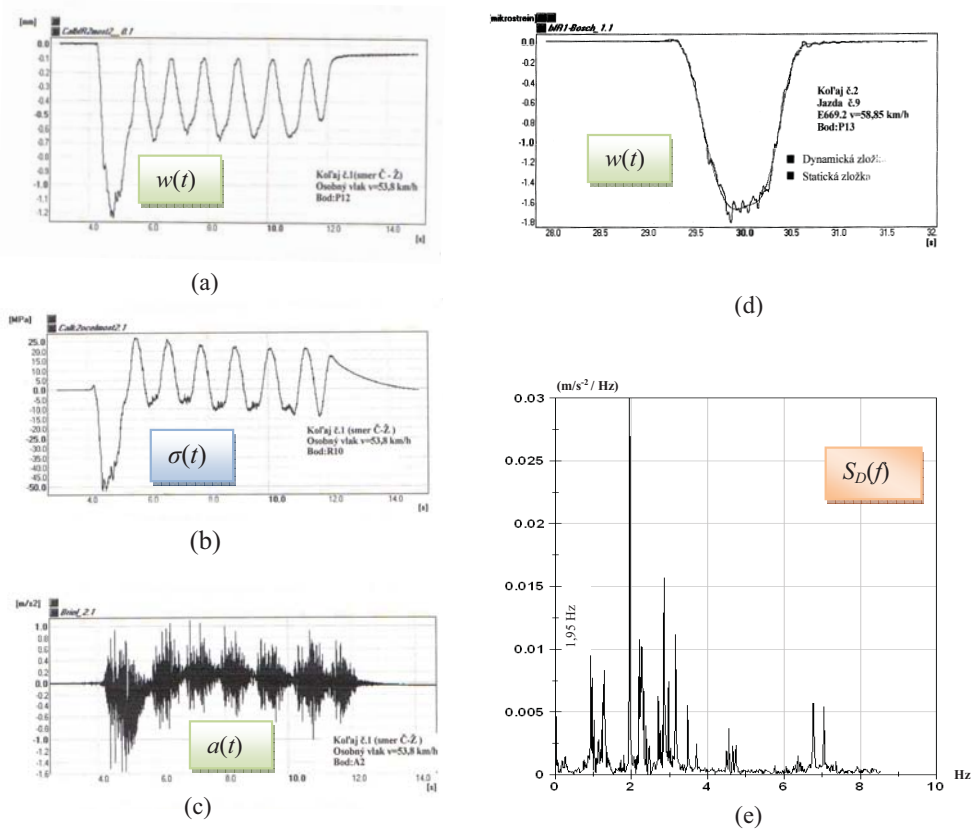

Fig. 8: Experimental analysis procedure results examples

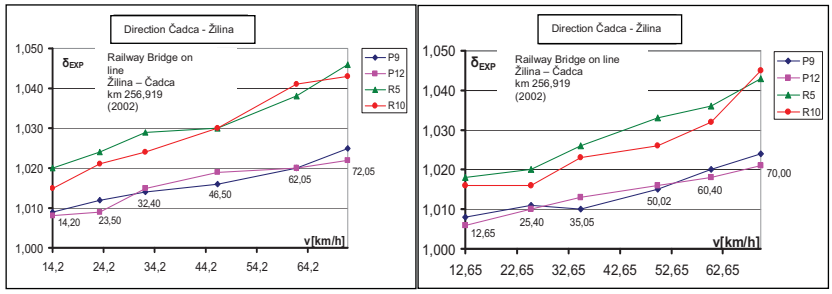

Legend: P9, P12, R5, R10

Bosh LVTD sensors

Kistler 9232A piezoelectric gauges

Fig. 9: Dynamic load factor δ_{OBS} against speed of the testing locomotive motion

5. Conclusions

This paper presents an overview of the in–service performance assessments of an SCC short–span bridge superstructure. A field load testing and visual inspections for the assessments of the SCC bridge durability under an actual service environment were conducted. Based on the presented results the following conclusions can be drawn:

- The maximum deflection from two SLT (2002, 2007) was *max w* = 1.88 mm from both SLT. The maximum value of SLT is 59.53 % lower than the maximum theoretical value of FEM. It means that the SCC bridge superstructure may be designed with a less restrictive design deflection.
- The dynamic responses in 2002, 2007 (monitoring) also show that the passage of the trains produces insignificant vibrations, the maximum dynamic deflection effective value w_{rms} = 0.48 mm (2002) and w_{rms} = 0.32 mm (2007). This is attributed to the difference between the natural frequency of the SCC bridge superstructure and the forcing frequency of the passing locomotive and trains.
- After five years of bridge service, DLF values of the SCC bridge are well compared with values DLT measured in the initial tests (2002). All experimental DLF values are lower than prescription by the *Slovak standards* DLF values. Therefore there is no need to post the load limit and the capacity–rating evaluation and for the SCC bridges can use rating factor of the existing methods for the conventional materials such as the allowable stress and load–factor.
- The predicted dynamic behavior of the bridge by a simplified FEM analysis calculation was compared to the measured one. Despite both the complex structural layout of the bridge (Fig. 2,3) and simplifying assumptions of the model (Fig. 4), obtained results showed good agreement for all experimentally identified damped natural frequencies in the basic frequency range 0 – 11 Hz (2002, 2007) and these are well compared with the theoretical values, Tab. 2.
- Although the data on the in–service performance of SCC Bridge are not enough, the results may provide a baseline data for the future capacity rating assessments and also serve as part of a long-term performance of the examined SCC bridge superstructure.

Acknowledgement

We kindly acknowledge the research project *VEGA,* Nr.G1/0169/12 granted by *Scientific Grant Agency of the Slovak Republic Ministry of Education.* We should also like to thank the *Civil Engineering Faculty – University of Žilina* for additional feed in this field research activity.

References

Baťa, M., Plachý, V., Sýkora, J., Bílý, V. & Polák, M. (1994) Static and dynamic tests of bridges, in: *Proc. of Czech – US Bridge Conference*, Praha.

Benčat, J. et al. (2007) *Report on dynamic monitoring results of the bridge on railway Žilina – Dětmarovice v km 256,919*, Report No. 6 – 3 – 42/SvF/07, ŽU/Žilina.

Benčat, J. et al. (2003) *Report on static and dynamic test results of the bridge on railway Žilina – Dětmarovice v km 256,919*, Report No. 6 – 3 – 19/SvF/03, ŽU/Žilina.

Bendat, J. S. & Piersol A. G. (1993) *Engineering applications of correlation and spectral analysis*, (2nd edition), Wiley Interscience, New York.

Design documentation. (2001), SUDOP Košice.

Slovak Standard No.73 6209 – *Loading test of bridges*.

Slovak Standard No.73 6203 – *Loading of bridges.*

The Steel Construction Institute. (2001) *Structural design of stainless steel*, SCI Publication P291, Ascot, UK.

18th International Conference
ENGINEERING MECHANICS 2012
Svratka, Czech Republic, May 14 – 17, 2012

pp. 117–122
Paper #323

INPUT SHAPING CONTROL OF ELECTRONIC CAMS

P. Beneš[*], M. Valášek[**], O. Marek[***]

Abstract: *The paper deals with the input shaping control of electronic cams that eliminates their residual vibrations. The models of several different kinds of electronic cams are described, i.e. the simple traditional one, the serial one, the parallel one, the multi-input one. Then the input shaping control and its generalization is described. The generalization means the shaper of arbitrary time length and/or of arbitrary rate combined with the set of shaping functions of reentry kind. It is demonstrated and explained that some more complex shaping functions in comparison with the simple Heaviside pulse shapers are more robust against model misalignment. This generalized input shaping control is applied to different kinds of electronic cams.*

Keywords: ***Input shaping, electronic cams, residual vibration, reentry commands***

1. Introduction

Conventional cam drives in modern machines can be replaced by properly controlled servomotors (Jirásko, 2010). This concept is generally called an electronic cam and can be further divided into several groups according to system structure – e.g. serial, parallel or multi-input electronic cams. The demand for fast and precise positioning is crucial in all mentioned cases but it could be easily corrupted by the residual vibration. To suppress the unwanted dynamics of flexible system the standard control input can be reshaped in such a way that it doesn't excite flexible modes or, more generally, that all the energy put into flexible modes is completely relieved at the end of the travel (Miu, 1989). The difference between original unshaped and shaped signal as well as the response of the two-mass model is shown in Fig. 1.

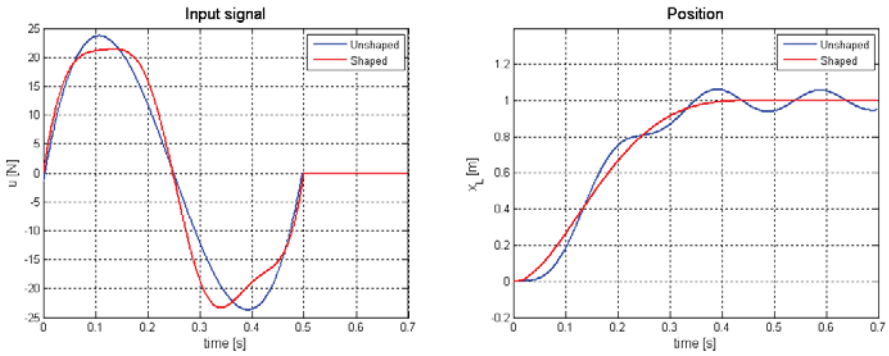

Fig. 1:Comparison of shaped and unshaped control input.

2. Necessary conditions

The control input that ensures no-vibration positioning has to fulfill some necessary conditions. For the system described using state space formulation as

$$\dot{\boldsymbol{y}} = \boldsymbol{A}\boldsymbol{y}(t) + \boldsymbol{B}\boldsymbol{u}(t), \tag{1}$$

[*] Ing. Petr Beneš: Fakulta strojní, ČVUT v Praze; Technická 4; 166 07, Praha 6; CZ, e-mail: petr.benes@fs.cvut.cz

[**] Prof. Ing. Michael Valášek, DrSc.: Fakulta strojní, ČVUT v Praze; Technická 4; 166 07, Praha 6; CZ, e-mail: michael.valasek@fs.cvut.cz

[***] Ing. Ondřej Marek: VÚTS, a.s.; U Jezu 525/4, 461 19, Liberec; CZ, e-mail: ondrej.marek@vuts.cz

these conditions can be derived in the form

$$\sum_{l=1}^{n} U_l(s)|_{s=\boldsymbol{A}} \cdot \boldsymbol{b}_l = e^{-\boldsymbol{A}T}\boldsymbol{y}(t_2) - e^{-\boldsymbol{A}T}\boldsymbol{y}(t_1), \tag{2}$$

where $U_l(s)$ is the finite time Laplace transform (Miu, 1989) of the l-th input, $\boldsymbol{b}_l$ is the corresponding column of $\boldsymbol{B}$ matrix, t_1 and t_2 is the start and the finish time, n is the number of inputs. The solution $u_l(t)$ in the time domain is the inverse Laplace transform of $U_l(s)$.

Now this approach would be applied to the simple electronic cam that can be modeled as a two mass spring-dumper system in Fig. 2.

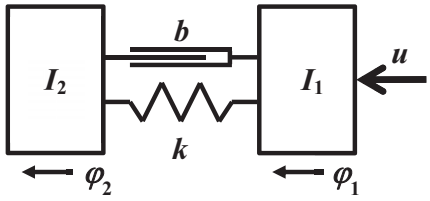

Fig. 2: Two-mass model of the electronic cam.

This system is described by the equation

$$\boldsymbol{M}\ddot{\boldsymbol{x}}(t) + \boldsymbol{B}\dot{\boldsymbol{x}}(t) + \boldsymbol{K}\boldsymbol{x}(t) = \boldsymbol{F}(t), \tag{3}$$

where

$$\boldsymbol{x} = \begin{bmatrix}\varphi_1\\ \varphi_2\end{bmatrix}, \boldsymbol{M} = \begin{bmatrix}I_1 & 0\\ 0 & I_2\end{bmatrix}, \boldsymbol{B} = \begin{bmatrix}b & -b\\ -b & b\end{bmatrix}, \boldsymbol{K} = \begin{bmatrix}k & -k\\ -k & k\end{bmatrix}, \boldsymbol{F} = \begin{bmatrix}u\\ 0\end{bmatrix}. \tag{4}$$

No-vibration conditions in the final position Φ_f of point-to-point translation are

$$\boldsymbol{x}_f = \begin{bmatrix}\Phi_f\\ \Phi_f\end{bmatrix}, \dot{\boldsymbol{x}}_f = \begin{bmatrix}0\\ 0\end{bmatrix}. \tag{5}$$

The differential equation of the second order (3) can be rewritten as a set of first order equations and transform to the Jordan canonical form

$$\underbrace{\begin{bmatrix}\dot{y}_1\\ \dot{y}_2\\ \dot{y}_3\\ \dot{y}_4\end{bmatrix}}_{\dot{\boldsymbol{y}}} = \underbrace{\begin{bmatrix}0 & 1 & 0 & 0\\ 0 & 0 & 0 & 0\\ 0 & 0 & p & 0\\ 0 & 0 & 0 & p^*\end{bmatrix}}_{\boldsymbol{A}} \underbrace{\begin{bmatrix}y_1\\ y_2\\ y_3\\ y_4\end{bmatrix}}_{\boldsymbol{y}} + \underbrace{\begin{bmatrix}0\\ 1\\ 1\\ 1\end{bmatrix}}_{\boldsymbol{B}} u, \tag{6}$$

where p and p^* are complex conjugated poles of flexible modes.

The boundary conditions (5) are transformed to the equation

$$\boldsymbol{y}(t_2) = [\Phi_f; 0; 0; 0]^T. \tag{7}$$

Assuming $t_1 = 0$ and zero initial conditions equation (2) can be rewritten in the component form

$$\begin{aligned} \frac{dU(s)}{ds}|_{s=0} &= \Phi_f,\\ U(s)|_{s=0} &= 0,\\ U(s)|_{s=p} &= 0,\\ U(s)|_{s=p^*} &= 0. \end{aligned} \tag{8}$$

This simple analytical formulation of necessary conditions for no-vibration translations used by Bhat & Miu (1991) is the result of the system description in the canonical form. Other state space representations usually need a numerical solution of (2).

Described approach leads to the control input in the form of pre-computed curve. However if it is rewritten to the form of a dynamical block it acts like a filter that transform any arbitrary signal to no-vibration one (Beneš & Valášek, 2008). And in contrast with patented input shaping technique by Singhose & Seering (1990) the length of this shaper is not dependent on the system natural frequency and can be set arbitrary.

3. Additional conditions and the control input synthesis

There are an infinite number of input functions $u(t)$ that fulfill equations (8). But these only ensure zero residual vibration. Therefore additional restrictions have to be applied e.g. for the to time domain continuity of the input signal

$$u(0) = 0, u(t_2) = 0. \tag{9}$$

Other restrictions are defined by maximal torque and rate of the actuator available etc.

The straight forward method of the control input synthesis is to assume analytical form of the control input with some variable parameters, e.g. the polynomial function with unknown coefficients

$$u(t) = \sum_{i=0}^{n} a_i \cdot t^i. \tag{10}$$

The exact value of parameters a_i is then calculated with respect to (8) and all other defined restrictions. It is possible to use some optimization methods as well.

Generally the number of parameters should be at least the same as the number of restricted conditions, however a smart choice of an analytical form of the input could automatically filled some of them. For example this form of a control input

$$u(t) = \sum_{i=1}^{n} a_i \cdot \sin\left(\frac{2\pi \cdot i}{t_2} t\right) \tag{11}$$

automatically filled conditions (9).

4. Serial electronic cam

The two-mass model in Fig. 2 is probably the most common demonstrator of different input shaping methods. Speaking about electronic cams the two masses represent the actuator (index 1) and the cam (index 2). The solution of the two-mass problem ensures precise positioning of the cam only. But in real systems the cam is connected to the rest of the system that usually has its own flexibility. The modified serial structure consisted of three bodies is in Fig. 3.

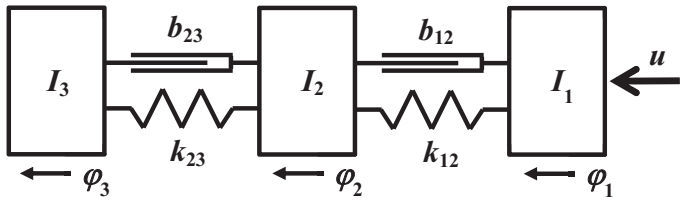

Fig. 3: Serial structure of electronic cam.

This system has two pairs of complex conjugated flexible modes and the rigid body mode. For simulation experiments it was described according to (1) and the control input was considered in the form of a polynomial function. Coefficient were calculated using (2) for $t_1 = 0\,s$, $t_2 = 1\,s$ and $\Phi_f = 1\,rad$. The value of all masses was set to 1 Nm^2, stiffness 100 *Nm/rad* and the dumping was neglected. The simulated system response is shown in Fig. 4.

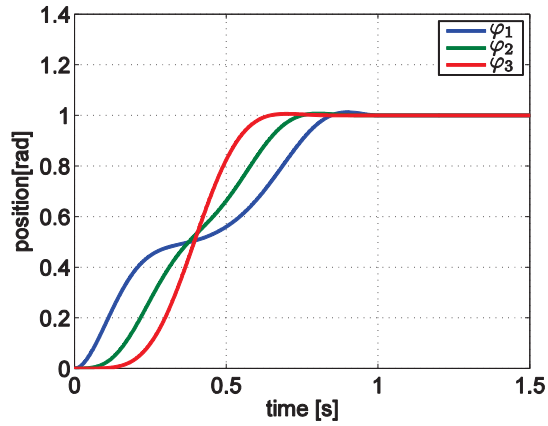

Fig. 4: Serial electronic cam – system response.

5. Parallel/two-input electronic cam

Input shaping techniques are usually applied only to systems with a single input. However many systems has two or more actuators. The schema of simple electronic cam with two parallel inputs is shown in Fig. 5. The position of the cam I_2 is controlled by actuators I_1 and I_3. Both actuators act on the same axis. The real application of this structure is that I_3 is primary force element, e.g. asynchronous motor, but with low accuracy of positioning. The I_1 is a fast servo motor that ensures precise positioning and/or vibration suppression.

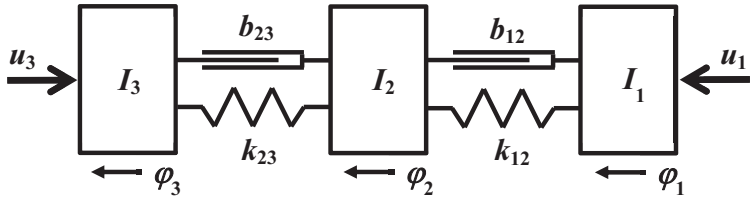

Fig. 5: Parallel/two-input structure of electronic cam.

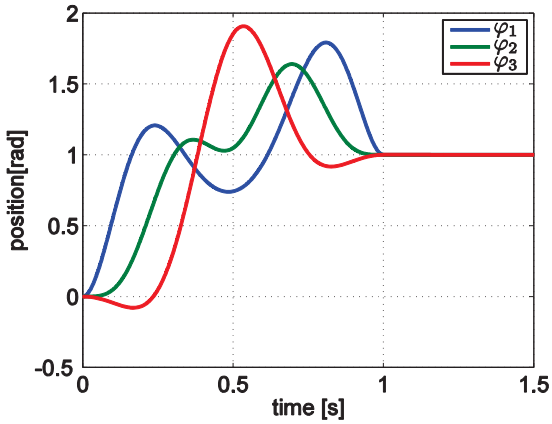

Fig. 6: Two-input electronic cam – system response.

Parameters of the model were the same as in the previous chapter and the control input u_1 was considered in the form of a polynomial function (10). The input u_3 was set as a constant. The values of coefficients were calculated using (2). Simulated system response is shown in Fig. 6. Note that there is

no residual vibration but all the masses slightly "overshoot" the final position during the travel. The reason is that no restrictions were defined to deal with this problem, but it is possible to add them to existing calculating procedure.

6. Robustness

Being a feed-forward method all control shaping techniques need precise system models. The vibration suppression is in fact caused by placing zeros of the control input into the poles of the system. Therefore incorrect system model causes that the control input is not design properly and vibrations are not canceled. To increase robustness to modeling errors it is possible to formulate additional constrains that either introduced more zeros to the control input or increase the order of existing ones. The price for that is the increase of necessary acting force or longer settling time. Comparison of spectral analysis of a standard shaper and a robust one is in Fig. 7.

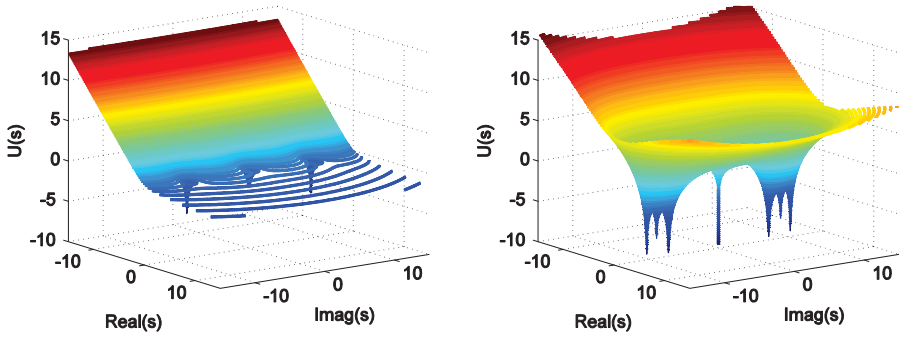

Fig. 7: Spectral analysis of a) standard shaper b) robust shaper.

7. Experiment

The test stand that was used for an experimental evaluation of simulations is in Fig. 8. Its structure is similar to Fig. 2, but the gearbox with ratio 1:5 was added. So for desired position $\varphi_2(t_2) = 2\pi\ rad$ the motor position has to be $\varphi_1(t_2) = 10\pi\ rad$. The settling time was $t_2 = 0{,}5\ s$. The control input was in the form (11) and two zeros were added to control input nearby modeling system poles.

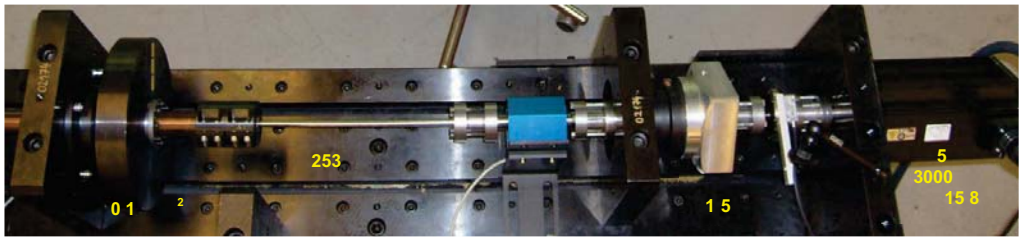

Fig. 8: Test stand.

The computed control input and the system response are in Fig. 9 and Fig. 10. The experiment proved simulation results and no vibration appeared.

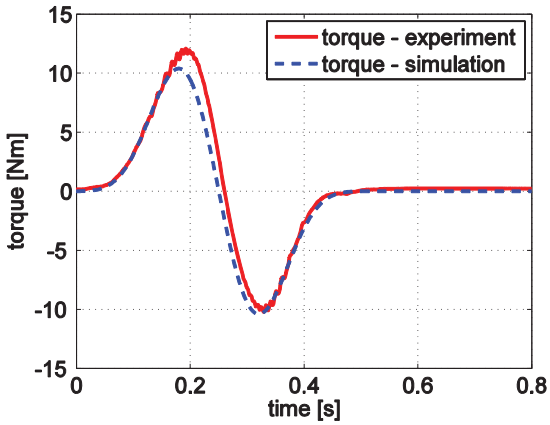

Fig. 9: Experiment – control input.

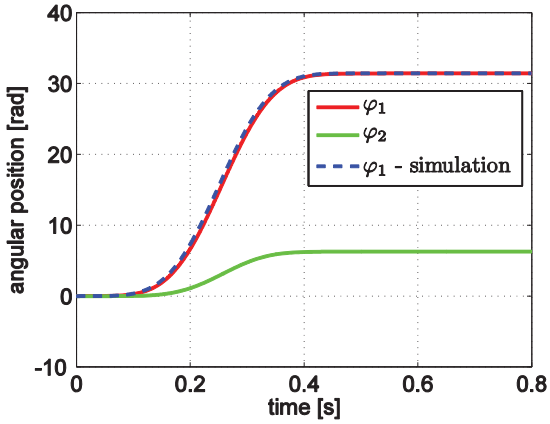

Fig. 10: Experiment – system response.

8. Conclusions

The presented approach to control of electronic cams and other flexible systems combines advantages of two different control shaping techniques. It produces command shapers of arbitrary length with reentry property as well. It is opened to formulation of additional constrains that ensure robustness to modeling errors.

Acknowledgement

The research has been supported by the Czech Science Foundation, project No. GAP101/11/2110.

References

Beneš, P. & Valášek, M. (2008) Input Shaping Control with Reentry Commands on Prescribed Duration. *Applied Computational Mechanics*, Vol. 2, no.2, pp.227-234.

Bhat, S.P. & Miu, D.K. (1991) Solutions to Point-to-Point Control Problem Using Laplace Transform Technique. *Journal of Dynamics Systems, Measurements and Control*, Vol. 113, pp.425-431.

Jirásko, P. (2010) *Application Methodology of Electronic Cams in Drives of Working Members of Production Machine Mechanisms, PhD. thesis*, TUL, Liberec (in Czech).

Miu, D.K. (1993) *Mechatronics, Electromechanics and Contromechanics.* Springer-Verlag, New York.

Singer, N. & Seering, W. (1990) Preshaping Command Inputs to Reduce System Vibration. *Journal of Dynamics Systems, Measurements and Control*, Vol. 112, pp.76-82.

18th International Conference
ENGINEERING MECHANICS 2012
Svratka, Czech Republic, May 14 – 17, 2012

pp. 123–128
Paper #345

IMPLEMENTATION OF DIRECT NUMERICAL SIMULATION OF VISCOUS INCOMPRESSIBLE FLOW

M. Beňo[*], B. Patzák [**]

Abstract: *The method for solving viscous incompressible flows, based on Glowinski, Pan,Hesla & Joseph (1998), is presented for the direct numerical simulation of viscous incompressible flow.It uses a finite element discretization in space and an operator-splitting technique for discretization in time. Quadratic approximation is employed for velocity flow and linear approximation for pressure on triangle elements. The goal is to develop more efficient and accurate numerical tool for computing viscous flows. The accuracy of the presented method has been confirmed on two common cases by implementation in Matlab program: the Poiseuille flow test, and on driven cavity flow test.*

Keywords: ***finite element, liquid flow, operator splitting, Navier-Stokes equations.***

1. Introduction

The aim of this article is to present a method for solving viscous incompressible flows. The finite element implementation is based on the incompressible Navier-Stokes equations on structured two dimensional triangular meshes using operator splitting for time discretization (Glowinski 2003). The fractional-time-step scheme described by Marchuk (1990) has been employed. Liquid is supposed to be incompressible and Newtonian. The advantage of this method is that no repeated remeshing is required. Also the assembled mass matrix remains constant and so it does not have to be assembled at every time step. By splitting one time step into three successive substeps the discretization enables better approximation of results. Pressure is computed in this case in the first sub-step while velocity is computed at each substep. To discretize the domain the Taylor-Hood triangular elements have bed used with second degree polynomic approximation of velocity and first degree polynomic approximation of pressure.

2. Problem formulation

2.1. The governing equations

Assume incompressible viscous Newtonian fluid occupying at the given time $t \in (0,T)$, delimited domain $\Omega \subset \mathbf{R}^2$ with boundary Γ. Let denote by $x = \{x_i\}_{i=1}^2$ a generic point in Ω. Let further denote by $u(x,t)$ velocity and by $p(x,t)$ pressure, both governed by Navier-Stokes equations:

$$\rho \frac{\mathrm{d}\mathbf{u}}{\mathrm{d}t} = \rho \mathbf{g} + \nabla . \boldsymbol{\sigma} \text{ on } \Omega \text{ - momentum equation,} \tag{1}$$

$$\nabla . \boldsymbol{u} = 0 \text{ on } \Omega. \text{ – incompressibility condition,} \tag{2}$$

where ρ is density of the fluid, $\mathbf{u}$ is velocity of the fluid, and $\boldsymbol{\sigma}$ is fluid stress. For an incompressible Newtonian viscous fluid, the stress is decomposed into its hydrostatic and shear components,

$$\boldsymbol{\sigma} = -p\mathbf{I} + 2\eta\mathbf{D}[\mathbf{u}], \tag{3}$$

where p is hydrostatic pressure in the fluid, η is the viscosity (assumed constant), and $2\eta\mathbf{D}[\mathbf{u}]$ is rate-of-strain tensor.

[*] Ing. Matej Beňo: Faculty of Civil Engineering, Czech Technical University; Thákurova 7; 166 29, Prague; CZ, e-mail: matej.beno@fsv.cvut.cz

[**] Prof. Dr. Ing. Bořek Patzák: Faculty of Civil Engineering, Czech Technical University; Thákurova 7; 166 29, Prague; CZ, e-mail:borek.patzak@fsv.cvut.cz

Relations (1)-(3) are to be supplemented by the appropriate initial conditions

$$\mathbf{u}(0) = \mathbf{u}_0 \text{ on } \Omega, \tag{4}$$

$$\nabla.\mathbf{u}_0 = 0, \tag{5}$$

and the boundary conditions

$$\mathbf{u} = \mathbf{u}_\Gamma(t) \text{ on } \Gamma, \tag{6}$$

$$\int_\Gamma \ \mathbf{u}_\Gamma(t)\,\hat{\mathbf{n}} = 0, \tag{7}$$

where $\hat{\mathbf{n}}$ is unit normal vector pointing out of the Γ.

2.2. Finite Element formulation

Let introduce spaces of approximation and test functions of velocities and pressure:

$$\mathbb{W}_h = \{v_h \in C^0(\Omega)^2, \forall T \in \mathcal{T}_h\},$$

$$\mathbb{W}_{oh} = \{v_h \in \mathbb{W}_h, v_h = 0 \; on \; \Gamma\},$$

$$L_h = \{q_h \in C^0(\Omega), \forall T \in \mathcal{T}_h\},$$

$$L_{0h} = \left\{q_h \in L_h \middle| \int_\Omega \ q_h dx = 0\right\}.$$

By using these finite-dimensional spaces we arrive at the following finite-element approximation of the problem (1)-(7):

Find $\mathbf{u}_h \in \mathbb{W}_{0h}$, $p \in L_{0h}$ satisfying:

$$\int_\Omega \ \left(\rho\left(\frac{\mathrm{d}\mathbf{u}_h}{\mathrm{d}t}\right) + (\mathbf{u}_h.\nabla)\mathbf{u}_h\right).\mathbf{v}_h dx - \int_\Omega \ p_h\,\nabla.\mathbf{v}_h dx + \int_\Omega \ 2\eta\mathbf{D}[\mathbf{u}] : \mathbf{D}[\mathbf{v}]dx = 0 \tag{8}$$

for all $\mathbf{v}_h \in \mathbb{W}_{0h}$,

$$\int_\Omega \ q_h\,\nabla.\mathbf{u}_h = 0 \ \text{ for all } q_h \in L_h, \tag{9}$$

$$\mathbf{u}_\mathrm{h}(0) = \mathbf{u}_{0h} \text{ on } \Omega, \tag{10}$$

where $\mathbf{u}_{0h}$ is an approximation of $\mathbf{u}_0$ satisfying the compatibility conditions

$$\int_\Omega \ q_h\,\nabla.\mathbf{u}_{0h} = 0 \ \text{ for all } q_h \in L_h. \tag{11}$$

Since, in (8), $\mathbf{u}$ is divergence-free and satisfies a Dirichlet boundary condition on all of Γ, we can write:

$$\int_\Omega \ 2\eta\mathbf{D}[\mathbf{u_h}] : \mathbf{D}[\mathbf{v_h}]dx = \int_\Omega \ \eta\nabla\mathbf{u_h} : \nabla\mathbf{v_h}\,dx \text{ for all } \mathbf{v}_h \in \mathbb{W}_{0h}.$$

3. Time discretization by operator splitting

3.1. Principle operator splitting:

As stated by Glowinski (2003) numerical solutions of the relations (1)-(7) is not trivial due to the following reasons:

- The above equations are nonlinear
- Handling of the incompressibility condition (2)
- The above equations are system of partial differential equations, coupled through the nonlinear term $(\boldsymbol{u}.\nabla)\boldsymbol{u}$, the incompressibility condition $\nabla.\boldsymbol{u} = 0$, and sometimes through the boundary conditions.

In the following sections, we show that a time discretization by operator splitting will partly overcome the above difficulties; in particular, decoupling of difficulties associated with the nonlinearity from those associated with the incompressibility condition. To introduce operator

splitting, the approach by Glowinski & Pironneau (1992) will be used. Let assume the following initial value problem:

$$\frac{\mathrm{d}\varphi}{\mathrm{d}t} + A(\varphi) = 0,$$
$$\varphi(0) = \varphi_0,$$

where A is an operator (possibly nonlinear, and even multivalued) from a Hilbert space H into itself and where $\varphi_0 \in$ H. There are numerous splitting operators to solve this problem (see Glowinski 2003).

3.2. Fractional-step scheme

In this work, the fractional-step scheme described by Marchuk (1990) is employed. Let assume decomposition of the operator A into the following nontrivial decomposition:

$$A = A_1 + A_2 + A3,$$

(by nontrivial, we mean A1, A2 and A3 are individually simpler than A). In the following, Δt is a time step.

Set $\varphi^0 = \varphi_0$, for n>= 0, φ^n being known we compute $\varphi^{n+1/3}$, $\varphi^{n+2/3}$ and φ^{n+1} as follows

$$\frac{\varphi^{n+\frac{1}{3}} - \varphi^n}{\Delta t} + A_1\left(\varphi^{n+\frac{1}{3}}\right) = f_1^{n+1},$$
$$\frac{\varphi^{n+\frac{2}{3}} - \varphi^{n+\frac{1}{3}}}{\Delta t} + A_2\left(\varphi^{n+\frac{2}{3}}\right) = f_2^{n+1},$$
$$\frac{\varphi^{n+1} - \varphi^{n+\frac{2}{3}}}{\Delta t} + A_3(\varphi^{n+1}) = f_3^{n+1}.$$

By applying operator splitting to the problem (8-11) we obtain (with $0 \le \alpha, \beta \le 1$ and $\alpha + \beta = 1$):

Find: $\mathbf{u}^{n+1/3} \in \mathbb{W}_h$ and $p^{n+1/3} \in L_h$

$$\rho \int_\Omega \frac{\mathbf{u}^{n+1/3} - \mathbf{u}^n}{\Delta t} . \mathbf{v} dx - \int_\Omega p^{n+1/3} \nabla . \mathbf{v} dx = 0 \text{ for all } \mathbf{v}_h \in \mathbb{W}_{0h} \quad (12)$$

$$\int_\Omega q \nabla . \mathbf{u}^{n+1/3} dx = 0 \text{ for all } q_h \in L_h. \quad (13)$$

Find: $\mathbf{u}^{n+2/3} \in \mathbb{W}_h$

$$\rho \int_\Omega \frac{\mathbf{u}^{n+2/3} - \mathbf{u}^{n+1/3}}{\Delta t} . \mathbf{v} dx - \rho \int_\Omega \left(\mathbf{u}^{n+1/3} . \nabla\right) \mathbf{u}^{n+2/3} . \mathbf{v}\, dx + 2\alpha\eta \int_\Omega \mathbf{D}\left[\mathbf{u}^{n+2/3}\right] : \mathbf{D}[\mathbf{v}]\, dx = 0 \quad (14)$$

for all $\mathbf{v}_h \in \mathbb{W}_{0h}$.

Finally find $\mathbf{u}^{n+1} \in \mathbb{W}_h$

$$\rho \int_\Omega \frac{\mathbf{u}^{n+1} - \mathbf{u}^{n+2/3}}{\Delta t} . \mathbf{v} dx + 2\beta\eta \int_\Omega \mathbf{D}[\mathbf{u}^{n+1}] : \mathbf{D}[\mathbf{v}]\, dx = 0 \text{ for all } \mathbf{v}_h \in \mathbb{W}_{0h}. \quad (15)$$

3.3 Finite element approximation

The triangular Taylor-Hood element has been used, with the quadratic velocity and linear pressure interpolation (see Figure 1).

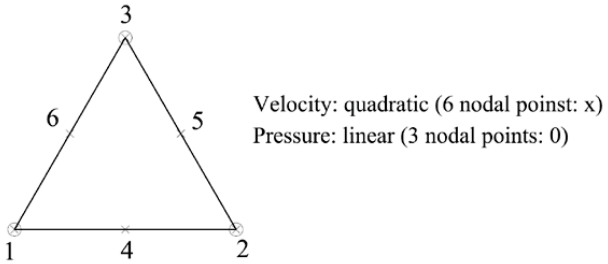

Figure 1: The Taylor-Hood element.

The interpolation functions for velocity have following term:

$$N_1 = 1 - 3\xi - 3\eta + 4\xi\eta + 2\xi^2 + 2\eta^2,$$
$$N_2 = -1\xi + 2\xi^2,$$
$$N_3 = -1\eta + 2\eta^2,$$
$$N_4 = 4\xi - 4\xi\eta - 4\xi^2,$$
$$N_5 = 4\xi\eta,$$
$$N_6 = 4\eta - 4\xi\eta - 4\eta^2,$$

for pressure, linear interpolation is used

$$L_1 = 1 - \xi - \eta,$$
$$L_2 = \xi,$$
$$L_3 = \eta,$$

where ξ, η are isoparametric coordinates.

The particular variables are approximated on the elements as linear combinations of interpolation functions and nodal values:

$$u(\xi,\eta) = \sum_{i=1}^{6} N_i u_i,$$
$$v(\xi,\eta) = \sum_{i=1}^{6} N_i v_i,$$
$$p(\xi,\eta) = \sum_{i=1}^{3} L_i p_i,$$

where u_i, v_i a p_i are the corresponding nodal values. The concept of isoparametric elements is used, where the geometry of an element is approximated using quadratic interpolation:

$$x(\xi,\eta) = \sum_{i=1}^{6} N_i x_i,$$
$$y(\xi,\eta) = \sum_{i=1}^{6} N_i y_i,$$

where $x_i$and $y_i$are the coordinates of the node points in the element. By differentiating this, we express the derivative operators as

$$\begin{bmatrix} \frac{\partial}{\partial x} \\ \frac{\partial}{\partial y} \end{bmatrix} = \begin{bmatrix} \frac{\partial x}{\partial \xi} & \frac{\partial y}{\partial \xi} \\ \frac{\partial x}{\partial \eta} & \frac{\partial y}{\partial \eta} \end{bmatrix} \begin{bmatrix} \frac{\partial}{\partial \xi} \\ \frac{\partial}{\partial \eta} \end{bmatrix},$$

The integrals in the weak form are evaluated numerically using the Gaussian quadrature formula (Sarada and Nagaraj 2010).

This method has been implemented in the Matlab; yet further, particles including extensions and modification of liquid to fresh concrete flow will already be implemented in the C++.

4. Numerical validations:

The accuracy of prototype Matlab implementation has been verified using two benchmark problems: the Poiseuille flow between parallel plates and driven cavity flow.

4.1. Poiseuille flow

In this classic test, the steady state velocity and pressure distributions is simulated for a fluid moving laterally between two plates whose length and width is much greater than a distance separating them. The geometry, boundary and initial conditions are illustrated on Fig 2. The domain is divided into 400 elements, the height is 1 and the length is 4. The stationary profile of velocity profile at outflow is quadratic. The mass density is $\rho = 1.0\ kg/m^3$, and the viscosity is $\eta = 10^{-2} Pa\ s$. The results correspond with analytic solution.

When time step $\Delta t = 0.005$ is chosen the implemented simulations renders results in time $t = 1{,}5\ s$

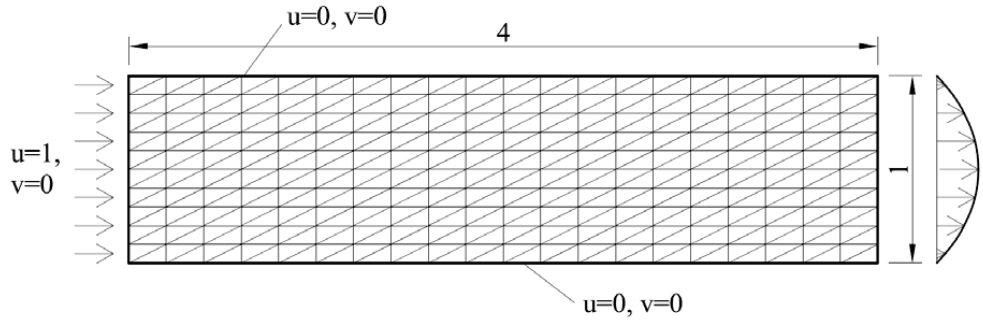

Figure 2: The geometry and the boundary conditions of flow in tube test. The used mesh consists of 861 nodes and 400 elements.

4.2. Driven Cavity flow

The driven cavity flow is a typical problem applied to verify numerical model in fluid dynamics. We simulate the flow inside closed cavity and compare the results with the model developed by the other researches (Botella and Peyret, 1998; Rabenold, 2005). Figure 3 shows geometry of the problem, computational mesh and applied boundary conditions. The viscosity is set to $\eta = 10^{-2} Pa\ s$, and the Reynold's number is computed as $1/\eta$ (based on geometry of size 1 and maximum velocity 1). The mass density is $\rho = 1.0\ kg/m^3$, and the time step is $\Delta t = 0.01$. The results are in good agreement, even though the present values are restricted to the 30x30 grid points (see table No. 1).

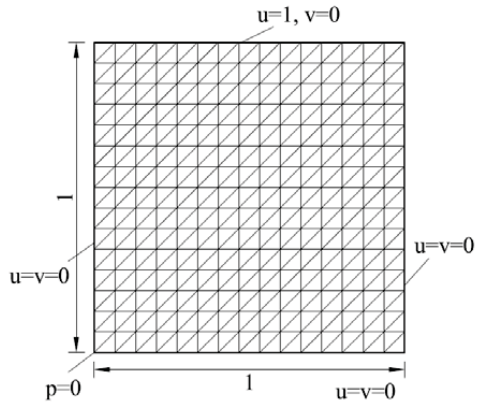

Figure 3: The geometry and the boundary conditions of driven cavity flow test. The used mesh consists of 961 nodes and 450 elements.

Tab. 1: Velocity extreme through cavity centerlines at $Re = 100$

method	u_{min}	v_{min}	v_{max}
Present	-0.2165	-0.2493	0.1771
Botella and Peyret	-0.21279	-0.25266	0.17854
Rabenold	-0.2140424	-0.2538030	0.1795728

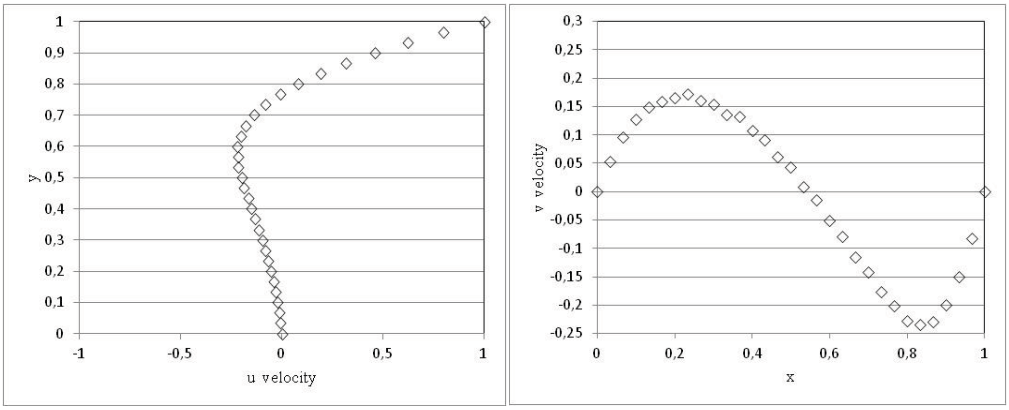

Figure 4: Velocity profiles through cavity centerlines at $\eta = 10^{-2} Pa\ s$ and 30 x 30 grid size.

5. Conclusion

Presented work describes formulation and implementation of non-stationary, incompressible flow finite element solver. The Tayler-Hood elements (P2-P1) have been implemented. For time discretization the operator splitting method is used and it reduces computation of velocity and pressure together to one time substep whereas in other substeps only velocity is being solved. The model is verified using standard benchmark tests from the literature.

Acknowledgement

This work has been supported by the Grant Agency of the Czech Technical University in Prague, grant No. 12/027/OHK1/1T/11.

References

Barrett, K.E (2004) Multilinear Jacobians for isoparametric planar elements. *Finite Elements in Analysis and Design* 40, pp. 821-853

Bittnar, Z., Šejnoha, J. (1992) *Numerické metody mechaniky 1,* CTU Press*, Prague*

Botella, O., Peyret, R. (1998) Benchmark spectral results on lid-driven cavity flow, *Computers&Fluids*, 27, 4, pp. 421-433

Glowinski, R., Pan, T.-W., Hesla, T.I., J oseph, D.D. (1998) A distributed Lagrange multiplier-fictitious domain method for particulate flows. *Int. J. Multiphase Flows* 25, pp. 755–794.

Glowinski, R. (2003) Finite Element Methods for Incompressible Viscous Flow, in: *Handbook of Numerical Analysis*, vol. 9 (P.G. Ciarlet, J.L. Lions eds), North-Holland, Amsterdam, pp. 3-76.

Glowinski, R., Pironneau, O. (1992) Finite element methods for navier-stokes equations. *Annual Reviews Fluid Mech*. 24, pp. 167-204

Marchuk, G.I (1990) Splitting and Alternating Direction Methods, in *Handbook of Numerical Analysis*, vol. 1 (P.G. Ciarlet, J.L. Lions eds), North-Holland, Amsterdam, pp. 197-462.

Rabenold, P.T (2010) Lid-driven flow in a rectanglar cavity with corner obstacles, http://www-users.math.umd.edu/~rabenold/enme646_project.pdf

Rathod, H.T., Shajedul Karim, Md. (2002) An Explicit integration scheme based on recursion for the curved triangular finite elements. *Computers and Structures,* 80, pp. 43-76

Sarada, J., Nagaraja, K.V. (2010) Generalized Gaussian quadrature rules over two-dimensional regions with linear sides. *Applied Mathematics and Computation*, 217, 12, pp. 5612-5621.

18th International Conference
ENGINEERING MECHANICS 2012
Svratka, Czech Republic, May 14 – 17, 2012

pp. 129–135
Paper #277

THE INVERSE KINEMATICS OF N-SERIAL ROBOTIC CHAIN IN DIFFERENT QUADRANTS OF WORKING SPACE

Z. Bobovský[*], F. Trebuňa[**]

Abstract: *Inverse kinematics of mechanic system is area of solution at many universities and scientific research institutions. This paper dealt with of solution problem of inverse kinematic by cyclic coordinate descent method (CCD). This method allows use n-link chain mechanism without complicated changing of control algorithm. The article is focuses on the issue of setting the number of elements of mechanism. Also presents a modified method the incremental CCD, which is compared with this method. From the perspective of number of cycles required to achieve the desired position with increasing number of links and from the perspective of changing quadrant of working space.*

Keywords: ***Inverse kinematic, n-serial, robotic chain.***

1. Inverse kinematic problem

Inverse kinematic problem can be described as „finding" the right parameters for each kinematic joint of mechanism to achieve the desired result in a pre-defined position of member. The available literature provides several definitions for this problem. In defined shape of mechanism, fig. 1, we know where its base is. With the control system and sensors know the current mechanism shape and position of the end point of the mechanism. If we define a new position in which to get the mechanism end point, for the computation algorithm, the actual end point position is starting position and its task is to calculate values for individual joints q1 to q_n, so the end point has the desired position with reasoning error limit (Wang, 1991).

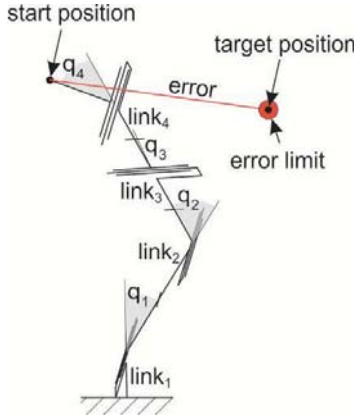

Fig. 1: Problem of inverse kinematic solution

There are several computation methods that are described in available literature. Whatever the method using Jacobian and their subsequent modifications (Wang, 1991; Mostýn, & Skařupa, 2000; Skařupa & Mostýn, 2002) or other methods (Mukundan, 2008), the biggest problem with these methods arises with the redundant manipulators, when the desired position is possible to achieve by the infinity combinations of q_i values.

[*] Ing. Zdenko Bobovský, PhD.: Department of applied mechanics and mechatronic, Technical University of Košice, Letná street 9; 040 01, Košice; SVK, e-mail: zdenko.bobovsky@tuke.sk
[**] Dr.h.c. mult. prof. Ing. František Trebuňa, CSc.: Department of applied mechanics and mechatronic, Technical University of Košice, Letná street 9; 040 01, Košice; SVK, e-mail: frantisek.trebuna@tuke.sk

2. Cyclic calculation

This method allows computing the inverse kinematics of redundant mechanisms with principle of gradual calculation parameters for each kinematics joint separately.

2.1 Cyclic coordinate descent

In this method there is gradual calculation for each kinematic joint separately from the last joint in a series of mechanism to the first. This cycle is repeated until it reaches desired position of the end point of mechanism respectively until value of error isn't smaller then error limit. The q value is a calculated difference between actual angle and desired angle. This q value can be limited by the maximum value of step size. The algorithm of calculation in basic form for one "finding" point with defined max step size and without optimization algorithm is shown (Bobovský, et al., 2011; Trebuňa & Bobovský, 2011).

2.2 Incremental cyclic coordinate descent

This method allows with last link "follow" desired point. Procedure of computation is shown (Bobovský, et al., 2011; Trebuňa & Bobovský, 2011). The algorithm is for one "finding" point with defined a max step size and without an optimized algorithms.

3. Number of cycles

Between a main criteria for choose the right inverse kinematics algorithm belongs a number of calculation cycles to achieve desired task and a time of computation. Computation times are changed depending on the type of computer on which the calculation is performed. Therefore, we only present the number of cycles required to achieve the desired position. The step size of the computation method CCD is 1° because of the twisting mechanism at a higher step value (Bobovský, et al. (2011)). The step size of method iCCD is 90°, when mechanism moves with a defined path between two points or without a defined path and the maximum possible number of cycles is n*100 for one point. Path is divided into parts of unit length.

Starting position of end point is $x_p = n$ a $y_p = 0$ and desired position of the mechanism is defined by fig. 2. The total number of 44 points distributed throughout the mechanism working space.

Link n has unit length and error limit is set to 0,01. The computation was made in application programmed in MATLAB©.

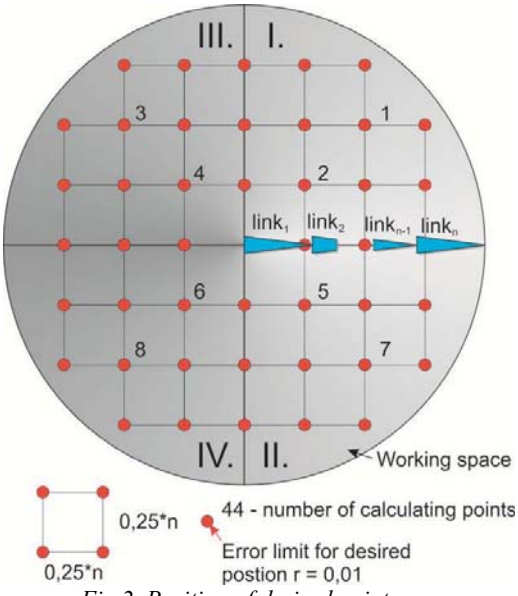

Fig 2. Position of desired points

3.1 Moving at defined path

When mechanism moves with defined path of end point for the total number of 44 required points, we obtained data on which we created the graphs, that shows the number of cycles required to achieve the desired point and the error from the desired point when reaching limits or error when reaching the maximum number of cycles for a given number of degrees of freedom (DOF). Fig. 3 shows the characteristics for point 1, shown in fig. 2. Based on the graph, for increasing number of DOF to achieve point 1, the CCD method leads to a sharp increase in required number of cycles. While the method iCCD lead to a linear increase in the required number of cycles. The positioning error in reaching the desired position leads to an increasing in the number of cycles of links in mechanism that don't reaches the desired position for n *100 cycles for one point of path.

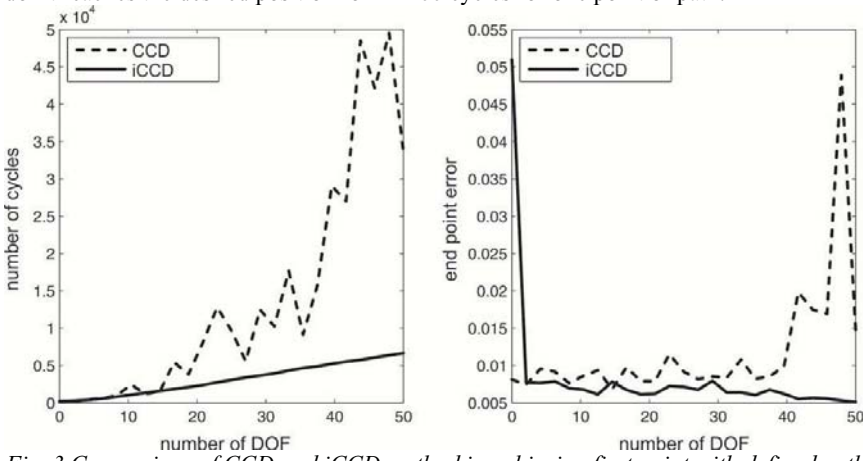

Fig. 3 Comparison of CCD and iCCD method in achieving first point with defined path (a – number of cycles, b – error at end of calculation)

Fig. 4 shows the characteristics for point 2. shown in fig. 2. Based on the graph, for increasing number of DOF, CCD method leads to faster achieving the desired point 2. While at the iCCD method there is a double number of cycles. The positioning error in reaching the desired position leads to an increasing in the number of cycles of links in mechanism that don't reaches the desired position for n *100 cycles for one point of path.

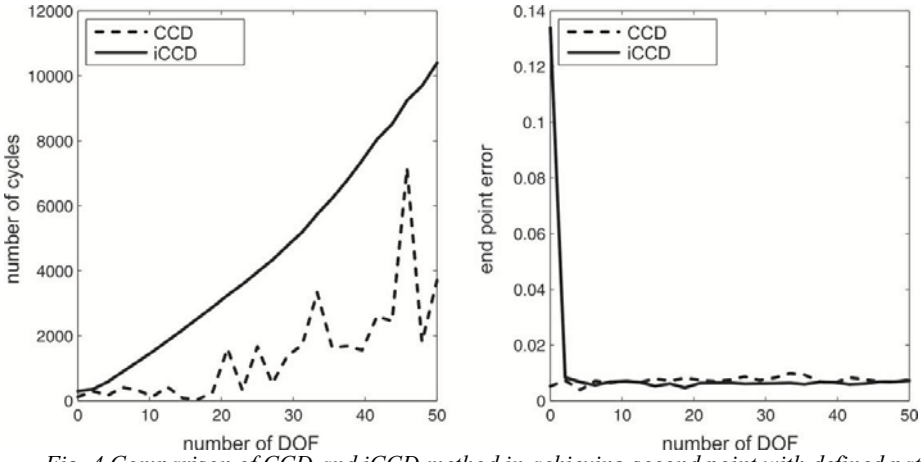

Fig. 4 Comparison of CCD and iCCD method in achieving second point with defined path (a – number of cycles, b – error at end of calculation)

3.2 Moving without defined path

When mechanism moves without defined path of end point for the total number of 44 required points, we obtained data on which we created the graphs, that shows the number of cycles required to achieve the desired point and the error from the desired point when reaching limits or error when reaching the maximum number of cycles for a given number of degrees of freedom (DOF). Fig. 5 shows the characteristics for point 1, shown in fig. 2. Based on the graph, for increasing number of DOF to achieve point 1, the CCD method leads to a faster achieving the desired point. But with higher DOF the mechanism don't achieve the desired point. While the method iCCD lead to a linear increase in the required number of cycles. The positioning error in reaching the desired position leads to an increasing in the number of cycles of links in mechanism that don't reaches the desired position for n *100 cycles for one point of path.

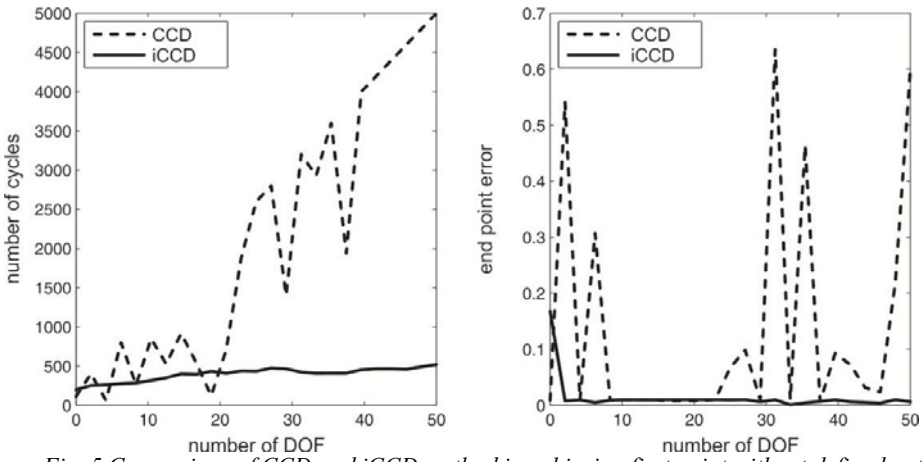

Fig. 5 Comparison of CCD and iCCD method in achieving first point without defined path (a – number of cycles, b – error at end of calculation)

Fig. 4 shows the characteristics for point 2. shown in fig. 2. Based on the graph, for increasing number of DOF, CCD method leads to faster achieving the desired point 2. While at the iCCD method there is an increasing number of cycles to 20%. The positioning error in reaching the desired position leads to an increasing in the number of cycles of links in mechanism that don't reaches the desired position for n *100 cycles for one point of path.

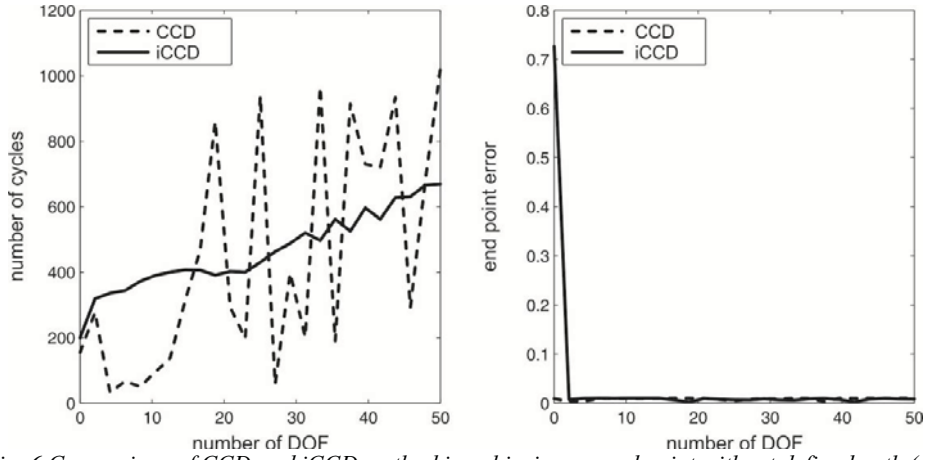

Fig. 6 Comparison of CCD and iCCD method in achieving second point without defined path (a – number of cycles, b – error at end of calculation)

4. Comparison

The following section compares the results for the desired points located in different quadrants. The goal is to show how changing the number of cycles required to achieve those points, depending on quadrant. In first case are compared points 1, 3, 5 and 7 shown in fig. 2 and in second case 2, 4, 5 and 6 also shown in fig. 2.

4.1 Moving at defined path

When moves on a defined path, which is divides into unit length. The method CCD occurs in different quadrants for different characteristic of graphs, fig. 7a) and fig. 8a). While characteristics at method iCCD have same behavior for quadrant I. and II., and the same for III. and IV. quadrant, fig. 7b) and fig. 8b). The same thing happened in both compared cases.

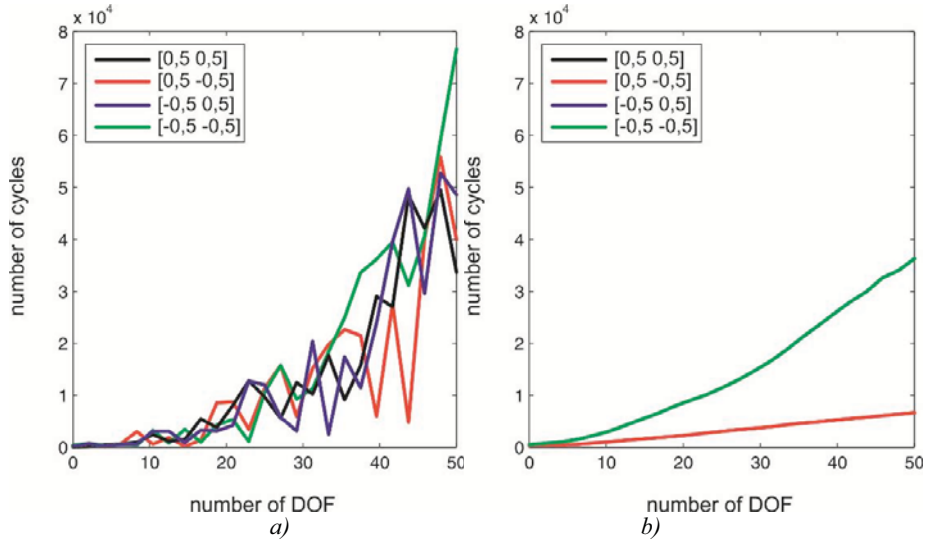

Fig. 7 Number of cycles required to achieve desired position with defined path for points 1, 3, 7 and 8 (a – CCD, b – iCCD)

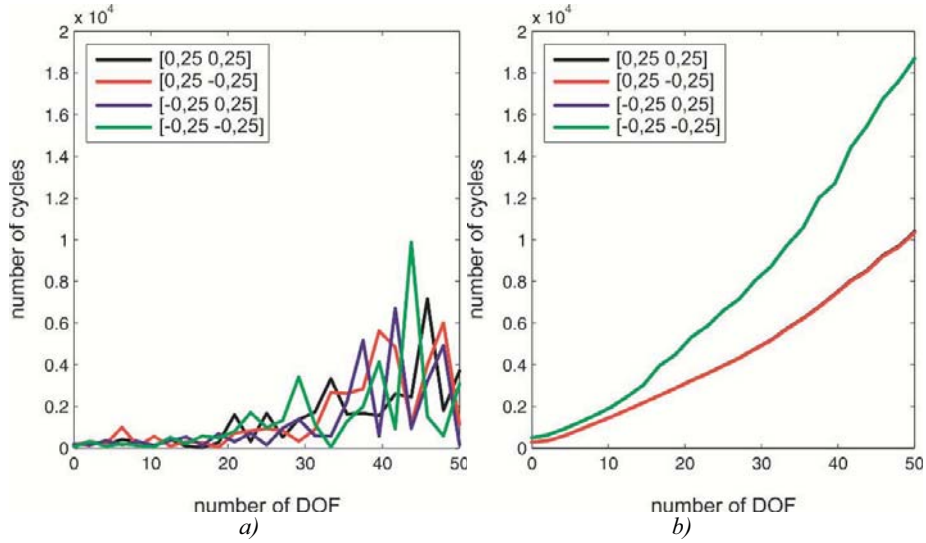

Fig. 8 Number of cycles required to achieve desired position with defined path for points 2, 4, 5 and 6 (a – CCD, b – iCCD)

4.2 Moving without a defined path

When moves without a defined path. The method CCD occurs in different quadrants for different characteristic of graphs, fig. 9a) and fig. 10a). Limiting factor is the maximum number of cycles. While the method iCCD in the first case, fig. 9b) have same behavior for quadrant I. and II., and the same for III. and IV. quadrant. In second case, fig. 10) occurs for I. and II. quadrant of the subtle difference between characteristics. For III. And IV. quadrants are the characteristics same.

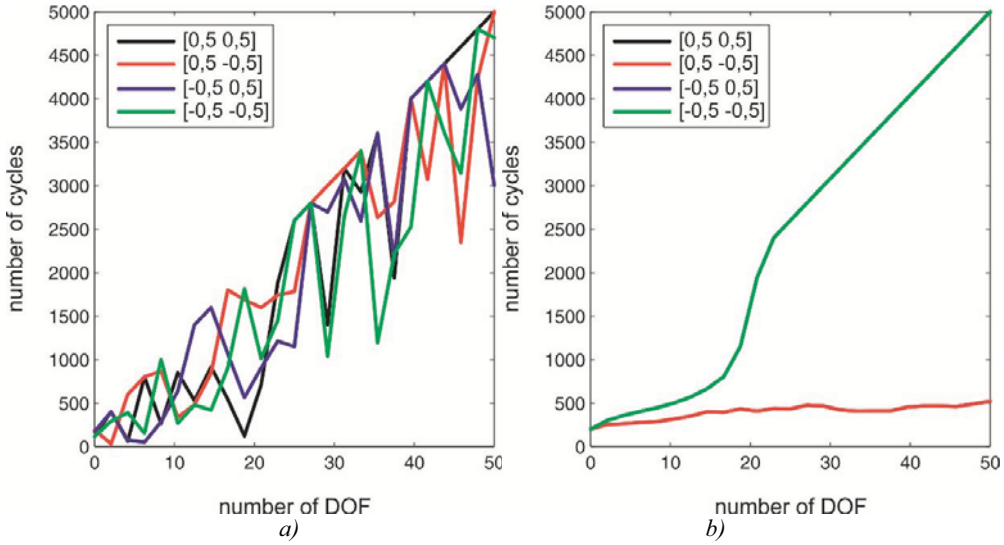

Fig. 9 Number of cycles required to achieve desired point without defined path for points 1, 3, 7 and 8 (a – CCD, b – iCCD)

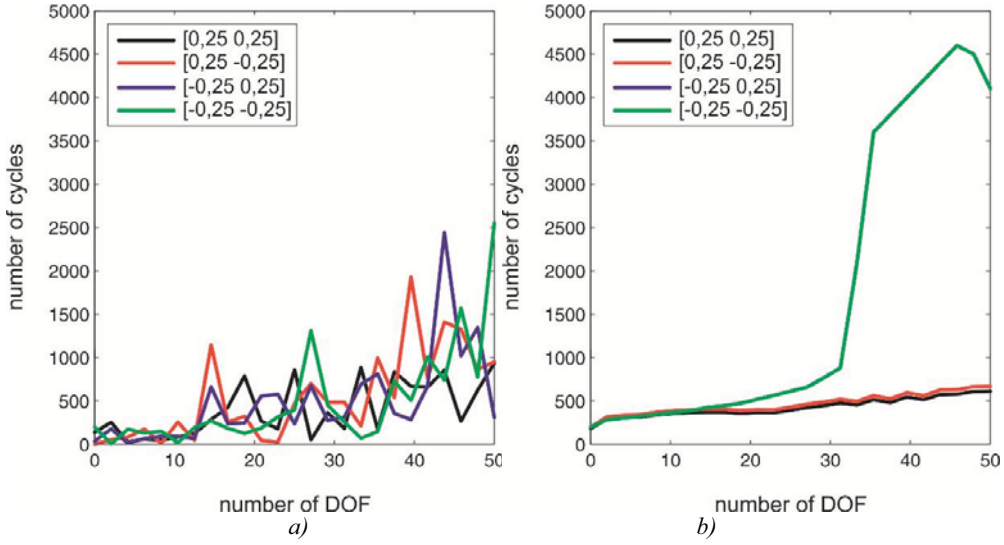

Fig. 10 Number of cycles required to achieve desired point without defined path for points 2, 4, 5 and 6 (a – CCD, b – iCCD)

5. Conclusions

The inverse kinematics of mechanical systems is a complex issue. To date, there are several methods for its solution. Not all are applicable to mechanisms with more degrees of a freedom because of the complex and the subsequent compilation of Jacobian and his numerical complexity. This article presents a comparison of the CCD method and its modified version incremental CCD in terms of a cycle number for different quadrants of mechanism working space.

When comparing these methods the results obtained we conclude that the calculation using method of iCCD is convenient at "finding" a single position of moving at the defined path if the desired point is close to actual position of the end point. Method of CCD is useful for distance points. To achieving the final position is to perform additional calculations at higher density of points within the mechanism working space.

Acknowledgement

The paper has been created realization of project "Centrum výskumu riadenia technických enviromentálnych a humánnych rizík pre trvalý rozvoj produkcie a výrobkov v strojárstve" (IMTS:26220120060), based on operating program support Research and Development financed from European Regional Development Fund and of project applied study - Stimuly "Komplexný modulárny robotický systém strednej kategórie s vyššou inteligenciou" (Req-00169-0001).

References

Bobovský, Z., Jezný, J. & Hroncová, D. (2011) Effect of step angle in inverse kinematics of serial chain robot, in: *MMaMS 2011 : Modelling of Mechanical and Mechatronical Systems: proceedings of the 4th international conference*: Herľany, Slovakia, 20. - 22. 9. 2011. - Košice : TU, 2011 S. 22-31. - ISBN 978-80-553-0731-2

Mostýn, V. & Skařupa, J. (2000) *Teorie průmyslových robotů*. 1. vydání, Košice: Edícia vedeckej a odbornej literatúry – Strojnícka fakulta TU v Košiciach, Vienala Košice, 2000, 150 str.; ISBN 80-88922-35-6;

Mukundan, R. (2008) A fast inverse kinematics solution for an n-link joint chain, *5th International Conference on Information Technology and Applications (ICITA 2008)*, URL: http://ir.canterbury.ac.nz/bitstream/10092/1555/1/12610087_ICITA08.pdf

Skařupa, J. & Mostýn, V. (2002) *Metody a prostředky návrhu průmyslových a servisních robotů*. Vienala Košice, ISBN 978-80-88922-55-1

Trebuňa, F. &Bobovský, Z., (2011) Cyclic calculation of inverse kinematics for n-link serial mechanism, in: *Acta Mechanica Slovaca.* Roč. 15, č. 3, (2011), In press - ISSN 1335-2393

Wang, T. Li-Ch. & Chen, Ch. Ch. (1991) A combined optimization method for solving the inverse kinematics problem of mechanical manipulators, *Transactions on robotics and automation*, vol. 7, no. 4, 1991, URL: http://www.cse.ohio-state.edu/~parent/classes/788/Sp06/ReferenceMaterial/IK/WC91.pdf

18th International Conference
ENGINEERING MECHANICS 2012
Svratka, Czech Republic, May 14 – 17, 2012

pp. 137–145
Paper #140

COMPLEX MODEL OF THE LOWER URINARY TRACT

M. Brandner [*], J. Egermaier [**], H. Kopincová [***], J. Rosenberg[****]

Abstract: *The complex model of the lower part of the urinary tract is introduced. It consists of the detrusor smooth muscle cell model and the detailed 1D model of the urethra flow. The nerve control is taken into account. In future this model will allow to simulate the influence of different drugs and mechanical obstructions in the bladder neck and urethra. A general muscle model involving the calcium dynamics in the smooth muscle cell and the growth and remodelling theory will be shortly introduced. For the modelling calcium dynamics the approach from Koenigsberger at al. (2008) was adopted. The model includes the ATP consumption calculation according to Hai and Murphy (1992). The main part is devoted to the development of a simple bladder model and the detrusor contraction during voiding together with the detailed model of the urethra flow.*

Keywords: ***urinary tract, bladder, urethra fluid flow, steady state preserving***

1. Introduction

The voiding is a very complex process. As we can see from Fig. 1 it consists of the transfer of information about the state of the bladder filling in to the spinal cord. Next part is the sending of the action potentials to the smooth muscle cells of the bladder. Even this process is not simple and includes the spreading of the action potential along the nerve axon and the transmission of the mediator (Ach - acetylcholine) in the synapse. The action potential starts the process of the smooth muscle contraction.

The smooth muscles have a lot of different forms in contradiction with the striated muscles. They are present in vesicles, arteries and others hollow organs.

Although the own biological motor - sliding between actin and myosin fueled by hydrolysis of ATP- is the same here as well as in striated and heart muscles, there are important differences between these basic types of muscles and also between smooth muscles in different organs. The sliding between actin and myosin causing the change of the form (length) of the muscle cell and its stiffness can be observed as a kind of growth and remodeling. This approach described e.g. in Rosenberg and Hynčík (2008) and Rosenberg and Hynčík (2007) is used in this model. It should be mentioned that a lot of different smooth muscle cells (SMC) models exist. They are based either on Huxley model where the calcium dynamics is not taken into account in details or on the contrary the calcium dynamics and the phosphorilation is modeled very precisely but the mechanochemical coupling is based on the work on Hai and Murphy (1992) where the stress in the muscle cell depends linearly on the amount of the bonded crossbridges either phosphorilized or unphosphorilized (e.g. Parthimos at al. (2007), Koenigsberger at al. (2008), where the model is applied to the SMC in the vessels).

To be able to describe the very complex processes in the SMC in the efficient form it is necessary to use the irreversible thermodynamics. This approach was described in Rosenberg and Svobodová (2010).

Using all these approaches the algorithm published in Rosenberg (2011b) was developed. In this contribution we join on the results of this paper. The simple model of the whole bladder and the detailed 1D model of the urethra flow is added. Some examples of the numerical experiments are shown.

[*]Doc. Ing. Marek Brandner, Ph.D.: NTIS New Technologies for Information Society, University of West Bohemia in Pilsen, Univerzitni 8; 306 14, Pilsen; Czech republic, e-mail: brandner@kma.zcu.cz
[**]Ing. Jiří Egermaier, Ph.D.: Department of Mathematics, University of West Bohemia in Pilsen, Univerzitni 8; 306 14, Pilsen; Czech republic, e-mail: jirieggy@kma.zcu.cz
[***]Ing. Hana Kopincová, Ph.D.: NTIS New Technologies for Information Society, University of West Bohemia in Pilsen, Univerzitni 8; 306 14, Pilsen; Czech republic, e-mail: kopincov@kma.zcu.cz
[****]Prof. Ing Josef Rosenberg, DrSc.: Department of Mechanics, University of West Bohemia in Pilsen, Univerzitni 8; 306 14, Pilsen; Czech republic, e-mail: rosen@kme.zcu.cz

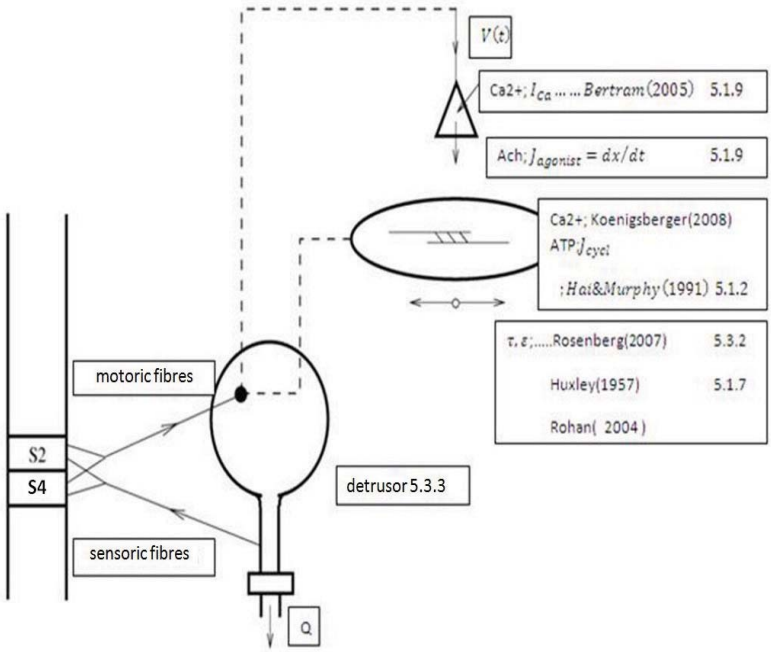

Fig. 1:

2. Bladder contraction

As it was already mentioned, the whole model of the bladder contraction is described in Rosenberg (2011a). It consists of the following parts:

- Model of the time evolution of the Ca2++ concentration - five equations Koenigsberger at al. (2008). The Ca2++ intracellular concentration is the main control parameter for the next processes and finally for the smooth muscle contraction. Its increase depends on the flux $J_{agonist}$ of the mediator (in this case acetylcholine) via the nerve synapse.
- Model of the time evolution of the phosporilation of the light myosin chain - three equations Hai and Murphy (1992). The muscle cell contraction is caused by the relative movement of the myosin and actin filaments. For this it is necessary that the phophorilation of the mentioned light myosin chain on the heads of the myosin occurs. Knowing this process also the time evolution of the ATP consumption (J_{cycl}) can be determined. The ATP (adenosintriphosphate) is the main energy source for the muscle contraction.

3. Model of the own contraction based on the GRT and the irreversible thermodynamics

The growth and remodelling theory Dicarlo and Quiligotti (2002) together with the laws of irreversible thermodynamics with internal variables was applied in Rosenberg and Svobodová (2010) to describe the mechano-chemical coupling of the smooth muscle cell contraction. The product of the chemical reaction affinity (the ATP hydrolysis) with its rate plays an important role in the discussed model. Further it can be assumed that the rate of the ATP hydrolysis depends on the ATP consumption. The corresponding equations in the non-dimensional form are following:

$$\dot{x} = \frac{g}{h}\left[\tau' - zy(x-1)\right] = k_1\left[\tau' - zy(x-1)\right], \tag{1}$$

$$\dot{y} = \frac{y}{k_2}\left[x\tau' - \frac{1}{2}zy(x-1)^2 + C'\right], \tag{2}$$

where

$$\begin{aligned} \dot{z} &= \mathrm{sgn}(m)\cdot\left[r - \frac{1}{2}z(x-1)^2\right], \\ x &= \frac{l'}{l'_r}, y = l'_r, z = k, \\ \frac{l}{l_0} &= x\cdot y \\ k' &= k\sqrt{\frac{|m|}{g}}, \\ l'_r &= \frac{l_r}{l_0}, \\ t' &= \frac{t}{\sqrt{g|m|}}. \end{aligned} \tag{3}$$

l_0 is the initial length of the muscle fibre, l_r its length after stimulation when the fibre is unloaded (s. c. resting length), l the actual length (when the contraction is isometric this is the input value), t' the stress and k is the fibre stiffness. The non-dimensional values are labeled with the single quote mark. The others symbols are the parameters. The most important parameter is C'. Using the irreversible thermodynamics we can obtain the following relations

$$\begin{aligned} C' &= p\cdot(C - a_{chem}Y)\sqrt{\frac{|m|}{g}}, \\ C\sqrt{\frac{|m|}{g}} &= C_0 + C_t e^{q\left(\frac{l}{l_0} - \frac{l}{l_0}|_{opt}\right)^2}, \\ p &= p_0 e^{s\left(\frac{l}{l_0} - \frac{l}{l_0}|_{opt}\right)^2}, \end{aligned} \tag{4}$$

where for the afinity of the chemical reactions especially for the hydrolysis of the ATP gilt

$$a_{chem} = -Q\cdot Y. \tag{5}$$

Q is the constant and Y is the concentration of ATP. For its time evolution gilts Pokrovski (2005)

$$\dot{Y} = -QQ\cdot Y + L\cdot J_{cycle}. \tag{6}$$

Here QQ is the damping parameter. Than the whole model is finished because the ATP consumption J_{cycl} as a function of the Ca2+ concentration in the cytoplasm was already determined.

4. Bladder and voiding model

To model the contraction of the bladder during the voiding process we will use the very simple model according Laforet and Guiraud (2007) and Arts at al. (1991). The bladder is modelled as a hollow sphere with the output corresponding to the input into urethra.

For the pressure in the bladder the following formula is introduced in Laforet and Guiraud (2007)

$$p = \frac{V_{sh}}{3V}\cdot\tau, \qquad \tau = \frac{F}{S}, \tag{7}$$

where V_{sh} is the volume of the wall, V the inner volume, τ stress in the muscle fibre, S the inner surface and F the force in the muscle cell.

For the flux q gilts

$$q = \frac{dV}{dt}, \tag{8}$$

where ρ is the density of the fluid.

Using the formulas for the isotonic contraction, we can at first obtain the relation for the volume. It gilts

$$l' = \frac{l}{l_0} = x \cdot y \tag{9}$$

and then

$$V = \kappa \cdot (x \cdot y)^3, \tag{10}$$

where κ is the constant which in the theoretical case if only one cell will occupy the circumference of the spherical bladder will be $1/6\pi^2$. Putting this formula into the equation for q and using the equations for the derivatives of x and y mentioned before we obtain the equation, from which we can calculate τ:

$$\tau = \frac{\frac{q}{3\kappa(x\cdot y)^2} + \left[k_1 z y^2 (x-1) + \frac{z y^2 x}{2k_2}(x-1)^2 - \frac{xy}{k_2}C'\right]}{k_1 y + \frac{x^2 y}{k_2}}. \tag{11}$$

For the pressure gilts then

$$p = \frac{V_{sh}}{3\kappa \cdot (x \cdot y)^3} \cdot \frac{\frac{q}{3\kappa(x\cdot y)^2} + \left[k_1 z y^2 (x-1) + \frac{z y^2 x}{2k_2}(x-1)^2 - \frac{xy}{k_2}C'\right]}{k_1 y + \frac{x^2 y}{k_2}}. \tag{12}$$

This will be putted into the equations for the isotonic contraction.

5. Urethral flow

We now briefly introduce a problem describing fluid flow through the elastic tube represented by hyperbolic partial differential equations with the source term. In the case of the male urethra, the system based on model in Stergiopulos at al. (1993) has the following form

$$\begin{aligned} a_t + q_x &= 0, \\ q_t + \left(\frac{q^2}{a} + \frac{a^2}{2\rho\beta}\right)_x &= \frac{a}{\rho}\left(\frac{a_0}{\beta}\right)_x + \frac{a^2}{2\rho\beta^2}\beta_x - \frac{q^2}{4a^2}\sqrt{\frac{\pi}{a}}\lambda(Re), \end{aligned} \tag{13}$$

where $a = a(x,t)$ is the unknown cross-section area, $q = q(x,t)$ is the unknown flow rate (we also denote $v = v(x,t)$ as the fluid velocity, $v = \frac{q}{a}$), ρ is the fluid density, $a_0 = a_0(x)$ is the cross-section of the tube under no pressure, $\beta = \beta(x,t)$ is the coefficient describing tube compliance and $\lambda(Re)$ is the Mooney-Darcy friction factor ($\lambda(Re) = 64/Re$ for laminar flow). Re is the Reynolds number defined by

$$Re = \frac{\rho q}{\mu a}\sqrt{\frac{4a}{\pi}}, \tag{14}$$

where μ is fluid viscosity. This model contains constitutive relation between the pressure and the cross section of the tube

$$p = \frac{a - a_0}{\beta} + p_e, \tag{15}$$

where p_e is surrounding pressure.

Presented system (13) can be written in the compact matrix form

$$\mathbf{u}_t + [\mathbf{f}(\mathbf{u}, x)]_x = \boldsymbol{\psi}(\mathbf{u}, x), \tag{16}$$

with $\mathbf{q}(x,t)$ being the vector of conserved quantities, $\mathbf{f}(\mathbf{q}, x)$ the flux function and $\boldsymbol{\psi}(\mathbf{q}, x)$ the source term. This relation represents the balance laws. For the following consideration, we reformulate this problem to the nonconservative form.

5.1. Nonconservative problems

We consider the nonlinear hyperbolic problem in nonconservative form

$$\begin{aligned} \mathbf{u}_t + \mathbf{A}(\mathbf{u})\mathbf{u}_x &= \mathbf{0},\ x \in \mathbf{R},\ t \in (0,T), \\ \mathbf{u}(x,0) &= \mathbf{u}_0(x),\ x \in \mathbf{R}, \end{aligned} \tag{17}$$

The numerical schemes for solving problems (17) can be written in fluctuation form

$$\frac{\partial \mathbf{U_j}}{\partial t} = -\frac{1}{\Delta x}[\mathbf{A}^-(\mathbf{U}^-_{j+1/2}, \mathbf{U}^+_{j+1/2}) + \mathbf{A}(\mathbf{U}^-_{j+1/2}, \mathbf{U}^+_{j-1/2}) + \mathbf{A}^+(\mathbf{U}^-_{j-1/2}, \mathbf{U}^+_{j-1/2})], \tag{18}$$

where $\mathbf{A}^{\pm}(\mathbf{U}^-_{j+1/2}, \mathbf{U}^+_{j+1/2})$ are so called fluctuations. They can be defined by the sum of waves moving to the right or to the left. The directions are dependent on the signs of the speeds of these waves, which are related to the eigenvalues of matrix $\mathbf{A}(\mathbf{u})$. In what follows, we use the notation $\mathbf{U}^+_{j+1/2}$ and $\mathbf{U}^-_{j+1/2}$ for the reconstructed values of unknown function. Reconstructed values represent the approximations of limit values at the points $x_{j+1/2}$. The most common reconstructions are based on the minmod function (see for example Kurganov and Tadmor (2000)) or ENO and WENO techniques Črnjarič-Zič at al. (2004).

The reconstruction can be applied to each component of $\mathbf{u}$. But this approach does not work well in general. It is better to apply the reconstruction to the characteristic field of $\mathbf{u}$. It means that each jump is decomposed to the eigenvectors $\mathbf{r}$ of Jacobian matrix $\mathbf{A}(\mathbf{u})$.

$$\mathbf{U}_{j+1} - \mathbf{U}_j = \sum_{p=1}^{m} \alpha^p_{j+1/2} \mathbf{r}^p_{j+1/2}. \tag{19}$$

Then the reconstruction based on minmod function can be defined by following

$$\begin{aligned} \mathbf{U}^+_{j+1/2} &= \mathbf{U}_{j+1} + \sum_p \phi^{p,+}_{I+1/2} \alpha^p_{j+1/2} \mathbf{r}^p_{j+1/2}, \\ \mathbf{U}^-_{j+1/2} &= \mathbf{U}_{j} + \sum_p \phi^{p,-}_{I+1/2} \alpha^p_{j+1/2} \mathbf{r}^p_{j+1/2}, \end{aligned} \tag{20}$$

where

$$\phi^{p,\pm}_{I+1/2} = \mp \frac{1}{2} \left(1 + \mathrm{sgn}(\theta^p_{I+1/2})\right) \min(1, |\theta^p_{I+1/2}|) \tag{21}$$

and

$$I = \begin{cases} j - 1/2, & \text{if } s^p_{j+1/2} \geq 0, \\ j + 3/2, & \text{if } s^p_{j+1/2} < 0. \end{cases} \tag{22}$$

The function $\theta^p_{j+1/2}$ can be determined by the following way

$$\theta^p_{j+1/2} = \frac{\alpha^p_{j+1/2} \mathbf{r}^p_{j+1/2} \cdot \mathbf{r}^p_{I+1/2}}{\alpha^p_{I+1/2} \mathbf{r}^p_{I+1/2} \cdot \mathbf{r}^p_{I+1/2}}. \tag{23}$$

When the problem (17) is derived from the conservation form (16), i.e. $\mathbf{f}'(\mathbf{u}) = \mathbf{A}(\mathbf{u})$ is the Jacobi matrix of the system, fluctuations can be defined as follows

$$\begin{aligned} \mathbf{A}(\mathbf{U}^-_{j+1/2}, \mathbf{U}^+_{j-1/2}) &= \mathbf{f}(\mathbf{U}^-_{j+1/2}) - \mathbf{f}(\mathbf{U}^+_{j-1/2}), \\ \mathbf{A}^-(\mathbf{U}^-_{j+1/2}, \mathbf{U}^+_{j+1/2}) &= \mathbf{F}^-_{j+1/2} - \mathbf{f}(\mathbf{U}^-_{j+1/2}), \\ \mathbf{A}^+(\mathbf{U}^-_{j-1/2}, \mathbf{U}^+_{j-1/2}) &= \mathbf{f}(\mathbf{U}^+_{j-1/2}) - \mathbf{F}^+_{j-1/2}. \end{aligned} \tag{24}$$

5.2. Decompositions based on augmented system

This procedure is based on the extension of the system (13) by other equations (for simplicity we omit viscous term). This was derived in George (2008) for the shallow water flow. The advantage of this step is in the conversion of the nonhomogeneous system to the homogeneous one. In the case of urethra flow we obtain the system of four equations, where the augmented vector of unknown functions is $\mathbf{w} = [a, q, \frac{a_0}{\beta}, \beta]^T$. Furthermore we formally augment this system by adding components of the flux function $\mathbf{f}(\mathbf{u})$ to the vector of the unknown functions. We multiply balance law (16) by Jacobian matrix $\mathbf{f}'(\mathbf{u})$ and obtain following relation

$$\mathbf{f}'(\mathbf{u})\mathbf{u}_t + \mathbf{f}'(\mathbf{u})[\mathbf{f}(\mathbf{u})]_x = \mathbf{f}'(\mathbf{u})\boldsymbol{\psi}(\mathbf{u}, x). \tag{25}$$

Because of $\mathbf{f}'(\mathbf{u})\mathbf{u}_t = [\mathbf{f}(\mathbf{u})]_t$ we obtain hyperbolic system for the flux function

$$[\mathbf{f}(\mathbf{u})]_t + \mathbf{f}'(\mathbf{u})[\mathbf{f}(\mathbf{u})]_x = \mathbf{f}'(\mathbf{u})\boldsymbol{\psi}(\mathbf{u}, x). \tag{26}$$

In the case of the urethra fluid flow modelling we add only one equation for the second component of the flux function i.e. $\phi = av^2 + \frac{a^2}{2\rho\beta}$ (the first component q is unknown function of the original balance law), which has the form

$$\phi_t + (-v^2 + \frac{a}{2\rho\beta})(av)_x + 2v\phi_x - \frac{2av}{\rho}\left(\frac{a_0}{\beta}\right)_x - \frac{a^2 v}{\rho\beta^2}\beta_x = 0. \tag{27}$$

Finally augmented system can be written in the nonconservative form

$$\begin{bmatrix} a \\ q \\ \phi \\ \frac{a_0}{\beta} \\ \beta \end{bmatrix}_t + \begin{bmatrix} 0 & 1 & 0 & 0 & 0 \\ -\frac{q^2}{a^2} + \frac{a}{\rho\beta} & 2\frac{q}{a} & 0 & -\frac{a}{\rho} & -\frac{a^2}{\rho\beta^2} \\ 0 & -\frac{q^2}{a^2} + \frac{a}{\rho\beta} & 2\frac{q}{a} & 2\frac{q}{\rho} & -\frac{aq}{\rho\beta^2} \\ 0 & 0 & 0 & 0 & 0 \\ 0 & 0 & 0 & 0 & 0 \end{bmatrix} \begin{bmatrix} a \\ q \\ \phi \\ \frac{a_0}{\beta} \\ \beta \end{bmatrix}_x = \mathbf{0}, \tag{28}$$

briefly $\mathbf{w}_t + \mathbf{B}(\mathbf{w})\mathbf{w}_x = \mathbf{0}$, where matrix $\mathbf{B}(\mathbf{w})$ has following eigenvalues

$$\lambda^1 = v - \sqrt{\frac{a}{\rho\beta}}, \lambda^2 = v + \sqrt{\frac{a}{\rho\beta}}, \lambda^3 = 2v, \lambda^4 = \lambda^5 = 0 \tag{29}$$

and corresponding eigenvectors

$$\mathbf{r}^1 = \begin{bmatrix} 1 \\ \lambda^1 \\ (\lambda^1)^2 \\ 0 \\ 0 \end{bmatrix}, \mathbf{r}^2 = \begin{bmatrix} 1 \\ \lambda^2 \\ (\lambda^2)^2 \\ 0 \\ 0 \end{bmatrix}, \mathbf{r}^3 = \begin{bmatrix} 0 \\ 0 \\ 1 \\ 0 \\ 0 \end{bmatrix}, \mathbf{r}^4 = \begin{bmatrix} \frac{-a}{\rho\lambda^1\lambda^2} \\ 0 \\ \frac{a}{\rho} \\ 1 \\ 0 \end{bmatrix}, \mathbf{r}^5 = \begin{bmatrix} \frac{-a^2}{\rho\beta^2\lambda^1\lambda^2} \\ 0 \\ \frac{a^2}{2\rho\beta^2} \\ 0 \\ 1 \end{bmatrix}. \tag{30}$$

We have five linearly independent eigenvectors. The approximation is chosen to be able to prove the consistency and provide the stability of the algorithm. In some special cases this scheme is conservative and we can guarantee the positive semidefiniteness, but only under the additional assumptions (see Brandner at al. (2009)).

The fluctuations are then defined by

$$\begin{aligned} \mathbf{A}^-(\mathbf{U}^-_{j+1/2}, \mathbf{U}^+_{j+1/2}) &= \begin{bmatrix} 0 & 1 & 0 & 0 & 1 \\ 0 & 1 & 0 & 0 & 1 \end{bmatrix} \cdot \sum_{p=1, s^{p,n}_{j+1/2}<0}^{m} \gamma^p_{j+1/2}\mathbf{r}^p_{j+1/2}, \\ \mathbf{A}^+(\mathbf{U}^-_{j+1/2}, \mathbf{U}^+_{j+1/2}) &= \begin{bmatrix} 0 & 1 & 0 & 0 & 1 \\ 0 & 1 & 0 & 0 & 1 \end{bmatrix} \cdot \sum_{p=1, s^{p,n}_{j+1/2}>0}^{m} \gamma^p_{j+1/2}\mathbf{r}^p_{j+1/2}, \\ \mathbf{A}(\mathbf{U}^+_{j-1/2}, \mathbf{U}^-_{j+1/2}) &= \mathbf{f}(\mathbf{U}^-_{j+1/2}) - \mathbf{f}(\mathbf{U}^+_{j-1/2}) - \boldsymbol{\Psi}(\mathbf{U}^-_{j+1/2}, \mathbf{U}^+_{j-1/2}), \end{aligned} \tag{31}$$

where $\boldsymbol{\Psi}(\mathbf{U}^-_{j+1/2}, \mathbf{U}^+_{j-1/2})$ is a suitable approximation of the source term and $\mathbf{r}^p_{j+1/2}$ are suitable approximations of the eigenvectors (30).

5.3. Steady states

The steady state for the augmented system means $\mathbf{B}(\mathbf{w})\mathbf{w}_x = \mathbf{0}$, therefore $\mathbf{w}_x$ is a linear combination of the eigenvectors corresponding to the zero eigenvalues. The discrete form of the vector $\Delta\mathbf{w}$ corresponds to the certain approximation of these eigenvectors. It can be shown Brandner at al. (2009) that

$$\Delta \begin{bmatrix} A \\ Q \\ \Phi \\ \frac{a_0}{\beta} \\ \beta \end{bmatrix} = \begin{bmatrix} \frac{\bar{A}}{\rho}\frac{1}{\widetilde{\lambda^1\lambda^2}} \\ 0 \\ \frac{\bar{A}}{\rho}\frac{\widetilde{\lambda^1\lambda^2}}{\widetilde{\lambda^1\lambda^2}} \\ 1 \\ 0 \end{bmatrix} \Delta\left(\frac{a_0}{\beta}\right) + \begin{bmatrix} \frac{\bar{A}^2}{\rho\beta_{j+1}\beta_j}\frac{1}{\widetilde{\lambda^1\lambda^2}} \\ 0 \\ \frac{\bar{A}^2}{\rho\beta_{j+1}\beta_j}\frac{\widetilde{\lambda^1\lambda^2}}{\widetilde{\lambda^1\lambda^2}} - \frac{\tilde{A}^2}{2\rho\beta_{j+1}\beta_j} \\ 0 \\ 1 \end{bmatrix} \Delta\beta, \tag{32}$$

where $\bar{A} = \frac{A_j + A_{j+1}}{2}$, $\bar{\beta} = \frac{\beta_j + \beta_{j+1}}{2}$, $\tilde{A}^2 = \frac{A_j^2 + A_{j+1}^2}{2}$, $\tilde{V}^2 = |V_j V_{j+1}|$, $\bar{V}^2 = \left(\frac{V_j + V_{j+1}}{2}\right)^2$ and

$$\widetilde{\lambda^1\lambda^2} = -\tilde{V}^2 + \frac{\bar{A}\bar{\beta}}{\rho\beta_{j+1}\beta_j}, \qquad \overline{\lambda^1\lambda^2} = -\bar{V}^2 + \frac{\bar{A}\bar{\beta}}{\rho\beta_{j+1}\beta_j}. \tag{33}$$

Therefore we use vectors on the RHS of (32) as approximations of the fourth and fifth eigenvectors of the matrix $\mathbf{B}(\mathbf{w})$ to preserve general steady state.

5.4. Positive semidefiniteness

Positive semidefiniteness of this scheme is shown in George (2008) for the case of shallow water equation. It is based on a special choice of approximations of the eigenvectors (30). This, in the case of urethra flow, is more complicated because of the structure of the eigenvectors. Some necessary conditions for approximation of these eigenvectors are presented in Brandner at al. (2009).

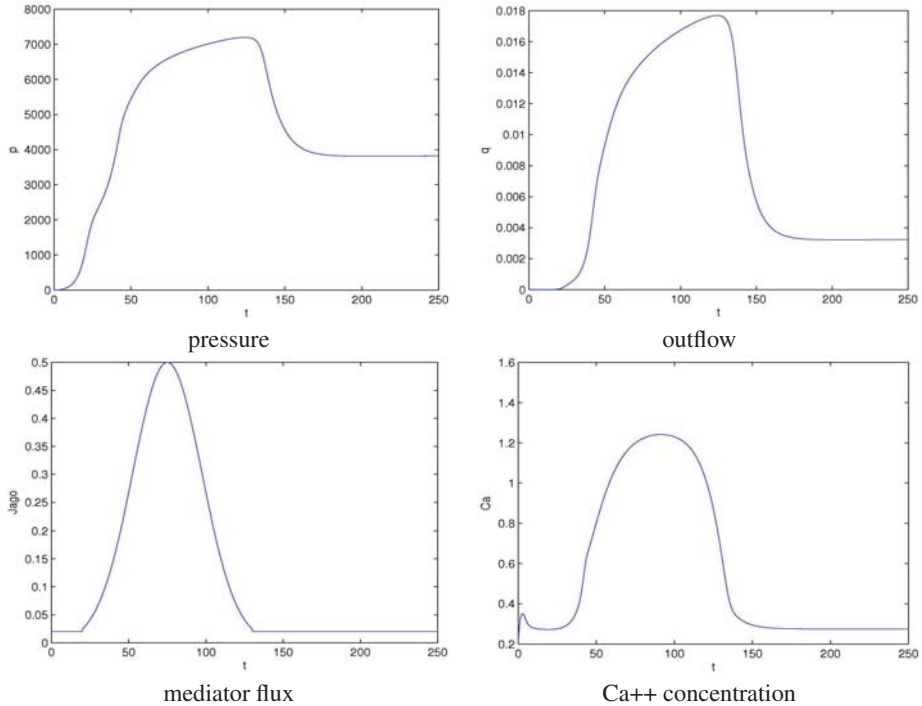

Fig. 2: Time evolution of the quantities at the bladder neck.

6. Numerical experiment

Now we present numerical experiment based on the system of differential equations described detrusor smooth muscle cell model (12 equations) and urethral flow (30 equations). The equations describing urethral flow are based on spatial high-resolution discretization of the urethra (15 finite volumes) described in section 5.2. The parameters used in this experiment are the same as in Rosenberg (2011a). The figures 2 illustrate time evolution of the quantities at the bladder neck. For the further application it is necessary to fit the parameters because of non-dimensionality of the equations describing the muscle contraction.

1. For the simplicity the precious modelling of the synapse is neglected and the mediator flux $J_{agonist}$ is chosen - see Fig. 2. The IC units are used although in the medical paper are used for intravesical pressure cmH_2O (1 cmH_2O = 0.1 kPa) and for the outflow ml/s. The concentration is measured in μM where M=mol/l.

2. At the Fig. 3 there are shown the cross-section area, velocity and flow rate along the whole urethra in two different times after beginning of voiding.

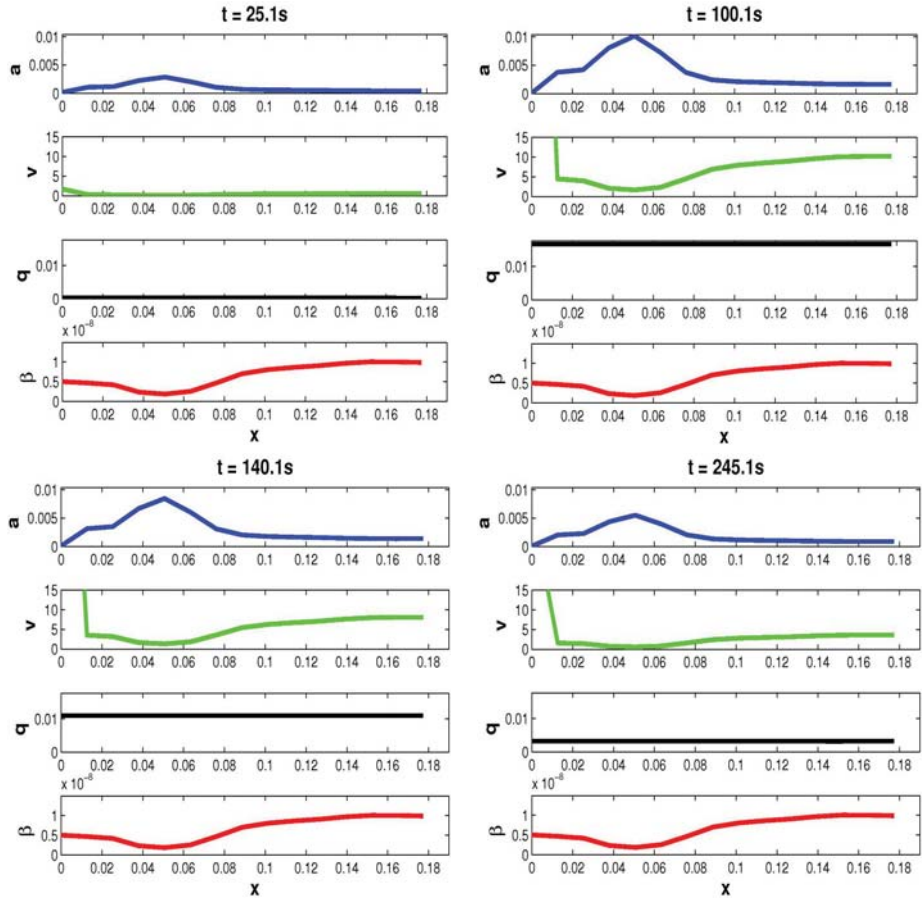

Fig. 3: Time evolution of the quantities through the urethra (cross section area, velocity, flow rate, tube compliance).

7. Conclusion

We presented the complex model of the lower part of the urinary tract. A simple bladder model and the detrusor contraction model were developed during voiding together with the detailed model of urethra flow. The urethra flow was described by the high-resolution positive semidefiniteness method, which preserves general steady states. For the practical application the identification of the parameters is necessary.

Acknowledgments

This work was supported by the European Regional Development Fund (ERDF), project NTIS - New Technologies for Information Society, European Centre of Excellence, CZ.1.05/1.1.00/02.0090 and the project SGS-2010-077 Support of Biomechanics at the Faculty of Applied Sciences, University of West Bohemia in Pilsen.

References

Arts, T., Bovendeerd, P.H.M., Prinzen, F.W., Reneman, R.S. (1991), Relation between left ventricular cavity pressure and volume and systolic fiber stress and strain in the wall. In: *Biophys. J.*,1991, vol. 59, p. 93-102

Brandner, M., Egermaier, J., Kopincová, H. (2009), Augmented Riemann solver for urethra flow modelling. In: *Mathematics and Computers in Simulations*, Vol. 80, No. 6, pp. 1222-1231

Črnjarič-Zič, N., Vukovič, S., Sopta, L. (2004), Balanced finite volume WENO and central WENO schemes for the shallow water and the open-channel flow equations. *Journal of Computational Physics*, Vol. 200, No. 2, pp. 512-548,

Dicarlo, A. and Quiligotti, S. (2002), Growth and balance. In: *Mechanics Research Communications 29*, Pergamon Press, 2002, p. 449-456.

George, D., L. (2008), Augmented Riemann Solvers for the Shallow Water Equations over Variable Topography with Steady States and Inundation. In: *Journal of Computational Physics*, Vol. 227, pp. 3089-3113.

Hai, C.M. and Murphy, R.A. (1992), Adenosine 5'-triphosphate consumption by smooth muscle as predicted by the coupled four-state crossbridge model. In: *Biophysical Journal*,1992, vol. 61, no. 2, p. 530-541

Koenigsberger, M., Sauser, R., Seppey, D., Beny, J.-L., Meister, J.-J. (2008), Calcium dynamics and vosomotion in arteries subject to isometric, isobaric and isotonic conditions. In: *Biophysical Journal* Vol. 95, 2008 p. 2728-2738

Kurganov, A., Tadmor, E. (2000), New High-Resolution Central Schemes for Nonlinear Conservation Laws and Convection-Diffusion Equations. In: *Journal of Computational Physics*, Vol. 160, No. 1, pp. 241-282

Laforet, J. and Guiraud, D. (2007), Smooth Muscle Model For Functional Electric Stimulation Applications. In: *Proceedings of the 29th Annual International Conference of the IEEE EMBS*, Cite Internationale, Lyon. France August 23-26. 2007

Parthimos, D., Edwards, D.H., Hill, C.E., Griffith, T.M. (2007), Dynamics of a three-variable nonlinear model of vasomotion: Comparison of theory and experiment. In: *Biophysical Journal*, 2007, vol. 93. p. 1534-1556

Pokrovski, V.N. (2005), Extended thermodynamics in a discrete/system approach. In: *European Journal of Physics*, 2005, vol. 26, p. 769-781

Rosenberg, J. (2011a), Smooth muscle model applied to bladder. In: *Proceeding of the 4th International conference Modelling of mechanical and mechatronic systems MMaMS 2011, Sept. 20-22*, Herlany, Slovakia.

Rosenberg, J. (2011b), Modelling of the voiding process. In: *Extended abstracts, 27th Conference with international participation Computational Mechanics 2011 November 7.-9.*, 2011, Plzeň.

Rosenberg, J. and Hynčík, L., (2007), Contribution to the simulation of growth and remodelling applied to Muscle fibre stimulation. In: *Short communication of the 1st IMACS International Conference on Computational Biomechanice and Biology ICCBB 2007, Sept. 10-13*, 2007, Plzeň, p. 1-4

Rosenberg, J. and Hynčík, L., (2008), Modelling of the influance of the stifness evolution on the behaviour of the Muscle fibre. In: *Human Biomechanice 2008*, International Conference, 29.9.-1.10.2008 Praha, Czech Republic

Rosenberg, J. and Svobodová, M. (2010), Comments on the thermodynamical background to the growth and remodelling theory applied to the model of muscle fibre contraction. In: *Applied and Computational Mechanics*, 2010, vol 4, no. 1 p. 101-112.

Stergiopulos, N., Tardy, Y., Meister, J.-J. (1993), Nonlinear Separation of Forward and Backward Running Waves in Elastic Conduits. In: it Journal of Biomechanics, Vol. 26, pp. 201-209

18th International Conference
ENGINEERING MECHANICS 2012
Svratka, Czech Republic, May 14 – 17, 2012

pp. 147–150
Paper #61

SINGULAR CASES OF PLANAR AND SPATIAL PARALLEL MANIPULATOR

L. Brezina[*], L. Houfek[**]

Abstract: *Singularities are places in the workspace of the robot where kinematic equations have no solution. It is of course desired to minimize number of such places in the workspace. The analysis of these places is then important from the construction point of view where singularities might be suppressed by suitable changes in design of construction. The paper deals with description of singular cases types of a parallel manipulator and their analysis via analysis of the determinants of the system Jacobians. This is demonstrated for two examples – planar and spatial parallel manipulator.*

Keywords: ***Parallel manipulator, singular cases, Jacobian matrices .***

1. Introduction

Parallel mechanisms are generally based on closed – loop kinematic chain which leads to very high stiffness of such a mechanism and related properties as high positioning accuracy and repeability, possibility of mounting of the actuators to the base thus achieving of high accelerations. On the other hand such a construction has also its drawbacks. It is among others smaller workspace which is restricted by singularity areas. These are defined as places in the workspace where direct or inverse kinematics has no solution. The appearance of such a singularity may cause fast changes in accelerations and force effects which may lead to loosing of the controllability or destruction of the device or its parts.

The methods for the singularity detection are either numerical or graphical. The numerical methods are often based on the analysis of determinants of Jacobian matrices (Sefrioui & Gosselin, 1992 or Belda & Stejskal, 2003), i.e. on the analysis of the presence of the solution for the kinematics. There are also sometimes used geometry methods, i.e. based on the Grassmann geometry (Merlet, 1989). The proposed article presents a singularity analysis for a spatial and planar manipulator via the method analyzing determinants of Jacobian matrices.

2. Analysis method

The method is based on the analysis of determinants of Jacobian matrices as was already mentioned. The singularity is detected for the singular value of the determinant. The behavior of the manipulator is also rapidly getting worse for the determinants which are “close to zero” – how close to zero must the determinant be to observe the unacceptable behavior have to be tested individually for each manipulator. The Jacobians are typically obtained in the following way.

The relation between joint and cartesian coordinates may be expressed as

$$f\left(q,z\right)=0, \tag{1}$$

where $q=\left[q_1,q_2,...,q_n\right]^T$ is the vector of the joint coordinates and $z=\left[z_1,z_2,...,z_n\right]^T$ is the vector of the Cartesian coordinates.

[*] Ing. Lukas Brezina, Ph.D..: Institute of Soldi Mechanics, Mechatronics and Biomechanics, Brno University of Technology, Technicka 2; 616 69, Brno; CZ, e-mail: brezina.l@fme.vutbr.cz

[**] Ing. Lubomir Houfek, Ph.D..: Institute of Soldi Mechanics, Mechatronics and Biomechanics, Brno University of Technology, Technicka 2; 616 69, Brno; CZ, e-mail: houfek@fme.vutbr.cz

Jacobians of the systems are then defined as

$$\Phi_q = \begin{bmatrix} \frac{\partial f_1}{\partial q_1} & \mathrm{L} & \frac{\partial f_1}{\partial q_n} \\ \mathrm{M} & \mathrm{O} & \mathrm{M} \\ \frac{\partial f_n}{\partial q_1} & \mathrm{L} & \frac{\partial f_n}{\partial q_n} \end{bmatrix}, \Phi_z = \begin{bmatrix} \frac{\partial f_1}{\partial z_1} & \mathrm{L} & \frac{\partial f_1}{\partial z_n} \\ \mathrm{M} & \mathrm{O} & \mathrm{M} \\ \frac{\partial f_n}{\partial z_1} & \mathrm{L} & \frac{\partial f_n}{\partial z_n} \end{bmatrix} \tag{2}$$

There are then three possible situations (the determinants are consequently analyzed for the whole workspace:

a) $\det \Phi_q = 0$ and $\det \Phi_z \neq 0$ for the singularities of the first type,

b) $\det \Phi_q \neq 0$ and $\det \Phi_z = 0$ for the singularities of the second type,

c) $\det \Phi_q = 0$ and $\det \Phi_z = 0$ for the combined singularities.

3. Spatial mechanism analysis

The spatial mechanism for the analysis is consisting of six extendible links and a platform (Fig. 1). The effector has six degrees of freedom.

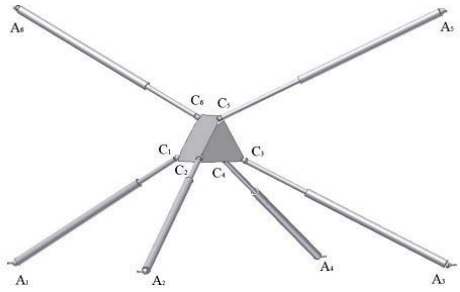

Fig. 1 Analysed spatial 6 DOF parallel manipulator

The relation between the joint and Cartesian coordinates is

$$\begin{aligned} f_i = &\left(n_x C_{ix} + o_x C_{iy} + w_x C_{iz} + x_{c1} - A_{ix}\right)^2 + \left(n_y C_{ix} + o_y C_{iy} + w_y C_{iz} + y_{c1} - A_{iy}\right)^2 + \\ &+ \left(n_z C_{ix} + o_z C_{iy} + w_z C_{iz} + z_{c1} - A_{iz}\right)^2 - S_i^2 = 0 \end{aligned} \tag{4}$$

for $i = 1, ..., 6$, where

$$R = \begin{bmatrix} \cos\psi\cos\nu & -\cos\psi\sin\varphi & \sin\psi \\ \sin\varphi\sin\psi\cos\nu + \cos\varphi\sin\nu & -\sin\varphi\sin\psi\sin\nu + \cos\varphi\cos\nu & -\sin\varphi\cos\psi \\ -\cos\varphi\sin\psi\cos\nu + \sin\varphi\sin\nu & \cos\varphi\sin\psi\sin\nu + \sin\varphi\cos\nu & \cos\varphi\cos\psi \end{bmatrix} = \begin{bmatrix} n_x & o_x & w_x \\ n_y & o_y & w_y \\ n_z & o_z & w_z \end{bmatrix}$$

and $C_{ix,y,z}$ are (cartesian) coordinates of the platform points, $A_{ix,y,z}$ are coordinates of the base points, x_{c1}, y_{c1}, z_{c1} are describing translation of the platform point C_1, ψ, ν, φ are Euler angles and S_i are link lengths (joint coordinates).

The equation (4) may be used for the derivation of the system Jacobians according to (2). Consequently are analyzed singularities (Fig. 2, 3).

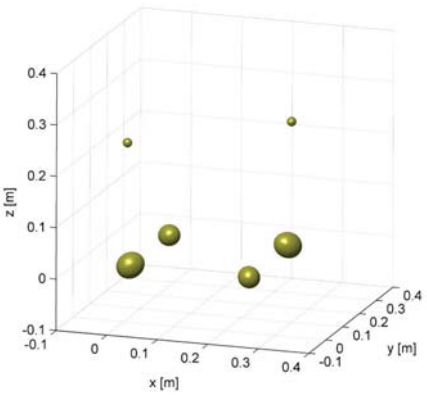

Fig. 2 Singular areas of the first type for $\psi, \nu, \varphi = 0°$

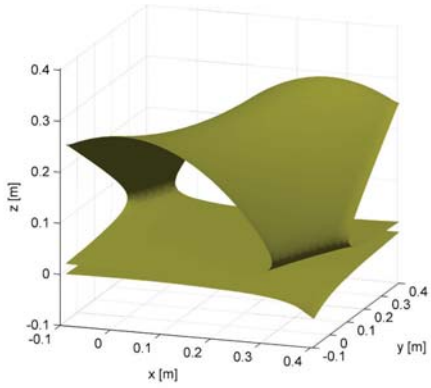

Fig. 3 Singular areas of the second type for $\psi, \nu, \varphi = 0°$

The following examples are mapping the workspace of the manipulator for the different orientations of the platform (Fig. 4- 7).

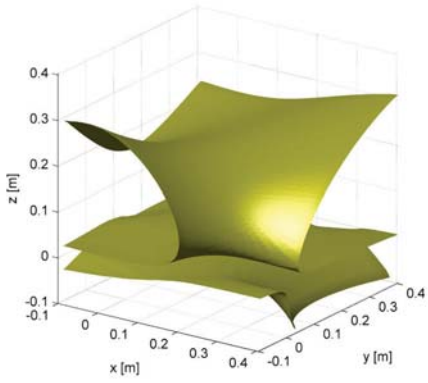

Fig. 4 $\psi = 5°, \nu = 0°, \varphi = 0°$

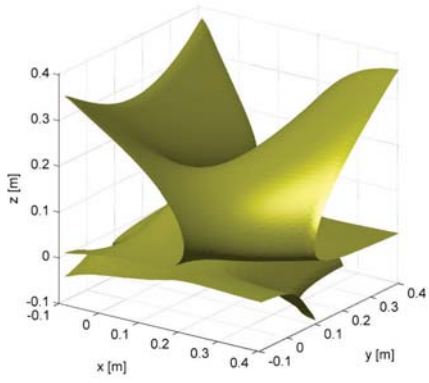

Fig. 5 $\psi = 5°, \nu = 5°, \varphi = 0°$

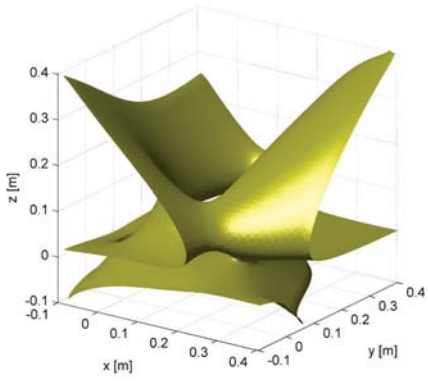

Fig. 6 $\psi = 5°, \nu = 5°, \varphi = 5°$

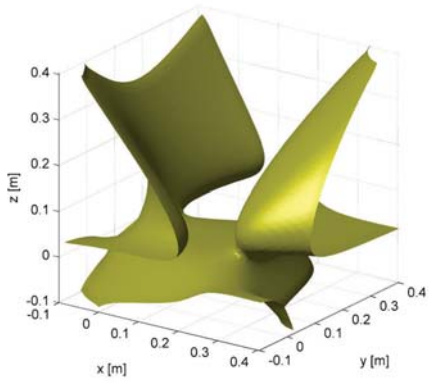

Fig. 7 $\psi = 10°, \nu = 5°, \varphi = 5°$

4. Planar manipulator

The planar manipulator is classical 3RPR 3 DOF parallel mechanism according to Fig. 8. It consists of the three extendable links and triangular effector.

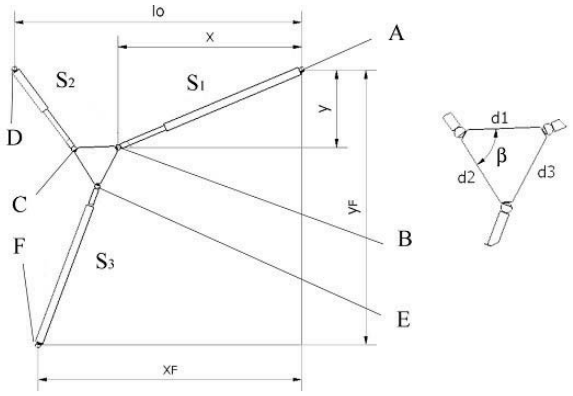

Fig. 8 3RPR parallel manipulator

The singularities (Fig. 9, 10) are analyzed in the same manner as for the spatial example.

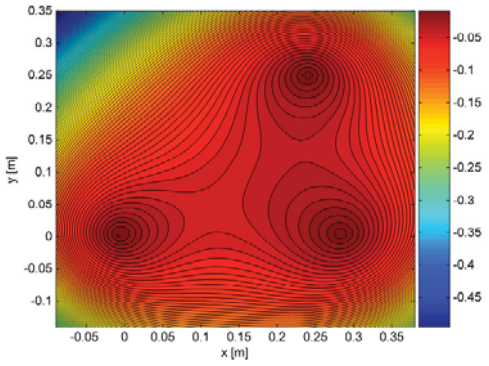

Fig. 9 Singularities of the first type $\varphi = 0°$

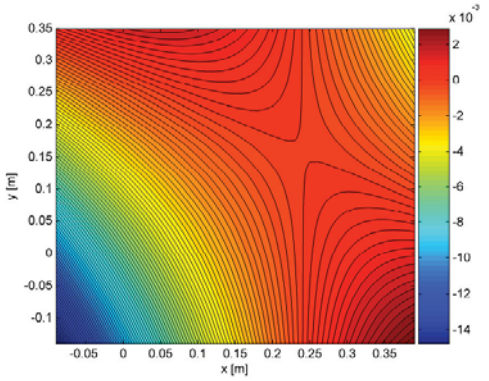

Fig. 10 Singularities of the second type $\varphi = 0°$

5. Conclusions

The article describes possible areas of singularities in a parallel manipulator workspace. There were analyzed singularities for the spatial and planar manipulator via the method analyzing determinants of the system Jacobians. The study is useful especially for the trajectory planning purposes where the avoiding of singularities is important because of the mechanism damage prevention.

Acknowledgement

This work was supported from FSI-S-11-15 "Design, testing and implementation of control algorithms with use of nonlinear models of mechatronics systems".

References

Belda, K. & Stejskal, V. (2003) Singular cases of the planar parallel robot. *Proceedings, Engineering mechanics*.

Merlet, J. P. (1989) Singular configurations of parallel manipulators and Grassmann geometry. *The international journal of robotics research*, 8, 5, pp. 1099 – 1113.

Sefrioui, J. & Gosselin, C. M. (1992) Singularity analysis and representation of planar parallel manipulators. *Robotics and autonomous systems*, 10 pp. 209 – 224.

18th International Conference
ENGINEERING MECHANICS 2012
Svratka, Czech Republic, May 14 – 17, 2012

pp. 151–158
Paper #238

FLOW BASED VIBRATIONS OF SLUICE GATES – PHYSICAL AND NUMERICAL MODELLING

M. Brouček[*], V. Jirsak[**], M. Králík[***], P. Nowak[†], L. Satrapa[‡], M. Zukal[§]

Abstract: *The first part of the paper presents results from laboratory experiments simulating hydrodynamic load acting on the large model of sluice gate located on spillway. Vibrations of the gate as one of the key aspects of durability and reliability of sluice gates as outlet works were measured together with forces in operating mechanism and pressures in surroundings. The second part is focused on numerical modelling of the executed experiments and aims at possible approaches for reliability assessment of sluice gates. The influence of the shape of the gate bottom on induced vibrations and possible cavitation is discussed in both parts.*

Keywords: ***Sluice gates, Physical modelling, Numerical modelling, Vibration***

1. Introduction

Reliability of flood gates installed on emergency spillways of hydraulic structures become widely discussed topic after major flood events struck Czech Republic in 1997 and 2002. Malfunction of flood gates followed by overtopping of the dam with all the related impacts is a primary cause in more than 25 % cases worldwide (Cassidy, 2000). Although no serious case of malfunction on important hydraulic structures during floods was reported in Czech Republic so far, increased probability of accidents can be expected despite regular maintenance as most of the gates are rapidly approaching the end of their designed service life.

The scope of the present contribution involves hydraulic and dynamic analysis of flow under the sluice gates. The importance of the issue of discharge under the sluice gate and possible vibration of the gate and foundation structure follows from operational grounds as well as from the reliability point of view. Hygienic standards also influence the necessity for deep understanding of this topic. Theoretical part of the paper is aimed at discharge under and over the sluice gate.

The experimental part focuses on description of principles used for measurement and evaluation of values on physical model constructed in the hydraulic laboratory at the CTU in Prague, Faculty of Civil Engineering. Pressures acting on the foundation structures and vertical forces acting on the gate structure under the steady state, gate lifting or lowering conditions measured on the physical model are presented in the experimental section.

The last section of this paper describes numerical model of sluice gate created in ANSYS Workbench environment while using ANSYS CFX code for modelling of flow and ANSYS Mechanical code for structural analysis. It comments the results obtained by applying one-way fluid-

[*] Ing. Miroslav Brouček: Czech Technical University in Prague, Faculty of Civil Engineering, Thákurova 7; 166 29, Prague; CZ, e-mail: miroslav.broucek@fsv.cvut.cz

[**] Ing. Václav Jirsák: Czech Technical University in Prague, Faculty of Civil Engineering, Thákurova 7; 166 29, Prague; CZ, e-mail: vaclav.jirsak@fsv.cvut.cz

[***] Ing. Martin Králík, Ph.D.: Czech Technical University in Prague, Faculty of Civil Engineering, Thákurova 7; 166 29, Prague; CZ, e-mail: martin.kralik@fsv.cvut.cz

[††] Dr. Ing. Petr Nowak: Czech Technical University in Prague, Faculty of Civil Engineering, Thákurova 7; 166 29, Prague; CZ, e-mail: petr.nowak@fsv.cvut.cz

[‡] doc. Ing. Ladislav Satrapa, CSc.: Czech Technical University in Prague, Faculty of Civil Engineering, Thákurova 7; 166 29, Prague; CZ, e-mail: satrapa@fsv.cvut.cz

[§] Ing. Milan Zukal, Ph.D.: Czech Technical University in Prague, Faculty of Civil Engineering, Thákurova 7; 166 29, Prague; CZ, e-mail: zukal@fsv.cvut.cz

structure interaction where hydrodynamic forces calculated in fluid part are used as boundary condition for the structural part. First ten eigenfrequencies and corresponding shapes of the laboratory model were determined by modal analysis and are presented in the final part of the numerical section.

2. Theory

2.1. Overfall spillway discharge

Water flowing over obstruction or construction called spillway is generally regarded as overfall. The highest point of the spillway is called spillway crest or the edge of spillway. Flow over spillway results in changes in pressure and flow velocity. Upstream and downstream water surface level difference is of importance.

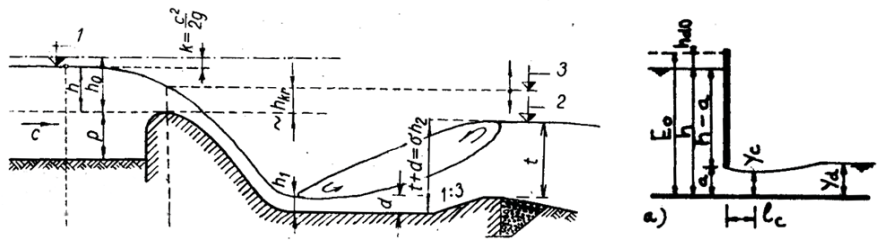

(a) (b)

Fig. 1: Calculation schemes: (a) Overfall spillway, (b) Discharge under sluice gate

Bazin`s equation can be used for calculation of spillway discharge under the conditions of steady flow which is not influenced by the tailwater level.:

$$Q = mb_0\sqrt{2g}\mathrm{h}^{3/2} \tag{1}$$

Where Q stands for spillway discharge [$m^3.s^{-1}$], m for coefficient of discharge [-], b_0 for effective width of spillway [m], g for gravitational acceleration = 9,81 $m.s^{-2}$ and h for head [m].

2.2. Discharge under sluice gate

Discharge under the sluice gated which is not influenced by tailwater is regarded as free flow discharge or perfect discharge. For discharge calculation the tailwater level, the shape of the edge of sluice gate and channel bottom, the influence of side structures, the height of gate opening, the transition of outflow stream into the tailwater all have to be taken into consideration. Assumptions used for calculation of model discharge are as follows. Atmospheric pressure is acting on both head and tailwater and the gate opening has rectangular shape. The characteristic value is therefore flow rate calculated on one meter of width of sluice gate denoted as q. Under the assumption of free and steady flow following equation can be used to calculate the discharge:

$$Q = \mu_v a\mathrm{b}\sqrt{2g(E_0 - y_c)} \tag{2}$$

Where Q stands for discharge under the gate [$m^3.s^{-1}$], μ_v for discharge coefficient [-], b for width of gate opening [m], a for height of gate opening [m], g for gravitational acceleration = 9,81 $m.s^{-2}$, E_0 for energy head and y_c for smallest the flow depth [m].

2.3. Basic Static analysis – material for model

Basic static analysis using elastic theory was carried out for the purpose of material selection for laboratory model. Static scheme selected for skin plate and cross beam is clear from following figure. Material SIMOLUX was selected based on the calculated values of deflections. Table 1 presents results calculated from simple static and 3D numerical analysis for selected material under the hydrostatic conditions as well as measured value of deflection and deflection calculated using finite code ANSYS Mechanical, where loading was derived from fluid dynamic calculations (more in Section 4.3.), for the hydrodynamic load with 30 mm gate opening.

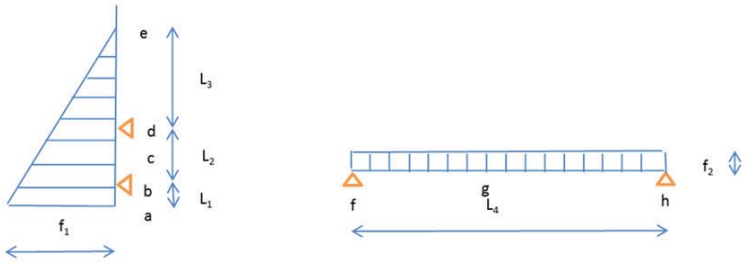

Fig. 2: Static scheme for basic 2D calculations of skin plate and cross beam

Tab. 1: Stress and deformation of laboratory model of sluice gate made of SIMOLUX

Source	Hydrostatic load	Hydrodynamic load
Deflection at point e – top middle (mm)		
Simple 2D analysis	2.9	----
FEM 3D analysis	2.8	1.10
Measured	----	1.45

3. Physical modelling

Physical model can faithfully represent the structure, under the certain conditions, and thus provide answers to numerous hydraulic, static and dynamic conditions. In order to obtain valid results from hydraulic research it is necessary to follow restrictions based on the type of the problem. In this case Froud`s Law of Comparison was used. Several similar models, which complement and extend each other's range of interest, have to be built, so that obtained results can be generalized. The models should cover whole range of possible topologies, hydraulic conditions and loading cases.

During the physical modelling all sorts of variables are measured and logged. For example, both static and dynamic action of water on the foundation structure, on the sluice gate structure, on the operating rod and their response and also hydraulic conditions in front and behind the gate. Typically, water pressure, force in operating rod and water levels are measured for selected flow or discharge rate. Thomson's spillway was used to measure flow rate, pressure probes to gather pressure distribution along the spillway, cylindrical gauges to measure deformations of the sluice gate and position of the water surface and force transducers to gain the force in time distribution in the operating rods. Table 2 shows typical result of measured and derived hydraulic variables on models with different shape of a spillway crest.

Tab. 2: Stress and deformation of laboratory model of sluice gate made of SIMOLUX

Variable	Spillway no. 1	Spillway no. 2	Spillway no. 3	Spillway no. 4
Description	Negative pressure overfall shape	Negative pressure overfall shape	Jambor sill	Jambor sill
h / h_a (-)	2.2	1.3	-	-
s (m)	-	-	0.03	0.1
h_a (m)	0.05	0.085	-	-
h (m)	0.12	0.12	0.12	0.5
b (m)	0.53	0.53	0.53	0.5
m (-)	0.53	0.52	0.52	0.55

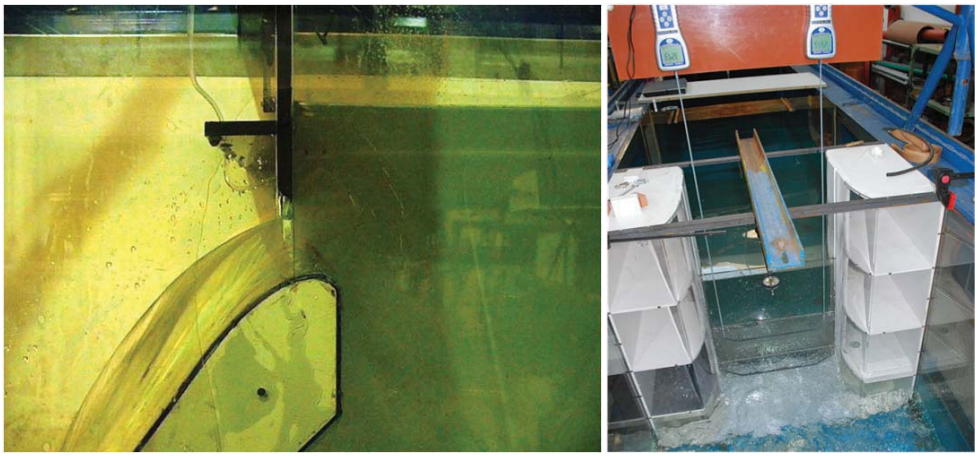

(a) (b)

Fig. 3: Laboratory models: (a) Spillway no. 1 – set-up 9, (b) Spillway no. 5 – set-up 2

Coefficient of discharge m derived from measured values on spillway no. 3 varies in range 0.51 to 0.54 and discharge coefficient μ_v varies between 0.782 and 0.87 both depending on the head. These values are different from usually used and published (e.g. Gabriel et. al., 1989; Kolář, Patočka and Bém, 1983) as the standard range for m is 0.43 to 0.5 and for μ_v it is 0.7 to 0.75. All these differences obtained by physical modelling will be subjected to future detailed research and the influence of tailwater will be included. Left part of the following figure presents measured values of pressure variations acting on foundation structure Fig. 4 (a) while on the right side the force in the operating rod is plotted against time during lifting the gate. Both figures contain data for different shape of the spillway model (i.e. spillway no. 1, no. 2 and no. 3)

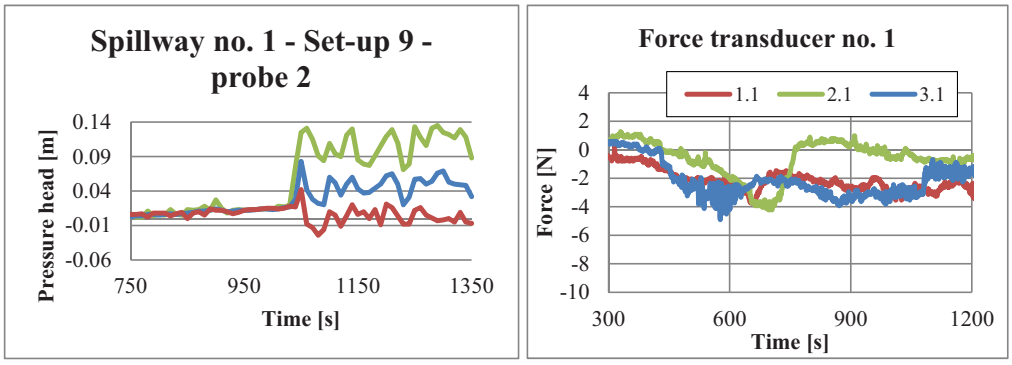

(a) (b)

Fig. 4: Measured values during gate lifting for different spillway models: (a) Pressure acting on the foundation structure, (b) Force in operating rod

Presented results clearly demonstrate the differences in pressure and force fluctuations and the time where bottom part of the gate loses contact with the water surface and free overfall state is reached. Fig. 5 (a) shows force fluctuation in operating rod measured on the spillway no. 5 under the steady conditions. The position of the gate opening (20 mm) was kept constant as well as the flow rate. The tailwater was not influencing the discharge under the gate and so all the observed vibration are only induced by the water flowing under the gate. Force magnitude is related to the net self-weight of the gate, which was used to set 0 on transducers. Fig. 5 (b) on the other hand presents absolute values

of forces in case of 30 mm gate opening but influenced by the tailwater, i.e. with submerged hydraulic jump that affects the downstream part (beams) of the gate structure.

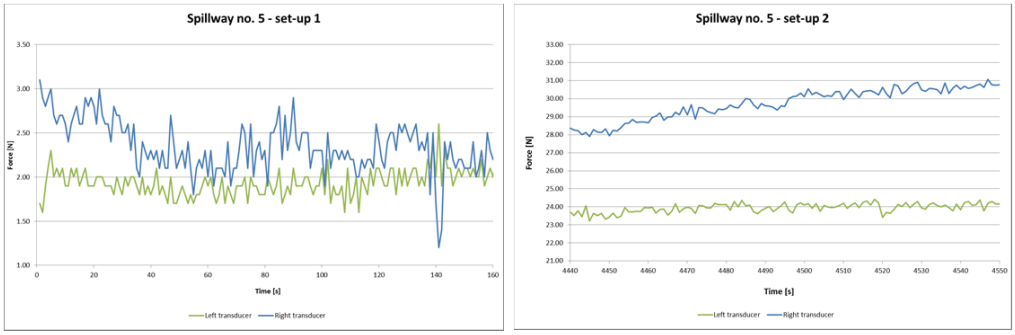

(a) (b)

Fig. 5: Measured forces: (a) Without the influence of tailwater, (b) Tailwater influenced

All the measured sets of data were carefully analysed using FFT. The logging frequency of the transducers was 1 Hz. Vibrations induced without the influence of tailwater did not show any significant differences from vibrations induced only by water flowing under the gate.

4. Numerical modelling

Numerical model of sluice gate was created in ANSYS Workbench environment while using ANSYS CFX code for solving the flow based problem (CFD) and ANSYS Mechanical for structural analysis.

4.1. Model description for CFD

Axis symmetry of the problem was applied in order to decrease the computation time. Sufficient length of the intake and outlet channel was incorporated into the model geometry to stabilize the flow conditions around the gate and also to exclude the direct influence of boundary conditions. Otherwise all the dimensions were taken from the physical model in laboratory. The CFD model topology was created in the Rhinoceros 4.0. software and consequently imported and modified in the ANSYS Geometry. Mesh was created in the ANSYS Meshing tool using the automatic mesh generator. The mesh consists of tetrahedron elements with significant refinement in the area around the bottom edge of the gate. The model consists of total three million elements.

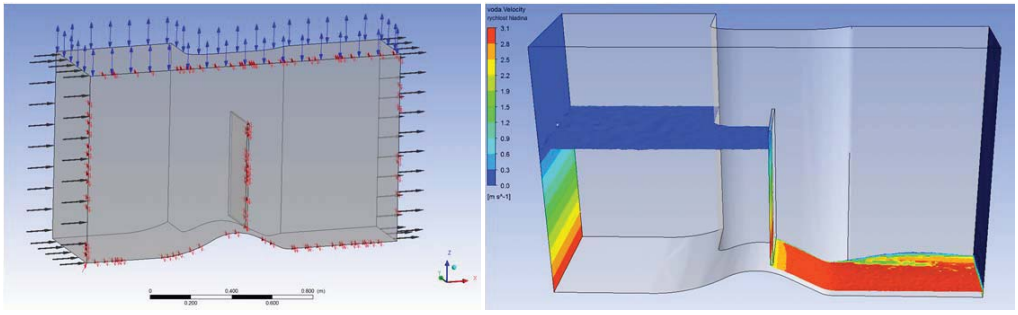

(a) (b)

Fig. 6: CFD model: (a) Topology with boundary conditions, (b) Velocities distribution in m.s^{-1}

4.2. Fluid flow modelling

The flow problem was calculated in ANSYS CFX code using following boundary conditions: ontake channel edge – constant water surface level; outlet channel edge – free flow with zero hydrostatic pressure for set-up no. 1 and raising tailwater level so the hydraulic jump will be positioned just under the gate for set-up no. 2. Top of the model was opened to the air pressure while the rest of the surfaces are considered impermeable. The model setup is clear from Fig. 6 (a).

The initialization of the steady computation of the free discharge under the sluice gate without the influence of the tailwater was executed employing homogenous multiphase water-air model with time step 0.1 s and a standard k-ε model of turbulence. Subsequently, the time step was increased to 0.5 s and the multiphase model was set to "mixture". Figures 6 (b) and 7 (a) present calculated velocity distribution and pressure acting on the gate respectively.

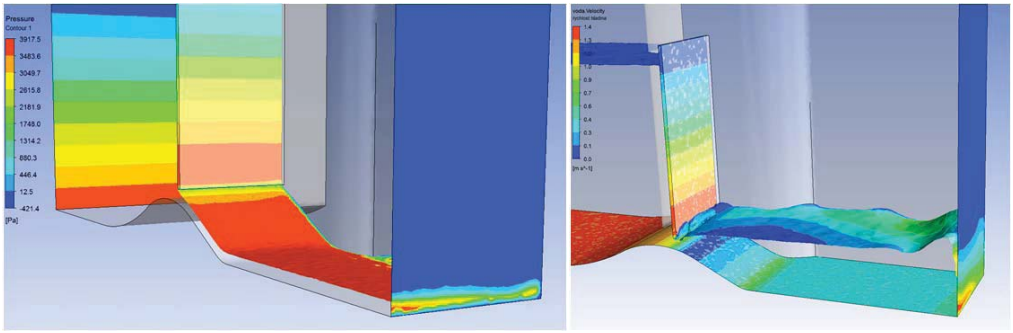

(a) (b)

Fig. 7: CFD model: (a) Pressure acting on the gate without the tailwater influence, (b) hydrostatic pressure (water surface) with the rising tailwater level

Unsteady solver with a time step 0.01 s and 5 iterations in each step was used to calculate the discharge influenced by the tailwater. Example of the results can be seen in Fig. 7 (b). Rising tailwater changes nature of the hydraulic jump and shifts into the close proximity of the bottom edge of the gate. The stream interacts with the bottom part of the gate and together with small wave action on the upstream face causes vibration of the entire gate construction. Time dependent forces with dynamic part having frequency approximately 2.1 s were obtained by the integration of pressures along the surface of the gate. Figure 8 shows fluctuation of forces acting on the bottom and downstream side.

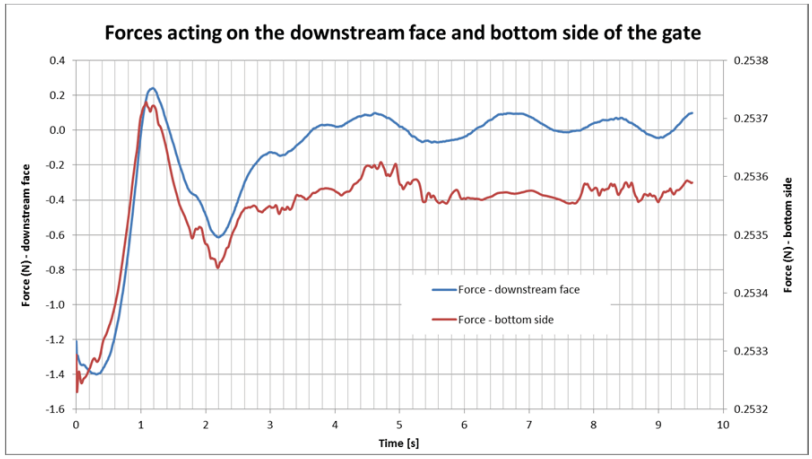

Fig. 8: Fluctuation of forces in numerical model obtained by pressures integration

4.3. Structural analysis – stress, strain and modal analysis

ANSYS Mechanical was used to perform structural analysis of the sluice gate model. Hydrodynamic load calculated using CFD as described in the section above was used as the loading boundary condition. The used method corresponds with the one-way fluid-structure interaction analysis.

The model topology was, as in the case of CFD, prepared in Rhinoceros 4.0 code and meshing was done in ANSYS Meshing code using automatic mesh generator. Hexahedral elements with nodes in the middle of sides of the elements were used. The structural model consists of approximately twenty thousand elements. Isotropic elastic material model with SIMOLUX parameters, i.e. 1270 kg.m^{-3} density, Young's modulus equals 1900 MPa and 0.2 for Poisson ratio.

The boundary conditions for structural analysis were set as follows: axes of symmetry – frictionless support; operating rod – vertical displacement constrain; wheels – horizontal displacement constrain; whole domain – self weight; skin plate – hydrodynamic load calculated by CFD for discharge uninfluenced by tailwater. All the applied boundary conditions are clear from Fig. 9.

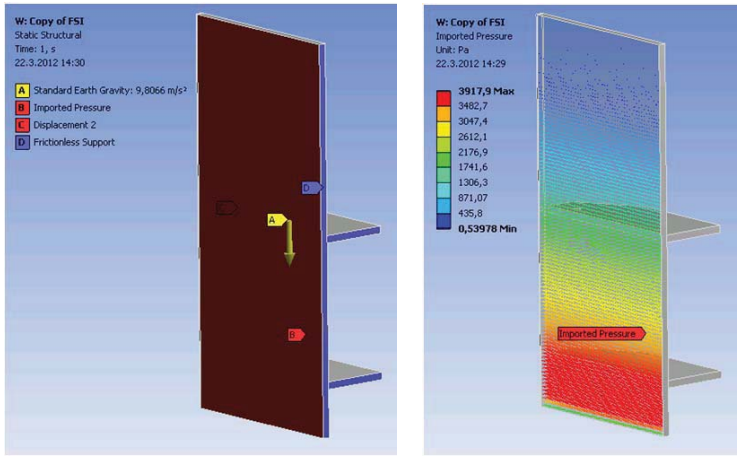

Fig. 9: Boundary conditions applied in stress-strain analysis (pressures in Pa)

Calculated deflection of the middle top of the sluice gate under the conditions described above was 1.1 mm. Maximal principal stress in wheels was 10 MPa while in cross beams 0.5 MPa. Typical results are shown in the following figure.

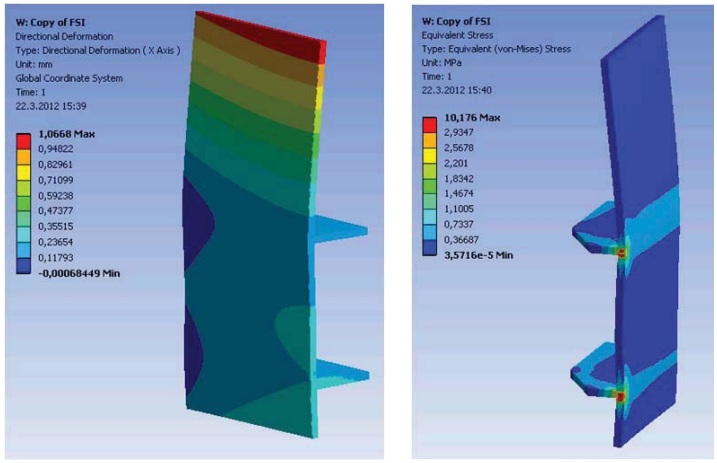

(a) (b)

Fig. 10: Stress-strain analysis (a) horizontal deflection (mm), (b) Von-Mises stress (MPa)

First ten eigenfrequencies and corresponding shapes were obtained by modal analysis and are presented in Fig 11.

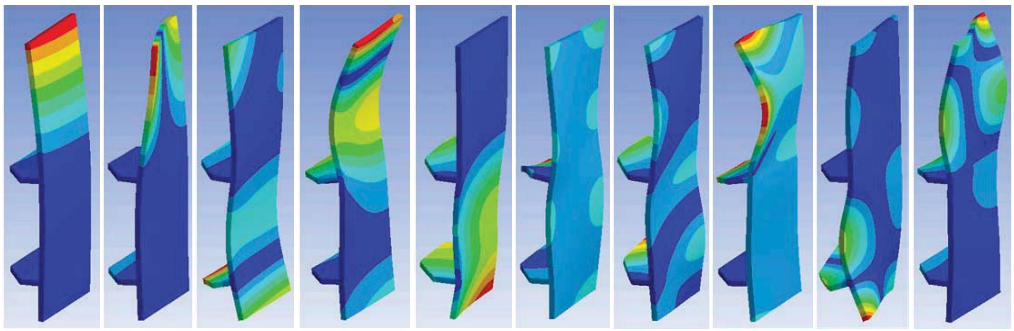

1	2	3	4	5	6	7	8	9	10
22.8	83.9	98.4	128.4	139.4	176.8	221.9	240.7	245.5	276.4

Fig. 10: Eigenfrequencies (Hz) and corresponding shapes

Although agreement between calculated discharge 30.4 l/s and measured discharge 29.9 l/s present suitability of CFD for numerical modelling of discharge under the sluice gate mounted on the Jambor sill, the difference in deflection calculated in the structural analysis part and measured is, however, larger than expected.

5. Conclusions

An extensive experimental program was started in order to properly evaluate vibration of sluice gates induced during discharge and their influence on the safety and reliability of the gates. As a part of this program CFD simulations and one-way fluid structure interaction calculations were carried out to verify the possibility of substituting numerical modelling for demanding physical modelling. Even with no calibrating procedure employed the hydraulic results are in reasonably good agreement with measured values of discharge and pressures. The results obtained from structural analysis show, however, the necessity of calibration of the material characteristics and model topology.

Hydrodynamic loading acting in the horizontal direction on the gate structure is mainly caused by the upstream water surface wave action and tailwater influence which shifts the hydraulic jump backwards to contact with the gate. Oscillations of the pressure in the hydraulic jump are then transferred to the gate structure. Hydraulically sharp or unsuitably shaped bottom edge of the gate can be the source of vibration even without the tailwater influence.

Acknowledgement

The financial support of the project No. VG20102014056 provided by the Ministry of the Interior of the Czech Republic is gratefully acknowledged.

References

Bubeník, M. (2000) Maintenance concerning the reliable operation of spillway gates on dams in Czech Republic. Q79. R20. *20th ICOLD Congress*. Beijing. China.

Cassidy, J. J. (2000) Gated spillways and dam safety. *Hydropower & Dams*. **6**. 71-75

Gabriel, P. et al. (1989) *Jezy - Weir structures*. Czech Republic. (in Czech).

International Commision of Large Dams – ICOLD (1996) Vibrations of hydraulic equipment for dams. *ICOLD Bulletin 102*

Kolář, V., Patočka, C. and Bém, J. (1983) *Hydraulika - Hydraulics*. Czech Republic. (in Czech).

Mouvet, L.C., Darbre, G.R. (2000) Probabilistic treatment of uncertainties: Malfunctioning of dischrage works and sliding of concrete dam under earthquake. Q76. R14. *20th ICOLD Congress*. Beijing. China

Pohl, R. (2000) Failure frequency of gates and valves at dams and weirs. *Hydropower & Dams*. **6**. 77-82

18th International Conference
ENGINEERING MECHANICS 2012
Svratka, Czech Republic, May 14 – 17, 2012

pp. 159–160
Paper #216

ON EFFECTIVE IMPLEMENTATION OF THE NON-PENETRATION CONDITION FOR NON-MATCHING GRIDS PRESERVING SCALABILITY OF FETI BASED ALGORITHMS

T. Brzobohatý [*], O. Vlach [**], Z. Dostál [***]

Abstract: *The point of this work is to extend our results obtained for elastic contact problems to the contact problems with non-matching grids which necessarily emerge, e.g., in the solution of transient contact problems or in contact shape optimization. We want to get good approximation and the constraint matrix B with nearly orthogonal rows. We consider both standard engineering approaches such as node to segment, or mortar elements. We give simple bounds on the singular values of the resulting matrix B and results of numerical experiments, including both the academic examples and some problems of practical interest. We conclude that the normalized orthogonal mortars proposed by Wohlmuth can be used to approximate the non-penetration conditions in a way that complies with the requirements of the FETI methods.*

Keywords: ***contact problems, Mortar elements, TFETI, scalability.***

1. Introduction

Mathematical models of contact include the inequalities which make the contact problems strongly nonlinear. In spite of this, a number of interesting results have been obtained by modifications of the methods that were known to be scalable for linear problems, in particular of the FETI domain decomposition method introduced by Farhat and Roux for parallel solution of linear problems. Using this approach, a body is partitioned into non-overlapping subdomains, an elliptic problem with Neumann boundary conditions is defined for each subdomain, and intersubdomain field continuity is enforced via Lagrange multipliers. The Lagrange multipliers are evaluated by solving a relatively well conditioned dual problem of small size that may be efficiently solved by a suitable variant of the conjugate gradient algorithm. Later Farhat (Mandel and Roux) introduced a "natural coarse problem" whose solution was implemented by auxiliary projectors so that the resulting algorithm became scalable.

It has been soon observed that duality based domain decomposition methods may also be successful for the solution of variational inequalities that describe equilibrium of a system of elastic bodies in unilateral contact. Recently, we obtained the theoretical results that guarantee the scalability also for contact problems, see Dostál et all (2010, 2012, 201x); Sadowská et all (2011).

The scalability results were originally proved for matching grids. In this case, the boolean matrix B which imposes the "gluing" conditions and non-penetration conditions has nearly orthogonal rows, which turns out to be a key ingredient of the proofs of optimality. By nearly orthogonal we mean that the matrix B has singular values distributed in a given positive interval that does not depend on the discretization parameter. For linear problems, B can be effectively reduced to the matrix with orthogonal rows; this was used by Klawonn and Widlund to improve the estimates of the rate of convergence. The orhogonalization of constraints that they use comprises multiplication of constraints that is not admissible for inequalities that describe the non-penetrations.

The point of this paper is to extend the results mentioned above to the contact problems with non-matching grids which necessarily emerge, e.g., in the solution of transient contact problems or in contact

[*]Ing. Tomáš Brzobohatý, PhD.: IT4Innovations Centre of Excellence, VŠB-Technická univerzita Ostrava, 17. listopadu 15/2172; 708 33, Ostrava-Poruba; CZ, e-mail: tomas.brzobohaty@vsb.cz
[**]Ing. Oldřich Vlach, PhD.: IT4Innovations Centre of Excellence, VŠB-Technická univerzita Ostrava, 17. listopadu 15/2172; 708 33, Ostrava-Poruba; CZ, e-mail: oldrich.vlach2@vsb.cz
[***]Prof. RNDr. Zdeněk Dostál, CSc.: IT4Innovations Centre of Excellence, VŠB-Technická univerzita Ostrava, 17. listopadu 15/2172; 708 33, Ostrava-Poruba; CZ, e-mail: zdenek.dostal@vsb.cz

shape optimization. We want to get both good approximation and B with nearly orthogonal rows. We consider both standard engineering approaches such as node to segment, (see Wriggers (2005)) or mortar elements (see Wohlmuth (2001, 2011); Laursen et all (2005)). We give simple bounds on the singular values of the resulting matrix B and results of numerical experiments, including both the academic examples and some problems of practical interest such as the the gears in fig. 1. We conclude that the normalized orthogonal mortars proposed by Wohlmuth can be used to approximate the non-penetration conditions in a way that complies with the requirements of the FETI methods.

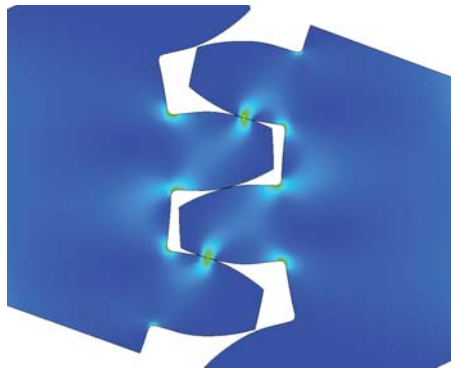

Fig. 1: von Misses stress in the real world example

Acknowledgments

This work was supported by the European Regional Development Fund in the IT4Innovations Centre of Excellence project (CZ.1.05/1.1.00/02.0070).

References

Farhat, C., Mandel, J. and Roux, F.-X., (1994), Optimal convergence properties of the FETI domain decomposition method, *Computer Methods in Applied Mechanics and Engineering*, Vol. 115, No. 3-4, pp. 365–385.

Dostál, Z., Markopoulos, A., Brzobohatý, T., Horyl, P. and Kozubek, T., (2010), Scalable TFETI algorithm for two dimensional multibody contact problems with friction. *Journal of Computational and Applied Mathematics*, Vol. 235, pp. 403–418.

Dostál, Z., Kozubek, T., Brzobohatý, T., Markopoulos, A., Vondrák, V. and Horyl, P., (2012), Theoretically supported scalable TFETI algorithm for the solution of multibody 3D contact problems with friction, *Computer Methods in Applied Mechanics and Engineering*, Vol. 205–208, pp. 110–120.

Sadowská, M., Kozubek, T., Dostál, Z., Markopoulos, A. and Bouchala, J., (2011), Scalable Total BETI based solver for 3D multibody frictionless contact problems in mechanical engineering, *Engineering Applicarions with Boundary Elements*, Vol. 35, pp. 330–341.

Dostál, Z., Kozubek, T., Brzobohatý, T., Markopoulos, A. and Vlach, O., Scalable TFETI with preconditioning by conjugate projector for transient frictionless contact problems of elasticity, *accepted in Computer Methods in Applied Mechanics and Engineering*.

Wriggers, P., (2005) *Contact Mechanics*. Springer, Berlin.

Wohlmuth, B.I., (2001), *Discretization Methods and Iterative Solvers Based on Domain Decomposition*, Lecture Notes in Computer Science and Engineering, 17, Springer, Berlin.

Wohlmuth, B.I., (2011), Variationally consistent discretization schemes and numerical algorithms for contact problems. *Acta Numerica*, Vol. 20, pp. 569–734.

Yang, B., Laursen, T.A. and Meng, X.N., (2005), Two dimensional mortar contact methods for large deformation frictional sliding, *Int. J. Numer. Meth. Engng.*, Vol. 62, No. 9, pp. 1183–1225.

18th International Conference
ENGINEERING MECHANICS 2012
Svratka, Czech Republic, May 14 – 17, 2012

pp. 161–168
Paper #208

HIERARCHICAL MULTISCALE MODELLING OF POROUS MEDIA WITH APPLICATIONS IN BIOMECHANICS

R. Cimrman[*], E. Rohan[**]

Abstract: *We consider materials with different levels of porosity at different scales. Homogenization theory provides a natural way of upscaling fluid-structure interaction problem posed at the smallest scale to higher levels of porosities in a sense that effective material coefficients (stiffness, permeability, Biot coefficients etc.) at a higher level are obtained by applying homogenization to the lower level. This approach leads to a convenient hierarchical description of the porous medium, suitable for multiscale modelling - in the contribution we present numerical examples motivated by bone tissue poromechanics.*

Keywords: ***poroelasticity, homogenization, multiscale modelling, double porosity.***

1. Introduction

Porous fluid saturated materials with different levels of porosities are abundant in nature and can be engineered as well to conform with requirements in technical practice. This paper describes one approach to modeling of the mechanical behavior of fluid-saturated cortical bone tissue. The multiscale model presented here is based on the theory of homogenization and provides an efficient computational tool which can be used firstly to study influence of the bone structure on the mechanical properties, namely on the stiffness and on the overall strength, secondly to study the mechano-transduction: how the macroscopic loading determines local deformation and microflows in the hierarchical porous structure. The latter phenomenon is tightly related to evolutionary processes which on a longer time scale lead to tissue remodeling and growth.

In the present study we focus on one sub-topic of the homogenization-based bone modelling. Namely, we provide homogenization-based formulae which enable to compute the poroelasticity coefficients for a given geometry and topology of micro- and mesoscopic levels. We describe an arrangement of porosities, each one forming a separate connected system, which are connected by a quasipermeable, or an impermeable interface; then the homogenized problem results in two different pressures. At the mesoscopic scale we take into account the Darcy flow in the poroelastic matrix, although in the mesoscopic channels the fluid is assumed to be static with no pressure gradients.

Only the main results relevant for computer implementation are reported here, as the derivation of the homogenization formulae is beyond the scope of this paper. In Section 2. we discuss modelling assumptions and introduce all formulae and equations constituting the two-level homogenized model. The hierarchical homogenization is implemented in our in-house finite element code; in Section 3. we illustrate the hierarchical upscaling procedure using a numerical example.

2. Hierarchical model of double porosity

We consider a poroelastic medium saturated by fluid. The porosity of the medium is formed at two levels, distinguishable by different sizes of pores, see Fig. 1. These are connected by a weakly permeable interface, so that the model also describes a situation of disconnected porosities, see Rohan and Cimrman (2012).

[*]Ing. Robert Cimrman Ph.D.: New Technologies Research Centre, UWB in Plzeň; Univerzitní 8, 306 14 Plzeň; CZ, e-mail: cimrman3@ntc.zcu.cz
[**]Prof. Dr. Ing. Eduard Rohan: Dept. of Mechanics and Dept. of Mathematics, Faculty of Applied Sciences, UWB in Plzeň; Univerzitní 22, 306 14 Plzeň; CZ, e-mail: rohan@kme.zcu.cz

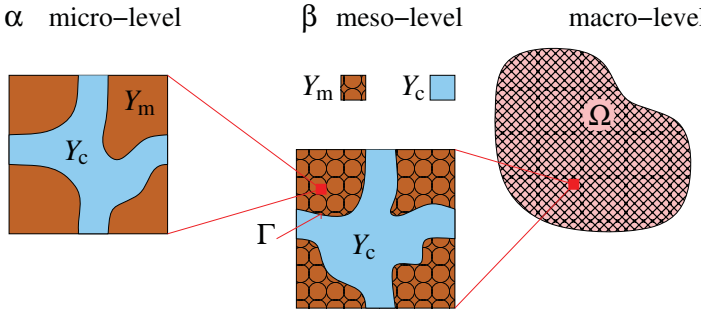

Fig. 1: The two-level heterogeneous structure: α-level is formed by a single connected porosity Y_c^α; the matrix Y_m^α is formed by the solid. At the β-level, the homogenized structure of the α-level forms the material situated in the matrix Y_m^β. Representative periodic cells are depicted.

The two levels, further labeled by superscripts α and β are associated with the "microscale" and the "mesoscale", respectively. In bone modelling, the two levels correspond to the canaliculo-lacunar and the Haversian porosities.

At the microscale level, we consider an elastic solid phase forming a porous skeleton filled with fluid. We assume only moderate pressure gradients at the mesoscopic scale, such that the fluid is static. The pores can form a connected porosity, or mutually separated inclusions: in the first case only one scalar pressure value represents the pressure field in the porosity. By homogenizing this two-phase medium we obtain a Biot-type model describing at the mesoscale the upscaled poroelastic microstructure α, cf. Auriault and Sanchez-Palencia (1977).

At the mesoscale the above mentioned α-poroelasticity model describes the material occupying the matrix of the meso-structure β; at this "higher" level the canals can exchange the fluid with the microscopic pores of the α level due to a weakly permeable interface. For upscaling from the meso- to the macroscopic scale, we take into account a slow flow in the "dual porosity" associated with the microscopic scale.

In this paper we only report the main results relevant for a computer implementation. Homogenization at each scale level proceeds in two steps:

1. Find effective (homogenized) coefficients by solving auxiliary problems for several characteristic (or corrector) functions, cf. Rohan et al. (2012b); Rohan and Cimrman (2011);

2. Compute the homogenized coefficients that can be used for the higher level and/or "global" (homogenized) model of the current level. Due to linearity of the problems, those steps are decoupled in a sense that the computation of the homogenized coefficients for the global level is valid for any point having the corresponding "microstructure".

Let us consider the scale parameter ε, describing the ratio of the characteristic sizes, L^α and L^β, of the two levels, i.e. $\varepsilon = L^\alpha/L^\beta$. By superscript $^\varepsilon$ we indicate dependence of functions and other parameters on ε. We use the same symbol also for upscaling from meso- to macro-scale: $\varepsilon = L^\beta/L^{macro}$.

Let us denote Ω^ℓ the domain at level $\ell = \alpha, \beta$. We assume that the domain Ω^ℓ is obtained from a periodic microstructure generated by a representative unit cell Y^ℓ decomposed as follows

$$Y^\ell = Y_m^\ell \cup Y_c^\ell \cup \Gamma_Y^\ell \,, \quad Y_c^\ell = Y^\ell \setminus Y_m^\ell \,, \quad \Gamma_Y^\ell = \overline{Y_m^\ell} \cap \overline{Y_c^\ell} \,, \quad \ell = \alpha, \beta \,, \tag{1}$$

where Y_m^ℓ is the matrix, Y_c^ℓ are the channels and Γ_Y^ℓ is the matrix–channels interface. Without loss of generality we can define $Y = (]0,1[)^3$ to be the unit cube, so $|Y| = 1$. As a result of (1), the domain Ω^ℓ is defined by $\bigcup_{k\in\mathbb{K}^\varepsilon} \varepsilon(Y^\ell + k)$ with $\mathbb{K}^\varepsilon = \{k \in \mathbb{Z}^3, \varepsilon(Y^\ell + k) \subset \Omega^\ell\}$.

The homogenization procedure starts with a model at the microscale, see Rohan and Cimrman (2012), written in terms of the displacement vector $\boldsymbol{u}^{\alpha,\varepsilon}$ of the matrix and the fluid pressure $p^{\alpha,\varepsilon}$ in pores, and the following material parameters, which form the input of the model:

- $\mathbb{D}^\varepsilon$: the elasticity fourth-order tensor of the matrix,
- γ: the fluid compressibility,
- ν: the fluid viscosity.

For each microstructure we also compute the porosities (volume fractions of pores) $\phi^\ell = |Y_c^\ell|/|Y^\ell|$, $\ell = \alpha, \beta$.

The upscaling procedure of the heterogeneous continuum consists in the limit analysis of the ε dependent model with respect to $\varepsilon \to 0$. For this we use the periodic unfolding method Cioranescu et al. (2008); Griso and Rohan (2007).

2.1. Homogenization results for level α

The two steps of the solution algorithm involve:

Corrector problems First, let us introduce some notation:

$$\begin{aligned} a_m^\alpha(\boldsymbol{w}, \boldsymbol{v}) &= \fint_{Y_m^\alpha} (\mathbb{D}\boldsymbol{e}_y(\boldsymbol{w})) : \boldsymbol{e}_y(\boldsymbol{v}) \,, \\ \boldsymbol{\Pi}^{ij} &= (\Pi_k^{ij}) \,, \quad i,j,k = 1,2,3 \text{ with } \Pi_k^{ij} = y_j \delta_{ik} \,, \end{aligned} \tag{2}$$

where denotes $\boldsymbol{e}_y(\boldsymbol{w})$ is the small strain tensor (derivatives w.r.t. Y domain coordinates y). By $\mathbf{H}^1_\#(Y_m)$ we mean $\mathbf{H}^1$ space of vector functions periodic in Y_m. The problem for the characteristic responses then reads: Find $(\boldsymbol{\omega}^{ij}, \boldsymbol{\omega}^P) \in \mathbf{H}^1_\#(Y_m) \times \mathbf{H}^1_\#(Y_m)$ satisfying

$$\begin{aligned} a_m^\alpha\left(\boldsymbol{\omega}^{ij} + \boldsymbol{\Pi}^{ij}, \boldsymbol{v}\right) &= 0 \,, \quad \forall \boldsymbol{v} \in \mathbf{H}^1_\#(Y_m) \,, \\ a_m^\alpha\left(\boldsymbol{\omega}^P, \boldsymbol{v}\right) &= \fint_{\Gamma_Y} \boldsymbol{v} \cdot \boldsymbol{n}^{[m]} \,\mathrm{dS}_y \,, \quad \forall \boldsymbol{v} \in \mathbf{H}^1_\#(Y_m) \,. \end{aligned} \tag{3}$$

Homogenized coefficients Using the characteristic responses (3) obtained at the microscopic scale the effective properties of the deformable porous medium are given by

$$A_{ijkl}^\alpha = a_m^\alpha\left(\boldsymbol{\omega}^{ij} + \boldsymbol{\Pi}^{ij}, \boldsymbol{\omega}^{kl} + \boldsymbol{\Pi}^{kl}\right) \,, \quad B_{ij}^\alpha = -\fint_{Y_m} \mathrm{div}_y \boldsymbol{\omega}^{ij} \,, \quad M^\alpha = a_m^\alpha\left(\boldsymbol{\omega}^P, \boldsymbol{\omega}^P\right) \,, \tag{4}$$

where $\mathbb{A}^\alpha$ is the skeleton stiffness corresponding to the dried medium, $\boldsymbol{B}^\alpha$ are the Biot-type stress coefficients associated with pressure in channels Y_c^α and M^α is effective Biot compressibility modulus. Obviously, the tensors $\mathbb{A}^\alpha = (A_{ijkl}^\alpha)$ and $\boldsymbol{B}^\alpha = (B_{ij}^\alpha)$ are symmetric; moreover $\mathbb{A}^\alpha$ is positive definite and $M^\alpha > 0$.

2.2. Homogenization results for level β

The two steps of the solution algorithm involve:

Corrector problems To define the local problems for corrector functions, we need the following bilinear forms which involve the homogenized coefficients computed in (4):

$$\begin{aligned} a_m^\beta(\boldsymbol{w}, \boldsymbol{v}) &= \fint_{Y_m^\beta} \mathbb{A}^\alpha \boldsymbol{e}_y(\boldsymbol{w}) : \boldsymbol{e}_y(\boldsymbol{v}) \,, \\ b_m^\beta(p, \boldsymbol{v}) &= \fint_{Y_m^\beta} p \hat{\boldsymbol{B}}^\alpha : \boldsymbol{e}_y(\boldsymbol{v}) \,, \quad \hat{\boldsymbol{B}}^\alpha := \boldsymbol{B}^\alpha + \phi^\alpha \mathbf{I}. \end{aligned} \tag{5}$$

It is worth noting that upscaling from the meso- to the macro-level does not lead to any fading memory terms involving time convolutions, in contrast with upscaling of the double porosity media, cf. Rohan

et al. (2012b); Rohan and Cimrman (2010). As a counterpart to the α level, see (3), the characteristic responses, i.e., displacement modes at the mesoscopic level, satisfy the following problems: find $\boldsymbol{w}^{ij}, \hat{\boldsymbol{w}}, \bar{\boldsymbol{w}} \in \mathbf{H}^1_{\#}(Y_m^\beta)$ such that

$$\begin{aligned} a_m^\beta\left(\boldsymbol{w}^{ij}+\boldsymbol{\Pi}^{ij},\,\boldsymbol{v}\right)=0 \quad \forall \boldsymbol{v}\in\mathbf{H}^1_{\#}(Y_m^\beta)\,,\\ a_m^\beta\left(\hat{\boldsymbol{w}},\,\boldsymbol{v}\right)=b_m^\beta\left(1,\,\boldsymbol{v}\right) \quad \forall \boldsymbol{v}\in\mathbf{H}^1_{\#}(Y_m^\beta)\,,\\ a_m^\beta\left(\bar{\boldsymbol{w}},\,\boldsymbol{v}\right)=-(1-\phi^\alpha)\oint_{\Gamma_Y^\beta}\boldsymbol{v}\cdot\boldsymbol{n}^{[m]} \quad \forall \boldsymbol{v}\in\mathbf{H}^1_{\#}(Y_m^\beta)\,. \end{aligned} \tag{6}$$

The pressure fluctuation associated with the α-level porosity is driven by the characteristic pressure response: find $\eta^1 \in H^1_{\#}(Y_m^\beta)/\mathbb{R}$ such that

$$\oint_{Y_m^\beta}\boldsymbol{K}\nabla_y(\eta^i+y_i)\cdot\nabla_y\psi=0 \quad \forall \boldsymbol{v}\in H^1_{\#}(Y_m^\beta)\,. \tag{7}$$

The permeability $\boldsymbol{K}$ can be computed using the standard homogenization of the Stokes flow considered in a connected α-porosity generated by Y_c^α, see e.g. Hornung (1997); Sanchez-Palencia (1980).

Homogenized coefficients The homogenized coefficients describing the material behaviour at the β level are computed as follows:

$$\begin{aligned} \mathbb{A}^\beta=(A^\beta_{ijkl}),\quad A^\beta_{ijkl}=a_m^\beta\left(\boldsymbol{w}^{ij}+\boldsymbol{\Pi}^{ij},\,\boldsymbol{w}^{kl}+\boldsymbol{\Pi}^{kl}\right)\,,\\ \boldsymbol{B}^\beta=(B^\beta_{ij}),\quad B^\beta_{ij}=b_m^\beta\left(1,\,\boldsymbol{w}^{ij}+\boldsymbol{\Pi}^{ij}\right)\,,\\ \bar{\boldsymbol{B}}^\beta=(\bar{B}^\beta_{ij}),\quad \bar{B}^\beta_{ij}=(1-\phi^\alpha)\phi^\beta\delta_{ij}+a_m^\beta\left(\boldsymbol{w}^{ij},\,\bar{\boldsymbol{w}}\right)\,,\\ \boldsymbol{K}^\beta=(K^\beta_{ij}),\quad K^\beta_{ij}=\oint_{Y_m^\beta}\boldsymbol{K}\nabla_y(\eta^i+y_i)\cdot\nabla_y(\eta^j+y_j)\,, \end{aligned} \tag{8}$$

where $\mathbb{A}^\beta$ is the skeleton stiffness corresponding to the dried medium, $\boldsymbol{B}^\beta$ and $\bar{\boldsymbol{B}}^\beta$ are the Biot-type stress coefficients associated with two pressures, p^α pressure field in the matrix (in the α-level pores) and $\bar{p}^\beta$ a single scalar pressure in the β-level channels, respectively, and $\boldsymbol{K}^\beta$ is the effective permeability. There are three effective Biot compressibility modulae

$$M^\beta=a_m^\beta\left(\hat{\boldsymbol{w}},\,\hat{\boldsymbol{w}}\right)\,,\quad \bar{M}^\beta=a_m^\beta\left(\bar{\boldsymbol{w}},\,\bar{\boldsymbol{w}}\right)\,,\quad N^\beta=a_m^\beta\left(\hat{\boldsymbol{w}},\,\bar{\boldsymbol{w}}\right)\,, \tag{9}$$

which constitute the following compressibility matrix:

$$\mathbb{M}^\beta=\begin{bmatrix} M^\beta+M^\alpha+\gamma\phi^\alpha & N^\beta \\ N^\beta & \bar{M}^\beta+\gamma\phi^\beta \end{bmatrix}\,. \tag{10}$$

Macroscopic equations The macroscopic behaviour of the double porosity fluid saturated medium is described by the triplet $(\boldsymbol{u}, p^\alpha, \bar{p}^\beta) \in \mathbf{H}^1(\Omega^\beta)\times L^2(\Omega^\beta)\times\mathbb{R}$ which satisfies the macroscopic equations (we use the abbreviation $\Omega=\Omega^\beta$)

$$\begin{aligned} \int_\Omega \mathbb{A}^\beta\boldsymbol{e}(\boldsymbol{u}):\boldsymbol{e}(\boldsymbol{v})-\int_\Omega\boldsymbol{e}(\boldsymbol{v}):\left[\boldsymbol{B}^\beta,\bar{\boldsymbol{B}}^\beta\right][p^\alpha,\bar{p}^\beta]^T=\int_{\partial\Omega}(1-\phi^\beta)\hat{\boldsymbol{g}}^\alpha\cdot\boldsymbol{v}\,\mathrm{dS}_x\\ +\int_\Omega(1-\phi^\beta)\hat{\boldsymbol{f}}^\alpha\cdot\boldsymbol{v}\,,\\ \int_\Omega[q^\alpha,\bar{q}^\beta]\left[\boldsymbol{B}^\beta,\bar{\boldsymbol{B}}^\beta\right]^T:\boldsymbol{e}(\dot{\boldsymbol{u}})\\ +\int_\Omega\boldsymbol{K}^\beta\nabla p^\alpha\cdot\nabla q^\alpha+\int_\Omega\kappa^\beta(p^\alpha-\bar{p}^\beta)(q^\alpha-\bar{q}^\beta)\\ +\int_\Omega[q^\alpha,\bar{q}^\beta]\cdot\mathbb{M}^\beta[\dot{p}^\alpha,\dot{\bar{p}}^\beta]^T=-J^\beta_{\mathrm{ext}}\bar{q}^\beta+\int_{\partial\Omega}(1-\phi^\beta)q^\alpha\bar{w}_n\,\mathrm{dS}_x\,, \end{aligned} \tag{11}$$

for all triplets $(\boldsymbol{v}, q^\alpha, \bar{q}^\beta) \in \mathbf{H}^1(\Omega^\beta) \times L^2(\Omega^\beta) \times \mathbb{R}$, where $\kappa^\beta = \oint_{\Gamma_Y^{\beta\,\tilde{\varkappa}}}$ is the average interface permeability, $\hat{\boldsymbol{f}}^\alpha, \hat{\boldsymbol{g}}^\alpha$ are given forces, $\bar{w}_n$ is a draining flux outwards the α porosity and $J^\beta_{\rm ext}$ is a given overall drainage of the β-level connected pores. Obviously, the data must satisfy some solvability conditions.

If $\boldsymbol{K}^\beta$ or κ^β are nonvanishing, initial conditions must be supplied; one may consider the unloaded and undeformed state, or a steady state characterized by a single pressure value, i.e. $p^\alpha(x, \cdot) = \bar{p}^\beta(\cdot)$, $x \in \Omega^\beta$.

3. Numerical example

The homogenization results presented in previous sections were discretized by the finite element method and implemented in a standalone computer code based on our code SfePy, see Cimrman and contributors (2012). In this section we show some results obtained by this code.

For numerical illustration of effects of geometry of connected porosities on the level α we used the reference periodic cells of the micro structures shown in Fig. 2. Three cases were considered:

- **#1**: α-level porosity in Fig. 2 (a), β-level porosity in Fig. 2 (d),
- **#2**: α-level porosity in Fig. 2 (b), β-level porosity in Fig. 2 (d),
- **#3**: α-level porosity in Fig. 2 (c), β-level porosity in Fig. 2 (d),

that is, the diameters of α-level channels increased with the case number. The following material/geometrical

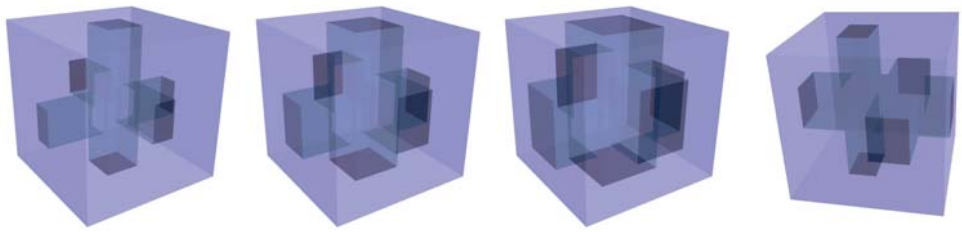

(a) (b) (c) (d)

Fig. 2: (a)-(c): reference cells for level α, case #1, #2 and #3. (d) reference cell with connected porosity for level β for all cases.

parameters were used:

coefficient	units	where	level	values
stiffness $\mathbb{D}$	GPa	Y_m	α	$\lambda = 17, \mu = 1.7$
kinematic fluid viscosity ν	m^2/s	Y_c	α	$\nu = 10^{-6}$
fluid compressibility γ	GPa^{-1}	Ω^β	macro β	$\gamma = 1.0$
interface permeability κ^β	m / (GPa s)	Ω^β	macro β	$\kappa^\beta = 10^{-6}$
porosity ϕ	1	case #1	α	$\phi = 0.119$
	1	case #2	α	$\phi = 0.236$
	1	case #3	α	$\phi = 0.376$
	1	all cases	β	$\phi = 0.185$

where the Lamé parameters defined the stiffness tensor as follows:

$$\mathbb{D} : D_{ijkl} \equiv \mu(\delta_{ik}\delta_{jl} + \delta_{il}\delta_{jk}) + \lambda\delta_{ij}\delta_{kl} \ .$$

Because a practical computation has to be related to a real scale of an existing microstructure, and because of scaling assumptions for fluid viscosity and interface permeability, we assumed the real value of $\varepsilon = 10^{-3}$ and scaled the values given above accordingly, when solving for the homogenized coefficients

coef.	$\boldsymbol{K}^{\alpha}$	$\boldsymbol{K}^{\beta}$
#1	$\begin{bmatrix} 4.44\cdot10^{-5} & 0 & 0 \\ 0 & 4.44\cdot10^{-5} & 0 \\ 0 & 0 & 1.40\cdot10^{-4} \end{bmatrix}$	$\begin{bmatrix} 3.62\cdot10^{-5} & 0 & 0 \\ 0 & 3.62\cdot10^{-5} & 0 \\ 0 & 0 & 1.14\cdot10^{-4} \end{bmatrix}$
#2	$\begin{bmatrix} 2.95\cdot10^{-4} & 0 & 0 \\ 0 & 2.95\cdot10^{-4} & 0 \\ 0 & 0 & 5.91\cdot10^{-4} \end{bmatrix}$	$\begin{bmatrix} 2.40\cdot10^{-4} & 0 & 0 \\ 0 & 2.40\cdot10^{-4} & 0 \\ 0 & 0 & 4.82\cdot10^{-4} \end{bmatrix}$
#3	$\begin{bmatrix} 1.06\cdot10^{-3} & 0 & 0 \\ 0 & 1.06\cdot10^{-3} & 0 \\ 0 & 0 & 1.74\cdot10^{-3} \end{bmatrix}$	$\begin{bmatrix} 8.63\cdot10^{-4} & 0 & 0 \\ 0 & 8.63\cdot10^{-4} & 0 \\ 0 & 0 & 1.42\cdot10^{-3} \end{bmatrix}$

Tab. 1: Homogenized permeability coefficients on levels α, β for cases #1, #2 and #3.

($\nu \to \nu/\varepsilon^2$, $\kappa^{\beta} \to \kappa^{\beta}/\varepsilon$). The computations resulted in the homogenized coefficients. Here we report only the permeabilities that are summarized in Tab. 1 for the three cases.

The macroscopic equations of level β (11) were solved on a cube domain with the following initial and boundary conditions:

- $\boldsymbol{u}(0,\cdot) = 0$, $p^{\alpha}(0,\cdot) = 0$, $\bar{p}^{\beta}(0,\cdot) = 0$,
- $\boldsymbol{u}(t,x) = 0$ for x in bottom face,
- pressure traction load on the top face, with magnitude equal to time step $\times 10^{-2}$ [GPa] up to step 10, then held on the value 10×10^{-2}, for 20 time steps, $t \in [0, 0.1]$.

In Fig. 3 we compare time histories of macroscopic solutions for the three cases and in Fig. 4 several snapshots of macroscopic solutions are shown. It can be seen that the connected porosity behaves in a viscoelastic manner because of the fluid flow in the interconnected pores. The influence of the pore geometry (radius) is clearly demonstrated.

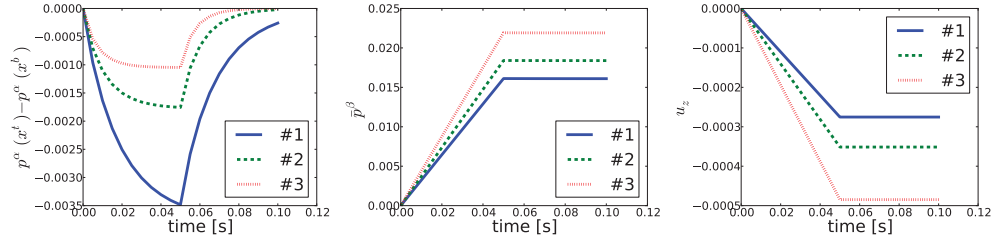

(a) (b) (c)

Fig. 3: Comparison of time histories of macroscopic solutions for the three cases: (a) difference between p^{α} in a point on the top face x^t and bottom face x^b; (b) $\bar{p}^{\beta}$, (c) z-displacement in x^t.

4. Conclusion

We have developed a two-level homogenized model of poroelastic media with weakly permeable interface between the two porosities. The two upscaling levels allow representing three scales which, however, should be separated in the sense of different enough characteristic lengths. As an advantage, the poroelastic coefficients can be computed for a given geometrical arrangement of micro- and meso-structures.

Since the model is intended to describe hierarchical structure of pores in the canaliculo–lacunar porosity of bone, we consider two "microscopic" levels with connected pores (Rohan et al., 2012a).

The homogenization procedure reported in this paper makes possible to treat an arbitrary geometry and topology of the pores, whereby the localization tensors and coefficients can be calculated as the response of the autonomous microscopic problems; this was demonstrated using a numerical example computed by our code (Cimrman and contributors (2012)). The assumption of the weakly permeable

#1

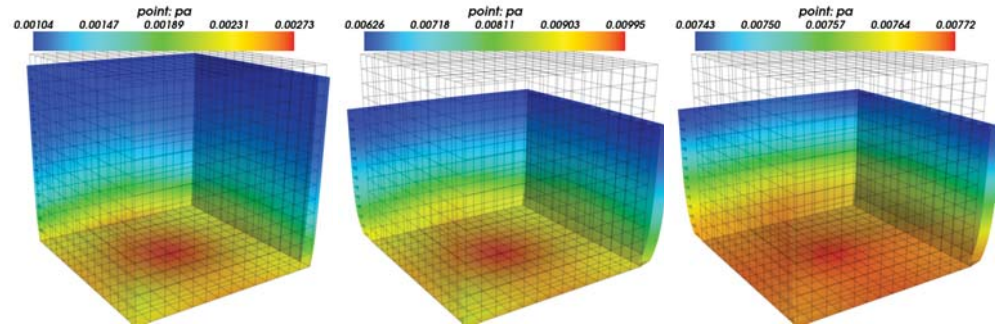

step 2 step 10 step 20

#2

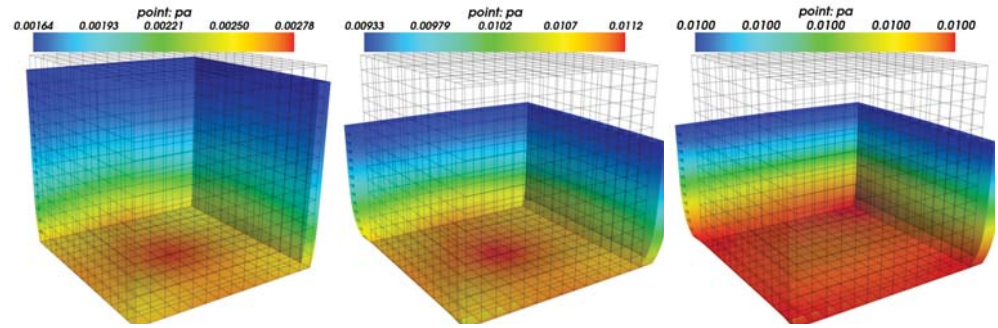

step 2 step 10 step 20

#3

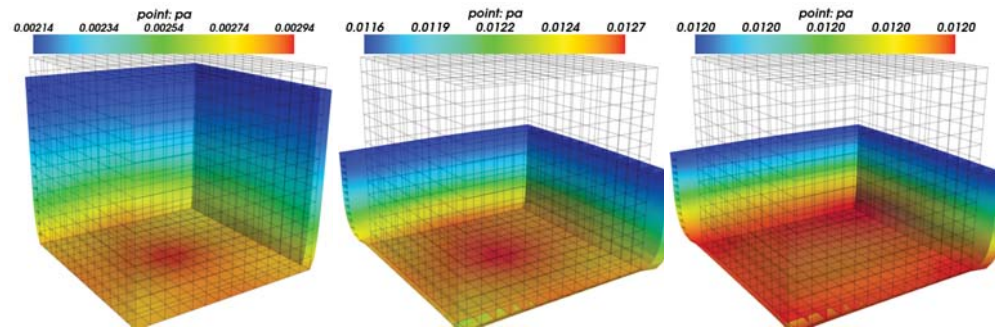

step 2 step 10 step 20

Fig. 4: Snapshots of macroscopic solutions ($10\times$ *magnified* $\boldsymbol{u}$, *color* = p^α) *in time steps 2, 10 and 20 for the case #1 (top), #2 (middle) and #3 (bottom).*

interface disables full connection of the two porosities; this situation is treated in a separate paper Rohan et al. (2012a), cf. Rohan et al. (2012b) for related issues of the double porous materials.

Acknowledgments

The research is supported in part by projects GACR 106/09/0740 of the Czech Republic. The work of E.R. was supported in part by the European Regional Development Fund (ERDF), project "NTIS - New Technologies for Information Society", European Centre of Excellence, CZ.1.05/1.1.00/02.0090.

References

Auriault, J. L. and Sanchez-Palencia, E. (1977). étude du comportement macroscopique d'un milieu poreux sature deformable. *Jour. de Mécanique*, 16(4):575–603.

Cimrman, R. and contributors (2012). SfePy: simple finite elements in python. http://sfepy.org.

Cioranescu, D., Damlamian, A., and Griso, G. (2008). The periodic unfolding method in homogenization. *SIAM Journal on Mathematical Analysis*, 40(4):1585–1620.

Griso, G. and Rohan, E. (2007). On the homogenization of a diffusion-deformation problem in strongly heterogeneous media. *Ricerche mat.*, 56:161–188.

Hornung, U. (1997). *Homogenization and porous media*. Springer, Berlin.

Rohan, E. and Cimrman, R. (2010). Two-scale modelling of tissue perfusion problem using homogenization of dual prous media. *Int. Jour. for Multiscale Comput. Engrg.*, 8:81–102.

Rohan, E. and Cimrman, R. (2011). Multiscale fe simulation of diffusion-deformation processes in homogenized dual-porous media. *Math. Comp. Simul.* In Press.

Rohan, E. and Cimrman, R. (2012). Hierarchical numerical modelling of nested poroelastic media. In *Proceedings of The Eleventh International Conference on Computational Structures Technology*, page submitted.

Rohan, E., Naili, S., Cimrman, R., and Lemaire, T. (2012a). Hierarchical homogenization of fluid saturated porous solid with multiple porosity scales. *Compte Rendus Acad. Sci./Mécanique*. Submitted.

Rohan, E., Naili, S., Cimrman, R., and Lemaire, T. (2012b). Multiscale modelling of a fluid saturated medium with double porosity: relevance to the compact bone. *Jour. Mech. Phys. Solids*, 60:857–881.

Sanchez-Palencia, E. (1980). *Non-homogeneous media and vibration theory*. Number 127 in Lecture Notes in Physics. Springer, Berlin.

18th International Conference
ENGINEERING MECHANICS 2012
Svratka, Czech Republic, May 14 – 17, 2012

pp. 169–176
Paper #15

AEROELASTIC CERTIFICATION OF LIGHT SPORT AIRCRAFT ACCORDING "LTF" REGULATION

J. Čečrdle[*]; V. Hlavatý [**]

Abstract: *Submitted paper deals with the aeroelastic certification of a light sport aircraft according the German regulation standard "LTF-UL". The procedure is simple, fast and low-cost, however it keeps the high standard regarding the quality and reliability of the obtained results. The procedure is based on the ground vibration test of the aircraft and flutter analyses based on the measured mode shapes. Paper is focused to the used experimental and analytical tools and methodologies. Whole process is demonstrated on the example of the FM-250 "Vampire II" light sport aircraft certification.*

Keywords: ***aeroelasticity, ground vibration testing, light sport aircraft, LTF regulation***

1. Introduction

In the Czech Republic, there have been a considerable growth in development and production of the light sport aircraft recently. New generation aircraft are lighter, aerodynamically refined and equipped by more powerful engines. It allows installation of advanced equipment, also flight performances are increasing. In many aspects, they expand to the higher aircraft category. However the design of such aircraft is ordinarily made with no regard to the aeroelasticity (e.g. under-balanced controls), also home-made alteration of the structure with possible negative influence to the aeroelastic stability (see Čečrdle (2010)) is a typical practice. Aeroelastic certification of these aircraft is based on the formal flight flutter tests, however due to the mentioned factors, there are additional requirements regarding aeroelasticity in some regulation standards. The typical example is the German national regulation standard "LTF-UL". It requires the ground vibration test and flutter analyses prior the flight flutter test for the aircraft with the design velocity over ***200 km.h^{-1}*** (section 629(3)). It is obvious, that the aeroelastic certification of the light sport aircraft must be fast, simple and low-cost. On the other side, the high standard of the results quality and reliability must be kept. The paper describes the certification procedure used at the VZLU. It is based on the ground vibration test of the aircraft and the flutter analysis using the measured modal characteristics. The procedure is demonstrated on the ***FM-250*** "Vampire II" aircraft example (fig.1). The duration of the whole procedure was about 20 workdays from the aircraft delivery to the analytical results available.

* Ing. Jiří Čečrdle, Ph.D.: Výzkumný a zkušební letecký ústav a.s., Beranových 130; 199 05 Praha - Letňany; tel.: +420.225 115 123, fax: +420 283 920 018; e-mail: cecrdle@vzlu.cz
** Ing. Václav Hlavatý: Výzkumný a zkušební letecký ústav a.s., Beranových 130; 199 05 Praha - Letňany; tel.: +420 225 115 178, fax: +420 283 920 018; e-mail: hlavaty@vzlu.cz

Fig. 1: FM-250 Vampire II aircraft (source: Flying Machines s.r.o.)

2. Ground Vibration Test

The purpose of the ground vibration test (***GVT***) is to get the modal parameters of the structure. These parameters, it means natural frequencies, mode shapes and modal masses are the input parameters for the follow-on flutter analyses. The ***FM-250*** aircraft test was performed on the completely equipped and weighted aircraft. The empty weight was ***280.5 kg***, plus ***2*** pilots of ***75 kg*** each and ***26 lt.*** of fuel representing ***50%*** of loading. The aircraft total mass was ***450 kg***. The control system (rolling, pitching, yawing) was free, there was used only soft rubber spring to fix a stick with no significant influence to the measured system. Due to the unstable vibrations, the elevator tab was fixed excluding the measurement of the tab flapping mode. Flaps were at the zero position excluding the skin modes and flap 2nd modes measurements.

The aircraft was suspended in the flight position by means of the rubber springs. The front belt was placed on the front fuselage and the rear belt was behind the wing. The natural frequencies of the aircraft on the suspension were ***1.1 Hz*** vertical, ***0.6 Hz*** lateral and ***0.5 Hz*** longitudinal.

Fig. 2: GVT test arrangement (source: VZLU)

Tab. 1: GVT results summary

#	mode title	f_0 [Hz]
1	Rudder Flapping (Fixed Pedals)	6.941
2	1st Symmetric Wing Bending	8.575
3	Tailplane Rolling	9.697
4	1st Fuselage Lateral Bending	10.57
5	1st Fuselage Vertical Bending	11.17
6	Antisymmetric Aileron Flapping (Fixed Sticks)	14.63
7	1st Antisymmetric Wing Bending	15.03
8	Symmetric Elevator Flapping (Fixed Sticks)	15.06
9	Symmetric Elevator Flapping (Free sticks)	15.21
10	1st Antisymmetric Wing In-plane Bending + Lateral Engine Vibrations	15.22
11	1st Symmetric Wing In-plane Bending	16.97
12	Symmetric Aileron Flapping	23.51
13	Antisymmetric Tailplane In-plane Vibration	24.39
14	Elevator Balance Tab Flapping	24.50
15	1st Symmetric Tailplane Bending	24.92
16	1st Engine Vertical Vibration	27.48
17	1st Fin Bending	28.93
18	1st Antisymmetric Wing Torsion	31.61
19	1st Symmetric Wing Torsion	32.33
20	2nd Symmetric Wing Bending	37.57
21	Antisymmetric Elevator Flapping	42.57
22	2nd Fuselage Vertical Bending	47.71
23	2nd Antisymmetric Wing Torsion	54.09
24	2nd Symmetric Wing Torsion	54.26
25	2nd Fuselage Lateral Bending	55.89
26	2nd Antisymmetric Wing Bending	62.97
27	2nd Symmetric Tailplane Bending	63.22
28	1st Symmetric Tailplane Torsion	68.42
29	1st Antisymmetric Tailplane Torsion	71.97
30	3rd Symmetric Wing Torsion	73.39
31	2nd Engine Vertical Vibration	75.46
32	1st Fin Torsion	86.98

The test arrangement is shown in fig.2. The measurements were performed by means of the ***PRODERA 2008*** test system. It includes circuits for the excitation, measurements and data acquisition as well as the algorithms for the vibration evaluation and the test control. There were used ***50 N*** exciters, the elevator tab flapping mode was excited by means of ***4 N*** exciter. The acquisition points grid contained ***139*** uni-axial accelerometers with the mass of ***0.001 kg***

each. The rigid chord of surfaces was assumed. The rough estimation of the natural modes distribution was measured by means of the swept sine excitation. Then the particular modes were investigated by means of the phase resonance method. Each mode was characterized by the natural frequency, mode shape, modal mass and damping ratio. The modal masses and damping ratios were obtained by means of the complex power method and by supplied energy method respectively. The exception was the elevator tab flapping mode for which the modal mass was set analytically due to the large play inside the actuation mechanism. Quality of the measured parameters were assessed by criteria functions (Δ and ***MIF***) characterizing the quality of the particular mode excitation. Natural frequencies and modal masses were corrected with respect to the additional mass and stiffness of the test device. Also the nonlinearities were evaluated by means of dependence of the natural frequency on the reference point displacement and as mechanical impedance respectively.

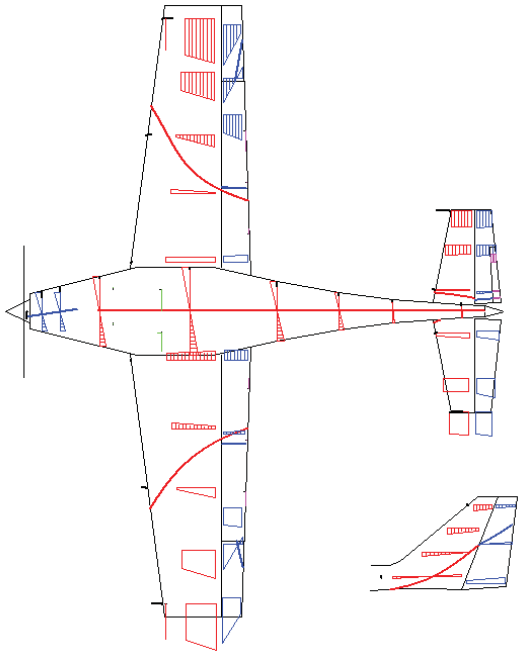

Fig. 3: GVT Example of mode shape visualization

The measured modes were divided into two sets: 1) significant modes of the main aerodynamic surfaces, controls and tabs and: 2) modes of auxiliary parts as flaps, landing gear, propeller blades etc. The former modes were used for the flutter calculations. These modes are summarized in tab.1. Fig.3 demonstrates the specific graphic format for the visualization of the mode shapes showing node lines and phase relations.

3. Flutter Analysis

According the **LTF-UL, section 629c** regulation, there must be performed the flutter analysis to prove no flutter appearance up to $1.2*V_D$ for the aircraft with V_D over $200\ km.h^{-1}$. Note that the V_D is the aircraft design velocity which usually exceeds the $200\ km.h^{-1}$ threshold. The analyses were based on the experimental modal model given by the ***GVT***. It is a common

practice, that the usage of the ***GVT*** based modal model is the only possibility due to no structural data (stiffness, inertia) available. For the purpose of analyses, the measured modal deformations were recalculated to the grid of points with 3-directional deformation. Also, the points were moved to the leading and trailing edge respectively in order to avoid the errors due to splining extrapolation. Finally, the data were transformed to the free format. For these purposes, the in-house ***SW*** tool was used. The grid of the measurement points used for the analyses is demonstrated in fig.4. It includes ***70*** points in total.

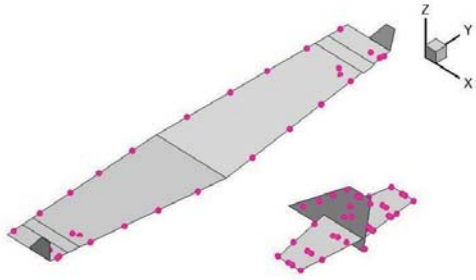

Fig. 4: Points used for analysis

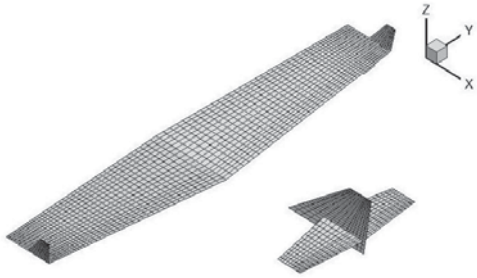

Fig. 5: Aerodynamic model - mesh

For the aeroelastic flutter analysis, the ***ZAERO*** system was used. The aerodynamic unsteady loads were given by the ***ZONA6*** Subsonic Unsteady Aerodynamic Theory. This theory solves the respective unsteady three dimensional linearized small disturbance potential equations of the subsonic aerodynamics. The ***FM-250*** aircraft aerodynamic model included the lifting surfaces only, influence of the fuselage body was neglected. The model includes both left and right hand side respecting the wing and tail unsymmetry (fixed aileron tab and elevator balancing tab on starboard side only). The aerodynamic mesh is shown in fig.5, it consists of ***2405*** aerodynamic elements in total. Aerodynamic matrices were calculated for the selected values of reduced frequency ranging from $k = 0.02$ to $k = 2.0$. Reduced frequency is dimensionless parameter including both flow velocity and frequency of vibrations. Aerodynamic forces are assumed to be dependent on the reduced frequency at a gentle rate, thus aerodynamic matrices are calculated for the selected values of reduced frequency and then interpolated. Considering the velocity range of interest (up to $1.2*V_D$), the Mach number was considered $M = 0.0$ (incompressible flow). This feasible simplification save the analysis effort. For the interpolation between structural grid and aerodynamic model, the "Infinite Plate splines" were used. The wing and fin surfaces were extended also to the fuselage area in order to avoid the unrealistic induced effects, however elements within the fuselage area were

splined by means of the "Zero Displacement Splines" which do not transfer the displacements and forces to the structure. The same is applied to the winglets as well, since there was no measurement point there. For the flutter stability solution, the g-method was employed. This method is based on the widely used ***P-K*** method, which includes the aerodynamic matrix into the stiffness matrix (real part) and the damping matrix (imaginary part). In addition, the g-method includes also first order damping term to the solution. Calculations were performed for a several altitudes ranging from ***H = 0*** to ***H = 3000 [m]***. The velocities were ranging from ***V = 10 m.s^{-1}*** to ***V = 200 m.s^{-1}***. The Mach number was considered ***M = 0.0*** for the whole range of velocities. Thus, the results for high velocities (over ***100 m.s^{-1}***) must be considered as artificial due to incompressible flow aerodynamics used. This is ordinary practice in the aeroelastic analysis, also called non-matched analysis. The artificial results are used to evaluate the rate of reserve in terms of the flutter stability with respect to the certification velocity (***1.2*V$_D$***). The structural damping was included via viscous model. There were considered: 1) no structural damping as a conservative estimation and 2) damping ratio of ***0.02*** as realistic estimation considering the ***GVT*** results. Analyses included those modes listed in tab.1.

Tab. 2: Flutter states list

#	abbr.	title	approx. f_{FL} [Hz]
1	RUDD	Rudder flutter	9.9
2	AILA	Antisymmetric wing aileron flutter	16.7
3	AILS	Symmetric wing aileron flutter	14.5
4	ETAB	Elevator tab flutter	15.2
5	ELEV(1)	Elevator control flutter	24.2
6	ELEV(2)	Elevator control flutter	23.3
7	WHTS	Wing and tail flutter	27.0
8	HTLA	Horizontal tail surface flutter	63.0

The list of the flutter states found is given in tab.2. There were found the flutter of the main lifting surfaces, controls and tabs. The most important ones are rudder, wing aileron and elevator flutter. Other instabilities with a character of low hump mode were suppressed by considering the non-zero structural damping (e.g. elevator tab flutter). The analysis was complex in order to assess the most critical flutter issues and major contributing factors. The lowest flutter speed has the rudder flutter. It was approaching the certification speed, nevertheless the flutter speeds considering the realistic structural damping are all over this threshold. The main contributing factor is low rudder flapping frequency. The next flutter states has a character of the wing bending torsional aileron flutter. The main contributing factor is the aileron static under-balancing as well as the flapping frequency. The elevator flutter appeared as two separated instabilities due to the structural and aerodynamic unsymmetry. The example of the ***V-g-f*** diagram is shown in fig.6.

Flutter speed dependence to the flight altitude is at a gentle rate. The most critical is the altitude of ***H = 0*** in the most cases. The influence of the structural damping shows the rate of change in terms of the stability increasing the velocity, the low influence of the structural damping means a high rate of change and vice versa. The summary of the flutter speeds is given in fig.7.

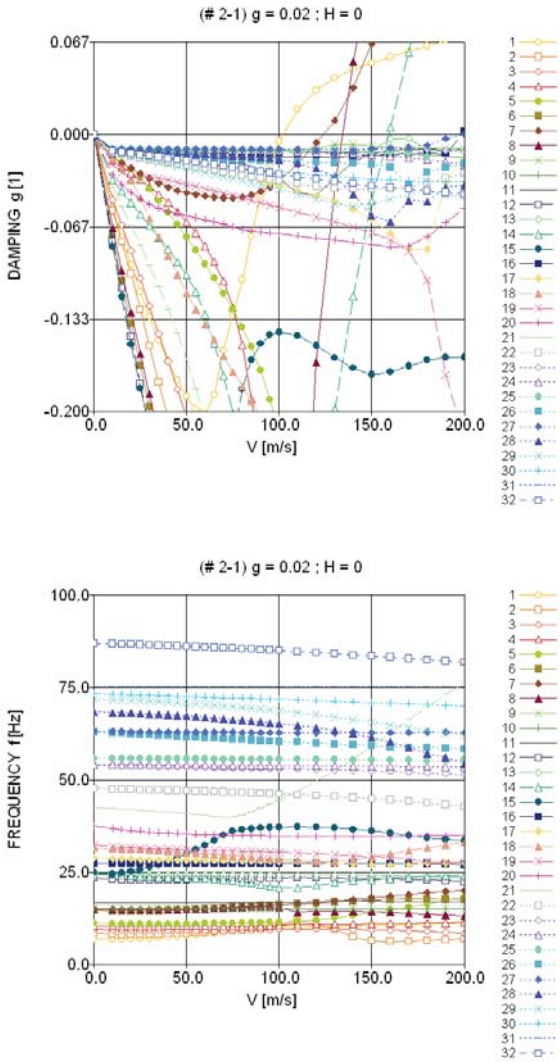

Fig. 6: V-g-f diagram example (g = 0.02; H = 0)

4. Conclusion

The paper deals with the assessment of the flutter stability of the light sport aircraft. It demonstrates the simple and fast certification procedure suitable for this aircraft category based on the ground vibration test of the aircraft and flutter analysis by means of the ***ZAERO*** system. The procedure is simple and fast, however it keeps the high standard with regard to the used experimental and analytical tools and the results reliability. The solution is demonstrated on the ***FM-250*** **"Vampire II"** light sport aircraft certification according German national airworthiness regulations **LTF-UL-2003, section 629**. Doing this, there was evidenced no flutter issue within the aircraft flight envelope.

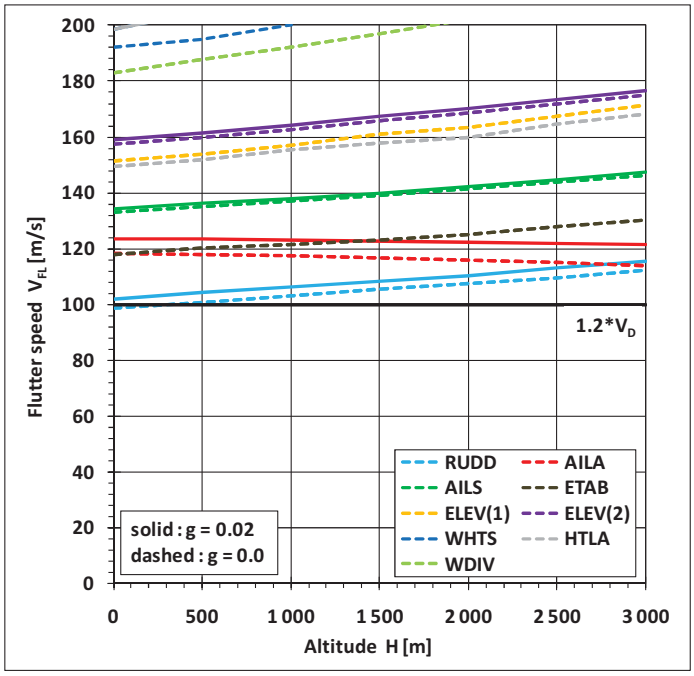

Fig. 7: Flutter speeds summary

5. References

Čečrdle, J. (2011) *Assessment of Aileron Tab Installation Influence to Aircraft Flutter Characteristics*, 52nd AIAA/ASME/ASCE/AHS/ASC Structures, Structural Dynamics, and Materials Conference (SDM), April, 4 - 7, 2011, Denver, CO, USA, AIAA-2011-1849

Weigel, K. (2009) *Development of Research Laboratory for Investigation of Light Aircraft Frequency Characteristics with an Emphasis on Aeroelastic Analysis*, Ph.D. Thesis, Czech Technical University, Prague, 2009

Čečrdle, J. – Gallovič, D. (2009) *NASPRO 3.0 – Software Tool for Transformation and Visualization of Aircraft Structure Modal Analysis Results*, Engineering Mechanics 2009, National Conference with International Participation, May 11 – 14, 2009, Svratka, Czech Republic, book of extended abstracts pp. 36 – 37, full text on CD-ROM, pp.175 - 179, ISBN 978-80-86246-35-2

Hlavatý, V. (2010) *Mobile Modal Test Laboratory at VZLU*, Czech Aerospace Proceedings, Vol.4/2010, pp.37-41, ISSN 1211-877X

(2003) Lufttüchtigkeitsforderungen für aerodynamisch gesteuerte Ultraleichtflugzeuge, LTF-2003-UL, 30.1.2003

18th International Conference
ENGINEERING MECHANICS 2012
Svratka, Czech Republic, May 14 – 17, 2012

pp. 177–186
Paper #88

EXPERIMENTAL DEVICE FOR TESTING OF SERVOMECHANISMS OF THE PASSIVE OPTOELECTRONIC RANGEFINDER

V. Čech[1], M. Červenka[2], P. Snopek[3], I. Trávníček[4], V. Václavík[5]

Abstract: *It is necessary to use quite a big gear ratio (from 150 to 300) to ensure an accurate control of the angular motions of passive optoelectronic rangefinder (POERF).Used zero-backlash gearings together with the features of rolling-contact bearings generate relatively high nonlinearities which make the achievement of demanded control accuracy of POERF complicated or even totally precluded. Experimental (Test) device for the described drives was constructed in OPROX company. The device was set into function by the composite authors of this article and at the moment, relevant measurements are being made. The aim is to use the testing measurements made on the device in order to design and verify a method and SW for initial and continuous identifications of the parameters of POERF nonlinear model of servo-drive. In this article we will provide basic information on mechanical design of the experimental device construction, control and power parts of servo-drive and on communication protocol including the measurement protocol (output data).*

Keywords: ***Experimental (Test) device, servo-drive, nonlinear system, passive optoelectronic rangefinder (POERF), measurement.***

1. Introduction

During the work on project KT-TA3/103 between 2007 and 2009 we discovered that zero-backlash servo-drives suitable for POERF are very nonlinear and it is impossible to achieve the demanded control quality when control algorithms based on linear theory of automatic control are used (Composite authors (2009)).

At that time, preliminary theoretic analyses were made (Čech, V. & Jevický, J. (2008a), Čech, V. & Jevický, J. (2008b), Čech, V. & Jevický, J. (2009)), and they verified the results acquired in experiments with servo-drives of POERF. Nevertheless, it was obvious that it is necessary to accomplish systematic experiments in order to form the basis for design of nonlinear model of servo-drive that must be implemented into servo-drive controllers so as to achieve the demanded quality of control. At the same time it was apparent that in order to accomplish these operations it will be necessary to construct a specialized experimental (test) device. In addition, it is essential to state that results of measurements mentioned in literature search are inadequate for our purposes.

The experimental (test) device (Fig. 1, 2, 3) was designed by composite authors of this article according to the conceptual design elaborated by V. Čech. The device was constructed and activated in OPROX company in cooperation with other sub-suppliers in 2011. Consequently, exploratory measurements have been made since August 2011 and they are about to be finished now. Mechanical structure was designed by M. Červenka. Power and control electronic units were designed and realized by P. Snopek and V. Václavík. Control and communication SW was realized by I. Trávníček. The measurements are made by I. Trávníček under the supervision of V. Čech.

[1] Doc. Ing. Vladimír Čech, CSc., Oprox Inc., Brno, Czech Republic, and University of Trencin, Fakulty of Special Technologies, Slovak Republic, e-mail: cech-vladimir@volny.cz

[2] Ing. Martin Červenka, Ph.D., Oprox Inc., Brno, Renneská 413/35, 639 00 Brno, Czech Republic, e-mail: martin.cervenka @oprox.cz

[3] Ing. Petr Snopek, Oprox Inc., Brno, Renneská 413/35, 639 00 Brno, Czech Republic, e-mail: petr.snopek@oprox.cz

[4] Bc. Ivo Trávníček, Oprox Inc., Brno, Renneská 413/35, 639 00 Brno, Czech Republic, and Brno Technical University, Fakulty of Mechanical Engineering, e-mail: i.travnicek@seznam.cz

[5] Ing. Vlastimil Václavík, Oprox Inc., Brno, Renneská 413/35, 639 00 Brno, CR, e-mail: vlastimil.vaclavik@oprox.cz

The aim of this article is to acquaint the specialists with the experimental device construction. In final part, examples of measurement results are stated to prove that zero-backlash drive with a set structure is really nonlinear.

2. Design of the experimental device

2.1. Design of the mechanical structure

Experimental device consists of (Fig. 1) the device 1, control computer 2 with particular SW and of power supply 3.

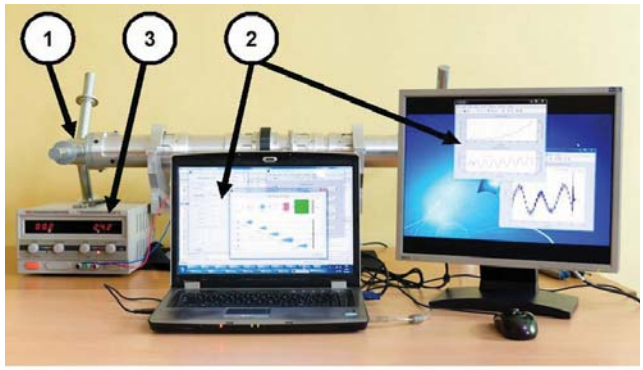

Fig. 1 General view of the Experimental device I.

In order to describe the full construction of the device we will use Fig. 2, 3, 4. In these pictures, there are single items/parts marked by identical arrowheads. The weight of the device is c. 32 kg and with side shanks for placement of weights it is c. 42 kg.

Output shaft (controlled object) 1 is placed with the use of rolling-contact bearings in the frame 2 of the device. The frame of the device 2 is pivoted on a base plate 3 with the use of a shaft 4. A control bar 12 is used to turn the frame 2 manually towards the base plate 3.

Manual turning will be used in the future to accomplish special experiments. For basic experiments that are being currently accomplished, the frame 2 is rigidly fixed to the base plate 3 by the use of stopping mechanism with a fixation screw 10.

On both sides of the output shaft 1 there are three side shanks where discs of different weights 11 can be placed and thus it is possible to change the moment of inertia of the output shaft (controlled system) in relatively high limits (bounds). The moment of inertia of the output shaft without the weights and side shanks (Fig. 2) is 0,014125 kgm^2. Maximal moment of inertia (6pcs of discs ea. 5 kg) is 1,205460 kgm^2.

Lightweight rolling-contact bearings 61818-2RS with inside diameter 90 mm by company SKF are used for placing the output shaft 1 into the frame 2.

Angular displacement of the output shaft 1 towards the frame 2 is measured by means of optic incremental sensor “SIGNUM RESM angle encoder” (arrowhead 8) by company RENISHAW plc, UK (www.renishaw.com) with outside diameter of the incremental ring 115 mm. On the surface of the incremental ring there are 18 000 line counts which correspond to basic resolution 0,35 mrad = 72 arc seconds. Overall resolution is amplified by the use of digital interpolation and the digital resolution can be up to 4000 higher (interpolation factor = 4, 20, ..., 4000). For example if the interpolation factor is 20 then the digital resolution equals 2,75 arc seconds = 0,013 mrad. In the following text we will use abbreviation RESM to refer to the sensor.

The respective servo-drive consists of (Fig. 2, 4) mechanical gearings, DC motor 5 with accessories, control and power unit 7 and power supplies 9.

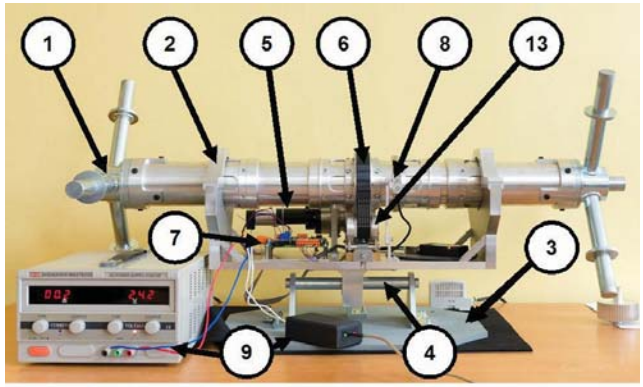

Fig. 2 General view of the Experimental device II.

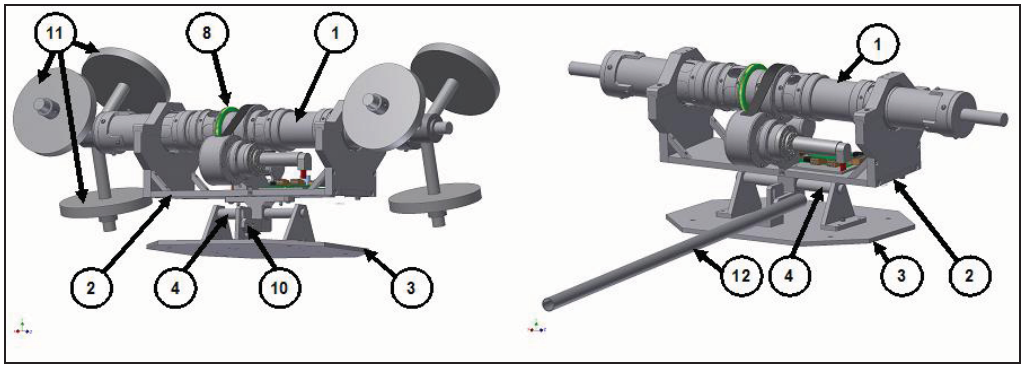

Fig. 3 Assembly of mechanical parts of the Experimental device

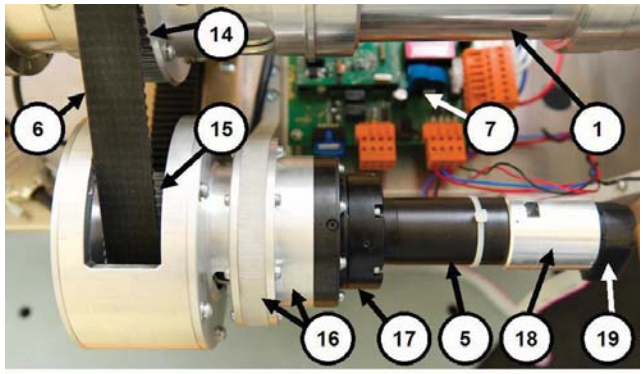

Fig. 4 Assembly of the servo-drive

Mechanical gearings comprise a harmonic drive gearing 17 and a belt drive 6.

Harmonic drive gearing (arrowhead 17) is type CPU-14A-100-M-06.XX-SP with gear ratio i_1 = 100 by company Harmonic Drive AG (www.harmonicdrive.de). Moment of inertia reflected to the gear input is $33 \cdot 10^{-7}$ kgm^2. It is filled with special grease for ambient temperature range from -30 to +50°C. The shaft of the DC motor (diameter 6 mm) is fastened to a hub of input shaft of the gearing by means of grub screws.

The belt drive is set from parts produced by company Gates Corporation, USA (www.gates.com). The drive is based on an indented belt PowerGrip® GT3 625 5MGT 25 (teeth pitch 5 mm, number of teeth 125, pitch length 625 mm, width of the belt 25 mm).

The belt 6 transmits motion from a driving indented pulley 15 to a driven indented pulley 14, which is fixed to the output shaft 1. The driven indented pulley 14 has 78 teeth. The driving indented pulley 15 is interchangeable. We have driving pulleys with 26, or 39 or 52 teeth at disposal so the gear ratio of the belt drive can be i_2 = 1,5 or 2,0 or 3,0. As a result we can make experiments with overall gear ratios $i_C = i_1 \cdot i_2$ = 150 or 200 or 300.

Tightening indented pulley 13 (22 teeth) placed on a slide carriage is used for tightening of the indented belt 6. Horizontal shift of the carriage is done with the use of an adjusting screw.

The driving pulley together with harmonic drive gearing and DC motor are fastened to the frame 3 by means of a console 16.

DC motor RE 35 (Graphite Brushes, 90 W) order number 273 759 is turned out by company Maxon motor (Switzerland), www.maxomotor.com. The DC motor 5 is fastened to a radial face of the harmonic drive gearing 17 with the use of a union flange.

The DC motor has the following basic parameters: number of pole pairs 1, number of commutator segments 13, nominal voltage 48 V, nominal current 0,915 A, nominal speed 2970 rpm, nominal torque 0,105 Nm, no-load speed 3810 rpm, starting current 4,16 A, stall torque 0,493 Nm, terminal resistance 11,5 Ω, terminal inductance 3,16 mH, rotor inertia $65{,}5 \cdot 10^{-7}$ kgm^2.

Accessories of the DC motor 5 mounted on its shaft: Brake AB 28 (24 V) order number 228 387 (arrowhead 18) and Encoder HEDL 5540 (5 V, 500 CPT, 3 channels) order number 110 512 (arrowhead 19). The whole set has order number 368 267. Resolution of encoder HEDL is 0,72° = 2592 arc seconds = 12,56 mrad. In the following text we will use abbreviation HEDL to refer to the sensor.

2.2. Design of control and power electronics

Control and power electronics unit 7 (Fig. 2, 4) is placed on the frame 3. Its photograph is in the picture Fig. 5.

Block diagram can be seen in the picture Fig. 6.

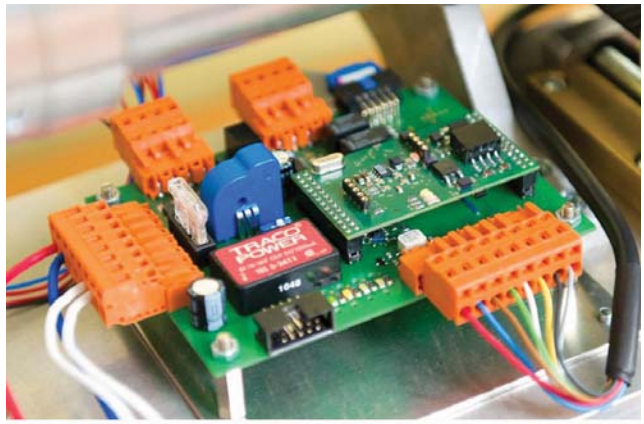

Fig.5 Assembly of power and control units

Servo-amplifier unit represents a basic element for proportional angular control of the servo-amplifier. The unit fulfils the requirements for highly precise settings of the required angular displacement whereas demanding power requirements of regulation are also met. In order to achieve these goals, modern methods for distributed measurement and control are applied. The unit has a maximum output power approx. 220 W at 24 V of continuous output power.

In order to fulfil the requirements for regulation the following characteristic components were used for assembling the servo-amplifier:

- hybrid controllers integrating standard peripheral circuits and powerful processing core usually used by digital signal processors DSP in one case
- highly integrated power stages with modern switching elements for fully digital power control
- modern communication standards
- sophisticated topology of multi-level feedback control

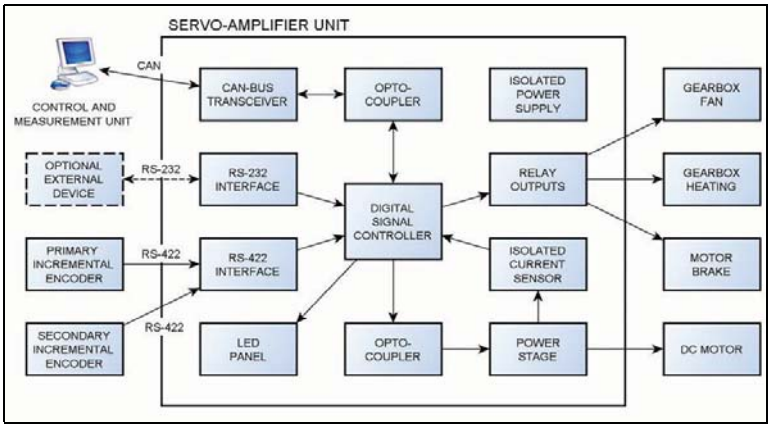

Fig. 6 Block diagram of power and control units

Description of block diagram (Fig. 6):

-*control and measurement unit* - control and measurement unit is based on PC compatible computer with Microsoft Windows operation system. PC computer is equipped with application SW, which sends commands via application interface and communication interface and receives status messages via CAN bus to which the control unit of the servo-amplifier is connected.

-*CAN bus transceiver and optocoupler* - galvanic isolated connection to CAN bus,

-*optional external device* - optional bi-directional communication line for additional devices,

-*RS-232 interface* - converts signal levels between optional external devices and digital signal controller

-*primary incremental encoder (HEDL)* - primary incremental encoder measures shaft turning angle

-*secondary incremental encoder (RESM)* - secondary incremental encoder measures turning angle of output shaft (controlled object) of the servomechanism

-*RS-422 interface* - converts signal levels between angle sensors and quadrature encoders of the digital signal controller

-*digital signal controller* - digital signal controller is equipped with DSP core, powerful timers for real time control, A/D convertors (12 bit), multi-channel quadrature input, CAN communication interface and PWM outputs (16 bit).

-*LED panel* - user interface for operational status of the servo-amplifier indication

-*isolated power supply* - power source for sensors, control electronics and isolated parts of output circuits

-*relay outputs* - high current outputs for general purpose

-*isolated current sensor* - Hall sensor for bipolar measuring of instantaneous current value in DC motor winding

-*power stage and optocoupler* - intelligent galvanic isolated power stage for proportional control of DC motor

-*gearbox fan and gearbox heating* - fan and heating elements for temperature stabilisation of the gear

-*motor brake* - permanent magnet single-face brake

-*DC motor* – DC motor with gearing and output shaft (controlled object)

2.3. Control and communication software

In the picture Fig. 7 there is a basic layout of the measuring system. DC motor is controlled by means of the servo-amplifier. Control commands for the servo-amplifier are sent through the use of CAN bus.

Sensors, that are connected to the same CAN bus, monitor the experimental device status.

In this developmental stage of the experimental device, usual PC (Fig.1, arrowhead 2) connected with the measuring system through the CAN bus is used for its controlling and monitoring the measured physical quantities.

Access of the user application to the CAN bus is provided by communication library (Fig. 7) connected with the communication circuit controllers.

The picture Fig. 8 shows the users interface Generator 1.3 that enables setting of measuring parameters. Generated measurement can be sent by means of pressing "Send to Stend (17)" and it starts moving according to the required signal. The measured results can be then monitored on PC and at the same time they are stored on a hard disk.

At current developmental stage the measurement is made only in an open loop, i.e. the control signal is not dependent on measured values from the sensors. It is possible to invoke a dialogue (Fig. 9) with an open regulation loop scheme of the system with the DC motor by pressing "Loop Settings (14)" – Fig. 8. The control loop (Fig. 9) starts with "Command signal" which represents position reference trajectory.

The DC motor functions as an integration part. The position reference signal needs to be differentiated with respect to time (Fig. 9) as it is necessary to get an output position response again in the open control loop. Servo-amplifier, DC motor and position sensor change the signal magnitude and therefore the signal has to be boosted by correction factor *Kp* (1), that provides units transition. After the boost of the signal by the correction factor *Kp,* we get voltage *u* in volts [V], that will be transmitted to motor clamps.

Application adjusts the voltage *u* to a form which is received by the servo-amplifier. Servo-amplifier needs the voltage to be divided into PWM duty cycle and direction DIR, and then it is transmitted to the DC motor (Fig. 9).

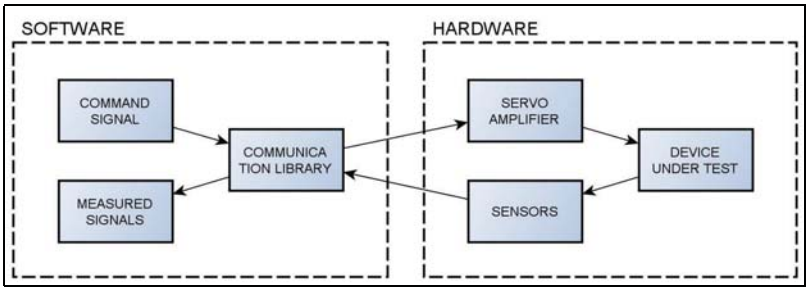

Fig. 7 Communication scheme

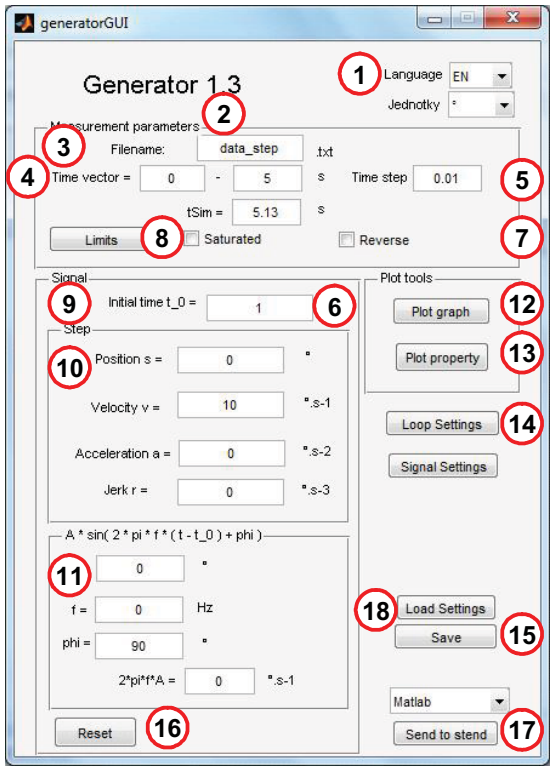

Fig. 8 Graphic interface – signal generator for the experimental device

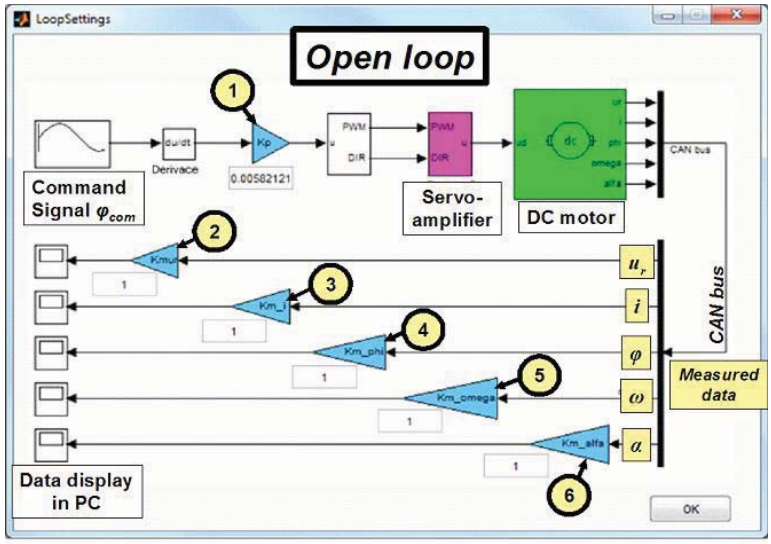

Fig. 9 Open regulation loop

Statuses are measured by means of DC motor and servo - amplifier sensors and those are then transmitted back into the PC by CAN bus. In order to get the measured quantities in SI units, the form in Fig. 9 is supplemented by another editing fields where it is possible to set correction coefficients for

voltage (2), current (3), turning angle of the rotor (4), angular velocity of the rotor (5) and angular acceleration of the rotor (6) of DC motor.

At present, the program Generator 1.3 can be used to develop only few basic command (referential) signal processes such as step in a position, step in speed, step in acceleration, and step in a jerk and harmonic signal. In part "Signal" (9) see Fig. 8 there are fields for command (referential) signal adjustment for DC motor control. Command (reference) signal shall be calculated as follows:

$$\varphi_{com} = \varphi_1(t) + \varphi_2(t), \tag{1}$$

where

$$\varphi_1(t) = \sum_{j=0}^{3} H(t-t_0) \cdot \varphi_C^{(j)} \cdot \frac{(t-t_0)^j}{j!}, \tag{2}$$

where

$H(t)$ is Heaviside step function (unit step function)

$t \in \langle t_{00}, t_K \rangle$ is continuous time (arrowhead (4)) with sampling period T (arrowhead (5)) [s]

t_0 is a moment from which the command signal is nonzero (arrowhead (6)) [s]

$\varphi_C^{(j)}$ is the size of the step of j^{th} derivation (j = 0, 1, 2, 3) – part „Signal" - arrowhead (10)

$$\varphi_2(t) = H(t) \cdot A \cdot sin(2\pi \cdot f \cdot (t-t_0) + \varphi_0), \tag{3}$$

where

CW/CCW – direction of motor rotation ("Reverse" - arrowhead (7))

f is frequency of harmonic command signal [Hz] (arrowhead (11))

A is amplitude of command signal [rad] (arrowhead (11))

φ_0 is initial stage of command signal [rad] (arrowhead (11))

Command signal – reference voltage (arrowhead (2)) can also be limited from bottom and top of its levels and its integration component can be saturated (arrowhead (8)).

Generated command signal can be displayed (arrowheads (12, 13)), set to zero (arrowhead (16)), and saved (arrowhead (15)) under the selected file name (arrowhead (3)).

"Send to Stend" – arrowhead (17) can initiate the simulation in connection with recording of measured data into the database.

3. Examples of measurement outputs

After the command signal parameters are defined, the measurement is made and measured values are sent back to PC. Results of each measurement are saved as text files that are labelled by key name and time when the measurement was made. Such file with results can be processed by e.g. MS Excell or Matlab.

Example of measurement outputs processing in programme Matlab is in Fig.10, where results of frequency analysis of measured signals are listed. Constant step in speed was set for the measurement i.e. the output shaft (controlled object) should have rotated (after the transient response) with constant speed. However, the speed of output shaft rotation actually changes due to nonlinear behaviour of the

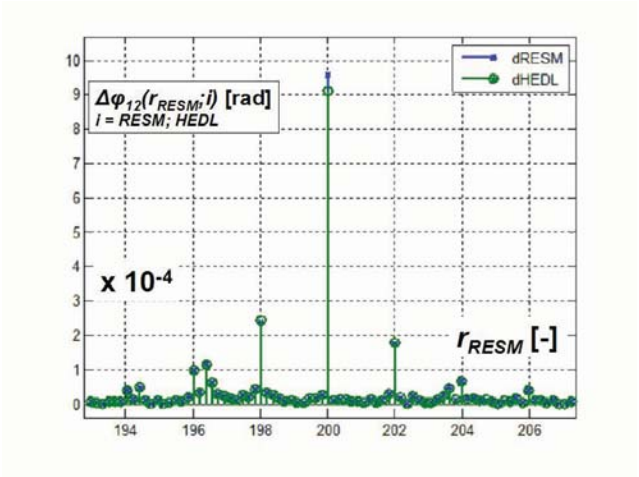

Fig. 10 The spectrum of positional inclinations depending on the position of the output shaft

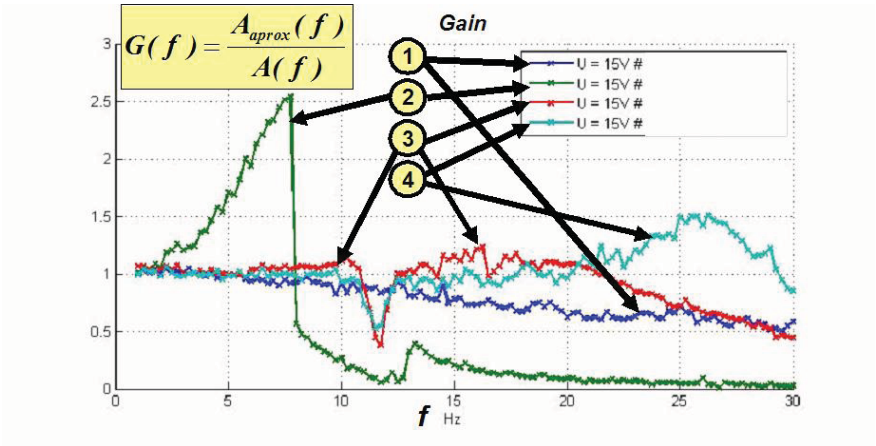

Fig. 11 Gain of the system at different tensions of the belt gear

system. This speed shift is not random but has a periodical pattern in dependence on absolute turning of the output shaft (sensor RESM). Fig. 10 shows, on a relative frequency r = 200 [-], a phenomenon which corresponds to a transfer of disturbed torque from DC motor rotating shaft to output shaft. Other significant harmonic items are at frequencies 198, 202, 196, 204 etc. These are effects of nonlinear behaviour of the system.

In Fig. 11 there are results of analysis for successive measurement which detects harmonic transfer function of the system and the effect of belt tension on system response. Gain of the system consists of point estimates of amplitude gain. Each curve in the graph connects point estimates of measurements with the same parameters, only the frequency f of harmonic command signal is changing. The system was excited by a concrete frequency for each point estimate and braking and damping down of the system preceded each new measurement.

First measurement was made without a belt (1), i.e. only gain to output shaft of the gearing was measured. In accordance with the graph in Fig. 11 we can assume that the system behaves as an inertial item.

While making the second measurement (2) the belt was added however it was not tense which means that the system works with a backlash. From the graph it is obvious that the process differs

significantly and a large drop of frequency about 8 Hz demonstrates nonlinear behaviour caused by the backlash. The experimental device is designed as a zero-backlash gearing so if the belt is tense enough, the nonlinearity of backlash type is not demonstrated. When measuring with slightly tense belt (3) and very tense belt (4) only decrease in gain around the frequency 12 Hz is reflected. It was found out that this decrease is caused by anti-resonance of output shaft 1 and the frame 2 against the base plate 3. When the frame structure with a base plate 3 were reinforced (stiffness reinforcement) this phenomenon in measured excitation range was not demonstrated. The effect of belt tense can be seen in Fig. 11 with excitation range about 26 Hz, where the increase of resonance arises (see measurement with very tense belt (4)).

4. Conclusions

We are currently working on improvements of the experimental device. We will report about their realisation and acquired results at some of the following conferences.

In the following period we will focus our effort on development of methodology for measurements and on design of software for automatic evaluation of measurements.

The design of nonlinear model of the servo-drive will be in progress concurrently with the evaluation of sufficiently extensive sets of measurements.

Acknowledgement

This work has originated under the support of financial means from the industrial research project of the Ministry of Industry and Trade of the Czech Republic – project code FR – TI 1/195: "Research and development of technologies for intelligent optical tracking systems".

References

Balátě, J (2004) Automatic Control, BEN, Praha, p. 664

Bolek, A, Kochman, J. et al. (1989) Parts of Machines, Volume I, SNTL Praha, p. 776

Bolek, A, Kochman, J. et al. (1990) Parts of Machines, Volume II, SNTL Praha, p. 712

Composite authors (2009): Final Research Report. *Program project MIT-ČR, "Tandem" - Program, Project Code: KT – TA3/103,* Project Title: „Výzkum high-end technologií a metod pro rozpoznávání pohybujících se objektů, stanovení parametrů pohybu objektů a pro systémy automatického sledování pohybujících se objektů". Oprox, Inc., Brno 2009, p. 177, appendices: 8/404.

Čech, V. & Jevický, J. (2008a) Simplified dynamic model of the transmission, *Book of Extended Abstracts of Engineering Mechanics 2008 and Proceedings on CD-ROM,* Editor Fuis, V. and Pásek, M., Svratka, 12. - 15. 5. 2008, pp. 44-45 and pp. 128-143, ISBN 978-80-87012-11-6.e.

Čech, V. & Jevický, J. (2008b) Simplified Dynamic Model of the Gearbox. *Proceedings of 24nd conference with International participation Computational Mechanics on CD-ROM*, Hrad Nečtiny, 3. - 5. 11. 2008, 2p., ISBN 978-80-7043-712-4

Čech, V. & Jevický, J. (2009) Simplified Dynamic Model of the Transmission II. *Book of Extended Abstracts of Engineering Mechanics 2009 and Proceedings on CD-ROM*, Svratka, 11. - 14. 5. 2009, s. 38 - 39 a s. 181 - 196, ISBN 978-80-86246-35-2 37.

Harmonic Drive Gearing, *Catalogue "Cup Type Component Sets & Housed units; CSF & CSG Series"*, www.HarmonicDrive.net

Juliš, K., Brepta, R. et al. (1987) *Mechanics, Volume II, Dynamics,* SNTL Praha, p. 688

Maxon motor, *Catalogue „Program 08/09"*, www.maxonmotor.com

Pfeiffer, O. & Ayre, A. & Keydel, CH. *Embedded Networking with CAN and CANopen.* Revised First Edition. Copperhill Technologies Corporation, 2008. ISBN 978-0-9765116-2-5

18th International Conference
ENGINEERING MECHANICS 2012
Svratka, Czech Republic, May 14 – 17, 2012

pp. 187–190
Paper #65

THE SECULAR EQUATION FOR SURFACE WAVES IN 2D ANISOTROPIC ELASTODYNAMICS

J. Červ*, J. Plešek*

Abstract: *The secular equation for the surface (Rayleigh–edge) waves propagating in a thin semiinfinite anisotropic elastic continuum is derived. The secular equation is obtained as a quartic one for the squared wave velocity. Some numerical examples are shown.*

Keywords: ***Composite laminates, Crystals, 2D anisotropic elasticity***

1. Introduction

The traditional way of deriving the secular equation for Rayleigh-edge waves propagating in the direction of the x_1-axis in an anisotropic elastic half-plane $x_2 \geq 0$ is to find a general steady-state solution for the displacement components that vanishes at $x_2 = \infty$. This involves the computation of quartic equation roots that depend not only on material constants but also on wave velocity. The secular equation (explicit or implicit) is then obtained by vanishing of the surface traction at $x_2 = 0$. For the solution of such secular equation it is necessary to precompute some roots of characteristic quartic equation. The method shown in this paper leads to explicit secular equation that depends on material constants only.

2. Preliminaries

We suppose that material and body axes of the 2D anisotropic linear elastic medium in the state of plane stress are denoted by X_1, X_2 and x_1, x_2 respectively. Third axis x_3 is identical with material axis X_3 and constitutes axis of possible rotation of principal material axes X_1, X_2 from body axes x_1, x_2. Due to the plane stress it holds $\sigma_{33} = \sigma_{23} = \sigma_{13} = 0$. In this paper we will assume that principal material axes X_1, X_2 coincide with body axes x_1, x_2. For considered material the relationship between the stress σ_{ij} and strain ε_{ij} components is given by

$$\begin{Bmatrix} \sigma_{11} \\ \sigma_{22} \\ \sigma_{12} \end{Bmatrix} = \begin{bmatrix} C_{11} & C_{12} & C_{16} \\ C_{12} & C_{22} & C_{26} \\ C_{16} & C_{26} & C_{66} \end{bmatrix} \cdot \begin{Bmatrix} \varepsilon_{11} \\ \varepsilon_{22} \\ 2\varepsilon_{12} \end{Bmatrix}, \tag{1}$$

where C_{ij} denote the elastic stiffnesses. The strain components ε_{ij} are related to the displacement components u_1, u_2 through

$$2\varepsilon_{ij} = \left(u_{i,j} + u_{j,i}\right), (i, j = 1,2). \tag{2}$$

The equations of motion, written in the absence of body forces, are

$$\sigma_{ij,j} = \rho \cdot \ddot{u}_i \,, \tag{3}$$

where ρ is the mass density and the comma denotes differentiation with respect to x_j (j=1,2).

* doc. Ing. Jan Červ, CSc. and Ing. Jiří Plešek, CSc.: Institute of Thermomechanics AS CR, v.v.i., Dolejškova 5, 182 00 Prague 8; CZ, e-mail: cerv@it.cas.cz

3. Rayleigh waves

The propagation of a Rayleigh wave along an edge of a semiinfinite 2D anisotropic medium is modeled. It is supposed that corresponding displacement and stress fields have the forms

$$u_s(x_1,x_2,t)=U_s(k\cdot x_2)\cdot e^{i\cdot k(x_1-c\cdot t)},\ \sigma_{rs}(x_1,x_2,t)=k\cdot\Sigma_{rs}(k\cdot x_2)\cdot e^{i\cdot k(x_1-c\cdot t)}\ (r,s=1,2)\quad , \tag{4}$$

where k is the wave number and c is the wave velocity. The boundary conditions of the problem are

$$\Sigma_{j2}(0)=0,\ U_j(\infty)=0\ ,\ (j=1,2). \tag{5}$$

Substituting (4) into (3), the equations of motion reduce to (the prime denotes differentiation with respect to $k\cdot x_2$)

$$i\cdot\Sigma_{11}+\Sigma'_{12}=-\rho\cdot c^2\cdot U_1\ ,\quad i\cdot\Sigma_{12}+\Sigma'_{22}=-\rho\cdot c^2\cdot U_2. \tag{6}$$

Since no boundary conditions are prescribed for σ_{11} and consequently also for Σ_{11} , this component may be eliminated. After some algebra we obtain a system of four ordinary differential equations of the first order for unknowns U_1, U_2, Σ_{12}, Σ_{22} . The system may be written in a matrix format

$$\begin{Bmatrix} U_1' \\ U_2' \\ \Sigma_{12}' \\ \Sigma_{22}' \end{Bmatrix}=\begin{bmatrix} i\dfrac{d_3}{d_1} & -i & \dfrac{C_{22}}{d_1} & -\dfrac{C_{26}}{d_1} \\ -i\dfrac{d_2}{d_1} & 0 & -\dfrac{C_{26}}{d_1} & \dfrac{C_{66}}{d_1} \\ \dfrac{d}{d_1}-\rho\cdot c^2 & 0 & i\dfrac{d_3}{d_1} & -i\dfrac{d_2}{d_1} \\ 0 & -\rho\cdot c^2 & -i & 0 \end{bmatrix}\cdot\begin{Bmatrix} U_1 \\ U_2 \\ \Sigma_{12} \\ \Sigma_{22} \end{Bmatrix}, \tag{7}$$

where d, d_1, d_2, d_3 are coupled by the relation

$$d=C_{11}\cdot d_1-C_{12}\cdot d_2+C_{16}\cdot d_3\ . \tag{8}$$

It is easily seen that the symbol d represents the determinant of stiffness matrix $\mathbf{C}$ (see (1)) and d_1, d_2, d_3 are subdeterminants of $\mathbf{C}$. From the positive definiteness of stiffness matrix $\mathbf{C}$ it follows that d, d_1 are positive. So we have

$$d>0\ \ \&\ \ d_1>0\ . \tag{9}$$

Denoting the stress vector **T** and displacement vector **U** as

$$\mathbf{T}=\{T_1\quad T_2\}^T\ ,\ \mathbf{U}=\{U_1\ \ U_2\}^T\ , \tag{10}$$

where $T_1=\Sigma_{12}$, $T_2=\Sigma_{22}$ then the above system of four equations may be rewritten as

$$\begin{Bmatrix} \mathbf{U}' \\ \mathbf{T}' \end{Bmatrix}=\begin{bmatrix} \mathbf{M}_1 & \mathbf{M}_2 \\ \mathbf{M}_3 & \mathbf{M}_4 \end{bmatrix}\cdot\begin{Bmatrix} \mathbf{U} \\ \mathbf{T} \end{Bmatrix}\quad . \tag{11}$$

The submatrices $\mathbf{M}_1$, $\mathbf{M}_2$, $\mathbf{M}_3$ and $\mathbf{M}_4$ are given by

$$\mathbf{M}_1=-i\cdot\begin{bmatrix} -\dfrac{d_3}{d_1} & 1 \\ \dfrac{d_2}{d_1} & 0 \end{bmatrix}\quad ,\quad \mathbf{M}_2=\begin{bmatrix} \dfrac{C_{22}}{d_1} & -\dfrac{C_{26}}{d_1} \\ -\dfrac{C_{26}}{d_1} & \dfrac{C_{66}}{d_1} \end{bmatrix}\quad ,$$

$$\mathbf{M}_3 = \begin{bmatrix} \dfrac{d}{d_1} - \rho \cdot c^2 & 0 \\ 0 & -\rho \cdot c^2 \end{bmatrix} = \begin{bmatrix} \dfrac{d}{d_1} & 0 \\ 0 & 0 \end{bmatrix} - \begin{bmatrix} \rho \cdot c^2 & 0 \\ 0 & \rho \cdot c^2 \end{bmatrix} \quad , \quad \mathbf{M}_4 = \mathbf{M}_1^{\,T} \, . \tag{12}$$

Besides this, it holds that

$$\mathbf{M}_1 = i \cdot \mathbf{N}_1 \, , \; \mathbf{M}_2 = \mathbf{N}_2 = \mathbf{N}_2^{\,T} \, , \; \mathbf{M}_3 = -\mathbf{N}_3 - \rho \cdot c^2 \cdot \mathbf{I} = \mathbf{M}_3^{\,T} \, , \; \mathbf{M}_4 = \mathbf{M}_1^{\,T} = i \cdot \mathbf{N}_1^{\,T} \, . \tag{13}$$

Symbols $\mathbf{N_1}$, $\mathbf{N_2}$, $\mathbf{N_3}$ appearing in the relation (13) are submatrices of the fundamental elasticity matrix $\mathbf{N}$ introduced by Ingebrigtsen and Tonning (1969). Symbol $\mathbf{I}$ is identity matrix of size 2. It is supposed that matrix $\mathbf{M_3}$ is not singular. It means that the Rayleigh wave propagates at a velocity distinct from that given by $\rho \cdot c^2 = d \big/ d_1$. With this assumption, the derivative of the second vector line of the system (11) yields relation for $\mathbf{U}'$. Substituting for $\mathbf{U}'$ into first vector line of (11) we get the relation for $\mathbf{U}$. Inserting the relation for $\mathbf{U}$ into second vector line of the system (11) gives after some matrix manipulations

$$\boldsymbol{\alpha} \cdot \mathbf{T}'' - i \cdot \boldsymbol{\beta} \cdot \mathbf{T}' - \boldsymbol{\gamma} \cdot \mathbf{T} = \mathbf{0} \, , \tag{14}$$

where real and symmetric matrices $\boldsymbol{\alpha}, \boldsymbol{\beta}, \boldsymbol{\gamma}$ are given by

$$\boldsymbol{\alpha} = \mathbf{M}_3^{\,-1} \, , \quad i \cdot \boldsymbol{\beta} = \mathbf{M}_1 \cdot \mathbf{M}_3^{\,-1} + \mathbf{M}_3^{\,-1} \cdot \mathbf{M}_1^{\,T} \, , \quad \boldsymbol{\gamma} = \mathbf{M}_2 - \mathbf{M}_1 \cdot \mathbf{M}_3^{\,-1} \cdot \mathbf{M}_1^{\,T} \, . \tag{15}$$

The system (14) for traction components $T_1 = \Sigma_{12}$, $T_2 = \Sigma_{22}$ is more convenient to work with than the corresponding system for displacement components, because the boundary conditions, instead of (5), are now homogeneous. It holds

$$T_j(0) = T_j(\infty) = 0 \, , \; (j = 1,2) \, . \tag{16}$$

The solution of (14) is assumed in the form

$$\mathbf{T}(k \cdot x_2) = \mathbf{T}_0 \cdot e^{i \cdot p \cdot k \cdot x_2} \quad , \tag{17}$$

where $\mathbf{T}_0 = \{T_{01} \; T_{02}\}^T$ is a constant vector and p is a complex number with $\mathrm{Im}(p) > 0$ to fulfil the boundary conditions at infinity. Introducing the solution (17) into the equation (14) we arrive at the following problem. It is necessary to solve the homogeneous system of two linear equations for unknowns T_{01} and T_{02} which are the components of the vector $\mathbf{T}_0$. The system has the form

$$\begin{bmatrix} -\alpha_{11} \cdot p^2 + \beta_{11} \cdot p - \gamma_{11} & \beta_{12} \cdot p - \gamma_{12} \\ \beta_{12} \cdot p - \gamma_{12} & -\alpha_{22} \cdot p^2 - \gamma_{22} \end{bmatrix} . \begin{Bmatrix} T_{01} \\ T_{02} \end{Bmatrix} = \begin{Bmatrix} 0 \\ 0 \end{Bmatrix} . \tag{18}$$

The homogeneous system (18) will have a nontrivial solution if and only if its determinant of the matrix is zero. This leads to a quartic characteristic equation in p. It has the form

$$\alpha_{11} \cdot \alpha_{22} \cdot p^4 - \alpha_{22} \cdot \beta_{11} \cdot p^3 + (\alpha_{11} \cdot \gamma_{22} + \alpha_{22} \cdot \gamma_{11}) \cdot p^2 - \beta_{11} \cdot \gamma_{22} \cdot p + \gamma_{11} \cdot \gamma_{22} = 0 \, , \tag{19}$$

where the real coefficients α_{ij} , β_{ij} , γ_{ij} correspond to matrices $\boldsymbol{\alpha}, \boldsymbol{\beta}, \boldsymbol{\gamma}$, respectively. If a quartic equation has real coefficients, then either i) all roots are real or ii) there is an even number of complex roots (i.e. 4 or 2 complex roots), in conjugate pairs, see Schwarz (1958). First case i) may be discarded due to assumption $\mathrm{Im}(p) > 0$. Second case ii) falls into three possibilities. There are two distinct roots $p_1 \neq p_2$ with positive imaginary parts. Then the general solution to (14) takes the form

$$\mathbf{T}(k \cdot x_2) = q_1 \cdot \mathbf{T}_0^{(1)} \cdot e^{i \cdot p_1 \cdot k \cdot x_2} + q_2 \cdot \mathbf{T}_0^{(2)} \cdot e^{i \cdot p_2 \cdot k \cdot x_2} \quad . \tag{20}$$

where $\mathbf{T}_0^{(1)}$, $\mathbf{T}_0^{(2)}$ correspond to p_1 , p_2 respectively. Symbols q_1, q_2 are arbitrary constants. Second possibility covers the case $p_1 = p_2$. It gives the general solution to (14) as

$$\mathbf{T}(k \cdot x_2) = q_1 \cdot \mathbf{T}_0^{(1)} \cdot e^{i \cdot p_1 \cdot k \cdot x_2} + q_2 \cdot k \cdot x_2 \cdot \mathbf{T}_0^{(1)} \cdot e^{i \cdot p_1 \cdot k \cdot x_2} \quad . \tag{21}$$

The case $p_1 = p_2$ seems to be not important from point of view of practical application. Third possibility is represented by only one root p_1 with positive imaginary part. Then the general solution to the equation of motion (14) has the form

$$\mathbf{T}(k \cdot x_2) = q_1 \cdot \mathbf{T}_0^{(1)} \cdot e^{i \cdot p_1 \cdot k \cdot x_2} \quad . \tag{22}$$

Due to boundary conditions at $x_2=0$ (see (16) where $T_1(0)= T_2(0)=0$ and the conditions that $T_{01}^{(1)}$, $T_{02}^{(1)}$ are not simultaneously zero we obtain $q_1=0$. It leads to trivial solution $\mathbf{T}(k \cdot x_2) = 0$, and therefore this possibility may now be safely discarded.

Applying zero boundary conditions at $x_2=0$ into (20) we get another homogeneous system in unknowns q_1, q_2. This system will have a nontrivial solution if the determinant is zero. It leads after some algebra to the desired secular equation that is quartic one in $\rho \cdot c^2$. All the coefficients of the secular equation are real and depend on material constants only.

Acknowledgement

This work was supported by the grant agency GA CR, projects P101/11/0288 and 101/09/1630 within the framework of project AV0Z20760514.

References

Ingebrigtsen K.A., Tonning A. (1969) Elastic surface waves in crystal. *Phys.Rev.*, 184, 77–103.

Schwarz Š. (1958) *Foundations of a theory of equations.* Publishing house of Czechoslovak Academy of Sciences, Prague (in Slovak).

18th International Conference
ENGINEERING MECHANICS 2012
Svratka, Czech Republic, May 14 – 17, 2012

pp. 191–201
Paper #87

COMPUTATIONAL STUDY OF SLUDGE PUMP DESIGN WITH VORTEX IMPELLER

M. Červinka*

Abstract: *This paper presents a computational study of sludge pump design with vortex impeller. It contains two design variants of vortex impeller, which is supported by CFD calculations in ANSYS Fluent. By modeling the problem in Fluent, it has been verified that such impellers could be fitted into the existing spiral casing with channel impeller. It was verified that the original operating parameters were maintained. Results of these design solutions and evaluation of effect of some construction modifications on the pump characteristics have been shown.*

Keywords: ***Sludge pump, vortex impeller, characteristics, design, Computational Fluid Dynamic.***

1. Introduction

Sludge pumps are used in many different branches of industry. We can find them in wastewater treatment plants, industry, home, etc. These pumps are very often used for polluted water pumping with abrasive particles. For this reason, these pumps can differ in construction, shape or used materials from classical hydrodynamic pumps. This paper describes a design of vortex impeller which can be fitted into existing spiral casing of original sludge pump with channel impeller. In the following chapters, this design will be introduced. It was proposed using the original operating parameters and the impeller is based on the principle of vortex impeller with commercial name TURO. These impellers are patented by Swiss company Egger. The second design variant of impeller is based on the vortex impeller which is called SuperVortex and is made by Danish company Grunfos. Models were created for both impellers and the CFD (Computational Fluid Dynamic) computations for both design variants were made to assess suitability of use. For solution and subsequent evaluation of this problem we used the values obtained from CFD calculations.

2. TURO impeller

The Turo impeller has lots of advantages. First, it is placed in a different position compared to the channel impellers; thus the large vortex under impeller is created. These impellers are used to pump polluted water with high content of abrasive particles therefore only approximately 15% of impurities get into contact with the impeller. For this reason there is less danger of abrasive wear than with classical channel impellers. Next advantage is that these impellers usually have a stable characteristic and in most cases only very low radial force acts on the impeller. Another advantage is a very simple construction. Efficiency of these types of impellers is between $\eta = (40 \div 55)$ %. A Working principle of this pump is shown in fig.1 and a typical pump with the Turo impeller is shown in fig. 2.

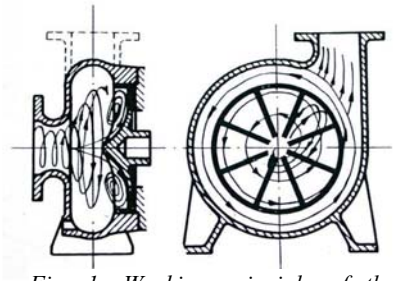

Fig. 1: Working principle of the Turo pump

Fig. 2: Typical pump with Turo impeller (Egger, 2008)

*Ing.Martin Červinka: Victor Kaplan's Department of Fluid Engineering, Institute of Energy, Brno University of Technology, Faculty of Mechanical Engineering, Technická 2896/2; 616 69, Brno; CZ, e-mail: y100967@stud.fme.vutbr.cz

3. Design of impellers

As mentioned above two models of impellers were created. At first the Turo impeller model was created. Basic equations described in (Feranec, 200?) were used to design this impeller. Original parameters of the pump are shown in Tab. 1. These parameters and known dimensions of spiral casing were used and main dimensions of Turo impeller were designed. The model of Turo impeller can be seen in fig. 3. Secondly, the other impeller model was created by cranking the vanes from the Turo impeller and by creating the so called spur. For this reason this impeller will be called "Turo with spur" and it can be seen in fig. 4.

3.1. Main dimensions of impeller

According to basic equations, main dimensions were created. In the following chapter, basic equations and calculated main dimensions can be seen.

Tab. 1: Original operating parameters.

Title	***Sign***	***Value***	***Unit***
Flow rate	Q	35.8	[l/s]
Head	H	21.5	[m]
Density	ρ	1050	[kg/m^3]
Speed	n	1450	[1/min]
Power	P	15	[kW]
Number of blades	z	8	[-]
Inlet, outlet angle of blade	β_1 , β_2	90	[°]

Diameter of impeller D_2

$$\Psi=\frac{g.H}{\frac{u_2^2}{2}}=\frac{2.g.H}{u_2^2} \tag{1}$$

$$u_2^2=\frac{2.g.H}{\Psi} \tag{2}$$

$$u_2=\sqrt{\frac{2.g.H}{\Psi}} \tag{3}$$

$$u_2=2\pi n.R_2=\sqrt{2.g.}\sqrt{\frac{H}{\Psi}} \tag{4}$$

$$D_2=84{,}8.\frac{1}{n}.\sqrt{\frac{H}{\Psi}}=84{,}8.\frac{1}{1450}.\sqrt{\frac{21{,}5}{1{,}17}}=\mathbf{0,\ 2507}[\mathrm{m}] \tag{5}$$

According to equations (1) – (4), we can obtain a final equation (5) for the impeller diameter. Based on this the value of diameter was chosen as ***D_2 = 0,25 m***

Impeller width b_2

$$\frac{b_4}{b_2} \cong 3 \tag{6}$$

$$b_2 = \frac{b_4}{3} = \frac{0,08}{3} = 0,026666 \Rightarrow 0,027 \quad [m] \tag{7}$$

Or by other equation

$$b_2 = (0,25 \div 0,3).D_s = 0,3.0,126 = 0,0378[m] \tag{8}$$

From results of equations (7) and (8), the value of impeller width was chosen as ***b_2 = 0,03 m***.

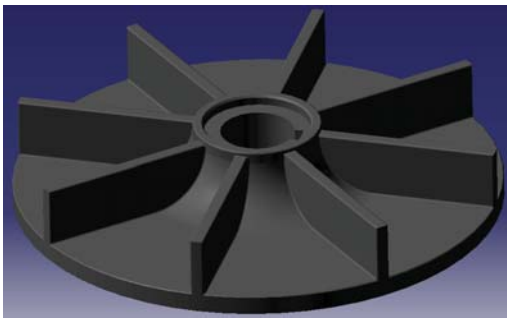

Fig. 3: The Turo impeller model

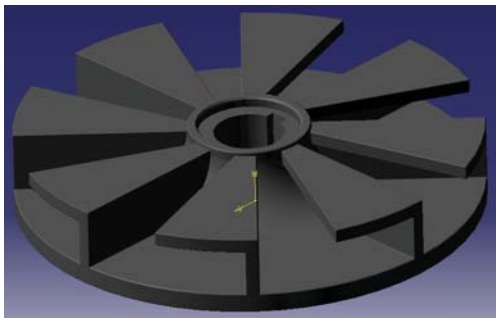

Fig. 4: The Turo with spur impeller model

3.2. Design of CFD model

Geometrical models of both impellers were created in Gambit 2.4.6. The computational mesh contained approximately 6 million hexahedral cells; the worst cell had skewness equal to 0. 7711. The whole model was split into 5 volumes: impeller, space above impeller, spiral casing, suction and displacement. The computation was done in ANSYS Fluent 12. 1 and 2 equation k- ε viscosity model with non – equilibrium wall function was used. A steady calculation with second order upwind was performed. To create all of these characteristics, an overall range of flow rate must be taken into account. Following design points were computed: ***1,25* Q_N*** (45 $l.s^{-1}$); ***Q_N*** (36 $l.s^{-1}$); ***0,75* Q_N*** (27 $l.s^{-1}$); ***0,5* Q_N*** (18 $l.s^{-1}$); ***0,25* Q_N*** (9 $l.s^{-1}$) and finally, last point ***0,1* Q_N*** (3,6 $l.s^{-1}$) for better projection of characteristics at low flow rate was added.

4. Evaluation

4.1. Characteristics of pump

A focus was put on the following characteristics Y – Q, η – Q, P – Q. As stated in (Pochylý et. al., 2009), the Y – Q characteristic should be considered as stable if the following condition of stability is fulfilled across the whole range of the flow rate:

$$\frac{\partial Y}{\partial Q} < 0 \tag{9}$$

The characteristics of pump with Turo impeller are shown in fig. 5, 6, and 7; the characteristic is stable across the whole range of flow rate. The power characteristic has almost a linear shape although there is a slight deviation near the shut-off point due to inaccuracies in the calculation. According to the general theory, the progress of these characteristics can be assessed as correct. At a design optimum we obtained head H = 22,23 m, power P = 13385 W and efficiency η = 58, 4%, which are higher values than original operating parameters.

The characteristics of pump with Turo with spur impeller are in principle the same as Turo. In fig. 5 the relation between specific energy and flow rate can be seen. It is as stable as the Turo impeller characteristic but the decrease of specific energy and related head can be seen. At the design optimum for Turo with spur impeller we obtained head H = 20, 47 m, power P = 12843 W and efficiency η = 56, 1%, i.e. a decrease compared to the original operating parameters. The difference of specific energy between the design variants is shown in fig. 8.

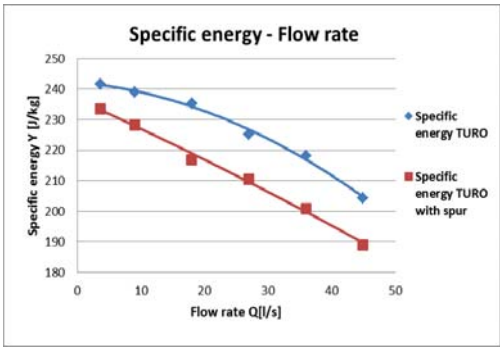

Fig. 5: Y – Q characteristics for both design variants

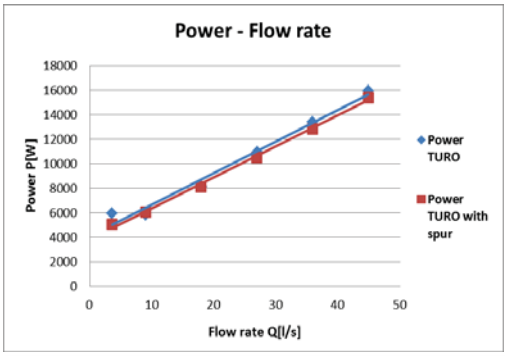

Fig. 6: P – Q characteristics for both design variants

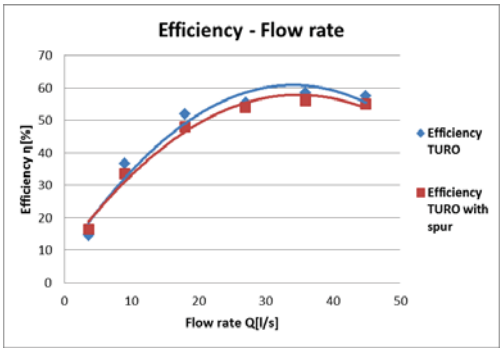

Fig. 7: η – Q characteristics for both design variants

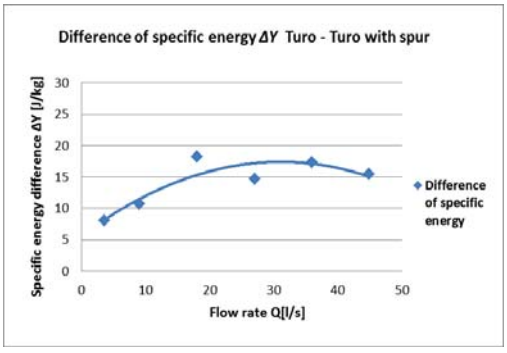

Fig. 8: The difference of specific energy between Turo and Turo with spur impellers

4.2. Specific energy in different volumes of pump

The characteristics of specific energy in dependence on flow rate for different volumes, as introduced in chapter 3.2, are shown in fig. 9 – 12. The characteristics for the Turo impeller are shown in fig. 9, 10 and for the Turo with spur are in fig. 11, 12. For both impeller volumes, characteristics are unstable at a low flow rates, which has a negative impact on total characteristics although they are considered as stable. Both variants have similar shapes of these characteristics for the same volumes.

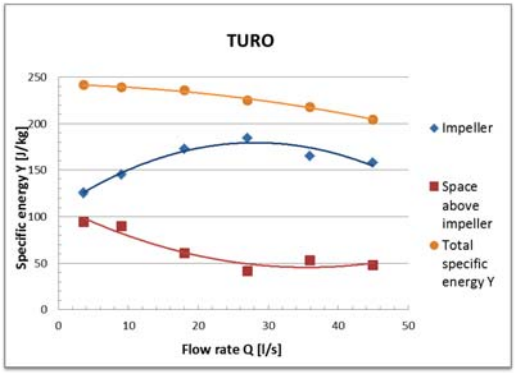

Fig. 9: Y – Q characteristics in specific volumes for Turo impeller

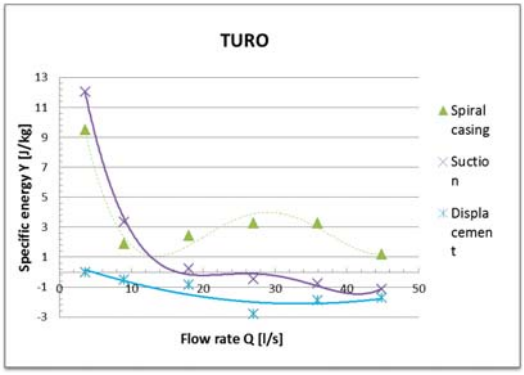

Fig. 10: Y – Q characteristics in specific volumes for Turo impeller

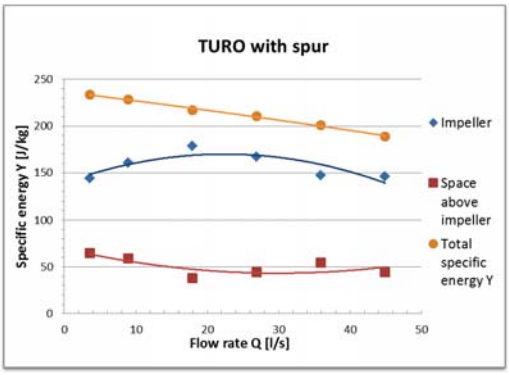

Fig. 11: Y – Q characteristics in specific volumes for Turo with spur impeller

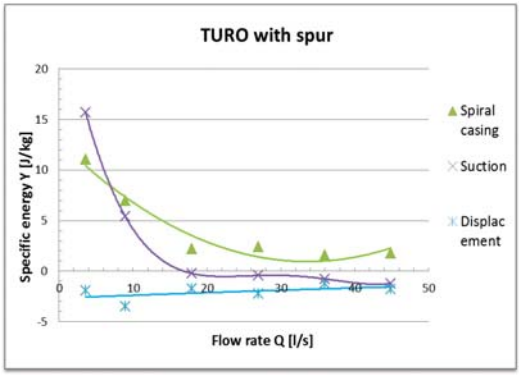

Fig. 12: Y – Q characteristics in specific volumes for Turo with spur impeller

4.3. Axial force

The axial force applied to impellers was obtained, like other values, from CFD computation. The axial force applied on impellers is shown in fig. 13 and the axial force applied only on impeller vanes for both design variants is shown in fig. 14. The axial force is oriented in positive direction of z – axis, i.e. it is negative values are directed into the impeller and the shaft is subjected to a compressive stress. Values of axial force for the Turo with spur are approximately three times larger than for the Turo. This is probably due to larger vanes of the Turo with spur; therefore fluid can act on the impeller by larger force. The axial force is not large for this type of pump; however it can be lowered by using construction adjustment stated in (Gančo, 1999). The best solution for these impellers is compensatory vanes at the back of supporting disk; these vanes can help to minimalize the effect of axial force.

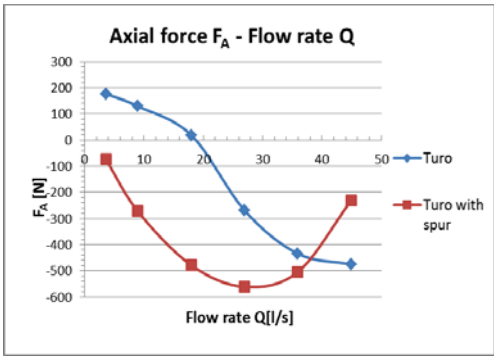

Fig. 13: Axial force on impellers

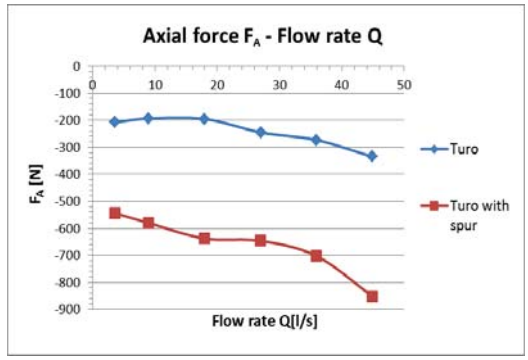

Fig. 14: Axial force on impeller vanes

4.4. Influence of construction modification

The influence of construction modification on pump characteristics was examined in this chapter. Three solutions of gap between the pump casing and the impeller were created. First solution was a conical gap with angle 15°, then a very small cylindrical gap, which was almost like wall behind the impeller and the last solution was a large cylindrical gap between these parts. For better illustration, these gaps are shown in fig. 15. The results from computation and evaluation of influence of each design variant are also shown. After obtaining results from CFD computation, we created all pump characteristics, which are shown in fig. 16, 17 and 18. The first solution (conical gap) shows the best results. The second solution (very small gap) has unstable Y – Q characteristic and the efficiency is lower than for conical gap. The large cylindrical gap has quite similar characteristics as a very small cylindrical gap. According to results presented in this chapter, it can be said that the conical gap with 15° angle achieved the best results and shapes of characteristics. The computation was made only for the Turo impeller.

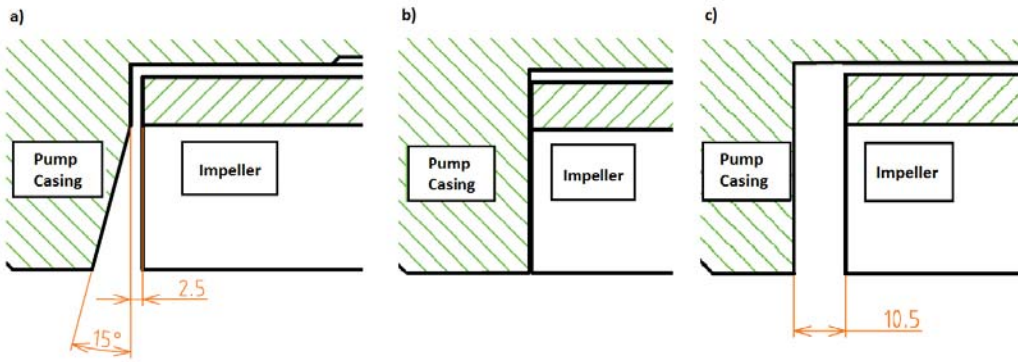

Fig. 15: Types of gaps a) Conical gap; b) Very small cylindrical gap; c) Large cylindrical gap

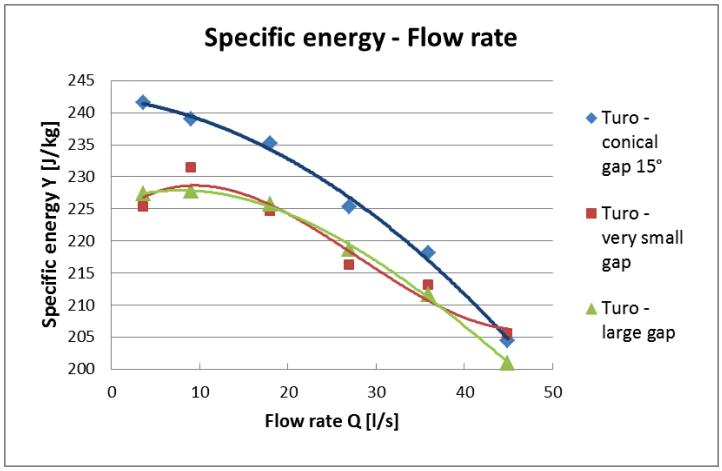

Fig. 16: Y - Q characteristics for different types of gaps

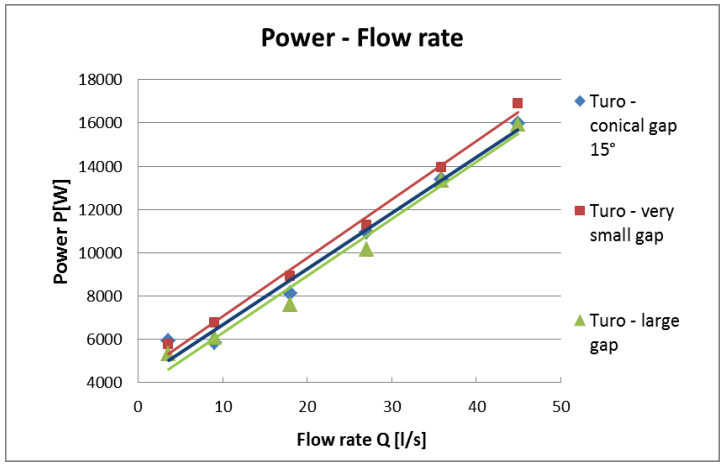

Fig. 17: P - Q characteristics for different types of gaps

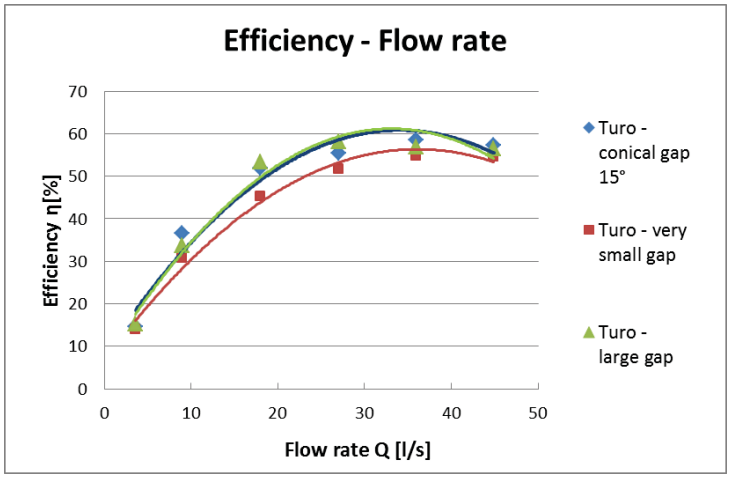

Fig. 18: η – Q characteristics for different types of gaps

4.5. Rotational motion in pump

The model of the whole pump is quite extensive and it is hard to show the behavior of fluid in each part. Velocity vectors and differences between design variants of impeller are shown. The graphic interpretation gives us a possibility to show vortices occurring in our model space, fluid behavior, etc.

4.5.1 Turo impeller

The main focus was put on fluid behavior in the inter vane channel. Velocity vectors are displayed in created cuts, which are shown in fig. 19. Velocity vectors in the impeller space are shown in fig. 20 – 23. Firstly, we considered an inlet to the impeller as it is whole upper face but the figures below show that the fluid began to leave the impeller in the region of larger radius. That is caused by rotation and vortex movement in the impeller. The figures also illustrated that the main vortex in the channel has counter-clockwise direction of rotation (fig. 20, 21) and it is opposite towards the output radius of the impeller (fig. 23). Therefore, the main vortex changes the direction of rotation as the fluid goes through inter blade channel. The magnitude of relative velocities is highest at impeller inlet, i.e. the area of small diameter of the impeller.

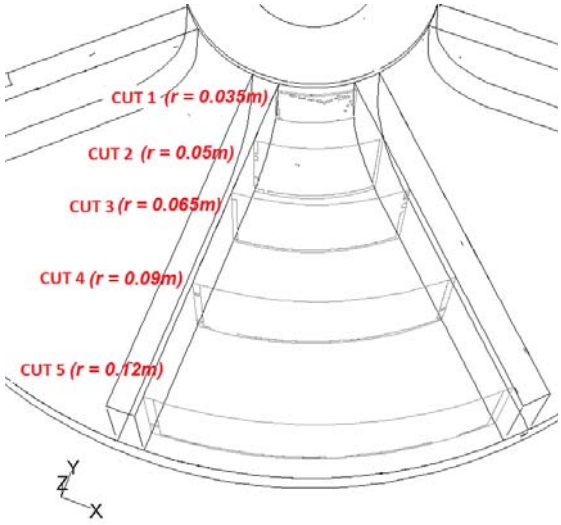

Fig. 19: The cuts in vane channel

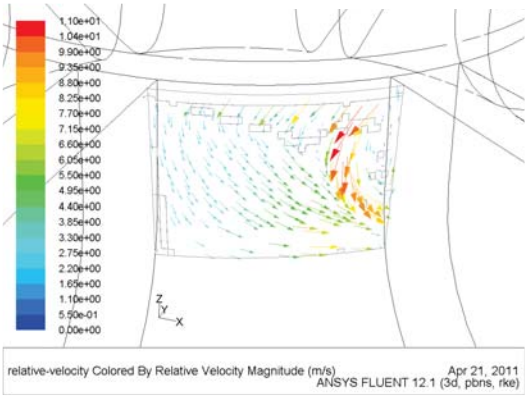

Fig. 20: Relative velocity vectors in cut no.1

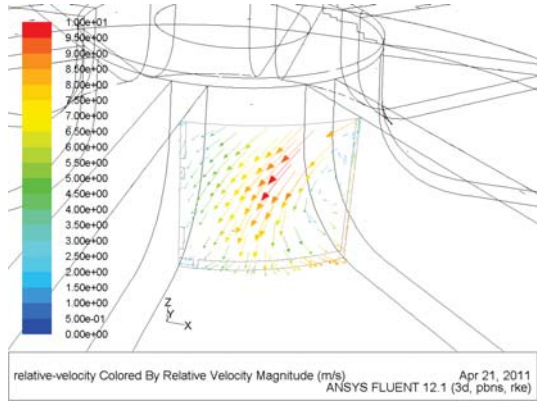

Fig. 21: Relative velocity vectors in cut no.2

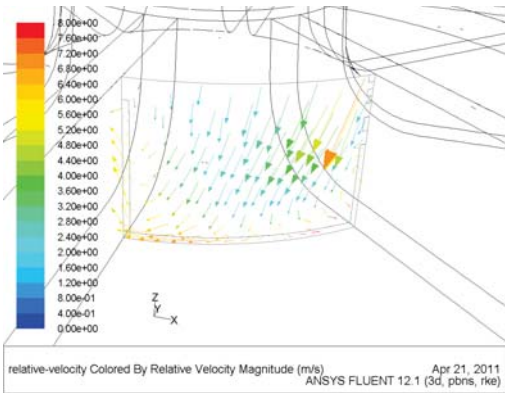

Fig. 22: Relative velocity vectors in cut 3

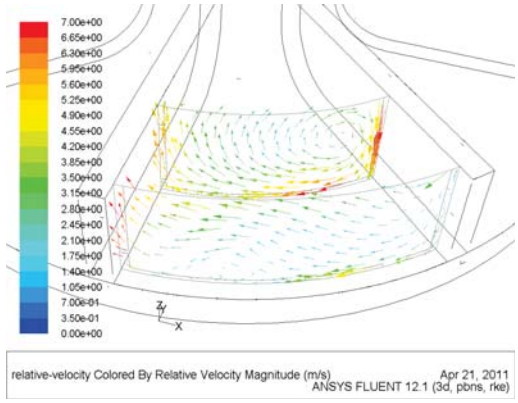

Fig. 23: Relative velocity vectors in cut no.4 and no.5

4.5.2 Turo with spur

The evaluation of the fluid motion in the pump space was also made for the Turo with spur impeller. For this design, velocity vectors in the same cuts are shown and only small differences between both impellers can be seen. The velocity vectors in the cuts are shown in fig. 24 - 27. At the inlet to the inter blade channel of impeller a negative property of the spur can be observed; it shrinks the inlet area such that the fluid cannot flow into the channel as well as for Turo impeller. According to Grundfos Company, which produces SuperVortex impellers, the spur should prevent the occurrence of small disturbing vortices nearby the impeller. Unfortunately, this property cannot be confirmed from achieved results due to limitations of our hardware capacity and this would probably need a finer computational mesh in this area.

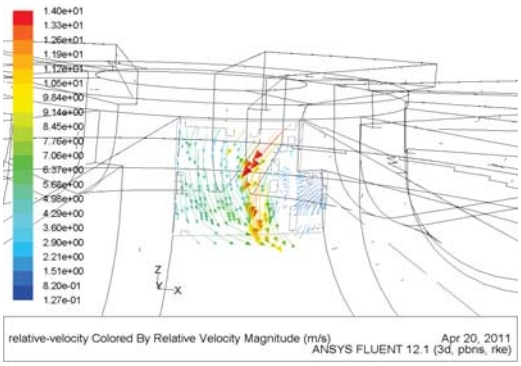

Fig. 24: Relative velocity vectors in cut 1

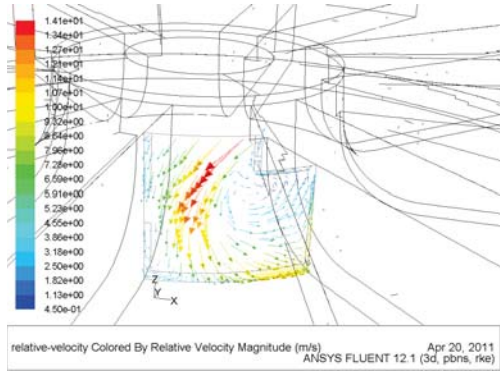

Fig. 25: Relative velocity vectors in cut 2

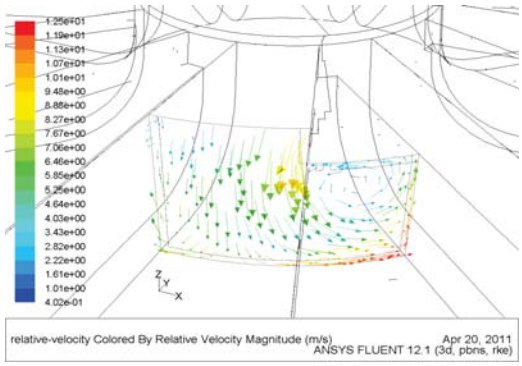

Fig. 26: Relative velocity vectors in cut 3

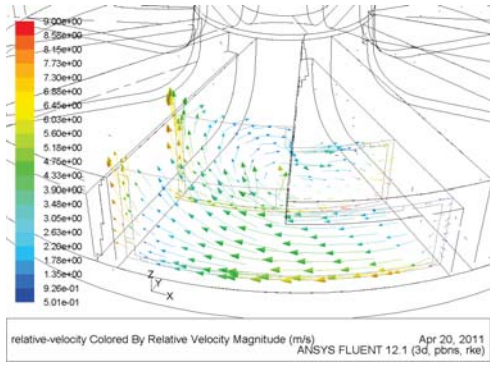

Fig. 27: Relative velocity vectors in cut 4 and 5

The differences at the inlet to impellers can be seen in fig. 28, 29. An interesting property of spur is that it prevents the flow of fluid into the impeller channel. It negatively affects the pump characteristic and it causes a decrease of the characteristic as is described in chapter 4.1.

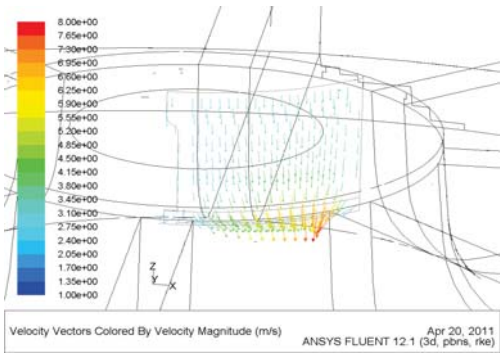

Fig. 28: Relative velocity vectors in inlet section above impeller for the Turo impeller

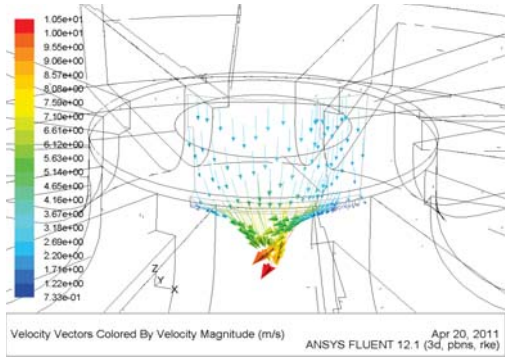

Fig. 29: Relative velocity vectors in inlet section above impeller for the Turo with spur impeller

5. Conclusions

Basic equations for design of Turo impeller are presented in this paper. The Turo impeller fulfilled operating parameters of the original pump. From achieved results it would be possible to change only the impellers with just a slight construction adaptation of the pump casing. The Turo with spur impeller was based on the principle of SuperVortex impeller; a decrease of characteristics values can be seen in this variant. The reason of this decrease follows from the fact that the spur has been designed such that it overlaps a part of the vane channel which caused a partial blockage. To improve this we can design the spur from the middle of the vane so that it would not block the fluid at inlet. We cannot confirm that the spur has a proper function because the results are not as predicative as we needed. The axial force acting on impellers of this type of pumps is not large. Moreover, it can be improved by some construction adjustments as mentioned in chapter 4.3. Both impellers have a stable Y – Q characteristic; this is very important in terms of occurrence of undesired pressure and flow pulsations. Finally, the influence of construction design of some parts of pump casing on pump characteristics was examined. This paper has shown three different solutions of a gap between the impeller and the pump casing. From results shown in chapter 4.4, it can be seen to what extent the

characteristic can be influenced by this change. There is an evident overall decrease of Y - Q characteristic for a very small gap while this characteristic becomes unstable, which is unacceptable. The large gap, which was created as cylindrical, again shows decrease of Y – Q characteristic and in the area of low flows it is on boundary of stability. From obtained results, the original conical gap can be assessed as the best solution of these design variants.

Acknowledgement

The author is grateful for funding and supporting this research to the Grant Agency of Czech Republic under project "Mathematical and Numerical Modeling of Flow in Pipe Junction and its Comparison with Experiment" with registration number 101/09/1539 as well as the junior research grant with sign FSI-J-12-21/1698 and the senior research grant FSI-S-12-2, which are provided by VUT, FSI.

References

Pochylý, F.; Haluza, M.; Drábková, S. (2009) "Stability of Q-Y characteristic of centrifugal pump". *In Engineering Mechanics 2009 – book of extended abstract, Svratka, Czech Republic, May 11-14, 2009*, ISBN 978-80-86246-35-2, pp. 989-996.

Pochylý, F.; Haluza, M.; Klas, R. (2009) "The stability of Y(Q) characteristic curve*". IAHR Symposium on Hydraulic Machinery and Systems, Timisoara, Romania, September 20-24, 2010*, pp. 1-6.

Feranec, M. (200?) *Aplikácie čerpadiel system Turo na čerpanie znečistených kvapalín*. Olomouc: Sigma - výzkumný ústav.

Gančo, M. (1999) *Axiálna sila hydrodynamických čerpadiel s radiálnym obežným kolesom*. Bratislava: Slovenská technická univerzita v Bratislavě.

Egger, Emile & Cie SA. (2008) *Turo vortex pumps* [online]. Egger. Available at WWW: http://www.eggerpumps.com/index.php?id=6&L=2.

18th International Conference
ENGINEERING MECHANICS 2012
Svratka, Czech Republic, May 14 – 17, 2012

pp. 203–210
Paper #12

SCALABLE ALGORITHM FOR NON-LINEAR PROBLEMS OF SOLID MECHANICS

J. Dobiáš, S. Pták*, Z. Dostál, T. Kozubek, A. Markopoulos**

Abstract: *The paper is concerned with a novel algorithm for solution to contact problems stemming from the TFETI (Total Finite Element Tearing and Interconnecting) domain decomposition method. The TFETI method is based on idea that the compatibility between non-overlapping sub-domains, into which the original domain is partitioned, is enforced by the Lagrange multipliers. The distinctive feature of the TFETI consists in the fact that the method also enforces the Dirichlet boundary conditions by means of the Lagrange multipliers. The TFETI based technique converts the original contact problem to the quadratic programming one with the equalities and simple bound constraints. Our new algorithm exhibits both parallel and numerical scalabilities so that it enables us to effectively solve steady-state problems of deformable bodies undergoing contact, geometric and material non-linear effects. In this paper we propose algorithm with nested iteration strategy, where its inner part consists of a new version of our previously developed MPRGP and SMALBE algorithms and the outer loop iterates on the geometric and material non-linearities. Numerical experiments include solutions to steady-state problems with non-linear effects and their results document that the proposed algorithms are robust, highly accurate and exhibit both parallel and numerical scalabilities.*

Keywords: ***Contact non-linearity, Geometric non-linearity, Material non-li-nearity, Domain decomposition, Scalability.***

1. Introduction

Dostál *et al.* analysed in (1) problem of frictionless contact problem between solid bodies, while they considered both geometrically and materially linear cases. Therein they suggested a new in a sense optimal version of their own previously developed algorithm based on TFETI (Total Finite Element Tearing and Interconnecting) domain decomposition method. The goal of this paper is to apply this new algorithm to the contact problems accompanied by both geometric and material non-linear phenomena, and to show that it can yield, even under these conditions, good results.

The FETI domain decomposition method was introduced by Farhat and Roux (2) as a parallel finite element solver for the self-adjoint elliptic partial differential equations. Its key idea is a decomposition of the spatial domain into non-overlapping sub-domains that are 'glued' by Lagrange multipliers, so that, after eliminating the primal variables, or displacements, the original problem is reduced to a small, relatively well conditioned, typically equality constrained quadratic programming problem that is to be solved iteratively. Later Farhat, Mandel and Roux (3) modified the basic FETI algorithm so that they were able to prove its numerical scalability, i.e. asymptotically linear complexity.

The partition of the original domain into sub-domains usually generates some 'floating' sub-domains with not enough prescribed displacements, so that their stiffness matrices are singular in steady-state cases and implementation of FETI then includes the computation of their kernels. However, stable evaluation of the bases of the kernels, though theoretically clear in exact arithmetic context, is tricky in the presence of the round-off errors. To overcome this difficulty, Dostál *et al.* (4) suggested enforcement of all the Dirichlet boundary conditions by the Lagrange multipliers so that all the sub-domains were treated as totally unconstrained. This version of FETI is referred to as the Total FETI (TFETI). Since the

*Ing. Jiří Dobiáš, CSc., Ing. Svatopluk Pták, CSc.: Institute of Thermomechanics, Academy of Sciences of the Czech Republic, Dolejškova 5, 182 00 Praha 8, Czech Republic, e-mail: jdobias@it.cas.cz
**Prof. RNDr. Zdeněk Dostál, DSc., Doc. Ing. Tomáš Kozubek, PhD., Ing. Alexandros Markopoulos, PhD.: Technical University in Ostrava, 17. listopadu 15, 708 00 Ostrava-Poruba, Czech Republic, e-mail: zdenek.dostal@vsb.cz

kernels of stiffness matrices of all the sub-domains are the same and known beforehand, this approach removed the problems with identification of these kernels.

Even though the FETI class methods were originally developed for numerical solution to linear elliptic partial differential equations, it turned out that they were even more successful for the solution to contact problems. The reason is that any FETI method reduces in effect for free the more general inequalities introducing the conditions of non-penetration of bodies to the bound constraints. The FETI based algorithm for contact problems was proposed by Dostál *et al.* in (5). The numerical scalability of this algorithm was demonstrated by numerical experiments.

The organisation of the paper is as follows. Section 2. introduces the TFETI for contact problems. Section 3. is briefly concerned with a new version of SMALBE and MPRGP, which are the algorithms stemming from the TFETI. The concepts of numerical and parallel scalabilities are explained in Section 4.. Section 5. outlines the overall computational strategy and we present there an algorithm that enables TFETI to be applied to solution to the contact, geometric and material non-linear effects. Section 6. shows results of numerical experiments and Section 7. concludes the paper.

2. Problem Formulation

For simplicity, let us consider a system of two solid deformable bodies in contact which occupy in reference configuration domain $\Omega = \Omega^m \cup \Omega^s$, where m denotes master body and s stands for slave body. Assume that their boundaries are subdivided into three disjoint parts Γ_u^i, Γ_f^i, and Γ_c^i, $i = m, s$, with prescribed Dirichlet, Neumann, and potential contact conditions, respectively.

The strong version of governing equations of the static equilibrium is as follows

$$\sigma_{ij}(\mathbf{u})_{,j} = f_i \quad \text{in} \quad \Omega, \tag{1}$$

where $\boldsymbol{\sigma}$, $\mathbf{u}$, and $\mathbf{f}$ denote stress tensor, displacement vector and loading vector, respectively. The Dirichlet and Neumann boundary conditions are, respectively, as reads

$$\mathbf{u} = 0 \quad \text{on} \quad \Gamma^u, \tag{2}$$

$$\sigma_{ij}(\mathbf{u}) \cdot \nu_j = p_i \quad \text{on} \quad \Gamma^f. \tag{3}$$

The variational formulation is to be obtained if we consider the constrained minimisation problem

$$\mathbf{u} \in \mathcal{K}, \qquad \mathcal{J}(u) \leq \mathcal{J}(v) \quad \forall v \in \mathcal{K}, \tag{4}$$

where $\mathcal{K}$ is a non-empty, closed, convex set of all feasible displacements. The quadratic functional

$$\mathcal{J}(\mathbf{v}) = \frac{1}{2} a(\mathbf{v}, \mathbf{v}) - \ell(\mathbf{v}) \tag{5}$$

is generated by a self-adjoint, positive definite bilinear form

$$a(\mathbf{v}, \mathbf{w}) = \sum_{i \in \{s,m\}} \int_{\Omega^i} \boldsymbol{\sigma}(\mathbf{v}^i) : \boldsymbol{\epsilon}(\mathbf{w}^i) dx \tag{6}$$

and accounts for internal forces. The linear functional

$$\ell(\mathbf{v}) = \sum_{i \in \{s,m\}} \int_{\Omega^i} \mathbf{f} \cdot \mathbf{v} dx + \sum_{i \in \{s,m\}} \int_{\Gamma^i}^{f} \mathbf{p} \cdot \mathbf{v} dx \tag{7}$$

accounts for the volumetric forces and tractions on the Neumann boundary.

To apply the TFETI domain decomposition, we tear each body from the part of the boundary with the prescribed Dirichlet boundary conditions, decompose each body into sub-domains and introduce new connecting conditions on the fictitious intersubdomain boundaries and on boundaries with imposed

Dirichlet conditions. The connecting conditions requires continuity of the displacements and of their normal derivatives across the intersubdomain boundaries.

Applying the standard finite element procedures while in addition considering TFETI method, we can express the governing equations of a contact problem in discretised form as follows

$$\mathbf{K}\mathbf{u} = \mathbf{f} - \mathbf{B}_I^\top \boldsymbol{\lambda}_I - \mathbf{B}_E^\top \boldsymbol{\lambda}_E, \tag{8a}$$

$$\mathbf{B}_I \mathbf{u} \leq \mathbf{c}_I, \tag{8b}$$

$$\mathbf{B}_E \mathbf{u} = \mathbf{c}_E, \tag{8c}$$

where $\mathbf{K}$ denotes a stiffness matrix with sparse positive semidefinite diagonal blocks corresponding to individual sub-domains. In accordance with the TFETI method, the kernels of all the sub-domains are the same and known beforehand. The matrix $\mathbf{B}_I$ and the vector $\mathbf{c}_I$ introduce the linearised non-interpenetration conditions. Similarly the matrix $\mathbf{B}_E$ and the vector $\mathbf{c}_E$ enforce the prescribed displacements along the part of the boundary with the Dirichlet conditions. $\boldsymbol{\lambda}_I$ and $\boldsymbol{\lambda}_E$ stand for the components of the vector of Lagrangean multipliers, while we shall use

$$\boldsymbol{\lambda} = \begin{bmatrix} \boldsymbol{\lambda}_I \\ \boldsymbol{\lambda}_E \end{bmatrix}, \quad \mathbf{B} = \begin{bmatrix} \mathbf{B}_I \\ \mathbf{B}_E \end{bmatrix} \quad \text{and} \quad \mathbf{c} = \begin{bmatrix} \mathbf{c}_I \\ \mathbf{c}_E \end{bmatrix}.$$

Eqn. (8a) has a solution iff $\mathbf{f} - \mathbf{B}^\top \boldsymbol{\lambda}$ belongs to the range of $\mathbf{K}$ and therefore the following relationship holds

$$\mathbf{R}^\top (\mathbf{f} - \mathbf{B}^\top \boldsymbol{\lambda}) = \mathbf{0}, \tag{9}$$

where $\mathbf{R}$ denotes the full rank matrix with columns spanning the kernel of $\mathbf{K}$. Since all the sub-domains are totally unconstrained, the kernels of the sub-domains are known beforehand and are to be assembled directly.

It is necessary to eliminate the primal variable $\mathbf{u}$ from eqn. (8a). It can easily be verified that if $\mathbf{u}$ is a solution to eqn. (8a), then there exists such a vector $\boldsymbol{\alpha}$ that

$$\mathbf{u} = \mathbf{K}^\dagger (\mathbf{f} - \mathbf{B}^\top \boldsymbol{\lambda}) + \mathbf{R}\boldsymbol{\alpha}, \tag{10}$$

where $\mathbf{K}^\dagger$ is any symmetric positive definite matrix satisfying the first Moore–Penrose condition $\mathbf{K}\mathbf{K}^\dagger\mathbf{K} = \mathbf{K}$, or it is the $\{1\}$-inverse.

Substituting eqn. (10) into eqn. (8a), we get the following minimisation problem

$$\min \ \frac{1}{2} \boldsymbol{\lambda}^\top \mathbf{B}\,\mathbf{K}^\dagger\,\mathbf{B}^\top \boldsymbol{\lambda} - \boldsymbol{\lambda}^\top \mathbf{B}\,\mathbf{K}^\dagger \mathbf{f} \quad \text{s. t.} \quad \boldsymbol{\lambda}_I \geq \mathbf{0} \quad \text{and} \quad \mathbf{R}^\top (\mathbf{f} - \mathbf{B}^\top \boldsymbol{\lambda}) = \mathbf{0}. \tag{11}$$

Let us now introduce the standard FETI notations

$$\mathbf{F} = \mathbf{B}\mathbf{K}^\dagger\mathbf{B}^\top, \quad \mathbf{G} = \mathbf{R}^\top\mathbf{B}^\top, \quad \mathbf{e} = \mathbf{R}^\top\mathbf{f}, \quad \mathbf{d} = \mathbf{B}\mathbf{K}^\dagger\mathbf{f}. \tag{12}$$

After some algebraic manipulation, we obtain the following formulation

$$\min \ \frac{1}{2} \boldsymbol{\lambda}^\top \mathbf{P}\mathbf{F}\mathbf{P}\boldsymbol{\lambda} - \boldsymbol{\lambda}^\top \mathbf{P}\mathbf{d} \quad \text{s. t.} \quad \boldsymbol{\lambda}_I \geq \mathbf{0} \quad \text{and} \quad \mathbf{G}\boldsymbol{\lambda} = \mathbf{0}, \tag{13}$$

where

$$\mathbf{P} = \mathbf{I} - \mathbf{Q} \quad \text{and} \quad \mathbf{Q} = \mathbf{G}^\top (\mathbf{G}\mathbf{G}^\top)^{-1}\mathbf{G} \tag{14}$$

stand for the orthogonal projectors on the kernel of $\mathbf{G}$ and the range of $\mathbf{G}^\top$, respectively. The point of the last step is to introduce preconditioning by the natural coarse grid projector.

The problem (13) is to be solved efficiently by the algorithms presented in the following section.

3. MPRGP and SMALBE Algorithms

We have shown that application of the TFETI methodology to the contact problems converts the original problem to the quadratic programming problem with bound and equality constraints and well-conditioned regular part of the Hessian matrix. Such problems are to be solved very efficiently by the recently proposed algorithms. A unique and qualitatively new feature of these algorithms is the rate of convergence in the bounds on the regular part of the Hessian, independent of the representation of constraints. See (1) for details.

The problem (13) is first reduced by Semi-Monotonic Augmented Lagran-geans with Bound and Equality constraints (SMALBE) method to the se-quence of bound constrained quadratic programming problems. SMALBE accepts inexact solutions of auxiliary bound constrained problems solved approximately in the inner loop until the norm of the projected gradient is proportional to the feasibility error, and updates the regularisation parameter until the value of the Lagrangian increases. These auxiliary problems are to be solved efficiently by the Modified Proportioning with Reduced Gradient Projection (MPRGP) method in the inner loop. It was proved by Dostál and Horák (6) that application of FETI or TFETI with natural coarse grid preconditioning to a contact problem can be combined with SMALBE and MPRGP to obtain algorithm with asymptotically linear, i.e. optimal, complexity. A unique feature of MPRGP is the rate of convergence which is independent of the inequality constraints. Moreover, the algorithm enjoys the finite termination property even for dual degenerate problems, so that it does not suffer from oscillations often attributed to this type of algorithms.

Detailed description of these algorithms is beyond the scope of this paper.

4. Numerical and Parallel Scalabilities

The performance of a domain decomposition based iterative method depends on two important properties, namely numerical and parallel scalabilities. Such a method is said to be numerically scalable if the condition number of the problem does not grow or grows weakly with the ratio of the sub-domain size and the mesh size. The parallel scalability represents ability of an algorithm to achieve larger speed-ups for a larger number of processes.

5. Non-linear Algorithm

The primary interest of this work is the development of effective strategy for fully non-linear problems, where, in addition to the contact interaction, the kinematics of the body system are not confined to small strains, and where the material response is potentially non-linear and inelastic.

The strains can be evaluated by means of the following in general non-linear relationship

$$\boldsymbol{\epsilon} = \mathbf{B_s}(\mathbf{u}) \cdot \mathbf{u}, \tag{15}$$

where $\mathbf{B}_s$ denotes an appropriate matrix relating strains with nodal displacements.

The stresses are computed by solving this constitutive equation

$$\boldsymbol{\sigma} = \sum_{nelem} \int_0^{\boldsymbol{\epsilon}} \mathbf{D} \mathrm{d}\boldsymbol{\epsilon}, \tag{16}$$

where $\mathbf{D}$ stands for the tangent material matrix. Its particular form depends on applied material model. We sum over $nelem$ elements.

The MPRGP and SMALBE algorithms are directly applicable to solution to the contact problem, which itself is a strongly non-linear phenomenon indeed, but with other conditions linear. Any additional non-linear effect necessitates employment of the nested iteration strategy, where the inner loop is concerned with TFETI based solver, while the outer loop iterates on the material/geometric non-linear effects and contact geometry update so that it might achieve equilibrium.

Consider the state of equilibrium of the system. Employing the modified Newton-Raphson iterative method, the governing equilibrium equations is as follows

$$\mathbf{K}^{(i-1)}\,\Delta\mathbf{u}^{(i)} = \mathbf{f}_{ext} - \mathbf{f}_{int}^{(i-1)}. \tag{17}$$

$\mathbf{K}$, $\mathbf{f}_{ext}$ and $\mathbf{f}_{int}$ denote the stiffness matrix, the vector of external nodal loading, and vector of internal nodal forces, respectively. The right superscript (i) stands for the current number of iteration. $\Delta\mathbf{u}^{(i)}$ denotes the displacement increment at each iteration, while the total displacement is updated as follows

$$\mathbf{u}^{(i)} = \mathbf{u}^{(i-1)} + \Delta\mathbf{u}^{(i)}. \tag{18}$$

Then we can in turn compute the strain tensor, stress tensor and internal forces as reads

$$\boldsymbol{\epsilon}^{(i)} = \mathbf{B}_s\left(\mathbf{u}^{(i)}\right)\mathbf{u}^{(i)}, \tag{19a}$$

$$\boldsymbol{\sigma}^{(i)} = \sum_{nelem}\int_0^{\boldsymbol{\epsilon}^{(i)}} \mathbf{D}\mathrm{d}\boldsymbol{\epsilon}, \tag{19b}$$

$$\mathbf{f}_{int}^{(i)} = \sum_{nelem}\int_{\Omega^{(i)}} \mathbf{B_s}^{\top}(\mathbf{u}^{(i)})\,\boldsymbol{\sigma}(\boldsymbol{\epsilon}^{(i)})\,\mathrm{d}\Omega^{(i)}. \tag{19c}$$

Equations (17) to (19) describe the problem in terms of the primal variables, i.e. displacements. The stiffness matrix and RHS vector of eqn. (17) have to be transformed in the sense of Section 2. in order that the problem might be computed by MPRGP/SMALBE algorithms for the Lagrangian multipliers. Then we can return to the primary variables, i.e. the displacement increments.

The simplified solution algorithm is shown in the following flowchart.

Initial step: Assemble stiffness matrix $\mathbf{K}$ and $\mathbf{B}_E$;
Set $i = 0$, $\mathbf{u}^0 = 0$, $\mathbf{f}_{int}^0 = 0$;

Step 1: Evaluate contact conditions $\mathbf{B}_I^{(i)}$;

Step 2: Solve contact problem by **MPRGP/SMALBE** for $\boldsymbol{\lambda} \rightarrow \Delta\mathbf{u}$,
$\mathbf{u}^{(i)} = \mathbf{u}^{(i-1)} + \Delta\mathbf{u}$.

Step 3: Compute the strain tensor $\boldsymbol{\epsilon}^{(i)}$ and stress tensor $\boldsymbol{\sigma}^{(i)}$.

Step 4: Integrate the equivalent internal forces $\mathbf{f}_{int}^{(i)}$.

Step 5: Assemble the residual load vector $\mathbf{res}^{(i)} = \mathbf{f}_{int}^{(i)} - \mathbf{f}_{ext}$;
check on convergence criteria $\frac{\|\Delta\mathbf{u}\|}{\|\mathbf{u}^{(i)}\|} < \eta_1$, $\frac{\|\mathbf{res}^{(i)}\|}{\|\mathbf{f}_{ext}\|} < \eta_2$;
If fulfilled then STOP,
otherwise set $i \leftarrow i + 1$ and go to **Step 1**.

6. Numerical Experiments

This section presents results of two sets of numerical experiments with the proposed algorithms. The first one is concerned with analysis of a bolt and nut contact problem and the second one shows results concerning the numerical and parallel scalabilities. All the numerical experiments were carried out with our in-house general purpose finite element package PMD (**P**ackage for **M**achine **D**esign) (7).

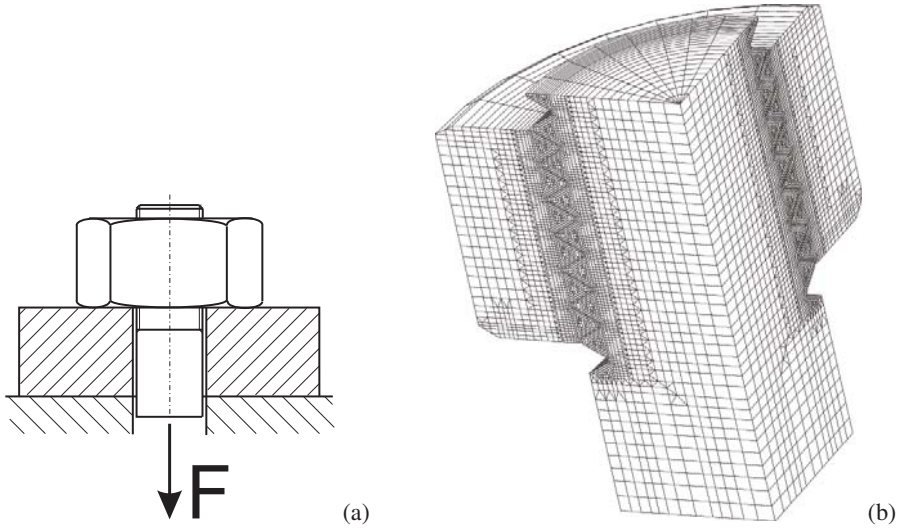

Fig. 1: Bolt & nut problem; (a) schematic sketch, (b) mesh.

6.1. Bolt and Nut Contact Problem

Consider a bolt and nut of 30 mm diameter and the metric thread. The nut rests on a washer and the bolt is loaded by a force **F** according to fig. 1(a). The problem is semi-coercive in the sense that we did not prescribe any constraints for the bolt in the direction of its axis. The motion of the bolt is restricted only by the surfaces in contact. Fig. 1(b) shows the finite element mesh, which was strictly created in accordance with the corresponding technical standard, apart from the thread that is not in form of the helix but rings. The problem is modelled with linear penta/hexahedra and we modelled only one quarter because of the symmetry. Numbers of primal and dual variables are 95052 and 1296, respectively, for the case with decomposition into two sub-domains. We consider both the geometric and material non-linear effects. The material properties for linearly–elastic–perfectly–plastic material model are as follows: Young's modulus $E = 2.1 \times 10^{11}\ Pa$, Poisson's ratio $\nu = 0.3$ and yield stress $\sigma_Y = 250MPa$. We used the von Mises yield criterion.

Fig. 2 shows distribution of von Mises stresses for three levels of loading. The first column depicts results for load $F = 3.8kN$, the second one for $F = 11.3kN$, and the third one for $F = 22.6kN$. The upper row represents results with applied elastic material model and the lower one with the plastic model.

6.2. Numerical and Parallel Scalabilities

Consider contact of two identical elastic cubes of size $a = 10\ mm$ and of the following material properties: Young's modulus $E = 2.1 \times 10^{11}$ Pa and Poisson's ratio $\nu = 0.3$. The computational model is discretised by tri-linear cubical elements and decomposed into cubical sub-domains, while their ratio $\frac{H}{h} = 10$. Considering parallel treatment, each sub-domain is assigned one processor.

The upper part of table 1 shows numbers of primal and dual variables for various decompositions. The lowest row demonstrates the numerical scalability of our algorithm. It reads numbers of the Hessian multiplications, which are the most important indicators of the performance of the algorithm and correspond to the numbers of iterations. It is obvious that the number of iterations increases only mildly with refinement of the mesh in the case that the ratio $\frac{H}{h}$ is held constant, which is in good agreement with theory.

It is clear from table 2 that our algorithm exhibits the parallel scalability.

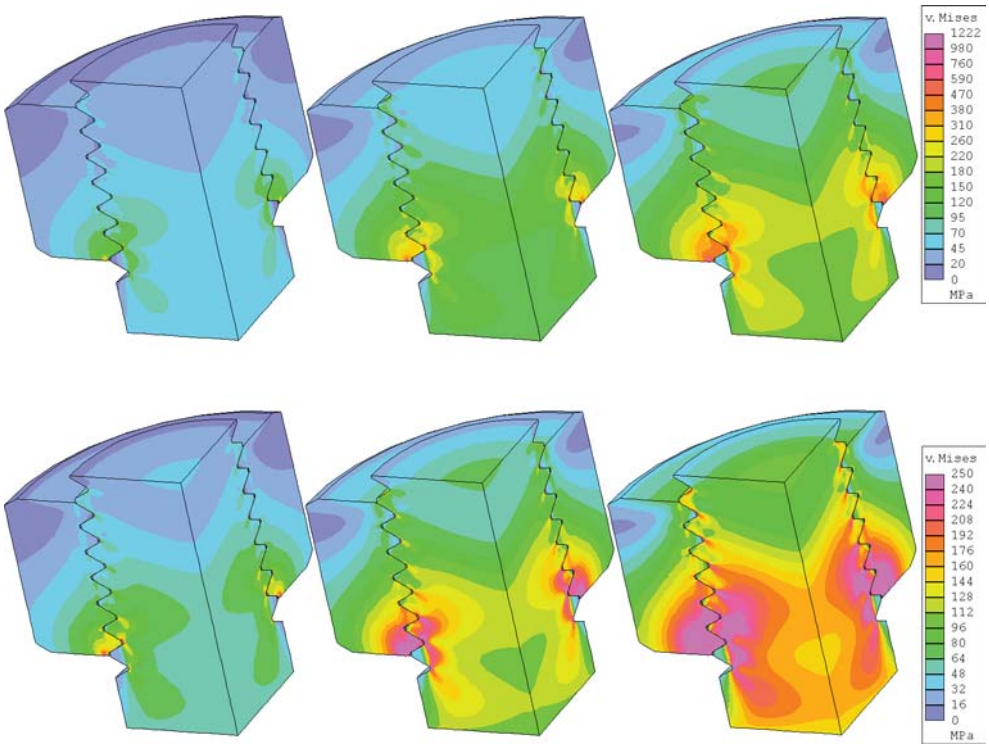

Fig. 2: Von Mises stress distribution.

Tab. 1: Numerical Scalability.

Subdomains	16	54	128	250
Primal variables	196 608	663 552	1 572 864	3 072 000
Dual variables	21 706	81 652	214 699	443 920
Hessian multiplications	60	63	67	69

Tab. 2: Parallel Speed-up.

Processors	2	4	8	16	24
Solver	1.76	3.66	7.57	15.30	22.89
Preprocessor	1.70	3.61	7.55	15.24	22.81
Total	1.73	3.63	7.56	15.27	22.85

7. Conclusion

New version of the algorithms MPRGP and SMALBE stemming from the TFETI domain decomposition method were applied to solution to contact problems accompanied by geometric and material non-linear effects. It was shown that they yield accurate solution, their converge rate is high and they exhibit both numerical and parallel scalabilities, which is essential for their application to the high performance computers.

Acknowledgments

The authors would like to acknowledge the support of GA CR through grant number 101/08/0574 and AS CR through grant number AV0Z20760514.

References

[1] Dostál, Z., Kozubek, T., Vondrák, V., Brzobohatý, T. & Markopoulos, A., Scalable TFETI algorithm for the solution of contact problems of elasticity. *International Journal for Numerical Methods in Engineering*, Vol 82, No.11, pp 1384–1405, 2010.

[2] Farhat, C. & Roux, F.X., A method of finite element tearing and interconnecting and its parallel solution algorithm. *International Journal for Numerical Methods in Engineering*, Vol 32, No.12, pp 1205–1227, 1991.

[3] Farhat, C., Mandel, J. & Roux, F.X., Optimal convergence properties of the FETI domain decomposition method. *Computer Methods in Applied Mechanics and Engineering*, Vol 115, No.5, pp 365–385, 1994.

[4] Dostál, Z., Horák, D. & Kučera, R., Total FETI - an easier implementable variant of the FETI method for numerical solution of elliptic PDE. *Communications in Numerical Methods in Engineering*, Vol 22, No.6, pp 1155–1162, 2006.

[5] Dostál, Z., Horák, D., Kučera, R., Vondrák, V., Haslinger, J., Dobiáš, J. & Pták, S., FETI based algorithms for contact problems: scalability, large displacements and 3D Coulomb friction. *Computer Methods in Applied Mechanics and Engineering*, Vol 194, No.2–5, pp 395–409, 2005.

[6] Dostál, Z. & Horák, D., Theoretically supported scalable FETI for numerical solution of variational inequalities. *SIAM Journal of Numerical Analysis*, Vol 45, No.6, pp 500– 513, 2007.

[7] PMD, www.it.cas.cz/manual/pmd

18th International Conference
ENGINEERING MECHANICS 2012
Svratka, Czech Republic, May 14 – 17, 2012

pp. 211–222
Paper #92

LATTICE MODELING OF CONCRETE FRACTURE INCLUDING THE EFFECT OF MATERIAL SPATIAL RANDOMNESS

J. Eliáš[*], **M. Vořechovský** [**]

Abstract: *The paper presents stochastic discrete simulations of concrete fracturing. The spatial material randomness of local material properties is introduced into a discrete lattice-particle model via an autocorrelated random field generated by the Karhunen–Loève expansion method. The stochastic discrete model is employed to simulate failure of three-point-bent beams with and without a central notch notch. The effect of spatial randomness on the peak load and energy dissipation is studied.*

Keywords: ***lattice model, concrete, fracture, stochastic simulations, material randomness, fracture energy, flexural failure.***

1. Introduction

It has been widely recognized that mechanical properties of materials exhibit a spatial variability. The seminal theory of Weibull (1939) offered simple and powerful tool to determine the probabilistic distribution of structural strength. However, applicability of the Weibull theory is limited to brittle structures with no redistribution prior to the peak load. The Weibull theory lacks any length scale and rupture of infinitely small volume directly causes failure of the whole structure. The absence of any characteristic length scale also results in spurious infinite strength of infinitely small structures (Vořechovský, 2010). Moreover, the Weibull theory assumes that strength of every material point is independent of its surroundings. However, many structures are made of quasibrittle materials like concrete, ceramics, rocks or ice. These structures have the ability to partially redistribute released stresses and thus their failure is triggered by rupture of some representative volume of finite size. Also the Weibull assumption of independence stands out against the natural expectation that the local strength fluctuate rather continuously inside a structure.

The advantage of Weibull theory comes from the fact that the mechanics of failure does not interact with the stochastic model – only elastic stress field is needed. Extension of the Weibull theory for finite internal material length scale requires knowledge of changes in the stress field during the redistribution prior to the peak load. The redistribution can be mimicked by the nonlocal Weibull theory of Bažant and Xi (1991) and Bažant and Novák (2000), where probability of failure of material point depends not only on its local stress but also on stress in its surroundings. Therefore, local stress is replaced by nonlocal stress obtained by nonlocal averaging of the (local) elastic stress field (Bažant and Jirásek, 2002). The nonlocal Weibull theory agrees for the large sizes with the local one. For intermediate structural sizes, it predicts higher strengths than the local Weibull theory thanks to possible stress redistribution. Unfortunately, in the in the case of very small structures, the theory is not applicable because the approximation or stress redistribution by nonlocal averaging is too simplistic. Though the nonlocal averaging helps to introduce the material internal length, it is not able to correctly reflect possible spatial correlations of local material properties.

A laborious option of structural strength estimation is represented by stochastic failure simulations that include proper mechanics of stress redistribution. Such a stochastic analysis can be performed using the finite element method with a sophisticated material constitutive law (Vořechovský, 2007;

[*]Ing. Jan Eliáš, Ph.D.: Institute of Structural Mechanics, Faculty of Civil Engineering, Brno University of Technology, Veveří 331/95; 602 00, Brno; CZ, e-mail: elias.j@fce.vutbr.cz
[**]Doc. Ing. Miroslav Vořechovský, Ph.D.: Institute of Structural Mechanics, Faculty of Civil Engineering, Brno University of Technology, Veveří 331/95; 602 00, Brno; CZ, e-mail: vorechovsky.m@fce.vutbr.cz

Vořechovský and Sadílek, 2008). Failure of highly heterogeneous materials can also be advantageously modeled via discrete models. These models can be *deterministic*: Grassl and Rempling (2008); Van Mier and Van Vliet (2003); Bolander and Saito (1998) or *stochastic*: Grassl and Bažant (2009); Alava et al. (2006). In this study, we adopt the lattice particle-model developed by G. Cusatis (Cusatis and Cedolin, 2007) for modeling of concrete fracturing. Spatial material fluctuations are introduced by modeling the material properties as realizations of a random field.

The following Section 2. briefly describes the deterministic mechanical (lattice) model and Section 3. elucidates how the spatial randomness is incorporated into the model. The model is then used for numerical simulations of failure of notched and unnotched three-point bent beams. The results are presented in Sections 4. (notched beams) and 5. (unnotched beams).

2. Deterministic model

Modeling of the initiation and propagation of cracks in quasibrittle materials exhibiting strain softening has been studied for several decades. Although this is a difficult task complicated by the distributed damage dissipating energy within a fracture process zone (FPZ) of non-negligible size, realistic results have been achieved by several different approaches; see e.g. Bažant and Planas (1998). The present study is based on the cohesive crack model (Barenblatt, 1962; Hillerborg et al., 1976; Bažant and Planas, 1998) called sometimes the fictitious crack model. It relies on an assumption that the cohesive stress transmitted across the crack is released gradually as a decreasing function of the crack opening, called the cohesive softening curve. Its main characteristic is the total fracture energy, G_F – a material constant representing the area under the softening curve.

In heterogeneous materials, the dissipation of energy takes place within numerous meso-level cracks inside the FPZ. Direct modeling of such distributed cracking calls for representation of the material meso-level structure. Models capable to efficiently incorporate the concrete meso-structure should be used. For this purpose, the present analysis will be based on the discrete lattice-particle developed by Cusatis and Cedolin (2007), which is an extension of Cusatis et al. (2003, 2006).

The material is represented by a discrete three-dimensional assembly of rigid cells. The cells are created by tessellation according to pseudo-random locations and radii of computer generated aggregates/particles. Every cell contains one aggregate (Fig. 1a,b). The cells are interconnected by set of three nonlinear springs (normal - n and two tangential - t_1, t_2) placed at the interfaces between the cells, representing the mineral aggregates in concrete and its surroundings. On the level of rigid cell connection, the cohesive crack model is used to represent cracking in the matrix between the adjacent grains. The inter-particle fracturing is assumed to be of damage-mechanics type and is modeled using a single damage variable ω applied to all three directions $i = n$, t_1 and t_2. Forces F_i in the springs can thus be evaluated from their extensions Δu_i by

$$F_i = (1 - \omega) k_i \Delta u_i \tag{1}$$

where k_i is elastic spring stiffness. The damage parameter ω depends on Δu_i and on the previous loading history of each connection. For a detailed description of the connection constitutive law or other model features, see Cusatis and Cedolin (2007). The confinement effect (present in the full version of the model) is neglected here as it was estimated that confinement does not play any important role in the studied type of experiment.

Beams of depths $D = 300$ mm, span-depth ratio $S/D = 2.4$ and thickness $t = 0.04$ m, were modeled. The maximal aggregate diameter was 9.5 mm. The minimal grain diameter was selected as 3 mm. Aggregates' diameters within the chosen range were generated using the Fuller curve. The parameters of the connection constitutive law, which were mostly taken similar to those in Cusatis and Cedolin (2007), were: matrix elastic modulus $E_c = 30$ GPa; aggregate elastic modulus $E_a = 90$ GPa; meso-level tensile strength $\sigma_t = 2.7$ MPa; meso-level tensile fracture energy $G_t = 30$ N/m; meso-level shear strength $\sigma_s = 3\sigma_t = 8.1$ MPa; meso-level shear fracture energy $G_s = 480$ N/m; meso-level compressive strength $\sigma_c = 42.3$ MPa; $K_c = 7.8$ GPa; $\alpha = 0.25$; $\beta = 1$; $\mu = 0.2$; $n_c = 2$.

To save computer time, the lattice-particle model covers only the region in which cracking was expected. Surrounding regions of the beams were assumed to remain linear elastic and were therefore

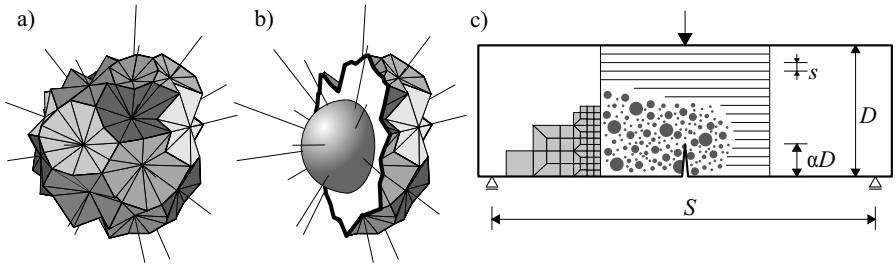

Fig. 1: a) One cell of the lattice-particle model and b) its section revealing the aggregate. c) Geometry of the beams simulated in three-point-bending.

modeled by standard 8-node isoparametric finite elements. The elastic constants for these elements were identified by fitting a displacement field with homogeneous strain to displacements of particle system subjected to low-level uniaxial compression. The macroscopic Young's modulus and Poisson ratio were found to equal $\bar{E} = 34.7$ GPa and $\bar{\nu} = 0.19$. The finite element mesh was connected to the system of particles by introducing interface nodes treated as auxiliary zero-diameter particles (Eliáš and Bažant, 2011). These auxiliary particles have their translational degrees of freedom prescribed by shape (or interpolation) functions of the nearest finite element. The rotations of the auxiliary particles were unconstrained.

3. Stochastic model

In the described discrete model, we assign material properties of each inter-particle connection according to a stationary autocorrelated random field. The value of the c-th realization of the discretized field at spatial coordinate $\boldsymbol{x}$ will be denoted $\boldsymbol{H}^c(\boldsymbol{x})$. For a given coordinate $\boldsymbol{x}_0$, $\boldsymbol{H}(\boldsymbol{x}_0)$ is a random variable H of cumulative distribution function (cdf) $F_H(h)$. Since we work with stationary random fields, the cdf $F_H(h)$ is identical for any position $\boldsymbol{x}_0$. Recent studies by Bažant and co-workers (Bažant and Pang, 2007; Bažant et al., 2009) showed that, when H represents strength of a quassibrittle material, $F_H(h)$ can be approximated by a Gaussian distribution onto which a power-law tail is grafted from the left at a probability about 10^{-4}–10^{-3}.

$$F_H(h) = \begin{cases} r_f \left(1 - e^{-\langle h/s_1 \rangle^m}\right) & 0 \le h \le h_{gr} \quad \text{(2a)} \\ F_H(h_{gr}) + \dfrac{r_f}{\delta_G\sqrt{2\pi}} \displaystyle\int_{h_{gr}}^{h} e^{-(h-\mu_G)^2/2\delta_G^2} \mathrm{d}h & h > h_{gr} \quad \text{(2b)} \end{cases}$$

where $\langle x \rangle = \max(x, 0)$, $s_1 = s_0 r_f^{1/m}$, m is the Weibull modulus (shape parameter) and s_0 is scale parameter of the Weibull tail, μ_G and δ_G are the mean value and the standard deviation of the Gaussian distribution that provides the Gaussian core. The Weibull-Gauss juncture at point at h_{gr} requires that that $(\mathrm{d}F_H/\mathrm{d}h)|_{h_{gr}^+} = (\mathrm{d}F_H/\mathrm{d}h)|_{h_{gr}^-}$. r_f is a scaling parameter normalizing the distribution to satisfy $F_H(\infty) = 1$. The distribution has in total 4 independent parameters.

The spatial fluctuation of the field is characterized through an autocorrelation function. It determines the spatial dependence pattern between the random variables at any pair of nodes. The correlation coefficient ρ_{ij} between two field variables at coordinates $\boldsymbol{x}_i$ and $\boldsymbol{x}_j$ can be assumed to obey the squared exponential function:

$$\rho_{ij} = \exp\left[-\left(\frac{\|\boldsymbol{x}_i - \boldsymbol{x}_j\|}{d}\right)^2\right] \tag{3}$$

It brings a new parameter d called the autocorrelation length.

To digitally simulate the stationary random field described by the random variable cdf F_H and correlation length d in the discrete model, we need to generate N realizations of the discretized random field $\boldsymbol{H}^0(\boldsymbol{x})$, $\boldsymbol{H}^1(\boldsymbol{x}), \ldots, \boldsymbol{H}^{N-1}(\boldsymbol{x})$ at the facet centers of the model. This is achieved using the

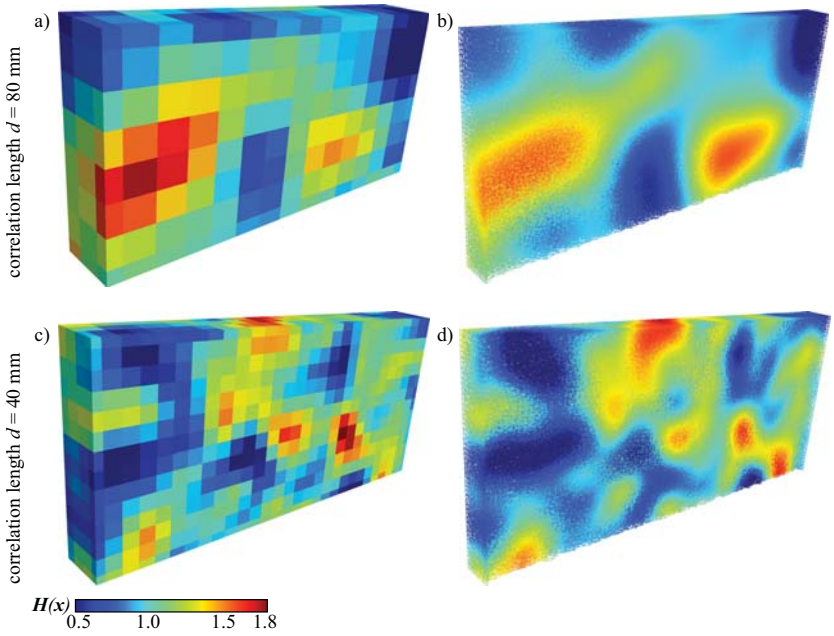

Fig. 2: Left: one realization of the autocorrelated random field $\boldsymbol{H}$ on a grid of spacing d/3 for $d = 80$ mm (top) and $d = 40$ mm (bottom). Right: realization of the field $\boldsymbol{H}$ at the element centers of the lattice-particle model.

the Karhunen–Loève expansion based on the spectral decomposition of covariance matrix $\boldsymbol{C}$, where $C_{ij} = \rho_{ij}$. This procedure decompose the correlated Gaussian variables $\widehat{\boldsymbol{H}}(\boldsymbol{x}_i)$ into independent standard Gaussian variables ξ_k that are easy to generate. $c-$th realization of the Gaussian random field $\widehat{\boldsymbol{H}}^c(\boldsymbol{x})$ is then obtained using K standard Gaussian random variables by the following expression

$$\widehat{\boldsymbol{H}}^c(\boldsymbol{x}) = \sum_{k=1}^{K} \sqrt{\lambda_k} \xi_k^c \boldsymbol{\psi}_k(\boldsymbol{x}) \tag{4}$$

where λ and $\boldsymbol{\psi}$ are the eigenvalues and eigenvectors of the covariance matrix $\boldsymbol{C}$. The value K is the number of eigenmodes/variables considered. In practice, it suffices to employ only a reduced number of eigenmodes $K \ll$ order of $\boldsymbol{C}$. In particular, K can be selected such that $\sum_{k=1}^{K} \lambda_k$ corresponds to about 99% of the trace of the covariance matrix $\boldsymbol{C}$ (Vořechovský, 2008). The vectors of independent standard Gaussian variables $\boldsymbol{\xi}$ are generated by Latin Hypercube Sampling using the mean value of each subinterval. The spurious correlation of the variables is then minimized by reordering their K realizations (Vořechovský and Novák, 2009).

A non-Gaussian random field can be generated by isoprobabilistic transformation of the underlying Gaussian field as

$$\boldsymbol{H}^c(\boldsymbol{x}) = F_H^{-1}(\Phi(\widehat{\boldsymbol{H}}^c(\boldsymbol{x}))) \tag{5}$$

Such a transformation, however, distorts the correlation structure of the field. Thus, when generating Gaussian field $\widehat{\boldsymbol{H}}$, the correlation coefficients must be modified (Vořechovský, 2008). This is here performed using the approximate method of HongShuang et al. (2008).

The realizations of the random field need to be evaluated for every shared facet (inter-particle bond) of the discrete mechanical model (at its center). This can be computationally extremely demanding for a large number of facets (large covariance matrix) and a short correlation length d (many eigenvalues needed, large K). We therefore adopted the expansion optimal linear estimation method - EOLE (Li and Kiureghian, 1993), which can significantly reduce the time of random field generation. Instead of

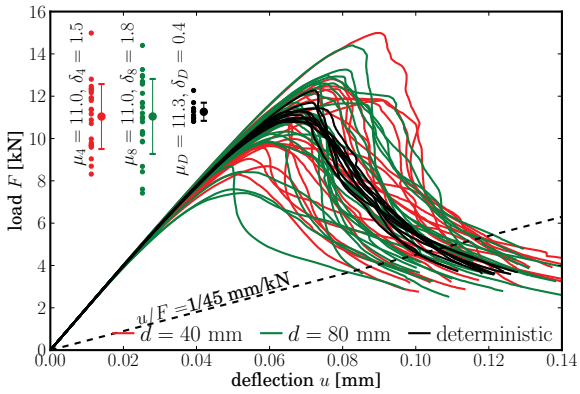

Fig. 3: Load-deflection curves for simulations of TPB beams with notch.

the facet centers, the random field is initially generated on a regular grid of nodes with spacing $d/3$ (see Fig. 2). The values of the random field at the facets are then obtain from expression

$$\widehat{\boldsymbol{H}}^c(\boldsymbol{x}) = \sum_{k=1}^{K} \frac{\xi_k^c}{\sqrt{\lambda_k}} \boldsymbol{\psi}_k^T \boldsymbol{C}_{xg} \tag{6}$$

where λ and $\boldsymbol{\psi}$ are now eigenvalues and eigenvectors of the covariance matrix of the grid nodes, and $\boldsymbol{C}_{xg}$ is a covariance matrix between facet center at coordinates $\boldsymbol{x}$ and the grid nodes. After the Gaussian random field values at facet centers are obtained by EOLE (Eq. 6), they need to be transformed to the non-Gaussian space by Eq. 5.

Besides the significant time savings, another advantage of using EOLE is that one can simply use the same field realization for several different granular positions. By keeping the c-th realization of decomposed variables $\boldsymbol{\xi}^c$ unchanged, the field realization can be adapted for any configuration of the facets in the discrete model.

Structural strength of a quasibrittle material is typically governed by two important material properties, namely the material strength and fracture energy. Realistic fracture models should therefore incorporate random spatial variability of at least these two variables. It is reasonable to consider the material strength fully correlated with the fracture energy (Grassl and Bažant, 2009). Furthermore, in the proposed lattice model, we also include the shear strength f_s and mode-II fracture energy G_s, which are again assumed to fully be correlated to the tensile strength f_t and mode-I fracture energy G_t, respectively. Assuming identical coefficient of variation (cov), we can use the same realizations of the random field to generate values of material strengths and fracture energies. For X substituted by any of the four mentioned mechanical properties, we can write

$$X(\boldsymbol{x}) = \bar{X}\boldsymbol{H}(\boldsymbol{x}) \tag{7}$$

where $\bar{X}$ stands for mean value of the particular property. The mean value of the (field) random variable H has to equal 1.

In this study, the following parameters of the Weibull-Gauss grafted distribution (Eq. 2a) were used: $m = 24$; $s_1 = 0.486$ MPa; $h_{gr} = 0.364$ MPa; $\delta_G = 0.25$. These values provide overall mean value μ_H=1; standard deviation $\delta_H \approx$0.25 and grafting probability $F_H(h_{gr}) \approx 10^{-4}$. Two correlation lengths d were considered: a shorter length $d_4 = 40$ mm (according to Grassl and Bažant (2009)) and a longer length $d_8 = 80$ mm (according to Vořechovský (2007)). The computation is performed with $N = 24$ realizations of the random field for each correlation length.

4. Simulations of bending of notched beams

The first set of beams (depth $D = 300$ mm, span $S = 2.4D$, thickness $t = 40$ mm) loaded in three-point-bending were modeled with a central notch up to 1/6 of its depth. Ten deterministic simulations were

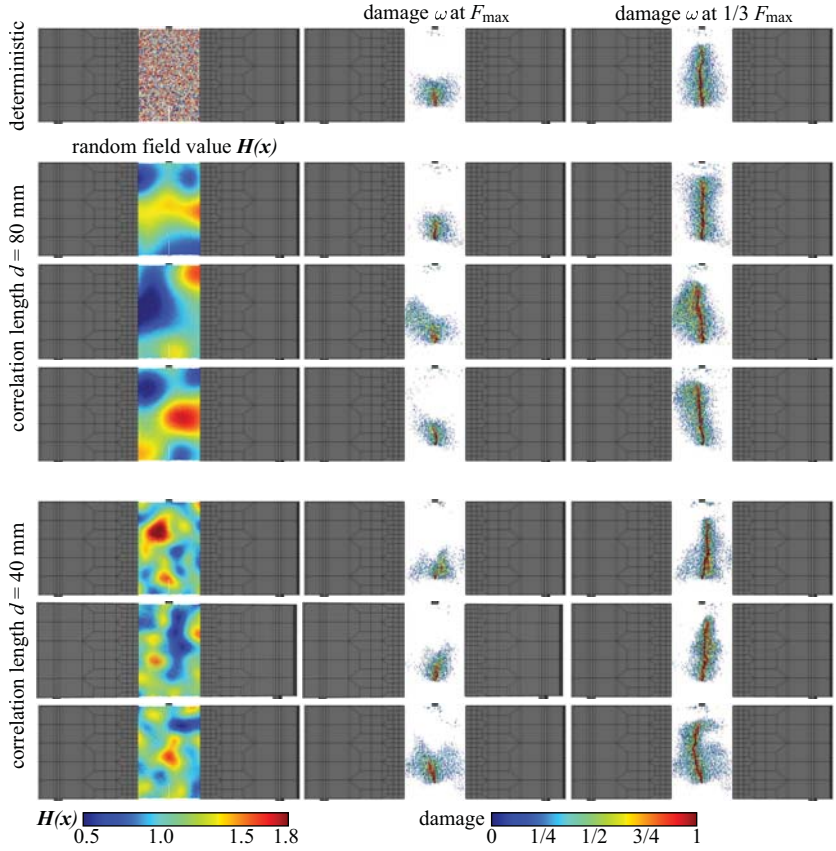

Fig. 4: Realizations of random field $\boldsymbol{H}$ (left) and corresponding damage patterns developed in bent notched beams at the peak force (middle) and after the load dropped to $1/3$ of its maximum (right).

computed. These simulations exhibit a certain scatter because of the pseudo-random granular positions differing for each realization. For both correlation lengths 40 and 80 mm, 24 simulations with spatial material randomness were performed. All the simulations were terminated when the magnitude of the loading force dropped to 1/3 of the maximal reached load $F_{\max}$. To ensure numerical stability in the presence of softening, the simulations were controlled by prescribing an increase of the crack mouth opening displacement (CMOD) in every step.

The notch present in the model induces a stress concentration at the notch tip. Therefore, high stresses occur only in a small area above the notch tip. Therefore, a crack initiates and propagates always from the notch tip. In stochastic calculations with rather large correlation length, local strength fluctuations within the region of high-stresses diminishes because of the imposed spatial correlation. Thus, the peak load $F_{\max}$ depends mostly on a single value of the random field realization at the notch tip location. In other words, a random field with correlation length greater than the length/width of FPZ can be, in the vicinity of the crack tip, viewed as a random constant – random field becomes a random variable at that region.

The obtained load-deflection curves are shown in Fig. 3. The figure also shows the maximal loads $F_{\max}$ in its upper left corner. The effect of the spatial strength fluctuations on the mean value of maximum load is negligible. The mean value of $F_{\max}$ is, for the deterministic calculation, $\mu_d = 11.3$ kN and, for stochastic simulations with $d = 40$ and 80 mm $\mu_4 = \mu_8 = 11.0$ kN. However, the standard deviations of the peak load are significantly influenced by the material randomness. The standard deviation of deterministic calculations (given solely by random aggregate position) is $\delta_d = 0.4$ kN. Significant increase in the standard deviation is observed for both correlation lengths: $\delta_4 = 1.5$ kN ($d = 40$ mm)

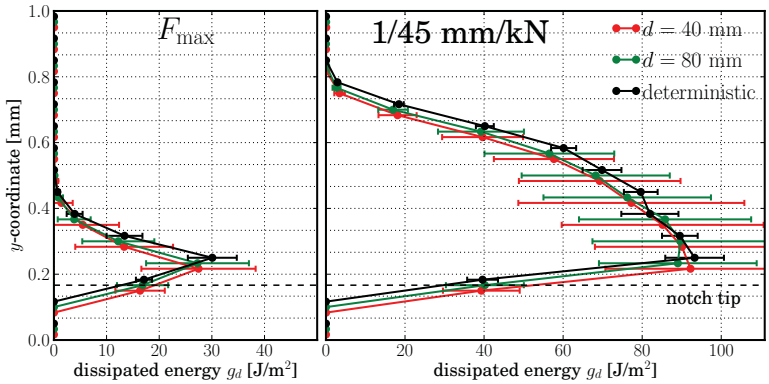

Fig. 5: Energy per unit ligament area g_d dissipated in notched beams up to a) maximal load and b) reference beam compliance $1/45$ mm/kN in dependence on the vertical position in the beam.

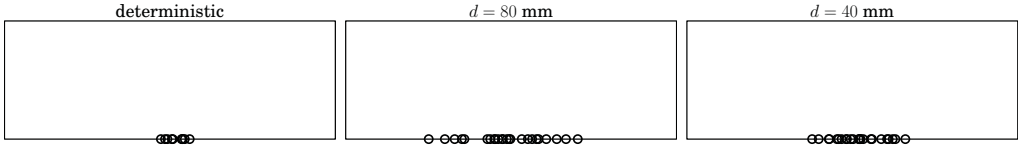

Fig. 6: Points of crack initiation of unnotched beams for various degrees of randomness.

and $\delta_8 = 1.8$ kN ($d = 80$ mm). Since the maximal load of the beam is given by local meso-level strength of a small area above the notch tip, we believe that the fluctuation rate does not influence the standard deviation (unless it is so small that material parameters vary significantly inside the FPZ).

For several selected realizations, the computed damage patterns (damage parameter ω from Eq. 1) at the peak load and at the termination of the simulations are showed in Fig. 4 together with the corresponding random field realization. Even though one can notice that the crack is slightly attracted (repelled) by areas of low (high) strength, the macrocrack trajectory is similar to the deterministic case (dictated by the singular stress field).

In order to compare energy dissipation in the beams, we need to determine simulation stages where the same portion of the ligament has already been damaged. Therefore, we select a stage when equivalent crack lengths (according to LEFM) are equal. Thus, all the models should have at that (reference) stage the same (reference) compliance, chosen as 1/45 mm/kN (Fig. 3). The depth of specimen was divided into horizontal stripes of depth s (Fig. 1c). All the energy dissipated at inter-particle contacts within a specific stripe was summed into variable G_d. One can normalize that energy by ligament area as $g_d = G_d/st$. The mean values and standard deviations of g_d are plotted in Fig. 5 for every stripe at the peak load and at the reference compliance stages. The figure confirms that the mean energy dissipation in notched tests does not change when the spatial material randomness is applied. Similarly to the peak force behavior, standard deviations of dissipated energy increase when randomness is present.

5. Simulations of bending of unnotched beams

The second simulation set focused on bending of unnotched beams where cracks initiate from a smooth bottom surface. Ten deterministic simulations and $N = 24$ simulations with random field for each correlation length were performed. To control the simulation, one needs to find some monotonically increasing variable, here again the CMOD was used. For unnotched beams with spatially fluctuating meso-level strength, the location of the macrocrack and thus the position of the crack mouth is not known in advance. Therefore, several short overlapping intervals were monitored simultaneously and the controlling CMOD was chosen to be the maximum one over them. Note, that other possibility of controlling variable might be the total energy dissipation in the specimen (Gutiérrez, 2004).

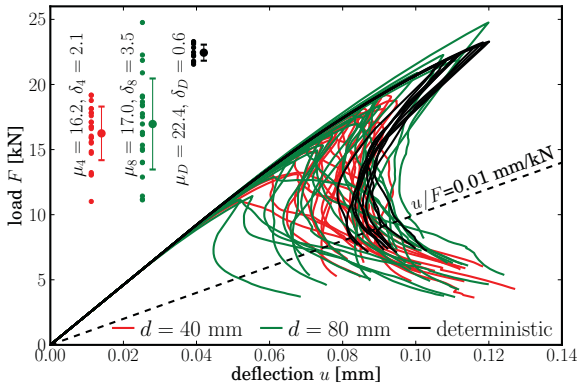

Fig. 7: Load-deflection curves for simulations of TPB beams without notch.

The variations in position of the crack mouth of the macrocrack are documented in Fig. 6. The Figure demonstrates the fundamental difference between notched and unnotched simulations. When no notch is present, the high-level stress region is much larger, located along the bottom central part of the specimen. Material strength and fracture energy fluctuate within the region and allow the macrocrack to "choose a weak spot" to initiate from. The higher is the distance form the midspan, the lower tensile stress appears. In the process of crack(s) formation, the stress field with a certain ability of redistribution increases towards the barrier (randomly varying strength and energy). The crack would start far from the midspan only when the material strength (and energy) of all points closer to the midspan is higher than in the surrounding. It is thus expectable (and confirmed by Fig. 6) that short correlation length, resulting in fluctuations that generate the weak spots more frequently, shrinks the zone where the macrocrack initiates. Indeed, the initiation zone for correlation length $d = 80$ mm is wider than for $d = 40$ mm.

Load deflection curves obtained from all the performed simulations are plotted in Fig. 7. The upper left corner shows the mean values and standard deviations of the peak load $F_{\max}$. The more fluctuating is the local strength, the weaker spot is statistically present and thus the lower is the mean value: $\mu_d = 22.4$ kN (deterministic), $\mu_8 = 17.0$ kN ($d = 80$ mm), $\mu_4 = 16.2$ kN ($d = 40$ mm). The standard deviation of the maximal force is low for the deterministic set, where $\delta_d = 0.6$ kN (cov$_d$=2.7%). For the correlation length 80 mm, it increases rapidly to $\delta_8 = 3.5$ kN (cov$_8$=21%). When the fluctuation rate increases more ($d = 40$ mm), the standard deviation of $F_{\max}$ decreases back to $\delta_4 = 2.1$ kN (cov$_4$=13%). This trend simply comes from the fact that the standard deviation of the local strength in the weakest spot inside some fixed region decreases with decreasing correlation length. Theoretically, the maximal standard deviation of $F_{\max}$ should be obtained for $d \approx \infty$ (a situation when the random field can be represented by a random variable – a random constant over the specimen volume).

Fig. 8 presents several selected realizations of the random field $\boldsymbol{H}$ and the computed damage patterns. One can see that the damage patterns differ for different levels of randomness. In the deterministic case, the damaged region at the peak load stage spans continuously the whole bottom area and the damage intensity directly depends on the distance from the midspan. For a random local strength and local fracture energy, the damage regions are more localized around low random field values. There is usually one such region for correlation length $d = 40$ mm and several low strength regions for $d = 80$ mm.

To compare the energy dissipation, we again choose some reference compliance that marks stages with the same LEFM crack length. The reference compliance now equals to 1/100 mm/kN (Fig. 7). Contrary to results from notched simulations, summation of total energy dissipated in stripes (per unit ligament area) is dependent on material randomness. In Fig. 9, deterministic calculations show higher values of dissipated energy g_d both for the peak force stage and for the stage at the reference compliance. This is caused by two factors: i) the localized macrocrack propagates in stochastic simulations through areas of lower meso-level strength and meso-level fracture energy, thus less energy is dissipated in total; ii) Distributed pre-peak cracking outside the macrocrack occurs mostly for deterministic simulation and thus it increases its total energy dissipation. Note that from about the middle of the specimens depth

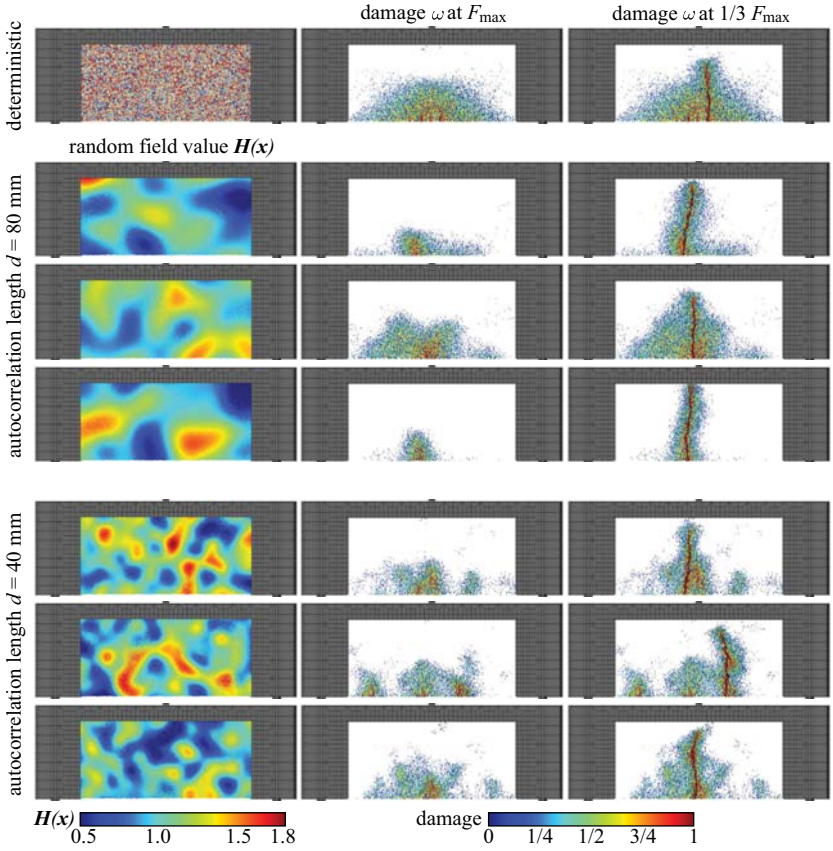

Fig. 8: Realizations of random field $\mathbf{H}$ *(left) and corresponding damage patterns developed in bent beams without notch at the peak force (middle) and after the load dropped to* $1/3$ *of its maximum (right).*

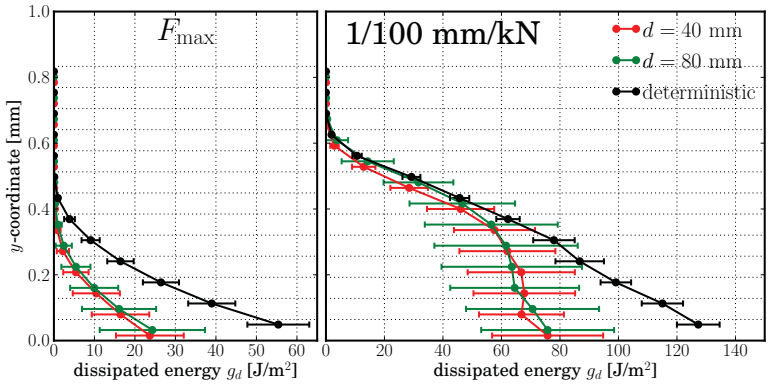

Fig. 9: Energy per unit ligament area dissipated in unnotched beams up to a) maximal load and b) reference beam compliance $1/100$ mm/kN *in dependence on vertical position in the beam.*

upwards, the energy dissipation of deterministic and stochastic simulations again match each other. This is because the crack at that depth cannot choose the weak region as it has already localized and the stress field forces the crack to grow from the current crack tip; and no pre-peak distributed cracking takes place there.

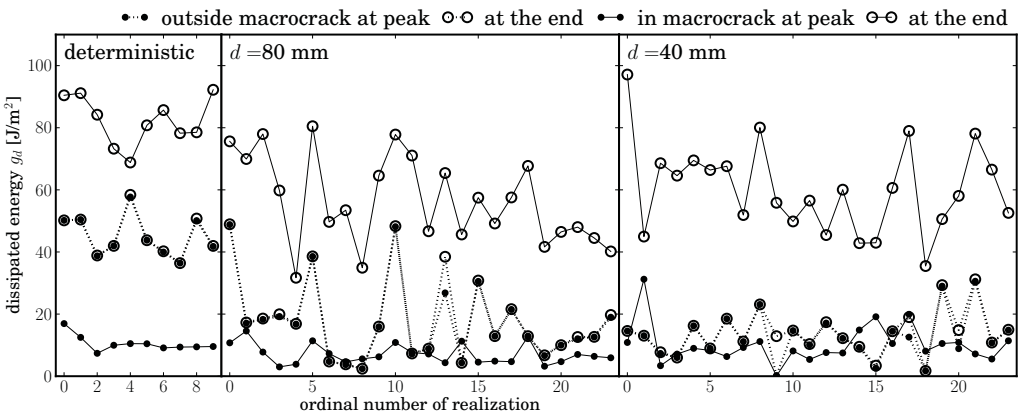

Fig. 10: Energy dissipation inside and outside the macro-crak at the peak load and at the reference compliance stages for every simulation.

Finally, we focus on a deeper analysis of the energy dissipation along the bottom surface. In the bottom boundary stripe of width $2d_{\max} = 19$ mm, the dissipated energies (per unit ligament area) inside and outside the macrocrack were evaluated for stages at the peak load and at the reference compliance. These values are plotted in Fig. 10 separately for each simulation. The results document that distributed cracking outside macrocrack in the most bottom layer after the peak is reached is close to zero. The amount of energy dissipated *outside* a macrocrack is much higher for the deterministic simulations than for those with random fields. Some of the simulations for $d = 80$ mm reached the value of the deterministic model, which can be explained by an absence of a locally weak spot and subsequent extensive pre-peak distributed cracking (see Fig. 8, third row). The energy dissipated *inside* the macrocrack at the reference compliance is clearly higher in the deterministic case than in the stochastic one. This is due to the positive correlation of local meso-level energy and meso-level strength at the inter-particle bonds. Since the macrocrack propagates through locally weaker areas, it also dissipates less energy there. Aspects related to correlation between the local tensile strength and fracture energy have been discussed by Vořechovský and Novák (2004).

6. Conclusions

We analyzed the influence of material spatial randomness on the peak load and the energy dissipation using a discrete lattice-particle model that reflects the concrete meso-scopic structure, i.e. the aggregate composition. The spatial material randomness was introduced by simultaneous scaling of the local meso-level strength and fracture energy of inter-particle bonds by realizations of autocorrelated random field. Two basic cases of three-point-bent beams were investigated: i) beams with a notch and ii) beams without a notch (the modulus of rupture test). Numerical results generally confirm theoretical expectations.

It has been found that:

- for the simulation with a sufficiently deep notch, the crack is forced to start at the notch tip. Therefore, the mean value of the maximal load for notched beam simulations does not change when material spatial randomness applies. However, the standard deviation of the maximal load increases when strength randomness is introduced. Also, the energy dissipation in deterministic and random media exhibit the same mean but an increasing standard deviation for the random cases.

- In the case of unnotched beams, the macrocrack initiates in a locally weaker spot.When a shorter correlation length of material properties is applied, the weaker is statistically the initiation spot and therefore the mean of the maximal load is lower. Standard deviations of the maximal load increase when randomness applied, however the shorter correlation lengths lead to a decrease of the standard deviation.

- Energy dissipated in unnotched beams is dependent on the randomness of the material. Two effects responsible for the dependency were identified. i) Change of the dissipated energy due to correlation of the local meso-level fracture energy and low meso-level strength of inter-particle bonds through which the macrocrack propagates. Depending on the sign of the energy-strength cross-correlation, this effect may increase or decrease the dissipated energy. For the current settings of the model, the lower is the local meso-level strength, the lower is also the local fracture energy and the lower is the energy dissipated inside the macrocrack. ii) The pre-peak distributed cracking has a tendency to localize only in weaker areas and thus the material dissipated less energy outside the macrocrack when random field is applied.

Acknowledgments

The financial support received from the Czech Science Foundation under Project No. P105/11/P055 and the Ministry of Education, Youth and Sports of the Czech Republic under Project No. LH12062 is gratefully acknowledged.

References

Alava, M. J., Nukala, P. K. V. V., and Zapperi, S. (2006). Statistical models of fracture. *Advances in Physics*, Vol. 55, No. 3-4, pp. 349–476.

Barenblatt, G. I. (1962). Mathematical theory of equilibrium cracks in brittle fracture. *Advances in Applied Mechanics*, Vol. 7, pp. 55–129.

Bažant, Z. P., and Jirásek, M. (2002). Nonlocal integral formulations of plasticity and damage: Survey of progress. *ASCE's Journal of Engineering Mechanics*, Vol. 128, No. 11, pp. 1119–1149.

Bažant, Z. P., Le, J.-L., and Bazant, M. Z. (2009). Scaling of strength and lifetime distributions of quasibrittle structures based on atomistic fracture mechanics. *Proceeding of the National Academy of Sciences, USA*, Vol. 106, No. 28, pp. 11484–11489.

Bažant, Z. P., and Novák, D. (2000). Probabilistic nonlocal theory for quasibrittle fracture initiation and size effect. I. Theory. *ASCE's Journal of Engineering Mechanics*, Vol. 126, No. 2, pp. 166–174.

Bažant, Z. P., and Pang, S.-D. (2007). Activation energy based extreme value statistics and size effect in brittle and quasibrittle fracture. *Journal of the Mechanics and Physics of Solids*, Vol. 55, pp. 91–131.

Bažant, Z. P., and Planas, J. (1998). *Fracture and size effect in concrete and other quasibrittle materials.* CRC Press.

Bažant, Z. P., and Xi, Y. (1991). Statistical size effect in quasi-brittle structures: II. Nonlocal theory. *ASCE's Journal of Engineering Mechanics*, Vol. 117, No. 7, pp. 2623–2640.

Bolander, J. E., and Saito, S. (1998). Fracture analyses using spring networks with random geometry. *Engineering Fracture Mechanics*, Vol. 61, pp. 569–591.

Cusatis, G., Bažant, Z., and Cedolin, L. (2003). Confinement-shear lattice model for concrete damage in tension and compression: I. theory. *ASCE's Journal of Engineering Mechanics*, Vol. 129, pp. 1439–1448.

Cusatis, G., Bažant, Z., and Cedolin, L. (2006). Confinement-shear lattice csl model for fracture propagation in concrete. *Computer Methods in Applied Mechanics and Engineering*, Vol. 195, pp. 7154–7171.

Cusatis, G., and Cedolin, L. (2007). Two-scale study of concrete fracturing behaviour. *Engineering Fracture Mechanics*, Vol. 6, pp. 3–17.

Eliáš, J., and Bažant, Z. (2011). Fracturing in concrete via lattice-particle model. In Onate, E., and Owen, D., editors, *2nd international conference on particle-based methods - fundamentals and applications*, p. 12, Barcelona, Spain. CD ROM.

Grassl, P., and Bažant, Z. P. (2009). Random lattice-particle simulation of statistical size effect in quasi-brittle structures failing at crack initiation. *ASCE's Journal of Engineering Mechanics*, Vol. 135, pp. 85–92.

Grassl, P., and Rempling, R. (2008). A damage-plasticity interface approach to the meso-scale modelling of concrete subjected to cyclic compressive loading. *Engineering Fracture Mechanics*, Vol. 75, pp. 4804–4818.

Gutiérrez, M. A. (2004). Energy release control for numerical simulations of failure in quasi-brittle solids. *Communications in Numerical Methods in Engineering*, Vol. 20, No. 1, pp. 19–29.

Hillerborg, A., Modéer, M., and Petersson, P.-E. (1976). Analysis of crack formation and crack growth in concrete by means of fracture mechanics and finite elements. *Cement and Concrete Research*, Vol. 6, pp. 773–782.

HongShuang, L., ZhenZhou, L., and XiuKai, Y. (2008). Nataf transformation based point estimate method. *Chinese Science Bulletin*, Vol. 53, No. 17, pp. 2586–2592.

Li, C.-C., and Kiureghian, A. D. (1993). Optimal discretization of random fields. *ASCE's Journal of Engineering Mechanics*, Vol. 119, No. 6, pp. 1136–1154.

Van Mier, J. G. M., and Van Vliet, M. R. A. (2003). Influence of microstructure of concrete on size/scale effects in tensile fracture. *Engineering Fracture Mechanics*, Vol. 70, pp. 2281–2306.

Vořechovský, M., and Novák, D. (2004). Modeling statistical size effect in concrete by the extreme value theory. In Walraven, J., Blaauwendaad, J., Scarpas, T., and Snijder, B., editors, *5^{th} International Ph.D. Symposium in Civil Engineering, held in Delft, The Netherlands*, Vol. 2, pp. 867–875, London, UK. A.A. Balkema Publishers. ISBN 90 5809 676 9.

Vořechovský, M. (2007). Interplay of size effects in concrete specimens under tension studied via computational stochastic fracture mechanics. *International Journal of Solids and Structures*, Vol. 44, pp. 2715–2731.

Vořechovský, M. (2008). Simulation of simply cross correlated random fields by series expansion methods. *Structural Safety*, Vol. 30, pp. 337–363.

Vořechovský, M. (2010). Incorporation of statistical length scale into weibull strength theory for composites. *Composite Structures*, Vol. 92, No. 9, pp. 2027–2034.

Vořechovský, M., and Novák, D. (2009). Correlation control in small-sample monte carlo type simulations i: A simulated annealing approach. *Probabilistic Engineering Mechanics*, Vol. 24, pp. 452–462.

Vořechovský, M., and Sadílek, V. (2008). Computational modeling of size effects in concrete specimens under uniaxial tension. *International Journal of Fracture*, Vol. 154, pp. 27–49.

Weibull, W. (1939). The phenomenon of rupture in solids. In *Royal Swedish Institute of Engineering Research*, Vol. 153, pp. 1–55, Stockholm.

18th International Conference
ENGINEERING MECHANICS 2012
Svratka, Czech Republic, May 14 – 17, 2012

pp. 223–230
Paper #164

TIME-DISCRETE INTEGRATION OF FINITE DEFORMATION

Z. Fiala *

Abstract: *Some necessary implications for the time-discrete integration of finite deformations will be discussed together with particular schemes, when the geometrical structure of the space of Cauchy-Green deformation tensors, implicitly contained in the principle of virtual power, is taken into account. All these time-discrete schemes reflect this geometrical structure in that the actual integration of corresponding evolution equation of deformation process takes place in the subset of positive-definite symmetric matrices (with non-Euclidean geometry), instead of in the linear space of symmetric matrices (with Euclidean geometry) as usual.*

Keywords: ***Finite deformation, time-discrete integration, Runge – Kutta – Munthe-Kaas method.***

1. Introduction

The conference paper is intended to draw attention to one of consequences, namely, the time-discrete approximation of finite deformation, when seeing a deformation process as a curve in the space of deformation tensors – in the sense of Noll and Seguin (2010), though using a rather different mathematical infrastructure and, moreover, employing natural geometry of this space, inherited from the principle of virtual power, see Fiala (2011, 2008). This approach provides exact and geometrically consistent procedure for linearization and integration of deformation process in time variable.

STARTING POINT: From the viewpoint of finite deformations, a deformation process can be represented pointwise by a trajectory $\mathbf{C} : I \to Sym^+(3,\mathbb{R})$ – the configuration space consisting of the set of all positive-definite symmetric matrices (*right Cauchy-Green deformation tensors*).

Note that $\partial\mathbf{C}_t = 2\mathbf{F}^T\mathbf{dF} \in sym(3,\mathbb{R})$ – the linear vector space of all symmetric matrices, where $\mathbf{d}$ is the *rate-of-deformation* tensor (stretching) – symmetric velocity gradient, and $\mathbf{F}$ is deformation gradient. One can then prove (Fiala (2011, 2008)) the following proposition.

PROPOSITION: Within small deformations, a deformation process superposed on initially strained body, characterized by the initial deformation field $\mathbf{C}$, is represented by a trajectory in the linear vector space of all symmetric matrices $sym(3,\mathbb{R}) \equiv T_{\mathbf{C}}Sym^+(3,\mathbb{R})$ – the tangent space to the manifold $Sym^+(3,\mathbb{R})$ at a point $\mathbf{C}$, i.e. the space of all vectors emanating from $\mathbf{C}$.

Based on the *power of internal forces*, we introduce Riemannian metric on $Sym^+ \equiv Sym^+(3,\mathbb{R})$ to become a manifold with Riemannian geometry, so that we shall be able to analyse deformation process by means of tools of differential geometry. Similarly we set $sym \equiv sym(3,\mathbb{R})$. Let us consider the stress power

$$\frac{\delta E_i}{\delta t} := \int_{\mathcal{S}} (\sigma : d)\, dv = \int_{\mathcal{S}} g^{ik} g^{jl} \sigma_{kl}\, d_{ij}\; dv = \int_{\mathcal{B}} B_t^{ik} B_t^{jl} K_{kl}\, \tfrac{1}{2}\, \partial C_{t\,ij}\, dV = \tag{1}$$

$$= \int_{\mathcal{B}} \mathrm{tr}(\mathbf{B}_t \mathbf{K}_t \mathbf{B}_t (\tfrac{1}{2}\, \partial \mathbf{C}_t))\, dV = \int_{\mathcal{B}} \mathrm{tr}(\mathbf{C}_t^{-1} \mathbf{K}_t \mathbf{C}_t^{-1} (\tfrac{1}{2}\, \partial \mathbf{C}_t))\, dV = \int_{\mathcal{B}} \mathrm{tr}(\mathbf{P}_t (\tfrac{1}{2}\, \partial \mathbf{C}_t))\, dV, \tag{2}$$

where symbol σ, as usual, stands for the Cauchy stress field, $\mathbf{K}_t$ for the *convective stress* and $\mathbf{P}_t = \mathbf{C}_t^{-1}\mathbf{K}_t\mathbf{C}_t^{-1}$ for the *2nd Piola-Kirchhoff stress*.

Now, consulting the analytical mechanics (Marsden et al. (1999)), we can interpret

$$\mathbf{\Omega}_{\mathbf{C}}(\,.\,,.\,) := \mathrm{tr}\left(\mathbf{C}^{-1}(.)\mathbf{C}^{-1}(.)\right) \tag{3}$$

* RNDr. Zdeněk Fiala, CSc., Institute of Theoretical and Applied Mechanics AS CR, v. v. i., The Academy of Sciences of the Czech Republic, Prosecká 809/76, 190 00, Prague 9 CZ; e-mail: fiala@itam.cas.cz

as the Riemannian metric on Sym^+ at the point $\mathbf{C}$ – a particular deformation state, and, as a consequence, the convective stress $\mathbf{K}_t$ as the *vector* and the 2nd Piola-Kirchhoff stress $\mathbf{P}_t$ as the *covector fields* along deformation process $\mathbf{C}_t$. Interestingly – in view of the *logarithmic strain* $\log(\mathbf{C})$, a *geodesic* (i.e. straight line) $\mathbf{C}_t$ connecting two deformation states $\mathbf{C}_1$ and $\mathbf{C}_2$ then reads

$$\mathbf{C}_t = \mathrm{Exp}_{\mathbf{C}_0}(t\mathbf{H}) := \mathbf{C}_0 \exp(t\mathbf{C}_0^{-1}\mathbf{H}), \tag{4}$$

where $\mathbf{H} = \mathbf{C}_0 \log(\mathbf{C}_0^{-1}\mathbf{C}_1)$, and exp, log stands for matrix exponential, resp logarithm.

Now, we can draw conclusions of the geometrical structure of Sym^+ for the *time-discrete integration* of finite deformations. If we calculate, starting from a given deformation state of a body $\mathbf{C}_t$, a deformation increment $\partial\mathbf{C}_t$, based on linearized equations and prescribed increments of external loading and displacement, the new resultant deformation $\mathbf{C}_{t+\Delta t}$ then is obtained by mapping this deformation increment to the space of all deformations Sym^+ starting at the initial state – i.e. by mapping the vector $\partial\mathbf{C}_t$ from the tangent space $T_{\mathbf{C}_t}Sym^+$ at the point $\mathbf{C}_t$ into the space Sym^+. This mapping can be formally expressed in terms of a general formula

$$\mathbf{C}_{t+\Delta t} = \mathrm{Exp}_{\mathbf{C}_t}(\Delta t\, \partial\mathbf{C}_t)\,. \tag{5}$$

In our context of Sym^+, the generalized exponential map (2) adds up an increment of deformation $\mathbf{H} \equiv \partial\mathbf{C}_0 \in T_{\mathbf{C}_0}Sym^+$ to the deformation $\mathbf{C}_0 \in Sym^+$, so that the resulting deformation $\mathbf{C}_1(\mathbf{H}) = \mathrm{Exp}_{\mathbf{C}_0}(\mathbf{H})$ stays in the space of deformations Sym^+. This would not be the case if we just set $\mathbf{C}_1(\mathbf{H}) = \mathbf{C}_0 + \mathbf{H}$ due to neglecting the "shape" of Sym^+ within the linear vector space of symmetric tensors sym.

CONSEQUENCE: Resulting deformation $\mathbf{C}_1(\mathbf{H})$ from adding an increment of deformation $\mathbf{H}$ to the deformation $\mathbf{C}_0$ is given by

$$\mathbf{H} \longmapsto \mathbf{C}_1(\mathbf{H}) \equiv \mathrm{Exp}_{\mathbf{C}_0}(\mathbf{H}) := \mathbf{C}_0 \exp(\mathbf{C}_0^{-1}\,\mathbf{H}) = \tag{6}$$

$$= \mathbf{C}_0 + \mathbf{H} + \tfrac{1}{2!}\,\mathbf{H}\mathbf{C}_0^{-1}\,\mathbf{H} + \tfrac{1}{3!}\,\mathbf{H}\mathbf{C}_0^{-1}\,\mathbf{H}\mathbf{C}_0^{-1}\,\mathbf{H} + \ldots \tag{7}$$

The approach mentioned above is nothing but the forward or explicit Euler's scheme, only conditionally stable, for *evolution equation* of deformation process

$$\partial\mathbf{C}_t = 2\mathbf{C}_t\mathbf{D} \tag{8}$$

evolving on Sym^+, where $\mathbf{D} = \mathbf{F}^{-1}\mathbf{dF}$, which is constant along geodesics.

After having summed up basic facts related to time-discrete integration of finite deformations in this introduction, we shall first discuss the geometry of the underlying configuration space Sym^+ and the properties of evolution equation of finite deformation on this space. Then we introduce methods of its solution in terms of Runge – Kutta – Munthe-Kaas (RKMK), and finely briefly mention another closely related method – again based on Lie group approach.

2. Configuration space Sym^+ – a playing field for finite deformations

Geometry of this space is explained in Fiala (2009), where further references are included. Here, I am going to highlight just some facts, which are substantial for exposition of time-discrete integration. Sym^+ is made up of all possible Cauchy-Green deformation tensors $\mathbf{C}$, in any point X of reference configuration $\mathcal{B}$.

$$\mathbf{C} = \mathbf{F}^T\mathbf{F} \tag{9}$$

As usual, $\mathbf{F}$ denotes deformation gradient of Φ. Cauchy-Green deformation tensors are represented by positive-definite symmetric matrix, and describe local geometry in the vicinity of $x = \Phi(X) \in \mathcal{S}$ in actual configuration from the viewpoint of an observer in reference configuration. In fact, $\mathbf{C}(X)$ in $X \in \mathcal{B}$ is related to an image of metric tensor $\mathbf{g}(x)$ in $x \in \mathcal{S}$ via the deformation Φ.

Since $\mathbf{F} \in GL$ – the group of nonsingular matrices with group operation of matrix multiplication, we have a natural map

$$p : GL \to Sym^+ \qquad \mathbf{F} \mapsto \mathbf{C} := \mathbf{F}^T\mathbf{F}. \tag{10}$$

Let us consider two successive deformations resulting in one single deformation and their deformation gradients

$$\Phi = \Phi_2 \circ \Phi_1 \qquad \mathbf{F} = \mathbf{F}_2\mathbf{F}_1. \tag{11}$$

Then

$$\mathbf{C} = \mathbf{F}_1^T\mathbf{C}_{12}\mathbf{F}_1, \tag{12}$$

where the resulting Cauchy-Green deformation tensors $\mathbf{C}$ is obtained by "translating" by an "amount" $\mathbf{F}_1$ of the Cauchy-Green deformation tensor $\mathbf{C}_{12}$ (standing for the deformation in state 1 with respect state 2). This is nothing but an operation of symmetry on Sym^+ with respect to already introduced metric (3) via group GL:

$$R : GL \times Sym^+ \to Sym^+ \qquad (\mathbf{F}, \mathbf{C}) \mapsto \mathbf{F}^T\mathbf{C}\mathbf{F}. \tag{13}$$

This operation is called *right translation*, since $R(\mathbf{F}_2\mathbf{F}_1, .) = R(\mathbf{F}_1, R(\mathbf{F}_2, .))$.

There is also similar approach leading to left translation L related to the Piola deformation tensor $\mathbf{B} = \mathbf{F}\mathbf{F}^T$, for which order of composition of transformations $L(\mathbf{F}_2\mathbf{F}_1, .) = L(\mathbf{F}_2, L(\mathbf{F}_1, .))$, compared to order of matrix multiplication in GL, does not reverse.

Before turning to evolution equation we need yet to specify some properties of Sym^+. Since many elements of GL have the same image in Sym^+, the map (10) does not have an inverse. But taking into account polar decomposition of nonsingular matrices $\mathbf{F} = \mathbf{R}\mathbf{U}$, we can introduce the isotropy subgroup $O \subset GL$, which is the group of orthogonal matrices

$$O := \left\{\mathbf{R} \in GL \,|\, \mathbf{R}^T\mathbf{R} = \mathbf{I}\right\}, \tag{14}$$

so that all elements in the *right coset* $[\mathbf{U}] := \{\mathbf{R}\mathbf{U} \,|\, \mathbf{R} \in O\}$ will have the same image $\mathbf{U}^2 \in Sym^+$, and resulting in factorisation of GL into disjoint right cosets. The correspondence between right coset space GL/O and Sym^+

$$\pi : GL/O \to Sym^+ \qquad [\mathbf{F}] \mapsto \mathbf{C} := \mathbf{G}^T\mathbf{G} \quad \text{for some } \mathbf{G} \in [\mathbf{F}] \tag{15}$$

is now one-to-one, and in addition to that, it is diffeomorphism.

Moreover, we can carry over the operation of matrix multiplication in GL to operation of right translations on GL/O via

$$\rho : GL \times GL/O \to GL/O \qquad (\mathbf{G}, [\mathbf{F}]) \mapsto [\mathbf{F}\mathbf{G}], \tag{16}$$

so that the folowing diagram is commutative

$$\begin{array}{ccc} GL/O & \xrightarrow{\ \pi\ } & Sym^+ \\ {\scriptstyle \rho_{\mathbf{G}}}\uparrow & & \uparrow{\scriptstyle R_{\mathbf{G}}} \\ GL/O & \xrightarrow{\ \pi\ } & Sym^+ \end{array}$$

That is

$$\pi \circ \rho_{\mathbf{G}} = R_{\mathbf{G}} \circ \pi, \tag{17}$$

where $\rho_{\mathbf{G}}(.) := \rho(\mathbf{G}, .)$ and $R_{\mathbf{G}}(.) := R(\mathbf{G}, .)$ for any $\mathbf{G} \in GL$. We call this property *equivariance*, which means that instead of studying the action of GL on Sym^+, we can equally well study the action of GL on GL/O.

3. Evolution equation for finite deformations

After having computed an increment of deformation $\mathbf{d}(v) = sym(\nabla v)$ superposed on a deformed configuration Φ_1 with deformation gradient $\mathbf{F}_1$ and deformation tensor $\mathbf{C}_1$, we have then to update deformation tensor to get the resulting $\mathbf{C}_2$ in terms of the initial $\mathbf{C}_1$ and computed deformation rate

$\partial \mathbf{C}_1 = 2\mathbf{F}_1^T \mathbf{d}(v)\mathbf{F}_1$. Since $\mathbf{F}^T\mathbf{dF} = \mathbf{C}_t\mathbf{F}^{-1}\mathbf{dF} = \mathbf{C}_t\mathbf{D}$, see Fiala (2008), we thus obtain the *evolution equation* for deformation process in finite deformations

$$\partial \mathbf{C}_t = 2\mathbf{C}_t\mathbf{D} \left(= 2\mathbf{D}^T\mathbf{C}_t\right) \in T_{\mathbf{C}_t} Sym^+, \tag{18}$$

evolving on $Sym^+ \subset sym$. Its time-discrete integration then gives us the desired formulae for updating deformation tensors $\mathbf{C}_t$. Note that $\mathbf{D} = \mathbf{F}^{-1}\mathbf{dF}$ is constant along geodesics.

If the equation (18) evolved on the space of symmetric tensors sym, which is linear vector space, we could use Runge – Kutta method, but not in our case of $Sym^+ \subset sym$. In fact, the curve $\mathbf{C}_t$ lies in Sym^+, and so $\partial \mathbf{C}_t \in T_{\mathbf{C}_t} Sym^+$ is the tangent to this curve, i.e. a vector in Sym^+ at its initial point $\mathbf{C}_t$. Since Sym^+ has non-Euclidean geometry, we cannot identify the space of points with the space of all vectors emanating from a point, as is the case for linear vector spaces (with Euclidean geometry), and so the classical Runge – Kutta method is inapplicable. Nevertheless, due to correspondence between the right coset space GL/O and Sym^+, and specific properties of Lie groups GL and O, it is still possible to extend this approach into modified Runge – Kutta – Munthe-Kaas method, which is now usable in our space. The key point is that these spaces possess *"sufficient" amount of "basic" movements*, so that we can still compare different vector spaces at different points, though with a bit complicated formulae in comparison with linear vector spaces (cf. section 5.), for which they simply reduces to identities.

In general, consider a differential equation of the form

$$\partial \mathbf{C} = \mathbf{H}(\mathbf{C}), \qquad t \geq 0, \qquad \mathbf{C}(0) = \mathbf{C}_0, \tag{19}$$

where $\mathbf{H}(\mathbf{C})$ is a tangent vector field on Sym^+. Whenever convenient, we allow $\mathbf{H}$ to be a function of time $\mathbf{H} = \mathbf{H}(t, \mathbf{C})$. The *flow* of a vector field $\mathbf{H}$ is the solution operator

$$\Psi_{t,\mathbf{H}} : Sym^+ \to Sym^+, \tag{20}$$

such that

$$\mathbf{C}(t) = \Psi_{t,\mathbf{H}}(\mathbf{C}_0) \tag{21}$$

solves (19). Note that the vector field $\mathbf{H}$ and the solution operator $\Psi_{t,\mathbf{H}}$ are related by differentiation

$$\mathbf{H}(\mathbf{C}_t) = \left.\frac{d}{dt}\Psi_{t,\mathbf{H}}(\mathbf{C}_t)\right|_{t=0}. \tag{22}$$

Let us now discuss the right-hand side of equation (18) from the viewpoint of basic movements. It is a simple task to prove that

$$\partial \mathbf{C}_t = \mathbf{D}^T\mathbf{C}_t + \mathbf{C}_t\mathbf{D} \tag{23}$$

$$= \mathbf{U}_t \left(\mathbf{R}^{-1}\mathbf{dR}\right) \mathbf{U}_t, \tag{24}$$

where $\mathbf{F}_t = \mathbf{R}_t\mathbf{U}_t$ and $\mathbf{U}_t^2 = \mathbf{C}_t$.

Now, denoting by $R^{\mathbf{C}_0} := R(., \mathbf{C}_0)$, i.e.

$$R^{\mathbf{C}_0} : GL \to Sym^+ \qquad \mathbf{F} \mapsto \mathbf{F}^T\mathbf{C}_0\mathbf{F}, \tag{25}$$

and by $Q^{\mathbf{U}_0}$

$$Q^{\mathbf{U}_0} : Sym^+ \to Sym^+ \qquad \mathbf{B} \mapsto \mathbf{U}_0\mathbf{B}\mathbf{U}_0, \tag{26}$$

then evidently

$$R^{\mathbf{C}_0}(\mathbf{I}) = \mathbf{C}_0 \tag{27}$$

$$Q^{\mathbf{U}_0}(\mathbf{I}) = \mathbf{U}_0^2 = \mathbf{C}_0, \tag{28}$$

and the corresponding vector spaces at $\mathbf{I}$ for both GL and Sym^+ transforms into $T_{\mathbf{C}_0} Sym^+$ by

$$R^{\mathbf{C}_0}_* \equiv T_{\mathbf{I}} R^{\mathbf{C}_0} : T_{\mathbf{I}} GL \to T_{\mathbf{C}_0} Sym^+ \qquad \mathbf{D} \mapsto \mathbf{D}^T\mathbf{C}_0 + \mathbf{C}_0\mathbf{D} \tag{29}$$

$$Q^{\mathbf{U}_0}_* \equiv T_{\mathbf{I}} Q^{\mathbf{U}_0} : T_{\mathbf{I}} Sym^+ \to T_{\mathbf{C}_0} Sym^+ \qquad \hat{\mathbf{D}} \mapsto \mathbf{U}_0\hat{\mathbf{D}}\mathbf{U}_0. \tag{30}$$

Remind that $T_{\mathbf{C}}Sym^+$ is a vector space of all vectors emanating from a point $\mathbf{C} \in Sym^+$, and similarly for the vector space $T_{\mathbf{G}}GL$.

That is,

$$\mathbf{D} = \mathbf{F}^{-1}\mathbf{dF} \in T_{\mathbf{I}}GL \tag{31}$$

$$\hat{\mathbf{D}} = \mathbf{R}^{-1}\mathbf{dR} \in T_{\mathbf{I}}Sym^+ \tag{32}$$

and equation (18) reads

$$\partial\mathbf{C}_t = R_*^{\mathbf{C}_t}(\mathbf{D}_t) \equiv R_*(\mathbf{D}_t)(\mathbf{C}_t) \tag{33}$$

$$= Q_*^{\mathbf{U}_t}(\hat{\mathbf{D}}_t) \equiv Q_*(\hat{\mathbf{D}}_t)(\mathbf{C}_t)\,, \tag{34}$$

where now $\mathbf{D}_t$ is a curve in the vector space of all matrices $\mathfrak{gl} := T_{\mathbf{I}}GL$, and $\hat{\mathbf{D}}_t$ a curve in the vector space of all symmetric matrices $sym := T_{\mathbf{I}}Sym^+$. These equations are called **equations of Lie type** (Munthe-Kaas (1999); Iserles et al. (2000)).

Actually, we made use of an identification $TGL \approx GL \times \mathfrak{gl}$ and $TSym^+ \approx TSym^+ \times sym$, called the *right trivialization*, where $TSym^+$ stands for a disjunct union of all vector spaces $T_{\mathbf{C}}Sym^+$ indexed by $\mathbf{C} \in Sym^+$ and similarly for TGL. Note also that $\mathfrak{gl} := T_{\mathbf{I}}GL = sym \oplus skew$, that is $T_{[\mathbf{I}]}GL/O \equiv sym$ and $T_{\mathbf{I}}O = skew$, see Fiala (2009) and references therein. Notation $skew$ stands for the vector space of all skew-symmetric matrices.

4. Limitations of Runge – Kutta method

The classical ν-stage Runge – Kutta method (Hairer et al. (1993)) is defined by constants $\{a_{k,l}\}_{k,l=1}^{\nu}$, $\{b_l\}_{l=1}^{\nu}$ and $\{c_k\}_{k=1}^{\nu}$, usually written as a *Butcher tableau*

$$\begin{array}{c|cccc} c_1 & a_{1,1} & a_{1,2} & \dots & a_{1,\nu} \\ c_2 & a_{2,1} & a_{2,2} & \dots & a_{2,\nu} \\ \vdots & \vdots & \vdots & \ddots & \vdots \\ c_\nu & a_{\nu,1} & a_{\nu,2} & \dots & a_{\nu,\nu} \\ \hline & b_1 & b_2 & \dots & b_\nu \end{array} \tag{35}$$

Applied to a standard vector equation $\boldsymbol{y}' = \boldsymbol{f}(t, \boldsymbol{y})$ on $\mathbb{R}^n$, a single step of length h from $\boldsymbol{y}_n = \boldsymbol{y}(t_n)$ to updated $\boldsymbol{y}_{n+1} = \boldsymbol{y}(t_n + h)$ is given first by solving following system of equations for $\boldsymbol{f}_l$

$$\left.\begin{array}{l} \boldsymbol{f}_k = \boldsymbol{f}(t_n + c_k h, \boldsymbol{y}_n + h\boldsymbol{\theta}_k) \\ \text{where } \boldsymbol{\theta}_k = \sum_{l=0}^{\nu} a_{k,l}\boldsymbol{f}_l \end{array}\right\} \qquad k = 1, \dots, \nu \tag{36}$$

and then followed by

$$\boldsymbol{y}_{n+1} = \boldsymbol{y}_n + h\boldsymbol{\theta}, \quad \text{where } \boldsymbol{\theta} = \sum_{l=0}^{\nu} b_l \boldsymbol{f}_l\,. \tag{37}$$

That is, the Runge – Kutta method starts by calculating the the rate of change $\boldsymbol{\theta}$ as a weighted average of estimates of the rate of change of $\boldsymbol{y}$ at several points $t_n + c_k h$ within the interval t_n to t_{n+1}.

Notice that $\boldsymbol{y}$ is a point whereas $\boldsymbol{f}(t, \boldsymbol{y})$ a vector at $\boldsymbol{y}$, which can be translated to the origin of coordinates without a change. In fact, $\mathbb{R}^n$ plays a triple role here: the space of points, then the additive group of translation operating on the space of point, and finally the vector space, on which the actual integration is carried out.

In our case, the space of points is the space Sym^+ made up of all Cauchy-Green deformation tensors, and the transformation group GL stands for the group of translation. Since Runge – Kutta method (RK) demands for $\mathbb{R}^n$, we have to resort to a related linear vector space, which is naturally isomorphic to $\mathbb{R}^n$, provided we properly transform all the quantities and desired operation to this vector space and back to Sym^+. The previous section suggests two of them: either the tangent space $T_{\mathbf{I}}Sym^+$ at the identity matrix $\mathbf{I}$, being equal to the space of all tangents to deformation processes passing through undeformed state – the vector space of all symmetric matrices sym, or $T_{\mathbf{I}}GL$ identified with the vector space of all matrices $\mathfrak{gl}$.

5. Runge – Kutta – Munthe-Kaas method (RKMK)

Following Munthe-Kaas (1999), we point out the role of actions (25) and (26) for constructing modified RK method on general homogeneous spaces: First, instead of seeking the discretization directly on a homogeneous space, we find an element of the group whose action induces the approximation. In fact, in (33) and (34) we expressed evolving equation (19) in the form

$$\partial \mathbf{C}_t = \mathbf{\Lambda}_*(\mathbf{\Delta}_t)(\mathbf{C}_t), \qquad t \geq 0, \qquad \mathbf{C}(0) = \mathbf{C}_0, \tag{38}$$

where either $\mathbf{\Lambda}_* : \mathfrak{gl} \times Sym^+ \to TSym^+$ with a curve $\mathbf{\Delta}_t = \mathbf{D}_t \subset \mathfrak{gl}$, or $\mathbf{\Lambda}_* : sym \times Sym^+ \to TSym^+$ with $\mathbf{\Delta}_t = \hat{\mathbf{D}}_t \subset sym$. In case of time-independent $\mathbf{\Delta}$, the solution of (38), and thus of (19), is given explicitly (Theorem 2.8, Iserles et al. (2000)) in terms of the actions (25) or (26)

$$\mathbf{C}(t) = \mathbf{\Lambda}(\mathbf{\Gamma}_t, \mathbf{C}_0), \qquad t \geq 0, \qquad \mathbf{\Gamma}_0 = \mathbf{I}, \tag{39}$$

where

$$\mathbf{\Gamma}_t = \mathrm{EXP}(t\Delta_0), \qquad \text{i.e.} \quad \partial \mathbf{\Gamma}_0 = \mathbf{\Delta}_0. \tag{40}$$

EXP stands for the matrix exponential. Otherwise, (39) approximates the solution for short times. Equation for Γ_t on corresponding spaces then reads

$$\partial \mathbf{\Lambda}(\mathbf{\Gamma}_t, \mathbf{C}_0) = \mathbf{\Lambda}_*(\mathbf{\Delta}_t)(\mathbf{C}_t), \qquad t \geq 0, \qquad \mathbf{\Gamma}_0 = \mathbf{I}. \tag{41}$$

That is, instead of approximating $\mathbf{C}(t)$, we seek an approximate action $\mathbf{\Gamma}_t$ that carries $\mathbf{C}(0)$ to $\mathbf{C}(t)$. Moreover, even though the group GL, resp the space Sym^+ are nonlinear objects, it is possible to transform the problem to their related linear spaces $\mathfrak{gl} = T_{\mathbf{I}}GL$, resp $sym = T_{\mathbf{I}}Sym^+$. In these spaces we can already apply calssical RK method and so, after transformating back, we get desired numerical approximation. Coming to terms with all the subtleties results in RKMK method presented in section 5. Notice that the first approach relies on group action GL, whereas the second one makes use of a direct map between the homogeneous space Sym^+ and the linear vector space sym.

As for EXP, let us remind relation of the spaces Sym^+ and GL with their tangent spaces sym and $\mathfrak{gl}$. For more see, for example, Marsden et al. (1999). Denote by $\exp$ and $\mathfrak{exp}$ the usual matrix exponential, but related to different spaces. Whereas $\exp$ maps all sym onto all Sym^+ in one-to-one way, for GL this property does not apply completely. Still, the map $\mathfrak{exp} : \mathfrak{gl} \to GL$ is one-to-one in some vicinity of $\mathfrak{gl}$ at the null matrix $\mathbf{0}$, which is maped onto near vicinity of GL of the identity matrix $\mathbf{I}$, see Fiala (2009). That is, only for those $\mathbf{G} \in GL$ sufficiently close to $\mathbf{I} = \mathfrak{exp}(\mathbf{0})$, there exists precisely one $\mathbf{g} \in \mathfrak{gl}$, such that $\mathbf{G} = \mathfrak{exp}(\mathbf{g})$, with its line segment $\mathfrak{exp}(t\mathbf{g})$ completely lying in this vicinity for $|t| \leq 1$. In other word, for any $\mathbf{g} \in \mathfrak{gl}$, one can still find sufficiently small $\varepsilon > 0$, such that a line segment $\mathfrak{exp}(t\mathbf{g})$ is all in this vicinity for $|t| \leq \varepsilon$.

During an analysis of the evolution equation for finite deformations, we naturally established two linear vector spaces, namely $sym \equiv T_{\mathbf{I}}Sym^+$ and $\mathfrak{gl} \equiv T_{\mathbf{I}}GL$. In appendix, a transformation of deformation rate fields on Sym^+ and corresponding vector fields on these linear vector spaces is briefly summarized, so that we can now express the evolution equation here.

The equation on linear vector space (sym or $\mathfrak{gl}$) for sufficiently small t reads (see Appendix)

$$\partial \mathbf{\Theta}_t = \mathbf{d}\mathrm{EXP}^{-1}_{\mathbf{\Theta}_t}(\mathbf{\Delta}_t)(\mathbf{C}_t), \qquad t \geq 0, \qquad \mathbf{\Theta}_0 = \mathbf{0}. \tag{42}$$

Now, we can apply RK method to obtain ν-stage Runge – Kutta – Munthe-Kaas method (Munthe-Kaas (1999)) solving our equation $\partial \mathbf{C}_t = \mathbf{\Lambda}_*(\mathbf{\Delta}_t)(\mathbf{C}_t)$, which evolves on Sym^+. Using the *Butcher tableau* (35), one step of RKMK method consists in solving following system of equations for δ_l

$$\left.\begin{aligned} &\mathbf{\Delta}_k = \mathbf{\Delta}\big(t_n + c_k h, \mathbf{\Lambda}\big(\mathrm{EXP}(h\mathbf{\Theta}_k), \mathbf{C}_n\big)\big) \\ &\text{where } \mathbf{\Theta}_k = \textstyle\sum_{l=0}^{\nu} a_{k,l}\delta_l \\ &\qquad \delta_l = \mathbf{d}\mathrm{EXP}^{-1}_{\mathbf{\Theta}_l}(\mathbf{\Delta}_l) \end{aligned}\right\} \qquad k = 1, \ldots, \nu \tag{43}$$

then followed by an update

$$\mathbf{C}_{n+1} = \mathbf{\Lambda}\big(\mathrm{EXP}(h\mathbf{\Theta}), \mathbf{C}_n\big), \qquad \text{where } \mathbf{\Theta} = \sum_{l=0}^{\nu} b_l \delta_l \,. \tag{44}$$

Again, $\mathbf{\Lambda}$ stands for the actions (25) or (26), EXP and $\mathbf{d}\mathrm{EXP}^{-1}$ for their corresponding matrix exponentials and their inverse differentials.

In particular:

- forward Euler ($\nu = 1$), cf. (5)

$$\begin{array}{c|c} 0 & 0 \\ \hline & 1 \end{array} \qquad\qquad \mathbf{\Theta} = \mathbf{\Delta}(t_n, \mathbf{C}_n) \tag{45}$$

- trapezoidal = modified Euler ($\nu = 2$), for example

$$\begin{array}{c|cc} 0 & 0 & 0 \\ 1 & 1/2 & 1/2 \\ \hline & 1/2 & 1/2 \end{array} \qquad \begin{aligned} \delta_1 &= \mathbf{\Delta}(t_n, \mathbf{C}_n) \\ \delta_2 &= \mathbf{\Delta}\big(t_n + h, \Lambda\big(\mathrm{EXP}(\tfrac{1}{2} h(\delta_1 + \delta_2), \mathbf{C}_n)\big)\big) \\ \mathbf{\Theta} &= \tfrac{1}{2}(\delta_1 + \delta_2) \end{aligned} \tag{46}$$

6. Conclusions

We analysed the evolution equation for finite deformations. We proved that instead of considering it on the linear vector space of symmetric matrices sym, it actually evolves on its subset – the manifold of symmetric positive definite matrices $Sym^+ \subset sym$, so that the usual time-discrete integration schemes are inapplicable. However, thanks to the specific geometry of Sym^+, due to the principle of virtual power, the modified RK method, namely the Runge – Kutta – Munthe-Kaas method applies. Moreover, the closely related Magnus expansion method, based on the same geometric approach, might prove especially useful for highly-oscillatory problems, see Iserles et al. (2000).

Appendix

To find out the evolution equation on linear vector space, we have yet to work out how to transform deformation rates. For details, see Engø (2000), for preliminaries, for example Marsden et al. (1999). This section is rather technical and is meant only as a reference.

In $T\exp$, the symbol T denotes the tangent lift of a map $\exp$ between manifolds to a map between corresponding tangent bundles (manifolds of vectors) $Tsym$ and $TSym^+$. Since for vector space sym in general $Tsym \approx sym \times sym$, and for Sym^+ in particular $TSym^+ \approx Sym^+ \times T_{\mathbf{I}} Sym^+ \equiv Sym^+ \times sym$, a vector space $T_{\mathbf{\Theta}} sym$ at $\mathbf{\Theta} \in sym$ can be directly identified with sym and a vector space $T_{\mathbf{C}} Sym^+$ at $\mathbf{C}$ with sym through the translation $Q^{\mathbf{U}}$ by $\mathbf{U}$, for which $\mathbf{C} = \mathbf{U}^2$. That is

$$\begin{array}{ccccccc} sym & \xrightarrow{\;id\;} & Tsym & \xrightarrow{\;T\exp\;} & TSym^+ & \xrightarrow{\;(Q^{\mathbf{U}})^*\;} & sym \\ {\scriptstyle \partial\mathbf{\Theta}}\uparrow & & {\scriptstyle \partial\mathbf{\Theta}}\uparrow & & \uparrow{\scriptstyle \partial\mathbf{C}} & & \uparrow{\scriptstyle \mathbf{\Delta}} \\ sym & \xrightarrow{\;id\;} & sym & \xrightarrow{\;\exp\;} & Sym^+ & \xrightarrow{\;Id\;} & Sym^+ \end{array}$$

where $(Q_{\mathbf{U}})^* = (Q_{\mathbf{U}})_*^{-1}$. Id and id are respective identity mappings, and in the upper rightmost corner, we made use of the equivalence $T_{\mathbf{I}} Sym^+ \approx sym$. Due to commutativity of the diagram, we eventually conclude

$$\partial\mathbf{\Theta} = \mathbf{d}\exp_{\mathbf{\Theta}}^{-1}\big(\mathbf{\Delta}\big)(\mathbf{C}), \qquad \mathbf{C} = \exp\mathbf{\Theta} \tag{47}$$

where $\partial\mathbf{\Theta}$ is a vector field on sym, and $\mathbf{\Delta}$ a vector field on Sym^+ in right trivialization. Both fields correspond to $\partial\mathbf{C}$ – the deformation rate field on Sym^+. The diagram for $\mathfrak{gl}$ and GL looks similar, see Engø (2000).

Finally, we cite expressions for the inverse of differential of the exponential mapping **d**EXP (inverse of the right-trivialized tangent of the exponential map *T*EXP).

First consider case of $\exp : sym \to Sym^+$. Let now $\mathbf{\Theta} = \mathbf{R}\mathbf{\Lambda}\mathbf{R}^{\mathrm{T}} = \sum \lambda_i P_i$ be the spectral decomposition of $\mathbf{\Theta}$, where $\mathbf{\Lambda}$ is the corresponding diagonal matrix with diagonal entries λ_i and P_i corresponding projectors, then (Bhatia (2007))

$$\mathbf{d}\exp^{-1}_{\mathbf{\Theta}}(\mathbf{\Delta}) := \mathbf{R}\left[\log^{[1]}(\mathbf{\Lambda}) \circ (\mathbf{R}^{\mathrm{T}}\mathbf{\Delta}\mathbf{R})\right]\mathbf{R}^{\mathrm{T}} \tag{48}$$

$$= \sum_i \sum_j \log^{[1]}(\lambda_i, \lambda_j) P_i \, \mathbf{\Delta} P_j, \tag{49}$$

where the *Hadamard (or Schur) product* $\mathbf{A} \circ \mathbf{B}$ of two matrices $\mathbf{A}$ and $\mathbf{B}$ is defined to be the matrix whose (i,j)-entry is $A^j_i B^j_i$, and the 3×3 symmetric matrix $\log^{[1]}(\mathbf{\Lambda})$ has numbers

$$\log^{[1]}(\lambda_i, \lambda_j) = \frac{\log(\lambda_i) - \log(\lambda_j)}{\lambda_i - \lambda_j} \quad \text{if } i \neq j \tag{50}$$

$$\log^{[1]}(\lambda_i, \lambda_i) = \log'(\lambda_i) = \frac{1}{\lambda_i} \tag{51}$$

as its (i,j)-entries. At point $\mathbf{0} \in sym$ the mapping $\mathbf{d}\exp^{-1}_{\mathbf{0}} = \mathbf{I}$.

Second, making use of the relation $\mathfrak{exp} : \mathfrak{gl} \to GL$ between vector space $\mathfrak{gl}$ and the original space GL results in following relations. Denoting by $[\mathbf{\Theta}, \mathbf{\Delta}] := \mathbf{\Theta}\mathbf{\Delta} - \mathbf{\Delta}\mathbf{\Theta}$, it can be proved, see Munthe-Kaas (1999); Iserles et al. (2000); Engø (2000),

$$\mathbf{d}\mathfrak{exp}^{-1}_{\mathbf{\Theta}}(\mathbf{\Delta}) = \mathbf{\Delta} - \tfrac{1}{2}[\mathbf{\Theta}, \mathbf{\Delta}] + \tfrac{1}{12}[\mathbf{\Theta}, [\mathbf{\Theta}, \mathbf{\Delta}]] + ... = \sum_{j=0}^{\infty} \frac{B_j}{j!}[\mathbf{\Theta}, [\mathbf{\Theta}, [..., [\mathbf{\Theta}, \mathbf{\Delta}]...]]], \tag{52}$$

where B_j are j'th Bernoulli numbers. The first few coefficients are

$$\frac{B_j}{j!} = \begin{cases} 0 & \text{for } k \text{ odd, and } k \neq 1 \\ 1, -\frac{1}{2}, \frac{1}{12}, -\frac{1}{720}, \frac{1}{30240}, -\frac{1}{1209600} & \text{for } k = 0, 1, 2, 4, 6, 8. \end{cases} \tag{53}$$

Acknowledgments

The support of the grant GAČR 103/09/2101, as well as RVO : 68378297 is gratefully acknowledged.

References

Bhatia, R. (2007), *Positive definite matrices*, Princeton University Press, Princeton.

Engø, K. (2000), On the construction of geometric integrators in the RKMK class. *BIT*, Vol 40, No.1, pp 41-61.

Fiala, Z. (2011), Geometrical setting of solid mechanics. *Annals of Physics*, Vol 326, No.8, pp 1983-1997.

Fiala, Z. (2008), Geometry of finite deformations, linearization, and incremental deformations under initial stress/strain. In: *Engineering Mechanics 2008* (V. Fuis et al. eds). Svratka, CD ROM, paper #215, 20pp.

Fiala, Z. (2009), Is the logarithmic time derivative simply the Zaremba-Jaumann derivative? In: *Engineering Mechanics 2009* (J. Náprstek et al. eds). Svratka, CD ROM, paper, 14pp.

Hairer, E., Nørsett, S. P., Wanner, G. (1993), *Solving ordinary differential equations I: Nonstiff problems*, Springer, Berlin.

Iserles, A., Munthe-Kaas, H. Z., Nørsett, S. P., Zanna, A. (2000), Lie-group methods. *Acta Numerica*, Vol 9, pp 215-365.

Marsden, J. E., Ratiu, T. S. (1999), *Introduction to mechanics and symmetry*, Springer, New York.

Munthe-Kaas, H. (1999), High order Runge-Kutta methods on manifolds. *Applied Numerical Mathematics*, Vol 29, No.1, pp 115-127.

Noll, W., Seguin B. (2010), Basic concepts of thermomechanics. *Journal of Elasticity*, Vol 101, No.2, pp 121-151.

18th International Conference
ENGINEERING MECHANICS 2012
Svratka, Czech Republic, May 14 – 17, 2012

pp. 231–237
Paper #241

COMPARISON OF COMPOSITE MATERIAL DEGRADATION ASSESMENT METHODS USING ACOUSTIC ANALYSIS AND LASER VIBROMETRY

T. Fíla [*], S. Urushadze [**], D. Kytýř [*], J. Valach [*], M. Šperl [**]

Abstract: *Assessment of degradation rate of material can be carried out by many experimental techniques differing in complexity and sophistication. A relatively simple method based on acoustic analysis is described in this contribution. Degradation of material's properties due to fatigue loading is detectable in decrease of their modulus of elasticity that can be derived from natural frequencies of specimens, which were acquired by the presented method. These measurements utilize self-designed device capable of specimen excitation and acquisition of its vibration. The recorded signal is then processed by spectral analysis enabling determination of natural frequencies. Usefulness of the above mentioned acoustic method can be seen in the fact that the measured changes of material's parameters are comparable to those obtained by laser vibrometry, which is by several orders more expensive technique.*

Keywords: ***natural frequency, material degradation, laser vibrometer, acoustic measurement***

1. Introduction

Reliable assessment of material degradation rate is very actual and discussed problem. Degradation rate can be carried out by many experimental techniques. Measurement of material sound exposure and so its typical acoustic characteristic is one of them. The characteristic is mainly represented by natural frequency and attenuation decrement. These magnitudes correspond with Young's modulus. Their changes represent material state and its degradation [Pirner & Urushadze, (2004)]. Use of these premises led to development of custom-designed acoustic measurement device that has been able to determine specimens natural frequencies and their decreases due to continuous material degradation [Fíla et al., (2011)]. Effort to prove that data acquired by this device and technique are correct and can be compared with other similar method led to comparative experiment. Laser vibrometer was selected as comparative device. Experiment setup, progress and conclusion are discussed in this paper.

2. Basic principles of acoustic testing device

Basic principle of acoustic testing is based on fact, that if it was possible to measure sound characteristics of specimen repeatedly with constant conditions, any measurable change in natural frequency value would be labeled as material degradation indication [Rojek et al., (2007)]. Custom-designed testing device was fabricated in order to accomplish this premise. Device description can be divided in two parts. Their functions are following:

– Specimen fasteners - Specimen is hanged up by two needles. This constraint enables specimen's moves with one degree of freedom (rotation round fasteners). Specimen can rock on needles during mechanical impacts on its surface. Fastening scheme is shown in Fig. 1.

– Working part - This part consists of alluminium tube that can be set and locked in four directions (angulary vertical, angulary horizontal, tube's end height and tube's end distance from specimen surface). This arrangement allows testing repeatedly at same conditions. Overall view of the acoustic measurement device is displayed in Fig. 2

[*] Bc. Tomáš Fíla, Ing. Daniel Kytýř Ph.D., Ing. Jaroslav Valach Ph.D.: CTU in Prague, Faculty of Transportation Science, Department of Mechanics and Materials, Na Florenci 25, 110 00 Prague 1, CZ, e-mail: [xfila, kytyr, valach]@fd.cvut.cz
[**] Ing. Shota Urushadze Ph.D., Ing. Martin Šperl P.hD.: Academy of Sciences of the Czech Republic, Institute of Theoretical and Applied Mechanics, v. v. i, Prosecká 809/76, 190 00 Prague 9, CZ, e-mail: [urushadze, sperl]@itam.cas.cz

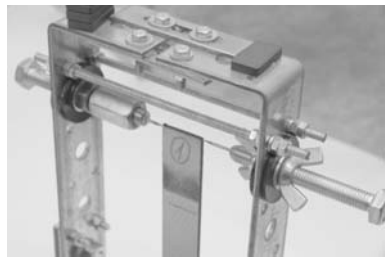

Fig. 1: Fastening of specimen to the acoustic device

Small pellet made of steel is inserted in alluminium tube that provides rigid lead to specimen surface. Sound emitted during impact is recorded by microphone fixed to the device and analyzed. Sound analysis is provided by transformation to get frequency spectrum. Sound is filtered and trimmed to normalized length prior natural frequency peaks determination.

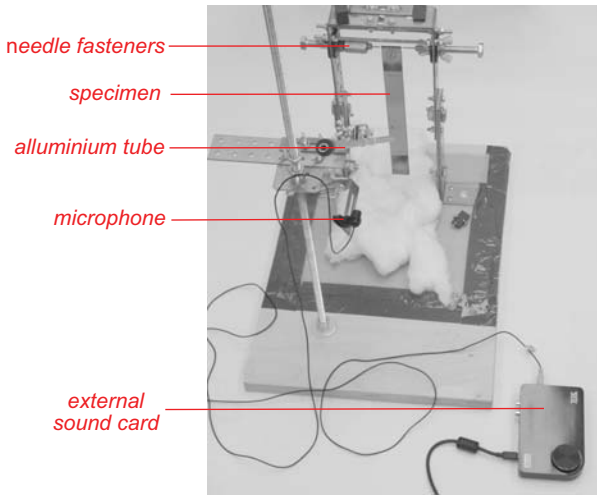

Fig. 2: Acoustic device with fastened specimen and external sound card

3. Material

Specimens of C/PPS composite material were measured. Carbon fiber/polyphenylene sulphide (C/PPS) composite is relatively new material used in aerospace industry and in other hi-tech applications. The matrix, that is made of thermoplastics, represents the main difference to more common composites based on epoxy resin, i.e. thermosets. Young modulus of this composite reaches 400 GPa and material mechanical properties are fully comparable with metal alloys [Kytýř et al., (2011)].

4. Experiment description

Comparative experiment of acoustic measurement and laser vibrometer was done. Laser vibrometer uses principles similar to acoustic measurement and is suitable for measurement of dynamic response and determination of fatique degradation [Pirner & Urushadze, (2002)].

Places appropriate for pellet impacts and for microphone and vibrometer positioning were selected. Pellet has to strike on specimen's surface clearly without any double-clicks or secondary impacts on

laboratory desk. Furthermore, impact has to be sufficiently strong to produce enough sound energy for appropriate recording. Constant position of microphone during whole experiment had to be carefully adjusted and strictly adhered. Close distance causes distorted recordings (limitations of sound card sensitivity). By constrast, large distance causes absence of higher frequencies in the spectrum because of their higher attenuation. The setup could not be determined exactly with use of any empirical rules. It had to be adjusted by sensitive measurement and calibration. Aluminium tube gradient was set to 45 degrees and microphone distance was maintained 135 mm from specimen surface during all tests.

Every specimen was marked on three places. First two places served as a designation of impact zone (approximately in the center and on the bottom of specimen). Third place secured constant positioning of laser vibrometer sensor. The points were selected on basis of natural modes calculated using finite element simulation of modal analysis and are shown in Fig. 3.

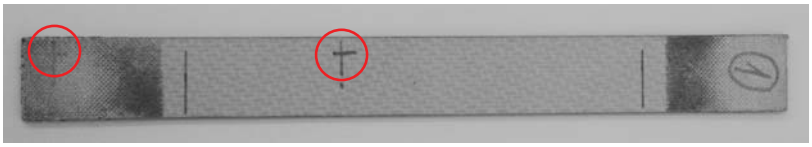

Fig. 3: Measured specimen with designated impact zones

Sound recordings were taken with 96 kHz sampling frequency and 24-bit quality. Vibrometer recordings were taken with 100 kHz sampling frequency and in maximal possible 24-bit quality. Recordings were captured simultaneously for each specimen. Every click had its own ordinal number that allowed data evaluation for both recordings with synchronous time. Specimens were repeatedly measured after degradation by given number of cycles. Measurement were made for 0, 1000, 10 000, 50 000 and 100 000 cycles.

Recorded data were evaluated using MATLAB and DEWESOFT software. Data influented by negative noise (in case of vibrometer floor vibrations and undesirable sound in case of microphone) were excluded from the analysis. The data were then normalized to identical length. This was very important for time synchronization and consequential results comparation. Bandpass filter was applied for elimination of undesirable low and high frequencies (below 50 Hz and above 5000 Hz in this case). Finally, spectral analysis was carried out and natural frequency was determined. Overall experiment setup is shown in Fig. 4.

5. Results

Four specimens (no. 1, 2, 3, 4) were used at the beginning of experiment. Results seemed to be satisfactory after evaluation of first two tests. Therefore, only two specimens (no. 1, 2) were selected to continue in rest of the experiment (due to lack of samples for other research). Unfortunately, specimen no. 2 cracked prematurely with degradation of only 77 000 cycles. This was probably caused by combination of large loading force (75 percent of material strength), high frequency of loading and repeated fastening into fatique testing machine [Meyers & Chawla, (2009)]. For these reasons results of first two tests are presented for all four specimens and last results only for specimen no. 1.

First results consists of evaluation of the first natural frequency that was very easy to be measured by laser vibrometer. Results of the measurement are shown in Tab. 1 (abbreviation M means microphone data and D represents vibrometer data). Values in the table represent mean values of natural frequencies calculated for each click (every specimen was measured ten times). The highest values of standard deviation were 0.47 Hz in case of laser vibrometer and 2.17 Hz in case of microphone. Data in Tab. 1 representing first natural frequency value was not be able to determine degradation rate of specimen.

However, potentional decrease of lower frequencies was hidden in measurement inaccuraccy. The decrease was more significant in higher frequencies and could be measured. Natural frequency approximately 3 000 Hz was chosen for determination of the decrease. The frequency was still able to be satisfactory measured by laser vibrometer and its occurrence in vibrometer frequency spectrum was al-

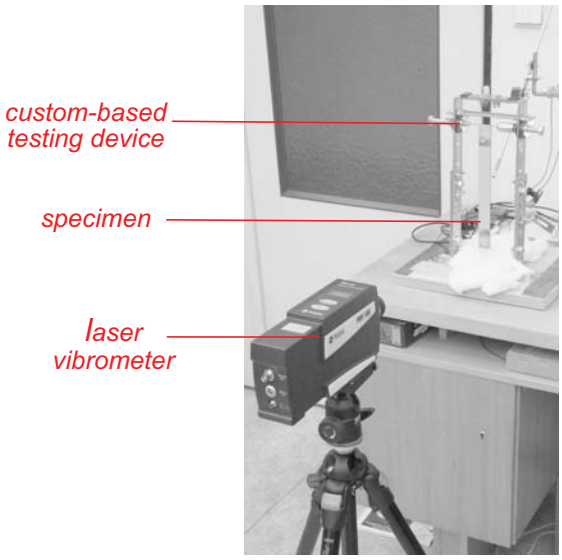

Fig. 4: Acoustic testing device and laser vibrometer during measurement

Tab. 1: First natural frequency results (mean values)

No.	Position	0 cycles		1000 cycles		10000 cycles		50000 cycles		100000 cycles	
		M	V	M	V	M	V	M	V	M	V
		[Hz]	[Hz]	[Hz]	[Hz]	[Hz]	[Hz]	[Hz]	[Hz]	[Hz]	[Hz]
1	Center	154.857	151	150.25	151	151	152	153.8	151	149.4	151
	Bottom	149.375	151	149.222	151	149	152	148.1	151	146	151
2	Center	146.5	150	148.09	149	148.778	149	151.5	149		
	Bottom	153	150	148.875	150	148.778	149	146.5	149		
3	Center	153.143	151	148.875	150						
	Bottom	149.6	150	148.222	150						
4	Center	147.875	149	146.333	149						
	Bottom	149.6	149	144.44	149						

most regular. Characteristic frequency spectrum measured by vibrometer and by microphone is shown in Fig. 5.

Mean values of selected natural frequency near 3 000 Hz are shown in Tab. 2 and Tab. 3 (abbreviation C means center mark on specimen surface, B represents bottom mark). Its decrease values are shown in Tab. 4. Graphical summary of the data is displayed in Fig. 6.

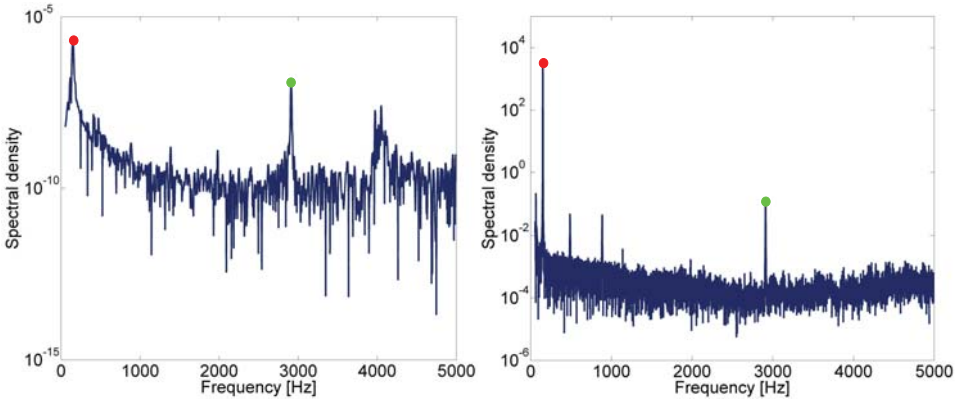

Fig. 5: Frequency spectrum measured by microphone (left) and by vibrometer (right) - (specimen no. 2, 1000 cycles, click no. 9). Red dot represents first natural frequency peak, green dot represents natural frequency peak used for evaluation of degradation.

Tab. 2: Selected natural frequency (approx. 3000 Hz) results measured by vibrometer (mean values)

No.	0 cycles		1000 cycles		10000 cycles		50000 cycles		100000 cycles	
	C	B	C	B	C	B	C	B	C	B
	[Hz]	[Hz]	[Hz]	[Hz]	[Hz]	[Hz]	[Hz]	[Hz]	[Hz]	[Hz]
1	2960	NaN	2940	2941	2933	2933	2900	2900	2886	NaN
2	2933	2934	2909	2909	2899	2899	2881	2881		
3	2933	NaN	2917	2916						
4	2921	NaN	2900	2901						

Tab. 3: Selected natural frequency (approx. 3000 Hz) results measured by microphone (mean values)

No.	0 cycles		1000 cycles		10000 cycles		50000 cycles		100000 cycles	
	C	B	C	B	C	B	C	B	C	B
	[Hz]	[Hz]	[Hz]	[Hz]	[Hz]	[Hz]	[Hz]	[Hz]	[Hz]	[Hz]
1	2959	2959	2941	2941	2930	2930	2901	2901	2887	2886
2	2934	2931	2909	2910	2898	2897	2881	2881		
3	2932	2931	2916	2916						
4	2920	2922	2901	2899						

Tab. 4: Mean values of natural frequency decrease (approx. 3000 Hz)

No.	1000 cycles		10000 cycles		50000 cycles		100000 cycles	
	M [Hz]	V [Hz]	M [Hz]	V [Hz]	M [Hz]	V [Hz]	M [Hz]	V [Hz]
1	-18	- 19.5	-29	-27	-58	-60	- 72.5	- 74
2	-23	- 24.5	-35	-34.5	-51.5	-52.5		
3	-15.5	- 16.5						
4	-21	- 20.5						

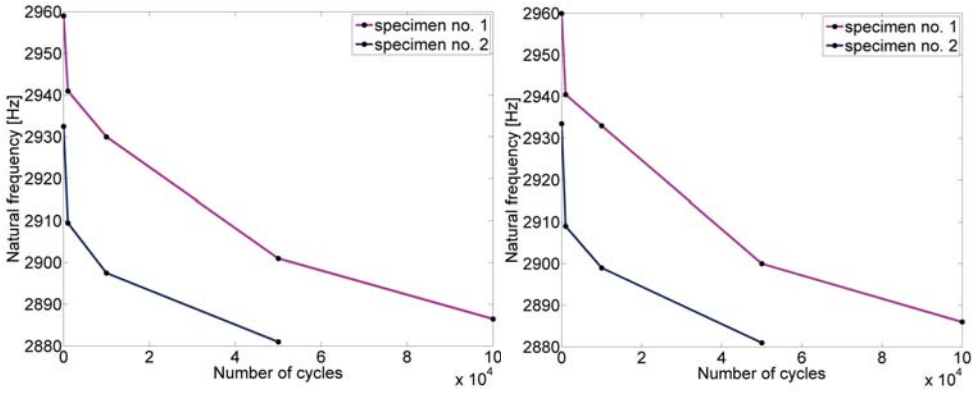

Fig. 6: Frequency decrease measured by microphone (left) and by vibrometer (right)

6. Conclusions and discussion

Correlation between natural frequency value and number of cycles of the specimen was confirmed. Data measured using acoustic method are fully comparable with data measured by laser vibrometer. Differences of spectral density peaks position (natural frequencies) reached repeatedly maximally 5 Hz. Absolute error of natural frequency determination remained constant through whole frequency spectrum. However, natural frequency decrease could not be determined in case of first natural frequency. The decrease was too small to be measured at lower frequencies (in this case up to 1000 Hz). The decrease was able to be determined at higher natural frequency (about 3000 Hz) where measurement using laser vibrometer began to be more complicated because of higher level of noise. Measurement by acoustic method at these frequencies did not produce any problems and results reached high accuracy. To conclude, the acoustic measurement using custom-designed experimental device proved ability to evaluate material degradation. This was proved in terms of precision, reproducibility and reliability by the comparative experiment.

Acknowledgments

The research has been supported by RVO: 68378297, by the Grant Agency of the Czech Republic (grant No. P105/10/2159), Grant Agency of the Czech Technical University in Prague (grant No. SGS12/205/OHK2/3T/16) and Ministry of Education and Sports (research plan No. MSM6840770043).

References

Fíla, T., Kytýř, D., Valach, J., Šperl, M.,(2011), Assesment of C/PPS Composites Degradation Indicators Using Acoustic Measurement, In: *Experimental Stress Analysis 2011*

Kytýř, D., Valach, J., Doktor, T., Jiroušek, O., (2011), Assessment of C/PPS Composites Degradation Indicators Using Acoustic Measurement, In: *Engineering Mechanics 2011*

Meyers, M., Chawla, K., (2009), *Mechanical behaviour of materials - second edition*, Cambridge university press, Cambridge, ISBN - 978-0-521-86675-0, pp. 713–759

Pirner, M., Urushadze, S., (2004) *Dynamic response as a tool for damage identification*, International Applied Mechanics, Vol. 40, No. 5, pp. 487–505

Pirner, M., Urushadze, S., (2002), *Structural damage assessment using dynamic response*, Acta Technica, CSAV, Vol. 47, No. 4, pp. 445–466

Rojek, M., Stabik, J., Sokól, S., (2007), *Fatique and ultrasonic testing of epoxy-glass composites*, Acta Technica, Journal of Achievements in Materials and Manufacturing Engineering, Volume 20, No. 1, pp. 183–186

Valach, J., Kytýř, D., Doktor, T., Sekyrová, K., Králík, V., Němeček, J., (2011), *Comparison of mechanical properties of CFRP laminate obtained from full-scale test and extrapolated from local measurement*, Chemické listy, Vol. 105, No. 17, pp. S729–S732

18th International Conference
ENGINEERING MECHANICS 2012
Svratka, Czech Republic, May 14 – 17, 2012

pp. 239–244
Paper #220

DESIGN AND USE OF NOVEL COMPRESSION DEVICE FOR MICROTOMOGRAPHY UNDER APPLIED LOAD

T. Fíla, P. Zlámal, P. Koudelka, O. Jiroušek, T. Doktor, D. Kytýř *

Abstract: *This paper deals with modification and usage of custom-designed compression device, that allows real time X-ray tomography scanning of specimen under applied pressure. In this case microtomography is used to obtain data required to determine specimens morphology and to develop 3D material model (especially for cellular materials such as bones, metal foams and quasi-brittle materials or particle composites such as concrete or cementitious composites). Important design changes were made in the existing device frame to increase its load capabilities, stiffness and to accomodate a larger specimen. Finally device displacement measurements were conducted and calibration experiment was carried out.*

Keywords: ***X-ray, microtomography, compression device, optical strain measurements***

1. Introduction

X-ray tomography is a method that facilitates generation of reliable and accurate 3D models of solid bodies and also development of material models using scanning of loaded specimens [Jiroušek & Jandejsek et al., (2011)]. These models can be used to study material morphology and additionally to use the data for development of finite element (FE) model of a studied material, e.g. trabecular bone [Jiroušek & Zlámal et al., (2011)] and quasi-brittle materials (such as stones, concrete). According to these techniques many design requirements had to be met. Loading device has to be very compact to fit in the X-ray scanning device and simultaneously it has to be as X-ray transparent as possible. Such material testing method is specific and the testing device has to be constructed with utilization of a custom design. Significant upgrade of previously designed machine capable of performing material measurements in X-rays is described in this paper.

2. Original device design

Described machine was designed and built in 2008. Primary, it was designed for compressional loading of trabecular bone specimens during X-ray tomography [Zlámal et al., (2008), Jiroušek & Zlámal et al., (2011)]. Nowadays, it is used also as a general purpose material testing machine. The device is displayed in Fig. 1. The loading frame of the device has been fabricated using high tech polymer [Zlámal et al., (2008)]. Polymeric material used as a body of machine is transparent for X-ray. However, the machine has been equipped by two oval holes in the body (see Fig. 1) for better manipulation and fastening of the specimen. The main disadvantage of the holes inheres in complicated reconstruction of the object using the filtered back projection method. Further development of the device has led to significant change in the device design.

The following requirements had to be satisfied:

– to accomodate larger specimen (cube with edge length 100 mm)

– ability to perform tests with very high loading forces (up to 25 kN)

– to increase the overall stiffness of the device

*Bc. Tomáš Fíla, Ing. Petr Zlámal, Bc. Petr Koudelka, Doc. Ing. Ondřej Jiroušek Ph.D., Ing. Tomáš Doktor, Ing. Daniel Kytýř Ph.D., Academy of Sciences of the Czech Republic, Institute of Theoretical and Applied Mechanics, v. v. i, Prosecká 809/76, 190 00 Prague 9, CZ, [fila, zlamal, koudelkap, jirousek, doktor, kytyr]@itam.cas.cz

Following limitations had to be eliminated:

– diversion of upper jaw under large loading force applied to heterogenous porous material

– X-ray noise caused by existing openings in the machine's polymeric body

Fig. 1: Device design prior to the modification

3. Modified design

To avoid the problems with manipulation windows in the existing design, construction with bayonet lock has been introduced. Bayonet lock allows for better manipulation with specimen and easier change of machines experimental setup. Both bayonets as well as the upper body are made of high strength duralumin 7075 with Young's modulus 72 GPa and strength 480 MPa (according to manufacturer's material datasheet). Upper part of the bayonet is constructed as duralumin body with wall thickness 5 mm. This part is considered to be absolutely rigid (based on results of FE simulation with load 25 kN). Maximal displacement calculated in the FE simulation was $5\mu m$. Bottom part of the device consists of three parts: bottom bayonet, flange used for fastening to the base desk and a composite tube. The composite tube is made of carbon fibre composite MTM57/T700S(12k)-150-35. This material exhibits excellent mechanical characteristics in tension while quaranteeing very low X-ray absorbtion. According to the data provided by manufacturer the material was used for fabrication of medical sockets for commercial CT scanners. Young's modulus of MTM is 125 GPa in the fibre direction and its strength is 2481 MPa. Sufficient tube wall thickness has been calculated as 0.65 mm using FE simulation and analytical model. Bottom part of the body (lower bayonet, flange and composite tube) has been permanently glued together by PL20 epoxide with shear strength 45 MPa (according to manufacturer's measurements). First experiment have proved that device is very stiff and can be used for loading up to 25 kN. Overall view of the new machine design and its parts in detail are shown in Fig. 2.

Another problem that had to be resolved was connected to flexural rigidity of the upper jaw. To ensure perfect vertical movement of the upper jaw during loading, a slide assembly was inserted into the machine's mechanism. Its functionallity has been verified in a sequence of experiments up to 13.5 kN in which horizontal movement of the jaw was observed with high resolution CCD camera. Slide assembly consists of bearing made of alloy with 60% PTFE and 40% percent bronze and inner shaft made of stainless steel. Maximal effectivity and functionallity of the part has been calculated using appropriate formulas [Černoch, (1977)]. Slide assembly has been manufactured with maximal precision and with, theoretically, zero clearence. Slide assembly visualization is displayed in Fig. 3.

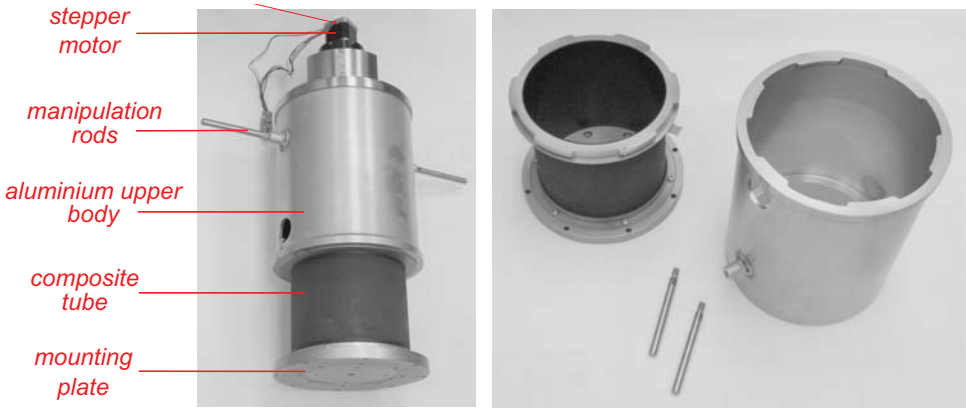

Fig. 2: Overall view of new design and description (left). Detailed view of assembly parts (right)

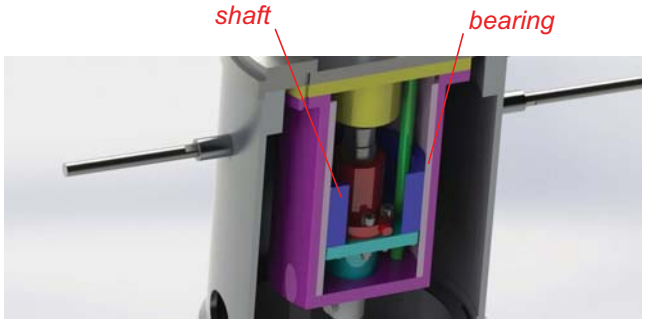

Fig. 3: Detail of slide assembly - bearing (light pink) and shaft (blue)

4. Initial testing and problems

Initial mechanical tests were performed to prove the stiffness and strength of the device. Loading force was increased in steps and device deformations were carefully observed by CCD camera. The only problem was caused by stepper motor that could not actuate the assembly due to its low performance. This problem appeared at load approximately 7 kN and was ad-hoc resolved by mounting of new stepper motor of higher torque capacity.

5. Experiment - displacement measurement

Manipulation and operation with the device is suitable for inserting in the shielded box of the micro-CT device. However, its stiffness had to be measured by a reliable method. Stiffness of the device is very important property. To capture the softening behaviour of loaded specimen the elastic strain was plotted to assess effects of device deformation tendency. Comparative experiment with both bodies (polymeric and composite) was carried out and measured deformations were confronted.

Displacements were measured optically using digital image correlation (DIC). DIC is reliable, precise, contactless method that enables measuremets of deformations without influencing the specimen. All image data were acquired using macro objective (Canon EF 180 mm f/3.5L Macro USM, Canon, Japan) mounted on a 15 MPix body (Canon EOS 7D, Canon, Japan). Composite tube was measured by DIC without any modifications to the surface because of its natural texture (see Fig. 4). Polymeric body was markered by dots required for correlation feasibility. Verification experiment was carried out by displacement driven loading with loading rate of 5 μm/s up to maximum force value 10 kN. Designated

zone on device surface was captured in eqvuidistant time intervals. Images have been then processed by digital image correlation toolkit [Jandejsek et al., (2010)] based on Lucas-Kanade algorithm [Lucas & Kanade, (1981)]. Displacement and deformation in vertical direction were determined and the results were compared with numerical and/or analytical calculations. Experiment setup is shown in Fig. 5.

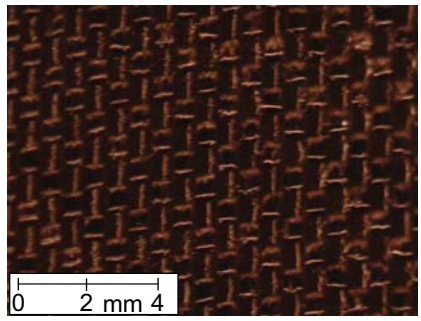

Fig. 4: Detailed view of the surface of the composite loading frame

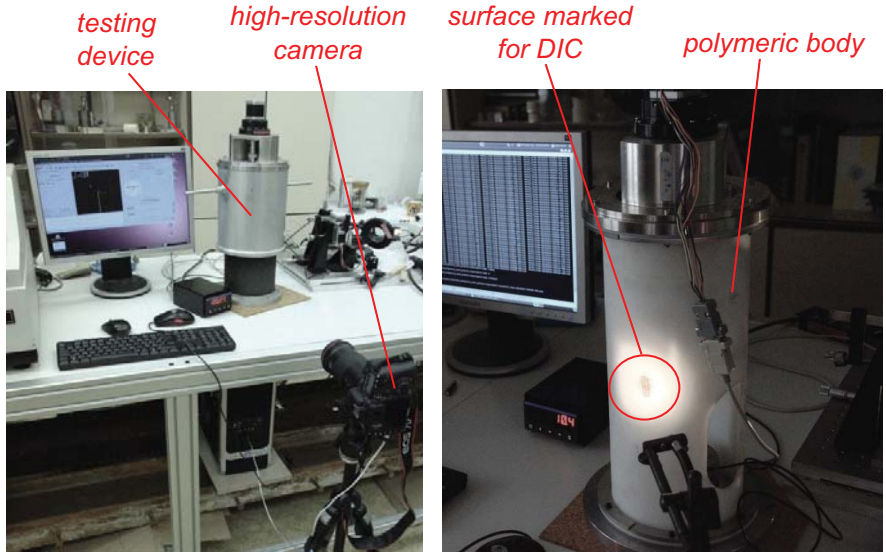

Fig. 5: Both device designs during experiment - optical measurement of displacements and deformations

Composite tube consists of 5 layers with fibre orientation 0, 45, 90, -45, 0 (orientation to force direction) and shows mechanical anisotropic behaviour. Overall Young's modulus was calculated using following equations [Meyers & Chawla, (2009), Meissner & Zilvar, (1987)] (updated for 5 layers):

$$E = \frac{2 \cdot E11 + E22 + 2 \cdot E45}{5} \tag{1}$$

$$\frac{1}{E45} = \frac{\cos^4\left(\frac{\pi}{4}\right)}{E11} + \frac{\sin\left(\frac{\pi}{4}\right)}{E22} + \left(\frac{1}{G12} - \frac{2 \cdot \nu}{E11}\right) \cdot \sin^2\left(\frac{\pi}{4}\right) \cdot \cos^2\left(\frac{\pi}{4}\right) \tag{2}$$

Material properties of MTM composite (according to manufacturer's datasheet) are shown in Tab. 1. Numerical solution has been done using ANSYS software with 8-noded shell elements. Results and

comparison with digital image correlation data are displayed in Tab. 2. Linear behaviour of device was proved and it is graphically shown in Fig. 6.

Tab. 1: Material properties of MTM composite

Young's modulus in fibre direction (E11)	127 GPa
Young's modulus perpendiculary fibre direction (E22)	7.9 GPa
Poisson's ratio	0.3
Shear modulus (G12)	3 GPa

Tab. 2: Comparison of overall z-direction displacement calculated and measured

	Composite tube	Polymeric body
Analytic solution	0.0697 mm	not calculated
Numerical solution	0.0694 mm	0.141 mm (relevant to measured place), max. 0.188 mm
Digital image correlation	0.0741 mm	0.764 mm

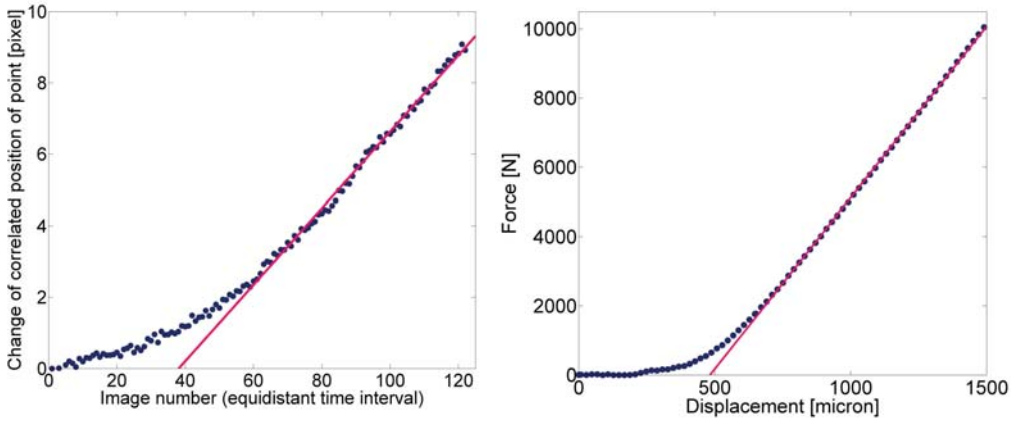

Fig. 6: Displacement and force diagram

Displacement and strains in the original (polymeric) body has been calculated in ANSYS software using solid elements. Results and comparison is summarized in Tab. 2. Numerical solution for displacement in vertical direction is shown in Fig. 7. Measured overall displacement of composite tube is very close to the analytical and numerical solution. High load capability of the redesigned device was verified and is realeased to loads up to 25 kN. On the contrary, the polymeric body was designed for loads up to only 2 kN and measured results confirmed that displacement and deformation at higher loads are too large for material testing.

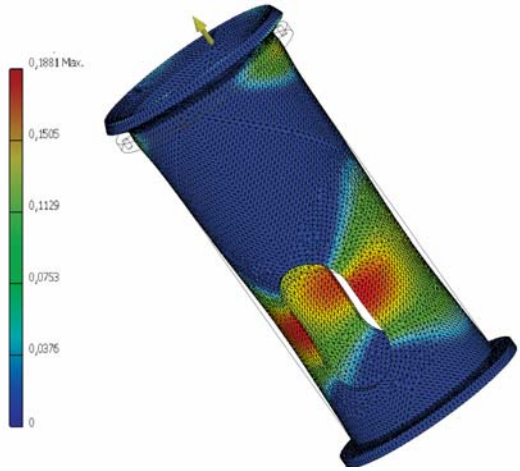

Fig. 7: Displacement in vertical direction [mm]

6. Conclussion and discussion

New upgraded design of device has been constructed. New design makes the device significantly stiffer which is important not only for higher loads but also for fracture toughness tests. Material more transparent for X-rays has been used to obtain more precise, more relevant and more accurate data. Linear behaviour of the device and its stiffness was measured and was considered as adequate to calculations and expectations. To conclude, prospective behaviour of device has been verified and device is suitable for considered experiments.

7. Acknowledgements

Support of the Grant Agency of the Czech Republic (Grant No. P105/10/2305, P105/11/1551 and P105/12/082) and support of RVO: 68378297 is gratefully acknowledged.

References

Černoch (1977), *Strojně technická příručka*, SNTL, Praha, pp. 666 – 689

Jandejsek, I., Valach, J., Vavřík, D., (2010), Optimization and Calibration of Digital Image Correlation Method. In: *Experimentální analýza napětí 2010*, (Šmíd, P.), Univerzita Palackého v Olomouci, Olomouc, pp 121–126.

Jiroušek, O., Jandejsek, I., Vavřík, D., (2011), *Evaluation of strain field in microstructures using micro-CT and digital volume correlation*, Journal of Instrumentation, Praha, Vol. 0, No. 1, pp. 60

Jiroušek, O., Zlámal, P., Žák O., (2009), Real time observation of trabecular bone microstructure during micromechanical testing, In: *Engineering Mechanics 2009 - Book of extended abstracts*, Institute of Theoretical and Applied Mechanics v. v. i., Academy of Sciencies of the Czech Republic, pp. 116-117

Jiroušek O., Zlámal P., Kytýř D., and Kroupa M. (2011), Strain analysis of trabecular bone using time-resolved X-ray microtomography, *Nucl. Instrum. Meth. A*, Vol 633, No. S1, pp S148–S151.

Lucas, B., Kanade T., An iterative image registration technique with an application to stereo vision, In: *Proceedings of Imaging Understanding Workshop*, pp 121-130 Optimization and Calibration of Digital Image Correlation Method. In: *Experimentální analýza napětí 2010*, (Šmíd, P.), Univerzita Palackého v Olomouci, Olomouc, pp 121-126.

Meissner, B., Zilvar, V., (1987), *Fyzika polymerů - Struktura a vlastnosti polymerních materiálů*, SNTL, Praha, pp. 276-289

Meyers, M., Chawla, K., (2009), *Mechanical behaviour of materials - second edition*, Cambridge university press, Cambridge, ISBN - 978-0-521-86675-0, pp. 765-814

Zlámal, P., Jiroušek, O., Vavřík, D., (2008), *A Novel Compression/tension Device for Investigation of Trabecular Bone Failure Using Real-time micro-CT Imaging*, 7th Youth Symposium on Experimental Solid Mechanics, Volume 1, 1st Edition, Division of Biomedical Engineering and Experimental Mechanics

18th International Conference
ENGINEERING MECHANICS 2012
Svratka, Czech Republic, May 14 – 17, 2012

pp. 245–254
Paper #271

DISCRETE TOPOLOGY OPTIMIZATION OF PLANAR CABLE-TRUSS STRUCTURES BASED ON GENETIC ALGORITHMS

V. C. Finotto*, M. Valášek**

Abstract: *This paper demonstrates the application of Genetic Algorithms to design optimal lightweight Cable-Truss structures, which are structures composed by bars and prestressed cables and offer a high potential in robotics. The optimal lightweight structure shape is determined through a discrete topology optimization process which starts from a ground grid of nodes and interconnect them using cables or bars in order to obtain optimal results. The optimal solution is considered to have the lower mass and highest stiffness, such relation is expressed in the parameter stiffness-to-mass ratio. The objective function of the optimization problem evaluates the bending stiffness and the mass of the feasible solutions searching for the maximum stiffness-to-mass ratio. Symmetric structural response is desired once that in movable machines the majority of the structures are moving parts in which forces can assume different directions during working cycle, as a result the algorithm must find solutions with are symmetric in the axis perpendicular to the loading direction. Simulations are also presented showing comparisons between Cable-Truss and Truss structures under the same boundary conditions, population and iterations. Structural static response is computed using nonlinear finite element iterative procedure. Examples with optimized modular layout of a 2D robotic arm are shown, which presents improvement of Cable-Truss structures in comparison with Truss structures in all cases that have been simulated.*

Keywords: ***Cable-Truss structures, Genetic Algorithms, Discrete Topology Optimization, lightweight design.***

1. Introduction

Lightweight structures research is based not only in material science but also in structural mechanics, processing and design. Is important noting that the scientific aim is to develop knowledge for the specific phenomena occurring in these areas and in the interface between them, in order to achieve increased performance for a wide range of structural applications (LsAA,2010). In addition, the main lightweight structures include tensile/tension structures, frame supported, air supported, air inflated, cable net, cable-and-strut, geodesic domes, and grid shells. In lightweight designing, different structural elements are used, which can be optimized, combined or substituted using different methods. However, assigning a single all-encompassing definition for all applications is an extremely complex task and consequently the meaning of the term lightweight structure varies accordingly to application and field of research. In the structural field, lightweight structures can be defined as those which shape is determined through an optimization process to efficiently carry the loads from a critical loading case regardless of the type of material employed (LsAA, 2010).

In the research of lightweight structures, trusses have attracted tremendous interest due to their extensive application in the contracture of infrastructures and space structures. Research works have focused on material characteristics, truss joint design, processing and construction of structural components. In recent years, influence of cables in such structures has also been investigated (Liao, 2009).

The term cable-truss is often taken to describe a structural member consisting of bars and prestressed cables. Cable elements can only withstand tension forces and are used not only to maintain stability and strength of truss system but also to decrease the structure weight, since the weight density of truss members is usually much higher than in cable elements (Liao, 2009). Cable elements are in

* Ing. Vitor Cores Finotto: Faculty of Mechanical Engineering, Department of Mechanics, Biomechanics and Mechatronics, ČVUT in Prague, Technická 4, 166 29, Prague, Czech Republic, e-mail: VitorCores.Finotto@fs.cvut.cz

** Prof. Ing. Michael Valášek, DrSc. : Faculty of Mechanical Engineering, Department of Mechanics, Biomechanics and Mechatronics, ČVUT in Prague, Technická 4, 166 29, Prague, Czech Republic, e-mail: Michael.Valasek@fs.cvut.cz

essence non-linear elements which undergo large displacements, in order to take this feature into account nonlinear finite element analysis is performed in order to compute static structural response of cable trusses.

Lightweight design of cable-trusses aims to obtain optimal mass reduction with minimal losses in stiffness, therefore structural optimization is essential. Such task can be divided into sizing, shape and topology optimization, among these, the later yields more material savings and greater complexity (Su, 2009).

Discrete topology optimization approaches are typically based on Evolutionary Algorithms (EAs), which are adaptive methods used for stochastic search and optimization (Hajela, 1995). Among several EAs, Genetic Algorithms (GAs) have been widely used in discrete topology optimization (Rozvany, 2009, Hajela, 1995, Balling, 2006), they consist of an adaptive heuristic search algorithms based on the principles of natural biological evolution. As such, they represent an intelligent exploitation of a random search used to solve optimization problems.

The objective of this work is to provide a topology optimization method for cable-truss structures. Differently than common approaches for discrete topology optimization, the proposed method decides not only the interconnection between nodes, but also if this interconnection is going to be performed by bar or cable. For that, ground structure approach is used, which consists of using a fix grid of nodes and explore the combinations of interconnection between nodes using cable and bar elements.

In addition, genetic algorithm is used for searching for the best solution and nonlinear finite element procedure is applied for computing static structural response. Stiffness-to-mass ratio is adopted as optimization criteria since it relates the stiffness performance in a determined direction and mass, which are both aimed when designing lightweight structures.

Furthermore, differently than previous researches, symmetric structural static response is aimed once the main target is to use cable-trusses for designing lightweight movable machines. Such application differs from civil engineering as forces can assume different directions during working cycle. This behavior demands that structural stiffness cannot rely only in cable elements since changes in force direction can lead to their compression.

Examples with optimal layout of a 2D cantilever beam are presented. The simulations aim to compare the stiffness-to-mass ratio of cable-trusses and trusses for different slenderness ratios. The obtained results indicate that Cable-Trusses reached improvement in all cases.

2. Cable-truss Structures

Cable-truss structures can be described as a system of straight bars and cables joined at their ends from a rigid framework. Similarly to trusses the objective is to transfer applied loads to the supports in the form of axial forces. Although trusses and cable-trusses are actually three-dimensional structures, most can be reduced to planar cases, such approximation is adopted in this work since it reduces computational cost and also brings a deeper insight of the structure dependences.

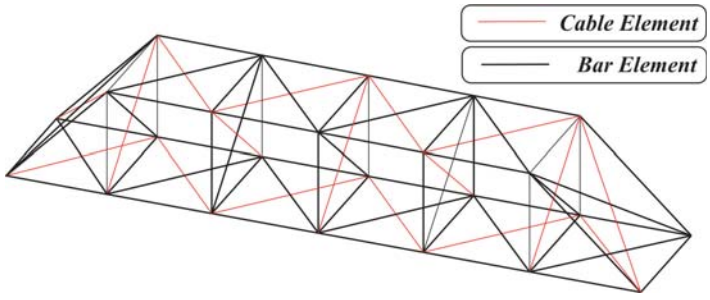

Fig. 1: Cable-Truss Structure.

As for trusses, planar cable-trusses idealization is subject to three main assumptions: (1) all external forces are applied at joints; (2) joints are considered frictionless hinges; (3) each element is only subjected to axial stress, which are constant along its length.

Planar cable-truss structures having simple configurations and fewer members can be solved analytically, however for complex cable-truss systems numerical procedures are needed. Structural static response is usually computed by nonlinear finite element iterative procedures, where the numerical model is based on the characteristics of structural members, which can be simulated as bar element (compression-tension) or cable element (tension-only). The formulation of such elements is presented along the following lines.

The stiffness of a bar element, shown in Figure 2, is given by $E_b A_b / L_b$, where E_b is the modulus of elasticity, $A_b$is the cross-sectional area and L_b is the length. This stiffness is projected into two-dimensional space composing a 4x4 element matrix. Considering that the material is linearly elastic and loads are applied at nodes, the elastic stiffness matrix, $[k_b]_e$, for one node of the bar element can be written as:

$$[k_b]_e = \frac{E_b A_b}{L_b}\begin{bmatrix} l^2 & lm \\ lm & m^2 \end{bmatrix}, \tag{1}$$

where, l and m are direction cosine values of the angles between local axis, x̃, and global axes, X and Y, as depicted in Figure 2a. This way, there is no need of coordinates transformation.

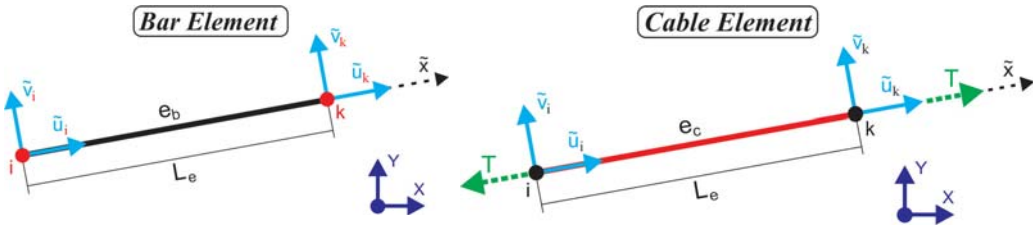

(a) (b)

Fig. 2: Bar and Cable Elements

Note that, though, cables exhibit geometrically nonlinear behavior which demands nonlinear analysis as strains are small but displacements are large as a reason of high flexibility. Moreover, cables cannot resist shear, axial pressure forces or bending moments (Nuholgu, 2010, Karoumi, 1999). Therefore, structural analysis of systems having cable elements is relatively complex since linear analysis, where elastic deformations and displacements are assumed to be small, is not often applicable and calculations divergence occurs rather frequently (Nuholgu, 2010).

If the material is linearly elastic material and forces are applied just in nodes, the stiffness matrix for only one node of planar cable element, $[k_c]_e$, can be written as the sum of its elastic and geometrical stiffness matrices, $[k_E]_e$ and $[k_G]_e$, respectively. In order to avoid coordinate transformations the stiffness matrix can also be expressed in terms of direction cosines between local and global axes as shown in Eq.2.

$$[k_c]_e = [k_E]_e + [k_G]_e = \frac{E_c A_c}{L_{c0}}\begin{bmatrix} l^2 & lm \\ lm & m^2 \end{bmatrix} + \frac{T}{L_c}\begin{bmatrix} (1-l^2) & -lm \\ -lm & (1-m^2) \end{bmatrix}, \tag{2}$$

where E_c is the cable elasticity modulus, A_c is the cable cross-sectional area, L_{c0} is the initial length of the element and L_c is the current length of the cable element. Note that, T relates to the applied tightening force usually applied to the system in order to increase cable rigidity. Sag effect in cables is taken into account by considering null tension on the element once it is submitted to compression.

The global stiffness matrix, $[K_g]$, of the cable-truss structure is then assembled by combining cable and bar elements for a determined topology, as defined in Eq.3.

$$\left[K_g\right] = \sum_{e=1}^{N} \left[k_i\right]_e, \tag{3}$$

where $\left[k_i\right]_e$ is the stiffness matrix of bar or cable element and N is total number of elements. After the assembly of global stiffness matrix and inclusion of support conditions the global set of equilibrium equations is formulated as:

$$\left[K_g\right]\{q\} = \{F_e\} + \{F_T\} = \{F\}, \tag{4}$$

where $\{q\}$ is the displacement vector, $\{F_e\}$ is the external imposed loads, and $\{F_T\}$ is the vector of initial nodal forces, which is computed based on the tightening forces applied to cable elements. It is important noting that the vector of initial nodal forces is design-dependent through the change of element length, positioning and initial strain applied to each element.

The solution of the nonlinear equations is not trivial because the stiffness of cable elements can be affected by its displacement. Thus, algorithms are needed to compute static structural response of the cable-truss structure. The most commonly used method is the so called Newton-Raphson method, which corresponds to an iterative procedure that uses the estimation of the structural response from previous steps, requiring several iterations before the system attains equilibrium. At the beginning of $(i-1)$ steps the imbalance force (residual force), R, can be written as:

$$\left\{R\left(\{q\}^{i-1}\right)\right\} = \left[K_g\right]\{q\}^{i-1} - \{F\}, \tag{5}$$

If the imbalance force at the beginning of the i-th step, $\left\{R\left(\{q\}^{i}\right)\right\}$, is expanded in a low order Taylor series, hence:

$$\begin{aligned} \left\{R\left(\{q\}^{i}\right)\right\} &= \left\{R\left(\{q\}^{i-1}\right)\right\} + \left.\frac{\partial R}{\partial \{q\}}\right|_{\{q\}^{i-1}} \delta\{q\}, \\ &= \left\{R\left(\{q\}^{i-1}\right)\right\} + \left[K_g\right]_{\{q\}^{i-1}} + \delta\{q\}, \end{aligned} \tag{6}$$

where $\{q\}^{i-1}$ is the displacement vector in the *(i-1)th* step. Setting $\left\{R\left(\{q\}^{i}\right)\right\} = 0$ it is possible to find the increment in displacement created by the imbalance force by solving the system:

$$\delta\{q\} = -\left(\left[K_g\right]_{\{q\}^{i-1}}\right)^{-1}\left(\left[K_g\right]\{q\}^{i-1} - \{F\}\right). \tag{7}$$

Nodal displacements are then updated using increments obtained in equation (7):

$$\{q\}^{i} = \{q\}^{i-1} + \delta\{q\}. \tag{8}$$

The above steps are repeated until the ratio of magnitude of the displacement increment vector to the previous displacement is met, which corresponds to the convergence criteria usually adopted. For further details of Newton-Raphson procedures see (Bathe, 1996).

3. Discrete Topology Optimization

The proposed discrete topology optimization method searches for the best interconnectivity between nodes, and also for the elements in each interconnection. For that, ground structure approach is used, in which all possible interconnections are performed based on an initial grid of nodes, as illustrated in Fig.3.

Note that, increasing the amount of nodes in the ground structure sharply increases the number of feasible solutions since more structural elements are used for forming the cable-truss system. Moreover, the nodes from ground structure can be deactivated when they are not used, however, these nodes cannot be moved during the optimization process.

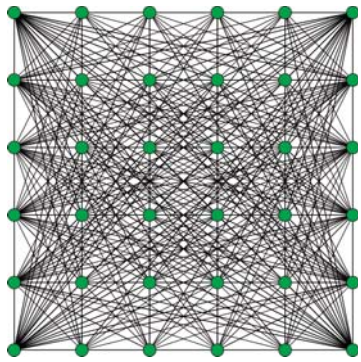

Fig. 3: Planar Gournd Structure

Since the main target in the lightweight design is to obtain optimal mass reduction with minimal losses in stiffness, topology optimization has been adopted in this work. Such method not only presents benefits regarding material saving, but also can be used as a first step in a multi-level optimization process (Carlos, 2000).

To achieve more complex structures, modular design can be used decrease design parameters when modeling cable-trusses. Such approach is commonly used in truss design, e.g., crane structures as illustrated in Fig.4a. Modularity in design consists in patterning basic modules to form more complex structures, as shown in Fig.4b. It can be also noticed that building time and cost is reduced by using a limited number of cross-sections in its structural members.

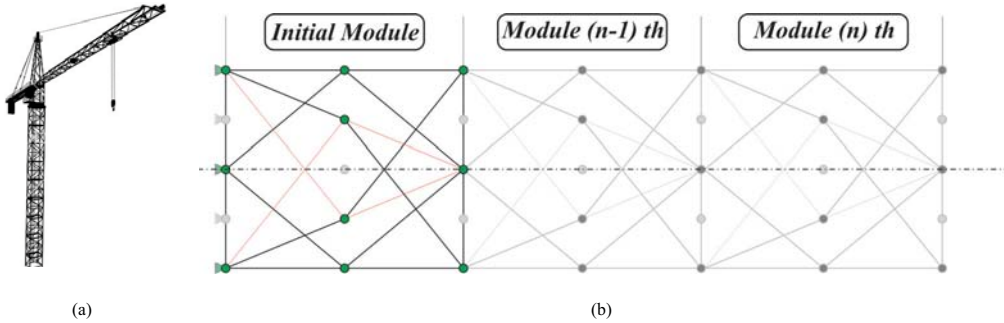

Fig. 4: Modular Design in Truss(a) and Cable-truss structures(b).

In order to attend lightweight requirements, the optimization process criteria should take into account the stiffness of the structure as well as its mass. Stiffness analysis can be performed through the definition of the overall system stiffness using the Cartesian stiffness matrix (Carbone, 2010). One of the possible uses of this approach consists in: a) selecting a specific node which characterize the structural behavior, b) loading the structure, and c) evaluating the displacements on the selected node to determine in which direction the structure presents higher stiffness. By this approach, the structural stiffness-to-mass ratio can be written as follows:

$$stm = \left(\frac{F_{jl}}{q_{il}}\right) m_t^{-1}, \tag{9}$$

where F_{jl} is the force applied at node j in the direction l, q_{il} is the displacement of node i in the direction l, and m_t is the total mass of the structure. Such index for stiffness performance has the advantage of having full physical meaning for single loading cases. Nonetheless, it does not take into consideration structural stiffness in different directions, which may lead to structures with reduced isometric stiffness properties.

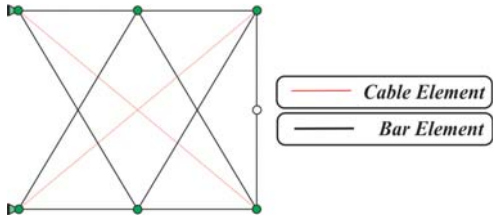

Fig. 5: Kinematically stable cable-truss structure

In addition, during the stochastic search of the optimal topology several kinematically instable or structurally invalid structures appear (Su 2009). Such structures, exemplified in Fig.5, should be filtered in order to increase convergence and decrease computational cost. Consequently, the filter presented in Eq.10, evaluates the degrees of freedom (dof) of the structure, which must be lesser or equal to 0.

$$dof_s = 2n_s - m_s - c_s, \tag{10}$$

where n is the number of nodes being actively used in the structure, m_s is the number of members, and c_s is the number of degrees of freedom. Note that, the subscript s implies that the aforementioned equation refers to each structure being evaluated during the stochastic search instead of the ground structure. In this sense, the optimization problem can be formulated as:

$$\begin{cases} \max \Rightarrow stm_s = (stiffness - to - mass\ ratio) \\ s.t. \\ dof_s \leq 0\ (Kinematical\ Stability\ Constraints) \end{cases}. \tag{11}$$

4. Genetic Algorithms

Genetic Algorithms (GAs) are adaptive methods which can be used for searching and optimization problems, performing a stochastic search and optimization. Compared to traditional optimization methods, such as calculus-based and enumerative strategies, GAs are robust, global, and may be applied generally without recourse to domain-specific heuristics. Although performance is affected by these heuristics, EAs operate on a population of potential solutions, applying the principle of survival of the fittest to produce successively better approximations to a solution (Mitchell, 1996, Han, 2002).

Individuals in a population compete for resources and mates. Those individuals most successful in each competition, e.g., the structures with higher stiffness to mass ratio, will produce more offspring than those that performed poorly. Genes from fittest individuals propagate throughout the population so that two good parents will sometimes produce offspring that are better than either parent. As a consequence, each successive generation will become more suited to their environment. To sum up, it can be said that GAs aim to use selective breeding of the solutions to produce offspring better than the parents by combining information from the chromosomes (Mitchell, 1996). In addition, GAs uses highly customizable genetic operators; selection, cross over and mutation, to perform the search for the optimal solution.

Traditional binary-vector encoding is commonly used for discrete topology optimization of trusses (Hajela, 1995, Balling, 2006). In order to encode cable-truss structures element properties have been encoded into integer numbers (0, 1 and 2), where 0 represents disconnection between two nodes, 1 and 2 relates to bar and cable element, accordingly.The GA with Nonlinear finite element solver used in this work was programmed in MATLAB. The logic of the program flows as shown in Fig.6 and in the procedure below:

[1.Start]: User provides number of nodes used, slenderness ratio of the structure, applied loads, and geometrical information about bars and cables.

[2.Generation of Ground Structure]: Symmetric ground structure is build using nodal matrix provided by user.

[3.Initial population]: Generate random population of n chromosomes (suitable solutions for the problem).

[4.Stability and Validity Checking]: Eq.10 is used to determine kinematically instable structures, which are repaired and reinserted into the population. The repair operation consists in stochastically adding bars to the original structure until stability is achieved.
[5.Decoding] : Population is decoded into bars, cables and disconnections.

[6.Nonlinear Structural Analysis]: Newton-Raphson procedure, see section 2, is used for computing static structural response and stiffness-to-mass ratio for each individual of the population.

[7.Evaluation] If the best solution of the population is better than the previous overall solution found by the algorithm, then the overall solution is updated. Otherwise, the worst individual of the current population is substitute by previous best solution.

[8.Test] If the end condition is satisfied, go to step [11]. If not, go to next step.

[9.New population] Create a new population by repeating following steps until the new population is complete:

> **[Selection]** Select two parent chromosomes from a population according to their fitness (the better fitness, the bigger chance to be selected).
>
> **[Crossover]** With a crossover probability of 0.9, cross over the parents to form a new offspring (children).
>
> **[Mutation]** With a mutation probability of 0.1, mutate new offspring at each locus (position in chromosome).

[10.Loop] Return to step [4].

[11.End] Best structure is stored.

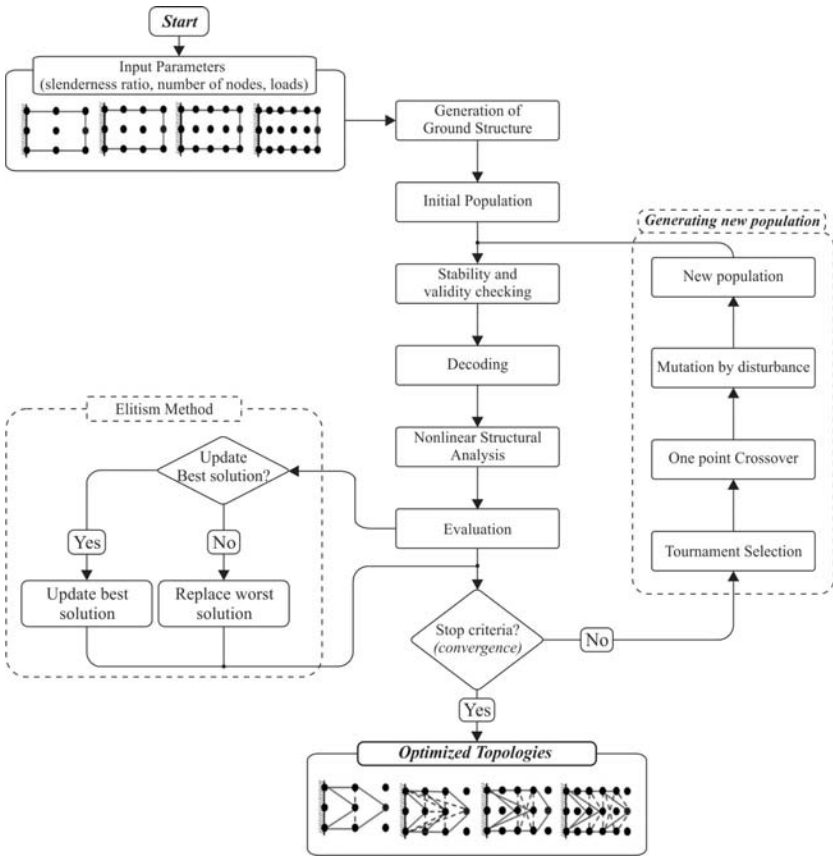

Fig. 6: GA applied to topology optimization of Cable-Trusses

5. Study Case - Cantilever Optimization

The design of optimal planar cable-trusses comprises the choice of several design parameters, such as, the ratio between cable and bar cross section areas, pre-stress, slenderness ratio (sl) of the structure, materials, among others. Discrete topology optimization was performed for a robotic arm which is approximated by a horizontal cantilever beam, an additional constraint was used for maintaining a minimum set of nodes which represents the structure. After obtaining the optimal topology, the structure is analyzed using different number of modules increasing the slenderness ratio. In all configuration the structure is submitted to a punctual load of 500N in the mid of the end of the last column of nodes, as shown in Fig.7.

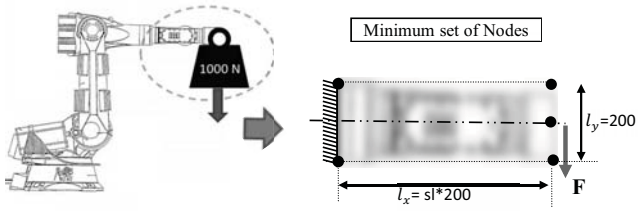

Fig. 7: Study case boundary conditions

The main input parameters for the algorithm are the cross section areas bars and cables which are $700\,mm^2$ and $40\,mm^2$ respectively, the strain on cables have been considered as 5.2e0-5, the population for simulations has been selected as 80 and the number of iterations as 5000, each simulation has been repeated 3 times and best results were selected for each structure.

The simulations compares the results in terms of stiffness-to-mass ratio for Cable-Truss and Truss structures under the same environment and boundary conditions, the target is to analyze which structure provides higher stiffness to mass ratio. Using a ground structure with fifteen nodes, as shown in Fig.8a., the method proposed searched for maximum stiffness-to-mass ratio. Same environment and boundary conditions are used for optimizing truss and cable-truss structures. Results of the topology optimization are shown in Fig.8.

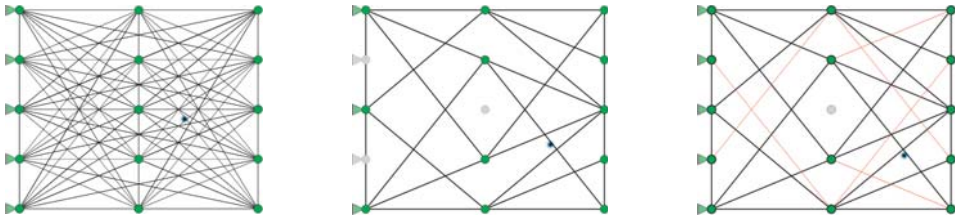

Fig.8: Optimal Structures obtained by discrete topology optimization

Structures obtained during topology optimization were used as initial modules to build more complex structures. It is important noting that by increasing the number of modules the slenderness ratio of the structure increases in the same proportion. Structures containing from 1 to 10 modules, where Fig. 9 depicts structures using 10 modules, were analyzed and results are shown in table 1.

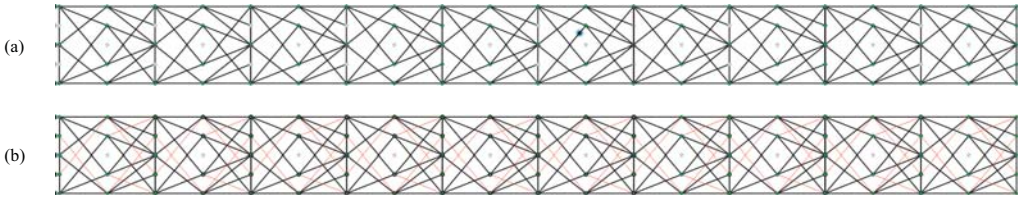

Fig. 9: a) Truss Structure using10 Modules b) Cable-truss Structure using10 Modules

Tab. 1: Stiffness to mass ratio of Optimized Structures.

	Truss (S-t-m)	Cable truss (S-t-m)
Sl=1	44996.79966	48149.45852
Sl=2	4835.850861	5193.808638
Sl=3	1019.162564	1103.527095
Sl=4	322.5478356	351.0791844
Sl=5	130.7810331	142.8265765
Sl=6	62.38712922	68.28822800
Sl=7	33.35000572	36.56401106
Sl=8	19.38779245	21.28215362
Sl=9	12.01891870	13.20573900
Sl=10	7.838589176	8.619098703

As it can be seen on the simulation results table, Cable-Truss structures presented higher stiffness-to-mass ratio in all cases, presenting average improvement 8.9% when compared to optimized Truss structures, as shown in Fig.10.

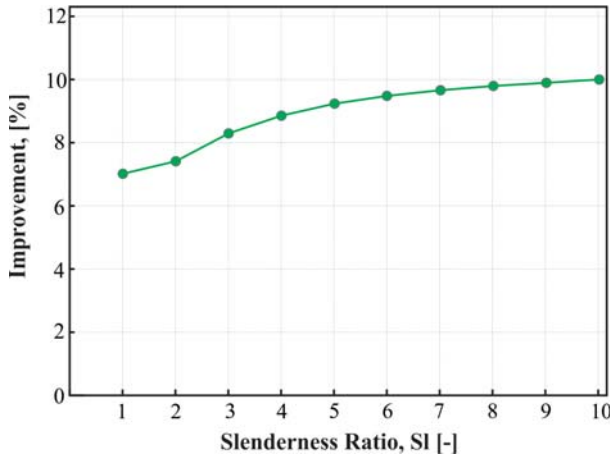

Fig. 10: Improvement in S-t-m of Cable-Trusses in comparison with Trusses

Furthermore, the length of the vector which encodes individuals increases quickly with the growth problems scale, leading the GAs to have troubles in convergence. Such problem is potentialized when analyzing cable-trusses since: a) the number of possible elements to interconnect to nodes increases the number of feasible solutions, b) cables cannot resist compression leading thus to a sharp increase in the number of kinematically instable structures during the stochastic search, and c) the evaluation of Eq.4 requires the use of iterative solution, which is computationally costly since inversion of the stiffness matrix must be performed several times.

6. Conclusions

In this article, a methodology for topology optimization of cable-trusses was presented. By combining Genetic Algorithm and Nonlinear Finite Element Method optimized cable-trusses were found. Such structures where obtained for an initial module, which was then patterned in order to form more complex structures.

Comparisons between optimized symmetric truss and cable-truss structures were performed for different number of modules. Results indicated that, in all cases, the stiffness-to-mass ratio of cable-trusses was higher than those obtained for trusses. Moreover, optimized symmetric cable-trusses have shown an average improvement of 8.9% when compared to optimized symmetric truss structures.

For further maximization of the stiffness-to-mass ratio complementary analysis are recommended. These include, for instance, optimization of cable-trusses considering the use of different modules as the slenderness ratio increases. As result, such study shall bring higher stiffness-to-mass ratio since the topology of the initial module may change as more modules are being used.

Acknowledgements

Our thanks to the research project GACR 101/08/H068, Research of new principle of mechanical and biomechanical systems with intelligent behavior, and to the European Brazilian Network of Academic Exchange (EUBRANEX) for funding this research.

References

Balling, R. J., Briggs, R. R., Gillman, K. (2006) Multiple optimum size/shape/topology designs for skeletal structures using a genetic algorithm, *Journal of Structural Engineering*, vol. 132, pp. 1158-1165.

Bathe K. J. (1996) *Finite Element Procedures*, Prentice Hall.

Carbone G., Ceccarelli M. (2010) Comparison if indices for stiffness performance evaluation., *Frontiers of Mechanical Engineering in China*, Volume 5, Number 3, pp.270-278.

Carlos A. et al. (2000) Multiobjective Optimization of Trusses using Genetic Algorithms, *Computers and Structures,* Vol. 75 , pp. 647-660.

Hajela, P., Lee, E. (1995) Genetic algorithms in truss topological optimization, *International Journal of Solids and Structures*, vol. 32, pp. 3341-3357.

Han, K., Kim, J. (2002) Quantum-Inspired Evolutionary Algorithm for a Class of Combinatorial Optimization. *IEEE Transactions on evolutionary computation,* Vol. 6, No. 6, pp. 20-40.

Karoumi R. (1999) Some modelling aspects in the nonlinear finite element analysis of cable supported bridges, *Computers and Structures* 71, pp.397-412.

Leonard J. W. (1988) *Tension structures*. New York: McGraw-Hill.

Liao, L., Baisong, Du. (2009) Finite Element Analysis of Composite Truss Structures Containing Pre-tensioned Cables, *The Seventeenth Annual International Conference on Composites (ICCE-17)*, pp. 56-58.

LsAA, (2010) Lightweight Structures Association of Australasia, *Lightweight structures Definition*. Available at http://www.lsaa.org/, June, 2010.

Mitchell, D. M. (1996) *An Introduction to Genetic Algorithms*. MIT Press.

Rajan, S. D. (1995) Sizing, shape, and topology design optimization of trusses using genetic algorithm, J*ournal of Structural Engineering*, vol. 121, pp. 1480-1487.

Rozvany, G. I.(2001) Aims, scope, methods, history and unified terminology of computer-aided topology optimization in structural mechanics, *Structural and Multidisciplinary Optimization*, vol. 21, pp 90-108.

Rozvany, G. I. N. (2009) A critical review of established methods of structural topology optimization, *Structural and Multidisciplinary Optimization* vol. 37, pp. 217-237.

Su, R., Gui, L., Fan, Z. (2009) Topology and Sizing Optimization of Truss Structures Using Adaptive Genetic algorithm with Node Matrix Encoding, *Fifth International Conference on Natural computation*, IEEE Computer Society. pp. 485–491.

18th International Conference
ENGINEERING MECHANICS 2012
Svratka, Czech Republic, May 14 – 17, 2012

pp. 255–261
Paper #6

RESONANCE BEHAVIOUR OF SPHERICAL PENDULUM – INFLUENCE OF DAMPING

C. Fischer, J. Náprstek, S. Pospíšil*

Abstract: *Experimental and numerical model of a uni-directionally driven pendulum-based tuned mass damper is presented in the paper. Stability of the motion in a vertical plane is analysed in the theoretically predicted resonance region. For the experimental part, special experimental frame is used, allowing independent change of linear viscous damping in the both perpendicular directions. The introduced damping is. Mathematical model respects the non-linear character of the pendulum and allows to introduce asymmetrical damping. Sensitivity of the resonance behaviour on the change of damping in both directions is studied and commented in the paper. The stability of the system is analysed experimentally and compared with numerical and theoretical results.*

Keywords: ***spherical pendulum, tuned mass damper, damping***

1. Introduction

A typical tuned mass damper is a pendulum. This low cost passive device used at tall masts and towers is very popular for its reliability and simple maintenance, see e.g. (Haxton, 1974; Náprstek and Pirner, 2002). However, dynamic behaviour of such substructure is significantly more complex than it is supposed by widely used simple linear single degree-of-freedom (SDOF) models working in one vertical plane. Such a conventional linear model is satisfactory only if the amplitude of kinematic excitation at the suspension point is very small and if its frequency remains outside a resonance frequency domain, which is possible only at the cost of lower efficiency of the damper. To improve the design of pendulum, a spherical pendulum should be considered.

The detailed review of the topic has been published by the authors recently in (Pospíšil et al., 2011). The mathematical model follows the approach presented in (Náprstek and Fischer, 2009). However, some historical remarks is worth to mention.

Auto-parametric systems have been intensively studied for the last four decades. The horizontally forced spherical pendulum was first studied by Miles (1962), who considered this problem of the stability of planar oscillations with respect to non-planar perturbations for small amplitude forcing in a neighbourhood of resonance using truncated equations. He found that planar solutions become unstable with respect to non-planar perturbations in particular parameter ranges and that there are stable non-planar oscillations. A more detailed later study (Miles, 1984) analysed a number of bifurcation diagrams for planar and non-planar motions as well as chaotic motion. Some experimental results have been presented by (Triton, 1986), where a good agreement with the theoretical results is demonstrated.

The present article exploits the analytical approach to the subject described in (Náprstek and Fischer, 2009) and compares it with some experimental findings. The movement of the pendulum is described in two coordinates θ, φ on a spherical surface respecting the non-linear interaction of both components, or in two cartesian coordinates ξ, ζ, representing the projection of the pendulums bob to the x, y plane. It means that the pendulum response is described by a system of two second-order non-linear ordinary differential equations. Interaction of both equations follows from non-linear terms only.

In the experimental as well in numerical approach the uni-directional harmonic excitation is supposed. If the excitation frequency belongs to the resonance region, post-critical states can emerge. These

*RNDr. Cyril Fischer, Ph.D., Ing. Jiří Náprstek, DrSc., doc. Ing. Stanislav Pospíšil, Ph.D.: Institute of Theoretical and Applied Mechanics, AS CR, v.v.i., Prosecká 76, Prague 9, Czech Republic, e-mail: {fischerc|naprstek|pospisil}@itam.cas.cz

states are characterized by either highly increased in-plane response, or by more or less complicated space trajectories of various types. The shape of this motion stabilizes for increasing frequency in a nearly elliptic "horizontal" trajectory. Above the upper limit of the resonance domain an existence of a stable deterministic solution in the vertical plane resumes. The existence and stability level of individual solutions or response types are dependent on pendulum geometry and excitation structure. It is obvious that such a type of response destroys effectiveness of the tuned mass damper.

In this article, a pendulum is examined using a specially developed experimental rig. It contains kinematically driven pendulum suspended from the Cardan joint. The damping can be arbitrarily adjusted by means of two independent magnetic units attached to the frame and to the supporting axes of rotation. These units are able to reproduce the linear viscous damping for both degrees of freedom. The stability of the system is analysed experimentally and numerically for several values of the damping.

2. Mathematical model

The spherical pendulum will be considered as a strongly non-linear dynamic system with kinematic external excitation in the suspension point, see Fig. 1.

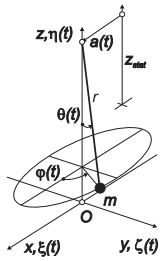

Fig. 1: Outline of the idealized model

The mathematical model follows from the balance of kinetic and potential energies. Using Hamilton's principle, an approximate Lagrangian system in x, y-coordinates for components ξ, ζ can be obtained (see detailed derivation in (Náprstek and Fischer, 2009)):

$$\left.\begin{aligned} \ddot{\xi} + \frac{1}{2r^2}\xi\frac{\mathrm{d}^2}{\mathrm{d}t^2}(\xi^2+\zeta^2) + 2\beta_\xi\dot{\xi} + \omega_0^2\left(\xi + \frac{1}{2r^2}\xi(\xi^2+\zeta^2)\right) &= -\ddot{a} \qquad (a) \\ \ddot{\zeta} + \frac{1}{2r^2}\zeta\frac{\mathrm{d}^2}{\mathrm{d}t^2}(\xi^2+\zeta^2) + 2\beta_\zeta\dot{\zeta} + \omega_0^2\left(\zeta + \frac{1}{2r^2}\zeta(\xi^2+\zeta^2)\right) &= 0 \qquad (b) \end{aligned}\right\} \tag{1}$$

The viscous damping has been introduced in a form of the Rayleigh function and denoted as β_ξ, β_ζ in (1). Accuracy of the mathematical model depends on the amplitude of the response, as the assumption of the small angle θ has been adopted. Natural frequency ω_0 of the corresponding linear pendulum is given by $\omega_0^2 = g/r$, where r is the suspension length of the pendulum and g is the gravitational acceleration. Neglecting the non-linear terms in (1), the system would broke up into two independent linear equations. Thus, the interaction of both the equations is given by non-linear terms only.

As the harmonic excitation $a(t) = a_0 \sin(\omega t)$ acts in the ξ direction only, the basic type of motion takes course in the vertical (xz)-plane if the time history starts under homogeneous initial conditions. With increasing amplitude of the excitation $a(t)$, the auto-parametric stability loss can occur and the post-critical state of the auto-parametric resonance arises.

3. Experimetnal analysis

The stability problems are, in general, very sensitive to boundary and initial conditions. Therefore, any simulation machine and its mechanical parts needs to be well prepared and manufactured to avoid

creating parasitical influences, which are very difficult to eliminate. This applies not only to a complicated kinematic mechanism but also to the relatively simple spherical pendulum. The authors use an experimental pendulum, designed to comply the assumptions of the theoretical and numerical model. This pendulum is suspended from Cardan joint attached to a trolley moving on two parallel miniature rails. Two magneto-dynamic units allow to introduce viscous damping in the practically full range from (almost) zero to the critical value. For detail of the set-up see (Pospíšil et al., 2011).

The length of the pendulum was 0.41 m, mass of its bob was significantly greater than it was in the previous experiments to increase inertia and thus to lower the minimal relative damping. Fundamental eigenfrequency of the pendulum was measured as $f_0 = 0.76$ Hz, i.e. $\omega_0 = 4.8\text{rad} \cdot \text{s}^{-1}$. Response of the pendulum was measured for excitation frequencies ranging from $f_l = 0.73$ Hz to $f_u = 0.97$Hz with increments $\Delta f = 0.002$ Hz, (i.e. range $\omega = 4.587 \ldots 6.095\text{rad} \cdot \text{s}^{-1}$). To cover the full range of the resonance interval, the each sweep was started for excitation frequency slightly higher than the eigenfrequency of the pendulum and small initial disturbance was given to the pendulum. Then was the excitation frequency gradually changed in small increments up or down to cover the whole frequency range. Each frequency was kept constant for three minutes and angles of the pendulum were measured and recorded. To eliminate the transition effects, only the last minute of each record was taken into account in the post-processing.

Figure 2 shows maximal and minimal measured amplitudes ($^\circ$) depending on the excitation frequency ($\omega, \text{rad.s}^{-1}$). Responses for several values of damping coefficients ($\beta_\xi = \beta_\zeta = 0.04, \ldots 1.2$) are shown in the individual rows. The alongside ξ and transversal ζ components are in the left and right hand columns respectively. Three curves are present in each plot, they represent maximal, minimal and mean values of the amplitudes. When all three curves coincide, the response of the pendulum is harmonic. If the minimal and maximal curve form a stripe, multi-harmonic or chaotic type of the response takes place. However, this simple criterion is not able to distinguish chaotic and multi-harmonic response.

4. Numerical analysis

In order to get an overview concerning the system behaviour in the vicinity of resonance frequency intervals several numerical analyses using the governing differential system (1) have been performed. For numerical simulation, default numerical procedure NDSolve from package Wolfram Mathematica and $M = 2$ variant of implicit Gear method (routine `gear2`) from the GNU Scientific Software Library (Galassi et al., 2009) have proved themselves to be the most stable and efficient. Adaptive step control is used in both numerical methods. Due to a high number of necessary simulation to obtain a single resonance curve, the parallel algorithm has been developed to exploit the computational power of the 2 cpu / 16-thread computer.

To assess the correspondence of numerical simulation and experimental results, let us compare the Figs 2 and 3. The both figures show the resonance curves, obtained form measured and computed data respectively. The qualitative behaviour in the lower end of the resonance interval is rather comparable. On the other hand, a quite significant difference can be seen in the upper part of the studied frequency interval, namely for low damping coefficients $\beta_\xi = \beta_\zeta \in \{0.04, 0.05\}$. It appears, that the experimental pendulum was able to follow the (less stable) upper branch of the solution during the sweep-up simulation much better than it was the numerical solution. This behaviour is also different from the measurements published by the authors in (Pospíšil et al., 2011). It seems that the only explanation for such a "stability on upper branch" is the increased mass of the bob of the pendulum. It is worth to mention, that after some change in the excitation or other noticeable artificial disturbance the pendulum jumped to the standard (lower and planar) stable branch of the response.

It is necessary to confess, that quantitative agreement between numerical simulation and experimental results for a single set of input parameters and a single time history was not so good. Even for carefully selected initial conditions the numerical model was not able to follow the trajectory of the experimental pendulum. This behaviour is not surprising, as the mathematical model (1) has been derived with the assumption of small amplitude of the response. Moreover, the significant dependence of instant frequency of the response on its instant amplitude is clearly seen from the experimental data.

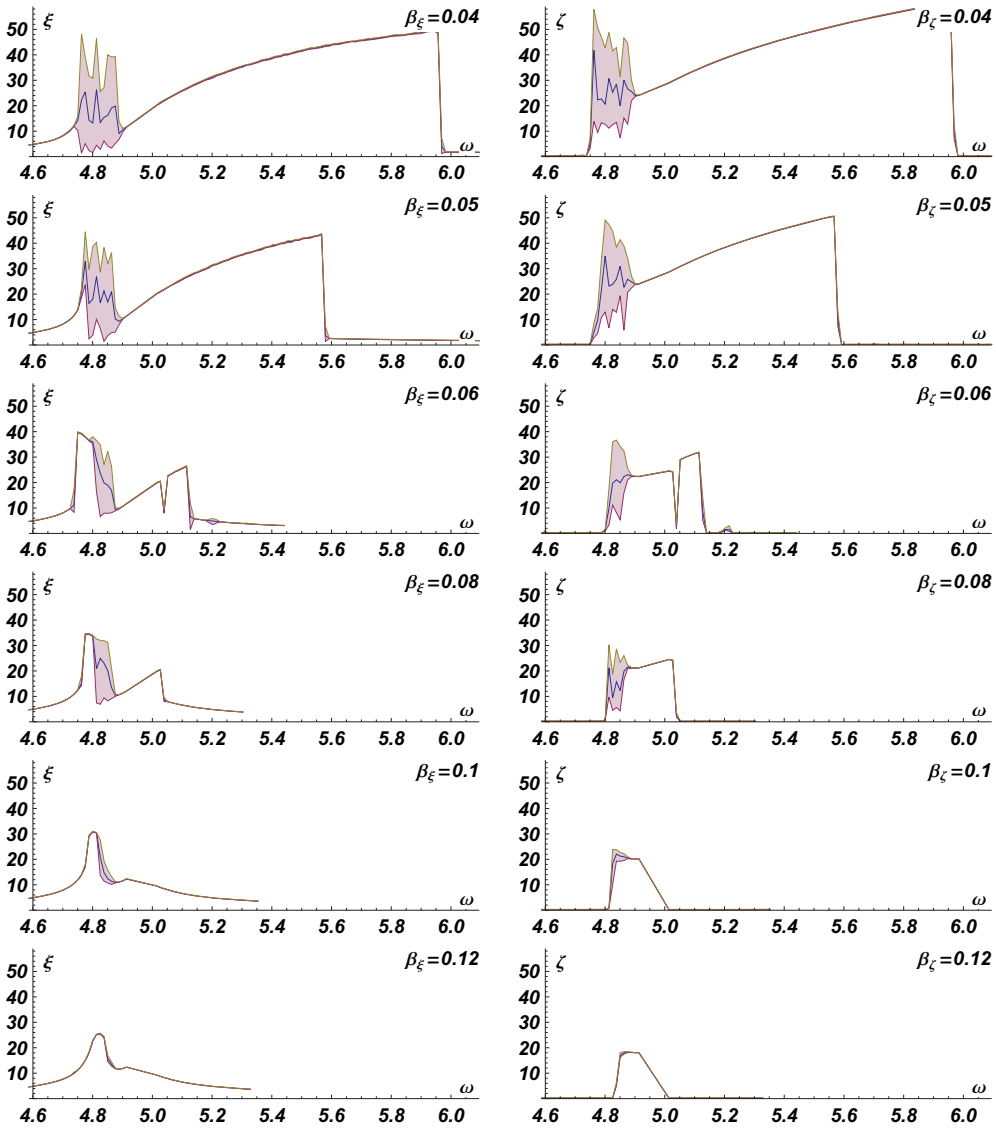

Fig. 2: Experimental pendulum: measured amplitudes ($\cdot^\circ$) of the response depending on excitation frequencies $\omega = 4.6 \ldots 6.1\,\mathrm{rad.s}^{-1}$ for several values of damping coefficients, same in the both directions. Longitudinal movement (ξ) is on the left hand side, transversal response (ζ) on the right hand side. For each plot, maximal, minimal and mean amplitudes are shown.

Having roughly assessed the validity of the numerical model introduced by Eq. (1) let us study the influence of individual damping coefficients on the overall response of the system in the both directions. The figure 4 shows selected results obtained during the extensive parametric study. For the interval of excitation frequencies $\omega \in (4.6, 6.1)$ and the values of damping coefficients $\beta_\xi, \beta_\zeta \in (0.005, 0.12)$, the equation (1) was repeatedly integrated and the maximal amplitudes in both directions was recorded. There are 10 pairs of colour plots in figure 4. Each pair corresponds to a single excitation frequency $\omega \in \{4.7, 4.72, \ldots, 4.88\}$ to cover area surrounding the eigenfrequency of the pendulum. In each pair, left plot shows response in longitudinal direction (ξ) and right plot corresponds to the transversal direction. Values on the horizontal axis of each plot represent the damping coefficients β_ξ, whereas the vertical axis stands in values of the damping coefficients β_ζ. Finally, the colour map shows the distribution of

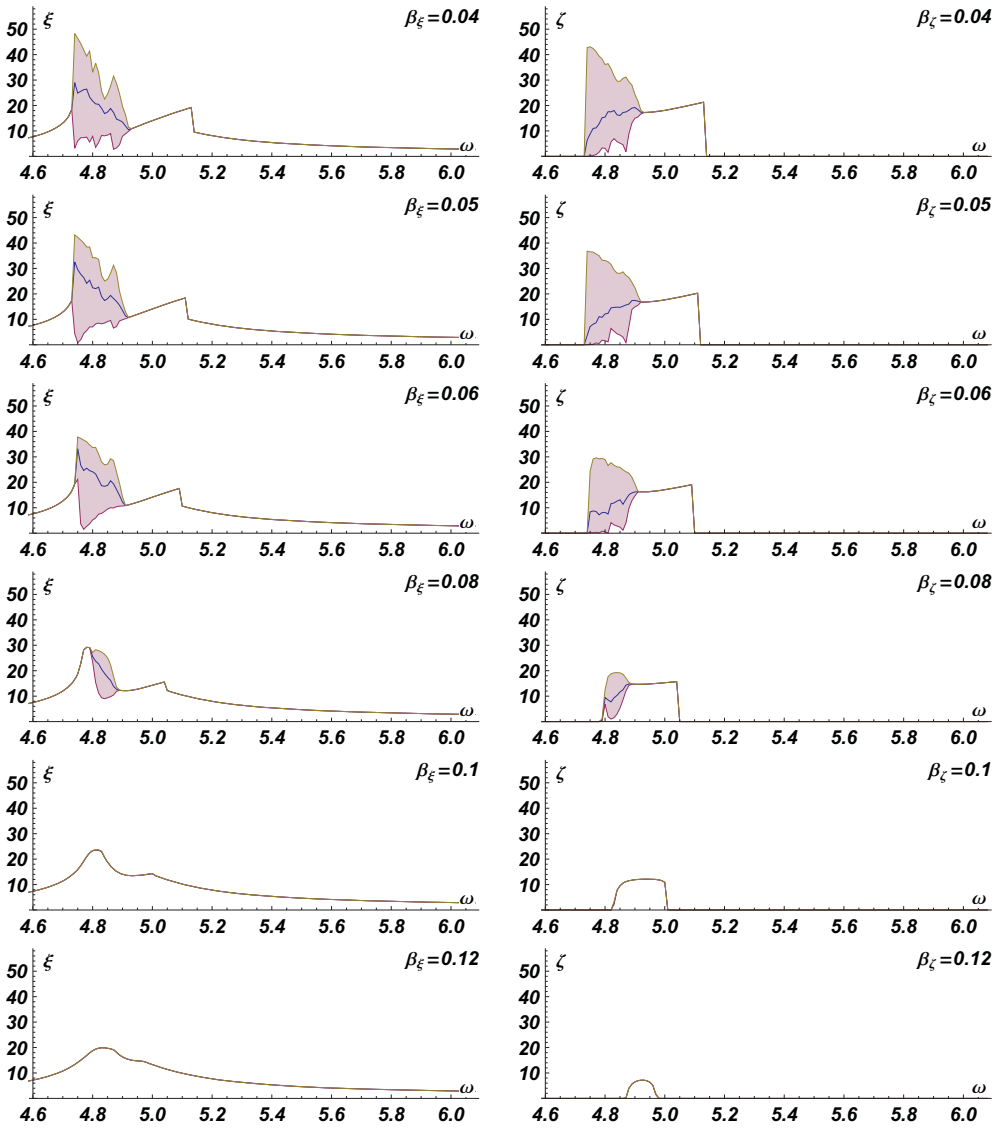

Fig. 3: Numerical integration: computed amplitudes ($\cdot^\circ$) of the response depending on excitation frequencies $\omega = 4.6 \ldots 6.1\,\mathrm{rad.s}^{-1}$ for several values of damping coefficients, same in the both directions. Longitudinal movement (ξ) is on the left hand side, transversal response (ζ) on the right hand side. For each plot, maximal, minimal and mean amplitudes are shown. Parameters of the model were chosen to meet geometrical properties of the experimental set-up.

the maximal amplitudes of xi and ζ in the left and right plot respectively. The dark blue colour indicates negligible or small amplitude of the response, whereas bright yellow and brown colours show the high response. The black dots in the each plot point at the discrete values of β used in simulation.

Several remarks can arise from observation of the figure 4. Firstly, it appears, that the presence of the spatial character of the system response does not depend significantly on the value of damping coefficient β_ζ (transversal motion). Similarly, the overall amplitude of the response seems to be influenced mostly by β_ξ (longitudinal motion) and far less by β_ζ. Secondly, the spatial response in the lower part of the resonance interval have higher amplitudes, but can be suppressed by smaller values of damping β_ξ. The lower amplitudes which appear in the upper part of the resonance interval need higher damping β_ξ to be

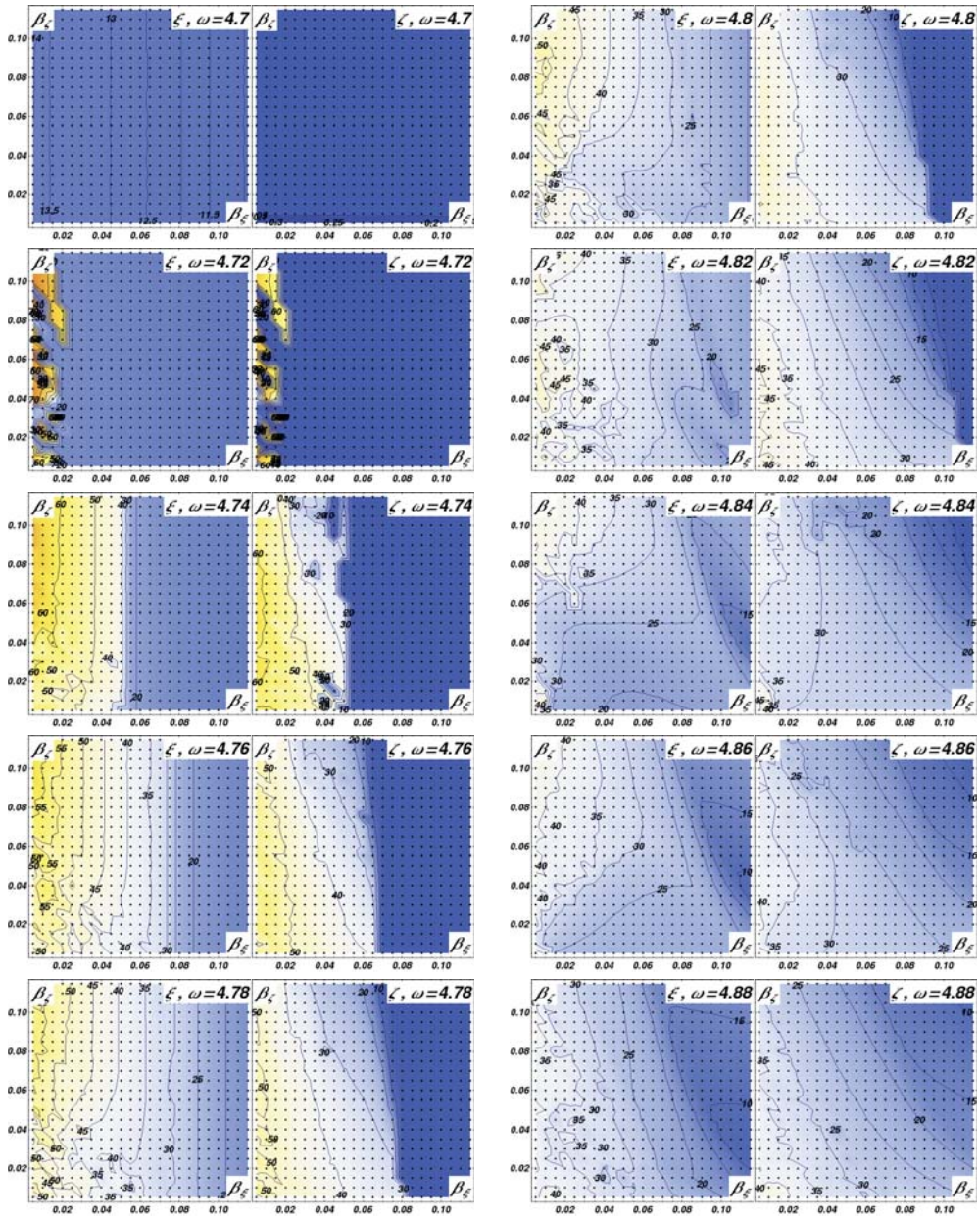

Fig. 4: Maximal amplitude of the response depending on the values of damping coefficients in the both directions $\beta_\xi, \beta_\zeta \in (0.005, 0.12)$ for excitation frequencies $\omega =\in \{4.7, 4.72, \ldots, 4.88\}$. For each frequency the left plot shows response in longitudinal direction (ξ) and right plot corresponds to the transversal direction.

wiped off. Third, it is not always true, that the higher damping (in transversal direction) automatically means the lower response (cf. ξ plots for $\omega > 4.78$ in fig. 4).

There are some problematic points in the presented study. Firstly, the complete bunch of simulation was performed with fixed initial conditions, more or less randomly chosen. Thus, this numerical analysis was not able to cover up the variety of possible stable branches. Secondly, remarks from the previous paragraph can be roughly explained form the structure of the equation (1). It is not clear, whether they

represent the behaviour of a real pendulum, or just its mathematical idealization. The further experimental study should cover up at least some cases of unsymmetrical damping.

5. Conclusions

It has been shown before that widely used linear model of the damping pendulum is acceptable only in a very limited extent of parameters concerning pendulum characteristics and excitation properties. In this work, two degrees of freedom experimental and non-linear numerical models was studied. The harmonic kinematic external excitation in the suspension point was applied in both cases. The viscous damping was varied in the analysis, independently in the numerical model and jointly in the present set of experimental results.

Various types of the response of the pendulum have been encountered for excitation frequency in the resonance frequency interval: in-plane, periodic or chaotic. The character of the response depends on structural parameters: frequency and amplitude of excitation, geometry of the pendulum and damping coefficients. It has been shown, that initiation of the spatial response is more sensitive to damping in the direction of excitation, whereas even a relatively high damping in the transversal direction does not prevent the spatial movement.

Dependence of the amplitude of the experimental pendulum on the values of damping is not surprising. On the other hand, reasonable correspondence between experimental measurements and numerical model has been confirmed. The qualitative correlation of numerical/experimental results has been observed. However, the assumption of small amplitude depreciate the quantitative relation of numerical and experimental results. For better results, the numerical model should be adopted to comprise dependence of instantaneous amplitude and frequency of the pendulum.

There are some open problems yet. The numerical analysis of the influence of damping should cover the additional (multiple) branches of the stable motion. The next experiments are necessary to validate the unsymmetrical influence of the values of damping coefficients.

From the practical point of view, it is highly recommended to design the damping pendulum absorber in such a way that any occurrence of non-linear resonance effects is avoided. If not, negative influence of the pendulum in the resonance domain is to be expected in both along-wind as well as in cross-wind directions. The experiments will continue with the application of more excitation amplitudes and damping values varying in both principal vibration planes.

Acknowledgments

The support of the Czech Scientific Foundation No. 103/09/0094, Grant Agency of the ASCR No. A200710902 as well as the support of RVO: 68378297 and AV 0Z 2071913 are gratefully acknowledged.

References

Galassi, M. et al. (2009) *GNU Scientific Library Reference Manual - Third Edition*, available on-line `http://www.gnu.org/software/gsl/` (April 2011).

Haxton, R. S., Barr, A. D. S. (1974) The autoparametric vibration absorber. *ASME J. Appl. Mech.* 94, pp. 119–125.

Miles, J. W. (1962) Stability of forced oscillations of a spherical pendulum. *Quart. J. Appl. Math.* 20, pp. 21–32.

Miles, J. W. (1984) Resonant motion of spherical pendulum. *Physica D* 11, pp. 309–323.

Náprstek, J., Fischer, C. (2009) Auto-parametric semi-trivial and post-critical response of a spherical pendulum damper. *Comput. Struct.* 87, pp. 1204–1215.

Náprstek, J., Pirner, M. (2002), Non-linear behaviour and dynamic stability of a vibration spherical absorber. In: *Proc. 15th ASCE Engineering Mechanics Division Conference* (A. Smyth et al. eds). Columbia Univ., New York, CD ROM, paper #150, 10 pp.

Pirner, M. (1994), Dissipation of kinetic energy of large-span bridges. *Acta Technica, CSAV*, Vol 39, pp 407-418.

Pospíšil, S., Fischer, C., Náprstek, J. (2011) Experimental and theoretical analysis of auto-parametric stability of pendulum with viscous dampers. *Acta Technica CSAV*, Vol 56, 4, pp. 359-378.

Tritton, D. J. (1986) Ordered and chaotic motion of a forced spherical pendulum. *Eur. J. Phys.* 7, pp. 162–169.

18th International Conference
ENGINEERING MECHANICS 2012
Svratka, Czech Republic, May 14 – 17, 2012

pp. 263–268
Paper #221

FORCE-TORQUE CONTROL METHODS FOR INDUSTRIAL ROBOTS

L. Flekal, T. Kubela, A. Pochylý, V. Singule*

Abstract: *The paper deals with Force – Torque control methods for industrial robots. The key aspect of these methods is to control a contact between a tool and a workpiece when either the tool or the workpiece is mounted on the robot flange. Real-time control of contact forces and moments is necessary. It is suitable to use it on a variety of industrial operations such as grinding, deburring, other machining operations or automatic assembly. The experimental set-up is based on a KUKA robot with FTC sensor (SCHUNK FTC-050) mounted on the robot and an external PLC system used for main control and connecting other essential sensors and devices. Main practical results are concerned with a design of specific end effector for a specific workpiece and with determining the contact between a workpiece and the surface maintaining a constant force during robot motion.*

Keywords: ***Force-torque control, industrial robots, real-time control, PLC, robot motion***

1. Introduction

Industrial robots programming is still a difficult and annoying task and expert knowledge is necessary in most cases. Due to this disadvantage the industrial robots are mainly used in fixed installations and they are used for repeatable tasks and programmed by an expert.

One of the greatest limitations and also one of the greatest space for further research represent a robot interaction with the worker. In many cases, it would be useful alow this interaction and it can help with robots integration to new industry fields. Nowadays the worker and the robot are usually separated trough some type of safety system.

Other important space for further research is in a need to automate the applications that are nonstandard for robots. Need to control the contact forces and moments between the robot and its environment is essential for this type of operations to ensure a right task performance. One of the representatives of this field are finishing operations (Boque, 2009; Pires, et al., 2002) like grinding, polishing, deburring, etc.

The next demand is concerned with a new robot programming technique that is based on human robot interaction and cooperation. Needles, to say that safety is the biggest task for this approach, because the robot workspace is fully shared with the worker. This technique allows the tasks to be frequently and easily changed and robots can be programmed online by demonstration of non-expert.

To use a robotic cell for finishing operation or human robot interaction, there is a need to ensure right force-torque feedback based on a force-torque sensor (Perry, 2002). Various control architectures can be applied (Bigras et al., 2007; Blomdell et al., 2005; Caccavale et al., 2005). The best way would be a force controller based on the complete model of the robot. Due to closed architecture of the robots that rarely allows a direct control of motor torque, this type of controller is difficult to implement on the actual range of industrial robots. Due to this fact, in this project we applied a cascade force controller even though we know that it does not take into account the whole model of the robot and only a tool position can be controlled.

* Institute of Production Machines, Systems and Robotics, Faculty of Mechanical Engineering, Brno University of Technology, Technická 2, Brno, 616 69, Czech Republic

2. Industrial demands

This project of force-torque control of industrial robots is motivated by real industrial demands. In collaboration with our industrial partner Blumenbecker Prag s.r.o. we received various components for testing and currently we are dealing mainly with components intended for finishing operations.

To answer the needs, the project have been initiated (we successfully asked for funding – Ministry of Industry and Trade of the Czech Republic) and we established a research platform based on academic-industry partnership.

Specific workpiece for grinding and deburring from our industrial partner is shown in Fig. 1, it is a coupling for chains. Surfaces that must be manufactured are shown in yellow in Fig. 2.

Fig. 1. A component example

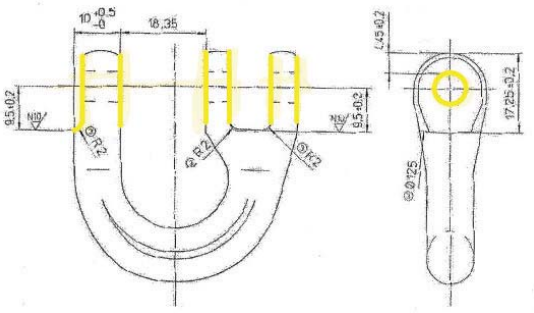

Fig. 2. Surfaces for manufacturing

As be seen from figure 1, this component is hard to be grasp by conventional end effector with simple parallel jaws and more specific and complicated procedure had to been used for this workpiece.

3. Design of the end effector

A basic principle of object grasping is presented in the following Fig. 3. A 2-finger parallel gripper equipped with angled prismatic inserts (parts 1 and 2) is used to grasp the component. As additional supporting element, a pneumatic cylinder (part 3) is used to hold the component using another prismatic element.

Fig. 3. A basic principle of object grasping

The described principle have some difficulties, a part is actually forced out by parallel jaws during pressing process. This force is reduced by selecting a proper tilt angle of prismatic inserts and by supporting pneumatic cylinder called "nose". A suitable material, with sufficient friction coefficient, need to be used for prismatic inserts. However, details concerned with this procedure are not covered in this contribution.

From the beginning the idea was to create the end effector to grasp all components from the whole production range of chain couplings and various alternatives of the end effector have been designed. Mainly due to large weight of the end effector it was decided to produce a device for grasping limited production range. Final design of the end effector is shown in Fig. 4.

Fig. 4. A model of the end effector

4. Control methodology

The following figure shows the hardware structure of robotic cell (Fig. 5). Data from the force-torque sensor (SCHUNK FTC-50) is sent to the PLC (Embedded PC Beckhoff) via serial connection RS232. Information about the contact force and torques are processed in the PLC and control deviation is processed here too. Control deviation is sending to the robot controller via DeviceNet interface. In the robot controller KUKA RSI (Robot Sensor Interface) is used to fulfill the condition of real-time data processing, it is a software package for communication with sensors and other devices in defined 12ms cycle.

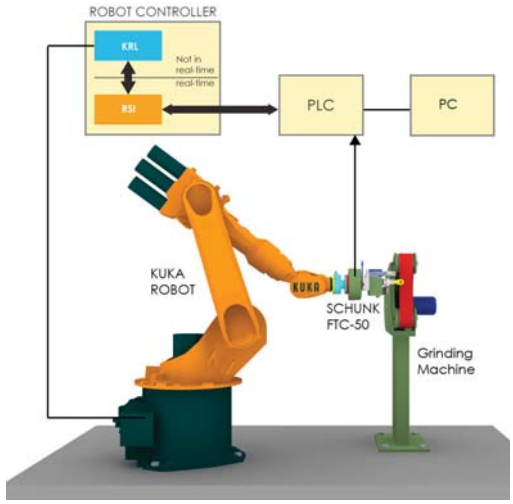

Fig. 5. Main structure of the robotic cell with general control structure

The following figure shows block diagram of control system (Fig. 6). Data from force torque sensor is processed by the gravity compensation block (f_{cont}) than it is compared with desired force (f_{des}) and after that it is processed by a couple of the PID controller (Reg I and Reg II). First of them is used for greater deviation on the beginning of the contact. Second of them is used for smaller deviation.

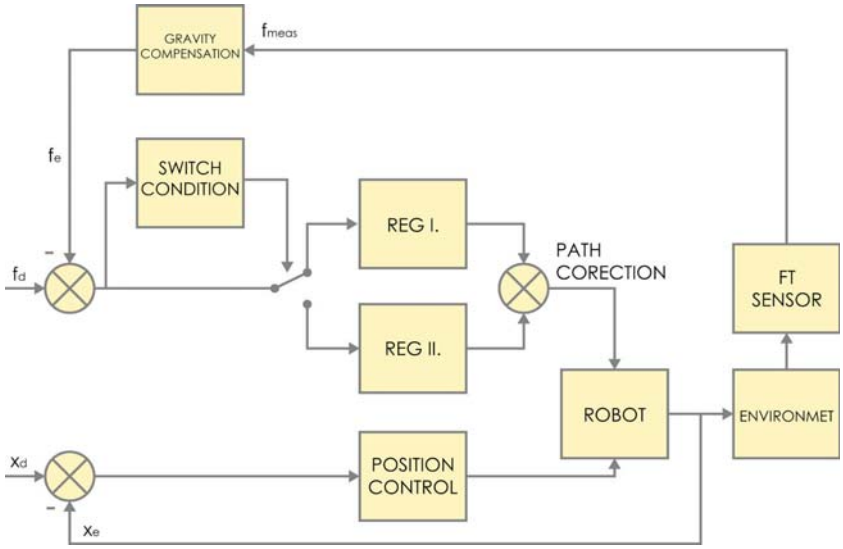

Fig. 6. Main block diagram of control structure

5. Machinery stiffness

For more accurate regulators constants adjustments some experimental measurements of used machinery stiffness have been made. Measurements was made on belt grinding machine and universal grinding machine Protool. Force torque sensor mounted on the flange of the industrial robot and the

end effector with grasped object was used for push against the grinder. Amount of contact force was measured by force torque sensor and position (grinder deflection) was measured by the robot control system (Fig. 7).

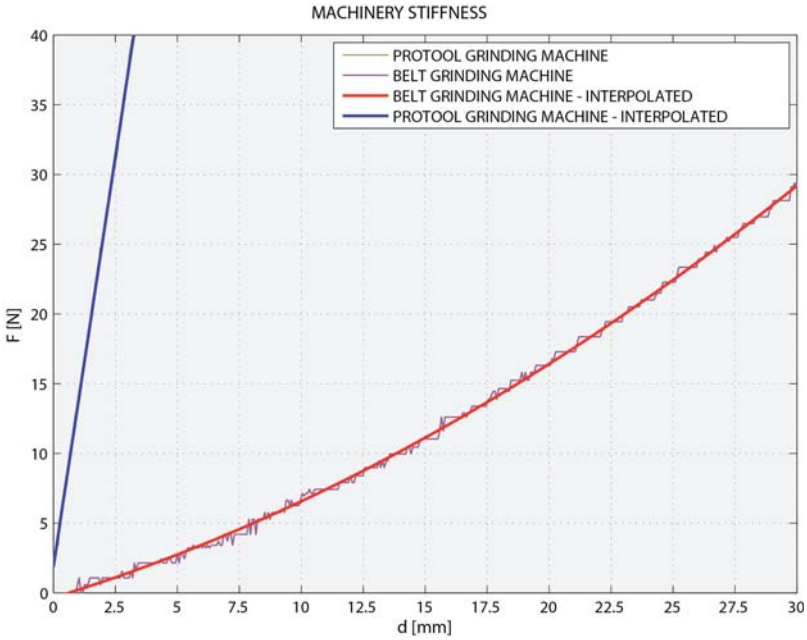

Fig. 7. Measurements of used machinery stiffness

A important advantage of this method for measure stiffness is that it is take into account stiffness of all parts (robot, sensor, end effector, grinders) due to this, data shown in figure reflect stiffness of all parts in kinematic chain. It is essential for proper control adjustment.

6. Results

Finally we present pilot results of the force-torque control based on the control structure described above. The following Fig. 8 shows example of time behavior of the contact force.

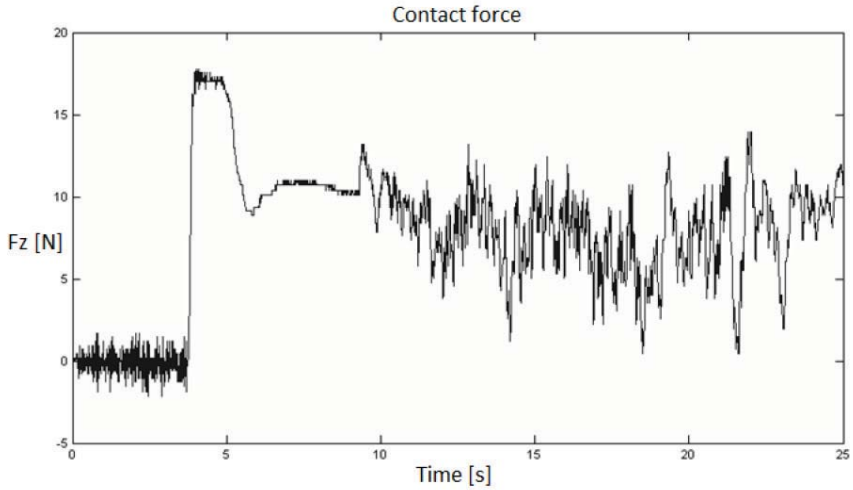

Fig. 8. Contact force during the robot motion along the surface

The desired contact force to maintain while the robot is in contact with the surface is set to 10N. The big increase in strength on 4 seconds is for first contact between robot an its environment (grinding machine). The interval between 6 and 9 seconds is for maintaining the contact force on a single robot position and interval after that is for maintain the constant contact force during robot motion. As can be seen the robot gaining and losing the contact during motion and the process need to be further optimized and this will be the main part of our future work.

7. Conclusion

Pilot results were presented using the control architecture described above where a desired contact force with object surface can be controlled allowing the robot follow object profiles.

All data processing and control algorithms is processed in the external PLC system (Embedded PC Beckhoff. Due to this, the control is independent on robot controller, it is important advantage of described control architecture. The only condition for KUKA robot controller is in need of RSI (Robot Sensor Interface) software package to be installed to fulfill the condition of real-time data processing.

Acknowledgement

This work has been supported and funded by the Ministry of Industry and Trade of the Czech Republic within the industrial research and development program TIP (2009); project number FR-T11/169: Adaptive Force-Torque Control of Robots for Industrial Applications.

References

Bogue, R., (2009) Finishing robots: a review of technologies and applications. *Industrial Robot*, Vol. 36, No.1, pp. 6-12.

Pires, J.N., Ramming, J., Rauch, S., Araujo, R. (2002) Force/torque sensing applied to industrial robotic deburring. *Sensor Review*, Vol. 22, No. 3, pp. 232-241.

Perry, D. (2002) Optimize your robot´s performance by selecting the right force/torque sensor system. *Industrial Robot,* Vol.29, No.5, pp. 395-398.

Bigras, P., Lambert, M., Perron, C. (2007) New formulation for an industrial robot force controller: Real-time implementation on a KUKA robot, in: *Proceedings of the IEEE International Conference on Systems, Man and Cybernetics (SMC 2007)*, Montreal, QC, Canada, pp. 2794-2799.

Blomdell, A. et al. (2005) Extending an Industrial Robot Controller: Implementation and Applications of a Fast Open Sensor Interface, *IEEE Robotics & Automation Magazine*, Vol. 12, No. 3, pp. 85-94.

Caccavale, F., Natale, C., Siciliano, B., Villiani, L. (2005) Integration for the next generation: embedding force control into industrial robots. *IEEE Robotics & Automation Magazine*, Vol. 12, No. 3, pp. 53-64.

18th International Conference
ENGINEERING MECHANICS 2012
Svratka, Czech Republic, May 14 – 17, 2012

pp. 269–279
Paper #318

BLAST PERFORMANCE OF FRC COMPOSITES

M. Foglar[*], M. Kovář[**]

Abstract: *The paper presents ways of numerical modeling of RC and FRC slabs subjected to blast loading. The models are based on experiments which were described at the EM2011, the experiments are performed in the military training area Boletice with the cooperation with the Czech Army. The use of racture energy as the key quantity in the modeling of FRC in comparison to RC is studied.*

Keywords: ***blast loading, fiber concrete, reinforced concrete.***

1. Introduction

This paper presents the primary results of two sets of field tests of blast performance of reinforced concrete and reinforced concrete specimens with plastic fibers. The tests were performed in cooperation with the Czech Army corps and Police of the Czech Republic at the military training area Boletice using real scale precast slabs and 25 kg of TNT charges placed in distance from the slab for better simulation of real in-situ conditions.

2. Field tests of blast performance of reinforced concrete and reinforced concrete specimens with plastic fibres

2.1. Specimens

This paper continues the research presented at Engineering Mechanics in 2011 (Foglar & al., 2011).

The specimens are designed in real scale of a small span bridge in as concrete slabs, 6m long, 1,5m wide and 0,3m thick. For reinforcing details, see referenced paper.

Five specimens were used in total during the experiments performed in 2010 and 2011. Three of the specimens were made of C30/37 grade concrete (specimen No. 1 (2010), 2 (2010) and 5 (2011)), two of C55/67 grade concrete (No. 3 (2011) and 4 (2011)). Polypropylene 54mm long synthetic fibres were used in three of the specimens. The fibre dosage was following: specimen No. 1 - 0kg/m3, No. 2 – 4,5kg/m^3, No. 3 - 0 kg/m^3, No. 4 – 4,5 kg/m^3 and No. 5 - 9kg/m^3. The dosage of the fibres was kept low as it can be achieved on-site. The fiber tensile strength is 620-758MPa, the shape combines monofilament and fibrillated shape (slightly corrugated and blended with fibrillated PolyPropylene fibers).

2.2. Results of the experiments

The experiments showed the beneficiary effect of added fibers on blast performance of the specimens.

The specimen No. 1, C30/37, no fibres, is regarded as the reference specimen. This specimen is the most damaged one by the blast loading. The area of the puncture is 0,43m^2, volume 0,12m^3, which represents 4,4% of the total volume of the specimen. Total volume of the damaged concrete (puncture + spalling) is 0,23m^3, which represents 8,5% of the total volume of the specimen. The sides of the specimen were damaged severely. The deflection was 295mm on the left side and 310mm on the right

[*] Ing. Marek Foglar, Ph.D.: Department of concrete and masonry structures, Czech Technical University, Thákurova 7; 166 29, Prague; CZ, e-mail: marek.foglar@fsv.cvut.cz

[**] Ing. Martin Kovář: Department of concrete and masonry structures, Czech Technical University, Thákurova 7; 166 29, Prague; CZ, e-mail: martin.kovar@fsv.cvut.cz

side of the specimen. The shape of deflection was similar to deflection from uniformly distributed loading.

The specimen No. 2, C30/37, 4,5kg/m^3 PP fibres was less damaged. The area of the puncture is 0,26m^2, volume 0,08m^3, which represents 2,9% of the total volume of the specimen. Total volume of the damaged concrete (puncture + spalling) is 0,15m^3, which represents 5,6% of the total volume of the specimen. The area of puncture was reduced by 40% in comparison to specimen No. 1, the total volume of damaged concrete was reduced by 35% in comparison to specimen No. 1. The left side of specimen No. 2 was not damaged, the damage of the right side was reduced by more than 50%. The deflection was 365mm on the left side and 380mm on the right side of the specimen. The shape of deflection was similar to deflection from point loading in the mid-span of the specimen. The deflection was increased by 19% in comparison to specimen No. 1.

The specimen No. 5, C30/37, 9kg/m^3 PP fibres was less damaged. Total volume of the damaged concrete (puncture + spalling) is 0,06m^3, which represents 2,2% of the total volume of the specimen. There was no puncture, the total volume of damaged concrete was reduced by 75% in comparison to specimen No. 1. The sides of specimen No. 5 were not damaged. The deflection was 255mm on the left side and 265mm on the right side of the specimen. The shape of deflection was similar to deflection from point loading in the mid-span of the specimen. The deflection was decreased by 16% in comparison to specimen No. 1.

The specimen No. 3, C55/67, no fibres was less damaged. The area of the puncture is 0,02m^2, volume 0,01m^3, which represents 0,4% of the total volume of the specimen. Total volume of the damaged concrete (puncture + spalling) is 0,2m^3, which represents 7,4% of the total volume of the specimen. The area of puncture was reduced by 95% in comparison to specimen No. 1, the crushed concrete remained within the reinforcement matrix, total volume of damaged concrete was reduced by 15% in comparison to specimen No. 1. The damage to the sides was reduced by 85%. The deflection was 285mm on the left side and 290mm on the right side of the specimen. The shape of deflection was similar to deflection from uniformly distributed loading. The deflection was increased by 10% in comparison to specimen No. 1.

The specimen No. 4, C55/67, 4,5kg/m^3 PP fibres was less damaged; its damage was similar to specimen No. 5. Total volume of the damaged concrete (puncture + spalling) is 0,05m^3, which represents 1,9% of the total volume of the specimen. There was no puncture, the total volume of damaged concrete was reduced by 22% in comparison to specimen No. 1. The sides of specimen No. 5 were not damaged. The deflection was 300mm on the left side and 305mm on the right side of the specimen. The shape of deflection was similar to deflection from point loading in the mid-span of the specimen. The deflection was increased by 15% in comparison to specimen No. 1.

The differences in puncture and spalling of concrete on the soffit of the slabs can be found in Table 1. The effect of blast loading on top and bottom surfaces of the specimens can be found in Fig. 1.

Tab. 1: Comparison of blast performance of specimens.

Specimen No.	**1**	**2**	**3**	**4**	**5**
Concrete	C30/37	C30/37	C55/67	C55/67	C30/37
Fibres	-	4,5kg/m^3	-	4,5kg/m^3	9,0kg/m^3
Puncture – top surface	0,43 m^2	0,26 m^2	0,02 m^2	-	-
Concrete spalling (soffit) < concrete cover	2,35 m^2	1,89 m^2	1,51 m^2	0,73 m^2	0,61 m^2
Concrete spalling (soffit) > concrete cover	1,71 m^2	1,09 m^2	1,2 m^2	0,44 m^2	0,37 m^2
Concrete spalling (top surface) < concrete cover	0,43 m^2	0,26 m^2	0,89 m^2	0,68 m^2	0,66 m^2
Concrete spalling (top surface) > concrete cover	0,43 m^2	0,26 m^2	0,29 m^2	0	0,08 m^2
Concrete spalling (left side) < concrete cover	0,52 m^2	0,05 m^2	0,08 m^2	0	0
Concrete spalling (left side) > concrete cover	0,35 m^2	0	0,02 m^2	0	0
Concrete spalling (right side) < concrete cover	0,34 m^2	0,16 m^2	0,08 m^2	0	0
Concrete spalling (right side) > concrete cover	0,23 m^2	0,11 m^2	0,02 m^2	0	0
Volume of crushed concrete	0,23 m^3	0,15 m^3	0,20 m^3	0,05 m^3	0,06 m^3
Permanent deflection	0,31 m	0,37 m	0,28 m	0,30 m	0,26 m

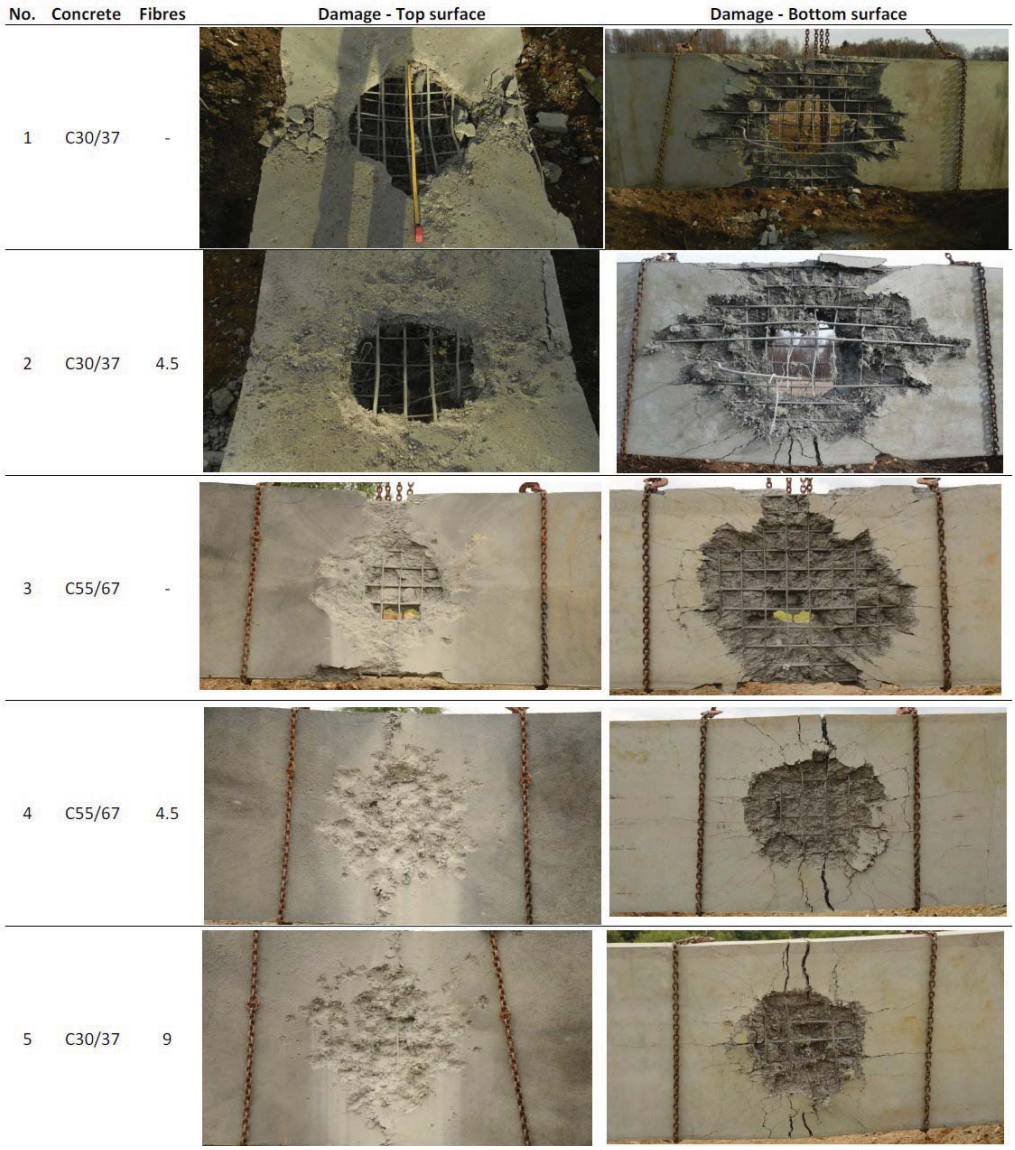

Fig. 1: Top and bottom surface of the RC specimen with plastic fibers after the blast.

3. Numerical modeling

A numerical model of the experiment was prepared for the purpose of further research. The process of model set-up is described in the following text. The model was calibrated according to the outcomes of the experiments described in the previous chapter.

3.1. Numerical solution of fast dynamic phenomena

Fast dynamic phenomena can be solved by the method of explicit time integration (finite difference method, differential method, see Fig, 2) the equation of motion can be expressed as

$$M_n \cdot u_n'' + C_n \cdot u_n' + K_n \cdot u_n = p_n \tag{1}$$

is solved in time t_n, hence at the start of fixed time step.

The method is based on linear displacement change. The velocity

$$u'_{n+1/2} = \frac{1}{\Delta t_{n+1/2}}(u_{n+1} - u_n) \tag{2}$$

is inserted into equation of acceleration

$$u'' = \frac{1}{\Delta t_n}(u'_{n+1/2} - u'_{n-1/2}) \tag{3}$$

u_{n+1} remains unknown in Eq. (1). The displacement in time t_{n+1} is

$$\begin{aligned}&(\frac{1}{\Delta t^2}M_n + \frac{1}{2\Delta t}C_n)\cdot u_{n+1} = \\ &p_n - (K_n - \frac{2}{\Delta t^2}M_n)\cdot u_n - (\frac{1}{\Delta t^2}M_n - \frac{1}{2\Delta t}C_n)\cdot u_{n-1}\end{aligned} \tag{4}$$

The matrixes M and C are diagonal; the solution is fast and simple.

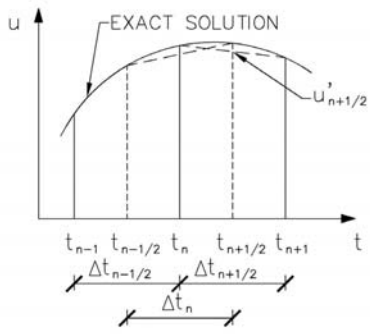

Fig. 2: The explicit time integration method (finite difference method)

In the method of explicit time integration, the system is in equilibrium only at time t_n, but not at time t_{n+1}. The time step depends on the highest natural frequency of the structural system. If the time step is adequately small, the method is numerically stable. The method of explicit time integration solves small number of equations in very small time steps in duration of approximately 10^{-6} – 10^{-8} s. The method of explicit time integration is suitable only for processes of a very short duration.

3.2. Numerical modeling of the experiments

LS-DYNA solver was developed for non-linear analysis of fast dynamic phenomena like blast or impact. Within the calculation, the FEM mesh can adapt by deleting elements whose resistance was depleted; these FEM elements "erode".

The model composes of several parts. The air forms boundaries of the model; the explosive (e.g. TNT) transfers the energy from the blast to FE elements of the air, where the blast wave propagates. The concrete specimen is modeled by solids, reinforcement by beam elements. For example of the model, see Fig. 3.

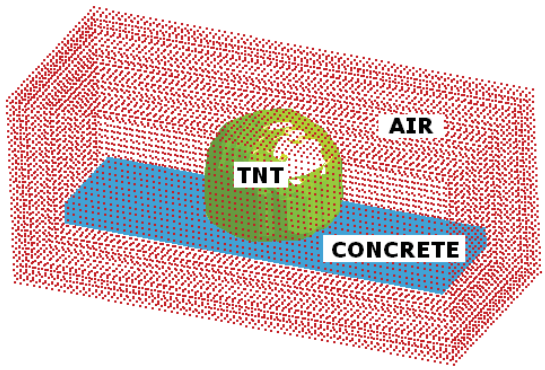

Fig. 3: Set-up of the FE model

The air is modeled using the 009-Null material and forms the undeformable FE network. The concrete specimen is modeled by the 159- CSCM_Concrete material model (brittle material model with damage (Murray (2007)); similar approach to concrete modeling is used by Coughlin et al. (2010)). The explosive is modeled by the 008-High explosive burn material model. The blast overpressure is calculated by the JWL equation of state (EOS):

$$p = A\left(1 - \frac{\omega}{R_1 V}\right)e^{-R_1 V} + B\left(1 - \frac{\omega}{R_2 V}\right)e^{-R_2 V} + \frac{\omega E}{V} \tag{5}$$

The material parameters of the used model (including strain-rate dependent response) were automatically generated in the LS-DYNA from the particular concrete compressive strength. The material properties of the FRC (fracture energy and others) are currently tested, see below.

3.2.1. 2D model

As the first step, a 2Dmodel was prepared. Its goal was to show basic characteristics of the experiment, e.g. the time when the blast overpressure wave reaches the surface of the specimen, the time when the elements at the soffit the specimen start to erode, etc. The blast overpressure wave reaches the surface of the specimen at 0,25 ms, see Fig. 4.

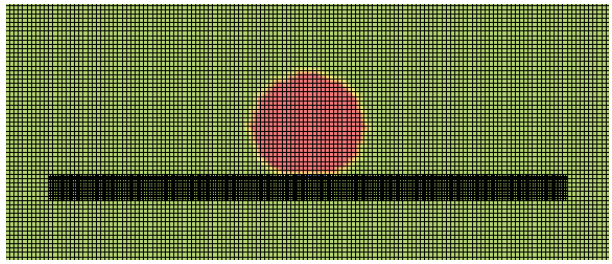

Fig. 4: Blast overpressure wave at 0,25 ms

The first finite elements start to erode at 0,4 ms, see Fig. 5.

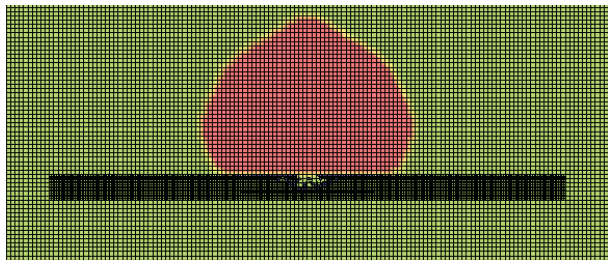

Fig. 5: Blast overpressure wave at 0,5 ms

Fig. 6 compares the video-recorded blast overpressure wave during the experiment with the FE model; element erosion can be spotted under the hypocenter.

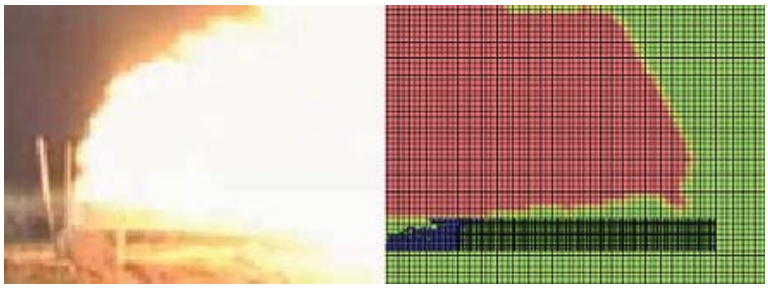

Fig. 6: Experiment vs. FE model

3.2.2. 3D model of reinforced concrete specimens

The 3D reinforced concrete model was prepared to mitigate the weaknesses of the plain concrete model using real dimensions of longitudinal and transverse reinforcement incl. links (steel reinforcement modeled as beam elements). The mesh size was chosen 30mm for concrete and reinforcement and 50mm for air.

The first elements erode when the blast overpressure wave reaches the surface under the hypocenter at 0,25 ms.

In the following phase, more FE erode, the damage of the specimen increases and spalling at the soffit takes place. For results at 1 ms from the blast, top surface and soffit, see Fig. 7, 8. Fig. 7 shows plastic strain (crack development) for plain concrete. Fig. 8 compares two slabs with different concrete grade (C30/37xC55/67 reinforced concrete).

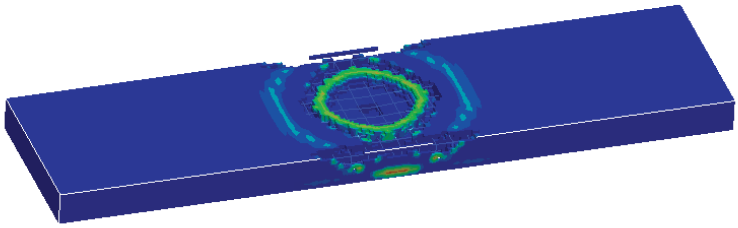

Fig. 7: Top view of the plain concrete specimen after the blast (t = 1 ms)

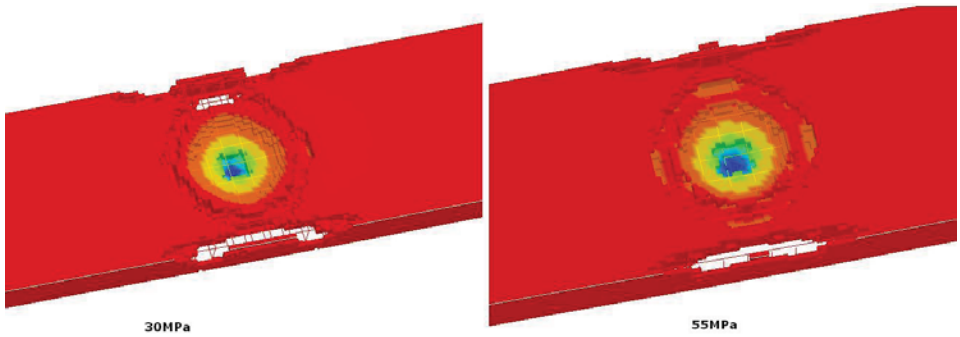

Fig. 8: Damage of two reinforced concrete specimens (left C30/37, right C50/67) (t = 1 ms)

The results of numerical modeling show good agreement with the experiments for reinforced concrete specimens.

3.3. 3D model of reinforced concrete specimens with PP fibers

The behavior of fiber concrete subjected to blast load is quite different from the behavior of plain (respectively reinforced) concrete specimens. At plain concrete, the specimen fails in tension after reaching its tensile strength. At fiber concrete, the stiffness of the specimen decreases after the tensile strength is reached (strain softening). The fibers take over the tensile stress during strain softening and the material performs with a residual tensile strength (approximately 1/3 of the original tensile strength according to fiber type, dosage and geometry). The difference between stress-strain diagrams of plain concrete and fiber concrete can be seen in Fig. 9.

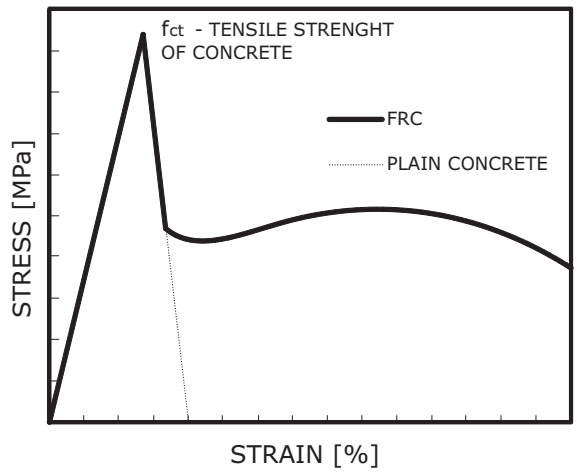

Fig. 9: Stress-strain diagram of concrete material model with damage

The material model of plain concrete MAT159_CSCM (material model with damage and plasticity, Murray, Y.D. (2007)) used in LS-DYNA solver has to be recalibrated to perform according to the presented description, i.e. to provide ductile behavior. For the analytical decription of the MAT159_CSCM material model, see Fig. 10.

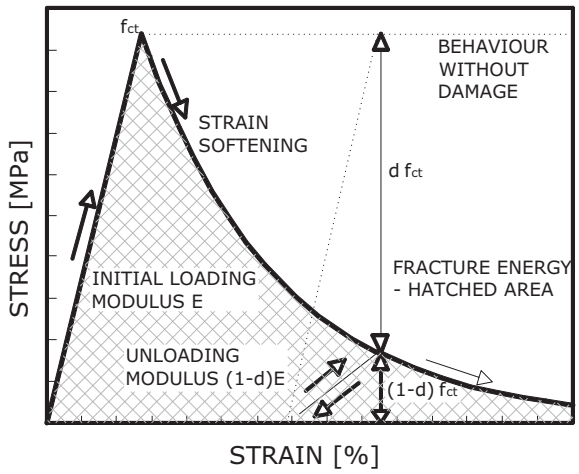

Fig. 10: Stress-strain diagram of concrete material model with damage

The key to MAT159_CSCM material model recalibration lies in tuning its unloading part to describe behavior of fiber concrete while the loading part can remain unchanged (the difference of plain concrete and fiber concrete can be neglected). The fracture energy G_f can be can be expressed as an integral of the area below the stress-strain diagram:

$$G_f = \int_0^{\infty} (1-d) f_{ct} dx \tag{6}$$

Where: d is the damage (from 0 to 1) and f_{ct} is the tensile strenght.

According to this approach, the integral of the fracture energy is used for verification of the value of the fracture energy.

The FRC material model was calibrated according to experiments decribed by Drahorad, Foglar et al. (2011). The experiments studied the strain-rate effect of FRC specimens (700x150x150mm) subjected to 4 points bending (see Fig. 11). The concrete mix properties and fiber dosage were the same as in the field experiments. The finite elements size in the numerical model used for evaluation of the experiments was chosen the same as in the full scale 3D models described in the preceeding paragraphs, as the blast modeling is highly scale-sensitive.

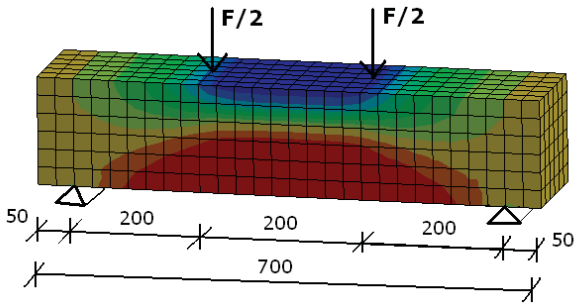

Fig. 11: Layout of the control experiment (mm)

The calibration models were prepared using LS-DYNA for plain concrete and both dosages of PP fibers. The fracture energy in tension and shear of the material model of plain concrete was modified to obtain similar integral of the fracture energy both from the experiments and the numerical evaluation.

For comparison of the force-deflection (F-δ) diagrams of plain concrere, 4,5kg/m^3 and 9kg/m^3 PP fibers FRC both experimental and numerical, see Fig. 13. The area of the force-deflection deigram was limited to the deflection of 8mm.

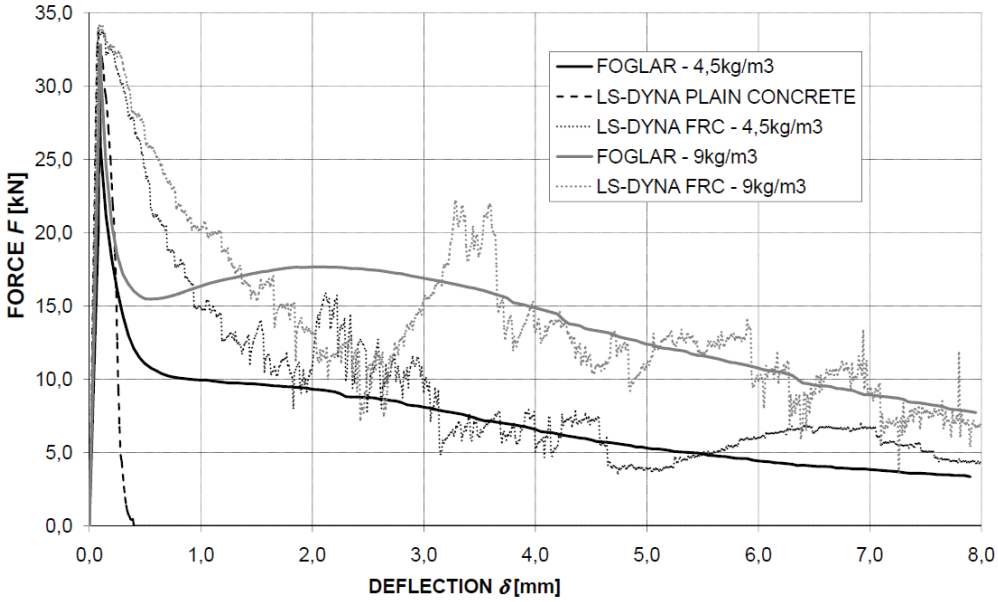

Fig. 13: Force – deflection diagram of material models

The obtained values of the fracture energy for various concrete strength classes and fiber dosages can be seen in Table 2.

Tab. 2: Hodnoty lomových energií různých betonů

Specimen	Fracture energy [N/m]
LS-DYNA – plain concrete	5,6
C30/37 – 4,5 kg/m^3 - experimental	62,0
C30/37 – 4,5 kg/m^3 - numerical	68,6
Foglar C30/37 – 9 kg/m^3	109,3
LS-DYNA – FRC with 9 kg/m^3	102,9

The calibrated material model was used in the 3D models described in the previous chapter. For example of the result of the modeling, see Fig. 14.

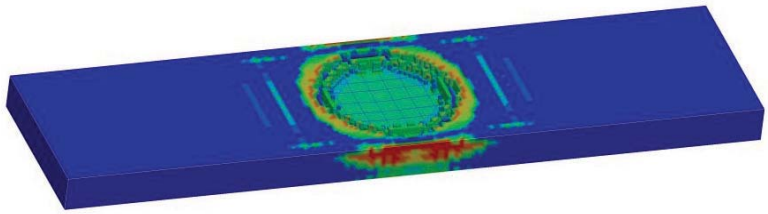

Fig. 14: Top view of the FRC specimen after the blast (t = 1 ms)

The results of numerical modeling show very good agreement with the experiments for specimens with added fibers.

4. Conclusions

The paper continued the paper presented at Engineering Mechanics 2011 with the results for high performance concrete and higher fiber dosages.

The experiments showed beneficiary effect of added fibres on blast performance of the specimens. The experiments also showed beneficiary effect of increased concrete compressive strength on blast performance of the specimens. Combination of fibres and increased compressive strength proved itself to be very effective for improving the blast performance.

The way of modeling of fiber concrete subjected to blast loading by increasing the facture energy of plain concrete MAT159_CSCM material model was presented and evaluated. The model calibration was performed according to small scale experiments. The results of numerical modeling show very good agreement with the experiments for specimens with added fibers.

Other ways of modeling of fiber concrete subjected to blast loading lie in changing the area of plasticity of the material model or in modeling of the dispersed reinforcement. These methods require much more effort to be invested, yet the result remains questionable.

Acknowledgement

This paper was supported by the Czech Ministry of Industry and Trade project FR-TI3/531 and the and the CTU project No. SGS12/029/OHK1/1T/11.

References

Coughlin A.M., Musselman E.S., Schokker A.J., D.G. Linzell (2010), Behavior of portable fiber reinforced concrete vehicle barriers subject to blasts from contact charges, *International Journal of Impact Engineering*, Volume 37, Issue 5, pp. 521-529.

Drahorád M., Foglar M., Smiřinský S., Veselý M. (2012), Užití dynamického faktoru nárůstu pevnosti betonu pro zkrácení doby zkoušek vláknobetonových vzorků, *Beton TKS 1/2012,* pp. 74-79.

Foglar M., Sochorová E., Kohoutková A. (2011), Field tests of blast performance of reinforced concrete and fibre reinforced cocncrete specimen, *Engineering mechanics*, pp. 143-146.

Millard, S.G. & al. (2010) Dynamic enhancement of blast resistant ultra high performance fiber-reinforced concrete under flexural and shear loading. *International Journal of Impact Engineering*, 37, 4, pp. 405-413.

Murray, Y.D. (2007), *User Manual for LS-DYNA Concrete Material Model 159*, US Department of transportation, FHWA-HRT-05-062

Murray, Y.D. (2007), *Evaluation of LS-DYNA Concrete Material Model 159*, US Department of transportation, FHWA-HRT-05-063

18th International Conference
ENGINEERING MECHANICS 2012
Svratka, Czech Republic, May 14 – 17, 2012

pp. 281–286
Paper #243

OPTIMIZATION OF CONCENTRATING STRUCTURES FOR RIVER REGULATION WITH THE USE OF CFD

P. Fošumpaur*

Abstract: *Currently, a project to improve navigation conditions on the Elbe River downstream the Střekov waterwork is preparing. Concentrating structures are important elements in this concept from the 19th century. This paper describes an optimization of newly designed concentrating structures in the frame of the Elbe regulation with the use of computational fluid dynamics (CFD). Analysis is also based on experiences with historical spur dikes. The results were compared with measurement on the physically based model and in situ.*

Keywords: ***concentrating structures, spur dikes, computational fluid dynamics***

1. Introduction

The historical development of modifications of navigable reaches of the Elbe and Vltava rivers shows early stages of such interventions simultaneously with early settlements in the river valleys in medieval times. Modifications of riverbeds reflected the human need for rational utilization of river conditions while reducing harmful effects of water at times of floods and hydrological droughts. The early interventions were effected for various purposes, which included harnessing the power of water for driving mills, sawmills and iron mills by building solid weirs as early as in the 13th century. Another notable purpose for modifying watercourses was to achieve navigability, starting in earnest during the reign of Charles IV in the 14th century.

In technical terms, two basic methods for achieving navigability of watercourses can be discriminated (Novak et al., 2007). The first one is waterway channelisation, when the design width of the waterway and the navigation depth are achieved by regulating interventions and construction of concentrating structures– spur dikes. The other method, canalisation, is concerned with the construction of a cascade of weirs and locks. In the Czech Republic, navigable reaches of the Vltava and Elbe rivers are for the most part made navigable by canalisation, while channelisation was previously implemented only at the lower Elbe from the Střekov barrage to the border between the Czech Republic and Germany. However, at times of low flow rates navigation is suspended. Efforts are being made to ensure undisrupted navigability by developing a project of a Děčín barrage, designed to ensure navigation depths from Děčín to the state border using additional concentrating structures.

This paper focuses on proposals for concentrating structures as well as spur dikes, in the form of longitudinal or transverse dikes within the riverbed designed to ensure sufficient navigation depths even at low flow rates. Requests by environmental organisations resulted in the need to ensure that the space between the spur dikes and the banks are not gradually slogged up with sediments for environmental reasons. The objective is to safeguard the space as a living environment for aquatic organisms and populations living on rocky bottoms. Following a research using a 3D mathematical model, a suitable design of the spur dikes has been devised and optimised, and subsequently verified using a physical model developed by a hydraulic laboratory (Fosumpaur et al., 2010). The first testing spur dikes have been constructed in-situ on the lower Elbe with evaluation of a piloting operation ongoing.

* Doc. Dr. Ing. Pavel Fošumpaur: Czech Technical University, Faculty of Civil Engineering, Department of Hydraulic Structures, Thákurova 7; 166 29, Prague 6; CZ, e-mail: fosumpaur@fsv.cvut.cz

2. Historical overview

The modern history of improving navigability of the Elbe and Vltava rivers begun in the 19th century with systematic modifications of the riverbeds, regular maintenance and construction of docks. These interventions would have been carried out predominantly by the firm of the industrialist and shipbuilder Vojtěch Lanna from České Budějovice. The company has gradually amassed a considerable fleet of dredgers, steam-tugs and barges, as well as other engineering ships, used to carry out majority of channelisation and canalisation measures on Czech rivers. Between the years 1833 and 1862, the company channelled the Vltava, including longitudinal spur dikes to decrease the width of the riverbed, resulting in an increase of the navigation depth and elimination of shallows. The commencement of steam navigation on the Elbe and the subsequent signing of navigation treaties in 1844 obliged the Austrian monarchy to dredge an international stretch of the Elbe to the required depth and to ensure proper maintenance. The legal frame for modern navigability interventions was laid down by the imperial waters act No. 93 passed in 1869 and followed up in 1870 by corresponding acts passed by national assemblies in the individual countries forming the monarchy.

In the next stage of improving navigability, between the years 1880 and 1920, the Elbe was further narrowed through further gradual modifications. Where the watercourse had been particularly broad, channelling was achieved by using concentrating structures, discontinuous in most cases, combined with transverse spur dikes and original bank fortifications. The dikes, as well as the bank reinforcements, were made of quarry stone ripraps, secured at the foot by a levelled quarry stone fill. Some spaces behind the concentrating structures would later be used for storage of material dredged from the river bottom.

Combined continuous structures in particular have been spontaneously covered in sediment, with some also filled in with refuse, such as the top part of the branch "Svádovské rameno", which had been filled in with fly-ashes from the boiler station of the Setuza plant in Ústí nad Labem between 1945 and 1949 (Zajícová, 2007).

Fig. 1: Svádov following the construction of concentrating structures and before the 2002 floods (Zajicova, 2007).

At other sites, the space between the spur dikes and the riverbank has not aggraded in more than 150 years in operation. This finding has lead us to study the design differences between individual historical spur dikes and to devise ways of further optimisation based on modern computing approaches. An example of such a spur dike is the setting at Nebočady, where the spur dikes were built in latter 19th century and lie directly adjacent to the natural monument of Nebočady alluvial plain with a dead end branch and a peninsula in between the branch and the main riverbed. The structure of the spur dikes at Nebočady is supplemented with a feeding shallow ditch featuring a slightly decreased crest at the transition between the transverse and oblique segments. The function of the shallow ditch is quite apparent from the images in Fig. 2, made under conditions of volumetric flow rate of approximately Q_{180d}. The photos clearly demonstrate the feeding function of the shallow ditch, affecting desirably the current behind the spur dikes at water levels mildly exceeding overflow edge of the ditch. The area behind the dikes is subject to a continuous flow, preventing sedimentation.

Fig. 2: Spur dikes near Nebočady and a detail of the feeding area.

3. Methods

To simulate flow conditions for different types of spur dikes a turbulent *k-ε* model was used. Reynolds equation for the turbulent flow of a real liquid is given by the formula:

$$\rho \frac{\partial \overline{\mathbf{u}}}{\partial t} - \mu \nabla . \nabla \overline{\mathbf{u}} + \rho \overline{\mathbf{u}} . \nabla \overline{\mathbf{u}} + \nabla \overline{p} + \nabla \left(\overline{\rho \mathbf{u}' \otimes \mathbf{u}'} \right) = \mathbf{F} \tag{1}$$

where **F** is the unit body force. In our case $F_x = F_y = 0$ and F_z = -g. The turbulent component is approximated by means of what is called turbulent stress and individual turbulent models differ mutually just by the manner of their description (Wilcox, 1998). In practical applications, *k-ε* turbulent model is used that belongs to the most favourite at the present time due to its relative simplicity and sufficient reliability of the solution for the majority of engineering tasks. The turbulent momentum transport in the *k-ε* model is given by the relation:

$$\begin{aligned} \left(\overline{\mathbf{u}' \otimes \mathbf{u}'} \right) &= -\nu_T \left(\nabla \overline{\mathbf{u}} + (\nabla \overline{\mathbf{u}})^T \right) \\ \nu_T &= C_\mu \frac{k^2}{\varepsilon} \end{aligned} \tag{2}$$

where ν_T is the turbulent viscosity and C_μ is the model constant (see below). This assumption leads to the following form of the momentum equation and the continuity equation:

$$\begin{aligned} &\rho \frac{\partial \overline{\mathbf{u}}}{\partial t} - \nabla . \left[\left(\mu + \rho C_\mu \frac{k^2}{\varepsilon} \right) . \left(\nabla \overline{\mathbf{u}} + (\nabla \overline{\mathbf{u}})^T \right) \right] + \rho \overline{\mathbf{u}} . \nabla \overline{\mathbf{u}} + \nabla \overline{p} = \mathbf{F} \\ &\nabla . \overline{\mathbf{u}} = 0 \end{aligned} \tag{3}$$

The transport equation of the turbulent kinetic energy *k* is given by the equation:

$$\begin{aligned} &\rho \frac{\partial k}{\partial t} - \nabla . \left[\left(\mu + \rho \frac{C_\mu}{\sigma_k} \frac{k^2}{\varepsilon} \right) \nabla k \right] + \rho \overline{\mathbf{u}} . \nabla k = \\ &= \rho C_\mu \frac{k^2}{\varepsilon} \left(\nabla \overline{\mathbf{u}} \right)^2 - \rho \varepsilon \end{aligned} \tag{4}$$

and the equation of the dissipation of turbulent energy *ε*:

$$\begin{aligned} &\rho \frac{\partial \varepsilon}{\partial t} - \nabla . \left[\left(\mu + \rho \frac{C_\mu}{\sigma_\varepsilon} \frac{k^2}{\varepsilon} \right) \nabla \varepsilon \right] + \rho \overline{\mathbf{u}} . \nabla \varepsilon = \\ &= \rho C_{\varepsilon 1} C_\mu k \left(\nabla \overline{\mathbf{u}} \right)^2 - \rho C_{\varepsilon 2} \frac{\varepsilon^2}{k} \end{aligned} \tag{5}$$

The k-ε model contains following constants that were deduced by experimental research according to Table 1:

Tab. 1: Parameters of k-ε turbulent model.

C_μ	$C_{\varepsilon 1}$	$C_{\varepsilon 2}$	σ_k	σ_ε
0,09	0,1256	1,92	1,0	1,3

To assess the risk of sedimentation of particles in the space behind the spur dikes the fall velocity has to be calculated. Falling particle achieves its fall velocity when the resultant of gravity force and buoyancy force equals the drag force. Resultant of gravity force and buoyancy force is:

$$G_v = V\mathrm{g}\left(\rho_p - \rho\right) = \frac{1}{6}\pi d^3 \mathrm{g}\left(\rho_p - \rho\right), \tag{6}$$

where V is the volume of the particle with diameter d, g is the gravity acceleration, ρ_p is the density of the particle (~2700 kg.m^{-3}) and ρ is the density of the fluid (1000 kg.m^{-3} for water). The drag force is given according the formula:

$$F = \frac{C_D}{8}\pi d^2 w^2 \rho\,, \tag{7}$$

where C_D is the drag coefficient and w is the fall velocity. The value of the fall velocity is according to formulas (6) and (7):

$$w = \sqrt{\frac{4}{3}\frac{d\left(\rho_p - \rho\right)g}{C_D \rho}}\,. \tag{8}$$

The value of the drag coefficient C_D depends on the Reynolds number. Final values of the fall velocity for different hydraulic conditions according the Reynolds number and particle diameter describe following equations (Miedema, Vlasblom, 1996). For the laminar regime for particles with diameter $d \leq 0{,}1$ mm the reduced Stokes equation was used:

$$w = 424\frac{\left(\rho_p - \rho\right)}{\rho}d^2\,. \tag{9}$$

For the particles with diameter 0,1 mm < d < 1 mm a Budryck equation is valid:

$$w = \frac{8{,}925}{d}\sqrt{1 + 95\frac{\left(\rho_p - \rho\right)}{\rho}d^3} - 1\,, \tag{10}$$

and in the turbulent regime for particles with diameter d > 1 mm the Rittinger equation was used:

$$w = 87\sqrt{\frac{\left(\rho_p - \rho\right)}{\rho}d}\,. \tag{11}$$

In equations (9) to (11) the particle diameter is in [mm] and the fall velocity is in [mm.s^{-1}]. Following Table 2 summarizes fall velocities according to equations (9) to (11) for particles of different diameter.

Tab. 2: Fall velocity for different particles

D [mm]	0.004	0.01	0.02	0.05	0.063	0.1	0.25	0.5	1
w [mm.s^{-1}]	0.01	0.07	0.29	1.80	2.86	7.21	66	81	113

4. Results

The final design for the flow-through spur dikes was optimised in accordance with simulations of flow-rate fields between the Elbe riverbank and the spur dike. The objective was to determine the shape of spur dikes that would prevent sedimentation of clay and suspended silt particles behind the spur dikes. The resulting spur dike design is shown in Fig. 3. Individual spur dikes feature a longitudinal section 70 to 100 meters long and an oblique part forming an angle with the riverbank of 45°, at a length of approximately 50 metres. The crest of the longitudinal spur dike section is at the water achieved at volumetric flow rate of Q_{180d}. The area behind the spur dikes is washed by water fed by a localised drop in the crest height at the transverse segment, achieved by means of a shallow ditch across the crest. The shallow ditch slopes at a rate of 1:5 from the level of Q_{180d} to Q_{345d}, the width of the overflow edge of the shallow ditch is 10 m. The cross-section of the rock-formed spur dikes is of a trapezoid shape with a width at the crest of 1 m and slopes of 1:5 towards the riverbank and 1:3 towards the watercourse axis. The crest is intended to widen at the termination of the longitudinal section to as much as 10 m. Fig. 4 shows the velocity field around the spur dike modeled by a 3D mathematical model at a flow rate of Q_{180d}. The results confirmed the suitability of the design, which was appreciated as the optimal and subsequently verified using a hydraulic model.

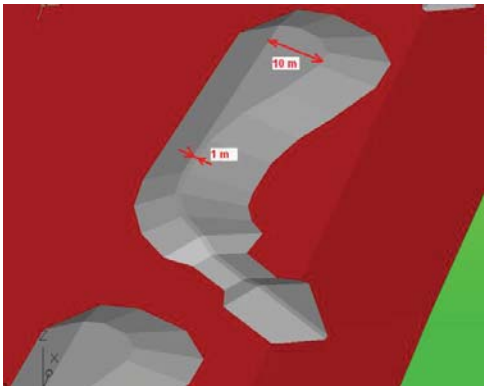

Fig. 3: Optimized spur dike.

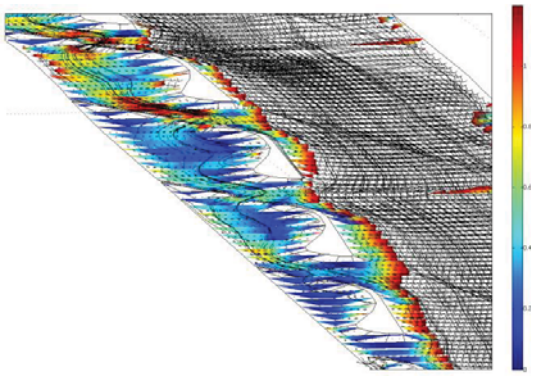

Fig. 4: 3D simulation – velocity field [m.s^{-1}].

The risk of sedimentation was assessed in a simplified form using a comparison between the sedimentation and dragging velocities as per Fig. 5. If the resultant for the sedimentation velocity *w* and the flow velocity *u* for the water current intersects the bed behind a spur dike between two feeding shallow ditches sedimentation will occur, and vice versa. The drag velocity was estimated as the current velocity according to the simulation using the 3D mathematical model.

Analysis of the sedimentation issue is further based on the presumption that the maximum distance L between adjacent spur dikes is up to 100 m, and the depth of water behind spur dikes at Q_{180d} is approximately H = 1.0 m.

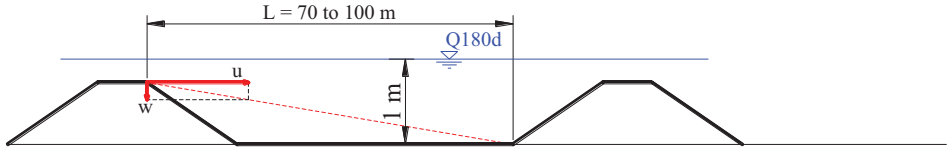

Fig. 5: Sedimentation assessment scheme.

The results obtained demonstrated that sedimentation of clay particles d < 4μm was not possible, and the sedimentation of suspended silt particles of 4 μm < d < 63 μm was not possible for all

practical purposes. On the other hand, sedimentation of fine sand particles of 63 μm < d < 250 μm cannot be ruled out, in particular in areas of no current during low flow rates. During periods of increased flow rates, re-transportation of settled sand particles can be expected due to turbulence. Medium-size sand particles of 250 μm < d < 1000 μm are rare in suspended sediment in the lower Elbe (up to 4% ratio) according to Rudis et al. (1999).

A follow-up investigation using a hydraulic model verified the stability of directing spur dikes under flood conditions. The investigation was conducted in the water management laboratory of the Faculty of Civil Engineering of the Czech Technical University in Prague. Stability of the spur dike design was confirmed up to and including the investigated volumetric flow rate of Q_{100}.

5. Conclusions

The research focused on designing a suitable shape of concentrating spur dikes with a view of improving navigability at the lower Elbe below the planned Děčín barrage to the state border between the Czech Republic and Germany. The key purpose of spur dikes is to ensure sufficient navigation depth even under conditions of low volumetric flow rates on the Elbe. An important requirement in the research was the reduction of sedimentation of suspended clay and silt particles in the area between the spur dikes and the riverbank. Historical spur dikes at the lower Elbe had been designed for the most part to lead to complete targeted aggradation. The initial inspiration for the research was therefore taken from spur dikes near Nebočady where partial washing of the riverbed behind the spur dikes is ensured at flow rates exceeding Q_{180d}. The shape of the spur dikes was further optimised using a 3D mathematical modeling. The optimisation aimed to determine the spur dike design that would best prevent sedimentation of suspended clay and silt particles. The results obtained from the 3D modeling were subsequently verified on a physical model, focusing particularly on stability under flood flow rates, with positive results. Initial pilot spur dike projects were constructed in the target area of the lower Elbe in 2010, with a currently ongoing evaluation of their function in terms of river navigation and sedimentation of small suspended particles. The initial results of the measurements fully support the proposed solution.

Acknowledgement

This research has been supported by the research program NAKI of the Ministry of Culture of the Czech Republic, on "Methodology and prevention and preservation tools of cultural heritage endangered by floods", No.: DF11P01OVV009.

References

Fosumpaur, P., Kralik, M. & Zukal, M. (2010) Physical and numerical modeling in the research of hydraulic structures, in: *Proc. of the Int. Conf. on modeling and simulation*, CTU in Prague.

Miedema, S.A. & Vlasblom, W.J. (1996) Theory for Hopper sedimentation, in: *Proc. 29th Annual Texas A&M Dredging Seminar*. New Orleans.

Novak, P., Moffat, A. I. B., Nalluri, C. & Narayanan, R. (2007) *Hydraulic structures*. Fourth edition, Taylor and Francis, 2007.

Rudis, M., Zalesky, J. & Kos, J. (1999) Experimental study of re-suspension of cohesive sediments of Elbe river, in: *Proc. of the 28.th Bienial Congress of IAHR*, Theme E3, p. 380, Graz-Austria, 1999.

Wilcox, D.C. (1998) *Turbulence Modeling for CFD*. 2nd edition, DCW Industries Inc., California.

Zajicova, P. (2007) Regulated Elbe reach Strekov-Hrensko, service of waterway and influence of floods on navigation, in: *Proc. Int. Conf. Vodni toky 2007*. Hradec Kralove-Czech Rep.

18th International Conference
ENGINEERING MECHANICS 2012
Svratka, Czech Republic, May 14 – 17, 2012

pp. 287–290
Paper #270

CHARACTERISTIC OF DAMAGE TO THE STRUCTURAL ELEMENT BY CREATING ITS "DEGRADATION PROFILE"

J. Frankl*

Abstract: *This paper presents results of experimental establishment of the extent of damage and changes in strength of a wooden structural element (a rafter base) through the creation of its "degradation profile." The tested part of the structural element was divided into segments by the means of a regular network from which standard test specimens were made with dimensions of 20x20x30 mm on which strength tests under compression along the fibres of wood were carried out. Readings were divided, according to the decrease in the property observed against the values of healthy (undamaged) wood, into 4 quality groups and then transferred back to the network of segments. A graphic model description of the shape and course of degradation of wood caused by wood-destroying fungi was created, marked as the "degradation profile of an element".*

Keywords: ***Wood, Timber, Wood-destroying Fungi, Degradation profile.***

1. Introduction

Durability and reliability of wooden structures and individual wooden structural elements in-built in buildings are considerably affected by the activities of many destructive biological agents. Among the most important biological pests are wood-damaging fungi. There is a considerable amount of information available about their morphology and principles of their destruction effect on wood (Schmidt 2006, Beach-Andersen 1995, Reinprecht 1996). Information on the changes in mechanical properties of wood due to their effects is available mainly based on experiments conducted under laboratory conditions (Singh 1994, Reinprecht 2008). Relatively little attention has been so far paid to the effects of wood-damaging fungi on changes in mechanical properties of wood under real conditions of actual structures.

The performed experiment was aimed at detecting the decrease in mechanical properties - compression strength along the fibres in wood samples prepared from a structural element (the bottom part of a rafter) damaged by the activities of wood-damaging fungi in a roof frame structure of a real building.

What was chosen for the experiment was the bottom part (the base) of a rafter from a roof beam structure of a historic building in the centre of Prague. According to the data collected from the construction documentation, the roof beam structure dates back from 1866 - 1868 when the last known reconstruction of the building was taking place. The roof beam structure of the building's gable roof consisted of 13 trusses. The tested part comes from a rafter on the western side of truss No. 8 (Fig. 1). The rafter base was damaged by wood-damaging fungi (brown rot). The damage took place long time ago. At the time of the survey of the quality condition of wood elements and the realization of repairs, wood-damaging fungi were in a non-active stage. By performing laboratory analysis using the cultivation method, the presence of viable germs of wood-damaging fungi of the *Trametes* and *Gloeophyllum* genera was identified in fragments of wood from the damaged part.

2. Methodology:

Part of the rafter, separated for experimental tests, was 60 cm long with a cross section of 12 x 15 cm (width x height). The damage by wood-damaging fungi observable with the naked eye covered the distance of approx. 40 cm from the end of the element. It was mostly of superficial nature which

* Ing. Jiří Frankl, Ph.D.: Institute Theoretical and Apllied Mechanics, v.v.i., Academy of Sciences of Czech Republic, Prosecká 76; 190 00, Prague; CZ, e-mail: frankl@itam.cas.cz

Fig. 1: View of the roof beam structure.

passed from the top surface of the element to the core (central) sections due to the activities of the fungi of the *Gloeophyllum* genus.

With regards to the required size of the test specimens, the dimensions of the tested wooden element and the technological capabilities (handling and woodworking machines), the division of the element "roughly" into a regular network of 12 x 5 x 4 segments of the size of approx. 45 x 25 x 25 mm was selected. More exact test samples of the required size of 20 x 20 x 30 mm were then made from individual segments, where possible. The difference in the sizes of segments and test samples covered losses during the processing (offcut) and allowed to partly offset the natural wood defects (knots, cracks). The division of part of the element by transverse and longitudinal cuts into individual segments and the production of test samples is clear from Fig. 2. Given the extensive damage to some parts and due to the natural defects of the wood, it was not possible, despite this measure, to prepare test samples from some of the segments Fig. 3.

In test samples prepared from individual segments, a test of the limit of compression strength in the direction of fibres was performed. The test was performed using the Testatron load testing apparatus as per the CSN 490110 Czech National Standard. Before the tests, humidity of test samples was adjusted in a climatic chamber to the prescribed 12 %. The testing apparatus and examples from the test of the samples are shown in Fig. 4.

The force at the limit of strength was measured using the load testing apparatus (Fmax). The compression strength was then calculated using formula (1), whereby σ is compression strength, $\mathbf{F_{max}}$ is the force at the strength limit and **a**, **b** are dimensions of the loaded surface.

$$\sigma = \mathbf{F}_{max} / \mathbf{a} * \mathbf{b} \tag{1}$$

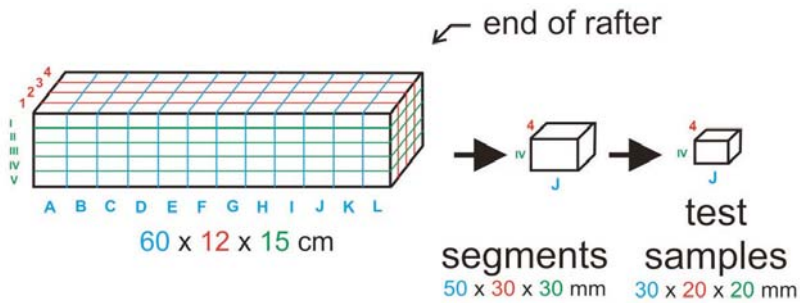

Fig. 2: Division of parts of the rafter into individual segments, their marking and the scheme of the production of test samples.

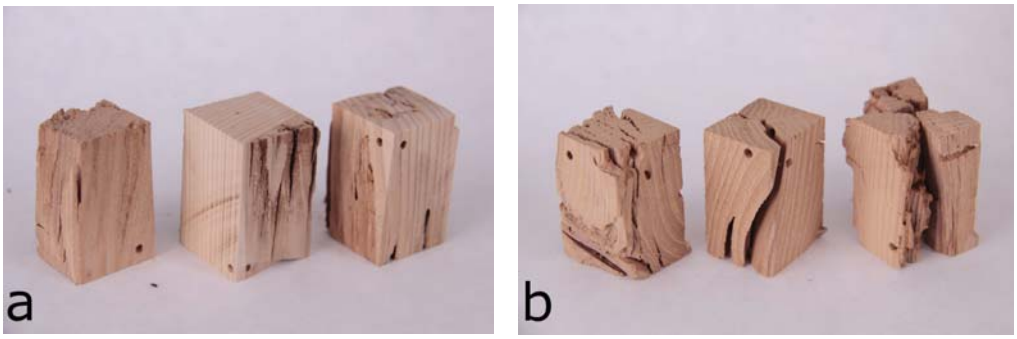

Fig. 3: Examples of segments originated by cutting beams before the production of exact test samples, a) segments with the potential to produce a test sample, b) segments with no opportunity to produce a test sample.

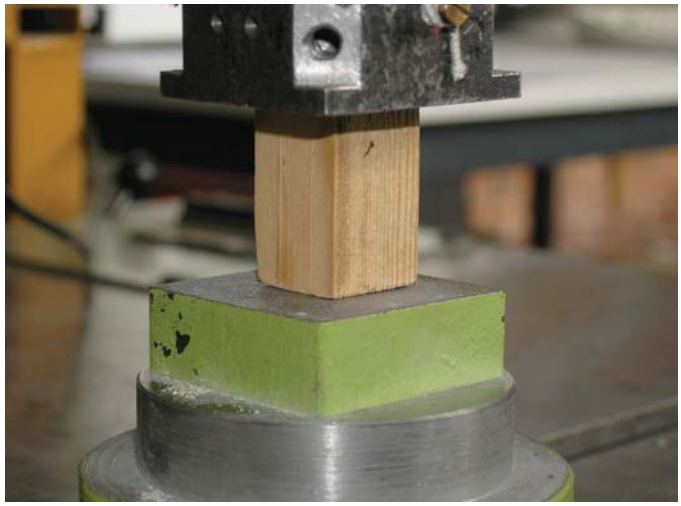

Fig. 4: Tests of mechanical properties of the wood - test of the compression strength in the direction of fibres.

In test samples prepared from individual segments of part of the rafter, the limits of compression strength of the wood in the direction of the fibres were ascertained as ranging from 31.7 to 2.9 MPa. The interval of values of the limit of strength was, for simplification purposes and in order to provide a graphic depiction of the degradation profile of the element, divided into four groups according to the degree of damage or rather the size of the change in the mechanical property under review. The division into groups is clear from Tab. 1.

Based on this division, a degradation profile was prepared, i.e. the graphic depiction of the changes in the wood strength due to degradation by wood-damaging fungi in individual parts of the base part of the rafter. The drawing of the degradation profile in longitudinal sections of rafters (in the pre-selected network of 12 x 5 x 4 segments) is shown in Fig. 5.

3. Conclusions

The experiment presents a considerable impact of destructive wood-damaging fungi on mechanical properties of the attacked wood. From the results of the tests of compression strength of wood and from the processed degradation profile, what is clear is a significant spread of values of strength of wood in individual segments of the element under review. This spread corresponds to the macroscopically observable accompanying phenomena of destruction caused by cellulosevorous

Tab. 1: division of the damage of the elements by wood-damaging fungi into five groups depending on the change (drop) in the monitored mechanical property.

wood	decrease in property (tentative)	limit in compression strength in the direction of fibres
	[%]	[MPa]
sound	0 – 10	31,7 – 28,5
damaged	10 – 40	28,5 – 19,0
strongly damaged	40 – 70	19,0 – 9,5
completly damaged	70 – 100	9,5 – 0

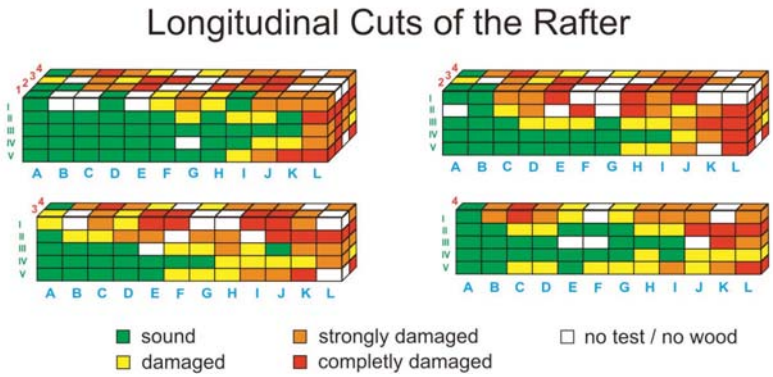

Fig. 5: Examples of segments originated by cutting beams before the production of exact test samples, a) segments with the potential to produce a test sample, b) segments with no opportunity to produce a test sample

wood-damaging fungi (darkening of wood, fissures, disintegration into minuscule particles). The results show that the transition zone between the heavily damaged timber (with a decrease in strength by more than 50%) and healthy wood is relatively narrow and varies in the order of millimetres. The degradation profile of the damaged element reveals changes in shape and considerable reduction of the effective cross section (of sound wood) in the element at the place it was deposited on the top plate.

Spatial descriptions of degradation profiles of elements may serve as a basis for assessing the residual bearing capacity and determining the life of structures in relation to the type of biological damage.

Acknowledgement

The paper was prepared with the support of a grant of the Grant Agency of the Czech Republic, Grant No. P105/11/P628.

References

Beach-Andersen J. (1995) The Dry Rot Fungus and Other Fungi in Houses, *Hussvamp Laboratoriets Forlag*, Holte, Denmark, 139 pp., ISBN 87-89560-22-1

Reinprecht L. (1996) Procesy degradacie dreva, 1. vydanie, *TU Zvolen*, Zvolen, Slovakia

Reinprecht L. (2008) Ochrana dreva, *Vydavat'elstvo TU vo Zvolene*, Zvolen, Slovakia, 453 pp. ISBN 978-80-228-1863-6

Schmidt O. (2006) Wood and Tree Fungi. *Springer Verlag*, Berlin, Heidelberg, Germany, ISBN 3-540-32138-1

Singh J. (1994) Building mycology – Management of decay and healt in buildings. (1994), *E & FN Spon*, UK

18th International Conference
ENGINEERING MECHANICS 2012
Svratka, Czech Republic, May 14 – 17, 2012

pp. 291–294
Paper #276

CHANGES IN PHYSICAL PROPERTIES OF WOOD DAMAGED BY ACTIVITIES OF WOOD-DAMAGING FUNGI

J. Frankl*

Abstract: *This paper presents results of experimental, laboratory establishment of the extent of changes in physical properties (swelling, water absorbability) of timber (spruce) damaged by the activity of wood-damaging fungi. The experiment was carried out using standard test samples (20 x 20 x 30 mm) prepared from new timber and subsequently exposed to the activities of wood-damaging fungi (Serpula lacrymans, Trametes versicolor) under optimal growth conditions for the period of 15 to 60 days. Changes in physical properties were observed in the damaged samples as per the CSN 490126 and CSN 490104 Czech National Standards. The experiment proved significant changes in the observed properties depending on the fungi type and duration of the activity thereof.*

Keywords: ***Wood, timber, physical properties wood-damaging fungi.***

1. Introduction

A lot of destructive biological agents affect wooden structural elements inbuilt in buildings. Among the most important destructive agents are wood-damaging fungi. Their morphology and principles of their destructive activity (decomposition of wood) are relatively well described in expert literature (Schmidt 2006, Reinprecht 1996). Less attention is paid to changes in physical or mechanical properties of wood due to their activities or the attention is focused on the types of wood-damaging fungi and tree species that are practically not used in construction industry (Reinprecht 2008).

The carried out experiment was aimed at detecting the decrease in physical properties of spruce wood due to the activities of cellulosevorous and lignivorous fungi. As a representative of a group of cellulosevorous fungi (brown rot) *Serpula lacrymans* was selected, as a representative of the lignivorous group of wood-damaging fungi (soft, white, spongy rot) *Trametes versicolor* was selected. Within the experiment, what was monitored was a change in selected properties depending on the duration of exposure to wood-damaging fungi.

2. Methods and results

Test samples of the size of 20 x 20 x 30 mm with clearly discernible fibre orientation were produced from dried spruce lumber (CSN 490101). The produced samples were dried in a drier at 103±2°C to a constant weight (at zero moisture) and then weighed and precisely measured. Subsequently, they were conditioned in a climatic chamber to achieve moisture content of wood of 12%.

Test samples were then placed into cultivation boxes with wort culture medium and active mycelia growth of the given wood-damaging fungus. The culture, at the time the samples were inserted, was 7 days old. Samples were in series by thirty pieces (for each type of the fungus and the time of activities) exposed to the activities of the wood-damaging fungi for the periods of 15, 30, 45 and 60 days (Fig. 1). Cultivation was taking place in a laboratory environment under optimal growth conditions (Bayer, Týn 1996). Upon expiry of the determined period of cultivation, samples were removed from cultivation boxes, washed and slowly dried until the moisture content of wood of 12% was achieved (Fig. 2).

* Ing. Jiří Frankl, Ph.D.: Institute Theoretical and Apllied Mechanics, v.v.i., Academy of Sciences of Czech Republic, Prosecká 76; 190 00, Prague; CZ, e-mail: frankl@itam.cas.cz

Fig. 1: Cultivation of samples in cultivation boxes after 45 days of exposure to wood-damaging fungi a) Serpula lacrymans, b) Trametes versicolor.

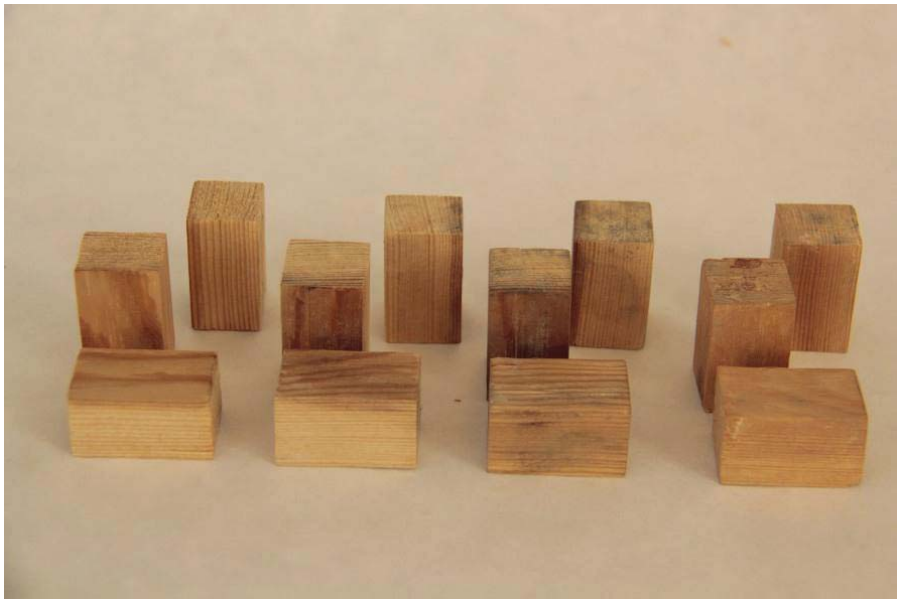

Fig. 2: Test samples after the end of the damage by wood-damaging fungi (Trametes versicolor - 30 days).

Later, the swelling test (CSN 490126) and the absorbability test (CSN 490104) were simultaneously carried out using the damaged samples and reference samples (without any damage). Test samples were immersed in a container with distilled water so as not to touch the bottom, walls and each other and were sunk at least 10 mm below the surface (ensured by a net). In the samples, what was continuously measured was a change in dimensions (the swelling test) until the stabilized condition was reached, i.e., until the difference between two consecutive measurements (within 24 hours) was less than 0.02 mm. At the same time, the samples were weighed (the absorbability test) until the stabilized condition was reached, i.e., until the difference between two consecutive measurements (within 24 hours) was less than 0.1%. After the stabilized condition was reached, all the tested samples were measured and weighed and changes in the observed physical properties evaluated (Fig. 3.).

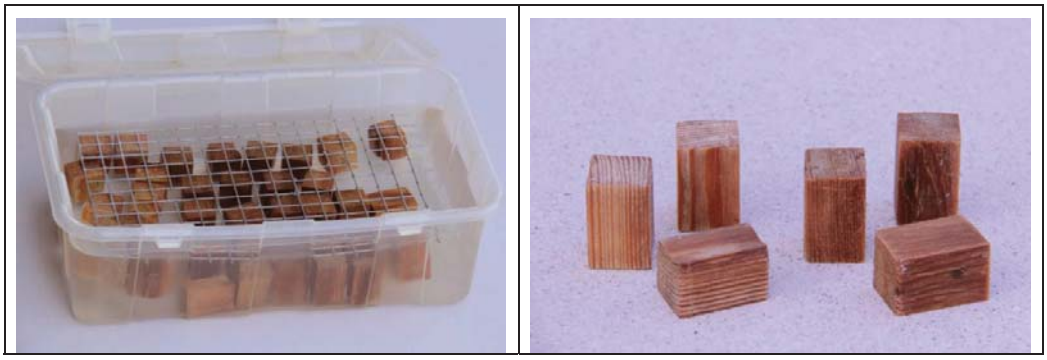

Fig. 3: Test samples during the test of physical properties

The absorbability of wood, W_{max}, as a percentage, is calculated using the following formula:

$$W_{max} = ((m_W - m_0) / m_0) * 100 \quad (1)$$

Where m_0 [g] is the weight of a test sample after having been dried to zero moisture and m_W [g] is the weight of the test sample after soaking.

The largest swelling of wood α_{max} as a percentage is calculated using the following formulas:

$$\alpha_{max\,(r,\,t,\,a)} = ((l_{max\,(r,\,t,\,a)} - l_{min\,(r,\,t,\,a)}) / l_{min\,(r,\,t,\,a)}) * 100 \quad (2)$$

For the radial, tangential and along the fibres directions (r, t and a coefficients).

And according to the following formula - for the total volume (**V** coefficient):

$$\alpha_{max\,(V)} = ((l_{max\,r} * l_{max\,t} * l_{max\,a}) - (l_{min\,r} * l_{min\,t} * l_{min\,a})) / (l_{min\,r} * l_{min\,t} * l_{min\,a}) * 100 \quad (3)$$

Where l_{max} is the dimensions of test specimens for moisture content equal to or greater than the limit of hydroscopicity of cell walls (after soaking) and l_{min} is the dimensions of test specimens during drying to zero moisture.

The identified average values of observed physical properties of spruce wood and their changes due to the effects of selected wood-damaging fungi for periods of varying duration are summarized in Tab. 1.

Tab. 1: Changes in physical properties of spruce wood (absorbability, swelling) caused by exposure for varied periods of time to wood-damaging fungi Serpula lacrymans and Trametes versicolor.

		Serpula lacrymans				Trametes versicolor				Reference
		15 days	30 days	45 days	60 days	15 days	30 days	45 days	60 days	
absorbability	[%]	95,9	127,4	151,1	153,1	107,4	140,7	146,4	178,9	59,5
comp. to the ref. samples	[%]	+ 61	+ 114	+ 154	+ 157	+ 80	+ 136	+ 146	+ 200	
swelling	[%]	15,9	16,2	17,9	18,9	18,7	13,6	13,4	12,5	12.1
comp. to the ref. samples	[%]	+ 31	+ 34	+ 47	+ 56	+ 54	+ 12	+ 11	+ 3	

3. Conclusions

The experiment has proved a considerable impact of destructive activities of wood-damaging fungi on physical properties of spruce wood used for building purposes. In case of effects of the cellulosevorous wood-damaging fungus Serpula lacrymans, there was an overall increase in absorbability of up to 153,1% in samples exposed to the wood-decaying fungus for 60 days during the experiment (compared to the reference samples). In swelling, there was an increased increase in dimensions (compared to reference samples) of up to 56% in samples exposed to the activities of the wood-damaging fungus for 60 days. In case of the effects of the lignivorous wood-damaging fungus Trametes versicolor, there was, in the course of the experiment (compared to reference samples), an overall increase in absorbability of up to 200% in samples exposed to the effects of the wood-damaging fungus for 60 days. In swelling, there was an increased increase in dimensions (compared to the reference samples) of up to 54% in samples exposed to the activities of the wood-damaging fungus for 15 days.

The experiment has proved a significant impact of activities of wood-damaging fungi on physical properties of wood. However, it is necessary to take into account the fact that it took place in the laboratory (sterile) environment under optimal growth conditions. In the real environment of buildings and wooden structures, where the wood degradation process is influenced by a number of other factors, the speed and the extent of changes in physical properties may be considerably different.

Acknowledgement

The paper was prepared with the support of a grant of the Grant Agency of the Czech Republic, Grant No. P105/11/P628.

References (EM Reference Chapter style)

Bayer J., Týn Z. (1996) Ochrana Dřeva, Grada Publishing, Praha, CR, 97 pp. ISBN 80-7169-275-1

Reinprecht L. (1996) Procesy degradacie dreva, 1. vydanie, *TU Zvolen*, Zvolen, Slovakia

Reinprecht L. (2008) Ochrana dreva, *Vydavaťelstvo TU vo Zvolene*, Zvolen, Slovakia, 453 pp. ISBN 978-80-228-1863-6

Schmidt O. (2006) Wood and Tree Fungi. *Springer Verlag*, Berlin, Heidelberg, Germany, ISBN 3-540-32138-1

18th International Conference
ENGINEERING MECHANICS 2012
Svratka, Czech Republic, May 14 – 17, 2012

pp. 295–299
Paper #293

ANALYSIS OF DEFLECTION OF REINFORCED CONCRETE ELEMENTS AFTER DEMOULDING

M. Frantová[*], P. Štemberk[**]

Abstract: *The content of this article is strut-and-tie modelling including the behaviour of early age concrete and analysis of deflections of reinforced concrete elements after demoulding. Mechanical properties of early age concrete are significantly influenced by ongoing hydration. Good knowledge of the behaviour of concrete at early age plays an important role in setting the deadline for removal of formwork and props. Material parameters and time-dependent deformation such as creep and shrinkage were in this work determined based on measurements and by using the microstructure development function. The results are deflections depending on the time of demoulding and the influence of support by props. The results are compared with the limit values. The proposed analysis of the instant of demoulding may be of practical use and can lead to proper intervals or technological breaks and can reduce the amount of formwork required for construction.*

Keywords: ***Deflection, development of microstructure, early-age concrete, formwork stripping, strut-and-tie model.***

1. Introduction

In building construction process, fast formwork dismantling is a very significant issue. There is always a purpose to reuse the formwork or to apply a load to the structure from the adjacent elements. The technological break between concreting and formwork removal and the time when structure can be loaded represents the most important time period in construction of reinforced concrete elements. Because of this, it is important to study the properties of concrete not only in long term, but also in early age just after formwork removal. Other criteria besides the speed of construction are the price of construction affected by the price of formwork rent, etc. Reduction of time necessary for formwork rent and minimizing of time necessary for technological breaks leads to cost savings.

The paper is based on work Štemberk & Tsubaki (2003) dealing with behaviour of concrete at early age and the microstructure development function. This work deals relatively deeply and correctly with the concrete behaviour in the beginning of hydration. Application of this function on particular construction is mentioned in Frantová (2007) where real numbers of short time strain of bridge deck loaded by concrete mix truck in early age of concrete only few hours are evaluated.

For particular application, analysis of elements using strut-and-tie models (STM) is used in the paper, which can be used for design of reinforced concrete structures because of their simplicity when obtaining results. The procedure of STM definition and calculations are available for instance in Reineck (2002).

2. Material model for early-age concrete

Mechanical properties of solidifying and afterwards hardening concrete are cardinally influenced by hydration when microstructure of concrete develops in this period very fast. When modelling the solidifying and hardening concrete it is important to take into consideration the influence of ongoing hydration that can be described by development of microstructure, which represents the process of solidifying and afterwards hardening of concrete. This process depends on various factors as is the

[*] Ing. Michaela Frantová, PhD.: Department of Concrete and Masonry Structures, Faculty of Civil Engineering, Czech Technical University in Prague, Thakurova 7, 166 29 Prague 6; CZ, e-mail: michaela.frantova@fsv.cvut.cz

[**] Doc. Ing. Petr Štemberk, PhD.: Department of Concrete and Masonry Structures, Faculty of Civil Engineering, Czech Technical University in Prague, Thakurova 7, 166 29 Prague 6; CZ, e-mail: stemberk@fsv.cvut.cz

composition of concrete mixture, the shape of structure and the external conditions such as temperature and the curing period. Strength of concrete grows exponentially in the early age but already after few days its exponential growth is over.

Mechanical properties of concrete at early ages are hard to be tested. Most of the researches made on microstructural evolution were based on data from pull-out and penetration tests, whose performance is rather difficult and time-consuming. Moreover, there are not many results that have been presented. Therefore, a reasonable estimation of concrete properties is a better alternative.

Generally, regarding modelling of mechanical properties, the type of equation is not a major point, but it is convenient to have such an equation as (1) for practical use.

$$h(t_n) = a_5 \cdot \left(\frac{a_3 t_n^{a_2}}{a_1 + a_3 t_n^{a_2}} \right)^{a_4} \tag{1}$$

Function (1) represents time-dependant evolution of microstructure, described in Štemberk & Tsubaki (2003). In this study it is used to define, firstly, compressive strength and, secondly, the modulus of elasticity of concrete at early age, which is necessary to know for STM calculations.

3. Application of material model for analysis of deflections

The element for application of assumptions is defined as a simply supported beam with the span of 6 metres and cross-section 0.3 x 0.6 m with lower reinforcement 6Ø20 and top reinforcement 2Ø12. Stirrups were for simplification assumed as two-legged Ø8 all over the length of the beam with the spacing of 200 mm. The strut-and-tie model was used. The calculation model was created using the 1D finite element method

$$K(t) \cdot u = \Delta f, \tag{2}$$

where $K(t)$ is the stiffness matrix that changes in time. This is caused by development of concrete properties, in other words, the modulus of elasticity in time.

Uniform loading due to self-weight was assumed as point loading acting in upper joints. Figure 1, where it was divided partially on Δf that was loading the construction step-by-step. Using this approach it was tried to increase the accuracy of the internal forces calculation of the deformed structure. However, assuming very small strains, the effect is negligible.

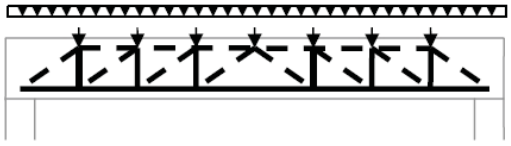

Fig. 1: Recalculation of loading to joints.

3.1. Formwork stripping of whole element

In the first case, the removal of formwork of whole element at the same time was assumed, see Figure 2. In Figure 3, deformations based on the removal of formwork at the time period 20 minutes are shown. If we assume the limit deflection L/250, construction complains the requirement at the time 9 hours after removal of formwork.

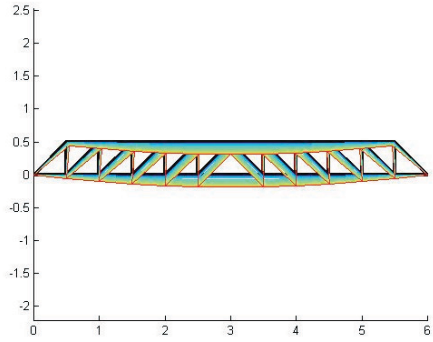

Fig. 2: Deflection after one-shot formwork removal (not in scale)

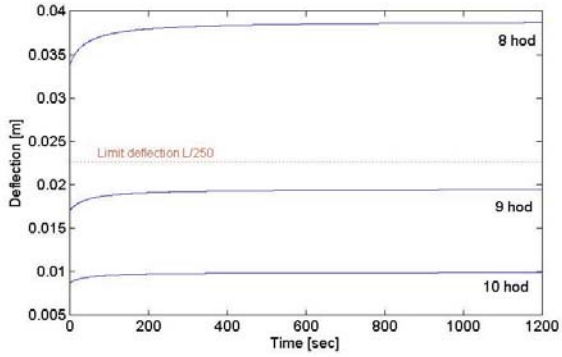

Fig. 3: Deflection after formwork removal

3.2. Step-by-step formwork stripping

In the practice, the beams demoulded are step-by-step based on the type of the formwork system. Separate states will appear after formwork removal, as can be seen in Figures 5, 6, 7 and 8 (deflections are not in scale). States are affected by the used formwork system.

In our case, it was opted for length of segment of 3 metres. It means two segments for the whole beam.

In Figure 5, removal of formwork from the left half of the beam is assumed while the right half is still being propped. The duration of this process is assumed 15 minutes. Immediately after beginning of the next step, the beam is supported by props in the first third of its length and the other half of the beam is demoulded. Similarly as in the first step, the period of 15minutes was assumed (Figure 6), after which the beam was supported by props in the second third (Figure 7). Now the beam is demoulded and left 15 minutes on the props. In the last step (Figure 8), removal of props follows. This is a theoretical option only, because from the experience it is known that props remain supporting the construction much longer. This is also visible from the Figure 9 in last stage of the formwork removal.

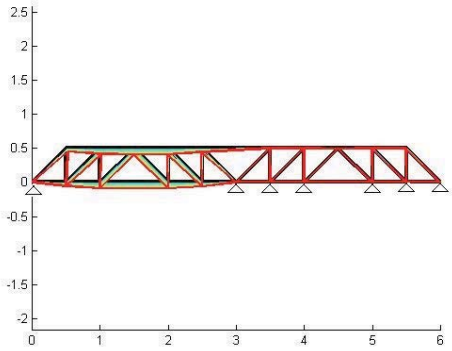

Fig. 5: Deformation after 15 minutes after demoulding from the left side

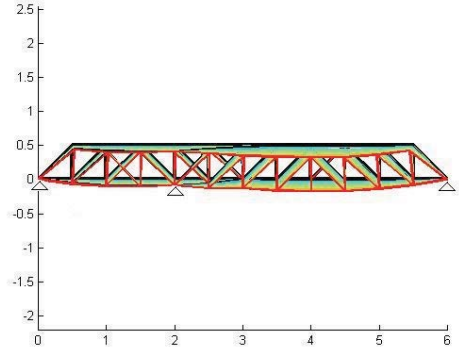

Fig. 6: Deformation after 30 minutes after propping in the first third of span and demoulding another half of the beam

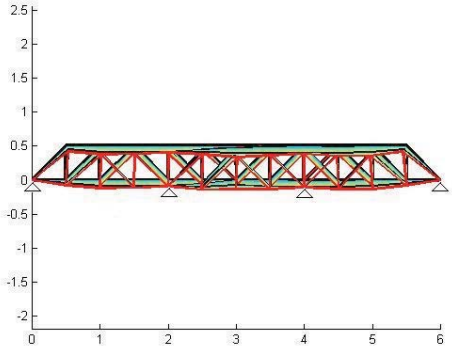

Fig. 7: Deformation after 45 minutes after propping in thirds of span

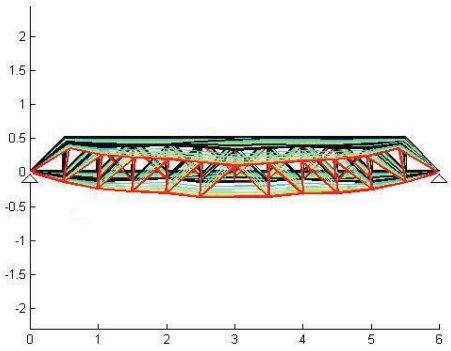

Fig. 8: Deformation after 60 minutes without props

Figure 9 expresses the largest deflections at individual time periods after demoulding. It is obvious that a big part of the deformation is caused directly by the last stage of demoulding. This is caused by higher stress in the struts that were not as big in the previous stages of demoulding. If additional possible loading was assumed, especially the period of the last stage would be very important and leaving the props on their positions would be decisive for the deflection.

So it means that leaving the props on their positions for a longer time period would cause the deflection not to change essentially as it can be seen in Figure 9. In the case of hasty removal of props, the deflection would be by 35% larger. However, also in the case of demoulding at the 8th hour the deflection is close to the value of the limit deflection $L/250$, which is 24 mm.

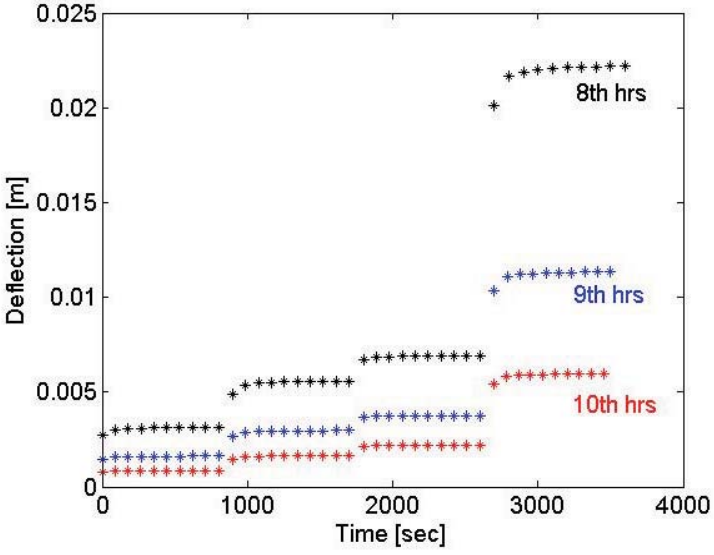

Fig. 9: Deflection based on the various time of demoulding

Values gathered by the proposed model provide very short values of time for possible demoulding. However, it should be kept in mind that the assumptions of experimental measurement were assumed, when the period of loading was 20 minutes and the level of loading was 30% of the concrete compression strength. It was tried to maintain these conditions. The model of the beam was simplified by the strut-and-tie model. Using this simplification, possible cracks are not taken into consideration, which would essentially influence the deflections. Also the cracks appearing on the verge of reinforcement and concrete might have played an important role.

4. Conclusions

In this study, a method to predict the earliest instant for formwork stripping is presented. Considering the early-age concrete, most of the final strength will be achieved after a relatively short time, though some further strength gain can occur according to the type of cement and admixtures. Therefore, the function of evolution of microstructure was used to define the time-dependent gain of concrete stiffness.

The studied element is a simply supported beam with 6 metres of span. That has been replaced by a strut-and-tie representation and was modelled using 1D finite element method. From the results of the presented work it can be seen that reinforced concrete elements loaded only by self-weight can comply with the deflection requirements already after a very short time after concreting. In the presented case it was the 8^{th} and 10^{th} hour. In the case of total formwork removal by one-shot, the value of 9 hours was approached. Respecting the process of formwork removal, one can speak about 8^{th} hours. If the props supporting the structure are left in place longer, the time for formwork removal would be even shorter and the structure could be also additionally loaded.

Acknowledgement

The work was created within the scope of the CTU in Prague, project SGS11/107/OHK1/2T/11, which is gratefully acknowledged.

References

Štemberk P. & Tsubaki T. (2003) Modeling of Solidifying concrete under One-Dimensional Loading, in: *Proceedings of JCI*, Vol.25, No.1, pp. 587-592.

Frantová M. (2007) Investigation of Bridge Deck Strain during Construction, In: *Modern Building Materials, Structures and Techniques*. Vilnius: VGTU Technika, 2007, pp. 246-247.

Reineck, K.-H. (2002) Examples for the Design of Structural Concrete with Strut-and-Tie Models, ACI International SP-208.

18th International Conference
ENGINEERING MECHANICS 2012
Svratka, Czech Republic, May 14 – 17, 2012

pp. 301–308
Paper #251

NEW DESIGNS OF EXTERNAL FIXATORS FOR TREATMENT IN TRAUMATOLOGY

K. Frydrýšek[*], O. Učeň[**], T. Kubín[**], L. Pleva[***], L. Žilka[****], V. Sládeček[*****]

Abstract: *This paper reports about the new design of external fixators invented at the VŠB - Technical University of Ostrava and at the Trauma Centre of The University Hospital in Ostrava together with MEDIN a.s. company. These fixators are intended for the treatment of open, unstable and complicated fractures in traumatology and orthopaedics for humans or animals. The new design is based on the development of Ilizarov and other techniques (i.e. shape and weight optimalization based on composite materials, application of smart materials, nanotechnology, low X-ray absorption, antibacterial protection, patient's comfort, reduction in the duration of the surgical treatment, and cost).*

Keywords: ***biomechanics, traumatology, design, experiments, numerical modelling***

1. Introduction

According to current studies and research, performed at VŠB – Technical University of Ostrava and Traumatology Centre of the University Hospital of Ostrava (Ostrava, Czech Republic) and Trauma Hospital of Brno (Brno, Czech Republic), for examples see references Pleva (1999), Podešva (2002), Stacha (2005), Rozum (2008), Pokorný & Paša et all (2007), Janečka (2011), Frydrýšek et all (2011), Frydrýšek (2012) and mentioned web page, the current design of external fixators can be modified, see Fig. 1. Fixators can be applied in traumatology, surgery and orthopaedics for treatments such as: open and unstable (complicated) fractures, limb lengthening, deformity correction, consequences of poliomyelitis, foot deformities, hip reconstructions, etc. Hence, external fixators can be used for treatment of humans and animals.

External fixation, see Fig. 1, is a surgical treatment usually used to set bone fractures in which a cast (plaster) would not allow proper alignment of the fracture. In this kind of reduction, holes are drilled into uninjured areas of bones around the fracture and special bolts or wires are screwed into the holes. Outside the body, rods and curved pieces of metal with special joints connect the bolts to make a stiff support. The complicated fracture can be set in the proper anatomical configuration. Since the bolts pierce the skin, proper cleaning to prevent infection at the site of surgery must be performed. External fixation is usually used when internal fixation is contraindicated, or as a temporary solution. During its use, it is also possible to use and exercise the broken limbs and even walk.

However, a modern design of these fixators is needed to satisfy new trends in medicine, see the following text.

[*] Assoc. Prof. M.Sc. Karel Frydrýšek, Ph.D., ING-PAED IGIP: Department of Mechanics of Materials, Faculty of Mechanical Engineering, VŠB – Technical University of Ostrava, 17. listopadu 15/2172; 708 33, Ostrava; CZ, e-mail: karel.frydrysek@vsb.cz

[**] M.Sc. Oldřich Učeň, Ph.D. & M.Sc. Tomáš Kubín, Ph.D.: Department of Production Machines and Design, Faculty of Mechanical Engineering, VŠB – Technical University of Ostrava, 17. listopadu 15/2172; 708 33, Ostrava; CZ, e-mail: oldrich.ucen@vsb.cz, tomas.kubin@vsb.cz

[***] Assoc. Prof. MUDr., Leopold Pleva, CSc.: Trauma Centre, University Hospital in Ostrava, 17. listopadu 1790, 708 52, Ostrava, CZ, e-mail: leopold.pleva@fnspo.cz

[****] M.Sc. Luboš Žilka: MEDIN, a.s., Vlachovická 619, 592 31 Nové Město na Moravě, e-mail: lubos.zilka@medin.cz

[*****] M.Sc. Václav Sládeček, Ph.D.: Department of Electronics, Faculty of Electrical Engineering and Computer Science, VŠB – Technical University of Ostrava, 17. listopadu 15/2172; 708 33, Ostrava; CZ, e-mail: vaclav.sladecek@vsb.cz

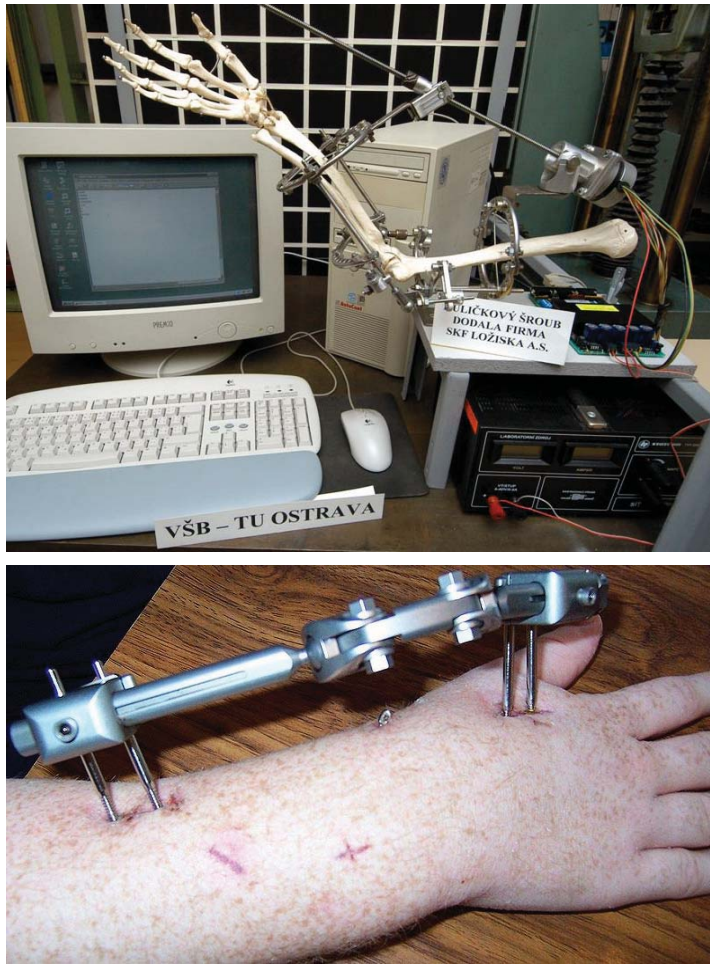

Fig. 1: Current design of external fixators

2. New Ways for Designing External Fixators

Scientific and technical developments, together with medical care and medical practice, bring new demands for designs of external fixators. These demands should be solved by: applications of new smart materials, new design, measuring of the real loadings and numerical modelling and experiments. These points are mutually connected.

Applications of new smart materials should satisfy the following requirements:

a) Low X-ray absorption (i.e. X-ray invisible) for the outer parts of fixators, see Fig. 2. The outer parts of fixators are usually made of metal (titanium, duralumin, stainless steel), which are visible in X-ray diagnostic. Sometimes, the surgeons must repeat X-ray diagnostics (from different points of view) during the operation, because it is difficult to see the broken limbs. Therefore, it is important to make the outer parts X-ray invisible, which leads to shortening the operating time and reducing radiation exposure for patients and surgeons.

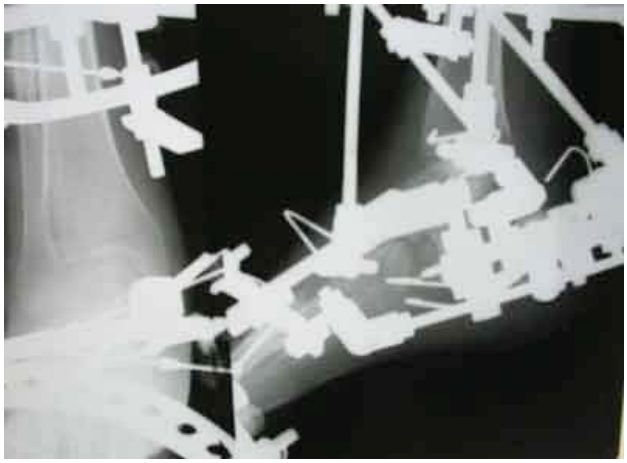

Fig. 2: Problems with high X-ray absorption (it is difficult to see broken limbs because there is too so much metal parts)

b) Application of nanoadditives containing selected metal-based nanoparticles on the surface of the outer parts of the fixators may allow for growth inhibition of several pathogens present on human skin and thus prevent or reduce possible infection. Nanotechnology allows a built-in antibacterial protection for solid products, coatings and fibres. Antibacterial protection gives products an added level of protection against damaging microbes such as, bacteria, mould and mildew that can cause cross-contamination and product deterioration. Antibacterial nanotechnology, combined with regular cleaning practices, helps to improve hygiene standards and provides extra protection wherever it is used. For more information see references Tokarský et all (2009), Valášková et all (2009) and Frydrýšek et all (2011).

c) Proper mechanical properties (stiffness of the whole system of fixators, fatigue testing, etc.) is based on laboratory testing of new smart materials.

d) Weight optimalization - to avoid the overloading of limbs fixed by external construction. This is based on the application of numerical methods and experiments.

It is possible to satisfy all these demands with a new material which uses proper plastics (polymers), because some current solutions based on light metals (aluminium, titanium etc.) are visible in X-ray diagnostic, see Fig. 2 and 3.

Fig. 3: Design of external fixators a) Based on metals (current design, heavier, expensive, etc.) b) Based on reinforced polymers (new design, lighter, cheap, more friendly etc.)

A **new design** should be made according to shape, ecological perspective, a patient's comfort, reducing the time of the surgical operation and reducing the overall cost. Technical aesthetics of fixators also have impacts on the psyche of the patients (i.e. "friendly-looking design of fixators"). For example, patients usually have better feelings, easier motion and physiotherapy with fixators made up from lighter composites (reinforced plastics) than heavier metals, see Fig. 3. In addition, polymers are easy recycled.

During the patient's treatment is important to do **measurements of the real loadings and stiffness of the external fixators** (laboratory measurement and measurement in vivo - painlessly) and data processing are needed. The original type of measuring is very important for future possible enhancements. This is based on strain gauge measurement and applied statistics and the Simulation-Based Reliability Assessment (SBRA) Method, see references Marek et all (2003), Frydrýšek (2010), Kala (2011), Frydrýšek (2012) and Fig. 4. This type of measuring and processing in vivo has never been applied before to the solution of problems of external fixators. This new solution promises new (so far not investigated) information about real loadings of external fixators during the treatments of patients. In a structural reliability assessment the concept of a limit state separating a multidimensional domain of random (stochastic) variables into "safe" and "unsafe" domains has been generally accepted and is increasingly used in structural reliability theory and in design applications.

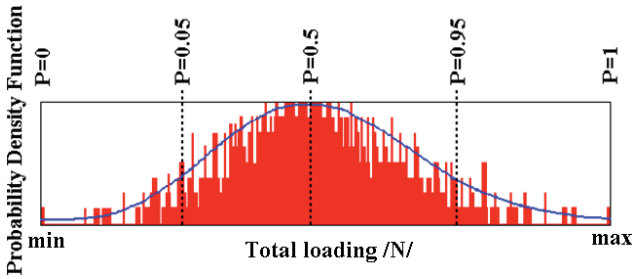

Fig. 4: Typical loading spectrum of an external fixator (overloading is included)

Numerical modelling and experiments (based on the previous skills, see references Pleva (1999), Podešva (2002), Stacha (2005), Pokorný & Paša et all (2007), Rozum (2008), Frydrýšek (2010), Frydrýšek et all (2011), Janečka (2011) and Frydrýšek (2012), as support for research and design, are a very important part of the solution, see Fig. 5, 6, 7 and 8 (i.e. application of FEM and experiments – fixator for fractures of pelvis and its acetabulum) and Fig. 9 (i.e. applications of FEM – fixator for fractures of limbs).

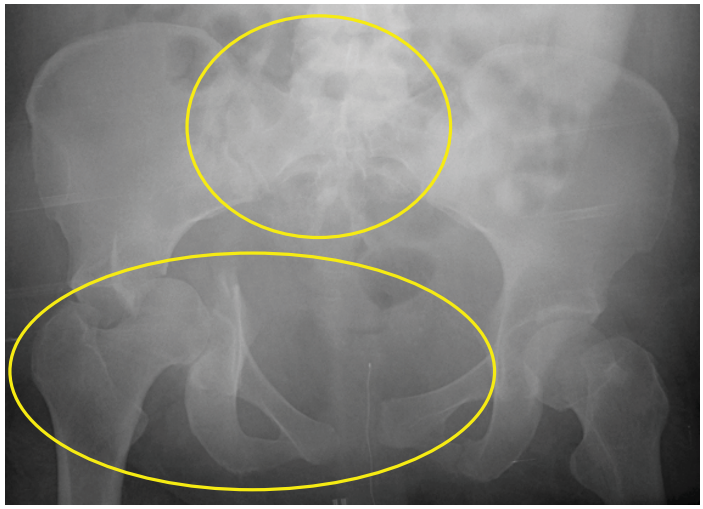

Fig. 5: Fracture of pelvis and acetabulum and its treatment (anteroposterior radiograph - transverse with posterior wall acetabular fracture).

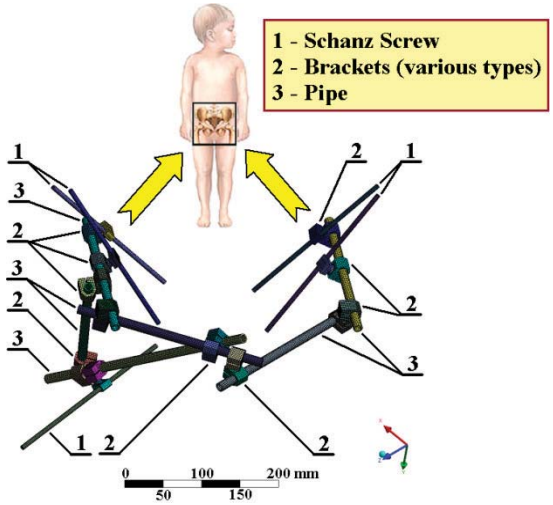

Fig. 6: Application of the external fixator for treatment of pelvis and its acetabulum

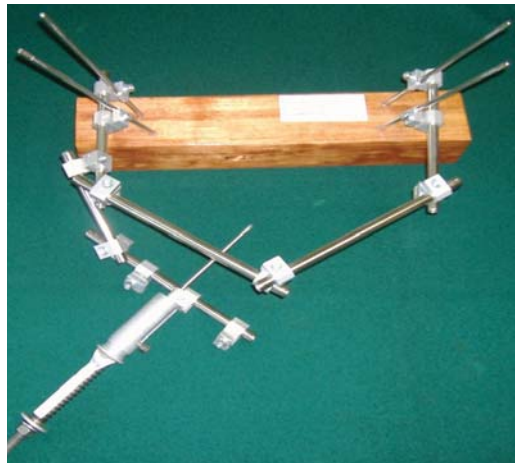

Fig. 7: Prototype of the external fixator for pelvis and acetabulum and its measurement

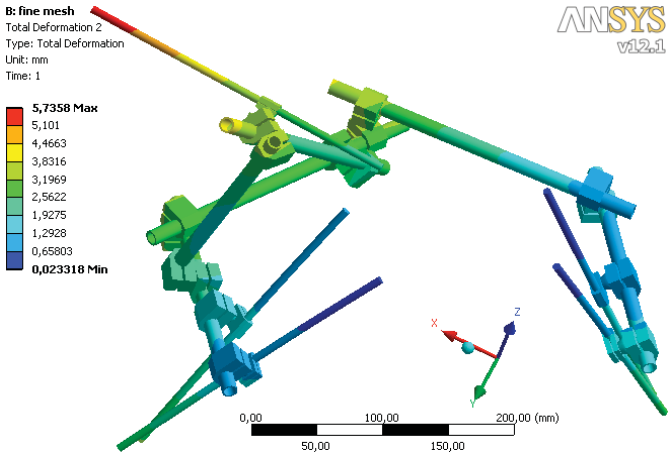

Fig. 8: FE modelling of external fixator for pelvis and acetabulum (total displacement for tensile loading 100 N).

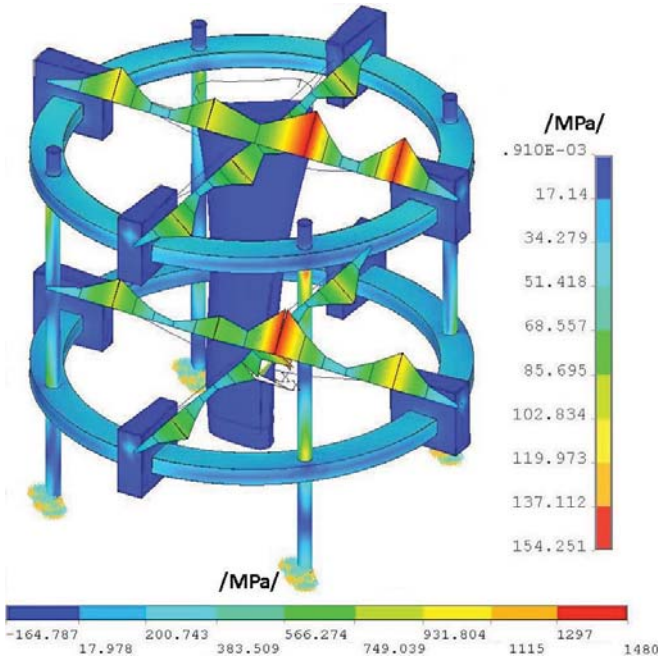

Fig. 9: FE modelling of external fixator for limbs (Equivalent von Mises stress distribution).

It is also important to focus on a **new design of rehabilitation aids connected with the new design of external fixators** presented in the former text.

Therefore, we are in the process of proposing the new continuous passive motion system based on the development of the first model, see Fig. 1a (i.e an electronically controled electro-mechanical device, fully programmable with LCD display, lower limb flexion mobilization unit, a noiseless torque gear motor with seat conveyer for excellent flexion angle setting). This new machine can be used for problems of septic arthritis, ligament tendon healing, for the treatment of intra-artricular fractures etc. The machine has a provision for treatment time, setting of flexion angle and extension provision, hold on flexion and hold on extension cyclic time. The machine also can be used for improvement of blood circulation, reduction of venous engorgement of deep venous thrombosis, extra and intra adhesions, joint stiffness and pain reduction etc.

The whole device consists of (can be formed by) the following elements:

- External fixator of any type.
- Special hinge system connecting both the parts of the external fixator in the place of the elbow and enabling both the parts of the fixator to move.
- Two demountable brackets fixed in particular parts of the external fixator.
- Motor driving unit with accessory equipment mounted between the two brackets producing the movement of both the parts of the fixator.
- Electronic control unit of the fixator motor drive.

Main engineering characteristics:

- Output of the drive 50 W
- Supply voltage 12 – 24V
- Current input up to 5 A
- Max. time of extremity bend by 90 - 20 s

Possible a variant of the small power unit:

- External – linear actuators
- Microstepping Driver R356 (see Fig. 10)

Fig. 10: Possible a variant of the small power unit.

The external fixator of the elbow joint with a motor drive mechanism and the hinge system will enable the timely rehabilitation of the elbow and will prevent late functional limitations that are the most serious complications at using the existing methods of healing limb fractures by external fixators, and that in many cases, result in the arthrodesis of the elbow joint.

3. Conclusions

Report about the new ways to design of external fixators, based on the results of previous research, was presented. Hence, the new designs and materials of fixators will satisfy the ambitious demands of modern traumatology, surgery and economics.

VŠB - Technical University of Ostrava (Faculty of Mechanical Engineering, Faculty of Metalurgy and Material Engineering, Faculty of Electrical Engineering and Computer Science and Centre of Nanotechnology) together with University Hospital of Ostrava and Trauma Hospital of Brno are now in the middle of a process creating a new design for external fixators. Hence, they are in cooperation with the Czech producers MEDIN (Nové Město na Moravě, Czech Republic) and ProSpon (Kladno, Czech Republic).

The new proposed designs cannot be more specifically described here, for confidentiality reasons.

Acknowledgement

This work was supported by the Ministry of Industry and Trade of the Czech Republic as the part of project № MPO FR-TI3/818 named “External Fixation”.

References

Frydrýšek K. (2010) *Pravděpodobnostní výpočty v mechanice 1 (Probabilistic Calculations in Mechanics 1)*, Faculty of Mechanical Engineering, VŠB - Technical University of Ostrava, Ostrava, ISBN 978-80-248-2314-0, Ostrava, Czech Republic, pp. 1-149, written in Czech language.

Frydrýšek, K. (2012): Probabilistic Approaches Used in the Solution of Design for Biomechanics and Mining, p. 304, In: Bérenguer, Ch., Grall, A., Soares, C., G.: *Advances in Safery, Reliability and Risk Management*, ISBN 978-0-415-68379-1, CRC Press/Balkema, Taylor and Francis Group, London, UK, pp. 1900-1905.

Frydrýšek, K., Koštial, P., Barabaszova, K. & Kukutschová, J. (2011) New ways for Designing External Fixators Applied in Treatment of Open and Unstable Fractures, in: *World Academy of Science, Engineering and Technology*, ISSN 2010-376X (print version) ISSN 2010-3778 (electronic version), vol. 7, issue 76, pp. 639–644.

Janečka, M. (2011) *Výzkum a vývoj zevního fixátoru na pánev (acetabulum), včetně experimentálního měření a počítačového modelování*, thesis of Ph.D. work, VŠB – Technical University of Ostrava, Ostrava, Czech Republic, pp. 1-17, written in Czech language.

Kala, Z. (2011) Sensitivity Analysis of Steel Plane Frames with Initial Imperfections, in *Engineering Structures*, vol.33, no.8, , pp. 2342-2349.

Marek, P., Brozzetti, J., Guštar, M. & Tikalsky, P. (2003) *Probabilistic Assessment of Structures Using Monte Carlo Simulation Background, Exercises and Software*, (2nd extended edition), ISBN 80-86246-19-1, ITAM CAS, Prague, Czech Republic.

Pokorný, V., Paša, L., Valentová, J. (2007) Osteosyntéza zlomenin dlouhých kostí ruky. In: *Úrazová chirurgie*, Praha, ISSN 1211-7080, 2007, vol. 15 (2), pp.28-35.

Podešva, R. (2002) *External Fixture Simulation for Treatment of Open Unstable Fractures with Computer Equipment Utilization*, Ph.D. thesis written in Czech language, Faculty of Mechanical Engineering, VŠB – Technical University of Ostrava, Czech Republic, pp.89.

Pleva, L. (1999) *External Fixator for Treatment of Acetabulum Fractures*, final report of the project IGA MZ ČR, reg. č. 3522-4, written in Czech language, FNsP – Ostrava-Poruba, Czech Republic, pp.77.

Rozum, K. (2008) *External Fixators for the Treatment Open Unstable Fractures*, inaugural work written in Czech language, FME, VŠB – Technical University of Ostrava, Czech Republic, 2008, ISBN 978-80-248-1670-8, pp.43.

Stacha, R. (2005) *Development of External Fixator for an Elbow Including Experimental Check and Computer Simulations*, Ph.D. thesis written in Czech language, Faculty of Mechanical Engineering, VŠB – Technical University of Ostrava, Czech Republic, pp.98.

Tokarský, J., Čapková, P., Rafaja, D., Klemm, V., Valášková, M., Kukutschová, J., Tomášek, V. (2009) Adhesion of Silver Nanoparticles on the Clay Substrates; Modeling and Experiment, in *Applied Surface Science*, ISSN: 0169-4332, , doi:10.1016/j.apsusc.2009.11.037.

Valášková, M., Simha Martynková, G., Matějka, V., Barabaszová, K., Plevová, E., Měřínská, D. (2009) Organovermiculite Nanofillers in Polypropylene", in *Applied Clay Science*, ISSN 0169-1317, 43, , pp. 108–112.

http://aplmech.vsb.cz/zevni-fixace/

18th International Conference
ENGINEERING MECHANICS 2012
Svratka, Czech Republic, May 14 – 17, 2012

pp. 309–315
Paper #195

NUMERICAL SIMULATION OF TRANSITIONAL FLOWS WITH LAMINAR KINETIC ENERGY

J. Fürst *

Abstract: *The article deals with the numerical solution of transitional flows. The single point k-k_L-ω model of Walters and Cokljat (2008) based on the use of a laminar kinetic energy transport equation is considered. The model doesn't require to evaluate integral boundary layer parameters (e.g. boundary layer thickness) an is therefore suitable for implementation into codes working with general unstructured meshes. The performance of the model has been tested for the case of flows over a flat plate with zero and non-zero pressure gradients. The results obtained with our implementation of the model are compared to the experimental data of ERCOFTAC.*

Keywords: ***Turbulence, transition, Navier–Stokes equations***

1. Introduction

The laminar-turbulent transition plays very important role in many flows of engineering interest. It has big impact on the heat transfer and losses. Unfortunately most of the state-of art turbulence models (e.g. Menters SST $k-\omega$ model, EARSM model of Hellsten) completely fail with the prediction of transition. However there are some attempts to modify basic models (e.g. low Reynolds model of Wilcox (1998), TSL model of Zheng et al. (1998)) with promising results, the experience shows that this approach is not capable of reliably capturing all factors that affect transition, see Menter et al. (2006).

The algebraic models based on empirical correlations (see e,g, Straka and Příhoda (2010)) offers simple approach with sufficient accuracy. On the other hand the implementation into a general unstructured code is quite difficult due to necessity of some non-local information (momentum boundary layer thickness, intermitency at wall, etc.). Therefore the applicability of these models is more-less limited to research/academic codes using structured meshes.

This article deals with the RANS-based transitional model developed by Walters and Cokljat (2008). The three-equation model is based on the low Reynolds $k-\omega$ model with an equation for the so called laminar kinetic energy k_L expressing the energy of stream-wise fluctuations in pre-transitional region. The main advantage of the model is its local formulation, it means that it can be easily implemented into unstructured solvers. Moreover it can (at least in principle) handle flows in complex geometry. Unfortunately the description of the model in Walters and Cokljat (2008) contains some errors (probably typos) which lead to strong underestimation of the friction in turbulent region. The aim of the aritcle is to show the correct version of the model and to test the performance of the model for simple flows over flat plate.

* Doc. Ing. Jiří Fürst, PhD.: Fac. of Mech. Eng., Czech Technical University in Prague, Karlovo nám. 13; 121 35, Prague; CZ, e-mail: Jiri.Furst@fs.cvut.cz

2. Mathematical model

2.1. Navier–Stokes equations

The viscous compressible flows is described by the set of Favre–averaged Navier–Stokes equations:

$$\frac{\partial \rho}{\partial t} + \frac{\partial (\rho u_j)}{\partial x_j} = 0, \tag{1}$$

$$\frac{\partial (\rho u_i)}{\partial t} + \frac{\partial (\rho u_i u_j)}{\partial x_j} + \frac{\partial p}{\partial x_i} = \frac{\partial (t_{ij} + \tau_{ij})}{\partial x_j}, \tag{2}$$

$$\frac{\partial (\rho E)}{\partial t} + \frac{\partial [(\rho E + p) u_j)}{\partial x_j} = \frac{\partial}{\partial x_j} \left[u_i (t_{ij} + \tau_{ij}) + \left(\frac{\mu}{Pr} + \rho \alpha_\theta \right) \frac{\partial h}{\partial x_j} \right], \tag{3}$$

where ρ is the density, u_i are the components of the velocity vector, p is the static pressure, E is the specific total energy, $h = E + p - u_i u_i/2$ is the specific enthalpy, t_{ij} is the mean viscous stress tensor, $\tau_{ij} = -\overline{\rho u_i' u_j'}$ is the Reynolds stress tensor, μ is the viscosity, Pr is the Prandtl number, and α_θ is the turbulent thermal diffusivity.

We assume perfect gas (the air) with $p = (\kappa - 1)(\rho E - \rho u_i u_i/2)$ where $\kappa = 1.4$ is the constant specific heat ratio. The flow is Newtonian with constant viscosity μ, hence $t_{ij} = 2\mu(S_{ij} - \frac{1}{3} S_{ll} \delta_{ij})$ where $S_{ij} = (\partial u_i/\partial x_j + \partial u_j/\partial x_i)/2$.

2.2. Turbulence model

The turbulence model is based on the Boussinesq hypothesis

$$\tau_{ij} = 2\rho\nu_T (S_{ij} - \frac{1}{3} S_{ll} \delta_{ij}) - \frac{1}{3} \rho k \delta_{ij}, \tag{4}$$

where ν_T is the turbulent kinematic viscosity and k is the turbulent kinetic energy.

We assume a three equation model of Walters and Cokljat (2008) with the transport equations for the turbulent kinetic energy k_T,the laminar kinetic energy k_L, and the turbulent frequency ω. The equations are

$$\frac{D(\rho k_T)}{Dt} = \rho (P_{k_T} + R_{BP} + R_{NAT} - \omega k_T - D_T) + \frac{\partial}{\partial x_j} \left[\left(\mu + \frac{\rho \alpha_T}{\sigma_k} \right) \frac{\partial k_t}{\partial x_j} \right], \tag{5}$$

$$\frac{D(\rho k_L)}{Dt} = \rho (P_{k_L} - R_{BP} - R_{NAT} - D_L) + \frac{\partial}{\partial x_j} \left[\mu \frac{\partial k_t}{\partial x_j} \right], \tag{6}$$

$$\frac{D(\rho \omega)}{Dt} = \rho \left[C_{\omega 1} \frac{\omega}{k_T} P_{k_T} + \left(\frac{C_{\omega R}}{f_W} - 1 \right) \frac{\omega}{k_T} (R_{BP} + R_{NAT}) - C_{\omega 2} \omega^2 \right.$$
$$\left. + C_{\omega 3} f_\omega \alpha_T f_W^2 \frac{\sqrt{k_T}}{d^3} \right] + \frac{\partial}{\partial x_j} \left[\left(\mu + \frac{\rho \alpha_T}{\sigma_\omega} \right) \frac{\partial \omega}{\partial x_j} \right]. \tag{7}$$

The various terms in the equations represents production, destruction, transport, and diffusion. However the structure of the model is more-less clear, there is a confusion in the definition of individual terms in the literature. The original Walters and Leylek's model (see Walters and Leylek (2004)) uses $k_T - k_L - \epsilon$ formulation. The model was later re-formulated using $k_T - k_L - \omega$ (see Walters and Leylek (2005) or Holloway et al. (2004)) and the current version was published in Walters and Cokljat (2008). Unfortunately it seems that the last article contains some errors. Therefore we will write here all individual terms and we will comment the differences of our version with respect to the original article.

The production of turbulent and laminar kinetic energy is

$$P_{k_T} = \nu_{T,s} S^2, \tag{8}$$

$$P_{k_L} = \nu_{T,l} S^2, \tag{9}$$

where $S = \sqrt{2 S_{ij} S_{ij}}$. The "small-scale" eddy viscosity is defined as

$$\nu_{T,s} = f_\nu f_{INT} C_\mu \sqrt{k_{T,s}} \lambda_{eff}, \tag{10}$$

where $k_{T,s}$ is the effective small-scale turbulence

$$k_{T,s} = f_{SS} f_W k_T. \tag{11}$$

The wall-limited turbulence length scale λ_{eff} and damping function f_W is

$$\lambda_{eff} = \min(C_\lambda d, \lambda_T), \tag{12}$$

$$\lambda_T = \sqrt{k_T}\omega, \tag{13}$$

$$f_W = \left(\frac{\lambda_{eff}}{\lambda_T}\right)^{\frac{2}{3}}, \tag{14}$$

here d is the wall distance. Note that the article Walters and Cokljat (2008) does not include the exponent $2/3$ in the definition of f_W. The original model Walters and Leylek (2004) as well as the Walters and Leylek (2005) do include the exponent. The origins of the $2/3$ exponent come from the $k-\epsilon$ formulation where the turbulent integral length scale is

$$\lambda_T = \frac{k_T^{\frac{3}{2}}}{\epsilon}, \tag{15}$$

therefore f_W actually limits the length scale to λ_{eff}.

The following terms are according to Walters and Cokljat (2008)

$$f_\nu = 1 - \exp\left(-\frac{\sqrt{Re_T}}{A_\nu}\right), \tag{16}$$

$$Re_T = \frac{f_W^2 k_T}{\nu\omega}, \tag{17}$$

$$f_{SS} = \exp\left[-\left(\frac{C_{ss}\nu\Omega}{k_T}\right)^2\right], \tag{18}$$

$$C_\mu = \frac{1}{A_0 + A_S\left(\frac{S}{\omega}\right)}. \tag{19}$$

The intermitency factor f_{INT} is

$$f_{INT} = \min\left(\frac{k_T}{C_{INT}(k_T + k_L)}, 1\right). \tag{20}$$

Note that the factor f_{INT} is defined with k_L in nominator in Walters and Cokljat (2008), but the article Walters and Leylek (2005) gives correct form with k_T.

The production of laminar kinetic energy k_L is assumed to be given by large-scale near wall turbulence

$$k_{T,l} = k_T - k_{T,s}. \tag{21}$$

The production term is then given by the equation (9) where

$$\nu_{T,l} = \min\left\{f_{\tau,l} C_{l1} \frac{\Omega\lambda_{eff}^2}{\nu}\sqrt{k_{T,l}}\lambda_{eff} + \beta_{TS} C_{l2} Re_\Omega d^2\Omega, \frac{k_L + k_{T,l}}{2S}\right\}. \tag{22}$$

Here

$$Re_\Omega = \frac{d^2\Omega}{\nu}, \tag{23}$$

$$\beta_{TS} = 1 - \exp\left(-\frac{\max(Re_\Omega - C_{TS,crit}, 0)^2}{A_{TS}}\right), \tag{24}$$

$$f_{\tau,l} = 1 - \exp\left(-C_{\tau,l}\frac{k_{tau_l}}{\lambda_{eff}^2\Omega^2}\right). \tag{25}$$

The dissipation ϵ_{Tot} is divided to an isotropic ($k_T\omega$) and anisotropic ($D_{T/L}$) part (similarly as in the low Reynolds Launder and Sharma $k-\epsilon$ model) with

$$D_T = \nu\frac{\partial\sqrt{k_T}}{\partial x_i}\frac{\partial\sqrt{k_T}}{\partial x_i}, \tag{26}$$

$$D_L = \nu\frac{\partial\sqrt{k_L}}{\partial x_i}\frac{\partial\sqrt{k_L}}{\partial x_i}. \tag{27}$$

However the the balance between the dissipation ϵ_{Tot} and diffusion $\frac{\partial}{\partial y}\left(\nu\frac{\partial k_{T/L}}{\partial y}\right)$ in the laminar sublayer suggests the same formula multiplied by 2 (see e.g. Launder-Sharma $k-\epsilon$ model or the older versions of $k-k_L-\epsilon$ and $k-k_l-\omega$) model, the above mentioned form was proposed in the new model and used in our calculations.

The turbulent diffusivity α_T is

$$\alpha_T = f_\nu C_{\mu,std}\sqrt{k_{T,s}}\lambda_{eff}, \tag{28}$$

and the damping function f_ω is

$$f_\omega = 1-\exp\left[-0.41\left(\frac{\lambda_{eff}}{\lambda_T}\right)^4\right]. \tag{29}$$

The remaining terms R_{BP} and R_{NAT} express the laminar-turbulent transition in terms of the energy transfer from k_L to k_T. They are of the form

$$R_{BP} = C_R\beta_{BP}k_L\omega/f_W, \tag{30}$$

$$R_{NAT} = C_{R,NAT}\beta_{NAT}k_L\Omega. \tag{31}$$

The bypass transition is driven by the β_{BP} function

$$\beta_{BP} = 1-\exp\left(-\frac{\phi_{BP}}{A_{BP}}\right), \tag{32}$$

$$\phi_{BP} = \max\left(\frac{k_T}{\nu\Omega}-C_{BP,crit},0\right), \tag{33}$$

and the natural transition by the β_{NAT} function

$$\beta_{NAT} = -\exp\left(-\frac{\phi_{NAT}}{A_{NAT}}\right), \tag{34}$$

$$\phi_{NAT} = \max\left(Re_\Omega-\frac{C_{NAT,crit}}{f_{NAT,crit}},0\right), \tag{35}$$

$$f_{NAT,crit} = 1-\exp\left(-C_{NC}\frac{\sqrt{k_L}d}{\nu}\right). \tag{36}$$

The turbulent kinematic viscosity used in the momentum equations is then

$$\nu_T = \nu_{T,s}+\nu_{T,l}. \tag{37}$$

The turbulent thermal diffusivity α_θ is then

$$\alpha_\theta = f_W\frac{k_T}{k_T+k_L}\frac{\nu_{T,s}}{Pr}+(1-f_W)C_{\alpha,\theta}\sqrt{k_T}\lambda_{eff}. \tag{38}$$

The coefficient $C_{\omega2}=0.92$ is constant in the original article. Nevertheless the correct form is

$$C_{\omega2} = 0.92f_W^2. \tag{39}$$

case	$U[\mathrm{m\,s^{-1}}]$	$k_T[\mathrm{m^2\,s^{-2}}]$	$\omega[\mathrm{s^{-1}}]$	$Tu[\%]$	$\mu_{T,std}/\mu[-]$
T3A	5.4	0.047 63	23.8	3.30	12
T3B	9.2	1.128 27	56.8	9.43	120
T3A-	19.8	0.048 57	23.8	0.91	12
T3C2	5.5	0.055 58	35.0	3.50	10

Tab. 1: Inlet conditions for flat plate calculations at $x = -0.05\,\mathrm{m}$, here $\mu_{T,std} := C_{\mu,std}\rho k_T/\omega$.

The other constants are

$$
\begin{array}{ccc}
A_0 = 4.04 & C_{INT} = 0.75 & C_{\omega 1} = 0.44 \\
A_S = 2.12 & C_{TS,crit} = 1000 & C_{\omega 3} = 0.3 \\
A_\nu = 6.75 & C_{R,NAT} = 0.02 & C_{\omega R} = 1.5 \\
A_{BP} = 0.6 & C_{l1} = 3.4 \cdot 10^{-6} & C_\lambda = 2.495 \\
A_{NAT} = 200 & C_{l2} = 10^{-10} & C_{\mu,std} = 0.09 \\
A_{TS} = 200 & C_R = 0.12 & Pr = 0.85 \\
C_{BP,crit} = 1.2 & C_{\alpha,\theta} = 0.035 & \sigma_k = 1 \\
C_{NC} = 0.1 & C_{SS} = 1.5 & \sigma_\omega = 1.17 \\
C_{NAT,crit} = 1250 & C_{tau,l} = 4360 &
\end{array}
$$

3. Simulation of flows over a flat plate

The model has been validated using T3 series of experimental flat plate test cases of ERCOFTAC. The T3A, T3B, and T3A- test cases had zero stream-wise pressure gradients with free-stream turbulence of 3%, 6%, and 1% respectively Coupland (1990a). The T3C2 has favorable pressure gradient in the first part of the plate followed by the adverse pressure gradient in the second part, see Coupland (1990b).

The calculation was carried out with OpenFOAM package with our implementation of the $k-k_L-\omega$ model. The numerical solution was obtained with finite volume method using SIMPLEC scheme for compressible flows (see eg. Ferziger and Perić (1999)).

The zero-pressure gradient cases (i.e. T3A, T3A-, and T3B) were calculated using a rectangular domain $\Omega = [-0.05, 2.9] \times [0, 0.175]\mathrm{m}$ where the flat plate starts at $x = 0\mathrm{m}$. The mesh consists of 635×105 cells where 600 cells were at the plate and 35 cells in the inlet region. The mesh was refined in the vicinity of the inlet edge (see fig. 1) and in the wall normal direction with $y_1 \approx 10^{-5}\mathrm{m}$ i.e. $y^+ \leq 1$.

The following boundary conditions were prescribed:

inlet: at the inlet plane ($x = -0.05\,\mathrm{m}$) we prescribe the velocity vector u_i, the temperature ($T = 293.15\,\mathrm{K}$), the turbulent kinetic energy k_T, the laminar kinetic energy $k_L = 0\,\mathrm{m^2\,s^{-2}}$, and the specific dissipation rate ω. The pressure is calculated with the homogeneous Neumann condition $\partial p/\partial n = 0$.

wall: at the wall ($x = 0\,\mathrm{m}$ to $2.9\,\mathrm{m}$ and $y = 0\,\mathrm{m}$) we prescribe non-slip condition for velocity ($u_i = 0\,\mathrm{m/s}$), the homogeneous Neumann condition for pressure $\partial p/\partial n = 0$, zero turbulent and laminar kinetic energy $k_T = k_L = 0\,\mathrm{m^2\,s^{-2}}$, and the homogeneous Neumann condition for the specific dissipation rate $\partial\omega/\partial n = 0$.

outlet: at the outlet ($x = 2.9\,\mathrm{m}$) we prescribe the static pressure $p = 101\,\mathrm{kPa}$ and we use homogeneous Neumann conditions for all remaining quantities.

symmetry: at the rest of the boundary (the upper boundary at $y = 0.175\,\mathrm{m}$ and the lower boundary in front of the plate) we assume symmetry condition for all variables (i.e. the slip condition).

We use constant dynamic viscosity $\mu = 1.8 \times 10^{-5}\,\mathrm{Pa\,s}$ and the ideal gas constant $R = 287\,\mathrm{J\,kg^{-1}\,K^{-1}}$. The parameters of inlet flows are are given in the table 1.

The figure 1 shows comparison of computed skin friction for T3A and T3B case with the experimental data of ERCOFTAC. One can see that the ready-made implementation of the model (labeled by OF

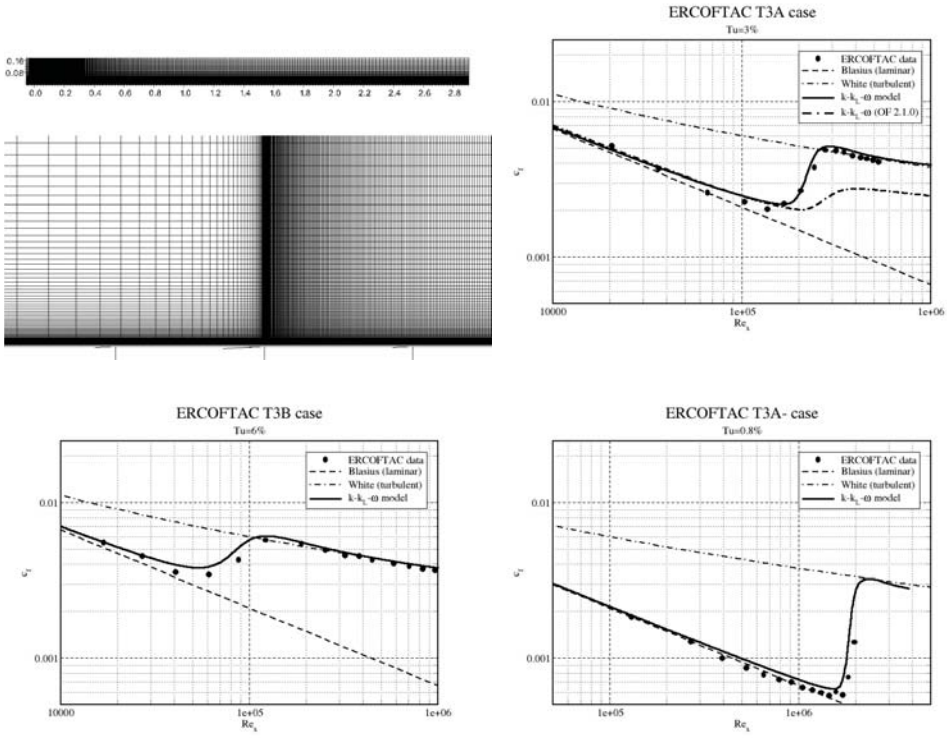

Fig. 1: Friction coefficient for zero-pressure gradient flows over a flat plate (ERCOFTAC T3A, T3B, T3A- cases).

2.1.0 at the figure) fails even with T3A case. On the other hand our implementation of corrected model gives quite good agreement with experimental data form ERCOFTAC database. The results show that the transition onset is very well captured in T3A and T3A- cases. In the T3B case with high turbulence intensity the transition seems to be shifted little bit upstream.

For the non-zero pressure gradient case (T3C2) we use

For the flow with pressure gradient (T3C2 case) we assume a domain with shaped upper boundary (see fig. 2). The shape was constructed in order to match the velocity distribution in the ERCOFTAC experiment. Fig. 2 shows the comparison of experimental data with the calculated velocity distribution at $y = 0.05\,\mathrm{m}$. The calculated skin friction coefficient[**] shows that the model predicts the transition onset to late. On the other hand the transition length is underpredicted, so the position of transition end is captured at right position.

4. Conclusion

The results indicate that the model of Walters and Cokljat (2008) is able (after all necessary corrections with respect to the original article) to predict the laminar-turbulent transition for simple flows over flat plate. Future work will be oriented to the implementation of the model to our in-house code and to its applications for flows in turbine cascades.

[**]The c_f as well as the Reynolds number Re_x was related to local velocity magnitude $U_{0.05}(x)$ at $y = 0.05\,\mathrm{m}$.

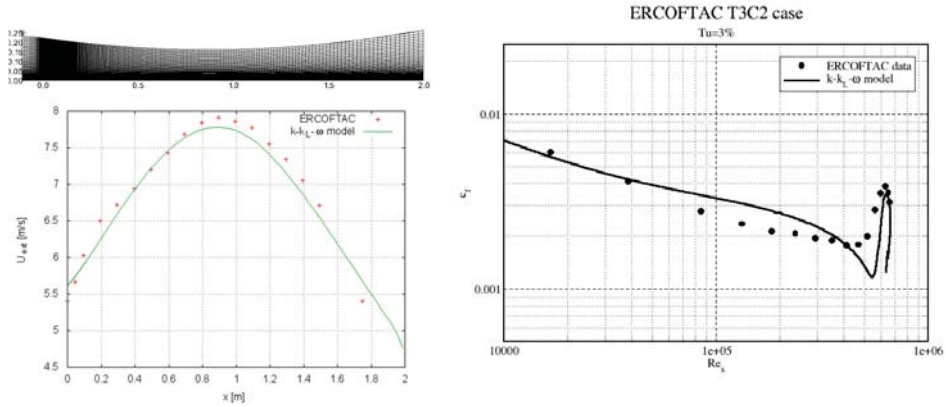

Fig. 2: Domain, the velocity at $y = 0\,05m$ and the friction coefficient for T3C2 ERCOFTAC cases.

Acknowledgments

The work was supported by the Grant no. P101/10/1329 and P101/12/1271 of the Grant Agency of Czech Republic. The author would like to thank prof. K. Walters for the clarification of the model.

References

Coupland, J. (1990a). Ercoftac special interest group on laminar to turbulent transition and retransition: T3a and t3b test cases. Technical report, ERCOFTAC.

Coupland, J. (1990b). Ercoftac special interest group on laminar to turbulent transition and retransition: T3c test cases. Technical report, ERCOFTAC.

Ferziger, J. H. and M. Perić (1999). *Computational Methods for Fluid Dynamics*. Springer.

Holloway, D. S., D. K. Walters, and J. D. Leylek (2004). Prediction of unsteady, separated boundary layer over a blunt body for laminar, turbulent, and transitional flow. *Int. Journal for Numerical Methods in Fluids 45*, 1291–1315.

Menter, F. R., R. B. Langtry, S. R. Likki, Y. B. Suzen, P. G. Huang, and S. Völker (2006). A correlation-based transition model using local variables - Part I: Model formulation. *Journal of Turbomachinery 128*, 413–422.

Straka, P. and J. Příhoda (2010). Laminar-turbulent boundary layer transition modelling for turbomachinery flows. *Czech Aerospace Proceedings 4*, 10–12.

Walters, D. K. and D. Cokljat (2008). Three-equation eddy-viscosity model for Reynolds-averaged Navier-Stokes simulations of transitional flow. *Journal of Fluids Engineering 130*, 121401–14.

Walters, D. K. and J. H. Leylek (2004). A new model for boundary layer transition using a single-point RANS approach. *Journal of Turbomachinery 126*, 193–202.

Walters, D. K. and J. H. Leylek (2005). Computational fluid dynamics study of wake-induced transition on a compressor-like flat plate. *Journal of Turbomachinery 127*, 52–63.

Wilcox, D. C. (1998). *Turbulence Modeling for CFD* (Second Edition ed.). DCW Industries, Inc.

Zheng, X., C. Liu, F. Liu, and C.-I. Yang (1998). Turbulent transition simulation using the $k - \omega$ model. *Int. J. Numer. Meth. Engng. 42*, 907–926.

18th International Conference
ENGINEERING MECHANICS 2012
Svratka, Czech Republic, May 14 – 17, 2012

pp. 317–321
Paper #162

FINITE ELEMENT CONTACT-IMPACT ALGORITHM IN EXPLICIT TRANSIENT ANALYSIS

D. Gabriel, J. Kopačka, J. Plešek [*] M. Ulbin [**]

Abstract: *This work addresses three issues in computational modelling of contact-impact problems: i) overviews a contact algorithm proposed by these authors, ii) local search treatment based on the modification of the Nelder-Mead simplex method, iii) discusses an algorithmic aspects of contact algorithm in conjunction with the explicit time integration scheme. The talk closes with the presentation of several numerical examples including the longitudinal impact of two thick plates, for which analytical solution is available.*

Keywords: ***FEM, contact-impact, explicit dynamics, local contact search***

1. Introduction

In the context of the finite element method, a frictionless three-dimensional contact-impact algorithm using pre-discretization penalty formulation was proposed (Gabriel et al., 2004). The key feature of this algorithm is that the local search and the penalty constraint enforcement are performed on the Gausspoint level of linear/quadratic serendipity elements rather than the nodal level of a finite element mesh. The method is shown to be consistent with the variational formulation of a continuum problem, which enables incorporation of higher-order elements with midside nodes to the analysis. Owing to a careful description of kinematics of contacting bodies when the non-linearized definition of penetration has been introduced, the displacement increments in the course of one load step are permitted to be large. Thus, the extension to geometrically nonlinear problems is straightforward. The algorithm proves to be robust, accurate and symmetry preserving—no master/slave surfaces have been introduced.

In proposed algorithm the local search represents measuring penetration of a Gauss point through the counterpart's object surface. It is necessary first to define the outward normal and then to compute its intersection with a curved surface, establishing distance. Although appearing trivial at first glance the numerical solution process is far from being easy, especially when dealing with severely distorted surfaces. In Ref. (Gabriel et al., 2010) several methods for the solution of non-linear algebraic systems were thoroughly tested: the Newton-Raphson method, the least square projection, the steepest descent method, Broyden's method, BFGS method and the simplex method. The effectiveness of these methods was performed by means of the benchmark configuration of distorted contact segment from static solution of bending of two rectangular plates over a cylinder (Gabriel et al., 2004). The most fitting method turned out the modification of the Nelder-Mead simplex method (Nelder and Mead, 1965), which belongs to very popular and simple direct search technique that has been widely used in unconstrained optimization problems.

In this paper, we focused on the performance of the Nelder-Mead simplex method for local contact search treatment in dynamic contact-impact problem. First, the formulation of a closest point projection problem is presented in Section 2. The idea of the Nelder-Mead method is outlined in Section 3. Finally, the effectiveness of contact algorithm with implemented Nelder-Mead simplex method for contact search procedure is demonstrated by test example of the longitudinal impact of two thick plates in Section 4.

[*] Ing. Dušan Gabriel, Ph.D., Ing. Ján Kopačka, Ing. Jiří Plešek, CSc., Institute of Thermomechanics AS CR, v.v.i., Dolejškova 5, 182 00 Praha 8, tel.: +420 266 052 026, e-mail: gabriel@it.cas.cz
[**] Doc. Dr. Miran Ulbin, Faculty of Mechanical Engineering, University of Maribor, Smetanova 17, 2000 Maribor, tel: +386 2 220 7705, e-mail: ulbin@uni-mb.si

2. Formulation of the closest point projection

Let us consider the slave quadrature point $\mathbf{y}_s \in \mathbb{E}^3$ and the master segment γ_c. The aim of the local contact search is to calculate the parametric coordinates $\xi_1, \xi_2 \in [-1, 1]$ corresponding to projection $\bar{\mathbf{y}}(\xi_1, \xi_2) \in \mathbf{E^3}$ of the quadrature point $\mathbf{y}_s$ (see Fig. 1).

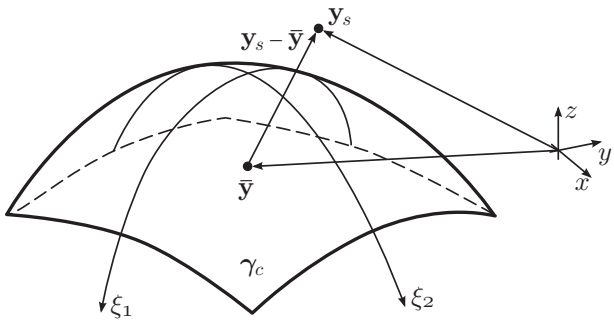

Fig. 1: Formulation of the minimization problem

Such a point has to satisfy

$$\bar{\mathbf{y}} = \min_{\mathbf{y} \in \gamma_c} \{(\mathbf{y}_s - \mathbf{y}) \cdot (\mathbf{y}_s - \mathbf{y})\} \tag{1}$$

where the minimization of the inner product on $\mathbb{E}^3$ instead of more natural Euclidean norm has been used. Hence, the minimized function is defined as

$$f = (\mathbf{y}_s - \mathbf{y}) \cdot (\mathbf{y}_s - \mathbf{y}) \tag{2}$$

The necessary condition for local extremum is

$$\begin{aligned} (\mathbf{y}_s - \mathbf{y}) \cdot \frac{\partial \mathbf{y}}{\partial \xi_1} &= 0, \\ (\mathbf{y}_s - \mathbf{y}) \cdot \frac{\partial \mathbf{y}}{\partial \xi_2} &= 0 \end{aligned} \tag{3}$$

The master segment γ_c is parametrized by

$$\mathbf{y}(\xi_1, \xi_2) = \sum_{i=1}^{n} N_i(\xi_1, \xi_2) \mathbf{Y}_i \tag{4}$$

where $N_i(\xi_1, \xi_2) : \mathbb{R} \times \mathbb{R} \to \mathbb{R}$ are the shape functions, n is the number of nodes and $\mathbf{Y}_i \in \mathbb{E}^3$ are the global coordinates of nodes. Note that the partial derivations are constant and Eqn. (3) is system of linear equations for linear triangular segments. If higher order elements are taken into account, Eqn. (3) results in the system of non-linear algebraic equations. The inequality constraints $|\xi_1|, |\xi_2| \leq 1$ for isoparametric segment γ_c are not explicitly imposed. The solution of the unconstrained problem lying outside the permissible range indicates that the quadrature point does not penetrate onto the master segment.

3. Nelder-Mead simplex method

Let us consider the minimization of the function f (2). The points $\mathbf{x}_i^k,\ i = 1, 2, 3$ define the current simplex in two-dimensional space. We set up

$$\mathbf{x}_h^k = \arg\max_i \left(f\left(\mathbf{x}_i^k\right)\right), \tag{5}$$

$$\mathbf{x}_l^k = \arg\min_i \left(f\left(\mathbf{x}_i^k\right)\right) \tag{6}$$

as the points with maximum and minimum function value, respectively. Further, we define

$$\bar{\mathbf{x}}_i^k = \frac{\sum_{\substack{i=1 \\ i\neq h}}^{2} \mathbf{x}_i^k}{2} \tag{7}$$

as the center of the points $\mathbf{x}_i^k$ with $i \neq h$. At each stage $\mathbf{x}_h^k$ is replaced by a new point. In Ref. (Nelder and Mead, 1965), three operations are applied: reflection, contraction, and expansion. In our modification only the reflection is considered. It is defined by

$$\mathbf{x}^* = \bar{\mathbf{x}}_i^k + \alpha\left(\bar{\mathbf{x}}_i^k - \mathbf{x}_h^k\right), \tag{8}$$

where α is the reflection coefficient (positive constant). We choose α simply equal to one. Thus, the simplex preserves regularity. In case that $f(\mathbf{x}^*) \geq f(\mathbf{x}_h^k)$ the vertex with second highest value is reflected instead of $\mathbf{x}_h^k$. When one of the vertices has still the same position, it indicates that the simplex rotates above a local extremum. Therefore, the simplex edge length a is halved after m iterations. The number of iteration m can be estimated by the empiric formula

$$m = 1.65n + 0.05n^2, \tag{9}$$

where $n = 2$ for two-dimensional case.

4. Longitudinal impact of two plates

The longitudinal impact of two thick plates was studied, for which the analytical solution was available (Brepta and Valeš, 1987). Despite the problem is two-dimensional one it could be used for testing different methods for three-dimensional local contact search. The plates dimensions were: thickness $2d = 5$ mm, length 2.5 mm. Young's modulus, Poisson's ratio and density, respectively, were $E = 2.1 \times 10^5$ MPa, $\nu = 0.3$, $\rho = 7800\,\mathrm{kg/m^3}$. The plates made contact with initial velocity $v_0 = 1$ m/s prescribed at time $t = 0$ s (Fig. 2).

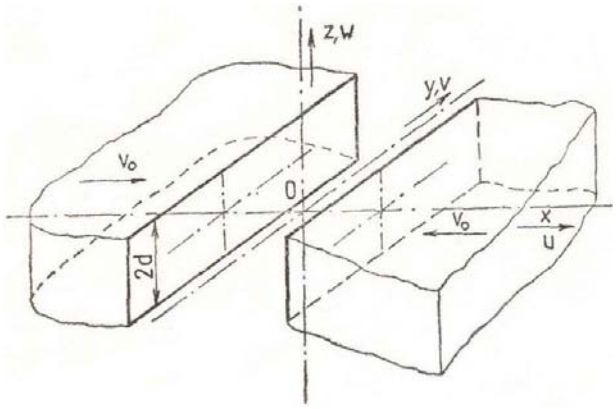

Fig. 2: Longitudinal impact of two plates

The analytical solution (Brepta and Valeš, 1987) utilizing the Laplace transform is rather complex. The distributions of displacements and stresses are cast in the form of infinite series of improper integrals which are evaluated numerically. For illustration, theoretical positions of wave fronts for a short time after impact are plotted in Fig. 3. At the instant the faces of the plates come into contact there are aroused elementary dilatation waves at all points of the contact area. The envelope of these waves is represented

by a wave with a plane wave front, propagating in both directions at speed of dilatation waves c_1. From the boundary points A, D of the contact area emanates a reflected wave which continues propagating in perpendicular direction to x, y plane at speed c_1. Behind the dilatation wave the transversal waves proceeds at speed c_2. In the region bounded by plane wave fronts of the dilatation wave and by circular wave fronts of the wave starting from the points A and D, the state of stress is the same as that encountered by a longitudinal impact of half-spaces.

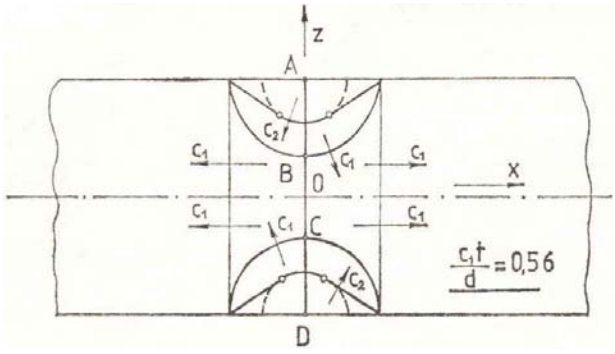

Fig. 3: Theoretical position of wave fronts for $c_1 t/d = 0.56$ after (Brepta and Valeš, 1987)

In view of symmetry, only one half of the plates was discretized using 100×100 eight-node linear brick elements per each plate. For the integration of equilibrium equations, the central difference with the lumped mass matrix was employed. The time step was chosen very small corresponding to the dimensionless Courant number C$o = 0.125$.

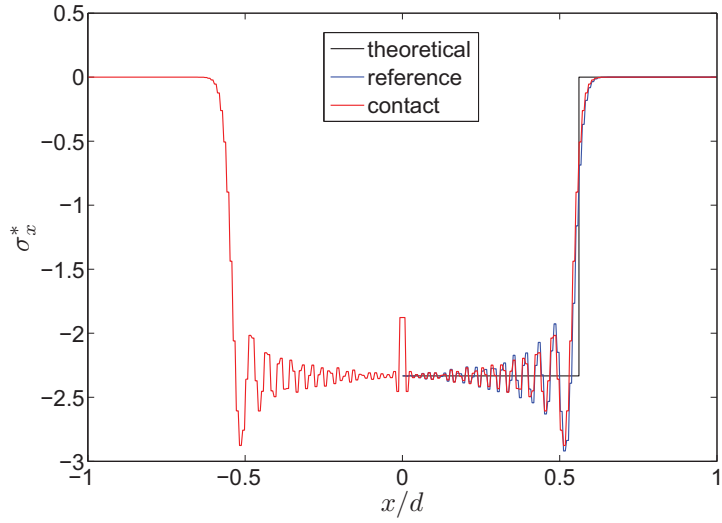

Fig. 4: Longitudinal stress distribution σ_x^* along x-axis for $z/d = 0$

The normalized longitudinal stress distribution $\sigma_x^* = \sigma_x c_1/\Lambda v_0$ (Λ is Lamé's constant) along x-axis is drawn in Fig. 4. The results are plotted for normalized time $c_1 t/d = 0.56$ and coordinate $z/d = 0$, for which no reflections from boundaries occur. Except the contact analysis a symmetric reference calculation was performed, where the longitudinal displacements of the front-end nodes of the plate were fixed.

In Fig. 4 the contact solution is plotted by red line while the solution based on the reference calculation is denoted by blue line. In addition, the theoretical solution corresponding to uniaxial strain condition is plotted by the black line. Quite a good agreement between the contact and reference calculation was observed. It should be emphasized that the symmetry of longitudinal stress distributions was perfectly preserved in contact analysis. Thus, the capability of the Nelder-Mead simplex method implemented in local search procedure was confirmed. It is clear that the numerical solution was influenced by dispersion errors caused by both FE spatial and time discretization. In comparisons with the continuum solution the speed of the longitudinal wave was slower. This fact follows from the theoretical dispersion diagrams derived in Ref. (Plešek et al., 2010).

The normalized transversal stress distribution $\sigma_z^* = \sigma_z c_1/\Lambda v_0$ along z-axis is drawn in Fig. 5. In contrast to graphs in previous Fig. 4 these distributions are strongly influenced by the longitudinal and transversal waves reflected from the boundary of plate. Before the arrival of these waves the solution is identical to the constant values $\sigma_z^* = -1$ corresponding to a half-space impact problem. It should be pointed out that the accuracy of analytical solution is strongly influenced by the number of terms included in the series of improper integrals (Brepta and Valeš, 1987). The analytical solution plotted in this paper was derived from the summation of the first 300 terms of this series.

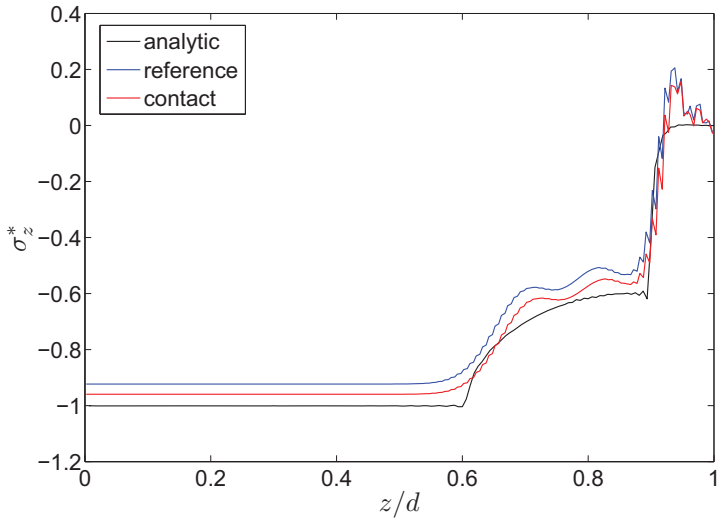

Fig. 5: Transversal stress distribution σ_z^* along z-axis for $x/d = 0.4$

Acknowledgments

This work was supported by projects ME10114, GAP101/12/2315 and GA101/09/1630 in the framework of AV0Z20760514.

References

Gabriel, D., Plešek, J. and Ulbin, M. (2004), Symmetry preserving algorithm for large displacement frictionless contact by the pre-discretization penalty method. *Int. J. Num. Met. Engng*, **61**, pp 2615–2638.

Gabriel, D., Kopačka, J., Plešek, J., Ulbin, M. (2010), Assesment of methods for calculating the normal contact vector in local search. *4th European Conference on Computational Mechanics (ECCM 2010)*, Paris, Computational Structural Mechanics Association, CD-ROM.

Nelder, J.A., Mead, R. (1965), A simplex method for function minimization. *The Computer Journal*, **7**, pp 308–313.

Brepta, R., Valeš, F. (1987), Longitudinal impact of bodies. *Acta Technica ČSAV*, **32**, pp 575–602.

Plešek, J., Kolman, R., Gabriel, D. (2010), Dispersion Error of Finite Element Discretizations in Elastodynamics, *Computational Technology Reviews*, (B.H.V. Topping et al. eds). Saxe-Coburg Publications, pp 251–279.

18th International Conference
ENGINEERING MECHANICS 2012
Svratka, Czech Republic, May 14 – 17, 2012

pp. 323–333
Paper #67

DETERMINATION OF BURST PRESSURE OF THIN-WALLED PRESSURE VESSELS

Ľ. Gajdoš, M. Šperl[1]

Abstract: *A simple fracture-mechanics based method is described for assessing a part-through crack in the wall of a pipe subjected to internal pressure of liquid and/or gas. The method utilizes simple approximate expressions for determining the fracture parameters K, J, and employs these parameters to determine critical dimensions of a crack on the basis of equality between the J-integral and the J-based fracture toughness of the pipe steel. The crack tip constraint is taken into account by the so-called plastic constraint factor C, by which the uniaxial yield stress in the J-integral equation is multiplied. The results of the prediction of fracture conditions are verified by burst tests on test pipes.*

Keywords: ***Fracture mechanics, J integral, pressure vessels, burst tests***

1. Introduction

In thin-walled gas pipelines, similarly as in other (especially welded) structures, we should expect defects to occur. Under certain conditions, the defects can grow and they will gradually shorten the residual life of gas pipelines. Using fracture mechanics we can assess the threat that such defects can pose to the pipeline wall taking into account whether a brittle, quasi-brittle or ductile material is involved. A model description of crack-containing systems, based on the stress intensity factor (SIF), K, can be used for brittle and quasi-brittle fracture, and in addition for subcritical fatigue growth, corrosion fatigue and stress corrosion [1], [2]. In these cases, the surface crack is usually located in the field of one of the membrane tensile stress components or in the field of bending stress, or in a combination of these two stresses. In comparison with the dimensions of the crack and the cross section of the pipeline the extent of the plastic zone at the crack tip is small. If the gas pipeline is made of a high toughness material, the plastic strains become extensive before the crack reaches instability. Hence, some elasto-plastic fracture mechanics methods, such as J-integral, crack opening displacement, the two-criterion method or some other procedure, should be employed to assess the fracture condition of the pipeline [3], [4]. Because the method of determination of burst pressure of thin-walled pressure vessels utilizes simple approximate expressions for determining the fracture parameters K, J, a brief background of some fracture-mechanics formulae will be made first.

2. A brief background of some fracture-mechanics formulae

SIF for an axial through crack

The stress intensity factor can be determined by equation (1)

$$K_I = M_T \sigma_\varphi \sqrt{\pi c} \tag{1}$$

Where $\sigma_\varphi = pD/2t$ is the hoop stress, and

M_T is the Folias correction factor, taking account of curvature of a pipe

One of the most widely used expressions to determine the Folias factor is the following [5]:

$$M_T = \sqrt{1 + 1.255\frac{c^2}{Rt} - 0.0135\frac{c^4}{R^2 t^2}} \tag{2}$$

[1] Ing. Ľubomír. Gajdoš, CSc., Ing. Martin Šperl, PhD., Institute of Theoretical and Applied Mechanics AS CR, v.v.i., Prosecká 76, 190 00 Prague 9, Czech Republic, e-mail {gajdos|sperl}@itam.cas.cz

where R is the mean radius of the pipe, and
t is the pipe wall thickness

SIF for an axial part-through crack

Various methods are used for analyzing the problem of axial semi-elliptical surface cracks in the wall of a cylindrical shell (Fig. 1).

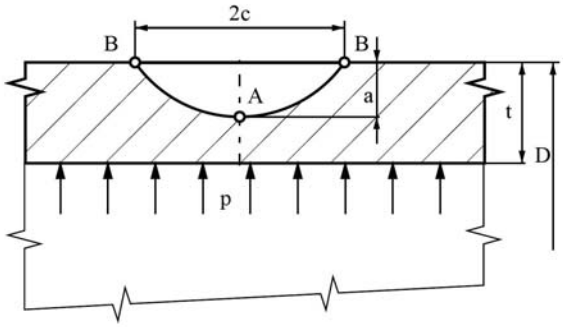

Fig. 1 An external longitudinal semi-elliptical crack in the wall of a cylindrical shell

A very good estimate of the stress intensity factor for such a crack is given by expression (3).

$$K_I = \left[M_F + \left(E_{(k)}\sqrt{c/a} - M_F \right) \left(\frac{a}{t} \right)^p \right] \frac{\sigma_\varphi \sqrt{\pi a}}{E_{(k)}} M_{TM} \tag{3}$$

This is an adjusted form of the Newman solution [6] for a thin-walled shell. Here

M_F - a function depending on the crack geometry (on the ratio a/c),

$E_k = \int_0^{\pi/2} \sqrt{1 - \frac{c^2 - a^2}{c^2} \sin^2 \theta} \, d\theta$ - an elliptical integral of the second kind

p - the function depending on the crack geometry (on the ratio a/c) and on the relative crack depth (on the ratio a/t)

$M_{TM} = \frac{\left(1 - \frac{a/t}{M_T} \right)}{1 - a/t}$ - the correction factor for curvature of a cylindrical shell and for an increase in stress owing to radial strains in the vicinity of the crack tip

Functions M_F and p differ in form for the lowest point of the crack tip (point A in Fig. 1) and for the crack mouth on the surface of the cylindrical shell (point B in Fig. 1).

The next fracture-mechanics parameter we need for determination of the burst pressure of a pipeline is J integral. The actual magnitude of this quantity will be compared to its critical value – the fracture toughness. From this comparison a magnitude of the burst pressure will result.

3. Engineering methods for determination of J integral

3.1 FC method

This method was proposed in Addendum A16 of the French nuclear code [7] as the J_s method. It stems from the second option of describing the transition state between ideally elastic and fully plastic

behaviour of material, that is to say from the function $f_2(L_r)$ of the R6 method [8]. This function takes the form:

$$f_2(L_r) = \left(\frac{E\varepsilon_{ref}}{L_r R_e} + \frac{L_r^{\,3} R_e}{2E\varepsilon_{ref}} \right)^{-1/2} \tag{4}$$

where
$L_r = \sigma/\sigma_L$ (σ – applied stress, σ_L – stress at the limit load)
R_e is the yield stress
E is Young´s modulus
ε_{ref} is the reference strain corresponding to the reference (nominal) stress σ_{ref}

If we identify function $f_2(L_r)$ with function $f_3(L_r) = \left(\frac{J}{J_e} \right)^{-\frac{1}{2}}$ and express L_r as σ_{ref} / R_e and elastic J integral J_e as K^2 / E', where $E' = E$ for plane stress state and $E' = E / (1-\nu^2)$ for plane strain state, we have:

$$J = \frac{K^2}{E'} \left(\frac{E.\varepsilon_{ref}}{\sigma_{ref}} + \frac{\sigma_{ref}^{\,3}}{2E.R_e^{\,2}.\varepsilon_{ref}} \right) \tag{5}$$

The stress σ_{ref} in the above equation is a nominal stress – i.e. a stress acting in the plane where the crack occurs. Taking into consideration the description of the stress-strain dependence by the Ramberg-Osgood relation (6) and adjusting Eq. (5) we obtain the *J*-integral in the form (7).

$$\frac{\varepsilon}{\varepsilon_0} = \frac{\sigma}{\sigma_0} + \alpha \left(\frac{\sigma}{\sigma_0} \right)^n \tag{6}$$

$$J = \frac{K^2}{E'} \left[A + \frac{0.5(\sigma/\sigma_0)^2}{A} \right] \tag{7}$$

where

$$A = 1 + \alpha \left(\frac{\sigma}{\sigma_0} \right)^{n-1} \tag{8}$$

As the pipeline is a body of finite dimensions, stress σ in Eqs. (7) and (8) is a nominal stress – i.e. a stress acting in the plane where the crack occurs. Referring to the R6 method [8] this stress for the pipe containing longitudinal part-through thickness crack may be written as:

$$\sigma = \frac{\sigma_\phi}{1 - \frac{\pi a c}{2t(t+2c)}} \tag{9}$$

In eq. (9) $\sigma_\phi = \frac{pD}{2t}$ is the hoop stress and the meaning of the symbols *a, c,* and *t* is clear from Fig.2.

3.2 GS method

The GS method was derived by Gajdoš and Srnec [9] on the basis of the limit transition of *J*-integral, formally expressed for a semi-circular notch, to a crack, with the variation of the strain energy density along the notch circumference being approximated by the third power of the cosine function of the polar angle. If the stress-strain dependence is further expressed by the Ramberg-Osgood relation (6) with $\varepsilon_0 = \sigma_0 / E$, (α, n – material constants) it can be arrived at Eq. (10)

$$J = \frac{K^2}{E'} \left[1 + \frac{2\alpha n}{(n+1)} \left(\frac{\sigma}{\sigma_0} \right)^{n-1} \right] \tag{10}$$

where σ is the nominal stress in the reduced cross-section of a body. For a pipe containing longitudinal part-through thickness crack it may be determined by the relation (9).

4. Accounting the constraint

The crack tip constraint is accounted here by a simple procedure based on the so-called plastic constraint factor on yielding, C. This factor is given by the ratio of the stress needed to obtain plastic macrostrains under constraint conditions to the yield stress at a homogeneous uniaxial state of stress [10]. The C factor can be expressed by the relation (11)

$$C = \frac{\sigma_1}{\sigma_{HMH}} \tag{11}$$

where $\sigma_{HMH,}$ the Huber-Mises-Hencky stress, is put equal to the yield stress.

Let us now consider the state of stress at the crack tip in a thick-walled body, where the stress perpendicular to the crack plane, σ_1, and the stress in the direction of the crack, σ_2, are equal, and the stress in the direction of the thickness of the body, σ_3, is governed by the expression $\sigma_3=\nu(\sigma_1+\sigma_2)$. Then, based on the HMH criterion and assumed elastic conditions ($\nu \cong 0.33$), the plastic constraint factor $C \approx 3$. If the stress in the thickness direction, $\sigma_{3,}$ falls within $2\nu\sigma_1$ and zero (thin-walled body), the value of the plastic constraint factor will range between $C = 1$ and $C = 3$. These data can be used to assess fracture conditions in gas pipelines with surface part-through cracks, employing a C-factor which has to be experimentally determined. After determination of the C factor the value of $C\sigma_0$ would be used instead of the yield stress σ_0 in relations for the calculation of *J*-integral.
The C factor was experimentally investigated at the Institute of Theoretical and Applied Mechanics of the Academy of Science of the Czech Republic in the framework of a broader project concerned with research of the reliability and operational safety of high pressure gas pipelines. Fracture conditions were investigated on five pipe bodies, made of steels X52, X65 a X70, with cycling-induced cracks. Data on the pipe bodies used, cracks in the walls, and mechanical and fracture-mechanical material properties of the bodies are given in Table 1.

Tab. 1. Summary of data concerning the assessment of the fracture behaviour of pipe bodies

Material	X 52	X 65	X 65	X 70	X 70
D (mm)	820	820	820	1018	1018
t (mm)	10.2	10.7	10.6	11.7	11.7
c (mm)	50	100	100	127	115
a (mm)	7.0	7.7	7.0	6.7	7.1
a/t	0.686	0.720	0.660	0.573	0.607
a/c	0.14	0.077	0.07	0.053	0.062
p (MPa)	8.05	9.71	9.86	9.86	9.55
$p/p_{0.2}$	1.034	0.750	0.769	0.800	0.775
σ_0 (MPa)	313	496	496	536	536
α	2.40	5.34	5.34	5.92	5.92
n	6.25	8.45	8.45	9.62	9.62
C	2.1	2.4	2.4	2.0	2.07
J_{cr} (N/mm)	487	432	432	439	439
- T/σ_0	0.672	0.575	0.544	0.606	0.611
- *Q*	0.667	0.591	0.546	0.648	0.651

The individual rows in the table show the following data (top to bottom): body diameter *D*, body wall thickness *t*, half-length of longitudinal part-through crack *c*, crack depth *a*, relative crack depth *a/t*, aspect ratio *a/c* of a semi-elliptical crack, fracture pressure *p*, ratio of fracture pressure *p* and pressure $p_{0.2}$ corresponding to the hoop stress at the yield stress, yield stress in the circumferential direction of the body σ_0, Ramberg-Osgood constant α, Ramberg-Osgood exponent *n*, plastic constraint factor *C*, *J*-integral critical value J_{cr}, determined as J_m (corresponding to attaining the maximum force at the "force – force point displacement" curve), T-stress to yield stress ratio T/σ_0, and *Q* parameter. Values of σ_0, α and *n* were derived from tensile tests and the values of J_{cr} from fracture tests run on

CT specimens. Values of the fracture pressure p were read at the moment the ligament under the crack in the pipe body ruptured. Values of the plastic constraint factor on yielding, C, were determined on the basis of J-integral in such a way that agreement was reached between the predicted and experimentally established fracture parameters for the given crack and fracture toughness of the material. The J-integral value was calculated from the GS method [9] on the one hand and the French nuclear code [7] on the other hand.

It should be noted that in determining the C factor the critical value of J-integral established on CT specimens was considered– namely J_{cr} = 439 N/mm for steel X70, J_{cr} = 432 N/mm for steel X65 and J_{cr} = 487 N/mm for steel X52. It was found out by a computational analysis of CT specimens, employed to construct the R curve, that the Q parameter for these specimens had been Q = 0.267. A comparison of this with the Q parameter for pipe bodies (Q ≈ -0.55 ÷ -0.65) reveals that the constraint in the CT specimens was much higher. This implies that the real fracture toughness – i.e. the critical value of J-integral, J_{cr} – was higher in the pipe bodies. The real C factor for a cracked pipe body is lower, so that the J-a curve for a pipe body is steeper than that for CT specimens with a greater C factor [11]. Due to this, the J integral for the axial part-through crack reaches the corresponding higher fracture toughness (for a lower constraint) for the same crack depth as the J integral with a higher C factor reaches lower fracture toughness (determined on CT specimens). The situation is illustrated in Fig.2.

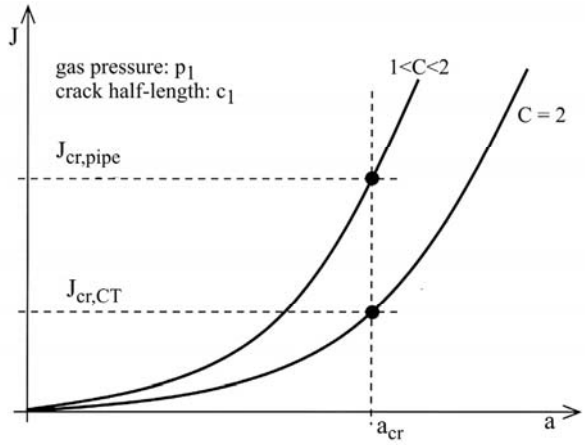

Fig. 2 Schematic J-a dependence for (i) a CT specimen, and (ii) a pipe with an axial part-through crack

Normalized T–stress values in Table 1 were obtained by the use of the plane solution – i.e. solution for an infinite length of a crack oriented longitudinally along the pipe. The problem was solved in the Institute of Physics of Materials, Brno, by the finite elements method. The solution included two steps: (i) a corresponding FEM network was established and corresponding boundary conditions were formulated for each crack depth, (ii) magnitudes of the stress intensity factor and the T-stress were calculated for each FEM network by means of the FEM system CRACK2D with hybrid crack elements. Values of the Q parameter were derived from $Q - T/\sigma_0$ curves, obtained by O´Dowd and Shih [12] by modified boundary layer analysis for different values of the strain coefficient (Ramberg-Osgood exponent, n). Strictly speaking, the Q parameter values from Table 1 do not correspond accurately to values for the examined cracks, because T-stresses were not computed for real semi-elliptical cracks, but for cracks spreading along the entire length of pipe body ($a/c \approx 0$). Nevertheless, with regard to the fact that the ratio of the depth to the surface half-length of examined cracks (a/c) was close to zero ($a/c=0.053 \div 0.14$), we can assume that the differences between real values of the Q parameter and the values listed in Table 1 will be small. Relations between the C and the Q parameter will be discussed later.

5. Burst tests

For burst tests of pipe bodies it is usually sufficient that the length of the pipe between the welds of dished bottoms is at least 3.5 D. Such a length permits placing a number of starting cuts axially along the length of the body. The cuts are made to initiate crack growth when the body is subsequently pressurized by a fluctuating pressure of water. They can be made in several ways, of which one uses a thin grinding wheel. The smallest real functional thickness of such a wheel is about 1.2 mm and the corresponding width of the cuts made with it is approximately 1.5 mm. Depending on the type of pipes of which gas pipelines are built (seamless, spirally welded, longitudinally welded) the starting cuts can be provided in the base material, transition region or the weld metal, their orientation being axial, circumferential or along the spiral weld. The depth of an initiated fatigue crack must be at least 0.5 mm along the whole perimeter of the cut tip so that the cut with the initiated crack at its tip can be considered as a crack after the pipe body has been subjected to cycling. This value follows from work of Smith and Miller [13].

As it was seen in the preceding section, the results of burst tests are presented in Table 1. The cracks were made in such a way that the test pipes were first provided with working slits and the check slits. The latter slits were of the same surface length as the working slits but their depth was greater. These check slits functioned as a safety measure to prevent cracks that developed at the working slits from penetrating through the pipe wall. For illustration, a DN1000 test pipe body of the working length 3.5 m is shown in Fig. 3.

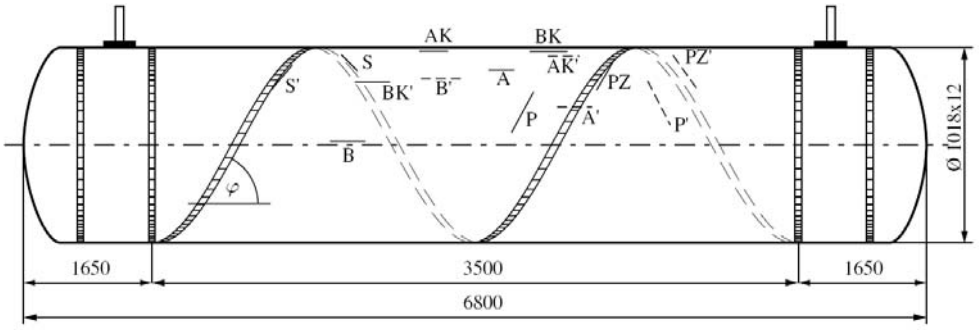

Fig.3 Test pipe body DN1000 with marking the starting cuts

The check slits are denoted in Fig. 3 by a supplementary letter K. The material of the test pipe body is a thermo-mechanically treated steel X70 according to API specification. The pipe is spirally welded, the weld being inclined at an angle of $\varphi = 62°$ to the pipe axis. It is provided with starting cuts oriented either axially or in the direction of the strip axis (i.e. in the direction of the spiral) and then along or inside the spiral weld. The cuts differ in length ($2c$ = 115 mm or 230mm) and depth (a = 5, 6.5, 7, and 7.5 mm). We are particularly interested in axial (longitudinal) slits situated aside welds because these are sites where axial cracks will be formed in the basic material of the pipe.

Efforts were made in the fracture tests to keep the circumferential fracture stress below the yield stress, because the operating stress in gas pipelines is virtually around one half of the yield stress (and does not exceed two thirds of the yield stress even in intrastate high-pressure gas transmission pipelines). Calculations reveal that in order to comply with this, the depth of the axial semi-elliptical cracks should be greater than one half of the wall thickness. Oblique cracks should be even deeper, as the normal stress component opening these cracks is smaller. If the crack depth is to have a certain magnitude before the fracture test is begun, the depth of the starting slit should be smaller than this magnitude by the fatigue extension of the crack along the perimeter of the slit tip. At the same time, we should bear in mind that the higher the fatigue extension of the crack, the better the agreement with a real crack.

5.1 Procedure of the tests

After the starting slits were made, the test pipes were subjected to water pressure cycling to produce fatigue cracks in the tips of the starting slits. The cycling was carried out in a pressurizing system, which included a high-pressure water pump, a collecting tank, a regulator designed to control the amount of water that was supplied and, consequently, the rate at which the pressure is increased in the pipe section. This was effected by opening by-pass valves. A scheme of the pressurizing system is shown in Fig. 4.

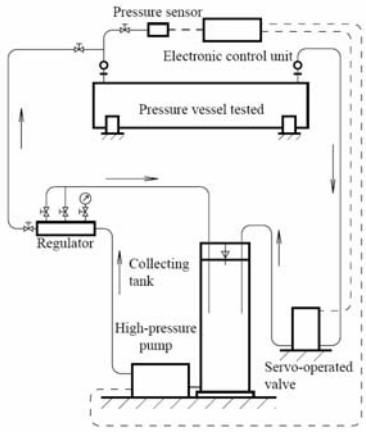

Fig.4 Pressurizing system used for cyclic pressure tests of a test pipe body

In cycling the cracks, the water pressure fluctuated between p_{min} = 1.5 MPa and p_{max} = 5.3 MPa, and the number of pressure cycles was between 3 000 and 4 000. The period of a cycle was approximately 150 seconds. The cycling went on until a crack, initiated in one of the check slits, became a through crack. This moment was easy to detect, because it was accompanied by a water leak. By choosing an appropriate difference between the depths of the working slits and the check slits it was possible to obtain a working crack depth (= starting slit depth + fatigue crack extension) approximately of the required size. To run a test for a fracture, however, it was necessary to remove the check slit which had penetrated through the wall of the test pipe from the body shell and to repair the shell, e.g. by welding a patch in it.

After removing the check slit with a crack which penetrated through the wall, and repairing the shell of the test pipe, the pipe was loaded by increasing water pressure to burst. The test procedure, which was common to all test pipes, will now be briefly described for the DN1000 pipe shown in Fig. 3. As the figure suggests, slits A, A′, B and B′ were oriented along the axis of the pipe. The nominal length of notches B, B′ had twice the length of notches A, A′, but they were shallower. As mentioned above, cracks at the slit tips were extended by fluctuating water pressure, and this proceeded until the cracks from the check slits (BK, BK′) grew through the wall and a water leak developed. Then the damaged parts of the shell were cut out, patches were welded in their place, and the test pipe was monotonically loaded to fracture at the location of crack B or B′. The burst of the test pipe at crack B is shown in Figs. 5 and 6 (in detail).

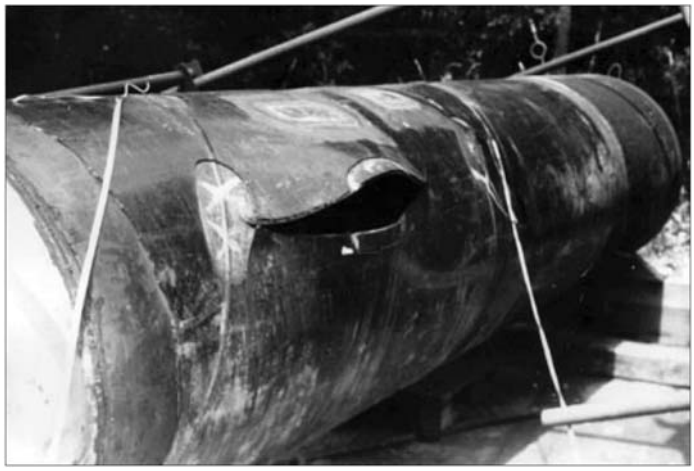

Fig.5 Burst initiated on the slit B with a fatigue crack

Fig.6 Burst initiated on the slit B - detail

Evidently, at the instant of fracture the crack spread not only through the remaining ligament, but also lengthwise. It means the LBB criterion was not observed. After removing the part of the pipe shell with crack B, a patch was welded in and the second burst test followed. In the Table 2 there are extracted from Table 1 the numerical values of the geometrical parameters, the J-integral fracture values, the Ramberg-Osgood constants, the fracture pressure and the fracture depth for cracks B and B´, respectively.

5.2 Prediction of fracture parameters

Fracture parameters for a cracked pipe, i.e. the crack size for a given pressure and/or the pressure for a given crack size, can be predicted by solving Eq. 12 (GS method) or Eq. 13 (FC method) for the unknown fracture parameter (e.g. crack depth a and/or pressure p).

$$\frac{K^2}{E'}\left[1+\frac{2\alpha n}{(n+1)}\left(\frac{\sigma}{C\sigma_0}\right)^{n-1}\right]=J_{cr} \tag{12}$$

$$\frac{K^2}{E'}\left[A+\frac{0.5\left(\sigma/C\sigma_0\right)^2}{A}\right]=J_{cr} \tag{13}$$

In the above equations K is given by Eq. 3, σ is given by Eq. 9 and A is $A=1+\alpha\left(\frac{\sigma}{C\sigma_0}\right)^{n-1}$.

J_{cr} in Eq. 12 and 13 is the critical magnitude of the J integral – the fracture toughness – taken here as the value J_m and α, n, σ_0 are the Ramberg-Osgood parameters of the steel in the hoop direction.

As it can be deduced from Table 1 the crack B fractured first, namely when the water pressure reached the value p = 9.55 MPa. The damaged part of the pipe shell was then cut out, the fracture surfaces were released to enable their fractographic examination. The missing part of the shell was replaced by welding a patch on it. In the second burst test the crack B´ fractured at the pressure p = 9.86 MPa. After cutting out the damaged part of the pipe shell the fracture surfaces were released and were then subjected to fractographic examination. The results are digestedly presented in Table 2.

Tab 2. Some characteristics referring to crack B and crack B´

Characteristics	Crack B	Crack B´
CRACK DIMENSIONS		
half-length, c (mm)	115	127
depth in fracture, a_f (mm)	7.1	6.7
RAMBERG-OSGOOD PARAMETERS		
α / n /σ_0 (MPa)	5.92 / 9.62 /536	5.92 / 9.62 /536
FRACTURE TOUGHNESS		
$J_{cr} = J_m$ (N/mm)	439	439
FRACTURE PRESSURE		
p_f (MPa)	9.55	9.86

It is seen from here that the crack depth at fracture was 7.1 mm for crack B and 6.7 mm for crack B´. These values are also shown in the last two columns of Table 1.

Now let us predict the fracture conditions according to engineering approaches, and compare the prediction results with real fracture parameter values (pressure, crack depth). As it was already stated the procedure for verifying the predictive engineering methods involves determining either the fracture stress for a given (fracture) crack depth or the fracture crack depth for a given (fracture) pressure. To illustrate this, we select the latter case – i.e. determining the fracture depth of a crack for a given (fracture) pressure. We will not use directly Eqs. 12 and 13 but general dependences of the J integral (given by the left-hand side of Eqs. 12 and 13) on the crack depth a. Fig. 7 shows the J-integral vs. crack B depth dependences, as determined by the FC and GS predictions for the fracture hoop stress corresponding to the measured fracture pressure. When using appropriate equations to determine J integrals, the following parameters were used: D = 1018 mm; t = 11.7 mm ; $p = p_f$ = 9.55 MPa; c = 115 mm; α = 5.92; n = 9.62; $\sigma_0 = 2.07 \times 536 = 1110$ MPa (i.e. C = 2.07).

Similarly, Fig. 8 shows J - a dependences for crack B´.

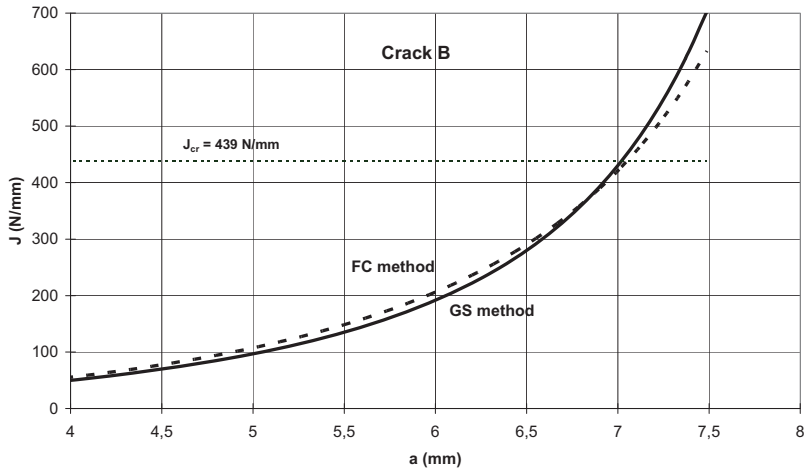

Fig.7 Prediction of the fracture depth for the crack B ($p = p_f$ = 9.55 MPa and C = 2.07)

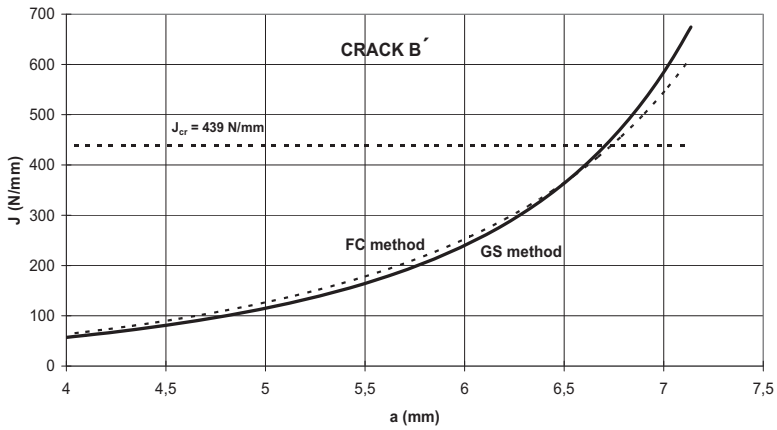

Fig.8 Prediction of the fracture depth for the crack B´ ($p = p_f = 9.86$ MPa and C = 2.0)

6. Conclusions

On the basis of both experimental work and a fracture-mechanical evaluation of experimental results, an engineering method has been worked out for assessing the geometrical parameters of critical axial crack-like defects in a high-pressure gas pipeline wall for a given internal pressure of a gas.
The method makes use of simple approximate expressions for determining fracture parameters K, J, and it accommodates the crack tip constraint effects by means of the so-called plastic constraint factor on yielding, C. Involving this idea in the fracture analysis leads to multiplication of the uniaxial yield stress by the C factor in the expression for determining the J-integral.

Two independent approximate equations for determining the J-integral provided very close assessments of the critical geometrical dimensions of part-through axial cracks.

With the use of the crack assessment method proposed, the critical gas pressure in a pipeline can also be determined for a given crack geometry.

Acknowledgment

This work was supported by RVO: 68378297 and by the grant projects P105/10/2052 and P105/10/P555 of the Grant Agency of the Czech Republic.

References

[1] J. Zemánková: Instability of Surface Defects in a Thin-Walled Linepipe (in Czech). Research Report V-KMtr-157/84, CTU Prague, 1984

[2] M.R. Ayatollahi and H. Khoramishad: Stress Intensity Factors for an Axially Oriented Internal Crack Embedded in a Buried Pipe. Int. Journal of Pressure Vessels and Piping 87 (2010), pp. 165 – 169

[3] T.L. Anderson: Fracture Mechanics: Fundamentals and Applications. 3rd Edition. New York: CRC Press; 2005

[4] C. Betegon and J.W Hancock: Two-Parameter Characterization of Elastic-Plastic Crack-Tip Fields. Journal of Applied Mechanics 58 (1991), pp. 104 – 110

[5] E.S. Folias: On the Theory of Fracture of Curved Sheets. Engineering Fracture Mechanics, No.2, Vol.2, 1970, pp. 151-164

[6] J.C. Newman: Fracture Analysis of Surface and Through-Cracked Sheets and Plates, Engineering Fracture Mechanics, Vol.5, No.3, 1973, pp. 667-689

[7] RCC-MR: Design and Construction Rules for Mechanical Components of FBR Nuclear Island. First Edition (AFCEN - 3-5 Av. De Friedeland Paris 8), 1985

[8] I. Milne, R. A. Ainsworth, A. R. Dowling and A. T. Stewart: Assessment of the Integrity of Structures Containing Defects. CEGB Report No. R/H/R6 – Rev.3, Central Electricity Generating Board, London, U.K., 1986

[9] L. Gajdoš and M. Srnec: An Approximate Method for J Integral Determination. Acta Technica CSAV, Vol.39, No.2, 1994, pp.151-171

[10] Ľ. Gajdoš: Structural Integrity of Pressure Pipelines. Transgas, 80-86616-03-7, Prague, Czech Republic, 2004

[11] Ľ. Gajdoš and M. Šperl : Application of a Fracture-Mechanics Approach to Gas Pipelines. Proceedings of World Academy of Science, Engineering and Technology. Vol.73, January 2011, pp. 480 - 487

[12] N. P. O´Dowd and C. F. Shih: Family of Crack-Tip Fields Characterized by a Triaxiality Parameter – I. Structure of Fields. Journal of the Mechanics and Physics of Solids, Vol.39, 1991, pp. 898-1015

[13] Smith, R. A. & Miller, K. J. (1977). Fatigue Cracks at Notches. International Journal of Mechanical Sciences, Vol.19, pp. 11-22

18th International Conference
ENGINEERING MECHANICS 2012
Svratka, Czech Republic, May 14 – 17, 2012

pp. 335–342
Paper #348

AN ENHANCED NUMERICAL SOLUTION OF BLASIUS EQUATION BY MEANS OF THE METHOD OF DIFFERENTIAL QUADRATURE

A. Guran [*] **, J. Gwinner** [**]

Abstract: *The differential quadrature method (DQM) is used to solve the two-dimensional Blasius boundary layer problem which is described by a third-order nonlinear differential equation. The governing nonlinear equation of boundary-value Blasius problem is first converted to a pair of nonlinear initial-value problems and then solved by both the DQ method and classical fourth-order Runge-Kutta method (RK4). It is revealed that as compared to the RK4, the DQ method can achieve much higher order of accuracy for the numerical results using larger time step sizes.*

Keywords: ***Differential quadrature method (DQM); Blasius equation; Fourth-order Runge-Kutta method (RK4); Convergence and accuracy of DQ solutions.***

1. Introduction

The Blasius boundary layer is an example of two-dimensional boundary layer problems. The Blasius problem models the behavior of two-dimensional steady state laminar viscous flow of an incompressible fluid over a semi-infinite flat plate. The governing equation of the problem is

$$f'''(\eta) + \frac{1}{2} f(\eta) f''(\eta) = 0 \quad , \quad 0 \le \eta \le \infty \tag{1}$$

where η and f(η) are the dimensionless coordinate and stream function, respectively (Schiliching, 2004). The boundary conditions for equation (1) are

$$f(0) = f'(0) = 0 \quad , \quad f'(\infty) = 0 \tag{2}$$

The problem was first solved by Blasius using a series expansions method. But the proposed analytic series solution does not converge at all. In fact, the obtained analytic solution is valid only for small values of η (i.e., the series solution converges only within a finite interval [0, η0] where η0 is an unknown constant which can be determined numerically or analytically). Howarth (Howarth, 1938) solved the Blasius equation numerically and found $\eta 0 \approx 1.8894/0.33206$. Furthermore, Asaithambi (Asaithambi, 2005) solved the Blasius equation more accurately and obtained this number as $\eta 0 \approx 1.8894/0.332057336$. Due to the limitation of Blasius power series solution, many attempts have been made to obtain the solutions which are valid on the whole domain of the problem. Some researchers have solved the problem numerically and some analytically or semi-analytically. Applying the homotopy analysis method (Liao, 1997), Liao obtained an analytic solution for the Blasius equation which is valid in the whole region of the problem (Liao, 1998; Liao,1999). Using the variational iteration method (He,1997), He constructed a five-term approximate-analytic solution for the Blasius equation which is also valid for large values of η (He,1999). However, the solutions obtained were not very accurate. The Adomian decomposition method (ADM) has also been used by some researchers to find analytic solutions for the Blasius equation (Allan and Syam, 2005; Wang, 2004; Abbasbandy, 2007). A homotopy perturbation solution to this problem was presented by He (He, 2003; He, 2004). Fang et al. (Fang et al., 2006), Cortell (Cortell, 2005), Ahmad (Ahmad, 2007), and Ahmad and Al-Barakati (Ahmad, 2009) also solved the Blasius problem using various numerical and analytical methods. From the review of the proposed schemes in (Liao, 1997; Ahmad and Al-Barakati, 2009), two general limitations may be observed: (1) The proposed approximate-analytic methods can not yield accurate solutions when a rather small number of solution terms are used, (2) Many calculations

[*] Professor, Technical University of Munich (Germany), Director, Institute of Structronic, 275 Slater Street, 9th Floor,Ottawa, Canada. Corresponding Author, ardeshir.guran@mcgill.ca

should be done to construct the resulting semi-analytic solutions and this increases considerably the CPU time especially when a large number of terms of solutions are to be used. The above-mentioned limitations can be eliminated by using the higher-order methods such as the differential quadrature method (DQM).The DQ method is capable of yielding high accurate numerical solutions using very few grid points. So far, the DQ method has been efficiently employed in a variety of problems in engineering, mathematics, and physical sciences and is emerging as a powerful numerical discretization tool. However, the DQ method has its difficulty in implementation to the problems with irregular and complex geometry. Since the time domain has no such difficulty, the strengths of higher-order accuracy of the DQ method can be fully exploited in approximating the time derivatives.

In this work, we first convert the Blasius equation to a pair of initial-value problems (Na, 1979) and then solve the pair of initial-value problems by the DQ method. The resultant initial-value problems are also solved by the conventional fourth-order Runge-Kutta method (RK4). The efficiency, accuracy, and convergence of the DQ time integration method are then investigated and analyzed. It is demonstrated that the DQ method gives better accuracy than the RK4 using much larger time steps.

2. Differential quadrature method

Let $f(t)$ be a solution of a differential equation and $0 = t_1, t_2, \ldots, t_m = T$ be a set of sample points in the time domain. According to the DQ method, the first-order derivative of the function $f(t)$ at any sample time points can be approximated by the following formulation (Bellman and Casti, 1971; Shu, 2001; Bert and Malik , 1996)

$$\dot{f}(t_i) = \sum_{j=1}^{m} A_{ij} f(t_j) \quad \text{or} \quad \dot{f}_i = \sum_{j=1}^{m} A_{ij} f_j \tag{3}$$

where m is the number of sample points in the time domain, $f(t_j)$ represents the functional value at a sample time point t_j, $\dot{f}(t_i)$ indicates the first-order derivative of $f(t)$ at a time point t_i, and A_{ij} is the weighting coefficient of the first-order derivative. The weighting coefficients can be determined by the functional approximations in the time domain. Using the Lagrange interpolation polynomials as the approximating functions (say test functions), Quan and Chang (Quan and Chang, 1989) obtained the following algebraic formulations to compute the first-order weighting coefficients

$$A_{ik} = \begin{cases} \dfrac{M^{(1)}(t_i)}{(t_i - t_k) M^{(1)}(t_k)} & i \neq k, \quad i,k = 1,2,\ldots,m \\ -\sum\limits_{j=1, j\neq i}^{m} A_{ij} & i = k, \quad i = 1,2,\ldots,m \end{cases} \tag{4}$$

where $M^{(1)}(t)$ is defined as

$$M^{(1)}(t_i) = \prod_{j=1, j\neq i}^{m} (t_i - t_j) \tag{5}$$

In this work, we used the non-uniformly spaced sample points (i.e, the Chebyshev-Gauss-Lobatto sample points) for calculation of weighting coefficients. These points are given by

$$t_i = T/2 \left[1 - \cos\left(\frac{(i-1)\pi}{m-1} \right) \right], \quad i = 1,2,\ldots,m \tag{6}$$

where T is the time span.

3. Conversion of Blasius boundary-layer problem to a pair of initial-value problems

The boundary-layer problem (1) can be transformed to the following pair of initial-value problems (Na, 1979)

$$\begin{cases} g'''(\alpha) + 0.5 g(\alpha) g''(\alpha) = 0 \\ g(0) = g'(0) = 0, \quad g''(0) = 1 \end{cases} \tag{7}$$

and

$$\begin{cases} f'''(\eta) + 0.5 f(\eta) f''(\eta) = 0 \\ f(0) = f'(0) = 0, \quad f''(0) = [g'(\infty)]^{-3/2} \end{cases} \tag{8}$$

4. DQ analogs of the pair initial-value problems

From equations (7) and (8), it may be seen that the only difference between two resultant initial-value problems is related to the value of the second-order derivative initial condition. Thus, the procedure for two initial-value problems is actually the same. To be applicable the procedure for both the initial-value problems, we consider the following equation

$$F'''(\eta) + 0.5 F(\eta) F''(\eta) = 0 \tag{10}$$

with general initial conditions

$$F(0) = F_0, \quad F'(0) = F_0', \quad F''(0) = F_0'' \tag{11}$$

where F_0, F_0', and F_0'' are constants.

The third-order initial-value problem (10) can be converted into a set of first-order initial-value problems as in the following

$$\begin{cases} x' = y \\ y' = z \\ z' = -0.5xz \end{cases} \tag{12}$$

with initial conditions

$$x(0) = F_0, \quad y(0) = F_0', \quad z(0) = F_0'' \tag{13}$$

From the quadrature rule, equation (3), the first-order derivatives of functions x, y, and z can expressed as

$$x_i' = \sum_{j=1}^{m} A_{ij} x_j \quad , \quad y_i' = \sum_{j=1}^{m} A_{ij} y_j \quad , \quad z_i' = \sum_{j=1}^{m} A_{ij} z_j \tag{14}$$

Substituting equation (14) in (12) yields

$$\begin{cases} \sum_{j=1}^{m} A_{ij} x_j = y_i \\ \sum_{j=1}^{m} A_{ij} y_j = z_i \\ \sum_{j=1}^{m} A_{ij} z_j = -0.5 x_i z_i \end{cases} \quad i = 1,2,\ldots,m \tag{15}$$

Applying the initial conditions (13) in (15) yields

$$\begin{cases} \sum_{j=2}^{m} A_{ij} x_j + A_{i1} F_0 = y_i \\ \sum_{j=2}^{m} A_{ij} y_j + A_{i1} F_0' = z_i \\ \sum_{j=2}^{m} A_{ij} z_j + A_{i1} F_0'' = -0.5 x_i z_i \end{cases} \quad i = 2,3,\ldots,m \tag{16}$$

Equation (16) is a nonlinear system of algebraic equations which can be solved by iterative methods. In this work, we use the Newton-Raphson method to solve system (16). Our numerical experiment for the present problem showed that only 3-5 iterations are sufficient to achieve accurate solutions using the Newton-Raphson method.

5. A step-by-step DQ in time

When very long-term solutions are required, it is more convenient to apply the DQ method as a step-by-step time integration scheme. In this technique, the time domain of interest is first divided into several time elements. The DQ method in then applied to each time element independently. Note that the solutions at the end of each time element will be used as initial conditions for the next time element (for more details of this technique see Refs. (Guran and Ahmadi, 2011)).

6. Numerical results and discussion

As it was mentioned earlier, we should first determine the magnitude of L (defined in equation (9)). This parameter can be obtained using the solution of equation (7). To solve equation (7) using the scheme described in Sec. 5, we divide the time domain into n equal DQM time element with m sample time points (per DQM time element). The total number of sample time points and the average time step can be obtained as, respectively, (Guran and Ahmadi, 2011)

$$M_{tot} = n\,(m\text{-}1) + 1 \tag{17}$$

$$\Delta t = T/(\,M_{tot}\,\text{-}1) = T/(\,n\,(m\text{-}1)) \tag{18}$$

where T is the length of time span. Figure 1 presents the variations of $g(\alpha)$ with α for different values of n (number of time elements) and m (number of time points per time element). It can be seen that by increasing n and/or m, the DQ solutions are converged rapidly. Note that the DQ solution results at m time points are utilized to obtain the solutions at all the time points located in time interval $[0, t_m]$ (where t_m is the length of DQ time elements) via the Lagrange interpolation scheme. Thus we are able to find a continuous representation for the function $g(\alpha)$ using the Lagrange interpolation scheme.

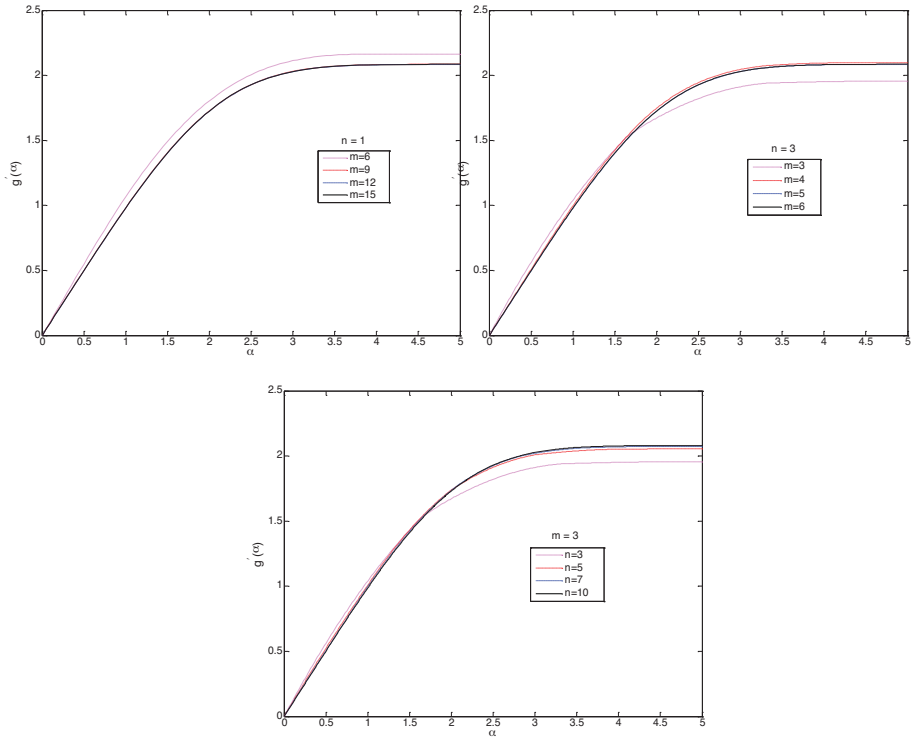

Fig. 1: Convergence and accuracy of DQ solutions with respect to the number of sample time points, m, and number of time elements, n.

It is interesting that the DQ method yields converged and rather accurate solutions using only m=3 time points. Note that m=3 is the smallest number of sample time points which can be used for the solution of present problem using the DQ method. This is due to the fact that the present problem is a third-order nonlinear equation and has three initial conditions given at the initial time point. It can also be seen from figure (1) that as α increases $g(\alpha)$ approaches to a constant value. This constant value is actually the magnitude of L. Note that in the cases shown in figure (1), the values of α is in the range $0 \leq \alpha \leq 5$. It is clear that to determine the magnitude of L ($=g(\infty)$), it in not required to solve the initial-value problem (7) at all the domain $0 \leq \alpha \leq \infty$. For example, as it can be seen from figure (1), one can solve the problem at the interval $0 \leq \alpha \leq 5$ to find an approximation of L. However, through numerical experiments we found that the most accurate L values can be obtained if the problem (7) is solved in the domain $0 \leq \alpha \leq 10$. Table 1 gives the results for L. An excellent rate of convergence can be observed. It can be seen that the DQ results are converged without instability for an increase in n and m. It can also be observed that by increasing the number of sample time points per time element, i.e., m, a smaller number of time elements, i.e., n, are required to obtain solutions with identical accuracies and vice versa (i.e., by increasing n a smaller m are required). However, when m is too small, the rate of convergence is slow and very large values of n are required to achieve accurate solutions.

Tab. 1: Convergence and accuracy of the DQ solution for $L = g'(10)$

n	***m*=7**	***m*=9**	***m*=11**	***m*=13**	***m*=15**
2	2.07125099256072	2.08616508333382	2.08552625546298	2.08535915160828	2.08542031533568
3	2.08086107493813	2.08573633901879	2.08539005571989	2.08541016274351	2.08540913792848
5	2.08564569949467	2.08540031913574	2.08540939693684	2.08540917319786	2.08540917643640
10	2.08540977491746	2.08540917461438	2.08540917646167	2.08540917643749	2.08540917643791***
15	2.08540923283780	2.08540917639232	2.08540917643792*	2.08540917643791**	2.08540917643791
20	2.08540918655018	2.08540917643358	2.08540917643791	2.08540917643790	2.08540917643791
30	2.08540917732140	2.08540917643774	2.08540917643791	2.08540917643791	2.08540917643791

*Δt_{DQ}=0.06666, **Δt_{DQ}=0.05555, ***Δt_{DQ}=0.07143,

In other words, the rate of convergence of solutions is more sensitive to m than n. Thus, to obtain accurate solutions with a reasonable time step, one should first choose the correct value of m and then increase n to reach to required accuracy. From Table 1, it is also observed that the magnitude of L is found to be converged up to fifteen digits. In Table 2 the DQ solutions are compared with those of RK4. Note that the sizes of time steps for two schemes are set to be equal to provide a reasonable comparison between two schemes.

Tab. 2: Convergence and accuracy of DQ solution for $L = g'(10)$ and comparison with RK4 solution

Method	***m*=7**	***m*=11**	***m*=15**
DQ (n=2)	2.07125099256072	2.08552625546298	2.08542031533568
RK4*	6.67115504023E+4	2.01369359611100	2.08539498816094
DQ (n=5)	2.08564569949467	2.08540939693684	2.08540917643640
RK4	2.08539777120960	2.08540721539089	2.08540861092003
DQ (n=10)	2.08540977491746	2.08540917646167	2.08540917643791
RK4	2.08540817139355	2.08540903063789	2.08540913673422
DQ (n=20)	2.08540918655018	2.08540917643791	2.08540917643791
RK4	2.08540910423540	2.08540916658843	2.08540917381891

*Note that the time steps for RK4 are so chosen that they are equal to those of DQM (i.e., $\Delta t_{RK4} = \Delta t_{DQM} = T/(n(m\text{-}1))$ and T=10 here)

To check the accuracy of DQ and RK4 solutions, shown in Tables 1 and 2, the problem is solved again using the RK4 and with very small time steps and the solutions are cited in Table 3.

Tab. 3: Convergence and accuracy of RK4 solution for $L = g'(10)$

Δt=0.1	**Δt=0.01**	**Δt=0.002**	**Δt=0.001**	**Δt=0.0005**
2.08540903063789	2.08540917642120	2.08540917643787	2.08540917643789	2.08540917643787

By comparing the DQ results with those of RK4, one can conclude that the DQ method needs much larger time steps to achieve accurate solutions. This illustrates the superiority of the DQ time integration method over the classical RK4. From the RK4 solutions shown in Table 2, one can also observe the numerical instability of RK4 when n=2 and m=7. In fact, when the time step is too large, the RK4 may encounter some numerical instability as seen in Table 2.

Tables 4-6 present convergence and accuracy of DQ time integration scheme for the solution of Blasius equation (i.e., equation (8)). A single time element is employed (i.e., n=1). The results of RK4

are also included for comparison. Rapid convergence and stability of the numerical solutions versus increasing DQ number of sample time points are obvious. Note that the DQ solutions are converged up to eight digits. Since the time steps are so large, the RK4 and DQ solutions match only to four decimal positions. This is due to the fact that the RK4 needs much smaller time step sizes than DQM to achieve results with identical accuracies.

Tab.4: Convergence and accuracy of DQ solution for $f(5)$ (n=1) and comparison with the RK4 solution

Method	*m*=6	*m*=7	*m*=9	*m*=11	*m*=13	*m*=15	*m*=20
DQ	3.2522253	3.2717815	3.2842311	3.2832062	3.2832779	3.2832734	3.2832736
RK4	3.2847702	3.2839304	3.2834541	3.2833406	3.2833037	3.2832890	3.2832778

Tab. 5: Convergence and accuracy of DQ solution for $f'(5)$ (n=1) and comparison with the RK4 solution

Method	*m*=6	*m*=7	*m*=9	*m*=11	*m*=13	*m*=15	*m*=20
DQ	0.9874834	0.9886335	0.9917923	0.9915237	0.9915431	0.9915418	0.9915419
RK4	0.9903180	0.9910017	0.9913909	0.9914847	0.9915157	0.9915282	0.9915381

Tab. 6: Convergence and accuracy of DQ solution for $f''(5)$ (n=1) and comparison with the RK4 solution

Method	*m*=6	*m*=7	*m*=9	*m*=11	*m*=13	*m*=15	*m*=20
DQ	0.0164112	0.0159920	0.0158999	0.0159073	0.0159067	0.0159068	0.0159068
RK4	0.0181004	0.0168513	0.0161596	0.0159995	0.0159482	0.0159279	0.0159125

Table 7 gives the convergence and accuracy of RK4 solutions with respect to time step sizes. The DQ results with Δt=1/4 =0.25 are also included for comparison. It can be seen that the DQ solutions with Δt=1/4 and RK4 solutions with Δt=1/20 are coincident to each other. Needless to say the DQ method is more efficient than RK4. We also compared our solutions with those of Howarth (Howarth, 1938) and we found that both results agree well with each other.

Tab. 7: Convergence and accuracy of RK4 for the solution of Blasius equation and comparisons with the DQ results

	Δt=1/4	Δt=1/7	Δt=1/10	Δt=1/12	Δt=1/16	Δt=1/20	DQ (Δt=1/4)
$f(5)$	3.28327697	3.28327398	3.28327374	3.28327370	3.28327367	3.28327367	3.28327367
$f'(5)$	0.99153882	0.99154159	0.99154183	0.99154186	0.99154189	0.99154190	0.99154190
$f''(5)$	0.01591136	0.01590723	0.01590690	0.01590684	0.01590681	0.01590680	0.01590680

Figure 2 presents the accuracy, convergence, and stability of DQ time integration method for computing the long-term solutions. It is seen that the DQ time integration scheme is also very efficient for time integration over long time duration. But care should be taken in choosing proper values of n and m. From figure 2 it is observed that when m is incorrectly chosen, the DQ time integration scheme may also be possible to yield inaccurate solutions. From the results shown in this figure and those cited in Tables 1-6, one can also concluded that the number of time points per time element, i.e., m, can not be too small. If m be too small, we then should use a large number of time element n to obtain accurate solutions and this increases the CPU time considerably. One the other hand, m can not be too large. If m be too large, the resulting DQ time integration scheme may be increasingly unstable. This is actually due to the fact that the DQ weighting coefficient matrices tend to be ill-conditioned by increasing the number of sample time points. The present authors recommend that m be in the range $5 \le m \le 15$. If m be in the above range, one needs not to be worried about efficiency and stability of DQ method. In Table 8 the DQ solutions with $\Delta t = 0.34965$ are compared with those of RK4 with $\Delta t = 0.25$ and $\Delta t = 0.1$ for different values of η. It can be seen that the DQ results with $\Delta t = 0.34965$ are better in accuracy than those obtained using RK4 with $\Delta t = 0.25$. Also, one can observe the numerical instability of RK4 for long-term solutions when $\Delta t = 0.25$. In other words, the RK4 solutions with $\Delta t = 0.25$ encounter a convergence problem and approach to infinity after $\eta = 35$. It can also be seen that the RK4 solutions with $\Delta t = 0.1$ are high accurate, since as η increases $f'(\eta)$ approaches to unity and $f''(\eta)$ approaches to zero. The DQ solutions with $\Delta t = 0.34965$ are also accurate, but their accuracy is less than those of RK4 with $\Delta t = 0.1$.

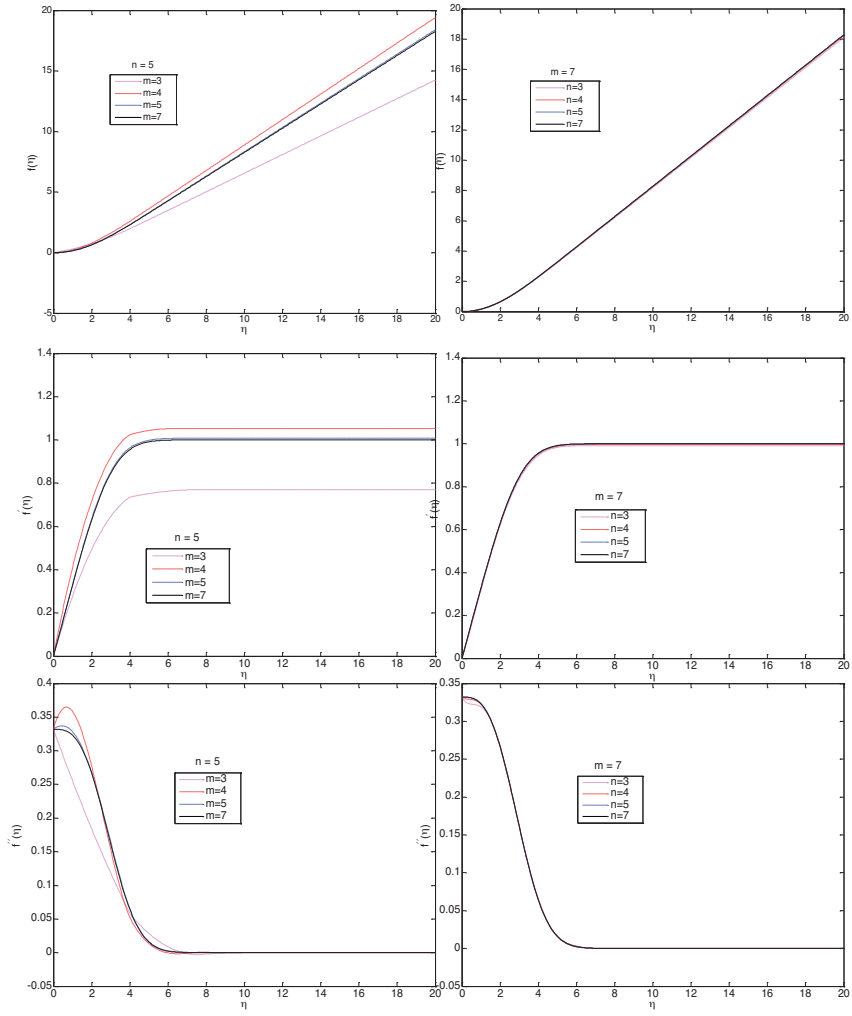

Fig. 2: Convergence and accuracy of the DQ method for the solutions of Blasius equation.

Tab. 8: Convergence and accuracy of RK4 for the solution of Blasius equation and comparisons with the DQ results

η	DQ(n=13,m=12: Δt = 0.34965)			RK4 (Δt = 0.25)			RK4 (Δt = 0.1)		
	$f(\eta)$	$f'(\eta)$	$f''(\eta)$	$f(\eta)$	$f'(\eta)$	$f''(\eta)$	$f(\eta)$	$f'(\eta)$	$f''(\eta)$
0.5	0.0414928	0.1658853	0.3309111	0.0414937	0.1658852	0.3309110	0.0414928	0.1658853	0.3309110
2.5	0.9963114	0.7512599	0.2174116	0.9963139	0.7512585	0.2174121	0.9963112	0.7512597	0.2174116
5.0	3.2832745	0.9915421	0.0159068	3.2832769	0.9915388	0.0159113	3.2832737	0.9915418	0.0159069
7.5	5.7792195	0.9999821	5.5261E-5	5.7792192	0.9999811	5.5849E-5	5.7792180	0.9999818	5.5273E-5
10	8.2792143	1.0000002	8.4437E-9	8.2792122	0.9999994	9.4693E-9	8.2792123	0.99999998	8.4588E-9
15	13.279215	1.0000002	4.361E-16	13.279209	0.9999994	2.862E-19	13.279212	0.99999998	1.736E-20
20	18.279217	1.0000002	6.458E-25	18.279207	0.9999994	9.377E-29	18.279212	0.99999998	1.686E-37
25	23.279218	1.0000002	1.289E-28	23.279204	0.9999994	3.180E-31	23.279212	0.99999998	1.667E-59
30	28.279219	1.0000002	2.892E-33	28.279201	0.9999994	9.181E-26	28.279212	0.99999998	1.404E-85
35	33.279220	1.0000002	8.721E-42	33.279198	0.9999994	2.333E-13	33.279212	0.99999998	9.27E-114
40	38.279221	1.0000002	2.454E-45	-9.8323E2	-9.8592E4	-2.1425E7	38.279212	0.99999998	5.78E-141
45	43.279221	1.0000002	2.417E-49	- *Infinity*	- *Infinity*	- *Infinity*	43.279211	0.99999998	7.72E-164
50	48.279223	1.0000002	1.151E-53	- *Infinity*	- *Infinity*	- *Infinity*	48.279211	0.99999998	6.34E-180

7. Conclusion

In this paper, the DQ method is employed to solve the well-known Blasius boundary layer problem. The efficiency, accuracy, and convergence of the DQ method are investigated and analyzed. It is shown that the DQ method can predict the behavior of Blasius boundary layer accurately. Numerical comparisons between the DQ time integration method and RK4 reveal that the DQ method is a promising and effective tool for handling the nonlinear systems of ordinary differential equations.

References

Abbasbandy S. A (2007) numerical solution of Blasius equation by Adomian's decomposition method and comparison with homotopy perturbation method. Chaos Solitons & Fractals; 31: pp. 257-60.

Ahmad F. (2007) Degeneracy in the Blasius problem. *Electron J Differ Equations*; 92: pp. 1-8.

Ahmad F, Al-Barakati WH. (2009) An approximate analytic solution of the Blasius Problem. Commun Nonlinear Sci Numer Simul;14: pp. 1021-4.

Allan FM, Syam MI. On the analytic solutions of the nonhomogeneous Blasius problem. *J Comput Appl Math* 2005;182:362-71.

Asaithambi A. (2005) Solution of the Falkner-Skan equation by recursive evaluation of Taylor coefficients. *J Comput Appl Math*;176: pp. 203-14

Bellman RE, Casti J. (1971) Differential quadrature and long term integrations. *J Math Anal Appl*; 34: pp. 235-8.

Bert CW, (1996) Malik M. Differential quadrature method in computational mechanics: a review. *ASME J Appl Mech Rev*;49: pp. 1-28.

Cortell R. (2005) Numerical solution of the classical Blasius flat-plate problem. *Appl Math Comput*; pp. 170:706-10.

Fang T, Guo F, Lee CF. (2006) A note on the extended Blasius Problem. Appl Math Lett; 19: pp. 613-7.

Guran A, Ahmadi G., (2011) Computational Approaches to the Lorenz System, *Proceedings of AMiTaNS'11, American Institute of Physics*.

Guran, A. , J. Gewinner (2011) A fast convergent solution of Blasius equation by means of differential quadrature, *II Annual Meeting of the Georgian Mechanical Union*, 15-17 december, Tbilisi, Georgia.

He JH. (2003) A simple perturbation approach to Blasius equation. Appl Math Comput; 140: pp. 217-22.

He JH. (2004) Comparison of homotopy perturbation method and homotopy analysis method. *Appl Math Comput*; pp. 156:527-39.

He J. (1997) A new approach to nonlinear partial differential equations. Commun Nonlinear Sci Numer Simul;2(4): pp. 230-35.

He J. (1999) Approximate analytical solution of Blasius equation. Commun Nonlinear Sci Numer Simul; 4(1): pp.75-8.

Howarth L. (1938) On the solution of the laminar boundary layer equations. *Proc Roy Soc London*; 164: pp. 547-79

Liao SJ. A (1997) kind of approximate solution technique which does not depend upon small parameters, Part 2: an application in fluid mechanics. *Int J Nonlinear Mech*; 32(5): pp. 815-22.

Liao SJ. (1998) An explicit, totally analytic solution of laminar viscous flow over a semi-infinite flat plate. Commun Nonlinear Sci Numer Simul; 3(2): pp. 53-57.

Liao SJ. A (1999) uniformly valid analytic solution of two dimensional viscous flow over a semi-infinite flat plate. *J Fluid Mech*; 385: pp. 101-28.

Na TY. (1979) Computational methods in engineering boundary value problems. Academic Press;.

Quan JR, Chang CT. (1989a) New insights in solving distributed system equations by the quadrature methods, Part I: Analysis. Comput Chem Eng; 13: pp. 779-788.

Schiliching H. (2004) Boundary layer theory. 8th ed. McGraw-Hill Inc.

Shu C. (2000) Differential quadrature and its application in engineering. New York: Springer publication.

Wang L. (2004) A new algorithm for solving classical Blasius equation. *Appl Math Comput*; 157: pp. 1-9.

18th International Conference
ENGINEERING MECHANICS 2012
Svratka, Czech Republic, May 14 – 17, 2012

pp. 343–344
Paper #121

NONLINEAR FINITE ELEMENT ANALYSIS OF CIRCULAR REINFORCED CONCRETE COLUMNS RETROFITTED BY STEEL JACKETS

A. Guran[1], M. Zakariaey[2]

Abstract: *This paper after a review of confinement methods for strengthening reinforced concrete structures uses a finite element technique to study the nonlinear behavior of circular reinforced concrete retrofitted with steel jackets under cyclic loading. Optimal thicknesses of the steel jackets are obtained and tabulated according to the geometry of columns. The numerical results are compared to experimental results of Priestley et al (1996) and Hwang and Kuo (2000).*

Keywords: ***Steel jacket, shear strength, finite element method, reinforced concrete column.***

1. Introduction

As the reinforced concrete structures continue to age, the need foreffective retrofittreatments has increased. Many building and bridge structuralcomponents no longerprovide capacity sufficient to meet the required code standards.Seismic upgrading and reinforcement protection are two of the majorissues requiring retrofits. Further,many aging structural members no longer provide the load capacity ofthe original design because of steel corrosion, concrete cracking, orother damage.

Currently applied methods for retrofitting reinforved concrete columns includesteel jacketing (Priestly et al, 1994, 1996), fiber reinforcedpolymer(FRP) jacketing (Saeedii et al ...), and Prefabricated CageSystem (PCS) reinforcement (Adam et al). All three methods havebeen shown to effectively in increase the strenth and capacity ofreinforced concrete columns.

2. Finite Element Analysis of Circular Columns Retrofitted by Steel Jackets

Figure 1 shows the configuration the circular concrete columnretrofited by steel jacket. The elements selected for finite elementanalysis using ANSYS are: 8 node element SOLID65 with 3 degrees offreedom (for concrete), 8 node element SOLID45 with 3 degrees offreedom (for steel), and 3D element TARGE 170 (forcontact between concrete and jacket), bar element LINK8 (forreinforcements).

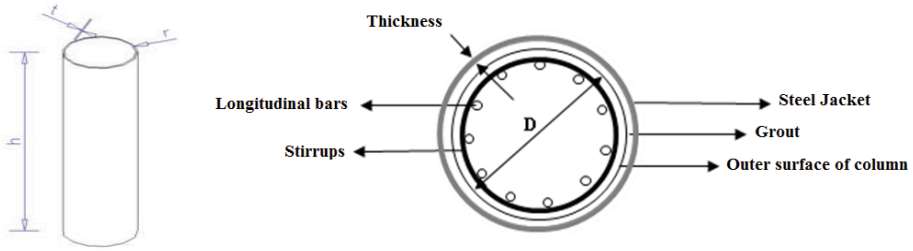

Fig. 1: circular concrete column retrofitted by steel jacket.

The geometry of the column and material properties ofconcete, steel jacket and reinforcements are taken from Priestly et al (1994). The cyclic load applied on top of the column in horizontaldirection is shown in figure 2.

[1] Professor, Technical University of Munich (Germany), Director, Institute of Structronic, 275 Slater Street, 9th Floor,Ottawa, Canada. Corresponding Author, ardeshir.guran@mcgill.ca

[2] Research Assistant, Institute of Structronic, 275 Slater Street, 9th Floor,Ottawa, Canada.

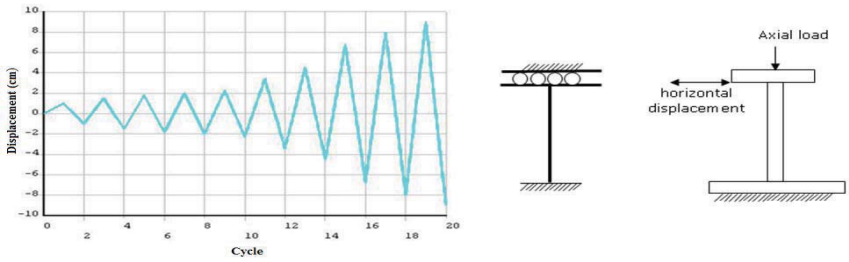

Fig. 2: Transverse loading: Horizontal Displacement control

Figure 3 shows the comprison of the finite element analysis with thoseof experiments by Priestly et al (1994) and by Huang Hwang and Kuo(2000).

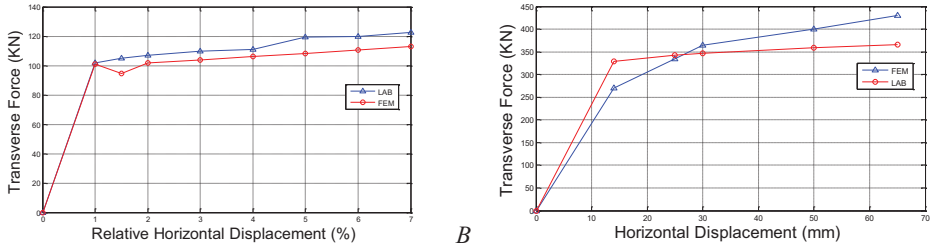

A *B*

Fig. 3: A. Comparison of envelopes for FEM model and experiments (Priestley et al, 1994)
B. Comparison of envelopes for FEM model and experiments (Hwang and Kuo, 2000)

Using the fact that optimal thickness corresponds to the situation inwhich the yielding in steel jacket and cracks in concrete occurressimultaneously together with transfer of load from concrete to steeljacket a procedure is proposed to calculate the optimum thickness ofthe column.

3. Concluding Remarks

In conclusion, the following remarks can be made. More details are given in full length version of this paper which is available in CD proceeding of conference.

1. The Steel Jackets are beneficial in Earthquake Design of structures
2. Thickness and tensile strength of steel jackets have significant influence on increasing the strength against Earthquake
3. Compressive strength of R.C has significant effects on Earthquake resistance of columns retrofitted by steel jackets
4. Effects of axial loads and reinforcement on strength of column are not drastic.
5. A procedure for determination of optimal thickness of steel jacket for maximum shear strength was proposed. The results are tabulated according to height and diameter of the columns.

References

Garzón-Roca, J., et al. (2011). "Behaviour of RC columns strengthened by steel caging under combined bending and axial loads." Construction and Building Materials 25(5): 2402-2412.

Saiidi, M. S., F. Martinovic, et al. (2004). "Assessment of Steel and Fiber Reinforced Plastic Jackets for Seismic Retrofit of Reinforced Concrete Columns with Structural Flares." Journal of Structural Engineering 130(4): 609-617.

Hwang S-J and Kuo, W-W, (2000). "Recent Advances in Seismic Retrofit of Rc Structures in Taiwan", Department of Construction Engineering National Taiwan University of Science and Technology, Taipei, Taiwan.

Priestley, M.J.N., Seible, F., Xiao Y., and Verma R. (1994), " Steel jacket Retrofitting of Reinforced Concrete Bridge Columns for Enhanced Shear Strength", part1,2, ACI Structural Journal, v.91

Priestley, M.J.N., Seible, F. and Calvi, G.M. ,(1996), ”Seisemic Design & Retrofit of Bridges” ,John Wiley & Sons,INC.

18th International Conference
ENGINEERING MECHANICS 2012
Svratka, Czech Republic, May 14 – 17, 2012

pp. 345–353
Paper #138

NUMERICAL SIMULATION OF TWO-PHASE FLOW IN A LOW PRESSURE STEAM TURBINE STAGE

J. Halama *, **J. Fořt** **

Abstract: *The paper deals with the numerical solution of two phase unsteady flow in a steam turbine stage performed by in-house numerical code. The main issues related to the flow model, numerical method and problem formulation are presented. The effect of droplet size of incoming wet steam is discussed.*

Keywords: ***Finite volume method, turbine, nucleation, wet steam, CFD.***

1. Introduction

The paper presents the results of recent work aimed at the simulation of steam flow with non-zero wetness at the inlet. The problem formulation requires the complete information about the structure of incoming liquid phase. It is relatively easy to estimate the inlet wetness, however the flow models have other unknowns, which have to be set. The presented model is based on the transport equations for three moments. The values of these moments for the inlet boundary condition have been estimated using numerical simulation of upstream expansion. Numerical test have shown, that numerical solution is quite sensitive to the given values of moments. This phenomenon has been studied for the steady flow in the nozzle. Similar effects have been observed in the case of unsteady flow in a turbine stage.

2. Flow model

Consider the flow of steam with velocity, pressure and temperature corresponding to the conditions within the low pressure part of a steam turbine. The rapid expansion of steam leads to non-equilibrium phase change, i.e. the condensation appears 'later', when the steam temperature drops sufficiently below the saturation temperature. This 'sub-cooling' is typically $30 - 40\ K$. Consider the liquid phase in the form of high amount of small spherical droplets dispersed in vapor and having the same velocity as the vapor. There is a mass exchange between vapor and droplets due to phase change. The flow model is based on the conservation of mass, momentum and energy for the mixture and the transport equation for the mass fraction of liquid phase. Such kind of model, known also as 'mixture model', is commonly used, e.g. Dykas et al (2003), Young (1992) or Šejna and Lain (1994). The droplet size is an important parameter. In reality there is a whole spectra of droplet sizes in the elemental volume of mixture. Flow models are mostly based on the average radius approximation, therefore the mentioned set of transport equations has to be complemented at least by the transport equation for the number of droplets, e.g. Dykas et al (2003). Here we consider three additional transport equations for the moments according to Hill (1966) to obtain higher precision of average droplet size prediction and to be able to add some simple model of droplet size distribution, for details see Halama et al (2010). The moments read:

$$Q_0 = N, \qquad Q_1 = \sum_{i=1}^{N} r_i, \qquad Q_2 = \sum_{i=1}^{N} r_i,^2 \tag{1}$$

*Jan Halama: Department of Technical Mathematics, Faculty of Mechanical Engineering, Czech Technical University in Prague, Karlovo nam. 13, 121 35, Prague; CZ, e-mail: jan.halama@fs.cvut.cz
**Jaroslav Fořt: Department of Technical Mathematics, Faculty of Mechanical Engineering, Czech Technical University in Prague, Karlovo nam. 13, 121 35, Prague; CZ, e-mail: jaroslav.fort@fs.cvut.cz

where N denotes the total number of droplets per unit mass and r_i is the radius of $i-th$ droplet. The average droplet radius is approximated by $r = \sqrt{Q_2/Q_0}$. The full system of transport equations reads

$$\frac{\partial \mathbf{W}}{\partial t} + \frac{\partial \mathbf{F}(\mathbf{W})}{\partial x} + \frac{\partial \mathbf{G}(\mathbf{W})}{\partial y} = \mathbf{Q}, \tag{2}$$

$$\mathbf{W} = \begin{bmatrix} \rho \\ \rho u \\ \rho v \\ e \\ \rho\chi \\ \rho Q_2 \\ \rho Q_1 \\ \rho Q_0 \end{bmatrix}, \mathbf{F} = \begin{bmatrix} \rho u \\ \rho u^2 + p \\ \rho uv \\ (e+p)u \\ \rho\chi u \\ \rho Q_2 u \\ \rho Q_1 u \\ \rho Q_0 u \end{bmatrix}, \mathbf{G} = \begin{bmatrix} \rho v \\ \rho vu \\ \rho v^2 + p \\ (e+p)v \\ \rho\chi v \\ \rho Q_2 v \\ \rho Q_1 v \\ \rho Q_0 v \end{bmatrix}, \mathbf{Q} = \begin{bmatrix} 0 \\ 0 \\ 0 \\ 0 \\ \frac{4}{3}\pi r_c^3 J\rho_l + 4\pi\rho Q_2 \dot{r}\rho_l \\ r_c^2 J + 2\rho Q_1 \dot{r} \\ r_c J + \rho Q_0 \dot{r} \\ J \end{bmatrix},$$

where ρ, u, v and e denotes the mixture density, velocity components and total energy per unit volume respectively. The symbol χ denotes the mass fraction of liquid phase (wetness). Under the perfect gas assumption the system is closed by the equation

$$p = \frac{(\gamma-1)(1-\chi)}{1+\chi(\gamma-1)}\left[e - \frac{1}{2}\rho(u^2+v^2) + \rho\chi L\right], \tag{3}$$

for further details see Šejna and Lain (1994) and Halama et al (2011). The common pressure for both phases is considered. The system (2) turns into the 2D Euler equations for the one phase flow if liquid phase vanishes ($\chi = Q_0 = Q_1 = Q_2 = 0$).

The specific heat ratio reads

$$\gamma = \frac{c_p}{c_p - R_v}, \tag{4}$$

where R_v is the gas constant for vapor and the specific heat at constant pressure c_p is a function of temperature in form

$$c_p = c_0 + c_1 T + c_2 T^2 + c_3 T^3. \tag{5}$$

According to the perfect gas assumption the vapor temperature

$$T = \frac{p}{\rho_v R_v}, \quad \rho_v = (1-\chi)\rho. \tag{6}$$

The number of suddenly born droplets per second in unit volume is given by the nucleation rate according to classical theory in Becker and Doering (1935)

$$J = \sqrt{\frac{2\sigma}{\pi m_v^3}} \cdot \frac{\rho_v^2}{\rho_l} \cdot \exp\left(-\beta \cdot \frac{4\pi r_c^2 \sigma}{3k_B T}\right) \qquad [m^{-3}s^{-1}], \tag{7}$$

where the surface tension σ of water is a function of temperature and it is corrected by the coefficient β proposed in Petr and Kolovratník (2001) to get better agreement with reality

$$\beta = 1.328 p_{cor}^{0.3}, \tag{8}$$

where p_{cor} $[bar]$ denotes the pressure at the intersection of the isentropic expansion from reservoir conditions (p_0 and T_0) with the steam saturation line in the Mollier diagram, see the Fig. 1. The just born droplet has radius equal to the critical radius

$$r_c = \frac{2\sigma}{L\rho_l \ln(T_s/T)} \qquad [m], \tag{9}$$

where $L(T)$ is the latent heat of condensation/evaporation and $\rho_l(T)$ denotes the density of water. The saturation temperature T_s is computed using industrial formulation of steam properties IAPWS-IF97. Droplet growth is computed as

$$\dot{r} = \frac{\lambda_v(T_s - T)}{L\rho_l(1 + 3.18 \cdot Kn)} \cdot \frac{r - r_c}{r^2} \qquad [ms^{-1}], \tag{10}$$

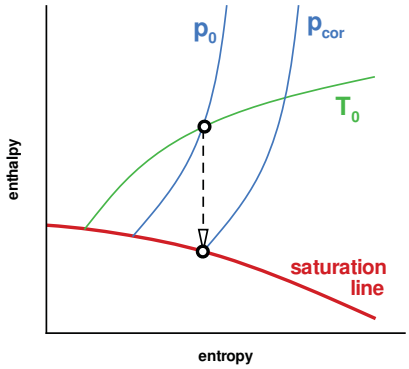

Fig. 1: Definition of p_{cor}.

with

$$Kn = \frac{\eta_v \cdot \sqrt{2\pi R_v T}}{4rp} \tag{11}$$

where vapor thermal conductivity λ_v and vapor viscosity η_v are functions of temperature.

We consider a certain limit value χ_{min} for wetness in order to avoid big computational errors (e.g. division by numbers going to zero, ...). The average radius is therefore computed as

$$r = \begin{cases} 0, & \chi \leq \chi_{min}, \\ \sqrt{Q_2/Q_0}, & \chi > \chi_{min}. \end{cases} \tag{12}$$

Flow models based on the average size of droplets may not work properly in certain conditions, therefore according to Sopuch (1996) we split the evaluation of source term $\mathbf{Q}$ into four cases

1. $T \geq T_s$ and $r \leq r_{min}$: all droplets have disappeared, i.e. set $\chi = Q_0 = Q_1 = Q_2 = 0$
2. $T \geq T_s$ and $r > r_{min}$: droplets are evaporating, set $r_c = 0$ in Eq. (10)
3. $T < T_s$ and $r \leq r_c$: consider nucleation only, set $\dot{r} = 0$
4. $T < T_s$ and $r > r_c$ nucleation and droplet growth according to the above formulas

The value of r_{min} is chosen appropriately.

There can be a problem with direct evaluation of droplet growth speed according to the Eq. (10), since the critical radius goes to infinity, when the vapor temperature approaches the saturation temperature. From the mathematical point of view this growth is controlled by the term $(T_s - T)$, which is going to zero at the same time, so the droplet growth speed $\dot{r}$ remains finite. However direct implementation of the Eq. (10) in the numerical code is dangerous, since the product of 'almost infinity' with 'almost zero' has unpredictably unstable behavior. Therefore we consider both equations (9) and (10) together in the form

$$\dot{r} = \frac{\lambda_v (T_s - T)}{L\rho_l (1 + 3.18 \cdot Kn)} \frac{r - r_c}{r^2} = \frac{\lambda_v}{L\rho_l (1 + 3.18 \cdot Kn)} \left(\frac{T_s - T}{r} - \frac{2\sigma}{L\rho_l r^2} \cdot \frac{T_s - T}{\ln \frac{T_s}{T}} \right), \tag{13}$$

where the term $\dfrac{T_s - T}{\ln \frac{T_s}{T}}$ ('zero' divided by 'zero' for T going to T_s) is approximated using the first six terms of Taylor expansion

$$\frac{T_s - T}{\ln \frac{T_s}{T}} = T \frac{\frac{T_s}{T} - 1}{\ln \frac{T_s}{T}} = 1 + \frac{1}{2}\vartheta - \frac{1}{12}\vartheta^2 + \frac{1}{24}\vartheta^3 - \frac{19}{720}\vartheta^4 + \frac{3}{160}\vartheta^5, \qquad \vartheta = \frac{T_s}{T} - 1. \tag{14}$$

This approximation yields stable numerical algorithm for cases with steam parameters close to saturation line.

3. Numerical method

Presented flow model includes convection, nucleation and droplet growth phenomena, which have very different time scales. Current numerical method is based on the splitting method of Strang (1968), where each phenomena is treated by individual numerical method. We use symmetrical splitting, i.e. we solve three successive equations

$$\frac{\partial \mathbf{W}^*}{\partial t} = \mathbf{Q}(\mathbf{W}^*) \tag{15}$$

$$\frac{\partial \mathbf{W}^{**}}{\partial t} = -\frac{\partial \mathbf{F}^c(\mathbf{W}^{**})}{\partial x} - \frac{\partial \mathbf{G}^c(\mathbf{W}^{**})}{\partial x} \tag{16}$$

$$\frac{\partial \mathbf{W}^{***}}{\partial t} = \mathbf{Q}(\mathbf{W}^{***}), \tag{17}$$

where $\mathbf{W}^*(t) = \mathbf{W}(t)$, $\mathbf{W}^{**}(t) = \mathbf{W}^*(t + \Delta t/2)$ and $\mathbf{W}^{***}(t) = \mathbf{W}^{**}(t + \Delta t)$. The solution $\mathbf{W}^{***}(t + \Delta t/2)$ corresponds to the solution $\mathbf{W}(t + \Delta t)$ of the original un-split system (2). The single step of Lax-Wendroff finite volume method is applied for (16) and several steps of Runge-Kutta method evaluate the source term contribution in (15) and (17). The algorithm of splitting method reads

$$\begin{aligned} \mathbf{W}_K^{(j+1)} &= \mathcal{RK}(\mathbf{W}_K^{(j)}, \frac{\Delta t}{2m}),\ j = 0, \ldots, m-1 \\ \mathbf{W}_K^{(m+1)} &= \mathcal{FV}(\mathbf{W}_K^{(m)}, \Delta t) \\ \mathbf{W}_K^{(j+1)} &= \mathcal{RK}(\mathbf{W}_K^{(j)}, \frac{\Delta t}{2m}),\ j = m+1, \ldots, 2m \end{aligned} \tag{18}$$

where $\mathbf{W}_K^{(0)} = \mathbf{W}_K^n$, $\mathbf{W}_K^{n+1} = \mathbf{W}_K^{(2m+1)}$, $\mathcal{FV}(\mathbf{W}_K^n, \Delta t)$ denotes one step of Lax-Wendroff method with initial data $\mathbf{W}_K^n$ and time step Δt (subscript $\cdot_K$ denotes the K-th cell and superscript $\cdot^n$ n-th time level). Similarly $\mathcal{RK}(\mathbf{W}_K^n, \Delta t)$ denotes one step of the Runge-Kutta method. The local number of sub-steps is $m = \Delta t/\tau$, where τ is the time scale of condensation and Δt is the time step of finite volume method for the equation (16). Domain of solution is discretized by the body fitted quadrilateral structured mesh.

4. Wet steam flow in the convergent-divergent nozzle

Current numerical method has been verified for the case of steam flow in the Barschdorff nozzle, for details see Halama et al (2011). There have been performed also computations of steam flow in a turbine cascade and turbine stage. All cases have been chosen to have steam temperature slightly below saturation temperature and zero wetness at the inlet, nucleation then starts inside the domain. Recent work has been aimed at the case of flow with nonzero wetness at the inlet. Since it is practically impossible to get reliable information about the droplet size structure of incoming steam, some basic numerical study for case of flow in a nozzle has been performed. The inlet boundary condition besides the the value of wetness requires also the values for moments, which have been estimated using numerical simulation of upstream expansion. The values of moments can be thus subjected to certain error. The following test cases investigate the sensitivity of numerical solution on the values of moments of incoming wet steam, in other words the sensitivity on the size of incoming droplets. Consider the geometry of Barschdorff nozzle from Barschdorff (1971) and three flow cases, which differ only in moments of incoming wet steam. The outflow static pressure corresponds to the design conditions of nozzle, this means supersonic velocity at the outlet and therefore no outlet boundary condition. Parameters of the flow cases are given in the Table 1.

Computed pressure, Mach number, wetness and average radius distributions along the nozzle axis are presented in the Fig. 2. The inflow droplet size in the case 1D-A is comparable to the critical radius, therefore the droplet growth given by the Eq. (13) is close to zero and the vapor sub-cooling grows til the rear part of the nozzle. The nucleation, which starts at the rear part is hardly noticeable, since the inflow vapor contains too many (too small) droplets so the number of newly born droplets does not increase much the number of already existing droplets. The wetness rise due to the nucleation is also small. If we consider bigger droplets at the nozzle inlet, see the case 1D-B, droplets gradually grow and

Tab. 1: Parameters of considered flow cases.

case	1D-A	1D-B	1D-C
$p_{0,inlet}\ [Pa]$	21061	21061	21061
$T_{0,inlet}\ [K]$	334.3	334.3	334.3
$\chi_{inlet}\ [-]$	0.349	0.349	0.349
$Q_{0,inlet}\ [kg^{-1}]$	$0.118 \cdot 10^{23}$	$0.111 \cdot 10^{19}$	$0.111 \cdot 10^{13}$
$Q_{1,inlet}\ [mkg^{-1}]$	$0.112 \cdot 10^{12}$	$0.111 \cdot 10^{11}$	$0.111 \cdot 10^{7}$
$Q_{2,inlet}\ [m^2kg^{-1}]$	$0.392 \cdot 10^{3}$	$0.111 \cdot 10^{3}$	$0.111 \cdot 10^{1}$

the sub-cooling is small, it means that local wetness is close to the local equilibrium wetness. Since the sub-cooling is small, there is no nucleation. The last case 1D-C considers the biggest droplets at the inlet. Wetness rise due to droplet growth is negligible compared to the case 1D-B since the total surface of droplets which is proportional to the second moment Q_2 is small. The vapor sub-cooling grows and downstream the throat nucleation starts, which yields significant droplet size drop. The present model with single average size of droplets is no more suitable for such case, because it is not able to distinguish two groups of droplets with very different sizes. All three cases refer to the considerable sensitivity

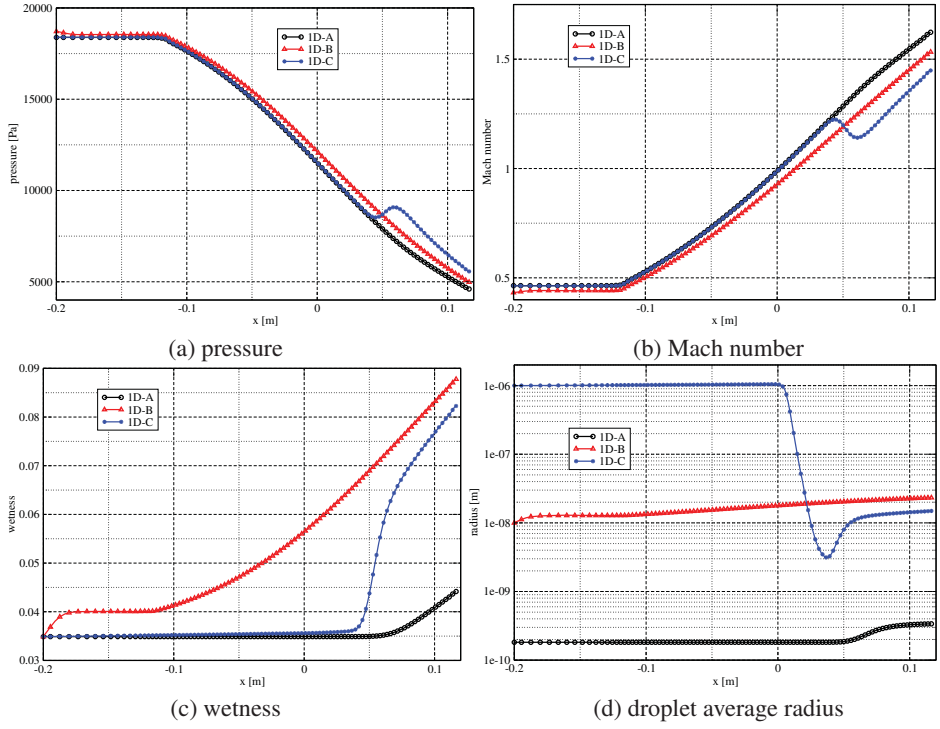

(a) pressure (b) Mach number

(c) wetness (d) droplet average radius

Fig. 2: The distributions along nozzle axis.

of condensing steam flow model on the structure of liquid phase at the inlet. Therefore one has to be very careful with the estimation of inlet boundary conditions as well as with conclusions about results of numerical simulation.

5. Stator-rotor interaction

Here we present the first results of unsteady stator-rotor interaction with the non-zero wetness at the inlet. A two-dimensional case corresponds to the cylindrical cut from the real annular stage projected onto plane. The set of equation (2) is solved in the coordinate system attached to the each respective blade cascade, i.e. in the absolute frame for stator and in the relative frame for the rotor. Numerical domain consists of 8 stator and 11 rotor blade passages to keep the original ratio of stator to rotor number of blades. Computational grid consists of single H-type structured block per each blade channel. The single stator channel is discretized by 112x45 points and the single rotor one using 141x33 points, see the Fig. 3.

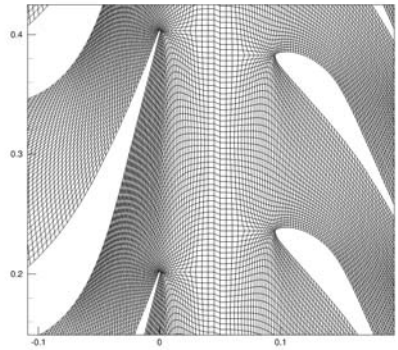

Fig. 3: Detail of computational grid at stator-rotor interface.

Initial computations have been performed for inlet boundary conditions related to the case 1D-A for the nozzle and outlet static pressure $4165\ Pa$. Numerous tests with relaxed time step, increased artificial dissipation etc. were performed to suppress the appearance of oscillations in the stator cascade. The regularization of droplet growth model, see the Eq. (13) and (14), helped to stabilize the numerical algorithm, although some oscillations of solution in the stator cascade remained, see the wetness isolines in the Fig. 4. These oscillation have most probably their origin in 'too small' size of droplets . The

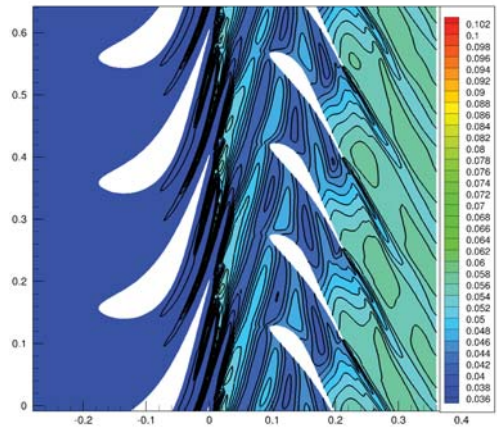

Fig. 4: Wetness contours at $t = t_0$ for 'too small' droplets at the inlet

values of moments for that case have been obtained from numerical solution in upstream stage, where

nucleation took place close to stage outlet and the numerical simulation under-predicted the size of droplets. Therefore we further present the case with 'bigger' droplets (the moments Q_i were modified).

We compare two cases. The case 1, which models only convection of wet steam, i.e. the source term including nucleation and droplet growth is omitted. The case 2 considers the solution of complete system with nucleation and droplet growth. Both cases have the same boundary conditions, the inlet boundary conditions corresponds to the case 1D-B for the nozzle in the previous section. The outlet static pressure is $4165\ Pa$. The Fig. 5 shows isolines of pressure in two consequent positions of rotor cascade during the rotor movement of one rotor pitch (the time necessary for the rotor shift of one pitch is denoted as τ_R). The flow field in the stator cascade does not contain shock waves, the pressure field between stator and rotor is without strong gradients. The structure of isolines for different rotor positions is thus very similar. The following figures 6 - 8 show isolines of wetness, vapor sub-cooling and average droplet radius respectively. These figures does not contain the results of case 1, since this case models only pure convection of vapor with parameters given by the inlet boundary conditions, i.e. the Figures 6 - 8 for the case 1 would show only a constant value everywhere.

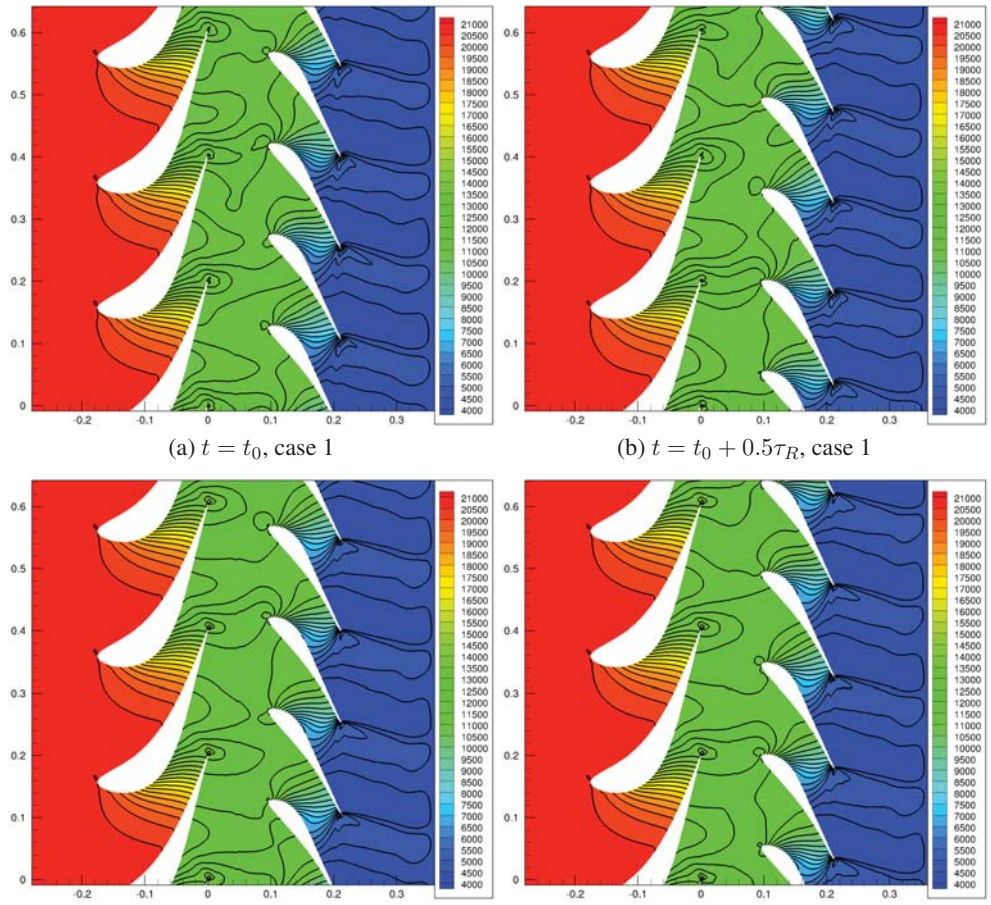

(a) $t = t_0$, case 1 (b) $t = t_0 + 0.5\tau_R$, case 1

(c) $t = t_0$, case 2 (d) $t = t_0 + 0.5\tau_R$, case 2

Fig. 5: Pressure field.

6. Conclusions

Current numerical method has been successfully extended for the cases with non-zero wetness of incoming steam. The droplet growth model has been regularized. The numerical method has stable behavior

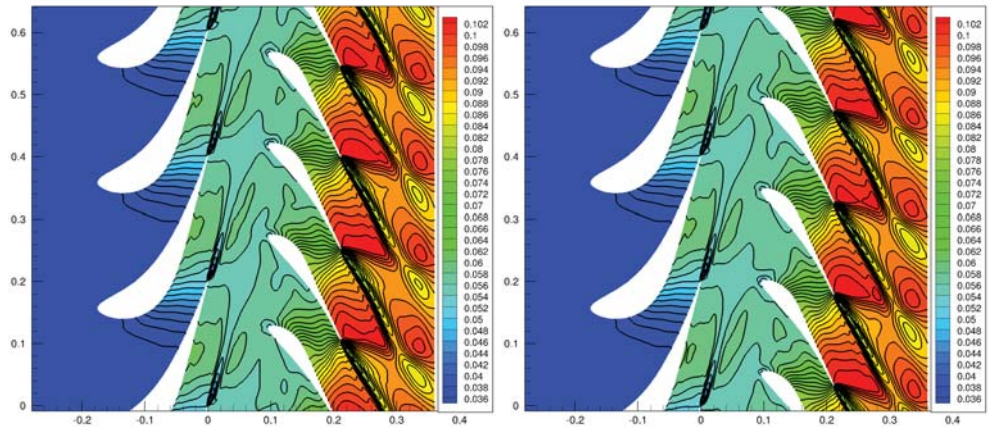

(a) $t = t_0$, case 2 (b) $t = t_0 + 0.5\tau_R$, case 2

Fig. 6: Wetness contours.

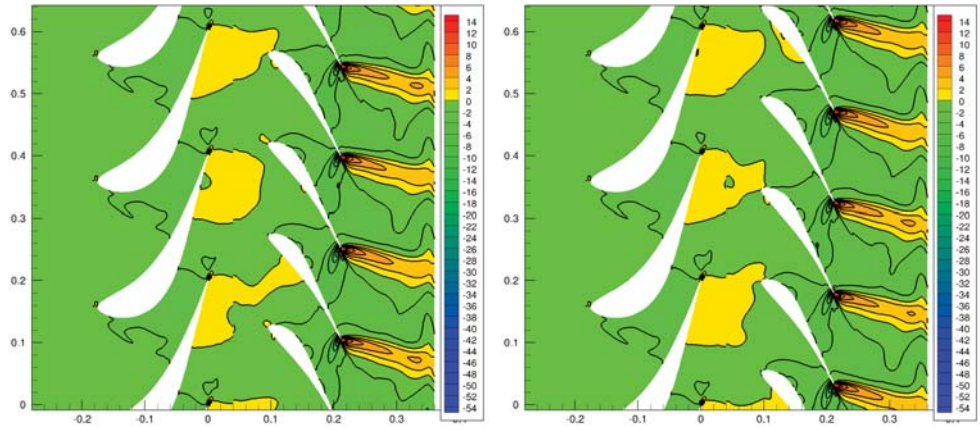

(a) $t = t_0$, case 2 (b) $t = t_0 + 0.5\tau_R$, case 2

Fig. 7: Vapor sub-cooling contours.

in the case of steady flow in a nozzle as well as unsteady flow in a turbine stage. The sensitivity of numerical results on the droplet size of incoming steam has been reported. The results achieved for cases with identical wetness and different sizes of droplets at the inlet have shown, that the droplet size has a non-negligible effect also for pressure distribution in the whole computational domain. One has to be careful with the problem formulation, since the values of moments at the inlet has to be usually estimated by numerical simulation and thus they may be deteriorated by some errors. This work showed the need for improved droplet growth model to get more reliable droplet size prediction.

Acknowledgments

This work was supported by the grant No. 101/11/1593 of Grant Agency of the Czech Republic and by the grant No. SGS10/244/OHK2/3T/12 of Grant Agency of the Czech Technical University in Prague.

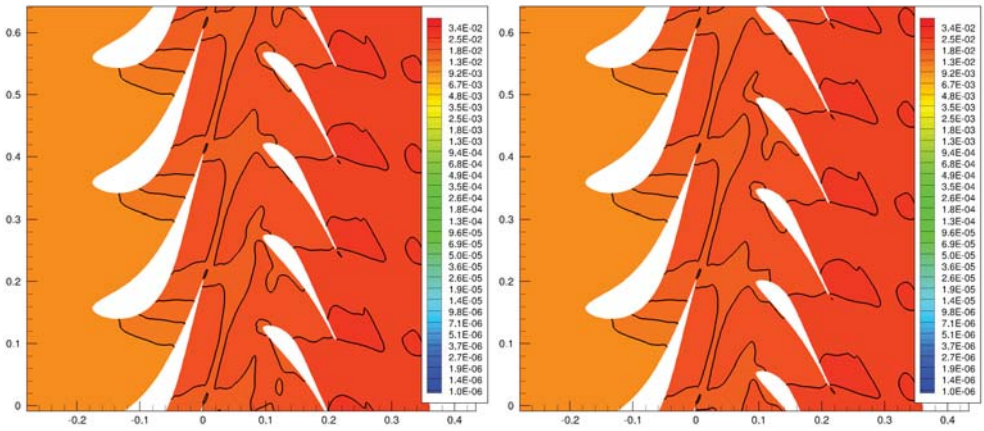

(a) $t = t_0$, case 2 (b) $t = t_0 + 0.5\tau_R$, case 2

Fig. 8: Average droplet size $[\mu m]$.

References

Becker, R., Döring, W. (1935), Kinetische Behandlung der Keimbildung in übersättingten Dämpfen. *Journal Ann. d. Physik*, Vol. 24, No. 8.

Petr, V., Kolovratník, M. (2001), Heterogenous Effects in the Droplet Nucleation Process in LP Steam Turbines, *4th European Conference on Turbomachinery*, Firenze.

Hill, P. G. (1966), Condensation of water vapor during supersonic expansion in nozzles, part 3, *Journal of Fluid Mechanics*, Vol.3, 593–620.

Strang, G., (1968), On the construction and comparison of difference schemes, *SIAM Journal of Numerical Analysis*, Vol. 5, 506–517.

Barschdorff, D., (1971), Verlauf der Zustandgroesen und gasdynamische Zuammenhaenge der spontanen Kondensation reinen Wasserdampfes in Lavalduesen, *Forsch. Ing.-Wes.*, Vol. 37, No. 5, (in german).

Dykas, S., Goodheart, K., Schnerr, G.H., (2003), Numerical study of accurate and efficient modeling for simulation of condensing flow in transonic steam turbines, *5th European conference on Turbomachinery*, Prague, 751–760.

Young, J.B., (1992), Two-Dimensional, Nonequilibrium, Wet–Steam Calculations for Nozzles and Turbine Cascades, *Journal of Turbomachinery*, vol 114.

Šejna, M., Lain, J. (1994), Numerical modelling of wet steam flow with homogenous condensation on unstructured triangular meshes, *Journal ZAMM*, vol. 74, no. 5, 375–378.

Šťastný, M., Šejna, M., (1995), Condensation effects in transonic flow through turbine cascade, *Proceedings of the 12th international conference of the properties of water and steam*, Begel House, 711–719.

, Sopuch P., (1996), Kinetics of phase change vapor-liquid and its numerical simulation, *Doctoral thesis*, IT CAS CR, (in Czech).

Halama, J., Fořt, J., Seifert, M., (2010), Numerical solution of wet steam flow with a priori droplet size distribution, *Proceedings of Conference 'Topical Problems of Fluid Mechanics'*, Prague, 63–66.

Halama, J., Benkhaldoun, F., Fořt, J., (2011), Flux schemes based finite volume method for internal transonic flow with condensation, *International Journal for Numerical Methods in Fluids*, vol. 65, no. 8, 953–968.

18th International Conference
ENGINEERING MECHANICS 2012
Svratka, Czech Republic, May 14 – 17, 2012

pp. 355–361
Paper #74

TESTING OF MECHANICAL PROPERTIES OF NATURAL STONES USED AS A BUILDING MATERIAL

H. Hasníková*

Abstract: *Further presentation of some destructive and non-destructive methods for investigation of mechanical properties of natural stone quarried and used as a building material in Bohemia in the past is the aim of the paper. Tested samples were made both from virgin material from existing quarries (e.g. sandstone from Hořice) and from material got from historical constructions (various sandstones from the Charles Bridge in Prague), which was built-in for a long time. The flexural strength, the compressive strength and Young modulus were obtained from the basic destructive tests. Before these tests the identical samples were investigated non-destructively by ultrasound and so called peeling test so that the two ways of testing could be compared at the end.*

Keywords: ***Mechanical properties, non-destructive testing, natural stone, historical buildings***

1. Introduction

Historical buildings are part of cultural heritage and have to be maintained as the other structures to survive for next generations. Diagnosis of structures works not only with structure condition from static point of view, but also with condition of used material. Material properties are influenced e.g. by loading of the structure or environment. Preliminary diagnosis operates with both destructive and non-destructive testing. Methods of non-destructive testing are easy to handle mostly and could be done in-situ; do not leave any damages and give quick results. The results should be taken as a primary estimation. Destructive testing operates with samples cut from the structure. Results are exact, but the process is more time-consuming and leaves marks at the structure. Both ways of testing have their advantages and it is very useful to combine them.

2. Experimental work

2.1. Material specification

Various types of sedimentary rocks, which have been found in Prague region in medieval ages, were tested. Virgin samples from existing quarries have been investigated so that new material could be compared with material already used in the structure; they were made from marlit stone, so called opuka stone, travertine and fine grained quartz sandstone from Hořice. Opuka stone is one of the most typical historical materials used in medieval ages in Prague and is composed of clay and calcareous elements with organic components (sponge and foraminifer shells). Horizontal layering is conditioned by lamination which manifests as alteration of lighter and darker laminae of thickness of 1-2 mm. The average value of bulk density is 2080 kg.m^{-3} and porosity of "opuka" stone is 21.28 %.

Generally in the past travertine was used for monumental structures, because it resists very well to weathering. Nowadays it is one of the most popular natural stones used as a decorative element of facades. Travertine composes from bifurcated clusters of micrite (calcite) and as accessories have been identified small quartz clasts inside the stone. Pores distribution resulting from mercury porosimetry shows that there is not one dominant characteristic pore diameter but it varies from 10 μm

* Ing. Hana Hasníková: Institute of Theoretical and Applied Mechanics AS CR, v. v. i., Prosecká 809/76, 190 00, Prague; CZ, e-mail: hasnikova@itam.cas.cz

to 100 μm. The origin of pores is connected with decomposition of organic material buried in created sediment. The average value of bulk density is 2530 kg.m^{-3} and porosity of travertine is 21.28 %.

Sandstone from Hořice quarry is often used for reconstructions of historical buildings in Prague region. Quartz and kaolinite are the main mineralogical components of the stone; it also contains light fragments of clay in some places. There are flakes of mica as an accessory in the stone. Cement is composed from kaolinite. The average value of bulk density is 1810 kg.m^{-3} and porosity of Hořice sandstone is 25.84 %.

The other sandstone samples were made from stone blocks taken from the Charles Bridge. Light pinkish-grey hard porous arkose is coarse grained sandstone from Žehrovice. Clast´s main component is quartz, the other participating elements are fine-grained quartzite, siltstones and feldspar. There are heavy metals and flakes of mica as accessories in the stone. The average value of bulk density is 2110 kg.m^{-3} and porosity of arkose is 16.59 %.

Hard sandstone with ferruginous cement from Petřín quarry is dark brown quartz stone with claystone fragments as accessories. Clasts compose of quartz, "iron quartz" and siltstones. Stratums were obvious at the samples. The oldest part of cement, limonite-goethite acts as a corrosion sealant, which is covered by the others - kaolinite, apatite, quartz and potassium feldspar cements. The average value of bulk density is 2020 kg.m^{-3} and porosity of sandstone is 24.84 %.

Middle grained crumble porous sandstone from Nehvizdy quarry has horizontal layering conditioned by alternation of middle grained lamins and fine grained lamins. Main component of both clasts and cement is quartz. Yellow coloured cement is also made of quartz, here in the form of discontinuous coat on the surface of grains. The average value of bulk density is 1940 kg.m^{-3} and porosity of sandstone is 24.33 %.

2.2. Specimens and test conditions

The initial shape and size of test specimens in a form of beams was chosen according to the specifications for testing of mechanical characteristics. Therefore, the basic specimen dimensions were 50 mm x 50 mm x 300 mm as the European Standard EN 12372:2006 dealing with flexural strength requires. The test specimens were manufactured within standard tolerance limits and dimensions were measured with accuracy of 0.1 mm (as required by EN 13373). Compression test specimens were grinded according to the standard tolerance (ČSN EN 1926) from remaining beam halves after bending tests. Dimensions of these cubes were 50 mm x 50 mm x 50 mm, also measured with accuracy of 0.1 mm.

All the specimens were tested in the laboratories of ITAM with environment basically specified by temperature and relative humidity. Specimens themselves were conditioned for two physical states - the dry conditions and fully water saturated conditions; described in the Czech Standard ČSN EN 1936. Before testing the specimens were stored in a climatic chamber (for standard tests in "dry conditions") at 70°C ± 5°C till an equilibrium state of moisture content which was measured by weighing in intervals of 24 ± 2 hours with accuracy of 0.1 g. At the equilibrium state the mass do not change more than 0.1 % of the mass of the test specimen. After drying and before testing specimens stayed in an environment with the temperature of 20°C ± 5°C and very low humidity till the temperature is balanced, the test then was carried out within 24 hours.

Fully water saturated conditions were arranged by long-term storage of specimens in a container with water so that all the pores could be filled by water. The water absorption was natural because no vacuum or negative pressure was used. Specimens were also weighed in intervals of 24 ± 2 hours with accuracy of 0.1 g and at fully saturated state it was assumed, that the mass does not change more than 0.1 % of the mass of test specimen.

2.3. Test set up and measured quantities

Ultrasonic tests carried out on basic specimens before bending, because following the orientation of sedimentation layers and controlling an assumed direction of ultrasonic transmission is easier on the beams than on the cubes. Non-destructive peeling test that focuses mainly on near surface cohesion characteristics were made on beams before bending, too.

The ultrasonic speed propagation was measured in longitudinal direction, i.e. ultrasound propagation goes along the beam. Device used for testing was UKS 12 produced by Geotron Elektronik. It composes of a generator of electric impulses, two transducers (a transmitting one and a receiving one) and microsecond timer. The timer has a screen where a received wave is shown so that the time of wave´s passaging through the sample could be read. Frequency used for measurements was 20 kHz. Test conditions followed Czech technical standard ČSN EN 14579: Natural stone test methods – Determination of sound speed propagation (a Czech version of the European Standard EN 14579:2004) and composition is shown on *Fig. 1*.

Ultrasound velocity c [km.sec^{-1}] has been calculated according to (1):

$$c = \frac{L}{t} \tag{1}$$

Dynamic modulus of elasticity could be calculated from ultrasound speed propagation c and bulk density ρ [kg.m^{-3}] of the material, see (2) below:

$$E = c^2 \rho \tag{2}$$

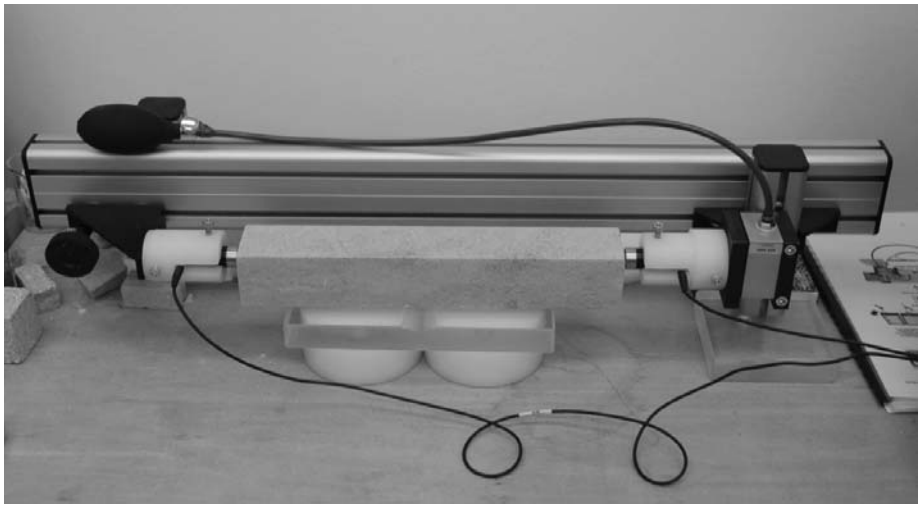

Fig. 1: *Tested beam sample with transmitting transducer (left) and receiving transducer (right)*

Peeling test is used for determination of material's surface strength. It can be used for surface degradation and/or for assessment of surface properties improvement by consolidation agent application. In the course of the test set of adhesive strips (made of pressure-sensitive tape) is in sequence attached and then removed from the same surface area and weight of the removed material is determined by laboratory scales. The process model expects some asymptotic value of removed material to reached by the end of the test (and denoted as A [g]). This value characterizes surface strength and should be related to the material's overall strength. The values of A should be indirectly proportional to material's strength.

Peeling was studied using double side opaque plastic tape 18 mm in width and 40 mm in length (Doppelband Stark 50 kg). The strips were stuck to the surface and smoothed with gentle finger pressure. Thereafter they were removed by pulling at an angle of 90°, and weighed on a balance with sensitivity of 0.0001 g, for better illustration see *Fig. 2*. The peeled off material was determined as the difference between the weight of the tape after removal from the surface and the weight of the clean tape before application. One measurement set consisted of 10 strips.

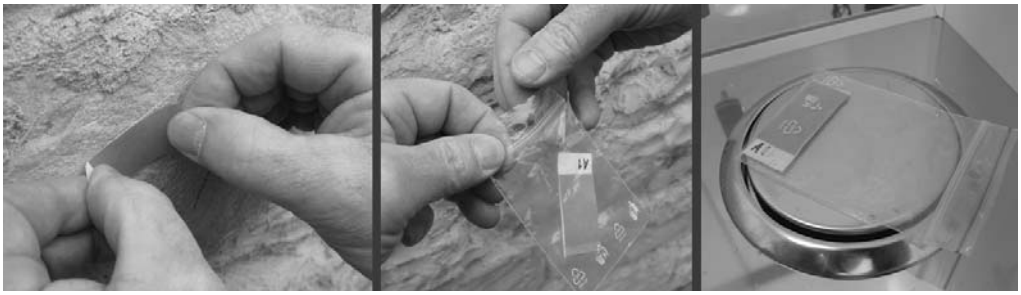

Fig. 2: Basic steps of peeling test; a) strip being attached to the surface, b) saving removed material, c) weighing by laboratory scales

If the released material decreases with increasing number of peelings, and the results approach a nonzero value, use nonlinear regression of the measured data for each place where the measurements were made. The form (3) describing the sequence of weights of the removed material *m(n)* has been suggested and the explanation of constants *A*, *B* and *C* is demonstrated on *Fig. 3*.

$$m(n) = A + Be^{-Cn} \tag{3}$$

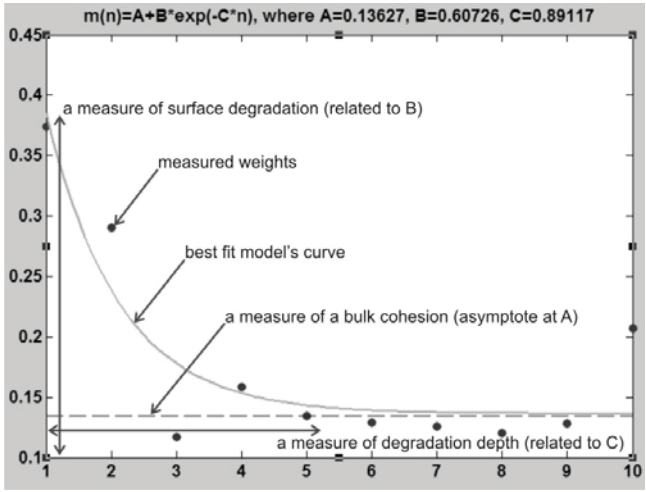

Fig. 3: Typical evaluation diagram of peeling test

The flexural strength R_{tf} is represented by the normal stress σ_x in marginal parts of the cross section induced by the bending moment M_y. The inner force is caused by maximal force F_{max} at the moment of damage. In final calculations used in ČSN EN 12372: Natural stone test methods – Determination of flexural strength under concentrated load (a Czech version of the European Standard EN 12372:2006), see equation (4) below, the moment of inertia I_y represents the dimensions of the specimen that were measured with accuracy of 0.1 mm. The *z*-variable with zero value in a centre of gravity represents a position of an extreme stress within the cross section. In the equation (4) *l* is a distance between supports, *b* is a width and *h* is a height of a cross section.

$$\sigma_x(z) = \frac{M_y}{I_y} z \rightarrow R_{ft} = \frac{\frac{1}{4} l F_{\max}}{\frac{1}{12} b h^3} \frac{h}{2} = \frac{3 l F_{\max}}{2 b h^2} \tag{4}$$

Loading device used for testing was an electromechanical load frame „WOLPERT“ with the maximum force capacity of 100 kN, a load cell Lukas 10 kN and a deformation sensor HBM LVDT μm. Test arrangement is apparent in *Fig. 4*, the crosshead speed was 0,15 mm/min. All the tests kept to conditions given by the Czech technical standard ČSN EN 12372: Natural stone test methods –

Determination of flexural strength under concentrated load (a Czech version of the European Standard EN 12372:2006).

Young's modulus of elasticity has been calculated according to (5); ΔF and $\Delta\varepsilon$ are read from line approximating the linear part of working diagram (area from 0.2 F_{max} to 0.5 F_{max}).

$$E = \frac{\Delta F l^3}{48 I_y \Delta\varepsilon} \tag{5}$$

The compressive strength R_c is represented by normal stress σ_x caused by maximal force F_{max} at the moment of damage operating on area A defined by base dimensions a and b, see (6) below. Base dimensions were measured with accuracy of 0.1 mm. Calculation is used in ČSN EN 1926: Natural stone test methods – Determination of uniaxial compressive strength (a Czech version of the European Standard EN 1926:2006).

$$\sigma_x = \frac{N_x}{A} \rightarrow R_c = \frac{F_{\max}}{A} = \frac{F_{\max}}{ab} \tag{6}$$

Loading devices used for testing were a servohydraulic MTS 250 load frame (load cell MTS 250 kN) and an electromechanical load frame „WOLPERT" of the maximum force capacity of 100 kN, (a load cell MTS 100 kN). Test arrangement is apparent in *Fig. 4* and the crosshead speed was 0.45 mm/min. All the tests keep to conditions given by the Czech technical standard ČSN EN 1926: Natural stone test methods – Determination of uniaxial compressive strength (a Czech version of the European Standard EN 1926:2006).

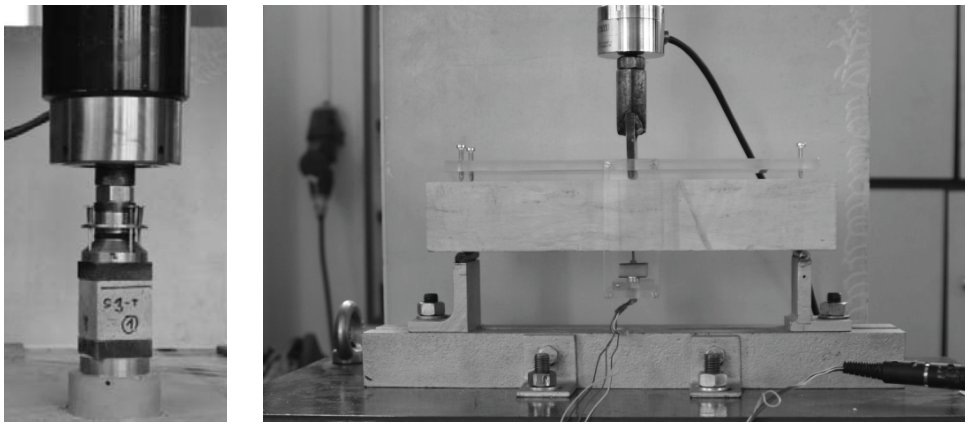

Fig. 4: Loading arrangement for a) compressive strength, b) flexural strength

2.4 Results

Basic mechanical properties have been evaluated by both destructive and non-destructive methods for two conditions of the specimens. In *Tab. 1* there are summarized results for dry samples, peeling test included, and in *Tab. 2* there are results for fully saturated samples.

Tab. 1: Summary of the results for dry material

Stone Dry samples	Flexural strength R_{ft} [MPa]	Compressive strength R_c (Average value) [MPa]	Peeling test A *1000 [g]	Ultrasound Speed Prop. (Longitudinal direction) [km/s]
Marlit stone	12.55	52.50	2.04	3.70
Travertine	8.34	51.81	1.46	5.14
Arkose	3.58	26.70	3.10	2.64
Hořice sandstone	3.06	23.59	6.22	2.74
Petřín sandstone	2.72	19.37	1.73	2.93
Nehvizdy sandstone	0.68	7.93	63.07	1.83

Tab. 2: Summary of the results for fully saturated material

Stone Saturated samples	Flexural strength R_{ft} [MPa]	Compressive strength R_c (Average value) [MPa]	Ultrasound Speed Propagation (Longitudinal direction) [km/s]
Marlit stone	7.97	47.11	3.21
Travertine	8.27	39.80	5.38
Arkose	2.02	19.45	1.90
Hořice sandstone	1.80	22.76	2.19
Petřín sandstone	1.06	12.96	2.62
Nehvizdy sandstone	0.33	12.54	1.42

About five samples of each material for each condition have been tested. The average values were used to create final comparative diagrams. It has been observed that dry samples were more resistant to mechanical loading than saturated samples. Demonstration of the situation is in *Fig. 5*; both flexural and compressive strength was higher for dry samples.

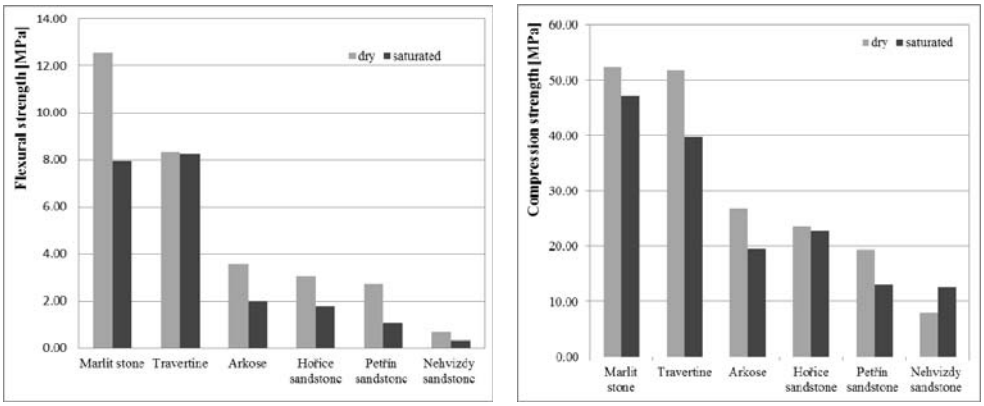

Fig. 5: Comparison of dry and fully saturated material; a) flexural strength, b) compressive strength

Non-destructive testing of natural stones have been made by ultrasound and peeling test. Ultrasound speed propagation have been measured for both dry and saturated samples, so that comparison could be made. For all the materials with regularly distributed pores, not travertine, the ultrasound velocity was higher in dry samples than in saturated ones, see *Fig. 6a* below. Peeling test results confirmed that the materials with the lower compressive strength should have higher A-value, see *Fig. 6b*.

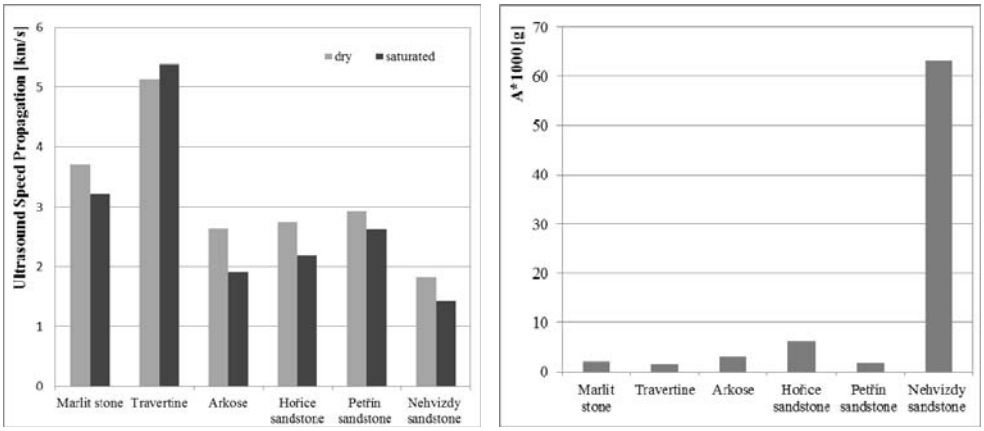

Fig. 6: a) Comparison of ultrasound velocity in dry and fully saturated material; b) peeling test

To compare destructive and non-destructive testing of natural stones, modulus of elasticity have been calculated. Dynamic modulus of elasticity calculated from ultrasound velocity varies from static one evaluated from bending tests in general. The difference in this case is bigger, but it could be caused by

many heterogeneities in the samples. Similar values could be observed for materials that have small diameter of the most frequent pore. Peeling test results could corellate with compressive strength as is shown in *Fig. 7b* below.

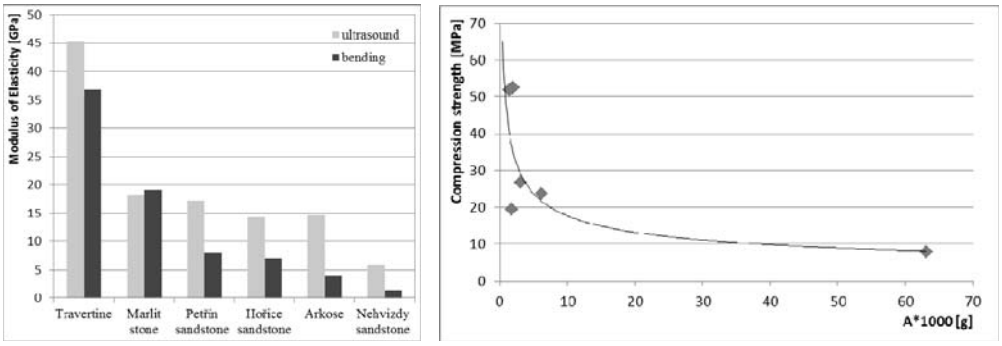

Fig. 7: a) Comparison of MoE got from bending tests and ultrasound tests, b) comparison of peeling tests and compression tests

3. Conclusions

Various types of sedimentary rocks used as a building material in the past have been investigated. Destructive and non-destructive testing was used for evaluation of basic mechanical properties. Series of laboratory test have also been used for observation how humid materials behave during the tests. This was simulated by two basic states of the stones; dry and fully saturated materials have been tested. Both destructive and non-destructive testing reacts to humidity of the material. With increasing humidity the flexural strength, compressive strength and even the ultrasound velocity decrease. Peeling test could be used for preliminary testing of materials; it provides an estimation of material resistance to mechanical loading based on surface strength. It is more relevant for new material that for one already used in structure, where degradation caused by environment has to be taken into account.

Acknowledgement

Laboratory tests took place at Institute of Theoretical and Applied Mechanics of the Academy of Science of the Czech Republic as a part of project STONECORE (FP-2007-SSP-5A).

References

EN 12372:2006 Natural stone test methods – Determination of flexural strength under concentrated load

EN 13373:2003Natural stone test methods - Determination of geometric characteristics on units

EN 1926:2006 Natural stone test methods – Determination of uniaxial compressive

EN 1936:2006 Natural stone test methods - Determination of real density and apparent density, and of total and open porosity

EN 14579:2004 Natural stone test methods – Determination of sound speed propagation

Drdácký M.; Rescic, S.; Slížková Z.; Tiano, P.; Valach J. (2011) Standardization of peeling tests for assessing the cohesion and consolidation characteristics of historic stone surfaces, *Materials and Structures*, 2011

Vasconcelos G., Lourenço P.B., Alves C.A.S., Pamplona J. (2008) Ultrasonic evaluation of the physical and mechanical properties of granites, *Ultrasonics,*48, 5, pp. 453-466

18th International Conference
ENGINEERING MECHANICS 2012
Svratka, Czech Republic, May 14 – 17, 2012

pp. 363–375
Paper #175

OPTIMAL SEMI-ACTIVE PREVIEW CONTROL OF A QUARTER CAR MODEL WITH MAGNETORHEOLOGICAL DAMPER WITH RESPECT TO TIRE LIFT OFF

F. Havelka*, M. Musil**

Abstract: *A quarter car model with magnetorheological (MR) damper is studied. An adopted experimentally verified non – linear hysteretic mathematical model is used to represent the MR damper. Approaching road disturbances are measured by a sensor. Optimal preview control strategy for fully active suspension is derived with respect to road holding, suspension rattle space and ride comfort. Continuous inverse mathematical model of the MR damper for the use of control is derived such that force generated by MR damper matches the control force of fully active system if possible. In the simulations, the effect of tire lift off is modeled using a continuous mathematical function.*

Keywords: ***quarter car, MR damper, optimal preview control, tire lift off***

1. Introduction

In recent years active and semi-active suspensions have been investigated due to their ability to adapt to various types of road excitations. Compared with passive suspension systems, which can only dissipate the energy present in the system, active suspension systems can supply the flow of energy into the system and can generate forces which are independent of the state of the system. Effective compromise between passive and active suspension systems are semi-active suspensions. Semi-active suspension systems are less expensive than the active ones, they require much less energy intensive source and even if the source of energy fails they can still operate as passive suspension systems.

In this paper a magnetorheological damper is utilized in the suspension system as a semi-active part. An experimentally verified non-linear hysteretic mathematical model is used to represent the dynamics of the MR damper. A basic quarter car model is utilized to simulate the vertical dynamics of vehicle. For the use of control algorithm a continuous inverse mathematical model of the MR damper is derived. Dissipative force generated by the MR damper tries to match the one generated by a fictive ideal active system. Optimal preview control strategy for the fully active system with respect to road holding, suspension rattle space and ride comfort is derived such that it is supposed that approaching road disturbances are measured by a sensor and are known within a certain distance ahead. Active and semi-active suspension systems with preview are examined in vehicle travelling over a bump and in both cases the effect of tire lift off is investigated.

2. Quarter car model with idealized active suspension and with consideration the tire lift off

To simulate the vertical dynamics of vehicle, the quarter car model is utilized – figure 1a.). The equations of motion with consideration the tire lift off problem are follows:

$$\begin{aligned} m_1\ddot{y}_1 &= -k_1\left(y_1 - y_2\right) + u - m_1 g \\ m_2\ddot{y}_2 &= -k_2\left(y_2 - w\right)\left[1 - H\left(y_2 - w\right)\right] - k_1\left(y_2 - y_1\right) - u - m_2 g \end{aligned} \tag{1}$$

where *H(-)* is the heaviside step function and *u* is the force generated by active control element, which dynamics is neglected.

* Ing. Ferdinand Havelka: Institute of Applied Mechanics, Faculty of Mechanical Engineering, Slovak University of Technology, Námestie slobody 17; 812 31, Bratislava 1; SK, e-mail: ferdinand.havelka@stuba.sk

** doc., Ing. Miloš Musil, Ph.D.: Institute of Applied Mechanics, Faculty of Mechanical Engineering, Slovak University of Technology, Námestie slobody 17; 812 31, Bratislava 1; SK, e-mail: milos.musil@stuba.sk

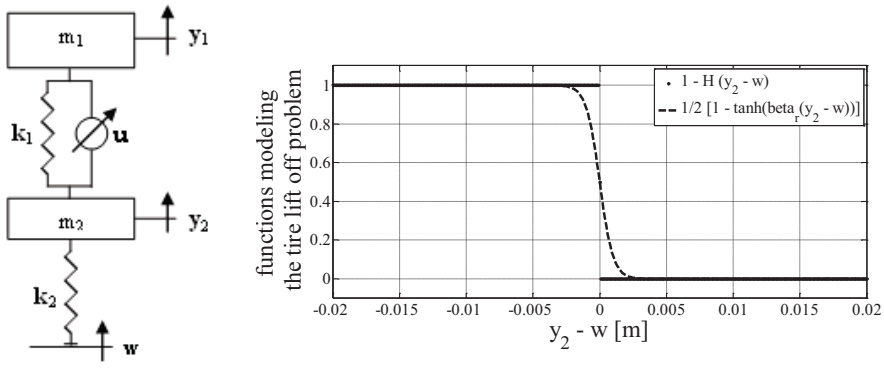

a.) *b.)*

Fig. 1: a.) quarter car model with active suspension
b.) functions modeling the tire lift off problem

The function modeling the tire lift off problem can be rewritten into form:

$$1-H\left(y_2-w\right)=\frac{1}{2}\left[1-\operatorname{sgn}\left(y_2-w\right)\right]\cong\frac{1}{2}\left\{1-\tanh\left[\beta_r\left(y_2-w\right)\right]\right\} \tag{2}$$

where now the function *tanh(-)* is a continuous function and β_r is a coefficient large enough.

Noting the relation (2), equations of motion in the matrix form are:

$$\mathbf{M}_\mathbf{a}\ddot{\mathbf{q}}_\mathbf{aA}+\mathbf{K}_\mathbf{aL}\mathbf{q}_\mathbf{aR}+\mathbf{K}_\mathbf{aN}\mathbf{q}_\mathbf{aR}\mathbf{e}_\mathbf{a}\tanh\left(\beta_r\mathbf{q}_\mathbf{aR}\right)=\mathbf{b}_\mathbf{ag}g+\mathbf{b}_\mathbf{u}u \tag{3}$$

where

$$\begin{gathered}\mathbf{M}_\mathbf{a}=\begin{bmatrix}m_1&0\\0&m_2\end{bmatrix},\ \mathbf{K}_\mathbf{aL}=\begin{bmatrix}k_1&0\\-k_1&\frac{k_2}{2}\end{bmatrix},\ \mathbf{K}_\mathbf{aN}=\begin{bmatrix}0&0\\0&-\frac{k_2}{2}\end{bmatrix},\ \mathbf{e}_\mathbf{a}=\begin{bmatrix}0\\1\end{bmatrix}^T,\\ \mathbf{b}_\mathbf{ag}=-\begin{bmatrix}m_1\\m_2\end{bmatrix},\ \mathbf{b}_\mathbf{u}=\begin{bmatrix}1\\-1\end{bmatrix},\ \mathbf{q}_\mathbf{aA}=\begin{bmatrix}y_1\\y_2\end{bmatrix},\ \mathbf{q}_\mathbf{aR}=\begin{bmatrix}y_1-y_2\\y_1-w\end{bmatrix}\end{gathered} \tag{4}$$

Transformation from absolute to the relative coordinates is realized through the equation:

$$\mathbf{q}_\mathbf{aR}=\mathbf{T}_\mathbf{aA}\mathbf{q}_\mathbf{aA}+\mathbf{T}_\mathbf{aw}w \tag{5}$$

where

$$\mathbf{T}_\mathbf{aA}=\begin{bmatrix}1&-1\\0&1\end{bmatrix},\ \mathbf{T}_\mathbf{aw}=\begin{bmatrix}0\\-1\end{bmatrix} \tag{6}$$

Combining equation (3) and differentiated equation (5), state space model of system in the figure 1 a.) is obtained:

$$\dot{\mathbf{x}}_\mathbf{a}=\mathbf{A}_\mathbf{aL}\mathbf{x}_\mathbf{a}+\mathbf{A}_\mathbf{aN}\mathbf{x}_\mathbf{a}\mathbf{E}_\mathbf{a}\tanh\left(\beta_r\mathbf{x}_\mathbf{a}\right)+\mathbf{B}_\mathbf{a}u+\mathbf{G}_\mathbf{a}\mathbf{f}_\mathbf{gw} \tag{7}$$

where

$$\begin{gathered}\mathbf{A}_\mathbf{aL}=\begin{bmatrix}\mathbf{O}_\mathbf{a}&\mathbf{T}_\mathbf{aA}\\-\mathbf{M}_\mathbf{a}^{-1}\mathbf{K}_\mathbf{aL}&\mathbf{O}_\mathbf{a}\end{bmatrix},\ \mathbf{A}_\mathbf{aN}=\begin{bmatrix}\mathbf{O}_\mathbf{a}&\mathbf{O}_\mathbf{a}\\-\mathbf{M}_\mathbf{a}^{-1}\mathbf{K}_\mathbf{aN}&\mathbf{O}_\mathbf{a}\end{bmatrix},\ \mathbf{E}_\mathbf{a}=\begin{bmatrix}\mathbf{e}_\mathbf{a}^T\\\mathbf{o}_\mathbf{a}\end{bmatrix}^T,\ \mathbf{B}_\mathbf{a}=\begin{bmatrix}\mathbf{o}_\mathbf{a}\\\mathbf{M}_\mathbf{a}^{-1}\mathbf{b}_\mathbf{u}\end{bmatrix},\\ \mathbf{G}_\mathbf{a}=\begin{bmatrix}\mathbf{G}_\mathbf{ag}&\mathbf{G}_\mathbf{aw}\end{bmatrix},\ \mathbf{G}_\mathbf{ag}=\begin{bmatrix}\mathbf{o}_\mathbf{a}\\\mathbf{M}_\mathbf{a}^{-1}\mathbf{b}_\mathbf{ag}\end{bmatrix},\ \mathbf{G}_\mathbf{aw}=\begin{bmatrix}\mathbf{T}_\mathbf{aw}\\\mathbf{o}_\mathbf{a}\end{bmatrix},\ \mathbf{f}_\mathbf{gw}=\begin{bmatrix}g\\\dot{w}\end{bmatrix},\ \mathbf{x}_\mathbf{a}=\begin{bmatrix}\mathbf{q}_\mathbf{aR}\\\dot{\mathbf{q}}_\mathbf{aA}\end{bmatrix}\end{gathered} \tag{8}$$

where $\mathbf{O}_\mathbf{a}$ and $\mathbf{o}_\mathbf{a}$ are zero matrix and vector respectively of appropriate dimensions.

3. Optimal linear preview control of idealized active suspension

Optimal linear control without preview has been widely utilized in active suspensions regulation. As was shown by many authors, e.g. (Hać & Youn, 1991; Hać, 1992; Thompson & Pearce, 1998), optimal linear control with preview, i.e. the case when approaching road disturbances are known within a certain distance ahead, reduces variances of car body acceleration, suspension travel and tire deflection at the same time compared with the no preview case.

In this section, optimal linear preview control of idealized active suspension is derived. Incoming road disturbances are measured by a sensor at some distance ahead of the vehicle. The tire lift off effect is not considered in the deriving. The equations of motion for such a problem are:

$$\mathbf{M}_\mathbf{a}\ddot{\mathbf{q}}_\mathbf{aA} + \mathbf{K}_\mathbf{a}\mathbf{q}_\mathbf{aR} = \mathbf{b}_\mathbf{u}u \tag{9}$$

where

$$\mathbf{K}_\mathbf{a} = \begin{bmatrix} k_1 & 0 \\ -k_1 & k_2 \end{bmatrix} \tag{10}$$

The remaining variables are described above. Combining equation (9) and differentiated equation (5), state space model of idealized active suspension with preview and without consideration the tire lift off effect is obtained:

$$\dot{\mathbf{x}}_\mathbf{a} = \mathbf{A}_\mathbf{a}\mathbf{x}_\mathbf{a} + \mathbf{B}_\mathbf{a}u + \mathbf{G}_\mathbf{aw}\dot{w} \tag{11}$$

where

$$\mathbf{A}_\mathbf{a} = \begin{bmatrix} \mathbf{O}_\mathbf{a} & \mathbf{T}_\mathbf{aA} \\ \mathbf{-M}_\mathbf{a}^{-1}\mathbf{K}_\mathbf{a} & \mathbf{O}_\mathbf{a} \end{bmatrix} \tag{12}$$

The state vector $\boldsymbol{x}_a$ contains relative displacements $\mathbf{q}_\mathbf{aR}$ (suspension and the tire deflections) and absolute velocities $\dot{\mathbf{q}}_\mathbf{aA}$ (car body and the wheel velocities) – see (8). Such a description leads to the velocity of road disturbances at the input. It is assumed that the road disturbances *w(t)* (and also its derivation) are measured at the distance l_p in front of the vehicle, i.e. at time t the preview information about incoming road disturbances is available from the time t up to time $t + t_p$, where $t_p = l_p/v$ is the preview time and v is the vehicle velocity. The active force generator is optimized in regard to ride comfort, suspension rattle space and road holding. Corresponding variables to be minimized are car body acceleration, suspension deflection and tire deflection.

$$\mathbf{z} = \begin{bmatrix} \ddot{y}_1 & y_1 - y_2 & y_2 - w \end{bmatrix}^T \tag{13}$$

and in state space form

$$\mathbf{z} = \mathbf{C}_\mathbf{a}\mathbf{x}_\mathbf{a} + \mathbf{D}_\mathbf{a}u + \mathbf{H}_\mathbf{a}\dot{w} \tag{14}$$

Then the performance index involves appropriately weighted variances of optimized variables (13) that are to be minimized and weighted variance of active force that is also to be minimized:

$$J = \lim_{T\to\infty}\frac{1}{T}\int_0^T \left[q_1\ddot{y}_1^2 + q_2\left(y_1 - y_2\right)^2 + q_3\left(y_2 - w\right)^2 + Ru^2 \right] dt \tag{15}$$

or using (13) in the generalized matrix form

$$J = \lim_{T\to\infty}\frac{1}{T}\int_0^T \left(\mathbf{z}^\mathbf{T}\mathbf{Q}\mathbf{z} + u^\mathbf{T}Ru \right) dt \tag{16}$$

where

$$\mathbf{Q} = \begin{bmatrix} q_1 & 0 & 0 \\ 0 & q_2 & 0 \\ 0 & 0 & q_3 \end{bmatrix} \tag{17}$$

Constants q_1, q_2 and q_3 are weighting constants chosen by the designer that determine the tradeoff between the optimized variables. **Q** is weighting matrix and R is control cost constant.

After substituting for $\boldsymbol{z}$, the argument of the integral (16) after some adjustment has the form

$$\mathbf{z}^{\mathrm{T}}\mathbf{Q}\mathbf{z}+u^{\mathrm{T}}Ru=\mathbf{x}_{\mathbf{a}}^{\mathrm{T}}\mathbf{Q}_{\mathbf{1}}\mathbf{x}_{\mathbf{a}}+u^{\mathrm{T}}R_{1}u+\dot{w}^{\mathrm{T}}Q_{2}\dot{w}+2\mathbf{x}_{\mathbf{a}}^{\mathrm{T}}\mathbf{N}_{\mathbf{1}}u+2\mathbf{x}_{\mathbf{a}}^{\mathrm{T}}\mathbf{N}_{\mathbf{2}}\dot{w} \tag{18}$$

where

$$\mathbf{Q}_{\mathbf{1}}=\mathbf{C}_{\mathbf{a}}^{\mathrm{T}}\mathbf{Q}\mathbf{C}_{\mathbf{a}},\quad R_{1}=\mathbf{D}_{\mathbf{a}}^{\mathrm{T}}\mathbf{Q}\mathbf{D}_{\mathbf{a}}+R,\quad Q_{2}=\mathbf{H}_{\mathbf{a}}^{\mathrm{T}}\mathbf{Q}\mathbf{H}_{\mathbf{a}},\quad \mathbf{N}_{\mathbf{1}}=\mathbf{C}_{\mathbf{a}}^{\mathrm{T}}\mathbf{Q}\mathbf{D}_{\mathbf{a}}\quad \mathbf{N}_{\mathbf{2}}=\mathbf{C}_{\mathbf{a}}^{\mathrm{T}}\mathbf{Q}\mathbf{H}_{\mathbf{a}} \tag{19}$$

Then the Hamiltonian H for this issue is in the form

$$\mathbf{H}=\frac{1}{2}\left(\mathbf{x}_{\mathbf{a}}^{\mathrm{T}}\mathbf{Q}_{\mathbf{1}}\mathbf{x}_{\mathbf{a}}+u^{\mathrm{T}}R_{1}u+\dot{w}^{\mathrm{T}}Q_{2}\dot{w}+2\mathbf{x}_{\mathbf{a}}^{\mathrm{T}}\mathbf{N}_{\mathbf{1}}u+2\mathbf{x}_{\mathbf{a}}^{\mathrm{T}}\mathbf{N}_{\mathbf{2}}\dot{w}\right)+\boldsymbol{\lambda}^{\mathrm{T}}\left(\mathbf{A}_{\mathbf{a}}\mathbf{x}_{\mathbf{a}}+\mathbf{B}_{\mathbf{a}}u+\mathbf{G}_{\mathbf{aw}}\dot{w}-\dot{\mathbf{x}}_{\mathbf{a}}\right) \tag{20}$$

where $\boldsymbol{\lambda}$ is a vector of Lagrange multipliers. The necessary conditions for the optimum of **H** are

$$\frac{\partial\mathbf{H}}{\partial u}=0\quad\wedge\quad\frac{d}{dt}\left(\frac{\partial\mathbf{H}}{\partial\dot{\mathbf{x}}_{\mathbf{a}}}\right)=-\frac{\partial\mathbf{H}}{\partial\mathbf{x}_{\mathbf{a}}} \tag{21}$$

From the first condition we obtain the active control force u

$$\frac{\partial\mathbf{H}}{\partial u}=0:\quad u^{\mathrm{T}}R_{1}+\mathbf{x}_{\mathbf{a}}^{\mathrm{T}}\mathbf{N}_{\mathbf{1}}+\boldsymbol{\lambda}^{\mathrm{T}}\mathbf{B}_{\mathbf{a}}=0\quad\Rightarrow\quad u=-R_{1}^{-1}\left(\mathbf{N}_{\mathbf{1}}^{\mathrm{T}}\mathbf{x}_{\mathbf{a}}+\mathbf{B}_{\mathbf{a}}^{\mathrm{T}}\boldsymbol{\lambda}\right) \tag{22}$$

From the second necessary condition

$$\frac{d}{dt}\left(\frac{\partial\mathbf{H}}{\partial\dot{\mathbf{x}}_{\mathbf{a}}}\right)=-\frac{\partial\mathbf{H}}{\partial\mathbf{x}_{\mathbf{a}}}:\quad\dot{\boldsymbol{\lambda}}^{\mathrm{T}}=-\left(\mathbf{x}_{\mathbf{a}}^{\mathrm{T}}\mathbf{Q}_{\mathbf{1}}+u^{\mathrm{T}}\mathbf{N}_{\mathbf{1}}^{\mathrm{T}}+\dot{w}^{\mathrm{T}}\mathbf{N}_{\mathbf{2}}^{\mathrm{T}}+\boldsymbol{\lambda}^{\mathrm{T}}\mathbf{A}_{\mathbf{a}}\right) \tag{23}$$

After substituting the control force – in relation (22) – into (23) and after some adjustment we obtain

$$\dot{\boldsymbol{\lambda}}=-\left(\mathbf{Q}_{\mathbf{n}}\mathbf{x}_{\mathbf{a}}+\mathbf{A}_{\mathbf{n}}^{\mathrm{T}}\boldsymbol{\lambda}+\mathbf{N}_{\mathbf{2}}\dot{w}\right) \tag{24}$$

where

$$\mathbf{Q}_{\mathbf{n}}=\mathbf{Q}_{\mathbf{1}}-\mathbf{N}_{\mathbf{1}}R_{1}^{-1}\mathbf{N}_{\mathbf{1}}^{\mathrm{T}},\quad\mathbf{A}_{\mathbf{n}}=\mathbf{A}_{\mathbf{a}}-\mathbf{B}_{\mathbf{a}}R_{1}^{-1}\mathbf{N}_{\mathbf{1}}^{\mathrm{T}} \tag{25}$$

Substitution the control force – in relation (22) – into the state equation (11) gives

$$\dot{\mathbf{x}}_{\mathbf{a}}=\mathbf{A}_{\mathbf{n}}\mathbf{x}_{\mathbf{a}}-\mathbf{B}_{\mathbf{a}}R_{1}^{-1}\mathbf{B}_{\mathbf{a}}^{\mathrm{T}}\boldsymbol{\lambda}+\mathbf{G}_{\mathbf{aw}}\dot{w} \tag{26}$$

From the linear structure of equations (24) and (26) the proposed solution follows

$$\boldsymbol{\lambda}(t)=\mathbf{P}(t)\mathbf{x}_{\mathbf{a}}(t)+\mathbf{r}(t) \tag{27}$$

where

$$\mathbf{P}(T)=\mathbf{P}_{\mathbf{T}},\quad\mathbf{r}(T)=0,\quad\boldsymbol{\lambda}(T)=\mathbf{P}_{\mathbf{T}}\mathbf{x}_{\mathbf{a}}(T) \tag{28}$$

where $\mathbf{r}(t)$ is a vector dependent on the excitation $\dot{w}(t)$ and T is the duration of the problem. Differentiation (27) according to time gives

$$\dot{\boldsymbol{\lambda}}(t)=\dot{\mathbf{P}}(t)\mathbf{x}_{\mathbf{a}}(t)+\mathbf{P}(t)\dot{\mathbf{x}}_{\mathbf{a}}(t)+\dot{\mathbf{r}}(t) \tag{29}$$

Substitution the relations (27) into (26) and next (24) and (26) into (29) after some manipulation yields

$$\left(\dot{\mathbf{P}}+\mathbf{P}\mathbf{A}_{\mathbf{n}}+\mathbf{A}_{\mathbf{n}}^{\mathrm{T}}\mathbf{P}-\mathbf{P}\mathbf{B}_{\mathbf{a}}R_{1}^{-1}\mathbf{B}_{\mathbf{a}}^{\mathrm{T}}\mathbf{P}+\mathbf{Q}_{\mathbf{n}}\right)\mathbf{x}_{\mathbf{a}}=-\dot{\mathbf{r}}+\left(-\mathbf{A}_{\mathbf{n}}^{\mathrm{T}}+\mathbf{P}\mathbf{B}_{\mathbf{a}}R_{1}^{-1}\mathbf{B}_{\mathbf{a}}^{\mathrm{T}}\right)\mathbf{r}-\left(\mathbf{P}\mathbf{G}_{\mathbf{aw}}+\mathbf{N}_{\mathbf{2}}\right)\dot{w} \tag{30}$$

Whereas $\mathbf{x}_{\mathbf{a}}(t)$ and $\dot{w}(t)$ are arbitrary vectors, relation (30) is valid only when both sides of (30) are zero vectors, which implies

$$\begin{aligned}-\dot{\mathbf{P}}&=\mathbf{P}\mathbf{A}_{\mathbf{n}}+\mathbf{A}_{\mathbf{n}}^{\mathrm{T}}\mathbf{P}-\mathbf{P}\mathbf{B}_{\mathbf{a}}R_{1}^{-1}\mathbf{B}_{\mathbf{a}}^{\mathrm{T}}\mathbf{P}+\mathbf{Q}_{\mathbf{n}}\\ \dot{\mathbf{r}}&=\left(-\mathbf{A}_{\mathbf{n}}^{\mathrm{T}}+\mathbf{P}\mathbf{B}_{\mathbf{a}}R_{1}^{-1}\mathbf{B}_{\mathbf{a}}^{\mathrm{T}}\right)\mathbf{r}-\left(\mathbf{P}\mathbf{G}_{\mathbf{aw}}+\mathbf{N}_{\mathbf{2}}\right)\dot{w},\quad\mathbf{r}(T)=0\end{aligned} \tag{31}$$

If the problem duration T approaches infinity, $T \to \infty$, the first equation from relations (31) can be rewritten as

$$\mathbf{P}\mathbf{A}_\mathbf{n} + \mathbf{A}_\mathbf{n}^\mathrm{T}\mathbf{P} - \mathbf{P}\mathbf{B}_\mathbf{a} R_1^{-1}\mathbf{B}_\mathbf{a}^\mathrm{T}\mathbf{P} + \mathbf{Q}_\mathbf{n} = \mathbf{O} \tag{32}$$

where now **P** is a nonnegative definite symmetric solution of the algebraic Riccati equation (32).
The second equation from relations (31) is integrated backwards and uses all the future information about the derivative of the road input $\dot{w}(t)$ up to time $t = T$. Nevertheless $\dot{w}(t)$ for $\tau > t + t_p$ is not available, because at time t the preview information about incoming road disturbances is available from the time t only up to time $t + t_p$, therefore $\dot{w}(t)$ for $\tau > t + t_p$ is replaced by its expectation which is zero. This yields zero solution for $\mathbf{r}(\tau)$ for $\tau \geq t + t_p$.

$$\dot{\mathbf{r}} = \left(-\mathbf{A}_\mathbf{n}^\mathrm{T} + \mathbf{P}\mathbf{B}_\mathbf{a} R_1^{-1}\mathbf{B}_\mathbf{a}^\mathrm{T}\right)\mathbf{r} - \left(\mathbf{P}\mathbf{G}_\mathbf{aw} + \mathbf{N}_\mathbf{2}\right)\dot{w}, \quad \mathbf{r}\left(t + t_p\right) = 0 \tag{33}$$

After some substitutions

$$\dot{\mathbf{r}} = -\mathbf{A}_\mathbf{c}^\mathrm{T}\mathbf{r} - \mathbf{G}_\mathbf{r}\dot{w}, \quad \mathbf{r}\left(t + t_p\right) = 0 \tag{34}$$

where

$$\mathbf{A}_\mathbf{c} = \mathbf{A}_\mathbf{n} - \mathbf{B}_\mathbf{a} R_1^{-1}\mathbf{B}_\mathbf{a}^\mathrm{T}\mathbf{P}, \quad \mathbf{G}_\mathbf{r} = \mathbf{P}\mathbf{G}_\mathbf{aw} + \mathbf{N}_\mathbf{2} \tag{35}$$

The solution of equation (34) is given by following integral:

$$\mathbf{r}(t) = e^{-\mathbf{A}_\mathbf{c}^\mathrm{T} t}\left[\mathbf{c}_\mathbf{r} - \int_1^t e^{\mathbf{A}_\mathbf{c}^\mathrm{T}\tau}\mathbf{G}_\mathbf{r}\dot{w}(\tau)d\tau\right] \tag{36}$$

With respect to $\mathbf{r}(t + t_p) = 0$, the vector integration constant $\mathbf{c}_r$ is obtained

$$\mathbf{o} = e^{-\mathbf{A}_\mathbf{c}^\mathrm{T}\left(t+t_p\right)}\left[\mathbf{c}_\mathbf{r} - \int_1^{t+t_p} e^{\mathbf{A}_\mathbf{c}^\mathrm{T}\tau}\mathbf{G}_\mathbf{r}\dot{w}(\tau)d\tau\right] \;\Rightarrow\; \mathbf{c}_\mathbf{r} = \int_1^{t+t_p} e^{\mathbf{A}_\mathbf{c}^\mathrm{T}\tau}\mathbf{G}_\mathbf{r}\dot{w}(\tau)d\tau \tag{37}$$

Substituting $\mathbf{c}_r$ obtained in (37) into (36) after some manipulations gives

$$\mathbf{r}(t) = \int_t^{t+t_p} e^{\mathbf{A}_\mathbf{c}^\mathrm{T}(\tau - t)}\mathbf{G}_\mathbf{r}\dot{w}(\tau)d\tau \tag{38}$$

Now, state a substitution $\sigma = \tau - t$. Integral (38) after performing the substitution and switching the limits of integration is transferred to form

$$\mathbf{r}(t) = \int_0^{t_p} e^{\mathbf{A}_\mathbf{c}^\mathrm{T}\sigma}\mathbf{G}_\mathbf{r}\dot{w}(t + \sigma)d\sigma \tag{39}$$

For determination of $\boldsymbol{r}(t)$ it is necessary to solve the integral (39) at each time.
Finally, substituting $\boldsymbol{\lambda}$ – equation (27) – into the one for the control force – equation (22) – and with respect to (32) and (39), after some manipulations, the active control force is obtained

$$u = -R_1^{-1}\left(\mathbf{N}_\mathbf{1}^\mathrm{T} + \mathbf{B}_\mathbf{a}^\mathrm{T}\mathbf{P}\right)\mathbf{x}_\mathbf{a} - R_1^{-1}\mathbf{B}_\mathbf{a}^\mathrm{T}\mathbf{r} \tag{40}$$

After the introduction of substitutions

$$\mathbf{K}_\mathbf{b} = R_1^{-1}\left(\mathbf{N}_\mathbf{1}^\mathrm{T} + \mathbf{B}_\mathbf{a}^\mathrm{T}\mathbf{P}\right), \quad \mathbf{K}_\mathbf{f} = R_1^{-1}\mathbf{B}_\mathbf{a}^\mathrm{T} \tag{41}$$

the relation (40) has the form

$$u = -\mathbf{K}_\mathbf{b}\mathbf{x}_\mathbf{a} - \mathbf{K}_\mathbf{f}\mathbf{r} \tag{42}$$

It can be seen that the active control force consists of the feedback gain $\mathbf{K}_\mathbf{b}$ and of the feedforward gain $\mathbf{K}_\mathbf{f}$. The feedforward part of the active control force $\mathbf{K}_\mathbf{f}\mathbf{r}(t)$ is a function of incoming road disturbances – integral (39) – which implies that it tries to eliminate the effect of these approaching road excitation on the vehicle.

With respect to (42), the state equation (11) of idealized fully active system can be rewritten as

$$\dot{\mathbf{x}}_\mathbf{a} = \left(\mathbf{A}_\mathbf{a} - \mathbf{B}_\mathbf{a}\mathbf{K}_\mathbf{b}\right)\mathbf{x}_\mathbf{a} - \mathbf{B}_\mathbf{a}\mathbf{K}_\mathbf{f}\mathbf{r} + \mathbf{G}_\mathbf{aw}\dot{w} \tag{43}$$

4. MR damper – hydromechanical and mathematical model

Hydromechanical and mathematical model of the MR damper were identified by the author in publication (Úradníček, 2008), where they were designed on the basis of model of an electrorheological damper compiled in publication (Hong & Choi, 2005).

Hydromechanical parameters of the hydromechanical model of the MR damper – figure 2 a) – are:
C_1, C_2, C_4 – compressibility of the volumes front of, behind the piston and of gas storage
A_1, A_2, A_4, A_f – cross-sectional area of the bottom, top part of the piston and cross-sectional area of the membrane and of the grooves
p_1, p_2, p_4 – pressures of the MR fluid front of, behind the piston and of gas storage
I_f – inertia of the MR fluid flowing through the grooves of the piston
R_f – hydraulic resistance of the MR fluid flowing through the groove of the piston
Δp_{MR} – pressure drop in the groove of the piston caused by friction force
y_r – displacement of the MR fluid flowing through the groove of the piston relative to piston
y_p – displacement of the piston of the MR damper
y_m – displacement of the membrane separating the MR fluid from gas
Overall pressure drop in front of and behind the piston is:

$$\Delta p = p_2 - p_1 = I_f A_f \ddot{y}_r + R_f A_f \dot{y}_r + \Delta p_{MR} \tanh\left(\beta_d \dot{y}_r\right) \tag{44}$$

The parameter β_d allows us to regulate the friction force near zero velocity of motion of the MR fluid flowing through the grooves. The function tanh (-) ensures the consistency of the mathematical model.

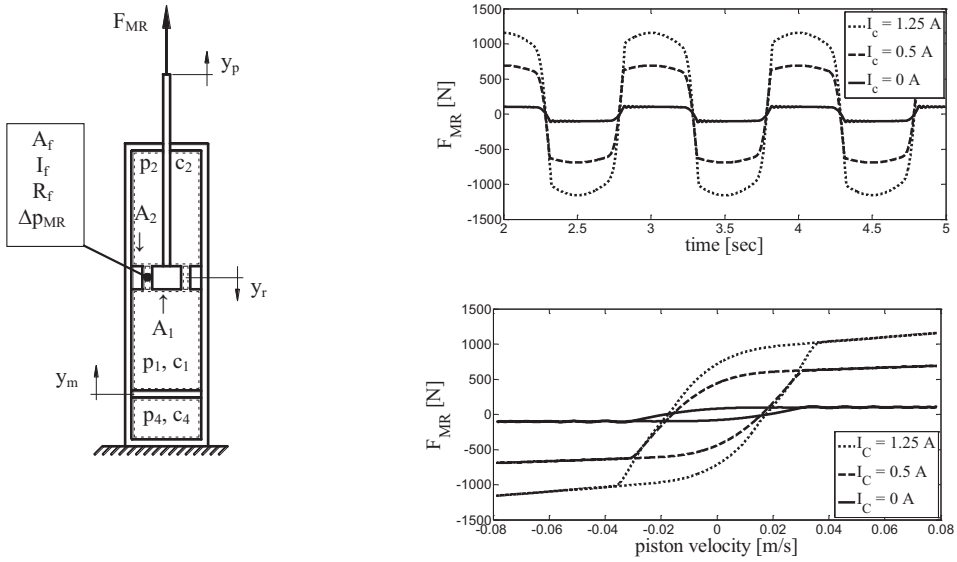

a.) *b.)*

Fig. 2: a.) hydromechanical model of the MR damper b.) dynamical characteristics of the MR damper

Maintain the continuity of the volumes front of, behind the piston and of gas storage describe following relations:

$$\begin{aligned} c_1 p_1 &= -\left(A_1 - A_f\right) y_p + A_f y_r + A_4 y_m \\ c_2 p_2 &= \left(A_2 - A_f\right) y_p - A_f y_r \\ c_4 p_4 &= A_4 y_m \end{aligned} \tag{45}$$

Since the cross-sectional areas A_1 and A_2 are approximately equal, they can be approximated by their mean value $A_p \approx (A_1 + A_2) / 2$.
Pressures in front of the piston and of gas storage are also approximately equal – $p_1 \approx p_4$.

Pressure drop in front of and behind the piston with respect to relations (45) and the above assumptions after some manipulation is:

$$p_2 - p_1 = -A_f \left(\frac{1}{c_1 + c_4} + \frac{1}{c_2} \right) y_r + \left(A_p - A_f \right) \left(\frac{1}{c_1 + c_4} + \frac{1}{c_2} \right) y_p \tag{46}$$

By substituting the equation (46) into (44) and by multiplying by the approximate area, the equation of motion of the hydromechanical model of the MR damper in the figure 2 a.) is obtained.

$$I_f A_f A_p \ddot{y}_r + R_f A_f A_p \dot{y}_r + \Delta p_{MR} A_p \tanh\left(\beta_d \dot{y}_r\right) + A_f \left(\frac{1}{c_1 + c_4} + \frac{1}{c_2} \right) A_p y_r = \left(A_p - A_f \right) \left(\frac{1}{c_1 + c_4} + \frac{1}{c_2} \right) y_p \tag{47}$$

After substitutions

$$\begin{aligned} &m_f = I_f A_f A_p, \quad c_f = R_f A_f A_p, \quad F_y = \Delta p_{MR} A_p, \\ &k_{f_1} = A_f \left(\frac{1}{c_1 + c_4} + \frac{1}{c_2} \right) A_p, \quad k_{f_2} = \left(A_p - A_f \right) \left(\frac{1}{c_1 + c_4} + \frac{1}{c_2} \right) \end{aligned} \tag{48}$$

the equation of motion (47) is transferred to form

$$m_f \ddot{y}_r + c_f \dot{y}_r + F_y \tanh\left(\beta_d \dot{y}_r\right) + k_{f_1} y_r = k_{f_2} y_p \tag{49}$$

The damping force of the MR damper is proportional to the pressure difference in front of and behind the piston

$$F_{MR} = \left(p_2 - p_1 \right) A_p \tag{50}$$

By substituting (44) into (50) with respect to substitutions (48) the damping force of the MR damper is obtained

$$F_{MR} = m_f \ddot{y}_r + c_f \dot{y}_r + F_y \tanh\left(\beta_d \dot{y}_r\right) \tag{51}$$

With respect to the equation of motion (49) for the damping force also applies

$$F_{MR} = k_{f_2} y_p - k_{f_1} y_r \tag{52}$$

In publication (Úradníček, 2008) author experimentally identified the parameters of the MR damper LORD RD – 1005 – 3 on the basis of mathematical model described by relations (49) and (51) as functions of electric current flowing through the coil of the MR damper (for the range of electric current 0 – 1.25 A):

$$\begin{aligned} &m_f = d_5 \qquad c_f\left(I_c\right) = c_1 I_c + d_1 \qquad F_y\left(I_c\right) = a_2 I_c^3 + b_2 I_c^2 + c_2 I_c + d_2 \\ &\beta_d = 80 \qquad k_{f_1}\left(I_c\right) = b_3 I_c^2 + c_3 I_c + d_3 \qquad k_{f_2}\left(I_c\right) = b_4 I_c^2 + c_4 I_c + d_4 \end{aligned} \tag{53}$$

The values of the parameters of the approximate functions (53) are in the table 1.

Tab. 1: Values of the parameters of the approximate functions (53)

i	a_i	b_i	c_i	d_i
1	0	0	1685	21.5
2	- 368.19	216.5	952.02	98.61
3	0	- 772967.93	1657383.84	76527.7
4	0	- 1271919	2571391.71	173556.34
5	0	0	0	1.45

Some dynamical characteristics of the identified mathematical model of the MR damper – equations (49) and (51) – excited by a harmonic force of amplitude *12.5 mm* and frequency *1 Hz* for different electric currents are in the figure 2 b.).

5. Quarter car model with MR damper and with consideration the tire lift off

The mathematical model of the semi-active MR damper described in the previous section is implemented in the quarter car model described in the second section. So the idealized fully active suspension is replaced by the MR damper. In the equations of motion (1) the active control force u is replaced by the one generated by the MR damper – F_{MR}.

$$\begin{aligned} m_1\ddot{y}_1 &= -k_1\left(y_1-y_2\right)+F_{MR}-m_1 g \\ m_2\ddot{y}_2 &= -k_2\left(y_2-w\right)\left[1-H\left(y_2-w\right)\right]-k_1\left(y_2-y_1\right)-F_{MR}-m_2 g \end{aligned} \tag{54}$$

Dynamics of the MR damper is described by the relations (49) and (51) in the previous section. It is useful to utilize the relation (52) instead of the relation (51) for the expression of the damping force of the MR damper.

$$\begin{aligned} m_f\ddot{y}_r + c_f\dot{y}_r + F_y\tanh\left(\beta_d\dot{y}_r\right)+k_{f_1}y_r &= k_{f_2}y_p \\ F_{MR} &= k_{f_2}y_p - k_{f_1}y_r \end{aligned} \tag{55}$$

In the case of using the MR damper in the quarter car suspension the piston displacement y_p with respect to the figure 2 a.) and equations of motion (54) is replaced by the suspension deflection $y_2 - y_1$.

$$\begin{aligned} m_f\ddot{y}_r + c_f\dot{y}_r + F_y\tanh\left(\beta_d\dot{y}_r\right)+k_{f_1}y_r &= -k_{f_2}\left(y_1-y_2\right) \\ F_{MR} &= -k_{f_2}\left(y_1-y_2\right) - k_{f_1}y_r \end{aligned} \tag{56}$$

By substituting the MR damping force from the second relation of (56) into (54) the equations of motion of the quarter car model with MR damper and with consideration the tire lift off in the matrix form are

$$\mathbf{M_s}\ddot{\mathbf{q}}_{\mathbf{sA}} + \mathbf{B_{sL}}\dot{\mathbf{q}}_{\mathbf{sA}} + \mathbf{B}_{sN}\tanh\left(\beta_d\dot{\mathbf{q}}_{\mathbf{sA}}\right)+\mathbf{K_{sL}}\mathbf{q_{sR}}+\mathbf{K_{sN}}\mathbf{q_{sR}}\mathbf{e_s}\tanh\left(\beta_r\mathbf{q_{sR}}\right)=\mathbf{b_{sg}}g \tag{57}$$

where

$$\mathbf{M_s}=\begin{bmatrix} m_1 & 0 & 0 \\ 0 & m_2 & 0 \\ 0 & 0 & m_f \end{bmatrix},\ \mathbf{B_{sL}}=\begin{bmatrix} 0 & 0 & 0 \\ 0 & 0 & 0 \\ 0 & 0 & c_f \end{bmatrix},\ \mathbf{B_{sN}}=\begin{bmatrix} 0 & 0 & 0 \\ 0 & 0 & 0 \\ 0 & 0 & F_y \end{bmatrix},\ \mathbf{K_{sN}}=\begin{bmatrix} 0 & 0 & 0 \\ 0 & -k_2/2 & 0 \\ 0 & 0 & 0 \end{bmatrix} \tag{58}$$

$$\mathbf{K_{sL}}=\begin{bmatrix} k_1+k_{f_2} & 0 & k_{f_1} \\ -\left(k_1+k_{f_2}\right) & \dfrac{k_2}{2} & -k_{f_1} \\ k_{f_2} & 0 & k_{f_1} \end{bmatrix},\ \mathbf{e_s}=\begin{bmatrix} 0 \\ 1 \\ 0 \end{bmatrix}^T,\ \mathbf{b_{sg}}=-\begin{bmatrix} m_1 \\ m_2 \\ 0 \end{bmatrix},\ \mathbf{q_{sA}}=\begin{bmatrix} y_1 \\ y_2 \\ y_r \end{bmatrix},\ \mathbf{q_{sR}}=\begin{bmatrix} y_1-y_2 \\ y_2-w \\ y_r \end{bmatrix}$$

Transformation from absolute to the relative coordinates is realized through the equation:

$$\mathbf{q_{sR}}=\mathbf{T_{sA}}\mathbf{q_{sA}}+\mathbf{T_{sw}}w \tag{59}$$

where

$$\mathbf{T_{sA}}=\begin{bmatrix} 1 & -1 & 0 \\ 0 & 1 & 0 \\ 0 & 0 & 1 \end{bmatrix},\ \mathbf{T_{sw}}=\begin{bmatrix} 0 \\ -1 \\ 0 \end{bmatrix} \tag{60}$$

Combining equation (57) and differentiated equation (59), state space model is obtained:

$$\dot{\mathbf{x}}_\mathbf{s}=\mathbf{A_{sL}}\mathbf{x_s}+\mathbf{A_{sr}}\mathbf{x_s}\mathbf{E_s}\tanh\left(\beta_r\mathbf{x_s}\right)+\mathbf{A_{sd}}\tanh\left(\beta_d\mathbf{x_s}\right)+\mathbf{G_s}\mathbf{f_{gw}} \tag{61}$$

where

$$\mathbf{A}_{sL}=\begin{bmatrix}\mathbf{O}_s & \mathbf{T}_{sA}\\ -\mathbf{M}_s^{-1}\mathbf{K}_{sL} & -\mathbf{M}_s^{-1}\mathbf{B}_{sL}\end{bmatrix},\quad \mathbf{A}_{sr}=\begin{bmatrix}\mathbf{O}_s & \mathbf{O}_s\\ -\mathbf{M}_s^{-1}\mathbf{K}_{sN} & \mathbf{O}_s\end{bmatrix},\quad \mathbf{A}_{sd}=\begin{bmatrix}\mathbf{O}_s & \mathbf{O}_s\\ \mathbf{O}_s & -\mathbf{M}_s^{-1}\mathbf{B}_{sN}\end{bmatrix}$$
$$\mathbf{E}_s=\begin{bmatrix}\mathbf{e}_s^T\\ \mathbf{o}_s\end{bmatrix}^T,\quad \mathbf{G}_s=\begin{bmatrix}\mathbf{G}_{sg} & \mathbf{G}_{sw}\end{bmatrix},\quad \mathbf{G}_{sg}=\begin{bmatrix}\mathbf{o}_s\\ \mathbf{M}_s^{-1}\mathbf{b}_{sg}\end{bmatrix},\quad \mathbf{G}_{sw}=\begin{bmatrix}\mathbf{T}_{sw}\\ \mathbf{o}_s\end{bmatrix},\quad \mathbf{x}_s=\begin{bmatrix}\mathbf{q}_{sR}\\ \dot{\mathbf{q}}_{sA}\end{bmatrix} \tag{62}$$

where $\mathbf{O}_s$ and $\mathbf{o}_s$ are zero matrix and vector respectively of appropriate dimensions.

6. Continuous inverse mathematical model of the MR damper

Mathematical model of the MR damper works such – see relations (56) – that for given electric current and for kinematic variables the damping force F_{MR} is calculated. An inverse model of the MR damper designed for the use of control should calculate the control electric current for given kinematic variables and for required damping force.

In section 3 the optimal preview control and corresponding active control force were derived. In this section as required damping force F_{MR} that is trying to be matched by the MR damper the active control force u from section 3 is taken. In some situations the active force is physically unable to be achieved by the MR damper. This problem is solved below.
As it was pointed out the active control force that would be generated by fully active system is trying to be matched by the one generated by the MR damper, so with respect to the second relation of (56) it can be written

$$\begin{aligned} F_{MR} &= u\\ -k_{f_2}\left(y_1-y_2\right)-k_{f_1}y_r &= u\end{aligned} \tag{63}$$

For the use of control it is appropriate to replace the variables $k_{f1}(I_c)$ and $k_{f2}(I_c)$ from relations (53) by linear functions $k_{f1r}(I_r)$ and $k_{f2r}(I_r)$ and for given range of control electric current to optimize their parameters by the least squares method – see figure (3)

$$k_{f_{1r}}\left(I_r\right)=c_{3r}I_r+d_{3r},\qquad k_{f_{2r}}\left(I_r\right)=c_{4r}I_r+d_{4r} \tag{64}$$

These relations (64) are used only in the inverse model of the MR damper for calculating the required electric current.

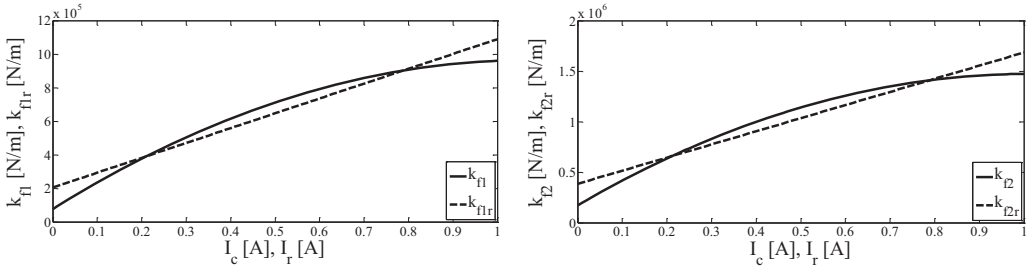

Fig. 3: Comparison of the functions used in the mechanical and jn the inverse model of the MR damper see relations (53) and (64

After mentioned replacement the second relation of (63) now has the form

$$-k_{f_{2r}}\left(y_1-y_2\right)-k_{f_{1r}}y_r=u \tag{65}$$

By substituting (64) and (42) – relation for calculating the active control force u – into (65) we obtain

$$\begin{aligned} &-\left(c_{4r}I_r+d_{4r}\right)\left(y_1-y_2\right)-\left(c_{3r}I_r+d_{3r}\right)y_r=\\ &=-K_{b_1}\left(y_1-y_2\right)-K_{b_2}\left(y_2-w\right)-K_{b_3}\dot{y}_1-K_{b_4}\dot{y}_2-\mathbf{K}_{\mathbf{f}}\mathbf{r}\end{aligned} \tag{66}$$

where

$$\mathbf{K_b} = \begin{bmatrix} K_{b_1} & K_{b_2} & K_{b_3} & K_{b_4} \end{bmatrix}^T, \quad \mathbf{x_a} = \begin{bmatrix} y_1 - y_2 & y_2 - w & \dot{y}_1 & \dot{y}_2 \end{bmatrix}^T \tag{67}$$

After some manipulations the required control electric current is obtained

$$I_r = \frac{\left(\mathbf{K_{I_n}} + \mathbf{K_{b_s}}\right)\mathbf{x_s} + \mathbf{K_f}\mathbf{r}}{\mathbf{K_{I_d}}\mathbf{x_s}} \tag{68}$$

where

$$\begin{aligned} \mathbf{K_{I_n}} &= \begin{bmatrix} -d_{4r} & 0 & -d_{3r} & 0 & 0 & 0 \end{bmatrix}, \quad \mathbf{K_{b_s}} = \begin{bmatrix} K_{b_1} & K_{b_2} & 0 & K_{b_3} & K_{b_4} & 0 \end{bmatrix} \\ \mathbf{K_{I_d}} &= \begin{bmatrix} c_{4r} & 0 & c_{3r} & 0 & 0 & 0 \end{bmatrix}, \quad \mathbf{x_s} = \begin{bmatrix} y_1 - y_2 & y_2 - w & y_r & \dot{y}_1 & \dot{y}_2 & \dot{y}_r \end{bmatrix}^T \end{aligned} \tag{69}$$

If this fictive required electric current I_r flew through the coil of the MR damper, the ideal control active force would be achieved. The required electric current I_r calculated from the relation (68) can be any real number (also negative, which is physically impossible). But there are some restrictions of electric control current. Working range of the electric current is limited to *0 – 1 A*. Instead of commonly used saturation a continuous function is utilized for the calculation of theoretical control electric current for used MR damper (Havelka, 2010) – see figure 4

$$I_{ct} = \frac{1}{2}\left\{1 + \tanh\left[\alpha\left(I_r - \frac{1}{2}\right)\right]\right\} \tag{70}$$

The parameter α was optimized by the least squares method to match the commonly used saturation.

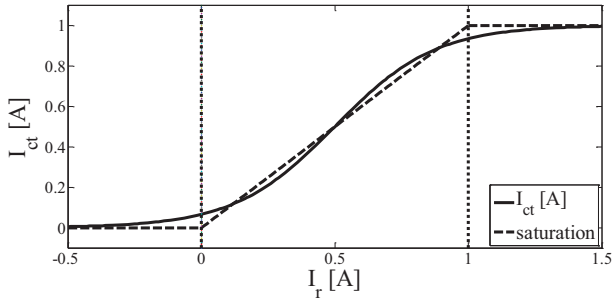

Fig. 4: Comparison of commonly used saturation and the designed continuous function I_{ct} [A]

Since the response time of an actual MR damper to the theoretical required control electric current I_{ct} is not immediate but time-delayed, this effect can be included into the model using a first order filter

$$\dot{I}_c(t) = -\frac{1}{T_{MR}}\left[I_c(t) - I_{ct}(t)\right] \tag{71}$$

where T_{MR} is the time constant of the MR damper set to *20 ms* and I_c is the actual electric current applied to the model (53) of the MR damper. It further means that the system matrices $\mathbf{A_{sL}}$ and $\mathbf{A_{sd}}$ of the state space model (61) are also dependent on the applied electric current I_c.

7. Simulations and results

To significantly demonstrate the benefits of preview control the vehicle model was let to travel over a bump and further it was supposed that all the state variables are measured. The bump is described by equation

$$w(t) = \left\{H\left(t - t_{bs}\right) - H\left[t - \left(t_{bs} + t_b\right)\right]\right\}\frac{b_h}{2}\left\{1 - \cos\left[2\pi\frac{1}{t_b}\left(t - t_{bs}\right)\right]\right\} \tag{72}$$

where t_{bs} is the "starting" time of the bump, b_h is the height of the bump and $t_b = b_l / v$ is the duration time of the bump where v is the vehicle velocity.

Values used during the simulations are listed below.

Bump parameters: $b_l = 0.5\ m;\ b_h = 0.05\ m$

Quarter car parameters: $m_1 = 288.9\ kg;\ m_2 = 28.58\ kg;\ k_1 = 14\ 000\ N/m;\ k_2 = 155\ 900\ N/m;$

Weighting constants: weight to ride comfort $q_1 = 1$; weight to suspension rattle space $q_2 = 10^3$; weight to road holding $q_3 = 10^4$; weight to penalizing the active control force $r = 0$

Control electric current calculation: $c_{3r} = 884\ 415;\ d_{3r} = 205\ 355;\ c_{4r} = 1\ 299\ 475;\ d_{4r} = 385\ 540;\ \alpha = 2.65$

The quarter car equipped with fully active idealized suspension was let to travel over a bump at velocity *4 m/s* – figure 5. The preview distance in front of the front wheel was set to *1.6 m*. This implies the preview time $t_p = 0.4\ sec.$

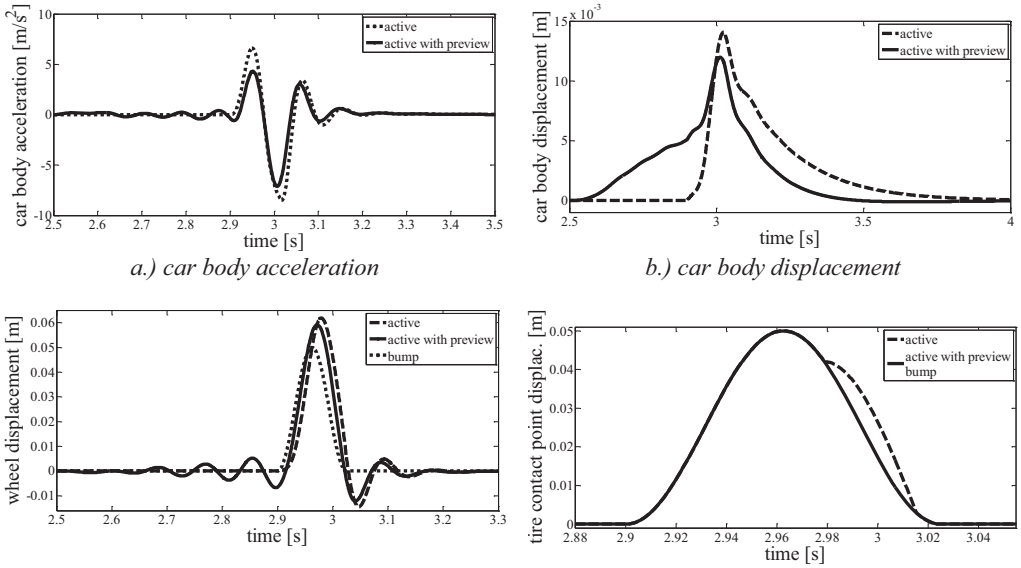

a.) car body acceleration *b.) car body displacement*

c.) wheel displacement *d.) tire contact point diplacement*

Fig. 5: Responses of the quarter car model traveling over a bump equipped with fully active system controlled by "active" and "active with preview" control strategies

In Figure 5 car body acceleration and car body, wheel and tire contact point displacements of fully active quarter car model traveling over a bump controlled by "active" and "active with preview" control strategies are shown. In all cases the active preview control strategy provides lower amplitudes and also smaller variances. As shown in Figure 5 c.) – the preview controlled active suspension acts the wheel before the bump excitation comes to smoothly lift it over the bump and avoids the tire lift off the road compared with the no preview case when the undesired tire lift off effect occurs – Figure 5 d.).

Then the quarter car equipped with the MR damper in suspension was let to travel over a bump at velocity *3.5 m/s* – figure 6. The preview distance in front of the front wheel was set to *1.6 m*. This implies the preview time $t_p = 0.457\ sec.$

Figure 6 shows that the semi-active MR damper with the preview case provides some small improvement in car body displacement compared with the no preview case, but in terms of the wheel displacement no difference between the preview and no preview case can be observed.

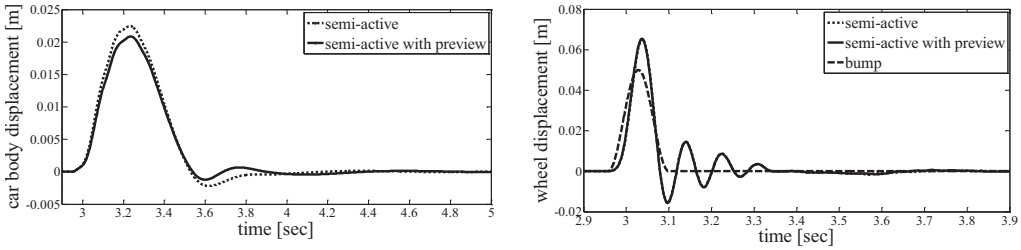

a.) car body displacement *b.) wheel displacement*

Fig.6: Responses of the quarter car model traveling over a bump equipped with MR damper controlled with "no preview" and "preview" control strategies

This is because the semi-active MR damper is unable to supply energy into the system and cannot generate forces when there is no changing suspension deflection, i.e. the MR damper cannot act the system before the excitation comes – see figure 7 b.).

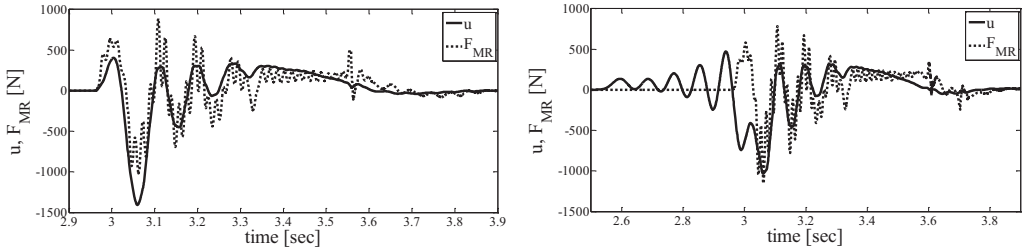

a.) no preview case *b.) preview case*

Fig.7: Required active force "u" and the actual control force of the MR damper "F_{MR}" in the quarter car model traveling over a bump controlled with" no preview" and "preview" control strategies

The control electric current is trying to change the MR fluid properties to achieve the required active control force – see figures 8 and 7 b.) from the time *2.5 sec* up to time *3 sec* – but during this time period there is no changing suspension deflection so the MR damper can produce no force – see F_{MR} in the figure 7 b.) during this period.

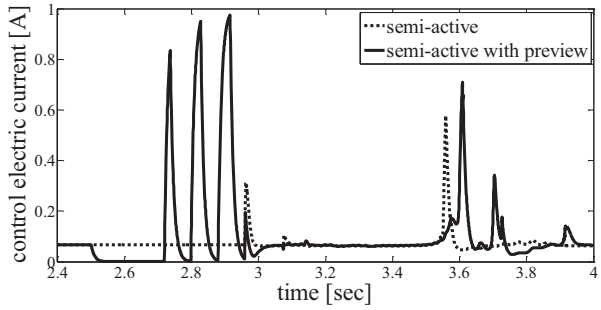

Fig.8: Control electric current flowing through the coil of the MR damper in the quarter car model traveling over a bump controlled with" no preview" and "preview" control strategies

8. Conclusions

The preview controlled active suspension acts the vehicle before the excitation comes, i.e. prepares the vehicle for approaching road disturbances to smoothly travel over them and reduces the probability of undesired tire lift off effect. Active suspension with preview compared with the no preview case provides lower maximum amplitudes and smaller variances of car body acceleration, suspension travel and tire deflection at the same time.

In the case of utilizing the semi-active MR damper in suspension difference between the preview and no preview control strategies almost diminishes. This is because MR damper is only able to dissipate the energy present in the system and cannot generate independent forces when there is no changing suspension deflection.

Acknowledgement

This work was supported by grant Vega 1/0197/12.

References

Hać, A. (1992) Optimal Linear Preview Control of Active Vehicle Suspension. *Vehicle System Dynamics*, 21, pp.167-195.

Hać, A. & Youn, I. (1991) Optimal Semi-Active Suspension with Preview Based on a Quarter Car Model, in*: American Control Conference, 1991*, Boston, MA, USA, pp.433-438.

Havelka, F. & Zuščík, M. & Musil, M. (2010) Návrh spojitého inverzného matematického modelu magnetoreologického tlmiča pre riadenie, in*: Noise and Vibration in Practice: Proceedings of the 15th international acoustic conference, 2010*, Kočovce, Slovensko, pp.53-56.

Hong, S. R. & Choi, S. B. (2005) A hydro-mechanical model for hysteretic damping force prediction of ER damper: experimental verification. *Journal of Sound and Vibration,* 285, pp.1180-1188.

Prabakar, R. S. & Sujatha, C. & Narayanan, S. (2009) Optimal semi-active preview control response of a half car vehicle model with magnetorheological damper. *Journal of Sound and Vibration,* 326, 3-5, pp.400-420.

Thompson, A. G. & Pearce, C. E. M. (1998) Physically Realisable Feedback Controls for a Fully Active Preview Suspension Applied to a Half-Car Model. *Vehicle System Dynamics*, 30, pp.17-35

Úradníček, J. (2008) Multidisciplinárna optimalizácia modelu odpruženia vozidla vybaveného semiaktívnym magnetoreologickým tlmičom. *Kandidátska dizertačná práca*. STU v Bratislave SjF, Bratislava.

18th International Conference
ENGINEERING MECHANICS 2012
Svratka, Czech Republic, May 14 – 17, 2012

pp. 377–381
Paper #249

COMPUTATIONALLY EFFICIENT ALGORITHMS FOR EVALUATION OF STATISTICAL DESCRIPTORS

J. Havelka [*], A. Kučerová [**], J. Sýkora [***]

Abstract: *Homogenization methods are becoming the most popular approach to modelling of heterogeneous materials. The main principle is to represent the heterogeneous microstructure with an equivalent homogeneous material. When dealing with the complex random microstructures, the unit cell representing exactly periodic morphology needs to be replaced by a statistically equivalent periodic unit cell (SEPUC) preserving the important material properties in the statistical manner. One of the statistical descriptors suitable for SEPUC definition is the lineal path function. It is a low-order descriptor based on a more complex fundamental function able to capture certain information about the phase connectedness. Its main disadvantage is the computational cost. In this contribution, we present the reformulation of the sequential C code for evaluation of the lineal path function into the parallel C code with Compute Unified Device Architecture (CUDA) extensions enabling the usage of computational potential of the NVIDIA graphics processing unit (GPU).*

Keywords: ***Lineal path function, homogenization, statistically equivalent periodic unit cell, graphics processing unit.***

1. Introduction

Modelling of random heterogeneous materials is a multi-disciplinary problem with a wide range of relevant engineering applications. The unifying theoretical framework is provided by homogenization theories, which aim at the replacement of the heterogeneous microstructure with an equivalent homogeneous material, e.g. Torquato (2002). Currently, two main approaches are available: (i) computational homogenization and (ii) effective media theories. While the first class of methods studies the distribution of local fields within a typical heterogeneity pattern using a numerical method, the second group estimates the response analytically on the basis of limited geometrical information (e.g. the volume fractions of constituents) of the analysed medium.

It is generally accepted that detailed discretisation techniques, and the Finite Element Method (FEM) in particular, remain the most powerful and flexible tools available. Despite of the tedious computation time, it provides us details of local stress and strain fields. Moreover, it is convenient to characterize the material heterogeneity by introducing the concept of a Periodic Unit Cell (PUC) (Vorel, 2009) or Statistically Equivalent Periodic Unit Cell (SEPUC), see Zeman and Šejnoha (2007); Vorel et al. (2012) for more details. On the other hand, if only the overall (macroscopic) response is demanded variable, it is sufficient to introduce structural imperfections in a cumulative sense using one of the averaging schemes, e.g. the Mori-Tanaka method (Vorel and Šejnoha, 2009). If the effective material parameters of complex microstructure (see Figure 1) are demanded, the homogenization technique based on the SEPUC can be utilized. Furthermore, this approach allows us to reduce the computation cost by generating smaller unit cell describing the real structure. The generation of the SEPUC is based on optimization of an appropriate statistical descriptor. One most commonly used group of descriptors embodies a set of general n-point probability functions, applicable to an arbitrary two-phase composite. A different statistical function deserves attention when phase connectivity information is to be captured in more

[*] Jan Havelka: Faculty of Civil Engineering, Czech Technical University in Prague, Thákurova 7/2077; 166 29, Prague; CZ, e-mail: jan.havelka.1@fsv.cvut.cz
[**] Ing. Anna Kučerová, Ph.D.: Faculty of Civil Engineering, Czech Technical University in Prague, Thákurova 7/2077; 166 29, Prague; CZ, e-mail: anicka@cml.fsv.cvut.cz
[***] Ing. Jan Sýkora, Ph.D.: Faculty of Civil Engineering, Czech Technical University in Prague, Thákurova 7/2077; 166 29, Prague; CZ, e-mail: jan.sykora.1@fsv.cvut.cz

detail, as e.g. for medium in Figure 1. Therefore we focus here on usage of the lineal path function. The principal drawback concerns its evaluation, which is non-negligible time-consuming, especially when evaluated many times within the optimization process. Hence, we present an accelerated implementation of the lineal path function on the GPU. The following section details the definition of the lineal path

Fig. 1: Three cuts through trabecular bone microstructure obtained by micro Computed Tomography (Jiroušek et al., 2008)

function. The Section 3. discusses its algorithmic formulation and Section 4. presents the resulting speed-up obtained at GPU in comparison with the sequential CPU formulation together with concluding remarks.

2. Lineal path function

The lineal path function (Lu and Torquato, 1992) is one of the low-order microstructural descriptors based on a more complex fundamental function which contains more detailed information about phase connectedness and hence certain information about long-range orders (Zeman, 2003).

The fundamental function can defined as

$$\lambda_r(\mathbf{x}_1, \mathbf{x}_2, \alpha) = \begin{cases} 1, \text{ if } \mathbf{x}_1\mathbf{x}_2 \subset D_r(\alpha), \\ 0, \text{ otherwise}, \end{cases} \tag{1}$$

i.e., a function which equals to 1 when the segment $\mathbf{x}_1\mathbf{x}_2$ is contained in the phase r for the sample α and zero otherwise. The lineal path function, denoting the probability that the $\mathbf{x}_1\mathbf{x}_2$ segment lies in the phase r, then follows directly from the ensemble averaging of this function

$$L_r(\mathbf{x}_1, \mathbf{x}_2) = \overline{\lambda_r(\mathbf{x}_1, \mathbf{x}_2, \alpha)}. \tag{2}$$

Under the assumptions of statistical homogeneity and isotropy, the function simplifies to

$$L_r(\mathbf{x}_1, \mathbf{x}_2) = L_r(\mathbf{x}_1 - \mathbf{x}_2) = L_r(\|\mathbf{x}_1 - \mathbf{x}_2\|). \tag{3}$$

Obviously, if the points $\mathbf{x}_1$ and $\mathbf{x}_2$ coincide, the lineal path function takes the value of volume fraction of the phase r. On the other hand, for points $\mathbf{x}_1$ and $\mathbf{x}_2$ that are far apart the lineal path function vanishes.

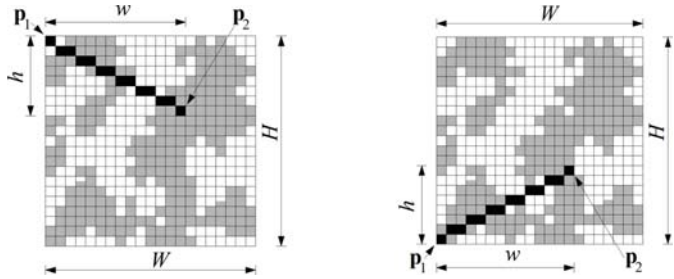

Fig. 2: Schema of the lineal path function

3. Algorithmic formulation

The generation of SEPUC is usually based on digital images, which are discretised representation of a studied medium. The segments are then defined as a set of pixels connecting two pixels $\mathbf{p}_1$ and $\mathbf{p}_2$ with the coordinates within the image $\mathbf{p}_i = (w, h)$, and , where W and H are the dimensions of the image (see Figure 2). The sets of pixels for segments starting in $\mathbf{p}_1 = (1, 1)$ and ending in $\mathbf{p}_2 = (w, h)$ are obtained by algorithm given in Bresenham (1965). The group of segments is complemented by the ones starting in $\mathbf{p}_1 = (1, H)$ and ending in $\mathbf{p}_2 = (w, h)$ to cover all possible lengths and orientations within the image. Once having the defined segments, the computation of lineal path function involve simple translations of each segment throughout the image and the comparison whether all pixels of the segment at a given position correspond to image pixels with the value representing the investigated phase.

Since the generation of segments can be done only once for a given image size, this part of the code does not necessarily need to be so fast. The crucial part of the code is the translation of the segment and the comparison with the image, which is called repeatedly for any new image created during the optimization of the SEPUC. Having a single CPU, the translations and comparisons needs to be performed sequentially, see Figure 3. Last years witnessed increasing popularity of parallel computations on GPUs.

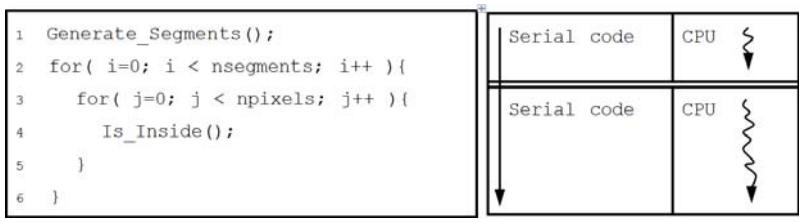

Fig. 3: Schema of the sequential code

The reason is the high performance at relatively low cost. Moreover, the CUDA simplifies the GPU-based software development by using the standard C language, see NVIDIA Corporation (www). We used the high number of simple GPU threads to compute the translations and comparisons of segments simultaneously, see Figure 4.

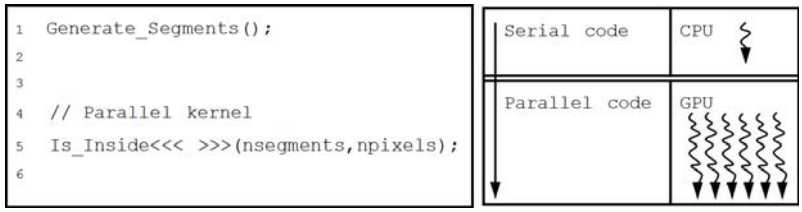

Fig. 4: Schema of the parallel code

4. Conclusions

We have compared the sequential variant of lineal path function calculation on a single CPU with the parallel one using the GPU. The particular computations were performed on INTEL Core i7 CPU 950 @ 3.07 GHz, 12 GB RAM, GPU - NVIDIA QUADRO 4000 with Microsoft Windows Enterprise SP 1 operating system and the CUDA v. 4.0 compute capability. The efficiency of GPU parallelism was demonstrated on evaluation of lineal path function for 10 two-dimensional images with the size varying from 50x50 px to 500x500 px, see Figure 5(c). Two distinct calculations of lineal path function were considered. The originally developed algorithm covering all possible segments in the domain and enhanced method with constraint of first zero segment in given direction. Table 1 shows the amount of time necessary for one evaluation of lineal path function depending on the image size and chosen method.

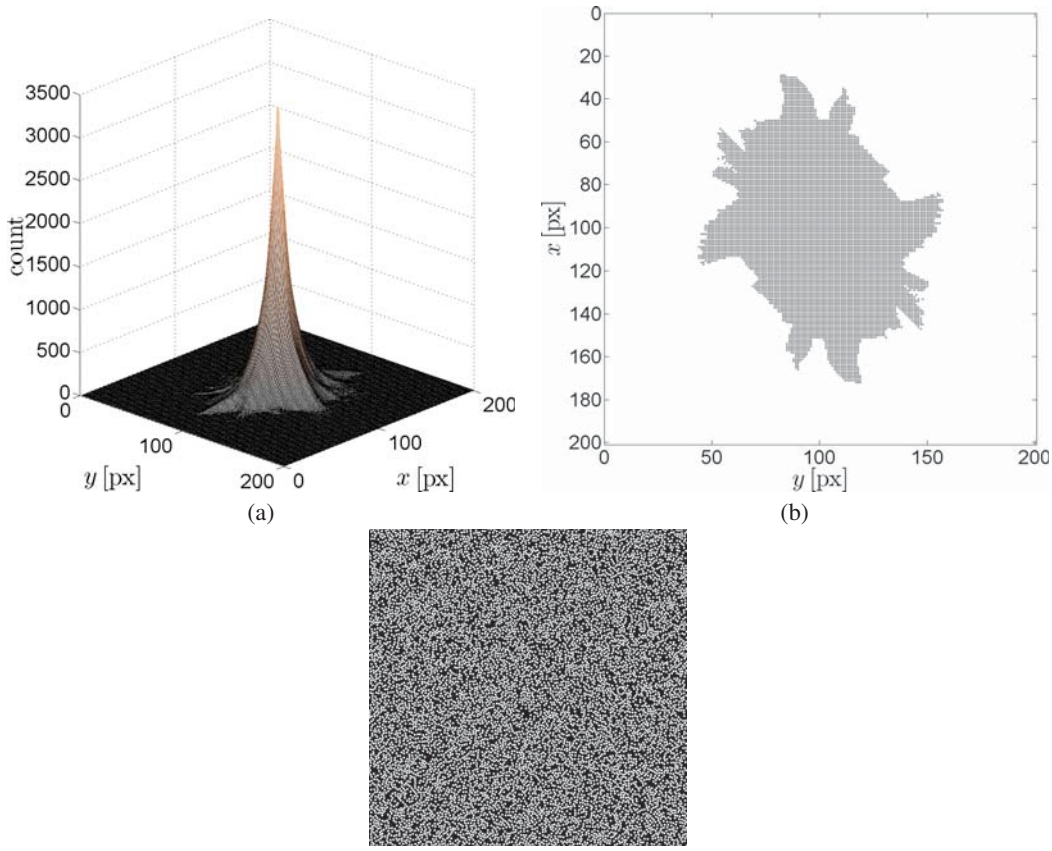

Fig. 5: (a) Lineal path function, (b) lineal path function (view X-Y), (c) testing image 500x500 px

One can see that for very small images, the usage of CPU outperforms the GPU because of additional time spent by copying the data from main memory RAM to GPU memory. Nevertheless, the parallelism of GPU gains for images larger than 50x50 px and the time savings increase rapidly.

Acknowledgments

The financial support of this work by the Czech Science Foundation (project No. 105/12/1146) is gratefully acknowledged.

References

Bresenham, J.E. (1965), Algorithm for computer control of a digital plotter. *IBM System journal*, Vol 4, No.1, pp 25-30.

Jiroušek, O., Vavřík, D., Jakůbek, J. and Dammer, J. (2008), Correlation of trabecular bone mechanical properties to its microstructure using CT-based FE modeling. *Proc. Engineering Mechanics*, Institute of Thermomechanics AS CR, Prague.

Lu, B. and Torquato, S. (1992), Lineal-path function for random heterogeneous materials. *Physical Review E*, Vol 45, No.2, pp 922-929.

NVIDIA Corporation (www), http://developer.nvidia.com/page/home.html. 2701 San Tomas Expressway Santa Clara, CA 95050, USA.

Torquato, S. (2002), *Random heterogenous materials*. Springer-Verlag, New York.

Standard				*Enhanced*				
D/ML [px]/[px]	GPU [s]	CPU [s]	**ratio**	D/ML [px]/[px]	GPU [s]	CPU [s]	**ratio**	**overall speedup**
50/50	0.179	0.328	**1.83**x	50/50	0.156	0.265	**1.69**x	**2.10**x
100/100	1.075	4.617	**4.29**x	100/100	0.722	2.371	**3.28**x	**6.39**x
150/150	3.957	21.653	**5.47**x	150/150	1.954	8.018	**4.10**x	**11.08**x
200/200	10.209	66.425	**6.51**x	200/200	3.621	14.742	**4.07**x	**18.34**x
250/250	22.276	169.245	**7.59**x	250/250	6.427	27.612	**4.29**x	**26.33**x
300/300	43.429	357.022	**8.22**x	300/250	8.413	42.338	**5.03**x	**42.44**x
350/350	76.644	649.195	**8.47**x	350/250	10.909	63.304	**5.80**x	**59.51**x
400/400	127.841	1127.897	**8.82**x	400/250	13.481	84.287	**6.25**x	**83.67**x
450/450	209.693	1821.911	**8.69**x	450/250	18.608	122.569	**6.59**x	**97.91**x
500/500	315.951	2846.712	**9.01**x	500/250	21.145	139.698	**6.61**x	**134.64**x

Tab. 1: Comparison of CPU and GPU performance (D=dimension of testing image in pixels, ML=maximal length of segment in pixels)

Vorel, J. (2009), *Multi-scale modeling of composite materials*. Ph.D. thesis, CTU in Prague, Prague.

Vorel, J. and Šejnoha, M. (2009), Evaluation of homogenized thermal conductivities of imperfect carbon-carbon textile composites using the Mori-Tanaka method. *Structural Engineering and Mechanics*, Vol 33, No.4, pp 429-446.

Vorel, J., Zeman, J., Šejnoha, M. and Tomková, B. (2012), Homogenization of plain weave composites with imperfect microstructure: Part II-Analysis of real-world materials. submitted for publication.

Zeman, J. (2003), Analysis of Composite Materials with Random Microstructure. *CTU Reports*, Ph.D. thesis, Vol 7, No.3, CTU Press, Prague.

Zeman, J. and Šejnoha, M. (2007), From random microstructures to representative volume elements. *Modelling and Simulation in Materials Science and Engineering*, Vol 15, No.4, pp 325-335.

18th International Conference
ENGINEERING MECHANICS 2012
Svratka, Czech Republic, May 14 – 17, 2012

pp. 383–389
Paper #225

EVALUATION OF WEDGE-SPLITTING TEST RESULTS FROM QUASI-BRITTLE PRISMATIC SPECIMENS USING THE DOUBLE-*K* FRACTURE MODEL

I. Havlíková[*], T. Pail[**], V. Veselý[***], D. Vořechovská[****], Z. Keršner[*****]

Abstract: . *The fracture-mechanical parameter values of concrete, a quasi-brittle composite material, are determined from records of experiments on specimens with stress concentrators. One of the fracture models applicable to concrete is the double-K model. This model combines the concept of cohesive forces acting on the effective crack increment with a criterion based on the stress intensity factor. The outputs of the model are critical crack tip opening displacement and fracture toughness values, including the initiation stress intensity factor value corresponding to the beginning of stable crack propagation. In this paper, a method of calculation by means of the double-K fracture model is verified using published data and the results of a pilot wedge-splitting test performed by the authors.*

Keywords: ***Double-K fracture model, concrete, prismatic specimen, wedge-splitting test.***

1. Introduction

Cement-based composites are one of the most widely used building materials. Concrete may be classified as a so-called quasi-brittle material. Studying the mechanical response of specimens made of such composites under static and dynamic/fatigue loading is complicated due to their highly nonlinear nature. Numerical tools for modelling both elastic (elastic-plastic) behaviour and also the fracture process are commonly used to predict or assess the response of structures fabricated from quasi-brittle materials. Such tools − often based on the finite element method (Červenka et al., 2007) or physical discretization of the continuum (Frantík, 2007) − are usually equipped by exploiting a type of nonlinear fracture model simulating the cohesive nature of cracking of quasi-brittle material (Bažant & Planas, 1998; Karihaloo, 1995; Shah et al., 1995). The parameters of this fracture model are determined from records of fracture tests; this is carried out either using evaluation methods built on the principle of the used non-linear fracture model, e.g. the work of fracture method (RILEM, 1985) or the size effect method (RILEM, 1990), or using inverse analysis with the possible application of advanced identification methods (Štafa & Frantík, 2010).

The utilization of existing methods for the evaluation of test records can result in the obtaining of fracture parameter values influenced by both the size and shape of the test specimen and the test geometry (the boundary conditions of the test). Such parameters cannot be used as relevant inputs to an analysis using the above-mentioned numerical tools. A similarly distorted description of the fracture may be indirectly caused by utilization of the methods for evaluation of the fracture model parameters – through the identification methods used – if this procedure is applied to the results of only one type of test and specimen size/shape. The effects of the specimen's size/geometry/free boundaries directly affect the recorded load–deflection or the load–crack mouth opening displacement diagram by means of which the inverse analysis is carried out. Note that both groups of methods for determination of the parameters of quasi-brittle fracture models have been studied by the authors' team for several years (see e.g. Veselý et al., 2007, 2009, 2010, and 2011).

[*] Ing. Ivana Havlíková: Brno University of Technology, Faculty of Civil Engineering, Institute of Structural Mechanics, Veveří 331/95; 602 00, Brno; CZ, e-mail: havlikova.i@fce.vutbr.cz

[**] Ing. Tomáš Pail: ditto, e-mail: pail.t@fce.vutbr.cz

[***] Ing. Václav Veselý, Ph.D.: ditto, e-mail: vesely.v1@fce.vutbr.cz

[****] Ing. Dita Vořechovská, Ph.D.: ditto, e-mail: vorechovska.d@fce.vutbr.cz

[*****] doc. Ing. Zbyněk Keršner, CSc.: ditto, e-mail: kersner.z@fce.vutbr.cz

Research into the above-mentioned effects of the characteristics of the specimen or the test has been the subject of considerable attention in recent decades. Various methods are used for the determination of the characteristics of fracture models for concrete test geometries on notched specimens; the three-point bending of notched beams or wedge-splitting of compact notched specimens (Brühwiler & Wittmann, 1990; Karihaloo, 1995) are among the most common. The model referred to as the "double *K*" (double-*K* or double-*G* – see Reinhardt & Xu, 1999, Xu & Reinhardt, 1999a, b, c; Xu et al., 2003, Xu et al. 2006, Zhao et al., 2007, Xu & Zhang, 2008; Kumar & Bara, 2009; Zhang & Xu, 2011) is similar in this respect. In principle, this model combines the concept of cohesive forces acting on the faces of the fictitious (effective) crack increment with a criterion based on the stress intensity factor (SIF). This model can determine the critical crack tip opening displacement and the fracture toughness and is capable of describing different levels of crack propagation: an initiation part, which corresponds to the beginning of stable crack growth (at the level of reaching the stress intensity factor, $K_{Ic,ini}$), and a part featuring unstable crack propagation (after reaching the unstable fracture toughness, $K_{Ic,un}$).

In this paper, a selected method of calculation exploiting the double-*K* fracture model parameters is verified using published data (Zhang & Xu, 2011). Subsequently, it is employed in processing the results of the authors' own pilot wedge-splitting test performed on a prismatic concrete specimen. Note that the shape function of the wedge-splitting test specimen used in the evaluation procedure was prepared from data published in Seitl et al. (2011).

2. Evaluation of the wedge-splitting test on concrete specimens

The geometry of a prismatic-shaped specimen for use in wedge-splitting tests (WST) is shown in Fig 1, where D is specimen depth, $2H$ is specimen width, B is specimen thickness and a_0 is the initial notch length. A sketch of the loading force decomposition is shown in Fig. 1 right and consists of applied vertical load P_V, normal reaction N, friction force F_f, horizontal force applied on the specimen P_H and wedge angle θ.

The horizontal splitting force P_H can be calculated as:

$$P_H = \frac{P_V}{2\tan\theta} \tag{1}$$

where $\theta = 15°$ in our case.

The execution of this test on a selected concrete specimen is shown in Fig. 2. The input data are summarized in Tab. 1 for two tested concrete specimens: i) data from the literature (Zhang & Xu, 2011), denoted as Specimen 1, and ii) data from the authors' own afore-mentioned pilot wedge-splitting experiment (Specimen 2).

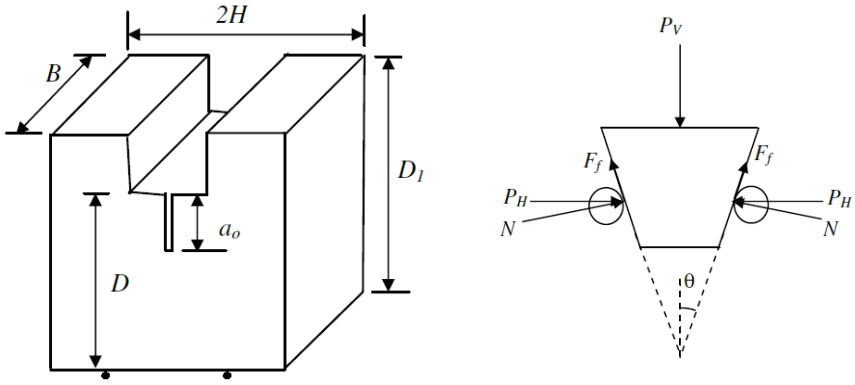

Fig. 1: Specimen geometry and force diagram.

Fig. 2: Wedge-splitting test configuration and a detail of a cracked concrete specimen (photo by Táňa Holušová).

Tab. 1: Input parameters.

Parameter	Symbol	Unit	Specimen 1	Specimen 2
Depth	D	mm	200	130
Width	$2H$	mm	200	150
Thickness	B	mm	199	70
Notch depth	a_0	mm	80	25
Thickness of holder	H_0	mm	2	5
Load from the linear part	P_i	N	7856	2799
Crack mouth opening displacement for P_i	$CMOD_i$	mm	0.026	0.117
Maximum load	P_{max}	N	10023	4443
Crack mouth opening displacement for P_{max}	$CMOD_c$	mm	0.0898	0.2386

2.1. Calculation of double-*K* fracture parameters

The analytical method for WST was developed (Xu & Reinhardt, 1999c) as an alternative to the experimental approach (Xu & Reinhardt, 1999a) used to assess double-*K* fracture toughness parameters. This procedure is based on a linear asymptotic superposition assumption (Xu & Reinhardt, 1999b) and requires numerical investigation of the cohesive toughness $K_{Ic,c}$, which represents the growth of unstable fracture toughness $K_{Ic,un}$ above the level of the initiation fracture toughness $K_{Ic,ini}$ due to cohesive stress transfer in the fictitious crack zone. This relation is given by the equation:

$$K_{Ic}^{un} = K_{Ic}^{ini} + K_{Ic}^{c} \tag{2}$$

and can be explained as an increase in the crack resistance caused by aggregates interlocking in the fracture process zone (FPZ) located in front of the stress-free crack tip. Once the cohesive toughness $K_{Ic,c}$ is solved analytically, the value of $K_{Ic,ini}$ can be evaluated by Eq. (2) and therefore it is only necessary to obtain a smaller number of measured parameters from a recorded *P–CMOD* diagram in comparison with the experimental approach.

2.1.1. Determination of the unstable fracture toughness $K_{Ic,un}$

The unstable fracture toughness $K_{Ic,un}$ is defined as the critical stress intensity factor created by the maximum load P_{max} at the effective crack tip and can be expressed as the resistance to unstable crack

propagation. To evaluate this parameter one can use the following linear elastic fracture mechanics (LEFM) formula (Xu & Reinhardt, 1999a, b, c):

$$K_{\mathrm{Ic}}^{un} = \frac{P_{\max}}{BD}\sqrt{D}F\left(\alpha_c = \frac{a_c + H_0}{D + H_0}\right) \tag{3}$$

$$F(\alpha_c) = \frac{(2+\alpha_c)(0.886 + 4.64\alpha_c - 13.32\alpha_c^2 + 14.72\alpha_c^3 - 5.6\alpha_c^4)}{(1-\alpha_c)^{3/2}} \tag{4}$$

where the maximum load $P_{\max}$ and the critical effective crack length a_c are the input parameters readily obtained from the measured *P–CMOD* diagram, H_0 represents the thickness of the clip extensometer holder and B, D are the specimen dimensions according to Fig. 1.

To evaluate Eq. (4) it is necessary to evaluate the critical effective crack length a_c at the unstable loading condition ($P_{\max}$) by solving the following nonlinear equation proposed by Murakami (1987):

$$CMOD_c = \frac{P_{\max}}{BE}V\left(\alpha_c = \frac{a_c + H_0}{D + H_0}\right) \tag{5}$$

$$V(\alpha_c) = \left[2.163 + 12.219\alpha_c - 20.065{\alpha_c}^2 - 0.9925{\alpha_c}^3 + 20.609{\alpha_c}^4 - 9.9314{\alpha_c}^5\right] \times \left(\frac{1+\alpha_c}{1-\alpha_c}\right)^2 \tag{6}$$

where $CMOD_c$ is the critical crack mouth opening displacement due to the maximum load $P_{\max}$ and E is Young's modulus, which can be determined either through a compressive cylinder test or through the calculation method given in the RILEM recommendation (RILEM, 1990).

2.1.2. Determination of cohesive fracture toughness $K_{\mathrm{Ic},c}$

The cohesive fracture toughness can be described as the energy dissipated by cohesive forces distributed along the critical fictitious crack zone. To calculate the cohesive fracture toughness $K_{\mathrm{Ic},c}$, bilinear distribution of the cohesive stress is assumed. Generally, the cohesive stress function $\sigma(w)$ expresses the relation between the cohesive stress σ and the fictitious crack opening displacement w. Four parameters are necessary to uniquely define this function, namely the tensile strength f_t, the cohesive stress σ_s, the crack opening displacement w_s at the slope discontinuity of the bilinear curve, and the critical crack opening displacement w_0 at which the cohesive stress σ drops to zero. These four parameters can be determined using expressions given e.g. in the CEB-FIP design code. The following parameter values of the bilinear cohesive stress function were used in this paper: f_t = 3.546 MPa, σ_s = 0.599 MPa, w_s = 0.02363 mm and w_0 = 0.16177.

At the maximal load $P_{\max}$ the crack becomes unstable and the corresponding opening at the tip of the stress-free crack (the origin of the fictitious crack) is termed the critical crack tip opening displacement, $CTOD_c$. Depending on the value of $CTOD_c$, two cases exist for the cohesive stress distribution along the fictitious crack length at the critical state (Zhang & Xu, 2011).

Case I is supposed to hold for $CTOD_c < w_s$, and the corresponding distribution of cohesive stress in the FPZ is linearly distributed according to the formula:

$$\sigma_1(x) = \sigma(CTOD_c) + \frac{x - a_0}{a_c - a_0}\left(f_t - \sigma(CTOD_c)\right) \tag{7}$$

where $\sigma(CTOD_c)$ is the cohesive stress at the tip of the initial crack with the length a_0 at the critical state. This can be obtained using Eq. (8) according to the cohesive stress function:

$$\sigma(CTOD_c) = \sigma_s(w_s) + \frac{w_s - CTOD_c}{w_s}\left(f_t - \sigma_s(w_s)\right) \tag{8}$$

Case II is supposed to hold when $w_s < CTOD_c < w_0$, and in this case, the corresponding cohesive stress distribution is bilinear and can be expressed for $a_0 \le x \le a_s$ as:

$$\sigma_2(x) = \sigma(CTOD_c) + \frac{x - a_0}{a_s - a_0}\left(\sigma_s(w_s) - \sigma(CTOD_c)\right) \qquad (9)$$

or for $a_s \le x \le a_c$ this can be rewritten as:

$$\sigma_3(x) = \sigma_s(w_s) + \frac{x - a_s}{a_c - a_s}\left(f_t - \sigma_s(w_s)\right) \qquad (10)$$

where, in both equations, $\sigma_s(w_s)$ is the cohesive stress corresponding to the crack opening displacement w_s, f_t is the tensile strength, a_0 is the initial notch depth (initial crack length) and a_s is the effective crack length corresponding to $CTOD = w_s$, which can be obtained by solving the following nonlinear equation:

$$w_s = CMOD_c\left(\left(1 - \frac{a_s}{a_c}\right)^2 + \left(1.081 - 1.149\frac{a_c}{D}\right)\left(\frac{a_s}{a_c} - \left(\frac{a_s}{a_c}\right)^2\right)\right)^{1/2} \qquad (11)$$

In Eq. (11) $CMOD_c$ is the crack opening mouth displacement at the critical point, D is the specimen depth according to Fig. 1 and a_c is the critical effective length mentioned above.

Once the distribution of cohesive stress in the FPZ is known, one can calculate the cohesive fracture toughness $K_{Ic,c}$ by integrating the following expression:

$$K_{Ic}^{c} = \int_{a_0/a_c}^{1} \frac{2\sqrt{a_c}}{\sqrt{\pi}}\sigma(U)F(U,V)dU \qquad (12)$$

where $F(U,V) = \frac{3.52(1-U)}{(1-V)^{3/2}} - \frac{4.35 - 5.28U}{(1-V)^{1/2}} + \left(\frac{1.30 - 0.30U^{3/2}}{\left(1-U^2\right)^{1/2}} + 0.83 - 1.76U\right)\left[1 - (1-U)V\right]$ (13)

and where the substitutions $U=x/a_c$, $V=a_c/D$ are used: $\sigma(U)$ is the cohesive stress according to formulas (7, 9, 10) and $F(U,V)$ is the characteristic Green function. To evaluate Eq. (12) a special numerical integration method is necessary to handle the singularity at the integral boundary.

2.2. Results of calculations

This paper is primarily focused on the functionality of the double-*K* fracture model. The results of the calculations of the values of selected parameters of this model can be found in Tab. 2. The values in parentheses for "Specimen 1" are taken from Zhang & Xu (2011).

Tab. 2: The resulting values.

Parameter	Symbol	Unit	Specimen 1	Specimen 2
Critical effective crack length	a_c	mm	119.59 (119.84)	31.62
SIF (unstable fracture)	K_{Ic}^{un}	MPa·m$^{1/2}$	1.557 (1.557)	0.918
SIF (cohesive toughness)	K_{Ic}^{c}	MPa·m$^{1/2}$	0.868 (0.885)	0.141
SIF (initiation toughness)	K_{Ic}^{ini}	MPa·m$^{1/2}$	0.689 (0.672)	0.777
Critical crack tip opening	$CTOD_c$	mm	0.03992 (0.03938)	0.101

3. Conclusions

The concept of the double-*K* fracture model is not currently used in the Czech Republic (except for in a study reported in the paper Keršner & Matesová (2001), which focused on three-point bending of

notched prismatic concrete specimens), but the worldwide scientific and professional public interest in this model has recently been increasing. A technical committee (TC) of the RILEM international fellowship (International Union of Laboratories and Experts in Construction Materials, Systems and Structures), related to the double-*K* concept and headed by Prof. Shilang Xu and Dr. Shailendra Kumar, was established in October 2011. The task of the new technical committee is to examine the crack stability criteria related to the double-*K* fracture model, whose use has been shown to be independent of the sample size, and on the basis of further extensive experimental and numerical verification, to attempt to prepare a RILEM document which will be usable for international standardization activities in the field of concrete and concrete structures. Note that the double-*K* model criteria are used to assess the safety of large concrete structures (dams) in Chinese national standard No. DL/T5332-2005, issued in 2005.

In this paper, the utilization and results of a method for calculation of the double-*K* fracture model parameters were shown. The procedure was programmed and verified using published data and the results of the authors' own pilot wedge-splitting test. The applicability of the used approach was demonstrated via the comparison of the evaluated results of WST experiments on prismatic-shaped concrete specimen with published data.

Acknowledgement

This outcome has been achieved with the financial support of the Czech Scientific Foundation, project No. P104/11/0833, and of the Ministry of Education of the Czech Republic, project No. MSM0021630519.

References

Bažant, Z. P. & Planas, J. (1998) *Fracture and Size Effect in Concrete and other Quasibrittle Materials*. CRC Press, Boca Raton, Florida.

Červenka, V., Jendele, L. & Červenka, J. (2007) *ATENA Program documentation – Part 1: theory*. Červenka Consulting, Prague.

Brühwiler, E. & Wittmann, F. H. (1990) The wedge splitting test, a new method of performing stable fracture mechanics tests. *Engineering fracture mechanics*, Vol. 35, 117–125.

Frantík, P. (2007) FyDiK application, http://www.kitnarf.cz/fydik, 2007–2011.

Karihaloo, B. L. (1995) *Fracture mechanics of concrete*. Longman Scientific & Technical, New York.

Keršner, Z. & Matesová, D. (2001) Jak funguje model „dvojí K" u betonových vzorků. Sborník *Problémy lomové mechaniky*, Brno, 60–63, ISBN 80-214-1906-7. In Czech.

Kumar, S. & Barai, S. V. (2009) Equivalence between stress intensity factor and energy approach based fracture parameters of concrete. *Engineering Fracture Mechanics.* 76:1357–1372.

Murakami, Y. (1987) *Stress Intensity Factor Handbook I, II, III*. Pergamon Press, Oxford.

Reinhardt, H. W. & Xu, S. (1999) Crack extension resistance based on the cohesive force in concrete. *Engineering Fracture Mechanics.* 64:563–587.

RILEM Committee FMT 50 (1985) Determination of the fracture energy of mortar and concrete by means of three-point bend test on notched beams. *Mater. Struct*., 18, 285–290.

RILEM Committee FMT 89 (1990) Size effect method for determining fracture energy and process zone size of concrete. *Mater. Struct*., 23, 461–465.

Seitl, S., Veselý, V. & Řoutil, L. (2011) Two-parameter fracture mechanical analysis of a near-crack-tip stress field in wedge splitting test specimen. *Computers and Structures*, 89, 1852–1858

Shah, S. P., Swartz, S.E. & Ouyang, Ch. (1995) *Fracture mechanics of structural concrete: applications of fracture mechanics to concrete, rock, and other quasi-brittle materials*. John Wiley & Sons, Inc., New York.

Štafa, M. & Frantík, P. (2010) Model for high precision approximation of load deflection diagrams. In: Proc. of conference *Engineering Mechanics 2010*, Svratka. ISBN 978-80-87012-26-0.

Veselý, V., Frantík, P. & Keršner, Z. (2009) Cracked volume specified work of fracture. In B.H.V. Topping, L.F. Costa Neves and R.C. Barros (eds), *Proc. of 12th Int. Conf. on Civil, Structural and Environmental Engineering Computing*, Funchal, 2009. Civil-Comp Press.

Veselý, V., Keršner, Z., Němeček, J., Frantík, P., Řoutil, L. & Kucharczyková, B. (2010) Estimation of fracture process zone extent in cementitious composites. *Chemické Listy*, vol. 104 (2010), s382–s385. ISSN 0009-2770.

Veselý, V., Řoutil, L. & Keršner, Z. (2007) Structural geometry, fracture process zone and fracture energy. In: Carpinteri Al., Gambarova, P., Ferro, G., Plizzari, G. (eds.), *Proc. of Fracture Mechanics of Concrete and Concrete Structures (FraMCoS-6)*, Catania, Italy, 2007. Taylor & Francis/Balkema, vol. 1, 111–118.

Veselý, V., Řoutil, L. & Seitl, S. (2011) Wedge-Splitting Test – Determination of Minimal Starting Notch Length for Various Cement Based Composites. *Key Engineering Materials*, Vol. 452-453, 77–80.

Xu, S. & Reinhardt, H. W. (1999a) Determination of double-K criterion for crack propagation in quasi-brittle fracture, Part I: Experimental investigation of crack propagation. *International Journal of Fracture.* 98:111–149.

Xu, S. & Reinhardt, H. W. (1999b) Determination of double-K criterion for crack propagation in quasi-brittle fracture, Part II: Analytical evaluating and practical measuring methods for three-point bending notched beams. *International Journal of Fracture.* 98:151–177.

Xu, S. & Reinhardt, H. W. (1999c) Determination of double-K criterion for crack propagation in quasi-brittle fracture, Part III: Compact tension specimens and wedge splitting specimens. *International Journal of Fracture.* 98:179–193.

Xu, S., Reinhardt, H. W., Wu, Z. & Zhao, Y. (2003) Comparison between the double-K fracture model and the two parameter fracture model. *Otto-Graf-Journal.* Vol. 14, 131–158.

Xu, S. & Zhang, X. (2008) Determination of fracture parameters for crack propagation in concrete using an energy approach. *Engineering Fracture Mechanics.* 75:4292–4308.

Xu, S., Zhao, Y. & Wu, Z. (2006) Study on the average fracture energy for crack propagation in concrete. *Journal of Materials in Civil Engineering.* 817–824.

Zhang, X. & Xu, S. (2011) A comparative study on five approaches to evaluate double-K fracture toughness parameters of concrete and size effect analysis. *Engineering Fracture Mechanics.* 78:2115–2138.

Zhao, Y., Xu, S. & Wu, Z. (2007) Variation of fracture energy dissipation along evolving fracture process zones in concrete. *Journal of Materials in Civil Engineering.* 625–633.

18th International Conference
ENGINEERING MECHANICS 2012
Svratka, Czech Republic, May 14 – 17, 2012

pp. 391–397
Paper #211

FRACTURE PROPERTIES OF CEMENTITIOUS COMPOSITES REINFORCED WITH CARBON NANOFIBERS/NANOTUBES

P. Hlaváček[*], V. Šmilauer[**]

Abstract: *The main objective of this work is to determine the mechanical properties of a new cementitious nano-composite material. Carbon nanotubes/nanofibers were synthesized directly on the particle surfaces (Portland cement, fly ash, sand). Mixing these carbon-modified particles with ordinary Portland cement creates a cementitious binder, where the carbon nanofibers are perfectly dispersed in the volume. Previous attempts to create nano-reinforced composite materials suffered from flocculation and improper dispersion of admixed nanofibers. Now, the hybrid material can be intermixed directly with water creating strong and brittle composite.*

Keywords: ***Carbon, nanotubes, mortar, paste, fracture energy***

1. Introduction

The main objective of this work is to determine the mechanical properties of the cement paste/mortar reinforced with carbon nanofibres/nanotubes (CNF/CNT) directly synthesized on the cement and sand particles. The synthesis of the CNF/CNT directly on the particles surface brings the advantage in elimination of the tedious dispersion process. The cement hybrid material (CHM – cement with carbon nanofibers) can be directly mixed with water and/or sand, creating a strong and quasi-brittle composite material. Fig. 1 shows the SEM image of the CHM, the Portland cement particles are completely covered with the CNF.

CNT/CNF reinforcement on the nanoscale brought fruitful results for a variety of materials (Hammel et al., 2004). Previous experiments have shown the twofold increase of paste compressive strength (Nasibulina et al., 2010). This would imply reduction of cementitious binders in ordinary concrete in a similar manner as replacement by supplementary cementitious materials. Unfortunately, several experiments are carried out by physicists, who are unfamiliar with cement science. The consequence is in improperly-conducted experiments which are hardly reproducible in their labs and worldwide. Experimental evidence still presents the basis of scientific approach and the reproducibility forms the stepping stone in science. This is another goal of presented article.

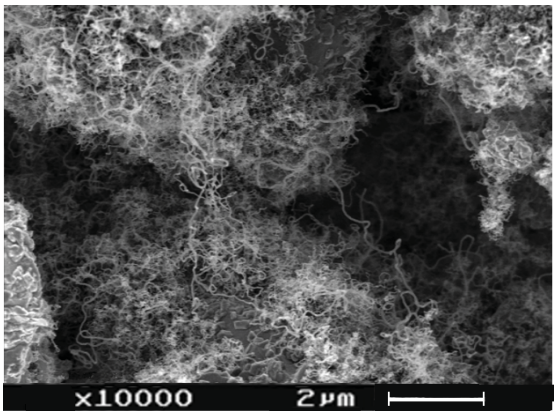

Fig 1. SEM image of the CNF synthesized directly on the cement grains surface. Reprinted from L. Nasibulina et al. (2010).

To elucidate the effect CNF/CNT on surfaces, two batches from CHM and modified sand were prepared. Samples in the first batch were prepared from the CHM and water in the case of paste, or CHM, water and unmodified sand in the case of

[*] Ing. Petr Hlaváček: Faculty of Civil Engineering, Czech Technical University in Prague; Thákurova 7; 166 29, Prague 6; CZ, e-mail: petr.hlavacek@fsv.cvut.cz

[**] doc. Ing. Vít Šmilauer, Ph.D.: Faculty of Civil Engineering, Czech Technical University in Prague; Thákurova 7; 166 29, Prague 6; CZ, e-mail: vit.smilauer@fsv.cvut.cz

mortar. The second batch was fabricated from ordinary Portland cement, water and sand with surface synthesized carbon nanofibers.

Fracture energies and compressive strengths of these cement-based composites were determined. It was found that for the case of CHM batch, the compressive strength of the cement paste increases with the amount of CHM in the mixture. On the contrary, the compressive strength of mortar decreases with the amount of CHM in the mixture. This phenomenon is partially explained by the ITZ behavior and CHM properties. The measurements on the second batch show almost no change in the fracture energy with the addition of carbon-modified sand. The explanation lies in a small length of the CNF/CNT (about two μm) compared to the length of ITZ (about 20 μm).

2. Materials and methods

2.1. Cement binder, CHM, sand

The cement, CEM I 42.5 R originated from Mokrá, the Czech Republic, was used as the source material for all specimens. Specific Blaine surface had the value of 355 m^2/kg for the coarse cement and 587 m^2/kg for finely-ground cement. The chemical composition is given in the Table 1.

The cement hybrid material (CHM) and the carbon-modified sand were synthesized by L. Nasibulina et al. by the chemical vapor deposition method (Nasibulina et al., 2010). The Portland sulfate-resistant cement (CEM I 42.5N) was used as the base for CNF/CNT growth resulting in CHM, see Table 1 for the chemical composition. In the synthesis, acetylene was utilized as the main carbon source for its low decomposition temperature and affordability; CO and CO_2 presents promoting additives (Nasibulina et al., 2010). The CNF/CNT growth runs at temperature about 600°C in fluidized bed reactor see Fig. 2 for the scheme of the reactor. The CNT typically grown on the cement particles are 30 nm in diameter and 3 μm in length (La Mudimela et al., 2009), the specific surface area of CNT is about 10 – 20 m^2/g. CNT exhibit elastic modulus in the range of 180 - 588 GPa and tensile strength from 2 to 6 GPa (La Mudimela et al., 2009; Li et al., 2005).

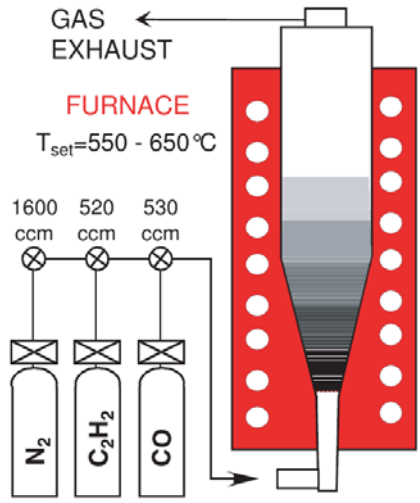

Fig 2. Scheme of the fluidized bed reactor, overtaken from L. Nasibulina et al. (2010).

Table 1: Oxide Component Content of CHM Base Cement and Cement originated from Mokrá

Component	Content (wt%)	
	CHM-Base Cement	Mokrá Cement
CaO	63.1	65.6
SiO2	20.2	19.0
SO3	3.0	4.0
Fe2O3	4.0	3.5
Al2O3	2.2	5.0
MgO	2.0	1.1
K2O	0.3	1.1
Na2O	0.5	0.1

In the batch with CHM, pure silica sand with the fraction 0 – 2 mm, was utilized in the mortar specimens. Three fractions PG1 (0 – 0.25 mm), PG2 (0.25 – 1 mm) and PG3 (1 – 2 mm) were mixed in the ratio 1:1:1. In the batch with carbon-modified sand, sand fraction 0 – 1 mm was mixed with the carbon modified sand in the mass ratio 0 – 0.3.

2.2. Specimen preparation

Two sets of samples were prepared and cast into steel form:

- Cement grains with synthesized carbon nanotubes – Five cement paste sets and five mortar sets were cast. The water/binder ratio was set to 0.35 and the carbon nanotubes/paste ratio varied from 0.0 to 0.038. The CHM was intermixed with the pure cement and (in case of mortar) with the dry silica sand; the water with superplasticizer was added at the end. Table 2 shows the batch compositions.
- Sand particles with synthesized carbon nanotubes – Five sets with the coarse cement and five sets with the fine cement were cast. The water/binder ratio was set to 0.5 and the carbon-modified sand/mortar ratio varied from 0.0 to 0.2. The Portland cement was intermixed with dry sand and carbon-modified sand; the water with superplasticizer was added at the end. Table 3 shows the batch compositions.

Table 2: Carbon-modified cement paste and mortar composition; weight fractions per one sample.

Sample		Total binder weight	Cement hybrid material	Water/ binder ratio	Total water weight	Super plasticizer (63% water)	Sand fraction 0 - 2 mm
CHM	Paste	234 g	0 - 70 g	0.35	81.9 g	0.47 g	–
	Mortar	75 g	0 - 22.5 g	0.35	26.25 g	0.38 g	225 g

Table 3: Carbon-modified sand mortar composition; weight fractions per one sample GC - ground cement, Blaine surface 587 m^2/kg, RC – raw cement 355 m^2/kg.

Sample		Total binder weight	Fine cement	Water/ binder ratio	Total water weight	Super plasticizer (63% water)	Sand fraction 0 - 1 mm	Carbon – modified cement
Carbon–modified sand	Mortar RC	75 g	–	0.5	37.5 g	0.3 g	157.5 – 225 g	0 – 67.5 g
	Mortar GC	75 g	75 g	0.5	37.5 g	0.3 g	157.5 – 225 g	0 – 67.5 g

Hand stirring of each specimen took four minutes, consecutive vibrating and form filling took extra four minutes. The specimens sized 40x40x80 mm were cured in the water bath at ambient temperature.

After 28 days of curing, the specimens were cut on diamond saw; in the case of the paste specimens were cut to nine parts (approx. 13x13x80 mm), in the case of mortar to four parts (approx. 19x19x80 mm). According to RILEM standards for mechanical testing (RILEM, 1985) notches were sawn in the middle of the beams to the 45% of the height. The production of such small-sized specimens is much more efficient than direct casting into small molds. The casting and vibration of small amount of material is ineffective and the quality of specimens (including surface defects or material inhomogenity) is significantly worse than the quality reached by cutting from larger bodies.

2.3. Assessment of fracture energy

The fracture energy, G_f, was determined according to the RILEM standard (1985). See Fig. 3 for the experiment scheme. Three point displacement-controlled bending test was carried out to obtain the load-displacement curve. The work of external force P could be calculated as

$$W_f = \int_0^{u_i} P du \tag{1}$$

where P is the external force, u is the load-point displacement and u_i presents the final displacement at which the load is equal to zero. The average (effective) fracture energy in the ligament, according to the RILEM standart, is defined as

$$G_f = \frac{W_f}{bl}, \quad l = d - a_0 \tag{2}$$

where l represents the length of the ligament, b the thickness of the beam, d the total height of the beam and a_0 is the depth of the nodge. The support span L was in case of mortar set to 65 mm and in case of cement paste set to 50 mm.

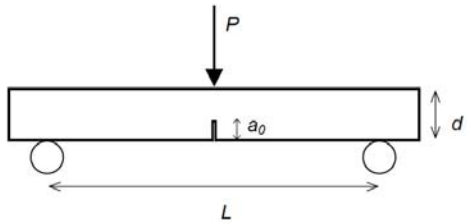

Fig. 3 Scheme of the three point bending test used for the fracture energy determination.

3. Results and discussion

3.1. Compressive strength

The results on the CHM-based paste samples show that replacing 3.5% cement with the CHM could increase the compressive strength by 25%, in our case from the average value of 56 MPa to the average 70 MPa. However, in the case of CHM-based mortar samples, the increase of CHM led to decrease of compressive strength. The mortar samples with 7% replaced cement exhibit a 15% lower

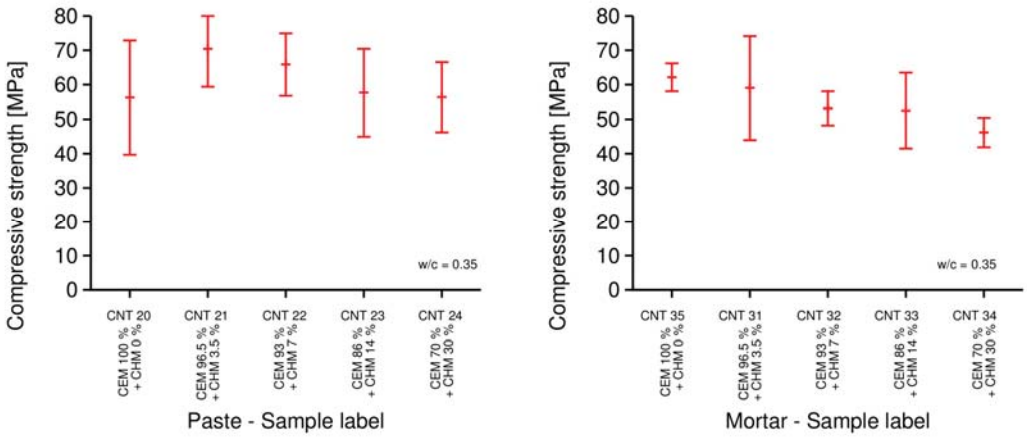

Fig 4. Compressive strength of mortar and paste samples with different cement/CHM ratii.

compressive strength, in our case decrease from the average of 62 MPa to the average of 53 MPa. See Fig. 4 for the compressive strengths of mortar and paste samples with different cement/CHM ratii.

The results on the mortar made from fine cement with the carbon-modified sand show that replacing 30% of sand with the carbon modified sand could increase the compressive strength by 25%, in our case from the average value of 44 MPa to the average 58 MPa. It should be noticed, that the compressive strength of the mortar based on the coarse cement with unmodified sand is 57 MPa. See Fig. 5 for the compressive strengths of mortar samples with different mass ratii of carbon modified sand/raw sand.

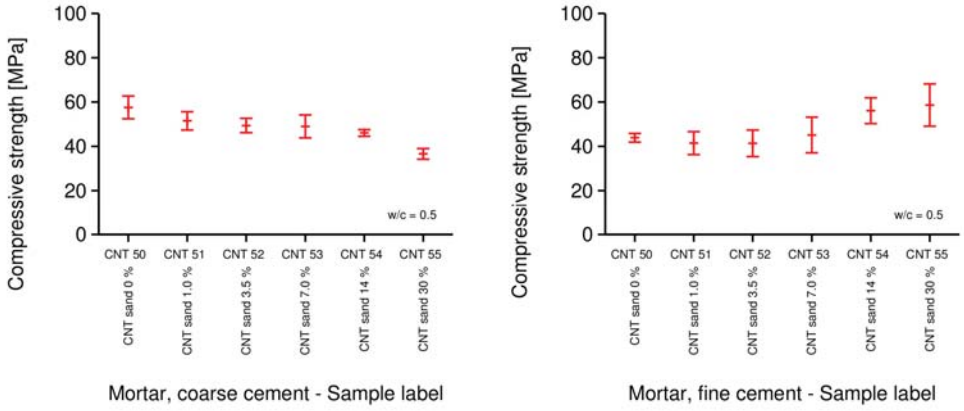

Fig.5 Compressive strength of mortar with different weight ratii of carbon modified sand/raw sand, left coarse cement, right fine cement.

3.2. Fracture energy

The fracture energy results are depicted in the Figs. 6 and 7. The CHM paste samples exhibit a significant increase in the fracture energy even in a small amount of cement replacement by CHM. Replacing 3.5% of cement causes an increase in the fracture energy by 14%. The mortar CHM samples do not exhibit almost any change in the fracture energy. The mortars prepared from carbon-modified sand and from the finely ground cement exhibit slight increase in the fracture energy.

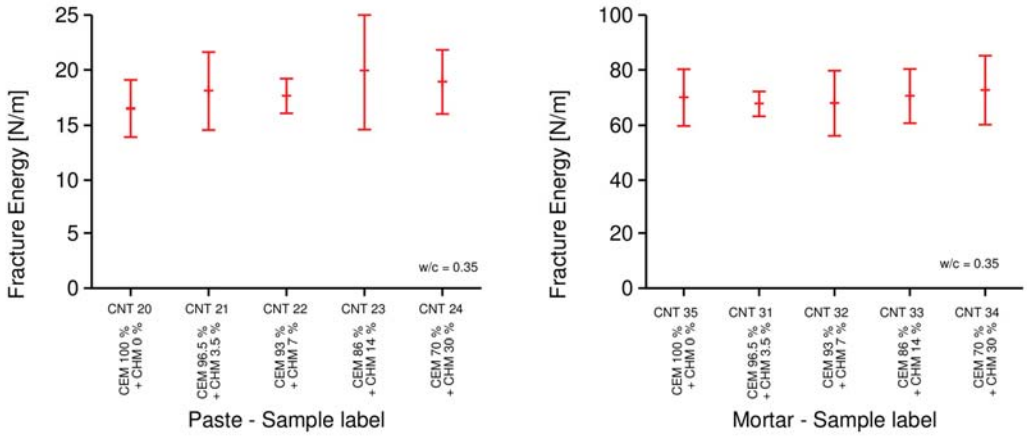

Fig.6 Fracture energy of CHM-based paste and mortar samples with different cement/CHM ratii.

3.3 Discussion and hypotheses

Let us introduce some hypotheses partially explaining the behavior of cement paste/mortar with the CHM. The paste samples reinforced with the CNT/CNF exhibit the expected increase in the compressive strength as well as in the fracture energy. Raki et al. (2010) hypothesized that the CNT act as a nano-reinforcement agent improving the C-S-H gel properties. Makar & Chan (2010) thought that the carbon nanotubes appear as nucleating sites for the cement hydration product.

In the case of the carbon-modified cement, the decrease in compressive strength on CNT-reinforced mortar samples could be caused by the higher amount of water in the ITZ which was pushed out by the extremely hydrophobic carbon nanotubes. Preliminary experiments with high compacted (60 MPa) mortar samples with the w/c ratio 0.35 do not exhibit the compressive strength reduction.

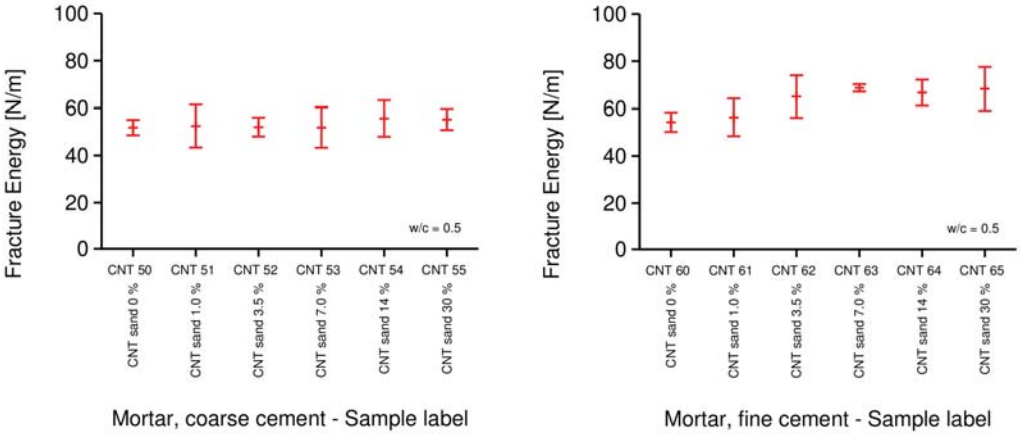

Fig.7 Fracture energy of mortar with different weight ratii of carbon modified sand/raw sand, left coarse cement, right fine cement.

From calorimetric tests carried out at our laboratory is evident, that the CNT/CNF does not affect the long-term (understand days) reaction kinetics, and do not prevent the cement particles from hydration.

The changes in the compressive strengths from the Figure 5 required additional measurements of density to identify the source of strength gain. The plot of compressive strength of all mortar samples versus the density is given in Figure 8. As is obvious from this figure, the mortars prepared from the carbon-modified sand do not exhibit any evident effect of CNT to the compressive strength and all the changes from Figure 5 could be explained by different densities of the samples.

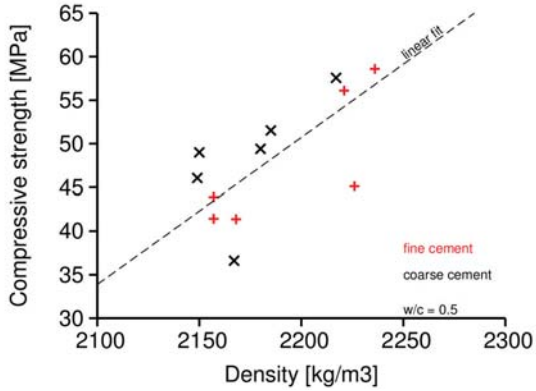

Fig.8 Dependence of compressive strength on density of mortar from carbon-modified sand.

The increase in the fracture energy for the fine-cement mortar with the carbon-modified sand (Figure 7 left) compared with no change in the fracture energy for the coarse-cement mortar (Figure 7 right) indicates a small length of the CNT. Meaning the CNT are unable to bridge the ITZ in the case of coarse-cement mortar. The ITZ closely corresponds to the cement particles mean diameter, which can be recalculated from the Blaine surface. The ITZ corresponds to 20 μm for the coarse cement (Blaine 355 m^2/kg) and, 3-4 μm for the fine cement (Blaine 587 m^2/kg). Since the CNT are only about 2 μm long they have no chance to improve the micromechanical properties of the ITZ in the case of the coarse cement. On the other hand this CNT can help in the case of the finely ground cement.

4. Conclusion

The cement pastes/mortars reinforced with CNT/CNF directly synthesized on the surface of the cement grains exhibit comparable mechanical properties as the cement pastes/mortars reinforced with the separately added carbon nanotubes as introduced in Metaxa et al. (2010). Previous attempts to create nano-reinforced composite materials suffered from the flocculation and improper dispersion of separately added nanofibers/nanotubes. The main advantage of this new method presents the elimination of the demanding CNT/CNF dispersion; now, the hybrid material can be intermixed directly with water and/or sand, creating a strong and quasi-brittle composite similar to ordinary cement paste/mortar.

Since we have not proven any evident effect of CNT/CNF to the compressive strength of mortar, dare we say that our results are in strong contrary to the measurements of Ludvig et al. (2011) and Nasibulina et al. (2010), who published a 2-3x increase in compressive strength of mortar when the CNT/CNF are used. Unfortunately these sources do not provide densities or porosities of the measured samples and thus the results remain questionable.

Acknowledgement

Authors gratefully acknowledge support from the Czech Science Foundation under grant GAČR 103/09/H078 and from the Czech Technical University in Prague under grant No. SGS12/116/OHK1/2T/11.

References

Nasibulina, L. et al. (2010) Direct Synthesis of Carbon Nanofibers on Cement Particles. *Journal of the Transportation Research Board*, No. 2142, 96-101, doi:10.3141/2142-14.

Hammel, E., et al. (2004) Carbon nanofibers for composite applications. *Carbon*; 42; 1153 –1158.

La Mudimela, P. et al. (2009) Synthesis of carbon nanotubes and nanofibers on silica and cement matrix materials. *Journal of Nanomaterials*, doi:10.1155/2009/526128.

Li, G.Y., Wang, P.M. & Zhao, X. (2005) Mechanical behavior and microstructure of cement. *Carbon*, 43, 1239–1245.

RILEM TCS, (1985) RILEM Determination of the fracture energy of mortar and concrete by means of three-pointbend tests on notched beams. *Materials and Structures*, vol. 18, issue 106, 285-290.

Raki, L. et al. (2010) Cement and Concrete Nanoscience and Nanotechnology. *Materials*, vol. 3, 918-942; doi:10.3390/ma3020918.

Makar, J.M. & Chan, G.W. (2009) Growth of Cement Hydration Products on Single-Walled Carbon Nanotubes. *Journal of the American Ceramic Society*, 92, (6), pp. 1303-1310, DOI: 10.1111/j.1551-2916.2009.03055.x.

Metaxa, Z.S., Konsta-Gdoutos, M.S. & Shan, S.P. (2010) Mechanical Properties and Nanostructure of Cement-Based Materials Reinforced with Carbon Nanofibers and Polyvinyl Alcohol (PVA) Microfibers. *Advances in the Material Science of Concrete*, SP-270—10.

Ludvig, P. et al. (2011) Tailoring the innate properties of Portland cement: the application of carbon nanotubes. *7th Central European Congress on Concrete Engineering*, Balatonfüred.

18th International Conference
ENGINEERING MECHANICS 2012
Svratka, Czech Republic, May 14 – 17, 2012

pp. 399–402
Paper #161

FEM SIMULATION OF AN INTEGRATED LONGITUDINAL AND TANGENTIAL WAVE PROBE

P. Hora [*], **O. Červená** [**]

Abstract: *The aim of contribution is the finite element modeling of integrated longitudinal and shear wave probe. This type of probe was investigated by Cheng-Kuei Jen and Makiko Kobayashi in Jen (2007). Finite element calculations are performed in the commercial environment COMSOL Multiphysics. The ultrasonic transducer excitation was modeled as total force load. The received ultrasonic signal was obtained by integration of velocities at place of ultrasonic transducer. Though these simplifications the resulting ultrasonic signals are in good agreement with results presented by Cheng-Kuei Jen and Makiko Kobayashi.*

Keywords: ***Ultrasonic probe, FEM modeling.***

1. Introduction

Non-destructive testing (NDT) of materials are commonly performed to identify and characterize of defects and damage in metals, metal alloys, composites and other materials. Furthermore, the increasing demand to improve the performance, increase reliability and extend the life of transportation vehicles, structures and engineering systems, requires the use of systems that have integrated capabilities with built-in sensors that perceive and process in-service information and take actions to accomplish desired operations and tasks. It is established that ultrasonic methods are widely used for real-time, in-situ or off-line NDT and evaluation of large metallic and composite structures including airplanes, pressure vessels and pipelines, Kundu (2004).

Because of their subsurface inspection capability, elastic property characterization ability, fast inspection speed, simplicity and cost-effectiveness, there has been considerable interest in ultrasonic NDT. Common limitations of current piezoelectric ultrasonic transducers (UT) are (a) lack of suitability for use on curved surfaces and (b) the difficulty for use at temperatures higher than 100°C. Therefore the objective of this investigation is to develop integrated longitudinal, shear, Rayleigh surface and Lamb plate acoustic wave transducers and flexible high temperature UT operated at least up to 150°C, Jen (2007).

2. Integrated longitudinal and shear wave probe

Various efforts have been devoted to the development of piezoelectric UTs of large bandwidth and high efficiency and they may be supplied by several companies. However, it is understood that S waves may be advantageous over P waves for NDT and characterization of materials because liquid and gas medium do not support S waves. In addition, for the evaluation of material properties, sometimes it is important to measure shear modulus and viscoelastic properties in which S wave properties are a requisite. Furthermore, a UT setup to generate and receive both P and S waves at the same sensor location would be also of interest.

The mode conversion from P to S wave due to reflection at a solid-air interface was reported in Achenbach (1973); Graff (1975). It means that the P wave UT together with P-S mode conversion caused by the reflection at a solid-air interface can be effectively used as a S wave probe as shown in Fig. 1. P waves in this figure generated by an P wave UT reach a solid-air interface and reflected as PP

[*]Doc. Ing. Petr Hora, CSc.: Institute of Thermomechanics AS CR, v. v. i., Dolejškova 1402/5; 182 00, Prague; CZ, e-mail: hora@cdm.it.cas.cz
[**]RNDr. Olga Červená: Institute of Thermomechanics AS CR, v. v. i., Dolejškova 1402/5; 182 00, Prague; CZ, e-mail: cervena@cdm.it.cas.cz

and PS waves. The equations governing the reflection and mode conversion with respect to the P wave incident angle α can be given in Eqs.1-3, Achenbach (1973); Graff (1975), where c_1 and c_2 are P and S wave velocities in the solid, respectively, and R_{PP} and R_{PS} are energy reflection coefficients of the P and S waves, respectively.

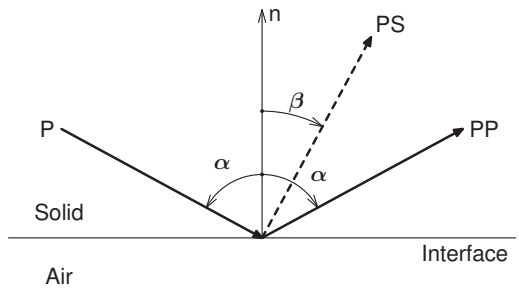

Fig. 1: Reflection and mode conversion wave at solid–air interface.

$$\frac{c_1}{\sin\alpha} = \frac{c_2}{\sin\beta} \tag{1}$$

$$R_{PP} = \left(\frac{\cos^2 2\beta - (c_2/c_1)^2 \sin 2\alpha \sin 2\beta}{\cos^2 2\beta + (c_2/c_1)^2 \sin 2\beta \sin 2\alpha} \right)^2 \tag{2}$$

$$R_{PS} = \frac{4\,(c_2/c_1)^2 \cos^2 2\beta \sin 2\alpha \sin 2\beta}{\left(\cos^2 2\beta + (c_2/c_1)^2 \sin 2\beta \sin 2\alpha \right)^2} \tag{3}$$

In this study, a steel with the P wave velocity c_1 = 5770.8 m/s and S wave velocity c_2 = 3138.5 m/s at room temperature was used as the substrate. These values are corresponding to the elastic properties of the substrate material in FEM analysis. Fig. 2 depicts the relation of angle of reflection to angle of incidence. The used angles of incidence are plotted by dashed lines. Fig. 3 shows the calculated energy reflection coefficient based on Eqs. 2 and 3 for the mild steel substrate. It indicates that the maximum energy conversion rate from the P wave to the PS wave is 97.8% at α = 67.3°, and the reduction of the energy conversion rate is within 1% in the α range between 60.8° and 73.0°.

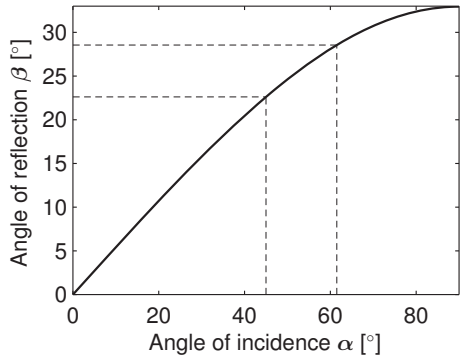

Fig. 2: Angle of reflection (β) vs. angle of incidence (α).

By considering this criterion, $\alpha+\beta$ is required to be 90°. From Eq. 1, which is the Snells law, we can obtain α = 61.46° ($\alpha = \arctan(c_1/c_2)$). At this angle, the conversion rate is 97.03% that is only 0.79%

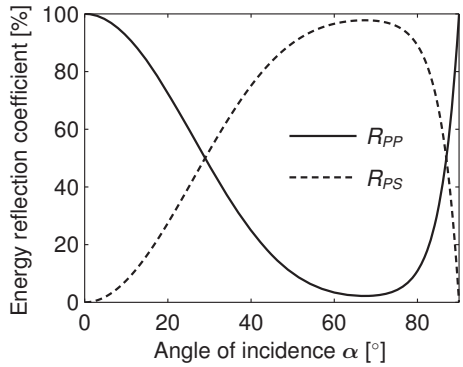

Fig. 3: Energy reflection coefficient vs. angle of incidence (α).

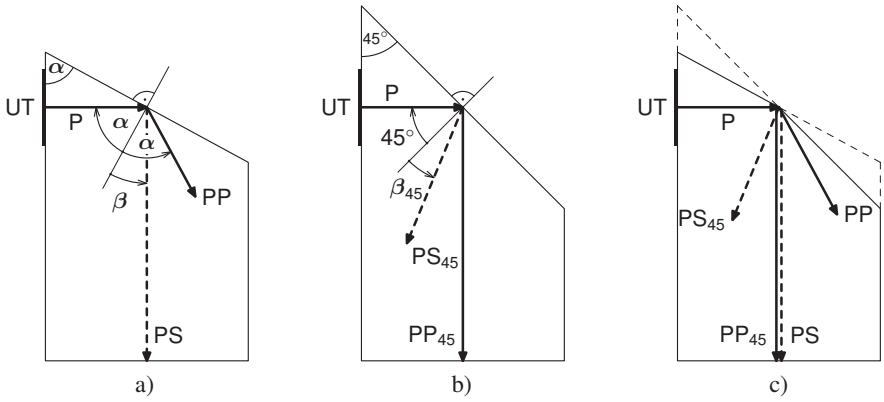

Fig. 4: Cases of the studied ultrasonic probes.

smaller than the maximum conversion rate at 67.3°, based on the result in Fig.3. Therefore, Fig. 4a) shows the schematic design developed for this study.

In Fig. 4b) the schematic diagram of an integrated P wave UT probe with the P wave UT is located in a plane parallel to the direction of PP wave where $\alpha = 45°$ is shown.

In Jen (2007) is shown, how to generate and receive both P and S waves at the same time. The S wave probe shown in Fig. 4a) can be modified to achieve such a purpose. In fact, it simply makes a slanted surface with an angle 45° from the intersection of the slanted plane and the line from the center of the P UT as shown in Fig. 4c). The 45° angle plane will reflect the energy of the P wave into the PP_{45} wave normal to the probing end as shown in Fig. 4c). Therefore, in principle, the upper part of the P wave, generated from P UT, can be used to produce the PS wave and the lower part to produce the PP_{45} wave.

3. FEM modeling

FEM modeling was performed for all three cases of probes depicted in Fig. 4. FE time dependent calculations are performed in the commercial environment COMSOL Multiphysics with the Structural Mechanics Module, COMSOL (2012). The plane strain was used as an application mode.

The probe width was 16 mm and middle of P UT (h) was located at 20 mm from probe end for each cases. The P UT size (w) was 6 mm. The steel with Young's modulus 200 GPa, Poisson's ratio 0.29 and density 7870 kg/m^3 was chosen as the substrate material of probe.

The quadrilateral mapped mesh with maximal element edge 0.2 mm is created. Elements are the Lagrange–Quadratic type. Number of elements for case a) and c) was 9760, for case b) was 11200. Number of degrees of freedom for case a) and c) was 78890, for case b) 90482.

The P UT was modeled as total force load in x-direction:

$$F_x(t,y) = \cos^2\left(\frac{y-h}{w}\pi\right)(1-\cos(2\pi ft/N))\sin(2\pi ft), \quad t \in \langle 0, 1\mu\mathrm{s}\rangle, \quad y \in \langle h - w/2, h + w/2\rangle$$

where f = 0.5 MHz is frequency, N = 5 is number of cycles, and t is time. The others edges were free.

Calculations were done in time interval from 0 to 30 μs with time step 0.01 μs. Relative tolerance of solution was 1×10^{-4}, absolute tolerance 1×10^{-8}. Method BDF with maximum BDF order equals to 2 was used for this time analysis. The received ultrasonic signal was obtained by integration of velocities at place of ultrasonic transducer.

4. Conclusions

The contribution deals with the finite element modeling of integrated longitudinal and shear wave probe that was described by Cheng-Kuei Jen and Makiko Kobayashi. Finite element calculations were performed for three cases of probes: the first one used the reflected S wave, the second one the reflected P wave and the third one used both S wave and P wave. The ultrasonic transducer excitation was modeled as total force load. The integration of velocities at place of ultrasonic transducer was used as the received ultrasonic signal.

The effect of the reflected PP wave for cases a) and c) is negligible due to the low value of the energy reflection coefficient $R_{PP} \approx 3\%$ for given angle of incidence α = 61.46°. The influence of the reflected PS_{45} wave for cases b) and c) is insignificant because of the dimension of the substrate has been chosen so that the reflected PS_{45} wave from the probing end does not enter into the aperture of the P UT. Though some simplifications the results are in good agreement with work of Cheng-Kuei Jen and Makiko Kobayashi.

The analyze of the P UT size and location will be our further aim. The area of the P UT will be adjusted so that the amplitudes of the reflected PS and PP_{45} waves will be nearly the same.

Acknowledgments

The work has been supported by the Institute Research Plan AV0Z20760514 and by the grants GA CR No 101/09/1630.

References

Jen, Ch.-K., Kobayashi, M., (2007), Integrated and Flexible High Temperature Piezoelectric Ultrasonic Transducers. In: *Ultrasonic and advanced methods for nondestructive testing and material characterization* (C.H. Chen ed.) Wolrd Scientific, New York, chap. 2

Kundu, T., (2004), *Ultrasonic Nondestructive Evaluation: Engineering and Biological Material Characterization*, CRC Press, New York.

Achenbach, J. (1973), *Wave Propagation in Elastic Solids*, North-Holland, New York.

Graff, K.F. (1975), *Wave Motion in Elastic Solids*, Dover, New York.

COMSOL, Inc., http://www.comsol.com

18th International Conference
ENGINEERING MECHANICS 2012
Svratka, Czech Republic, May 14 – 17, 2012

pp. 403–417
Paper #129

EXPERIMENTAL INVESTIGATION OF AIR PRESSURE AND ACOUSTIC CHARACTERISTICS OF HUMAN VOICE. PART 1: MEASUREMENT *IN VIVO*

J. Horáček[*], V. Radolf[*], V. Bula[*], J. Veselý[*], A. M. Laukkanen[**]

Abstract: *This contribution is aimed to provide material that can be used to develop more realistic physical models of voice production. The experimental methodology and the results of measurement of subglottal, oral (substitute for subglottic) and acoustic air pressure (captured at a distance of 20 cm in front of the subject's mouth) are presented. The data were measured during ordinary speech production and when the acoustic impedance and mean supraglottal resistance were raised by phonating into differently sized tubes in the air and having the other end submerged under water. The results presented in time and frequency domain show the physiological ranges and limits of the measured pressures in humans for normal and extreme phonation.*

Keywords: ***Biomechanics of voice, measurement of oral pressure, voice exercises, phonation into tubes.***

1. Introduction

This pilot study is a beginning of the experimental investigation of human voice source substitute by complex physical models of phonation. The modelling follows the previous measurements of vocal folds vibration and acoustic, flow and pressure characteristics of human voice production on simplified models of human voice production carried out on a special test facility in the dynamics laboratory of the Institute of Thermomechanics (see Horáček et al. 2011). The main purpose of the present contribution is to present the methodology tests of experimental techniques and laboratory equipment used for *in vivo* measurement and to obtain real physiological data for normal and some extreme ways of human phonation. A similar study performed afterwards on the test rig will enable a comparison of the results obtained *in vivo* and *in vitro* measurements. This comparison will follow in a later article. For simulation of extreme phonation situations the acoustic impedance of human vocal tract was artificially increased by prolonging of the vocal tract with different tubes or straws and by phonation into water, which makes the phonation more difficult due to loading the human phonatory system by additional hydrodynamic pressure.

Straws and tubes are widely used in vocal exercising and voice therapy (see, e.g. Laukkanen et al. 2012). In Scandinavia a resonance tube method has been used. For a description of the method in more detail, see e.g. Simberg and Laine (2007). Research results have been obtained showing that phonation into a tube may improve laryngeal setting towards a more economic and efficient voice production (Laukkanen et al. 1998, Laukkanen et al. 2008) and that the vocal tract setting may be changed improving sound energy transfer from the vocal tract and thus increasing sound pressure level and loudness. In the studies phonation into air has been used. The present study compares phonation in a resonance tube with the other end in air with that when the outer end is submerged into water and with phonation into a straw. It is of particular interest how much air pressure is needed in phonation and what happens to the voice quality during phonation into a tube or straw.

[*] Ing. Jaromír Horáček, DrSc., Ing. Vojtěch Radolf, Ph.D., Ing. Vítězslav Bula, Ing. Jan Veselý, Institute of Thermomechanics, Academy of Sciences of the Czech Republic, Dolejškova 1402/5, 182 00, Prague 8, CZ, e-mails: jaromirh@it.cas.cz, radolf@it.cas.cz, bula@it.cas.cz, vesely@it.cas.cz.

[**] Prof. Anne-Maria Laukkanen, Ph.D.: Speech and Voice Research Laboratory, School of Education, University of Tampere; FIN-33014, Tampere; Finland, e-mail: Anne-Maria.Laukkanen@uta.fi.

2. Material and methods

One female voice trainer, phonated first in a normal way (in speech mode) on [pa:pa], [pi:pi], [pu:pu] at comfortable pitch and loudness, and then into several plastic straws and a resonance tube in the air and with the other end submerged from 2 cm down to 25 cm below water surface into a big aquarium – see the measurement schema in Fig. 1.

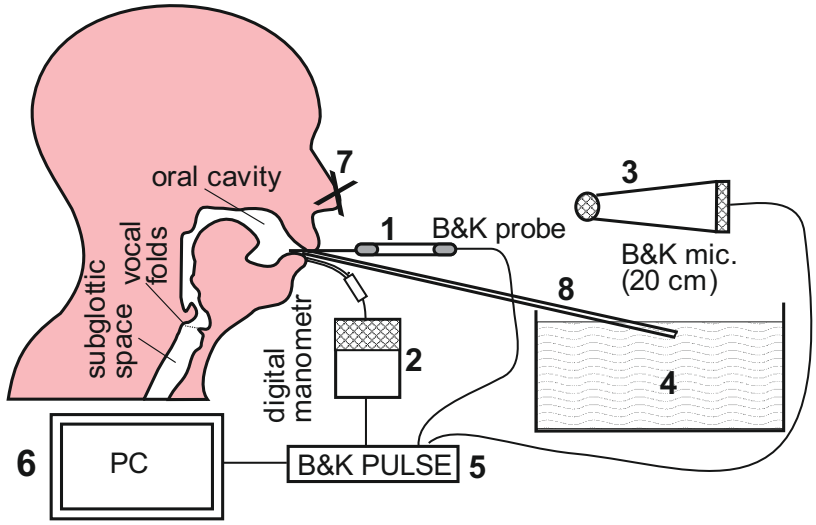

Fig. 1 – Schema of the measurement set up: 1 - B&K microphone probe 4182, 2 – digital manometer Greisinger Electronic GDH07AN, 3 – sound level meter B&K 2239, 4 – aquarium, 5 – B&K measurement system PULSE 10 with Controller Module MPE 7537 A, 6 – personal computer, 7 – clip, 8 – impedance tube.

Tab. 1 – Types of tubes used for increasing of acoustic impedance of the vocal tract.

impedance tube	L – length [mm]	d – inner diameter [mm]
narrow plastic stirring straw	127	2.5
resonance glass tube	264	6.8
drinking straw	150	5.8
long plastic tube	990	4.5

Air pressure was measured intraorally using the B&K special microphone probe type 4182 designed for measurement of acoustic pressure in small cavities in the frequency range between 1 Hz and 20 kHz, and the digital manometer Greisinger Electronic GDH 07AN, the pressure sensor part of which was connected with the oral cavity by a small compliant plastic tube of about 8 cm length and inner diameter of about 1.5 mm. The tubes and straws used are summarized in Table 1. The subject was keeping the lips firmly sealed around the tube or straw and the two probes at the corner of the mouth to measure oral pressure. Pressure during the production of voiceless plosive [p] and manual shuttering of the other end of the tube gave an estimate of subglottic pressure. The nose was closed with a clip to prevent any leakage of air through the nose. A similar approach of measurement technique was used by Titze (2009) for measurement of phonation threshold pressure in occluded vocal tract.

Acoustic signal was recorded using B&K sound level meter type 2239 with the microphone at a distance of 20 cm from the subject's mouth. The recording was made using 32.8 kHz sampling frequency, and 16-bit amplitude accuracy. The measured signals were joint to the PC controlled B&K

measurement system PULSE 10 with the controller module MPE 7537A. Each phonation trial was recorded for 20 s and afterwards the data were transferred in the WAV and ASCI formats and under sampled to 16 kHz for evaluation of the measured signals in the time and frequency domains by using the Matlab. The subglottal pressure p_{sub}, the mean air pressure p_{av}, the mean root square pressure p_{rms} inside and outside the vocal tract, the pressure spectra, the spectrograms, the fundamental voice frequencies F0 and the formant frequencies F1-F5 were analyzed for each trial from the time records of the pressure signals.

Acoustic analysis was done in Matlab by averaging the frequency spectra calculated by FFT using 1s time windows with 75% overlap (see thin lines in Figures 2-12). Then the resulting spectra were averaged in the frequency bands (windows) equal to the fundamental frequency F0 with overlap of F0-10 Hz. Thus the new curves of "filtered spectra" were obtained (see thick lines in Figures 2-12) and the maxima of these curves were considered as formants.

3. Results

The subglottal pressure was measured using the effect of the vocal tract occlusion by production of the consonant [p] during an ordinary phonation on [pa:pa], [pi:pi], [pu:pu] or by manually repeated shuttering of the outer end of the tube during sustained phonation into it. The subglottal pressure was read from the time signal just when the outer end of the tube was closed and the vocal folds were opened and not vibrating, and consequently when the air pressure in the oral cavity was equal to the pressure in lungs. This occlusion or shuttering was repeated several times during each trial that was 20 s long in total.

The measured results are summarized in Tables 2-6 and in Figures 2-12.

Tab. 2 – Acoustic characteristics for ordinary phonation with occluded vocal tract – pressures and frequencies.

ordinary	**subglot.**	**oral**	**outside**	**fund.freq.**	**resonances – formants**				
phonation	p_{sub}	p_{av}	p_{rms}	F0	F1	F2	F3	F4	F5
	[Pa]	[Pa]	[Pa]	[Hz]	[Hz]	[Hz]	[Hz]	[Hz]	[Hz]
[pa:pa]	1000	0	0.064	164	780	1210	2840	3630	4250
[pi:pi]	710	0	0.065	172	330	2470	3730	/	/
[pu:pu]	800	15	0.077	170	350	660	2850	3720	4250

The results for phonation on [pa:pa], [pi:pi], [pu:pu] without using any impedance tube are summarized in Table 2 for the measured pressures and frequencies and the results for phonation [pu:pu] are shown in Fig. 2. The estimated subglottal pressure p_{sub} was, in general, considered as the pressure maximum achieved during the whole trial, e.g. $p_{sub} \approx 800$ Pa at the time instant t=2.5 s when the spectrogram of the oral pressure signal clearly shows no vocal folds vibration during production of the voiceless consonant [p] – see Fig. 2. A decrease of the subglottal pressure at the beginning of each occlusion event (e.g. at time t=2 s) was possible to detect in nearly all trials. A reason of it can be a physiological reaction of the subject on a sharp closure of the oral cavity. Mean oral pressure p_{av} during phonation of the vowel [u:] is possible to evaluate from the time signal when the vocal folds are vibrating and the vocal tract is opened at the lips (see e.g. the time interval at about t=6 s where the mean oral pressure was about 15 Pa due to the radiation losses. It is possible to detect the fundamental frequency F0=170 Hz and the higher harmonics (partials) in the spectrogram during phonation on [u:] as well as in the spectrum of the acoustic pressure measured during the whole trial outside the vocal tract. The formant frequencies F1-F5 were evaluated from the spectrum using especially developed program in Matlab. Clearly detectable formant frequencies are underlined in the Tables 2-6. The data for each trial were evaluated from the time records in the same manner. Maximum subglottal pressures measured for ordinary phonation with occluded vocal tract were found between 710 and 1000 Pa. Mean oral pressure was found to be around zero for phonation on [a:] and [i:] because of a larger

mouth opening than for the vowel [u:]. The fundamental frequency varied between 164 and 172 Hz. The lowest formant frequencies, in general, correspond to the formants found in humans (Baken & Orlikoff, 2000). It can be noted that according to Hirano (1981) the mean subglottal pressure for normal vowel phonation is in the range of 400-2600 Pa, and up to maximum 5 kPa in extremes.

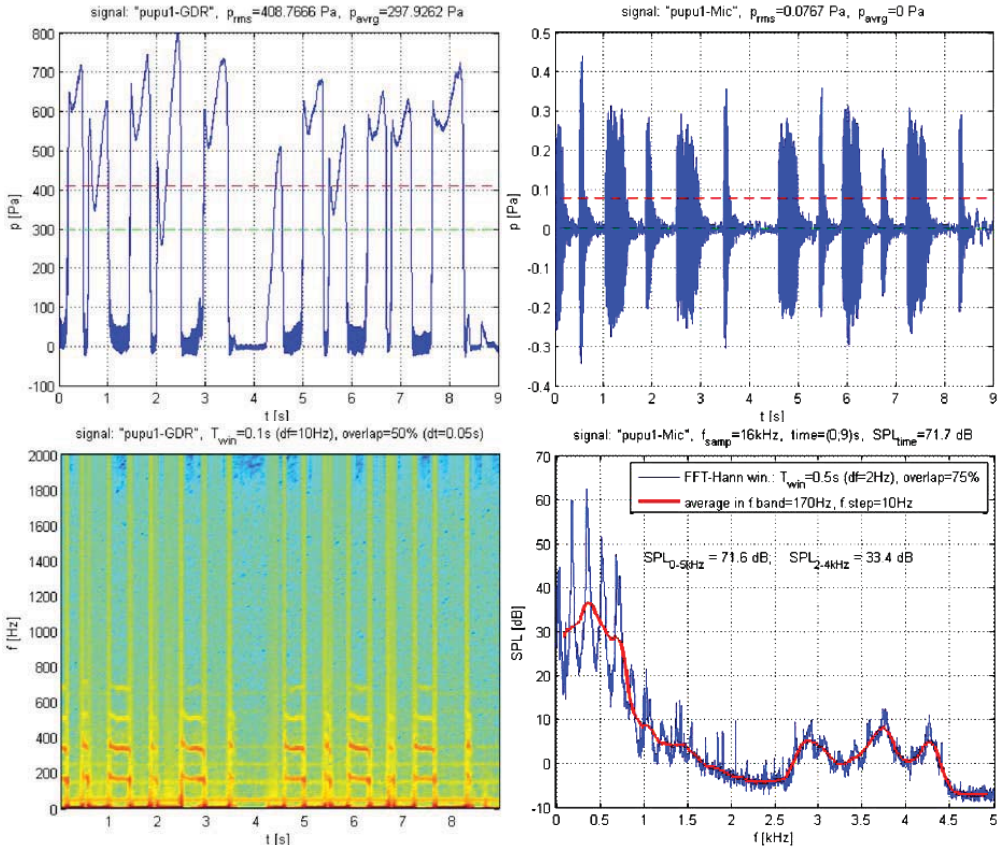

Fig. 2 – Measurement of the phonation [pu:pu]: 1) the oral pressure and its spectrogram (left), 2) the sound signal 20 cm in front of the lips and its spectrum (right).

Tab. 3 – Acoustic characteristics for phonation into the drinking straw – pressures and frequencies.

phonation	**subgl.**	**oral**	**outside**	**fun.fr.**		**resonances – formants**				
drinking straw into	p_{sub} [Pa]	p_{av}/p_{rms} [Pa]	p_{rms} [Pa]	F0 [Hz]	f_b^* [Hz]	F1 [Hz]	F2 [Hz]	F3 [Hz]	F4 [Hz]	F5 [Hz]
air	1200	38/132	0.055	168	/	170	1080	1480	2600	3750
H_2O (2cm)	950	317/-	0.076	150	10-25*	220	360	670	1030	1400
H_2O (5cm)	1250	532/-	0.080	152	15-25*	220	320	600	1040	1440

*frequency interval of bubbling

The results of phonation into a drinking straw for the measured pressures and frequencies are summarized in Table 3 and shown in Figs. 3-5, corresponding to the three ways of phonation: into air and water in the depth of about 2 cm and 5 cm below the water surface. All measured time records and spectrograms for the shuttered phonation are similar like in the previous case for an ordinary

phonation, the maximum of the subglottal pressure p_{sub} was achieved at the time instants when no vocal folds oscillation was possible to detect in the spectrograms of the oral pressure, see e.g. a short time interval at about t=9 s in Fig. 3 when a maximum p_{sub}=1200 Pa was achieved, and on the other hand a short time interval just before time t=8 s when the subglottal pressure was much lower ($p_{sub} \approx 650$ Pa) because the vocal folds were vibrating and interrupting the airway that joins the subglottal and supraglottal spaces. Substantial increase in the mean oral pressure p_{av} is related to the hydrodynamic pressure in addition to the pressure looses in the tube itself, see p_{av}=38 Pa in Table 3 for phonation into air. The higher harmonics and formants are clearly visible in Fig. 3 in the spectrum of the oral pressure measured by the B&K microphone probe, and the pressure $p_{rms} \approx 132$ Pa was possible to evaluate in the oral cavity for phonation into air.

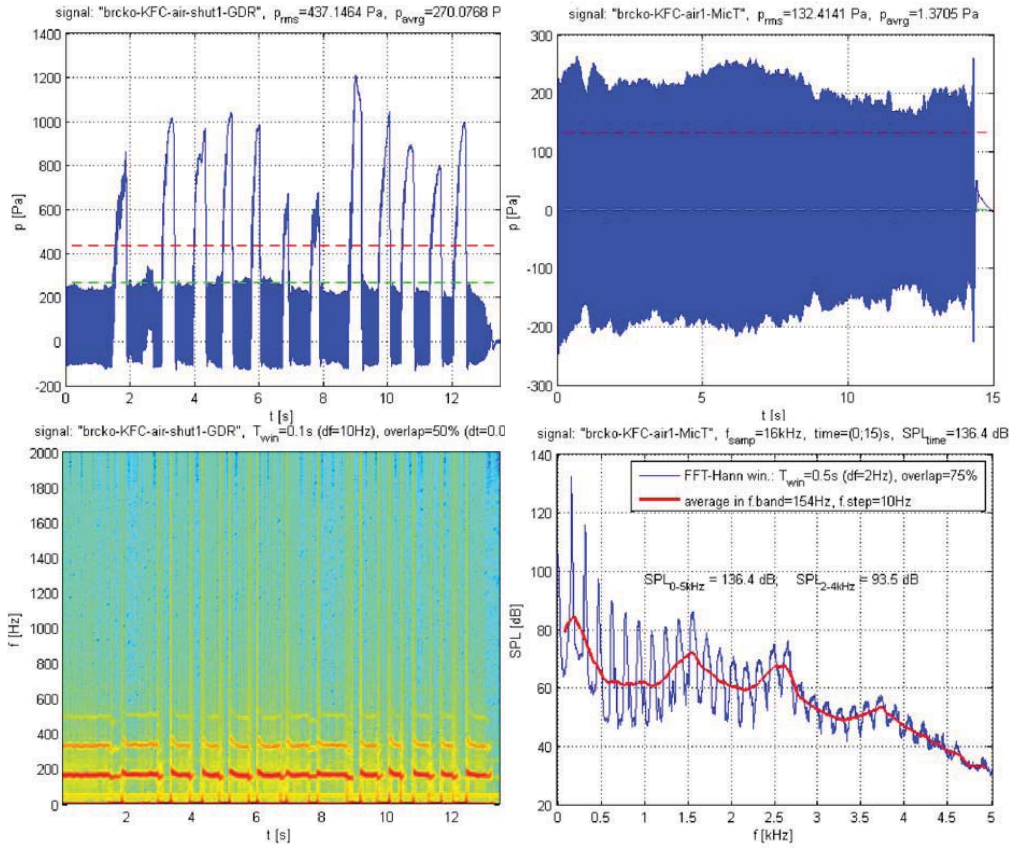

Fig. 3 Measurement of the phonation into drinking straw: 1) oral pressure and its spectrogram (left), 2) sound signal in the mouth and its spectrum (right).

For phonation into water, the frequencies corresponding to water bubbling were detected in the spectra in the lowest frequency region between about 10 Hz and 25 Hz, see Fig. 4 where these frequencies can be identified clearly in the oral pressure signal. It is interesting to note that the subglottal pressure did practically not increased for phonation into water and only slightly compared to the value for normal phonation in Table 2. It might be caused by an air leakage between the straw or two pressure probes and the lips. The fundamental frequency for phonation into water decreased while the mean oral pressure substantially increased and the pressure p_{rms} outside the vocal tract was comparable in all cases to the ordinary phonation with the occluded vocal tract. We can note that the effects of phonation into this type of a drinking straw on the vocal tract setting were studied by Laukkanen et al. (2012) using magnetic resonance imaging technique.

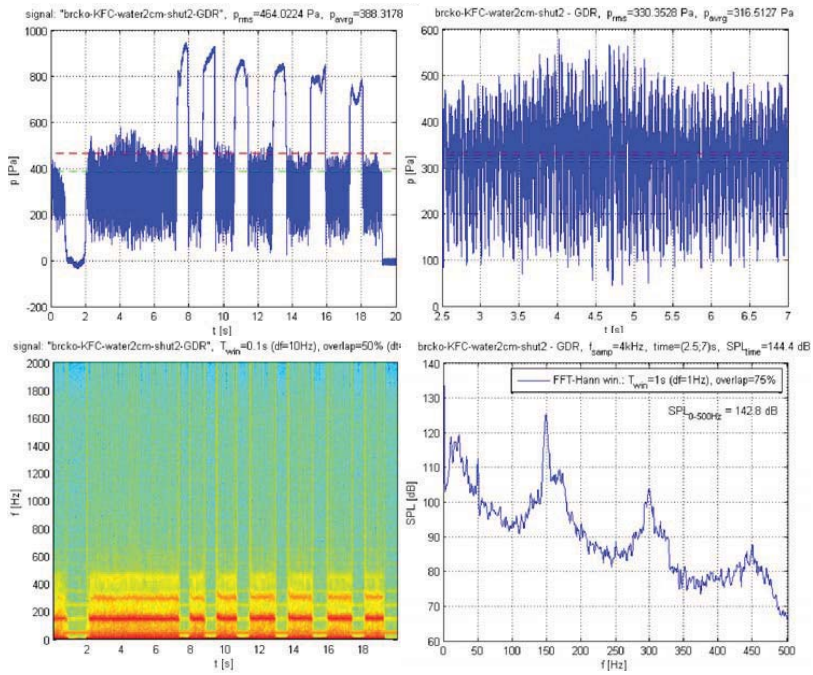

Fig. 4 Measurement of the phonation into a drinking straw submerged 2 cm under water: 1) oral pressure and its spectrogram (left), 2) sound signal in the mouth and its detailed spectrum showing effect of water bubbling in the low frequency range (right).

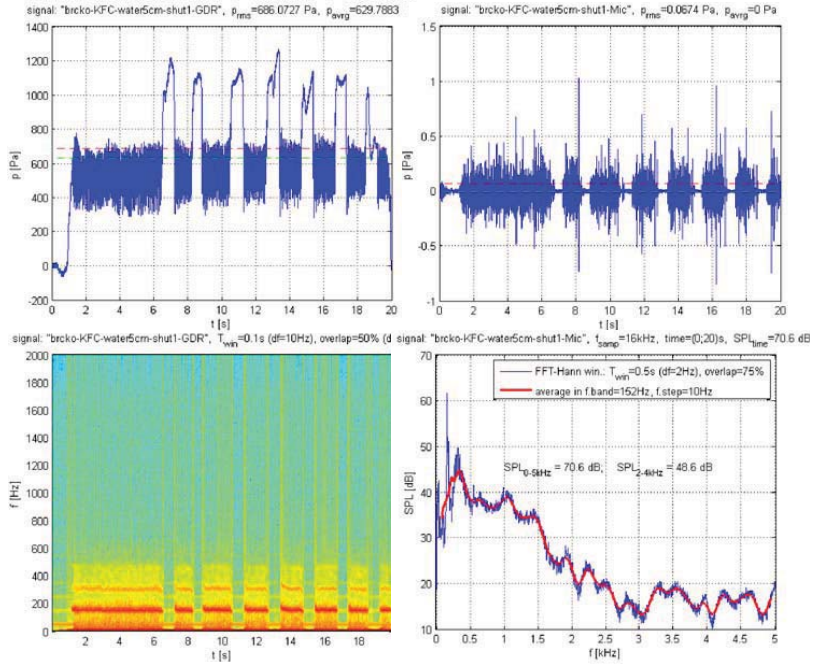

Fig. 5 Measurement of the phonation into a drinking straw submerged 5 cm under water: 1) oral pressure and its spectrogram (left), 2) sound signal 20 cm in front of the lips and its spectrum (right).

The results measured for phonation into the narrow plastic stirring straw are summarized in Table 4 and presented in Figs. 6 and 7 for phonation into air and into water. The subglottal pressure was substantially higher than for both the ordinary phonation and the drinking straw phonation and similarly, the mean oral pressure was higher. The fundamental phonation frequency decreased by phonation into water in a similar way like for the drinking straw. For phonation into air the lowest resonances F2=1700 Hz and F3=2700 Hz are clearly detected in the oral pressure signal measured by the B&K probe. We can note that the effects of phonation into similar stirring straws on the vocal tract setting were studied by Titze et al (2002), Laukkanen et al. (2008) and Titze (2009).

Tab. 4 – Acoustic characteristics for phonation into the narrow plastic stirring straw – pressures and frequencies.

phonation	**subgl.**	**oral**	**outside**	**fun.fr.**		**resonances – formants**				
stirring straw into	p_{sub} [Pa]	p_{av} [Pa]	p_{rms} [Pa]	F0 [Hz]	f_b* [Hz]	F1 [Hz]	F2 [Hz]	F3 [Hz]	F4 [Hz]	F5 [Hz]
air	1430	571	0.020	166	/	115	1730	2640	3830	4140
H_2O (2cm)	1400-1650	700-850	0.036	150	5-30*	440	850	1070	1450	1900

*frequency interval of bubbling

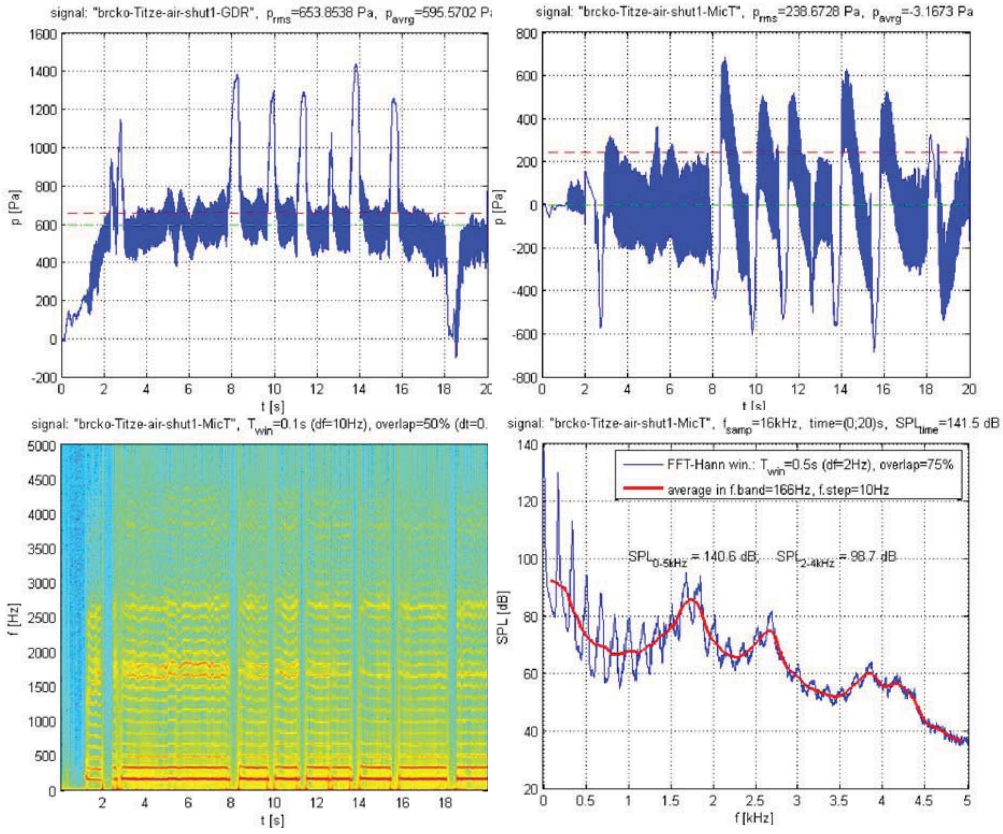

Fig. 6 Measurement of the phonation into the narrow plastic stirring straw: 1) oral pressure and its spectrogram (left), 2) sound signal in the mouth and its spectrum (right).

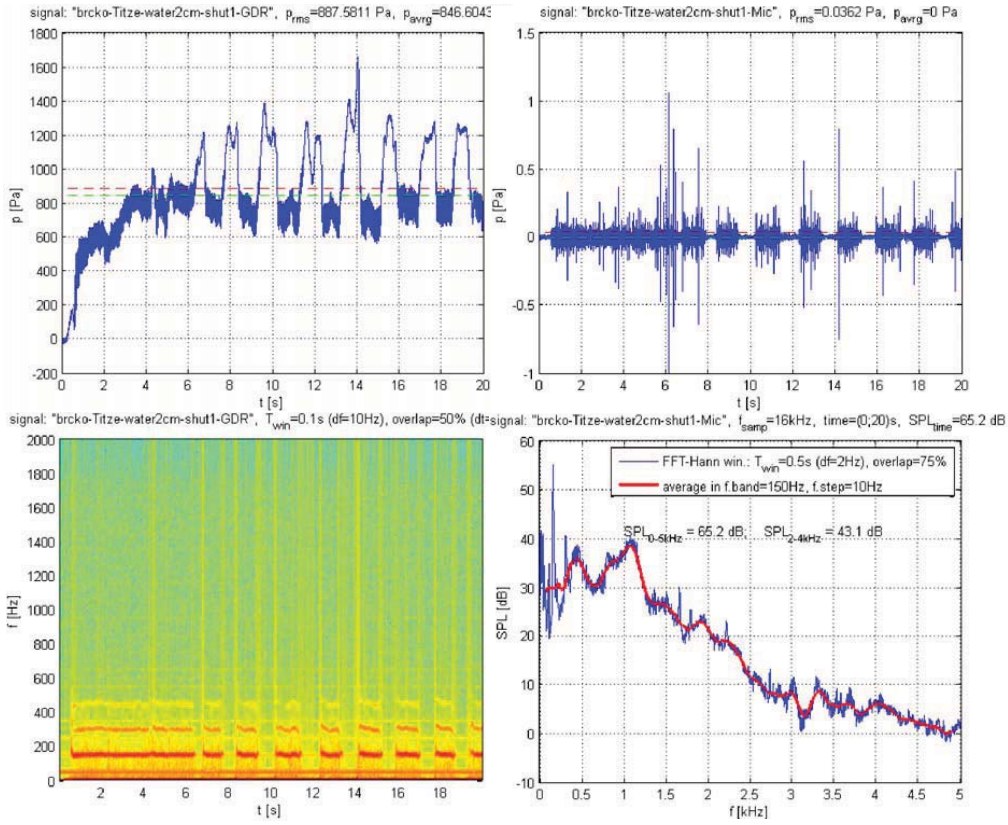

Fig. 7 Measurement of the phonation into the narrow plastic stirring straw submerged 2 cm under water: 1) oral pressure and its spectrogram (left), 2) sound signal 20 cm in front of the lips and its spectrum (right).

Tab. 5 – Acoustic characteristics for phonation into the glass tube (so called resonance tube) – pressures and frequencies.

phonation	**subgl.**	**oral**	**outside**	**fun.fr.**		**resonances – formants**				
glass tube	p_{sub}	p_{av}/p_{rms}	p_{rms}	F0	f_b*	F1	F2	F3	F4	F5
into	[Pa]	[Pa]	[Pa]	[Hz]	[Hz]	[Hz]	[Hz]	[Hz]	[Hz]	[Hz]
air	900	52/34	0.077	146	/	620	1300	1910	2520	3180
H_2O (2cm)	1150	251/107	0.115	156	18*	680	1100	1450	2540	
H_2O (10cm)	1700	1068/-	0.092	152	15*	430	600	1100	1500	
H_2O (15cm)	2450	1605/117	0.074	158	15*	450	1000	1500	1900	2200

*frequency of bubbling

The measurements for phonation into the resonance glass tube are presented in Table 5 and in Figs. 8-11. The subglottal pressure for phonation into air was comparable with the phonation [pu:pu] and lower than for phonation into the drinking straw as well as for the stirring straw. The mean oral pressure given by the tube impedance was comparable with phonation [pu:pu] and into the drinking tube, and substantially lower than for the stirring straw. The fundamental frequency was considerably lower than for the ordinary phonation with the occluded vocal tract and increased for phonation into

water. The subglottal pressure as well as the mean oral pressure p_{av} increased with the water depth due to the hydrodynamic pressure. The root mean square oral pressure p_{rms} also increased considerably by phonation into the water, nearly four times compared to phonation into air, i.e. from about 123.8 dB in air up to 135.3 dB for the water depth 15 cm. We should note that the maximum oral pressure p_{rms}=132 Pa i.e. 136.4 dB, was obtained for phonation into the drinking straw. In general, the SPL measured outside the vocal tract was between 60 dB and 75 dB in all cases.

Substantial differences were found in the spectra of the pressure signals measured inside the oral cavity by the B&K microphone probe and outside measured by the B&K sound level meter (see Figs. 9 and 11). Especially, some low frequency and dominant formants at about 600 Hz in Fig. 9 and at about 300 Hz in Fig. 11 measured outside the vocal tract are not detected in the spectra of the oral pressure. The dominant frequency of the water bubbling was at about 18 Hz for phonation into the water depth 2 cm and 15 Hz for the higher water levels. The difference found in the spectra inside and outside the vocal tract can be attributed to a high intensity of bubbling; moreover it may be also influenced by a plastic foil by which it was necessary to cover the aquarium especially for the higher water levels.

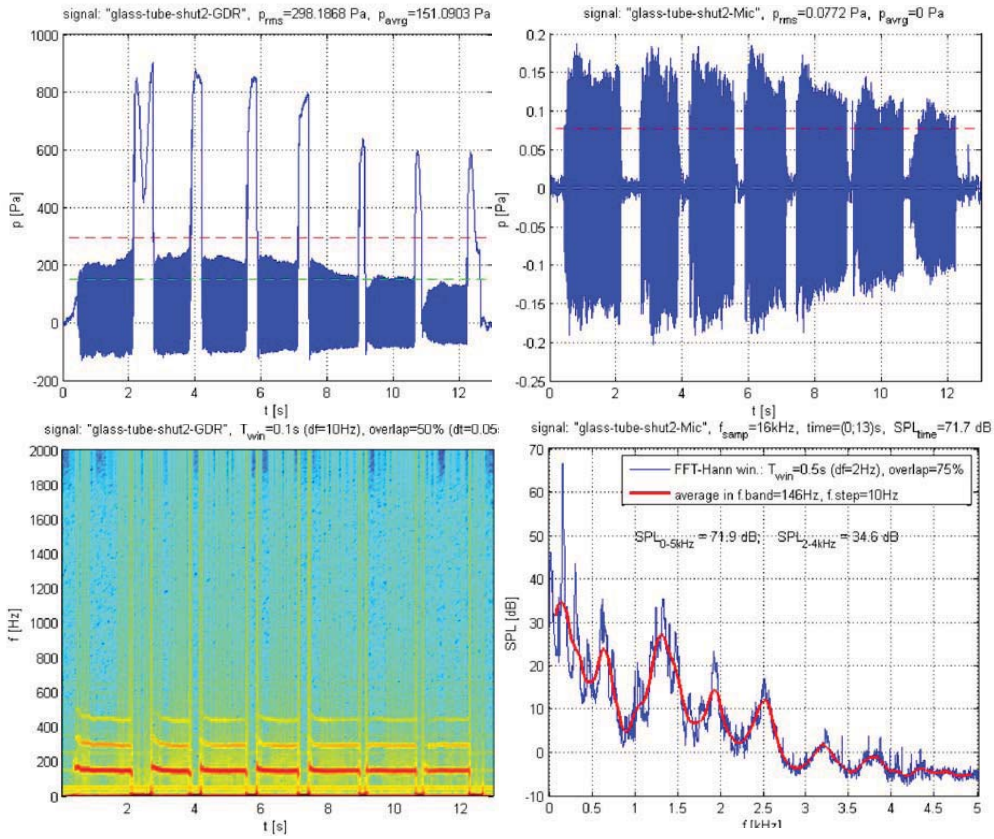

Fig. 8 Measurement of phonation into the glass (resonance) tube: 1) oral pressure and its spectrogram (left), 2) sound signal 20 cm in front of the lips and its spectrum (right).

Extreme phonation was compared between male and female subjects by phonation into the very long plastic tube. Table 4 and Fig. 12 show the differences between female and male phonation when the water depth was continuously changed during the phonation from 0 cm (phonation into air) down to about 25 cm and shuttering the tube end. The measured maximum of the subglottal pressure for the female subject was about p_{sub}=2.55 kPa and for the male subject p_{sub}= 3.25 kPa, and similarly the mean oral pressure p_{av} measured in male was about 460 Pa higher than in female.

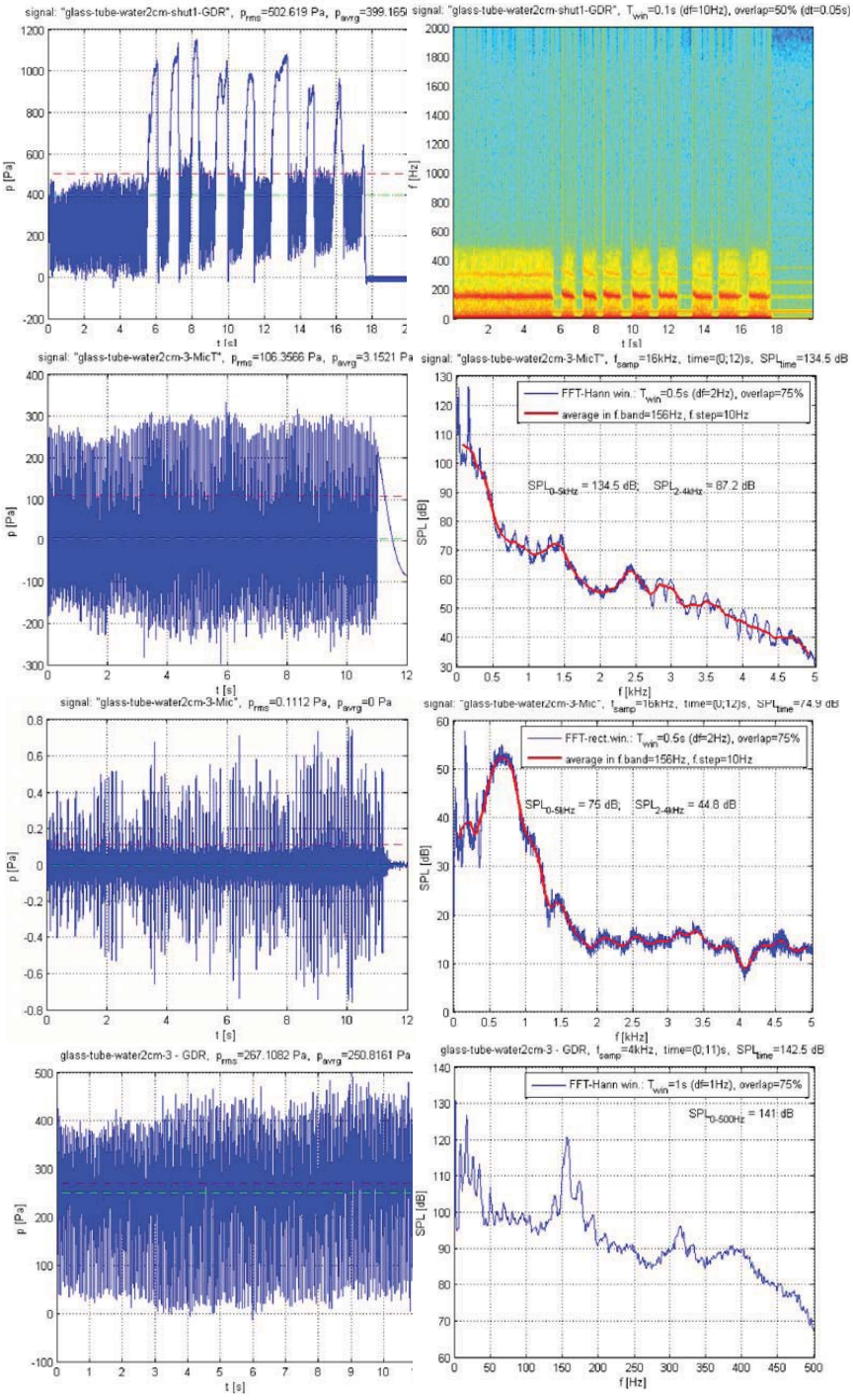

Fig. 9 Measurement of the phonation into a resonance glass tube submerged 2 cm under water: 1) oral pressure and its spectrogram (upper panel), 2) sound signal in the mouth and its spectrum (2nd panel), 3) sound signal 20 cm in front of the lips and its spectrum (3rd panel), 4) oral pressure and detail of its spectrum showing bubbling effect in the lowest frequency range (bottom).

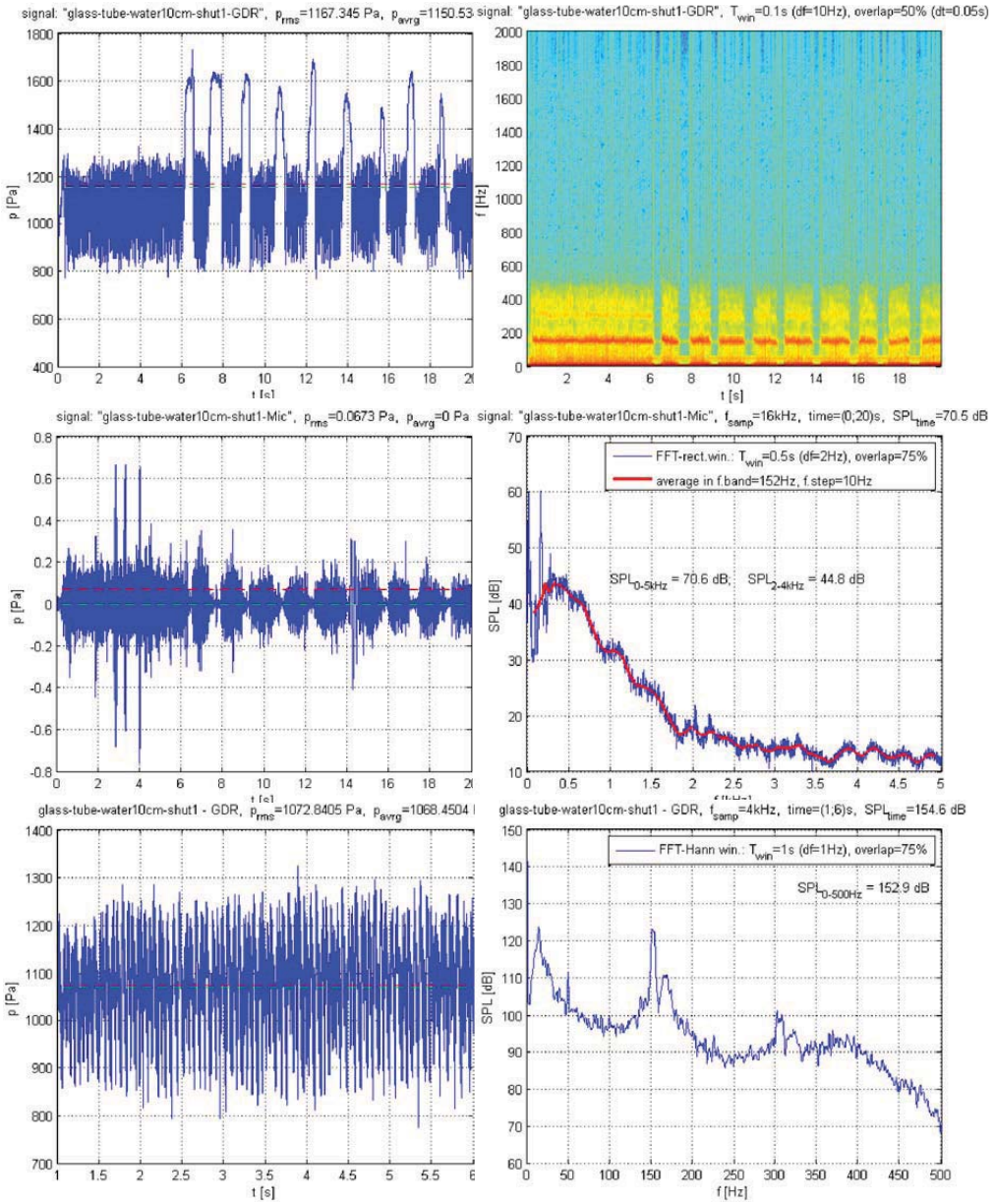

Fig. 10 Measurement of the phonation into a resonance glass tube submerged 10 cm under water: 1) oral pressure and its spectrogram (upper panel), 2) sound signal 20 cm in front of the lips and its spectrum (2nd panel), 3) oral pressure and detail of its spectrum showing bubbling effect in the lowest frequency range (bottom).

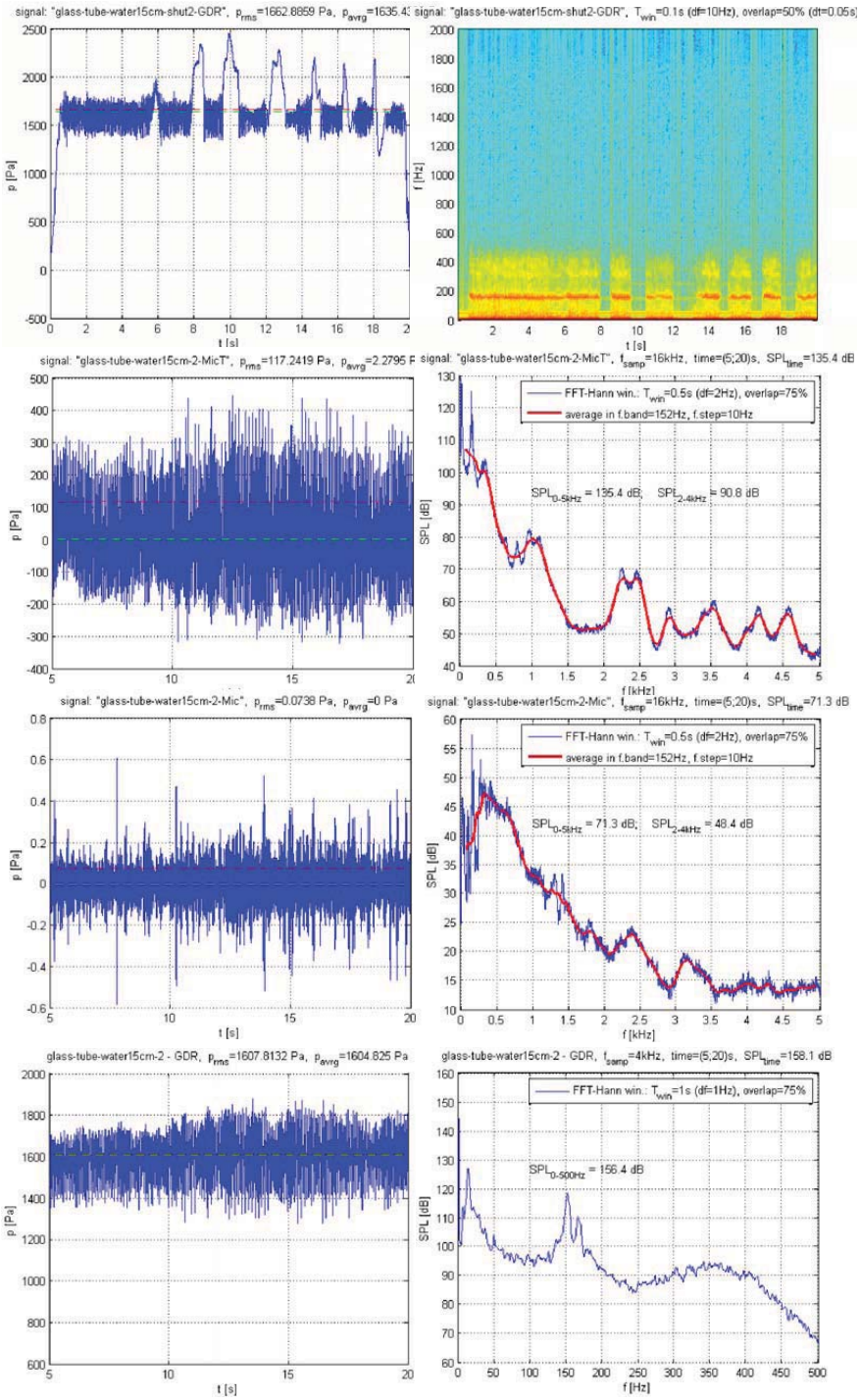

Fig. 11 Measurement of the phonation into a resonance glass tube submerged 15 cm under water: 1) oral pressure and its spectrogram (upper panel), 2) sound signal in the mouth and its spectrum (2nd panel), 3) sound signal 20 cm in front of the lips and its spectrum (3rd panel), 4) oral pressure and detail of its spectrum showing bubbling effect in the lowest frequency region (bottom panel).

Tab. 6 – Acoustic characteristics for phonation into the long plastic tube varying the submerge depth in water from zero to a maximum of about 23 cm under the water for female and up to about 25 cm for male – pressures and frequencies.

phonation	**subgl.**	**oral**	**outside**	**fun.fr.**	**resonances – formants**					
into a long tube	p_{sub} [Pa]	p_{av} [Pa]	p_{rms} [Pa]	F0 [Hz]	F1 [Hz]	F2 [Hz]	F3 [Hz]	F4 [Hz]	F5 [Hz]	F6 [Hz]
female	750 - 2550	250 - 2290	0.042	156	360	550	1030	2500	3260	4040
male	2000 - 3250	250 - 2750	0.060	115	280	1140	1640	2250	3560	4120

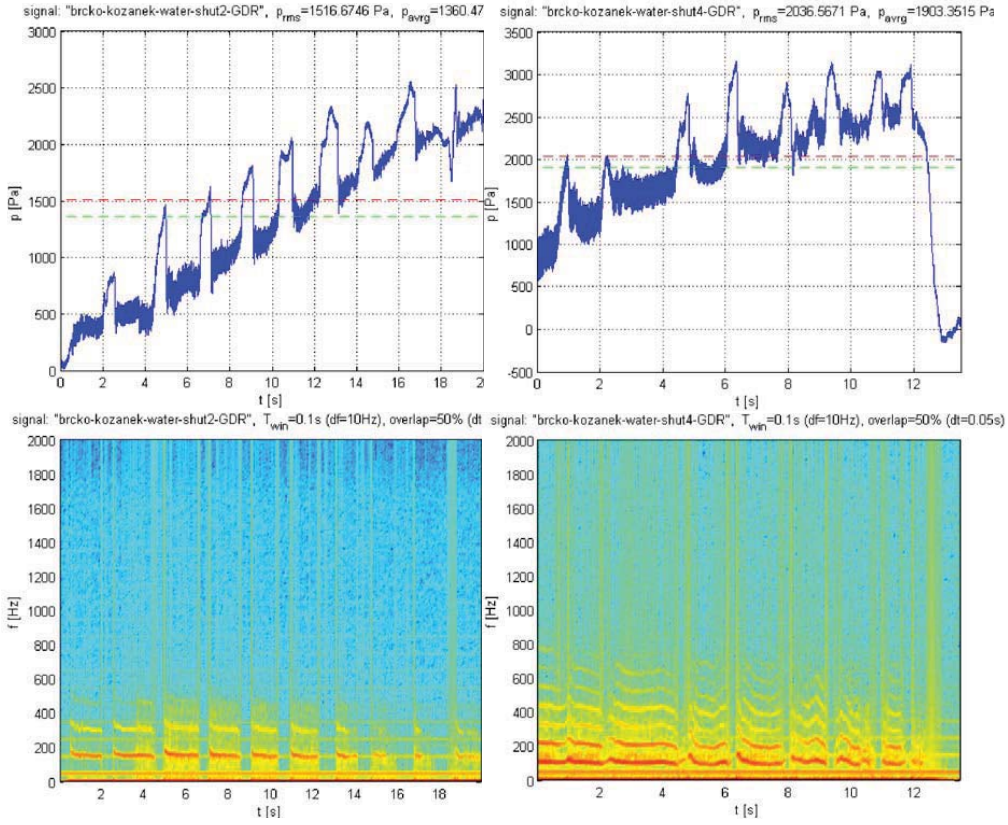

Fig. 12 Measurement of phonation into long plastic tube ("1 m") starting in air and submerging the tube continuously deeper and deeper into water: 1) female phonation (F0=156 Hz) up to about 23 cm H_2O, 2) male phonation (F0=115 Hz) up to about 25 cm H_2O.

4. Discussion and concluding remarks

According to the results in Tables 1-6 for the female phonation the subglottal pressure p_{sub} varied in all cases studied between 710 Pa and 2550 Pa, the mean oral pressure p_{av} varied from 0 Pa for phonation on [a:] and [i:] to the maximum 2290 Pa for phonation into the long plastic tube at about 23 cm under the water. The fundamental frequency F0 varied between 146 and 172 Hz. Water bubbling frequency varied in the interval between 5 Hz and 30 Hz for all cases studied.

The air pressure used for phonation into the resonance tube in the air was approximately the same as in vowel phonation. Phonation into straw offers a higher resistance, as already presented by Titze et al. (2002). The subglottal pressure p_{sub} measured in our case for phonation into the stirring straw was 1430 Pa and the oral pressure p_{av}=571 Pa; for phonation into the resonance tube we measured p_{sub}=900 Pa and p_{av}=52 Pa (see Tabs. 4 and 5) These values corresponds well with the measurements by Titze et al. They measured p_{sub} approximately from 1 to 2.5 kPa for the male and the oral pressure in the range 0-1.5 kPa in the lowest pitch (F0=147 Hz). For the female the lowest pitch was 220 Hz, the subglottal pressure varied between 1.5-2.5 kPa, and the oral pressure approximately between 0.5-1.8 kPa. Titze estimated lung pressure needed for phonation into a resonance tube (30 cm in length, 7.5 mm inner diameter) in air: 0.73 kPa and for the smallest stirring straw (11.5 cm in length, 2 mm inner diameter) 5.13 kPa assuming the air flow rate 0.2 l/s. Similar estimation was done for the oral pressure: 90 Pa for a resonance tube and 4.6 kPa for the stirring straw. Titze et al. (2002) concluded that the male who had considerably more practice with this type of phonation raised lung pressure by ca 100%, while the female raised it by 50%.

The subglottal pressure as well as the oral pressure measured for the resonance tube 2 cm under water was higher than in the air, but lower than needed for the straws. The highest pressures were measured for the resonance tube 15 cm under water.

The maximum root mean square pressure inside the oral cavity 136.4 dB was measured for phonation into the drinking straw, however many p_{rms} values for the signal from the B&K probe were not possible to evaluate due to difficulties with fixing correctly the two probes in addition to a straw or tube between the subject's lips. It is the reason why many p_{rms} values measured inside the oral cavity are missing in the tables.

A higher subglottic pressure is needed with increasing the water depth that also offers a higher pressure oscillation in the vocal tract. Voice therapy tradition pays attention to that tube 10 cm or deeper under water should only be used for a short time and proper guidance of phonation is needed (see Simberg and Laine, 2007). With a higher supraglottic resistance a higher subglottic pressure and tighter adduction of the vocal folds is needed. However, the air pressure inside the glottis also increases, thus reducing collision between the vocal folds.

Acoustic results show that the fundamental frequency F0 lowers with the hydrodynamic pressure for the drinking and stirring straws submerged into water, however an opposite tendency was measured for phonation into the resonance tube where F0 being the lowest for phonation into air.

Similar measurements were performed on a physical model of phonation, and the results of both measurements will be compared in another paper. The results of the present studies will be used for testing the models of the vocal fold prosthesis in the laboratory.

Acknowledgements

The study was supported by the Grant Agency of the Czech Republic by the project GAČR P101/12/1306: Biomechanical modelling of human voice production - way to artificial vocal folds.

References

Baken R.J. & Orlikoff R. (2000) *Clinical Measurement of Speech and Voice*. 2nd edition. Singular.

Hirano M. (1981) *Clinical examination of voice*. Disorders of Human Communication 5. G.E. Arnold, F. Winckel and B.D. Wyke (eds.), Springer – Verlag, Wien.

Horáček J., Uruba V., Radolf V., Veselý J. & Bula V. (2011) Airflow visualization in a model of human glottis near the self-oscillating vocal folds model. *Applied and Computational Mechanics,* **5**, 1, pp. 21-28.

Laukkanen A-M., Lindholm P., Vilkman E. (1998) Vocal exercising and speaking related changes in glottal resistance. A pilot study. *Logopedics Phoniatrics Vocology*, **23**, 2, pp. 85-92.

Laukkanen A-M., Titze I.R., Hoffman H., Finnegan E.M. (2008) Effects of a semi-occluded vocal tract on laryngeal muscle activity and glottal adduction in a single female subject. *Folia Phoniatrica et Logopaedica,* **60**, pp. 298-311.

Laukkanen A-M., Horáček J., Krupa P. & Švec J.G. (2012) The effect of phonation into a straw on the vocal tract adjustments and formant frequencies. A preliminary MRI study on a single subject completed with acoustic results. *Biomedical Signal Processing and Control,* **7**, 1, pp. 50– 57.

Simberg S. & Laine A. (2007) The resonance tube method in voice therapy: Description and practical implementations, *Logopedics Phoniatrics Vocology.* **32**, pp. 165–170.

Titze I.R, Finnegan E.M., Laukkanen A-M., Jaiswal S. (2002) Raising lung pressure and pitch in vocal warm-ups: The use of flow-resistance straws. *Journal of Singing*, **58**, 4, pp. 329-338.

Titze I.R. (2009) Phonation threshold pressure measurement with a semi-occluded vocal tract. *Journal of Speech, Language, and Hearing Research,* **52,** pp. 1062-1072.

Vampola T., Laukkanen A-M., Horáček J. & Švec J.G. (2011) Finite element modelling of vocal tract changes after voice therapy. *Applied and Computational Mechanics,* **5**, 1, pp. 77-88.

Vampola T., Laukkanen A-M., Horáček J. & Švec J.G. (2010) Vocal tract changes caused by phonation into a tube: A case study using computer tomography and finite-element modeling. *Journal of Acoustical Society of America*, **129**, 1, pp. 310-315.

18th International Conference
ENGINEERING MECHANICS 2012
Svratka, Czech Republic, May 14 – 17, 2012

pp. 419–426
Paper #185

COMPARISON OF IMPLICIT-GRADIENT DAMAGE-PLASTIC MODELS

M. Horák [*], **M. Jirásek** [**]

Abstract: *Damage mechanics coupled with the theory of plasticity is a suitable framework for description of the complex behavior of materials such as concrete [Grassl and Jirásek (2006)], steel [Engelen, Geers and Baaijens (2003)], or bone [Charlebois, Jirásek and Zysset (2010)]. However, the classical theory fails after the loss of ellipticity of the governing differential equation. From the numerical point of view, loss of ellipticity is manifested by the patholocical dependence of the results on the size and orientation of the finite elements. This paper describes two different formulations of coupled damage-plastic models, and their nonlocal enhancements based on the implicit gradient approach. The difference between the formulations is discussed and illustrated by a numerical example.*

Keywords: ***damage, plasticity, nonlocal continuum, implicit-gradient formulation***

1. Introduction

This paper presents coupled damage-plasticity models. Continuum damage mechanics is suitable for the description of stiffness degradation due to the growth of defects such as micro-voids and micro-cracks, while plasticity theory describes permanent deformations of a material induced e.g. by slip mechanisms. However, standard damage-plasticity models with softening would lead to a pathological sensitivity of the numerical solution, converging to physically meaningless results. In this contribution, two different ways of coupling damage with plasticity are considered, and a method that can provide an objective description of localized inelastic processes is described.

2. Plasticity

The main feature of plasticity models is irreversibility of plastic strain. We restrict our attention to the associative plasticity with isotropic hardening or softening under small strain. The basic equations include an additive decomposition of the total strain into an elastic (reversible) part and a plastic (irreversible) part,

$$\boldsymbol{\varepsilon} = \boldsymbol{\varepsilon}_e + \boldsymbol{\varepsilon}_p, \tag{1}$$

the stress-strain law,

$$\boldsymbol{\sigma} = \mathbb{D}_e : \boldsymbol{\varepsilon}_e, \tag{2}$$

the definition of the yield function

$$f(\boldsymbol{\sigma}, \kappa) = \tilde{\sigma}(\boldsymbol{\sigma}) - \sigma_Y(\kappa) \tag{3}$$

loading-unloading conditions in the Kuhn-Tucker form,

$$f(\boldsymbol{\sigma}, \kappa) \leq 0 \qquad \dot{\lambda} \geq 0 \qquad \dot{\lambda} f(\boldsymbol{\sigma}, \kappa) = 0, \tag{4}$$

flow rule as the evolution law for plastic strain

$$\dot{\boldsymbol{\varepsilon}}_p = \dot{\lambda} \frac{\partial f}{\partial \boldsymbol{\sigma}}, \tag{5}$$

[*] Ing. Martin Horák: Faculty of Civil Engineering, Czech Technical University in Prague; Thakurova 7/2077; 166 29, Prague; CZ, e-mail: Martin.Horak@fsv.cvut.cz
[**] Prof. Ing. Milan Jirásek, DrSc.: Faculty of Civil Engineering, Czech Technical University in Prague; Thakurova 7/2077; 166 29, Prague; CZ, e-mail: Milan.Jirasek@fsv.cvut.cz

evolution law for cumulated plastic strain,

$$\dot{\kappa} = \sqrt{\dot{\boldsymbol{\varepsilon}}_p : \dot{\boldsymbol{\varepsilon}}_p}, \tag{6}$$

and the isotropic hardening (softening) law, described by the function $\sigma_Y(\kappa)$ that is embedded in the definition of the yield function (3). In the equations above, $\boldsymbol{\sigma}$ is the stress tensor, $\mathbb{D}_e$ is the elastic stiffness tensor, $\tilde{\sigma}$ is a seminorm of the stress tensor, λ is the plastic multiplier, κ is the cumulated plastic strain and σ_Y is the current yield stress. An overdot marks the derivative with respect to time. To describe the behavior of a specific material, a concrete form of the stress seminorm has to be introduced. In the subsequent chapters, we will use the Mises yield condition, which belongs to the most used yield criteria and defines the stress seminorm as

$$\tilde{\sigma}(\boldsymbol{\sigma}) = \sqrt{\frac{3}{2}\boldsymbol{s} : \boldsymbol{s}} \tag{7}$$

where $\boldsymbol{s}$ is the deviatoric part of the stress. Note that for Mises plasticity, yielding has a purely deviatoric character.

2.1. Implementation

To implement the constitutive model into a displacement-driven finite element code, an algorithm for the evaluation of the stress increment from a given strain increment must be developed. This procedure is usually called the stress-return algorithm. The stress return algorithm is based on the elastic-plastic operator split, which consists of a trial elastic predictor followed by the return mapping algorithm. In the first step, the trial stress

$$\boldsymbol{s}^{tr} = 2G\left(\boldsymbol{e}^{n+1} - \boldsymbol{e}_p^n\right) \tag{8}$$

is computed. Here, G is the shear modulus of elasticity and $\boldsymbol{e}$ is the deviatoric part of the strain. If the trial stress satisfies the condition of plastic admissibility, $F(\boldsymbol{\sigma}^{tr}, \kappa^n) \leq 0$, the step is elastic and the trial stress $\boldsymbol{\sigma}^{tr}$ is accepted as the actual stress $\boldsymbol{\sigma}^{n+1}$. If the trial stress violates the yield condition, the step is plastic and the return mapping algorithm has to be used. Here we describe the so-called radial-return algorithm [Krieg and Key (1976)], which represents a radial projection of the trial stress onto the yield surface. The formula for $\boldsymbol{s}^{n+1}$ has the following form:

$$\boldsymbol{s}^{n+1} = \boldsymbol{s}^{tr} - 2G\Delta\boldsymbol{e}_p \tag{9}$$

After using the discrete version of equation (5) in combination with equation (9), we arrive at

$$\boldsymbol{s}^{n+1} = \boldsymbol{s}^{tr} - \sqrt{6}G\Delta\kappa\frac{\boldsymbol{s}^{n+1}}{\|\boldsymbol{s}^{n+1}\|} \tag{10}$$

Clearly, $\boldsymbol{s}^{n+1}$ and $\boldsymbol{s}^{tr}$ are colinear, thus

$$\frac{\boldsymbol{s}^{n+1}}{\|\boldsymbol{s}^{n+1}\|} = \frac{\boldsymbol{s}^{tr}}{\|\boldsymbol{s}^{tr}\|} \tag{11}$$

Substituting (11) into (10), the radial mapping of the trial stress onto the yield surface is obtained:

$$\boldsymbol{s}^{n+1} = \left(1 - \frac{\sqrt{6}G\Delta\kappa}{\boldsymbol{s}^{n+1}}\right)\boldsymbol{s}^{n+1} \tag{12}$$

Moreover, the yield criterion must be fullfiled at the end of the step:

$$f(\boldsymbol{s}^{n+1}, \kappa^n + \Delta\kappa) = 0 \tag{13}$$

Substitution equation (12) into (13) leads to one nonlinear scalar equation for $\Delta\kappa$. For linear hardening plasticity, in the form $\sigma_Y(\kappa) = \sigma_0 + H\kappa$, this equation is reduced to a linear equation, and $\Delta\kappa$ can be obtained directly as

$$\Delta\kappa = \frac{f^{tr}}{3G + H} \tag{14}$$

where $f^{tr} = f(\boldsymbol{s}^{tr}, \kappa^n)$, H is the plastic modulus, and σ_0 is the initial yield stress.

3. Coupling of damage and plasticity

In this section, a brief description of the continuum damage mechanics and its coupling with the plasticity theory is discussed, see [Maugin (1992)] for more details. The isotropic damage mechanics is considered, which means that one single scalar damage variable is introduced. The damage variable describes the reduction of stiffness and strength of material due to the creation, coalescence and growth of voids and microcracks. There exists at least two ways of coupling the plasticity theory to the damage mechanics. The first approach is based on the formulation of the plasticity problem in the effective (i.e. undamaged) stress space. The second approach relies on the plasticity formulated in the nominal (i.e. damaged) stress space. For both approaches, the stress-strain law has the form

$$\boldsymbol{\sigma} = (1-\omega)\bar{\boldsymbol{\sigma}} = (1-\omega)\mathbb{D}_e : (\boldsymbol{\varepsilon} - \boldsymbol{\varepsilon}_p) \tag{15}$$

where $\bar{\boldsymbol{\sigma}}$ is the effective stress and ω is the damage variable that ranges from zero (virgin material) to one (completely damaged material).

For the model based on effective stress, equations (2)–(5) are reformulated in the effective stress space

$$\bar{\boldsymbol{\sigma}} = \mathbb{D}_e : (\boldsymbol{\varepsilon} - \boldsymbol{\varepsilon}_p), \tag{16}$$

$$f(\bar{\boldsymbol{\sigma}}, \kappa) = \tilde{\sigma}(\bar{\boldsymbol{\sigma}}) - \bar{\sigma}_Y(\kappa), \tag{17}$$

$$f(\bar{\boldsymbol{\sigma}}, \kappa) \leq 0 \qquad \dot{\lambda} \geq 0 \qquad \dot{\lambda} f(\bar{\boldsymbol{\sigma}}, \kappa) = 0, \tag{18}$$

$$\dot{\boldsymbol{\varepsilon}}_p = \dot{\lambda} \frac{\partial f}{\partial \bar{\boldsymbol{\sigma}}}, \tag{19}$$

Moreover, the damage law is needed. Usually it is postulated as

$$\omega = g(\kappa) \tag{20}$$

For the second group of models, all equations are formulated in terms of nominal stress. However, this formulation can be rewritten in terms of the effective stress, and the hardening (softening) function would by given by

$$\bar{\sigma}_Y = \frac{\sigma_Y}{(1 - g(\kappa))} \tag{21}$$

In the first case, the evolution of damage and the effective yield stress is prescribed, while in the second case the evolution of the nominal yield stress and damage is prescribed. Since the nominal stress is directly available from the stress-strain diagram, it may be simpler to describe it directly and then consider the effective yield stress as a derived quantity. The models are fully equivalent; however, it is neccesary to pay attention when constructing the nonlocal extension. Nonlocal extension of both classes of models will be described in the next chapter.

3.1. Implementation

Implementation of the formulation based on the effective stress is very similar to the implementation of pure plasticity and consist of the return mapping algorithm followed by the explicit evaluation of damage. To implement a damage plastic model based on the nominal stress, the formula for the trial stress has to be changed to

$$\boldsymbol{s}^{tr} = (1-\omega^n) 2G \left(\boldsymbol{e}^{n+1} - \boldsymbol{e}_p^n \right) \tag{22}$$

Again, if the trial stress satisfies the yield condition, the step is elastic and the trial stress is accepted as the actual stress. If the trial stress violates the yield condition, the step is plastic and the return mapping algorithm has to be used. The formula for $\boldsymbol{s}^{n+1}$ reads

$$\boldsymbol{s}^{n+1} = \boldsymbol{s}^{tr} - 2G\Delta\omega \left(\boldsymbol{e}^{n+1} - \boldsymbol{e}_p^n \right) - (1-\omega^{n+1}) 2G \Delta \boldsymbol{e}_p^n \tag{23}$$

After substitution of (5) into (23), multiplication of the second term by $\dfrac{1-\omega^n}{1-\omega^n}$, and some algebra, we get

$$\boldsymbol{s}^{n+1} = \frac{1-\omega^{n+1}}{1-\omega^n} \boldsymbol{s}^{tr} - (1-\omega^{n+1}) \sqrt{6} G \Delta\kappa \frac{\boldsymbol{s}^{n+1}}{\| \boldsymbol{s}^{n+1} \|} \tag{24}$$

Obviously, $\boldsymbol{s}^{n+1}$ and $\boldsymbol{s}^{tr}$ are colinear; therefore, we arrive at the radial return mapping of the trial stress onto the yield surface:

$$\boldsymbol{s}^{n+1} = \left(\frac{1-\omega^{n+1}}{1-\omega^n} - \frac{(1-\omega^{n+1})\sqrt{6}G\Delta\kappa}{\|\boldsymbol{s}^{tr}\|} \right) \boldsymbol{s}^{tr} \tag{25}$$

Combining the yield criterion (13) with (25) leads to one scalar nonlinear equation

$$\sqrt{\frac{3}{2}} \left(\frac{1-\omega(\kappa^n+\Delta\kappa)}{1-\omega(\kappa^n)} \left\| \boldsymbol{s}^{tr} \right\| - (1-\omega(\kappa^n+\Delta\kappa))\sqrt{6}G\Delta\kappa \right) - \sigma_Y(\kappa^n+\Delta\kappa) = 0 \tag{26}$$

with $\Delta\kappa$ as the unknown. This equation can be solved iteratively, for example by the Newton method.

4. Implicit-gradient regularization

In the previous section, two formulations coupling damage mechanics to the theory of plasticity were described, and their numerical implementation was presented. Now we focus on the regularization of the coupled damage-plastic models by the implicit-gradient formulation, with nonlocal cumulated plastic strain. In the regularized implicit-gradient formulation, the constitutive equations are enhanced by the nonlocal cumulated plastic strain, which is computed from a Helmholtz-type differential equation

$$\bar{\kappa} - l^2\nabla^2\bar{\kappa} = \kappa \tag{27}$$

with homogeneous Neumann boundary condition

$$\frac{\partial\bar{\kappa}}{\partial\boldsymbol{n}} = \boldsymbol{0}. \tag{28}$$

In the equations above, l is a length scale parameter, ∇ is the Laplace operator, and $\boldsymbol{n}$ is an outer normal.

To regularize the constitutive model properly, attention must be paid to its localization properties. For the local model, localization can occur if the tangent plastic modulus, i.e., the derivative of σ_Y with respect to κ, becomes equal to or less than the critical value H_c derived by the localization analysis based on the acoustic tensor [Ottosen and Runesson (1991)]. For a model with an associated flow rule, this critical value is never positive. Therefore, localization cannot happen before peak, but at peak or after peak it may occur. It can be shown that a nonlocal model provides a proper regularization (nonzero width of the localized process zone and nonzero dissipation) if the derivative of the nominal yield stress with respect to the local κ, denoted as H_L, remains above H_c. To be on the safe side, we would like to keep H_L positive, because $H_c \leq 0$.

For instance for a model with

$$\sigma_Y = \sigma_Y(\bar{\kappa}) \tag{29}$$

we have $H_L = 0$ and there is a danger of localization into an arbitrarily thin layer. This is the so-called basic nonlocal plastic model, which can be improved by the overnonlocal formulation, with

$$\sigma_Y = \sigma_Y(\hat{\kappa}) \tag{30}$$

where

$$\hat{\kappa} = m\bar{\kappa} + (1-m)\kappa \tag{31}$$

is the overnonlocal variable. In this case, $H_L = (1-m)\sigma'_Y$ where σ'_Y is the derivative of σ_Y with respect to its argument. If the nominal yield stress is decreasing, we have $\sigma'_Y < 0$ and then the condition $H_L > 0$ is satisfied for $m > 1$. However, this formulation fails if σ'_Y is changing from positive to negative values (first hardening, then softening), because the condition $H_L > 0$ cannot be satisfied in both ranges with the same constant m.

The standard nonlocal formulation of a damage-plastic model is based on

$$\sigma_Y = (1-g(\hat{\kappa}))\bar{\sigma}_Y(\kappa) \tag{32}$$

The local plastic modulus is given by

$$H_L = -(1-m)g'\bar{\sigma}_Y + (1-g)\bar{\sigma}'_Y \tag{33}$$

and the condition $H_L > 0$ translates into

$$\bar{\sigma}'_Y > \frac{(1-m)g'\bar{\sigma}_Y}{1-g} \tag{34}$$

where $\bar{\sigma}'_Y$ is the derivative of function $\bar{\sigma}_Y$ with respect to its argument and corresponds to the plastic modulus of the elastoplastic model without damage. The condition can be satisfied at least in two ways:

- using $\bar{\sigma}'_Y > 0$ and $m = 1$, which is the formulation with the usual nonlocal variable and with hardening elastoplastic part, see [Grassl and Jirásek (2006)];
- using $\bar{\sigma}'_Y \geq 0$ and $m > 1$, which is the overnonlocal formulation with an elastoplastic part that can contain a plateau (perfect plasticity without hardening) but must not soften, see [Charlebois, Jirásek and Zysset (2010)].

Localization capabilities of different implicit-gradient formulations will be explored in the next chapters by a representative numerical example.

4.1. Implementation of implicit gradient model

The implementation of the implicit gradient formulation is based on mixed finite elements. We start from the strong form of the set of governing differential equations

$$\nabla \cdot \boldsymbol{\sigma} = \mathbf{0} \tag{35}$$

$$\bar{\kappa} - l^2\nabla^2\bar{\kappa} = \kappa \tag{36}$$

Following the standard procedure, equations (35) and (36) are recast in the weak form,

$$\int_V (\nabla \cdot \boldsymbol{\sigma}) \cdot \boldsymbol{\eta} \, \mathrm{d}\boldsymbol{x} = 0 \tag{37}$$

$$\int_V (\bar{\kappa} - l^2\nabla^2\bar{\kappa})\eta \, \mathrm{d}\boldsymbol{x} = \int_\mathrm{V} \kappa\eta \, \mathrm{d}\boldsymbol{x} \tag{38}$$

where $\boldsymbol{\eta}$ and η are suitable test functions. The displacements and the nonlocal cumulative plastic strains are approximated at the element level by

$$\boldsymbol{u} = \boldsymbol{N}\boldsymbol{d} \qquad \bar{\kappa} = \boldsymbol{N}_{\bar{\kappa}}\boldsymbol{d}_{\bar{\kappa}} \tag{39}$$

where $\boldsymbol{N}$ and $\boldsymbol{N}_{\bar{\kappa}}$ are matrices containing the shape functions and $\boldsymbol{d}$ and $\boldsymbol{d}_{\bar{\kappa}}$ are vectors with the corresponding degrees of freedom (nodal displacements and nodal values of the nonlocal cumulated plastic strain). After discretization, we obtain the set of nonlinear algebraic equations

$$\left\{ \begin{array}{c} \boldsymbol{f}_{int} \\ \\ \boldsymbol{\phi}_{int} \end{array} \right\} = \left\{ \begin{array}{c} \boldsymbol{f}_{ext} \\ \\ \mathbf{0} \end{array} \right\} \tag{40}$$

in which $\boldsymbol{f}_{int}$ and $\boldsymbol{f}_{ext}$ are the standard internal and external forces and $\boldsymbol{\phi}_{int} = \int_V (\boldsymbol{N}_{\bar{\kappa}}^T\boldsymbol{N}_{\bar{\kappa}}\boldsymbol{d}_{\bar{\kappa}} + l^2\boldsymbol{B}_{\bar{\kappa}}^T\boldsymbol{B}_{\bar{\kappa}}\boldsymbol{d}_{\bar{\kappa}} - \kappa\boldsymbol{N}_{\bar{\kappa}}^T) \, \mathrm{d}\boldsymbol{x}$ are generalized internal forces. The set of nonlinear equations is solved by the Newton-Raphson iteration scheme. This numerical method requires a tangent matrix, which is obtained by differentiating the internal force vector with respect to the nodal unknowns:

$$\boldsymbol{K} = \begin{bmatrix} \dfrac{\partial \boldsymbol{f}_{int}}{\partial \boldsymbol{d}} & \dfrac{\partial \boldsymbol{f}_{int}}{\partial \boldsymbol{d}_{\bar{\kappa}}} \\ \\ \dfrac{\partial \boldsymbol{\phi}_{int}}{\partial \boldsymbol{d}} & \dfrac{\partial \boldsymbol{\phi}_{int}}{\partial \boldsymbol{d}_{\bar{\kappa}}} \end{bmatrix} \tag{41}$$

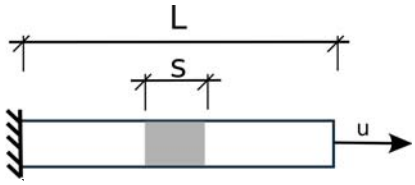

Fig. 1: Uniaxial tension test: Geometry and Loading

where

$$\frac{\partial \boldsymbol{f}_{int}}{\partial \boldsymbol{d}} = \int_V (1-\omega)\boldsymbol{B}^T \frac{\partial \boldsymbol{\theta}}{\partial \boldsymbol{\varepsilon}} \boldsymbol{B}\, \mathrm{d}\boldsymbol{x} \qquad \frac{\partial \boldsymbol{f}_{int}}{\partial \boldsymbol{d}_{\bar{\kappa}}} = -\int_V \frac{d\omega}{d\kappa} \boldsymbol{B}^T \bar{\boldsymbol{\sigma}} \boldsymbol{N}_{\bar{\kappa}}\, \mathrm{d}\boldsymbol{x}$$

$$\frac{\partial \boldsymbol{\phi}_{int}}{\partial \boldsymbol{d}} = -\int_V \boldsymbol{N}_{\bar{\kappa}}^T \frac{\partial \boldsymbol{\theta}_\kappa}{\partial \boldsymbol{\varepsilon}} \boldsymbol{B}\, \mathrm{d}\boldsymbol{x} \qquad \frac{\partial \boldsymbol{\phi}_{int}}{\partial \boldsymbol{d}_{\bar{\kappa}}} = \int_V \left(\boldsymbol{N}_{\bar{\kappa}}^T \left(1 + \frac{\partial \boldsymbol{\theta}_\kappa}{\partial \bar{\kappa}} \right) \boldsymbol{N}_{\bar{\kappa}} + l^2 \boldsymbol{B}_{\bar{\kappa}}^T \boldsymbol{B}_{\bar{\kappa}} \right) \mathrm{d}\boldsymbol{x}$$

In the equations above, $\boldsymbol{B}$ and $\boldsymbol{B}_{\bar{\kappa}}$ are matrices containing derivatives of the shape functions, $\dfrac{\partial \boldsymbol{\theta}}{\partial \boldsymbol{\varepsilon}}$ corresponds to classical elasto-plasto-damage stiffness and functions $\boldsymbol{\theta}_\kappa$ is supplied by the return mapping algorithm.

5. Numerical example

Simulation of a one-dimensional bar in tension is carried out to demonstrate regularization properties of different implicit-gradient formulations of plasticity coupled to isotropic damage. Geometry of the problem is plotted in Fig. 1, the material and geometrical parameters are summarized in Tab. 1. Influence of the nonlocal formulation on the profile of damage along the bar is studied. Isotropic linear hardening of the effective yield stress and exponetial evolution of damage is considered:

$$\bar{\sigma}_Y = \sigma_0 + H\kappa \tag{42}$$

$$\omega = 1 - \mathrm{e}^{-\mathrm{a}\kappa} \tag{43}$$

This yields to the nominal stress in the form

$$\sigma_Y = (1 - \mathrm{e}^{-\mathrm{a}\kappa})(\sigma_0 + \mathrm{H}\kappa) \tag{44}$$

At first, the over-nonlocal regularization based on nonlocal damage is considered, i.e. $\omega = g(\hat{\kappa})$. In this approach, the nonlocal cumulated plastic strain affects only the damage variable, while plasticity is formulated in the effective stress space and therefore remains local. The advantage of this approach is in a simple implementation based on the local return mapping algorithm followed by an explicit evaluation of the damage variable. The second class of models considered here is based on the over-nonlocal averaging of the nominal yield stress, $\sigma_Y = \sigma_Y(\hat{\kappa})$. Fig. 2 and Fig. 3 show the distribution of damage along the bar for different stages of loading for the first approach and the second approach, respectively. Finally, Fig. 4 compares the distribution of the damage variable obtained by the formulation based on the effective stress and by the formulation based on the nominal stress.

6. Conclusions

We have presented two formulations coupling plasticity with damage, and introduced two different implicit-gradient regularization schemes which lead to an objective description of localized failure processes. We have shown that even if the local models are fully equivalent, the nonlocal formulation can lead to substantially different results; therefore it is neccesary to pay attention when constructing the nonlocal extension. Further research will focus on the comparison of the computational efficiency of both models, and on extensions of the gradient regularization to more general yield conditions.

Length of bar	L	100 mm
Length of imperfection	s	20 mm
Cross-sectional area	A	100 m
Young's modulus	E	20 GPa
Isotropic hardening law	$\sigma_Y = \sigma_0 + H\kappa$	
Initial yield stress	σ_0	2 MPa
Initial yield stress (imperfection)	σ_0	1.8 MPa
Hardening modulus	H	600 MPa
Damage law	$\omega = 1 - \exp^{-a\kappa}$	
Dimensionless damage parameter	a	300
Characteristic length	l	5 mm

Tab. 1: Uniaxial tension test: Geometrical and material parameters

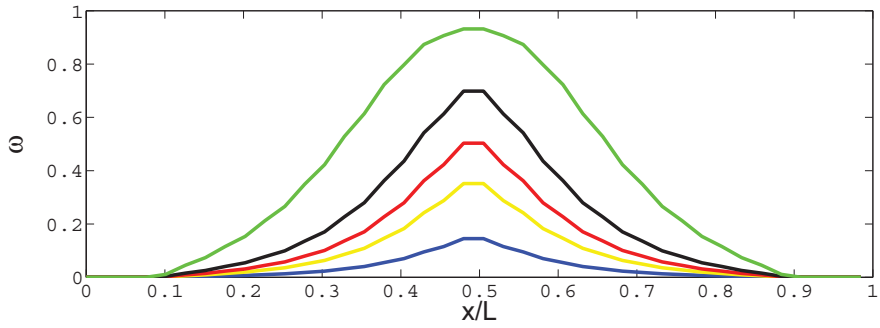

Fig. 2: Evolution of damage profile for formulation 1

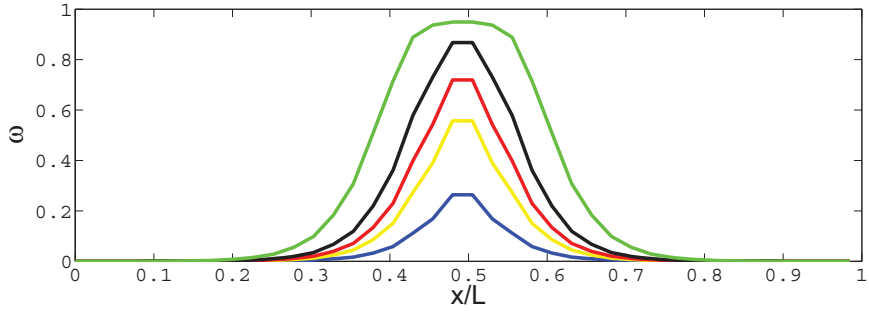

Fig. 3: Evolution of damage profile for formulation 2

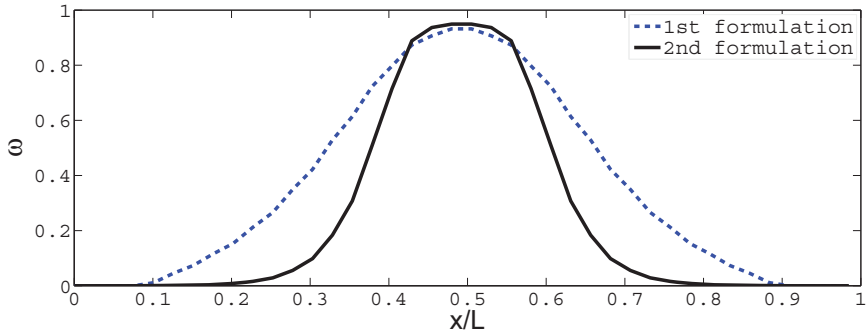

Fig. 4: Comparison of damage distribution

Acknowledgments

Financial support of of the Czech Technical University in Prague under project SGS12/027/OHK1/1T/11 is gratefully acknowledged.

References

Grassl P., and Jirásek M. (2006), Plastic model with non-local damage applied to concrete. *International Journal for Numerical and Analytical Methods in Geomechanics*, Vol 30, pp 71-90.

Charlebois, M., Jirásek, M. and Zysset, Ph. (2010), A nonlocal constitutive model for trabecular bone softening in compression. *Biomechanics and Modeling in Mechanobiology*, Vol 9, pp 597-611.

Engelen R.A.B., Geers M.G.D., Baaijens, F.P.T. (2003), Nonlocal implicit gradient-enhanced elasto-plasticity for the modelling of softening behaviour. *International Journal of Plasticity*, Vol 19, pp 403-433.

Krieg, R. D. and Key, S. W. (1976), Implementation of a time dependent plasticity theory into structural computer programs. *Constitutive Equations in Viscoplasticity: Computational and Engineering Aspects*, ASME, New York.

Maugin, G. (1992), The Thermomechanics of Plasticity and Fracture. *Cambridge University Press.*

Ottosen, N. and Runesson, K. (1991), Properties of discontinuous bifurcation solutions in elastoplasticity. *International Journal of Solids and Structures*, Vol 27, pp 401-421.

18th International Conference
ENGINEERING MECHANICS 2012
Svratka, Czech Republic, May 14 – 17, 2012

pp. 427–432
Paper **#224**

THE STUDY OF MECHANICS OF DEFORMATION BEHAVIOUR OF SERVICE ROBOTS GRIPPING SYSTEMS

M. Horák[*], F. Novotný[**]

Abstract: *This paper presents an analysis of the gripping system and contact links with a vertical plane of contact. It focuses on comparing the classic gripping elements and elements which combined methods of gripping force deducing with the using of different physical principles (vacuum, friction and adhesion). The first part of the paper describes the behavior of suction cups used as standard during radial loading using a computer simulation depending on rigidity of an elastomer sealing rim of the suction cup. The second part illustrates structural modifications of the suction cup by means of a bearing supporting plate having a material with an adhesion layer on the contact boundary and allowing the down-pressure to be regulated depending on mechanical properties of the object kept.*

Keywords: ***Gripping element, suction cup, vacuum, adhesion, contact.***

1. Introduction

In most cases it concerns applications combining the latest smart vacuum technology with high-tech systems of multi-angle industrial robots having six degrees of freedom that replace standard single-purpose manipulators step by step. When handling of jumbo formats of sheets having boundary dimensions ca. 3 x 6 m, nowadays a cooperation of two robots placed on a common travelling device is used. It is obvious that a handling task like this makes high demands for providing the parallel motion of both robots. Possible inaccuracies in positioning (Horák, 2005) find distinct expression in an undesirable loading of the sheet gripped, excessive loading of the robot wrist and vacuum gripping elements.

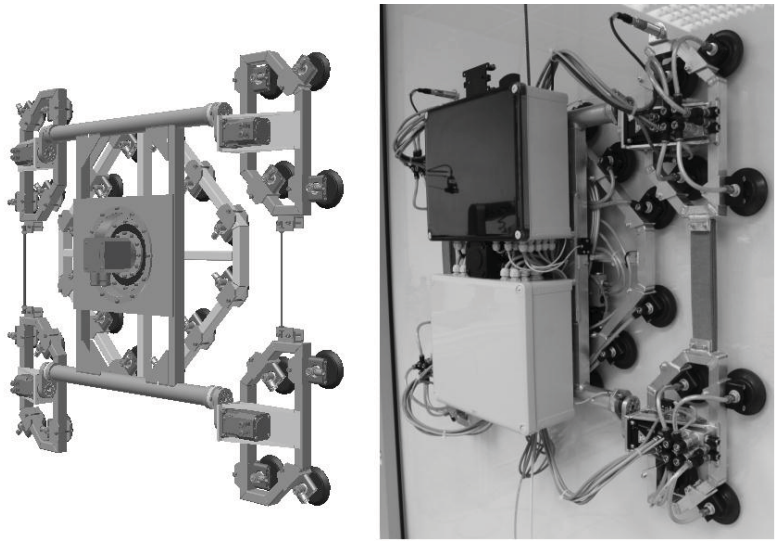

Fig. 1: Developed service robot platform for a motion on the vertically oriented glass walls

[*] Ing. Marcel Horák, Ph.D.: Technical University of Liberec, Faculty of Mechanical Engineering, Department of Glass Producing Machines and Robotics; Studentská 1402/2; 461 17, Liberec; CZ, e-mail: marcel.horak@tul.cz

[**] doc. Ing. František Novotný, CSc.: Technical University of Liberec, Faculty of Mechanical Engineering, Department of Glass Producing Machines and Robotics; Studentská 1402/2; 461 17, Liberec; CZ, e-mail: frantisek.novotny@tul.cz

The use of suction cups in the field of holding-down systems, such as locomotion devices (chassis) of service robots allowing the autonomous motion on vertically oriented walls, is a reciprocal task (Fig. 1). As for the systems based on the stepping principle of the robot motion (Novotný & Horák & Plavec, 2011), changes in the center of gravity distance occur, which has a negative impact on the loading pattern of particular suction cups subjected to radial and axial forces as well as to tilting moments depending on the geometry of the chassis kinematics (climbing robot).

It is necessary to specify such safety level so that the gripping or holding-down system satisfied the requirements for the stable keeping in the all regimes of loading. Thus, authors put the accent on an analysis of deformation behavior of suction cups with a rigid body and flexible sealing rim. The basic aim is focused to modify the contact areas of the suction cup in order to increase their load capacity in radial direction when a preservation of the vacuum level, because during the robot motion on the vertical walls the suction cups are overtaxed in the radial direction.

2. Deformation analysis of standard suction cup – computer model

The contact of the suction cup and sheet in accordance with the classic power conception has been already analyzed in (Novotný & Horák, 2008), where it was found that a resultant value of the safety coefficient is in the region of 14 to 20 respecting changes in the friction character in any position of the gripping plane. To have the full picture, the classic power analysis was supplied experimentally verified results of the computer simulation using the finite-element method, when an adequate numerical model of the standard suction cup was created (Fig. 2) respecting material properties of TPU (Horák, 2008) for the description of which the Mooney-Rivlin rheological model was used, when it is valid that

$$\frac{F}{2A_0\left(\lambda_1-\frac{1}{\lambda_1^2}\right)}=c_{10}+\frac{c_{01}}{\lambda_1}, \tag{1}$$

where F = force, λ_1 = deformation, c_{10} and c_{01} is Mooney-Rivlin material constant and A_0 is the cross section initial area during uniaxial tension test (1). When the test results are known, it's possible to determine the material constants from main stress in dependency on the actual deformation λ_1. In the other cases it can be used the relations (2) and (3) for the determination of material constants depending on the modulus of elasticity E.

$$c_{01}\cong\frac{1}{4}c_{10}, \tag{2}$$

$$6\cdot\left(c_{10}+c_{01}\right)\cong E\,. \tag{3}$$

Boundary conditions describing the character of frictional conditions were set on the basis of the laboratory test results. It was demonstrated that the friction coefficient values have been dependent substantially on a state of the contact material surface (glass), which is resumed clearly in the diagram in Fig. 3.

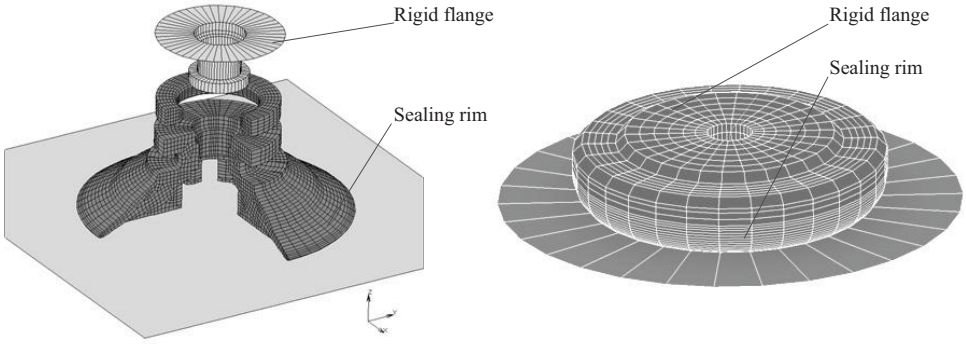

Fig. 2: Computer models for two basic types of standard suction cups

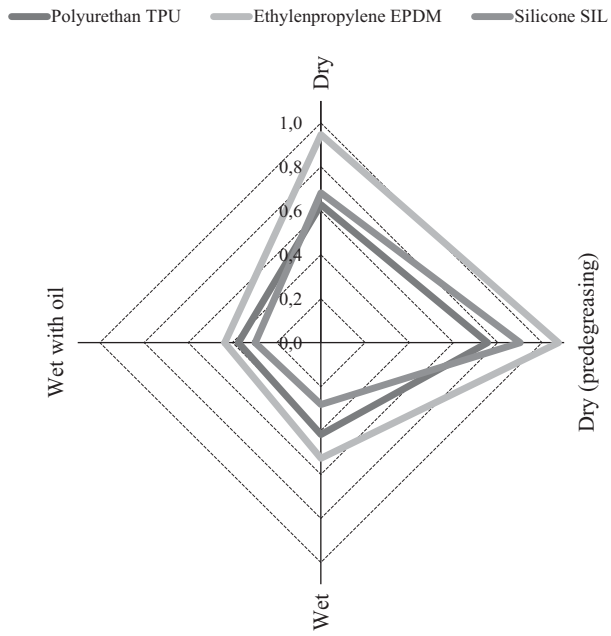

Fig. 3: Friction coefficient

The computer model was also optimized from standpoint of a variable active surface of the suction cup depending on the loading profile; this surface is defined by the suction cup effective diameter (important for the suction cup without a rigid body). The actual contact area corresponding to the loading level was detected in view of the state of contacting bodies (the contact quality) during each step of the calculation. This effect contributed greatly to obtaining of the representative computer model of the suction cup behavior during external loading.

3. Computer simulation results

During the computer simulation of the suction cup (with the rigid body - rigid bearing plate) deformation behavior (the geometrical diameter of 60 mm), the series of calculations was carried out. Subsequently the model created (Fig. 4) allows an influence of the sealing rim rigidity on a course of the contact profile shift to be evaluated depending on the radial loading force F_{RAD} value.

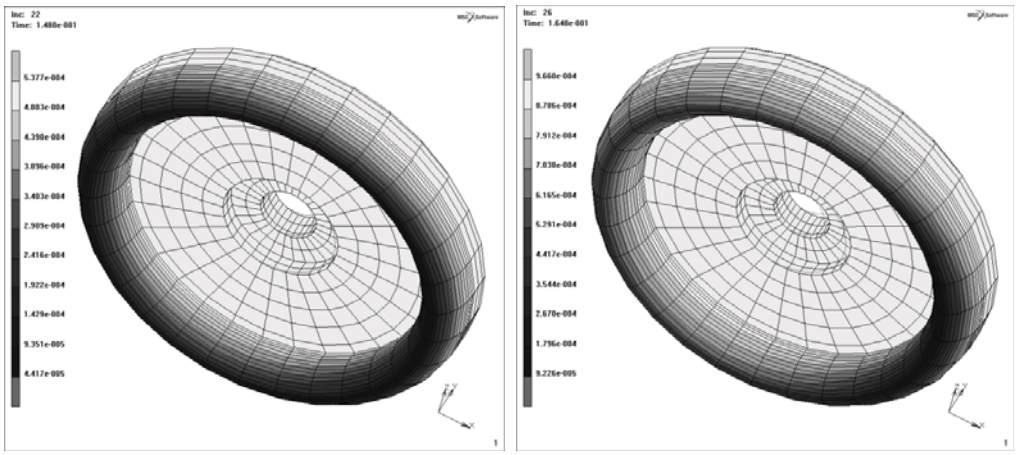

F_{RAD} = 120 N F_{RAD} = 160 N

Fig. 4: Deformation of the suction cup's sealing edge in axis x (vacuum level -60 kPa)

Being based on a series results, the course of the contact profile shift in the plane perpendicular to the suction cup axis was analyzed in detail at pre-selected points owing to the action of the external radial force. The course characters depending on the elastic modulus in the range 2-30 MPa and the friction coefficient 0.8 are shown in diagrams in Figures 5 and 6. The real behaviour of the sealing rim is replaced by the Mooney-Rivlin material model (MSC.Marc, 2004, MSC.Marc, 2005).

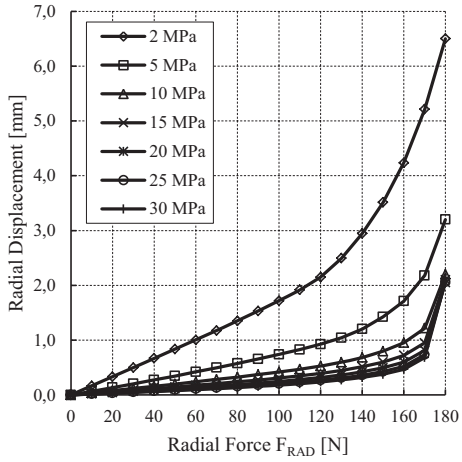

Fig. 5: Distance of the suction cup center

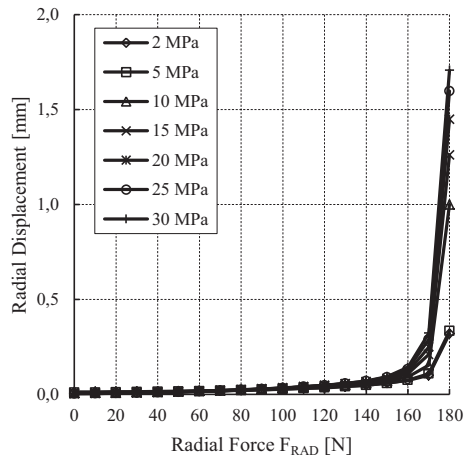

Fig. 6: Distance of profile edge

From the standpoint of the contact stability, the given results show that primary shifts of the contact profile of the suction cup occur already in the radial loading range from 60 to 120 N. The range from 120 to 140 N is to be found on the contact stability limit. Any next increase of the loading results in a collapse and subsequently it leads to the suction cup shifting in the plane of loading (Novotný & Horák, 2009, Novotný & Horák, 2010).

4. Combined vacuum adhesive gripping element

The proposed design solution combining the vacuum gripping element (GE) with a rigid flange, a flexible sealing rim, and a withdrawable positionable plate treated by an adhesive layer is a one possibility to increase the radial load capacity (Horák & Novotný, 2011).

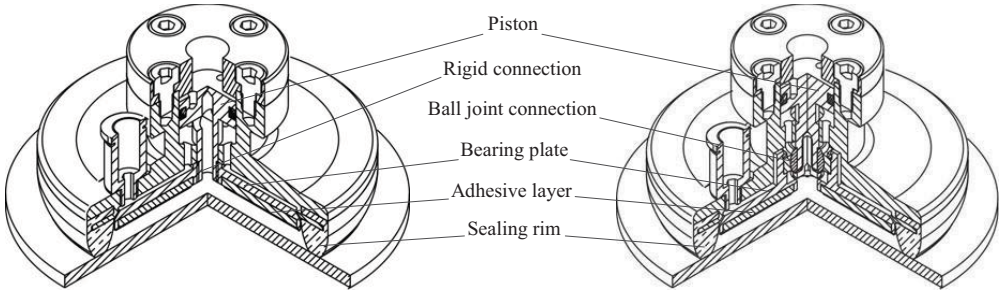

Fig. 7: GE without flatness compensation

Fig. 8: GE with flatness compensation

The technical solution concept is illustrated in Fig. 7 which comprises a detailed section of the gripping element configuration with a rigid threaded connection of the bearing plate and the piston. Fig. 8 shows the solution enabling to adjust automatically the adhesive layer or the bearing plate orientation depending on an orientation of the object contact surface (the plate and the piston are connected through a ball joint) in position when the adhesive insert is out of the contact with the object handled.

4.1. Results of laboratory tests

The aim of tests was to verify a utility of the solution in terms of an increase in the element load capacity particularly in the radial (tangential) direction as well as to analyze the gripping system behavior at various vacuum levels, and in different degree of the bearing plate putting out or putting in owing to the handled object, and also to define its optimal position. Results of primary tests are shown in diagrams in Figures 9 and 10.

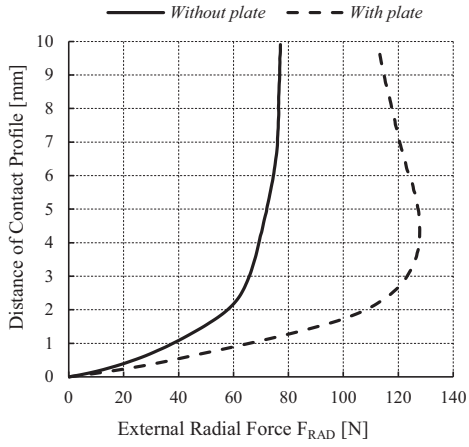

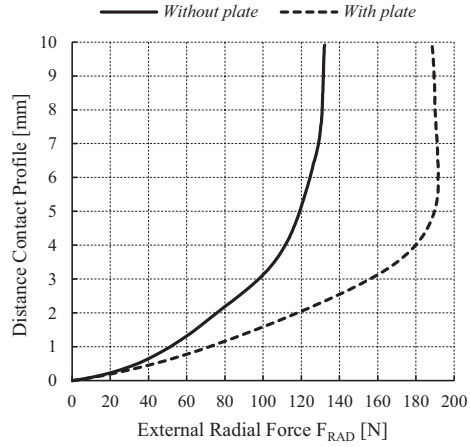

Fig. 9: Rad. distance of profile (vacuum -40 kPa) *Fig. 10: Rad. distance of profile (vacuum -80 kPa)*

4.2. Tests evaluation

From the diagrams given it results that the adhesive layer together with the bearing plate affects evidently the gripping (contact) stability and finds expression in a marked increase of the load capacity (Fig. 11) which is dependent on the observed level of the contact profile shift and vacuum, and ranges from 31% to 94%. As for a pure stabile character of the contact defined by the determined maximum shift 0.5mm, the load capacity increase as high as **60 %** at average.

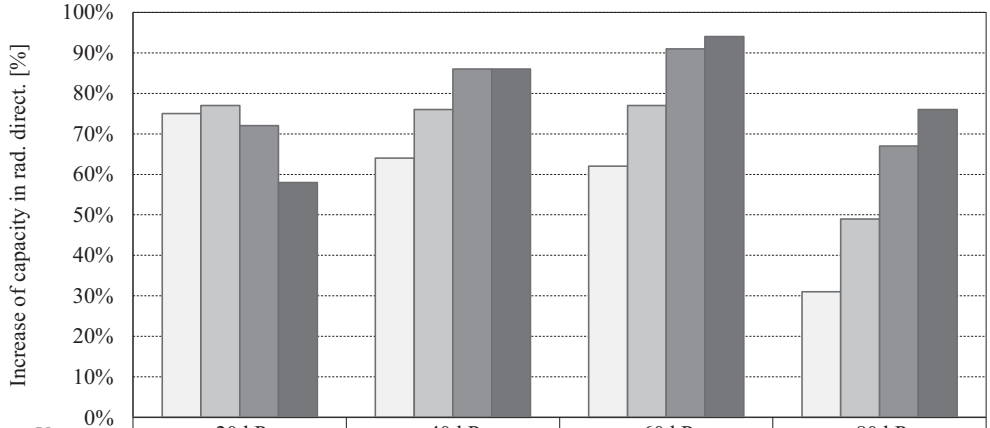

Displacement \ Vacuum	- 20 kPa	- 40 kPa	- 60 kPa	- 80 kPa
0,5 mm	75%	64%	62%	31%
1,0 mm	77%	76%	77%	49%
1,5 mm	72%	86%	91%	67%
2,0 mm	58%	86%	94%	76%

Fig. 11: The increase in load capacity of gripping element in the radial direction

5. Conclusions

The paper submitted describes possibilities of an industrial utilization of adhesive layers for designing gripping elements. The computer model of the vacuum gripping element used as standard was prepared, and the effect of the sealing rim rigidity on the contact stability was analyzed during external loading in the contact plane.

The main part was focused on problems related to increasing the load capacity of elements in radial direction by reason of unprecedented demands on vacuum gripping heads in connection with the new production technologies and methods. A vacuum-adhesive gripping element was designed and tested in laboratory. Provided clean operation, it was shown during tests that the use of adhesive layers leads to increasing of the radial load capacity at tens of per cents in comparison with standard solutions whereas the vacuum level is kept.

Acknowledgement

This work was supported by the Research plan No. MSM 4674788501 and OP Research and Development for Innovation: Centre for Nanomaterials, Advanced Technologies and Innovation, CZ.1.05/2.1.00/01.0005.

References

Horák, M. (2005) Dynamická manipulace s tenkými deskami skla. *Disertační práce*, Liberec: Technická univerzita v Liberci, 2005. 133 s.

Novotný, F. & Horák, M. & Plavec, M. (2011) Mobilní plošina pro pohyb po vertikální stěně. *Utility model No. 22900*, http://spisy.upv.cz/UtilityModels/FullDocuments/FDUM0022/uv022900.pdf

Novotný, F. & Horák, M. (2008) Robot Handling in Automatic Flat Glass Production. *Acta Mechanica Slovaca*, 12 [2008], č. 2-A, s. 419-430. ISSN 1335-2393.

Horák, M. (2008). Dynamická manipulace s plochým sklem. Liberec: TU v Liberci. 2008. 165 s., ISBN 978-80-7372-425-2.

MSC.Marc® (2004) Nonlinear Finite Element Analysis of Elastomers. *Technical paper*, p. 66.

MSC.Marc® (2008) Manual Volume A - Theory and User Information. p. 793.

Novotný, F. & Horák, M. (2009) Computer Modelling of Suction Cups used for Window Cleaning Robot and Automatic Handling of Glass Sheets. *MM Průmyslové spektrum - MM Science Journal*, č. 2, MKČR E 7645. p. 113-116. ISSN 1803-1269. www.mmscience.eu/20090304.

Novotný, F. & Horák, M. (2010) Problems of Loading Capacity of Suction Cups in the Radial Direction. In: *Proceedings of the Fifth International Conference on Optimisation of the Robots and Manipulators*, Calimanesti, Romania, p. 70-74, ISBN 978-981-08-5840-7, doi: 10.3850/978-981-08-5840-7_S2-4.

Horák, M. & Novotný, F. (2011) Podtlakový úchopný prvek. *Utility model No. 22075*, *Patent No. 302959*, http://spisy.upv.cz/UtilityModels/FullDocuments/FDUM0022/uv022075.pdf, http://spisy.upv.cz/Patents/FullDocuments/302/302959.pdf

Horák, M. & Novotný, F. (2011) Increases in the Radial Capacity of Vacuum Gripping Elements. *MM Science Journal, October 2011*, Special Edition - 20th International Workshop on Robotics in Alpe-Adria-Danube Region (RAAD), October 5-7 2011, MKČR E 7645, www.mmscience.eu, p. 122-127. ISSN 1803-1269 (Print), ISSN 1805-0476 (On-line)

18th International Conference
ENGINEERING MECHANICS 2012
Svratka, Czech Republic, May 14 – 17, 2012

pp. 433–448
Paper #41

APPLICABILITY OF EXISTING INDEXES OF NON-PROPORTIONALITY OF DAMPING IN CASE OF THEORETICAL MODEL OF SLENDER STRUCTURE WITH INSTALLED TMD

S. Hračov[*], S. Pospíšil[**], J. Náprstek[***]

Abstract: *The paper analyzes an applicability of to date published indexes of non-proportionality in the case of a linear viscously damped numerical model of slender structure equipped with tuned mass damper (TMD). The installation of TMD into the structure not only reduces the level of undesired vibration, but it can also cause due to damping element of TMD a significant increase of damping non-proportionality. The paper recommends the most suitable indexes for such a type of structure and points out to impropriety of the others. The point of view of is also focus on the validity of the existing criterions for neglecting of non-diagonal terms of a modal damping matrix. Only indexes and criterions based on the properties of the modal damping matrix were taking into account. The verifications of validity and recommendations for usage of particular indexes and criterions were performed using analysis of the dynamic response of an existing structure on harmonic excitation with and without neglecting of non-diagonal terms of modal damping matrix. The applicability was also checked using analysis of particular complex eigen-modes.*

Keywords: ***Indexes of non-proportionality of damping, tuned mass damper, slender structure***

1. Introduction

Numerically efficient solution of a dynamic response of linear viscously damped numerical models of real structures using modal superposition method (MSM) see e.g. Hart & Wong (2000) motivates many authors to set boundaries, to which the inaccuracy of a solution with neglecting of non-diagonal terms of a modal damping matrix is still acceptable. Simultaneously, they attempted to quantify an extent of non-proportionality of the damping by means of indexes of various types.

The first group of indexes of non-proportionality is related to complex eigen-modes. Prater & Singh (1986) defined two indexes based on calculations of surfaces that form individual components of complex eigen-modes in the complex plane. Another two indexes suggested by these authors are functions of phase differences between individual complex components. Similarly in Bhaskar (1999), an index related to a modal area, which creates components of the complex eigen-modes in the complex plane was proposed. The second index defined in this paper is based on a placement of components of complex eigen-modes in the complex plane and on their relative position to the position of components of eigen-modes of the same proportionally (classically) damped system. Three indexes based on relation of a real and a complex part of eigen-modes formulated Liu et al. (2000). Prells & Friswell (2000) proposed an index of non-proportionality equal to a norm of difference between orthonormal matrix generated from complex eigen-modes and a unit matrix. All above mentioned indexes require calculation of complex eigen-values and eigen-modes. Thus almost all the main numerical advantages of subsequent and prospective using of MSM are lost. More accurate results of the calculation of the response with negligible added computational time in comparison with MSM could be reached by complex mode superposition method

[*] Ing. Stanislav Hračov, Ph.D.: Institute of Theoretical and Applied Mechanics AS CR, v.v.i.; Prosecká 76; 140 00, Prague; CZ, e-mail: hracov@itam.cas.cz

[**] doc. Stanislav Pospíšil, Ph.D.: Institute of Theoretical and Applied Mechanics AS CR, v.v.i.; Prosecká 76; 140 00, Prague; CZ, e-mail: pospisil@itam.cas.cz

[**] Ing. Jiří Náprstek, DrSc.: Institute of Theoretical and Applied Mechanics AS CR, v.v.i.; Prosecká 76; 140 00, Prague; CZ, e-mail: naprstek@itam.cas.cz

see Hurty & Rubinstein (1964). This method utilizes the previously calculated complex eigen-modes to uncouple the system of differential equation of the numerical model.

More useful from the point of view of the computational time is the second group of indexes and criterions, which do not require the previous calculation of complex eigen-modes. The indexes are derived from a distribution of damping elements in the modal damping matrix, from a mutual frequency distances between the dominant frequency of a loading and individual eigen-frequencies and between eigen-frequencies themselves. In this paper short summary of till now published indexes and criterions of this type are presented. The focus is aimed especially at their applicability for numerical models of slender structures equipped with a tuned mass damper. On an example of real structure errors in response on harmonic excitation that are caused by neglecting of non-diagonal terms of the modal damping matrix are investigated together with indexes and criterions for selected damping ratios of absorber. On the basis of mutual relation of errors and criterions and of indexes and calculated complex eigen-modes the most appropriate ones are recommended.

2. Theoretical background

The discrete mathematical model of structure and its response can be described by very well-known system of differential equations of the second order:

$$\mathbf{M}\ddot{\mathbf{x}}(t)+\mathbf{C}\dot{\mathbf{x}}(t)+\mathbf{K}\mathbf{x}(t)=\mathbf{p}(t) \tag{1}$$

K, **M** and **C** are the stiffness, mass and damping matrices respectively; **x***(t)* and **p***(t)* are the displacement and force vectors. The key to analysis of the response of the governing system (1) using MSM is the transformation:

$$\mathbf{x}(t)=\mathbf{X}\mathbf{q}(t) \tag{2}$$

where **q***(t)* is a vector of principal (modal) co-ordinates and **X** is the matrix, columns of which are real eigen-modes of the undamped system. The substitution (2) leads to set of uncoupled differential equations, if the modal damping matrix:

$$\tilde{\mathbf{C}}=\mathbf{X}^{\mathbf{T}}\mathbf{C}\mathbf{X} \tag{3}$$

is diagonal i.e. it fulfills the relation:

$$\mathbf{K}\mathbf{M}^{-1}\mathbf{C}=\mathbf{C}\mathbf{M}^{-1}\mathbf{K} \tag{4}$$

In this case the mathematical expression of viscous damping is called proportional or classical. When the modal damping matrix is not diagonal the equations in principal coordinates are coupled. The simplest method to obtain uncoupled equations is to neglect the non-diagonal terms of this modal damping matrix. Nevertheless this method could lead to significant error in calculation of the response due to omitting of a presence of a mechanical interaction between eigen-modes.

3. Indexes of non-proportionality and criterions for neglecting of non-diagonal terms of modal damping matrix

In this chapter to date published indexes of non-proportionality and criterions which are based on properties of modal damping matrix are summarized. Short comments on their limitations and usability are attached to their mathematical formulations.

The basic and the most general requirement and criterion for the neglecting of non-diagonal terms of modal damping matrix is a diagonal dominance of the modal damping matrix:

$$\left|\tilde{C}_{ii}\right| > \sum_{\substack{j=1 \\ j\neq i}} \left|\tilde{C}_{ij}\right| \qquad pro\ \forall i \tag{5}$$

The first relevant criterion for possible omitting of the mechanical interaction between eigen-modes was suggested by Hasselman (1976). He expressed the condition for possible ignoring of non-diagonal terms in a form:

$$\sqrt{\frac{2\zeta_r}{\left(\omega_s/\omega_r\right)^2-1}} \ll 1 \tag{6}$$

where ζ_r is a damping ratio of the r-th eigen-mode given by:

$$\zeta_r = \widetilde{C}_{rr}/2\omega_r \tag{7}$$

and ω_s is the s-th and ω_r is the r-th eigen-frequency of the undamped system. However it is supposed, that a ratio of both examined eigen-frequencies is smaller than unity:

$$\omega_s/\omega_r > 1 \tag{8}$$

Next assumption of a usability of the condition (6) is:

$$\widetilde{C}_{rs}/\widetilde{C}_{rr} < 1 \tag{9}$$

Generally, the Hasselman's criterion removes the main difference between non-classically and classically damped systems. It supposes also high mechanical interaction of eigen-modes of classically damped systems which lies close to each other.

Similar to condition (6) Warburton & Soni (1977) defined a criterion based on a solution of the response on harmonic excitation in a form:

$$\zeta_r < \varepsilon \left| \frac{\tilde{C}_{rr}}{2\tilde{C}_{rs}} \left(\frac{\omega_s^2}{\omega_r^2} - 1 \right) \right|_{\min s} \tag{10}$$

Coefficient ε expresses the maximal value of desired and acceptable error in determination of the response. For problems in practice the authors recommended the value of ε equal:

$$\varepsilon = 0,05 \tag{11}$$

This value should correspond to relative error up to 10 percent. In comparison to criterion (6) the condition (10) is taking into account a ratio of diagonal and non-diagonal terms of modal damping matrix.

In the paper of Prater & Singh (1986) three indexes non-proportionality are published. For the purposes of their mathematical expressions authors divided the modal damping matrix into a sum of diagonal matrix $\mathbf{C}_\mathrm{d}$ and matrix $\mathbf{\Gamma}$ which has zero diagonal terms:

$$\tilde{\mathbf{C}} = \mathbf{C}_d + \mathbf{\Gamma} \tag{12}$$

The first generalized index is defined as the quotient between the sum of non-diagonal terms of the transformed damping matrix and the sum of all its terms:

$$\delta_1 = \sum_{i=1}^{n}\sum_{j=1}^{n}\left|\Gamma_{ij}\right| / \sum_{i=1}^{n}\sum_{j=1}^{n}\left|\tilde{C}_{ij}\right| \tag{13}$$

Index (13) indicated the degree of non-proportionality of the damping of the system as a whole. In problems where the response is investigated only in given frequency range or when only few eigen-modes are coupled due to the damping, it is recommended to use the modified index (13) in a form:

$$\delta_{1i} = \sum_{j=1}^{n}\left|\Gamma_{ij}\right| / \sum_{j=1}^{n}\left|\tilde{C}_{ij}\right| \tag{14}$$

which is valid for i-th eigen-mode. The second index proposed by Prater & Singh (1986) is given by ratio of the determinants of matrices $\mathbf{\Gamma}$ and $\mathbf{C}_\mathrm{d}$:

$$\delta_2 = \frac{\left|\mathbf{\Gamma}\right|}{\left|\tilde{\mathbf{C}}\right|} \tag{15}$$

Since the determinant is scalar, no index of particular eigen-mode can be formulated. The third proposed index is based on comparison of the response of a system with full modal damping matrix and the same system with modal damping matrix with diagonal terms only. The response of both systems on harmonic load is given by solution of following system of differential equations:

$$\left(-\omega^2\mathbf{I}+\mathrm{i}\,\omega\tilde{\mathbf{C}}+\mathbf{\Lambda}\right)\mathbf{q}=\mathbf{f} \tag{16}$$

The vector of amplitudes of harmonic forces is assumed as a unity vector **f**:

$$\mathbf{f}=\left[1,1,\ldots,1\right]^{\mathrm{T}} \tag{17}$$

The loading frequencies ω are chosen equal to the damped eigen-frequencies with damping ratios given by equation (7) in which one can expect the highest response:

$$\omega=\omega_{di}=\sqrt{1-\zeta_i^2}\,\omega_i \tag{18}$$

The proposed response based index of i-th eigen-mode is then given by ratio of difference between amplitude of steady state response of approximate $\hat{q}_i$ and full modal system q_i and amplitude q_i:

$$\delta_{3i}=\frac{\left|\left(\left|q_i\right|-\left|\hat{q}_i\right|\right)\right|}{\left|q_i\right|} \tag{19}$$

To quantify the amplitude q_i the whole matrix system (16) must be solved. In the case of system with neglected non-diagonal terms of modal damping matrix for amplitude $\hat{q}_i$ it holds:

$$\hat{q}_i=\frac{1}{-{\omega_{di}}^2+\omega_i^2+\mathrm{i}\,\omega_{di}\tilde{C}_{ii}} \tag{20}$$

It is also possible to define the overall index as an arithmetic mean:

$$\delta_3=\frac{1}{n}\sum_{i=1}^{n}\delta_{3i} \tag{21}$$

Authors recommended omitting of non-diagonal terms of modal damping matrix if following conditions are fulfilled:

$$\delta_1\ll 1 \qquad \delta_2\ll 1 \qquad \delta_3\ll 1 \tag{22}$$

From the point of view of numerical difficulty the index δ_1 is the most appropriate. Index δ_2 was determined by authors as the less useful. The third index δ_3 could serve as indicator of error rate of the response of variously modified damped systems.

Tong et al. (1994) defined an index for quantifying the damping non-proportionality as:

$$I=\left(\sigma_{\max}-\sigma_{\min}\right)/\left(\sigma_{\max}+\sigma_{\min}\right) \tag{23}$$

σ_{max} and σ_{min} are the maximum and minimum eigen-values of matrix **H**:

$$\mathbf{H}=\tilde{\mathbf{C}}_d^{-1}\tilde{\mathbf{C}} \tag{24}$$

Coefficient I is zero for classically damped system. With increasing of the non-proportionality of the damping the coefficient approximates the unity. Authors defined an upper bound of the relative error of the response caused by neglecting of non-diagonal terms in the case of harmonic load as follows:

$$E\left(\omega\right)\le I\left(\tilde{\mathbf{C}}\right)+\left(\frac{\max(\tilde{C}_{ii})}{\min(\tilde{C}_{ii})}\right)^{1/2} \tag{25}$$

The degree of non-proportionality of the damping based on relations of the non-diagonal and diagonal terms of the modal matrix was presented by Venancio-Filho et.al. (2001):

$$\chi_r = \max \left| \frac{\tilde{C}_{rs}^2}{\tilde{C}_{rr}\tilde{C}_{ss}} \right| \tag{26}$$

However, the limiting value of coefficient (26) for approximative solution by neglecting of non-diagonal terms of the modal damping matrix was not given.

Bhaskar (1995) proposed an index which originates from the solution of the response of the system on harmonic excitation. For i-th eigen-mode it has a form:

$$\kappa_i = \frac{\sum_{j=1}^{n} \left| \Gamma_{ij} \right|}{\left(\left(1/\omega^2 \right) \left(\omega_i^2 - \omega^2 \right)^2 + \tilde{C}_{ii}^2 \right)^{1/2}} \tag{27}$$

For diagonally dominant modal matrix the coefficient κ_i should fulfill a condition:

$$0 \le \kappa_i < 1 \tag{28}$$

Coefficients (27) include not only the terms of modal damping matrix but also a frequency of the loading and a relation of the loading frequency to the eigen-frequencies. If one is interested only in upper bound of non-proportionality of the damping, the coefficient (27) could be simplified in a form:

$$\kappa_i \le \frac{\sum_{j=1}^{n} \left| \Gamma_{ij} \right|}{\tilde{C}_{ii}} \tag{29}$$

Gawronski & Sawicki (1997) derived an upper bound of the relative error of the response in modal coordinates for the case of neglecting of non-diagonal terms of modal damping matrix. The condition of the error of i-th modal coordinate is given by:

$$\frac{\left| q(\omega_i) - \hat{q}(\omega_i) \right|}{\left| q(\omega_i) \right|} \le \frac{\nu_i \sigma_i}{2\xi_i \omega_i} \tag{30}$$

where coefficient σ_i is given by a sum of terms of the *i*-th row of the non-diagonal matrix $\boldsymbol{\Gamma}$:

$$\sigma_i = \sum_k \left| \Gamma_{ik} \right| \tag{31}$$

Coefficient ν_i is the maximum from a series:

$$\nu_i = \max_{k \ne i} \left(\nu_{i,k} \right) \tag{32}$$

Coefficient $\nu_{i,k}$ is scalar, which is given by ratio of modal amplitudes of *i*-th and *k*-th eigen-mode in the case of harmonic load with frequency ω_k:

$$\nu_{i,k} = \frac{\left| f_i \right| / \left| f_k \right|}{\xi_i / \xi_k \left(\left(\omega_i / \omega_k \right)^2 + \left(\left(\omega_i / \omega_k \right)^2 - 1 \right)^2 / 4\xi_i^2 \right)^{1/2}} \tag{33}$$

The prerequisite of using the condition (30) is a small ratio of modal loadings:

$$\frac{\left| f_i \right|}{\left| f_k \right|} \ll 1 \tag{34}$$

The requirement (34) is very conservative and for many system impossible to fulfill.

4. Applicability of indexes and criterions in case of real structure equipped with TMD

4.1. Specification of structure

The indexes and criterions from previous chapter were calculated and analyzed for the case of a linear discrete numerical model of existing TV tower equipped with TMD. Absorber in a form of pendulum was installed into a laminate extension of a top of the tower, due to possible excessive vibrations caused by a wind load. The vortex-shedding effect on the cylindrical extension without absorber could cause danger stresses in laminate from the point of view of material fatigue and life-time of the structure. TMD was designed and tuned to be the most effective in vibrations in the second eigen-mode i.e. eigen-frequency of the tower. The weight of absorber is 1 tone, which is 1/10 of a generalized (effective) mass of the second eigen-mode. TMD has usually higher damping properties than the part of the structure, where it is installed, and thus, it could represent an significant origin of non-proportionality of the damping.

4.2. Relative errors of response of numerical model on harmonic excitation due to approximate solution

The discrete numerical model of structure was created in CALFEM, which is Matlab toolbox for computing by the finite elements method. Basic model without TMD had 15 nodes, each with 3 degrees of freedom. The absorber was subsequently modeled as a concentrated mass connected to the top of the tower with Kelvin-Voigt damping term and had one degree of freedom in horizontal direction. Adding this degree of freedom into the model resulted in increasing of total number of eigen-modes by one. This eigen-mode was associated due to tuning of absorber to the second eigen-mode of the basic system. It means, that model with absorber had two eigen-modes, which are similar in shape. However, they differ especially in a phase between absorber and the top of the tower see Figure 1.

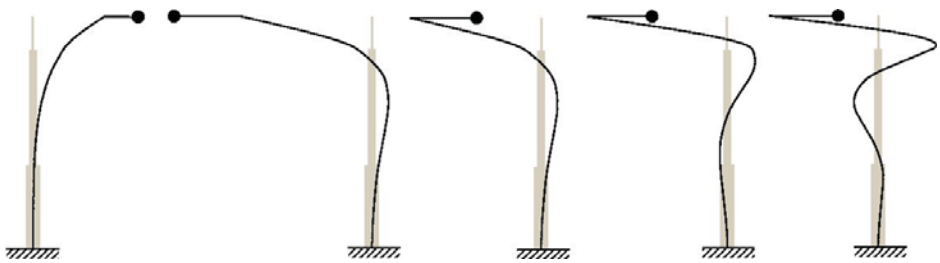

Fig. 1: The first five eigen-modes and eigen-frequencies of the structure with absorber (in parentheses the corresponding eigen-frequencies of the basic system without absorber)

At first, the steady state response of the structure with absorber on a harmonic force located at the top of the tower was calculated. The response were analyzed for an interval of the frequency of the loading force (f = 0 ÷ 3 Hz), where the first four eigen-modes of the basic system lie. Damping matrix of the basic system was proportional to the combination of the mass and stiffness matrix. Multiplicative coefficients related to these stiffness and mass matrices were calculated from the given structural damping ratio (ζ= 0,005) for the first two eigen-frequencies of the basic system. Factor of the damping non-proportionality of the system has been examined as follows: a set of various damping ratio of the TMD (dashpot absorber) was used (ζ_{TMD} = 0 ÷ 0,8), while constant structural damping was kept. First seven eigen-modes were used for reduction of the matrix system (1) using transformation (2) and two different solutions of response of this reduced model were assumed. The first one concerned the direct solution of the reduced system with full modal damping matrix. The second one took into account only the diagonal terms of the modal damping matrix. Relative errors of amplitudes

of steady state response of the top of the tower ε_{Ytop} and absorber ε_{Ytmd} and of the phase difference between the top and the absorber ε_{φ} caused by the second approximate solution were calculated for a set of ζ_{TMD}. Specifically, the relative errors were determined for the first four dominant peaks of frequency-amplitude curves see Figure 2, which lay near the eigen-frequencies of the undamped system and where the highest response was noticeable. On Figure 2 only the part of investigated frequency interval with the second and third peak is shown, for which the errors were the most significant. The peak corresponding to the third eigen-frequency was not identifiable for nonzero damping ratio ζ_{TMD} and it wasn't included in the analysis. The relative errors in determination of the frequency of the peaks ε_f together with all previously defined errors are summarized in the Table 1.

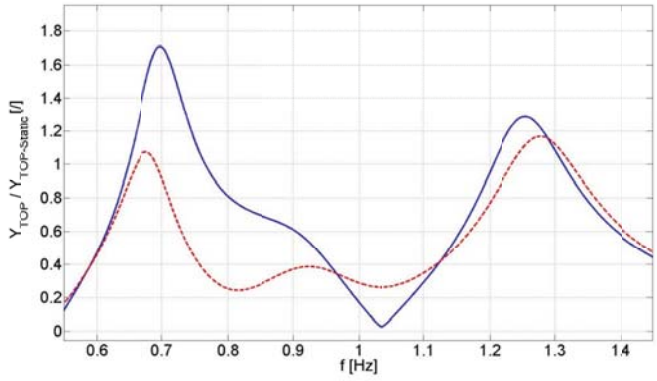

Fig. 2: Dynamic magnification factor of amplitude of the top of the tower as a function of driving frequency of the load for exact and approximate solution
(Blue solid line – exact solution, red dashed line – approximate solution; $\zeta_{TMD} = 0{,}2$)

Tab. 1: Relative errors of the response caused by approximate solution for various values of ζ_{TMD}
(In parentheses the corresponding eigen-frequencies of the structure with absorber)

Peak n.	**1** (f_1= 0,378 Hz)				**Peak n.**	**2** (f_2= 0,679 Hz)			
ζ_{TMD} [/]	0	0,2	0,5	0,8	ζ_{TMD} [/]	0	0,2	0,5	0,8
ε_f [%]	< 0,1	< 0,1	< 0,1	0,26	ε_f [%]	< 0,1	3,15	9,65	10,48
ε_{Ytop} [%]	0,01	2,11	12,69	29,61	ε_{Ytop} [%]	0,03	37,15	79,40	89,61
ε_{Ytmd} [%]	0,01	-0,7	0,38	2,68	ε_{Ytmd} [%]	0,01	19,09	56,23	68,18
ε_{φ} [%]	0,7	9,12	12,76	26,33	ε_{φ} [%]	0,28	10,89	17,50	10,09
Peak n.	**3** (f_4= 1,275 Hz)				**Peak n.**	**4** (f_5= 2,12 Hz)			
ζ_{TMD} [/]	0	0,2	0,5	0,8	ζ_{TMD} [/]	0	0,2	0,5	0,8
ε_f [%]	< 0,1	-1,75	-6,46	-5,47	ε_f [%]	< 0,1	-0,28	-1,04	-2
ε_{Ytop} [%]	0,02	9,16	45,74	68,60	ε_{Ytop} [%]	0,01	-1,97	0,38	9,33
ε_{Ytmd} [%]	0,02	2,66	20,30	34,28	ε_{Ytmd} [%]	0,03	-3,99	-10,44	-13,82
ε_{φ} [%]	0,57	19,32	33,04	31,24	ε_{φ} [%]	0,27	19,81	33,21	40,57

The table shows, that neglecting of mechanical interaction between eigen-modes resulted in significant errors in amplitudes of the top of the tower especially for the frequencies corresponding to the second and the third peak for nonzero ζ_{TMD}. These resonant frequencies lie very close to the tuning frequency of the absorber and thus are more influenced by it than the frequencies of the first and fourth peak.

With increasing of the damping of the absorber the errors also increase. This fact isn't generally valid for every numerical model of the structure with absorber. It depends as well as on a chosen model of classical viscous damping of the basic structure and numerical model of the absorber as on the difference of damping ratios of the eigen-modes of the structure and ζ_{TMD}. The ζ_{TMD} of a real absorber installed into the existing tower was from practical point of view set equal 20%. This value of ζ_{TMD} is optimal for reduction of vibrations with frequencies close to the second eigen-frequency of the basic structure. However, this value of ζ_{TMD} is 40 times higher than the damping ratio of this second eigen-mode. The relative error of the amplitude of the response of the top of the tower is in this case significant and is equal almost 40% for the second peak see Table 1 and Figure 2. Similarly, the maximal and appreciable error of amplitude of the absorber is equal 20%. It follows, that the non-proportionality of the damping is in this practical case substantial. Amplitudes of approximate solution are for almost every studied case lower than for exact solution. This fact could be explained by the mechanical interaction between eigen-modes for non-classically damped system. It could be also interpreted by different modal damping of eigen-modes for both solutions see Table 2. The final results of the response are strongly affected by a number of eigen-modes of undamped system being taken into the consideration. The controlling calculation of the response of the full system (1) on the same excitation showed, that using a set of first seven eigen-modes resulted to acceptable maximal absolute error less than 0,1%.

The influence of non-proportionality of the damping on the individual eigen-modes could be also illustrated by different phases of their components. The components of the first six complex eigen-modes, which correspond to displacements of the tower, are for the practical value of ζ_{TMD} depicted in the complex plane on Figure 3. The most influenced are the second, the third and the fourth complex eigen-mode. Their components have different phases i.e. they don't lie in the complex plane on one line. On the other hand, the fifth, the sixth and especially the first eigen-mode almost correspond to the real undamped eigen-modes, which are characterized by same phase of all components.

Tab. 2: Damping ratios of eigen-values of approximate (ζ_{APP}) and real (ζ) numerical model for various values of ζ_{TMD}

1st eigen-value					**2nd eigen-value**				
ζ_{TMD} [/]	0	0,2	0,5	0,8	ζ_{TMD} [/]	0	0,2	0,5	0,8
ζ [/]	0,0047	0,0067	0,0087	0,0093	ζ [/]	0,0027	0,0597	0,0585	0,0381
ζ_{APP} [/]	0,0047	0,0068	0,0100	0,0132	ζ_{APP} [/]	0,0027	0,0651	0,1586	0,2522
3rd eigen-value					**4th eigen-value**				
ζ_{TMD} [/]	0	0,2	0,5	0,8	ζ_{TMD} [/]	0	0,2	0,5	0,8
ζ [/]	0,0033	0,1105	0,4505	0,8485	ζ [/]	0,0054	0,0551	0,0574	0,0385
ζ_{APP} [/]	0,0033	0,0986	0,2415	0,3844	ζ_{APP} [/]	0,0054	0,0594	0,1404	0,2215
5th eigen-value					**6th eigen-value**				
ζ_{TMD} [/]	0	0,2	0,5	0,8	ζ_{TMD} [/]	0	0,2	0,5	0,8
ζ [/]	0,0093	0,0182	0,0266	0,0282	ζ [/]	0,0156	0,0178	0,0208	0,0230
ζ_{APP} [/]	0,0093	0,0187	0,0327	0,0467	ζ_{APP} [/]	0,0156	0,0179	0,0213	0,0247

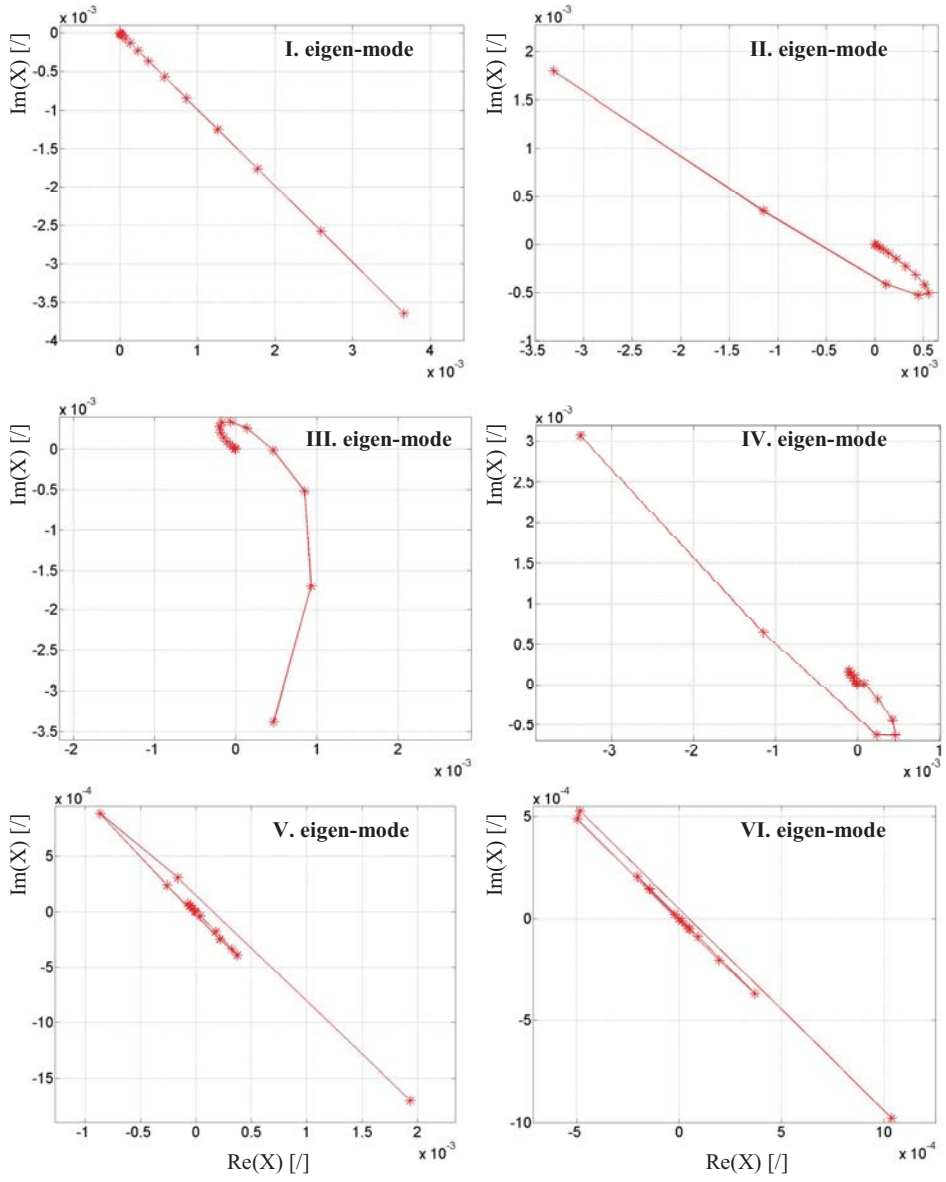

Fig. 3: Components of first six complex eigen-modes of structure in complex plane (ζ_{TMD} = 0,2)

4.3. Calculation of indexes of non-proportionality and criterions as functions of damping ratio of the absorber

For the investigated numerical model and for a set of ζ_{TMD} the previously defined indexes and criterions were calculated. In this chapter their values and recommendations of their applicability in case of structures with absorber are given. The guidelines are based on comparison of the indexes and criterions with complex character of the eigen-modes and relative errors given in Table 1. The focus was aimed especially to errors of amplitude of the top of the tower.

The most general indication of non-proportionality of the damping is the non-fulfillment of the diagonal dominance of the modal damping matrix. In Table 3 the ratio of absolute value of diagonal term and the sum of absolute values of non-diagonal terms for each row of modal damping matrix as a function of ζ_{TMD} is evaluated. The cases for which the requirement of dominance is fulfilled are printed in bold. From the table it follows, that the modal damping matrix isn't diagonally dominant for

all analyzed values of ζ_{TMD}. The requirement of dominance is fulfilled only for zero ζ_{TMD} and for eigen-modes, which aren't associated with the second eigen-mode of the basic system. The decrease of ratios with increase of ζ_{TMD} corresponds with increase of the extent of the non-proportionality of the damping.. Nevertheless, the diagonal dominance of the modal matrix could serve only as additional not the decisive criterion for neglecting the non-diagonal terms. It follows from the fact, that although relative errors for zero ζ_{TMD} are small, the modal damping matrix isn't diagonally dominant.

Tab. 3: Ratio of absolute value of diagonal term and the sum of absolute values of non-diagonal terms for each row of modal damping matrix as function of ζ_{TMD}

ζ_{TMD} [/]	Eigen-mode (row) n.					
	1	2	3	4	5	6
0	**1,453**	0,422	0,583	**1,539**	**7,917**	**34,642**
0,2	0,084	0,235	0,373	0,334	0,286	0,691
0,5	0,049	0,226	0,361	0,312	0,198	0,326
0,8	0,040	0,223	0,358	0,307	0,176	0,236

The values of the left side of the condition (6) suggested by Hasselman (1976) is graphically presented for particular eigen-modes and for various ζ_{TMD} on Figure 4.

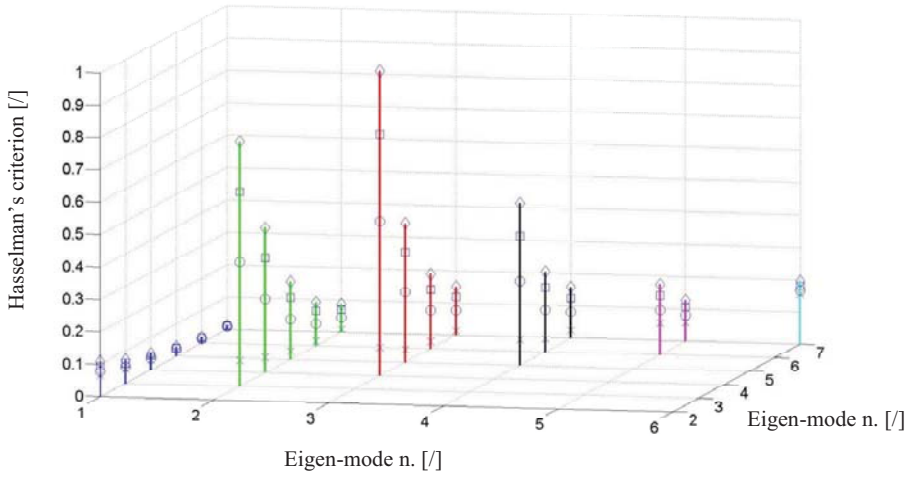

Fig. 4: Graphical expression of Hasselman's criterion for neglecting of mechanical interaction of eigen-modes for various ζ_{TMD} (×...ζ_{TMD} =0; o...ζ_{TMD} =0,2; □...ζ_{TMD} =0,5;◊ ...ζ_{TMD} =0,8)

The significant mechanical interaction between the second and third, the third and fourth as well as between the fourth and the fifth eigen-mode was determined. On the other hand, small interaction between the first eigen-mode and the others were found out. However these results come from frequency proximity of these eigen-modes rather than from a distribution of damping in the system. It could be demonstrated on the example of the mechanical interaction of the sixth and the seventh eigen-mode. Relatively high value of interaction (0,2) didn't change significantly with increasing of the ζ_{TMD} and also didn't correspond to negligible error in calculation of the response using approximate solution. It should be also noted, that condition (9), which is required for using Hasselman's criterion and which is related to ratios of diagonal a non-diagonal terms of modal damping matrix, is fulfilled only for zero ζ_{TMD}. However, the main disadvantage and the reason of

unusability of Hasselman's criterion is the fact that it finds out the mechanical interaction even between eigen-modes of classically damped models.

Criterion suggested by Wartburton & Soni (1977) for neglecting of non-diagonal terms of modal damping matrix was expressed by means of boundary value ε_b of the coefficient ε see Table 4 and Figure 5. For smaller values of ε than ε_b the condition (10) is fulfilled, for higher values it is not. In comparison to Hasselman's criterion the proposed criterion could identify the classically damped system due to ratio of diagonal and non-diagonal terms of the modal damping matrix. In this case the coefficient ε_b is theoretically zero. The authors proposed for problem in practice value of ε_b equal 5%. This value should correspond to maximal achievable error of response equal 10%. For the first eigen-mode the assumption of a small mechanical interaction based on analysis of the relative errors and complex eigen-modes was confirmed with exception of the highest ζ_{TMD}. For the lowest ζ_{TMD} a small non-proportionality of whole system was also confirmed. For higher values of ζ_{TMD} especially the practical one the coefficient ε_b for particular eigen-modes shows relatively good agreement with errors of the top of the tower given in Table 1. On Figure 5a there is depicted the coefficient ε_b as a function of ζ_{TMD} for the first six eigen-modes. It shows almost the linear dependency of ζ_{TMD} on ε_b i.e. increase of the ε_b with increase of ζ_{TMD}. The decreasing of the value of ε_b with increasing of ζ_{TMD} occurs only for values of ζ_{TMD} lower than a specific ζ_{TMD} for which the damping matrix is the best approximation of the classically damped one see Figure 5b. This specific value of ζ_{TMD} is in our case close to damping ratio of the first and second eigen-mode of structure without absorber.

Tab. 4: Boundary value ε_b of parameter ε of criterion of particular eigen-modes suggested by Wartburton & Soni (1977) for various ζ_{TMD}

ζ_{TMD} [/]	Eigen-mode n.					
	1	2	3	4	5	6
0	0,0010	0,0052	0,0071	0,0051	0,0009	0,0003
0,2	0,0129	0,1993	0,2734	0,2586	0,0536	0,0157
0,5	0,0336	0,5059	0,6942	0,6542	0,1354	0,0396
0,8	0,0543	0,8126	1,1151	1,0497	0,2172	0,0635

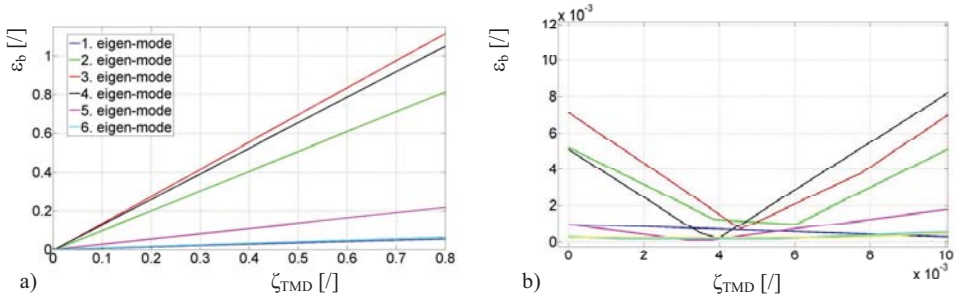

Fig. 5: Boundary values ε_b of parameter ε of criterion of particular eigen-modes suggested by Wartburton & Soni (1977) as function of ζ_{TMD}

The summation based indexes δ_{1i} of particular eigen-modes, which was proposed by Prater & Singh (1986), are depicted as a function of ζ_{TMD} on Figure 6. All of these indexes are increasing with increasing of ζ_{TMD}. Only for lower values of ζ_{TMD} than specific value of ζ_{TMD}, which was defined in previous paragraph, the indexes have decreasing trend see Figure 6b. The values of indexes δ_{1i} for chosen ζ_{TMD} are also quantified in Table 5. From the Table 5 and from the Figure 6b follow, that for zero ζ_{TMD} the first four eigen-modes are highly coupled. It doesn't correspond with errors of solution of the response obtained from the analysis of numerical model and also with a character of complex eigen-modes. The behaviour of indexes also shows, that for practical and higher

values of ζ_{TMD} the most influenced eigen-mode by damping term of absorber is the first one. It is in contrast to an expected and confirmed presumption, that the most influenced eigen-modes are the second, the third and the fourth one.

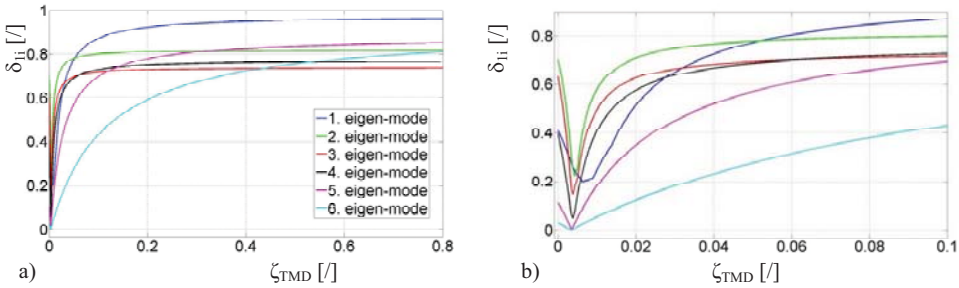

Fig. 6: Indexes δ_{1i} of particular eigen-modes as function of ζ_{TMD} (Prater & Singh (1986))

Tab. 5: Indexes of non-proportionality of damping δ_{1i} for various values of ζ_{TMD}

ζ_{TMD} [/]	Eigen-mode n.					
	1	2	3	4	5	6
0	0,408	0,703	0,632	0,394	0,112	0,028
0,2	0,922	0,810	0,729	0,750	0,778	0,592
0,5	0,954	0,816	0,735	0,762	0,835	0,754
0,8	0,962	0,817	0,737	0,765	0,850	0,809

Another calculated response based indexes δ_{3i} of particular eigen-modes see Figure 7 and Table 6 express very well the trend of behaviour of obtained errors of peaks of the response in frequencies near the corresponding eigen-frequencies. However, the calculation of indexes requires the solution of the response of the whole system with full modal damping matrix. And thus no advantage of calculation of indexes in comparison with the solution of the real and full problem is gained.

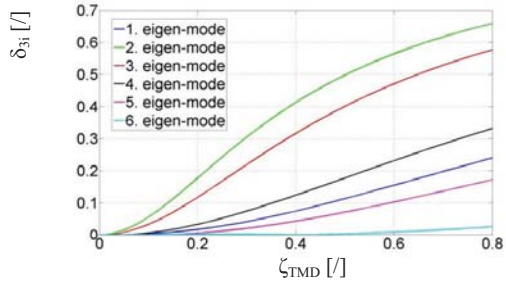

Fig. 7: Indexes δ_{3i} of particular eigen-modes as function of ζ_{TMD} (Prater & Singh (1986))

Tab. 6: Indexes of non-proportionality of damping δ_{3i} for various values of ζ_{TMD}

ζ_{TMD} [/]	Eigen-mode n.					
	1	2	3	4	5	6
0	3,8e-5	9,3e-4	1,1e-4	6,3e-5	1e-5	7,8e-6
0,2	0,017	0,177	0,117	0,033	0,005	0,002
0,5	0,113	0,498	0,401	0,177	0,071	0,003
0,8	0,240	0,659	0,577	0,332	0,172	0,025

The values of the generalized determinant based index δ_2 and generalized indexes δ_1 and δ_3 of the investigated numerical model suggested by Prater & Singh (1986) are for chosen ζ_{TMD} given in Table 7. Index δ_2 indicates the unrealistically high value of non-proportionality of the damping. Even for the realistic value of ζ_{TMD} equal 0,2 it exceeds the border of total non-proportionality of the system given by one. The other generalized indexes δ_1 and δ_3 are strongly affected by the number of eigen-modes taking into account. Assuming in the solution of indexes one additional eigen-mode, which is minimally influenced by absorber i.e. is almost classical, results in decreasing of both generalize indexes δ_1 and δ_3.

Tab. 7: Generalized indexes of non-proportionality of damping δ_{1-3} for various values of ζ_{TMD}

Index	ζ_{TMD} [/]			
	0	0,2	0,5	0,8
δ_1	0,089	0,693	0,762	0,781
δ_2	2,6e-8	1,773	466,7	8022
δ_3	1,7e-4	0,050	0,181	0,287

The values of index *I* defined by Tong et al. (1994) show very high non-proportionality of the system almost in the whole interval of investigated values of ζ_{TMD} see Figure 8 and Table 8. Only in a narrow interval of ζ_{TMD} in the neighborhood of specific ζ_{TMD} the index is minimized. This specific value of ζ_{TMD} corresponds as it was previously defined to the best approximation of the damping matrix to its classically damped form. The values of the index don't correspond to the results of analysis of the error. For all chosen ζ_{TMD} the value of index are almost one, which stands for the total non-proportionality of the damping. However, the errors caused by approximate solution are especially for zero ζ_{TMD} less significant than it could be expected from the value of index. This conclusion of unusability of this index is also supported by the excessive values of upper bounds of the relative errors given by (25) for all ζ_{TMD} see Table 8.

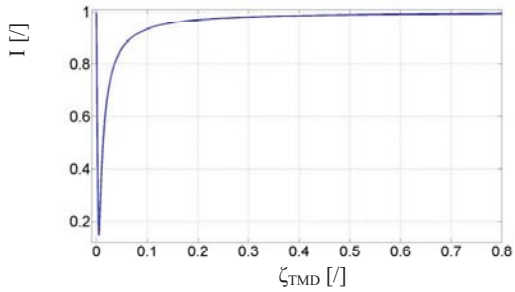

Fig. 8: Index of non-proportionality of damping I as function of ζ_{TMD} (Tong et al. (1994))

Tab. 8: Index of non-proportionality of damping I and upper bound of error of response for various values of ζ_{TMD}

ζ_{TMD} [/]	0	0,2	0,5	0,8
I	0,995	0,97	0,990	0,994
E	9,56	8,423	8,705	9,466

The prerequisite of the diagonal dominance of the modal damping matrix for a quantification of the non-proportionality of the individual eigen-mode using indexes defined by Bhaskar (1995) has been confirmed. The value of indexes is close to one which represents the absolute non-proportionality even for the ζ_{TMD}= 0,2 see Figure 9. For higher values of ζ_{TMD} the indexes are higher than one. On the

figure the indexes of each eigen-mode were calculated for driving frequencies of the loading equal to the first six eigen-frequencies of the structure with absorber. Only indexes of eigen-modes for which driving frequencies are not equal to their corresponding eigen-frequencies are depicted. The indexes of particular eigen-modes and corresponding eigen-frequencies are summarized in Table 9.

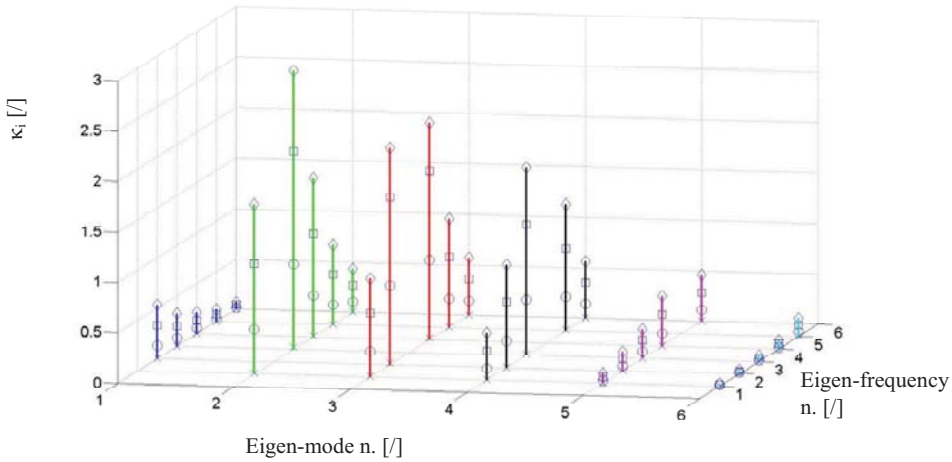

Fig. 9: Indexes of non-proportionality κ_i of particular eigen-modes for driving frequencies of loading equal to eigen-frequencies of the system with absorber for various ζ_{TMD} (Bhaskar (1995)) (×...ζ_{TMD} =0; o...ζ_{TMD} =0,2; □...ζ_{TMD} =0,5;◊ ...ζ_{TMD} =0,8)

Tab. 9: Maximal values of indexes of non-proportionality κ_i of particular eigen-modes and their corresponding eigen-frequencies for various values of ζ_{TMD} (Bhaskar(1995))

ζ_{TMD} [/]	Eigen-frequency and eigen-mode n.					
	1	2	3	4	5	6
0	0,688	2,370	1,715	0,650	0,126	0,029
0,2	11,843	4,262	2,683	2,992	3,501	1,448
0,5	20,609	4,433	2,773	3,202	5,052	3,068
0,8	25,123	4,477	2,796	3,258	5,671	4,239

The upper bounds of the relative errors in modal coordinates derived by Gawronski & Sawicki (1997) are given for investigated model in Table 10.

Tab. 10: Relative errors of modal displacements due to neglecting of non-diagonal terms of modal damping matrix for various values of ζ_{TMD} (Gawronski & Sawicki (1997))

ζ_{TMD} [/]	Eigen-mode n.					
	1	2	3	4	5	6
0	0,029	0,082	0,055	0,045	0,008	0,002
0,2	3,713	1,923	0,345	1,386	0,263	0,101
0,5	15,829	4,485	0,727	3,382	0,928	0,244
0,8	30,715	6,327	0,935	4,915	1,657	0,378

Calculated upper bounds of errors are for ζ_{TMD} equal and higher than 20% very high. The highest bound was obtained for the modal displacement which corresponds to the first eigen-mode of the

system. Although the influence of the damping term of the absorber should be more significant in case of the second, the third and the fourth eigen-mode. We can't directly compare the errors of generalized displacements and errors of modal displacements. However we can't expect for these excessive upper bounds such a real level of relative errors of the response in generalized co-ordinates.

The coupling indexes χ_r of individual eigen-modes defined by Venancio-Filho et al. (2001) are given in Table 11. Under assumption, that zero stands for minimum and one for maximum non-proportionality, it follows that in all investigated cases index is very high. This fact doesn't correspond with calculated character of complex modes and relative errors.

Tab. 11: Indexes of non-proportionality of damping of particular eigen-modes for various values of ζ_{TMD} (Venancio-Filho et al. (2001))

ζ_{TMD} [/]	Eigen-mode n.					
	1	2	3	4	5	6
0	0,050	0,430	0,430	0,108	0,009	0,001
0,2	0,277	0,880	0,880	0,846	0,467	0,120
0,5	0,508	0,950	0,950	0,934	0,695	0,261
0,8	0,627	0,968	0,968	0,958	0,787	0,364

5. Conclusions

The article deals with an applicability of till now published indexes of non-proportionality of the damping in the case of slender structure (TV tower) equipped with absorber which is subjected to the harmonic excitation. The focus is also aimed at criterions for neglecting of non-diagonal terms of the modal damping matrix of its numerical model. These terms express the coupling of modal coordinates i.e. the mechanical interactions of individual eigen-modes. The applicability is assessed using comparison of indexes and criterions with character of complex eigen-modes and with relative errors of the response that are caused by neglecting of non-diagonal terms for selected values of damping ratios of absorber. From the practical point of view the errors corresponding to the dominant peaks of response curve of the top of the tower were taking into account. None of investigated indexes and criterions did fully correspond to the obtained solutions. The summation based index suggested by Prater & Singh (1986), indexes proposed by Bhaskar (1995) and Venancio-Filho et al. (2001) indicated very high values of non-proportionality particularly for the first four eigen-modes for all selected damping ratios of absorber. Even for zero damping ratio for which the calculated errors of the response were negligible and also for the first eigen-mode, which is almost identical with real eigen-mode of the undamped system. Also the generalized index suggested by Tong et al. (1994), determinant based index proposed by Prater & Singh (1986) indicated almost total non-proportionality of the system for all investigated cases. The analysis confirmed that criterion suggested by Hasselman (1976) couldn't be used because it supposes the mechanical interaction between individual eigen-modes even for classically damped structures. The relatively good agreement between calculated relative errors and proposed criterions was obtained for criterion proposed by Warburton & Soni (1977). The boundary values of its parameter ε for which the criterion is still fulfilled could also serve as an approximate index of non-proportionality of particular eigen-modes. Analysis of the response also highlights the necessity of prerequisite of non-proportional damping, when passive damping equipment is installed into the structure and when the detailed behavior is investigated.

Acknowledgement

The kind support of the Czech Science Foundation No. 103/09/0094, Grant Agency of the ASCR No. A200710902, Ministry of Industry and Trade No. MPO TIP FR-TI3/654 and RVO 68378297 research plan is gratefully acknowledged.

References

Bhaskar, A. (1995) Estimates of errors in the frequency response of non-classically damped system. *Journal of Sound and Vibration*, 184 (1), pp. 59–72.

Bhaskar, A. (1999) Mode shapes during asynchronous motion and non-proportionality indexes. *Journal of Sound and Vibration*, 224 (1), pp. 1–16.

Gawronski, W., Sawicki, J. T. (1997) Response errors of non-proportionally lightly damped structures. *Journal of Sound and Vibration*, 200 (4), pp. 543–550.

Hart, G. C. & Wong, K. (2000) *Structural Dynamics for Structural Engineers*. John Wiley & Sons, Inc., New York

Hasselsman, T. K. (1976) Modal coupling in lightly damped structures. *AIAA Journal*, 14, pp. 1627–1628.

Hurty, Walter C, & Rubinstein, Moshe F, (1964) *Dynamics of Structures*, Englewood Cliffs: Prentice-Hall,Inc,

Liu, K., Kujath, M. R. & Zheng, W. (2000) Quantification of non-proportionality of damping in discrete vibratory systems. *Computer and Structures*, 77 (5), pp. 557–569.

Prater, G. & Singh, R. (1986) Quantification of the extent of non-proportional viscous damping in discrete vibratory systems. *Journal of Sound and Vibration,* 104(1), pp. 109-125.

Prells, U. & Friswell, M. I. (2000) A measure of non-proportional damping. *Mechanical System and Signal Processing*, 14 (2), pp. 125–137.

Tong, M., Liang, Z., Lee, G. C. (1994) An index of damping non-proportionality for discrete vibrating systems. *Journal of Sound and Vibration*, 174, pp. 37–55.

Venancio-Filho, F., Wang, Y.K., Lin, F.B., Claret, A.M. & Ferreira, W.G. (2001) Dynamic Analysis of Nonproportional Damping Structural Systems Time and Frequency Domain Methods, *Transactions*, SMiRT 16, Washington DC.

Warburton, G. B. & Soni, S. R. (1977) Errors in response calculations for non-classically damped structures. *Earthquake Engineering and Structural Dynamics*, 5, pp. 365–376.

18th International Conference
ENGINEERING MECHANICS 2012
Svratka, Czech Republic, May 14 – 17, 2012

pp. 449–451
Paper #49

UTILIZATION OF INSTANT REALITY SOFTWARE FOR MOTION VISUALIZATION

J. Hrbáček*, T. Novotný*

Abstract: *The article deals with the ways of virtual models motion visualization in Instant Reality software based on variable input signals. Further use of this visualization is in virtual reality imaging. Paper includes the possibility of using internal software tools such as events and sensors for simultaneous changes of transformations based on differently generated signals. The output of the work is to verify the acquired knowledge on a simple application task.*

Keywords: ***Instant Reality, events, sensors, signals.***

1. Introduction

Many companies spend a lot of money by moving heavy or huge devices across the whole country, in order to present their products to potential buyers. They should consider using a stereoscopic presentation, because then only things they need to move are notebook and easily moveable presentation device. The stereoscopic presentation allows its user to perceive the depth (3rd dimension) of an object projected on two dimensional screens. In order to create a great immersion in the virtual projection, the object motion should be realistic as well. To accomplish this, the dynamic simulation should be involved.

Perhaps the most optimized solution for stereoscopic projection is use of Virtual Reality Modeling Language (VRML) as a graphical output of any mathematical software which can create dynamic simulation. However not every mathematical software has its own VRML viewer and because of this, the Instant Reality software is a great solution as an external graphics viewer. This paper refers to the ways of exporting data from mathematical software, such as MatLab, to the Instant Reality software and creating the real motion directly in Instant Reality.

2.1. Background

The stereoscopic presentation is commonly used, but motion visualization has its faults. The main fault is that the motion is only an animation, so the movement is uniform. Real objects do not move only uniformly, but they also accelerate and decelerate.

There is software for animating virtual objects, such as Autodesk 3D Max. It is great for animating complex motion, for example animation of the whole manufacturing process. But it also has many disadvantages, e.g. it cannot easily make a non-uniform motion and it also generates a redundant amount of values in the interpolators, which has a negative influence on computing power of the work station and it can cause lags in the animation.

3. Materials and Methods

In VRML code there is one powerful tool which allows an object to move and this tool is called an interpolator (Orientation and Position Interpolators). Interpolators have two input parameters. The first parameter (key) contains the time points, when the object is needed to be. The second parameter (keyValue) contains the transformation data, where the object is needed to be. The interpolator itself

* Ing. Jakub Hrbáček, Ing. Tomáš Novotný, ING-PAED IGIP: Institute of Production Machines, Systems and Robotics, Faculty of Mechanical Engineering, Brno University of Technology, Technická 2896/2; 616 69, Brno; CZ, emails: y101623@stud.fme.vutbr.cz, novotny.t@fme.vutbr.cz

computes all the values between the defined points (Žára, 1999), but because it is a linear interpolator, computed data lie on the line between two defined points so that is very easy to establish a uniform motion, as it is shown in Fig.1.

However, in order to make a non-uniform motion there have to be much more defined points and even then it is hard to compute these values by yourself. That is why the dynamic simulation software is used. It can compute all values needed to make an acceleration and deceleration or general non-uniform motion.

Syntax Example of Position Interpolator:

```
DEF PI PositionInterpolator {
    key [0, 0.3, 0.8]
    keyValue [0 0 0, 0 3 1, -1 5 0]
}
```

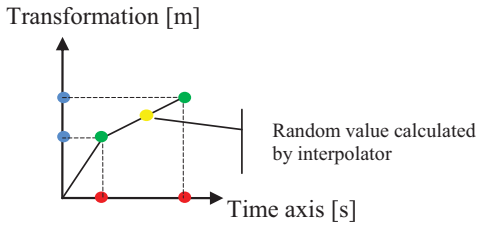

Fig. 1: Linear Interpolation

There are three simple ways to export data calculated in dynamic simulation software. This software should have the ability to save calculated data into simple txt file or similar file format. To extract manually this saved data from txt file is very easy, but the syntax of interpolator is quite clear, so the data should by formatted to its right form. However this way of exporting could be a little time consuming so in order to automate the export a simple program should be written.

The second way of exporting is quite conditioned. The condition is in obtaining MatLab software. MatLab has a 3D animation tool box, which can display simulation itself in VRML integrated viewer (Humusoft s.r.o., 2000). The serious disadvantage is obvious, because if you have a stereoscopic cluster system programmed for a specific VRML viewer, you cannot use a MatLab. Fortunately the MatLab is able to create VRML code with data obtained in dynamic simulation inserted directly into the interpolators so simulations can be viewed in extern VRML viewer. This solution is much faster than the first one.

The third solution uses a timer (TimeSensor) which is generated by VRML itself. This solution also requires using a Script node, because of this a certain programming skill is required. The Script node allows using scripting languages, but only two of them, so far. One of them is ECMAScript, also known as JavaScript, which is appropriate for simple tasks, like converting data type and mathematical functions. And they are mathematical functions which send the data to object transformation parameters so it can move by mathematically defined curve and acceleration.

```
DEF p Script {

    eventIn SFFloat set_start
    eventOut SFRotation value_changed
    eventOut SFVec3f tr_changed
    url "javascript:
    function set_start (hodnota) {
        value_changed[0]=1; value_changed[1]=value_changed[2]=0;
        value_changed[3]=10*Math.sin(50*hodnota)
            tr_changed[0]=tr_changed[2]=0
            tr_changed[1]=3*Math.cos(40*hodnota) ;
    }"
}
```

Fig. 2: Example of Simple Script

4. Results

Every way of extracting data has its advantages and also its disadvantages.

The first way can be used for dynamic simulation software without any graphical display; moreover it could serve as its graphical output. But export automation or manual export could be very time consuming process.

The second solution is conditioned by obtaining MatLab software what could be main problem for smaller companies which cannot afford it. But this solution is much faster and it also allows viewing the simulations in extern VRML viewer, because MatLab can generate a VRML code by using special block in 3D animation toolbox called VRSink. This VRML code is complete therefore there is no need of data formatting.

The third solution is the most optimized solution, because it does not burden the computation power of workstation. Nevertheless to accomplish this it is necessary to have certain knowledge of programming ECMAScript or Java and to solve the differential equations analytically in order to create motion equations as a mathematical function.

5. Conclusion

Even though the stereoscopic principle has been known almost for a whole century, the possibilities of virtual reality technologies did not even scratch its surface. No one can really predict a new application of virtual reality or its next connection to the systems that already exist.

But for now a very impressive application of virtual reality is 3-Dimensional graphical interpretation of objects and their motion that really exists. In order to simulate the real behavior dynamic simulations should be included.

This text deals with a few possibilities of data export from dynamic simulation software to a VRML code. Every way has its advantages and disadvantages which are not easy to compare, so each way should be used for a specific need.

There is another way of data export, but it has not been established yet. The VRML itself did not have any interface for an external signal until 1999, after that the Extern Authoring Interface (EAI) was added. Thanks to EAI and Java programming language the virtual model should be able to connect directly to a data stream. So the next step of the research is to establish a connection to MatLab data stream in order to create a real-time control.

References

Humusoft s. r. o. Virtual Reality Toolbox: User's Manual. Prague (2000). ISBN 80-7080-373-8.

Žára, Jiří. (1999) Laskavý průvodce virtuálními světy. Computer Press.

18th International Conference
ENGINEERING MECHANICS 2012
Svratka, Czech Republic, May 14 – 17, 2012

pp. 453–460
Paper #95

EXPANSION LIMIT ESTIMATION OF PISTOL HOLLOW POINT BULLET PENETRATING THE BLOCK OF SUBSTITUTE MATERIAL

J. Hub[*], J. Komenda[**], M. Novák[***]

Abstract: *The article presents a numerical model of expansion pistol hollow point bullet penetrating the block of simulator representing the organic material (tissue). The hollow point bullet has an expansion ability to increase its wound potential, but only in case of exceeding the specific limit impact velocity. The simulation using FEM system Ansys Autodyn v14 presents 2D results of estimation the bullet velocity limit for expansion occurrence based on experiments. Also the analysis and influencing factors of the penetration process are presented as well. The results obtained help to evaluate the bullet post-penetrating characteristics.*

Keywords: ***Pistol cartridge, expansion bullet, wound effect, expansion limit, FEM simulation.***

1. Introduction

Expansion bullets, so called hollow point bullets, are characterized by functional deformation of the front part (so called expansion) while penetrating a soft target. Functional deformation of the expansion bullets in the target increases its radial dimensions and its front cross section (Rosenberg, 2002). The bullet transmits more energy into the target and is therefore considered as the bullet with enhanced wound potential. Pistol cartridges with these bullets are prohibited in the civil sector and the ammunition is applied especially for special police units. Among such ammunition is the cartridge Action 5, which is used in the experiments and analysis described in this article. The cartridge Action 5 is of the caliber 9 mm Luger with a homogeneous brass bullet with front expansion hollow covered with a plastic cap (see Fig. 1, 2). The basic ballistic characteristics of this cartridge are shown in Table 1. The cartridge is the product of the company RUAG Ammotech and is ranked among others in service of some security forces within the Czech Republic.

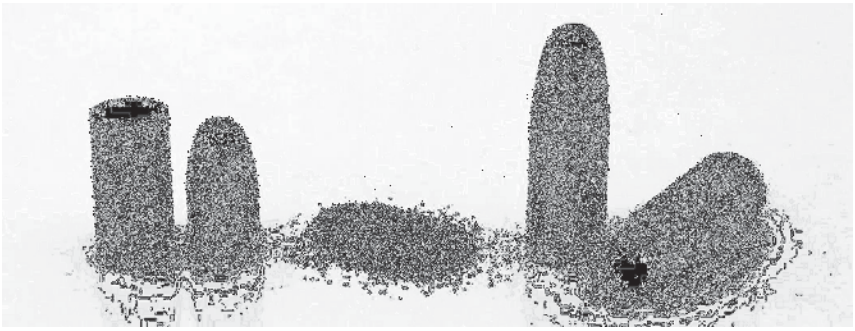

Fig. 1: The cartridge Action 5 (right) and its components – from the left the cartridge case with the primer, the bullet of caliber 9 mm and propellant charge (powder)

[*] Ing. Juraj Hub, Ph.D.: Department of Aircraft and Rocket Technology, University of Defense, Kounicova 65, 662 10 Brno; CZ, e-mail: juraj.hub@unob.cz

[**] Assoc. Prof. Ing. Jan Komenda, CSc.: Department of Weapons and Ammunition, University of Defense, Kounicova 65, 662 10 Brno; CZ, e-mail:jan.komenda@unob.cz

[***] Ing. Miroslav Novák, Ph.D.: Prototypa-ZM, Hudcova 533/78c, 612 00 Brno; CZ, e-mail: miroslav.novak@prototypa.cz

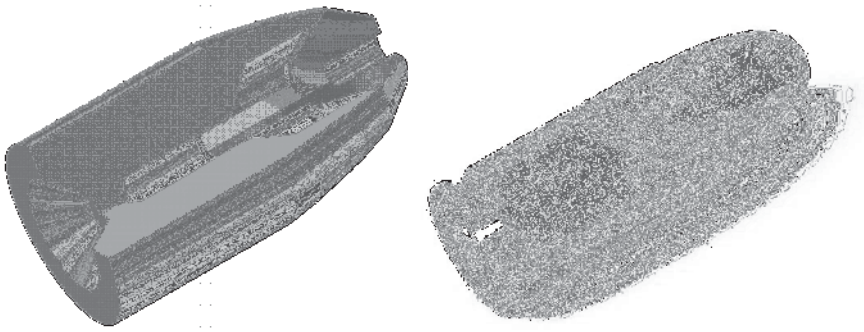

Fig. 2: Longitudinal cut of the bullet and cartridge Action 5; on the left the model used in FEM simulation and on the right the actual cartridge; the plastic cap is visible in the front part of the bullet

Tab. 1: Ballistic characteristics of the bullet Action 5

Weight of the bullet m_b [g]	6.1
Initial bullet velocity v_0 [m/s]	460
Initial momentum of the bullet H_0 [kg · m/s]	2.8
Initial bullet energy E_0 [J]	645
Initial specific bullet energy e_0 [MJ/m^2]	10.1/4.1*

Note: * Initial specific bullet energy is the initial bullet energy related to the cross section of the bullet. The values of the specific energy are valid for the bullet before the deformation / after the deformation in the substitute material. The cross-sectional area of the front part of the bullet increases from the original undeformed value 64 mm^2 to the value 156 mm^2 corresponding to the deformation diameter 14.1 mm, that means an increase of the cross section area of 145 %.

2. Expansion features of the bullet Action 5

A certain problem of the expansion bullets is their specific deformation behavior at different impact velocities and during penetration of different types of targets. In particular, different impact velocities can cause significant differences in wound effect and piercing ability of the same bullet in relation to an identical target. Important functional characteristics of the expansion behavior of each bullet are the expansion coefficient and the expansion velocity limits.

The coefficient of expansion of the bullet K_e is defined as the ratio of the maximum radial dimension of the bullet after and before the deformation, respectively, thus the ratio of diameter of the cylinder circumscribing the deformed shape of the bullet and the caliber of the bullet, see Fig. 3:

$$K_e = \frac{D}{d} \tag{1}$$

The increase of the bullet deformation causes the increase of the coefficient of expansion and the wound potential. In practice, the coefficient of expansion falls within the range of 1 to 2.

Deformation of the bullet generally increases with an impact velocity penetrating the live target, or its substitution, while other conditions remain the same. A very low impact velocity causes no deformation of the bullet. After reaching a particular minimum impact velocity, the bullet begins to deform. In practical terms, this velocity is not essential. In terms of assessing the effects of bullet such deformation of the bullet is significant, at which the maximum diameter of the bullet exceeds the origin bullet caliber. Impact velocity, at which such deformation is reached, is known as the lower limit (velocity limit) of the bullet expansion. This velocity has only approximate importance in practice and therefore the size of the velocity range at which the bullet shows increased wound effect.

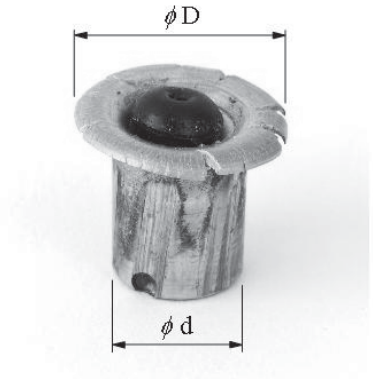

Fig. 3: Radial dimensions of expanded bullet required for expansion coefficient estimation; the bullet Action 5 with standard deformation caused by penetration of the substitute material – ballistic gel – with the expansion coefficient of the value 1.57 (shot No. 4)

In practice it is usually chosen the initial, and thus the impact, velocity of the bullet onto a target in order to provide the maximum deflection of the bullet with the maximum coefficient of expansion and thus with the maximum effect. Such an impact velocity is known as the upper limit (velocity limit) of the bullet expansion. The deformation of the bullet remains unchanged with further increasing of the bullet impact velocity. At a certain velocity threshold it may lead to disintegration of the bullet. This limit velocity is the limit of destruction (destructive limit). Reaching or exceeding this velocity leads to decreasing of the wound potential of the bullet while the piercing ability of the bullet increases.

The bullet expansion limits are independent of the thickness of the material which penetrates the bullet. The process of expansion of the bullet is usually completed at the track of just a few centimeters after impacting the block and afterwards the shape of the bullet remains unchanged. Therefore the experimental determination of the limits of expansion is sufficient to run at a relatively short track of the bullet penetration in the material on which the expansion process of the bullet is completed.

Knowing the limits of expansion is important for the proper choice of ballistic properties of the cartridge as a part of its development regarding to optimizing the wound effect of the bullet. To achieve the maximum level of wound effect, it is desirable that an expansion bullet hits the target with the velocity corresponding to the upper limit of expansion, eventually of slightly higher rate, without exceeding the limit of bullet destruction. Lower impact velocity leads to reduction of wound effect of the bullet when comparing to the upper limit. Higher impact velocity and exceeding the destruction limit reduces the wound potential more significantly. When shooting at a greater distance, the bullet impact velocity decreases and thereby reduces the wound effect of the bullet. The rate of decline of the impact velocity determines the rate of expansion decline of the bullet effect on the target with respect to the width of interval between the lower and the upper limit of expansion, respectively.

A different impact velocity of the expansion bullet may significantly affect the rate of wound effect. Paradoxically, an unexpanded bullet with a low impact velocity penetrates deeper into the target with respect to the fast bullet that expands. In the case of penetration of the target the slower unexpanded bullet leaves the target with higher velocity than a fast expanded bullet. For a slow bullet the transferred energy rate is low and the bullet is not only less effective towards the selected target, but can also threaten more non-participating neighborhood in the case of penetrating the target.

3. Shooting experiments

Shooting experiments were conducted by the ammunition Action 5 of identical series (cartridge stamping 9x19 SX A5 - DAG10E0842) from the ballistic measuring device 9x19 NATO-H onto uncovered gel blocks of density 15% at distance of 5 m from the muzzle of the ballistic measuring device, see Fig. 4. The prismatic gel block has the length of 0.3 m and rectangle cross-section

perpendicular to the bullet trajectory has dimensions 0.2 m x 0.14 m, see Fig. 5. Velocity of the bullet $v_{2.5}$ was measured using non-contact optical gates with the base 1 m and this velocity is considered equal to the velocity of gel block impact v_{imp}. Velocity of the bullet after the penetration of the block v_{res} was measured using two high-speed cameras Redlake HG-100K and MotionXtra N4.

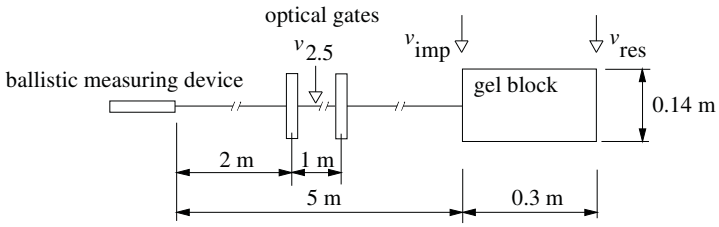

Fig. 4: Experimental scheme

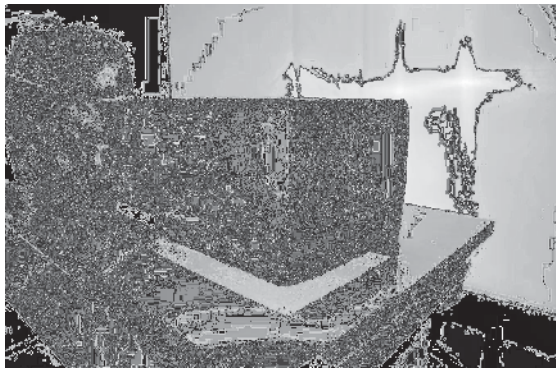

Fig. 5: Experimental gel block in firing position in shooting range Prototypa, Brno

Two kinds of Action 5 cartridges were used for the experimental shooting – original cartridges and delaborated cartridges with modified propellant with lower weight in order to reduce the velocity of the bullet. Dimensional and weight characteristics of the bullets are shown in Table 2. The aim of the experiments was to achieve different impact velocities to prove various expansion behavior of the bullet penetrating the substitute material. In addition, the experiment results and observations are necessary inputs for simulation part of the presented work as well.

Tab. 2: Characteristics of bullets used in experiment

No of shot	Propellant weight	Bullet weight	Velocity $v_{2.5} = v_{imp}$	Velocity v_{res}	Bullet length L	Bullet diameter D	Coef. of expansion K_e
	g	g	m/s	m/s	mm	mm	1
1	0.30	6.03	248	105	15.2	9.0	1.00
2	0.35	6.01	349	80	14.8	9.2	1.02
3	0.40	6.02	395	44	13.7	12.0	1.33
4	0.44	5.97	454	36	13.4	14.1	1.57

The temperature of the bullet and gel block, respectively, was 20°C and ambient temperature in Prototypa shooting range was 10°C.

Deformed bullets are shown in Fig. 6 along with simulation results.

The course of the impact velocity of the bullets v_{imp} with respect to the residual velocity v_{res} is shown on graph in Fig. 8 along with simulation results.

4. FEM simulations

In order to simulate the penetration process an explicit nonlinear transient hydrocode Autodyn v14.0 was used, implemented into Finite Element Method system Ansys Workbench. The model of the bullet and gel block was created using 2D axial symmetry, so only a half of the parts of all components were modeled.

The model of the bullet Action 5 was created upon real geometry with equal main dimensions. The geometry was slightly simplified in order to model the suitable mesh. The volume and density of the brass bullet body and plastic cap was modified in order to achieve equal total weight of the bullet. The simulation gel block does not fully respect the original prismatic shape of the gel block due to the axial symmetry used within FEM model. The shape of the simulation gel block is cylinder with diameter of 0.14 m and length of 0.3 m.

The bullet uses mesh-based Lagrangian method and the gel block uses mesh-free particle based Smooth Particle Hydrodynamics (SPH) method. Therefore the model for the gel block is suitable only for simulation the opening process of the block cavity during penetration process and does not cover the process of cavity closing. The character and discretization of the model of both the bullet and gel block is shown in Fig. 6.

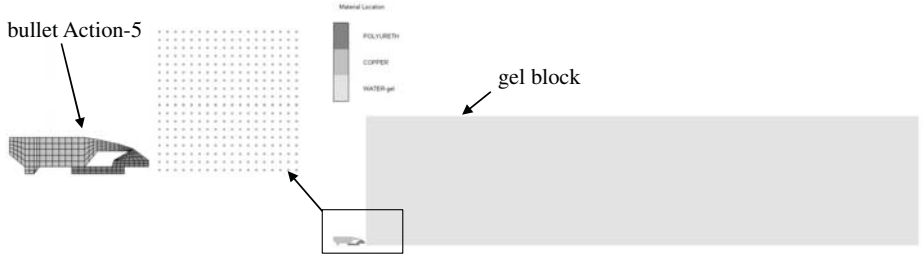

Fig. 6: FEM model of the bullet Action 5 and the gel block using axial symmetry

The rotation of the bullet caused by barrel bore and air drag are not considered. The simulation methodology is based on (Hazell, 2009; Hub, 2011).

All material models of the bullet and the gel block were retrieved from the Autodyn material library and they are in some cases modified. The bullet consists of the brass body and the plastic cap.

The material behavior of the brass body represents the modified copper material and is described through the shock equation of state (EOS) and the strength model. The brass body uses EOS (Steinberg, 1996) with following parameters: $\rho = 8354$ m · s^{-3}, $\Gamma = 2.0$, $C_0 = 3958$ m · s^{-1} and $S_1 = 1.497$. The Piecewise Johnson-Cook constitutive strength model contains the following parameters: $G = 68800$ MPa, $Y_0 = 120$ MPa, $\varepsilon_{P1} = 0.3$, $Y_1 = 450$ MPa, $Y_2 = 450$ MPa, $m = 1$.

The plastic cap follows the modified polyurethane model with density $\rho = 1265$ kg · m^{-3}, linear EOS with bulk modulus $K = 2000$ MPa and the elastic strength model with shear modulus $G = 5$ MPa.

The ballistic gel material represents the modified water model with EOS using parameters $C_0 = 1647$ m · s^{-1} and $S_1 = 1.921$. The density of gel block varies upon impact velocity of the bullet as the parameter to achieve the correspondence between experimental and simulation results. The density of simulation model of the gel block has the value of 520 kg · m^{-3} for the shot No. 1, next 650 kg · m^{-3} for No. 2, next 740 kg · m^{-3} for No. 3 and 750 kg · m^{-3} for No. 4.

The initial condition for the simulation represents the impact velocity of the bullet and it is equal to the velocities $v_{2.5}$ and v_{imp} according to the values shown in Table 2. The output simulation parameters are the geometry of deformed bullet after the penetration and residual velocity of the bullet after penetrating the gel block. Those parameters will be compared to experiments.

The example of graphical result of FEM simulation is shown in Fig. 7 for both the shot No. 1 (the lowest impact velocity) and for the shot No. 4 (the higher impact velocity), respectively.

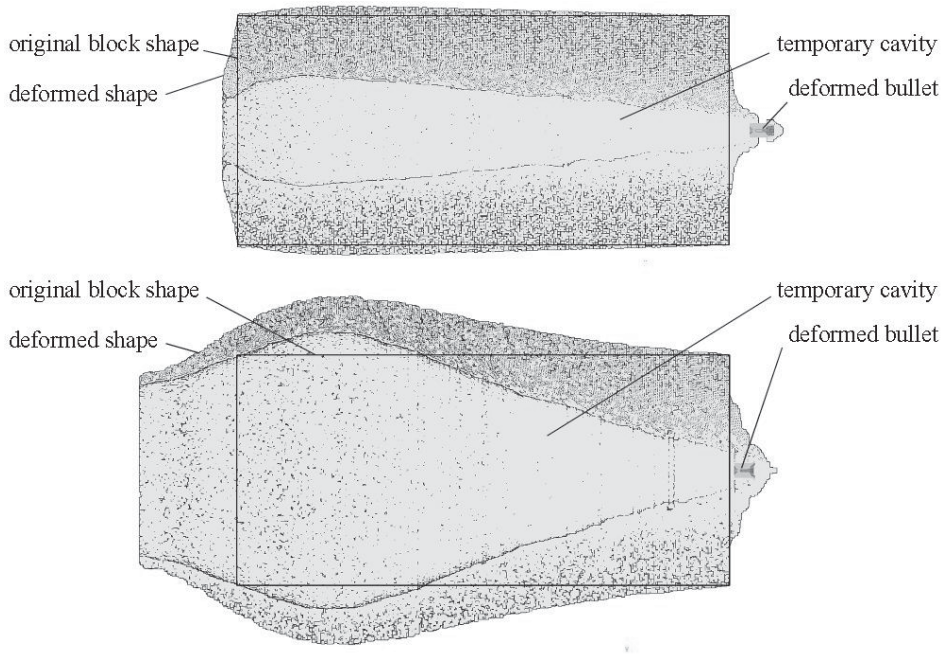

Fig. 7: Simulation results of penetrated gel block by the bullet Action 5; upper picture represents the shot No. 1 (impact velocity 248 m/s), the bottom picture the shot No. 4 (impact velocity 454 m/s)

The simulation results shown in Fig. 7 introduce a large temporary cavity made by penetrating bullet. Similar cavity was observed also on experiments. The volume of the cavity is larger for the bullet with higher level of expansion that means also higher impact velocity of the bullet and higher wound potential.

5. Simulation results and comparing to experiments

The FEM simulations using Ansys Autodyn aims to find good correlation for character and deformation of the bullet after penetration process. The second comparing parameter is residual velocity of the bullet after penetration of the gel block with respect to impact velocity of the bullet.

Every bullet showed some extent of the expansion after penetration of the gel block and the level of this extent varied upon the impact bullet velocity. Geometrical parameters of the bullets are contained in Table 3 and deformed shapes of the bullets are shown in Fig. 8.

Tab. 3: Comparing the experimental and simulation results

No of shot	Impact velocity	Bullet length L			Bullet max. diameter D			Residual velocity v_{res}		
		L_{exp}	L_{sim}	Δ_L	D_{exp}	D_{sim}	Δ_D	$v_{res,exp}$	$v_{res,sim}$	Δ_v
	m/s	m/s	m/s	%	mm	mm	%	mm	mm	%
1	248	15.2	14.8	3	9.0	9.0	0	105	110	5
2	349	14.8	14.1	5	9.2	9.2	0	80	79	1
3	395	13.7	13.4	2	12.0	10.5	14	44	45	2
4	454	13.4	12.4	8	14.1	12.2	16	36	37	3

No. 1	No. 2	No. 3	No. 4
248 m/s	349 m/s	395 m/s	454 m/s

Fig. 8: Bullets after penetration of the gel block – upper line shows the experimental results and the bottom line the simulation results

The bullets with lower velocity showed smaller expansion, the bullet No. 4 shows the greatest expansion with original propellant weight and original shooting velocity. In all cases the plastic cap was pushed inside of the bullet hollow. Every bullet penetrating the gel block was caught in the soft catch located behind the gel block without any secondary deformations.

The comparison of the change of bullet dimensions as well as the experimental and simulation velocities of the bullet after penetrating the gel block is shown in Table 3. The symbol Δ means a deviation of compared values calculated as the difference between compared values divided by the lower value of those compared.

According to the deviations shown in Table 3, the simulation follows the experimental values with respect to dimensions of the bullet very well and quite well with respect to the residual velocities.

The graph in Fig. 9 shows the course of impact velocity with respect to the decrease of residual velocity for both experimental and simulation values. The relative decrease of the residual velocity is equal to the ratio between the difference of impact and residual velocities divided by the impact velocity expressed in percentage units:

$$\bar{v}_{res} = \frac{v_{imp} - v_{res}}{v_{imp}} \cdot 100 \qquad (2)$$

On the other hand, the decrease of the residual velocity shows how much velocity of the impacting bullet was consumed by the penetration process. The course is not linear and between the impact velocities 349 m/s and 395 m/s occurs a break region where the behavior of the expansion process changes its effect on deceleration of the bullet in the gel block. We consider this effect as increased influence of expansion shape of the bullet. It is probably caused by exceeding the caliber diameter by expanded front part of the bullet. This effect should be investigated in detail in the future and it would be helpful to conduct more shooting experiments with impact velocities between the values of 349 m/s and 395 m/s.

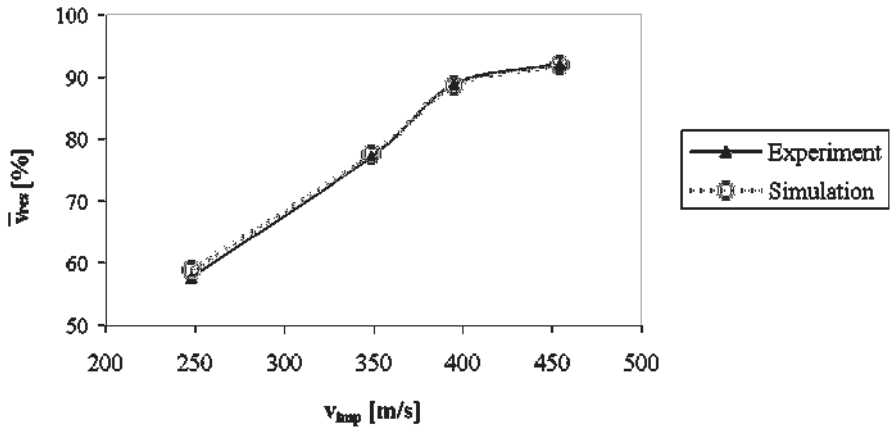

Fig. 9: Graph of the dependance of the decrese of residual velocity of the bullet with respect to the impact velocity

6. Conclusion

The above analysis in the article represents a detail view on the function of expansion bullet when penetrating a soft target (e.g. living tissue or its technical substitution). The results of the experiments and FEM simulations show fairly good correspondence. Based on the analysis of the function of the cartridge Action 5 in the terminal ballistics it can be stated that the basic characteristics of ballistic cartridge correspond to the physical and mechanical properties of the cartridge, i.e. the ballistic performance of the cartridge makes it possíble to reach optimum deformation of the bullet in soft targets (Jedlička, 2011).

According to presented anlysis it is possible to estimate following expansion velocity limits:

- lower expension limit – approx. 248 m/s (shot No. 1)
- expansion limit with expansion coefficient equal to 1 – approx. 349 m/s (shot No. 2)
- upper expansion limit – between 395 m/s and 454 m/s (shots No. 3 and 4).

Analysis of results allows to introduce the lower expansion limit of pistol bullet Action 5 and to estimate other limits of this cartridge. For their precise determination it is necessary to carry out further experiments with mentioned cartridge Action 5.

Acknowledgement

The work presented in this paper has been supported by the Ministry of Interior of the Czech Republic (security research project VG20112015037).

References

Hazell, P. (2009) Numerical simulations and experimental observations of the 5.65-mm L2A2 bullet perforating steel targets of two hardness values. *Journal of Battlefield Technology*, March 2009, Vol. 6, pp.1-4.

Hub, J., Komenda, J. & Racek, F. (2011) Ballistic resistance of duralumin sheet metal plate using forward obstacle, in: *Proc. Int. Conf. In Military Technology* (R. Jalovecky & A. Steffek eds), University of Defense, Brno, pp.1663-1682.

Jedlička, L., Komenda, J. & Beer S. (2011) Ballistic analysis of small arms cartridge, in: *Proc. Int. Conf. In Military Technology* (R. Jalovecky & A. Steffek eds), University of Defense, Brno, pp.1717-1726.

Rosenberg M. R. (2002) *Waffen und Einsatzmunition der Polizei*. Motorbuch Verlag, Stuttgart.

Steinberg, D. J. (1996) *Equation of state and strength properties of selected materials.* Lawrence Livermore National Laboratory, Livermore.

18th International Conference
ENGINEERING MECHANICS 2012
Svratka, Czech Republic, May 14 – 17, 2012

pp. 461–468
Paper #128

SENSITIVITY ANALYSIS OF SMALL PUNCH TEST

J. Hůlka, P. Kubík, J. Petruška[1]

Abstract: *The paper deals with numerical simulation of penetration test called Small Punch Test (SPT). SPT is used to determine basic mechanical properties from a tiny piece of material. There are no generally accepted standards for this type of testing until now. The testing procedure drew a great interest in the last decade. "Code of Practice" was created based on the CEN Workshop 2007, which recommends both geometry, experiment performance and its evaluation. To obtain the mechanical properties from SPT is an indirect computational task. One of possible approaches to obtain yield strength and ultimate strength is the use of an inverse numerical simulation. There is a need to define the important variables, that will substantially influence the inverse simulation.*

Keywords: ***SPT, FEM, sensitivity analysis***

1. Introduction

Material properties of any component can change during their operation. The knowledge of the current values is desirable especially for extending service life of the component. To enable the evaluation of structural steels mechanical properties, penetration test of small bodies called the Small Punch Test is intensively developed. This non-standard type of test is preferred if there is shortage of material for samples. It is common for example in part of nuclear power plants, turbines, rotors, etc. The principle of SPT is punch penetration through the flat disc-shaped specimen. Schematic test arrangement is shown in Figure 1. The specimen is clamped between the upper and lower die and the punch penetrates the specimen up to failure. Punch displacement and reaction forces are recorded during the test. Punch can be either a ceramic ball or punch of steel with hemisphere ending.

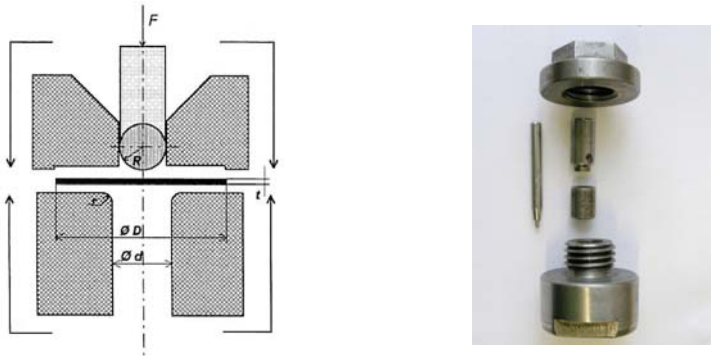

Fig. 1: Schematic representation of experimental assembly

Small Punch Test method originated in the early eighties of the last century in the U.S., where Manahan (1981) first published the method. Development of this method was under way parallel in Japan, too. The method focused on assessing the effect of irradiation on the material properties used in thermonuclear reactors. The biggest milestone in the development of this method was the establishment of document CWA 15627:2007 D/E/F on the basis of the CEN Workshop in 2007, which become the industry standard. This "Code of Practice" recommends not only the geometry of sample and tools, but also the testing course and its evaluation.

[1] Ing. Jiří Hůlka, Ing. Petr Kubík, Prof. Ing. Jindřich Petruška, CSc.: Institute of Solid Mechanics, Mechatronics and Biomechanics, Brno University of Technology; Technická 2896/2; 616 69 Brno; tel.: +420 777838541, e-mail: hulka@c-box.cz

For commercial use of this method, several technologies were developed cut the test specimen from the bulk of tested structures. They can be divided into two groups. The first is based on grinding off the sample and the second is based on electrosparking.

2. Numerical model variation

We are trying to simulate a real experiment with the help of finite element model (FEM). Our goal is to achieve computationally an identical force-deflection response, which is recorded from the experiment. The sensitivity analysis helps us to consider importance of variables that occur in the FE model. In this paper we analyse the influence of the following variables:

- FE mesh density
- modelling tools as rigid bodies
- influence of sample thickens
- influence of material model
- influence of friction between punch and sample
- influence of friction and forces among dies and sample

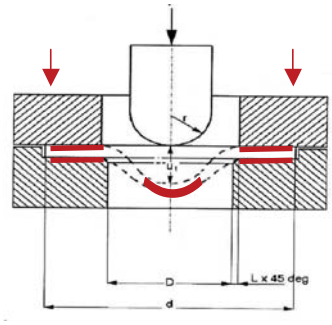

Fig. 2: Locations with friction influence

3. Material model

Very ductile austenitic steel ASTM A316L is investigated in our case. Specimens were made from rolled plate with a thickness of 20mm. We expected anisotropic mechanical properties because of rolling. To verify our assumption, the plate was cut in three directions, namely 0° in the longitudinal, diagonal 45° and 90° lateral direction. This is illustrated in Figure 3. Three specimens were made from prepared parts for uniaxial smooth tension test in every direction. Samples were made with longer clamping head, from which the SPT samples were made.

The average results of tensile tests in various directions of the plate are in Figure 4. It is possible to conclude from the results, that samples even at 45°do not show significant anisotropy. Material will be considered isotropic.

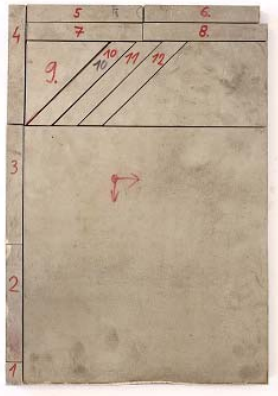

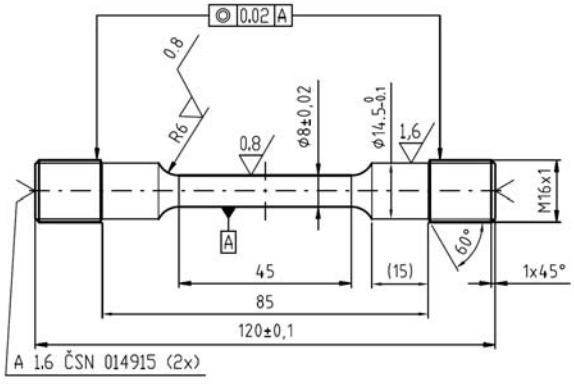

Fig. 3: Plate for the samples production (left), sample for uniaxial tension test (right)

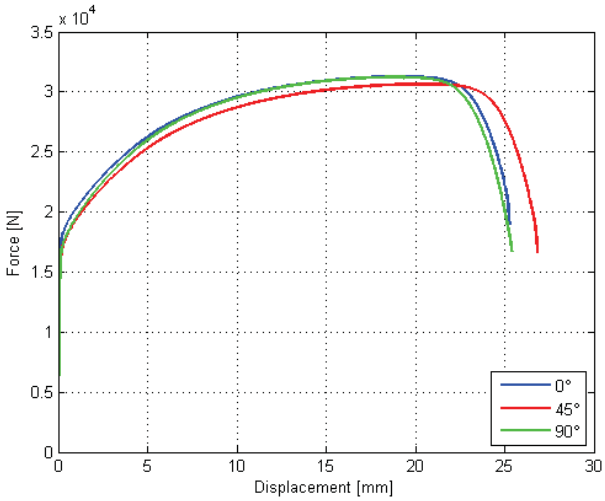

Fig. 4: Average values of tensile tests in three directions

The true stress-true strain curve is used as input data for elastic-plastic analysis. The uniaxial stress condition of circular smooth sample is valid only until ultimate strength. Strain value is commonly higher then break point, so it is necessary to calibrated the material model with help of parallel numerical simulation, as shown in Figure 5. There is used MLR correction recommended by Mirone (2006) or the initial estimate of the curve correction. Trial and error correction was used for greater accuracy. Figure 5 shows multilinear material model.

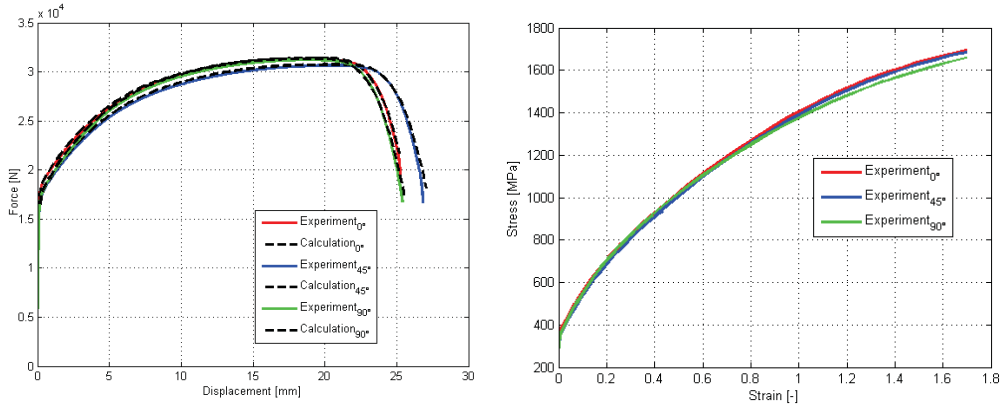

Fig. 5: Calibrated material model curves (left), the curves truth stress-strain (right)

4. SPT experiments

SPT samples were made from used tensile specimen's heads. In cooperation with Material & Metallurgical research Ltd. Ostrava, five penetration tests were performed in each of the direction. Experimental results are displayed in Figure 6. Considerable dispersion of measured values partly explains this sensitivity analysis. Fractures in the lower displacement are observed for some of the samples. Differences in fracture location are observed too. This issue will be investigated further.

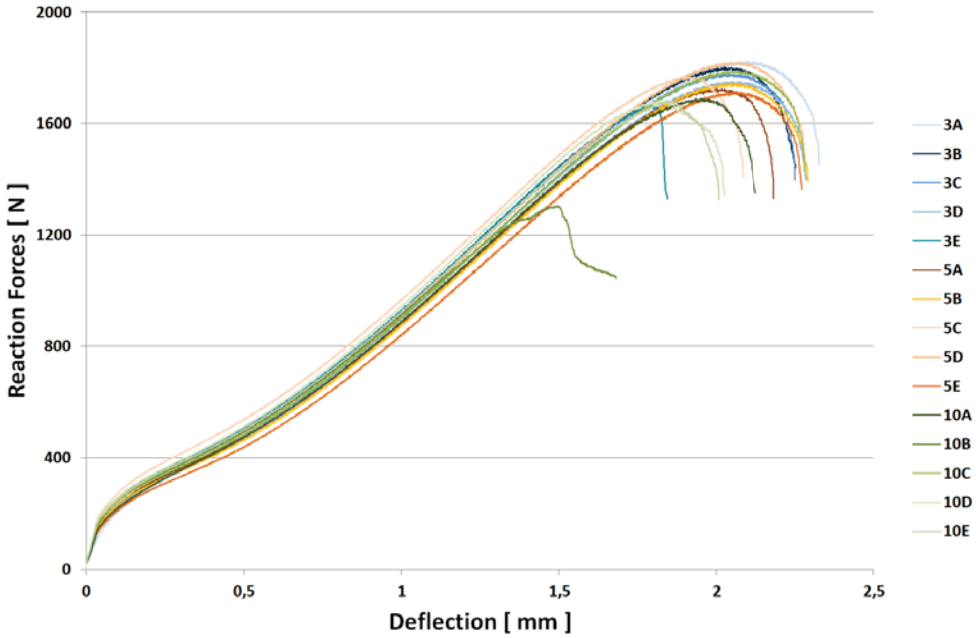

Fig. 6: SPT experiments

Tab. 1: Thickness of samples measured before the experiment

3=0°		10=45°		5=90°	
3A	0,505	***10A***	0,500	***5A***	0,490
3B	0,500	***10B***	0,495	***5B***	0,495
3C	0,505	***10C***	0,500	***5C***	0,505
3D	0,495	***10D***	0,505	***5D***	0,500
3E	0,505	***10E***	0,500	***5E***	0,485

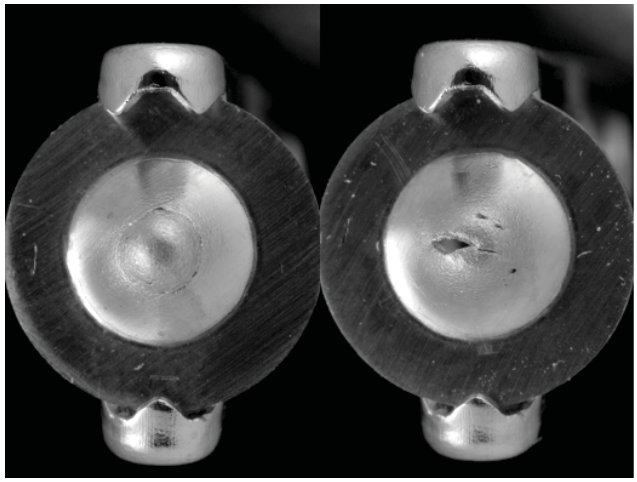

Fig. 7: SPT samples after the experiment with the standard (left) and unusual fracture (right)

5. Model of Small Punch Test

The computational model of SPT was created in explicit Abaqus code. Geometry of FE model is identical to the experiment assembly and recommended CWA 15627 except punch diameter, which is recommended 2,5mm. Geometry of FE model is in Figure 8.

Tools were modelled as “Rigid Body” and axisymmetrical FE model was used. Punch is moved in the y-axis direction. Contact force is prescribed to the upper die and the lower one is fixed.

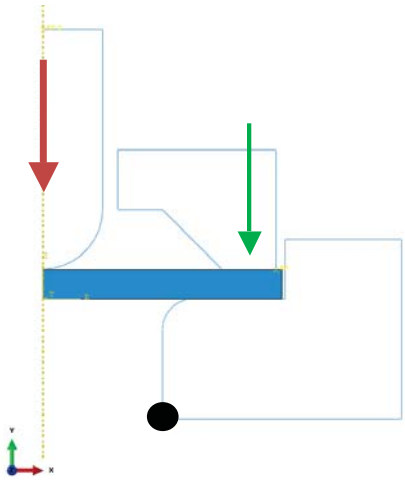

Specimen diameter	8,0 mm
Specimen thickness	0,5 mm
Punch radius	1,0 mm
Inner diameter of lower die	4,0 mm
Lower die radius	0,5 mm

Fig. 8: Geometry of FE model with dimensions

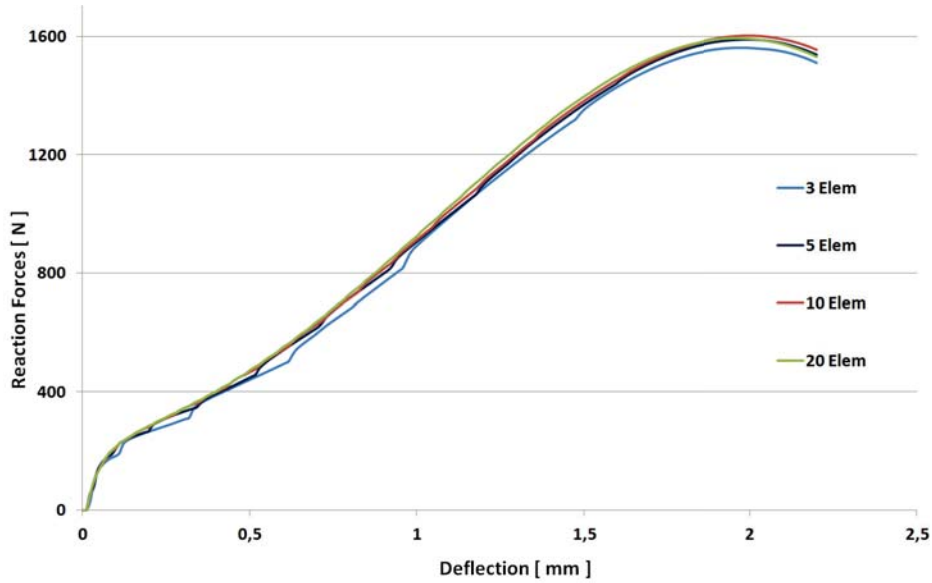

Fig. 9: Influence of FE density

6. Sensitivity analysis

Knowledge of variables based on sensitivity analysis is important for inverse problem. To minimize the scattering of measured values is necessary for quality output from the numerical simulation. We assume an ideal experimental tools shape in our case.

6.1 FE mesh density

Fixed upper and lower die represent the default state of the model. Coulomb friction model is used with the coefficient f=0,1. The same friction coefficient is used between the punch – sample and dies – samples. Material model is used for 90° (transversal direction).

The graph in Figure 9 shows that the model is adequately described with 5 - 10 elements in the through thickness direction of the sample.

6.2 Tools deformation

There is an effort to model tools as rigid bodies to shorten calculation time and to make the model more efficient. Displacement difference due to the punch deformation is shown in Figure 10. Displacements are measured between the ends of the punch. Tools were modelled as elastic bodies.

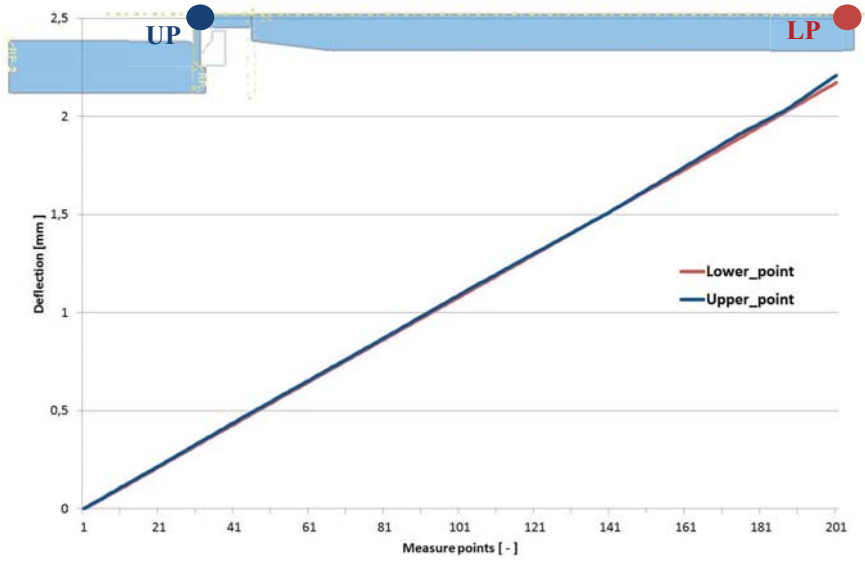

Fig. 10: Displacement differences on punch

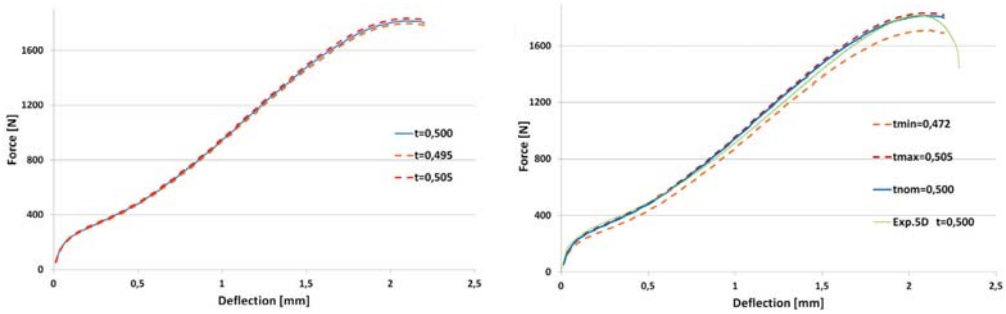

Fig. 11: Reaction forces according CWA thickness tolerances (left) and real values (right)

6.3 Influence of sample thickness

Samples production is not easy. Although there are mechanical productions of samples, most of them are produced by hand. Thickness and flatness of samples is prescribed by CWA. Table 1 shows the thickness-tolerance, which is recommended +-1% of the sample thickness (+-0,005mm). We assume ideal flatness of the sample in FE model and only the influence of thickness is studied. There is force dispersion according CWA tolerance on the left part of Figure 11. The right part of the figure shows force dispersion with real thicknesses used in the experiments.

6.4 Influence of friction between punch and sample

We distinguish between two places with friction in the model. One is the interface between the punch and the sample. The second is between the matrix and the sample, as shown in Figure 2. Friction coefficient is changed between the punch and the sample, see Figure 12. Coefficient of friction between the dies and sample was f=0,1.

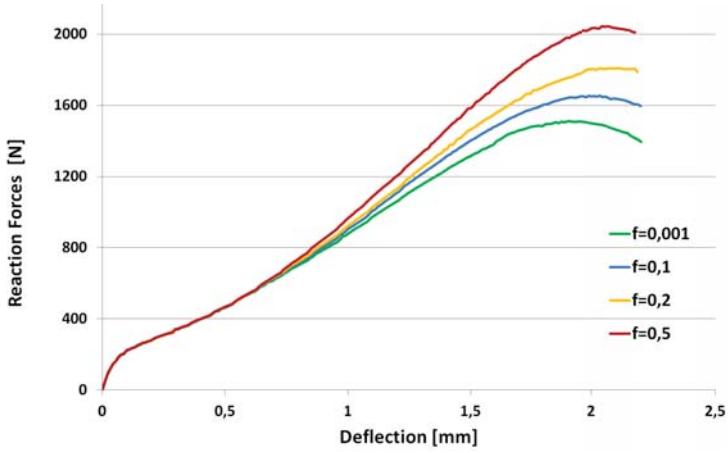

Fig. 12: Influence of friction coefficient variability between punch and sample

6.5 Influence of friction and upper die pressure variability

In Figure 13, we can see simulation results to quantify the effect of upper die pressure and friction variability on the test results.

6.6 Influence of material model calibration

It is always important to perform parallel numerical simulation by material model calibration. Differences in forces response using a model without material hardening after the yield stress, ultimate strength and material models calibrated at 0° and 90° direction are in Figure 14.

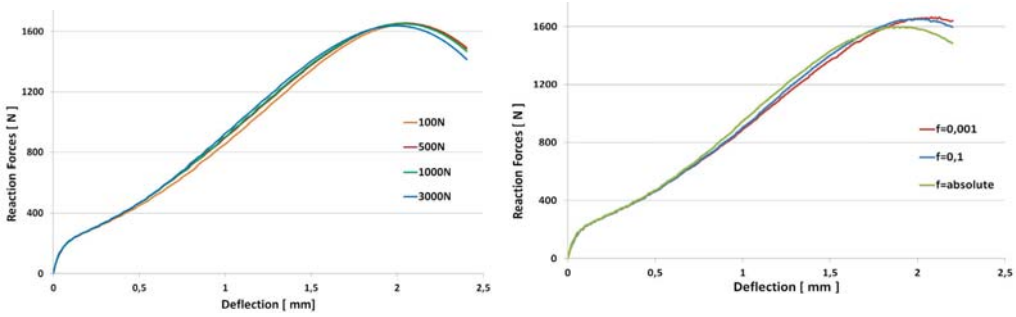

Fig. 13: Effect of die pressure (left) and friction coefficient value

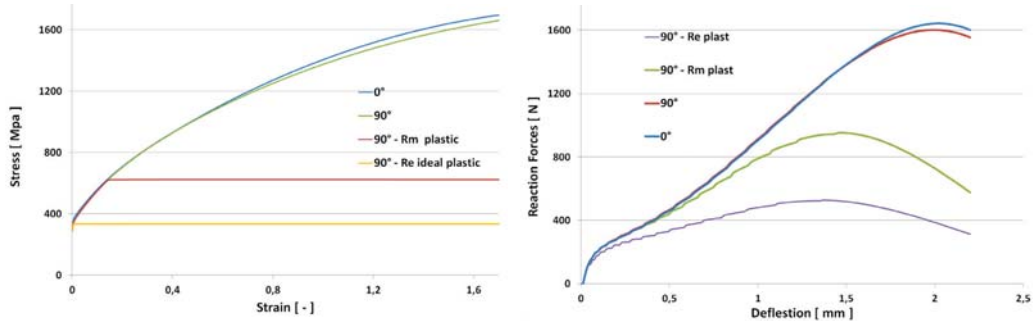

Fig. 14: Effect of material model to response forces

7. Conclusion

This paper presents a sensitivity analysis of SPT. Uniaxial tensile tests did not confirm the strong anisotropy of the material. SPT samples were prepared from heads of tensile specimens. Considerable dispersion of data was found from fifteen tests.

Sensitivity analysis was focused on the variables affects in the test. There are well calibrated material models, finite element density, value of the friction coefficient, the actual thickness of sample and tool deformation.

True stress – strain curve is the input to the elastic-plastic material model. The graph in Figure 14 shows that the maximum reaction force of SPT lies in the extrapolated part of curve which is obtained from uniaxial tensile test. This is reason to pay close attention to the calibration of the true stress-strain curve.

The value of Coulomb's friction coefficient plays a dominant role in the second part of test. At that time there is relative movement between the specimen and the punch. Static value of friction was used in chapter 6.4. Distribution of friction as static and dynamic one will be subject to further sensitivity analysis.

It is not easy to keep the prescribed thickness tolerance. This is due to small dimension of specimen and mostly handmade samples.

The influence of friction and pressure among dies and sample is not significant. Deformations of tools are not significant, too. Figure 9 shows, that a suitable mesh density of sample is 5-10 elements in thickness.

Acknowledgement

Financial help of the grant projects GA101/09/1630 and FSI-S-11-11/1190 is gratefully acknowledged.

References

CEN WORKSHOP AGREEMENT „Small Punch Test method for Metallic Materials" (2007) CWA 15627:2007: D/E/F, Decenber 2007

Egan P., Whelan M.P., Lakestani F., Connelly M.J. (2007) Small punch test: An approach to solve the inverse problem by deformation shape and finite element optimization. *Comp. Mat. Science*.40, 33-39

Hurst R., Matocha K.(2010) The European Code of Practice for Small Punch Testing – where do we go from here? *Metallurgical Journal*, 63, 5-11.

Manahan M., Argon A., Harling O. (1981) The development of a miniaturized disk bend test for the determination of post-irradiation mechanical properties. *J. of Nuclear Mat.*, 103-104, 1545-1550.

Mirone G. (2006) Role of stress triaxiality in elastoplastic characterization and ductile failure prediction. *Eng. Fract. Mech.*, 74, 1203-1221

18th International Conference
ENGINEERING MECHANICS 2012
Svratka, Czech Republic, May 14 – 17, 2012

pp. 469–475
Paper #275

THE DETERMINATION OF THE KINEMATIC QUANTITIES BY USING THE HIGH-SPEED DIC METHOD

R.Huňady[*], M. Hagara[**], M. Schrotter[***]

Abstract: *A measuring of deformations and displacements of a moving object can be considered for one of the most complicated tasks in the experimental mechanics. Thanks to modern optical methods like method of digital image correlation, we are able to record displacements during the time variable actions such as dynamic loading or motion. The article deals with possibilities of using high-speed digital image correlation for determination of some kinematic quantities of rotating objects.*

Keywords: ***motion, kinematic quantities, digital image correlation***

1. Introduction

The kinematics can be integrated from theoretical aspect as part of classic physics. Its main objective is description of point/body movement or system of points/bodies but it does not deal with forces which cause this movement. For description of this movement it is necessary to find out the trajectory of this motion and also the velocity and acceleration. In practice kinematics can serve for determining a range of movement of some mechanism or for finding out velocities or accelerations of its components movement.

There is a plenty of sensors for measuring of kinematics quantities which utilize various physical methods and can be divided as follows:

- according to a signal output and an operating principle
  a) with analog signal (resistive, capacitive, inductive, inductactive, ultrasound, optoelectronic, piezoelectric,...)
  b) with discrete signal (electrocontact, image, oscillatory, magnetic with Hall probe, optoelectronic, optronic, incremental, absolute,...)
- according to a kind of measured quantity
  a) position sensor
  b) velocity sensor
  c) acceleration sensor
- according to a contact with an investigated object
  a) contact
  b) non-contact

To the position sensors we can include also rpm sensors so called tachometers. Tachometers can be divided according to transfer of rotation frequency to an output signal as follows:

a) hydraulic tachometers

[*] Ing. Róbert Huňady, PhD.: Department of Applied Mechanics and Mechatronics, Faculty of Mechanical Engineering, Technical University of Košice, Letná 9; 042 00, Košice; SK, e-mail: robert.hunady@tuke.sk

[**] Ing. Martin Hagara: Department of Applied Mechanics and Mechatronics, Faculty of Mechanical Engineering, Technical University of Košice, Letná 9; 042 00, Košice; SK, e-mail: martin.hagara@tuke.sk

[***] Ing. Martin Schrotter: Department of Applied Mechanics and Mechatronics, Faculty of Mechanical Engineering, Technical University of Košice, Letná 9; 042 00, Košice; SK, e-mail: martin.schrotter@tuke.sk

b) pneumatic tachometers

c) tachometers with non-electric output (mechanical, resonant, chronometric, stroboscopic)

d) tachometers with electrical output

Likewise, they can be divided into contact and non-contact.

In some cases it is convenient to use for measurement non-contact methods which do not disturb measured structure. Among modern non-contact methods which are more and more popular nowadays belongs also digital image correlation (DIC).

2. Digital image correlation

Digital image correlation is a non-contact optical method served for identification of spatial displacements and strains of investigated object. Three-dimensional displacements are determined by correlation of digital images obtained by CCD cameras during movement of an investigated object.

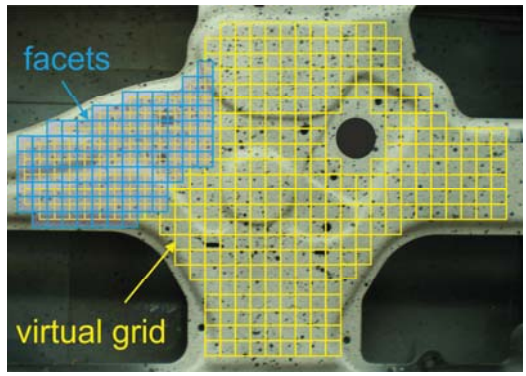

Fig. 1: Random black and white pattern created on the surface of investigated object

The object surface is in software application automatically divided into small image elements called facets. Each of these facets contains a characteristic contrast random pattern usually created by spraying of black stochastic dots on a white background (Fig.1). This pattern imitates the object contour, moves and/or deforms together with it. Displacement fields are determined by correlation of corresponding facets determined on digital images before and after object movement.

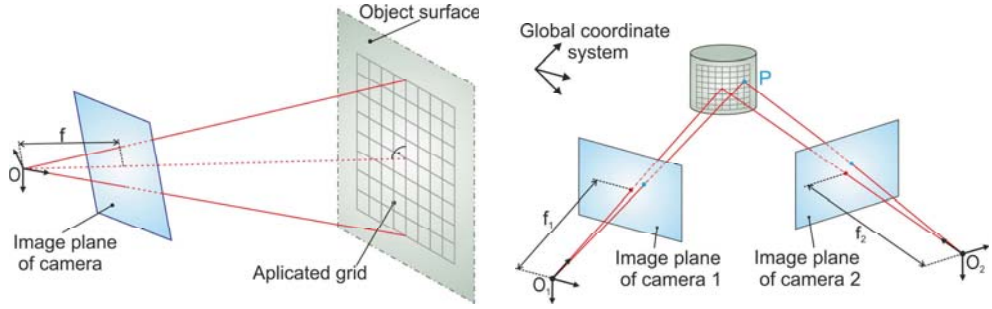

Fig. 2: The principal of 2D (left) and 3D (right) digital image correlation

If one camera with perpendicular position to investigated object is used for sampling images displacements can be determined just in plane parallel to image plane of camera (Fig. 2 left). This configuration is called two-dimensional digital image correlation (2D-DIC).

A three-dimensional digital image correlation (3D-DIC) is used in spatial analysis. In this case the determination of 3D-displacement could not be realized by one camera. For this reason two cameras are used to capture images from two different locations and directions (Fig. 2 right). This configuration allows studying mainly flat objects or planar objects with small curvature. Nowadays systems with three, four, six or eight cameras are developed to observe spatial objects from all

directions. Discrete values of displacements in three mutually perpendicular directions of each investigated point are obtained as output from correlation system. Subsequently it is necessary to process these data numerically to obtain required kinematic quantities (Sutton et al., 2009; Siebert et al., 2005; Pan et al., 2009; Yoshizawa, 2009; Siebert et al., 2009).

3. Motion analysis of an object with constant rotary movement

The investigated object was a cooling fan of an automobile Škoda Felicia powered by stabilized generator with constant voltage 5V.

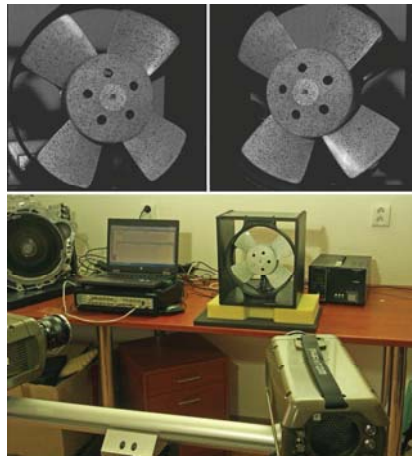

Fig. 3: Cameras configuration and views of investigated cooling fan from both cameras

Since a frequency of rotation of the cooling fan was relatively high, it was necessary to perform a high-speed measurement with a sampling frequency FS=5000fps to obtain continuous displacements of rotating fan. By this high frequency cameras shutter time was too short to get enough light onto the sensor. Therefore it was required to use a high-performance point source of white light to illuminate the fan during measurement. Likewise it was necessary to ensure that the whole investigated object could be seen by both cameras. Since fuzzy images could introduce some inaccuracies in a form of correlation errors captured images had to be really sharp with optimal contrast. Total acquisition time was prescribed to 0,5s and 2500 images were captured by both cameras. Cameras configuration and views of investigated cooling fan obtained by both cameras can be seen in the Fig. 3.

A reconstructed contour of the investigated area is depicted in the Fig. 4. Displacements were investigated in three points lying in the same straight line. These points are in the Fig. 4 depicted by green dots and marked by numbers from 1 to 3.

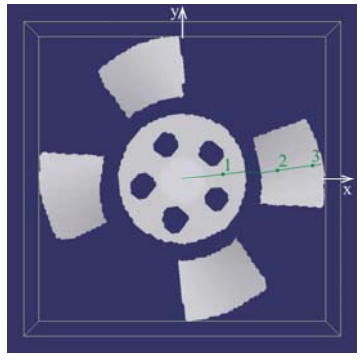

Fig. 4: Reconstructed contour of cooling fan after correlation with selected investigated points

The time dependences of displacements of each point in *x* and *y* directions (see Fig. 5) were consequently imported into Matlab and numerically processed. Trajectories of these three points can be seen in the Fig. 6.

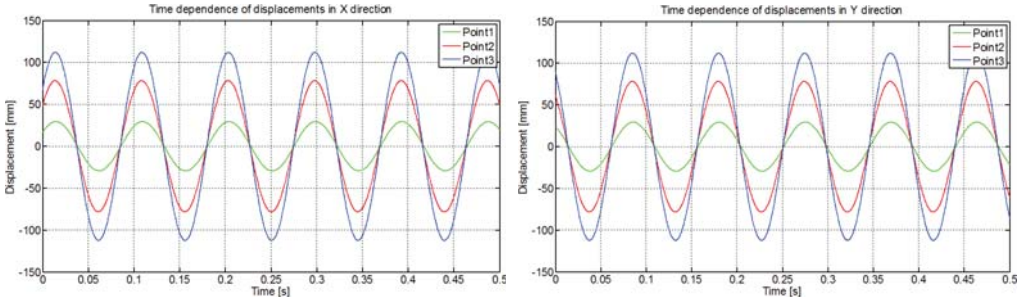

Fig. 5: Time dependence of chosen points displacements in directions x, y

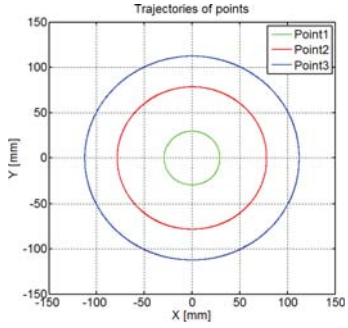

Fig. 6: Trajectories of cooling fan chosen points

Rotation frequency f_o of the cooling fan with constant rotary movement was determined from the frequency dependences of displacements in *x* and *y* direction. The time dependences of displacements were transformed into a frequency domain by Fast Fourier Transform (FFT). Frequency spectrums of displacements of each investigated point are depicted in the Fig. 7.

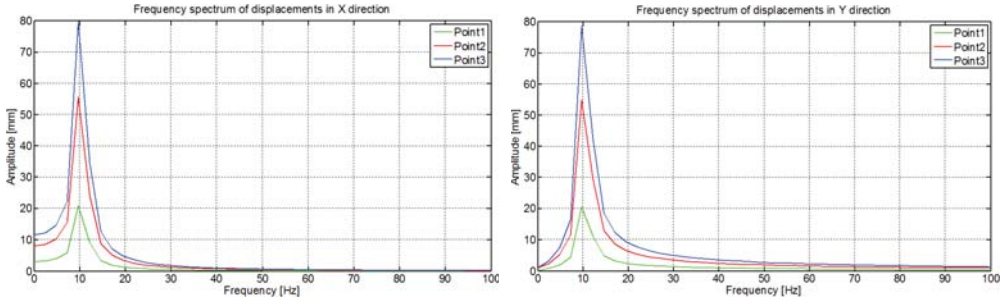

Fig. 7: Frequency spectrum of displacements in directions x,y

Because time dependences of displacements obtained by measurement represented set of discrete values it was necessary to utilize method of numerical differentiation for obtain another kinematic parameters (for instance velocity, angular velocity etc.) (Rizwan, 2008). Derivation of arbitrary function *f*(*t*) with respect to time t can be expressed by term:

$$f'(t) = \lim_{\Delta t \to 0} \frac{f(t+\Delta t) - f(t)}{\Delta t}. \qquad (1)$$

When the table values are equidistant in terms of time and Δt is assumed small enough (fig. 7) we can obtain formula for numeric differentiation by derivation of interpolation formulas expressed by the

help of differences. For three successive values it is possible to obtain assumption of first and second differentiation of given function by terms:

$$f'(t) = \frac{f(t+\Delta t) - f(t-\Delta t)}{2\Delta t}, \tag{2}$$

$$f''(t) = \frac{f(t+\Delta t) - 2f(t) + f(t-\Delta t)}{\Delta t^2}. \tag{3}$$

By using of presented terms the angular velocity ω of cooling fan rotations was determined by numerical differentiation of rotation angle φ:

$$\omega(t) = \frac{\varphi(t_{i+1}) - \varphi(t_i)}{\Delta t}, \tag{4}$$

where:

$$\varphi(t) = \arctan\frac{y(t)}{x(t)}, \tag{5}$$

$$\Delta t = \frac{1}{F_S}. \tag{6}$$

Time dependence of rotation angle and angular velocity are graphically depicted in the fig. 8 and fig. 9.

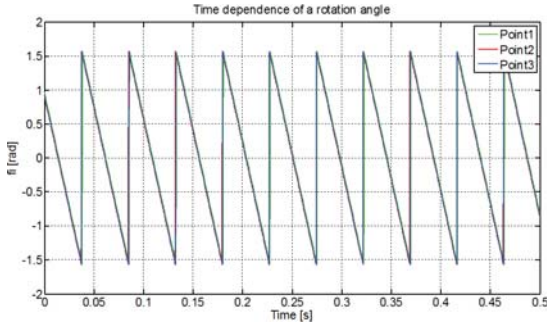

Fig. 8: Time dependence of rotation angle of cooling fan

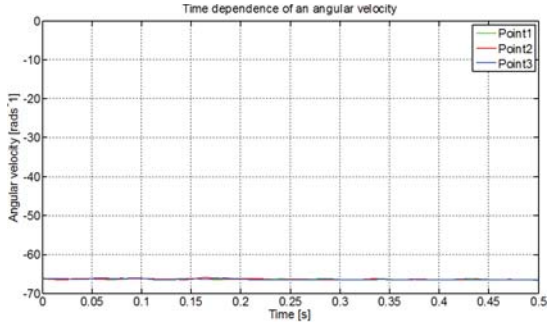

Fig. 9: Time dependence of angular velocity of cooling fan (after smoothing)

The velocity of particular points was determined by two methods. In the first case known frequency f_o of cooling fan rotation determined from frequency dependence of displacements was used. For calculation of velocities in this case was used:

$$v(t) = 2\pi f_o r(t), \tag{7}$$

where:

$$r(t) = \sqrt{x(t)^2 + y(t)^2}. \tag{8}$$

Dependence of velocities of particular points is for this approach showed in the fig. 10.

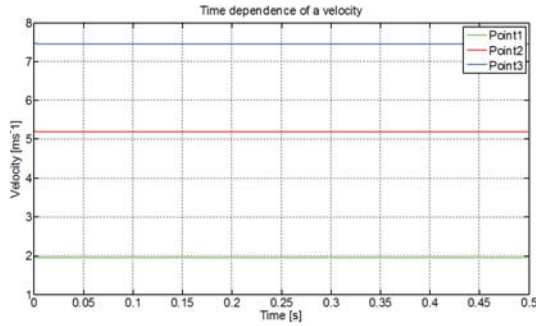

Fig. 10: Time dependence of velocity of chosen points

In the second one the velocity of cooling fan points was defined upon time dependence of angular velocity ω obtained by numerical differentiation. In contrast to former case it is possible to apply this computation also by accelerated or decelerated rotation movement. Velocities were determined according to:

$$v(t) = \omega(t)\, r(t) \tag{9}$$

For this instance the time dependence of velocities of particular points is showed in the fig.11.

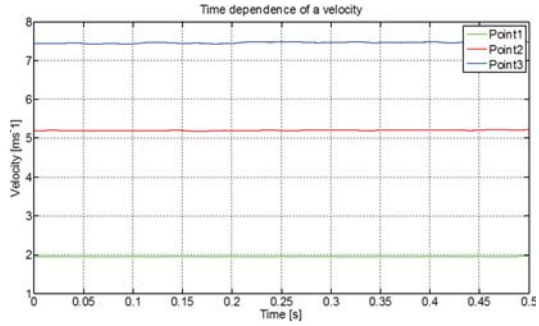

Fig. 11: Time dependence of velocities of selected points

4. Conclusions

Using of digital image correlation method is a convenient choice to solve a lot of strength or dynamic problems of mechanics. It does not face to almost any restrictions of investigated materials and can be used for various conditions. Operating software of correlation system offers background with intuitive interface which considerably facilitates researcher's work.

One of the restrictions by DIC movement analysis can be a fact that investigated object has to be situated in visual field of all cameras for all the time. With respect to that correlation systems use to be mostly formed by two cameras it is possible to use them particularly for solving of flat objects. With increasing number of cameras it is not so easy to ensure illuminating conditions equal for all respective cameras. Because of that it is necessary to exclude all shadows and reflections from snapshots. Another obstruction can be technical parameters of CCD cameras. Confined inner memory of cameras allows take 16000 snapshots with full resolution what gives rise to shorter acquisition time by higher sampling frequencies. Because of increasing sampling frequency the illumination of image is decreasing due to faster shutter time there is need to use more powerful source of light.

By investigation of rotary object movement the correlation error is increasing due to increasing distance of investigated points from centre of rotation. This phenomenon is due to that by higher speeds is displacement of points between two particular correlated snapshots higher. Because the numerical differentiation does not work with continuous values but with discrete ones it installs certain

inaccuracy to calculation. This inaccuracy obtained by higher sampling frequencies is not such strong to influence accuracy of results.

The same way i.e. by sampling of displacements and their consecutive numerical processing in Matlab it is possible to perform analysis of decelerated motion. The results obtained by investigation of physical pendulum decelerated movement were verified by means of simulation in program MSC Adams/View and are described in other technical publications.

As correlation system is created by high speed digital cameras there is possibility to use it also for investigation of objects vibrations. Operating software of correlation system enables direct performing of spectral analysis from measured values which serves for acquirement of natural frequencies of investigated motion. By using of complementary program Modan 1.0 which was created on Technical University of Košice, the Faculty of mechanical engineering and the Department of applied mechanics and mechatronics, we can obtain not only natural frequencies of vibrations but also corresponding modal shapes. In this way we can perform experimental modal analysis directly on rotating components of construction (Trebuňa et al., 2010; Huňady et al., 2011).

Acknowledgement

This contribution is the result of the project implementations: „Center for research of control of technical, environmental and human risks for permanent development of production and products in mechanical engineering“ (ITMS:26220120060) supported by the Research & Development Operational Programme funded by the ERDF and „Development of unconventional experimental methods for mechanical and mechatronic systems“ supported by Scientific Grant Agency VEGA MŠ SR (Project No. 1/0937/12).

References

Huňady, R., Bobovský, Z. & Hagara, M. (2011) Methodology for determination of modal parameters by digital image correlation. In: MMaMS 2011 - Modelling of Mechanical and Mechatronical Systems, Herľany, Slovakia, pp. 193-201.

Pan B. & al. (2009) Two-dimensional digital image correlation for in-plane displacement and strain measurement: a review. In: IOP Publishing - Measurement, science and technology, no. 20.

Rizwan, B. (2008) Introduction to Numerical Analysis Using Matlab, Infinity Science Press, ISBN 978-0-7637-7376-2.

Siebert T. & al. (2005) New features in digital image correlation techniques. In: 22nd DANUBIA-ADRIA Symposium on Experimental Methods in Solid Mechanics, Parma, Monticelli Terme.

Siebert, T., Wood, R. & Splithoff, K. (2009) High Speed Image Correlation for Vibration Analysis. In: 7th International Conference on Modern Practice in Stress and Vibration Analysis, IOP Publishing.

Sutton, M., Orteu, J. J. & Schreier, H. (2009) Image Correlation for Shape, Motion and Deformation Measurements - Basic Concepts, Theory and Applications, Springer Science + Business Media, LLC, 321 p., ISBN: 978-0-387-78746-6.

Trebuňa, F. & Huňady, R. (2010) Využitie digitálnej obrazovej korelácie na určovanie vlastných tvarov a frekvencií sústavy. In: Jemná mechanika a optika, vol. 55, no. 10, p. 276-279, ISSN 0447-6441.

Trebuňa, F., Huňady, R. & Znamenáková, M. (2010) Using of digital image correlation method for experimental determination of modal parameters, In: Experimentální analýza napětí 2010: 48th International scientific conference: Velké Losiny, Czech Republic, Olomouc: Univerzita Palackého, p. 451-458, ISBN 978-80-244-2533-7.

Yoshizawa T. (2009) Handbook of Optical Metrology – Principles and Applications. CRC Press, Taylor & Francis Group, 730 p., ISBN: 978-0-8493-3760-4.

18th International Conference
ENGINEERING MECHANICS 2012
Svratka, Czech Republic, May 14 – 17, 2012

pp. 477–482
Paper #9

SOFTWARE PREDICTION OF NON-STATIONARY HEATING OF SHELL MOULDS FOR MANUFACTURE OF ARTIFICIAL LEATHERS

M. Hušek*, A. Potěšil**

Abstract: *In the design of non-stationary heating of shell moulds for the production of artificial leathers for vehicle interiors using infrared emitters, virtual simulations are of great importance. Virtual heating was used in a number of practically solved problems and has become irreplaceable in the complex process of technical preparation of the artificial leathers manufacture. It is based on combination of suitable informatics tools complemented by specific functions. Optimal temperature distribution on the styling mould surface is achieved only by suitable positioning of infra-red emitters, correct identification of positions of control thermocouples on the heated mould surface and setup of corresponding parameters of the regulation system. Development of the technology of virtual heating has been supported by the project MPO TIP 2009 under the registration number FR-TI1/266.*

Keywords: ***Artificial leather, shell mould, non-stationary heating, radiation heating, finite element method.***

1. Introduction

In the last few years, the company Magna Exteriors & Interiors Bohemia, s.r.o (hereafter Magna) has been dealing with an innovation project " Innovation of technology of artificial leathers manufacture". The artificial leathers are major styling elements of softened interior components in vehicles. An example of such a product is a dashboard, which represents a complicated part in terms of design, complexity of styling shapes, dimensions and process energy.

Within the innovation of the so called “Slush technology”, workers of the company Magna acknowledge necessity of a complex approach with participation of a number of experts from the Technical University of Liberec and the company LENAM, s.r.o. This synergy resulted in acceleration of preparation of the technology in question and increased efficiency in batch production.

The issue of virtual heating in the final stages of the above-mentioned project is mainly implementation of software application IREviewBlender in the preparatory stages of the artificial leather manufacture. This process would not be possible without prior knowledge of everyday realities and technical complications in the production itself. That is why the individual functionalities of the developed application were optimized and confronted with the experienced workers responsible for the technical preparation of production as early as at the project start.

2. Methodology

The procedure of artificial leather manufacture is as follows: a sufficient amount of powder of thermoplastic polymer based on PU or PVC is applied on a hot metal shell mould face. The powder melts and sinters into a thin compact layer. Having cooled the mould, the finished product is stripped from the mould. The mould gives the artificial leather appropriate desirable shape and precise impression of the mould surface at the same time, which is usually a fine embossed design. With the view of productivity it is desirable that the heating and cooling of the mould were as fast as possible. The procedure of high-quality sintering of artificial leathers, however, necessitates keeping rather a narrow interval of sintering temperature – approximately 20°C.

*Ing. Martin Hušek, Technická univerzita v Liberci, Studentská 2, Liberec 1, CZ, e-mail: martin.husek@tul.cz

** Doc. Ing. Antonín Potěšil, CSc.: LENAM, s.r.o., Klostermannova 690/15; 460 01, Liberec; CZ, e-mail: antonin.potesil@lenam.cz

2.1. Procedure of Design of Non-stationary Mould Heating

Preparation of heating is divided into two basic stages, as illustrated in fig. 1.

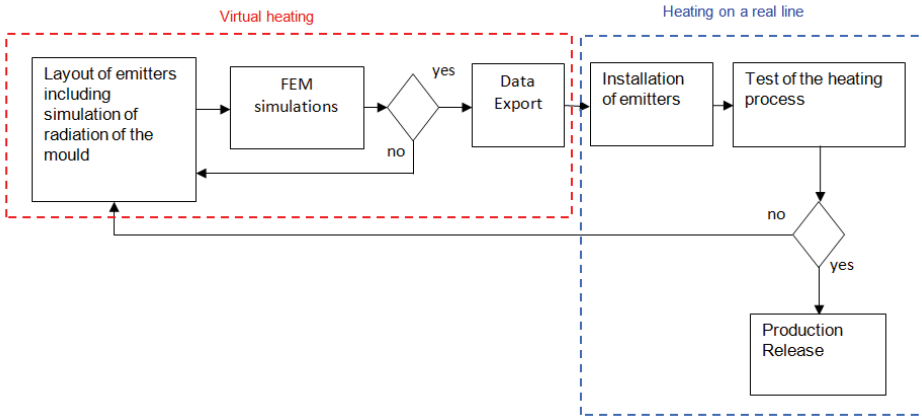

Fig. 1: Flowchart of the procedure of heating layout

The first working stage is the design of virtual heating. It is based on the first estimation of positions of infra-red emitters according to the needed amount of heat necessary for heating the given amount of material. These efforts result in simulation of the heat flux density distribution. This is followed by finite element computation of temperatures in the selected time steps. In this stage of determination of heating, virtual experimentation with simulation of the regulated heating of the model of the system in question begins. The desired result is a satisfactory uniform temperature distribution over the whole mould surface. In case of reaching an optimal result, the data for manual or robotic placement of holders of infra-red emitters around the mould are exported. Further tests of heating are realized on the test or batch line. In that case heating is already evaluated according to the quality of the manufactured leather. The leather is thoroughly examined and imperfections caused by over-heating or insufficient heating of the given area are looked for. These problems are solved by changing the position of the concrete emitter directly on the line or by intervention in the regulation parameters. Having completed these procedures, heating is released for the batch production.

2.2. IREviewBlender

IREviewBlender is an application based on extension of freeware environment Blender by functionalities that enable positioning of emitters over the mould relief. The main tasks of the application are:

1) Building a virtual model of a real module of shell mould heating, consisting of relevant components of a flow line (frames for shell mould fixation, frame for emitters clamping and other special structures), see fig.2.
2) Application of various types of infra-red emitters as needed and within the technical limitations (emitters of various shapes, numbers, layout and power properties), see fig. 3.
3) Simulation of the heat flux distribution on the surface of a shell mould and optimization of the positions of infra-red emitters above the mould and their control thermocouples on the shell mould, which is necessary for successful control of non-stationary temperature field, see fig.4.
4) Export of the results into a suitable format for the needs of control temperature-structural FEM analyses in CAE systems, see fig.5.
5) Export of the topological data (coordinates) for emitters and thermocouples for safe and non-collision placement of emitters on the real supporting structure and placement of corresponding thermocouples on the mould (output image files or files with transformation matrixes for positioning by a robotic arm).

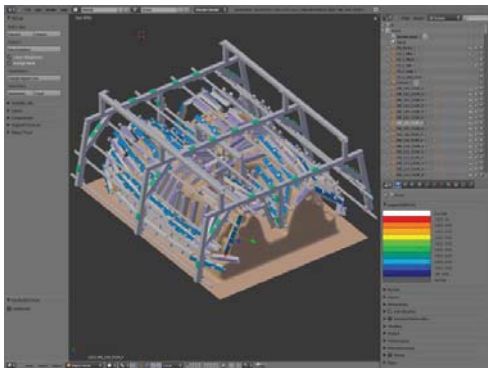

Fig. 2: Assembled model

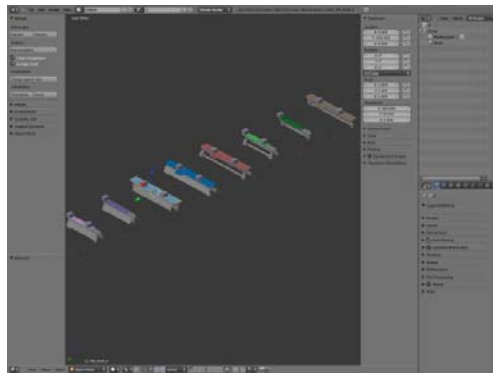

Fig. 3: Database of emitters

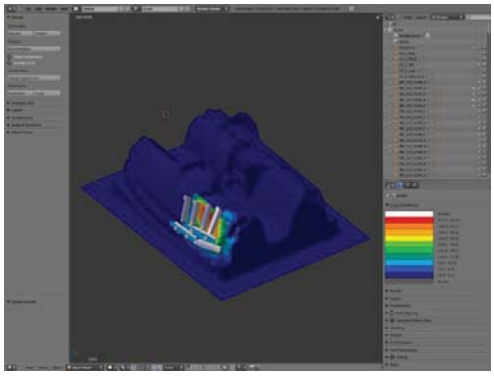

Fig. 4: Heat flux

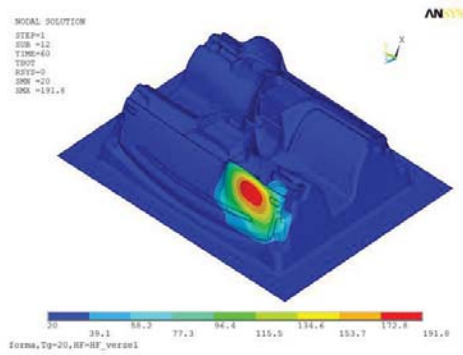

Fig. 5: Temperature calculation in sw ANSYS

3. Implementation into Manufacture

As early as during programming of the basic functions of the application IREviewBlender, a number of practical tasks had been dealt with. This was the only way of getting the feedback concerning necessity and correctness of its functionalities and adding further useful functions according to the current needs of the operators of this production technology. The following chapters present selected and resolved problem situations.

3.1. Design of Heating for Batch Production

One of many solved tasks was positioning of emitters above the mould for batch production of artificial leathers. The two situations differed considerably. The starting point was the data and experience acquired during the design of heating of a prototype mould illustrated in the previous pictures. Besides the determination of positions and types of the applied emitters it was also necessary to make design changes and to add a frame structure for fixation of special emitters in the middle of the mould – see fig. 6.

.

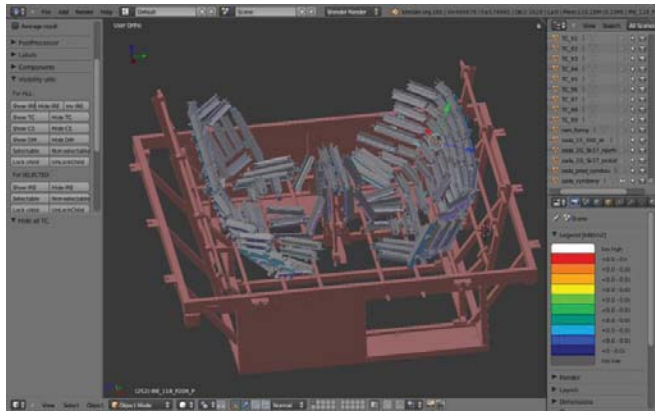

Fig. 6: Fixation of emitters

3.2. Design of Heating of the Cleaning Station

Each mould has to be cleaned up after repeated usage in the production cycle and its surface must be covered with special separation and protection preparations at precisely defined temperature range for precisely defined time.

The cleaning procedure will be run in automatic mode of a specially designed line, of a so called cleaning station, exploiting robot for application of chemicals. The workstation has to be universal for various types and shapes of moulds. Technical specifications are defined by requirements of maximum delivered and switch powers for individual emitters arranged into several sections.

It was evident from the beginning that some automatic movements of whole groups of emitters should be applied. This is the only way of adapting the positions of emitters to various types and shapes of moulds. Fig. 7 illustrates three configurations of emitters layout. For better lucidity only the fixing elements – so called holders are depicted.

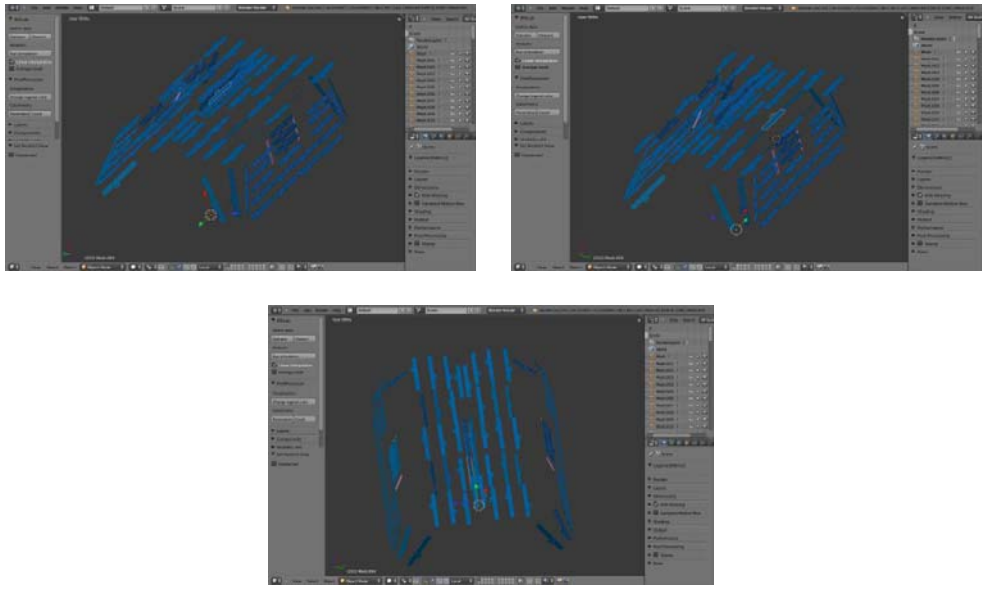

Fig. 7: Three group positions of the emitters

3.3. Test Mould Design

Another requirement of workers of technical preparation of artificial leather manufacture, which has been successfully resolved, was design of a so called test mould and its heating. Prior to launching a new product on the basis of PVC or PU it is essential to realize a number of tests with powder mixture on test moulds so that the prototype or batch production of leathers was not restricted. These moulds are usually equipped with dividing grooves of various shapes and areas with several styling reliefs.

For this purpose, a test mould has been designed for the test line, see fig. 8. Its undulated shape serves for testing the functionalities of virtual heating and for searching important criteria for optimal positioning of emitters in IREviewBlender. Further application of this mould is in testing genetic algorithms for optimization of the emitters layout, which is dealt with by experts of the Technical University of Liberec.

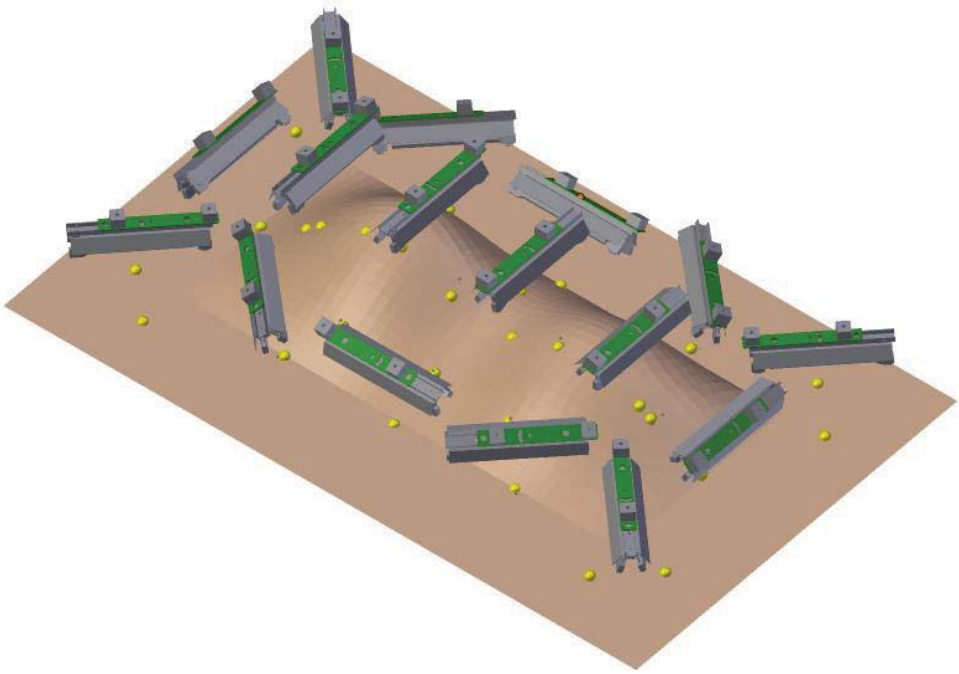

Fig. 8: Test Mould

4. Conclusions

The introduction of the paper presents problems of design of non-stationary heating of thin-walled shell moulds by a large number of infra-red emitters in the manufacture of artificial leathers. The leathers are used in production of softened interior parts mainly in cars.

In the second part, the process of design of non-stationary heating is dealt with. As having been mentioned, the whole design process begins with virtual heating. This includes design of positions of emitters above the mould surface and data preparation for temperature-structural FEM computations. The whole virtual process is completed by data export for physical installation of emitters in the flow line or test line, where further heating tests are performed.

In the last part of the paper there are mentioned some practical cases, which confirm that virtual heating of moulds is irreplaceable part of a complex technical preparation of manufacture of artificial leathers. The application of IREviewBlender allowed reaching the solution in a way more effective than using the standard CAD systems.

Acknowledgement

It is a pleasant duty of the authors of the paper to thank their team colleagues from the company LENAM, s.r.o. for their important contribution to the project solution, also to thank Mr. Jiří Hnídek from the Technical University of Liberec for consultancy support of programming in the graphical environment Blender and last but not least to thank Mr. Jaroslav Kozák from the company Magna for precious information related to the technology of manufacture of artificial leathers.

Acknowledgements belong as well to further unnamed colleagues from the partner Technical University of Liberec, faculty of Mechatronics, who work on other related topics within the project, oriented to identification of non-stationary temperature fields of moulds and regulation algorithms controlling the radiation processes of heating.

Development of the technology of virtual heating was realized within the project MPO TIP 2009 registered under the registration number FR-TI1/266.

References

Potěšil, A. (2011) Non-stationary heating of shell moulds in the process of manufacture of artificial leathers. 17th International Conference ENGINEERING MECHANICS 2011, Svratka, Czech Republic, 9 – 12 May 2011.

18th International Conference
ENGINEERING MECHANICS 2012
Svratka, Czech Republic, May 14 – 17, 2012

pp. 483–487
Paper #303

DES SIMULATION OF SEPARATION CONTROL FOR FLOW OVER HUMP

T. Hyhlík[*], M. Matějka[**], V. Skála[***]

Abstract: *Article deals with numerical solution of the separation control using Detached Eddy Simulation turbulence model. Numerical computation was done using commercial code Fluent. Vortex structures was visualized from the numerical solution. The strong influence of side walls to the character of the flow field is visible. The effect of the flow control was observed. Computed flow field is compared with experimental data obtained from hot wire measurement in the traversing plane. Significant deviations between numerical simulation and hot wire measurement are found. Numerical simulation of the three dimmensional flow controlled flow field is still challenge for present CFD.*

Keywords: ***Detached Eddy Simulation, Flow Control, Hump, Vortex Structures***

1. Introduction

Separation occurs in the wide range of application in the engineering practice. Separated flow has negative impact on performance because it reduces pressure loss, increase noise etc.

Control of turbulent flow by using oscillatory perturbation generated by synthetic jet actuator can be effective in influencing flow separation (Gatski & Rumsey, 2004). The main advantage of flow control by using synthetic jet actuators against steady suction or blowing is their energy consumption and not least they do not require piping system. Oscillatory flow control is effective mainly in the case when introduced two dimensionally because there are generated vortex structures which are responsible for the momentum transfer across the shear layer.

Our geometrical configuration is inspired by the work of Seifert & Pack (2002) which also forms the basis for few CFD validation workshops (Gatski & Rumsey, 2004) but the numerical simulation of flow controlled separation is still an open problem. Our previous works were focused to visualization and identification of vortex structures, pressure measurement, constant temperature anemometry measurement and to the methods of flow control (Matějka et al., 2011, Matějka et al. 2009, Matějka & Popelka 2010).

2. Experimental Setup

Experiments were conducted in low speed Eiffel type wind tunnel with *300 mm x 200 mm* test section. The dimension of hump is *400 mm x 300 mm x 50 mm (l x w x h)*. The hump has built in a synthetic jet generator to control flow field behind it. The position of output slot is marked in the figure 1.

Data acquisition was carried out by using constant temperature anemometry. Measurement was done by using a single sensor probe in the traversing plane behind the hump. Traversing plane is marked by red colour in the figure 2a.

[*] Ing. Tomáš Hyhlík, Ph.D.: CTU in Prague, FME, Department of Fluid Dynamics and Thermodynamics, Technická 4, 166 07, Prague, CZ, e-mail: tomas.hyhlik@fs.cvut.cz

[*] [*] Ing. Milan Matějka, Ph.D.: CTU in Prague, FME, Department of Fluid Dynamics and Thermodynamics, Technická 4, 166 07, Prague, CZ, e-mail:milan.matejka@fs.cvut.cz

[*] [**] Ing. Vladislav Skála: CTU in Prague, FME, Department of Fluid Dynamics and Thermodynamics, Technická 4, 166 07, Prague, CZ, e-mail:VladislavSkala@seznam.cz

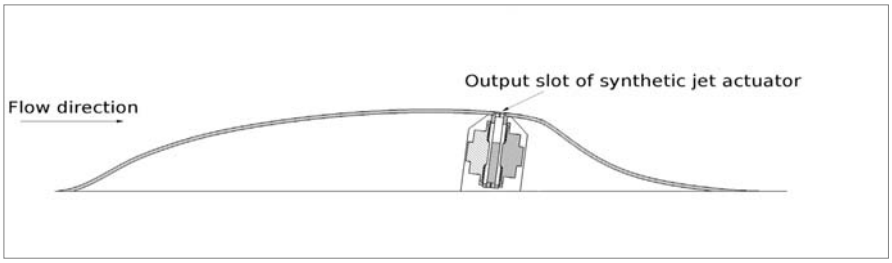

Fig. 1: Hump with synthetic jet actuator

The design of synthetic jet generator is based on requirement to obtain maximum intensity of the synthetic jet with minimum input energy (Kordík et al. 2010). Therefore, the exciting frequency of synthetic jet generator should correspond to its resonant frequency. Two loudspeakers arranged by two in one cavity and 9 cavities in one line were used. The synthetic jet actuators were excited by using amplitude frequency modulation. Carrying frequency $fc = 370\ Hz$ is the resonant frequency of synthetic jet actuator. The value of modulation frequency $f_{AM} = 60\ Hz$ was chosen with respect to the Strouhal number

$$F^{+} = \frac{fx}{U_{\infty}} \quad , \tag{1}$$

Stokes number of output orifice

$$St_o = \frac{fh^2}{\nu} \tag{2}$$

and oscillatory momentum coefficient

$$c_{\mu} = \frac{\rho_0 u_0^{'2} h}{1/2\rho_{\infty} U_{\infty}^2 l} \quad . \tag{3}$$

The value of Strouhal number was $F^{+} = 1.2$, Stokes number of output orifice was $St_o = 6.6$ and oscillatory momentum coefficient was $c_{\mu} = 0.0047$.

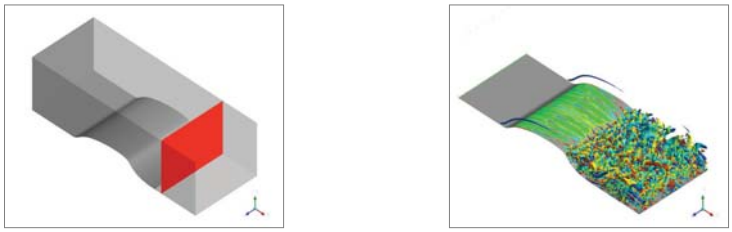

(a) Location of traversing plane behind the hump (b) Visualized vortex structures behind the hump

Fig. 2: Computational domain

3. Numerical Simulation

Unsteady numerical simulation of the flow field with influence of synthetic jet was done by using commercial code Fluent. In this case half of the channel is simulated on 14.5 million cells by using non iterative time advancement method with second order implicit scheme. Fractional step scheme is used for pressure velocity coupling. Convective terms are discretized by using bounded central differencing scheme in momentum equations otherwise second order upwind scheme is used. Turbulence modelling is based on Delayed Detached Eddy Simulation variant of SST k-ω model

(Menter et al. 2003). The inflow velocity of $8\ ms^{-1}$ was set up, i.e. $Re = 215000$. Velocity boundary condition close to the synthetic jet actuator slot exit was set with carrying frequency $fc = 370\ Hz$ and modulation frequency $f_{AM} = 60\ Hz$ and with amplitude $17\ ms^{-1}$.

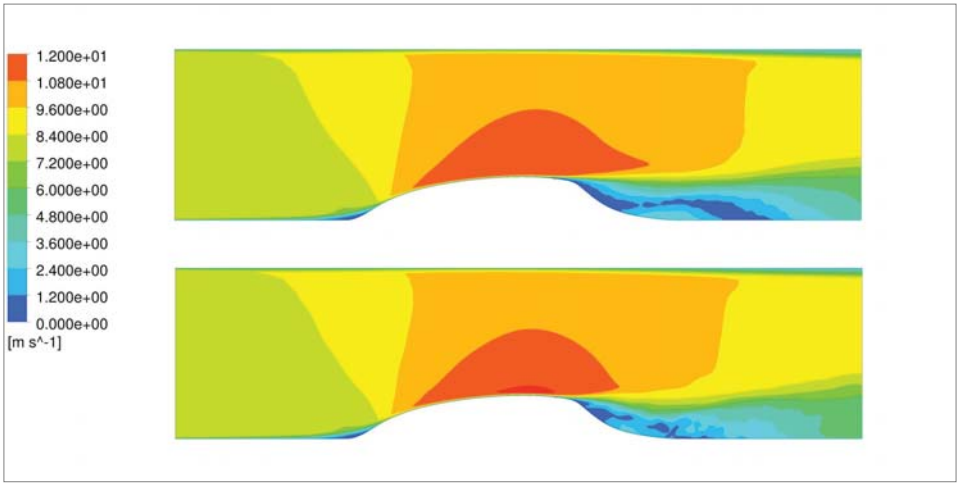

Fig. 3: Contours of mean velocity in the symmetry plane, upper without influence of synthetic jet, lower with influence of synthetic jet

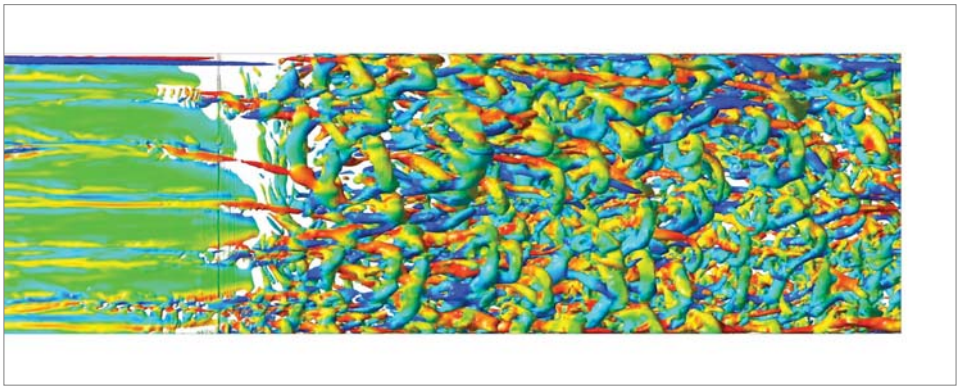

Fig. 4: Vortex structures behind the hump without influence of synthetic jet visualized using swirling strength criterion; only half of the channel in visible

4. Results

The figure 2b shows complex three dimensional vortex structures behind the hump. Vortexes are visualized by using swirling strength method where colour is based on component of swirling velocity in the direction of the main flow. The influence of synthetic jet generator can be observed on the creation of downstream traveling vortex packs. Observed vortex packs are present through the whole width of the channel.

There are complex vortex structure behind the hump for both cases, i.e. synthetic jet controlled and uncontrolled flow field. Figure 4 shows vortex structures for the case without influence of synthetic jet. It is very interested in that there are not big dominant secondary vortexes close to the upper side wall but instead of it there are few small vortexes.

The effect of synthetic jet flow control is clearly visible on figure 3 where contours of mean velocity in the symmetry plane are shown for both the case without influence of synthetic jet and with influence of synthetic jet. Flow control in this case significantly reduce size of separation zone.

Velocity profile from the numerical computation in the traversing plane is presented in the figure 5a and deviation of measured and computed mean velocity normalized by inflow velocity is in the figure 5b. Significant deviation in the regions close to the side walls can be seen. Maximum observed deviation close to the left side wall is very close to *60 %.*

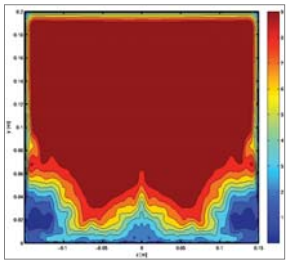

(a) Velocity profile from the numerical computation in [ms^{-1}]

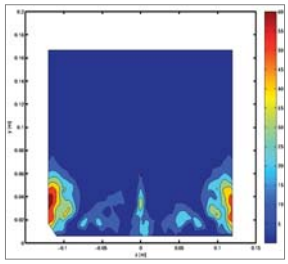

(b) Normalized deviation of the measured and computed mean velocity in [%]

Fig. 5: Mean velocity profile in the traversing plane

RMS velocity profile from the numerical computationn is presented in the figure 6a and deviation of measured and computed RMS velocity normalized by inflow velocity is in the figure 6b. Maximum deviations are present close to the side walls and maximally reach 35 % close to the left side wall.

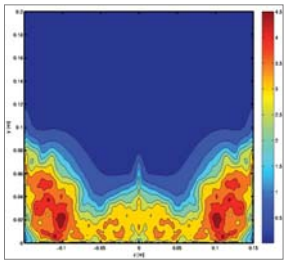

(a) RMS velocity profile from the numerical computation in [ms^{-1}]

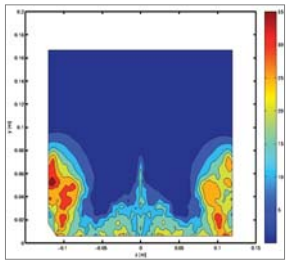

(b) Normalized deviation of measured and computed RMS velocity in [%]

Fig. 6: RMS velocity profile in the traversing plane

5. Conclusion

Investigation of the flow field in the channel with wall hump which is affected by the synthetic jet generator has been made. The focus was placed both on the comparison of measured and computed velocity data in the traversing plane and on the identification of vortex structures influencing the flow field. It was shown that there are significant deviations of mean velocity and RMS velocity in the regions near the side walls. In the middle part of the channel, where the side walls do not affect strongly flow field good agreement is obtained between hot wire anemometry data and computation. The significant deviations close to the side wall can be caused by the influence of traversing probe to the flow field and mainly by lack of knowledge about boundary conditions in the slot exits which are based on synthetic jet characteristic measured as a synthetic jet into quiscent air and approximated by harmonic function.

Acknowledgement

The work has been supported by Czech Science Foundation under grant No. GA 101/08/1112.

References

Gatski, T. B. & Rumsey C. (2004) Langley Research Center Workshop: CFD Validation of Synthetic Jets and Turbulent Separation Control, NASA

Kordík, J., Trávníček Z. & Šafařík P. (2010) Experiments on Resonance Frequencies of Synthetic Jet Actuators. In: *Journal of Flow Visualization and Image Processing,* 2010, Vol. 17, Issue 3, pp. 203-214

Matějka, M., Hyhlík, T. & Pick P. (2011) Visualization of Effect of the Flow Control to the Flow Field of Hump. In: *Flow Visualization and Image Processing (PSFVIP-8),* Moscow, Lomonosov Moscow State University, pp. 47-50

Matějka, M., Pick P., Procházka P. & Nožička J. (2009) Experimental Study of Influence of Active Methods of Flow Control on the Flow Field Past Cylinder. In: *Journal of Flow Visualization and Image Processing*, Vol. 16, Issue 4, pp. 353-366

Matějka, M. & Popelka L. (2010) An influence of Amplitude Modulation of Synthetic Jet to the Flow Field of the Wake. In: *Experimental Fluid Mechanics 2010*, Liberec, Technical University of Liberec, vol. 1, pp. 410-416

Menter, F. R., Kuntz M. & Langry R. (2003) Ten Years of Experience with the SST Turbulence Model. In: *Turbulence, Heat and Mass Transfer 4*, Begell House Inc., pp. 625-632

Seifert, A. & Pack L. G. (2002) Active Flow Separation Control on Wall-Mounted Hump at High Reynolds Numbers. In: *AIAA Journal*, Vol. 40, No. 7, pp. 1363-1372

18th International Conference
ENGINEERING MECHANICS 2012
Svratka, Czech Republic, May 14 – 17, 2012

pp. 489–498
Paper #90

NUMERICAL ANALYSIS OF THERMAL FIELDS IN THE INSULATED COVER OF TIRE CURING PRESSES

M. Hynek*, P. Votapek**

Abstract: *Regardless what type of rubber curing chamber is used (steam dome curing press or mold with heated plates) it is reasonable to insulate the chamber cover properly. However, quite often the heat losses though the joints of the metal parts of the chamber cover are underestimated. Numerical analyses can help in an effort to estimate the thermal fields and the resulting heat losses. However, the main problem for such analyses is a realistic specification of thermal boundary conditions especially in case of heat convection. In this paper, an alternative way of setting of convection boundary condition is proposed. Instead of strict specification of convection parameters, which are very difficult to estimate, it is proposed to incorporate a simple thermal boundary layer based only on heat conduction. By this modification no boundary conditions need to be prescribed right on the surface of the analyzed structure and the resulting temperature distribution on the surface has more freedom to classify the actual design of the analyzed structure in particular locations.*

Keywords: ***curing press, heat losses, heat transfer coefficients, FEM thermal analysis***

1. Introduction

It is well known that motion of a fluid with respect to a surface with heat generation is accompanied with a specific form of heat transfer referred to as convection. If the motion of flow is generated by external forces (e.g. wind, air conditioning, fan or pump), it is called forced convection. If it is driven merely by gravity forces, it is called free (or natural) convection. In most cases, both types of convection affect the studied structure and the values of local heat transfer coefficient differ according to location.

Proper evaluation of local heat transfer coefficients based on experimental measurements is extremely complicated and in many situation even impossible. In laboratory conditions, however, there can be exploited several optical measurement methods, such as PLIF (Planar Laser-Induced Fluorescence). This method is based on the principle that atoms or molecules excited with laser spontaneously emit light (observed as fluorescence) which is affected by various parameters such as the concentration of a certain species in a fluid and the temperature. Signals from CCD cameras are then processed to provide 2-D spatial information on concentration, velocity or temperature maps in fluid flows with resolution under 1 mm. From these 2D maps it is possible to evaluate the temperature distribution also in the thermal boundary layer and subsequently the local heat transfer coefficients can be determined from the temperature gradient in the thermal boundary layer (see section 2).

Another method destined for nondestructive testing and inspection, which can also be used in heat transfer measurements, is holographic interferometry. The basic principle of holography lies in its ability to record two slightly different scenes and to display the difference between them. Holographic pictures in general can record motion, deformations, stress, temperature and other continual physical fields. Typically, optical lasers are used nowadays in holographic interferometry giving an accuracy of a half wavelength of the laser (i.e. up to 10^{-3} mm). Again, the detailed knowledge of the temperature field close to the surface allows us to determine the temperature gradient in the thermal boundary layer. Unfortunately, such measurements are hardly performable in real conditions of a plant.

* Doc. Ing. Martin Hynek, Ph.D.: Department of Machine Design, Faculty of Mechanical Engineering, University of West Bohemia; Univerzitní 22; 306 14, Pilsen; CZ, e-mail: hynek@kks.zcu.cz

** Ing. Petr Votápek: Department of Machine Design, Faculty of Mechanical Engineering, University of West Bohemia; Univerzitní 22; 306 14, Pilsen; CZ, e-mail: pvotapek@kks.zcu.cz

One could propose that running a numerical simulation in order to qualitatively compare heat passage through several variants of a structure might be conducted just with a unified, somehow estimated, heat transfer coefficient. Unfortunately, using a convection boundary condition by setting a specific value of heat convection coefficient and an approached temperature of the fluid (i.e. the temperature just outside the thermal boundary layer) will inevitably influence the temperature distribution in the analyzed structure. Instead, it is suggested here to incorporate a sandwich-like thermal boundary layer directly into the finite element model. As this thermal boundary layer consists of several sub-layers based on heat conduction only, there is no need to solve the problem as a coupled analysis of heat conduction and fluid flow in the boundary layer.

2. Determination of heat transfer coefficients from temperature gradient

It is a fact that the heat transfer coefficient for a specific location on the surface depend on many factor, such as the difference between the temperature of the fluid and the surface, shape, spatial orientation and roughness of the surface, fluid flow velocity, state of the velocity boundary layer and other factors.

Instead of taking all these factors into account it is advised to consider the following presumption. It is assumed that the molecules closest to the heated surface do not move relative to this surface and hence the thin sub-layer of the thermal boundary layer adjacent to the surface is subject to pure heat conduction. Written in an equation, it applies:

$$q_y = -\lambda_S \frac{dT(y)}{dy}, \tag{1}$$

where $\lambda_S[W.m^{-1}.K^{-1}]$ stands for thermal conductivity of the boundary sub-layer closest to the surface and q_y is the density of thermal flux in *y*-direction (see Fig. 1). Reported values of λ_S for dry air at temperatures 0 °C and 100 °C are 0.0237 $W.m^{-1}.K^{-1}$ and 0.0307 $W.m^{-1}.K^{-1}$, respectively.

Let us recall the well-known Newton's law for convective heating or cooling:

$$q_X = \alpha_X (T_{WX} - T_\infty), \tag{2}$$

where $a_X[W.m^{-2}.K^{-1}]$ stands for the local heat transfer coefficient at location *X*, T_{WX} denotes wall temperature at location *X*, T_∞ is the approached temperature of the fluid and q_X is the density of thermal flux at location *X* (again, in *y*-direction).

Admitting that all heat transmitted in convection from the surface to the surrounding fluid must be conducted through the stationary sub-layer of the thermal boundary layer leads to the equation:

$$\alpha_X (T_{WX} - T_\infty) = -\lambda_S \left(\frac{dT(y)}{dy} \right)_{WX}, \tag{3}$$

and hence it follows for the mean value of the heat transfer coefficient on an area A:

$$\alpha_X = \frac{1}{A} \int_A \frac{-\lambda_S}{(T_{WX} - T_\infty)} \left(\frac{dT(y)}{dy} \right)_{WX} dA, \tag{4}$$

where the location *X* takes the place of all points of the area *A* on the heated surface. The evaluation of thermal gradients $\left(\frac{dT(y)}{dy}\right)_{WX}$ can be accomplished from measurements of temperature distribution in thermal boundary layer by means of holographic interferometry or PLIF method. Further information about this approach can be found in Holman (1972) or in Pavelek et al. (2003) where Fig. 1 was taken from.

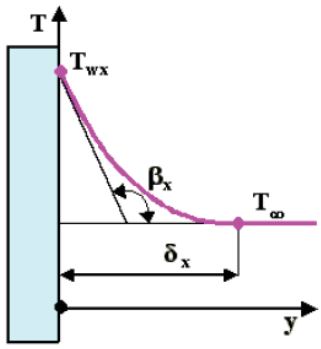

Fig. 1: Temperature profile in thermal boundary layer (δ_X denotes the thickness of the thermal boundary layer which is typically several millimeters)

3. Sandwich-like model of the thermal boundary layer

Applying the principle described in the previous section to the whole thickness of the thermal boundary layer turned out to be very useful for FEM thermal analyses. As mentioned earlier in the text, using a convection boundary condition by setting a specific value of heat convection coefficient and the approached temperature will inevitably influence the temperature distribution in the analyzed structure. To avoid this undesired effect, the thermal boundary layer can be divided into *N* sub-layers (each specified with a reasonable value of thermal conductivity) and included in the FEM model of analyzed structure. Setting the approached temperature outside the outer sub-layer provides more freedom in calculation of the resulting temperature distribution on the surface of the structure.

It should be stressed that pure heat conduction was assumed in individual sub-layers. However, in reality, only a thin sub-layer closest to the surface can be considered stationary. Therefore, as the distance of a particular sub-layer from the surface increases, its artificial value of heat conduction coefficient λ_T^i should increase accordingly to reflect the fact that heat is transferred more intensely due to increasing influence of both free and forced convection. The specific values of coefficients λ_T^i ($i = 1..N$) need to be set in such a manner that the resulting temperature distribution through the thermal boundary layer is in agreement with relevant experimental measurement or published results. For the purpose of thermal calculations presented in this paper a temperature profile published in Čížek (2005) was adopted (see Fig. 6).

In notation of the previous section the density of the artificial heat flux density is introduced as:

$$q_T = \alpha_T(T_{WX} - T_\infty) = -\lambda_{ML}\left(\frac{dT(y)}{dy}\right)_{WX}, \tag{5}$$

where $\lambda_{ML}[W.m^{-1}.K^{-1}]$ stands for heat conductivity of the whole thermal boundary layer evaluated according to the common theory of heat conduction in multilayer structures introducing terms of conduction resistance R_i for individual sub-layers with thicknesses t_i :

$$R = \frac{\delta_X}{\lambda_{ML}\,A} = \sum_i R_i = \sum_i \frac{t_i}{\lambda_T^i\,\mathrm{A}}, \qquad i = 1..N \tag{6}$$

Having known λ_{ML} together with the temperature profile in boundary layer and the wall temperature distribution makes it possible to easily evaluated heat flux through the area *A*:

$$Q_A = \alpha_T\,A\,(T_{WX} - T_\infty) = -\lambda_{ML}A\left(\frac{dT(y)}{dy}\right)_{WX}. \tag{7}$$

4. Application example - FEM thermal analysis of the insulated cover of a curing press

The approach described in the previous section was applied to the thermal analysis of the insulate cover of a large curing press for vulcanization of heavy machinery tires (see Fig. 2). The maximum press force of this particular steam dome press was 900 t, the production cycle was about 80 min., the temperature of the heating steam was 160 °C and the mean temperature of the surrounding air was about 40 °C (see Fig. 3). The main task was to propose cost-effective design changes in order to reduce the heat losses through the cover and to quantify the resulting power sawing.

Fig. 2: Analyzed curing press

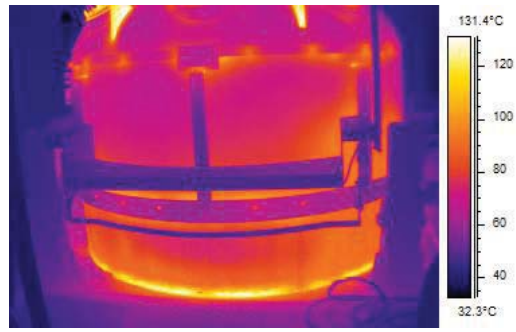

Fig. 3: Snapshot from a thermovision camera

The problem was solved as steady-state thanks to long production times. The geometry of the steam dome made it possible to analyze only an axisymmetrical FEM model. Special attention was paid to three areas where individual parts of the dome are joined together and the cover insulation is fixed to the steel structure of the dome and protected with sheetmetal. While the lower and the upper area represent welded joints, the middle area matches the place where the upper part of the dome is pressed against the circumferential sealing which is fixed in the lower part of the dome (see Fig. 4).

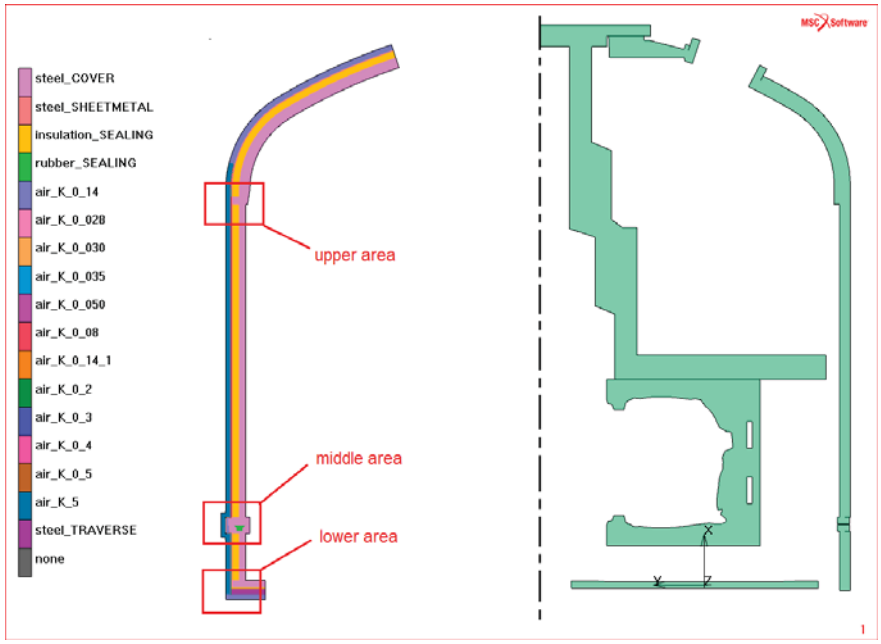

Fig. 4: Axisymmetrical FEM model (left) and the corresponding steam dome press geometry (right)

Critical for the analyzed FEM model was the implementation of the artificial multi-layer thermal boundary layer on the outer surface of the dome cover. The definition of heat conduction coefficients for individual sub-layers (e.g. "K_0_028" refers to $\lambda_T^i = 0.028\, W.m^{-1}.K^{-1}$) as well as the overall thickness of the artificial boundary layer (set to 4.5 mm) is shown in Fig. 5. These values of λ_T^i and the corresponding sub-layer thicknesses were determined by trial and error method until the calculated temperature distribution character in the boundary layer resembled the measured data from Fig. 6.

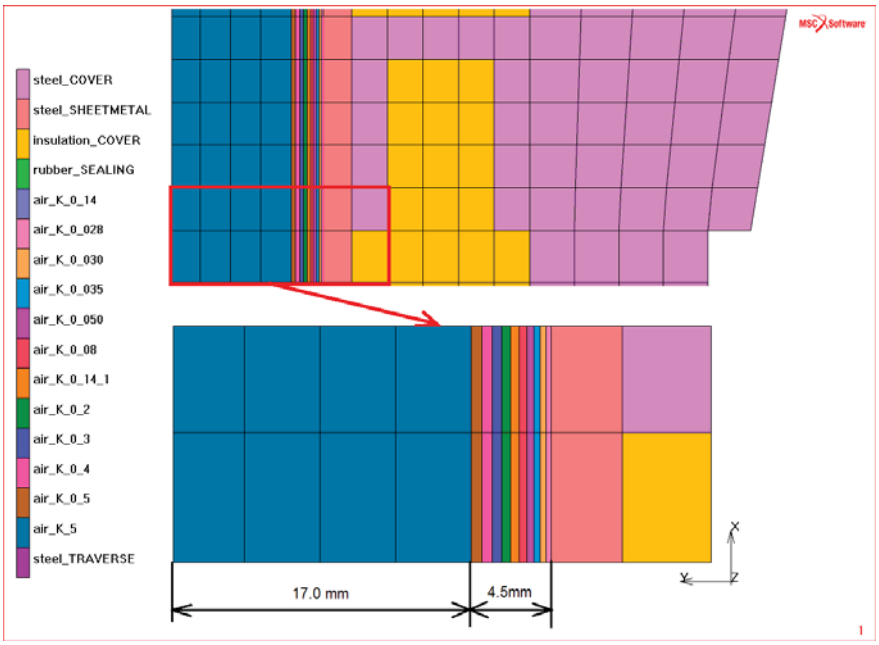

Fig. 5: A detailed view of the artificial thermal boundary layer

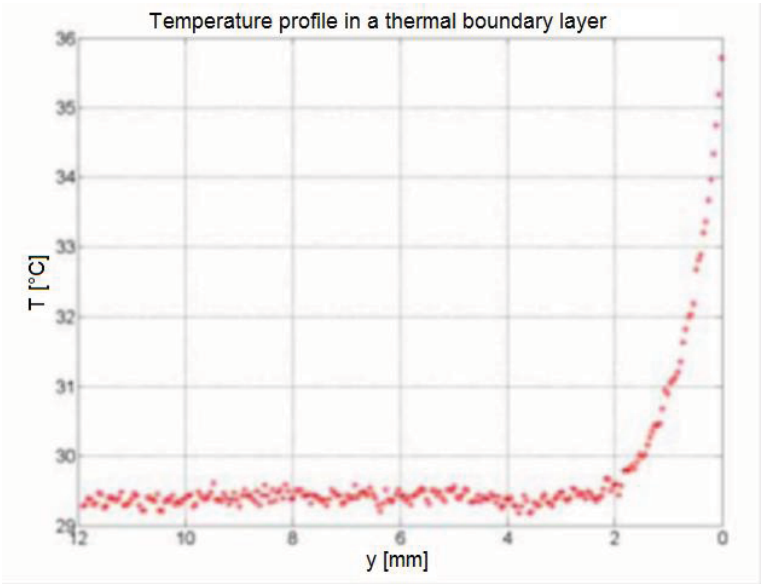

Fig. 6: A typical temperature profile in a thermal boundary layer measured with PLIF, published in Čížek (2005).

In Fig. 7 there are presented detailed views of the FEM model in all three monitored areas. From the material specified for individual FEM elements the design of the press cover can be deduced. On the left the original design and on the right the variant with proposed modifications are shown.

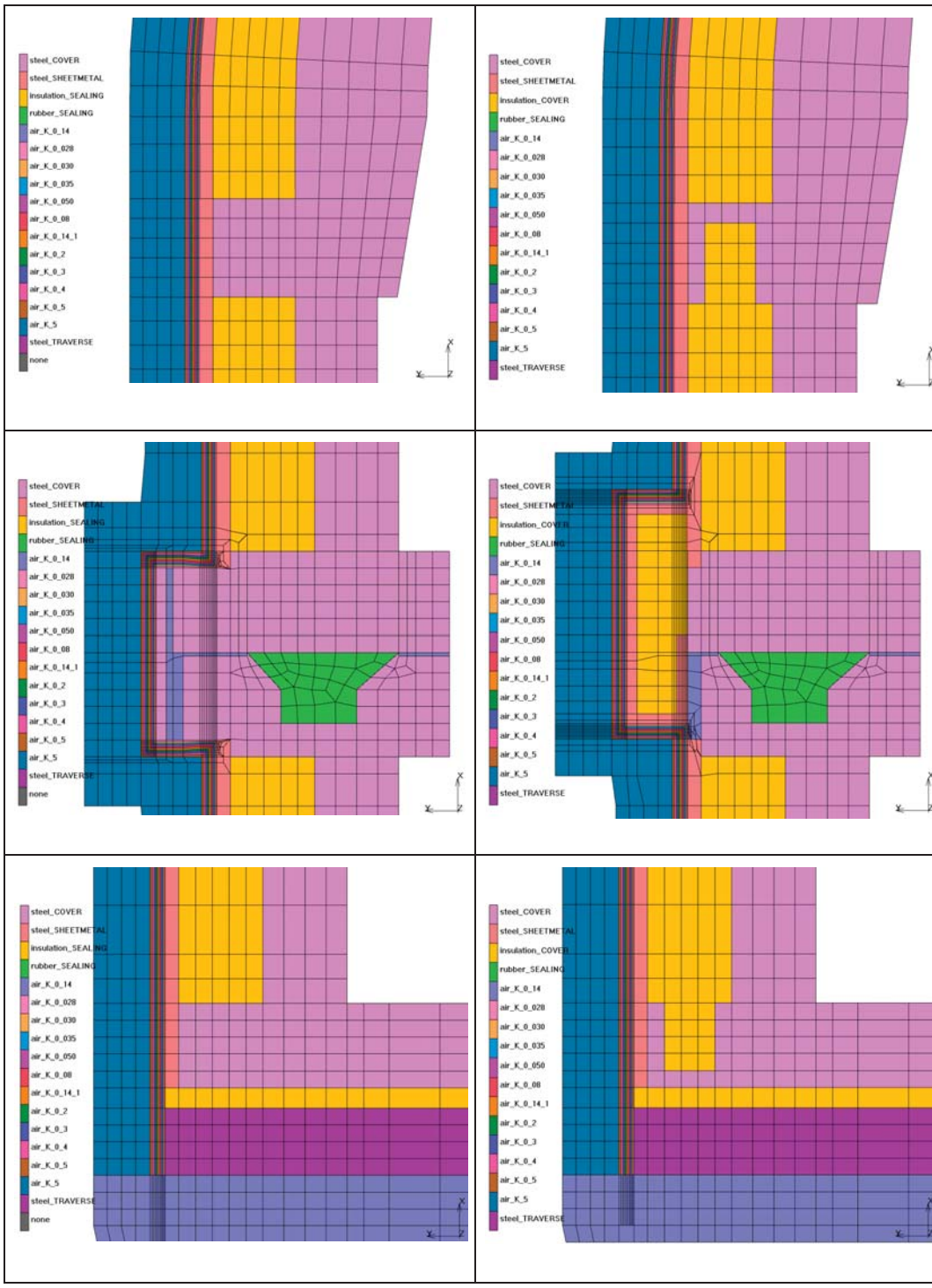

Fig. 7: Design changes between the original (left) and the modified (right) variants of the press cover

Fig. 8 presents the steady state temperature fields in the monitored areas. In each picture of Fig. 8 there is denoted a zone on the surface where heat fluxes will be evaluated and compared.

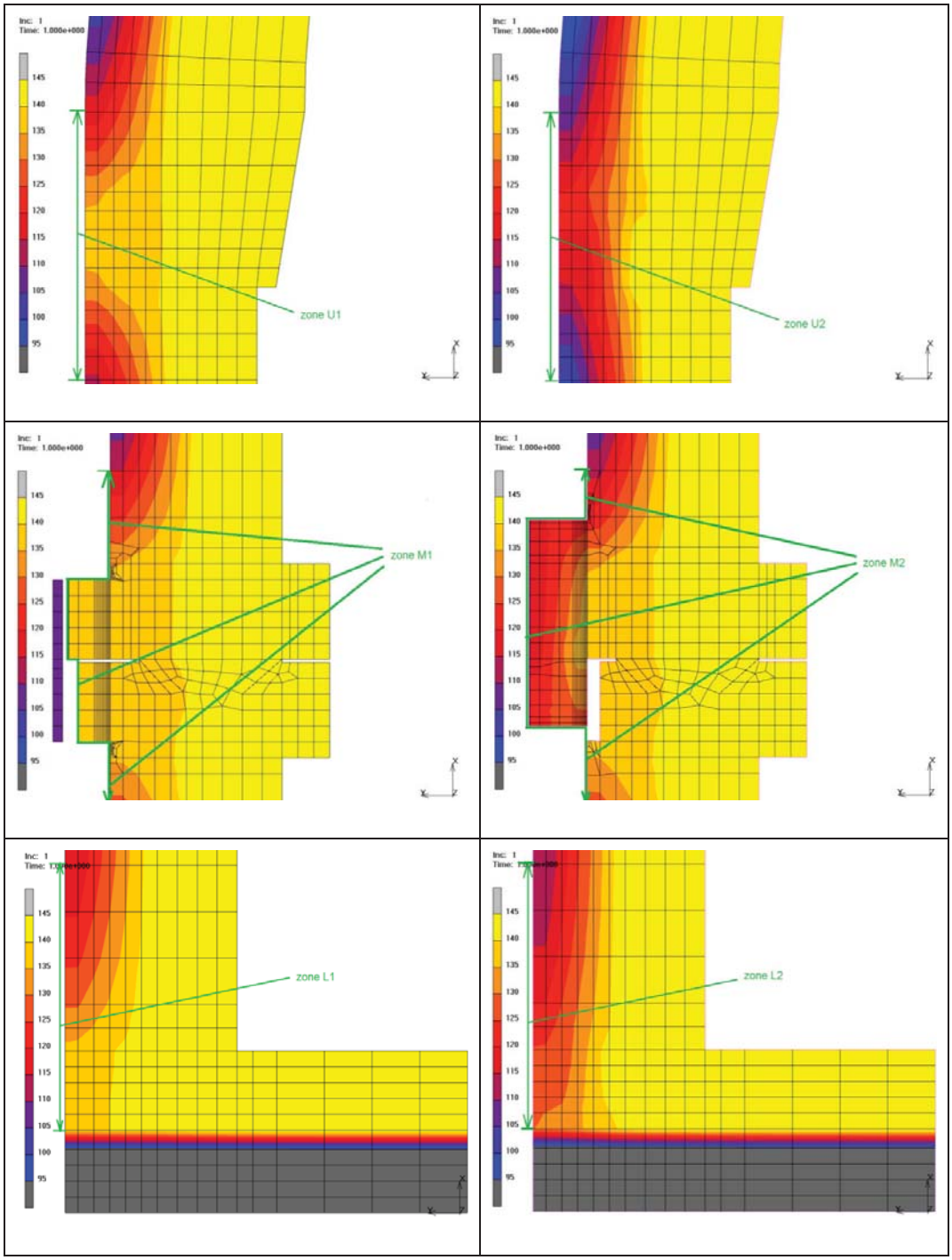

Fig. 8: Steady state temperature fields in the original (left) and the modified (right) variants

The curves plotted in Fig. 9 represent path plots of wall temperature on the surface of each zone, i.e. the position on x-axis of the plot corresponds to cumulative length of the edges of involved finite elements and the values on y-axis are nodal temperatures on the surface of the monitored zones.

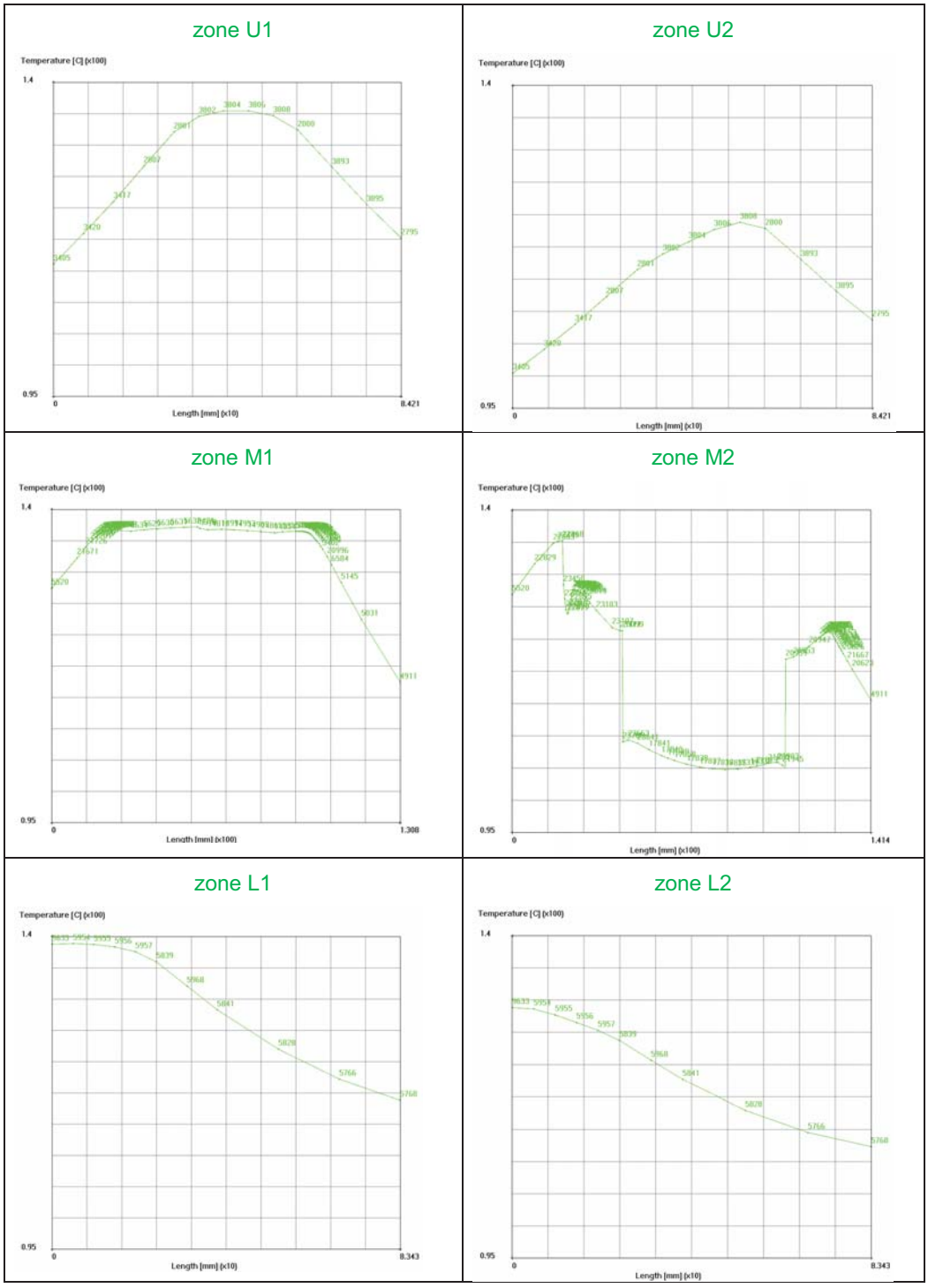

Fig. 9: Path plots of wall temperature for individual zones of interest

In Fig. 10, path plots of the whole cylindrical part of the press cover are compared for both original and modified design. Fig. 11 demonstrates that temperature profiles in the boundary layer depend strongly of the location on the surface of the cover. However, but their characteristic form is in agreement with the measured data from Fig. 6.

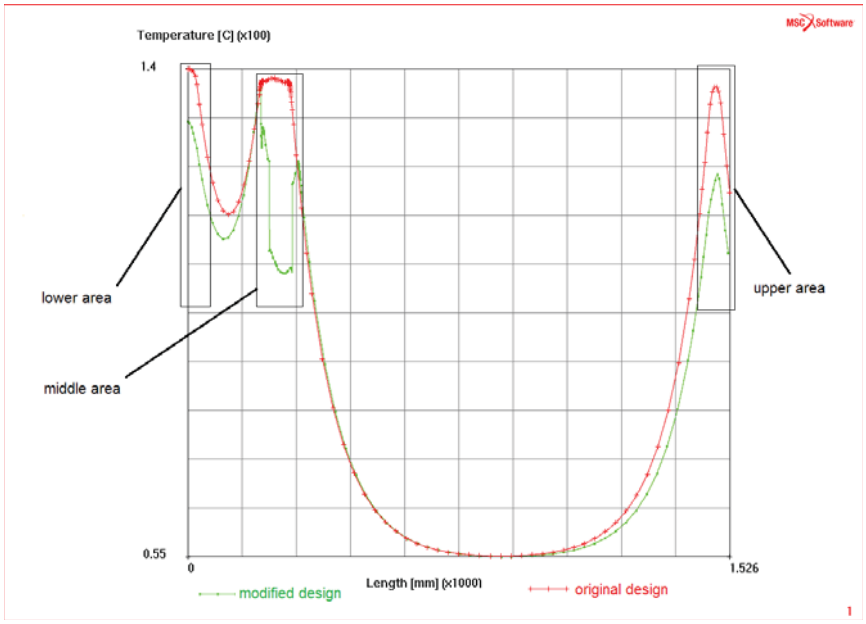

Fig. 10: Path plots of wall temperature for the whole cylindrical section of the press cover

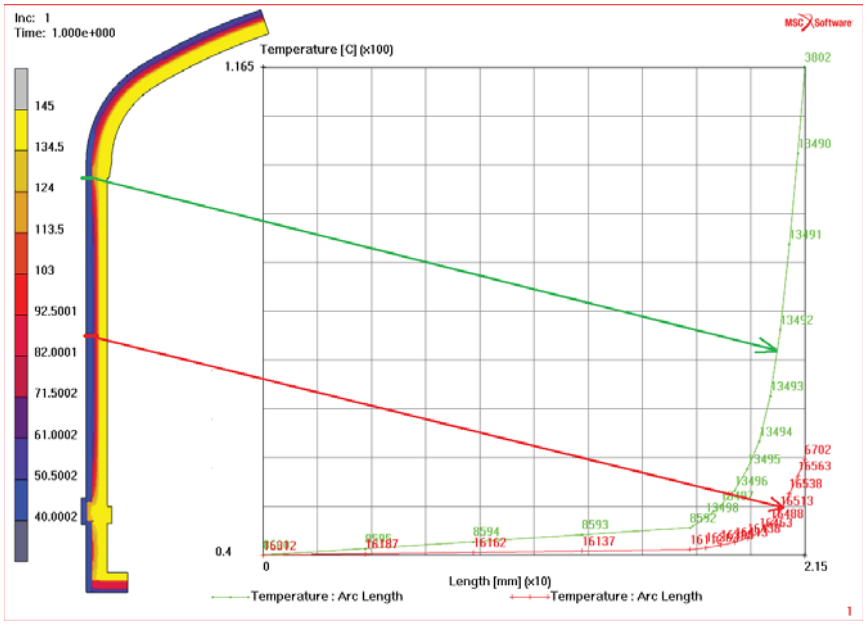

Fig. 11: Temperature profiles in the boundary layer plotted for two specific locations (the modified variant is visualized here): in the zone **2** *the wall temperature is 116.5 °C, in the middle of the cylindrical section the wall temperature drops to 55 °C*

5. Conclusions

The proposed sandwich-like model of thermal boundary condition in a simplified FEM model of the curing press cove enabled a quantitative assessment of heat losses reduction resulting from the proposed design modifications. Applying the equation (7) to individual monitored zones as well as to the whole cylindrical section of the press cover estimates the values of heat fluxes (for summary, see Tab.1). The presented results confirm that even simple design changes helping to avoid thermal bridging are always worth to take into account.

Tab. 1: Heat fluxes through evaluated areas of the curing press cover evaluated on both original and modified variant

Monitored area	$Q_A[W.m^{-2}]$ **original design**	$Q_A[W.m^{-2}]$ **modified design**	**Power saving [%] modified on original**
upper	2.56	2.15	16
middle	4.11	2.59	37
lower	2.89	2.28	21
whole cylindrical surface	21.15	19.14	9.5

Acknowledgement

The research was performed as a part of the postgraduate study focused on the increasing energy efficiency of technological processes and therefore the authors are grateful to all consultants who contributed to this topic.

References

Bejan, A. (1995): Convection heat transfer, New York: Wiley. ISBN 0-471-57972-6

Čížek, J. (2005): Měření teplotních polí v tekutinách, http://stc.fs.cvut.cz/History/2005/Papers/D_P/cizek_12107.pdf

Holman, J. P. (1972): Heat transfer. Fourth edition. Tokyo, McGraw-Hill Kogakusha, Ltd.

Jícha, M. (1989): Přenos tepla a látky. Skripta VUT, Brno

Lédl,V., Vít,T., Psota,P., Doleček,R. (2011): Holografic Interferometry used for of Temperature Fiel in Fluid, Engineering and Technology 59, World Academy of Science www.waset.org/journals/waset/v59/v59-447.pdf

Meyer, K.E., Larsen, P.S., Guillard,F., Westergaard,C.H. (2002): Temperature and velocity fields in natural convection by PIV and LIF, Proceedings of 11th International Symposium on Applications of Laser Techniques to Fluid Mechanics, Paper 35.1., Lisbon

Pavelek, M. a kol. (2003): Termomechanika. Skripta VUT, Brno, http://ottp.fme.vutbr.cz/~pavelek/optika/1810.htm

18th International Conference
ENGINEERING MECHANICS 2012
Svratka, Czech Republic, May 14 – 17, 2012

pp. 499–505
Paper #52

INFLUENCE OF WATER TEMPERATURE ON HEAT TRANSFER COEFFICIENT IN SPRAY COOLING OF STEEL SURFACES

M. Chabičovský, M. Raudenský, M. Hnízdil *

Abstract: *Cooling of stainless steel surfaces with flat fan nozzles was studied experimentally. Several configurations of jets and pressures were tested. Tests were done with variable coolant (water) temperatures (20 °C, 40 °C, 60 °C and 80 °C). The influence of coolant temperature on the heat transfer coefficient was investigated. An increase in coolant temperature caused a significant decrease of the Leidenfrost temperature (temperature at which the character of boiling is changed - the film boiling is changed into nucleate boiling). Changing the water temperature from 20 °C to 80 °C caused a change of the Leidenfrost temperature of about 140 °C. Furthermore it was observed that in a high temperature region (above Leidenfrost temperature) the heat transfer coefficient has the highest value for the lowest water temperature and for the high coolant temperature (80 °C) the cooling intensity is the lowest.*

Keywords: ***Spray cooling, Heat Transfer, Leidenfrost temperature, cooling with hot water***

1. Introduction

This article is based on an experimental study, which was conducted in the Heat Transfer and Fluid Flow Laboratory (Brno University of Technology). The cooling of stainless steel surfaces with flat fan nozzles and the influence of different factors on heat transfer coefficient (HTC) was studied. Because the water temperature in cooling processes in the metallurgical industry changes during the year, one of the goals was to find if the cooling intensity and the Leidenfrost temperature is influenced by the water temperature. The Leidenfrost temperature (Leidenfrost point) is defined as the temperature at which the character of boiling changes. Film boiling is changed into nucleate boiling (see Fig.1).

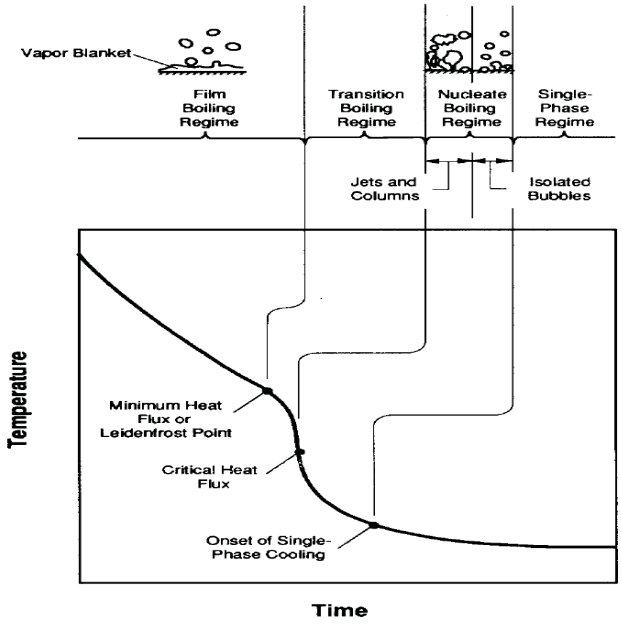

Fig. 1: Temperature-time history of a surface during quenching in bath of liquid (Bernardin & Mudawar, 2002)

The practical importance in the metallurgical industry of the Leidenfrost temperature is that above this temperature is a small heat flux and below is a large one. Water temperature can change the character of the heat transfer (boiling regime) and it can cause problems with process control.

* Ing. Martin Chabičovský, Prof. Ing. Miroslav Raudenský, CSc, Ing. Milan Hnízdil: Heat Transfer and Fluid Flow Laboratory, Brno University of Technology, Technická 2896/2; 616 69, Brno; CZ, e-mail: chabicovsky@lptap.fme.vutbr.cz

Many articles about cooling in metallurgical industry and factors which have the biggest influence on heat transfer have been written in technical journals. Only a small number of them deal with the influence of coolant temperature. Some authors studied, both in theory and practice, the parameters of water droplets (including their temperature) and their influence on cooling and the Leidenfrost point (Bernardin & Mudawar, 1999), (Raudenský & Boháček, 2009). A generalization of models for a single droplet to spray does not lead to results that are measurable in industry (Raudenský & Boháček, 2009). In the experimental study in the Heat Transfer and Fluid Flow Laboratory (Raudenský et al., 2011) the influence of water temperature on cooling with mist nozzles for an austenitic steel plate was measured. In addition the research at the University of British Columbia in Canada (Xu & Gadala, 2006) showed the influence of coolant temperature on cooling in spray cooling for 7 mm thin carbon plates.

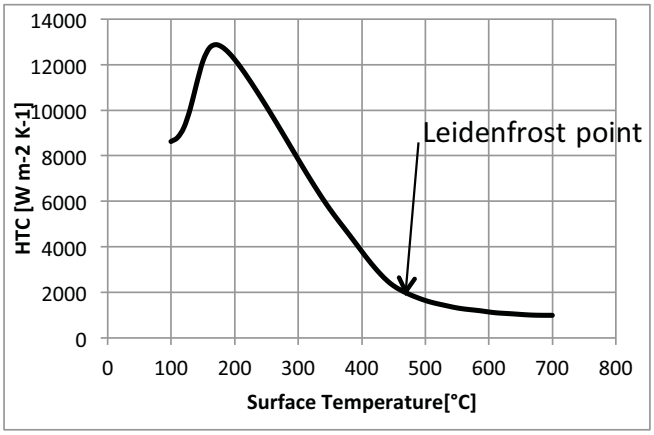

Fig. 2: Typical dependence of HTC on surface temperature in spray cooling

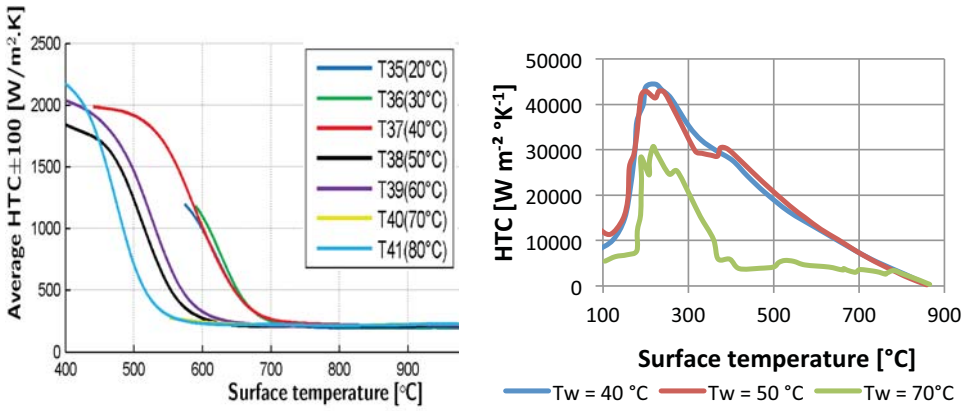

Fig. 3: Influence of water temperature on heat transfer coefficient. Left graph adapted from paper (Raudenský et al., 2011). Right adapted from paper (Xu & Gadala, 2006).

It can be inferred from the dependence of heat flux on the surface temperature and the knowledge of eq. (1)

$$\dot{q} = HTC(T_S - T_W) \tag{1}$$

that the change of cooling intensity is caused only by the difference between the surface temperature T_S and the water temperature T_w and it is not connected with the shape of the HTC curve. It is not true. The change of cooling intensity is mainly caused by changing the type of boiling. As it was shown in Raudenský et al. (2011) and Xu & Gadala (2006), the increase of coolant temperature caused the decrease of the Leidenfrost temperature, which is connected with changing of type of boiling.

2. Experimental measurements

2.1 Experimental apparatus

An experimental apparatus developed for linear moving of the hot test sheet under nozzles was used in experiments. The nozzles were located above or under the hot sheet. The movement of the holder with the test plate was provided by an electric engine, which was connected to the holder by a steel wire. The girder was rotatable. It allowed upper, bottom and side cooling. The collector with nozzles was connected to a manometer and a water tank. The water tank was equipped with a heater. It allowed adjusting of the water temperature from 20 °C to 90 °C. The water from the water tank was pumped to the collector. The sheet holder was equipped with a position sensor. Thermocouples were welded on the underside of the test sheet (see Fig. 4). Information about the temperature of the test sheet, water temperature and position of the test sheet was recorded in a data acquisition system (datalogger). The information was transferred from the datalogger into the computer after the experiment.

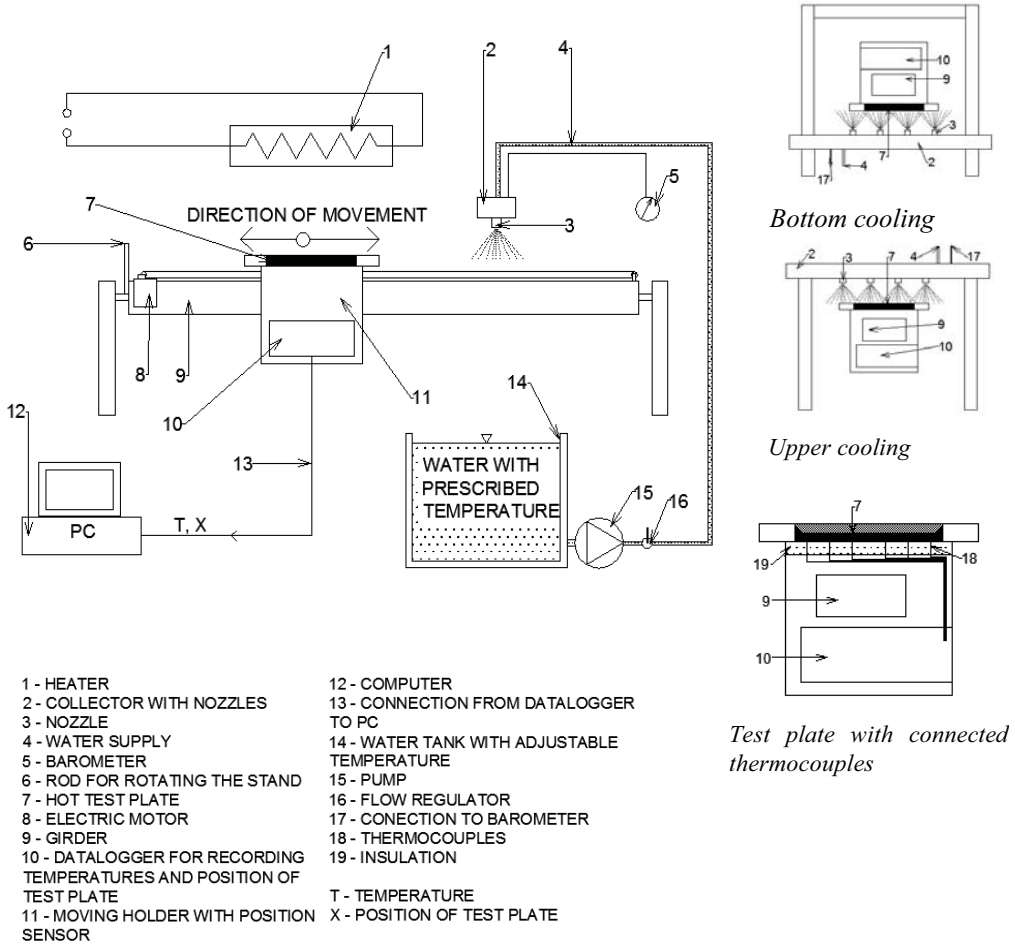

Test plate with connected thermocouples

Fig. 4: Schematic diagram of experimental apparatus

2.2 Experimental procedure

First the cooling section and the test sheet were prepared. A predetermined number and type of the nozzles was connected to the supporting frame. The thermocouples were connected on the test sheet. The test sheet was placed into the furnace and heated. The experiment started after reaching the target

temperature 900 °C. The datalogger started recording information about the temperature and location of the test sheet. The pump was switched on and the flow rate was adjusted. Heating was stopped. The test sheet was removed from the furnace and repeatedly passed through the cooling section with prescribed velocity (see Fig. 5). When the test sheet was sufficiently cooled, the pump was switched off and the movement of the test sheet was stopped. Data recording was stopped and the obtained data were transferred into the computer. This was followed by subsequent data processing and numerical computation of surface temperature and HTC using inverse task (Raudenský, 1993).

Fig. 5: Example of upper cooling experiment

2.3 Program of experiments

Commercially available flat fan nozzles were used for experiments with different water temperatures. The initial temperature of stainless steel sheet was 900 °C. All experiments were conducted with water pressure 3 bar and velocity of the test sheet 0.8 ms^{-1}. Some experiments were conducted with upper cooling and others with bottom cooling. Each experiment was conducted with a different temperature. The temperatures tested in the experiments were 20 °C, 40 °C, 60 °C and 80 °C for upper cooling and 40 °C and 60 °C for bottom cooling. Experiments TEMP20U, …, TEMP80U indicate upper cooling experiments and TEMP40B, TEMP60B indicate bottom cooling experiments (Tab. 1).

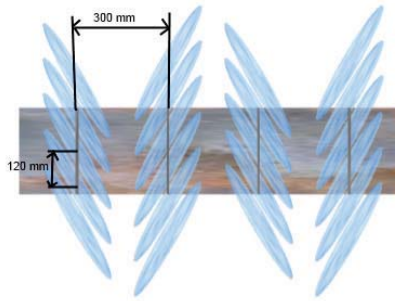

Fig. 6: Illustration of nozzles position above sheet

Tab. 1 Table of testing parameters

Experiment	Step between nozzle widthwise	Velocity	Water Pressure [bar]	Water Temperature [°C]
TEMP20U	120 mm	0.8 m/s	3	20
TEMP40U				40
TEMP60U				60
TEMP80U				80
TEMP40B	120 mm	0.8 m/s	3	40
TEMP60B				60

3. Results

The measured temperatures were recomputed to the surface temperatures and the heat transfer coefficient was computed by the inverse task (Raudenský, 1993). The dependence of the heat transfer coefficient on the surface temperature for various water temperatures in top cooling experiments is shown in Fig. 7. This graph shows the shift of the Leidenfrost temperature to lower temperatures with increase of the coolant temperature. The change of water temperature from 20 °C to 80 °C caused the change of about 140 °C of the Leidenfrost temperature. A similar result was obtained for bottom cooling experiments (Fig. 8). These results match results for austenitic plate presented in Raudenský et al. (2011) and for carbon steel in Xu & Gadala (2006).

Furthermore it was observed that in a high temperature region the heat transfer coefficient decreases with increasing coolant temperature (Fig. 9 and Fig. 10). It is interesting that the value of the heat transfer coefficient is nearly the same for water temperatures 40 °C and 60 °C (Fig. 9). These results can be expected, but are inconsistent with results presented in Raudenský et al. (2011) for mist nozzles. This could be caused by different type of nozzles (mist nozzles) and the general experiment configuration.

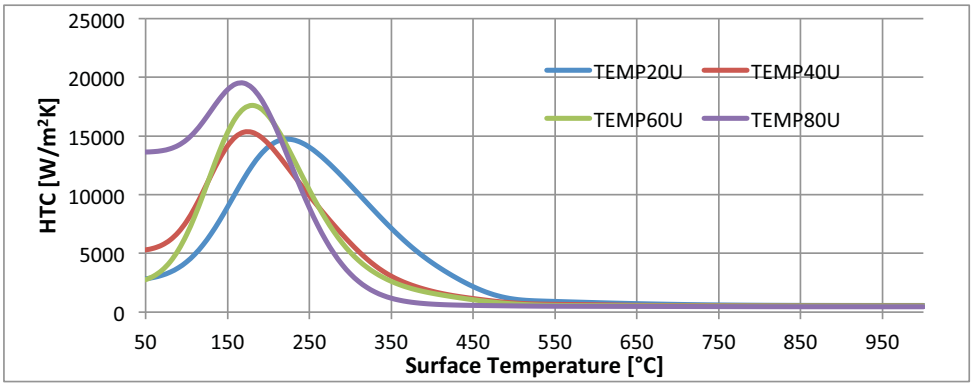

Fig. 7: Upper cooling

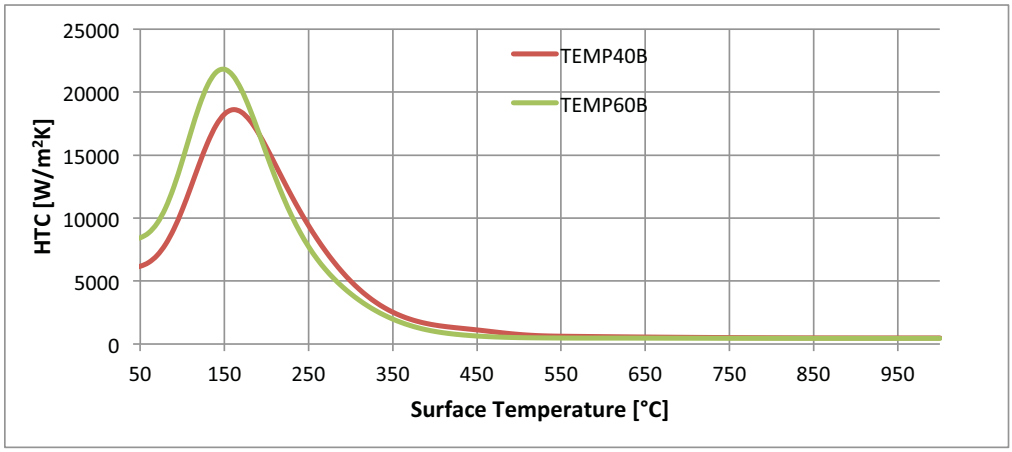

Fig. 8: Bottom cooling

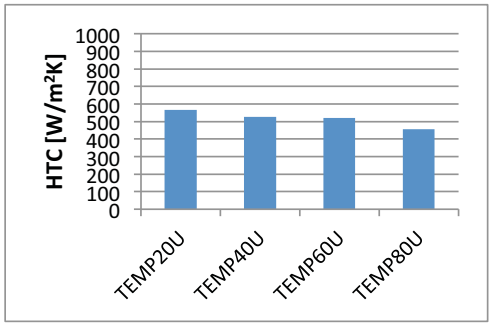

Fig. 9: Upper cooling in high temperature area

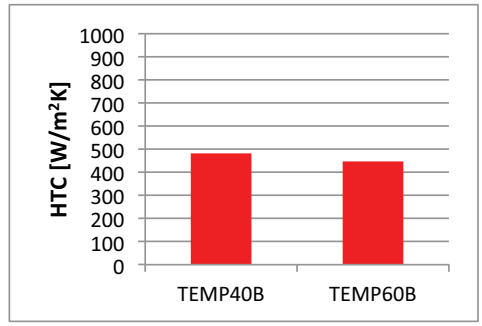

Fig. 10: Bottom cooling in high temperature area

A simple explanation of the shift of the Leidenfrost temperature may be as follows. Hot water does not need as much heat as cold water to reach the boiling temperature. Heat needed to heat water to boiling temperature is small compared with the heat required to change phase from liquid to gas. The time required to heat warmer water is a bit shorter than for colder water. This small shorten of the time needed to heat water can cause a decrease of Leidenfrost temperature. There is no need to supply so much heat from the surface to incoming water and so a steam layer can be formed even at lower surface temperatures. Another thing which may cause a shift of the Leidenfrost temperature could be decrease of water viscosity with increasing water temperature. Proper justification would require further research.

4. Conclusion

Experimental investigation showed the influence of coolant temperature on Leidenfrost temperature in cooling stainless steel sheets. The change of water temperature from 20 °C to 80 °C caused the change of 140 °C of the Leidenfrost temperature. This result is in agreement with results for austenitic steel (Raudensky et al., 2011) and for carbon steel (Xu & Gadala, 2006). This result has applications in the metallurgical industry, where the temperature of cooling water changes during the year. This change of coolant temperature causes a change of cooling intensity and it leads to undesirable material properties. Furthermore it was observed, that in the high temperature region the heat transfer coefficient decreases with increasing coolant temperature and the value of the heat transfer coefficient is nearly same for water temperatures 40 °C and 60 °C.

Acknowledgement

The paper presented has been supported by the internal grant of the Brno University of Technology No. FSI-S-11-20.

References

Bernardin, J. D. & Mudawar, I. (1999). The leidenfrost point: Experimental study and assessment of existing models. *Journal of Heat Transfer*, 121(4), pp. 894-903.

Bernardin, J. D. & Mudawar, I. (2002) A cavity activation and bubble growth model of the leidenfrost point. *Journal of Heat Transfer*, 124(5), pp. 864-874.

Bernardin, J. D. & Mudawar, I. (2004) A leidenfrost point model for impinging droplets and sprays. *Journal of Heat Transfer*, 126(2), pp.272-278.

Bernardin, J. D., & Mudawar, I. (2005) Transition boiling heat transfer of droplet streams and sprays. *Paper presented at the American Society of Mechanical Engineers, Heat Transfer Division, (Publication) HTD*, 376 HTD(2), pp. 201-210.

Horský, J. & Raudenský, M. & Tseng, A. (2005) Heat Transfer Study of Secondary Cooling in Continuous Casting. *AISTech 2005*. Ohio, pp. 1-11.

Raudenský, M. (1993) Heat transfer coefficient estimation by inverse conduction algorithm. *International Journal of Numerical Methods for Heat and Fluid Flow*, 3(3), pp. 257-266.

Raudenský, M. & Boháček, J. (2009) Leidenfrost Phenomena at Hot Sprayed Surface. *In 7th ECI International Conference on Boiling Heat Transfer.* pp. 1-9.

Raudenský, M. & Hnízdil, M. & Lee, S. & Kim, S. & Hwang, J. (2011) Influence of Water Temperature on Cooling Intensity of Mist Nozzles in Continuous Casting. *In 19th Conference on Materials and Technology. Ljubljana 2011*. pp. 60-70.

Xu, F & Gadala, M. S. (2006) Heat transfer behavior in the impingement zone under circular water jet. International Journal of Heat and Mass Transfer, Volume 49, Issues 21–22, pp. 3785-3799, ISSN 0017-9310.

18th International Conference
ENGINEERING MECHANICS 2012
Svratka, Czech Republic, May 14 – 17, 2012

pp. 507–512
Paper #72

SIMULATION OF VEHICLE TRACK DYNAMIC LOADING

M. Chalupa[1], R. Vlach[2]

Abstract: *The contents of article describes design of the vehicle track computational model and example of testing procedure of the track dynamic loading simulation. The proposed approach leads to an improvement of track vehicle course stability. The computational model is built for MSC. ADAMS, AVT computational simulating system. Model, which is intended for MSC computational system, is built from two basic parts. The first one is represented by geometrical part, while the second one by contact computational part of the model. The aim of the simulating calculation consist in determination of change influence of specific vehicle track constructive parameters on changes of examined qualities of the vehicle track link and changes of track vehicle course stability. The work quantifies the influence of changes of track preloading values on the demanded torque changes of driving sprocket. Further research possibilities and potential are also presented.*

Keywords: ***tracked vehicles, track, computational simulation, dynamic loading simulation.***

1. Introduction

Presented research analysis the problem of bad course holding of specific track vehicle when driven at a speed exceeding 65 km.h^{-1}. It is possible to identify the reasons of this effect and to propose potential possibilities of its elimination (Chalupa, 2001). Proposal of the design changes that would enable the safe increasing of the maximum vehicle speed is desired and would be very useful for practical use.

This problem can be solved by use of mathematical computer simulation (Rolc, 2008) and (Chalupa, 2007). It is necessary to built the mathematical model of the examined object, and powerful computing simulating system must be available (Chalupa, 2007) and (Koucký, 2011). The mathematical model described in this work is built for modelling in MSC.ADAMS.AVT computational system (ADAMS/MSC, 2003) and (Chalupa, 2007). The ambition of this work is to create a generalised computational model usable not only for the simulation of vehicle track but also for the general vehicle undercarriage dynamic properties. The results of such modelling could be practically used in mathematical modelling and analysing of individual undercarriage parts behaviour during vehicle ride. It is necessary to define the main possibilities of track vehicle course holding improvement by simultaneous increase of maximum speed vehicle.

The first part of the simulation is focused on collecting the data on undercarriage design parameters under different vehicle course holding conditions and increasing maximum speed. These preliminary simulations are focused on monitoring of the influence of changes in supporting axes reaction forces in relation with changes of track links weight and initial tension of track. Such changes can influence the general vehicle course holding. It is well known that design parameters have relevant influence on dynamic loading of some undercarriage parts. The complete calculation of this influence is subject of the second part of the presented work. Following part of the simulation is focused on

[1]Assoc.Prof. Milan Chalupa, MSc. CSc., Department of Mechanical Engineering, Faculty of Military Technology, University of Defence, Kounicova 65, 662 10 Brno, Czech Republic, milan.chalupa@unob.cz www.unob.cz
[2] Assoc. Prof. Radek Vlach, MSc. Ph.D..Institute of Solid Mechanics, Mechatronics and Biomechanics, Faculty of Mechanical Engineering, Brno University of Technology, Technická 2896/2, 616 69 Brno, Czech Republic, vlach@uvee.fee.vutbr.cz www.vutbr.cz

determination of possible changes of sprocket wheel torque in relation with changes of initial tension of track. According to torque required on driving wheel (absorbed to override the resistance of the vehicle track), it is possible to determine other parameters of undercarriage design, that are greatly affecting maximum vehicle speed.

The paper presents possible modeling method for the selected type of vehicle track in point two and results of simulating computer modeling of vehicle track dynamic loading performed by vehicle running in point three.

2. Computational model

The computational simulating system MSC.ADAMS.AVT is used for the computational modelling and simulating. This system can be used for the analysis of kinetic and dynamic characteristics of the modelling mechanic system and its animation. Model intended for MSC computational system must be built from two basic parts. These parts of the model are: geometrical and contact computational parts (ADAMS/MSC, 2003). Geometrical part of computational model must consists of basic parts of the vehicle undercarriage movable parts. The model involves road wheels (Fig. 1), supporting rollers, driving sprocket (Fig. 2), idle wheel and track line on which individual track links are connected by couplings (Fig. 3). The parts are defined by components with real geometrical shape. The critical aspect at this point is to keep the flat contact.

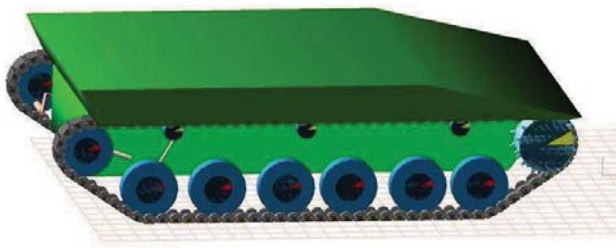

Figure 1: Geometrical part of computational model

The main parts of the track link are as follows: the body with two guiding detents and two connected eyes with pins, couplings, and retaining screws. There are 84 track links on each track.

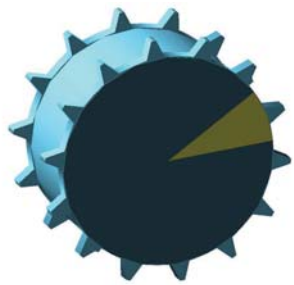

Figure 2: Geometrical model of the sprocket wheel

Axel arms, shock absorbers and torsion bars are defined as simplified shape components, thus without contact components. This type of the components is generated from the offer of universal track vehicles undercarriage components. They are defined by input data such as basic design dimensions, weight, moment of inertia, stiffness, absorbing and number of parts.

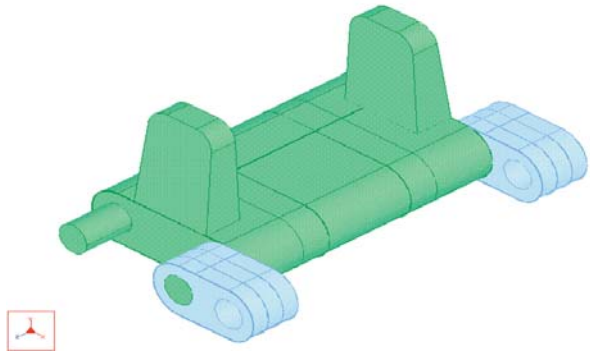

Figure 3: Geometrical model of the track link and connecting clip

Contact part of computational model must involve impact and frictional forces system (ADAMS/MSC, 2003). To guarantee the highest accuracy and practicality, the impact and frictional forces of the individual undercarriage parts are defined in such way (Vlach, 2008), that the whole model resembles the reality as much as possible. These contact forces are described in Adams System by impact force Eq. (1):

$$F = -k'(q - q_0)^n - cq' \qquad (1)$$

where: $q-q_0$..penetration of bodies in contact, k - contact stiffness, c – damping coefficient, $\dot{q}$ - sliding velocity of bodies in contact, n - stiffness force exponent

Contact model is described by characteristic of sliding velocity influence on friction coefficient (Fig. 4), (Chalupa, 2007) and (Vlach, 2008).

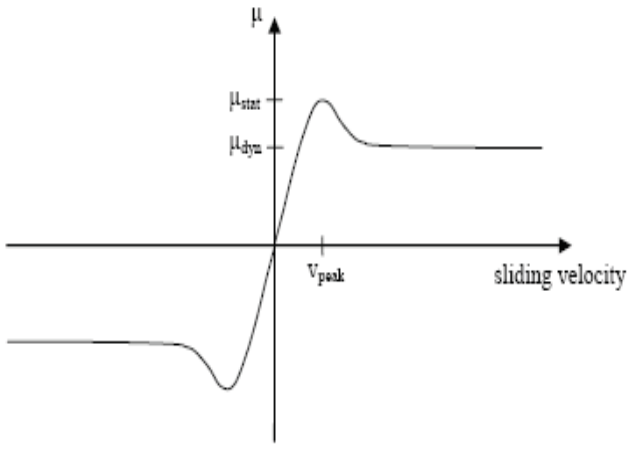

Where:
μ_{stat} - static friction coefficient,
μ_{dyn} - dynamic friction coefficient

Figure 4: Course of friction

3. Results of calculation

The aim of the simulating calculation to determine the influence of change of specific vehicle track constructive parameters on changes of examined qualities of the vehicle track link. These are determined especially by intensity changes of the reaction force of the carrying elements of track links bodies.

The ten of tested parameters are radius of driving wheel, radius of tightening wheels, initial tension track, weight of track link, stiffness of connection plugs track link, resistance against turning of clutches plugs link, geometry of driving rib of track link, weight of bearing rollers, radius of bearing rollers, stiffness of assessment of base of bearing rollers.

Simulation calculations were performed with using of computation model displayed in figure 1. As can be seen from introduced example in graph 1, reduction of the initial torsion of track for about 10 000 Nm causes decrease of required torque value from 10 181 Nm to 9 369 Nm. It represents approximately 7.5 %. Increasing of initial track tension for about 10 000 Nm causes increasing of required torque value from 10 181 Nm to 13 553 Nm, which is about 33 %. It is thus possible to conclude that there is a big influence of changes in initial torsion of track on driving sprocket required torque.

Graph 1: Course of required torque moment values on initial track torsion

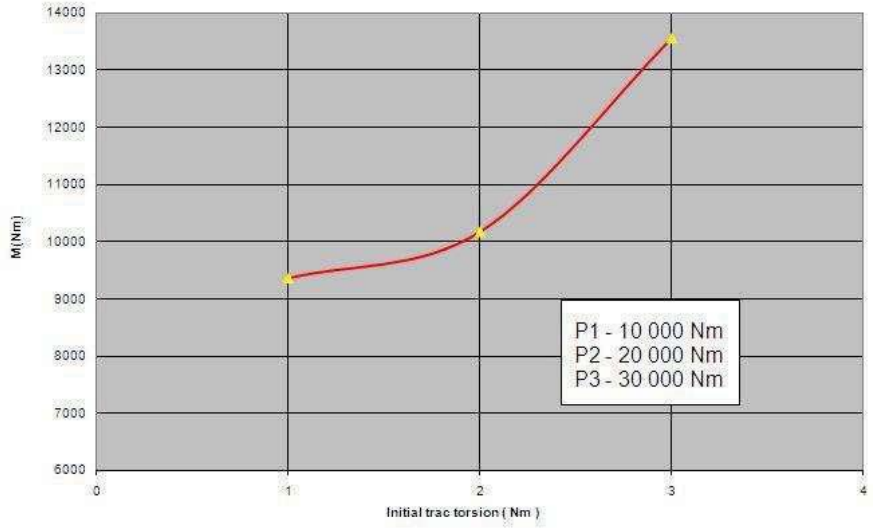

This parameter influences vehicle course holding and improves maximum speed of the vehicle. It seems to be very promising and important to perform the full analysis of this phenomenon (influence of this design parameter) in the future. The results of previously performed basic simulating calculations shown the big influences of changes in reaction forces supporting rollers axes on changes of track links weight and initial tension of track. It is clear that this design parameters have big influence on dynamic loading of some undercarriage parts and therefore a maximum speed of vehicle. The same influence of changes of required torque on sprocket wheel in relation with changes of driving sprocket diameter were approved as well. This parameter influences vehicle course holding and improves maximum speed of the vehicle. This phenomenon will be the subject of our forthcoming research when full calculation will be performed.

4. Further research plans

Application of the advanced simulation will be performed as a consequent step with the aim of assembling the approximation relation y_o of monitored parameters R_x, , F_{pr}, k_p a m_x.

1. Composite plan simulations assembly for 4 parameters (Vlach, 2008).
2. Implementation of 24 simulating calculations according to composite plan.
3. Assesment of regression function
   According to proposed model simulations, it is possible to derive the approximation relation (regression function) formulating the dependence of element velocity on above mentioned factors, which are easy to determine. Created regression quadratic model has a following form (in relation to variables):

$$y = \beta_0 + \sum_{j=1}^{n} \beta_j x_j + \sum_{j=1}^{n} \beta_{jj'} x^2_j + \sum_{j<j'}^{n\,n} \beta_{jj'} x_j x_{j'} + \varepsilon \tag{2}$$

where: β - regression coefficient, x_j - monitored parameter, n - number of parameters

The form of approximation equation:

$$\begin{aligned} y_0 = {} & \beta_0 + \beta_1 R + \beta_2 F_{pr} + \beta_3 k_p + \beta_4 m + \beta_5 R^2 + \beta_6 F^2_{pr} + \beta_7 k^2_p + \beta_8 m^2 + \beta_9 R{\cdot}F_{pr} + \\ & \beta_{10} R{\cdot}k_p + \beta_{11} R{\cdot}m + \beta_{12} k_p{\cdot}F_{pr} + \beta_{13} m{\cdot}F_{pr} + \beta_{14} k_p{\cdot}m + \beta_{15} R{\cdot}F_{pr} + \beta_{16} m{\cdot}R{\cdot}k_p + \\ & \beta_{17} m{\cdot}R{\cdot}F_{pr} + \beta_{18} m{\cdot}k_p F_{pr} + \beta_{19} m{\cdot}F_{pr}{\cdot}k_p{\cdot}R + \varepsilon \end{aligned} \tag{3}$$

where: β - regression coefficient, R - monitored parameter (diameter of driving wheel),
F - monitored parameter (initial tension force of track),
k – monitored parameter (track geometry), m - monitored parameter (track link weight),
n - number of parameters

4. Final verification of mathematical model
   Final verification is provided by comparison of the physical dependence value y obtained from the measurement and regression function y_o corresponding point.

5. Conclusion

The paper describes one of the possible ways how to create the computational model of real track vehicle movement mechanism in software environment MSC.ADAMS.AVT. Vehicle track design and recommendation for upgrading mathematical model is emphasised. The objective is to create computation simulation for the purpose of finding the basic information on track component parts and undercarriage performance of moving vehicle.

The similar simulations were already performed. They analysed the influence of changes in reaction force values on axes of supporting rollers depending on changes in weight track link, changes of track radius and sizing changes in initial tension track. Their results approved, that influence of changes of track radius, initial tension and track link weight, on changes of reaction forces on supporting rollers of undercarriage influence are significant and they are worth of further investigation.

This research also confirmed previously published results of simulating calculations analysing influence of changes in driving and track adjusting wheels on required driving wheel torque. Proposed calculations quantify the influence ratio of movement and dynamic loading on elements of vehicle chassis.

One of the main benefits of the proposed analysis is the possibility of determination, which constructional changes can lead to an objective improvement. This can be defined as a track vehicle directional improvement and improvement of maximum speed increase, simulated apart from other factors, not only by track construction, but also by the whole track kinetic and suspension track vehicle undercarriage mechanism.

Acknowledgement

The research was performed under support of Research plan 0000401 of Faculty of Military Technologies of University of Defence in Brno, Czech Republic.

References

ADAMS/MSC/ (2003), Tracked Vehicle Toolkit version 2003.0, Documentation, MSC.Software, Sweden.

Chalupa, M., Kotek, V., Vlach, R. , (2001) Research of design of vehicle track for high speed. Final report of Research program POV MO 03171100014. VA Brno, pp.1 – 115.

Chalupa,M., Kratochvíl, C., Kotek, V., Heriban, P. (2007) "Computer Method of Analysis of Driving System Dynamic Properties." In: "AT & P Journal Plus". Bratislava: HMH s.r.o., 841 02 Bratislava 42, ISSN 1336-5010.

Chalupa, M. (2007) "Simulation Metod of Analysis of Driving System Dynamic Properties". In: Proceedings of the International conference "48th International conference of Departments of Mechanical Engineering", Smolenice 12.-14.9. 2007", STU v Bratislavě, SR, 2007, ISBN 978-80-227-2708-2, pp.48 -56.

Chalupa, M, Veverka, J, , (2007). Dynamic Loading Simulation of Vehicle Track . In: Proceedings of the International conference „Engineering mechanics 2007.", Svratka, CR, ISBN 978-80-87012-06-2, pp. 82 – 90.

Chalupa, M, Veverka, J. (2007). "Computerized Dynamic Loading Simulation of Vehicle Track." In: Proceedings of the International conference „Dynamics of Rigid and Deformable bodies 2007", Ústí nad Labem, CR ISBN 978-80-7044-914-1, pp. 231 – 238.

Koucký, M. and Vališ, D. (2011) „Some aspects of sequential systems design." In Proceedings 17th ISSAT International Conference on Reliability and Quality in Design. Piscataway : International Society of Science and Applied Technologies,. ISBN 978-0-9763486-7-2, ,pp. 62-66.

Rolc, S., Adamík, L., Buchar, J., Severa, L. (2008) Plate response to buried charge explosion, Material Science Forum, Vol 566, ISBN 0-87849-465-0, pp. 83-88.

Vlach, R., Chalupa, M. (2008). The methodology of track mathematical model verification data measuring of tracked vehicle BMP 2, Methodology of measuring, University of Defence Brno, VTUO Slavičín, division Vyškov, CR, ISBN 978-80-7231-608-9, pp. 1 – 15.

18th International Conference
ENGINEERING MECHANICS 2012
Svratka, Czech Republic, May 14 – 17, 2012

pp. 513–521
Paper #60

MOTION OF ROTATING SPHERICAL PARTICLES TOUCHING A WALL

Z. Chára[*], P. Vlasák[**], I. Keita[***]

Abstract: *The paper deals with an analysis of motion of rotating spherical particle in calm water, when the particle is in contact with a smooth, horizontal wall. The motion was visualized by a fast digital camera at 1000 frames/second. Based on software analysis the particle trajectories as well as rotational velocities were determined. Values of vertical, horizontal and rotational velocities were used as input parameters for numerical model and the results are compared with experimental data. Experiments were performed with glass particle of diameter 25 mm, initial values of rotational speeds varied from 500 to 3000 revolution per minute.*

Keywords: ***Particle rotation, particle trajectory, Magnus force.***

1. Introduction

Particle motion and particle-wall collision play an important role in many industrial processes involving suspension flows. The collisions affect particle accumulation and dispersion and inter-phase transport and mixing. Compared to a dry collision the kinetic energy of a particle in a liquid environment is dissipated by viscous stresses in the liquid and by inelasticity during collision (Li et al., 2012). The ratio of particle inertia to viscous forces is quantified through the Stokes number, $St = (1/9)(\rho_p/\rho_f)Re$, where Re is the particle Reynolds number based on impact velocity. Barnocky & Davis (1988) experimentally examined the impact of a sphere on a surface covered by a thin layer of liquid to investigate the critical Stokes number. The work by Davis et al. (2002) also used a thin layer of liquid but they measured the impact and rebound velocity to determine the effective coefficient of restitution. Joseph et al. (2001) measured the approach and rebound of a fully immersed collision to determine the coefficient of restitution as function of the Stokes number. They showed that below a Stokes number of approximately 10 no rebound of the particle occurs and for a Stokes number grater than 1000 the particle rebound is not affected by the surrounding fluid. A lot of computational studies have also considered the problem of particle collision in a liquid. Leweke et al. (2004) computed the flow generated by a particle colliding normal to a surface without rebound. Their simulations showed the development of vortex rings around the particle.

Although many papers deal with the particle-wall collision a little is known about the collision when the particle rotates. The aim of this contribution is to analyze a movement of the rotating particle, calculate a theoretical trajectory of the particle and compare it with the experimental observation.

2. Experimental set-up

The experiments with rotating spherical particle were realized in a water tank of dimensions 40 x 28 x 20 centimeters. The tank was filled with water up to a level 60 mm above the bed. The bed was formed by a glass plate of thickness 19 mm. The particle was a glass sphere of diameter 25 mm and density 2470 kg/m^3. Water temperature was 24^{o}C. The sphere was sped up in a special spinning device situated above the water level. The sphere was held between cups and rotated about a horizontal axis

[*] Ing. Zdeněk Chára, CSc.: Institute of Hydrodynamics AS CR, v. v. i., Pod Pat'ankou 30/5; 166 12, Prague; CZ, e-mail: chara@ih.cas.cz

[**] prof. Pavel Vlasák, DrSc.: Institute of Hydrodynamics AS CR, v. v. i., Pod Pat'ankou 30/5; 166 12, Prague; CZ, e-mail: vlasak@ih.cas.cz

[***] Ibrahima Keita, PhD.: Institute of Hydrodynamics AS CR, v. v. i., Pod Pat'ankou 30/5; 166 12, Prague; CZ

with an initial angular velocity ω_0, which was measured by a tachometer. When the trigger was released, the springs pulled the cups apart, allowing the ball to fall freely in water. The spinning device ensured the required spherical rotation in the given plane and translational velocity of the ball was reached by free fall. The device allowed the sphere to spin up to 6 500 revolutions per minute (rpm), but in these experiments a range of 500-3000 rpm was used. Since the device was above water level the particle passed through the surface and this passing slightly modified its movement. Consequently even a non-rotating particle did not move only vertically but with some horizontal shift. After a collision with the bed, the particle rebounded and the combined translational and rotational motion continued.

The particle movement in water was recorded with a frequency of 1000 frames per second using a digital video camera NanoSence III+. Hairlines were drawn along two perimeters of the particle to make it possible to visualize the particle rotation. Only experiments in which the plane of the particle trajectory was parallel to the plane of the video camera objective were chosen.

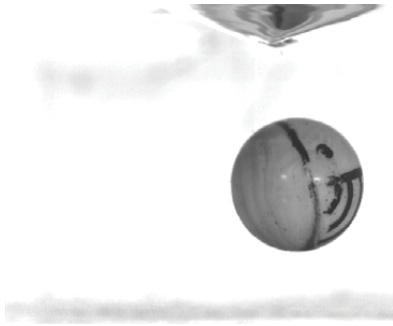

Fig.1: Original image taken from camera

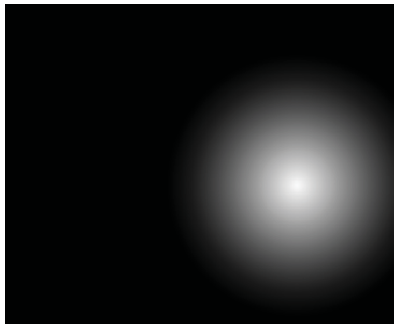

Fig.2: Convolution between 2D filter and original image

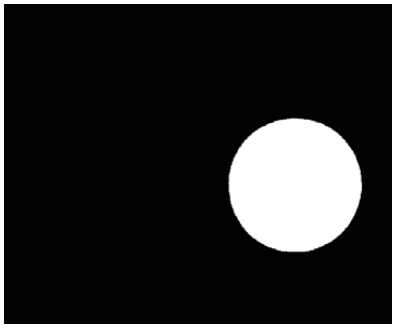

Fig.3: Particle shape after binary operation

Typical picture taken from the camera is shown in Fig. 1. To analyze the particle movements we applied functions implemented in Matlab Image Processing Toolbox. Firstly we chose a 2-D filter with circular shape and then we performed a convolution between the original image and the 2-D filter. The result is shown in Fig. 2, where the maximum white intensity corresponds to the particle centre. Even if the original image has a relatively high scale factor (13.6 pixels/mm) the trajectory based on the image pixels is inaccurate (see Fig. 4). Fig. 4 shows both the trajectories and the vertical velocities calculated from the particle trajectories. As can be seen in Fig. 4 using only pixels resolution to determine the velocity lets to enormous errors. To improve the resolution of the image we applied a fitting of the white intensity in the convolution image (Fig. 2). In both vertical and horizontal direction we used a polynominal curve of the fifth degree to approximate the white intensity. And we suppose that the position of the particle centre corresponds to the maximum of the white intensity. This way seems to give much better results compared with previous one. Another possibility how to improve the particle center identification is to convert the original image into binary one, (Fig. 3), and on this image perform some binary operations. This approach gives the best results, (Fig. 4), but constant conditions regarding the image contrast are required. If we know a position of the particle center the translational velocity components can be easily calculated.

The rotational velocities were determined from the following idea. The spherical particle was marked by two lines (like meridian and equator) which form two planes going through the centre of the particle (point C). In each time step we chose arbitrarily two points (A,B) on the equator (or meridian) and looked for a normal vector of the plane (ACB). If time series of the normal vectors is known, the 2D rotational velocity can be calculated.

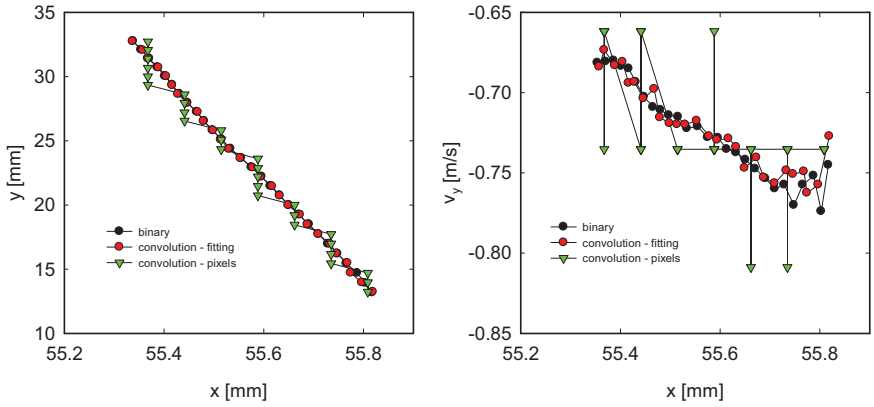

Fig.4: Comparison of different ways of particle location (left-trajectory, right –vertical velocity)

3. Discussion of the results

The particle motion in fluids is described by a set of ordinary differential equations taking into account interaction of several forces like submerged gravitational force, drag force, force due to the added mass, Magnus and history forces and torque acting on a rotating particle. History force was not considered due to the relatively large particle diameter and high Reynolds number (Re > 6000) in a vicinity of the wall. So, the system of the equations was considered in the following form

$$m\frac{d\vec{u}}{dt} = \vec{F}_g + \vec{F}_d + \vec{F}_m + \vec{F}_M, \qquad I\frac{d\vec{\omega}}{dt} = \vec{M} \tag{1}$$

where $\boldsymbol{m}$ is particle weight, $\boldsymbol{F_g}$, $\boldsymbol{F_d}$, $\boldsymbol{F_m}$ and $\boldsymbol{F_M}$ are gravitational, drag, added mass and Magnuse forces respectively. $\boldsymbol{I}$ is the particle momentum of inertia, $\boldsymbol{\omega}$ is rotational velocity and $\boldsymbol{M}$ is the drag torque given by the formula

$$\vec{M} = -C_\omega \frac{\rho_f}{2} \vec{\omega} |\vec{\omega}| r^5 \tag{2}$$

where C_ω is dimensionless drag torque coefficient. The reliable experimental and theoretical data of the coefficient C_ω are described by Sawatzki (1970). The drag force was determined by the following expression

$$\vec{F}_d = \left[\frac{24}{Re} \left(1 + 0.15\, Re^{0.687} \right) \right] \left(\rho_f / 2 \right) \pi (d/2)^2 \vec{u} |\vec{u}| \tag{3}$$

and Magnus force was given as

$$\vec{F}_M = C_M \frac{\pi d^3}{6} \rho_f \left[\vec{\omega} \times \vec{u} \right] \quad \left(= \frac{C_{LR}}{\Gamma} \frac{\pi d^3}{16} \rho_f \left[\vec{\omega} \times \vec{u} \right] \right) \tag{4}$$

where C_M is the dimensionless Magnus force coefficient. In the bracket there is another expression for Magnus force which can be found in literature and where the lift coefficient is used instead the Magnus force coefficient ($C_{LR} = 8\Gamma/3\ C_M$). Γ is dimensionless parameter sometimes called as dimensional angular velocity ($\Gamma = 2Re_\omega/Re$). The theoretical analysis of the Magnus force was performed by Rubinov & Keller (1961) for very small values of the Reynolds numbers and they deduced $C_M = 0.75$. In the range of moderate Reynolds numbers ($550 < Re < 1600,\ \Gamma < 0.7$) Tsuji et al. (1985) observed trajectories of a sphere which collided with an inclined plate submerged in water and they suggested $C_M = 0.15 \pm 0.04$. Oesterle & Dinh (1998) proposed the following formula for the lift coefficient ($10 < Re < 140,\ 1 < \Gamma < 7$)

$$C_{LR} = 0.45 + \left(2\Gamma - 0.45 \right) \exp\left(-0.075\, \Gamma^{0.4}\, Re^{0.7} \right), \quad Re < 140 \tag{5}$$

In our experiments the range of Reynolds numbers was from 1000 to 20 000 and the range of non-dimensional angular velocity from 0.5 to 10. As was mentioned above the particle trajectories were used to calculate the vertical as well as the horizontal velocity components. Time resolution was given by the camera frame rate and for all tested cases $\Delta t = 0.001$ sec. First of all we analyzed the angular velocities and the results we compared with particle drag torque to determine the coefficient of drag torque, C_ω. Fig 5 shows time series of the measured angular velocities for the initial values of rotational velocities – 500, 1000, 2000 and 3000 rpm. The particle always rotated in counter-clockwise direction.

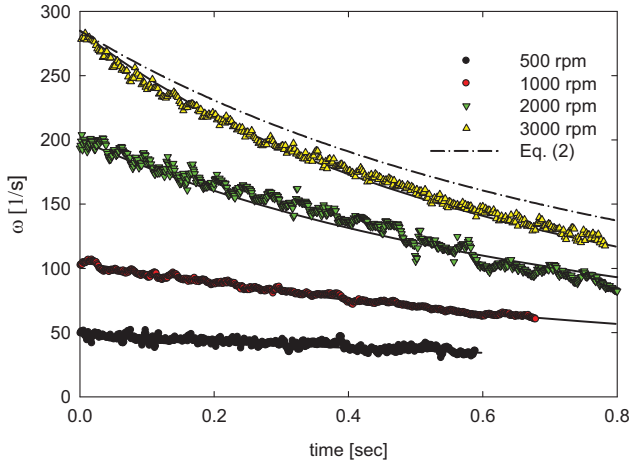

Fig.5: Time series of angular velocities

As can be seen in Fig. 5 the angular velocities monotonically decrease in time which means that negligible changes of angular velocities occurred during particle-bed collisions (at least the changes

lay in a range of experimental errors). We approximated the data of angular velocities by the Equation (2) with the coefficient of drag torque taken directly from Sawatzki (1970) data. The approximation is shown as a dash-dot line in Fig. 5 and in a whole range of time interval the line is above the experimental data. To get a better approximation (solid lines in Fig. 5) the drag torque coefficient is suggested to be slightly modified according to the formula

$$C_{\omega} = 1.3\ C_{\omega\ Sawatzki} \tag{6}$$

The aim of this paper is to analyze the particle trajectories and with help of equation set (1) calculate the trajectories with initial values of both translational and rotational velocities taken from the experiments. Figs. 6, 7 and 8 show particle trajectories for the non-rotating particle and for the particle with rotation 1000 and 3000 rpm. The left part of the figures show time series of the vertical particle position, the right part shows the particle positions in the *x-y* plane (***x*** is horizontal coordinate and goes from left to right, ***y*** is vertical coordinate and goes from bottom to upwards). The interruption of the trajectory for the non-rotating particle is due to a relatively small water depth. When the particle went up after the first collision with the bed, the particle nearly touched a water level and when the particle started again to settle a part of the water level was pulled down. Since the non-rotating particle had a small but not a negligible value of horizontal velocity it moved along the bottom (see Fig. 6, right). The initial trajectory of the rotating particle is going down from the left to the right do to the counter-clockwise rotation and hence due to the Magnus force. Depending on the angle of the first trajectory the particle either reversed its movement immediately after the first collision, (Fig. 7, right), or continued forward and reversed after the second collision, (Fig. 8, right).

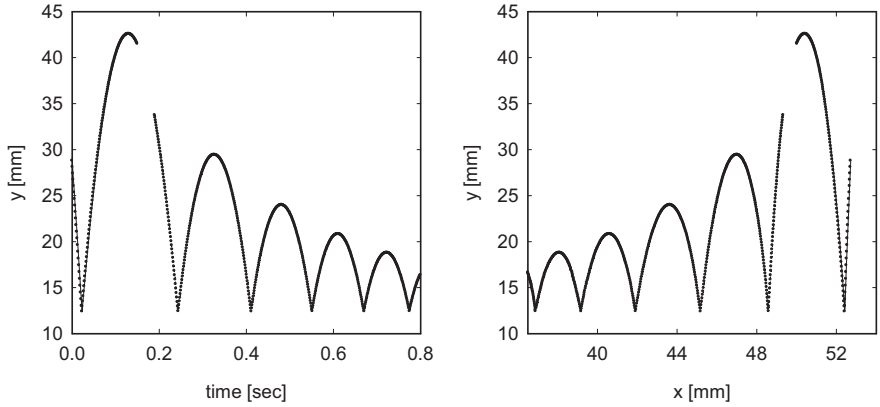

Fig.6: Trajectories of non-rotating particle

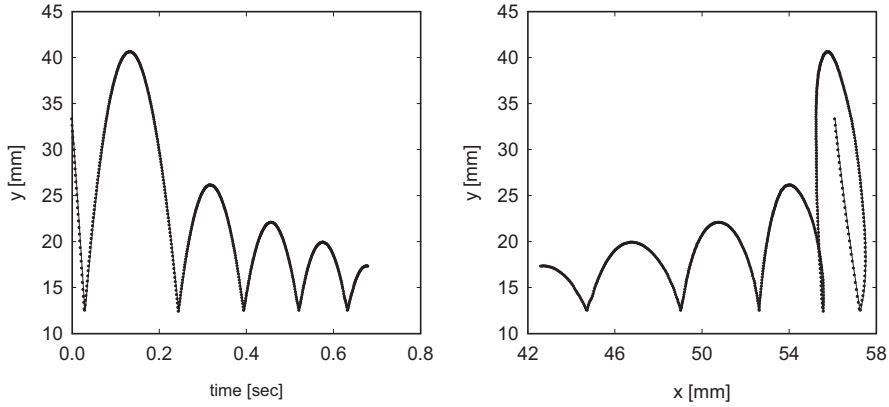

Fig.7: Trajectories of rotating particle with initial rotation 1000 rpm

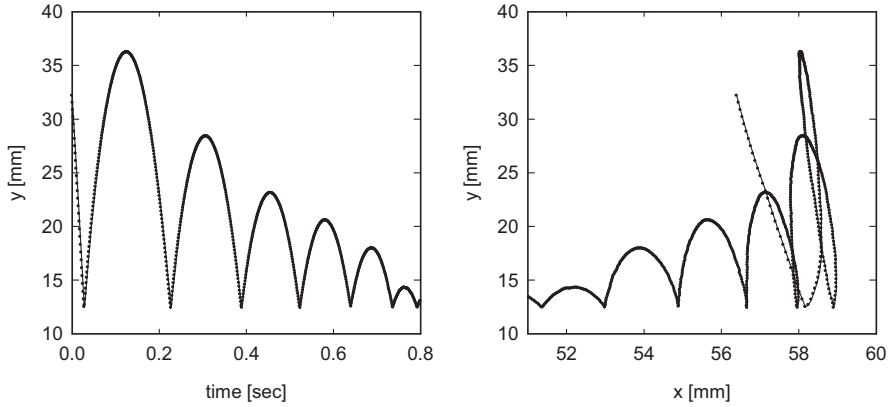

Fig.8: Trajectories of rotating particle with initial rotation 3000 rpm

Figs. 9, 10 and 11 show the translational particle velocities determined from trajectories of the particle center. Blue lines in these figures show the velocities in horizontal direction, red lines show the vertical velocity component. While the vertical velocities changed for a very short time during the collision process, somewhat different behavior was observed for the horizontal velocities in the case of rotating motion. The horizontal velocities increased and just before the collision they decreased. After the collision the horizontal velocities continued to decrease, but the time derivate of the horizontal velocity is much higher compared to the time derivate of the vertical velocities. This situation is clearer in Fig. 12 where a detail of time series of the first rebound is shown for initial rotation 1000 and 3000 rpm and for different angles of incoming trajectories. The angels are between the trajectories and a normal vector of the bed. The higher is the angle the higher is the horizontal velocity before the impact. The origin of time coordinate corresponds to the time of the collision. As can be seen in Fig. 12 the particle strongly accelerates in the horizontal direction just after the impact. The acceleration acts in direction of the Magnus force and it is restricted to a region close to the bed (up to a distance 0.2D). The acceleration depends on the initial conditions of rotation, the higher is the rotation, the higher is the acceleration.

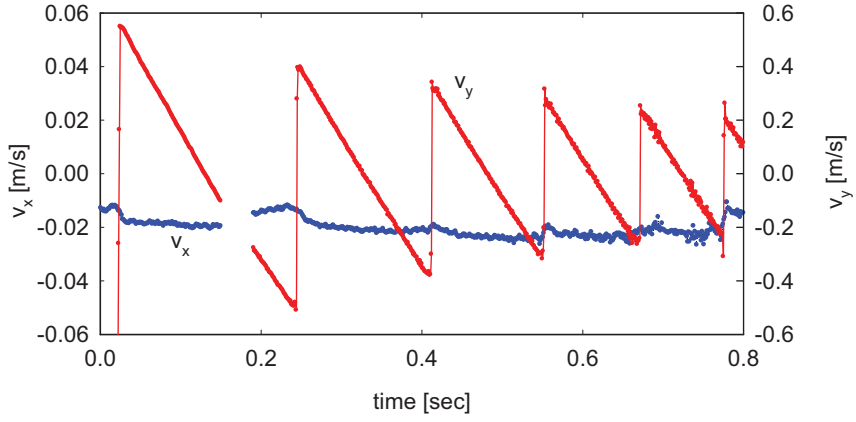

Fig.9: Translational velocities of non-rotating particle (blue - horizontal, red - vertical velocities)

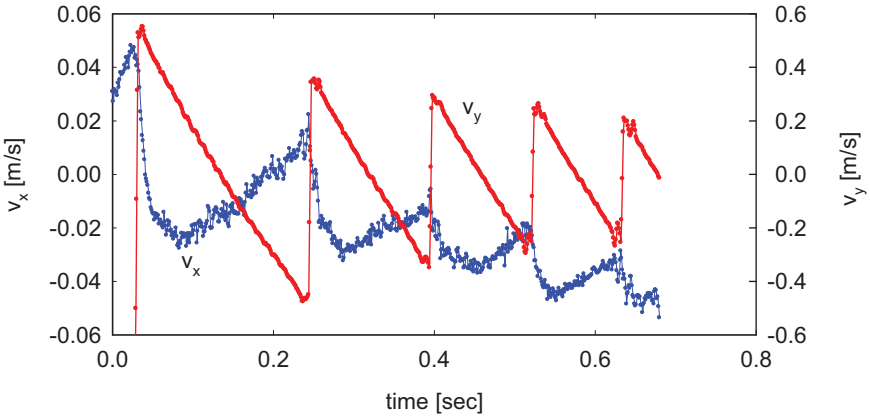

Fig.10: Translational velocities of rotating particle - 1000 rpm

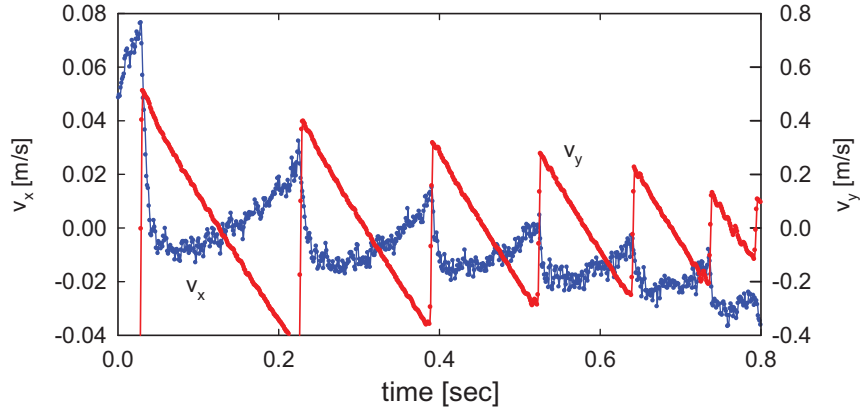

Fig.11: Translational velocities of rotating particle - 3000 rpm

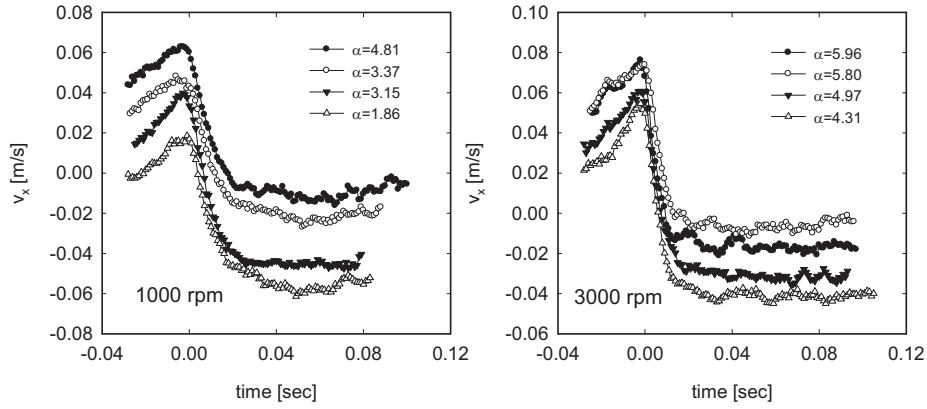

Fig.12: Horizontal velocity component of rotating particle after the first rebound

Another interesting feature can be concluded from the time series of the horizontal velocities and the vertical position of the particle. Between two impacts the particle quickly accelerates and then slowly decelerates but the point of transition does not correspond to the point where the particle

reaches the maximal position above the bottom and where the vertical velocity changes the direction. The point of transition precedes the maximal position of several tens of milliseconds.

As we know the particle trajectories and the translational and rotational velocities just after the impact and supposing that the Magnus force coefficient is constant over each individual jump we could solve the Equations (1). The Magnus force coefficient was determined for each jump to obtain the best coincidence between the measured and the calculated trajectories. Figs. 13 and 14 show calculated (red lines) and measured (blue lines) values of the particle trajectories and the translational velocities for a case of the initial rotation 1000 rpm.

All values of the Magnus force coefficients were plotted together versus initial values of the non-dimensional angular velocity Γ_0, ($\Gamma_0 = 2Re_{\omega out}/Re_{out}$). The results are shown in Fig. 15 and the Maguns force coefficient can be approximated by the equation

$$C_M = \frac{0.523}{3.49 + \Gamma_0} \tag{7}$$

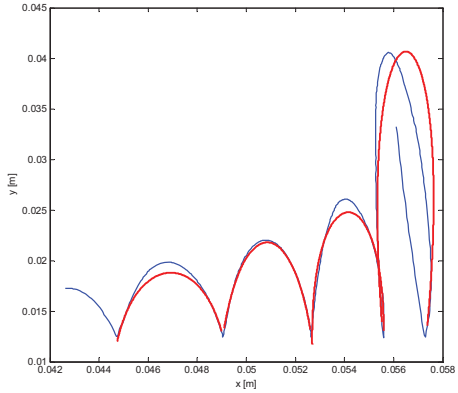

Fig.13: Comparison between calculated (red lines) and measured (blue lines) trajectories of rotating particle – 1000 rpm

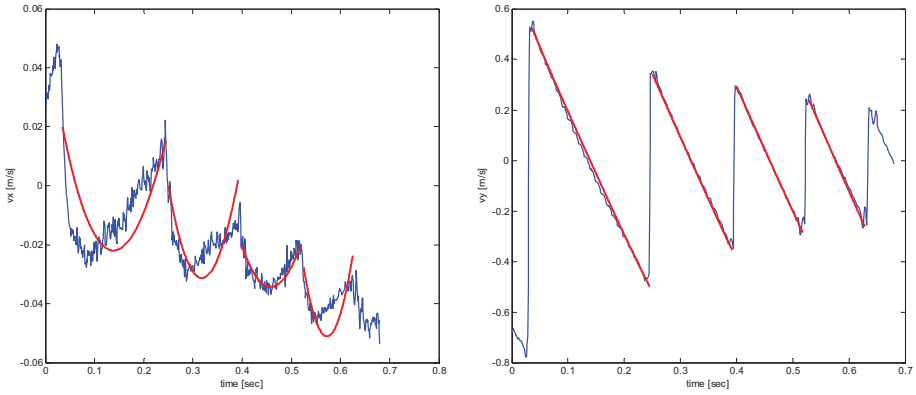

Fig.14: Comparison between calculated (red lines) and measured (blue lines) translational velocities of rotating particle – 1000 rpm

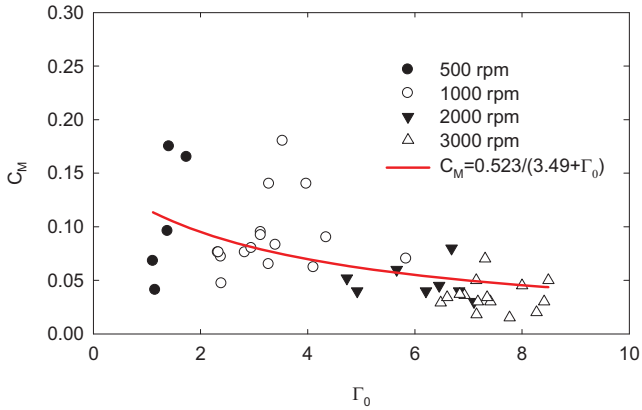

Fig.15: Dependence of Magnus force coefficients, (C_M), on initial values of non-dimensional angular velocities, (Γ_0)

4. Conclusion

Movements of the spherical particles rotating in calm water and touching the horizontal bed were visualized and analyzed. Due to very low values of dynamic friction coefficients no changes of the angular velocities were observed during collision process. The angular velocities monotonically decreased during time and the drag torque acting on the particle could be described by Equation (2) where a modification of the drag torque coefficient is suggested according to the Equation (6).

Measured values of translational and angular velocities just after the collision were used as initial parameters for numerical simulations of the particle movements. The Magnus force coefficients were determined for each jump to obtain the best coincidence between the measured and the calculated trajectories. The Magnus force coefficient can be approximated by the Equation (7).

Acknowledgement

The support under project No. 103/09/1718 of the Grant Agency of the Czech Republic and RVO: 67985874 is gratefully acknowledged.

References

Barnocky, G. & Davis, R.H. (1988) Elastohydrodynamics collision and rebound of sphere: experimental verification. *Phys. Fluids*, 31, pp. 1324-1329.

Davis, R.H., Rager, D.A. & Good, B.T. (2002) Elastohydrodynamic rebound of sphere from coated surface. *J. Fluid Mech*., 468, pp. 479-497.

Joseph, G.G., Zenit, R., Hunt, M.L. & Rosenwinkel, A.M. (2001) Particle-wall collisions in a viscous fluid. *J. Fluid Mech.*, 443, pp. 329-346.

Leweke, T., Thompson, M.C. & Hourigan, K. (2004) Vortex dynamics associated with the collision of a sphere with a wall. *Phys. Fluids* 16 (9), pp. 74-77

Li, X., Hunt, M.L. & Colonius T. (2012) A contact model for normal immersed collisions between a particle and a wall., *J. Fluid Mech.*, 691, pp. 123-145.

Oesterle, B. & Dinh, T.B. (1998) Experiments on the lift of a spinning sphere in the range if intermediate Reynolds numbers. *Experiments in Fluids*, 25, pp. 16-22

Rubinov, S.I. & Keller, J.B. (1961) The transverse force on a spinning sphere moving in a viscous fluid. *J. Fluid Mech*., 11, pp. 447-459.

Sawatski, O. (1970) Das Stromungsfeld um eine rotierende Kugel. *Acta Mechanica,* 9, pp. 159-214.

Tsuji, Y., Morikawa, Y. & Mizuno, O. (1985) Experimental measurements of the Magnus force on a rotating sphere at low Reynolds numbers. *ASME J. Fluid Eng.*, 107, pp. 484-488.

18th International Conference
ENGINEERING MECHANICS 2012
Svratka, Czech Republic, May 14 – 17, 2012

pp. 523–529
Paper #78

NUMERICAL SIMULATION AND EXPERIMENTS WITH THE PROFILE NACA 0012

Š. Chládek, I. Zolotarev, V. Uruba*

Abstract: *This paper introduces the new model of the airfoil and describes both aeroelastic experiments and numerical simulation with the profile NACA 0012. The aeroelastic is the science which studies the flow-structure interaction. The flow field can cause change of the position of the solid body and the body due to the change of its position influences the flow field. Mathematical description of the interaction has to involve both the equations of the fluid dynamic and the equations of motion of the solid body. The first results will be presented from the measuring in the dynamic laboratory and from the measuring in the wind tunnel. The main aim of the experimental part of this research is to cause a self oscilated motion of the airfoil and to measure the transient flow field during this motion. The numerical part should be identical with the experimental dates.*

Keywords: ***Aeroelastic, flow-structure interaction, identification***

1 Introduction

The interaction of the airfoil and fluid flow belongs to a large group of fluid-structure interaction. This interaction takes place in many technical disciplines, e.g. from civil engineering to human vocal tract computation. It is desirable to be able to describe and compute this field of study. The paper describes first steps with the new model of the airfoil, which is used both for numerical simulation and for the experiments.

2 Structural design

The model of an airfoil NACA 0012 is a symmetrical profile with the length of the chord 100 mm with two degrees of freedom. In comparison to the previous aeroelastic models which have been used in the Institute of Thermomechanics it differs in the solution of airfoil – frame attachment. That models can vibrate vertically and rotate around the elastic axis. It was possible to separate these two motions. In this new stand both degrees of freedom are realized by vertically movement. The combination of two vertical displacements gives the final rotation and translation. The scheme with the basic dimensions is shown in Figure 1. The airfoil (position 1) is fastened to the small beam (position 2) and the beam is fastened to the plate with two leaf springs (position 3). The springs are made from phosphor bronze. The plate is attached to the frame with only one screw in the ways it is possible to change the angle of attack. The small beam (position 2) is equipped with 13 holes, so it is possible to change the position among the wing and the springs. It causes changes in dynamic properties of the wing, moreover the holes allow to add mass which also change the static and dynamic properties. Important part of the stand is rod (position 4) for holding the airfoil in constant horizontal position against the flow.

*Ing.Štěpán Chládek, Ing. Igor Zolotarev, CSc., doc.Ing.Václav Uruba, CSc., Institute of Thermomechanics AS CR, v. v. i., Dolejškova 5, 18200 Praha 8, e-mail: chladek@it.cas.cz, igor@it.cas.cz, uruba@it.cas.cz

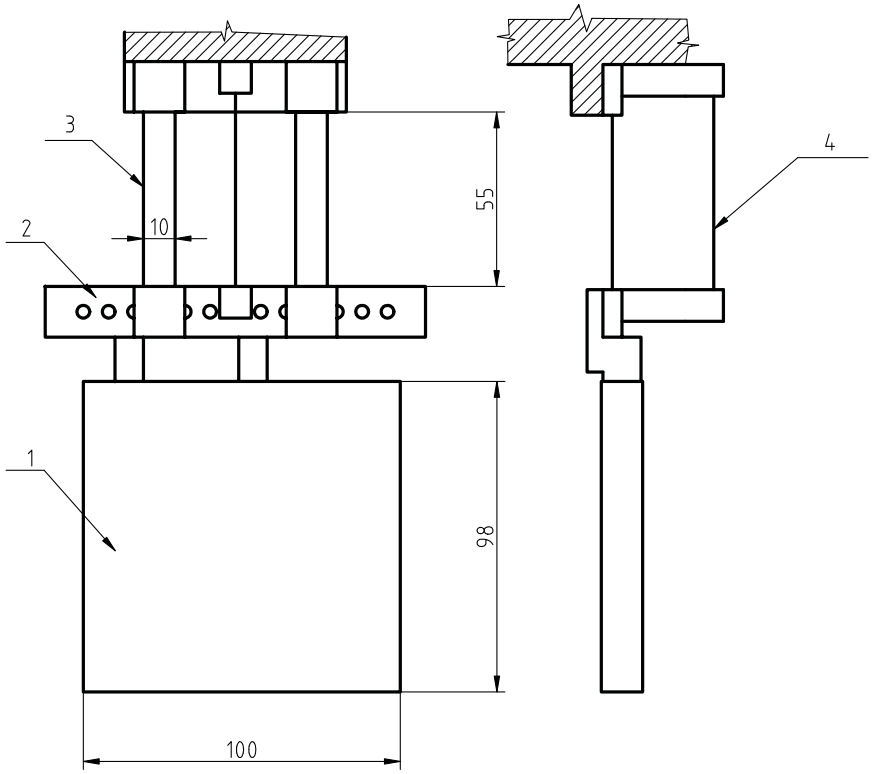

Fig. 1: Design of the airfoil with important dimensions [mm]

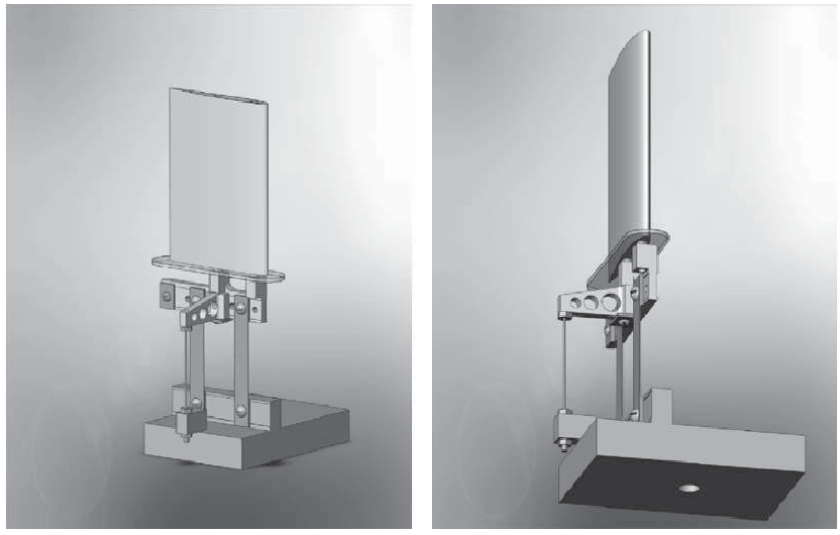

Fig. 2: CAD model of the airfoil stand (from Uruba (2009))

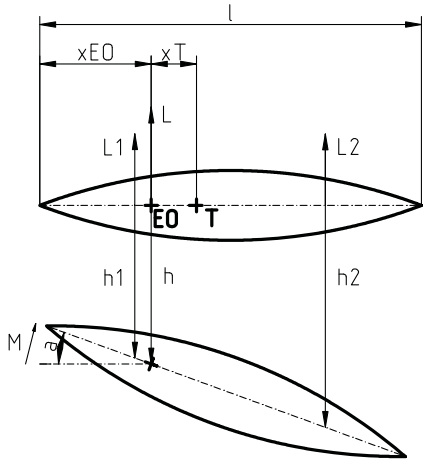

Fig. 3: Basic coordinations and forces acting on the airfoil.

2.1 Mathematical model of the structure

The mathematical model of the prof le consists of system of ordinary differential equations (ODE) of motion. These equations can be derived for example using Lagrange equations and from the law of total energy conservation. They are generaly nonlinear, but for small motion they can be linearized. The prof le can vertically vibrate with two degrees of freedom. Let us denote $y = (h_1, h_2)^T$ a position vector which describes the vertical translation at the points of connection among the springs and the airfoil and $\mathbf{M}, \mathbf{B}, \mathbf{K}$ the mass, damping and stiffness matrices. Then we can write the equation of motion in the form (1)

$$\mathbf{M}\ddot{\mathbf{y}}(t) + \mathbf{B}\dot{\mathbf{y}}(t) + \mathbf{K}\mathbf{y}(t) = \mathbf{f}(t) \tag{1}$$

Vector $\mathbf{f}(t) = (-L_1(t), -L_2(t))^T$ contains the lift forces acting on the leaf springs. In many aeroelastic applications there are considered instead of two lift forces just one lift force, which acts on the elastic axis and one torsional moment. The vector of forces looks like then $\tilde{\mathbf{f}}(t) = (-L_1(t), M(t))^T$**.** It is possible to use basic geometrical transformation to transform equation (1) to the equation of motion with the position vector in the form $\tilde{y} = (h, \alpha)^T$. If we know the transformation matrix R, we can express the coordition like (2)

$$\tilde{y}(t) = \mathbf{R}y(t), \mathbf{R} = \frac{\mathbf{1}}{\mathbf{x_{EO2}} + \mathbf{x_{EO1}}} \begin{pmatrix} \mathbf{x_{EO2}} & \mathbf{x_{EO1}} \\ -1 & 1 \end{pmatrix} \tag{2}$$

If is used the transformation relation (2) and the corresponding derivation to the equation (1), after few modif cation it will be obtained

$$\mathbf{R^T M R}^{-1}\ddot{\tilde{\mathbf{y}}}(t) + \mathbf{R^T B R}^{-1}\dot{\tilde{\mathbf{y}}}(t) + \mathbf{R^T K R}^{-1}\tilde{\mathbf{y}}(t) = \mathbf{R^T f}(t) \tag{3}$$

With the following substitution $\tilde{\mathbf{M}} = \mathbf{R^T M R}^{-1}, \tilde{\mathbf{B}} = \mathbf{R^T B R}^{-1}, \tilde{\mathbf{K}} = \mathbf{R^T K R}^{-1}$ a $\tilde{\mathbf{f}}(t) = \mathbf{R^T f}(t)$ it can be written the f nal equation

$$\tilde{\mathbf{M}}\ddot{\tilde{\mathbf{y}}}(t) + \tilde{\mathbf{B}}\dot{\tilde{\mathbf{y}}}(t) + \tilde{\mathbf{K}}\tilde{\mathbf{y}}(t) = \tilde{\mathbf{f}}(t) \tag{4}$$

The very important factor for next computation is the identif action of static and dynamic properties of the model.

Table 1: Dynamic characteristics of the model from the experiment

Mode No.	Natural frequency $[Hz]$	Damping ratio [%]
1	31.75	2.04
2	40	1.74

3 Mathematical fluid flow model

The problem is solved using finite volume method in the commercial software Fluent. Numerical code has been prepared for the fluid-structure interaction problem and nowadays it will be created a structural mesh of the channel with the airfoil. It is considered viscous laminar incompressible flow, which is modelled in Fluent by the Navier-Stokes equations. Considering the character of the task it has to be dealt with the mesh motion. It is solved using spring - based smoothing method, where edges between any two nodes are idealized as a springs. Any motion at a given boundary disturbes an equilibrium of the mesh and it is used an iterative algorithm to find a new position of all nodes to setup new equilibrium again. Of course, this solution is useful for only small motions.

4 Dynamic properties of the model

The aim of the measurement in the laboratory of dynamic and vibration is to gain both the basic idea about the system properties and the data for the system identification.

4.1 Experiment

It was needed to measure the frequency spectrum of the airfoil. This measurement gives an idea about the model properties. It has been used for a modal testing the devices from the company Brüel & Kjær. The actuator was modal hammer B&K 8230-002 and the sensor was accelerometer B&K 4519-002. It has been measured in the frequency range $(0, 200)$ Hz and there are two important peaks, see Figure 4. The values of natural frequencies and damping ratios from the experiment are presented in Table 1.

Further, it has been was changed the position among the airfoil and the leaf springs and it was measured the natural frequencies of the system. The results are shown in the Figure 5. Considering the graph could be concluded: when changing the airfoil-frame position, its two natural frequencies change significantly. As mentioned above, in the case of self-feeding oscillation is necessary to keep the natural frequencies as close as possible at a flow speed $v = 0\,m.s^{-1}$. The ideal configuration should be either position 3 or position 4, where the number denotes the hole of the beam (Figure 1, position 2).

4.2 System identification

Very important process is the identification of the system. The identified model is an input not only to the fluid-structure interaction but also to the predictive algorithm for flutter onset. For the identification process it has been used the following experiment. The airfoil was attached to frame at two points and in these two points were measured in four combination (position of actuator vs. position of sensor) the complex frequency transfers. From these transfers were computed the eigenvalues of the model, for more information see Horacek (2005). The eigenvalues of the system are listed in Table 2.

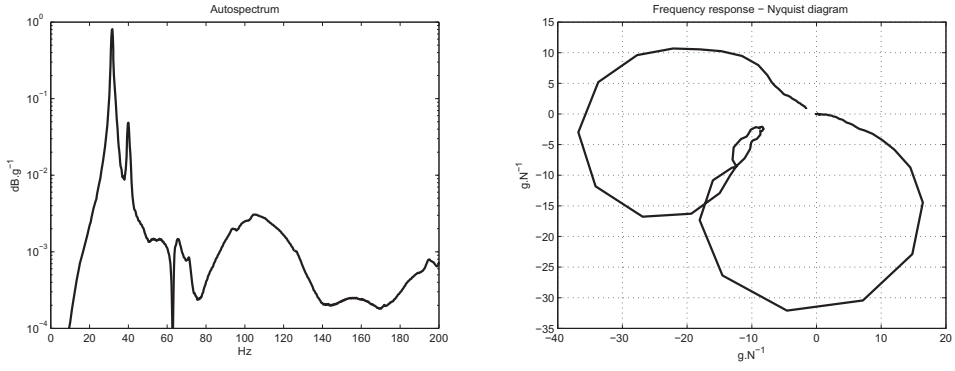

Fig. 4: Autospectrum

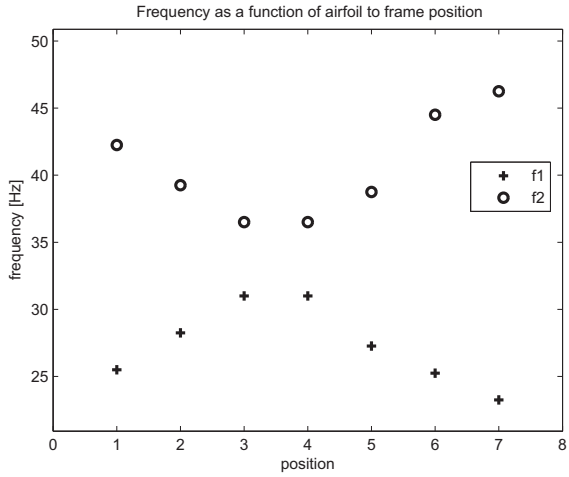

Fig, 5: Natural frequencies as a function of the airfoil to frame position

Table 2: Eigenvalues of the airfoil from the identif cation

Eigenvalue	Real part	Imaginary part
s1	-2.55	201.4
s2	-1.72	250

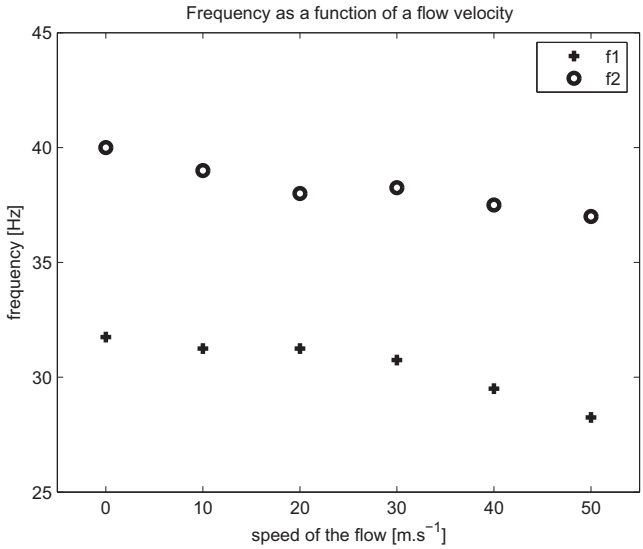

Fig. 6: Natural frequencies of the airfoil as a function of the f ow speed

5 Measurement in the wind tunnel

It has been measured in the wind tunnel in the Institute of Thermomechanics with this prof le. It has been used the wind tunnel operating at highest velocity of the f ow approximately $50 m.s^{-1}$. The f ow speed was not set up directly, but it was calculated from the pressure difference. This measurement has prooved also a feasibility of the experiment. The conf guration of the experiment has been tested with good results. The airfoil can be excited with a modal hammer, moreover there is a space for vibrator in a case of need.

During the f rst experiment it has been measured the frequency spectrum of the prof le as a function of the f ow speed. The angle among the f ow and the airfoil was set to $\alpha = 0 rad$. It has been changed the f ow speed with the difference $\Delta v = 10 m.s^{-1}$ in the range $v \in (0, 50) m.s^{-1}$. It has been used the same devices Brüel & Kjær as in the laboratory of dynamics. The results are shown in the Figure 6.

It has not been reached the f utter during this f rst measurement with the limit speed of the f ow $u_\infty = 50 m.s^{-1}$. It was not possible to increase the f ow speed, moreover the method, which will be used for the f ow f eld mapping, PIV (particle image velocimetry) needs for correct results speed of the f ow no more than $30 m.s^{-1}$. It should be done some structural changes on the stand to change its modal properties, either to replace the leaf springs with another type or to add some mass.

6 Conclusions

This paper describes current situation about the new prof le NACA 0012 in the Institute of Thermomechanics. There are two parallel parts of research, one focuses on the experiments both in the laboratory of dynamics and vibration and in the wind tunnel, the second one concentrates on the numerical simulation. One of the global aim of the experimental branch is to set up self-feeding oscillation (f utter) and to measure the transient f ow f eld during this motion. The numerical part consists of correct identif cation and f uid-structure interaction problem simulation. The mathematical model ot the wing is in good agreement with the measurement.

Acknowledgement

The research was supported by the project of the Grant Agency of the Czech Republic by the project No. 101/09/1522 of the Grant Agency of the Czech Republic „Experimental research of unsteady f ow patterns around vibrating airfoil with application in aeroelasticity“.

References

Dowell, E.H. (1995), *Modern Course in Aeroelasticity*, Kluwer Academic Publishers, Dodrecht

Uruba, V., Jonáš, P., Tsymbalyuk, V. (2009), *Navrh experimentalniho zarizeni pro vyzkum nestacionarniho proudeni v okoli kmitajiciho prof lu*, Interaction and Feedbacks 2009, Praha.

Horacek, J., Kozanek, J., Luxa, M., Vanek, F., Vesely, J., Vlcek, V. (2005), *Experimentalni vyzkum nestacionarnich aeroelastickych jevu optickymi metodami.*, Research Report No. Z 1369/05, Institute of Thermomechanics AV CR, Praha.

Horacek, J., Kozanek, J., Vesely, J. (2005), *Dynamic and stability properties of an aeroelastic model*, Engineering Mechanics, pp. 413-424

18th International Conference
ENGINEERING MECHANICS 2012
Svratka, Czech Republic, May 14 – 17, 2012

pp. 531–536
Paper #300

FATIGUE CRACK GROWTH AND DELAMINATION IN FIBER METAL LAMINATE (GLARE) DURING LOADING WITH POSITIVE MEAN STRESS

A. Chlupová[*], V. Kozák[**]

Abstract: *The aim of the paper is to present the results of a study on the damage of fiber metal laminate (GLARE) subjected to the low cycle fatigue loading with positive mean stress. The fatigue crack initiation and growth was observed on the surface of notched specimens and then the individual layers of fatigued specimens were removed by chemical etching and polishing to obtain data about cracks length and delamination shape and area. Mechanism of initiation and crack growth in this type of materials differs from homogeneous monolithic materials. The fatigue life in term of number of cycles to crack initiation depending on amplitude of local plastic deformation and local stress in the notch root was evaluated.*

Keywords: ***Fatigue, laminate, crack initiation, crack growth, delamination***

1. Introduction

Fibre metal laminates (FMLs) were developed at Delft University of Technology in Netherlands (Roebroeks 1991). These hybrid laminates consist of fibre reinforced plastic layers, so-called prepregs alternating with metal sheets of aluminium alloy. This combination connects outstanding fatigue resistance and high strength properties of glass fibre composite and ductility of metal layers.

FMLs can be strengthened by different kinds of fibres (Chlupova 2002). Material in this study with commercial name GLARE contains as reinforcing fibres the high strength S-glass fibres. For the metal sheets, the aluminium alloy 2024-T3 of thickness 0.4 mm is used (Prasilova 1998).

The concept of hybrid materials was developed primary for aviation applications (Vasek 1999) and presently is used as a fuselage of Airbus A380 (Hinrichsen 2002); nevertheless it can have very wide range of employment as a material for automotive and ship industry, wind power plants, sports, up to unusual applications such as manufacturing of music instruments or prosthesis in medicine.

FMLs possess different kinds of properties and their anisotropy allows tailoring material exactly according to the stress-strain fields acting in particular structural part (Chlupova et al. 2001). Basic mechanical properties such as strength and stiffness are comparable to conventional materials. The other properties like impact and fire resistance, formability, manufacturability, reparability, weight savings, low costs of production etc. offer in many cases significant advantages and are in the centre of attention (Yaghoubi 2012, Moussavi-Torshizi 2010, Park 2010). The drawback of this material can be seen in the lack of knowledge, i.e. due to insufficient data and information about material characteristics the designers aren't able to make the right decisions at design of structural parts and hesitate to apply FMLs for broader industrial applications.

The aim of this work is to present results obtained at study of fatigue properties of one kind of FML. Contrary to the monolithic metal materials the GLARE exhibits among others longer fatigue life and extremely elongated stadium of fatigue crack propagation which makes this material safer and damage tolerant. Zehnder in his work compared two types of materials: 1) homogeneous material and 2) layered material made of metal and plastics laminas without fibres, show that plastic layers operate as a barrier and a kind of bridging element (Zehnder1997). The glass fibre layers in GLARE can

[*] Ing. Alice Chlupová, Ph.D.: Institute of Physics of Materials, Academy of Sciences of the Czech Republic, Žižkova 22; 616 62, Brno; CZ, e-mail: prasil@ipm.cz

[**] Ing. Vladislav Kozák, CSc.: Institute of Physics of Materials, Academy of Sciences of the Czech Republic, Žižkova 22; 616 62, Brno; CZ, e-mail: kozak@ipm.cz

therefore even more improve the mentioned barrier and bridging effect. Glass fibre layers have very positive effect on postponing of initiation and on retardation of propagation of already initiated fatigue cracks. This fact elongates efficiently fatigue life and increases safety of structural parts made of this kind of material (Prasilova 1998).

2. Experiment

Material used for investigation: GLARE 2 have unidirectional fibre orientation. Flat specimens having dimensions 200x50mm and thickness: t = 1.4, 3.1 and 6.5 mm (i.e. with number of layers 3/2, 6/5 and 12/11) were provided with different kind of notches: specimens with central semicircular or circular notch or two side shallow notches with stress concentration factor K_t = 1.2, 2.4 and 3.2.

The cyclic loading was performed in force control regime, i.e. different levels of stress amplitudes were chosen with parameter of asymmetry of R = 0.04. Specimens were loaded by computer controlled servohydraulic testing machine MTS 880 at room temperature. Maximum applied stress in cycle σ_{max} varied from 90 to 450 MPa in individual test.

Fatigue crack initiation and growth was observed in-situ on the surface of notched specimens. The surface metal layer at the notch root area was mechanically grinded and polished before the loading to facilitate observation of crack initiation and growth. Observation and measurement of crack length during loading was performed using microscope QUESTAR QM-100 and CCD camera. The data acquisition during loading was performed. Loading was terminated at length of surface layers about 10 mm or at number of cycles 10^6. After test termination the destructive analysis was performed. Individual layers of laminate were removed by means of chemical etching and mechanical grinding and polishing. A level of material degradation inside of laminate was evaluated (i.e. for cracks the number, length, place and direction of growth were investigated; for delamination the size and shape were assessed).

3. Results

FMLs are very complex material which means that damage in this type of material is even more complex problem. The damage can occur at different levels as is seen in *Fig. 1*.

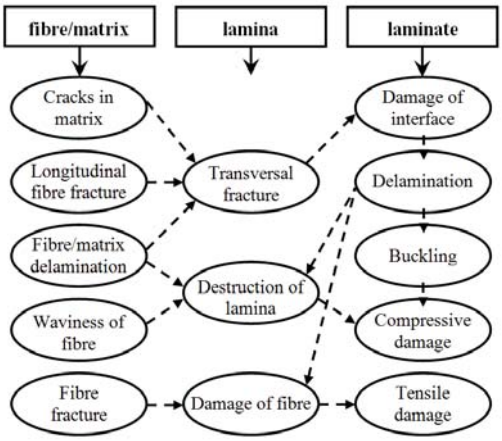

Fig. 1: Different types and levels of damage in hybrid laminates.

Mechanism of initiation and crack propagation differs from the mechanism of initiation in homogeneous monolithic materials. Fatigue cracks initiate first in metal layers in inner layers of laminate. The cracks initiated always at metal prepreg interface even in case of surface metal layer. The latest is the initiation in surface layers nevertheless the crack growth on surface of specimen was the fastest. The crack front in FMLs is not continuous, it is created by crack fronts in individual layers laying usually not in one plane and with the maximum length on the surface of specimen. It is

different from the crack front in monolithic metal materials where it is continuous, in one plane and curved with maximum length inside of material.

The initiation place is usually under some angle from the notch root (*Fig. 2a*). The deflection depends on the type of notch and applied stress (in case of central circular hole it was about 7 to 12 degree at lower applied stresses and 5 to 20 degree for higher applied stresses). The wide range of deflection angles of crack initiation place is connected mainly to: 1) fibre structure with intact fibres directly in the notch root which prevent crack initiation and 2) cut fibres acting as defects are situated at certain angle. Between areas of continuous and cut fibres i.e. outside the notch root there is a high level of shear stress on fibre-matrix interface and high level of interlaminar elastic and plastic deformations. The initiation in the notch root is therefore less probable (see *Fig. 2b*).

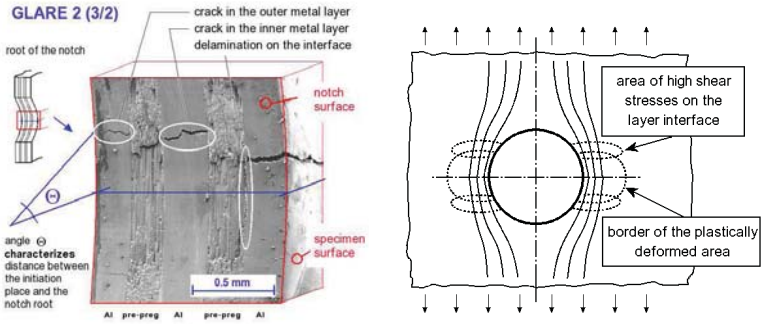

Fig. 2: a) Deflection of crack initiation angle and b) shear stress in the fibre reinforced lamina with circular notch.

Shortly after initiation the cracks are radial i.e. they grow perpendicularly to the edge of the notch. After some propagation period (approximately when cracks reach length corresponding to the notch radius) the cracks deflect to the direction perpendicular to applied loading. From comparison of situation inside and on surface of laminate it is obvious that number of cracks in metal layers inside of laminate is bigger and crack length is smaller.

Number of cycles to crack initiation N_{in} and to elongation to defined length N_f were evaluated in dependence on applied stress level. Obtained results for different notch and different thickness of specimens from unidirectional material GLARE 2 are shown in *Fig. 3*.

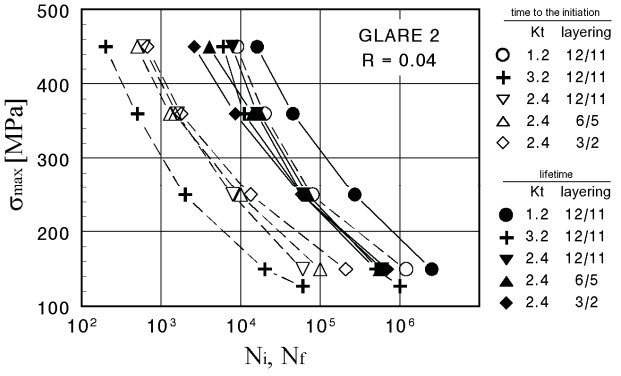

Fig. 3: Number of cycles to crack initiation and up to end of testing for specimens with different lay-up and different notches.

Measured data were then used for finite element method calculation of local plastic deformation in the notch root ε_{pl}. At calculations in 2D analysis by means of ABACUS software the elasto-plastic behaviour of metal layers and internal stresses in unidirectional laminate GLARE 2 were taken into account (Chlupová, 2001). A plastic deformation in metal layers was calculated according to experimentally measured monotonic hardening curve of aluminium alloy 2024-T2, the residual

stresses caused by laminate preparation method were taken into account. Results of FEM calculations of plastic deformation for specimen with central circular notch are graphically represented in *Fig. 4*.

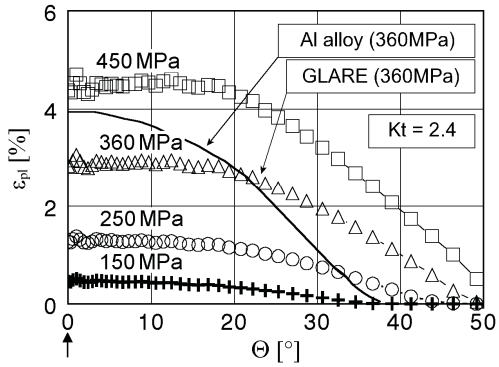

Fig. 4: Results of FEM calculations for specimen with central circular notch.

Calculated amplitude of local plastic deformation in aluminium layers in the notch root was then displayed in dependence of number of cycles to initiation (see *Fig. 5a*). As it is seen from the plot, all data points obtained for different stress concentration factors K_t lie on one curve.

$$\varepsilon_{a,pl,l} = 0{,}036 \cdot N_{in}^{-0{,}214} \tag{1}$$

Amplitude of local plastic deformation in notch root can be therefore considered to be the parameter determining number of cycles to fatigue crack initiation in notched specimens from the material GLARE, similarly like in the case of homogeneous materials (Polák 1991).

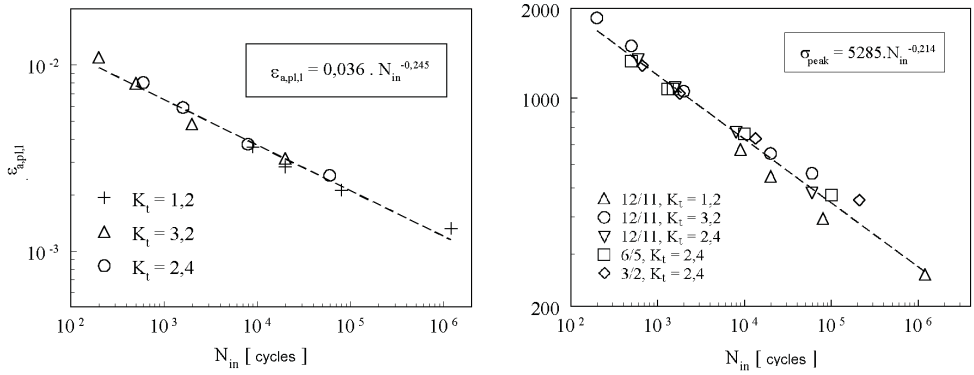

Fig. 5: Dependence of number of cycles to crack initiation (N_{in}) on a) amplitude of local plastic deformation in the notch root and b) local peak stress in aluminium layers the notch root of specimen.

Local plastic deformation in the notch root is induced by local stress σ_{peak}, which is given by maximum applied stress σ_{max}. The value of local stress can be calculated using stress concentration factor in metal layers $K_{t,Al}$ and internal residual stress in metal layers $\sigma_{r,Al}$ as follows:

$$\sigma_{peak} = \sigma_{\max} K_{t,Al} + \sigma_{r,Al} \tag{2}$$

In the Fig. 5b there is the dependence of number of cycles to initiation on calculated local peak stress according to equation (2) for different thicknesses and different notch factors together with approximation of data by power function:

$$\sigma_{peak} = 5285 \cdot N_{in}^{-0{,}214} \tag{3}$$

Relationship between N_{in}, $K_{t,Al}$, $\sigma_{r,Al}$ and σ_{max} given by eq. (2) and (3) explains experimentally observed lower number of cycles to crack initiation in thicker laminates. In laminates with higher number of layers (12/11) due to curing cycle in autoclave the higher tensile residual stress in metal layers are present, i.e it results in higher level of local stress in the notch root σ_{peak} and consequently the lower number of cycles to crack initiation. This trend is more pronounced for lower levels of applied stress σ_{max}.

Delamination is one kind of damage in laminates which is related to crack initiation and growth (see *Fig. 6a*). Delamination for this type of material has nearly elliptical shape. The delamination size can be thus characterised by ratio b/l, where l is crack length and b is the height of delamination in the notch root. These two parameters are also axis of "half-ellipse" which can be used as a good approximation of delamination shape. The appearance of delaminated areas on the resin rich surface of prepreg after removing of metal layer with four cracks in specimen loaded at maximum applied stress 450 MPa are exhibited in *Fig. 6b*.

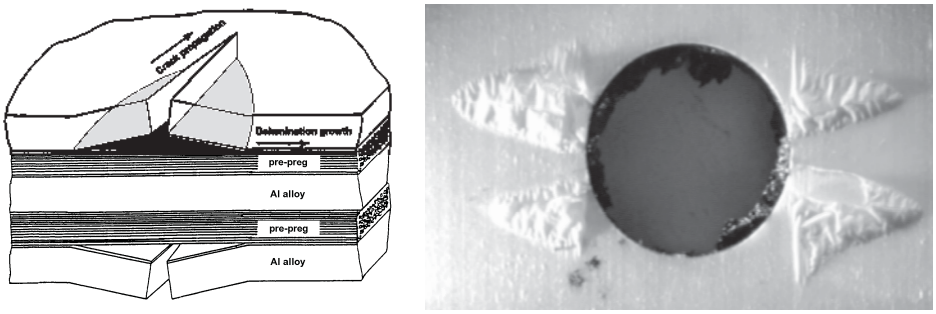

Fig. 6: a) Scheme of relationship between crack growth, delamination and fibres bridging the opening crack; b) real shape and range of delamination.

As soon as the crack in metal layer is initiated simultaneously the delamination appears as a result of shear stresses on layers interface. The size of delamination depends on many factors such as crack length, crack growth rate, fibres properties and fibres volume fraction but predominantly on quality of adhesion on interface. The presence of delamination of certain size is essential to create optimal conditions for outstanding fatigue resistance; nevertheless a judging of effect of adhesion quality is difficult due to its antagonistic influence on delamination. Strong adhesion results in small delamination. In the extreme: in the case of no delamination, the length of fibres actively acting on crack closure would be so small that crack wouldn't open and crack would stop. On the other hand at these conditions the loading of short part of fibres would be so enormous that it would cause the failure of fibres. The right function of fibres and their bridging effect wouldn't be thus possible. Weak adhesion results in big delamination and significant decrease of bearing capacity. In the extreme: it would cause debonding of laminate along the fibre-matrix interface. In that case the transfer of loading through shear stresses from metal to prepreg layers and vice versa wouldn't be possible.

4. Conclusions

Fatigue behaviour of fibre metal laminates containing as a reinforcing material glass fibres was studied. It was found that FMLs exhibit different mechanism of initiation and growth of fatigue cracks than homogeneous monolithic metallic materials. Cracks initiate first inside of laminate, exhibits shorter period of crack initiation and strongly elongated period of crack growth. Number of cracks initiated from the notch is higher and the place is transferred out of the root of notch.

The situation in inner and outer layers of laminate differs slightly – the initiation in inside layers is earlier, nevertheless the growth is slower than on surface. Prepreg acts as an effective barrier against crack growth from one layer to another. Cracks thus grow separately and independently. Crack growth was monitored in relation to growth direction and growth rate.

Relations for prediction of number of cycles to crack initiation and fatigue life of notched specimens from laminate were specified. The dependence of initiation on local plastic deformation and/or local stress in the notch root of metal layers was evaluated.

The delamination for both types of material (GLARE2 and GLARE 3) was found to be dependent on type of material, crack length and location in the metal-prepreg interface closer or farther from the specimen surface.

Delamination area is proportional to crack length, which induced it. Range of delamination is affected by level of shear stresses at metal-prepreg interface. It was found that the shape of delamination in material GLARE can be approximated by an ellipse. The higher is the level of maximum applied stress the higher range of delamination it evokes. The proper function of laminate, i.e. bridging effect of reinforcing fibres on growing crack, can be assured only by optimum strength of adhesion which causes suitable delamination area.

Acknowledgement

Financial support of projects GACR 106/09/1954 and RVO 68081723 is acknowledged.

References

Chlupova, A. (2001) Fatigue behavior of laminate composites, *Ph.D. Thesis*, Technical University of Brno.

Chlupova, A., Heger, J., Vasek, A. (2001) Fatigue crack initiation and early growth in GLARE 3 fiber metal laminate subjected to mixed tensile and bending loading. *Acta Polytechnica* Vol. **41**, pp: 33–36.

Chlupova, A. & Dymacek, P. (2002) Mechanical behaviour of hybrid laminates with carbon fibers. *Metallic Mater.* Vol. 40, pp. 195–208.

Hinrichsen, J. (2002) The material down-selection process for A3XX , *Around Glare: A new aircraft material in context*, pp 127-144.

Moussavi-Torshizi, S.E., Dariushi, S., Sadighi, M., Safarpour, P. (2010) A study on tensile properties of a novel fiber/metal laminates, *MatSciEng A*, Vol. 527, pp: 4920-4925.

Park, S.Y., Choi, W.J., Choi, H.S. (2010) A comparative study on the properties of GLARE laminates cured by autoclave and autoclave consolidation followed by oven postcuring, *Int. Journal of advanced manufacturing technology*, Vol. 49 pp: 605-613.

Polak, J. (1991) *Cyclic Plasticity and Low Cycle Fatigue Life of Metals*, Academia, Praha.

Prasilova, A. & Vasek, A. (1998) Retarding effect of reinforcing fibers on early crack growth in fatigued notched laminate GLARE2, *Engineering Mechanics*, Vol. 5, No.3, pp. 219-223.

Roebroeks, G.H.J.J. (1991) Towards GLARE – the development of a fatigue insensitive and damage tolerant aircraft material. *Ph.D. Thesis*, Delft University of Technology.

Vasek, A., Dymacek, P. & Vogelesang, L.B. (1999) Fatigue strength of L610-P wing-fuselage attachment lug made of glare 2 fibre-metal laminate, *Fatigue design and reliability*, Vol. 23, pp: 73-81.

Yaghoubi, A.S., Liu, Y., Liaw, B. (2012) Stacking Sequence and Geometrical Effects on Low-Velocity Impact Behaviors of GLARE 5 (3/2) Fiber-Metal Laminates, *Journal of thermoplastic composite materials* Vol. 25 pp: 223-247.

Zehnder, A.T., Swenson, D.V., Pienkos, T.J. (1997) Polymer reinforcements for retarding fatigue crack growth in metals, *International journal of fracture*, Vol. 84, pp: 307-323.

18th International Conference
ENGINEERING MECHANICS 2012
Svratka, Czech Republic, May 14 – 17, 2012

pp. 537–541
Paper #223

EXPERIMENTAL MEASUREMENT OF FULL-FIELD STRAINS IN THE VICINITY OF U-NOTCH IN DUCTILE MATERIAL

I. Jandejsek[*], O. Jiroušek[**], D. Vavřík[***]

Abstract: *The paper deals with the measurement of full-field displacements and strains evolution in the vicinity of the U-notch in the flat high-ductile aluminum specimen during its loading. The full-field displacements are measured using Digital Image Correlation method in a set of vertices of a triangular mesh reflecting the presence of the stress concentrator. From the known displacements strain distribution is computed. The resulting strain field is compared with simultaneous strain gauge measurement. These strain gauges are located just in a few well-defined positions and serve for correction of a systematical error caused by rigid-body motion of the specimen during loading. The experimental results are used as referential for Finite Element simulation using the same triangular mesh.*

Keywords: ***Full-field strain measurement, DIC, fracture mechanics.***

1. Introduction

Precise experimental measurement of strain/stress distribution in the vicinity of sharp notches and cracks in high ductile metals such as aluminum alloy is necessary for reliable determination of physical processes accompanying fracture evolution. Intensities of elastic and plastic deformations can be used for validation of different fracture toughness approaches, verification of FEM models and determination of a suitable material model. Nowadays experimental optical methods provide full-field measurement of displacements and strains of the specimen analyzed. One of these methods is an image processing technique generally known as Digital Image Correlation (DIC), [Peters, 1982]. The technique utilizes a sequence of images that represents a process of a specimen surface deformation. In this sequence DIC observes displacements of individual templates of some pattern employing a correlation technique. The template is a small rectangular part of the pattern that contains a distinguishable distribution of gray-scale intensities. Displacement field obtained from this method is utilized for consequent calculation of the strain fields. However, it turns out that the DIC method is error prone when the specimen undergoes even slight rigid body rotations and displacements changing camera-specimen distances during the test. In such cases the consequent changes in magnification cause systematical errors in measured strains. In this study combination of simultaneous optical and strain gauge measurement was employed for correction of this error.

One of the DIC method advantage is that one can define an arbitrary grid of vertices at which the particular displacements are measured. Therefore it is beneficial to use the same DIC measurement grid as it is used in the FEM numerical model. This allows direct and easy comparison between experimental and FEM results. The identical linear triangular mesh was employed for both experimental DIC measurement and numerical model in this study. Results obtained by both techniques show a very good correlation.

[*] Ing. Ivan Jandejsek: Institute of Theoretical and Applied Mechanics AS CR, v. v. i., Prosecká 809/76; 190 00, Prague 9; CZ, e-mail: jandejs@itam.cas.cz

[**] Doc. Ing. Ondřej Jiroušek, PhD.: Institute of Theoretical and Applied Mechanics AS CR, v. v. i., Prosecká 809/76; 190 00, Prague 9; CZ, e-mail: jirousek@itam.cas.cz

[***] Ing. Daniel Vavřík, PhD.: Institute of Theoretical and Applied Mechanics AS CR, v. v. i., Prosecká 809/76; 190 00, Prague 9; CZ, e-mail: vavrik@itam.cas.cz

2. Experiment

A high ductile Aluminum alloy (ČSN 424415.21) 2 mm thick flat specimen with a symmetric central slit (MT configuration) was employed for the fracture experiment. The stress-strain diagram of the material obtained from conventional tension test, chemical composition of the material and its mechanical properties are summarized in Fig. 1. The geometry of the specimen is depicted in Fig. 2. The U-notch was pre-machined by spark out technology and its radius was 150 μm. It is very difficult to obtain a sharp pre-crack in such ductile material. Conventional fatigue method here fails because of large plasticity that develops during cycling.

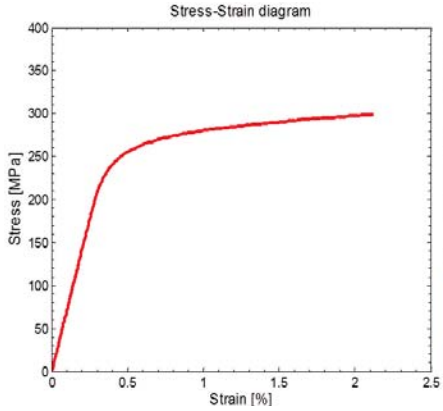

Al-alloy
(ČSN 42 4415.21)

Chemical composition [%]

Al	Cu	Mg	Mn	Si	Fe	Ti	Zn	Cr
94,61	0,03	4,79	0,14	0,12	0,21	0,02	0,01	0,02

Mechanical properties

Modulus of Elasticity E [Mpa]	Poisson ratio ν	Yield point $R_{p0.2}$ [Mpa]
70 600	0,3	252

Fig. 1: Mechanical parameters of the material.

The speckled pattern (black background, white speckles) used for DIC measurement was prepared on one side of the specimen using an airbrush gun. Three strain gauge rosettes (0/45/90) were installed in the well-defined positions on the opposite side of the specimen; see Fig. 2. These positions were selected for precise measurement of the nominal strains in sufficient distance away from concentrator, where the assumption of relatively homogenous strains is valid. The strain gauges were primary installed to correct influence of rigid body motions for DIC measurement. Such movements which change distance camera-specimen are reflected in the DIC measurement as a systematic error. This systematic error has the form of a linear surface; therefore the error can be subtracted from the knowledge of the correct strains measured at least in three non-collinear positions.

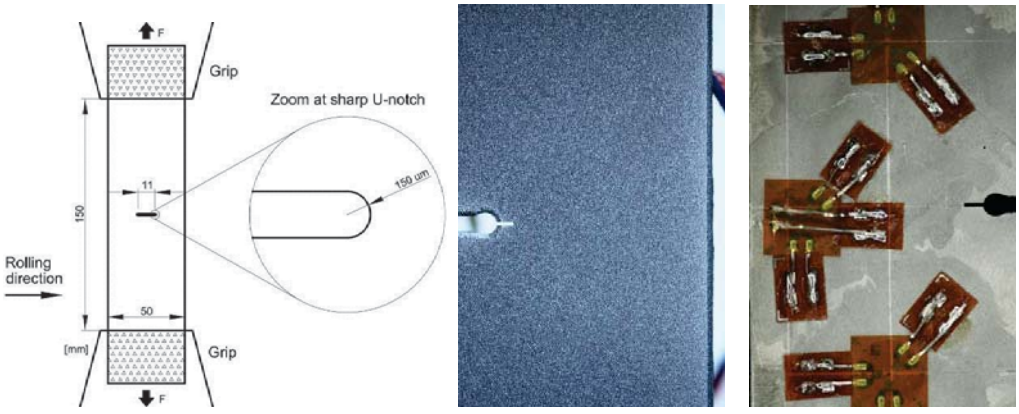

Fig. 2: Geometry of the specimen tested (left). Speckled pattern for the DIC measurement prepared on the front side of the specimen that was optically observed (middle). Three strain gauge rosettes installed on the opposite side of the specimen, right.

The specimen was subjected to uni-axial tension loading (opening mode I) under the condition of constant grip displacement velocity 1 mm/min. Remote force F was measured by a 50kN load cell with read-out frequency 1 Hz. The resulting load vs. grip displacement diagram is show in Fig. 3. The speckled surface was optically observed during the test. The images were acquired by a 15 MPixel

camera (Canon EOS500D, Canon Inc., Japan) and a macro-lens (Canon Ultrasonic EF 180mm f/3,5 L, Canon Inc., Japan) with frequency 1 image per 5 sec. during loading until the macroscopic fracture occurred. The surface of the specimen was illuminated by circular diffusion light due to avoidance of reflection artifacts. Images were stored in 3168x4752px RAW format and transformed to gray-scale color space. The experimental setup is shown in Fig. 3.

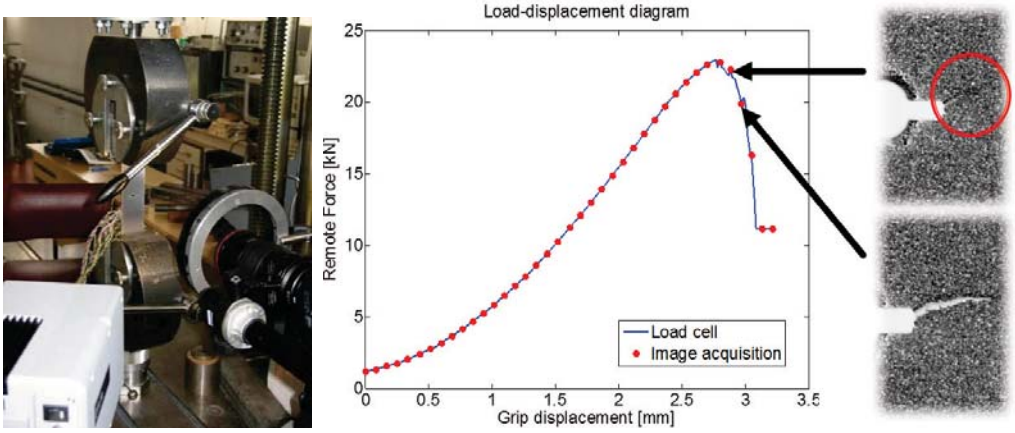

Fig. 3: Experimental setup from the front view (left). The loading diagram: remote force versus grip displacement, red circles highlights the states at which the images were acquired (right).

2.1. DIC measurement vs. FEM model

Our own Digital Image Correlation (DIC) system [Jandejsek, 2010] was employed for evaluation of the full-field displacements. A triangular mesh was generated in the ANSYS system using linear triangular (PLANE42) elements. Vertices of the triangular mesh were used as the input points at which displacements were measured using the DIC algorithm. The mesh was adjusted to reflect the presence of the stress concentrator. The FEM model is shown in Fig. 4 (one half of the specimen due to symmetry) with enlarged part of the mesh that was used for DIC measurement (only this part was optically observed).

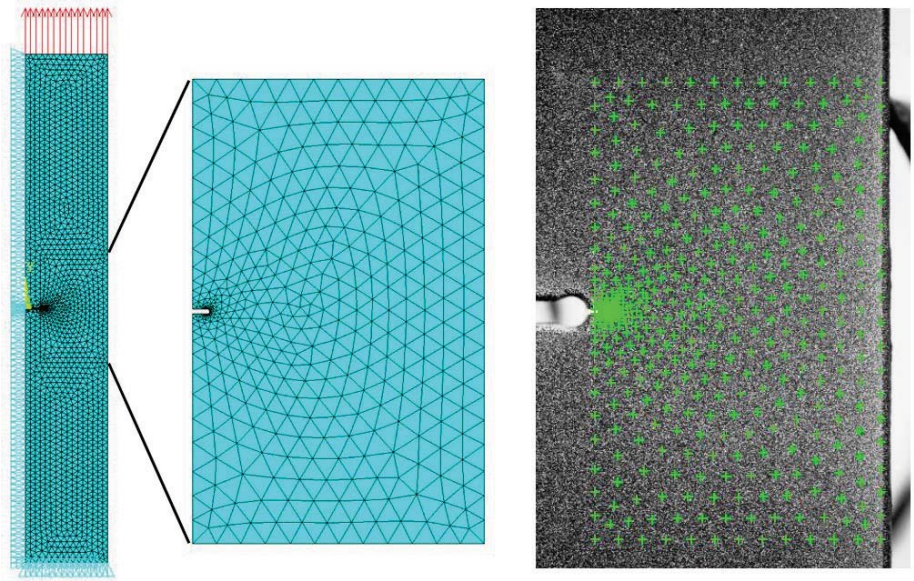

Fig. 4: The FEM model with the generated triangular mesh in the ANSYS (left). Part of the mesh used as the measurement grid for the DIC method (right).

From the known nodal displacements, strain tensor at every triangular element was computed. For more accurate evaluation of the strains from measured displacements which are unavoidable noisy, a smoothing procedure based on spline function approximation was used. Due to the presence of relatively large strains at the vicinity of the notch tip, the finite Green-Lagrange strain tensor was used instead of conventional infinitesimal (small) strain tensor. The Green-Lagrange strain tensor is defined as:

$$\varepsilon_{G-L} = \frac{1}{2}\left(F^T F - I\right) \tag{1}$$

where F is the deformation gradient obtained from affine transformation of a particular triangle of the mesh. The full-field nominal strains ε_1, ε_2 were than corrected using values of measured strains from the strain gauge rosettes. The resulting contour plots of the nominal strains ε_1, ε_2 of the elastic-plastic state at remote force 16,81kN before and after strain gauge corrections are shown in Fig. 5 and Fig. 6. There is an asymmetry clearly visible in the ε_1 field. This assymetry inducted by material non homogeneity or geometry imperefection was latery pronounced by the direction of the crack propagation, compare with Fig. 3.

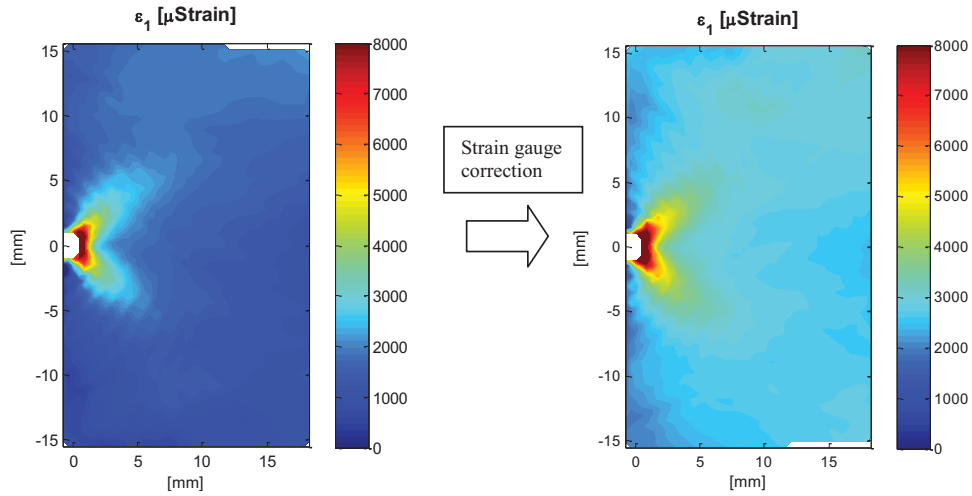

Fig. 5: Nominal strains ε_1 [μ-Strain] in the vicinity of the notch measured by the DIC method at the state of remote force 16.81kN, without strain gauge correction (left), after correction (right).

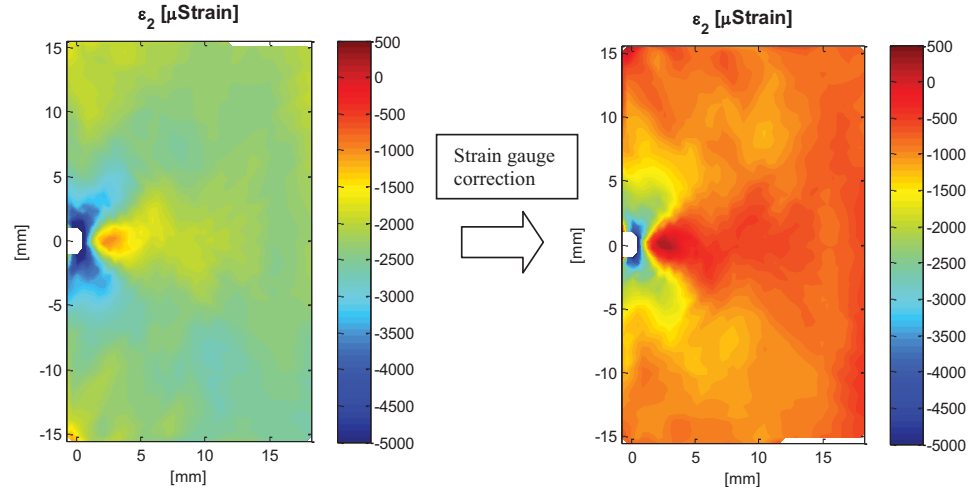

Fig. 6: Nominal strains ε_2 [μ-Strain] in the vicinity of the notch measured by the DIC method at the state of remote force 16.81kN, without strain gauge correction (left), after correction (right).

Subsequently, the numerical model using the same triangular mesh as in the experiment was computed by FEM in ANSYS system. Due to the symmetry only half part of the specimen was modeled. The problem was considered as plane stress with thickness and the multi-linear material model based on experimental data obtained from conventional tension test was used. The resulting contour plots of the FEM results at the force 16,81kN are shown in Fig. 7. Strain field is symmetric due to symmetric FE model. It can be seen that the field ε_2 obtained by FEM shows more localized deformations than the experimental result, compare with Fig. 6. It is explained by using the smoothing procedure in DIC measurement. It will be solved by using a more adoptive filter in the future work.

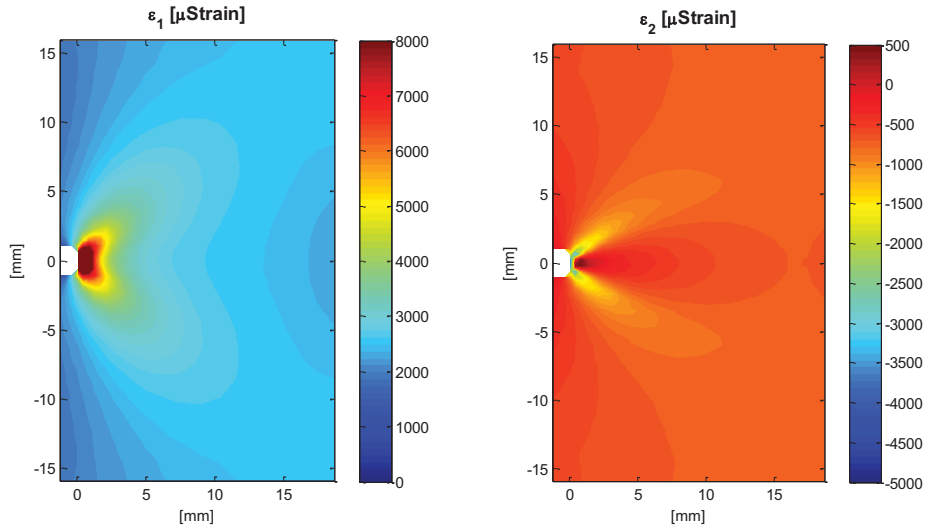

Fig. 7: Nominal strains ε_1 (left) and ε_2 (right) [μ-Strain] in the vicinity of the notch computed by FEM at remote force 16.81kN.

3. Conclusions

It can be concluded, that the above described enhanced DIC method in conjunction with the strain gauge measurement enables precise measurement of the full-field strains. The full-field nominal strains were successfully evaluated in the vicinity of the U-Notch in the thin plate of the high-ductile aluminum alloy. With the help of three non-collinear strain gauge rosettes the measurements were corrected for the rigid body movements. Correlation for the rigid-body movement of the specimen during the experiment was found to be very important and limiting aspect of such measurements when strains are measured using a DIC applied to the surface of the specimen. Displacements were measured in a triangular FE mesh to enable direct comparison with FE results. The comparison with the FEM model proved that method is sufficiently accurate to measure both elastic and plastic deformation.

Acknowledgement

The research has been supported by Grant Agency of the Czech Republic (grant No. P103/09/2101).

References

Peters, W.H. & Ranson, W.F. (1982) Digital imaging techniques in experimental stress analysis. *Opt Eng 21*, pp.427-431.

Jandejsek, I., Valach, J. & Vavřík, D. (2010) Optimization and Calibration of Digital Image Correlation Method, in: *Proc. Experimental Stress Analysis 2010*, Olomouc, pp.121-126.

Jandejsek, I., Vavřík, D. (2011) Experimental Methods for Evaluation of the Energy Balance in Vicinity of the Crack, in: *Proc. Experimental Stress Analysis 2011*, Olomouc, pp.135-138.

18th International Conference
ENGINEERING MECHANICS 2012
Svratka, Czech Republic, May 14 – 17, 2012

pp. 543–549
Paper #206

LARGE-SCALE MICRO-FINITE ELEMENT SIMULATION OF COMPRESSIVE BEHAVIOR OF TRABECULAR BONE MICROSTRUCTURE

O. Jiroušek, P. Zlámal *

Abstract: *Microstructural finite element analysis has become a standard technique for evaluation of mechanical properties of trabecular bone. Due to the high complexity of the trabecular bone microstructure, the FE models have a very large number of elements (about 1 million elements per cubic cm in 50 μm^3 resolution). To perform FE analysis of the microstructural FE models based on micro-CT scanning of whole bone samples (e.g. vertebral bodies) it is needed to solve 10^7 – 10^8 equations. This article deals with comparison of approaches using voxel-based microstructural FE models to calculate the overall mechanical properties of trabecular bone.*

Keywords: ***voxel FE models, elastic properties, trabecular bone, parallel computing, MPI***

1. Introduction

Inverse estimation of material properties (namely stiffness and strength) of trabecular bone using FE models of its microstructure is important not only as a nondestructive tool for early prediction of osteoporotic fracture, but can be successfully applied in other research areas, e.g. in animal models to study effect of various growth factors on bone formation.These microstructural FE models are used to perform a numerical simulation of mechanical experiment. Usually, the micro-FE model is subjected to unit load in three mutually perpendicular directions and elastic constants are determined from the 'virtual experiment'.

With the growth of computer power of today's computers it is now possible to solve large systems of algebraic equations arising from discretization of differential equations using the finite element method. This enables to use very detailed FE models of trabecular bone microstructure for inverse determination of their overall mechanical properties [van Rietbergen et al (1999), Niebur et al (2000)]. In these microstructural models, tissue material properties are usually assumed to be isotropic and homogeneous and are determined using either nanoindentation [Rho et al (1997), Zysset et al (1999), Jirousek et al (2011)] or from micromechanical tests performed on individual trabeculae [Jungmann et al (2011), Doktor et al (2011), Lorenzetti et al (2011)].

The early models of the trabecular bone microstructure involved only small volume of the bone [Muller et al (1995)], but solving large number of equations on parallel architectures using either shared [Natarajan (1991)] or distributed memory [Johan el al (1994), Hodgson and Jimack (1997)] architecture enabled to use this inverse modeling to compute the overall stiffness and strength of whole bones [MacNeil et al (2008), Eswaran et al (2007)]. One possibility for FE modeling of whole bones is to use continuum FE models of whole bones [Taddei et al (2004)] with spatially variable material properties, i.e. material properties are prescribed to each finite element based on the tissue density obtained based on the tissue density in the material point [Pahr and Zysset (2009)]. In this case, the inner microstructure is not taken into account and is reflected only by the different density. These FE models are computationally far less demanding, but their ability to reflect the real microstructure as well as changes of the tissue material properties due to metabolic diseases, e.g. deficiency of the bone mineral is at least questionable.

With the advancement of X-ray imaging systems, particularly with growing resolution and physical dimensions of modern X-ray flat panel detectors it is now possible to acquire tomographic images of

*Doc. Ing. Ondřej Jiroušek, Ph.D., Ing. Petr Zlámal: Institute of Theoretical and Applied Mechanics, Prosecká 76, 190 00 Prague 9; CZ, e-mail: {jirousek, zlamal}@itam.cas.cz

whole bones with resolution sufficient to capture its inner structure. These flat panel detectors convert X-ray photons not absorbed by the inspected object into visible-light photons using a scintillating material. A layer of photodiodes converts these photons into electrons which activate corresponding pixels in a layer of amorphous silicone. The activated pixels are used to generate the high-quality, high-resolution digital image in a computer. Modern X-ray flat panel detectors have several megapixel resolution with typical pixel size 50-200 μm.

One possibility to develop the FE model of trabecular bone architecture is to use smooth-boundary tetrahedral models. This technique has been popular in early 1990s but requires extra user intervention to develop these models. Marching Cubes Algorithm [Lorensen and Cline (1987)] is needed to find the surface of the trabecular bone and because of the complexity of the architecture this procedure usually involves user-intervention both in the process of tissue segmentation and in the smoothing/optimization of the surface (triangular) mesh. Moreover, resulting FE models can have even more degrees of freedom than directly generated voxel models.

Easier approach in terms of model development is to convert the segmented 3-D image data to a voxel model. In this procedure, every voxel (spatial pixel) in the sequence of microtomographic images is directly converted to one hexahedral element. It has been shown [Chevalier et al (2007)] that these models can be used for inverse estimation of elastic properties and strength of trabecular bone. Since the procedure to develop a voxel model is quite straightforward it can be used to develop a micro-FE model of whole bones. However, to solve even only a linear static analysis (single solution of a set of linear algebraic equations) large memory is needed to store the sparse system matrix. For example – the volume of an average human vertebral (L4) body is 45×10^3 mm^3. With micro-CT images taken at 50 μm^3 resolution and with average porosity 85%, one gets a FE model with approximately 48 million elements.

In the present study a parallel solution strategy is described for solving such a large problem in parallel utilizing existing open-source programs. Our main aim was to demonstrate the scalability of proconditioned conjugate gradient (PCG) parallel solver for large linear elasticity problems. Two architectures are used, one distributed shared memory (DSM) system (SGI Altix), second shared memory system (Intel Xeon X5560) tested using two problems of different size. The larger problem (rat vertebra) is solved on SGI Altix 4700 series equipped with 56 2-core Intel Itanium-2 processors and SGI's NUMAlink processor interconnect with 288 GB RAM. The smaller problem (sample of human trabecular bone) is solved using a 16-core system based on Intel Xeon X5560 processors with 48 GB RAM. Voxel FE model of rat vertebra is developed based on micro-CT images taken in 50 μm^3 resolution. Total number of unknowns in these models was approximately 14.10^6 and $1{,}7.10^6$, respectively. The models are used for inverse estimation of the rat vertebrae stiffness in the inferosuperior direction and in case of the human bone sample for orthotropic properties inverse calculation.

2. Materials and Methods

2.1. Micro-CT scanning of trabecular bone microstructure

To develop high-resolution micro-FE model of trabecular bone at different resolution, two experiments were performed. In the first experiment, only a cylindrical sample has been extracted from human proximal femur. The sample (diameter 5 mm and height 8 mm) was mounted on a rotating table and placed in a shielded X-ray box. A complete tomography (360 projections, 1° increment) of the sample was performed to capture its microstructure. For the tomographic measurements an X-ray source (Hamamatsu L8601-01 with 5 μm focal spot size) and Medipix-2* (256×256 square pixels, 55×55 μm^2 each) detector were used. Acquired tomographic projections were beam hardening (BH) corrected using a set of aluminum calibrators covering the full attenuation range of the bone specimen using a procedure described in Vavrik and Jakubek (2009).

The second experiment involved scanning whole vertebra. In this case L4 vertebra of a laboratory rat has been chosen. To improve the spatial resolution in this case of a specimen with larger physi-

*Medipix collaboration home page: http://medipix.web.cern.ch/MEDIPIX/

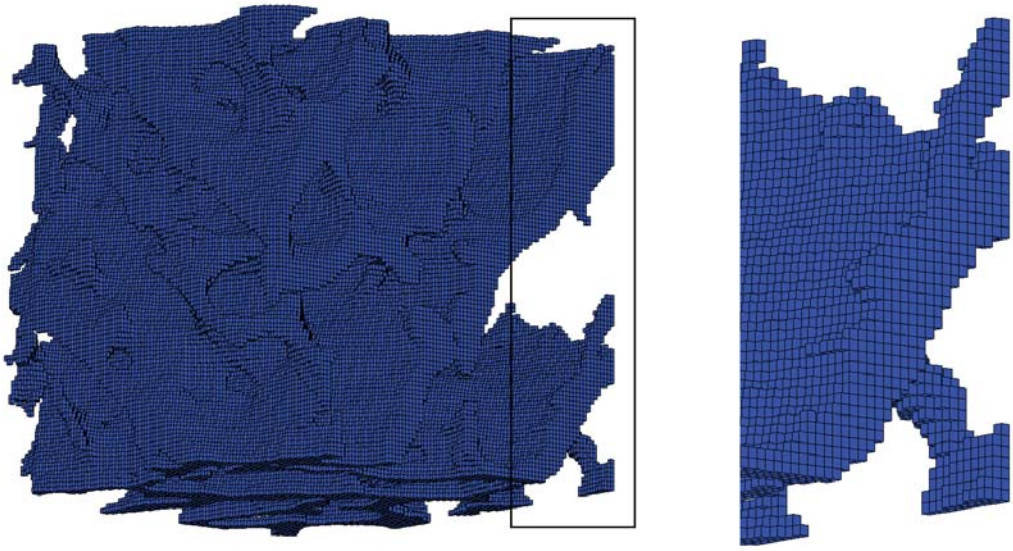

Fig. 1: FE model of the trabecular bone microstructure (left) developed based on the micro-CT image data (100x100x100 voxels) showing the microstructure represented using linear hexahedral elements. Detail (right) showing individual elements.

cal dimensions, a flat panel X-ray detector C7942CA-22 (Hamamatsu Photonics K.K.) with resolution 2368×2240 px and physical dimensions 120×120 mm was used. Scanning sequence consisted of 360 scans with 0.5° step.

2.2. Development of the voxel micro-FE models

The cross-sectional image data were reconstructed from the sinograms using either FBP (filtered back-projection) or OSEM (ordered subsets expectation maximization) methods. Both FBP and OSEM provided similar results with OSEM resulting in more homogeneous background. However, both techniques resulted in a set of images suitable for easy application of segmentation with a global threshold. The threshold value is set automatically based on the Otsu's method with chooses the threshold to minimize the intraclass variance of the black and white pixels [Otsu (1979)].

For the micro-FE model of the vertebra, only a subregion was selected – the cortical shell and internal trabecular structure of the vertebral body was considered. The endplates and the posterior processes has been mathematically removed. These parts were excluded from the inverse computation of the overall stiffness due to simplify the load application and specification of the boundary conditions. Direct conversion from micro-CT volumetric data to voxel micro-FE models requires only setting appropriate threshold to distinguish between the bone and empty space. The threshold value was chosen iteratively using one selected reconstructed cross-section of the vertebra.

2.3. Inverse calculation of the stiffness and strength

To compute the overall stiffness of the vertebral body in the infero-superior direction a unit displacement has been prescribed on the top surface of the vertebral body. The lower surface of the body was fixed (all nodes with minimal z-coordinate were prescribed zero displacements in three directions). Based on our previous nanoindentation results [Jirousek et al (2011)] the tissue-level material properties were prescribed: Young's modulus of elasticity E_{TISSUE}=15 GPa, Poisson's ratio: μ_{TISSUE}=0.2.

From the volume data, 100×100×100 voxels were selected in the middle part for easy comparison of orthotropic elastic properties. The coordinate axes were aligned such as to keep Z-axis in the direction of

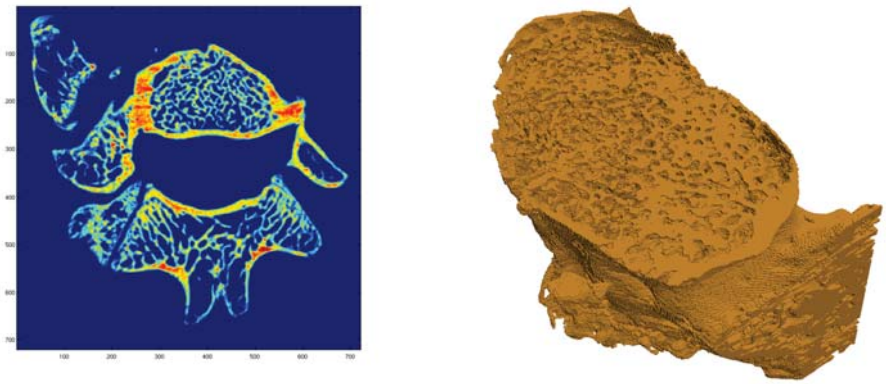

Fig. 2: Cross-sectional image data of the whole rat vertebra and the FE model created from the vertebral body part showing the microstructure represented using hexahedral elements

loading during the experiment. Total number of nodes was 566,790 for the $100\times100\times100$ voxel model and 4,791,142 for the FE model of rat vertebra. Prior the computations, the FE models were verified for mesh connectivity.

2.4. Parallel computation using PCG solver

The critical part of the FE computation of such a large model is the solver. For the current micro-FE analyses of voxel models of trabecular bone is one level element-by-element preconditioned conjugate gradient (EBE-PCG) Hughes et al (1987) considered as the most frequently used solver. The solver takes advantage of the identical size of every element in the voxel model (every element has exactly the same stiffness matrix) and it is very memory efficient (it does not compute the global stiffness matrix) since it requires only a matrix-vector product. However, due to its slow convergence and poor scalability, this solver is efficient only for problems of moderate size (under 1 million elements) and can be successfully used for the solution of small-volume samples of trabecular bone. For large models of whole bones or for nonlinear material models (plasticity) this solver is inefficient. An example of this inefficiency is given in van Rietbergen et al (2003) where linear elastic analysis of a micro-FE model of the proximal femur with 96 million elements using the EBE-PCG solver with a convergence tolerance of 10^{-3} took 25,000 CPU hours (almost 7 weeks of wall-clock time) on 30 processors of an SGI-Origin2000 computer with 250MHz-R10000 processors using 17 GB of memory.

For our computations, PCG solver with 1.10^{-8} tolerance was chosen for all considered FE models [Bangerth et al (2007), Bangerth et al (2011)]. Prior the computations with the largest system (rat vertebra, $\sim15.10^6$ unknowns) the convergence and speedup was tested using smaller FE models. These models were obtained by cutting the trabecular bone microstructure to smaller connected volumes with variable number of degrees of freedom (DOF). The cutting resulted in three FE models: i) small ($\sim$10,000 DOFs), ii) middle ($\sim$400,000 DOFs) and iii) large($\sim$3,000,000 DOFs).

On the SGI Altix 4700 the PCG solver scaled nicely up to 32 CPUs (more CPUs were not tested due to the workload of the computer by other users). Of course, the smallest FE model was not tested for more than 2 CPUs, since the solver took less then 3 seconds to converge on 1 CPU on the SGI Altix and less than 2 seconds on 1 core of Intel Xeon X5560. However, when number of unknows was larger than 100,000 the problems scaled very nicely on the SGI Altix system. As one can see from Tab. 1 the Intel Xeon X5660 system scaled nicely only up to 8 processor cores. Time needed to finish the large model using all 16 CPU cores was even larger when only 8 CPU cores were used. This might be caused by the fact, that the system was not fully-dedicated for the only task and there was no scheduling system available.

Tab. 1: Solver time and speedup for the middle-size model (400,000 DOFs) using PCG solver on SGI Altix 4700 architecture (Intel IA-64 Madison)

number of CPUs	solver time [s]	number of iterations	speedup [-]
1	663	205	1
2	404	250	1.6
4	250	265	2.7
8	106	275	6.3
16	59	286	11.2
32	30	303	22.1

Tab. 2: Solver time and speedup for large model (3,000,000 DOFs) using PCG solver on 16-core shared-memory Intel Xeon X5560 system

number of CPUs	solver time [s]	number of iterations	speedup [-]
1	1194	479	1
2	653	496	1.8
4	366	514	3.3
8	208	525	5.7
16	211	545	5.7

For the large problem, the SGI Altix was tested only from 8 CPUs up, since the NUMAlink architecture does not allow to allocate more than 2 GB RAM per processor and the memory needed for this problem was larger then the limit for smaller number of CPUs when used in parallel.

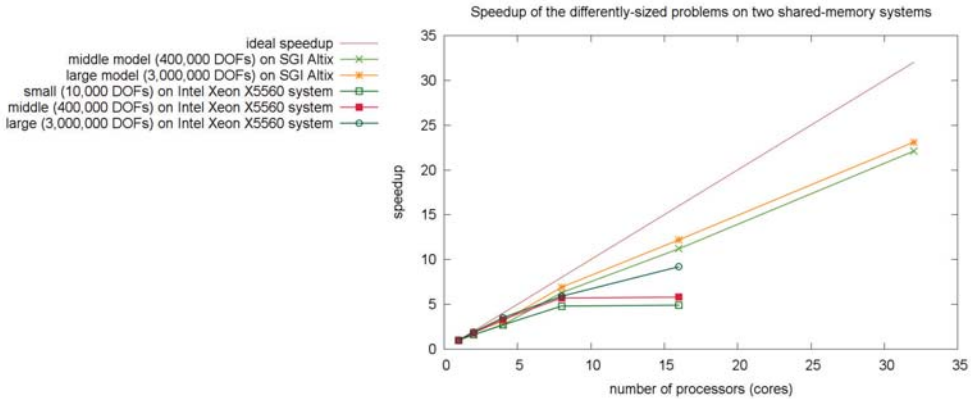

Fig. 3: Speedup of the PCG solver for differently-sized problems on the two architectures

3. Conclusions

In the paper, solution strategy for large-scale FE models originating from micro-CT data of trabecular microstructure of whole bones was presented. These micro-FE models are intended for validation of computationally less-demanding numerical models, but can be successfully used for numerical studies of implant-bone interaction, for studies of different approaches to vertebroplasty or in animal models for verification and comparison of drug treatments.

Results from the FE simulations were written in large ASCII files in both VTK (visualization toolkit, [Schroeder et al (2003)]) and GMV (general mesh viewer, [Ortega (2005)]) formats. The advantage of using VTK format lies in the easy postprocessing with Paraview [Henderson (2007)] which takes advantage of the multicore system (ParaView can be configured for visualization clusters using MPI parallel server on the same machine that is running the GUI).

From the inverse calculation of the orthotropic properties of micro-FE model of trabecular bone sample E_X=1.06 GPa, E_Y=1.97 GPa and E_Z=1.86 GPa were determined with agreement to previously published results, see Jirousek and Zlamal (2011).

Since the memory requirements for the PCG solver are slightly over 1 GB per million DOFs, one can easily compute the maximal number of unknowns solvable on a shared memory system. In our computations, a specialized program for partitioning graphs and FE meshes which produces fill reducing orderings for sparse matrices, METIS [Karypis and Kumar (1999)] was used. One limitation exists for the SGI Altix systems - the memory available for one processor is limited (in our configuration, each processor is eqquipped with 2 GB RAM) and therefore the user must decide how to partition the problem not to exceed the memory available for the single processor. On the other hand, the extensibility of the Altix 4700 is remarkable – the system can contain up to 2048 dual-core Itanium 2 processors (connected by the NUMAlink 4 interconnect) equipped by up to 128 TB of memory.

As a conclusion, it can be stated, that for very-large problems with more than 10 million unknowns the EBE-PCG solver (despite its low memory requirements) is inconvenient due to its slow convergence. In this case, more powerful and more scalable strategy should be employed, such as the Algebraic Multigrid (AMG) solvers, such in Eswaran et al (2007).

Acknowledgments

The research has been supported by RVO: 68378297 and by the Czech Science Foundation (grant No. P105/10/2305).

References

J.-Y. Rho, T. Y. Tsui, G. M. Pharr. (1997), Elastic properties of human cortical and trabecular lamellar bone measured by nanoindentation. *Biomaterials*, Vol 18, No. 20, pp. 1325–1330.

P. K. Zysset, X. E. Guo, C. E. Hoffler, K. E. Moore, S. A. Goldstein. (1999), Elastic modulus and hardness of cortical and trabecular bone lamellae measured by nanoindentation in the human femur. *Journal of Biomechanics*, Vol 32, No. 10, pp. 1005–1012.

O. Jirousek, J. Nemecek, D. Kytyr, J. Kunecky, P. Zlamal, T. Doktor. (2011), Nanoindentation of trabecular bone-comparison with uniaxial testing of single trabecula. *Chemicke Listy*, Vol 105, No. 17, pp. s668–s671.

B. Van Rietbergen, R. Muller, D. Ulrich, P. Ruegsegger, R. Huiskes. (1999), Tissue stresses and strain in trabeculae of a canine proximal femur can be quantified from computer reconstructions. *Journal of Biomechanics*, Vol 32, No 2, pp. 165–173.

G. L. Niebur, M. J. Feldstein, J. C. Yuen, T. J. Chen, T. M. Keaveny. (2000), High-resolution finite element models with tissue strength asymmetry accurately predict failure of trabecular bone. *Journal of Biomechanics*, Vol 33, No 12, pp. 1575–1583.

R. Jungmann, M. E. Szabo, G. Schitter, R. Yue-Sing Tang, D. Vashishth, P. K. Hansma, P.J. Thurner. (2011), Local strain and damage mapping in single trabeculae during three-point bending tests. *Journal of the Mechanical Behavior of Biomedical Materials*, Vol 4, No. 4, pp. 523–534.

T. Doktor, O. Jirousek, D. Kytyr, P. Zlamal, I. Jandejsek. (2011), Real-time X-ray microradiographic imaging and image correlation for local strain mapping in single trabecula under mechanical load. *Journal of Instrumentation*, Vol 6, No. 11 , Art.No. C11007.

S. Lorenzetti, R. Carretta, R. Muller, E. Stussi. (2011), A new device and method for measuring the elastic modulus of single trabeculae. *Medical Engineering and Physics*, Vol 33, No. 8, pp. 993–1000.

R. Muller, P. Ruegsegger. (1995) Three-dimensional finite element modelling of non-invasively assessed trabecular bone structures. *Medical Engineering and Physics*, Vol 17, No. 2, pp. 126–133.

R. Natarajan. (1991), Finite element applications on a shared-memory multiprocessor: Algorithms and experimental results. *Journal of Computational Physics*, Vol 94, No. 2, pp. 352–381.

B. C. Hodgson, P. K. Jimack. (1997), A domain decomposition preconditioner for a parallel finite element solver on distributed unstructured grids. *Parallel Computing*, Vol 23, No. 8, pp. 1157–1181.

Z. Johan, K. K. Mathur, S. L. Johnsson, T. J. R. Hughes. (1994), Scalability of finite element applications on distributed-memory parallel computers. it Computer Methods in Applied Mechanics and Engineering, Vol 119, No. 12, pp. 61–72.

J. A. MacNeil, S. K. Boyd. (2008) Bone strength at the distal radius can be estimated from high-resolution peripheral quantitative computed tomography and the finite element method. *Bone*, Vol 42, No. 6, pp. 1203-1213.

S. K. Eswaran, H. H. Bayraktar, M. F. Adams, A. Gupta, P. F. Hoffmann, D. C. Lee, P. Papadopoulos, T. M. Keaveny. (2007), The micro-mechanics of cortical shell removal in the human vertebral body. Computer Methods in Applied Mechanics and Engineering, Vol 196, No. 3132, pp. 3025-3032.

F. Taddei, A. Pancanti, M. Viceconti. (2004), An improved method for the automatic mapping of computed tomography numbers onto finite element models. *Medical Engineering and Physics*, Vol 26, No. 1, pp. 61–69.

D. H Pahr and P. K Zysset. (2009), A comparison of enhanced continuum FE with micro FE models of human vertebral bodies. *Journal of Biomechanics*, Vol 42, No. 4, pp 455–62.

W. E. Lorensen, H. E. Cline. (1987), Marching Cubes: A high resolution 3D surface construction algorithm. *Computer Graphics*, Vol. 21, No. 4, pp. 163–169.

Y. Chevalier, D. Pahr, H. Allmer, M. Charlebois, P. Zysset. (2007), Validation of a voxel-based FE method for prediction of the uniaxial apparent modulus of human trabecular bone using macroscopic mechanical tests and nanoindentation. *Journal of Biomechanics*, Vol 40, No. 15, pp. 3333–3340.

D. Vavrik, J. Jakubek. (2009), Radiogram enhancement and linearization using the beam hardening correction method. *Nuclear Instruments and Methods in Physics Research Section A*, Vol 607, No 1, pp 212–214.

N. Otsu. (1979). A Threshold Selection Method from Gray-Level Histograms. *IEEE Transactions on Systems, Man, and Cybernetics*, Vol. 9, No. 1, pp. 62–66.

T. J. R. Hughes, R. M. Ferencz, and J. O. Hallquist. (1987), Large-scale vectorized implicit calculation in solid mechanics on a Cray X-MP/48 utilizing EBE preconditioned conjugate gradients, *Computer Methods in Applied Mechanics and Engineering*, Vol 61, pp 215-248.

B. van Rietbergen, R. Huiskes, F. Eckstein, and P. Ruegsegger. (2003), Trabecular bone tissue strains in the healthy and osteoporotic human femur. *Journal of Bone and Mineral Research*, Vol 18, No. 10, pp 1781–1788.

G. Karypis and V. Kumar. (1999), A Fast and Highly Quality Multilevel Scheme for Partitioning Irregular Graphs. *SIAM Journal on Scientific Computing*, Vol. 20, No. 1, pp. 359392.

W. Bangerth and R. Hartmann and G. Kanschat. (2007) deal.II – a General Purpose Object Oriented Finite Element Library. *ACM Transactions on Mathematical Software*, Vol 33, No. 4, pp. 24/1–24/27.

W. Bangerth, C. Burstedde, T. Heister, M. Kronbichler. (2011), Algorithms and Data Structures for Massively Parallel Generic Finite Element Codes. *ACM Transactions on Mathematical Software*, Vol 38, No. 2, pp. 14:1–14:28.

W. Schroeder et al. (2003) The Visualization Toolkit. 3rd Edition. Kitware Inc.

F. A. Ortega. GMV 3.8. General Mesh Viewer Users Manual. (2005), Los Alamos National Laboratory, http://www-xdiv.lanl.gov/XCM/gmv

A. Henderson. (2007), ParaView Guide, A Parallel Visualization Application. *Kitware Inc.*

O. Jirousek, and P. Zlamal. (2011) Microstructural models of trabecular bone -comparison of CT-based FE models. *17^{th} International Conference Engineering Mechanics 2011*, Vol 1, No. 1, pp. 247–250.

18th International Conference
ENGINEERING MECHANICS 2012
Svratka, Czech Republic, May 14 – 17, 2012

pp. 551–555
Paper #205

MEASUREMENT OF STRAINS IN CONCRETE BY INTERFEROMETRIC FIBRE OPTIC SENSORS

D. Jiroutová[*], M. Vokáč[**], P. Bouška[***]

Abstract: *In recent years, fiber-optic technology appeared in measurement technology and sensors. The great advantage of fiber-optic technology is lifespan and measurement which is not influenced by electromagnetic fields. Therefore, the large cable length can be used. For the same reasons, the optic fibers are used in computer networks. A number of physical principles can be used for measuring. In the case of measuring strains in the concrete, a relatively simple and economically favorable principle of low-coherence interferometer can be used. These interferometric extensometers were used to measure strains in the pre-stressed concrete railway sleepers stored in the laboratory. Thus, effects of creep and shrinkage of concrete were monitored. The experiment was supplemented by tests on the accompanying specimens, i.e., the concrete strength, modulus of elasticity and shrinkage and creep measurements. Experimentally obtained data was compared with standard assumptions for the design of concrete structures EN 1992-1-1.*

Keywords: ***Fiber-optic sensor, concrete, strain, shrinkage, creep.***

1. Introduction

The appearance, quality, durability and safety of constructions are the most important parameters for design process in the civil engineering. The structural monitoring during construction and monitoring of reliability and durability of structure use different methods of watching its "health" and their goal is to provide accurate and "in-time" information about structure status. The most frequently monitored parameters in concrete structures are strain, vibration, temperature, displacement and deformation, humidity, cracks opening, etc.

During the life of concrete structures, creep and shrinkage are caused by influences of several processes in material, external loading and environmental condition. These two parameters are variable over time and can significantly influence the final value of the strain. Creep and shrinkage of structures can be calculated through a variety of methods based on evaluations of similar parameters (material properties and surroundings conditions) with different importance. Therefore, it is necessary to choose a suitable prediction method of creep and shrinkage behavior for structure design spatially in case of pre-stressed concrete structure such as a bridge build by cantilever method.

For this reason, displacement and deformation are the most watched parameters in the structures. The monitoring of these parameters can be performed in the short term, middle term, long term or during the whole lifespan of the structures. The whole range of conventional sensors (i.e. strain gauge, videoextensometer etc.) is used for strain monitoring in structures. Selection of appropriate conventional method depends on the application, the measurement range to the desired accuracy and other parameters.

In the last few years, the field of structure monitoring of bridges, tunnels, dams, power stations, stadiums, historic buildings, as well as piping systems, etc., is increasingly utilizing systems based on fiber-optic technologies. Compared to traditional methods, the fiber-optic technology exhibit many advantages such as higher quality measurements, higher reliability, easier installation and

[*] Ing. Dita Jiroutová: Klokner Institute, Czech Technical University in Prague, Šolínova 7; 166 08, Prague; CZ, e-mail: Dita.Jiroutova@klok.cvut.cz

[**] Ing. Miroslav Vokáč, Ph.D.: Klokner Institute, Czech Technical University in Prague, Šolínova 7; 166 08, Prague; CZ, e-mail: Miroslav.Vokac@klok.cvut.cz

[***] Doc. Ing. Petr Bouška, CSc.: Klokner Institute, Czech Technical University in Prague, Šolínova 7; 166 08, Prague; CZ, e-mail: Petr.Bouska@klok.cvut.cz

maintenance, insensitivity to the environment (mainly to the electromagnetic field), corrosion resistance, safety in explosive and flammable environments, the possibility of long-term monitoring and lower cost per lifetime. There is a large variety of fiber-optic sensors working on different physical principles. Results in this article were obtained by fiber-optic sensors working on principle of low-coherence interferometer.

2. Theoretical background

The total strain in concrete structure ε_c consists of strain due to stress ε_σ, shrinkage ε_{SH}, creep ε_d and strain caused by temperature ε_T (1). Strain due to creep and shrinkage is dominant is strain monitoring of pre-stressed structure, therefore, the evaluation of these structure measuring shall take into account these phenomena and the entire job is more complicated. The experimental results led to a number of standards, recommendations and models for calculating the coefficient or creep. The model according to EN 1992-1-1 was chosen for strain course calculation by reason of simple application, adequate accuracy and sufficient number of important parameters.

$$\varepsilon_c = \varepsilon_\sigma + \varepsilon_d + \varepsilon_{SH} + \varepsilon_T \tag{1}$$

Total strain calculated according to model EN 1992-1-1 was compared with experimental data of total strain obtained on monitoring structure. Total strain of monitored pre-stressed sleeper was measured by long-gauge optical fibers SOFO. This type of sensors was chosen by reason of possibility installation them into body of the structure, adequate accuracy and mainly ability of strain measurement along the structure, not only at local point. The SOFO sensor can be used for the whole lifespan structure monitoring without continuous data recording; it is one of their advantages. The SOFO interferometric sensor was developed at the Swiss Federal Institute of Technology in Lausanne and now are manufactured by SMARTEC.

SOFO sensor consists of a measurement fiber and reference fiber installed in the structure. The total strain of the structure is then result in a change of the length difference between these fibers. The low-coherence double Michelson interferometer is used to make an absolute measurement. The first interferometer is made of the PA tube with measurement and reference fibers and the second low-coherence interferometer with mobile mirror is placed into the portable reading unit (Glišić & Inaudi, 2007), Figure 1.

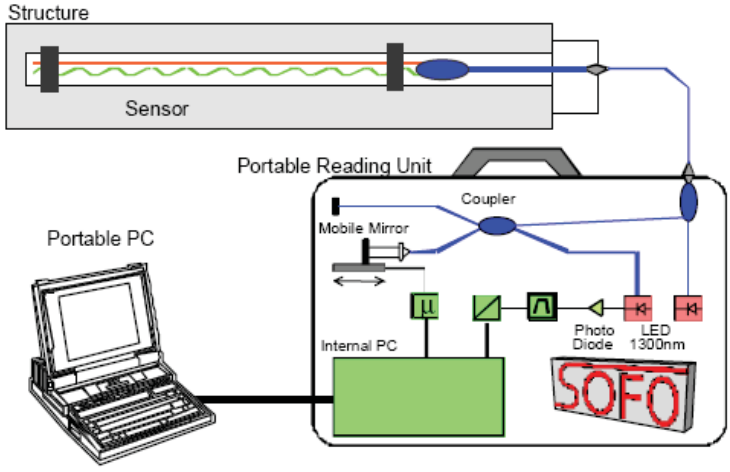

Fig. 1: Setup of the SOFO interferometric sensor system (Inaudi (2004))

3. Experimental

SOFO interferometric extensometers were used to measure strains in the pre-stressed concrete railway sleepers stored in the laboratory conditions. Thus, effects of creep and shrinkage of concrete were monitored. Concreting of two reinforced concrete sleepers B91 S were conducted by the ŽPSV a.s. company in Nové Hrady on September 20, 2010. The fiber-optic extensometers were installed on steel reinforcement of sleepers before casting of concrete. Four fiber-optic extensometers with active length 0,5 m marked with serial number (9088, 9089, 9090 and 9091) were installed on the pre-stressing wires at the center span of sleeper – two extensometers on each sleeper. Location of extensometers is shown on scheme in Figure 2. In addition, two temperature sensors Ni 1000 (see Figure 2) marked with serial number 0301 and the 0302 were also installed. These two pre-stressed concrete railway sleepers were monitoring for 467 days in laboratory of Klokner Institute. Thus, obtained data of total strain was compared with theoretical prediction of total strain calculated according to EN 1992-1-1.

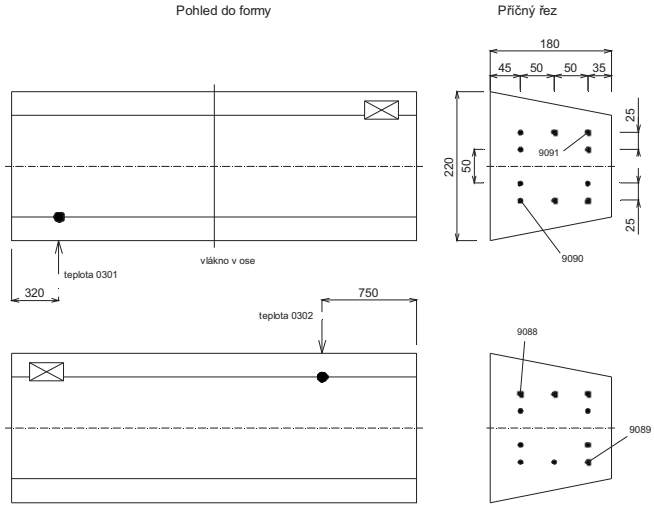

Fig. 2: Location of SOFO fiber-optic extensometers on reinforced concrete sleepers B91 S.

Table 1: Concrete strength determine according to EN 12390

Specimen No.	Specimen diameter [mm]	Specimen high [mm]	Weight [g]	Bulk density [kg·m^{-3}]	Load [kN]	Cylinder strenght f_{cm} [MPa]
Date of the test: 29.9. 2010 – 9 days						
1	149,6	301,0	12979	2453	901	51,3
2	149,4	301,3	12983	2458	1231	70,2
3	150,3	301,5	13011	2432	1193	67,2
Average value:				**2450**		**63,0**
Date of the test: 18.10. 2010 – 28 days						
4	151,3	301,5	13169	2431	701	39,0
5	150,5	301,5	13137	2449	1413	79,4
6	150,0	302,0	13032	2444	1156	65,5
Average value:				**2440**		**61,5**

The parameters of model EN 1992-1-1 for strain prediction were obtained by experiments carried out on fundamental concrete elements (cylinder samples) made from same concrete recipe as monitored structure. Additional necessary experiments were tests of concrete strength, modulus of elasticity tests, shrinkage and creep measurements. Concrete strength was determined according to

EN 12390 on six test specimens at the age 9 days (three test specimens) and 28 days (three test specimens). Test specimens were made from same concrete recipe as the monitored pre-stressed railway sleepers in the same day. Results of concrete strength are shown in Table 1. Next important material parameter is modulus of elasticity. This parameter was determined according to ISO 6784 on the same test specimens as concrete strength. Values of elasticity modulus are stated in Table 2. Average concrete strength and elasticity modulus at the age 28 days were used in creep and shrinkage model according to EN 1992-1-1.

Table 2: Elasticity modulus determine according to ISO 6784

Specimen No.	Specimen diameter [mm]	Stress in cross-section [MPa]			Strain [10^{-3}]			Elasticity modulus E_{cm} [GPa]
		Lower level σ_d	Upper level σ_h	$\Delta\sigma$	$\Delta\varepsilon_1$	$\Delta\varepsilon_2$	$\varnothing\,\Delta\varepsilon$	
Date of the test: 29.9. 2010 – 9 days								
1	149,6	0,5	22,5	21,96	0,535	0,403	0,469	46,8
2	149,4	0,5	22,5	22,02	0,612	0,659	0,636	34,6
3	150,3	0,5	22,3	21,76	0,490	0,598	0,544	40,0
Average value:								**40,5**
Date of the test: 18.10. 2010 – 28 days								
4	151,3	0,5	25,6	25,10	0,599	0,617	0,608	41,3
5	150,5	0,5	22,5	21,98	0,566	0,505	0,536	41,0
6	150,0	0,5	26,0	25,54	0,541	0,706	0,624	41,0
Average value:								**41,0**

One component of total strain is shrinkage. For this reason, the shrinkage measuring was conducted on three test specimens 100 x 100 x 500 mm made from same concrete recipe as the monitored pre-stressed railway sleepers. Results from these experiments are shown in Figure 3. Average values of experimental data were compared with shrinkage calculated according to EN 1992-1-1 (see Figure 3). There is shown relative good agreement between experimental dates of shrinkage and calculated values.

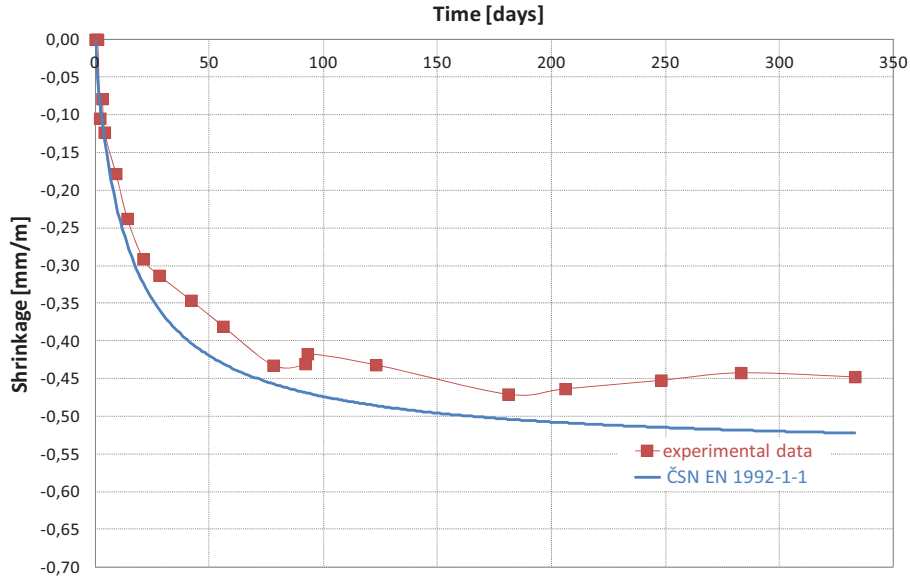

Fig. 3: Comparison of experimental shrinkage and calculated prediction of shrinkage according to EN 1992-1-1

All of these experimental data were used for prediction of total strain according to EN 1992-1-1. This prediction is shown in Figure 4. In Figure 4 are shown experimental data obtained from measuring of total strain in two pre-stressed concrete railway sleepers by four SOFO interferometric extensometers.

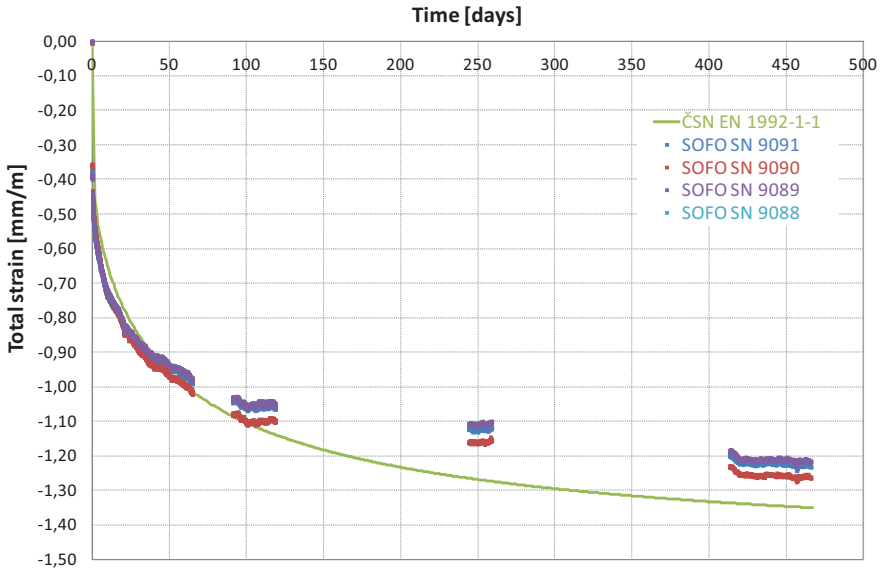

Fig. 4: Comparison of experimental total strain and calculated (EN 1992-1-1) prediction of total strain

4. Conclusions

The comparison of experiment and chosen model proved the applicability of this model EN 1992-1-1 with adequate accuracy for strain describing structures with same concrete recipe. Above mentioned mathematical model can be used for calculation other characteristics of pre-stressed reinforced concrete sleeper. Furthermore, this relatively simple experiment conducted on railway sleepers verified applicability of the fiber-optic extensometers for monitoring of pre-stressed concrete structures.

Acknowledgement

This research and paper was supported by the project GAČR P104/10/2359.

References

Glišić, B. & Inaudi, D. (2007) *Fibre Optic Methods for Structural Health Monitoring*. John Wiley & Sons Ltd, Londýn, 262 p.

Inaudi, D. (2004) SOFO Sensors for Static and Dynamic Measurements. In: *Proceedings of the 1st FIG International Symposium on Engineering Surveys for Construction Works and Structural Engineering*. Nottingham, p. 1-10.

18th International Conference
ENGINEERING MECHANICS 2012
Svratka, Czech Republic, May 14 – 17, 2012

pp. 557–568
Paper #317

NUMERICAL ANALYSIS OF A BRIDGE PIER SUBJECTED TO TRUCK IMPACT

P. Jiříček, M. Foglar*,

Abstract: *The paper presents description and comparison of the procedures prescribed by the European standard EN 1991-1-7 for bridge pier impact load. The methods incorporate static and dynamic analysis and are compared with a outcomes from a detailed FEM model of a truck prepared in the AUTODYN software. The outcomes are evaluated and conclusions are drawn.*

Keywords: ***Impact loading, numerical modelling.***

1. Introduction

In some cases of the structural arrangement, the vehicle impact can represent the decisive loading for the design of bridge substructure.

In the present design standards, the Eurocodes, there is a special part dealing with the accidental load caused from impact of road vehicles, trains, vessels etc., EN 1991-1-7. In the most common design cases the less sophisticated method based on an equivalent static load is used in the design praxis. The other method based on dynamic analysis is ignored because it is more demanding and requires performing of a special dynamic analysis.

The two methods provided within this standard are described and compared among each other. Later, the two methods are compared to the outcomes from a detailed FEM model of a truck prepared in the AUTODYN software.

2. Vehicle impact loading according to EN 1991-1-7

The standard EN 1991-1-7 (2007) provides procedures for assessing load from impact of road vehicles, trains, vessels etc.

The load can be obtained by:

- Equivalent static load
- Dynamic analysis

2.1. Equivalent static load

The equivalent static load should provide the same effect as a vehicle impacting the structure. This simplification can be used for:

- Verification of the static equilibrium
- Verification of the structural resistance
- assessing of the deflection caused by the impact

The load is divided according to the part of the structure it influences:

- Impact of the substructure
- Impact of the superstructure

* Ing. Pavel Jiříček, Ing. Marek Foglar, Ph.D.: Fac. of Civil Engineering, CTU in Prague, Thákurova 7; 166 29, Prague; CZ, e-mails: marek.foglar@fsv.cvut.cz, pavel.jiricek@fsv.cvut.cz

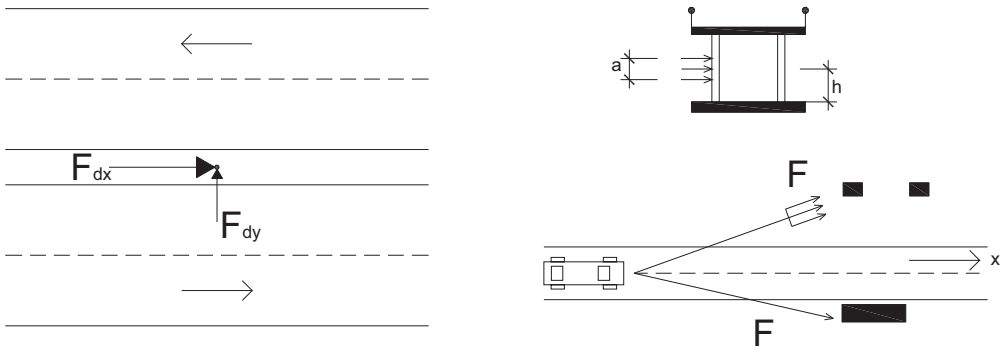

Fig. 1: left: definition of the impact forces; right: vertical alignment of the impact force (according to EN 1991-1-7 (2007))

Table 1: Design values of the impact forces on bridges over road network (according to EN 1991-1-7 (2007))

Category of the communication	Force Fdx [kN]	Force Fdy [kN]
Motorways and main roads	1000	500
Other roads	750	375
Local roads	500	250

The load to substructure can be taken from *Table 1*, explained in *Fig. 1*. The longitudinal and transverse forces do not act simultaneously.

The impact force acts in the height *h* (*Fig. 1*) and can be redistributed to an area with the height *a*. Values of the variables are provided within the cited design standard.

2.2. Dynamic analysis

A more detailed procedure for assessing the impact load is provided in Appendix C of EN 1991-1-7.

The impact bifurcates to soft and hard impact. In the case of the hard impact, the impacting vehicle deflects while the impacted structure remains stiff and unmoved. On the contrary, during the soft impact the impacted structure deflects (e.g. safety barriers). The hard impact can be used in the case of a vehicle impacted bridge pier.

The maximum dynamic force is defined as change of momentum in time:

$$F_0 = \frac{m \cdot v_r}{\Delta t} \tag{1}$$

where v_r is the speed of the impacting vehicle at the time of the impact

m is the mass of the impacting vehicle $m = \rho AL$

Δt is the duration of the impact (force impulse) $\Delta t = \sqrt{m/k}$

k is the equivalent stiffness of the impacting vehicle vztahem $k = EA/L$

E is the modulus of elasticity

A is the cross-sectional area

L is the length of the impacting vehicle

ρ is the volumetric mass of the impacting vehicle.

The impacting force is constant during the impact or increases linearly (*Fig. 2*).

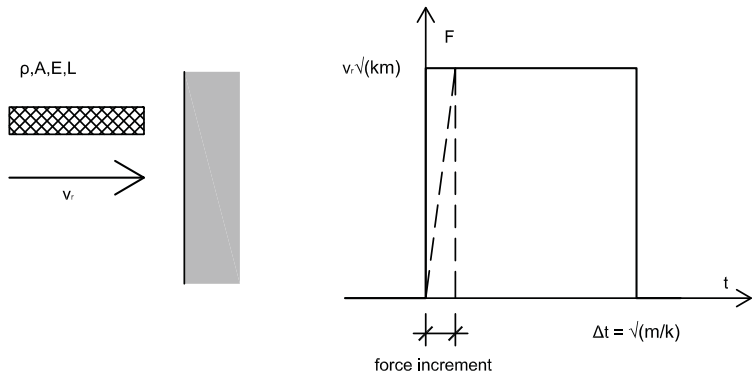

Fig. 2: Model of the impact, F = dynamic interaction force (according to EN 1991-1-7, (2007))

Table. 2: Design values of the mass of the impacting vehicle and the dynamic impact force F0; (according to EN 1991-1-7 (2007))

Category of the communication route	mass	speed	deceleration	impact force	breaking distance
	m	***v0***	***a***	***F0***	d_b [a)]
	[kg]	**[km/h]**	**[m/s²]**	**[kN]**	**[m]**
Motorway	30 000	90	3	2 400	20
Road in a urban are[a)]	30 000	50	3	1 300	10

[a)] speed reduced to 50 km/h

3. The assessment procedure according to EN 1991-1-7

The vehicle impact load is regarded as an accidental loading by the EN 1991-1-7. Therefore an accidental load combination has to be set-up.

In general, an accidental load combination can be analytically described as:

$$E_d = E\left\{G_{k,j}; P; A_d; \left(\psi_{1,1} or \psi_{2,1}\right)Q_{k,1}; \psi_{2,i}Q_{k,i}\right\} \quad j \geq 1; i > 1 \tag{2}$$

where the combination in the brackets {} can be written as:

$$\sum_{j\geq 1} G_{k,j} "+" P "+" A_d "+" \left(\psi_{1,1} or \psi_{2,1}\right)Q_{k,1} "+" \sum_{i>1} \psi_{2,i}Q_{k,i} \tag{3}$$

where the choice of the combination values $\psi_{1,1}$ or $\psi_{2,1}$ lies on the particular accidental design load. The combination can contain the design accidental load (impact, fire, etc.) or is related to the sesign situation following the accidental loading where $A = 0$.

4. Numerical modelling

This part of the paper is focused on application of the procedures described in the previous paragraphs. The utilization of the equivalent static force and the use of the dynamic analysis is compared to a 3D FEM model of a struck impacting a bridge pier.

4.1. Description of the bridge the impact loads are applied on

The impact loads are applied on a typical prestressed concrete two span bridge (see *Fig. 3* and *Fig. 4*). The superstructure is connected to a frame pier which is located in the median of a motorway. This bridge was built in 2005 by the joint venture of the companies STRABAG and SMP Construction as a part of the D3 motorway in south from Prague in the Czech Republic. Both the substructure and the superstructure are made of concrete C30/37. The span lengths are 25,750 and 21,735m. The middle pier is assessed to vehicle impact, the effect of the safety barriers is neglected.

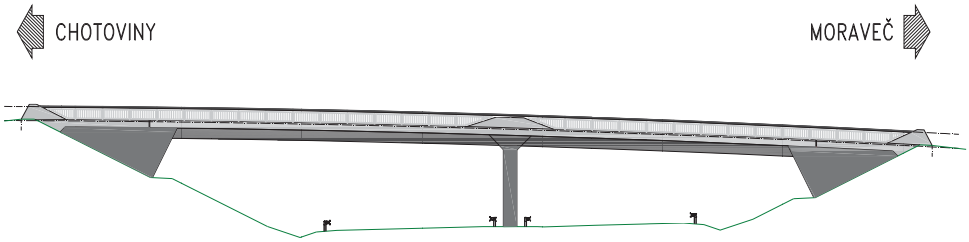

Fig. 3: View of the assessed bridge near Chotoviny

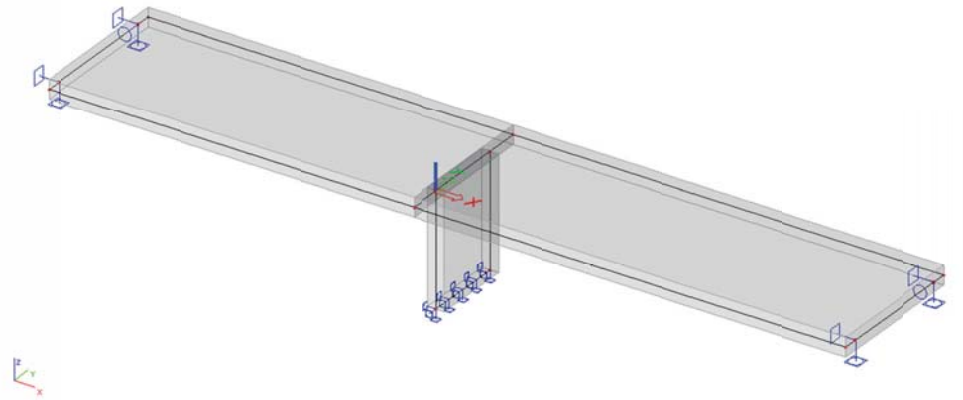

Fig. 4: Schematic slab FEM model of the bridge near Chotoviny.

4.2. Application of the equivalent static force

When using the equivalent static force for assessing a bridge pier subjected to impact load (EN 1991-1-7, (2007)), the impact forces are applied according to *Table 1*. The forces are placed in the most adverse position (*Fig. 5*), but do not act simultaneously. The impact forces are distributed on the centre-line of the slab which is modelling the bridge pier (*Fig. 6*). The distributed load acts from 0,5 to 1,5m above the crossed motorway.

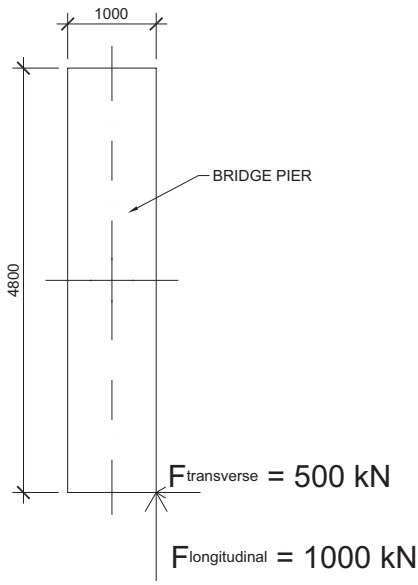

Fig. 5: Location of the impact forces

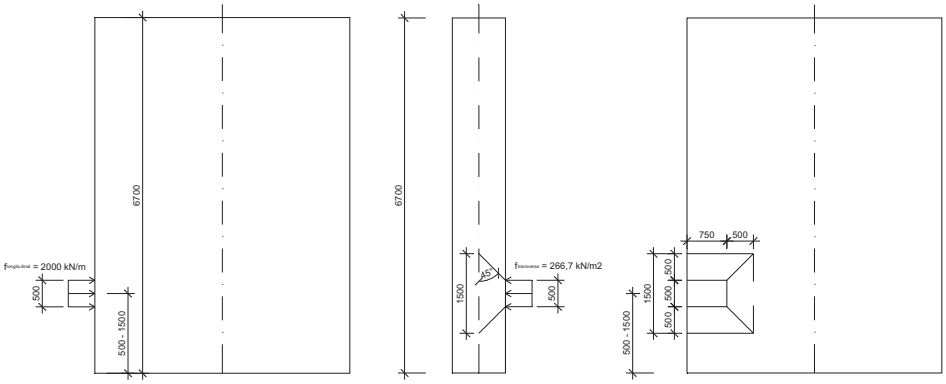

Fig. 6: Areal distribution of the impact forces on the bridge pier centre-line

The effect of the equivalent impact load on the bridge pier is assessed by a linear FEM analysis. The accidental load combination according to EN 1990 (2007) (see Eq. 6 and 7) is used for combining the effects of self weight, dead load and traffic load (LM1 according to EN 1991-2 (2005)) if it acts adversely.

The shear combined with the effect of torsion is the decisive load case, utilization of the cross-section is 60%, see *Table 3*.

Tab. 3: Summary of truck impact modelled with the use of the equivalent static force

	Impact direction	Decisive loading	Maximal impact force	Utilization	Dynamic coefficient
Truck impact	longitudinal	shear	1000,00 kN	60%	×
	transverse	shear	500,00 kN	60%	×

4.3. Dynamic analysis

When using the Appendix C for assessing a bridge pier subjected to impact load (EN 1991-1-7, (2007)). The impact force acts under the angle of 10° (*Fig. 7* and *Table 2*) from the horizontal axis of the motorway; for simplification, the impact angle is taken 0° and the force acts in the direction of the traffic on the motorway.

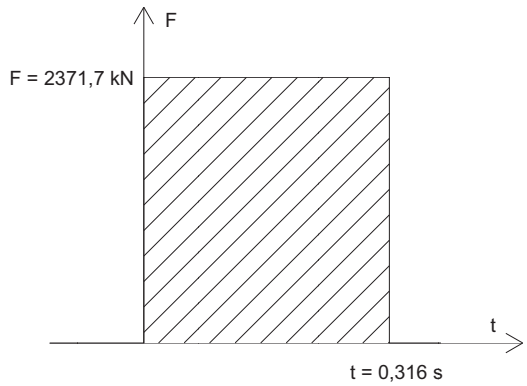

Fig. 7: Time distribution of the impact force for the dynamic analysis

In the following step, the dynamic system with two degrees of freedom is set up (*Fig. 8*).

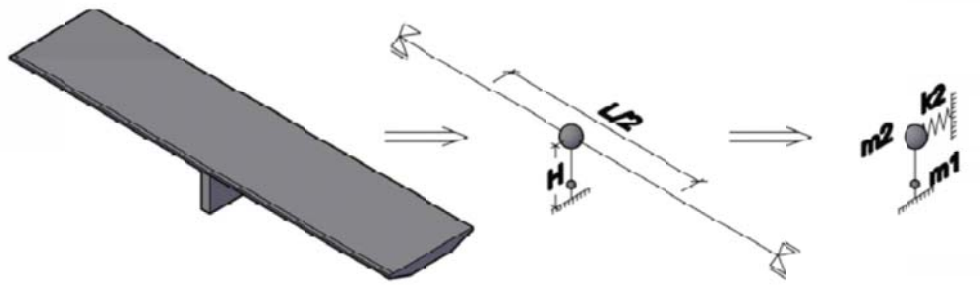

Fig. 8: Setting up the dynamic system of the bridge pier subjected to truck impact

The bridge pier is modelled by a cantilever which is supported by as spring on its free end. The stiffness of the spring *k2* corresponds to the lateral bending stiffness of the superstructure supported at bridge bearings. The mass *m2* is taken as the mass of the upper half of the bridge pier and the middle part of the superstructure (self weight + dead load) as can be seen in *Fig. 9*. The mass *m1* is taken as the mass of the lower part of the bridge pier and is located in the spot of the vehicle impact (1,5m above the motorway). In the next step, the matrix of docility and the matrix of damping of the dynamic system is prepared (Rayleighs damping, damping coefficient taken 7% for reinforced concrete). In this case, the matrix of mass is

$$M = \begin{bmatrix} 40{,}2 & 0 \\ 0 & 670{,}7 \end{bmatrix} \cdot 10^3 \text{ kg},$$

the matrix of docility is

$$\delta = \begin{bmatrix} 0{,}026917 & 0{,}021283 \\ 0{,}021283 & 0{,}186188 \end{bmatrix} \text{ mm}$$

and the matrix is

$$C = \begin{bmatrix} 32213{,}00 & -3653{,}47 \\ -3653{,}47 & 8820{,}28 \end{bmatrix} \cdot 10^3 \text{ kg/s}.$$

From the known input values, the dynamic response of the system is obtained with the use of direct integration of the equation of motion (Fig. 9).

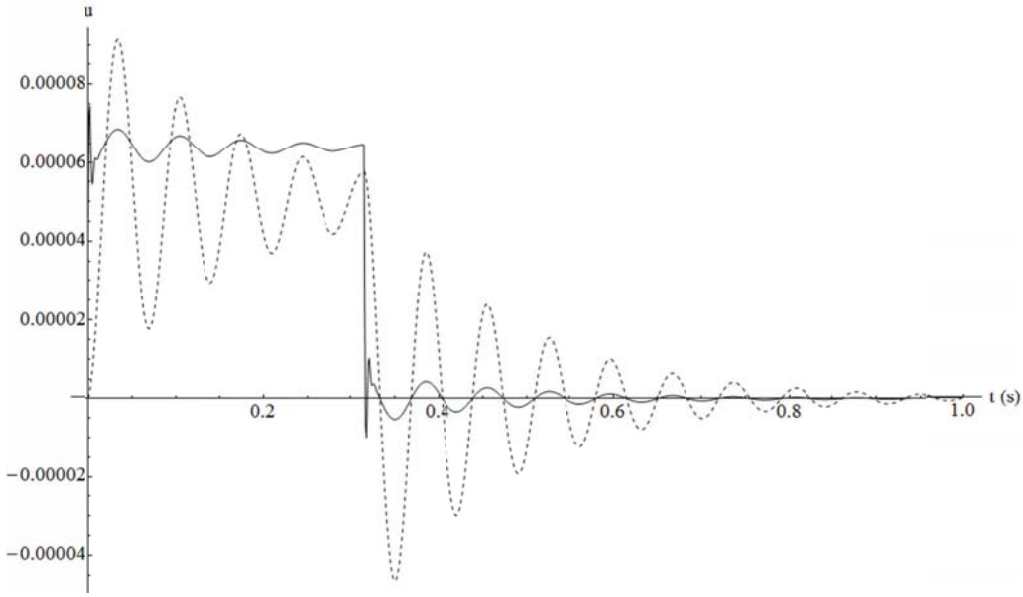

Fig. 9: Dynamic response of the system to the impact load, - - deflection at the top of the bridge pier, — deflection at the spot of the impact

The force couple causing the maximal deflection is determined reversely from the matrix of docility (3038,82;-337,28) [kN]. The 2D model of the bridge pier is then loaded by these forces and the resultant internal forces are determined.

The initial impact force in the direction of the traffic is 2371,7 kN, but the force causing the maximum deflections is 3038,82 kN; the resulting dynamic coefficient is 1,3).

The shear is the decisive load case, utilization of the cross-section is 80%, see *Table 4*.

Tab. 4: Summary of truck impact modelled with the use of the dynamic analysis

	Impact direction	Decisive loading	Maximal impact force	Utilization	Dynamic coefficient
Truck impact	longitudinal	shear	3038,82 kN	80%	1,3
	transverse	×	×	×	×

4.4. Nonlinear numerical analysis

Unlike both of the procedures for assessing a bridge pier subjected to vehicle impact incorporated in the EN 1991-1-7 which (based on simplifying assumptions) provide impact loading for the structure, the method described in this part aims to model a real truck hitting a bridge pier in full scale and then obtain the impact load reversely. The truck impact model is prepared in the ANSYS AUTODYN software.

The truck IVECO Trakker ADN140T50 (*Fig. 10 and 11*) was taken as the hitting vehicle. The 3D computational model was prepared in the RHINOCEROS 4.0 software using 2D and 3D finite elements which represent the decisive structural parts of the vehicle.

Fig. 10: The truck IVECO Trakker ADN140T50

Fig. 11: Computational model of the truck

The FE-modell is composed of a main frame carrying the motor (*Fig. 12*), a cab with the bumper (*Fig. 13*) and the load of the truck (for achieving the maximum allowable load). The main frame is composed of two horizontal U-profiles (309,0 x 80,0 x 10,0 mm), the motor block (3D brick element) and supplemental elements (thickness 10mm) which are connecting the cab. The cab (including the housing) is modelled by 2mm thick 2D elements; the bumper is modelled by 5mm thick 2D elements. The truck load is modelled by a steel block with reduced mass for obtaining the desired total weight 32 tonnes.

The material model used for the truck is linear steel without damage (material model with damage would increase the computing time, which is already now at approximately 96hrs). The finite elements which reach the limit deformation are eroded (i.e. dismissed from the model), but their mass and velocity stay within the system. This approach is satisfactory since the goal of the truck FE model is only to transmit the load to the bridge pier, not to perform a "crash-test study" of the truck.

The geometrical model is meshed using the Lagrange's network with an element size of 50mm.

The vehicle is moved with a speed of 90km/h towards the bridge pier.

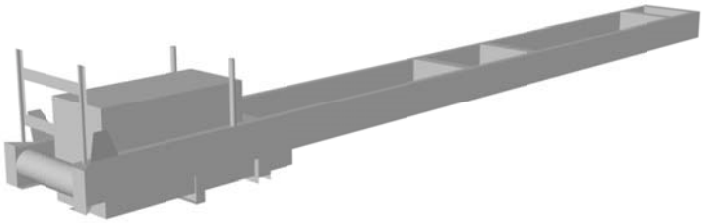

Fig. 12: Computational model of the main frame carrying the motor

Fig. 13: Computational model of the cab including the bumper

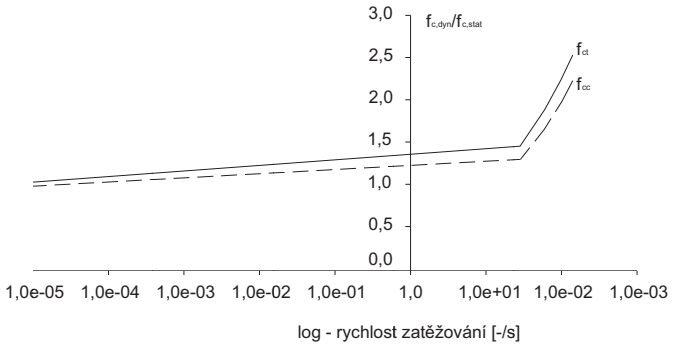

Fig. 14 Increase of the strength (both tensile and compressive) depending on the speed of loading (according to CEB-FIP Model Code 1990 (1993))

The material of the bridge pier was chosen to illustrate its behaviour when subjected to blast; the two main aspects are:

- Damage of the material when subjected to ultimate loading

- Increase of the strength (both tensile and compressive) depending on the speed of loading (dynamic increase factor)

The material model RHT for brittle materials with damage was chosen for concrete. This model incorporates the strain-rate effect, which describes the increase of strength with the speed of loading (*Fig. 14*).

The concrete bridge pier is modelled without reinforcement; the concrete strength class was taken C30/37. The effect of the safety barriers is neglected, the 32 tonne vehicle hits the pier in the direction of the traffic in the speed of 90km/h (*Fig. 15*).

The elements of the pier erode when reaching 100% damage. The elements of the vehicle erode when reaching the ultimate deformation; the erosion increases the energetic instability of the system with the use of Lagrange's network, which sets boundaries to the used element size.

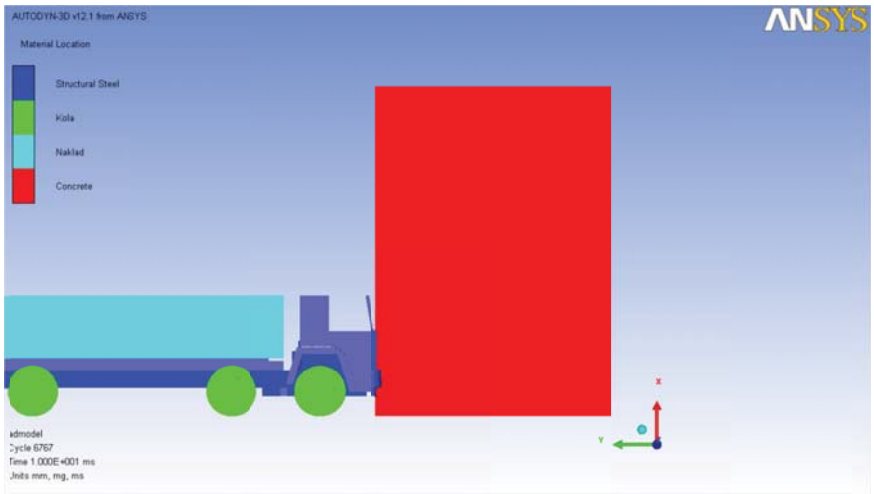

Fig. 15: The 32 tonne truck hitting the bridge pier.

The truck speed in at the moment of the impact together with the speed of the vehicle during the impact was taken from the FE model (Fig. 16). The total duration of the impact was 334ms.

The acting impact force was obtained from the change of the momentum using Eg. 1 (*Fig. 17*), the unlikely local extremes were neglected. The maximum impact force is 5762,65 kN (9707,76 kN local extreme).

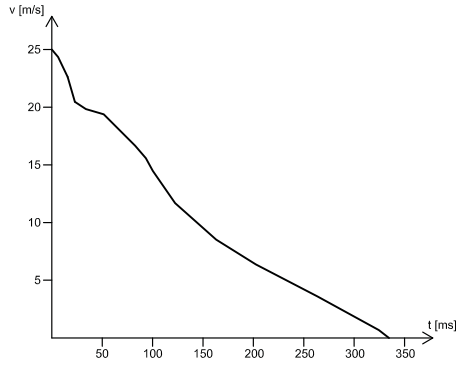

Fig. 16: Speed of the vehicle during the impact

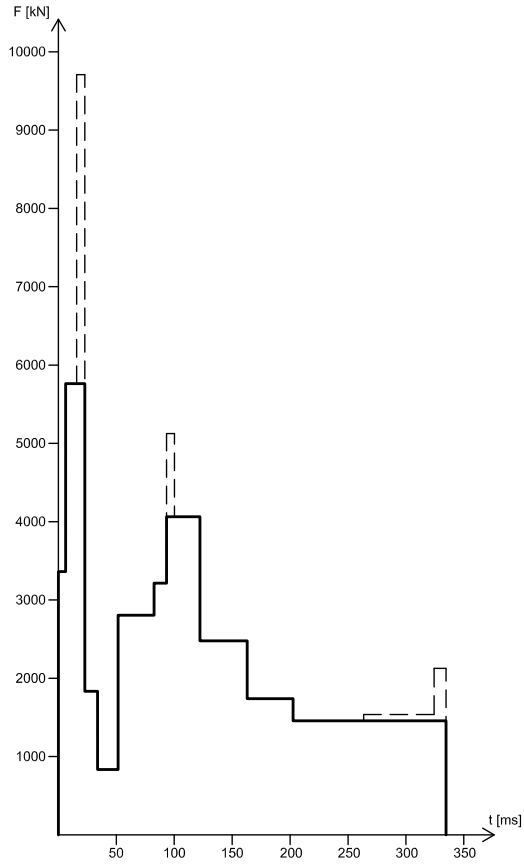

Fig. 17: The acting impact force during the impact, - - real time dependence, — the time dependence used in the assessment

With the known course of the impact force the same procedure as in the previous part is used.

From the known input values, the dynamic response of the system is obtained with the use of direct integration of the equation of motion. The force couple causing the maximal deflection is determined reversely from the matrix of docility (6471,64;-580,75) [kN] (*Fig. 18*). The 2D model of the bridge pier is then loaded by these forces and the resultant internal forces are determined.

The initial impact force in the direction of the traffic is 5762,65kN (9707,76 kN local extreme), but the force causing the maximum deflections is 6471,64 kN (10802,05 kN local extreme); the resulting dynamic coefficient is 1,12).

As in the previous chapter, shear is the decisive load case, utilization of the cross-section is 170% (280% for the local extreme), see *Table 5*.

Tab. 5: Summary of truck impact modelled with the use of a real vehicle

	Impact direction	Decisive loading	Maximal impact force	Utilization	Dynamic coefficient
Truck impact	longitudinal	shear	6471,64 kN	170%	1,12
	transverse	×	×	×	×

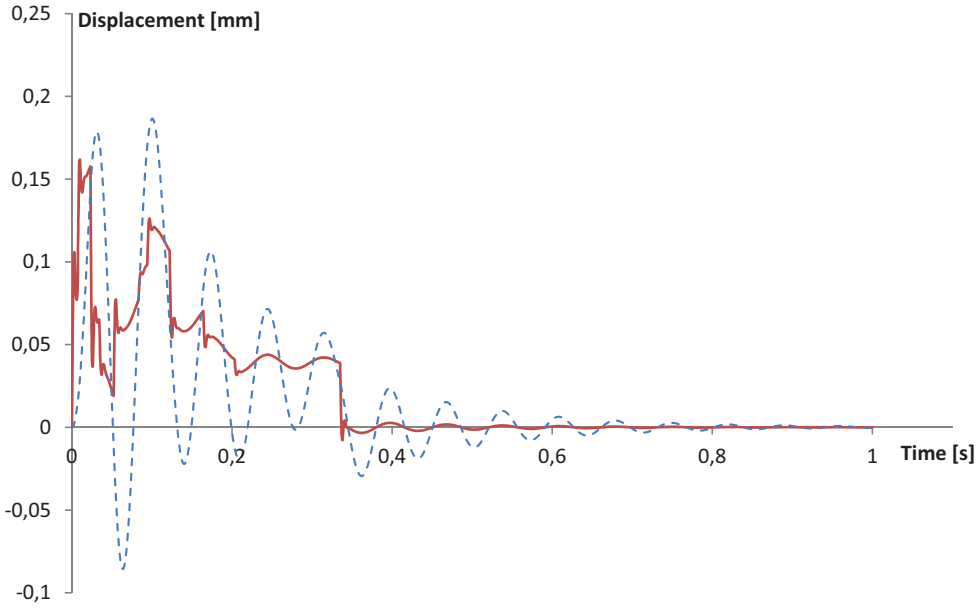

Fig. 18: Dynamic response of the system to the real truck impact load, - - deflection at the top of the bridge pier, — deflection at the spot of the impact

5. Conclusions

Three different approaches to vehicle impact were assessed. The first two are incorporated in the EN 1991-1-7 design code: the equivalent static load and the dynamic analysis. The pier of the modelled bridge provided satisfactory resistance to the impact loading. The commonly used method, the equivalent static load provided smaller loading and utilization than the load provided by the dynamic analysis. The equivalent static force was three times smaller than the impact force obtained by the dynamic analysis.

The third tested approach lied in full-scale modelling of the impacting truck. A non-linear computational model of a 32 tonne truck impacting the concrete pier was prepared. From the speed of the vehicle during the impact, the acting impact force during the 334 ms long impact was calculated. This force is two times higher than the impact force obtained by the dynamic analysis and six times higher than the equivalent static force. Thusly the resistance of the bridge pier is not satisfactory when using regular standard approaches for its assessment.

It is questionable whether to use the force calculated from the full-scale modelling of the impacting truck for the assessment of the bridge pier cross-section according to present design standards. The bridge pier experienced some cracking and erosion of crushed concrete elements. By the opinion of the authors, the damaged pier should be loaded by the design load and its residual bearing capacity verified by the means of a non-linear analysis. This analysis will be performed in the ongoing research.

Acknowledgement

This paper was supported the Czech Ministry of Industry and Trade project FR-TI3/531.

References

ČSN EN 1991-1-7 (2007) *Zatížení konstrukcí, Obecná zatížení – Mimořádná zatížení*. ÚNMZ.

ČSN EN 1990 (2007) *Zásady navrhování konstrukcí*. ÚNMZ.

ČSN EN 1991-2 (2005) *Zatížení konstrukcí, Zatížení mostů dopravou*. ÚNMZ.

CEB-FIP (1993) *Model Code 1990* Comité Euro-International du Béton.

18th International Conference
ENGINEERING MECHANICS 2012
Svratka, Czech Republic, May 14 – 17, 2012

pp. 569–578
Paper #252

SIMULATION OF PITTING FORMATION IN GEARING

J. Jurenka*, M. Španiel**

Abstract: *In the presented article is presented a numerical simulation approach of pitting arise phenomena on the gear teeth. The basic assumption of the presented approach was that pitting (pits on the contact surfaces) is a result of fatigue crack propagation under (rolling) contact loading conditions. The solution approach consisted of numerical simulations of fatigue cracks growth in the FEM framework. Fatigue crack growth simulations are based on evaluation of the so called Paris law in conjunction with FEA of crack tip loading conditions and fracture criteria evaluation. Penetration of the fluid lubricant into fatigue (pitting) cracks is simulated using special cavity finite elements, which allow to introduce so called lubricant closure inside crack. A simplified distribution of residual stresses in the surface layers of teeth is included as well. The simulations were carried out under the commercial code ABAQUS CAE FEM programme which allows to develop in-house codes using the Python scripting language. Mentioned programme codes are the basis of all FEA including the simulation of the contact loading conditions and the incremental crack growth.*

Keywords: ***gears, pitting, FEM simulation, crack propagation.***

1. Introduction

Pitting is understood as fatigue damage of components caused by cyclic contact load, when material particles come off and shallow pits arise in contact surface. Pitting is most often related to damage of contact surface of gear teeth (Fig. 1), but it also occurs on working surface of rolling bearing or on heads of rails and railway's wheels. Pitting formation leads to degradation (in extreme case to loss) of functionality of afflicted device, to escalation of vibrations, noise and other negative effects. Therefore, appreciable attention is given to study of this damage with purpose of reducing or eliminating these negative effects.

Fig. 1: Pitting damage of real gear.

Physical fundamentals of pitting formation are so complex, that there are still being used special empirical relations for determination of lifetime (of for example gear sets), which require experimental data gained from tests carried out directly on gear sets in special test stands. These experiments are time-consuming and also costly.

* Ing. Josef Jurenka: Czech Technical University in Prague; Technická 4, 166 07, Prague 6; CZ, e-mail: Josef.Jurenka@fs.cvut.cz

** Doc. Miroslav Španiel, CSc: Czech Technical University in Prague; Technická 4, 166 07, Prague 6; CZ, e-mail: Miroslav.Spaniel@fs.cvut.cz

Many attempts to mathematical description of pitting wear were implemented in recent years. The basic assumption of these attempts is that initiation and fatigue crack propagation are in progress before pit rise. The results of experiments indicate that pitting cracks propagate from contact surface into material of surface layer at first and after cracks reach a specific deep, they curve and turned backward towards the surface. Finally, end-fracture results in detachment of a material particle, as a result of which the pit is originated.

Two main domains are discussed in conjunction with approaches to the numerical simulation of pitting damage rise process. The basic assumption of the first group is that a pressured fluid lubricant penetrates into cracks and influences its growth. This approach can be represented e.g. by Fajdiga et al. (2004), who simulate fatigue crack growth from a surface initial crack and contact loading approximated by pressure distribution corresponding to the EHD lubrication theory. In the second group of approaches other possible damage mechanisms of pitting rise are assumed. E.g. Ding et al. (2003) simulate pitting rise from subsurface initial cracks.

The presented article belongs to the first group of the above mentioned approaches. The fatigue crack growth is numerically simulated by finite element method. The crack growth starts from the surface initial crack. The contact conditions between real gear teeth near the pitting crack mouth are computed and the pressured fluid lubricant penetration into pitting crack is assumed.

2. Implemented phenomenological fatigue crack growth theories

The basic assumption of the presented crack growth simulations is validity of the small scale yielding (SSY) conditions. In another words, the initial cracks are so long that the material can be modelled as an isotropic continuum and a dimension of crack tip plastic zone is negligible compared to the total crack length.

Then the rate of fatigue cracks propagation can be described by phenomenological theory – the Paris law, which is usually expressed as a relation of crack growth rate against stress intensity factor amplitude. In the pitting crack simulations the crack growth predictions were based on the fracture mechanics criterion – J-integral. The application of J-integral criterion was enforced by nonlinear character of performed FE analyses (stress intensity factors are not supported), where the gear meshing has to be solved under large deformation condition. With respect to that, the modification of Paris law relation is required and consists in substitution of stress intensity factor amplitude by amplitude of J-integral (1).

$$\frac{\mathrm{d}a}{\mathrm{d}N} = C(\Delta J)^m, \tag{1}$$

where C and m are material parameters and ΔJ is a J-integral amplitude.

The fatigue crack growth direction corresponds to the direction in which the maximum energy release rate is achieved. Under SSY conditions the criterion of maximum energy release rate is equal to maximal J-integral criterion and is equivalent to the maximal tangential stress criterion.

3. Experimental works

Experimental works were carried out at two basic levels. Firstly, simple so called CT test specimens were employed to provide data for validation of the crack growth prediction models under program ABAQUS and secondly, shortened fatigue tests of the real gearing were carried out using special testing machine (Niemann closed testing chain, Fig. 2 - Petr, K. 2010) to provide real pits shapes and gearing lifetime. More detailed information about used experimental equipment can be seen in the paper Jurenka (2011).

The both CT specimens and testing gears were manufactured from the 18CrNiMo7-6 material. After heat finishing (gears tempering and contact surfaces cementing into deep approximately 0.7 - 0.9 mm and hardening to final hardness approximately 58-60 HRC) the following characteristics of the material can be mentioned: Young's modulus 210 000 MPa, yield stress 1100 MPa, strength 1250 MPa. The estimated Paris law parameters are the following: C=1.42e-5 mm/[cycle.(N.mm)1.3] and m=1.3.

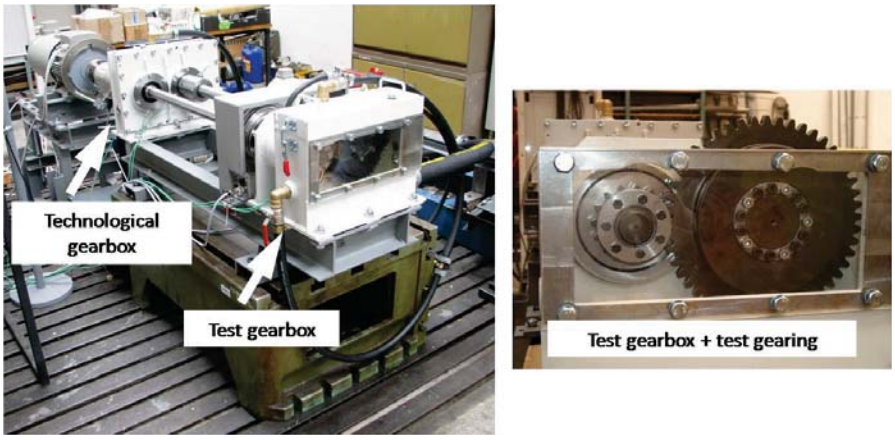

Fig. 2: Gear testing equipment (Petr, K. 2010).

Six tests were carried out. Digital pictures of teeth contact surfaces were made in the fixed time interval during the testing with time increment 2.5 hours. An example of time series of surface fatigue damage pictures is shown in the Fig. 3. Tested gearings were designed according to norm ISO 6336/1996 to limit durability approximately 30 hours under given loading conditions. Each test was stopped after formation of large pit or more smaller pits (maximal permissible pitting damage pollution of contact surface is 4%). The average life time of tested gearing was approximately 54 hours Fig. 4.

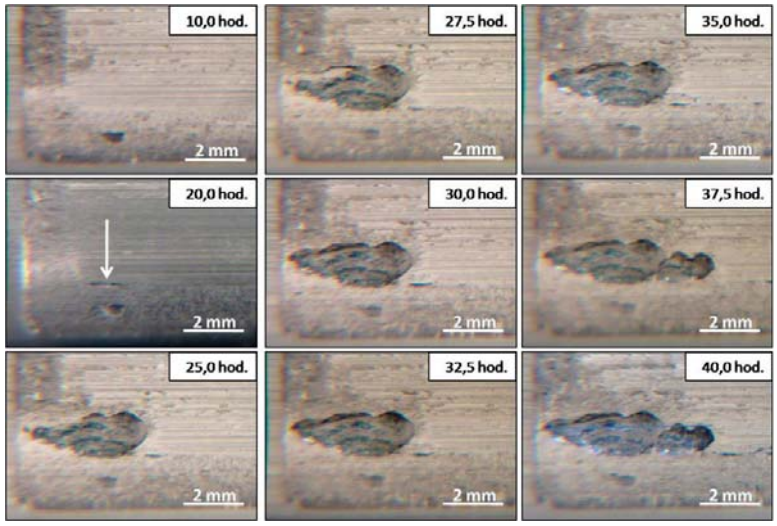

Fig. 3: Pitting damage formation during gears testing.

For providing more complete and accurate information about formation of observed pits, the detailed metallographic samples were created and analyzed. Material cuts were carried out through the biggest pits, and in the region of the tooth root, and region of the tooth head, of the pinion. The experimental tests results are shown in the Fig. 5, where the topology of four analyzed pits is displayed by the curved lines in context to the pinion tooth geometry. The direction of pitting crack initiation along the contact surface is shown by arrows.

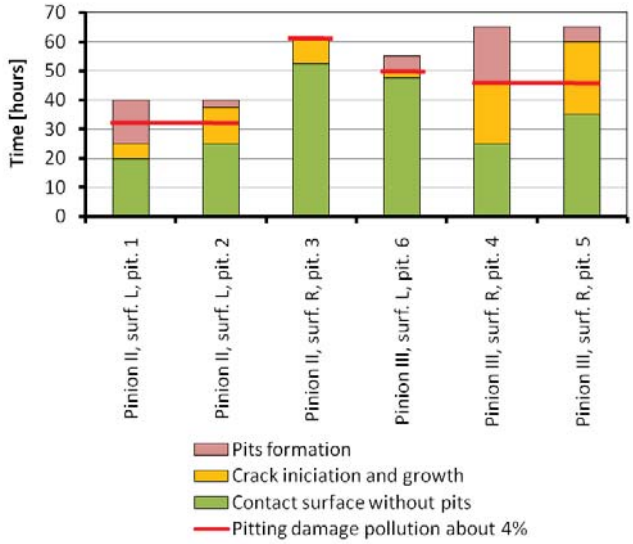

Fig. 4: Pitting damage formation during gears testing - gearing lifetime.

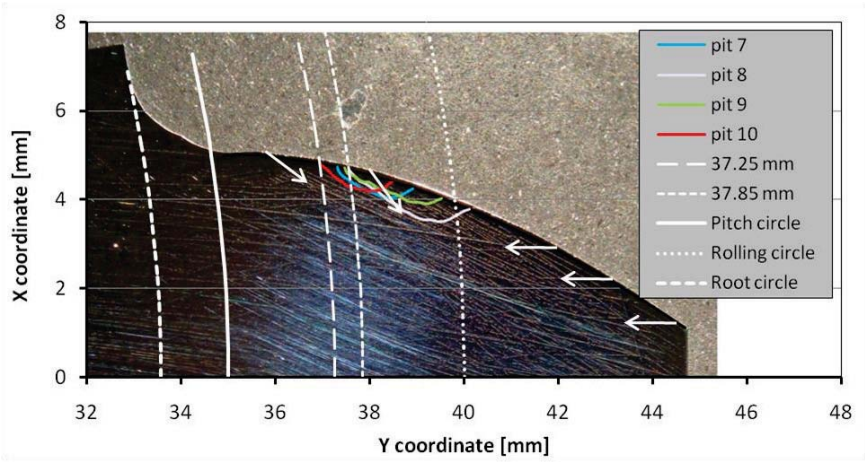

Fig. 5: Pitting damage formation during gears testing - pit topology and initial crack orientations (arrows) - metallographic sample.

According to presented pictures sequence in the Fig. 3 and pictures of metallographic samples, the probable process of pitting damage formation can be estimated:

- Pitting cracks start to propagate especially from the so called one tooth meshing contact area, thus the pitting damage is concentrated in this domain. In this domain the pitting cracks growth from tooth root to the tooth head.
- Relatively straight crack mouth could be a result of propagation of many short cracks in the critical domain of contact surface, from which the magistral crack is created subsequently. Presence of mentioned short cracks can lead to the creation of initial small pits in the critical region around the magistral crack mouth.
- The initial assumption, that the pits are created by fatigue crack growth, can be confirmed by the analysis of material particles, which were found in the oil tank. The dimensions and shape some of these particles correspond very well with formed pits (Fig. 6). So the pits were created by breaking off one or more relatively large material particles. This is in compliance with mentioned pictures sequence in the Fig. 3.

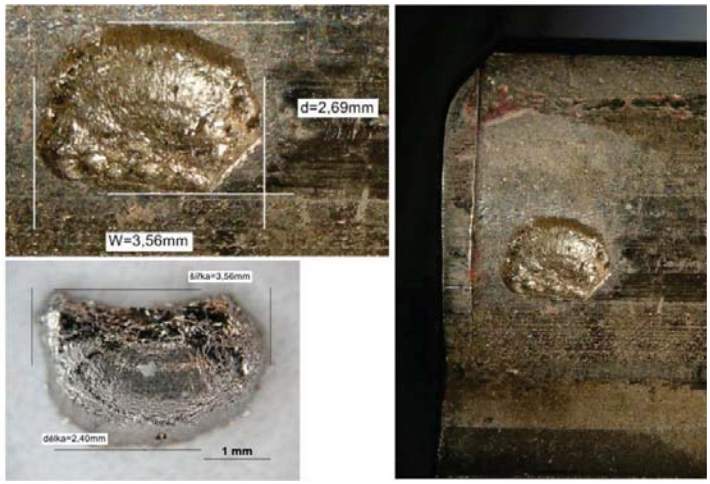

Fig. 6: Magistral pit and inverse material particle.

4. Pitting crack growth simulations

Simulations were performed under the commercial FEM code ABAQUS, which provides both computation tools for evaluation fracture mechanics criterion J-integral and Python language interface for in-house programme codes (developed at the Faculty of Mechanical Engineering CTU in Prague) submitting, which provide full automatic FE model creation and simulation control.

4.1. FE model and simulation flow

The numerical prediction of pitting formation presented in this article is based on the simulations of the gearing contact conditions, which induce boundary conditions for subsequent fatigue crack growth computational predictions. Basic mechanical quantities defining contact conditions are: contact pressure, shear stress, relative slip range and rate. Actually these quantities could be affected by both properties of fluid lubricant used and contact surface roughness. In the FE models the complex tribological relations (so called EHD lubrication conditions) are approximated by friction coefficient *f*, whose value can be in the range of 0.01-0.1 and special cavity model, which allows to include pressured fluid lubricant penetration into the pitting cracks. The residual pressure distribution in the subsurface layers was approximately estimated on the basis of experimental measurement using X-Ray diffraction. Linear elastic isotropic material model was assumed and all FE analyses are assumed as quasistatic and planar considering plane strain conditions.

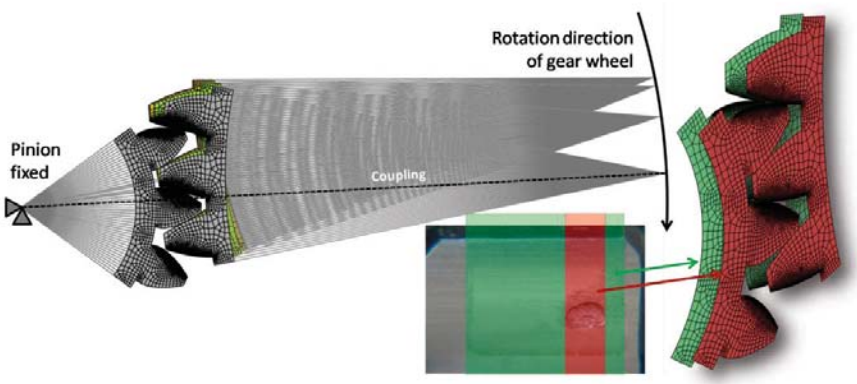

Fig. 7: The basic model concept.

The parametric FE model is conceived as the planar model, which combines two 2D models (one with pitting crack and one without) to simulate kvasi-3D contact conditions during gearing meshing. (Fig. 7).These two 2D models are merged in the gear ring regions and their thicknesses correspond to the thickness of cracked respectively non-cracked contact surface.

The initial crack is included in the FE model before the simulation start (Jurenka, 2011). Between modelled crack surfaces the special cavity finite elements (F2D2) are defined to simulate penetration of pressured lubricant into crack during gearing meshing. The law of mass flow q of pressure lubricant is defined by the simple relation:

$$q = C_v \Delta p\,, \tag{2}$$

where C_v is the viscous resistance coefficient and Δp is the pressure gradient. The value of C_v is approximately estimated using analytical equation for laminar flow into thin slot as:

$$\frac{q}{\rho} = \frac{b}{12 \cdot \eta} \frac{\Delta p}{l} h^3\,, \tag{3}$$

where ρ is a lubricant density, b is a crack width, l is a crack length and h is a distance between crack surfaces. η is the dynamic viscosity of lubricant, which is a function of the pressure inside lubricant according to relation:

$$\eta = \eta_0 \cdot \exp\left(\alpha \cdot \overline{p}\right), \tag{4}$$

where η_0 is dynamic viscosity for 0 pressure, α is the piezo-coefficient of lubricant and $\overline{p}$ is a actual pressure inside lubricant. On the basis of comparison of relation (2) and (3) the relation for C_v estimation is given:

$$C_v = \frac{12 \cdot \eta \cdot l}{b \cdot h^3}\,, \tag{5}$$

Cavity volumes are defined between crack surfaces. These volumes correspond to the crack extension increments (Fig. 8). The mass flow between each two neighboring cavity volumes q_i (i = 1, ..., N, N is number of volumes, resp. crack extensions) is given by relation (2). In the cavity model the $\overline{p}$ corresponds to average pressure between neighboring cavity volumes, and the value of both $\overline{p}$ and Δp result from actual loading during gear meshing. The first cavity volume is connected with the contact surface and is pressured by actual contact pressure.

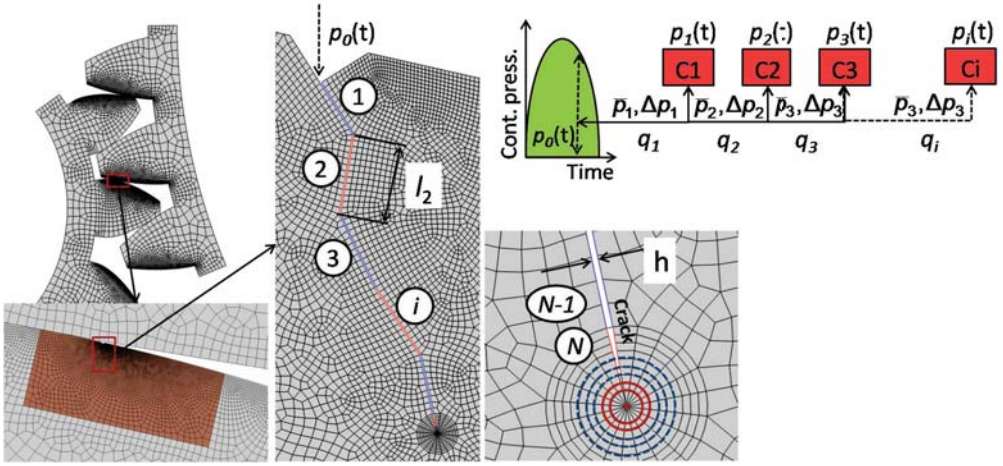

Fig. 8: The basic model concept.

In the FE model the residual stress distribution is defined as initial condition using several sublayers with constant residual pressure (Fig. 9). The distribution was approximately estimated on the basis of X-Ray diffraction residual stress measurement and theoretical knowledge (Neckář, F., 1991).

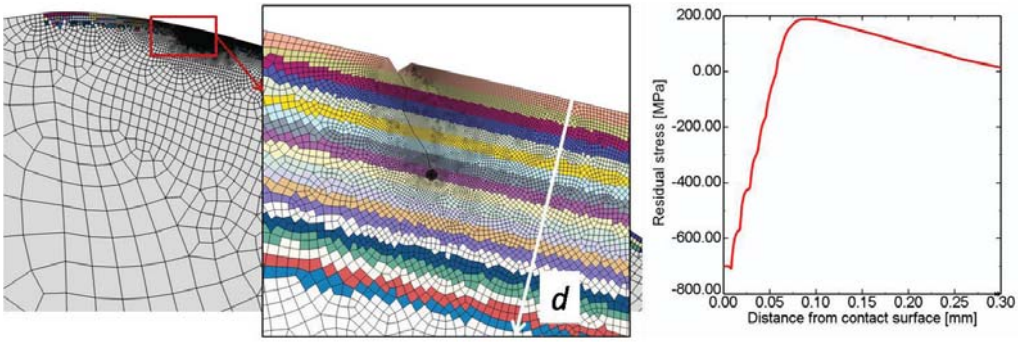

Fig. 9: Application of Residual stress distribution.

The basic scheme of simulation of pitting crack propagation is shown in the Fig. 9. In the first step the contact pressure distribution in the crack mouth is calculated. Subsequently the incremental crack growth is simulated in the loop as long as the final pit shape is achieved. In each computational iteration of the solution loop (item 2.1 in the Fig. 9) the J-integral is calculated in the several directions in front of the crack tip (Fig. 10). The probably crack extension direction is evaluated in the item 2.2 (Fig. 9) either as the direction, in which the maximum of J-integral was calculated (Španiel, M., 2008), or as an average direction calculated from all J-integral values bigger than the threshold value. It is assumed, that the crack can growth only if it is opened. Thus if the contact between crack surfaces arise (pressure in the cavity is not able to open crack), then the crack can not growth. In the last part of the solution loop (item 2.3, Fig. 10), the model crack is extended and FE model is modified.

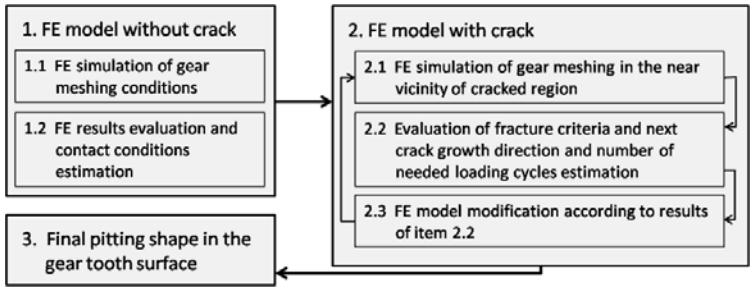

Fig. 10: Block schema of pitting simulation under ABAQUS.

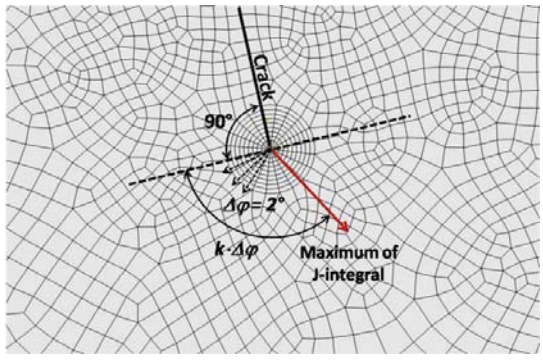

Fig. 11: Crack direction estimation.

With respect to the complex physical background leading to pitting formation, which can not be fully experimentally explained, the developed FE model was created in the relatively general form. This means, that they contains many parameters, which can be change independently and its influence on the pitting crack growth can be evaluated. The basic model parameters are listed in the Tab 1.

Tab. 1: The basic FE model parameters.

FEM model parameter	Min value	Max value
Friction coefficient on the teeth contact surfaces - f [-]	0,01	0,15
Friction coefficient between crack surfaces - f_c [-]	0,3	1
Initial crack length - a_{ini} [μm]	10	50
Initial crack angle between crack and contact surface - φ [°]	25	160
Crack extension increment length - l [μm]	10	50
Initial crack location on the contact surface (diameter of circle with center in the pinion axis) - ρ [mm]	37,25	37,85
Kinematic viscosity coefficient of fluid lubricant - υ [mm^2/s]	1	300
Dynamic viscosity coefficient of fluid lubricant - η_0 [MPa·s]	0,89e-9	0,27e-6
Piezo-coefficient of fluid lubricant - α [mm^2/N]	0,02	0,02
Density of fluid lubricant - ρ' [kg/m^3]	890	890
Initial crack surfaces distance - h [mm]	1e-6	1e-4

4.2. Results of simulations and discussion

The presented research of pitting damage phenomenon is based on both experimental results of real gearing tests and numerical simulations of pitting crack propagation under contact loading conditions. The main goal of performed numerical simulations is to provide information, which can confirm or confute above mentioned theory of pitting damage formation.

The simulated crack behavior (crack growth direction) is analyzed with respect to:

- The location of contact region between gear teeth according to the crack mouth,
- gearing meshing conditions,
- the stress field around the whole crack,
- the possibility of fluid lubrication penetration inside the crack,
- the J-integral values, and
- the residual stress distribution.

Numerical model is defined by many parameters, whose values can not be experimentally verified. The detailed sensitivity study of the influence of selected parameters on the pitting crack behavior has to be done. In the first stage the possibility of growth of initial pitting cracks is assessed.

In the presented simulation the following parameters were assumed (Tab. 2):

Tab. 2: Assumed FE model parameters.

FEM model parameter	Value
Friction coefficient on the teeth contact surfaces - f [-]	0,01
Friction coefficient between crack surfaces - f_c [-]	1
Initial crack length - a_{ini} [μm]	15
Initial crack angle between crack and contact surface - α [°]	30, 60, 90, 120, 150
Crack extension increment length - l [μm]	20
Initial crack location on the contact surface (diameter of circle with center in the pinion axis) - ρ [mm]	37,55
Dynamic viscous of fluid lubricant - η_0 [MPa·s]	0,89e-9 ÷ 0,27e-6
Initial crack surfaces distance - h [mm]	1,6e-4

The attention was focus on the initial stage of pitting cracks propagation in the presented article. With respect to the experimental observation the influent of small pits in the crack mouth region on

the pitting crack growth was studied. The several basic configurations were assumed (Fig. 12). The initial small pit deeps were chosen as a) 0,001; b) 0,01; c) 0,03; d) 0,05 and e) 0,08 mm. The initial crack length was equal to 0,015 mm and the initial crack angle was 30° against to the contact surface.

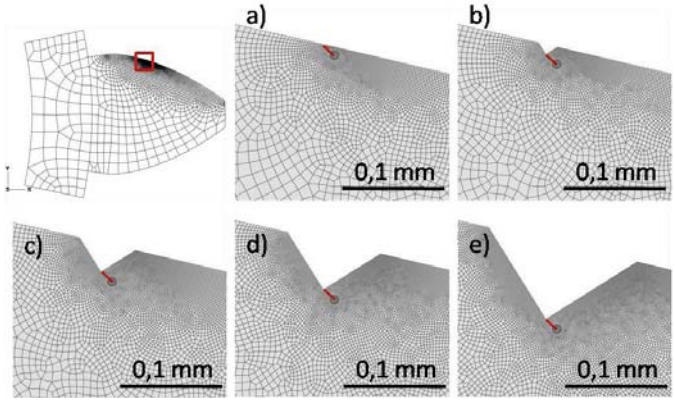

Fig. 12: Initial pitting cracks configuration.

The shape of pitting cracks after several simulation loops (several cracks extensions) with respect to the initial small pit dimension is shown in the Fig. 13. The initial configuration before the first simulation run is shown in the Fig. 12. The advance cavity model according to the Fig. 8 was used and residual stress was neglected. The model crack surface distance was 1,6e-4 mm.

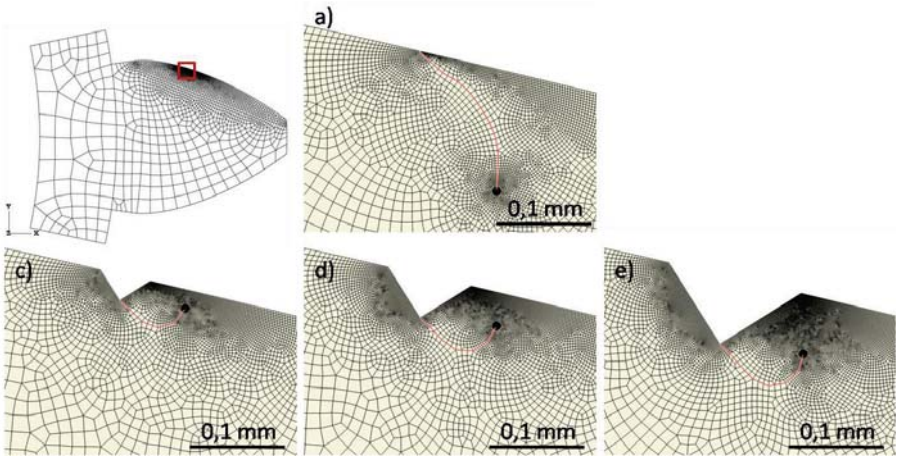

Fig. 13: Pitting cracks shapes.

The predicted lifetimes, resp. number of loading cycles needed to simulated cracks growth is for presented cracks listed in the Tab. 3. These results show, that it is possible to use the developed FE model to simulation of pitting damage formation. The mentioned results are in a relative good agreement with experimental data from qualitative point of view and it seams, that it is possible to validate FE model on the basis of sensitivity study of its parameters.

5. Conclusions

The achieved results show, that the chosen numerical approach to the simulation of pitting damage formation can be used. However the developed FE model is very complex due to credible description of physical background. Many parameters can be change and experimental verification of their values does not exist. From this point of view, the large sensitivity study of the most important parameters has to be done. On the basis such complex results, the FE model can be finally validate.

The main result and outputs of the above mentioned research are:

- The complex parametric FE model for pitting crack growth was created.
- The advance cavity model for simulation of penetration of pressured fluid lubricant into pitting cracks was introduced.
- The methodology for implementation of residual stress into subsurface layers of material was developed.
- The complex experimental tests of real gears were performed and evaluated.

In the future the attention will be focused on the extension of experimental base. Especially, on the validation of fatigue cracks growth under non-proportional mixed model loading conditions.

In the simulation domain, the large sensitivity study of FE model parameters will be carried out and the real heat treatment of contact surfaces will be simulated in the special program code SYSWELD to achieved more accurate information about residual stress distribution.

Tab. 3: Crack growth rate prediction.

Crack increments	a)			b)			d)			e)		
	J-int.	No. cycles	Time	J-int.	No. cycles	Time	J-int.	No. cycles	Time	J-int.	No. cycles	Time
	J [Nmm]	N []	t [h]	J [Nmm]	N []	t [hour	J [Nmm]	N []	t [hour	J [Nmm]	N []	t [hour
1	0.0139	3.65E+05	4.19	0.1441	1.75E+04	0.20	0.1713	1.40E+04	0.16	0.1758	1.35E+04	0.16
2	0.0437	8.24E+04	0.95	0.0797	3.77E+04	0.43	0.1239	2.13E+04	0.24	0.1334	1.93E+04	0.22
3	0.0771	3.94E+04	0.45	0.1366	1.87E+04	0.22	0.1160	2.32E+04	0.27	0.1001	2.81E+04	0.32
4	0.1103	2.47E+04	0.28	0.1497	1.66E+04	0.19	0.2374	9.14E+03	0.11	0.1984	1.15E+04	0.13
5	0.1388	1.84E+04	0.21	0.0720	4.30E+04	0.49	0.2607	8.09E+03	0.09	0.2763	7.50E+03	0.09
6	0.0600	5.46E+04	0.63				0.2076	1.09E+04	0.12	0.2722	7.65E+03	0.09
7	0.0563	5.93E+04	0.68							0.2109	1.07E+04	0.12
8	0.0729	4.24E+04	0.49									
9	0.0980	2.89E+04	0.33									
10	0.1398	1.82E+04	0.21									
suma		**7.33E+05**	**8.43**		**1.34E+05**	**1.54**		**8.65E+04**	**0.99**		**9.82E+04**	**1.13**

Acknowledgement

This research was supported by the Czech Science Foundation (no.101/06/1427) and Josef Božek Research Center of Engine and Automotive Engineering.

References (EM Reference Chapter style)

Ding, Y., Rieber, N., F. (2003) Spalling formation mechanism for gears, Wear 254

Fajdiga, G., Flašker, J., Glodež, S. (2004) The Influence of different parameters on surface pitting of contacting mechanical elements, Engineering Fracture Mechanics 71

Jurenka, J., Španiel, M. (2011) Simulation of fatigue crack propagation under contact loading conditions, in: *Proc. Fatigue design 2011*,W6.4, 8 p., Centre technique des industries mechaniques, Senlis, France

Neckář, F., Kvasnička, I (1991): Vybrané statě z úběru materiálu. 1. vyd. Praha: eS ČVUT, 88s. ISBN 80-01-00696-4.

Petr, K., Kanaval, J., Dynybyl, V. (2010) Modification and Non-standard methods of increasing tooth flank surface, In international conference on gears, Düsseldorf: VDI Verlag, p. 1439-1442. ISBN 978-3-18-092108-2.

Španiel, M. - Jurenka, J. - Kuželka, J. (2008) Verification of FE model of fatigue crack propagation under mixed mode conditions, In: MECCANICA, Vol. 43, ISSN 1572-9648.

18th International Conference
ENGINEERING MECHANICS 2012
Svratka, Czech Republic, May 14 – 17, 2012

pp. 579–584
Paper #196

MATERIAL NON-LINEAR BEAM ELEMENT WITH SHEAR CAPACITY

J. Kabeláč *

Abstract: *The paper describes a new formulation of beam elements for deformational variant of FEM, which respects non-linear material behaviour. This formulation considers combination of shear and axial loading and is suitable for short or torque beams similarly to the Timoshenko theory. Non-uniform warping and influence of transversal contraction are not considered in the formulation. The cross section can be of arbitrary known shape and composed of more materials. The presented element respect real distribution shear stress over cross section taking material non-linearity into consideration*

Keywords: ***beam element, FEM, material non-linearity, shear, torque***

1. Introduction

More economical usage of materials at technical objects is connected with the development of simulation tools. A similar situation is at beam construction which is abundantly represented in technical practice. Just use of material non-linearity provides reserves in material usage. Besides that in practice more and more emphasis is placed on robustness of simulation tools without neccessarity of deep knowledge of service. Frequent use of some materials makes correct use of linear models impossible, for example reinforced concrete. For these reasons, based on practical requests of users, the following formulation of beam element was developed. Geometry of the presented element is shown on fig. 1.

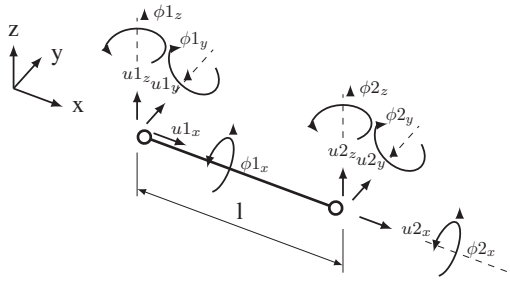

Fig. 1: Beam element

During making solution about used formulation of the element that should be implemented an extensive research of available formulations in commercial CAE software's (Nastran, Abaqus, Marc, Ansys) was done. All softwares provides a lot of formulations of the beam element including material non-linearity. Their definition it is possible to find for example here Crisfield (2000),Němec (2010) and Zienkiewicz (2000). Detail assessment shows that there is provided robust and sufficient solution for Euler formulation of the element for uniaxial stress in all software's. But in case of shear stress the situation is dismal. Here are provided solutions for Timoshenko formulation as well but detail analysis proves that these solutions are very simplified. For example Ansys provides the element BEAM 188/189. This element however supposes constant shear strain over cross section and strain corresponding to linear torsion. But real stress distribution at shear loading is different (for example Grutmann (1999)). In other

*Ing. Jaromír Kabeláč; FEM Consulting, Veveří 331/94; 602 00, Brno, CZ, jaromir.kabelac@seznam.cz

CAE software's the situation is similar. Even literature search did not provide more complex formulation for material non-linearity.

None of available formulations of the beam element respect real distribution shear stress over cross section taking material non-linearity into consideration.

Solution of plastic torque is known for long time (for example here Chakrabarty (2006)). Numeric solution of plastic torque for an arbitrary cross section is defined here Gruttmann (2001). By small modification the author extend this solution to general shear loading Kabeláč (2011). The model for axial part of stress is generally known (good description in Crisfield (2000)). By combining of these solutions we obtain real stress distribution over cross section at arbitrary combination of beam loading. In that way formulated cross section behaviour is combined with appropriate shape function. Result of this combination is here presented formulation of beam element, which respects real shear stress distribution over arbitrary cross section.

Use of various cross section characteristics, specified by an user, increases demands on an user and is a source of possible mistakes. Therefore we left numerical values as input and the only input is a shape of cross section or FEM mesh of cross section. On this mesh more materials can be defined. It means the model is also usable for composite cross section.

The represented model is valid for small strain, straight prismatic beam and free warping of cross section. The influence of transversal contraction is not considered. In connection to co-rotational formulation its involving in geometric non-linearity is easy.

2. Formulation

The final formulation of beam element with the shear influence and considering of material non-linearity is connection of following analyses:

1. **Distribution of deformations along beam**. A classical formulation of beam elements does not seem to be suitable for this propose. A simplified formulation was used with constant strain along axis of beam. From here transversal deformations are interpolated by quadratic function and the other deformations are interpolated linearly.

$$\mathbf{\Psi} = [\frac{du_x}{dx}, \frac{d\phi_y}{dx}, \frac{d\phi_z}{dx}, \frac{d\phi_x}{dx}, \theta_y, \theta_z]^T \quad ; \quad \mathbf{\Psi} = \mathbf{\Xi}.\mathbf{u} \tag{1}$$

2. **Strain over cross section**. In view of the formulation strain over cross section is defined by three components ε_x , γ_{xy} and γ_{xz} the other components are zero. These components are defined by current unknown warping function w and components of strain along axis of beam.

$$\boldsymbol{\varepsilon}_i = \mathbf{B_i}.\mathbf{w_i} + \mathbf{G_i}.\mathbf{\Psi} \tag{2}$$

3. **Calculation of warping function**. Based on described process of strain over cross section and using of equilibrium equations a particular PDE problem can be formulated. Considering used material model it is a non-linear problem. This problem can be by variational principles transformed to classical non-linear FEM problem over mesh of cross section. The result is an actual warping function and then stress over cross section.

$${}^k\mathbf{F} = \sum_i^{elem} \int_{\Omega_i} \mathbf{B}_i^T.\boldsymbol{\sigma}({}^k\boldsymbol{\varepsilon}_i).d\Omega_i = 0 \Rightarrow \mathbf{w} \tag{3}$$

4. **Calculation of cross section internal forces V and tangential stiffness matrix of cross section D**. Based on known warping function and stress over cross section it is easy to define final internal forces and stiffness matrix of cross section.

$$\mathbf{V} = [N_x, M_y, M_z, M_x, V_y, V_z]^T = \sum_i^{elem} \int_{\Omega_i} \mathbf{G_i}^T.\boldsymbol{\sigma_i}(\boldsymbol{\varepsilon_i}).d\Omega_i \quad ; \quad \mathbf{D} = \frac{\partial V_i}{\partial \Psi_j} \tag{4}$$

5. **Internal forces $\mathbf{R}$ and tangential stiffness matrix of beam element $\mathbf{K}$.**

$$\mathbf{R} = l.\mathbf{\Xi}^T.\mathbf{V} \quad ; \quad \mathbf{K_t} = l.\mathbf{\Xi}^T.\mathbf{D}.\mathbf{\Xi} \tag{5}$$

2.1. Beam shape function

It is a known and generally widespread solution for Timoshenko beam in linear area. But it is not possible to find a direct relation between deformation in grid and skew from shear by this solution. For this reason a simplified formulation was developed. Process of rotation along beam is linear interpolation of rotation in grid. Shape functions are used here.

$$\eta \in < -1, 1 > \tag{6a}$$

$$N_1 = \frac{1}{2}(1 - \eta) \tag{6b}$$

$$N_2 = \frac{1}{2}(1 + \eta) \tag{6c}$$

$$x = l.N_2 \tag{6d}$$

$$\phi_z = N_1.\phi 1_z + N_2.\phi 2_z \tag{7}$$

It means the element has constant curvature in deformation. In this case bend must be interpolated by quadratic polynomial.

$$u_y = N_1.u1_y + N_2.u2_y + \alpha.Nc \tag{8}$$

$$Nc = 1 - \eta^2 \tag{9}$$

Coefficient α is excluded as follows. Skew is obtained from the relation:

$$\theta_z = -\phi_z + \frac{du_y}{dx} \tag{10}$$

To avoid shear locking of the element, the skew must be constant.

$$\frac{d\theta_z}{dx} = 0 \tag{11}$$

By solution of this equation it is excluded parameter α and for skew and transversal deformation is valid:

$$u_y = N_1.u1_y + N_2.u2_y - \frac{L}{8}(\phi 2_z - \phi 1_z).Nc \tag{12}$$

$$\theta_z = \frac{1}{L}(u2_y - u1_y) - \frac{1}{2}(\phi 1_z + \phi 2_z) \tag{13}$$

It remains to express the relation between deformation in grid and strain of beam by transforming into 3D:

$$\boldsymbol{\Psi} = \begin{bmatrix} \frac{du_x}{dx} \\ \frac{d\phi_y}{dx} \\ \frac{d\phi_z}{dx} \\ \frac{d\phi_x}{dx} \\ \theta_y \\ \theta_z \end{bmatrix} = \frac{1}{l} \begin{bmatrix} u_{2x} - u_{1x} \\ \phi_{2y} - \phi_{1y} \\ \phi_{2z} - \phi_{1z} \\ \phi_{2x} - \phi_{1x} \\ -u_{2z} + u_{1z} - \frac{l}{2}\left(\phi_{2y} + \phi_{1y}\right) \\ u_{2y} - u_{1y} - \frac{l}{2}\left(\phi_{2z} + \phi_{1z}\right) \end{bmatrix} = \boldsymbol{\Xi}.\mathbf{u} \tag{14}$$

In that way formulated element has a great advantage which lies in a fact that strain of beam are constant.

2.2. Strain over cross section

In accordance with St'Venant theory free warping is occurring over cross section. Free warping is defined by currently unknown warping function $\mathbf{w}$. Examples of warping functions are shown on fig. 2 for different shear loading.

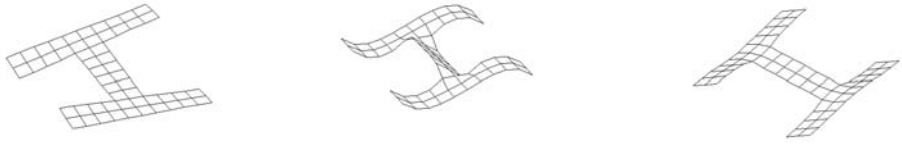

torque shear shear

Fig. 2: Example of warping function on I - profile

For strain over cross section it could be written.

$$\boldsymbol{\varepsilon} = \begin{bmatrix} \varepsilon_x \\ \gamma_{xy} \\ \gamma_{xz} \end{bmatrix} = \begin{bmatrix} \frac{\partial u_x}{\partial x} \\ \frac{\partial u_x}{\partial y} + \frac{\partial u_y}{\partial x} \\ \frac{\partial u_x}{\partial z} + \frac{\partial u_z}{\partial x} \end{bmatrix} = \begin{bmatrix} \frac{du_x}{dx} + z\frac{d\phi_y}{dx} - y\frac{d\phi_z}{dx} \\ \frac{\partial w}{\partial y} + \theta_z - z\frac{d\phi_x}{dx} \\ \frac{\partial w}{\partial z} - \theta_y + y\frac{d\phi_x}{dx} \end{bmatrix} \tag{15}$$

Interpolation of warping function $\mathbf{w}$ by shape functions over mesh of cross section pursuant to FEM principles is used. Warping function is clearly defined by values in grids of mesh $\mathbf{w_i}$. If $\mathbf{B}$ is derivation matrix of shape function, than for strain it is possible to write:

$$\boldsymbol{\varepsilon} = \mathbf{B}.\mathbf{w} + \mathbf{G}.\boldsymbol{\Psi} \tag{16}$$

$$\mathbf{G} = \begin{bmatrix} 1 & z & -y & 0 & 0 & 0 \\ 0 & 0 & 0 & -z & 0 & 1 \\ 0 & 0 & 0 & y & -1 & 0 \end{bmatrix} \tag{17}$$

2.3. Derive warping function

In the paper Kabeláč (2011) there was described analysis how to define warping function $\mathbf{w}$ by FEM :

$$\Omega \quad : \quad \frac{\partial \sigma_x}{\partial x} + \frac{\partial \tau_{xy}}{\partial y} + \frac{\partial \tau_{xz}}{\partial z} = 0 \tag{18a}$$

$$\Gamma \quad : \quad \tau_{xy}.n_y + \tau_{xz}.n_z = 0 \tag{18b}$$

In view of the formulation of the element the first derivation is zero. By using of variational principle and FEM principles the problem is transformed into system of non-linear equations.

$$\mathbf{F} = \sum_i^{elem} \int_{\Omega_i} \mathbf{B}_i^T.\boldsymbol{\sigma}(\boldsymbol{\varepsilon}_i).d\Omega_i = 0 \Rightarrow \mathbf{w} \tag{19}$$

$$\mathbf{K_F} = \frac{\partial F_i}{\partial w_j} \tag{20}$$

These equations are supplemented by conditions for warping function.

$$N = \int_\Omega w.E.d\Omega = 0 \tag{21a}$$

$$M_y = \int_\Omega z.w.E.d\Omega = 0 \tag{21b}$$

$$M_z = \int_\Omega -y.w.E.d\Omega = 0 \tag{21c}$$

Which can be written down as:

$$\mathbf{L}.\mathbf{w} = 0 \tag{22}$$

Here arbitrary material model can be used and defined as follows:

$$\boldsymbol{\sigma} = f(\boldsymbol{\varepsilon}) \tag{23}$$

$$\mathbf{D}_m = \frac{\partial f_i}{\partial \varepsilon_j} \tag{24}$$

The result is warping function defined by values in grid of mesh $\mathbf{w_i}$ for actual deformations $\boldsymbol{\Psi}$. More details in Kabeláč (2011).

2.4. Internal forces and tangential stiffness matrix of cross section

To express searching warping function $\mathbf{w}$ it is possible to express internal forces of cross section by simple relation.

$$\mathbf{V} = \sum_i^{elem} \int_{\Omega_i} \mathbf{G_i}^T.\boldsymbol{\sigma_i}(\boldsymbol{\varepsilon_i}).d\Omega_i \tag{25}$$

Where $\boldsymbol{\varepsilon_i}$ is expressed by relation (16). It remains to express tangential stiffness matrix of cross section $\mathbf{D}$, whih is obtained by derivation of relation (25) according to $\boldsymbol{\Psi}$.

$$\mathbf{D} = \frac{\partial V_i}{\partial \Psi_j} = \sum_i^{elem} \int_{\Omega_i} \mathbf{G_i}^T.\mathbf{D_m}.\left(\mathbf{G_i} + \mathbf{B_i}.\mathbf{dw_i}\right).d\Omega_i \tag{26}$$

$$\mathbf{dw} = \frac{\partial w_i}{\partial \Psi_j} \tag{27}$$

Derivation $\mathbf{w}$ according to $\mathbf{\Psi}$ is a result of solution of system of linear equations.

$$\begin{bmatrix} \mathbf{K_F} & \mathbf{L} \\ \mathbf{L}^T & \mathbf{0} \end{bmatrix} \cdot \begin{bmatrix} \mathbf{dw} \\ -\boldsymbol{\lambda} \end{bmatrix} = \begin{bmatrix} \mathbf{H} \\ \mathbf{0} \end{bmatrix} \tag{28}$$

$$\mathbf{H} = \sum_{i}^{elem} \int_{\Omega_i} \mathbf{B_i}^T.\mathbf{D_m}.\mathbf{G_i}.d\Omega_i \tag{29}$$

2.5. Internal forces and tangential stiffness matrix of beam

One last step is necessary to make. Because strain $\mathbf{\Psi}$ is constant along axis of beam for internal forces in grids of beam element is valid.

$$\boxed{\mathbf{R} = \int_0^l \mathbf{\Xi}^T.\mathbf{V}.dx = l.\mathbf{\Xi}^T.\mathbf{V}} \tag{30}$$

And for tangential stiffness matrix of beam:

$$\boxed{\mathbf{K} = \int_0^l \mathbf{\Xi}^T.\mathbf{D}.\mathbf{\Xi}.dx = l.\mathbf{\Xi}^T.\mathbf{D}.\mathbf{\Xi}} \tag{31}$$

3. Conclusions

The element presented here is robust enough for practical use. Cross section can have arbitrary origin point. It can be composed of more materials and the formulation is independent on material model. A disadvantage of the element is neglecting of non-uniform warping especially in prevailing shear loading. The element will be tested in future and it is supposed to be implemented in commercial CAE software.

Acknowledgements

This contribution has been prepared with the financial support of the company FEM Consulting.

References

Crisfield, M.A. (2000) *Non-linear Finite Element Analysis of Solids and Structures*, Vol. 1, John Wiley & Sons Ltd., West Sussex UK.

Gruttmann, F., Sauer, M., Wagner, W. (1999) Shear Stresses in Prismatic Beams with Arbitrary Cross Sections, *International Journal for Numerical Methods in Engineering*, Vol. 45 No., pp. 865–889.

Gruttmann, F., Wagner, W. (2001) Finite Element Analysis of Saint-Venant Torsion Problem with Exact Integration of the Elastic-Plastic Constitutive Equations, *Computer Methods in Applied Mechanics and Engineering*, 190, pp. 3831-3848.

Chakrabarty, J. (2006) *Theory of plasticity*. Elsevier Butterworth-Heinemann, Oxford.

Kabeláč, J. (2011) Shear stress on arbitrary composite cross section, *Aplied Mechanics 2011*, Velké Bílovice, Czech Republic,Ústav fyziky materiálů AV ČR, Brno.

Kabeláč, J. (2011) Shear stress on arbitrary cross section including plasticity, *Engineering Mechanics 2011*, Svratka, Czech Republic, Institute of Thermomechanics, Academy of Sciences of the Czech republic, Prague.

Němec, I. et al. (2010) *Finite element analysis of structures*, Shaker Verlag, Aachen, Germany.

Zienkiewicz, O.C., Taylor, R.L. (2000) *The Finite Element Method, Vol.1 , The Basic*, 5th, Elsevier Butterworth-Heinemann, Oxford UK.

18th International Conference
ENGINEERING MECHANICS 2012
Svratka, Czech Republic, May 14 – 17, 2012

pp. 585–592
Paper #326

SIMULATION OF THE BEHAVIOUR OF A 3D LINK OF A KNITTED FABRIC MADE OF NI-TI TO THE MECHANICAL LOADING

J. Kafka*

Abstract: *The models of knitted fabrics are geometrically complicated systems. The simulations of the knitted fabrics models have to include nonlinearities in a form of the geometry, contact and in some case in a form of the material. These nonlinearities increase the computational time. One of the simplifications is the geometrical simplification. The model of the knitted fabric can be transfer from 3D to 2D model. That removes the contact. How large influence has this simplification, we can determine with a model of one link. The creation of this model and the results of the simulation for the link are described thereinafter.*

Keywords: ***shape memory alloy, knitted fabric, non-linear simulation***

1. Introduction

Technical textiles are used in many industries such as geoengineering, agroengineering, civil engineering, health service and transport facilities. The technical textiles have unique characteristics, which are the reasons, why they are tested in new fields of application. That brings new needs of testing of not only mechanical properties. One of the several possibilities of testing of the behaviour of the technical textiles to the mechanical loading is simulation by way of the finite element method. This method can be in some cases the only possibility.

In this article is described a link of a knitted fabric, which is made from Ni-Ti material. Ni-Ti is one of the materials, which is part of the shape memory alloy materials (SMA). SMAs are a unique group of materials, which has the property to recover their shape, when the temperature is increased. Further these materials are capable of absorb large elastic deformations to 10%.

Simulations of the mechanical behaviour of the Ni-Ti knitted fabrics, in which I am engaged, include nonlinearities in the form of the large deformations, contact and material. In consequence of these nonlinearities are the computational simulations of large models of the knitted fabrics time-consuming. One of the possibilities, how the time-consuming of the FEM simulations can be reduced, is a disestablishment of the contact nonlinearity. The contact nonlinearity can be removed only in the case, that the influence of the frictional forces is inconsiderable. The investigation of the influence of the frictional forces is the main aim of the simulations, which are described thereinafter.

2. Geometrical model

For a creation of a geometrical model of a 3D link of Ni-Ti knitted fabrics is used Dalidovic`s model. This model simplifies the geometry of the knitted fabrics by means of abscissas and semicircles. The shape of the Dalidovic`s geometry model of the knitted fabric is figured in Figure 1. The geometrical model, which is applied for the following simulations, is in Figure 2.

* Ing. Jiří Kafka: Department of engineering mechanics, Technical university of Liberec, Studentská 2; 46117, Liberec; CZ, e-mail: jiri.kafka@tul.cz

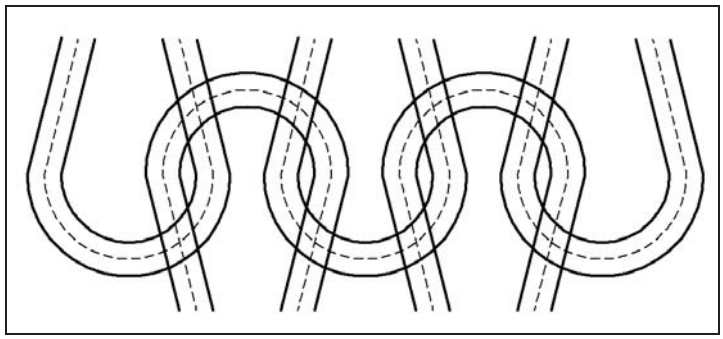

Fig. 1: Dalidovic`s model of the knitted fabrics.

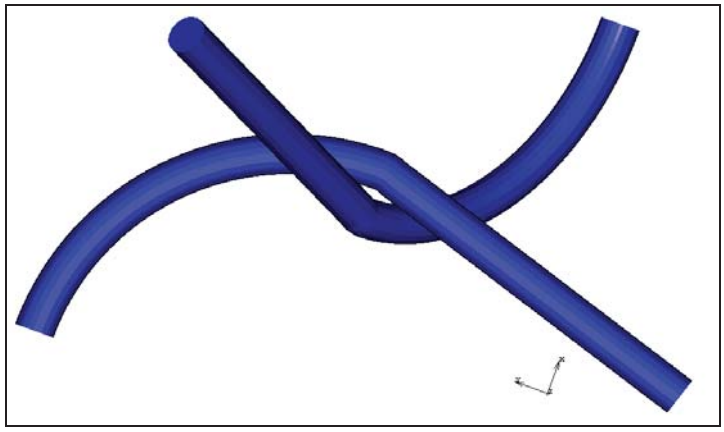

Fig. 2: Geometrical model of the 3D link of the knitted fabrics.

3. Finite element mesh

A three dimensional mesh of elements is created from 2D elements QUAD4, which are created on one of two end sections of the thin wire of the knitted fabrics. These 2D elements are applied for the creation of 3D elements. The two dimensional elements are pulled in the direction of the axis of the thin wire. As a result are 3D elements HEX8, which are an eight/node, isoparametric, arbitrary hexahedral. These linear solid elements are converted to HEX20 elements, which are represented by three-dimensional 20-node bricks with Herrmann formulation. These elements use triquadratic interpolation functions to represent the coordinates and displacements and can be used for large strain behaviour.

The both parts of the geometrical model of the knitted fabrics have an equable geometry, hence the finite element mesh of one thin wire of the knitted fabrics is used for the definition of the second thin wire. The final FE model is shown in Figure 3 and Figure 4. The parameters of the FE mesh are described in Table 1.

Tab. 1: Parameters of the finite element mesh.

Type and number of elements	Number of nodes
Element 35 – HEXA20	-
11400	53238

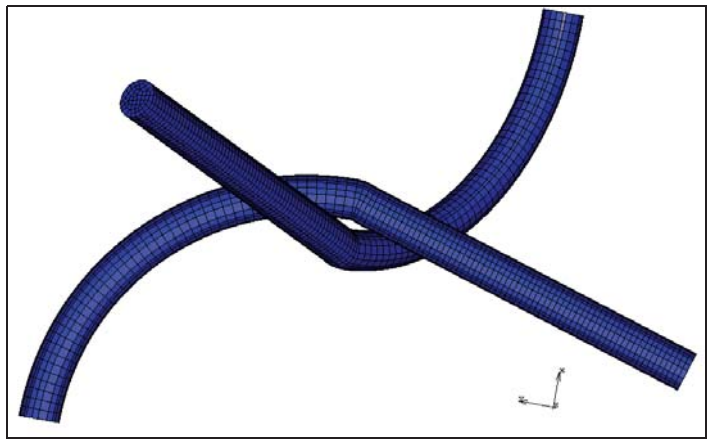

Fig. 3: Finite element mesh of the 3D link of the knitted fabrics.

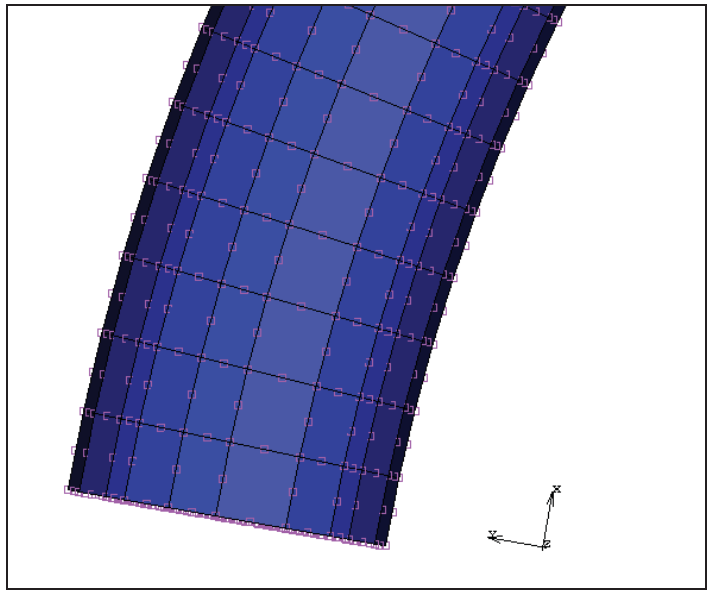

Fig. 4: A detail of the nodes of the FE mesh.

4. Boundary conditions

The influence of the friction is observed on two types of the mechanical loading. The first type of the mechanical loading is a tension of one thin wire in the lengthwise direction of the knitted fabrics. The second thin wire of the knitted fabrics is fixed in the initial position. The boundary conditions for the fixed parts of the 3D link are transformed into the direction of the thin wire as shown the Figure 5.

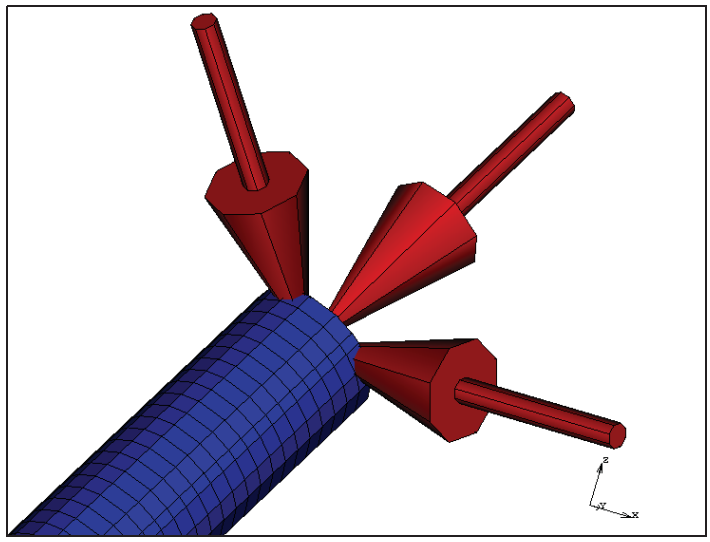

Fig. 5: The transformed boundary conditions for the fixed wire.

The second type of the simulations is a tension of one thin wire in the cross direction of the knitted fabrics. The second wire is fixed as well as in the first simulation.

The tension for the both simulations is defined by means of displacements. Maximal displacement is 0,5mm. All boundary conditions are defined on the end sections of the thin wires of the 3D link. The both type of boundary conditions are shown on Figure 6.

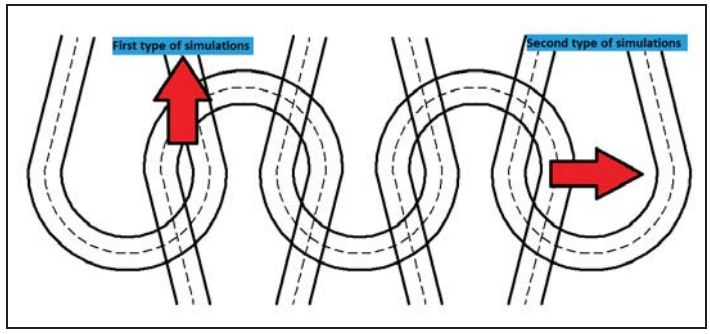

Fig. 6: The boundary conditions for both simulations.

5. Material and material model

One of the materials, which belong to SMAs, is called Nitinol (Ni-Ti). The chemical composition of Ni-Ti is 55.82 wt. % nickel (Ni). Nickel gives the fibers superelastic behaviour above 10°C. SMAs have two phases, each with a different crystal structure and therefore different properties. One of the phases is a high temperature phase called *austenite* (A) and the other is the low temperature phase called *martensite* (M). Austenite has a generally cubic crystal structure and martensite has tetragonal, orthorhombic or monoclinic crystal structure. The change from one structure to the other is called as martensitic transformation.

For the simulations of the behaviour of the 3D link of the knitted fabric is the material model defined by the help of structural material model for the shape memory alloy or more precisely Auricchio`s model. This material model is described by Helmholtz free energy.

$$\psi = \psi_{el} + \psi_{ch} + \psi_{tr} + \psi_{id} + I_{\varepsilon L} \tag{1}$$

This material model can be for tension cases replaced by trilinear material model.

6. Contact

For both simulations is for the contact between the wires of the 3D link of the knitted fabric used arctangent model, which belongs to the group of Coulomb friction models. This friction model is based on a continuously differentiable function in terms of the relative sliding velocity.

$$\sigma_t = -\mu\sigma_n \cdot \vec{t} \tag{2}$$

7. Parameters of the computations

All the variants of the simulations have the same computational parameters. A step of the simulation is set with a fixed and equally small increment. The small increment is important for a finding a contact between the thin wires of the 3D link of the knitted fabric in every step of the computation. During the simulations the large deformations rise. That is the reason, why the third part of the relation for the strain cannot be neglected.

$$\frac{\partial u_j}{\partial x_i} + \frac{\partial u_i}{\partial x_j} + \frac{\partial u_j}{\partial x_i}\frac{\partial u_i}{\partial x_j} \tag{3}$$

8. Results

For both types of the simulations are used the results for the displacement 0,25mm. The maximal displacement 0,5mm is too large. Below I show the results for contact normal forces, contact friction forces, principal stresses, normal stresses and shear stresses.

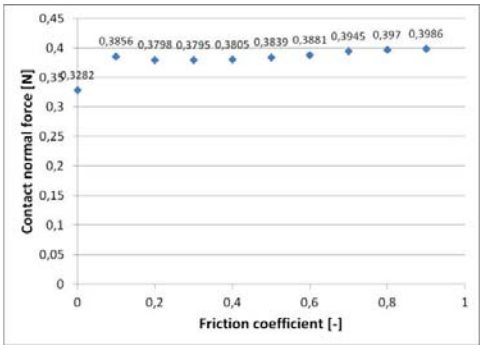

Fig. 7: The contact normal force [N] for the first type of the simulations.

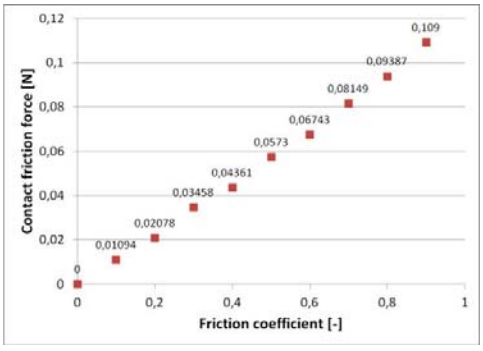

Fig. 8: The contact friction force [N] for the first type of the simulations.

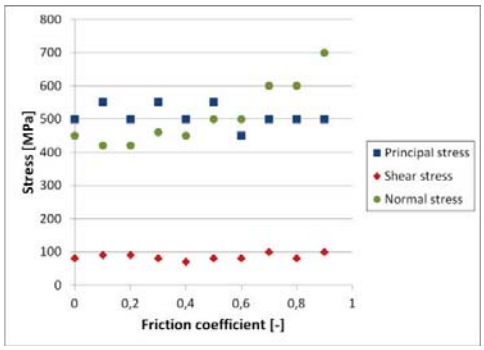

Fig. 9: The stresses [MPa] for the first type of the simulations.

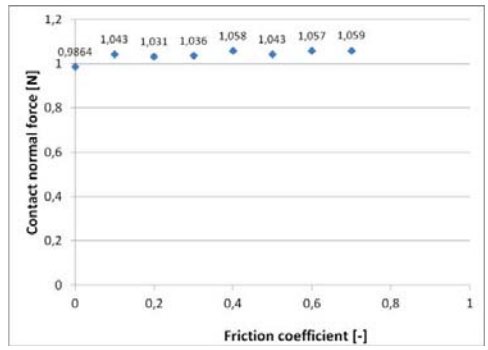

Fig. 10: The contact normal force [N] for the second type of the simulations.

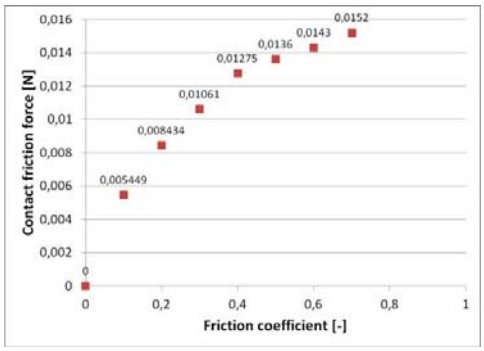

Fig. 11: The contact friction force [N] for the second type of the simulations.

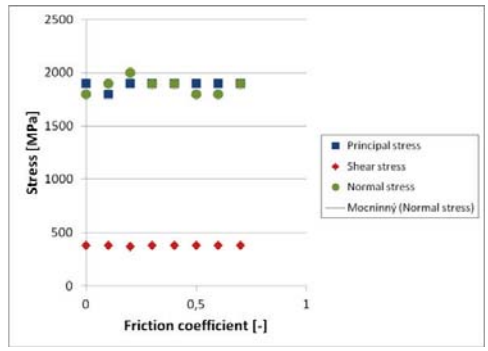

Fig. 12: The stresses [MPa] for the second type of the simulations.

The results show, that only the contact friction force changes in depending on the friction coefficient, which is given the definition of the contact friction force. The contact normal force has large changes, but only for the first type of the simulations and for large friction coefficients, which are unrealistic for our materials. Other variables are unchanging in depending on the friction coefficient.

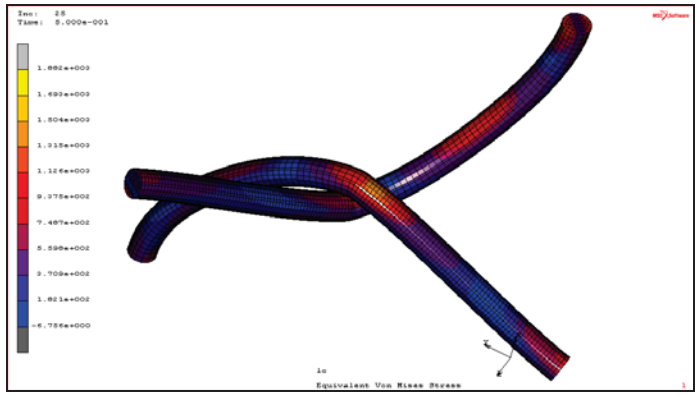

Fig. 13: Von Mises stress [MPa] for the second type of the simulations.

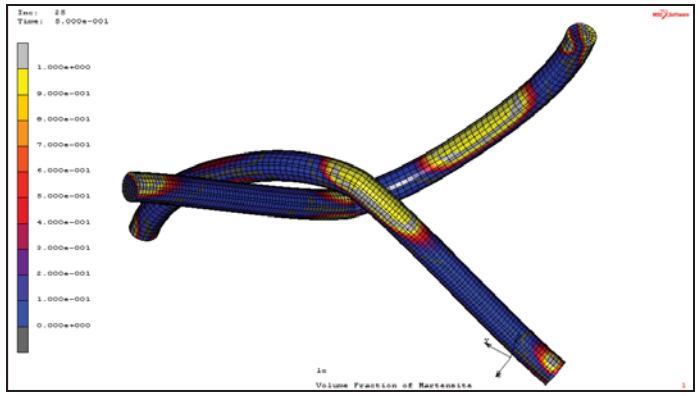

Fig. 14: The volume fraction of martensite.

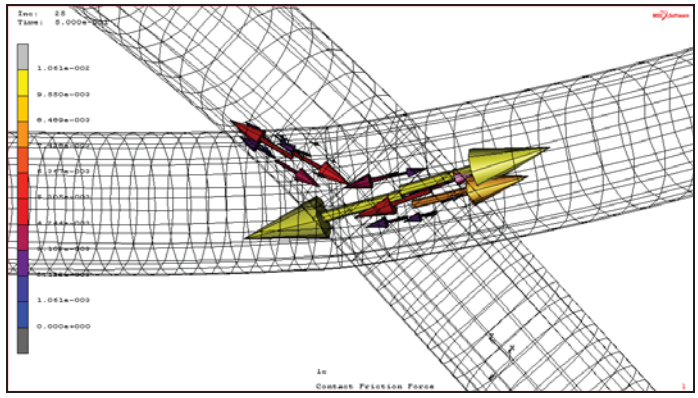

Fig. 15: The contact friction force [N].

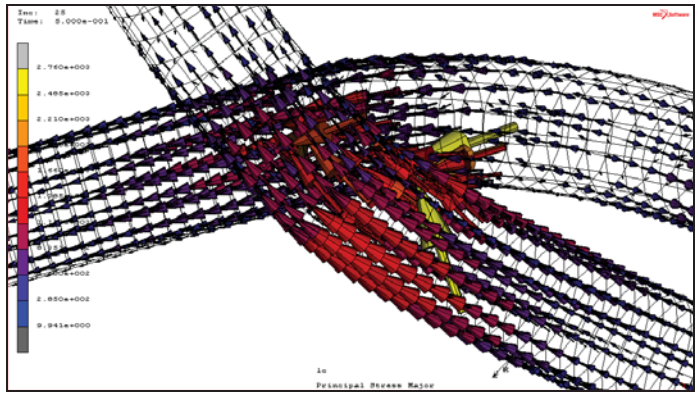

Fig. 16: The principal stress major [MPa].

9. Conclusion

The results of both simulations show, that we can the influence of the friction, if we do not research the friction or heat, which is generated from the friction. Other variables are independent on the friction coefficient. The changes of these variables are shown only for large friction coefficients. The main result of these simulations is the simplified geometrical model of the knitted fabric, which will be used for simulations of large models of the knitted fabrics.

Acknowledgement

Acknowledge the support from project SGS (Student Grant Competition) at Faculty of Mechanical Engineering at Technical university of Liberec, int. n. 2820.

References

Renkens, W. & Kyosev, Y. (2011) Geometry modeling of warp knitted fabrics with 3D form. *Textile Research journal*, 81(4), 437, pp.437-443.

Kharkova, G., Kononova, O., Krasnikovs, A., Eiduks, M., Machanovskis, E. & Dyelyitis, K. (2011) Elastic properties of cotton fabric based polymer composities. *Engineering for rural development,* pp.402-407.

Lomov, S., Moese, M., Stalmans, R., Trycinski, G., Humbeeck, J. V. & Verpoest, I. (2011) Finite element modeling of SMA textiles: superelastic behaviour. *The Journal of the Textile Institure*.

Ramakrishne, S. (1997) Characterization and modeling of the tensile properties of plain weft-knit fabric-reinforced composites. *Composite Science and Technology*, 57.

Reese, S., & Christ, D. (2008) Finite deformation pseudo-elasticity of shape memory alloys – Constitutive modeling and finite element implementation. *International Journal of Plasticity*, 24, pp.455-482.

18th International Conference
ENGINEERING MECHANICS 2012
Svratka, Czech Republic, May 14 – 17, 2012

pp. 593–606
Paper #285

SYMBOLIC ANALYSIS OF A MECHATRONIC DRIVE USING THE PROGRAM SAMD

J. Kalous[1], **D. Biolek**[2], **Z. Kolka**[1]

Abstract: *The paper presents practical application of the new developed program SAMD on a mechatronic drive unit, consisting of a PWM dc-to-dc converter and a permanent-magnet dc motor, to get results of both its symbolic and semisymbolic analyses. Above all it is shown how to create individual purpose-oriented models of that drive to obtain transfer functions, poles and zeroes, frequency characteristics and step responses for both the input supply voltage and the controlling duty ratio.*

Keywords: ***mechatronic drive, PWM dc-to-dc converter, permanent-magnet dc motor, symbolic analysis, program SAMD.***

1. Úvod

Mechatronické pohony procházejí v současné době rychlým vývojem především díky tomu, že se v nich bezprostředně uplatňují nejrychleji se rozvíjející obory elektrotechniky, zejména výkonové elektroniky a číslicové řídící a regulační techniky, a to bez ohledu na to, zda jde o pohony s motory střídavými nebo s motory stejnosměrnými.

Až do nedávné doby byly stejnosměrné motory řízených či regulovaných pohonů zpravidla napájeny ze střídavé elektrické sítě přes řízené tyristorové usměrňovače. V případech, kdy v dané konkrétní aplikaci byl k dispozici pouze stejnosměrný elektrický zdroj s konstantním napětím (např. akumulátorová baterie, diodový usměrňovač apod.), bylo možné řídit či regulovat stejnosměrný motor pouze prostřednictvím ztrátové odporové regulace (reostat, odporový napěťový dělič, výkonový zesilovač), což samozřejmě snižovalo energetickou účinnost celého pohonu. V současné době je dána možnost překonat tento vážný nedostatek použitím spínaných stejnosměrných měničů s impulsní šířkovou modulací, jejichž energetická účinnost překračuje i 95 %.

V počátečním stadiu projektování jakéhokoliv řízeného či regulovaného mechatronického pohonu je obvyklé získat co největších množství informací o statických a dynamických vlastnostech hnacího motoru a jeho napájecí jednotky, které ve vzájemné součinnosti představují akční člen pohonu. Jde zejména o následující kvantitativním ukazatele: stabilita soustavy, velikosti pólů a nul a jejich rozložení v Gaussově rovině komplexní proměnné, činitel zesílení a amplitudové a fázové frekvenční charakteristiky pro řídící (akční) veličinu atp.

V tomto příspěvku, který bezprostředně navazuje na příspěvek Kalous et al. (2010) je ukázáno, jak využít nově vyvinutý program SAMD (z angl. **S**ymbolic **A**nalysis of **M**echatronic **D**rives) k získání podkladů pro analýzu zejména dynamických vlastností akčního členu stejnosměrného mechatronického pohonu, tvořeného zvyšovacím spínaným stejnosměrným měničem a stejnosměrným motorem s permanentními magnety.

2. Model spínače s impulsní šířkovou modulací

Spínané stejnosměrné měniče (SpSSM) jsou výkonové elektronické obvody, které umožňují s vysokou účinností měnit velikost stejnosměrného napětí čili plní ve stejnosměrných elektrických obvodech obdobnou funkci jako transformátory v obvodech střídavých. Obecně obsahují výkonový

[1] Doc. Ing. Jaroslav Kalous, CSc., Prof. Dr. Ing. Zdeněk Kolka, ÚREL FEKT VUT Brno, Purkyňova 118, 612 00 Brno, KalousJaroslav@upcmail.cz, kolka@feec.vutbr.cz

[2] Prof. Ing. Dalibor Biolek, CSc., katedra elektrotechniky, Fakulta vojenských technologií, Univerzita obrany v Brně, Kounicova 65, 662 10 Brno, dalibor.biolek@unob.cz

stejnosměrný vstup a výstup a řídící vstup ve tvaru sledu pravoúhlých impulsů s opakovacím kmitočtem řádu desetitisíců až statisíců impulsů za sekundu a s nastavitelnou šířkou (obr. 1).

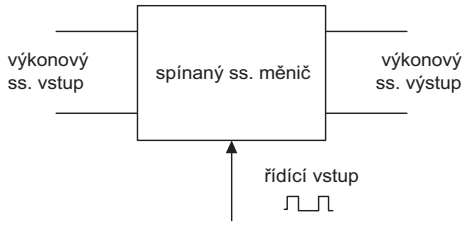

Obr. 1 Blokové schéma stejnosměrného měniče

Na obr. 2 jsou pro ilustraci uvedena principiální obvodová schémata snižovacího a zvyšovacího SpSSM, k jejichž výkonovému vstupu je připojen ss. zdroj napětí U_s, k výkonovému výstupu je připojena rezistorová zátěž R_o. Svorkami *a-p-c* je v obou schématech vymezen tzv. spínač s impulsní šířkovou modulací (spínač s IŠM), složený z aktivního spínače *S* (tranzistor typu BJT, MOSFET, IGBT apod.) a z výkonové polovodičové diody *D* ve funkci tzv. pasivního spínače. Ke svorce *a* je připojen aktivní spínač *S*, ke svorce *p* je připojena dioda *D,* svorka *c* je společná pro obě elektronické součástky.

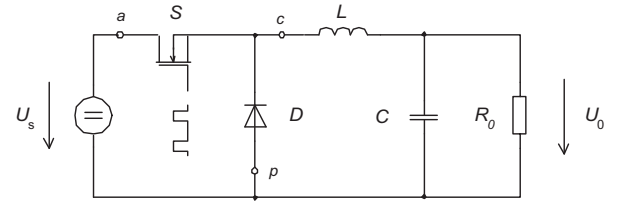

a) snižovací měnič

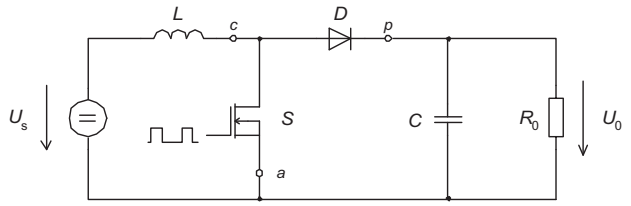

b) zvyšovací měnič

Obr. 2 Principiální schémata spínaných stejnosměrných měničů

Spínač s IŠM je „srdcem“ všech SpSSM a pracuje následovně. V časovém intervalu $0 < t \le dT_{sp}$ každé spínací periody T_{sp} je aktivní spínač *S* sepnut a dioda *D* je v nevodivém stavu, zatímco v časovém intervalu $dT_{sp} < t \le T_{sp}$ je aktivní spínač *S* rozpojen a dioda *D* je ve vodivém stavu. Veličina $d \in (0,1)$ je tzv. *střída spínání*, vyjadřující poměrnou část spínací periody, v níž je aktivní spínač *S* sepnut a dioda *D* je v nevodivém stavu. Zavedeme ještě tzv. *doplňkovou střídu spínání* $d' = 1 - d$, vyjadřující zbývající poměrnou část periody, v níž je aktivní spínač *S* rozpojen a dioda *D* je ve vodivém stavu.

V počítačových analýzách a simulacích SpSSM se hojně používá metoda, založená na tzv. průměrovaných modelech spínačů s IŠM (Dijk, 1995; Kalous, 2004). Tato metoda byla vyvinuta s cílem snazšího vytváření tzv. obvodových modelů SpSSM s IŠM na základě obvodových schémat SpSSM. Vychází z následující myšlenky.

Zatímco pasivní prvky SpSSM (rezistory, cívky, kondenzátory) lze oprávněně považovat za prvky lineární, je spínač s IŠM prvkem nelineárním, určujícím obecně nelineární charakter chování celého

měniče. Pracuje jako jednopólový dvoupolohový přepínač. Schéma ideálního spínače s IŠM je spolu s přiřazenými napětími a proudy uvedeno na obr. 3.

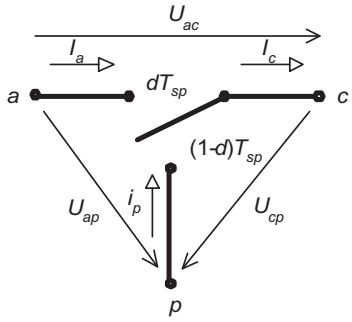

Obr. 3 Ideální spínač s IŠM

Vyjdeme-li z výše uvedeného popisu činnosti reálného spínače s IŠM, potom pro okamžité hodnoty ss. proudů ve spínači platí

$$I_a(t)=\begin{cases} I_c(t) & \text{pro } 0 \le t < dT_{sp}, \\ 0 & \text{pro } dT_{sp} \le t < T_{sp}, \end{cases}$$
$$I_p(t)=\begin{cases} 0 & \text{pro } 0 \le t < dT_{sp}, \\ I_c(t) & \text{pro } dT_{sp} \le t < T_{sp}, \end{cases} \tag{1}$$

Obdobně pro okamžité hodnoty ss. napětí ve spínači platí

$$U_{cp}(t)=\begin{cases} U_{ap}(t) & \text{pro } 0 \le t < dT_{sp}, \\ 0 & \text{pro } dT_{sp} \le t < T_{sp}, \end{cases}$$
$$U_{ac}(t)=\begin{cases} 0 & \text{pro } 0 \le t < dT_{sp}, \\ U_{ap}(t) & \text{pro } dT_{sp} \le t < T_{sp}. \end{cases} \tag{2}$$

Průměrné hodnoty proudů a napětí v periodě spínání pro konstantní střídu spínání $d = d_0$ jsou potom rovny

$$\bar{I}_a = \frac{1}{T_{sp}}\int_0^{T_{sp}} I_a(t)\mathrm{d}t = d_0\bar{I}_c, \qquad \bar{I}_p = \frac{1}{T_{sp}}\int_0^{T_{sp}} I_p(t)\mathrm{d}t = (1-d_0)\bar{I}_c = d_0'\bar{I}_c,$$
$$\overline{U}_{cp} = \frac{1}{T_{sp}}\int_0^{T_{sp}} U_{cp}(t)\mathrm{d}t = d_0\overline{U}_{ap}, \qquad \overline{U}_{ac} = \frac{1}{T_{sp}}\int_0^{T_{sp}} U_{ac}(t)\mathrm{d}t = (1-d_0)\overline{U}_{ap} = d_0'\overline{U}_{ap}. \tag{3}$$

Vztahy pro průměrné hodnoty proudu $\bar{I}_a$ a napětí $\overline{U}_{cp}$ jsou definičními vztahy průměrovaného ideálního spínače s IŠM.

Jestliže střída spínání d není konstantní, platí pro malé odchylky průměrných hodnot proudů a napětí vztahy

$$\tilde{\bar{I}}_p = d_0\tilde{\bar{I}}_c + \bar{I}_{c0}\tilde{d}, \qquad \tilde{\bar{I}}_p = d_0'\tilde{\bar{I}}_c - \bar{I}_{co}\tilde{d},$$
$$\tilde{\overline{U}}_{cp} = d_0\tilde{\overline{U}}_{ap} + \overline{U}_{ap0}\tilde{d}, \qquad \tilde{\overline{U}}_{ac} = d_0'\tilde{\overline{U}}_{ap} - \overline{U}_{ap0}\tilde{d}, \tag{4}$$

které vypočítáme pomocí totálních diferenciálů vztahů (3). Indexem 0 jsou v nich označeny hodnoty veličin v pracovním bodě a vlnovkou nad jednotlivými veličinami jsou označeny jejich malé odchylky v okolí pracovního bodu.

Model spínače s IŠM, do nějž je zahrnut vliv ztrát, vyvolaných pulsující složkou proudu $\tilde{i}_a(t)$ v pasivních prvcích, připojených mezi svorkami $a - p$ spínače, se od modelu ideálního poněkud liší.

Pro případ konstantní střídy spínání $d = d_0$ je model takového spínače s IŠM definován vztahy (Vorpérian, 1990)

$$\bar{I}_a = d_0 \bar{I}_c, \qquad \bar{U}_{ap} = \frac{1}{d_0}\bar{U}_{cp} + d_0' r_e \bar{I}_c \tag{5}$$

kde r_e je ekvivalentní rezistor, jehož velikost je obecně funkcí sériového ztrátového odporu kondenzátoru a zatěžovacího odporu měniče.

Pro případ, kdy střída spínání není konstantní, platí pro malé odchylky průměrných hodnot proudů a napětí vztahy

$$\tilde{\bar{I}}_a = d_0 \tilde{\bar{I}}_c + \bar{I}_{c0}\tilde{d}, \qquad \tilde{\bar{U}}_{ap} = \frac{1}{d_0}\tilde{\bar{U}}_{cp} + d_0' r_e \tilde{\bar{I}}_c - \frac{U_d}{d_0}\tilde{d}, \tag{6}$$

kde

$$U_d = \bar{U}_{ap0} + (d_0 - d_0')r_e \bar{I}_{c0}. \tag{7}$$

Na základě vztahů (5) až (7) byly pro knihovnu programu SAMD vytvořeny dva lineární submodely spínače s IŠM, jejichž schématické značky spolu s orientačními šipkami proudů jsou uvedeny na obr. 4 (Biolek & Biolková, 2007).

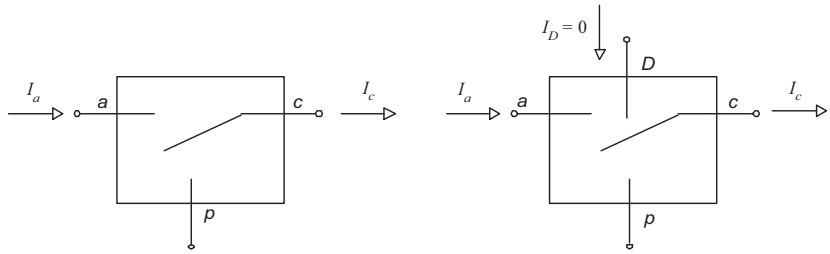

a) model pro d = konst *a) model pro d = var*

Obr. 4 Schématické značky modelů spínače s IŠM

Zatímco model pro konstantní střídu spínání se použije k výpočtu funkcí typu „přenos vstupního napětí“, model pro proměnnou střídu spínání se použije pro výpočty funkcí typu „přenos střídy spínání“.

3. Symbolické a semisymbolické analýzy pohonu a jeho částí

Jako příklad uvažujme akční člen stejnosměrného mechatronického pohonu, tvořeného zvyšovacím SpSSM a stejnosměrným motorem s permanentními magnety (PMDC motor). Celý pohon je napájen z dvanácti voltové akumulátorové baterie. Předpokládá se, že rychlost otáčení motoru bude regulována prostřednictvím změny přenosu napětí SpSSM. Motor bude pracovat při zadaném vstupním napětí 30 V buď naprázdno nebo při zatížení momentem dané velikosti. Uvedený příklad pohonu včetně parametrů je převzat z Lyshevski (2000).

Parametry PMDC motoru jsou následující: indukčnost vinutí kotvy L_a = 4 mH, odpor vinutí kotvy R_a = 3,2 Ω, činitel magnetického pole $c\Phi$ = 0,105 V s rad^{-1} = 0,105 N m A^{-1}, hmotný moment setrvačnosti $J = 5.10^{-5}$ kg m^2 a činitel proporcionálního tlumení $b = 1.10^{-5}$ N m s rad^{-1}.

Pro zadané provozní podmínky musí mít zvyšovací SpSSM ustálený přenos napětí M_U = 2,5, čemuž odpovídá ustálená střída spínání d_0 = 0,6. Aby měnič pracoval jak při chodu naprázdno, tak při zatížení v nepřerušovaném proudovém režimu, byly pro kmitočet spínání f_{sp} = 200 kHz určeny následující parametry jeho prvků: indukčnost cívky L = 0,7 mH a odpor jejího vinutí R_L = 20 mΩ, kapacita kondenzátoru C = 3 mF a jeho sériový ztrátový odpor R_C = 0,15 Ω.

3.1 Stejnosměrný motor s permanentními magnety

Obvodový model PMDC motoru pro přenos vstupního napětí do úhlové rychlosti, vytvořený schématickým editorem programu SAMD, je uveden na obr. 5.

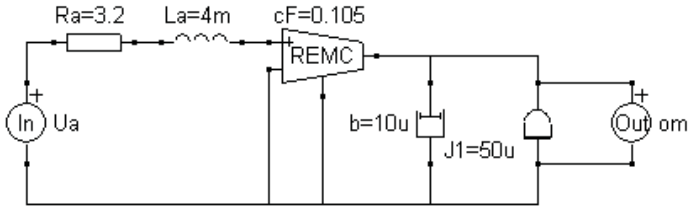

Obr. 5 Obvodový model PMDC motoru pro přenos vstupního napětí

Výsledky výpočtu výše uvedeného přenosu, který je v SAMDu označen jako přenos typu effort-to-effort K_{ee}, poskytne program v následujícím tvaru:

```
_____________symbolic_____________________
cF
---------------------------------------
cF^(2) +Ra*b
+s*( Ra*J1 +La*b )
+s^(2)*( La*J1 )

_____________semisymbolic_________________
Multip. Coefficient =  5.25000000000000E+0005

 1.00000000000000E+0000
---------------------------------------
 5.52850000000000E+0004
 8.00200000000000E+0002 * s
 1.00000000000000E+0000 * s^(2)


_________________zeros_____________________
none

_________________poles_____________________
-7.23820573952289E+0002
-7.63794260477100E+0001
```

Získaný výsledek lze přepsat do obvyklého symbolického a semisymbolického tvaru operátorového přenosu

$$K_{ee}(s) = \frac{\omega(s)}{U_a(s)} = \frac{c\Phi}{L_a J_1 s^2 + (R_a J_1 + L_a b)s + \left((c\Phi)^2 + R_a b\right)} = 5{,}25.10^5 \frac{1}{s^2 + 8{,}002.10^2 s + 5{,}529.10^4}. \quad (8)$$

Je zřejmé, že uvedený přenos nemá žádnou nulu a má dva reálné záporné póly, jimž odpovídají časové konstanty τ_1 = 1,382 ms a τ_2 = 13,09 ms.

Kromě toho SAMD poskytne též přechodovou charakteristiku v semisymbolickém tvaru

```
_____________step response_________________
9.49624672153389E+0000
 1.12028386911409E+0000*exp(-7.23820573952289E+0002*t)
-1.06165305906479E+0001*exp(-7.63794260477100E+0001*t)
```

čemuž odpovídá matematický výraz

$$h_{\omega}(t) = 9{,}466 + 1{,}12e^{-\frac{t}{1{,}38.10^{-3}}} - 10{,}62e^{-\frac{t}{13{,}09.10^{-3}}}. \quad (9)$$

Přechodová charakteristika tedy obsahuje kromě stejnosměrné složky i dvě aperiodické složky s řádově odlišnými velikostmi a časovými konstantami.

3.2 Zvyšovací spínaný stejnosměrný měnič

Pro zvyšovací SpSSM je třeba vytvořit v editoru SAMDu dva obvodové modely a to jednak pro přenos vstupního napětí do napětí výstupního a jednak pro přenos střídy spínání do výstupního napětí..

Průměrovaný obvodový model zvyšovacího SpSSM pro přenos vstupního napětí, vytvořený schématickým editorem programu SAMD, je uveden na obr. 6. Ze srovnání tohoto modelu se zapojením zvyšovacího SpSSM na obr. 2b je zřejmé, že skutečný spínač s IŠM mezi svorkami *c-a-p* byl nahrazen modelem dle obr. 5a. Navíc byly do modelu doplněny ztrátové rezistory R_L a R_C cívky a kondenzátoru. Velikost zatěžovacího odporu R_z odpovídá zatěžovacímu momentu motoru 0,6 N m. Ekvivalentní rezistor r_e v průměrovaném modelu spínače s IŠM je v tomto případě dán paralelní kombinací sériového ztrátového odporu kondenzátoru R_c a zatěžovacího odporu R_z (Biolek & Biolková, 2007).

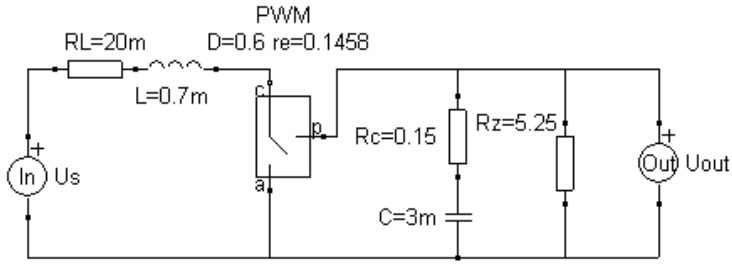

Obr. 6 Obvodový model zvyšovacího SpSSM pro přenos vstupního napětí do výstupního napětí

Výsledky výpočtu přenosu vstupního napětí do výstupního napětí, odpovídající přenosu typu effort-to-effort, poskytne SAMD v následujícím tvaru:

```
_____________symbolic_____________________
Rz -D*Rz
+s*( C*Rc*Rz -C*Rc*D*Rz )
---------------------------------------
D^(2)*Rz +D*re -D^(2)*re +Rz -2*D*Rz +RL
-s*( C*Rc*D^(2)*re +2*C*Rc*D*Rz -C*Rc*D^(2)*Rz -C*Rc*D*re +C*D^(2)*re*Rz -C*Rc*Rz -
        RL*C*Rc -C*D*re*Rz -L -RL*C*Rz )
+s^(2)*( L*C*Rz +L*C*Rc )

_____________semisymbolic_________________
Multip. Coefficient =  8.33333333333333E+0001

 2.22222222222222E+0003
 1.00000000000000E+0000 * s
---------------------------------------
 7.89234567901235E+0004
 1.73621728395062E+0002 * s
 1.00000000000000E+0000 * s^(2)

_____________________zeros_____________________
-2.22222222222222E+0003

_____________________poles_____________________
-8.68108641975308E+0001 + j  2.67184076335775E+0002
```

-8.68108641975308E+0001 - j 2.67184076335775E+0002

Získaný výsledek lze přepsat do symbolického a semisymbolického tvaru operátorového přenosu

$$K_{ee}(s)=\frac{U_{out}(s)}{U_s(s)}=\frac{b_1 s+b_0}{a_2 s^2+a_1 s+a_0}=8{,}333.10^1\,\frac{s+2{,}222.10^3}{s^2+1{,}736.10^2 s+7{,}892.10^4}\,. \tag{10}$$

Závislosti koeficientů polynomů v čitateli b_0, b_1 a ve jmenovateli a_0, a_1, a_2 přenosu (10) na parametrech analyzovaného SpSSM jsou zřejmé z výsledkového textu v části „symbolic“.

Je zřejmé, že uvedený přenos má jednu nulu a dva komplexně sdružené póly, všechny leží v levé části Gaussovy roviny komplexní proměnné. To znamená, že daný zvyšovací SpSSM je stabilní.

Kromě toho SAMD poskytne též přechodovou charakteristiku v semisymbolickém tvaru

_____step response_____
2.34638968839945E+0000
-2.34638968839945E+0000*exp(-8.68108641975308E+0001*t)*cos(2.67184076335775E+0002*t)
-4.50471393772513E-0001*exp(-8.68108641975308E+0001*t)*sin(2.67184076335775E+0002*t).

čemuž odpovídá matematický výraz

$$h_{\overline{U}_{out}}(t)=2{,}346+2{,}389\,e^{-\frac{t}{11{,}52.10^{-3}}}\cos\left(267{,}2\,t-2{,}952\right). \tag{11}$$

Přechodová charakteristika obsahuje kromě stejnosměrné složky exponenciálně tlumenou střídavou složku se stejně velkou amplitudou, s časovou konstantou $\tau = 11{,}52$ ms a s frekvencí $f = 42{,}52$ Hz.

Linearizovaný průměrovaný obvodový model zvyšovacího SpSSM pro přenos střídy spínání do výstupního napětí, vytvořený schématickým editorem programu SAMD, je uveden na obr. 7. Od modelu na obr. 6 se liší v tom, že byl použit čtyřpólový model spínače s IŠM dle obr. 5b a jako vstup slouží „zdroj napětí“ označený symbolem střídy spínání *d*. Číselné hodnoty parametrů linearizovaného spínače s IŠM stejně jako velikosti napětí U_{ap}, proudu I_c a zatěžovacího odporu R_z odpovídají zatěžovacímu momentu motoru 0,6 N m.

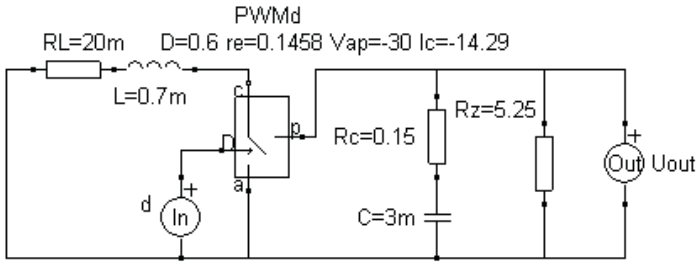

Obr. 7 Obvodový model zvyšovacího SpSSM pro přenos střídy spínání do výstupního napětí

Výsledky výpočtu přenosu střídy spínání do výstupního napětí, odpovídající nepochybně přenosu typu effort-to-effort, poskytne SAMD v následujícím tvaru:

_____symbolic_____
re*Ic*Rz +D*Vap*Rz +D^(2)*re*Ic*Rz -2*D*re*Ic*Rz +RL*Ic*Rz -Vap*Rz
+s*(C*Rc*D*Vap*Rz +C*Rc*D^(2)*re*Ic*Rz -2*C*Rc*D*re*Ic*Rz +C*Rc*re*Ic*Rz -
C*Rc*Vap*Rz +L*Ic*Rz +RL*C*Rc*Ic*Rz)
+s^(2)*(L*C*Rc*Ic*Rz)

D^(2)*Rz +D*re -D^(2)*re -2*D*Rz +Rz +RL
-s*(C*Rc*D^(2)*re -C*Rc*Rz -C*Rc*D^(2)*Rz -C*Rc*D*re +C*D^(2)*re*Rz +2*C*Rc*D*Rz -
RL*C*Rc -C*D*re*Rz -L -RL*C*Rz)
+s^(2)*(L*C*Rz +L*C*Rc)

```
_____________semisymbolic_____________
Multip. Coefficient = -2.08395833333333E+0000

-2.52831770024548E+0006
 1.08447925711176E+0003 * s
 1.00000000000000E+0000 * s^(2)
-------------------------------------
 7.89234567901235E+0004
 1.73621728395062E+0002 * s
 1.00000000000000E+0000 * s^(2)

_________________zeros_________________
-2.22222222222222E+0003
 1.13774296511046E+0003

_________________poles_________________
-8.68108641975308E+0001 + j  2.67184076335775E+0002
-8.68108641975308E+0001 - j  2.67184076335775E+0002
```

Získaný výsledek lze přepsat do symbolického a semisymbolického tvaru operátorového přenosu

$$K_{ee}(s) = \frac{U_{out}(s)}{d(s)} = \frac{b_2 s^2 + b_1 s + b_0}{a_2 s^2 + a_1 s + a_0} = -2{,}084\,\frac{s^2 + 1{,}084.10^3 s - 2{,}528.10^6}{s^2 + 1{,}736.10^2 s + 7{,}892.10^4} \tag{12}$$

Závislosti koeficientů polynomů v čitateli b_0, b_1, b_2 a ve jmenovateli a_0, a_1, a_2 přenosu (12) na parametrech analyzovaného SpSSM jsou zřejmé z výsledkového textu v části „symbolic“.

Je zřejmé, že uvedený přenos má dvě nuly, z nichž jedna leží v pravé části Gaussovy roviny komplexní proměnné. V důsledku toho má analyzovaný zvyšovací SpSSM při přenosu střídy spínání do výstupního napětí charakter dynamického členu s neminimální fází. Dva komplexně sdružené póly přenosu (12) jsou samozřejmě stejné velikosti jako v případě přenosu (9), takže daný SpSSM je i v tomto případě stabilní.

Přechodová charakteristika, kterou vypočítá SAMD, má semisymbolický tvar

```
_____________step response_____________
 6.67597309473158E+0001
-6.88436892806491E+0001*exp(-8.68108641975308E+0001*t)*cos( 2.67184076335775E+0002*t)
-2.94724498796548E+0001*exp(-8.68108641975308E+0001*t)*sin( 2.67184076335775E+0002*t),
```

jemuž odpovídá matematický výraz

$$h_{\overline{U}_{out}}(t) = 0{,}6676 + 0{,}7488\, e^{-\frac{t}{11{,}52.10^{-3}}} \cos(267{,}2t - 2{,}737). \tag{13}$$

V něm byly velikosti stejnosměrné složky a amplitudy střídavé složky stonásobně zmenšeny, což odpovídá skokové změně střídy spínání o velikosti 0,01. Amplituda střídavě složky je srovnatelná s velikostí stejnosměrné složky.

3.3 Stejnosměrný mechatronický pohon se zvyšovacím spínaným měničem

Pro stejnosměrný mechatronický pohon se zvyšovacím SpSSM je třeba vytvořit v editoru SAMDu dva obvodové modely, první pro přenos vstupního napětí do výstupní rychlosti motoru a druhý pro přenos střídy spínání do téže rychlosti.

Průměrovaný obvodový model stejnosměrného mechatronického pohonu se zvyšovacím SpSSM pro přenos vstupního napětí, vytvořený schématickým editorem programu SAMD, je uveden na obr. 8. Předpokládá se, že pohon bude pracovat buď naprázdno nebo zatížený ustáleným momentem 0,6 N m. Ekvivalentní rezistor r_e v průměrovaném modelu spínače s IŠM je v tomto případě dán pouze sériovým ztrátovým odporem kondenzátoru R_C.

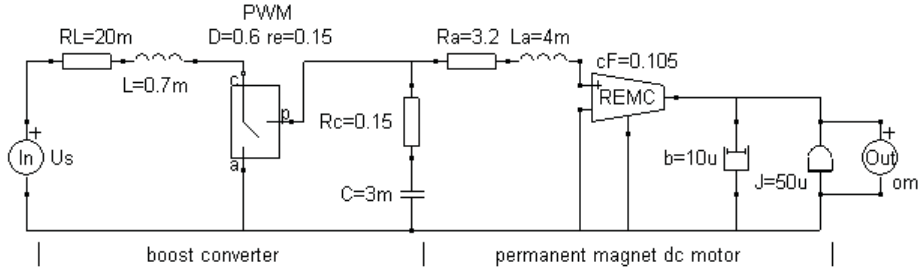

Obr. 8 Obvodový model pohonu pro přenos vstupního napětí do rychlosti

Výsledky výpočtu přenosu vstupního napětí do výstupního rychlosti PMDC motoru, odpovídající přenosu typu effort-to-effort, poskytne SAMD v následujícím tvaru:

```
_____________symbolic_____________________
 -cF +D*cF
-s*( C*Rc*cF -C*Rc*D*cF )
---------------------------------------
 -Ra*b +2*D*cF^(2) -D^(2)*Ra*b +2*D*Ra*b -D*re*b -cF^(2) -D^(2)*cF^(2) -RL*b +D^(2)*re*b
+s*( 2*D*La*b -L*b -D*re*J -C*D*re*Ra*b +C*D^(2)*re*Ra*b -C*Rc*D*re*b
        +2*C*Rc*D*cF^(2) -D^(2)*La*b -C*D*re*cF^(2) -D^(2)*Ra*J +2*C*Rc*D*Ra*b -
        C*Rc*D^(2)*cF^(2) +2*D*Ra*J +C*D^(2)*re*cF^(2) -La*b -C*Rc*D^(2)*Ra*b -
        RL*C*cF^(2) -RL*C*Rc*b -C*Rc*cF^(2) +C*Rc*D^(2)*re*b +D^(2)*re*J -RL*J -
        C*Rc*Ra*b -Ra*J -RL*C*Ra*b )
-s^(2)*( C*D*re*La*b -2*C*Rc*D*Ra*J +C*D*re*Ra*J -2*D*La*J +C*Rc*D^(2)*La*b -
        C*D^(2)*re*La*b +D^(2)*La*J +C*Rc*D*re*J +C*Rc*Ra*J -C*Rc*D^(2)*re*J
        +RL*C*Ra*J +L*C*Rc*b +RL*C*Rc*J +L*J +L*C*cF^(2) -2*C*Rc*D*La*b +L*C*Ra*b
        +RL*C*La*b +C*Rc*D^(2)*Ra*J +C*Rc*La*b +La*J -C*D^(2)*re*Ra*J )
-s^(3)*( C*D*re*La*J +L*C*La*b +RL*C*La*J +L*C*Ra*J +C*Rc*La*J +L*C*Rc*J
        +C*Rc*D^(2)*La*J -C*D^(2)*re*La*J -2*C*Rc*D*La*J )
-s^(4)*( L*C*La*J )

_____________semisymbolic_________________
Multip. Coefficient =  4.50000000000000E+0007

 2.22222222222222E+0003
 1.00000000000000E+0000 * s
---------------------------------------
 4.21352380952381E+0009
 7.39698380952381E+0007 * s
 3.09267738095238E+0005 * s^(2)
 9.51985714285714E+0002 * s^(3)
 1.00000000000000E+0000 * s^(4)

_________________zeros_____________________
-2.22222222222222E+0003

_________________poles_____________________
-6.30822885042182E+0002
-1.22657996946038E+0002 + j  2.70221112370774E+0002
-1.22657996946038E+0002 - j  2.70221112370774E+0002
-7.58468353514534E+0001
```

Získaný výsledek lze přepsat do symbolického a semisymbolického tvaru operátorového přenosu

$$K_{ee}(s)=\frac{\overline{\omega}(s)}{U_s(s)}=\frac{b_1 s+b_0}{a_4 s^4+a_3 s^3+a_2 s^2+a_1 s+a_0}=4{,}5.10^7\,\frac{s+2{,}222.10^3}{s^4+9{,}52.10^2 s^3+3{,}093.10^5 s^2+7{,}397.10^7 s+4{,}214.10^9}. \quad (14)$$

Závislosti koeficientů polynomů v čitateli b_0, b_1 a ve jmenovateli a_0, a_1, a_2, a_3, a_4 přenosu (14) na parametrech analyzovaného SpSSM jsou zřejmé z výsledkového textu v části „symbolic“.

Je zřejmé, že uvedený přenos má jednu nulu, dva reálné póly a dvojici komplexně sdružených pólů. Všechny leží v levé části Gaussovy roviny komplexní proměnné. To znamená, že daný mechatronický stejnosměrný pohon se zvyšovacím SpSSM je stabilní.

Kromě toho SAMD poskytne též přechodovou charakteristiku v semisymbolickém tvaru

```
_____step response_____
2.37331042900413E+0001
 6.17522523926224E-0001*exp(-6.30822885042182E+0002*t)
-3.05089075970093E+0001*exp(-7.58468353514534E+0001*t)
 6.15828078304176E+0000*exp(-1.22657996946038E+0002*t)*cos( 2.70221112370774E+0002*t)
-4.32643606343418E+0000*exp(-1.22657996946038E+0002*t)*sin( 2.70221112370774E+0002*t),
```

čemuž odpovídá matematický výraz

$$h_{\overline{\omega}}(t)=23{,}73+0{,}6175e^{-\frac{t}{1{,}59.10^{-3}}}-30{,}51e^{-\frac{t}{13{,}2.10^{-3}}}+7{,}526e^{-\frac{t}{8{,}15.10^{-3}}}\cos(270{,}2t-0{,}6124) \quad (15)$$

Přechodová charakteristika tedy obsahuje kromě stejnosměrné složky dvě aperiodické složky s řádově odlišnými časovými konstantami τ_1= 1,59 ms a τ_2= 13,2 ms a exponenciálně tlumenou střídavou složku s časovou konstantou τ = 8,15 ms a s frekvencí f = 43 Hz. Dominantní složkou přechodové charakteristiky je aperiodická složka o velikosti 30,31 rad s^{-1}, amplituda střídavé složky představuje cca 25 % velikosti dominantní složky. Navíc časová konstanta tlumení střídavé složky je ve srovnání s časovou konstantou dominantní složky o něco více než poloviční.Z toho vyplývá, že kmitání výstupní rychlosti je téměř zanedbatelné. O tom se lze v SAMDu snadno přesvědčit zobrazením jejího časového průběhu (pro úsporu místa není v tomto článku uveden).

Pro posuzování dynamických vlastností daného mechatronického pohonu je třeba znát i průběh frekvenční charakteristiky. Program SAMD nabízí jednak kmitočtovou charakteristiku ve tvaru Nyquistova diagramu a jednak ve tvaru logaritmických kmitočtových charakteristik (Bodeho diagramy). Na obr. 9 je uvedena logaritmická amplitudová frekvenční charakteristika a na obr. 10 pak logaritmická fázová frekvenční charakteristika pro přenos vstupního napětí do výstupní rychlosti.

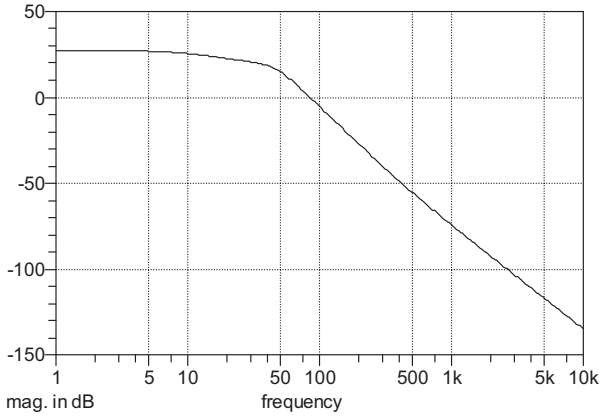

Obr. 9 Logaritmická amplitudová frekvenční charakteristika pro přenos vstupního napětí

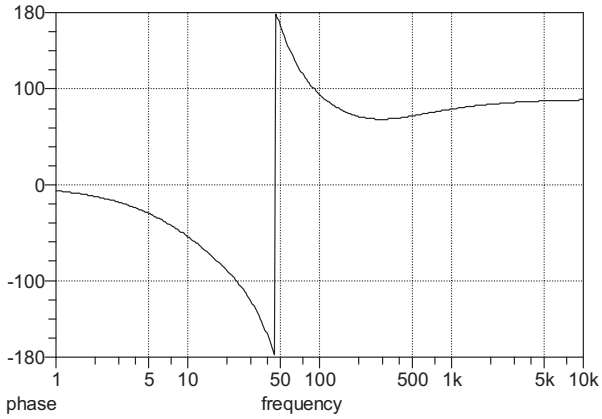

Obr.10 Logaritmická fázová frekvenční charakteristika pro přenos vstupního napětí

Linearizovaný průměrovaný obvodový model stejnosměrného mechatronického pohonu se zvyšovacím SpSSM pro přenos střídy spínání, vytvořený schématickým editorem programu SAMD, je uveden na obr. 11. Od modelu na obr. 8 se liší v tom, že byl použit čtyřpólový model spínače s IŠM dle obr. 5b a jako vstup slouží „zdroj napětí" označený symbolem střídy spínání *d*. Číselné hodnoty parametrů linearizovaného spínače s IŠM stejně jako velikosti napětí U_{ap}, proudu I_c a zatěžovacího odporu R_z odpovídají zatěžovacímu momentu motoru 0,6 N m.

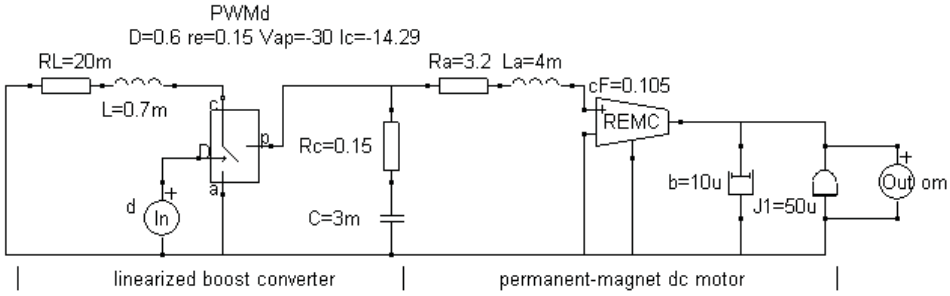

Obr. 11 Linearizovaný obvodový model pohonu pro přenos vstupního napětí do rychlosti

Výsledky výpočtu přenosu střídy spínání do výstupní rychlosti PMDC motoru, odpovídající přenosu typu effort-to-effort, poskytne SAMD v následujícím tvaru:

```
_____________symbolic_____________
 -re*Ic*cF -D*Vap*cF -D^(2)*re*Ic*cF +2*D*re*Ic*cF -RL*Ic*cF +Vap*cF
-s*( C*Rc*D*Vap*cF +C*Rc*D^(2)*re*Ic*cF -2*C*Rc*D*re*Ic*cF +C*Rc*re*Ic*cF -
       C*Rc*Vap*cF +L*Ic*cF +RL*C*Rc*Ic*cF )
-s^(2)*( L*C*Rc*Ic*cF )
---------------------------------------
2*D*Ra*b -cF^(2) -D^(2)*Ra*b -Ra*b -D*re*b +2*D*cF^(2) -D^(2)*cF^(2) -RL*b +D^(2)*re*b
-s*( La*b +L*b +D*re*J1 +C*D*re*Ra*b -C*D^(2)*re*Ra*b +C*Rc*D*re*b +C*Rc*cF^(2)
       +D^(2)*La*b +C*D*re*cF^(2) +D^(2)*Ra*J1 +C*Rc*Ra*b +C*Rc*D^(2)*cF^(2) +Ra*J1 -
       C*D^(2)*re*cF^(2) -2*D*La*b +C*Rc*D^(2)*Ra*b +RL*C*cF^(2) +RL*C*Rc*b -
       2*C*Rc*D*cF^(2) -C*Rc*D^(2)*re*b -D^(2)*re*J1 +RL*J1 -2*C*Rc*D*Ra*b -2*D*Ra*J1
       +RL*C*Ra*b )
-s^(2)*( C*D*re*La*b +C*Rc*Ra*J1 +C*D*re*Ra*J1 +La*J1 +C*Rc*D^(2)*La*b -
       C*D^(2)*re*La*b +D^(2)*La*J1 +C*Rc*D*re*J1 -2*C*Rc*D*Ra*J1 -C*Rc*D^(2)*re*J1
       +RL*C*Ra*J1 +L*C*Rc*b +RL*C*Rc*J1 +L*J1 +L*C*cF^(2) +C*Rc*La*b +L*C*Ra*b
       +RL*C*La*b +C*Rc*D^(2)*Ra*J1 -2*C*Rc*D*La*b -2*D*La*J1 -C*D^(2)*re*Ra*J1 )
```

```
-s^(3)*( C*D*re*La*J1 +L*C*La*b +RL*C*La*J1 +L*C*Ra*J1 -2*C*Rc*D*La*J1 +L*C*Rc*J1
        +C*Rc*D^(2)*La*J1 -C*D^(2)*re*La*J1 +C*Rc*La*J1 )
-s^(4)*( L*C*La*J1 )

_____________semisymbolic_____________
Multip. Coefficient = -1.12533750000000E+0006

-2.52618436691215E+0006
 1.08543925711176E+0003 * s
 1.00000000000000E+0000 * s^(2)
---------------------------------------
 4.21352380952381E+0009
 7.39698380952381E+0007 * s
 3.09267738095238E+0005 * s^(2)
 9.51985714285714E+0002 * s^(3)
 1.00000000000000E+0000 * s^(4)

_________________zeros_____________________
-2.22222222222222E+0003
 1.13678296511046E+0003

_________________poles_____________________
-6.30822885042182E+0002
-1.22657996946038E+0002 + j  2.70221112370774E+0002
-1.22657996946038E+0002 - j  2.70221112370774E+0002
-7.58468353514534E+0001
```

Získaný výsledek lze přepsat do symbolického a semisymbolického tvaru operátorového přenosu

$$K_{ee}(s)=\frac{\overline{\omega}(s)}{\widetilde{d}(s)}=\frac{b_2 s^2+b_1 s+b_0}{a_4 s^4+a_3 s^3+a_2 s^2+a_1 s+a_0}=-1{,}125.10^6\,\frac{s^2+1{,}085.10^3 s-2{,}256.10^6}{s^4+9{,}52.10^2 s^3+3{,}093.10^5 s^2+7{,}397.10^7 s+4{,}214.10^9}. \qquad (16)$$

Závislosti koeficientů polynomů v čitateli b_0, b_1, b_2 a ve jmenovateli a_0, a_1, a_2, a_3, a_4 přenosu (16) na parametrech analyzovaného SpSSM jsou zřejmé z výsledkového textu v části „symbolic“.

Je zřejmé, že uvedený přenos má dvě nuly, z nichž jedna leží v pravé části Gaussovy roviny komplexní proměnné. V důsledku toho má analyzovaný mechatronický pohon se zvyšovacím SpSSM při přenosu střídy spínání do výstupního rychlosti PMDC motoru charakter dynamického členu s neminimální fází. Dva reálné póly a dvojice komplexně sdružených pólů přenosu (16) jsou samozřejmě stejné velikosti jako v případě přenosu (14), takže daný SpSSM je i v tomto případě stabilní.

Přechodová charakteristika, kterou vypočítá SAMD, má semisymbolický tvar

```
_____________step response_________________
 6.74687062067722E+0002
 2.72965971705198E+0001*exp(-6.30822885042182E+0002*t)
-9.25177733370800E+0002*exp(-7.58468353514534E+0001*t)
 2.23194074132558E+0002*exp(-1.22657996946038E+0002*t)*cos( 2.70221112370774E+0002*t)
-9.46482188129187E+0001*exp(-1.22657996946038E+0002*t)*sin( 2.70221112370774E+0002*t),
```

jemuž odpovídá matematický výraz

$$h_{\overline{\omega}}(t)=6{,}747+0{,}2730\,e^{-\frac{t}{1{,}59.10^{-3}}}-9{,}252\,e^{-\frac{t}{13{,}2.10^{-3}}}+2{,}424\,e^{-\frac{t}{8{,}15.10^{-3}}}\cos 270{,}2\left(270{,}2t-0{,}4011\right). \qquad (17)$$

V něm byly velikosti stejnosměrné složky i obou aperiodických složek a amplitudy střídavé složky stonásobně zmenšeny, což odpovídá skokové změně střídy spínání o velikosti 0,01. Dominantní složkou přechodové charakteristiky je v tomto případě aperiodická složka o velikosti 9,252 rad s^{-1}, amplituda střídavé složky představuje cca 26 % velikosti dominantní složky. Navíc časová konstanta

tlumení střídavé složky je ve srovnání s časovou konstantou dominantní složky o něco více než poloviční. Z toho vyplývá, že kmitání výstupní rychlosti je téměř zanedbatelné. O tom se lze v SAMDu snadno přesvědčit zobrazením jejího časového průběhu (pro úsporu místa není v tomto článku uveden).

Pro posuzování dynamických vlastností daného mechatronického pohonu při přenosu střídy spínání do výstupní rychlosti je třeba znát i průběhy frekvenční charakteristiky pro chod naprázdno a pro chod se zatížením momentem 0,6 N m. Na obr. 12 jsou uvedeny logaritmické amplitudové frekvenční charakteristiky a na obr. 13 pak logaritmické fázové frekvenční charakteristiky pro přenos střídy spínání do výstupní rychlosti a uvedená zatížení.

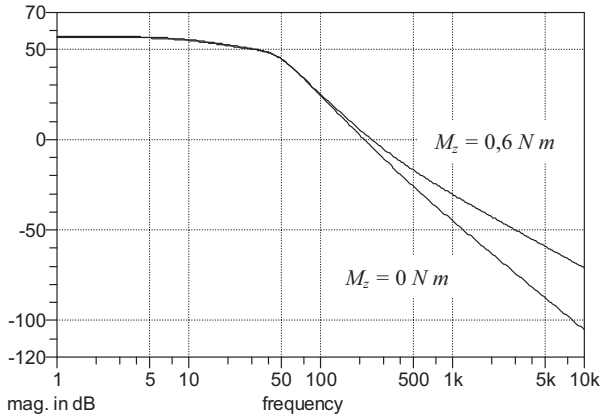

Obr. 12 Logaritmické amplitudové frekvenční charakteristiky pro přenos střídy spínání

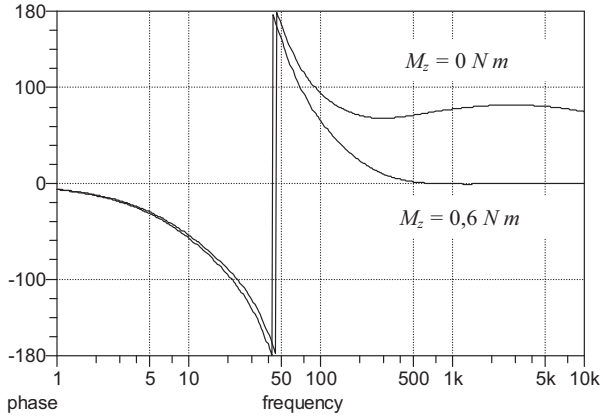

Obr. 13 Logaritmické fázové frekvenční charakteristiky pro přenos střídy spínání

Z průběhů jak amplitudové tak i fázové frekvenční charakteristiky pro přenos střídy spínání je patrné, že jejich tvary závisí na zatížení motoru. U amplitudové charakteristiky je zřejmé, že při zatížení motoru je frekvence, při které tato charakteristika prochází nulou vyšší než při chodu naprázdno a navíc se zmenšuje její strmost. Fázová charakteristika vykazuje při vyšších frekvencích nulový fázový posuv.

Výše uvedenými postupy byly zjištěny a analyzovány přenosy vstupního napětí a střídy spínání do výstupní rychlosti pohonu. Podobně lze v případě potřeby zjišťovat a analyzovat přenosy obou uvedených veličin např. do výstupního napětí zvyšovacího SpSSM nebo do proudu kotvy PMDC motoru přesunutím výstupního bloku Out v obvodových modelech mezi příslušné uzly nebo do příslušné větve a volbou typu přenosu typu effort-to-flow pro případ výpočtu přenosů do proudu kotvy PMDC motoru.

4. Závěr

V příspěvku je na příkladu akčního členu mechatronického stejnosměrného pohonu, tvořeného zvyšovacím SpSSM a PMDC motorem ukázáno, jakým způsobem lze pomocí programu SAMD analyzovat jeho základní dynamické vlastnosti při přenosu vstupního napětí a při přenosu střídy spínání do výstupní rychlosti motoru, které jsou výchozím podkladem pro návrhy přímého nebo zpětnovazebního řízení a regulace celého pohonu. Ukázalo se, že vzhledem ke snadnosti vytváření účelově orientovaných obvodových modelů v grafickém editoru uvedeného programu, vycházejících v případě elektrických a elektronických obvodů z jejich obvodových schémat a v případě mechanických částí z obdobných ekvivalentních schémat, a vzhledem ke snadnosti formulace příslušných přenosů lze považovat program SAMD za významný příspěvek k analýzám projektovaných nebo již realizovaných mechatronických pohonů.

Poděkování

V příspěvku jsou prezentovány dílčí výsledky výzkumu, který je podporován Grantovou Agenturou ČR v rámci řešení projektu č. P102/10/1665.

Odkazy

Biolek, D. & Biolková, V. (2007), Symbolická analýza DC-DC měničů s impulsovou šířkovou modulací. *Slaboproudý obzor,* 63 (2007), No. 3 – 4, pp. 29 – 32.

Dijk, E. et al (1995), PWM-Switch Modeling of DC-DC Converters, in *IEEE Trans. on Power Electronics,* 1995, Vol. 10, No. 6, 659 – 664.

Kalous, J. (2004), Dvě metody modelování stejnosměrných měničů s impulsní šířkovou modulací, *Sborník Univerzity obrany v Brně,* řada B, 2004, č. 2, 77 – 96)

Kalous, J. (2006), Modelování spínaných stejnosměrných měničů. *Slaboproudý obzor,* 62 (2006), No. 3 – 4,. P1 – P10.

Kalous, J., Biolek, D., Kolka, Z. (2010), Project of a Program for Symbolic Analyses of Mechatronic Drives, in *Proc. of Int. Conf. on Engineering Mechanics 2010* (I. Zolotarev, ed), Inst. of Thermomechanics, AS CR, v.v.i., Prague, May 2010.

Lyshevski, S. E. (2000), *Electromechanical Systems, Electric Machines, and Applied Mechatronics,* CRC Press LLC, 2000.

Vorpérian, V.(1990), Simplified Analysis of PWM Converters Using Model of PWM Switch, Part I: Continuous Conduction Mode, *IEEE Trans. On Aerospace and Electronic Systems,* 1990, Vo. 26, No. 3, 490 – 496.

18th International Conference
ENGINEERING MECHANICS 2012
Svratka, Czech Republic, May 14 – 17, 2012

pp. 607–619
Paper #322

SIMULATION OF FLIGHT CONTROL OF A HUMMINGBIRD LIKE ROBOT NEAR HOVER

M. Karásek, A. Preumont *

Abstract: *Interest in Micro Air Vehicles (MAVs) capable of hovering is gradually increasing because they can be a low-cost solution for security applications or remote inspection. Much research has centred on designs inspired by insects and hummingbirds, where the propellers are replaced by flapping wings. It is assumed that that flapping wings improve, at small scales, both manoeuvrability and energy efficiency. This numerical work based on quasi-steady aerodynamics applies to a hummingbird robot with a pair of flapping wings and a 12 cm wingspan. We construct a control derivatives matrix that estimates the effect of each wing kinematics parameter on the cycle averaged wing forces and forms the key stone of the flight controller. We implement the controller in a simulation model with rigid body dynamics and "continuous" (i.e. not averaged) aerodynamics. The simulation results show that the controller stabilizes the robot attitude and controls the flight in 4 DOF (translation in any direction + yaw rotation) by modifying only 2 wing kinematic parameters per wing - the flapping amplitude and the mean wing position. Other control parameters are possible. Thus, various mechanical design solutions can be studied in the future.*

Keywords: ***Micro Air Vehicle, flapping wings, control.***

1. Introduction

Micro Air Vehicles (MAVs) are small flying robots with remote or autonomous operation designed to fly indoors or outdoors. They are being used by private companies as well as law enforcement units for aerial photography, terrain reconnaissance and video surveillance. A vast majority of MAVs is based on fixed and rotary wings.

MAVs with flapping wings have been researched intensively during recent years. These bio-inspired designs mimicking hummingbirds and insects are believed to combine energy efficient lift production, capability of hovering flight and high maneuverability. First successful flapping wing MAVs had dragonfly morphology (de Croon et al., 2009), see Fig. 1 left. Nano Hummingbird (Keennon et al., 2012) is the first man-made flapping wing MAV to take-off, hover and fly in any direction. The researchers managed to integrate avionics, flapping and control mechanisms and a battery sufficient for 11 min flight into a robot of 19 g with 16.5 cm wingspan (Fig. 1 right).

DelFly Micro
by TU Delft
(de Croon et al., 2009)
weight 3.07 g
wingspan 10 cm
endurance 3 min

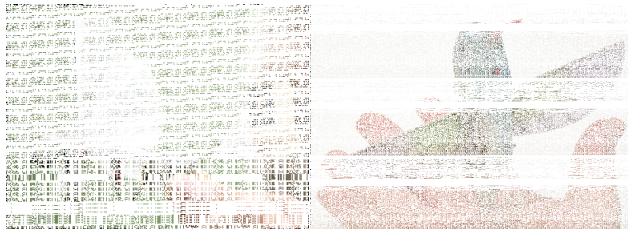

Nano Hummingbird
by AeroVironment Inc.
(Keennon et al., 2012)
weight 19 g
wingspan 16.5 cm
endurance 4-11 min

Fig. 1: Examples of MAVs with flapping wings

Characteristic features of flapping flight include high flapping frequencies (from 15 Hz in large hummingbirds to hundreds of Hz in insects) and high angles of attack. The aerodynamic mechanisms of

*Ing. Matěj Karásek, Prof. André Preumont: Active Structures Laboratory, Université Libre de Bruxelles, CP 165/42, Av.F.D.Roosevelt 50; 1050, Brussels; BE, e-mail: matej.karasek@ulb.ac.be

flapping wings responsible for high lift production were described in (Sane, 2003; Shyy et al., 2010). Studies on flapping flight stability and control mechanisms, recently reviewed by (Orlowski & Girard, 2012), show that the flapping flight is naturally unstable. It is controlled by modifications of wing trajectory.

Many simulations of flapping flight have been carried out, the majority of them uses quasi-steady aerodynamics derived from thin airfoil theory using blade elements theory (Sane & Dickinson, 2002). Various control approaches were successfully used: pseudo-inverse allocation + PID (Orlowski et al., 2010), output-feedback LQR (Deng et al., 2006a,b), back-stepping and feedback linearization (Rakotomamonjy et al., 2010) or Central Pattern Generator control that mimicks spinal cords (Chung & Dorothy, 2010).

In this numerical work, based on quasi-steady aerodynamics and rigid body dynamics, we present a control strategy that is similar to cascade control of quadrocopters (Michael et al., 2010). Flight is controlled in 4 DOF (any direction + turning); vertical flight and turning is controlled directly, while flight forward/backward and sideways is achieved by body pitching and rolling respectively. We parametrize the wing kinematics and study the effect of each parameter on cycle averaged forces and moments generated by the wing. From the results we construct a control derivatives matrix (similar to (Doman et al., 2010)), that is used to transform the control forces/moments into wing motion changes. We discuss the selection of control parameters as these are crucial for design of wing mechanism in future robot. Finally we test the control performance with a selected set of control parameters in simulation.

2. Mathematical model

2.1. Wing motion

Motion of a flapping wing can be described by 3 angles (Fig. 2): sweep angle ϕ, deviation angle δ and wing inclination angle α^*. They are measured from the mean stroke plane, which is inclined from the body horizontal plane $x_B y_B$ by Θ.

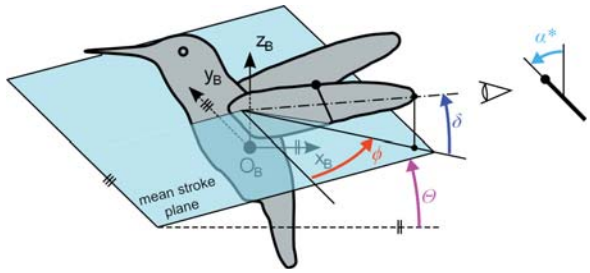

Fig. 2: Wing motion angles: sweep angle ϕ, deviation angle δ and inclination angle α^*

In the current study we assume harmonic motion in all three DOFs according to equations

$$\begin{aligned} \phi &= \phi_0 + \phi_m cos(2\pi f t) \\ \alpha^* &= \alpha_0 + (\pi/2 - \alpha_m) sin(2\pi f t - \varphi_\alpha) \\ \delta &= \begin{cases} \delta_{m1} sin(2\pi f t) \\ \delta_{m2} sin(4\pi f t) \end{cases} \end{aligned} \tag{1}$$

where t is time. The motion is parameterized by 9 parameters (Fig. 3): flapping frequency f, mean stroke plane angle Θ, sweep angle amplitude ϕ_m and offset ϕ_0; inclination angle amplitude α_m, offset α_0 and phase shift φ_α; deviation angle amplitude δ_{m1} (resulting into an oval trajectory) or δ_{m2} (resulting into a "figure 8" trajectory).

2.2. Quasi-steady aerodynamics

We use quasi steady approach (Sane & Dickinson, 2002) to model the forces generated by flapping wings. The wing is assumed to be flat and rigid. The model was derived from steady flow thin airfoil

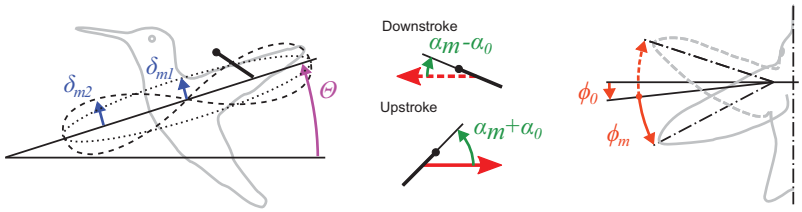

Fig. 3: Wing motion angles: sweep angle ϕ, deviation angle δ and angle of attack α

theory using blade element theory. Experimentally obtained force coefficients published by (Dickinson et al., 1999) include, at least partially, the effects of "unsteady" flow mechanisms typical for flapping flight.

We consider two force components: translational force and rotational force. Because they result mainly from pressure field distribution around the wing they are placed to the center of pressure (CP). We neglect the effect of added mass inertia of the surrounding fluid (virtual mass force) as its contribution to the total force is very small.

The necessary wing geometry parameters are displayed in Fig. 4, definitions are given in (Ellington, 1984). S is the surface of a single wing, R is the wing length, $\bar{c}$ is the mean chord length, $\hat{r} = r/R$ is non-dimensional position of a wing blade and $\hat{c} = c/\bar{c}$ is the normalized chord length, $\hat{x}_0$ is the non-dimensional position of the rotational axis. Similar to other studies we assume the center of pressure (CP) is located, in chord-wise direction, at the rotational axis. The span-wise CP location R_{CP} is determined by the product of wing length R and the radius of second moment of inertia $\hat{r}_2$.

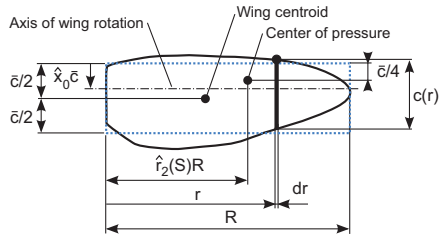

Fig. 4: Wing geometry parameters

According to (Deng et al., 2006a) the total force can be expressed, in normal and tangential direction of the wing, as

$$
\begin{aligned}
F_{T,tr} &= 0.5\rho S U_{CP}^2 C_T(\alpha) \\
F_{N,tr} &= 0.5\rho S U_{CP}^2 C_N(\alpha) + \pi\left(\frac{3}{4} - \hat{x}_0\right)\rho\dot{\alpha}\frac{U_{CP}}{\hat{r}_2}\bar{c}^2 R\int_0^1 \hat{r}\hat{c}^2(\hat{r})d\hat{r}
\end{aligned}
\tag{2}
$$

where ρ is the air density and $C_N(\alpha)$ and $C_T(\alpha)$ are the force coefficients given as a function of angle of attack α by expressions

$$
\begin{aligned}
C_N(\alpha) &= 3.4\sin(\alpha) \\
C_T(\alpha) &= \begin{cases} 0.4\cos^2(2\alpha) & 0 \le |\alpha| < \frac{\pi}{4} \\ 0 & \frac{\pi}{4} \le |\alpha| < \frac{3\pi}{4} \\ -0.4\cos^2(2\alpha) & \frac{3\pi}{4} \le |\alpha| < \pi \end{cases}
\end{aligned}
\tag{3}
$$

2.3. Center of pressure velocity and angle of attack

To express the CP velocity we introduce three coordinate frames: global frame G, body-fixed frame B and wing-fixed frame W. They are displayed in Fig. 5. A left superscript is used to indicate the frame in

which a vector or matrix is expressed. The CP velocity is a resultant of body absolute motion (velocity $\mathbf{v_{GB}}$, angular velocity $\boldsymbol{\omega}_{\mathbf{GB}}$) and the wing rotation around the body (angular velocity $\omega_{\mathbf{BW}}$). Using the simultaneous motion theory we can express the velocity of CP in W frame as

$$^{\mathbf{W}}\mathbf{v_{GCP}} = \mathbf{R_{WB}}\left(^{\mathbf{B}}\mathbf{v_{GB}} + {}^{\mathbf{B}}\boldsymbol{\omega}_{\mathbf{GB}} \times {}^{\mathbf{B}}\mathbf{r_{BCP}}\right) + {}^{\mathbf{W}}\boldsymbol{\omega}_{\mathbf{BW}} \times {}^{\mathbf{W}}\mathbf{r_{WCP}} \tag{4}$$

where $\mathbf{r_{WCP}}$ and $\mathbf{r_{BCP}}$ is the CP position in the wing frame and in the body frame respectively. $\mathbf{R_{WB}}$ is the matrix of rotation from wing frame to body frame (given by wing position angles ϕ, δ and α^*).

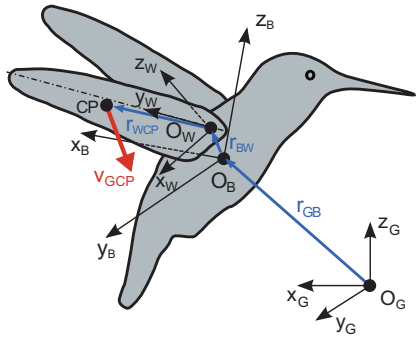

Fig. 5: Coordinate frames and center of pressure velocity

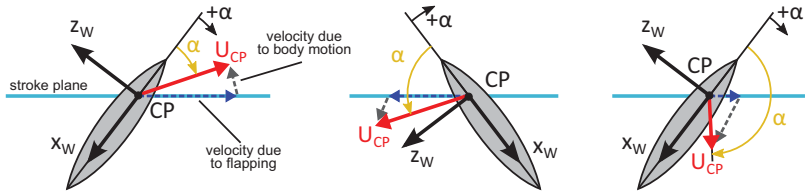

Fig. 6: Angle of attack in various situations

The angle of attack is measured between the wing chord and the velocity vector of the wing. Since not only the magnitude but also the direction of CP velocity changes, the aerodynamic angle of attack is also affected as can be seen in Fig. 6. Situations, where angle of attack is negative or greater than 90° are also sketched. The magnitude of the CP velocity vector in $x_W z_W$ plane of the wing is

$$U_{CP} = \sqrt{{}^{W}v_{GCPx}^2 + {}^{W}v_{GCPz}^2} \tag{5}$$

According to Fig. 6 the angle of attack can be computed as

$$\alpha = \text{atan2}(-{}^{W}v_{GCPz}, -{}^{W}v_{GCPx}) \tag{6}$$

where the atan2 function returns values between $-\pi$ and π.

2.4. Body dynamics

The dynamics of the flying robot can be described, under rigid body assumption, by Newton-Euler motion equations. Similar to an aircraft (e.g. (Padfield, 2007)) we obtain 12 ordinary differential equations with 12 unknown coordinates - velocity (u, v, w), angular velocity (p, q, r), position (x, y, z) and orientation expressed by Roll-Pitch-Yaw angles $(\varphi, \vartheta, \psi)$ - see Fig.7. By omitting the equations for position

and heading (yaw) angle ψ the system is reduced to 8 equations

$$\begin{aligned}
\dot{u} &= -(wq - vr) + X/m + g\sin\vartheta \\
\dot{v} &= -(ur - wp) + Y/m - g\cos\vartheta\sin\varphi \\
\dot{w} &= -(vp - uq) + Z/m - g\cos\vartheta\cos\varphi \\
I_{xx}\dot{p} &= (I_{yy} - I_{zz})\,qr + I_{xz}\,(\dot{r} + pq) + L \\
I_{yy}\dot{q} &= (I_{zz} - I_{xx})\,pr + I_{xz}\left(r^2 - p^2\right) + M \\
I_{zz}\dot{r} &= (I_{xx} - I_{yy})\,pq + I_{xz}\,(\dot{p} - qr) + N \\
\dot{\varphi} &= p + q\sin\varphi\tan\vartheta + r\cos\varphi\tan\vartheta \\
\dot{\vartheta} &= q\cos\varphi - r\sin\varphi
\end{aligned} \tag{7}$$

where m is the body mass. I_{xx}, I_{yy}, I_{zz} and I_{xz} are the non-zero moments and product of inertia in body frame (products I_{xy} and I_{yz} are both zero due to body symmetry). Aerodynamic forces and moments are represented by vectors (X, Y, Z) and (L, M, N) respectively.

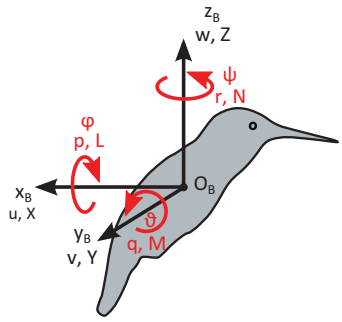

Fig. 7: Definition of body coordinates

We transform the wing forces (2) into body frame as follows

$$[X, Y, Z]^T = \sum_i [X_i, Y_i, Z_i]^T = \sum_i \mathbf{R_{BWi}}\,[F_{Ti}, 0, F_{Ni}]^T \tag{8}$$

$$[L, M, N]^T = \sum_i {}^{\mathbf{B}}\mathbf{r_{BCP_i}} \times [X_i, Y_i, Z_i]^T \tag{9}$$

where index i stands for the left and the right wing. $\mathbf{R_{BW}}$ is the transformation matrix from B frame to W frame ($\mathbf{R_{BW}} = \mathbf{R_{WB}}^T$) and ${}^{\mathbf{B}}\mathbf{r_{BC}}$ is the CP (force application point) position expressed in the body frame as

$${}^{\mathbf{B}}\mathbf{r_{BC}} = {}^{\mathbf{B}}\mathbf{r_{BW}} + \mathbf{R_{BW}}\,{}^{\mathbf{W}}\mathbf{r_{WCP}} \tag{10}$$

with ${}^{\mathbf{B}}\mathbf{r_{BW}} = [\pm w/2, 0, l_1]^T$ defining the position of the right/left wing base in the body frame and ${}^{\mathbf{W}}\mathbf{r_{WCP}} = [0, \pm R_{CP}, 0]^T$ defining the CP position inside the right/left wing frame.

2.5. System linearization

The mathematical model introduced in previous sections is nonlinear and was used in simulations. For control design a linear model is preferred.

The system dynamics (7) include aerodynamic forces and moments (8-9) that are functions of wing motion parameters $\mathbf{p} = [f, \Theta_L, \phi_{mL}, \phi_{0L}, \alpha_{mL}, \alpha_{0L}, \varphi_{\alpha L}, \delta_{m1L}, \delta_{m2L}, \Theta_R, \cdots, \delta_{m2R}]^T$, system state $\mathbf{x} = [u, v, w, p, q, r, \varphi, \vartheta]^T$ and time t. Assuming the flapping frequency is much higher than the bandwidth of the system, the aerodynamic forces can be replaced by their cycle averaged values (mean values over one wingbeat), e.g.

$$\overline{X} = \int_0^{\frac{1}{f}} X(\mathbf{x}, \mathbf{p}, t)\mathrm{d}t = \overline{X}(\mathbf{x}, \mathbf{p}) \tag{11}$$

that depend only on $\mathbf{x}$ and $\mathbf{p}$. We use small perturbation theory to rewrite the states and wing motion parameters as

$$\mathbf{x} = \mathbf{x_e} + \delta\mathbf{x}, \quad \mathbf{p} = \mathbf{p_e} + \delta\mathbf{p} \tag{12}$$

where subscript e signifies the equilibrium values and δ is the perturbation. We approximate the aerodynamic forces and moments by the linear terms of Taylor's expansion. For force in x-axis we obtain

$$\overline{X}(\mathbf{x},\mathbf{p}) = \overline{X}_e(\mathbf{x_e},\mathbf{p_e}) + \sum_{i=1}^{6} \frac{\partial \overline{X}}{\partial x_i}\delta x_i + \sum_{j=1}^{n} \frac{\partial \overline{X}}{\partial p_j}\delta p_j \tag{13}$$

where $\overline{X}_e$ is the cycle averaged force generated in equilibrium and n is number of wing kinematic parameters. The terms of the first summation are the derivatives with respect to body velocities and angular velocities called the stability derivatives. If taken with an opposite sign they represent aerodynamic damping. The second summation terms are the derivatives with respect to changes in wing motion. They are called the control derivatives. Further the overbar notation for cycle averages is dropped and the notation of the derivatives is shortened in the following manner

$$\frac{\partial \overline{X}}{\partial u} = X_u\,, \quad \frac{\partial \overline{X}}{\partial v} = X_v\,, \quad \ldots \quad , \quad \frac{\partial \overline{X}}{\partial f} = X_f\,, \quad \frac{\partial \overline{X}}{\partial \Theta} = X_\Theta\,, \quad \ldots \tag{14}$$

In this study we consider only near hover flight. Thus, all the equilibrium states are zero ($u_e = v_e = w_e = p_e = q_e = r_e = \varphi_e = \vartheta_e = 0$) and the perturbed states are equal to their absolute values ($\delta\mathbf{x} = \mathbf{x}$). The wing motion parameters $\mathbf{p_e}$ must ensure the trim: the z-force must be in balance with the gravity force ($Z_e = mg$), while the remaining forces and moments need to be zero ($X_e = Y_e = L_e = M_e = N_e = 0$).

First we suppose the wing kinematics does not change ($\delta\mathbf{p} = \mathbf{0}$). Instead, we assume we can apply an arbitrary external force or moment on the body. According to previous works on passive stability (Taylor & Thomas, 2002; Taylor et al., 2003; Zhang & Sun, 2010) as well as to our results there exists no aerodynamic coupling between the longitudinal and lateral system. By neglecting second order terms, we can rewrite the equations as two linear subsystems represented in state space as

$$\begin{aligned} \left[\dot{u}, \dot{w}, \dot{q}, \dot{\vartheta}\right]^T &= \mathbf{A_{long}}\,[u, w, q, \vartheta]^T + \mathbf{B_{long}}[X, Z, M]^T \\ [\dot{v}, \dot{p}, \dot{r}, \dot{\varphi}]^T &= \mathbf{A_{lat}}\,[v, p, r, \varphi]^T + \mathbf{B_{lat}}[Y, L, N]^T \end{aligned} \tag{15}$$

where the system and control matrices, $\mathbf{A}$ and $\mathbf{B}$, are expressed as

$$\mathbf{A_{long}} = \begin{bmatrix} \frac{X_u}{m} & \frac{X_w}{m} & \frac{X_q}{m} & g \\ \frac{Z_u}{m} & \frac{Z_w}{m} & \frac{Z_q}{m} & 0 \\ \frac{M_u}{I_{yy}} & \frac{M_w}{I_{yy}} & \frac{M_q}{I_{yy}} & 0 \\ 0 & 0 & 1 & 0 \end{bmatrix}, \quad \mathbf{A_{lat}} = \begin{bmatrix} \frac{Y_v}{m} & \frac{Y_p}{m} & \frac{Y_r}{m} & -g \\ \frac{L_v I_{zz} + N_v I_{xz}}{I_{xx}I_{zz} - I_{xz}^2} & \frac{L_p I_{zz} + N_p I_{xz}}{I_{xx}I_{zz} - I_{xz}^2} & \frac{L_r I_{zz} + N_r I_{xz}}{I_{xx}I_{zz} - I_{xz}^2} & 0 \\ \frac{L_v I_{xz} + N_v I_{xx}}{I_{xx}I_{zz} - I_{xz}^2} & \frac{L_p I_{xz} + N_p I_{xx}}{I_{xx}I_{zz} - I_{xz}^2} & \frac{L_r I_{xz} + N_r I_{xx}}{I_{xx}I_{zz} - I_{xz}^2} & 0 \\ 0 & 1 & 0 & 0 \end{bmatrix}$$

$$\mathbf{B_{long}} = \begin{bmatrix} \frac{1}{m} & 0 & 0 \\ 0 & \frac{1}{m} & 0 \\ 0 & 0 & \frac{1}{I_{yy}} \\ 0 & 0 & 0 \end{bmatrix}, \qquad \mathbf{B_{lat}} = \begin{bmatrix} \frac{1}{m} & 0 & 0 \\ 0 & \frac{I_{zz}}{I_{xx}I_{zz} - I_{xz}^2} & \frac{I_{xz}}{I_{xx}I_{zz} - I_{xz}^2} \\ 0 & \frac{I_{xz}}{I_{xx}I_{zz} - I_{xz}^2} & \frac{I_{xx}}{I_{xx}I_{zz} - I_{xz}^2} \\ 0 & 0 & 0 \end{bmatrix} \tag{16}$$

In the following section a controller will be designed, assuming the external forces and moments as inputs. In reality, these will be generated by the wings. From the approximation in (13) we can write a relation between cycle averaged forces/moments and modifications of wing kinematics parameters $\mathbf{\Delta p}$ as

$$[X, Y, Z, L, M, N]^T = \mathbf{J}\Delta\mathbf{p} \tag{17}$$

where $\mathbf{J}$ is the matrix of control derivatives defined as

$$\mathbf{J} = \begin{bmatrix} X_{p_1} & X_{p_2} & \cdots & X_{p_n} \\ Y_{p_1} & Y_{p_2} & \cdots & Y_{p_n} \\ \vdots & \vdots & \ddots & \vdots \\ N_{p_1} & N_{p_2} & \cdots & N_{p_n} \end{bmatrix} \tag{18}$$

The kinematic parameters modifications that should produce desired forces/moments are estimated by a pseudoinverse of the previous relation

$$\mathbf{\Delta p} = \mathbf{J}^{+}[X, Y, Z, L, M, N]^T \tag{19}$$

3. Control design

In the previous section we have presented the complete mathematical model which is necessary to perform an open loop simulation. The next task is to develop a 4DOF flight controller, allowing us to fly foreward/backward, up/down and sideways and to steer by changing the heading angle. As we show further the system itself is unstable. Thus, the controller also needs to stabilize the attitude.

This section applies to a robot with wing and body properties of a typical hummingbird (Tab.1,2). We take the mass of a ruby-throated hummingbird (Chai et al., 1996) and estimate the inertia and wing base position according to a simplified 3D model in Catia with typical body dimensions. We used Matlab image processing to obtain the wing geometry parameters from an image of a real hummingbird wing profile (Fig. 8). Wing kinematic parameters for equilibrium (i.e. hover) $\mathbf{p_e}$ are in Tab. 3. They were chosen to satisfy the trim condition with a relative error below 0.5% while being close to real animal observations (Tobalske et al., 2007).

Tab. 1: Aerodynamic parameters

R (mm)	$\bar{c}$ (mm)	S (mm^2)	$\hat{x}_0$ (-)	$\int_0^1 \hat{r}\hat{c}^2(\hat{r})d\hat{r}$ (-)	$\hat{r}_2$ (-)	ρ (kg.m^{-3})
48	12.7	611	0.25	0.428	0.492	1.2

Tab. 2: Body parameters

m (g)	I_{xx} (g.mm^2)	I_{yy} (g.mm^2)	I_{zz} (g.mm^2)	I_{xz} (g.mm^2)	l_1 (mm)	w (mm)
4.32	492	557	411	-220	10	14

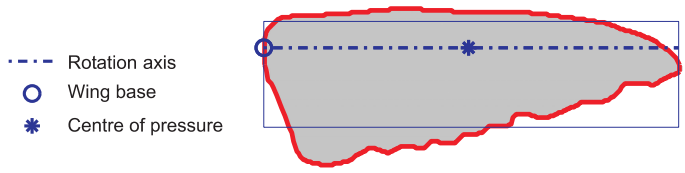

Fig. 8: Hummingbird wing profile

3.1. System matrices

We evaluate the stability derivatives in hover as follows. We keep the wing kinematics constant and symmetric for both wings ($\mathbf{p_e}$). We pick several values of one of the velocities from a defined neighborhood around zero while keeping the others in zero. In each case we calculate the vector of cycle averaged forces and moments in body frame. The relationships between the averaged forces/moments and the

Tab. 3: Wing kinematics for hover

f (Hz)	Θ (°)	ϕ_m (°)	ϕ_0 (°)	α_m (°)	α_0 (°)	φ_α (°)	δ_{m1} (°)	δ_{m2} (°)
48	0	70	0	30	0	0	0	0

varying velocity can be plotted - the derivatives are represented by a tangent to the curves in the origin. We proceed similarly to get the derivatives with respect to the remaining velocities. We find out that many of them are zero, so we only keep X_u, X_q, Y_v, Y_p, Z_w, L_v, L_p, M_u, M_q and N_r. This justifies splitting the system into longitudinal and lateral part. It further reveals that vertical translation and yaw rotation are aerodynamically decoupled from the remaining motions.

The expressions in the system matrices reduce to

$$\mathbf{A_{long}} = \begin{bmatrix} \frac{X_u}{m} & 0 & \frac{X_q}{m} & g \\ 0 & \frac{Z_w}{m} & 0 & 0 \\ \frac{M_u}{I_{yy}} & 0 & \frac{M_q}{I_{yy}} & 0 \\ 0 & 0 & 1 & 0 \end{bmatrix}, \quad \mathbf{A_{lat}} = \begin{bmatrix} \frac{Y_v}{m} & \frac{Y_p}{m} & 0 & -g \\ \frac{L_v I_{zz}}{I_{xx}I_{zz}-I_{xz}^2} & \frac{L_p I_{zz}}{I_{xx}I_{zz}-I_{xz}^2} & \frac{N_r I_{xz}}{I_{xx}I_{zz}-I_{xz}^2} & 0 \\ \frac{L_v I_{xz}}{I_{xx}I_{zz}-I_{xz}^2} & \frac{L_p I_{xz}}{I_{xx}I_{zz}-I_{xz}^2} & \frac{N_r I_{xx}}{I_{xx}I_{zz}-I_{xz}^2} & 0 \\ 0 & 1 & 0 & 0 \end{bmatrix} \tag{20}$$

In the longitudinal system a vertical motion is fully decoupled from the rest. In the lateral system all three motions are coupled. While the sideways motion and roll are coupled aerodynamically, yaw and roll are coupled due to non-zero inertia product I_{xz}. Thus, it would be possible to avoid this coupling by designing a robot with mass distribution that would be symmetrical around all the three body axes.

Calculation of system poles gives results that are in accordance with previous stability studies (reviewed in (Orlowski & Girard, 2012)). Both systems, longitudinal and lateral, have similar pole structure resulting into one unstable oscillatory natural mode and two (fast and slow) stable natural modes and need to be stabilized.

3.2. Control strategy

We have shown in the preceding section that the system can be split into 3 decoupled subsystems - longitudinal dynamics (u,q), vertical dynamics (w) and lateral + yaw dynamics (v,p,r). Moreover, lateral and yaw dynamics are coupled by inertia product I_{xz} - there is no aerodynamic coupling. We can take an advantage of this decoupling and use a decentralized cascade control strategy similar to quadrocopters (Michael et al., 2010). The controller is formed by two loops. An inner loop is stabilizing the attitude (roll φ and pitch ϑ) by respective moments L, M. An outer loop controls the flight. Flying up/down and turning is controlled directly by Z force and N moment. Forwards/backwards and sideways flight is controlled indirectly by body inclination around pitch and roll axis. The controller scheme is in Fig. 9.

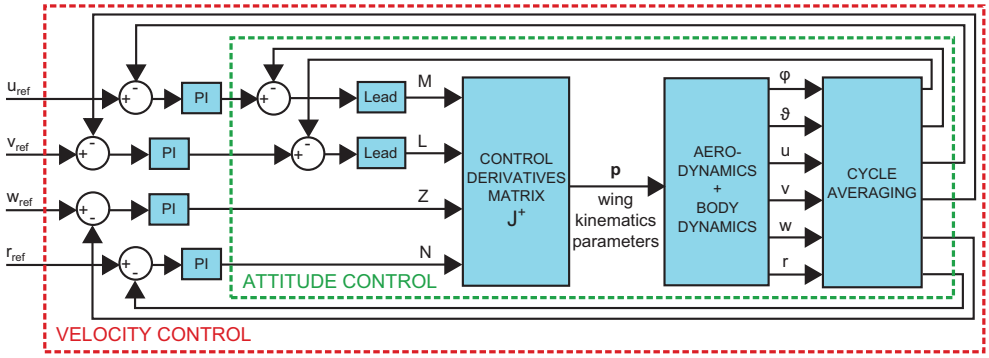

Fig. 9: Cascade control: the inner loop controls attitude, the outer loop controls velocity

Since we develop the controller for a cycle averaged linear system, the best performance is achieved with a discrete design. The sampling frequency is equal to the flapping frequency. The attitude in the inner loop, φ and θ, is controlled by a pair of lead compensators. The velocities in the outer loop, u, v, w and r, are controlled by 4 PI controllers. The control gains were tuned for the linearized system (15) using standard techniques.

3.3. Control derivatives

The forces from the controller are transformed into wing motion by the control derivatives matrix (18). We compute the control derivatives in nearly the same way as the stability derivatives. Since we are around hover we keep the body velocities and angular velocities zero. We chose one parameter, p_i, that we will vary around its equilibrium p_{ei}. All the other parameters are kept in equilibrium $\mathbf{p_e}$. We evaluate the cycle averaged forces and moments for each value. If we plot the averaged forces/moments as a function of the selected parameter, the control derivatives are given by the slopes of tangents to the resulting curves in p_{ei}.

We split the results into two parts. When applying the wing kinematic changes symmetrically on both wings (subscript S) only the longitudinal system forces and moment (X, Z and M) are modified. The linearized relationship can be written as

$$[X, Z, M]^T = \mathbf{J_S} \left[f_S, \phi_{mS}, \phi_{0S}, \alpha_{mS}, \alpha_{0S}, \varphi_{\alpha S}, \delta_{m1S}, \delta_{m2S}, \Theta_S\right]^T \tag{21}$$

To see the importance of each parameter we divide the row belonging to moment by characteristic length R_{CP}. The normalized matrix, with units N/Hz or N/°, is evaluated as

$$\hat{\mathbf{J}}_\mathbf{S} = \begin{array}{c} \\ X \\ Z \\ \frac{M}{R_{CP}} \end{array} \begin{array}{c} \begin{array}{ccccccccc} \phi_{mS} & \phi_{0S} & \alpha_{mS} & \alpha_{0S} & \varphi_{\alpha S} & \delta_{m1S} & \delta_{m2S} & \Theta_S & f_S \end{array} \\ \left[\begin{array}{ccccccccc} 0 & 0.212 & 0 & -1.07 & 0 & 0.107 & 0 & -0.739 & 0 \\ 1.21 & 0 & 0.446 & 0 & -0.248 & 0 & 1.18 & 0 & 1.77 \\ 0 & -0.519 & 0 & -0.240 & 0 & 0.702 & 0 & -0.192 & 0 \end{array}\right] \end{array} \tag{22}$$

For asymmetric changes of wing kinematics (subscript A) only the lateral system force and moments (Y, L and N) are affected. We get

$$[Y, L, N]^T = \mathbf{J}_A \left[\phi_{mA}, \phi_{0A}, \alpha_{mA}, \alpha_{0A}, \varphi_{\alpha A}, \delta_{m1A}, \delta_{m2A}, \Theta_A\right]^T \tag{23}$$

where the control derivatives matrix, normalized as above, is

$$\hat{\mathbf{J}}_\mathbf{A} = \begin{array}{c} \\ Y \\ \frac{L}{R_{CP}} \\ \frac{N}{R_{CP}} \end{array} \begin{array}{c} \begin{array}{cccccccc} \phi_{mA} & \phi_{0A} & \alpha_{mA} & \alpha_{0A} & \varphi_{\alpha A} & \delta_{m1A} & \delta_{m2A} & \Theta_A \end{array} \\ \left[\begin{array}{cccccccc} -0.288 & 0 & 0.0956 & 0 & 0.401 & 0 & -0.136 & 0 \\ -1.03 & 0 & -0.615 & 0 & 0.176 & 0 & -1.76 & 0 \\ 0 & 0.0628 & 0 & -1.63 & 0 & 0.0317 & 0 & -0.828 \end{array}\right] \end{array} \tag{24}$$

By studying the matrices above we can identify two groups of parameters according to their effect on generated forces and moments. The first group includes flapping frequency f, sweep amplitude ϕ_m, angle of attack amplitude α_m, phase shift φ_α and amplitude of figure eight-like deviation δ_{m2}. If we modify these parameters symmetrically on both wings, we control the vertical force Z. If we modify these parameters, excluding the flapping frequency, asymmetrically (with positive sign on left wing and with negative sign on right wing) we modulate the L moment (roll) and Y force.

The second group includes sweep angle offset ϕ_0, angle of attack offset α_0, amplitude of oval-like deviation δ_{m1} and mean stroke plane inclination Θ. Symmetric changes of these parameters result into M moment (pitch) and X force modulation. Same parameters taken asymmetrically modify the yaw moment N.

3.4. Choice of control parameters

In the real robot design the number of parameters needed to control the flight needs to be minimized. The matrices (22) and (24) show, that we only need two parameters per wing to generate independently

the four control forces/moments Z, L, M and N. While this approach leaves us no control of the "parasite" forces X and Y, it allows a simpler design of the future robot wing motion mechanism. Another parameter per wing is necessary to assure that X and Y is zero. However, when tested in simulation the controller performance decreased compared to the simpler two parameter per wing controller. Our explanation is that the additional constraints actually reduce the effect of the parameter change on the control force/moment.

For the selected pair of parameters p_1, p_2 we construct a reduced control derivatives matrix

$$\mathbf{J_{red}} = \begin{bmatrix} Z_{p_{1L}} & Z_{p_{1R}} & Z_{p_{2L}} & Z_{p_{2R}} \\ L_{p_{1L}} & L_{p_{1R}} & L_{p_{2L}} & L_{p_{2R}} \\ M_{p_{1L}} & M_{p_{1R}} & M_{p_{2L}} & M_{p_{2R}} \\ N_{p_{1L}} & N_{p_{1R}} & N_{p_{2L}} & N_{p_{2R}} \end{bmatrix} \tag{25}$$

Finally, we transform the control forces/moments into wing kinematic parameters as

$$[p_{1L}, p_{1R}, p_{2L}, p_{2R}]^T = \mathbf{J_{red}}^{-1}[X, L, M, N]^T \tag{26}$$

There are many possible choices of the two control parameters. Since we "ignore" the effect on X and Y forces, full rank of the reduced control derivatives matrix $\mathbf{J_{red}}$ does not guarantee successful control. Moreover we base the control design on the linearized model, while the original system is nonlinear. This requires that the control performance of each combination needs to be tested in nonlinear simulation. In the real robot the final choice of the control parameters will also be constrained by the feasibility of the wing control mechanism design of each choice.

In the next section we present results for ϕ_m and ϕ_0 chosen as control parameters. Their effects on generated force/moments are sketched in Fig. 10.

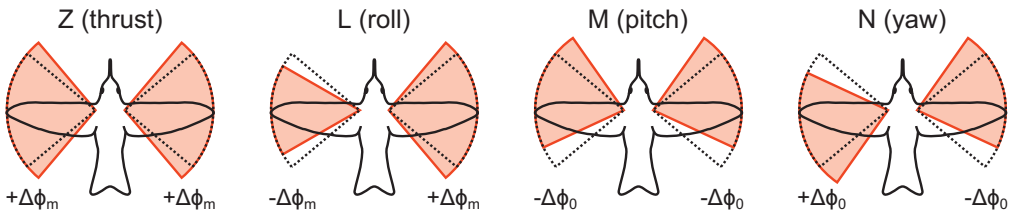

Fig. 10: Control force and moments generated through wing kinematics parameters ϕ_m and ϕ_0

4. Simulation results

We evaluated the controller performance by simulations in Matlab/Simulink. The simulation model included nonlinear models of aerodynamics and 6 DOF body dynamics, as described in chapters 2.1.-2.4.. The simulation results are presented for two test trajectories in the four controlled DOFs (velocities u,v,w, angular velocity r). The flight was controlled by the sweep angle amplitude ϕ_m and sweep angle offset ϕ_0.

In the first trajectory we applied a step command in each DOF, one after another, to show the control performance in each single DOF with the coupling effects with the rest of the nonlinear system. The results are in Fig. 11 left. We observe that the longitudinal and vertical dynamics are decoupled from the rest of the system, as indicated by the linearized model. The high frequency oscillation is caused by the pulsating forces due to flapping motion, however the mean values are closely following the linear results. The lateral dynamics and yaw dynamics are coupled, as predicted by the linearization. The control performance in lateral direction is worse than expected, but the system remains stable. The flapping oscillation in lateral and yaw system occurs only when the wing kinematics differs between the wings, but again the mean value follows the command.

The time behavior of the control parameters shows that the necessary changes in wing kinematics are very small. Although the control parameters should be zero in hovering flight according to linearized

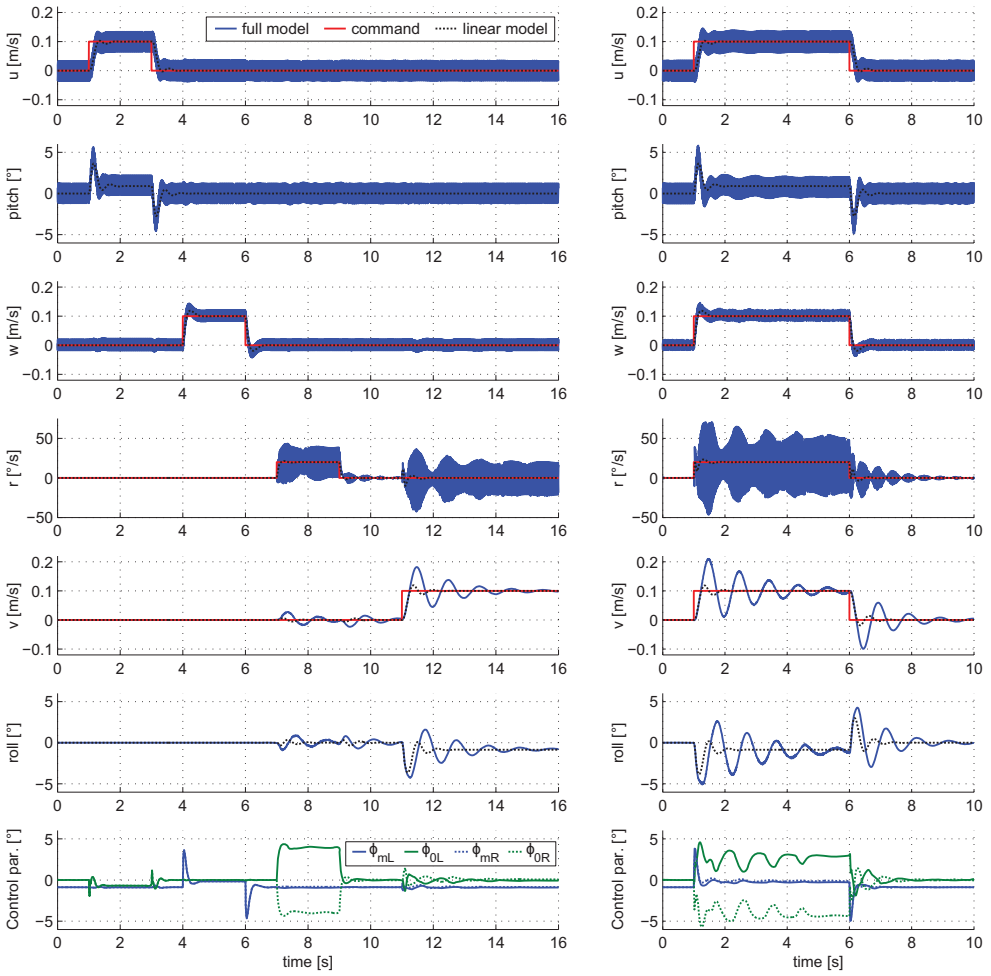

Fig. 11: Step response: step commands one after another for each controlled DOF (left), all step commands at once (right)

model, we observe that sweep amplitude ϕ_m is approximately -1° when all commands are zero. The explanation is that the flapping motion induces a body oscillation that changes the velocity of the wing and subsequently also the angle of attack. This results into slight increase of the cycle averaged lift force that is then compensated by decreasing the sweep amplitude.

The control parameter peaks during the step commands are all below $5°$ and could be further decreased if the controller was tuned less aggressively. The only exception is the rotation around yaw axis (step in r) during which the sweep offset ϕ_0 remains relatively high (but still below $5°$). This is however in accordance with the control derivatives matrix (24), where we can see that the effect of ϕ_0 on yaw moment R is relatively low. A more effective parameter for yaw control may be chosen in future.

In the second trajectory the step command was sent to all the DOFs at once to reveal any control cross-coupling effects and evaluate the potential decrease of control performance. We can see in Fig. 11 right that apart from slight increase of transition times there is no significant change in the overall performance and also the control parameters remain in a similar range.

5. Conclusions

In this paper we presented a simulation model of a hummingbird sized tailless flapping-wing flying robot. The mathematical model was based on rigid body dynamics and quasi steady aerodynamics.

First, we showed by employing system linearization and cycle averaging techniques that the system is decoupled and can be split into separate subsystems for vertical, longitudinal and lateral+yaw dynamics.

Then we parameterized the wing motion and studied the effect of each parameter on the cycle averaged forces. From the results we built a control derivatives matrix. We showed, that the parameters can be split into two groups. The first group parameters can produce a lift force, when changes are applied symmetrically on both wings, and a roll moment, when applied asymmetrically. The second group parameters produce pitch or yaw moments when being modified symmetrically or asymmetrically. Thus, to generate the necessary control force and moments only two wing parameters per wing are necessary. Several choices of the control parameters are possible. The control derivatives matrix was used to transform the control forces and moments into wing motion changes.

Finally, the controller was implemented into the simulation model and tested. We chose sweep (flapping) amplitude and sweep offset (mean wing position) as the control parameters. The controller showed good performance with almost no cross-coupling effects. Apart from lateral dynamics, the nonlinear system response was almost identical with the one of the linearized system. The control performance in sideways flight is decreased, yet still acceptable. The linear approximation of non-linear behavior of lateral dynamics seems to be less precise. A better control of lateral direction flight might be searched in the future.

The results of this study will be further used in the development of the flapping wing robot. We have shown that several choices of the two control parameters are possible. An implementation of these parameters into mechanical design of the robot will be researched in future.

Acknowledgments

The research of M. Karásek is supported by FRIA grant from F.R.S. - FNRS (FC 89554).

References

Chai, P., Harrykissoon, R., & Dudley, R. (1996) Hummingbird hovering performance in hyperoxic helliox: effects of body mass and sex. *Journal of Experimental Biology*, 199, pp.2745–2755.

Chung, S. & Dorothy, M. (2010) Neurobiologically inspired control of engineered flapping flight. *Journal of Guidance, Control, and Dynamics*, 33, 2, pp.440–453.

de Croon, G., de Clerq, K., Ruijsink, R., Remes, B., & de Wagter, C. (2009) Design, aerodynamics, and vision-based control of the delfly. *International Journal of Micro Air Vehicles*, 1, 2, pp.71–97.

Deng, X., Schenato, L., Wu, W. C., & Sastry, S. S. (2006a) Flapping flight for biomimetic robotic insects: part I-system modeling. *IEEE Transactions on Robotics*, 22, 4, pp.776–788.

Deng, X., Schenato, L., & Sastry, S. (2006b) Flapping flight for biomimetic robotic insects: part II-flight control design. *IEEE Transactions on Robotics*, 22, 4, pp.789–803.

Dickinson, M. H., Lehmann, F.-O., & Sane, S. P. (1999) Wing rotation and the aerodynamic basis of insect flight. *Science*, 284, 5422, pp.1954–1960.

Doman, D. B., Oppenheimer, M. W., & Sigthorsson, D. O. (2010) Wingbeat shape modulation for flapping-wing micro-air-vehicle control during hover. *Journal of Guidance, Control, and Dynamics*, 33, 3, pp.724–739.

Ellington, C. P. (1984). The aerodynamics of hovering insect flight. II. Morphological parameters *Philosophical Transactions of the Royal Society of London. Series B, Biological Sciences*, 305, 1122, pp.17–40.

Keennon, M., Klingebiel, K., Won, H., & Andriukov, A. (2012) Development of the Nano Hummingbird: A Tailless Flapping Wing Micro Air Vehicle. in: *50th AIAA Aerospace Sciences Meeting including the New Horizons Forum and Aerospace Exposition*, pp. 1–24.

Michael, N., Mellinger, D., Lindsey, Q., & Kumar, V. (2010) The grasp multiple micro uav testbed. *IEEE Robotics and Automation*, 17, 3, pp.56–65.

Orlowski, C., Anouck, G., & Shyy, W. (2010). Open loop pitch control of a flapping micro-air vehicle using a tail and control mass. In *2010 American Control Conference, Marriott Waterfront, Baltimore*, pp.536–541.

Orlowski, C. T. & Girard, A. R. (2012) Dynamics, stability, and control analyses of flapping wing micro-air vehicles. *Progress in Aerospace Sciences*, in press.

Padfield, G. D. (2007) *Helicopter Flight Dynamics: The Theory and Application of Flying Qualities and Simulation Modeling*. Blackwell Science Ltd., Washington DC, 2nd edition.

Rakotomamonjy, T., Ouladsine, M. & Le Moing, T. (2010) Longitudinal modelling and control of a flapping-wing micro aerial vehicle. *Control Engineering Practice*, 18, 7, pp.679–690.

Sane, S. P. (2003) The aerodynamics of insect flight. *Journal of Experimental Biology*, 206, pp.4191–4208.

Sane, S. P. & Dickinson, M. H. (2002) The aerodynamic effects of wing rotation and a revised quasi-steady model of flapping flight. *Journal of Experimental Biology*, 205, pp.1087–1096.

Shyy, W., Aono, H., Chimakurthi, S., Trizila, P., Kang, C.-K., Cesnik, C., & Liu, H. (2010) Recent progress in flapping wing aerodynamics and aeroelasticity. *Progress in Aerospace Sciences*, 46, 7, pp.284–327.

Taylor, G. K., Nudds, R. L., & Thomas, A. L. R. (2003) Flying and swimming animals cruise at a Strouhal number tuned for high power efficiency. *Nature*, 425, pp.707–711.

Taylor, G. K. and Thomas, A. L. R. (2002) Animal flight dynamics II. Longitudinal stability in flapping flight. *Journal of Theoretical Biology*, 214, 3, pp.351–370.

Tobalske, B. W., Warrick, D. R., Clark, C. J., Powers, D. R., Hedrick, T. L., Hyder, G. A., & Biewener, A. A. (2007) Three-dimensional kinematics of hummingbird flight. *Journal of Experimental Biology*, 210, 13, pp.2368–2382.

Zhang, Y. & Sun, M. (2010) Dynamic flight stability of a hovering model insect: lateral motion. *Acta Mech. Sinica*, 26, 2, pp.175–190.

18th International Conference
ENGINEERING MECHANICS 2012
Svratka, Czech Republic, May 14 – 17, 2012

pp. 621–624
Paper #313

COMPARATIVE ACOUSTIC ANALYSIS OF PLANE DOUBLE-WALL AND MULTILAYERED SANDWICH BAFFLES

S. Karczmarzyk*

Abstract: *A comparison of the transmission loss (TL) for different double-wall and multilayered sandwich baffles are presented in the paper. For prediction the TL values of the double-wall baffles the well known (in the literature) model is used. For prediction the TL for the multilayered (not only three-layer) sandwich baffles a local elastodynamic model of the present author is employed. Physical parameters some of the structures considered are the same as those occurring in the reality. Conclusions resulting from the analysis are convergent with conclusions existing in the literature on multi-panel structures lined with elastic materials.*

Keywords: ***Double-wall, multi-layer sandwich panel, local model, acoustic analysis, transmission loss.***

1. Introduction

A baffle is any device that hinders passage of sound in order to reduce the sound pressure in a specified region (Ko, 1981). The multi-wall, and in-particular two-wall, baffles are considered e.g. in the papers (Bolton et al., 1996 and Tadeu et al., 2004). Usually, the two-wall baffles are composed of two rigid walls and of a soft porous material inserted between the walls in order to make the baffle more efficient. Bolton et al. (1996) investigated three possible concepts (configurations) of usage of the soft material i.e., UU configuration, BU configuration and BB configuration, where U means the soft material unbonded with the rigid wall whereas B means the soft material bonded with the rigid wall. One of the main conclusions of the investigation is expressed as follows: "the BB configuration should be used because of its better performance in the low frequency range".

Let us note that the BB configuration can be considered as a three-layer sandwich baffle. In this paper double-wall baffles without the soft material between the walls and different sandwich baffles are compared in the lower frequency range, 16-500 Hz, by comparing the TL values.

2. Double-wall model

In order to obtain the TL for a double-wall baffle, composed of two identical infinite isotropic walls with an air gap between them, the model widely reported in the literature was used. It is first noted that for a double-wall baffle, with or without a soft material between the walls, the ratio p_i/p_t, where p_i, p_t denote the incident and transmitted pressures, respectively, can be expressed formally as follows,

$$\frac{p_i}{p_t} = \frac{p_i}{p_{32}} \frac{p_{32}}{p_{31}} \frac{p_{31}}{p_{22}} \frac{p_{22}}{p_{21}} \frac{p_{21}}{p_{12}} \frac{p_{12}}{p_t} \tag{1}$$

Symbols pk1 and pk2 in (1) denote the pressures on sides 1 and 2, respectively, of k-th layer, while subscripts k=1,2,3 denote the wall far of the acoustic wave, the soft material layer or the gap between the walls and the wall incident by the acoustic wave, respectively. At the interfaces of the baffle the following equalities are satisfied,

$$\frac{p_{31}}{p_{22}} = \frac{p_{21}}{p_{12}} = 1 \tag{2}$$

* Dr. Eng. Stanisław Karczmarzyk, DrSc.: Institute of Machine Design Fundamentals, Warsaw University of Technology, Narbutta 84; 02-524, Warsaw; PL, e-mail: karczmarzyk_st@poczta.onet.pl

Due to (2) the expression (1) is in the following form,

$$\frac{1}{\tau_\theta} = \frac{p_i}{p_t} = \frac{p_i}{p_{32}} \frac{p_{32}}{p_{31}} \frac{p_{22}}{p_{21}} \frac{p_{12}}{p_t} \tag{3}$$

The following expressions, for the ratios occuring in (3), can be found in the literature – as for instance in the work by Okura (2007),

$$\begin{aligned} &\frac{p_i}{p_{32}} = \frac{Z_{22} + jm\omega + \rho c/\cos\theta}{2(Z_{22} + jm\omega)}, \quad \frac{p_{32}}{p_{31}} = 1 + j\frac{m\omega}{Z_{22}}, \quad \frac{p_{22}}{p_{21}} = \frac{\cosh(jkd\cos\theta + \delta)}{\cosh\delta}, \quad k = \omega/c, \\ &\frac{p_{12}}{p_t} = 1 + j\frac{m\omega\cos\theta}{\rho c}, \qquad Z_{22} = \frac{\rho c}{\cos\theta}\coth(jkd\cos\theta + \delta), \qquad \delta = \coth^{-1}(1 + j\frac{m\omega\cos\theta}{\rho c}) \end{aligned} \tag{4}$$

Symbols, c, ρ, d, m, θ, ω, in expressions (4), denote, sound speed in the air, density of the air, distance (gap) between the walls, surface density of the wall, incident angle of the acoustic wave and radian frequency of the acoustic wave, respectively.

The transmission loss (TL), in particular for the double-wall baffle, is defined as follows,

$$TL_\theta = 10\log\left|p_i / p_t\right|^2 \tag{5}$$

It is noted that the theory predicts, depending on value of the term β, the coincidence frequency for the double-wall baffle,

$$\beta = (\omega/c)d\cos\theta < 1 \quad \Leftrightarrow \quad f_c = \sqrt{2\rho c^2/md}\,/(2\pi\cos\theta) \tag{6}$$

The coincidence frequencies predicted by formula (6) are low i.e., they appear first on the left-hand side in the charts TL vs frequency. It is seen from (6) that the coincidence frequecy of the double-wall baffle increases with increasing the incident angle.

The coincidence frequency defined by formula (6) is specific for the double-wall baffle. It does not appear for the solid baffle as for instance the sandwich one. Moreover, the theory by Okura (2007) predicts other coincidence frequencies specific for the double-wall baffle. To outline the problem the following explicit formula, given by Okura (2007), is applied,

$$TL_\theta = 10\log\left[\,1 + 4a^2\cos^2\theta(\cos\beta - a\sin\beta\cos\theta)^2\right], \quad a = \frac{\omega m}{2\rho c}, \quad \beta = \frac{\omega d}{c}\cos\theta \tag{7}$$

Upon basis of (7) the following relationships are valid,

$$TL_\theta = 0 \;\Leftrightarrow\; \begin{cases} \theta = \pi/2 \\ or \\ \theta \neq \pi/2 \end{cases}, \quad \cos\beta - a\sin\beta\cos\theta = 0 \tag{8}$$

The equation appearing in (8) admits existence of other coincidence frequencies – specific for the double-wall baffles. Since the coincidence frequencies expected form equation (8) are much higher than the coincidence frequency defined by formula (6) they are not discussed here more widely.

3. Local model of multilayered sandwich baffle

The local model used to obtain the numerical results for the sandwich structures was presented in first reference of the author (Karczmarzyk, 2011). An outline of the model is given in second reference of the author (Karczmarzyk, 2011).

It is noted that all through-the-thickness boundary and compatibility conditions, for displacements and stresses, as well as the cross-sectional warping in each layer have been included in the model. Therefore the model is able to predict accurately both the coincidence frequencies and the TL for a wide spectrum of layered structures including the multilayered sandwich panels.

4. Numerical results

Computations of the TL were made, following the procedure outlined in section 3, for the following three structures: double-wall baffle with different gaps between the walls, three-layer sandwich baffle and five-layer sandwich baffle. The results have been computed for the incident angle equal to 30 degrees within frequency range 16-500 Hz.

The double-wall infinite baffle considered here is composed of two identical isotropic walls and of a gap between them filled with air. The computations were made for the following data of the wall: thickness=25 mm, Young's modulus=2.6 GPa, Poisson's ratio=0.185, density=770 kg/m3. The TL values were calculated for the following four gaps: d=25 mm, d= 50mm, d=75 mm and d=100mm.

Parameters of the three-layer baffle are as follows: thicknesses of layers (mm) – 12, 25, 12, Young's moduli (GPa) – 4.6, 2.1, 4.6, Poisson's ratios – 0.185, 0.185, 0.185, densities (kg/m3) – 1000, 670, 1000. Parameters of the five-layer sandwich baffle are as follows: thicknesses of layers (mm) – 12, 2, 21, 2, 12, Young's moduli (GPa) – 4.6, 17, 2.3, 17, 4.6, Poisson's ratios – 0.185, 0.42, 0.185, 0.42, 0.185, densities (kg/m3) – 1000, 11400, 760, 11400, 1000.

It is explained that parameters of the walls in the double-wall baffle as well as parameters of the sandwich baffles are taken from paper by Yano et al. (2005). All the numerical results, obtained by the present author, are presented in Fig. 1. The line denoted by 3-layer concerns the three-layer sandwich baffle and the line named 5-layer refers to the five-layer sandwich baffle.

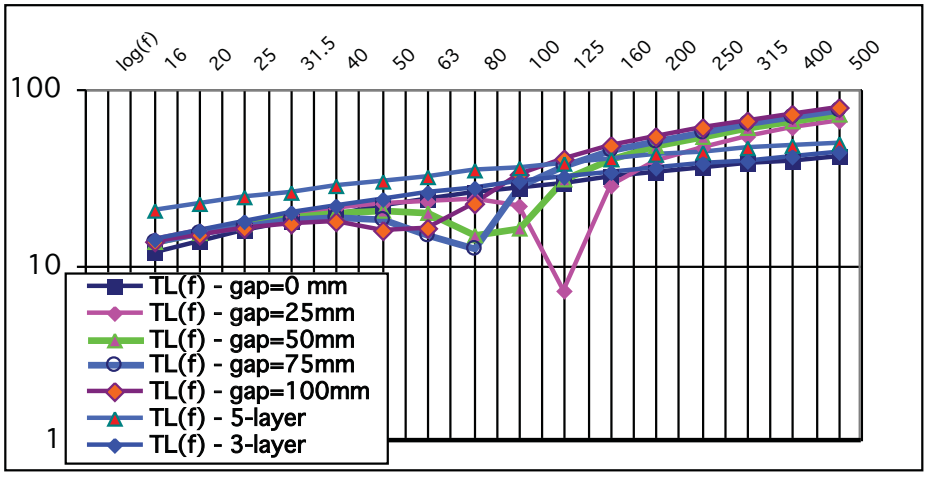

Fig. 1: Dependence of the TL on frequency for the double-wall and sandwich baffles.

It is seen in Fig. 1 that, within the range considered, the double-wall baffles have at least three basic deficiencies comparing with the sandwich baffles. First, the TL of the double-wall baffle is lower than TL of the sandwich three-layer baffle within the range 16-f_3 Hz and it is lower than TL of the sandwich five-layer baffle within the range 16-f_5 Hz, while f_3, f_5 are dependent on (width of) the gap between the walls. For instance when the gap is 50 mm wide the f_5 is close to 160 Hz and f_3 approaches 125 Hz. Decreasing the gap to 25 mm results in increasing f_5 up to 250 Hz and f_3 up to 180-200 Hz. Second, the TL of the double-wall baffles significantly decreases in vicinity of the coincidence frequency defined by formula (6). It is reminded that the coincidence frequency is specific for the double-wall baffle and does not exist, within the low range of frequencies, for the sandwich baffles. Third, it is noted that thicknesses of the sandwich baffles are lower than total thicknesses of the double-wall baffles. For the gap 50 mm wide the double-wall baffle is 2 times thicker than each of the sandwich baffles considered here. The above analysis confirms the conclusion of Bolton et al. (1996) cited in the introduction.

Since TL of the five-layer baffle is much higher for the lower frequencies than TL of all the double-wall baffles therefore the TL for the five-layer structure is presented in Fig. 2 in a wide frequency range, 16-20000 Hz. The results show that the five-layer baffle can be attractive in acoustic applications. It is explained that the critical coincidence frequency for the baffle equals 7036,18 Hz.

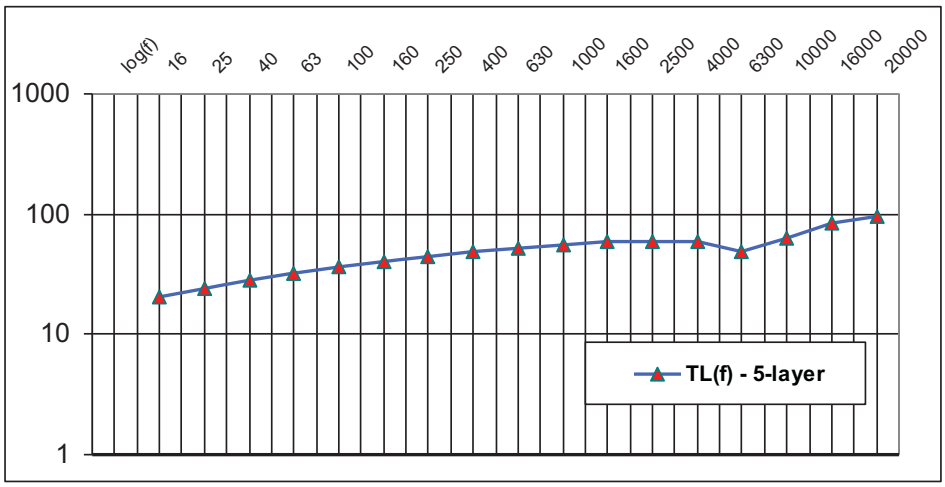

Fig. 2: Dependence of the TL on frequency, in a wide range, for the five-layer baffle.

5. Conclusions

The TL for double-wall baffles and three-layer and five-layer sandwich baffles have been compared in the paper in frequency range 16-500 Hz. Some advantages of the sandwich baffles over the double-wall counterparts have been pointed out. In particular, the five-layer sandwich baffle seems to be attractive in acoustic applications since it is much more thin and more efficient in reducing of passage of sound, in the frequency range considered, than the double-wall baffle.

Above statement is also valid when higher frequencies are considered. For frequencies higher than 500 Hz the TL of the double-wall baffle is much higher than TL for the five-layer baffle however in both the cases the TL is high enough to hinder passage of sound in a satisfactory level.

References

Bolton, J.S., Shlau, N.-M. & Kang, Y.J. (1996) Sound transmission through multi-panel structures lined with elastic porous materials. *Journal of Sound and Vibration*, 191, 3, pp. 317-347.

Karczmarzyk, S. (2011) Local model of plane acoustic waves propagation in multilayered infinite sandwich structures. *Archives of Mechanics*, 63, 5-6, pp. 573-598.

Karczmarzyk, S. (2011) Acoustic characteristics of plane multilayered sandwich infinite-infinite structures, in: *Book of full texts 17th Int.Conf. Engineering Mechanics 2011* (V. Fuis ed.), Inst. of Thermomechanics, Academy of Sciences of the Czech Republic, v.v.i. – branch Brno, Svratka, pp. 275-278.

Ko, S.-H. (1981) Flexural wave baffling by use of a viscoelastic material. *Journal of Sound and Vibration*, 75, 3, pp. 347-357.

Okura, K. (2007) Design of sound insulation, in*: Vibration Damping, Control, and Design* (C.W. de Silva ed.), The University of British Columbia, Vancouver, Canada, pp.19.1-19.10.

Tadeu, A., Antonio, J. & Mateus, D. (2004) Sound insulation provided by single and double walls – a comparison of analytical solutions versus experimental results. *Applied Acoustics*, 65, pp. 15-29.

Yano, H., Tachibana, H., Sakamoto, S. & Matsumoto, T. (2005) Alleviation of the coincidence effect in double-layered plasterboards composing multiple drywall systems, in*: Proc. of The 2005 Congress and Exposition on Noise Control Engineering*, Rio de Janeiro, Brasil, available in the internet.

18th International Conference
ENGINEERING MECHANICS 2012
Svratka, Czech Republic, May 14 – 17, 2012

pp. 625–629
Paper #20

DEPENDENCE OF SALTATION PARAMETERS ON BED ROUGHNESS AND BED POROSITY

I. S. Kharlamova[*], P. Vlasák[**]

Abstract: *In numerical models of bed load transport a bed structure of channel could be described by two parameters, a size of bed particles and a standard deviation of normal distribution of bed particles in the vertical direction. The present paper deals with the effect of bed parameters on average length and height of one jump of saltating particle. A new formula was proposed for bed roughness based on size and standard deviation of the normal distribution of the bed particles. The dependences of length and height of the jump on the diameter of the saltating and bed particles were determined for different variation of vertical distribution of the bed particles.*

Keywords: ***Saltation parameters, saltation length, saltation height, bed structure, normal distribution of bed particles, bed roughness.***

1. Introduction

Saltation is a type of bed-load transport of solid particles in natural channels. During saltation the conveyed particles move along rough bed periodically jumping and colliding with bed particles. Parameters of motion of solid particles and its behaviour depend significantly on bed structure.

The goal of the present paper is to find a dependence of average parameters of saltation motion, such as length and height of one jump, on size of bed particles and on their vertical distribution with respect to the bed plane.

Present research is conducted on the base of simulation models of motion of spherical particles in the channel with rough bed, (Lukerchenko et al., 2009).

2. Bed geometry

The present investigation is an extension of the preceding one, in which a model of rough bed was presented (Kharlamova et al., (2011). Saltating particle during its motion collides with bed particles. The bed particles are grouped on the bed in small areas, which are appearing exactly in that place where saltating particle tent to lend. All bed particles are spherical grains of the same size; the size can be the same or different from the size of saltating particle. Bed particles are organized in particular ways in horizontal and vertical directions. Projections of all particles onto horizontal plane touch each other forming a compact hexagonal lattice, Fig. 1*a*. In vertical direction the bed particles are distributed along *y*-axis according to Gaussian distribution with standard deviation σ around mean bed level, Fig. 1*b*. After collision of the saltating particle with a bed particle the bed particle remains in the same position, while the saltating particle after some energy dissipation continues its motion in the stream. The process of particle's motion continues in such a way until the saltating particle gets stuck into the space between bed particles or until it performs a given numbers of jumps.

The above mentioned bed model allows changing size of bed particles and their vertical distribution around given bed level, it means change of the bed structure. Thickness of bed layer and its porosity can be controlled by stochastic distribution of bed particles around mean bed level and by their size.

[*] Mgr. Irina S. Kharlamova: Institute of Hydrodynamics ASCR, v.v.i., Pod Pat'ankou 30/5; 166 12, Prague 6; CZ, e-mail: kharlamova@ih.cas.cz

[**] Prof. Ing. Pavel Vlasák, DrSc.: Institute of Hydrodynamics ASCR, v.v.i., Pod Pat'ankou 30/5; 166 12, Prague 6; CZ, e-mail: vlasak@ih.cas.cz

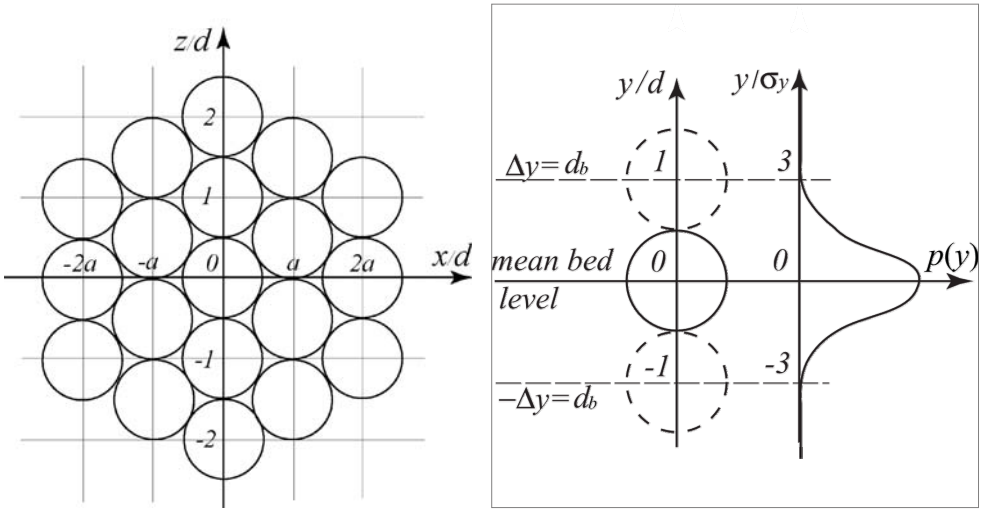

a) b)

Fig. 1. Bed structure in the present model: a) in the x-z plane particles form a compact hexagon; b) examples of distribution of bed particles along y-axis with Gaussian distribution with standard deviation σ = d_b/3 around mean bed level.

Twenty various bed geometries were analysed; these were formed by four different values of standard deviation, i.e. σ = 0, 0.08d_b, 0.17d_b and 0.33d_b; and by five different sizes of the bed particles, i.e. d_b = 3, 4, 5, 6 and 7 mm. Two sets of numerical experiment were conducted. The first simulation provided a situation where the size of saltating particle was equal to size of bed particles ($d = d_b$). In the second simulation the size of saltating particle remained constant and equal to 3 mm; size of the bed particles varied from 3 to 7 mm.

3. The investigation. Calculation of the shear velocity and bed roughness

In order to investigate the change of saltation parameters with variation of bed particle's sizes, it was assumed that the saltation process occurs in the channel with a constant flow rate, Q, and variable bed roughness. In this case it is necessary to know the relationship between bed roughness, k_s, and characteristic flow velocity – shear velocity, u_*.

In the literature there are several experimental studies which determine this connection: Wilson (1987), Yalin (1992), Van Rijn (1993), Sumer et al. (1996), Camenen et al. (2006). The work of Camenen et al. (2006) combines all experimental data from the abovementioned papers and presents a dependence of the equivalent bed roughness on different parameters such as bed shear stress, settling velocity of the bed particles and Froude number. However, the connection formula is very cumbersome and, as authors claim themselves, does not have any physical meaning:

$$\frac{k_s}{d_b} = 0.6 + 1.8\, W_s^{1.2}\, F^{-2.4}\, \tau_*^{1.7}, \tag{1}$$

where $W_s = [(s-1)^2/(gv)]^{1/3} w_s$ – dimensionless settling velocity; s – ratio of solid particles' density and liquid density, for sand and water s = 2.65; g = 9.81 – gravitational acceleration; ν – kinematic viscosity of water; w_s – sedimentation (settling) velocity of the bed grains; $F = U_{av}/\sqrt{gH}$ – Froude number; $U_{av} = Q/(bH)$ – average velocity in the channel; Q – flow rate; H – water depth; b – width of the channel; $\tau_* = u_*^2/((s-1)\, g\, d_b)$ – dimensionless bed shear stress.

We proposed a simple relationship between bed roughness, k_s, and a size of bed particles, d_b, and their vertical distribution, σ :

$$k_s = 6\sigma + 0.5d_b \,. \tag{2}$$

According to definition of the value of bed roughness, it is a distance between the smallest depression and the highest protrusion of bed formation, and it is also a random value in natural channels. According to (2) for standard deviation $\sigma = 0.33\ d_b$ the value $k_s = 2.5\ d_b$ is close to another simple formula for k_s, (Yalin, 1992): $k_s = 2\ d_b$, when the value of the bed shear stress τ_* is less than 1. When the standard deviation is equal zero, $\sigma = 0$, the bed roughness is minimum, $k_s = 0.5\ d_b$, as is clear from Fig. 1,2.

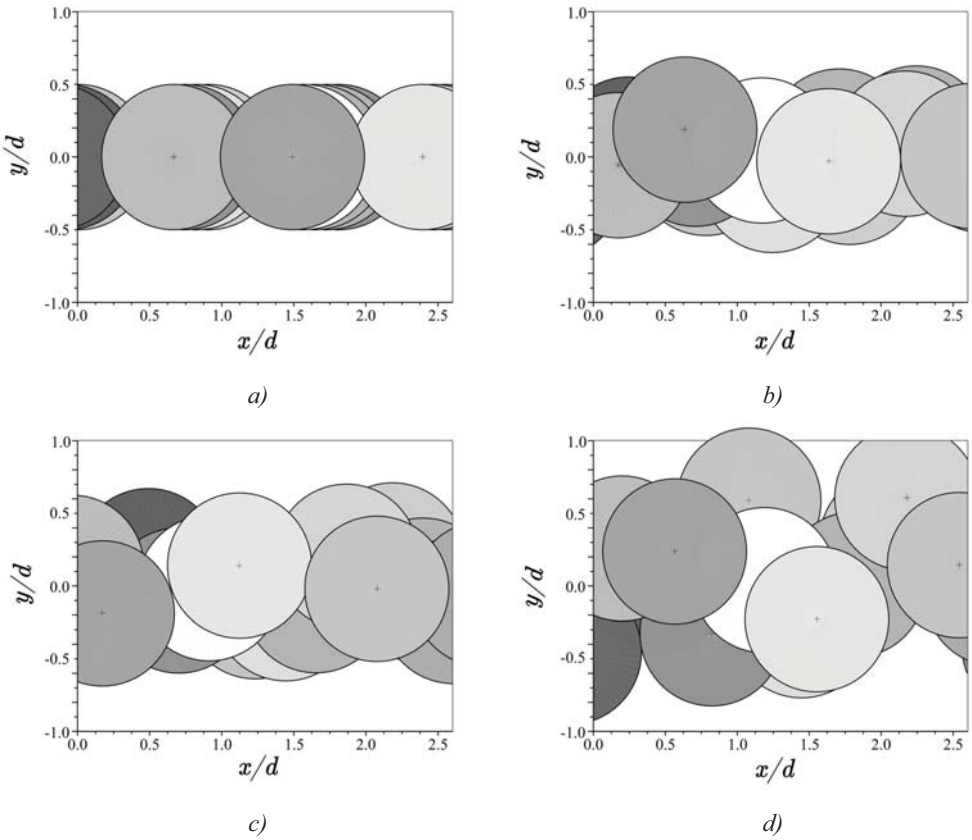

Fig. 2. Examples of distribution of bed particles:
a) standard deviation σ = 0, b) σ = 0.08d_b, c) σ = 0.17d_b, d) σ = 0.33d_b.

Value of shear velocity, u_*, can be determined from the channel parameters, including bed roughness k_s and a logarithmic law distribution of turbulent velocity profile in an open channel:

$$u(y) = \frac{u_*}{\kappa}\ln\left(\frac{y}{y_0}\right), \quad y_0 = 0.11\frac{\nu}{u_*} + 0.033k_s \,. \tag{3}$$

Integrating (3) by depth of the channel and taking into account the width of the channel, a relationship between parameters of the channel and shear velocity can be obtained:

$$U_{av} = \frac{Q}{Hb} = \int_{y_0}^{H} u(y)dy\,, \tag{4}$$

$$\frac{Q}{Hb} = \frac{u_*}{\kappa}\ln\left(\frac{H}{y_0}\right) - \frac{u_*}{\kappa}\left(1 - \frac{y_0}{H}\right). \tag{5}$$

Solving equation (5) and (2) the values of shear velocity and bed roughness can be obtained. For calculation of the values of these the following parameters of the channel, flow and particles were used: flow rate, Q, in channel is constant and equal $25{\cdot}10^{-3}$ m^3/s, channel width, b, is 25 cm, depth of water, H, is 10 cm, kinematic viscosity, ν, and density of water, ρ, consequently equal 10^{-6} s/m^2 and 10^3 kg/m^3, density of solid particles (sand) is $2.65{\cdot}10^3$ kg/m^3, and Karman constant $\kappa = 0.41$. The value of the flow rate Q was chosen so large so that it could allow realising a situation with developed, steady saltation when the saltating particle could perform up to 100 jumps.

4. Results

In result of the first set of numerical experiment the average saltation parameters – length and height of one jump – were calculated. The size of bed particles and the saltating particle was the same and equaled consistently to 3, 4, 5, 6, 7 mm, and standard deviation in normal distribution, σ, was 0, 0.08, 0.17, and 0.33 d_b, see Fig. 3.

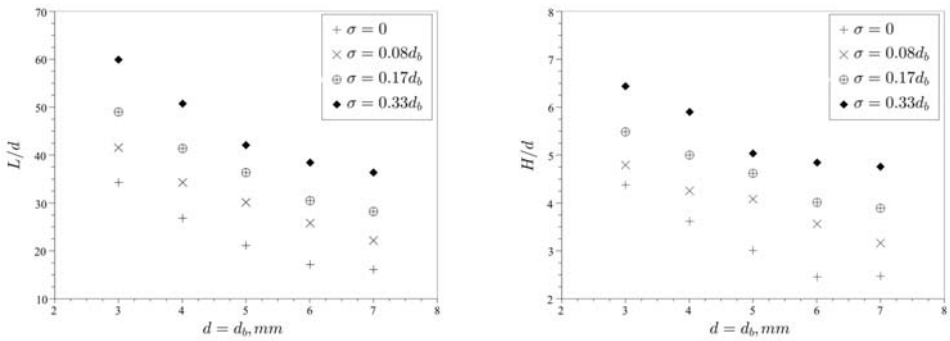

a) *b)*

Fig. 3. Dependences of average saltation length and height on diameter of saltating particle at various standard deviations, diameter of bed particles is the same as that of the saltating particle.

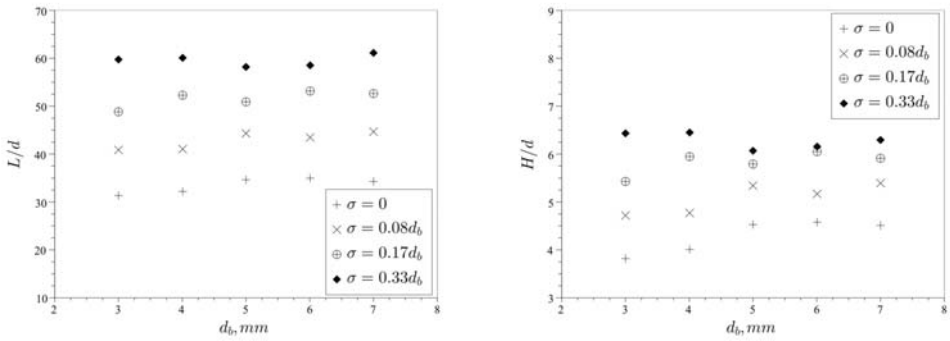

a) *b)*

Fig. 4. Dependences of average saltation length and height of one jump on diameter of the bed particles at various standard deviations, diameter of saltating particle is 3 mm.

As can be seen from the graphs, the dependences are nearly linear; parameters decrease with increasing the diameter and with decreasing the standard deviation. Thus the smaller saltating particle and bed porosity the longer its jumps.

In the second simulation set the size of saltating particle was constant and equal to 3 mm, sizes of bed particles equaled 3, 4, 5, 6, 7 mm, standard deviation equaled 0, 0.08, 0.17, and 0.33 d_b. The results of this simulation are shown in Fig. 4.

Saltating particle has approximately the same values of length and height of its jump at various sizes of bed particles. The larger standard deviation the larger length and height. The form of saltating jump does not change with various ratios between diameters of saltating and bed particles.

Saltating particle with 3 mm diameter at motion along porous bed (standard deviation $\sigma = 0.33\ d_b$, bed particles more then 5 mm) tends to stick into the holes in the bed and, as a consequence, makes a small numbers of jumps (20 from predesigned 100).

5. Conclusions

As a result of modelling different bed geometries saltation parameters (length, height of one jump) were obtained.

It was conducted that for the equal saltating and bed particles (less than $d \leq 5$ mm) the dependences of length and height on the diameter of particles ($d = d_b$) were nearly linear. The length and height of the jumps strongly depend on particle size d and on standard deviation σ - they increase with decreasing particle diameter d and with increasing standard deviation, σ (bed porosity).

For constant diameter of the saltating particle d and varying size of the bed particles d_b, other tendencies were observed. The length and height of the jumps with varying diameter of bed particles remain approximately constant with slight tendency to increase; they also increase with increasing bed porosity (σ). However, in the case of large bed porosity and small saltating particles, the saltating particles tend to stick into the bed among bed particles, and therefore they make only a limited numbers of jumps.

Acknowledgement

Support under the project No. 103/09/1718 of the Grant Agency of the Czech Republic and the Institutional Research Plan No. AV0Z20600510 of the Academy of Sciences of the Czech Republic are gratefully acknowledged.

References

Camenen B., Bayram A., Larson M. (2006) Equivalent Roughness height for plane bed under steady flow. *Journal of Hydraulic Engineering*, 132, 11, pp.1146-1158.

Kharlamova I.S., Kharlamov A.A., Chara Z., Vlasak P. (2011) Modelling of bed in process of particle saltation in channel, in: *Book of full text of Engineering Mechanics 2011* (V. Fuis ed.), Svratka, Czech Republic, pp.279-282.

Lukerchenko, N., Piatsevich, S., Chára, Z., Vlasák, P. (2009) 3D numerical model of the spherical particle saltation in a channel with a rough fixed bed. *Journal of Hydrology and Hydromechanics*, 57, 2, pp.100-112.

Sumer B., Kozakiewez A., Fredse J., Deigaard R. (1996) Velocity and concentration profiles in sheet flow layer of movable bed. *Journal of Hydraulic Engineering*, 122, 10, pp.549-558.

Van Rijn L. (1993) *Principles of sediment transport in rivers, estuaries, and coastal seas.* Aqua, The Netherlands.

Wilson K. (1987) Analysis of bed load motion at high shear stress *Journal of Hydraulic Engineering,* 113, 1, pp.97-103.

Yalin M. (1992) *River mechanics*, Pergamon, Oxford, U.K.

18th International Conference
ENGINEERING MECHANICS 2012
Svratka, Czech Republic, May 14 – 17, 2012

pp. 631–637
Paper #188

MODELING OF FRESH CONCRETE FLOW USING XFEM

F. Kolařík [*], **B. Patzák** [**]

Abstract: *Modeling of fresh concrete flow is interesting problem from both theoretical and practical point of view and its application to self compacting concrete casting simulations is a subject of active research with important practical aspects. Practical importance is especially in application to self compacting concrete, which is highly actual. It is usually modeled in eulerian description of motion as a problem of two immiscible fluids (concrete as a Bingham fluid and air as a Newtonian fluid). Due to different physical properties of these fluids, there are discontinuities of velocity and pressure fields at the interface. In this paper, the eXtended Finite Element Method (XFEM) is used allowing the standard FE approximation space with tailor made functions across the interface to resolve the discontinuities.*

Keywords: ***Flow, concrete, XFEM, Bingham model, level set***

1. Introduction

This paper deals with eXtended Finite Element Method (XFEM) and its implementation in flow problems. Especially, it is focused on its application to fresh concrete flow. In modeling of flow problems using standard Finite Element Method (FEM) fluid is usually considered as a single homogeneous continuous medium. There are in principle three ways, how to describe the motion of continuous medium. In Lagrangian description, motion of each point is described in the framework of reference configuration. This approach, usually used in structural mechanics, is not suitable for fluid description, because of large deformations which require frequent re-meshing. In Eulerian description the motion is connected to actual configuration and therefore convective term is present and the Navier-Stokes equations governs the motion of the fluid. In this case, computation can be done on a fixed grid and no re-meshing is needed. On the other hand, one needs to use some stabilization due to convective terms and also LBB condition has to be satisfied. The advantages of both approaches have been combined in Arbitrary Lagrangian Eulerian formulation which is often used to model fluid-structure interactions. In the present work, Eulerian formulation is used. Modeling of fresh concrete flow in the context of Eulerian formulation is typically done using so called immiscible fluids concept (as a free surface flow), first proposed in (Chessa and Belytschko (2003)). For example, in case of fresh concrete flow, one fluid represents concrete and the other one represents air. Since both fluids are immiscible, the interface between them can be always captured. There are different possibilities, how to track the interface. In FEM context, Volume Of Fluid (see Gopala and Van Wachem (2008)) and level-set method (Sethian (1999), Osher and Fedkiw (2003)) are suitable choices. Since the flow is modeled using XFEM, the level-set method is used in this work. The level-set method describes interface as a zero level set of higher dimensional function. Usually, that function is chosen as a signed distance function. Motion of the interface is then governed by simple convective equation. Extended Finite Element Method enriching the standard continuous approximation of velocity and pressure fields by discontinuous enrichment functions along the interface is then used to discrete governing equations.

2. Governing equations

As was mentioned before, problem is described by Navier-Stokes equations. In this work, only 2D flow is considered. Let $\Omega \subset R^2$ be open set with boundary $\partial\Omega$. Boundary $\partial\Omega$ is decomposed to four mutually disjoint parts Γ_D, Γ_N, $\Gamma_{SWF}$and Γ_{OUT}, on which we prescribe Dirichlet boundary condition,

[*]Ing. Filip Kolařík: Department of Mechanics, Faculty of Civil Engineering, CTU in Prague, Thákurova 7, 166 27, Prague; CZ, e-mail: filip.kolarik@fsv.cvut.cz
[**]Prof. Dr. Ing. Bořek Patzák : Department of Mechanics, Faculty of Civil Engineering, CTU in Prague, Thákurova 7, 166 27, Prague; CZ, e-mail: borek.patzak@fsv.cvut.cz

Neumann boundary condition, so called "slip with friction" boundary condition, "penetration with resistance" (Volker (2002)) and so called "do nothing" boundary condition. The whole problem can be formulated as follows:

$$\rho\frac{\partial \boldsymbol{u}}{\partial t} + \rho\left(\boldsymbol{u}\cdot\boldsymbol{\nabla}\right)\boldsymbol{u} - \boldsymbol{\nabla}\cdot\boldsymbol{\sigma} - \rho\boldsymbol{b} = \boldsymbol{0} \quad \text{in } \Omega \tag{1}$$

$$\boldsymbol{\nabla}\cdot\boldsymbol{u} = 0 \quad \text{in } \Omega \tag{2}$$

$$\boldsymbol{u} = \boldsymbol{g} \quad \text{on } \Gamma_D \tag{3}$$

$$\boldsymbol{u} = \boldsymbol{h} \quad \text{on } \Gamma_N \tag{4}$$

$$\boldsymbol{u}\cdot\boldsymbol{t} + \beta^{-1}\,\boldsymbol{n}\cdot(\boldsymbol{\tau} - p\boldsymbol{\delta})\cdot\boldsymbol{t} = 0 \quad \text{on } \Gamma_{SWF} \tag{5}$$

$$\boldsymbol{u}\cdot\boldsymbol{n} + \alpha\,\boldsymbol{n}\cdot(\boldsymbol{\tau} - p\boldsymbol{\delta})\cdot\boldsymbol{n} = 0 \quad \text{on } \Gamma_{SWF} \tag{6}$$

$$\boldsymbol{n}\cdot(\boldsymbol{\tau} - p\boldsymbol{\delta}) = 0 \quad \text{on } \Gamma_{OUT}. \tag{7}$$

Unknown fields are then velocity $\boldsymbol{u}$ and pressure p. Density ρ, body forces $\boldsymbol{b}$ and functions $\boldsymbol{g}$ and $\boldsymbol{h}$ are prescribed. Parameters β and α in equations (5) and (6) are assumed to be constant. Outer normal vector to the boundary is denoted as $\boldsymbol{n}$, tangent vector as $\boldsymbol{t}$. Standard decomposition of stress tensor $\boldsymbol{\sigma}$ into deviatoric stress $\boldsymbol{\tau}$ and hydrostatic pressure p is used. Strain rate tensor (8) is defined as symmetric part of velocity gradient:

$$\boldsymbol{D} = \frac{1}{2}\left(\boldsymbol{\nabla}\boldsymbol{u} + (\boldsymbol{\nabla}\boldsymbol{u})^T\right). \tag{8}$$

Constitutive law for air can be considered as one-parameter (viscosity μ) Newtonian fluid (9). It is well known that fresh concrete flow can be described by at least two parameters. The first one is yield stress τ_0 which introduces minimal stress necessary for concrete flow. The second parameter, plastic viscosity, μ_{pl} governs the main flow. Despite its simplicity, practical simulations have proved, that it is a suitable choice for describing fresh concrete behavior. The Bingham model (10) is described by following equations:

$$\boldsymbol{\tau} = \mu\boldsymbol{D} \tag{9}$$

$$\begin{cases} \boldsymbol{\tau} = \left[\mu_{pl} + \frac{\tau_0}{\sqrt{\boldsymbol{J_2^e}}}\right]\boldsymbol{D} & ;\, |\boldsymbol{J_2}| \le \tau_0 \\ \boldsymbol{D} = \boldsymbol{0} & ;\, |\boldsymbol{J_2}| \ge \tau_0 \end{cases} \tag{10}$$

where $\boldsymbol{J_2^e}$ is the second invariant of deviatoric strain tensor and $\boldsymbol{J_2}$ is second invariant of deviatoric stress tensor, which is defined as:

$$\boldsymbol{J_2} = \frac{1}{2}\boldsymbol{\tau} : \boldsymbol{\tau} \tag{11}$$

The second invariant of strain rate tensor is defined similarly.

3. Description of the interface

Generally speaking, there are two major approaches for description of the interface. So called interface tracking and interface capturing methods. First group of methods uses deforming mesh to track the interface and describes the interface in explicit manner. As it was mentioned before, in flow problems it is usual to use fixed grid and describe the motion in eulerian sense. Therefore, interface capturing methods have been developed (Sethian (1999)).They describes the interface in some implicit sense. One of the most often used methods of this group is so called level-set method which is applied in this work as well. In this method, interface is represented as a zero level set of some scalar function ϕ. Here, ϕ has been chosen as a signed distance function, which is defined by following property:

$$\phi(\boldsymbol{x}) = \pm \min_{\boldsymbol{x}^* \in \Sigma} ||\boldsymbol{x} - \boldsymbol{x}^*|| \tag{12}$$

The sign in the definition depends on which fluid occupies the point x, Σ denotes the interface between both fluids. Since the interface is changing in time, the level-set representation has to be updated at each time step. Motion of the interface is governed by level-set transport equation:

$$\frac{\partial \phi}{\partial t} + \boldsymbol{u} \cdot \boldsymbol{\nabla} \phi = 0 \qquad \text{in } \Omega \text{ x } [0, T] \tag{13}$$

where $\boldsymbol{u}$ is convective velocity of the fluid. Of course, to solve (13), the proper boundary and initial conditions are needed.

4. Spatial dicretization and XFEM

Since both fluids in our model have different physical properties (density and viscosity), there are discontinuities in velocity and pressure fields along the interface. In general, one can distinguish between two types of discontinuities: strong and weak discontinuities. Strong discontinuity is present when there is a jump in a function. Weak discontinuity arises, when there is a jump in derivative of the function. Example of both types of discontinuities is typically two phase flow with surface tension, where the jump in pressure field (strong discontinuity) and jump in derivative of velocity field, or jump in strain rate tensor (weak discontinuity) occur. Proper description of discontinuities in terms of standard FEM is impossible because functions from approximation space are continuous. It is possible to refine mesh in sub-domains where one expects some discontinuities in the solution. In the case of two phase flow, such a solution is not efficient because the interface is evolving in time and therefore frequent re-meshing would be necessary. Contrary to this, treatment of discontinuities is very easy and natural using XFEM. The main idea behind XFEM is to enrich approximation space with tailored global (defined in whole domain) functions which can describe discontinuities in the solution. Choice of these functions depends on solved problem and on our a priori knowledge of solution. In our case, approximation of unknown function in XFEM has following form:

$$\boldsymbol{u^h}(\boldsymbol{x}, \boldsymbol{t}) = \underbrace{\sum_{i \in I} N_i(\boldsymbol{x}) \boldsymbol{u_i}(\boldsymbol{t})}_{standard\ FE\ approx.} + \underbrace{\sum_{i \in I^*} M_i(\boldsymbol{x}) \boldsymbol{a_i}(\boldsymbol{t})}_{enrichment} \tag{14}$$

where $N_i(\boldsymbol{x})$ is standard FE shape function belonging to node i, I is the set of all nodes in computational domain Ω, $M_i(\boldsymbol{x})$ is enrichment function belonging to node i and I^* is the set of enriched nodes (which is subset of I). Note, that enrichment function $M_i(\boldsymbol{x})$ is defined as multiplication of proper global shape function, which stores "the knowledge" behind enrichment and "partition of unity" (PU) function:

$$M_i(\boldsymbol{x}) = N_i(\boldsymbol{x})[\psi(\boldsymbol{x}) - \psi(\boldsymbol{x_i})] \qquad \forall \text{ i} \in I^* \tag{15}$$

In (15), ψ is so called global enrichment function, which is defined on whole domain Ω and $N_i(\boldsymbol{x})$ is standard FE shape function. In general, one can use any set of functions with PU property instead of FE shape functions. Note, that global enrichment function ψ is "shifted" to ensure Kronecker-δ property hold. In two phase flow, when interface is described by level-set method, the enrichment functions for strong (16) and weak (17) discontinuities can be constructed easily as:

$$\psi_{sign}(\boldsymbol{x}) = sign(\phi(\boldsymbol{x})) = \begin{cases} -1 & : \phi(\boldsymbol{x}) \leq 0 \\ 0 & : \phi(\boldsymbol{x}) = 0 \\ 1 & : \phi(\boldsymbol{x}) \geq 0 \end{cases} \tag{16}$$

for strong discontinuity and

$$\psi_{abs} = abs(\phi(\boldsymbol{x})) \tag{17}$$

for weak discontinuity. As was proposed in (Fries (2003)), enrichment function in form 17 can leads to sub-optimal convergence because of presence of parasite terms in blending elements (elements in which only some nodes are enriched). In this paper, so-called "Ramp function", first published in (Fries (2003)), is used to overcome problems in blending elements.

Modeling of fresh concrete flow is a two fluid problem without the surface tension. Therefore, both velocity and pressure fields are enriched by "abs-enrichment" function. Namely:

$$\boldsymbol{u^h}(\boldsymbol{x},\boldsymbol{t}) = \sum_{i\in I} N_i(\boldsymbol{x})\boldsymbol{u_i}(\boldsymbol{t}) + \sum_{i\in I^*} N_i(\boldsymbol{x})\left[abs(\phi(\boldsymbol{x})) - abs(\phi(\boldsymbol{x_i})\right]\boldsymbol{a_i}(\boldsymbol{t}) \tag{18}$$

$$p^h(\boldsymbol{x},t) = \sum_{i\in I} N_i(\boldsymbol{x})p_i(t) + \sum_{i\in I^*} N_i(\boldsymbol{x})\left[abs(\phi(\boldsymbol{x})) - abs(\phi(\boldsymbol{x_i})\right]b_i(t) \tag{19}$$

Provided that proper function spaces are defined (see Tezduyar and Osawa (2000)), weak formulation of (1) - (7) states as follows: find $\boldsymbol{u^h} \in S_u^h$ and $p^h \in S_p^h$ such that $\forall \boldsymbol{w^h} \in V_u^h, \forall q^h \in V_p^h$:

$$\begin{aligned}
&\int_\Omega \rho \boldsymbol{w^h}\frac{\partial \boldsymbol{u^h}}{\partial t}d\Omega + \int_\Omega \rho \boldsymbol{w^h}\cdot(\boldsymbol{u^h}\cdot\boldsymbol{\nabla u^h})d\Omega + \int_\Omega \boldsymbol{\nabla w^h} : \boldsymbol{\tau(u^h)}d\Omega - \int_\Omega \boldsymbol{w^h}\cdot p^h d\Omega \\
&- \int_\Omega \boldsymbol{w^h}\cdot\boldsymbol{b}d\Omega - \int_{\partial\Omega}\boldsymbol{w^h}\cdot(\boldsymbol{\tau}-p\delta)\cdot\boldsymbol{n}dS + \int_\Omega q^h\boldsymbol{\nabla}\cdot\boldsymbol{u^h}d\Omega \\
&+\sum_{el}\left[\int_{\Omega_e}\tau_{SUPG}(\boldsymbol{u^h}\cdot\boldsymbol{\nabla w^h})\cdot\left(\rho\frac{\partial \boldsymbol{u^h}}{\partial t} + \rho\boldsymbol{w^h}\cdot(\boldsymbol{u^h}\cdot\boldsymbol{\nabla u^h}) - \boldsymbol{\nabla}\cdot\tau(\boldsymbol{u^h}) + \nabla p^h - \boldsymbol{b}\right)d\Omega_e\right] \\
&+\sum_{el}\left[\int_{\Omega_e}\tau_{PSPG}\frac{1}{\rho}\nabla q^h\cdot\left(\rho\frac{\partial \boldsymbol{u^h}}{\partial t} + \rho\boldsymbol{w^h}\cdot(\boldsymbol{u^h}\cdot\boldsymbol{\nabla u^h}) - \boldsymbol{\nabla}\cdot\tau(\boldsymbol{u^h}) + \nabla p^h - \boldsymbol{b}\right)d\Omega_e\right] \\
&+\sum_{el}\left[\int_{\Omega_e}\tau_{LSIC}\boldsymbol{\nabla}\cdot\boldsymbol{w^h}\rho\boldsymbol{\nabla}\cdot\boldsymbol{u^h}d\Omega_e\right] = 0
\end{aligned} \tag{20}$$

Terms in the first two lines follows from standard Galerkin discretization, the third line represents stabilization term due to convection effects, the fourth line provides PSPG stabilization for elements not satisfying LBB condition and the last line provides another stabilization in higher velocity flow. Stabilization parameters $\tau_{SUPG}, \tau_{PSPG}, \tau_{LSIC}$ are chosen according to (Tezduyar and Osawa (2000)). Note, that in that work, finite elements linear in both velocity and pressure were used and therefore terms with $\boldsymbol{\nabla\tau}$ vanishes. Moreover, due to relatively small flow velocity of concrete, only PSPG stabilization is needed, because linear element does not satisfy the LBB condition.

Level-set function, as a scalar function, is discretized by the same shape functions as pressure:

$$\phi^h(\boldsymbol{x}) = \sum_{i\in I} N_i(\boldsymbol{x})\phi_i \tag{21}$$

5. Temporal discretization and solving scheme

After spatial discretization, we have system of non-linear ordinary differential (in time) equations, which has in general form:

$$(\boldsymbol{M}+\boldsymbol{M_\delta})\,\boldsymbol{a} + (\boldsymbol{N(u)}+\boldsymbol{N_\delta(u)}) + (\boldsymbol{K}+\boldsymbol{K_\delta})\,\boldsymbol{u} + \boldsymbol{K}_\mu\boldsymbol{u} + (\boldsymbol{G}+\boldsymbol{G_\delta})\,\boldsymbol{p} = \boldsymbol{F}+\boldsymbol{F_\delta} \tag{22}$$

$$\boldsymbol{G^T u} + \boldsymbol{M_\epsilon a} + \boldsymbol{N_\epsilon(u)} + \boldsymbol{K_\epsilon u} + \boldsymbol{G_\epsilon p} = \boldsymbol{E}+\boldsymbol{E_\epsilon} \tag{23}$$

Terms $\boldsymbol{M}, \boldsymbol{N(u)}, \boldsymbol{K}, \boldsymbol{G}, \boldsymbol{F}, \boldsymbol{E}$ in (22) and (23) follows from standard Galerkin discretization and represents time dependent term, convective term, diffusive term, term connected to pressure and terms represents boundary conditions. Terms with δ subscript are due to the SUPG stabilization, terms with ϵ are due to the PSPG stabilization and $\boldsymbol{K_\mu}$ follows from LSIC stabilization.

5.1. Solution scheme

Solution scheme introduced in (Patzák and Bittnar (2009)) can be described as follows:

1. Temporal discretization by θ-scheme.

$$\begin{aligned} \boldsymbol{a}^{t+\Delta t} &= \boldsymbol{a}^{t} + \boldsymbol{\Delta a} \\ \frac{\boldsymbol{u}^{t+\Delta t} - \boldsymbol{u}^{t}}{\Delta t} &= \alpha \boldsymbol{a}^{t+\Delta t} + (1-\alpha)\boldsymbol{a}^{t} \\ \boldsymbol{p}^{t+\Delta t} &= \boldsymbol{p}^{t} + \boldsymbol{\Delta p} \end{aligned} \tag{24}$$

2. Evaluation (prediction)

$$\begin{aligned} \boldsymbol{u} &= \boldsymbol{u}^{t} + \boldsymbol{\Delta a}^{t} \\ \boldsymbol{a} &= \boldsymbol{a}^{t} \\ \boldsymbol{p} &= \boldsymbol{p}^{t} \end{aligned} \tag{25}$$

3. Computing of velocity and pressure increments

$$\begin{aligned} \boldsymbol{M}^{*}\boldsymbol{\Delta a} - \boldsymbol{G}^{*}\boldsymbol{\Delta p} &= \boldsymbol{R} \\ (\boldsymbol{G}^{\boldsymbol{T}})^{*}\boldsymbol{\Delta a} + \boldsymbol{G}_{\boldsymbol{\epsilon}}\boldsymbol{\Delta p} &= \boldsymbol{Q} \end{aligned} \tag{26}$$

where

$$\begin{aligned} \boldsymbol{M}^{*} &= \boldsymbol{M} + \boldsymbol{M}_{\boldsymbol{\delta}} + \alpha\Delta t\left(\frac{\partial \boldsymbol{N}}{\partial \boldsymbol{u}} + \frac{\partial \boldsymbol{N}_{\boldsymbol{\delta}}}{\partial \boldsymbol{u}} + \boldsymbol{K} + \boldsymbol{K}_{\boldsymbol{\delta}}\right) \\ \boldsymbol{G}^{*} &= \boldsymbol{G} + \boldsymbol{G}_{\boldsymbol{\delta}} \\ (\boldsymbol{G}^{\boldsymbol{T}})^{*} &= \boldsymbol{M}_{\boldsymbol{\epsilon}} + \alpha\Delta t\left(\frac{\partial \boldsymbol{N}_{\boldsymbol{\epsilon}}}{\partial \boldsymbol{u}} + \boldsymbol{K}_{\boldsymbol{\epsilon}} + (\boldsymbol{G}^{\boldsymbol{T}})\right) \\ \boldsymbol{R} &= \boldsymbol{F} + \boldsymbol{F}_{\boldsymbol{\delta}} - [(\boldsymbol{M} + \boldsymbol{M}_{\boldsymbol{\delta}})\,\boldsymbol{a} + (\boldsymbol{N}(\boldsymbol{u}) + \boldsymbol{N}_{\boldsymbol{\delta}}(\boldsymbol{u})) + (\boldsymbol{K} + \boldsymbol{K}_{\boldsymbol{\delta}})\,\boldsymbol{u} + \boldsymbol{K}_{\mu}\boldsymbol{u} + (\boldsymbol{G} + \boldsymbol{G}_{\boldsymbol{\delta}})\,\boldsymbol{p}] \\ \boldsymbol{Q} &= \boldsymbol{E} + \boldsymbol{E}_{\boldsymbol{\epsilon}} - \left[\boldsymbol{G}^{\boldsymbol{T}}\boldsymbol{u} + \boldsymbol{M}_{\boldsymbol{\epsilon}}\boldsymbol{a} + \boldsymbol{N}_{\boldsymbol{\epsilon}(\boldsymbol{u})} + \boldsymbol{K}_{\boldsymbol{\epsilon}}\boldsymbol{u} + \boldsymbol{G}_{\boldsymbol{\epsilon}}\boldsymbol{p} = \boldsymbol{E} + \boldsymbol{E}_{\boldsymbol{\epsilon}}\right] \end{aligned} \tag{27}$$

4. Evaluation of velocity and pressure

$$\begin{aligned} \boldsymbol{a} &\leftarrow \boldsymbol{a} + \boldsymbol{\Delta a} \\ \boldsymbol{p} &\leftarrow \boldsymbol{p} + \boldsymbol{\Delta p} \\ \boldsymbol{u} &\leftarrow \boldsymbol{u} + \Delta t\alpha\boldsymbol{\Delta a} \end{aligned} \tag{28}$$

5. Repeat steps 2.-4. until convergence is reached.

6. Solve the level set equation with computed velocity field $\boldsymbol{u}$. This is done using positive explicit scheme described for example in (Barth and Sethian (1998)).

7. Proceed with next time step.

6. Numerical example

Implementing of XFEM in combination with moving interface by level-set method is quite complicated task and there is a lack of suitable benchmark tests. To illustrate the prototype implementation of XFEM and its application, the application to structural behavior of composite cantilever with circular inclusions is presented. The geometry and structured FE mesh are shown in $Fig.1$ together with stress magnitude contours. Note, that the discretization is based on structured, regular grid and is not capturing the circular

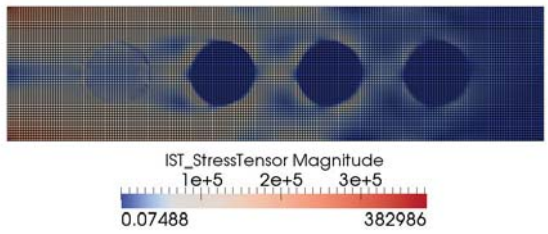

Fig. 1: Cantilever with weakened holes - stress magnitude contours

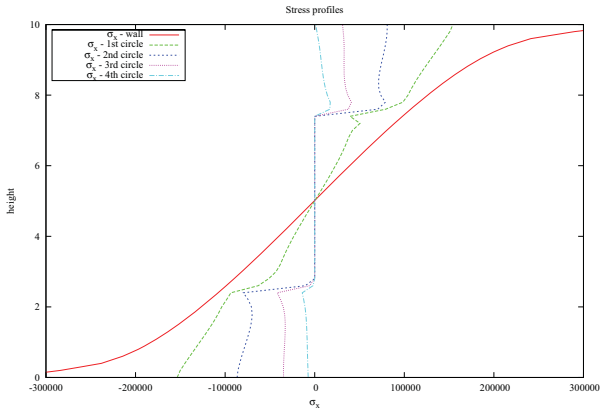

Fig. 2: The stress profile

inclusion geometry which is captured by introducing weak discontinuity enrichment in velocity field with kinks located at material interfaces. Material of cantilever is linear elastic with Young modulus $E = 3 \cdot 10^4 MPa$, weakened holes have Young modulus $E = 0.1 MPa$. Poisson ratio is equal to 0.3. Since there are different material properties, so-called "abs enrichment" was used, because of weak discontinuity in displacement (or strong discontinuity in strains and stresses). Constant continuous load with intensity 1 kN/m has been prescribed on the top surface of the beam. In $Fig.1$, contours of stress magnitude are shown. It can be seen, that in weakened holes the stress is nearly zero as the material has very small Young Modulus. In $Fig.2$, normal stress profiles at the restraint, resp. at the cut through each hole center is plotted shown. Again, it can be seen, that the stress is concentrated near the hole, while the hole itself is not under the stress.

7. Conclusions

In this paper, the numerical model for fresh concrete casting simulations was presented. The problem is treated as flow of a two immiscible homogeneous fluids with different physical properties. The concrete is considered as two-parametric Bingham fluid, the air is modeled as a standard Newtonian fluid. The interface between both fluids is describeb in sense of level-set method. Extended finite element method is then used to resolve description of discontinuities in velocity and pressure fields across the interface. Since there is no surface tension in this problem, presenting discontinuity is only weak and therefore, so-called "abs enrichment" is used. The prototype XFEM implementation is illustrated on structural analysis of composite cantilever with circular inclusions.

Acknowledgments

This work was supported by the Grant Agency of the Czech Technical University in Prague, grants No. SGS12/026/OHK1/1T/11 and New Industrial Technologies for Tailor-made Concrete Structures at Mass Customized Prices TailorCrete, . 7E10055.

References

Barth, T.; Sethian, J.A. (2009), Numerical Schemes for the HamiltonJacobi and Level Set Equations on Triangulated Domains. *Journal of computational physics*, 145 1-40.

Chessa, J.; V.; Belytschko, T. (2003), An extended finite element method for two phase flow. *ASME J. Appl. Mech.*, Vol 70, 10-17.

Fries, T. (2008), A corrected XFEM approximation without problems in blending elements. *Int. J. Numer. Methods Eng.*, Vol 75, 530-532.

Gopala, V.; Van Wachem, B. (2008), Volume of fluid methods for immiscible-fluid and free-surface flows. *Chemical Engineering Journal*, Vol 141, pp 204-221.

Osher S.,Fedkiw R. (2003) *Level Set Methods and Dynamic Implicit Surfaces*, Springer, Berlin.

Patzák, B.; Bittnar, Z. (2009), Modeling of fresh concrete flow. *Computers and Structures*, 87 (15), pp 962-969.

Sethian, J. (1999), *Level Set Methods and Fast Marching Methods* second ed., Cambridge University Press, Cambridge.

Tezduyar, T. ; Osawa, Y. (2000), Finite Element Stabilization parameters computed from element matrices and vectors. *Computer Methods in Applied Mechanics and Engineering,*, Vol 190, is. 3-4, pp 411 - 430.

Volker, J. (2002), Slip with friction and penetration with resistance boundary conditions for the NavierStokes equationsnumerical tests and aspects of the implementation. *Journal of Computational and Applied Mathematics*, Vol 147, No.2, pp 287-300.

18th International Conference
ENGINEERING MECHANICS 2012
Svratka, Czech Republic, May 14 – 17, 2012

pp. 639–655
Paper #235

LTB RESISTANCE OF BEAMS INFLUENCED BY PLASTIC RESERVE OR LOCAL BUCKLING

Y. Koleková[*], I. Baláž[**]

Abstract: *The results of original procedure concerning calculation of the values of the critical moments M_{cr} using approximate formulae convenient for educational and standardization purposes are presented. The authors formulae are today used in many international and national standardization documents (e.g. in several Eurocodes and their National Annexes), in engineering practice of 32 countries and in educational process at many Universities (e.g. in EPU de São Paulo, EPFL Lausanne, etc.). New C_1 values are presented for beams under combination of uniform loading and unequal end moments. Development of useful modification of Eurocode formulae for lateral torsional buckling resistance $M_{b,Rd}$, which enable to show very clearly the influence of plastic resistance and local buckling on LTB resistance of metal (steel, stainless steel, aluminium) and timber beams calculated by any of 4 Eurocode methods.*

Keywords: ***Critical moment, LTB resistance, steel and aluminium beams, Eurocodes.***

1. Introduction

In different Eurocodes: EN 1993-1-1 (2005), EN 1993-1-4 (2006) for steel, EN 1995-1-1 (2004) for timber, EN 1994-1-1 (2004) for composite steel and concrete and EN 1999-1-1 (2007) for aluminium alloys structures, different ways of calculations of critical moments and resistances of laterally unrestrained beams are used. It was shown in the papers Baláž, I. – Koleková, Y. (2000 b, c, 2002 a, b, 2004 a, b) that rules of different Eurocodes concerning lateral torsional buckling could be unified. In this paper EN 1993-1-1 (2005) (ENV 1993-1-1, 1992), EN 1993-1-4 (2006) and EN 1999-1-1 (2007) will be analysed. Lateral torsional buckling of timber structures including analysis of EN 1995-1-1 rules was analysed in Baláž, I. – Koleková, Y. (2004 a, b) and in Baláž (2005).

2. Critical moment M_{cr}

Critical moment M_{cr} is an important quantity, which is needed for calculation of relative slenderness $\bar{\lambda}_{LT}$. The value of M_{cr} may be calculated: (i) more exactly by using a computer program, or (ii) approximately by using various less or more exact approximate formulae of different authors or standards, which have different forms.

The approximate Clark-Mrázik 3-factors formula (see Baláž, I. – Koleková, Y., 2000 c, 2002 a, b) has the best form and it is much more convenient than 1-factor formulae, see e.g. in Roik, K. – Carl, J. – Lindner, J. (1972). Similar 3-factors formula was used also in European prestandards ENV 1993-1-1 (1992) and in ENV 1999-1-1 (1998). Authors showed several times (Baláž, I., 1999, Baláž, I. – Koleková, Y., 1999, 2000, 2002, Koleková, Y., 1999) that using of values of factors C_1, C_2, C_3 taken from tables of ENV 1993-1-1 (1992) or from ENV 1999-1-1 (1998) leads in many cases to incorrect values of critical moments. Despite of this fact the factors C_1, C_2, C_3 defined in ENV 1993-1-1 (1992) and ENV 1999-1-1 (1998) are still used in practise, in many good books (e.g. in Hirt, M.A. – Bez, R., 1998, Hirt, M.A. – Bez, R. – Nussbaumer, A., 2007)) and also in Access Steel available in Internet. Authors criticized their use in drafts prEN 1993-1-1 and prEN 1999-1-1 and consequently the informative annex containing the ENV tables was completely removed from EN 1993-1-1 (2005),

[*] Assoc. Prof. Ing. Yvona Koleková, PhD.: Department of Structural Mechanics, Faculty of Civil Engineering, Slovak University of Technology, Radlinského 11; 813 68, Bratislava; SK, e-mail: yvona.kolekova@stuba.sk

[**] Prof. Ing. Ivan Baláž, PhD.: Department of Metal and Timber Structures, Fakulty of Civil Engineering, Slovak University of Technology, Radlinského 11; 813 68, Bratislava; SK, e-mail: ivan.balaz@stuba.sk

which now does not contain any M_{cr} formulae. New more general formulae and tables enabling to compute M_{cr} developed by authors in Baláž, I. – Koleková, Y. (2000 b) were fully accepted for Annex I of drafts and later also of final version of EN 1999-1-1 (2007). In Fruchtengarten, J. (2005) a lot of various formulae were evaluated in the frame of parametric study by comparing them with exact results of program PEFSYS and it was concluded that proposal of Baláž, I. – Koleková, Y. (2000 b) gives the most exact results. Factors C_1, C_2, C_3 computed by authors Baláž, I. – Koleková, Y. (2000 b) and their formula for calculating of elastic critical moment M_{cr} are used in several National Annexes, e.g. in Slovak (STN EN 1993-1-1/NA, 2007), Czech (ČSN EN 1993-1-1, 2006), Austrian (ÖNORM B 1993-1-1, 2007) and Belgian (2005) National Annexes to Eurocode EN 1993-1-1 (2005), because this Eurocode gives no details of calculation of M_{cr}. Authors results are used also in tables used in the following publications: Deutscher Ausschluß für Stahlbau (2005), ECCS Technical Committee 8 – Stability (2006), Design Manual For Structural Stainless Steel. (2006), Excerpt from the Background Document to EN 1993-1-1 (2010).

According to authors proposal the elastic critical moment M_{cr} can be computed from the formula

$$M_{cr} = \mu_{cr} \frac{\pi\sqrt{EI_z GI_t}}{L} \tag{1}$$

where

$$\mu_{cr} = \frac{C_1}{k_z}\left[\sqrt{1+\kappa_{wt}^2 + (C_2\zeta_g - C_3\zeta_j)^2} - (C_2\zeta_g - C_3\zeta_j)\right] \tag{2}$$

three non-dimensional parameters are

$$\kappa_{wt} = \frac{\pi}{k_w L}\sqrt{\frac{EI_w}{GI_t}}, \quad \zeta_g = \frac{\pi z_g}{k_z L}\sqrt{\frac{EI_z}{GI_t}}, \quad \zeta_j = \frac{\pi z_j}{k_z L}\sqrt{\frac{EI_z}{GI_t}} \tag{3}$$

and three factors C_1, C_2, C_3 depend on the loadings, end restraint conditions, shape of the cross-section and C_1 also on torsional properties. The details and numerical values see in Tables 1-4 or in Tables 1 and 2 in Baláž, I. – Koleková, Y. (2000 b), Tables I.1 - I.4 in EN 1999-1-1 (2007) or Tables NB.3.1-NB.3.4 in STN EN 1993-1-1/NA (2007).

Our general formula (1) becomes very approximate formula used in German standard DIN 18 800 (1990, 2008) in the case of double symmetric cross-section ($z_j = 0$ mm) when our more refined values of factor C_2 are replaced by rough value 0,5 used in DIN 18 800 (1990, 2008). The meaning of our factor C_1 is the same as the meaning of the factor ζ used in DIN 18 800 (1990, 2008), Table 10.

Factor C_1 depends on bending moment distribution, boundary conditions and parameter κ_{wt}. In Baláž, I. – Koleková, Y. (2000 b), in EN 1999-1-1 (2007) or in STN EN 1993-1-1/NA (2007) a linear interpolation between values $C_{1,0} = C_1(\kappa_{wt} = 0)$ and $C_{1,1} = C_1(\kappa_{wt} = 1)$ is proposed. For $\kappa_{wt} \geq 1$ it is proposed in Baláž, I. – Koleková, Y. (2000 b), in EN 1999-1-1 (2007) and in STN EN 1993-1-1/NA (2007) to use an approximation $C_1(\kappa_{wt} \geq 1) \approx C_{1,1} = C_1(\kappa_{wt} = 1)$. For many loading cases the difference between values $C_{1,0} = C_1(\kappa_{wt} = 0)$ and $C_{1,1} = C_1(\kappa_{wt} = 1)$ is negligible, that is why many authors of various publications even do not inform, which value of C_1 they use. Eurocode EN 1993-1-1 (2005) uses C_1 in Table A.1, formulae BB.5 and BB.9 without any definition . Here it is an advise to users of EN 1993-1-1 (2005): you can use relevant values of C_1 given in Baláž, I. – Koleková, Y. (2000 b), in EN 1999-1-1 (2007) or in STN EN 1993-1-1/NA (2007), or you can use an approximation $C_1 = (k_c)^{-2}$, where k_c is a correction factor for relevant moment distribution (see Table 6.6 in EN 1993-1-1 (2005)).

Tab. 1: Values of factors C_1 and C_3 corresponding to various end moment ratios ψ, values of buckling length factor k_z and cross-section parameters ψ_f and κ_{wt}.

End moment loading of the simply supported beam with buckling length factors $k_y = 1$ for major axis bending and $k_w = 1$ for torsion

Loading and support conditions. Cross-section monosymmetry factor ψ_f	Bending moment diagram. End moment ratio ψ. M-side / ψM-side	k_z [2)]	Values of factors					
			C_1 [1)]		C_3			
			$C_{1,0}$	$C_{1,1}$	$\psi_f = -1$	$-0{,}9 \le \psi_f \le 0$	$0 \le \psi_f \le 0{,}9$	$\psi_f = 1$
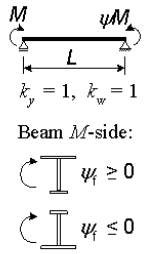 $k_y = 1,\ k_w = 1$ Beam M-side: $\psi_f \ge 0$ $\psi_f \le 0$	M_{cr} ψ=+1	1,0	**1,000**	**1,000**	**1,000**			
		0,7L	**1,016**	**1,100**		**1,025**	**1,000**	
		0,7R	**1,016**	**1,100**		**1,025**	**1,000**	
		0,5	**1,000**	**1,127**		**1,019**		
	M_{cr} ψ=+3/4	1,0	**1,139**	**1,141**		**1,000**		
		0,7L	**1,210**	**1,313**		**1,050**	**1,000**	
		0,7R	**1,109**	**1,201**		**1,000**		
		0,5	**1,139**	**1,285**		**1,017**		
	M_{cr} ψ=+1/2	1,0	**1,312**	**1,320**	**1,150**	**1,000**		
		0,7L	**1,480**	**1,616**		**1,160**	**1,000**	
		0,7R	**1,213**	**1,317**		**1,000**		
		0,5	**1,310**	**1,482**	**1,150**	**1,000**		
	M_{cr} ψ=+1/4	1,0	**1,522**	**1,551**	**1,290**	**1,000**		
		0,7L	**1,853**	**2,059**	**1,600**	**1,260**	**1,000**	
		0,7R	**1,329**	**1,467**		**1,000**		
		0,5	**1,516**	**1,730**	**1,350**	**1,000**		
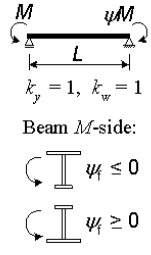 $k_y = 1,\ k_w = 1$ Beam M-side: $\psi_f \le 0$ $\psi_f \ge 0$ $\psi_f = \frac{I_{fc} - I_{ft}}{I_{fc} + I_{ft}}$	M_{cr} ψ = 0	1,0	**1,770**	**1,847**	**1,470**	**1,000**		
		0,7L	**2,331**	**2,683**	**2,000**	**1,420**	**1,000**	
		0,7R	**1,453**	**1,592**		**1,000**		
		0,5	**1,753**	**2,027**	**1,500**	**1,000**		
	M_{cr} ψ = -1/4	1,0	**2,047**	**2,207**	**1,65**	**1,000**	**0,850**	
		0,7L	**2,827**	**3,322**	**2,40**	**1,550**	**0,850**	**-0,30**
		0,7R	**1,582**	**1,748**	**1,38**	**0,850**	**0,700**	**0,20**
		0,5	**2,004**	**2,341**	**1,75**	**1,000**	**0,650**	**-0,25**
	M_{cr} ψ = -1/2	1,0	**2,331**	**2,591**	**1,85**	**1,000**	$1{,}3 - 1{,}2\psi_f$	**-0,70**
		0,7L	**3,078**	**3,399**	**2,70**	**1,450**	$1 - 1{,}2\psi_f$	**-1,15**
		0,7R	**1,711**	**1,897**	**1,45**	**0,780**	$0{,}9 - 0{,}75\psi_f$	**-0,53**
		0,5	**2,230**	**2,579**	**2,00**	**0,950**	$0{,}75 - \psi_f$	**-0,85**
	M_{cr} ψ = -3/4	1,0	**2,547**	**2,852**	**2,00**	**1,000**	$0{,}55 - \psi_f$	**-1,45**
		0,7L	**2,592**	**2,770**	**2,00**	**0,850**	$0{,}23 - 0{,}9\psi_f$	**-1,55**
		0,7R	**1,829**	**2,027**	**1,55**	**0,700**	$0{,}68 - \psi_f$	**-1,07**
		0,5	**2,352**	**2,606**	**2,00**	**0,850**	$0{,}35 - \psi_f$	**-1,45**
	M_{cr} ψ = -1	1,0	**2,555**	**2,733**	**2,00**	$-\psi_f$		**-2,00**
		0,7L	**1,921**	**2,103**	**1,55**	**0,380**	**-0,580**	**-1,55**
		0,7R	**1,921**	**2,103**	**1,55**	**0,580**	**-0,380**	**-1,55**
		0,5	**2,223**	**2,390**	**1,88**	$0{,}125 - 0{,}7\psi_f$	$-0{,}125 - 0{,}7\psi_f$	**-1,88**

1) $C_1 = C_{1,0} + (C_{1,1} - C_{1,0})\kappa_{wt} \le C_{1,1}$, ($C_1 = C_{1,0}$ for $\kappa_{wt} = 0$, $C_1 = C_{1,1}$ for $\kappa_{wt} \ge 1$)

2) $0{,}7L$ = left end fixed, $0{,}7R$ = right end fixed

Tab. 2: Values of factors C_1, C_2 and C_3 corresponding to various transverse loading cases, values of buckling length factors k_y, k_z, k_w, cross-section monosymmetry factor ψ_f and torsion parameter κ_{wt}.

Loading and support conditions	Buckling length factors			Values of factors								
				C_1 [1)]		C_2			C_3			
	k_y	k_z	k_w	$C_{1,0}$	$C_{1,1}$	⊥ $\psi_f = -1$	⊥⊤⊥ $-0,9 \le \psi_f \le 0,9$	⊤ $\psi_f = 1$	⊥ $\psi_f = -1$	⊥⊤⊥ $-0,9 \le \psi_f \le 0,9$	⊤ $\psi_f = 1$
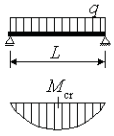	1	1	1	1,127	1,132	0,33	0,459	0,50	0,93	0,525	0,38
	1	1	0,5	1,128	1,231	0,33	0,391	0,50	0,93	0,806	0,38
	1	0,5	1	0,947	0,997	0,25	0,407	0,40	0,84	0,478	0,44
	1	0,5	0,5	0,947	0,970	0,25	0,310	0,40	0,84	0,674	0,44
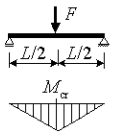	1	1	1	1,348	1,363	0,52	0,553	0,42	1,00	0,411	0,31
	1	1	0,5	1,349	1,452	0,52	0,580	0,42	1,00	0,666	0,31
	1	0,5	1	1,030	1,087	0,40	0,449	0,42	0,80	0,338	0,31
	1	0,5	0,5	1,031	1,067	0,40	0,437	0,42	0,80	0,516	0,31
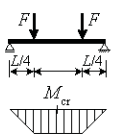	1	1	1	1,038	1,040	0,33	0,431	0,39	0,93	0,562	0,39
	1	1	0,5	1,039	1,148	0,33	0,292	0,39	0,93	0,878	0,39
	1	0,5	1	0,922	0,960	0,28	0,404	0,30	0,88	0,539	0,50
	1	0,5	0,5	0,922	0,945	0,28	0,237	0,30	0,88	0,772	0,50
						$\psi_f = -1$	$-0,5 \le \psi_f \le 0,5$	$\psi_f = 1$	$\psi_f = -1$	$-0,5 \le \psi_f \le 0,5$	$\psi_f = 1$
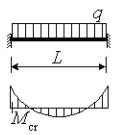	0,5	1	1	2,576	2,608	1,00	1,562	0,15	1,00	-0,859	-1,99
	0,5	0,5	1	1,490	1,515	0,56	0,900	0,08	0,61	-0,516	-1,20
	0,5	0,5	0,5	1,494	1,746	0,56	0,825	0,08	0,61	0,002712	-1,20
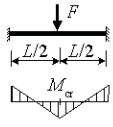	0,5	1	1	1,683	1,726	1,20	1,388	0,07	1,15	-0,716	-1,35
	0,5	0,5	1	0,936	0,955	0,69	0,763	0,03	0,64	-0,406	-0,76
	0,5	0,5	0,5	0,937	1,057	0,69	0,843	0,03	0,64	-0,0679	-0,76

1) $C_1 = C_{1,0} + (C_{1,1} - C_{1,0})\kappa_{wt} \le C_{1,1}$, ($C_1 = C_{1,0}$ for $\kappa_{wt} = 0$, $C_1 = C_{1,1}$ for $\kappa_{wt} \ge 1$).

2) Parameter ψ_f refers to the middle of the span.

3) Values of critical moments M_{cr} refer to the cross section, where M_{max} is located

Tab. 3: Relative non-dimensional critical moment μ_{cr} for cantilever $(k_y = k_z = k_w = 2)$ loaded by concentrated tip load F.

Loading and support conditions	$\frac{\pi}{L}\sqrt{\frac{EI_w}{GI_t}} = k_w \kappa_{wt} = \kappa_{wt0}$	$\frac{\pi z_g}{L}\sqrt{\frac{EI_z}{GI_t}} = k_z \zeta_g = \zeta_g$	(T) (C) / (C) (T)		$\frac{\pi z_j}{L}\sqrt{\frac{EI_z}{GI_t}} = k_z \zeta_j = \zeta_{j0}$			(C) (T) / (T) (C)	
			-4	-2	-1	0	1	2	4
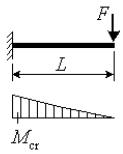	0	4	0,107	0,156	0,194	0,245	0,316	0,416	0,759
		2	0,123	0,211	0,302	0,463	0,759	1,312	4,024
		0	0,128	0,254	0,478	1,280	3,178	5,590	10,730
		-2	0,129	0,258	0,508	1,619	3,894	6,500	11,860
		-4	0,129	0,258	0,511	1,686	4,055	6,740	12,240
	0,5	4	0,151	0,202	0,240	0,293	0,367	0,475	0,899
		2	0,195	0,297	0,393	0,560	0,876	1,528	5,360
		0	0,261	0,495	0,844	1,815	3,766	6,170	11,295
		-2	0,329	0,674	1,174	2,423	4,642	7,235	12,595
		-4	0,364	0,723	1,235	2,529	4,843	7,540	13,100
	1	4	0,198	0,257	0,301	0,360	0,445	0,573	1,123
		2	0,268	0,391	0,502	0,691	1,052	1,838	6,345
		0	0,401	0,750	1,243	2,431	4,456	6,840	11,920
		-2	0,629	1,326	2,115	3,529	5,635	8,115	13,365
		-4	0,777	1,474	2,264	3,719	5,915	8,505	13,960
	2	4	0,335	0,428	0,496	0,588	0,719	0,916	1,795
		2	0,461	0,657	0,829	1,111	1,630	2,698	7,815
		0	0,725	1,321	2,079	3,611	5,845	8,270	13,285
		-2	1,398	3,003	4,258	5,865	7,845	10,100	15,040
		-4	2,119	3,584	4,760	6,360	8,385	10,715	15,825
	4	4	0,845	1,069	1,230	1,443	1,739	2,168	3,866
		2	1,159	1,614	1,992	2,569	3,498	5,035	10,345
		0	1,801	3,019	4,231	6,100	8,495	11,060	16,165
		-2	3,375	6,225	8,035	9,950	11,975	14,110	18,680
		-4	5,530	8,130	9,660	11,375	13,285	15,365	19,925

a) For $z_j = 0$, $z_g = 0$ and $\kappa_{wt0} \le 8$: $\mu_{cr} = 1{,}27 + 1{,}14\,\kappa_{wt0} + 0{,}017\,\kappa_{wt0}^2$.

b) For $z_j = 0$, $-4 \le \zeta_g \le 4$ and $\kappa_{wt} \le 4$, μ_{cr} may be calculated also from formulae (I.7) and (I.8), where the following approximate values of the factors C_1, C_2 should be used for the cantilever under tip load F:

$C_1 = 2{,}56 + 4{,}675\,\kappa_{wt} - 2{,}62\,\kappa_{wt}^2 + 0{,}5\kappa_{wt}^3$, if $\kappa_{wt} \le 2$

$C_1 = 5{,}55$ if $\kappa_{wt} > 2$

$C_2 = 1{,}255 + 1{,}566\,\kappa_{wt} - 0{,}931\,\kappa_{wt}^2 + 0{,}245\,\kappa_{wt}^3 - 0{,}024\kappa_{wt}^4$, if $\zeta_g \ge 0$

$C_2 = 0{,}192 + 0{,}585\,\kappa_{wt} - 0{,}054\,\kappa_{wt}^2 - (0{,}032 + 0{,}102\,\kappa_{wt} - 0{,}013\,\kappa_{wt}^2)\,\zeta_g$, if $\zeta_g < 0$

Tab. 4: Relative non-dimensional critical moment μ_{cr} for cantilever $(k_{\mathrm{y}} = k_{\mathrm{z}} = k_{\mathrm{w}} = 2)$ loaded by uniformly distributed load q

Loading and support conditions	$\frac{\pi}{L}\sqrt{\frac{EI_{\mathrm{w}}}{GI_{\mathrm{t}}}} = k_w \kappa_{wt} = \kappa_{wt0}$	$\frac{\pi z_{\mathrm{g}}}{L}\sqrt{\frac{EI_{\mathrm{z}}}{GI_{\mathrm{t}}}} = k_z \zeta_g = \zeta_{g0}$	(T) (C) (C) (T)		$\frac{\pi z_{\mathrm{j}}}{L}\sqrt{\frac{EI_{\mathrm{z}}}{GI_{\mathrm{t}}}} = k_z \zeta_j = \zeta_{j0}$			(C) (T) (T) (C)	
			-4	-2	-1	0	1	2	4
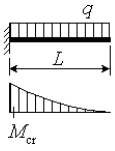	0	4	0,113	0,173	0,225	0,304	0,431	0,643	1,718
		2	0,126	0,225	0,340	0,583	1,165	2,718	13,270
		0	0,132	0,263	0,516	2,054	6,945	12,925	25,320
		-2	0,134	0,268	0,537	3,463	10,490	17,260	30,365
		-4	0,134	0,270	0,541	4,273	12,715	20,135	34,005
	0,5	4	0,213	0,290	0,352	0,443	0,586	0,823	2,046
		2	0,273	0,421	0,570	0,854	1,505	3,229	14,365
		0	0,371	0,718	1,287	3,332	8,210	14,125	26,440
		-2	0,518	1,217	2,418	6,010	12,165	18,685	31,610
		-4	0,654	1,494	2,950	7,460	14,570	21,675	35,320
	1	4	0,336	0,441	0,522	0,636	0,806	1,080	2,483
		2	0,449	0,663	0,865	1,224	1,977	3,873	15,575
		0	0,664	1,263	2,172	4,762	9,715	15,530	27,735
		-2	1,109	2,731	4,810	8,695	14,250	20,425	33,075
		-4	1,623	3,558	6,025	10,635	16,880	23,555	36,875
	2	4	0,646	0,829	0,965	1,152	1,421	1,839	3,865
		2	0,885	1,268	1,611	2,185	3,282	5,700	18,040
		0	1,383	2,550	4,103	7,505	12,770	18,570	30,570
		-2	2,724	6,460	9,620	13,735	18,755	24,365	36,365
		-4	4,678	8,635	11,960	16,445	21,880	27,850	40,400
	4	4	1,710	2,168	2,500	2,944	3,565	4,478	8,260
		2	2,344	3,279	4,066	5,285	7,295	10,745	23,150
		0	3,651	6,210	8,845	13,070	18,630	24,625	36,645
		-2	7,010	13,555	17,850	22,460	27,375	32,575	43,690
		-4	12,270	18,705	22,590	26,980	31,840	37,090	48,390

a) For $z_{\mathrm{j}} = 0$, $z_g = 0$ and $\kappa_{wt0} \le 8$: $\mu_{cr} = 2{,}04 + 2{,}68\,\kappa_{wt0} + 0{,}021\,\kappa_{wt0}^2$.

b) For $z_{\mathrm{j}} = 0$, $-4 \le \zeta_{\mathrm{g}} \le 4$ and $\kappa_{\mathrm{wt}} \le 4$, μ_{cr} may be calculated also from formula (I.7) and (I.8),

where the following approximate values of the factors C_1, C_2 should be used for the cantilever under uniform load q:

$C_1 = 4{,}11 + 11{,}2\,\kappa_{\mathrm{wt}} - 5{,}65\,\kappa_{\mathrm{wt}}^2 + 0{,}975\,\kappa_{\mathrm{wt}}^3$, if $\kappa_{\mathrm{wt}} \le 2$

$C_1 = 12$ if $\kappa_{\mathrm{wt}} > 2$

$C_2 = 1{,}661 + 1{,}068\,\kappa_{\mathrm{wt}} - 0{,}609\,\kappa_{\mathrm{wt}}^2 + 0{,}153\,\kappa_{\mathrm{wt}}^3 - 0{,}014\,\kappa_{\mathrm{wt}}^4$, if $\zeta_{\mathrm{g}} \ge 0$

$C_2 = 0{,}535 + 0{,}426\,\kappa_{\mathrm{wt}} - 0{,}029\,\kappa_{\mathrm{wt}}^2 - (0{,}061 + 0{,}074\,\kappa_{\mathrm{wt}} - 0{,}0085\,\kappa_{\mathrm{wt}}^2)\,\zeta_{\mathrm{g}}$, if $\zeta_{\mathrm{g}} < 0$

In this paper we give values of $C_1(\kappa_{wt} = 0{,}235)$ for a lot of new moment distributions valid for beam supported at both ends by "forks", with double symmetric cross-section, for which parameter $\zeta_j = 0$ and there is no need to know value of C_3. These C_1 values may be used also for continuous girders being on the safe side. Investigated loading case is shown in Figure 1.

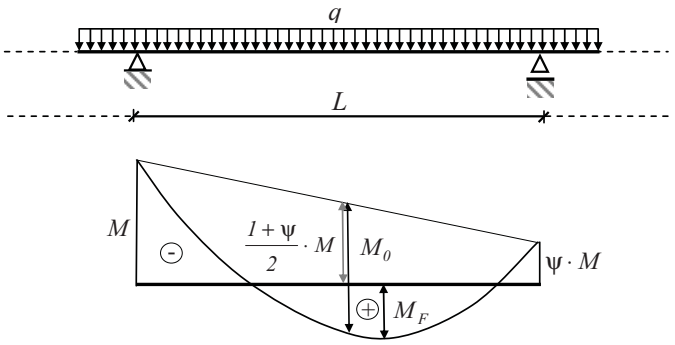

Fig.1: Investigated loading case

The following was taken into account:

$$-1 \le \psi \le 1, \qquad M_0 = \frac{1}{8} qL^2 \ge 0, \qquad M \le 0, \qquad M_F = M_0 + \frac{1+\psi}{2} M + \frac{(1-\psi)^2}{16} \frac{M^2}{M_0} \tag{4}$$

$$|M|_{max} = |M| \quad \text{if} \quad \sqrt{\frac{1+\psi}{2}} - sign(M) \frac{3+\psi}{4} \frac{|M|}{M_0} > 1, \qquad \text{otherwise} \quad |M|_{max} = M_F \tag{5}$$

Elastic critical moment M_{cr} may be calculated from the formula (1) for cases $\zeta_g = 0$. For cases $\zeta_g \neq 0$, because we have not relevant values of factor C_2 for various cases, we can use an approximate value $C_2 = 0{,}5$ for all cases as it was done also in DIN 18 800 (1990, 2008). Then

$$\mu_{cr} \approx \frac{C_1}{k_z} \left[\sqrt{1 + \kappa_{wt}^2 + (0{,}5\zeta_g)^2} - 0{,}5\zeta_g \right] \tag{6}$$

The numerical values of factor C_1 were calculated for $\kappa_{wt} = 0{,}235$ and different moment distributions defined by parameters ψ, M_0 / M by an efficient computer program CalcMcr Version 1.9 developed by the authors and they may be used also for the beams with any κ_{wt} values. C_1 values were computed for combination of 21 end moments ratios ψ = -1; -0,9; -0,8; -0,7; -0,6; -0,5; -0,4; -0,3; -0,2; -0,1; 0; 0,1; 0,2; 0,3; 0,4; 0,5; 0,6; 0,7; 0,8; 0,9; 1, and 11 moment ratios M_0 / M = 0; - 0,25; - 0,5; - 0,75; - 1; - 1,25; - 1,5; - 1,75; - 2; -10; - ∞ (see Table 5 and Figure 2). $C_1 \approx 1{,}16$ for M_0 / M = - 10 and $C_1 = 1{,}13$ for $M_0 / M = -\infty$ for all ψ values. Similar table as Table 5 was created also for $0 \le M_0 / M \le \infty$, but it is not given here because of limited size of the paper. Location of the elastic critical moment M_{cr} is identical with location of maximum moment $|M|_{max}$.

Similar tables like Table 1 were created also for four other loadings and boundary conditions:

(i) point load F in the middle of the beam span combined with support moments,

(ii) two point loads F acting in quarters of the beam span combined with support moments,

(iii) cantilever under uniform loading q and

(iv) cantilever under tip load F.

Computer program CalcMcr Version 1.9 enables for these 4 loading cases to take into account exactly, according to (1) and (2), also point of load q, F application related to shear center and mono-symmetry of cross-sections.

Tab. 5: Values of factor $C_1(\kappa_{wt} = 0{,}235; \psi; M_0 / M)$. *Boundary conditions:* $k_y = 1,\ k_z = 1,\ k_w = 1$.

C_1	M_0 / M										
ψ	**0**	**- 0,25**	**- 0,5**	**- 0,75**	**- 1**	**- 1,25**	**- 1,5**	**- 1,75**	**- 2**	**-10**	**- ∞**
1	**1,00**	**1,28**	**1,75**	**2,67**	**4,36**	**4,61**	**2,59**	**1,69**	**1,24**		
0,9	**1,06**	**1,37**	**1,93**	**3,03**	**4,70**	**4,14**	**2,36**	**1,58**	**1,23**		
0,8	**1,11**	**1,46**	**2,11**	**3,40**	**5,05**	**3,66**	**2,14**	**1,47**	**1,22**		
0,7	**1,17**	**1,56**	**2,29**	**3,77**	**5,31**	**3,19**	**1,92**	**1,36**	**1,21**		
0,6	**1,24**	**1,68**	**2,52**	**4,11**	**5,07**	**2,78**	**1,75**	**1,26**	**1,21**		
0,5	**1.32**	**1,82**	**2,77**	**4,34**	**4,54**	**2,48**	**1,63**	**1,22**	**1,20**		
0,4	**1,39**	**1,95**	**3,01**	**4,65**	**4,01**	**2,18**	**1,49**	**1,18**	**1,19**		
0,3	**1,48**	**2,11**	**3,26**	**4,77**	**3,34**	**1,98**	**1,39**	**1,20**	**1,19**		
0,2	**1,58**	**2,27**	**3,49**	**4,64**	**2,84**	**1,80**	**1,30**	**1,20**	**1,19**		
0,1	**1,68**	**2,44**	**3,73**	**4,26**	**2,47**	**1,64**	**1,23**	**1,19**	**1,18**		
0	**1,79**	**2,61**	**3,83**	**3,74**	**2,23**	**1,53**	**1,20**	**1,19**	**1,18**	**1,16**	**1,13**
-0,1	**1,90**	**2,79**	**3,99**	**3,26**	**1,96**	**1,39**	**1,18**	**1,18**	**1,17**		
-0,2	**2,03**	**2,96**	**3,97**	**2,76**	**1,79**	**1,29**	**1,19**	**1,18**	**1,17**		
-0,3	**2,15**	**3,11**	**3,75**	**2,38**	**1,63**	**1,23**	**1,19**	**1,18**	**1,17**		
-0,4	**2,28**	**3,28**	**3,29**	**2,10**	**1,49**	**1,21**	**1,19**	**1,18**	**1,17**		
-0,5	**2,40**	**3,27**	**2,84**	**1,92**	**1,40**	**1,21**	**1,19**	**1,17**	**1,17**		
-0,6	**2,54**	**3,18**	**2,47**	**1,70**	**1,30**	**1,20**	**1,19**	**1,17**	**1,16**		
-0,7	**2,65**	**2,93**	**2,19**	**1,56**	**1,25**	**1,21**	**1,19**	**1,17**	**1,16**		
-0,8	**2,65**	**2,83**	**1,99**	**1,49**	**1,25**	**1,21**	**1,19**	**1,17**	**1,16**		
-0,9	**2,64**	**2,77**	**1,81**	**1,43**	**1,26**	**1,21**	**1,19**	**1,17**	**1,16**		
-1	**2,62**	**2,71**	**1,63**	**1,36**	**1,26**	**1,22**	**1,19**	**1,17**	**1,16**		

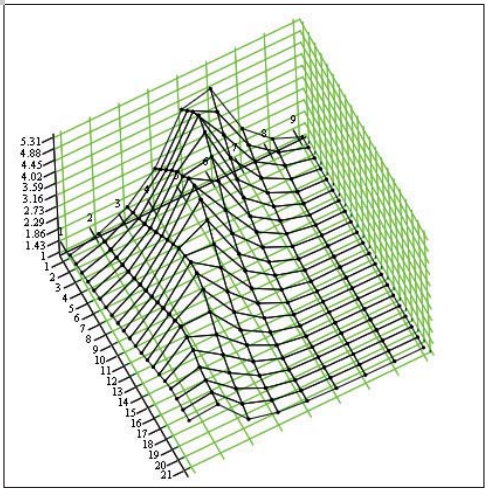

C_1

Fig. 2: $C_1(\kappa_{wt} = 0{,}235; \psi; M_0 / M)$ *for* $-1 \le \psi \le 1$ *(21 values) and for* $-\infty \le M_0 / M \le 0$ *(11 values)*

All above mentioned tables are more general containing both $C_{1,0} = C_1(\kappa_{wt} = 0)$ and $C_{1,1} = C_1(\kappa_{wt} = 1)$ values, what enables to obtain more exact C_1 value for any κ_{wt} by using an interpolation.

3. Design buckling resistance moment $M_{b,Rd}$

The design buckling resistance moment $M_{b,Rd}$ as it is defined in Eurocodes is described in paragraph 3.1. After modifications of Eurocode formulae the influence of plastic reserve and local buckling may be shown. This is done in paragraph 3.2.

3.1 $M_{b,Rd}$ according to Eurocodes EN 1993-1-1 (2005), -1-4 (2006) and EN 1999-1-1 (2007)

A laterally unrestrained member subject to major axis bending should be verified against lateral-torsional buckling as follows

$$\frac{M_{Ed}}{M_{b,Rd}} \leq 1{,}0 \tag{7}$$

where M_{Ed} is the design value of the moment.

The characteristic $M_{b,Rk}$ and design $M_{b,Rd}$ buckling resistance moment of a laterally unrestrained beam should be taken as

$$M_{b,Rk} = \chi_{LT} W_y f_y, \qquad M_{b,Rd} = \frac{M_{b,Rk}}{\gamma_{M1}} \tag{8}$$

where f_y is the yield strength (in EN 1999-1-1 (2007) symbol f_o is used),

γ_{M1} is partial safety factor of material which may be defined in national annex. The recommended values are given in Table 6.

Tab. 6: Recommended values of partial factor γ_{M1}

EN	EN 1993-1-1 (2005)	EN 1993-1-4 (2006)	EN 1993-2 (2006)	EN 1999-1-1 (2007)
γ_{M1}	1,0	1,1	1,1	1,1

The value of reduction factor χ_{LT} for lateral torsional buckling depends on relative slenderness $\bar{\lambda}_{LT}$, and imperfection factor α_{LT}

$$\chi_{LT} = \frac{1}{\Phi_{LT} + \sqrt{\Phi_{LT}^2 - \beta \bar{\lambda}_{LT}^2}}, \qquad \chi_{LT} \leq 1{,}0 \tag{9}$$

$$\Phi_{LT} = 0{,}5\left[1 + \alpha_{LT}(\bar{\lambda}_{LT} - \bar{\lambda}_{LT,0}) + \beta \bar{\lambda}_{LT}^2\right] \tag{10}$$

where $\beta = 1$ in 6.3.2.2 and value $\beta = 0{,}75$ is recommended in 6.3.2.3 of EN 1993-1-1 (2005), (β may be changed in National Annex for rolled I-sections and equivalent I-sections in 6.3.2.3).

α_{LT} is an imperfection factor depending on buckling curve and it is defined in Eurocodes (Table 7),

$\bar{\lambda}_{LT,0}$ is the limit of the horizontal plateau (Table 7),

$\bar{\lambda}_{LT} = \sqrt{\frac{W_y f_y}{M_{cr}}}$ is the relative slenderness, (11)

M_{cr} is the elastic critical moment for lateral torsional buckling (see paragraph 2.).

Tab. 7: Values of imperfection factor α_{LT}

EN	Limits		α_{LT}	$\bar{\lambda}_{LT,0}$
EN 1993-1-1 (2005) 6.3.2.2 General case [EN 1993-2 (2006)]	Rolled I-sections	$h/b \leq 2$	0,21	0,2
		$h/b \leq 2$	0,34	
	Welded I-sections	$h/b \leq 2$	0,49	
		$h/b \leq 2$	0,76	
	Other cross-sections		0,76	
EN 1993-1-1 (2005) 6.3.2.3 Rolled I-sections and equivalent I-sections [EN 1993-2 (2006)]	Rolled I-sections	$h/b \leq 2$	0,34	0,4
		$h/b \leq 2$	0,49	
	Welded I-sections	$h/b \leq 2$	0,49	
		$h/b \leq 2$	0,76	
EN 1993-1-4 (2006)	Cold formed sections and hollow sections (welded and seamless)		0,34	
	Welded open sections and other sections for which no test data are available		0,76	0,4
EN 1999-1-1 (2007)	Class 1 and class 2 cross-sections		0,1	0,6
	Class 3 and class 4 cross-sections		0,2	0,4

W_y is the appropriate section modulus as follows:

$W_y = W_{pl,y}$ for Class 1 or 2 cross-sections

$W_y = W_{el,y}$ for Class 3 cross-sections

$W_y = W_{eff,y}$ for Class 4 cross-sections.

Instead of this explicit definition of W_y used in EN 1993-1-1 (2005), the implicit formulae are used in ENV 1993-1-1 (1992) $W_y = \beta_w W_{pl,y}$ and in ENV 1999-1-1 (1998) and in EN 1999-1-1 (2007) $W_y = \alpha_w W_{el,y}$. Shape factors β_w and α_w are defined in Table 8.

Tab. 8: Values of shape factors β_w *in EN 1993-1-1 (2005) and* α_w *in EN 1999-1-1 (2007)*

Cross-section class	EN 1993-1-1 (2005), factor β_w	EN 1999-1-1 (2007), factor α_w	
		Without welds	With longitudinal welds
1	1	W_{pl}/W_{el} *)	$W_{pl,haz}/W_{el}$ *)
2	1	W_{pl}/W_{el}	$W_{pl,haz}/W_{el}$
3	W_{el}/W_{pl}	$\alpha_{3,u}$	$\alpha_{3,w}$
4	W_{eff}/W_{pl}	W_{eff}/W_{el}	$W_{eff,haz}/W_{el}$

*) NOTE: These formulae are on the conservative side.
For more refined value, recommendations are given in EN 1999-1-1 (2007), Annex F.

In Table 8 the various section moduli W and $\alpha_{3,u}, \alpha_{3,w}$ are defined as:

W_{pl} plastic modulus of gross section

W_{eff} effective elastic section modulus, obtained using a reduced thickness t_{eff} for the class 4 parts (see 6.2.5.2 in EN 1999-1-1 (2007))

$W_{el,haz}$ effective elastic modulus of the gross section, obtained using a reduced thickness $\rho_{o,haz}t$ for the HAZ material (see 6.2.5.2 in EN 1999-1-1 (2007))

$W_{pl,haz}$ effective plastic modulus of the gross section, obtained using a reduced thickness $\rho_{o,haz}t$ for the HAZ material (see 6.2.5.2 in EN 1999-1-1 (2007))

$W_{eff,haz}$ effective elastic section modulus, obtained using a reduced thickness $\rho_c t$ for the class 4 parts or a reduced thickness $\rho_{o,haz}t$ for the HAZ material, whichever is the smaller (see 6.2.5.2 in EN 1999-1-1 (2007))

$\alpha_{3,u} = 1$ or may alternatively be taken as

$$\alpha_{3,u} = 1 + \frac{\beta_3 - \beta_{mcp}}{\beta_3 - \beta_2} \frac{W_{pl} - W_{el}}{W_{el}} \tag{12}$$

$\alpha_{3,w} = W_{el,haz} / W_{el}$ or may alternatively be taken as

$$\alpha_{3,w} = \frac{W_{el,haz}}{W_{el}} + \frac{\beta_3 - \beta_{mcp}}{\beta_3 - \beta_2} \frac{W_{pl,haz} - W_{el,haz}}{W_{el}} \tag{13}$$

where:

β_{mcp} is the slenderness parameter for the most critical part in the section (see EN 1999-1-1 (2007))

β_2 and β_3 are the limiting values for that same part according to Table 8.

The critical part is determined by the lowest value of $(\beta_2 - \beta)/(\beta_3 - \beta)$.

For aluminium alloys cross-sections without welds it can be written

$$\beta_w = \alpha_w \frac{W_{el}}{W_{pl}}, \quad \alpha_w = \beta_w \frac{W_{pl}}{W_{el}} \tag{14}$$

3.2 Modified formulae of $M_{b,Rd}$ showing plastic reserve and local buckling influence

There are two possible forms how to express the characteristic lateral torsional buckling resistance of member in bending:

a) the form utilising as reference moment the plastic moment resistance of cross section $W_{pl}f_y$ as it is used in EN 1993-1-1 (2005) for steel members and EN 1993-1-4 (2006) for stainless steel members:

$$M_{b,Rk} = \chi_{LT}\beta_W W_{pl} f_y \tag{15}$$

with $$\chi_{LT}\beta_w = \frac{M_{b,Rk}}{W_{pl}f_y} = \frac{\beta_w}{\Phi_{LT} + \sqrt{\Phi_{LT}^2 - \beta(\sqrt{W_{pl}f_y / M_{cr}}\sqrt{\beta_W})^2}}, \quad \text{if} \quad \sqrt{\frac{W_{pl}f_y}{M_{cr}}} \le \frac{\bar{\lambda}_{LT,0}}{\sqrt{\beta_W}} \tag{16}$$

otherwise $$\chi_{LT}\beta_W = M_{b,Rk} / W_{pl}f_y = \beta_W \tag{17}$$

where $$\Phi_{LT} = 0{,}5\left[1 + \alpha_{LT}(\sqrt{W_{pl} f_y / M_{cr}}\sqrt{\beta_W} - \bar{\lambda}_{LT,0}) + \beta(\sqrt{W_{pl} f_y / M_{cr}}\sqrt{\beta_W})^2\right] \quad (18)$$

with $\beta_w = 1$ for class 1, 2, $\beta_W = W_{el} / W_{pl}$ for class 3 sections and $\beta_W = W_{eff} / W_{pl}$ for class 4 sections.

b) the form utilising as reference moment the elastic moment resistance of cross section $W_{el} f_y$ as it is used in EN 1999-1-1 (2007) for design of aluminium members:

$$M_{b,Rk} = \chi_{LT} \alpha_W W_{el} f_y \quad (19)$$

with $$\chi_{LT}\alpha_w = \frac{M_{b,Rk}}{W_{el} f_y} = \frac{\alpha_w}{\Phi_{LT} + \sqrt{\Phi_{LT}^2 - \beta(\sqrt{W_{el} f_y / M_{cr}}\sqrt{\alpha_W})^2}}, \quad \text{if} \quad \sqrt{\frac{W_{el} f_y}{M_{cr}}} \le \frac{\bar{\lambda}_{LT,0}}{\sqrt{\alpha_W}} \quad (20)$$

otherwise $$\chi_{LT}\alpha_W = M_{b,Rk} / W_{el} f_y = \alpha_W \quad (21)$$

where $$\Phi_{LT} = 0{,}5\left[1 + \alpha_{LT}(\sqrt{W_{el} f_y / M_{cr}}\sqrt{\alpha_W} - \bar{\lambda}_{LT,0}) + \beta(\sqrt{W_{el} f_y / M_{cr}}\sqrt{\alpha_W})^2\right] \quad (22)$$

with $\alpha_w = W_{pl} / W_{el}$ for class 1, 2, $\alpha_W = 1$ for class 3 sections and $\alpha_W = W_{eff} / W_{el}$ for class 4 sections.

This modification may be done for formulae of all methods defining lateral buckling curves used in EN 1993-1-1 (2005): (i) general case in 6.3.2.2, with or without utilising 6.3.2.2(4), which means that $\chi_{LT} = 1$ in interval $0 \le \bar{\lambda}_{LT} \le \bar{\lambda}_{LT,0}$, (ii) rolled I-sections or equivalent welded sections in 6.3.2.3 with or without utilising factor f defined in 6.3.2.3(2).

According to 6.3.2.3(2) of EN 1993-1-1 (2005) the design buckling resistance moment may be increased by dividing by factor f, which may be defined in National Annex. The following minimum values are recommended in EN 1993-1-1 (2005):

$$f(k_c, \sqrt{W_{pl} f_y / M_{cr}}\sqrt{\beta_W}) = 1 - 0{,}5(1 - k_c)\left[1 - 2(\sqrt{W_{pl} f_y / M_{cr}}\sqrt{\beta_W} - 0{,}8)^2\right] \quad (23)$$

but $$f(k_c, \sqrt{W_{pl} f_y / M_{cr}}\sqrt{\beta_W}) \le 1{,}0 \quad (24)$$

The factor f defined by (23) is smaller than 1 only in the interval

$$\max\left[\bar{\lambda}_{LT,0};\ 0{,}1\right] \approx \max\left[\bar{\lambda}_{LT,0};\ 0{,}8 + \sqrt{0{,}5}\right] \le \sqrt{W_{pl} f_y / M_{cr}}\sqrt{\beta_W} \le 0{,}8 + \sqrt{0{,}5} \approx 1{,}5 \quad (25)$$

The correction factor k_c for different moment distributions is given in Table 9a and in Table 6.6 in EN 1993-1-1 (2005)). In corrigendum EN 1993-1-1 (2005) from April 2009 it is recommended to use k_c values for calculation of C_1 values used in EN 1993-1-1 (2005) in Table A.1, formulae BB.5 and BB.9. The comparisons in Table 9b show that C_1 values calculated from k_c values are only approximate ones. It is better to use more exact C_1 values of authors published in Baláž, I. – Koleková, Y. (2000 b), in EN 1999-1-1 (2007) or in STN EN 1993-1-1/NA (2007).

It is very important to mention that all k_c values compared in Table 9b relate to the cross-section in the middle of the span and they are valid for boundary conditions $k_z = 1$ (both beam ends are restrained against lateral movement and free to rotate in plan) and $k_w = 1$ (both beam ends are restrained against rotation about longitudinl axis and free to warp).

Tab. 9a: k_c from EN 1993-1-1 (2005)

Moment distribution	k_c
$\psi = 1$	1,0
$-1 \le \psi \le 1$	$\frac{1}{1{,}33 - 0{,}33\psi}$
	0,94
	0,90
	0,91
	0,86
	0,77
	0,82

Tab. 9b: Comparison of C_1 values of authors with k_c^{-2}

k_c	$1/k_c^2 \approx C_1$	$C_{1,0} = C_1(\kappa_{wt} = 0)$	$C_{1,1} = C_1(\kappa_{wt} = 1)$
1 $\psi = 1$	1	1	1
0,924 $\psi = 0{,}75$	1,172	1,139	1,141
0,858 $\psi = 0{,}5$	1,357	1,312	1,320
0,802 $\psi = 0{,}25$	1,556	1,522	1,551
0,752 $\psi = 0$	1,769	1,770	1,847
0,708 $\psi = -0{,}25$	1,995	1,753	2,027
0,669 $\psi = -0{,}5$	2,235	2,331	2,591
0,634 $\psi = -0{,}75$	2,489	2,547	2,852
0,602 $\psi = -1$	2,756	2,555	2,733
0,94	1,132	1,127	1,132
0,90	1,235	0,5*2,576=1,288	0,5*2,608=1,304
0,91	1,208	-	-
0,86	1,352	1,348	1,363
0,77	1,687	1,683	1,726
0,82	1,487	-	-

*) Values 2,576 and 2,608 relate to M_{max} and 0,9, 1,235, 1,288 and 1,304 relate to M in midspan

Distribution of modified lateral torsional buckling curves defined in 6.3.2.2 with utilising 6.3.2.2(4) is shown in Fig.3. The ends of plateaux are denoted by relative slenderness values $\bar{\lambda}_{LT,0} = 0.4$, $\bar{\lambda}_{LT,0} / \sqrt{0.85} = e = 0{,}434$ and $\bar{\lambda}_{LT,0} / \sqrt{0.7} = f = 0{,}478$ (Fig.3). Note the discrepancies in member resistances ($M_{el} > M_{pl}$) at these points when 6.3.2.2(4) is utilised.

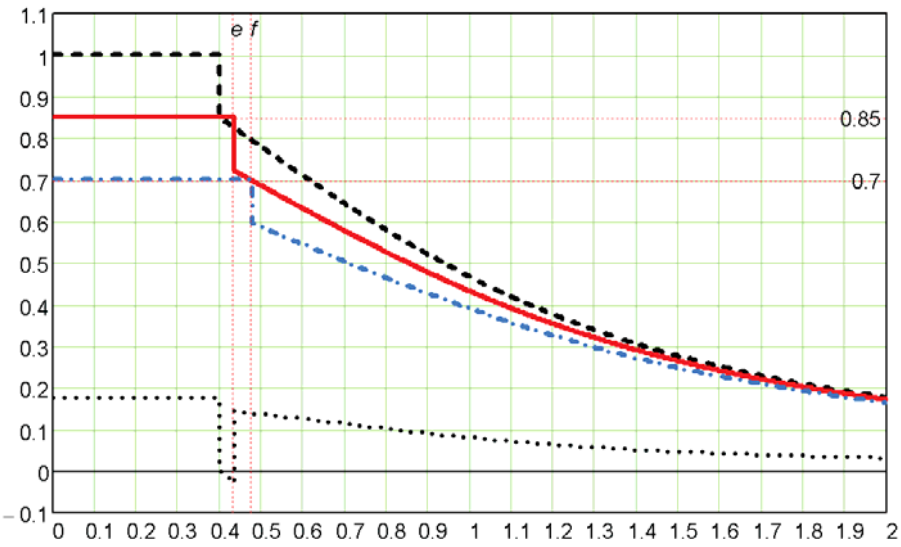

Fig. 3: Functions $\chi_{LT}\beta_W = f(\sqrt{W_{pl} f_y / M_{cr}})$ based on EN 1993-1-1 (2005), 6.3.2.2 calculated for imperfection factor $\alpha_{LT} = 0{,}76$, relative slenderness defining end of the plateau $\bar{\lambda}_{LT,0} = 0{,}4$, $\beta = 1$ and for (i) $\beta_w = 1$ (black dashed line), (ii) $\beta_w = W_{el} / W_{pl} = 0{,}85$ (red solid line) and (iii) $\beta_w = W_{eff} / W_{pl} = 0{,}7$ (blue dot-and-dashed line). Plastic reserve of member is defined by the ordinates of the bottom black dotted line, which should be multiplied by 100 to obtain plastic reserve in %.

4. Conclusions

The paper is devoted to (i) critical moment M_{cr} and (ii) lateral torsional buckling resistance moment $M_{b,Rd}$ of metal (steel and aluminium) beams.

The original results of the authors are presented concerning calculation of M_{cr} by using approximate formulae convenient for standardization and educational purposes and for engineering practice. The results are based on large parametrical studies (Baláž, I., 1999-2001, 2005, 2007, Baláž, I. – Koleková, Y., 1999-2001, 2002, Koleková, Y., 1999) which showed that procedure used in prestandard Eurocodes ENV 1993-1-1 (1992) and ENV 1999-1-1 (1998) may lead in many cases to incorrect results. Authors results, which were the first time published in (Baláž, I. – Koleková, Y., 1999 a, b, 2000 b, c, 2002 a, b) are today used in many international and national standardization documents including Eurocodes (Belgian National Annex, 2005, Czech National Annex ČSN EN 1993-1-1, 2006, Austrian National Annex ÖNORM B 1993-1-1, 2007, Slovak National Annex STN EN 1993-1-1/NA, 2007, Design Manual For Structural Stainless Steel, 2006, Deutscher Ausschluß für Stahlbau, 2005, ECCS Technical Committee 8 – Stability, 2006, Excerpt from the Background Document to EN 1993-1-1, 2010, EN 1999-1-1, 2007). The correctness and the exactness of results based on authors results (Table 1-4) were verified in habilitation thesis (Koleková, Y., 1999) and later also in two independent Brazilian and Slovak PhD thesis (Fruchtengarten, J., 2005, Živner, T., 2010). The Brazilian PhD thesis stated that M_{cr} values calculated on the basis of the authors results are the best among all used approximate formulae. Procedure of M_{cr} calculation based on authors results were introduced in the engineering practice of many countries. In Slovakia it was thanks to courses for the engineers in practice organized by Universities and Slovak Chamber of Civil Engineers and the textbooks written for them (Baláž, I., 2007, 2010, 2012) and for the university students. It was also showed how the procedure used for many years in Czechoslovak, Czech and Slovak standards may be improved (Baláž, I., 1980, 1997, 1998, 2000), Baláž, I. – Živner, T., 2007). The detailed numerical examples were published in the above mentioned textbooks and in the several papers (e.g. Baláž, I. (2012). The authors created for engineers in practice and for students at Universities the original computer program CalcMcr.

New C_1 values derived by authors for uniform loading combined with end moments are presented in Table 5 and Figure 2.

The Table 9a, b shows that using of k_c values recommended in corrigendum EN 1993-1-1 (2005) from April 2009 for calculation of C_1 values may lead to approximate values, which may be used in correct way only if user knows that: (i) relating boundary conditions are $k_z = 1$ (both beam ends are restrained against lateral movement and free to rotate in plan) and $k_w = 1$ (both beam ends are restrained against rotation about longitudinal axis and free to warp and that (ii) k_c values compared in Table 9b with authors more exact C_1 values are valid for M in midspan and not to cross-section were M_{max} is located.

The paper presents also the way how the Eurocode formulae (EN 1993-1-1, 2005), EN 1993-1-4, 2006), EN 1999-1-1, 2007) for calculation of lateral torsional buckling resistance $M_{b,Rd}$ may be modified to show clearly influence of plastic reserve and local buckling on beam resistance (paragraph 3.2 and Figure 3). This may be very useful for engineers in practice. The much more similar diagrams as it is on Figure 3 were published in (Baláž, I. – Koleková, Y., 2007, 2008, 2009).

The paper is devoted to the lateral torsional buckling resistance of metal (steel, stainless steel, aluminium) beams, but the presented results may be used also for design and verification of structures made of other structural materials (timber, concrete, composite steel and concrete structures). The results relating to lateral torsional buckling of: (i) timber beams authors solved in the papers (Baláž, I., 2001, 2005, Baláž, I. – Koleková, Y., 2004 a, b), (ii) concrete beams in (Baláž, I. – Živner, T., 2006), (iii) aluminium beams in (Baláž, I. – Valach, P., 1997, Baláž, I. – Koleková, Y. – Ároch, R., 1998, Baláž, I. – Koleková, Y., 2000 a, 2007, 2008). The influence of beam end stiffeners was solved in (Živner, T., 2010, Živner, T. – Baláž, I., 2010).

The second author is the member of 5 working Evolution Groups: EG EN 1993-1-1, EG EN 1993-1-3, EG EN 1993-1-5, EG EN 1993-2 and EG EN 1999-1-1. All members of EGs are very active without any financial support on the European level. Even accommodation, travel, food and other expenses must be covered by own budget of EGs members. EGs are responsible for maintenance of existing Eurocodes (creating of Corrigenda and Amendments) and for further development of the next generation of Eurocodes. Nobody else from Slovak republic is member of EGs.

We spent blessed moments in investigation of these problems during several years despite of the fact that financial support was very poor. The reasons of poor funding were: a) the funding into the science in Slovakia is for long time deeply undersized comparing with all other EU countries, b) only the results published in current journals are highly evaluated even when they are without any useful application, c) journals with high impact factors are preferred despite of the fact that the European Association of Science Editors already in November 2007 issued an official statement recommending "that journal impact factors are used only – and cautiously – for measuring and comparing the influence of entire journals, but not for the assessment of single papers, and certainly not for the assessment of researchers or research programs", d) a well known specialist from the Institute of Construction and Architecture, Slovak Academy of Sciences in Bratislava evaluated our first grant application for this project in 1999 and in his review he gave us the lowest possible grades and used the following wordings: "investigators – underaverage; scientific team composition – inadequate; expected contributions – not important; scientific goals – obsolete, everything was already solved".

Acknowledgement

The authors acknowledge support by the Slovak Scientific Grant Agency under the contracts No. 1/1101/12.

References

Baláž, I. (1980) Klopenie nosníkov v zmysle revidovanej ČSN 73 1401. *Staveb. Čas.* 28, č.6, VEDA, Bratislava, s. 465-478.

Baláž, I. (1997) Comparison of Different Design Curves for Lateral Torsional Buckling of Rolled and Welded Steel Beams, in: *Proc. of 18th Czecho-Slovak International Conference on Steel Structures and Bridges `97* . Brno, p. 2 / 3 – 2 / 11.

Baláž, I. (1998) Klopenie nosníkov podľa STN 73 1401: 1997, in: *Zborník prednášok z konferencie „Súčasný stav európskych a slovenských technických noriem a ich aplikácie v stavebníctve."* SvF TU Košice. Košice, s. 41-48.

Baláž, I. (1999 a) Buckling of monosymmetric beams – conjured problem, in: *Proc. Eurosteel 2nd European Conference on Steel Structures,* Praha, pp.701-704.

Baláž, I.: (1999 b) Kritické momenty pri klopení podľa STN 73 1401, in: *Zborník prednášok z XXV. Celoštátneho aktívu „Stratégia rozvoja oceľových konštrukcií."* Lipovce, s.77-82.

Baláž, I. (1999 c) Klopenie kovových nosníkov, in: *Zborník XI. Mezinárodní vědecké konference.* VUT Brno, s. 63-66.

Baláž, I. (2000) Kapitola 6.8.2 "Prúty namáhané ohybom" str.104 – 112 a „Príloha H" str. 235 – 250. in: P. Juhás a kol.: *Navrhovanie oceľových konštrukcií. Komentár k STN 73 1401: 1998.* SÚTN Bratislava, str. 1 – 260. ISBN 80-88971-06-3.

Baláž, I. (2001) Klopenie drevených nosníkov, in: *Zborník prednášok z konferencie „Výstavba a obnova budov"*, výstava PRO DOMO. Košice. Dom techniky Košice, s. 27-32.

Baláž, I. (2005) Lateral torsional buckling of timber beams. *Wood Research*, 50(1), pp.51-58.

Baláž, I. (2007 a) Klopenie nosníkov v STN EN 1993-1-1 a EN 1999-1-1. in: *Zborník odborných prednášok*, *1. časť.* ESF SÚTN Nové európske normy na navrhovanie kovových konštrukcií – Eurokód 3 a 9. STU Bratislava. S. 84 – 94 a in: *Zborník odborných prednášok*, *2.časť*, s. 1 – 8.

Baláž, I. (2007 b) Kapitola 6: Klopenie ohýbaných nosníkov. Prúty namáhané kombinovane osovou silou N_{Ed} a ohybovým momentom M_{Ed} podľa STN EN 1993-1-1 In: *Zborník SKSI*: Baláž, I. – Ároch, R. – Chladný, E. – Kmeť, S. – Vičan, J.: Navrhovanie oceľových konštrukcií podľa Eurokódov STN EN 993-1-1: 2006 a STN EN 1993-1-8: 2007. Bratislava, s.96-131.

Baláž, I. (2010) Kapitola 6: Klopenie ohýbaných nosníkov. Prúty namáhané kombinovane osovou silou N_{Ed} a ohybovým momentom M_{Ed} podľaSTN EN 1993-1-1 In: *Zborník SKSI:* Baláž, I. – Ároch, R. – Chladný, E. – Kmeť, S. – Vičan, J.: Navrhovanie oceľových konštrukcií podľa EurokódovSTN EN 1993, časti -1-1:2006 a

-1-8: 2007, podľa ich národných príloh NA: 2007 a NA: 2008 a ich opráv AC: 2009 a AC: 2009.Bratislava, s.107-267.

Baláž, I. (2012) Klopenie kovových nosníkov aj podĺa eurokódov, in: *Zborník 17. konferencie statikov "Statika stavieb 2012"*, Piešťany, s.7-20.

Baláž, I., Koleková, Y. (1999 a) Buckling of monosymmetric beams – conjured problem, in: *CD-ROM 2nd part. Eurosteel 2nd European Conference on Steel Structure,* Praha, 21 pages.

Baláž, I., Koleková, Y. (1999 b) Stability of monosymmetric beams, in: *Proc. of the 6th International Colloquium "Stability and ductility of steel structures"* , Timisoara, pp.57-64.

Baláž, I., Koleková, Y. (2000 a) Lateral Torsional Buckling of Unwelded and Welded Steel and Aluminium Beams. *Slovak Journal of Civil Engineering.* 2000/3, pp.1-7.

Baláž, I., Koleková, Y. (2000 b) Proposals for Improvements of Lateral Torsional Buckling Eurocodes Rules, in: *Proc. of 19th Czech and Slovak International Conference "Steel Structures and Bridges 2000".* Štrbské Pleso, High Tatras, pp.81-86.

Baláž, I., Koleková, Y. (2000 c) Critical Moments of Beams and Girders. Clark – Mrázik formula, in: *Proc. of 19th Czech and Slovak International Conference "Steel Structures and Bridges 2000".* Štrbské Pleso, High Tatras, pp.87-94.

Baláž, I., Koleková, Y. (2000 d) Klopenie nosníkov a konzol podľa noriem STN 73 1401 a ČSN 73 1401. Analýza a návrhy na vylepšenie, in: *Zborník XXVI. celoštátneho aktívu pracovníkov odboru oceľových konštrukcií: "Kovové konštrukcie a mosty. Súčasný stav a prespektívy rozvoja."* SvF ŽU Žilina, SSOK ZSVTS Bratislava. Rajecké Teplice, pp.13-18.

Baláž, I., Koleková, Y. (2000 e) Besselove funkcie použité pri výpočte Mcr konzoly obdĺžnikového prierezu zaťaženej silou F, in: *Zborník XXVI. celoštátneho aktívu pracovníkov odboru oceľových konštrukcií: "Kovové konštrukcie a mosty. Súčasný stav a prespektívy rozvoja."* SvF ŽU Žilina, SSOK ZSVTS Bratislava. Rajecké Teplice, pp.19-24.

Baláž, I., Koleková, Y. (2002 a) Critical Moments, in: *Proc. of Internal Colloquium on Stability and Ductility of Steel Structures,* Budapest, pp.31-38.

Baláž, I., Koleková, Y. (2002 b) Clark-Mrázik Formula for Critical Moments, in: *Proc. of Internal Colloquium on Stability and Ductility of Steel Structures*, Budapest, pp.39-46.

Baláž, I., Koleková, Y. (2004 a) Factors C1, C2, C3 for computing elastic critical moments Mcr, in: *Zborník VI. sympózia Drevo v stavebných konštrukciách so zahraničnou účasťou*. Kočovce, pp.29-34.

Baláž, I., Koleková, Y. (2004 b) Resistance of timber beams to out-of-plane buckling, in: *Zborník VI. sympózia Drevo v stavebných konštrukciách so zahraničnou účasťou*, Kočovce, pp.35-42.

Baláž, I., Koleková, Y. (2007) Lateral torsional buckling of beams, resistances and critical moments, in: *Proc. Hommages à René Maquoi*, Liège, pp.39-50.

Baláž, I., Koleková, Y. (2008) Odolnosť nosníkov z hliníkových zliatin a ocele v klopení, in: *CD zborník príspevkov z Medzinárodnej vedeckej konferencie SvF STU*. Bratislava, sekcia 02, blok D, príspevok č.25, str.1-8.

Baláž, I., Koleková, Y. (2009) Interesting results obtained by modifying of Eurocode formulae for stability of members*. Sborník: 22. Česká a slovenská konference. Ocelové konstrukce a mosty 2009*. AN CERM, Brno, s. 7-14.

Baláž, I., Koleková, Y., Ároch, R. (1998) Lateral Torsional Buckling of Unwelded and Welded Steel and Aluminium Beams. *Second World Conference on Steel in Construction*. San Sebastián 11-13, poster.

Baláž, I. - Plačko, B. (1980) Posudzovanie nosníkov na klopenie. *Technický zpravodaj OK*. Příloha - pomůcky a směrnice. VŽSKG Ostrava, č.3, s.1-51.

Baláž, I., Valach, P. (1997) Lateral Torsional Buckling of Unwelded Aluminium Beams, in: *Zborník prednášok zo VI. vedeckej konferencie SvF TU v Košiciach.* 8. sekcia. Kovové a drevené konštrukcie. Košice, s.87-92.

Baláž, I., Živner, T. (2006) LTB of Unrestrained Steel Beams According to EN 1993-1-1 and Positive Influence of Metal Sheeting Acting as Shear Diaphragm, in: *Zborník prednášok 21. českej a slovenskej medzinárodnej konferencie.* Bratislava, KKDK SvF STU Bratislava, s.117-126.

Baláž, I., Živner, T. (2007) Kritické ohybové momenty obojstranne votknutých nosníkov v článku H.2 normy STN 73 1401: 1998, in: *Zborník VIII. Vedeckej konferencie s medzinárodnou účasťou.* Stavebná fakulta TU Košice, s.19-24.

Belgian National Annex (2005) for the EN 1993 Part 1-1 IBN Committee „Steel Structures". Version 28.10.2005.

ČSN EN 1993-1-1 (2006*) Eurokód 3: Navrhování ocelových konstrukcí – Část 1-1: Obecná pravidla a pravidla pro pozemní stavby* Národní příloha NB **(**informativní), pp.95-98.

Design Manual For Structural Stainless Steel. (2006), 3rd edition. Appendix B: Lateral torsional buckling. Euro Inox and SCI, pp. 109-112.

Deutscher Ausschluß für Stahlbau (2005). *Out-of-plane stability of plane structural frames*. Baláž, I. – Koleková, Y.: Annex 1. Design aid to determining the elastic critical moments M_{cr} for lateral torsional buckling. Aachen, pp.14-29.

DIN 18 800 (1990) *Stahlbauten. Teil 2 Stabilitätsfälle, Knicken von Stäben und Stabwerken*. DIN, Beuth, Berlin.

DIN 18 800 (2008) *Stahlbauten. Teil 2 Stabilitätsfälle, Knicken von Stäben und Stabwerken*. DIN, Beuth, Berlin.

ECCS Technical Committee 8 – Stability (2006*) Rules for Member Stability EN 1993-1-1. Background documentation and design guidelines*. No.119. Brussels, 259 pages.

EN 1993-1-1 (2005) *Eurocode 3: Design of Steel Structures. Part 1-1: General Rules and Rules for Buildings* CEN Brussels.

EN 1994-1-1 (2004) *Eurocode 3: Design of Composite Steel and Concrete Structures. Part 1-1: General Rules and Rules for Buildings* CEN Brussels.

EN 1995-1-1 (2004) *Eurocode 3: Design of Timber Structures. Part 1-1: General Rules and Rules for Buildings* CEN Brussels.

EN 1999-1-1 (2007) *Eurocode 9: Design of Aluminium Structures. Part 1-1: General Structural Rules*. CEN Brussels.

ENV 1993-1-1 (1992) *Eurocode 3: Design of Steel Structures. Part 1-1: General Rules and Rules for Buildings* CEN Brussels.

ENV 1999-1-1 (1998) *Eurocode 9: Design of Aluminium Structures. Part 1-1: General Rules and Rules for Buildings* CEN Brussels.

Excerpt from the Background Document to EN 1993-1-1 (2010) Baláž, I., Koleková, Y.: Chapter 7.2 Design Aids. 7.2.1 Hand formulae for the determination of M_{cr}. Flexural buckling and lateral torsional buckling on a common basis: Stability assessments according to Eurocode 3. Stahlbau Leichtmetallbau. Aachen, pp.60-67.

Fruchtengarten, J. (2005) *Sobre o estudo da flambagem lateral de vigas de aço por meio da utilizaçoã de uma teoria não-linear geometricamente exata*, Dissertação (Mestrado), Departamento de Engenharia de Estruturas e Fundações, Escola Politécnica da Universidade de São Paulo. São Paulo, 226 pages.

Hirt, M.A., Bez, R. (1998) *Stahlbau. Grundbegriffe und Bemessungsverfahren*, 1st German Edition, Ernst & Sohn, A Wiley Company, Berlin.

Hirt, M.A., Bez, R., Nussbaumer, A. (2007) *Stahlbau. Grundbegriffe und Bemessungsverfahren*, 2nd German Edition, Ernst & Sohn, A Wiley Company, Berlin.

Koleková, Y. (1999) *Elastic Critical Moments of the Thin-Walled Beams with Monosymmetric Cross-Section.* (In Slovak). Thesis for docent habilitation. Faculty of Civil Engineering. Slovak University of Technology. Bratislava, 121 pages.

ÖNORM B 1993-1-1 (2007) *Eurocode 3: Bemessung und Konstruktion von Stahlbauten. Teil 1-1: Allgemeine Bemessungsregeln*. Nationale Festlegungen zu ÖNORM EN 1993-1-1, nationale Erläuterungen und nationale Ergänzungen. Ausgabe 2007-02-01. Wien.

Roik, K., Carl, J., Lindner, J. (1972) *Biegetorsionsprobleme gerader dünnwandiger Stäbe*. Berlin, München, Düssledorf. Ernst & Sohn, 252 pages.

STN EN 1993-1-1/NA (2007) *Navrhovanie oceľových konštrukcií. Časť 1-1: Všeobecné pravidlá a pravidlá pre budovy.* Národná príloha. S.1-24. SÚTN Bratislava.

STN EN 1999-1-1 + A1 (2011). *Navrhovanie hliníkových konštrukcií. Časť 1-1: Všeobecné pravidlá pre konštrukcie.* Preklad európskej normy. S.1-220. SÚTN Bratislava.

Živner, T., Baláž, I. (2010) Vplyv čelnej dosky na klopenie nosníkov, in: *Zborník 36.aktívu pracovníkov odboru oceľových konštrukcií. Oceľové, drevené a kompozitné konštrukcie a mosty.* Hotel Boboty,Terchová – Vrátna. ŽU v Žiline, SSOK. Str. 25-32.

Živner, T. (2010) *Stabilitné problémy ohýbaných nosníkov*. PhD Thesis. STU v Bratislave, pp.1-228.

18th International Conference
ENGINEERING MECHANICS 2012
Svratka, Czech Republic, May 14 – 17, 2012

pp. 657–663
Paper #24

B-SPLINE FINITE ELEMENT METHOD IN ONE-DIMENSIONAL ELASTIC WAVE PROPAGATION PROBLEMS

R. Kolman [*], **J. Plešek**[*], **M. Okrouhlík**[*]

Abstract: *In this paper, the spline variant of finite element method (FEM) is tested in one-dimensional elastic wave propagation problems. The special attention is paid to propagation of stress discontinuities as an outcome of the shock loading and also to spurious oscillations occurring near theoretical wave-fronts. Spline variant of FEM is a modern strategy for numerical solution of partial differential equations. This method is based on spline basic functions as shape, testing functions in FEM content. For examples, B-splines, T-splines, NURBS and more others could be applied. For one-dimensional problems, B-spline representation is sufficient. B-spline basis functions are piecewise polynomial functions. It was shown, that B-spline shape functions produce outstanding convergence and dispersion properties and also appropriate frequency errors in elastodynamics problems. In this initial work, accuracy, convergence and stability of the B-spline based FEM are studied in numerical modelling of one-dimensional elastic wave propagation of stress discontinuities. For the time integration, the Newmark method, the central difference method and the generalized-α method are employed.*

Keywords: ***elastic wave propagation, B-spline based finite element method, spurious oscillations.***

1. Introduction

A modern approach in the finite element analysis is the isogeometric analysis (IGA), see Cottrell et al. (2009), where shape functions are based on varied types of splines. For example, B-spline, NURBS, T-spline and others are used for spatial discretization. This approach has an advantage that the geometry and approximation of the field of unknown quantities is prescribed by the same technique. Another benefit is that the approximation is smooth.

It was shown for the IGA approach, that the optical modes did not exist unlike higher-order Lagrangian finite elements, see Cottrell et al. (2006); Hughes et al. (2008). Further, dispersion and frequency errors for the isogeometric analysis were reported to decrease with the increasing order of spline, see Cottrell et al. (2009). IGA, where continuous piecewise higher order polynomials are used as shape functions, improves the dispersion errors and frequency spectrum in comparison with Lagrangian finite elements. The spline based FEM with the small dispersion errors and the variation diminishing property, see Piegl and Tiller (1997), could eliminate the spurious oscillations, which are the outcome of the Gibb's effect and dispersion behaviour of FEM based on the continuous Galerkin's approximation method, see Chin (1975) and Belytschko and Mullen (1978). The convergence and accuracy of IGA in explicit elastodynamics have been shown in the paper Auricchio et al. (2012).

For one-dimensional problems, the B-spline basis functions could be used for spatial discretization. Generally, the B-spline basis functions for bounded solids are not uniform due to the end point interpolating property, see Fig. 1. For this reason, the non-homogeneity of basis functions near the boundary of the domain produces the dispersion and attenuation behaviour, see Kolman et al. (2011). The homogeneous spline shape functions are very important for wave propagation problems, because they produce repeating rows of mass and stiffness matrices. Thus the B-spline FEM in an unbounded domain does not produce optical modes unlike higher-order Lagrangian FEM, see Hughes et al. (2008).

A lot of methods for the numerical solution of wave propagation problems in elastic solids have been developed, for example finite difference method, finite volume method, front tracking algorithms, space-time treatment methods, oscillations filtering by postprocessing, finite element spatial discretization with

[*]Ing. Radek Kolman, Ph.D., Ing. Jiří Plešek, CSc., Prof. Ing. Miloslav Okrouhlík, CSc.: Institute of Thermomechanics, Academy of Sciences of the Czech Republic, Dolejškova 1402/5; 182 00, Prague; CZ, e-mail: {kolman;plesek;ok}@it.cas.cz

the finite difference in time (semidiscretization), discontinuity Galerkin's method and variational construction method and more others. Details for references see Belytschko and Hughes (1986), Hughes (1983), Park et al. (2012). In this paper, only the semidiscretization method is tested in one-dimensional elastic wave propagation of sharp wave fronts and stress discontinuities. For the spatial discretization, the continuous Galerkin's approximation method is employed, see Hughes (1983). In this initial work, accuracy, convergence and stability of the B-spline based FEM is studied in numerical modelling of one-dimensional elastic wave propagation of stress discontinuities. For the time integration, the Newmark method, see Newmark (1959) or Subbaraj and Dokainish (1989), the central difference method, see Dokainish and Subbaraj (1989), and the implicit form of the generalized-α method , see Chung and Hulbert (1993), are employed.

2. B-SPLINE BASED FINITE ELEMENT METHOD

In this section, the basis of B-spline based finite element method is shortly introduced. In Computer-Aided Design (CAD), a B-spline curve is given by the linear combination of B-spline basis functions $N_{i,p}$, see book of Piegl and Tiller (1997),

$$\mathbf{C}(\xi) = \sum_{i=1}^{n} N_{i,p}(\xi)\,\mathbf{B}_i \tag{1}$$

where $\mathbf{B}_i, i = 1, 2, \ldots, n$ are corresponding coordinates of control points. B-spline basis functions $N_{i,p}(\xi)$ are prescribed by the Cox-de Boor recursion formula, see Piegl and Tiller (1997). For a given knot vector Ξ, $N_{i,p}(\xi)$ are defined recursively starting with piecewise constants ($p = 0$)

$$N_{i,0}(\xi) = \begin{cases} 1 & \text{if} \quad \xi_i \le \xi \le \xi_{i+1} \\ 0 & \text{otherwise} \end{cases} \tag{2}$$

For $p = 1, 2, 3, ...$, they are defined by

$$N_{i,p}(\xi) = \frac{\xi - \xi_i}{\xi_{i+p} - \xi_i} N_{i,p-1}(\xi) + \frac{\xi_{i+p+1} - \xi}{\xi_{i+p+1} - \xi_{i+1}} N_{i+1,p-1}(\xi) \tag{3}$$

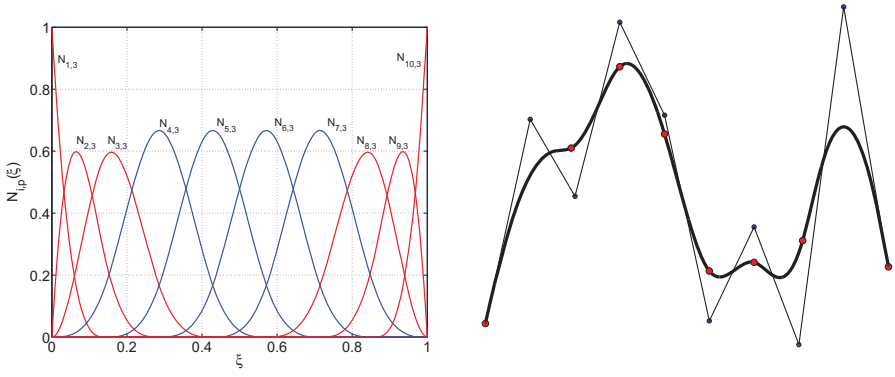

Fig. 1: Cubic B-spline basis functions (on the left) and an open cubic B-spline curve interpolating end points (on the right) for ten control points and the uniform knot vector. Red lines correspond to non-uniform basis functions and blue lines correspond to uniform (homogeneous) basis functions. The number of non-uniform basis functions depends on the polynomial order.

A knot vector in one dimensional case is a non-decreasing set of coordinates in the parameter space, written $\Xi = \{\xi_1, \xi_2, ..., \xi_m\}$, where $\xi_i \in R$ is the i-th knot, i is the knot index, $i = 1, 2, \ldots, m$, where $m = n + p + 1$, p is the polynomial order, and n is the number of basis functions. The main properties of B-spline basis functions are introduced in book Piegl and Tiller (1997). The knot vector for an open

B-spline curve interpolating end points should be in the form $\Xi = \{a, \ldots, a, \xi_{p+2}, \ldots, \xi_n, b, \ldots, b\}$, where values are usually set as $a = 0$ and $b = 1$. The multiplicity of the first and last knot value is $p + 1$. If the values ξ_{p+1} up to ξ_{n+1} are chosen uniformly, the knot vector Ξ is called uniform, otherwise non-uniform, see Piegl and Tiller (1997). An example of cubic B-spline basis functions and an open cubic B-spline curve interpolating end points with its control polygon is displayed in Fig. 1.

In the B-spline based FEM, see book Cottrell et al. (2009), the approximation of the displacement field u^h is given by

$$u^h(\xi) = \sum_{i=1}^{n} N_{i,p}(\xi)\, u_i^{\mathrm{B}} \tag{4}$$

where u_i^{B} is the component of the vector of control variables – displacements corresponding to the control points. Remark, the linear B-spline FEM is identical with the standard linear FEM. In the following text, the continuous Galerkin's approximation method for the numerical solution of partial differential equations is employed, see book Hughes (1983). Spatial discretization of elastodynamics problems by the finite element method leads to, see Hughes (1983),

$$\mathbf{M}\ddot{\mathbf{u}} + \mathbf{K}\mathbf{u} = \mathbf{R} \tag{5}$$

Here, $\mathbf{M}$ is the mass matrix, $\mathbf{K}$ the stiffness matrix, $\mathbf{R}$ is the time-dependent load vector, $\mathbf{u}$ and $\ddot{\mathbf{u}}$ contain control point variables–displacements and accelerations. Mass matrix, stiffness matrix and load vector are defined by the same relationships as the standard FEM, see Hughes (1983). The element stiffness and mass matrices are given by

$$\mathbf{K} = \int_V E\mathbf{B}^{\mathrm{T}}\mathbf{B}\, \mathrm{d}V, \qquad \mathbf{M} = \int_V \rho\mathbf{N}^{\mathrm{T}}\mathbf{N}\, \mathrm{d}V \tag{6}$$

where E is the modulus of elasticity, ρ is the mass matrix, $\mathbf{B}$ is the strain-displacement matrix, $\mathbf{N}$ stores the displacement shape functions and integration is carried over the non-deformed domain V. Global matrices are assembled in the usual fashion. Mass matrix defined by the relationship (6) is called the consistent mass matrix. In this paper, the diagonal mass matrix is put together by 'row sum' method, see Hughes (1983). If the theory of linear elastodynamics is considered, then the mass matrix $\mathbf{M}$ and the stiffness matrix $\mathbf{K}$ are constant. These matrices are evaluated by the Gauss-Legendre quadrature formula, see Hughes (1983).

3. FINITE ELEMENT RESPONSE AND NUMERICAL INTEGRATION

For an undamped system in the current configuration at time t, we get the equations of motion in the form resulting from the finite element semidiscretization $\mathbf{M}\ddot{\mathbf{u}} = \mathbf{F}_{\text{res}}$ where the residual vector is $\mathbf{F}_{\text{res}} = \mathbf{R} - \mathbf{F}_{\text{int}}$. Generally, $\mathbf{F}_{\text{int}}$ is the vector of the internal control points forces corresponding to element stresses. In the linear elasticity theory, the interval forces are given $\mathbf{F}_{\text{int}} = \mathbf{K}\mathbf{u}$. The aim of computational procedures used for the solution of transient problems is to satisfy the equation of motion, not continually, but at discrete time intervals only. It is assumed that in the considered time span $[0, t_{max}]$ all the discretized quantities at times $0, \Delta t, 2\Delta t, 3\Delta t, \ldots, t$ are known, while the quantities at times $t + \Delta t, \ldots, t_{max}$ are to be found. The quantity Δt, being the time step, need not necessarily be constant throughout the integration process. We consider the constant time step Δt in the following text.

In this paper, the B-spline based FEM response of the elastic bar is computed numerically by the Newmark method with parameters $\beta = 1/4$, $\gamma = 1/2$, see the paper Newmark (1959), with the consistent mass matrix and the central difference method, see the paper Dokainish and Subbaraj (1989), with the lumped mass matrix by the 'row sum' method are employed. Implementation of the both methods is prescribed in work Okrouhlik (2008). The last method of the direct time integration is the implicit generalized-α method, see Chung and Hulbert (1993), with consistent mass matrix. The predictor-corrector explicit form of the implicit generalized-α method was implemented, see Hulbert and Chung (1996). The generalized-α method is an extension of the Newmark method that exhibits algorithmic damping. This second order algorithmic damping introduced to improve the shortcoming. This method achieves high-frequency dissipation while minimizing unwanted low-frequency dissipation. The dissipation effect of the generalized-α method is controlled by the spectral radius in the high-frequency limit

$\rho_\infty \in [0,1]$. The value of $\rho_\infty = 0$ eliminates the high-frequency response (known as asymptotic annihilation). On the other side, setting $\rho_\infty = 1$ eliminates the algorithmic damping and the trapezoidal time-integration is considered. The value of $\rho_\infty = 0.8$ is recommended with respect to dissipation, dispersion and period time elongation, see paper Chung and Hulbert (1993). The values of $\rho = 0.8$ and $\rho = 0.5$ are tested in connection with B-spline discretization.

4. Problem description

In this contribution, the crucial test is a problem of axial elastic waves propagation in a free-fixed "thin" bar under the force loading prescribed by the Heaviside step function. The scheme of the task is depicted on Fig. 2. The shock loading generates stress and velocity jumps propagating by theoretical wave speeds. The parameters of the task are set: the bar length $L = 1\,m$, the cross-section $A = 1\,m^2$, Young's modulus $E = 1\,Pa$, the mass density $\rho = 1\,kg/m^3$ and the amplitude of impact pressure $\sigma_0 = 1\,Pa$. The analytical solution of this impact problem could be found in book Kolsky (1963), where the displacement field $u(x,t)$ without a wave reflection in the time range $t \in [0, L/c_0]$ is derived in the form

$$u(x,t) = v_0\,(t - x/c_0)\,H(t - x/c_0), \tag{7}$$

where the impact velocity is given by $v_0 = \sigma_0/\sqrt{E\rho}$ and $H(t)$ is the Heaviside time step function defined in book Kanwal (1998). Wave speed in an elastic bar is prescribed by the relationship $c_0 = \sqrt{E/\rho}$, see Kolsky (1963).

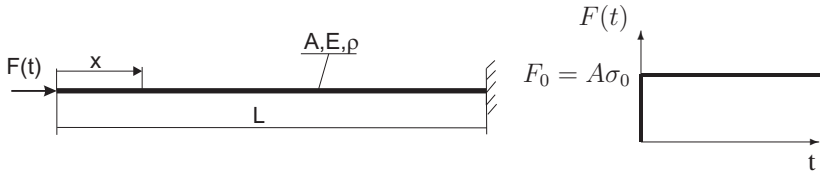

Fig. 2: Scheme of an elastic free-fixed bar under a shock loading.

5. Finite element response

The response of the elastic bar is computed numerically by the Newmark method, see Newmark (1959), with the consistent mass matrix , by the central difference method, see Dokainish and Subbaraj (1989), with the lumped mass matrix with respect to the 'row sum' method and by the implicit generalized-α method, see Hulbert and Chung (1996), with the consistent mass matrix. Details for the numerical implementation see the works Okrouhlik (2008) and Grosu and Harari (2007).

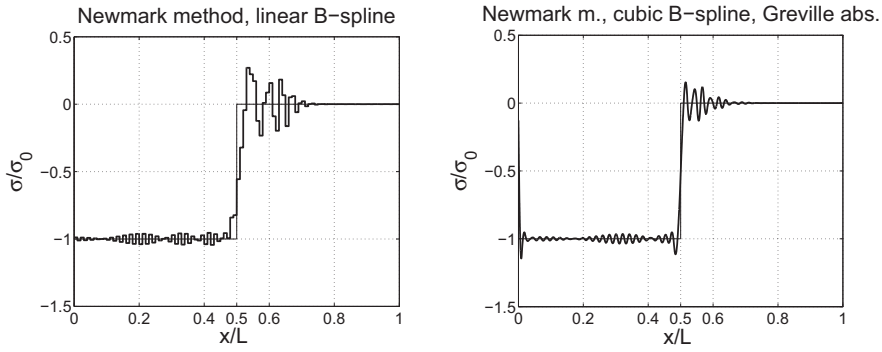

Fig. 3: Stress in an elastic bar under the shock loading at time $t = 0.5L/c_0$ computed by the Newmark method for linear (on the left) and cubic (on the right) B-splines.

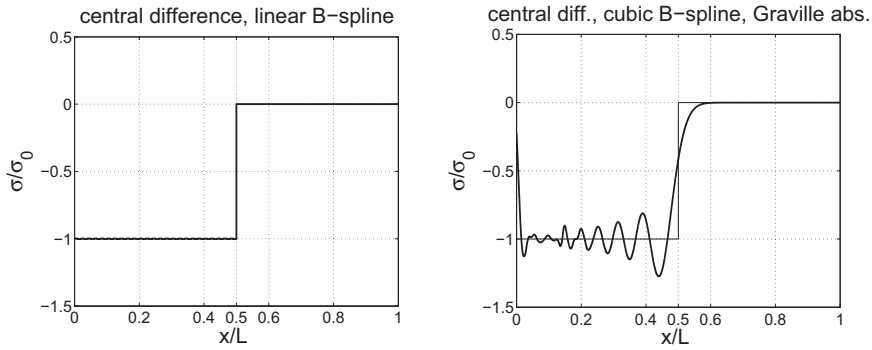

Fig. 4: Stress in an elastic bar under the shock loading at time $t = 0.5L/c_0$ computed by the central difference method for linear (on the left) and cubic (on the right) B-splines.

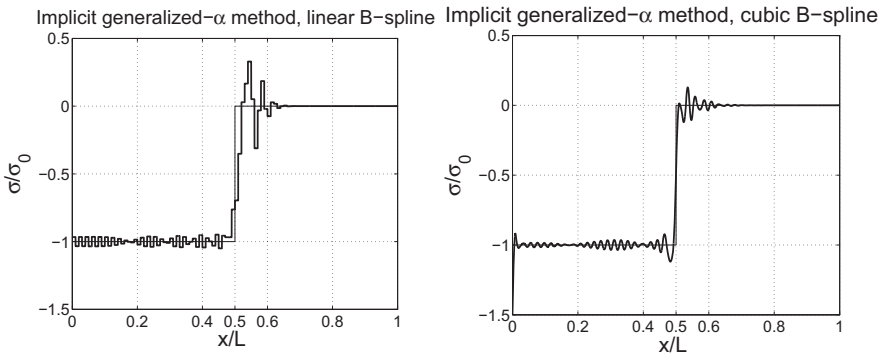

Fig. 5: Stress in an elastic bar under the shock loading at time $t = 0.5L/c_0$ computed by the implicit generalized-α method with $\rho_\infty = 0.8$ for linear (on the left) and cubic (on the right) B-splines.

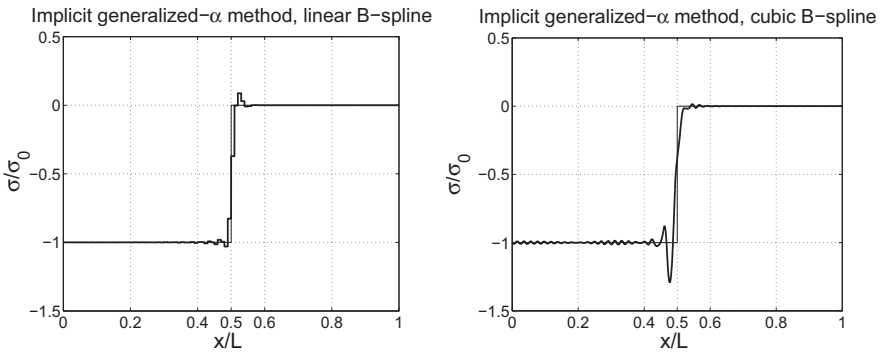

Fig. 6: Stress in an elastic bar under the shock loading at time $t = 0.5L/c_0$ computed by the implicit generalized α-method with $\rho_\infty = 0.5$ for linear (on the left) and cubic (on the right) B-splines.

Time step for the Newmark method is chosen as $\Delta t^{NM} = 1/8\, T_{min}$, where T_{min} is the minimal vibration period of the whole system (5). It is valid $T_{min} = 2\pi/\omega_{max}$, where ω_{max} is the maximum eigenfrequency of the whole system (5). The period elongation error for the Newmark method with this time step is smaller than 5%, see Hughes (1983). Time step for the central difference method is set with respect to the stability limit and good dispersion behaviour. Practically, time step is chosen as $\Delta t^{CDM} = 0.99999 \Delta t_{crit}$, where the critical value is given by critical time step $\Delta t_{crit} = 2/\omega_{max}$, see paper Park (1977). The time step for the implicit form of generalized-α method is chosen with respect to the stability limit, see paper Hulbert and Chung (1996).

The bar is discretized by linear ($p = 1$) and cubic ($p = 3$) B-splines with $N = 101$ control points. For the linear B-spline discretization, the knot vector is used uniform, Piegl and Tiller (1997), and the control points are distributed uniformly with constant distances. For the cubic B-spline discretization, the knot vector is also employed uniform, but the control points are given by the Greville abscissa, see Greville (1967). Thus, this parameterization is linear. It means that the mapping from the parametric space to the geometrical one is linear and Jacobians of this transformation are constant values. This linear parametrization produces smaller dispersion and frequency errors than the uniform one, see paper Kolman et al. (2011). On the other side, the higher-order spline discretization with the linear parameterization shows the 'outlier frequencies' but with the smaller frequency errors that the non-linear parameterization, see Hughes et al. (2008). The 'outlier frequencies' correspond to the vibration of bar borders. These non-physical high frequencies influence the value of time step, and, in generally, also the accuracy and stability of the direct time integrations.

The courses of dimensionless stress σ/σ_0 along the bar computed by the Newmark method are depicted on Fig. 3 at time $t = 0.5L/c_0$. The results for the central difference method are shown on Fig. 4. For the implicit generalized-α method, the stress waveforms are presented for spectral radius $\rho = 0.8$ on Fig. 5 and for $\rho = 0.5$ on Fig. 6. The theoretical wavefront takes place in half of the bar and the stress value in the overlaying area should hold the magnitude $\sigma = -\sigma_0$.

6. Discussion and conclusions

In the numerical test of stress discontinuity propagation computed by B-spline variant of FEM, the oscillations near sharp wave-fronts are smaller than for the classical FEM due to the variation diminishing property and smaller dispersion errors. The post-shock oscillations are typical for the central difference method due to the 'row sum' diagonal mass matrix. This diagonal mass matrix is only of second order accuracy and also it produces unsuitable frequency spectrum. On the other side, the Newmark method and the implicit form of the generalized-α method produce the both types of oscillations, both post-shock and front-shock oscillations. However, the front-shock oscillations are dominant. Jumps in behaviour of a stress function obtained by the implicit form of the generalized-α method with high level of frequency dissipation are well approximated. Nevertheless, the total energy is not preserved. The best results have been obtained by the central difference method for the combination - uniform linear finite elements, lumped mass matrix and time step near the critical time step. In this case, dispersion effect and period elongation are reciprocally eliminated.

The post- and front-oscillations could be explained by dispersion behaviour of FEM for the consistent and diagonal mass matrices. The consistent mass matrix overestimates the wave speed. Thus, distortion of the wave-front comes up. Spurious oscillations occur in the front of the theoretical wave-front. On the other side, the diagonal mass matrix underestimates the wave speed and spurious oscillations occur behind of the theoretical wave-front. This effect for the central difference method is more intensified by higher-order non-homogeneous B-spline shape functions due to the end point interpolating property. The higher-order B-spline discretization with the 'row sum' diagonal mass matrix of second order accuracy produces frequency spectrum with extensive errors. The maximal frequency defines the global critical time step. But inside a bar, the local appropriate time step should be chosen considerably lower. Therefore, the central difference method integrates equations of motion with the time step performed for producing poor dispersion characteristics.

Acknowledgments

This work was supported by the grant projects GPP101/10/P376, GA101/09/1630, GAP101/11/0288 and GAP101/12/2315 under AV0Z20760514.

References

Auricchio F., Beirao da Veiga L., Hughes T.J.R., Reali A. and Sangalli G. (2012), Isogeometric collocation for elastostatics and explicit dynamics, ICES REPORT 12-07, The Institute for Computational Engineering and Sciences, The University of Texas at Austin.

Belytschko, T. and Mullen, R. (1978), On dispersive properties of finite element solutions. In: *Modern Problems in Elastic Wave Propagation* (J. Miklowitz et al. eds). New York: Wiley, pp 67-82.

Belytschko, T. and Hughes, T.R.J. (1986), *Computational method for transient analysis*, Amsterdam: North Holland.

Chin, R.C.Y. (1975), Dispersion and Gibb's phenomenon associated with difference approximations to initial boundary-value problems, *Journal of Computational Physics*, Vol 18, pp 233-247.

Chung, J. and Hulbert,G.M. (1993), A Time integration algorithm for structural dynamics with improved numerical dissipation: The generalized-α method, *Journal of Applied Mechanics*, Vol 60, pp 371-375.

Cottrell, J.A., Reali, A., Bazilevs, Y. and Hughes, T.J.R. (2006), Isogeometric analysis of structural vibrations, *Comput. Methods Appl. Mech. Engrg.*, Vol 195, pp 5257-5296.

Cottrell, J.A., Hughes, T.J.R., and Bazilevs, Y. (2009), *Isogeometric Analysis: Toward Integration of CAD and FEA*, John Wiley & Sons, New York.

Dokainish, M.A. and Subbaraj, K. (1989), A survey of direct time-integration methods in computational structural dynamics - I. Explicit methods, *Computers & Structures*, Vol 32(6), pp 1371-1386.

Greville, T.N.E. (1967), On the normalization of the B-splines and the location of the nodes for the case of unequally spaced knots, *Inequalities*, Shiska, O. (Eds.), Academic Press, New York.

Grosu, E. and Harari, I. (2007), Stability of semidiscrete formulations for elastodynamics at small time steps, *Finit Elements in Analysis and Design*, Vol 43, pp 533-542.

Hughes, T.J.R. (1983), *The Finite element method: Linear and dynamic finite element analysis*, New York: Prentice-Hall, Englewood Cliffs.

Hughes, T.J.R., Reali, A. and Sangalli, G. (2008), Duality and unified analysis of discrete approximations in structural dynamics and wave propagation: Comparison of p-method finite Elements with k-method NURBS, *Comput. Methods Appl. Mech. Engrg.*, Vol 197, pp 4104-4124.

Hulbert, G.M. and Chung, J. (1996), Explicit time integration algorithms for structural dynamics with optimal numerical dissipation, *Comput. Methods Appl. Mech. Engrg.*, Vol 137, pp 175-188.

Kanwal, R.P. (1998), *Generalized functions: Theory and technique*, Birkhuser, Boston.

Kolman, R., Plešek, J., Okrouhlík. M and Gabriel, D. (2011), *Dispersion errors of B-spline based finite element method in one-dimensional elastic wave propagation*. In: *Computational Methods in Structural Dynamics and Earthquake Engineering ECCOMAS 2011* (M. Papadrakakis et al. eds.). Corfu, Greece, pp 1-12.

Kolsky, H. (1963), *Stress wave in solids*, New York: Dover Publications.

Newmark, N.M. (1959), A method of computation for structural dynamic, *Journal of the Engineering Mechanics Division*, Vol 85, pp 67-94.

Okrouhlík, M. (Eds.) (2008), *Numerical methods in computational mechanics*, Educational Series, Institute of Thermomechanics AS CR, Prague, *http://www.it.cas.cz/files/u1784/Num_ methods_in_CM.pdf*.

Park, K.C. (1977), Practical aspect of numerical time integration, *Computures & Structures*, , Vol 7, pp 343-353.

Park, K.C., Lim, S.J., and Huh, H. (2012), A method for computation of discontinuous wave propagation in heterogeneous solids: basic algorithm description, Preprint MNE4285, to appear submitted to *International Journal for Numerical Methods in Engineering*.

Piegl, L. and Tiller, W. (1997), *The NURBS book*, Springer-Verlag.

Subbaraj, K. and Dokainish, M.A. (1989), A survey of direct time-integration methods in computational structural dynamics - II. Implicit methods, *Computers & Structures*, Vol 32(6), pp 1387-1401.

18th International Conference
ENGINEERING MECHANICS 2012
Svratka, Czech Republic, May 14 – 17, 2012

pp. 665–671
Paper #178

FRICTIONLESS CONTACT OF ELASTIC BODIES: COMPARISON OF TREATMENT IN FINITE ELEMENT ANALYSI AND ISOGEOMETRIC ANALYSIS

J. Kopačka, R. Kolman, D. Gabriel, J. Plešek *

Abstract: *Artificial oscillations in contact force due to non-smooth contact surface are treated by isogeometric analysis (IGA). After brief overview of B-splines and Non-Uniform Rational B-Splines (NURBS) representation, the mortar-based contact algorithm is presented in the frictionless small deformation regime. Contact constraints are regularized by penalty method. The contact algorithm is tested by means of contact patch test.*

Keywords: ***Isogeometric analysis, Contact analysis, NURBS***

1. Introduction

The main difficulty in contact analysis is non-smoothness. It arises from inequality constraint as well as the geometric discontinuities inducted by spatial discretization. Contact analysis based on traditional finite elements utilizes element facets to describe a contact surface. The facets are C^0 continuous so that surface normal can experience jump across facet boundaries leading to artificial oscillations in contact force.

There were attempts to treat the geometric discontinuities by smoothing the contact surfaces using splines interpolation. These remedies introduce an additional geometry on the top of the existing finite element mesh. This adds an additional layer of data management and increasing computational overhead. Details and further references can be found in Wriggers (2006).

Another remedy to the geometric discontinuity provides isogeometric analysis (IGA). The fundamental idea is to accurately describe a physical domain of interest by proper representation (e.g. NURBS) and then utilize the same basis for analysis. This is in contrast with the classical finite element method where the basis is given in advance by the element type and so that the physical domain could be approximated inaccurately. More detailed description could be found in Cottrell et al. (2009).

Isogeometric NURBS-based contact analysis has some additional advantages: preserving geometric continuity, facilitating patch-wise contact search, supporting a variationally consistent formulation, and having a uniform data structure for the contact surface and the underlying volumes.

Geometric basis and formulation for frictionless isogeometric contact has been given in Lu (2010). Sharp corners or C^0 edges that can exist on the interface of patches present a challenge to contact detection. A strategy to seamlessly deal with sharp corners has been proposed in this reference. Herein, the contact constraints are regularized by penalty method and contact virtual work is discretized by finite strain surface-to-surface contact element. Both one-pass and two-pass algorithm are tested.

In Temizer et al. (2011), finite deformation frictionless quasi-static thermomechanical contact problems are considered. Two penalty-based contact algorithms are studied herein. The former is called knot-to-surface (KTS) algorithm. It is the straightforward extension of the classical node-to-surface (NTS) algorithm. Since NURBS control points are not interpolatory, contact constraints are enforce directly at the physical points of the quadrature points. It is shown in this reference that this approach is

*Ing. Ján Kopačka, Ing. Radek Kolman, Ph.D., Ing. Dušan Gabriel, Ph.D., Ing. Jiří Plešek, CSc.: Institute of Thermomechanics AS CR, v.v.i., Academy of Science of the Czech Republic, Dolejškova 1402/5; 182 00, Prague 8; CZ, e-mail: {kopacka,kolman,gabriel,plesek}@it.cas.cz

over-constrained and therefore not acceptable if a robust formulation with accurate tractions is desired. The latter is called mortar-KTS algorithm. In this algorithm a mortar projection to control pressures is employed to obtain the correct number of constraints.

The penalty-based mortar-KTS algorithm has been extended to frictional contact in Lorenzis et al. (2011) and Temizer et al. (2012). The mortar-KTS algorithm has been also studied in conjugation with augmented Lagrangian method in Lorenzis et al. (2012). Isogeometric frictionless contact analysis using non-conforming mortar method in two-dimensional linear elasticity regime has been presented in Kim (2011).

In this paper, we present mortar-based frictionless isogeometric contact algorithm in small deformation regime. The main contribution of this work is to prepare an implementation of the IGA procedures for further investigation. After brief overview of B-Splines and NURBS representation in section 2., the isogeometric contact algorithm is presented in section 3. The robustness of the algrithm is chacked by means of contact patch test in section 4.

2. B-splines and NURBS

This section gives a brief overview of the main concerns of B-splines and NURBS. For more detailed description as well as efficient algorithms see Piegl and Tiller (1997). Throughout this paper we use p to indicate the polynomial degree, n to indicate the number of basis functions, d_p to indicate the number of parametric dimensions, and d_s to indicate the number of spatial dimensions.

Let $\boldsymbol{\Xi}^i$, $i = 1, \dots d_\mathrm{p}$ be the open non-uniform knot vector associated with i^{th} parametric dimension of a patch

$$\boldsymbol{\Xi}^i = \left\{ \underbrace{\xi^i_1, \dots, \xi^i_{p_i+1}}_{p_i+1 \text{ equal terms}}, \xi^i_{p_i+2}, \dots, \xi^i_{n_i}, \underbrace{\xi^i_{n_i+1}, \dots, \xi^i_{n_i+p_i+1}}_{p_i+1 \text{ equal terms}} \right\}. \tag{1}$$

The knot vector is a non-decreasing sequence of parametric coordinates. The knot vector is said to be non-uniform if the knots are unequally spaced in the parametric space. If the first and the last knot value appears $p_i + 1$ times, the knot vector is called open. Open knot vectors are interpolatory at the corners of patches. It means that the boundary of a B-spline object with d_p parametric dimensions is itself a B-spline object of $d_\mathrm{p} - 1$.

The B-spline basis functions are defined by Cox-de Boor recursion formula. For $p = 0$

$$N_{j,0}(\xi) = \begin{cases} 1 & \xi \in [\xi_j, \xi_{j+1}), j = 1 \dots n \\ 0 & \text{otherwise,} \end{cases} \tag{2}$$

and for $p > 0$

$$N_{j,p}(\xi) = \frac{\xi - \xi_j}{\xi_{j+p} - \xi_j} N_{j,p-1}(\xi) + \frac{\xi_{j+1+p} - \xi}{\xi_{j+1+p} - \xi_{j+1}} N_{j+1,p-1}(\xi). \tag{3}$$

B-splines are known to be unable to exactly describe some curves, whereas rational functions can. NURBS (Non-Uniform Rational B-Splines) was developed to extend interpolatory capability of the B-splines. The extension originates from projection geometry of conic sections. A p^{th} degree NURBS basis function is defined by

$$R^p_j(\xi) = \frac{N_{j,p}(\xi) w_j}{\sum_{\hat{j}=1}^{n} N_{\hat{j},p}(\xi) w_{\hat{j}}}, \tag{4}$$

where w_j is referred to as the j^{th} weight.

Multivariate NURBS objects can be constructed simply by tensor product of univariate NURBS basis functions (4). For $d_\mathrm{p} = 2$

$$R^{p_1,p_2}_{j_1,j_2}(\xi^1, \xi^2) = R^{p_1}_{j_1}(\xi^1) \otimes R^{p_2}_{j_2}(\xi^2) = \frac{N_{j_1,p_1}(\xi^1) N_{j_2,p_2}(\xi^2) w_{j_1,j_2}}{\sum_{\hat{j}_1=1}^{n_1} \sum_{\hat{j}_2=1}^{n_2} N_{\hat{j}_1,p_1}(\xi^1) N_{\hat{j}_2,p_2}(\xi^2) w_{\hat{j}_1,\hat{j}_2}} \tag{5}$$

and similarly for the higher parametric dimension. With NURBS basis functions at hand we can finally introduce surface discretization by

$$\mathbf{x}(\xi^1,\xi^2)=\sum_{j_1=1}^{n_1}\sum_{j_2=1}^{n_2}R_{j_1,j_2}^{p_1,p_2}(\xi^1,\xi^2)\mathbf{P}_{j_1,j_2}, \tag{6}$$

where $\mathbf{P}_{j_1,j_2}\in\mathbb{R}^{d_\mathrm{s}}$ is the control net, i.e., array of coordinates of control points. Adopting the isogeometric concept, an analogous interpretation is used for unknown displacement field and its variation. Utilizing proper connectivity arrays according to Cottrell et al. (2009), one can write

$$\mathbf{x}(\boldsymbol{\xi})=\sum_{A=1}^{n_\mathrm{cp}}N_A(\boldsymbol{\xi})\mathbf{x}_A\qquad \mathbf{u}(\boldsymbol{\xi})=\sum_{A=1}^{n_\mathrm{cp}}N_A(\boldsymbol{\xi})\mathbf{u}_A\qquad \delta\mathbf{u}(\boldsymbol{\xi})=\sum_{A=1}^{n_\mathrm{cp}}N_A(\boldsymbol{\xi})\delta\mathbf{u}_A, \tag{7}$$

where $\boldsymbol{\xi}=(\xi^1,\xi^2)\in\mathbb{R}^{d_\mathrm{p}}$, A is the index of global basis function and n_cp is the number of control points. It is also useful to consider local mappings defined over one individual knot span which can be interpreted as a finite element

$$\mathbf{x}(\boldsymbol{\xi})=\sum_{a=1}^{n_\mathrm{ec}}N_a(\boldsymbol{\xi})\mathbf{x}_a\qquad \mathbf{u}(\boldsymbol{\xi})=\sum_{a=1}^{n_\mathrm{ec}}N_a(\boldsymbol{\xi})\mathbf{u}_a\qquad \delta\mathbf{u}(\boldsymbol{\xi})=\sum_{a=1}^{n_{ec}}N_a(\boldsymbol{\xi})\delta\mathbf{u}_a, \tag{8}$$

where a is the number of local basis function, and n_ec is the number of element control points.

3. Isogeometric contact treatment

In this section we present isogeometric treatment of small displacement frictionless contact between two elastic deformable bodies. We adopt mortar-KTS algorithm according to Temizer et al. (2011) and customize it for the small displacement regime. For more detailed description of computational contact, the reader is referred to Wriggers (2006).

3.1. Contact kinematics

Consider two elastic bodies Ω_1 and Ω_2 in contact without friction. The size and the location of the contact boundary $\Gamma_\mathrm{c}=\partial\Omega_1\cap\partial\Omega_2$ is unknown. For its determination, a function which measures the distance between the bodies is introduced

$$d(\boldsymbol{\xi}):=\left\|\mathbf{x}_\mathrm{s}-\mathbf{x}_\mathrm{m}(\boldsymbol{\xi})\right\|,\quad \mathbf{x}_\mathrm{m}\in\partial\Omega_1,\ \mathbf{x}_\mathrm{s}\in\partial\Omega_2. \tag{9}$$

With the aid of this function one can assign to each slave point $\mathbf{x}_\mathrm{s}\in\partial\Omega_2$ a master point $\bar{\mathbf{x}}_\mathrm{m}\in\partial\Omega_1$ by the closest point projection

$$\boldsymbol{\nabla}d(\boldsymbol{\xi})=\frac{\partial\mathbf{x}_\mathrm{m}(\boldsymbol{\xi})}{\partial\boldsymbol{\xi}}\cdot\left[\mathbf{x}_\mathrm{s}-\bar{\mathbf{x}}_\mathrm{m}(\boldsymbol{\xi})\right]=\mathbf{0}. \tag{10}$$

This is a system of non-linear algebraic equations with respect to $\boldsymbol{\xi}=(\xi_1,\ldots,\xi_{d_\mathrm{p}})$. Different methods for its numerical solution were studied in Gabriel et al. (2011). Customizing to the isogeometric analysis is straightforward. It consists in replacing basis functions and its derivatives. The closest projection point as well as related variables will be indicated by the bar symbol further in this paper (e.g. $\bar{\mathbf{x}}_\mathrm{m}$, $\bar{\boldsymbol{\xi}}$).

With the closest point, $\bar{\mathbf{x}}_\mathrm{m}$, at hand we can define the normal gap as

$$g_\mathrm{N}=(\mathbf{x}_\mathrm{s}-\bar{\mathbf{x}}_\mathrm{m})\cdot\bar{\mathbf{n}}_\mathrm{m}=(\mathbf{u}_\mathrm{s}-\bar{\mathbf{u}}_\mathrm{m})\cdot\bar{\mathbf{n}}_\mathrm{m}+g_0, \tag{11}$$

and its variation

$$\delta g_\mathrm{N}=\left(\delta\mathbf{u}^1-\delta\bar{\mathbf{u}}^2\right)\cdot\bar{\mathbf{n}}_\mathrm{m}, \tag{12}$$

where $\mathbf{u}_\mathrm{s}$ and $\bar{\mathbf{u}}_\mathrm{m}$ are displacements of the slave and master points respectively, and g_0 is the initial normal gap.

3.2. Contact constraints

Non-penetration condition dictates that normal gap has to be non-negative. If the gap is closed, it has to generate pressure. These two natural criteria can be written as Karush-Kuhn-Tucker (KKT) condition for contact

$$g_{\mathrm{N}} \geq 0 \tag{13}$$

$$t_{\mathrm{N}} \leq 0 \quad \text{on } \Gamma_{\mathrm{c}}, \tag{14}$$

$$t_{\mathrm{N}} g_{\mathrm{N}} = 0 \tag{15}$$

where the third equality is called complementary condition. It states that either the gap or the contact traction has to be zero. One of the possibilities how to regularized the KKT conditions is the penalty method. The regularized normal contact constraint reads as

$$t_{\mathrm{N}} = \epsilon \langle g_{\mathrm{N}} \rangle , \quad \langle g_{\mathrm{N}} \rangle = \begin{cases} g_{\mathrm{N}} & \text{if } g_{\mathrm{N}} \leq 0 \\ 0 & \text{otherwise} \end{cases}, \tag{16}$$

where ϵ_{N} is the penalty parameter.

3.3. Weak form

Contact boundary value problem can be formulated in a weak sense by

$$\delta\Pi(\mathbf{u}, \delta\mathbf{u}) = \delta\Pi_{\mathrm{int}}(\mathbf{u}, \delta\mathbf{u}) + \delta\Pi_{\mathrm{ext}}(\mathbf{u}, \delta\mathbf{u}) + \delta\Pi_{\mathrm{c}}(\mathbf{u}, \delta\mathbf{u}) = 0, \tag{17}$$

subjected to (13). The terms on the right hand side denote virtual work due to internal forces, virtual work due to external forces and virtual work due to contact forces respectively. Assuming the validity of the action-reaction principle, contact virtual work can be expressed as

$$\delta\Pi_{\mathrm{c}}(\mathbf{u}, \delta\mathbf{u}) = \int_{\Gamma_{\mathrm{c}}} \epsilon_{\mathrm{N}} g_{\mathrm{N}} \delta g_{\mathrm{N}} \, \mathrm{d}\Gamma \tag{18}$$

3.4. Discretized form

By substituting (8) into (11) and (12), the normal gap and its variation becomes

$$g_{\mathrm{N}} = \left[\sum_{a=1}^{n_{\mathrm{ec}}^{\mathrm{s}}} R_a^{\mathrm{s}}(\boldsymbol{\xi}^{\mathrm{s}}) \mathbf{u}_a^{\mathrm{s}} - \sum_{a=1}^{n_{\mathrm{ec}}^{\mathrm{m}}} R_a^{\mathrm{m}}(\bar{\boldsymbol{\xi}}) \mathbf{u}_a^{\mathrm{m}} \right] \cdot \bar{\mathbf{n}}^{\mathrm{m}} + g_0(\bar{\boldsymbol{\xi}}), \tag{19}$$

$$\delta g_{\mathrm{N}} = \left(\sum_{a=1}^{n_{\mathrm{ec}}^{\mathrm{s}}} R_a^{\mathrm{s}}(\boldsymbol{\xi}^{\mathrm{s}}) \delta\mathbf{u}_a^{\mathrm{s}} - \sum_{a=1}^{n_{\mathrm{ec}}^{\mathrm{m}}} R_a^{\mathrm{m}}(\bar{\boldsymbol{\xi}}) \delta\mathbf{u}_a^{\mathrm{m}} \right) \cdot \bar{\mathbf{n}}^{\mathrm{m}}. \tag{20}$$

Defining the vectors

$$\mathbf{u} = \begin{bmatrix} u_1^{\mathrm{s}} \\ \vdots \\ u_{n_{\mathrm{ec}}^{\mathrm{s}}}^{\mathrm{s}} \\ u_1^{\mathrm{m}} \\ \vdots \\ u_{n_{\mathrm{ec}}^{\mathrm{m}}}^{\mathrm{m}} \end{bmatrix} \qquad \delta\mathbf{u} = \begin{bmatrix} \delta u_1^{\mathrm{s}} \\ \vdots \\ \delta u_{n_{\mathrm{ec}}^{\mathrm{s}}}^{\mathrm{s}} \\ \delta u_1^{\mathrm{m}} \\ \vdots \\ \delta u_{n_{\mathrm{ec}}^{\mathrm{m}}}^{\mathrm{m}} \end{bmatrix} \qquad \mathbf{N} = \begin{bmatrix} R_1^{\mathrm{s}}(\boldsymbol{\xi}^{\mathrm{s}}) \bar{\mathbf{n}}_{\mathrm{m}} \\ \vdots \\ R_{n_{\mathrm{ec}}^{\mathrm{s}}}^{\mathrm{s}}(\boldsymbol{\xi}^{\mathrm{s}}) \bar{\mathbf{n}}_{\mathrm{m}} \\ -R_1^{\mathrm{m}}(\bar{\boldsymbol{\xi}}) \bar{\mathbf{n}}_{\mathrm{m}} \\ \vdots \\ -R_{n_{\mathrm{ec}}^{\mathrm{m}}}^{\mathrm{m}}(\bar{\boldsymbol{\xi}}) \bar{\mathbf{n}}_{\mathrm{m}} \end{bmatrix}, \tag{21}$$

equations (19) and (20) can be cast in matrix form as

$$g_{\mathrm{N}} = \mathbf{N}^{\mathrm{T}} \mathbf{u} + g_0, \tag{22}$$

$$\delta g_{\mathrm{N}} = \delta\mathbf{u}^{\mathrm{T}} \mathbf{N}. \tag{23}$$

3.5. Mortar-KTS contact algorithm

In the spirit of the mortar method, the the contact virtual work is expressed as

$$\delta\Pi_{\mathrm{c}}(\mathbf{u},\delta\mathbf{u}) = \sum_{A} \epsilon_{\mathrm{N}} g_{\mathrm{N}_A} \delta g_{\mathrm{N}_A} \, A_A, \tag{24}$$

where summation is extended to the active control points. The control point normal gap and its variation are defined as the weighted average, with the basis functions as weights

$$g_{\mathrm{N}_A} = \frac{\int_{\Gamma_{\mathrm{c}}} R_A g_{\mathrm{N}} \,\mathrm{d}\Gamma}{\int_{\Gamma_{\mathrm{c}}} R_A \,\mathrm{d}\Gamma} \qquad \delta g_{\mathrm{N}_A} = \frac{\int_{\Gamma_{\mathrm{c}}} R_A \delta g_{\mathrm{N}} \,\mathrm{d}\Gamma}{\int_{\Gamma_{\mathrm{c}}} R_A \,\mathrm{d}\Gamma}. \tag{25}$$

An active control point is one for which $g_{\mathrm{N}A} \leq 0$. The 'area of competence' of a control point is defined as

$$A_A = \int_{\Gamma_{\mathrm{c}}} R_A \,\mathrm{d}\Gamma. \tag{26}$$

Substituting (25) and (26) into (24) yields

$$\delta\Pi_{\mathrm{c}} = \sum_{A} \frac{\epsilon_{\mathrm{N}}}{\int_{\Gamma_{\mathrm{c}}} R_A \,\mathrm{d}\Gamma} \int_{\Gamma_{\mathrm{c}}} R_A g_{\mathrm{N}} \,\mathrm{d}\Gamma \int_{\Gamma_{\mathrm{c}}} R_A \delta g_{\mathrm{N}} \,\mathrm{d}\Gamma. \tag{27}$$

Substituting (22) and (23) into (27)

$$\delta\Pi_{\mathrm{c}} = \delta\mathbf{u}^{\mathrm{T}} \sum_{A} \frac{\epsilon_{\mathrm{N}}}{\int_{\Gamma_{\mathrm{c}}} R_A \,\mathrm{d}\Gamma} \left(\int_{\Gamma_{\mathrm{c}}} R_A \mathbf{N} \,\mathrm{d}\Gamma \int_{\Gamma_{\mathrm{c}}} R_A \mathbf{N}^{\mathrm{T}} \,\mathrm{d}\Gamma \mathbf{u} + \int_{\Gamma_{\mathrm{c}}} R_A g_0 \,\mathrm{d}\Gamma \int_{\Gamma_{\mathrm{c}}} R_A \mathbf{N} \,\mathrm{d}\Gamma \right). \tag{28}$$

Finally, the contact residual vector is immediately obtained from (28)

$$\mathbf{G}_{\mathrm{c}} = \mathbf{K}_{\mathrm{c}} + \mathbf{F}_{\mathrm{c}}, \tag{29}$$

where by gauss integration

$$\mathbf{K}_{\mathrm{c}} = \sum_{A} \frac{\epsilon_{\mathrm{N}}}{\sum_{g=1}^{n_{\mathrm{gp}}} R_A(\boldsymbol{\xi}_g) w_g j_g} \sum_{g=1}^{n_{\mathrm{gp}}} R_A(\boldsymbol{\xi}_g) \mathbf{N} w_g j_g \sum_{g=1}^{n_{\mathrm{gp}}} R_A(\boldsymbol{\xi}_g) \mathbf{N}^{\mathrm{T}} w_g j_g, \tag{30}$$

$$\mathbf{F}_{\mathrm{c}} = \sum_{A} \frac{\epsilon_{\mathrm{N}}}{\sum_{g=1}^{n_{\mathrm{gp}}} R_A(\boldsymbol{\xi}_g) w_g j_g} \sum_{g=1}^{n_{\mathrm{gp}}} R_A(\boldsymbol{\xi}_g) g_0(\boldsymbol{\xi}_g) w_g j_g \sum_{g=1}^{n_{\mathrm{gp}}} R_A(\boldsymbol{\xi}_g) \mathbf{N} w_g j_g, \tag{31}$$

where w_g are Gauss-Legendre weights, j_g are the Jacobian determinant, both evaluated at Gaussian quadrature point $g = 1, \ldots, n_{\mathrm{gp}}$.

4. Contact patch test

In this section we present a three-dimensional version of the contact patch test acoording to Taylor and Papadopoulos (1991). Dimensions are depicted in the Fig. 1. Both blocks are subjected to a pressure $p = 1F/UL^2$. The same material with $\nu = 0.3$ and $E = 1000F/UL^2$ is used for both blocks. The analytical solution is $\sigma_z = -1F/UL^2$.

Either of the blocks is discretized by one trivariate NURBS patch of order $p = 1$ in each parametric dimension. The knot vectors are

$$\boldsymbol{\Xi}^i = \left\{ \begin{array}{cccccccc} 0 & 0 & 0.25 & 0.5 & 0.75 & 1 & 1 \end{array} \right\}, i = 1, \ldots, 3. \tag{32}$$

There are four nonzero knot spans which are depicted by the black grid in the Fig. 2. There are contours of the z-displacement field in the Fig. 2. The constant partial derivative with respect to z implies constant pressure in both blocks. The same results has been obtained for tri-quadratic and tri-cubic NURBS patches.

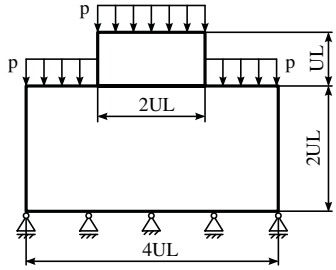

Fig. 1: The contact patch test according to Taylor and Papadopoulos (1991). UL is the unit length, $p = 1F/UL^2$ is the presuure.

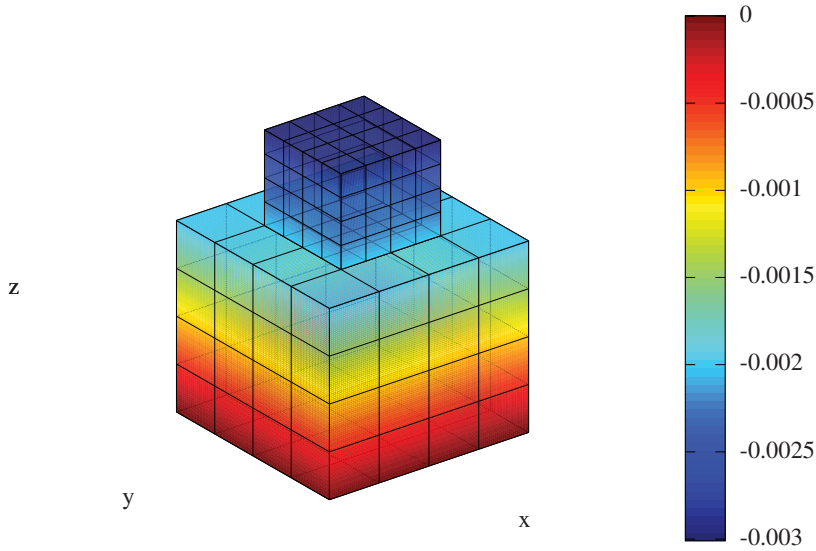

Fig. 2: Z-displacement field. The constant partial derivative with respect to z implies constant pressure.

5. Conclusions

The frictionless mortar-based isogeometric contact algorithm in small deformation regime has been outlined. The correct implementation of the contact algorithm has been successfully tested by means of contact patch test. Indeed, one cannot make serious conclusins based on one numerical example. Therefore, we will continue in the assessment of the algorithm in the further work.

Acknowledgements

This work was supported by the Grant Agency of the Czech Republic under grant numbers GAP101/12/2315, GPP101/10/P376, GA101/09/1630 in the framework of AV0Z20760514.

References

Wriggers, P. (2006), *Computational Contact Mechanics*, Springer, Berlin.

Cottrell, J.A., Hughes, T.J.R., Bazilevs, Y. (2009), *Isogeometric Analysis: Toward Integration of CAD and FEA*, John Wiley & Sons, New York.

Temizer, I., Wriggers, P., Hughes, T.J.R. (2011), Contact treatment in isogeometric analysis with NURBS. *Comput. Methods Appl. Mech. Engrg.*, Vol 200, pp 1100-1112.

Lu, J. (2010), Isogeometric contact analysis: Geometric basis and formulation for frictionless contact. *Comput. Methods Appl. Mech. Engrg.*, Vol 200, pp 726-741.

De Lorenzis, L., Temizer, I., Wriggers, P., Zavarise, G. (2011), A large deformation frictional contact formulation using NURBS-based isogeometric analysis. *Int. J. Numer. Meth. Engng.*, Vol 87, pp 1278-1300.

Kim, J.Y., - Youn, S.K. (2011), Isogeometric contact analysis using mortar method. *Int. J. Numer. Meth. Engng.*.

Temizer, I., Wriggers, P., Hughes, T.J.R. (2012) Three-dimensional mortar-based frictional contact treatment in isogeometric analysis with NURBS. *Comput. Methods Appl. Mech. Engrg.*, Vol 209-212, pp 115-128.

De Lorenzis, L., Wriggers, P., Zavarise, G. (2012) A mortar formulation for 3D large deformation contact using NURBS-based isogeometric analysis and the augmented Lagrangian method. *Comput. Mech.*, Vol 49, pp 1-20.

Piegl, L., Tiller, W. (1997) *The NURBS Book (Monographs in Visual Communication)*. Second Edition, Springer-Verlag.

Gabriel, D., Kopačka, J., Plešek, J., Ulbin, M. (2010), Assesment of methods for calculating the normal contact vector in local search. In: *In ECCM 2010*, Computational Structural Mechanics Association, Paris, 2 pp..

Taylor, R. L., Papadopoulos, P. (1991) On a patch test for contact problems in two dimensions. *Nonlinear Computational Mechanics*, pp 690-702, Springer, Berlin.

18th International Conference
ENGINEERING MECHANICS 2012
Svratka, Czech Republic, May 14 – 17, 2012

pp. 673–679
Paper #182

NUMERICAL MODELLING OF THE REINFORCEMENT CORROSION

P. Koteš[*], M. Brodňan[**]

Abstract: *The reinforcement corrosion is the phenomenon that highly affects the reliability and durability of reinforced concrete structures. From that reason, a lot of researchers in Slovakia and in the world pay their attention to reinforcement corrosion. In the frame of the research work, the reinforced concrete girder bridges were diagnosed and observed. These bridges are influenced by reinforcement corrosion of main girders. The paper is concerned with detection and simulation of corrosion of steel reinforcement in the reinforced concrete. The cracking response of the reinforced concrete beams due to the corrosion effect of the steel reinforcement was analyzed. The effect of corrosion was simulated by the nonlinear numerical analysis using the program ATENA.*

Keywords: ***Crack, reinforcement, corrosion, numerical modeling, concrete.***

1. Introduction

Reinforced concrete is a versatile, economical and successful construction material. Usually, it is durable and resistant material, performing well throughout its service life. However, sometimes it does not perform adequately as it is expected. It is due to poor design, construction, inadequate materials selection and severe environment than anticipated or a combination of those factors (Broomfield, 1997).

The corrosion of reinforcing steel in concrete, due to severe environment, is the phenomenon that highly affects the reliability and durability of reinforced concrete structures. In the frame of the research work of Department of Structures and Bridges at the University of Žilina, reinforced concrete girder bridges were diagnosed and observed. Simultaneously, the bridge was evaluated and its remaining lifetime was estimated.

The considered bridges are situated in the villages Kolárovice and Topolčianky (Fig. 1). The bridge´s structural system is created by the reinforced concrete single span girder with theoretical span of 10.006 m (Kolárovice) or 13.60 m (Topolčianky). The width of road is 7.51m and the overall width of bridge is 9.51m (Kolárovice) and in the case of bridge in Topolčianky, the road width is 6.00 m and the overall width is 7.80 m. The bridge obliqueness is 45° and 80°.

Fig. 1: Diagnosed bridges in villages Kolárovice and Topolčianky.

[*] Ing. Peter Koteš, Ph.D.: Department of Structures and Bridges, Civil Engineering Faculty, University of Žilina, Univerzitná 8215/1; 010 26, Žilina; SK, e-mail: kotes@fstav.uniza.sk

[**] Ing. Miroslav Brodňan, Ph.D.: Department of Structures and Bridges, Civil Engineering Faculty, University of Žilina, Univerzitná 8215/1; 010 26, Žilina; SK, e-mail: brodnan@fstav.uniza.sk

In the case of bridge near Kolarovice, from the results of the bridge diagnostics follows that the concrete has quality of C30/37 and the beams are reinforced by rebar of the type A (10 210) in two layers (5ϕA30 in the lower layer and 2ϕA30 in the upper layer). Accordingly, the reinforcement corrosion was indicated. The corrosion caused the diameter loss from the initial value of 30 mm to the actual average value of 29.3 mm (the minimal measured value is 28.7 mm) and also caused the dropping out the concrete cover. The concrete cover is 30 mm.

Alike in the case of bridge near Topolčianky, from the results of the bridge diagnostics follows that the concrete has quality of C16/20 and the beams are reinforced by rebar of the type C (10 452) also in two layers (5ϕC35 in the lower layer and 2ϕC35 in the upper layer). The corrosion caused the diameter loss from the initial value of 35 mm to the actual average value of 33.99 mm (the minimal measured value is 33.50 mm) and also caused the dropping out the concrete cover. The concrete cover is just 15 mm.

From the results of the bridge evaluation follows that the remaining lifetime of bridges is about 20 years (Koteš & Vičan, 2006; Kala & Omishore, 2009). From those results, the urgency of bridge reconstruction or strengthening in order to increase its load-carrying capacity is evident.

The reinforcement corrosion of main girders influenced the remaining lifetime severely. The corrosion does not only decrease the reinforcement cross-section, but also causes the cracks and dropping out the concrete cover. It means that the flexural stiffness is decreasing. The corrosive reduction rate (rust) causes the pressure at surrounding concrete by increasing its volume. So, the tension stresses are appearing. The micro cracks are created after exceeding of concrete tension strength. The micro cracks are getting connected into longitudinal cracks by subsequent increasing of corrosive reduction rate volume. The cracks with corrosive reduction rate are able to cause the decreasing of bond between concrete and reinforcement and following dropping out of concrete cover. The same effect occurs also at some places of spandrel beams (Fig.1).

For the purpose of the better comprehension of crack formation and development, the numerical model of reinforcement corrosion in concrete cross-section was created in computer program ATENA.

2. Numerical models of reinforcement corrosion

2.1. 2D numerical model

The girder bridge near Kolárovice was used for numerical modeling. Firstly, the numerical model of reinforcement corrosion was created in the 2D module ATENA. Only cross-section of the T-girder with real dimensions was modelled (Fig. 2).

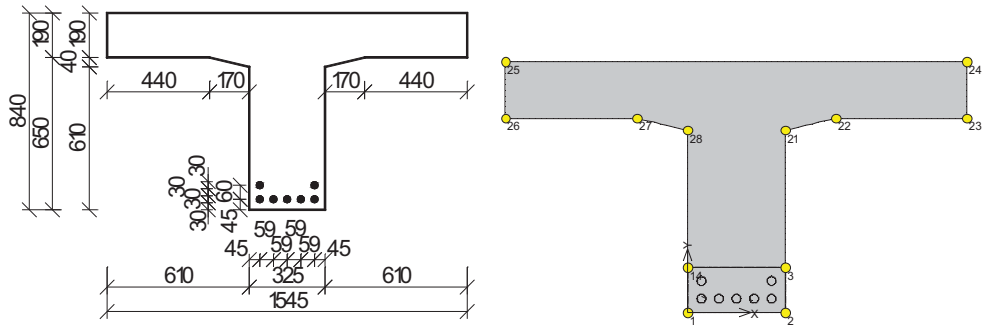

a) Cross-section of T-girder *b) 2D numerical model*

Fig. 2: Cross-section of T-girder and numerical model.

The material model of concrete „Concrete-SBETA Material“ with compression strength $f_{cu} = 40.0$ N.mm^{-2}, derived from CEB-FIP MC 90, was applied for concrete. The basic properties of this material model are: tensile strength, fracture energy and the equivalent uniaxial law. This material

model provides objective results due to formulations based on energetic principles and its dependency on the finite element mesh is negligible. The main reinforcement in the RC girder was modelled as a 3D Bilinear Steel von Mises element with yield strength of $f_y = 200.0$ N.mm^{-2}. Others characteristics are calculated by software ATENA on the basis of redefined formulas. The rigid contacts between concrete and reinforcement were considered.

The concrete part of the cross-section was divided into two parts – the upper part was divided into macro elements with dimensions 20x20 mm (the influence of corrosion on cracks was not expected) and the bottom part was divided into macro elements with dimensions 2x2 mm. The reinforcement was also divided into macro elements with dimensions 2x2 mm.

The reinforcement corrosion modeling was the most important part of the problem. It was chosen in such a way in modeling that the increase of reinforcement volume acts as load on the T-girder cross-section. In general, the reinforcement cross-section area is decreased due to corrosion, but the corrosion product (rust), on the contrary, increases its volume, what means the increase of the cross-section area of reinforcement.

The increase of reinforcement volume can be given by percentage. The increasing percentage "p" depends on corrosion type and its products and it achieves the values from 4% to 12%. The value p = 8% was chosen in this case. However, this is just increasing percentage of the corrosion rate area. Thus, it was needed to find the total percentage of growth of corroded reinforcement area and corrosion rate together. The corrosion – increase of full reinforcement cross-section – was modeled using the function "shrinkage" with minus sign (swelling). This way of corrosion modeling was verified in (Koteš et al., 2006; Koteš et al., 2008).

If the corrosion rate area $A_{s1,rozd}(t)$ is considered be increasing with time for about percentage "p", the entire reinforcement area including corrosion rate area (Fig. 3) is equal to

$$A_{s1,celk}(t) = A_{s1}(t) + A_{s1,rozd}(t)\cdot(1+p) = \frac{\pi}{4}\cdot\left(\phi^2\cdot(1+p) - \phi^2(t)\cdot p\right), \tag{1}$$

where ϕ is the reinforcement diameter,

$\phi(t)$ is the changed reinforcement diameter in time.

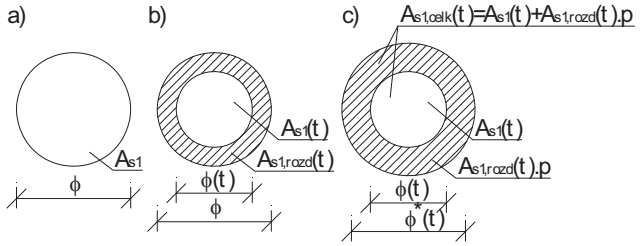

Fig. 3: Change of reinforcement cross-section area due to corrosion.

Vice versa, it is also possible to derive the new reinforcement diameter taking into account area increasing

$$\phi^*(t) = \sqrt{\phi^2\cdot(1+p) - \phi^2(t)\cdot p}\,. \tag{2}$$

The percentage increase "p*" taking into account changing of the whole reinforcement area is given by:

$$A_{s1,celk}(t) = A_{s1}\cdot(1+p^*) \;\Rightarrow\; p^* = \frac{A_{s1,celk}(t)}{A_{s1}} - 1\,. \tag{3}$$

The changing of the whole reinforcement area means that the remaining carrying part of reinforcement $A_{s1}(t)$ decreases and the corrosion rate area $A_{s1,rozd}(t)$ increases. The initial value of diameter ϕ = 30.0 mm, the reduced diameter in time ϕ (t) = 28.7 mm and the percentage p = 8% were considered in the numerical model. So, the final increase of reinforcement area is p* = 0,678 %. For better observing of cracks formation and development, the value p* was divided into ten loading steps.

2.2. 3D numerical model

The 2D model created is not perfect because it considers the transverse cracks only. The cracks across the longitudinal axis cannot be modeled in 2D. Thus, the 3D model was created in ATENA to obtain better understanding of the crack formation and development. The 3D model of the half length of the girder is shown in Fig. 4.

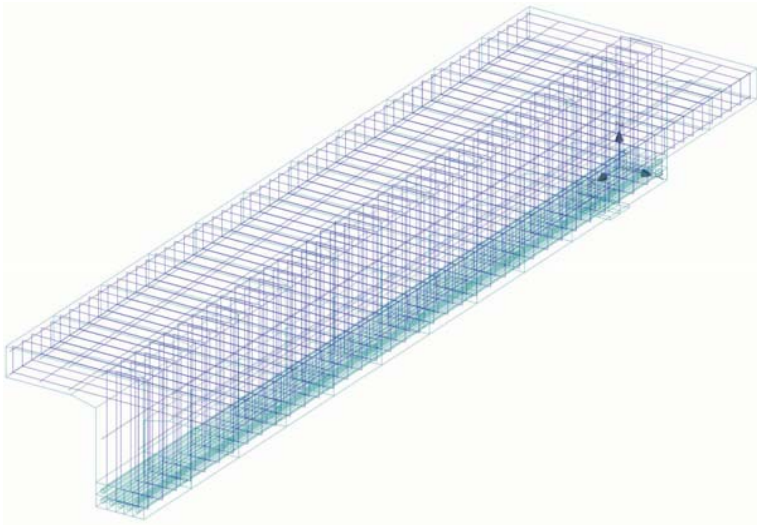

Fig. 4: 3D numerical model.

In this case, the material models of concrete „CC3DNonLinCementitious2“ with compression strength f_{cu} = 40.0 N.mm^{-2} was applied for concrete. The main reinforcement in the RC girder was modeled again as a 3D Bilinear Steel von Mises element with yield strength of f_y = 210.0 Nmm^{-2}. Other characteristics are calculated by software ATENA on the basis of redefined formulas. The rigid contacts between concrete and reinforcement were again considered. The list of used materials is given in Tab. 1. The two models were created: model 1 – without transverse stiffeners (just main reinforcement) and model 2 – with transverse stiffeners (using stirrups).

Tab. 1: Review of used material characteristics – 3D model.

Material	Material element
Concrete C30/37	3D Nonlinear Cementitious 2, f_{cu} = 40.0 N.mm^{-2} (C30/37)
Main reinforcement 5ϕA30	3D Bilinear Steel Von Mises, E = 210.10^3 N.mm^{-2}; f_y = 200 N.mm^{-2}
Stirrups ϕA8 and reinforcement in slab ϕA10	Reinforcement, bilinear, E = 210.10^3 N.mm^{-2}; f_y = 200 N.mm^{-2}
Steel plate	3D Elastic Isotropic, E = 210.10^3 N.mm^{-2}; f_y = 210 N.mm^{-2}

In the 3D model, the concrete part of cross-section was divided into 11 parts – the upper part was divided into macro elements with dimensions 200x200 mm (the influence of corrosion on cracks was not expected) and the bottom 10 parts were divided into macro elements with dimensions 20x20 mm. The reinforcement was also divided into macro elements with maximal dimensions 20x20 mm.

In this case, the corrosion was considered just in the middle of the span, not along the full length.

3. Results of numerical model

3.1. 2D model

In the 2D model, the cracks formation and development were observed in the T-girder cross-section. From this reason, the monitoring points were situated in various places of cross-section. The parameters like cracks width or strains in direction x or y were observed in these points. There were 21 monitoring points in cross-section of numerical model (Fig. 5).

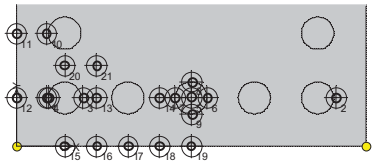

Fig. 5: Monitoring points in cross-section.

The crack formation and development in cross-section are shown in Fig. 6. There is possible to see the consecutive cracks development from the bulk towards the edges of the figure. The majority of cracks, with maximum width, occurred just inside. The cracks were connected into edge cracks causing the concrete cover dropping out. Moreover, they caused large failure of concrete inside the concrete cross-section and therefore the bond between concrete and reinforcement was decreased. The main compressive and tensile stresses are shown in Fig. 7.

a) Step 2 *b) Step 5* *c) Step 10*

Fig. 6: Cracks formation and development in loading steps.

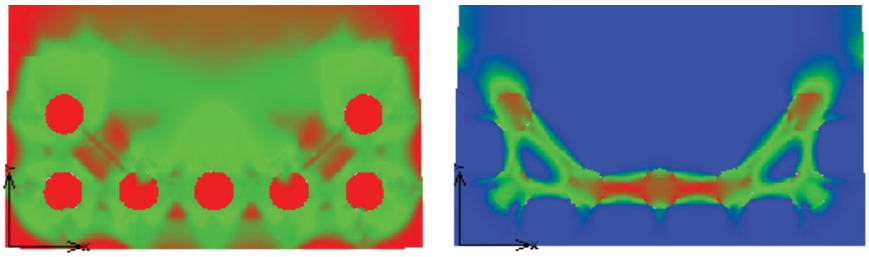

a) The main compression stresses in step 2 *b) The main tension stresses in step 2*

Fig. 7: Main stresses $\sigma_{1,2}$ in step 2.

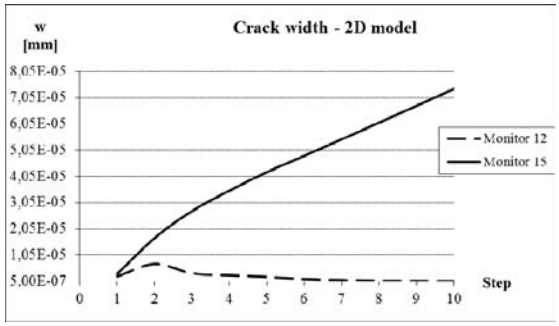

Fig. 8: Cracks development – 2D model.

The crack width at the two monitoring point 15 and 12 in the 2D model is shown in Fig. 8. It can be seen in the figure that the crack width at the monitor point 15 is monotonically increasing, whereas at the monitor point 12 the crack width decreases, after a small initial increase. This is due to repartitioning of the compression and tension stresses in the cross-section.

3.2. 3D model

Once again, the monitoring points were situated in various places of the cross-section or in macroelements. The parameters like cracks width or strains and deformations in directions x, y or z were observed at these points.

The crack formation and development in cross-section in the middle of the girder of both models are shown in Fig. 9. It is possible to observe the consecutive cracks development from the bulk towards the edges like in the 2D model. The majority of cracks with maximum width again occurred just inside. This 3D model also confirms that the cracks are getting connected into edge cracks causing the concrete cover dropping out. The crack pattern is similar to the 2D model (Fig. 6). The crack width development of both models is shown in Fig. 10.

a) Model 1 - without transverse stiffeners *b) Model 2 - with transverse stiffeners*

Fig. 9: Cracks formation and development – cross-section in middle of girder.

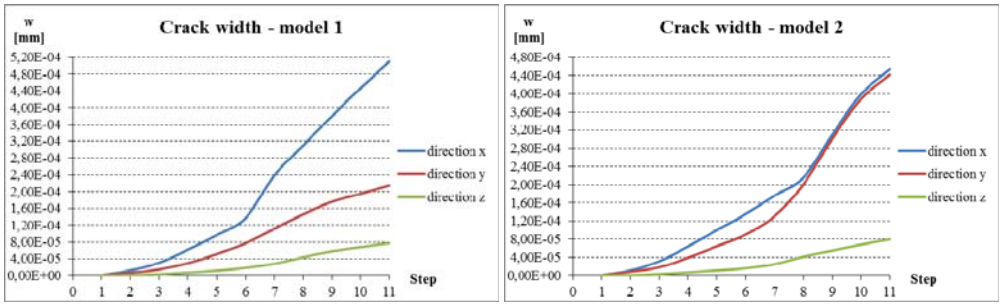

a) Model 1 *b) Model 2*

Fig. 10: Cracks development – 3D models.

4. Conclusions

The results concerning the reinforcement corrosion numerical modeling are presented in the paper. The influence of reinforcement corrosion on the crack formation and propagation were observed in the cross-section of the T-girder. In the paper was shown that already a small corrosion (percentage of corroded reinforcement area) caused the micro crack formation and propagation inside the cross-section near reinforcement.

Small differences between the 2D and 3D models are probably due to repartitioning of the compression and tension stresses, not only in the cross-section (directions y, z - 2D model), but also in the full girder volume (directions x, y, z – 3D models).

From the results of the 3D models (model 1 - without transverse stirrups, model 2 - with transverse stirrups) follows that the stirrups (transfers stiffeners) did not influence greatly the crack pattern (Fig. 9) at cross-section – in both models were achieved approximately the same crack development. However according to expectation, the stirrups did influence the crack width (Fig. 10). Using the stirrups causes the crack width to decrease in longitudinal direction about 11 % (direction x). Nevertheless, the limit crack width was exceeded in both models without using vertical loading induced bending stresses. The crack width in the vertical direction (direction z) is not markedly changed.

The micro cracks are getting connected into edge cracks due to corrosion increase, which can lead to concrete cover dropping out. In that case, the sufficient strength and bonding of concrete cover is not ensured. Consequently, using some types of strengthening (e.g. gluing of FRP materials on concrete cover) is limited or is not possible to apply.

Practically, it means the need to insist on better diagnostics, to check the degree of failure of concrete cover and to control the bonding between concrete and reinforcement. Based on correct diagnostics, it is recommended to decide if the existing concrete cover is better to retain or is it preferable to replace it by the new concrete cover.

Acknowledgement

This work was supported by Research Project no. 1/0517/12 of Slovak Grant Agency.

References

Broomfield, J.P. (1997) *Corrosion of steel in concrete. Understanding, investigation and repair.* E&FN Spon, London, 240 p.

Koteš, P. & Brodňan, M. & Šlopková, K. (2008) Simulation of corrosion of reinforcement in reinforced concrete, in: *Proceedings of the 2nd International Conference on Concrete Modeling*, Delft, The Nederlands, pp. 761-766.

Koteš, P. & Brodňan, M. & Šlopková, K. & Kotula, P. (2010) Numerical modelling of reinforcement corrosion in reinforced concrete, *Journal "Ochrona przed korozją"*, volume 53, number 6, ISSN 0473-7733, pp. 307-309.

Koteš, P. & Vičan, J. (2006) Experiences with Reliability-based Evaluation of Existing Concrete Bridges in Slovakia, in: *Proceedings of the abstracts The Second International fib Congress and Proceedings of the papers on CD (ID 16-6)*, Naples, Italy, pp. 566-567.

Kala, Z. & Omishore, A. (2009) Applications of Advanced Variance-based Methods in Civil Engineering, in: *Proc. of the Lightweight Structures in civil Engineering*, Warsaw (Poland), pp.68–73.

18th International Conference
ENGINEERING MECHANICS 2012
Svratka, Czech Republic, May 14 – 17, 2012

pp. 681–690
Paper #268

PARTIAL SAFETY FACTORS FOR EVALUATION OF EXISTING BRIDGES ACCORDING TO EUROCODES

P. Koteš [*], J. Vičan [**]

Abstract: *In the paper, the partial safety factors for materials and load effects recommended according to Eurocode for bridge members subjected to bending are presented. In the frame of research activities of the Department of structures and bridges, the modified reliability levels for existing bridge evaluation were derived. Firstly, these levels were used for determining partial safety factors for material. Closely, the partial safety factor of steel and concrete were determined depending on the age of the bridge and on the remaining lifetime of the bridge. New modified reliability levels for evaluation of existing bridges are also affected the partial safety factors of loads.*

Keywords: ***Bridge, existing structure, evaluation, partial safety factors.***

1. Introduction

Bridges are considered to be an inseparable and strategically very important part of the transportation infrastructure and they should have such parameters not to become the limiting component of the communication capacity and traffic reliability. In the past, bridge maintenance, repair and rehabilitation activities were performed on an "as-needed" basis. This changed in the late 1960s, when a series of bridge failures focused public attention on the deterioration of existing bridges, motivating governments to initiate standardized bridge inspection and evaluation procedures. Data collected through these inspection activities formed the basis for future computer based bridge management systems (BMS) (Lauridsen et al., 1998; Thompson et al., 1998; Vičan et al., 1998).

The evaluation of existing concrete bridge structures is the most important process in the global Bridge Management System (BMS) because of providing the basic information about existing bridges required from the viewpoint of decision making process related to the optimal bridge maintenance and rehabilitation strategy. Therefore, the existing bridge evaluation should be made not only as the result of periodic inspection on the base of subjective evaluation of actual bridge condition but from the viewpoint of the bridge reliability i.e. from the viewpoint how the actual bridge condition affects the bridge reliability for remaining bridge lifetime. Thus, the bridge evaluation becomes relevant when the significant deviations from the project descriptions are found, when some relevant damage is observed or when the bridge lifetime has gone beyond planned one, etc.

The paper deals with the determination of the modified reliability levels for evaluation of existing concrete bridges. The theoretical approach taking into account the conditional probability was used. The modified levels depend on the age of the bridge and on the planned remaining lifetime and, moreover, influence the partial safety factors of materials and loads.

2. Reliability-based evaluation of existing concrete bridges

The reliability level for newly designed bridges for whole lifetime T_d ($T_d = 100$ years), which is represented by failure probability $P_{f,d}$ ($P_{f,d} = 7.2 \cdot 10^{-5}$) or by reliability index β_d ($\beta_d = 3.8$), is given in a Eurocode. However, the reliability level for evaluation of existing bridges for remaining lifetime t_r is not given in the Eurocodes.

[*] Ing. Peter Koteš, Ph.D.: Department of Structures and Bridges, Civil Engineering Faculty, University of Žilina, Univerzitná 8215/1; 010 26, Žilina; SK, e-mail: kotes@fstav.uniza.sk

[**] Prof. Ing. Josef Vičan, Ph.D.: Department of Structures and Bridges, Civil Engineering Faculty, University of Žilina, Univerzitná 8215/1; 010 26, Žilina; SK, e-mail: vican@fstav.uniza.sk

Generally, the process of the existing bridge evaluation has various differences in comparison with the reliability assessment of newly designed bridge. In the case of the existing bridge structure, new information concerning the actual bridge condition is available which is unknown in the design phase. The certificates of material properties, measurements of actual bridge geometry, collection load data, results of proof load testing and especially results of the periodic inspections regularly performed within lifetime of the observed bridge are the major resources of this information. The extra information unknown in the design phase can be used not only for verification of the correct bridge performance or for detection of possible mistakes concerning the computational model assumptions or calculations but also helps to reduce some uncertainty related to the bridge member resistance and load parameters entering the evaluation process.

In abroad, the problem of evaluation of existing bridges was solved in frame of the developing Bridge Management Systems based on computer-aided expert systems. The reliability-based evaluation of existing bridges is preferred in the works of American (Nowak & Gruni, 1994; Frangopol & Estes, 1997) and Canadian (Allen, 1992; Bartlett et al., 1992) authors. Theoretical outputs of these scientific studies create the background of the contemporary Canadian (Reel & Agorwal, 1997) and Ontario (OHBDC, 1991) standards for the evaluation of existing road bridges and determining their load carrying capacities in the form of Live Load Rating Factors (LLRF). Both standards are based on the probability model of the structural reliability verification with the differentiated reliability level depending on the bridge component importance in the whole bridge structure.

In the area of Europe, several authors and institutions have focused their research activities on this problem last years (Wong ar al., 2005; Draft BD 79, 2000). A publication of the Joint Committee on Structural Safety (JCSS) (Diamantidis, 2001) is being developed. This publication contains some practical and operational recommendations and rules for the assessment of existing structures.

3. Reliability analysis

From the bridge reliability view point, the reduction of the load and resistance parameter uncertainties decreases failure probability of existing bridge structure that means the possibility to admit lower reliability level for evaluation of existing bridge than it is in the case of newly designed one.

In the theoretical analysis, it is assumed that the bridge structural element was designed for total lifetime T with corresponding reliability index β given by formula

$$\beta = \left(m_R - m_S\right) \Big/ \sqrt{s_R^2 + s_S^2} \tag{1}$$

where m_R, s_R are the basic parameters of the normally distributed random variable resistance R of a bridge structural elements,

m_S, s_S are the basic parameters of the normally distributed random variable load effects S of the same bridge element.

The bridge inspection was performed at the time $t_{insp} < T$ during which the observed structural element was found to be without relevant failure due to overcrossing its limit states. This positive information expresses that resistance R of the observed structural element satisfies the following relation

$$R > max\ (S_i) \quad for\ \ i = 1\ \ldots\ldots\ N(t). \tag{2}$$

The load effects S_1, S_2 …. S_n are mutually independent normally distributed and occur in succession but randomly in time and N(t) means the random number of them within time interval (0, t). N(t) is considered as the random variable having Poisson distribution with parameter λ(t) (intensity of load effects) which is constant or linearly dependent on time t according to relation

$$\lambda(t) = \lambda_0 + \left(\lambda_{insp} - \lambda_0\right) \cdot t \Big/ t_{insp}\ , \tag{3}$$

where λ_o is the value of parameter λ at the time t = 0,

$\lambda_{t,insp}$ is the value of parameter λ at the time t = t_{insp} of the periodic inspection.

If the following formula is considered

$$L(t) = \int_0^t \lambda(\tau) d\tau \,, \tag{4}$$

then time occurrence of individual sets of load effects S_i satisfies the following dependence

$$P(N(t) = n) = L(t)^n \cdot e^{-L(t)} / n!, \; for \; n = 0,1 \ldots k. \tag{5}$$

If the parameter λ(t) is constant in time, the following relation may be obtained using the relation (3)

$$L(t) = \lambda \cdot t \,, \tag{6}$$

and if the parameter is linearly dependent on time, using substitution (3) to (4) is obtained

$$L(t) = \lambda_0 \cdot t + \left(\left(\lambda_{insp} - \lambda_0 \right) \cdot t^2 \right) / \left(2 \cdot t_{insp} \right). \tag{7}$$

As has been shown in Ditlevsen & Madsen (1996), the updated failure probability P_{fu} of the observed structural element at the time period (t_{insp}, T) should be obtained by means of the conditional probability according to the formulae

$$P_{fu} = \left(P_f(T) - P_f(t_{insp}) \right) / \left(1 - P_f(t_{insp}) \right). \tag{8}$$

The corresponding updated reliability index β_u of the observed structural element for the remaining time period (t_{insp}, T = T_d) can be determined in accordance with

$$\beta_u = -\Phi^{-1}\left(P_{fu} \right), \tag{9}$$

where Φ^{-1} is the inverse distribution function of standardized normal distribution N(0,1).

The failure probability $P_f(T)$, $P_f(t_{insp})$ can be obtained for normally distributed bridge element resistance R and normally distributed load effects S_i using the following formulae for complete probability (Ditlevsen & Madsen, 1996)

$$P_f(T) = P\left[\max(S_i)(i = 1 \ldots N(T) > \mathrm{R} \right] = \int_{-\infty}^{\infty} \left(1 - e^{-L(T)\Phi\left(-\frac{x - m_S}{s_S} \right)} \right) \cdot \varphi\left(\frac{x - m_R}{s_R} \right) \cdot \frac{1}{s_R} dx \,, \tag{10}$$

where φ is the probability density function of standardized normal distribution N(0,1).

Using the information (2), the updated reliability index β_u can be greater than designed index β_d. Next, we are able to solve back the adjusted target failure probability P_{ft} (target reliability index β_t) for which the element should be evaluated for remaining lifetime (T-t_{insp}) so that we can achieve the required value of the target failure probability P_{ft} with minimal one inspection. The change of the updated reliability index β_u and the target reliability index β_t in time is shown in Fig. 1 in dependence on time of inspection and on the values of the parameter λ. From the Fig. 1 can be seen that the updated reliability index β_u is increasing in time (markedly in the end of lifetime). From this reason, the target reliability index β_t is decreasing in time.

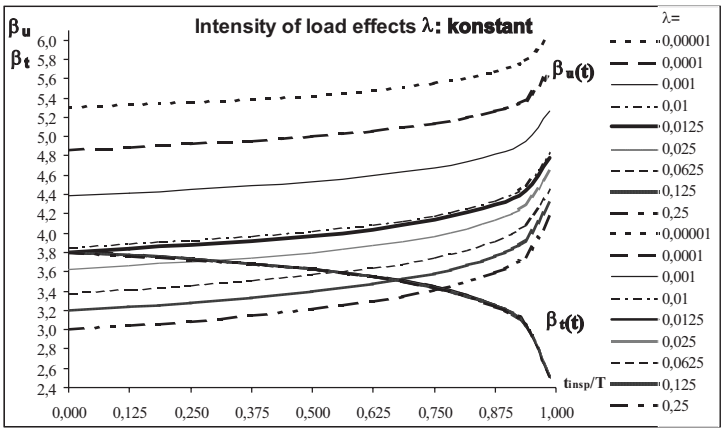

Fig. 1: Updated reliability index β_u and the target reliability index β_t in dependence on inspection time.

The reliability level given by failure probability P_{ft} or by reliability index β_t shown in Fig. 1 depends just on the full remaining lifetime ($T - t_{insp}$) – from time of inspection t_{insp} to the end of the lifetime T. But practically, it is usually to evaluate the structure for shortening lifetime – us selected time interval. For example, it can be time between two inspections or if the structure does not satisfy for full remaining lifetime ($T- t_{insp}$). In this case, the structure can be evaluated on shortening remaining lifetime – planned remaining lifetime t_r.

The theoretical approach is the same as above mentioned. But, the lifetime T of the member should be shortening to determine the required reliability of observed member for planned interval t_r. It means that the whole lifetime is not T = 100 years, but it is equal to sum $t_{insp}+t_r$.

This approach is important for bridge owner, because it gives to owner ability to save the funds. The results are shown in Fig. 2.

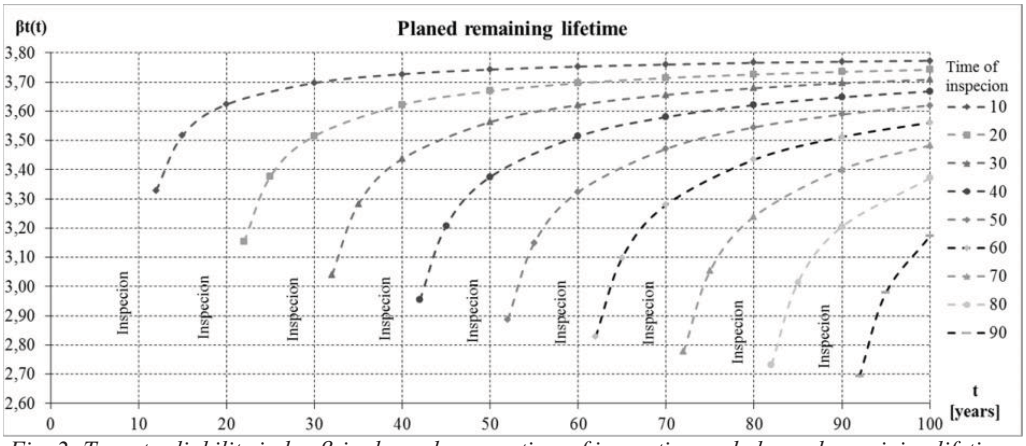

Fig. 2: Target reliability index β_t in dependence on time of inspection and planned remaining lifetime.

4. Reliability levels

The obtained reliability levels depend on the age of the bridge and on the planned remaining lifetime. The results of the reliability levels for bridge element not respecting the degradation due to regularly performed maintenance are shown in Tab. 1.

Tab. 1: Reliability levels for existing bridge evaluation not respecting degradation.

Remaining lifetime	The age of the bridge [years]									
	10. years		20. years		30. years		40. years		50. years	
[years]	β_t	P_{ft}	β_t	P_{ft}	β_t	P_{ft}	β_t	P_{ft}	β_t	P_{ft}
2	3.328	$4.38\cdot10^{-4}$	3.153	$8.09\cdot10^{-4}$	3.039	$1.19\cdot10^{-3}$	2.954	$1.57\cdot10^{-3}$	2.886	$1.96\cdot10^{-3}$
5	3.517	$2.19\cdot10^{-4}$	3.377	$3.67\cdot10^{-4}$	3.282	$5.16\cdot10^{-4}$	3.208	$6.68\cdot10^{-4}$	3.149	$8.21\cdot10^{-4}$
10	3.623	$1.46\cdot10^{-4}$	3.515	$2.20\cdot10^{-4}$	3.437	$2.94\cdot10^{-4}$	3.375	$3.70\cdot10^{-4}$	3.323	$4.46\cdot10^{-4}$
20	3.697	$1.09\cdot10^{-4}$	3.622	$1.46\cdot10^{-4}$	3.563	$1.83\cdot10^{-4}$	3.514	$2.21\cdot10^{-4}$	3.471	$2.59\cdot10^{-4}$
30	3.727	$9.70\cdot10^{-5}$	3.669	$1.22\cdot10^{-4}$	3.621	$1.47\cdot10^{-4}$	3.58	$1.72\cdot10^{-4}$	3.545	$1.97\cdot10^{-4}$
40	3.743	$9.08\cdot10^{-5}$	3.696	$1.09\cdot10^{-4}$	3.656	$1.28\cdot10^{-4}$	3.621	$1.47\cdot10^{-4}$	3.589	$1.66\cdot10^{-4}$
50	3.753	$8.72\cdot10^{-5}$	3.714	$1.02\cdot10^{-4}$	3.679	$1.17\cdot10^{-4}$	3.648	$1.32\cdot10^{-4}$	3.62	$1.47\cdot10^{-4}$
60	3.76	$8.48\cdot10^{-5}$	3.726	$9.72\cdot10^{-5}$	3.696	$1.10\cdot10^{-4}$	3.668	$1.22\cdot10^{-4}$		
70	3.766	$8.31\cdot10^{-5}$	3.735	$9.38\cdot10^{-5}$	3.708	$1.05\cdot10^{-4}$				
80	3.77	$8.18\cdot10^{-5}$	3.742	$9.12\cdot10^{-5}$						
90	3.773	$8.07\cdot10^{-5}$								

Remaining lifetime	The age of the bridge [years]							
	60. years		70. years		80. years		90. years	
[years]	β_t	P_{ft}	β_t	P_{ft}	β_t	P_{ft}	β_t	P_{ft}
2	2.828	$2.35\cdot10^{-3}$	2.777	$2.75\cdot10^{-3}$	2.732	$3.15\cdot10^{-3}$	2.692	$3.56\cdot10^{-3}$
5	3.098	$9.75\cdot10^{-4}$	3.053	$1.13\cdot10^{-3}$	3.014	$1.29\cdot10^{-3}$	2.978	$1.45\cdot10^{-3}$
10	3.279	$5.22\cdot10^{-4}$	3.239	$6.00\cdot10^{-4}$	3.204	$6.78\cdot10^{-4}$	3.172	$7.57\cdot10^{-4}$
20	3.434	$2.97\cdot10^{-4}$	3.401	$3.35\cdot10^{-4}$	3.371	$3.74\cdot10^{-4}$		
30	3.512	$2.22\cdot10^{-4}$	3.483	$2.48\cdot10^{-4}$				
40	3.561	$1.85\cdot10^{-4}$						

5. Partial safety factors

New modified reliability levels for evaluation of existing bridges given in Tab. 1 affect the values of partial safety factors for material resistance and for loads, also. In the practical design, the reliability levels are transformed to the design values of the material resistance and loads. In the partial safety factors method, the design values of material resistance and loads are determined by means of characteristic values and appropriate partial safety factors. Loads and resistance are treated as random variables and are described by bias factors λ (expressing ratio of mean value to nominal value) and by coefficient of variation v.

5.1. Partial safety factors for material

Considering normally distributed random variable resistance, the partial safety factors of concrete and reinforcement (EN 1991-1-1, 2002) are given by formulae

$$\gamma_M = \frac{R_k}{R_d} = \frac{1-\beta_k \cdot v_R}{1-\alpha_R \cdot \beta_t \cdot v_R}, \tag{11}$$

where R_k is the characteristic value of the material resistance,

R_d is the design value of the material resistance,

$\alpha_R = 0.8$ is the sensitivity coefficient,

v_R is the coefficient of variation of material resistance,

$\beta_k = 1.645$ is the reliability index corresponding to probability 5 % (valid for characteristic values),

β_t is the recommended target reliability index depending on the age of the bridge and on the planned remaining lifetime (Tab. 1).

To determine values of partial safety factors, the basic statistical characteristics shall be known, especially coefficient of variation v_R. In the case of partial safety factor γ_c for concrete, the value of variation coefficient v_R was backward calculated from formulae (11) for $\gamma_c = 1.50$ (for new designed bridges) and reliability index $\beta_t = 3.80$. So, the value of coefficients of variation $v_R = 0.172$ was used for determining the partial safety factors of concrete.

Using mentioned parameters, new values of partial safety factors for concrete were determined considering the planned remaining lifetime and a bridge age. The determined values are shown in Tab. 2.

Tab. 2: The partial safety factor γc for concrete strength valid for existing bridge evaluation

Planned remaining lifetime t_r [years]	γ_c - age of bridge [years]		
	< 60 years	60-80 years	> 80 years
< 2	1.21	1.20	1.15
2 – 10	1.35	1.31	1.30
10 – 20	1.40	1.36	1.34
20 – 40	1.43	1.41	
> 40	1.45		

In the case of the partial safety factor γ_S for reinforcement, it is possible to use the value of $v_R = 0.081$, which is corresponding to partial safety factor $\gamma_s = 1.15$ for reinforcement (for new designed bridges) and reliability index $\beta_t = 3.80$. The determined values of the partial safety factors for reinforcement are shown in Tab. 3. For the serviceability limit state were determined values $\gamma_c = \gamma_c = 1.0$ and $\gamma_s = 1.0$.

Tab. 3: The partial safety factors γs for reinforcement valid for bridge existing evaluation

Planned remaining lifetime t_r	γ_s - age of bridge [years]		
[years]	< 60 years	60-80 years	> 80 years
< 2	1.10	1.10	1.06
2 – 10	1.11	1.11	1.10
10 – 20	1.13	1.12	1.11
20 – 40	1.14	1.13	
> 40	1.14		

5.2. Partial safety factors for loads

The load of the bridges is given in the code STN EN 1991-2 (2006). The load models are an important part of evaluation. The basic load combination for road bridges is a simultaneous occurrence of permanent load and variable load. The code STN EN 1991-2 (2006) specifies the characteristic loads, partial safety factors for newly designed bridges and the load combinations. However, the calculation of load partial safety factors for evaluation of existing bridges requires knowledge of the statistical models of singular loads, in particular distribution function, density function, standard deviation, coefficient of variation, time variation and correlation with other load components.

Permanent loads

The partial safety factors of permanent loads respecting the recommended modified reliability levels (expressed by β_t) given in Tab. 1 considering normally distributed random variables were established using the formulae

$$\gamma_{G,i} = \gamma_{Sd} \cdot \frac{S_d}{S_k} = \gamma_{Sd} \cdot \frac{\mu_{G,i} \cdot (1 + \alpha_S \cdot \beta_t \cdot v_G)}{\mu_{G,i}} = \gamma_{Sd} \cdot (1 + \alpha_S \cdot \beta_t \cdot v_{G,i}) , \qquad (12)$$

where S_k is the characteristic value of load,

S_d is the design value of load,

$\alpha_S = 0.7$ is the sensitivity coefficient of loads,

$\gamma_{Sd} = 1.05$ is the partial safety factor of model uncertainties,

$v_{G,i}$ are the coefficients of variation of single permanent loads.

According to standard STN EN 1990/A1/NA (2007), the permanent loads are divided into cast-in-place made produces with recommended value of partial safety factor $\gamma_G = 1.35$ (for new designed bridges) and factory-made produces and transported to construction with recommended value of partial safety factor $\gamma_G = 1.25$ (for new designed bridges). The value of variation coefficient v_R is equal to $v_G = 0.107$ for cast-in-place made produces and $v_G = 0.072$ for factory-made produces and transported to construction.

The new recommended partial safety factors of permanent loads depending on the age of bridges and on planned remaining lifetime are shown in Tab. 4 and Tab. 5.

Tab. 4: The partial safety factors of permanent loads - cast-in-place made produces

Planned remaining lifetime	$\gamma_{G,i}$ - age of bridge [years]		
t_r [years]	< 60 years	60-80 years	> 80 years
< 2	1.29	1.28	1.27
2 – 10	1.32	1.31	1.31
10 – 20	1.33	1.32	1.32
20 – 40	1.34	1.33	
> 40	1.34		

Tab. 5: The partial safety factors of permanent loads - factory-made produces and transported to construction

Planned remaining lifetime	$\gamma_{G,i}$ - age of bridge [years]		
t_r [years]	< 60 years	60-80 years	> 80 years
< 2	1.21	1.20	1.20
2 – 10	1.23	1.23	1.22
10 – 20	1.24	1.24	1.23
20 – 40	1.25	1.24	
> 40	1.25		

Variable loads

The variable loads are random variables with Gumble distribution according to STN EN 1990 (2009). The partial safety factors of variable loads respecting the recommended modified reliability levels (expressed by β_t) given in Tab. 1 considering Gumble distributed random variables were also established using the formulae

$$\gamma_Q = \gamma_{Sd} \cdot \frac{S_s}{S_k} = \gamma_{Sd} \cdot \frac{\mu_Q \cdot \left\{1 - v_Q[0,449 + 0,778 \cdot ln(-ln\Phi(\alpha_S \cdot \beta_t)]\right\}}{\mu_Q \left\{1 - v_Q[0,449 + 0,778 \cdot \ln(-\ln(0,95)]\right\}}, \qquad (13)$$

where S_k is the characteristic value of load,

S_d is the design value of load,

$\alpha_S = 0.7$ is the sensitivity coefficient of loads,

$\gamma_{Sd} = 1.05$ is the partial safety factor of model uncertainties,

v_Q is the coefficients of variation of variable load.

The variable loads are different to variable loads of road bridges and variable loads of railway bridges. In the case of road bridges according to standard STN EN 1990/A1/NA (2007), the partial safety factor is equal to $\gamma_Q = 1.35$ and in the case of road bridges, the partial safety factor is equal to $\gamma_Q = 1.40$ (for new designed bridges). The value of variation coefficient v_Q is equal to $v_Q = 0.1944$ for loads on road bridges and $v_Q = 0.2414$ for loads on railway bridges considering the formulae (13).

The new recommended partial safety factors of variable loads depending on the age of bridges and on planned remaining lifetime are shown in Tab. 6 and Tab. 7.

Tab. 6: The partial safety factors of variable loads on road bridges

Planned remaining lifetime	$\gamma_{Q,i}$ - age of bridge [years]		
t_r [years]	< 60 years	60-80 years	> 80 years
< 2	1.17	1.14	1.12
2 – 10	1.26	1.23	1.22
10 – 20	1.29	1.27	1.26
20 – 40	1.31	1.30	
> 40	1.32		

Tab. 7: The partial safety factors of variable loads on railway bridges

Planned remaining lifetime	$\gamma_{Q,i}$ - age of bridge [years]		
t_r [years]	< 60 years	60-80 years	> 80 years
< 2	1.19	1.16	1.14
2 – 10	1.29	1.27	1.25
10 – 20	1.33	1.30	1.29
20 – 40	1.35	1.34	
> 40	1.37		

6. Conclusions

The paper presents the results of the research concerning the reliability levels for evaluation of existing bridges. The modified reliability levels for evaluation were determined and they depend on the bridge age and on planned remaining lifetime. The values of the levels are valid for members subjected to bending. Theoretical reliability basis for modification of partial safety factor method due to allowing for the major differences between existing bridge evaluation and design of the new ones is presented.

In final consequence, the lower reliability levels reflect into the partial safety factors of materials and loads. In the paper are shown determined partial safety factors for concrete γ_c, partial safety factor for reinforcement γ_s and partial safety factors for permanent loads $\gamma_{G,i}$ and variable loads $\gamma_{Q,i}$.

Acknowledgement

This work was supported by Research Project no. 1/0364/12 supported by Slovak Grant Agency.

References

Allen, D.E. (1992) Canadian Highway Bridge Evaluation: Reliability Index. *Canadian Journal of Civil Engineering.* Volume 19, pp. 987-991.

Bartlett, F.M. & Buckland, P.G. & Kennedy, D.J. (1992) Canadian Highway Bridge Evaluation: Derivation of Clause 12 of CAN/CSA – 56 – 88. *Canadian Journal of Civil Engineering.* pp. 1007-1016.

Diamantidis, D. (2001) *Probabilistic Assessment of Existing Structures*. Rilem Publications S.A.R.L. Cachan Cedex.

Ditlevsen, O. & Madsen, H.O. (1996) *Structural Reliability Methods*. John Wiley and sons.

Draft BD 79 (2000) *Level 4 and Level 5 – Methods of Assessment for Bridges*. WS Atkins. London.

EN 1991-1-1 (2002) Eurocode 1: *Action on structures – Part 1-1: General actions – Densities, self-weight, imposed loads for buildings.* CEN Brussele.

Frangopol, D.M. & Estes, A.C. (1997) System Reliability for Condition Evaluation of Bridges. In: *IABSE Workshop "Evaluation of Existing Steel and Composite Bridges"*. Lausanne, pp.47-56.

Lauridsen, J. & Bjerrum, J. & Andersen, N.H. & Lassen, B. (1998) Creating a Bridge Management System. *Structural Engineering International.* Volume 3:pp. 216-220.

Nowak, A.S. & Gruni, H.N. (1994) Calibration of the Ontario Highway Bridge Code 1991 Edition. Canadian *Journal of Civil Engineering.* Volume 21, pp.25-35.

OHBDC (1991) *Ontario Highway Bridge Design Code.* 3rd edition. Ministry of Transportation. Downsview. Ontario,

Reel, R.S. & Agorwal, A.C. (1997) Reliability-Based Section of the Draft Canadian Highway Bridge Design Code. In: *IABSE workshop "Evaluation of Existing Steel and Composite Bridges"*. Lausanne, pp. 17-24.

STN EN 1990 (2009) *Basis of structural design.* SUTN, p. 86.

STN EN 1990/A1 (2006) *Basis of structural design. Amendment A1.* SUTN, p. 28.

STN EN 1990/A1/NA (2007) *Basis of structural design. Amendment A1. National annex.* SUTN, p. 8.

STN EN 1991-2 (2006) *Action on structures. Part 2: Traffic loads on bridges.* SUTN, p. 136.

STN EN 1991-2/NA (2007) *Action on structures. Part 2: Traffic loads on bridges. National annex* SUTN, p. 16.

Thompson, P.D. & Small, E.P. & Johnson, M. & Marshall, A.D. (1998) The Pontis Bridge Management System. *Structural Engineering International.* Volume 4, pp.303-308.

Vičan, J. at all. (1998) *Bridge Management System – Methodology of the Existing Road Bridge Evaluation.* Final Report for Slovak Road Administration. University of Žilina, (in Slovak).

Wong, S.M. & Hobbs, R.E. & Onof, C. (2005) Element and System Risk Considerations in Highway Bridge Assessment. In: *Proc. of 4th International Conference on Current and Future Trends in "Bridge Design. Construction and Maintenance".* Kuala Lumpu,

18th International Conference
ENGINEERING MECHANICS 2012
Svratka, Czech Republic, May 14 – 17, 2012

pp. 691–701
Paper #218

COMPARATIVE STUDY ON NUMERICAL AND ANALYTICAL ASSESSMENT OF ELASTIC PROPERTIES OF METAL FOAMS

P. Koudelka, O. Jiroušek, T. Doktor, P. Zlámal, T. Fíla *

Abstract: *Recently, titanium metal foams are being considered as a suitable replacement for substituting trabecular bone microstructure especially for their similar pore distribution. The most common methods for determination of compressive effective elastic properties of such materials involve different approaches based on finite element analysis (FEA) of their microstructure. The internal geometry is usually modeled by two different methods - directly on the basis of a series of CT scans or using one of discretization schemes. However, all these techniques require highly specialized hardware, software and significant amount of computational time. In this paper, the effective elastic properties of the metal foam are instead obtained by analytical modulus-porosity relations and results are compared with previous FE based analysis.*

Keywords: ***metal foams, modulus-porosity relations, finite element method, compressive behavior, effective elastic properties***

1. Introduction

Metal foams are highly porous materials that possess unique combination of mechanical, acoustic and electromagnetic properties. At very low specific weights and thus high specific stiffnesses, they are able to absorb significant amount of deformation energy while guaranteeing other properties such as high fire and heat resistance, noise attenuation and shielding of electromagnetic devices (Banhart, 2001). Combination of these characteristics attracts application of metal foams in many engineering fields from interior design and equipment to civil engineering and vehicle construction.

The recent development of many cost-effective production techniques increases their potential for substitution of legacy engineering practices and/or substitution of the most commonly used materials. Particularly, metal foams will be potentially able to outperform certain types of polymer foams and honeycomb structures in light of mechanical and environmental properties respectively.

Furthermore, open-cell metal foams manufactured from biocompatible materials (i.e. pure Titanium, Ti-Ni alloys, etc.) successfully mimic natural characteristics of human bones. Usage of titanium and its alloys as fusion implants is one of the most important developments in the field of biomechanics and biomaterials. Such structural implants offer high corrosion resistance, good mechanical properties and exceptional biocompatibility among other biomaterials. Open-pore structure with mean pore dimensions of 200 – 500 μm is susceptible of transport of body fluids and also the ingrowth of new bone tissue. By modifying the morphology, amount, size and orientation of pores, mechanical characteristics can be adjusted to particular bone tissue, which gives the opportunity to assess optimal characteristics compatible with the bone. This is the key parameter in bone implant applications because it prevents the stress-shielding problem existing in the implantation of bulk materials due to the mismatch of mechanical properties.

During the last decades, there has been much effort dedicated to understanding of the porosity dependence of the effective elastic constants of cellular metals. Numerous relations derived from various constitutive laws have been developed as a result of extensive theoretical and experimental work. The most of the relationships give the variation of elastic constants in terms of porosity. However, many of the suggested laws contain fitting parameters whose mechanical and physical explanation is either

* Bc. Petr Koudelka, Doc. Ing. Ondřej Jiroušek, PhD., Ing. Tomáš Doktor, Ing. Petr Zlámal, Bc. Tomáš Fíla: Institute of Theoretical and Applied Mechanics AS CR, Prosecká 76; 190 00, Praha 9; CZ, e-mail: [koudelkap,jirousek,doktor,zlamal,fila]@itam.cas.cz

unclear or values of the parameters do not correspond to microstructural characteristics of the material. This indicates that the derivation of the microstructure-property relationships for porous metals (with both open- and closed-cell pores) is still an open issue and in many cases other parameters (i.e. pore shape and distribution) have to be taken also into account.

In this paper, effective elastic properties in compression predicted by various models for modulus-porosity relations are compared to experimental and numerical results of compressive behavior of Alporas aluminium closed-cell foam and Optinium open-cell biocompatible titanium foam. Experimental values of elastic modulus and porosity of Alporas foam were assessed on the basis of quasi static compressional loading and weighting of the sample respectively.

2. Materials

2.1. Alporas

Alporas® is a closed-cell aluminium foam developed in late 80's and produced by Japan manufacturer Shinko Wire Co., Ltd. Structure of this material is typically constituted by large inner pores of polyhedral shape with average size 4.5 mm. Cell walls that create complex random inner structure are typically $100\,\mu$m thick with overall porosity approximately $90\,\%$ (Miyoshi, 1998), although it can be manufactured at different levels of porosity saying that polyhedron cells become spherical at porosities under $70\,\%$. Foam is manufactured using special unnormalized alloy containing $97\,\%$ of aluminium, $1.5\,\%$ of calcium and $1.5\,\%$ of titanium (Miyoshi, 1998). Because material properties of this alloy are not provided by the manufacturer, the material models typically use mechanical properties of $98\,\%$ aluminium as stated in (Konstantinidis, 2005).

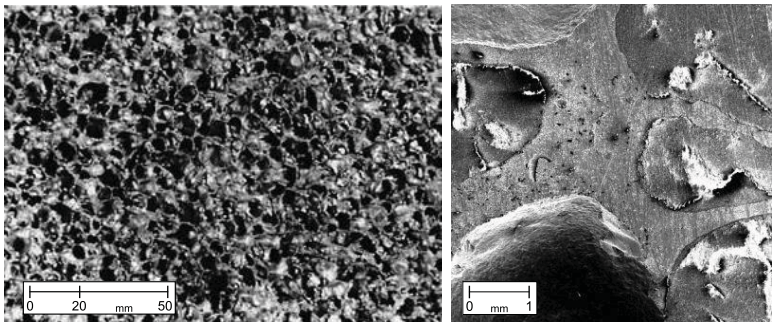

Fig. 1: Alporas - macroscopic structure (left), surface of the cell wall captured using SEM - specimen prepared for nanoindentation experiment (right)

2.2. Optinium

Optinium© foam is manufactured using commercial grade CP4 titanium powder which is transformed to open-pore structure using a propellant (space holder technique, see Singh (2009b)). Final porous structure reaches effective porosity of $60-65\,\%$ and as has been shown in a permeability study of these materials (Singh, 2009a), the pore and interconnect sizes are almost independent of relative density, but foam strut thickness decreases with increasing porosity. Implants manufactured from this material are ideal for their bone integration and ongrowth potential. The combination of bone-like mechanical properties with the interconnecting porosity leads to excellent biological fixation, a method that has already been proven in endoprosthetics. Main usage of the implants is the surgical treatment of degenerate discs of the lumbar spine and restoration of initial height of the intervertebral disc space.

3. Finite element analysis

Determination of mechanical characteristics of cellular materials using finite element (FE) analysis is strongly dependent on microstructure modeling scheme. The internal structure can be generated directly

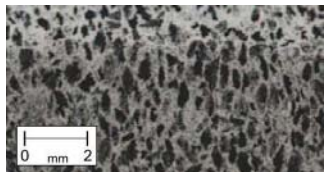

Fig. 2: Macroscopic structure of Optinium

from samples of the real material or using one of several discretization methods. Direct modeling of the internal structure is based on computed-tomography scanning of specimens. This approach facilitates FE representation of the internal structure including all of its irregularities and defects (Vavřík, 2011). Simultaneously, material properties at the level of the individual cells can be assessed by nanoindentation with high reliability and reproducibility (Jiroušek, 2009; Králík, 2011); moreover Digital Volumetric Correlation (DVC) method can be used to identify the three-dimensional strain field in the loaded microstructure (Jiroušek, 2011). Instead of modeling the complex internal structure of metal foam directly, a unit cell approach is often used. Internal structure of cellular materials can be then represented by miscellaneous two- and three-dimensional models according to the various cellular forms. In the preceding FE study (Koudelka, 2011) the beam-only discretization with cubic cells (Fig. 3) was used intentionally to investigate its suitability for modeling of closed-cell foams and trabecular bones. It has been shown that this discretization scheme, originally developed for modeling of open-cell foams, is suitable for also assessment of elastic characteristics of Alporas closed-cell foam (Fig. 4). Declared elastic modulus of Alporas (in the range from 0.4 GPa to 1.0 GPa) was acquired with model relative density in interval $0.08 - 0.13$, which is consistent with real mechanical characteristics while significantly reducing amount of computational time.

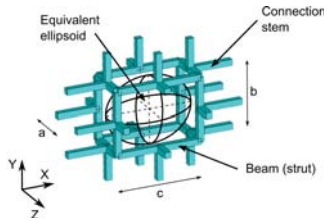

Fig. 3: Gibson-Ashby's cell with corresponding equivalent ellipsoid

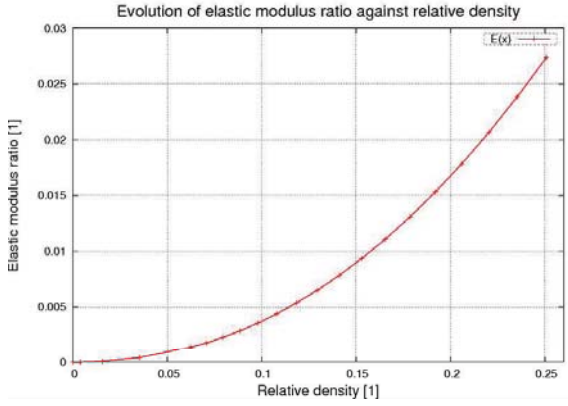

Fig. 4: Evolution of relative elastic modulus plotted against relative density - FE simulations of Alporas

4. Effective elastic moduli of porous metals

From the view of micromechanics, cellular metals can be considered as a special case of multiphase mixtures or materials with microstructure. The effective elastic properties can be predicted when mechanical characteristics of material components and microstructural details are known. Microstructural information of the lowest order involve volume fractions of constituent phase whereas higher order information stands for pore size, shape and orientation including their statistical characteristics (Markov, 2000; Milton, 2003; Nemat-Nasser, 1999; Torquato, 2002).

Effective elastic modulus E_{e} can be then considered as a function of phase moduli E_{i} and the lowest-order only (porosity ϕ_{i}) microstructural information (Pabst, 2004a):

$$E_{\mathrm{e}} = f(E_{\mathrm{i}}, \phi_{\mathrm{i}}) \tag{1}$$

where $E_{\mathrm{i}},\ i \in (0, 1, \ldots, n)$ are the phase moduli of all n constituent phases and ϕ_{i} are the volume fractions of the n phases.

For porous metals where the void phase exhibits approximately zero mechanical properties one can assume that the void phase is redundant and therefore write the following basic assumptions: $\phi_1 \equiv 1-\phi$, $\phi_2 \equiv \phi$ and for void phase with zero elastic modulus: $E_2 = 0,\ E_1 \equiv E_0$.

This provides for definition of Hashin-Shtrikman (HS) bound for the effective elastic modulus as:

$$E_{\mathrm{HS}} = \frac{9K_{\mathrm{HS}}G_{\mathrm{HS}}}{3K_{\mathrm{HS}} + G_{\mathrm{HS}}} \tag{2}$$

where G_{HS} ans K_{HS} are HS bounds for the shear and bulk modulus respectively (Hashin, 1963). In general, HS bounds are valid for microstructure called Hashin assemblage, which consists of polydisperse composite spheres containing concentric spherical inclusions. In the case of macroscopically isotropic porous material, Hashin assemblage would be approximated by a material containing hollow spheres with an infinitely wide size distribution.

In the case of porous materials relative elastic modulus is the most frequently defined as:

$$E_{\mathrm{r}} = \frac{E_{\mathrm{e}}}{E_0} \tag{3}$$

where E_{e} is the effective elastic modulus and E_0 is the elastic modulus of matrix phase or solid skeleton phase (for closed-cell and open-cell materials respectively). Linear dependence between the relative elastic moduli and porosity can be considered at very low porosities:

$$E_{\mathrm{r}} = 1 - [E]\,\phi \tag{4}$$

where $[E]$ is the intrinsic elastic modulus defined as (Pabst, 2003):

$$[E] \equiv -\lim_{\phi \to 0} \frac{E_{\mathrm{r}} - 1}{\phi} \tag{5}$$

In the special case of a cellular material with spherical pores and solid phase Poisson's ratio $\upsilon_0 = 0.2$ or $\upsilon_0 = 0.33$ the intrinsic elastic modulus is equal to two ($[E] = 2$) and any deviations from this value may be inflicted by discrepancies from sphericity of pore shapes or discrepancies of the solid phase Poisson's ratio (Pabst, 2006a). This model also predicts a critical porosity parameter $\phi_{\mathrm{c}} = [E]^{-1} \leq 1$ representing a point where the effective elastic modulus reaches zero and the material looses its integrity.

4.1. Nonlinear models

Porosity dependence of the effective elastic moduli is usually nonlinear. The applicability of modulus-porosity relations is often stated to be controlled by the approximate isometry and not only by the sphericity of pores. This is supported by the fact that Coble-Kingery relation in the form (Coble, 1956):

$$E_{\mathrm{r}} = 1 - [E]\,\phi + ([E] - 1)\phi^2 \tag{6}$$

which reduces to:

$$E_{\mathrm{r}} = (1 - \phi)^2 \tag{7}$$

for porous material with spherical pores and solid phase Poisson ratio $\upsilon_0 = 0.2$ is in the same form as a special case of power-law relations, functional equation approach, differential approach and semi-empirical Gibson-Ashby model derived by fitting large set of experimental data irrespective to spherical pore shape or isolated-pore topology. As a result, the connectedness of pores itself does not exclude the use of any modulus-porosity relation.

The mechanical properties of foams can be modeled by considering deformation mechanisms of individual cells (Ashby, 2004). Open-cell foams deform by bending followed at large loads by the formation of plastic hinges within the cell walls. Relative elastic modulus is then defined as:

$$E_{\mathrm{r}} = \alpha \left(\frac{\rho_{\mathrm{f}}}{\rho_0}\right)^{\eta} \tag{8}$$

where ρ_{f} is density of the foam, ρ_0 is density of the matrix material, α and η are constants related to cell geometry.

In closed-cell foams, bending of the cell walls is accompanied by stretching of the cell faces (Gibson, 1997). The relation for the relative elastic modulus has then a linear density term, which is related to face stretching, and square term related to edge bending:

$$E_{\mathrm{r}} = C\varphi^2 \left(\frac{\rho_{\mathrm{f}}}{\rho_0}\right)^2 + C(1 - \varphi)\left(\frac{\rho_{\mathrm{f}}}{\rho_0}\right) \tag{9}$$

where C is a constant related to cell geometry and φ is the fraction of solid contained in the cell edges. It should be noted that experimental verification of these relations exhibits problems with the determination of φ for high foam's relative densities (above $30\,\%$) because there is no distinction between cell edges and faces. Furthermore, either the cell size effect and cell anisotropy effect on mechanical properties are not incorporated in the Gibson-Ashby's model.

Other considered relations based on exponential and power laws are the most commonly used for determination of modulus-porosity dependence of ceramic materials. In case of porous metals considered in this paper, the modified exponential relation, Mooney-type exponential relation, Archie type relation, Phani-Niyogi relation and Pabst-Gregorová relation are studied.

The modified exponential relation appears in the form (Mooney, 1951):

$$E_{\mathrm{r}} = \exp\left(\frac{-[E]\phi}{1 - \phi}\right) \tag{10}$$

Derivation of this equation has been given via the functional equation approach (Pabst, 2004b) and trivial case for porous material with spherical pores leads to the prediction:

$$E_{\mathrm{r}} = \exp\left(\frac{-2\phi}{1 - \phi}\right) \tag{11}$$

This model results in zero relative modulus only in the case of $100\,\%$ porosity. To allow for zero relative modulus at porosities lower than $100\,\%$, additional parameter of critical porosity has to be introduced, which leads to the Mooney-type exponential relation (Mooney, 1951):

$$E_{\mathrm{r}} = \exp\left(\frac{-[E]\phi}{1 - \frac{\phi}{\phi_{\mathrm{c}}}}\right) \tag{12}$$

Power-law relations are in the simplest form represented by the Archie-type relation (Archie, 1942):

$$E_{\mathrm{r}} = (1-\phi)^{[E]} \tag{13}$$

This equation does not exhibit problem with zero relative modulus at $100\,\%$ porosity and again the critical porosity parameter can be introduced to allow zero relative modulus at porosities lower than $100\,\%$. This results in a Krieger-type power-law relation (Krieger, 1972), often called Phani-Niyogi relation (Phani, 1987):

$$E_{\mathrm{r}} = \left(1-\frac{\phi}{\phi_{\mathrm{c}}}\right)^{[E]\phi_{\mathrm{c}}} \tag{14}$$

All these exponential and power-law relations can be derived via the functional equation approach and their semi-empirical character is given by the fact that intrinsic elastic modulus may not be reliably known due to variations in pore shape and difficulties in assessment of pore size distribution and connectivity. Thus, reliable estimates of critical porosities are not available.

Pabst-Gregorová model (Pabst, 2004c) has been found heuristically and appears in the form:

$$E_{\mathrm{r}} = \left(1-[E]\phi+([E]-1)\phi^2\right)\frac{\left(1-\frac{\phi}{\phi_{\mathrm{c}}}\right)}{(1-\phi)} \tag{15}$$

This relation ensures zero relative elastic moduli for the case $\phi = \phi_{\mathrm{c}}$. When critical porosity of the material with spherical isometric pores is considered to be equal to 1, the relation reduces to the Coble-Kingery relation (Eq. 6).

5. Results

The hereinbefore mentioned relations were applied to prediction of relative elastic moduli of porous aluminium and titanium. Elastic characteristics of pore-free macroscopically isotropic matrix materials which are necessary input information for calculation of the relative moduli were taken from literature (Miyoshi, 1998; Singh, 2009b) and are listed in Tab. 1.

Tab. 1: Elastic characteristics of pore-free aluminium and titanium alloys used for manufacturing of Alporas and Optinium respectively (CP stands for "Commercially Pure")

	Alporas	Optinium
Elastic property	CP Aluminium	CP4 Titanium
E [GPa]	69	112.3
υ [1]	0.33	0.317

Tab. 2: Elastic characteristics of reference materials

Material property	Alporas	Optinium
E [GPa]	0.826	10.4
porosity [1]	0.914	0.639

Internal structure of the studied materials is constituted of large overlapping void inclusions (closed pores) of polyhedral shape and skeleton-like open pore structure with considerable variation in the size

and orientation of the pores and hence the foam struts in case of Alporas and Optinium respectively. This may lead to preliminary estimates of intrinsic elastic moduli significantly divergent from benchmark value of 2.

For Alporas, however, when the data are fitted with master curve using the Archie-type relation (Eq. 13) which seems to be the most promising among other models, the resulting intrinsic tensile modulus obtained via this equation is $[E] = 1.84$ for experimental results and $[E] = 2.11$ for FE results. When the Phani-Niyogi relation (Eq. 14) is used for fitting with critical porosity as a additional parameter, the intrinsic tensile modulus is $[E] = 2.36$, the critical porosity exceeds unity giving $\phi_{\mathrm{C}} = 1.13$ for experimental data and $[E] = 2.11$, $\phi_{\mathrm{C}} = 1.01$ for FE results. Similarly, when the Pabst-Gregorová (Eq. 15) model is considered in its complex form with both fitting parameters (intrinsic elastic modulus and critical porosity), fitted values are again close to benchmark ones with experimental $[E] = 1.95$, $\phi_{\mathrm{C}} = 1.01$ and numerical $[E] = 2.03$, $\phi_{\mathrm{C}} = 1.00$. It is apparent that if one lets vary freely the intrinsic elastic modulus in the power-law equations (making it adjustable fit parameter) the resulting intrinsic tensiel modulus is always approximately 2. Although internal structure of Alporas is composed of overlapping polyhedral cells and not spherical ones (that are indicated by the intrinsic elastic modulus equal to 2), it can be interpreted as a clear confirmation of the approximate isometricity of pores and also foam's isotropic mechanical characteristics. As contrasted to porosity dependence of porous ceramics, exponential-law models are completely unsatisfactory for metal foams with modified exponential model (Eq. 10)resulting in value $[E] = 0.44$ a and $[E] = 0.88$ for experimental and numerical results respectively. This result indicates significant deviation from spherical pore shape but visual comparison of fitting curve and numerical results shows diametrically different evolution of the fit model. By contrast, evolution of the Mooney-type model (Eq. 12)fits the numerical curve well with intrinsic elastic moduli $[E] = 0.88$ and $[E] = 1.6$ for experimental and numerical results respectively. Nevertheless, the corresponding critical porosity values amount to experimental $\phi_{\mathrm{C}} = 1.01$ and numerical $\phi_{\mathrm{C}} = 1.29$ that is clearly nonsense from the physical reality (Tab. 3, Fig. 5).

Tab. 3: Fit parameters determined for the master curve of the porosity dependence of the elastic modulus of Alporas and Optinium metal foams using power- and exponential-law models

		Alporas		Optinium	
Relation	Fit model	$[E]$	ϕ_{C}	$[E]$	ϕ_{C}
Archie	$E_{\mathrm{r}} = (1-\phi)^{[E]}$	2.11	–	2.20	–
Phani-Niyogi	$E_{\mathrm{r}} = \left(1-\frac{\phi}{\phi_{\mathrm{c}}}\right)^{[E]\phi_{\mathrm{c}}}$	2.11	1.01	1.89	0.92
Pabst-Gregorová	$E_{\mathrm{r}} = \left(1-[E]\phi+([E]-1)\phi^2\right)^{\frac{\left(1-\frac{\phi}{\phi_{\mathrm{c}}}\right)}{(1-\phi)}}$	2.03	1.00	2.08	1.01
Modified exponential	$E_{\mathrm{r}} = \exp\left(\frac{-[E]\phi}{1-\phi}\right)$	0.88	–	1.37	–
Mooney	$E_{\mathrm{r}} = \exp\left(\frac{-[E]\phi}{1-\frac{\phi}{\phi_{\mathrm{c}}}}\right)$	1.60	1.29	1.37	1.01

Analogous results have been obtained for Optinium foam with exponential models predicting large deviations from actual curves representing modulus-porosity dependence of this type of foam. Foam exhibits different relative stiffnesses in directions perpendicular and parallel to compaction direction due to eccentric spaceholders used during the production process. This kind of pore geometry and macroscopic material characteristics is essential according to intended usage of this material. PlivioPore implant system is indicated for posterior lumbar intercorporeal fusion using osteoconductive titanium implants from Optinium ensuring excellent both primary and secondary stability. This is primarily achieved by virtue of rotation principle during embedding of the implant into spinal column. Firstly, the implant is fully inserted into the intervertebral disc space using the implant holder and consequently rotated by 90 degrees to its desired position (Synthes, 2007). Such utilization principle and surgical technique require highest material stiffness in directions perpendicular to transverse and sagital plane where most loads are transferred. These material characteristics can be predicted by power-law equations, as in the case of Alporas (see Tab. 3). Moreover, both exponential-law models are suitable for prediction of modulus-porosity

dependence of this material with intrinsic elastic moduli $[E] = 1.37$ and critical porosity $\phi_C = 1.01$ indicating anisometry of the internal structure due to nonspherical spaceholders.

Table 4 summarizes results obtained by fitting the master curves using Gibson-Ashby's equations (Eqs. 8, 9). For Optinium, if one lets vary both fitting parameters freely, optimal master curve characterizing porosity-dependence of this foam is achieved with $\alpha = 1.78$ and $\eta = 2.82$. This is in contrast with previous theoretical and experimental works with $\alpha = 2.03$ and $\eta = 2$ according to experimental study of Dillard (2004) and $\alpha = 0.6$ and $\eta = 1.6$ according to theoretical model of strut bending of Ashby (2004). Values of constants in these experimental and numerical studies were obtained for nickel-based open-cell foam indicating that any of the models is not applicable in general and must be adapted to particular studied material. When $\eta = 2$ is considered, the optimal value of α amounts to 1.01 which is consistent with more detailed structural mechanics analysis of a low density, open-cell, Kelvin foam with tetrakaidecahedral cells and struts with a Plateau border shape (Warren, 1997). FE simulations of Kelvin foam lead to prediction of $\alpha = 0.98$ and comparison with experimental data suggests that $\alpha = 1$ can be used for a wide variety of open-cell foams. By contrast, application of Gibson-Ashby's equation for porosity dependence of elastic modulus for closed-cell foams is limited due to difficulties in determination of fraction of solid contained in the cell edges. FE simulations of a unit tetrakaidecahedral closed-cell with flat faces give $\varphi = 0.32$ for relative densities less than 0.2 (Simone, 1998). For such low relative densities, the second linear density term dominates, implying that cell face stretching is the more significant mechanism of deformation in closed-cell foams. Similar simulations on tetrakaidecahedral closed-cells and Weaire-Phelan closed-cells give $\varphi = 0.311$ (Kraynik, 1999). Fitting using these values give optimal constant equal to approximately 1.5 but, as was observed at exponential-law models, comparison of fitting curve and numerical results shows diametrically different evolution of the fit model. If one lets fraction of solid contained in the cell edges vary freely as a additional fitting parameter, master curve fits the actual modulus-porosity dependence well. Yet, optimal fit model values are $C = 2.14$ and $\varphi = 1.02$ which is nonreasonable value for closed-cell foams corresponding to all of the foam's solid contained in the cell edges (Fig. 6).

Tab. 4: Fit parameters determined for the master curve of the porosity dependence of the elastic modulus of Alporas and Optinium metal foams using Gibson-Ashby's models

		Alporas		Optinium	
Structure	Fit model	α	η	C	φ
Open-cell	$E_r = \alpha \left(\frac{\rho_f}{\rho_0}\right)^{\eta}$	1.78	2.82	–	–
Closed-cell	$E_r = C\varphi^2 \left(\frac{\rho_f}{\rho_0}\right)^2 + C(1-\varphi)\left(\frac{\rho_f}{\rho_0}\right)$	–	–	1.03	2.14

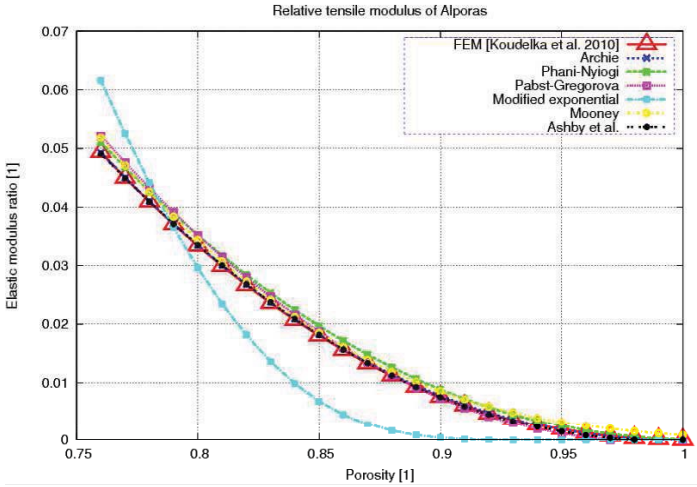

Fig. 5: Evolution of relative elastic modulus plotted against porosity for Alporas showing master curves determined by fitting using equations listed in Tabs. 3 and 4

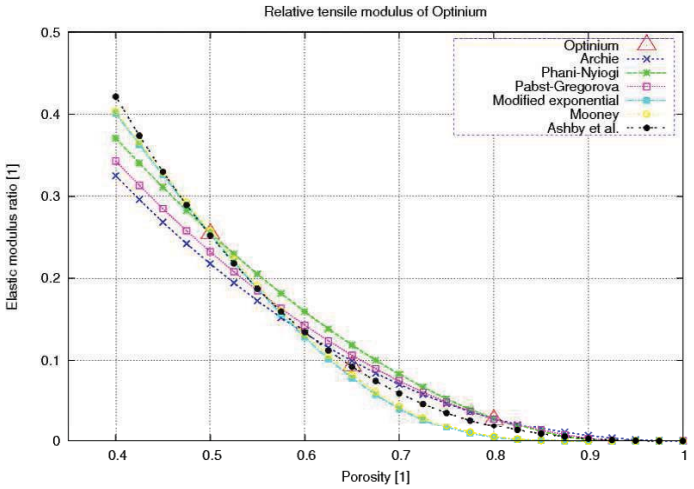

Fig. 6: Evolution of relative elastic modulus plotted against porosity for Optinium showing master curves determined by fitting using equations listed in Tabs. 3 and 4

6. Conclusion

Several exponential- and power-law equations have been introduced in order to obtain a master curve characterizing as precisely as possible the general trend of the porosity dependence of the elastic moduli. Predictions given by these mathematical models have been applied to mechanical behavior of Alporas closed-cell aluminium foam and Optinium open-cell titanium biocompatible foam. Based on the concept of intrinsic elastic moduli a brief overview of modulus-porosity relations has been given including exponential and power-law expressions as well as Gibson-Ashby's relations for both types of studied foams, among them also the relations with critical porosity. It has been shown that for materials with microstructure types investigated here, both the modified exponential relation and Mooney type relation provide unsatisfactory predictions of the actual porosity dependence of Alporas. Power-law models proved to be well suitable for determination of modulus-porosity dependence of both studied foams whereas Gibson-Ashby's semi-empirical equations are only suitable for predictions of modulus-porosity dependence of

Optinium. From the view of computational resources, modulus-porosity predictions assessed by fitting of aforementioned equations is incomparably simpler than performing sets of FE simulations - irrespective of direct or indirect microstructural modeling. Experimental verification of modulus-porosity predictions implies custom manufactured samples of cellular materials as both Alporas and Optinium foams are produced only at 90 % and 65 % levels of porosity respectively.

Acknowledgment

The research has been supported by Czech Science Foundation (grant no. P105/12/0824) with support of the RVO: 68378297. The financial support is gratefully acknowledged.

References

Archie, G.E. (1942), The electrical resistivity log as an aid in determining some reservoir characteristics, *Trans. AIME (Am. Inst. Min. Metall. Eng.), Vol. 146, 1942*, 54-67.

Banhart, J. (2001), *Prog. Mater. Sci., Vol. 46*, 559-632.

Ashby, M.F., Gibson L.J., Evans, A.G., Fleck, N.A., Hutchinson, J.W., Wadley, H.N.G. (2004), Metal Foams: A Design Guide, *Butterworth-Heinemann Publications*.

Coble, R. L., Kingery, W. D., (1956), Effect of porosity on physical properties of sintered alumina, *J. Am. Ceram. Soc., Vol. 39*, 377-385.

Dillard, T. (2004), Caractérisation et simulation numérique du comportement Mécanique des mousses de nickel: morphologie tridimensionnelle, réponse élastoplastique et rupture, *Thése de doctorat, Ecole Nationale Supérieure des Mines de Paris*.

Gibson, L.J., Ashby, M.F. (1997), Cellular Solids - Structure and Properties, second ed., *Cambridge University Press, UK*.

Hashin, Z., Shtrikman, S. (1963), A variational approach to the theory of the elastic behaviour of multiphase materials, *Journal of the Mechanics and Physics of Solids, Vol. 11, No. 2, 1963*, 127-140.

Imwinkelried T. (2007), Mechanical properties of open-pore titanium foam, *J Biomed Mater Res A 2007, Vol. 81A, No. 4*, 964-970.

Jiroušek, O., Jandejsek, I., Vavřík, D. (2011), Evaluation of strain field in microstructures using micro-CT and digital volume correlation, *Journal of Instrumentation, Vol. 6*, 1-5, ISSN 1748-0221.

Jiroušek, O., Němeček, J., Zlámal, P. (2009), Combining Nanoindentation and Real-Time Tomography for Micro Finite Element Models of Materials with Complex Inner Structure, *Proc. of the 12. International conference on Civil, structural and environmental enginering computing*, Civil-Comp Press, 165-175, ISBN 978-1-905088-32-4.

Konstantinidis, I.Ch., Papadopoulos, D.P., Lefakis, H., Tsipas, D.N. (2005), Model for determining mechanical properties of aluminum closed-cell foams, *Theoretical and Applied Fracture Mechanics, Vol. 43*, 157-167.

Koudelka, P., Jiroušek, O., Valach, J. (2011), Determination of mechanical properties of materials with complex inner structure using microstructural models, *MTM - Machines, Technologies, Materials. International virtual journal for science, technics and innovations for the industry, Vol. 5, No. 3*, 39-42.

Králík, V., Němeček, J. (2011), Two-scale model for prediction of macroscopic elastic properties of aluminium foam, *Chemické Listy, Vol. 105, No. 17, 2011*, 672-675.

Kraynik, A.M., Neilsen, M.K., Reinelt, D.A., Warren W.E. (2011), Foam micromechanics, Foams and Emulsions, *Proceedings of the NATO Advanced Study Institute on Foams, Emulsions and Cellular Materials*, Kluwer Academic Publishers, Dordrecht, 259-286.

Krieger, I. M. (1972), Rheology of monodisperse lattices, *Adv. Colloid Interf. Sci., Vol. 3*, 111-136.

Markov, K. Z. (2000), Elementary micromechanics of heterogeneous media, *Heterogeneous Materials - Micromechanics Modeling Methods and Simulations*, 1-162.

Milton, G. W. (2003), The Theory of Composites, *Cambridge University Press*.

Miyoshi, T., Itoh, M., Akiyama, S., Kitahara A. (1998), Aluminium foam, "ALPORAS": The Production Process, Properties and Applications, *Materials Research Society Symposium Proc. Vol. 521*.

Mooney, M. (1951), The viscosity of a concentrated suspension of spherical particles, *J. Colloid Sci., Vol. 6*, 162-170.

Nemat-Nasser, S., Hori, M. (1999), Micromechanics - Overall Properties of Heterogeneous Materials (2nd ed.), *North-Holland/Elsevier*.

Pabst W., Gregorová, E., Tichá, G. (2006a), Elasticity of porous ceramics - A critical study of modulus-porosity relations, *Journal of the European Ceramic Society, Vol. 26*, 1085-1097.

Pabst W., Gregorová, E. (2003), Derivation of the simplest exponential and power-law relations for the effective tensile modulus of porous ceramics via functional equations, *J. Mater. Sci. Lett., Vol. 22*, 1673-1675.

Pabst W., Gregorová, E. (2006b), Effective elastic moduli of alumina, zirconia and alumina-zirconia composite ceramics, *Ceramics and Composite Materials: New Research*, Nova Science Publishers.

Pabst W., Gregorová, E. (2004a), Effective elastic properties of aluminazirconia composite ceramics - Part 2: Micromechanical modeling, *Ceramics-Silikáty, Vol. 48*, 14-23.

Pabst W., Gregorová, E. (2004b), Mooney-type relation for the porosity dependence of the tensile modulus of ceramics, *J. Mater. Sci., Vol. 39*, 3213-3215.

Pabst W., Gregorová, E. (2004c), New relation for the porosity dependence of the effective tensile modulus of brittle materials, *J. Mater. Sci., Vol. 39*, 3501-3503.

Phani, K. K. and Niyogi, S. K. (1987), Young's modulus of porous brittle solids, *J. Mater. Sci., Vol. 22*, 257-263.

Simone, A.E., Gibson, L.J. (1998), Effects of solid distribution on the stiffness and strength of aluminum foams, *Acta Mater., Vol. 46*, 2139-2150.

Singh, R., Lee, P.D., Lindley, T.C., Dashwood, R.J., Ferrie, E., Imwinkelried, T. (2009a), Characterization of the structure and permeability of titanium foams for spinal fusion devices, *Acta Biomater 2009, Vol. 5, No. 1*, 477-487.

Singh, R., Lee, P.D., Lindley, T.C., Kohlhauser, C., Hellmich, C., Bram, M., Imwinkelried, T., Dashwood, R.J. (2009b), Characterization of the deformation behavior of intermediate porosity interconnected Ti foams using micro-computed tomography and direct finite element modeling, *Acta Biomaterialia, Vol. 6, 2010*, 2342-2351.

Synthes Gmbh (2007), PlivioPore. Open-porous, osteoconductive structure for optimized fusion. Technique Guide.

Torquato, S. (2002), Random Heterogeneous Materials - Microstructure and Macroscopic Properties, *Springer, New York, 2002*.

Vavřík, D., Dammer, J., Jakůbek, J., Jeon, I., Jiroušek, O., Kroupa, M., Zlámal, P. (2011), Random Heterogeneous Materials - Microstructure and Macroscopic Properties, *Nuclear Instruments and Methods in Physics Research, Section A: Accelerators, Spectrometers, Detectors and Associated Equipment, Vol. 633, 2011*, 152-155.

Warren, W.E., Kraynik, A.M. (1997), Linear elastic behavior of a low density Kelvin foam with open cells, *ASME J. Appl. Mech., Vol. 64*, 787-794.

18th International Conference
ENGINEERING MECHANICS 2012
Svratka, Czech Republic, May 14 – 17, 2012

pp. 703–707
Paper #215

EXPERIMENT E6/0,2 WITH LATERAL PASSIVE PRESSURE ROTATION ABOUT THE TOE

P. Koudelka[*], J. Valach[**], J. Bryscejn[***]

Abstract: *The paper gives information on a repeated long-term experiment E6/0,2 with lateral pressure at rest and passive pressure during wall rotation about the top towards into tested granular mass. The experiment was successfully finished in the last year 2011 and (together with a previous experiment E5/0,2) it should prove gained results which appear distinct from a theory of EUROCODE 7-1 contemporaneously used. Both experiments monitored and registered both pressure components and mass deformation and displacements into the sandy mas.*

Keywords: ***Lateral earth pressure, pressure at rest, passive pressure, physical experiments, ideally non-cohesive sand, mass deformation, slip surface, bi-component pressure sensor.***

1. Introduction

A basic research of earth/lateral pressure based on physical and numerical experiments has begun in 1998 at the institute of the authors and it has continued. The physical research should prove behaviour of ideally non-cohesive granular mass during three basic types of structure movement towards active and passive directions The first research period in 1998-2000 aimed on active pressure and in 2001-2002 on the first long/term experiment with passive pressure (E3/0.2) but during this the first side glass tables cracked. Despite it the experiment went off successfully to finish. In the course of the second period was developed experimental equipment on the second and the third (contemporary) stages. The first experiment with passive pressure E3/0,2 (2001-2) was repeated like experiment E5/0,2 (2010) in a frame of the second research period such as a long-term operation test of the new experimental equipment. It brought similar results however, with lower pressure values. The experiment E5/0,2 had to be repeated and this, the last carried out experiment E6/0,2 is presented in the paper.

2. Experimental equipment

The actual advanced equipment (see Figs 1a,b) has the same size and it is fully controlled by two computers (the first for front wall movement and data monitoring and registration, the second for visual monitoring and photo registration) and reaches up very suitable characterizations: max. *active* wall movement of 300 mm, max. *passive* wall movement of 242 mm, arbitrarily *slow* front wall movement of velocity from of 3.684 to of >0 mm/min. i.e. arbitrarily slow movement, max. pressing force cca 2870 kN, 5 bi-component pressure sensors in front moved wall, 1 three-component sensor and 5 bi-component pressure sensors in back solid wall, 2 potential movement sensors, 1 optoelectronic movement sensor, 1 impulse summator, max. recording frequency 1000 Hz. The equipment can afford a huge quantity of data of 803 MB/day.

Deformation of the sample and displacements into it are monitored visually. Slip surfaces and uplifts of the sample mass are monitored through the right transparent side due to red strips into the mass (see Fig.1a). Locations of the strips are registered a stabile photo camera about per day during

[*] Ing. Petr Koudelka, DrSc.: Institute of Theoretical and Applied Mechanics, Czech Academy of Sciences, Prosecká 76; 190 00 Prague 9; CZ, e-mail: koudelka@itam.cas.cz

[**] Ing. Jaroslav Valach, PhD.: Institute of Theoretical and Applied Mechanics, Czech Academy of Sciences, Prosecká 76; 190 00 Prague 9; CZ, e-mail: valach@itam.cas.cz

[***] Ing. Jan Bryscejn: Institute of Theoretical and Applied Mechanics, Czech Academy of Sciences, Prosecká 76; 190 00 Prague 9; CZ, e-mail: bryscejn@itam.cas.cz

Fig. 1. Experimental equipment with transparent glass sides before experiment E6/,02 with non-cohesive sandy sample into:
a) Lateral view at right equipment side (left). The moved front wall with five bi-component pressure sensors is left, back stabile wall with six pressure sensors is right.
b) Front view at hardware facilities in front of the experimental equipment (right). Red frame bearing six black cameras is left.

the front wall movement. Also, the locations of the strips are measured manually in the time intervals. Displacements of black little globes located in front sample part in net of 50/50 mm are monitored by cameras set through the transparent left side (see in Fig.1b left). Visual registration data of cameras are stored separately in the second separate computer (see Fig.1b right). A detailed description of the equipment can be found in Koudelka P. and Bryscejn J. 2010.

3. Experiment E6/0,2

The experiment belongs to the set of basic physical experiments whose should repair and prove the lateral/earth pressure theory:
- *active pressure:* three repeated experiments with pressure at rest and active pressure (structure rotations about the toe and top and translative motion – carried out 1998 - 2000,
- *passive pressure:* three repeated experiments with pressure at rest and passive pressure (structure rotations about the toe and top and translative motion).

Thus, altogether two times six experiments without experiment E3/0.2 that was performed using the original simple equipment of which results probably will not be fully comparable.

The basic physical research for the more advanced theory and its development has continued from April 8, 2010 to be completed the experiments with pressure at rest and passive pressure, i.e. double repeated long-term experiments for rotations about the top and the toe and for translative motion. The firstly, the experiments E5/0,2 and E6/0,2 with rotation about the top and an ideally non-cohesive sand have been begun using a velocity of wall toe movement of 0.005 mm/min. (near to natural processes - 50 times faster than finger nail growth or 53 times faster than continental drift). The following repeated experiment E6/0,2 was entered 25.3.2011 on and finished successfully on 19.12.2011. A history of the experiment E6/0,2 see in Table 1. A detailed description of the equipment function during the experiment (operation test) can be found in Koudelka P., Valach J. and Bryscejn J. 2011. Contemporarily (in March 2012), the first experiment with *passive* rotation *about the toe* E5/0,1 is running from 28.2.2012.

3.1. Sample

The same material (quartz sand) under the same compaction is used for samples of all experiments. Principal physical properties of the sample were found as follows: unit weight γ= 15.697 kN/m^3, effective angle of shearing resistance ϕ_{ef} = 38.5°, effective cohesion c_{ef} = 0, residual angle of shearing resistance ϕ_r = 31°, structure-ground interface friction angle δ = 12.8°, moisture w = 0.3 %.

Table 1. History of experiment E6/0,2 - Rotation about the top

E5/0,2	Date			Movement		
Phase [1] [Note]	Start [day]	End [day]	Time [2] [h/m/s]	Direction [act./pas]	Dist. max. [3] [mm]	Velocity [mm/min]
0a	25.03.2011	25.03.2011	0:59:59	active	- 0.200	0.005
recons.1	25.03.2011	31.03.2011	-	-	- 0.200	0
a0	31.03.2011	31.03.2011	1:14:25	passive	- 0.020	0.005
recons.2	31.03.2011	07.04.2011	-	-	- 0.020	0
0p	07.04.2011	07.04.2011	1:40:16	passive	0.292	0.005
recons.3	07.04.2011	26.04.2011	-	-	0.292	0
p1	26.04.2011	03.05.2011	163:52:20	passive	47.950	0.005
recons.4	03.05.2011	01.09.2011	-	-	47.950	0
p2	01.09.2011	25.09.2011	578:02:28	passive	205.460	0.005

[1] Phases containing zero indicate movement in a branch of pressure at rest, similarly "a" branch of active pressure and "p" branch of passive pressure, Numbered phases "recons" indicate period's re-consolidation without a movement for research of time stability of the pressure.

[2] Time of continuous wall movement.

[3] Distance maximum of the wall toe at the phase end from its original position before the experiment start.

3.2. Hardware and software

The entire system is equipped with electronics and computers to enable controlling experiments and also proper data collection. It has single power plug 220V which leads to UPS which is backing up the crucial low-consumption devices and also the main computer. A stepper motor control unit is supplied from DC power source (40V/5A). Two kinds of software run on the main computer. InMotion program works with the stepper motor unit in two modes — program mode is used when the experiment is in progress and realizes slow steady motion of the front wall; the second mode is used for controlling the motor on demand for various purposes, e.g. during the setup of experiment. Program NextView is software which collects data from all sensors and saves it for later processing at desired sampling rate. It shows also actual data in both numerical and graphical manners. Signals of the pressure sensors, temperature sensor and analog potentiometric sensors are conditioned, amplified and led to 16bit A/D convertors, then via interfacing USB devices (BMCM) into the measuring computer. Two digital displacement sensors (resolution 10 nm), found next to potentiometric sensors, are connected into the PC via internal card. The second computer is used for controlling of a camera system.

4 Results

The experiment brought an extreme quantity of basic NextView data of *1.508 GB* (time data and sensor data without visual monitoring data and photos). The data quantity needs a special technology (software, approaches etc.) of which development is running. At all events, size of experimental results does not make it possible to transfer data in a suitable format and to analyze them in short time and of course, to present the complete results in one paper. Complete analyses and evaluations of particular aspects of the granular mass behaviour in detail will be present step by step further. A digest of the results follows below.

The front wall rotation about the top influences the maximal movement of the toe. The wall is very rigid and it behaves like solid structure and due to it movements of other wall points depend on the toe movement linearly according to their distance to the top. That is for all results are regarded to a relevant toe movement.

4.1. Data

Data collected during whole experiment as well as the rest phases are saved to disk in NextView's proprietary data format (.lfx). The sampling rate of these datasets differs. So, to be obtained human-understandable results, these data are exported to ASCII format first. This leads into huge amount of data (~68 GB), so the decimation process takes place here. It is done via several short scripts written in Matlab language. This lessens amount of the data reasonably, so it can be put into several well-arranged Excel tables. For this purpose, a macro in Excel was developed. The original data with high sampling rates will be used in subsequent evaluation process.

Very important movement of the front wall toe was measured using five independent techniques: potential movement sensors, optoelectronic movement sensor, impulse summator and the maximum distance of the toe after the experiment from its original location by electronic micrometer. There were not found significant differences. A position of the front wall top (not moved) was controlled by the second potential movement sensor. Movement values presented in the Paper are data according to the lower potential movement sensor in all experimental phases except of the last one (p2) for which are used data according to the measurement after the experiment by electronic micrometer.

4.2. Deformations and slip surfaces

Deformations of the red strips and displacements of the black little globes during the first three phases, i.e. both active and passive pressure at rest, and also changes of the sample surface, were not visible. A slight uplift of the lower strips could be monitored up the toe movement of 10-20 mm. The toe movement of 47,95 mm at the end of the fourth phase (p1 – movement for full passive pressure according to EC 7-1) appears to be critical and the red strips on right side of the sample shoved:

- A front part of the sample behind the front moved wall was uplifted yet in upper area (depth of 0 – 0.6 m) at the maximal values of 18–21 mm in distances about of 0.8 m from the wall. The uplift was visible to depth of 0.9 m and fell to of 8 mm on a level of 0.9 m.
- This wall movement appeared critical because simultaneously, *the first slight slip displacement* was monitored at the strip level of 0.9 m in a distance from the wall of 0.58 m.

This sample state is illustrates in Fig. 2 (photo is not so obvious).

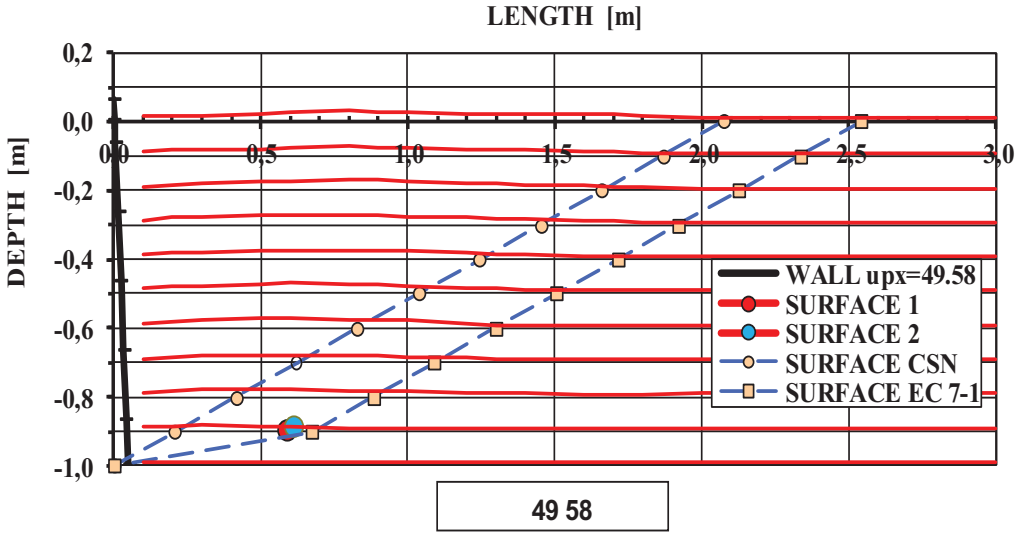

Fig. 2: Deformation of the sample front part according to the red strips and beginning the first slip surfaces Nos. 1, 2 in a strip of depth of -0,9 m comparatively to theoretical slip surfaces according to ČSN 73 0037 and EC 7-1 after passive movement of the toe of 49.58 mm.

4.3. Pressures

Pressure analyses will be performed after the data transformation in xls format that is running. Contemporarily, it can be stated the passive pressure maximum has been found after the toe wall

movement of 124.3 mm and its value has been 102.4 kPa. This value is near to maximal passive pressure value of 107.8 kPa which had been found before during the experiment E5/0,2 after toe movement of 60.0 mm and the value of 102.3 kPa had been found after toe movement of 87.1 mm.

5 Conclusion

In spite of the analyses of data are not carried out a preliminary conclusion appears possible. Granular mass of the experiment E6/0,2 behaved similarly to the experiment E5/0,2. It can be seen obviously in figures of Figs. 3a,b which make it possible to compare visible mass changes (slip surfaces including) after experiments.

Fig. 3: View at right sides of the samples (granular masses of the same sand of size of 0.3 mm.
a) Experiment E6/0,2 after toe movement of 212.3 mm(left).
b) Experiment E5/0,2 after toe movement of 226.9 mm (right).

Both pressure results of the repeated experiments E5/0,2 and E6/0,2 appear similar too. Differences are in an interval of a temperature influence and could be caused also a bit of incorrectness of the masses.

Acknowledgement

The Grant Agency of the Czech Republic and the Grant Agency of the Czech Academy of Sciences provided financial support of the connected research (GP Nos.103/02/0956, 103/05/2130, 103/07/0557, 103/08/1617, P105/11/-1160 and A2071302 resp.). The authors would like to thank them all for support.

References

ČSN 73 0037 (1992) *Earth pressure acting on structures*, 52 ps. Prague: Vydavatelstv norem. (In Czech)

EUROCODE 7-1 2004 *Geotechnical design – Part 1: General rules*. CEN, Bruxeles.

Koudelka, P. (2000) Nonlinear bicomponent lateral pressures and slip surfaces of granular mass. *Proc. IC GeoEng2000*, Melbourne, Technomic Publ.Co.Inc., Lancaster/Basel, p.72 (ps.8).

Koudelka, P. (2008) Granular Mass Behaviour Under Passive Pressure. Proc. *6th IC Case Histories in Geotechnical Engineering*, Arlington (USA), University of Missouri-Rolla, Rolla (Missouri), Shamsher Prakash, ISBN 1-8870009-14-0, # 5.35.

Koudelka, P., Bryscejn, J. (2010) Original Experimental equipment for Slow Processes of Lateral Pressure in Granular Masses. *48th Int. Scientific Conference on Experimental Stress Analysis*, Velké Losiny, Proc. ISBN 978-80-244-2533-7, eds. P. Šmíd, P. Horváth, M. Hrabovský, pp.177-184.

Koudelka P., Valach J. and Bryscejn J. (2011) Operation Test of a New Experimental Technology for Research of Lateral Pressure. *49th Int. Scientific Conference on Experimental Stress Analysis*, Znojmo, Proc. ISBN 978-80-214-4275-7, pp. 155-160.

18th International Conference
ENGINEERING MECHANICS 2012
Svratka, Czech Republic, May 14 – 17, 2012

pp. 709–718
Paper #56

CRACK ANALYSIS IN MAGNETOELECTROELASTIC SOLIDS

S. Krahulec[*], J. Sladek[**], V. Sladek[***], P. Stanak[****]

Abstract: *The paper discusses about crack analysis in magnetoelectroelastic solids. 2-D crack problems are considered. There are applied various electromagnetic boundary conditions on the crack-faces. The definition of the electromagnetic boundary conditions on the crack-faces plays an important role in the crack analysis of magnetoelectroelastic materials. Two extreme cases - the fully permeable and the fully impermeable crack surfaces are analysed. The finite element method is applied to solve crack boundary value problems. The coupling among magnetic, electrical and mechanical fields is adequately considered in magnetoelectroelastic solids subjected to external loads.*

Keywords: ***magnetoelectroelastic composites, crack opening displacement***

1. Introduction

Smart materials are widely used in practical engineering applications. It can be observed coupling effect between mechanical and electric fields (piezoelectric), mechanical and magnetic fields (piezomagnetic), mechanical and electric and magnetic fields (magnetoelectroelactic), etc. An electric potential is produced when a piezoelectric element is under stress or strain loading. This effect is called direct piezoelectric effect. When a mechanical deformation is produced by an electric field, it is a converse piezoelectric effect (Song at al., 2006). Magnetoelectric materials induce the polarization by a magnetic field, or conversely induce magnetization by an electric field Nan (1994). These materials are promising for a wide range of applications, such as four-state memories, magnetic field sensors and magnetically controlled optoelectric devices. It is important to analyze magnetoelectroelastic material for fracture resistance, because it is brittle. The electric and magnetic boundary conditions on the crack-faces are determined by the measure of shielding of the electric and magnetic fields. Thus, it is important to define the electromagnetic boundary conditions on the crack-faces. There are frequently considered two extreme cases. The first it is the fully permeable crack. This type does not shield the electric and magnetic field. The second one is fully impermeable crack, which shields the electric and magnetic field completely. The boundary value problems with cracks can be solved by several methods. For example finite element method (Enderlein at al., 2005), boundary element method (García-Sánchez et al., 2007) and meshless method (Sládek at al., 2008).

2. Basic equations of magnetoelectroelasticity

The coupling of the mechanical, electrical and magnetic fields in magnetoelectroelastic solids (Nan, 1994) is given by the following constitutive equations

$$\sigma_{ij} = c_{ijkl}\varepsilon_{kl} - e_{kij}E_k - d_{kij}H_k \tag{1}$$

[*] Ing. Slavomír Krahulec: Institute of Construction and Architecture, Slovak Academy of Science, 845 03 Bratislava, Slovakia, e-mail: slavomir.krahulec@savba.sk

[**] Prof. Ing. Ján Sládek, DrSc.: Institute of Construction and Architecture, Slovak Academy of Science, 845 03 Bratislava, Slovakia

[***] Prof. RNDr. Vladimír Sládek, DrSc.: Institute of Construction and Architecture, Slovak Academy of Science, 845 03 Bratislava, Slovakia

[****] Ing. Peter Staňák: Institute of Construction and Architecture, Slovak Academy of Science, 845 03 Bratislava, Slovakia, e-mail: peter.stanak@savba.sk

$$D_j = e_{jkl}\varepsilon_{kl} + h_{jk}E_k + \alpha_{jk}H_k \tag{2}$$

$$B_j = d_{jkl}\varepsilon_{kl} + \alpha_{kj}E_k + \gamma_{jk}H_k \tag{3}$$

where

$$\varepsilon_{ij} = \frac{1}{2}\left(u_{i,j} + u_{j,i}\right) \tag{4}$$

$$E_i = -\psi_{,i} \tag{5}$$

$$H_i = -\mu_{,i} \tag{6}$$

The strain tensor ε_{ij}, electric field vector E_i and magnetic intensity vector H_i are related to independent variables - displacement , electrical potential and magnetic potential denoted by u_i , ψ and μ, respectively. σ_{ij}, D_i, B_i represent the stress tensor, the electric displacements, and the magnetic inductions, respectively. Material parameters are the elastic coefficients c_{ijkl} , dielectric permittivities h_{jk} and magnetic permeabilities γ_{jk} . Finally, e_{kij} , d_{kij} and α_{jk} are the coefficients for the piezoelectric, piezomagnetic, and magnetoelectric coupling, respectively.

For plane-deformation problems the constitutive equations can be written in a matrix form (Parton and Kudryavtsev, 1988)

$$\begin{bmatrix}\sigma_{11}\\ \sigma_{33}\\ \sigma_{13}\end{bmatrix} = \begin{bmatrix}c_{11} & c_{13} & 0\\ c_{13} & c_{33} & 0\\ 0 & 0 & c_{44}\end{bmatrix}\begin{bmatrix}u_{1,1}\\ u_{3,3}\\ u_{1,3}+u_{3,1}\end{bmatrix} - \begin{bmatrix}0 & e_{31}\\ 0 & e_{33}\\ e_{15} & 0\end{bmatrix}\begin{bmatrix}-\psi_{,1}\\ -\psi_{,3}\end{bmatrix} - \begin{bmatrix}0 & d_{31}\\ 0 & d_{33}\\ d_{15} & 0\end{bmatrix}\begin{bmatrix}-\mu_{,1}\\ -\mu_{,3}\end{bmatrix} =$$

$$= \mathbf{C}\begin{bmatrix}\varepsilon_{11}\\ \varepsilon_{33}\\ 2\varepsilon_{13}\end{bmatrix} - \mathbf{L}\begin{bmatrix}E_1\\ E_3\end{bmatrix} - \mathbf{K}\begin{bmatrix}H_1\\ H_3\end{bmatrix} \tag{7}$$

$$\begin{bmatrix}D_1\\ D_3\end{bmatrix} = \begin{bmatrix}0 & 0 & e_{15}\\ e_{31} & e_{33} & 0\end{bmatrix}\begin{bmatrix}u_{1,1}\\ u_{3,3}\\ u_{1,3}+u_{3,1}\end{bmatrix} + \begin{bmatrix}h_{11} & 0\\ 0 & h_{33}\end{bmatrix}\begin{bmatrix}-\psi_{,1}\\ -\psi_{,3}\end{bmatrix} + \begin{bmatrix}\alpha_{11} & 0\\ 0 & \alpha_{33}\end{bmatrix}\begin{bmatrix}-\mu_{,1}\\ -\mu_{,3}\end{bmatrix} =$$

$$= \mathbf{G}\begin{bmatrix}\varepsilon_{11}\\ \varepsilon_{33}\\ 2\varepsilon_{13}\end{bmatrix} + \mathbf{H}\begin{bmatrix}E_1\\ E_3\end{bmatrix} + \mathbf{A}\begin{bmatrix}H_1\\ H_3\end{bmatrix} \tag{8}$$

$$\begin{bmatrix}B_1\\ B_3\end{bmatrix} = \begin{bmatrix}0 & 0 & d_{15}\\ d_{31} & d_{33} & 0\end{bmatrix}\begin{bmatrix}u_{1,1}\\ u_{3,3}\\ u_{1,3}+u_{3,1}\end{bmatrix} + \begin{bmatrix}\alpha_{11} & 0\\ 0 & \alpha_{33}\end{bmatrix}\begin{bmatrix}-\psi_{,1}\\ -\psi_{,3}\end{bmatrix} + \begin{bmatrix}\gamma_{11} & 0\\ 0 & \gamma_{33}\end{bmatrix}\begin{bmatrix}-\mu_{,1}\\ -\mu_{,3}\end{bmatrix} =$$

$$= \mathbf{R}\begin{bmatrix}\varepsilon_{11}\\ \varepsilon_{33}\\ 2\varepsilon_{13}\end{bmatrix} + \mathbf{A}\begin{bmatrix}E_1\\ E_3\end{bmatrix} + \mathbf{M}\begin{bmatrix}H_1\\ H_3\end{bmatrix} \tag{9}$$

Governing equations for magnetoelectroelastic body under static loading conditions are given by the force equilibrium and the scalar Maxwell's equations as

$$\sigma_{ij,j} + X_i = 0 \tag{10}$$

$$D_{j,j} - \Pi = 0 \tag{11}$$

$$B_{j,j} = 0 \tag{12}$$

where X_i and Π represent the body force vector and the volume density of free charges, respectively.

The Dirichlet boundary conditions of magnetoelectroelastic body are given as follows

$$\begin{aligned} u_i &= U_i, \quad \text{on} \quad \partial\Omega_u \\ \psi &= V, \quad \text{on} \quad \partial\Omega_v \\ \mu &= A, \quad \text{on} \quad \partial\Omega_a \end{aligned} \tag{13}$$

where U_i, V and A are prescribed the mechanical displacement, the electric potential and the magnetic potential, respectively.

The Neumann boundary conditions of magnetoelectroelastic body are

$$\begin{aligned} t_i &= \sigma_{ij} n_j = T_i, \quad \text{on} \quad \partial\Omega_t, \quad \partial\Omega = \partial\Omega_u \cup \partial\Omega_t \\ q &= D_i n_i = -Q, \quad \text{on} \quad \partial\Omega_q, \quad \partial\Omega = \partial\Omega_v \cup \partial\Omega_q \\ s &= B_i n_i = -S, \quad \text{on} \quad \partial\Omega_s, \quad \partial\Omega = \partial\Omega_a \cup \partial\Omega_s \end{aligned} \tag{14}$$

where T_i, Q, S and n_i are the traction vector, the normal component of the electric displacement vector, the normal component of the magnetic induction and unit outward vector components.

A general boundary value problem in a magnetoelectroelastic solid is uniquely specified by the governing equations (10)-(12), constitutive equations (7)-(9) and boundary conditions (13)-(14). The FEM is applied to solve above stated boundary value problem. For this purpose, we will utilize the COMSOL computer code for multi-physics problems.

The governing equation for a transient dynamic problem with inertial and damping term is written in COMSOL as

$$e_a u_{,tt} + d_a u_{,t} + \nabla.\Gamma = F \quad \text{in } \Omega \tag{15}$$

where u is independent variable. The mass and damping coefficients are denoted by e_a and d_a, respectively, and will be excluded in the static analysis. The "scalar" F is the source term. The "flux vector" Γ is represented by equation

$$\Gamma = c\nabla u + \alpha u - \gamma \tag{16}$$

in which coefficients c, α and γ are the diffusion coefficient, the flux convection coefficient and the flux source term, respectively.

The symbols used in Eq. (15) can be represented for particular governing equations (10)-(12) completed with the constitutive equations (7)-(9) as

$$\Gamma = \begin{pmatrix} -\begin{bmatrix} \sigma_{11} \\ \sigma_{33} \\ \sigma_{13} \end{bmatrix} \end{pmatrix} = \begin{pmatrix} -\begin{bmatrix} c_{11}u_{1,1} + c_{13}u_{3,3} + e_{31}\psi_{,3} + d_{31}\mu_{,3} \\ c_{13}u_{1,1} + c_{33}u_{3,3} + e_{33}\psi_{,3} + d_{33}\mu_{,3} \\ c_{44}(u_{1,3} + u_{3,1}) + e_{15}\psi_{,1} + d_{15}\mu_{,1} \end{bmatrix} \end{pmatrix}, \quad \nabla = \mathbf{D}_u^T := \begin{pmatrix} \partial_1 & 0 & \partial_3 \\ 0 & \partial_3 & \partial_1 \end{pmatrix}, \quad F = \begin{pmatrix} X_1 \\ X_3 \end{pmatrix} \tag{17}$$

$$\Gamma = \begin{pmatrix} \begin{bmatrix} D_1 \\ D_3 \end{bmatrix} \end{pmatrix} = \begin{pmatrix} e_{15}(u_{1,3} + u_{3,1}) & -h_{11}\psi_{,1} & -\alpha_{11}\mu_{,1} \\ e_{31}u_{1,1} + e_{33}u_{3,3} & -h_{33}\psi_{,3} & -\alpha_{33}\mu_{,3} \end{pmatrix}, \quad \nabla = \mathbf{D}_\psi^T := \begin{pmatrix} \partial_1 & \partial_3 \end{pmatrix}, \quad F = \Pi \tag{18}$$

$$\Gamma = \begin{pmatrix} \begin{bmatrix} B_1 \\ B_3 \end{bmatrix} \end{pmatrix} = \begin{pmatrix} d_{15}(u_{1,3}+u_{3,1}) & -\alpha_{11}\psi_{,1} & -\gamma_{11}\mu_{,1} \\ d_{31}u_{1,1}+d_{33}u_{3,3} & -\alpha_{33}\psi_{,3} & -\gamma_{33}\mu_{,3} \end{pmatrix}, \quad \nabla = \mathbf{D}_\mu^T := \begin{pmatrix} \partial_1 & \partial_3 \end{pmatrix}, \quad F = 0 \tag{19}$$

3. Finite element formulation

Introducing the virtual displacement δu_i , virtual electric potential $\delta\psi$ and virtual magnetic potential $\delta\mu$, equations (10)-(12) can be rewritten as

$$\int_\Omega (\sigma_{ij,j} + X_i)\delta u_i d\Omega + \int_\Omega (D_{j,j} - \Pi)\delta\psi d\Omega + \int_\Omega B_{j,j}\delta\mu d\Omega = 0 \tag{21}$$

The equation (21) as well as the boundary equations (14) and relations (4)-(6) can be represented equivalently as

$$\begin{aligned} &-\int_\Omega \sigma_{ij}\delta\varepsilon_{ij}d\Omega + \int_{\partial\Omega_u} \sigma_{ij}n_j\delta u_i d(\partial\Omega) + \int_{\partial\Omega_t} T_i\delta u_i d(\partial\Omega) + \int_\Omega X_i\delta u_i d\Omega - \int_\Omega D_i\delta E_i d\Omega \\ &+\int_{\partial\Omega_v} n_i D_i\delta\psi d(\partial\Omega) - \int_{\partial\Omega_q} Q\delta\psi d(\partial\Omega) - \int_\Omega \Pi\delta\psi d\Omega - \int_\Omega B_i\delta H_i d\Omega + \int_{\partial\Omega_a} n_i B_i\delta\mu d(\partial\Omega) \\ &-\int_{\partial\Omega_s} S\delta\mu d(\partial\Omega) = 0 \end{aligned} \tag{22}$$

The field variables u_i , ψ and μ can be approximated by the shape functions N_u , N_ψ and N_μ and the unknown nodal degrees of freedom $\mathbf{u}_k$, ψ_k and μ_k

$$\mathbf{u}_e = N_u(\xi_1,\xi_2)\mathbf{u}_k, \ \mathbf{u}_e = \begin{pmatrix} u_1 \\ u_3 \end{pmatrix}_e, \ \mathbf{u}_k = \begin{pmatrix} u_1 \\ u_3 \end{pmatrix}_k, \quad \psi_e = N_u(\xi_1,\xi_2)\psi_k, \quad \mu_e = N_u(\xi_1,\xi_2)\mu_k. \tag{23}$$

Usually, the matrices B_u , B_ψ and B_μ are introduced for simplification

$$\mathbf{B}_u = \mathbf{D}_u N_u, \quad \mathbf{B}_\psi = \mathbf{D}_\psi N_\psi , \quad \mathbf{B}_\mu = \mathbf{D}_\mu N_\mu \tag{24}$$

where the transposed matrices to $\mathbf{D}_u$, $\mathbf{D}_\psi$ and $\mathbf{D}_\mu$ have been defined in Eqs. (17)-(19). Recall that the matrices $\mathbf{D}_u$, $\mathbf{D}_\psi$ and $\mathbf{D}_\mu$ involve the derivatives with respect to global Cartesian coordinates x_1 and x_3 , which are expressed in terms of the derivatives with respect to the local coordinates on elements as

$$\begin{pmatrix} \partial/\partial x_1 \\ \partial/\partial x_3 \end{pmatrix} = [J]^{-1}\begin{pmatrix} \partial/\partial\xi_1 \\ \partial/\partial\xi_2 \end{pmatrix}, \quad [J]^{-1} = \begin{pmatrix} \partial\xi_1/\partial x_1 & \partial\xi_2/\partial x_1 \\ \partial\xi_1/\partial x_3 & \partial\xi_2/\partial x_3 \end{pmatrix}. \tag{25}$$

The element energy functional is resulted from equations (22), (24) and (1)-(3)

$$\begin{aligned} \delta F_u^e = &-\delta\mathbf{u}_k^T\left\{\left(\int_{\Omega^e}\mathbf{B}_u^T\mathbf{C}\mathbf{B}_u d\Omega\right)\mathbf{u}_k + \left(\int_{\Omega^e}\mathbf{B}_u^T\mathbf{L}\mathbf{B}_\psi d\Omega\right)\psi_k + \left(\int_{\Omega^e}\mathbf{B}_u^T\mathbf{K}\mathbf{B}_\mu d\Omega\right)\mu_k\right\} \\ &+\delta\mathbf{u}_k^T\left\{\left(\int_{\partial\Omega_u^e}\mathbf{B}_u^T\mathbf{N}\mathbf{C}\mathbf{B}_u d(\partial\Omega)\right)\mathbf{u}_k + \left(\int_{\partial\Omega_u^e}\mathbf{B}_u^T\mathbf{N}\mathbf{L}\mathbf{B}_\psi d(\partial\Omega)\right)\psi_k\right. \\ &\left.+\left(\int_{\partial\Omega_u^e}\mathbf{B}_u^T\mathbf{N}\mathbf{K}\mathbf{B}_\mu d(\partial\Omega)\right)\mu_k\right\} + \delta\mathbf{u}_k^T\int_{\Omega^e}N_u^T\mathbf{X}d\Omega + \delta\mathbf{u}_k^T\int_{\partial\Omega_t^e}N_u^T\mathbf{T}d(\partial\Omega) = 0 \end{aligned} \tag{26}$$

$$\begin{aligned}\delta F_{\psi}^{e} = &-\delta\psi_k^T\left\{\left(\int_{\Omega^e}\mathbf{B}_{\psi}^T\mathbf{G}\mathbf{B}_u d\Omega\right)\mathbf{u}_k+\left(\int_{\Omega^e}\mathbf{B}_{\psi}^T\mathbf{H}\mathbf{B}_{\psi} d\Omega\right)\psi_k+\left(\int_{\Omega^e}\mathbf{B}_{\psi}^T\mathbf{A}\mathbf{B}_{\mu} d\Omega\right)\mu_k\right\}\\ &+\delta\psi_k^T\left\{\left(\int_{\partial\Omega_v^e}N_{\psi}^T\mathbf{n}\mathbf{G}\mathbf{B}_u d(\partial\Omega)\right)\mathbf{u}_k+\left(\int_{\partial\Omega_v^e}N_{\psi}^T\mathbf{n}\mathbf{H}\mathbf{B}_{\psi} d(\partial\Omega)\right)\psi_k\right.\\ &\left.+\left(\int_{\partial\Omega_v^e}N_{\psi}^T\mathbf{n}\mathbf{A}\mathbf{B}_{\mu} d(\partial\Omega)\right)\mu_k-\left(\int_{\Omega^e}N_{\psi}^T\Pi d\Omega\right)\right\}-\delta\psi_k^T\left(\int_{\partial\Omega_q^e}N_{\psi}^T Q d(\partial\Omega)\right)=0\end{aligned} \tag{27}$$

$$\begin{aligned}\delta F_{\mu}^{e} = &-\delta\mu_k^T\left\{\left(\int_{\Omega^e}\mathbf{B}_{\mu}^T\mathbf{R}\mathbf{B}_u d\Omega\right)\mathbf{u}_k+\left(\int_{\Omega^e}\mathbf{B}_{\mu}^T\mathbf{A}\mathbf{B}_{\psi} d\Omega\right)\psi_k+\left(\int_{\Omega^e}\mathbf{B}_{\mu}^T\mathbf{M}\mathbf{B}_{\mu} d\Omega\right)\mu_k\right\}\\ &+\delta\mu_k^T\left\{\left(\int_{\partial\Omega_a^e}N_{\mu}^T\mathbf{n}\mathbf{R}\mathbf{B}_u d(\partial\Omega)\right)\mathbf{u}_k+\left(\int_{\partial\Omega_a^e}N_{\mu}^T\mathbf{n}\mathbf{A}\mathbf{B}_{\psi} d(\partial\Omega)\right)\psi_k\right.\\ &\left.+\left(\int_{\partial\Omega_a^e}N_{\mu}^T\mathbf{n}\mathbf{M}\mathbf{B}_{\mu} d(\partial\Omega)\right)\mu_k\right\}-\delta\mu_k^T\left(\int_{\partial\Omega_s^e}N_{\mu}^T S d(\partial\Omega)\right)=0\end{aligned} \tag{28}$$

where $\mathbf{n}=\begin{pmatrix}n_1 & n_3\end{pmatrix}$, $\mathbf{N}=\begin{pmatrix}n_1 & 0 & n_3\\ 0 & n_3 & n_1\end{pmatrix}$.

Assuming that $\delta F_u=\sum\delta F_u^e$, $\delta F_{\psi}=\sum\delta F_{\psi}^e$ and $\delta F_{\mu}=\sum\delta F_{\mu}^e$ with using the abbreviations

$$\mathbf{K}_{uu}^e=\left(\int_{\Omega^e}\mathbf{B}_u^T\mathbf{C}\mathbf{B}_u d\Omega\right)-\left(\int_{\partial\Omega_u^e}\mathbf{B}_u^T\mathbf{N}\mathbf{C}\mathbf{B}_u d(\partial\Omega)\right),$$

$$\mathbf{K}_{u\psi}^e=\left(\int_{\Omega^e}\mathbf{B}_u^T\mathbf{L}\mathbf{B}_{\psi} d\Omega\right)-\left(\int_{\partial\Omega_u^e}\mathbf{B}_u^T\mathbf{N}\mathbf{L}\mathbf{B}_{\psi} d(\partial\Omega)\right),$$

$$\mathbf{K}_{u\mu}^e=\left(\int_{\Omega^e}\mathbf{B}_u^T\mathbf{K}\mathbf{B}_{\mu} d\Omega\right)-\left(\int_{\partial\Omega_u^e}\mathbf{B}_u^T\mathbf{N}\mathbf{K}\mathbf{B}_{\mu} d(\partial\Omega)\right),\quad \mathbf{f}_u^e=\int_{\Omega^e}N_u^T\mathbf{X}d\Omega+\int_{\partial\Omega_t^e}N_u^T\mathbf{T}d(\partial\Omega)$$

$$\mathbf{K}_{\psi u}^e=-\left(\int_{\Omega^e}\mathbf{B}_{\psi}^T\mathbf{G}\mathbf{B}_u d\Omega\right)+\left(\int_{\partial\Omega_v^e}N_{\psi}^T\mathbf{n}\mathbf{G}\mathbf{B}_u d(\partial\Omega)\right),$$

$$K_{\psi\psi}^e=-\left(\int_{\Omega^e}\mathbf{B}_{\psi}^T\mathbf{H}\mathbf{B}_{\psi} d\Omega\right)+\left(\int_{\partial\Omega_v^e}N_{\psi}^T\mathbf{n}\mathbf{H}\mathbf{B}_{\psi} d(\partial\Omega)\right),$$

$$K_{\psi\mu}^e=-\left(\int_{\Omega^e}\mathbf{B}_{\psi}^T\mathbf{A}\mathbf{B}_{\mu} d\Omega\right)+\left(\int_{\partial\Omega_v^e}N_{\psi}^T\mathbf{n}\mathbf{A}\mathbf{B}_{\mu} d(\partial\Omega)\right),\quad f_{\psi}^e=\int_{\Omega^e}N_{\psi}^T\Pi d\Omega+\int_{\partial\Omega_q^e}N_{\psi}^T Q d(\partial\Omega)$$

$$\mathbf{K}_{\mu u}^e=-\left(\int_{\Omega^e}\mathbf{B}_{\mu}^T\mathbf{R}\mathbf{B}_u d\Omega\right)+\left(\int_{\partial\Omega_a^e}N_{\mu}^T\mathbf{n}\mathbf{R}\mathbf{B}_u d(\partial\Omega)\right),$$

$$K_{\mu\psi}^e=-\left(\int_{\Omega^e}\mathbf{B}_{\mu}^T\mathbf{A}\mathbf{B}_{\psi} d\Omega\right)+\left(\int_{\partial\Omega_a^e}N_{\mu}^T\mathbf{n}\mathbf{A}\mathbf{B}_{\psi} d(\partial\Omega)\right),$$

$$K_{\mu\mu}^e=-\left(\int_{\Omega^e}\mathbf{B}_{\mu}^T\mathbf{M}\mathbf{B}_{\mu} d\Omega\right)+\left(\int_{\partial\Omega_a^e}N_{\mu}^T\mathbf{n}\mathbf{M}\mathbf{B}_{\mu} d(\partial\Omega)\right),\quad f_{\mu}^e=\int_{\partial\Omega_s^e}N_{\mu}^T S d(\partial\Omega) \tag{29}$$

and assembling the matrices into global matrix, the discretized equations can be written as

$$\begin{bmatrix}\mathbf{K}_{uu} & \mathbf{K}_{u\psi} & \mathbf{K}_{u\mu}\\ \mathbf{K}_{\psi u} & K_{\psi\psi} & K_{\psi\mu}\\ \mathbf{K}_{\mu u} & K_{\mu\psi} & K_{\mu\mu}\end{bmatrix}\begin{bmatrix}\mathbf{u}\\ \psi\\ \mu\end{bmatrix}=\begin{bmatrix}\mathbf{f}_u\\ f_{\psi}\\ f_{\mu}\end{bmatrix} \tag{30}$$

or

$$\mathbf{Kx} = \mathbf{F} \tag{31}$$

where $\mathbf{K}$ is the stiffness matrix of the structure, $\mathbf{x}$ is the vector of unknown quantities and $\mathbf{F}$ is the loading vector.

4. Boundary conditions for crack-face

In this paper, two extreme boundary conditions on crack faces are considered, i.e., the fully impermeable and the fully permeable conditions. The electrical and magnetic boundary conditions on crack faces along x_1 for fully impermeable example are given as

$$\begin{aligned} D_3(\mathbf{x}\in\partial\Omega_c^+) &= D_3(\mathbf{x}\in\partial\Omega_c^-) = 0 \\ B_3(\mathbf{x}\in\partial\Omega_c^+) &= B_3(\mathbf{x}\in\partial\Omega_c^-) = 0 \end{aligned} \tag{32}$$

where $\partial\Omega_c^+$ and $\partial\Omega_c^-$ are the upper and the lower crack faces, respectively.

The fully permeable crack face boundary conditions along x_1 are given by

$$\begin{aligned} D_3(\mathbf{x}\in\partial\Omega_c^+) &= D_3(\mathbf{x}\in\partial\Omega_c^-),\ \psi(\mathbf{x}\in\partial\Omega_c^+) - \psi(\mathbf{x}\in\partial\Omega_c^-) = 0 \\ B_3(\mathbf{x}\in\partial\Omega_c^+) &= B_3(\mathbf{x}\in\partial\Omega_c^-),\ \mu(\mathbf{x}\in\partial\Omega_c^+) - \mu(\mathbf{x}\in\partial\Omega_c^-) = 0 \end{aligned} \tag{33}$$

5. Numerical examples

It is considered a magnetoelectroelastic straight strip. It can be solved as a 2-D problem under plane deformation conditions with the width of the strip $w = 2.5m$ and height $h = 3m$. The central crack with length $a = 1m$ along the axis x_1 is assumed. On the top and bottom surfaces of the strip, we consider either single pure loadings (a pure electrical load D_0, a pure magnetic load B_0, a pure mechanical load σ_0) or combinations of such pure loadings, while the lateral sides are traction free and with vanishing normal components of the electric displacement and magnetic induction vectors. A quarter of the strip is analyzed because of bi-axial symmetry. On the symmetry cuts, the normal displacements and tangential traction vector components are vanishing as well as the normal components of the electric displacement and magnetic induction vectors disappear. Thus, on the bottom of the quarter of the strip except the crack face we have $u_3 = 0$, $t_1 = 0$, $Q = 0$, $S = 0$, while on the right lateral $u_1 = 0$, $t_3 = 0$, $Q = 0$, $S = 0$. As long as the impermeable crack is assumed, Q and S are vanishing on the surface of the crack, while in the case of permeable crack the potentials ψ and μ are vanishing on both crack faces as long as no potentials are applied on the crack surface.

For the magnetoelectroelastic material, we chosen the $BaTiO_3$-$CoFe_2O_4$ composite (Li, 2000):

$$c_{11} = 22.6\cdot10^{10}\,Nm^{-2},\ c_{13} = 12.4\cdot10^{10}\,Nm^{-2},\ c_{33} = 21.6\cdot10^{10}\,Nm^{-2},\ c_{44} = 4.4\cdot10^{10}\,Nm^{-2},$$

$$e_{15} = 5.8\,Cm^{-2},\ e_{31} = -2.2\,Cm^{-2},\ e_{33} = 9.3\,Cm^{-2},$$

$$h_{11} = 5.64\cdot10^{-9}\,C(Vm)^{-1},\ h_{33} = 6.35\cdot10^{-9}\,C(Vm)^{-1}.$$

$$d_{15} = 275.0\,N(Am)^{-1},\ d_{31} = 290.2\,N(Am)^{-1},\ d_{33} = 350.0\,N(Am)^{-1},$$

$$\alpha_{11} = 5.367\cdot10^{-12}\,Ns/VC,\ \alpha_{33} = 2737.5\cdot10^{-12}\,Ns/VC.$$

$$\gamma_{11} = 297.0 \cdot 10^{-6} Wb(Am)^{-1} \ , \ \gamma_{33} = 83.5 \cdot 10^{-6} Wb(Am)^{-1}$$

The quarter of the strip is covered by 8400 linear quadrate finite elements.

In Figs. 1-4, the numerical results are given for all considered cases of single loadings: (i) pure mechanical load $\sigma_0 = 1Pa$; (ii) pure electrical load $D_0 = 1C/m^2$; (iii) pure magnetic load $B_0 = 1Vs/m^2$. Fig. 1 shows the distribution of the electric potential along the crack face for the fully impermeable crack condition. It can be seen that the electrical potential is negative, if a pure electrical load is applied. A similar behaviour can be observed for the magnetic potential (Fig.2) on the crack face under fully impermeable crack conditions, but the negative magnetic potential is appears if a pure magnetic load is applied and its magnitude is smaller than the value corresponding to a pure electrical load.

More interesting is the crack opening displacement shown in Fig. 3. and Fig.4. For the fully impermeable crack faces (Fig. 3.), a considerable opening of crack is caused by a pure magnetic loading and a pure electrical loading, though it is still slightly lower than in the case of a pure mechanical loading. For the fully permeable crack faces, however, the inverse behaviour is observed, when the main opening is caused by a pure mechanical loading, while the crack opening displacement is negative (crack closure) under a pure magnetic loading.

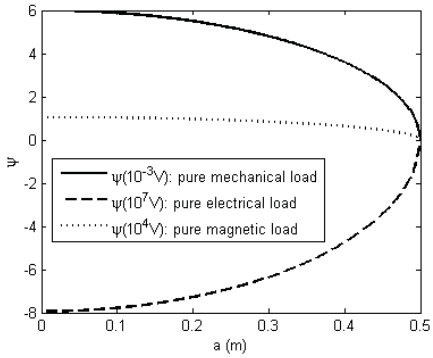

Fig. 1. Variation of the electrical potential on the crack face for the fully impermeable crack condition under a various loads.

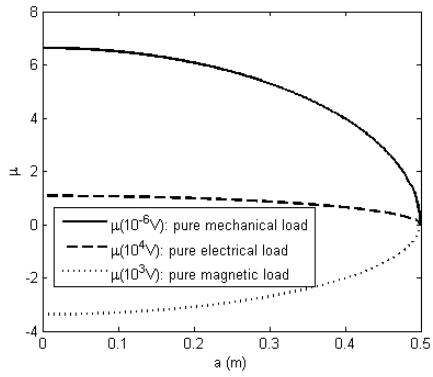

Fig. 2. Variation of the magnetic potential on the crack face for the fully impermeable crack condition under a various loads.

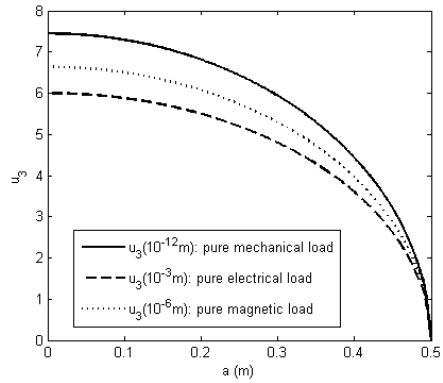

Fig. 3. Variation of the crack displacement for the fully impermeable crack condition under a various loads.

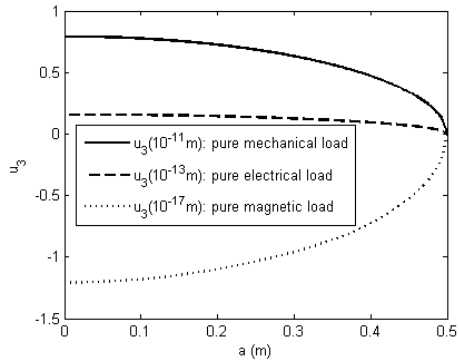

Fig. 4. Variation of the crack displacement for the fully permeable crack condition under a various loads.

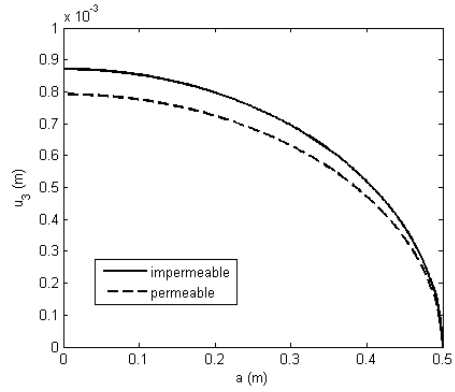

Fig. 5. Influence of the electromagnetic conditions on the crack displacement under a combined load.

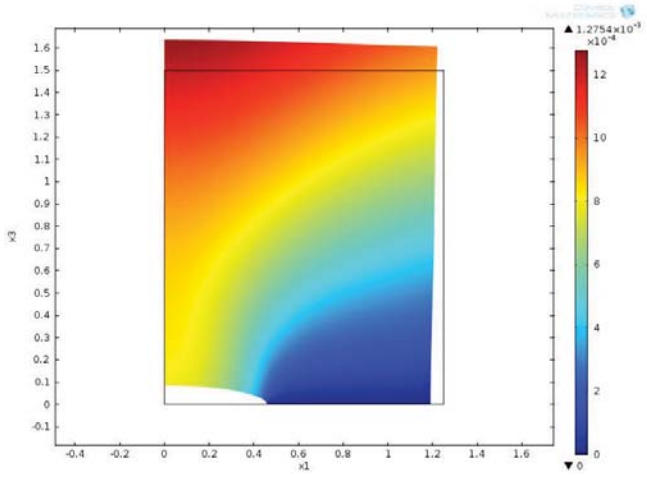

Fig. 6. Deformation of the quarter of the strip in direction x_3 for the fully permeable crack condition under combined load.

In the last example (Fig.5. and Fig. 6.), combined loading by mechanical load $\sigma_0 = 10^8 Pa$ with electrical load $D_0 = 10^{-2} C/m^2$ and magnetic load $B_0 = 10 Vs/m^2$ are applied. The influence of the crack electromagnetic boundary conditions on the crack opening displacement u_3 along the crack surface is shown in Fig. 5, when a combined loading is applied to the strip. A larger crack opening displacement appears in the case of fully impermeable electro-magnetic boundary conditions on the crack faces. Fig. 6. illustrates the displacements u_3 in a quarter of the strip under combined loading for the fully permeable crack conditions.

6. Conclusions

2-D crack problems in homogeneous magnetoelectroelastic composites are analyzed by finite element method using the commercial code COMSOL. The relevant governing equations are realized within the general framework for the partial differential equations. The mechanical and electromagnetic responses are studied under pure and/or combined mechanical and electro-magnetic loadings with assuming either permeable or impermeable electro-magnetic boundary conditions on the crack surface.

The coupling among the mechanical and electro-magnetic fields is confirmed by induced mechanical and electro-magnetic responses induced by pure single (pure mechanical, or electrical, or magnetic) loadings as well as by combined loadings. The crack opening displacements are dependent on the electro-magnetic boundary conditions applied on the crack surface. It has been found that the magnetic loading leads to crack closure.

References

Song, G., Sethi, V., Li H.-N. (2006) Vibration control of civil structures using piezoceramic smart materials: A review. *Engineering Structures* 28, , 1513-1524.

Nan, C.W. (1994) Magnetoelectric effect in composites of piezoelectric and piezomagnetic phases, *Phys. Rev. B* 50 6082-6088.

Enderlein, M., Ricoeur, A., Kuna, M. (2005) Finite element techniques for dynamic crack analysis in piezoelectrics, *International Journal of Fracture* 134, 191-208.

Parton, V.Z., Kudryavtsev, B.A. (1988) *Electromagnetoelasticity, Piezoelectrics and Electrically Conductive Solids.* Gordon and Breach Science Publishers, New York,.

García-Sánchez, F. , Rojas-Díaz, R., Sáez, A., Zhang, Ch. (2007) Fracture of magnetoelectroelastic composite materials using boundary element method (BEM), *Theoretical and Applied Fracture Mechanics* 47 192-204.

Sladek, J., Sladek, V., Solek, P., Pan, E. (2008)Fracture analysis of cracks in magneto-electro-elastic solids by the MLPG, *Computational Mechanics* 42 697-714.

Li, J.Y. (2000) Magnetoelectroelastic multi-inclusion and inhomogeneity problems and their applications in composite materials. *International Journal of Engineering Science* 38, 1993-2011.

18th International Conference
ENGINEERING MECHANICS 2012
Svratka, Czech Republic, May 14 – 17, 2012

pp. 719–724
Paper #125

MODELING OF MACROSCOPIC ELASTIC PROPERTIES OF ALUMINIUM FOAM

V. Králík[*], J. Němeček[**]

Abstract: *This paper is focused on the prediction of macroscopic elastic properties of highly porous aluminium foam. The material is characterized by a closed pore system with very thin pore walls and large air pores. Intrinsic material properties of cell wall constituents are assessed with nanoindentation whereas analytical homogenizations are employed for the assessment of the cell wall elastic properties. Very good agreement was found between the various analytical estimates. Two-dimensional microstructural FEM model was applied to obtain effective elastic properties of the upper material level. for which the Young's modulus reached 1.11 GPa. The value is by ~30% lower than the range of experimental values obtained from experimental compression tests. It follows from the 2-D approximation that the 2-D model underestimates the stiffness, by ~30% compared to the real case constrained in 3-D. Therefore, more appropriate 3-D model based on microCT data will be prepared in the future work.*

Keywords: ***metal foam, porous system, nanoindentation, micromechanical properties, homogenization.***

1. Introduction

Traditionally, materials are tested on large samples by macroscopic methods that can give overall (or effective) properties. Together with the development of experimental techniques in the past, microstructural and micromechanical properties have become important in the description of the material behavior since they could give answers on the origin of many macrolevel phenomena.

Aluminium foams belong to the up-to-date structural materials with high potential to many engineering applications. This highly porous material with a cellular structure is known for its attractive mechanical and physical characteristics. The application of this material is very wide. Some structural and functional applications of aluminium foams for industrial sector which covers mainly automotive, aircraft but also building industries have been reviewed e.g. by Banhart (2001).

In general, mechanical properties of metal foams are governed by two major factors: (i) cell morphology (shape, size and distribution of cells) and (ii) material properties of the cell walls (Miyoshi et al., 1998). However, measurement of mechanical properties of the cell walls is a difficult problem that cannot be solved with conventional methods due to their small dimensions, low local bearing capacity and local yielding and bending of the cell walls. These problems can be overcome using micromechanical methods, namely nanoindentation, in which the load–displacement curve is obtained in the sub-micrometer range.

In this study, micromechanical analysis of a commercially available aluminium foam Alporas® (Shinko Wire Co., Ltd) was performed. Nanoindentation technique was applied to access elastic properties of the distinct phases within the cell walls. Based on these results, overall effective elastic properties (Young's modulus) of the solid phase were evaluated by several homogenization schemes. To calculate the effective elastic properties at the whole structural level (including the air pores) microstructural FEM model was applied.

[*] Ing. Vlastimil Králík: Faculty of Civil Engineering, Department of Mechanics, Czech Technical University in Prague, Thákurova 2077/7; 166 29, Prague; CZ, e-mail: vlastimil.kralik@fsv.cvut.cz

[**] Doc. Ing. Jiří Němeček, Ph.D.: Faculty of Civil Engineering, Department of Mechanics, Czech Technical University in Prague, Thákurova 2077/7; 166 29, Prague; CZ, e-mail: jiri.nemecek@fsv.cvut.cz

2. Material characterization

2.1. Structure of Al-foam

The properties of Al-foam depend directly on the shape and structure of the cells, therefore description of its structure is very important. The Alporas foam is characterized by a hierarchical microstructure with the system of closed pores. An internal structure of the aluminum foam is shown in Fig. 1. The most important structural characteristic of a cellular solid is its relative density, ρ / ρ_s (where ρ is the foam density and ρ_s is the density of the solid, i.e. Al). The fraction of pore space in the foam can be defined by its porosity (1- ρ / ρ_s) (Gibson, 1997). The porosity was detected by weighing of a sufficiently large foam sample and by taking into account the density of pure aluminum (2700 kg/m^3). The relative density was assessed as 0.0859 and porosity reached 0.914, i.e. 91.4%.

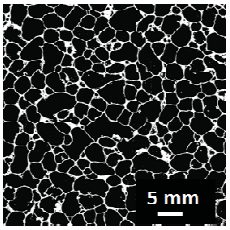

Fig. 1. Overall view on a typical structure of aluminium foam

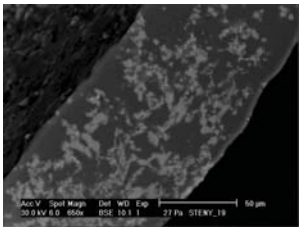

Fig. 2. ESEM image of a cell wall

Other important parameters for the description of the internal foam structure are both distribution of cell wall thicknesses and pore size and shape characteristics. These geometric parameters of the cell structure are crucial for the selection of the homogenization schemes and modeling mechanical performance. A high resolution optical image of the foam surface on a cross-section embedded to blackwashed gypsum was prepared. Prior to imaging the specimen was mechanically polished with fine SiC papers to receive smooth and flat surface. Size of the scanned area was 112 × 158 mm (which is sufficiently large to represent a structural level of the material).

The cell wall thickness assessed as the minimum distance between neighboring pores was evaluated using image analysis. Distribution of the cell wall thicknesses for is shown in Fig. 3. The distribution shows a significant peak, i.e. a characteristic thickness, around L~61 μm. The majority of cell wall thicknesses lies between 20 to 200 μm.

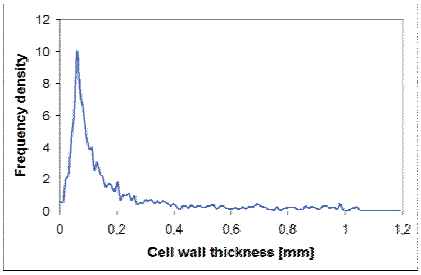

Fig. 3 Distribution of cell wall thickness

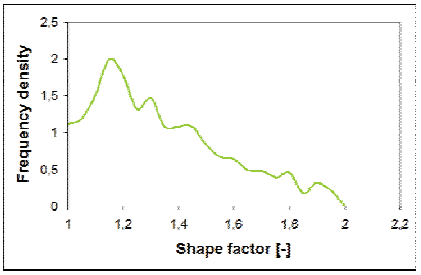

Fig. 4 Distribution of shape factor

A characteristic size of each pore was also estimated with the help of image analysis. Some small corrections and noise filtering in the binary image was necessary to help the algorithm automatically identify all individual pores. The pores are almost spherical or polyhedral shape due to a high foaming ratio.In the analysis, the pores were replaced by equivalent ellipses. Further, a shape factor computed as the ratio between the longer and shorter axes of the ellipse was obtained. Distribution of the values of shape factor is shown in Fig. 4. The mean value of shape factor was 1.15. This value indicates that the shape of the pores is nearly circular with a small flattening.

An equivalent pore diameter assuming circular pores was also calculated. The distribution of this equivalent pore diameters can be seen in Fig. 5. The equivalent diameters of pores are distributed over a range of 0.2 mm to 6 mm and the mean value of the equivalent diameter is 2.9 mm.

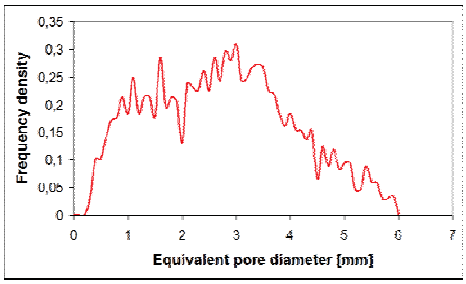

Fig. 5 Distribution of equivalent diameter

2.2. Definition of the model

At least two characteristic length scales can be distinguished for the material: the cell wall level and the foam level. Therefore, two-scale microstructural model for the prediction of macroscopic elastic properties on the whole foam level is proposed based on the utilization of nanoindentation data received on cell walls (Němeček et al., 2011; Hasan et al., 2008). The model covers:

- **Level I** (the cell wall level).

In this level, characteristic dimension of the cell wall defined by the mean midspan wall thickness is L~61 µm. This level consists of prevailing aluminium matrix (Al-rich area) with embedded heterogeneities in the form of Ca/Ti-rich areas (Králík et al., 2011). Distinct elastic properties of the microstructural constituents were assessed using nanoindentation at this level.

- **Level II** (the foam level).

At this level, the whole foam containing large pores with an average diameter ~2.9 mm are considered. Cell walls are considered as homogeneous having the properties that come from the Level I homogenization.

3. Level I homogenization

Firstly, intrinsic elastic properties of the microstructural constituents were assessed by nanoindentation at this level. Detailed description of the experimental part can be found in Němeček et al., 2011. Two-phase system (major Al-rich and minor Ca/Ti-rich phase) was assumed in the statistical deconvolution algorithm (Constantinides et al., 2006) to obtain Young's moduli and volume fractions of the two phases (Tab. 1). Poisson's ratio 0.35 was considered for both phases. Based on these results, effective elastic properties (Young's modulus) of the solid phase were evaluated by selected analytical homogenization schemes, namely Voigt and Reuss bounds, Mori-Tanaka method and self-consistent scheme (Zaoui, 2002). The homogenized elastic modulus for the cell wall is summarized in Tab. 2. Very close bounds and insignificant differences in the elastic moduli estimates by the schemes were found.

Tab. 1: Elastic moduli and volume fractions of the two microstructural phases from deconvolution

Input values from nanoindentation	Mean E (GPa)	St.dev. (GPa)	Volume fraction
Al-rich zone	61.9	4.6	0.638
Ca/Ti-rich zone	87	17	0.362

Tab. 2: Effective values of Young's modulus computed by different homogenization schemes at Level I

Scheme	Mori-Tanaka	Self-consist. scheme	Voigt bound	Reuss bound
$E_{eff,\ Level\ I}$ (GPa)	70.076	70.135	71.118	69.195

4. Level II homogenization

At this level, cell walls are considered as a homogeneous phase having the properties that come from the Level I homogenization. The cell walls create a matrix phase and the large air pores can be considered as inclusions in this homogenization.

At first, effective elastic properties of the Level II were estimated with the same analytical schemes used in Level I. The volume of air pores was evaluated experimentally (Section 2.1) on our samples as 91.41 %. The homogenized elastic modulus for the Level II structure is summarized in Tab. 3. It is clear from Tab. 3 that the analytical schemes show a high dispersion of results. None of the schemes used here give appropriate results compared to experiments. Nevertheless, the correct solution should lie between Voight and Reuss bounds that are, in this case, quite distant (Tab. 3). The Mori-Tanaka ends up close to the average phase value, whereas the self-consistent scheme tends to reach lower stiffness value (i.e. the air) due to the very large volume fraction of pores.

Tab. 3: Effective values of Young's modulus computed by different analytical homogenization schemes at Level II

Scheme	Mori-Tanaka	Self-consist. scheme	Voigt bound	Reuss bound
$E_{eff,\ Level\ II}$ (GPa)	3.1510	0.0012	6.0200	0.0011

At second, the more appropriate two dimensional microstructural FEM model was applied. The model geometry was generated from high resolution optical images of Al-foam cross-section, whose preparation is described in section 2.1. Size of the selected representative area was 60×60 mm and was rotated about both coordinate axes (axes of symmetry). Resulting area with a size of 120×120 mm was thus created to represent a higher structural level of the material. At this image, pore centroids were detected, Delaunay triangulation applied and Voronoi cells created. Then, an equivalent 2D-beam structure was generated from cell boundaries (Fig. 6). As a first estimate, uniform cross-sectional area was prescribed to all beams (~8.59 % of the total area).

The aim of the numerical analysis was to determine the effective elastic constants using the micromechanical approach in which the homogenized medium (a composite) should exhibit the same deformation behavior as the microscopically inhomogeneous sample in an average sense, In this analysis, prescribed macroscopic strain $\mathbf{E}$ is imposed on the boundaries of the RVE and microscopic strains and stresses are solved in the RVE. Volumetric averaging of microscopic stresses leads to the assessment of an average macroscopic stress and finally estimation of effective stiffness parameters.

The key issue of the computation is the size of RVE and application of boundary conditions around the domain. Since the RVE size is always smaller than an infinite body, any constraints can strongly influence the results. Application of the kinematic boundary conditions leads to the overestimation of effective stiffness and it can give an upper bound, whereas the static boundary conditions give a lower bound (Šmilauer, 2006). The best solution is usually provided by applying periodic boundary conditions to RVE which are, however, difficult to implement into commercial codes.

Nevertheless, the influence of the boundary conditions on microscopic strains and stresses in the domain decrease in distant points from the boundary. The size of our domain (120×120 mm) allowed us to solve the problem with kinematic boundary conditions. For homogenization, considerably smaller region (20×20 mm) was used. Microscopic strains and stresses were computed inside this

smaller area which was still sufficiently large to describe the material inhomogeneities and to serve as material RVE.

The whole domain (120×120 mm) was subjected to homogeneous macroscopic strain in one axial direction ($\mathbf{E}=\{1,0,0\}^T$) by imposing prescribed displacement to one domain side (Fig. 6). The test was performed using Oofem software package (Patzák et al., 2001) and microscopic strains and stresses solved in the domain. Strains and stresses (structural forces for the case of beams, respectively) inside the smaller area (20×20 mm) were averaged and used for computation of the homogenized stiffness matrix (one column in the matrix, respectively). Assuming material isotropy, the (1,1) member at the material stiffness matrix is given by:

$$L_{11} = E\frac{(1-\nu)}{(1+\nu)(1-2\nu)},$$

in which E is the Young's modulus and ν Poisson's ratio, respectively. Since the Poisson's ratio of the whole foam is close to zero (as confirmed by experimental measurements) the L_{11} member coincides with the Young's modulus E. For the tension test in x-direction (Fig.6), the homogenized Young's modulus was found to be E_{hom} = 1.11 GPa.

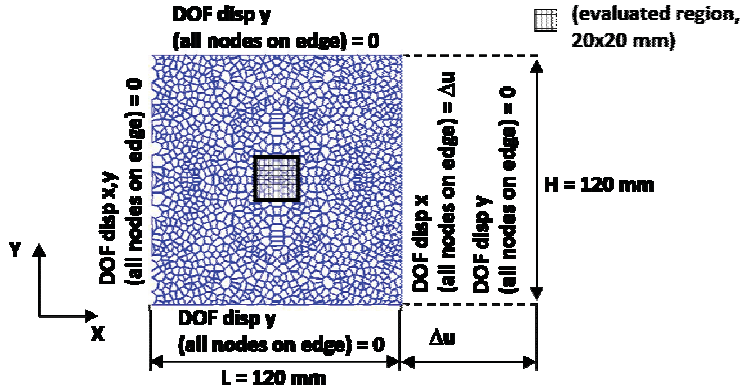

Fig. 6. 2D-beam structure with prescribed boundary conditions.

Such stiffness is comparable with the range of experimental values (0.4−1 GPa) reported for Alporas® e.g. by Ashby et. al. (2002). It is lower than first results obtained from our currently running experimental measurements (uniaxial compression test on 30×30×60 mm Alporas blocks) that indicate E≈1.45 GPa. The lower stiffness obtained from two-dimensional model can be explained by the lack of additional confinement appearing the three-dimensional case. Therefore, the results of the simplified 2-D model can be treated as a first estimate of the Level II material properties which need to be refined. The real confinement of a 3-D cell structure can hardly be captured in 2-D computation and leads to the necessity of the 3-D computation.

5. Conclusions

The microstructure of Al-foam was studied by image analysis and phase properties assessed with nanoindentation. Important parameters such as relative density (0.0859), porosity (0.914), distribution of cell wall thicknesses, distribution of equivalent pore diameters and shape factors of pores were determined. Two-scale micromechanical model was proposed for the assessment of foam effective elastic properties. Elastic parameters of cell walls (Level I) were obtained from statistical nanoindentation results from which one dominant and one minor mechanical phase were separated by the deconvolution algorithm. Application of analytical homogenization schemes showed very similar results of effective cell wall elastic properties ($E_{Level\text{-}I} \approx 70$ GPa). This value together with corresponding volume fraction of cell walls and large pores were used in micromechanical up-scaling to the upper level (Level II). Effective elastic properties of Level II were estimated with the same analytical schemes used in Level I. However, the analytical methods do not give satisfactory results in

this case. Therefore more appropriate two dimensional microstructural FEM model was applied. Homogenized Young's modulus reached 1.11 GPa. The estimated value was lower by 30% compared to experimental results (1.45 GPa). It is primarily due to the three dimensional effects (cell shape, additional confinement) that cannot be captured in the two dimensional model. Therefore, further development of the numerical model (influence of beam stiffness variations, size of RVE, extension to 3-D) and extending an experimental program is planned in the near future.

Acknowledgement

Support of the Czech Science Foundation (GAČR P105/12/0824) and the Grant Agency of the Czech Technical University in Prague (SGS12/116/OHK1/2T/11) is gratefully acknowledged.

References

Ashby M. F., Evans A., Fleck N. A., Gibson L. J., Hutchinson J. W., Wadley H. N. (2002) Metal foams: a design guide, Materials & Design, 23, 1.

Banhart J. (2001) Manufacture, characterisation and application of cellular metals and metal foams. Progress in Materials Science, 46, 6, pp.559-632.

Constantinides G., Chandran K.R., Ulm F.-J. & Vliet K.V. (2006) Grid indentation analysis of composite microstructure and mechanics: Principles of validation, Mat. Sci. and Eng., 430, 1-2, pp.189-202.

Gibson L. J., Ashby M. F. (1997) *Cellular solids – Structure and properties*. Cambridge University Press, Cambridge.

Hasan M.A., Kim A. & Lee H.-J. (2008) Measuring the cell wall mechanical properties of Al-alloy foams using the nanoindentation method, Composite Structures, 83, 2, pp.180-188.

Miyoshi T., Itoh M., Akiyama S. & Kitahara A. (1998) Aluminium foam, "ALPORAS": The production process, properties and application, Mat. Res. Soc. Symp. Proc., 521, pp.133-137.

Němeček J., Králík V., Vondřejc J., Němečková J. (2011) Identification of micromechanical properties on metal foams using nanoindentation, in: *Proceedings of the Thirteenth International Conference on Civil, Structural and Environmental Engineering Computing* (Edinburgh: Civil-Comp. Press), pp. 1-12.

Patzák B., Bittnar Z.(2001) Design of object oriented finite element code, Advances in Engineering Software, 32, 10-11, pp. 759-767.

Šmilauer V. (2006) Elastic properties of hydrating cement paste determined from hydration models, Doctoral thesis, Czech Technical University in Prague.

Zaoui A. (2002) Continuum Micromechanics: Survey, Journal of Engineering Mechanics, 128, 8, pp.808-816.

18th International Conference
ENGINEERING MECHANICS 2012
Svratka, Czech Republic, May 14 – 17, 2012

pp. 725–732
Paper #70

THE LAMINAR FLOW SOLUTION IN THE PLANE BY EIGENMODE EXPANSION

H. Krausová*

Abstract: *The paper deals with non-stationary laminar flow solution of an incompressible fluid. The Navier-Stokes equation is used for the description of this motion and it is solved by means of an expansion into a series of eigenmodes of vibration. A mathematical model, which assumes planar flow with specific boundary conditions, can be generalized to the spatial problem with different types of boundary conditions. The influence of the individual eigenmodes of vibration on the form of unsteady flow is evident.*

Keywords: ***Navier-Stokes equation, modal analysis, eigenmodes***

1. Introduction

The paper proposes a solution to a non-stationary laminar flow of incompressible fluid using an expansion into a series of eigenmodes of vibration. Pressure drop is chosen as the boundary conditions for this problem. After finding the equation for the velocity function, individual eigenmodes of vibration, partial sums and their time development were then drawn.

2. Problem definition

The Navier-Stokes equation (without the convective term) was used as the mathematical model of the aforementioned flow:

$$\rho \frac{\partial c_i}{\partial t} + \frac{\partial p}{\partial x_i} - \mu \frac{\partial^2 c_i}{\partial x_j^2} = 0. \tag{1}$$

While solving this equation, only the case of the planar flow in a pipe was considered (*fig. 1*):

$$\rho \frac{\partial c_1}{\partial t} + \frac{\partial p}{\partial x_1} - \mu \frac{\partial^2 c_1}{\partial x_2^2} = 0. \tag{2}$$

The flow with the pressure drop was considered and hence the pressure at the ends of pipe was chosen as the boundary conditions:

$$\begin{aligned} x_1 = 0 &: \; p(0,t) = p_1(t), \\ x_1 = L &: \; p(L,t) = p_2(t). \end{aligned} \tag{3}$$

In order to solve this problem, initial conditions for velocity and pressure are required. Initial velocity was chosen as zero and initial pressure was prescribed by using a general function φ, which depends only on the position in axis x_1.

$$\begin{aligned} t = 0 : p(x_1, 0) &= \varphi(x_1, 0), \\ c_1(x_2, 0) &= 0. \end{aligned} \tag{4}$$

* Ing. Hana Krausová: Energy Institute, Faculty of Mechanical Engineering, Brno University of Technology, Technická 2896/2; 616 69 Brno; CZ, e-mail: hana.mating@gmail.com

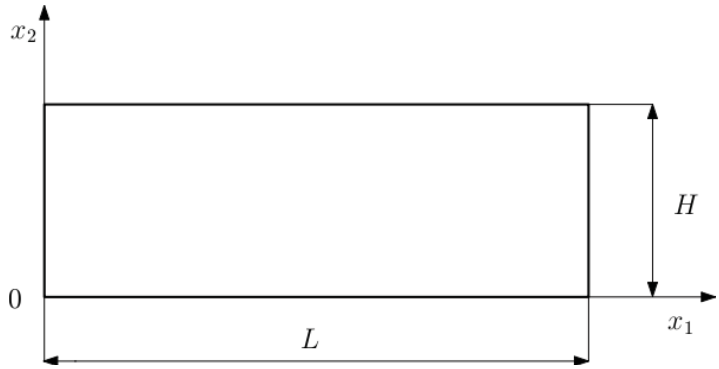

Fig. 1: Planar pipe

On comparing the dependencies of velocity and pressure with the variables in equation (2), it was found out that pressure derivative is a time dependent function. Using boundary conditions (3), the equation for pressure was obtained:

$$p(x_1, t) = p_1(t) - \frac{p_1(t) - p_2(t)}{L}\, x_1. \tag{5}$$

Equation (2) was then transformed into the following form:

$$\frac{\partial c_1}{\partial t} - \nu\, \frac{\partial^2 c_1}{\partial x_2^2} = \frac{p_1(t) - p_2(t)}{\rho L}. \tag{6}$$

The solution of the homogeneous part of this equation was considered to be in the form:

$$c_1(x_2, t) = e^{st}\, w(x_2), \tag{7}$$

where s is the eigenvalue and w is the eigenvector of velocity.

Using equation (7), the partial differential equation (6) was transformed to the ordinary differential equation:

$$sw - \nu\, \frac{\partial^2 w}{\partial x_2^2} = 0, \tag{8}$$

with zero boundary conditions for the eigenmode shape of velocity:

$$\begin{aligned} x_2 = 0 &: w = 0, \\ x_2 = H &: w = 0. \end{aligned} \tag{9}$$

The solution of equation (6) is discussed in further detail in section 2.3. The following sections give important properties of eigenvalue and eigenmode shapes of velocity, which are later used to find the solution.

2.1. Eigenvalue and eigenmode shapes of velocity

In order to solve equation (8), it is required to find out more information about the form of eigenvalue s. An estimate was performed which showed that the eigenvalue is negative real number:

$$s = -\nu\, \frac{\int_0^H \frac{\partial w}{\partial x_2}\, \frac{\partial w^*}{\partial x_2}\, dx_2}{\int_0^H w\, w^*\, dx_2} = -\alpha, \qquad \alpha \in \mathbb{R}^+. \tag{10}$$

Another fact that needs to be considered is that the eigenvectors are orthogonal. This was observed after comparing equation (8) for the k-th and l-th term of eigenmode shapes of velocity w_k and w_l^*:

$$(s_k - z_l) \int_0^H w_k \, w_l^* \, dx_2 = 0, \tag{11}$$

where z_l is the eigenvalue for the l-th term of eigenmode shapes of velocity.

From this equation two conclusions can be made:

- Eigenvalues are equal for the same indices:

$$s_k = z_l, \quad \text{for } k = l. \tag{12}$$

- Eigenvectors are orthogonal real functions:

$$\int_0^H w_k \, w_l^* \, dx_2 = 0. \tag{13}$$

2.2. Determination of the velocity function

The general solution of homogeneous partial differential equation of second order (8):

$$sw - \nu \frac{\partial^2 w}{\partial x_2^2} = 0, \tag{14}$$

has the form:

$$w(x_2) = A \sinh\left(\sqrt{\frac{s}{\nu}} \, x_2\right) + B \cosh\left(\sqrt{\frac{s}{\nu}} \, x_2\right). \; A, B \in \mathbb{C}. \tag{15}$$

Using the first boundary condition (9), that is:

$$x_2 = 0 : w = 0, \tag{16}$$

it was found out that constant B is zero. Hence the eigenmodes will be only a function of hyperbolic sine:

$$w(x_2) = A \sinh\left(\sqrt{\frac{s}{\nu}} \, x_2\right). \tag{17}$$

From the second boundary condition the following expression was obtained

$$\sinh\left(\sqrt{\frac{s}{\nu}} \, H\right) = 0. \tag{18}$$

Using the property (10) that the eigenvalue is a real number, an expression for constant α was derived:

$$\alpha = \nu \left(\frac{k\pi}{H}\right)^2. \tag{19}$$

Using the boundary conditions, an equation for the eigenvalue and also the form of the eigenmodes was found. However, the constant A in the function for eigenmode shapes of velocity has still to be determined. This constant was found by using the orthogonality condition:

$$\int_0^H w_k \, w_k^* \, dx_2 = 1. \tag{20}$$

After that, the constant for the k-th term of eigenmode shapes of velocity was found to be of the form:

$$A_k = -\,i\,\sqrt{\frac{2}{H}}. \tag{21}$$

Final form of the eigenmode shapes of velocity is solely the sine function:

$$w_k = \sqrt{\frac{2}{H}}\,sin\left(\frac{k\pi}{H}\,x_2\right). \tag{22}$$

2.3. Eigenmode expansion

In the previous section, only the homogeneous part of equation (8) was discussed. Here the complete solution of equation (6) will be considered:

$$\frac{\partial c_1}{\partial t} - \nu\,\frac{\partial^2 c_1}{\partial x_2^2} = \frac{p_1(t) - p_2(t)}{\rho L}, \tag{23}$$

accompanied by the boundary and initial conditions:

$$\begin{aligned} x_2 = 0: &\quad c_1(0,t) = 0, \\ x_2 = H: &\quad c_1(H,t) = 0, \\ t = 0: &\quad c_1(x_2,0) = 0. \end{aligned} \tag{24}$$

Solution of this equation was approached by using an expansion into a series of eigenmodes of vibration in the form:

$$c_1(x_2,t) = \sum_{k=1}^{\infty} a_k(t)\,w_k(x_2). \tag{25}$$

Substituting this form of velocity function into equation (23) the following equation was obtained:

$$\sum_{k=1}^{\infty}\left(\frac{\partial a_k(t)}{\partial t} - s_k\,a_k(t)\right) w_k = \frac{p_1(t) - p_2(t)}{\rho L}. \tag{26}$$

This equation can be simplified according to the orthogonality (13) and orthonormality (20) condition to the form:

$$\frac{\partial a_k(t)}{\partial t} - s_k\,a_k(t) = \sqrt{\frac{2}{H}}\,\frac{H}{k\pi}\,\frac{p_1(t) - p_2(t)}{\rho L}\,[1 - (-1)^k]. \tag{27}$$

This last equation accompanied by the initial condition:

$$t = 0 : a(0) = 0, \tag{28}$$

was solved using Laplace transformation. During an inverse transformation, convolution theorem was used and for the next computation constant change of pressure Δp was considered.

Expression for time dependent function $a_k(t)$ is:

$$a_k(t) = \sqrt{\frac{2}{H}}\,\frac{H^3}{(k\pi)^3\rho L\nu}\,[1 - (-1)^k]\,(1 - e^{s_k t})\,\Delta p. \tag{29}$$

Substituting the equation for time dependent function (29) back into equation (25) the following expression was obtained:

$$c_1(x_2,t) = \frac{2H^2\Delta p}{\pi^3 \rho L \nu} \sum_{k=1}^{\infty} \frac{1-(-1)^k}{k^3} \left(1 - e^{s_k t}\right) \sin\left(\frac{k\pi}{H} x_2\right), \tag{30}$$

where eigenvalue is:

$$s_k = -\nu \left(\frac{k\pi}{H}\right)^2. \tag{31}$$

2.4. Result comparison

The result obtained was confirmed by comparing the maximal velocity achieved through the calculation (30) with the exact value. But nevertheless it was a restricted case. The considered time interval t was large enough and the equation was approximated only by the first eigenmode:

$$c_1\left(\frac{H}{2}\right) = \frac{4}{\pi^3} \frac{H^2}{\rho L \nu} \Delta p \doteq \frac{H^2}{7.75\, \rho L \nu} \Delta p. \tag{32}$$

While exact value (Šob, 2002) for velocity in the middle of pipe is:

$$c_1\left(\frac{H}{2}\right) = \frac{H^2}{8\, \rho L \nu} \Delta p. \tag{33}$$

Mentioned results differ only by 4%, hence it can be said that approximation by the first eigenmode is quite accurate. By increasing the number of eigenmodes, a more precise value for the maximal velocity will be obtained.

2.5. Graphical assessment

For the following graphical assessment these values for the variables were used:

$H = 0.09$ m, $\rho = 1000\ \mathrm{kg \cdot m^{-3}}$,

$L = 12$ m, $\nu = 10^{-6}\ \mathrm{m^2 \cdot s^{-1}}$.

$\Delta p = 300$ Pa,

From the equation (30) it can be easily seen that the velocity profile is composed only from odd eigenmode shapes of velocity, because the time dependent function $a_k(t)$ for even eigenmodes is zero. The first four eigenmodes are drawn in the following figures:

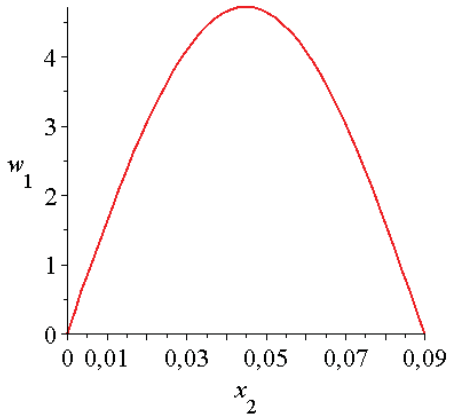

(a) First

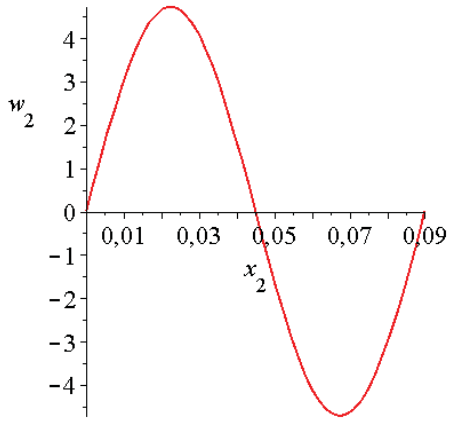

(b) Second

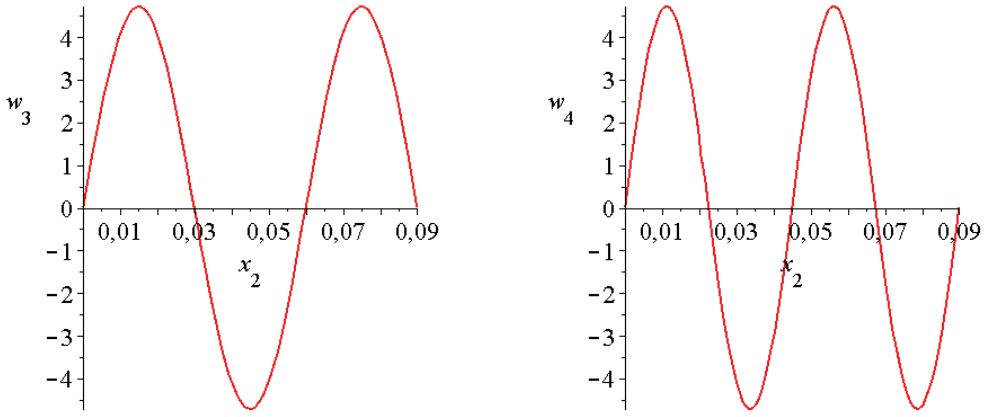

(c) Third (d) Fourth

Fig. 2: Eigenmodes of vibration

Final form of velocity function is given by equation (30). The partial sums of this series are plotted against time $t = 200$ s. This stretch of time was chosen randomly, however it was not chosen to be long enough for the stabilization of the velocity profile.

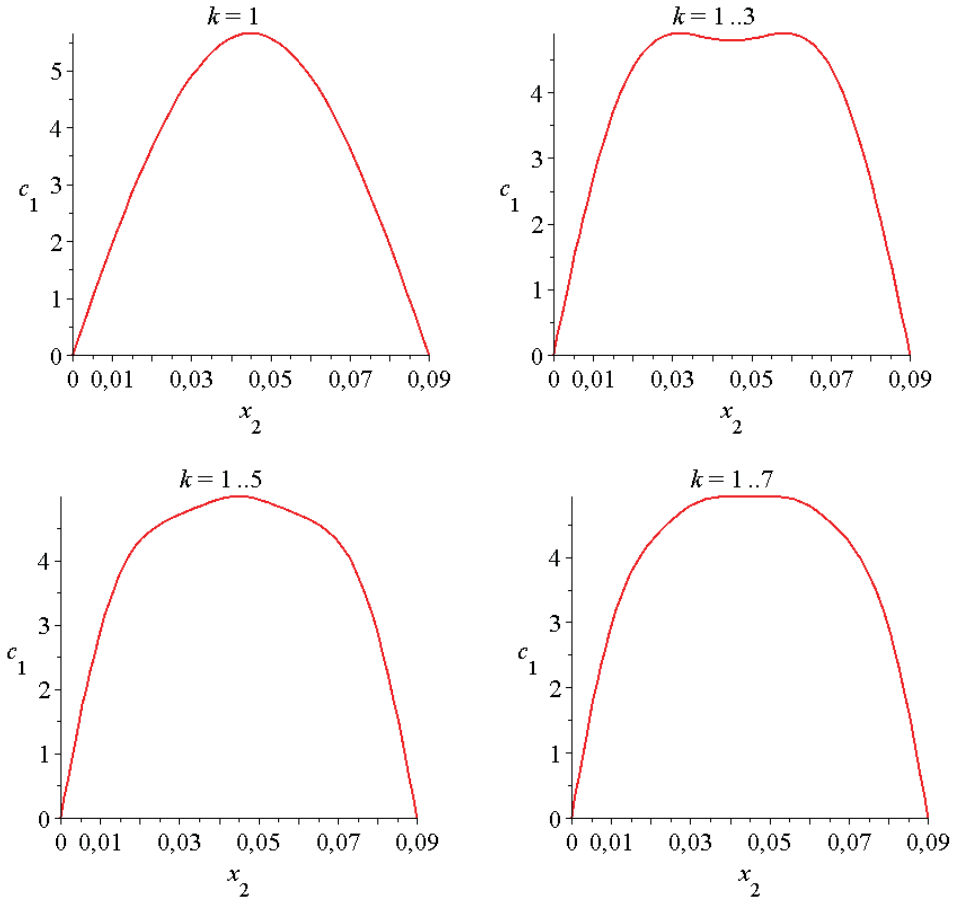

Fig. 3: The partial sums of velocity function

From these graphs, it can be shown that after summing seven eigenmodes, the shape of the velocity profile is getting closer to profile of laminar flow despite the fact that the profile is not completely stabilized. Odd eigenmodes cause symmetric velocity profile which is expected by our case of start-up flow.

Next the time dependence of the velocity when twenty eigenmode of vibrations are summed was then observed.

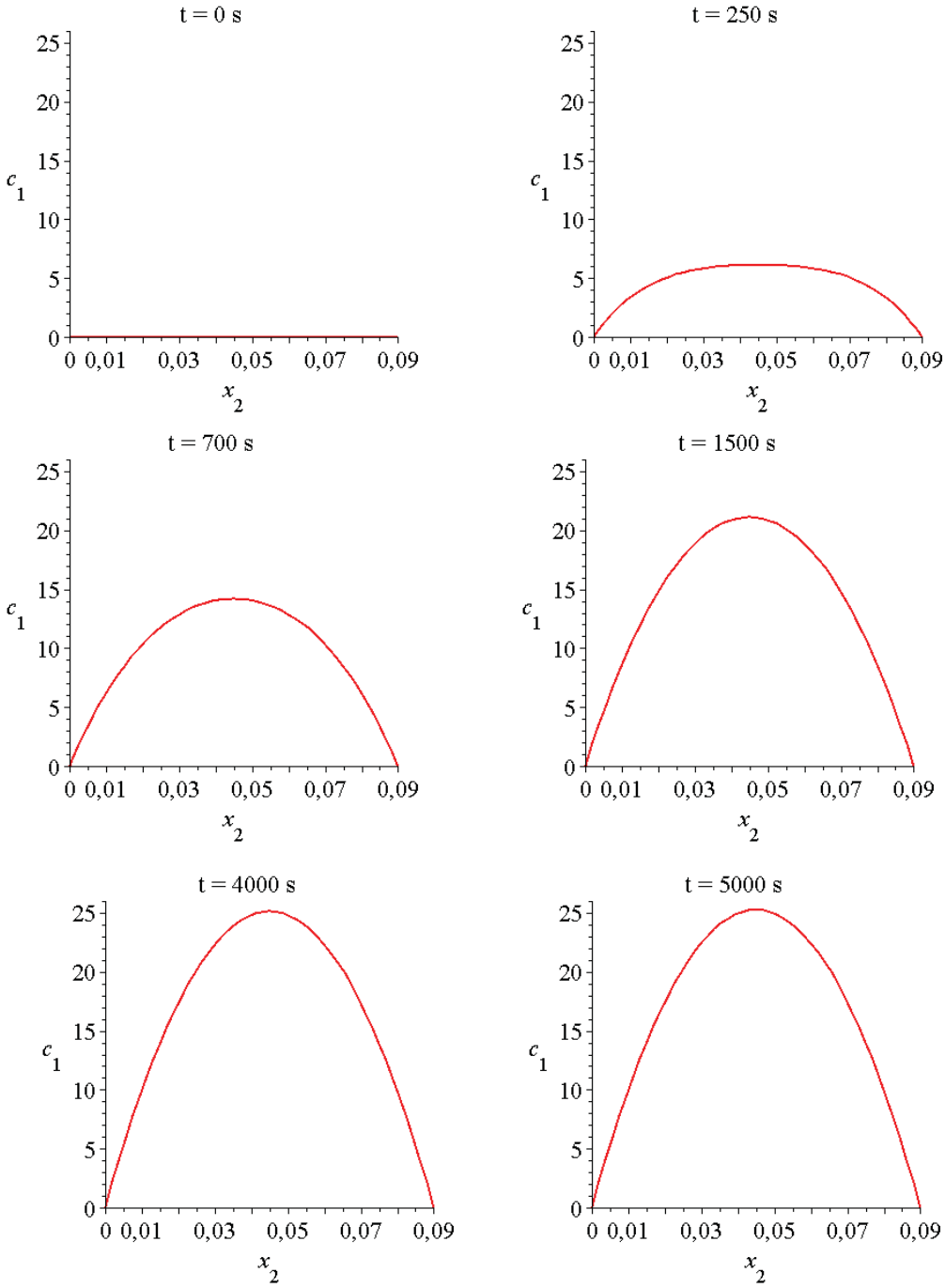

Fig. 4: Time dependence for ten odd eigenmode shapes of velocity

2.6. Comparison

From literature, it is common knowledge that for a time step long enough, the flow is considered as stationary, hence equation (2) has the form:

$$\frac{\partial p}{\partial x_1} - \mu \frac{\partial^2 c_1}{\partial x_2^2} = 0. \tag{34}$$

Analytical solution of this equation with zero boundary condition for velocity on walls of the pipe is a quadratic function of coordinate x_2:

$$c_1(x_2) = \frac{\Delta p}{2\mu L}(H x_2 - x_2^2). \tag{35}$$

This expression can also be obtained from equation (30) for a long enough time t:

$$c_1(x_2) = \frac{4H^2 \Delta p}{\pi^3 \rho L \nu} \sum_{\substack{l=1 \\ k=2l-1}}^{\infty} \frac{1}{k^3} \sin\left(\frac{k\pi}{H} x_2\right). \tag{36}$$

For summation of the series equation (Kadlec & Kufner, 1969) was used:

$$\sum_{n=1}^{\infty} \frac{\sin nx}{n^3} = \frac{2\pi^2 x - 3\pi x^2 + x^3}{12}. \tag{37}$$

This sum of series holds for all summing indices, so it is necessary to transform this expression to only odd summing indices. To obtain only odd summing indices, the property that sum over all summing indices is equal to sum over odd and even indices was used. Hence using equation (37), expression (35) was obtained, which is the same to the analytical solution of equation (34).

3. Conclusions

This paper described the solution of the Navier-Stokes equation for non-stationary flow of an incompressible fluid. This solution is based on an expansion into a series of eigenmodes of vibration. The proposed approach considers the solution of velocity function as a combination of eigenmode shapes of velocity and time dependent function. Specific solution to the presented problem depends only on the odd eigenmode shapes of velocity since even eigenmodes were zero. The graphical part of this paper illustrated the achieved results.

Acknowledgement

The financial support of the Specified Research Grants No. FSI-J-12-21/1698, No. FSI-S-12-2 and NETME Centre project - New technologies for Mechanical Engineering CZ.1.05/2.1.00/01.0002 is gratefully acknowledged.

References

Brdička, M., Samek, L. & Sopko, B. (2000) *Mechanika kontinua*. Academia, Prague.

Kadlec, J. & Kufner, A. (1969) *Fourierovy řady*. Academia, Prague.

Krausová, H. (2009) *Navier-Stokesova rovnice – řešení laminárního proudění*. Bachelor's thesis. BUT, FME, Brno.

Pochylý, F. & Fialová, S. (2009) *Řešení laminárního proudění rozvojem podle vlastních tvarů kmitu*. Research work, BUT, FME, Brno.

Šob, F. (2002) *Hydromechanika*. Academic Publisher CERM, Brno.

18th International Conference
ENGINEERING MECHANICS 2012
Svratka, Czech Republic, May 14 – 17, 2012

pp. 733–739
Paper #312

APLICATION OF HIGH-RESOLUTION X-RAY RADIOGRAPHY FOR MONITORING THE PENETRATION DEPTH OF CONSOLIDANTS IN NATURAL BUILDING STONES

F. Krejci[*], J. Jakubek[*], M. Slavikova[**], P. Kotlik[**]

Abstract: *For conservation of the built cultural heritage the application of conservation products like consolidants or water repellents is often used. A natural stone is, however, a complicated heterogeneous porous system making the process of consolidation dependent on many variables. The selection of a suitable consolidant and consolidation conditions therefore remains a complex issue. The impregnation depth is a key factor for the assessment of the treatment efficiency. So far, the methods used for monitoring the penetration depth usually require a cut of the investigated stone. These destructive approaches, however, significantly reduces the number and choice of the investigated cuts. The methods, furthermore, do not allow dynamical studies of the impregnation process. The combination of state-of-the-art hybrid pixel semiconductor detectors with newly available micro-focus X-ray sources makes X-ray radiography an ideal non-destructive tool for the penetration depth monitoring. In this contribution, we present results of high-resolution X-ray radiography applied for the penetration depth monitoring of polymer consolidants in the Opuka stone.*

Keywords: ***X-ray radiography, computed tomography, stone, consolidation, penetration depth, Opuka.***

1. Introduction

Stone impregnation with consolidating materials is an important process of stone conservation. Due to aggressive contaminants and weather effects (repeated wetting, freezing and continuous capillary action), the interaction between the building stone of monuments and the environment results in changes of the mechanical properties of the stone (Price 1996). As a result of such degradation and corrosion processes the solidness of the monument can deteriorate. The consolidation might be characterized as a targeted act leading to recovery of the mechanical properties of the damaged stone. The consolidation itself is usually realized by saturation of the damaged stone by various consolidants. The process is consequently evaluated as successful if the damaged part of the stone gains the missing binder and the part is attached to the healthy core of the stone (Bayer 2009).

A natural stone is, however, usually a complex heterogeneous porous system in which the degraded part of the stone differs from the healthy part in absorbability, porosity, composition, etc. This makes the consolidation process dependent on many variables. It is thus difficult to choose the right consolidant which will penetrate well in stone parts - both damaged and healthy (Bayer 2009). The consolidation is moreover an irreversible intervention on the stone and, if the consolidating substance does not penetrate at a sufficient depth, there is the risk of further accelerated stone degradation resulting in the loss of the valuable historic material (Pinto et al. 2007, Snethlage & Wendler 2005). Monitoring the penetration depth thus plays a key role in the assessment of the stone consolidation efficiency.

[*]Ing. Frantisek Krejci: Institute of Experimental and Applied Physics, Czech Technical University in Prague, Horska 3a/22, Prague 2, 12800, Czech Republic; CZ, e-mail: frantisek.krejci@utef.cvut.cz

[*]Ing. Jan Jakubek, Ph.D.: Institute of Experimental and Applied Physics, Czech Technical University in Prague, Horska 3a/22, Prague 2, 12800, Czech Republic; CZ, e-mail: jan.jakubek@utef.cvut.cz

[**]Ing. Monika Slavikova, Institute of Chemical Technology, Department of Chemical Technology of Monuments Conservation, Technicka 5, Prague 6, 166 28, Czech Republic, e-mail: slavikom@vscht.cz

[**]Doc. Ing. Petr Kotlik, CSc. Institute of Chemical Technology, Department of Chemical Technology of Monuments Conservation, Technicka 5, Prague 6, 166 28, Czech Republic, e-mail: petr.kotlik@vscht.cz

1.1 Opuka stone

Cretaceous sandy marlstone, called in the Czech Republic and other eastern European countries "Opuka", was a common building stone in Bohemia from the beginning of stone architecture in the early mediaeval epoch. As the most ancient building stone in Prague, Opuka was used for historical monumental edifices such as churches, fortresses, castles, fortifications as well as burgher's houses. The consolidation of this stone thus plays a key role in preservation of the Czech building cultural heritage. The occurrence of this stone and the respective monuments are recorded also in Poland, Germany and France.

The Opuka stone is specific with its fine-porous structure in which the pore size with size less than 0.1 μm prevails. These small pores can even account for up to 98 % of the total pore volume. Due to very high content of small pores, in comparison with sandstone and limestone, the impregnation of Opuka stone gives the worst results (Šrámek 1992). Although the stone shows high water absorption, the speed of capillary action is very slow and in practical restoration aims the consolidation of Opuka stone still remains an issue (Kotlík 2000). For a successful consolidation of the stone it is very important to know the time needed for achieving a sufficient penetration depth and the dependence of the penetration depth on the stone type and conditions during consolidation.

1.2 Penetration depth monitoring

Most of the methods for monitoring the penetration depth of consolidants have limited use due to their destructive nature (the methods always require a stone cut). Such a destructive approach significantly reduces the number and choice of studied cuts in the sample. Moreover, dynamical studies, which are crucial for penetration depth assessment, are practically not feasible. Instrumental methods for monitoring the penetration depth in a destructive way include scanning electron microscopy, infrared microscopy with Fourier transform, micro-drilling and non-destructive ultrasonic measurement (Casadio & Toniolo 2004). Color reactions for monitoring the penetration depth include staining the stone cut with iodine vapor or specific reagents (e.g., catalyst of organosilanes can be stained with a solution of diphenylthiocarbazone, Bayer 2009). Hydrophobic properties of consolidants can be used to visualize the consolidated part by wetting.

1.3 X-ray radiography

X-ray radiography is relatively non-destructive methods newly explored for direct monitoring of the stone consolidation (V. Cnudde et al. 2004, V. Cnudde et al. 2009, Slavikova et al. 2012). The possibility of monitoring consolidation as a dynamic process and measuring a 3-D distribution of the consolidant in the stone makes the approach an outstanding tool with many advantages over other methods.

Using this technique, the visualization of the consolidant inside the stone depends on the contrast in X-ray absorption between the mineral constituents of the stone material and the consolidant itself. Besides the stone sample parameters, the quality of the resultant visualization is dependent on the CT configuration used given by the X-ray source parameters (used photon flux, tube spectrum) and in particular by the X-ray detector. In the case, when the total amount of the consolidation product applied is very small, the contrast between the treated and untreated part of the stone is very small and the exact localization of the penetration depth and the consolidant distribution in the stone remains very difficult to determine. A clear visualization of the consolidant is then often accomplished by doping these consolidation products with a contrast agent that causes a higher attenuation for X-rays (e.g. 3-bromopropyltrimethoxysilane, Brunetti et al. 2004, Slavikova et al. 2012).

By adding a product with higher attenuation for X-rays to the original conservation products, higher contrast can be created between the stone material and the conservation products. On the other hand, due to doping of the original products, the process of consolidation can be in certain characteristics significantly influenced (the penetration ability of consolidants is often not exactly the same as the penetration ability of commercial consolidation products). As these differences are reduced with decreasing concentration of the contrast agent, the application of X-ray radiography with high sensitivity enabling detection of very small variations in attenuation in the stone is desired.

Recent advances in semiconductor technology allow for the construction of hybrid planar pixelated detectors. The pixel detectors of Medipix type (X. Llopart et al. 2001, X. Llopart et al. 2007)

contain highly integrated signal electronics with a digital counter per pixel. Thus, each individual X-ray photon impinging on the detector is processed independently – the signal is amplified, discriminated and counted. Moreover, the counter is incremented without any dark current and with full suppression of electronic noise. Thanks to the digital integration, the result (e.g. radiograph) is absolutely linear and the dynamic range is virtually unlimited (in practice limited just by the number of detected photons, Jakůbek 2007). Such advantages do not exist in other types of detectors such as charge integrating devices (e.g. flat panels and CCDs) which suffer from limited dynamic range, limited linearity, noise integration and non-zero dark current. In this contribution, we present the application of Medipix detector technology for monitoring the penetration depth of consolidants in the Opuka by means of X-ray radiography.

2. Materials and methods

1.4 Stone materials

Three kinds of Opuka were used for consolidation monitoring – gold Opuka from Přední Kopanina (Central Bohemia near Prague), grey Opuka from Přibylov (East Bohemia) and decalcified Opuka from Džbán (North West Bohemia). Decalcified Opuka is a special stone which has naturally lost much of its binder (calcium carbonate). In our studies, decalcified Opuka simulates a vastly degraded stone with high porosity, poor mechanical properties and low resistance to structural deterioration. On the other hand, the so called gold and gray Opuka represent a healthy rock part with narrow pore size distribution and much lower total porosity than decalcified Opuka. At present, the gold and grey Opuka is often used for restoration of stone monuments (Kotlík 2000).

The stone samples were consolidated and after seven days their radiograms were measured. The samples were stored at 20°C and 50 % air relative humidity. As the X-ray radiographic system was not able to measure large stone samples (due to limited area of the used pixel detector), stone samples were therefore cut with a diamond saw Minosecar to blocks of 0.5 × 0.5 × 4 cm (see Fig. 1). In order to prevent evaporation of consolidant from the impregnated stone and the capillary action from the side walls, the vertical sides of the samples were covered with a carnauba wax layer. The wax impregnation of the side walls ensures that the consolidation mixture penetrates only the lower sample base. Without the wax treatment the flow profile of the consolidant would be influenced by the interaction with the sample surface and would not represent the behavior in larger stone blocks.

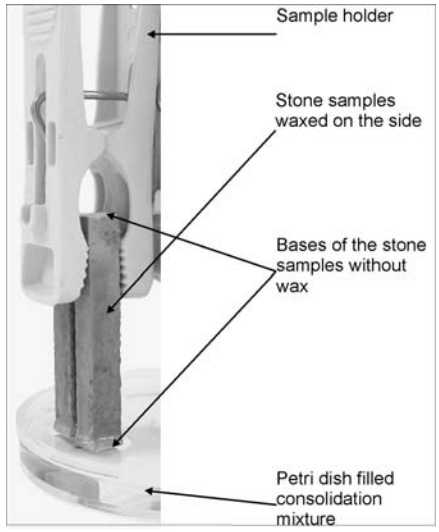

Fig. 1 Experimental setup used for the stone samples consolidation. The sedimentary layers of the impregnated sample are perpendicular to the surface of the consolidation mixture. The wax impregnation of the side walls ensures that the consolidation mixture penetrates only the lower sample base (i.e., only vertically).

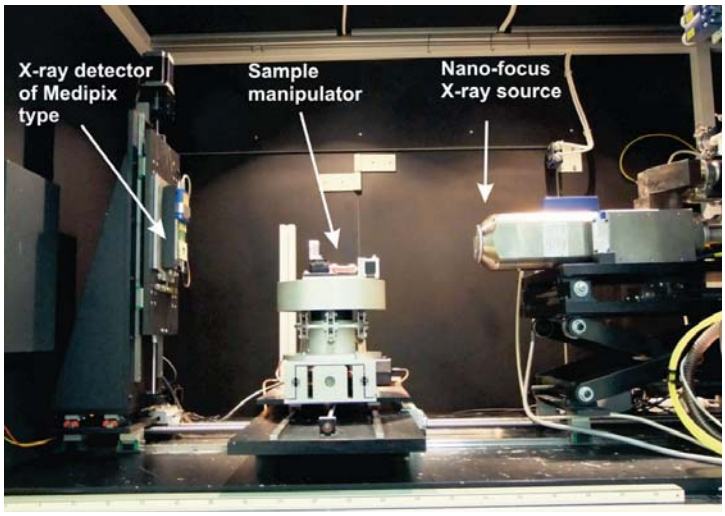

Fig. 2 X-ray micro-radiography setup at the Institute of Experimental and Applied Physics of the CTU in Prague used in the measurement.

1.5 Consolidants

For X-ray radiography measurements a commercial consolidant was mixed with a suitable contrast compound enhancing the attenuation of X-rays. To study the influence of the contrast agent to measured quantities, three mixtures of different contrast agent concentrations were prepared for our experiments. The mixtures are denoted in the text as follows: ID (concentration of the contrast agent 97 %), IED (48.5 %) and IEDE (4.3%). The consolidation mixtures were prepared from Dynasylan 40 (Et40), (3-iodopropyl)trimethoxysilane (I- MEOS) and dibutyltin dilaurate (DBTDL) catalyst which was added as an accelerator of polycondensation (Brus & Kotlík 1996),. Dynasylan 40 (Evonk Degussa Corporation) is a mixture of tetramers and pentamers of tetraethoxy orthosilicate. The iodinated silane (3-iodopropyl)trimethoxysilane is a contrast agent for X-ray radiography from Sigma Aldrich.

1.6 X-ray radiography and micro-tomography measurement

The X-ray imaging experiments were carried out in the compact radiography system developed at the IEAP CTU in Prague (J. Jakůbek et al. 2006). The setup (see Fig. 2) is equipped with a X-ray tube from Feinfocus. During the experiments the X-ray tube was operated with a transmission tube head FXT-160.51 and a broad polychromatic spectrum of a W–Be target spot at 50 keV. The size of the X-ray focal spot has of Gaussian shape with sigma ~1 μm. As an X-ray sensor, we used the position sensitive Timepix digital single photon counting device (X. Llopart et al. 2007) with a 300 μm thick Si sensor arranged into a matrix of 256 × 256 square pixels of 55 μm pitch giving a total detection area of 14×14 mm^2.

During all measurements the Timepix detector was operated in counting (so-called Medipix) mode. In our studies, although the number of photons reaching the detector is relatively low (mostly hard X-rays traverse the 5 mm thick stone for which the efficiency of a silicon sensor is low), sufficient contrast is achieved just by prolongation of the measurement exposure time (typically no longer than 60 s). Images were acquired at 50 keV X-ray tube voltage and 30 μA target current. The measured radiographic data were corrected for the beam-hardening effect using a signal-to-thickness calibration (Jakůbek 2007). From the measured radiographs the penetration depth of the consolidant can be directly evaluated.

By scanning the sample at many angles and by suitable image reconstruction, high resolution tomographic images can be obtained with micrometer-scale resolution. This technique allows displaying the stone structure in various virtual cuts, which enables precise monitoring of the consolidant distribution in the sample. For the studies of the consolidation on the stone capillary level,

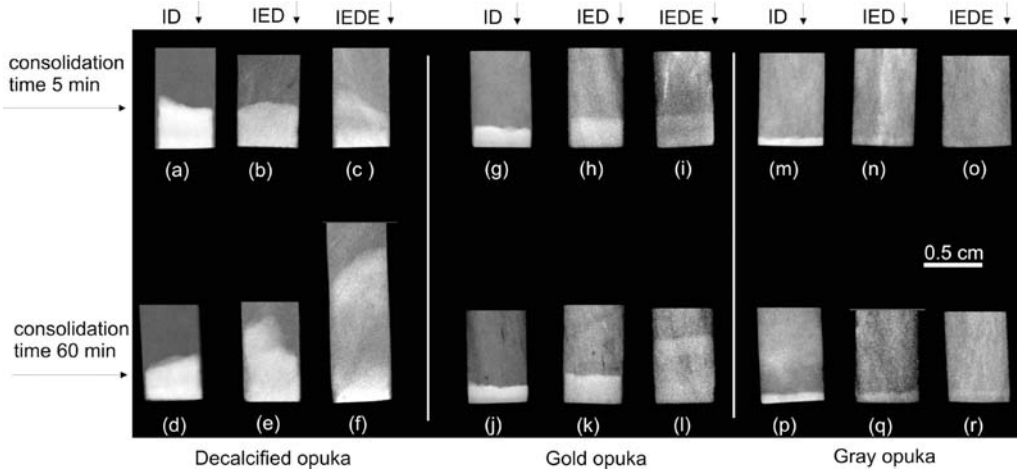

Fig. 3 X-ray radiographs of three different Opuka stone samples impregnated for 5 min (above) and 60 min (below) with consolidation mixtures ID, IED, IEDE (see text). The penetration of consolidants is visualized in white. Besides the penetration depth monitoring it is also possible to visualize Opuka stone sedimentary layers (nicely visible in radiograms (h),(n) and (e)) or consolidant distribution inhomogenities – for example, the consolidants flow is divided into two fronts in radiograms (c), (f), and (i)) (Slavikova et al. 2012).

tomography of a small sample (total imaged volume ~1 mm^3) with spatial resolution 9 µm was also measured. 3-D tomographic reconstruction was calculated from 181 projections acquired with one degree step using an adapted iterative expectancy maximization method accelerated by ordered subsets. The projection images were acquired at 50 keV with 30 µA target current and exposure time 15 s.

3. Results

The resulting radiographs enable monitoring the penetration depth of the used consolidant in a very simple, reliable and non-destruction way (see Fig. 3). In comparison with most of the conventionally

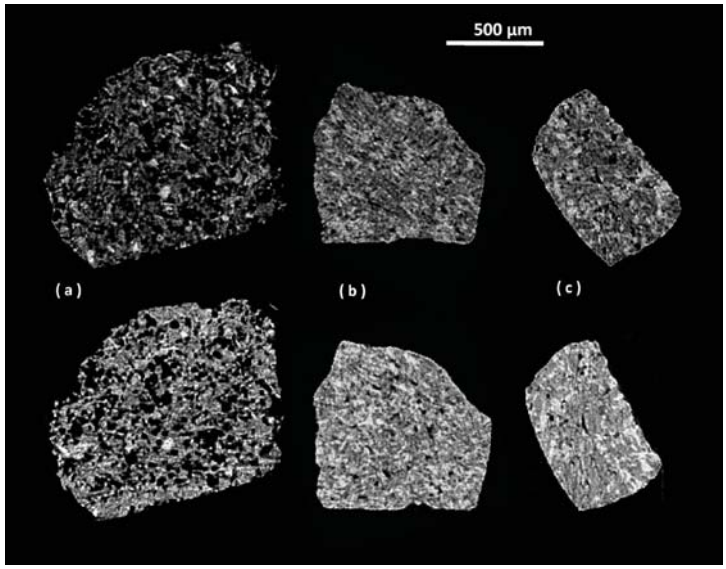

Fig. 4 High-resolution computer tomography of three Opuka stones before (above) and after the consolidation (below). (a) decalcified Opuka, (b) gold Opuka, (c) gray Opuka. All images are visualized at the same gray-scale (Slavikova et al. 2012).

used techniques, it is possible to study a large number of stone samples giving possibility to find appropriate combination of the consolidated stone, consolidant and consolidation conditions such as consolidation time. Dynamical monitoring (X-ray movie) of the consolidation process is possible as well – see Slavikova et al. 2012.

To demonstrate the feasibility of studying the consolidation on a stone capillary level, high resolution tomography of a small stone part before and after the consolidation has been carried out (see Fig. 4). This feature opens the possibility for a whole range of further studies. Topics like porosity changes visualization inside stone samples during impregnation can be investigated, as well as the investigation how the products react inside different stone types. Thanks to the quality of the measured images and their digital nature, further image analysis is possible.

4. Conclusions

We have demonstrated that the application of X-ray radiography utilizing semiconductor particle-counting detectors stands out as a powerful tool in research of consolidants inside natural building stones. The capabilities of this technique have been demonstrated on simple projections X-ray radiography as well as computed tomography used for monitoring of consolidant in Opuka. The study can provide not only a basic step for additional knowledge on the suitability of investigated products for the treatment of the Opuka stone type, but also the study can serve as an instrumental and methodological work applicable for treatment of other stone types.

X-ray micro-radiography technique appears as an ideal tool for finding appropriate combinations of stones, consolidants and consolidation time. Even though this technique cannot compete ultimate with spatial resolution, e.g., from electron microscopes, the main advantage lies in the possibility of non-destructive stone volume visualization (i.e., the method is not just superficial).

Due to mixing with a contrast agent, the penetration ability of consolidants is not exactly the same as the penetration ability of commercial consolidation products. These differences are reduced with decreasing concentration of the used contrast agent. Application of X-ray radiography demands setups with high sensitivity enabling detection of very small changes in attenuation in the stone. A further significant improvement in pixel detector sensitivity is expected with the application of novel sensor materials with higher atomic number such as CdTe and GaAs.

Acknowledgement

Work supported by research grants No. 21/2010 and No. 21/2011 and MSM 6046137302 of the Ministry of Education, Youth and Sport and research grant P105/11/1551 of the Grant Agency of the Czech Republic. This work is a part of the student research projects A2_FCHT_2010_20 and A2_FCHT_2011_008. Research carried out in frame of the Medipix Collaboration.

References

Bayer, K. (2008), Možnosti hodnocení efektivity konsolidace porézních anorganických materiálů, in: Padesát let používání organokřemičitanů na území České republiky, *Proceedings of ICOMOS* (in Czech), Národní muzeum, Národní památkový ústav, 35–42.

Brunetti, A. et al. (2004), Visualization of monomer and polymer imide porous stones by using X-ray tomography, *Nuclear Instruments and Methods in Physics Research B*, 222, 235-241.

Brus, J. & Kotlík, P. (1996), Consolidation of stone by mixtures of alkoxysilane and acrylic polymer, *Studies in Conservation*, 41, 109-119.

Casadio, F. & Toniolo L. (2004), Polymer treatments for stone conservation: methods for evaluating penetration depth, *JAIC*, 43 3-21.

Cnudde, V. et al. (2004), X-ray micro-CT used for the localization of water repellents and consolidants imide natural building stones, *Material Characterization*, 53, 259-271.

Cnudde ,V. et al. (2009), The use of X-ray tomography in the study of water repellents and consolidants, *Engineering Geology*, 103, 84-92.

Jakůbek, J. (2007), Data processing and image reconstruction methods for pixel detectors, *Nuclear Instruments and Methods in Physics Research A*, 576, 223-234.

Jakůbek, J. et al. (2006), Compact system for high resolution X-ray transmission radiography, in-line phase enhanced imaging and micro CT of biological samples, *IEEE Nuclear Science Symposium Conference Proceeding*, 1077 – 1080

Kotlík, P. (2000), Opuka, STOP (Society for Technology protection of monuments), (in Czech), Praha.

Llopart, X., et al. (2001), *IEEE Transactions on Nuclear Science* , 49, 2279-2283.

Llopart, X., et al. (2007),, Timepix, a 65k programmable pixel readout chip for arrival time, energy and/or photon counting measurements , *Nuclear Instruments and Methods in Physics Research A*, 581, 485.

Pinto, P. F. et al. (2007), The role of treatment procedure, *Journal of Cultural Heritage,* 9, 38–53.

Price, C. A. (1996), Stone conservation: an overview of current research, *The Getty Conservation Institute*, Santa Monica.

Slavikova, M. et al. (2012), X-ray radiography and tomography for monitoring the penetration depth of consolidants in Opuka – the building stone of Prague monuments, *Journal of Cultural Heritage*, in print.

Snethlage, R. & Wendler, E. (2005), Chenical Conservation of Stone Structures, *Ullmann's Encyclopedia of Industrial Chemistry.*

Šrámek, J. (1992), Relationships between mineralogy, physical – mechanical properties and durability of cretaceous calcitic spongolities, Proceedings, *7th International congress on deterioration and conservation of stone,* Lisbon - Portugal, 57–66.

18th International Conference
ENGINEERING MECHANICS 2012
Svratka, Czech Republic, May 14 – 17, 2012

pp. 741–744
Paper #30

MOBILE ROBOT TRACKING USING IMAGE PROCESSING

J. Krejsa[*], S. Věchet[**], T. Ripel[**]

Abstract: *During the evaluation of autonomous mobile robot navigation routines the determination of true robot position on its track is essential. The paper presents simple yet reliable method of tracking robot position using processing of images acquired from the devices positioned above the operation space. The method consists of two steps for each image: detection of the robot in image space and transfer of its coordinates to operation space.*

Keywords: ***Mobile robot, image processing, object tracking.***

1. Introduction

To evaluate the quality of localization and path planning routines (Věchet 2011) with real robots, the determination of true position of the robot must be performed. This paper proposes simple yet reliable method of tracking the position of the robot based on the processing of robot images acquired by bird eye positioned camera. The method was used when the quality of Extended Kalman filter based localization was evaluated, as described by Krejsa (2012), focused on the utilization in the prototype of presentation robot Advee (Ripel 2011).

Proposed method consists of two steps. During the first stage the position of the robot in the image space is found, using the detection of marks placed on the robot. In the second stage found coordinates are recalculated into operational space, providing the correction of imprecise image acquiring device mounting, optic flow imperfections, etc.

2. Detection in image space

The sequence of the robot images is acquired from the digital camera mounted above the operational space, as indicated on Fig. 1.

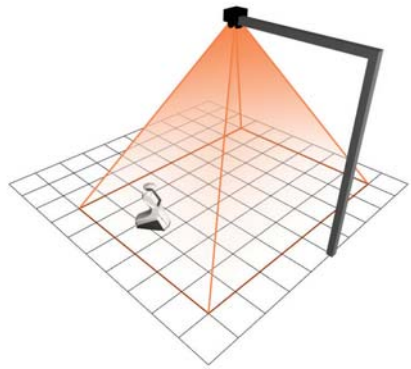

Fig. 1. The principle of image acquiring

[*] Ing. Jiří Krejsa, PhD.: Institute of Thermomechanics ASCR, v.i.i, Brno department, Technická 2, 616 69, Brno, CZ, e-mail: krejsa@fme.vutbr. cz

[**] Ing. Stanislav Věchet, PhD., Ing. Tomáš Ripel: Faculty of Mechanical Engineering, Brno University of Technology, Technická 2, 616 69, Brno, CZ, e-mail:vechet.s@fme.vutbr.cz

Two devices were used to acquire the images, differing in resolution and optical systems, in particular Canon 350D with Canon EF20/f2.8 lens and Pixelink PLB-762G camera with Edmund Optics SZ110M lens. Both devices were positioned 3650 mm above the operational space of the robot. Two white marks with diameter of 21.5mm were placed on the sides of the robot in 607mm relative distance. The mounting of the devices is illustrated on Fig. 2.

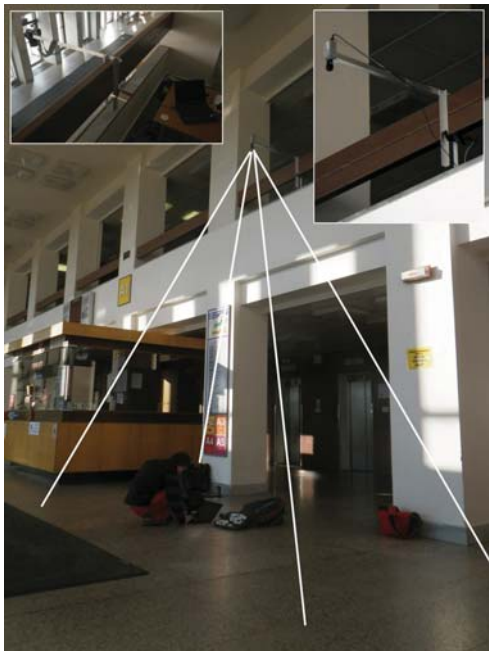

Fig.2. Image acquiring - particular devices mounting

Different optics result in different field of view and therefore the covered operational space. Canon 350D chip has the resolution of 3456 x 2304 pixels and with given optics covers the area of 4.7 x 3.3m, with the final resolution of 1.4mm/pixel. Pixelink camera chip has the resolution of 752 x 480 pixels, covers the area of 10.1 x 6.5m thus producing the final resolution of 13mm/pixel.

Both devices are controlled from the computer, frame rate was set to 1s for the Canon camera due to the duration of image data saving, frame rate for the Pixelink camera was set to 0.5s, even though several experiments were performed with higher frame rates (Pixelink device is capable of maximum 60 fps).

Image data were acquired and saved and then processed offline, therefore there was no demand for optimized image processing with respect to computational requirements. Acquired images were processed in following way, with examples of actual images shown on Fig. 3:

- Format processing: raw to grayscale; region of interest (ROI) determination
- Thresholding ROI with given adaptive threshold value
- Evaluation of the intensity sums of rectangular image blocks uniformly covering the region of interest, with parametrically given overlay.
- Determination of priority blocks by sorting the blocks according to the intensity sum and selection of the blocks with given minimal distance in image space.
- Calculation of precise position of the marks in priority blocks using COG procedure.

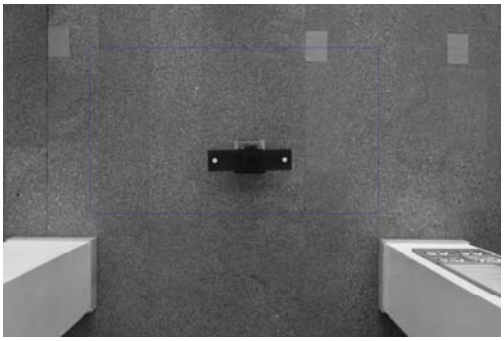

Original image in grayscale with ROI

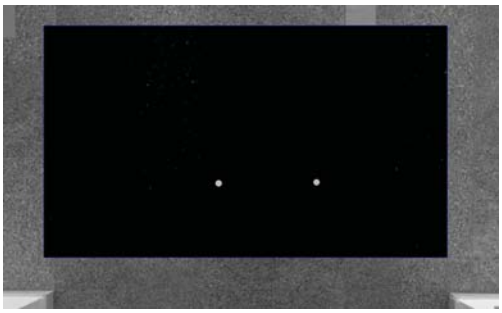

ROI thresholding

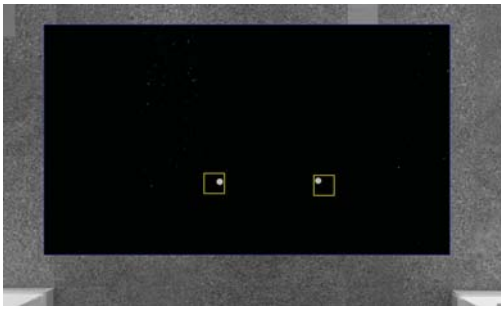

Detected priority blocks holding the condition of minimal distance

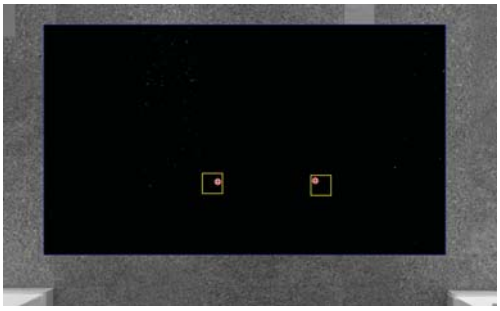

Determination of exact position using COG procedure for priority blocks

Fig. 3. Image processing of acquired images

Images are processed in batch, with constant parameters of block sizes, its overlay and minimal distance between the blocks. Other parameters are variable during the processing, in particular the threshold and region of interest boundaries. Image processing outputs the positions of detected marks in image space in the form of text file for further processing.

3. Recalculation to operational space

Once the position of the marks is found, the next stage is to determine the position of the marks in the operational space. Due to the imperfections in camera mounting and optical flow the values can not be simply multiplied by a constant, but the nonlinear transformation is necessary. The transformation uses the set of calibration points in the operational space, for which the real position $[x_r, y_r]$ is known and corresponding position in image space $[x_o, y_o]$ can be found. The points from both operational and image space are first centered into the center of image space and then transformed to polar coordinates. Thus the coordinates $[\rho_r, \varphi_r]$ and $[\rho_o, \varphi_o]$ are obtained. The transformation from image to operational space is then performed using polynomial of the 4th order:

$$\begin{aligned}\rho_r = \; & a_0 + a_1\rho_o + a_2\varphi_o + a_3\rho_o\varphi_o + a_4\rho_o^2 + a_5\varphi_o^2 + a_6\rho_o^2\varphi_o + a_7\rho_o\varphi_o^2 + \\ & a_8\rho_o^3 + a_9\varphi_o^3 + a_{10}\rho_o^3\varphi_o + a_{11}\rho_o\varphi_o^3 + a_{12}\rho_o^2\varphi_o^2 + a_{13}\rho_o^4 + a_{14}\varphi_o^4 \\ \varphi_r = \; & a_{15} + a_{16}\rho_o + a_{17}\varphi_o + a_{18}\rho_o\varphi_o + a_{19}\rho_o^2 + a_{20}\varphi_o^2 + a_{21}\rho_o^2\varphi_o + a_{22}\rho_o\varphi_o^2 + \\ & a_{23}\rho_o^3 + a_{24}\varphi_o^3 + a_{25}\rho_o^3\varphi_o + a_{26}\rho_o\varphi_o^3 + a_{27}\rho_o^2\varphi_o^2 + a_{28}\rho_o^4 + a_{29}\varphi_o^4\end{aligned}$$

To determine the unknown coefficients of the polynomial, at least 30 equations are required, represented by 15 calibration points. In performed experiments dozens of points were used, determining the coefficients by least squares optimization.

Quality of the transformation was verified using translation motion of the robot through the whole observed region and checking the distance between the marks, that should remain constant during the motion. Pixelink camera distortion was found substantially smaller, however due to the lower resolution and larger viewing angle of the optics the average error in the distance is higher. In particular the standard deviation is 0.43 mm for the Canon camera and 2.92 mm for Pixelink camera. In both cases, however, the values correspond to subpixel precision of marks detection in image space.

The example of comparison of true trajectory detected from image processing and the estimate generated by Extended Kalman filter based localization technique for the experimental robot Leela is shown in Fig. 4.

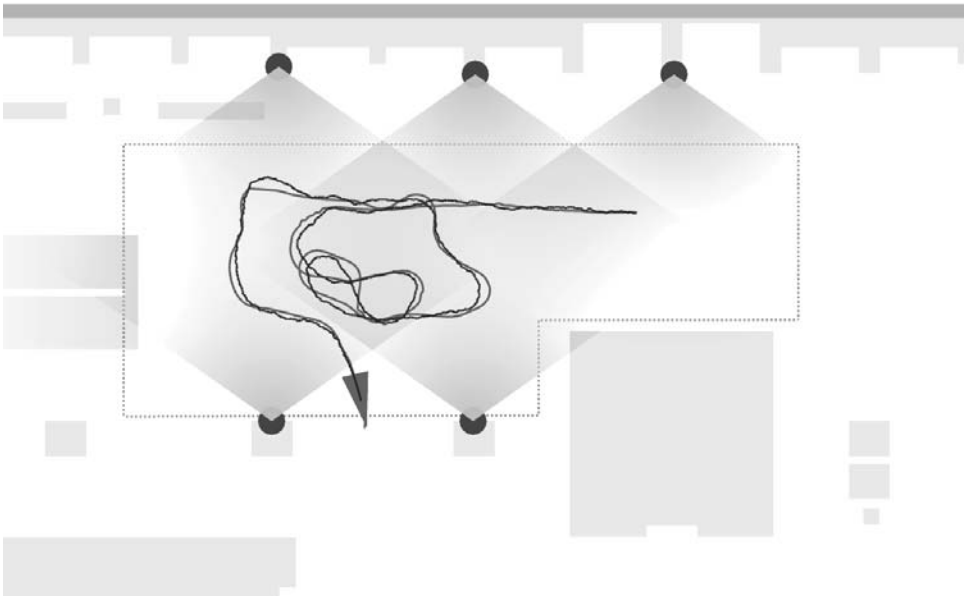

Fig. 4. Comparison of true trajectory of the robot and EKF based localization estimate

4. Conclusions

Presented method is simple and easy to implement. The processing was performed offline, but the computational requirements are low enough to perform online tracking. The method depends on possibility to mark the robot with at least two markers. The precision of the method depends on the rate between the image resolution and covered operational space, the image detection can reach subpixel precision.

Acknowledgement

Results were supported by ASCR via research plan AV0Z20760514 and by Brno University of Technology under project FSI-S-11-15.

References

Krejsa J., Věchet S. (2012): Infrared beacons based localization of mobile robot, *Electronics and Electrical Engineering*, 1(117), 2012, pp. 17-22

Věchet S., Krejsa J. (2011): Concurrent mapping and localization based on potential fields, in Proceedings of *Engineering Mechanics 2011*, Svratka, pp. 647-650

Ripel T., Hrbáček J. (2011): Complex mechanical design of autonomous robot Advee, in *Mechatronics, recent technological and scientific advances*, Springer, pp. 121-130

18th International Conference
ENGINEERING MECHANICS 2012
Svratka, Czech Republic, May 14 – 17, 2012

pp. 745–754
Paper #298

THE PROBABILISTIC CALCULATING OF FATIGUE CRACK PROPAGATION USING FCPROBCALC PROGRAM

M. Krejsa*

Abstract: *The paper gives examples of the probabilistic assessment of a steel cyclic loaded structure. Fatigue progression of the cracks from the edge and from the surface is used as a basis for proposing a system of inspections. The newly developed method Direct Optimized Probabilistic Calculation (DOProC method) was used for solution. The method was applied in FCProbCalc software.*

Keywords: ***DOProC method, FCProbCalc, Fatigue Crack, Inspection of Structure, Safety Margin.***

1. Introduction

Reliability of bearing structures which are subject to load cycles is affected considerably by degradation processes being, in particular, the result of fatigue of the basic material. Methods are under development now which would detect failures and defects, if any, resulting from initiation cracks. Linear fracture mechanics is among alternative methods. Mechanical engineering experts have been dealing with such issues for many years. Results have been gradually taken over and implemented into designs of the loading structures in buildings. Because input variables include uncertainties and reliability should be taken into account, probabilistic methods should be used in investigation into the propagation rate of the fatigue crack.

This paper describes the use of the original method and method which is under development now: the Direct Optimized Probabilistic Calculation ("DOProC") can be used for a probabilistic design and assessment of reliability of structures with the specified designed probability of failure, without using any simulation techniques - Janas et al. (2009); Janas et al. (2009). The DOProC method deals, as the other probabilistic methods, with tasks where at least certain input quantities are of a random nature. In many cases, this calculation method is very efficient and provides accurate estimates of resulting probabilities. Only a calculation error and an error resulting from discretizing of input and output quantities are involved there.

DOProC method has proved to be a good solution, among others, in probabilistic analysis of fatigue crack propagation in constructions subject to cyclical loads. Detailed methods with examples of the probabilistic assessment for a construction subject to fatigue load are available, a particular attention being paid to cracks from the edge and those from the surface. Similarly to other probabilistic analysis, this information is used as a basis for designing a system of inspections of the cyclic load construction, e.g. Moan (2005), Straub (2009), Chen et al. (2011), Krejsa et al. (2011), the aim being to analyze real propagation of fatigue cracks in those structural details which tend most to be damaged by fatigue. If no fatigue cracks are found, the analysis of inspection results give conditional probability during occurrence.

In order to improve quality of probabilistic calculations, a special software - FCProbCalc - was developed. Using this software, it is possible to monitor effectively and flexibly development of fatigue damage in structures, to determine times for inspections and to ensure that the construction will be fit for operation in terms of fatigue safety. The methods and application can considerably improve estimation of maintenance costs for the structures and bridges subject to cyclical loads.

*Doc. Ing. Martin Krejsa, Ph.D.: Department of Structural Mechanics, Faculty of Civil Engineering, VSB - Technical University Ostrava, Ludvika Podeste 1875/17; 708 00, Ostrava-Poruba; CZ, e-mail: martin.krejsa@vsb.cz

2. Direct Optimized Probabilistic Calculation (DOProC)

The Direct Optimized Probabilistic Calculation ("DOProC") has been under development since 2002. Principles of DOProC method which can be used for various types of probabilistic tasks have been described in theory in many publications. The calculation procedure for a certain task in DOProC method is clearly determined by its algorithm, while Monte Carlo simulation methods generate calculation data for simulation on a random basis, e.g. Konecny et al. (2007), Krivy et al. (2007).

Similarly as with the other probabilistic methods, Kralik (2009), input random quantities in DOProC (such as the load, geometry, material properties, or imperfections) are described using the non-parametric (empirical) distribution in histograms. This technique can be also used for parametric divisions. The distribution is typically based on observations, being often long-lasting ones. A computational procedure is being developed now, the aim being to implement into DOProC method the statistic dependence of input parameters.

In DOProC method, each calculation of the failure probability, p_f, is, however, limited by the number of random input variables. If there are too many random variables, the application is extremely time demanding - even if high-performance computers are used. The number of necessary computational operations and time needed for the calculation is also influenced by the number of intervals in each input random variable. This influences, in turn, accuracy of final probabilities. Therefore, efforts have been made to optimize calculations in order to reduce the number of operations, keeping, at the same time, reliable calculation results. The goal of optimizing techniques is to minimize the computational time and to maintain correctness and high accuracy even in relatively demanding probabilistic tasks. This is the reason why the method includes in its name the word "Optimized".

DOProC method has been used, so far, in probabilistic assessment of combined load or reliability of cross-sections and systems consisting of statically determined or undetermined load carrying constructions, e.g. Janas et al. (2003), in probabilistic assessment of load carrying constructions which are subject to shocks in probabilistic analysis of steel-fibre reinforced concrete mixtures or in probabilistic assessment of reliability of anchored reinforcement or arc reinforcement in underground and long mine works with a special focus on anti-slipping properties.

It is possible to use ProbCalc in DOProC probabilistic calculations (see Fig. 1). ProbCalc is a software application which is still under development. It is rather easy and simple to implement quite a complicated analytical transformation model of a probabilistic task defined using a text-oriented editor. In more complex numerical calculation models, there is a chance to use the procedure programmed by the user as DLL (with a dynamic library extension). The optimizing techniques have been implemented into ProbCalc and can be combined now in the probabilistic calculation.

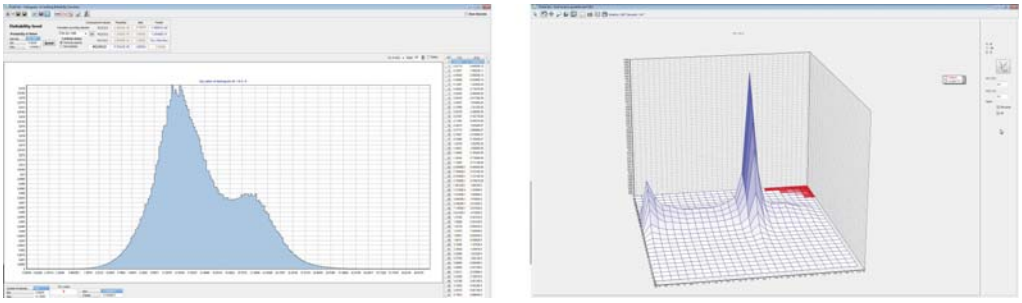

Fig. 1: Desktop of the ProbCalc software (left) and calculated 3D chart of reliability function (right).

More advanced user knowledge is required then to enter the probabilistic tasks in ProbCalc. It is essential to know, at least, general basics of algorithms because this influence the way of defining the computational model and selection of the best optimizing procedure. This weakness is removed if the application software is customized for a specific probabilistic task, this being, for instance, the case of FCProbCalc.

3. Probabilistic calculation of fatigue crack propagation

Occurrence of initiation cracks and crack propagation in structures subject to fatigue load has been known for a long time. The process is closely connected with fabrication of the steel structures, Kala (2005), and, in particular, with creation of details which tend to be damaged by fatigue. The key difference is between initiation of cracks resulting from steelmaking inclusions and those created during fabrication of structural details. Regarding the former, it takes a long time until it reaches the surface, while the latter is at the surface from the beginning of the loading. Standardized approaches of previous EC standards suppose that surface cracks were not present there. The acceptable damage method which is described in the new standard admits random occurrence of surface cracks. The major difference is that a fatigue crack might not be fragile, but could be ductile. In real components of steel structures and bridges, the latter is more frequent that the former which is used in experimental measurements in processed small test-pieces. This fact is not a new phenomenon. It has been known for a long time and has been mentioned, for instance, by Anderson (2005). During the designing, fabrication and processing of details, nobody, however, paid attention to random occurrence of initiation cracks from surface areas (from the surface or from the edge).

Three sizes are important for the characteristics of the propagation of fatigue cracks. These are the initiation size, the detectable size and the final acceptable size which occurs prior to failure caused by a fragile or ductile crack. The fatigue crack damage depends on a number of stress range cycles. This is a time factor in the course of reliability for the entire designed service life. In the course of time, the failure rate increases, while the reliability drops.

The topic is discussed in two levels that affect each other: the probabilistic solution to the propagation of the fatigue crack and uncertainties in determination of quantities used in the calculation. When investigating into the propagation, the fatigue crack that deteriorates a certain area of the structure components is described with one dimension only: a. In order to describe the propagation of the crack, the linear elastic fracture mechanics is typically used. It is based on the Paris-Erdogan law, e.g. Sanford (2003):

$$\frac{\mathrm{d}a}{\mathrm{d}N} = C \cdot (\triangle K)^m \ , \tag{1}$$

where C, m are material constants Carpinteri et al. (2007), a is the crack size and N is the number of loading cycles.

The initial assumption is that the primary design should take into account the effects of the extreme loading resulting from the ultimate state of carrying capacity method. Then, the fatigue resistance should be assessed. This means, the reliability margin in the technical probability method is:

$$Z_{(R,S)} = RF = R - S \ , \tag{2}$$

where R is the random resistance of the element and S represents random variable effects of the extreme load.

When using (1), the condition for the acceptable crack length a_{ac} is:

$$N = \frac{1}{C} \int_{a_0}^{a_{ac}} \frac{\mathrm{d}a}{\triangle K^m} > N_{tot} \ , \tag{3}$$

where N is the number of cycles needed to increase the crack from the initiation size a_0 to the acceptable crack size a_{ac}, and N_{tot} is the number of cycles throughout the service life.

The equation for the propagation of the crack size (1) needs to be modified for this purpose. The state of stress near the crack face is described using ΔK (the stress intensity coefficient) which depends on the loading (bending, tension), size and shape of the fatigue crack, and geometry of the load-bearing component. If the $\Delta\sigma$ stress range and axial stress-load of the flange are constant, the following relation applies:

$$\Delta K = \Delta\sigma \cdot \sqrt{\pi a} \cdot F_{(a)} \ , \tag{4}$$

where $F_{(a)}$ is the calibration function which represents the course of propagation of the crack. After the change of the number of cycles from N_1 to N_2, the crack will propagate from the length a_1 to a_2. Having

modified (1) and using (4), the following formula will be achieved:

$$\int_{a_1}^{a_2} \frac{\mathrm{d}a}{(\sqrt{\pi a} \cdot F_{(a)})^m} = \int_{N_1}^{N_2} C \cdot (\triangle\sigma)^m \, \mathrm{d}N \ . \tag{5}$$

If the length of the crack a_1 equals to the initial length a_0 (this is the assumed size of the initiation crack in the probabilistic approach) and if a_2 equals to the final acceptable crack length a_{ac} (this is the acceptable crack size which replaces the critical crack size a_{cr} if the crack results in a brittle fracture), the left-hand side of the equation (5) can be regarded as the resistance of the structure $R_{(a_{ac})}$:

$$R_{(a_{ac})} = \int_{a_0}^{a_{ac}} \frac{\mathrm{d}a}{(\sqrt{\pi a} \cdot F_{(a)})^m} \ . \tag{6}$$

If the upper integration limit a_d is used, the resistance of the structure $R_{(a_{ad})}$ can be specified similarly. Similarly, it is possible to define the cumulated effect of loads that is equal to the right side (randomly variable effects of the extreme load) (5):

$$S = \int_{N_0}^{N} C \cdot (\triangle\sigma)^m \, \mathrm{d}N \ = C \cdot (\triangle\sigma)^m \cdot (N - N_0) \ , \tag{7}$$

where N is the total number of oscillations of stress peaks ($\Delta\sigma$) for the change of the length from a_0 to $a_{a_{ac}}$, and N_0 is the number of oscillations in the time of initialization of the fatigue crack (typically, the number of oscillations is zero).

It is possible to define a reliability function RF:

$$RF_{(\mathbf{X})} = R_{(a_{ac})} - S_{(N)} \ . \tag{8}$$

where $\mathbf{X}$ is a vector of random physical properties such as mechanical properties, geometry of the structure, load effects and dimensions of the fatigue crack.

The analysis of the reliability function (8) gives a failure probability p_f:

$$p_f = P(RF_{(\mathbf{X})} < 0) = P(R_{(a_{ac})} < S_{(N)}) \ . \tag{9}$$

3.1. Probabilistic calculation of fatigue cracks propagating from the edge

A tension flange has been chosen for applications of the theoretical solution suggested in the studies Tomica et al. (2007). Depending on location of an initial crack, the crack may propagate from the edge or from the surface (see Fig. 2). Regarding the frequency, weight and stress concentration, those locations rank among those with the major hazard of fatigue cracks appearing in the steel structures and bridges.

A flange without stress concentration is used for confronting the both cases depending on the location of the crack initiation. The cases are different in calibration functions $F_{(a)}$ - and in weakened surfaces which are appearing during the crack propagation.

For the crack propagating from the edge, the calibration function is:

$$F_{(a)} = 1.12 - 1.39 \cdot \frac{a}{b} + 7.32 \cdot \left(\frac{a}{b}\right)^2 - 13.8 \cdot \left(\frac{a}{b}\right)^3 + 14.0 \cdot \left(\frac{a}{b}\right)^4 \ , \tag{10}$$

where a is the length of the crack and b is the width of the flange Janssen et al. (2002); (see Fig.2).

The acceptable crack size a_{ac} can be described then by a formula resulting from the deduced weakening of the cross-section area of the flange:

$$a_{ac} = b \cdot \left(1 - \frac{\sigma_{\max}}{f_y}\right) \ . \tag{11}$$

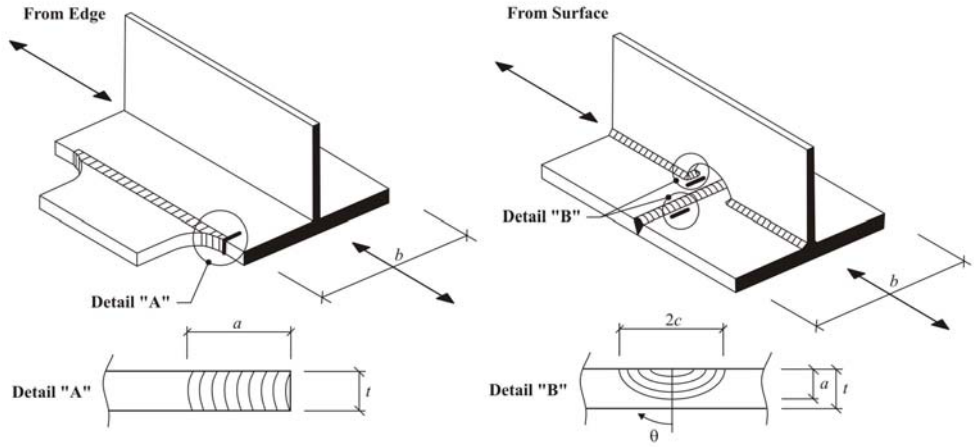

Fig. 2: Characteristic propagation of cracks from the outer edge (left) and from the surface (right).

3.2. Probabilistic calculation of fatigue cracks propagating from the surface

A similar approach can be used to determine the acceptable size of a crack propagating from the surface. The bending component can be neglected for welded steel two-axis symmetric I-profiles where the fatigue crack appears in the lower tension flange. The flange is loaded only by the normal stress resulting from the axial load - tension: $\sigma_m = \sigma$.

It is rather difficult to deduce analytically the acceptable size of the crack propagating from the surface. In accordance with Krejsa et al. (2010), the shape is replaced with a semi-elliptic curve where the ellipsis axes are a (the crack depth) and c (a half of the crack width) - see Fig. 2. The area of the surface crack depends on the number of N loading cycles and is described by the following formula:

$$A_{cr(N)} = \frac{1}{2} \cdot \pi \cdot a_N \cdot c_N \ . \tag{12}$$

During propagation of the fatigue crack from the surface, it is not enough to monitor only one crack size (which would be sufficient, for instance, for a crack propagating from the edge). In that case, the crack size needs to be analyzed for directions of the both semi-axes: a and c. The propagation of the fatigue crack from the surface in the a direction depends on the propagation in the c direction. Crack velocity propagation is described by (1). In Krejsa et al. (2010) there is a formula for calculation of the crack depth Δa as a result of an increased width of the Δc crack:

$$\Delta a = \left\{ \frac{1}{\left[1.1 + 0.35 \cdot \left(\frac{a}{t}\right)^2 \cdot \sqrt{\frac{a}{c}}\right]} \right\}^m \cdot \Delta c \ . \tag{13}$$

The crack sizes for a and c are during the propagation limited by upper limit values:

$$2 \cdot c \leq 0,4 \cdot b_f \quad a \leq 0,8 \cdot t_f \ , \tag{14}$$

If these upper limit values are exceeded, the fatigue crack propagates differently. Krejsa (2011) gives also the formula for the mutual dependence of the sizes in a and c:

$$c = 0.3027 \cdot \frac{a^2}{t} + 1.0202 \cdot a + 0.00699 \cdot t \ . \tag{15}$$

When determining the acceptable crack size, a modified relation (12) using (13) and (15), should be taken as a basis. After modification:

$$\sigma_{\max} \cdot \frac{b_f t_f}{b_f t_f - \frac{1}{2} \cdot \pi a \cdot \left(0.3027 \cdot \frac{a^2}{t_f} + 1.0202 \cdot a + 0.00699 \cdot t_f \right)} \leq f_y \ , \tag{16}$$

It is difficult to describe the a crack size directly explicitly. In order to calculate the acceptable crack size a_{ac}, it is necessary to use a numerical iteration approach where restrictions resulting from (16) should be taken as a basis.

3.3. Determination of inspections of structures subject to fatigue

Because it is not certain in the probabilistic calculation whether the initiation crack exists and what the initiation crack size is and because other inaccuracies influence the calculation of the crack propagation, a special inspection is necessary to check the size of the measurable crack in a specific period of time. The acceptable crack size influences the time of the inspection. If no fatigue cracks are found, the analysis of inspection results give conditional probability during occurrence.

While the fatigue crack is propagating, it is possible to define following random phenomena that are related to the growth of the fatigue crack and may occur in any time, t, during the service life of the structure. Then:

- $U_{(t)}$ **phenomenon:** No fatigue crack failure has not been revealed within the t-time and the fatigue crack size $a_{(t)}$ has not reached the detectable crack size a_d . This means:

$$a_{(t)} < a_d \ , \tag{17}$$

- $D_{(t)}$ **phenomenon:** A fatigue crack failure has been revealed within the t-time and the fatigue crack size $a_{(t)}$ is still below the acceptable crack size a_{ac}. This means:

$$a_d \leq a_{(t)} < a_{ac} \ , \tag{18}$$

- $F_{(t)}$ **phenomenon:** A failure has been revealed within the t-time and the fatigue crack size $a_{(t)}$ has reached the acceptable crack size a_{ac}. This means:

$$a_{ac} < a_{(t)} \ . \tag{19}$$

Using the phenomena above, it is possible to define probability for their occurrence in any t-time. Those three phenomena cover the complete spectrum of phenomena that might occur in the t-time. This means:

$$P(U_{(t)}) + P(D_{(t)}) + P(F_{(t)}) = 1 \ . \tag{20}$$

The probabilities of random phenomena can be determined in any period of time, t, using, for instance, DOProC method. The probabilistic calculation is carried out in time steps where one step equals to one year of the service life of the construction. When the failure probability (for the F phenomenon) reaches the designed failure probability p_d, the inspection should be carried out in order to find out fatigue cracks, if any, in the construction element. The inspection provides information about real conditions of the construction. Such conditions can be taken into account when carrying out further probabilistic calculations. The inspection in the t time may result in any of the three mentioned phenomena. Using the inspection results for the t time, it is possible to define the probability of the mentioned phenomena in another times: $T > t_I$. For that purpose, the conditional probability should be taken into consideration.

3.4. Using the conditioned probability to determine times to inspect the construction

If the crack is not revealed within the t-time, this may mean that there is not any fatigue crack in the construction element. This might be an initiative phase of nucleation of the fatigue crack (when a crack appears in the material) and this phenomenon is not taken into account in the fracture mechanics.

Even if the fatigue crack is not revealed it is likely that it exists but the fatigue crack size is so small that it cannot be detected under existing conditions.

In order to fix the time for the next inspection, it is necessary to determine the conditioned probabilities, $P(F_{(T)} \mid U_{(t_I)})$ and/or $P(F_{(T)} \mid D_{(t_I)})$, which can be expressed using the Bayes' formula:

$$P(F_{(T)} \mid U_{(t_I)}) = \frac{P(F_{(T)}) - P(F_{(t_I)}) - P(D_{(t_I)}) \cdot P(F_{(T)} \mid D_{(t_I)})}{P(U_{(t_I)})} , \tag{21}$$

$$P(F_{(T)} \mid D_{(t_I)}) = \frac{P(F_{(T)}) - P(F_{(t_I)}) - P(U_{(t_I)}) \cdot P(F_{(T)} \mid U_{(t_I)})}{P(D_{(t_I)})} . \tag{22}$$

If redistribution of stress from a point that is weakened by the crack is not taken into account, the crack propagation crack is usually rather high in the practical range of measurable values. If a fatigue crack is found during the inspection of the construction, it is necessary to monitor the safe growth of the crack or to take actions that will slow down or stop further propagation of the fatigue crack. In order to time the inspections well, the equation which defines the failure probability in $T > t_I$ is most important - provided that no fatigue cracks have been revealed during the last inspection. It is clear from the equation that the results of the failure probability are influenced by mutual relations between the three crack sizes - the initiation crack size, measurable crack size and acceptable crack size.

When the failure probability reaches the designed failure probability p_d, an inspection should be carried out in order to reveal fatigue cracks, if any, in the construction component. The inspection may result in one of the mentioned phenomena with corresponding probabilities. The entire calculation can be repeated in order to ensure well-timed inspections in the future.

4. FCProbCalc software

FCProbCalc was developed using the aforementioned techniques. By means of FCProbCalc, it is possible to carry out the probabilistic calculation of propagation of fatigue cracks in a user friendly environment. The attention is paid to propagation of fatigue cracks from the surface and edge. On the basis of these data, times for the first and next inspections are determined, the goal being to identify fatigue damage to structural details which most tend to be damaged by fatigue.

The reference probabilistic calculation used input quantities from the publication which had included the probabilistic assessment of a steel/reinforced concrete bridge on the highway in a point where a longitudinal beam connects to a transversal beam. Tables 1 and 2 show the input quantities which were entered deterministically and stochastically. The required reliability was expressed by the reliability index $\beta = 2$ which corresponds to the failure rate of $p_d = 0.02277$.

Using FCProbCalc it is possible to specify propagation of fatigue crack from the edge for a certain time interval - the resistance of the structure $R_{(a_d)}$ and $R_{(a_{ac})}$ (numerical integration using Simpson's rule with 1000 differences was used), Fig. 3), load effect S as well as probability of elementary phenomena U, D and F which are the source information for determination of the time of the first inspection. If no fatigue damage is found during the inspection, times for next inspections have been determined on the basis of the conditioned probability.

The calculated probabilities of the random phenomena, U, D and F (Fig. 4), are the source information for next inspections of the bridge based on the conditioned probability. If the edge crack cannot be detected during the first inspection in the 50$^{\text{th}}$ year of operation, the next inspection will take place in the 58$^{\text{th}}$ year of operation. And if the crack is not identified there again, the next year of inspection is the 63$^{\text{th}}$ year. After that year, the inspection intervals will become shorter considerably (operation years: 66,

Tab. 1: Overview of variable input quantities expressed in a histogram with parametric distribution of probabilities

Quantity	Type	Mean value	Standard deviation
Oscillation of stress peaks $\Delta\sigma$ [MPa]	Normal	30	3
Total number of oscillation of stress peaks per year N [-]	Normal	10^6	10^5
Yield stress f_y [MPa]	Lognormal	280	28
Nominal stress in the flange plate σ [MPa]	Normal	200	20
Initial size of the crack a_0 [mm]	Lognormal	0.2	0.05
Smallest detectable size of the crack a_d [mm]	Normal	10	0.6

Tab. 2: Overview of input quantities expressed in a deterministic way

Quantity	Value
Material constant m	3
Material constant C	$2.2 \cdot 10^{13}$
Width of the flange plate b_f [mm]	400
Thickness of the flange plate t_f [mm]	25
Nominal probability of failure p_d	0.02277

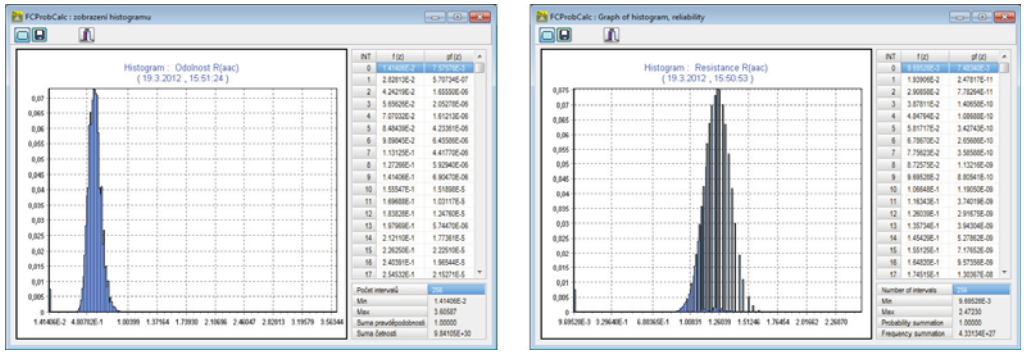

Fig. 3: FCProbCalc program output: Resulting histogram of the structural resistance $R(a_{ac})$ for propagation of fatigue crack from the edge (left) and from the surface (right).

69, 71, 73 and 74). If the crack is not identified during the 75$^{\text{th}}$ year, it can be assumed that - if the input values have not changed (in particular, the intensity and efficiency of the operation load) - the medium value of the initial crack will be less than 0.2 mm or there is not any fatigue crack at all.

The similar approach is used in the probabilistic calculation for propagation of a fatigue crack from surface (calculated time of inspections in years: 110, 123, 131, 137, 142 and 147).

The Fig. 5 shows the graphic results of the inspections calculated using DOProC method.

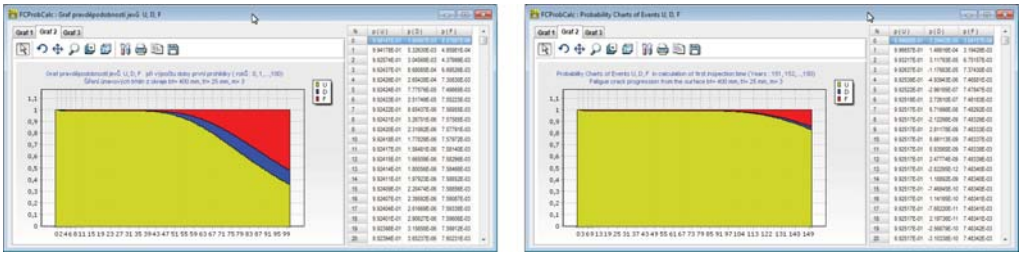

Fig. 4: FCProbCalc program output: Probabilities of the phenomena U, D and F for the propagation of fatigue crack from the edge (0 to 100 years of operation, left) and for the propagation of fatigue crack from the surface (0 to 150 years of operation, right).

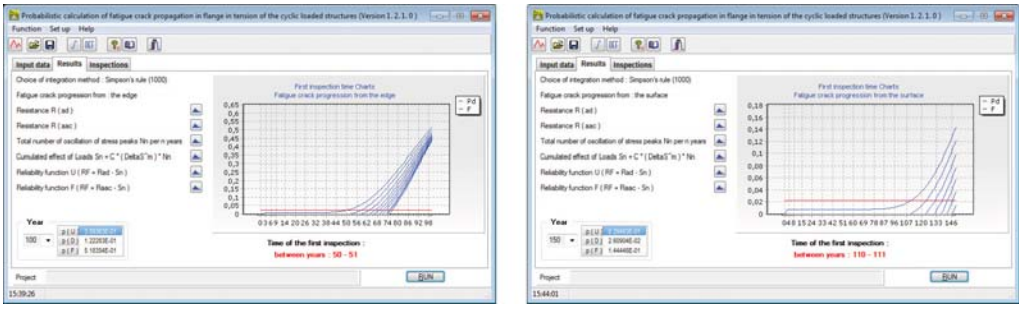

Fig. 5: FCProbCalc program output: failure probability p_f , depending on the years of operation for the propagation of fatigue crack from the edge (0 to 100 years of operation, left) and for the propagation of fatigue crack from the surface (0 to 150 years of operation, right).

5. Conclusions

This paper addresses application of the new probabilistic method, DOProC, for probabilistic assessment of steel structures which are subject to load cycles and which tend to suffer from fatigue cracks. The method was included into FCProbCalc which is the software which makes it possible to solve very efficiently the probabilistic task of fatigue crack propagation in a user-friendly environment.

FCProbCalc was used for the probabilistic assessment of fatigue damage to a bridge structure where cracks were propagating from both the surface and edge. Times were specified for inspections of the bridge structure, where the purpose was to monitor occurrence of certain fatigue cracks. The comparison proved that velocity of propagation of the fatigue crack from the surface is considerably slower than that from the edge.

It should be pointed out that FCProbCalc still provides many other options to be used. Future development of this software will focus, in particular, on numerical integration in calculation of structural resistance and on impacts of the chosen numerical methods and input parameters on the computational time and final accuracy of the calculations in the context of the time of the proposed inspections.

Appendix

For a lite version of FCProbCalc and for other software products based on DOProC method please visit web pages **http://www.fast.vsb.cz/popv** , Janas et al. (2012).

Acknowledgments

The paper was published thanks to the financial support granted to the project "Creation of educational program for civil engineers in the Moravian-Silesian Region". The project registration number is CZ.1.07/3.2.07/02.0060.

References

Anderson, T. L. (2005) *Fracture mechanics: fundamentals and applications*. Third edition, CRC Press, Taylor & Francis Group, Boca Raton, Florida. ISBN 0-8493-1656-1.

Carpinteri, A. & Paggi M. (2007) Self-similarity and crack growth instability in the correlation between the Paris' constants. *Engineering Fracture Mechanics*, vol. 74, issue 7, pp 1041–1053 (13 p), DOI 10.1016/j.engfracmech.2006.12.007.

Chen, N. Z., Wang, G. & Soares, C. G. (2011) Palmgren-Miner's rule and fracture mechanics-based inspection planning. *Engineering Fracture Mechanics*, vol. 78, issue 18, pp 3166–3182 (17 p), DOI 10.1016/j.engfracmech.2011.08.002.

Janas, P., Krejsa, M. & Kolos, I. (2003) Reliability assessment of structure expressed to impact. *Proceedings of national conference with international participation Engineering Mechanics 2003,* Svratka. Editors Naprstek, J. and C. Fischer. (10 s). ISBN 80-86246-18-3.

Janas, P., Krejsa, M.& Krejsa, V. (2012) *ProbCalc Software and DOProC Method*. Web pages. [on-line]. http://www.fast.vsb.cz/popv. VSB – Technical University Ostrava.

Janas, P., Krejsa, M. & Krejsa, V. (2009) Structural Reliability Assessment using a Direct Determined Probabilistic Calculation. *Proceedings of the 12th International Conference on Civil, Structural and Environmental Engineering Computing*, Civil–Comp Press, Stirlingshire, Scotland. Paper 79, ISBN 978-1-905088-31-7.

Janas, P., Krejsa, M. & Krejsa, V. (2009) Using the Direct Determined Fully Probabilistic Method for determination of failure. *Proceedings of the European Safety and Reliability Conference, Esrel 2009*. Taylor & Francis Group, London, ISBN 978-0-415-55509-8 (set of 3 volumes + CD-ROM), ISBN 978-0-203-85975-9 (e-book).

Janssen, M., Zuidema, J. & Wanhill, R. J. H. (2002) *Fracture Mechanics*. Second edition, Delft University Press. ISBN 90-407-2221-8.

Kala, Z. (2005) Sensitivity Analysis of the Stability Problems of Thin–Walled Structures. *Journal of Constructional Steel Research*, vol. 61, issue 3, pp 415–422 (8 p), DOI 10.1016/j.jcsr.2004.08.005.

Konecny, P., Tikalsky, P. J. & Tepke, D. G. (2007) Performance Evaluation of Concrete Bridge Deck Affected by Chloride Ingress. *Transportation Research Record*, issue 2028, pp 3–8 (6 p), DOI 10.3141/2028-01.

Kralik, J. (2009) *Reliability Analysis of Structures Using Stochastic Finite Element Method*. Slovak university of technology in Bratislava. (143 s) ISBN 978-80-227-3130-0.

Krejsa, M. & Tomica V. (2010) Calculation of Fatigue Crack Propagation Using DOProC Method. *Transactions of the VSB – Technical University of Ostrava*, no.1, vol.X, Civil Engineering Series, paper #11 (9 p), DOI 10.2478/v10160-010-0011-6. Publisher Versita, Warsaw, ISSN 1213-1962 (Print) ISSN 1804-4824 (Online).

Krejsa, M. & Tomica V. (2011) Determination of Inspections of Structures Subject to Fatigue. *Transactions of the VSB – Technical University of Ostrava*, no.1, vol.XI, Civil Engineering Series, paper #7 (11 p), DOI 10.2478/v10160-011-0007-x. Publisher Versita, Warsaw, ISSN 1213-1962 (Print) ISSN 1804-4824 (Online).

Krejsa, M. (2011) *Using DOProC Method for Structural Reliability Assessment*. Habilitation thesis, VSB – TU Ostrava. ISBN 978-80-248-2385-0.

Krivy, V. & Marek P. (2007) Probabilistic Design of Steel Frame Structures. *Stahlbau*, vol. 76, issue 1, pp 12–20 (13 p), DOI 10.1002/stab.200710003.

Moan, T. (2005) Reliability–based management of inspection, maintenance and repair of offshore structures. *Structure and Infrastructure Engineering*, vol. 1, issue 1, pp 33–62 (30 p), DOI 10.1080/15732470412331289314, Taylor & Francis Ltd.

Sanford, R. J. (2003) *Principles of Fracture Mechanics*. Pearson Education, Inc., U.S.A. ISBN 0-13-092992-1.

Straub, D. (2009) Stochastic Modeling of Deterioration Processes through Dynamic Bayesian Networks. *Journal of Engineering Mechanics*. DOI 10.1061/(ASCE)EM.1943-7889.0000024.

Tomica, V. & Krejsa, M. (2007) Optimal Safety Level of Acceptable Fatigue Crack. *Proceedings of 5th International Probabilistic Workshop*, Ghent, Belgium. Edited by L.Taerwe and D.Proske. (12 p). ISBN 978-3-00-022030-2.

18th International Conference
ENGINEERING MECHANICS 2012
Svratka, Czech Republic, May 14 – 17, 2012

pp. 755–761
Paper #163

MODELLING OF THE CEILING SLAB FROM THE HOLLOW CORE PANELS IN ANSYS PROGRAM

J. Kršík[*], J. Křiváková[**]

Abstract: *The aim of this paper is to describe modeling of the Ceiling slab from the hollow core panels in ANSYS program. The real load tests are used from NO. VTT-S-07311-06 from VTT Technical Centre of Finland.. Several simplifications are accepted. The calculated deformations are compared with deformations from the load test at the end.*

Keywords: ***Ansys, Prestress, Concrete, Hollow Core Panel, Deformations***

1. Úvod

Popsaná úloha je zaměřena na vytvoření MKP modelu stropní desky ze 4 kusů dutinových stropních panelů typu SPIROLL s předem předpjatou výztuží. Modelovaná deska byla v roce 2006 fyzicky vyrobena a podrobena zatěžovacím zkouškám smykové pevnosti ve Finském výzkumném institutu VTT pod číslem VTT-S-07331-06 (Pajari, 2006). Porovnávání výsledků numerického modelu a skutečného experimentu provedeného ve Finsku má sloužit k verifikaci MKP modelu, který bude dále sloužit k výpočtu extrémních hodnot převážně smykových napětí v nebezpečných průřezech spřažených stropních desek tvořených předpjatými stropními panely vyráběnými v České Republice firmou Goldbeck Prefabeton s.r.o. Uspořádání skutečného testu je vidět z obr. 1. Modelována je symetrická pravá polovina zatěžovacího testu.

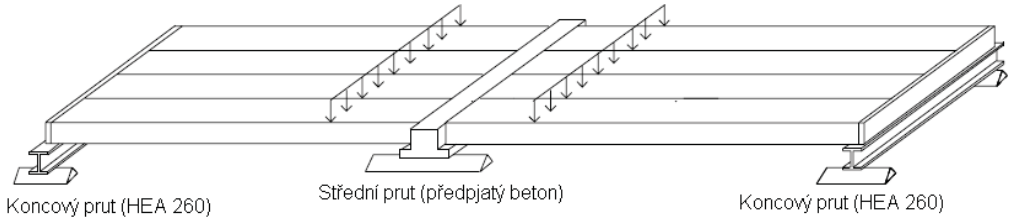

Obr. 1 Přehled uspořádání zatěžovacího testu[1]

Modelovaná stropní deska má tloušťku 0,4 m, délku 9 m a šířku 4,8 m. Deska je sestavena ze 4 panelů o šířce 1,2 m. Na levé straně je deska podepřena předpjatým betonovým prutem, který je v příspěvku modelován pouze tuhostí podpůrných pružin. Tato podpora přenáší 86,7 % proměnného zatížení. Na pravé straně je deska podepřena ocelovým prutem HEA 260. Tento prut je rovněž modelován pouze jako tuhost podpůrných pružin a přenáší zbývajících 13,3 % proměnného zatížení. Stálé zatížení je tvořeno vlastní hmotností desky a je rovnoměrně rozloženo na obě podpory. Proměnné zatížení, které je vyvozeno přes složitou zatěžovací soustavu, narůstá, až do porušení desky smykem.

[*] Ing. Jakub Kršík: Institute of Structural Mechanics, Brno University of Technology, Veveří 331/95; 602 00, Brno; CZ, e-mail: krsik.j@fce.vutbr.cz

[**] Ing. Jarmila Křiváková, CSc.: Institute of Structural Mechanics, Brno University of Technology, Veveří 331/95; 602 00, Brno; CZ, e-mail: krivakova.j@fce.vutbr.cz

[1] Research report No. VTT-S-07331-06, PAJARI, Matti. VTT Research Centre of Finland, 2006

2. Popis tvorby stropní desky

Model 1 panelu

Všechny betonové objemové části, jsou vytvořeny z objemových konečných prvků SOLID 185. Nejprve je vytvořena síť čela panelu (obr. 2) z pomocných plošných prvků SHELL 181, které jsou po vytvoření objemového modelu odstraněny. Čelo je následně protaženo do délky podél přímky s podélným dělením 50 mm. Hustota sítě čela panelu a dělení po délce panelu bylo zvoleno s ohledem na podepření, zatížení a požadované výsledky. Předpínací výztuž je modelována z dvouuzlových konečných prvků BEAM 188. V každém panelu je celkem 13 předpínacích lan napnutých ve výrobně na napětí 1000 MPa. Toto napětí je dále v modelu snižováno o ztráty pružným přetvořením betonu, relaxací předpínací výztuže a ztrátu pokluzem v kotevní oblasti (Navrátil, 2008). Hodnota pokluzu lan je uvažována 2,5 mm v čele panelu a délka vlivu pokluzu je kotevní délka 1,25 m.

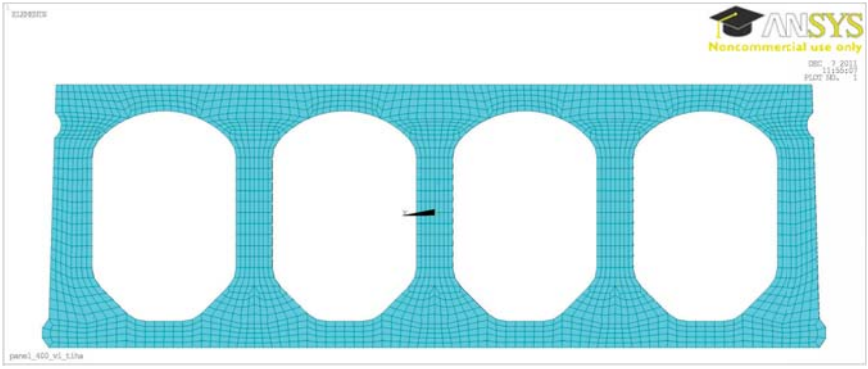

Obr. 2 Síť konečných prvků čela panelu

Model stropní desky

Spřažená stropní deska je vytvořena ze čtyř panelů zmonolitněných mezipanelovou zálivkou. V místech uložení jsou dutiny panelů zality do hloubky 50 mm stejným zálivkovým betonem. Dále je do každé spáry vložena tzv. zálivková výztuž z oceli A500HW o průměru 16 mm a délky 1150 mm.

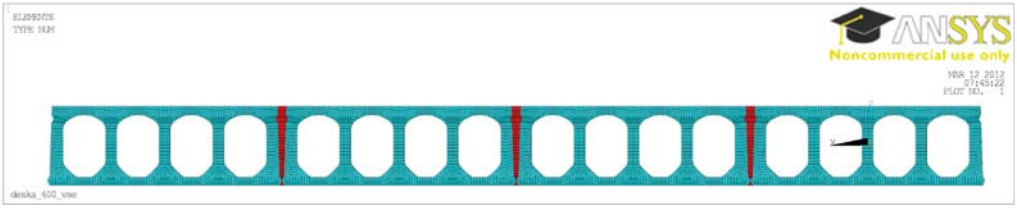

Obr. 3 Přední pohled na desku, včetně mezipanelové zálivky

Modely použitých materiálů jsou shrnuty v tabulce 1. Hodnoty vycházejí ze skutečných zkoušek, které byly provedeny po ukončení zatěžovacího testu.

Tab. 1: Použité materiálové charakteristiky

N.O	**Jméno**	**Typ**	**Objemová hmotnost** [kg/m^3]	**Modul pružnosti** [Pa]	**Poissonovo číslo** [-]	**Mez pevnosti** [Pa]
1	Beton předpjatých panelů	Beton	2386	$35 \cdot 10^9$	0,2	$44{,}5 \cdot 10^6$
2	Předpínací výztuž	Předpínací ocel	7850	$190 \cdot 10^9$	0,3	$1630 \cdot 10^6$
3	Beton mezipanelové zálivky	Beton	2196	$29{,}7 \cdot 10^9$	0,2	$33{,}1 \cdot 10^6$

4	Zálivková výztuž	Ocel	7850	$200 \cdot 10^9$	0,3	$500 \cdot 10^6$
5	Beton zalití čel	Beton	2196	$29{,}7 \cdot 10^9$	0,2	$33{,}1 \cdot 10^6$
6	Roznášecí podložky	Ocel	7850	$210 \cdot 10^9$	0,3	$355 \cdot 10^6$

Betonové části jsou modelovány multilineárním pracovním diagramem s izotopickým zpevněním vytvořeným aproximací parabolického pracovního diagramu dle ČSN EN 1992-1-1 3.1.7. Materiálovým modelem předpínací výztuže je bilineární pracovní diagram s izotopickým zpevněním odpovídající ČSN EN 1992-1-1 3.3.6 (2005). Materiálový model ostatních ocelových materiálů je lineární pracovní diagram vyhovující požadavkům výše uvedené normy.

Jednotlivé body zlomů multilineárních a bilineárních pracovních diagramů jsou shrnuty do tabulky 2. Počátek je vždy v 0 a tangenta první větve (tj. mezi body 0 a 1) se musí rovnat modulu pružnosti. Příslušné pracovní diagramy jsou také zobrazeny na obrázku 4. Na vodorovné ose je vynesena poměrná deformace ε a na svislé ose je tahové, nebo tlakové napětí.

Celkové množství konečných prvků na desce a hmotnost příslušné části je uvedena v tabulce 3.

Tab. 2: Multilineární a bilineární charakteristiky pracovních diagramů materiálů

N.O	**Bod 1**		**Bod 2**		**Bod 3**		**Bod 4**	
	ε [-]	f [Pa]	ε [-]	f [Pa]	ε [-]	f [Pa]	ε [-]	f [Pa]
1	0,0005	$17{,}5 \cdot 10^6$	0,001	$32{,}0 \cdot 10^6$	0,0015	$41{,}0 \cdot 10^6$	0,002	$44{,}5 \cdot 10^6$
2	0,00858	$1{,}63 \cdot 10^9$	0,035	$1{,}86 \cdot 10^9$				
3	0,0005	$14{,}9 \cdot 10^6$	0,001	$24{,}8 \cdot 10^6$	0,0015	$30{,}5 \cdot 10^6$	0,002	$33{,}1 \cdot 10^6$
4	0,0025	$500 \cdot 10^6$	0,035	$500 \cdot 10^6$				
5	0,0005	$14{,}9 \cdot 10^6$	0,001	$24{,}8 \cdot 10^6$	0,0015	$30{,}5 \cdot 10^6$	0,002	$33{,}1 \cdot 10^6$
6	0,0017	$355 \cdot 10^6$	0,035	$355 \cdot 10^6$				

Tab. 3: Počet použitých konečných prvků a jejich celková hmotnost

N.O	**Jméno**	**Typ**	**Počet konečných prvků** [ks]	**Hmotnost dílčí části** [kg]
1	Beton předpjatých panelů	SOLID 185	1 424 160	18 726,9
2	Předpínací výztuž	BEAM 188	9 360	341,3
3	Beton mezipanelové zálivky	SOLID 185	65 880	795,0
4	Zálivková výztuž	BEAM 188	69	5,4
5	Beton zalití čel	SOLID 185	33 708	637,0
6	Roznášecí podložky	BEAM 188	832	36,2
	Celkem		1 534 009	20 541,8

Proměnné zatížení na desce je umístěno ve vzdálenosti 1,2 m od čela desky. Při takto umístěném zatížení dojde nejprve k porušení desky smykem. V zatěžovacím testu je zatížení přenášeno přes složitou zatěžovací soustavu. Tato soustava je do modelu zjednodušena svou hmotností $F_{z1} = 0{,}66$ kN a $F_{z2} = 6{,}22$ kN. Zatížení je rozdílné pro krajní panely – index 1 a pro střední panely – index 2. Hodnota zatížení, při níž došlo k porušení smykem je v zatěžovacím testu $F_1 = 295{,}1$ kN a $F_2 = 292{,}2$ kN. Toto zatížení je přepočteno na roznášecí podložky o rozměrech 0,1 x 1,155 m jako tlak o hodnotě $P_1 = 2{,}561$ MPa a $P_2 = 2{,}584$ MPa. Hodnota a směr působení zatížení je zobrazena na obrázku 5.

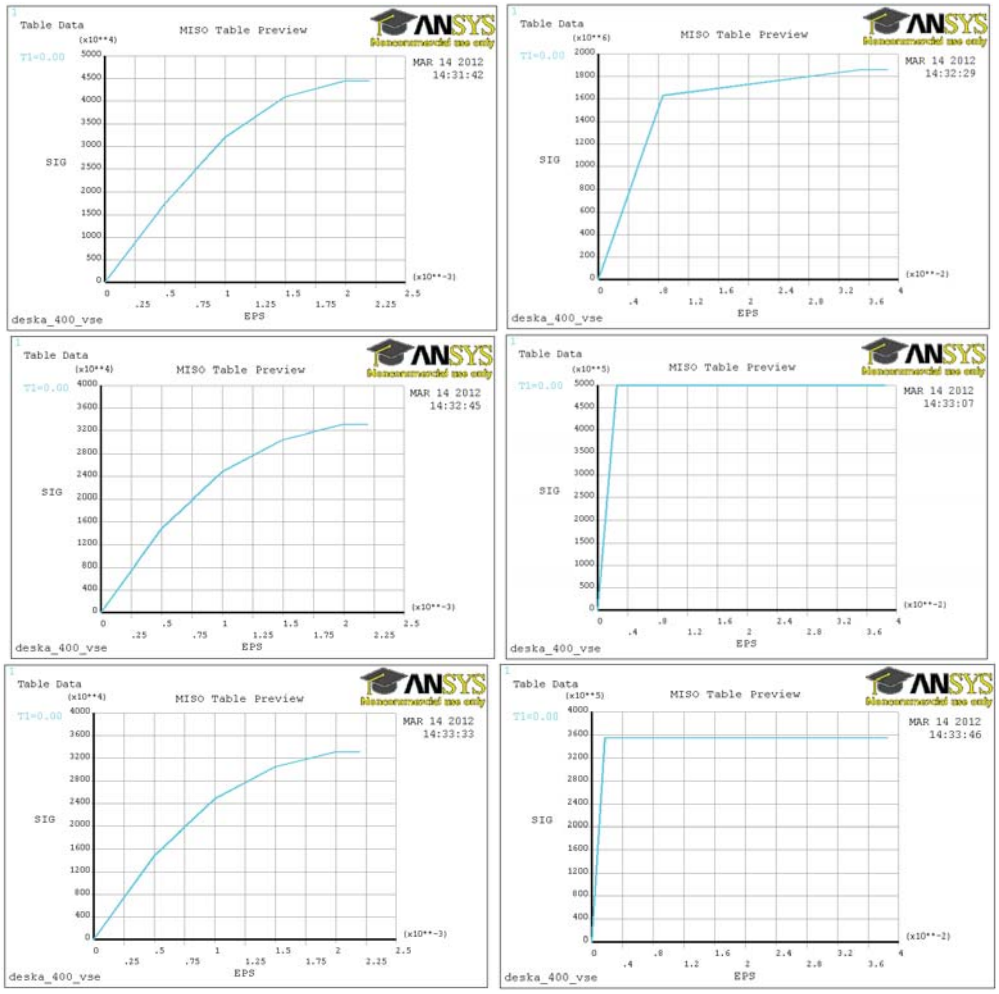

Obr. 4 Multilineární a bilineární charakteristiky použitých materiálů

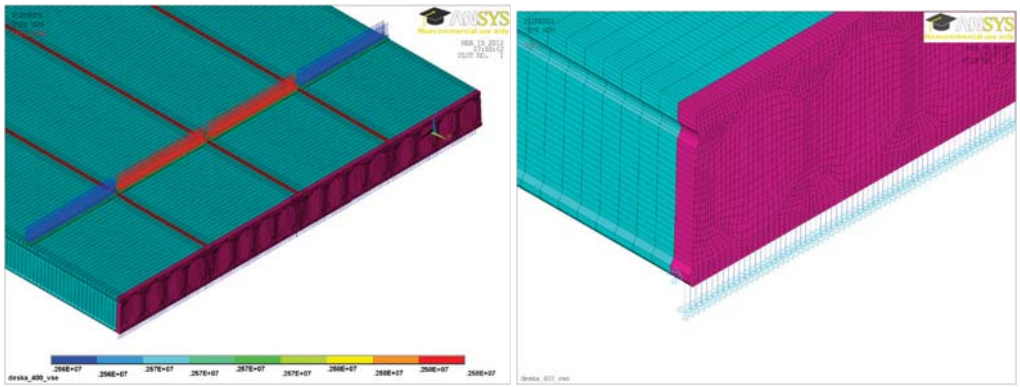

Obr. 5 Zatížení na desce a detail pružného podepření

Podepření je modelováno jako pružné pomocí dvouuzlových konečných prvků LINK 11 s definovanou tuhostí v souboru reálných konstant. Použité prvky mají délku 100 mm. Jedním uzlem jsou chyceny k betonové desce a v druhém uzlu mají definované přetvoření 0 mm ve všech směrech (vetknutí). Tuhost K je určena iteračně podle následujícího algoritmu:

Krok 1: Vložení velmi vysoké hodnoty tuhosti. Použita převrácená hodnota průhybu, která byla naměřena uprostřed rozpětí v zatěžovacím testu (1). Kde q je spojité zatížení nad příslušnou podporou, které je určeno jako součet 1/2 z stálého zatížení (hmotnost desky) a 86,7 % z proměnného zatížení v případě podpory 1 (betonový prut) nebo 13,3 % z proměnného zatížení v případě podpory 2 (ocelový prut). L je délka podpůrné konstrukce, což je 4,8 m. W je hodnota poklesu naměřená v zatěžovacím testu při kolapsu desky uprostřed rozpětí podpůrného prutu. w = 7,6 mm pro podporu 1 a w = 5,9 mm pro podporu 2.

$$K = EI = \frac{5}{384} \cdot \frac{q \cdot l^4}{w} \tag{1}$$

Použitá tuhost podpory 1 je $K_1 = 217{,}8$ MNm^2

Použitá tuhost podpory 2 je $K_2 = 63{,}6$ MNm^2

Krok 2: Zjištění reakcí R_n v jednotlivých podporách, kde n je číslo podpory. Vypočtení poklesu jednotlivých podpor w_n z rovnice ohybové čáry (2) (Šmiřák, 1999). Kde EI je tuhost z kroku 1, x_n je x-ová souřadnice podpory n, L je délka podpory L = 4,8 m. Tyto vypočtené poklesy podpor jsou požadovány od pružného podepření, takže následuje úprava tuhostí K_n podle vztahu (3). Tímto je každé pružině vložena jiná hodnota tuhosti. Reakce jsou zobrazeny na obrázku 6. Zvláště pěkně je vidět vyšší hodnota reakce pod žebry panelů a nižší hodnota reakce pod dutinami.

$$w_n = \frac{q}{24EI} \cdot x_n \cdot \left(L^3 - 2Lx_n{}^2 + x_n{}^3\right) \tag{2}$$

$$K_n = \frac{R_n}{w_n} \tag{3}$$

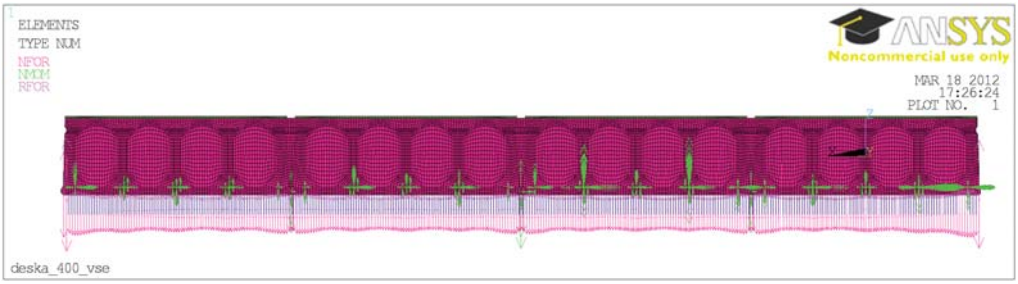

Obr. 6 Deformace pružné podpory

Krok 3: Zjištění reakcí R_n a úprava tuhostí K_n podle vztahu (3) pro nové reakce R_n. Tyto reakce jsou jiné, protože dojde k přerozdělení vnitřních sil z důvodů rozdílné tuhosti pružin.

Krok 4: Opakování kroku 3 dokud není změna reakce R_n zanedbatelná. Jako kritérium je zvolena poměrná změna reakce R_n o 5 % pro dvě následující iterace alespoň na 90 % pružin.

Jednotlivé kroky iterace vyžadují opakované spouštění celého výpočtu se změnou tuhosti pružin. Přičemž právě vždy dvě pružiny jsou definovány shodným elementem a reálnou konstantou. Konstrukce je symetrická. Celkem je definováno 688 pružin a 4 pevné posuny 0 mm jako okrajová podmínka (2 pro každý podpůrný prut). Z toho vyplývá, že je definováno celkem 688 elementů typu LINK 11 seskupených do souboru elementů o 344 položkách, kde má každý vlastní reálnou konstantu.

3. Nastavení výpočtu

Výpočet je proveden metodou Newton-Rhapson v 10 zatěžovacích krocích a je použit přímý řešič pro řídké matice. Výsledky jsou ukládány pro každý zatěžovací krok. Jsou povoleny velké deformace a není povoleno automatické snížení počtu zatěžovacích kroků v případě rychle konvergence.

Řešič sestavil soustavu 5 137 840 lineárních rovnic. Její řešení výše uvedenou metodou pro všechny zatěžovací kroky trvalo 12 hodin. Ke konvergenci docházelo v průměru po dvou iteračních krocích.

Konfigurace použitého počítače je následující:

Procesor: 2 x Intel® Xenon® X5650 2,67 GHz (6 jader každý), technologie 32 nm
RAM: 49 150 MB

4. Výsledky

Z důvodů velké časové náročnosti provedení iterace tuhosti podepření jsou prezentovány výsledky po 1. iteraci tuhosti podepření. Tj. hodnota tuhosti je stejná pro všechny pružiny.

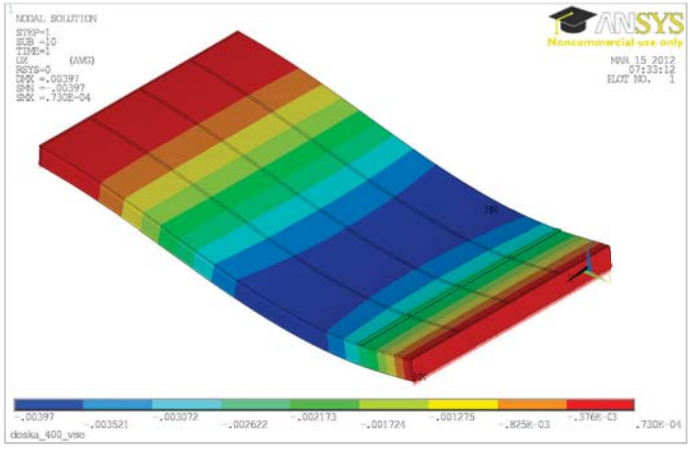

Obr. 7 Deformace desky po prvním kroku iterace tuhosti podepření

Na obrázku 7 je vidět deformace desky pod zatížením. Vypočtené deformace jsou ve vzdálenosti 1,4 m od čela desky a 3,9 m od čela desky. Tyto deformace jsou zobrazeny na obrázku 8.

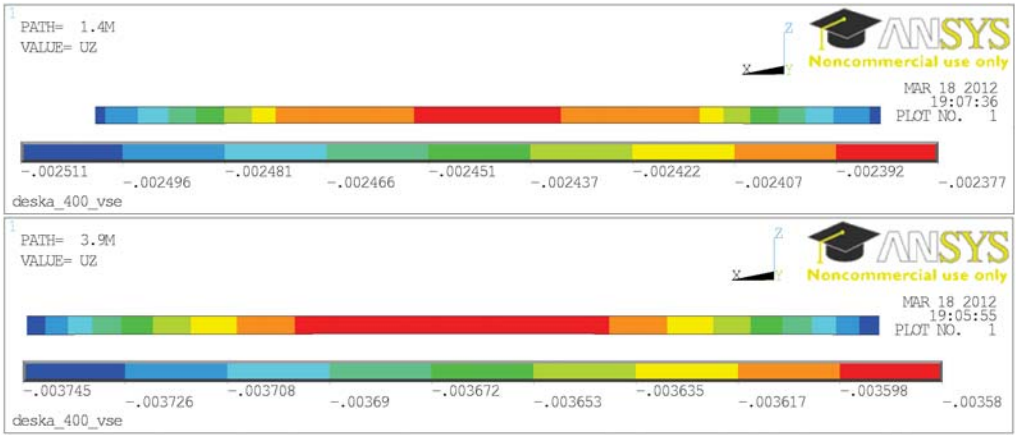

Obr. 8 Průběh deformace desky ve vzdálenosti 1,4 a 3,9 m od čela po prvním iteračním kroku

Průběh smykových napětí v rovině YZ (rovina v níž leží žebra desky) je zobrazen na obrázku 9. Pro vykreslení průběhu smykových napětí bylo nutno změnit barevnou škálu výsledků na 0 – 3,5 MPa. Důvodem je vznik velmi velké špičky smykových napětí na hraně roznášecí podložky o hodnotě okolo 8 MPa, která značně zhrubuje přesnost automaticky generované barevné škály.

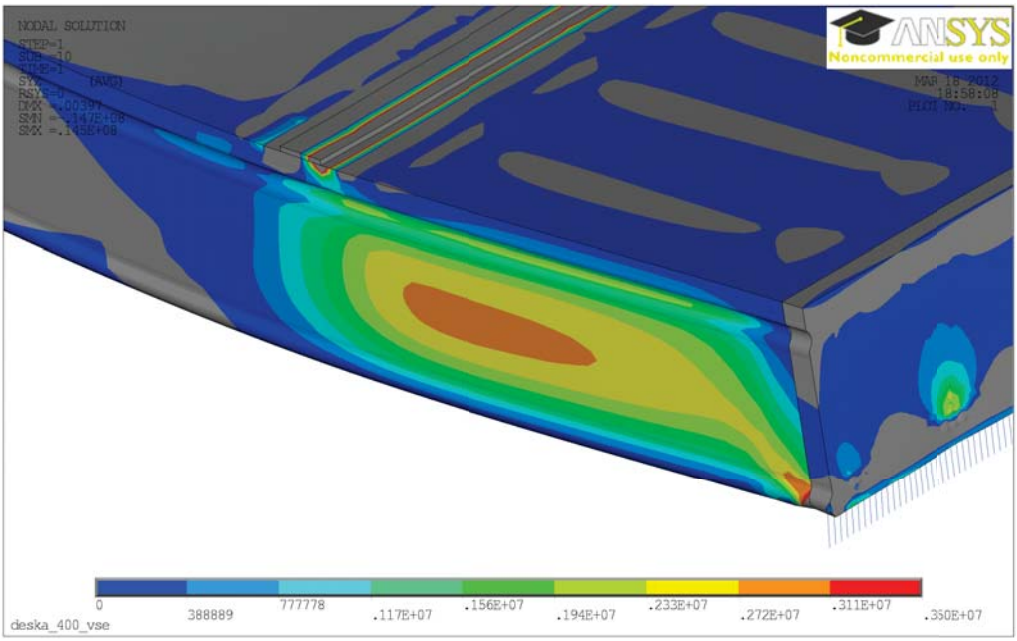

Obr. 9 Průběh smykových napětí po prvním kroku iterace tuhosti podepření

5. Závěr

Průběhy smykových napětí lze srovnávat s skutečným zatěžovacím testem. V zatěžovacím testu se při stejném zatížení náhle objevila smyková trhlina ve stejných místech, jako se vypočetlo zvýšené smykové napětí. Kořeny trhliny začali vznikat pod roznášecími podložkami a v místě podepření. Toto místo vzniku trhlin je na obrázku 8 prokázáno. Stejně tak je prokázáno pole zvýšeného smykového napětí mezi roznášecí podložkou a podepřením.

Odchylky vypočtených výsledků od naměřených jsou způsobeny hlavně použitím zjednodušených materiálových charakteristik, neuvažováním pružno-plastického chování betonu, a také je uvažován zjednodušený model předpětí, jehož charakteristiky jsou převzaty od výrobce panelů.

Reference

ČSN EN 1992-1-1 (2005) Eurocode 2: Design of concrete structures – Part 1-1: General reles and rules for buildings. *Český normalizační institut,* Prague.

Krsik, J. (2012) Modelování dutinového panelu Spiroll v programu ANSYS, in*: 14th International Conference of PhD Students – JUNIORSTAV 2012* Brno University of Technology, Brno, p. 274

Navrátil, J. (2008) *Předpjaté betonové konstrukce*, Akademické nakladatelství CERM, s.r.o., Brno.

Pajari, M. (2006) *Load test on hollow core slab floor with prestressed concrete beam*. Research report NO VTT-S-07331-06, Technical Research Centre of Finland (VTT), Helsinki, 76 p.

Šmiřák, S (1999) *Pružnost a plasticita I pro distanční studium,* Akademické nakladatelství CERM, s.r.o., Brno.

18th International Conference
ENGINEERING MECHANICS 2012
Svratka, Czech Republic, May 14 – 17, 2012

pp. 763–774
Paper #214

NUMERICAL ANALYSIS OF COUPLED HEAT AND MOISTURE TRANSFER BASED ON KUNZEL MODEL

J. Kruis [*], **J. Maděra** [**]

Abstract: *Coupled heat and moisture transfer is still more often used in many civil engineering problems. In connection with concrete and plasters, the Künzel model is very popular. Unfortunately, very different orders of material parameters have devastating influence on the condition number of matrices obtained after space and time discretization of problems. It results in severe numerical difficulties. This contribution deals with some strategies leading to better numerical behaviour of the coupled transport processes.*

Keywords: ***coupled heat and moisture transport, Künzel model, condition number, non-symmetric systems of equations.***

1. Introduction

Continuous rapid development of computers enables solution of very complicated and complex problems. Whereas single-physics problems dominated in the past because of limited computer power, multi-physics problems have become a standard in recent years. In civil engineering, the multi-physics problems are usually represented by hydro-thermo-mechanical problems. The coupled heat and moisture transfer is used in connection with concrete ageing, problems in soils and rocks, plaster design, reconstruction of historical buildings, etc.

In the past, the temperature and moisture distribution in structures was estimated and the temperature and relative humidity or the water content were assumed as material parameters of mechanical models. Nowadays, simultaneous analysis of mechanical behaviour together with the temperature and moisture distribution can be performed.

There are several models of heat and moisture transfer depending whether the convection or diffusion phenomena prevails. Comprehensive list of models can be found in reference Černý and Rovnaníková (2002). The coupled heat and moisture transfer in buildings or building components is usually described by the Künzel model which is summarized in section 2.

The material coefficients depend on the actual values of temperature and relative humidity and they are not constant. It means, the conductivity matrix of material has to be computed in every time step. In some configurations, the conductivities are very small and it leads to serious numerical problems because there are zero diagonal matrix entries. In such cases, appropriate degrees of freedom should be removed from the system and they can be returned back when the conductivities become physically important.

2. Künzel model of coupled heat and moisture transport

In 1995, Künzel proposed in reference Künzel (1995) a model of coupled heat and moisture transfer suitable for building components.

The Künzel model of coupled heat and moisture transport is based on the relative humidity, φ, and temperature, T. Instead of the relative humidity, water content, w, can be also used but it is generally non-continuous variable while the relative humidity is always continuous. The continuity of a variable is

[*] doc. Ing. Jaroslav Kruis, Ph.D.: Department of Mechanics, Faculty of Civil Engineering, Czech Technical University in Prague, Thákurova 7; 166 29, Prague; CZ, e-mail: jk@cml.fsv.cvut.cz
[**] Ing. Jiří Maděra, Ph.D.: Department of Materials Engineering and Chemistry, Faculty of Civil Engineering, Czech Technical University in Prague, Thákurova 7; 166 29, Prague; CZ, e-mail: madera@fsv.cvut.cz

an advantage in the finite element method. The relative humidity is defined by the relationship

$$\varphi = \frac{p_v}{p_{vs}(T)} \,, \tag{1}$$

where p_v denotes the partial pressure of water vapour and $p_{vs}(T)$ denotes the saturated water vapour pressure which depends on the temperature. The water content, w, can be expressed as a function of the relative humidity, φ. The partial pressure of saturated water vapour in the air has the form

$$p_{vs}(T) = e^{23{,}5771 - \frac{4042{,}9}{T - 37{,}58}} \,. \tag{2}$$

The vapour diffusion flux density has the form

$$\boldsymbol{q}_v = D_m \nabla m + D_T \nabla T \approx D_m \nabla m = -\delta \nabla p_v \,, \tag{3}$$

where D_m (kg/m/s) is the mass-related diffusion coefficient, m (-) is the mass fraction of water vapour related to the total mass of the vapour and air mixture, D_T (kg/m/s/K) is the thermo-diffusion coefficient, T is the temperature, δ (kg/m/s/Pa) is the water vapour diffusion coefficient in air, p_v (Pa) denotes the water vapour partial pressure. The contribution $D_T \nabla T$ is usually negligible and the mass fraction of water vapour related to the total mass of the vapour and air mixture can be replaced by the water vapour partial pressure. The water vapour diffusion coefficient in air has the form

$$\delta = \frac{2{,}306.10^{-5}}{R_v T} \left(\frac{T}{273{,}15} \right)^{1{,}81} \,, \tag{4}$$

where $R_v = 461{,}5$ J/K/kg. Furthermore, in the case of small capillaries, water vapour diffusion resistance factor, μ, has to be introduced and the vapour diffusion flux density has the form

$$\boldsymbol{q}_v = -\frac{\delta}{\mu} \nabla p_v = -\delta_p \nabla p_v \,, \tag{5}$$

where δ_p (kg/m/s/Pa) denotes the water vapour permeability. With the help of (1), the vapour diffusion flux density can be written in the form

$$\boldsymbol{q}_v = -\delta_p \nabla p_v = -\delta_p p_{vs} \nabla \varphi - \delta_p \varphi \frac{\mathrm{d}p_{vs}}{\mathrm{d}T} \nabla T \,. \tag{6}$$

Liquid conduction is described by the liquid flux density (kg/m^2/s) in the form

$$\boldsymbol{q}_l = -D_w(w) \nabla w \,, \tag{7}$$

where $D_w(w)$ (m^2/s) denotes the capillary transport coefficient. The liquid conduction can be also described by the Darcy's formula

$$\boldsymbol{q}_l = K_1 \nabla p_k \,, \tag{8}$$

where K_1 (kg/m/s/Pa) is the permeability coefficient and p_k (Pa) denotes the capillary suction stress. With the help of Kelvin's formula, the capillary suction stress can be written in the form

$$p_k = -\varrho_w R_0 T \ln \varphi \,, \tag{9}$$

where ρ_w (kg/m^3) is the density of water and R_0 (J/kg/K) denotes the gas constant for water vapour. Equation (8) can be rearranged into new form

$$\boldsymbol{q}_l = -K_1 \varrho_w R_0 \ln \varphi \nabla T - K_1 \varrho_w R_0 T \frac{1}{\varphi} \nabla \varphi \approx -K_1 \varrho_w R_0 \frac{T}{\varphi} \nabla \varphi \,. \tag{10}$$

The term $K_1 \varrho_w R_0 \ln \varphi \nabla T$ is significantly smaller than the other and therefore it is usually neglected. The liquid flux density can be also written in the form

$$\boldsymbol{q}_l = -D_\varphi \nabla \varphi \,, \tag{11}$$

where D_φ (kg/m/s) is the liquid conduction coefficient. Comparison of (11), (7) and (10) reveals relationships among the particular material parameters

$$D_\varphi = D_w \frac{\mathrm{d}w}{\mathrm{d}\varphi} = K_1 \varrho_w R_0 \frac{T}{\varphi} \,. \tag{12}$$

Balance equation for the moisture has the form

$$\frac{\partial w}{\partial t} = -\mathrm{div}(\boldsymbol{q}_l + \boldsymbol{q}_v) + S_w \,, \tag{13}$$

where S_w (kg/m^3/s) denotes the moisture source or sink. Substitution of (11) and (6) into the balance equation (13) results in

$$\begin{aligned} \frac{\partial w}{\partial t} &= \mathrm{div}\left(D_\varphi \nabla\varphi + \delta_p p_{vs} \nabla\varphi + \delta_p \varphi \frac{\mathrm{d}p_{vs}}{\mathrm{d}T} \nabla T \right) + S_w = \\ &= \mathrm{div}\left(\left(D_\varphi + \delta_p p_{vs}\right) \nabla\varphi + \delta_p \varphi \frac{\mathrm{d}p_{vs}}{\mathrm{d}T} \nabla T \right) + S_w \,. \end{aligned} \tag{14}$$

The time derivate on the left hand side can be further modified

$$\frac{\partial w}{\partial t} = \frac{\mathrm{d}w}{\mathrm{d}\varphi} \frac{\partial \varphi}{\partial t} = h_{\varphi\varphi} \,. \tag{15}$$

Heat transport is described by the well known balance equation

$$\frac{\partial H}{\partial t} = \frac{\partial (H_s + H_w)}{\partial t} = -\mathrm{div}\boldsymbol{q}_T + S_h \,, \tag{16}$$

where H (J/m^3) denotes the total enthalpy, H_s (J/m^3) denotes the enthalpy of dry material, H_w (J/m^3) denotes the enthalpy of material moisture, $\boldsymbol{q}_T$ (J/m^2/s=W/m^2) denotes the heat flux density and S_h (W/m^3) denotes the heat source or sink. The Fourier law has the form

$$\boldsymbol{q}_T = -\lambda \nabla T \,, \tag{17}$$

where λ (W/m/K) denotes the thermal conductivity of the moist material and T (K) denotes the temperature. The source or sink of heat can be written in the form

$$S_h = -h_v \mathrm{div}\boldsymbol{q}_v \,, \tag{18}$$

where h_v (J/kg) denotes the latent heat of phase change and $\boldsymbol{q}_v$ (kg/m^2/s) denotes the vapour diffusion flux density.

With respect to (6), the balance equation has the form

$$\begin{aligned} \frac{\partial H}{\partial t} &= -\mathrm{div}\boldsymbol{q}_T + S_h = \mathrm{div}(\lambda \nabla T) + h_v \mathrm{div}\left(\delta_p p_{vs} \nabla\varphi + \delta_p \varphi \frac{\mathrm{d}p_{vs}}{\mathrm{d}T} \nabla T \right) = \\ &= \mathrm{div}\left(\lambda \nabla T + h_v \delta_p p_{vs} \nabla\varphi + h_v \delta_p \varphi \frac{\mathrm{d}p_{vs}}{\mathrm{d}T} \nabla T \right) = \\ &= \mathrm{div}\left(h_v \delta_p p_{vs} \nabla\varphi + \left(\lambda + h_v \delta_p \varphi \frac{\mathrm{d}p_{vs}}{\mathrm{d}T} \right) \nabla T \right) \,. \end{aligned} \tag{19}$$

Similarly to the mass balance equation, the left hand side can be written in the form

$$\frac{\partial H}{\partial t} = \left(\frac{\mathrm{d}H_s}{\mathrm{d}T} + \frac{\mathrm{d}H_w}{\mathrm{d}T} \right) \frac{\partial T}{\partial t} = \left(\varrho C + \frac{\mathrm{d}H_w}{\mathrm{d}T} \right) \frac{\partial T}{\partial t} = h_{TT} \,, \tag{20}$$

where ϱ (kg/m^3) denotes the density of material and C (J/kg/K) is the heat capacity coefficient.

Let new notation be introduced in the form

$$\begin{pmatrix} \boldsymbol{q}_\varphi \\ \boldsymbol{q}_T \end{pmatrix} = \begin{pmatrix} \boldsymbol{D}_{\varphi\varphi} & \boldsymbol{D}_{\varphi T} \\ \boldsymbol{D}_{T\varphi} & \boldsymbol{D}_{TT} \end{pmatrix} \begin{pmatrix} \boldsymbol{g}_\varphi \\ \boldsymbol{g}_T \end{pmatrix} = \\ = \begin{pmatrix} D_\varphi + \delta_p p_{vs} & \delta_p \varphi \dfrac{\mathrm{d}p_{vs}}{\mathrm{d}T} \\ h_v \delta_p p_{vs} & \lambda + h_v \delta_p \varphi \dfrac{\mathrm{d}p_{vs}}{\mathrm{d}T} \end{pmatrix} \begin{pmatrix} \nabla\varphi \\ \nabla T \end{pmatrix} . \tag{21}$$

With the new notation, the balance equations have the form

$$h_{\varphi\varphi} \frac{\partial \varphi}{\partial t} = \operatorname{div} \left(\boldsymbol{D}_{\varphi\varphi} \nabla\varphi + \boldsymbol{D}_{\varphi T} \nabla T \right) , \tag{22}$$

$$h_{TT} \frac{\partial T}{\partial t} = \operatorname{div} \left(\boldsymbol{D}_{T\varphi} \nabla\varphi + \boldsymbol{D}_{TT} \nabla T \right) . \tag{23}$$

3. Initial and boundary conditions

The balance equations (22) and (23) are valid in domain Ω which has boundary Γ. The boundary of the domain Ω is split into parts Γ_T, Γ_φ, where the Dirichlet boundary conditions are prescribed (prescribed values), Γ_{qT}, $\Gamma_{q\varphi}$, where the Neumann boundary conditions are prescribed (prescribed fluxes) and Γ_{NT} and $\Gamma_{N\varphi}$, where the Newton (Cauchy) boundary conditions are prescribed. The parts Γ_T, Γ_{qT} and Γ_{NT} are disjoint and their union is the whole boundary Γ. The same is valid for the parts Γ_φ, $\Gamma_{q\varphi}$ and $\Gamma_{N\varphi}$.

The Dirichlet boundary conditions have the form

$$\varphi(\boldsymbol{x}, t) = \overline{\varphi}(\boldsymbol{x}, t), \qquad \boldsymbol{x} \in \Gamma_\varphi , \tag{24}$$
$$T(\boldsymbol{x}, t) = \overline{T}(\boldsymbol{x}, t), \qquad \boldsymbol{x} \in \Gamma_T , \tag{25}$$

where $\overline{T}(\boldsymbol{x}, t)$ denotes the prescribed temperature on the part Γ_T and $\overline{\varphi}(\boldsymbol{x}, t)$ denotes the prescribed relative humidity on the part Γ_φ. The Neumann boundary conditions have the form

$$\boldsymbol{q}_\varphi(\boldsymbol{x}, t) = \overline{\boldsymbol{q}}_\varphi(\boldsymbol{x}, t), \qquad \boldsymbol{x} \in \Gamma_{q\varphi} , \tag{26}$$
$$\boldsymbol{q}_T(\boldsymbol{x}, t) = \overline{\boldsymbol{q}}_T(\boldsymbol{x}, t), \qquad \boldsymbol{x} \in \Gamma_{qT} , \tag{27}$$

where $\overline{\boldsymbol{q}}_\varphi(\boldsymbol{x}, t)$ denotes the prescribed moisture flux on the part $\Gamma_{q\varphi}$ of the boundary and $\overline{\boldsymbol{q}}_T(\boldsymbol{x}, t)$ denotes the prescribed heat flux on the Cauchy boundary conditions part Γ_{qT}. The Newton (Cauchy) boundary conditions have the form

$$\boldsymbol{q}_\varphi(\boldsymbol{x}, t) = \beta_\varphi (p(\boldsymbol{x}, t) - p_\infty(\boldsymbol{x}, t)) \boldsymbol{n}, \qquad \boldsymbol{x} \in \Gamma_{N\varphi} , \tag{28}$$
$$\boldsymbol{q}_T(\boldsymbol{x}, t) = \beta_T (T(\boldsymbol{x}, t) - T_\infty(\boldsymbol{x}, t)) \boldsymbol{n}, \qquad \boldsymbol{x} \in \Gamma_{NT} , \tag{29}$$

where $p_\infty(\boldsymbol{x}, t)$ denotes the ambient water vapour pressure and β_φ is the mass transfer coefficient, both defined in the part $\Gamma_{N\varphi}$. The pressures are transformed to the relative humidity with the help of relationship (1). $T_\infty(\boldsymbol{x}, t)$ is the ambient temperature and β_T is the heat transfer coefficient, both defined in the part Γ_{NT}.

Besides the boundary conditions, the initial conditions are prescribed in the form

$$\varphi(\boldsymbol{x}, 0) = \varphi_0(\boldsymbol{x}), \qquad \boldsymbol{x} \in \Omega, \tag{30}$$
$$T(\boldsymbol{x}, 0) = T_0(\boldsymbol{x}), \qquad \boldsymbol{x} \in \Omega, \tag{31}$$

where $\varphi_0(\boldsymbol{x})$ denotes the initial relative humidity and $T_0(\boldsymbol{x})$ denotes the initial temperature.

4. Discretization of the differential equations

The finite element method is used for spatial discretization of the partial differential equations (22) and (23). The weighted residual statement is applied to the mass balance equation assuming $(\delta\varphi) = 0$ on Γ_φ and $(\delta T) = 0$ on Γ_T. The brackets are used for weight functions $(\delta\varphi)$ and (δT) because there are some material parameters denoted by δ.

The mass balance equation multiplied by the test function $(\delta\varphi)$ has the form

$$\int_\Omega (\delta\varphi)\Big(h_{\varphi\varphi}\frac{\partial\varphi}{\partial t} - \operatorname{div}\big(\boldsymbol{D}_{\varphi\varphi}\nabla\varphi + \boldsymbol{D}_{\varphi T}\nabla T\big)\Big)\mathrm{d}\Omega = 0 \tag{32}$$

and the energy balance equation multiplied by the test function (δT) has the form

$$\int_\Omega (\delta T)\Big(h_{TT}\frac{\partial T}{\partial t} - \operatorname{div}\big(\boldsymbol{D}_{T\varphi}\nabla\varphi + \boldsymbol{D}_{TT}\nabla T\big)\Big)\mathrm{d}\Omega = 0\,. \tag{33}$$

Applying Green's theorem, the weak formulation for the mass transfer yields

$$\begin{aligned}\int_\Omega (\delta\varphi)h_{\varphi\varphi}\frac{\partial\varphi}{\partial t}\mathrm{d}\Omega + \int_\Omega \nabla(\delta\varphi)\boldsymbol{D}_{\varphi\varphi}\nabla\varphi\mathrm{d}\Omega + \int_\Omega \nabla(\delta\varphi)\boldsymbol{D}_{\varphi T}\nabla T\mathrm{d}\Omega + \\ - \int_{\Gamma_{q\varphi}\cup\Gamma_{N\varphi}} (\delta\varphi)\boldsymbol{D}_{\varphi\varphi}\frac{\mathrm{d}\varphi}{\mathrm{d}\boldsymbol{n}}\mathrm{d}\Gamma - \int_{\Gamma_{qT}\cup\Gamma_{NT}} (\delta\varphi)\boldsymbol{D}_{\varphi T}\frac{\mathrm{d}T}{\mathrm{d}\boldsymbol{n}}\mathrm{d}\Gamma = 0\end{aligned} \tag{34}$$

and the weak formulation for heat transfer

$$\begin{aligned}\int_\Omega (\delta T)h_{TT}\frac{\partial T}{\partial t}\mathrm{d}\Omega + \int_\Omega \nabla(\delta T)\boldsymbol{D}_{T\varphi}\nabla\varphi\mathrm{d}\Omega + \int_\Omega \nabla(\delta T)\boldsymbol{D}_{TT}\nabla T\mathrm{d}\Omega - \\ - \int_{\Gamma_{q\varphi}\cup\Gamma_{N\varphi}} (\delta T)\boldsymbol{D}_{T\varphi}\frac{\mathrm{d}\varphi}{\mathrm{d}\boldsymbol{n}}\mathrm{d}\Gamma - \int_{\Gamma_{qT}\cup\Gamma_{NT}} (\delta T)\boldsymbol{D}_{TT}\frac{\mathrm{d}T}{\mathrm{d}\boldsymbol{n}}\mathrm{d}\Gamma = 0\,.\end{aligned} \tag{35}$$

In the finite element method, the temperature T and relative humidity φ are approximated in the form

$$\varphi = \boldsymbol{N}_\varphi(\boldsymbol{x})\boldsymbol{d}_\varphi\,, \tag{36}$$

$$T = \boldsymbol{N}_T(\boldsymbol{x})\boldsymbol{d}_T\,, \tag{37}$$

and the gradients of the temperature and relative humidity are also needed

$$\nabla\varphi = \boldsymbol{B}_\varphi(\boldsymbol{x})\boldsymbol{d}_\varphi\,, \tag{38}$$

$$\nabla T = \boldsymbol{B}_T(\boldsymbol{x})\boldsymbol{d}_T\,. \tag{39}$$

In the previous equations, $\boldsymbol{N}_\varphi(\boldsymbol{x})$ denotes the matrix of approximation functions for the relative humidity, $\boldsymbol{N}_T(\boldsymbol{x})$ denotes the matrix of approximation functions for the temperature, $\boldsymbol{B}_\varphi(\boldsymbol{x})$ is the matrix of gradients of the approximation functions collected in the matrix $\boldsymbol{N}_\varphi(\boldsymbol{x})$, $\boldsymbol{B}_T(\boldsymbol{x})$ is the matrix of gradients of the approximation functions collected in the matrix $\boldsymbol{N}_T(\boldsymbol{x})$, $\boldsymbol{d}_\varphi$ denotes the vector of nodal relative humidities and $\boldsymbol{d}_T$ denotes the vector of nodal temperatures. The approximations of weight functions have the form

$$(\delta\varphi) = \boldsymbol{N}_{(\delta\varphi)}(\boldsymbol{x})\boldsymbol{d}_{(\delta\varphi)}\,, \tag{40}$$

$$(\delta T) = \boldsymbol{N}_{(\delta T)}(\boldsymbol{x})\boldsymbol{d}_{(\delta T)}\,, \tag{41}$$

where the notation is similar to the previous one.

Using approximations (36)–(39) in equations (34) and (35), a set of the first order differential equations is obtained in the matrix form

$$\begin{pmatrix} \boldsymbol{K}_{\varphi\varphi} & \boldsymbol{K}_{\varphi T} \\ \boldsymbol{K}_{T\varphi} & \boldsymbol{K}_{TT} \end{pmatrix}\begin{pmatrix} \boldsymbol{d}_\varphi \\ \boldsymbol{d}_T \end{pmatrix} + \begin{pmatrix} \boldsymbol{C}_{\varphi\varphi} & \boldsymbol{C}_{\varphi T} \\ \boldsymbol{C}_{T\varphi} & \boldsymbol{C}_{TT} \end{pmatrix}\begin{pmatrix} \dot{\boldsymbol{d}}_\varphi \\ \dot{\boldsymbol{d}}_T \end{pmatrix} = \begin{pmatrix} \boldsymbol{f}_\varphi \\ \boldsymbol{f}_T \end{pmatrix}\,. \tag{42}$$

The matrices $\boldsymbol{K}_{\varphi\varphi}$, $\boldsymbol{K}_{\varphi T}$, $\boldsymbol{K}_{T\varphi}$ and $\boldsymbol{K}_{TT}$ create the conductivity matrix of the problem and they have the form

$$\boldsymbol{K}_{\varphi\varphi} = \int_\Omega \boldsymbol{B}^T_{(\delta\varphi)} \boldsymbol{D}_{\varphi\varphi} \boldsymbol{B}_\varphi \mathrm{d}\Omega, \quad \boldsymbol{K}_{\varphi T} = \int_\Omega \boldsymbol{B}^T_{(\delta\varphi)} \boldsymbol{D}_{\varphi T} \boldsymbol{B}_T \mathrm{d}\Omega, \tag{43}$$

$$\boldsymbol{K}_{T\varphi} = \int_\Omega \boldsymbol{B}^T_{(\delta T)} \boldsymbol{D}_{T\varphi} \boldsymbol{B}_\varphi \mathrm{d}\Omega, \quad \boldsymbol{K}_{TT} = \int_\Omega \boldsymbol{B}^T_{(\delta T)} \boldsymbol{D}_{TT} \boldsymbol{B}_T \mathrm{d}\Omega\,, \tag{44}$$

where the conductivity matrices of material $\boldsymbol{D}_{\varphi\varphi}$, $\boldsymbol{D}_{\varphi T}$, $\boldsymbol{D}_{T\varphi}$ and $\boldsymbol{D}_{TT}$ are diagonal matrices and the diagonal entries are equal to appropriate conductivities

$$d_{\varphi\varphi} = D_w \frac{\mathrm{d}w}{\mathrm{d}\varphi} + \delta_p p_{vs}, \quad d_{\varphi T} = \delta_p \varphi \frac{\mathrm{d}p_{vs}}{\mathrm{d}T}, \tag{45}$$

$$d_{T\varphi} = h_v \delta_p p_{vs}, \quad d_{TT} = \lambda + h_v \delta_p \varphi \frac{\mathrm{d}p_{vs}}{\mathrm{d}T}\,. \tag{46}$$

The matrices $\boldsymbol{C}_{\varphi\varphi}$, $\boldsymbol{C}_{\varphi T}$, $\boldsymbol{C}_{T\varphi}$ and $\boldsymbol{C}_{TT}$ create the capacity matrix of the problem and they have the form

$$\boldsymbol{C}_{\varphi\varphi} = \int_\Omega \boldsymbol{N}^T_{(\delta\varphi)} \boldsymbol{H}_{\varphi\varphi} \boldsymbol{N}_\varphi \mathrm{d}\Omega, \quad \boldsymbol{C}_{\varphi T} = \int_\Omega \boldsymbol{N}^T_{(\delta\varphi)} \boldsymbol{H}_{\varphi T} \boldsymbol{N}_T \mathrm{d}\Omega, \tag{47}$$

$$\boldsymbol{C}_{T\varphi} = \int_\Omega \boldsymbol{N}^T_{(\delta T)} \boldsymbol{H}_{T\varphi} \boldsymbol{N}_\varphi \mathrm{d}\Omega, \quad \boldsymbol{C}_{TT} = \int_\Omega \boldsymbol{N}^T_{(\delta T)} \boldsymbol{H}_{TT} \boldsymbol{N}_T \mathrm{d}\Omega, \tag{48}$$

where the capacity matrices of material $\boldsymbol{H}_{\varphi\varphi}$, $\boldsymbol{H}_{\varphi T}$, $\boldsymbol{H}_{T\varphi}$ and $\boldsymbol{H}_{TT}$ are diagonal matrices and the diagonal entries are equal to appropriate capacities

$$h_{\varphi\varphi} = \frac{\mathrm{d}w}{\mathrm{d}\varphi}, \quad h_{\varphi T} = 0, \tag{49}$$

$$h_{T\varphi} = 0, \quad h_{TT} = \rho C \; + \frac{\mathrm{d}H_w}{\mathrm{d}T}\,. \tag{50}$$

The vectors $\boldsymbol{f}_\varphi$ and $\boldsymbol{f}_T$ contain prescribed nodal fluxes and have the form

$$\boldsymbol{f}_\varphi = \int_{\Gamma_{qT} \cup \Gamma_{NT}} \boldsymbol{N}^T_{(\delta\varphi)} \hat{q}_\varphi \mathrm{d}\Gamma, \quad \boldsymbol{f}_T = \int_{\Gamma_{q\varphi} \cup \Gamma_{N\varphi}} \boldsymbol{N}^T_{(\delta T)} \hat{q}_T \mathrm{d}\Gamma\,, \tag{51}$$

where $\hat{q}_\varphi$ denotes the mass boundary fluxes and $\hat{q}_T$ denotes the heat boundary fluxes.

5. Numerical solution

From the numerical point of view, coupled problems are described by balance equations which have the form of partial differential equations. The exact solution cannot be obtained with respect to non-linearities hidden in the material models. Another obstacle is caused by very general domains which are solved in real engineering problems. Therefore, numerical methods have to be used.

The balance equations (42) can be written in the form

$$\begin{pmatrix} \boldsymbol{C}_{\varphi\varphi} & \boldsymbol{C}_{\varphi T} \\ \boldsymbol{C}_{T\varphi} & \boldsymbol{C}_{TT} \end{pmatrix} \begin{pmatrix} \dot{\boldsymbol{d}}_\varphi \\ \dot{\boldsymbol{d}}_T \end{pmatrix} + \begin{pmatrix} \boldsymbol{K}_{\varphi\varphi} & \boldsymbol{K}_{\varphi T} \\ \boldsymbol{K}_{T\varphi} & \boldsymbol{K}_{TT} \end{pmatrix} \begin{pmatrix} \boldsymbol{d}_\varphi \\ \boldsymbol{d}_T \end{pmatrix} = \begin{pmatrix} \boldsymbol{f}_\varphi \\ \boldsymbol{f}_T \end{pmatrix} = \begin{pmatrix} \boldsymbol{f}_{\varphi\varphi} + \boldsymbol{f}_{\varphi T} \\ \boldsymbol{f}_{T\varphi} + \boldsymbol{f}_{TT} \end{pmatrix}, \tag{52}$$

where the vectors $\boldsymbol{f}_T$ and $\boldsymbol{f}_\varphi$ denote prescribed nodal fluxes and they can be further split to two contributions. The vector $\boldsymbol{f}_\varphi$ is the sum of vectors $\boldsymbol{f}_{\varphi\varphi}$ and $\boldsymbol{f}_{\varphi T}$ which represent contributions to the nodal fluxes caused by temperature changes and humidity changes. The meaning of other contributions is similar.

The system of differential equations (52) can be written more compactly in the form

$$\boldsymbol{C}(\boldsymbol{d})\dot{\boldsymbol{d}} + \boldsymbol{K}(\boldsymbol{d})\boldsymbol{d} = \boldsymbol{f}\,, \tag{53}$$

where the dependency of the stiffness, conductivity, capacity and coupling matrices on the attained values of variables is explicitly denoted. $\Delta \boldsymbol{d}$ and $\Delta \dot{\boldsymbol{d}}$ denote increments of nodal variables and their time derivatives.

The system (53) has to be solved by an incremental method. Time discretization is based on the $\boldsymbol{v}$-form of the generalized trapezoidal method Hughes (1987) defined by the relationships

$$\boldsymbol{d}_{n+1} = \boldsymbol{d}_n + \Delta t \boldsymbol{v}_{n+\gamma} \,, \tag{54}$$

$$\boldsymbol{v}_{n+\gamma} = (1-\gamma)\boldsymbol{v}_n + \gamma \boldsymbol{v}_{n+1} \,, \tag{55}$$

where $\boldsymbol{v}$ denotes the first derivatives of nodal values with respect to time and γ is a parameter from the range $[0, 1]$. The subscript n denotes the time step and it serves also as an index in the incremental method, called the outer iteration loop. It is assumed that all variables are known at the time t_n and variables at the time t_{n+1} are searched.

Substitution of expressions defined in equations (54) and (55) to the system of differential equations (53) leads to relationship

$$\left(\boldsymbol{C}_n + \Delta t \gamma \boldsymbol{K}_n\right) \boldsymbol{v}_{n+1} = \boldsymbol{f}_{n+1} - \boldsymbol{K}_n \left(\boldsymbol{d}_n + \Delta t (1-\gamma) \boldsymbol{v}_n\right) \,, \tag{56}$$

where $\boldsymbol{C}_n$ and $\boldsymbol{K}_n$ denote the capacity and stiffness/conductivity matrices evaluated with the help of values $\boldsymbol{d}_n$. The system of algebraic equations (56) is generally non-linear and the Newton-Raphson method Bittnar and Šejnoha (1996) has to be used at each time step.

The trial solution $\boldsymbol{v}_{n+1,0}$ of the system of equations (56) is used for computation of the trial nodal values $\boldsymbol{d}_{n+1,0}$ which are obtained from equations (55) and (54). Substitution of the trial solution back to the system of equations (56) with modified matrices does not generally lead to equality. An iteration loop, called the inner iteration loop, in every time step is based on residual which is computed from the relationship

$$\begin{aligned} \boldsymbol{r}_{n+1,j} &= \boldsymbol{f}_{n+1} - \boldsymbol{K}_n \left(\boldsymbol{d}_n + \Delta t (1-\gamma) \boldsymbol{v}_n\right) \\ &- \left(\boldsymbol{C}_{n+1,j} + \Delta t \gamma \boldsymbol{K}_{n+1,j}\right) \boldsymbol{v}_{n+1,j} \,, \end{aligned} \tag{57}$$

where $\boldsymbol{C}_{n+1,j}$ and $\boldsymbol{K}_{n+1,j}$ denote the matrices evaluated for $\boldsymbol{d}_{n+1,j}$ and j is the index in the inner loop. Correction of nodal time derivatives are computed from the equation

$$\left(\boldsymbol{C}_{n+1,j} + \Delta t \gamma \boldsymbol{K}_{n+1,j}\right) \Delta \boldsymbol{v}_{n+1,j+1} = \boldsymbol{r}_{n+1,j} \tag{58}$$

and new time derivatives are in the form

$$\boldsymbol{v}_{n+1,j+1} = \boldsymbol{v}_{n+1,j} + \Delta \boldsymbol{v}_{n+1,j+1} \,. \tag{59}$$

It has to be noted that the permanent recalculation of matrices $\boldsymbol{K}$ and $\boldsymbol{C}$ with respect to actual nodal values is very computationally demanding. In such a case, the matrix of the system of equations $\boldsymbol{C}(\boldsymbol{d}) + \Delta t \gamma \boldsymbol{K}(\boldsymbol{d})$ has to be always factorized and it requires additional computational time. The numerical examples show that the modified Newton method, which changes the system matrix only at the beginning of a new time step is the best choice. More details can be found in references Kruis and Koudelka and Krejčí (2010) and Kruis and Koudelka and Krejčí (2012).

6. Numerical experiments

In order to show possible difficulties, coupled heat and moisture transfer described by the Künzel model on a rectangular two-dimensional domain is assumed. Rectangular finite elements with bi-linear basis functions are used. The quadrilateral element contains four nodes and therefore there are eight degrees of freedom in the case of heat and moisture transfer on each element. The degrees of freedom are located in vector

$$\boldsymbol{d}_e^T = (\varphi_1, \varphi_2, \varphi_3, \varphi_4, T_1, T_2, T_3, T_4) \,. \tag{60}$$

Tab. 1: Material parameters.

density of material	ϱ=16.5 kg/m^3
water vapour diffusion resistance factor	μ=58 (-)
capillary transport coefficient	$D_w = 6.2 \times 10^{-12}$ m^2/s
	$\dfrac{\mathrm{d}H}{\mathrm{d}T} = \varrho c$
heat capacity coefficient	$c = 1567$

Tab. 2: Thermal conductivity.

0.00000	0.0393
0.00219	0.0423
0.03040	0.0443
0.03968	0.0484
0.06349	0.5130

With respect to the ordering of degrees of freedom in the vector $\boldsymbol{d}$, the matrix of basis functions has the form

$$\boldsymbol{N} = \begin{pmatrix} \boldsymbol{N}_\varphi & \boldsymbol{0} \\ \boldsymbol{0} & \boldsymbol{N}_T \end{pmatrix} = \begin{pmatrix} N_1 & N_2 & N_3 & N_4 & 0 & 0 & 0 & 0 \\ 0 & 0 & 0 & 0 & N_1 & N_2 & N_3 & N_4 \end{pmatrix} . \tag{61}$$

The matrix of partial derivatives has the form

$$\boldsymbol{B} = \begin{pmatrix} \dfrac{\partial \varphi}{\partial x} \\ \dfrac{\partial \varphi}{\partial y} \\ \dfrac{\partial T}{\partial x} \\ \dfrac{\partial T}{\partial y} \end{pmatrix} = \begin{pmatrix} \dfrac{\partial \boldsymbol{N}_\varphi}{\partial x} & \boldsymbol{0} \\ \dfrac{\partial \boldsymbol{N}_\varphi}{\partial y} & \boldsymbol{0} \\ \boldsymbol{0} & \dfrac{\partial \boldsymbol{N}_T}{\partial x} \\ \boldsymbol{0} & \dfrac{\partial \boldsymbol{N}_T}{\partial y} \end{pmatrix} = \begin{pmatrix} \boldsymbol{B}_\varphi & \boldsymbol{0} \\ \boldsymbol{0} & \boldsymbol{B}_T \end{pmatrix} . \tag{62}$$

The conductivity matrix of an element has the form

$$\boldsymbol{K} = \int_{\Omega_e} \boldsymbol{B}^T \boldsymbol{D} \boldsymbol{B} \, \mathrm{d}\Omega \, , \tag{63}$$

where the matrices $\boldsymbol{B}$ and $\boldsymbol{D}$ are defined by relationships (62) and (21) respectively. Ω_e denotes the element area. The conductivity matrix is assembled from four blocks in the form

$$\begin{pmatrix} \boldsymbol{B}_\varphi & \boldsymbol{0} \\ \boldsymbol{0} & \boldsymbol{B}_T \end{pmatrix}^T \begin{pmatrix} \boldsymbol{D}_{\varphi\varphi} & \boldsymbol{D}_{\varphi T} \\ \boldsymbol{D}_{T\varphi} & \boldsymbol{D}_{TT} \end{pmatrix} \begin{pmatrix} \boldsymbol{B}_\varphi & \boldsymbol{0} \\ \boldsymbol{0} & \boldsymbol{B}_T \end{pmatrix} = \begin{pmatrix} \boldsymbol{B}_\varphi^T \boldsymbol{D}_{\varphi\varphi} \boldsymbol{B}_\varphi & \boldsymbol{B}_\varphi^T \boldsymbol{D}_{\varphi T} \boldsymbol{B}_T \\ \boldsymbol{B}_T^T \boldsymbol{D}_{T\varphi} \boldsymbol{B}_\varphi & \boldsymbol{B}_T^T \boldsymbol{D}_{TT} \boldsymbol{B}_T \end{pmatrix} . \tag{64}$$

If the diagonal conductivity matrices of material, $\boldsymbol{D}_{\varphi\varphi}, \boldsymbol{D}_{TT}$, are zero or very close to zero, zero or nearly zero entries appear on the main diagonal of the conductivity matrix of an element and on the main diagonal of the conductivity matrix of problem.

Let the material parameters summarized in table 1 be used. Table 2 contains the thermal conductivity which is given by measured data.

The conductivity matrix of material, $\boldsymbol{D}$, in the Künzel model is defined in (21). The matrix evaluated at the beginning of the analysis has the form

$$\boldsymbol{D}_K = \begin{pmatrix} D_\varphi + \delta_p p_{vs} & \delta_p \varphi \dfrac{\mathrm{d}p_{vs}}{\mathrm{d}T} \\ L_v \delta_p p_{vs} & (\lambda + L_v \delta_p \varphi \dfrac{\mathrm{d}p_{vs}}{\mathrm{d}T}) \end{pmatrix} = \begin{pmatrix} 9.895512 \times 10^{-9} & 2.68344 \times 10^{-10} \\ 2.418454 \times 10^{-2} & 4.013119 \times 10^{-2} \end{pmatrix} . \quad (65)$$

There are obvious differences in orders of particular matrix entries. The eigenvalues of the matrix are

$$\lambda_1 = 9.733798 \times 10^{-9} , \quad (66)$$
$$\lambda_2 = 4.013119 \times 10^{-2} , \quad (67)$$

and their ratio is

$$\kappa = 4.123 \times 10^{6} . \quad (68)$$

In order to fix ideas, a plane stress problem is analyzed and compared with the coupled heat and moisture transport. Let the Young modulus be $E = 50$ GPa and the Poisson ratio $\nu = 0.2$. The stiffness matrix of elastic material subjected to plane stress conditions has the form

$$\boldsymbol{D}_{ps} = \begin{pmatrix} \frac{E}{1-\nu^2} & \frac{E\nu}{1-\nu^2} & 0 \\ \frac{E\nu}{1-\nu^2} & \frac{E}{1-\nu^2} & 0 \\ 0 & 0 & \frac{E}{2(1+\nu)} \end{pmatrix} = 10^6 \begin{pmatrix} 52\,083 & 10\,417 & 0 \\ 10\,417 & 52\,083 & 0 \\ 0 & 0 & 20\,833 \end{pmatrix} . \quad (69)$$

The eigenvalues of the stiffness matrix of the material are

$$\lambda_1 = 20833 \times 10^{6} , \quad (70)$$
$$\lambda_2 = 41666 \times 10^{6} , \quad (71)$$
$$\lambda_3 = 62500 \times 10^{6} \quad (72)$$

and the ratio of the largest and smallest eigenvalues results in the condition number

$$\kappa = 3 . \quad (73)$$

The larger condition number, the worse behaviour of many iterative method and greater cancellation errors. Comparison of the condition numbers (73) for plane stress and (68) for the coupled heat and moisture transfer reveals that the transport problem behaves much worse than the plane stress problem.

The conductivity matrix of the whole problem has the following smallest and largest eigenvalues

$$\lambda = \begin{pmatrix} 0.000000001366664 \\ \vdots \\ 0.085677899281368 \end{pmatrix} \quad (74)$$

and the condition number is

$$\kappa = 6.269 \times 10^{7} . \quad (75)$$

The conductivity matrix of the whole problem has no kernel because there have to be Dirichlet boundary conditions somewhere on domain boundary.

The generalized trapezoidal rule generates the following matrix $\boldsymbol{C}_n + \Delta t \gamma \boldsymbol{K}_n$. The smallest and largest eigenvalues are

$$\lambda = \begin{pmatrix} 0.0000669816805 \\ \vdots \\ 132.3215121202840 \end{pmatrix} \quad (76)$$

and the condition number is

$$\kappa = 1.975 \times 10^6 \,. \tag{77}$$

It is slightly better than the condition number of the conductivity matrix of the whole problem $\boldsymbol{K}$ because the capacity matrix is non-singular and positive definite.

The conductivity matrix of material $\boldsymbol{D}_K$ based on the Künzel assumption is populated by entries with very different order of magnitude. The better moisture insulation, the larger difference in orders of magnitude. Theoretically, a perfect hydrophobic material leads to zero term $d_{\varphi\varphi} = D_\varphi + \delta_p p_{vs}$ which results in a zero row and column in the conductivity matrix of a finite element $\boldsymbol{K}$. Moreover, there could be a zero column and row in the matrix of the whole problem which make difficulties for solvers of linear algebraic systems of equations. In the case of real materials, the diagonal term $D_\varphi + \delta_p p_{vs}$ is not exactly equal to zero but it could be very small and rows and columns in the global matrix could be nearly zero. The condition number of the global matrix is very large in such cases. It causes severe problems to iterative solvers because the rate of convergence usually depends on the condition number. If a direct solver is used for such systems of equations, significant cancellation errors could occur.

If materials with extremely small moisture conductivities are used, numerical difficulties may occur when significant moisture fluxes are presents. Such situation emerges e.g. near boundary where moisture flux is defined by external conditions. If an insulation material is close to the structure surface, the model is unable to transport the moisture flux from the exterior into structure. It results in non-balanced fluxes and the non-linear solver tends to reduce the length of time step. When the time step length is smaller than reasonable threshold, e.g. 10^{-3} s, the solver announces problems and it stops. This phenomena is illustrated in figures 1 and 2. The distribution of relative humidity along the coordinate axis is depicted in figure 1 while the time behaviour of the relative humidity at point near the external surface is visible in figure 2. The red line represents the relative humidity for structure with insulation near the surface. It means, there are extremely small moisture conductivities. On the other hand, the blue curve shows the relative humidity for structure without an insulation. Another examples can be found in references Kočí et al (2012) and Kočí et al (2010).

Zero columns and rows can be removed from the system of equations but it is not easy in real world problems. It is difficult to recognize small value nearly equal to zero because of a hydrophobic material with extremely small conductivity and small matrix entries caused by inappropriate scale of variables. The decision which numbers could be removed from the system of equations has to be based on evaluation of the heat and moisture fluxes. Contributions to the fluxes from particular gradients are evaluated and they are compared. The moisture flux contains two contributions

$$\boldsymbol{q}_\varphi = \boldsymbol{q}_{\varphi\varphi} + \boldsymbol{q}_{\varphi T} \,, \tag{78}$$

where

$$\boldsymbol{q}_{\varphi\varphi} = (D_\phi + \delta_p p_{vs})\nabla\varphi \,, \tag{79}$$

$$\boldsymbol{q}_{\varphi T} = \delta_p \varphi \frac{\mathrm{d}p_{vs}}{\mathrm{d}T}\nabla T \,. \tag{80}$$

Similarly for the heat flux

$$\boldsymbol{q}_T = \boldsymbol{q}_{T\varphi} + \boldsymbol{q}_{TT} \,, \tag{81}$$

where

$$\boldsymbol{q}_{T\varphi} = h_v \delta_p p_{vs} \nabla\varphi \,, \tag{82}$$

$$\boldsymbol{q}_{TT} = (\lambda + h_v \delta_p \varphi \frac{\mathrm{d}p_{vs}}{\mathrm{d}T})\nabla T \,. \tag{83}$$

If some of the contributions $\boldsymbol{q}_{\varphi\varphi}, \boldsymbol{q}_{\varphi T}, \boldsymbol{q}_{T\varphi}, \boldsymbol{q}_{TT}$ are significantly smaller than others in the vicinity of a node, the appropriate variable (temperature or relative humidity) is removed from the node and the appropriate degree of freedom is removed from the discrete system. This operation represents perfect barrier and no flux is possible there.

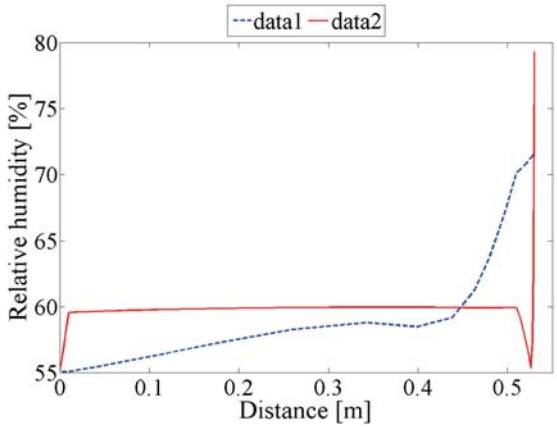

Fig. 1: Distribution of the relative humidity along the thickness.

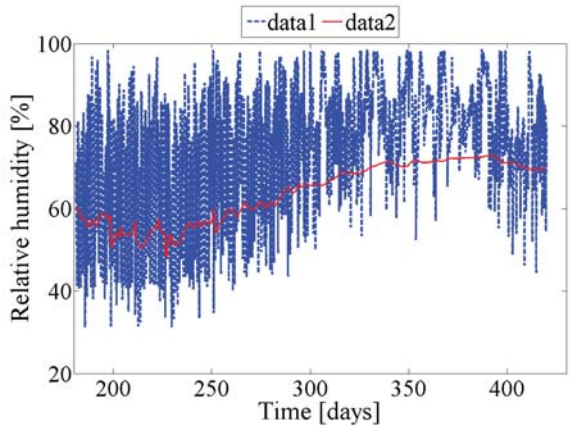

Fig. 2: Behaviour of the relative humidity in time at point near external boundary.

7. Conclusions

Modification of the algorithm for solution of coupled heat and moisture transfer based on the Künzel model was introduced. It evaluates contributions to the moisture and heat fluxes and it adaptively deals with the degrees of freedom defined in nodes of finite element mesh. If some fluxes are smaller than the others, the appropriate degrees of freedom are removed from the system and perfect insulation is obtained. When material parameters change their values, the degrees of freedom are returned to the system.

Acknowledgments

Financial support for this work was provided by project number P105/10/1682 of Czech Science Foundation. The financial support is gratefully acknowledged.

References

Hughes, T.J.R. (1987), *The Finite Element Method. Linear Static and Dynamic Finite Element Analysis*, Prentice-Hall, Inc., Englewood Cliffs, New Jersey 07632.

Bittnar, Z., Šejnoha, J. (1996), *Numerical Methods in Structural Mechanics*, ASCE Press, New York, Thomas Telford, London.

Černý, R., Rovnaníková, P. (2002), *Transport Processes in Concrete*, Spon Press, Taylor & Francis Group, London and New York.

Künzel, H. M. (1995), *Simultaneous Heat and Moisture Transport in Building Components*, Fraunhofer Institute of Building Physics, Fraunhofer IRB Verlag Stutgart.

Kruis, J. and Koudelka, T. and Krejčí, T. (2012), Multi-physics Analyses of Selected Civil Engineering Concrete Structures. *Communications in Computational Physics*, Vol 12, pp 885-918, doi:10.4208/cicp.031110.080711s.

Kruis, J. and Koudelka, T. and Krejčí, T. (2010), Efficient computer implementation of coupled hydro-thermo-mechanical analysis, *Math. Comput. Simulat*, Vol 80, pp 1578-1588.

Kočí, V., Maděra, J., Černý, R. (2012), Exterior thermal insulation systems for AAC building envelopes: computational analysis aimed at increasing service life. *Energy and Buildings*, Vol. 47, No. 1, pp 84-90.

Kočí, J., Kočí, V., Maděra, J., Rovnaníková, P., Černý, R. (2010), Computational analysis of hygrothermal performance of renovation renders In: *Advanced Computational Methods and Experiments in Heat Transfer XI*, WIT Press, Southampton, pp 267-277.

18th International Conference
ENGINEERING MECHANICS 2012
Svratka, Czech Republic, May 14 – 17, 2012

pp. 775–788
Paper #297

EIGENVIBRATION OF ROAD BRIDGES: MEASUREMENT AND NUMERICAL ANALYSIS

J. Kruis [*], M. Polák [**], T. Koudelka [***], T. Plachý [†].

Abstract: *Experimental and numerical analysis of existing highway concrete prestressed bridges were performed. In order to obtain good agreement between the numerical and experimental analyses, three-dimensional finite element models of the bridges were used. The eigenfrequencies and eigenmodes were obtained by the subspace iteration method with Gram-Schmidt orthonormalization in the reduced problem. The eigenfrequencies and eigenmodes obtained from the numerical analysis and from the experiment were compared and very good agreement was attained.*

Keywords: ***highway bridges, eigenmodes, eigenfrequencies, experimental analysis, subspace iteration method.***

1. Introduction

Highway bridges are subjected to experimental analysis of their vibration before they are put into service. The aim of experimental analysis is to determine eigenfrequencies and eigenmodes of the bridges. In order to perform the experiments smoothly and as much precisely as possible, it is useful to determine the eigenfrequencies and eigenmodes by numerical analysis in advance. Sensors should be located in antinodes because of significant displacements which can be measured more precisely than small displacements near the vibration nodes, Polák et al (2005).

The bridges analysed are highway concrete prestressed bridges in Prague. They are six-span structures made from the concrete C35/45-XF2+XD1. The length of the left bridge is 560.976 m (71.999 + 84.248 + 101.905 + 115.170 + 115.153 + 72.501) while the right bridge has the length 551.540 m (72.000 + 83.737 + 99.952 + 112.436 + 112.246 + 71.169). Both bridges are horizontally curved with radius 747.5 m and 753.75 m for the left and right bridge, respectively.

The cross sections of the bridges are changing along the length with respect to the quadratic parabola. The maximum height of the cross section is 6.5 m over the piers while only 3.135 m in the span centers. Each pier is created by four columns with a variable cross section.

2. Finite Element Model

With respect to the complicated bridge geometry, a three-dimensional finite element model was created. The model is based on brick finite elements with eight nodes and linear approximation functions. The three-dimensional model was used because of the curved shape of the bridge. In order to generate the mesh as easily as possible, the bridge was modelled as a straight one and a special short computer code was developed which bends the original mesh into the curved one. Special attention was devoted to the bridge bearings. In order to describe the bearings correctly, local coordinate systems were defined in the nodes of the mesh because of the movable supports.

[*] doc. Ing. Jaroslav Kruis, Ph.D.: Department of Mechanics, Faculty of Civil Engineering, Czech Technical University in Prague, Thákurova 7; 166 29, Prague; CZ, e-mail: jk@cml.fsv.cvut.cz
[**] doc. Ing. Michal Polák, CSc.: Department of Mechanics, Faculty of Civil Engineering, Czech Technical University in Prague, Thákurova 7; 166 29, Prague; CZ, e-mail: polak@fsv.cvut.cz
[***] Ing. Tomáš Koudelka, Ph.D.: Department of Mechanics, Faculty of Civil Engineering, Czech Technical University in Prague, Thákurova 7; 166 29, Prague; CZ, e-mail: koudelka@cml.fsv.cvut.cz
[†] Ing. Tomáš Plachý, Ph.D.: Department of Mechanics, Faculty of Civil Engineering, Czech Technical University in Prague, Thákurova 7; 166 29, Prague; CZ, e-mail: plachy@fsv.cvut.cz

Tab. 1: The subspace iteration method.

definition of initial vectors $\boldsymbol{V}_0$, $k = 0$
iterate $k = 0, 1, 2, \ldots$
$\tilde{\boldsymbol{V}}_{k+1} = \boldsymbol{K}^{-1}\boldsymbol{M}\boldsymbol{V}_k$
$\tilde{\boldsymbol{V}}_{k+1} \to \boldsymbol{V}_{k+1} : \boldsymbol{V}_{k+1}^T\boldsymbol{M}\boldsymbol{V}_{k+1} = \boldsymbol{I}$
$\boldsymbol{\Omega}_{0,k+1} = \boldsymbol{V}_{k+1}^T\boldsymbol{K}\boldsymbol{V}_{k+1}$
if $k > 1$ and $\boldsymbol{\Omega}_{0,k+1} - \boldsymbol{\Omega}_{0,k} < \varepsilon\boldsymbol{I}$, break

In the finite element model, the bridge piers were replaced by a set of 588 springs. The bridge piers were modelled separately because they are also curved and even non-prismatic. Each pier was described by its three-dimensional model and all neccessary stiffnesses were obtained. The bridge stiffeners near the bridge supports were also modelled by spring elements.

The mesh contains 51 642 nodes, 39 750 finite brick elements, 588 bar elements representing the bridge piers and stiffeners, 154 926 unknowns (degrees of freedom). The equation of motion of undamped free vibration has the form

$$\boldsymbol{M}\ddot{\boldsymbol{d}} + \boldsymbol{K}\boldsymbol{d} = \boldsymbol{0}\,, \tag{1}$$

where $\boldsymbol{M}$ is the mass matrix, $\boldsymbol{K}$ is the stiffness matrix, $\ddot{\boldsymbol{d}}$ is the vector of nodal accelerations and $\boldsymbol{d}$ is the vector of nodal displacements. The eigenvalue problem is described by the equation

$$(\boldsymbol{K} - \omega_0^2\boldsymbol{M})\boldsymbol{v} = \boldsymbol{0}\,, \tag{2}$$

where $\boldsymbol{v}$ is the eigenvector and ω_0 is the natural circular frequency. The eigenfrequencies and eigenvectors were computed by the subspace iteration method which is a generalization of the inverse iteration method. Instead of one vector used in the inverse iteration, the subspace method deals with several vectors simultaneously located in the modal matrix $\boldsymbol{V}$. Columns of the modal matrix $\boldsymbol{V}$ are orthonormalized in every iteration step and approximations of the eigenvalues are computed in the form

$$\boldsymbol{\Omega}_0^2 = \boldsymbol{V}^T\boldsymbol{K}\boldsymbol{V}\,. \tag{3}$$

The orthonormalization is based on the Gram-Schmidt method. The subspace iteration is summarized in table 1. More details about the method can be found in references Hughes (1987) and Bittnar and Šejnoha (1996).

The system of linear algebraic equations is solved by a sparse direct solver based on the modified minimum degree algorithm which can be found e.g. in reference Kruis (2006). The stiffness matrix is stored in a symmetric compressed row storage scheme and 5,386,635 matrix entries are stored before factorization while after it there are 108,925,929 matrix entries due to fill-in phenomenon. The sparse direct solver was used because the classical $\boldsymbol{L}\boldsymbol{D}\boldsymbol{L}^T$ factorization based on the skyline storage scheme leads to unacceptable memory requirement. The symbolic QG factorization takes 1.330 s and the real factorization takes 187.350 s.

3. Experimental Modal Analysis

The experimental modal analysis was performed for both highway bridges. The scheme and the procedure of the modal analysis were the same for both bridges. The electrodynamic exciter TIRAVIB 5140 was used for excitation. The position of the exciter was determined based on the calculated eigenmodes to be able to excite basic natural modes of the bridge, it was placed in one third of the 4th span on the left side of the bridge cross section. The driving force was measured using three force transducers S35 LUKAS located between the exciter and the bridge. The force transducers were connected to one

channel to measure the total driving force. The response of the bridge was measured by six acceleration transducers B12/200 Hottinger Baldwin Messtechnik (HBM). The transducers were connected to the multianalyzer DEWETRON 5000.

The response measurement was done only from the 3rd to the 6th span of the bridge because of the character of the calculated eigenmodes which have the amplitudes of the mode shapes much higher in the spans No. 3, 4 and 5 than in the first two spans. The lengths of the 3rd, 4th and 5th measured spans of the bridge were divided into ten equal parts - 10 cross sections and the length of the 6th span was divided in four parts - 4 cross sections. The response was measured in five points in each cross section on the upper road surface. The point positions were determined based on the finite element model and they corresponded to the positions of some element nodes of the finite element model. The total number of measured cross sections was 35 and the total number of measured points was 175 on each bridge. The transducers were mounted on five steel weights, which were put to all points of one cross section at once, thus the response was measured in all points of the cross section simultaneously. The vibration of the bridge was measured in the vertical direction in all points in the first part of the experiment and in the horizontal direction in the second part.

The reference acceleration transducer B12/200 HBM was added to the basic measurement system to have the possibility to use the second measurement and the evaluation technique Ambient Vibration Testing (AVT). The reference transducer was placed near the exciter. The temperature was measured during the experiments with respect to the methodology published in reference Polák and Plachý (2010).

The time data records of the response were saved during the measurement and evaluated in off line mode on the control computer. The Frequency Response Function (FRF) was evaluated for each point of measurement

$$H_{rS}(if) = \frac{\ddot{w}_r(if)}{F_s(if)} \,, \tag{4}$$

where i is the imaginary unit, $w_r(if)$ is the measured acceleration in the point r in frequency domain, which was induced by excitation force $F_s(if)$ acting in the point S. The values of the Frequency Response Functions $H_{rS}(if)$ were determined as an average of the 8 measurements with 75% overlap of the windows. The length of each signal window in time domain was 64 s, the frequency range of the window was set to 10 Hz. According to the fact that the excitation force could be affected by additional dynamic forces caused e.g. by wind during the experiment and these forces could not be measured, the Operating Deflection Shapes Frequency Response Functions (ODS FRF) were evaluated. The function ODS FRF is a complex function, which can be expressed by the real and the imaginary part or by magnitude and phase functions. The magnitude function is expressed just as a frequency spectrum of the measured response but the phase function is a phase of the measured response related to the phase measured in the reference point S. The evaluation of the natural frequencies and modes of vibration of the bridges were done in the software MEScopeVES of the company Vibrant Technology, Inc.

4. Results

Because the finite element mesh was obtained from a mesh of virtual straight bridge by bending, the numerical analysis was performed on both meshes. The reason is to show the influence of apposite mesh on dynamic behaviour.

The relative difference between the calculated and measured eigenfrequencies is given in the code ČSN 73 6209 in the form

$$\Delta_{(j)} = \frac{f_{(j)cal} - f_{(j)obs}}{f_{(j)cal}} 100(\%) \,, \tag{5}$$

where $f_{(j)cal}$ denotes the j-th calculated eigenfrequency and $f_{(j)obs}$ denotes the j-th observed (measured) eigenfrequency. The permissible range for the relative difference has the form

$$r = \pm(14 + \frac{f_{(j)cal}}{f_{(min)cal}}) \leq \pm 25(\%) \,. \tag{6}$$

Tab. 2: Measured and computed eigenfrequencies and circular eigenfrequencies.

j	$\omega_{0,i}$ (s^{-1})		$f_{(j)cal}$ (Hz)		$f_{(j)obs}$ (Hz)	$\Delta_{(j)}$ (%)	r(%)
	straight	curved	straight	curved	measured		
1	5.862073	5.211826	0.932978	0.829487	0.78	5.96	±14.7
2	6.548391	6.452192	1.042208	1.026898	0.88	14.3	±14.9
3	6.975418	6.941419	1.110172	1.104761	1.05	4.95	±15.0
4	7.251255	7.144612	1.154073	1.137100	1.23	-8.17	-15;+10
5	8.066984	7.852371	1.283900	1.249743	1.30	-4.02	±15.1
6	8.614414	9.555517	1.371026	1.520807	????	????	????
7	9.976354	9.828060	1.587786	1.564184	1.50	4.10	±15.4
8	10.960545	10.948090	1.744424	1.742442	????	????	????
9	12.502974	12.334055	1.989910	1.963025	1.80	8.30	±15.7
10	14.295015	14.079335	2.275122	2.240795	????	????	????

Table 2 summaries eigenfrequencies obtained from the numerical analysis and measured on existing structure. The relative differences and permissible ranges are also included. Question marks indicate values which were not obtained with required reliability.

First ten calculated eigenmodes are depicted in figures 1–10. The eigenmodes of virtual straight bridge are in the left hand side of figures while the eigenmodes of the real curved bridge are in the right hand side.

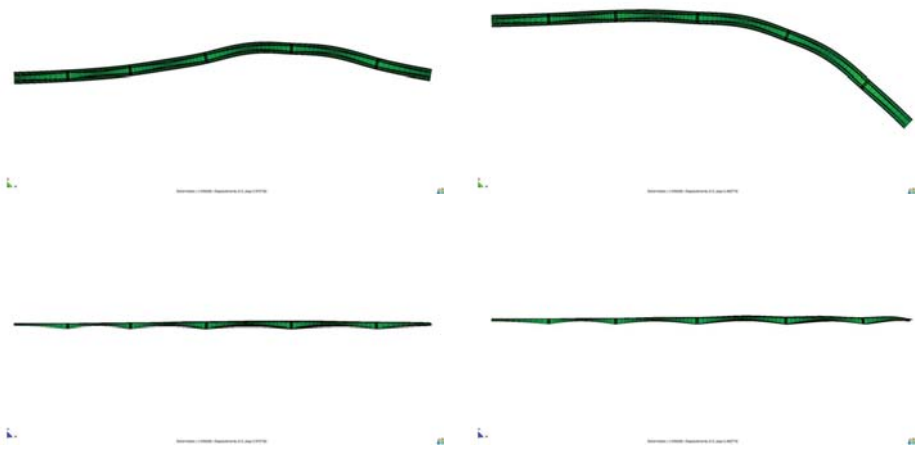

Fig. 1: 1st eigenmode.

The eight natural frequencies and natural mode shapes were evaluated during an experimental modal analysis on both bridges in the frequency range from 0.5 to 2.5 Hz and the natural torsional mode with the corresponding natural frequency 4.80 Hz for the left bridge and 4.74 Hz for the right bridge. The evaluated natural modes are shown in figures 11–18.

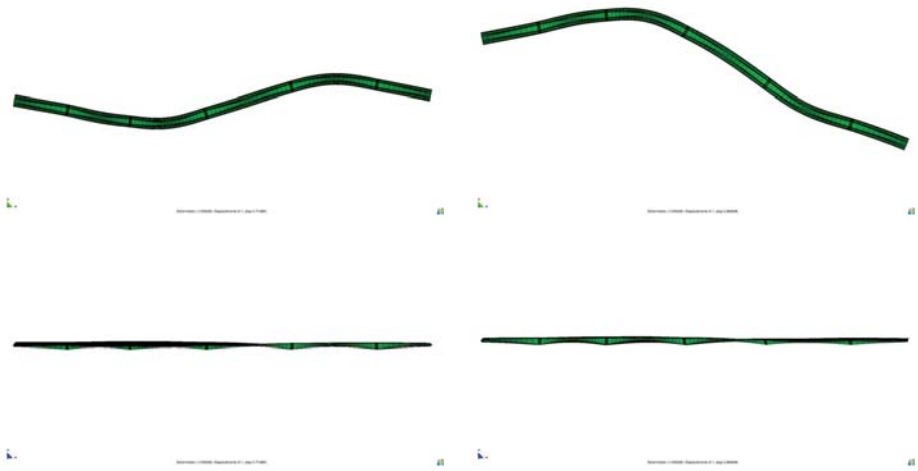

Fig. 2: 2nd eigenmode.

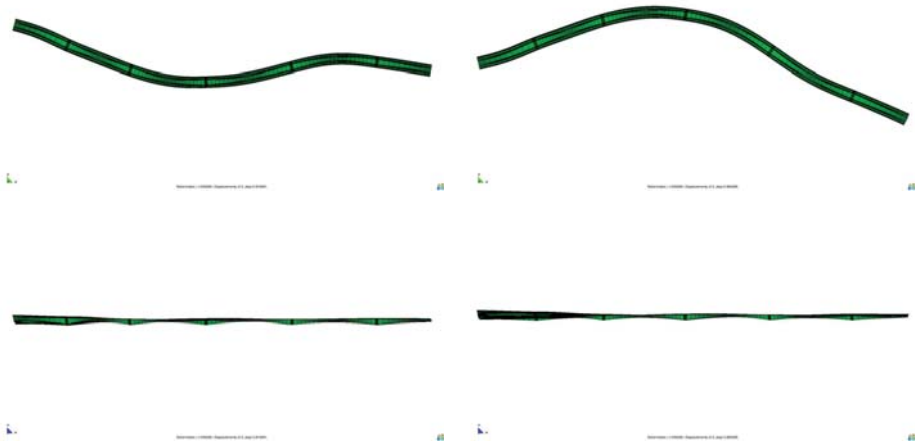

Fig. 3: 3rd eigenmode.

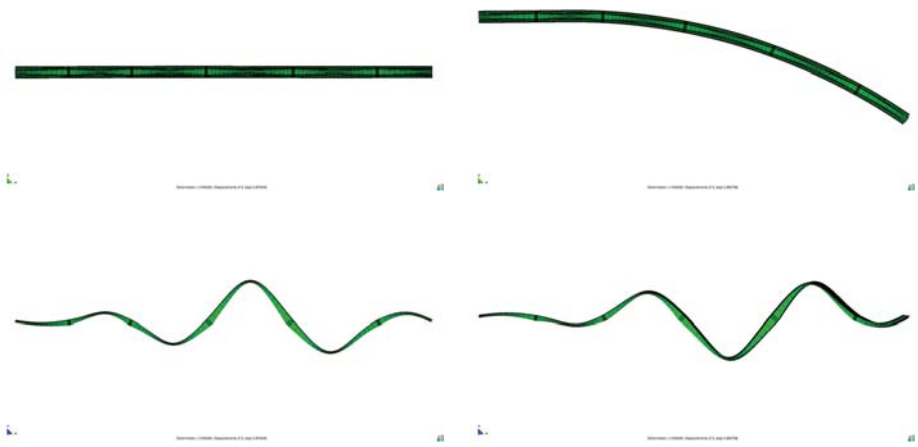

Fig. 4: 4th eigenmode.

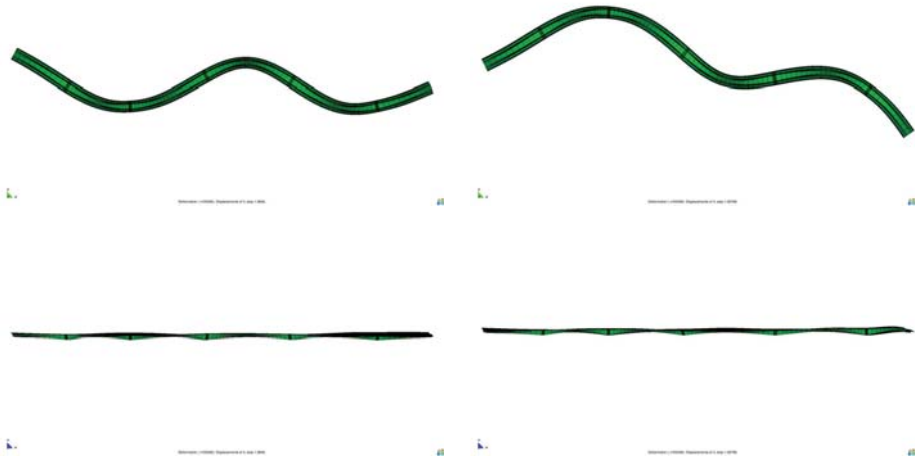

Fig. 5: 5th eigenmode.

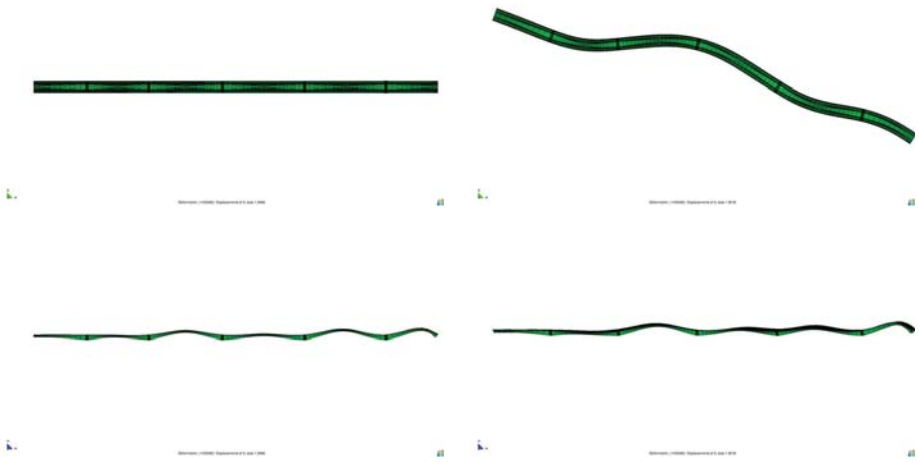

Fig. 6: 6th eigenmode.

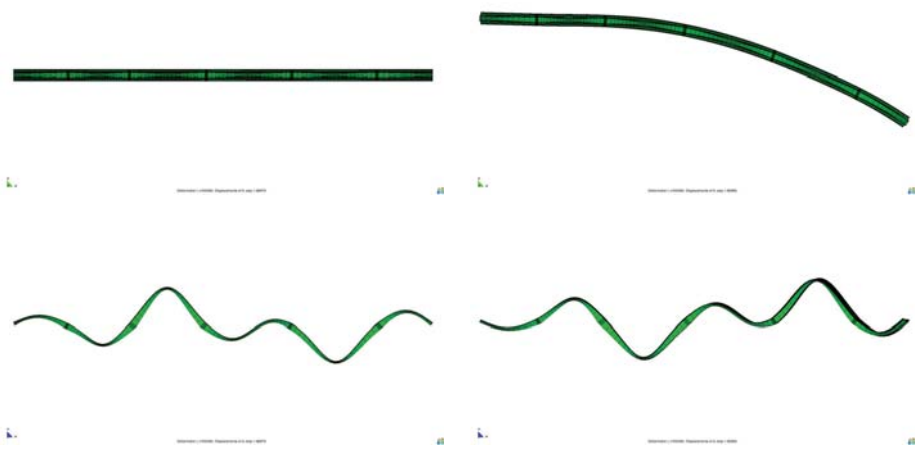

Fig. 7: 7th eigenmode.

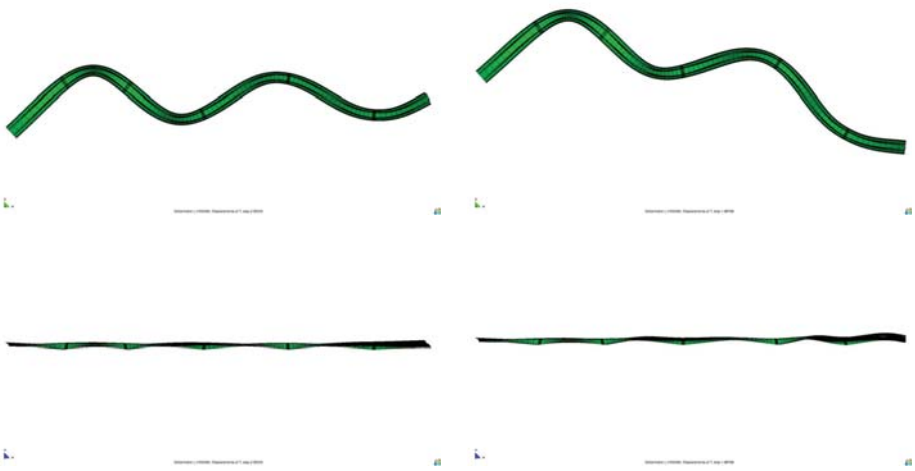

Fig. 8: 8th eigenmode.

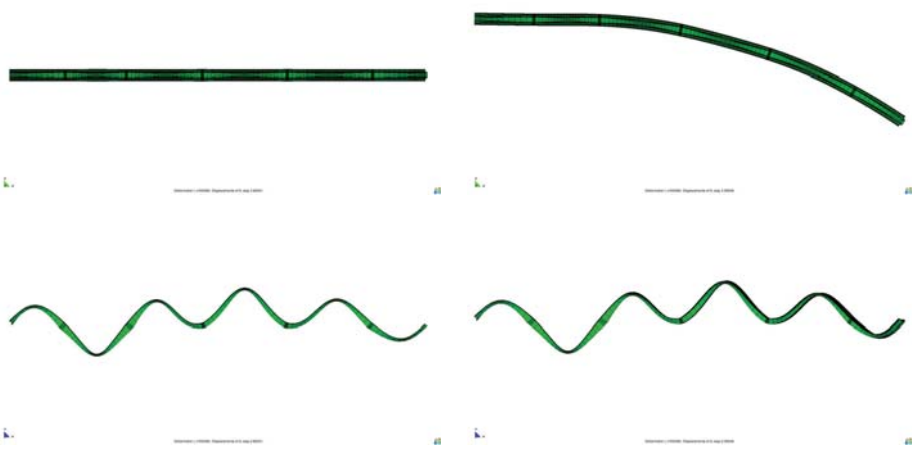

Fig. 9: 9th eigenmode.

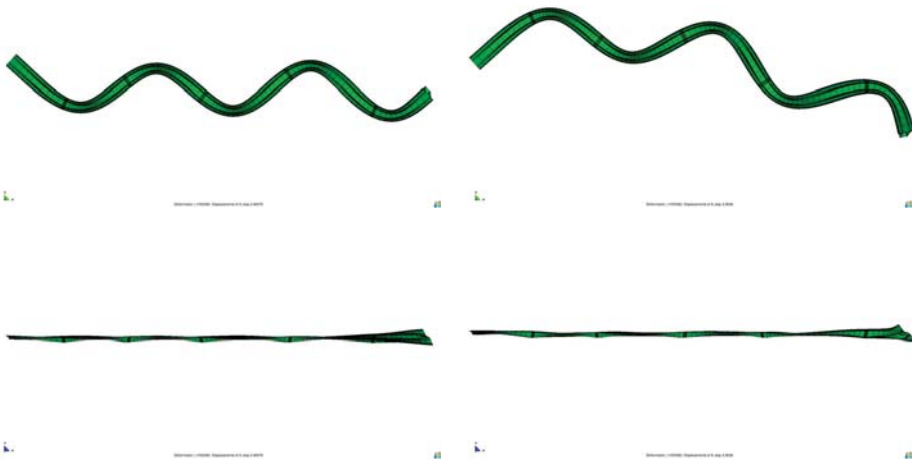

Fig. 10: 10th eigenmode.

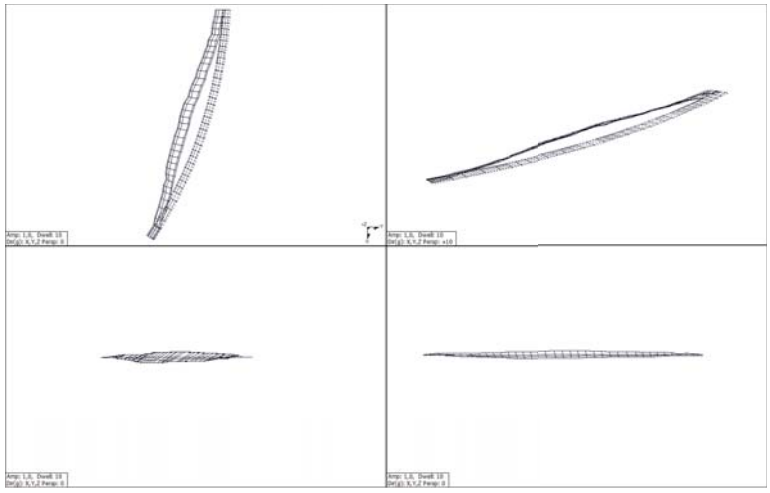

Fig. 11: 1st eigenmode.

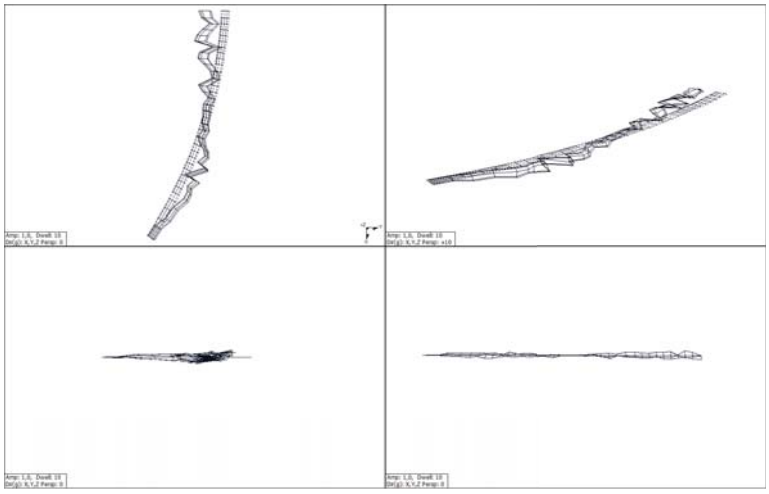

Fig. 12: 2nd eigenmode.

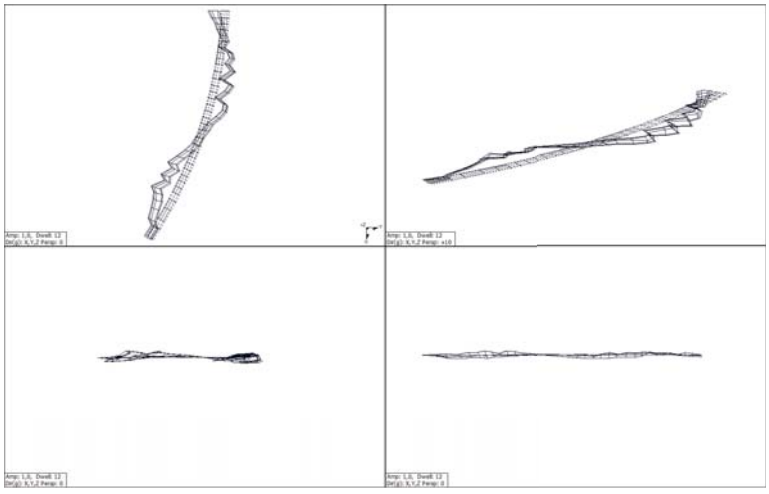

Fig. 13: 3rd eigenmode.

5. Conclusions

The measured eigenfrequencies and eigenmodes were compared with the eigenfrequencies and eigenmodes obtained from numerical analysis based on the finite element three-dimensional model because of the curved shape of the bridges. All compared eigenfrequencies satisfy conditions given in the code ČSN 73 6209. The experimentally obtained eigenmodes contain the same number of vibration nodes and lines as the numerically obtained eigenmodes. Moreover, the vibration lines are located in the same bays of the bridges.

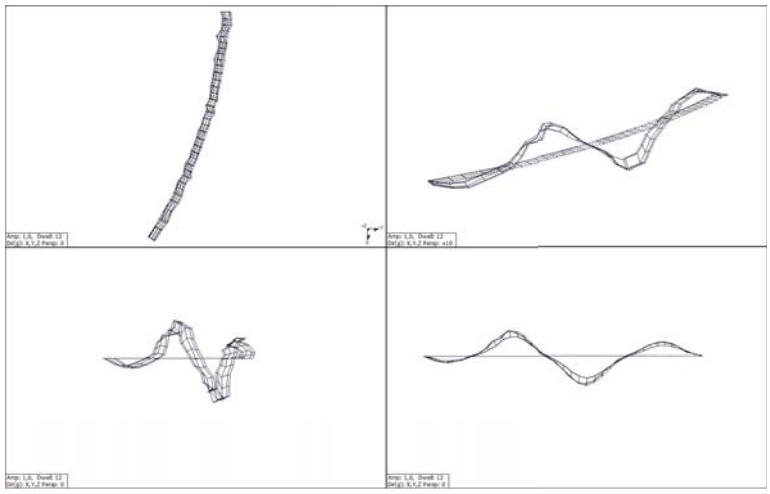

Fig. 14: 4th eigenmode.

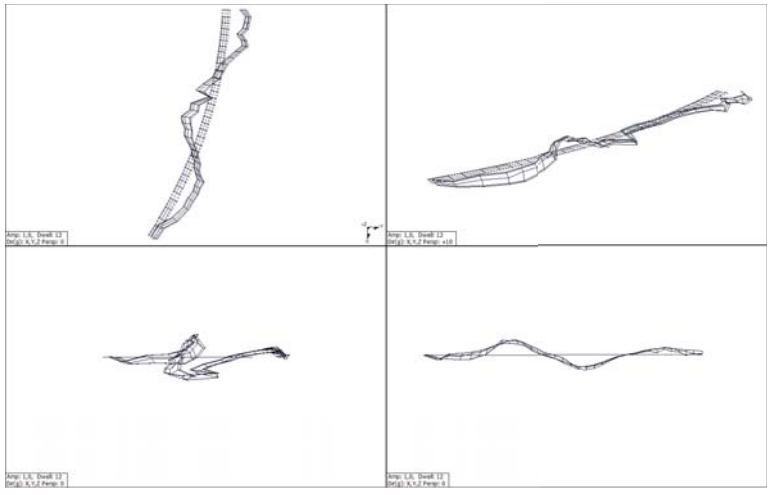

Fig. 15: 5th eigenmode.

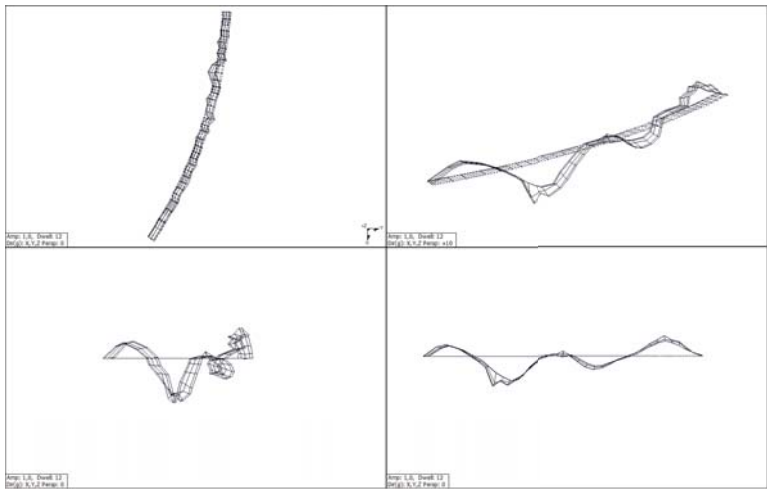

Fig. 16: 7th eigenmode.

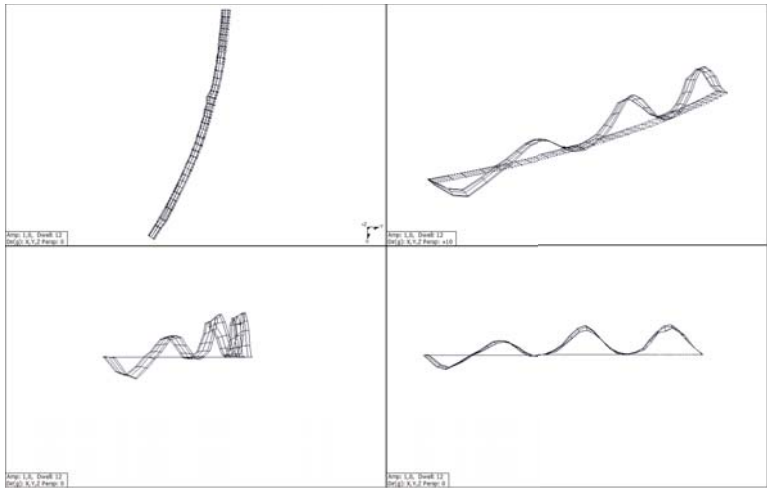

Fig. 17: 9th eigenmode.

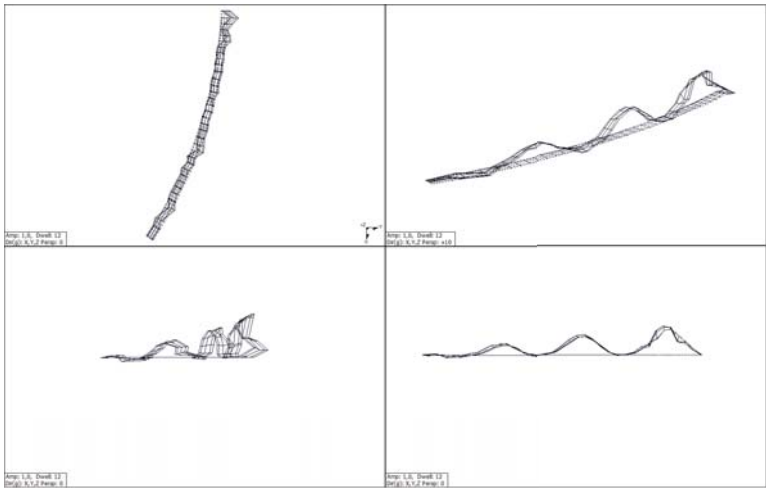

Fig. 18: 10th eigenmode.

Acknowledgments

This work was supported by the Grant Agency of the Czech Technical University in Prague, grant No. SGS12/027/OHK1/1T/11 and SGS12/117/OHK1/2T/11. The financial support is gratefully acknowledged.

References

Hughes, T.J.R. (1987), *The Finite Element Method. Linear Static and Dynamic Finite Element Analysis*, Prentice-Hall, Inc., Englewood Cliffs, New Jersey 07632.

Bittnar, Z., Šejnoha, J. (1996), *Numerical Methods in Structural Mechanics*, ASCE Press, New York, Thomas Telford, London.

Kruis, J. (2006) *Domain Decomposition Methods for Distributed Computing*, Saxe-Coburg Publications, Kippen, Stirling, Scotland, UK.

Polák, M., Plachý, T. (2010) Long-Time Monitoring of Thermal Actions on a Prestressed Concrete Bridge Structure. In.: *Proc. 48th International Scientific Conference on Experimental Stress Analysis* (Šmíd P et al. eds). Olomouc: Palacky University, pages 369-376.

Polák, M., Plachý, T., Rotter, T., Ryjáček, P. (2005) Study of dynamic behavior of two road bridges and their numerical models In.: *Proc. 6th International Conference on Structural Dynamics EURODYN 2005* (C. Soize et al. eds.). Millpress Science Publishers, vol. 3, p. 1669-1674.

18th International Conference
ENGINEERING MECHANICS 2012
Svratka, Czech Republic, May 14 – 17, 2012

pp. 789–792
Paper #130

A NUMERICAL STUDY OF THE BICYCLE HELMET DROP TEST

O. Krupička, M. Šudrich, J. Vyčichl *

Abstract: *The study focused on helmet drop tests conducted in numerical software LS–DYNA. For this purpose new virtual models of the test–head according to ČSN EN 960 (2007) and impact pad were created. A modified model of a bicycle helmet, utilized in earlier studies and obtained from 3D scan of a real bicycle helmet, was also used. The models had similar properties as a real drop test has. The aim was to find out the output value of the model head acceleration during impact and determination of Head Injury Criterion.*

Keywords: ***Bicycle, Helmet, HIC, Impact, LS–DYNA***

1. Introduction

The aim of the study was the creation of virtual drop test of bicycle helmets which would be a close approximation to an actual helmet drop test. The main target of this study was to obtain acceleration and Head Injury Criterion (HIC) values on the test–head during impact. The influence of the impact angle of the helmet at pad, for two types of bicycle helmet, was also observed. This was ensured by the appropriate choice of materials for used models and defining of the virtual test in FEM software. Numerical analysis was conducted in LS–DYNA Solver and modification of models in LS–PrePost.

2. Virtual models

The creation of the test–head and impact pad, for simplicity, was conducted directly in Design Modeler in Workbench. The helmet was created by scanning real bicycle helmet, which had been purchased by Department of Mechanics and Materials on Faculty of Transportation Sciences.

2.1. Test–head model

The test–head model for study was modeled according to ČSN EN 960 (2007). The base of the virtual model consisted of parallel planes. The base plane was perpendicular to the vertical axis. A reference plane was derived from the base plane as well as other planes. The distances of the base and the reference plane were different for each head model as well as the distance between the other planes. According to the table values, in ČSN EN 960 (2007), there was part of head above and below the reference plane modeled.

For analysed model, there was chosen a head of size M that corresponds to the inner helmet circumference 600mm, total height of 247mm and volume 4.86dm^3. For the numerical analysis, structural steel was used for test–head as material. The density of material was adjusted to 1153.10kg/m^3, so the height of test–head was 5,60kg.

2.2. Bicycle helmet model

A Virtual model of a bicycle helmet was created earlier by Micka and Vyčichl (2007) using a 3D hand–scanner. After the scanning process, some improvements were needed in Blender and Netgen software. The purpose of these improvements was to simplify the whole surface of the helmet.

* Bc. Ondřej Krupička, Bc. Martin Šudrich, Ing. Jan Vyčichl, Ph.D.: Czech Technical University in Prague, Faculty of Transportation Sciences, Konviktská 20; 110 00, Prague 1; CZ, e-mail: ondra.krupicka@gmail.com, msudrich@gmail.com, vycichl@fd.cvut.cz,

Tab. 1: Material properties

	Structural steel	EPS	ABS
Material type	Elastic	Crushable foam	Modified piecewise linear plasticity
Young's modulus	200.00GPa	62.73MPa	3.00GPa
Density	7850.00kg/m^3	100.00kg/m^3	1040.00kg/m^3
Poisson's ratio	0.30	0.01	0.40
Maximum tensile stress	x	1.30MPa	x
Dumping coefficient	x	0.20	x
Yield stress	x	x	60.00MPa
Tangent modulus	x	x	1.02MPa

Expanded Polystyrene (EPS) material is, by Mills and Gilchrist (2008), one of the most common materials for bicycle helmet today and Acrylonitrile Butadiene Styrene (ABS) polymer is a common material for the helmet shell. It was necessary to use a crushable foam type material. For the purpose of the study the material library of Micka (Jíra and Jírová) was utilised. It contained both EPS, including working curve for 100kg/m^3, and ABS polymer for the shell. For the properties of both materials, see in Tab. 1. The weight of the helmet was 0.21kg.

For the purposes of the study, there were two types of helmet created without any mounting system. The first represented an In–Mold bicycle helmet with a shell of ABS on the top surface, while the second helmet represented a Double–In–Mold with the ABS shell on all surfaces. These shells, both with the same material properties, were created at the end in LS–PrePost after final assembly and meshing.

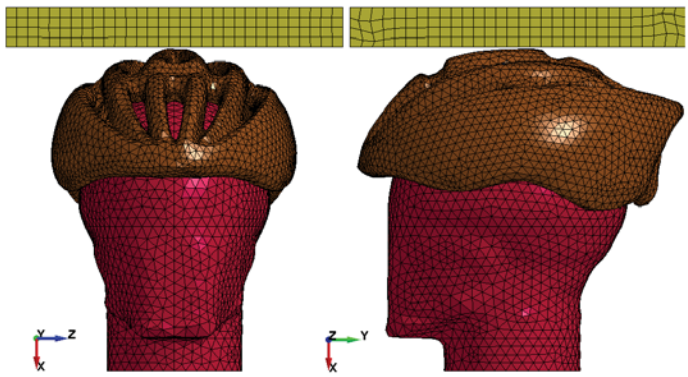

Fig. 1: Visualization of virtual models after mesh applied

2.3. Impact pad

An impact pad was created with a simple block shape. It is formed with the width of 300mm, length 300mm and a height of 35mm. As a pad material, structural steel (density 7850kg/m^3) was selected in the LS–PrePost.

2.4. Completation and boundary conditions in LS–Prepost

When the helmet was ready, the test–head and impact pad were added. Because of academic license problems in ANSYS Workbench, all models were exported in STEP format and final preparation was conducted in LS–PrePost.

The mesh was created in LS–PrePost. Due to the helmet shape the mesh was unstable in some areas so manual repair was needed. Models with the mesh applied are shown on Fig. 1. The test–head was formed by 56 457 elements (Tetrahedron) and 10 420 nodes. The helmet was formed by 52 127 elements (Tetrahedron) and 11 350 nodes. The ABS shell of the helmet was in both cases (In–Mold and Double–In–Mold) defined from the nodes forming the foam. For this reason, the definition of contact between the two parts of the helmet was not needed. The contact between the pad, the helmet and the test–head were defined as automatic surface to surface.

The helmet and test–head were evaluated at the beginning of the simulation at an initial velocity of 6.26m/s, always in the direction of vertical axis of the test–head. The chosen value corresponded to a free fall from a height of 2m just before impact. The height of 2m is a standard height for real bicycle helmet tests according to ČSN EN 1078 (1998). The tests were always calculated assuming a gravity acceleration of 9.81m/s^2. The pad is supported at all nodal points of its bottom surface. The termination time was set to 0.02s to verify convergence.

2.5. Impact angles of helmet and test–head

For study influence of impact angle, 7 model situations were created for both types of helmets. The helmet and test–head were fixed and only the location of the pad was changed. For base fall of system, the vertical axis for model head is perpendicular to the impact surface. In other situations, the pad is rotated by 30°, 60° and 90° to the front and by the same angles to the side.

3. Head Injury Criterion

The Head Injury Criterion (HIC) is usually formulated as a function of the instantaneous acceleration, see Payne and Patel (2001). The acceleration in the center of the gravity of the test–head and its maximum value were investigated on the falling system.

The human brain is very susceptible to accelerate, especially under action of a high value exceeding hundred times acceleration of the gravity. The time period, over which the acceleration takes effect, is very important. The brain is able to survive, without permanent damage, extreme acceleration values of about 200g but only up to 2ms. In values around 80g, the period during which there is irreversible damage, is much longer. In this case, it may be up to 200ms. The acceleration of 300g is critical for the human brain. Exceeding this limit leads to irreversible damage. HIC score was determined using the equitation 1.

$$HIC = \left\{ (t_2 - t_1) \left[\frac{1}{t_2 - t_1} \int_{t_1}^{t_2} a(t)\,\mathrm{d}t \right]^{2,5} \right\} max \tag{1}$$

4. Conclusions

In LS–DYNA Solver all situations were solved and then it was important to determine the acceleration of the test–head during impacts. In situations where the impact pad was rotated by 90° to the side and to the front, contact was made between the test–head and pad. It was caused by the absence of the mounting system of the helmet. Only in these 4 situations, the maximum acceleration value exceeded 300g, in other situations it did not. In most cases the g–value was around 180g for a very short time.

Then HIC for 15ms was determined; because the values were less favorable. The resulting HIC values are given in Tab. 2. The difference between both helmets was not so evident in the resulting values. However, in most cases, the maximum value of acceleration was higher for Double–In–Mold

Tab. 2: HIC score

Impact pad rotated to the side				
	Base impact	30°	60°	90°
In-Mold helmet	287,85	270,80	183,99	562,75
Double-In-Mold helmet	292,98	288,17	172,52	548,83
Impact pad rotated to the front				
	Base impact	30°	60°	90°
In-Mold helmet	287,85	281,35	230,92	371,86
Double-In-Mold helmet	292,98	278,35	202,08	371,85

helmet than In–Mold helmet, while HIC values were not. The results show that the size of the area under the curve of acceleration for Double–In–Mold helmet is smaller. The HIC score is almost the same or smaller then for In–Mold helmet. It is also evident from a sample graph on Fig. 2.

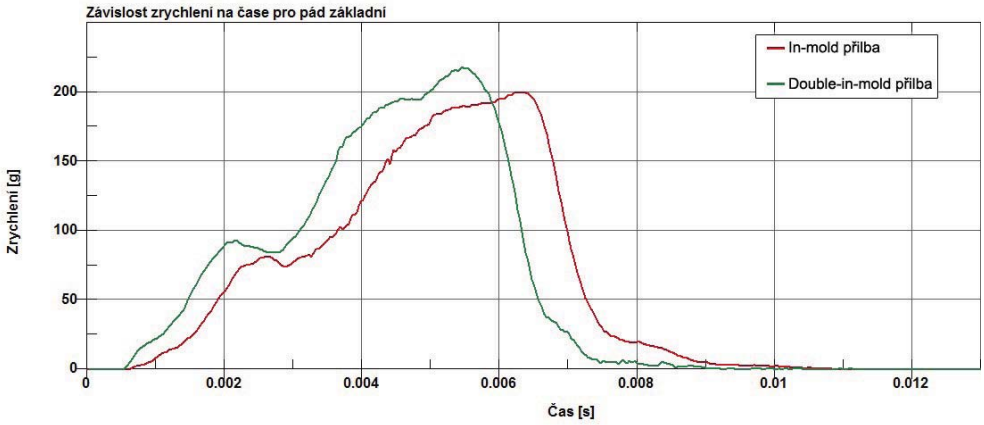

Fig. 2: Sample of acceleration-time diagram - base impact

Acknowledgments

This study has been supported by research plan of the Ministry of Education MSM6840770043 and by Grant of Czech Technical University Student's Grant Competition SGS12/163/OHK2/2T/16.

References

ČSN EN 960 (2007), Makety hlavy pro zkoušení ochranných přileb.

ČSN EN 1078 (1998), Přilby pro cyklisty a pro uživatele skateboardů a kolečkových bruslí.

Micka, M., Jíra, J., and Jírová, J. (2010), Modelování pádové zkoušky helmy v ANSYS LS-DYNA. In: *ANSYS Users Meeting, 2010.*

Payne, A. R., and Patel, S. (2001), Head Injury Criteria. *Injury Mechanisms and Injury Criteria, Project 427519.* http://www.eurailsafe.net/subsites/operas/HTML/Section3/Section3.3frm.htm.

Micka, M. and Vyčichl, J. (2007), Tvorba modelu přilby z 3D skenování. In: *15. ANSYS Users Meeting, 2007.*

Mills N.J.and Gilchrist A. (2008), Oblique impact testing of bicycle helmets. In: *International Journal of Impact Engineering* Vol. 35, pp 1075-1086.

18th International Conference
ENGINEERING MECHANICS 2012
Svratka, Czech Republic, May 14 – 17, 2012

pp. 793–796
Paper #126

MACRO-MECHANICAL PROPERTIES OF NANOTEXTILES ON PLGA BASE – TENSILE STRENGTH

V. Křelinová[*], P. Tesárek[**], I. Klicmanová[***], P. Ryparová[****], J. Mukařovský[*****]

Abstract: *The paper presents the results measured during the macro-mechanical study of properties of nanotextiles based on poly-(lactide-co-glycolite) acid (PLGA). These nanotextiles are extensively used in biomedicine and many other applications, and therefore it is important to reach a certain level of mechanical properties so that they can be used properly. Very easy and cheap method, so called passportization, can be utilized for investigation of nanotextile microscopic properties. For the testing of macro-mechanical properties it is possible to use common testing methods like in case of textiles and membranes (e.g. water vapor barriers). The results of tensile strength related to the width of tested sample are presented in this paper. Finally, certain aspects limiting the use of common testing methods (especially nanotextile weight per unit area) are discussed.*

Keywords: ***nanotextiles, nanofibers, mechanical properties, tensile strength, PLGA.***

1. Introduction

Macro-mechanical properties are lately investigated even in case of nano-materials. The following text is specifically focused on nanofibre materials based on polymers and their macro-mechanical properties. The tested nanotextiles were spun using "NanoSpider" technology (Elmarco Ltd.) that works on principle of needleless electrospinning where the cylinder (cathode) is connected to a high voltage source covering itself with a thin film of polymer solution. The anode is created by a slab on which are the nanofibres formed. The electric field pulls out, elongates and thins the fibers that are finally collected on the slab. The resulting fibers have typical thickness from tens to hundreds of nanometers.

The process of electrospinning itself is dependent on many parameters: choice of polymer type and viscosity of its water solution, or different solvent solution. The NanoSpider technology enables setting of electrode distance, setting of spinning voltage, setting of substrate fabric speed and spin speed of cylinder cathode. Environmental parameters like temperature and humidity of the air are also of a great importance.

Extremely fine nanofibres can't exist independently and they need a kind of support (at least during the electrospinning), i.e. material that would assure sufficient mechanical resistance. There exist several possibilities, which supporting the material: it can be a polymeric support textile (spunbond), a sheet based on cellulose, or certain types of "classical" textiles. Except the price there is important the adhesion of nanofibres to the supporting surface (by manipulation the support and the nanofibres mustn't separate). The electrospinning technology enables production of nanotextiles

[*] Ing. Veronika Křelinová: Faculty of Civil Engineering, Czech Technical University in Prague, Thákurova 7; 16629, Prague; CZ, e-mail: veronika.krelinova@fsv.cvut.cz

[**] Ing. Pavel Tesárek, Ph.D.: Faculty of Civil Engineering, Czech Technical University in Prague, Thákurova 7; 16629, Prague; CZ, e-mail: tesarek@fsv.cvut.cz

[***] Iveta Klicmanová: Faculty of Civil Engineering, Czech Technical University in Prague, Thákurova 7; 16629, Prague; CZ, e-mail: iveta.klicmanova@fsv.cvut.cz

[****] Mgr. Pavla Ryparová: Faculty of Civil Engineering, Czech Technical University in Prague, Thákurova 7; 16629, Prague; CZ, e-mail: pavla.ryparova@fsv.cvut.cz

[*****] Ing. Jan Mukařovský, Ph.D.: Faculty of Civil Engineering, Czech Technical University in Prague, Thákurova 7; 16629, Prague; CZ, e-mail: jan.mukarovsky@fsv.cvut.cz

within a certain range of weight per unit area. Using this technology it is possible to produce nanotextiles with the width of up to 4 meters (Li et al., 2002). The produced nanotextiles, depending on the weight per unit area, can be applied with or without supporting material (spunbond). The nanofibres are macroscopically hardly accessible and so just the reproducibility of the same nanostructure in repeatable production procedure is a very delicate problem.

The above mentioned facts tend to the need for investigation of macro-mechanical properties. Besides there are other mainly macroscopic properties (especially the weight per unit area) that can specifically describe the micro structure of nanotextiles. Such properties are subsequently used for passportiazation of nanotextiles (Krňanský et al., 2010), i.e. an easy and cheap method how to check the microscopic properties of produced nanotextiles based on measured macroscopic properties. The mechanical test of nanotextiles can be performed using conventional testing techniques (Huang el al., 2001).

For the macro-mechanical testing there were used nanotextiles based on Poly-(lactide-co-glycolite) acid (PLGA). Such nanotextiles are largely used, for instance, in biomedicine (Paipitak et al, 2010).

2. Experimental methods and samples

The PLGA based nanotextiles were spun in the Center for Nanotechnology in Civil Engineering, at the Faculty of Civil Engineering, Czech Technical University (CTU) in Prague. This center uses the Elmarco NS Lab 500 S, the laboratory device for electrospinning of nanofibres with spinning electrode width of 500 mm. The PLGA solution (ration 50:50) for electrospinning were prepared as 2.3% solution where 0.23 g of PLGA were stirred with 4 ml of dimethyl chloride (DMC, Sigma Aldrich) and subsequently 6 ml of dimethylformamide (DMF) were added.

The nanotextile samples with the length of 40 mm and width between 21 and 25 mm were cut out from the PLGA based nanotextile. The nanotextile layer was subsequently carefully separated from the spunbond. The samples' weights per square meter were determined from their dimensions (micrometric set) and measured with the accuracy of 0.0005 g.

The ends of tested samples were strengthened by a paper tape to prevent damage of the PLGA nanotextile before testing, respectively during preparation of a tensile test. The tensile strength tests were carried out on LabTest 4.100SP1 device at the Faculty of Civil Engineering of CTU in Prague. The measuring range was set to 50 N maximum where the accuracy exceeds 0.1 % (at 2 N force). The samples were loaded with constant speed until failure. The resulting forces were determined from the testing device software.

The arrangement of the tensile strength test is showed on Fig. 1 and 2.

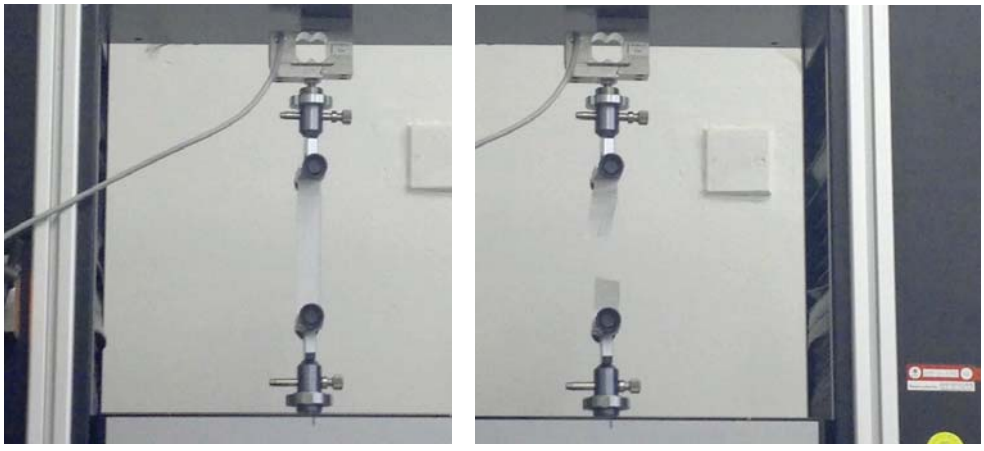

Fig. 1, 2: Arrangement of tensile strength test – during testing (left), after failure (right)

3. Experimental results

The resulting forces were unified by dividing them by the width of the sample (N/m). For the weight per square meter of 3.1 (± 10 %) g/m^2 the resultant force reaches 7.4 E-5 (± 10 %) N/m. The results were determined as the arithmetic mean of 6 measurements.

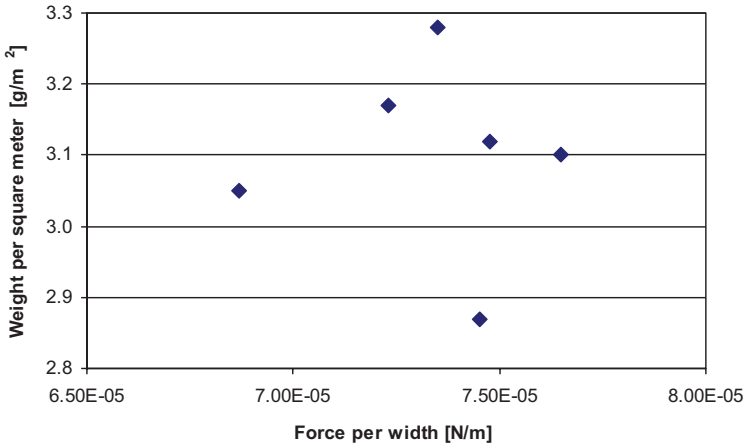

Fig. 3: Measured results of tested PLGA nanotextile samples

4. Conclusions

The nanotextile tensile strength testing showed the feasibility of such a testing. There are certain critical aspects limiting the testing of nanotextiles on common equipment (pull test devices). From the practical point of view it is possible to work with polymeric nanotextiles that have weight per unit area more than 1 g/m^2 (Krňanský et al., 2011). Working with nanotextiles with lower weight per unit area is very complicated because of the nanofibre surface tension when the nanotextiles tend to wrap up. Other aspect is a treatment of the nanotextile sample ends that must be strengthened before fastening in the clips (Andrady, 2008).

In a similar way like the nanotextile weight per unit area correlates with water vapor diffusion permeability (Krňanský et al., 2010) it is presumable that the tensile strength (in combination with e.g. weight per unit area) is related to certain macroscopic and/or microscopic properties that can be efficiently used for the passportization.

In the next step, it is proposed to move the nanotextile testing into micro-level, e.g. using AFM (Atomic Force Microscopy) and nanoindentation devices (Tesárek & Němeček, 2011), and finally compare the results obtained in macro a micro level.

Acknowledgement

This outcome has been achieved with the financial support of the Grant Agency of the Czech Republic (P108/12/0891 – Nucleation on strongly curved surfaces of PLGA nanofibers) and the Czech Technical University in Prague (SGS12/110/OHK1/2T/11 – The use of nanotechnology in construction).

Special thanks belong to the Center for Nanotechnology in Civil Engineering at Faculty of Civil Engineering of Czech Technical University in Prague where the nanotextile production and testing was carried out.

References

Andrady, L. A. (2008): *Science and technology of polymer nanofibers*, New Jersey, pp. 213-215.

Huang, L., Nagapudi, K., Apkarian, R. & Chaikof E.L. (2001) Engineered collagen-PEO nanofibers and fabrics. *J Biomater Sci Polym Edn*, 12, 9, pp. 979-94.

Krňanský, J., Tesárek, P. & Mukařovský, J. (2010): *Passportization of PVA based nanofibres spun on NS LAB 500S device and verification of their basic properties*, Research report 2010, Cideas, Prague.

Krňanský, J., Tesárek, P., Mukařovský, J. & Ryparova. P. (2011): Verification of basic properties of PVA based nanofibres spun on NS LAB 500S device, Research report 2011, Cideas, Prague, pp. 147-147.

Li, W.J., Laurencin, C.T., Caterson, E.J., Tuan, R.S. & Ko, F.K. (2002). Electrospun nanofibrous structure: A novel scaffold for tissue engineering. *J Biomed Mater Res*, 60, 4, pp. 613-621.

Paipitak, K., Pornpra, T., Moingkontalanf, P., Techitdheer, W. & Pecgarapa, W. (2010): Characterization of PVA-Chitosan Nanofibers Prepared by Electrospinning. *Procedia Engineering, The 2nd International Science, Social Science, Engineering and Energy Conference 2010* (I-SEEC 2010), pp. 101-102.

Tesárek, P. & Němeček, J. (2011): Microstructures and micro-mechanical study of gypsum. *Chemické listy*, 105, 17, pp. 852-853.

18th International Conference
ENGINEERING MECHANICS 2012
Svratka, Czech Republic, May 14 – 17, 2012

pp. 797–809
Paper #246

SEQUENTIAL DESIGNS OF EXPERIMENTS FOR SAMPLING-BASED SENSITIVITY ANALYSIS

A. Kučerová [*], E. Janouchová [**]

Abstract: *The sensitivity analysis is a basic tool for investigating the sensitivity of a model response to its inputs. One widely used strategy to assess the sensitivity is based on a set of simulations for a given sets of input parameters, i.e. points in the design space. An estimate of the sensitivity can be then obtained by computing correlations between the input parameters and the chosen components of the model response. The accuracy of the sensitivity prediction depends on the choice and the number of design points called the design of experiments. Moreover, once the design of experiments is created, the obtained sensitivity prediction may be inaccurate because of the insufficient number of design points. To improve the prediction, new design points should be sequentially added into the existing design. The aim of the presented paper is to review and compare available criteria determining the quality of the sequential design of experiments suitable for sampling-based sensitivity analysis.*

Keywords: ***Sequential design of experiments, Space-filling, Orthogonality, Latin Hypercube Sampling, Sampling-based sensitivity analysis***

1. Introduction

Sensitivity analysis (SA) is an important tool for investigating properties of complex systems. It is an essential part of inverse analysis procedures (Kučerová (2007)) and is also closely related to response surface modelling (Helton et al (2006)) or uncertainty analysis (Helton et al (2006)). To be more specific, SA provides some information about the contributions of individual system parameters/model inputs to the system response/model outputs. A number of approaches to SA has been developed, see e.g. Saltelli et al (2000) for an extensive review. The presented contribution is focused on widely used sampling-based approaches (Helton et al (2006)), particularly aimed at an evaluation of Spearman's rank correlation coefficient (SRCC), which is able to reveal a nonlinear monotonic relationship between the inputs and the corresponding outputs.

When computing the SA in a case of some real system using expensive experimental measurements or some computationally exhaustive numerical model, the number of samples to be performed within some reasonable time is rather limited. Randomly chosen sets of input parameters do not ensure appropriate estimation of related sensitivities. Therefore the sets must be chosen carefully. A review and comparison of several criteria, which can govern the stratified generation of input sets called as a design of experiments (DOE), is presented in Janouchová and Kučerová (2011).

Another important aspect of a DOE generation is a choice of the number of design points. A small DOE does not have to give us the required accuracy of the sensitivity prediction and one has to increase the number of design points so as to achieve the accuracy improvement. Once having the time-consuming measurements for the original small design, adding new points into the existing design is more efficient than generation of the whole larger DOE. The subject of adding new points to the initial design is considered e.g. in Crombecq et al (2011), where the authors use sequential space-filling designs for surrogate modeling. In this paper we follow the results presented in Janouchová and Kučerová (2011) for small DOEs and focus on sequentially generated DOEs based on the chosen criteria and their comparison in terms of sensitivity prediction.

[*] Ing. Kučerová, Ph.D.: Faculty of Civil Engineering, Czech Technical University in Prague, Thákurova 7/2077; 166 29, Prague; CZ, e-mail: anicka@cml.fsv.cvut.cz

[**] Eliška Janouchová: Faculty of Civil Engineering, Czech Technical University in Prague, Thákurova 7/2077; 166 29, Prague; CZ, e-mail: eliska.janouchova@fsv.cvut.cz

The following section reviews the criteria for optimization of a DOE, which are available in literature. Section 3. includes some comments on widely used methods for stratified generation of a DOE and Section 4. deals with generation of optimal sequential DOEs. Section 6. presents the comparison of the optimal sequential designs quality for usage in sampling-based SA for theoretical analytical functions, while the results for structural models are given in Section 7. Concluding remarks are summarized in Section 8.

2. Criteria for assessing optimal designs

A number of different criteria for assessing the quality of particular DOE can be found in literature. In general, they can be organized into groups with respect to the preferred DOE property. The most widely preferred features are

- *space-filling* property, which is needed in order to allow for evaluation of sensitivities valid for the whole given domain of admissible input values, so-called design space;
- *orthogonality*, which is necessary to assess the impact of individual input parameters.

Other main objectives can be preferable in particular applications of DOE. In response surface methodology, reduction of noise and bias error can become more important than the orthogonality (Goel et al (2008)). Nevertheless, no special objectives were formulated for the case of sampling-based SA, so we employ the common ones.

2.1. Space-filling criteria

Let us recall four widely used space-filling criteria.

Audze-Eglais objective function (AE) proposed in Audze and Eglais (1977) is based on a potential energy among the design points. The points are distributed as uniformly as possible when the potential energy E^{AE} proportional to the inverse of the squared distances among points is minimized, i.e.

$$E^{\mathrm{AE}} = \sum_{i=1}^{n} \sum_{j=i+1}^{n} \frac{1}{L_{ij}^2}\,, \tag{1}$$

where n is the number of the design points and L_{ij} is the Euclidean distance between points i and j.

Euclidean maximin (EMM) distance is probably the best-known space-filling measure (Johnson et al (1990); Morris and Mitchell (1995)). It states that the minimal distance $L_{\min,ij}$ between any two points i and j should be maximal. In order to apply the minimization procedure to all presented criteria, we minimize the negative value of a minimal distance E^{EMM}, i.e.

$$E^{\mathrm{EMM}} = -\min\{..., L_{ij}, ...\}, \quad i = 1...n, \quad j = (i+1)\,...\,n\,. \tag{2}$$

Modified L_2 discrepancy (ML_2) is a computationally cheaper variant of a discrepancy measure, which is widely used to assess precision for multivariate quadrature rules (Fang and Wang (1994)). Here, the designs are normalized in each dimension to the interval $[0, 1]$ and then, the value of ML_2 is computed according to

$$E^{\mathrm{ML}_2} = \left(\frac{4}{3}\right)^k - \frac{2^{(1-k)}}{n} \sum_{d=1}^{n} \prod_{i=1}^{k} (3 - x_{di}^2) + \frac{1}{n^2} \sum_{d=1}^{n} \sum_{j=1}^{n} \prod_{i=1}^{k} [2 - \max(x_{di}, x_{ji})]\,, \tag{3}$$

where k is the number of input parameters, i.e. the dimension of the design space and x_{di} and x_{ji} are the i-th coordinates of the d-th and j-th points, respectively. Since the evaluation of discrepancy for

a large design can be time-consuming, some efficient algorithms are proposed e.g. in Heinrich (1996). To achieve the best space-filling property of DOE, the value of ML_2 should be minimized.

D-optimality criterion (Dopt) was proposed in Smith (1918) as a pioneering work in the field of DOE for regression analysis. This criterion minimizes the variance associated with estimates of regression model coefficients by minimizing the determinant of the so-called dispersion matrix $(\mathbf{Z^T Z})^{-1}$ or equivalently, by maximizing the determinant of the so-called information matrix $(\mathbf{Z^T Z})$ (de Aguiar et al (1995)). Again, in order to apply a minimization procedure, but to avoid the inversion of the information matrix, we can minimize negative value of the determinant of the information matrix, i.e.

$$E^{\mathrm{Dopt}} = -\det(\mathbf{Z^T Z})\,, \tag{4}$$

where $\mathbf{Z}$ is a matrix with evaluated regression terms in the design points. An important shortcoming of this criterion concerns a choice of the number of regression terms to be included into the information matrix, because few terms can lead to the D-optimal DOE with duplicated points. In this contribution we employ a Bayesian approach as described in Hofwing and Strömberg (2010) or Janouchová and Kučerová (2011).

2.2. Orthogonality-based criteria

There are two well-know approaches to evaluate the orthogonality of a DOE. The most popular one is based on correlation among the samples' coordinates, the other one is a conditional number.

Conditional number (CN) is commonly used in numerical linear algebra to examine the sensitivities of a linear system (Cioppa and Lucas (2007)). Here, we use conditional number of $\mathbf{X}^T\mathbf{X}$, where $\mathbf{X}$ is a matrix of the design points' coordinates, so-called design matrix

$$\mathbf{X} = \begin{bmatrix} x_{11} & x_{12} & \cdots & x_{1k} \\ x_{21} & x_{22} & \cdots & x_{2k} \\ \vdots & \vdots & & \vdots \\ x_{n1} & x_{n2} & \cdots & x_{nk} \end{bmatrix}, \tag{6}$$

where n is the number of the design points and k is the dimension of the design space and the columns are centred to sum to 0 and scaled to the range $[-1, 1]$. The conditional number is then defined as

$$E^{\mathrm{CN}} = \mathrm{cond}(\mathbf{X^T X}) = \frac{\lambda_\mathbf{1}}{\lambda_\mathbf{n}}\,, \tag{7}$$

where λ_1 and λ_n are the largest and smallest eigenvalues of $\mathbf{X}^T\mathbf{X}$, respectively, therefore the E^{CN} is greater or equal to 1. Values closer to 1 correspond to more orthogonal DOE, therefore the conditional number should be minimized.

Pearson product-moment correlation coefficient (PMCC) is a standard measure of a linear dependence between two variables. Having two variables x_i and x_j, the PMCC is defined as

$$c_{ij} = \frac{\mathrm{Cov}\,(x_i, x_j)}{\sigma_{x_i}\sigma_{x_j}} = \frac{\sum_{a=1}^{n}(x_{ai} - \overline{x_i})(x_{aj} - \overline{x_j})}{\sqrt{\sum_{a=1}^{n}(x_{ai} - \overline{x_i})^2 \sum_{a=1}^{n}(x_{aj} - \overline{x_j})^2}}\,, \tag{8}$$

where

$$\overline{x_i} = \frac{1}{n}\sum_{a=1}^{n} x_{ai} \quad \text{and} \quad \overline{x_j} = \frac{1}{n}\sum_{a=1}^{n} x_{aj}\,. \tag{9}$$

The PMCC takes a value between -1 and 1 and positive values indicate that the value of x_i tends to increase together with increasing value of x_j, while negative values indicate decreasing value of x_i with increasing value of x_j. Zero value stands for no linear relationship between x_i and x_j. In order to obtain

orthogonal DOE in a multi-dimensional design space, the PMCC needs to be evaluated for each pair of columns in the design matrix (7). As a result, one obtains a $k \times k$ symmetrical correlation matrix

$$\mathbf{C} = \begin{bmatrix} c_{11} & c_{12} & \cdots & c_{1k} \\ c_{21} & c_{22} & \cdots & c_{2k} \\ \vdots & \vdots & & \vdots \\ c_{k1} & c_{k2} & \cdots & c_{kk} \end{bmatrix} . \tag{10}$$

In the case of an orthogonal DOE, the correlation matrix $\mathbf{C}$ is equal to identity matrix. To achieve an orthogonal DOE, one can, for instance, minimize the maximum $|c_{ij}|$ as in Cioppa and Lucas (2007) or the sum of squares of the elements above the main diagonal of $\mathbf{C}$ as it is done in engineering softwares (Novák (2011); Novák et al (2011)) as well as in presented results, i.e.

$$E^{\mathrm{PMCC}} = \sqrt{\sum_{i=1}^{k} \sum_{j=i+1}^{k} c_{ij}^2} . \tag{11}$$

Spearman's rank correlation coefficient (SRCC) can be used to capture a nonlinear but monotonic relationship between two variables and therefore, it can be efficiently applied for estimation of correlations in sampling-based SA (Helton et al (2006)). The idea is to replace the values of x_{ai} and x_{aj} by their corresponding ranks $r(x_{ai})$ and $r(x_{aj})$ and then the SRCC can be computed as

$$\rho_{ij} = 1 - \frac{6 \sum_{a=1}^{n} \left(r(x_{ai}) - r(x_{aj}) \right)^2}{n(n^2 - 1)} . \tag{12}$$

In case of a multi-dimensional design space, the orthogonality of the DOE can be similarly to (11) achieved by minimizing

$$E^{\mathrm{SRCC}} = \sqrt{\sum_{i=1}^{k} \sum_{j=i+1}^{k} \rho_{ij}^2} . \tag{13}$$

Kendall tau rank correlation coefficient (KRCC) is an alternative measure of a nonlinear dependence between two variables. In particular, it is based on the number of concordant ($T_{c,ij}$) and discordant ($T_{d,ij}$) pairs of samples according to

$$\tau_{ij} = \frac{T_{c,ij} - T_{d,ij}}{n(n-1)/2} , \tag{14}$$

and again, the orthogonal DOE can be obtained by minimizing

$$E^{\mathrm{KRCC}} = \sqrt{\sum_{i=1}^{k} \sum_{j=i+1}^{k} \tau_{ij}^2} . \tag{15}$$

3. Latin Hypercube Sampling

Since the optimization of DOE defined on real domains becomes computationally exhaustive even at moderate number of dimensions or design points, practical applications are usually restricted to the optimization of the so-called Latin Hypercube (LH) designs (Iman and Conover (1980)). LH sampling provides a possibility to represent prescribed probabilistic distribution of particular variables and hence, it can be efficiently applied in uncertainty analysis (Helton et al (2006)). The idea is to divide the range of each variable x_j into n disjoint intervals of equal probability and one value x_{ij} is selected from each interval. This selection can be either random or commonly prescribed to the centre of the interval. Then, the n values for each variable are randomly coupled without replacement with n values of other variables resulting in n vectors of variables where each discrete value of each variable is used only once.

The discretisation itself is quite useful for simplification of the optimization process. Therefore, we focus our attention mainly to the optimization of DOE in discrete domains assuming that continuous domains are usually also discretised so as to make the optimization process manageable. Of course, the LH restriction simplifies the optimization even more, since the search space is significantly reduced. However, it is not obvious, whether such restriction excludes the best solutions regarding the objective of SA. Hence, we examine here both the LH designs as well as *free* designs without any prescribed restrictions on points position.

4. Sequential designs of experiments

When generating experimental designs sequentially, lack of knowledge about the resulting number of design points leads obviously to worse properties of the resulting designs than the one-shot DOEs. Nevertheless, an optimization of a large one-shot DOE can become too complex and thus a sequential design can achieve better qualities than the result of one-shot DOE optimization stuck in a local extreme.

The authors in Crombecq et al (2011) present a review of a different procedures for one by one generated sequential designs and compare their qualities with one-shot DOEs in terms of projected and intersite distance. In general, the aim of the described procedures is to provide DOEs with good space-filling and orthogonal property, but they cannot be used for reliability analysis, since the DOEs do not fulfil any probability distribution.

Other authors focus on LH designs which allow to maintain the probability distributions of particular variables. Vořechovský (2009) proposed strategies for adding new points into an existing LH design based on sequential refinement of the domain discretisation. The methods, however, suffer from highly increasing number of points to be added.

In this contribution we focus on a humble goal to compare the qualities of sequential designs obtained by sequential addition of a constant number of new points, preserving the original discretisation and optimized to the individual criteria described in Section 2.. We assume that adding of a constant number of points, which can be handled by an optimization process, should provide a DOE with better qualities than sequential one by one DOEs.

5. Generation of Optimal Design of experiments

We start our comparison by generating small designs having 10 points in two-dimensional discrete domain. The both variables are defined always in ten equally distant discrete values. Each design is optimized according to one of the criteria described in Section 2.. One set of LH designs is optimized with the LH constrains, the other set of *free* designs is optimized without any constrains.

Since the designs are not excessively complex, the Simulated Annealing method (Kirkpatrick et al (1983); Černý (1985)) was applied to optimize each criterion. The procedure slightly differs for the free and for the LH designs. While in the first case a single loop of the algorithm involves a sequential selection of a design point and its random movement to any unoccupied position, in the latter case the algorithm randomly chooses two points and then switches one of their randomly chosen coordinates. The acceptance of a new solution is driven by the Metropolis criterion

$$\exp\left(\frac{f_{\text{old}} - f_{\text{new}}}{T}\right) \geq U\,, \tag{16}$$

where f_{old} and f_{new} stand for values of a criterion for an actual and for a new solution, respectively. T denotes the algorithmic temperature initially set to $T_{\max} = 10^{-3}$ and gradually reduced by a multiplicative constant $T_{\text{mlt}} = \left({}^{T_{\max}}/_{10^{-6}}\right)^{1/100}$ after each ${}^{n_{\max}}/_{10}$ iterations or sooner if the number of accepted movements reaches the value ${}^{n_{\max}}/_{100}$. The entire algorithm terminates after $n_{\max} = 10^6$ criterion evaluations.

Of course, there is no guarantee that the global optimum is achieved, nevertheless, more frequent falls to local extremes also reflect the shortcoming of a particular criterion. Hence, we decided to present the obtained results without any deeper search for more robust and reliable optimization method.

The optimization process was performed 100 times for each criterion and the obtained designs were then employed as initial designs for sequential designs generation. Larger designs were generated sequentially in three steps by adding 10 new points into the existing designs. The following optimization process is very similar to the optimization of the initial designs. The difference consists of optimization only of the added points positions, while the optimized criterion is evaluated for the whole new design.

There are presented two methods for generating sequential designs in this paper. The first one is based on unrestricted selection of new points according to the optimized criterion and both the free DOEs as well as LH DOEs were employed as initial ones. Figs. 1 and 2 show examples of resulting designs of this first method. The plotted examples are chosen among the other designs for their worst result in the sum of the minimal distances to other points. The aim is to show the worst results one can obtain by optimizing particular criteria.

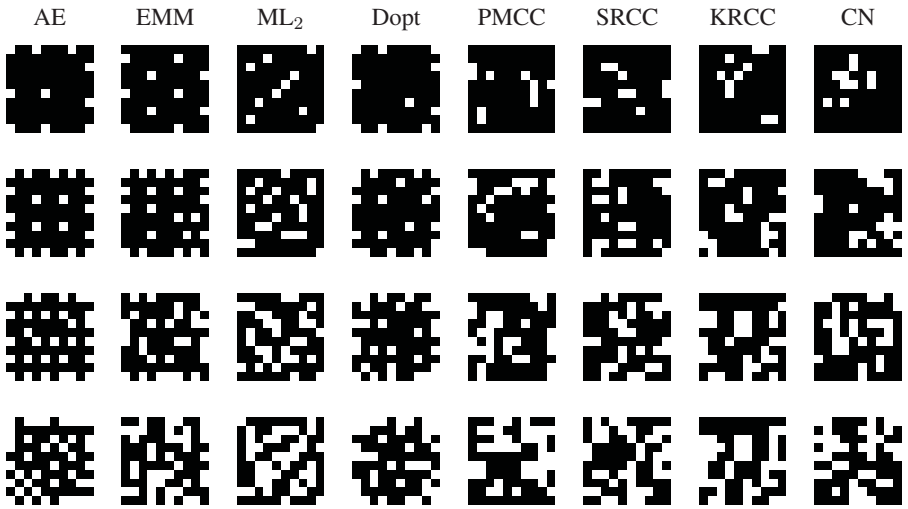

Fig. 1: Sequential free designs.

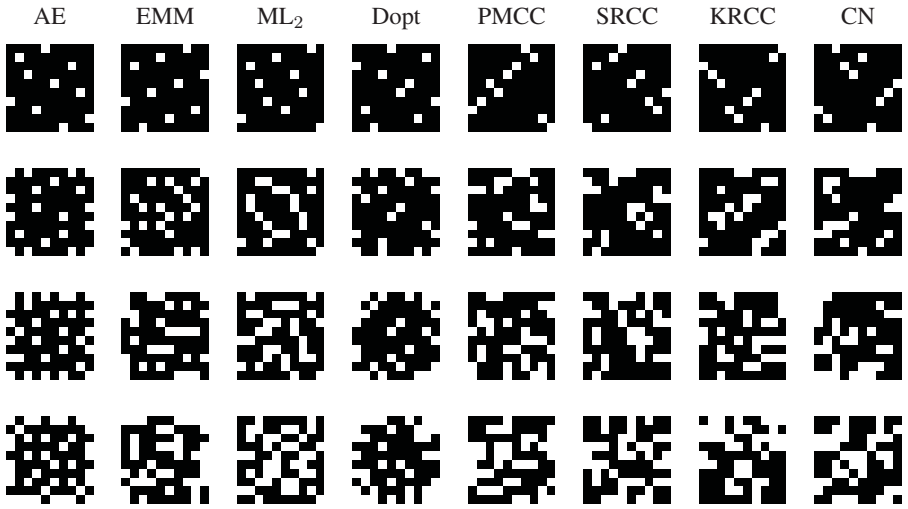

Fig. 2: Sequential free designs from original LH designs.

The second method preserve the LH constrains also for the added points and thus, the equal number of points are located in each column or row. Here the LH designs are used as the initial designs. The resulting DOEs obtained by this method are presented in Fig. 3.

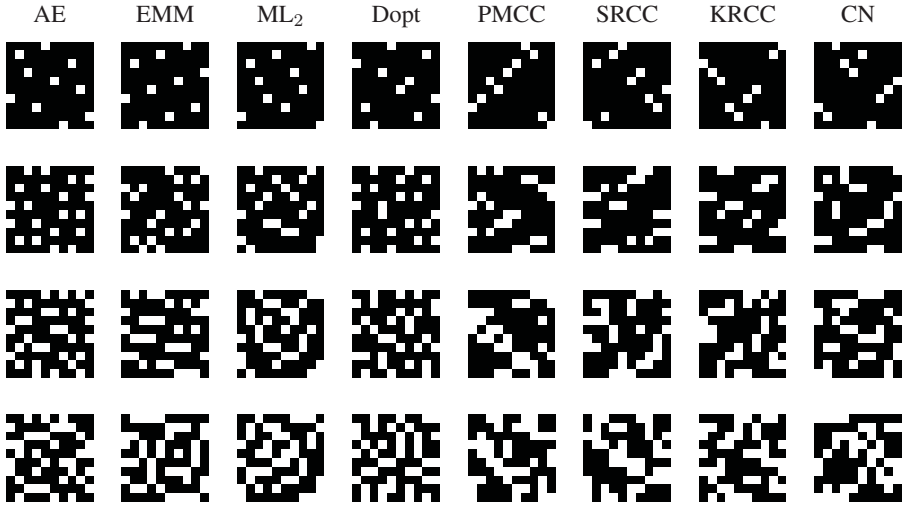

Fig. 3: Sequential mixed LH designs from original LH designs.

6. Sensitivity analysis on a set of mathematical functions

The SRCC criterion has been shown that it can significantly improve the results in estimating the importance of model parameters in sensitivity analysis for the case of nonlinear monotonic models (Helton et al (2006)).

Having the numerical model given as

$$z = f(x_1, x_2, \ldots, x_k) \tag{17}$$

relating the model response z and the model parameters x_i, the impact of the parameter x_i to the model response z can be estimated by evaluating their Spearman's rank correlation $\rho_{x_i,z}$ according to

$$\rho_{x_i,z} = 1 - \frac{6\sum_{a=1}^{n}\left(r(x_{ai}) - r(z_a)\right)^2}{n(n^2-1)}\,, \tag{18}$$

where x_{ai} are values of particular model parameter corresponding to points in DOE and z_a are values of model responses corresponding to these points.

In engineering practice, the majority of the numerical models fulfil the condition of a monotonic relationship between the model parameters and the model response. Therefore, to support the study of optimal DOE quality in sampling-based SA, we performed a comparison for a list of nonlinear but monotonic models. The shapes of the chosen models plotted for the case of square 10×10 domain are shown in Figure 4 together with corresponding parameter-response correlations obtained for the **Full** design consisting of all feasible design points (here 100 points).

Then, the parameter-response correlations were estimated using the all obtained optimal designs and the differences among correlations $\tilde{\rho}$ obtained by the optimal designs and correlations ρ obtained by the full designs are stored. The error measure ϵ in the parameter-response correlations evaluated for a given function is considered as an average difference between each parameter and model response correlation obtained by an optimal and a full design, i.e.

$$\epsilon = \frac{1}{k}\sum_{i=1}^{k}\left|\tilde{\rho}_{x_i,z} - \rho_{x_i,z}\right|. \tag{19}$$

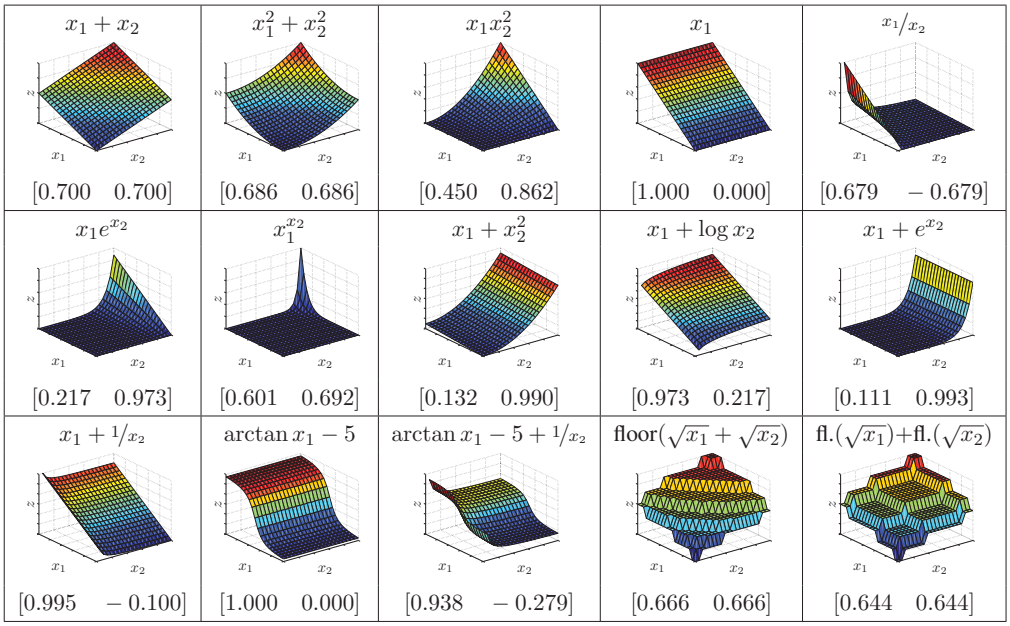

Fig. 4: Shapes of 15 functions for sensitivity analysis with the corresponding values of parameter-response correlations.

The statistics over the obtained values of errors ϵ is presented in Figure 5 using the box plots.

For an easier evaluation of particular criteria, the mean and maximal errors over all models multiplied by 100 are listed in Table 1.

Tab. 1: Mean and maximal errors in correlation predictions for theoretical models.

			AE		**EMM**		**ML$_2$**		**Dopt**		**PMCC**		**SRCC**		**KRCC**		**CN**	
		points	mean	max	mean	max	mean	max	mean	max	mean	max	mean	max	mean	max	mean	max
1st method	free	10	5.9	32.0	6.2	29.4	5.1	20.5	4.5	33.6	8.4	51.4	7.3	48.5	7.5	46.5	8.6	59.9
		20	3.3	16.5	4.6	19.7	3.1	14.3	2.9	20.7	5.1	34.2	4.4	32.4	4.4	29.9	4.4	37.4
		30	2.1	12.0	4.3	17.1	2.2	10.6	3.0	17.4	3.6	25.2	3.3	22.7	3.2	26.1	2.9	22.0
		40	1.5	10.0	4.1	16.0	1.7	8.5	2.5	13.0	2.6	19.0	2.4	23.4	2.5	19.6	2.2	17.0
		overall	**3.2**	**17.6**	**4.8**	**20.6**	**3.0**	**13.5**	**3.2**	**21.2**	**4.9**	**32.5**	**4.4**	**31.8**	**4.4**	**30.5**	**4.5**	**34.1**
	LH	10	6.7	28.9	9.8	31.1	4.5	11.2	6.8	20.3	5.5	31.4	5.8	28.4	5.6	33.0	5.3	30.7
		20	2.9	20.2	5.6	23.8	2.8	13.5	3.5	20.3	4.2	25.2	3.9	31.4	3.9	25.7	3.6	25.7
		30	2.0	12.6	4.5	16.5	2.0	9.5	3.0	15.3	3.1	19.1	2.9	23.7	2.9	20.0	2.7	22.6
		40	1.8	10.6	4.3	18.6	1.7	8.3	2.4	13.6	2.5	16.5	2.3	16.9	2.3	14.8	2.2	17.9
		overall	**3.4**	**18.1**	**6.1**	**22.5**	**2.8**	**10.6**	**3.9**	**17.4**	**3.8**	**23.1**	**3.7**	**25.1**	**3.7**	**23.4**	**3.5**	**24.2**
2nd method	LH	10	6.7	28.9	9.8	31.1	4.5	11.2	6.8	20.3	5.5	31.4	5.8	28.4	5.6	33.0	5.3	30.7
		20	4.8	15.4	7.1	25.3	2.8	10.2	6.0	19.3	3.1	20.8	3.1	18.5	3.0	18.6	3.0	25.2
		30	2.6	11.3	5.3	22.9	2.3	8.7	2.5	9.6	2.1	21.8	2.2	18.2	2.3	17.5	2.2	20.5
		40	2.5	9.0	4.9	19.2	1.6	5.9	2.3	8.8	1.6	11.3	1.6	12.6	1.8	15.5	1.7	15.1
		overall	**4.2**	**16.2**	**6.8**	**24.6**	**2.8**	**9.0**	**4.4**	**14.5**	**3.1**	**21.3**	**3.2**	**19.4**	**3.2**	**21.2**	**3.1**	**22.9**

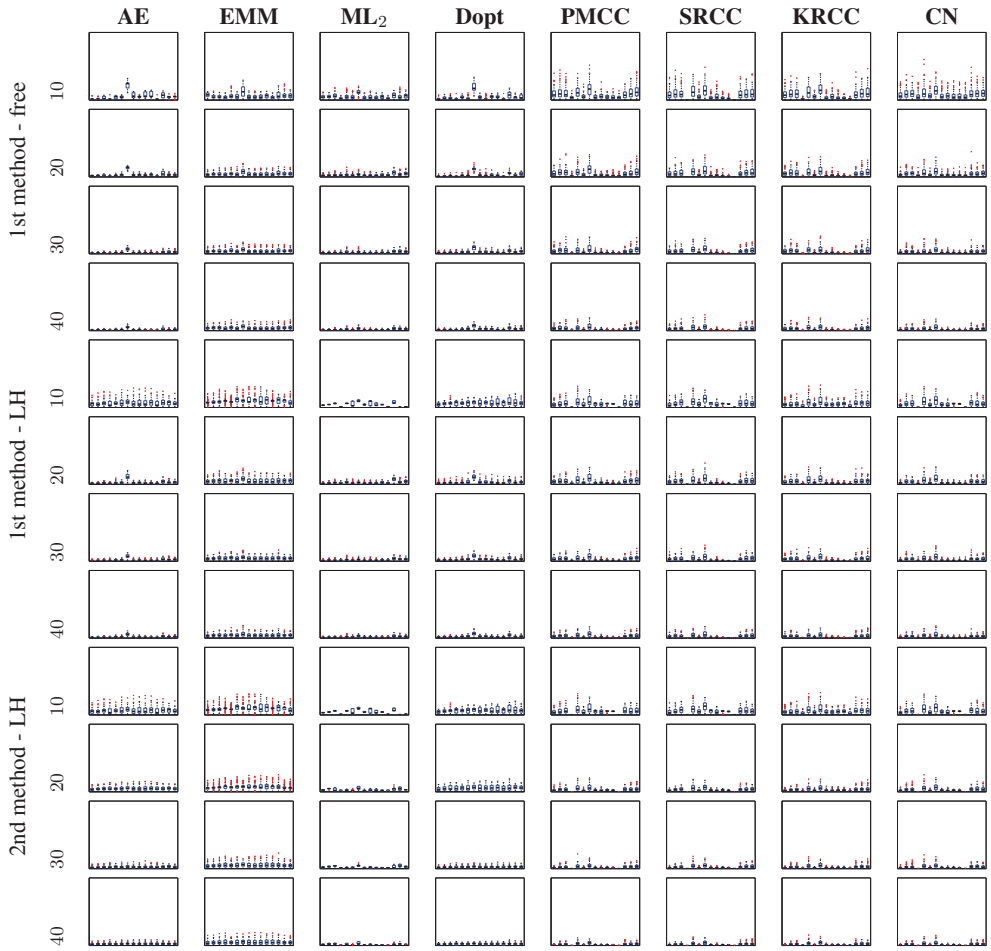

Fig. 5: Statistics on results of criteria in estimating parameter-response correlations for theoretical models. Each rectangle contains 15 *box plots representing the distribution of errors in correlation prediction for particular models depicted in Figure 4. The scale is* 0 *at the bottom and* 1 *at the top per rectangle. Furthermore, each rectangle refers to the optimal designs according to one criterion associated with the corresponding column and to the chosen number of the design points and the type of restriction applied associated with the corresponding row.*

7. Sensitivity analysis on truss structures

The sensitivity analysis study presented in the previous section is aimed on two-dimensional theoretical problems. Therefore, this section is devoted to illustrative engineering problems with higher number of dimensions. We have chosen two models of truss structures commonly used as benchmarks for sizing optimization.

The first one represents a ten-bar truss structure (Venkaya (1971)) shown in Figure 6. The design variables are the cross-sectional areas of the bars. This benchmark is defined with two types of variables: continuous and discrete one. Here we focus on a discrete formulation with discrete values of cross-sectional areas together with values of material properties and loading taken from Lemonge and Barbosa (2003). All ten cross-sectional areas have the same 42 feasible discrete values (in^2): 1.62, 1.80, 1.99, 2.13, 2.38, 2.62, 2.63, 2.88, 2.83, 3.09, 3.13, 3.38, 3.47, 3.55, 3.63, 3.84, 3.87, 3.88, 4.18, 4.22, 4.49, 4.59, 4.80, 4.97, 5.12, 5.74, 7.22, 7.97, 11.50, 13.50, 13.90, 14.20, 15.50, 16.00, 16.90, 18.80, 19.90, 22.00, 22.90, 26.50, 30.00, 33.50.

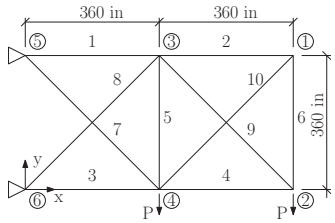

Material:	Aluminum
Specific weight:	0.1 lb/in^3
Young's modulus:	10^7 psi
Loading P:	100 kips

Fig. 6: Scheme of a ten-bar truss structure together with material parameters and values of applied loading.

The second model concerns a 25-bar truss structure with a geometry, material properties and loading given in Figure 7. Thanks to the symmetry of the structure, the bars can be organized into eight groups. The bars in one group have the same cross-sectional areas and hence, there are only eight design variables. These variables are again discrete with 30 feasible values (in^2): 0.1, 0.2, 0.3, 0.4, 0.5, 0.6, 0.7, 0.8, 0.9, 1.0, 1.1, 1.2, 1.3, 1.4, 1.5, 1.6, 1.7, 1.8, 1.9, 2.0, 2.1, 2.2, 2.3, 2.4, 2.5, 2.6, 2.8, 3.0, 3.2, 3.4, see **?**.

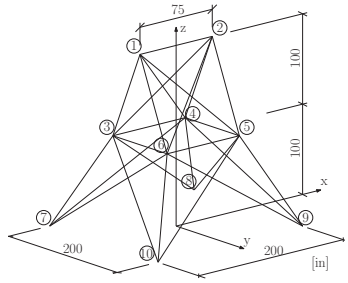

Material:	Aluminum
Specific weight:	0,1 lb/in^3
Young's modulus:	10^7 psi

Nodal loads

Node	F_x	F_y	F_z
1	1.0	-10.0	-10.0
2	0.0	-10.0	-10.0
3	0.5	0.0	0.0
6	0.6	0.0	0.0

Fig. 7: Scheme of a 25-bar truss structure together with material parameters and values of applied loading.

The response of these models consists of three components: total weight of the structure w, maximal deflection d and maximal stress s. Because of higher dimensions of these problems, we have generated the optimal DOEs only with LH restriction, since they can be optimized more easily. This restriction automatically specifies the number of corresponding design points, which has to be equal to the number of feasible values (42 for the ten-bar truss and 30 for the 25-bar truss).

A simulated annealing method with the same parameters as described in Section 5. but with a maximum of 10^7 iterations was employed to generate 20 optimal DOEs using each criterion under the study. The parameter-response correlations were then estimated using the obtained optimal DOEs and compared with the correlations computed using the **Large** DOEs consisting of $2 \cdot 10^7$ samples generated by Monte Carlo method. The statistics on the errors ϵ in estimation of parameter-response correlations is demonstrated again in terms of box plots independently for each criterion and each model response component, see Figure 8.

For clearer summarization of the obtained results, the mean and maximal errors in correlation predictions multiplied again by 100 are listed in Table 2.

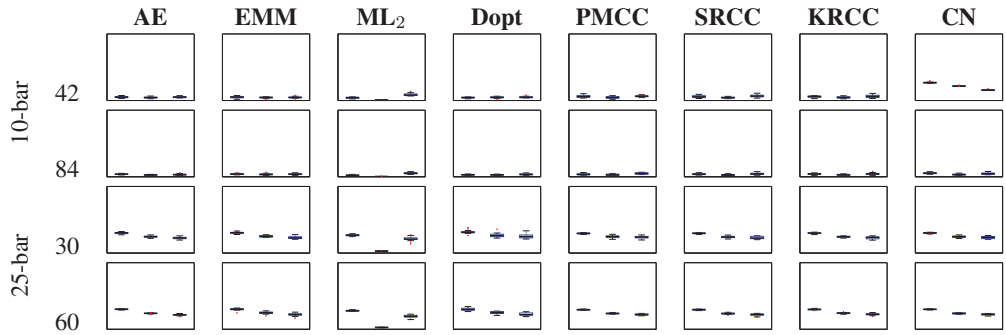

Fig. 8: Statistics on results in estimation of parameter-response correlations for structural models. Each rectangle contains three box plots representing the distribution of the errors in correlation prediction for particular model responses: the total weight w, the maximal deflection d and the maximal stress s. The scale is 0 at the bottom and 1 at the top per rectangle. Each rectangle refers to optimal designs according to one criterion associated with the corresponding column and to the chosen structure associated with the corresponding row.

Tab. 2: Mean and maximal errors in correlation predictions for structural models.

Model		AE		EMM		ML_2		Dopt		PMCC		SRCC		KRCC		CN	
		mean	max	mean	max	mean	max	mean	max	mean	max	mean	max	mean	max	mean	max
10-bar	42																
	w	5.1	7.5	4.9	7.5	4.1	5.5	4.3	5.4	6.2	10.3	5.9	9.2	5.8	7.5	27.0	29.7
	d	4.5	6.7	4.4	5.6	0.7	1.1	4.6	6.5	4.5	7.3	4.3	6.2	4.7	7.1	21.7	23.0
	s	5.1	7.3	4.7	7.7	8.9	13.9	5.1	8.0	6.5	9.2	6.8	11.0	6.6	10.7	15.7	17.7
	overall	**4.9**	**7.5**	**4.7**	**7.7**	**4.6**	**13.9**	**4.7**	**8.0**	**5.7**	**10.3**	**5.7**	**11.0**	**5.7**	**10.7**	**21.5**	**29.7**
	84																
	w	3.9	5.1	4.1	6.1	2.3	3.6	3.0	4.2	3.7	6.3	3.9	6.1	4.1	5.8	5.4	7.7
	d	2.7	3.6	3.6	6.7	0.4	0.7	2.9	4.0	3.1	5.0	2.7	4.6	2.9	4.4	3.4	5.5
	s	3.3	5.7	3.9	6.0	5.4	7.7	3.7	5.8	5.0	6.7	4.3	7.7	4.4	8.0	4.8	8.0
	overall	**3.3**	**5.7**	**3.9**	**6.7**	**2.7**	**7.7**	**3.2**	**5.8**	**3.9**	**6.7**	**3.6**	**7.7**	**3.8**	**8.0**	**4.5**	**8.0**
25-bar	30																
	w	30.0	32.3	30.4	33.5	26.8	28.9	31.6	38.3	29.5	30.8	29.6	30.7	29.9	31.4	30.0	31.2
	d	24.6	27.2	25.1	27.5	23.6	28.3	26.8	35.7	24.4	28.1	24.1	27.1	24.3	25.8	24.5	27.2
	s	22.6	25.9	23.2	27.6	21.2	27.4	25.2	33.4	23.8	27.2	23.0	26.0	22.7	25.8	23.4	26.3
	overall	**25.7**	**32.3**	**26.2**	**33.5**	**23.9**	**28.9**	**27.9**	**38.3**	**25.9**	**30.8**	**25.6**	**30.7**	**25.6**	**31.4**	**26.0**	**31.2**
	60																
	w	30.0	30.9	30.0	31.9	27.8	29.5	30.2	34.1	29.4	30.4	29.4	30.4	29.9	31.4	29.9	30.9
	d	23.9	25.1	24.7	27.7	22.5	25.5	24.9	27.3	23.8	25.3	23.6	25.6	24.2	26.5	23.8	25.1
	s	21.6	23.7	22.3	25.8	19.3	22.6	22.6	26.4	22.1	23.9	21.9	23.9	22.5	25.1	22.2	23.8
	overall	**25.2**	**30.9**	**25.7**	**31.9**	**23.2**	**29.5**	**25.9**	**34.1**	**25.1**	**30.4**	**25.0**	**30.4**	**25.5**	**31.4**	**25.3**	**30.9**

8. Conclusions

This paper reviews eight criteria used for sequential optimization of a design of experiments and presents a comparison of the resulting designs when employed for a sampling-based SA on 15 theoretical and two structural models. The overall results can be summarized in several following conclusions:

- The quality of all the optimal DOEs can be improved by adding of new points and the conclusions valid for small designs remains mostly valid also for the larger sequential designs.
- The best result was achieved by the ML_2 criterion, which is very robust and thus the obtained DOEs provided very small errors in sensitivity predictions with very small variance. The LH designs optimized with respect to ML_2 criterion provide better results and they are also more easily optimized. Therefore they can be recommended for the practical usage.
- Orthogonality-based criteria provide good results on theoretical problems when applied for generation LH designs, but the resulting errors have higher variance and which lower their fidelity.

- An interesting effect can be noticed on D-optimal designs. While the small D-optimal free designs have significantly better results than the small D-optimal LH designs, this difference decreases with increasing number of points and the larger D-optimal LH designs have the same or smaller errors than the D-optimal free designs of the same size.
- Also AE criterion achieved very good results when applied to free designs, but the variance is again relatively high.
- Worse results were obtained using EMM criterion.

The presented results revealed that the ML_2 criterion, which is not very popular, can provide very good results when applied for the generation of the DOE for sampling-based sensitivity analysis. The results obtained for 25-bar structure were unsatisfactory for all the studied criteria. This can be caused by too small number of samples in the generated designs. However, the larger designs did not improve the results significantly.

Acknowledgments

The financial support of this work by the Czech Science Foundation (project No. 105/11/P370) is gratefully acknowledged.

References

de Aguiar, P. F. and Bourguignon, B. and Khots, M. S. and Massart, D. L. and Phan-Than-Luu, R. (1995), D-optimal designs. *Chemometr Intell Lab*, Vol 30, No.2, pp 199-210.

Alam, F. M. and McNaught, K. R. and Ringrose, T. J. (2004), A comparison of experimental designs in the development of a neural network simulation metamodel. *Simulation Modelling Practice and Theory*, Vol 12, No.7-8, pp 559-578.

Audze, P. and Eglais, V. (1977), New approach for planning out of experiments. *Problems of Dynamics and Strengths*, Vol 35, pp 104-107, Zinatne Publishing House.

Černý, J. (1985), Thermodynamical approach to the traveling salesmanproblem: An efficient simulation algorithm. *Journal of Optimization Theory and Applications*, Vol 45, pp 41-51.

Cioppa, T. M. and Lucas, T.W. (2007), Efficient Nearly Orthogonal and Space-Filling Latin Hypercubes. *Technometrics*, Vol 49, No. 1, pp 45-55.

Crombecq, K. and Laermans, E. and Dhaene, T. (2011), Efficient space-filling and non-collapsing sequential design strategies for simulation-based modeling. *European Journal of Operational Research*, Vol 214, No. 3, pp 683-696.

DuMouchel, W. and Jones, B. (1994), A simple Bayesian modification of D-optimal designs to reduce dependence on an assumed model. *Technometrics*, Vol 36, No. 1, pp 37-47.

Fang, K. T. and Wang, Y. (1994), *Number-theoretic Methods in Statistics*, Chapman & Hall, London.

Goel, T. and Haftka, R. T. and Shyy, W. and Watson, L. T. (2008), Pitfalls of using a single criterion for selecting experimental designs. *Int J Numer Meth Eng*, Vol 75, No. 2, pp 127-155.

Goel, T. and Haftka, R. T. and Shyy, W. (2009), Comparing error estimation measures for polynomial and kriging approximation of noise-free functions. *Struct Multidiscip O*, Vol 38, No. 5, pp 429-442.

Heinrich, S. (1996), Efficient Algorithms for Computing the L_2-discrepancy. *Math Comput*, Vol 65, No. 216, pp 1621-1633.

Helton, J. C. and Johnson, J. D. and Oberkampf, W. L. and Sallaberry, C. J. (2006), Sensitivity analysis in conjunction of with evidence theory representations epistemic uncertainty. *Reliab Eng Syst Safe*, Vol 91, No. 10-11, pp 1414-1434.

Helton, J. C. and Johnson, J. D. and Sallaberry, C. J. and Storlie, C. B. (2006), Survey of sampling-based methods for uncertainty and sensitivity analysis. *Reliab Eng Syst Safe*, Vol 91, No. 10-11, pp 1175-1209.

Hofwing, M. and Strömberg, N. (2010), D-optimality of non-regular design spaces by using a Bayesian modification and a hybrid method. *Structural and Multidisciplinary Optimization*, Vol 42, No. 1, pp 73-88.

Iman, R. L. and Conover, W. J. (1980), Small sample sensitivity analysis techniques for computer models, with an application to risk assessment. *Communications in Statistics - Theory and Methods*, Vol A9, No. 17, pp 1749-1842.

Janouchová, E. and Kučerová, A. (2011), Competitive Comparison of Optimal Designs of Experiments for Sampling-based Sensitivity Analysis. *Computers & Structures*, submitted for publication, e-print: arXiv:1201.0942.

Johnson, M. and Moore, L. and Ylvisaker, D. (1990), Minimax and maximin distance designs. *Journal of Statistical Planning and Inference*, Vol 26, No. 2, pp 131-148.

Kirkpatrick, S. and Gelatt, Jr., C., and Vecchi, M. P. (1983), Optimization by Simulated Annealing. *Science*, Vol 220, pp 671-680.

Kučerová, A. (2007), *Identification of nonlinear mechanical model parameters based on softcomputing methods*, Ecole Normale Supérieure de Cachan, Laboratoire de Mécanique et Technologie, Ph.D. Thesis.

Lemonge, A.C.C. and Barbosa, H.J.C. (2003), An adaptive penalty scheme for genetic algorithms in structural optimization. *International Journal for Numerical Methods in Engineering*, Vol 59, pp 703-736.

Morris, M. D. and Mitchell, T. J. (1995), Exploratory designs for computer experiments. *Journal of Statistical Planning and Inference*, Vol 43, No. 3, pp 381-402.

Novák, D. and Vořechovský, M. and Rusina, M. (2011), *FREET v. 1.5 - program documentation*, Brno/Červenka consulting, Prague, User's and Theory Guides.
`http://www.freet.cz`

Novák, J. (2011), *Generator of optimal LHS designs SPERM v. 2.0.*, Centre for Integrated Design of Advanced Structures (CIDEAS), Czech Technical University in Prague.
`http://www.cideas.cz/ke stazeni/sperm/`

Saltelli, A. and Chan, K. and Scott, E. M. (2000), *Sensitivity analysis*, NY:Wiley, New York.

Smith, K. (1918), On the standard deviations and interpolated values of an observed polynomial function and its constants and the guidance they give towards a proper choice of the distribution of observations. *Biometrika*, Vol 1/2, pp 1-85.

Toropov, V. V. and Bates, S. J. and Querin, O. M. (2007), Generation of Extended Uniform Latin Hypercube Designs of Experiments. In: *Proceedings of the Ninth International Conference on the Application of Artificial Intelligence to Civil, Structural and Environmental Engineering* (A. Smyth et al. eds). B.H.V. Topping, Civil-Comp Press, Stirlingshire, Scotland. Paper 7, CD-ROM.

Venkaya, V. B. (1971), Design of optimum structures. *Computers & Structures*, Vol 1, pp 265-309.

Vieira, H. and Sanchez, S. and Kienitz, K. H. and Belderrain, M. C. N. (2011), Generating and improving orthogonal designs by using mixed integer programming. *European Journal of Operational Research*, Vol 215, No. 3, pp 629-638.

Vořechovský, M. (2009), Hierarchical Subset Latin Hypercube Sampling for correlated random vectors. In: *Proceedings of the First International Conference on Soft Computing Technology in Civil, Structural and Environmental Engineering*, B.H.V. Topping and Y. Tsompanakis, Civil-Comp Press, Stirlingshire, Scotland. Paper 53, CD-ROM.

18th International Conference
ENGINEERING MECHANICS 2012
Svratka, Czech Republic, May 14 – 17, 2012

pp. 811–814
Paper #98

NUMERICAL ANALYSIS OF FRACTURED FEMUR WITH INTERNAL OSTEOSYNTHESIS

V. Kunášek*, J. Jírová

Abstract: *The internal osteosynthesis method of the thighbone diaphysis allows use of some different types of devices in dependence on complexity and a type of the diaphysis fracture. The aim of this project is a numerical stress analysis in case of two types osteosynthesis plates applied to two different thighbone diaphysis fractures. We simulated incidents, when a pacient's broken leg was too early however fully treated and his thighbone did not begin to recovery yet. In these extreme incidents the whole stresses are carried by the plates. The modeling and calculations was done using FEM software ANSYS Workbench.*

Keywords: ***Biomechanics, Internal osteosynthesis, Femur, Finite element method, ANSYS Workbench***

1. Introduction

This paper disserts about numerical analyses of two internal osteosynthesis methods used in fractured human thighbone therapy. The aim is a comparison of stress distribution in two types of osteosynthesis plates applied to two types of the thighbone diaphysis fractures, oblique and wedge, ones which represent the most common fractures of the thighbone diaphysis caused by light traffic accidents. In the project we analysed 5 models: a virtual model of unbroken thighbone, virtual model of an oblique fractured thighbone with wave plate implementation, virtual model of wedge fractured thighbone with wave plate implementation, virtual model of oblique fractured thighbone with straight plate implementation and virtual model of wedge fractured thighbone with straight plate implementation.

2. Virtual models

The virtual models used in our analyses were made up by the fractured thighbone, two types of plate with cortical screws and cortical filler in case of the wave plate. All models were imported or created in ANSYS Workbench (fig.1).

2.1. Thighbone

The original `*.x_t` format of 470 mm tall left thighbone virtual model is provided by author (Dr. Marcello Papini, University Ryerson, Toronto, Canada) for noncomercial use. This model was imported to ANSYS Workbench DesignModeler where we modified a volume of the cancellous bone and made diaphysis fractures. A form of the cancellous bones inside both epiphyses of the femur were greatly simplified.

The thighbone diaphysis fractures used in our thesis represent the most common fractures of the thighbone diaphysis which have been caused by light traffic accidents- maximum impact speed was 25km/h (Drábek, 2009).

2.2. Plates and screws

The virtual model of the 230 mm tall wave plate was created in ANSYS Workbench DesignModeler in the base of the original `*.stl` model provided for this project purposes by its producer, ©Litos

*Bc. Václav Kunášek, Doc. Ing. Jitka Jírová, CSc.: Department of Mechanics and Materials, Czech Technical University in Prague, Faculty of Transportation Sciences, Konviktská 20, 110 00, Praha 1; CZ, e-mail: vaclav.kunasek@seznam.cz, jirova@fd.cvut.cz

company. Our virtual model represented a little simplified contrary to original geometry especially use of cylindrical screw holes in our model. The real use of the wave plate internal osteosynthesis is related with implementation of the cortical filler between the wave-middle part of the plate and femur diaphysis. We used a simple filler of cuboid design in our analyses.

The straight plate virtual model is based on our wave plate model and has not any real template. This plate was made up by straightening wave plate middle part because of the objective stress distribution comparison between the plate with wave and the same plate without wave.

Analogous to screw holes were created all virtual models of cortical screws. We designed cylindrical screws according to their litos dimension template with the lenght agreed to robustness of the femur diaphysis and the diameter of model cylindrical screws corresponded to outer diameter of the litos original screws.

Fig. 1: Complete four virtual models of fractured femur diaphyses with internal osteosyntheses

2.3. Finite element model

We compromised mesh quality in dependence on sophistication of parts of our model systems between hardware requirements to numerical analysis and precision of results. Our models consisted of 28 000 to 37 000 elements (size of elements: 2.5- 8mm). The finite element model was done in ANSYS Workbench Mesher. The femur, plates and screws were meshed by solid tetrahedron elements. The cortical filler was meshed by cuboid elements.

2.4. Material properties

Our models contained four types of materials. There were a material model of a cortical bone, cancellous bone, *Titanium Grade 1* for plates and $TiAl_6V_4$ for cortical screws. We used the homogeneous linear isotropic mechanical properties for all used virtual models because of simplifying and agility of the analyses. There was need to know two mechanical characteristics: Young's modulus and Poisson's ratio (tab.1).

2.5. Initial conditions and loads

The thighbone was loaded by force of 2500N that occurred on a proximal side of the thighbone head. A vector of the force occurred in axis (Z axis) intersected the center of the femur head on the proximal side and the center of distal epiphysis. We used the support of distal parts of both condyluses that allowed free displacement in ortoghonal plane (represented by X axis and Y axis) to the force vector (represented by Z axis). Similar to the real experiment, we allowed a rotation around Z axis in our analyses.

In our analyses, were used three types of contact types. First contact type (in ANSYS Workbench called *Bounded*) ensuring compagination of joined parts was used in cases of appositions of plates to

Tab. 1: Material properties

Material	Young's modulus [MPa]	Poisson's ratio [-]
Cortical bone	17600	0.25
Cancellous bone	350	0.25
$TiAl_6V_4$	115000	0.34
Titanium Grade 1	103000	0.34

screws, screws to diaphyses parts of the damaged thighbone, for appositions of the wave plate to the cortical filler and for joints of cancellous bone to the cortical bone. The second contact type called *frictional* was used for appositions of proximals to distals faces of the fractured thighbones and for diaphyses to the cortical filler contacts in cases of the wave plate use. This contact type allows frictional sliding of contact faces (cortical bone to cortical bone) with friction coefficient equal to 0.15 (Landor, 2010). The last used contact type, *Frictionless*, allowed sliding of contact faces without friction. For simplification of all analyses, we used this contact type in cases of appositions of plates to the thighbone diaphyses.

3. Validation of virtual thighbone

There was required to validate our virtual model of the thighbone before the main numerical analyses of fractured thighbones with internal osteosynthesis. This task proceeded per experiments (Jírová et al.,1989) which contained stress values at medial and lateral side of a loaded real human thighbone. We used identic initial conditions and loads for this publication for unbroken thighbone validation and for next other analyses.

During the validation (fig.2), we analysed and compared stress values in 13 points at lateral diaphysis side and stress values in 13 points at medial diaphysis side of our virtual model and the most corresponding human 470 mm tall thighbone (Jírová et al.,1989).

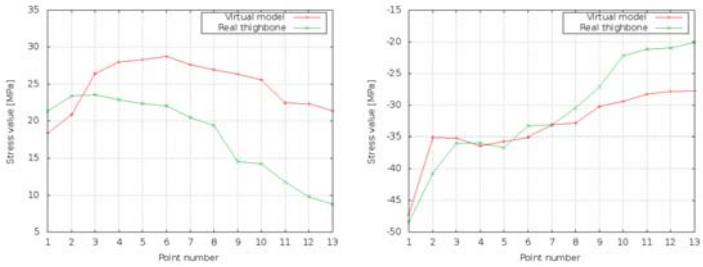

Fig. 2: Graphically compared stress results: lateral side- tensile stress (left graph), medial side- compression stress (right graph)

The stress results in graphs (fig.2) pointed at some diferences between a real human thighbone and our virtual model. These differences were at first caused by different geometry structure of a real thighbone and our virtual model especially by lenght of thighbone neck, at second by different robustness of the cortical bone of diaphyses parts, at third by different conception of a cancellous bone and finally the results could be different due to the finite element quality of our virtual models.

4. Results

Results of stress values on the undamaged thighbone were sufficiently comparable with each other for us to continue in numerical analyses of damaged thighbones with internal osteosyntheses. This project's

aim was focused on numerical comparison of marked tensile stress values at screws and the wave plate contrary to the straight plate implemented to the fractured thighbone (by oblique and wedge fractures). We observed the stress results at plates, screws and contact faces of fragmented thighbones, safety factor of the cortical bone and relative deformations of both fragmented parts of the fractured thighbone.

Firstly analysed magnitude represented the screws and plates tensile stress distribution. The specific type and form of the oblique fracture influenced the stress distribution more than in the case of wedge fracture because the oblique faces of fracture allowed a sliding of proximal part in distal part of the fractured thighbobe. This fact caused redundant straining of the last screw in proximal part and especially first screw in distal part of the fractured thighbone. The results with use of the wave plate showed lower stress values (almost half) than with the straight plate. The stress results in the case of the wedge fractured thighbone diaphysis showed almost equal stress distribution along all screws and screw holes in both cases of the used plates.

Secondly a high value of the loading force caused mutual contacts of the proximal to distal parts of the fractured thighbones and mutual contacts of the fractured thighbones to plates. Therefore there was necessary to analyse the compression stress on these faces. In all analyses, we registered the higher compression stress values on the contact faces of the proximal parts of the fractured thighbone. The stress results in case of the wave plate, oblique fractured thighbone combination showed more than half stress result values contrary to use of the straight plate again.

The last analysed magnitude was the safety factor of the cortical bone. Safety factor had been bearing to compression stress on the contact faces of the model described in the last paragraph. This magnitude is characterised by ratio of ultimate compression strenght to the Equivalent (von-Mises) stress of the cortical bone, used 124 MPa (Valenta et al., 1985). The results in cases of the fractured thighbones with both types of plates were not positive. We registered the vaules of safety factor less than limit value 1 in cases of all analysed samples of the fractured thighbone with internal osteosyntheses. The most affected areas in cases of models with the wedge fractures were located at the contact faces of proximal parts of the fractured thighbones. In case of samples with oblique fracture the most damaged areas were located on lateral sides of proximal parts of the thighbone under central parts of the plates. These presented areas of the cortical bone had been probably more destructed.

5. Conclusions

The aim of this project was to compare the stress results at loaded virtual models of fractured thighbones with internal osteosyntheses. We focused mostly on the tensile stress on plates and screws, compressive stress on contact faces of fractured parts of the thighbones (proximal and distal part) and finally on the safety factor of the cortical bone. We registered better ability of the wave plate to stress distribution in all our analyses. Evidently lower values of the tensile stress in case of the analysed loaded oblique fractured thighbone with the wave plate implementation contrary to straight plate. Also the compression stress analyses showed more favorable results for wave plate osteosynthesis than use of the straight plate. Finaly, the wave plate allowed less destruction of the cortical bone than the straight plate.

Acknowledgments

The project has been supported by the research plan of the Ministry of Education, Youth and Sports MSM6840770043.

References

Valenta et al. (1985), *Biomechanika*, Academia, Praha.

Jírová et al. (1989), *Silová interakce dříku náhrady kyčelního kloubu s kostí*, ÚTAM, Praha.

Drábek (2009), *Interakce lidského těla s interiérem vozidla*, Vlastimil Drábek,Olomouc.

Landor, I., Horák, Z., Vlček, M. (2010), *Biomechanical analyses of distal radius*, ČVUT- Fakulta strojní,Praha.

Kovanda, J., Riccardo, R. (1999), *Vehicle- human interaction*, Edizioni Spiegel, Milano, Italy.

18th International Conference
ENGINEERING MECHANICS 2012
Svratka, Czech Republic, May 14 – 17, 2012

pp. 815–824
Paper #226

INFLUENCE OF GEOMETRIC PARAMETERS ON THE STIFFNESS OF TRADITIONAL DOVETAIL TIMBER JOINT

J. Kunecký[*], R. Cacciotti[**], M. Kloiber[***]

Abstract: *The paper presents the development of numerical modeling for a traditional dovetail timber joint. The objective is to find the influence of its geometrical properties on the mechanical stiffness of the joint as well as to assess the main problems and limitations faced during the numerical modeling of the structure. An experiment with a replicated timber joint was used to validate the model. Material properties were ascertained and contact adjustment was made. Parametric study was performed: two angles of the joint beams (α, β) were varied. Suitable ranges of the angles for each type of loading were found. Main limitations and problems present in the modeling are depicted in the discussion.*

Keywords: ***Historical construction, timber joint, numerical modeling.***

1. Introduction

1.1. Motivation

Historical buildings represent for contemporary professionals and researchers a seamless source of inspired engineering solutions which, if opportunely applied, provide feasible modern applications. The development of such practical potential, however, cannot prescind from an accurate exploration of the peculiarities of modern and traditional realities and an adequate assessment of their interaction (Vinař et al., 2010). From this perspective traditional carpentry and timber assembly techniques require a deeper understanding of the context in which they were developed in order to address the safety and functional requirements imposed by current design practice. The following considerations should be made:

The making of carpentry joints in the past was commonly grounded on empirical rules and its design strictly context-specific. The consequent lack of experimental and analytical evidence interferes with the establishment of reliable behavior models and the outlining of recommendations for rehabilitation or strengthening of timber structures. The result is a knowledge gap in the building codes and international standard that necessitates integration.

The heterogeneity of timber joints characteristics constitutes a true challenge for modeling process: the variation of geometrical parameters and the material nonlinearity imposes the development of a comprehensive methodology aimed at reducing standardization errors and at overcoming modeling limitations to a satisfactory extent.

Although research concerning specifically wood connections is somewhat limited, considerable leaps forward are being made (Burnet at Al.). In Czech Republic, for example, the *´Design and Assessment of Timber Joints of Historical Structures´* project, funded by the Ministry of Culture (DF12P01OVV004, February 2012), aims at tackling the above mentioned issues with extensive research in traditional joint testing and implementation of their mechanical behavior through experimental approach and numerical modeling, this study being one of its preliminary step.

[*] Ing. Jiří Kunecký, PhD. : Institute of theoretical nad applied mechanics AS CR, v.v.i, Prosecká 76, 190 00, Prague, CZ, email: kunecky@itam.cas.cz

[**] Mgr. Riccardo Cacciotti : Institute of theoretical nad applied mechanics AS CR, v.v.i, Prosecká 76, 190 00, Prague, CZ, email: cacciotti@itam.cas.cz

[***] Ing. Michal Kloiber, PhD. : Institute of theoretical nad applied mechanics AS CR, v.v.i, Prosecká 76, 190 00, Prague, CZ, email: kloiber@itam.cas.cz

1.2. Objectives

The main objective of the analysis is to individuate and quantify the influence of the variation of parameters of a traditional dovetail timber joint and develop a suitable numerical model for a specific case.

The objectives are:

- To find the influence of parameters of geometry and determine the main limitation of modeling

- To understand the behavior of the joint under load, especially for further experimental testing leading to determination of its bearing capacity

1.3. Oblique dovetail halving joint

The joint under analysis is an oblique dovetail halving joint (Fig. 1). It combines two different carpentry methods, dovetailing and halving, to provide for an improved performance in specific building components such as roof trusses. Such combination, in the middle Ages, was frequently adopted for right-angled or oblique joints subjected to particularly preponderant axial forces.

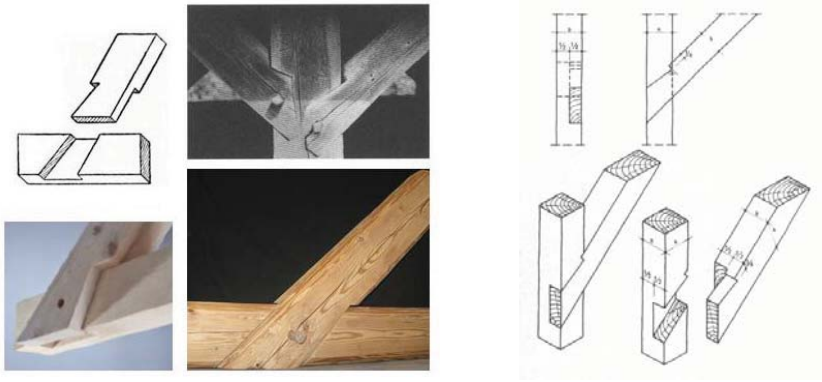

Fig.1: Examples (left) and typical geometry (right) of oblique dovetail timber joint (Gerner et al., 2003)

Dovetailing is a common technique widespread in woodworking joinery which consists in shaping the end of one member as a dovetail pin and in cutting a matching slot in a second member to be connected in order to ensure good interlocking. Such joint presents mainly resistance to pulling.

Halving consists in cutting half the depth of the timber section. This is one of the simplest methods of connecting two pieces of timber, especially where it is desired to make frames and bracket supports for either inside or outside use.

In the oblique dovetail halving joint the connecting members are at an angle to each other. Such method is mainly used for bracing of frames and can be occasionally observed with both its sides dovetailed.

1.3.1. Typical geometry

As a prerequisite for modelling it is necessary to individuate the main geometrical characteristics of the joint. A geometrical standardisation is possible by taking into consideration the ´golden rules´ used by handcraft men directly on site. Such rules, found in both modern literature and historic manuals, outline the general proportions with which cuts should be made in the timber elements.

The diagram in Fig. 1 shows a schematic layout of an oblique dovetail halving joint (Gerner et al., 2003). The vertical beam presents a cut of depth equal to half its breadth and two non-parallel oblique cuts on the height side to allow for interlocking with the dovetail. The oblique beam has a longitudinal halving for a length equal the height of the vertical beam; the halved section has a right-angle triangular shape cut of base equal to one sixth of the height of the oblique beam section and opposite vertex being the corner of the beam itself.

2. Methods

2.1. Outline of the work

A parametric FE model is presented to clearly explore the reaction of the joint to different loading phases. Experimental techniques are thoroughly applied to appropriately adjust and validate the model. Specific experiments are performed: material testing is required in order to determine mechanical parameters and the contact surfaces' behavior (wood-steel, wood-wood) is analyzed to specify contact characteristics in the joint. The paragraphs below outline the joint assembly and material tests and the necessary contact adjustment. The model is verified by comparing and cross-checking the measured and modeled values of its mechanical behavior. A sensitivity analysis, for different geometric parameters of the joint, is also performed.

2.2. Experiments

2.2.1. Dovetail joint experiment

The tested joint is prepared by assembling two beams of old dry timber coming from a historic roof built during the eighteenth century (see Fig. 2). The general layout and the geometrical details of the tested joint are shown in Fig. 3. Both beam 1 and 2 present a cross section of 175x150mm and intersect at an angle of 50°. Beam 1 is a 928 mm long timber element showing on one side a cut 216 mm wide at the top and 245 mm wide at the bottom of the beam. The difference between the two measurements reveals that the two sides of the slot in the beam are not parallel but one is inclined about 10° more than the other one with respect to the vertical. Beam 2 is 880mm long with a projection on the vertical plane of 743 mm. The height of the halved section is 182 mm and presents a cut at 60° with the horizontal on the leeward side of the beam. A hole of about 30 mm of diameter, located at the point of intersection of the beams axes, allows for dowel interlocking.

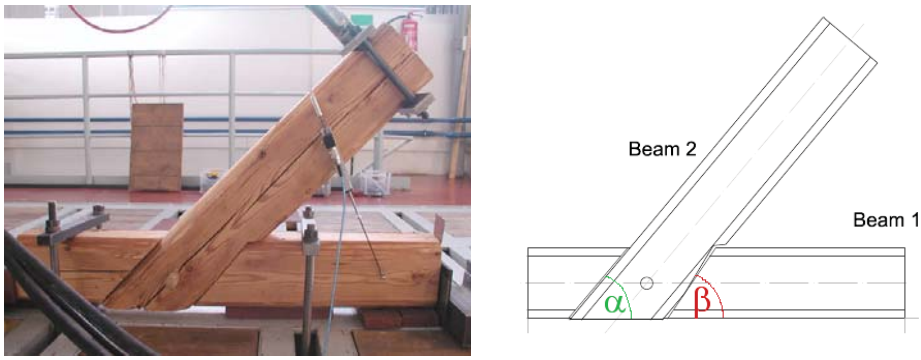

Fig. 2. The tested timber joint (left), simplified geometry with important parameters (right)

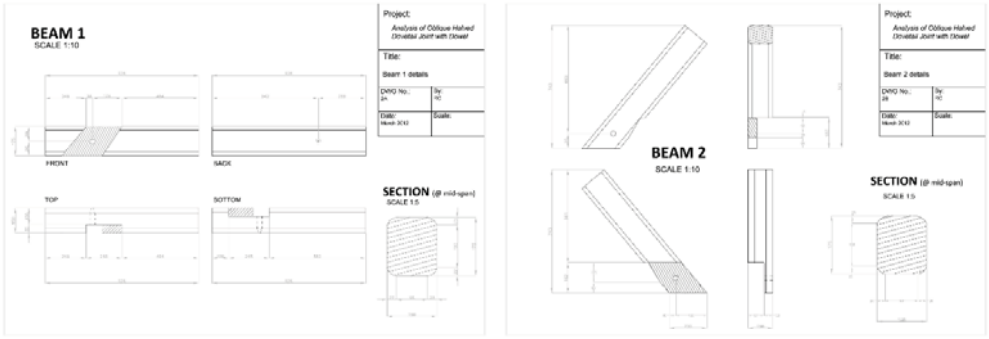

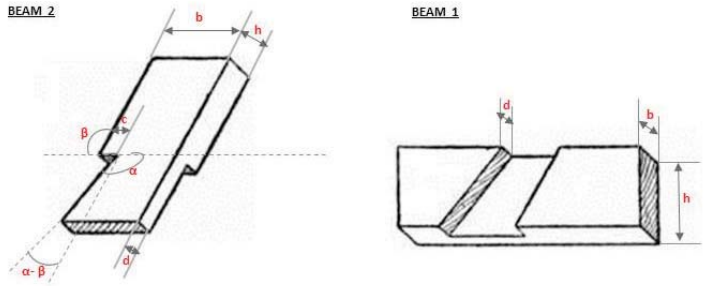

		Theory	Measured
BEAM 1	b (mm)	-	150
	h (mm)	-	175
	d	0,5b	0,333b
BEAM 2	b (mm)	-	230
	h (mm)	-	175
	c	0,167b	0,152b
	d	0,5h	0,353h
	α	55°	60°
	θ	45°	50°
	α-θ	10°	10°

Fig. 3. Geometry of the experimental joint (top) compared with literature data (bottom)

The table shown in Fig. 3 outlines the ratios between the relevant dimensions of cuts on the two timber members. Such data provides useful information for quantifying the divergent ranges of geometrical parameters of the analyzed joint. It can be seen how the measured joint differs slightly from the theoretical geometry (see par. 1.3.1) mainly due to manufacturing constraints and adaptation of dimensions during the assembly phase.

During testing the joint is subjected to cyclic loading produced by a servo hydraulic MTS actuator (cylinder) with a capacity of 25 kN, connected to a steel frame. The rotational response of the joints is measured indirectly by means of the potentiometer Megatron SPR 18-S-100 (5kΩ).

During the session the displacement of beam 2 is recorded to be ±10 cm. The controlled amplitude of such displacement is increased at every cycle with a constant step equal to 4 mm. The frequency of each cycle is equal to a value of 0,1 Hz.

2.2.2 Determination of material properties

Specimens of dimensions 30x30x30 mm were cut from the unloaded sections of the tested beam. Compression was applied by using standard testing machine with constant strain rate 0,0002/s. The magnitude of such loading conditions and the related sample responses are shown in Fig. 4.

Unfortunately a number of constraints derived from the nature of the empirical analysis precluded an exact determination of all those coefficients needed for modeling the orthotropic nature of wood (E_x, E_y, E_z, G_{xy}, G_{yz}, G_{xz}, μ_{xy}, μ_{yz}, μ_{xz}). Therefore material parametric values available in the literature, typical for the type of wood tested, are integrated in the implementation of the model (Požgaj et al., 1997). Although measured data reflect partially the general trend presented in the bibliographical references (E_x:E_y:E_z=27:2:1) the absolute values obtained during testing considerably diverge to standard ones outlined in *Picea abies* (possibly due to 250 years old dry state of specimen). The approach pursued, which will be described in greater detail in the next sections, consists in scaling the unknown parameters G_{xy}, G_{yz}, G_{xz}, μ_{xy}, μ_{yz}, μ_{xz} accordingly to the ratio between measured Young's moduli and theoretical values (Tab. 1.). The axes considered during modeling are respectively XYZ ~ LRT.

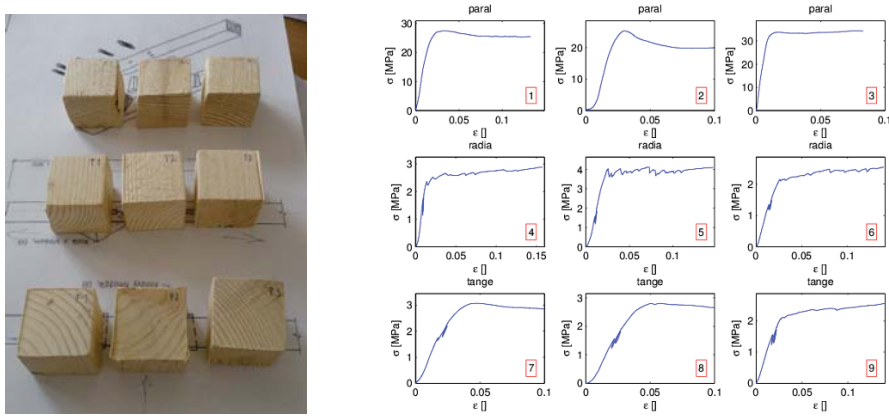

Fig. 4. The samples of old wood tested (parallel to grain/longitudinal, radial, tangential orientation of annual rings)

It is important to underline that the results of testing are strongly influenced by the location of the specimen's cube in the original beam and its orientation. The number of annual rings in the cross-sectional area also show to have a certain impact on the measured moduli. In order to overcome this interference and as there exist the methodological need to model the wood as a continuum these values were averaged to the mean number of annual rings.

Tab. 1. Material properties used in the modeling of the timber joint [MPa]

E_x	E_y	E_z	G_{xy}	G_{yz}	G_{xz}	μ_{xy}	μ_{yz}	μ_{xz}
2180	186	92	92	12.5	150	0.023	0.014	0.687

2.2.3 Experiments for contact adjustment

In order to appropriately determine the contact adjustment, the wood was tested by the following (see Fig. 5):

a) a 25x25mm steel cube pressing the sample

b) a 30x30x30mm timber cube (30x30x30 mm) cut from the historical material available is pressed against a wood joist. Orientation of fibers is set to be longitudinal pressured to radial orientation of joist.

In these experiments force-deflection curves are recorded.

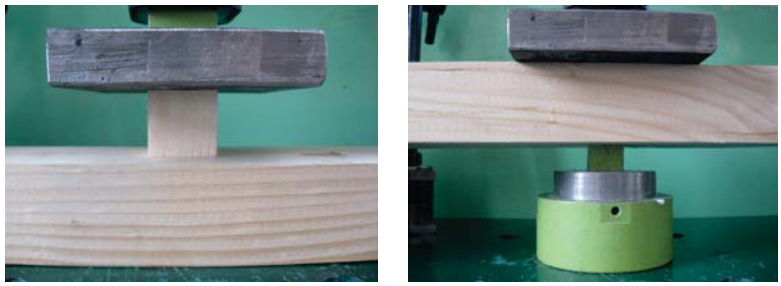

Fig. 5. Contact experiments

2.3 Numerical modelling

2.3.1 Model description

The FE model is built by using ANSYS finite element software. For simplification of the problem and in order to avoid continuous divergent solutions only few elements were considered. The quadratic SOLID95 hexahedral element type was chosen. The model is shown in Fig. 6.

It has to be noted that the timber dowel shown on the tested joint is not considered in modeling for the following reasons:

- the paper focuses on investigating the role of generic geometric parameters of the dovetail joint. The presence of the dowel, by further restricting localized movements, would produce deformations with plastic/cracking behavior, which falls outside the concern of this preliminary study on wood.
- the validation of the proposed model is mainly based on bending and in this perspective the role of the dowel would not have considerable significance.

The model presents orthotropic material properties without plasticity because of lack of experimental data about plastic behavior along the tested sample (results from the material testing are valid only on the continuum level, however, locally will be probably the deformations higher near the jaws). All the DOFs are removed according to those of the tested joint (see Figs. 2 and 6). Three types of loading are considered: tension compression and bending. The parameters varied for the purpose of this study were the two angles *(α,β)* shown in Fig. 2, which mostly influence the behavior of the structure under loading. Static friction between the beams was set to be 0.5. A 2mm gap between the two beams of the joint was also modeled.

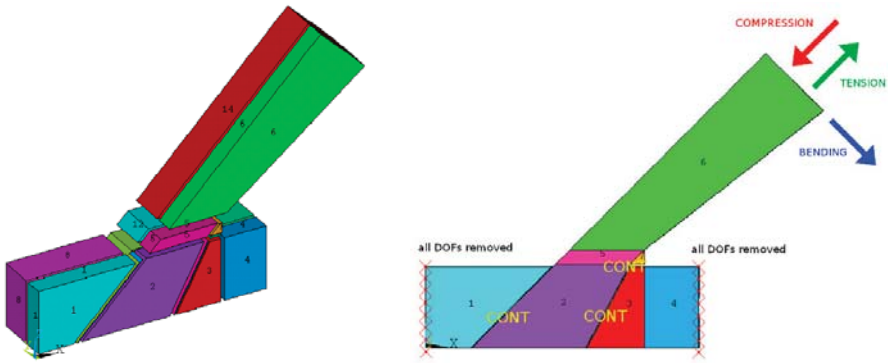

Fig. 6. The finite element model of the joint (left), loading and contact description of the joint (right)

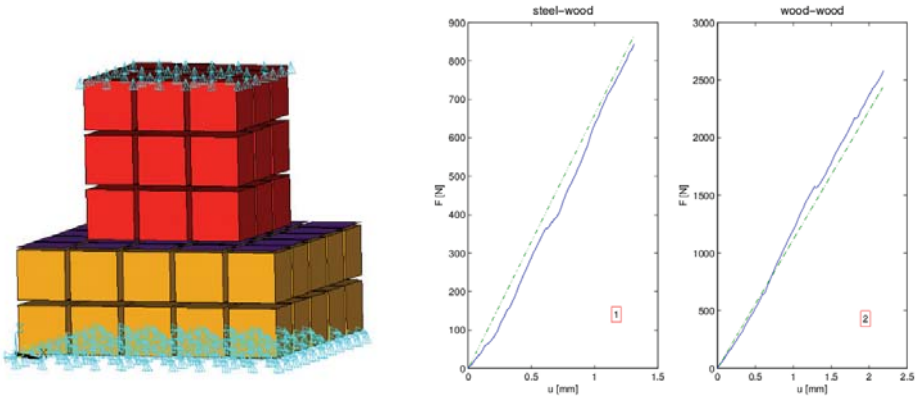

Fig. 7. Contact model – shrinked elements (left), contact validation results (right)

2.3.2 Contact adjustment

To understand well the behavior of contacts between the beams under static conditions, an additional simple FE model was created (see Fig. 7). Surface to surface contact was chosen for the analysis using quadratic contact elements CONTA174 and TARGE170. Augmented Lagrangian formulation of the contact was used with some additional adjustment of the contact parameters. Contact elements were precisely inserted between the 3D elements and node positions were carefully reviewed. The comparison between numerical model and experiments was shown in Fig. 7. The first section of the graphs, representing the state before cracking the tensioned top grains of the joist was neglected (because this phenomenon was not considered in the numerical modeling). The contact behavior was considered to be relatively precise and was applied to the dovetail joint model (see Fig. 6 CONT).

3. Results

3.1 Validation

The model was loaded in bending as per the above mentioned joint test. As discussed before the role of the dowel was considered to be negligible for this type of loading. Comparison between the results from experimental measurement and numerical computations is presented in Fig. 8. It stems out that the bending stiffness of the numerical model is higher than that of the measured joint. However such discrepancy can be justified by considerations of different nature:

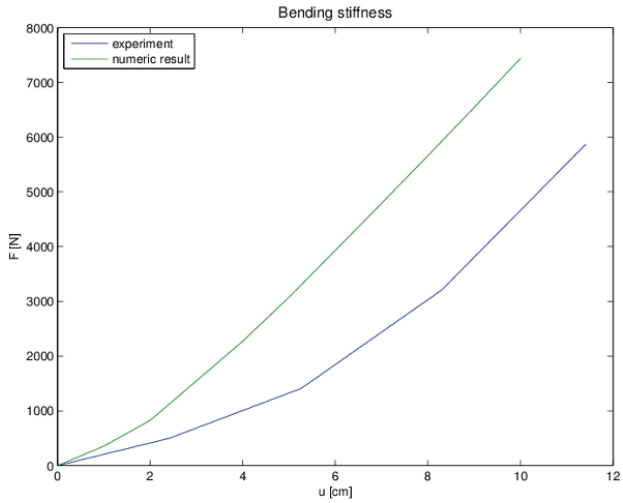

Fig. 8. Comparison between numerical model and experimental data

- the problem cannot be exactly modeled because of the heterogeneity of wood and the lack of an appropriate number of material testing
- model does not consider the drying cracks that can be instead observed on the historical beam
- the simplified model pursued by this study does not purposely take into account the plasticity of wood
- the surface of the beams on the sides of the joint cuts is made using traditional techniques and therefore not completely planar
- cracking of wood heard during the experimental testing cannot be included in the numerical model

Because of these reasons it is possible to say, that the validation is not made in the meaning of preciseness, but in the meaning of the context. The paper is focused on determination of the role of the geometry of the joint and not on acquisition of precise numbers absolutely (it is, in fact, not possible using FE but only using a set of experiments).

3.1 Parametric study

In the parametric study the two angles (α,β) were varied in the range of α ranging from 30° to 70° with a step of 5°. β is varied from *actual* α+2°to α+22° with a step of 5°. The reason is clear – the dovetail should always have higher β angle than α angle. The tensile and compressive loading was applied in the axis of the loaded beam 2. Bending was always perpendicular to this axis. Results from the simulations are shown in Figs. 9-11.

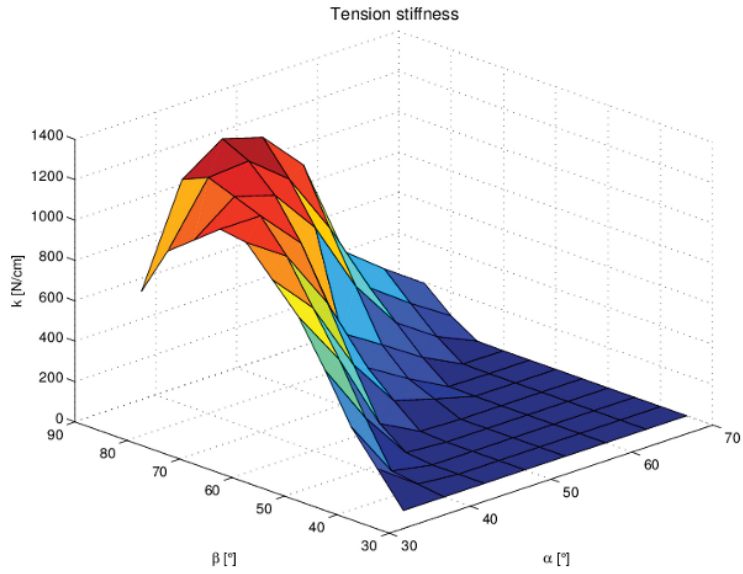

Fig. 9. Beam loaded in tension in axis of the beam 2

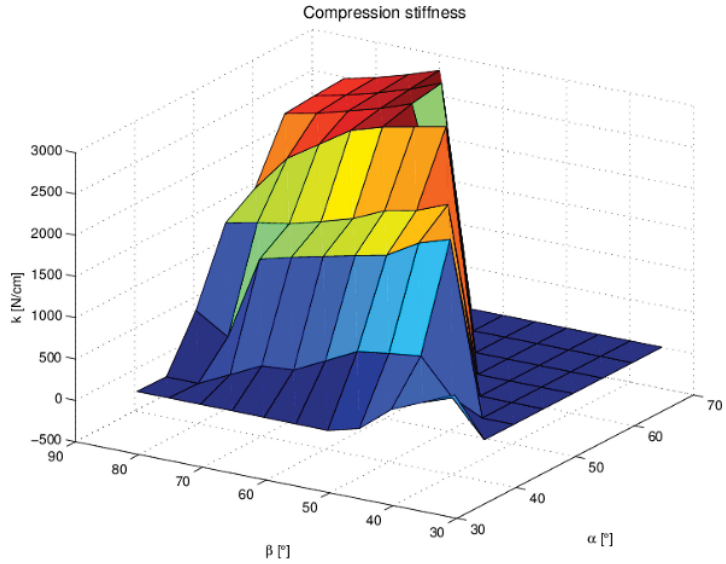

Fig. 10. Beam loaded in compression in axis of the beam 2

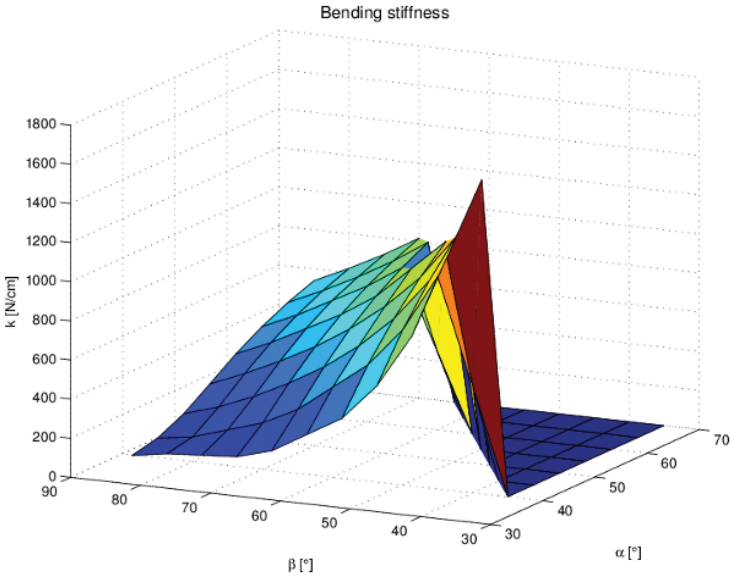

Fig. 11. Beam loaded inbending perpendicular to the axis of the beam 2

According to the computations made for beam two being loaded in tension, it is best to use 45° angle of the beam with nearly right angle β. For the compressive test, it is the best option to choose higher than 45° of angle α with small difference between the α and β. If the beam 2 is supposed to be loaded in bending it is good to choose only slightly higher β than α. The best solution is always based on the function of the truss in the structure and should be chosen suitably.

5. Discussion and conclusion

Although the results show clear conclusions, they should be read with attention because of many limitations.

- It is clear that for compressive loading the worst values for 30° are caused mainly by the missing timber dowel that enables the structure to slide. The behavior with the dowel will be modeled in future studies already programmed, in order to improve the modeling of traditional joints.
- Compressive stiffness of the joint depends on the size of the hook (see Figs. 1, 2 and 6), probably more than on the geometry itself what clarifies the high stiffness when the angles are higher.
- Material uncertainty and the scaling of material parameters should be advocated: we were looking for trends more than absolutely precise solution. In the future more material samples from more locations of the beam will be measured and averaged. Because the values of Young's moduli are not so well correlated with the values from literature (although such old wood is not mentioned) it is possible, that an error in the measured data could be present. However, because all the measurements were made on the same machine (material, contact), the relative results of the work should be not invalidated.
- Drying - cracking problems will probably remain, however, more fresh wood will be used in the next models.

This preliminary study posed one big question: how precisely it is possible to model the mechanical behavior of traditional timber joints? The answer could be that it showed many uncertainties and unknowns in the modeling and showed the way for ongoing research.

Acknowledgement

The work was supported by a kind sponsorship of grant of Ministry of Culture # DF12P01OVV004 called „*Design and Assessment of Timber Joints of Historical Structures"*. It is also gratefully acknowledged the support of grant #DF11P01OVV002.

References

Burnet D.T. et al. (2003) - Structural properties of pegged timber connections as affected by end distance. Forest product journal, vol.53, p. 53-57, 2003.

Gerner M. (2003) – *Tesařské spoje*, GRADA Praha 2003, ISBN 80-247-0076-X

Požgaj A. (1997) – *Štruktúra a vlastnosti dreva,* PRÍRODA Bratislava 1997, ISBN 80-07-00960-4

Vinař J. (2010) – *Historické krovy: Typologie, průzkum, opravy*, GRADA Praha 2010, ISBN 978-80-247-3038-7

18th International Conference
ENGINEERING MECHANICS 2012
Svratka, Czech Republic, May 14 – 17, 2012

pp. 825–834
Paper #177

EARLY DEFECT DETECTION OF ACETABULAR IMPLANTS

D. Kytýř, O. Jiroušek, P. Zlámal, T. Doktor[*], I. Jandejsek [**]

Abstract: *The paper is focused on possibilities of modern X-ray detectors and micro-focus X-ray source for investigation of early degradation processes of acetabular implants. To simulate the most adverse activity (downstairs walking) a hip joint simulator was developed. The experimental setup was designed for cyclic loading of polyethylene acetabular cup implanted into the human pelvic bone and fixed by commercial polymethyl methacrylate bone cement. To predict the bone degradation numerical analysis of detailed three-dimensional model of the acetabular cup and the cement mantle implanted in a bone block was performed. Using large area flat panel detector and microfocus X-ray source it is possible to investigate micro-damage propagation and detect early defect in the bone-implant interface.*

Keywords: ***bone–cement interface, computed tomography, crack detection, hip simulator***

1. Introduction

Total hip arthroplasty has emerged as one of the most successful interventions in orthopaedics. In spite of the successful use of the total endoprosthesis there is still a number of problems connected with the artificially created co-existence and interaction between the bone tissue and the technical substances of the endoprosthesis. From an engineering perspective these must be designed with the sufficient mechanical strength and be able to endure the biological environment in which they are placed. In order to reduce the incidence of an implant failure, it is important that the entire system is fully characterized; from the anatomy of the joint and the biological response, through to the micro-structure of the material and the design geometry.

Micro-motions and consecutive loosening of the acetabular implant is one of the most serious therapeutic complications which often occurs several years after the implantation. Worldwide experiences demonstrate that $80\,\%$ of all revised endoprosthesis are damaged by the aseptic loosening. The important part in the this process is remodelling of bone tissue as a result of the change of the stress field after the implantation. Living bone tissue is continuously in the process of growing, strengthening and resorption; a process called bone remodelling. Initial cancellous bone adapts its internal structure by trabecular surface remodelling to accomplish its mechanical function as a load bearing structure. In the case of cemented acetabular implants the remaining cartilage is removed from the acetabulum and the shape is adapted to the original one by means of a spherical milling machine. With this procedure a roughly spherical bed is obtained. The size and character of the contact stress distribution in subchondral bone influences the cement mantle degradation and the primary stability of the implant.

2. Materials and methods

To determine the degradation caused by cyclic mechanical loading radiological investigation have been used. Cement layer degradation were investigated using using hip simulator. To predict the bone degradation numerical analysis of detailed three-dimensional model of the acetabular cup and the cement mantle implanted in a bone block was performed. Image data from μCT were used to reconstruct the complex geometry of the inner structure of the trabecular bone and the interface between the pelvic bone and the implant. Visualization of trabecular bone structure and cement layer changes (damage accumulation) provided information about implant instability progress.

[*]Daniel Kytýř, Ondřej Jiroušek, Petr Zlámal, Tomáš Doktor: Institute of Theoretical and Applied Mechanics AS CR, v. v. i., Prosecká 76, 190 00 Prague 9, email: {kytyr, jirousek, zlamal, doktor}@itam.cas.cz
[**]Ivan Jandejsek: Czech Technical University in Prague, Institute of Experimental and Applied Physics, Horská 3a/22, 128 00 Praha 2 email: jandejs@itam.cas.cz

2.1. Hemipelvic bone specimen

The experiments and measurements were carried out using wet anatomical specimen of a hemipelvic bone from female donor. With regards to microtomography device detector size it was necessary to cut down the specimen to fit the detector. The bone was resected in ischial, pubic and iliac part; the acetabular area remained intact. Cemented acetabular cup with its rim made of ultra-high molecular weight polyethylene (UHMWPE) was implanted. For proper function of the cup and its fixation was essential that the layer of cement was equally strong across the interface between the surface of a polyethylene cup and machined acetabulum. Well compression into a bone bed and the grooves on the surface of the cup obviated case rotation and movement of the implant. The implantation procedure depicted on Fig.1 consists of four basic steps:

- After removal of large boundary osteophytes was acetabulum emended by rasper cutter at an angle of $45\,^{\circ}$ from the longitudinal axis of the patient
- Customized acetabulum was drilled to make a anchor slots for the bone cement
- The bone cement was formed into a shape of acetabular cup. The cap was placed and fixed. Horizontal declination of the cap from the frontal plane was $45\,^{\circ}$ The centration was facilitated by horizontal support arm of cap loader, which is parallel to the operating table and the longitudinal axis of the patient.
- Final location of the implant was checked using protractor on the vertical arm.

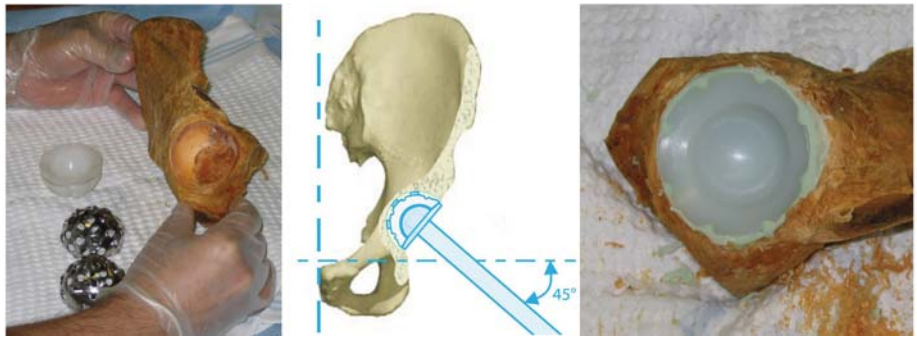

Fig. 1: Acetabular component implantation procedure

2.2. Bone specimen for material testing

Knowledge of material properties is a prerequisite to perform mechanical analysis, especially in case of numerical simulations. There is a very wide range of trabecular bone material properties ($E = 0.1 - 4.5\,\mathrm{GPa}$) reported in literature, see Dalstra (1993) and Hanson (2004), almost no correlation between the Young's modulus and anatomical location. To obtain mechanical properties of the trabecular bone time-resolved X-ray microtomography described in Jirousek & Zlamal (2011) and Digital Volume Correlation (DVC) presented by Jirousek & Jandejsek (2011) was employed.

Regard to the cancellous bone microstructure composed of trabeculae (approximately with length $1000\,\mu\mathrm{m}$ and thickness $150\,\mu\mathrm{m}$) the sapmle $12\,\mathrm{mm}$ high and $10\,\mathrm{mm}$ in diameter was drill out from proximal femur.

Special loading device was designed for this purpose. The frame of the device was made from plastic material with very low absorption of X-rays. The sample was fixed in an cylindrical chamber and loaded. The incremental loading with $100\,\mu\mathrm{m}$ increments up to $10\,\%$ deformation was applied in the experiment. The loading device was mounted on a rotational table and placed between the X-ray source and detector. Microfocus X-ray source L8601-01 (Hamamatsu Photonics K.K.)was used together with X-ray detector

Medipix-2, see Jakubek (2007), for the imaging. The detector chip is equipped with a single common backside electrode and a front side matrix of electrodes. The active area of the detector with $55\,\mu\mathrm{m}$ pitch provides images with resolution $256 \times 256\,\mathrm{px}$.

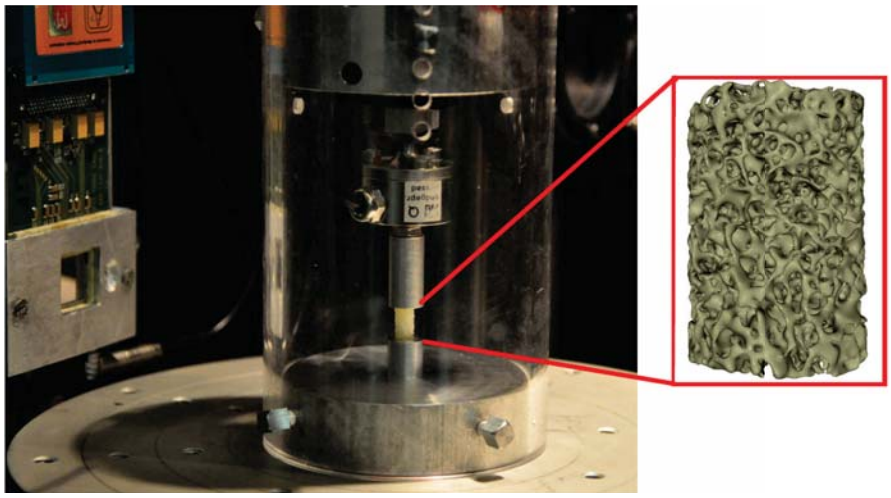

Fig. 2: Detail of loading device placed between X-ray source and detector with reconstructed specimen based on μCT data

DVC is a novel technique for 3D strain and deformation measurements across entire material volumes can be described in four steps: (i) control points in which the displacements will be tracked are defined in the image data, (ii) image correlation is performed in a $20 \times 20 \times 20\,\mathrm{px}$ image subvolume around the control point, (iii) displacement of each of the control points is computed by minimizing the 3D correlation coefficient by using nonlinear optimization techniques, (iv) the strains are computed from the established displacements and of the control points and overall mechanical properties ($E = 0.853\,\mathrm{GPa}$) are obtained.

2.3. Numerical analysis

To obtain a better information about stress distribution during the gait cycle (one step) and location of early defect regions the numerical simulation was performed. Finite element model of acetabular socket with cement layer and acetabular component was developed. The gait analysis (downstair gait cycle) consists of sequence of 20 loadsteps.

2.4. Model development

Based on implant manufacturer (Beznoska s.r.o.) datasheed detailed geometrical model was created. Four separately components was modeled. Femoral component was modeled as a spherical head with ($\oslash D = 32\,\mathrm{mm}$) and the cylindrical neck. Acetabular implant with inner diameter $32\,\mathrm{mm}$and outer diameter $49\,\mathrm{mm}$ was modeled with all construction detail without any simplification. The cement layer was created as a imprint of the implant and one surface and hemisphere at other side. The thickness of mantle was $3\,\mathrm{mm}$. This layer was surrounded by cylindrical socket bone socket.

10-node tetrahedral elements was chosen for meshing of all components because of the thin geometry and small radius of the cement mantle model. The simulation was assumed to be quasistatic, divided in 20 loadsteps. The loading force value and the direction of downstair walking in each load step was measured by Bergmann (2001). The contact was used for more accurate force transmission to the pelvis. The model was constrained by fixation of all degrees of freedom at the bottom part.

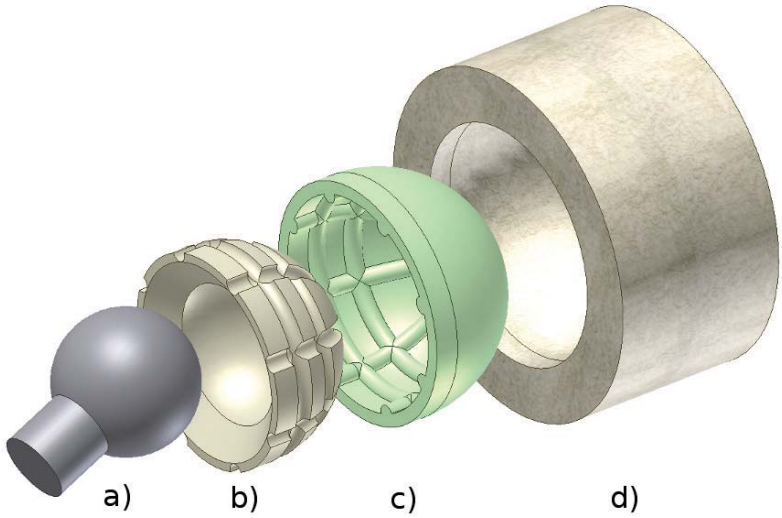

Fig. 3: Hip replacement CAD model composed of a) femoral component b) acetabular component c) cement layer d) bone socket

2.5. Contact definition

In accordance with Ansys modeling approaches, surface-to-surface contact was defined between head and acetabular component. Elastic modulus of steel femoral part was more than three hundred times higher than plastic cup; therefore the rigid-to-flexible method was used. The head and the inner hemisphere of the cup was meshed by special elements to model the femoro-acetabular interface. Both types of contact elements were second-order 8-nodes. For rigid-to-flexible contact designation the target surface is always the rigid surface and the contact surface is always the deformable surface. Contact elements are constrained against penetrating the target surface. However, target elements can penetrate through the contact surface. To ensure a proper function of the contact it is necessary that all contact and target element normals have opposite direction. Friction between the femoral head and the acetabular cup was neglected. For better numerical stability the femoral and acetabular component was connected by very flexible spar elements with no influence to stress distribution in pelvis.

2.6. Used materials

Material properties are described in Tab. 1. All materials were considered as isotropic linear elastic. Trabecular bone material properties were obtained by experimental measurement, the properties of the stainless steel, UHMWPE (ISO 5834 -2) and the bone-cement Palacos R (Heraeus Medical, GmbH) were provided by the manufacturers.

Tab. 1: Material properties

Material	Young's modulus [GPa]	Poisson's ratio [-]
Stainless steel	220	0.30
UHMWPE (ISO 5834 -2)	0.69	0.46
Bone cement	2	0.38
Trabecular bone	0.853	0.25

2.7. Numerical analysis results

In the Fig. 2.7. von Mises stress field distribution in the bone-cement interface during one step is depicted. At 20 % of the gait cycle the maximum stress 12.48 MPa was reached in area of the acetabular labrum. In this region the risk of potential damage is expected.

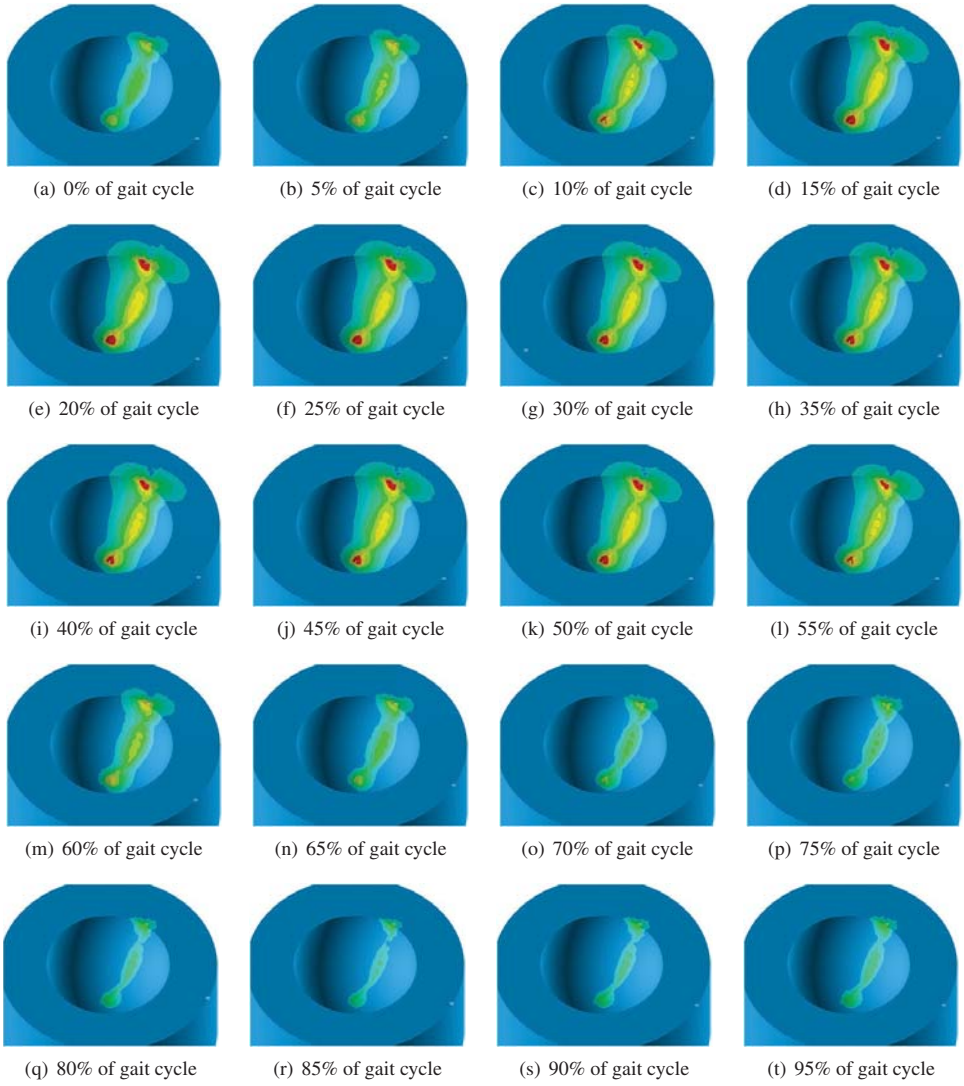

(a) 0% of gait cycle (b) 5% of gait cycle (c) 10% of gait cycle (d) 15% of gait cycle

(e) 20% of gait cycle (f) 25% of gait cycle (g) 30% of gait cycle (h) 35% of gait cycle

(i) 40% of gait cycle (j) 45% of gait cycle (k) 50% of gait cycle (l) 55% of gait cycle

(m) 60% of gait cycle (n) 65% of gait cycle (o) 70% of gait cycle (p) 75% of gait cycle

(q) 80% of gait cycle (r) 85% of gait cycle (s) 90% of gait cycle (t) 95% of gait cycle

Fig. 4: von Mises stress distribution in the bone-cement interface during the normal walking cycle

2.8. Fatigue testing

New hip joint simulator was designed to allow fatigue testing of the sample of pelvic bone with implanted cemented acetabular component. The simulator was designed as an accessory for Instron 1343 (Illinois Tool Works, Inc.). Fatigue tests were carried out using servo-hydraulic loading device. The force-driven loading had a sinusoidal run. The hip contact force of required direction and magnitude was applied to the implant using spherical femoral component head.

According to hip contact forces measurement presented by Bergmann (2001) mean value 1300 N and amplitude 1000 N (the peak value of the contact force corresponds to 260 % of body weight) were chosen to simulate the most unfavorable activity (downstairs walking).

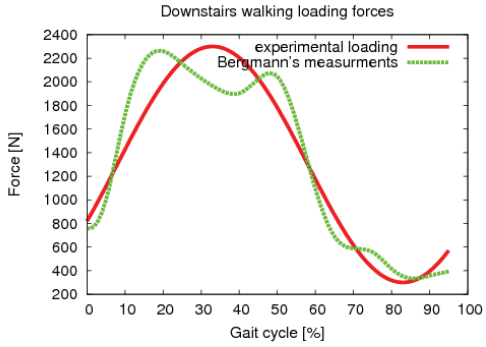

Fig. 5: Comparison of measured hip contact force and experimental loading

The correct position of the bone with the implant and loading force direction was fundamental. Bergmann (2001) measurements and setup of experiments carried out in University of Portsmouth were used. The implanted hemipelvis was mounted onto the loading device for $-8\,^{\circ}$ on the sagital plane and $-32\,^{\circ}$ on the transverse plane.

Lewis (2003) tested the effect of loading frequency on the fatigue live of acrylic bone cement. Usually, the experiments are performed with 1 Hz frequency to simulate normal walking. Various types of bone cement specimens were tested by compression test with 1 Hz and 10 Hz frequency. The main conclusion of this study was that the obtained results support the hypothesis that the test frequency (over the range used) does not exert a statistically significant effect on the fatigue live of the cements. According to possibilities of the loading device 4 Hz frequency was chosen for the test.

Fig. 6: The hip simulator

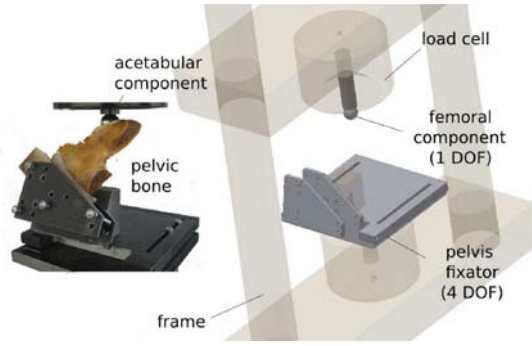

Fig. 7: Design of the hip simulator in detail

The experiment ran for eight hours per a day, that means approximately 115,000 cycles a day. The bone was moistened by saline solution to simulate the physiological conditions during the testing. The temperature in the laboratory was about 25 °C. Between the testing periods the bone was stored in the freezer with temperature $-15\,^{\circ}$C. Following Grasa (2005) prediction and results of numerical analysis described in section 2.7. the number of loading cycles before imaging with 25 % probability of damage was estimated to 250,000.

2.9. Tomography

High resolution micro-focus X-ray computed tomography (μCT) was used in the investigation of changes in the cement layer cement-bone interface and the actual trabecular bone at the microscopic level. The process of damage accumulation was monitored by repeated scanning. Imaging was performed four times a sample. First the pelvis resected by the dimensions of the corresponding size of the detector with intact acetabulum was scanned. After that the joint replacement was implanted and re-imaged. A quarter of a million load cycles were applied to the pelvis at the hip simulator. After this time some initialization damage of cement could be expected, therefore another scanning has been done. After 300,000 load cycles the pelvis damage was seen with the naked eye, therefore the loading test was completed and final imaging was done.

2.10. Microtomography measurement

To acquire the radiograph of acetabular region microtomography device in detail described in Jakubek (2006) was used. Manipulation with X-ray source, rotation table with specimen and detector was motorized. Stepper motors controlled by Pixelman software plug-in was employed.

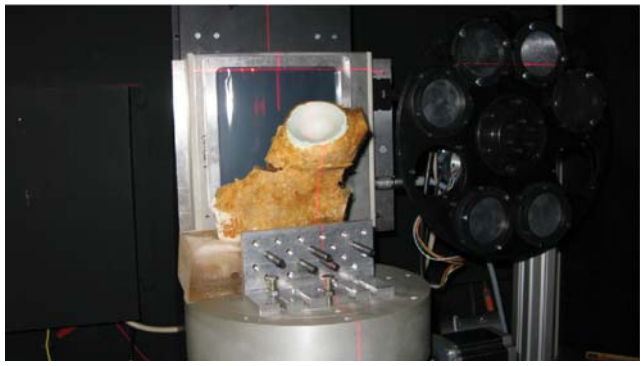

Fig. 8: Pelvis radiogram acquisition using microtomography device

Sequence of 360 projections with $1\,^{\circ}$ step was acquire using microfocus X-ray source and flat panel detector. Specimen was irradiated using X-ray source L8601-01 (Hamamatsu Photonics K.K.) with emission spot of $5\,\mu\mathrm{m}$. Large area ($120 \times 120\,\mathrm{mm}$)X-ray detector C7942CA-22 (Hamamatsu Photonics K.K.) allowed to obtain image data with resolution up to $2368 \times 2240\,\mathrm{px}$.

To minimize time of scanning the maximal power of the source (voltage $80\,\mathrm{kV}$ and current $125\,\mu\mathrm{A}$) was set. This ratio provide maximal signal to noise ratio in the radiograph. To other improvement of image quality 10 times $0.5\,\mathrm{s}$ acquisition was performed.

2.11. Corrections

Calibration measurements have been held for the noise reduction. Flat field (FF), dark field (DF) and beam hardening (BH) and correction were performed. FF corection (scanning without specimen) reduce the inhomogeneity across the chip. DF correction (scanning with disconnected source) avoids radiation background. BH correction, see Vavrik (2009), was performed to obtain equivalent absorbing characteristic.

2.12. Reconstruction

Tomographic reconstruction is a process which relies on mathematical algorithms to estimate the distribution search space based on 3D projection of 2D data and provides layers (slices) distribution. The sequence of corrected projections were used for object reconstruction. The image reconstruction procedure is based on Filtered Backprojection and Fan beam reconstruction algorithms.

2.13. Specimen visualization

High resolution models based on a sequence of 1100 slices with resolution $2368 \times 2240\,\mathrm{px}$ and $16\,\mathrm{bit}$ color depth were developed to investigate implant degradation during the loading. Projections obtained by μCT imaging were visualized using μCTvis&modeller software, see Vavrik (2011). A visualization of the whole specimen with implanted acetabular component from three different direction before mechanical testing is depicted in Fig. 9. A direct volume rendering technique was used for this purpose.

Fig. 9: Reconstructed acetabulum from different views

3. Results and discussion

A visualization of the damage propagation is shown in 10. There is intacted specimen on the left side. In the middle part the on the pelvis after 250,000 loading cycles crack propagation in trabecular bone structure (marked by the red rectangle) is clearly visible. On the visualization after 300,000 cycles depicted in the right part the crumbled cement particles are identified in green bordered area and cement mantle debonding is marked by the blue rectangle. All these three observed types of damage negatively influence stability of the implant.

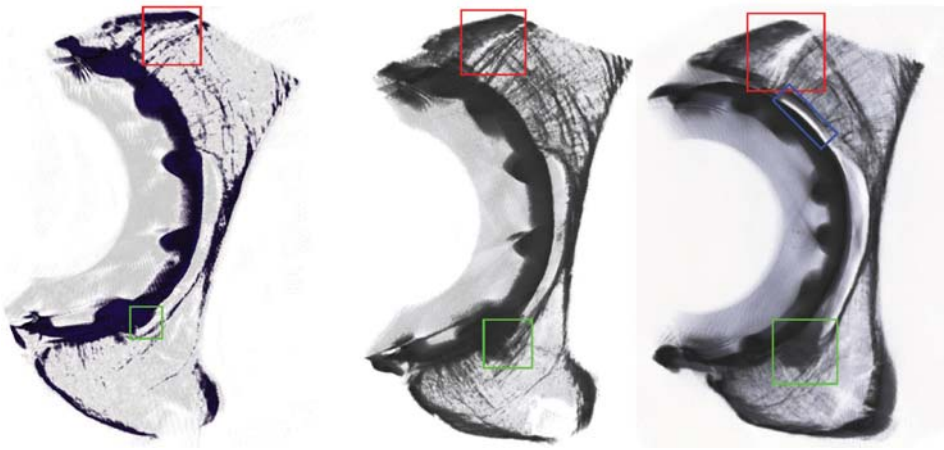

Fig. 10: Damage propagation in the bone structure and cement mantle

In accordance with the results obtained by the FE analysis – stress field with its maximum in region of acetabular labrum – the crack is observable in the same region.

3.1. Model accuracy

The accuracy of the reconstructed model depends on the input data and the reconstruction method. Radiograms could be improved by longer time of radiation. The quality of the reconstructed slices could be improved considerably by increasing the number of projections from 360 to 720 or 1440 in case of $360\,^\circ$ tomography. Using cone beam (inclusion of 3D beam divergence effect) results in better data but the required PC-time is not balanced by improvement of model accuracy. Longer radiation and higher number of projections was disapproved because the the X-ray source was loosing its stability with long time of radiation exposure. The other problem with higher number of projections was the hardware limit. The data matrices were exceeding the capacity of the RAM memory of all available computers. Therefore the accuracy of the reconstruction is optimal with respect to the available devices.

4. Conclusions

The aim of the research was to investigate the cemented bone–implant interface behavior (cement layer degradation and bone-cement interface debonding) with an emphasis on the techniques suitable to detect the early defects in the cement layer. The failure of total hip joint replacement was described in this work by the method combining of material testing, numerical simulation, ex vivo experiments and radiological imaging. Mechanical tests were carried out to obtain mechanical properties of trabecular bone and to compare these measurement procedures. Assessed material properties were used in numerical simulations.

The numerical analysis was performed to predict the degradation of acetabular replacement fixation. Detailed three-dimensional finite element model of the acetabular cup and the cement mantle implanted in a small bone block was developed. The analysis of the gait divided in 20 loadsteps ascertained stress field distribution at the bone-cement interface during the gait cycle. The places of maximum value of von Mises stress were in the acetabular labrum for all load steps considered. The place of maximum stress value corresponded well with the place where the initial crack occurred in the experiment. The performed experiments approved accuracy of the numerical model.

To simulate in vivo conditions a polyethylene acetabular cup was implanted into the human pelvic bone using commercial polymethyl methacrylate bone cement. The implanted cup was then loaded in a custom hip simulator to initiate fatigue crack propagation in the bone cement. The pelvic bone was then repetitively scanned in a micro-tomography device. Reconstructed tomography images showed failure processes that occurred in the cement layer during the first 300,000 cycles. Using large area flat panel detector and microfocus X-ray source it is possible to investigate micro-damage propagation in the bone-implant interface.

Presented hybrid experimental–numerical approach allow successful monitoring of cemented hip joint replacement degradation. Particularized three-dimensional finite element model of the acetabular cup and the cement mantle in a small bone block was developed. Numerical analysis was carried out and from stress distribution during gait cycle number of cycles with $25\,\%$ damage probability was estimated. Material properties of the trabecular bone in this model was obtained from mechanical tests. The implanted cup was then loaded in a custom hip simulator to initiate fatigue crack propagation in the bone cement. The crack propagation and debonding was observed using transmission radiography. The replacement degradation was observed at the place predicted by numerical model.

Acknowledgments

The research has been supported by RVO: 68378297, by the Grant Agency of the Czech Republic (grant No. P105/10/2305) and Ministry of Education and Sports (research plan No. MSM6840770040).

References

Bergmann G., Deuretzbacher G., Heller M.O., Graichen F., Rohlmann A., Strauss J. and Duda G.N. (2001), Hip contact forces and gait patterns from routine activities. *J. Biomech.*, Vol 34 No.7, pp 859–871.

Dalstra M., Huiskes R., Odgaard A. and van Erning L. (1993), Mechanical and textural properties of pelvic trabecular bone. *J. Biomech.*, Vol 26, No.4-5, pp 523–535,

Grasa J., Perez M.A., Bea J.A., Garca-Aznar M.J, and Doblare M. (2005), A probabilistic damage model for acrylic cements. Application to the life prediction of cemented hip implants. *Int. J. Fatigue*, Vol 27, No.8, pp 891–904.

Hanson N.A. and Bagi C.M. (2004), Alternative approach to assessment of bone quality using micro-computed tomography. *Bone*, Vol 35, No.1, pp 326–333.

Jakubek J. et al. (2006), Experimental system for high resolution X-ray transmission radiography, *Nucl. Instrum. Meth. A* Vol 563, No.1, pp 278–281.

Jakubek J. (2007), Data processing and image reconstruction methods for pixel detectors, *Nucl. Instrum. Meth. A*, Vol 576, No.1, pp 223–234.

Jirousek O., Zlamal P., Kytyr D., and Kroupa M. (2011), Strain analysis of trabecular bone using time-resolved X-ray microtomography. *Nucl. Instrum. Meth. A*, Vol 633, No.S1, pp S148–S151.

Jirousek O., Jandejsek I. and Vavrik D. (2011), Evaluation of strain field in microstructures using micro-CT and digital volume correlation, *JINST* Vol 6, pp C01039

Lewis G., Janna S. and Carroll M. (2003), Effect of test frequency on the in vitro fatigue life of acrylic bone cement. *Biomaterials*, Vol 24, No.6, pp 1111–1117.

Vavrik D. and Jakubek J. (2009), Radiogram enhancement and linearization using the beam hardening correction method,*Nucl. Instrum. Meth. A* Vol 607, No.1, pp 212–214.

Vavrik D. et al. (2011) Advanced X-ray radiography and tomography in several engineering applications, *Nucl. Instrum. Meth. A* Vol 633, No.S1, pp S152–S155.

18th International Conference
ENGINEERING MECHANICS 2012
Svratka, Czech Republic, May 14 – 17, 2012

pp. 835–841
Paper #306

COLLISION OF A ROTATING SPHERICAL PARTICLE WITH FLAT WALL IN LIQUID

N. Lukerchenko[*], Yu. Kvurt[**], Z. Chara[***], P.Vlasak[****]

Abstract. *The collision of the rotating spherical particle with a flat wall in liquid was studied experimentally. The glass and steel beads rotating in water and silicon oil were used. A high-speed video system recorded the bead motion before and after the collision. It was shown that the restitution coefficient depends not only on the Stokes number but also on the particle angular velocity; the restitution coefficient decreases with increasing of the rotational Reynolds number and decreasing of the Stokes number. These results can be useful in modelling of the two-phase flows near solid boundaries.*

Key words: ***restitution coefficient, spherical particle, particle rotation, liquid viscosity.***

1. Introduction

The mechanisms of solid particles collision with a solid boundary or with other particles is a subject of interest for many years, especially in case of a two-phase flow, like processes of mixing in chemical reactors, slurry pipeline transport, pneumatic transport, bed load transport and erosion in channel, particle sedimentation, fluidization, filtering and suspension thickening.

The modeling of particle-particle or particle-wall collisions requires a detailed understanding of the mechanics of impact and rebound. The energy dissipation due to an inelastic contact is usually characterized by a coefficient of restitution e, defined as the ratio of the rebound velocity to the impact velocity (normal components)

$$e = | v_r / v_i |, \tag{1}$$

where v_i and v_r are the impact and rebound velocities, respectively, i.e. the velocity just before and after the collision. The coefficient of restitution characterizes the energy losses during collision; the initial kinetic energy is transformed into elastic strain energy stored in the bodies and then restored into kinetic energy of the rebounding particle (Ruiz-Angulo & Hunt, 2010).

Under negligible fluid resistance, in a fully elastic collision coefficient of restitution can be approximately unity, $e \approx 1$, whereas for a perfectly plastic collision $e = 0$. Coefficient of restitution is less than one for the most part of collisions, i.e. collisions with inelastic losses. Inelasticity of the collision is evoked by plastic deformation, viscoelasticity or vibration. Their effects lead to energy losses, which are dependent on the impact velocity, and coefficient of restitution decreases with impact velocity with power law with small exponents (Gondret et all., 2002).

Most of the known studies deal with so called dry collisions, i.e. collisions in vacuum or gas, where the fluid resistance is negligible. Only a few works take into account effect of fluid viscosity on the coefficient of restitution and collision process, but we have not found any study dealing with the effect of particle rotation. For collision of solid particles in liquid surrounding, the effect of liquid is important and the restitution coefficient is often named the effective restitution coefficient.

[*] Nikolay Lukerchenko, PhD.: Institute of Hydrodynamics of Academy of Sciences of the Czech Republic, v.v.i.; Pod Patankou 30/5, 166 12, Prague 6; CZ, e-mail: lukerchenko@ih.cas.cz
[**] Dr. Yury Kvurt, CSc.: Institute of Problems of Chenical Physics of Russian Academy of Sciences; Chernogolovka, Moscow reg., 142432 Russia, e-kvurt@icp.ac.ru
[***] Ing. Zdeněk Chára, CSc.: Institute of Hydrodynamics AS CR, v. v. i., Pod Pat'ankou 30/5, 166 12 Prague 6; CZ, e-mail: chara@ih.cas.cz
[****] Prof. Ing. Pavel Vlasák, DrSc.: Institute of Hydrodynamics AS CR, v. v. i., Pod Pat'ankou 30/5, 166 12 Prague 6; CZ, e-mail: vlasak@ih.cas.cz

Davies et all. (1986) declared, that the pertinent number for the collision is not the Reynolds number, but the particle Stokes number which compares the particle inertia to the fluid viscous forces

$$St = (2/9)\,\rho_p\,|\,U\,|\,r\,/\,\mu = (1/9)\,(\,\rho_p\,/\,\rho_f\,)\,Re, \tag{2}$$

$$Re = d\,U\,\rho_f\,/\,\mu, \tag{3}$$

where ρ_p is a particle density, ρ_f is a fluid density, r is a particle radius, μ is fluid dynamic viscosity, and is a Reynolds number based on the particle impact velocity U and particle diameter d.

Let us suppose that the particle shape is spherical, it moves in liquid and collides with a plane wall. The rebound of the particle after collision depends on the material of particle and the wall, on impact velocity and the restitution coefficient $e = e\,(St)$, which is a function of the particle Stokes number. For $St < St_c$, where $St_c \approx 10$ is a critical Stokes number, the effective restitution coefficient is equal zero, and no rebound occurs. The restitution coefficient increases with increase of the Stokes number, and reaches the maximum value when the Stokes number is about 2000 – 3000. In this region the restitution coefficient is close to the value of restitution coefficient determined for a collision in gas or in vacuum (Gondret et all., 2002).

2. Experimental equipment and procedure

The goal of the present work is to examine experimentally the effect of liquid viscosity and of particle rotation on the restitution coefficient of the spherical particle rebounding from a plane wall in liquid. Two series of experiments were conducted. In the first series it was proved, that particle impact with wall causes the particle rotation. The second series deals with effect of particle rotation on the restitution coefficient. The experiments were focused on determining trajectory of a solid sphere falling in water onto a plane glass wall and evaluation of the effect of liquid viscosity and particle rotation on the restitution coefficient.

Water and silicon oil were used as a liquid; viscosity of the oil was about 200 higher than that of water, what made possible to obtain different values of Stokes number. Smooth glass and steel spherical particles of diameter d = 14, 16, and 19 mm were used. Hairlines were drawn along two perimeters of the particle with the angle of 90° to make it possible to visualize the particle rotation. A sheet of glass of thickness 21 mm was used as impact surface.

The particle was rotated about a horizontal axis in a spinning device developed in the Institute of Hydrodynamics AS CR, v. v. i., situated above the water level (see Fig. 1). The particle was held between cups and rotated around with an initial angular velocity ω_0, which was measured by a tachometer. When the trigger was released, the springs pulled the cups apart, allowing the particle to fall freely in water. The spinning device ensured the required particle rotation in the given plane and translational velocity of the particle was reached by free fall of the particle (Lukerchenko et all., 2012). The device allowed to spin the particle up to 6 500 rpm (revolutions per minute).

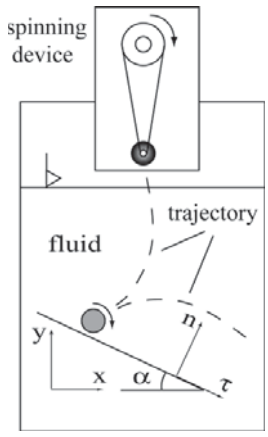

Fig. 1: Experimental setup.

Immediately before the collision the angular velocity becomes 1.5 – 2 times less than ω_0. After the collision with the wall, the particle rebounded and the combined translational and rotational motions were recorded with a frequency of 1000 frames per second by the digital video camera MotionPro X High-Speed CMOS Digital Camera. Only experiments in which the plane of the particle trajectory was parallel to the plane of the video camera objective were chosen. The software *MotionPro X Studio* was used for data processing.

3. Results and discussion

For example, in the case of bed load transport or multi-phase flows in chemical reactor, the motion of particles in fluid near solid wall results in the particle-wall collisions and, when the impact angel is not equal $\pi/2$, the sequent particle rotation. The particle angular velocity ω could reach values of a few tens or even hundreds of revolutions per minute during the particle saltation pattern. Let us now consider the spherical shape of a particle. The sphere rotation in fluid generates the secondary flow, the centrifugal effect will produce a swirling radial jet directed outward of the equatorial region of the sphere, which is reason for flow of fluid towards the poles in the direction of the axis of rotation. The pole-ward flow exert equal and opposite forces on each hemisphere so that the resultant force is zero in unbounded area. When the particle rotates around an axis parallel to the wall the presence of the wall generates forces in normal and tangential directions, which are functions of the rotational Reynolds number, particle relative distance from the wall, and relative roughness of the particle and the wall. In neighbourhood of a wall, the boundary destroys the symmetry around the particle and the particle becomes a subject of forces, which can dump the impact velocity, and in consequence decrease the restitution coefficient. The forces would affect motion of the particle, attract or repulse it when the particle moves towards the boundary. Small particle-wall gap would bring into play strong viscous effect, which causes repulsive forces (Liu and Prosperetti, 2010).

The value of the repulsive force depends on the angular velocity and roughness of the sphere surface. The larger roughness of the sphere surface gives the larger induced secondary fluid flow. In the case of a smooth sphere, the effect is noticeable for the large angular velocities only, whereas in the case of the rough sphere it can be observed even for the moderate or small angular velocity range. For the intensification of the secondary flow we used a golf ball with a rough surface (diameter d = 0.0428 m, mass m = 0.0458 kg). The glass wall was covered by the waterproof sandpaper and situated under angle of 25^0 to the horizontal vessel bed (see Fig. 1).

The main difficulty of data processing of the conducted experiments is that time of a collision duration is much smaller than the time period between two successive images ($\Delta t = 10^{-3}$ s) of the used camera. According to Gondret et all. (2002) the collision duration is typically 10^{-5} s (it was measured with a piezoelectric sensor). The values of the horizontal x and vertical y coordinates of two ends of a diameter (x_1 , y_1) and (x_2 , y_2) were obtained. The coordinates of the ball center (x_0, y_0) and the angle of the ball rotation φ were calculated as functions of time:

$$x_0\,(t) = 0.5[x_1\,(t) + x_2\,(t)\,], \tag{4}$$

$$y_0\,(t) = 0.5[y_1\,(t) + y_2\,(t)\,]; \tag{5}$$

$$\varphi\,(t + \Delta t) = \varphi\,(t) + \arccos\,[\boldsymbol{a}\,(t).\boldsymbol{a}(t + \Delta t)/d^2], \tag{6}$$

where

$$\boldsymbol{a}\,(t) = [x_2\,(t) - x_1\,(t); y_2\,(t) - y_1\,(t)\,] \tag{7}$$

is the vector coincided with the diameter. The dependences (4) – (6) were smoothed and then differentiated, and the translational and angular velocities immediately before and after the collision were calculated.

Fig. 2 shows the time dependences of the coordinates of the ends of the horizontal diameter (x_1 , y_1) and (x_2 , y_2) and of the ball center (x_0 , y_0) in the case without the ball rotation before the collision (ω_0 = 0). The slope angle of the plots allows us to define the components of the velocity of the ball center before and after the collision. As indicated in the picture the ball begins to rotate after the collision. The characteristics of the spherical particle motion before and after the collision for the experiments, where three different initial angular velocity ω_0 were used (ω_0 = 0; 4500, and 5200 rpm),

are given in Table 1. Immediately before the collision the angular velocity of the ball becomes 1.5 – 2 times less than the initial angular velocity ω_0 (Lukerchenko & Kvurt, 2011).

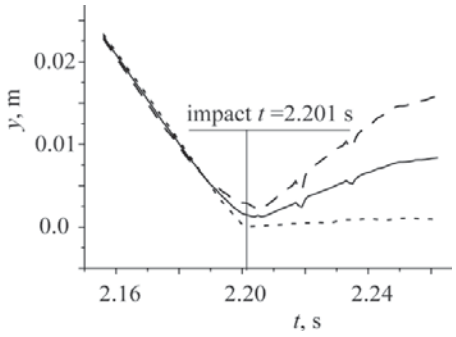

Fig. 2: Coordinates of the ends of the horizontal diameter (x_1,y_1) [- - -] *and* (x_2,y_2) [·····] *and of the ball center* y_0 [—] *versus time t before and after the particle impact* ($\omega_0 = 0$).

Table 1 shows that the maximum value of the restitution coefficient e is when the ball does not rotate before the collision ($Re_{\omega,r} = 0$). The rotational Reynolds number

$$Re_{\omega,r} = \omega \cdot r^2 \rho_f / \mu \tag{8}$$

is the dimensionless analogue of the angular velocity of a sphere. The larger angular velocity immediately before the collision corresponds to the smaller restitution coefficient. Based on these results, it can be conclude that the larger angular velocity immediately before the collision corresponds to the smaller value of the effective restitution coefficient.

Table 1: The characteristics of the ball motion before and after the collision.

No.	ω_0 [rpm]	$v_{i,n}$ [m/s]	$v_{r,n}$ [m/s]	e	St	ω_i [rpm]	$Re_{\omega,r}$
1	0	-0.39	0.27	0.70	1 850	0	0
2	4 500	-0.51	0.31	0.60	2 420	2 005	95 300
3	5 200	-0.75	0.35	0.46	3 570	3 065	145 500

Examples of experimental trajectories and velocity components for rotating glass spherical particle (diameter d = 16 mm) falling in water are illustrated in Fig. 3. The time between two successive images was $\Delta t = 10^{-3}$ s. Initial angular velocity $\omega_0 = 5\,800$ rpm, due to the pass through water level and drag in water the angular velocity just before the 1st impact was significantly less, only $\omega_1 = 3\,288$ rpm, and further $\omega_2 = 1\,846$ rpm, and $\omega_3 = 895$ rpm for the 2nd and 3rd impact, respectively. The three first impact and jump after the collision of the particle with horizontal glass plane wall were recorded.

The distance of the particle centre y_0 to the wall is displayed as a function of time t and of the horizontal coordinate x, respectively, in upper part of Fig. 3. The particle rotated in clockwise direction and due to the Magnus force its direction was downward and in negative x-axis direction. Both the trajectory in xy-plane and the record of $y_0 = f(t)$ show steady uniform motion before impact and gradual decrease of jump height due to the effect of the drag force and decreasing of the effective restitution coefficient. Interesting is effect of the particle rotation on change in x-direction during the first impact. The height of the jump gradually decreased in successive jumps on the contrary to length of the jumps.

The instantaneous particle velocity components in vertical (normal) and horizontal (tangential) direction were computed as the time derivative of the co-ordinate increment between two successive images, and the corresponding velocity components v_y and v_x were plotted as function of time in bottom part of Fig. 3, which illustrate character of velocity changes during collision. The values of velocity components just before and after collision (v_i and v_r, respectively) can be determined and used for the effective restitution coefficient e calculation, see Eq. (1). The particle vertical (normal) velocity component reached the maximum just before the first collision; during the individual jumps normal

velocity component reached very quickly maximum value and then gradually decreased due to drag of the surrounding liquid. This behaviour is, due to the viscosity of water, different from that of the particle in gas, where other forces than gravity are negligible. The jump trajectories are not parabolic.

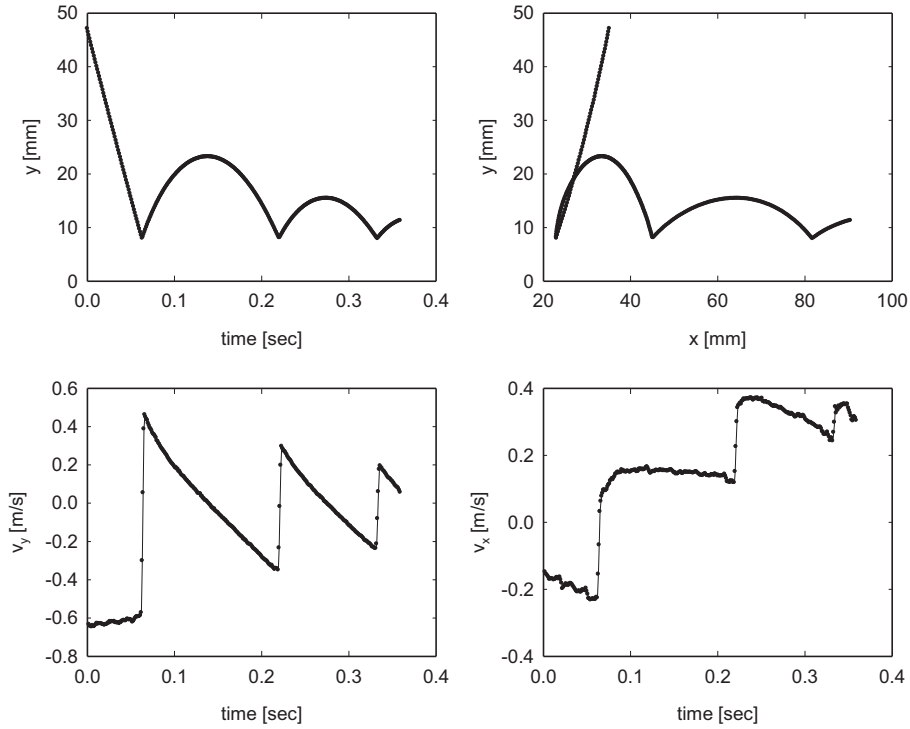

Fig. 3: Trajectories and velocity components of rotating glass spherical particle falling in water (diameter d = 16 mm, initial angular velocity ω_0 = 5 800 rpm).

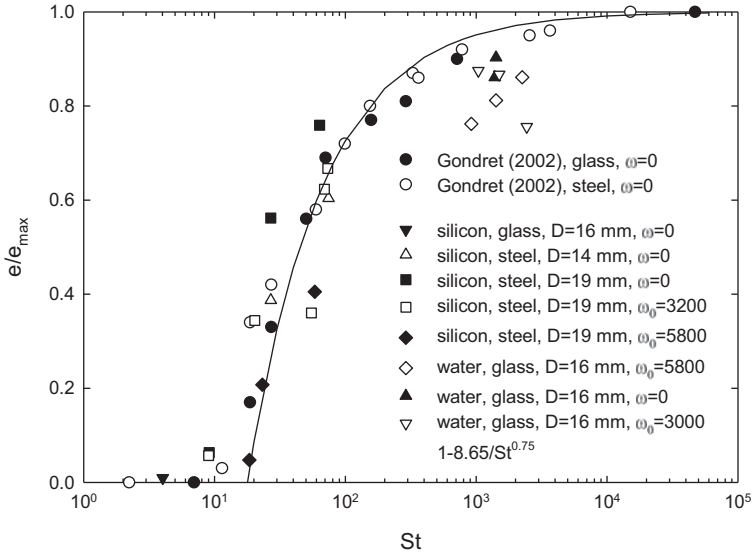

Fig. 4: Dependence of the dimensionless restitution coefficient *e/e_0 on the Stokes number St; comparison of present experiments with Gondret et all. (2002) results.*

The normal velocity decreased nonlinearly with time and its modulus was significantly smaller at the end of the jump than at the beginning. On the contrary, the tangential velocity increased after the particle collision due to the Magnus force.

As it was mentioned above, for particle impact in liquid the viscous effects are important, since the particle rebound depends on both, the plasticity and viscous losses. Fig. 4 shows the comparison of our experimental data of the restitution coefficient e with results of Gondret et all. (2002), Ruiz-Angulo & Hunt (2010). For current experiment water and silicon oil were used as liquid, smooth glass and steel spherical particles of diameter 14, 16, and 19 mm and resistant glass wall (of thickness 21 mm) was used as impact surface. The silicon oil of viscosity about 200 higher than that of water made possible to obtain results in region of low Stokes number with used particles of relatively large diameter. Fig. 4 shows that present experimental data of particles without rotation relatively well coincide with data from above mentioned literature. However, rotation of the particle entailed decreasing of the effective restitution coefficient. This finding is supported for instance by the data ◊ (glass particle in water, d = 16 mm, ω_0 = 5 800 rpm), which were also used for illustration of particle trajectories and velocity components in Fig. 3.

According to Ruiz-Angulo & Hunt (2010) the solid line

$$e/e_0 = 1 - 8.65/St^{0.75} \tag{9}$$

is the best fit of experimental data of experiments, which were conducted with no permanent deformation of either the impacted surface or of the particle (Joseph et all., 2001). The maximum coefficient of restitution e_0 is value measured with given particle and plane wall in air. This curve was used as a reference for elastic collisions, corresponding to the greatest possible value of the restitution coefficient at a given Stokes number (Ruiz-Angulo & Hunt, 2010). We can see that for low values of the Stokes number, below approximately St = 10, the particles did not rebound due to the viscous effect. For the relatively large Stokes number, i.e. $St > 10^3$, the viscous effect became negligible and the effective restitution coefficient reached the elastic limit, $e/e_0 = 1$.

For constant parameters of particle and carrier liquid the increase of the Stokes number depends on the impact velocity. In the Stokes number interval between St = 20 and St = 10^3, as the impact velocity increased, the energy consumed by plastic deformation increased and energy consummated to displace the fluid from area between particle and wall decreased. However, the used velocities did not cover the regimes of high impact velocities where the plastic deformation dominates the hydrodynamic effects.

4. Conclusions

The collision of the rotating glass and steel spherical particle with a flat wall in water and silicon oil was studied experimentally. It was conducted that the restitution coefficient depends not only on the Stokes number, but also on the particle angular velocity, the restitution coefficient decreases with increasing of the rotational Reynolds number.

It was confirmed, that the restitution coefficient increases with increase of the Stokes number, and reaches the maximum when the Stokes number $St > 10^3$, where the viscous effect became negligible and the restitution coefficient is close to the value of restitution coefficient determined for a collision in gas or in vacuum. For the Stokes number $St < St_c$, where $St_c \approx 10$ is the critical Stokes number, the effective restitution coefficient is equal zero, and no rebound occurs.

Acknowledgements

Support under the project No. 105/10/1574 of the Grant Agency of the Czech Republic and RVO: 67985874 of the Academy of Sciences of the Czech Republic are gratefully acknowledged. The authors are very grateful to Dr. Ibrahima Keita and Ing. Jiri Miles for the technical support of the experiments.

References

Davis, R.H., Serayssol J.-M. & Hinch E.J. (1986) The elastohydrodynamic collision of two spheres, *Journal of Fluid Mechanics*, 163, pp.479-497.

Gondret, P., Lance, M. & Petit, L. (2002) Bouncing motion of spherical particles in fluids. *Physics of Fluids,* 14(2), pp.643-652.

Joseph, G.G., Zenit, R., Hunt, M.L. & Rosenwinkel, A.M. (2001) Particle-wall collision in a viscous fluid, *Journal of Fluid Mechanics*, 433, pp.329-346.

Liu, Q. & Prosperetti, A. (2010) Wall effects on a rotating sphere, *Journal of Fluid Mechanics*, 657, pp.1-21.

Lukerchenko, N., Kvurt, Yu., Keita, I., Chara, Z. & Vlasak, P. (2012) *Particulate Science and Technology*, Vol. 30(1), p.55–67.

Lukerchenko, N. & Kvurt, Yu. (2011) Influence of a sphere rotation on the restitution coefficient for the collision in liquid, in: *Proc. 24th Int. Conf. Mathematical Metod in Engineering and Technology MMTT-24.* (V.V.Balakirev ed), Saratov State Technical University, Kiev (Ukraine), Vol.3., pp.20-23.

Ruiz-Angulo, A. & Hunt, M.L. (2010) Measurements of the coefficient of restitution for particle collisions with ductile surfaces in a liquid, *Granular matter*, 12, pp.185-191.

18th International Conference
ENGINEERING MECHANICS 2012
Svratka, Czech Republic, May 14 – 17, 2012

pp. 843–848
Paper #179

COMPUTATIONAL HOMOGENIZATION OF ACOUSTIC PROBLEM IN PERFORATED PLATES

V. Lukeš[*], E. Rohan[**]

Abstract: *We consider acoustic wave propagation described by Helmholtz equation and involving homogenized transmission conditions imposed along a thin perforated interface separating two halfspaces occupied by the acoustic medium. The homogenized transmission conditions are imposed on this perforated interface. The transmission conditions were obtained as the two-scale homogenization limit of the standard acoustic problem imposed in the layer perforated by a sieve-like obstacle with periodic structure. By using the sensitivity analysis we can solve the problem of an optimal design of the perforation to minimize the transmission loss in a domain embedding the interface. The perforated periodic structure is represented by a reference computational cell, whereby its geometry is controlled by the spline functions.*

Keywords: ***linear acoustics, homogenization, sensitivity analysis, transmission condition***

1. Introduction

Optimization of noise transmission in the acoustic fluid belongs to important merits of the acoustic engineering. Sieve-like structures are classical elements employed in noise-reducing devices. For example, in the exhaust silencers of the combustion engines the gas flows through ducts equipped with various sieves which in part may influence the transmission losses associated with acoustic waves propagating in the exhaust gas. In aerospace and automotive industry there are many applications related to acoustic waves and fluid flow where optimal design of the sieves (perforated slabs) is a challenging problem.

In the paper we deal with the acoustic transmission through a *perforated interface*, cf. Chen (1996); Bonnet-Bendhia and others (2005). The transmission conditions to be imposed on the interface plane were derived in Rohan and Lukeš (2010), using the asymptotic analysis. The limit model of an interface plane involves some homogenized impedance coefficients depending on the so-called microscopic problems; these are imposed in the *reference periodic cell* embedding an obstacle which represents the perforation. The two-scale modeling approach allows for an efficient treatment of complicated designs of perforations. The limit model was subjected to the sensitivity analysis in Rohan and Lukeš (2009). It resulted in the sensitivity formulas for the homogenized coefficients and we obtained the total variation of an objective function depending on the acoustic pressure w.r.t. the obstacle shape at the "microlevel".

An abstract optimization problem is formulated at three levels: at the "global" one the pressure field is controlled by an interface variable – the transversal acoustic momentum involved in the homogenized transmission condition; at the "homogenized interface" level, the interface variables are satisfy the non-local transmission conditions depending on the homogenized impedance parameters; finally, at the "microscopic level" these impedance (homogenized) parameters depend on solutions of auxiliary local problems featured by the shape of perforations.

2. Acoustic transmission through perforated interfaces

We consider the global problem of the wave propagation in a duct $\Omega \subset \mathbb{R}^3$ filled by the acoustic fluid. Ω is subdivided by perforated plane Γ_0 in two disjoint subdomains Ω^+ and Ω^-, so that $\Omega = \Omega^+ \cup$

[*]Ing. Vladimír Lukeš, Ph.D.: Department of Mechanics and New Technology for an Information. Society, Faculty of Applied Sciences, University of West Bohemia, Univerzitn 22, Plzeň, CZ, e-mail: vlukes@kme.zcu.cz
[**]prof. Dr. Ing. Eduard Rohan: Department of Mechanics and New Technology for an Information. Society, Faculty of Applied Sciences, University of West Bohemia, Univerzitn 22, Plzeň, CZ, e-mail: rohan@kme.zcu.cz

$\Omega^- \cup \Gamma_0$, see Figure 1 (obviously, much more general setting is possible). The acoustic pressure field p is discontinuous in general along Γ_0. In a case of no convection flow (the linear acoustics), the waves propagating in Ω are described by the following equations where κ is the wave number (i.e. frequency $\omega = \kappa c$)

$$\begin{aligned} \nabla^2 p + \kappa^2 p = 0 \quad & \text{in } \Omega^+ \cup \Omega^- \,, \\ \text{transmission conditions} \quad \mathcal{G}(\kappa, [p]^+_-, [\partial p/\partial n]^+_-) = 0 \quad & \text{on } \Gamma_0 \,, \\ r\mathrm{i}\kappa p + \frac{\partial p}{\partial n} = s2\mathrm{i}\kappa\bar{p} \quad & \text{on } \partial\Omega \,, \end{aligned} \tag{1}$$

where s, r and $\bar{p}$ are given data, $[\cdot]^+_-$ is the jump across Γ_0. $\frac{\partial p}{\partial n} = \boldsymbol{n} \cdot \nabla p$ is the normal derivative on Γ_0. The homogenized transmission conditions $\mathcal{G} = 0$ developed in Rohan and Lukeš (2010) introduce two internal variables on Γ_0: the "in-layer" acoustic potential p^0 and the "trans-layer" acoustic velocity g^0, which is coupled with the "off-layer" fields through: $\partial p/\partial n^\pm = \pm\mathrm{i}\kappa g^0$, so that $[\partial p/\partial n]^+_- = 0$. Boundary $\partial\Omega = \Gamma_w \cup \Gamma_{\mathrm{in}} \cup \Gamma_{\mathrm{out}}$ of the duct is split into walls and the input/output parts; by the constants r, s in $(1)_3$ different conditions on $\partial\Omega$ are respected: $r = s = 0$ on the duct walls Γ_w, whereas $r = s = 1$ on Γ_{in} and $r = 1$, $s = 0$ on Γ_{out}.

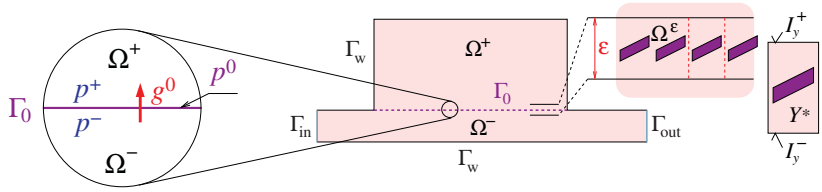

Fig. 1: Left: illustration of the transmission coupling – the acoustic pressure jump is proportional to the transverse acoustic velocity g^0. Center: the domain and boundary decomposition of the global acoustic problem considered. Right: perforated interface and the representative periodic cell $Y = Y^* \cup \overline{S}$.

3. Acoustic problem with homogenized sieve

We now formulate the *state problem* describing acoustic waves in open bounded domain Ω with immersed homogenized sieve represented by non-local transmission conditions. We need the following notation:

$$a_\Omega(p,\, q) = \int_\Omega \nabla p \cdot \nabla q \,, \quad (p,\, q)_\Omega = \int_\Omega pq \,, \quad \langle p,\, q\rangle_{\Gamma_0} = \int_{\Gamma_0} pq \,.$$

The problem is defined at two levels:

At the *global level* the interface conditions involve 3 geometrical parameters A, B, F which characterize the design of the sieve perforation; we define (summation $\alpha, \beta = 1, 2$)

$$\mathcal{A}(p,q) = \int_{\Gamma_0} A_{\alpha\beta}\partial_\beta p \partial_\alpha q \,, \quad \mathcal{B}(g,q) = \int_{\Gamma_0} B_\alpha g \partial_\alpha q \,, \quad \mathcal{F}(g,h) = \int_{\Gamma_0} Fgh \,. \tag{2}$$

The *global* problem is to find $(p.p^0, g^0) \in H^1(\Omega \setminus \Gamma_0) \times H^1(\Gamma_0) \times L^2(\Gamma_0)$ such that

$$\begin{aligned} a_\Omega(p,\, q) - \kappa^2 (p,\, q)_\Omega + \mathrm{i}\kappa \langle p,\, q\rangle_{\Gamma_{\mathrm{in-out}}} - \mathrm{i}\kappa \left\langle g^0,\, [q]^+_-\right\rangle_{\Gamma_0} &= 2\mathrm{i}\kappa \langle \bar{p},\, q\rangle_{\Gamma_{\mathrm{in}}} \\ \mathcal{A}(p^0, \phi) - \kappa^2 \varsigma^* \left\langle p^0,\, \phi\right\rangle_{\Gamma_0} + \mathrm{i}\kappa \mathcal{B}(g^0, \phi) &= 0 \,, \\ -\mathrm{i}\kappa \mathcal{B}(\psi, p^0) - \kappa^2 \mathcal{F}(g^0, \psi) + \mathrm{i}\kappa \frac{1}{\varepsilon^0} \left\langle [p]^+_-,\, \psi\right\rangle_{\Gamma_0} &= 0 \,, \end{aligned} \tag{3}$$

for all $(q, \phi, \psi) \in H^1(\Omega \setminus \Gamma_0) \times H^1(\Gamma_0) \times L^2(\Gamma_0)$, where ε_0 is the real thickness of the layer.

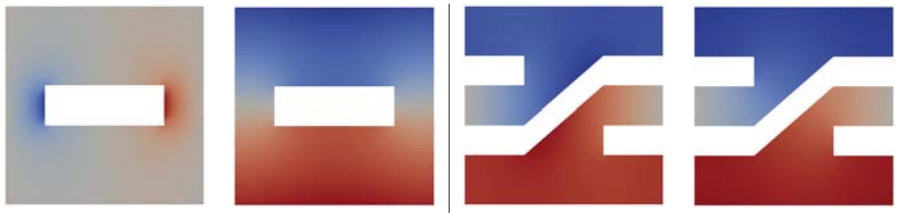

Tab. 1: Correctors π, ξ and homogenized coefficients for two different geometrical structures.

At the *local* level the geometrical parameters A, B, F are determined upon solving "microscopic problems". The perforation design is characterized by computational cell $Y = \Xi \times]-1/2, +1/2[$ with $\Xi =]0, b_1[\times]0, b_2[$, where the fluid occupies domain Y^* and $S = Y \setminus \overline{Y^*}$ represents a rigid obstacle, see Figure 1. Further $I_y^{\pm} = \Xi \pm (0, 0, 1)$ are the "lower" and "upper" faces of Y. In (3), $\varsigma^* = |Y^*|/|\Xi|$ is the porosity. Below the space $H^1_{\#}(Y^*)$ contains all Ξ-periodic functions in the Sobolev space $H^1(Y^*)$. The local problems read: find $\pi^\beta, \xi \in H^1_{\#}(Y^*)$ such that

$$\begin{aligned} \Big(\nabla_y \pi^\beta,\, \nabla_y \psi\Big)_{Y^*} &= -\int_{Y^*} \partial^y_\beta \psi \;, \quad \beta = 1, 2 \;, \\ (\nabla_y \xi,\, \nabla_y \psi)_{Y^*} &= -\left(\int_{I_y^+} \psi - \int_{I_y^-} \psi \right) \;, \end{aligned} \tag{4}$$

for all $\psi \in H^1_{\#}(Y^*)$, where $\nabla_y = (\partial/\partial y_\beta)$ and $(\,,\,)_{Y^*}$ is the inner product in $L^2(Y^*)$. Using the local responses, the geometrical parameters can now be computed, see (2) and Figure 1:

$$\begin{aligned} A_{\alpha\beta} &= \frac{1}{|\Xi|} \Big(\nabla_y(\pi^\beta + y_\beta),\, \nabla_y(\pi^\alpha + y_\alpha)\Big)_{Y^*} \;, \\ B_\alpha &= \fint_{Y^*} \partial^y_\alpha \xi = \fint_{I_y^+} \pi^\alpha - \fint_{I_y^-} \pi^\alpha \;, \qquad F = -\fint_{I_y^+} \xi - \fint_{I_y^-} \xi \;, \end{aligned} \tag{5}$$

where $\fint = |\Xi|^{-1} \int$. Note $F > 0$ and A is positive definite.

Table 1 illustrates how the homogenized coefficients and corrector functions depend on the geometrical arrangement of the reference cell Y.

4. Optimal design problem

One of the most frequently used criteria of optimality in acoustics is related to transmission loss (TL) evaluated using two pressures $p^{in} = p$ on Γ_{in}, $p^{out} = p$ on Γ_{out}, where p satisfies the *state problem* (3). In our numerical tests we observed some remarkable sensitivity of TL on the perforation design, see Rohan and Lukeš (2010). In the further sections we will employ the following objective function:

$$\Phi_{\rm TL}(p) = \hat{\Phi}(p^{in}, p^{out}) = 20\, log\left(\frac{|p^{in}|}{|p^{out}|}\right) - \widetilde{TL}. \tag{6}$$

Let the perforation design be controlled by design variables $\mathbf{d}$ which describe the shape of obstacle S and, thereby, the shape of domain Y^*, so that $\mathbf{d}$ influences the homogenized coefficients A, B, F involved in (3). Let us recall that these coefficients are integrals of functions π^β, ξ which are solutions of the microscopic problems (4) posed in Y^*. At the global level, $\mathbf{d}$ influences the overall acoustic fields (p, p^0, g^0).

We can now define the *optimal perforation design problem*:

$$\begin{aligned} &\min_{\mathbf{d}\in D_{adm}} \Phi(p, p^0, g^0) \\ &\text{subject to:} \quad (p, p^0, g^0) \text{ solves (3), where } A, B, F \text{ are given by (4),(5),} \end{aligned} \tag{7}$$

where D_{adm} is the set of admissible designs, constraining shape regularity of ∂S and typically some other features, like the size of the obstacle (thickness), or porosity of the interface.

To solve (7) using gradient-based methods, the sensitivity of Φ w.r.t. the design $\mathbf{d} = (d_i)$ must be supplied at any iteration (Φ can be substituted by Φ_{TL} or $-\Phi_0$, for instance). For this, any component d_i is associated with the *design velocity* field $\vec{\mathcal{V}}^i$ which can be constructed e.g. by solving an auxiliary elasticity problem in domain Y^* or it results from derivative of the spline-based parametrization of the reference cell mesh, see Fig. 2. The shape sensitivities $\delta A_{\alpha\beta}(\vec{\mathcal{V}}^i), \delta B_\beta(\vec{\mathcal{V}}^i), \delta F(\vec{\mathcal{V}}^i)$ and $\delta\zeta^*(\vec{\mathcal{V}}^i)$ of coefficients $A_{\alpha\beta}, B_\beta, F$ and ζ^* can be obtained, as described in Rohan and Lukeš (2009), using the general approach based on the material derivative.

The total design sensitivity $\delta\Phi(p, p^0, g^0; \vec{\mathcal{V}}^i) = \frac{\partial}{\partial d_i}\Phi$ is obtained by formula

$$\begin{aligned} \delta\Phi(p, p^0, g^0; \vec{\mathcal{V}}^i) = 2\Re\Big\{ &\int_{\Gamma_0} \delta A_{\alpha\beta}(\vec{\mathcal{V}}^i)\partial_\beta p^0 \partial\tilde{p}^0 - \kappa^2 \int_{\Gamma_0} \delta F(\vec{\mathcal{V}}^i) g^0 \tilde{g}^0 \\ &-\kappa^2\delta\zeta^*(\vec{\mathcal{V}}^i)\int_{\Gamma_0} p^0\tilde{p}^0 + \mathrm{i}\kappa\int_{\Gamma_0}\delta B_\alpha(\vec{\mathcal{V}}^i)\left(\partial_\alpha\tilde{p}^0\, g^0 - \partial_\alpha p^0\, \tilde{g}^0\right)\Big\}\ , \end{aligned} \tag{8}$$

where $(\tilde{p}, \tilde{p}^0, \tilde{g}^0) \in H^1(\Omega\setminus\Gamma_0)\times H^1(\Gamma_0)\times L^2(\Gamma_0)$ is the *adjoint state*, cf. Feijóo and others (2004), satisfying the *adjoint equation*, see Rohan and Lukeš (2009) for details,

$$\begin{aligned} &a_\Omega(\tilde{p},\, q) - \kappa^2(\tilde{p},\, q)_\Omega + \mathrm{i}\kappa\langle\tilde{p},\, q\rangle_{\Gamma_{\mathrm{in-out}}} - \mathrm{i}\kappa\left\langle\psi,\, [\tilde{p}]^+_-\right\rangle_{\Gamma_0} + \mathrm{i}\kappa\frac{1}{\varepsilon^0}\left\langle [q]^+_-,\, \tilde{g}^0\right\rangle_{\Gamma_0} \\ &+ \mathcal{A}(\tilde{p}^0,\phi) - \kappa^2\varsigma^*\left\langle\tilde{p}^0,\, \phi\right\rangle_{\Gamma_0} + \mathrm{i}\kappa\mathcal{B}(\psi,\tilde{p}) - \mathrm{i}\kappa\mathcal{B}(\tilde{g}^0,\phi) - \kappa^2\mathcal{F}(\tilde{g}^0,\psi) \\ &= -\frac{1}{2}\left(\partial_{\Re(p,p^0,g^0)}\Phi(p,p^0,g^0;q,\phi,\psi) - \mathrm{i}\partial_{\Im(p,p^0,g^0)}\Phi(p,p^0,g^0;q,\phi,\psi)\right)\ , \end{aligned} \tag{9}$$

for all $(q,\phi,\psi)\in H^1(\Omega\setminus\Gamma_0)\times H^1(\Gamma_0)\times L^2(\Gamma_0)$, where $\Re$ and $\Im$ is the real and the imaginary part, respectively.

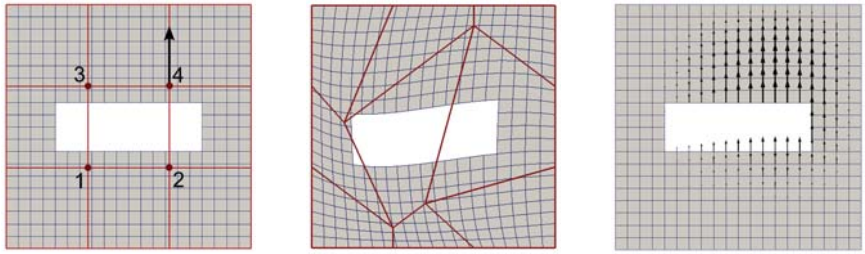

(A) (B) (C)

Fig. 2: (A): spline-based parametrization of the reference cell mesh, initial state; (B): FE mesh modified by moving position of the inner control points; (C): design velocity field $\vec{\mathcal{V}}$ associated with the shape perturbation – y-shift of control point 4.

4.1. Numerical example

We consider a 2D problem of acoustic waves in a waveguide equipped with a perforated plate, see Fig. 3, designed by repeating a reference cell which geometry is controlled by the spline functions. In the optimal design problem we allow four inner control points to move, see Fig. 2, so we have eight optimization parameters (two coordinates for each control point). The objective function to be optimized

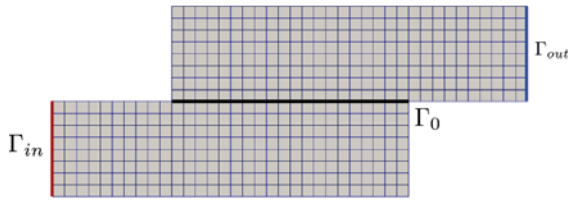

Fig. 3: Acoustic waveguide equipped with a perforated plate Γ_0.

is considered in such form to find a shape of the obstacle for which the transmission loss $TL(p)$ is close to a required value $\widetilde{TL}$. The results (local minima) were obtained by the SQP algorithm with box constraints which secure the "mesh deformation" during the design iterations.

We started the optimization with two different initial states given by the parametrization vectors $[0,0,0,0,0,0,0,0]$ (for rectangular shape), $[0,0,0,0,-0.3,0.3,-0.3,0.3]$ (for distorted shape), see Fig. 4, (A) and (B). In both cases, the optimization process resulted in the shape parametrized by the vector $[-0.304, 0.304, -0.304, 0.304, -0.276, -0.276, 0.276, 0.276]$, the final shape is depicted in Fig. 4(C). The box constraints were chosen as $\langle -0.35, 0.35\rangle$ for all eight parameters to secure the "safe mesh deformation". Figure 4(D) shows the shape ($[-0.25, 0.25, -0.25, 0.25, 0.25, -0.25, 0.25, -0.25]$) of the reference cell for which the transmission loss $\widetilde{TL}$ was computed. The fact, that the optimization finished in state Fig. 4(C) and not in Fig. 4(D), can be explained by the existence of multiple local minima of the used objective function.

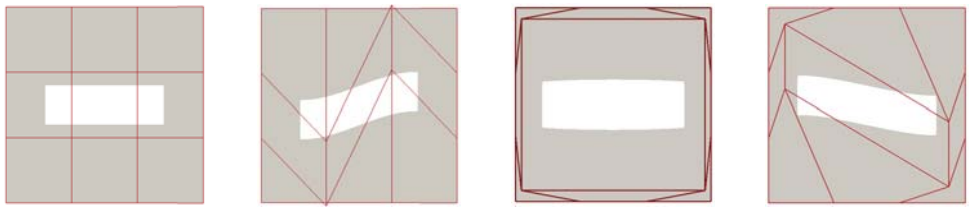

Fig. 4: (A) and (B): two different initial states used in optimization, parametrization: $[0,0,0,0,0,0,0,0]$ *(left),* $[0,0,0,0,-0.3,0.3,-0.3,0.3]$ *(middle); (C): final shape of the obstacle after optimization, param.:* $[-0.304, 0.304, -0.304, 0.304, -0.276, -0.276, 0.276, 0.276]$ *(D): the shape with param.* $[-0.25, 0.25, -0.25, 0.25, 0.25, -0.25, 0.25, -0.25]$ *for which* $\widetilde{TL}$ *was computed.*

5. Conclusion

The "multi-scale" homogenization approach is employed for an efficient treatment of the optimal perforation design. We use the spline parametrization to control the shape of the solid obstacle forming the perforation. The model and its sensitivity discussed in this paper are implemented in our in-house developed finite element based code *SfePy* (Cimrman and others (2012)). The numerical example demonstrate the ability of the optimization method to find an appropriate shape of the solid obstacle for a given transmission loss value.

Acknowledgments

This work was supported by the European Regional Development Fund (ERDF), project "NTIS – New Technologies for Information Society", European Centre of Excellence, CZ.1.05/1.1.00/02.0090 and by Czech Science Foundation, project GA101/12/2315.

References

Bonnet-Bendhia, A. S., Drissi, D., Gmati, N. (2005), Mathematical analysis of the acoustic diffraction by a muffler containing perforated ducts. *Mathematical Models and Methods in Applied Sciences*, Vol. 15(7), pp 1059–1090.

Chen, K.T. (1996), Study on the Acoustic Transmission Loss of a Rigid Perforated Screen. *Applied Acoustics*, Vol. 47(4), pp 303–318.

Cimrman, R. and others (2012), SfePy home page: http://sfepy.org

Feijóo, G.R., Oberai, A.A., Pinsky, P.M. (2004), An application of shape optimization in the solution of inverse acoustic scattering problems. *Inverse Problems*, Vol. 20, pp 199–228.

Rohan, E., V. Lukeš, V. (2009), Sensitivity analysis for the optimal perforation problem in acoustic transmission. *Appl. Comp. Mech.*, UWB Pilsen, Vol. 3, pp 111–120.

Rohan, E., Lukeš, V. (2010) Homogenization of the acoustic transmission through perforated layer. *J. of Comput. and Appl. Math.*, Vol. 234(6),pp 1876–1885.

18th International Conference
ENGINEERING MECHANICS 2012
Svratka, Czech Republic, May 14 – 17, 2012

pp. 849–855
Paper #14

THE USE OF RUBBER VIBRO-BASE ISOLATION TO DECREASE STRUCTURE DYNAMIC RESPONSE

D. Makovička*, D. Makovička**

Abstract: *The use of rubber or another elastomer in the foundation structure is an efficient solution to reduce vibrations propagating into the building structure through the subsoil. The principle of vibro-base isolation consists in inserting an elastic layer between the dual foundation plates, with protective hydroisolation against water flooding. The example of reinforced concrete structure of the building is used to show the efficiency of vibro-base isolation, comparing isolated versus non-isolated structures. This efficiency is assessed based on computational prognosis of vibration of the building floors. Non-stationary dynamic load by the measured vibrations due to technical seismicity caused by cars passing near the analyzed structure is used to calculate the building response. technical seismicity, insulation, building, dynamic analysis, response prognosis.*

Keywords: ***technical seismicity, vibro-base isolation, building, dynamic analysis, response.***

1. Introduction

The example of a residential building is used to illustrate the use of vibro-base isolation against the propagation of vibrations (Makovička & Makovička, 2009) from the subsoil to the protected building. The building (ground plan size roughly 90 ×21 m) has three underground storeys and graduated six (north side) up to ten (south side) storeys over the ground. The building is founded on a foundation plate on the level of the 3rd underground storey. Spatial model was chosen for dynamic analysis of the structure. Floor slabs, load-bearing walls, columns and beams were modelled as reinforced concrete monoliths made of concrete C30/37. Load-bearing walls in the longitudinal direction of the storeys over the ground were modelled as built of bricks. Staircase broadsteps and loggia slabs were simulated as precast slabs, hinge-connected to the structure walls.

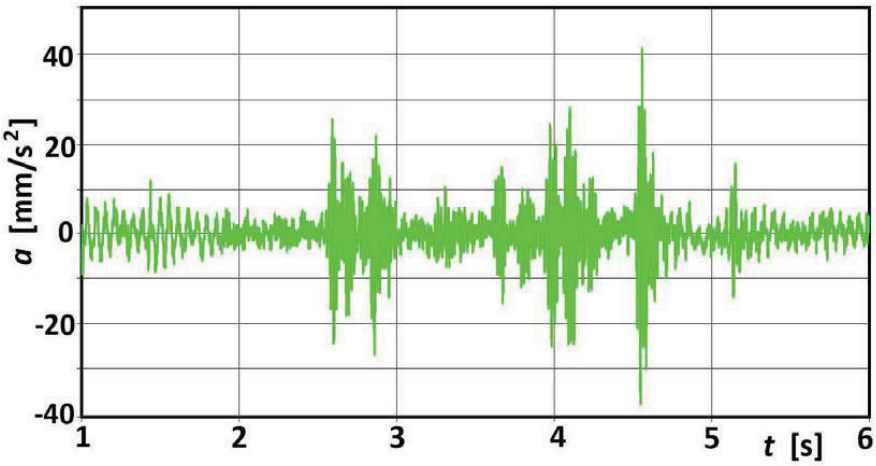

Fig. 1: Measured horizontal acceleration excited by an underground train pass below the building

* Doc. Ing. Daniel Makovička, DrSc.: Klokner Institute, Czech Technical University in Prague, Šolínova 7; 166 08, Prague 6; CZ, e-mail: daniel.makovicka@klok.cvut.cz

** Ing. Daniel Makovička, Jr.: Static and Dynamic Consulting, Šultysova 170; 284 01 Kutná Hora; CZ, e-mail: d.makovicka@makovicka.cz

Rubber antivibration blocks Ekodyn of the company Ekostar were chosen as isolation against vibrations caused by traffic. The rubber layer was designed to be placed underneath the entire ground plan of the building, and also on side walls of the underground storeys. The rubber layer would be laid using Ekodyn plates with the dimensions 500 × 500 × 30 mm for the horizontal isolation layer. Rubber thickness of 25 mm was used for the vertical layer.

2. Computational model and load

A 3D model of the whole structure was designed for the structure analysis, including underground storeys and the vibroisolation rubber layer. On the level of the floor of the 3rd underground storey, the computational model is placed on a multiple-layer subsoil structure. The foundation plate with the thickness 500 mm (upper foundation plate) is placed on the vibroisolation layer made of Ekodyn rubber blocks. Bottom concrete with the thickness 150 mm (lower foundation plate) is placed under the rubber layer, which is laid on the layer of the original subsoil formed by healthy slate (class R3). The footing bottom is below the underground water level. The relative structure damping value was chosen as 5% of the critical damping value.

Modelled rubber stiffness in the computational model respects the selected rubber type. The stiffness of the rubber blocks in their rotation around the vertical axis of the sample and stiffness of bend compression of the rubber around horizontal axes was neglected compared to the vertical and horizontal stiffness of the rubber samples.

The antivibration layer of the rubber plates was designed so that (a) its response to permanent and long-term loads in deflections is approximately uniform and does not exceed 10% to 15% of the rubber thickness, and so that (b) the dynamic response of the whole system fulfils the criteria of optimal vibration reduction compared to vibration of the base (Makovička, & Makovička, 2011, a,b).

As for the dynamic analysis of the structure, non-bearing parts of the structure were incorporated in the mass of the load-bearing elements as mean “blurred“ value of load caused by thin partition walls, floorings, etc. Similarly, the magnitude of the long-term live load components were incorporated in the mass of ceiling structures in the value of 50%.

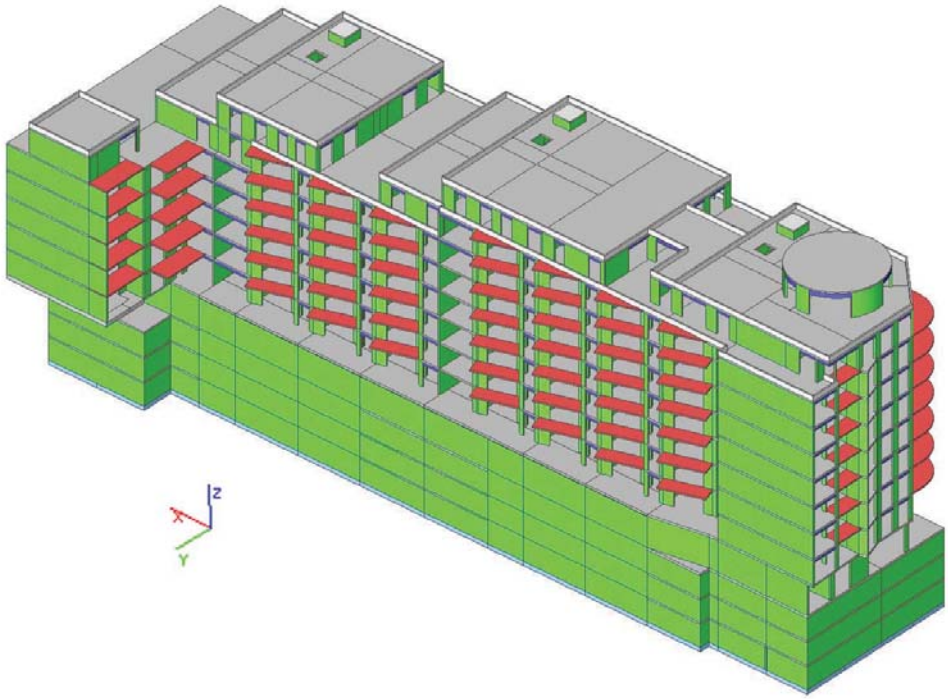

Fig. 2: Calculation model ... South-West view

Nonstationary dynamic excitation (Fig. 1) due to traffic was introduced to the model at selected points of the structure, in an approximately regular grid of points on the level of the foundation plate. Attenuation of dynamic excitation along the distance from the source was introduced to the structure model in steps, using bands of the approximate width of 10 m, graduated based on measured vibrations. Dynamic load was introduced to the structure at the same moment and with the same phase. Part of the measured acceleration record, incorporating the effect of B line metro passage in the duration of 1 s, was used for the dynamic calculation. This selected 1 s of the record includes several maximum non-stationary values of the measured acceleration of the vibrations and corresponds to the maximum excited vibration on a test foundation block inside the area of construction (free-field measurement).

The purpose of the calculation was to determine the relative response of individual building storeys compared to excitation on the foundation base level, at the place of rubber placement. For this reason, the response results were normalized.

3. Natural vibration

The calculation of natural vibration of the residential building was done for the model of the whole structure laid on the elastic vibroisolation layer.

In terms of dynamic response of the building to the effects of dynamic load caused by external sources (traffic), the lowest possible tuning of the building structure is decisive. This is manifested by flexural vibration of the building on the rubber on one hand, and by vertical and horizontal translative vibration of the building as a whole on the rubber or by torsional vibration of the whole structure or its parts.

Besides basic modes of natural vibration of the structure as a whole, natural vibration frequencies of floor slabs of individual storeys, inside walls and console of floor slabs (balconies) appear in the calculation results, which cause that the building response is slightly different on every storey and/or with loops at other stations.

For an illustration, the six lowest natural vibration modes are arranged in Tab. 1 including comments to these modes. The first 75 natural modes were used for the dynamic calculation of forced vibration.

Tab. 1: Natural vibration frequencies of the building and description of natural modes

Mode number	*Natural frequency [Hz]*	*Description of natural mode*
1	*2.28*	*Rotation of the whole building around axis x*
2	*3.54*	*Rotation of the building around axis x and twisting around axis z*
3	*4.25*	*Rotation of the building around axis y and twisting around axis z*
4	*5.83*	*Bending of the building in the direction y, bending of floor slabs*
5	*7.41*	*Bending of the building around axis x, bending of floor slabs*
6	*8.00*	*Bending of the building around axis x, bending of floor slabs, higher mode*

4. Vibration transfer through the foundation structure

The calculation of vibration transfer from the lower to the upper part of the foundation plate of the building was done for the model of the structure part laid on the elastic vibroisolation layer, lower foundation plate (base concrete), and subsoil layer (slate R3).

The interaction at the rubber and reinforced concrete foundation structure interface has an effect on vibration transmission to the building structure itself. Characteristics of this interaction depend on (a) intensity and frequency composition of dynamic load, (b) properties of the foundation structure and subsoil under foundation level, (c) properties of the rubber used, and (d) the upper part of the modelled structure of the whole building.

The same type of rubber is exposed to different types of stress (static load and deformation) in different parts of the foundation structure. In terms of evaluation of the concrete and rubber interaction, the average (most frequent) stress value (and resulting compression) for individual used rubber types must be determined. However, the resulting values are only average values, as well, and may show different behaviour in other conditions.

Vibration of the lower part of the (unsprung) foundation structure was normalized to the maximum value 1.0 (100%); the intensity of vertical and horizontal vibration of the upper part of the isolated foundation structure does not exceed 40%. Conservatively, vibrations of the lower foundation plate, due to passing through the rubber layer and thanks to interaction at the contact point between individual parts of the foundation structure, can be considered to become reduced approximately by 50%. Another positive consequence of using the rubber layer consists in changed intensities of individual dominant frequencies corresponding to natural frequencies of the system. The calculation results show very well that vibrations at frequencies of the order over 30 Hz become significantly attenuated and/or filtered off (Makovička & Makovička, 2011, b).

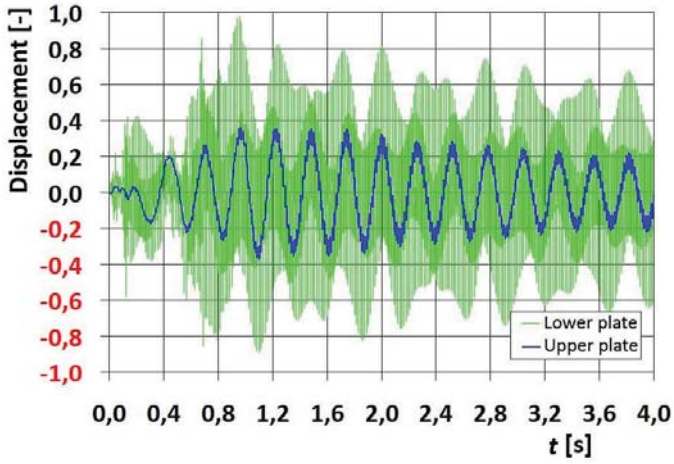

Fig. 3: Time histories of vertical vibration within the vibration transfer through foundation structure.

5. Forced vibration of the whole building

Calculations of forced vibration of the residential building were done for the model of the whole structure laid on the elastic vibroisolation layer, or as a variant, on the original slate R3 subsoil. Calculation of forced vibration of the structure was done using the method of dynamic excitation decomposition to the spectrum of natural vibration modes. The calculation determined the dynamic response of the structure, while the overall duration of the calculation was 1.000 s, and the calculation was done with the step of 0.005 s. The calculated values (displacements of the foundation plate and floor slabs) were normalized so that the maximum displacement value in the foundation plate was equal to 1. Maximum calculated response values are shown in Tab. 2. Normalized displacements of the structure make it possible to perform a simple comparison of the increased or decreased response of the structure.

Comparing the calculated response on the level of the foundation plate (at the place where the structure is laid on the rubber and at places where dynamic excitation is introduced) to the response on individual higher storeys, this ratio can be used to estimate the magnitude of vibration changes on individual storeys. This ratio depends on the structure tuning, thus on the effect of the building geometry, chosen cross-sections and thickness and load values, including the permanent component of live loads. This procedure is considerably conservative and on the safety side.

For the sake of comparison, the structure response to dynamic load was calculated also for the nonisolated building (without any inserted rubber); the resulting normalized values in displacements caused by vertical and horizontal excitation are shown in Tab. 2.

Tab. 2: Extremes of relative floor displacements under vertical and horizontal excitation

Floor level	Isolated structure				Nonisolated structure			
	Vertical		Horizontal		Vertical		Horizontal	
	u_z		u_y		u_z		u_y	
	Max	Min	Max	Min	Max	Min	Max	Min
-3rd Floor	1.00	-0.76	1.00	-0.83	1.00	-1.00	1.00	-1.00
-2nd Floor	1.22	-1.29	0.96	-1.07	1.43	-1.00	1.28	-1.89
-1st Floor	1.24	-0.97	0.89	-0.89	1.00	-1.00	1.12	-1.23
+1st Floor	0.87	-0.92	0.70	-0.59	0.85	-0.82	1.18	-1.49
+2nd Floor	0.74	-0.64	1.00	-1.02	0.70	-0.53	0.85	-0.91
+3rd Floor	0.70	-0.69	0.85	-0.76	0.54	-0.72	0.91	-0.95
+4th Floor	0.73	-0.72	1.08	-1.13	0.63	-0.51	0.81	-1.04
+5th Floor	0.66	-0.66	1.08	-0.93	0.63	-0.56	0.81	-1.19
+6th Floor	0.69	-0.71	0.85	-1.04	0.52	-0.47	1.09	-1.32

Tab. 3: Response comparison of isolated and nonisolated structure in frequency interval 1 to 20 Hz

Floor level	Isolated structure			Nonisolated structure		
	Tuning effect	Transfer through foundation	Effective acceleration	Tuning effect	Transfer through foundation	Effective acceleration
	[–]	[–]	[mm/s^2]	[–]	[–]	[mm/s^2]
Horizontal vibration						
-3rd to 1st FL, North part	1.00	0.5	1.01	2.66	1	9.71
2nd to 9th FL, North part	0.69	0.5	0.7	2.91	1	10.61
-3rd to 1st FL, South part	0.78	0.5	0.79	1.31	1	4.79
2nd to 9th FL, South part	0.52	0.5	0.53	1.76	1	6.43
Roof	1.34	0.5	1.35	2.89	1	10.55
Balconies	0.71	0.5	0.72	2.62	1	9.55
Vertical vibration						
-3rd to 1st FL, North part	2.54	0.5	2.79	1.90	1	6.77
2nd to 9th FL, North part	2.60	0.5	2.86	1.75	1	6.24
-3rd to 1st FL, South part	2.03	0.5	2.23	1.62	1	5.77
2nd to 9th FL, South part	2.67	0.5	2.94	1.36	1	4.83
Roof	3.44	0.5	3.78	4.26	1	15.15
Balconies	4.44	0.5	4.88	3.67	1	13.08

Comparison of both analyses indicates that the isolated structure shows significantly lower vibrations in acceleration (Tab. 3) than structures without any isolation (Makovička & Makovička, 2011, c).

Time courses of the response, or dominant frequencies of this response, respectively, provide another effect that plays an important role in dynamic response assessment. Time courses of forced vibration in the vertical direction with horizontal excitation were calculated for selected points within an axis, located over each other (Fig. 4). Thanks to springing of the building structure by the inserted rubber layer, the frequency signal of the response would be redistributed in the area of low frequencies, approximately on the level between 1 Hz to 15 Hz, 20 Hz at the maximum (Jacquet. & Heiland, 2002 and Roško & Králik, 2009). Higher frequency components of excitation are markedly damped and are be transmitted to the building by negligibly small vibration amplitudes compared to the low frequency components.

In the structure without any rubber layer, no redistribution of the frequency signal and attenuation of vibrations occur and/or they occur in a considerably lower extent. Individual parts of the structure then start vibrating at some of the dominant excitation frequencies that correspond to or approach the natural frequency (or higher harmonic frequencies) of the appropriate part of the structure.

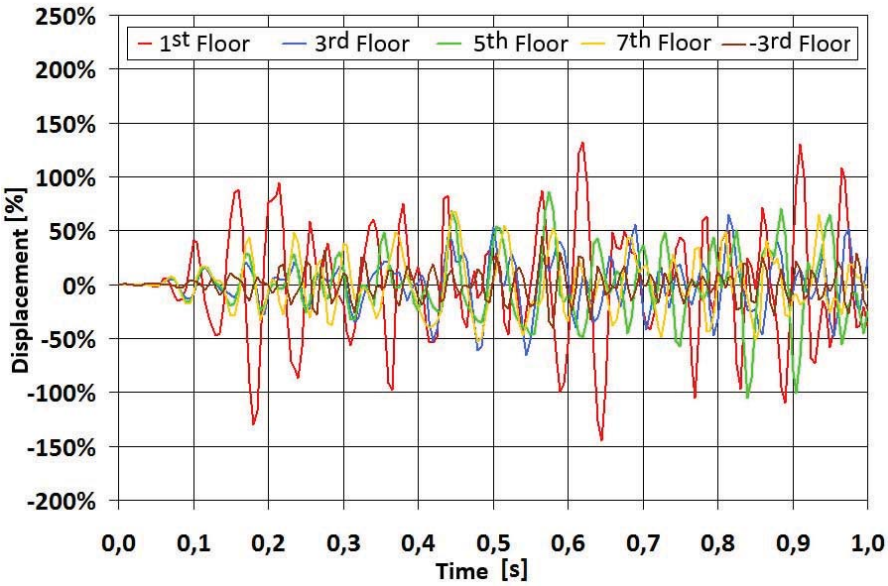

Fig. 4: Time courses for selected points of vertical vibration under horizontal excitation.

6. Conclusion

The aim of this paper is to assess the effect of building vibroisolation on the transfer of vibrations due to traffic from the subsoil environment. When metro trains pass in the tunnel in immediate vicinity of the building, dominant vibrations are propagated to the surroundings in the form of transient vibration.

Maximum measured intensities of vibrations at the construction site were used as non-periodic load of the building by technical seismicity caused by traffic effects. Based on calculation of static and dynamic response of the building, optimum distribution of the rubber in the foundation structure was designed. Furthermore, the calculation was used to predict floor vibration on individual storeys, and time courses of vibration at selected points were determined.

This paper compares calculated responses for an isolated and nonisolated building (Tab. 3). Comparison of the results clearly indicates the advantages of implementing vibroisolation in the foundation part of the building.

Acknowledgement

This research was supported as a part of the research projects in GAČR P105/11/1580 Transient response of structure under short-term dynamic or impact load due to seismic effects and explosions, for which the authors would like to thank the Agency.

References

Makovička, D. & Makovička, D., Jr. (2009) Response analysis and vibroinsulation of buildings subject to technical seismicity, in: *Earthquake Resistant Engineering Structures VII*, WIT Press, Southampton, UK, pp. 197-205.

Makovička, D. & Makovička, D. (2011, a) Vibrobase insulation of a building excited by the technical seismicity effect of tube railway operation, in: *Earthquake Resistant Engineering Structures VIII* (C.A.Brebbia & M.Maugeri eds), WIT Press, Southampton, UK, pp. 79-88.

Makovička, D. & Makovička, D. (2011, b) Springing of building structure in order to eliminate traffic vibrations, in: *EURODYN 2011: Proceedings of the 8th International Conference on Structural Dynamics*, Leuven, pp. 922-927

Makovička, D. & Makovička, D. (2011, c) Effect of vibro-insulation on restriction of vibration transfer from subsoil into the building, in: Fuis, Vladimír: *Engineering Mechanics 2011, 17th International Conference* (V.Fuis ed), Institute of Thermomechanics, Academy of Sciences of the Czech Republic, v.v.i. - Brno, pp.375-378

Jacquet, T. & Heiland, D. (2002) *Tieffrequente Bauwerken-Kopplungen als Schutz gegen Erschütterungen*, Gerb Berlin.

Roško, P. & Králik, J. (2009) Energy-based analysis and design of structures under seismic loading. in: Papadrakakis, M., Lagaros, N.D., Fragiadakis, M: *COMPDYN 2009: Thematic Conference on Computational Methods in Structural Dynamics and Earthquake Engineering* (M.Papadrakakis, N.D.Lagaros, M.Fragiadakis eds), Rhodes.

18th International Conference
ENGINEERING MECHANICS 2012
Svratka, Czech Republic, May 14 – 17, 2012

pp. 857–868
Paper #42

APPLIED METHOD FOR DESIGN OPTIMIZATION OF HYDROSTATIC GUIDEWAY ON REAL MACHINE TOOL

M. Mareš[*], E. Stach[**], T. Holkup[***]

Abstract: *The main advantages of hydrostatic bearings are: design flexibility, excellent structural damping, and zero friction at low speeds; this is a great opportunity for various types of machine tools. However, the need to determine many parameters at the design stage and a lack of a general approach to their optimization pose a large obstacle to wider application. This paper suggests a general iterative method for design optimization of hydrostatic bearings for linear and low-speed rotary axes. The method uses automated generation of load combinations, multi-objective optimization for determining design parameters and FEM for predicting structural deflection of machine frame parts.*

Keywords: ***Hydrostatic, guideway, bearing, optimization .***

1. Introduction

1.1. Background

Hydrostatic (HS) guideways represent one of the guidance types ensuring linear and rotating movement of machine tool parts that fulfil the above-mentioned requirements. The use of HS guideways in engineering is of a relatively recent date: with some earlier exceptions, this type was introduced in the 1960s and 1970s (Lewis, 1966). The main component of a HS guideway is a HS pocket containing pressurized fluid. This guideway type is a very good option for high-precision machines, machines requiring very small positioning steps, machines for hard machining (high damping needed), and large machines (design flexibility needed). Conditions for HS operation:

- Very thin fluid layer (gap height) in the bearing (*0.005* to *0.2 mm*);
- Very low fluid compressibility;
- Sufficient parallelism and planarity of bearing surfaces in all operating modes;
- Relatively constant viscosity of fluid (stable temperature).

In practice, a distinction is made between two types of HS guideways: open guideways (preloaded by gravity of parts or other dominant load) and closed guideways (mutually preloaded pockets placed opposite each other). The characteristic dimensions of HS pockets, the pressure distribution, and a graphic representation of open and closed guideway types are shown in Fig. 1. HS guideway can generally operate in two operating modes corresponding to the settings of the hydraulic unit and the flow control methods:

- Constant flow provided by the pump (One pump for each pocket, Flow dividers);
- Constant pressure provided by the pump (Control by means of constant hydraulic resistance such as capillary tube or orifice, advanced flow control such as PM flow controller (source: Hyprostatik) or membrane, self-compensating systems used especially for radial HS bearings).

[*] Ing. Martin Mareš: Research Center for Manufacturing Technology, Czech Technical University, Horská 3; 128 00, Prague; CZ, e-mail: M.Mares@rcmt.cvut.cz

[**] Ing. Eduard Stach: Research Center for Manufacturing Technology, Czech Technical University, Horská 3; 128 00, Prague; CZ, e-mail: E.Stach@rcmt.cvut.cz

[***] Ing. Tomáš Holkup, Ph.D.: Research Center for Manufacturing Technology, Czech Technical University, Horská 3; 128 00, Prague; CZ, e-mail: T.Holkup@rcmt.cvut.cz

Tab. 1: Nomenclature.

Symbol	Quantity	Units
c, C	Inner / outer pocket width	m
d, D	Inner / outer pocket length	m
l	Land width	m
b	Effective perimeter	m
A_{eff}	Effective area	m^2
R_T	Pocket hydraulic resistance	$Pa.s.m^{-3}$
R_K	Capillary tube hydraulic resistance	$Pa.s.m^{-3}$
l_K	Capillary tube length	m
r_K	Capillary tube radius	m
η	Dynamic viscosity	Pa.s
h	Gap height	m
h_0	Initial gap height	m
$h_{I,II,III,IV}$	Gap heights in HS pocket corners	m
h_D	Allowable gap height	m
p_p	Pump pressure	Pa
p_T	Pocket pressure	Pa
p_0	Atmospheric pressure	Pa
Q	Flow	$m^3.s^{-1}$
F	Load	N
F_T	Pocket reaction	N
$F_{max,mid,min}$	Maximal / medium / minimal load of reaction spectra	N
$h_{min,max}$	Minimal / maximal allowable gap height in working space	m
F_s	Force range defining maximum and minimum of pocket load	N
$F_{a,b,m}$	Crucial points of force – deflection characteristic	N
K	Stiffness	$N.m^{-1}$
k	Safety load coefficient	-
k_h	Safety gap height coefficient	-
rot X, rot Y	Pocket tilt in X / Y direction	rad
rot X_D, rot Y_D	Allowable pocket tilt in X / Y direction	rad
ε_D	Allowable pocket tilting	m

The advantages of HS guideways include: a very low friction coefficient; long service life (the guide surfaces do not touch); good damping in the direction perpendicular to the guide surfaces; and high stiffness (depending on the thickness of the pressure oil layer). Disadvantages include: a more complex design; demanding manufacturing process; demanding maintenance (the guideways are vulnerable to dirt); and costly operation.

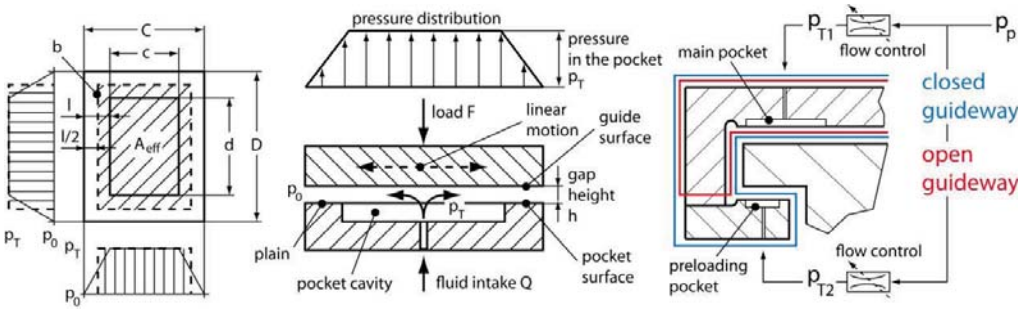

Fig. 1: HS pocket parameters and gudeway types (partially taken from(Brecher & Weck, 2006)).

A great deal of research has been dedicated to the design of HS pockets and its influence on guideway characteristics. A large number of these works focus exclusively on radial HS bearings. For example, paper (Sharma et al., 2002) compared the characteristics of HS pockets with circular, rectangular, elliptical and annular pocket cavity. He also considered different controllers, such as capillary, orifice and constant flow valve restrictors. He used the FEM method to analyse the properties of HS pockets. Another study worth mentioning is the follow-up study (Shie & Shih, 2010), where were (knowing the pump parameters and the gap height) found the optimum parameters for a radial HS bearing (such as orifice location and diameter and the ideal pocket cavity dimensions) using the FEM method and an optimization method combining Genetic Algorithms and Gray Relation Analysis. Some papers focus on HS pocket materials (Wang & Yamaguchy, 2002), the influence of the pressure medium properties (Wang & Yamaguchy, 2002), research on smart controllers (Slocum et al., 1995), and the effects of temperature on HS bearings (Ting & Mayer, 1971).

However, research on methods for design and optimization of entire motion axis guideways realized by a system of more HS pockets has been sporadic. There is a marginally related study by (Sharma et al., 1995), where were examined the differences in using sets of four and six hybrid HS pockets of comparable performance. In most of the available literature, however, research on entire HS planar guideways is only done as part of the design of the whole machine, and is not paid much attention (e.g. (Kim & Cho, 2006), or (Tlustý, 1993)). In an interesting project (Mekid, 2000) the author tried to further the research on the design of high-precision machines by introducing adjustable, preloading bearings for closed HS guideways.

1.2. General design method

The primary aim of this paper is to present an iterative approach to optimizing the entire design process for HS machine tool guideways (lacking in the available literature), combining the *finite element method* (FEM) and multiparametric, multi-criterion optimization. The method is robust, taking into account all possible load situations which can arise in operation, and is not dependent on the selection of a specific optimization criterion.

The first part of the paper is dedicated to a general description of the design optimization approach. It provides an overview of the outputs and applications of the partial results of the iteration process which include: reaction spectra based on a rigid FEM model; HS pocket parameters found through minimization and a well-selected object function; and force reactions and deformations computed on the basis of an FEM model of the entire machine, which are decisive for feasibility of the whole design.

In the second part of the paper, the approach is presented on an example of a real machine tool linear axis with a closed HS system controlled by constant hydraulic resistors—capillary tubes. *Genetic algorithms* (GA) have been used as a tool for optimizing dimensions for the HS pockets and the controllers. The HS pockets have been optimized with respect to the required force-deflection characteristics. The limits for the minimum pocket gap and the maximum allowable tilting of the HS pockets have been selected as the convergence criteria.

2. The design process

The iteration process is general, independent on the selected pocket shape, the type of HS guideway used (closed or open), or the selected type of control (constant flow, constant pressure, flow divider, capillary tube, membrane, orifice plate, etc.). It is applicable for any type of these elements with sufficient mathematical description from the fluid mechanics. Diagram in Fig. 2 shows the process for optimizing the position and design parameters of a HS pockets providing guideway of a machine tool moving axis. The iterative process can be divided into three parts, each of them with a specific result (see Fig. 2):

- Computing the reaction forces and adjusting the position of the HS pockets;
- Suggesting new characteristics for the next iteration step, taking into account the geometry and force boundary conditions;
- Checking for undesired conditions and checking the selected or prescribed criteria.

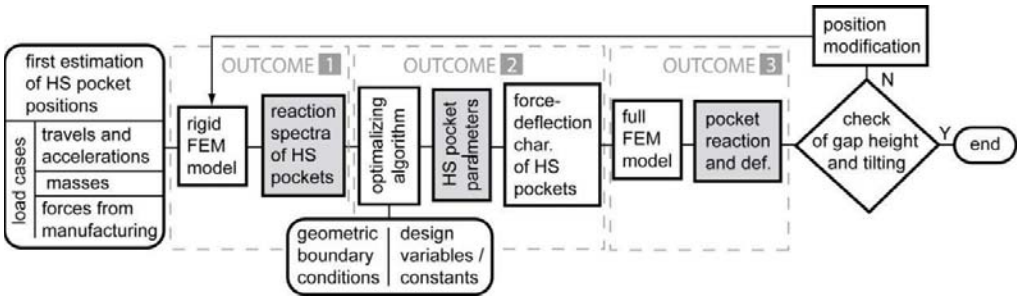

Fig. 2: Diagram showing the iterative design process.

2.1. Rigid FEM model

This design stage involves computations of a statistical distribution: the *reaction spectrum* (Fig. 3) in HS pockets using automatic load case generation and a rigid FEM model. In order to reduce computation time, the flexibility of the machine parts is not taken into account at this stage. The model considers the machine tool frame as rigid and uses spring elements with substituting stiffness for modelling the HS pockets. During the computations various relevant kinematic configurations, load configurations and machine acceleration combinations are generated.

In a case where the machine parts connected by the guideways could be considered as absolutely rigid, the reaction computations would end here, and the stage of designing the pocket geometry and accessory parameters would follow. However, this is generally not the case.

2.2. The optimization algorithm

The next step involves finding optimized pocket dimensions and flow controller parameters for the reaction spectra (possibly multiplied by a safety coefficient), using multiparametric optimization tools. A sensitive approach is necessary when setting the collision boundary conditions, and the geometric boundary conditions need to be respected. The optimization task can be defined as a minimization task.

Results of this design stage are parameters of HS pockets and their flow controllers together with resultant HS pocket force-deflection characteristics. These comply with all pre-defined limits, convergence criteria and safety factors.

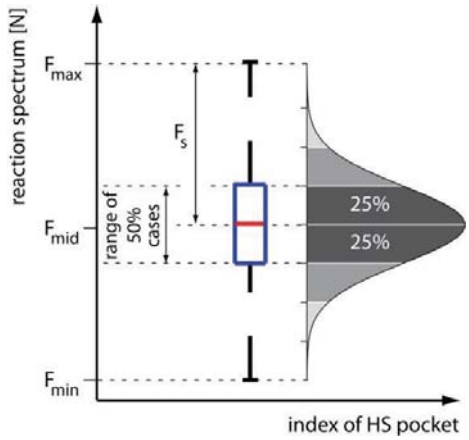

Fig. 3: Reaction spectrum of one bearing point.

2.3. A detailed FEM model

Mainly in order to check for various undesired conditions resulting from structural flexibility, a detailed FEM model of the whole system is created. Elements representing properties of each of the HS pockets are added at appropriate points between models of the two moving parts.

The FEM model is loaded with a *symmetrical load case* (corresponding to F_{mid} force resulting from the rigid FEM model shown in Fig. 3) which represents medium load from alternating (two-way) loads—the acceleration of the motion axes and the cutting forces. The model also needs to be in the medium kinematic position.

Based on the results of the detailed detailed FEM model (deformation of HS guideway and pocket tilting), the positions of the HS pockets are sensitively adjusted and new F_{mid} values for the reaction spectra are computed (condition: the force range F_s, which the pocket has to transfer, remains unchanged). The new spectra serve as input for the next iteration step.

3. Application

The design method is demonstrated on one half of the hydrostatic X axis of a real portal milling machine (Fig. 4).

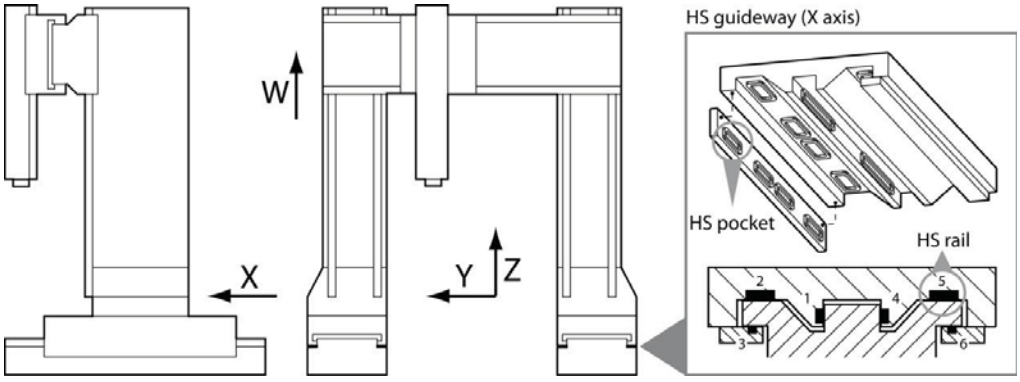

Fig. 4: A diagram showing a portal milling machine.

The design method can be applied to any assignment where sufficient and verified mathematical description of the HS components is available. The application example shown here uses the following input information for the iteration process (Fig. 2):

- Knowledge of the load cases;
- Pump and pressure medium parameters;
- Checking Required gap height.

The aim is to create a suitable HS guideway design (positions and geometry of the HS pockets) for a control system using capillary tubes. The design has to account for loading with the machine's own weight, reactions caused by axis acceleration, cutting forces and compliance of machine parts which influences the distribution of load on the pockets.

3.1. Reaction spectra of the HS pocket

Computations of the reaction spectra for the pockets are based on the 'rigid FEM model' which uses substituting spring elements for the HS pockets. The machine frame, however, is considered to be absolutely rigid. ANSYS FEM software is used for creating the rigid structure of nodes representing points of applied external forces, inertia forces and gravities. HS pockets are modeled as linear springs. The variations are generated and computed automatically using APDL (ANSYS parametric design language) routines. The specific input for the computations includes:

- The mass of the parts and the position of their centers of gravity;
- The positions and orientation of the pockets in relation to the selected coordinate system;

- Travel and acceleration of each axis;
- Maximum values of cutting forces in each direction;
- Some cases the stiffness of the drive of a given axis needs to be entered.

In the model case (the X axis of a portal milling machine) the HS guideways were designed as a system based on pairs of pockets preloaded against each other (close guideway - Fig. 1). The initial position of the pockets was selected intuitively. The description and distribution of the HS pockets on one half of the X axis of a portal milling machine is shown in Fig. 5. Through the iteration process (Fig. 2) the positions of the pairs of HS pockets, preloaded against each other, were adjusted with a view to finding their optimum distribution in terms of load and deflection.

At this design stage the computations automatically generate different kinematic configurations and load case combinations. In the example presented here the different configurations of the model are found along the *W*, *Y* and *Z* axes; the position of the portal on the *X* axis does not have an impact on the loading of its guideway (Fig. 4). Different combinations of acceleration and cutting forces needed to be taken into account as well. Acceleration potentially occurs along the *X*, *Y* and *Z* axes.

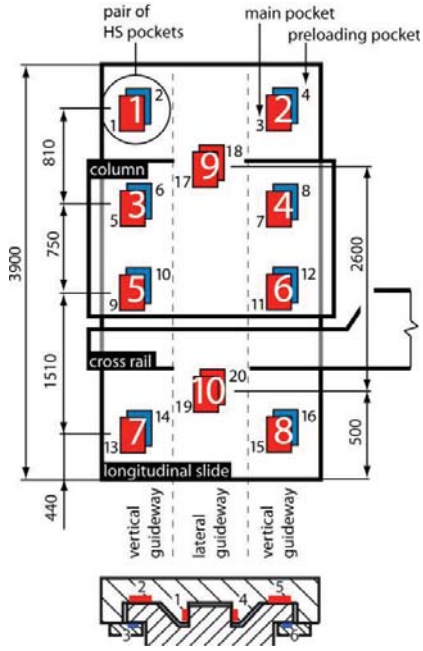

Fig. 5: Initial HS pocket positions.

Each of the three axes can reach one of two extreme positions; therefore, there are 2^3 kinematic configurations (the position of the portal does not have an impact on the *X* axis guideway). Combinations of acceleration and cutting forces also needed to be taken into account (again, for the *X*, *Y* and *Z* axes). After integrating the parts that move together, this represents a total of 2^9 load configurations. Therefore, altogether $2^3 * 2^9 = 4096$ load cases need to be examined, each of which can potentially be a case of extreme load for one of the points on the guideway.

The whole system is absolutely rigid, with the exception of the HS pocket substituting elements (all of them are considered to have the same stiffness) and the substituting elements for the X axis drives. The case where the drives are considered as highly (almost absolutely) rigid is closer to the real situation. When finding optimum pocket dimensions, however, the stiffness of the drives was considered to be zero, which means greater demands placed on the lateral pockets. The resulting reaction spectra for each HS pocket pair (the numbering corresponds to the system introduced in Fig. 5) obtained in the first iteration step are shown in Fig. 6.

As the longitudinal slide of the *X* axis is flexible due to its length and relative slenderness, the computed reaction spectra do not reflect the real situation accurately, and it is necessary to adopt an iteration approach to the design of the HS guideway of the *X* axis.

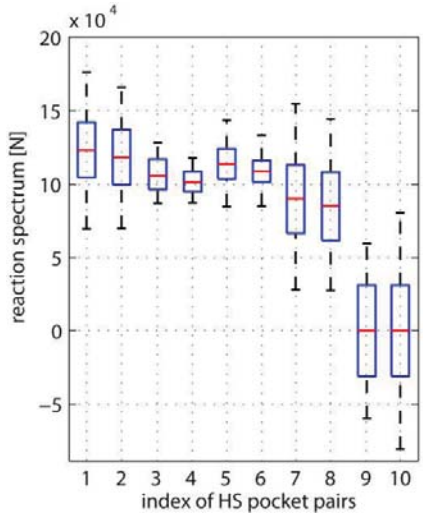

Fig. 6: Reactions in the pocket pairs; flexible positioning along the X axis.

3.2. Determining the HS pocket parameters

The HS system in question works in a mode of constant pressure set on the pump (p_p = *const.),* and regulation is ensured by constant hydraulic resistors (capillary tubes) placed before the HS pockets. A diagram representing the system is shown in the following figure.

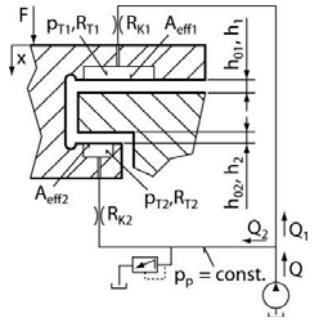

Fig. 7: Diagram representing the HS system.

The force characteristic of the system is the result of substituting the continuity equation (1) in the force balance equation of the HS system (2). The continuity equation:

$$\mathrm{Q_i} = \frac{p_{Ti}}{R_{Ti}} = \frac{p_p}{R_{Ti} + R_{Ki}} \rightarrow p_{Ti} = \frac{p_p \cdot R_{Ti}}{R_{Ti} + R_{Ki}}, \tag{1}$$

where the hydraulic resistances correspond to the following relations:

$$R_{Ti} = \frac{12 \cdot \eta \cdot l_i}{b_i \cdot \left(h_{0i} \mp x\right)^3} \text{ and } R_{Ki} = \frac{8 \cdot \eta \cdot l_{Ki}}{\pi \cdot r_{Ki}^4}, \text{ where } i = 1, 2.$$

The force characteristic of the pair of HS pockets preloaded against each other is determined by the following relations:

$$\mathrm{F} = p_{T1} \cdot A_{eff1} - p_{T2} \cdot A_{eff2}, \tag{2}$$

$$\mathrm{F} = p_p \cdot \left(A_{eff1} \cdot \frac{R_{T1}}{R_{T1} + R_{K1}} - A_{eff2} \cdot \frac{R_{T2}}{R_{T2} + R_{K2}} \right). \tag{3}$$

The stiffness of the bearing is then determined by a derivation of relation (3) according to the *x* coordinate:

$$K = \frac{dF}{dx}. \tag{4}$$

At this computation stage the aim is to find optimum parameters for the HS pockets. Some of the parameters are given (or selected) as fixed; other parameters as free, i.e. variable within prescribed limits:

- Fixed parameters (*p*): pump pressure, oil viscosity, one characteristic HS pocket dimension;
- Free parameters (*q*): the remaining pocket and capillary tube dimensions (Fig. 1).

These parameters, bound in equations expressing the force characteristic of the HS pocket pairs, have to meet the prescribed boundary conditions:

- Geometric boundary conditions - preventing contact between two neighboring pockets; respecting the structural space required for the HS pockets on the guideway;
- Force boundary conditions - the pairs of pockets need to safely transfer loads determined by the rigid FEM model.

GA (Houck et al., 1999) represent one of the options for obtaining optimum results from this multiparametric task. In the case presented here the genetic algorithms are created using *Matlab GA toolbox*.

A fitness function can be selected in many different ways (e.i. maximizing stiffness with minimizing oil flow and energy consumption), depending on the needs of a particular application. One of the possibilities for setting the fitness function is to minimize the working space of the HS pocket. Fig. 8 and detailed description provides more information about the selected fitness function.

The F_s force range (Fig. 3) defines the maximum and minimum load cases F_{max} and F_{min} (around the medium load position F_{mid}) to which the HS pocket pair is expected to be exposed during operation. Therefore, the minimization task using GA aims to situate the gap height under maximum load (in one direction or the other, marked as h_{min} and h_{max} in Fig. 3) within the prescribed range +/- k_h around the balanced position h_0 (loading with own weight). This first safety range must be selected appropriately at the beginning of the GA iteration process. The range has two direct impacts:

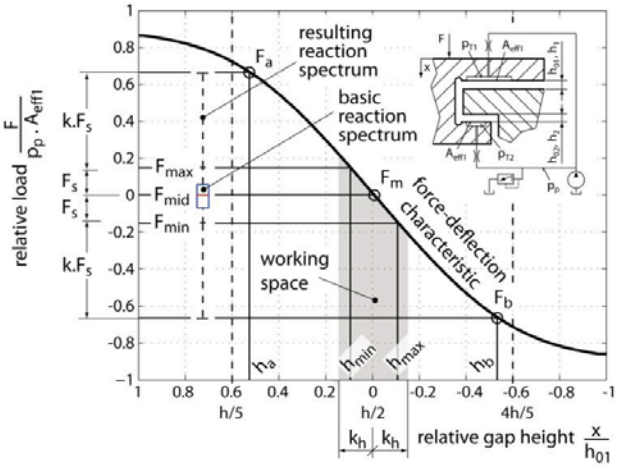

Fig. 8: The Force-deflection characteristic and description of the fitness function.

- It influences the slope of the force characteristic around the inflection point, and thus impacts on the stiffness of the bearing in the working space;
- By defining these limits the solution is 'forced' to be symmetrical and the inflection point of the characteristic (extreme stiffness of the bearing) moves to the center of the working space.

In order to prevent a collision between the pocket surface and the guide surface (i.e. to maintain a sufficient gap height), a second safety range was defined. On the horizontal axis of the chart in Fig. 3 this range is defined by the limit values of *20% (h/5)* and *80% (4h/5);* within these limits the force-deflection characteristic of a pair of pockets has to equal no more than the *k*-multiple of the F_s range, where *k* is an appropriately selected safety coefficient defining the *resulting reaction spectrum*. In the chart this range is defined by the F_a and F_b values . A flowchart representing the GA for obtaining an optimum force characteristic for the system based on pairs of pockets preloaded against each other is shown in Fig. 9.

The condition for ending the GA iteration process was a total of 20 generations where the fitness value remained basically unchanged. Where the result was not satisfactory from the point of view of both safety criteria, the limits for these criteria needed to be adjusted. In the opposite case the resulting characteristic of the HS pocket pair was saved in a file for further verification in the detailed FEM model.

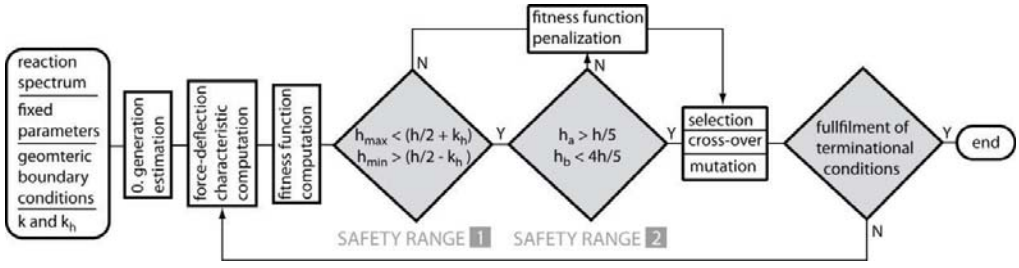

Fig. 9: Genetic algorithms based optimization.

3.3. Force reactions and deflections

The relevant conditions for the HS axes of the portal machine, which needed to be checked for in order to prevent undesired contact between the HS pocket surface and the guide surface were selected as the convergence criteria (in equations (5) and (7)) for the whole design process, include:

- The minimum gap height on the perimeter of the HS pocket (Fig. 10);

$$\min\{h_I, h_{II}, h_{III}, h_{IV},\} < h_D \tag{5}$$

- The tilting of the HS pocket in relation to the guide surface.

$$\text{rot X} < rot\,\text{X}_\text{D} \wedge \text{rot Y} < rot\,\text{Y}_\text{D} \tag{6}$$

However, as each of the HS pockets had different dimensions, the criterion defining the maximum allowable tilting (6) needed to be unified:

$$\max\{h_I, h_{II}, h_{III}, h_{IV},\} - \min\{h_I, h_{II}, h_{III}, h_{IV},\} < \varepsilon_D \tag{7}$$

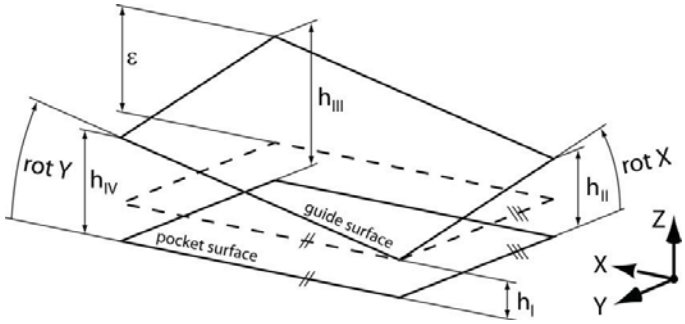

Fig. 10: Checking for undesired conditions of the HS pocket.

This check is performed for all pairs of HS pockets (Fig. 5) of the machine axis in question, in each iteration step of the design process, using the detailed FEM model of the whole machine loaded with a symmetrical load case (the F_{med} force from Fig. 3). The detailed FEM model of the whole machine is shown in Fig. 11.

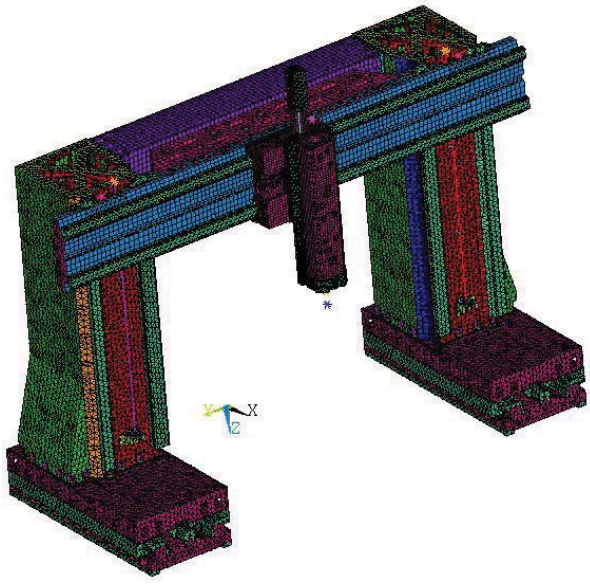

Fig. 11: Detailed FEM model of the machine.

Non-linear elements characterizing the force-deflection properties were added between the guideway parts in the direction of the *X* axis.The material and geometry of the model parts are defined by the specific brief. Connected mass elements: ca. *18 t*. Total mass of the model with connected masses: ca. *152 t*. The FEM model elements used in the ANSYS software: Solid45, Shell63, Mass21, Combin39.

In the detailed FEM model (Fig. 11) the guideways for the *Y*, *Z* and *W* axes (which are not part of the design process) are represented by linear springs with approximate stiffness. Non-linear elements characterizing the force-deflection properties of the HS guideway pockets (Fig. 8) were added between the guideway parts in the direction of the *X* axis.

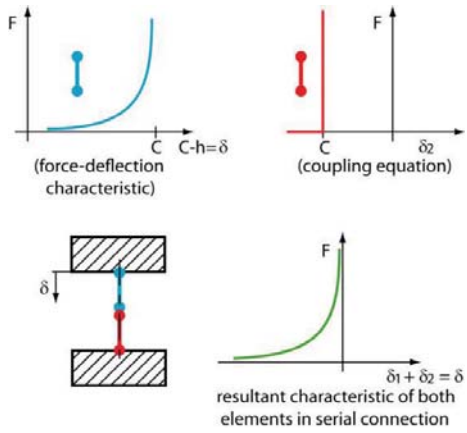

Fig. 12: Force-deflection characteristics of elements representing HS pockets.

Using ANSYS, each of the pockets is represented by a CONTA39 nonlinear spring and a preloading constraint equation to model the pocket characteristic and the nominal pocket gap as well, Fig. 12.

In case the conditions of inequations (5) and (7) are not met, the positions (numbers) of the HS pockets in the detailed model are sensitively adjusteded (according to detailed FEM model results) and new values for the medium load of the reaction spectra F_{mid} are computed (positions on the y axis of the chart in Fig. 6). The absolute magnitude of the reaction spectra (determined by the F_s value) does not change (based on the premise that data provided by the rigid FEM model correspond to all possible combinations of load cases, and their adjustment is not necessary due to the safety factors). In case the above-mentioned convergence criteria are met for the HS axis as a functional unit, the iteration process (Fig. 2) is terminated and the solution is considered to be complete.

4. Results

Satisfactory results were obtained-i.e. the convergence criteria (equations (5) and (7)) were met already in the second step of the iteration process shown in Fig 2. A comparison of iteration steps 0 (initial - Fig. 6) and 2 (final) is shown in Fig. 13.

During the process new pocket positions were found, their dimensions and capillary tube parameters were optimized; the number of pockets remained unchanged. As Fig. 13 shows, the reaction spectra (output from the rigid FEM model – Fig. 2) only change their position on the *y* axis (the position of medium load F_{med}); their magnitude (i.e. the range of the F_s forces) remains unchanged during the iteration process.

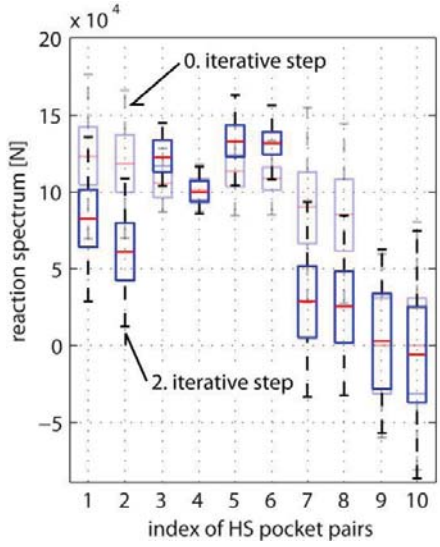

Fig. 13: Resulting reactions in the pocket pairs.

A total of 100 individuals in 500 generations were sufficient in each GA iteration step of the process shown in Fig. 9 to find suitable solutions (force-deflection characteristics of the HS pocket pairs) using GA.

The limits within which the resulting force characteristics of the HS pocket pairs have to be situated are determined by the coefficients k and k_h. For the vertical guideway the value of the safety coefficient k (a multiple of the load spectrum) equals *2.5*; for the lateral guideway (which already has large safety margins in the condition of zero drive stiffness) the value equals *2*. The k_h coefficient (defining the working space) is the same for both guideways and its values equals *0.01 mm*. Two examples of the resulting characteristics from the final, second iteration step of the whole design process for HS guideways of the X axis are shown in Fig. 14 (the marked areas and limits are the same as the marking in Fig. 5).

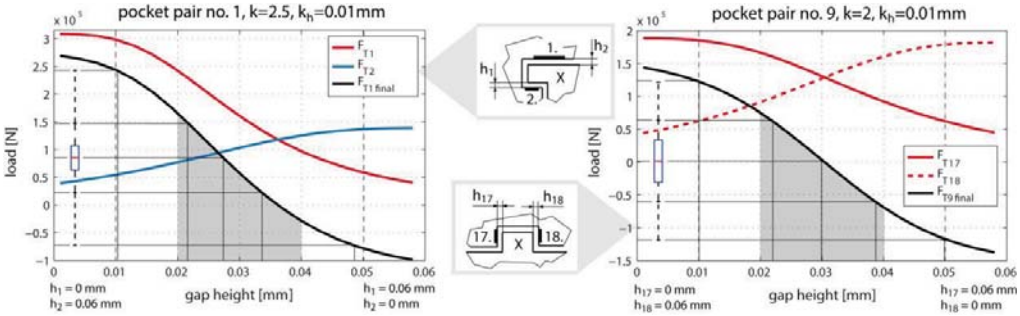

Fig. 14: An example of the resulting characteristics for pairs of HS pockets of the vertical (left) and lateral (right) guideway.

Due to loading (namely the weight of the parts) and to the overall flexibility of the longitudinal slide and the bed, significant local deflection occurred in the HS guideway of the X axis. The HS guideway pockets also tilted considerably, which reduced their load-bearing capacity.

Example results of the initial and the final design are shown in Fig. 15. The overall deflection after the longitudinal slide is loaded by the parts' own weight is shown.

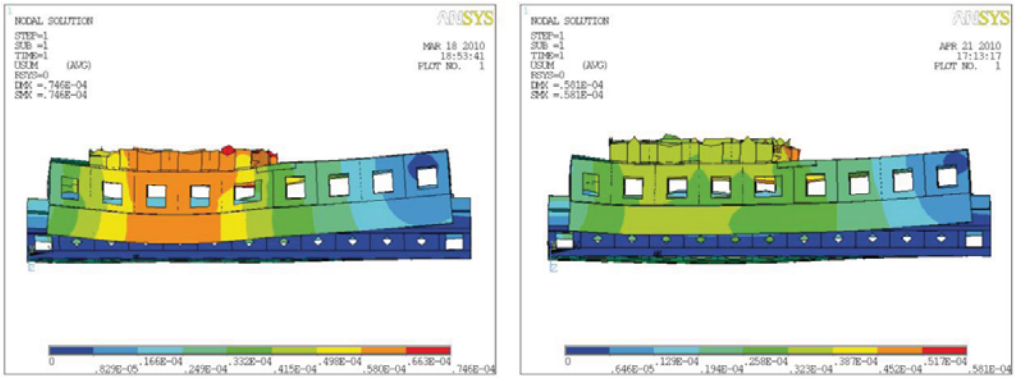

Fig. 15: Visualization of the results of the initial and the final design.

The convergence criteria (5) and (7) were set as follows: the minimum gap height on the perimeter of the pocket could not be less than $h_D = 0.010$ *mm*, and the tilting of the pocket in relation to the guide surface could not exceed the prescribed value of $\varepsilon_D = 0.007$ *mm.* When these criteria were met for all pockets of the HS guideway of the *X* axis, the design was considered to be complete.

5. Conclusions

An iterative approach to designing HS guideways for a machine tool has been presented, based on the finite element method (FEM) and an optimization method using the minimization task. The design aims to find suitable dimensions, location and number of HS pockets and controllers for the HS guideways in order to meet load-bearing requirements and minimize deflection.

The process was demonstrated on one half of the HS quideways of the *X* axis of a portal milling machine. Optimum results were obtained in the second iteration step. The whole iteration procedure has been automated.

The advantage of this design process combining multiparametric optimization and FEM lies in its robustness (the possibility to check for any parameter of the pocket or the guideway) and variability. The drawback are its demands on detailed FEM modeling. Any pocket shape and controller type can be taken into account, if their clear description exists in the fluid mechanics domain. Great variability of the optimization process is another indisputable advantage. The optimization can be based on any parameter or a combination of parameters. Instead of simple GA, the approach to designing HS guideways could be further developed by using NSGA II optimization (Deb et al., 2002), which does not use weight coefficients, and thus optimize the dimensions of the pockets and the controllers used from the point of view of more performance characteristics (e.g. adding stiffness and flow characteristics to force-deflection characteristics).

Acknowledgement

This research has been supported by the Czech Ministry of Education, Youth and Sports grant No. 1M0507.

References

Lewis, G.K. (1966), Flow and Load Parameters of Hydrostatic Oil Bearings for Several Port Shapes. *Journal Mechanical Engineering Science*, Vol.8, No.2, pp. 173-184.

Weck, M. & Brecher, Ch. (2006), *WerkzeugmaschinenKonstruktion und Berechnung*, ISBN 10 3-540-22502-1 Springer Berlin Heidelberg New York, Germany.

Sharma, S.C., Jain, S.C. & Bharuka, D.K. (2002), Influence of Recess Shape on the Performance of a Capillary Compensated Circular Thrust Pad Hydrostatic Bearing. *Tribology International* 35, pp. 347-356.

Shie, J.-S. & Shih, M.-Ch. (2010), A Study on Optimization Design of a Hydrostatic Bearing. *Proceedings of International Forum on Systems and Mechatronics*, pp. 1-6.

Wang, X. & Yamaguchy, A. (2002), Characteristics of Hydrostatic Bearing / Seal Parts for Water Hydraulic Pumps and Motors. Part 1: Experiment and Theory. *Tribology International* 35, pp.425-433.

Wang, X. & Yamaguchy, A. (2002), Characteristics of Hydrostatic Bearing / Seal Parts for Water Hydraulic Pumps and Motors. Part 2: On Eccentric Loading and Power Losses. *Tribology International* 35, pp.435-442.

Slocum, A.H., Scagnetti, P.A., Kane, N.R. & Brunner, Ch. (1995), Design of Self-Compensated, Water-Hydrostatic Bearings. *Precision Engineering* 17, pp. 173-185.

Ting, L.L. & Mayer, Jr., J.E. (1971), The Effect of Temperature and Inertia on Hydrostatic Thrust Bearing Performance. *Journal of Lubrication Technology*, pp. 307-312.

Sharma, S.C., Jain, S.C., Sinhasan, R. & Shalia, R. (1995), Comparative Study of the Performance of Six-Pocket and Four-Pocket Hydrostatic / Hybrid Flexible Journal Bearings. *Tribology International*, Vol.28, No.8, pp. 531-539.

Kim, S. & Cho, J.-W. (2006), Structural Characteristic Analysis of High-Precision Centraless Grinding Machine with a Concrete-filled Bed. *Internationa Journal of Precision Engineering and Manufacturing*, Vol.7, No.4, pp. 34-39.

Tlusty, J. (1993), High-Speed Machining. *Keynote Papers, Annals of the CIRP,* Vol.42, No.2, pp. 733-738.

Mekid, S. (2000), High Precision Linear Slide. Part I: Design and Construction. *International Journal of Machine Tool & Manufacture* 40, pp. 1039-1050.

Houck, Ch.R., Joines, J.A. & Kay, M.G. (1999), A Genetic Algorithm for Function Optimization: A Matlab Implementation, *North California State University*.

Deb, K., Pratap, A., Agarwal, S. & Meyarivan T. (2002), A Fast and Elitist Multiobjective Genetic Algorithm: NSGA-II, *IEEE Transactions on Evolutionary Computation*, Vol.6, No.2, pp. 182-197.

18th International Conference
ENGINEERING MECHANICS 2012
Svratka, Czech Republic, May 14 – 17, 2012

pp. 869–873
Paper #236

NUMERICAL SIMULATION OF 3D GLASS SAGGING PROCESS

I. Matoušek[*], M. Starý[**]

Abstract: *The article deals with possibilities of using the tools for computer modelling in glass industry with the intention on the sagging process. Possibilities of usage are demonstrated in 3D-models of rectangular glass sheets supported by simple mould. Numerical outputs are compared with verifying experimental results under laboratory conditions. Mentioned analysis allows identifying individual stages of the sagging process. Results of sensitivity analysis of chosen parameters are submitted in brief in the end of the article.*

Keywords: ***Glass, forming, sagging, bending, slumping.***

1. Introduction

Glass sagging process is ranked among the expanded glass technologies. It is used firstly for windscreen production; known is also a usage for a production of spherical optical elements and complex building elements, but also in an art glass manufacture. Glass sagging is a relatively complex technological process (Hyre, 2002), whereas its principle is based on the glass temperature dependence on glass rheological properties.

The principle of the method is notorious – glass sheet placed on a frame changes its shape under the influence of the gravity force at a given temperature corresponding to a viscosity under the deformation point (10^{10} Pas). The required shape is obtained through an interaction between the glass sheet, exposed to the viscous flow due to gravity forces, and the frame. The final shape is fixed due to viscosity increasing during the annealing process.

Glass products with more a more complex shapes and stricter dimension tolerances are required and products quality is more and more emphasized, so it is more and more difficult to obtain required aims through those traditional techniques of the product preparation. Therefore the need of an effective and accurate predictive computational model becomes increasingly crucial.

2. Experiment

For the purpose to analyze basic parameters of the glass sheet sagging process a special fixture, simple ring symmetrical along both vertical planes, has been projected (Fig. 1). Measurements were realized in the laboratory furnace with a special design (Fig. 3). Samples of glass sheet made of clear float soda-lime glass (Float glass by AGC with deformation point corresponding to the temperature of 593 °C) of an oblong shape with dimensions 100 x 150 x 2.1 mm has been put on the ring and subsequently they have been inserted together to a preheated laboratory furnace, in which sample has been heated up to the working temperature. As soon as the temperature in the whole cross section of the glass sheet exceeds deformation point sagging process starts. During the experiment a surface temperature of the glass sheet were measured by thermocouples from the top and the bottom side.

After a defined period of time (10, 20 and 40 minutes) the frame with the sagged sample was taken out of the laboratory furnace and annealed by the air. Consequently, the deflection along three basic curves (Fig. 2) was evaluated by means of a special gauging device with an optical laser sensor.

[*] Ing. Ivo Matoušek, Ph.D.: Department of Glass Producing Machines and Robotics, Technical University of Liberec, Studentská 1402/2; 461 17, Liberec; CZ, e-mail: ivo.matousek@tul.cz

[**] Ing. Michal Starý, Ph.D.: Department of Glass Producing Machines and Robotics, Technical University of Liberec, Studentská 1402/2; 461 17, Liberec; CZ, e-mail: michal.stary@tul.cz

The aim of experiments was the identification of boundary conditions, concretely the course of temperatures for a virtual model specification and an experimental evaluation of influence of chosen parameters on a course of sagging process. The measurement of samples sag was also used for the verification of computer model results.

Fig. 1: Experimental frame with sagged glass

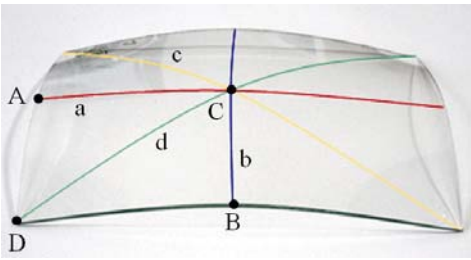

Fig. 2: Sample with measured lines and points

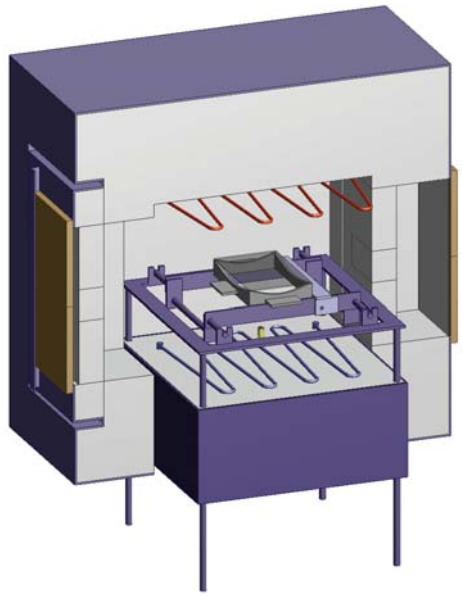

Fig. 3: Broken-out section of laboratory kiln

3. Virtual model

The flat glass gravity process is a complex couple thermo-mechanical problem characterized with strong interaction between the heat transfer and viscous flow of molten glass. Basic phenomena of the forming process are the distribution and the course of temperature fields in the sheet being shaped as well as viscosity changes with temperature.

Numerical modeling of glass forming is based on couple non-linear thermo-mechanical solution, described in the Lagrangian coordinate system by conversation equations, as follows:

$$\frac{\partial \sigma_{ij}}{\partial x_j} = b_i \tag{1}$$

$$\operatorname{div}\left(\lambda \operatorname{grad} T\right) = \rho\, c\, \dot{T} \tag{2}$$

where: σ_{ij} - the stress tensor, b - body force, T - temperature, λ - effective conductivity, c - specific heat.

Above temperature corresponding to the deformation point molten glass can be considered to be incompressible (ε_{ii} = 0). In this temperature interval the elastic part of the total strain is near insignificant and therefore constitutive behaviour of glass can be characterized by Newtonian model. Relation between equivalent von Misses $\bar{\sigma}$ stress and equivalent strain rate $\dot{\bar{\varepsilon}}$ is then defined through the Newtonian viscoplastic isochoric law, as follows:

$$\bar{\sigma} = 3\eta(T)\dot{\bar{\varepsilon}} \tag{3}$$

The viscosity of glass is highly dependent on temperature. In the glass forming range this dependence can be expressed by V-F-T model (Fulcher, 1925):

$$\log \eta(T) = A + \frac{B}{T - T_o} \tag{4}$$

where: A, B - temperature coefficients.

The critical factor of solved problem is the distribution of temperature fields in formed glass sheet. The sample is in the laboratory furnace heated by convection and radiation, which has a dominant influence. The heat transfer in the furnace is complicated by specific (molten) glass properties. Clear silica are semitransparent for infrared radiation, especially for near-infrared radiation and above the temperatures of 500 °C begins at heat transfer exert radiation (Fig. 4).

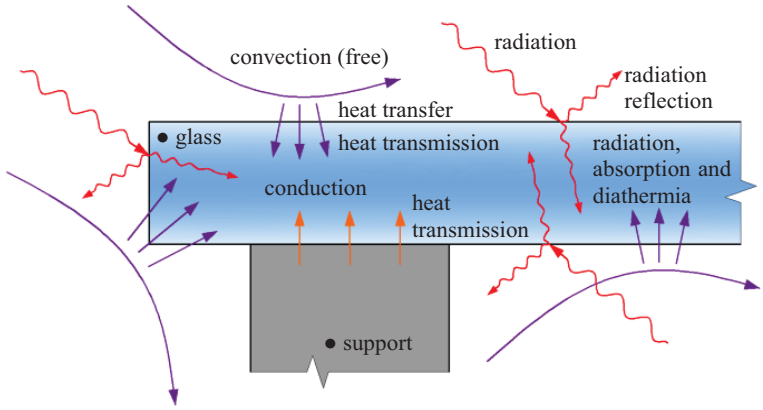

Fig. 4: Thermal transmittance at the sagging process

Considering the thickness of analyzed glass samples, there was used an effective conductivity and heat transfer in the system were realized by means of external subroutine. Geometrical characteristics were chosen according to the experimental model (Fig. 1), material properties of shaped glass were described through the rigid plastic model. The ring mould is assumed to be rigid (Fig. 5).

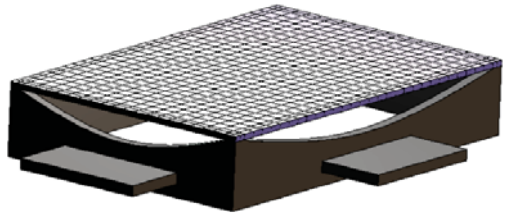

Fig. 5: Virtual model (FEM)

4. Results of virtual modelling

Numerical model allowed analyzing the course of the glass gravity bending process (Fig. 6 and 7).

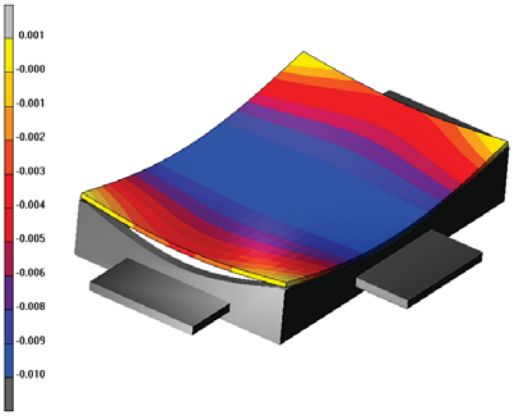

Fig. 6: Sagging on the ring at time 600 s

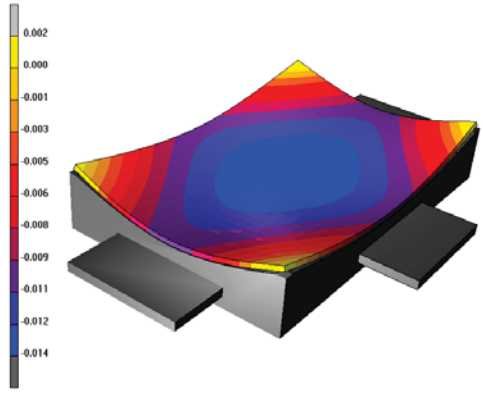

Fig. 7: Sagging on the ring at time 2400 s

Shaping behavior is demonstrable on Fig. 8 where the time flow of displacements is shown in four chosen points (see Fig. 2) for the defined boundary conditions. The sagging process (on the support ring shown in Fig. 1) itself consists of three different stages (see Fig. 9).

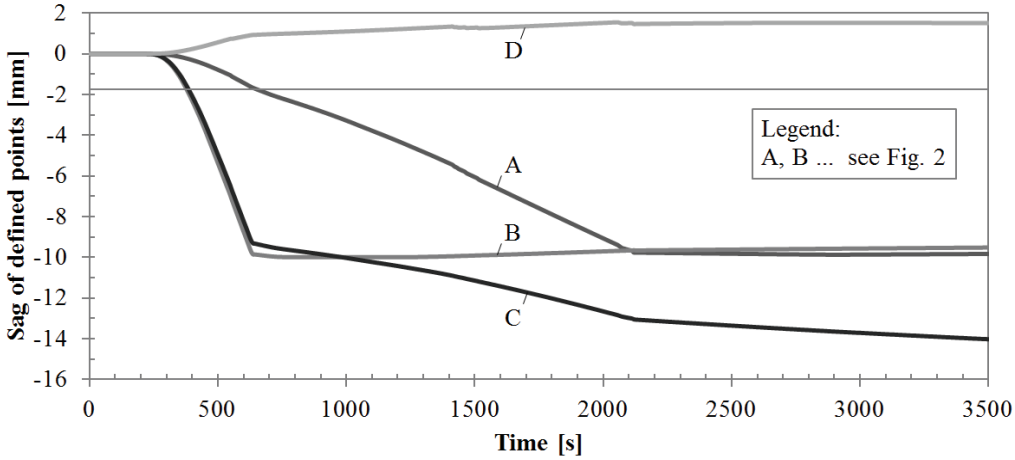

Fig. 8: Development of maximum displacement during sagging for defined points and sample thickness 2,1mm

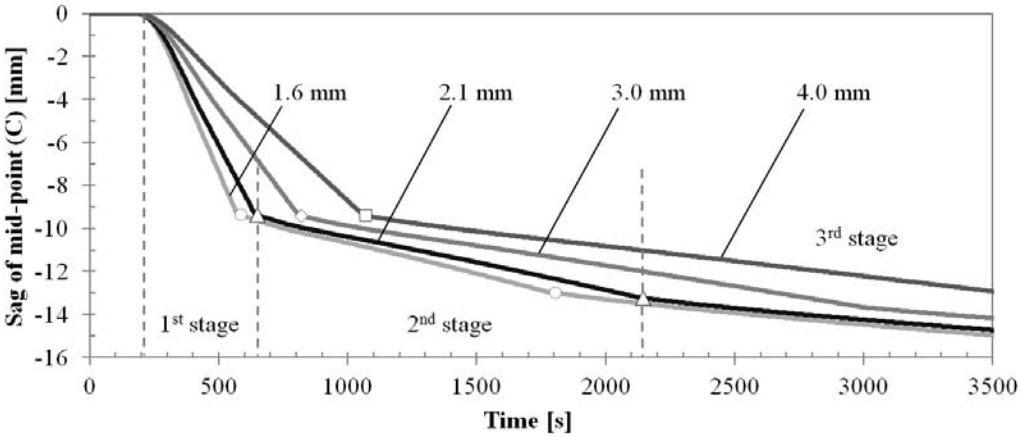

Fig. 9: Development of maximum displacement during sagging for various sample thicknesses

After warming through the cross section to the temperature above the temperature of deformation point glass sheet starts to deform (approx. 220 s from the moment of the sample feeding to the furnace for working temperature 618 °C and thickness 2.1 mm) - primarily along the longitudinal (longer) side. During the first stage samples deforms in similar way that is characteristic for the free bending between two supports. In the moment when sample comes to the contact with ring along longitudinal sides (Fig. 6 - for the sample thickness 2.1 mm, ca. 650 s after feeding glass sample into the furnace) the geometric conditions are modified, sample stiffness is changed that results in reduction of sagging velocity and the first stage is transformed to the second one. Sagging process continues with deformations along shorter side mainly. When the shorter sides come to the contact with the ring, velocity of sagging further decreases starts final stage (see Fig. 9).

The thermal field distribution in a shaped sheet was necessary to modify to obtain the equality of virtual model and experimental measurement. Laboratory furnace experiments were done by set control temperature of 630 °C. The stabile temperature on the upper surface of the sheet was 621 °C and on the bottom surface it was 613 °C due to these experiments. By this temperature distribution the maximal bend curve is moved to lower times, that means that sag bending runs faster then it corresponds to the experimental measurement. For this reason thermal flow intensity had to lowered down. The temperature of upper and bottom surface was decreased to 619 °C, respectively 612 °C.

According to these conditions there was in the time of 2400 s registered the distribution of displacements among curves showed on Fig. 10. The displacement behaviour along curves (for appointed range) is in really high equality with realized experiments, maximal deviation is under 1 %.

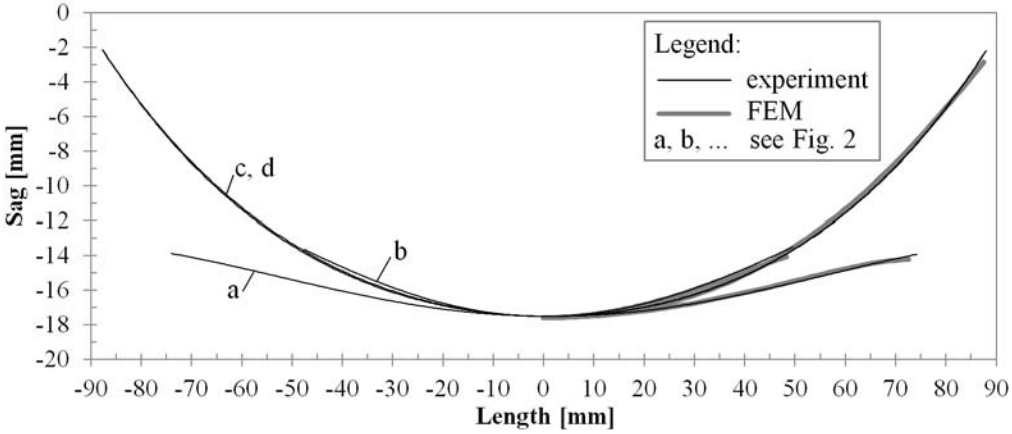

Fig. 10: Sample deflection along basic curves at time 2400 s and sample thickness of 2.1 mm

The numerical model verification allowed analyzing the influence of chosen parameters of sagging process. The sagging speed changes linearly with the viscosity change, the important characteristic is in this case except temperature also the quality of viscosity curve temperature dependency. The various thickness influence for simplified boundary conditions (the sample temperature is described by reference temperature) for the interval of 1.6 to 4.0 mm is shown on Fig. 9. The sagging speed in the first stage (and approximately in the second stage as well) of two blanks with various thickness is set by the square ratio of their thickness.

The sagging rate change in the gravity center due to the change in the thickness of glass sheet can be described by equation (5), generally, whereas for the 1st stage of the sagging process coefficient $c(l_l,l_t)$ is equal to 1.

$$v_2(z) = c(l_l, l_t)\frac{h_1^2}{h_2^2} v_1(z)\,, \tag{5}$$

where: $v_i(z)$ - sagging speed of the sample gravity center in vertical direction, h_i - sample thickness, $c(l_l, l_t)$ - geometrical coefficient, l - support distance along longitudinal (l_l) and transversal (l_t) axis.

5. Conclusions

In the paper a computer analysis of sagging process is presented. Comparison of numerical results with experiment validated the reliability of the numerical model. The sagging process on 3D support rings itself proceeds in three different stages and sagging rate decreases relatively markedly with the stiffness increase due to change of boundary conditions. Maximum sagging rate (at the sample gravity centre) changes linearly with the viscosity and with the square ratio of sample thickness.

Acknowledgement
The research was realized with the support of the research project MSM 4674788501 financed by the Ministry of Education of the Czech Republic.

References

Fulcher, G.S. (1925) Analysis of Recent Measurements of the Viscosity of Glasses. *Journal of American Ceramics Society*, 8, 6, pp.339-355.

Hottel, H. C., Sarofim, A. F. (1967) *Radiative heat transfer*. McGraw-Hill, New York.

Hyre, M. (2002) Numerical Simulation of Glass Forming and Conditioning. *Journal of American Ceramic Society*, 85, 5, pp. 1047-1056.

18th International Conference
ENGINEERING MECHANICS 2012
Svratka, Czech Republic, May 14 – 17, 2012

pp. 875–878
Paper #191

REINFORCED ELEMENTS OF STRUCTURES FROM THE GLUED LAMINATED TIMBER WITH HIGH PERFORMANCE LAMELLA

L. Melzerová*

Abstract: *The paper is concerned with an optimal design of high-strength reinforcing lamella made from glued laminated timber structure controlled by the lamella thickness and material. The stepping stone for the present analysis are the results of nondestructive bending tests of thirty beams with different types of reinforcing lamellas adopting two material variants. Six different thicknesses were examined. The FEM models are created such as to exactly represent the tested beams which allows for a reliable comparison of measured and simulated data, e.g. center point deflection. As a next step, new FEM models are created for one particular real beam made from glued laminated timber reinforced by high performance lamella. Both thickness and material of this lamella are modified in individual numerical simulations to estimate an optimal degree of reinforcement with respect to the maximum deflection allowable for a given loading.*

Keywords: ***Glued laminated timber, High performance lamellas, FEM models***

1. Introduction

The paper is concerned with the search for optimal thickness and material of reinforcing lamella introduced into glued laminated timber beam structures. An extensive experimental as well as numerical investigation of real glued laminated timber beams with no additional reinforcements has been described in detail in our previous work suggesting the need for a detailed evaluation of the influence of Young's modulus of elasticity in the fiber direction.

Hereinafter, we extend the previous work by considering an additional reinforcing element in terms of a high strength composite lamella glued at the bottom surface of the beam. Thirty such beams were examined experimentally. The first half of specimens was enhanced by glass-fiber (G) reinforced composite lamella, while carbon (C) fibers based composites were adopted in the second half of the specimens. Three different thicknesses of the reinforcing lamella were considered for each group of composites. Thickness of 2, 4, and 6 mm were assumed for carbon fiber composites (notation C2, C4 and C6). For glass fiber composites the thicknesses of 5, 10, and 15 mm were adopted (notation G5, G10 and G15). The experimental measurements, performed up to failure, were then compared with numerical simulations using again the Finite Element Method (FEM).

Each of the tested specimens was represented by a unique FEM model taking into account not only the type of reinforcing lamella but also the particular material composition of timber selected randomly when preparing the specimens. The center point deflection has been selected again to compare the experimental and numerical results. Next, one of the specimens was selected to numerically investigate the influence of thickness and material of the reinforcing lamella on the beam response.

2. FEM models of thirty reinforced real tested beams

This section describes the simulation part of the work carried out for thirty FEM models split into six groups labeled as C2, C4, C6, G5, G10 and G15 thus resulting into five models for each group. One particular example of such a beam is illustrated in Figure 1.

The center beam deflection is used to assess the degree of agreement between experimental work and numerical simulations. First, this criterion is exploited for a comparative loading of 24 kN of each force in Figure 2 used in our previous study to assess the impact of reinforcing lamella in comparison

* Ing. Lenka Melzerová, Ph.D.: CTU in Prague, Faculty of Civil Engineering, Department of Mechanics, Thákurova 7; 166 29, Prague; CZ, e-mail: melzerov@fsv.cvut.cz

to the beams with no reinforcement. The comparison between laboratory and numerical experiments is evaluated next for the maximum loading, see Figure 3. As expected, we have not achieved such a good agreement owing to the no nonlinear response prior to fatal failure in experiments not captured by purely elastic simulations. On the other hand, such loadings are not acceptable for real structures in use and therefore the nonlinear branch of loading curve linked to the evolution of cracks has not been investigated in this study. The third loading state considered 48 kN for each force as depicted in Figure 4. In this case, a perfect match between the laboratory measurements and numerical results was achieved.

Fig. 1: FEM model of one particular beam

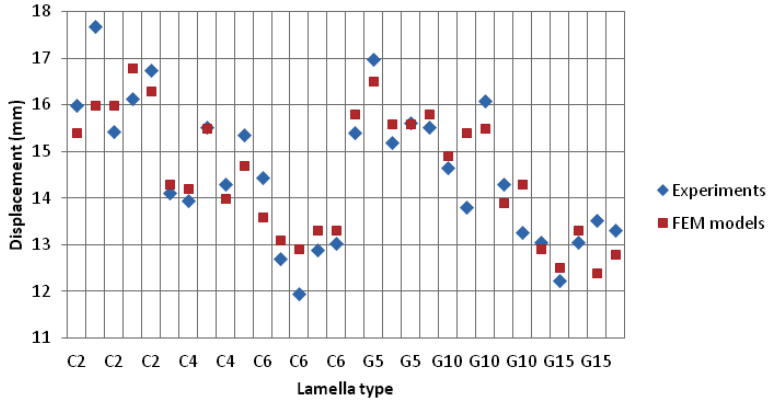

Fig. 2: Comparison between laboratory measurements and numerical simulations for thirty specimens loaded by two forces with the magnitude of 24 kN

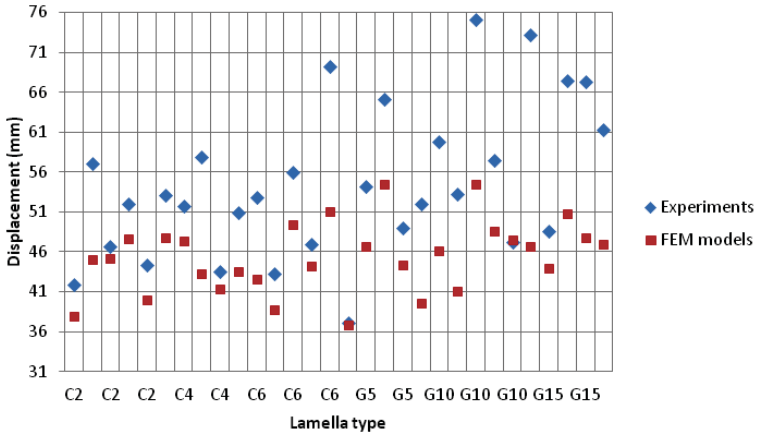

Fig. 3. Comparison between laboratory measurements and numerical simulations for thirty specimens subjected to maximum loading

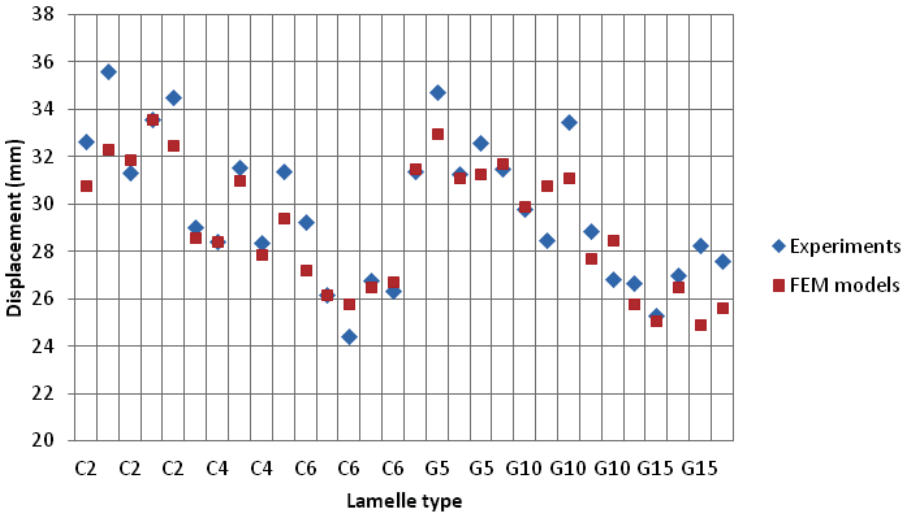

Fig. 4. Comparison between laboratory measurements and numerical simulations for thirty specimens loaded by two forces with the magnitude of 85 kN

3. FEM simulation of different thicknesses and materials of reinforced lamellas

The beam No. 16 was selected for the purpose of optimization. This beam experienced the lowest strength out of all investigated beams. It failed at the compression surface at the load level of 64 kN of each force. A randomly place lamella with low strength was introduced at the top, the most compressed, surface the during production step. The optimization procedure investigated the influence of the reinforcing lamella thickness and its material assuming the load level equal to 48 kN of each force, thus being well within the elastic response of the tested beam. The resulting deflections for both types of materials are plotted in Figure 5. The reinforcing lamellas assumed thickness from 2 to 20 mm with a 2mm step.

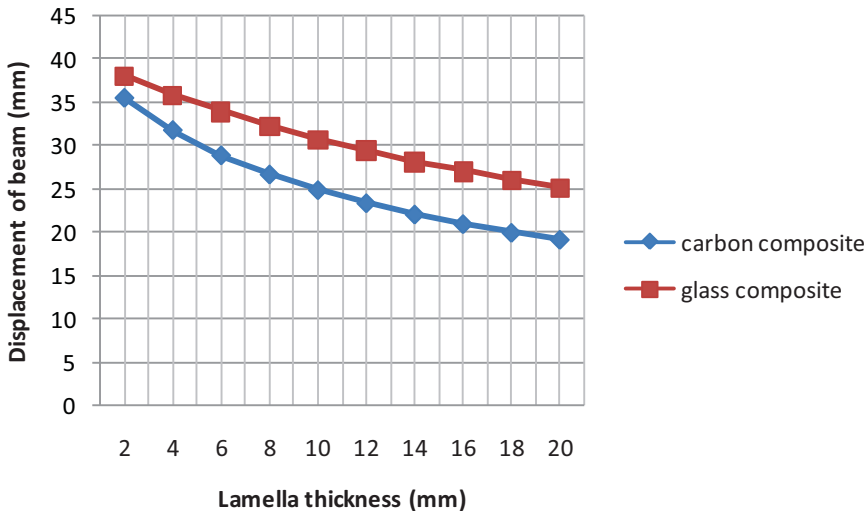

Fig. 5. Evolution of a center point deflection as function of the lamella thickness for the selected beam No. 16 for both types of composites for the loading level of 48 kN

4. Conclusions

It can be seen that the results provided by FEM simulations agree rather well with experimentally derived data. The positive impact of reinforcing lamella manifested by the reduction of maximum deflection is evident. The presented results allow for obtaining an optimal design with respect to three parameters (lamella thickness, deflection and loading). Optimizing thicknesses of both types of composite reinforcements enables to define an optimal reinforcing lamella for each of the beam. This will be subject of future research.

Acknowledgement

This outcome has been achieved with the financial support of the Ministry of Education, Youth and Sports of the Czech Republic, project No. LD12023 advanced methods for design, strengthening and evaluation of glued laminated timber and project No.SGS12/117/OHK1/2T/11.

References

Melzerova, L. and Kuklik, P. (2010) Variability of Strength for Beams from the Glued Laminated Timber, in *Proceedings of the 48th International Scientific Conference on Experimentalni Analyza Napeti 2010 Experimental Stress Analysis*, Smid P., Horvath P., Hrabovsky M., eds., pp. 257-260.

Melzerova, L. and Kuklik, P. (2010) Statistical Research of Mechanical Properties of Glued Laminated Timber Beams, *Metallurgy*, vol. 49, no. 2, pp. 376-380. ISSN 0543-5846.

Melzerova, L. and Kuklik P. (2011) Beams from the Glued Laminated Timber with the High Performance Lamellas and their FEM Models, in *Experimentalni Analyza Napeti 2011*, pp. 237-244.

Melzerova, L., Kuklik P. and Šejnoha M. (2011) Variable Local Modulus of Elasticity as Inputs to the FEM Models of Beams from the Glued Laminated Timber, in *2nd International Conference on Material Modelling.* Paris: TRANSVALOR-Presses des MINES, p. 313.

18th International Conference
ENGINEERING MECHANICS 2012
Svratka, Czech Republic, May 14 – 17, 2012

pp. 879–887
Paper #193

DYNAMIC BEHAVIOUR OF LOCOMOTIVE WITH AXLE-MOUNTED TRACTION MOTORS

T. Michálek*, J. Zelenka**

Abstract: *Especially in case of locomotives for freight operation, nose-suspended traction motors are usually used nowadays. This solution of traction drive is simple and relatively cheap; however, because of bearing of the traction motors directly on the axles, this solution contributes to increase the unsprung masses with all negative influences on dynamic interaction between the rail vehicle and the track, as well. Therefore, this paper deals with influence of nose-suspended traction drive of a locomotive on the dynamic interaction between the vehicle and the track. By means of simulations, dynamic behaviour of the locomotive with axle-mounted traction motors is compared with dynamic behaviour of a locomotive equipped with fully suspended traction drive.*

Keywords: ***Nose-suspended traction motor, dynamic interaction vehicle–track, simulations.***

1. Introduction

In framework of solving of R&D project "TIP" of the Ministry of Industry and Trade of the Czech Republic in years 2010–2012, Jan Perner Transport Faculty of the University of Pardubice co-operates with company CZ LOKO, a.s. at research and development of a new modular four-axled diesel-electric locomotive Class 744.0. Among others, computer simulations of running and guiding behaviour of the new locomotive are realized at Detached Branch of the Jan Perner Transport Faculty in Česká Třebová. Nowadays, the computer simulations create an integral part of development of new railway vehicles and allow assessing of dynamic behaviour of these vehicles in design stage and possibly optimizing of some parameters, as well. This work deals with dynamic interaction between the locomotive, which is equipped with axle-mounted nose-suspended traction motors, and the track. By means of simulations, dynamic effects of run of the locomotive equipped with nose-suspended traction motors are compared with a locomotive with fully suspended traction drive.

2. Locomotive Class 744.0

The locomotive Class 744.0 is a four-axled diesel-electric locomotive for shunting as well as track service which is equipped with new CZ LOKO bogies. These bogies are two-axled with wheel base of 2400 mm; each wheelset is driven by axle-mounted nose-suspended asynchronous traction motor TAM 1084 C6. Wheelset guiding is performed by means of connecting rods; primary as well as secondary suspension is realized by means of flexi-coil springs. Traction and breaking forces between the bogie frame and the vehicle body are transmitted by means of a central pivot. The wheelsets are equipped with a disc brake; the brake discs are mounted into the wheels. Detailed description of the new bogie is given for example in the paper (Kopal, 2009).

The locomotive Class 744.0 can be produced in various versions with a power of 800 up to 1500 kW and maximum speed up to 120 km/h. Total weight of a standard-gauged version of the locomotive can range from 64 up to 90 t. Besides the standard-gauged version, a broad-gauged version of the locomotive, which is designed according to the GOST standards, is being prepared for the track gauge 1520 mm, as well. Nowadays, a prototype of the standard-gauged version of the locomotive 744.001 is tested in framework of its authorisation process.

* Ing. Tomáš Michálek: University of Pardubice, Jan Perner Transport Faculty, Department of Rail Vehicles, Detached Branch Česká Třebová, Slovanská 452; 560 02, Česká Třebová; CZ, e-mail: tomas.michalek@student.upce.cz

** doc. Ing. Jaromír Zelenka, CSc.: University of Pardubice, Jan Perner Transport Faculty, Department of Rail Vehicles, Detached Branch Česká Třebová, Slovanská 452; 560 02, Česká Třebová; CZ, e-mail: jaromir.zelenka@upce.cz

3. Dynamic model of the locomotive

For purposes of computer simulations of dynamic behaviour of the locomotive, an original program system "SJKV" for multi-body simulations was used. This program system is being developed at the Detached Branch of the Jan Perner Transport Faculty in Česká Třebová and allows creating of various modifications for concrete rail vehicles. Detailed description of the program system "SJKV" is given in the paper (Zelenka, 2009). In framework of solving the R&D project "TIP", a new version of the program system named "SJKV-Lok744" was created. This modification of the program system allows investigation of dynamic behaviour of the standard-gauged as well as broad-gauged version of the locomotive Class 744.0 CZ LOKO; see also papers (Zelenka & Michálek, 2011; Kohout et al., 2011).

Because of time requirements and numerical stability of computations it is useful to consider only the important bodies (i.e. the bodies with a big weight) in the multi-body simulations. Therefore, dynamic model of the locomotive consists of seven rigid bodies: four wheelsets, two bogie frames and vehicle body. The other components are reduced to these "basic" bodies. Each rigid body of the dynamic model has 6 degrees of freedom and is defined by means of its mass, inertia moments as well as position of the centre of mass. Constituent bodies of the dynamic model are coupled by means elastic and damping joints which represent springs, dampers, elements of the wheelset guiding, bump stops etc. A schema of the dynamic model of the locomotive is shown in fig. 1.

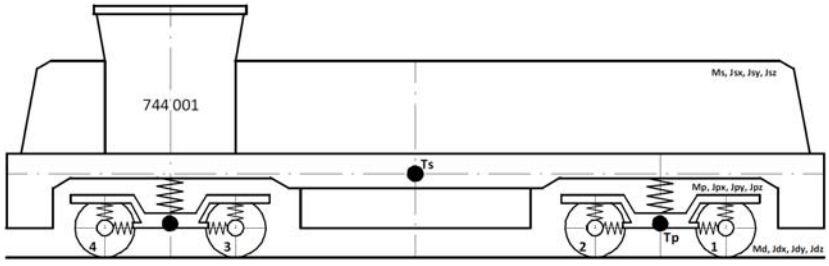

Fig. 1 Schema of dynamic model of the locomotive Class 744.0 CZ LOKO.

Besides to that, dynamic model of the track is created with reduced masses of rails which belong to each of wheels; these rails are coupled with the base by means of elastic and damping joints. For purposes of the simulations, wheel/rail contact is described by means of characteristics of wheel/rail contact geometry and it is considered as a one-point contact. Numerical solution of the model (i.e. solution of equations of motion) is based on finite differences method; see also the paper (Michálek & Zelenka, 2011), for example.

As it was stated above, the dynamic model of the locomotive is created only with seven "basic" rigid bodies and all the other elements have to be reduced to these bodies. Reduction of springs, dampers, elements of wheelset guiding etc. is relatively simple because of their mass which is very small in comparison with the "basic" bodies – i.e. vehicle body, bogie frames and wheelsets. However, reduction of components of the traction drive can be more problematic. In case of a fully suspended traction drive (for example drive with a hollow shaft), the traction motor including gearbox is fastened on the bogie frame and therefore we can suppose that the motor and bogie frame make a whole, i.e. one rigid body. However, the locomotive Class 744.0 is equipped with axle-mounted nose-suspended traction motors. Construction of the nose-suspended traction motor is very simple; the motor is mounted directly on the wheelset (by means of so-called nose bearings) and on the opposite side it is suspended on the bogie frame (by means of a flexible joint). A schema of the nose-suspended traction drive with rolling nose bearings is shown in fig. 2. The greatest advantage of the axle-mounted nose-suspended traction drive is just the simplicity and related lower price; therefore, this solution is often used on locomotives for freight operation. The greatest disadvantage of the nose-suspended traction motors is the fact that approximately 60 up to 80 % of the mass of the traction motor (including the gear transmission) creates unsprung masses; it is related with the three-point bearing of the traction motor on the wheelset and bogie frame. However, because of requirement on invariable position of the gearwheels (and the constructional solution – see fig. 2), the whole mass of the traction motor creates the unsprung mass in lateral direction. And it is generally known that a share of the unsprung masses has a significant influence on the dynamic interaction between the vehicle and the track.

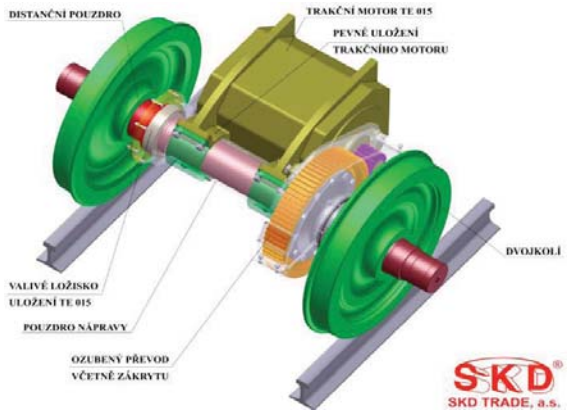

Fig. 2 Nose-suspended traction motor (Šlitr, 2007).

In framework of this work, two different alternatives of dynamic model of the locomotive were created. The first variant represents the locomotive Class 744.0 CZ LOKO with a total weight of 80 t equipped with the axle-mounted nose-suspended traction motors. The second one represents an imaginary locomotive which has the same parameters (total weight, masses and inertia moments of the bodies, characteristics of joints etc.) as the Class 744.0, but it is equipped with some kind of fully suspended traction drive. Therefore, mass of the traction motors does not increase the share of unsprung masses in this case. Relevant modifications of the dynamic model were performed in following way – in case of the locomotive equipped with nose-suspended traction drive, mass of the traction motors was "divided" between the wheelset and the bogie frame in the equations of motion of these bodies in vertical direction; it means:

$$\ddot{z}_d = g + \left(M_d + \frac{2}{3} \cdot M_{TM} \right)^{-1} \cdot \sum_{(i)} F_{dz,i}, \tag{1}$$

$$\ddot{z}_p = g + \left(M_p + 2 \cdot \frac{1}{3} \cdot M_{TM} \right)^{-1} \cdot \sum_{(i)} F_{pz,i}, \tag{2}$$

where $\ddot{z}_d$ is acceleration of wheelset in vertical direction, $\ddot{z}_p$ is acceleration of bogie frame in vertical direction, g is acceleration of gravity, M_d is mass of wheelset, M_p is mass of bogie frame, M_{TM} is mass of traction motor, $\Sigma F_{dz,i}$ represents forces, which act on the wheelset in vertical direction, and $\Sigma F_{pz,i}$ represents forces, which act on the bogie frame in vertical direction. In case of all other degrees of freedom (except rotational motion of the wheelset around its lateral axis), the whole nose-suspended traction motor is considered as a part of the wheelset in this dynamic model. Inertia moments of wheelset were modified on basis of CAD model of the bogie so that their values represent the whole rigid body "wheelset + traction motor". Thus, this modification takes into account the fact that approximately 70 % of the nose-suspended traction motor creates the unsprung mass in vertical direction and 100 % of mass of the motor creates the unsprung mass in lateral direction.

In case of the imaginary locomotive, which would be equipped with a fully suspended traction drive, relevant modification of dynamic model of this locomotive is based on the assumption that traction motors are fastened to the bogie frame. Therefore, mass of the traction motors is added to the mass of the bogie frame and inertia moments of the bogie frame are modified in relevant way. This condition is valid for all translational degrees of freedom in this case; for example the equations of motion of the wheelset and the bogie frame in vertical direction have following form now:

$$\ddot{z}_d = g + \frac{1}{M_d} \cdot \sum_{(i)} F_{dz,i}, \tag{3}$$

$$\ddot{z}_p = g + \left(M_p + 2 \cdot M_{TM} \right)^{-1} \cdot \sum_{(i)} F_{pz,i}. \tag{4}$$

4. Simulations of dynamic behaviour of the locomotives

The aim of this work is to compare the dynamic behaviour of a locomotive, which is equipped with an axle-mounted nose-suspended traction drive, with a locomotive with a fully suspended traction drive. This comparison was made by means of computer simulations of run of the locomotive Class 744.0 CZ LOKO with a total weight of 80 t and an imaginary locomotive with the same parameters, but with the fully suspended traction drive. Dynamic models of these locomotives, which were used for multi-body simulations in the program system "SJKV", are described in previous chapter.

It is generally known that the share of unsprung masses in running gear of a rail vehicle influences above all dynamics of wheel forces (i.e. the vertical forces acting in wheel/rail contact); the dynamic effects of the vehicle run on the track increase with increasing vehicle speed and decreasing quality of a track geometry. Therefore, the assessment of dynamic behaviour of the locomotives (Class 744.0 with nose-suspended traction drive and the imaginary locomotive with fully suspended traction drive) was performed for various speeds and under conditions of three various tracks (with various track geometry). In all cases, conditions of wheel/rail contact geometry and the friction coefficient in wheel/rail contact were identical – the wheel/rail contact with a value of equivalent conicity 0.207 and the friction coefficient 0.40 were used.

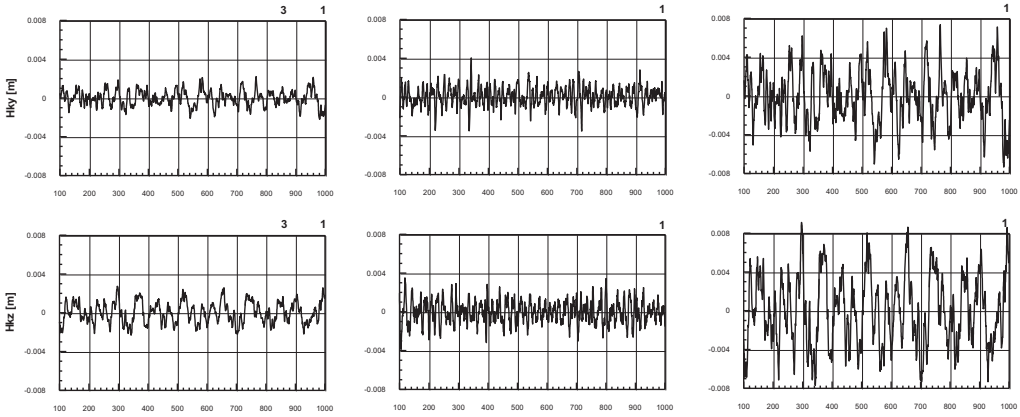

Fig. 3 Deviations of left rail position from the ideal position in horizontal (top) and vertical (bottom) direction for considered tracks – "T_OREk3" (left), "T_ChDo" (in the middle) and "T_ORE" (right).

Three various tracks were used at the simulations; these tracks are designated as "T_OREk3", "T_ChDo" and "T_ORE", and each of these tracks shows different level of quality of the track geometry. These simulation input data describing the track geometry were obtained from a super-structure measurement car or on the basis of so-called "ORE-track" which is given by means of a power spectral density of deviations of European tracks. All the simulations were performed in a straight track with a length of 900 m. According to the Appendix C of the European standard EN 14363, the quality of the track geometry is assessed by means of maximum values Δy_{max} and Δz_{max} and standard deviations s_y and s_z of deviations of the real rail position from the ideal position which is given by means of a track alignment. Values of these characteristics for considered tracks are given in tab. 1; records of deviation of the left rail from the ideal position in vertical and horizontal direction are shown in fig. 3. The track "T_OREk3" has the best quality; "T_ORE" has the worst quality.

Tab. 1 Maximum values and standard deviations of deviation of rail position from the ideal position.

Track	Δy_{max} [mm]	s_y [mm]	Δz_{max} [mm]	s_z [mm]
"T_OREk3"	2.21	0.80	2.74	1.08
"T_ChDo"	4.03	0.97	3.85	1.14
"T_ORE"	7.36	2.68	9.11	3.59

5. Simulation results

As it was mentioned, the share of unsprung masses influences above all the dynamics of wheel forces. Therefore, especially the wheel forces were observed at the simulations. In case of considered locomotives with a total weight of 80 t, the static wheel force (static load) has a value of 98.1 kN. During the run of the vehicle, the wheel forces oscillate around this static load value; level of these oscillations depends on vehicle speed as well as on quality of the track geometry.

At the simulations post-processing, time histories of the wheel forces were statistically processed. At first, the time histories were filtrated by means of upper limiting filter 20 Hz. Consequently, standard deviations of wheel force of the left wheel of the 1st wheelset were calculated from the filtered time histories. In fig. 4 there are compared obtained dependencies of these standard deviations on the vehicle speed from a range of 80 up to 160 km/h for all three considered cases given by the quality of the track geometry (see chapter 4).

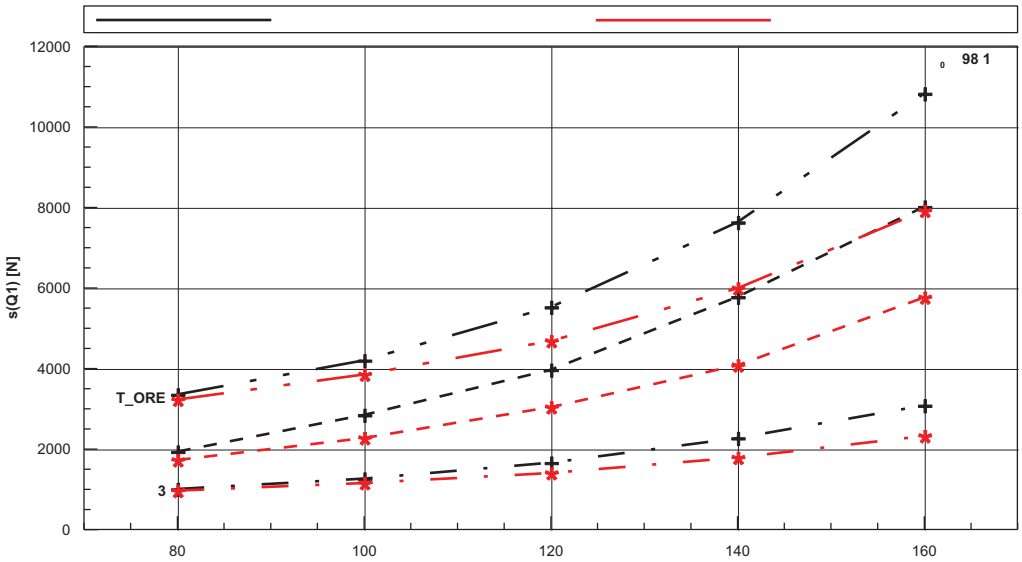

Fig. 4 Standard deviations of wheel force of the left wheel of the 1st wheelset in dependency on vehicle speed for all three considered cases of quality of the track geometry.

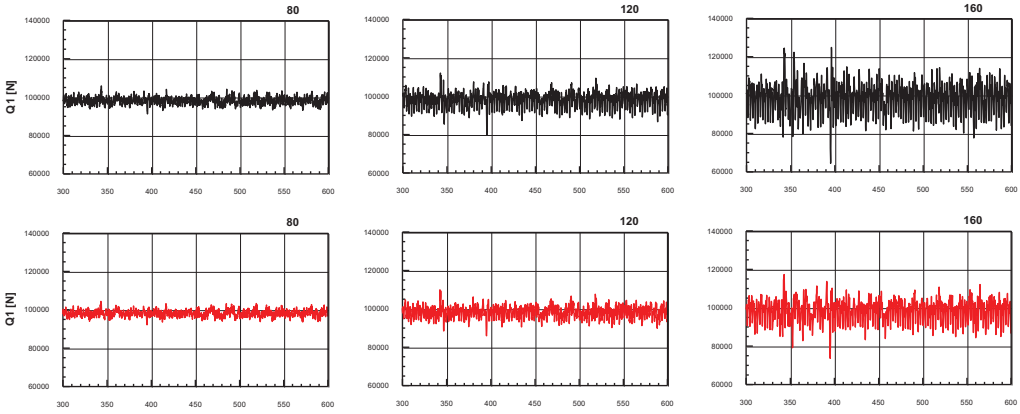

Fig. 5 Records of wheel force of the left wheel of the 1st wheelset on the track "T_ChDo" at speed of 80 km/h (left), 120 km/h (in the middle) and 160 km/h (right) for the locomotive equipped with nose-suspended traction drive (top) as well as with fully suspended traction drive (bottom).

From the graph in fig. 4 it is apparent that the dynamics of wheel forces depends strongly on the quality of the track geometry as well as on the vehicle speed. A difference between the locomotive equipped with axle-mounted nose-suspended traction drive and the locomotive with fully suspended traction drive is more significant with increasing speed, too. This statement is valid for all three tracks; in case of worse quality of the track geometry, the difference is certainly bigger. For example in case of the track "T_ChDo", relative value of the standard deviation of the wheel force (related to the static wheel load) reaches following values – in case of the locomotive with nose-suspended traction motors: 2.0 % (at speed 80 km/h), 4.1 % (120 km/h) and 8.2 % (160 km/h); in case of the locomotive with fully suspended traction drive: 1.8 % (80 km/h), 3.1 % (120 km/h) and 5.9 % (160 km/h). In fig. 5 there are shown records of wheel force of the left wheel of the 1st wheelset on the track "T_ChDo" for both alternatives of the locomotive at these speeds. Of course, maximum values of the relative standard deviation are reached on the worst track "T_ORE" – in case of locomotive with nose-suspended traction motors, the relative standard deviation has a value of 11.0 % at speed 160 km/h; in case of locomotive with fully suspended traction drive it is "only" 8.1 % at the same speed.

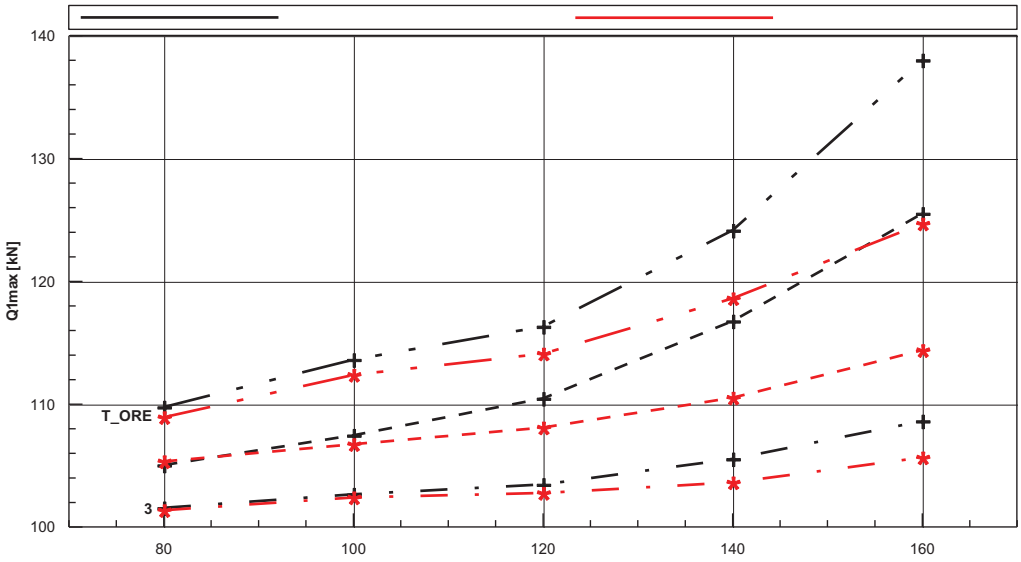

Fig. 6 Expected maximum values of wheel force for both alternatives of the locomotive with total weight of 80 t in dependency on vehicle speed according to the EN 14363.

The second method, which was used for the assessment of dynamic interaction between the vehicle and the track in vertical direction, was an evaluation of so-called expected values of maximum wheel forces according to the European standard EN 14363, which deals with testing of new or modernized railway vehicles in framework of their authorization process. This assessment was also used for both alternatives of the locomotive running at speeds from the range of 80 up to 160 km/h on the same three tracks. The filtered time histories (upper limiting filter 20 Hz) of wheel forces were also used at this method of evaluation. In this case, the time histories are divided into sections with a length of 250 m (± 10 %); then, it is necessary to determine for each assessed set of wheels in all these sections values of wheel forces, which correspond to a cumulative frequency of 99.85 %. After that, a mean value $M[Q_{max}]$ of these values and their standard deviation $S[Q_{max}]$ are calculated. The expected value of the maximum wheel force is given as:

$$Q_{\max} = M[Q_{\max}] + 2.2 \cdot S[Q_{\max}]. \tag{5}$$

In this concrete case, both wheels of the first wheelset were considered at computation of the expected values of maximum wheel force and the time histories of the wheel forces obtained from the simulations were divided into four sections with a length of 225 m. Results of this statistic assessment are presented in fig. 6. A limit value of the maximum wheel forces (according to the EN 14363) of both considered variants of the locomotive is 188.1 kN.

This method of assessment of the wheel forces confirms the above mentioned results obtained by means of the simplifier method using the standard deviations (see fig. 4). Although the limit value of the maximum wheel force is not exceeded in any case, it is evident that the difference between the locomotive with nose-suspended traction motors and the locomotive with fully suspended traction drive becomes to be more significant with increasing speed. Especially in case of worse quality of the track geometry, this difference is considerable at speeds higher than approximately 120 km/h. For example on the tracks "T_ChDo" and "T_ORE" – while the locomotive, which is equipped with nose-suspended traction drive, shows values of the maximum wheel force higher by approximately 2 % (than the locomotive with fully suspended traction drive) at speed 120 km/h, this difference has a value of approximately 10 % at speed 160 km/h.

Although the share of unsprung masses influences above all the dynamics of wheel forces, it certainly has an influence on interaction between the vehicle and the track in lateral direction, as well. As it was said, in case of the axle-mounted nose-suspended traction drive, approximately 60 up to 80 % of weight of the traction motor creates unsprung masses in vertical direction, but it is practically 100 % in lateral direction. However, an assessment of the lateral interaction between the vehicle and the track is more complicated. At first, the dynamic behaviour of rail vehicle in lateral direction is influenced by means of wheel/rail contact geometry very significantly. Especially at higher speeds, the stability of vehicle run can influence the results, as well. Then, it is also necessary to take into account that a simplified dynamic model of the locomotive was used at the simulations. From these reasons, an evaluation of the "lateral dynamics" was made only by means of standard deviations of lateral acceleration of the 1st wheelset in this stage – in a similar way as the assessment of wheel forces. Time histories of the lateral wheelset acceleration were also filtrated (upper limiting filter 20 Hz) before calculation of the standard deviations. In fig. 7 there are compared obtained dependencies of these standard deviations on the vehicle speed from a range of 80 up to 160 km/h for the tracks "T_ORE" (the worst quality of the track geometry) and "T_OREk3" (the best quality of the track geometry). In fig. 8 there are shown records of lateral acceleration of the 1st wheelset on the track "T_ORE" for both alternatives of the locomotive at various speeds; moving quadratic means are added there, as well.

The realized simulation results show following: from the point of view of the "lateral dynamics" during the run in a straight track, the difference between the locomotive with nose-suspended traction motors and the locomotive with fully suspended traction drive also exists. On the basis of fig. 7 it is possible to state that the "lateral dynamics" is related above all with the quality of track geometry and the difference between both variants of the locomotive are marked only at higher speeds.

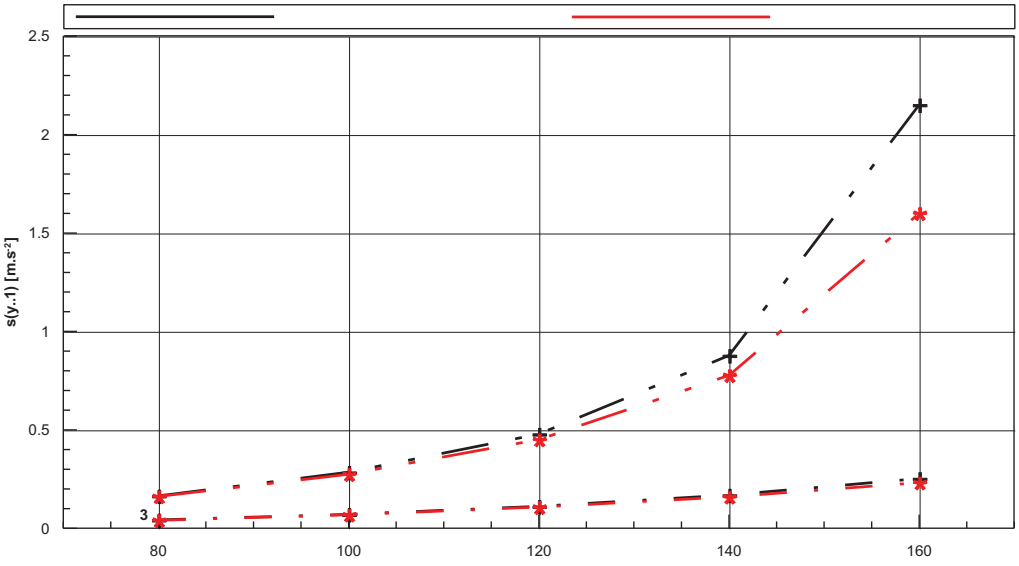

Fig. 7 Standard deviations of lateral acceleration of the 1st wheelset in dependency on vehicle speed on tracks "T_ORE" and "T_OREk3".

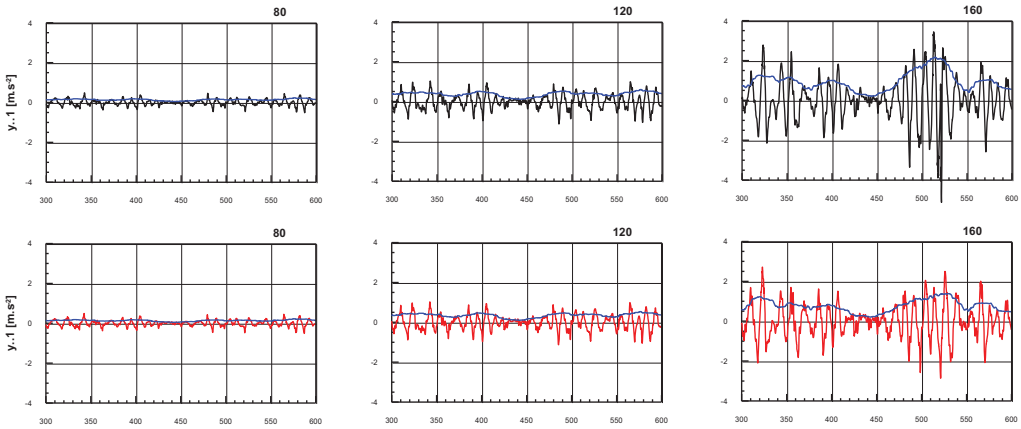

Fig. 8 Records of lateral acceleration of the 1st wheelset on the track "T_ORE" at speed of 80 km/h (left), 120 km/h (in the middle) and 160 km/h (right) for the locomotive equipped with nose-suspended traction drive (top) as well as with fully suspended traction drive (bottom); the blue lines in graphs present moving quadratic means with a window length of 25 m.

6. Conclusions

Nowadays, a traction drive using the axle-mounted nose-suspended traction motors is often used on locomotives for freight operation. This technical solution, which is conceptually very old, is very simple, robust and relatively cheap. However, the greatest disadvantage of the nose-suspended traction drive is a significant increase of unsprung masses in running gear of the vehicle in comparison with various types of fully suspended traction drives. Although relatively lightweight asynchronous traction motors are used today, their weight ranges in order of tons and approximately 60 up to 80 % of this weight is suspended directly on wheelset. The higher share of unsprung masses increases then the level of dynamic effects between the vehicle and the track with all negative impacts on stability of geometric position of the track, stress of the superstructure and the vehicle running gear etc.

In this paper, the new locomotive Class 744.0 CZ LOKO with a total weight of 80 t equipped with axle-mounted nose suspended traction drive is compared with an imaginary locomotive with fully suspended traction drive from the point of view of the dynamic interaction between the vehicle and the track. At various speeds from range of 80 up to 160 km/h, wheel forces as well as lateral wheelset accelerations were observed by means of computer simulations of vehicle run on straight tracks with various quality of the track geometry. The aim of this paper is to assess the differences between the dynamic behaviour of both mentioned conceptions of locomotive running gear.

From the point of view of "vertical dynamics" (i.e. the dynamics of wheel forces), the simulation results show that the predominant factor for the force interaction between the vehicle and the track is the quality of the track geometry. The dynamic effects of the vehicle run increase with increasing speed; in case of worse quality of the track geometry, this increase is more significant. However, the difference between the locomotive equipped with nose-suspended traction motors and the locomotive with fully suspended traction drive is also significant. In case of worse quality of the track geometry, these differences are substantial at speeds higher than approximately 120 km/h, although for example the limit value of the maximum wheel force according to the EN 14363 was not exceeded in any case.

From the point of view of "lateral dynamics", the assessment is more complicated, because for example the stability of run of the vehicle at higher speeds could also have a certain influence. Performed assessment using the lateral acceleration of wheelset shows that the dominant influence on the dynamic behaviour has the quality of the track geometry, again. However, a certain difference between both considered conceptions of the locomotive also exists. From the mentioned reasons, a more detailed investigation of an influence of conception of the locomotive running gear on the stability of run will be performed in the next stage of research of the dynamic behaviour of the new locomotive Class 744.0. Besides that, a special attention will be also paid to the influence of unsprung masses in locomotive running gear on dynamic effects of the vehicle run through the switches.

Nowadays, a prototype of the new locomotive 744.001 is tested on tracks in the Czech Republic. Results of these tests will be used for validation and possible improvement of the dynamic model of this locomotive which is being developed in framework of co-operation of the company CZ LOKO, a.s. and the Jan Perner Transport Faculty of the University of Pardubice.

Acknowledgement

This work was supported by R&D project No. FR-TI2/562 "Research and Development of a Modular Four-axled Locomotive" of the Ministry of Industry and Trade of the Czech Republic and by internal grant project No. 51030/20/SG520001 of the University of Pardubice.

References

ČSN EN 14363:2006 *Railway applications – Testing for the acceptance of running characteristics of railway vehicles – Testing of running behaviour and stationary tests*, (in Czech). Czech Institute for Normalization, Prague.

Kohout, M., Zelenka, J. & Michálek, T. (2011) Influence of parameter's change of locomotive CZ LOKO series 744.0 modified for track gauge 1520 mm on dynamic behaviour, (in Czech), in: *Proceedings of the 20th international conference "Current problems in Rail Vehicles – PRORAIL 2011", Volume II.*, University of Žilina, pp. 131-137.

Kopal, J. (2009) Running gear of CZ LOKO locomotives, (in Czech), in: *Proceedings of the 19th conference with international participation "Current problems in Rail Vehicles"*, University of Pardubice, pp. 1-6.

Michálek, T. & Zelenka, J. (2011) Reduction of lateral forces between the railway vehicle and the track in small-radius curves by means of active elements. *Applied and Computational Mechanics*, 2011, 5, pp. 187-196.

Šlitr, M. (2007) Modernisation of bearing of nose-suspended DC traction motor with rolling bearings and raised power, (in Czech), in: *Current trends in development and production of rail vehicles*, Czech Raildays 2007, Ostrava. URL: http://www.railvolution.net/czechraildays/2007/seminare/v_5.pdf [cit. 2012-03-13].

Zelenka, J. (2009) Running and guiding behaviour of two-axled diesel-electric locomotives CZ LOKO, (in Czech), *New Railway Technique*, 2009, 6, pp. 15-23.

Zelenka, J. & Michálek, T. (2011) Running and guiding behaviour of the locomotive class 744.0 CZ LOKO for the track gauge 1520 mm. *Транспорт Урала*, 2011, 28, pp. 59-63. URL: http://www.usurt.ru/transporturala/arxiv/028_1_20_2_1.pdf [cit. 2012-03-19].

18th International Conference
ENGINEERING MECHANICS 2012
Svratka, Czech Republic, May 14 – 17, 2012

pp. 889–892
Paper #58

COMPENSATION OF IRREGULAR MOTION OF A MACHINE TOOL FEED DRIVE AXIS

J. Moravec*

Abstract: *This contribution deals with the interaction of feed drive axes of NC machine tools, primarily focusing on the compensation of vibrations in the linear axis caused by a carried unbalanced rotating axis. These vibrations negatively influence both machining precision and surface quality. To suppress the effect of unbalanced mass, four compensators were designed as additive blocks supplementing the ordinary cascade control loop of the NC machine tool's feed drive axis. The paper also includes results of an experimental verification of these methods, carried out on a test bed which is a simplified model of a real NC machine tool.*

Keywords: ***Linear motor, Mass unbalance, Cascade loop.***

1. Úvod

U pohybové osy NC obráběcího stroje s přímým pohonem dochází k bezprostřednímu působení síly motoru na řízenou hmotu (např. suport s obrobkem, unášená kolébka nebo otočný stůl). Oproti pohonům nepřímým (s mechanickým převodem) zde odpadá urychlování hmot mechanických převodů, a to vytváří předpoklad pro dosažení vyšších zrychlení řízené hmoty. Přímý pohon je ale více choulostivý na působení vnějších sil (řezné síly, rázy, síly od nevývahy). Regulace je napadána přímo, bez ochranného efektu vložených převodů (vliv síly na regulaci se snižuje s kvadrátem vloženého převodu), a to vede ke snížení přesnosti obrábění a zhoršení kvality obrobeného povrchu. Tento problém je výrazný zejména u pohybových os s přímými pohony, které unášejí např. otočný stůl s obrobkem, nebo kolébku. V příspěvku představené metody kompenzace kmitů lineární osy vybuzené unášenou rotační osou s nevývahou jsou ověřeny na experimentálním stavu, který je zjednodušeným modelem pohybové osy NC obráběcího stroje.

Lineární osa je řízena kaskádně uspořádaným regulačním obvodem s proudovým (PI), rychlostním (PI) a polohovým (P) regulátorem. Dynamická poddajnost motoru (přenos mezi výchylkou řízené hmoty a vnější silou) podstatně závisí na nastavení konstant regulátorů rychlosti a polohy. Nastavení regulace je ale omezeno, např. poddajnou mechanikou stroje. Pro další potlačení vybuzených kmitů lineární osy je možné regulační obvod NC pohybové osy rozšířit o kompenzační bloky.

Byly navrženy čtyři metody kompenzace. Tři z metod jsou principiálně podobné (proudová, rychlostní a polohová kompenzace). Kompenzátory vypočítávají budící sílu, převádějí ji na signál s potřebnou dimenzí (proud, rychlost nebo poloha) a s potřebným fázovým předstihem jej přičítají do regulace tak, aby motor působil protisílou k poruchové síle od nevývahy. Pro naladění těchto kompenzátorů je nutné znát některé v provozu obtížně zjistitelné parametry (polohu, velikost nevývahy vůči lineární ose a vzdálenost jejího středu hmotnosti od osy rotace). Algoritmus čtvrté metody kompenzace přímo reaguje na vybuzené výchylky lineární osy a adaptivně, bez přednastavení parametrů nevývahy, vypočítává amplitudu i fázi kompenzačního signálu a přičítá jej do polohové zpětné vazby.

Pro ověření efektu kompenzace v ustálených i přechodových stavech byly kompenzační algoritmy experimentálně testovány při konstantní i proměnné úhlové rychlosti nevývahy a to při klidovém i pohybovém stavu lineární osy.

* Ing. Jan Moravec.: Výzkumné centrum pro strojírenskou výrobní techniku a technologii, České vysoké učení technické v Praze, Horská 3; 128 00, Praha 2; CZ, e-mail: j.moravec@rcmt.cvut.cz

2. Interakce rotační a lineární osy

Pohybová osa experimentálního stavu poháněná lineárním synchronním motorem s permanentními magnety (přímým pohonem) unáší prstencový motor s nevývahou, obr. 1. Rotace nevývahy vybuzuje kmity lineární osy. Průmět výsledné síly od nevývahy do lineární osy lze popsat vztahem

$$F_x(t) = -m_n \cdot r_n \cdot \left(\ddot{\varphi}(t)\sin\varphi(t) + \dot{\varphi}^2(t)\cos\varphi(t)\right) \tag{1}$$

kde m_n je hmotnost nevývahy, $\varphi(t)$ je natočení nevývahy a r_n je vzdálenost středu hmotnosti nevyváženého rotoru od jeho osy rotace.

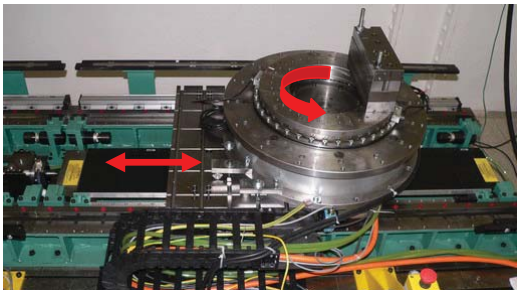

Obr. 1: Experimentální stav pro kompenzaci interakce rotační a lineární osy

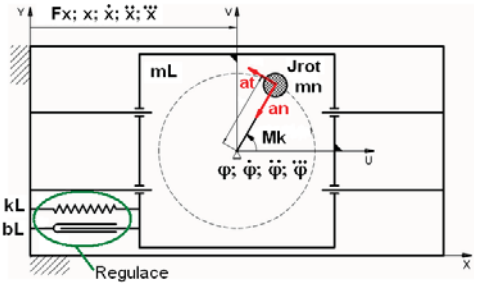

Obr. 2: Schéma experimentálního stavu

3. Kompenzátory s pevně nastavenými parametry

Proudová kompenzace

U synchronního motoru s permanentními magnety platí lineární vztah mezi proudem I_{sk} a silou motoru F_{mot}

$$F_{mot} = I_{sk} \cdot K_f \tag{2}$$

kde K_f [N.A^{-1}] je silová konstanta motoru. Frekvenční přenos mezi žádaným a skutečným proudem motoru je pro frekvence odpovídající otáčkám nevývahy prakticky jednotkový. Pro externí sílu působící na motor může být tedy snadno vypočítán proudový kompenzační signál a zaveden do proudové regulační smyčky motoru. Známe-li okamžitou polohu a velikost nevývahy vůči lineární ose, tak proudový kompenzační signál vytvářející protisílu k rušivé síle od nevývahy je

$$I_k(t) = -\frac{1}{K_f} \cdot m_n \cdot r_n \cdot \left(\ddot{\varphi}_{sk}(t)\sin\varphi_{sk}(t) + \dot{\varphi}^2_{sk}(t)\cos\varphi_{sk}(t)\right) \tag{3}$$

kde $\varphi_{sk}(t)$ je skutečné natočení nevývahy vůči lineární ose. Při derivování skutečné polohy nevývahy (změřené zpětnovazebním polohovým čidlem) ale vznikají problémy se zesílením šumu. Proto je skutečná poloha nevývahy počítána z polohy žádané, šumem nezatížené. Ve výpočtu pak musí být zohledněn frekvenční přenos polohové regulace prstencového motoru. Ten je zde nahrazen filtrem prvního řádu se shodným propustným pásmem f_p. Jeho Laplaceův obraz je

$$G_{ki}(s) = \frac{1}{\frac{1}{2\pi f_p}s + 1} \tag{4}$$

Laplaceův obraz skutečné polohy $\Phi_{sk}(s)$ počítané z polohy žádané je dán součinem obrazů náhradního filtru $G_{ki}(s)$ a žádané polohy $\Phi_{zad}(s)$

$$\Phi_{sk}(s) = G_{ki}(s).\Phi_{zad}(s) \tag{5}$$

U rychlostní a polohové kompenzace je kompenzační signál zaváděn na vstup rychlostní, resp. polohové zpětné vazby lineární osy. K vykompenzování vybuzené síly je zapotřebí stejný proud jako u kompenzace proudové daný vztahem (3). Rychlostní nebo polohový kompenzační signál musí být do

regulačního obvodu zavedeny s takovým předstihem a amplitudou, aby jejich proudový (silový) účinek v motoru kompenzoval právě vybuzenou sílu od nevývahy. Laplaceův obraz vztahu (3) pro proudový kompenzační signál $K_I(s)$ musí být u rychlostního kompenzátoru násoben kauzální náhradou přenosu mezi žádanou rychlostí a proudem $G_{VI}(s)$ a u polohového regulároru kauzální náhradou přenosu mezi žádanou polohou a proudem $G_{XI}(s)$. Kompenzační signál pro rychlostní kompenzátor bude tedy

$$K_R(s) \doteq K_I(s) \cdot G_{VI}(s) \tag{6}$$

a pro polohový kompenzátor

$$K_X(s) \doteq K_I(s) \cdot G_{XI}(s) \tag{7}$$

Do přenosových funkcí kompenzátorů je nutné přednastavit konstanty filtrů aproximujících náhradní přenosy a dále hmotnostní parametry nevývahy a její polohy vůči lineární ose. Určení těchto parametrů je v praxi obtížné a jsou zatíženy chybami. Proto byla vyvinuta metoda, která vybuzené výchylky lineárního motoru kompenzuje adaptivně, bez přednastaování jakýchkoli parametrů.

4. Adaptivní kompenzace

Adaptivní kompenzátor reaguje na vybuzené výchylky a nastavuje podle nich proporce kompenzačního signálu x_{komp} tak, aby skutečné výchylky lineárního motoru x_{skut} byly minimální. LMS algoritmus adaptivního filtru na zadané referenční frekvenci současně nastavuje amplitudu i fázi kompenzačního signálu x_{komp} tak, aby byl co nejpřesnějším odhadem harmonické složky vybuzené nevývahou a obsažené v polohové odchylce Δx. Referenční frekvence je odvozena od otáček nevývahy. Frekvenční přenos G(s) zahrnuje přenos motoru a jeho rychlostní regulace. Hodnota zpětné vazby x_{zv} je dána rozdílem

$$x_{zv} = x_{skut} - x_{komp} \tag{8}$$

Pokud je žádaná hodnota polohy $x_{zad}=0$ a pokud bude výstup filtru dokonalým odhadem frekvenční složky vybuzené nevývahou na jeho vstupu ($x_{komp}=\Delta x$) pak

$$\Delta x = x_{komp} = x_{zad} - x_{zv} = 0 - x_{zv} = -x_{zv} \tag{9}$$

$$x_{skut} = x_{zv} + x_{komp} = x_{zv} - x_{zv} = 0 \tag{10}$$

Za výše uvedených předpokladů jsou výchylky lineárního motoru vybuzené otáčením nevývahy zcela vykompenzovány. V kompenzátoru se nastavuje pouze jediná konstanta, ovlivňující konvergenci algoritmu.

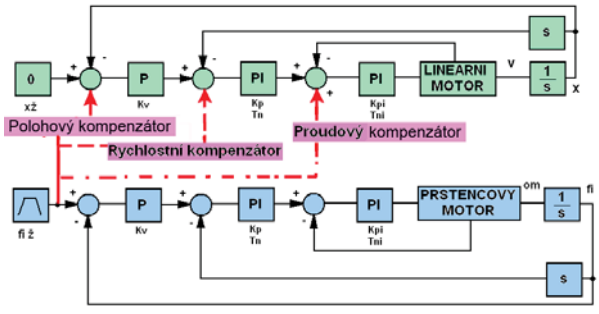

Obr. 3: Implementace kompenzátorů s pevně nastavenými parametry do regulačního obvodu lineárního motoru

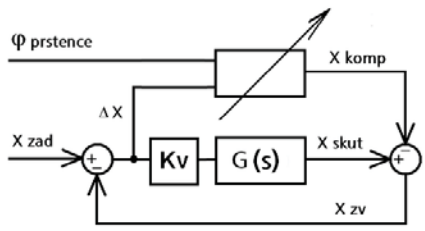

Obr. 4: Implementace adaptivního algoritmu do regulačního obvodu lineárního motoru

5. Experimentální ověření funkce kompenzátorů

Při experimentálním ověřování kompenzátorů byl lineární i prstencový motor řízen v polohové zpětné vazbě. Nevývaha byla roztáčena na konstantní úhlové rychlosti (rozběh a brzdění pomocí s-funkce s definovaným ryvem). Byl sledován kompenzační efekt při klidové žádané poloze lineárního motoru a dále při jeho pohybu konstantní rychlostí (rozběh a brzdění pomocí s-funkce s definovaným ryvem) a harmonickým pohybem. Výsledky experimentů jsou zachyceny na obr. 5 až obr. 8.

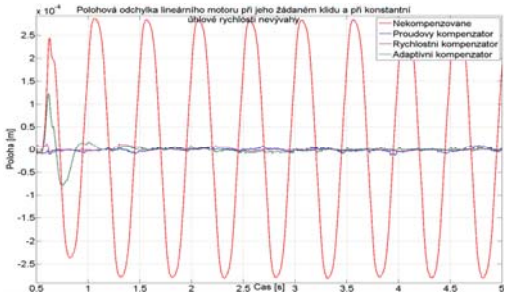

Obr. 5: Polohová odchylka lineárního motoru při jeho žádaném klidu a při konstantní úhlové rychlosti nevývahy

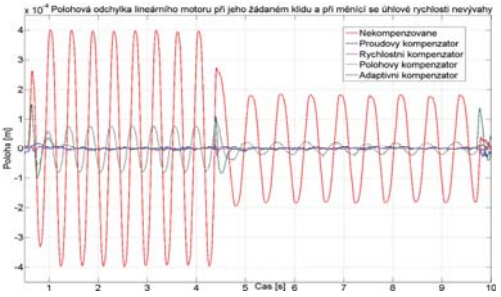

Obr. 6: Polohová odchylka lineárního motoru při jeho žádaném klidu a při měnící se úhlové rychlosti nevývahy

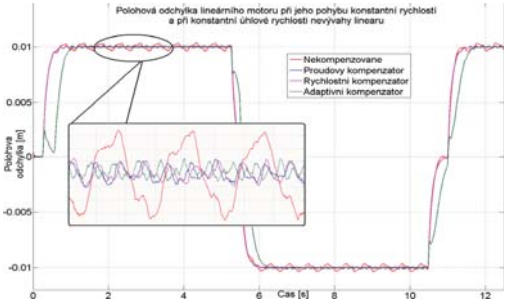

Obr. 7: Polohová odchylka lineárního motoru při jeho pohybu konstantní rychlostí a při konstantní úhlové rychlosti nevývahy (zbytkové vibrace ve výřezu nesouvisí s otáčením nevývahy)

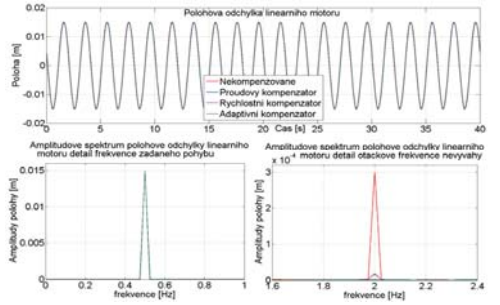

Obr. 8: Polohová odchylka lineárního motoru při jeho harmonickém pohybu a při konstantní úhlové rychlosti nevývahy

6. Závěr

Všechny kompenzátory snižují vybuzené výchylky lineárního motoru v přechodových i ustálených stavech otáčení nevývahy. Velmi výrazný je kompenzační efekt proudového, rychlostního a adaptivního kompenzátoru v ustálených stavech, vibrace jsou sníženy přibližně 40-krát, a to na úroveň několika inkrementů odměřovacího pravítka, obr. 5, obr. 6. Polohový kompenzátor snižuje vybuzené výchylky přibližně 5-krát. Nižší kompenzační efekt je zapříčiněn chybou přibližného odhadu náhradního přenosu mezi žádanou polohou a proudem. V přechodových stavech mají nejvýraznější efekt proudový a rychlostní kompenzátor. Kompenzátory snižují vybuzené výchylky i při pohybu lineárního motoru, obr. 7. Při jeho harmonickém pohybu má nejvýraznější kompenzační efekt adaptivní kompenzátor, který kompenzovanou harmonickou složku prakticky zcela potlačí, obr. 8.

Litaratura

Souček, P. (2004) *Servomechanismy ve výrobních strojích*, ČVUT v Praze.

Souček, P., Bubák, A., (2008) *Vybrané statě z kmitání v pohonech výrobních strojů*, ČVUT v Praze.

Haykin, S. (1996) *Adaptive Filter Theory*, third ed., Prentice-Hall, New Jersey, 1996.

Tyto výsledky byly získány za finančního přispění Ministerstva školství, mládeže a tělovýchovy v rámci podpory projektu výzkumu a vývoje 1M0507.

18th International Conference
ENGINEERING MECHANICS 2012
Svratka, Czech Republic, May 14 – 17, 2012

pp. 893–899
Paper #17

COMPARISON OF APPROACHES TO PREVENTION OF INJURIES, ACCIDENTS AND INCIDENTS BETWEEN THE CZECH REPUBLIC AND RUSSIA

L. Mukhametzianova[*], L. Kotek[**]

Abstract: *Important aspects of the design of machinery are estimation of their risks and assessment of operator safety. This article compares legislation in the field of industrial safety, and prevention of injuries, accidents and incidents in the Czech Republic and Russia. Information from the article could be beneficial especially for Czech (or European) enterprises, which try to enter the Russian region markets.*

Keywords: ***Machinery, safety of machinery, risk assessment, prevention of accidents, pressing and forging.***

Introduction

The development of legislation is important for industrial safety which regulates the minimum requirements for industrial processes. Currently, the safety of employees and nearby residents is considered one of the most important factors to be taken into account in any activities.

Legislative requirements vary from state to state; in advanced countries they are based on the fundamental principle - the employer is responsible for health of workers.

Industrial risks can be divided into several basic categories: physical hazards (employee is exposed to physical factors - temperature, pressure, forces, etc.), chemical hazards (effects of chemicals and chemical products) and ergonomic hazards resulting from the inappropriate interaction between the machinery equipment and human, or the impact of the working environment.

Safety in industry is a broad term that can be applied in the following areas:

- operation of machinery,
- operation of equipment containing hazardous chemical substances and products,
- operation of lifting equipment,
- operation of pressure equipment,
- operation of equipment for mining and processing of ores.

Important trading partner of the Czech Republic and the EU (European Union) is Russia. According to data given on the website BusinessInfo.cz, import to Russia in 2010 increased by 47.4% to 140.0 billion U.S. dollars compared to the same period of 2009. A considerable part of the import consists of machinery, equipment and vehicles. Therefore it is important for both countries to know the requirements concerning safety in the industry.

[*] Ing. Leisan Mukhametzianova : Institute of Production Machines, Systems and Robotics, Brno University of Technology, Street Technická 2896/2; 616 69, Brno; CZ, e-mail: leisan.muhamet@gmail.com

[**] Ing. Luboš Kotek, Ph.D.: Institute of Production Machines, Systems and Robotics, Brno University of Technology, Street Technická 2896/2; 616 69, Brno; CZ, e-mail: kotek.l@fme.vutbr.cz

1. Legislation

Prevention of accidents in the Czech Republic is regulated by legislation of European Union, as well as the specific legislation of the Czech Republic. In Russia there are federal laws that are in accordance with international laws (international treaties and conventions in particular with the European Union). In the Czech Republic there are the following laws and decrees relating to safety in industry:

- Government Decree No. 176/2008 Coll. «On technical requirements for machinery (Revised European engineering direction 2006/42/ES) [1];

- Decree No. 48/1982 Coll. of Czech Agency for work's safety, which contains the basic requirements to ensure safety of work and technical equipment [2];

- Law No. 59/2006 Coll. - The prevention of major accidents (Directive of European Parliament and the Council 2003/105/ED on the control of hazards of major accidents involving dangerous substances);

- Decree No. 19/1979 Coll. - which determines some requirements for ensuring safety of the particular lifting equipment;

- Government Decree No. 26/2003 Coll. – which determines technical requirements for pressure equipment;

- Law No. 44/1988 Coll. – on mining and Law No. 61/1988 Coll. On mining, explosives and state mining administration;

In Russia, these are the following laws and decrees:

- Technical regulation on safety of machinery and equipment TR TC 010/2011 [3];

- Regulations on safety of machining equipment. POT RO-14000-002-98 [4];

- Federal Law of 30 November 2011 No. 366-FZ "About ratification of the Convention of Prevention of Major Industrial Accidents (Convention No 174)";

- Federal Law of 21 July 1997 No. 116-FZ "On work safety of hazardous machining equipment ";

- Federal Law of 21 November 1995 No. 170-FZ "On the use of nuclear energy";

- Federal Law of 21 July 1997 No. 117-FZ "On safety of hydrostructures";

- Instructions for risk analysis of hazardous machining equipment (RC 03-418-01).

Approaches to prevention of accidents for each industry are specific. This article will describe legislative requirements of the Czech Republic and Russia in the field of prevention of accident in the operation of machinery.

2. Ensuring safety of machinery in the Czech Republic and Russia

2.1 Ensuring safety of machinery relating to the design of machinery

As early as a manufacturer designs machinery he has to define the parameters that ensure workers safety during assembling, dismantling, commissioning, as well as for self-dependent operation, and as part of technological systems in accordance with the requirements of operational documentation.

Safety of machinery in the designing process in the Czech Republic and Russia provides:

1) Identification of potential risks, such as:

1. Risks of mechanical hazard:

- Risk of loss of stability;

- Risk of break-up during operation;

- Risks due to falling or ejected objects;

- Risks due to surfaces, edges and corners;

- Risks related to combined machinery;
- Risks related to variations in operating conditions;
- Risks related to moving parts;
- Risks of uncontrolled movements;

2. Risks associated with other hazards:

- Electricity supply;
- Static electricity;
- Energy supply other than electricity;
- Incorrect installation;
- Extreme temperatures;
- Fire;
- Explosion;
- Noise;
- Vibration;
- Radiation;
- External radiation;
- Laser radiation;
- Emissions of hazardous materials and substances;
- Risk of being trapped in a machine;
- Risk of slipping, tripping or falling;
- Lightning strike.

2) Risk assessment - the machinery must be designed and constructed to take into account the results of risk assessment;

In Russia and Czech Republic the acceptable risk for machinery is also determined. In case a degree of risk is higher than acceptable, it is necessary to adjust the machinery for reducing the risk. Provided this is not possible or not economicaly efficient, it is necessary to include into the instruction manual the information that restricts the conditions for using of equipment, or add a notice of additional requirement for safety measures.

3) Determination of levels of physical factors (noise, infrasound, air and contact ultrasound, local and general vibration, electromagnetic fields) and the level of emission of hazardous and toxic substances to ensure a safe operation.

4) Preparation of the instruction manual - the manufacturer has to take into account not only the expected use of machinery but also any reasonable expectable use. The instruction manual has to notify of incorrect use of machinery.

In case the machinery is intended to be used by unskilled operators, the text and adjustment of instruction manual must take into account the level of general education and the abilities to understand that can be reasonably expected from such operators.

5) Consideration of ergonomic principles to reduce discomfort, fatigue and psychological stress of operators.

2.2 Ensuring safety of machinery during manufacturing, storage, transportation, use and disposal of machinery

Safety of machinery in terms of manufacturing, storage, transportation, use and disposal in the Czech Republic and Russia, provides:

1) Ensuring compliance with requirements on design and operational documentation;

2) Testing of machinery according to project documentation;

3) Risk assessment by manufacturer that is prior to launching and after overhaul;

4) Produce of warning labels or marks to notify of danger;

5) Use of safe materials and substances;

6) Use of guards and protection devices;

7) The information in the instruction manual to avoid misuse. In Russia the instruction manual also provides recommendations for safe disposal of equipment and its components.

8) State control over compliance with safety requirements.

2.3 Classification of machinery, safety requirements

Safety requirements for specific groups, types, models of machinery are established taking into account the features of destination, productivity and operating conditions of equipment. There is machinery for:

- Metalworking
- Woodworking
- Pressing and forging
- Casting

Table 1 shows a classification of machinery in the Czech Republic and Russia.

Tab. 1: Classification of machinery in the Czech Republic and Russia.

Machinery	**Classification group of machinery**	
	Czech Republic	**Russia**
- Lathes	Metalworking	Metalworking
- Drilling machines		
- Grinding machines		
- Milling Machines		
- Planing and shaping machines		
- Saws machines		
- Grinding machines		
- Gear cutting machines	-	Metalworking
- Electroerosive machines		
- Electrochemical machines		
- Ultrasound machines		
- Automatic line		
- Metal Cutting Shears	Punching and shearing	Metalworking
- Bending machines	Bending and	Metalworking

- Straightening machines	straightening of the material	
- Forging hammers	Forging by hammer	Pressing and forging
- Horizontal forging machines	-	Pressing and forging
- Hydraulic presses	Punching and shearing	Pressing and forging
- Mechanical drawing presses	Punching and shearing	-
- Press brakes		
- Friction Screw Presses		
- Vulcanizing presses		
- Rotary drum curing presses		
- Platen printing, folding and slotting machines		
- Machinery for the preparation of molding materials and mixtures	-	Casting
- Machines for casting into molds in shell	Casting	Casting
- Equipment for casting to the models		
- Casting machines		
- Centrifugal casting machines		
- Casting equipment for working with ingot mold		
- Casting machines for blast furnaces		
- Complexly mechanized and automatic molding line for casting and molding	-	Casting
- Moulding machines	Forming of material	Casting
- Injection and blow molding machines		
-Sandcasting machines		
- Reversing machines		
- Machines for cleaning castings, and easing	Releasing and cleaning castings	Casting
- Band sawing machines	Woodworking	Woodworking
- Circular sawing machines		
- Planing machines		
- Vertical shapers machines		
- Thickening machines	Woodworking	-
- Lathes	-	Woodworking
- Grinding machines		
- Drilling and slotting machines		
- Tenoning machines		

In table 2 there are requirements for hydraulic presses in the Czech Republic and Russia.

Tab. 2: The requirements for hydraulic presses in the Czech Republic and Russia.

Safety requirements	Czech Republic	Russia
Pressure control	1. Press should be protected in each hydraulic circuit by manometer, which allows to control operating pressure. Hydraulic circuits should be protected by relief valves for prevention excess pressure. 2. Presses driven by pressure from the central station should be protected by equipment to prevent a rapid pressure drop.	1. In the accumulators, piping of each press should be manometers to control the pressure. 2. Hydraulic equipments in all highest points should have valves to release air from fluid circuit, and in the lowest points – valves for descent of the working fluid.
Movement of the piston	1. Presses with vertical and horizontal movement of pressing piston should be protected by equipment to prevent undesired spontaneous movement due a leakage of pressure fluid at the reverse direction. 2. In case of working stroke position of the pressing piston should be permitted.	1. To prevent a rapid dropping or lifting of pressing piston with a sudden large liquid flow rate the main valve on the pipeline should be equipped with a device that automatically shut off flow of working fluid. 2. In the case of rapid dropping of pressing piston to eliminate the impact of piston on the foundation should be buffers, wooden pillows, etc. 3. The pressing piston should be covered by the hood, which should be closed with the catch. 4. For the presses, which consist of several units, the position of pressing piston should be seen on each press and pump, or about position of piston should inform alarms.
Press control	1. Press should be protected by device, which is possible at any time discontinue an operation, and with alarm, which notes that the press is in operation. 2. Press should be protected by switch, which blocks press operation in case of transfer of material to the press platform. 3. The design of the press should avoid sudden opening of the press.	1. The piping should have safety valves or other similar devices for the prevention of hydraulic impact. 2. Between pump and press should be lighting and acoustic alarm, interlocked with the triggering device of presses.
Pump	-	1. The pump should have a safety valve and turn off device. 2. If there are a few pumps, should be the device which disconnects each pump separately.

Safety of workers	1. Worker should be protected from burning or scalding in case of open press; heating medium inlets should be covered that their failure or other damage avoids injury. 2. In case of press operating the person shouldn't to stay on the hopper or enter into it. 3. The area of material immersion into the melting chamber should be protected to avoid injury done by steam blowing. 4. Filling the hopper should eliminate putting hands into the screw and plunger injection.	Manual and automatic systems shouldn't disconnect such devices in case that outage of these devices leads to injury.
Monitoring of safety	-	All parts of the press under the pressure of steam, air and liquid, periodically should by inspected and tested.

3. Conclusion

This article discusses legislation of the Czech Republic and Russia in the field of industrial safety. In particular, this article compares legislative requirements to ensure the safe operation of machines while their design, manufacture, storage, transportation, use and disposal. This article also deals with classification of machinery in the Czech Republic and Russia, in accordance to legislation. To describe the differences and similarities in the requirements of legislation, hydraulic press is chosen as an example. This article may be useful for Czech and European companies which wish to export their products to Russia, or move their production facilities.

Acknowledgement

This article has been supported by Project No. CZ.1.07/2.3.00/09.0162 with the title ―Knowledge and Skills in Mechatronics - Innovations Transfer to Practice.

These results were obtained with financial support of Brno University of Technology by the specific research program No. FSI-S-11-5 "Environmental and safety aspects of the development, manufacture and operation of machines."

References

BusinessInfo.cz [online]. [cit. 2012-03-15]. Accessible from: http://www.businessinfo.cz/cz/sti/rusko-zahranicni-obchod-zeme/6/1000580/

Government Decree No. 176/2008 Coll. *«On technical requirements for machinery»*

Decree No. 48/1982 Coll. of Czech Agency for work's safety, which contains the basic requirements to ensure safety of work and technical equipment.

Technical regulation on safety of machinery and equipment TR TC 010/2011.

Regulations on safety of machining equipment. POT RO-14000-002-98.

18th International Conference
ENGINEERING MECHANICS 2012
Svratka, Czech Republic, May 14 – 17, 2012

pp. 901–914
Paper #227

METHOD FOR CONSTRAINED DESIGNS OF EXPERIMENTS IN TWO DIMENSIONS

E. Myšáková *, **M. Lepš** **

Abstract: *This paper presents a new approach for generating a Design of Experiments in constrained and non-regular two-dimensional spaces. The methodology is based on the triangulation of the admissible space by Delaunay Triangulation method. Then, a heuristic smoothing method for generating uniform Finite Element meshes within the triangulated space is applied to obtain uniformly spaced designs. Although not 100% reliable, the proposed method can produce superior designs to already known optimal solutions.*

Keywords: ***Design of Experiments, constrained design spaces, non-regular design spaces, space-filling, Delaunay triangulation.***

1. Introduction

Space-Filling Design Strategies known as *a Design of Experiments* (DoE) constitute an essential part of any experimentation. Our contribution is aimed at one particular domain of constrained design spaces. The most frequent example is the case of *a mixture experiment*, where individual inputs form a unity volume or unity weight (Montgomery, 2000, Chapter 11-5). This only condition leads to the simplex space; further limits of individual inputs then form *a polytope*, still convex but generally irregular space. Therefore, all traditional DoEs (Montgomery, 2000) that are constructed for hypercube spaces cannot be applied here.

Although the problem is known for decades, the progress of methods for DoEs does not follow current development within the area of computer experiments (Fang et al., 2006). The main difference between classical and modern DoEs is the number of samples where, for the latter, the hundreds of samples is a usual scenario. Then, the classical approaches based on fixed small-sample templates (Cornell, 1973, 1979) cannot be used. Up-to-date, the authors have found only few references on DoEs in constrained design spaces. References (Petelet et al., 2010) and (Fuerle and Sienz, 2011) apply traditional Latin Hypercube (LH) designs to a bounding box followed by a Genetic Algorithm (GA) and hill-climbing optimization algorithms, respectively, to fulfil original constraints. Here, the LH methodology is merely used for minimization of the searched space than for nice properties of LH designs. Another approach is presented in (Hofwing and Strömberg, 2010), where interesting points are found by a GA and then, the final solution is located by sequential linear programming. The solution is in this case general, however, the computational demands are enormous.

In this paper a different approach based on *Delaunay triangulation* (DT) of an admissible domain and an utilization of nice properties of the `Distmesh` tool (DM) (Persson and Strang, 2004) is presented. Our results will be compared to seven constrained examples in two dimensions presented in (Hofwing and Strömberg, 2010), namely a placing of six design points in a triangle, parallelogram, pentagon, hexagon, heptagon, octagon and a search for a position of twelve design points in an irregular hexagon, see Fig. 1 for optima presented in (Hofwing and Strömberg, 2010).

The paper is organized as follows. Section 2 describes three frequent objective functions that are used for comparison of space-filling designs and that will be used hereafter. For other measures and their comparison, see reference (Janouchová and Kučerová, 2011). Next section is devoted to the short

*Eva Myšáková: Faculty of Civil Engineering, Czech Technical University in Prague, Thákurova 7, 166 29 Prague 6; CZ, e-mail:eva.mysakova@fsv.cvut.cz
**Ing. Matěj Lepš, Ph.D., Faculty of Civil Engineering, Czech Technical University in Prague, Thákurova 7, 166 29 Prague 6; CZ, e-mail:leps@cml.fsv.cvut.cz

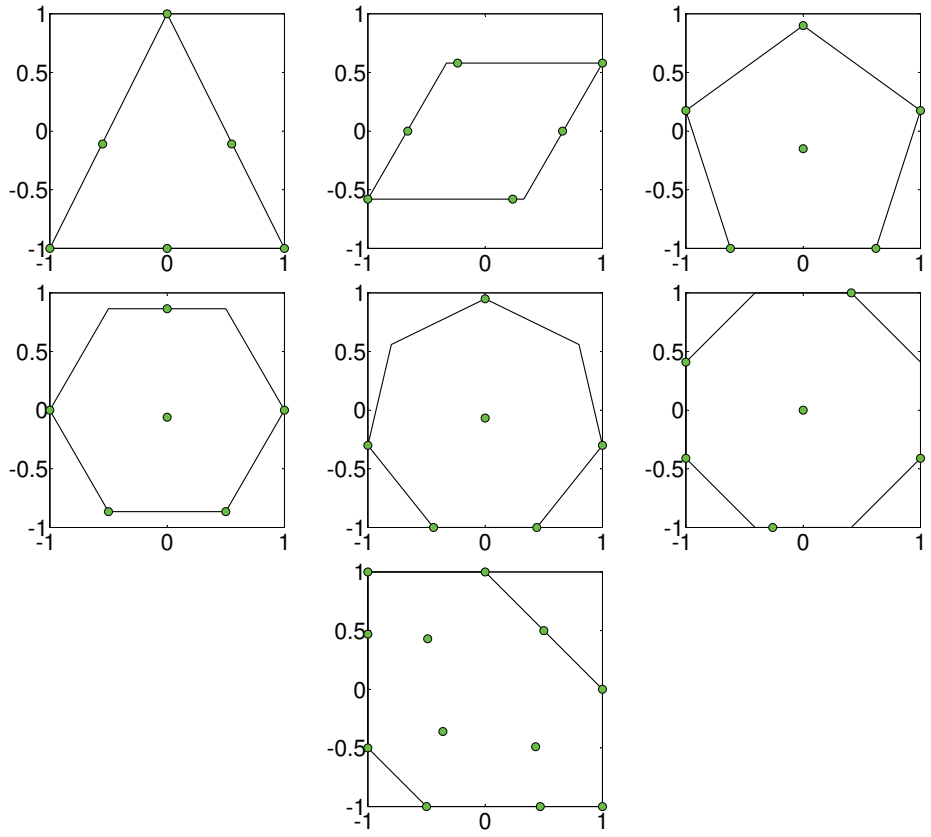

Fig. 1: Reference designs (Hofwing and Strömberg, 2010). Note that designs are created in a unitless domain $[-1, 1] \times [-1, 1]$*; the real designs are created by linear transformation to user-specific bounds.*

presentation of the methodology used in referencing paper (Hofwing and Strömberg, 2010) followed by our approach in Section 4. Finally, the fifth section presents comparison and analysis of obtained results.

2. Objective functions

Since we are interested in space-filling properties, three most common objective functions are examined. The first is *Euclidean Maximin* metric (EMM) (van Dam et al., 2009; Husslage, 2006) for its simplicity and easiness in visualization. The EMM is the minimal distance out of all distances between any two design points and is to be maximized:

$$E^{\mathrm{EMM}} = \min\{..., L_{ij}, ...\}, \quad i = 1, ..., n; \quad j = (i+1), ..., n \quad , \tag{1}$$

where n is the number of design points and L_{ij} is the Euclidean distance between points i and j. From the experiments point of view EMM expresses the worst case scenario of the closeness of two experiments. Even for computer experiments the assumption that an evaluation is costly is still valid. Therefore, the possible duplicity of two closed points remains a crucial task.

The second measure is *Audze-Eglais* objective function (AE) proposed by Audze and Eglais in (Audze and Eglais, 1977). It is based on an analogy with a potential energy of the set of points. The points are distributed uniformly when the potential energy E^{AE} proportional to the inverse of the squared distances among points is minimized, i.e.

$$E^{\mathrm{AE}} = \sum_{i=1}^{n} \sum_{j=i+1}^{n} \frac{1}{L_{ij}^2} \quad . \tag{2}$$

Since the objective is a sum of distances, it is not heavily disturbed by outliers from the potential energy point of view. Therefore, such measure represents an average property of the set of points.

The third objective function is *D-optimality* (Dopt) proposed by Kirsten Smith in (Smith, 1918). We minimize a negative value of a determinant of a linear information matrix $\mathbf{Z}$, i.e.

$$E^{\mathrm{Dopt}} = -\det(\mathbf{Z^T Z}) \,, \text{where} \tag{3}$$

$$\mathbf{Z} = \begin{bmatrix} 1 & x_{11} & x_{12} \\ 1 & x_{21} & x_{22} \\ \vdots & \vdots & \vdots \\ 1 & x_{n1} & x_{n2} \end{bmatrix} . \tag{4}$$

3. Genetic algorithm (GA) based method

A hybrid optimization method has been proposed in (Hofwing and Strömberg, 2010) to solve irregular DoE problems. It is based on the efficient combination of a Genetic Algorithm (GA) and a sequential linear programming (SLP) methodology. Firstly, the GA is used to locate crude positions of individual points and then, the SLP is applied to find nearest local optima. Particularly, a binary version of a GA and an interior point method from Matlab is utilized. The primary objective function is the presented D-optimality in its linear form. However, the global optima of such specified problem have duplicities, i.e. few points share same positions. Although duplicities can be sometimes welcomed, here they are assumed to be deficiencies of the particular designs. Therefore, the authors in (Hofwing and Strömberg, 2010) have applied Bayesian modification of an information matrix which is based on adding higher order terms into the matrix $\mathbf{Z}$. Particularly, examples from the referenced paper have been solved with added quadratic terms. Note that some additional constant must be added to diagonal elements of $(\mathbf{Z^T Z})$ to solve the singularity of the resulting matrix, see e.g. (DuMouchel and Jones, 1994) or (Janouchová and Kučerová, 2011) for more details. Although this methodology is able to find optimal solutions, not always they are global ones and also the computational demands are not low. Hence, a new method is presented in the next section.

4. Method using Delaunay triangulation (DT) and `Distmesh` tool (DM)

A triangulation is a term suitable for 2D, generally it means the partition of the domain by simplexes. Delaunay triangulation (DT) is the most popular triangulation method (Chen and Holst, 2011). It is based on a convex hull of given points V describing the admissible domain, where the convex hull is the smallest convex set containing all points in V. Then, DT triangulates the convex hull such that there is no point of V inside the circumsphere of any simplex in the triangulation.

Because it is relatively simple to create DT and then compute a volume and other properties of simplexes, see Appendix A, we have a rough estimation, how is the admissible region formed. An example of utilizing such methodology has been firstly presented in (Crombecq et al., 2009) for regular design spaces. We extended this idea for constrained design spaces by incorporating the `Distmesh` tool (DM) (Persson and Strang, 2004).

In our method the domain described by corner vertices is triangulated by DT and the desired number of random points is generated inside, see Fig. 2a). Each triangle will contain a portion of the required number of samples based on a ratio of its volume to the total volume of the admissible space. Since the `floor` command is used, the missing points to the total number of points are added to the biggest simplex, see e.g. illustrative example in Fig. 2a), where smaller triangles get only two points, whereas the

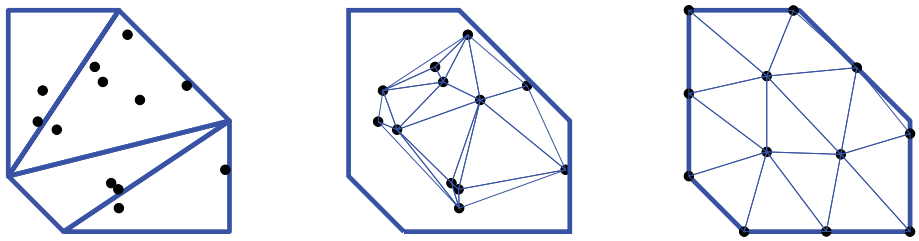

(a) Triangulation of the domain with randomly generated points.

(b) Triangulation of random points forming a truss-like structure.

(c) The final design after the application of the `Distmesh` tool.

Fig. 2: The generation of a uniform mesh from randomly generated points.

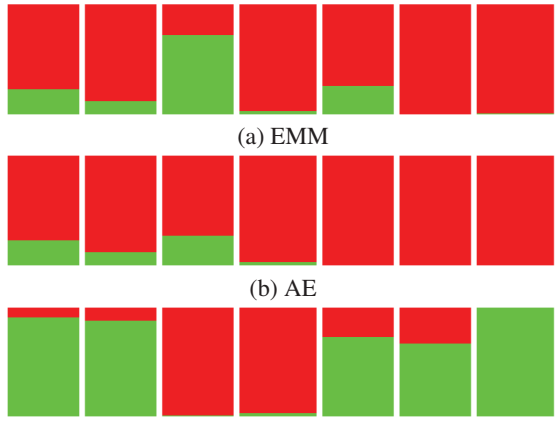

(a) EMM

(b) AE

(c) Dopt

Fig. 3: The comparison of the DM tool and the referenced algorithm (Hofwing and Strömberg, 2010) for three objectives; the vertical axis is the percentage of success (the bigger area, the better method), the horizontal axis stems for 7 individual examples (triangle, parallelogram, pentagon, hexagon, heptagon, octagon, irregular hexagon). Key: Red color = DM tool, Green color = referenced algorithm.

biggest triangle three plus three remaining. And again, since the computation of the simplexes' volumes is simple, see Appendix A, the procedure is very fast.

Then the DM tool is applied. The `Distmesh` tool is a heuristic smoothing algorithm for generating uniform meshes (Chen and Holst, 2011). It is well-known that the most uniform meshes for the Finite Element Method (FEM) are characterized with uniformly spaced nodes (but not vice-versa!). Therefore, we have tried utilized this nice property of the DM tool. The DM is based on a simple dynamical system of expanding pin-jointed structure, here characterized by the second mesh, see Fig. 2b). Those trusses that are too short are causing repulsive forces that move the too close nodes apart, see Fig. 2c) for the final solution. The main disadvantage apart from high computational demands is the need to return nodes that leave the prescribed admissible domain. The DM offers solutions for basic entities, polygon used in our computations is one of them, see the original paper (Persson and Strang, 2004) for more details.

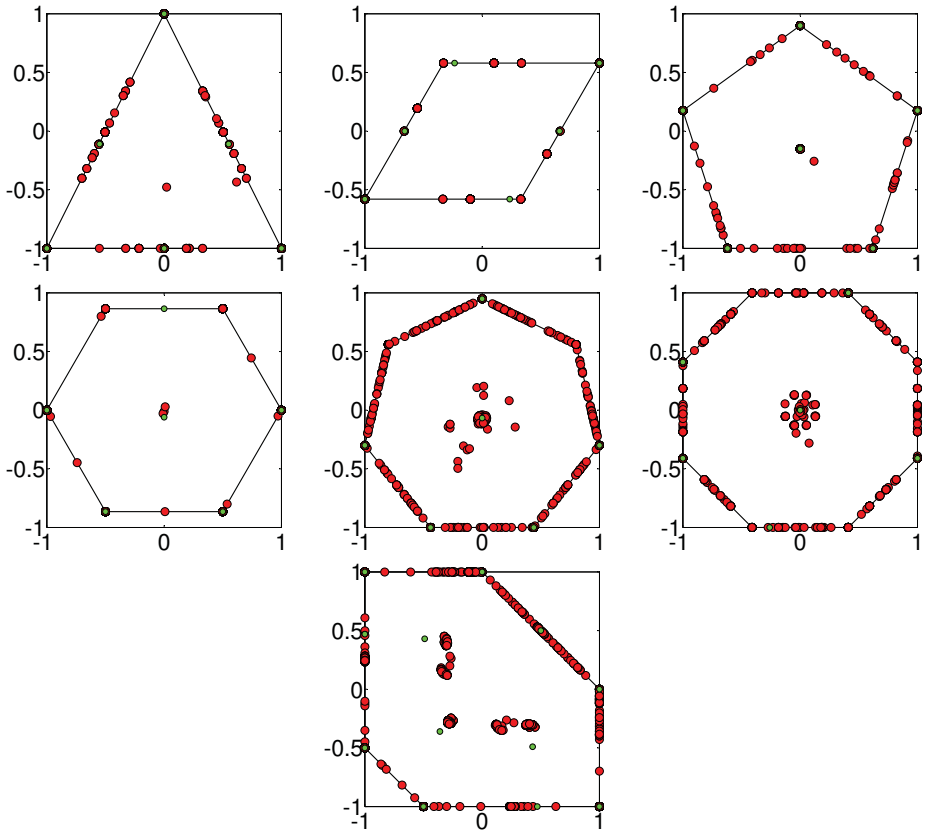

Fig. 4: Red points stems for the resulting design points from all 100 runs of the DM tool, green points are reference designs (Hofwing and Strömberg, 2010).

5. Results

The proposed procedure has been run one hundred times for the sake of statistics. However, the referenced paper (Hofwing and Strömberg, 2010) has only one value from one run, therefore the comparison of these two algorithms will not be precise. The detailed results for each solved example (triangle, parallelogram, pentagon, hexagon, heptagon, octagon, irregular hexagon) are presented in Tabs. 1–7 in Appendix B in the barchart form along with the visualization of the best and the worst designs of our procedure. The best designs for referenced procedure are already presented in Fig. 1. Figure 3 shows the relative winning score (RWS)[†] (Nosek and Lepš, 2011) for our method and the algorithm presented in (Hofwing and Strömberg, 2010). The RWS is a statistic of 100 runs divided into ones with better results than reference values and ones with worse. We can see that our method clearly wins in EMM and AE objectives, i.e. has attained a bigger area. The RWS comparison is used to save the space, for more detailed analysis see Figs. 6–7 in Appendix C, where the boxplot results of all hundred runs are shown. Last but not least, Fig. 4 shows the resulting design points from all hundred runs of our method on solved examples. Note that in several examples the local optima are created by rotating the optimal position of points around the center point.

Since the reference algorithm was optimized for Dopt objective function, it is not surprising that it wins in this objective, but not predominantly. In all but last example our methodology was able to find a

[†]Note that RWS graphs are plotted by Merlin Statistical Software for Microsoft Excel `http://www.heckgrammar.kirklees.sch.uk/index.php?p=10310`, particularly the *Mosaic Plot* has been used.

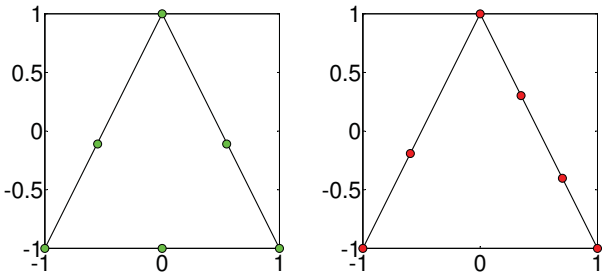

Fig. 5: Comparison of designs for Example 1 (triangle and 6 design points). Left picture shows the reference design (Dopt = -50.0598), right picture shows the design generated by the new method with the best result in the Dopt objective function (Dopt = -53.0001). Lower value is better.

superior solution even for the Dopt objective. Such situation is depicted in Fig. 5, where our solution (on right) attains a better Dopt value. The reason is probably in the added terms of Bayesian updating that does not allow the reference procedure to find the global optimum.

Since the codes have not been deeply optimized from implementation point of view, the analysis of computational demands cannot be rigorously done. However, we can state general requirements of the proposed method. The random generator used for the creation of the random points before applying the DM tool is very fast with no optimization cycle. The DM tool is the most demanding one. There is several Delaunay triangulations inside the loop of the Distmesh tool that are needed to preserve the inner structure to be physically consistent. And still, as is visible from the EMM performance, the Distmesh has problems with the quality of the boundary surface mesh, see also the discussion e.g. in (Chen and Holst, 2011).

6. Conclusions

The Design of Experiments for constrained spaces and computer experiments is relatively new and unexplored area. The constraints complicates the application of all contemporary DoE algorithms for regular design spaces. The presented paper is a pioneering work that brings a new methods and unpublished results. It is important to note that the presented method is independent on the number of dimensions as long as the procedure of returning points lying outside the prescribed domain in higher dimensions is provided. Using DT we are able to apply the DM tool on any irregular domain in N-dimensional space. Only the computational demands can limit the application in higher dimensions.

Acknowledgments

This work was supported by the Czech Science Foundation GAČR, grant No. P105/12/1146.

References

Audze, P. and Eglais, V. (1977). New approach for planning out of experiments. *Problems of Dynamics and Strengths*, 35:104–107. Zinatne Publishing House.

Chen, L. and Holst, M. (2011). Efficient mesh optimization schemes based on Optimal Delaunay Triangulations. *Computer Methods in Applied Mechanics and Engineering*, 200(9-12):967–984.

Cornell, J. A. (1973). Experiments with Mixtures: A Review. *Technometrics*, 15(3):437–455.

Cornell, J. A. (1979). Experiments with Mixtures: An Update and Bibliography. *Technometrics*, 21(1):95–106.

Crombecq, K., Couckuyt, I., Gorissen, D., and Dhaene, T. (2009). Space-filling sequential design strategies for adaptive surrogate modelling. In Topping, B. H. V. and Tsompanakis, Y., editors, *Proceedings of the First International Conference on Soft Computing Technology in Civil, Structural and Environmental Engineering*. Civil-Comp Press, Stirlingshire, UK.

DuMouchel, W. and Jones, B. (1994). A simple Bayesian modification of D-optimal designs to reduce dependence on an assumed model. *Technometrics*, 36(1):37–47.

Fang, K.-T., Li, R., and Sudjianto, A. (2006). *Design and modeling for computer experiments*. Chapman & Hall/CRC.

Fuerle, F. and Sienz, J. (2011). Formulation of the Audze–Eglais uniform Latin hypercube design of experiments for constrained design spaces. *Advances in Engineering Software*, 42(9):680 – 689.

Hofwing, M. and Strömberg, N. (2010). D-optimality of non-regular design spaces by using a Bayesian modification and a hybrid method. *Structural and Multidisciplinary Optimization*, 42:73–88.

Husslage, B. (2006). *Maximin Designs for Computer Experiments*. PhD thesis, Tilburg University.

Janouchová, E. and Kučerová, A. (Sent for publication, 2011). Competitive comparison of optimal designs of experiments for sampling-based sensitivity analysis. *Computers & Structures*.

MathPages (2011). Simplex volumes and the Cayley-Menger determinant. www pages: http://www.mathpages.com/home/kmath664/kmath664.htm.

Montgomery, D. C. (2000). *Design and Analysis of Experiments, 5th Edition*. Wiley, 5 edition.

Nosek, J. and Lepš, M. (2011). More practical graphical methodology for comparison of single-objective optimization algorithms. *Sent for publication*.

Persson, P.-O. and Strang, G. (2004). A simple mesh generator in MATLAB. *SIAM Review*, 46(2):329–345.

Petelet, M., Iooss, B., Asserin, O., and Loredo, A. (2010). Latin hypercube sampling with inequality constraints. *AStA Advances in Statistical Analysis*, 94:325–339.

Smith, K. (1918). On the standard deviations and interpolated values of an observed polynomial function and its constants and the guidance they give towards a proper choice of the distribution of observations. *Biometrika*, 1/2:1–85.

van Dam, E. R., Rennen, G., and Husslage, B. (2009). Bounds for maximin latin hypercube designs. *Operations Research*, 57:595–608.

A Computation of simplex volume

Because we know the coordinates of simplex vertices, we use the formula which requires these (and only these) inputs (MathPages, 2011).

The computation of a volume of a simplex in 2D (3 vertices):

$$V_2 = \frac{1}{2!}\begin{vmatrix} 1 & x_{1(1)} & x_{2(1)} \\ 1 & x_{1(2)} & x_{2(2)} \\ 1 & x_{1(3)} & x_{2(3)} \end{vmatrix}$$

The computation of a volume of a simplex in 3D (4 vertices):

$$V_3 = \frac{1}{3!}\begin{vmatrix} 1 & x_{1(1)} & x_{2(1)} & x_{3(1)} \\ 1 & x_{1(2)} & x_{2(2)} & x_{3(2)} \\ 1 & x_{1(3)} & x_{2(3)} & x_{3(3)} \\ 1 & x_{1(4)} & x_{2(4)} & x_{3(4)} \end{vmatrix}$$

The computation of a volume of a simplex in nD ($n+1$ vertices):

$$V_n = \frac{1}{n!}\begin{vmatrix} 1 & x_{1(1)} & x_{2(1)} & \dots & \dots & x_{n(1)} \\ 1 & x_{1(2)} & x_{2(2)} & \dots & \dots & x_{n(2)} \\ \vdots & \vdots & \vdots & \vdots & \vdots & \vdots \\ 1 & x_{1(n+1)} & x_{2(n+1)} & \dots & \dots & x_{n(n+1)} \end{vmatrix}$$

In the notation $x_{a(b)}$ a is a variable (dimension) and b is a design point.

B Results for seven individual examples

Legend for Tables 1-7: The results of 100 runs of the DM tool for 7 examples. The first row shows the results of the EMM metric (higher is better), the second row shows the results of the AE metric (lower is better) and the third row shows the results of the $Dopt$ objective (lower is better). The first column presents the barcharts of results of the selected objective over those 100 runs. The second column shows the best and the third column shows the worst designs according to the selected objective function, respectively. Green dash line is a reference value taken from (Hofwing and Strömberg, 2010), green points show reference designs.

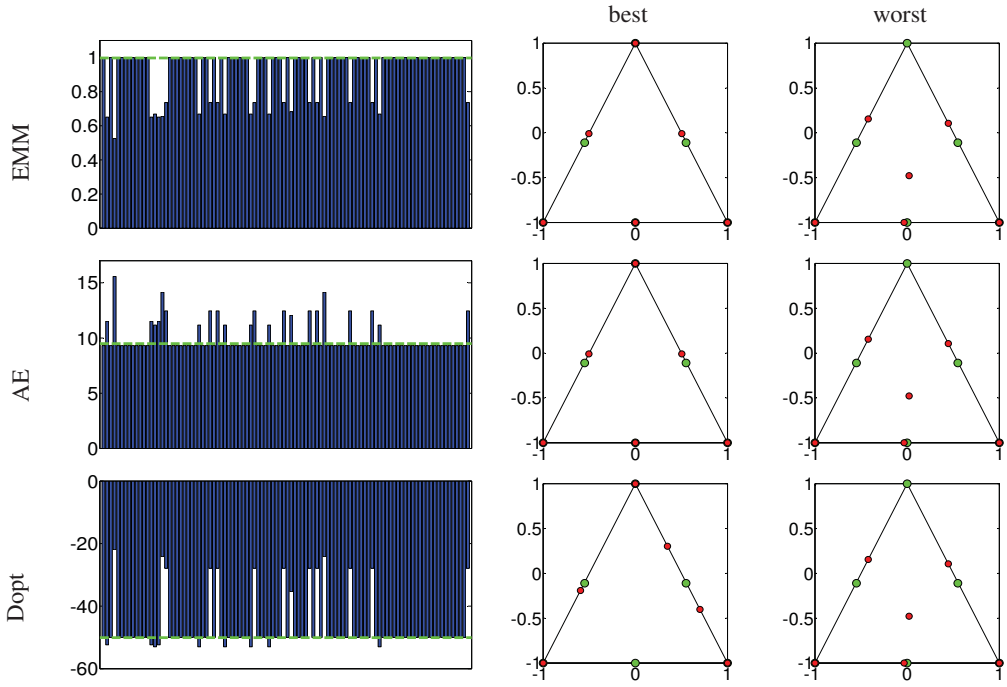

Tab. 1: Example 1 (triangle and 6 design points).

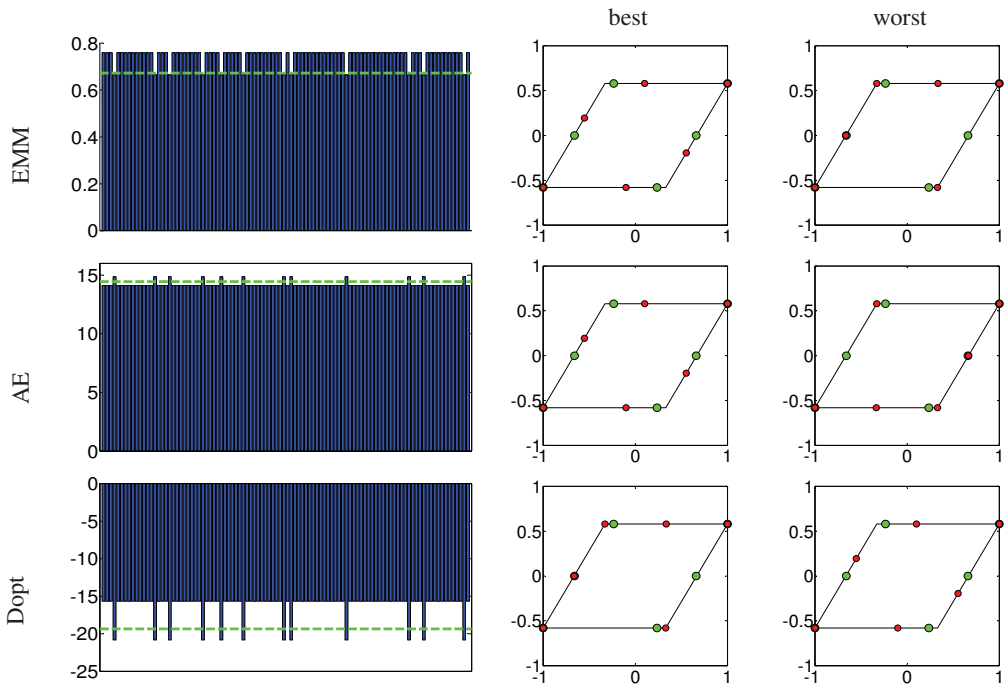

Tab. 2: Example 2 (parallelogram and 6 design points).

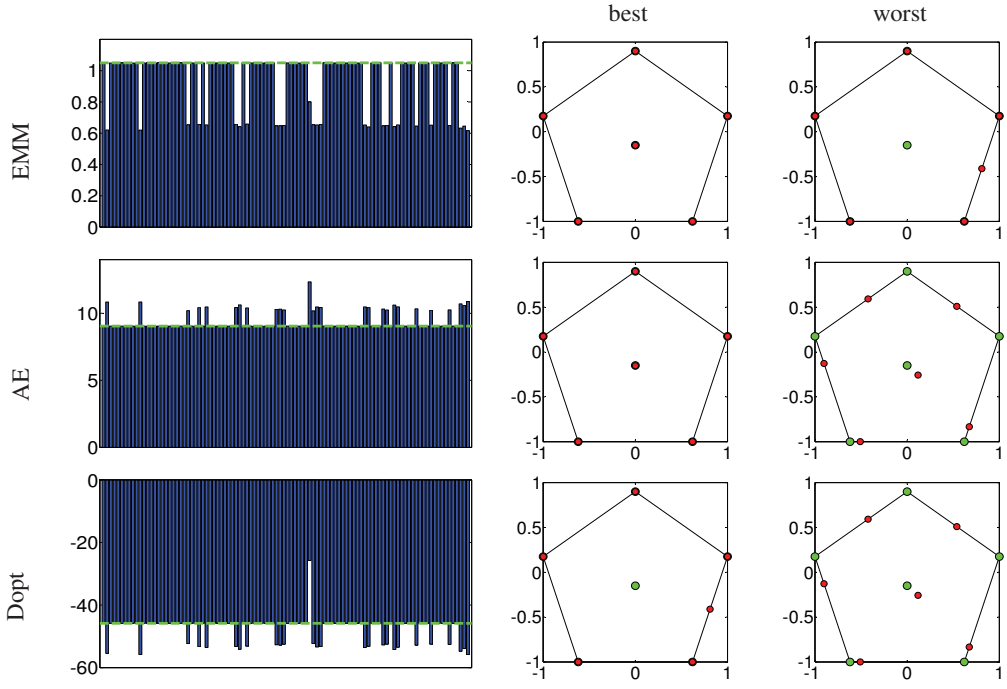

Tab. 3: Example 3 (pentagon and 6 design points).

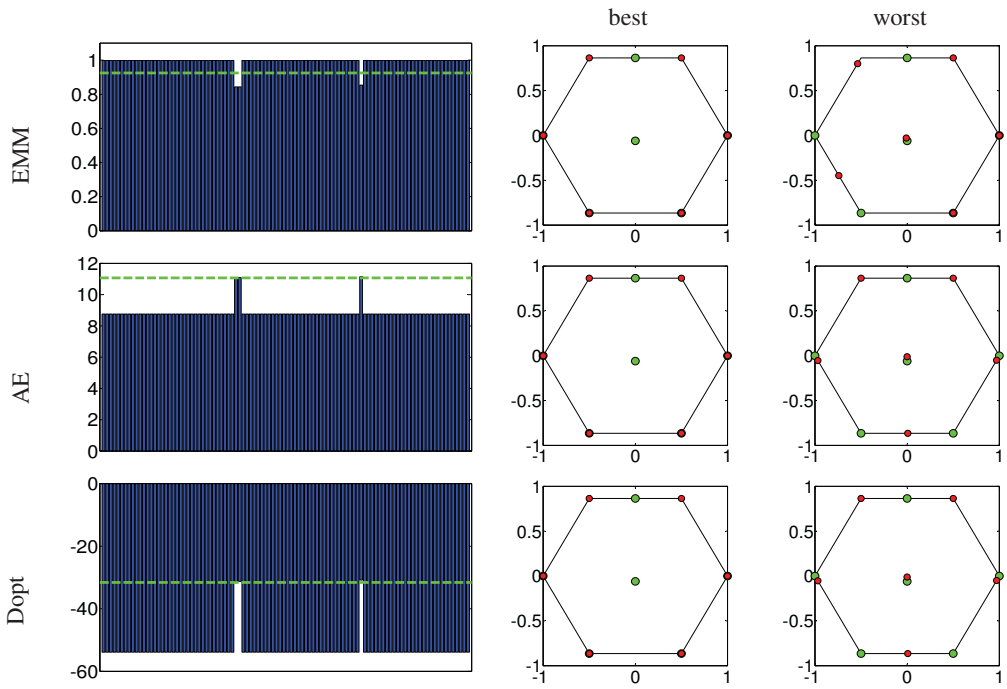

Tab. 4: Example 4 (hexagon and 6 design points).

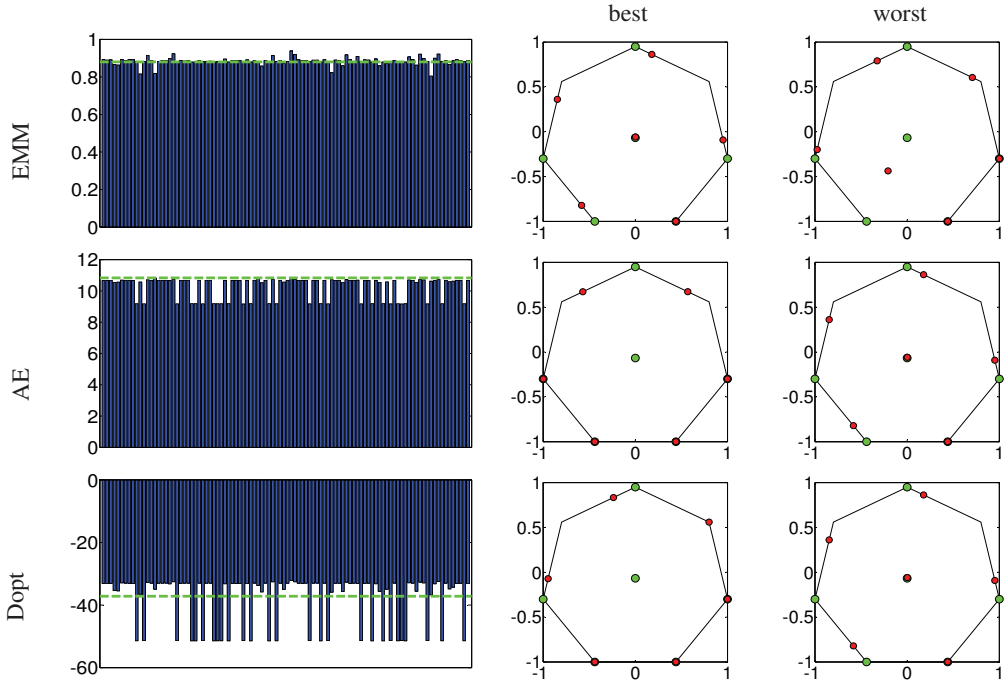

Tab. 5: Example 5 (heptagon and 6 design points).

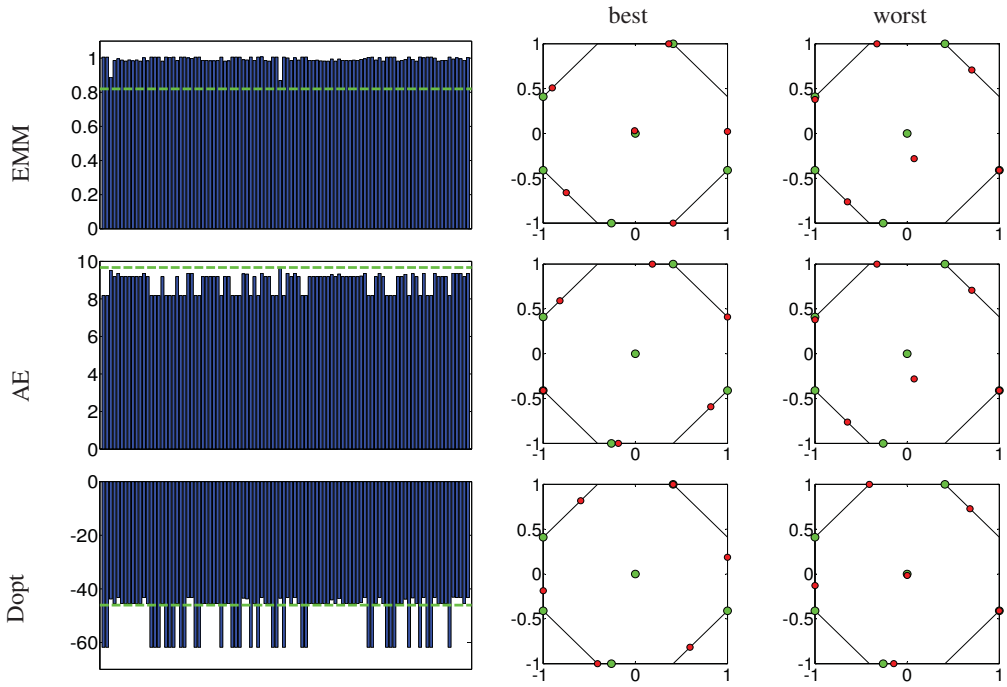

Tab. 6: Example 6 (octagon and 6 design points).

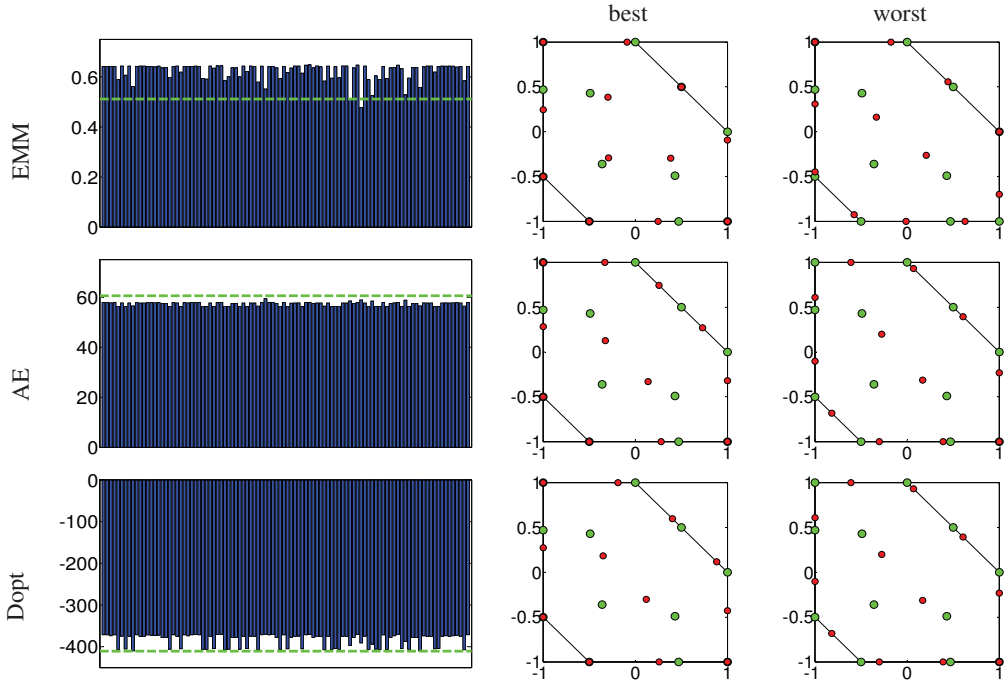

Tab. 7: Example 7 (irregular hexagon and 12 design points).

C Boxplot results

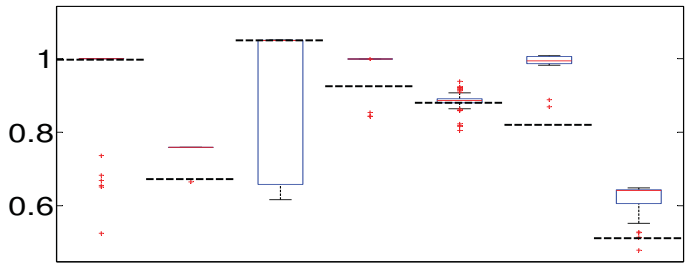

(a) EMM (higher is better)

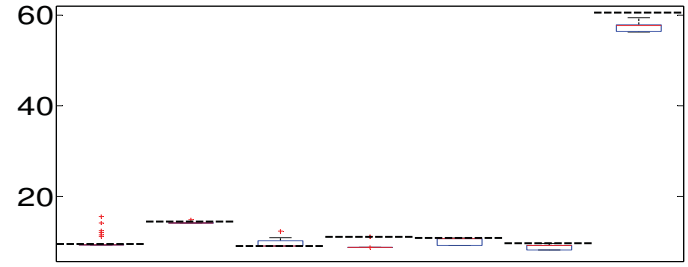

(b) AE (lower is better)

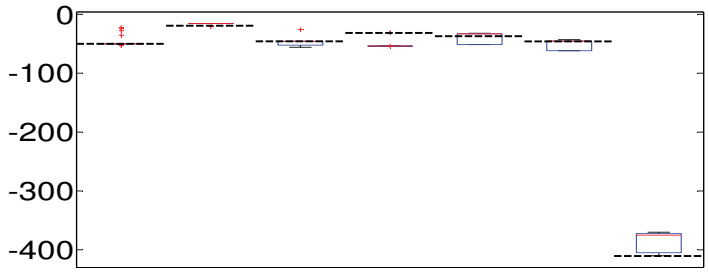

(c) Dopt (lower is better)

Fig. 6: The boxplots of results for 7 individual examples (triangle, parallelogram, pentagon, hexagon, heptagon, octagon, irregular hexagon) and three objective functions. Black dash lines are reference values taken from (Hofwing and Strömberg, 2010).

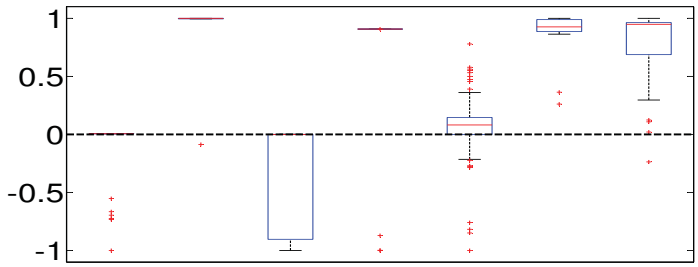

(a) EMM (higher is better)

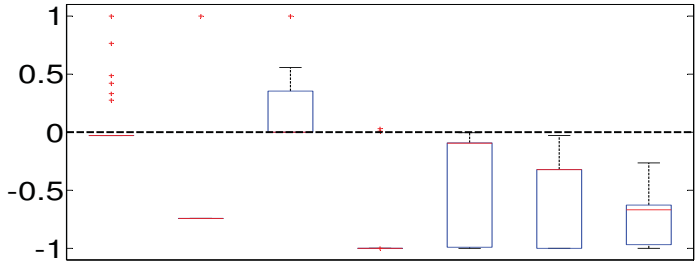

(b) AE (lower is better)

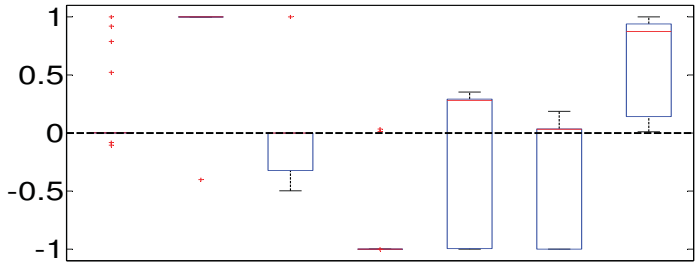

(c) Dopt (lower is better)

Fig. 7: The boxplots of results for 7 individual examples (triangle, parallelogram, pentagon, hexagon, heptagon, octagon, irregular hexagon) and three objective functions. Values are normalized. Black dash line is a reference value taken from (Hofwing and Strömberg, 2010).

18th International Conference
ENGINEERING MECHANICS 2012
Svratka, Czech Republic, May 14 – 17, 2012

pp. 915–926
Paper #32

GENERALIZED LINEAR MODEL WITH AERO-ELASTIC FORCES VARIABLE IN FREQUENCY AND TIME DOMAINS

J. Náprstek, S. Pospíšil [1]

Abstract: *Behavior of slender aero-elastic systems in a sub-critical domain including position of the lowest critical state is commonly investigated using double degree of freedom (DDOF) linear model. The most frequently used are neutral models treating aero-elastic forces as certain constants corresponding to system parameters and stream velocity. Although this approach is working well, it shows a number of shortcomings. For this reason modeling by flutter derivatives or indicial functions has been launched. However, these two groups of models have been developed separately one from each other. It seems they are rather isolated until now. Moreover they mostly suffer from various gaps in mathematical formulations and further treatment. The paper tries to put all three groups together on one common basis and to demonstrate linkage of them. This approach allows formulate more sophisticated models combining main aspects of all groups in question keeping the DDOF basis. These models correspond by far better to results of wind channel and full scale measurements.*

Keywords: ***Flutter derivatives, Indicial functions, Non-symmetric systems, Dynamic stability.***

1. Introduction

Slender prismatic structures exhibited to strong dynamic wind effects (bridge decks, towers, chimneys, etc.) are frequently analyzed using a double degree of freedom (DDOF) linear model working with heaving and torsional components of a cross-section, see e.g. Bartoli & Righi (2006). This aero-elastic model is often adequate to study the system response until the first critical state is reached. Relevant mathematical models appearing in literature differ in principle by way of composition of aero-elastic forces. This criterion enables to sort them roughly in three groups. The first group can be possibly called neutral models - aero-elastic forces are introduced as suitable constants independent from excitation frequency and time. The second one involves flutter derivatives - they respect the frequency dependence of aero-elastic forces, see Scanlan & Tomko (1971).

Finally the third is working with indicial functions - they are defined as kernels of convolution integrals formulating aero-elastic forces as functions of time, see Wagner (1929), Küssner (1954), Garrick (1938) and Scanlan, Beliveau & Budlong (1974). Second and third groups have been developing separately from each other and seem to be isolated until now, see **?** and Costa et al. (2007) for example. Moreover they mostly suffer from various gaps in mathematical formulations and further treatment. The paper tries to put all three groups together on one common basis and to demonstrate linkage of them. This approach allows formulate more sophisticated models combining main aspects of all groups keeping the DDOF basis. These models correspond by far better to results of wind channel and full scale measurements and seem to be very promising for the future investigation and practical applications.

For purposes of this study the bridge girder is considered as axially symmetric or almost symmetric with possible response components in heave u (vertical direction) and pitch φ (rotation around S point). An outline can be seen in Fig.1. In principle all types of above models have been investigating many years. Each of them has its advantages and shortcomings. However most of them suffer very often from mathematical gaps preventing their generalization and synthesis on formal basis in order to identify some special phenomena remaining hidden when dealing with heuristic approaches only. Let us characterize now briefly the groups of models mentioned above in forthcoming parts.

[1] Ing. Jiří Náprstek, DrSc., Doc.Ing. Stanislav Pospíšil, PhD.
Institute of Theoretical and Applied Mechanics ASCR, v.v.i.; Prosecká 76, 190 00 Prague 9,
tel. +420.286 892 515, e-mail: naprstek@itam.cas.cz, pospisil@itam.cas.cz

2. Neutral models

Neutral models are relatively the most simple and enable to provide many results analytically in a form of closed solution. These models have been extensively studied for instance in Pospíšil & Náprstek (2011).

Although there exist many versions of a basic formulation, in principle the most general model of neutral type can be expressed in the form:

$$\begin{aligned} \ddot{u} + b_m \cdot \dot{u} - hq \cdot \dot{\varphi} + \omega_u^2 \cdot u - p \cdot \varphi &= 0 \\ \ddot{\varphi} + q \cdot \dot{u} + b_I \cdot \dot{\varphi} + gp \cdot u + \omega_\varphi^2 \cdot \varphi &= 0 \end{aligned} \qquad (1)$$

where we have denoted: $\omega_u^2, \omega_\varphi^2-$ total eigen-frequencies in relevant components including stiffness and aero-elastic components; b_m, b_I- total damping parameters including internal structural damping and aero-elastic contribution; $q[(ms)^{-1}]$ or $p[m \cdot s^{-2}]$ gyroscopic or non-conservative forces of aero-elastic origin respectively; $g[m^{-2}], h[m^2]$ auxiliary constants serving for dimensional compatibility of the above equations (they can be regarded as certain characteristics of the cross-section).

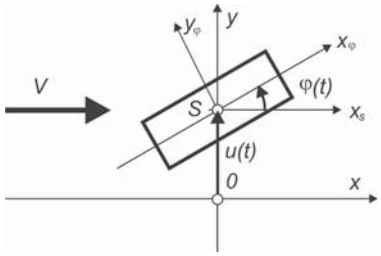

Fig. 1: Schematic DDOF model of a bridge symmetric cross-section under wind loading.

Parameters q, p in general don't include any static components which follow from elastic properties of the system itself, they consist only of aero-elastic terms vanishing for zero velocity of the air stream. So for stream velocity $V = 0$, the system (1) degenerates in two independent equations.

The main tool for stability investigation is, together with the system (1), its characteristic equation:

$$\begin{aligned} D = \lambda^4 + \lambda^3(b_m + b_I) + \lambda^2(\omega_u^2 + \omega_\varphi^2 + b_m b_I + hq^2) + \\ + \lambda(\omega_u^2 b_I + \omega_\varphi^2 b_m + (1 + gh)pq) + \omega_u^2\omega_\varphi^2 + gp^2 &= 0 \end{aligned} \qquad (2)$$

The resulting characteristic equation represents annuled polynomial of the fourth order $(n = 4)$ with roots $\lambda_1, \lambda_2, \lambda_3$ and λ_4. The trivial solution of system (1) is stable only if a real part of all four roots is negative. In other words, stability limits are given by conditions:

$$\mathrm{Re}(\lambda_i) = 0, \quad i \in (1, \ldots, 4) \qquad (3)$$

Consequently, the trivial solution of system (1) is stable in a domain representing an intersection of sub-domains $\mathrm{Re}(\lambda_i) < 0, \quad i \in (1, \ldots, 4)$.

The system (1) and the characteristic equation (2) can provide a lot of information regarding motion stability, critical velocities V_{crit}, system response on stability limits, etc. Consequently, it enables to predict flutter/divergence onset velocity as well as to estimate their shapes in a particular case. However aero-elastic coefficients in Eqs (1) are introduced as constants corresponding to certain conditions ruling around the cross-section. Anyway, these coefficients are functions of V and ω, and therefore some iterative process should follow balancing these effects in order to harmonize velocity V with velocity V_{crit}. Despite these shortcomings the applicability of neutral models is quite wide if the variability of the aero-elastic terms is approximately linear. Otherwise one of more sophisticated models should be used, as we will see in next two parts.

Strategy of the stability investigation can be based on Routh-Hurwitz inspection of Eq. (2). The detailed analysis and relevant results can be found e.g. in Náprstek & Pospíšil (2001), Náprstek, J. (2007). The most important types of aero-elastic stability loss (flutter and divergence) and their possible interactions are there given together with the conditions of their existence.

3. Models with flutter derivatives

Flutter derivatives have been introduced many years ago, see for instance Theodorsen (1935) and more recently Poulsen, Damsgaard & Reinhold (1992). Their various aspects have been investigated exten-

sively for a long time in the aircraft, civil and other branches of engineering. They have been introduced as functions in the frequency domain related to a particular cross-section without any link with other system parameters (inertia, elastic stiffness, internal damping). Nevertheless they can be understood as a certain extension of the damping and stiffness matrix elements. Flutter derivatives can be interpreted as amplitudes Q or M of the heaving forces or the pitching moments, respectively, which should reach a unit amplitude of one response component under harmonic external kinematic excitation, while remaining components are kept zero in the same time. Thus the flutter derivatives are the dimensionless functions of the excitation frequency ω, stream velocity V and geometric characteristic of the cross-section B $[m]$. They are combined in one dimensionless argument $\kappa = B\omega/V$. So the basic relations between kinematic and force components can be roughly outlined:

	$\dot{u}$	u	$\dot{\varphi}$	φ
$Q:$	$H_1(\kappa)$	$H_4(\kappa)$	$H_2(\kappa)$	$H_3(\kappa)$
$M:$	$A_1(\kappa)$	$A_4(\kappa)$	$A_2(\kappa)$	$A_3(\kappa)$
$Q:$	$A_{11}(\kappa)$	$A_{12}(\kappa)$	$A_{13}(\kappa)$	$A_{14}(\kappa)$
$M:$	$A_{21}(\kappa)$	$A_{22}(\kappa)$	$A_{23}(\kappa)$	$A_{24}(\kappa)$

; $\quad \kappa = \dfrac{B\omega}{V}$ (4)

where following notation has been introduced: $H_i(\kappa)$ or $A_i(\kappa)$ - amplitudes of flutter derivatives corresponding to heaving forces Q or pitching moments M amplitudes due to individual sets of unit kinematic harmonic excitations of a proper cross-section in an aerodynamic tunnel (notation and indexing corresponds to literature referenced); $A_{ij}(\kappa)$ - alternative notification of flutter derivatives assigned with respect to the table in Eq. (4);

Since we try to write down final formulae of Q or M amplitudes, there appear expressions of the type $\kappa A_{11}(\kappa)\cdot\dot{u}(t)$, $\kappa A_{23}(\kappa)\cdot\dot{\varphi}(t)$, etc. They are to see everywhere since classical until contemporary literature, e.g. [Scanlan] and many others. However, they are inconsistent mixing both frequency and time variables together. Subsequent integral transform would be unapplicable. Therefore respecting harmonic regime of the flutter derivatives (functions of ω) also displacements $u(t), \varphi(t)$ and their time derivatives should be expressed correspondingly, for instance in the form of their Fourier transform. It means in particular as $\mathrm{i}\omega U, U, \mathrm{i}\omega\Phi, \Phi$. So that with reference to notification (4) the heaving and pitching aero-elastic forces in the frequency domain can be written as follows:

$$\begin{aligned} Q(\omega) &= \mu_m V^2\ (\tfrac{\mathrm{i}\omega B}{V}\kappa A_{11} + \kappa^2 A_{12})\ U + \mu_m V^2(\tfrac{\mathrm{i}\omega B^2}{V}\kappa A_{13} + \kappa^2 B A_{14})\ \Phi, \quad \mu_m = \varrho/m \\ M(\omega) &= \mu_I V^2 B^2\ (\tfrac{\mathrm{i}\omega}{V}\kappa A_{21} + \tfrac{1}{B}\kappa^2 B A_{22})\ U + \mu_I V^2 B^2(\tfrac{\mathrm{i}\omega B}{V}\kappa A_{23} + \kappa^2 A_{24})\ \Phi,\ \mu_I = 2\varrho/I \end{aligned} \tag{5}$$

where m or I are a mass or mass inertia moment of the vibrating body and ϱ is a specific mass of the air.

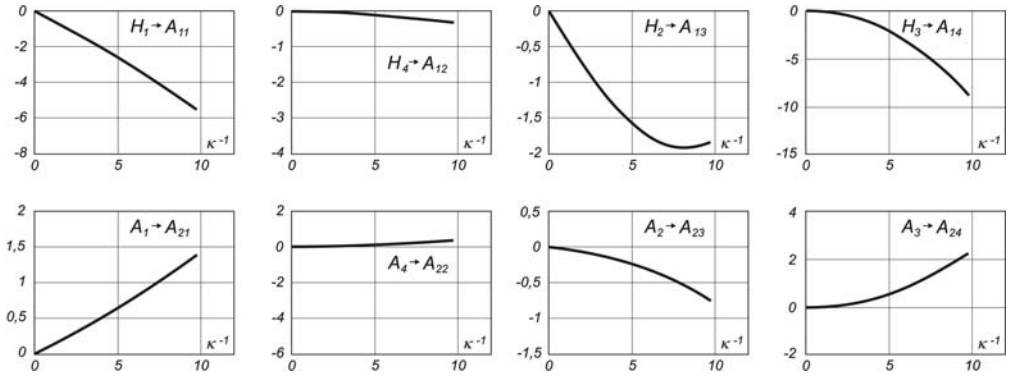

Fig. 2: Outline of flutter derivatives; rectangular cross-section, ratio 1:5; position of $A_{11} - A_{24}$ pictures correspond with table in Eq. (4).

The definition itself of flutter derivatives apparently implicates that they can serve only to develop a linear mathematical model as their application is based on the superposition principle. Flutter derivatives can be incorporate into the governing equations of type (1) only if these equations are expressed in the frequency domain. Hence the system (1) should be written in a form of the two-way Laplace transform (integration $t \in (-\infty, +\infty)$) to unify the basis of individual parts. Transformation exists if the system is stable and therefore influence of initial conditions disappear with increasing time. It means, however, that only steady state problems with explicit frequency $\omega = -\mathrm{i}\lambda$ can be investigated. Finally we write the complete system in the frequency domain, so that it has a character of an algebraic (unknowns $U,\ \Phi$) system:

$$\begin{matrix} Q: \\ M: \end{matrix} \left| \begin{matrix} \lambda^2 + \lambda \cdot (b_m + \mu_m VB \cdot \kappa A_{11}) + (\omega_u^2 + \mu_m V^2 \cdot \kappa^2 A_{12}) \ ; & \\ \lambda \cdot \mu_m VB^2 \cdot \kappa A_{13} + \mu_m V^2 B \cdot \kappa^2 A_{14} & \\ \lambda \cdot \mu_I VB^2 \cdot \kappa A_{21} + \mu_I V^2 B \cdot \kappa^2 A_{22} \ ; & \\ \lambda^2 + \lambda \cdot (b_I + \mu_I VB^3 \cdot \kappa A_{23}) + (\omega_\varphi^2 + \mu_I V^2 B^2 \cdot \kappa^2 A_{24}) & \end{matrix} \right| \cdot \left| \begin{matrix} U \\ \Phi \end{matrix} \right| = \left| \begin{matrix} 0 \\ 0 \end{matrix} \right| \tag{6}$$

The shape of flutter derivatives for the rectangular cross-section as they are plotted in Fig. 2 is commonly accepted. Let us go briefly through individual graphs in this figure. It can be observed that functions A_{ij} related with $\dot{u}, \dot{\varphi}$ are odd functions, while those related to u, φ are even with respect to the vertical axis. Indeed this fact can be shown also theoretically using Theodorsen functions, see Theodorsen (1935). Looking through Fig. 2, it is obvious that the courses of individual A_{ij} are not "dramatic". Hence with respect to the interval length needed on the $1/\kappa$ axis, only the first and the second terms of the odd or even polynomial expansions seems to be satisfactory to characterize A_{ij} in equations (6). Thus for instance:

$$A_{11} \approx a_{11}\frac{1}{\kappa} + b_{11}\frac{1}{\kappa^3}\ , \quad A_{12} \approx a_{12}\frac{1}{\kappa^2} + b_{12}\frac{1}{\kappa^4}\ , \quad \text{etc.} \tag{7}$$

where a_{ij} and b_{ij} are relevant dimensionless coefficients of the polynomial expansion. These coefficients can be obtained fitting relevant polynomials into experimental results.

Let us note that function values of A_{12} and A_{22} are markedly small. Indeed, dealing with a symmetrical cross-section and supposing perfectly uniform stream velocity in a wind tunnel, functions A_{12} and A_{22} should vanish identically. Their non-zero values presented in Fig. 2 are most probably the results of imperfections ruling in experiments. Despite this fact, these terms have been included to keep theoretical consistency of relevant matrices (many papers omit those and work with six derivatives only).

Let us introduce polynomial expansions Eqs (7) into Eqs (6). Being aware that $\omega^2 = \lambda^2$, one obtains a modified system:

$$\begin{matrix} Q: \\ M: \end{matrix} \left| \begin{matrix} q_{11},\ q_{12} \\ q_{21},\ q_{22} \end{matrix} \right| \cdot \left| \begin{matrix} U \\ \Phi \end{matrix} \right| = \left| \begin{matrix} 0 \\ 0 \end{matrix} \right| \tag{8}$$

$$\begin{aligned} q_{11} &= (\lambda^2 + \lambda(b_m + \mu_m VBa_{11}) + (\omega_u^2 + \mu_m V^2 a_{12})) - \mu_m(\tfrac{1}{\lambda}\tfrac{V^3}{B}b_{11} + \tfrac{1}{\lambda^2}\tfrac{V^4}{B^2}b_{12})\ , \\ q_{12} &= (\lambda\mu_m VB^2 a_{13} + \mu_m V^2 B a_{14}) - \mu_m(\tfrac{1}{\lambda}V^3 b_{13} + \tfrac{1}{\lambda^2}\tfrac{V^4}{B}b_{14})\ , \\ q_{21} &= (\lambda\mu_I VB^2 a_{21} + \mu_I V^2 B a_{22}) - \mu_I(\tfrac{1}{\lambda}V^3 b_{21} + \tfrac{1}{\lambda^2}\tfrac{V^4}{B}b_{22})\ , \\ q_{22} &= (\lambda^2 + \lambda(b_I + \mu_I VB^3 a_{23}) + (\omega_\varphi^2 + \mu_I V^2 B^2 a_{24})) - \mu_I(\tfrac{1}{\lambda}V^3 B b_{23} + \tfrac{1}{\lambda^2}V^4 b_{24})\ . \end{aligned} \tag{9}$$

The neutral models following Eqs (1) include system parameters, which implicitly incorporate the influence of surrounding air, for instance $b_m = b_{m,syst} + b_{m,air}$, etc. Depending on a strategy of a particular analysis the additional part $b_{m,air}$ is subsequently considered as a function of the stream velocity V, but any relation with the frequency ω is always omitted. Anyway, terms containing coefficients a_{ij} in Eqs (9) can be considered as a certain "first approximation", e.g. $b_{m,air} = \mu_m VCa_{11}$, $\omega_{u,air}^2 = \mu_m V^2 a_{12}$, etc. So that respecting terms with a_{ij}, one obtains result analogous with the neutral model Eqs (1), where

the dependence on the stream velocity V is obvious approaching zero with $V \to 0$. It is apparent, see Fig. 2, that a_{ij} can be positive or negative. Therefore introduction of terms with a_{ij} can result (on the level of the "first approximation") in an increase or a decrease of effective system parameters due to the aero-elastic effects. In particular non-conservative and gyroscopic character of the system follows solely from these terms as the system itself doesn't contain extra-diagonal elements. Non-symmetric character of the system results from character of a_{ij} signs:

$$a_{13} < 0, \quad a_{14} < 0, \quad a_{21} > 0, \quad a_{22} > 0 \tag{10}$$

and therefore symbolical link of some coefficients in Eqs (1) and elements specified in Eqs (9) can be written:

$$\begin{array}{ccc} -p = \mu_m V^2 B a_{14} < 0, & g = \mu_I a_{22}/\mu_m a_{14} < 0, & gp = \mu_I V^2 B a_{22} > 0, \\ q = \mu_I V B^2 a_{21} > 0, & h = \mu_m a_{13}/\mu_I a_{21} < 0, & -hq = \mu_m V B^2 a_{13} < 0. \end{array} \tag{11}$$

Coefficients b_{ij} represent the most simple quantification of the frequency ω influence within aero-elastic forces, see Eqs (9). Looking over Fig. 2 we can see, that the second terms in expansions Eqs (7) arithmetized by coefficients b_{ij} can be considered significantly smaller especially for rising ω.

In order to inspect the primary form of the differential system, let us make an inverse transform of Eqs (8), (9) back to the time domain. After tedious manipulation, the differential system including the influence of the flutter derivatives on the level of approximation Eqs (7) can be written as follows:

$$\begin{aligned} \ddot{u} \; & + b_m(\dot{u} - \eta^2\beta_{11} \int_{-\infty}^{t} u(\tau)\mathrm{d}\tau) - hq(\dot{\varphi} - \eta^2\beta_{13} \int_{-\infty}^{t} \varphi(\tau)\mathrm{d}\tau) \\ & + \omega_u^2(u - \eta^2\beta_{12} \int_{-\infty}^{t} (t-\tau)u(\tau)\mathrm{d}\tau) - p(-\eta^2\beta_{14} \int_{-\infty}^{t} (t-\tau)\varphi(\tau)\mathrm{d}\tau) \quad = \quad 0 \\ \ddot{\varphi} \; & + q(\dot{u} - \eta^2\beta_{21} \int_{-\infty}^{t} u(\tau)\mathrm{d}\tau) + b_I(\dot{\varphi} - \eta^2\beta_{23} \int_{-\infty}^{t} \varphi(\tau)\mathrm{d}\tau) \\ & + gp(\dot{u} - \eta^2\beta_{22} \int_{-\infty}^{t} (t-\tau)\varphi(\tau)\mathrm{d}\tau) + \omega_\varphi^2(\varphi - \eta^2\beta_{24} \int_{-\infty}^{t} (t-\tau)\varphi(\tau)\mathrm{d}\tau) \quad = \quad 0 \end{aligned} \tag{12}$$

Both of the systems (8), (12) can be immediately used for further investigation. The system (12) is an extension of (1). It demonstrates memory properties due to convolution integrals. In principle the integrals could be avoided differentiating twice both equations of the system. However resulting equations of the fourth order are less suitable for further analysis than the form of Eqs (12). Especially stability of the numerical solution of Eqs (12) is far better.

Nevertheless, let us focus to a main tool of the dynamic stability analysis. It follows from the system (8) representing a condition of its zero determinant. Provided the matrix of the system Eq. (8) is multiplied by a factor λ^2, the condition of the stability gets a form of the characteristic equation of the eight degree of the parameter λ:

$$a_0\lambda^8 + a_1\lambda^7 + a_2\lambda^6 + a_3\lambda^5 + a_4\lambda^4 + a_5\lambda^3 + a_6\lambda^2 + a_7\lambda + a_8 = 0 \tag{13}$$

$$\begin{aligned} a_0 \; &= \; 1 \, , && \text{(a)} \\ a_1 \; &= \; (b_m + b_I) + (\mu_m V B a_{11} + \mu_I V B^3 a_{23}) \, , && \text{(b)} \\ a_2 \; &= \; (\omega_u^2 + \omega_\varphi^2 + b_m b_I) + (\mu_m V^2 a_{12} + \mu_I V^2 B^2 a_{24} + b_m \mu_I V B^3 a_{23} + b_I \mu_m V B a_{11} \\ & \quad + \mu_m \mu_I V^2 B^4 (a_{11} a_{23} - a_{13} a_{21})) \, , && \text{(c)} \\ a_3 \; &= \; b_m \omega_\varphi^2 + b_I \omega_u^2 + \mu_m \omega_\varphi^2 V B a_{11} + \mu_I \omega_u^2 V B^3 a_{23} + \mu_I b_m V^2 B^2 a_{24} + \mu_m b_I V^2 a_{12} \\ & \quad + \mu_m \mu_I V^3 B^3 (a_{11} a_{24} + a_{12} a_{23} - a_{13} a_{22} - a_{14} a_{21}) \\ & \quad - \mu_I V^3 B b_{23} - \mu_m \tfrac{V^3}{B} b_{11} \, , && \text{(d)} \end{aligned} \tag{14}$$

$$
\begin{aligned}
a_4 &= \omega_u^2\omega_\varphi^2 + \mu_m\omega_\varphi^2 V^2 a_{12} + \mu_I\omega_u^2 V^2 B^2 a_{24} + \mu_m\mu_I V^4 B^2(a_{12}a_{24} - a_{14}a_{22}) \\
&\quad + \mu_m\mu_I V^4 B^2(-a_{23}b_{11} - a_{11}b_{23} + a_{21}b_{13} + a_{13}b_{21}) \\
&\quad - \mu_I b_m V^3 B b_{23} - \mu_m b_I \tfrac{V^3}{B} b_{11} - \mu_I V^4 b_{24} - \mu_m \tfrac{V^4}{B^2} b_{12} \,, \qquad \text{(e)} \\
a_5 &= \mu_m\mu_I V^5 B(-a_{11}b_{24} - a_{23}b_{12} - a_{12}b_{23} - a_{24}b_{11} \\
&\quad + a_{14}b_{21} + a_{22}b_{13} + a_{13}b_{22} + a_{21}b_{14}) \\
&\quad - \mu_I b_m V^4 b_{24} - \mu_m b_I \tfrac{V^4}{B^2} b_{12} - \mu_I\omega_u^2 V^3 B b_{23} - \mu_m\omega_\varphi^2 \tfrac{V^3}{B} b_{11} \,, \qquad \text{(f)} \\
a_6 &= \mu_m\mu_I V^6(-a_{12}b_{24} - a_{24}b_{12} + a_{14}b_{22} + a_{22}b_{14}) \\
&\quad - \mu_I\omega_u^2 V^4 b_{24} - \mu_m\omega_\varphi^2 \tfrac{V^4}{B^2} b_{12} + \mu_m\mu_I V^6(b_{11}b_{23} - b_{21}b_{13}) \,, \qquad \text{(g)} \\
a_7 &= \mu_m\mu_I \tfrac{V^7}{B}(-b_{14}b_{21} - b_{13}b_{22} + b_{11}b_{24} + b_{12}b_{23}) \,, \qquad \text{(h)} \\
a_8 &= \mu_m\mu_I \tfrac{V^8}{B^2}(b_{12}b_{24} - b_{14}b_{22}) \,. \qquad \text{(i)}
\end{aligned}
$$

As it has been mentioned terms containing b_{ij} are relatively small and represent a certain "correction" of the main part which is given by terms with a_{ij}. Moreover b_{ij} related with $\dot{u}, u$ are even significantly smaller than those related with $\dot{\varphi}, \varphi$. So it can be put approximately: $b_{11} \approx 0,\ b_{12} \approx 0,\ b_{21} \approx 0,\ b_{22} \approx 0$. Therefore in Eqs (14) coefficients $a_7, a_8 = 0$ and $a_3 - a_6$ get simpler. Roots $\lambda_7, \lambda_8 \neq 0$ and hence the remaining part of the characteristic equation Eq. (13) can be divided by λ^2. Finally the degree of the characteristic equation drops from eight to six. Thus let us rewrite this one together with simplified coefficients $a_0 - a_6$:

$$
a_0\lambda^6 + a_1\lambda^5 + a_2\lambda^4 + a_3\lambda^3 + a_4\lambda^2 + a_5\lambda + a_6 = 0 \qquad (15)
$$

$$
\begin{aligned}
a_0 &= 1 \,, \qquad \text{(a)} \\
a_1 &= (b_m + b_I) + (\mu_m V B a_{11} + \mu_I V B^3 a_{23}) \,, \qquad \text{(b)} \\
a_2 &= (\omega_u^2 + \omega_\varphi^2 + b_m b_I) + (\mu_m V^2 a_{12} + \mu_I V^2 B^2 a_{24} + b_m\mu_I V B^3 a_{23} + b_I\mu_m V B a_{11} \\
&\quad + \mu_m\mu_I V^2 B^4(a_{11}a_{23} - a_{13}a_{21})) \,, \qquad \text{(c)} \\
a_3 &= b_m\omega_\varphi^2 + b_I\omega_u^2 + \mu_m\omega_\varphi^2 V B a_{11} + \mu_I\omega_u^2 V B^3 a_{23} + \mu_I b_m V^2 B^2 a_{24} + \mu_m b_I V^2 a_{12} \\
&\quad + \mu_m\mu_I V^3 B^3(a_{11}a_{24} + a_{12}a_{23} - a_{13}a_{22} - a_{14}a_{21}) - \mu_I V^3 B b_{23} \,, \qquad \text{(d)} \\
a_4 &= \omega_u^2\omega_\varphi^2 + \mu_m\omega_\varphi^2 V^2 a_{12} + \mu_I\omega_u^2 V^2 B^2 a_{24} + \mu_m\mu_I V^4 B^2(a_{12}a_{24} - a_{14}a_{22}) \\
&\quad + \mu_m\mu_I V^4 B^2(-a_{11}b_{23} + a_{21}b_{13}) - \mu_I b_m V^3 B b_{23} - \mu_I V^4 b_{24} \,, \qquad \text{(e)} \\
a_5 &= \mu_m\mu_I V^5 B(-a_{11}b_{24} - a_{12}b_{23} + a_{22}b_{13} + a_{21}b_{14}) \\
&\quad - \mu_I b_m V^4 b_{24} - \mu_I\omega_u^2 V^3 B b_{23} \,, \qquad \text{(f)} \\
a_6 &= \mu_m\mu_I V^6(-a_{12}b_{24} + a_{22}b_{14}) - \mu_I\omega_u^2 V^4 b_{24} \,. \qquad \text{(g)}
\end{aligned} \qquad (16)
$$

Although Eq. (15) is approximate only, it is obvious that higher degree of the stream velocity influence is focused rather on the rotating component and its velocity: $\varphi,\ \dot{\varphi}$, while heaving component and its velocity corresponds rather with the neutral model in Eqs (1). The structure of Eqs (16) suggests some more possible simplifications canceling remaining b_{ij}. Such step would lead to full analogy with the neutral model (1).

4. Generalized Routh-Hurwitz method

Dynamic stability of MDOF systems is closely related with eigen values of the characteristic matrix. If their real parts are all negative, the system is stable. To carry-out a general and careful analysis, a strategy based on an inspection of the characteristic polynomial $P(\lambda)$ is preferable. In such a case properties of the characteristic matrix are reflected in polynomial roots. So that limits separating their negative and positive real part values should be found. A large group of methods for searching these limits is based on properties of the Hurwitz matrix $\mathbf{H} \in \mathbb{R}^{n\times n}$ and its diagonal sub-determinants. Then

the basic principle requests that all diagonal sub-determinants should be positive. Thus zero value of sub-determinants indicate individual stability limits. Here only a technique of this procedure will be outlined. For a rigorous mathematical proof, see monographs, i.e. Gantmacher (1966). Following scheme can be outlined:

$$P(\lambda) = a_0\lambda^n + a_1\lambda^{n-1} + a_2\lambda^{n-2} + \ldots + a_{n-1}\lambda + a_n \tag{17}$$

$$\mathbf{H} = \left\| \begin{array}{ccccc} a_1, & a_3, & a_5 & , \ldots, & a_{2n-1} \\ a_0, & a_2, & a_4 & , \ldots, & a_{2n-2} \\ 0, & a_1, & a_3 & , \ldots, & a_{2n-3} \\ 0, & a_0, & a_2 & , \ldots, & a_{2n-4} \\ 0, & 0, & a_1 & , \ldots, & a_{2n-5} \\ \ldots & \ldots & \ldots & \ldots & \ldots \\ \ldots & \ldots & \ldots & \ldots & \ldots \end{array} \right\| \quad ; \quad \begin{array}{l} a_{2k+1} = 0; \quad k > (n-1)/2 \\ a_{2k} = 0; \quad k > n/2 \end{array} \tag{18}$$

In other words, elements of the 1st row are coefficients of the odd powers λ completed with zeroes in the right part of the row. Similarly the 2nd row consists of coefficients of the even powers λ. The 3rd and 4th rows correspond with 1st and 2nd rows being shifted one element to the right. Similarly 5th and 6th rows, etc., as far as the last non-zero element a_{2k+1} or a_{2k} reaches right boundary of the row.

In order to facilitate and make more transparent the sub-determinants evaluation, the matrix $\mathbf{H}$ is subjected now to triangulation using the Routh algorithm (remembers the Gauss elimination process). In the first step: The odd rows remain intact. From the even rows are deducted the respective odd rows multiplied by the factor a_0/a_1. Further steps are analogous until the $(n-1)$th step is done. The whole process can outlined as follows:

$$\mathbf{H}_{(1)} = \left\| \begin{array}{ccccccc} a_1, & a_3, & a_5, & a_7, & \ldots, & a_{2n-1} \\ 0, & b_1, & b_3, & b_5, & \ldots, & b_{2n-3} \\ 0, & a_1, & a_3, & a_5, & \ldots, & a_{2n-3} \\ 0, & 0, & b_1, & b_3, & \ldots, & b_{2n-5} \\ 0, & 0, & a_1, & a_3, & \ldots, & a_{2n-5} \\ \ldots & \ldots & \ldots & \ldots & \ldots & \ldots \\ \ldots & \ldots & \ldots & \ldots & \ldots & \ldots \end{array} \right\| \quad \Longrightarrow \quad \ldots \mathbf{H}_{(n-1)} = \left\| \begin{array}{ccccc} a_1, & a_3, & a_5, & a_7, & \ldots \\ 0, & b_1, & b_3, & b_5, & \ldots \\ 0, & 0, & c_1, & c_3, & \ldots \\ 0, & 0, & 0, & d_1, & \ldots \\ 0, & 0, & 0, & 0, & \ldots \\ \ldots & \ldots & \ldots & \ldots & \ldots \\ \ldots & \ldots & \ldots & \ldots & \ldots \end{array} \right\| \tag{19}$$

where in $\mathbf{H}_{(1)}$ has been denoted: $b_1 = a_2 - a_3 \cdot a_0/a_1,\ b_3 = a_4 - a_5 \cdot a_0/a_1$, etc. The matrix $\mathbf{H}_{(n-1)}$ emerging after the $(n-1)$th step is triangular. Its diagonal sub-determinants can be evaluated easily:

$$\Delta_1 = a_1, \quad \Delta_2 = a_1 \cdot b_1, \quad \Delta_3 = a_1 \cdot b_1 \cdot c_1, \ \ldots \tag{20}$$

Hence we can state that the system is stable if it holds:

$$\Delta_i > 0, \quad i \in (1, n),\ a_0 > 0 \tag{21}$$

Although formulae Eq. (20) look to be simple, diagonal elements $a_1, b_1, c_1, d_1, ...$ are more and more complex. If a further analysis suffices to be numerical, then following a certain strategy of system parameter series, numerical value of all Δ_i can be evaluated for each system parameter combination. Then going throughout Δ_i values, a number of sign changes within $i \in (1, n)$ is inspected. If all Δ_i are positive, there are no sign changes and the system represented by the polynomial Eq. (17 is stable.

Let us add that the diagonal elements in the $\mathbf{H}_{n-1}$ matrix after the elimination process can be written in a closed form:

$$a_1 = \Delta_1, \quad b_1 = \Delta_2/\Delta_1, \quad c_1 = \Delta_3/\Delta_2, ... \quad x_1 = \Delta_{n-1}/\Delta_{n-2}, \quad z_1 = \Delta_n/\Delta_{n-1} = a_n \tag{22}$$

where x_1 or z_1 means diagonal element in the $n-1$ or n row, respectively. Very cumbersome but elementary process leading to formulae (22) has been omitted. On the other hand formulae (22) can be directly deduced from Eqs (20).

Routh-Hurwitz (RH) conditions Eq. (21) are necessary and satisfactory and therefore giving unique results. However, when an analytic investigation is necessary, then to use solely sub-determinants Δ_i in an analytic form is realistic until let say $n = 4$. Nevertheless RH conditions Eq. (21) can be combined with Descartes rule. This theorem requests positive value of all coefficients of the polynomial Eq. (17), i.e. $a_i > 0$, to keep real part of all roots negative. Because Descartes rule represents the set of necessary and not satisfactory conditions, it should be combined with RH conditions Eq. (21). The combination of both approaches makes possible to simplify the process of the stability analysis, as polynomial coefficients are incomparably simpler than RH determinants. Putting both sets together it can be shown that many of particular conditions are consequences of the others. Therefore as much minimized set of satisfactory conditions as possible should be selected. This selection can be done by sight until $n = 4$. For higher degree of a polynomial a formalized tool is necessary.

One possibility of an effective selection is offered by Liénard theorem. It is based on a knowledge that fulfilling conditions $a_i > 0$, RH conditions Eq. (21) are no more independent. For instance at $n = 4$ only one condition $\Delta_3 > 0$ is independent. With reference to Gantmacher (1966) for the proof and other mathematical details, we provide only instructions of the theorem application. Relevant conditions of negative real parts of polynomial (17) roots can be formulated in one of four versions:

$$\begin{array}{lllll} \text{(a)} & a_n > 0,\ a_{n-2} > 0, & \ldots, & \Delta_1 = a_1 > 0,\ \Delta_3 > 0, \ldots \\ \text{(b)} & a_n > 0,\ a_{n-2} > 0, & \ldots, & \Delta_2 > 0,\ \Delta_4 > 0, \ldots \\ \text{(c)} & a_n > 0,\ a_{n-1} > 0,\ a_{n-3} > 0, & \ldots, & \Delta_1 = a_1 > 0,\ \Delta_3 > 0, \ldots \\ \text{(d)} & a_n > 0,\ a_{n-1} > 0,\ a_{n-3} > 0, & \ldots, & \Delta_2 > 0,\ \Delta_4 > 0, \ldots \end{array} \tag{23}$$

It follows from formulations Eq. (23) that positivity either of all coefficients a_i or one of subsets $a_n, a_{n-2}, ..., a_n, a_{n-1}, a_{n-2}$ invalidates the full independency of the determinant conditions (21). Namely positiveness of the odd Hurwitz sub-determinants implicates positiveness of the even Hurwitz sub-determinants and vice versa.

Let us demonstrate the above algorithm for a system $n = 4$. Respective condition sets read:

$$\begin{array}{lll} \text{coefficients:} & a_0 > 0, \quad a_1 > 0, \quad a_2 > 0, \quad a_3 > 0, \quad a_4 > 0, & \text{(a)} \\ \text{sub-determinants:} & \Delta_1 = a_1 > 0, \qquad \Delta_2 = a_1 \cdot a_2 - a_3 \cdot a_0 > 0, & \text{(b)} \\ & \Delta_3 = a_3 \cdot \Delta_2 - a_4 \cdot a_1^2 > 0, \qquad \Delta_4 = a_4 \cdot \Delta_3 > 0. & \end{array} \tag{24}$$

The condition $\Delta_1 > 0$ is included in Eq. (24a), condition $\Delta_2 > 0$ must be fulfilled if $\Delta_3 > 0$ should be in force and $\Delta_4 > 0$ follows from (24a) and $\Delta_3 > 0$. Thus if conditions (24a) are valid then among RH sub-determinants only Δ_3 is independent and must be taken into account. So we can see, that such arrangement of conditions comply with the third version of the Liénard theorem, see Eq. (23c). This set of conditions is popular to process problems upto $n = 4$. Anyway, such condition sets can be proceed also by way of visual assemblage. However problems $n \geq 6$, which are under consideration, should be discussed using one version of the Liénard theorem, see Eq. (23).

Let us try to configure conditions for $n = 6$. First of all following coefficients of the polynomial should be positive, see Eq. (23c) or (23c):

$$a_0 = 1 > 0, \quad a_1 > 0, \quad a_3 > 0, \quad a_5 > 0, \quad a_6 > 0 \tag{25}$$

With respect to Eq. (23c) it should hold:

$$\Delta_1 > 0, \quad \Delta_3 > 0, \quad \Delta_5 > 0 \tag{26}$$

The condition $a_0 = 1 > 0$ is explicit and conditions $a_1 > 0$ and $\Delta_1 = a_1 > 0$ are identical. Consequently, considering conditions (25), only sub-determinants Δ_3 and Δ_5 are independent. Together with (25) they make the close set of satisfactory conditions determining the negative real part of polynomial $P(\lambda)$ roots for $n = 6$. For $n = 6$, respective sub-determinants have the form as follows, see basic form

of the $\mathbf{H}$ matrix (18):

$$\begin{aligned}
\Delta_2 &= a_1 \cdot a_2 - a_0 \cdot a_3, \\
\Delta_3 &= a_3\Delta_2 - a_1^2 a_4 + a_0 a_1 a_5 \\
\Delta_4 &= a_4\Delta_3 - a_2(a_5\Delta_2 - a_1^2 a_6) + a_0(a_1 a_4 a_5 - a_0 a_5^2 - a_1 a_3 a_6) \\
\Delta_5 &= a_5\Delta_4 + a_1 a_5 a_6 \Delta_2 - a_3 a_6 \Delta_3 - a_1^3 a_6^2 \\
\Delta_6 &= a_6\Delta_5
\end{aligned} \tag{27}$$

Redundancy of sub-determinants (27) (or independency of Δ_3 and Δ_5) when conditions (25) are taken into account is obvious. Going through Eqs (25) and (27) once again, we can see that also other versions of Liénard theorem are applicable, in particular (23d).

5. Numerical experiments related to real example

Let us recall conditions (25) and (26) together with Eqs (27). They should be carefully analyzed. Apparently the most transparent illustration of their character and interaction can be outlined in the plane $\omega_u^2 \times \omega_\varphi^2$. With the help of this pictures one can see the influence of individual parameters on the stability of the basic system while creating limits identifying the change in stability character. Conditions $a_i \geq 0$ and $\Delta_i \geq 0$, treated usually separately in the literature have now gained general meaning. Stability conditions may intersect mutually and thus create separated instability domains in which individual generalized forces need not be necessarily positive due to non-conservative and gyroscopic influences. Therefore traditionally discussed types of dynamic stability loss appear here as special cases of one general mechanism treated above. So that going through one can detect all types of instability dealing with the advanced "neutral" model proposed here.

The Fig. 3 shows the result of the analysis for the rectangular cross-section that has been analyzed in the wind tunnel. The characteristics of this cross-section is described in Table 1.

Tab. 1: Characteristics of the rectangular cross section and measured values of critical wind speed. $V_c^{(1)}$ is taken from the experiments, see Král et al. (2011) and $V_c^{(2)}$ results from the presented method respectively.

mass	inertia	width	frequency	frequency	damping	damping	speed	speed
m	I	B	ω_u	ω_φ	ζ_u	ζ_φ	$V_c^{(1)}$	$V_c^{(2)}$
$[kg/m]$	$[kgm]$	$[m]$	$[s^{-1}])$	$[s^{-1}]$	$[(\%]$	$[\%]$	$[m/s]$	$[m/s]$
4.02	0.0023	0.30	4.900	4.048	0.9	1.3	9.0	8.5

The graphs are actually the stability diagrams for certain value of the wind speed. For much simpler model that is described in the article by Pospíšil & Náprstek (2011) four planar curves divide the plane into several zones of stability and instability. By using the advanced neutral model the figure is more complicated, however the stability domains can be also observed. For example, the a_5 divide the plane $\omega_u^2 \times \omega_\varphi^2$ into two semi-planes where the right one is the stable zone. The Δ_4 is the most complicated condition being a result of combination of various a_i including Δ_3 and a_4, the latter one being a hyperbola with the axis in the second and fourth quadrant. This is know as a divergence stability conditions, see Pospíšil & Náprstek (2011).

Higher determinants Δ_5 and Δ_6 create complex parametric curves combining lower order determinants together, see Eqs (27). For example, in the figure with Δ_5, besides the lines, the parabolic shapes standing for the flutter condition, see Pospíšil & Náprstek (2011), are visible. The zone between those parabolas is the stable one, however with increase of the wind speed V this zone changes, the parabolic shapes may merge or undergo other transformation so that the stability domain is narrower in the general term of the word.

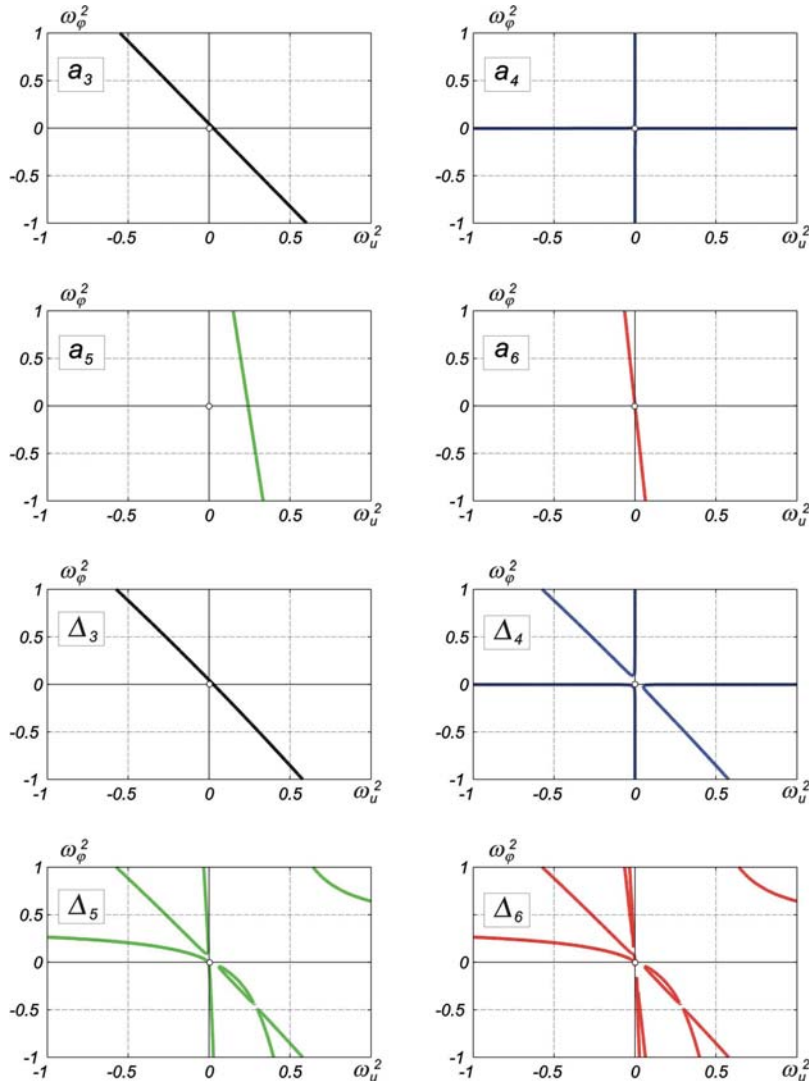

Fig. 3: Conditions of stability depicted in the frequency plain, $\omega_u^2 \times \omega_\varphi^2$.

The influence of the wind velocity can be seen more transparently at the different type of diagrams. The Fig. 4 illustrates the use of the described analysis for the evaluation of the critical wind speed, i.e. the speed when one of the conditions (25) and (26) is violated. Only the independent conditions are presented. In particular: $a_1 - a_6$, see Eq. (25) and two determinants Δ_3 and Δ_5, see Eq. (26). It can be seen from the Fig. 4 that the condition Δ_5 crosses the zero at the speed $V = 8.5\,m/s$. This corresponds quite well to the experimentally verified value $V = 9.0\,m/s$. Obviously, the critical speed depends much upon the measured value of structural damping.

Generally, the coefficients a_5, a_6 and the determinants Δ_5 and Δ_6 are very sensitive to precise determination of the flutter derivatives, which is usually very complicated task for both very low values of κ (higher values of the reduced wind velocity V) as well as for the values where the reduced frequency is very high. These regions determine the signs of the coefficients b_{ij}, which are used for the fitting

of the flutter derivatives. Higher order expansion would improve the analysis. On the other hand this improvement would be lost in doubling of the order of the characteristic polynomial (13).

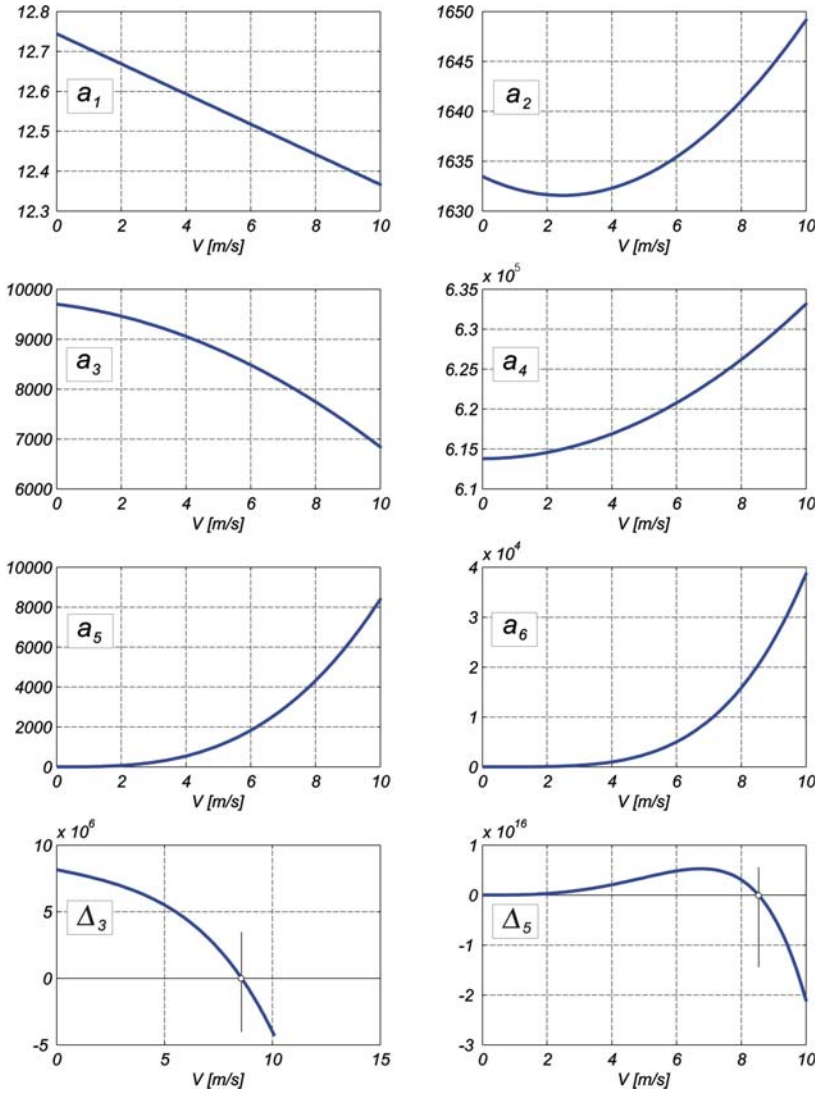

Fig. 4: Course of the some coefficients a_i and determinants Δ as function of velocity V. The point of the zero crossing at individual coefficients determines the loss of the stability, which may be of any kind.

6. Conclusion

Two types of double degree of freedom (DDOF) linear systems interacting with aero-elastic forces have been investigated and compared. The DDOF system under study describes inherent dynamic features of a slender prismatic beam attacked by a cross wind stream of a constant velocity (long bridge decks, guyed masts, towers, etc.). Relevant mathematical models of aero-elastic forces appearing in literature differ in principle by way of composition of aero-elastic forces. From this point of view two groups have been investigated: neutral models, where aero-elastic forces are introduced as suitable constants

independent from excitation frequency and time and models using flutter derivatives for modelling the aero-elastic forces.

The second group respects explicitly the stream velocity and the frequency of the system response. It succeeded to put both groups together on one common basis to demonstrate their linkage. The platform of qualitative investigation of aero-elastic critical states in a frequency plain has been significantly expanded with respect to the stream velocity. Memory effects ruling in aero-elastic DDOF system have been substantiated and compared in frequency and time domains. The approach presented allows to formulate more flexible models combining main aspects of both groups keeping the DDOF basis. This approach can be used for the analysis of practical flow-structure interaction problems. However, teh attention should be paid to the precise flutter derivatives measurement, especially in the both very low and very high frequency domains.

Acknowledgement

The support of the Czech Scientific Foundation No. 103/09/0094, Grant Agency of the ASCR No. A200710902 as well as the support of RVO 68378297 are gratefully acknowledged.

References

Bartoli, G., Righi, M. (2006) Flutter mechanism for rectangular prisms in smooth and turbulent flow. *J. Wind. Eng. Ind. Aerodyn.* 94, 275–291.

Caracoglia, L., Jones N.P. (2003) Time domain vs. frequency domain characterization of aeroelastic forces for bridge sections. *J. Wind. Eng. Ind. Aerodyn.* 91, 1135–1150.

Costa C., Borri C., Flamand O., Grillaud G. (2007): Time-domain buffeting simulations for wind-bridge interaction. *J. Wind. Eng. Ind. Aerodyn.* 95, (9-11), 991–1006.

Gantmacher, F.R. (1966) *Theory of Matrices* (in Russian). Nauka, Moscow.

Garrick, I.E. (1938) On Some Reciprocal Relations in the Theory of Nonstationary Flows. *NACA Technical Report No. 629*, 1938.

Král, R., Pospíšil, Náprstek, J., 2011. Experimental analysis of frequency tuning influence on the response stability of bridge girders under wind action. In: Proceedings of 13th International Conference on Wind Engineering, Amsterdam. 8 pgs.

Küssner, H.G. (1954) A general method for solving problems of the unsteady lifting surface theory in the subsonic range. *J. Aeronautical Sci.*, 21(1).

Náprstek, J., Pospíšil, S. (2001) Aeroelastic instability of a system with nonconservative and gyroscopic forces. In: *Proc. 11th Engineering Mechanics Conference* (A.Poživilová, J.Masák eds), IT ASCR, Svratka, , 8 pgs. CD ROM.

Náprstek, J. (2007) Domains and types of aeroelastic instability of slender beam. In: *Proc. Biennial Conference Mech. Vibration and Noise 2007*, Las Vegas: ASME, CD paper #DETC2007-34132, 10 pgs.

Náprstek, J., Pospíšil, S. (2012) Relation of flutter derivatives and indicial functions in linear aero-elastic models. In: *Proc. Dynamics of Machines 2012* (L. Pešek edt.). Inst. Termomechanics ASCR, Prague, pgs 95–102.

Pospíšil, S., Náprstek, J., (2011) General formulation of linear aeroelastic system stability and respective post-critical response types. In: *Proc. 13th Int. Conf. On Wind Engineering* (C. Geurts, B. Blocken eds). Tech. Univ. Eindhoven, Amsterdam, paper 177, 8 pgs.

Poulsen, N.K., Damsgaard, A. and Reinhold, T.A. (1992) Determination of flutter derivatives for the Great Belt Bridge. *J. Wind Eng. Ind. Aerodyn.* 41, 153–164.

Scanlan, R.H., Tomko, J.J. (1971) Airfoil and Bridge Deck Flutter Derivatives. *J. of Eng. Mech. ASCE* 97, 1717–1737.

Scanlan, R.H., Beliveau, J.G., Budlong, K. (1974) Indicial aerodynamic functions for bridge decks. *J. of Engrg. Mech. ASCE* 100, 657–672.

Theodorsen, T. (1935) General Theory of Aerodynamic Instability and the Mechanism of Flutter. *NACA Technical Report No. 496*.

Wagner, H. (1929) Über die Entstehung des dynamischen Auftriebes von Tragflügeln. *Zeit. Angew. Math. und Mech.*, 5(1), 17–35.

18th International Conference
ENGINEERING MECHANICS 2012
Svratka, Czech Republic, May 14 – 17, 2012

pp. 927–931
Paper #273

ANALYSIS OF VULNERABILITY OF CULTURAL HERITAGE AGAINST FLOODS

K. Nedvědová[*], V. Kostkanová, J. Frankl, R. Pergl[**]

Abstract: *Introducing first part of the project Methodology of Protection and Rescue of Cultural Heritage against Flood dealing with creating catalogue of damage on cultural heritage due to floods. The aim of this catalogue is to collect, synthesize and analyze possible known information about the damage linked with a particular object of protection and material.*

Keywords: ***Cultural Heritage, flood, material vulnerability, damage risk.***

1. Introduction

Flood is a natural phenomenon that cannot be avoided but in past years its impact is rapidly growing. During last 15 years we have been experiencing many severe flooding that influenced almost every part of the Czech Republic. Except damages of life and property there have been loss of historical monuments, devastation of sites and changes in historical landscape. Irreversible loss and great expenses spent to restoration and renewal led to the conclusion that integrated flood risk management is needed if we want protect effectively historic environment against flooding.

From the analysis of flood impact in selected towns and villages and from other European projects emerged series of serious facts:

- insufficient foreknowledge of owners and stakeholders about value of cultural heritage objects and necessity of special approach during remedial works, especially in heritage reservations and zones,
- inaccessibility of practical experience from floods in past years,
- lack of effective instructions for owners and administrators,
- lack of experience and methodic guidelines for local government in unusual situation happening on cultural heritage site,
- inappropriate use of materials during renovations,
- importance of proper maintenance and good technical condition of buildings,
- importance of preventive measures,
- absence of guidelines for flood protection planning on outstanding cultural heritage sites,
- need of transparency in legislative and processes of flood protection planning to achieve maximal efficiency and sensitivity,
- underestimated role of historical water works

2. Catalogue of damage

According to this experience our project Methodology of Protection and Rescue of Cultural Heritage against Flood was formed. First part of the project is dealing with creating catalogue of damage on cultural heritage due to floods. The aim of this catalogue is to collect, synthesize and analyze possible known information about the damage linked with a particular object of protection and material. Furthermore this catalogue analyzes possible damage vulnerability at these objects of cultural heritage. A special attention is paid to prevention and tends to recommend suitable measures for different

[*] Ing. arch Klára Nedvědová, Mgr. Vladislava Kostkanová, Ph.D., Ing. Jiří Frankl, Ph.D. , Institute of Theoretical and Applied Mechanics, AS CR v.v.i.,Prosecká 809/76, 190 00 Praha 9; CZ, e-mail: nedvedova@itam.cas.cz

[**] Ing. Robert Pergl, Faculty of Economics and Management, Czech University of Life Sciences Prague, Kamýcká 129, 165 21 Praha 6; CZ, email: pergl@pef.czu.cz

situations in this part. Both moveable and immoveable objects of cultural heritage are included in the catalogue.

Catalog will have an electronic form and should be available within wider informational server of Ministry of Environment ČR POVIS for free. Owners, administrators of the cultural heritage and professional public are considered as possible users. Catalogue should serve as a tool for assessing damage vulnerability for moveable and immovable cultural heritage.

The experiences from last recent floods in the Czech Republic (especially disastrous floods in 1997 and 2002) are used as inputs. Also the practical knowledge about possible damage and its prevention from specialists of different branches serves as an important resource.

A conceptual ontological map was created and it serves as a functional tool for creating the base of the damage vulnerability catalogue for various objects of cultural heritage. The catalogue is organized in two main parts. Input factors will be given to user to define his object of interest and characteristics of flooding. As input data are specified:

– characteristics of flooding – water height, dynamics, cleanness of water, period of occurrence, length of activity,

– temperature, moisture, season,

– construction system, technical state and material creating the object of interest

Based on these user defined inputs, output analysis is created:

– vulnerability of the object to probable damage,

– damage description, description of damage mechanism,

– recommended preventive measures

The vulnerability of flood damage is categorized according to the flood action and object type to three main degrees: a) no consequence or very small damage (resistant objects) b) medium damage or significant consequence c) critical consequence, total damage, destruction of the object. However finer categorization within these main degrees is also possible. Examples of recorded damage on cultural heritage in the past are demonstrated in the form of damage cards. There are described object characterization, flood action and damage description in detail. Performed reconstruction and protective measures are described as well.

3. Conclusions

Right prevention is considered as most effective measure and more sensitive towards objects itself. It reduces loss of cultural historic value and authenticity. The catalogue of the damage vulnerability due to floods will help to plan and optimize the correct prevention measures applied in time to protect the objects of cultural heritage in the future.

Acknowledgement

The research has been supported by the research grant NAKI DF11PO1OVV009 provided by MK ČR.

References

Drdácký, M., Binda L., Hennen I.Ch., Koepp, Ch., Lanza, L.G., Helmerich, R. (eds.) (2011) *CHEF – Cultural Heritage Protection against Flooding.* Institute of Theoretical and Applied Mechanics AS CR, v.v. i. Prague

Drdácký, M. (ed.) (2010) Special Issue: Flood impacts to Heritage Structures, *Journal of Performance of Constructed Facilities.* Vol. 24 No. 5

English Heritage (2004) *Flooding and Historic Buildings*, Technical Advice Note.

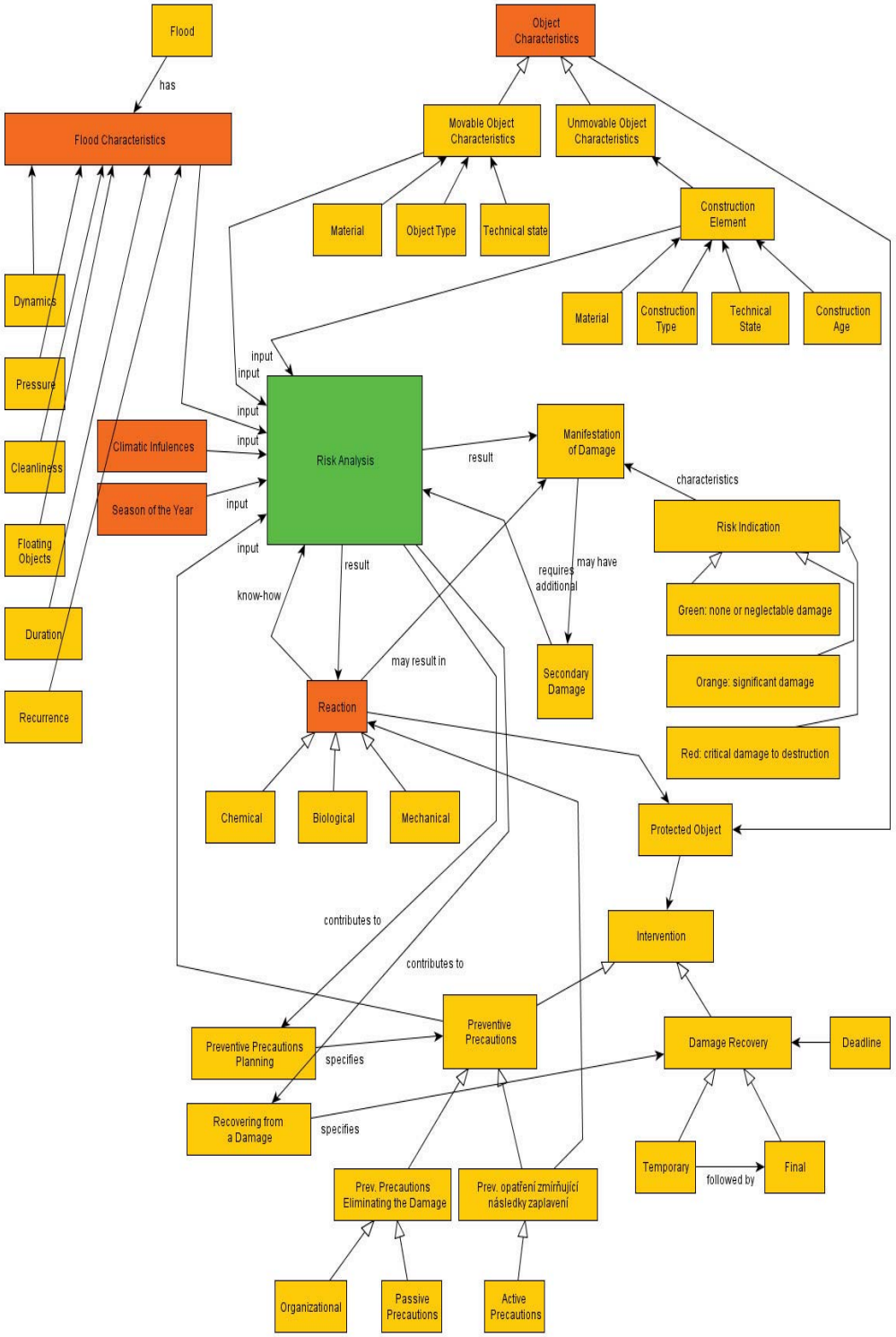

Fig. 1 A conceptual ontological map

CARD OF DAMAGE AT CULTURAL HERITAGE

Object – name, address:	Charles Bridge, Prague 1	Subscribed in: NKP, KP Lies in: UNESCO, Prague Protected Area
Object type:	Medieval stone bridge with 17 piers connected with 16 arches	
Construction description:	Stone bridge was built in 14th century, destroyed in historic floods and reconstructed (rebuilt) in every century thereafter construction materials: marly sandstone, sandstone in 20th century reconstructed foundations and bearing constructions: concrete, steel, sandstone formerly reconstructed or original foundations and piers: sandstone, wooden piles, wooden grate, bricks	
Object use:	Pathway for walkers, heritage, stands and artists, museum (in bridge towers)	
Description of the damaged construction, material	Subsoil of incohesive coarse river sandy gravels under foundation of pier No. 8 and 9. First pier ring based on wooden grate, which is founded on wooden piles of unknown length. Foundation of pier No. 9: millstones bellow the protective pier ring, perimeter rings founded on wooden sheet walls at the distance of 2 m from the pier trunk reaching the incohesive sandy gravels; stone fill, partly bricked	
Technical state before flood:	Technical state before flood not known in detail – exploration conducted after flood, but from historical sources known damage in the past during floods in 1432 and 1784, partly reconstructed in past Insufficient foundation depth in coarse river sediments of Vltava river (sands and gravels), which are sensitive to scour Original wooden foundations of the 8th and 9th piers from the 16th century partly repaired in 18th century	
Flood description:	August 2002, Vltava river, Q = 5 500 m^3/s (average normal Q = 150 m^3/s) Flood type: summer flood	
Acting factors, causes of the primary damage:	Acting force: dynamic action of streaming water - strong horizontal stream, Duration period: days	
Mechanism of damage:	Erosion of coarse river sediments as a consequence of strong dynamic impact of streaming water, scour of the pier foundations, founded in these sediments	
Manifestation of damage:	Potholes at the pier rings, which did not reached the original pier trunk Scoured cavern below the millstones – foundation of the 9th pier	
Secondary damage in consequence of the event	**Damage mechanism:** thread of the possible inclination of the foundations and piers, possible uneven settlements (were not present at the time of exploration) foundations are in metastable state	
	Damage manifestation: none at the upper construction thread of the crack formation due to uneven settlements and construction inclination possible thread of collapse of the whole pier construction during floods in the future	

Reconstruction measures	Reconstruction duration: 2004-2005, reconstruction of the damaged foundations founded into insufficient depth in scour sensitive river sedimetns, permanent protection of the foundations against scour 1. Prolongation of the foundation depth through the sheet pile wall combined with jet grouting into the ground layer of low permeable rock horizon 2. filling of the caverns by jet grouting
Prevention measures:	1. permanent scour protection of the pier 8th and 9th foundations, sheet pile wall was embedded into the ground layer of low permeability and connected with the bridge pier through a reinforced concrete beam 2. reconstruction of icebreakers (2003/2004) – protection against floating objects
Picture documentation:	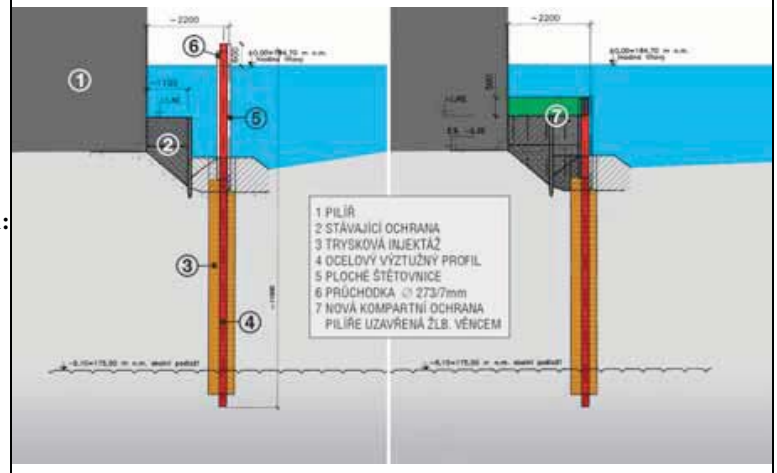
Reference/further information:	Remeš M. (2004) Karlův most — definitivní ochrana základů pilířů;. 8 a 9 časopis Zakládání staveb). 4/2004, pp. 2-4.

Fig. 2 Card of damage at cultural heritage – Charles Bridge (8th and 9th pillars)

18th International Conference
ENGINEERING MECHANICS 2012
Svratka, Czech Republic, May 14 – 17, 2012

pp. 933–944
Paper #261

MICROMECHANICS-BASED MODELS OF COCCIOPESTO MORTARS

V. Nežerka*, M. Somr, J. Zeman*****

Abstract: *The paper deals with homogenization and strength estimation of mortars containing crushed bricks or other clay products. These mortars, known as cocciopesto, were used mainly during the Byzantine period and by Romans. Cocciopesto exhibit quite extraordinary mechanical properties due to formation of C-S-H gel coating on the interface between lime matrix and crushed clay products. Based on literature study, it seems that no one has ever tried to estimate the properties of cocciopesto mortars using micromechanical modeling. The micromechanical approach and Mori-Tanaka homogenization technique provided an explanation for the characteristic behavior of these mortars, but they had to be modified for homogenization of coated particles. Mortar strength was estimated from magnitudes of the quadratic average of deviatoric strain in individual phases. The calculations confirmed the important role of the C-S-H gel coating on the mortar strength and stiffness. Despite the above mentioned simplifications and a few uncertainties, the model seems to be able to correctly predict the trends and serve for an optimization of the mortar composition towards desired properties.*

Keywords: ***cocciopesto, micromechanics, Mori-Tanaka method, C-S-H gel coating, strength estimation***

1. Introduction

The present conservation practice uses air lime or hydraulic lime mortars, because these are compatible with the original materials. The use of air lime presents problems with slow setting, inability to harden under water, lack of durability and poor mechanical strength. Therefore, the hydraulic lime-pozzolan mortars were widely used in the past and are still used nowadays for repairs. These mortars are of a higher porosity and lower strength than cement-based mortars, but they exhibit better durability.

Phoenicians were probably the first ones who added crushed clay products, such as burnt bricks, tiles or pieces of pottery, to the lime mortar in order to increase its durability and strength. Romans used this type of mortar in areas where other natural pozzolans were not available and called such material *cocciopesto*. The structures, mainly from the Byzantine period, have also very thick joints, often comparable to the size of bricks. Together with the enhanced mechanical properties of the cocciopesto mortar, the use of the thick joints probably results in the increased resistance to earthquake loading, since the non-linear behavior of the mortar allows for a better energy dissipation (Baronio et al., 1997).

By a closer investigation, it was found that the mortars containing crushed bricks exhibit a hydraulic character due to formation of C-S-H gel on the lime-brick interface. It was reported in many papers, dealing with the cocciopesto mortars, that a thin layer of the gel forms at the interface if the bricks are made of clay and burnt at the appropriate firing temperature (which is about 600-900°C (Maropoulou et al., 1995)). Since this component is responsible for some extraordinary properties of Portland cement concrete, it is conjectured that also the enhanced mechanical properties of the lime-crushed brick mortars can be attributed to the relatively high strength and stiffness of the C-S-H gel coating. The addition of crushed bricks should ensure the mortar hydraulicity, and therefore improve mechanical properties of the mortar, without the need for modern artificial substances or industrial by-products such as metakaolin or fly ash.

*Ing. Václav Nežerka: Faculty of Civil Engineering, Czech Technical University in Prague, Thákurova 7, 166 29 Praha 6, Czech Republic; e-mail: vaclav.nezerka@fsv.cvut.cz
**Ing. Michael Somr: Faculty of Civil Engineering, Czech Technical University in Prague, Thákurova 7, 166 29 Praha 6, Czech Republic; e-mail: michael.somr@fsv.cvut.cz
***Doc. Ing. Jan Zeman, Ph.D.: Faculty of Civil Engineering, Czech Technical University in Prague, Thákurova 7, 166 29 Praha 6, Czech Republic; e-mail: zemanj@cml.fsv.cvut.cz

The goal of this work is to investigate the influence of the C-S-H gel coating on the mortar behavior from the micromechanical point of view and provide a tool for the estimation mechanical properties based on mortar composition. Two works, (Pichler and Hellmich, 2011) and (Šmilauer et al., 2011), provided an inspiration for the development of micromechanical models. These works deal with composite materials, composed of a matrix, voids and aggregates and exploit the Mori-Tanaka method (Benveniste, 1987; Mori and K., 1973) to estimate the effective stiffness and strength of the composite. It is assumed that only the deviatoric stress is responsible for a failure of the material, therefore the quadratic average of the deviatoric stress in the lime matrix was chosen as an adequate indicator for the determination of mortar strength. Even though there are a few simplifications in these models, the results in Pichler and Hellmich (2011) and Šmilauer et al. (2011) quite well correspond to the available experimental data and therefore they should be applicable to the mortars with crushed bricks as well.

2. Stiffness Homogenization

The term inhomogeneity is understood as an inclusion of a material embedded in a matrix, having different material properties from those of the matrix. If a sample of an inhomogeneous material is subjected to the external load $\mathbf{E}$, then the average strain in individual phases can be calculated as $\mathbf{E}^{(r)} = \mathbf{A}^{(r)} : \mathbf{E}$, where $\mathbf{A}^{(r)}$ represents a strain concentration factor for a phase r. The superscript r attains the values from 1 (possibly even 0 if the matrix is included) to the number of phases n. The strain concentration factor can be calculated as follows:

$$\mathbf{A}_{\text{dil}}^{(r)} = [\mathbf{I} + \mathbf{S} : \mathbf{M}^{(0)} : (\mathbf{L}^{(r)} - \mathbf{L}^{(0)})]^{-1} \qquad \text{where} \qquad r = 1, ..., n \tag{1}$$

where $\mathbf{I}$ represents the fourth order unity tensor with components $I_{ijkl} = 1/2(\delta_{ik}\delta_{jl} + \delta_{il}\delta_{jk})$, where δ_{ij} is a Kronecker delta defined as $\delta_{ij} = 1$ for $i = j$, and $\delta_{ij} = 0$ otherwise; $\mathbf{S}$ is so called Eshelby tensor and its components for various inclusion shapes can be found, e.g., in Mura (1987), $\mathbf{M}^{(0)}$ is a compliance tensor representing the matrix, the $\mathbf{L}^{(r)}$ and $\mathbf{L}^{(0)}$ are stiffness tensors, representing the individual phases and the matrix, respectively.

The subscript dil in Eq. (1) stands for a "dilute distribution", because Eq. (1) is valid under the assumption that the inhomogeneity is embedded in an infinite matrix. The assumption of dilutely distributed non-interacting inhomogeneities is a starting point for a refinement of the model accounting for a mutual interaction of inhomogeneities, such as the Mori-Tanaka scheme introduced next.

2.1. Mori-Tanaka Scheme

The Mori-Tanaka model, (Benveniste, 1987; Mori and K., 1973), formally equals to that of a dilute distribution. However, the strain in individual inhomogeneities is not directly dependent on the externally applied load (macroscopic strain), but rather on a strain in the matrix, which is approximated by a constant field $\mathbf{E}^{(0)}$:

$$\mathbf{E}^{(r)} = \mathbf{A}_{\text{dil}}^{(r)} : \mathbf{E}^{(0)} \tag{2}$$

The relationship between the macroscopic strain and strain in the matrix can be found using a simple reasoning:

$$\begin{aligned} \mathbf{E} &= c^{(0)}\mathbf{E}^{(0)} + \sum_{r=1}^{n} c^{(r)}\mathbf{E}^{(r)} = c^{(0)}\mathbf{E}^{(0)} + \sum_{r=1}^{n} c^{(r)}\mathbf{A}_{\text{dil}}^{(r)} : \mathbf{E}^{(0)} = \\ &= \left(c^{(0)}\mathbf{I} + \sum_{r=1}^{n} c^{(r)}\mathbf{A}_{\text{dil}}^{(r)} \right) : \mathbf{E}^{(0)} \end{aligned} \tag{3}$$

where c, having a superscript (0) and (r), stands for a volume fraction of the matrix and inhomogeneities, respectively. The relationship between the average matrix strain and the macroscopic strain can be described simply as $\mathbf{E}^{(0)} = \mathbf{A}_{\text{MT}}^{(0)} : \mathbf{E}$, where

$$\mathbf{A}_{\text{MT}}^{(0)} = \left(c^{(0)}\mathbf{I} + \sum_{r=1}^{n} c^{(r)}\mathbf{A}_{\text{dil}}^{(r)} \right)^{-1} \tag{4}$$

is the Mori-Tanaka strain concentration factor. The strain in the individual inhomogeneities is then provided by

$$\mathbf{E}^{(r)} = \mathbf{A}_{\mathrm{dil}}^{(r)} : \mathbf{E}^{(0)} = \mathbf{A}_{\mathrm{dil}}^{(r)} : \mathbf{A}_{\mathrm{MT}}^{(0)} : \mathbf{E} \tag{5}$$

2.2. Effective Stiffness according to M-T Scheme

The relationship between the macroscopic stress $\boldsymbol{\Sigma}$ and strain $\mathbf{E}$ can be obtained as follows:

$$\boldsymbol{\Sigma} = \sum_{r=0}^{n} c^{(r)} \boldsymbol{\Sigma}^{(r)} = \sum_{r=0}^{n} c^{(r)} \mathbf{L}^{(r)} : \mathbf{E}^{(r)} = \sum_{r=0}^{n} c^{(r)} \mathbf{L}^{(r)} : \mathbf{A}^{(r)} : \mathbf{E} = \mathbf{L}^{\mathrm{eff}} : \mathbf{E} \tag{6}$$

where $\mathbf{L}^{\mathrm{eff}}$ is the effective stiffness tensor, and in case of the Mori-Tanaka scheme it can be obtained as

$$\mathbf{L}^{\mathrm{eff}} = \left(c^{(0)} \mathbf{L}^{(0)} + \sum_{r=1}^{n} c^{(r)} \mathbf{L}^{(r)} : \mathbf{A}_{\mathrm{dil}}^{(r)} \right) : \mathbf{A}_{\mathrm{MT}}^{(0)} \tag{7}$$

In the special case of an isotropic matrix containing isotropic spherical inhomogeneities, the Mori-Tanaka model yields an isotropic overall behavior, irrespective of the spatial arrangement of the phases. The effective stiffness of such composite can be then described by scalar constants, since the Eshelby tensor can be also decomposed into its volumetric and deviatoric part:

$$\mathbf{S} = \alpha^{(0)} \frac{1}{3} \delta_{ij} \delta_{kl} + \alpha^{(0)} \left(\mathbf{I} - \frac{1}{3} \delta_{ij} \delta_{kl} \right) = \alpha^{(0)} \mathbf{I}_{\mathrm{V}} + \beta^{(0)} \mathbf{I}_{\mathrm{D}} \tag{8}$$

where $\mathbf{I}_{\mathrm{V}}$ and $\mathbf{I}_{\mathrm{D}}$ are volumetric and deviatoric projection tensors, respectively. These tensors serve for a decomposition of any stress or strain tensor into its volumetric and deviatoric components. The scalar parameters $\alpha^{(0)}$ and $\beta^{(0)}$ depend, in case of spherical isotropic particles, only on the matrix Poisson's ratio:

$$\alpha^{(0)} = \frac{1 + \nu^{(0)}}{3\left(1 - \nu^{(0)}\right)} \qquad \text{and} \qquad \beta^{(0)} = \frac{2\left(4 - 5\nu^{(0)}\right)}{15\left(1 - \nu^{(0)}\right)} \tag{9}$$

These parameters are also called constraint constants and because of the entire isotropy (i.e., elastic and geometric) they can be expressed by scalar values. They relate the eigenstrains ε^t in individual phases to the total strain, and the decomposition into volumetric and deviatoric strain highlights their meaning:

$$\varepsilon_{kk} = \alpha \varepsilon_{kk}^{t} \qquad \text{and} \qquad \varepsilon_{ij} = \beta \varepsilon_{ij}^{t} \tag{10}$$

Using the equations (5), (8) and knowing that the elastic stiffness tensor can be decomposed into volumetric and deviatoric parts, $\mathbf{L} = 3K\mathbf{I}_{\mathrm{V}} + 2G\mathbf{I}_{\mathrm{D}}$, all the terms in Eq. (7) can be decompossed into their volumetric and deviatoric parts. Since the volumetric and deviatoric components are independent of each other, the effective bulk modulus can be, after a simple manipulation, expressed as

$$K^{\mathrm{eff}} = \frac{c^{(0)} K^{(0)} + \sum_{r=1}^{n} c^{(r)} K^{(r)} \left[1 + \alpha^{(0)} \left(\frac{K^{(r)}}{K^{(0)}} - 1 \right) \right]^{-1}}{c^{(0)} + \sum_{r=1}^{n} c^{(r)} \left[1 + \alpha^{(0)} \left(\frac{K^{(r)}}{K^{(0)}} - 1 \right) \right]^{-1}} \tag{11}$$

and the effective shear modulus as

$$G^{\mathrm{eff}} = \frac{c^{(0)} G^{(0)} + \sum_{r=1}^{n} c^{(r)} G^{(r)} \left[1 + \beta^{(0)} \left(\frac{G^{(r)}}{G^{(0)}} - 1 \right) \right]^{-1}}{c^{(0)} + \sum_{r=1}^{n} c^{(r)} \left[1 + \beta^{(0)} \left(\frac{G^{(r)}}{G^{(0)}} - 1 \right) \right]^{-1}} \tag{12}$$

2.3. Homogenization with Coated Particles

This section is devoted to the evaluation of the constraint constants for coated particles, relating the induced strain to the eigenstrain in individual phases, $\alpha^{(r)}$ and $\beta^{(r)}$, and obtaining the effective elastic properties. The spherical inclusion with a thin interlayer and embedded in a matrix is considered for the evaluation. This is an enormous simplification and it is also a good model for randomly oriented inhomogeneities, such as particles embedded in the mortar paste.

The whole procedure for a determination of the constraint constants, $\alpha^{(r)}$ and $\beta^{(r)}$ was taken from Luo and Weng (1987), where the theoretical background can be found. Motivated by Eshelby's observations, Luo and Weng (1987) undertook a similar study to find the elastic field in the inclusion (grain) and its coating, which is embedded in an infinitely extended matrix. They restricted their consideration to the case of a three-phase, spherically concentric solid. The solution of Luo and Weng is based on the equations for a general displacement field in spherical coordinates. The integration constants were found using the continuity conditions and equilibrium of stresses on the interface of individual phases.

The superscript (g) stands for the grain (or the inner inclusion), (c) stands for the coating and the superscript (m) is used in the quantities describing the surrounding matrix. The parameter c is defined as $c = (a/b)^3$ (see Fig. 1) and it has a physical meaning of the volume fraction of phases in a two-phase composite. The hydrostatic and deviatoric transformation problems are treated separately. Each phase, a grain, its coating and a surrounding matrix, is represented by its bulk modulus $K^{(r)}$ and shear modulus $G^{(r)}$. The geometry is described by the radius of a grain a and radius of its coating b, as depicted in the following figure:

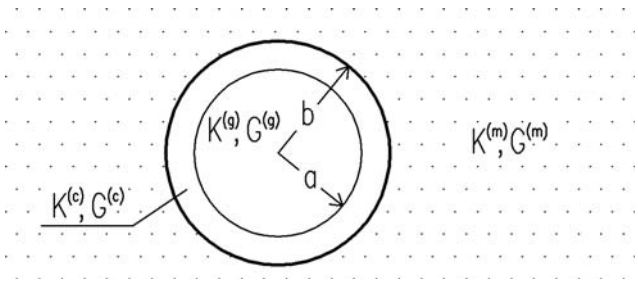

Fig. 1: A three-phase composite spherically concentric solid

Volumetric Part

The constraint constant for grain $\alpha^{(g)}$ is calculated as

$$\alpha^{(g)} = 3K^{(g)}\left[\left(3K^{(c)} + 4G^{(m)}\right) - 4c\left(G^{(m)} - G^{(c)}\right)\right]/p \tag{13}$$

where $c = (a/b)^3$ and p is

$$p = \left(3K^{(g)} + 4G^{(c)}\right)\left(3K^{(c)} + 4G^{(m)}\right) - 12c\left(K^{(g)} - K^{(c)}\right)\left(G^{(m)} - G^{(c)}\right) \tag{14}$$

The constraint constant for the coating of the grain, $\alpha^{(c)}$, is obtained as

$$\alpha^{(c)} = -4cK^{(g)}\left(G^{(m)} - G^{(c)}\right)/p \tag{15}$$

Deviatoric Part

The deviatoric constraint constant for the grain can be found in the form

$$\beta^{(g)} = a_1 - \frac{21}{5\left(1-\nu^{(g)}\right)}\, a_2 \tag{16}$$

and for the coating as

$$\beta^{(c)} = b_1 - \frac{21}{5\left(1-2\nu^{(c)}\right)}\frac{1-c^{\,5/3}}{1-c}\, b_2 \tag{17}$$

where the constants a_1 and a_2 can be calculated as

$$\begin{pmatrix} a_1 \\ a_2 \end{pmatrix} = \mathbf{R}^{-1} \tag{18}$$

and the terms b_1 and b_2, needed for the calculation of the deviatoric constraint constants for the coating, can be found as

$$\begin{pmatrix} b_1 \\ b_2 \\ b_3 \\ b_4 \end{pmatrix} = \mathbf{E}^{-1}\mathbf{F}\mathbf{K}^{-1}\mathbf{H}\mathbf{R}^{-1} \tag{19}$$

The individual matrices, needed for the calculation of coefficients a_1, a_2 and b_1, b_2, can be found in the Appendix.

Modification of Stiffness Homogenization

For the calculation of the effective moduli, the formulas (11) and (12) can be used in a slightly modified form. Namely, the constraint constants $\alpha^{(0)}$ and $\beta^{(0)}$ are substituted by the corresponding constants $\alpha^{(r)}$ and $\beta^{(r)}$, which remain $\alpha^{(0)}$ and $\beta^{(0)}$ in case of uncoated particles. However, coated grains are represented by $\alpha^{(g)}$ and $\beta^{(g)}$ and their coating by $\alpha^{(c)}$ and $\beta^{(c)}$.

3. Strength Estimation

The strength estimation is based on the J_2 yield criterion, i.e. that only the deviatoric part of the imposed load can cause a failure of the material. Therefore, it is necessary to calculate the deviatoric stress in individual components, which can be afterwards compared with a critical stress. Such approach was used by Pichler and Hellmich (2011) and it turned out to be suitable for an estimation of the compressive strength in cementitious materials.

Due to the assumed elastic linear behavior of the RVE, all imposed work is stored at each point as an elastic energy density, $W_\mathrm{e} = 1/2\,\boldsymbol{\sigma} : \boldsymbol{\varepsilon} = 1/2\,\boldsymbol{\varepsilon} : \mathbf{L} : \boldsymbol{\varepsilon}$, which can be decomposed into the volumetric and deviatoric parts, $W_\mathrm{e} = 1/2\,\sigma_\mathrm{m}\varepsilon_\mathrm{V} + 1/2\,\mathbf{s} : \mathbf{e}$. The quantity $\varepsilon_\mathrm{V} = 1/3\,\boldsymbol{\delta} : \boldsymbol{\varepsilon}$ represents the relative change of volume, $\mathbf{e}$ is obtained as $\mathbf{e} = \boldsymbol{\varepsilon} - \boldsymbol{\delta}\varepsilon_\mathrm{V}$ and it represents the deviatoric part of the strain tensor, $\sigma_\mathrm{V} = 1/3\,\boldsymbol{\delta} : \boldsymbol{\sigma}$ is the mean stress and $\mathbf{s} = \boldsymbol{\sigma} - \boldsymbol{\delta}\sigma_\mathrm{V}$ is the stress deviator.

The deviatoric part of the imposed work, $W_\mathrm{eD} = 1/2\,\mathbf{s} : \mathbf{e} = 1/(4G)\,\mathbf{s} : \mathbf{s}$, is proportional to the second invariant of the stress deviator, J_2, where

$$J_2 = 1/2\,\mathbf{s} : \mathbf{s} \tag{20}$$

and therefore $W_\mathrm{eD} = J_2/(2G)$. The quadratic average of the deviatoric stress is then $\|\mathbf{s}\| = \sqrt{2\,J_2}$

3.1. Quadratic Strain Averages

The expression for the quadratic average of the deviatoric strain field over a general phase, r, can be derived using the Hill's lemma

$$\langle U \rangle = \frac{1}{2}\langle \mathbf{E}^{(r)} : \mathbf{L}^{(r)} : \mathbf{E}^{(r)} \rangle = \frac{1}{2}\langle \mathbf{E}^{(r)} \rangle : \mathbf{L}^{\mathrm{eff}} : \langle \mathbf{E}^{(r)} \rangle = \frac{1}{2}\mathbf{E} : \mathbf{L}^{\mathrm{eff}} : \mathbf{E} \tag{21}$$

which expresses the equality between the average strain energy density, $\langle U \rangle$, in the RVE by means of the microscopic or macroscopic quantities (Gross and Seelig, 2006). From Eq. (21) the following equality can be obtained:

$$\mathbf{E} : \mathbf{L}^{\mathrm{eff}} : \mathbf{E} = \frac{1}{|\Omega|}\int_\Omega \boldsymbol{\varepsilon}(\mathbf{x}) : \mathbf{L}(\mathbf{x}) : \boldsymbol{\varepsilon}(\mathbf{x})\,\mathrm{d}\mathbf{x} \tag{22}$$

where Ω stands for the domain of the entire RVE, opposed to $\Omega^{(r)}$ denoting the domain of the single inclusion (inhomogeneity). The local strain $\boldsymbol{\varepsilon}(\mathbf{x})$ can be then decomposed into its volumetric and deviatoric part (responsible for the material failure):

$$\mathbf{E} : \mathbf{L}^{\mathrm{eff}} : \mathbf{E} = \frac{1}{|\Omega|}\int_\Omega \boldsymbol{\varepsilon}(\mathbf{x}) : [K(\mathbf{x})\mathbf{I}_\mathrm{V} + 2G(\mathbf{x})\mathbf{I}_\mathrm{D}] : \boldsymbol{\varepsilon}(\mathbf{x})\,\mathrm{d}\mathbf{x} \tag{23}$$

To extract the deviatoric part, it is convenient to differentiate the entire expression (23) with respect to $G^{(r)}$. The volumetric part vanishes and we obtain

$$\mathbf{E} : \frac{\partial \mathbf{L}^{\text{eff}}}{\partial G^{(r)}} : \mathbf{E} = \frac{1}{|\Omega|} \sum_{r=0}^{n} \int_{\Omega^{(r)}} 2\, \mathbf{e}^{(r)}(\mathbf{x}) : \mathbf{e}^{(r)}(\mathbf{x})\, \mathrm{d}\mathbf{x} \tag{24}$$

which can be after a simple manipulation:

$$\frac{1}{2}\, \mathbf{E} : \frac{\partial \mathbf{L}^{\text{eff}}}{\partial G^{(r)}} : \mathbf{E} = \frac{1}{|\Omega|} \frac{|\Omega^{(r)}|}{|\Omega^{(r)}|} \sum_{r=0}^{n} \int_{\Omega^{(r)}} \mathbf{e}^{(r)}(\mathbf{x}) : \mathbf{e}^{(r)}(\mathbf{x})\, \mathrm{d}\mathbf{x} \tag{25}$$

knowing that $c^{(r)} = |\Omega^{(r)}|/|\Omega|$, even more simplified:

$$\frac{1}{2}\, \mathbf{E} : \frac{\partial \mathbf{L}^{\text{eff}}}{\partial G^{(r)}} : \mathbf{E} = c^{(r)} \frac{1}{|\Omega^{(r)}|} \int_{\Omega^{(r)}} \mathbf{e}^{(r)}(\mathbf{x}) : \mathbf{e}^{(r)}(\mathbf{x})\, \mathrm{d}\mathbf{x} \tag{26}$$

The quadratic average of the deviatoric strain field over a general phase, r, is defined as (Pichler and Hellmich, 2011)

$$\|\mathbf{e}^{(r)}\| = \sqrt{\frac{1}{|\Omega^{(r)}|} \int_{\Omega^{(r)}} \frac{1}{2}\, \mathbf{e}^{(r)}(\mathbf{x}) : \mathbf{e}^{(r)}(\mathbf{x})\, \mathrm{d}\mathbf{x}} \tag{27}$$

and using Eq. (26), it can be also expressed as

$$\|\mathbf{e}^{(r)}\| = \sqrt{\frac{1}{4c^{(r)}}\, \mathbf{E} : \frac{\partial \mathbf{L}^{\text{eff}}}{\partial G^{(r)}} : \mathbf{E}} \tag{28}$$

The related quadratic average of the deviatoric stress field (see (20)) is used as an estimate for deviatoric stress peaks (Pichler and Hellmich, 2011):

$$\|\mathbf{s}^{(r)}\| = \sqrt{\frac{1}{|\Omega^{(r)}|} \int_{\Omega^{(r)}} \frac{1}{2}\, \mathbf{s}^{(r)}(\mathbf{x}) : \mathbf{s}^{(r)}(\mathbf{x})\, \mathrm{d}\mathbf{x}} = 2G^{(r)} \|\mathbf{e}^{(r)}\| \tag{29}$$

Assuming the elasto-brittle behavior, the elastic response can be expected until the quadratic deviatoric stress averages over each of the phases remain below a critical strength (Pichler and Hellmich, 2011):

$$\|\mathbf{s}^{(r)}\| \leq s_{\text{crit}}^{(r)} \tag{30}$$

4. Homogenization of Cocciopesto Mortar

The specific feature of cocciopesto mortars is that a thin layer of C-S-H gel is formed around the crushed brick particles and it should be taken into account in the calculation. A thickness of the C-S-H layer at the brick interface is assumed to be about 20 μm for the calculations; the backscattered electron image of the interface can be seen in Fig. 2, which is reproduced from Böke et al. (2006). However, the estimation of the C-S-H gel thickness on the brick interface is one of the deficiencies in the modeling. Another uncertainty is the elastic stiffness of the gel. There are basically two types of the gel present in the Portland cement. As reported in literature, e.g. Selvam et al. (2009), these are low and high-density C-S-H gel. For the calculation of the effective properties of cocciopesto mortars, values representing the low-density C-S-H gel were considered. The nanoindentation results showed that the low-density C-S-H phase has a mean stiffness of about 22 GPa (Constantinides and Ulm, 2004), the density of the gel in calculation was considered as 2000 $\mathrm{kg/m^3}$, as suggested in Jeffrey and Hamlin (2006) and Poisson's ratio as 0.20.

In the calculations it is assumed that 50% of the C-S-H gel occupies the voids, 30% of the C-S-H gel consumes a part of the lime matrix and the remaining 20% is assumed to consume a part of the brick phase. These values are only estimated, but they do not have any significant influence on the final results. Despite the uncertain material properties of the gel phase, the model should be capable to indicate trends.

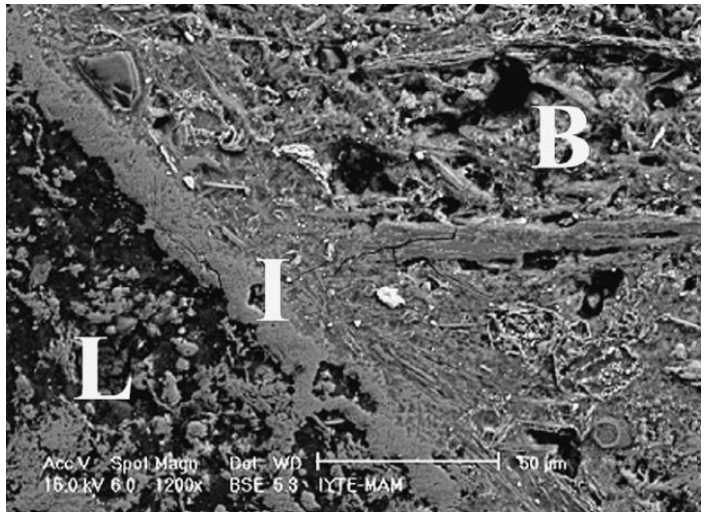

Fig. 2: Brick interface (I) between lime matrix (L) and brick aggregate (B), reproduced from Böke et al. (2006)

Based on a comprehensive literature study, e.g. Maropoulou et al. (2005), the mix proportions for the micromechanical homogenization of the cocciopesto mortar were determined as 4 mass portions of lime matrix, 3 mass portions of crushed bricks and 5 mass portions of siliceous sand in the hardened mortar. This composition should be similar to the historic mortars described by, for instance, Vitruvius. A porosity of the hardened mortar is varying according to the environment and technology. For the calculations, the porosity was considered to be 30% of the volume. The mechanical properties of the individual components, considered in the calculations, are summarized in Tab. 1. The properties of voids are set to be non-zero to avoid numerical complications.

Tab. 1: Properties of individual components used for calculations

	density	E	ν	tensile strength	source
	$[\mathrm{kg/m^3}]$	[MPa]	-	[MPa]	-
lime	1900	1800	0.25	0.4	Drdácký and Michoinová (2003)
siliceous sand	2600	70000	0.17	48	AZoM (2012)
clay brick	1600	2400	0.17	3.2	Hendricx et al. (2009)
voids	-	10^{-9}	10^{-3}	-	-

The summary of material properties in Tab. 1 indicates that the weakest constituent is the hardened lime matrix, having the tensile strength approximately 0.4 MPa. This value can vary according to curing time and technology. However, the value should not be higher than 0.7 MPa, which is still way smaller than the tensile strength of the other components.

4.1. Results and Discussion

The C-S-H gel coating significantly stiffens the crushed brick particles and its presence results in an increase of the effective mortars stiffness (see Fig. 3), even though the layer is relatively thin in comparison with the diameter of the brick particles.

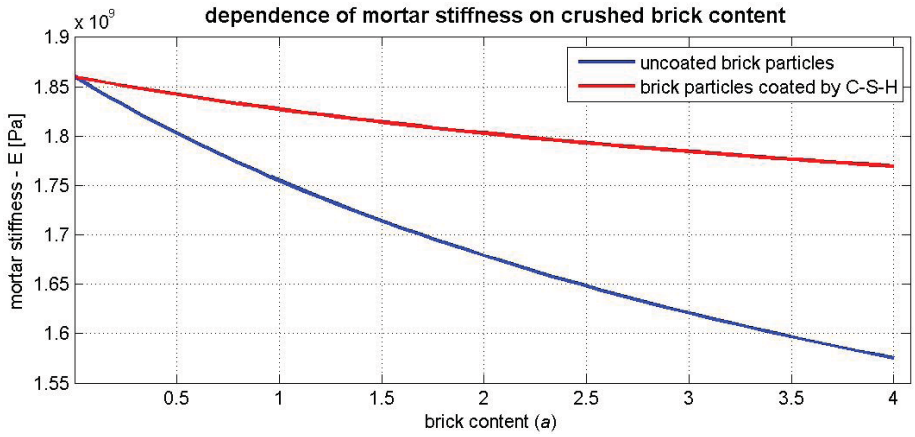

Fig. 3: The effective stiffness of mortars containing coated / uncoated crushed brick particles

It can be clearly seen from Fig. 3 that with the addition of crushed bricks without consideration of coating, the mortar stiffness is quite significantly reduced. However, for the mortar containing coated crushed brick particles the mortar stiffness reduction or increase is strongly dependent on the size of the added crushed brick particles. The variable parameter a (brick content) has a meaning of the mass portion in the mix (lime : brick : sand = 4 : a : 5). The calculation were done assuming the size of the brick particles to be 1 mm in diameter. From the nature of the Mori-Tanaka method, the crushed brick size distribution does not have any effect in case of uncoated particles, but plays a significant role in case of particles with coating.

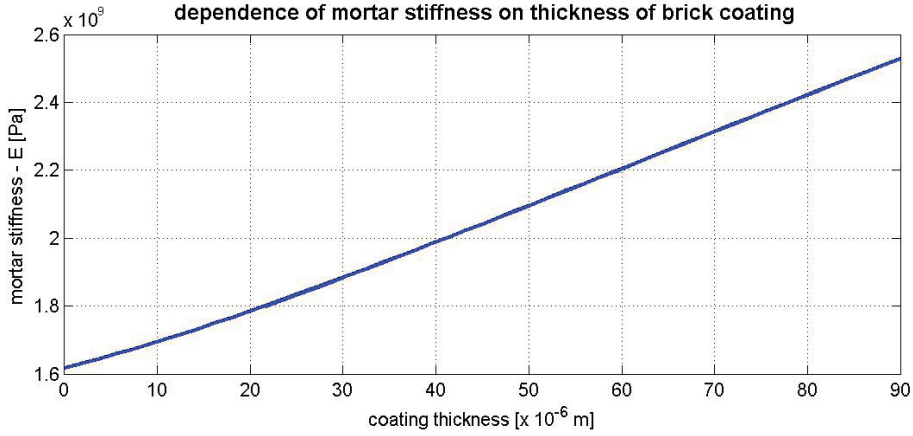

Fig. 4: A dependence of the effective mortar stiffness on coating thickness

If the C-S-H gel coating is formed, a bigger coating thickness should result in an increase of the effective mortar stiffness (see Fig. 4). The same increase of the effective mortar stiffness can be obtained if smaller crushed brick particles are added (see Fig. 5).

It can be concluded that the C-S-H gel formation on the interface of crushed brick particles results in an increase of the effective mortar stiffness. This increase is steep if the ratio of gel thickness to size of brick particles is relatively high (see Fig. 5), and that can be ensured by addition of crushed brick particles having a smaller diameter.

A reduction or increase of the deviatoric stress in the lime matrix is also strongly dependent on the ratio of coating thickness to size of crushed brick particles. If the added brick particles are smaller, the

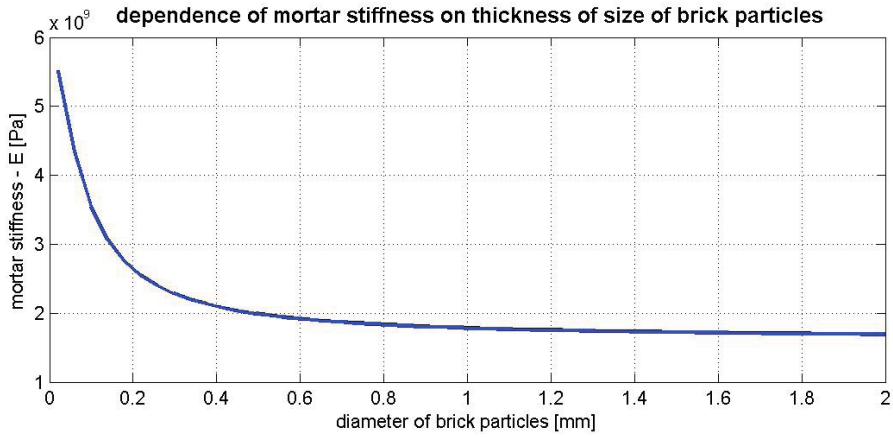

Fig. 5: A dependence of the effective mortar stiffness on a diameter of brick particles

effect of C-S-H gel coating becomes greater and the deviatoric stress within the lime matrix significantly decreases (see Fig. 6). The values on the y-axis in Fig. 6 represent the ratio of the quadratic average of the deviatoric stress in the lime matrix for particles approaching zero diameter (being the reference value), $\|\mathbf{s}^{(0)}(r \to 0)\|$, to the quadratic average of the deviatoric stress in the lime matrix for crushed brick particles of a variable size (on the x-axis), $\|\mathbf{s}^{(0)}\|$.

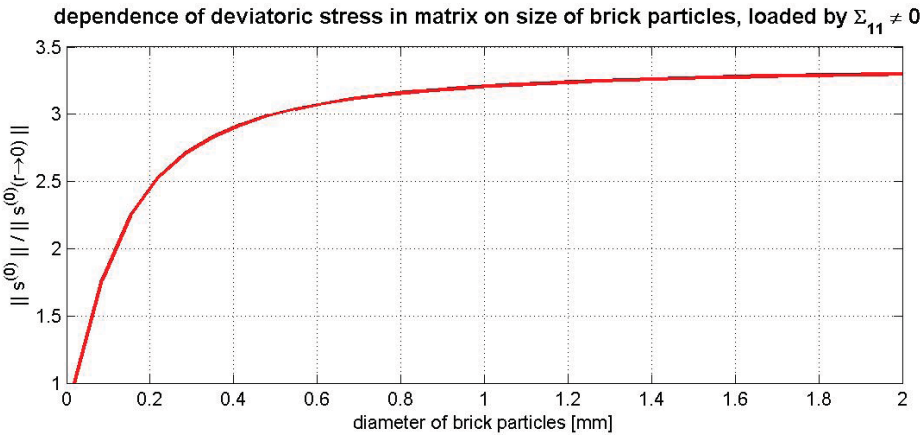

Fig. 6: A dependence of the deviatoric stress in matrix on a diameter of brick particles

From the calculations it seems reasonable to add a certain amount of finely ground bricks into to the mix, since it should result in a reduction of the deviatoric stress within the matrix. It can be concluded that big-size brick particles cause a mortar stiffness decrease and the small particles are responsible for a reduction the deviatoric stress in lime matrix. This reduction can be seen in Fig. 7, where the uniform crushed brick size distribution was modified in order to reduce the deviatoric stress in the lime matrix and to keep the mortar stiffness as low as possible. While in case of the uniform crushed brick size distribution the deviatoric stress within the lime matrix is increasing with the addition of crushed brick particles, it is being reduced with the addition of crushed bricks having a smaller diameter.

For the conservation mortars a low elastic modulus and sufficient strength are, together with ductility, usually required (Velosa et al., 2009). The proper composition of a mortar can be prepared using multiple fractions of crushed bricks. Fine brick particles in the mix should ensure a reduction of the deviatoric

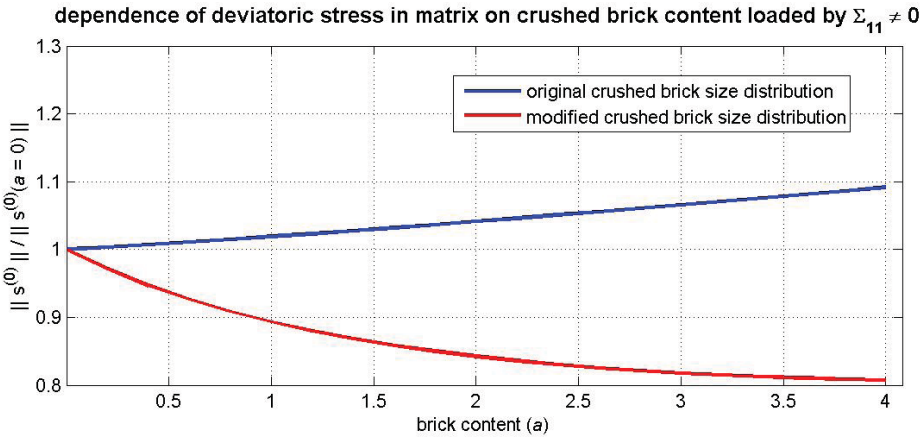

Fig. 7: A comparison of a uniform and modified size distribution crushed brick particles

stress in matrix, and therefore increase the mortar strength. On the other hand, bigger fractions make the mortar more compliant.

5. Conclusions

The calculations based on micromechanical approach revealed, confirmed or provided an explanation to the following facts:

- The assumption of C-S-H gel formation on the matrix-crushed brick interface has a major influence on behavior of the cocciopesto mortars, especially in case of small crushed brick fractions.
- The main factor influencing the behavior of the crushed bricks (or other clay products, such as tiles or pottery) in a mortar is the ratio of coating thickness to crushed brick size. It was also found that the addition of crushed bricks, having a bigger diameter, should make the mortar more compliant and cause an increase of the deviatoric stress in the matrix. The addition of crushed bricks of a small size results in the opposite behavior - the mortar becomes stiffer and the deviatoric stress in the lime matrix is reduced, ensuring a higher mortar strength.
- The proposed model also confirmed a negative effect of voids in lime mortars, since the increased porosity causes quite large increase of the deviatoric stress within the lime matrix, and therefore reduces the mortar strength (Nežerka, 2011).

However, the results provided in this work, cannot be considered as exact because of a few simplifications and uncertainties in the calculation. The Mori-Tanaka homogenization technique assumes the materials to behave linearly and it is expected that the C-S-H gel should have additional positive effect on the mortar strength if the non-linear behavior were considered. The thickness of the C-S-H gel coating, 20 μm, cannot be also taken as the exact universal value, since it is dependent on the amount and a chemical composition of the individual mortar constituents. There is also uncertainty around the reduction of porosity, if the C-S-H gel is formed.

Acknowledgments

The authors would like to thank for the financial support by the grant no. DF11P01OVV008.

References

AZoM, m. (2012). *Material Science publishing and information provision*. http://www.azom.com/article.aspx?ArticleID=1114.

Baronio, G., Binda, L., and Lombardini, N. (1997). The role of brick pebbles and dust in conglomerates based on hydrated lime and crushed bricks. *Construction and Building Materials*, 11:33–40.

Benveniste, Y. (1987). A new approach to the application of Mori-Tanaka theory in composite materials. *Mechanics of Materials*, 6:147–157.

Böke, H., Akkurt, S., Ípekoğlu, B., and Uğurlu, E. (2006). Characteristics of brick used as aggregate in historic brick-lime mortars and plasters. *Cement and Concrete Research*, 36:1115–1122.

Constantinides, G. and Ulm, F. (2004). The effect of two types of C-S-H on the elasticity of cement-based materials: Results from nanoindentation and micromechanical modeling. *Cement and Concrete Research*, 34:67–80.

Drdácký, M. and Michoinová, D. (2003). Lime mortars with natural fibres. *Britle Matrix Composites 7" Proceedings of the 7th Int. Symposium*, pages 523–532.

Gross, D. and Seelig, T. (2006). *Fracture Mechanics with an Introduction to Micromechanics*. Springer.

Hendricx, R. et al. (2009). Observation of the failure mechanism of brick masonry doublets with cement and lime mortars by X-ray CT. Technical report, Katholieke Universiteit Leuven.

Jeffrey, J. and Hamlin, M. (2006). A colloidal interpretation of chemical aging of the c-s-h gel and its effects on the properties of cement paste. *Cement and Concrete Research*, 36:30–38.

Luo, H. and Weng, G. (1987). On Eshelby's inclusion problem in a three-phase spherically concentric solid, and a modification of Mori-Tanaka's method. *Mechanics of Materials*, 6:347–361.

Maropoulou, A., Bakolas, A., and Anagnostopoulou, S. (2005). Composite materials in composite structures. *Cement and Concrete Composites*, 27:295–300.

Maropoulou, A., Bakolas, A., and Bisbikou, K. (1995). Characterization of ancient, Byzantine and later historic mortars by thermal and X-ray diffraction techniques. *Thermochemica Acta*, 269/270:779–995.

Mori, T. and K., T. (1973). Average stress in matrix and average elastic energy of materials with mixfitting inclusions. *Acta Metallurgica*, 21:571–574.

Mura, T. (1987). *Micromechanics of Defects in Solids*. Springer.

Nežerka, V. (2011). Micromechanics-Based Models of Cocciopesto Mortars. Master's thesis, Czech Technical University in Prague.

Pichler, B. and Hellmich, C. (2011). Upscaling quasi-brittle strength of cement paste and mortar: A multi-scale engineering mechanics model. *Cement and Concrete Research*, 41:467–476.

Selvam, P., Subramani, V., Murray, S., and Hall, K. (2009). *Potential Application of Nanotechnology on Cement Based Materials*. Mack-Blackwell Rural Transportation Center.

Velosa, A., Rocha, F., and Veiga, R. (2009). Influence of chemical and mineralogical composition of metakaolin on mortar characteristics. *Acta Geodynamica et Geomaterialia*, 153:121–126.

Šmilauer, V., Hlaváček, P., Škvára, F., Šulc, R., Kopecký, L., and Němeček, J. (2011). Micromechanical multiscale model for alkali activation of fly ash and metakaolin. *Journal of Materials Science*, pages 1–11.

Appendix

The individual matrices, needed for the calculation of coefficients a_1, a_2 and b_1, b_2 that are necessary for the determination of the deviatoric constraint constants (see Section 2.3.), can be found as

$$\mathbf{E} = \begin{bmatrix} 1 & -\dfrac{6\nu^{(c)}}{1-2\nu^{(c)}} & 3 & \dfrac{5-4\nu^{(c)}}{1-2\nu^{(c)}} \\ 1 & -\dfrac{7-4\nu^{(c)}}{1-2\nu^{(c)}} & -2 & 2 \\ 1 & \dfrac{3\nu^{(c)}}{1-2\nu^{(c)}} & -12 & \dfrac{-2\left(5-\nu^{(c)}\right)}{1-2\nu^{(c)}} \\ 1 & -\dfrac{7+2\nu^{(c)}}{1-2\nu^{(c)}} & 8 & \dfrac{2\left(1+\nu^{(c)}\right)}{1-2\nu^{(c)}} \end{bmatrix} \tag{31}$$

$$\mathbf{F} = \begin{bmatrix} 3 & \dfrac{5-4\nu^{(m)}}{1-2\nu^{(m)}} \\ -2 & 2 \\ -\dfrac{12G^{(m)}}{G^{(c)}} & \dfrac{-2\left(5-\nu^{(m)}\right)}{1-2\nu^{(m)}}\dfrac{G^{(m)}}{G^{(c)}} \\ \dfrac{8G^{(m)}}{G^{(c)}} & \dfrac{2\left(1+\nu^{(m)}\right)}{1-2\nu^{(m)}}\dfrac{G^{(m)}}{G^{(c)}} \end{bmatrix} \tag{32}$$

$$\mathbf{H} = \begin{bmatrix} 1 & -\dfrac{6\nu^{(g)}}{1-2\nu^{(g)}} \\ 1 & -\dfrac{7-4\nu^{(g)}}{1-2\nu^{(g)}} \end{bmatrix} \tag{33}$$

$$\mathbf{K} = \mathbf{G}\mathbf{E}^{-1}\mathbf{F} \tag{34}$$

$$\mathbf{R} = \mathbf{P} + \mathbf{Q}\mathbf{E}^{-1}\mathbf{F}\mathbf{K}^{-1}\mathbf{H} \tag{35}$$

where

$$\mathbf{G} = \begin{bmatrix} 1 & -\dfrac{6\nu^{(c)}c^{\,2/3}}{1-2\nu^{(c)}} & \dfrac{3}{c^{\,5/3}} & \dfrac{5-4\nu^{(c)}}{\left(1-2\nu^{(c)}\right)c} \\ 1 & -\dfrac{\left(7-4\nu^{(c)}\right)c^{\,2/3}}{1-2\nu^{(c)}} & -\dfrac{2}{c^{\,5/3}} & \dfrac{2}{c} \end{bmatrix} \tag{36}$$

$$\mathbf{P} = \begin{bmatrix} 1 & \dfrac{3\nu^{(g)}}{1-2\nu^{(g)}} \\ 1 & -\dfrac{7+2\nu^{(g)}}{1-2\nu^{(g)}} \end{bmatrix} \tag{37}$$

and finally

$$\mathbf{Q} = \frac{G^{(c)}}{G^{(g)}} \begin{bmatrix} -1 & -\dfrac{3\nu^{(c)}c^{\,2/3}}{1-2\nu^{(c)}} & \dfrac{12}{c^{\,5/3}} & \dfrac{2\left(5-\nu^{(c)}\right)}{\left(1-2\nu^{(c)}\right)c} \\ -1 & \dfrac{\left(7+2\nu^{(c)}\right)c^{\,2/3}}{1-2\nu^{(c)}} & -\dfrac{8}{c^{\,5/3}} & \dfrac{2\left(1+\nu^{(c)}\right)}{\left(1-2\nu^{(c)}\right)c} \end{bmatrix} \tag{38}$$

18th International Conference
ENGINEERING MECHANICS 2012
Svratka, Czech Republic, May 14 – 17, 2012

pp. 945–954
Paper #201

THE CRITERION OF CHOOSING THE PROPER SEEDING PARTICLES

J. Novotný[*], L. Manoch[**]

Abstract: *This paper is focused on the problem of the ability of seeding particles to follow the flow field. One of the most important factors influencing the resultant accuracy of the measurement is using the proper seeding particles for feeding the flow when measuring by Particle Image Velocimetry method – PIV. The aim of the paper is to provide comprehensible instruction for choosing the proper type of seeding particles with regard to the flow characteristics and required measurement accuracy. The paper presents two methods with the help of which it is possible to determine the seeding particles' ability to follow the flow field. The first method is based on the direct calculation of the phase lag and amplitude ratio between the particle and the fluid. The calculation is based on solution of the BBO equation for spherical particle. The other method results from the calculation of the particle time response, which defines the maximum frequency of disturbances, which are to be followed by the particle. In the conclusion, the method of choosing the seeding particles is proposed, depending on the required measurement accuracy.*

Keywords: ***PIV, seeding particles, BBO, accuracy***

1. Introduction

When measuring with the help of Particle Image Velocimetry the particle image shift in time Δ t is measured. Instead of measuring the liquid velocity, the distance of the particles covered in Δt is measured. The resultant measurement accuracy is i.a. influenced by the seeding particles' ability to follow the flow field, by the method of calculating the resultant shift and by other parameters by the help of which it is possible to identify the quality of obtained signal. Quite a few of authors dealt with the signal quality influence on the resultant accuracy of the measurement by the PIV method in the past decade. The authors most often deal with the influence of particular parameters (particle density, particle size, gradient, measured shift) on the resultant PIV measurement accuracy. Much attention is given to the influence of particular algorithms by the help of which the correlation plane is calculated. This paper is focuses only on the influence of seeding particles' ability to follow the flow field. Different authors, concerned themselves on the problem in the past. Their articles solve the movement of the spherical particle in the flow field in dependence on the amplitude ratio (phase lag) and Stokes number. The authors' use of the diagrams and conclusions is limited to the sizes of the particles, no longer commonly used. The resolution of the diagrams presented by the authors mentioned above doesn't allow precise reading of the required values. This paper aims to remedy the shortcomings. The particle's ability to follow the fluid movement is influenced by the density ratio of the particle and the liquid, by the shape and size of the particle and fluid viscosity. If we want to deal with the description of particle displacement in the flow field it is necessary to describe the displacement by means of the motion equation. The spherical or eventually at least oval-shaped seeding particles are ideal for the PIV measurement. The seeding particle displacement will be further solved on condition that the particle is spherical. This assumption is not always fulfilled; especially the solid particles made from SiO2 or AL2O3 do not fulfill the assumption, but this simplification is necessary and does not lower the quality of obtained data.

[*] Ing. Jan Novotný, Ph.D. : CTU in Prague Faculty of Mechanical Engineering Department of Fluid Dynamics and Thermodynamics, Technicka 4; 166 07, Prague; CZ, e-mail: jan.novotny@fs.cvut.cz
[**] Ing. Lukáš Manoch.: CTU in Prague Faculty of Mechanical Engineering Department of Fluid Dynamics and Thermodynamics, Technicka 4; 166 07, Prague; CZ, e-mail: lukas.manoch@fs.cvut.cz

2. Solutions of the BBO equation

The movement of the spherical particle carried by the viscosity liquid was already described by Basset. The equation derived by Basset is commonly classified as BBO equation. The other authors also concerned with the spherical particle displacement in both steady and unsteady flow are Basset, Boussinesq and Oseen. BBO equation can be written down in the form:
Where:

$$m_p \frac{du_P}{dt} = \frac{18\,\mu_F}{\rho_P d_P^2} m_P (u_F - u_P) - m_F \frac{Du_F}{Dt} + \frac{1}{2} m_F \left(\frac{Du_F}{Dt} - \frac{du_P}{dt}\right) + \\ + 9\sqrt{\frac{\rho_F \mu_F}{\pi}} \frac{m_P}{\rho_P d_P} \int_{t_0}^{t} \frac{\frac{Du_F}{D\tau} - \frac{du_P}{d\tau}}{\sqrt{t-\tau}} d\tau + (m_P - m_F) g. \tag{1}$$

u_p is velocity of the particle
u_F is fluid velocity
m_P is particle mass
m_F is mass of the fluid at particle-volume
d_P is particle diameter
μ_F is fluid viscosity
ρ_p is particle density

The given equation is valid for these cases:

- The size of the smallest vortices is several times bigger than the particle diameter;
- The Reynold's number calculated from the particle diameter and from the difference between liquid and particle velocity is lower than 1.
- The particles density in the liquid has to be low enough in order to prevent from interaction among the individual particles as well as to prevent the particles features from changing during the process of adding the particles to the fluid;
- The turbulence is homogeneous.

Quite a few of authors have made a detailed analysis of the influence of the particular equation terms (1) and thus we will not deal with it. Hjemfeld solved the equation (1) for the course of liquid velocity uF and particle velocity uP expressed with the help of Fourier's integral:

$$u_P = \int_0^{\infty} (\sigma \cos \omega t + \varphi \sin \omega t) d\omega \tag{2}$$

$$u_F = \int_0^{\infty} (\zeta \cos \omega t + \lambda \sin \omega t) d\omega \tag{3}$$

The expression for the velocity of the particle is the solution of the equation (1). In the equation (4), the velocity of the particle is expressed with the help of the liquid movement whose phase is shifted within an angle β and the amplitude is increased or decreased η-times:

$$u_P = \int_0^{\infty} \eta \begin{bmatrix} (\zeta \cos(\omega t + \beta) + \\ \varphi \sin(\omega t + \beta)) \end{bmatrix} d\omega \tag{4}$$

Where:

$$\eta = \sqrt{(1+f_1)^2 + f_2^2} \tag{5}$$

$$\beta = \tan^{-1}\left[\frac{f_2}{1+f_1}\right] \tag{6}$$

When introducing the particle and liquid density as $s = \sigma_P / \sigma_F$ and the non-dimensional Stokes number Ns defined according to:

$$Ns = \sqrt{\frac{\nu}{\omega D^2}} \tag{7}$$

Where:
ω is angular velocity corresponding to the maximum frequency of disturbances in flow,
ν is kinematic viscosity of flowing fluid,
D is size of the seeding particle.

it is possible to express the coefficients f1 and f2 as functions Ns, s and D, for more detail see. The dependence of the amplitude η and displacement angle β ratio on the Stokes number is mentioned by Hjelmfelt as well as Sommerfeld for several particle and liquid density ratios. The results of the equations solution, indicated by the authors, are unsatisfactory for most of the PIV measurements for two reasons. Either the authors mention fluid and particle density ratio within the range that is not used

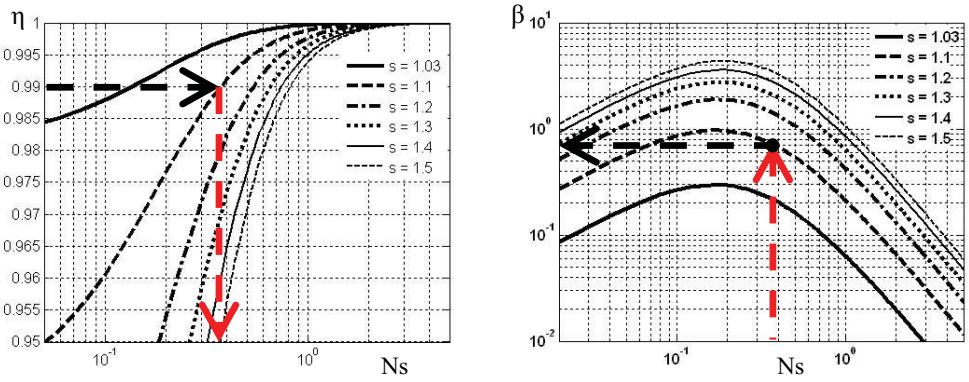

Fig. 1: Dependence of amplitudes ratio η and phase lag β on Stokes number Ns for particles flowing in water and for several values of density ratios

any longer at measuring by the PIV method [19], or they present the dependence of the phase lag (or actual and measured amplitude ratio) for the range of Stokes number obtained by PIV measurements very sporadically [40]. The resulting dependencies presented in those articles do not also meet the requirement for quick and precise determination of the range of application of different particle types, which are at the experimenter's disposal.

In order to generate the particular diagrams that enable to deduct the required data easily and quickly it is necessary to display the dependence of amplitudes ratio on Stokes number in the range of 0.95< η <1. At this range it is possible to read easily the Stokes number by which the given particle moves with an amplitude deviation lower than one percent of the total velocity in the given place. It is necessary to consider different specific gravities of fluid and particle to make the presented dependencies complex. At measuring in liquids, the particle and liquid density ratios occur in the range of c. 1.03-1.5 (the difference between the particle and liquid density). Based on the solution presented by, it appears that if the particle density is identical to the liquid density then the difference in the phase lag and in the measured amplitude from the real liquid movement is zero. Such particles closely follow the liquid flow in case the characteristic disturbance size in the liquid is minimally several times bigger than the particle diameter. At measuring in the gases the density ratios s occur in the range from 20 for the expanded polystyrene micro balls up to the 2250 for Aluminum powder particles. For the measurement by the PIV method at low velocities, it is also possible to use helium bubbles that reach the density ratio s dependent on their size in the range of 0.9-1.1. The size of the particles generated in this manner is c. 1 mm and their application is limited to the very slow flow of the order of ones of meters per second. The Stokes number is used for transparent plotting of the phase lag against the amplitude ratio dependent on the fluctuation frequency in the flow. It is evident from the definition of the Stokes number that with increasing frequency the Stokes number decreases whereas with decreasing particle diameter the Stokes number increases. The dependencies of η and β

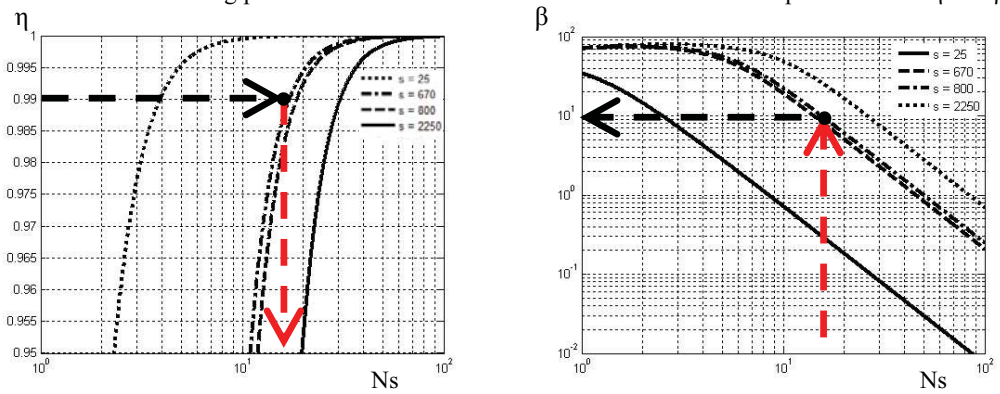

Fig. 2: Dependence of amplitudes ratio η and phase lag β on Stokes number Ns for particles flowing in air and for several values of density ratios.

on the Stokes number for the particular values of density ratio most frequent in the liquids and gases are displayed in the diagrams in Fig. 1 and 2.

3. Accuracy determination

The particle's ability to follow the flow field is shown in the diagrams in Fig. 1 to 4. It is possible to deduct the phase lag and particle and liquid amplitude ratio for the given frequency, and to read the particle and fluid density ratio. If we want to determine which particles are convenient for the existent experiment and which are not, it is necessary to determine the maximum frequency of disturbances which can be followed by the particles with given accuracy. For determination of the frequency that can be followed by the particles with the amplitude deviation lower than one percent (η=0.99) it is necessary to know:

- Mean value of particle diameter
- Specific density of particle and fluid
- Kinematic viscosity of fluid

It is possible to resume the determination of maximum frequency that can be followed by the particles in following points:
to determine the value of the Stokes number, for particular value of density ratio s, from diagram in Fig. 1 for η=0.99

for particles with diameter D and for the fluid with viscosity ν, to calculate the maximum frequency of disturbances that can be followed by the particles. For water and air, it is possible to deduct from the diagram Fig. 4.
to check if the calculated frequency is higher than the maximum frequency that we want to measure
If the calculated frequency is lower it is possible to use the given type of the particle in case that the phase lag deducted from the diagram in Fig. 2 or 4 is of the order of ones of degrees or smaller.
If the calculated frequency is lower than the maximum frequency that we want to measure it is recommended to use particles with smaller diameter or possibly the particles with lower value of specific density s.

In order to achieve the speed and integrity of the work it is necessary to introduce a diagram of dependence of the Stokes number on the frequency of disturbances for readily available seeding particles. This characteristic is plotted in diagrams in Fig. 4 which enable us to find quickly the searched frequency of disturbances in the flow for particular size of Stokes number and for the given particle. The usage of the suggested procedure at measuring in water and air is exemplified in the following paragraph.
In case that we measure in water at temperature of 20°C with particles with a mean diameter of 5 μm and specific density s=1.1 we can read from the diagram in Fig. 1 for η=0.99 the value of the Stokes number c. NS=0.35. The maximum frequency of disturbances which is measurable with given accuracy in water with such particle can be read from the diagram in Fig. 4 (eventually we can calculate it from the equation 4). The frequency that is followed by the particles with accuracy better than one percent and which was deducted from the diagram in Fig. 4 is 50 kHz. It is possible to consider this frequency as satisfactory for most cases of flow in water. For completeness' sake it is necessary to check the size of the phase lag. For value NS=0.35, the maximum phase lag with frequency of disturbances 40 kHz, β=0.7° can be read from the diagram in Fig. 2. It is possible to use the given particles in case that we assume the frequencies of disturbances in water lower than 50 kHz. Let's introduce the similar case for standard particles used at measuring in the air. Such particles are most frequently generated by fog generators and mean particle diameter value is c. 1 μm, specific density of particle/air is s=670. In this case, for η=0.99, s a d we can read the Stokes number NS=17 from the diagram in Fig. 3. The diagram in Fig. 5 allows us to determine, for the value NS and for the mean particle diameter 1 μm, the maximum frequency that can be followed by the particles i.e. 7 kHz. What remains to be checked is the size of the phase lag β=10°, deducted from the diagram in Fig. 2. The determined maximum value of disturbance frequency that can be followed by the particles, i.e. 7 kHz, and the phase lag 10° are not the optimum values for measurement in the air during which the frequencies of the order of tens of kHz are to be expected. Consequently, if we want to observe the processes in the air whose frequency is higher than 7 kHz it is necessary to choose more suitable seeding particles. When choosing the more suitable seeding particles we can make use of a table 1 that contains the most frequent types of seeding particles and their features, and the relevant values of frequencies which can be followed by them. The table clearly shows us that when choosing the more suitable seeding particles the mean value of particles diameter and their specific density s are very important parameters. In general, the smaller the particles diameter and the more the specific density approaches one, the bigger the ability of particles to follow the flow field. If we accordingly use the same particles with diameter d=0.3 μm then the maximum frequency for NS=17 read for such particles from diagram in Fig. 4 is 90 kHz.

4. The time response of the particle

If we neglect, in equation (1), all terms on the right side except the term expressing the drag force affecting the particle that moves in the flow field with velocity different from that of a liquid, then the equation (1) will change into the form of:

$$m\frac{du_P}{dt} = \frac{1}{2}C_D\frac{\pi d_P{}^2}{4}\rho_F(u_F - u_P)\left|u_F - u_P\right| \tag{8}$$

Where:

CD	drag coefficient of particle
D	seeding particle diameter
ρF	fluid density
uF	velocity of the fluid
uP	velocity of the particle
m	particle mass
du_p/dt	velocity gradient

It is a case of balance between an inertial force proportional to the mass of a particle and a drag force given by particle shape and size. By means of the equation (8) we can describe the situation when seeding particles are introduced into the flowing liquid whereas these particles have a different velocity than the fluid. Another example is the steady flow in a curved channel when due to the centrifugal acceleration the heavier particles can be moved from the original radius r at the entrance to the bigger radius r + Δr. The centrifugal acceleration can reach even the order of thousands of g by high velocities of the flow in the curved channel. In such a case it is necessary to verify the fault of the PIV measurement. If we introduce the Reynolds number of particle respecting the relative velocity of the particle in flowing fluid (u-v), and if the resulting Reynolds number calculated from the particle and fluid relative velocity is markedly smaller than one, it is possible to consider the flow around the particle to be creeping. The solution of equation (7) based on previous assumptions with constant flow velocity u= const., and with zero initial velocity of the particle v0=0 can be written down in following form:

$$u_P = u_F(1 - e^{-t/\tau_V}) \tag{9}$$

where τ_V is classified as time response of the particle:

$$\tau_V = \frac{\rho_P d_P^{\,2}}{18\mu_c} \tag{10}$$

The time response of the particle expresses the particles' ability to follow the liquid flow. It is the time interval during which the particle accelerates from zero velocity up to the value of c. 63.2 % of liquid

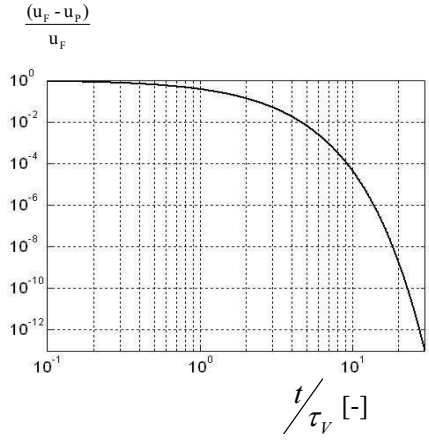

Fig. 3: The course of equalization of particle and liquid velocity in non-dimensional coordinates.

flow velocity. The response time of particle depends both on the particle size and material, and on viscosity of fluid that the particles move in. The response time of the same particles is different in environments with different viscosity. The time interval Δt during which the particle reaches

uP=0.99uF at constant liquid velocity uF is equal to c. 4.5 multiple of the particle response time τ_V.

For time interval equal to 10 multiple of τ_V, the difference between the liquid and particle velocity is only 4.5 thousandth of the percent. In the diagram in Fig. 3 we can follow the difference between the particle and liquid velocity depending on the multiples of the particle response time. The advantage of such projection is the fact that it enables us to follow the particle and liquid speed equalization independently of the size of the response time of particle which is to be used in the experiment. The concrete time interval during which the speed equalization of both velocities takes place with required accuracy is possible to obtain easily by multiplying of the deducted value by the response time of particle we want to use in the measurement.

It is evident from above mentioned that the smaller the particle time response the bigger the particle's ability to follow the sudden changes in the flow. Let's assume again a harmonic motion of the particle when calculating the maximum frequency which can be followed by the particle with the help of the time response. The frequency of such motion is equal to:

$$f = \frac{\omega}{2\pi} \tag{11}$$

At calculating the maximum frequency it is necessary to determine the angular velocity ω. In diagram 3, as mentioned earlier, it occurs that for 4.5 multiple of the particle response time the difference between the particle and fluid velocity is smaller than one percent. If the angular velocity is equal to the reciprocal value of 4.5 multiple of the time response we can calculate the maximum frequency of disturbances that can be followed by the particles according to equation:

$$f_{MAX} = \frac{1}{9\pi\tau_V} \tag{12}$$

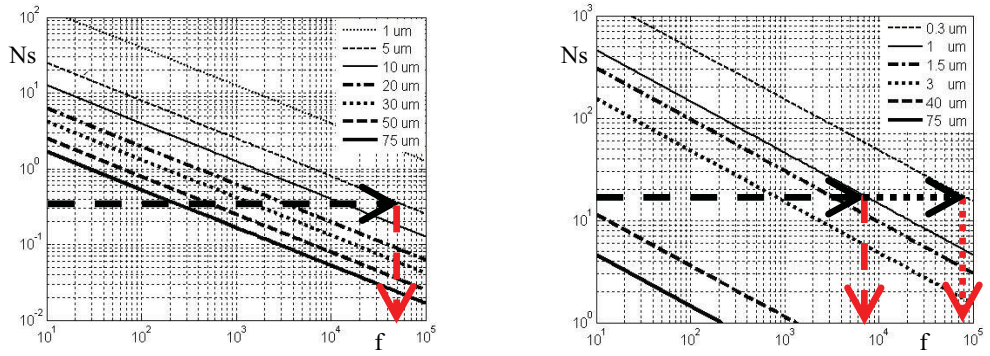

Fig.4: Dependence of Ns on dimensionless frequency for particles moving in water (A) and in air (B)

Tab 1: Parametres of particles used for measuring by the PIV method

Particles used for measuring in liquids Dynamic viscosity of water at 20 °C 1.002 10-3 [kgm-1s-1]				
Material of particle	Polyamide	Glass particles	Silvered glass particles	Fluorescent particles
Density[kgm-3]	1030	1100 [kgm-3]	1400 [kgm-3]	1500 [kgm-3]
Diameter [μm]	5 10 20	5 10 20	5 10 20	10 30 75
Response time of particle τv [μs]	1.42 5.71 22.84	1.5 6.10 24.4	1.9 7.76 31	8.32 74.850 467.81
fMAX - BBO	>100 kHz 79 kHz 18 Hz	50 kHz 11 kHz 2.6kHz	12 kHz 2.8 kHz 850 Hz	2.3 kHz 250 Hz 45 Hz
fMAX – τv	25 kHz 6.2 kHz 1.5 kHz	23 kHz 5.8 kHz 1.4 kHz	18 kHz 4.6 kHz 1.1 kHz	4.3 kHz 470 Hz 75 Hz
Particles used for measuring in liquids Dynamic viscosity of water at 20 °C 1.71 10-5 [kgm-1s-1]				
Material of particle	Oil	Water	Aluminium powder	Polystyrene microballs
Density [kgm-3]	800	1000	2700	30
Diameter [μm]	1 1.5 3	1 1.5 3	0.3	40 100
Response time of particle τ [μs]	2.60 5.85 23.40	3.25 7.31 29.24	0.79	155.95 714.75
fMAX - BBO	7 kHz 3.2 kHz 810 Hz	6 kHz 2.7 kHz 700 Hz	25 kHz	85 Hz 15 Hz
fMAX – τv	13.6 kHz 6 kHz 1.5 kHz	10.8 kHz 4.8 kHz 1.2 kHz	44.8 kHz	226 Hz 50 Hz

5. Conclusion

Based on the presented approaches it is possible to determine the maximum frequency of disturbances that can be followed by the concrete particles. The comparison of both methods is summarized in table 1 which contains the response times of individual particles as well as maximum frequencies based on BBO equation solution and based on the time response calculation. The comparison of both methods shows full correspondence between both approaches. From the results it is evident that if specific gravity of the particle and fluid approaches one, the maximum frequencies calculated by means of BBO equation are higher than the values determined by means of time response. On the contrary, at higher specific gravity the maximum frequency calculated by means of BBO equation is lower than value determined from time response. This behavior is given by the fact that the influence of particular BBO equation terms changes with changing particle and fluid density ratio. The measurement by the PIV method makes also use of different particles than those presented in table 1 with their maximum frequencies which is the reason why the paper proposes the method, for given particle type and given

fluid, with the help of which it is possible to easily and quickly determine the frequency to be followed by the particles with chosen accuracy.

6. Acknowledgment

This project has been supported by the MPO TA01010184

7. References

Adrian Ronald, J. (1986) Image shifting technique to resolve directional ambiguity in double-pulsed velocimetry, *Optical society of America.*

Astarita,T., G. Cardone. (2005) Analysis of Interpolation Schemes for Image Deformation Metods in PIV, *Experiments in Fluids 38*, 233-243, DOI 10.1007/S00348-004-0902-03.

Basset, A. B. (1888) A Treatise on Hydrodynamics, *Deighton, Bell and Co*., Cambridge.

Bolinder, J. (1990) On the Accuracy of Digital Particle Image Velocimetry system, *Technical report*, ISSN 0282-1990.

Byoung Jane K., Hyung Jim S. (2006) A Further Assessment of Interpolation schemes for Window Deformation in PIV*, Experiment in Fluids*, 499-511.

Byoung Jae K., Chetan Swarup, Hyung Jin Sung, *Interpolation for Image Deformation in PIV.*

Corsin, S., (1961) Lumely Appl. Csi. Res. A6 1961. 114.

Crowe C., Sommerfeld M., Tsuji Y., Multiphase Flows with Droplets and Particles, *CRC Press LLC Washington,* D.C.

Czarnecki, J., Dabros, T. (1980) Attenuation of the van der Waals Attraction Energy in the Particle/ Semi-Infinite*. Medium System due the Roughness of the Particle Surface*, J. Colloid Interface, 78, 25.

Gui, L., S. T. Wereley*,* (2002) A Correlation-Based Continuous Window-Shift Technique to Reduce the Peak-Loking Efect in Digital PIV Image Evaluation, *Experimental in Fluids 32*, 506 – 517,Springert Verlang 2002, DOI 10.1007/S00348-001-0396-1.

Gui L., Merzkirch W., Fri R., (2000) A Digital Mask Technique for Reducing the Bias Error of the Correlation-Based PIV Interrogation Algorithm, 30-35, *Experiments in Fluids*.

Hart D. P., (1999) Super-Resolution PIV by Recursive Local-Correlation, *Journal of Vizualization*, Vol 10.

Hesham El-Batsh, (2001) Modeling Particle Deposition on Compressor and Turbine Blade Surfaces, *PhD Thesis*, Vienna University of Technology, Pohlgasse 8/1/3, A-1120 Vienna.

Hinze, J. O., (1956) Turbulence, *McGraw-Hill*, New York.

Hjelmfelt A. T., Mockros L. F., Motion of Discrere Particles in a Turbulent Fluid, *Appl. Sci. Res. Vol. 16*, 149-161.

Liang, D.F., C.B. Jiang, Y.L. Li, (2002) A Combination Correlation-based Interrogation and Tracking Algorithm for Digital PIV evaluation. *Experiments in Fluids 33*, 684-695.

Linken R., C. Poelma, J. Westerweel, (2003) Compensation for Spatial Effects for Non-Uniform Seeding in PIV Interrogation by Signal Relocation, *5th international Symphosium on Particle Image Velocimetry*, Busan, Korea.

Nobach H.,. Honkanen M., (2005) Two-Dimensional Gausian Regression for Sub-Pixel Displacement Estimation in Particle Position Estimation in Particle tracking Velocimetry, *Experiments in Fluids 38*, 511-515.

Raffel M., C. Willert, J. Komphenhans, (2007) Particle Image Velocimetry, *Springer-Verlang*, Second Edition, Berlin, ISBN 978-3-540-72307-3.

Raffel, M., Ronneberger O., Kompenhans J., (1998) Advanced Evaluation Algorithms for Standart and dual Plane Particle Image Velocimetry, *Proc. 9th Intl. Symp. on Laser Techniques to Fluid Mechanics*, Lisbon (Portugal). 13–16 July.

Saffman P., G., (1965) The Lift on Small Sphere in Slow Shear Flow, *J. Fluid Mech. 22*, 385.

Scarano F.,, Riethmuler M., L., (2000) Advances in Iterative Multigrid PIV Image Processing, *Experiment in Fluids*, 851-860.

Scarano F., Riethmuller M. L., (1999) Iterative Multigrid Approach in PIV Image Processing with Discrete Window Offset, *Experiment in Fluids 26*, 513-523.

Scarano F., (2004) 2nd Derivatives Ccross-Correlation Based PIV Super-Resolution, *12th International Symposium on Aplications of Laser Techniques to Fluid Mechanics*, Lisbon, Portugal.

Sommerfeld M., (2000) Theoretical and Experimental Modeling of Particle Flows, *Von Karman Institute for Fluid Dynamics*, Lecture Series.

Westerweel,J.,Dabiri, D., and Gharib, M., (1997), The Effect of a Discrete Window offset on the Accuracy of Cross-Correlation Analysis of Digital PIV Recordings, *Experiment in Fluids 23*, 20-28.

Westerwel J., (1997) Fundamentals of Digital Particle Image Velocimetry, *Measurement science and technology 8*, 1379-1392, UK.

Westerweel J., (1993) Digital Particle Image Velocimetry - Theory and Application, *Delftse Universitarie Pers III, PhD Thesis*, Technische Universiteit Delft, ISBN 90-6275-881-9.

Westerweel J., (2000) Theoretical Analysis of the Measurementt Precision in Particle Image Velocimetry, *Experiments in Fluids s3-s12*, Springer - Verlang.

Westerweel J., (2005) Analysis interrogation With Low Ppixel Resolution, *SPIE*, 624-635.

18th International Conference
ENGINEERING MECHANICS 2012
Svratka, Czech Republic, May 14 – 17, 2012

pp. 955–967
Paper #172

EFFECT OF LINSEED OIL ON THE MECHANICAL PROPERTIES OF LIME MORTARS

C.P. Nunes[*], Z. Slížková[**], D. Křivánková[***], D. Frankeová[****]

Abstract: *Linseed oil was commonly used in former times as an additive for mortars to improve hydrophobicity. However, linseed oil has also an important role on the mechanical behaviour of mortars that is strongly dependent on the type of binder. The effect of linseed oil addition in 1.5% by the weight of the binder was studied in two different mortar mixtures: air lime mortar and air lime-metakaolin mortar. The degree and the order of carbonation and hydration reactions were studied by thermogravimetric analysis and flexural and compressive strength were evaluated along curing time: 14, 28, 60 and 90 days. The results point out that carbonation process was slightly improved by the addition of linseed oil whereas the hydraulic effect of the pozzolan metakaolin was reduced. However, it is the lower capillarity coefficient, which involves a water intake reduction that may be reported as the main factor improving the mechanical behaviour of lime with linseed oil mortar exposed to freeze-thaw cycles and hence, its durability in wet and freezing conditions.*

Keywords: ***Linseed oil, lime, metakaolin, mechanical strength, hydrophobic effect.***

1. Introduction

The scientific interest of mortars based in traditional formulations is that they show great compatibility with ancient building materials and hence fulfil the recommendations of ICCROM for use in repairs (Lanas & Alvarez, 2003). Furthermore, they have been widely used in modern work with decorative and protective purposes. Both uses require the mortars to be durable, which is also an important economic issue.

However, today's lime mortars with compositions similar to ancient mortars, and thus more suitable to ensure the aesthetical and functional compatibility with pre-existing materials, have presented durability problems mainly when exposed to weathering agents like water and freeze-thaw cycles (Veiga, 2003).

Nowadays air lime mortars are very porous and their mechanical strength and durability are low when exposed to water and frost even though if only occasionally. One way to improve the strength and durability of air lime mortars is to partially replace air lime by other materials such as pozzolanas. The promising pozzolanic material in this regard that has also been used in the past is metakaolin (Aggelakopoulou et al., 2011). The air lime-metakaolin mortar properly designed may be promising as repair mortar because it can achieve much higher mechanical strength than pure air lime mortar but it is not strong enough to generate stress that might lead to failure in the original system to be repaired (Fortes-Revilla et al., 2006; Slížková, 2009; Válek et al., 2010).

[*] Mgr. Cristiana P. Nunes: Institute of Theoretical and Applied Mechanics, Prosecká 809/76; 190 00, Prague; CZ, e-mail: nunes@itam.cas.cz

[**] Ing. Zuzana Slížková, Ph.D.: Institute of Theoretical and Applied Mechanics, Prosecká 809/76; 190 00, Prague; CZ, e-mail: slizkova@itam.cas.cz

[***] Mgr. Dana Křivánková: Institute of Theoretical and Applied Mechanics, Prosecká 809/76; 190 00, Prague; CZ, e-mail: krivankova@itam.cas.cz

[****] Mgr. Dita Frankeová: Institute of Theoretical and Applied Mechanics, Prosecká 809/76; 190 00, Prague; CZ, e-mail: frankeova@itam.cas.cz

The territory of Central Europe always lacked the natural pozzolanas, thus the artificial pozzolanas were supposed to be used. A possibility to obtain artificial pozzolanas presents calcination of some rocks, in particular consolidated sediments, such as clay shales. In the Czech Republic, there is a specific type of clay shale that is extracted from several mines. After burning at temperatures similar to the burning of kaolinite in metakaolin production, the Czech clay shale exhibits pozzolanic properties. Therefore, it has a potential for use in lime-pozzolana binders. (Vejmelková et al., 2011)

The hereby designated metakaolin corresponds to the burnt Czech clay shale. Besides being a national material, burnt Czech clay shale was selected taking into account the previous studies of lime-metakaolin mortars in the Czech Republic (Vejmelková et al., 2011; Slížková, 2009; Válek, 2007).

Lime mortars blended with pozzolanas and other additives seek to recover ancient techniques and improve lime mortars behaviour. However, there is much to learn about which additives to use, how to use them and in what suitable application fields (Veiga, 2003).

Since liquid transport is one of the key factors influencing durability (Roels, 2000) additives which grant hydrophobic properties to mortars have become of great interest to the scientific community (Blachnik, 2001; Stolz, 2007; Izaguirre et al., 2010).

The design of lime mortars with linseed oil additive has the main goal of ensuring a degree of internal hydrophobicity and, consequently, lessen the damage from salt and frost. However, data from literature show that addition of oils to lime mortars reduces their mechanical strength by partially inhibiting carbonation reactions (Oliveira & Santiago, 1992; Sá, 2002; Veiga, 2003; Čechová, 2009). Other studies indicate significant compressive strength increment (Rovnaníková, 2002; Sá 2005; Ventolà et al., 2011).

The main goal for using oil as an additive for mortars relies in its hydrophobic properties. Hence, it may be a very efficient additive to improve durability by restraining water penetration. Linseed oil was one of the main lipid additives used for mortars formulation in former times according to ancient treatises, e.g. Vitruvius (Maciel, 2009), Pliny (Bostock, 1857), Palladio (Tavernor & Schofield, 1997). However, there is lack of information about the formulation technique.

Čechová's (2009) recent study about the effect of linseed oil in lime based mortars gave a new insight on the potential of this ancient and widely used additive in the improvement of mortars properties for restoration purposes. The addition of 1%-w of linseed oil (by weight of binder) has proved to have a positive effect on the properties of different lime based mortars. It limits water absorption into mortar without significantly affecting the total open porosity or decreasing the degree of carbonation. On the other hand, lime mortars and lime with pozzolana mortars with 3 months of age with 1% and 3% oil showed significant strength reduction, particularly in the case of 3% oil addition.

Owing to the proved influence of oils on the mechanical properties and durability of mortars the aim of this paper is to study mechanical behaviour of hardened lime-based mortars (lime and lime-metakaolin) enriched with 1.5%-w linseed oil (to the weight of binder) and to relate it with its resistance to freeze-thaw cycles.

2. Experimental study

2.1. Materials

The materials used for the mortars preparation were all from local suppliers. Table 1 presents the materials and respective provider company.

All the mortars were prepared in laboratory conditions with a binder: aggregate proportion of 1:3 (by weight), using a siliceous sand as aggregate. Designations and proportions of the mortars are presented in Table 1. The percentage weight of linseed oil added in respect to the weight of binder was 1.5%. This proportion was chosen on the basis of the results achieved by Rovnaníková (2002) and Čechová (2009) that used proportions of 1%, 5% and 10% of boiled linseed oil (oil varnish) and 1% and 3% of raw linseed oil respectively.

The commercial hydrated air lime powder (class CL 90) was supplied by Vápenka Čertovy Schody a.s. Čerták® and the aggregate by Provodínské písky a.s. The hereby designated metakaolin

corresponds to burnt Czech clay shale Mefisto L_{05} and was supplied by České Lupkové Závody a.s. The raw linseed oil was supplied by GRAC s.r.o.

Tab. 1: Mortar designation and constitution (by weight).

Mortar code	Composition
L	Lime : Sand (1:3-w)
LO	Lime : Sand (1:3-w) + linseed oil
LM	Lime : Metakaolin : Sand (0,75:0,25:3-w)
LMO	Lime : Metakaolin : Sand (0,75:0,25:3-w) + linseed oil

2.2. Sample preparation and curing conditions

Binder and aggregate were mechanically mixed for 6 min using an automatic mortar mixer MATEST-E093 at low speed. Regarding mortars with linseed oil addition, binder and aggregate were mixed for 3min and a bit of dry mixture (approximately 50g) was blended with oil in a plastic cup and mixed manually for 3min. The oiled mixture was then added to the dry mixture and blended for plus 3min in the automatic mixer. Water was then added and the mixtures were blended for plus 3 min in the automatic mixer. The amounts of water were designed so that each mortar could get comparable consistencies using the flow table test (170 ±5mm).

Mortars were mechanically compacted in prismatic 20×20×100mm and 40×40×160mm casts with ten falls in each one of the two layers which completes the casts. A plastic foil was put on the bottom of the casts to facilitate de-moulding.

In order to analyse the characteristics of the different mortars along time, twenty 20×20×100mm and five 40×40×160mm specimens were prepared with each of the mortars. The samples were kept for one day inside the casts and then de-moulded. During the first day inside the casts and for six days further the samples were stored at 90±5% of relative humidity. The mortar beams were further stored until testing days under controlled ambience at a temperature of 20±5ºC and 60±10% on grid-lined shelves to ensure the contact of all the sides with air and homogeneous progress of the carbonation reaction. Table 2 summarizes results of water/binder ratio, consistency and air content obtained for the fresh mortars.

Tab. 2: Fresh mortars properties. The values correspond to the average of 3 values ± standard deviation and were determined through the preparation of 2kg of dry mortar.

Mortar Code	Water/binder ratio	Consistency [cm]	Air content [%]
L	1,04	16,8 ± 0,1	2,6 ± 0,1
LO	1,08	16,6 ± 0,1	5,4 ± 0,2
LM	0,96	17,1 ± 0,3	2,2 ± 0,1
LMO	1,02	16,5 ± 0,1	4,0 ± 0,1

2.3. Testing program and results

Samples to be mechanically tested were taken from the room with controlled ambience conditions and tested within half an hour later.

Five specimens 20×20×100mm of each mortar were tested after 14, 28, 60 and 90 days, so that the evolution of their characteristics could be analysed. For the characterization of 90 days of age mortars, five specimens 40×40×160mm of each mortar were also used. All the specimens of each mortar were used for flexural and compressive strength tests. Half of each specimen 20×20×100mm (five half parts) were used for compressive strength and half were used for carbonation rate determination by thermogravimetric analysis.

Half of each specimen 40×40×160mm 90 days of age were also used for bulk density, open porosity, pore size distribution and water absorption by capillarity determinations after being dried to constant mass at 60ºC.

2.3.1. Flexural and compressive strength

Flexural and compressive strength were determined based on the Czech standard ČSN EN 1015-11, in a universal traction machine, following the classic method of performing the compressive test with half samples obtained from the flexural test. Following the time intervals for strength testing of lime based mortars proposed by Lawrence et al., 2006, so far the specimens were tested at the ages of 14, 28, 60 and 90 days. In Table 3 flexural and compressive strength development of the mortars cured up to 90 days is given. Fig. 1 plots the graphics of mechanical strength results for specimens 40×40×160mm 90 days of age and Fig. 2 shows the mechanical strength development of 20×20×100mm samples along time.

A correlation between 20×20×100mm and 40×40×160mm values for all mortars with the age of 90 days cannot be established, particularly in the case of mortar L. The differences are assigned to the size effect influencing both the attained strength values (Drdácký et al., 2011) and the degree of reactions generating the strength gain, particularly carbonation reaction.

Tab. 3: Flexural and compressive strength (average values ± standard deviation) of mortars cured up to 14, 28, 60 and 90 days (Specimens 40x40x160mm).*

Mortar	Flexural strength [Mpa]					Compressive strength [Mpa]				
	14 d	**28 d**	**60 d**	**90 d**	***90 d**	**14 d**	**28 d**	**60 d**	**90 d**	***90 d**
L	0.33	0.36	0,59	1,51	**0,54**	0.44	0.73	1,24	1,51	**1,01**
	±0.03	±0.07	±0,05	±0,09	**±0,06**	±0.06	±0.06	±0,04	±0,09	**±0,03**
LO	0.41	0.54	0.70	1.77	**1.34**	0.63	1.11	1.60	1.50	**2,29**
	±0.03	±0.07	±0.05	±0.19	**±0.07**	±0.05	±0.07	±0.09	±0.10	**±0.20**
LM	1.86	2.16	1,80	1,68	**1,65**	5.82	6.76	4,83	5,55	**6,71**
	±0.55	±0.60	±0,14	±0,16	**±0,20**	±0.63	±0.57	±0,75	±0,57	**±0,65**
LMO	1.17	1.45	1.50	1.53	**1,26**	2.77	3.15	4.55	5.68	**4,02**
	±0.13	±0.15	±0.28	±0.39	**±0,36**	±0.25	±0.37	±1.19	±0.60	**±0,23**

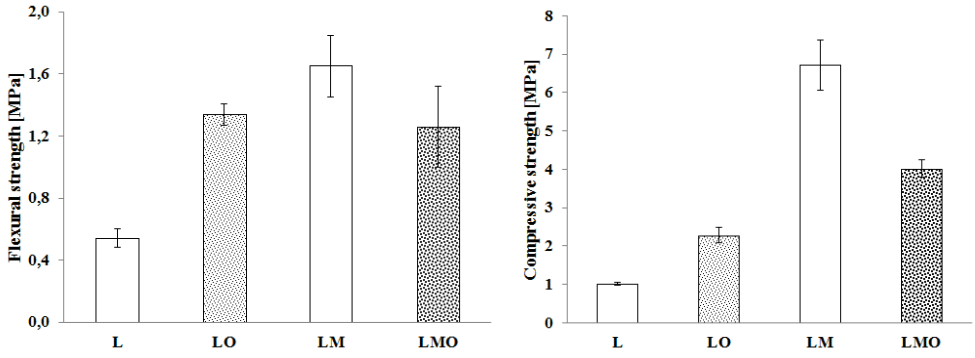

Fig. 1: Graphics of flexural and compressive strength of 90 days of age mortar specimens 40×40×160m.

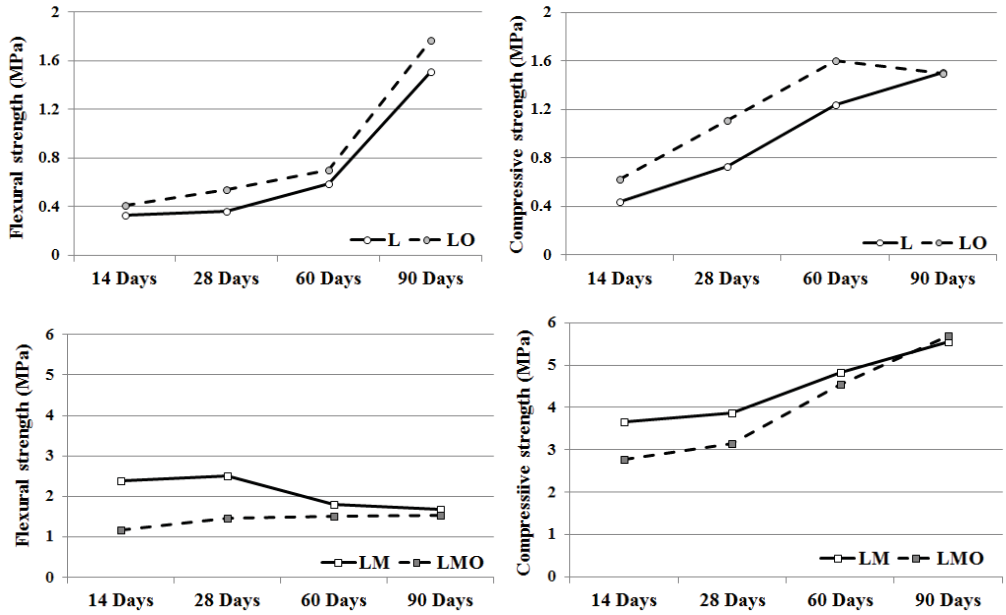

Fig. 2: Graphics of flexural and compressive strength development of mortar specimens 20×20×100mm up to 90 days of age.

2.3.2. Bulk density and open porosity

These tests were performed based on the on the Czech standard ČSN EN 1936 by total saturation with water under vacuum and hydrostatic weighing. Results of each mortar with 90 days are given on Table 4 in terms of average values and standard deviation.

Tab. 4: Bulk density and open porosity (average values ± standard deviation) of mortars 90 days of age.

Mortar	Bulk density [kg·m^{-3}]	Open porosity [%]
L	1767,82 ±0,18	32,01 ±0,19
LO	1645,33 ±9,99	34,44 ±0,58
LM	1688,80 ±0,95	34,35 ±0,13
LMO	1611,06 ±7,84	32,41 ±0,50

2.3.3. Mercury porosimetry

Pore size distribution was performed with a mercury porosimeter Quantachrome Poremaster® PM-60-13 with a specimen from each mortar with 90 days of age.

Two equivalent penetrometers were used with a 5cm^3 bulb and a total intrusion capacity of 0,500cm^3. Low pressure testing ranged from 6894,7Pa (1Psi) to 344737Pa (50Psi) and high pressure analysis from 275790,3 (40Psi) to 172368925Pa (30000Psi). Equilibration times were 15s for low pressure and 30s for high pressure. As mercury parameters, the following were used: advancing and receding contact angle = 140º; surface tension = 0,485 N/m; and density = 13,5487g/ cm^3.

Pore size distribution curves are plotted in Fig. 3 and represent the calculated pore size diameter of each mortar for the stated measurement conditions.

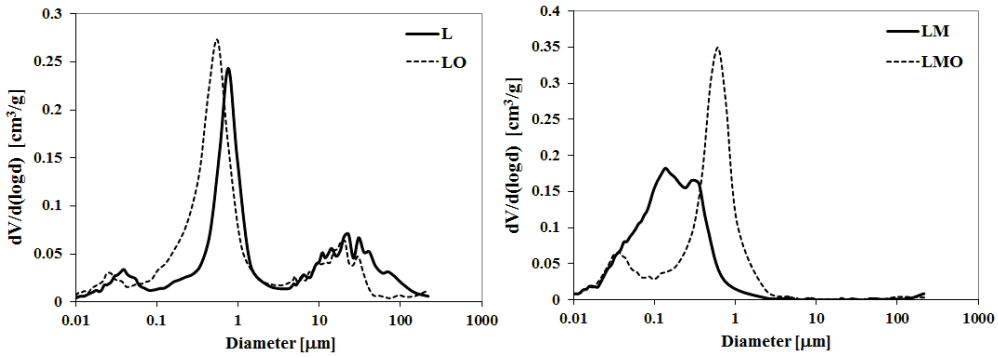

Fig. 3: Mercury intrusion curves of 90 days of age mortars.

2.3.4. Capillary water absorption

The test was performed based on the testing procedures of the Czech standards ČSN EN 1015-18 and ČSN EN 15801. Lateral surfaces of samples were sealed with epoxy resin. Half of each sample 40×40×160mm was immersed in 5mm of water (over absorbent textile) inside a covered box to maintain constant hygrothermal conditions and to limit the water evaporation from the samples. The weight of the absorbed water per unit of the exposed surface immerged, function of the square root of time (in hours), was registered. The tests were carried out until the absorption reached an asymptotic value. The capillary water absorption coefficient was determined by the angular coefficient of the curve. The results are presented in Table 5 and in Fig. 4.

Tab. 5: Capillary water absorption coefficient (average values of 4 samples ± standard deviation) of mortars 90 days of age.

Mortar	Capillary coefficient [kg·m^{-2}·h$^{-1/2}$]
L	2,77 ±0,03
LO	0,51 ±0,02
LM	0,97 ±0,03
LMO	0,42 ±0,02

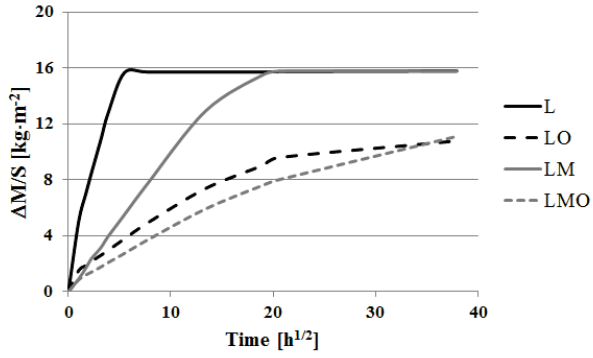

Fig. 4: Cappilarity water absorption test curves of mortars 90 days of age.

2.3.5. Thermogravimetric analysis - TGA

TGA was used in order to follow the progress of the hardening reactions of carbonation and hydration in the course of time. The analysis was carried out using a TA instrument, model SDT Q600-

TGA/DSC in static nitrogen atmosphere at a temperature range between 20-1000°C and at a controlled heating rate of 20°C/min. The first derivative of thermogravimetry was used in order to identify the hydrated and the carbonated phases at their characteristic decomposition temperatures, and to follow up their formation in time qualitatively.

For this analysis 20×20×100mm half of samples that remained from the mechanical tests were used. Table 6 reports the portlandite ($Ca(OH)_2$) content in the mortars along time and Fig. 5 shows the ratio between hydration and carbonation reactions in time. While products of hydration reaction are visible at the temperature range 100-370°C, the carbonation manifests as an increasing peak reaching maximum value between 700°C and 800°C.

Tab. 6: Portlandite content development determined by thermogravimetric analysis in mortars up to 90 days of age.

Test day	**Portlandite [$Ca(OH)_2$] (%)**			
	L	**LO**	**LM**	**LMO**
14	17,64	15,07	7,69	8,23
28	14,68	11,42	6,34	6,17
60	8,40	5,90	4,76	3,50
90	4,93	5,51	2,81	2,38

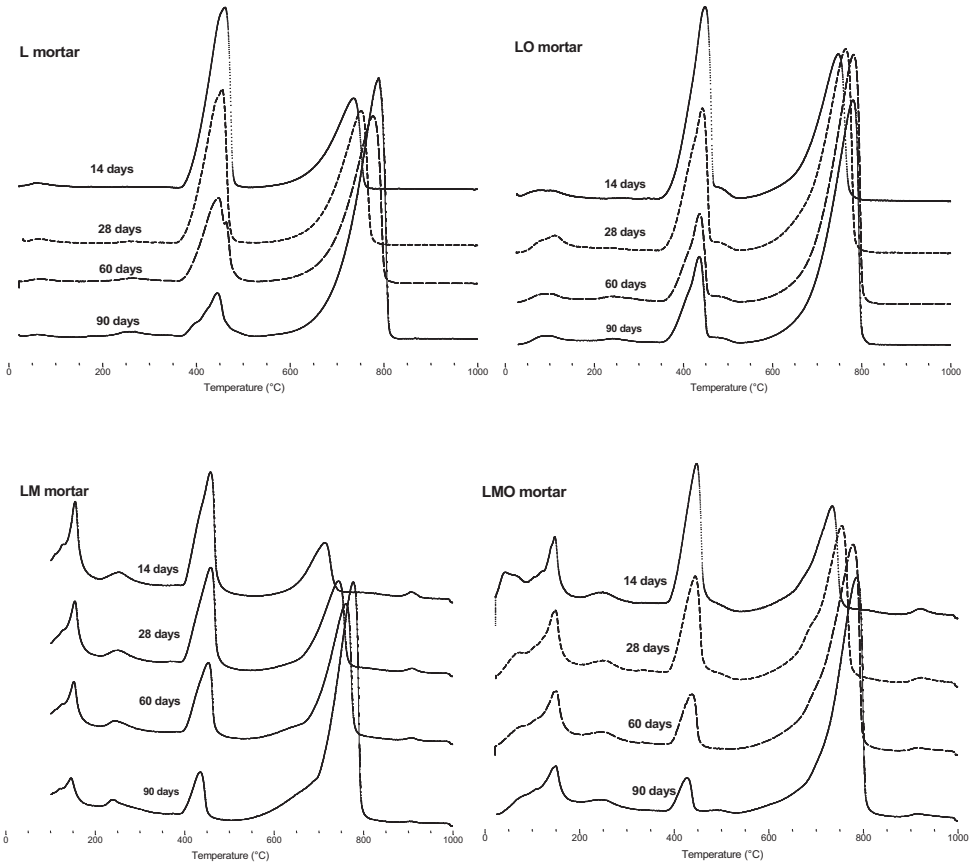

Fig. 5: DTG graphics of analysed mortars at 14, 28, 60 and 90 days of age.

2.3.6. Freeze-thaw testing program

Samples 40×40×160mm of lime and lime with linseed oil with 90 days of age were dried to constant mass at 60°C before being tested. The freezing tests were performed based on the Czech standard ČSN 72 2452. Samples were immersed in water at ambience temperature (20±5ºC) until achieving constant mass. After saturation in water samples were subjected to -20ºC (±5ºC) in a freezer during four hours and then thawed in water at ambience temperature (20±5ºC) for at least two hours before performing another cycle. Three samples were subjected to the freezing cycles and three samples were maintained immersed in water throughout the test (reference samples).

Lime mortar samples crumbled after one freezing cycle (Fig. 6.a). Under the binocular microscope microfissuration around the sand grains and powdering of binder could be observed on the fresh broken pieces (Fig.6.b).

Lime with linseed oil mortar was subjected to ten cycles after which the samples showed moderate degradation by binder powdering and, consequently, sand disintegration, particularly on the edges (Fig. 7.a). Under the binocular microscope micro-fissuration on the surfaces could be observed (Fig.7.b). Hence, after 10 cycles it was decided to perform flexural and compressive strength tests. Prior to the mechanical tests, samples were dried to constant mass at 60ºC. The results of mechanical strength after freezing tests are given in Table 7 and Fig. 8.

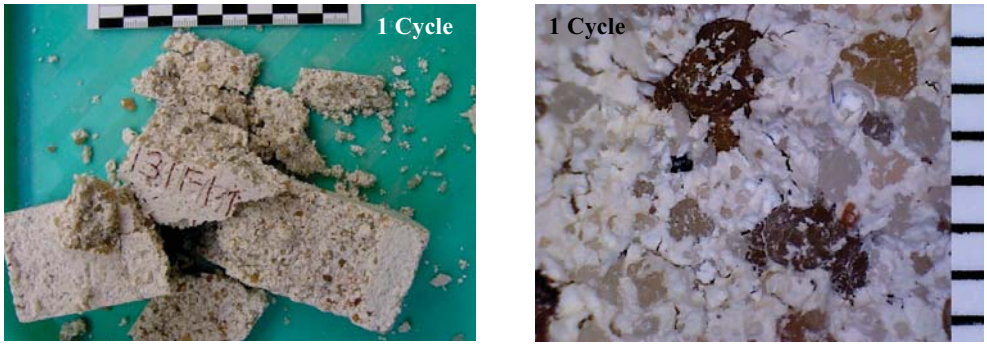

a) *b)*

Fig. 6: Aspect of L mortar 90 days of age after one freezing cycle: a) General view; b) Detailed view (millimeter scale).

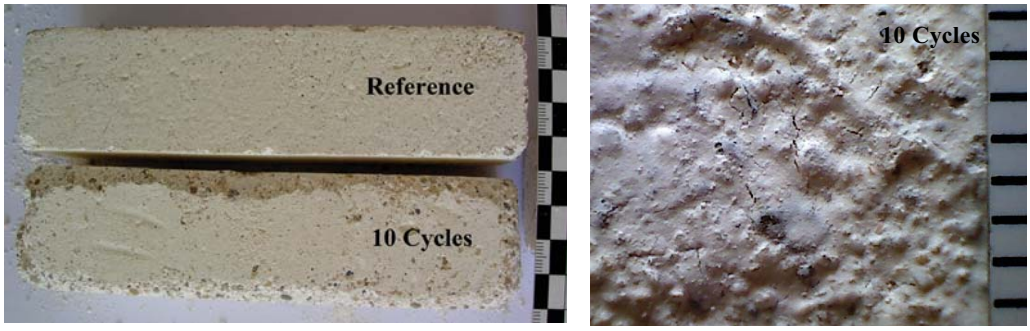

a) *b)*

Fig. 7: Aspect of LO mortar 90 days of age after10 freezing cycles: a) General view of a reference and aged sample; b) Detailed view of a sample after 10 freezing cycles (millimeter scale).

Tab. 7: Flexural and compressive strength (average values ± standard deviation) of mortars 90 days of age after the freezing test.

Mortar	Flexural strength [MPa]	Compressive strength [MPa]
LO – Not Aged	1.34 ±0.07	1,01 ±0,03
LO – Age Reference	0,32 ±0,04	0,69 ±0,12
LO – 10 Cycles	0,30 ±0,03	0,55 ±0,06

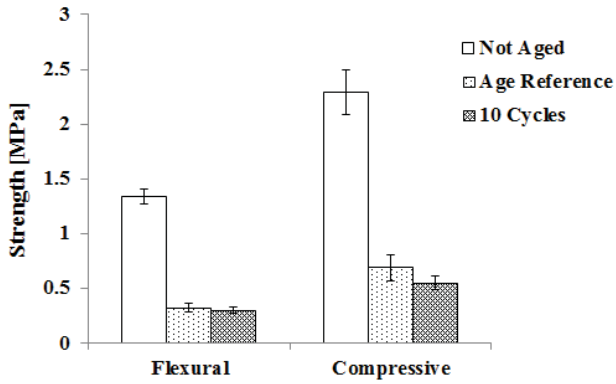

Fig. 8: Flexural and compressive strength for LMO mortar 90 days of age after freezing test.

3. Analysis and discussion of results

3.1. Mechanical strength

L and LO mortars indicate similar flexural strength development until 90 days of age. LO mortar has slightly higher values but significant regarding the compressive strength (Fig. 2). LO compressive strength increases till 60 days after when slightly drops to the same value of L mortar and TGA shows the same evolution for the carbonation rate (Fig. 5). However, 40×40×160mm specimens 90 days of age results indicate remarkably higher flexural and compressive strength values (148% and 127% strength increment, respectively) for LO mortar compared to L mortar (Fig. 1) . Hence, it can be assumed that linseed oil is improving mechanical strength on air lime mortar.

Lime-metakaolin mortars, LM and LMO, show different strength development behaviour. Contrary to the pure air lime mortars the flexural and compressive strength of LMO is significantly lower than that of LM, particularly at early ages (14 and 28 days) after which the values become practically equal (Fig. 2). Regarding these results, it must be taken into account that strengths determined at early ages (up to 28 days) are not conclusive because they are strongly influenced by the water content of the mortar. Values of 4×4×16cm samples 90 days of age show a marked difference between LM and LMO strengths (Fig. 1): oil addition promoted a reduction of 23% on flexural strength and 40% on compressive strength.

In lime-metakaolin mortars, hardening reactions are hydration and carbonation while calcium hydroxide mortars harden only due to carbonation reaction. Obviously, because of binder hardening, the mechanical strengths of lime mortars increase with curing time. In lime-metakaolin mortars, a combined reaction of hydration and carbonation takes place. Hydration reactions initiate first resulting in the formation of hydrated phases such as calcium silicate hydrate (CSH) and calcium aluminate hydrate (CAH) phases. This provides an initial set to the mortars. Subsequently carbonation of free lime takes place, which is mostly after 14 days (Cizer, 2009).

A combined reaction of hydration and carbonation takes place in lime-metakaolin mortar. Hydration reaction is the first reaction and carbonation of lime is the complementary reaction in the strength gain (Cizer, 2009). Under curing conditions used in the experiment (20ºC and 60%) the

hydration (pozzolanic) reaction prevailed within 28 days while the carbonation reaction prevailed afterwards. Carbonation dominance in hydration/carbonation completion causes the strength reduction in lime-metakaolin mortar during the monitored time period 28-90 days. Regarding LMO results, the addition of oil to lime-metakaolin mortar might inhibit CSH and/or CAH formation that are the main phase responsible for imparting strength to the mortar at early ages.

A possible explanation that can account for the strength improvement in lime mortar and strength reduction in lime-metakaolin mortar is that when oil is added into mortar, triacylglycerols undergo hydration resulting in formation of insoluble calcium salts of fatty acids (Rovnaníková, 2002). Due to their interaction with calcium they are well bounded in the mortar structure and the hydrophobic alkyl chain will cause mortar repellence (Rovnaníková, 2002) and maybe strength improvement in the case of lime mortars. Regarding lime-metakaolin mortar, the formation of insoluble calcium salts may prevent the formation of CSH and/or CAH phases by depleting calcium hydroxide.

3.2. Porosity and capillarity

Concerning density and open porosities although the air content values of fresh mortars with linseed oil addition are much higher than the reference mortars (Table 2), values of porosity of hardened mortars are very similar (Table 3). Hence, a relationship between mechanical properties and porosity cannot be established as it is usually possible (Pandley & Sharma, 2000; Lanas et al., 2003; 2006).

Rovnaníková (2002) achieved similar results on lime mortar enriched with 1% boiled linseed oil, i.e., air content of fresh mortar with linseed oil was significantly higher than that of the reference but hardened mortars had similar open porosity values. Čechová (2009) also obtained similar open porosity results for lime mortar and lime with natural pozzolana mortar three months of age with 1% linseed oil.

The mechanical strength differences cannot be explained regarding the porosity characteristics of hardened mortars nor the water/binder ratio that is also very similar in all mortars. However, the significantly higher air content values of mortars with linseed oil may actually play an important role on the higher rate of carbonation at young ages. In the case of the LO mortar, the high air content may account for the improvement of the carbonation rate by allowing better carbon dioxide diffusion within the mortar matrix.

Although the difference in the air content is very high, no significant changes were detected between curing evaporation curves of reference and modified mortars. However, difference in moisture content between LM and LMO mortars after 90 days was significant: mortar with oil addition has approximately less 3%-w moisture than the reference mortar. Table 8 presents the moisture content determined for 90 days of age mortar specimens by means of their drying at 60ºC to constant mass.

The differences in moisture content of reference and modified mortars may be explained by the pore size distribution curves (Fig. 3). The addition of oil to lime-metakaolin mortar strongly influences the porometry by shifting the size of the pores towards higher values hence promoting higher water evaporation which may account for the lowering of the mechanical strength of LMO mortar. Contrarily, oil addition to lime mortar shifts the pore size towards lower values but the influence is not so significant and the moisture content is not altered.

Tab. 8: Moisture content (average values ± standard deviation) of mortars 90 days of age.

Mortar code	Moisture content [%]
L	0,48 ± 0,06
LO	0,49 ± 0,08
LM	5,67 ± 2,41
LMO	2,77 ± 0,23

Porosity results are very similar between reference mortars and mortars with oil but the capillary coefficients are relevantly different. Capillary coefficient reduction promoted by the addition of oil on

L mortar is approximately 82% and on LM mortar 57% and these features cannot be explained on the basis of the porometry results (Fig. 3). Particularly in the case of lime-metakaolin mortars porometry, LMO pore sizes were shifted towards bigger pores: the peaks related to 0.14 μm and 0.32 μm pores in LM mortar were merged into a narrower unimodal distribution with a stronger peak centered on 0.59μm. The percentage of total intrusion volume remained similar: 32% for LM and 35% for LMO. It could be expected that such a modification of pore size generated by the oil addition would influence the water absorption coefficient taking into account that pores situated around 1μm have the highest effect on capillarity (Barsottelli et al., 2001). However, Wendler & Charola (2008) suggest that water will move by capillary transport only in pore sizes ranging from 10μm to 1mm so, according to these authors, the pore size distribution determined for both mortars will have no influence on water absorption by capillarity.

Nevertheless, the extremely slow capillary water absorption rate of mortars with linseed oil compared to the reference may be rather assigned to the hydrophobic effect of the oil that grants higher contact angle of water on the hydrophobic mortars surface and inhibits water penetration into the voids.

Porometry modification promoted by the addition of linseed oil may however contribute to the reduction of the mechanical strength of lime-metakaolin mortar.

3.3. Thermogravimetric analysis

Lime with linseed oil shows slightly faster carbonation rate up to 60 days of age as it is illustrated by the stronger peaks assigned to calcite formation (~750-800 ºC) and less pronounced peaks assigned to portlandite dehydroxilation (~400-475ºC) in DTG curves (Fig. 5). It can be assumed that the values of calcium hydroxide content are well correlated with mortars compressive strength development.

As abovementioned, in lime-metakaolin mortars, hydration reactions initiate first resulting in the formation of hydrated phases such as CSH and CAH phases. Subsequently carbonation of free lime takes place, which prevails mostly until 28 days of age.

It can be noticed that LM mortar peak concerning the presence of CAH phase (~230ºC) is slightly more pronounced than that of LMO throughout the curing time. CSH peak (~150ºC) is very strong at young ages in LM curve whereas in LMO is less strong but its decomposition is less affected during time. On the other hand, carbonation rate is slightly improved in LMO mortar after 28 days of curing.

Nevertheless, the differences in DTG curves of reference mortars and mortars with oil may be found to influence the mechanical strength negligibly.

3.3. Freeze-thaw resistance

Improved durability of lime mortar with linseed oil addition has been confirmed by testing their freeze-thaw resistance: lime mortar was destroyed after one cycle whereas lime with linseed oil endured ten cycles after which showed visual moderate degradation but mechanical strength significantly decreased. After ageing LO flexural strength value is close to that of lime mortar not aged while compressive strength is two times lower.

Unexpected is that reference samples, which have been kept immersed in water throughout the test, have similar mechanical strength compared to the specimens subjected to the freezing cycles. This behaviour outlines that the freezing test is not affecting significantly the mortar strength but it is rather the prolonged action of water that is probably promoting dissolution of the not-carbonated binder fraction.

Mechanical strength can be related to durability of the mortar: specimens with higher strength (LO) show higher resistance as it is usually reported (Lanas et al., 2006; Botas, 2009; Čechová, 2009). But in the present case this fact is mainly influenced by the hydrophobicity of the mortar that prevents water from penetrating the sample. Capillarity coefficients of the mortars confirm this assumption: the lower the amount of absorbed water, the better the mechanical performance and durability.

The same damage resistance behaviour is expected for lime-metakaolin mortar with linseed oil although its mechanical strength is lower compared to the reference.

4. Conclusions

Mechanical strength and porosity are important indirect parameters to assess mortar durability. In the case of linseed oil addition to lime based mortars the results indicate that the modification of the chemical composition of the mortar can have greater significance for the mortar durability by hindering water intake, thus lessening related problems.

The lower capillarity coefficient, which implies a water intake reduction, may be pointed as the main factor improving the performance of lime mortar with linseed oil exposed to freeze-thaw cycles and hence, its durability. The extremely slow capillary water absorption rate of mortars with linseed oil compared to the reference may be assigned to the hydrophobic effect of the oil that grants higher surface tension to the mortars thus inhibiting water penetration into the voids.

Although previous research studies outlined that oil addition to lime mortars decreases mechanical strength by restraining carbonation, the results obtained in the present study show the contrary. This is possibly due to a combination of different factors, particularly the chemical composition of the oil, the type of binder and the amount of oil added.

Regarding the results of the study by Čechová (2009) showing that linseed oil addition in 1%-w/w and 3%-w/w promotes a marked reduction of mechanical strength (particularly with 3%) it can be assumed that slight modifications on the amount of oil added to the mortar mixture can have great influence on the mechanical behaviour.

In the present study it was highlighted that porosity and carbonation rate has low influence on the mechanical behaviour of mortars with oil 90 days of age. The strength modification may be rather assigned to formation of insoluble calcium salts of fatty acids that are well bounded in the mortar structure improving strength in lime mortar and decreasing it in lime-metakaolin mortar. Furthermore, the new compounds formed by the oil addition seem to promote higher surface tension and prevent water absorption. However, one must take into account that the combination of the small variations determined for each parameter may play a significant role for the obtained modifications on mortar strength. Hence, air content and porometry may be outlined as the most important indirect contributing factors due to their influence in the moisture content during the curing process.

Further research developments focused on the chemistry of the processes will certainly contribute to clarify the questions on mortar strength and durability raised by the results reported.

Acknowledgement

The present study was supported by the Czech national project MK ČR NAKI DF11P01OVV0080 entitled “High Valuable and Compatible Lime Mortars for Application in the Restoration, Repair and Preventive Maintenance of the Architectural Heritage”.

References

Aggelakopoulou, E., Bakolas, A., Moropoulou, A. (2011) Properties of lime-metakolin mortars for the restoration of historic masonries. *Applied Clay Science*, 53, pp.15-19.

Barsottelli, M., Cellai G. F., Fratini, F., Manganelli Del Fà, C. (2001) The hygrometric behavior of some artificial stone materials used as elements of masonry walls. *Materials and Structures*, 34, pp. 211-216.

Čechová, E. (2009) *The effect of linseed oil on the properties of lime-based restoration mortars*. PhD thesis, UB, Bologna.

Cizer, O. (2009) *Competition between carbonation and hydration on the hardening of calcium hydroxide and calcium silicate binders*. PhD thesis, KU, Leuven.

Drdácký, M., Slížková, Z., O'Hagan, J.T. (2011) Non-standard testing and characterisation of mortars from historic masonry. in: *Abstracts of the 9th Australasian Masonry Conference*, J.Ingham, M.Dhanasekar & M.Masia (eds.), Univ. of Auckland, Queenstown , ISBN 978-0-473-18069-0, pp. 50-50 (full paper on CD, pp. 493-502).

Fortes-Revilla, C.; Martínez-Ramírez, S.; Teresa Blanco-Varela, M. (2006) Modelling of slaked lime-metakaolin mortar engineering characteristics in terms of process variables. *Cement and Concrete Composites*, 28, pp.458-467.

Izaguirre, A.; Lanas, J.; Álvarez, J.I. (2010) Ageing of lime mortars with admixtures: Durability and strength assessment. *Cement and Concrete Research*, 40, pp.1081-1095.

Bostock, J. & Riley, H.T.(1857) *Pliny: The natural history*. (translated from Latin to English), Vol. 6, H.G. Bohn, London.

Botas, S.M.S. (2009) *Avaliação do comportamento de argamassas em climas frios (Evaluation of mortars behavior in cold climates)*. Master Thesis, FCT-UNL, Lisbon.

Lanas, J. & Alvarez J.L. (2003) Masonry repair lime-based mortars: factors affecting the mechanical behaviour. *Cement and Concrete Research*, 33, pp.1867-1876.

Lanas, J., Sierra, R., Alvarez, J.I. (2006) Study of the mechanical behavior of masonry repair lime-based mortars cured and exposed under different conditions. *Cement and Concrete Research*, 36, pp.961-970.

Lawrence, R.M.H.; Mays, T.J., Walker P.; D'Ayala D. (2006) Determination of carbonation profiles in non-hydraulic lime mortars using thermogravimetric analysis, *Thermochimica*, pp.179-189.

Maciel, J. (1999) *Vitrúvio: Tratado de Arquitectura*. (Translated from Latin to Portuguese). 3rd Ed., UTL-IST, Lisbon.

Pandley, S.P. & Sharma, R.L. (2000) The influence of mineral additives on the strength and porosity of OPC mortar. *Cement and Concrete Research*, 30, pp.19-23

Oliveira, M. & Santiago, C. (1992) Organic additives in Brazilian lime mortars. in: *Lime and other alternatives cements*, Ed. Neville Hill, S. Holmes, D. Mather, Intermediate Technology Publications, pp.203-210.

Roels, Staf (2000) *Modelling unsaturated moisture transport in heterogeneous limestone*. PhD Thesis, KU, Leuven.

Rovnaníková, P. (2002) *Omítky*. STOP, 80-86657-00-0, Prague.

Sá, A.F.G. (2002) *Argamassa de cal aérea hidratada com incorporação de gordura e sua utilização em rebocos (Air lime hydrated mortars with incorporation of fat to be used as renders)*. Student Monograph, IST-UTL, Lisbon.

Sá, A.F.G. (2005) *Rebocos em Paredes de Pedra e Cal. (Renders in walls of lime and stone).* Master Thesis, IST-UTL, Lisbon.

Slížková, Z. (2009) Charakteristiky malt modifikovaných metakaolinem aplikovaných na historických objektech, in: *Proc. Seminář Metakaolin 2009*, Fakulta stavební VUT v Brně, Brno, pp.146-155.

Stolz, H.J. (2007) Oleochemicals: important additives for building protection, in: *Proc. 2nd National Congress in Building Mortars*, APFAC, Lisbon.

Tavernor, R. & Schofield, R. (1997) *Andrea Palladio: The four books on architecture. 1570*. (translated from Italian to English), MIT, Massachusetts.

Válek, J.; Slížková, Z.; Zeman, A. (2007) Mechanické a fyzikální zkoušky vápenných malt přida vkem metakaolinu a jejich vhodnost pro opravy památkově chráněných objektù. in: *Proc. Seminář Metakaolin 2*, Fakulta stavební VUT v Brně, Brno.

Veiga, R. (2003) As Argamassas na Conservação (Mortars in Conservation). in: *Actas das 1ª as Jornadas de Engenharia Civil da Universidade de Aveiro*. Aveiro University, Lisbon.

Vejmelková, E.; Keppert, M.; Rovnaníková, P; Keršner, Z; Černý, R. (2011) Properties of lime composites containing a new type of pozzolana for the improvement of strength and durability. *Composites: Part B*, doi:10.1016/j.compositesb.2011.11053 (article in press).

Ventolà, L.; Vendrell, M.; Giraldez, P.; Merino, L. (2011) Traditional organic additives improve lime mortars: New old materials for restoration and building natural stone fabrics. *Construction and Building Materials*, 25, pp.3313-3318.

Wendler, E. & Charola, A.E. (2008) Water and its interaction with porous inorganic building materials. in *Proc. Hydrophobe V: 5th International Conference on Water Repellent Treatment of Building Materials*, Aedification Publishers, pp. 57-74.

ČSN EN 1015-11, změny A1 Zkušební metody malt pro zdivo - Část 11: Stanovení pevnosti zatvrdlých malt v tahu za ohybu a v tlaku.

ČSN EN 1936 Zkušební metody přírodního kamene - Stanovení měrné a objemové hmotnosti a celkové a otevřené pórovitosti.

ČSN EN 1015-18 Zkušební metody malt pro zdivo - Část 18: Stanovení koeficientu kapilární absorpce vody v zatvrdlé maltě.

ČSN EN 15801 Ochrana kulturního dědictví – Metody zkoušení – Stanovení nasákavosti vody kapilárním vzlínáním.

ČSN 72 2452 Zkouška mrazuvzdornosti malty.

18th International Conference
ENGINEERING MECHANICS 2012
Svratka, Czech Republic, May 14 – 17, 2012

pp. 969–970
Paper #316

STRESS WAVE PROPAGATION IN THE INSTITUTE OF THEMOMECHANICS.

M. Okrouhlík*

Abstract: *The paper is devoted to a survey of old, recent and contemporary stress wave propagation tasks having been studied in the Institute of Thermomechanics (IT) within the period of the last sixty years. Scientific deeds as well as people who deserve admirations for achieving them are mentioned. Problems and employed analytical and numerical methods are shortly listed.*

Keywords: ***Historical survey, Stress wave propagation in solids, Institute of Thermomechanics.***

Investigation of stress wave propagation in solids was initiated by Rudolf Brepta in sixties of the last century. R. Brepta devoted his attention to analytical approaches based on the Fourier transform applied to spatial variables appearing in governing partial differential equations describing the wave processes in solids, followed by the Laplace transform applied to time variables.

The stress waves were treated within the scope of elastic continuum assumptions, i.e. small displacements and small strains mainly for isotropic elasticity satisfying equations

$$\frac{\partial \sigma_{ji}}{\partial x_j} = \rho \frac{\partial^2 u_i}{\partial t^2}, \quad \varepsilon_{ij} = \frac{1}{2}\left(\frac{\partial u_i}{\partial x_j} + \frac{\partial u_j}{\partial x_i} \right), \quad \sigma_{ij} = C_{ijkl}\, \varepsilon_{kl}\,.$$

At the end of sixties R. Brepta succeeded in building up an efficient team composed of young and enthusiastic people. In quick succession there came, listed in the order of their appearance, J. Beneš, F. Valeš, M. Okrouhlík, H. Šebková, J. Červ, and J. Trnka. Later the team was complemented by E. Veselý, I. Huněk, L. P. Plešek and I. Tvrdík.

The scope of problems having been solved by R. Brepta and by his team is, even by today's standard, impressive. The most significant tasks are listed in chronological order here.

Dispersion of longitudinal waves in prismatic bars of square and rectangular cross-sections, waves in one and two-dimensional lattices, torsional impact on thin discs, longitudinal impact of cylindrical bars, lateral impact of thick plates, transversal impact on a thin strip – F. Valeš, eccentric impact a thin bar – H. Šebková, a thin disc suddenly loaded by a radial point force and torsional impact on a shaft – J. Červ.

In most cases analytical formulas for time distribution of displacements, velocities and stress components were derived, programmed and numerically evaluated.

Later on, at the beginning of seventies, a systematic investigation of side effects and dispersion errors of discrete methods began. The dispersion phenomenon, originally treated by Brillouin, were mainly applied to finite element method approach to the solution of transient tasks in continuum mechanics leading to stiff differential equations whose solutions critically depend on the correct choice of time-step operator and the time step itself.

It appears that the dispersion topic is still alive. Today's investigation of this task in the IT is carried by a representative of younger generation of researchers, namely by Radek Kolman, a bright guy, who substantially contributed not only to the study of dispersion but also to that of isogeometric approach to discretization methods as well as to accuracy analysis of time integration operators.

Now, the stress wave propagation and impact tasks are pursued within a scope of computational mechanics and finite element technology. A substantial enhancement to IT personnel dealing with

* prof. Ing. Miloslav Okrouhlík, CSc., Institute of Thermomechanics AS CR, v.v.i., Dolejškova 1420/5, 18200 Prague 8, CR, e-mail: ok@it.cas.cz

computational mechanics, appeared back in 2003 when – after the SVUSS was dissolved – was the arrival of capable researches equipped with profound engineering skills accompanied by deep knowledge of mechanics, mathematics and programming. At that time J. Plešek, S. Pták and J. Dobiáš came to IT. All of them substantially contributed – among other things – to solving new stress wave tasks, getting new grants, and to subsequent publications of their results in good journals.

As an example one could mention a new contact-search approach implemented in contact impact procedures of PMD (Package for Machine Design – a home-made general finite element code, developed and maintained in IT) developed by Dušan Gabriel. His unique approach is based on the search of contact in Gauss points avoiding thus ambiguity of definitions of corner node normals.

Together with colleagues from Uppsala University a lot of effort was also devoted to efficiency of a percussive rock drilling process with consideration of wave energy radiation into the rock.

Another recent example of improvement of finite element technology – resulting in creating more efficient equation solvers for very large matrices, needed, among other things, for solution of transient tasks – is a new efficient code developed by P. Pařík based on fill-in minimization.

Computational skills, needed for solving complicated problems of engineering practice – included those related to fast transient tasks – are being constantly amended and revised. A comprehensive educational text, based on our experience, concentrating on classical and new computational methods was compiled recently.

Also our experimental colleagues who contributed to progress in understanding the nature of stress wave propagation should be mentioned. One of the founding fathers was M. Prokopec, who was Brepta's coauthor of the first Czech book devoted to stress wave propagation. J. Beneš, E.Veselý, J. Trnka and Z. Převorovský were his successors.

References

Okrouhlík, M. (2003) Rudolf Brepta – his life, work and people around him, Bulletin CSM, Vol. 2/2009. For extensive list of references see: http://baobab.cdm.cas.cz/brepta.

Lundberg, B., Okrouhlík, M. (2006) Efficiency of a percussive rock drilling process with consideration of wave energy radiation into the rock. *International Journal of Impact Engineering*. 32 (10) , pp. 1573-1583.

Okrouhlík, M. editor (2008) *Numerical methods in computational mechanics.* Institute of Thermomechanics, Prague, ISBN 978-80-87012-35-2.

18th International Conference
ENGINEERING MECHANICS 2012
Svratka, Czech Republic, May 14 – 17, 2012

pp. 971–974
Paper #169

CREEP SIZE EVOLUTION OF CEMENT PASTE PREPARED FROM PORTLAND CEMENT WITH CONTENT OF FLY ASH

P. Padevět[*], P. Bittnar[**]

Abstract: *The cement paste is basic part of concrete and may contain various additives. Fly ash is one of materials useable as an admixture in cement paste and concrete. Changes of properties of cement paste mixed with fly ash were observed during several months. Creep of dried and saturated cement paste was measured for one complete month. The measured data was evaluated and compared with results of computational model with a creep model B3.*

Keywords: ***Cement paste, creep, shrinkage, fly ash, B3 model of creep.***

1. Introduction

Among one of the hot topic waste materials the fly ash can count as well. The power plants in the Czech Republic produce annually 8 million tons of fly ash. Fly ash is generated as the secondary product by burning brown coal in the lignite power plants. The generated quantity of the fly ash is between 10 % and 30 % of the original volume of burned coal. From the perspective of chemistry, the fly ash is an inert material; the main component is SiO_2 and Al_2O_3 and CaO and SO4, suitable for building material. Conventional fly-ash contains up to 80 % glass phase, as the main component. Sulfur content (expressed as SO_3) usually does not exceed 1 %. In the high-temperature combustion of coal, it is not necessary to add ground limestone into burnt mixture.

The basic properties of cement paste can be described by material characteristics. One of these material properties is creep – especially basic creep. On the other hand, it is important to write that basic creep is not the most important characteristic in designers work. But in many cases the size of creep is the very important feature in the design of civil structures.

This paper is focused on properties of cement paste containing fly ash as an additive, not as like an activator. The characteristics of the cement paste mixed with ash from power plants have been defined in several previous works, e.g. (Padevět & Bittnar 2009). Tensile bending strength of cement paste with addition of fly ash reaches higher values than the pure cement paste. Very good values of tensile strength in bending were achieved when the weight ratio of cements and fly ash was 1:1.

2. Specimens and their preparation

The water/cement ratio was chosen 0.4. The content of 40 % of the quantity of water in cement allows a very good workability and also no segregation of cement in the initial phase of the cement hydration. Portland cement CEM I 42.5 R was used for production of specimens (Padevět & Bittnar 2009), cement without additives. The main attention was focused to amount of fly ash added to the mixture. As described above, very good material properties were achieved with a weight ratio of fly-ash and cement 50: 50.

The experiment was conducted with two types of specimens, one month and five months old cylinders of the same type. The value of creep was measured for 32 and 36 days. The ambient temperature was controlled between 19 – 20 °C with a maximum deviation of ±1 °C.

[*] Ing. Pavel Padevět, Ph.D.: Faculty of Civil Engineering, Czech Technical Unicersity in Prague, Thákurova 7; 166 29, Prague; CZ, e-mail: pavel.padevet@fsv.cvut.cz

[**] Ing. Petr Bittnar,.: Faculty of Civil Engineering, Czech Technical Unicersity in Prague, Thákurova 7; 166 29, Prague; CZ, e-mail: petr.bittnar@fsv.cvut.cz

3. Results

In the each set of specimens were two pieces dried and two pieces saturated with water. Basic creep was determined as the difference between creep and shrinkage. Differences between sizes of creep for various aged specimens are described in figure 1 - 4.

All specimens were loaded by plumbs during whole experiments. Between Fig. 1 and 2 (3 and 4 too) is viewable difference in first days. For dried specimens is characteristic instant increasing of the deformation and slowing increasing of deformation in next days. Deformation of water saturated specimens is increases gradually from start of loading.

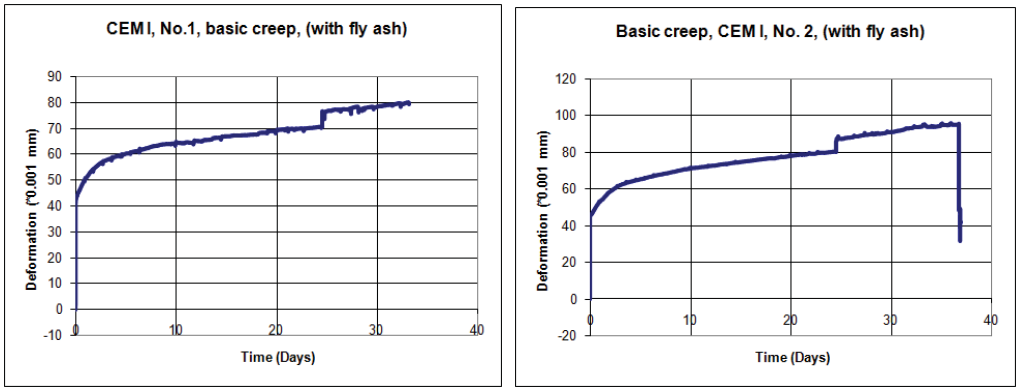

Fig. 1: Basic creep of dried specimens (in 1 month age).

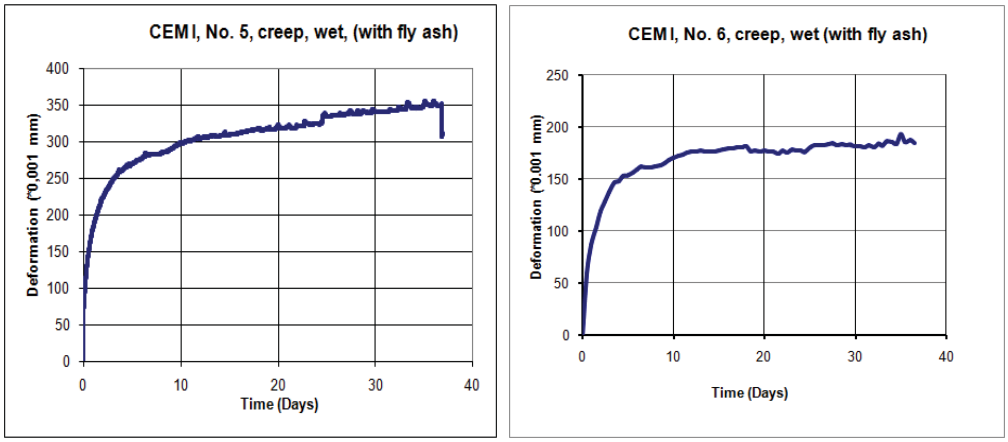

Fig. 2: Creep of water saturated specimens (in 1 month age).

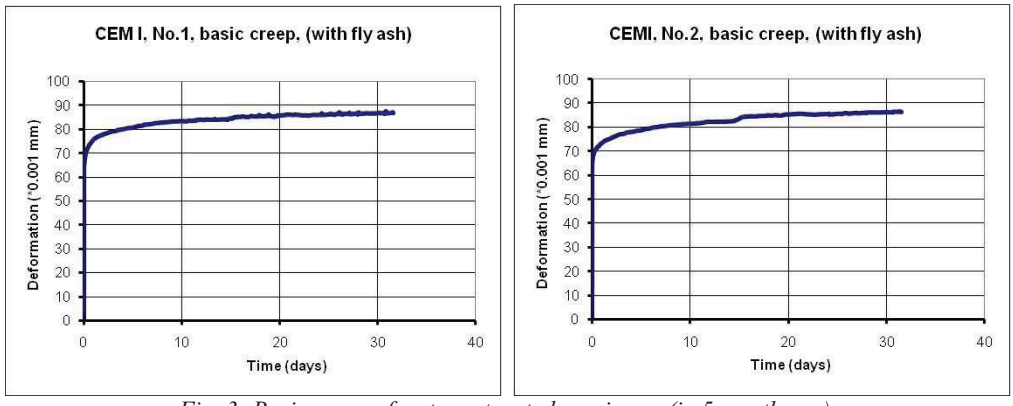

Fig. 3: Basic creep of water saturated specimens (in 5 month age).

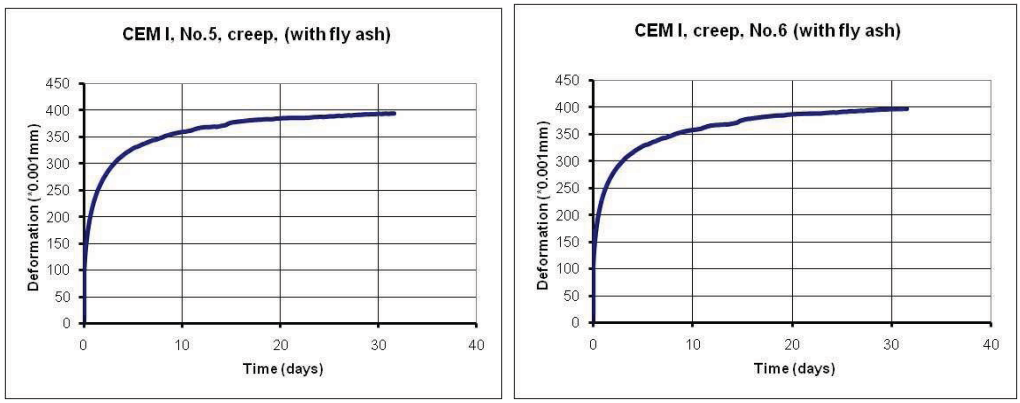

Fig. 4: Creep of water saturated specimens (in 5 month age).

Fig. 1:Basic creep of dried specimens (left – in 5 months age, right – in 1 month age).

Tab. 1: Size of creep (in microns) after 25 days.

Condition	1 month old specimens	5 month old specimens
dried	27	16
dried	37	17
saturated	225	225
saturated	130	220

4. Conclusions

The graphs show that the basic creep range is from value 25 to 30 microns over 25 days.

Water-saturated specimens (Van Mier 1997) reach very high values of creep size. Creep of these specimens (without the influence of shrinkage) reached values between 130 to 225 microns after 25 days. The age of the specimens has a significant influence on the size of creep at the initial stage of measurement. Basic creep of dried specimens shows differences in its size. This size depends on the age of cement paste. Size of creep is reduced with increasing age. In all cases, measurements of deformation solids, the increase was steepest during the first 5 days.

In the past, compliance tests were conducted by simulations of creep of the pure cement paste model B3 (Bažant, Baweja 1995). By simulation of the creeping cement paste mixed with the fly ash it is possible to achieve a good agreement between the model and the real measurements, although simulation is designated for concrete primary.

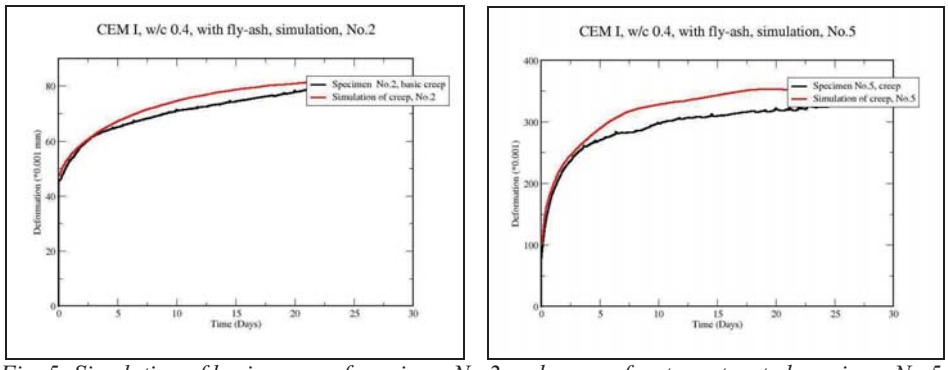

Fig. 5: Simulation of basic creep of specimen No.2 and creep of water saturated specimen No.5.

Acknowledgement
This work was supported by project GACR underNo. P104/11/2285.

References

Padevět P., Bittnar P., (2009) Measuring of Creep of Cement Paste Specimen, *Proceedings of the 2nd WSEAS International Conference on Applied Mathematics, Simulation, Modeling (ASM'09),* Athens, Greece, pp. 33-39.

Bažant, Z.P., Baweja, S., (1995) Creep and Shrinkage Prediction Model for Analysis and Design of Concrete Structure – Model B3, *Materials and Structures,* Vol. 28, pp. 357-365.

Van Mier, J.G.M., (1997) *Fracture Processes of Concrete* CRC Press, ISBN 0-8493-9123-7.

18th International Conference
ENGINEERING MECHANICS 2012
Svratka, Czech Republic, May 14 – 17, 2012

pp. 975–977
Paper #254

THE DEVELOPMENT OF THE SIZE OF FRACTURE ENERGY OF CEMENT PASTE WITH FLY ASH IN THE TIME

P. Padevět[*], O. Zobal[**]

Abstract: *The size of fracture energy of cement paste reaches values other than cement paste without admixtures. The cement paste increases the strength values in time. Paper describes experimental investigation on the field of material properties of cement paste, especially fracture energy.*

Keywords: ***Cement paste, Fracture Energy, Tensile Strength, Fly-ash, Bend Test, Prism Specimen.***

1. Introduction

The cement paste is material based only on two parts; water and cement (Neville, 1997). Properties of cement pastes are relatively well known. Particular, the compressive strength depends on the water/cement ratio w/c. Equally, an important factor for compressive strength, the water content in the material. Increasing the amount of water in cement paste allows the maturation of the cement paste.

Nowadays, much attention is focused on processing of waste materials. Very good usable waste material can be fly ash. This material is generated by burning coal to produce electricity in coal-fired power plants. This paper aims to evaluate the changing properties of cement paste if is into the paste added component of waste – fly-ash, typically.

2. Specimens

The advantage of the cement paste is the homogeneity. Homogeneous fine-grained materials are suitable for testing in smaller testing equipments. Therefore, the preparation of specimens was selected type of form 20 x 20 x 100 mm. Portland cement CEM I 42,5 R was used for production of specimens. Because the intention was not to use a plasticizer, was selected water-cement ratio 0.4. Grout with a water/cement ratio beyond the specified limit has high fluidity, which may cause segregation of cement and water. On the other hand, the grout may be too rigid and treated by practically no plasticizer. Consistency of 0.4 was chosen as a tougher type of cement paste. Specimens of cement paste were stored in the water basin for about 30 days. The specimens were removed from the water two days before testing. Subsequently, specimens were dried for 48 hours at 60 °C. Specimens prepared from fly ash and cement paste had w / c factor of 0.4.

3. Testing of specimens

Fracture energy was measured in the tests performed using the three-point bending test. Distance support the specimen was 80 mm. The notch was located in the middle of the range below the point where the applied load. To assessment the test were required two parameters, strength and vertical deflection of the specimen. For those of parameters it is possible to calculate the fracture energy of the test specimen. Before the tests were measured dimensions of each specimen.

Execution of experiments was carried out in the test machine MTS Alliance RT 30kN (Padevět, 2009). It is an electromechanical testing machine with a very subtle shift in the crosshead. By using relatively small specimens can achieve the desired results the test method.

[*] Ing. Pavel Padevět, Ph.D.: Faculty of Civil Engineering, Czech Technical Unicersity in Prague, Thákurova 7; 166 29, Prague; CZ, e-mail: pavel.padevet@fsv.cvut.cz

[**] Ing. Ondřej Zobal,.: Faculty of Civil Engineering, Czech Technical Unicersity in Prague, Thákurova 7; 166 29, Prague; CZ, e-mail: ondrej.zobal@fsv.cvut.cz

4. Results

The data obtained from tests carried out are summarized in graphs. The resulting graphs are shown in Fig.1. In the loading phase the specimen, there is a linear increase deformation of and strength. After reaching almost 90% strength is accelerate our growth deformation of the specimen. After reaching the ultimate strength is increasing with little deformation of to steep reduction strength of material.

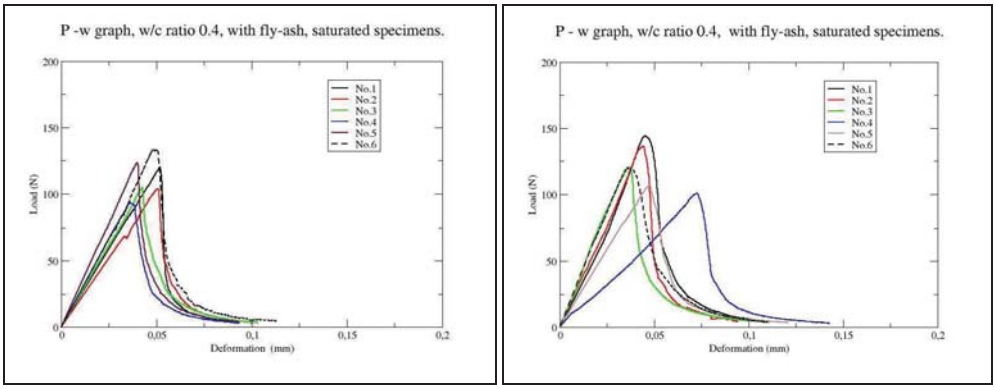

Fig. 1: P-δ graphs of water saturated specimens prepared using C/A 0.5/0.5 (left) and C/A 0.4/0.6(right).

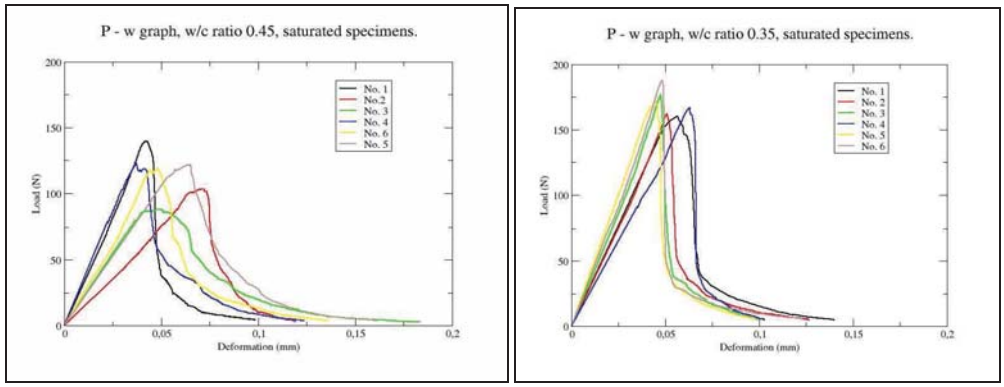

Fig. 2: P-δ graphs of water saturated specimens prepared using w/c 0.45 (left) and w/c 0.35(right) without fly ash.

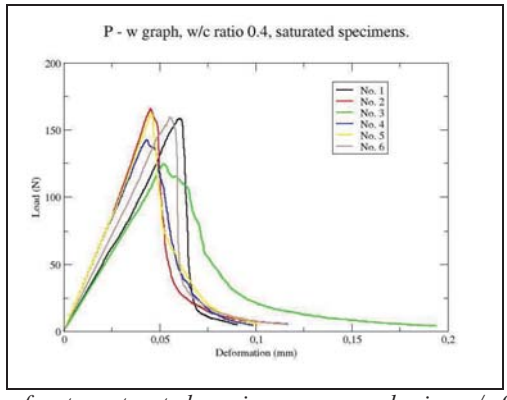

Fig. 2: P-δ graphs of water saturated specimens prepared using w/c 0.4 without fly ash.

Tab. 1: Fracture energy of cement paste.

w/c	Relation cement/fly ash	Fracture energy (N/mm)
0.4	0.5/0.5	16.66
0.4	0.4/0.6	18.73
0.35	--	26.74
0.40	--	24.13
0.45	--	22.02

5. Conclusions

Very interesting is the decrease of fracture energy of cement paste containing fly ash. Fracture energy for water-saturated specimens decreased by 18%, depending on the water / cement ratio increased from 0.35 to 0.45. Decline in value is up 30 % towards the value for the corresponding w/c ratio. Very interesting fact is the increasing value of fracture energy of cement paste, which contained a lower amount of cement and higher amount of ash. In conclusion, the value of fracture energy of cement paste with fly ash varies from 17 to 19 N/mm. On the other side fracture energy of cement paste without fly ash achieves values between 22 and 26.7 N/mm. The direct effect of humidity on the size of the fracture energy of cement pastes was not proved.

By contrast, significant changes in the fracture energy of cement paste in tensile strength, bending strength were no major changes. Comparison with values for w/c ratio we record a decrease of, but it is also depending on the amount of fly ash in the cement paste.

Reducing the strength of cement paste containing fly ash corresponds to the reduction volume weight. A very significant factor that has a definite influence on the mechanical properties of cement paste is the amount of fly ash in the mixture. Quantity ash is influencing factor in the case of fracture energy.

Acknowledgement
This work was supported by project GACR under No. P104/11/2285.

References

Padevět P., Bittnar P., (2009) Measuring of Creep of Cement Paste Specimen, *Proceedings of the 2nd WSEAS International Conference on Applied Mathematics, Simulation, Modeling (ASM'09),* Athens, Greece, pp. 33-39.

Neville, A.M., (1997) *Properties of Concrete*, John Wiley & Sons, (1997), ISBN 0-470-23527-6.

18th International Conference
ENGINEERING MECHANICS 2012
Svratka, Czech Republic, May 14 – 17, 2012

pp. 979–982
Paper #168

VIBRATIONS OF THE SLENDER ROD INDUCED BY THE TURBULENCE IN THE COOLANT FLOW

L. Pečínka[*], M. Švrček[**]

Abstract: *The theoretical model is presented. The vibrations are proposed to be random nature and are caused by random pressure fluctuation in the turbulent boundary layer surrounding the rod. The mean square of the amplitude of rod deflection is expressed using frequency response function to distributed loading and the spatial correlation density of the pressure fluctuations. The general expressions is derived and applied to slender rod with boundary condition pinned-pinned.*

Keywords: ***Fundamental frequency, frequency response function, transverse forces, spatial correlation density.***

1. Introduction

In the operation of nuclear power plants the fuel assenblies are surrounded by the axial turbulent flow and in consequence of pressure fluctuations acting on its surface. The problem is this one of random vibrations. In general several types of forces exists as follows

- the pressure forces which are considered to be independent of rod motion.
- the damping forces which are dependent on the lateral velocity of the rod
- the inertie forces which are dependent on the acceleration
- the elastic restoring forces which are dependent on the stiffness.

Special type of kinematic excitation represents independent mutual motion of upper and lower supports. This one is not included in this model.

2. Basic equations

Under the suppositions discussed in the previous chapter it can be shown that the mean square of the amplitude of deflection at the centre of the rod may be expressed as follows (Thomson 1965)

$$\langle y^2(t)\rangle = \frac{1}{M\omega_1^4}\int_0^{+\infty} H(f)H^{\star}(f)df \int_0^L\int_0^L R_f(x,x',f)\phi_1(x)\phi_1(x')\,dxdx' \qquad (1)$$

Where M ….. mass of the rod

ω_1 …. fundamentals circular frequency of the rod to distubuted loading

$H(f)$ … frequency response function of the rod to distributed loading

$H^*(f)$… komplex conjugate of $H(f)$

L …. length of the rod

ϕ_1 …. fundamentals mode of the rod

x, x'…. space variables

t …… time

[*] Ing. Ladislav Pečínka, CSc.: Institute Nuclear Research Institute Rez, Husinec-Rez 130, 250 68, CZ, e-mail: pel@ujv.cz

[**] Ing. Miroslav Švrček, : Institute Nuclear Research Institute Rez, Husinec-Rez 130, 250 68, CZ, e-mail: smi@ujv.cz

$R_f = \langle F(x,t)F'(x',t)\rangle$ where $F(x,t)$ and $F(x',t)$ denote values of the transverse forces at points x and x´ respectively at time t and the symbol $\langle\ \rangle'$ denotes time average per unit bandwith in this case at frequencyf. The term per unit bandwith is related to frequency under analysis.

For the evaluation of the spatial correlation R_f we will concentrate attention on the component of vibration in the plane containing cross section A-A, see Fig.1: Let us suppose unity of the rod length and homogeneous pressure field surrounding the rod. If we denote pressure diference between any point on the rod surfaře and a point diametrally oposite as „p“ and let positive „p“ is associated with the force directed toward the upper half on the figure then the force directed upward in the interval $d\theta$ is $F = pD/2\cos\theta\, d\theta$. Similarly the force on the interval $d\theta' is F' = pD_0/2\cos\theta'\, d\theta'$.

Based on the principles of integral calculus it is evident that the time mean square of the force F acting on the rod in the plane containing cross section A-A per unit rod length and per unit bandwith is

$$\langle F(x,t)F(x,t')\rangle' = \frac{D_0^2}{4}\int_{-\pi/2}^{\pi/2}\int_{-\pi/2}^{\pi/2}\langle \rho(x,\theta,t)\rho(x,\theta',t)\rangle' \cos\theta\cos\theta'\, d\theta\, d\theta' \tag{2}$$

Reavis (1967) postulated that exists a such positive value of α that we can suppose following approximation

$$\langle p(x,\theta,t)(p/x,\theta',t)\rangle' = \langle p^2(x,t)\rangle' e^{-\alpha|\theta-\theta'|} \tag{3}$$

Substituting (3) into (2) as the result we obtain

$$\langle F^2(x,t)\rangle' = \frac{D_0^2}{4}\langle p^2(x,t)\rangle' \int_{-\pi/2}^{+\pi/2}\int_{-\pi/2}^{+\pi/2} e^{-\alpha|\theta-\theta'|}\cos\theta'\cos\theta\, d\theta'\, d\theta \tag{4}$$

$$= \langle p^2(x,t)\rangle D_0^2\psi_D^2 \tag{5}$$

where

$$\begin{aligned}\psi_D^2 &= \frac{1}{4}\int_{-\pi/2}^{\pi/2}\int_{-\pi/2}^{\pi/2} e^{-\alpha|\theta-\theta'|}\cos\theta'\cos\theta\, d\theta\, d\theta' \\ &= \frac{1}{4(\alpha^2+1)}\left\{\alpha\pi + \frac{2}{\alpha^2+1}\left[1+e^{-\alpha\pi}\right]\right\}\end{aligned} \tag{6}$$

and represent effective rod diameter squared to actual rod diameter squared.

In eq. (5) the force $\langle F^2(x,t)\rangle'$ is expressed in terms of $\langle \rho^2(x,t)\rangle'$. It means that the peripherally distributed pressure loading is converted into a concentrated force loading.

From the supposition of the homogeneous boundary layer we can deduce that equation (3) depend not only on angles $|\theta-\theta'|$ but also on the coordinates $(x-x')$. It means that the following equation may be written

$$\frac{\langle F(x,t)F(x',t)\rangle'}{\langle F^2(x,t)\rangle'} = \frac{\langle p(x,t)\rho(x',t)\rangle'}{\langle p^2(x,t)\rangle'} \tag{7}$$

Based on the Gorman experiments (Gorman 1969) equation (7) may be rewritten as follows

$$\frac{\langle p(x,t)p(x',t)\rangle'}{\langle p^2(x,t)\rangle} = e^{-\alpha|x-x'|}\cos\beta(x-x') \tag{8}$$

where parameter α is different from α in equation (6). The following values are valid: $\alpha = 0.6$, $\beta = 1.0$.(Gorman 1969). Putting eq. (8) into eq. (1) and after simple rearrangement we can written

$$\int_O^L\int_O^L R_f(x,x',t)\varphi_1(x)\varphi_1(x')dx\,dx' = \\ = D_0^2\psi_D^2\int_O^L\int_O^L\langle p(x,t)\,p(x',t)\rangle\varphi_1(x)\varphi_1(x')dx\,dx' \tag{9}$$

and as the result we obtain

$$\langle y^2(t)\rangle = \frac{D_0^2\Psi_D^2}{M\omega_1^4}\langle p^2(x,t)\rangle'\int_0^{+\infty}\mathrm{H}(f)\mathrm{H}^*(f)df\int_0^L\int_0^L e^{-\alpha|x-x'|}\cos\beta(x-x')* \\ *\varphi_1(x)\varphi_1(x')dx\,dx' \tag{10}$$

3. Application on the slender rod with boundary condition pinned pinned

In this case the double integral in eq. (10) takes the form

$$\Psi_L^2 = \int_O^L\int_O^L e^{-\alpha|x-x'|}\cos\beta(x-x')\sin\frac{\pi x}{L}\sin\frac{\pi x'}{L}dx\,dx'$$

and finally

$$\langle y^2(t)\rangle = \frac{L^2D_0^2}{M\omega_1^4}\Psi_D^2\Psi_L^2\langle\rho^2(x,t)\rangle\int_O^{+\infty}\mathrm{H}_1(f)\mathrm{H}_1^*(f)df \tag{11}$$

Based on given boundary conditions and eq. (5), the integral in eq. (11) takes the form

$$\mathrm{I} = \int_O^{+\infty}\frac{\Omega^4 + 4D^2\Omega^2\omega^2}{\left[\left(\Omega^2-\omega^2\right)+i2D\Omega\omega\right]\left[\left(\Omega^2-\omega^2\right)-i2D\Omega\omega\right]}d\omega \tag{12}$$

The general glutation of eq. (12) is given in (4) and takes the form

$$\mathrm{I}_n = \int_O^{+\infty}\frac{\mathrm{P}_n(x)}{Q_n(x)Q_n(-x)}dx \tag{13}$$

where

$$\mathrm{P}_n|x| = A_0x^{2nL} + A_1x^{2n-4} + \ldots + A_{n-1}$$

$$Q_n|x| = B_0x^2 + B_1x^{n-1} + \ldots + B_n$$

For $n = 2$ the following expression is valid (Prudnikov 1981)

$$\mathrm{I}_2 = -\frac{\Pi i}{B_o}\frac{A_0 B_2 - A_1 B_0}{B_1 B_2 - B_3 B_0}$$

Since $B_0 = -1, \quad B_1 = i2D\omega, \quad B_2 = \Omega^2, \quad A_0 = 4D^2\Omega^2, \quad A = \Omega$

As the result obtain

$$\mathrm{I}_2 = \frac{\Omega}{4D}\left(1 + 4D^2\right) \doteq \frac{\Omega}{4D} \quad for\ D \langle\langle 1$$

And finally

$$\left\langle y^2(t)\right\rangle = \frac{L^2 D_0^2}{M\omega_1^4}\Psi_D^2\Psi_L^2\left\langle \rho^2(x,\mathrm{H})\right\rangle \frac{\pi f_1}{4D} \tag{14}$$

Conclusions

This paper represent theoretical analysis of the effects of boundary layer turbulence on fuel rod vibrafon. Some results of experimental investigations has been used. We will continue in this effort as follows

- Numercial evaluation of the values Ψ_L^2
- Assessment of mean square of the rod amplitude for the fuel rod of fuel assembly TVSA-T
- Application on the fuel assembly TVSA-T of NPP Temelin.

Preliminary numercial assessment showed that $\left\langle y(t)\right\rangle_{rms} = 3.04\mu m$

References

Thomson W.T. (1965) *Vibration Theory and Applications* Prentice Hall, New Jersey.

Reavis J.R. (1967) WVI – Westinghous Vibration Correlation for Maximum Fuel Element Displacement for Parallel Turbulent Flow *Thirteen Annual Meeting Americal Nuclear Society, June.*

Gorman D.J. (1969) *The Role of Turbulance in the Vibration of Reactor Fuel Element in Liquid Flow* Advanced Engineering Branch, Chalk River, Ontario , Rept. No AECL-3371.

Prudnikov A.P. et al. (1981) *Integrals an Series* Nauka Publishing, Moscow, Serie Mathematics and Physics, in Russian Language only

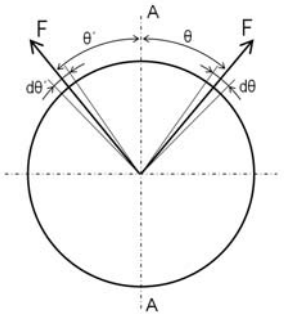

Fig. 1: Cross section A-A

18th International Conference
ENGINEERING MECHANICS 2012
Svratka, Czech Republic, May 14 – 17, 2012

pp. 983–988
Paper #281

LABORATORY OPTICAL MEASUREMENT OF MODEL BLADE VIBRATION UNDER ROTATION

L. Pešek, F. Vaněk, V.Bula, J.Cibulka*, B.Tryzna**

Abstract: *The optical method for the accurate laboratory measurement of blade vibration under rotation was proposed in IT AS CR. This method is based on the fast optical-elements that register time passages of the blades. The description of the method and first experimental results of the model blade vibration under rotation will be discussed.*

Keywords: ***blade, tip timing, optical measurement.***

1. Introduction

The turbine blade and blade disc dynamics research started in the laboratory Vibrodiagnostics and non-linear dynamics, IT AS CR in late 70th years of the last century with turbine blade development and testing in Skoda Works, Plzen. After 1989 the blade disc research was first aimed on vibration diagnostics of blades in service and their residual life estimation Daněk et al. (1993,2001). The latest research of dynamic behaviour of blade discs deals with non-linear blade couplings and usage of high-damping materials Pešek et al. (2008, 2009 and 2010).

For laboratory accurate contactless measurements of blade vibration under rotation the new optical method based on the optical displacement sensor was developed in IT AS CR. At first the optical sensor was assembled and tested under a static condition. Then the time responses of the sensor was tested under rotation and at last the circumferential vibration of the model blade wheel was evaluated. For the evaluation of the circumferential displacement of the blades the tip-timing method was used.

2. Design and static calibration of the optical sensor

The optical displacement sensor consists of minilaser FP-65/1A-LWL-SMA with the emissive power 10mW coupled with the optical fiber and the light beam detector Si-PIN diod SD200-11-31-241 with circular surface (∅5 mm) and response time 8ns. Homogennous parallel light beam transmission from the optical fibers is ensured by the collimators F-C5-S2-543 placed on the free ends of the fibers. For the light transmission between the laser and the collimator and the collimator and the PIN DIODE the optical multimode fibers ended by SMA connectors on both sides of the fibers.

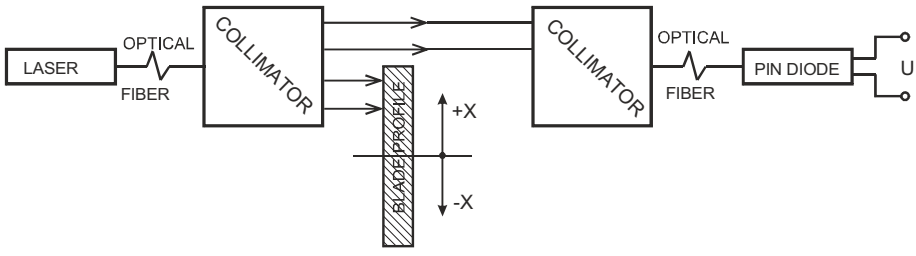

Fig.1 Scheme of the optical sensor measurement

* Ing. Luděk Pešek, CSc., Ing. František Vaněk, CSc., Ing. Vítězslav Bula, Jan Cibulka: Institute of Thermomechanics AS CR, v.v.i., Dolejškova 5, 18200 Praha 8, e-mail: pesek@it.cas.cz.

** Ing. Bohuslav Tryzna, CSc., Zálesí 1074, 14200 Praha 4, e-mail: b.tryzna@seznam.cz.

The output voltage change of the light detector is proportional to the intersection of the laser beam foot mark and the blade profile. Transfer relations between the output voltage and the incursion of the profile into the beam foot mark was ascertained by the calibration of the sensor by means of the x-y coordinate table SOND A1 with a step 0,01 mm (Fig.2).

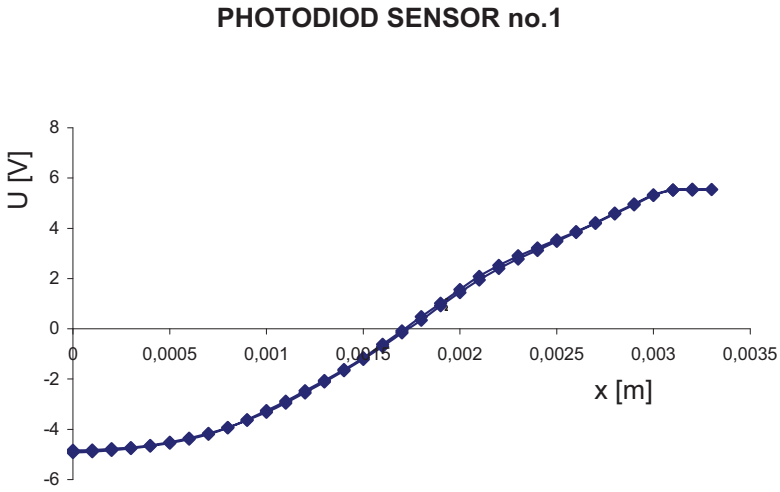

Fig.2 Output voltage of the light detector versus the blade incursion into the beam light

3. Experiment under rotation

The fixtures of the optical sensor were manufactured for the dynamic calibration on the test blade wheel. The cut view of the tested bladed disc with the electromagnet (EM) and the optical displacement sensor (ODS) is shown in the Fig.3. Diameter of the disc was ∅505mm. The disc is equipped with sixty prismatic beam blades (190mm length). The picture of the ODS set-up is visible on the Fig.4.

The strain-gauge was glued on the side surface of the blade at its root for measuring of the circumferential displacement. Its calibration was performed by the acceleration measurement of the blade tip at the impact excitation. The electromagnet UTM4 (Fig.3) excited the blades under rotation. The components of the electromagnetic force are both in axial and circumferential directions of the wheel (Pešek, 2009). Due to the position of the magnet, however, the axial force prevailed over circumferential force. Therefore for maximizing the excitation effect in the circumferential direction, the excitation frequency was tuned to the resonance frequency 332Hz of the first circumferential flexural mode of the blade and the revolution speed was set to the value 83rpm corresponding the 4^{th} engine order excitation.

The strain gauge, ODS, supply current of the electromagnet and phase mark signals of the forced vibration of the blade B30 were recorded with a sampling frequency 2MHz by the digital oscilloscope YOKOGAWA DL750.

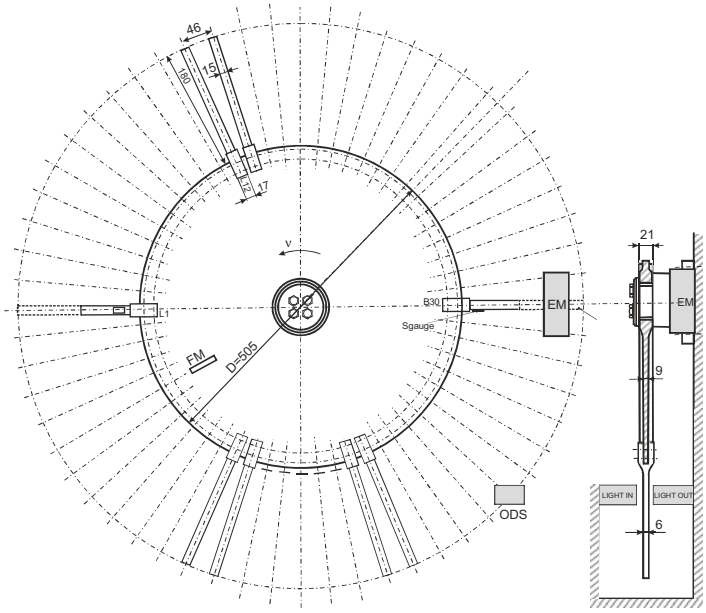

Fig.3 Sketch (front and side views) of the blade wheel with the electromagnet excitation (EM), strain gauge (Sgauge) and optical displacement sensor (ODS).

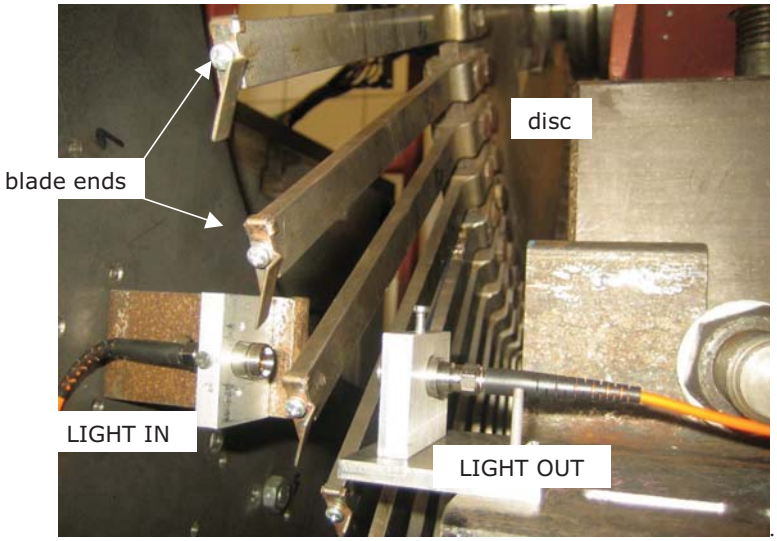

Fig.4 Picture of the experimental set-up.

First the time characteristics of the output voltage of the DIODE detector without the collimator and optical fiber were analyzed without the electromagnetic excitation for different revolution speeds (300, 700, 800rpm). The optical sensor ODS placed on the stator registered time passages of all blades. The results of voltage characteristics transformed from time to angle-position dependences are depicted for the six blade passage in the Fig. 5. Despite the high response time of the DIODE detector, the dependence of the characteristics on the revolution speed appears. Nevertheless the gradient of the diode opening and closing remains almost same in the operating range of speeds.

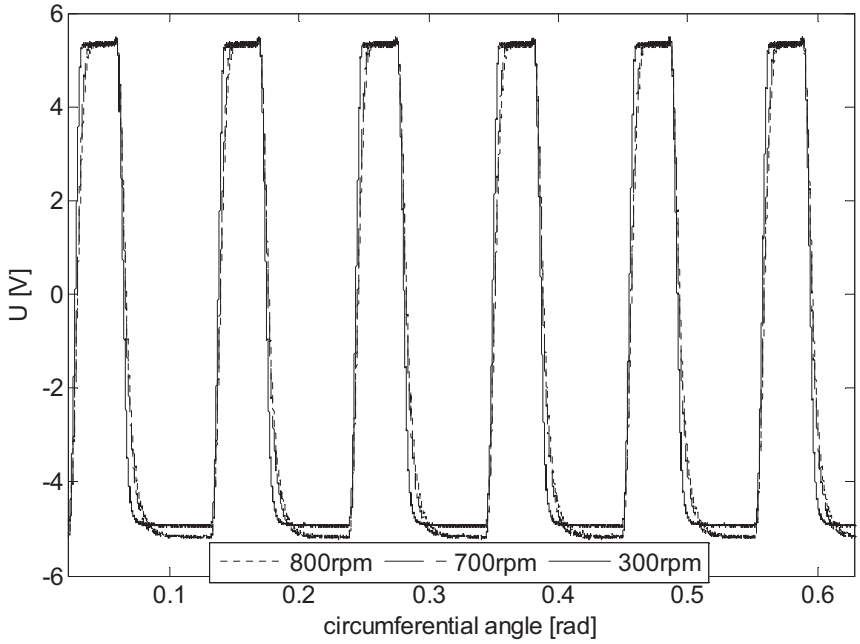

Fig.5 Position versus voltage dependences of the ODS sensor for 300, 700 and 800rpm in the period of the first six blades' passage.

After the analysis of the DIODE detector characteristics under rotation, the optical sensor (Fig.1) was tested for the blade vibration evaluation at the electromagnetic excitation. Besides the optical measurement of the blade passages, the passages of the rigid wheel with 60 notches were registered at the same time. Then the circumferential displacement Δv_{ij} of each blade tip *i*=1,2,..,60 was evaluated from the time differences $\Delta t_{ij} = t_{ijB} - t_{ijR}$ of the leading edge arrivals t_{ijB} of the blade passages and the leading edge arrivals t_{ijR} of the corresponding notch in each revolution *j*=1,2,..,n of the wheel. The displacements Δv_{ij} can be calculated from Δt_{ij} using the simple kinematic relation (Pešek, 2008)

$$\Delta v_{ij} = \Delta t_{ij} \dot{v}_{ij} = \Delta t_{ij} 2\pi f_{ij} r \,, \tag{1}$$

where f_{ij} is a revolution frequency (Hz), *r* is a distance of the ODS sensor from the rotation axis. The revolution frequency is evaluated from differences of trigger times of the phase mark for each revolution. The measured data were processed by the numerical program developed in the MATLAB.

The amplitude spectrum of the blade B30 vibration is drawn in the Fig. 6. The component of the circumferential vibration of amplitude 3μm and frequency 338Hz is close to the resonant frequency 332Hz. The level of vibration, however, was very low almost on the noise level of the strain-gauge measurement. Therefore for the time result comparison with the ODS measurement, the strain-gauge signal was substituted by the "noise-free" sinus characteristic with frequency 338Hz and amplitude 3 μm. The comparison of the ODS displacement of the blade B30 with the "filtered" and downsampled strain-gauge displacement is shown in the Fig.7. The downsampling is inevitable because the ODS blade displacement characteristic is sampled only by the revolution frequency for the configuration of one sensor on the whole perimeter.

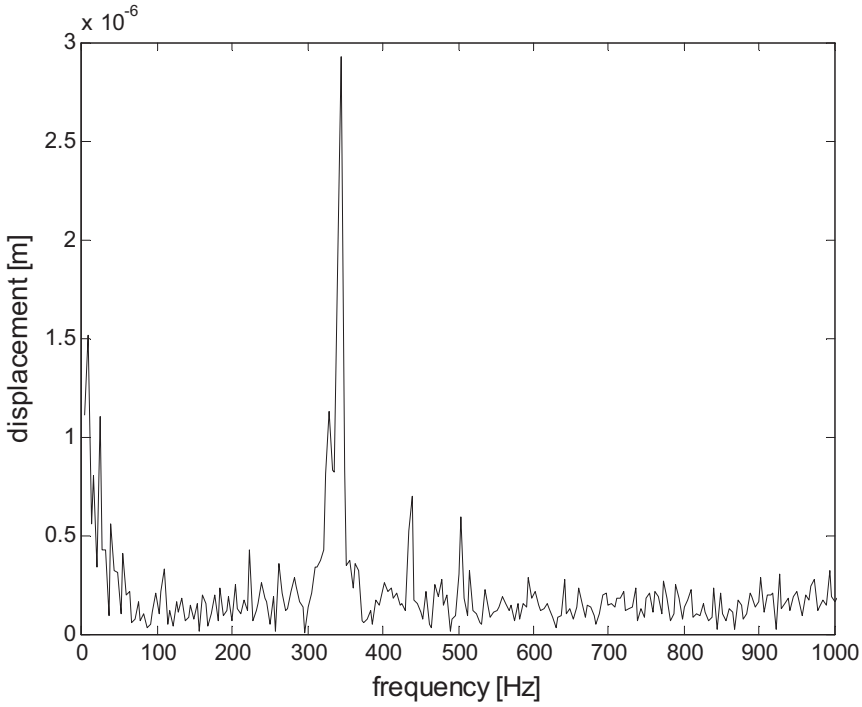

Fig.6 The amplitude spectrum of the blade B30 vibration.

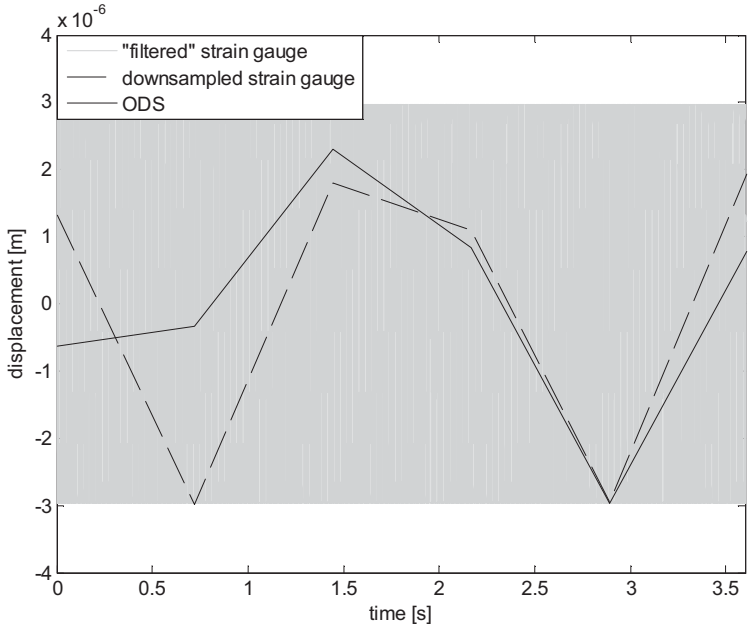

Fig.7 ODS and strain-gauge (filtered and downsampled) displacement time characteristics of the blade B30 at electromagnetic excitation and revolution 83rpm.

4. Conclusion

The new laboratory optical method for evaluation of displacements of rotating and vibrating blades was designed and implemented. The first results of the optical measurement of the blade vibration in non-rotating and rotating states were presented. The displacement of the blades were evaluated by the tip-timing method. The results were compared with the strain-gauge results of the blade vibration. The circumferential amplitudes of blade vibration caused by the weak electromagnetic excitation was very low (cca 3μm) under rotation. Nevertheless the vibration was detected by the optical measurement. The optical method will be futher tested for accurate contactless measurements of blade vibtration and callibrations of the sensors for vibrodiagnostics of the turbine blades.

Acknowledgement

This work has been elaborated in a frame of the grant project GA CR 101/09/1166 "Research of dynamic behavior and optimization of complex rotating system with non-linear couplings and high damping materials".

References

Daněk, O., Vaněk, F., Cibulka, J. (1993): Experimental Investigation of Turbine Blades in Service. Diagnostic of Rotating Machines in Power Plants. Springer , in: *Proc. Symposium on Diagnostic of Rotating Machines in Power Plants*, Udine.

Daněk O., Kozánek J., Pešek L., Procházka P., Vaněk F. (2001): Developement of Identification Methods of Dynamics Parameters of Rotationg Machinery Parts, in: *Proc. Int. Conf. on Structural Systems Identification*, Univerisity Kassel, pp.243-250.

Pešek, L., Vaněk, F., Procházka, P., Vaněk,P., Cibulka, J. (2008): Dynamics of Rotating Blade Disk Identified by Magneto-Kinematic Measuring System, in: *Proc. ISMA2008 Conference*, KU Leuven, pp.1-15.

Pešek L., Vaněk F., Procházka P., Vaněk P., Cibulka J.(2009): Development of excitation and measurement for identification of rotating blade discs, In: *8th Int. Conf. on Vibrations in Rotating Machines SIRM 2009*, Vienna, paper ID8, pp.1-10.

Pesek, L., Pust, L., Vanek, F., Vesely, Cibulka, J. (2010): Dynamics of model bladed disc with friction elements for vibration suppression, in: *Proc. 8th IFToMM International Conference on Rotor Dynamics*, MoD2-3, Seoul, Korea.

Pešek, L., Vaněk, F., Balda, M., Procházka, P., Vaněk, P. , Cibulka, J., Bula, V.: Developement of Vibrodiagnostic System of Tram Wheel For Damage Analysis, Engineering MECHANICS, Vol. 15, 2008, No. 6, p. 447–460.

18th International Conference
ENGINEERING MECHANICS 2012
Svratka, Czech Republic, May 14 – 17, 2012

pp. 989–992
Paper #250

DIGITAL IMAGE PROCESSING OF STRUCTURE RESPONSE

M. Petřík[*], P. Štemberk[**]

Abstract: *This paper deals with an easily available means of vibration measurement which is the digital image processing. A method is proposed whose internal procedures are described in detail and its applications are discussed. The usability verification of the method was performed on vibration measuring of different types of experimental structures. The flow chart of the method is also given. The cases of appropriate usage are discussed.*

Keywords: ***Digital image processing, dynamic test, digital camera, cyclic loading.***

1. Introduction

Vibration is a phenomenon known in structures which are subjected to dynamic loading. Good understanding of vibration behavior can be successfully applied in a wide range of engineering fields, such as mechanical engineering. In the case of civil engineering, some specific features need to be accounted for. The vibration of buildings and bridges can cause problems connected with fatigue of materials, reduced serviceability, stability and others. The external influences, such as earthquake (see Fig. 1), machines, traffic and other human activities are considered as the unfavorable vibration sources. This is the reason why measurement techniques for vibration tests are developed and experiments are conducted. The technological development gradually enables to use improved and more sophisticated measuring instruments. At the beginning, only simple mechanical instruments were used for displacement measuring. Expensive accelerometers which are commonly used today were developed quite recently. Nowadays, it is even possible to use wireless accelerometers and accessible accelerometer transmitter boards (used for example in some smartphones, computer peripherals and robotics), which can be purchase for very reasonable price. But, yet another less expensive possibility of today is the use of digital image processing, e.g. Štemberk and Kohoutková (2005), which requires a simple digital camera, a tripod, a measuring marker and a computer with proper software.

Fig. 1 Consequences of earthquake (Murty et al. 2001)

[*] Ing. Martin Petřík: Czech Technical University in Prague, Thakurova 7, 166 29 Prague 6, CZ, martin.petrik@fsv.cvut.cz

[**] doc. Ing. Petr Štemberk, Ph.D.: Czech Technical University in Prague, Thakurova 7, 166 29 Prague 6, CZ, stemberk@fsv.cvut.cz

2. Proposed digital-image-processing method

The method is based on the fact that every single point in a raster image (pixel) has its own specific values and also the unique coordinates. By utilizing this reality, it is possible to work with an image like with a digital matrix. The proposed digital image processing application was created with respect to the above mentioned facts. The whole method consists of the following three steps: recording, data processing and post-processing. The first step relies on placing of the measuring markers and the camera fixation. In general, the camera distance ranges from 0.5 to 10 meters, which depends on the size and the resolution of the camera sensor and the lens focal length. The data are subsequently processed (see Fig. 2) and the results post-processed, which includes numerical differentiation and plotting.

The recorded series of images, or a movie, is split into single images that are uploaded one-by-one in the software application. Then, the dynamic threshold dependent on the brightest and the darkest place of the image is determined. The threshold is used when the original image is converted into a binary image. The binary image contains only zeros (black) and ones (white), as can be seen in Fig. 3. The second step consists of searching for a continuous area composed of ones only. Then, the center of gravity of the area which contains only the ones is calculated and its coordinates are stored. The next images are automatically loaded and processed in the same manner. The last step consists of determination of the measuring point pixel size because it is necessary to multiply the results (pixels) by a ratio of the actual size to the pixel size.

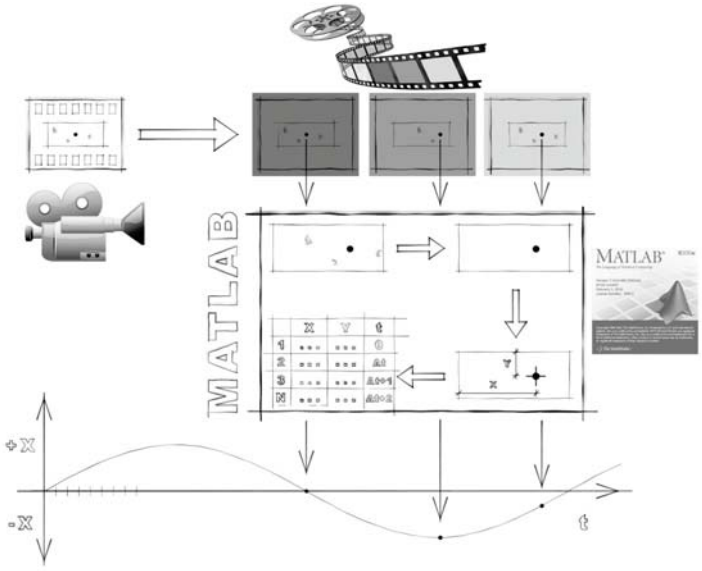

Fig. 2: Flow chart of proposed digital image processing method

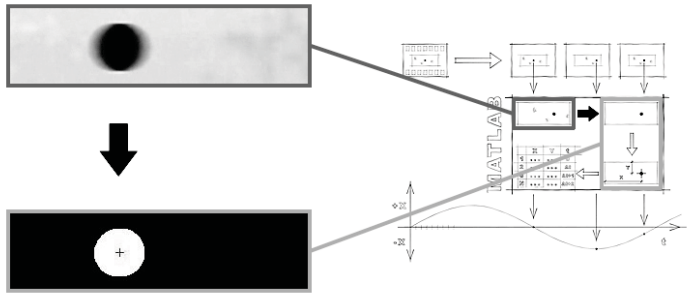

Fig. 3: Visualization of inner steps of digital image processing method

3. Application of proposed method

Three experimental structures were constructed in order to test proposed method, as can be seen in Fig. 4. The T-shaped concrete column (see Fig. 4A) was exposed to seismic loading until creation of plastic joint and subsequent collapse. The second experiment was concerned with steel frame structure with hydraulic strut and tie damping system (see Fig. 4B) and the same seismic loading. Two versions of the structure were tested. Comparison of the response is shown in Figs. 5 and 6. The last construction was type of wooden frame structure with tuned mass damper located in the last floor (see Fig. 4C). Free vibration caused by initial deviation was measured.

All the performed experiments proved usability of proposed method. It is appropriate to use digital image processing in case of measuring displacements of hardly accessible places, low budget and experiments with hazard of expensive accelerometers destruction.

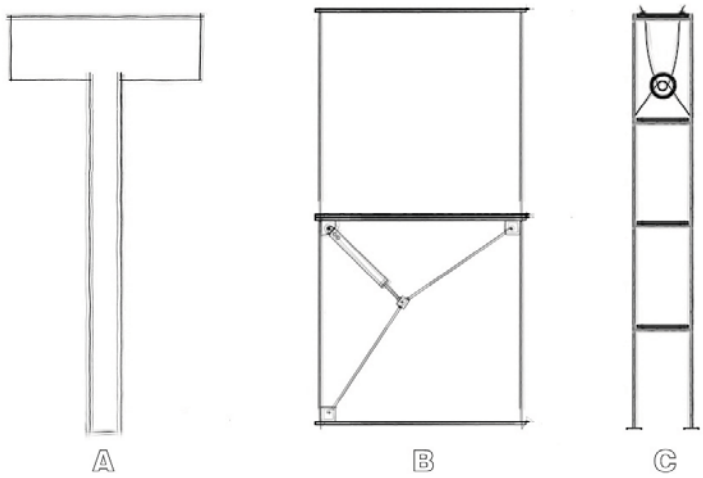

Fig. 4: Sketches of the experimental structures

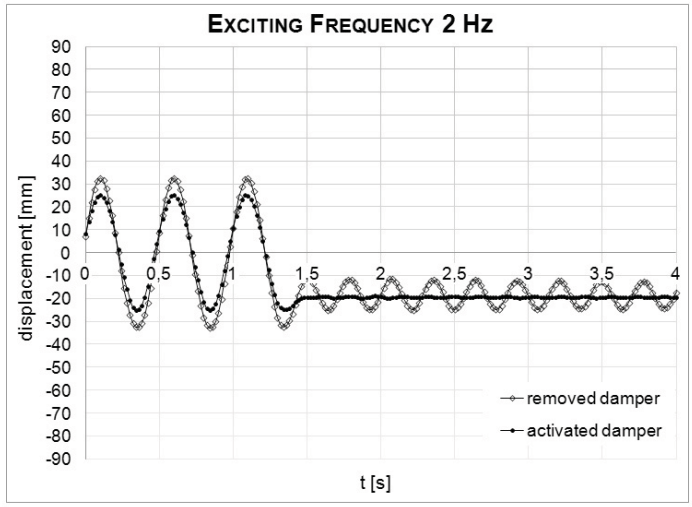

Fig. 5: Comparison of the response of the first floor

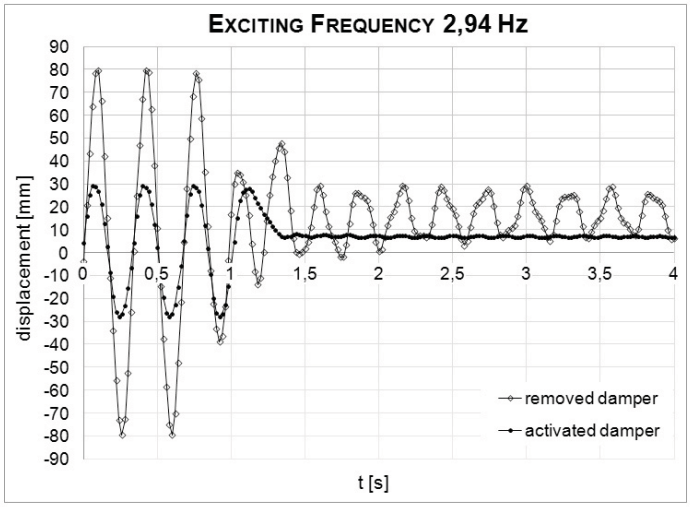

Fig. 6: Comparison of the response of the first floor (close to natural frequency)

4. Conclusions

It was shown that it is possible to apply digital image processing in measuring the displacement of cyclically loaded structures. This however assumes that certain rules and conditions, such as a sufficient measuring point resolution, the ratio of the vibration frequency to the video frequency and proper camera fixation, are satisfied. The proposed method is essentially wireless and also reasonably priced. On the other hand, using this method requires certain discipline and certain amount of experience with digital processing. The flow chart of the method and its inner steps were given. The procedure of measuring was discussed.

Acknowledgement

The financial support by the Czech Science Foundation, project P105/10/2098, and the CTU in Prague, project SGS11/107/O[HK1/2T/11, which is gratefully acknowledged.

References

Murty, C.V.R. et al. (2001) *The Seismic Performance of Reinforced Concrete Frame Buildings with Masonry Infill Walls*. New York: McGraw-Hill Professional.

Štemberk P. and Kohoutková A. (2005) Image-analysis-based measuring of lateral deformation of hardening concrete. *Materials Science* (Medžiagotyra), vol. 11(3), p. 292-296.

18th International Conference
ENGINEERING MECHANICS 2012
Svratka, Czech Republic, May 14 – 17, 2012

pp. 993–1000
Paper #81

DEVELOPMENT AND MODELING OF A BIOMECHATRONIC SENSOR EFFECTOR BOOT DEVICE

A. Platonov[*], L. Ilieva-Mitutsova[**], I.Chavdarov[***], N. Serbenyuk[*], O. Trifonov[*], V. Yaroshevsky[*]

Abstract: *In this paper we represent the development of a sensor effector boot mechatronic device for effective rehabilitation of patients in the early post-traumatic stage (1 month) after the occurrence of a serious spinal-cord trauma or poli-trauma. The device is portable with insurance for vertical position in the bed of the immovable patients. The device includes: a module for basing and fixation of the patient's leg, a sensor "SkinTouch" for measuring bio-electrical impedance in points on the skin of the foot, a mechanism for acupressure, a module for basing of a measuring sensor and a mechanism for acupressure, and also gives the possibility for their connection to various foot points for the programme performance of the procedures and PC controlled sensor and effector elements, connected to the physician s monitor. In the paper are presented the design, modelling and experimenting of the separated modules. The studies are carried in Bulgarian Academy of Sciences - Russian Academy of Sciences collaboration advance to develop a new device for treatment of spinal patients and creating new technologies of their rehabilitation.*

Keywords: ***boot mechatronic device, sensor, effector, rehabilitation, paraplegics.***

1. Introduction

Perspective and necessity of investigation on new sensors and effector mechatronic devices and technologies for locomotion rehabilitation are based on the results from the investigations on the physiological control locomotion mechanisms of humans and animals, performed in the Institute of Physiology "Pavlov" PAN (Gerasimenko et al.,1999), (Nikitin et al., 2001). Perspectives for a positive result of the rehabilitation at the locomotion pathology are derived in these investigations, as a result of a spinal cord trauma, main brain diseases or continuous muscle inactivity. At this stage a very important fact appears the application of the tactile feet stimulation of the injured limbs (Okhotsimsky, Nikitin, Gerasimenko et al., 2006). One of the methods of restoring the support-locomotion functions is to affect the neurons of the spinal cord using the limb reception system as a natural communication channel. Foot receptor activation is applied for that purpose. The study aim is to complete the following tasks: (i) to affect the extra receptors, which signals stimulate the central locomotion generator located in the spinal cord; (ii) to affect the nerve endings in the biologically active zones, stimulating the functioning of internal organs of a seriously disabled patient. The start of the procedure during the early post-traumatic stage (after the occurrence of a spinal cord trauma or poli-trauma) is considered to be appropriate for the decrease of atrophy speed. Due to patient's poor physical state, receptors stimulation is proposed at the start of recuperation procedure, only.

[*] Prof. Alexandr Platonov, DrSc: Keldysh Institute of Applied Mathematics, Russian Academy of Sciences, 4 Miusskaya Sq., 125047 Moscow, Russia, e-mail: platonov@keldysh.ru.

[**] Assoc. Prof. Lidia Ilieva-Mitutsova, Ph.D.: Assist.Prof. Vladimir Vitkov,: Institute of Mechanics, Bulgarian Academy of Sciences, Acad. G. Bonchev str., bl. 4, 1113 Sofia, e- mail: lidia@imbm.bas.bg

[***] Assoc. Prof. Ivan Chavdarov, Ph.D., Institute of system engineering and robotics, Bulgarian Academy of Sciences, Acad. G. Bonchev str., bl. 1, 1113 Sofia, Bulgaria, e-mail: ivan_chavdarov@dir.bg.

[*] Assis. Prof., Nicolay Serbenyuk, Ph.D.: Keldysh Institute of Applied Mathematics, Russian Academy of Sciences, 4 Miusskaya Sq., 125047 Moscow, Russia, e-mail: serb@ keldysh.ru.

[*] Assoc. Prof. Oleg Trifonov, Ph.D.: Keldysh Institute of Applied Mathematics, Russian Academy of Sciences, 4 Miusskaya Sq., 125047 Moscow, Russia, e-mai: tov@ keldysh.ru.

[*] Assoc. Prof. Viktor Yaroshevsky, Ph.D.: Keldysh Institute of Applied Mathematics, Russian Academy of Sciences, 4 Miusskaya Sq., 125047 Moscow, Russia, e-mai: yarosh@ keldysh.ru.

2. Methods

Developed mechatronic module can ensure treatment procedures by foot receptor activation on method of acupressure, combined with methods of reflexotherapy. It operates according to a previously prescribed program for acupressure at specific foot points, receptor activation along specific trajectory or affects foot reflex areas.

The module can ensure control measure the bioelectrical resistance by means of a specialized sensor (Platonov et al., 2010) Such a sensor is needed to design a high-spatial resolution map of acupuncture points of a patient's foot, and the map should be used to analyze the results of the treatment. The sensor measuring both the initial (pre-treatment) foot skin electro-conductivity, as well as the current one operating during the process of medical treatment, is of essential importance for the successful stimulation of patient's foot.

Product "Mechanical Desktop 2005" is applied for the creation of a virtual 3D model of the module. The program "MSC.visualNastran 4D 2002" for computer simulation is applied on the 3D model.

3. Technical solution of mechatronic sensor effector boot device

The device includes:

- a module for basing and fixation of the patient's leg,
- a sensor "SkinTouch" for measuring bio-electrical impedance in points of the foot skin,
- a mechanism for acupressure,
- a carriage module for basing of a measuring sensor and a mechanism for acupressure,
- a module for a plane motion and positioning of carriage module to various foot points for the programme performance of the procedures,
- PC controlled sensor and effector elements, connected to the physician's monitor.

Four variants of the module for founding of patient leg, measuring and acupressure are developed and modelled (Ilieva-Mitutsova L., Chavdarov I., et al., 2011). The objective of the work presented in this paper is the development of the module variant IV, being the most suitable one for a portable device for application in a patient's bed when the patient being stationary.

The mechanical modules are designed in Institute of mechanics, BAS. The specialized a sensor "SkinTouch" for measuring bio-electrical impedance in points of the foot skin is developed in the Institute of Applied Mathematics "Keldysh"-RAN. Down are presented the design and modelling of the separated modules.

3.1. Design of a module for basing and fixation of the patient's leg

3.1.1. Requirements to module for basing and fixation of the patient's leg

The designed module must meet the following requirements:

1. Sustainable basing the patient's leg, which is in a bed.
2. An accessibility to be ensured to maximum number of points on the foot with the aim to measure the bioelectrical resistance by means of a specialized sensor.
3. Accessibility to maximum number of points on the foot for automatic acupressure performance according to a programme assignment, individually for each patient.
4. Discomfort must not be created to the patient, and also not to influence the precision of the carried out measurements.
5. Basing to be possible at different patient's feet sizes.
6. Safety of the patients to be ensured of the device activity at arising programme or mechanical reasons.

3.1.2. View of the module for basing and fixation of the patient's leg

The developed module includes the following component, (*Fig. 1*): 1- heel support, 2 - foot fixations, 3 - regulated foot fixing of the leg.

The foot is based at support 1. Fixations 3 are prepared for the leg fixed above the ankle joint and in the front part of the foot, which location is regulated longitudinally according to the foot size.

The surface of the foot remains uncovered for a direct contact to each point for measurement of the skin electrical resistance and acupressure.

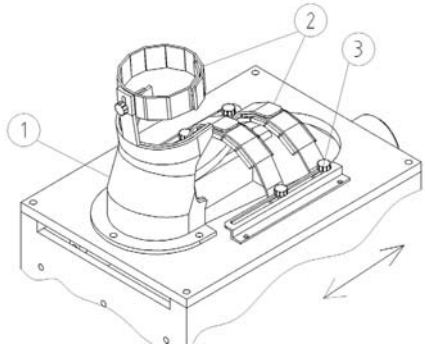

Fig.1: General view of the module for basing of the patient's leg

3.2. A carriage module for basing of a measuring sensor and a mechanism for acupressure

Combined module - carriage (*Fig. 2.*) comprises carriage 1, to which is immovably attached module for acupressure 2 and a measuring module 5. In the modules joints are included respectively two linear drives, by means of which a translation along axis Z is realised.

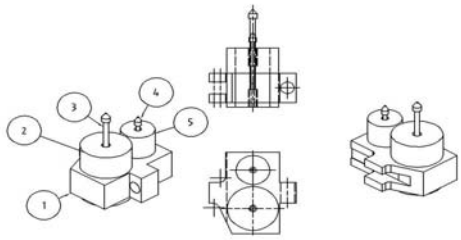

Fig.2: A carriage module for basing sensor and effector elements of device

The respective useful contact pressure of an electrode for measurement 4 is achieved by means of drive control and the external force (acupressure) is regulated by means of the executive mechanism 3.

3.3. A mechanism for acupressure

The mechanism for acupressure includes (*Fig.3.)* translation linear drive 1 and removable instrument with different number of pins 2 *(Fig.4.).*

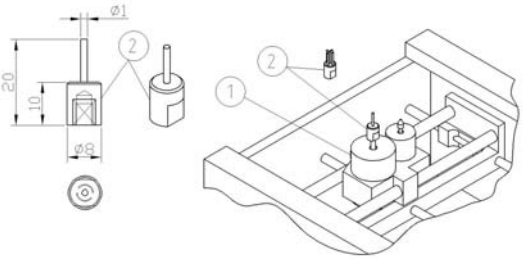

Fig. 3: A mechanism for acupressure

Effector instruments with different number of pins are applying for receptor activation by the method

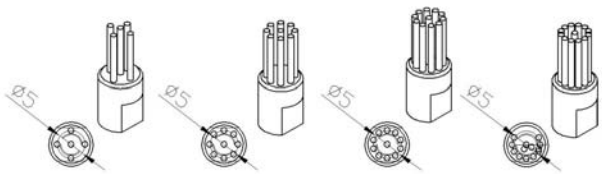

Fig. 4: Effector instruments with different number of pins

of skin-deep multi-pins acupressure combined with methods of reflexotherapy.

3.4. Design and modelling of a module for a plane motion and positioning of carriage to various foot points

Movement along axes X and Y is realised by two mechanisms respectively (*Fig. 5.*). The mechanism for longitudinal translation X includes: a foundation 1, a drive 2, a leading screw 3 and a guide 4 for translation along axis X. It is necessary, the run of this translation to be equal to the length of the foot $H_1 \approx 110$ to 150mm. The mechanism for translation along axis Y includes: a base-carriage 5, a drive 6, a gear 7 and a screw- carriage 9.

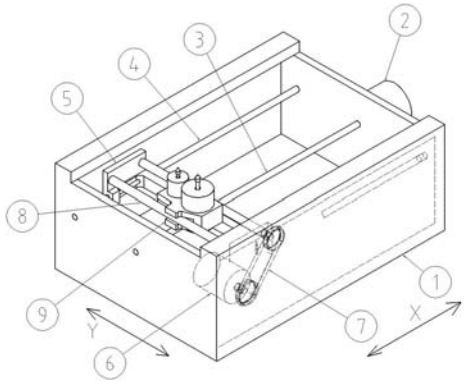

Fig.5: A module for a plane motion and positioning of carriage

The drive 6 is fixed on the base-carriage 5 witch by means of the gear 7 activates the screw- carriage 9. It moves by itself the carriage module 9 along axis Y lead on the guide 8. It is necessary, the translation run to be equal to the width of the foot $H_2 = Lp \approx 40$ to 60mm

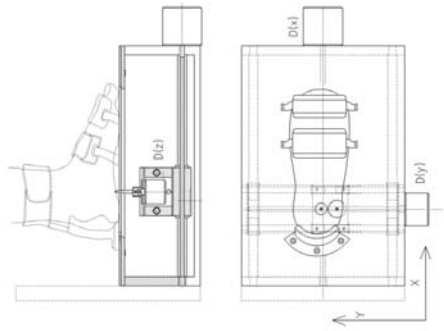

Fig.6: Basing of the patient's leg for the programme performance of the procedures

The *Fig.6.* shows the basing of the patient's leg on the module gives the possibility for connection sensor and effector instruments to various foot points for the programme performance of the procedures.

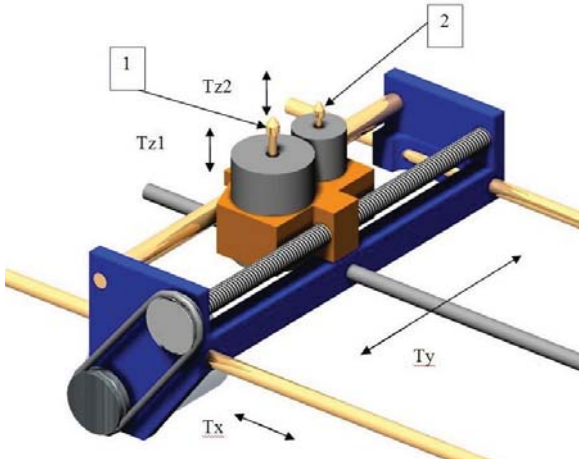

Fig.7: 3D model of mechanism for a plane motion and positioning of carriage for measurement and acupuncture

3.5 Development of the sensor "SkinTouch" for measuring bio-electrical impedance in a skin point

3.5.1 Proof of the design necessity of a specialized sensor for measuring bio-electrical impedance

The device measuring both the initial (pre-treatment) foot skin electro-conductivity, as well as the current one operating during the process of medical treatment, is of essential importance for the successful stimulation of patient's foot. Such a sensor is needed to design a high-spatial resolution map of acupuncture points of a patient's foot, and the map should be used to analyze the results of the treatment. The complexity of the registration needed originates in the measurement of current extremely low values. Note that current low value is due to the high ohm resistance of patient's foot skin, and to the restriction of voltage applied to patient's skin. That restriction is imposed to avoid not only injury or pain, but also data distortion due to the effect of voltage of the measuring instrument over the physiology of controlled processes.

A mechatronic approach for the measurement of human skin electro-conductivity is developed in the Institute of Applied Mathematics "Keldysh"-RAS (Platonov A. et al.,2010). The measurement method proposed is based on the use of a differential operational amplifier, controlled by a microprocessor. It is capable of maintaining stable ultra-small current (not larger than several μA) in the chain of the analogue-digital analyzer (ADA) of the skin resistance receptor. Signals coming from an analogue-digital converter (ADC) are used to apply microprocessor control of measurements. The ADC is switched to a differential operational amplifier. A special measuring device "SkinTouch" is designed to realize the software algorithms and analyze the capabilities of the proposed method. It is assembled using modern electronic compounds and schemes that guarantee the measurement accuracy required.

3.5.2. Technical description of the sensor "SkinTouch"

The basic function of the sensor device "SkinTouch", is to perform point measurements of the human skin resistance characteristics. Among its technical characteristics, one should note the ultra-low current of measurement, from 0, 5 to 2 μA, and the moderate potential difference (voltage) applied to the electrodes and not exceeding 7 V. Those characteristics exceed twice the characteristics of the existing equipment. They enable one to significantly decrease the measurement pattern distortion and minimize the unfavourable effects over the patient.

3.5.2.1. Requirements to the measurer of resistance characteristics

Methodically, the instrument for measurement of the resistance characteristics of human skin should satisfy the following requirements:

1. Measurements should be performed using low current in the range 0,1 - 1 μA.
2. Current value should be constant during measurement.
3. The measurable parameter should be the difference between the electrode potentials.
4. The working voltage between the electrodes should be within the range [0,1 – 1] V.
5. The maximal admissible difference between the electrode potentials should be 15 V.
6. The measurements performed should minimally affect patient's state.

Note that the designed sensor device "SkinTouch" satisfies the outlined requirements.

3.5.2.2 Principal scheme of the "SkinTouch"

The principal scheme of the measuring device "SkinTouch" is shown in *Fig.7.* The device basic compounds are:

- Microcontroller;
- Measuring unit;
- Generator unit;
- Supply sources.

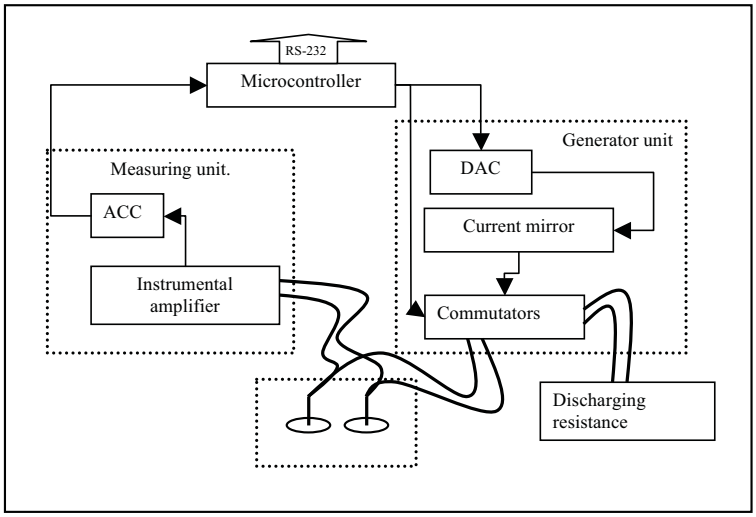

Fig.8: Principal scheme of the measuring device "SkinTouch"

The microcontroller coordinates performance of all other units, transition of measurement results to other devices along the channel RS-232, as well as receives of controlling commands.

The measuring unit consists of:

- Instrumental operational amplifier, with small value of leak current and incorporated means of protection against electrostatic discharges;
- Analogue-digital converter incorporated into the microcontroller

The generator unit consists of:

- Digital-analogue converter with current output, which provides the necessary range of the supporting current.
- Current mirror which exactly copies the supporting current of the ADC within the range of the electrodes supply voltage. The commutation unit is used to eliminate the electrode polarization.

The direction of current flowing between the measuring electrodes can be varied upon an order issued by the microprocessor. The unloading resistance is used for calibration and discharge of the electrode static charge.

Two direct current sources are used to supply the measuring device "SkinTouch". The first source, with voltage 3,5 V, is used to supply the instrument digital section. The second source provides two voltage values: + 3,5 V and – 3,5 V, and it supplies the instrument analogue section. Batteries or accumulators are used to reduce disturbances.

A prototype of the measuring device "SkinTouch" is assembled, and instrument tests are performed.

8. View and modelling of the sensor effector boot device

Product *Mechanical Desktop 2005* is applied for the creation of a virtual 3D model of the module.

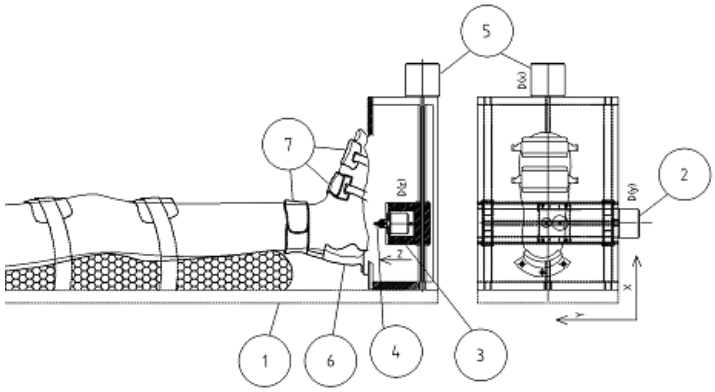

Fig.9: General view of the device in the bed of the immovable patient

The module components are following: 1- base, 2 - translation linear drive along axis Y, 3 - combined module-carriage, 4 - executive mechanism for acupressure, 5 - translation linear drive along axis X, 6 - heel support, 7 - foot fixations.

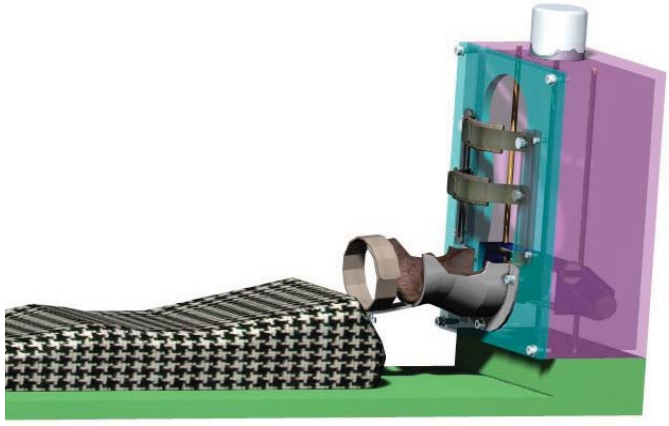

Fig.10. 3D model of a mechatronic sensor effector boot device

Module functions simulation is performed on the derived 3D model of the new device.

9. Conclusions

The conclusions derived after modelling and simulation help the successful realization and approbation of the separate modules and the prototype of the new device.

The program is derived for the performance of the rehabilitation heeling by means of the new portable mechatronic device. It is as follows:

1. Measuring the bioelectrical resistance to be performed in the foot points for each individual patient by means of a specialized sensor "***Skin Touch***". An individual chart of the acupuncture foot points of the patient is build up.
2. Planning and performing of treatments (acupresura) in definite points, along a defined trajectory or on a foot area.
3. Performing a periodical estimation and control of the treatment results by means of measuring of the bioelectrical resistance in definite foot points. The healing programme undergoes a consecutive variation, if necessary.

Clinical tests are going to be performed for assessment the efficiency of the new technology for rehabilitation of patients with spinal-cord trauma by means of the application of the new mechatronic boot device in the patient's bed within the frame of the first month after heavy damage. The results are valued in two directions:

- for the fundamental science, which investigate the adaptive processes and control of human locomotion, at absence of a link with the high regions of the nervous system after a trauma disconnection;

- for the rehabilitation practice, at a proved positive effect it is possible a routine application of the new technical device and technology of locomotion therapy.

Acknowledgement

This work was supported by a Bi-lateral project of BAS and RAS **"**Creation of new sensor and effector mechatronic devices for rehabilitation the locomotion abilities of the spinal cord of patients with a spinal-cord pathology" and Institutional Research Plan of IMECH of BAS.

References

Gerasimenko, Yu., Avelev, V., Makarovsky, A. et al.(1999) Neurokontrol of central pattern generator by means of epidural spinal cord stimulation. In: *From the Basic motor Control to Functional Recovery (*N. Ganchev and G. Ganchev eds), Publishing Hause of BAS Prof. M. Drinov, Sofia, pp. 484-488.

Nikitin O., Gerasimenko Yu. et al.(2001) Features of CPG activation in chronic spinalized cats under spinal cord stimulation, in*: Sensoriomotor control* (A. Kosev ed.), NATO, Scientific Affairs Division, LOS Press, 172-179.

Ilieva-Mitutsova L., Chavdarov I., Vitkov V., Yaroshevsky V.,(2011) A mechatronic module modeling for foot receptor activation, in: *Proceed.of Inter. Conf „Engineering Mechanics 2011",* (V.Fuis ed.), Inst.of Thermomechanics,ASCR, Prague, pp. 231-234.

Okhotsimsky D., Nikitin O., Gerasimenko Y. et al.(2006) A biomechanical stimulator for scientific-experimental study of the regeneration of spinal cord locomotion capabilities after traumatic break, in: *Proceed. of Inter. Conf. "Advanced Problems in Mechanics 2005", Minisymposium on Biomechanics,*(Nyashin Y.ed.), St. Petersburg, 394 – 400.

Platonov A., Vitkov V., Inieva-Mitusova L., Serbenyuk N., Trifonov O., Yaroshevskiy V. (2010) A high sensitivity device for measuring bio-electrical impedance of human skin, in: *Proceed. of Inter. Conf. "Advanced Problems in Mechanics 2010"*, htpp://apm-conf.spb.ru, St. Petersburg.

18th International Conference
ENGINEERING MECHANICS 2012
Svratka, Czech Republic, May 14 – 17, 2012

pp. 1001–1010
Paper #292

ESTIMATION OF THE CRITICAL TIME STEP FOR EXPLICIT INTEGRATION

J. Plešek, R. Kolman, D. Gabriel*

Abstract: *Explicit integration plays a key role in many problems of linear and non-linear dynamics. For example, the finite element method applied to spatial discretization of continua leaves a system of ordinary differential equations to be solved, which is often done by the central difference method. This and similar explicit schemes suffer from magnification of the round-off errors if the time step exceeds certain fixed length known as the critical time step.The corresponding critical Courant number (*Cr*, dimensionless time step) is inversely proportional to the maximum natural frequency of the system. The well known recommendation* $\mathrm{Cr} = 1$ *is deemed as the best. In fact, for some configurations this choice may dangerously overestimate the true value. It was shown in an earlier paper by the same authors that by increasing the number of elements in the finite element mesh one will paradoxically improve the mesh's stability towards its theoretical limit. The present paper refines some details, presenting small scale numerical tests. The first test involves a long truss/bar consisting of one row of elements whose critical Courant number changes as elements are added one after another. Since this increases the critical number one may pick up a time step such that it is supercritical to a certain mesh but becomes subcritical by merely adding one element. In a similar fashion, a square area is tested in the second example, using different arrangements of edge supports. It is concluded that the usual setting,* $\mathrm{Cr} = 1$*, is not entirely safe.*

Keywords: ***Explicit integration, Courant number, Critical time step, Wave propagation, Dispersion***

1. INTRODUCTION

Detailed analysis of accuracy and stability of finite element wave propagation solutions was presented in review paper Plešek et al. (2010) and references cited therein for various finite elements including consistent and lumped mass matrices. The critical Courant number limiting the length of the time step in explicit integration schemes, namely the central difference method, follows from the famous formula

$$\mathrm{Cr}_{\mathrm{crit}} = \frac{2}{\bar{\omega}} \tag{1}$$

where $\bar{\omega}$ is the dimensionless frequency

$$\bar{\omega} = \frac{\omega_{\max} H}{c_1} \tag{2}$$

with $\omega_{\max}$ being the maximum natural frequency of a finite element mesh, H the element size, and c_1 the speed of the fasted wave propagating in a continuum, typically the longitudinal wave. Nearly equally famous recommendation $\mathrm{Cr} = 1$ (or slightly less to be on the safe side) for linear finite elements, also known to engineers as "rule of thumb" is deemed to be best. In fact, this observation comes from dispersion analysis but, as it has been shown in Ref. Plešek et al. (2010), for some configurations it may dangerously overestimate the critical time step. It was also shown that by increasing the number of elements, N, in the finite element mesh one will improve the mesh's stability towards $\mathrm{Cr}_{\mathrm{crit}} = 1$ as $N \to \infty$, which is rather a paradoxical finding.

The present paper refines these details, presenting small scale numerical tests, which exemplify some peculiarities. The first test involves a long truss/bar consisting of one row of elements whose critical Courant number changes as elements are added one after another. Since this increases the critical number one may pick up a time step such that it is supercritical to a certain mesh but becomes subcritical by

*Ing. Jiří Plešek, CS., Ing. Radek Kolman, PhD., Ing. Dušan Gabriel, PhD., Institute of Thermomechanics, Dolejškova 5, Praha 8, 182 00, Czech Republic

merely adding one element. In a similar fashion, a square area is tested in the second example, using different arrangements of edge supports. It turns out that the numerical solutions to wave propagation may be strongly influenced by small variation of distant boundary conditions, which should normally be physically insignificant. Finally, the third illustration shows the direct numerical results relevant to the above mentioned choices of sub and supercritical times steps.

2. PROBLEM DESCRIPTION

This section concerns with essentials of wave propagation in homogeneous solids, finite element technology and dispersion computation.

2.1. Propagation of waves in an elastic isotropic continuum

The ith equation of motion in linear elastodynamics reads

$$(\Lambda + G)u_{j,ji} + Gu_{i,jj} = \rho\ddot{u}_i \tag{3}$$

In this equation, Λ and G are Lamé's constants, ρ is the mass density and u_i is the ith component of the displacement vector. Furthermore, a comma placed before subscripts refers to spatial differentiation whereas the superimposed dots denote the time derivatives. The summation convention on repeated indices is assumed. The Lamé constants Λ, G may be related to engineering constants E, ν as

$$\Lambda = \frac{\nu E}{(1+\nu)(1-2\nu)}, \qquad G = \frac{E}{2(1+\nu)} \tag{4}$$

where E and ν are Young's modulus and Poisson's ratio.

In an unbounded isotropic continuum, two types of planar waves exist: the longitudinal wave and two transversal waves, featuring mutually orthogonal polarisation. The longitudinal wave propagates with the speed

$$c_1 = \sqrt{\frac{\Lambda + 2G}{\rho}} \tag{5}$$

The speed of the two transversal waves is

$$c_2 = \sqrt{\frac{G}{\rho}} \tag{6}$$

The standard continuum is said to be *non-dispersive*. This is, by d'Alembert's solution, because the wave profile (wavelength) does not affect the velocity of propagation.

As a special case, one may consider a plane harmonic solution to Eqn. (3) as

$$u_i = U_i(\mathbf{x}) \exp(\mathrm{i}k\,(\mathbf{p}\cdot\mathbf{x} \pm ct)) \tag{7}$$

or its equivalent form

$$u_i = U_i(\mathbf{x}) \exp(\mathrm{i}(\mathbf{k}\cdot\mathbf{x} \pm \omega t)) \tag{8}$$

where $\mathrm{i} = \sqrt{-1}$ is the imaginary unit; $\mathbf{x}$ is a position vector; t is time; k is the wave number; $\mathbf{p}$ is the unit normal to the wave front; $\mathbf{k}$ is the wave vector, $\mathbf{k} = k\mathbf{p}$; c is the phase velocity; ω is the angular velocity; and U_i is the ith component of the amplitude vector at the point defined by the position vector $\mathbf{x}$. For a given wavelength λ, the wave number k may be computed from

$$k = \frac{2\pi}{\lambda} \tag{9}$$

The phase velocity c is related to ω and k by

$$c = \frac{\omega}{k} \tag{10}$$

Finally, the group velocity c_g is defined as

$$c_g = \frac{\mathrm{d}\omega}{\mathrm{d}k} \tag{11}$$

In non-dispersive systems, c is a constant and since $\omega = ck$, we get $c_g = c$. Thus, in the absence of dispersion the group velocity equals the phase velocity. On the other hand, $c_g \neq c$ indicates dispersion.

2.2. Finite element method

Spatial discretization by the finite element of an elastodynamic problem introduces the ordinary differential system

$$\mathbf{M}\ddot{\mathbf{u}} + \mathbf{K}\mathbf{u} = \mathbf{R} \tag{12}$$

Here, $\mathbf{M}$ is the mass matrix, $\mathbf{K}$ the stiffness matrix, $\mathbf{R}$ is the time-dependent load vector, and $\mathbf{u}$ and $\ddot{\mathbf{u}}$ contain nodal displacements and accelerations. The element mass and stiffness matrices are given by

$$\mathbf{M}_e = \int_V \rho \mathbf{H}^T \mathbf{H}\, \mathrm{d}V \tag{13}$$

and

$$\mathbf{K}_e = \int_V \mathbf{B}^T \mathbf{C}\mathbf{B}\, \mathrm{d}V \tag{14}$$

where $\mathbf{C}$ is the elasticity matrix, $\mathbf{B}$ is the strain-displacement matrix, $\mathbf{H}$ stores the displacement interpolation functions and integration is carried over the element domain. Global matrices are assembled in the usual fashion. Under plane strain conditions, the elastic matrix $\mathbf{C}$ takes the form

$$\mathbf{C} = \frac{E}{1-\nu^2} \begin{bmatrix} 1 & \nu & 0 \\ \nu & 1 & 0 \\ 0 & 0 & \frac{1-\nu^2}{2(1+\nu)} \end{bmatrix} \tag{15}$$

The mass matrix defined by Eqn. (13) is called the consistent mass matrix.

Explicit integration methods, such as the central difference method discussed later, require the mass matrix inverted. Thus, it is advantageous to have it diagonal or *lumped.* In contrast to consistent matrices, which are uniquely defined by the variational formulation, lumping procedures are not strictly prescribed. The only common principle is the ability of FEM to assemble diagonal global matrix from the element mass matrices, thus, lumping may be performed on an element basis. Out of many methods rendering the mass matrix diagonal we shall refer to the simplest: the row sum method (RS) for bilinear elements and the Hinton-Rock-Zienkiewicz method (HRZ) for quadratic elements—see Ref Plešek et al. (2010).

In the subsequent analysis, a regular $H_x \times H_y$ mesh composed of plane rectangular elements is considered with H_x and H_y measuring the length of element edges aligned with coordinate axes. It proves useful to define reference matrices $\bar{\mathbf{M}}_e$, $\bar{\mathbf{K}}_e$ for a parent element having unit properties E and ρ, unit thickness b and unit length $H_x = 1$. Then performing integration over the reference domain $1 \times r$ one gets

$$\mathbf{M}_e = brH_x^2 \rho \bar{\mathbf{M}}_e \tag{16}$$

and

$$\mathbf{K}_e = bE\bar{\mathbf{K}}_e \tag{17}$$

Therefore, a class of problems is defined by two constants: the Poisson ratio ν and the aspect ratio $r = H_y/H_x$. Within this class, the reference stiffness matrix $\bar{\mathbf{K}}_e$ is a function of ν and r whereas the reference mass matrix $\bar{\mathbf{M}}_e$ is independent of both. Denote by $\bar{\omega}_e$ the maximum natural frequency of a *single* element described by these unit matrices. For example, one may compute $\bar{\omega}_e = 2.39$ for the bilinear RS elements or $\bar{\omega}_e = 7.61$ for the quadratic serendipity HRZ elements.

2.3. Dispersion computation

The smooth solutions, Eqn. (7) and (8), no longer apply to discretized system (12). In this case, the speed of propagation of an harmonic wave depends on its angular frequency. According to Ref. Plešek et al. (2010), such dependence may be manifested by the dispersion plot shown in Fig. 1. In general, dispersion behaviour is investigated by considering an harmonic wave train travelling through unbounded mesh, which may be accomplished by prescribing periodic boundary conditions. Thus, the normalized frequencies read off the plot actually represent the limit natural frequencies corresponding to a very large (theoretically infinite) finite element mesh.

As in the preceding section, denote by $\bar{\omega}_\lambda$ the supreme value of the normalized angular frequency in Fig 1, e.g. $\bar{\omega}_\lambda = 2.00$ for bilinear elements and $\bar{\omega}_\lambda = 7.37$ for quadratic elements. It is worth mentioning

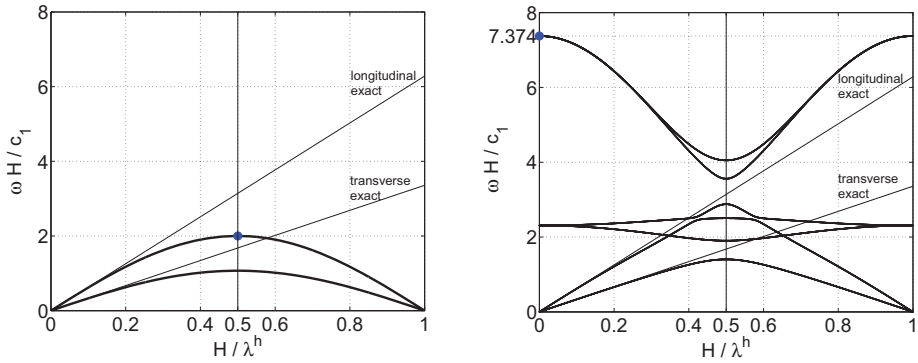

Fig. 1: Dispersion curves for bilinear (left) and serendipity (right) elements.

that $\bar{\omega}_\lambda < \bar{\omega}_e$ in every case. It should also be noted that the dispersion diagrams discussed in this text are entirely due to spatial dispersion, neglecting effects of time integration—refer to paper Plešek et al. (2010) for complete treatise. This by no means oversimplifies actual problems since they are namely these theoretical values that enter stability criteria.

2.4. Explicit time integration and numerical stability

As a representative of explicit schemes, reviewed in Reference Subbaraj and Dokainish (1989), the central difference method (CDM) will be discussed. Its discrete operator reads

$$\frac{1}{\Delta t^2}\mathbf{M}\mathbf{u}^{t+\Delta t} = \mathbf{R}^t - (\mathbf{K} - \frac{2}{\Delta t^2}\mathbf{M})\mathbf{u}^t - \frac{1}{\Delta t^2}\mathbf{M}\mathbf{u}^{t-\Delta t} \tag{18}$$

where $\mathbf{R}^t$ contains forces acting on the nodal points at time t. It is well known that CDM is only conditionally stable, Ref. Park (1977), that is

$$\Delta t \leq \frac{2}{\omega_{\max}} \tag{19}$$

where $\omega_{\max}$ is the maximum eigenfrequency of the finite element mesh. The highest frequency can be computed by the standard FE software, aiming at the lowest eigenvalue with $\mathbf{K}$ and $\mathbf{M}$ swapped. This method was indeed employed in all the numerical computations presented here. Alternatively, the crititical time step may be estimated analytically as in Ref. Flanagan (1981).

At this point, it is convenient to introduce the Courant dimensionless number defined as

$$\mathrm{Cr} = \frac{c_1 \Delta t}{H} \tag{20}$$

In elastodynamics, c_1 is the velocity of the longitudinal wave. Using the latter definition and that of $\bar{\omega}$ in Eqn. (2), the stability condition (19) can be rephrased as

$$\mathrm{Cr} \leq \frac{2}{\bar{\omega}} \tag{21}$$

or, defining $\mathrm{Cr}_{\mathrm{crit}}$, in the form of Eqn. (1). Inequality $\mathrm{Cr} \leq 1$ then exactly manifests the Courant-Friedrichs-Lewy stability condition for the linear truss element Subbaraj and Dokainish (1989) but for other elements it may not be generally valid. On the other hand, we know, by Fried's theorem Fried (1972), which is a direct consequence of Sturm's polynomial separation property, that the maximum frequency is bounded by $\bar{\omega}_e$ obtained as the maximum eigevalue taken over all the elements in the FE mesh.

If the mesh is regular, composed only of rectangular elements of the same aspect ratio (the so-called structured mesh), one may devise another estimate of the critical time step, which lends some interesting

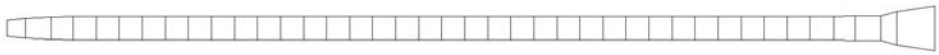

Fig. 2: Eigenvector corresponding to the highest frequency of a bar with free ends.

insight into the problem of numerical stability in general. One asymptotic case arises for the infinite mesh, when $\omega_{\max}$ equals the supremum taken over all the dispersion curves for the particular element, i.e., $\bar{\omega}_\lambda$ is exploited. Tentatively, one may conjecture

$$\bar{\omega}_\lambda \leq \bar{\omega} \leq \bar{\omega}_e \tag{22}$$

This expression is indeed valid for an abitrary body with free boundary, $\Gamma_u = \emptyset$, but *does not hold* for a constrained mesh, for instance, if some displacement boundary conditions are prescribed. The meaning of the statement (22) will be clarified in full by examples shown in the next section.

Finally, it should be pointed out, that precisely because of the inequality (22), the true frequency of a real mesh will probably be higher than the estimate stemming from dispersion theory. Hence, the popular formula $c_1 \Delta t = H$ for the determination of time step length is not entirely safe.

3. NUMERICAL EXPERIMENTS

Unit dimensions were set in the numerical tests as follows: mass density $\rho = 1$, Poisson's ratio $\nu = 0.3$, and Young's modulus $E = 0.7428\ldots$ so that $c_1 = 1$ and $c_2 = 0.5345\ldots$. Furthemore, plane strain square bilinear elements with edge length $H = 1$ and unit thickness, $b = 1$, were employed. The reason for chosing linear rather than quadratic elements to illustrate stability properties is that the difference between $\bar{\omega}_\lambda = 2.00$ and $\bar{\omega}_e = 2.39$ is greater for these elements. Having N elements in the mesh, the total mass is $m = N\rho H^2 b = N$.

3.1. Plane strain bar

As the first example we consider a plane strain bar whose length is variable depending on the number of elements used. Fig 2 shows the eigenmode corresponding to the bar's maximum frequency for 40×1 discretization. The value of frequencies computed for various Ns are listed in Tab. 1.

One important observation following the inspection of Tab. 1 is that starting from the 20×1 bar, the maximum frequency does not change within the first 8 digits, which suggests an existence of the limit. Alas, this limit, $\bar{\omega} = 2.16$, differs from the theoretical value $\bar{\omega}_\lambda = 2.00$. On the one hand, our sequence correctly starts at $\bar{\omega}_e = 2.39$ for 1×1 discretization, but on the other, the asymptotics $\mathrm{Cr}_{\mathrm{crit}} = 1$ has never been reached. Why is it so? The answer lies in Fig 2. Since only the free ends vibrate, the maximum eigenvalue does not depend on the bar's length but solely on this boundary effect. The limit solution will not fit the periodical boundary conditions characteristic of the dispersion approach.

Tab. 1: Critical Courant numbers for the bilinear finite element mesh of a free bar.

N	$\bar{\omega}$	$\mathrm{Cr}_{\mathrm{crit}}$
1x1	2.3904568	0.8366602
2x1	2.1837346	0.9158622
3x1	2.1865457	0.9146848
4x1	2.1664669	0.9231620
5x1	2.1649080	0.9238268
6x1	2.1621023	0.9250256
7x1	2.1616266	0.9252292
8x1	2.1612303	0.9253988
9x1	2.1611334	0.9254403
10x1	2.1610747	0.9254654
20x1	2.1610454	0.9254780
40x1	2.1610454	0.9254780
80x1	2.1610454	0.9254780
100x1	2.1610454	0.9254780

Another interesting observation follows from the graphical representation depicted in Fig. 3 on the log scale. Apart from the limit, there is a pronounced gap between the three and four element configurations. Selecting $\mathrm{Cr} = 0.92$, the time step is stable for the 4×1 mesh but unstable for the smaller 3×1 mesh. This motivates the critical test defined in Fig. 4.

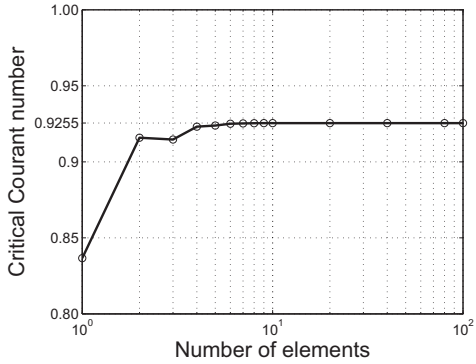

Fig. 3: Distribution of the critical Courant number for the bar with free ends.

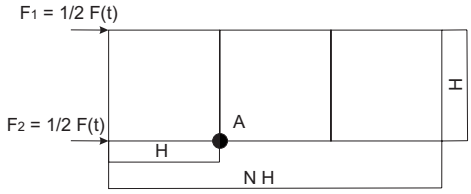

Fig. 4: Transient problem with Heaviside load; unstable configuration.

A three-element bar is loaded by the Heaviside step function $F(t) = 1$ for $t > 0$. Since $\mathrm{Cr} = 0.92 > \mathrm{Cr}_{\mathrm{crit}}$ one expects an incursion of instability after some time has elapsed but a stable solution if a four-element problem had been considered instead. In both the cases, parabolic displacement evolution

$$u(t) = \frac{F}{2m} t^2 = \frac{t^2}{2N} \tag{23}$$

applies to the motion of the whole body. The average acceleration, $1/N$, measured at the control point A for the 4×1 configuration equals 0.25. The existence of the stable solution is confirmed by plots shown in Fig. 5. The oscillatory course of acceleration history is due to waves reflection about the mean value 0.25, which matches the rigid body motion. By contrast, the unstable 3×1 problem exhibits the solution's uncotrolled blow up at about $t = 3000$, see Fig. 6. The instability commences even much earlier after several wave reflections, which is nicely captured in Fig. 7.

Let us return to the original eigenvalue problem shown in Fig. 2. This time the boundary conditions are modified by clamping the right end. The corresponding eigenvector and the frequencies computed are shown in Fig. 8 and Tab. 2, respectively. The same limit $\bar{\omega} = 2.16$ is reached already by the 8×1 discretization, which is not surprising. Indeed, the vibration modes roughly correspond to those of the free bar twice the length of the free-fixed bar. A more interesting fact is that the maximum frequency now *increases.* This is because the results converge to the same limit as before but for each N-element bar the constrained configuration has lower maximum frequency than the free one. The critical Courant number distribution is shown in Fig. 9

We close our discussion concerning this example with the remark that the conjecture (22) does not hold for a constrained problem. For example, for the free-fixed bar $\bar{\omega}_\lambda > \bar{\omega}_{1\times 1}$, because the maximu

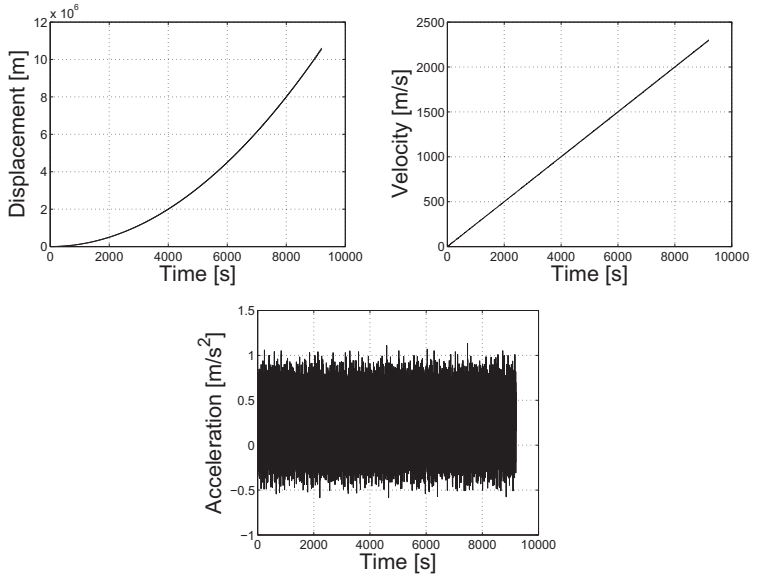

Fig. 5: Displacement, velocity and acceleration in the stable 4×1 *computation.*

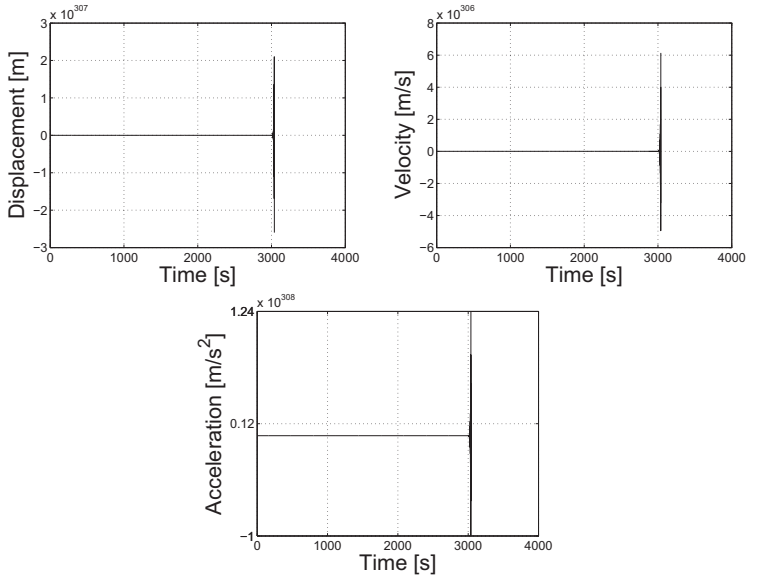

Fig. 6: Displacement, velocity and acceleration in the unstable 3×1 *computation.*

frequency has been reduced by the imposition of the boundary condition. Theoretically, one could even have had $\bar{\omega} = 0$ if all the nodes had been fixed. By contrast, $\bar{\omega}_e$ always forms the upper bound.

3.2. Plane strain square domain

Similar examples as in the preceding section may be analysed. Consider a plane strain square domain shown in Fig. 10 and the critical Courant number distributions for both (fixed and free) boundary configurations—Fig. 11.

In this case, convergence to the limit $\mathrm{Cr}_{\mathrm{crit}} = 0.99$ is observed. Similarly as for the free bar this number is slightly less than the theoretical value $\mathrm{Cr}_{\mathrm{crit}} = 1$. The reason can again been seen in Fig. 10, which

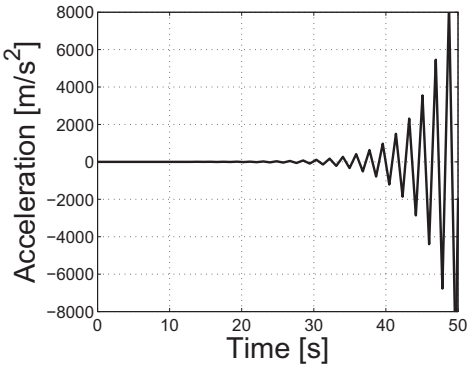

Fig. 7: Detail of acceleration build up.

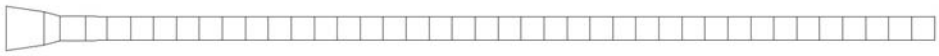

Fig. 8: A free-fixed bar.

suggests that it is the vibration of the corner elements that is responsible for the maximum frequency and is, in fact, independent of the mesh size.

A new phenomenon is detected with the constrained mesh. Comparing it with the free-fixed bar one notices that, here, zero displacements are prescribed along the whole boundary. This means that adding extra elements is merely equivalent to mesh refinement, which in turn implies the increase of the dimensionless maximum frequency. Since the mesh grading is regular and there are no boundary effects, monotonous convergence to the theoretical limit, $\mathrm{Cr}_{\mathrm{crit}} = 1$, follows. It is interesting to note that also in this situation $\bar{\omega} < \bar{\omega}_\lambda$, which violates condition (22) as the present problem is fully constrained.

4. CONCLUSIONS

It might seem at first glance that, except illustrating certain mathematical principles, the present study bears little importance to real-world computation. On the one hand, todays engineering problems are extremely large (rendernig $N \to \infty$ effectively) and, on the other, one may safely use the upper bound by calculating the maximum eigenvalue of a single element.

Tab. 2: Critical Courant numbers for the free-fixed bar.

N	$\bar{\omega}$	$\mathrm{Cr}_{\mathrm{crit}}$	N	$\bar{\omega}$	$\mathrm{Cr}_{\mathrm{crit}}$
1x1	1.8403500	1.0867498	8x1	2.1610454	0.9254780
2x1	2.1530847	0.9288998	9x1	2.1610454	0.9254780
3x1	2.1587386	0.9264670	10x1	2.1610454	0.9254780
4x1	2.1608547	0.9255597	20x1	2.1610454	0.9254780
5x1	2.1609985	0.9254981	40x1	2.1610454	0.9254780
6x1	2.1610395	0.9254805	80x1	2.1610454	0.9254780
7x1	2.1610425	0.9254793	100x1	2.1610454	0.9254780

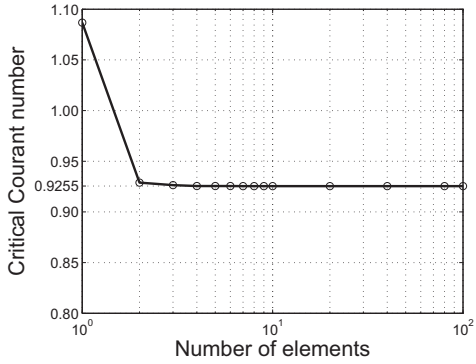

Fig. 9: Distribution of the Critical Courant number for the free-fixed bar.

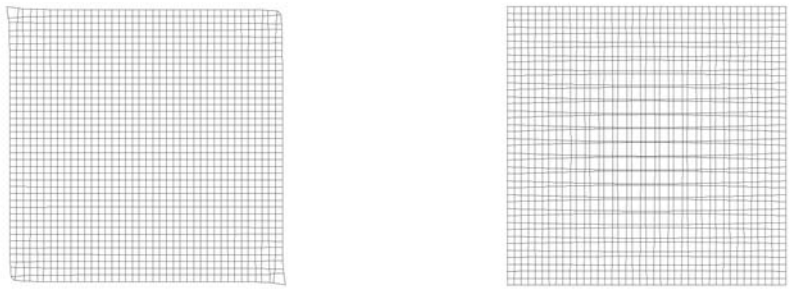

Fig. 10: Maximum eigenmode of a free square domain (left) and the domain with fixed edges (right).

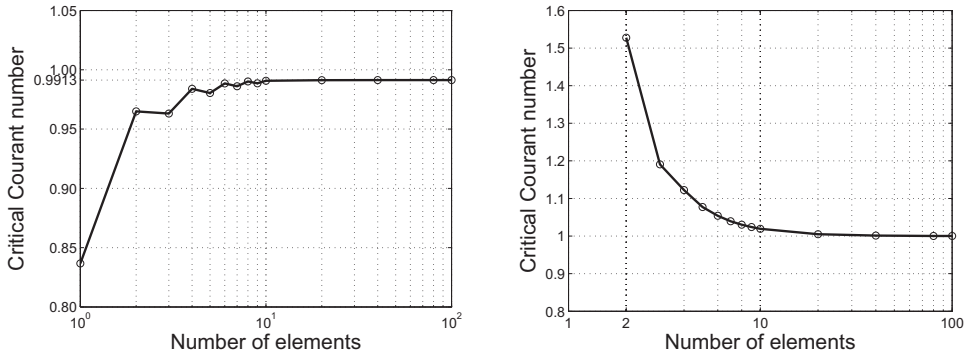

Fig. 11: Critical Courant numbers for free (left) and fixed domain (right).

It should be borne in mind that Fried's estimate, $\bar{\omega} \leq \bar{\omega}_e$, is only useful for a structured mesh when all the elements have the same spectrum. For an unstructured mesh, this information is hardly available and one must resort to other estimates. It is namely under such circumstances that the analysts use the $\bar{\omega}_\lambda$ limit derived from dispersion diagrams often unaware of its pitfalls. It must be emphasised that for the reasons exaplained in the paper the frequent recommendation $c_1 \Delta t = H$ is not entirely safe.

The examples involving free bodies clearly demonstrated the way the vibration of corner elements changed the stability limits. Hence, we conclude that even distant boundary conditions, which should normally be physically insignificant, may considerably influence numerical solution.

Acknowledgements

This work was supported by GACR 101/09/1630 granted project in the framework of AV0Z20760514 research plan.

References

Plešek, J. , Kolman, R., Gabriel, D. (2010) Dispersion errors of finite element discretizations in elasto-dynamics. *Computational Technology Reviews Vol. 1, Saxe-Coburg Publications,* 251–279.

Dokainish, M.A., Subbaraj, K. (1989) A survey of direct time-integration methods in computational structural dynamics - I: Explicit methods. *Computers & Structures*, **32**, 1371–1386.

Park, K.C. (1977) Practical aspect of numerical time integration. *Computers & Structures*, **7**, 343–353.

Flanagan, D.P., Belytschko, T. (1981) A uniform strain hexahedron and quadrilateral with orthogonal hourglass control. *Int. J. Num. Methods Engng.*, **17**, 679–706.

Fried, I. (1972) Bounds on the extremal eigenvalues of the finite element stiffness and mass matrices and their spectral condition number. *Journal of Sound and Vibration*, **22**, 407–418.

18th International Conference
ENGINEERING MECHANICS 2012
Svratka, Czech Republic, May 14 – 17, 2012

pp. 1011–1016
Paper #346

VARIANTS OF NAVIER-STOKES EQUATIONS

F. Pochylý[*], S. Fialová[**], H. Krausová[***]

Abstract: *The different variants of the Navier -Stokes equations are presented in the paper. The authors also present new variants to be used for qualitative analysis of the fluid flow. New variants can also be used for the numerical solution, especially for the method of control volumes.*

Keywords: ***Navier-Stokes equations, compressible liquid, bulk viscosity.***

1. Introduction

Nowadays, research in fluid flow is mainly focused on computational simulation. Often, however, a qualitative analysis of the problem is missing. Predicting the behavior of the pressure and the velocity fields can be based on qualitative analysis of the Navier -Stokes equations and continuity equation. Firstly, it is necessary to modify the above mentioned equations to a suitable form for analysis.

Recently, the questions of unsteady fluid motion are being solved. Modified Navier -Stokes equations into a new form might serve for these purposes. This form is suitable for qualitative analysis of the interaction of body with fluids, as well as for the new variant of the method of control volumes.

It is possible that the proposed modifications of the local gravity acceleration forces are already known. In this case, the author believes that the shown diversity of the Navier Stokes equations will serve to the readers.

Used symbols

x_i - Cartesian system coordination, y_i - rotating system coordination, t - time, $\mathbf{u}$ - translation, $\mathbf{v}$ - absolute velocity, $\mathbf{n}$ - outer normal vector to the liquid, $\mathbf{w}$ - relative velocity, $\boldsymbol{\omega}$ - angular velocity, δ_{ij} - Kronecker delta, ε_{ijk} - Levi-Civit tensor, $\boldsymbol{\Omega}$ - $\operatorname{rot}\mathbf{v}, \operatorname{rot}\mathbf{w}; \Delta\mathbf{v} = -\operatorname{rot}\boldsymbol{\Omega} + \operatorname{grad}\operatorname{div}\mathbf{v}$, η - dynamical viscosity. ξ - bulk viscosity, λ - second viscosity, ρ - density, $\mathbf{H}$ - magnetic field intensity, μ - surroundings permeability, $\mathbf{g}$ - gravity acceleration, $\mathbf{x}$ - (x_1, x_2, x_3), $\mathbf{y}$ - (y_1, y_2, y_3), Y – specific energy, $\mathbf{U}$ - tangential velocity, v - sound velocity, the sum convention is used in the paper.

2. Compressible liquid

As it is well known that the equation of force equilibrium of macroscopic fluid particle can be written in the form:

$$\rho \frac{dv_i}{dt} - \frac{\partial \sigma_{ij}}{\partial x_j} = G_i . \tag{1}$$

[*] Prof. Ing. František Pochylý, CSc.: Institute of Power Engineering, Brno University of Technology, Technická 2896/2; 616 69, Brno; CZ, e-mail: pochyly@fme.vutbr.cz

[**] Ing. Simona Fialová, Ph.D.: Institute of Power Engineering, Brno University of Technology; Technická 2896/2; 616 69, *Brno*; CZ, e-mail: fialova@fme.vutbr.cz

[***] Ing. Hana Krausová: Institute of Power Engineering, Brno University of Technology; Technická 2896/2; 616 69, Brno; CZ, e-mail: y100881@stud.fme.vutbr.cz

It is solved together with the continuity equation:

$$\frac{dp}{dt} + \rho v^2 \frac{\partial v_i}{\partial x_i} = 0. \tag{2}$$

It is possible to split the stress tensor σ_{ij} on the bases of superposition (de Groot and Mazur 1962) into two parts:

$$\sigma_{ij} = \tau_{ij} + \Pi_{ij} \tag{3}$$

The first part τ_{ij} is connected with the so called reversible thermodynamic phenomenon and is represented by the pressure function *p*, see the term:

$$\tau_{ij} = -p\delta_{ij}\,. \tag{4}$$

The irreversible part Π_{ij} includes the damping properties of the liquid. These properties may vary significantly for different types of fluids. Therefore it is necessary to seek constitutive relations for each fluid separately, where the stress tensor Π_{ij} depends on the strain rate tensor. According to this dependence, fluids are divided into so-called Newtonian and the other rheological fluids (e.g. Bingham).

In this paper we consider only the Newtonian fluids that are characterized by dependence:

$$\Pi_{ij} = 2\eta v_{ij} + \lambda \delta_{ij} v_{kk} \tag{5}$$

where λ is so-called second viscosity (Brdička et al., 2000; de Groot and Mazur, 1962; Pochylý et al., 2011).

Based on the kinetic theory of gases principle, Enskog (Brdička et al., 2000) derived the relationship:

$$\lambda = -\frac{2}{3}\eta\,. \tag{6}$$

On the basis of a series of experiments it was found (Pochylý et al. 2011) that this relationship is not endorsed and has to be supplemented by the value of bulk viscosity ξ, so that:

$$\lambda = \xi - \frac{2}{3}\eta. \tag{7}$$

The results of the experiments suggest that λ strongly depends on the frequency. For water, the following applies:

$$\lambda = \rho\frac{9800}{f}\ ;\quad f < 1000 H_z. \tag{8}$$

When we expressed $\frac{dv_i}{dt}$ in Euler approach and considering (4), (5), (7), can be (1) written in

the form: $$\rho\frac{\partial v_i}{\partial t} + \rho\frac{\partial}{\partial x_i}\left[\frac{1}{2}|\mathbf{v}|^2\right] - \rho\varepsilon_{ijk} v_j \Omega_k - (2\eta+\lambda)\frac{\partial^2 v_k}{\partial x_i \partial x_k} + \eta\varepsilon_{ijk}\frac{\partial \Omega_k}{\partial x_j} + \operatorname{grad} p = G_i\,, \tag{9}$$

or as a vector:

$$\rho\frac{\partial \mathbf{v}}{\partial t} + \rho\operatorname{grad}\left(\frac{1}{2}|\mathbf{v}|^2\right) - \rho\mathbf{v}x\boldsymbol{\Omega} - (2\eta+\lambda)\operatorname{graddiv}\mathbf{v} + \eta\operatorname{rot}\boldsymbol{\Omega} + \operatorname{grad} p = \mathbf{G}. \tag{10}$$

Vector $\mathbf{G}$ on the right side of (10) represents the bulk force. This effect is caused by external gravitational fields $\mathbf{G}_g$, or electromagnetic fields $\mathbf{G}_M$. For these forces the relations hold:

$$\mathbf{G}_g = \rho \mathbf{g}; \qquad \mathbf{G}_M = \mu \operatorname{rot} \mathbf{H} \times \mathbf{H} \tag{11}$$

In the text that follows, we neglect $\mathbf{G}_M$, as the influence of magnetic fields deserves a special attention.

In many technical applications, the specific energy Y is of an importance, defined by term:

$$Y = \frac{|\mathbf{v}|^2}{2} + \frac{p}{\rho} - \mathbf{g} \cdot \mathbf{x}. \tag{12}$$

For these purposes, it is appropriate to modify the expression for the gravitational force $\mathbf{G}_g$. We propose a new shape for $\mathbf{G}_g$. It is easy to show that the following holds:

$$\mathbf{G}_g = \rho \operatorname{grad}(\mathbf{g} \cdot \mathbf{x}). \tag{13}$$

By this definition of gravitational forces, the equation (10) can be modified by using the specific energy:

$$\rho \frac{\partial \mathbf{v}}{\partial t} + \rho \operatorname{grad} Y - \rho \mathbf{v} \times \boldsymbol{\Omega} - (2\eta + \lambda) \operatorname{graddiv} \mathbf{v} + \eta \operatorname{rot} \boldsymbol{\Omega} = 0. \tag{14}$$

When solving small oscillations of a body in the compressible fluid, equations (14) could be written using the translation $\mathbf{u}$. If we decompose the liquid field into its stationary and non-stationary components induced by small oscillations of the body, it can be written that (Pochylý, 2009).

$$p = -\rho v^2 \operatorname{div} \mathbf{u} \tag{15}$$

$$\begin{aligned} &\mathbf{v} = \mathbf{v}_0 + \mathbf{c}; \quad \mathbf{v}_0 = \mathbf{v}_0(\mathbf{x}); \quad \mathbf{c} = \mathbf{c}(\mathbf{x}, t) \\ &\boldsymbol{\Omega} = \boldsymbol{\Omega}_0 + \boldsymbol{\omega}; \quad \boldsymbol{\Omega}_0 = \boldsymbol{\Omega}_0(\mathbf{x}); \quad \boldsymbol{\omega} = \boldsymbol{\omega}(\mathbf{x}, t) \end{aligned}. \tag{16}$$

If we neglect in the equation (14) the small velocity components and when we express it using the translation

$$\mathbf{c} = \frac{\partial \mathbf{u}}{\partial t}, \tag{17}$$

it (1.10) can be written in the form:

$$\rho \frac{\partial \mathbf{c}}{\partial t} + \rho \operatorname{grad}(\mathbf{v}_0 \mathbf{c}) - \rho \mathbf{v}_0 \times \boldsymbol{\omega} - \rho \mathbf{c} \times \boldsymbol{\Omega}_0 - (2\eta + \lambda) \operatorname{graddiv} \mathbf{c} + \eta \operatorname{rot} \boldsymbol{\omega} - \rho v^2 \operatorname{graddiv} \mathbf{u} = 0 \tag{18}$$

This form of the equation allows using the ANSYS software environment, which is commonly used in the classical mechanics problems solutions.

3. Incompressible liquid

The incompressibility condition is expressed by the continuity equation in the form:

$$\operatorname{div} \mathbf{v} = 0. \tag{19}$$

on the basis of this equation, (14) can be simplified to the form:

$$\rho\frac{\partial \mathbf{v}}{\partial t}+\rho\,\mathrm{grad}\,Y-\rho\mathbf{v}\times\boldsymbol{\Omega}+\eta\,\mathrm{rot}\,\boldsymbol{\Omega}=0..\tag{20}$$

Equation (20) is easily written in the index symbolism in two versions:

$$\rho\frac{\partial v_i}{\partial t}+\rho\frac{\partial Y}{\partial x_i}-\rho\varepsilon_{ijk}\varepsilon_{klm}v_j\frac{\partial v_m}{\partial x_j}-\eta\frac{\partial^2 v_i}{\partial x_j\partial x_j}=0.\tag{21}$$

or in a simpler form:

$$\frac{\partial v_i}{\partial t}+\frac{\partial}{\partial x_j}\left(v_iv_j+\delta_{ij}\frac{p}{\rho}-\delta_{ij}g_kx_k-\frac{\eta}{\rho}\frac{\partial v_i}{\partial x_j}\right)=0.\tag{22}$$

For the investigation of the force effects between the liquid and the body it is suitable to write the equation (22) in the basic form (1), taking into account the substance's derivative.

$$\frac{dv_i}{dt}=\frac{\partial v_i}{\partial t}+\frac{\partial v_i}{\partial x_j}v_j\tag{23}$$

Under these assumptions, (1) can be written for example in the form:

$$\rho\frac{\partial v_i}{\partial t}+\rho\frac{\partial}{\partial x_j}\left(v_iv_j-\delta_{ij}g_kx_k\right)-\frac{\partial\sigma_{ij}}{\partial x_j}=0.\tag{24}$$

Assuming that the body is made up of multiple contiguous areas bounded by the surface S and the liquid is sealed in the field V in between Γ and S, you can write for the force $\mathbf{F}$ the relationship

$$\left(\mathbf{F}\right)_i=F_i=-\int_S\sigma_{ij}n_j\,dS.\tag{25}$$

After integration of (24) using the Gauss-Ostrogradsky theorem we obtain:

$$F_i=-\rho\int_V\frac{\partial v_i}{\partial t}dV-\rho\int_{S\cup\Gamma}\left(\rho v_iv_j-\delta_{ij}g_kx_k\right)n_j\,d\Theta+\int_\Gamma\sigma_{ij}n_j\,d\Gamma\,.\tag{26}$$

The forces analysis in the unsteady motion of the body in the liquid according to the relation (26) is complex, given that you cannot reliably determine the effect of volume integrals.

This deficiency can be removed by following the proposed modification. Easy to see that, assuming (19), it holds:

$$\frac{\partial v_i}{\partial t}=\frac{\partial}{\partial x_j}\left(\frac{\partial v_j}{\partial t}x_i\right)\tag{27}$$

Using this adjustment, (24) as well as (26) can be significantly simplified. Substituting into (24), (26) we obtain:

$$\frac{\partial}{\partial x_j}\left[\rho\frac{\partial v_j}{\partial t}x_i+\rho v_iv_j-\sigma_{ij}-\delta_{ij}\rho g_kx_k\right]=0\tag{28}$$

$$F_i = -\int_{S\cup\Gamma} \rho\left(\frac{\partial v_j}{\partial t}x_i + v_i v_j - \delta_{ij} g_k x_k\right) n_j d\Theta + \int_{\Gamma} \sigma_{ij} n_j d\Gamma. \tag{29}$$

The right side of the expression (29) is no longer dependent on the volume integrals and determines the additional effects of the liquid on the body.

Equation (28) can serve as a starting point for the solution of the non-stationary fluid mechanics problems, including unsteady body motion in the liquid.

For example, for a method of control volumes: By the integrating of (28) over the control volume ΔV bounded by the surface ΔS, the following equation can be obtained:

$$\iint_{\Delta S}\left(\rho\frac{\partial v_j}{\partial t}x_i + \rho v_i v_j - \sigma_{ij}\delta_{ij}\rho g_k x_k\right) n_j d\Delta S = 0 \tag{30}$$

4. Relative space

Suppose that the coordinate system (y_i) rotates to x_i by angular velocity $\boldsymbol{\omega}(\omega,0,0)$. Navier -Stokes equations in the system (y_i) can be written for incompressible liquid for example in the following two options:

$$\rho\frac{\partial \mathbf{w}}{\partial t} + \rho\boldsymbol{\omega}x(\boldsymbol{\omega}\times\mathbf{y}) - 2\rho\boldsymbol{\omega}\times\mathbf{w} - \eta\Delta\mathbf{w} + \operatorname{grad}(p - \rho\mathbf{g}\mathbf{y}) = 0 \tag{31}$$

$$\rho\frac{\partial \mathbf{w}}{\partial t} + \rho\operatorname{grad}[Y - U(\mathbf{v}\cdot\mathbf{U}) - \mathbf{g}\cdot\mathbf{y}] - \mathbf{w}x(2\boldsymbol{\omega} + \operatorname{rot}\mathbf{w}) - \eta\Delta\mathbf{w} = 0 \tag{32}$$

Also in the component form:

$$\rho\frac{\partial w_i}{\partial t} + \rho\frac{\partial}{\partial y_j}(w_i w_j) + \rho\omega^2\varepsilon_{i1k}\varepsilon_{k1m}y_m + 2\rho\omega\varepsilon_{i1k}w_k - \frac{\partial^2 w_i}{\partial y_j\partial y_j} + \frac{\partial}{\partial y_i}(p - \rho g_j y_j) = 0 \tag{33}$$

$$\rho\frac{\partial w_i}{\partial t} + \rho\frac{\partial}{\partial y_j}\left[w_i w_j - \frac{1}{2}|\mathbf{u}|^2\delta_{ij} + 2u_i w_j - \frac{\eta}{\rho}\frac{\partial w_i}{\partial y_j} + \delta_{ij}\left(\frac{p}{\rho} - g_k y_k\right)\right] = 0 \tag{34}$$

Adjusting

$$\frac{\partial w_i}{\partial t} = \frac{\partial}{\partial y_j}\left(\frac{\partial w_j}{\partial t}y_i\right) \tag{35}$$

Can be (34) rewritten into simpler form:

$$\frac{\partial}{\partial y_j}\left[\frac{\partial w_j}{\partial t}y_i + w_i w_j - \frac{1}{2}|\mathbf{u}|^2\delta_{ij} + 2u_i w_j - \frac{\eta}{\rho}\frac{\partial w_i}{\partial y_j} + \delta_{ij}\left(\frac{p}{\rho} - g_k y_k\right)\right] = 0 \tag{36}$$

The expression (36) expresses a new notation of Navier -Stokes equations in a rotating coordinate system suitable for further analysis

5. Conclusions

The paper presents some new findings, which can be used both for qualitative analysis of the flow, as well as to simplify the method of control volumes. The volume or the second viscosity is of particular importance. They can get more accurate results for reliable modeling of unsteady pressure pulsations. The essential findings presented in this study can be formulated as follows:

$$\lambda = \rho \frac{9800}{f}; \quad f < 1000 H_z \quad \text{for water}$$

$$\frac{\partial y_i}{\partial t} = \frac{\partial}{\partial x_j}\left(\frac{\partial y_i}{\partial t} x_i\right); \qquad g_i = \frac{\partial}{\partial x_i}(\mathbf{g} \cdot \mathbf{x})$$

Acknowledgement

This work was gratefully acknowledged by grant projects: P101/10/0209, FSI-S-12-2, NETME Centre ED0002/01/01.

References

Brdička, M., Samek, L. & Sopko, B. (2000) *Mechanika kontinua*. In Czech Academia, Prague.

de Groot, S. R., Mazur, P. (1962) *Non-Equilibrium Thermodynamics,* North Holland, Amsterdam, pp. 20-83.

Pochylý, F., Habán, V. & Fialová, S. (2011) Bulk Viscosity - Constitutive Equations. *International Review of Mechanical Engineering (IREME).* 2011. Vol. 5 N.(6). (20 p.). ISSN 1970-8734.

Pochylý, F. (2009) *Využití Lagrangeovy metody k řešení nestacionárního pohybu tělesa v kapalině.* Výzkumná zpráva VUT-EU13303-20-09, Brno (CZ) VUT FSI, p.7.

18th International Conference
ENGINEERING MECHANICS 2012
Svratka, Czech Republic, May 14 – 17, 2012

pp. 1017–1031
Paper #54

VALIDATION OF THE POINT-MASS MODELLING APPROACH FOR FIBRES IN THE INVERTED PENDULUM MODEL

P. Polach[*], M. Hajžman[**], O. Tuček[***]

Abstract: *Fibres, cables and wires can play an important role in design of many machines. One of interesting applications is replacing the chosen rigid elements of a manipulator or a mechanism with fibres. The main advantage of this design is achievement of a lower moving inertia, which can lead to a higher mechanism speed and lower production costs. A chosen inverted pendulum attached to a frame by two fibres serves as a typical testing system for the investigation of the fibres properties influence on the system dynamic response. Motion of the pendulum of this nonlinear system is investigated using the* ***alaska*** *simulation tool. The sophisticated point-mass fibre model is validated on the basis of the results obtained using a massless fibre model. In addition, the equation of motion based on the massless approach is studied in terms of solution existence and its uniqueness.*

Keywords: ***Inverted pendulum, fibres, multibody modelling, vibration.***

1. Introduction

One of interesting applications of cables or fibres is replacement of the chosen rigid elements of manipulators or mechanisms by those flexible elements (Chan, 2005). The main advantage of this design is the achievement of a lower moving inertia, which can lead to a higher machine speed and lower production costs. Drawbacks can be associated with the fact that cables should be only in tension (Smrž & Valášek, 2009; Valášek & Karásek, 2009) in the course of a motion. The possible cable modelling approaches should be tested and their suitability verified in order to create efficient mathematical models of cable-based manipulators mainly intended for the control algorithm design. The motion of the inverted pendulum driven by two fibres attached to a frame (see Fig. 1), which is a simplified representation of a typical cable manipulator, is investigated using the **alaska** simulation tool (and using an in-house software created in the MATLAB system). The influence of some parameters of this system has already been investigated. The influence of the actuated fibres motion on the pendulum motion in the case of their simultaneous harmonic excitation was investigated in Polach & Hajžman (2011c), in the case of non-symmetric harmonic excitation it was investigated in Polach & Hajžman (2012a). The effect of the fibres' mass on the pendulum motion was investigated in Polach et al. (2012), the effect of the fibres preload was investigated in Polach & Hajžman (2012b).

The sophisticated point-mass fibre model is validated on the basis of the results obtained using a massless fibre model. The correctness of the point-mass fibre model is partly evident from Polach et al. (2012), where results of simulations when considering relatively "light" fibre made of thin carbon fibres correspond well, up to the certain excitation frequency, with the results of simulations with massless fibre model (see also Chapter 5). In addition, in this paper the equation of motion based on the massless approach is studied in terms of solution existence and its uniqueness.

[*] Dr. Ing. Pavel Polach: Section of Materials and Mechanical Engineering Research, Výzkumný a zkušební ústav Plzeň s.r.o., Tylova 1581/46; 301 00, Plzeň; CZ, e-mail: polach@vzuplzen.cz

[**] Ing. Michal Hajžman, Ph.D.: Department of Computer-Aided Modelling, Výzkumný a zkušební ústav Plzeň s.r.o., Tylova 1581/46; 301 00, Plzeň; CZ, e-mail: hajzman@vzuplzen.cz

[***] Mgr. Ondřej Tuček: Department of Computer-Aided Modelling, Výzkumný a zkušební ústav Plzeň s.r.o., Tylova 1581/46; 301 00, Plzeň; CZ, e-mail: tucek@vzuplzen.cz

2. Possibilities of the cable modelling

The cable (fibre, wire etc.) modelling (Hajžman & Polach, 2011) should be based on considering the cable flexibility and the suitable approaches can be based on the flexible multibody dynamics (see Shabana, 1997). The simplest way how to incorporate cables in equations of motion of a mechanism is the force representation of a cable (e.g. Diao & Ma, 2009). It is assumed that the mass of cables is small to such an extent comparing to the other moving parts that the inertia of cables is negligible with respect to the other parts. The cable is represented by the force dependent on the cable deformation and its stiffness and damping properties. This way of the cable modelling is probably the most frequently used model in the cable-driven robot dynamics and control.

A more precise approach is based on the representation of the cable by a point-mass model (e.g. Kamman & Huston, 2001). The cable can be considered either flexible or rigid. It has the advantage of a lumped point-mass model. The point masses can be connected by forces or constraints.

In order to represent bending behaviour of cables their discretization using the finite segment method (Shabana, 1997) or so called rigid finite elements (Wittbrodt et al., 2006) is possible. Standard multibody codes (SIMPACK, MSC.ADAMS, **alaska** etc.) can be used for this purpose. Other more complex approaches can utilize nonlinear three-dimensional finite elements (Freire & Negrão, 2006) or can employ the absolute nodal coordinate formulation (ANCF) elements (Shabana, 1997).

Investigation of the possible approaches to the modeling of the system of inverted pendulum driven by fibres was investigated in Polach & Hajžman (2011a) and Polach & Hajžman (2011b). Implementation of the model based on the finite rigid elements into the **alaska** simulation tool proved to be unsuitable (Polach & Hajžman, 2011a). The ANCF elements cannot be implemented in the **alaska** simulation tool, verification on this approach was carried out utilizing the MATLAB system (Polach & Hajžman, 2011b).

3. Inverted pendulum

Already mentioned inverted pendulum, which is attached and driven by two fibres and affected by a gravitation force, was chosen as an example of the investigation of fibres' behaviour – see Fig. 1. When the pendulum is displaced from the equilibrium position (i.e. "upper" position) it is returned back to the equilibrium position by the tightened fibre.

The massless model is shown in Fig. 1 (the used model of the fibre based on the point-mass model with lumped point masses corresponding to the mass of the fibre is geometrically identical) – e.g. Polach & Hajžman (2011c). The models of the system of the inverted pendulum are considered to be two-dimensional.

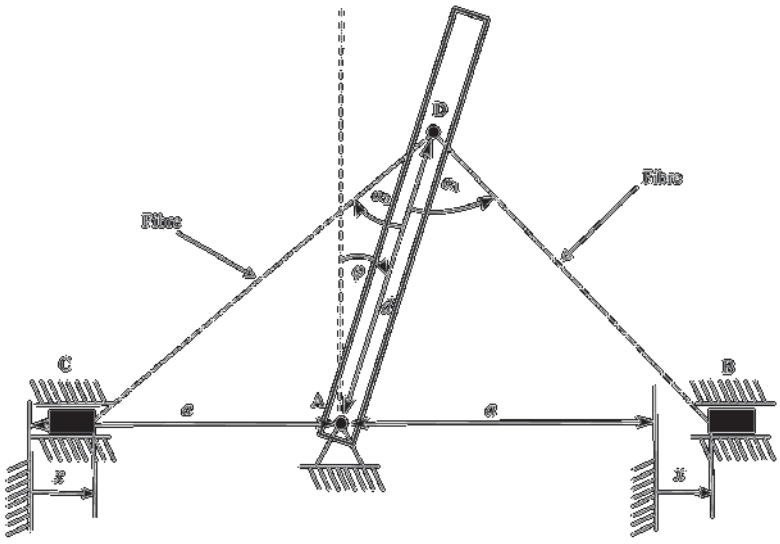

Fig. 1: Inverted pendulum actuated by the fibres.

The system kinematics can be described by angle φ (one degree of freedom) and prescribed kinematic excitation $x(t)$. The equation of motion is of the form

$$\ddot{\varphi} = \frac{1}{I_{\mathrm{A}}} \cdot \left(F_1(\varphi) \cdot d \cdot \sin \alpha_1(\varphi) - F_2 \cdot d \cdot \sin \alpha_2(\varphi) + m \cdot g \cdot \frac{l}{2} \cdot \sin \varphi \right), \tag{1}$$

where I_{A} is the moment of inertia of the pendulum with respect to the axis in point A (see Fig. 1), $\alpha_1(\varphi)$ and $\alpha_2(\varphi)$ are angles between the pendulum and the fibres, m is the mass of the pendulum, g is the gravity acceleration and l is the length of the pendulum. The forces acting on the pendulum from the fibre are

$$\begin{aligned} F_1(\varphi) &= \left[k_1 \cdot \left(l_1(\varphi) - l_0 \right) + b_1 \cdot \frac{\mathrm{d}l_1(\varphi)}{\mathrm{d}t} \right] \cdot H\left(l_1(\varphi) - l_0 \right), \\ F_2(\varphi) &= \left[k_2 \cdot \left(l_2(\varphi) - l_0 \right) + b_2 \cdot \frac{\mathrm{d}l_2(\varphi)}{\mathrm{d}t} \right] \cdot H\left(l_2(\varphi) - l_0 \right), \end{aligned} \tag{2}$$

where k_i ($i = 1, 2$) is the fibre stiffness, b_i ($i = 1, 2$) is the fibre damping coefficient and $H(\cdot)$ is the Heaviside function. It is supposed, that forces act in the fibres only when the fibres are in tension.

Original length l_0 of the fibres is supposed to be constant and actual lengths $l_1(\varphi)$ and $l_2(\varphi)$ of the fibres should be calculated in each time

$$\begin{aligned} l_1(\varphi) &= \sqrt{\left(d \cdot \cos \varphi \right)^2 + \left(a + x(t) - d \cdot \sin \varphi \right)^2}, \\ l_2(\varphi) &= \sqrt{\left(d \cdot \cos \varphi \right)^2 + \left(a - x(t) + d \cdot \sin \varphi \right)^2}. \end{aligned} \tag{3}$$

Each fibre is discretized using 10 point masses in the fibre model based on the point masses (e.g. Polach & Hajžman, 2011c). Each point mass is unconstrained (i.e. number of degree of freedom is 3) in two-dimensional model of the system of the inverted pendulum. The adjacent point masses are connected using spring-damper elements. Only axial (spring and damping) forces are considered in these spring-damper elements. The stiffness and the damping between the masses are determined in order to keep the global properties of the massless fibre model.

The kinematic excitation is given by function

$$x(t) = x_0 \cdot \sin\left(2 \cdot \pi \cdot f \cdot t \right), \tag{4}$$

where x_0 is the chosen amplitude of motion, f is the excitation frequency and t is time. The influence of the excitation frequency on the pendulum motion is investigated. Excitation in points designated B and C (see Fig. 1) is considered to be symmetrical (without any mutual phase shift) and of the same amplitude x_0.

4. Existence and uniqueness of the solution of the pendulum motion equation

Before the validation of the point-mass fibre model the existence and uniqueness of the solution should be studied. For sake of such an analysis the pendulum equation of motion based on the fibre modelling by massless approach (1) can be rewritten to form

$$\begin{aligned} &\ddot{\varphi}(t) = f\left(t, \varphi, \dot{\varphi} \right), \\ &\varphi(0) = 0, \\ &\varphi(T) = 0, \\ &t \in [0, T], \end{aligned} \tag{5}$$

where

$$f\left(t, \varphi, \dot{\varphi} \right) = B_0 \cdot F_1(\varphi) \cdot \sin \alpha_1(\varphi) - B_0 \cdot F_2(\varphi) \cdot \sin \alpha_2(\varphi) + B_1 \cdot \sin \varphi, \tag{6}$$

$$\sin\alpha_1(\varphi)=\frac{\cos\varphi}{l_1(\varphi)}\cdot\big(a+x(t)\big),$$
$$\sin\alpha_2(\varphi)=\frac{\cos\varphi}{l_2(\varphi)}\cdot\big(a-x(t)\big), \tag{7}$$
$$B_0=\frac{d}{I_A},\quad B_1=\frac{m\cdot g\cdot l}{2\cdot I_A},$$

$F_1(\varphi)$ and $F_2(\varphi)$ are given by expressions (2), $l_1(\varphi)$ and $l_2(\varphi)$ are given by expressions (3) and T is the time of the end of numerical simulation.

Function $x(t)$ is considered to be smooth function of property

$$\left|\dot{x}(t)\right|\le\tilde{K}. \tag{8}$$

From previous estimate it is easy to derive the following condition

$$\left|x(t)\right|\le K,$$

where from the physical point of view constant K fulfills

$$d-a<K<d+a.$$

Constants a, d, l_0, $\tilde{K}$, K, k_i (i = 1, 2), b_i (i = 1, 2) in equations (1), (2), (3), (8) are positive real numbers.

It is reasonable to suppose that velocity of pendulum is bounded, i.e. there is a positive constant R such that

$$\left|\dot{\varphi}(t)\right|\le R. \tag{9}$$

Based on expression (2) it can be seen that $F_i(\varphi)$ (i = 1, 2) is discontinuous due to appearing the Heaviside function. Hence function $f(t,\varphi,\dot{\varphi})$ on the right hand side of (5) is also discontinuous and nonlinear. Thus it is obvious that there is no solution for $\varphi\in C^2$, where C^k, k = 2, is space of all functions such that the k-th derivative exists and is continuous.

4.1. Preliminaries

Throughout this section a notation $|\cdot|$ for absolute value in $\mathbb{R}$ and space

$$C_0^1\big([0,T]\big)=\big\{u\in C^1\big([0,T],\mathbb{R}\big):u(t)=0,\ t\in\{0,T\}\big\}$$

will be used.

Let $T>0$ be given and let

$$f(t,u,v):[0,T]\times\mathbb{R}\times\mathbb{R}\to\mathbb{R}$$

be a mapping satisfying the Carathéodory conditions (e.g. Drábek & Milota, 2007; Rachůnková et al., 2009), which are

1. $f(t,u,v)$ is continuous in (u,v) for almost all $t\in[0,T]$,
2. $f(t,u,v)$ is measurable in t for fixed (u,v),
3. for each compact set $\kappa\subset\mathbb{R}^2$, there is a function $h(t)\in L_1\big([0,T]\big)$ such that

$$\left|f(t,u,v)\right|\le h(t)\ \text{ for a.e. } t\in[0,T]\ \text{ and all }(u,v)\in\kappa, \tag{10}$$

where L_1 is space of measurable functions such that $\int_0^T\left|h(t)\right|\cdot dt<\infty$.

Following theorems with proofs can be found in Rachůnková et al. (2009) and Schmitt & Thompson (2004).

Theorem 1 *Let* $f(t,u,v)$ *satisfy the Carathéodory conditions and assume that there is a function* $h(t)\in L_1([0,T])$ *such that*

$$|f(t,u,v)|\le h(t) \text{ for a.e. } t\in[0,T] \text{ and } \forall u,v\in\mathbb{R}. \tag{11}$$

Then problem (5) has a solution.

Theorem 2 *Let* $f(t,u,v)$ *satisfy the Carathéodory conditions and*

$$|f(t,u,v)-f(t,\overline{u},\overline{v})|\le A_0\cdot|u-\overline{u}|+A_1\cdot|v-\overline{v}|,\ \forall u,v,\overline{u},\overline{v}\in\mathbb{R},t\in[0,T], \tag{12}$$

where A_0, A_1 *are positive constants such that*

$$\frac{A_0\cdot T^2}{\pi^2}+\frac{A_1\cdot T}{\pi}<1. \tag{13}$$

Then problem (5) has a unique solution $\varphi\in C_0^1([0,T])$*, with* $\dot{\varphi}$ *absolutely continuous and equation (5) being satisfied almost everywhere.*

4.2. Main qualitative result

The solvability of problem (5) is investigated in this subchapter. It is known that there exist points in $[0,T]$ where function $f(t,u,v)$ is discontinuous and the Lebesgue measure of the set of these points is equal zero. Thus for almost all $t\in[0,T]$ is $f(t,u,v)$ continuous, it means the first condition of the Carathéodory conditions is satisfied. The second condition is obviously satisfied, too.

Now if the same *R* as in (9) is used $\kappa=[-R,R]\times[-R,R]$ can be chosen. Then the inequality (10) will be fulfilled with $h(t)$ in the form

$$\begin{aligned}|f(t,u,v)|&\le B_0\cdot\left|F_1(u,v)\cdot\frac{\cos u}{l_1(u)}\right|\cdot|a+x(t)|+B_0\cdot\left|F_2(u,v)\cdot\frac{\cos u}{l_2(u)}\right|\cdot|a-x(t)|+B_1\\&\le\left(C_0+C_1+(C_2+C_3)\cdot\left(d\cdot R\cdot(a+K)+\tilde{K}\cdot(a+K)+d\cdot\tilde{K}\right)\right)\cdot(a+K)=h(t),\end{aligned} \tag{14}$$

where

$$\begin{aligned}&C_0=B_0\cdot k_1\cdot\left(1+\frac{l_0}{|K+(a-d)|}\right),\quad C_1=B_0\cdot k_2\cdot\left(1+\frac{l_0}{|K-(a-d)|}\right),\\&C_2=\frac{B_0\cdot b_1}{(K+(a-d))^2},\quad C_3=\frac{B_0\cdot b_2}{(K-(a-d))^2}\quad,\end{aligned} \tag{15}$$

so $h(t)$ is element of L_1. Therefore $f(t,u,v)$ satisfies the Carathéodory conditions and assumptions of Theorem 1 too.

Condition (12) of Theorem 2 remains to be checked. It holds

$$\begin{aligned}&|f(t,u,v)-f(t,\overline{u},\overline{v})|\le B_0\cdot\left|F_1(u,v)\cdot\frac{\cos u}{l_1(u)}\cdot(a+x(t))-F_1(\overline{u},\overline{v})\cdot\frac{\cos\overline{u}}{l_1(\overline{u})}\cdot(a+x(t))-\right.\\&\left.\left(F_2(u,v)\cdot\frac{\cos u}{l_2(u)}\cdot(a-x(t))-F_2(\overline{u},\overline{v})\cdot\frac{\cos\overline{u}}{l_2(\overline{u})}\cdot(a-x(t))\right)\right|+B_1\cdot|\sin u-\sin\overline{u}|\le\\&B_0\cdot\left|\left|(-d)\cdot(v-\overline{v})\right|\cdot\frac{b_1\cdot(a+K)^2}{(K+(a-d))^2}+\left|d\cdot(v-\overline{v})\right|\cdot\frac{b_2\cdot(a+K)^2}{(K-(a+d))^2}\right|+B_1\cdot|u-\overline{u}|=\\&B_1\cdot|u-\overline{u}|+B_0\cdot\left(\frac{d\cdot b_1\cdot(a+K)^2}{(K+(a-d))^2}+\frac{d\cdot b_2\cdot(a+K)^2}{(K-(a+d))^2}\right)\cdot|v-\overline{v}|\quad.\end{aligned} \tag{16}$$

In estimations (14) and (16) inequalities

$$\left|\sin(\cdot)\right| \le 1, \quad \left|\cos(\cdot)\right| \le 1, \quad \left|\sin u - \sin \overline{u}\right| \le \left|u - \overline{u}\right|, \quad \left|H(\cdot)\right| \le 1,$$

$$\frac{1}{\sqrt{d^2 - 2 \cdot d \cdot \left(a \pm x(t)\right) \cdot \sin u + \left(a \pm x\right)^2}} \le \frac{1}{\left|K \pm (a-d)\right|}, \tag{17}$$

and (9) were used.

It can be seen comparing (13) and (16) that

$$A_0 = B_1$$

and

$$A_1 = d \cdot B_0 \cdot (a+K)^2 \cdot \left(\frac{b_1}{\left(K + (a-d)\right)^2} + \frac{b_2}{\left(K - (a+d)\right)^2} \right). \tag{18}$$

Finally if function $x(t)$ can be chosen such that $\left|x(t)\right| \le K = d$ then one gets

$$A_1 = \frac{d \cdot B_0 \cdot (a+d)^2}{a^2} \cdot (b_1 + b_2). \tag{19}$$

If inequality (13) holds for A_0, A_1 and T it was proven that unique solution

$$\varphi \in C_0^1\left([0,T]\right)$$

of (5) exists.

Now T can be chosen arbitrarily so it might happen that condition (13) would not be satisfied and problem (5) would not have a solution. Thus it is difficult to find or proof other theorem which has less restrictive condition then (13). So if T will be chosen in order to fulfil (13) then a unique solution exists, which is absolutely continuous.

5. Numerical simulations

5.1. Parameters of pendulum models

The most important model parameters (see Fig. 1) are: $l = 1$ m, $a = 1.2$ m, $d = 0.75$ m, $I_A = 3.288$ kg·m^2, $m = 9.864$ kg, stiffness $k_i = 8.264 \cdot 10^4$ N/m ($i = 1, 2$), damping coefficient $b_i = 5 \cdot 10^{-4} \cdot k_i$ N·s/m ($i = 1, 2$). In the case of the point-mass fibre model very low mass of fibre was considered (in contradiction to Polach & Hajžman, 2011a; Polach & Hajžman, 2012b; Polach & Hajžman, 2011c; Polach et al., 2012; Polach & Hajžman, 2012a): mass of one fibre is 0.1 grams. To compare: mass of the so far lightest considered (carbon) real fibre was 3.846 grams – Polach et al. (2012). The natural frequency of the linearized system of the inverted pendulum in equilibrium position at consideration the massless fibre model is 5.04 Hz.

5.2. Verification of the point-mass fibre model

The kinematic excitation amplitude (see Eq. (4)) $x_0 = 0.02$ m was chosen (as in Polach & Hajžman, 2011a; Polach & Hajžman, 2011c; Polach et al., 2012; Polach & Hajžman, 2012a and Polach & Hajžman, 2012b). Excitation frequency f was considered in the range from 0.1 Hz to 200 Hz.

Time histories and extreme values of pendulum angle φ (maximum value of pendulum angle at quasi-static loading is $\varphi = 1.52°$; minimum value of pendulum angle at quasi-static loading is logically $\varphi = -1.52°$) are the validated quantities. Selected results of the numerical simulations are presented in Figs 2 to 22. Simulation time is 10 seconds. It was tested that after this period the character of the system response to the kinematic excitation does not change (e.g. Polach & Hajžman, 2011c).

Generally, the pendulum motion is influenced by the excitation frequency of the moving fibres – Polach & Hajžman (2011a); Polach & Hajžman (2011c); Polach et al. (2012); Polach & Hajžman (2012a); Polach & Hajžman (2012b) and Figs 2 to 22.

Extreme values of pendulum angle φ at consideration the massless fibre model and the point-mass fibre model are given in Figs 2 and 3. Absolute differences of pendulum angle φ of point-mass fibre model, i.e. $\left(\varphi_{\max\,\text{massless}} - \varphi_{\max\,\text{point-mass}}\right)$ and $\left(\varphi_{\min\,\text{massless}} - \varphi_{\min\,\text{point-mass}}\right)$, are given in Figs 4 and 5. Relative differences of pendulum angle φ of point-mass fibre model, i.e. $\left(\varphi_{\max\,\text{massless}} - \varphi_{\max\,\text{point-mass}}\right)/\varphi_{\max\,\text{massless}}$ and $\left(\varphi_{\min\,\text{massless}} - \varphi_{\min\,\text{point-mass}}\right)/\varphi_{\min\,\text{massless}}$, are given in Figs 6 and 7 and in Tab. 1. For the purpose of comparing, Figs 2 to 7 show even dependences of plotted quantities of inverted pendulum attached using carbon fibres (Polach et al., 2012). Remarkable time histories of pendulum angle φ at various excitation frequencies are given in Figs 8 to 22.

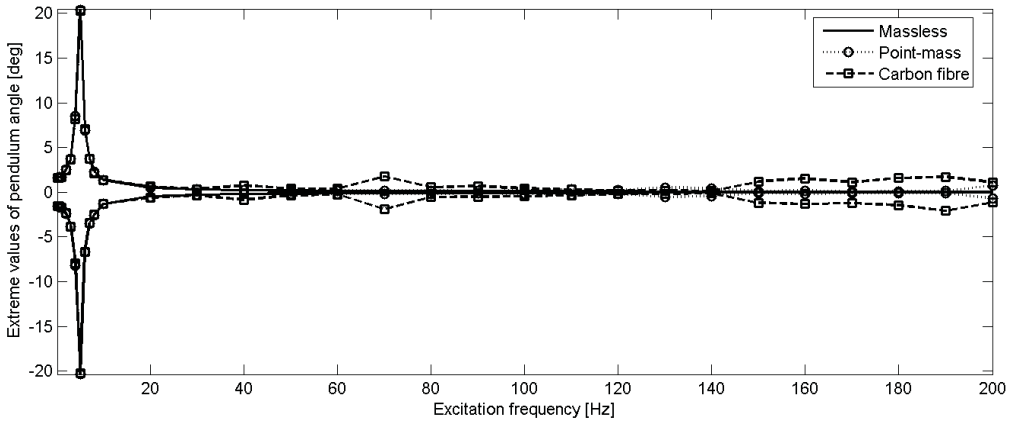

Fig. 2: Extreme values of time histories of pendulum angle φ in dependence on the excitation frequency (in the whole investigated frequency range).

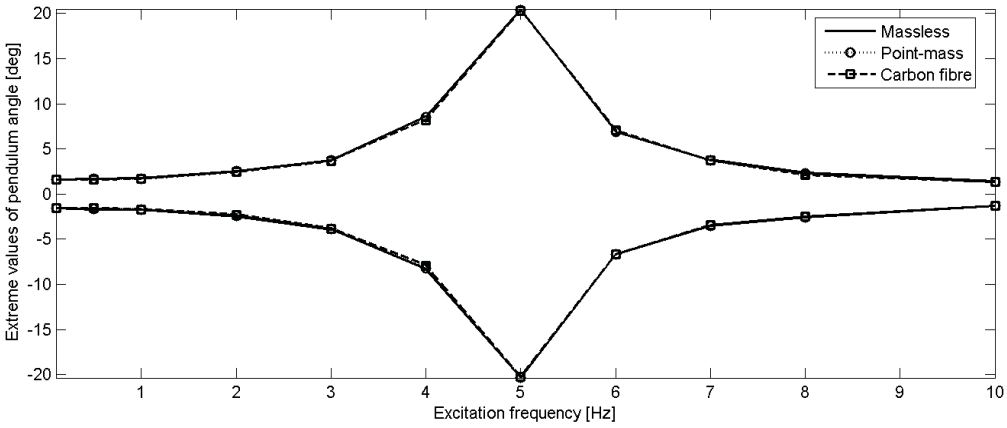

Fig. 3: Extreme values of time histories of pendulum angle φ in dependence on the excitation frequency (up to 10 Hz only).

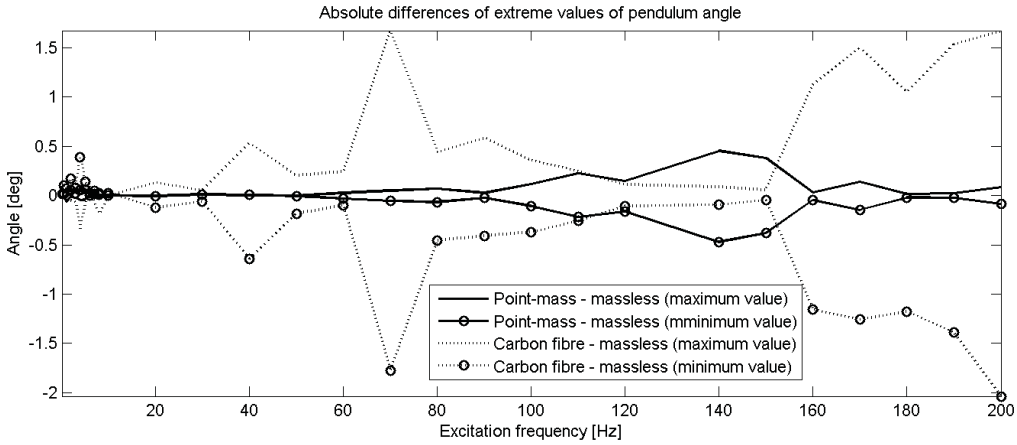

Fig. 4: Absolute differences of extreme values of time histories of pendulum angle φ in dependence on the excitation frequency (in the whole investigated frequency range).

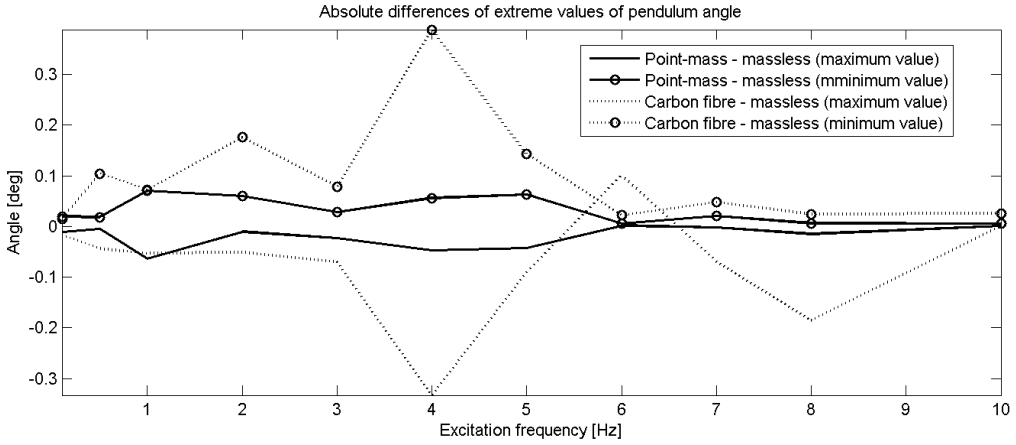

Fig. 5: Absolute differences of extreme values of time histories of pendulum angle φ in dependence on the excitation frequency (up to 10 Hz only).

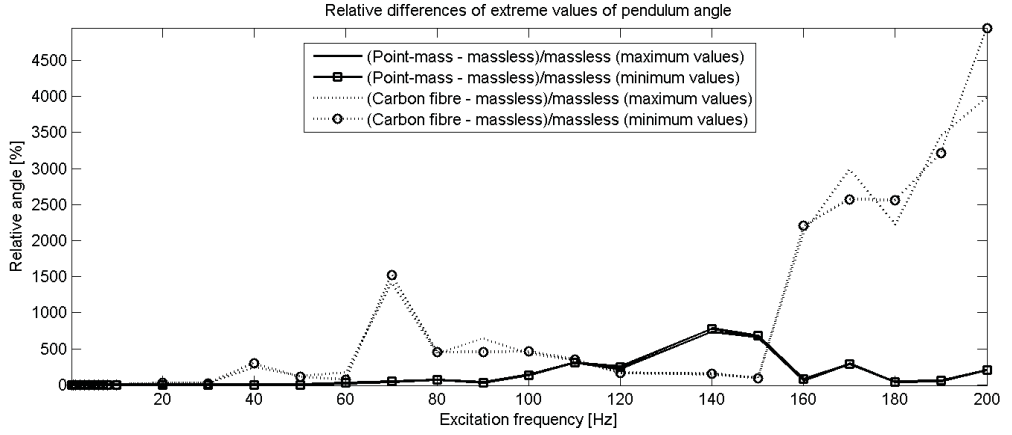

Fig. 6: Relative differences of extreme values of time histories of pendulum angle φ in dependence on the excitation frequency (in the whole investigated frequency range).

Tab. 1: Simulations results.

Excitation frequency f [Hz]	**Relative differences of minimum values of pendulum angle φ [%]**	**Relative differences of maximum values of pendulum angle φ [%]**
0.1	-1.2	-0.7
0.5	-1.1	-0.3
1	-4.0	-3.6
2	-2.4	-0.4
3	-0.7	-0.6
4	-0.7	-0.6
5	-0.3	-0.2
6	-0.1	0
7	-0.6	-0.1
8	-0.3	-0.7
10	-0.4	0.1
20	1.8	0
30	-3.2	3.5
40	-3.3	1.2
50	1.9	-0.1
60	23.4	19.2
70	46.2	42.8
80	65.8	66.1
90	26.5	29.3
100	131.8	142.0
110	303.6	305.1
120	249.7	218.0
140	776.3	734.0
150	678.4	662.9
160	80.4	56.0
170	290.8	277.9
180	39.0	34.3
190	58.4	53.4
200	206.8	206.7

From the courses of the quantities in Figs 2, 4 and 6 and from Tab. 1 it is evident that a good compliance of the results obtained at simulating with inverted pendulum models with the point-mass fibre model and with the massless fibre model is up to the excitation frequencies of approx. 50 Hz (see Figs 2 to 17). At higher excitation frequencies partly vibration of individual point masses and partly probably also influence of numerical errors at solving equations of motion apparently show up in the results of simulations (see Figs 18 to 22). This fact is evident especially from time histories of

pendulum angle φ at excitation frequencies 60 Hz and 70 Hz in Figs 18 and 19, in which time histories of pendulum angle φ of point-mass models with "slightly higher" mass of the "verified" fibre (by 10 %) and when considering carbon fibres are given in addition. Due to the change of the characters of time histories of pendulum angle φ at simulating with inverted pendulum models with the point-mass fibre model and with the massless fibre model (from the excitation frequencies 60 Hz) it is necessary to take the comparison of the extreme values of pendulum angle φ given in Figs 2, 4 and 6 and Tab. 1 cautiously (especially the relative differences of extreme values).

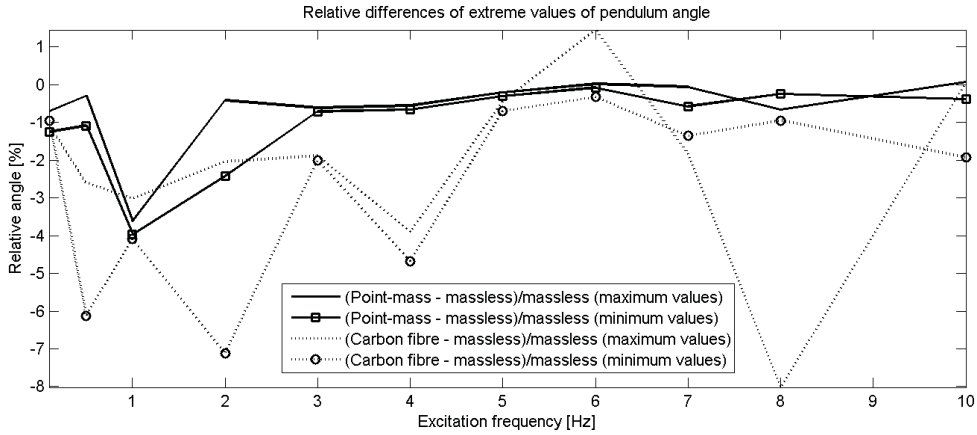

Fig. 7: Relative differences of extreme values of time histories of pendulum angle φ in dependence on the excitation frequency (up to 10 Hz only).

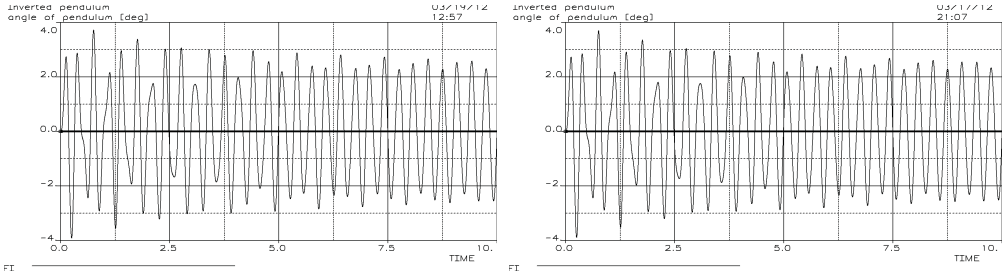

a) *b)*

Fig. 8: Time history of pendulum angle φ, excitation frequency f = 3 Hz, a) massless model, b) point-mass model.

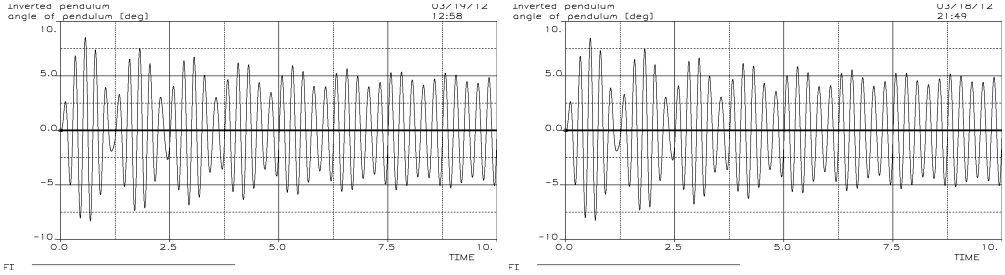

a) *b)*

Fig. 9: Time history of pendulum angle φ, excitation frequency f = 4 Hz, a) massless model, b) point-mass model.

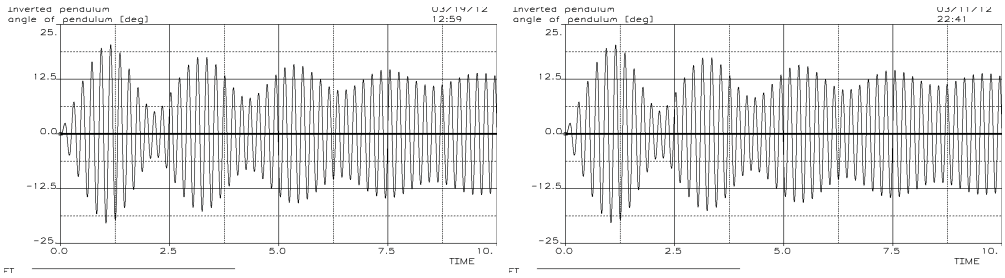

a) *b)*

Fig. 10: Time history of pendulum angle φ, excitation frequency f = 5 Hz, a) massless model, b) point-mass model.

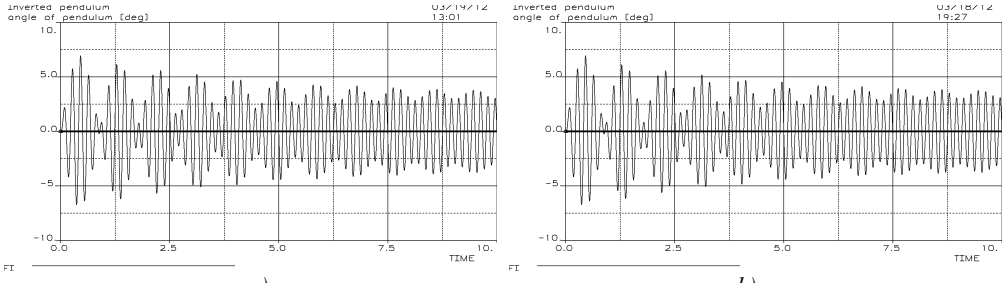

a) *b)*

Fig. 11: Time history of pendulum angle φ, excitation frequency f = 6 Hz, a) massless model, b) point-mass model.

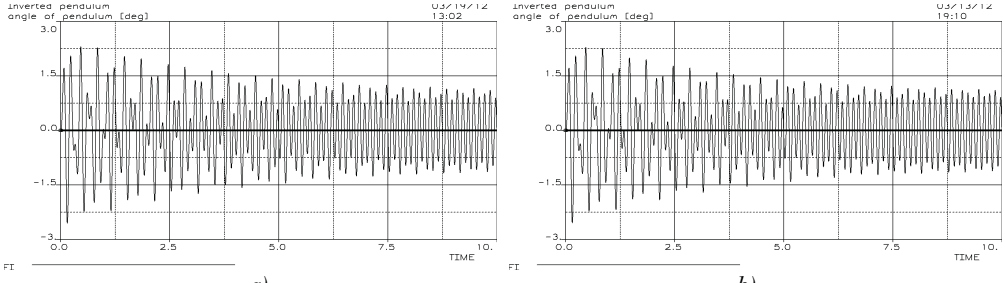

a) *b)*

Fig. 12: Time history of pendulum angle φ, excitation frequency f = 8 Hz, a) massless model, b) point-mass model.

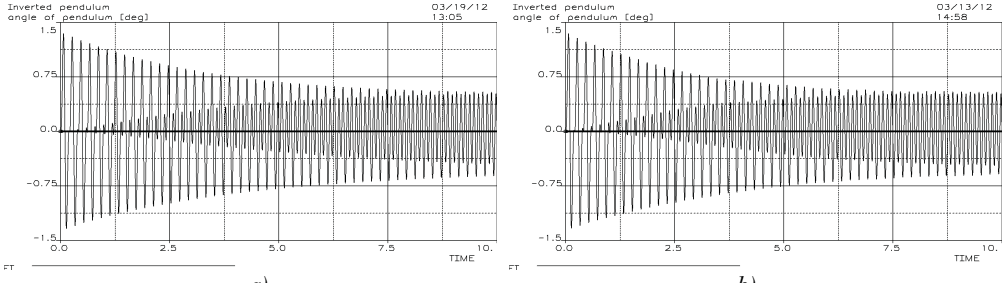

a) *b)*

Fig. 13: Time history of pendulum angle φ, excitation frequency f = 10 Hz, a) massless model, b) point-mass model.

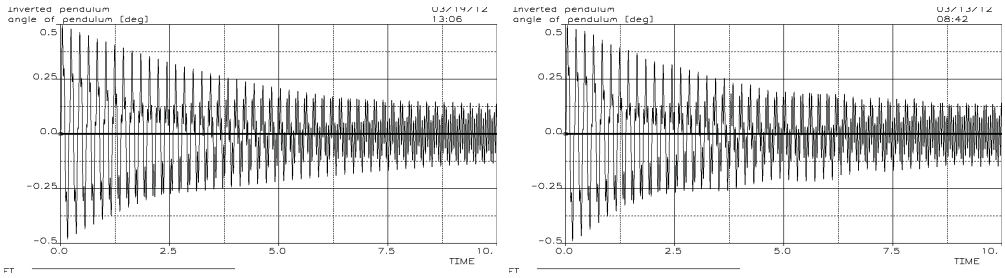

a) *b)*

Fig. 14: Time history of pendulum angle φ, excitation frequency f = 20 Hz, a) massless model, b) point-mass model.

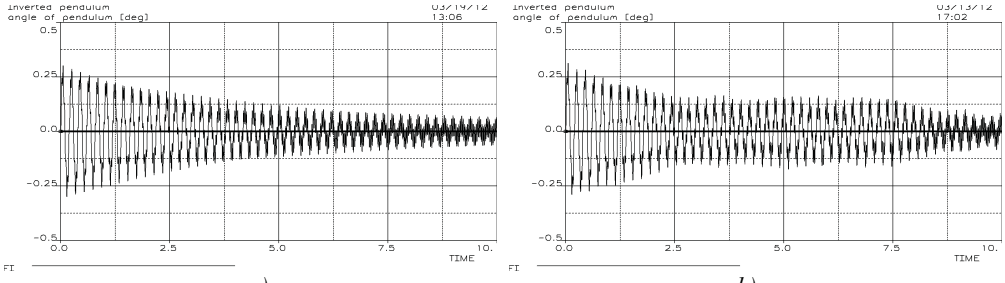

a) *b)*

Fig. 15: Time history of pendulum angle φ, excitation frequency f = 30 Hz, a) massless model, b) point-mass model.

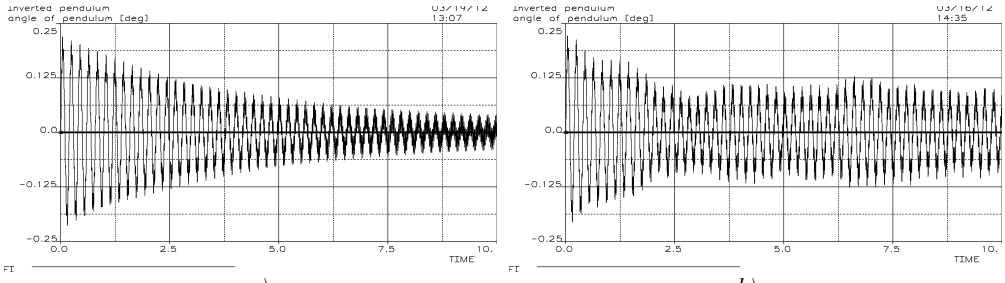

a) *b)*

Fig. 16: Time history of pendulum angle φ, excitation frequency f = 40 Hz, a) massless model, b) point-mass model.

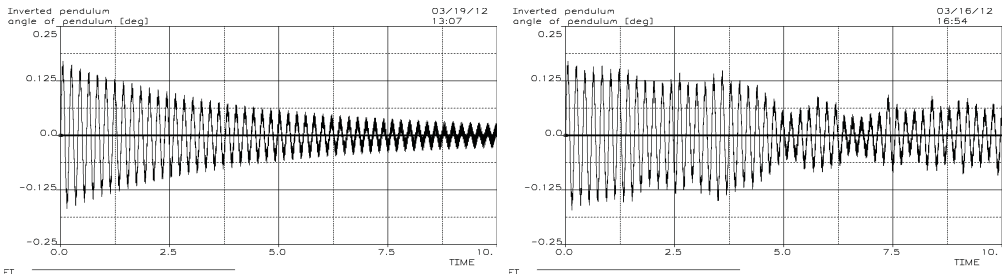

a) *b)*

Fig. 17: Time history of pendulum angle φ, excitation frequency f = 50 Hz, a) massless model, b) point-mass model.

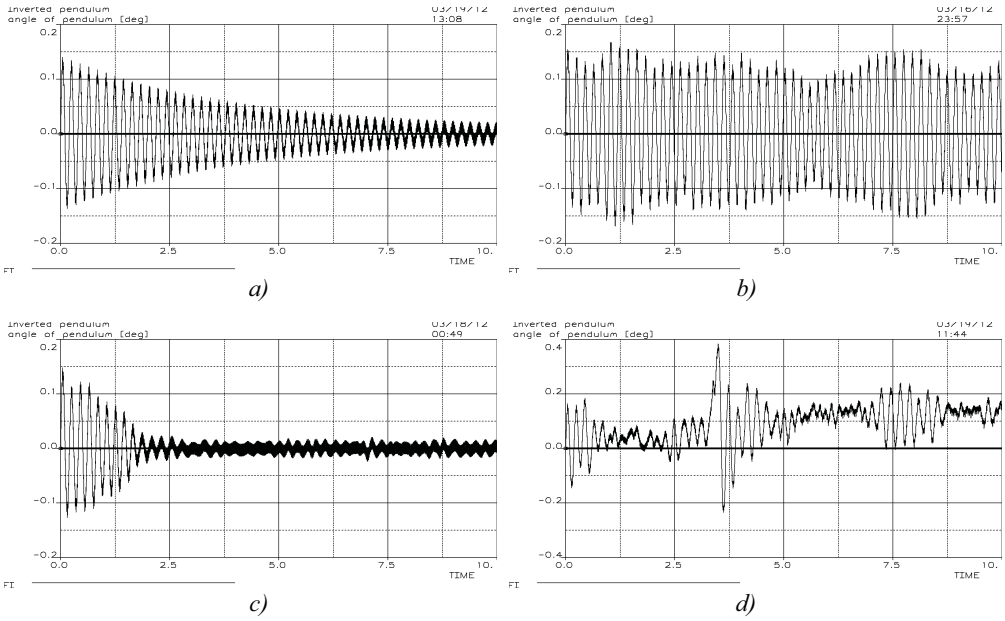

Fig. 18: Time history of pendulum angle φ, excitation frequency f = 60 Hz, a) massless model, b) point-mass model, c) point-mass model (fibre mass 0.11 grams), d) point-mass model of carbon fibre (other scale in vertical axis).

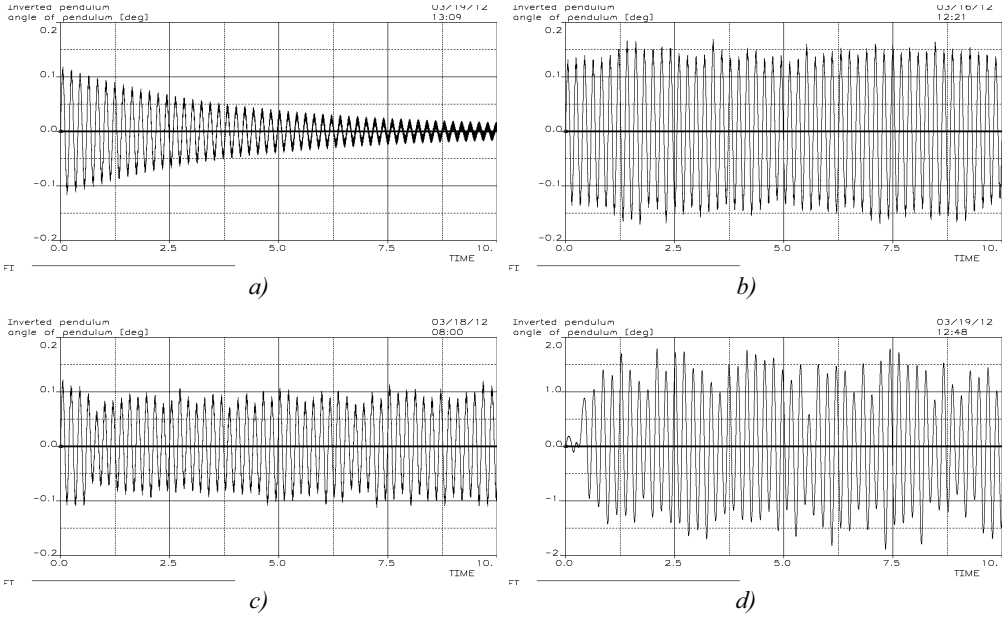

Fig. 19: Time history of pendulum angle φ, excitation frequency f = 70 Hz, a) massless model, b) point-mass model, c) point-mass model (fibre mass 0.11 grams), d) point-mass model of carbon fibre (other scale in vertical axis).

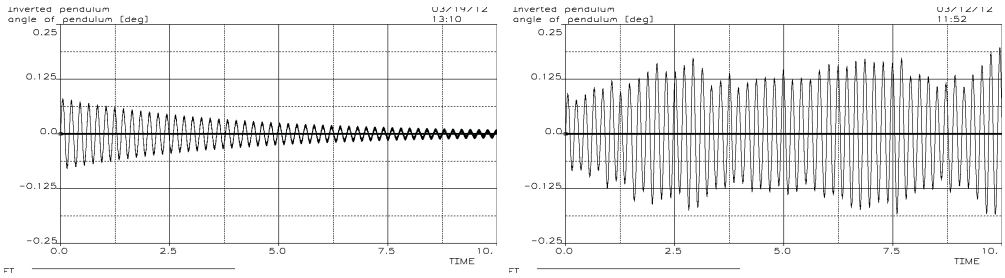

a) *b)*

Fig. 20: Time history of pendulum angle φ, excitation frequency f = 100 Hz, a) massless model, b) point-mass model.

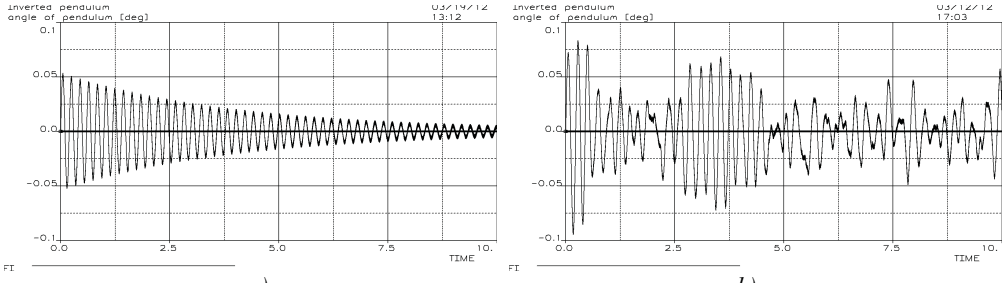

a) *b)*

Fig. 21: Time history of pendulum angle φ, excitation frequency f = 150 Hz, a) massless model, b) point-mass model.

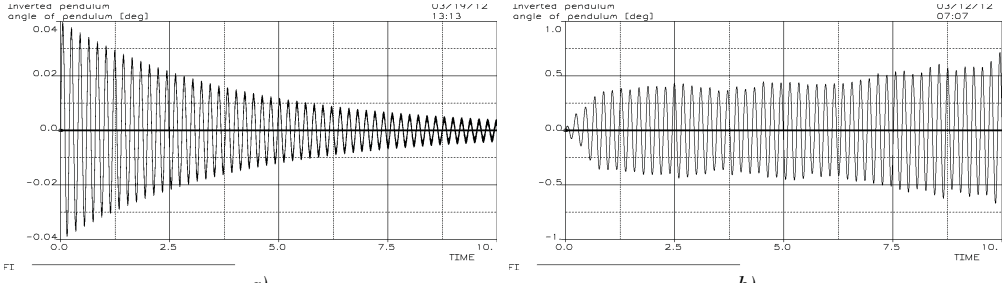

a) *b)*

Fig. 22: Time history of pendulum angle φ, excitation frequency f = 200 Hz, a) massless model, b) point-mass model (other scale in vertical axis).

6. Conclusions

The approach to the cable modelling based on the lumped point-mass representations for the investigation of the motion of the inverted pendulum was validated on the basis of the results obtained using the massless fibre model. It was proved that point-mass fibre model is well applicable up to the excitation frequency of approx. 50 Hz (which is generally sufficient for the control of the considered cable-based manipulators). At higher excitation frequencies partly vibration of individual point masses and partly probably also influence of numerical errors at solving equations of motion show up in the results of simulations. They are caused by considering almost massless fibres in the point-mass fibre model.

Experimental verification of the cable dynamics within the manipulator systems and research aimed at measuring the material properties of selected fibres are considered important steps in further research.

Acknowledgement

The paper has originated in the framework of solving No. P101/11/1627 project of the Czech Science Foundation entitled "Tilting Mechanisms Based on Fiber Parallel Kinematical Structure with Antibacklash Control" and institutional support for the long-time conception development of the research institution provided by Ministry of Industry and Trade of the Czech Republic.

References

Chan, E.H.M. (2005) *Design and Implementation of a High-Speed Cable-Based Parallel Manipulato*r. PhD Thesis, University of Waterloo.

Diao, X. & Ma, O. (2009) Vibration analysis of cable-driven parallel manipulators. *Multibody System Dynamics*, 21, 4, pp. 347-360.

Drábek, P. & Milota, J. (2007) *Methods of Nonlinear Analysis*. Birkhauser, Basel.

Freire, A. & Negrão, J. (2006) Nonlinear Dynamics of Highly Flexible Partially Collapsed Structures, in: *Proc. III European Conference on Computational Mechanics, Solids, Structures and Coupled Problems in Engineering* (C.A. Mota Soares, J.A.C. Martins, H.C. Rodrigues, J.A.C. Ambrósio, C.A.B. Pina, C.M. Mota Soares, E.B.R. Pereira & J. Folgado eds), Laboratório Nacional de Engenharia Civil, Lisbon, CD-ROM.

Hajžman, M. & Polach, P. (2011) Modelling of Cables for Application in Cable-Based Manipulators Design, in: *Proc. ECCOMAS Thematic Conference Multibody Dynamics 2011* (J.-C. Samin & P. Fisette eds), Université catholique de Louvain, Brussels, CD-ROM.

Kamman, J.W. & Huston, R.L. (2001) Multibody Dynamics Modeling of Variable Length Cable Systems. *Multibody System Dynamics*, 5, 3, pp. 211-221.

Polach, P. & Hajžman, M. (2011a) Approaches to the Modelling of Inverted Pendulum Attached Using of Fibres, in: *Proc. 4th International Conference on Modelling of Mechanical and Mechatronic Systems 2011* (A. Gmiterko ed.), Technical University of Košice, Herľany, CD-ROM (pp. 408-416).

Polach, P. & Hajžman, M. (2011b) Absolute nodal coordinate formulation in dynamics of machines with cables, in: *Proc. 27th Conference with International Participation Computational Mechanics 2011* (V. Adámek & M. Zajíček eds), University of West Bohemia in Plzeň, Plzeň, CD-ROM.

Polach, P. & Hajžman, M. (2011c) Investigation of Dynamic Behaviour of Inverted Pendulum Attached Using of Fibres, in: *Proc. 11th Conference on Dynamical Systems – Theory and Applications, Nonlinear Dynamics and Control* (J. Awrejcewicz, M. Kaźmierczak, P. Olejnik & J. Mrozowski eds), Department of Automatics and Biomechanics, Technical University of Łódź, Łódź, pp. 403-408.

Polach, P. & Hajžman, M. (2012a) Investigation of dynamic behaviour of inverted pendulum attached using fibres at non-symmetric harmonic excitation, in: *Proc. EUROMECH Colloquium 524 Multibody system modelling, control and simulation for engineering design* (J.B. Jonker, W. Schiehlen, J.P. Meijaard & R.G.K.M. Aarts eds), University of Twente, Enschede, pp. 42-43.

Polach, P. & Hajžman, M. (2012b) Effect of Fibre Preload on the Dynamics of an Inverted Pendulum Driven by Fibres, in. *Proc The 2nd Joint International Conference on Multibody System Dynamics* (P. Eberhard ed.), University of Stuttgart, Stuttgart, CD-ROM.

Polach, P., Hajžman, M., Šika, Z., Mrštík, J. & Svatoš, P. (2012) Effects of fibre mass on the dynamics of an inverted pendulum driven by cables, in: *Proc. National Colloquium with International Participation Dynamics of Machines 2012* (L. Pešek ed.), Institute of Thermomechanics Academy of Sciences of the Czech Republic, Prague, pp. 127-134.

Rachůnková, I., Staněk, S. & Tvrdý, M. (2009) *Solvability of Nonlinear Singular Problems for Ordinary Differential Equations*. Hindawi Publishing Corporation, New York.

Schmitt, K. & Thompson, R.C. (2004) *Nonlinear Analysis and Differential Equations – An Introduction*. Lecture Notes, University of Utah, Salt Lake City.

Shabana, A.A. (1997) Flexible Multibody Dynamics: Review of Past and Recent Developments. *Multibody System Dynamics*, 1, 2, pp. 189-222.

Smrž, M. & Valášek, M. (2009) New Cable Manipulators. In: *Proc. National Conference with International Participation Engineering Mechanics 2009* (J. Náprstek & C. Fischer eds)), Institute of Theoretical and Applied Mechanics Academy of Sciences of the Czech Republic, Svratka, CD-ROM (pp. 1209-1216).

Valášek, M. & Karásek, M. (2009) HexaSphere with Cable Actuation. *Recent Advances in Mechatronics: 2008-2009*, Springer-Verlag, Berlin, pp. 239-244.

Wittbrodt, E., Adamiec-Wójcik, I. & Wojciech, S. (2006) *Dynamics of Flexible Multibody Systems. Rigid Finite Element Method*. Springer, Berlin.

18th International Conference
ENGINEERING MECHANICS 2012
Svratka, Czech Republic, May 14 – 17, 2012

pp. 1033–1040
Paper #101

ANALYSIS OF MEASURED AND COMPUTED FORCE EFFECTS IN TRACTOR'S THREE-POINT LINKAGE DURING TILLAGE

P. Porteš[*], F. Bauer[**], J. Čupera[***]

Abstract: *The aim of the paper is an analysis of the measured and calculated force effects which act on tractor during tillage. Effects of the forces on individual driving wheels are analysed too. A mathematical model describing the transformation of force effect acting in the three-point linkage to loads in individual tractor wheels is developed. It is shown that the results of performed computations and theoretical analysis are in a good agreement. Based on the model, it is possible to use the measured force effects for precise determination of forces acting on the wheels. The influence of the length of the upper link on the loading of individual wheels and consequently on the traction performance of the tractor is determined.*

Keywords: ***three-point hitch, tillage, force effects, mathematical model.***

1. Introduction

The attached or trailed attachments are connected to tractor through three-point linkage, thus force effects acting on tractor are usually significantly different from effects of simple tractive forces, which typically exist in tractive tests. The adhesive loading of driving wheels is generally desirable, since it leads to maximal tractive efficiency. But this action is unfortunately connected with undesirable soil compaction, especially in case of ploughing systems moving in furrow. This fact was documented e.g. in Renius (1981), Upadhyaya et al (1985). Soil compaction can cause serious problems (Nosalewicz & Nosalewicz, 2011) and proper design of working system is thus critical (Cudzik et al, 2010). Adhesive loading of driving wheels is determining factor for achieving the maximal tractive efficiency of tractors. This efficiency consequently highly influences general efficiency of working system. Grečenko (1984) stated that typical difference between tractor performing ploughing and tractor being tested in tractive test is following: the wheeled tractor is moving (by one of its sides) in the furrow and thus it is inclined. In combination with power effects of the plough this inclination causes a different load of individual wheels (moving in the furrow and on the unploughed soil) and changes in the load of both axles. The tractor's tractive properties are thus affected (decreased), especially in the cases when differential lock is not used. This results in significant changes not only in the grip of driving wheels but also in an increased compaction of soil. Design and performance of an adjustable three-point hitch also highly influences the operation efficiency (Al-Jalil et al, 2001). Various data-acquisition systems and different strain gauges systems were used by several authors to evaluate the force effects in the three-point hitch (Al-Janobi, 1984; Al-Janobi, 2000) and/or transmission system (Kim et al, 2000). Also the general models of working tractor were developed (Kolator and Białobrzewski, 2011). The goal of this paper is to develop the precise mathematical model describing the transformation of force effect acting in the three-point linkage to loads in individual tractor wheels. Performed analysis can be used for further studies on dynamic properties of tractor units or other vehicles as described e.g. in Chalupa (2005) and/or Chalupa et al. (2009).

[*] Ing. Petr Porteš, Ph.D.: Institute of Automotive Engineering, Brno University of Technology; Technická 2896/2; 616 69 Brno; e-mail: portes@fme.vutbr.cz

[**] Prof. Ing. František Bauer, CSc.: Department of Engineering and Automobile Transport, Mendel University in Brno; Zemědělská 1; 613 00, Brno; CZ, e-mail:bauer@mendelu.cz

[***] Ing. Jiří Čupera, Ph.D. : Department of Engineering and Automobile Transport, Mendel University in Brno; Zemědělská 1; 613 00, Brno; CZ, e-mail:xcupera@node.mendelu.cz

2. Material and experimental methods

Forces measured in the discrete times in the three-point hitch links were selected as an input data: force in the right lift rod, force in the left lift rod, force in the right lower link, force in the left lower link, and force in the upper link (Fig. 2). The load cells measure solely the axial force in the links. It is given by their design and the fact that links are ended by spherical joint on both sides and thus loaded only along the axe. Lower links are the exception, because the sensors are exposed to the bending moment along the axe perpendicular to the plane positioned between lower and lift link. The sensors in the lower links are design in such way that they measure the axial force and do not sense bending. Verification of independence of measured force on the bending of the lower link is a part of experimental verification of calculation. Considering the fact that resulting force acting on the tractor is calculated as a spatial system, it is necessary to determine also the force directives (directions and points of application) altogether with the force magnitudes determined by sensors. Directions and points of application are given by the geometry of the three-point hitch. The forces lie in the lines connecting the joints at the ends of individual links. Thus the geometrical arrangement of the hitch must be determined for each position of the mechanism. The hitch has two degrees of freedom against the tractor: movement of the hitch upwards (change of lifting mechanism links angle, points E-DL-DR see (Fig. 1) and side movement. Both movements are measured by position sensors (potentiometers) and produce the input data for kinematic solution of the mechanism.

Following problems must be solved for determination of forces acting on tractor via three point hitch during tillage:

-mechanism kinematics. The result is a position of the three-point hitch in the space.

-static equilibrium of the forces acting in the spatial mechanism. The result is represented by vectors of force and moment acting on the tractor.

The multi-body software SAMS described in Poreš (1997) was used for creation and solving of the equations. The SAMS software enables both, static and dynamic analysis of the system. Due to large number of input parameters necessary for dynamic model, the static analysis was used to determine the acting forces. The building elements for creation of the mechanism models in SAMS are represented by rigid bodies connected by kinematic joints or constraints. The software works with relative coordinates. The kinematic joints connect the solids in open kinematic chains and enable relative movement of neighbouring elements in the chain. The kinematic constraints close the open chain into closed loop. Topology of the TPH multi-body model and the types of kinematic elements are presented in Fig. 1.

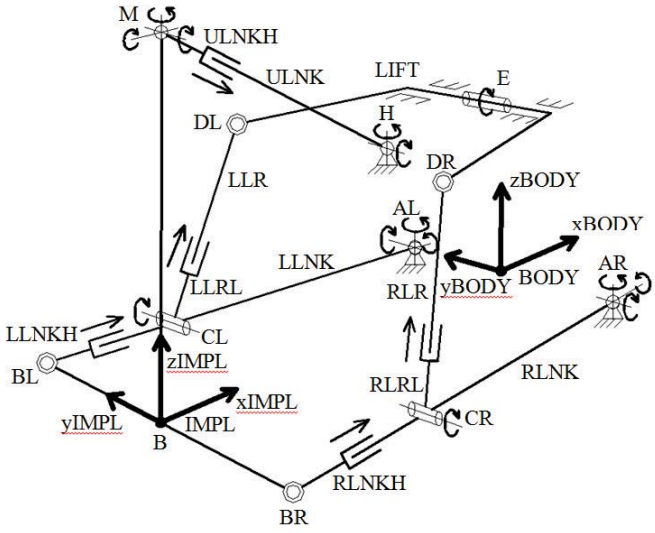

Fig. 1 Kinematic model of the tractor's three-point hitch

In order to determine the balance between forces measured in the links and forces acting on three-point hitch mechanism, the links had to be divided into two parts (in the position of sensor location) connected by translational joint enabling the sole reciprocal movement in the direction of the link axe and not enabling any reciprocal rotation. This arrangement allows adding the force element into the model. Both parts would be drawn together by the force equal to the force measured in the strain gauge. Reciprocal relative position of both parts is ensured by constant value of relative coordinate added to the model by translational joint. Each translational joint adds one degree of freedom to the model and corresponding added coordinate is independent value which could be prescribed.

The software SAMS involves the elements, which enable definition of the direction and points of application of the forces or moments of unknown magnitudes. The magnitude of the forces and moments is determined on the basis of dynamic or (as in this case) static equilibrium. These elements determine the unknown magnitudes of force and moment vector components acting on tractor in the origin of system of coordinates „IMPL“ (see Fig.2) and magnitude of moment lifting the hydraulic arms. The number of unknown magnitudes of force effects must be in the case of solving static equilibrium equal to the number of independent coordinates (number of degrees of freedom) in order to find equilibrium for any combination of force effects acting in the direction of any degree of freedom.

TPH mechanism has 7 (originally 2) degrees of freedom after adding of above described translational joints. The number of unknown magnitudes of force elements is also 7. 3 unknown components of force and 3 unknown components of moment acting on the body „IMPL“ (implement) and 1 magnitude of moment lifting the body „LIFT“ (connecting links lifting the mechanism).

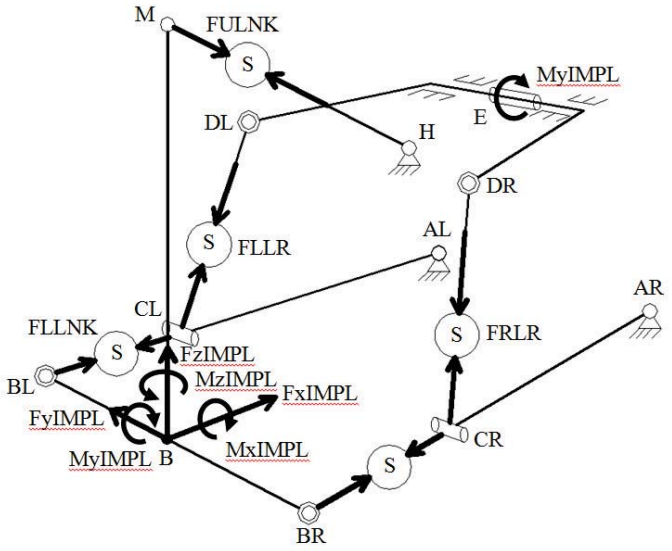

Fig. 2 Forces, moments and location of sensors (S) in tractor's three point hitch

The coordinate system „IMPL“ (implement) is an orthogonal right-rotating coordinate system positioned into the middle of the section of a line connecting points BL and BR (connection of lower links to the implement) and it is fixed to the body „IMPL“. The axe *z* directs from the origin of coordinate system to the point M (connection of upper link to the implement), the axe *y* lies on the connecting line of the points BR and BL and directs to the left (from the driver's view), and the axe *x* direct forward (see Fig. 1).

The „BODY“ (see Fig. 3) substitutes the whole tractor in the model, including rear wheels without front axle and wheels and without TPH. This body is connected with auxiliary mass less body "ARM" by spherical joint. The body „ARM“ is connected to the global frame by means of translational joint, enabling translational movement in the direction of its three axes. By this configuration the "BODY" has 6 degrees of freedom. The „BODY“ is also connected in the CFA location with body "FAXL" representing the front axle by the rotational joint. Another degree of freedom is thus added to the set,

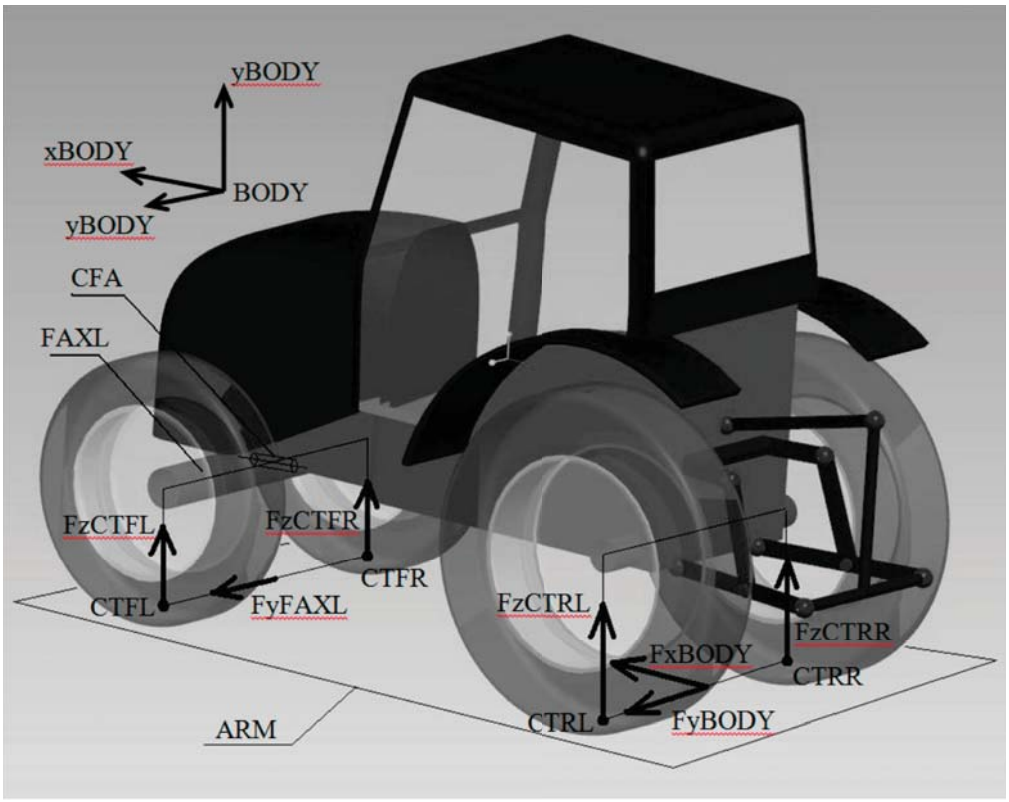

Fig. 3 Scheme of tractor model

which means 7 extra degrees of freedom in comparison with model described in the previous part of the text. Following 7 unknown magnitudes of forces and moments can be calculated (see Fig. 3): vertical reaction (wheel loading) FzCTFL, FzCTFR, FzCTRL, FzCTRR in the positions of contact between tyres and ground CTFL, CTFR, CTRL, CTRR; lateral force FyFAXL, resp. FyBODY acting on front, resp. rear axle in the height of ground; longitudinal driving force FxBODY acting in the centre of rear wheel track on rear axle (in the model acting on BODY).

The lateral force acting on front axle FyFAXL represents the sum of lateral forces acting on both front wheels. Its presence in the model is significantly important, because it influences distribution of the total vertical force acting on the front axle between individual wheels of the axle. This simplified model does not allow division of the lateral force acting on the front axle to the forces acting on individual wheels. The same applies for division of lateral force acting on rear axle FyBODY.

The field experiments were performed in the area located close to Slavkov u Brna on the black soil type, loess soil matrix, with the wheat as a pre-crop. The soil was treated by disc harrows (the depth of 8 cm) after the harvest of wheat. The average soil moisture by weight during the experiments was determined as 19.7 %. The ploughing was performed using the tractor Zetor 11741, six-cylinder engine SAME6WTE1, maximal output 78.2 kW at 2000 rpm – measured at PTO by dynamometer Schenk W 400. Maximal torque/revolutions 480 Nm/1400 rpm. Increase of torque: 35 %. Gear box – reverse, mechanical with three-stage torque multiplier. Front tires: 14,9 R 24; rear tires: 18,4 R38. Gross weight of the tractor: 5680 kg; the weight loading the front tire 2920 kg, which represents 51 % of total weight.

The plough Kverneland EM 85, model EM85-200-28, gross weight 1260 kg was used to perform the ploughing operation.

The forces acting in the three-point hitch were monitored using attached strain gauges. The force sensors located on the lift rods – see Fig. 2 (between CL and DL and/or CR and DR) measure solely

tensile and/or compression force. The maximal load in tension and compression is 60 kN. The sensors in lower links (between BL and CL; BR and CR) are during normal operation loaded also in bending, except tension and pressure. Their design eliminates these extra loads and solely axial tension loads are sensed. Maximum of 1 % nominal error is guaranteed by producer of the sensors. Schematics of the three-point hitch attached with strain gauges is shown in Fig. 2. The ploughing system was drawn by other tractor and the tractive force FxM in the tow rope was measured by strain gauge sensor Hottinger U2B-100. The maximal load in tension and compression is 100 kN. Uncertainty of measurement for mentioned load cell is 203,4 N, $U_{sensitivity}$ = 26,08 N, $Ut_{empcoeff}$= 26,08 N; $U_{linearity}$ = 200 N.

The testing plot (30 m in length) was indicated on the working area. There was enough space in front of the testing plot to achieve the stabilization of the working system. The forces in the three-point hitch were recorded at 250 Hz frequency and the values were directly transferred to the computer. Average values from 125 force measurements were used in the computational algorithm, which represents approximately 0.9 m of travel. In the total length of 30 m was thus received 34 values for each individual measurement. The forces in the individual links and rods as well as force FxM in the tow rope were recorded in the whole length of testing plot. Altogether, 4 sets of measurement were performed:

Set I: ploughing on the left side, deepness of the ploughing – 17 cm

Set II: ploughing on the right side, deepness of the ploughing – 17.5 cm

Set III: ploughing on the right side, deepness of the ploughing – 25 cm

Set IV: ploughing on the left side, deepness of the ploughing – 27 cm

3. Results and discussion

Figure 3 shows the course of computed and measured force FxP as a function of time for Set III measurement. The determined force effects in the three-point hitch and developed algorithm were used for calculation of force FxBODY. The force FxM represents the overall ploughing resistance, which includes plough resistance, rolling resistance and transmission mechanism resistance. The rolling resistance and resistance of rotating parts of transmission mechanism (FxD) were determined experimentally as follows. The plough was lifted into transport position and the complete working system was drawn on the rope. The received values were used for calculation of mean value of FxD. Experimentally determined plough resistance was consequently calculated using following formula:

$$\boldsymbol{FxP = FxM - FxD} \tag{1}$$

Experimentally determined plough resistance FxP was consequently compared with calculated plough resistance, defined using forces measured at three-point hitch and corresponding to theoretical driving force FxBODY. If the calculation of algorithm is correct, following formula must be valid:

$$\boldsymbol{FxP = FxBODY} \tag{2}$$

Received value of FxP force was compared with calculated force FxBODY with use of developed algorithm. Table 1 contains measured values of forces acting in the three-point hitch including plough resistance force FxP. Computed values of forces and their courses during ploughing are as an illustrative case shown in Fig. 2.

The Sets I, II, and IV are not presented, neither in tabular, nor graphical version, due to their large extent, but they are included in the final analysis – see Fig. 4. Listed calculated values represent the force effects acting on the tractor during ploughing. Calculated forces acting on front axle FzCTFL and FzCTFR exhibit negative values, which means that front axle is lightened during working procedure. As it was stated above (in Material and Experimental Methods), the front axle is loaded by 2920 kg, which is the weight sufficient for transmission of driving force from the wheels to the ground. It is evident from calculated values of FzCTRL and FzCTRR forces, that ploughing operation increase the load of both rear wheels. The calculated forces acting in the transverse direction in the *y* axis reach relatively low values with reference to adhesive forces (forces in *z* axis) and thus can not produce instability of the working system in transverse direction.

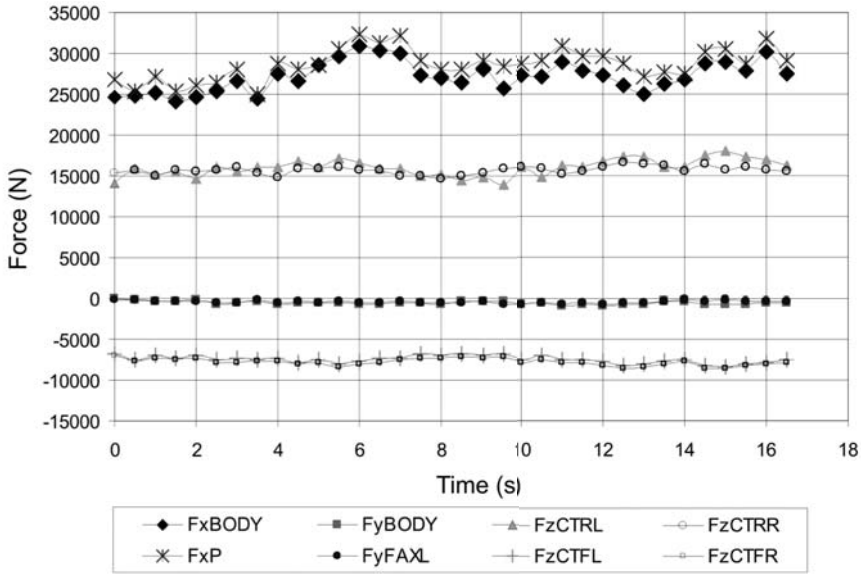

Fig. 3: Measured course of the force FxP and computed forces acting on ploughing tractor as a function of time – SET III

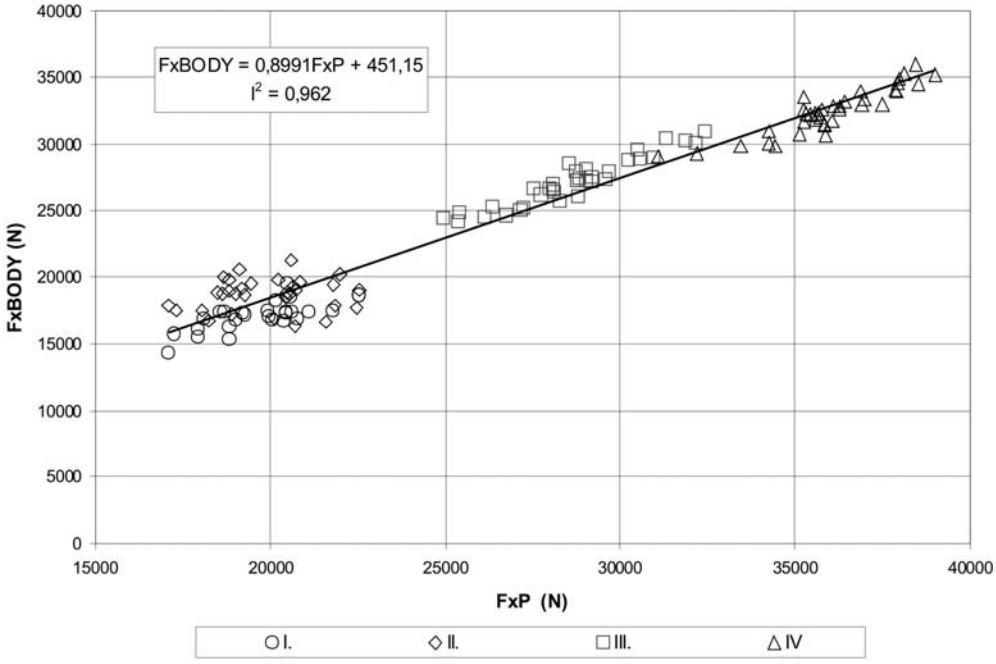

Fig. 4: Dependence of theoretically calculated plough resistance FxBODY on experimentally determined resistance FxP. I., II., III., and IV. denote measuring sets.

Ideally, the courses of FxBODY and FxP should overlap each other – see Fig. 3. The variations and differences are probably caused by inexact determination of rolling resistance and resistance of rotating parts in the transmission mechanism. The resistance forces were determined for ploughing system with plough in the transport position. The tractor's tires were loaded solely by weight of the machine (tractor) and the plough. But it is important to note, that forces acting on ploughing tractor are given by sum of plough weight and resistance forces acting on ploughing elements. The vertical components of ploughing elements resistance forces produce more intensive loads on tractor tires and thus increase the overall rolling resistance. This explanation is supported by the fact that experimentally determined plough resistance is bigger than calculated one. The verification of the mathematical model was performed by use of regression test, which involved dependence of theoretically determined plough resistance FxBODY on experimentally determined plough resistance FxP – see Fig. 4.

As it is obvious from regression analysis shown in Fig. 4, the measuring sets I and II are characterized by larger variation of calculated and measured values in comparison with sets III and IV, which exhibit smaller level of data scatter. This result can be explained as a consequence of a fact that measuring sets I and II were connected with 17 cm working depth of ploughing, while sets III and IV with 27 cm depth. The forces in case of sets I and II were thus lower indeed. This difference also produced larger exposure of the forces, which were not possible to measure chronologically together with other monitored force effects. This is especially the case of rolling resistance and/or forces of rotating parts of transmission mechanism, where larger variation of measured and calculated values was found. Presented results are in general accordance with conclusions presented by Bauer and Sedlák (2003).

Performed statistical analysis proven that calculated value of theoretical plough resistance FxBODY and experimentally determined value of plough resistance FxP clearly exhibit the linear dependence. The high value of determination coefficient approves the high dependence tightness. It can be concluded from the determination coefficient value $I^2 = 0.962$ that 96.2 % of calculated values variability is defined by proposed regression function. The results of regression analysis are listed in Table 3 and Table 4. The regression function was tested by F-test and the result of the test is included in Table 3. It is obvious that tested regression function very well describes the measured values. The performed t-test (and the results listed in Table 4) revealed that coefficient significance, where the coefficient represents the slope of the line) is very high. Test of the absolute term of equation approves its low significance.

Tab. 3: The test of regression function

	Difference	SS	MS	*F*	Significance F
Regresssion	1	5.2E+09	5.2E+09	3216.36	4.61E-92
Residua	127	2.05E+08	1615405		
Sum	128	5.4E+09			

Tab. 4: The test regression coefficients

	Coefficients	Error of the mean value	*t-stat*	*P* value
Limits	451.1531	439.2477	1.027104	0.306324
FxP (N)	0.899093	0.015853	56.71296	4.61E-92

4. Conclusions

The presented results and performed analysis approve that theoretically calculated plough resistance correspond to experimentally determined values. Thus it is possible to conclude that mathematical model is functional with satisfying level of accuracy and measured force values in the three-point

hitch can be used for calculation of force effects arising during ploughing operation on individual tractor wheels. If the force effects on individual wheels (with attachment connected to the three-point hitch) are known, it is possible to formulate and determine the traction characteristics. It is e.g. possible to evaluate, how different types of attachment connection influence the load of individual wheels. The change and alternation of the force effecting in the upper link of the three-point hitch, which can be influenced and determined by adjustable length, highly influences the final load of tractor's axes. It was experimentally determined and confirmed by consequent calculation with use of proposed algorithm, how exactly the length of the upper link influences the loading of individual wheels and thus traction performance of the tractor. The further research will be focused on detailed analysis of the different types of plough connection and its influence on loading of tractor's wheels, when considering weight of the machine, its inclination, and kinematics of the system.

Acknowledgement

The research has been supported by the grant project TP2/2012 – "Implementation of communication protocol according of SAE J1939 in agricultural tractor" financed by Mendel University in Brno and by European Regional Development Fund in the framework of the research project NETME Centre – New Technologies for Mechanical Engineering, project reg. No. CZ.1.05/2.1.00/01.0002, under the Operational Programme Research and Development for Innovation.

References

Al-Jalil, H. F., Khadir, A., Mukahal, W. (2001) Design and performance of an adjustable three-point hitch dynamometer. *Soil and Tillage Research*, 62, pp. 153-156.

Al-Janobi, A. (2000) A data-acquisition system to monitor performance of fully mounted implements. *Journal of Agricultural Engineering Research*, 75, pp. 167-175.

Bauer, F., Sedlák, P. (2003) Attached plows linkage influence on the load of tractor driving wheels. *Acta universitatis agriculturae et silviculturae Mendelianae Brunenesis,* 3, pp. 193-204.

Chalupa, M. (2005) Combined Metod of Driving System Dynamic Properties Analysis. *Magazine "Machinebuilding & Electrotechnics"*. Sofia, ISNN 0025-455X.

Chalupa, M., Veverka, J. and Vlach, R. (2009) Influence of Design Parameters on Vehicle Track Dynamic Loading. In *Proceedings of the 2nd International Multi-Conference on Engineering and Technological Innovation,* Orlando, pp. 365-369.

Cudzik, A., Białczyk, W., Czarnecki, J., Jamrozy, K. (2010) Traction properties of the wheel-turfy soil system. *International Agrophysics*, 4, pp. 343-350.

Grečenko, A. (1984). Operation on steep slopes state. *Journal of Terramechanics*, 21, pp. 181-194.

Kim, J. H., Kim, K. U., Wu, Y. G. (2000) Analysis of transmission load of agricultural tractors. *Journal of Terramechanics*, 37, pp. 113-125.

Kolatora, B., Białobrzewski, I. (2011) A simulation model of 2WD tractor performance. *Computers and Electronics in Agriculture*, 76, pp. 231-239.

Nosalewicz, A., Nosalewicz, M. (2011) Effect of soilcompaction on dehydrogenase activity in bulk soil and rhizosphere. *International Agrophysics*, 1, pp. 47-51.

Porteš, P. (1997) *Mathematical Modeling of Vehicle Handling*. Doctoral thesis. Brno University of Technology. Brno.

Renius, K. T. (1981) Traktoren, BLV Verlagsellschaft, Münschen

Upadhyaya, S.K., Kemble, L.J., Collins, N.E. and Camargo, F. A. (1985). Accurarcy of mounted implement draft prediction using strain gage mounted directly on three-point linkaeg system. *Transaction of the ASABE*, 28, pp. 40 - 46.

18th International Conference
ENGINEERING MECHANICS 2012
Svratka, Czech Republic, May 14 – 17, 2012

pp. 1041–1048
Paper #96

LIFETIME PREDICTION OF WIND LOADED MAST AND TOWERS WITH RESPECT TO LATERAL AND LONGITUDINAL WIND SPECTRUM

S. Pospíšil[*], J. Lahodný[**], V. Janata, S. Urushadze, R. Král, S. Hračov

Abstract: *The paper deals with a theoretical lifetime prediction of telecommunication towers, guyed masts and antenna's cantilevers and comparison with the long-term measurements. A simple and practical calculation method is presented. The wind load is described taking into account the probability distribution function of the mean velocity and corresponding wind pressures. The dynamic response of structure caused by the turbulence uses wind models for both longitudinal and lateral direction. Structural response takes into account the contribution of more vibration modes. Based upon this knowledge, the number of cycles for certain time period together with the residual time life prediction of antennas cantilevers and cables was determined.*

Keywords: ***Lifetime prediction, Masts, Towers, Fatigue, Wind, Spectrum.***

1. Introduction

Slender structures like masts and towers are repeatedly exposed to dynamic wind loading. The consequent vibration may cause the cumulating damage, which sometimes leads to the collapse of structure. To prevent the breakdown by timely replacement or reconstruction, or to predict the expenses for further tower operation, one should determine the remaining lifetime. A method for the determination of remaining life of guyed masts, antennas and guy ropes is presented in this article. It is based on the theoretical work described in Pospíšil et al. (1997) and it deals with the vibration caused not only by the longitudinal but also by the lateral wind turbulence monitored during a long-term measurement, the latter being in some cases of specific structural characteristics more important, see e.g. Repetto & Solari (2002). The age and regular inspection revealed that these components could be in danger with regards to the remaining life. Based on the long-term monitoring stress cycles by strain gauges the remaining life of the elements was determined. For practical as well as analytical reasons, it was compared with theoretical calculation and prediction using just the knowledge of dynamic characteristics of the structure and the wind.

2. Damage and fatigue model

There exists number of methods to determine the fatigue damage of a specimen, see for example Degrieck & Paepegem (2001), Benasciutti & Tovo (2005), Epaaratchchci & Clausen (2005), Wahl et al. (2001). For the sake of practical engineering analysis, the linear theory of damage accumulation is used, given in the mathematical form by the so-called Palmgren-Miner law:

$$D = \sum \frac{n_i}{N_{i,f}} \tag{1}$$

where n_i is the number of cycles with certain amplitude and $N_{i,f}$ is the total number of cycles to the damage, i.e. cycles corresponding to the *i*-th level of the load. Linear theory is based upon the assumption of the constant energy accumulated by one cycle and the characteristic amount of the energy in time of damage. The energy accumulation leads therefore to the summation of partial

[*] Doc. Ing. Stanislav Pospíšil, Ph.D.: Institute of Theoretical and Applied mechanics, CAS, Prosecká 76; 190 00, Prague; CZ, e-mail: pospisil@itam.cas.cz

[**] Ing. Jiří Lahodný, Ph.D..: Excon, a.s., Sokolovská 187; 190 00, Prague; CZ, e-mail:lahodny@excon.cz

damage. For the total collapse state holds $D = 1$. The relation between the damage and the number of cycles is not dependent on the level of the stresses. Some studies show, that in the case of cyclic loading with alternation of low and high amplitude cycles, the value $D = 1$ is very overrated and lead to the erroneous conclusion. Several modifications of the Palmgren-Miner criterion with the usage of non-linear equation for D involving the *i*-th level of the stresses can be found in Degrieck & Paepegem (2001). Before the analysis of the damage is performed according to the equation (1), there is a need to identify the amplitudes of individual cycles. The authors have chosen the rain-flow method for the separation of cycles into the stress ranges, see e.g. Amzallag et al. (1994).

3. Theoretical determination of number of cycles

There are several causes of the dynamic response of slender structures and consequently the sources of cyclic stresses. In the observed structures four sources were identified: a) the first one gives the number of load cycles caused by the fluctuation component of the wind acting in the direction of mean wind speed; b) the second part gives the number of cycles caused by lateral turbulent wind loads in the direction perpendicular; c) number of cycles caused by the direction changes in mean wind speed; d) number of cycles of the mast (or of the guy rope) caused by the shed vortices (Strouhal's effect).

The case c) needs some comments. For the determination of the stress range spectra, caused by changes of the mean wind speed and the wind direction changes, following simplifications are used.

It is assumed that the change of the mean velocity or direction occurs every 10 minutes, i.e. the period during which is the mean component of the wind velocity is considered as a constant. The stress range (hereafter labeled $\Delta_{\sigma,fl+mean}$, which occurs after this time is equal to the difference between the maximum value of the stress increase in the corresponding ten-minute interval and the minimum value of the stress increase in the previous interval.

$$\Delta_{\sigma,fl+\mathrm{mean}} = \sigma_{\max} - \sigma_{\min} \tag{2}$$

The maximum and minimum values of the stress increase $\sigma_{\max}$ and $\sigma_{\min}$ are defined as:

$$\sigma_{\max} = \sigma_{\mathrm{m}} + 3,7 \cdot \sigma_{Fl};\ \sigma_{\min} = \sigma_{\mathrm{m}} - 3,7 \cdot \sigma_{Fl} \tag{3}$$

where σ_m denotes the stress caused by the mean wind load and σ_{Fl} the standard deviation of the fluctuation component response in the corresponding ten-minute interval. Another simplification is introduced taking into account that the minima of the stress increases $\sigma_{\min}$ are approximately the same low values (near zero) for all mean wind velocities.

Number of cycles of the stress range by the stress range $\lambda_{\sigma,fl+mean}$ is defined as:

$$n_i = P_1 \cdot P_3 \cdot d_{10,\min} \tag{4}$$

where $d_{10,\min}$ is the number of the ten-minute intervals in the total lifetime of the structure.

3.1. Probability P1

We call P_1 the probability of occurrence of the mean wind speed, i.e. that the mean wind speed will lie in certain interval. This probability is based upon the knowledge of distributive function. We use Weibull distribution with parameters $k = 2$ and $c = 0.35 \cdot v_{\max}$ applicable for most locations in the Czech Republic. It may be written as:

$$f(\mu) = \frac{k}{c} \cdot \left(\frac{\mu}{c}\right)^{k-1} \exp\left[\left(-\frac{\mu}{c}\right)^{k}\right] \tag{5}$$

where μ is the ten-minutes wind speed according to ČSN EN Eurocode 1 (2007). Dividing the whole band into several intervals and integrating the curve in these intervals, we obtain the probability that the mean wind speed will lie in that interval.

3.2. Probability P2

The probability of the fluctuating stress component at certain mean wind speed is P_2. We use the assumption of Gaussian distribution around the mean stress. According to the standard ČSN EN Eurocode 3 (2008) the stress probability density function (PDF) at certain cross-section of the structure may be expressed as follows:

$$f(\tau) = \frac{1}{\sigma_\tau} \exp\left(\frac{-(\tau - \overline{\tau})^2}{2\sigma_\tau^2}\right) \tag{6}$$

where $\overline{\tau}$ is the mean stress value in the structural element and σ_τ is a stress standard deviation. The mean stress is calculated using mean wind speed from each interval. For the reference wind speed in order to calculate stresses we selected the upper limit of each interval. The stress standard deviation can be stated for example according to the standard ENV as $\sigma_\tau = \tau \cdot G/4$, where G is the gust factor, see ČSN P ENV 1993-3-1 (2000), Simiu & Scanlan (1996) . Let us assume that the stress response is composed from the harmonic components with the amplitudes $\tau_{ampl,fl,i}$. For each of these amplitudes we calculate the probability density function P_{2i} and consequently also the probability P_2 as the sum of all mean wind speed contributions; see Fig. 1.

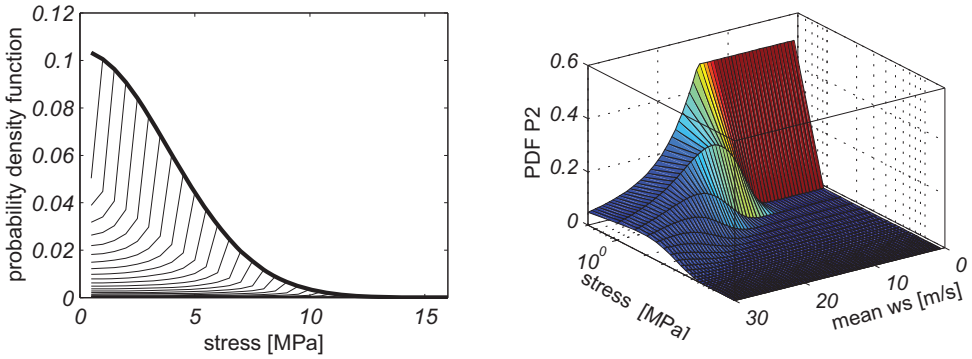

Fig. 1: Left: Probability density function of mechanical stress P_{2i} and partial probability density functions associated with the harmonic components. Right: Probability P_2 as the function of mean wind speed.

3.3 Probability P3

Alternatively we should consider also the occurrence frequency of the mean wind speed blowing in one direction. This we may call P_3. It is given by the fraction of the area bellow histogram (usually taken from the meteorological observations; wind rosette) and the area below the whole curve.

3.4 Probability P4

The probability P_4 expresses the fact that the structure vibrates in certain shape with certain frequency, close to one of the eigen-frequencies. It is the ratio between root mean square acquired by the integration of the response spectrum close to certain eigen-frequency respectively the background component of the response and the total integral of the response power spectrum over the whole frequency range.

3.5 Total number of the cycles due to wind fluctuation

The number of cycles with the amplitude of fluctuating component of the stresses $\tau_{ampl,fl,i}$ can be finally formed according to the practical formula, expressing the cumulative probability of mutually independent phenomena. We may write:

$$n_i = P_1 \cdot P_2 \cdot P_3 \cdot d_t \cdot \sum_{k=1}^{N} P_{4,f_k} \cdot f_k \tag{7}$$

where f_k is the *k*-th resonant frequency and d_t is the desired (projected) lifetime of the structure.

4. Damage assessment of existing structures-examples

In the period 2005-2011, the authors collected several measurements on several broadcast towers. The suitability of the procedure is documented on the analysis of towers and guyed masts. Two examples are presented here: The tower Veselský kopec (Example-1a), Vraní Vrch (Example-1b) and guyed mast Domamil with two sets of ropes (Example-2).

4.1. Data measurement

4.1.1. Wind characteristics

The ultrasonic anemometers in several elevations have measured the wind speed up to 60 m/s and the direction of the flow. The measured spectral density corresponded to EN spectra; see ČSN EN Eurocode 1 (2007). The characteristic profile is prevalently of category II as can be seen from Fig. 2.

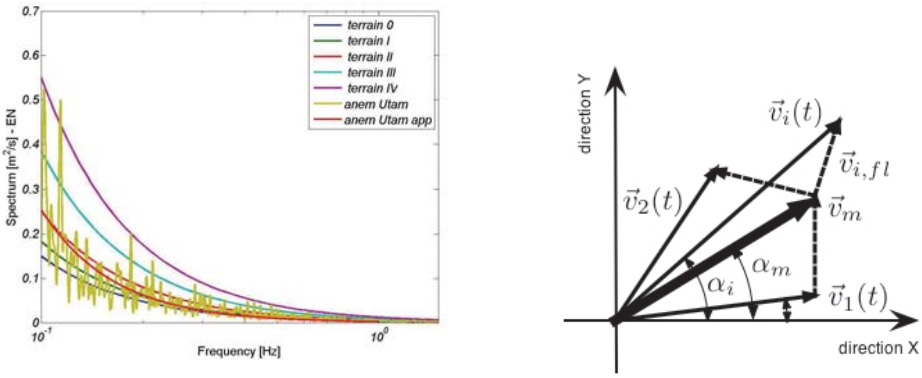

Fig. 2: Left: In order to analyze if the assumption of the load is based on the real values, the measured spectral densities were compared to theoretical ones given by the Eurocode. Right: Decomposition of the wind speed into its lateral and longitudinal components.

Decomposition of the velocity into the longitudinal and the lateral components was carried out as shown in Fig. 2. Wind speed is considered as a complex values and distribution is based on trigonometric relationship:

$$v_{\mathrm{fl,long}} = |\vec{v}| \cdot \cos(\alpha_{\mathrm{fl}});\ v_{\mathrm{fl,lat}} = |\vec{v}| \cdot \sin(\alpha_{\mathrm{fl}}) \tag{8}$$

4.1.2. Response measurement

Dynamic measurements consisted in determining of resonant frequency of the tower based on the evaluation of the ambient vibration of the structure. The dynamic measurement was taken from the acceleration time histories (in case of mast measurement) along the mast shaft or tower or from the strain gauges (in case of the rope measurement). Frequencies were evaluated directly from the assessed spectra by simple peak picking method and the shapes of vibration were identified. Also the logarithmic damping δ was evaluated from the measurements.

Strain measurements were carried out using strain gauges mounted on the tubular antenna or directly on the guy-rope tensioning rods, see Fig. 5. These strain gauges were connected to a bus and the numbers of cycles and the stress range was calculated using the Rainflow method. In the case of rope measurement, the stress range obtained from long-term measurements for calculation of damage accumulation were multiplied by the factor $\gamma = 1.10$ in order to include the influence of bending moments at the tailpiece of the rope and aeroelastic effects, see Fischer (1983). The measured number of cycles is extrapolated to the projected lifespan, usually 45 or 50 years.

4.2. Example 1-prediction for the towers (fiber reinforced cantilevers)

The fiber-glass cantilevers were about 20 m tall. They were made with the diameter of 1.9 m and with the wall thickness $12 \div 16$ mm. The determination of the fatigue can be based on literature references. This however may lead to uncertainties with regards to the lack of knowledge of the material parameters and past fabrication conditions. In this study we have used the properties of the fiber-glass elements taken from the experiments made at older antenna extensions, see Pirner & Fischer (1999). Their characteristics were closest to the characteristics of the laminates under examination and they were made in the same time period and with similar fabrication procedure describing the limit stress values for certain number of cycles.

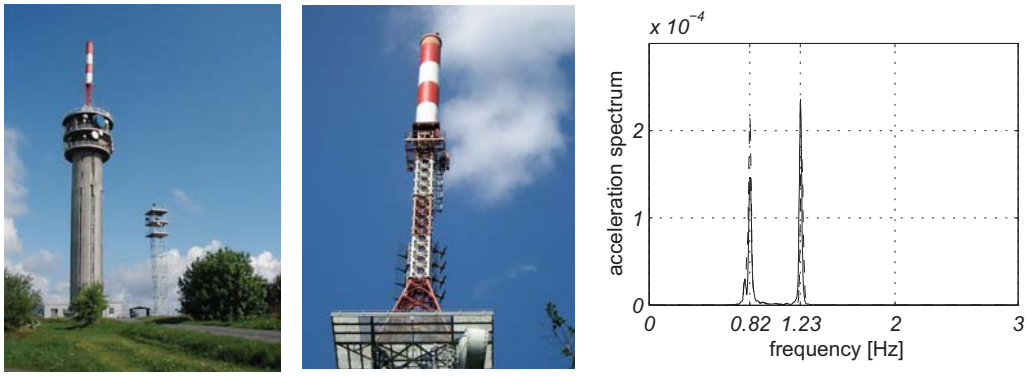

Fig. 3: Left: Photograph of the TV tower Veselský kopec (Example 1a), Middle: Vraní Vrch (Example 1b) with GRP antenna cantilevers. Right: Example of the spectral densities of the acceleration of a tower Veselský kopec to determine the resonance frequencies.

The forced vibration using two men swinging at the top was used to excite the towers. In case of strong wind, also the ambient wind excitation was analyzed and the resonant frequencies were determined. Also the wind speed, see Fig. 2, together with the spectrum have been measured. The spectral peaks of the response indicate usually the values of eigen-frequencies. It should be analyzed with care, however, because the influence of some mode shapes could be incorrectly concluded from the acceleration spectra of the whole tower and not just of the antenna cantilever. Fig. 3 (left) shows such an example; the structure as a whole vibrates predominantly with the first frequency 0.82 Hz; however, the dominant antenna's frequency was the second one with higher frequency equal to 1.23 Hz.

In case we know the measured values, we may set the number of cycles in every stress range according to Eq. 7. For the illustration, the probability, that the cantilever (depicted in Fig. 3. left) is vibrating in the first eigen-form is $P_{4,f1} = 0.06$, in the second $P_{4,f2} = 0.93$ and in the third and the fourth shape we may expect probability $P_{4,f3} = 0.00002$ and $P_{4,f4} = 0.00005$ respectively. Finally we may assess if it complies with the Palmgren-Miner criterion and/or determine the residual life of the structure.

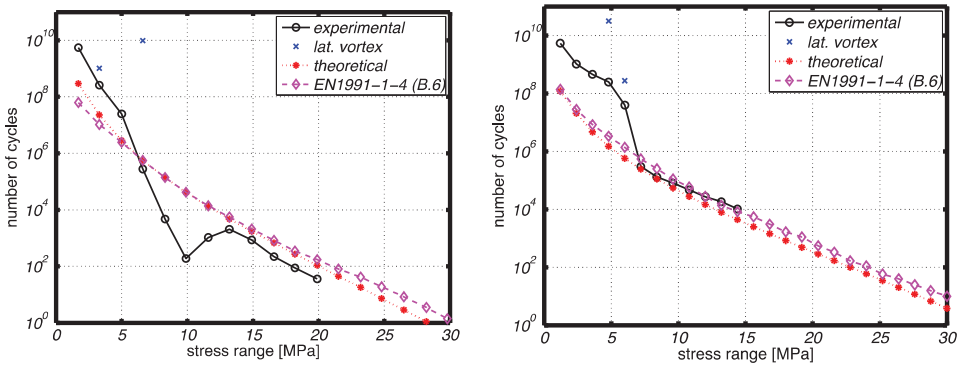

Fig. 4: Stress spectra ascertained from the strain-gauges measurement (circles) and number of cycles determined theoretically (red asterisks, magenta diamonds). Two blue crosses stand for the lateral vibration. Left: Example 1a (Veselský kopec), Right: Example b1 (Vraní vrch).

The suitability of the proposed method is demonstrated in Fig. 4, where the comparison between measured and calculated number of cycles is presented for the observed time interval. It is obvious, that there exists good agreement between proposed method and the measured values.

4.3. Example 2-prediction for the guy ropes

4.3.1. Response in the lateral direction

The calculation of the number of the cycles and the range of the stress is performed in the same manner as for the longitudinal direction of the wind except for the determination of the standard deviations of the fluctuation component, of the response and probability P_3.

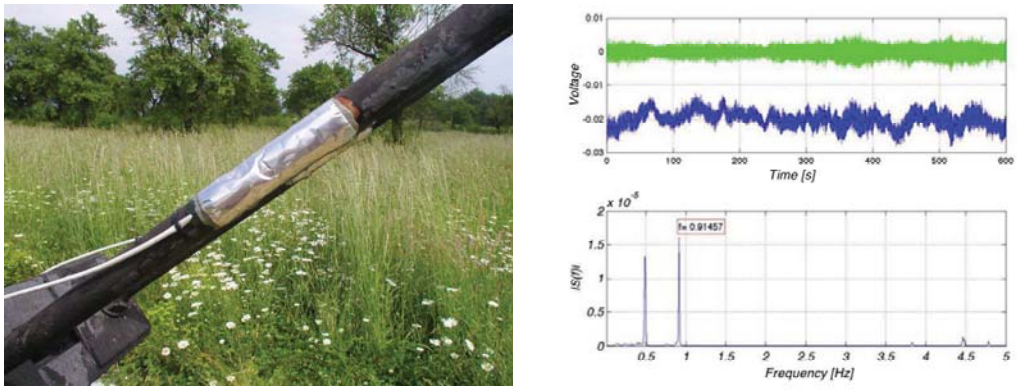

Fig. 5: Left-Strain-gauges glued at the guy rope. Right-stress time history and the spectral density of the response of lower rope.

Standard deviations of the resonant responses were determined approximately as $\sqrt{1/3} \cdot \sqrt{0.5} = 0.82$ times the standard deviations of the resonant response in the direction of the wind medium, see Madugula et al. (2002). The term $\sqrt{(1/3)}$ expresses the ratio of the approximate size of the fluctuation in the resonant frequency and in the perpendicular direction. It is considered that the size of aerodynamic damping for perpendicular direction is about 50 % compared to the aerodynamic damping for the direction of mean wind speed.

The probability that the wind will blow in the perpendicular direction is P_{3p}. It is derived from the probability P_3 by following simple approach considering the direction perpendicular to the most

frequent direction of the wind; with a possible deviation 45°. The probability value P_{3p} is equal to $1-P_3$.

4.3.2 Resonant components, net stress spectra

The probability P_4 expresses the influence of the background and the resonant responses respectively. It is given as the ratio of standard deviation of resonant responses and the background response respectively and the net dynamic response. This ratio is expressed in accordance with the definition of λ_3 (see Madugula et al. (2002)) as $1/\lambda_R$ where λ_R coefficient is considered to have a conservative value of 1.2 in our case).

The frequency of the background response as well as the resonant frequencies for the guys in the presented example can be seen on the Table 1, together with the individual probabilities P_4.

Tab. 1: The background and resonant frequencies of the lower cables 1 (left) and upper cables 2 (right) together with the individual values of the probability P_4.

	Lower cables		**Upper cables**	
	Freq. [Hz]	Probability P_4	Freq. [Hz]	Probability P_4
backgr. resp.	0,03	0,83	0,03	0,82
1. shape	0,43	0,03	0,29	0,02
2. shape	0,49	0,02	0,43	0,06
3. shape	0,76	0,05	0,49	0,07
4. shape	1,50	0,05	0,91	0,02
5. shape	1,80	0,02	1,10	0,01

Calculation of the tension in the guy rope was carried out for 3 different wind velocities. Based on the measurement of the wind spectra, the terrain category II was chosen and the static calculation used the patch load method according to ČSN EN Eurocode 1 (2007) was carried out. The coefficient of the maximum value (peak factor) was determined by the more accurate calculation according Sparling et al. (1993). Partial factor for fatigue loading was considered to have the value of $\gamma_{Ff}=1.00$ as recommended in ČSN EN Eurocode 3 (2008), article 9.5.

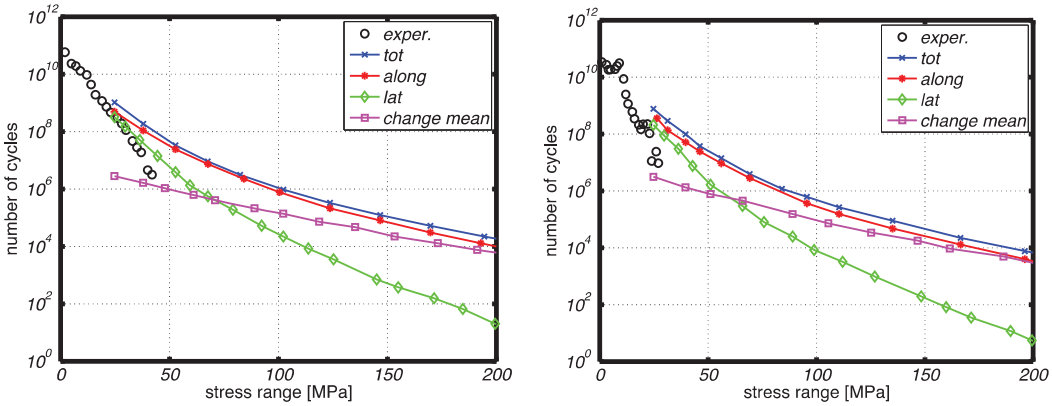

Fig. 6: Stress spectra ascertained from the strain-gauges measurement (blue circles) and total number of cycles determined theoretically with the use of known structure characteristics (green crosses). Red circles stand for stress spectra due to change of mean wind speed. Squares are the stress spectrum due to fluctuating lateral wind. Diamonds are due the along wind fluctuations. Left: Lower cables, Right: Upper cables.

5. Conclusions

The paper presented the analysis focused on the prediction of theoretical lifetime of antenna cantilever and mast guys and the comparison with long/short time measurements on the real structures. Examples of slender towers and masts subjected to the turbulent wind were presented. The wind load has been described by relatively simple formulas and the number of cycles during certain period was determined. The load description agreed very well with the measurements on the structure. Though there are differences in some of the stress ranges especially higher one which cannot be measured in the relatively short interval, there exists general agreement between theoretical predictions and onsite measurements, when correct assumption of the wind and the structure are employed. The work offers practical method for the clients to better estimate the service life of towers and their parts and to better organizes the maintenance work.

From the comparison obtained by theoretical calculation (for the measured wind speed) it is evident that the theoretical number of cycles is higher than measured ones, especially in the high stress range, which are significant from the lifetime point of view. This deviation may be caused by some conservative assumptions especially for lower wind speeds, which includes all kinds of excitation.

There are some open problems, behind the scope and limitation of this paper, like the correlation of the load with respect to the eigen-modes, superposition of lateral and longitudinal direction. However, in case there is attention paid to the short-term measurements of the dynamic characteristics of a structure, the method can give good results with regards to the lifetime prediction. This is useful when the structure is hardly accessible for the long-term monitoring.

Acknowledgement
The support for this work was provided by the projects of the Ministry of Industry and Trade No. MPO TIP FR-TI3/654, RVO: 68378297, the Czech Grant Agency by project No. GAČR 103/09/0094, the research project AV 0Z 2071913 and by the company České radiokomunikace a.s.

References

Amzallag, C., Gerey, J.P., Robert, J.L., Bahuaud, J. (1994) Standardization of the rain-flow counting method for fatigue analysis. *Fatigue*, Vol. 16, pp. 287-293.

Benasciutti, D., Tovo, R. (2005) Spectral methods for lifetime prediction under wide-band stationary random processes *International Journal of Fatigue, Vol.* 27, pp. 867-877.

ČSN EN 1991-1-4 Eurocode 1 (2007) Zatížení konstrukcí – Část 1-4: Obecná zatížení – Zatížení větrem.

ČSN EN 1993-3-1 Eurocode 3 (2008) Navrhování ocelových konstrukcí – Část 3-1: Stožáry a komíny – Stožáry.

ČSN P ENV 1993-3-1 (2000) Navrhování ocelových konstrukcí, část 3-1: Věže a stožáry.

Degrieck, Van Paepegem, W. (2001) Fatigue damage modeling of fiber-reinforced composite materials: review. *Appl Mech Rev* Vol. 54, No. 4, pp. 279-300.

Epaaratchchci, J. A., Clausen, D. P (2005) A new cumulative fatigue damage model for glass fiber reinforced plastic composites under step-discrete loading. *Composites*: Part A 36, pp. 1236-1245.

Fischer O. (1983) Secondary bending stresses in guy-ropes of guyed masts. *Acta Technica ČSAV*, No. 6, pp. 684-696.

Madugula, M.K.S. et al (2002) Dynamic Response of Lattice Towers and Guyed Masts. *ASCE*.

Pirner, M., Fischer, O. (1999) Long-time observation of wind and temperature effects on TV towers. *Journal of Wind Engineering and Industrial Aerodynamics*, Vol. 79, pp. 1-9.

Pospíšil, S., Bavestrello, F., De Col, M. (1997) A method for the calculation the number of cycles of the lattice tower due to the wind turbulence. *IASS WG 4*, Chicago.

Repetto, M. P., Solari, G. (2002) Dynamic crosswind fatigue of slender vertical structures. *Wind and Structures*, Vol. 5, No. 6, pp. 527-542.

Simiu, E., Scanlan, R. (1996) *Wind effects on structures*. Wiley, New York.

Sparling, B.F., Smith, B.W., Davenport, A.G. (1993) Simplified Dynamic Analysis Methods for Guyed Masts in Turbulent Wind. IASS WG 4, Prague.

Wahl N. et al. (2001) Spectrum fatigue lifetime and residual strength for fiberglass laminates in tension. *AIAA-0025.*

18th International Conference
ENGINEERING MECHANICS 2012
Svratka, Czech Republic, May 14 – 17, 2012

pp. 1049–1059
Paper #230

BRANCH AND BOUND METHOD FOR GLOBAL OPTIMA OF SIZE OPTIMIZATION BENCHMARKS

A. Pospíšilová [*], **M. Lepš** [**]

Abstract: *This contribution focuses on searching for global optima of size optimization benchmarks utilizing a method based on branch and bound principles. The goal is to show the process of finding these global optima on several examples. To minimize computational demands a suitable parallelization is used. Optima which can be found in available literature and optima obtained in this work are compared.*

Keywords: ***benchmarks, discrete sizing optimization, branch and bound method, global optima, parallel programming***

1. Introduction

A numerical optimization is nowadays a very popular tool for obtaining a different view on structures and materials. Shape of the structure, cross-sections, amount of reinforcement, thicknesses of sheets, design of concrete mixture and many other properties can be optimized. Recently, many heuristic algorithms are developed, tested on benchmarks and their efficiency is compared. To compare distinct optimization methods, it is appropriate to know the global optima of these benchmarks. The closer to the global optimum the gained value is, the better the method is. In the past, it was not possible to obtain these optima because of large computational demands. A computational power is growing every year therefore now seems to be the right time to deal with this issue.

This paper is trying to outline a process of searching for global optima of sizing discrete optimization benchmarks. Various optimization methods can be used for obtaining optima such as gradient methods (Shewchuk (1994)), heuristics methods (Dréo et al (2005)), or evolutionary algorithms (Eiben and Smith (2003)). These methods do not guarantee that the gained optimum is the global one because only a portion of the space is explored. Nevertheless, the advantage of these methods is that the optimum is found in a real time and the ability to obtain or at least approach a vicinity of a global optimum is considered as a sign of quality. In our work, we used a method based on branch and bound principles to obtain global optima and appropriate cross-sections. A good estimate of a lower and upper bounds reduces the searched space but still ensures that the global optima can be found. The algorithm presented in our paper is universal, i.e. it is applicable to other truss structures or a similar type of problems. We hope that the knowledge of global optima of studied benchmarks will improve the development of optimization methods.

2. Sizing optimization

Sizing optimization (Bendsoe and Sigmund (2003)) is one type of structural optimization that deals with truss-like structures. These structures are defined by topology, material, loading, supports, and a set of sections or alternatively minimum and maximum cross-sectional areas of the individual rods. The objective function is the weight of a structure and constraints are maximal stresses and maximal displacements, respectively. The goal is to find cross-sections for the given structure that satisfy prescribed constraints and have a minimal weight. The selection of cross-sections from the given set of sections defines a discrete optimization problem, whereas variables chosen from given limits leads to a continuous case. The

[*]Ing. Adéla Pospíšilová: Faculty of Civil Engineering, CTU in Prague, Thákurova 7; 166 29, Prague; CZ, e-mail: adela.pospisilova@fsv.cvut.cz
[**]Ing. Matěj Lepš, Ph.D.: Faculty of Civil Engineering, CTU in Prague, Thákurova 7; 166 29, Prague; CZ, e-mail: leps@cml.fsv.cvut.cz

continuous optimization problem can be efficiently solved by mathematical programming methods like gradient-based methods as will be shown later in the text. When using discrete variables, no such option is available. Thus our attention is aimed at the discrete case.

3. Discrete optimization problem

The goal is to find such combination of cross-sections from the given list of profiles that leads to minimal weight still fulfilling given constraints. Here, two methods that are able to find global optima for this discrete optimization problem are presented.

3.1. Enumeration

An *Enumeration* is the simplest method for obtaining a global optimum of the discrete optimization problem. It is necessary to compute values of an objective function and constraints for every combination of cross-sections from a given set. Therefore, the enumeration has very large computational demands. If there are n sections and k variables (i.e. rods or groups of rods) than n^k possible solutions exist, i.e. the problem grows exponentially with a growing number of variables. The application of the enumeration is therefore possible only for small structures or for analysis of the vicinity of some local optima.

3.2. Method based on branch and bound principles

A *branch and bound method* is another method for obtaining global optima. A. M. Land and A. G. Doig (see Land and Doig (1960)) invented this method for linear problems. It was modified for discrete problems and for mixed-discrete variables (see e.g. Arora (2002)) many times.

A branch and bound method is based on a division of a main problem to several subproblems, so-called branches. To estimate, which branches are to be evaluated, an existence of the lower and upper bounds needs to be assumed, i.e. the lower and upper bounds are used to restrict the searched space. The lower bound can be obtained by any continuous optimization method, because the global optimum with discrete design variables will never provide a lower value of the objective function than the global optimum with continuous design variables. The upper bound can be obtained by any heuristic method, because a local optimum always has a greater or equal value of the objective function than the global optimum. Since the constraints for the sizing optimization problem are more computationally demanding than the value of the objective function, they are calculated only for solutions that lie between lower and upper bounds. If we obtain a subproblem with a value of the objective function outside the given bounds, the rest of a branch is not calculated because global optimum cannot be located there. The more accurate estimates of the lower and upper bounds are, the narrower the searched space can be. Especially, the upper bound can be decreased during the calculation based on the already obtained objective function's values. Hence, the searched subspace will be reduced and a problem will be solved with less computational demands.

4. Continuous optimization problem

A continuous optimization problem is more complex than the discrete one because an infinite number of potential solutions exists in the space with real numbers. Therefore, it cannot be guaranteed that the found optimum is the global one. Nevertheless, it is possible to use powerful continuous optimization algorithms such as mathematical programming methods which are well established. Obtaining a potential global optimum with continuous variables is therefore less demanding than the solution of the optimization problem with discrete variables. The main disadvantage of this methodology is the uncertainty of a solution quality. It can be overcome by the following alternatives:

- The branch and bound method expects that the lower bound has the same (or higher) value of the objective function as the global optimum with continuous variables. Since the global optimum of the continuous problem cannot be generally known, the true lower bound cannot be ensured. As a solution, the lower bound is set to its lowest potential minimum i.e. without using any continuous optimization method. This process provides a real global optimum with discrete variables. In most

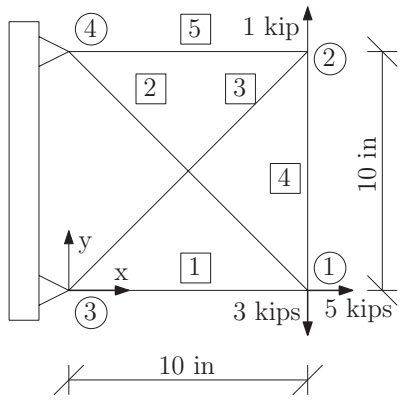

Fig. 1: The 5-bar truss

cases, however, the searched space will be extremely huge for computation of all possible solutions in a real time.

- Another approaches do not fully guarantee the acquisition of the global optimum. Nevertheless, the probability of obtaining the global optimum is acceptable. These approaches are based on an estimation of the global optimum with continuous variables and the value of its objective function. We use nonlinear programming that is implemented in MATLAB environment (e.g. `fmincon()` function). This routine is executed several times from random initial points. If the obtained optima do not differ from each other and the results are comparable to optima published in available literature, the estimate is considered as credible. If the gained optima differ from each other, then it is not possible to use them as the lower bound. The first approach (without using the continuous optimization method) is then used or the lower bound is estimated to be e.g. 20% lower than the best-gained value.

All continuous optima for problems mentioned below in this text were consistent with published optima. For the sake of certainty, the nonlinear programming method was launched with different starting vectors hundred times and the best solution was considered as the the lower bound.

5. Sizing optimization benchmarks

5.1. 5-bar truss

A representative example of a structure small enough for computational demands and bigger enough for branching purposes was necessary for developing the branch and bound algorithm. The topology of the structure was taken from reference Lee and Hajela (2001), constraints and a set of given cross-sections were chosen by authors.

A structure in Fig. 1 has four nodes and five rods and is made from aluminium. The density of the material is $0.1\ lb/in^3$ and Young's modulus is equal to $10^4\ ksi$. The allowable stress is limited to $\pm 60\ ksi$ in each rod and the displacements are limited to $\pm 0.06\ in$ along the horizontal and vertical directions. Continuous variables can assume values between lower $0.01\ in^2$ and upper bounds $0.1\ in^2$, respectively. Note that imperial units are used in the whole text because the gained solutions will be compared with published optima in available literature where imperial units are usually used.

A function of nonlinear programming `fmincon()` (The MathWorks (2011c)) offers four variants of optimization algorithms. In this paper, a Sequential quadratic programming (SQP) is a suitable algorithm for continuous sizing optimization problem. It is chosen by a command `options = optimset('Algorithm','active-set')`. Main idea is to convert a more complicated problem to a problem that is easier to solve. Here, the constrained nonlinear problem is solved using a sequence of parameterized unconstrained optimizations which, in the limit (of the sequence) converge to the constrained problem (The MathWorks (2011a)).

A starting point, i.e. a design variable vector composed of cross-sectional areas, an objective function, constraints and lower and upper bounds of variables are necessary as an input at the beginning of the algorithm. The objective function is a weight of the structure

$$m = f(A_i) = \rho \cdot \sum_{i=1}^{N} A_i \cdot L_i, \tag{1}$$

where $N = 5$ is a number of rods, A_i is a cross-sectional area and L_i is the length of a rod i and ρ is density of the material. Constraints are defined as inequalities such as

$$\max|\sigma_i| - 60 \leq 0, \tag{2}$$

$$\max|w_j| - 0.06 \leq 0, \tag{3}$$

where $\max|\sigma_i|$ is a maximal absolute value of stresses, j is an ordinal number of independent displacements and $\max|w_j|$ is a maximal absolute value of displacements. These values can be obtained by several methods. In this paper, the finite element method was used as is described e.g. in Pospíšilová (2010).

You can see the results for the continuous optimization problem of the 5-bar truss in Tab. 1. The objective function value of the optima gained with SQP algorithm is later used as the lower bound for the branch and bound method.

An identical topology of the 5-bar truss is used for the discrete optimization version. Material properties and constraints are also identical. The cross-sectional areas are chosen from the set $\{0.01, 0.02, \ldots, 0.1\}$ in^2. Since the structure has five rods ($k = 5$) and 10 cross-sectional areas ($n = 10$), the number of all possible solutions is $n^k = 10^5$. Therefore, the structure is small enough and the discrete global optimum can be obtained with the enumeration. The results obtained by the enumeration can be seen in Tab. 1.

The lower bound for the branch and bound method is set to the optimum value of the objective function obtained with continuous variables. The upper bound is set to the estimated weight 0.23 lb that is 25% greater than the global optimum value of the objective function gained by the enumeration. A space is searched systematically between these two bounds until the global optimum is found.

The steps of the algorithm can be described as follows:

1. First of all we have to decide which values will be used as initial. It is appropriate to begin with the lowest profiles and increase them because of minimization of the objective function. From a programming point of view, it is easier to use integer variables that are the ordinal numbers of the given set of cross-sectional areas - set M. For example, the initial design variable vector is `1 1 1 1 1`, which means that the first area (0.01 in^2) from the given set is attached to each rod. For numbering of rods see again Fig. 1.

2. The value of the objective function (a weight of a structure m) is then calculated and compared with the lower m_{min} and upper m_{max} bounds. If the weight of the structure is less than m_{min}, the algorithm will go to Step 3. If the structure weight is between m_{min} and m_{max} the algorithm will go to Step 4. If the weight of the structure is greater than m_{max}, the algorithm will go to Step 5.

3. The value of the objective function is less than m_{min}. It is necessary to find design variables' combination with greater weight than m_{min}. The last variable is raised to its maximum for faster progress of the algorithm as `1 1 1 1 10` and the value of the objective function is calculated and compared with m_{min}.

   (a) If the value of the objective function is still less than m_{min}, the algorithm searches for the design variables' combination with greater weight than the lower bound. This can be done as follows. The next-to-last variable is repeatedly raised by one, e.g. to (`1 1 1 2 10`). If the next-to-last variable value reaches its maximum it is decreased to its minimum and the third from the end variable value is raised by one. The algorithm will goes to Step 2 at the moment when all variables are set such that $m > m_{min}$.

Tab. 1: 5-bar truss optima

Variable	Units	Discrete optimization		Continuous optimization
		Enumeration	Branch and bound method	`fmincon()`
A_1	in^2	0.05	0.05	0.0500
A_2	in^2	0.01	0.01	0.01
A_3	in^2	0.06	0.06	0.0471
A_4	in^2	0.02	0.02	0.0167
A_5	in^2	0.01	0.01	0.01
m	lb	**0.179**	**0.179**	0.157
$\max \lvert w_j \rvert$	in	0.059	0.059	0.06
$\max \lvert \sigma_i \rvert$	ksi	59.371	59.371	60.006
w_{lim}	in	0.06	0.06	0.06
σ_{lim}	ksi	60	60	60

(b) If the value of the objective function is greater than the lower bound, the last variable value is decreased to its minimum (`1 1 1 1 1`) and is increased one by one (`1 1 1 1 2`, `1 1 1 1 3`, ..., etc.) until the weight is greater than m_{min}. If $m_{min} > m$ the algorithm goes to Step 2.

4. The value of the objective function is greater than m_{min} and less than m_{max}. The global optimum is located somewhere in this subspace. Therefore, the constraints are evaluated, i.e the stresses and displacements are calculated.

   (a) If the constraints are fulfilled, i.e. $\max \lvert \sigma_i \rvert \leq 60\ ksi$ and $\max \lvert w_j \rvert \leq 0.06\ in$, the upper bound is updated to the actual objective function value $m_{max} = m$. Thus the upper bound is pushed down towards the global optimum and the searched space is reduced. The last variable value is increased by one afterwards. If this variable value exceeds its maximal possible value of the cross-sectional area from a given set, e.g. `1 1 5 11 1`, its value is set to the minimal possible value and the next-to-this variable value is increased by one, i.e. `1 1 6 1 1`. The algorithm goes to Step 2.

   (b) If the constraints are not fulfilled, the value of the last variable is increased by one.

5. The value of the objective function is greater than m_{max}. The value of the last variable is decreased to its minimum, the next-to-last variable value is increased by one and the objective function value is calculated. If the variable exceeds its maximal possible value from the given set the algorithm acts as in Step 4a.

   (a) If the value of the objective function m is lower than m_{max}, the algorithm goes to Step 2.

   (b) If the objective function value m is greater than m_{max}, a value of the third variable increases by one and the value of the forth variable is set to its minimum. The algorithm continues in this way until the objective function value is less than m_{max}. If there is no such combination of cross-sectional areas, the task is terminated.

6. If all variable values are set to their maxima, the algorithm ends.

Fig. 2 shows a distribution of 5-bar truss potential solutions. A seagreen part shows a number of potential solutions below the lower bound where only the objective function values are calculated, i.e.

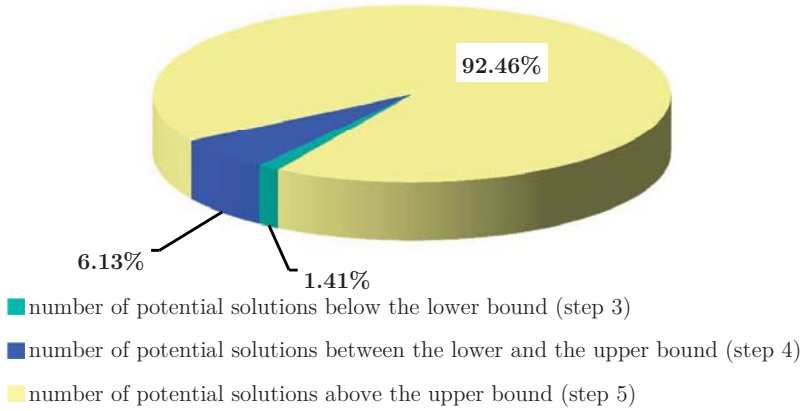

Fig. 2: A pie chart of a distribution of the 5-bar truss problem solutions solved by the branch and bound method

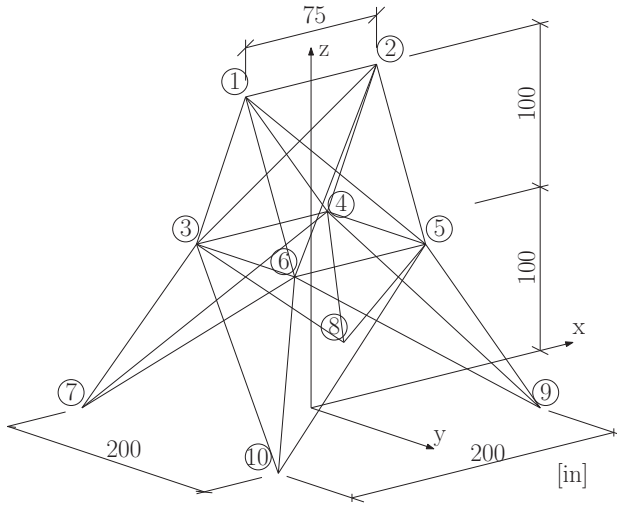

Fig. 3: The 25-bar truss

Step 3 of the algorithm. A blue part shows a number of potential solutions between the lower and the upper bound where values of the objective function as well as constraints are calculated. See Step 4 of the algorithm for more details. The global optimum is included in this subspace. A yellow part represents a number of potential solutions above the upper bound where only the objective function values are calculated. See Step 5 of the algorithm for more details. Tab. 1 presents results for the continuous optimization problem along with the results for the discrete problem solved by the enumeration and the branch and bound method. Since the enumeration calculates values of the objective function as well as constraints for all potential solutions it is not possible to omit the global optimum. Results obtained by both presented methods are identical and this comparison serves as verification of the branch and bound method.

5.2. 25-bar truss

A topology of this test problem has been firstly used in reference Fox and Schmit (1966). The structure has ten nodes and four supports (see Fig. 3); therefore there are 18 free displacements. The structure is symmetric thus some rods were linked to groups, listed in Tab. 2. The material is aluminium with density equal to $0.1\ lb/in^3$ and Young modulus equal to $10^4\ ksi$. The loading is defined in Tab. 3. Every

Tab. 2: Member grouping for the 25-bar truss

Group of bars	Conectivities
A_1	1-2
A_2	1-4, 2-3, 1-5, 2-6
A_3	2-5, 2-4, 1-3, 1-6
A_4	3-6, 4-5
A_5	2-4, 5-6
A_6	3-10, 6-7, 4-9, 5-8
A_7	3-8, 4-7, 6-9, 5-10
A_8	3-7, 4-8, 5-9, 6-10

Tab. 3: Loadings for the 25-bar truss (kips)

Node	F_x	F_y	F_z
1	1.0	-10.0	-10.0
2	0	-10.0	-10.0
3	0.5	0	0
6	0.6	0	0

cross-sectional area is chosen from the given group: 0.1, 0.2, 0.3, 0.4, 0.5, 0.6, 0.7, 0.8, 0.9, 1.0, 1.1, 1.2, 1.3, 1.4, 1.5, 1.6, 1.7, 1.8, 1.9, 2.0, 2.1, 2.2, 2.3, 2.4, 2.5, 2.6, 2.8, 3.0, 3.2 and 3.4 in^2, see reference Wu and Chow (1995). Continuous variables can assume values between a lower 0.1 in^2 and an upper bound 3.4 in^2, respectively. The allowable stress is set to ± 40 ksi in all rods and maximal allowable displacement is ± 0.35 in at all nodes along the x, y and z directions.

The same methodology was used for the 25-bar continuous optimization case as for the 5-bar truss problem. The results are shown in Tab. 4 and they are compared with the results published in available literature. The discrete case cannot be enumerated in a reasonable time because the number of potential solutions is $n^k = 30^8 = 6.561 \cdot 10^{11}$, where k is a number of rod groups. The discrete global optimum was gained with the branch and bound method, where the lower bound was set to the gained optimum from continuous optimization and the upper bound was set as the worst available solution from literature (see Rajeev and Krishnamoorthy (1992)). The algorithm is the same as in the 5-bar truss problem.

6. Parallelization

The 25-bar truss is relatively computationally demanding. Since the evaluation of solutions is independent to each other (except updating the upper bound m_{max} described in Step 4a of the algorithm), it is possible to run the method in a parallel way. Nowadays, modern computers are equipped with several core processors and thus it is appropriate to use this computational effort. MATLAB environment offers several tools of parallelization which are presented in this section.

The simplest parallelization method is to permit usage of all cores [1] by the `maxNumCompThreads()` command, see Luszczek (2009) for more information. There is no need to change a serial code; MAT-

[1] It is possible to permit only a subset of all available cores such as two cores out of four.

Tab. 4: Comparison of results for the 25-bar truss continuous case

Variable	Unit	Perez & Behdinan	this paper
		2007	2011
A_1	in^2	0.1	0.1
A_2	in^2	0.457	0.421
A_3	in^2	3.4	3.4
A_4	in^2	0.1	0.1
A_5	in^2	1.937	1.917
A_6	in^2	0.965	0.966
A_7	in^2	0.442	0.471
A_8	in^2	3.4	3.4
m	lb	483.84	**483.82**
$\max \lvert\sigma_i\rvert$	ksi	6.15	6.13
$\max \lvert w_j\rvert$	in	0.35	0.35
σ_{lim}	ksi	40	40
w_{lim}	in	0.35	0.35

LAB does all parallelization by itself. This variant of parallelization is not the best one because the user cannot mark appropriate parts for parallelization and also shared memory cannot be accessed.

Another possibility is to use a `parfor` loop instead of `for`. Every iteration of a `parfor` loop is independently executed on individual cores. For proper functioning of the `parfor` loop, it is necessary to prepare an appropriate number of processes/threads, so-called *labs*, by command `matlabpool open N`, where `N` is the number of opened labs. This reserves a collection of MATLAB worker sessions to run the loop iterations. The number of labs can be equal to the number of cores or less. Every lab has own part of the `parfor` loop. However, the user cannot specify any partition of data. It is also important to know that there is also no possibility to work with shared memory. Therefore it is not possible to update the upper bound value efficiently and therefore, this way of parallelization is not useful for the branch and bound method.

The last possibility mentioned here is the `spmd` method which means Single Programm Multiple Data, see e.g. The MathWorks (2011b) for more details. The `spmd` statement separates the block of a code to be run simultaneously on multiple labs. As well as in the `parfor` loop method, the command `matlabpool open N` open a required number of labs. Sending data to another lab is possible by the `labSend(data, X)` command, where `X` is the index of receiving lab where the data are sent. Then, it is necessary to receive the data by the `labReceive(Y)` command, where `Y` is the index of a lab from which the data will come. It is appropriate to split the data only at one, so-called *master*, lab and receive data with the others, so-called *slaves*. The master can process its own data as well.

The main problem here is to estimate a proper amount of data for every lab. If the data are sent too often the communication between the master and the slaves will take a plenty of time. In the 25-bar truss task, permutations with repetition are generated in advance for several groups of rods (i.e. four groups) and the remaining groups of rods (other four groups) are generated in the branch and bound method independently on each labs. In advance generated combinations are divided in the `for` loops to individual labs and then the algorithm continues as in the algorithm written for the 5-bar truss task. The maximal values of m_{max} are collected at the end of every iteration. The smallest one is chosen as a new

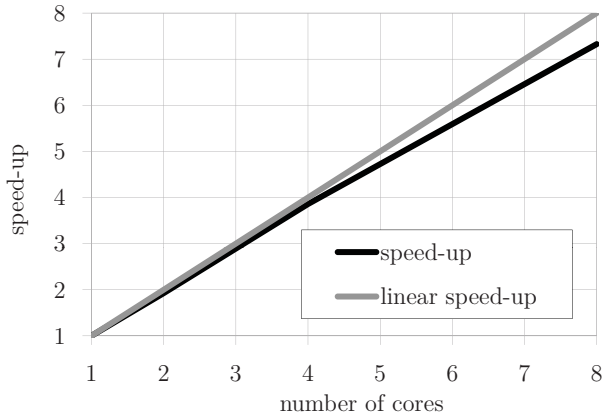

Fig. 4: A speed-up of the 25-bar truss problem solved by the parallel branch and bound method

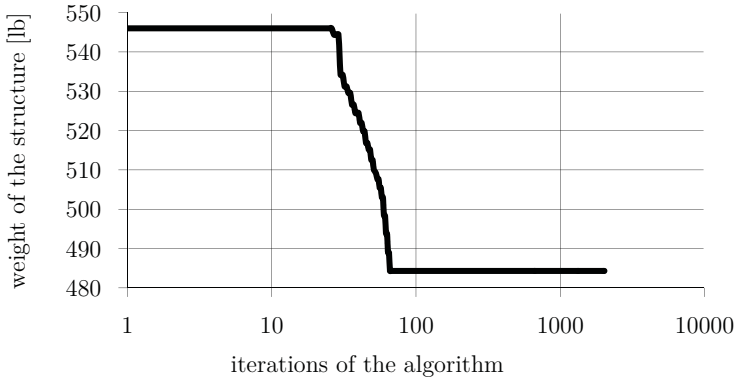

Fig. 5: A graph of the decreasing upper bound for the 25-bar truss problem

m_{max} and resent to every lab as an initial value of m_{max} for another iteration. If all data are used, the smallest value of m_{max} is taken as the global optimum.

For the parallel version of the algorithm, it is important how well the task is scaled, whether the parallelization is useful or not. Ideally, we would like to achieve linear scaling i.e. speed-up of n on n cores. However, it is very hard to obtain linear scaling, e.g. because of time spent on communications. Fig. 4 shows a graph where speed-up of the parallel algorithm is compared on 1 to 8 labs[2]. HP Xeon Z600 Workstation with two 4-cores processors Intel Xeon E5520, frequency 2.27GHz was used for computations within Matlab R2009a 64-bit in Debian GNU/Linux.

7. Conclusions

Fig. 5 shows a graph with the decreasing upper bound m_{max} for the 25-bar truss problem. The value of m_{max} determines the best solution in a progress of the algorithm. It can be interpreted as a convergence of the objective function to the global optimum. In advance generated combination were sent to eight labs by fifty. The number of iterations were $30^4/(8 \cdot 50) = 2025$. The global optimum was gained in the 66^{th} iteration. It is necessary to note that if the formulation of the task was in a different way, the global optimum would be gained in another iteration. Since a task is to find the global optima, the whole subspace of potential solutions must be search for and it is not possible to shorten the computation.

[2]It was not necessary to compute the whole task. Some variables have been fixed to prescribed values, here 2 out of 8 variables, and the algorithm has been run with this restriction.

Tab. 5: A comparison of results for the 25-bar truss discrete case from literature and the present work

Variable	Units	this paper	Kripka	Lemonge & Barbosa	Li & Liu	Wu & Chow	Coello	Rajeev & Krishnamoorthy
		B & B	SA	GA	PSO	GA	GA	GA
		2011	2004	2004	2009	1995	1994	1992
A_1	in^2	0.1	0.1	0.1	0.1	0.1	1.5	0.1
A_2	in^2	0.4	0.4	0.3	0.3	0.5	0.7	1.8
A_3	in^2	3.4	3.4	3.4	3.4	3.4	3.4	2.3
A_4	in^2	0.1	0.1	0.1	0.1	0.1	0.7	0.2
A_5	in^2	2.2	2.2	2.1	2.1	1.5	0.4	0.1
A_6	in^2	1	1	1	1	0.9	0.7	0.8
A_7	in^2	0.4	0.4	0.5	0.5	0.6	1.5	1.8
A_8	in^2	3.4	3.4	3.4	3.4	3.4	3.2	3
m	lb	**484.33**	**484.33**	484.85	484.85	486.29	539.78	546.01
$\max \lvert\sigma_i\rvert$	ksi	6.20	6.20	6.11	6.11	6.01	6.66	6.77
$\max \lvert w_j\rvert$	in	0.35	0.35	0.35	0.35	0.35	0.34	0.35
σ_{lim}	ksi	40	40	40	40	40	40	40
w_{lim}	in	0.35	0.35	0.35	0.35	0.35	0.35	0.35

Tab. 5 shows the optimum gained with the branch and bound method as well as optima obtained by heuristic algorithms found in literature. The obtained result by the branch and bound method is identical to the solution presented by author Kripka. He used the Simulated Annealing method. However, he did not search the whole subspace of possible solutions so he could not be sure that the obtained optimum is the global one. It can be seen that the results of the discrete and continuous case of the optimization problem are near to each other, see Tab. 4 and Tab. 5. Therefore, the solution is potentially correct. However, we can be sure that we have found the global optimum because we have systematically explored the whole space where the global optimum is located.

The branch and bound method is suitable for bigger structures. It does not enumerate all potential solutions of the optimization problem contrary to the enumeration method. The space is restricted to the subspace between the lower and the upper bound where the global optimum is located. The lower bound is obtained e.g. with some continuous optimization method. The constrained nonlinear programming using sequence of parameterized unconstrained optimization was used in this paper. The upper bound can be gained with some heuristic method which is fast and quite effective. The more accurate the value is, the efficient the branch and bound method is. The task will not be branched to so many subproblems.

Global optima for computational demanding tasks such as the 25-bar truss problem have not been published yet to the best authors' knowledge. We hope that by publishing the algorithm as well as the value of the global optimum we will introduce a standard of quality that will help to improve new optimization methods.

Acknowledgments

This work was supported by the Grant Agency of the Czech Technical University in Prague, grants No. SGS11/021/OHK1/1T/11 and No. SGS12/027/OHK1/1T/11 and the Czech Science Foundation GACR, grant No. P105/12/1146.

References

Arora, J. S. (2002), Methods for Discrete Variable Structural Optimization. In: *Recent Advantages in Optimal Structural Design* (S. A. Burns ed.). American Society of Civil Engineers, Reston (Virginia). Chapter 1, pp 1-40.

Bendsoe, M. P., Sigmund O. (2003), *Topology Optimization: Theory, Methods and Applications*, Springer.

Coello, C. A. C. (1994), Discrete Optimization of Trusses Using Genetic Algorithms. *EXPERSYS-94: Expert Systems Applications and Artificial Intelligence* (J. G. Chen et al. eds.), I.I.T.T. International, pp. 331-336.

Dréo, J., Pétrowski, A., Siarry, P. et al. (2005), *Metaheuristics for Hard Optimization: Methods and Case Studies*, Springer.

Eiben, A. E., Smith, J. E. (2003), *Introduction to Evolutionary Computing*, Springer.

Fox, R. L., Schmit, L. A. Jr. (1966), Advances in the Integrated Approach to Structural Synthesis. *Journal of Spacecraft and Rockets*, Vol 3, No.6, pp 858-866.

Kripka, M. (2004), Discrete Optimization of Trusses by Simulated Annealing. *Journal of the Brazilian Society of Mechanical Sciences and Engineering*, Vol 26, No.2, pp 170-173.

Land, A. H., Doig A. G. (1960), An Automatic Method of Solving Discrete Programming Problems. *Econometrica*, Vol 28, No. 3, pp. 497-520.

Lee J., Hajela P. (2001), Application of classifier systems in improving response surface based approximations for design optimization. In: *Computers & Structures*, Vol 79, Is. 3, pp 333-344.

Lemonge, A. C. C., Barbosa, H. J. C. (2004), An adaptive penalty scheme for genetic algorithms in structural optimization. *International Journal for Numerical Methods in Engineering*, Vol 59, No. 5, pp. 703-736.

Li, L. J., Huang, Z. B. and Liu, F. (2009), A heuristic particle swarm optimization method for truss structures with discrete variables. *Computers & Structures*, Vol 87, No. 7-8, pp. 435-443.

Luczczek, P. (2009), *Parallel Programming in MATLAB*. [online], last revision 20/07/09 [cit. 20/07/2009]. Available from `http://web.eecs.utk.edu/ luszczek/pubs/parallelmatlab.pdf`

Naylor, P. J. (2009), *Profiling, Optimization and Acceleration of MATLAB code*. [online], last revision 20/11/09 [cit. 20/11/2009]. Available from `http://www.enm.bris.ac.uk/staff/pjn/teaching/HPC/opt-notes.pdf`

Perez, R. E., Behdinan, K. (2007), Particle Swarm Optimization in Structural Design. In: *Swarm Intelligence, Focus on Ant and Particle Swarm Optimization* (F. T. S. Chan and M. K. Tiwari eds.). Itech Education and Publishing, Vienna, (Austria), pp 373-394.

Pospíšilová A. (2010). *Analysis of sizing optimization benchmarks* (in Czech), Bachelor Thesis, CTU in Prague, FCE, Department of mechanics, Prague.

Rajeev, S., Krishnamoorthy, C. S. (1992), Discrete Optimization of Structures Using Genetic Algorithms. *Journal of Structural Engineering*, Vol 118, No. 5, pp 1233-1250.

Shewchuk, J. R. (1994), *An Introduction to the Conjugate Gradient Method Without the Agonizing Pain*, School of Computer Science, Carnegie Mellon Univ., Pittsburgh, [online].

The MathWorks (2011), *Constrained Nonlinear Optimization Algorithms: Optimization Algorithms and Examples (Optimization Toolbox)*. [online], last revision 02/10/2011 [cit. 02/10/2011]. Available from `http://www.mathworks.com/help/toolbox/optim/ug/brnoxzl.html`

The MathWorks (2011), *Executing Simultaneously on Multiple Data Sets: Single Program Multiple Data (spmd) (Parallel Computing Toolbox)*. [online], last revision 02/10/2011 [cit. 02/10/2011]. Available from `http://www.mathworks.com/help/toolbox/distcomp/brukbno-2.html`

The MathWorks (2011), *Find minimum of constrained nonlinear multivariable function - MATLAB*. [online], last revision 02/10/2011 [cit. 02/10/2011]. Available from `http://www.mathworks.com/help/toolbox/optim/ug/fmincon.html`

The MathWorks (2011), *Getting Started with parfor: Parallel for-Loops (parfor) (Parallel Computing Toolbox)*. [online], last revision 02/10/2011 [cit. 02/10/2011]. Available from `http://www.mathworks.com/help/toolbox/distcomp/brb2x2l-1.html`

Wu, S.-J., Chow, P.-T. (1995), Steady-State Genetic Algorithms for Discrete Optimization of Trusses. *Computers & Structures*, Vol 56, No.6, pp 979-991.

18th International Conference
ENGINEERING MECHANICS 2012
Svratka, Czech Republic, May 14 – 17, 2012

pp. 1061–1071
Paper #219

SHAPE OPTIMIZATION BY PARTICLE SWARM ALGORITHM UTILIZING ISOGEOMETRIC ANALYSIS

A. Pospíšilová [*], **M. Lepš** [**], **D. Rypl** [***], **B. Patzák** [†]

Abstract: *The present paper describes the application of the particle swarm optimization (PSO) to the shape optimization of two-dimensional domains described by NURBS (non-uniform rational B-splines) and analyzed by the NURBS-based Isogeometric analysis. The regularization of the optimization problem, preventing undesirable clustering of control points of the underlying geometry leading to invalid geometry or parametrization, is achieved by controlling the magnitude of perturbation of design variables within PSO using a background mesh. This mesh, however, does not have to comply with requirements on a standard (e.g. FEM) computational mesh, as it does not have to follow the exact geometry. Thus construction of such mesh (Matlab* `Distmesh` *tool is utilized) is simple and does not introduce a bottleneck to the whole process. The capabilities and performance of the developed optimization strategy will be demonstrated on a standard benchmark problem.*

Keywords: ***Shape Optimization, Particle Swarm Optimization, NURBS, Isogeometric Analysis, Distmesh***

1. Introduction

Isogeometric analysis (IGA) (see papers Hughes (2005); Bazilevs (2006); Cottrell (2006, 2007, 2009); Zhang (2007)) is a recently introduced method which builds upon the concept of isoparametric elements and upgrades it to the geometry level. Although the original intention was to span the gap between the computer aided design (CAD) and the finite element method (FEM), the various advantages and range of applicability make the IGA an interesting alternative to the widely used FEM. It has been shown that the IGA outperforms the classical FEM in various aspects (accuracy, robustness, system condition number, etc.). Another distinct advantage of the IGA over the FEM consists in the conciseness of the parametrization of the design variable space, which makes the IGA attractive for the shape optimization problems.

The aim of this paper is to present the application of the particle swarm optimization (PSO) to the shape optimization of two-dimensional domains described by NURBS and analyzed by the NURBS-based IGA. The regularization of the optimization problem, preventing undesirable clustering of control points of the underlying geometry leading to invalid geometry or parametrization, is achieved by controlling the magnitude of perturbation of design variables within PSO using a background mesh.

The paper is organized as follows. The concept of the IGA is briefly recalled in Section 2. A method of the Particle Swarm Optimization is introduced in Section 3 and the `Distmesh` tool for mesh generating is shortly mentioned in Section 4. The final combination of all these methods is described in Section 5 and results are presented in Section 6.

[*]Ing. Adéla Pospíšilová: Faculty of Civil Engineering, CTU in Prague, Thákurova 7; 166 29, Prague; CZ, e-mail: adela.pospisilova@fsv.cvut.cz
[**]Ing. Matěj Lepš, Ph.D.: Faculty of Civil Engineering, CTU in Prague, Thákurova 7; 166 29, Prague; CZ, e-mail: leps@cml.fsv.cvut.cz
[***]doc. Dr. Ing. Daniel Rypl: Faculty of Civil Engineering, CTU in Prague, Thákurova 7; 166 29, Prague; CZ, e-mail: daniel.rypl@fsv.cvut.cz
[†]prof. Dr. Ing. Bořek Patzák: Faculty of Civil Engineering, CTU in Prague, Thákurova 7; 166 29, Prague; CZ, e-mail: borek.patzak@fsv.cvut.cz

2. Isogeometric Analysis

In the IGA, the approximation of the solution over the domain is based on the functions employed for the description of the underlying geometry of the domain itself. Therefore understanding of the NURBS based representation of the geometry (used in CAD) gives a good insight into the isogeometric concept. A NURBS patch is defined by a set of control points (topologically forming a regular grid of the dimension corresponding to the spatial dimension of the underlying parametric space), their weights, degree of the B-spline basis functions in each direction of the parametric space, and a so-called knot vector represented by a nondecreasing sequence of parametric coordinates for each direction defining the support for individual B-spline basis functions (in other words parametrization) in that particular direction. Note that the number of control points, degree of basis functions, and size of the knot vector in the particular parametric direction are not independent and must be mutually consistent. The data at the control points (for example the coordinates when the geometry is concerned, or the primary unknowns when the solution space is handled) are interpolated over the NURBS patch using the shape functions which are defined as weighted normalized tensor product of univariate B-spline basis functions in each of the parametric directions. For example, for a two-dimensional NURBS patch of a degree p in u-direction and degree q in v-direction, the basis function associated with a control point in the i-th row and j-th column of the grid of $N \times M$ control points is given by

$$R^{p,q}_{i,j}(u,v) = \frac{N^p_i(u) N^q_j(v)\, w_{i,j}}{\sum_{n=1}^{N} \sum_{m=1}^{M} N^p_n(u) N^q_m(v)\, w_{n,m}}, \tag{1}$$

where $w_{i,j}$ stands for the control point weight and $N^r_k(t)$ denotes the univariate B-spline basis functions of the degree r. Starting with the piecewise constant basis functions of a zero degree defined by

$$N^0_i(t) = \begin{cases} 1 & \text{if } t_i \leq t < t_{i+1}, \\ 0 & \text{otherwise}, \end{cases} \tag{2}$$

the basis functions for degree $p > 0$ are defined recursively as

$$N^p_i(t) = \frac{t - t_i}{t_{i+p} - t_i} N^{p-1}_i(t) + \frac{t_{i+p+1} - t}{t_{i+p+1} - t_{i+1}} N^{p-1}_{i+1}(t), \tag{3}$$

in which t_i (for $i = 1, 2, \ldots, N+p+1$) stands for entries of the knot vector and N denotes the number of control points (in the given direction). This is demonstrated in Figure 1a) where the cubic basis function N^3_i spanning four consecutive knot spans is obtained as linear combination of consecutive quadratic basis functions N^2_i and N^2_{i+1} spanning the first three and last three from those four knot spans, respectively. Figure 1b) then displays the hierarchical sequence for piecewise constant, linear, and quadratic basis functions built over an infinite uniform knot vector. For details concerning the definition of the B-spline basis functions and their properties the reader is referred to Piegl (1997).

An example of a quadratic NURBS curve (i.e. one-dimensional NURBS patch) defined by six control points and their weights and parameterized over the open knot vector[‡] $\{0, 0, 0, 1, 3, 3, 4, 4, 4\}$ is depicted in Figure 2a). The parametric equation of that particular curve is given by

$$\boldsymbol{r}(t) = \sum_{i=1}^{6} R_i(t) \boldsymbol{P}_i, \tag{4}$$

where $\boldsymbol{r}$ is the positional vector of a point on the curve corresponding to parameters $t \in \langle 0, 4 \rangle$ and $\boldsymbol{P}_i$ represents the individual control points. The colors of individual parts of the curve correspond to the individual non-zero knot spans (red: $0-1$, green: $1-3$, blue: $3-4$). The NURBS basis functions $R^2_i(t)$ as well as the B-spline basis functions $N^2_i(t)$ used to construct $R^2_i(t)$ are shown in Figure 2b) over the entire span of the knot vector. The curve interpolates those control points for which the corresponding basis function attains value one (knot value at which this occurs defines the parameter corresponding

[‡]Knot vector is called open if its first and last entry is repeated (degree + 1) times, which implies that the curve is passing through the first and last control point (see Piegl (1997) for details).

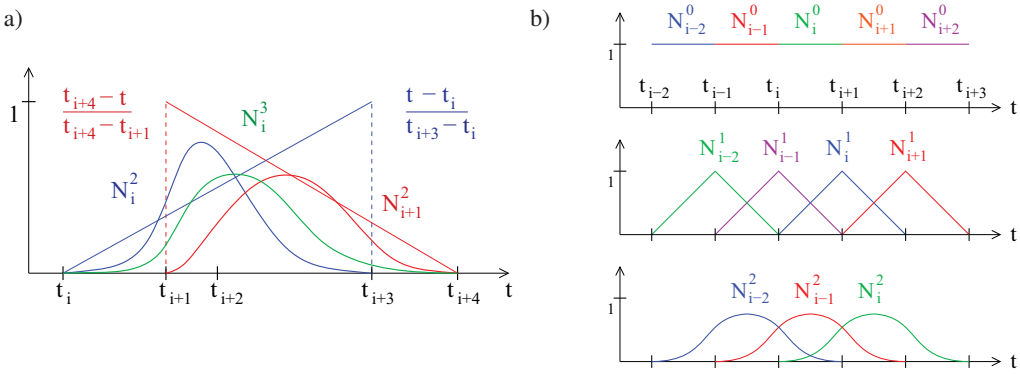

Fig. 1: B-spline basis functions: (a) construction of cubic basis function as linear combination of quadratic basis functions, (b) hierarchical sequence of piecewise constant, linear, and quadratic basis functions

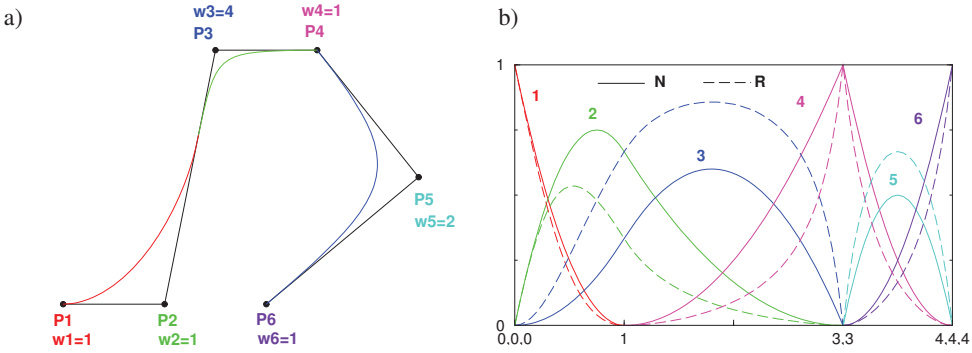

Fig. 2: Quadratic NURBS curve: (a) control polygon in black; numbers of individual control points and their weights (in parenthesis) in color corresponding to associated basis function; segments of the curve in red/green/blue corresponding to non-zero knot spans 0-1/1-3/3-4, (b) B-spline basis functions N_i and NURBS basis functions R_i corresponding to individual control points plotted over the entire span of the knot vector $\{0, 0, 0, 1, 3, 3, 4, 4, 4\}$

to that control point), the rest of the control polygon is only approximated. The curve is C^1 continuous everywhere except for the point corresponding to parameter 3 at which the continuity has been weakened by repeating that particular value in the knot vector twice.[§] Note the C^0 continuity of the B-spline basis function N_4 in Figure 2b) at parameter 3. The coincidence of the interface between the first (red) and the second (green) knot span on the curve with the intersection of the curve with its control polygon is a rule for quadratic curve only. Note that the red part of the curve (corresponding to the first knot span of size 1) is significantly larger than the green part (corresponding to the second knot span of size 2) despite the fact that the control polygon between control points 1 and 4 is symmetric with respect to the middle of its second segment. This is the consequence of the weight 4 applied at the third control point which results in the attraction of the curve toward the third control point.

The computational isogeometric mesh within the single NURBS patch is formed by partitioning the parametric space into the non-zero knot spans in each direction (in the example above, there are three such non-zero knot spans, see Figure 2). Since the shape functions within the single non-zero knot span

[§]Generally, multiplicity $k \leq p$ of a particular inner knot decreases the continuity of the basis functions of degree p at that knot to C^{p-k}.

are C^{∞}, the computation of characteristic components of the discretized governing differential equation (e.g. stiffness matrix, load vector, etc.) on each non-zero knot span is performed in the standard FE-like fashion, typically using the Gaussian numerical quadrature[¶].

The IGA has many features in common with the FEM (the shape functions form a partition of unity, they have the compact support, affine invariance applies, a numerical integration is employed, Neumann boundary conditions are satisfied naturally etc.) but there are some more or less significant differences. In the traditional FEM, the individual nodes are part of the computational domain, and corresponding degrees of freedom (DOFs) have the direct physical meaning (e.g. displacement in particular direction at the node), which is the direct consequence of the Kronecker delta property of the finite element shape functions. In the framework of the IGA, the control points of NURBS patches are generally not part of the physical computational domain. This implies that the application of Dirichlet boundary conditions is not straightforward and must be handled (often only approximately) within the available NURBS space. Except for the h-, p-, and hp-refinement strategies, the isogeometric concept offers also a higher order refinement methodology, known as k-refinement (see papers Hughes (2005); Cottrell (2007)), which has no analogue in the standard FEM and which is based on the fact that knot insertion (refinement of the parametric space) and degree elevation algorithms do not commute. Using the k-refinement, it is possible to increase the continuity across knot span boundaries (within a single NURBS patch) while limiting the growth of control variables. An important feature of the IGA analysis is the fact that due to a larger support of basis functions of quadratic degree and higher[‖] the number of control points necessary to obtain results of similar quality as that from the FEM using a basis function of the same degree, is smaller. The same also holds for the representation of the underlying geometry. This conciseness of parametrization makes the IGA attractive for the shape optimization problems as the size of the design variable space is kept limited while still preserving sufficient level of flexibility and geometrical continuity. Moreover, the approximation property of the B-spline basis functions (the actual geometry does generally not interpolate individual control points) eliminates the undesirable oscillations (know in the FEM) due to the interpolation nature of (typically Lagrangian) finite element basis functions and reduces the need for the regularization.

3. Particle Swarm Optimization

A lot of new metaheuristic optimization methods is inspired by nature. Algorithms simulate social behavior of animals, birds or insects or behave according to some physical phenomena. One of the main advantages of metaheuristics is that there is no need to determine a gradient of an objective function as in case of mathematical programming methods. Particle Swarm Optimization (PSO), as a member of Swarm Intelligence techniques, is a relatively new method firstly introduced in (Kennedy (1995)). It is based on a natural behavior of bird flocking or fish schooling. The flock acts like one organism. The whole flock as well as every individual, called particle, has its own memory. Particles share their best knowledge to each other thus the flock can find the optimal solution efficiently.

Each particle represents a potential solution in D-dimensional space. The i-th particle X_i is represented as $X_i = (x_{i1}, x_{i2}, x_{i3}, \ldots, x_{iD})$. Particles fly through the searched space with a velocity $V_i = (v_{i1}, v_{i2}, v_{i3}, \ldots, v_{iD})$. Every component of the velocity is updated according to the following equation

$$v_{id}^{j+1} = w \cdot v_{id}^{j} + c_1 \cdot rand() \cdot (p_{id} - x_{id}^{j}) + c_2 \cdot Rand() \cdot (p_{gd} - x_{id}^{j}), \quad d = i, \ldots, D \tag{5}$$

where w is the inertia weight, v_{id}^{j} is a velocity from the previous step, c_1 is the cognitive factor, c_2 is the social factor, p_{id} represents the best position of the particle i, p_{gd} represents the best swarm position and $rand()$ and $Rand()$ are two random scalars, vectors or matrices, respectively, in the range of [0,1] (Shi and Eberhart (1998)). The first addend of the Equation 5 is deterministic and represents an inertia of the particle. If there is a zero contribution from the second as well as the third addend, the particle will move only with inertia from the previous step and it does not stay in a local minimum. The second addend of

[¶]Note, however, that Gaussian numerical quadrature is generally not optimal and that there exist more efficient numerical integration schemes for the IGA.

[‖]Note, that for linear degree, the IGA analysis is identical with the FEM based on linear elements.

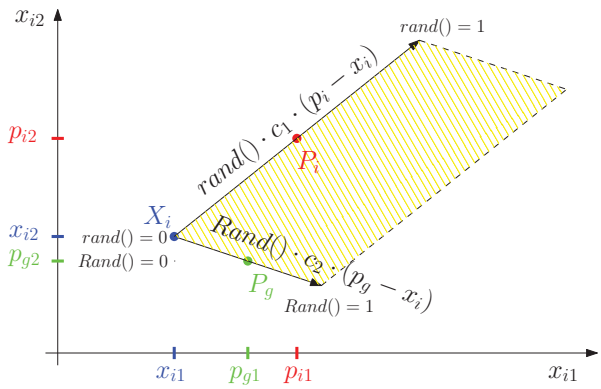

Fig. 3: Velocity update of one particle in 2D where $c_1 = c_2 = 2$

Equation 5 is stochastic because of the random function $rand()$. It provides movement of the particle towards its own best position. The third contribution is stochastic as well and provides shifting of the particle to the best swarm position. Fig. 3 illustrates stochastic contributions of Equation 5. Since each addend is scaled by a random number in the range of [0,1], the end of the velocity vector can be placed anywhere in the yellow hatched area.

The position of the particle x_{id}^j is then updated by

$$x_{id}^{j+1} = x_{id}^j + 1 \cdot v_{id}^{j+1} \tag{6}$$

where v_{id}^{j+1} is an actual velocity from Equation 5 and 1 has the meaning of the unit time.

There are two possibilities how to scale stochastic addends (Wilke et al (2007)). The first approach, a linear PSO, is using two random scalars as $rand()$ and $Rand()$ which multiply the magnitude of the cognitive and social vectors. The main disadvantage of this method is that particle will fly over the straight line at the end of the algorithm and whole space will not be searched. The second approach, a classical PSO, produces a two random vectors or two random diagonal matrices, respectively. The movement of particles is then diverse during the whole run. The classical approach is used hereafter.

The algorithm of the PSO can be described as follows.

1. The first step is to set up all coefficients and variables. We use values as listed in Table 1, see the next section for the discussion on the settings. Note that initial velocities can be zero or random. Non-zero velocities have a merit of diversity in the deterministic addend, and therefore, have been used in our implementation.

2. In the next step, the value of an objective function is calculated for all particles. The value is then compared with the best solution of the particle and with the best solution of the whole swarm. In case of better value in the actual iteration than in previous ones, the positions P_{gd} and P_{id} are updated.

3. Velocities are calculated for all particles according to Equation 5 and positions are updated by Equation 6.

4. The algorithm ends after reaching a maximum number of iterations selected at the first step.

The main drawback is that the PSO can move particles out of the admissible space. The easiest solution is to restrict a velocity or coordinates for a particle which flies outside. The three most frequent PSO approaches of controlling velocities (Čapek, 2008) are depicted in Fig. 4. An *absorbing wall* ensures the movement of the particle along the boundary, a *reflecting wall* bounces the particle back to the

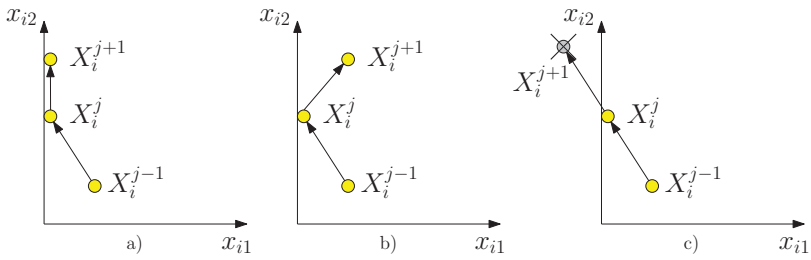

Fig. 4: Types of walls - (a) absorbing wall, (b) reflecting wall, (c) invisible wall

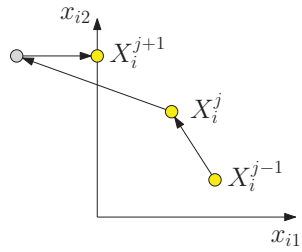

Fig. 5: Returning process for a particle which flies out of the solution space

admissible space and an *invisible wall* does not utilize updating of a particle position if the movement directs behind the boundary. In our implementation, another approach is used. The coordinates are limited to the given bounds, i.e. if the particle flies out of the admissible space, it is returned back to the boundary according to Fig. 5.

4. Mesh generation using $Distmesh$ tool

The `Distmesh` tool (DM) is a heuristic smoothing algorithm for generating uniform meshes (Chen and Holst, 2011). The DM is based on a simple dynamical system of expanding pin-jointed structure, here characterized by the second (background) mesh, see Fig. 6a). Those trusses that are too short are causing repulsive forces that move the too close nodes apart, see Fig. 6b) for the final solution. The main disadvantage apart from high computational demands is the need to return nodes that leave the prescribed admissible domain, i.e. the same problem encountered within the PSO. The DM offers similar procedure as is shown in Fig. 5 for basic entities. A polygon used in our computations to describe the background

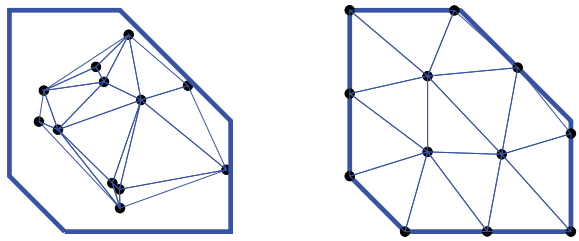

(a) Triangulation of random points forming a truss-like structure.

(b) The final mesh after the application of the `Distmesh` tool.

Fig. 6: An illustrative example of a generation of a uniform mesh from randomly generated points inside a polygon.

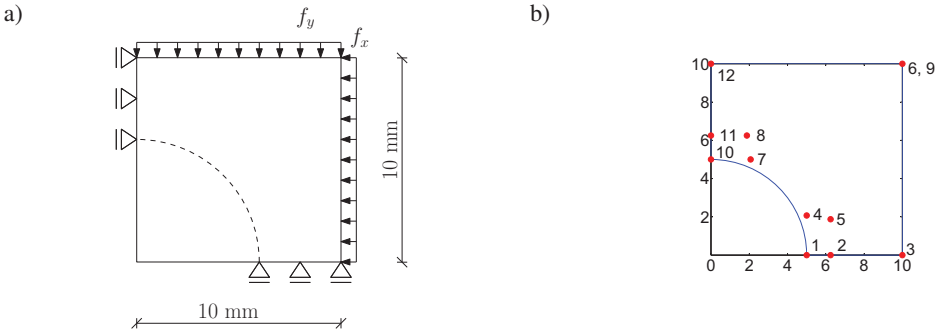

Fig. 7: (a) A square plate with an indicated hole and (b) starting positions of control nodes for one particle

mesh boundary is one of them, see the original paper (Persson, 2004) for more details. The background mesh, however, does not have to comply with requirements on a standard (e.g. FEM) computational mesh, as it does not have to precisely follow the exact geometry. Thus construction of such mesh can be simplified up to only two inner iterations of the DM and thus does not introduce a bottleneck to the whole process.

5. Shape optimization method

A combination of all methods mentioned above is applied on the benchmark structure depicted in Fig. 7 taken from (Norato et al, 2004). The plate is 10 mm high as well as wide and the thickness is 1 mm. It is symmetrically supported and symmetrically stretched, $f_x = f_y = -1$ N/mm. Young's modulus E is equal to 10 N/mm^2 and Poisson ratio ν equals to 0.3. Control nodes, placed on the structure, define a curve of a hole and a boundary polygon. The overall objective of the shape optimization is to find positions of the control nodes so that the shape of the benchmark structure has minimal compliance in the discretized form (Bendsøe and Sigmund, 2003)

$$\begin{aligned} & \min \ \mathcal{L} && = \tfrac{1}{2} f^T u, && (7)\\ s.t. \quad & \boldsymbol{K} u && = f, && (8)\\ s.t. \quad & V && = 70 \text{ mm}^2 && (9) \end{aligned}$$

with the stiffness matrix $\boldsymbol{K}$ and u and f as displacements and load vectors, respectively. Moreover, the total volume is restricted to 70% of the original volume, i.e. to $V_{max} = 70$ mm^2. Note that OOFEM software (Patzak (2012)) enhanced by the Isogeometric analysis (Rypl, 2012) is used for the computation of the compliance $\mathcal{L}$ and the volume V of the primary mesh as well.

The single objective optimization problem is therefore composed of the objective function $\mathcal{L}$ enhanced by the penalty function ensuring fulfilment of the volume constraint. The general shape of the penalty function used hereafter reads as

$$penalty_i = \left(\frac{\chi_i}{\alpha_{min}} \right)^{\beta} * MaxPen_i, \tag{10}$$

where χ_i is the value of the i-th equality constraint, violation of which by α_{min} percent is penalized with the $MaxPen_i$ value; a parameter β then influences the steepness of the penalty curve. Particularly, in case of the volume restriction, the penalty function is defined by

$$\chi_1 = \frac{V}{V_{max}} - 1, \quad MaxPen_1 = 2, \tag{11}$$

where V is the volume obtained from OOFEM using NURBS and V_{max} is the requested volume mentioned above. Other parameters are listed in Tab. 1.

Tab. 1: Coefficients for the PSO are following: c_1 is a cognitive factor, c_2 is a social factor, w is an inertia weight, $iter$ is the number of iterations, nop is the number of particles. Penalty functions have following coefficients: α_{min} is a distance where $MaxPen_i$ penalty is assigned and β is a shape parameter.

PSO					Penalty functions	
c_1	c_2	w	$iter$	nop	α_{min}	β
2	1	0.6	100	4	0.005	2

Then, one particle X_i in the PSO represents one potential solution. Since the plate is in 2D and has N control points, the vector X_i contains its all coordinates i.e. $2N$ components. The number of particles can be set to relatively low value e.g. 4 and the number of iterations can be restricted to 100. A cognitive factor is set to $c_1 = 2$ according to (Wilke et al (2007)) and a social factor to $c_2 = 1$. The second factor is set to lower value than in (Wilke et al (2007)) because we use a less number of particles and the social knowledge is not that important as the personal knowledge, i.e. we would like to keep the diversity of solutions. For the sake of completeness, all important coefficients are listed in Tab. 1.

Some nodes defining the boundary are forbidden to move because of prescribed supports. It is therefore necessary to distinguish which components of velocities can be zeros and non-zeros, respectively. If a movement of the node is allowed, the corresponding component in the velocity vector is at the start of the PSO set to a random value in the range of $[-1, 1]$. Otherwise, the component is zero. The initial positions of nodes are sums of starting positions depicted in Fig. 7b) and initial velocities according to Equation 6.

In the next step of the algorithm the `Distmesh` tool is used. It ensures that the nodes do not move towards each other by limiting the maximal length of the velocity terms to the half of the shortest edge connecting the given node within the background mesh. However, this does not ensure transposing of nodes as shown in Fig. 8a) and forming of unwanted loops on the boundary. This problem is solved by another penalty term

$$\chi_2 = V - V_{DM} \quad MaxPen_2 = 2, \tag{12}$$

where V is the volume obtained from Isogeometric analysis and V_{DM} is the volume obtained from the DM background mesh; i.e. we penalize big differences between these two meshes in terms of volumes, see Fig. 8c), which is usually the case of the loops on the boundary.

The last deficiency is an appearance of a peak with almost zero volume in pursuit of spreading out the points, see Fig. 8b). This is again solved by the penalty approach in terms of perpendicularity of

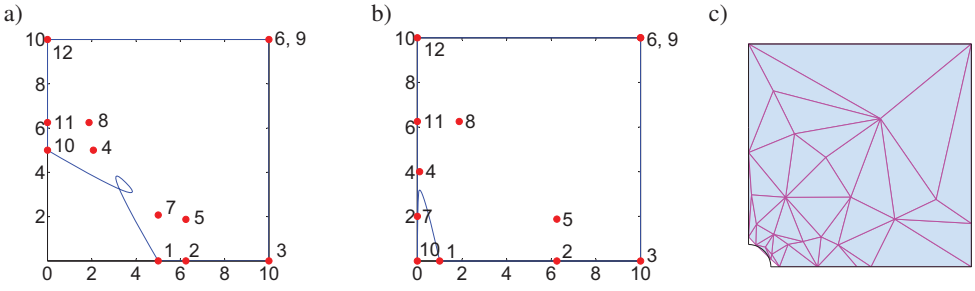

Fig. 8: (a) A loop which is created in case two nodes are transposed, (b) irregularity in corner nodes and (c) a difference between a real NURBS mesh and a background mesh from the `Distmesh` tool

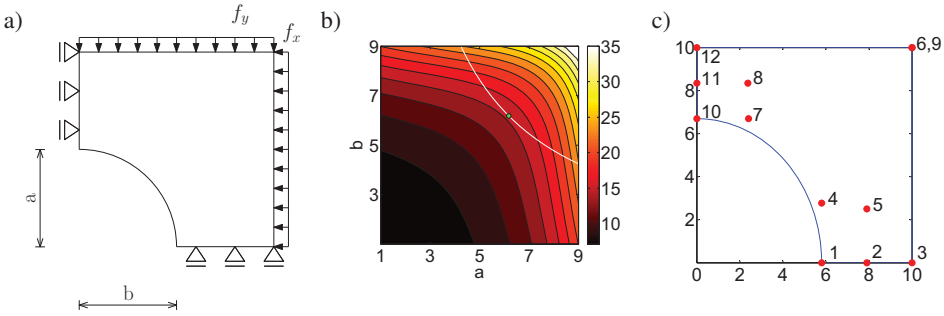

Fig. 9: (a) A parametric solution of a benchmark: (b) compliance of a parametric solution where a and b are in the range of [1,9] with a step of 0.1 mm and a white line representing a prescribed volume 70 mm^2 with the green point of an analytical optimum of a diameter of 6.18 mm ; (c) is the obtained parametric optimum

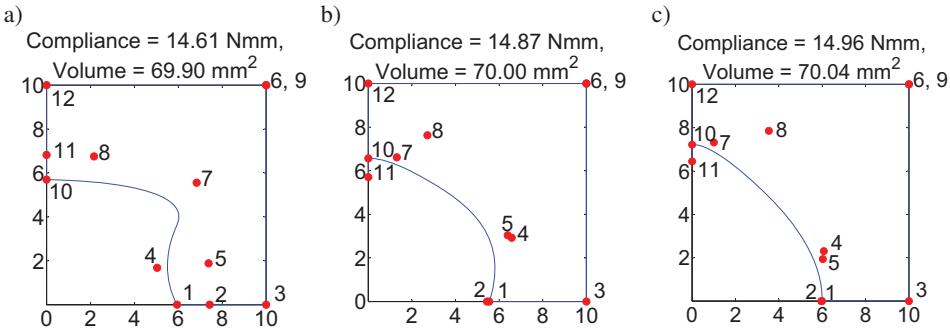

Fig. 10: Best solutions obtained in three runs of the PSO

quoins emerged in points 1 and 10 in Fig. 7b). Penalty function is used in the following form

$$\chi_3 = \sum_{j=1}^{2} \cos\phi_j, \quad MaxPen_3 = 0.1, \tag{13}$$

where ϕ_j is an angle of the boundary at points 1 and 10, respectively.

6. Results

The known analytical optimum of the selected benchmark is characterized by the ellipsoidal hole with different radii a and b for the prescribed loadings and a volume. Note that in case of $f_x = f_y$ the hole is circular. Therefore, we have simulated the problem with two parameters a and b in the range of [1,9] with step 0.1. The situation is depicted in Fig. 9a). The coordinates of curve's control nodes 1, 4, 7 and 10 in Fig. 9c) are proportionally rising up thus this simple model does not cover all possible solutions. The compliance for all values of parameters is depicted in Fig. 9b). The black points show solutions with a proper volume 70 mm^2. The objective function is minimized thus the optimum is the solution with the minimal compliance value lying on the curve given by those black points.

Three optima of the benchmark presented in Fig. 10 are obtained with the proposed method described in Section 5. It is clearly visible, that the problem is ill-posed since there are several local optima of the given problem with almost identical objective values closed to the global one, see comparison of values in Tab. 2 for the optima obtained by the parametric solution based on an analytical solution and by the

Tab. 2: Comparison of results for reference (Norato et al, 2004) and the presented method

author	method	compliance	volume
Norato et al (2004)	mesh 16x16	16.1653 Nmm	-
Norato et al (2004)	mesh 32x32	16.1928 Nmm	-
Norato et al (2004)	mesh 64x64	16.1952 Nmm	-
this paper	parametric solution	14.8140 Nmm	69.999 mm^2
this paper	method from Section 5	14.8712 Nmm	69.996 mm^2

presented approach. Also note the difference among values presented in (Norato et al, 2004) and IGA results probably caused by different discretizations.

7. Conclusion

The presented contribution has shown a nice combination of three methods. The Isogeometric analysis is a step towards a CAD which, as an addendum, has several advantages over the classical FEM analysis in obtaining mechanical responses of a structure. The precise description of the geometry predetermines IGA as a solution to the shape optimization problem. The Particle Swarm Optimization algorithm is then characterized by a physical meaning of a group of flying particles which can utilize the inner properties of the dynamics of particles. The shape optimization problem is difficult from the regularity point of view. Therefore, not only limitations within the PSO have been used in this work, but also the second, background mesh produced by the `Distmesh` tool has been utilized. The obtained solutions indicate the used benchmark as ill-conditioned. However, solutions closed to a symmetric analytical solution have been observed as well.

Acknowledgments

This work was supported by the Grant Agency of the Czech Republic - Projects No. 103/09/2009 and No. P105/12/1146. Their financial assistance is gratefully acknowledged.

References

Bazilevs, Y., Beirao de Veiga, L., Cottrell, J.A., Hughes, T.J.R., Sangalli, G. (2006), Isogeometric Analysis: Approximation, Stability and Error Estimates for h-refined Meshes, *Mathematical Models and Methods in Applied Sciences*, Vol. 16, No. 7 pp. 1031–1090.

Bendsøe, M. P. and Sigmund, O. (2003). *Topology Optimization: Theory, Methods and Applications*. Springer-Verlag.

Čapek, M. (2008), PSO optimalizace v MATLABu. *Mezinárodní konference Technical Computing Prague* 2008, pp. 18.

Cottrell, J.A., Reali, A., Bazilevs, Y., Hughes, T.J.R. (2006), Isogeometric Analysis of Structural Vibrations, *Computer Methods in Applied Mechanics and Engineering*, Vol. 195, pp. 5257–5296.

Cottrell, J.A., Hughes, T.J.R., Reali, A. (2007), Studies of Refinement and Continuity in Isogeometric Structural Analysis, *Computer Methods in Applied Mechanics and Engineering*, Vol. 196, pp. 4160–4183.

Cottrell, J.A., Hughes, T.J.R., Bazilevs, Y. (2009), *Isogeometric Analysis: Toward Integration of CAD and FEA*, John Wiley & Sons.

Chen, L. and Holst, M. (2011), Efficient mesh optimization schemes based on Optimal Delaunay Triangulations, *Computer Methods in Applied Mechanics and Engineering*, Vol. 200, No. 9-12, pp. 967-984.

Hughes, T.J.R., Cottrell, J.A., Bazilevs, Y. (2005), Isogeometric Analysis: CAD, Finite Elements, NURBS, Exact Geometry and Mesh Refinement, *Computer Methods in Applied Mechanics and Engineering*, Vol. 194, pp. 4135–4195.

Kennedy, J., Eberhart, R.C. (1995) Particle Swarm Optimization In: *IEEE International Conference of Neural Networks*, Vol. 4, pp. 1942–1948.

Norato, J., Haber, R., Tortorelli, D. and Bendsøe, M. P. (2004), A geometry projection method for shape optimization. *International Journal for Numerical Methods in Engineering*, Vol. 60, No. 14, pp. 2289-2312.

Patzák, B. (2012), OOFEM project home page, http://www.oofem.org.

Persson, P.-O., Strang, G. (2004), A Simple Mesh Generator in MATLAB *SIAM Review*, Vol. 46, No. 2, pp. 329–345.

Piegl, L., Tiller, W. (1997), *The NURBS Book*, Springer-Verlag.

Rypl, D., Patzák, B. (2012), From the Finite Element Analysis to the Isogeometric Analysis in an Object Oriented Computing Environment, *Advances in Engineering Software*, Vol. 44, No. 1, pp. 116–125.

Shi, Y. and Eberhart, R. (1998), A Modified Particle Swarm Optimizer. *IEEE International Conference on Evolutionary Computation* 1998, pp. 69-73.

Wilke, D. N., Kok, S. and Groenwold, A. A. (2007), Comparison of linear and classical velocity update rules in particle swarm optimization: Notes on diversity *International Journal for Numerical Methods in Engineering*, Vol. 70, No. 8, pp. 962-984.

Zhang, Y., Bazilevs, Y., Goswami, S., Bajaj, C., Hughes, T.J.R. (2007), Patient-specific Vascular NURBS Modeling for Isogeometric Analysis of Blood Flow, *Computer Methods in Applied Mechanics and Engineering*, Vol. 196, pp. 2943–2959.

18th International Conference
ENGINEERING MECHANICS 2012
Svratka, Czech Republic, May 14 – 17, 2012

pp. 1073–1080
Paper #198

BEM SHAPE OPTIMIZATION OF A HOLE IN COMPOSITE FOR MINIMUM LAGRANGIAN

P.P. Prochazka*

Abstract: *In composite materials a problem of optimal shape of hole is of great interest to designers and researchers. This problem seems to be theoretical but good application can be found in soil, fiber reinforced concretes, even steel structures, and, of course, in classical composites fabrication. Since an iteration process has to be constructed the problem can be identified as the problem of moving boundaries. From this conclusion the advantages of finite element method are suppressed and boundary elements should be prioritized. They do not require any improvement of the meshes in an arbitrary iterations step; the mesh can be selected in a reasonable way as it is auxiliary created only for necessary integration over the domain. The boundary element method appears to be extraordinarily advantageous in case the shape optimization is to be treated, although for classical arrangement fiber – matrix it also provides us with many affirmative properties. It had been proved elsewhere by the author that the minimum for Lagrangian of the material system leads to minimization of both the stresses and displacements. Consequently, minimization of Lagrangian is probably the best cost functional ever. Certain examples iteration process and of optimal shapes depending on the volume ratios of the hole will accompany the theoretical considerations.*

Keywords: ***Composite structures, shape optimization, heat transfer, homogenization of coefficient of conductivity.***

1. Introduction

The optimal shape of fiber is studied in a composite structure for optimal overall coefficient of conductivity. For the sake of simplicity a symmetric 2D unit cell is cut out of the structure, where one of the phases is a hole while the rest of the domain describing the unit cell is matrix with given material property, i.e. with given matrix conductivity. Heat transfer or harmonic problem is solved in this paper so that the linear conductivity equation mediates a representative formulation. The design parameters of the optimization problem are connected with the inner shape of matrix, which is assumed to be star-shaped. In this way, the optimization turns to a moving boundary problem so that boundary element method appears to be the most appropriate here. Using homogenization to get the overall properties the problem is not solvable uniquely and, moreover, can exceed the realistic situation. This is why reasonable constraints, or side conditions, should be defined, i.e. the admissible set of possible domains of the hole should be defined in realistically put forward. First of all, a reasonable condition is the restriction of volume (in 2D area) of the hole. Note that this restriction can be changed in next steps according to the requirements of user. On the other hand, this still must not be enough to meet a realistic situation, since the constraints are mostly formulated in integral form (potential energies, surface energies, volume – area, etc.), i.e. positive and negative signs appearing in these formulations can lead to a nonrealistic geometry. For that, additional restrictions on the shape characteristics should be applied to the admissible shape of the hole. Among such the length of diameters of the domain of the hole, tangential slope the inner boundary of the hole, vertical and/or horizontal restrictions on the length of rays starting from the center of the unit cell, etc. The mathematical formulation of homogenization of the heat transfer problem and the subsequent optimization will be suggested and numerical treatment of the problem envisaged provide a reasonable, fully usable in practice, layout.

As mentioned in many publications, e.g. Callis et al (2008), Kaminski (2003), plenty of approaches are available on how to solve these problems. Hereinafter similar procedure, established for elastic

* Prof. Ing. RNDr. Petr Prochazka, DrSc.: Czech Technical University in Prague, Civil Engineering, dept. Mechanics, Thakurova 7, 166 29 Prague 6; CZ, e-mail: petrp@fsv.cvut.cz

optimization problem in Prochazka (2009) will be applied for creating appropriate functional and calculating the optimal shape of the hole.

Classical approach in localization and homogenization of elastic composites belongs to Suquet (1985), and that of steady state heat transfer can be found also in Lévy (1985), in which periodic composites are studied. More or less this procedure is applied in this paper to unit cell concept. Optimization of the fiber shape in a composite structure due to heat load is discussed in Dvorak (1996), where the problem of a variance between given overall properties and calculated from the given material properties of phases is as small as possible.

2. Optimization problems in composite structures

General microstructure identification problem is treated in such a way that for given conductivity of both fiber and matrix (and, of course zero value of conductivity of the hole) with the given volume fractions of phases in the unit cell it is sought arrangement of the phases (in our case the hole) in a periodic cell so that the effective material constants of the periodic composite are as close as possible to maximum or minimum values. The problem in this study is considered for the linear conduction equation. It is necessary to note that although much more complicated problems occur in theory and practice, such as non-linear behavior of the conductivities, time-dependent behavior, high temperature effects, etc. The optimization itself belongs to the wide set of optimal control theories. Existence of solution can be proved under suitable hypotheses, as well as the convergence of numerical approximations. In the conduction case, the full characterization of G_δ-closure set (the set of all effective conductivities that result from taking the given phases in the given volume fraction mixed in any feasible micro-geometry) is known. The concept of composite media not only comes directly from the physical world but also provides a theoretically sound means for relaxation of variational problems - the problem of optimum topology design (see Delgado & Allaire (2011), Suzuki & Kikuchi (1991), for example). It is a classical result of the homogenization theory that composites can be replaced by a macroscopically homogeneous medium its material constants - the so called effective of overall constants or effective modules – depend on the micro-geometry in which the constituent phases form the mixture. Note that in classical theories of composites no respect had been taken to the shape of the phases. Modern theories deny this assumption and show that the shape of the phases can basically influence the properties of the composite at the macro-level. The set of all effective constants of mixtures of a given number of phases taken in a given proportion is called the G_δ-closure set and its knowledge is essential for the relaxation procedure. In the case of a scalar linear elliptic partial differential equation (the steady heat transfer equation), one of the phases may degenerate, i.e., a void or hole can be considered. However, for the case of the system of PDE's of linear elasticity, only a partial information about the G_δ-closure sets is available so far; namely we know how to minimize the complimentary energy for a given single macroscopic stress field. For the design with other (non-compliance) objective functions, the fu11 knowledge of the G_δ-closure set seems inevitable. So far, the following principal constructions are known:

Multiple rank laminates. The microstructure is a laminate (- layered composite) whose one or both components are again laminates that in turn can consist of laminates, etc. The layered rnicrostructure has the advantage that one can calculate the effective constants analytically. However, the scale levels of the subsequent laminations must be well separated which prohibits practical realization of these microstructures. For an example see Delgado & Allaire (2011), for example.

Coated ellipsoids construction. This construction is based on the fact that having a medium with the material constants that are equal to those of our desired microstructure, one can insert an ellipsoid of one phase with an ellipsoidal inclusion of the other phase where the ellipsoids have appropriately balanced dimensions, and the effective properties of the medium are not changed upon this insertion. Thus, one fills up the whole body with coated ellipsoids, but using infinitely many length scales, this time not even separated from one another. As a consequence, one cannot manufacture but a rough approximation of such a microstructure.

Vidgergauz' microstructure. One of the theories aiming to an extreme microstructure is the Vidgergauz microstructure, Vidgergauz (1989). It has the form of a properly shaped (oval-like) inclusion of one phase within the matrix of the other phase. The shape of the inclusion is found from

the optimality conditions that in this setting have the form that "the inclusions are equally strong", no one is preferred. However, the shapes of the inclusion have to be evaluated using elliptic integrals or other non-elementary functions. We note that although it is presented in the elasticity setting, similar results hold for the harmonic equation.

The aim of this work is to establish a numerical technique for the microstructure identification problem considering heat transfer as a typical for the Laplace equation. The optimal control theory is formulated as the problem of microstructure identification: Given the effective modules, what microstructure has its optimal from the point of view of the best overall conductivity - ideally, what microstructure attains the target? The last question is meaningful, as additional constraints may lead to restriction of the goal to ensure the realistic solution. As here the classical optimal shape design approach is based on the boundary variation technique, the class of admissible micro-geometries is restricted to a single inclusion (the hole).

3. Basic considerations and equations

Let the body representing the composite is denoted V and a unit cell is given as $\Omega \subset V \in R^2$ with its boundary $\partial\Omega$, which is supposed to be Lipschitz continuous, such as if the shape of the unit cell Ω is a square $(0,1)\times(0,1)$, for example. Isotropic phases $\Omega_\mathrm{f} \subset \Omega$ and $\Omega_\mathrm{m} \subset \Omega$ represent the fiber (hole) and matrix, respectively. The boundary of the fiber (i.e. the interfacial boundary Γ_C) is star shaped. Note that more general shapes are mentioned in Dvorak (1996), where a special treatment on how to simplify complicated unit cells is also discussed based on body transformations. The transformations create a group of base bodies.

The conservation law is assumed in the standard divergence form applied to temperature $u(y)$ as,

$$\frac{\partial}{\partial y_i}\left(c\,\frac{\partial}{\partial y_i}u\right) = 0 \tag{1}$$

where $c = c(y)$ is dependent on the position in Ω, consisting of two subdomains, fiber and matrix, which are equipped by different conductivity values $c_\mathrm{f} = 0$ (fiber) and c_m (matrix), where c_m is also constants. Note that the hole bears a negligible conductivity although this assumption is not an obstacle for generality. This means that the coefficient of conductivity c is defined as:

$$c(y) = c_\mathrm{f} \quad \text{for} \quad y \in \Omega_\mathrm{f} \quad \text{and} \quad c(y) = c_\mathrm{m} \quad \text{otherwise} \tag{2}$$

or

$$c(y) = c_\mathrm{f}\,\chi(y) + c_\mathrm{m}(1-\chi(y)) \tag{2a}$$

where χ is the characteristic function of the fiber.

The partial equations are written as

$$\nabla q = 0\,, \qquad q = c\nabla u \tag{3}$$

where ∇ is the nabla operator, and q is the flux vector, gradient of u.

For statistically isotropic material with the periodic boundary conditions an analog of the well known Hill condition holds valid as:

$$< q\nabla u >= \frac{1}{\operatorname{meas}\Omega}\int_\Omega q\nabla u\,\mathrm{d}\Omega =< q >< \nabla u >= \frac{1}{\operatorname{meas}\Omega}\int_\Omega q\,\mathrm{d}\Omega \times \frac{1}{\operatorname{meas}\Omega}\int_\Omega \nabla u\,\mathrm{d}\Omega \tag{4}$$

where meas Ω is the volume in 3D or area in 2D, mostly considered equal to unit.

4. Homogenization

In order to get relations between local and overall properties of the composite apply the overall flux q_0 to the composite and the real flux is then equal to

$$q = q_0 + q_1(u_1) \tag{5}$$

where the average of the fluctuation term u_1 is zero, similar to the elasticity problem. From (1) and (5) one gets:

$$\frac{\partial}{\partial y_i}\left[c(y)\left(\frac{\partial u_1}{\partial y_i}+q_0\right)\right]=0 \Rightarrow \frac{\partial}{\partial y_i}\left[c(y)\frac{\partial u_1}{\partial y_i}\right]=-\frac{\partial}{\partial y_i}\left[c(y)q_0\right] \tag{6}$$

in the sense of distributions. Eq. (6) is the starting equation for solving u_1 with u_0 given. This is an elliptic equation being defined in Ω. If comparing with the elasticity problem q_0 is a unit impulse and u_1 is the standard fluctuating term. Since also the Laplace equation (1) is linear, similar approach to that used in linear elasticity can also be applied hereinafter to decode the generalized terms, mainly see in the right hand side, for details see Prochazka & Valek (2012). From the detailed procedure it immediately follows instead of (6):

$$\frac{\partial}{\partial y_i}\left[c(y)\frac{\partial u_1}{\partial y_i}\right]=-q_C\delta_{\Gamma_C} \qquad \text{and the periodic boundary conditions,} \tag{7}$$

where q_C is a jump in the interfacial flow equals to

$$q_C(y)=[c_f-c_m]\,q_0 n^f(y)=[c_f-c_m]\,n^f(y) \tag{8}$$

as q_0 is considered as a unit impulse. Symbol δ_{Γ_C} is the distribution of Dirac's function along the interface between the phases. The formula is in compliance with Suquet (1987).

In the next text axisymmetry and star-shaped hole are supposed, i.e. there is a point (origin of the coordinate system) the rays from which cross the interfacial segment only and only once. For this reason the problem is solved in the first quadrant only.

5. Boundary element formulation

Since the shape optimization is closely related with a moving boundary problem the boundary element formulation seems to be extremely advantageous. Multiplying (7) by a function u_1^*, integrating successively over Ω_f and Ω_m, applying linear approximations over boundary elements and splitting the boundaries into that merging Γ_C and the remaining parts finally yields:

$$\begin{bmatrix} K_{11}^{\mathrm{f}} & K_{12}^{\mathrm{f}} \\ K_{21}^{\mathrm{f}} & K_{22}^{\mathrm{f}} \end{bmatrix} \begin{Bmatrix} u_{\mathrm{f}}^{\mathrm{out}} \\ u_{\mathrm{f}}^{\mathrm{in}} \end{Bmatrix} = \begin{Bmatrix} q_{\mathrm{f}}^{\mathrm{out}} \\ q_{\mathrm{f}}^{\mathrm{in}} \end{Bmatrix}, \quad \begin{bmatrix} K_{11}^{\mathrm{m}} & K_{12}^{\mathrm{m}} \\ K_{21}^{\mathrm{m}} & K_{22}^{\mathrm{m}} \end{bmatrix} \begin{Bmatrix} u_{\mathrm{m}}^{\mathrm{in}} \\ u_{\mathrm{m}}^{\mathrm{out}} \end{Bmatrix} = \begin{Bmatrix} q_{\mathrm{m}}^{\mathrm{in}} \\ q_{\mathrm{m}}^{\mathrm{out}} \end{Bmatrix}, \quad K_{ij} = B_{ik}^{-1} A_{kj} \quad \text{where} \quad A_{ij} u_j = B_{ij} q_j \tag{9}$$

where u and q are vectors of temperature and fluxes, respectively, their components are values at nodal points of the corresponding boundaries, A and B are square, generally not symmetric matrices of approximations, and quantities with superscript in are assigned to the nodal points at Γ_{C} and that with the superscript out are connected with the values outside of Γ_{C}. Since on Γ_{C} it holds $u_{\mathrm{f}}^{\mathrm{in}} = u_{\mathrm{m}}^{\mathrm{in}}$ and $q_{\mathrm{f}}^{\mathrm{in}} + q_{\mathrm{m}}^{\mathrm{in}} = q_C$, one eventually gets:

$$\begin{bmatrix} K_{11}^{\mathrm{f}} & K_{12}^{\mathrm{f}} & 0 \\ K_{21}^{\mathrm{f}} & K_{22}^{\mathrm{f}} + K_{11}^{\mathrm{m}} & K_{12}^{\mathrm{m}} \\ 0 & K_{21}^{\mathrm{m}} & K_{2}^{\mathrm{m}} \end{bmatrix} \begin{Bmatrix} u_{\mathrm{f}}^{\mathrm{out}} \\ u_{\mathrm{f}}^{\mathrm{in}} \\ u_{\mathrm{m}}^{\mathrm{out}} \end{Bmatrix} = \begin{Bmatrix} q_{\mathrm{f}}^{\mathrm{out}} \\ q_{\mathrm{C}} \\ q_{\mathrm{m}}^{\mathrm{out}} \end{Bmatrix} \tag{10}$$

where the matrix of the system is banded but generally not symmetric. Using periodic boundary conditions u and q follows from the previous equation for unit impulse q_0. Moreover,

$$q(y) = c(\frac{\partial u_1}{\partial y_i} + q_0) \Rightarrow < q >= c^* < \nabla u >,$$

where

$$c_i^* = \int_{\Omega} c(y)(1 + \frac{\partial u_1}{\partial y_i})\, \mathrm{d}\Omega(y) = c_{\mathrm{m}} \int_{\Omega_{\mathrm{m}}} (1 + \frac{\partial u_1}{\partial y_i})\, \mathrm{d}\Omega(y), \; i = 1,2 \tag{11}$$

and $c_{\mathrm{f}} \doteq 0$.

Now the main advantage of the boundary element formulation appears: applying the Green theorem to the latter relation leads us to interface integrals as:

$$c_i^* = c_{\mathrm{m}} \,\mathrm{meas}\, \Omega_{\mathrm{m}} + c_{\mathrm{m}} \int_{\Omega_{\mathrm{m}}} u_1 n_{\mathrm{i}}^{\mathrm{m}}\, \mathrm{d}\Omega(y) = c_{\mathrm{m}} \,\mathrm{meas}\, \Omega_{\mathrm{m}} + c_{\mathrm{m}} \int_{\Omega_{\mathrm{m}} \doteq \Gamma_{\mathrm{C}}} u_1 n_i^{\mathrm{m}}\, \mathrm{d}\Omega(y) + c_{\mathrm{m}} \int_{\Gamma_{\mathrm{C}}} u_1 n_i^{\mathrm{m}}\, \mathrm{d}\Omega(y) \tag{12}$$

so that the unpleasant volume integrals disappear. Note that $c_1^* = c_2^* = c^*$ because of the symmetry considered.

6. Optimization

Similarly to the optimization of beams, Prochazka & Lok (2009), the energy functional is formulated using Lagrangian multiplier λ bounding the given area of the hole. Hence, the problem can be established as:

$$= \frac{1}{2} \int_{\Omega} q \nabla u\, \mathrm{d}\Omega(y) - \lambda(\int_{\Omega^{\mathrm{f}}} d\Omega - \mathrm{meas}\, \Omega_{\mathrm{f}}) = \frac{1}{2} < q >< \nabla u > -\lambda(\int_{\Omega^{\mathrm{f}}} d\Omega - \mathrm{meas}\, \Omega_{\mathrm{f}}) \rightarrow \text{stationary} \tag{13}$$

which means that the above functional is minimum with respect to u but maximum in λ.

The shape of the hole is identified by radii p_s, $s = 1,2,\ldots,n$ of nodes located at the interface Γ_C. Because of the considered symmetry only the first quarter of unit cell (shaded) is observed.

In this way we obtain n triangles T_s, $s = 1,...,n$, which approximate the domain Ω_f. It obviously holds:

$$\int_{\Omega^f} d\Omega = \text{meas } \Omega_f = \sum_{s=1}^{n} \text{meas } T_s . \tag{14}$$

In certain cases of fiber volume ratio with combination of the given phase conductivities restrictive conditions have to be applied to the admissible beams of nodes at the interfacial boundary. This can be done in various ways. A typical lowest value of the length of any node at Γ_C is bounded from below by a given value $0 < p < p_s$ and the highest length is constrained by the conditions as $y_i < h < 1$, p, h are reals selected in advance.

If the above bounds on the beams are attained a special procedure needs to be used, see [3]. It requires an internal iteration, as the improvement of the boundary using collinear mapping to ensure the condition about constant fiber volume fraction.

7. Euler's equations

The stationary requirement leads to differentiation of the functional by the shape (design) parameters p_s

$$\lambda = \lambda_s \frac{\frac{1}{2} < \nabla u > \frac{\partial}{\partial p_s} < q >}{\frac{\partial}{\partial p_s} \int_{\Omega^f} d\Omega} , \quad s = 1,\ldots,n \tag{15}$$

The equation (15) requires λ to have the same value for any s. In other words, if this requirement were attained at any point on the "moving" part of the interfacial boundary the optimal shape of the trial body would be reached. For this reason the body of the composite structure should increase its area (in 3D its volume) at the nodal point of the boundary identified by p_s if λ is larger than the true value of the target, while it should decrease its value when λ is smaller than the correct Lagrangian multiplier. As, most probably, real value of the target is not known a priori, its estimate is done by averaging the current values at the nodal points. So, approximation of λ will be expressed as:

$$\lambda_{\text{approx}} = \frac{1}{n} \sum_{s=1}^{n} \lambda_s \tag{15}$$

Differentiation by λ completes the system of Euler's equations.

It remains to ensure that the fiber volume friction is constant with the value given a priori. For this aim a collinear mapping is applied after completing the shift of nodes at the interface. It can be done in such a way that assuming the current value of $\text{meas } \Omega^f_{\text{curr}}$, which is calculated from the current positions of the nodes mentioned, the prescribed $\text{meas } \Omega^f$ is reached by improving the triangles T_i by the value of

$$s = \sqrt{\frac{\text{meas}\,\Omega^{\text{f}}_{\text{curr}}}{\text{meas}\,\Omega^{\text{f}}}} \tag{16}$$

Brief description of algorithm:

1 set up the starting configuration fulfilling the condition of constant area of the hole

2 calculate c^* for the current configuration

3 set a successive unit shifts to nodal points p_s at Γ_C, calculate $c^*(p_s)$ the appropriate λ using substitution of derivatives by differences (central difference is used here and the step of difference is 0.0001)

4 compute λ_{approx} to get new positions of nodes at Γ_C

5 from the new positions get the area of the current Ω_{f}

6 using collinear mapping improve the positions of nodes to ensure the original fiber volume ratio

7 check up the constraint of the beams p_s and if fail occurs apply local iteration

8 Euclidean distance between current and previous energies λ_s should be less then given admissible error; if not, go to 2 and stop otherwise

8. Examples

Unit cell is considered with various fibers volume ratios. Since we compare energy densities at nodal points of the interfacial boundary, the relative energy density may be regarded as the comparative quantity influencing the movement of the boundary Γ_{C} in a proper direction. As said in the previous section, the higher value of this energy, the larger movement of the nodal point of Γ_{C} should aim at the optimum. The process of iterations will end if the Euclidean distance between current and previous energies be less then given admissible error. In the following examples $\text{meas}\,\Omega_{\text{m}}$ and also the conductivity and c_{m} are prescribed.

In the tests considered here $c_{\text{m}} = 1$, $\text{meas}\,\Omega_{\text{m}} = 0.6$ and $\text{meas}\,\Omega_{\text{m}} = 0.5$ with resulting optimal shape presented in Fig. 1 and being attained with relative error 1.8e-04 and 2.5e-04 after twenty seven and twenty two iterations using the step of iteration 0.1 to 0.005.

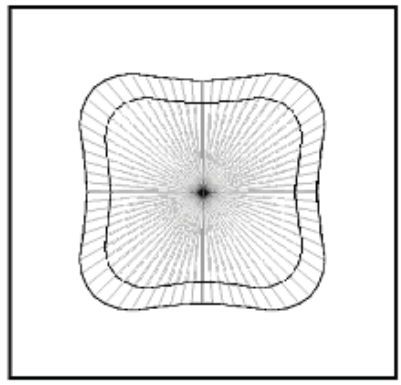

Fig. 1: Optimal shapes of holes for various area fractions

9. Conclusions

New optimization procedure is put forward in this paper based on homogenization technique. The problem which has been solved deals with homogenization of coefficients of the linear harmonic equation. The optimization is formulated in term of energy. A special constraint is adopted, which is involved in the formulation of optimal shape by Lagrangian multiplier, enabling us to show that the stationary point is attained for energy density being equal at each nodal point of the interfacial boundary. This condition leads us to an elegant and efficient numerical approach.

Acknowledgment

Financial support of the Grant agency of the Czech Republic, grant number P105/00/0266 is gratefully acknowledged.

References

Challis, V.J., Roberts, A.P. & Wilkins A.H. (2008) Design of three dimensional isotropic microstructures for maximized stiffness and conductivity. *Int. J. Solids and Structures*, **45**, (14-15), pp.4130-4146.

Kaminski, M. (2003) Homogenization of transient heat transfer problems for some composite materials. *Int. J. Engng. Sci.* **41**, pp. 1-29.

Prochazka, P.P., Dolezel, V. & Lok, T.-S. (2009) Optimal shape design for minimum Lagrangian. *Eng. Anal. with Bound. Elem*. **33**, pp. 447–455.

P.M. Suquet, P.M. (1985) Homogenization techniques for composite media. *Lecture Notes in Physics 272* (eds. E. Sanches-Palencia and A. Zaoi) Part IV, Sprinter Verlag Berlin, pp. 194-278.

Lévy, T. (1985) Fluids in porous media and suspensions. *Lecture Notes in Physics 272* (eds. E. Sanches-Palencia and A. Zaoi) Part II, Sprinter Verlag Berlin, pp. 64-119.

Dvorak, J. (1996) Optimization of composite materials, *PhD thesis*, Charles University, June 1996.

Delgado, G. & Allaire, G. (2011) Shape and Topology Optimization of Composite Materials with the level-set method. *EADS-Innovation Works.* Center of Applied Mathematics - Ecole Polytechnique, Jussieu, France.

Suzuki, K. & Kikuchi, N. (1991) A homogenization method for shape and topology optimization. *Comp. Meth. Appl. Mech. Engng*, **93**, pp. 291-318.

Vidgergauz, S.B. (1989) Regular strucutres with extremal elastic properties, *MTT* 24, pp. 57-63.

Prochazka P.P. & Valek, M (2012) Optimal Shape of Fibers in Composites Exposed to Combustion. To appear in *BETEQ 2012*.

18th International Conference
ENGINEERING MECHANICS 2012
Svratka, Czech Republic, May 14 – 17, 2012

pp. 1081–1085
Paper #37

MODELING OF FIBER BRIDGING IN MULTIPLY-CRACKING MORTAR

M. Přinosil*, P. Kabele**

Abstract: *The use of composite materials is one of current trends in civil engineering. Proper description of their behavior is one of prerequisites for correct and appropriate application of these materials. The subject of our research are fiber reinforced composite materials that exhibit tensile pseudo-ductile and strain hardening behavior. Response of a single fiber is one of many factors that affect the overall response of the composite. In the literature analytical relations describing the behavior of a fiber during its pull-out from the surrounding matrix can be found. Up to now, these models did not take into account the possibility that a fiber bridges more than one crack. In the present paper, we refine the model for one fiber by considering that it may cross several parallel cracks. A numerical study is performed to investigate the effect of this consideration on the relation between force acting in the fiber and its pull-out displacement.*

Keywords: ***Fiber-reinforced composite, fiber bridging, pseudo-ductility, strain hardening, multiple cracking***

1. Introduction

Historical monuments are at the present time subjected to various effects, which their builders couldn't take into account at the time of construction and which contribute to their deterioration. Excessive loads caused by temperature fluctuations or technical seismicity due to traffic and technological processes cause degradation and cracking of historical masonry. The cracks pave the way for penetration of water and contaminants into the masonry, which leads to further degradation. These cracks often formed in the masonry joints, because mortar is usually the weaker element. To alleviate the degradation we are developing a fiber reinforced mortar that under tensile stress undergoes multiple cracking as opposed to failing by a single brittle crack. During the multiple cracking process, a large number of fine cracks with controlled width forms, while the mortar retains macroscopic integrity. Keeping the small crack width may prevent penetration of contaminants. For these cases a methodology for systematic design of materials with brittle matrix reinforced with short fibers was developed (Li, 2003). This methodology employs micromechanics and fracture mechanics based models of the damage phenomena taking place at the level of the composite microstructure, such as fiber debonding and pullout and matrix cracking. It was successfully used, for example, for design of Engineered Cementitious Composites – ECC (Li, 2003). Our intention is to use this approach to develop a new lime mortar reinforced with short random fibers, which could be applied to restoration works on historic buildings. As part of this effort we further refine the existing micromechanical models to take into account previously neglected phenomena.

2. Single fiber response

Bridging effect of fibers crossing a crack in a brittle-matrix composite has a dominant influence on whether the material eventually exhibits multiple cracking (Marshall et al., 1988). When a fiber-bridged crack forms and opens, the fibers are being extracted from the surrounding matrix. This process can be divided into two main stages, which can be described by the relationship between force P on the pulled-out end of the fiber and displacement u at the same point. In the first stage, the fiber

* Ing. Michal Přinosil: Czech Technical University in Prague, Faculty of Civil Engineering, Department of Mechanics, Thákurova 7; 166 29, Prague; CZ, e-mail: michal.prinosil@fsv.cvut.cz

** prof. Ing. Petr Kabele, Ph.D.: Czech Technical University in Prague, Faculty of Civil Engineering, Department of Mechanics, Thákurova 7; 166 29, Prague; CZ, e-mail: petr.kabele@fsv.cvut.cz

gradually debonds from the matrix and as the force P increases. Assuming that debonding is resisted by fiber-matrix chemical bond strength G_d, that the debonded portion of the fiber elastically deforms, and that constant friction τ_0 acts on the debonded fiber-matrix interface, this stage can be described by Eq. (1). This stage is completed when the embedded end of the fiber becomes fully debonded from the matrix. The corresponding displacement of u then reaches the value of δ_c given in Eq. (2). A pull-out phase follows, during which the fiber slips out from the matrix while the contact area with the matrix diminishes. The pull-out phase is described by Eq. (3). The whole $P - u$ relation is shown in Fig. 1.

$$P_{deb} = \sqrt{\frac{\pi^2 \tau_0 E_f d_f^3}{2} u + \frac{\pi^2 G_d E_f d_f^3}{2}} \tag{1}$$

$$\delta_c = \frac{2\tau_0 L_e^2}{E_f d_f} + \sqrt{\frac{8 G_d L_e^2}{E_f d_f}} \tag{2}$$

$$P_{pull} = \pi d_f \tau_0 \left(1 + \frac{\beta(u - \delta_c)}{d_f}\right)(L_e - u + \delta_c) \tag{3}$$

In equations is E_f fiber elastic modulus, L_e is fiber embedment length, d_f is fiber diameter, τ_0 is frictional stress on debonded interface, G_d is fiber-matrix chemical bond strength and β is fiber-matrix interface slip-hardening parameter.

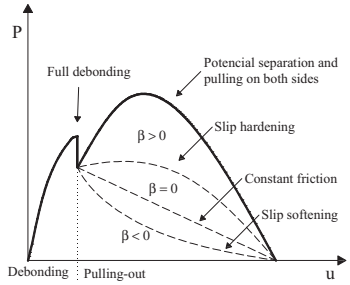

Fig. 1: Single fiber pull-out response

3. Probability of fiber bridging several cracks

The model described above adopts the assumption, that a fiber bridges only one crack. However, the length of fibers that are typically used in short-fiber reinforced mortars is in the order of 10 mm, while the crack to crack distance during multiple cracking can be as low as few mm. A question naturally arises, whether the $P - u$ relation described above is realistic in the multiply-cracking composites. Thus, the aim of this paper is to describe the influence of a state when a fiber bridges more than one crack.

First of all, let us investigate how many fibers may bridge more than one crack when the composite undergoes multiple cracking. To this end, we assume that fibers of length L_f are randomly distributed and oriented in the composite. Furthermore, we assume that matrix cracks, bridged by these fibers, are perfectly planar and parallel. The analytical relation derived below describes the probability with which a fiber passing through a fixed point P on a one crack crosses another crack at a distance d_c.

All possible cases of the position of the fiber end points fill the space corresponding to the sphere with radius L_e and center at point P. For one side of the crack it is a hemisphere. End points of fibers, which intersect the second crack, fill the space corresponding to the spherical cap of the hemisphere with a height L_e-d_c. (see Fig. 2). The ratio of the volume of the hemisphere and the spherical cap (Eq. 4) describes the probability with which a fiber intersects two parallel cracks with the given distance.

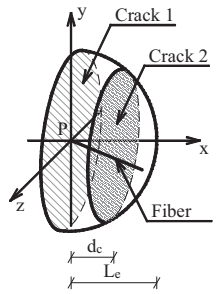

Fig. 2: Randomly oriented fiber in space with two parallel cracks

$$P(d_c) = \frac{(L_e - d_c)(2L_e^2 - L_e d_c - d_c^2)}{2L_e^3} \tag{4}$$

To verify the validity of the analytical relationship in Eq. (4), a numerical simulation was performed. We considered prismatic specimens of fiber reinforced composite with the same length of 200 mm but different square cross-sections with widths a) 50 mm b) 100 mm c) 200 mm.. Within these volumes, random fibers were generated keeping fiber volume fraction constant and equal to 2 %. Pairs of cracks (perpendicular to the specimen axis) with different mutual distances were inserted into each specimen and the number of fibers bridging both cracks was counted. The results for each specimen were averaged and the probability P was calculated. Figure 3 shows a very good agreement between the results of the analytical solution (Eq. 4) and numerical simulations.

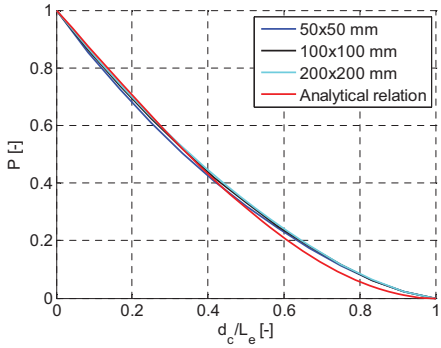

Fig. 3: Dependence of the number of fibers intersecting two parallel cracks on their distance

4. Crack spacing

At a crack plane, each fiber carries its bridging force. The fiber force decreases along its length with increasing distance from the crack plane due to transfer of the load to the surrounding matrix through the friction at the interface. At the end of debonded fiber-matrix interface (at distance d_c from the crack) the force is completely transferred to the matrix. Assuming constant frictional stress τ_0 along the interface, this force can be expressed as:

$$P(d_c) = \sqrt{\frac{\pi^2 G_d E_f d_f^3}{2}} + \pi d_f \tau_0 d_c \tag{5}$$

If we consider spatial randomness of fiber orientation, the number of fibers bridging a crack of unit area N_s is (Naaman 1972 referenced in Naaman, 2008):

$$N_s = \frac{2V_f}{\pi d_f^2} \tag{6}$$

And the area of crack corresponds to single fiber is:

$$A_m = \frac{\pi d_f^2}{2V_f} \tag{7}$$

The stress in matrix at distance d_c can be expressed as:

$$\sigma_m = P(d_c)/A_m \tag{8}$$

Assuming that a new crack forms when stress σ_m reaches the matrix tensile strength f_t, we can express the crack to crack distance for single fiber perpendicular to crack with sufficient embedment length as:

$$d_c = \frac{1}{\tau_0}\left(\frac{f_t d_f}{2V_f} - \sqrt{\frac{d_f G_d E_f (1+\eta)}{2}}\right) \tag{9}$$

Where $\eta = (E_f V_f)/(E_m V_m)$ expresses deformation of the matrix, V_m is matrix volume fraction, E_m is matrix elastic modulus, V_f is fiber volume fraction. For material and geometric parameters of typical ECC with PVA fibers d_f = 0,04 mm, L_e = 12 mm, E_f = 21 800 MPa, τ_0 = 2,21 MPa, G_d = 0,004 N/mm, E_m = 15900 MPa, f_t = 4,3 MPa and V_f = 0,02 we get d_c = 1,34 mm. From Eq. (4) we get that approximately 84 % of fibers crossing two cracks in this distance, which shows, that the possibility of fibers bridging multiple cracks should be taken into account.

5. Response of fiber bridging several cracks

For a description of behavior of single fiber bridging several cracks a numerical model was created and implemented in software MATLAB. This model utilizes the analytical relations of Eq. (1) – (3). We consider that a fiber bridges one main and one or two adjacent cracks. The distances between the main and adjacent cracks were being changed and we monitored the P_f - w relationship of the fiber at the main crack, where w crack opening and P_f is force in the fiber.

Cracks divide the fiber into several parts. Computation was controlled by displacement u_s on shorter of edge parts, because this part determines maximum force in the fiber P_f. During the debonding stage, separation occurs on every side of each crack. There is tunnel crack propagation along the fiber and debonded length L_{deb} is:

$$L_{deb} = \frac{P_f - \sqrt{\frac{\pi^2 G_d E_f d_f^3}{2}}}{\pi d_f \tau_0} \tag{10}$$

When the debonded length L_{deb} reaches the embedment length L_e on shorter edge part, pull-out phase occurs and force in fiber decreases in case $\beta = 0$. The crack beside shorter edge part is opening and others are closing due to fiber stiffness. Another case occurs when tunnels propagating from two nearby cracks meet. Debonding stops and when force P_f increases, only elastic deformation of fiber continues, which is restrained by frictional stress τ_0 at the interface. Displacement of fiber at any point can be described by equation:

$$u(x) = \frac{1}{E_f A_f}\int P_f - \pi d_f \tau_0 x \, dx \tag{11}$$

Considering, that center of full debonded part don't change its position on fiber and embedment length on this part corresponds to half distance of cracks d_c, we get contribution to the crack opening as elongation of fiber from half of this part:

$$u = \frac{2P_f d_c}{\pi E_f d_f^2} - \frac{\tau_0 d_c^2}{2E_f d_f} \tag{12}$$

Finally, we obtain crack opening w as the sum of pulled length on both sides of the crack:

$$w = \sum_{i=1}^{2} u_i \tag{13}$$

Where u_i is prescribed u_s for debonding or u for elastic deformation of the fiber from Eq. (12). Responses of fiber in the main crack are shown in Figure 4 and schematic drawings (possible states) at the end of debonding stage are shown in Figure 5.

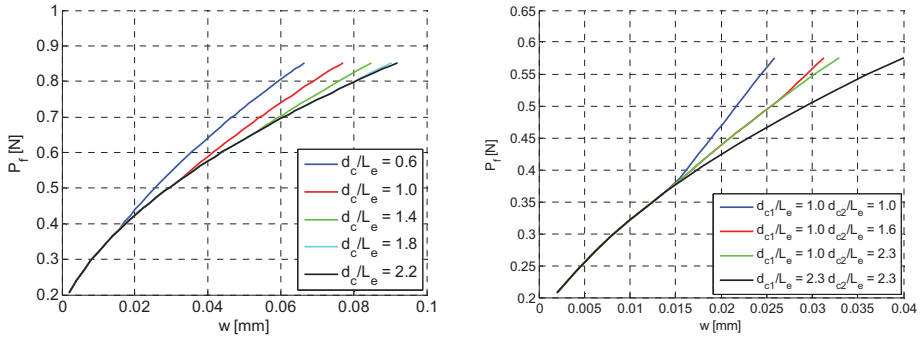

Fig. 4: Single fiber response for one nearby crack (left) and two nearby cracks (right)

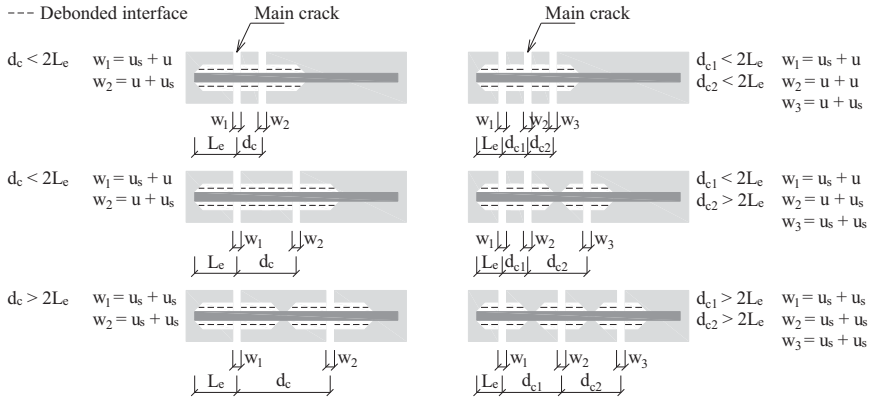

Fig. 5: Schematic drawings for different d_c – one nearby crack (left) and two nearby cracks (right)

6. Conclusions

According to the results, the single fiber response is affected by the interaction of cracks. This interaction occurs when $d_c < 2L_e$. It causes that for the same force P_f we get smaller crack opening w. Future work on this topic will be focused on examination how the interaction of cracks affects the behavior of cracks themselves.

Acknowledgement

The presented research has been carried out with financial support of the Czech Ministry of Culture, as part of the project no. DF11P01OVV008.

References

Li, V. C. (2003) On Engineered Cementitious Composites (ECC) – A review of the material and its applications. *Journal of Advanced Concrete Technology*, 1, 3, pp.215-230.

Marshall, D.B & Cox, B.N. (1988) A J-integral method for calculating steady-state matrix cracking stresses in composites. *Mechanics of Materials*, 7, 2, pp.127-133.

Naaman, A.E (2008) High Performance Fiber Reinforced Cement Composite. In: *High-Performance Construction Materials – Science and Applications* (C. Shi & Y. L. Mo eds.). World Scientific, Singapore, pp.91-154.

18th International Conference
ENGINEERING MECHANICS 2012
Svratka, Czech Republic, May 14 – 17, 2012

pp. 1087–1102
Paper #184

COMPUTER SIMULATION OF MUSICAL SINGER'S VOICE BASED ON MRI AND ACOUSTIC MEASUREMENTS

V. Radolf[*], A. Nissinen[****], A. M. Laukkanen[**], R. Havlík[***], J. Horáček[*]

Abstract: *An inverse method was used to estimate the vocal tract geometry as a 1 D model on the basis of acoustical characteristics of a professional musical singer before and after vocal exercising. The basic geometrical data for the model were obtained from magnetic resonance images (MRI) registered during sustained phonation of vowels [a:], [i:], [u:] produced in naive and professional ways (before and after exercising respectively). The model was used for numerical simulations of the voice signals. The results of simulation were compared to the acoustic recordings. According to the results, a singer's formant cluster was accomplished after exercising. It seemed to be due to lowering of the larynx and lengthening and narrowing of the epilarynx. The area ratio between the low pharynx and the epilarynx increased for [a:] but decreased for [i:] and [u:] after exercising being between 3.33 and 4.39. There was a qualitative agreement between 3D measurements of MRI and the results of modeling. The results suggest that for a singer's formant cluster a relatively low pharynx over epilarynx ratio may be sufficient, at least if the larynx lowers.*

Keywords: ***Biomechanics of voice, singer's and speaker's formant cluster, acoustic effects of vocal exercises.***

1. Introduction

In operatic singing, singers make use of a special voice quality in order to be heard over the orchestra without a microphone. The important acoustic component which determines the operatic quality of the voice, especially in male singers, is the so-called "singer's formant" (Sundberg, 1974, 2003; Titze, 2000). Similarly the voice quality of speakers, especially actors, is improved by the so-called "speaker's formant" (Leino, 1994; Leino et al., 2011).

Sundberg (1974) formulated an acoustic interpretation of singer´s formant as clustering of formants F3 – F5 in the vicinity of 3 kHz. According to the calculations by Fant (1960) such a situation can occur if the ratio of the cross-sectional area of the lower pharynx over the outlet of the epilaryngeal tube is six or higher. The physical modeling results by Sundberg supported the findings of Fant. Different results were obtained by Detweiler (1994) who investigated by MRI scanning the vowel phonation of tenor and baritone singers phonating vowel [a:] in modal register. According to her results, the subjects laryngopharyngeal/laryngeal outlet cross-sectional area ratios varied from 2.9:1 to 3.7:1, which wasn´t consistent with the hypotheses by Sundberg and Fant. Later, Sundberg (2003) criticized the Detweiler's way of measuring the areas, which was accomplished from the sagittal and transversal distances measured in 2D slices. The epilarynx tube, located just above the vocal folds, was also theoretically considered as a dominant source of clustering of formant frequencies especially when the cross-sectional area of this tube is approximately six times less than the area of the lower pharynx by Titze and Story (1997), and Story (2003). However, the physiological adjustment used in singers or in actors has not been known in sufficient details yet.

[*] Ing. Vojtěch Radolf, Ph.D. and Ing. Jaromír Horáček, DrSc.: Institute of Thermomechanics, Academy of Sciences of the Czech Republic; Dolejškova 1402/5; 182 00, Prague; CZ, e-mail: radolf@it.cas.cz and e-mail: jaromirh@it.cas.cz

[****] Antti Nissinen Ph.D, Dept. of Applied Physics, University of Eastern Finland, FI-70211, Kuopio, Finland, e-mail: antti.nissinen@uef.fi

[**] Prof. Anne-Maria Laukkanen, Ph.D.: Speech and Voice Research Laboratory, School of Education, University of Tampere; FIN-33014, Tampere; Finland, e-mail: Anne-Maria.Laukkanen@uta.fi

[***] MUDr. Radan Havlík, Ph.D.: AUDIO – Fon Centr. s.r.o.; Obilní trh 4; 602 00, Brno; CZ, e-mail: radan.ha@seznam.cz

The rationale of the present paper was to estimate the anatomical/geometrical adjustments and to model the acoustic changes that occur in the voice of a male professional musical actor after vocal warming up by vocal exercises.

2. MRI measurement and 3D vocal tract modeling

A Czech male musical actor (60 years, baritone) served as a subject in the magnetic resonance imaging investigation. Lying supine in the MRI machine he first produced the vowels [a:], [i:], [u:] in a naive technique and after ca 5 minute vocal exercising again in a professional "musical actor's" manner, aiming at the best voice quality. Each vowel sample was produced for at least 20 s to enable the MRI scanning. The samples were produced on a comfortable pitch, at approximately the same fundamental frequency. Being vocally trained, the subject was able to keep the articulation and phonation constant through a sustained vowel phonation. The subject's head position was stabilized with a support. Before starting the MRI measurement the subject phonated each sample with normal auditory feedback (i.e. without the MRI device on) and sustained the same phonation setting during MRI scanning. MRI scanning was performed at the Dept. of Medical Imaging, St. Anne's Faculty Hospital in Brno, using the 1.5 Tesla MRI device (Symphony Magnetom, Siemens). The imaging parameters were as follows: Field of view 236 x 270 mm, slice thickness 1.5 mm, acquisition time 20.07 s, number of averages 1, repetition time 5.49 s, echo time 2.88 s, number of sagittal images 44, resolution 512 x 448 pixels (cf. Laukkanen et.al., 2012).

For viewing the MR images (see Figure 1) and for measuring the changes of the vocal tract a Syngo FastView software (Siemens AG) and ITK Snap 2.0 were used. Lengths of different parts of the vocal tract were measured from midsagittal images as follows. Horizontal length (HL) was measured as the distance from the lips to the anterior lower edge of the anterior arch of Atlas. Vertical length (VL) was measured from the anterior lower edge of the anterior arch of Atlas down to the vocal folds. Total length (TL) of the vocal tract was calculated by adding HL and VL. Length of the epilaryngeal tube (EL) was measured from the collar of the epiglottis down to the vocal folds.

The 3D model of the vocal tract was reconstructed from the MRI images using Mimics (version 13.1, Materialise, Belgium). Especially the areas of the outlet of the epilarynx and the inlet of the low pharynx were studied from transversal slices of the 3D volume models of this part of the vocal tract, see Figure 2. The area of the inlet to the pharynx was studied just above the collar of epiglottis, while the area of the outlet of the epilarynx was studied just below the collar of epiglottis, at the point where the epilaryngeal tube and the sinus piriformes are separated. The region of interest (the region of the lower pharynx and upper epilarynx) of the vocal tract was segmented and the surface mesh of the focal tract was constructed. The surface meshes consisted of triangular elements. The cross sectional areas of the meshes were computed using Matlab. The cross sections were taken so that they were perpendicular with the midline of the mesh (vocal tract). In other words, the tangent of the midline determines the normal vector of the cross section. The area of each cross section was determined by modeling the cross section with a 2D mesh and summing the areas of the elements in the mesh. The ratio of the inlet to the pharynx over the outlet of the epilarynx was calculated from the areas.

3. Acoustic measurements

Due to noise and magnetic field no acoustic recording was possible during the MR imaging. For acoustic measurements the subject's voice was recorded during the same tasks afterwards in a sound-treated studio using the microphone Center 322 DATA LOGGER with software lingWAVES version 2.5 (sensitivity 30-130dB , sampling frequency of 44.1 kHz).

Acoustic analysis was done in Matlab by averaging frequency spectra calculated by FFT using 1s time windows with 75% overlap (see thin lines in Figure 4). Sound pressure level SPL was computed for each harmonics. Then the resulting spectra were averaged in the frequency bands (windows) equal to the fundamental frequency F0 with overlap of F0-10 Hz. Thus the new curves of "filtered spectra" were obtained (see thick lines in Figure 4) and the maxima of these curves were considered as formants.

4. MRI results

The MR images (see Figure 1) revealed lowering of the larynx from the fourth to the fifth vertebra, rising of the soft palate and thus a tighter closure of the velar port, prolongation of the vocal tract and of the epilaryngeal tube, widening of the mouth cavity due to a lower position of the tongue, narrowing and lengthening of the epilaryngeal and lower pharyngeal region and widening of the higher pharynx for [i:], and narrowing of it for [a:] and [u:] in phonation after the vocal exercising.

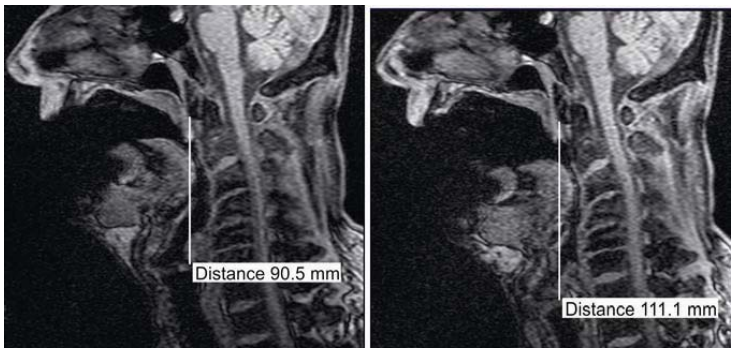

[a:] before and after warm-up

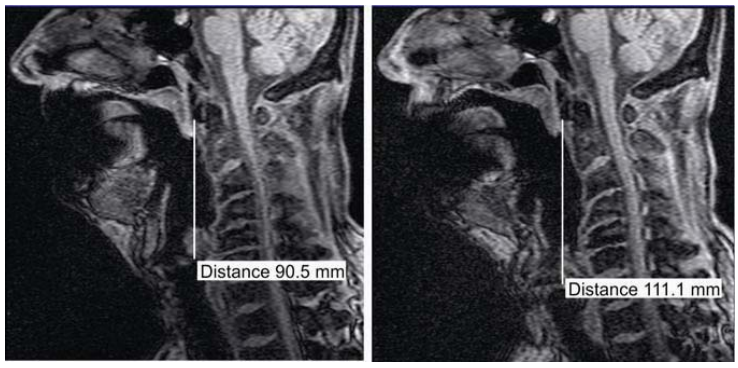

[i:] before and after warm-up

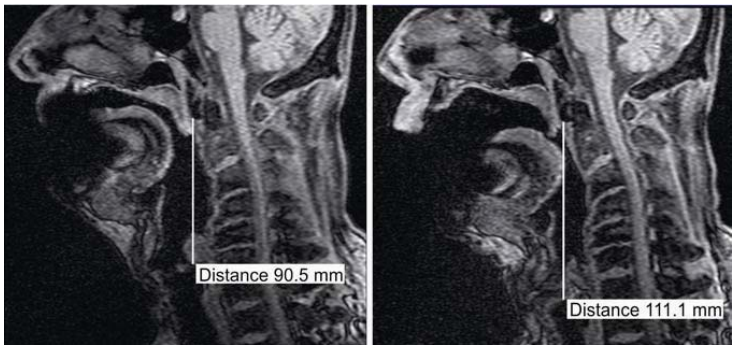

[u:] before and after warm-up

Fig. 1: Midsagittal MR images for the vowels [a:], [i:], [u:] before and after the vocal exercising.

The measured data for vocal tract length and its changes after warm up are summarized in Table 1 for all three vowels investigated.

The areas measured in the cross-sections at the end of the lower pharynx A_{ph} and at the upper end of the epilaryngeal tube A_{ep} and their ratios $R = A_{ph} / A_{ep}$ are summarized in Table 2. For all three vowels [a:], [i:] and [u:] after warm up the ratio was between R=3.33 and R=4.39, i.e. all ratios were lower than the value R=6 considered in the previous studies.

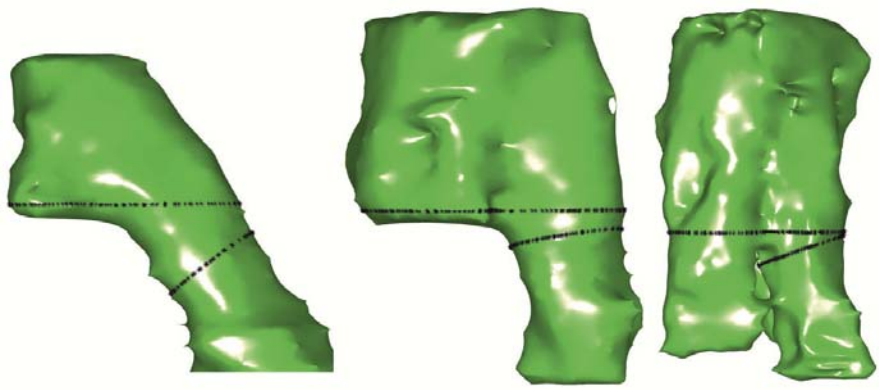

Fig. 2: The 3D volume models of the vocal tract in the region of the lower pharynx and the upper epilaryngeal tube for the vowels [a:], [i:] and [u:] with the marked cross-sections where the areas were measured (from left to right).

5. Acoustic results

The acoustic analyses showed that after exercising a cluster of two or three formants was formed for the vowel [a:] in the range of F3-F5 between 2 and 4 kHz, and similarly in the range of F2-F4 between 1.4 and 3.4 kHz for the vowel [i:] and in the range of F3-F4 between 1.8 and 3 kHz for the vowel [u:] (see Figure 4 and Table 3). Such clustering of the higher formants leads to a stronger speaker's/singer's formant. A weak resonance in the frequency region at about 1.6 kHz for the vowels [a:] and [u:] and at about 1.2 kHz for the vowel [i:] can be caused by a slight nasality, which corresponds well to the study by Vampola et al. (2008b), where the first oro/nasal formants were found in the frequency region above the formants F_1 and F_2 for the vowels [a:] and [u:] and between the formants F_1 and F_2 for the vowel [i:].

Tab. 1: Horizontal length of the vocal tract HL, vertical length of vocal tract VL, total length of vocal tract TL, length of the epilaryngeal tube EP and their changes after the warm-up for the vowels [a:], [i:] and [u:]. (MRI results)

distance [mm]	**[a:]**			**[i:]**			**[u:]**		
	before	after	change	before	after	change	before	after	change
HL	89	86.7	-2.3 %	89.7	90.5	0.8 %	89.4	94.3	4.9 %
VL	92.5	112.3	19.8	87.8	102.7	14.9	93.8	111.2	17.4
TL	181.5	199	17.5	177.5	193.2	15.7	183.2	205.5	22.3
EP	21	23	2	21	23	2	21	23	2

Tab. 2: Areas measured in cross-sections of the lower pharynx and of the upper epilarynx and their ratios before and after warm-up for the vowels [a:], [i:] and [u:]. (MRI results)

area [cm^2]	**[a:]**		**[i:]**		**[u:]**	
	before	after	before	after	before	after
A_{ph} (pharynx)	3.959	3.430	7.736	5.761	7.966	5.440
A_{ep} (epilarynx)	1.099	0.833	1.696	1.312	2.201	1.636
ratio ($R=A_{ph}/A_{ep}$)	3.60	4.12	4.56	4.39	3.62	3.33

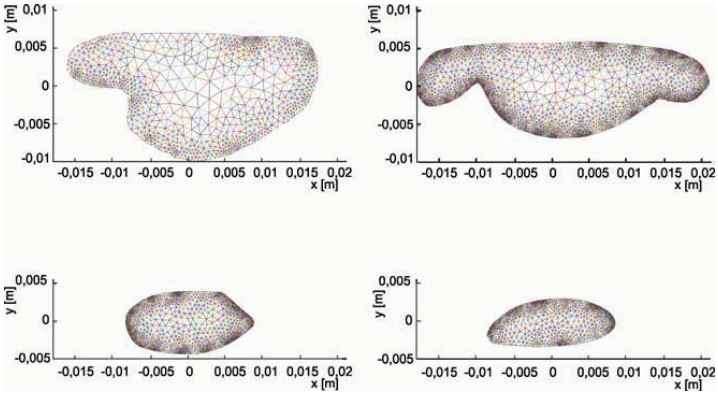

vowel [a:]

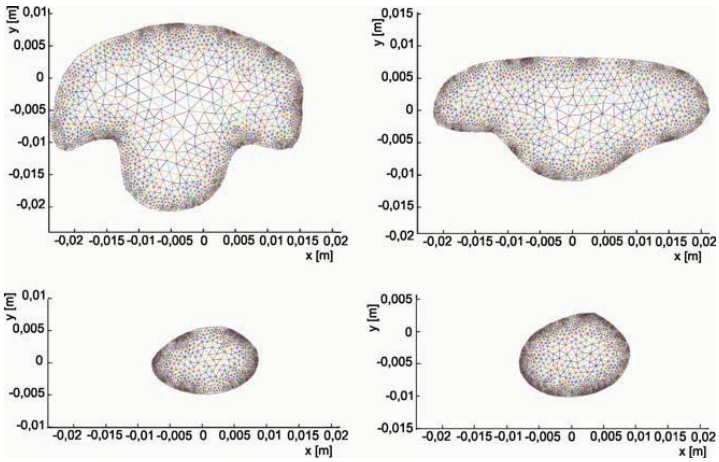

vowel [i:]

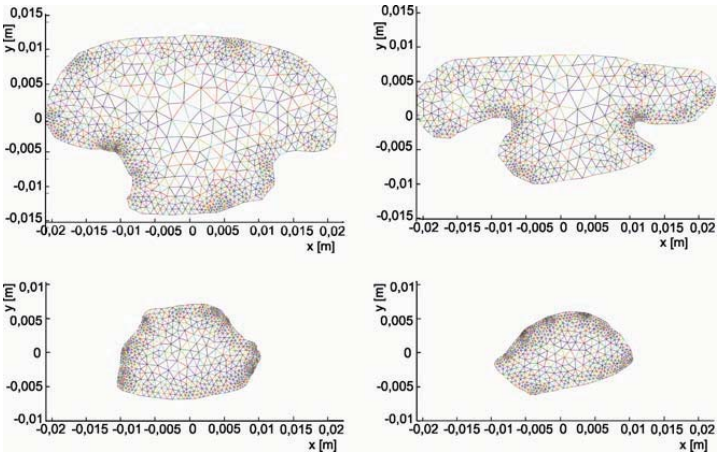

vowel [u:]

Fig. 3: Areas of the inlet of the low pharynx (upper panels) and the outlet of the epilarynx (lower panels) before (left) and after (right) voice exercising for phonation of vowels [a:], [i:], [u:].

6. Modeling approach

The possible vocal tract changes resulting in the formation of a speaker's (or singer's) formant cluster were also studied using a 1D mathematical model of voice production (Radolf, 2010). The 1D vocal tract model was developed from the 3D volume model obtained from the MR images (Vampola et al., 2008). The formant frequencies measured from the vowels [a:], [i:] and [u:] recorded from the subject of the present study before and after exercising were prescribed to the model and by a tuning procedure (changing the vocal tract shape, i.e. the size of area cross-sections) the best fitting vocal tract configurations were obtained. The length of the real vocal tract of the subject was measured using MRI data and the values given in Table 1 were used for both the epilaryngeal and total length of the vocal tract model before and after vocal exercising. Vocal tract channel was modeled as a system of conical elements of 4 mm in length except for the first and the last element, whose length was modified according to the total length of vocal tract given by Table 1.

The model is based on an analytical solution of 1D wave equation for acoustic wave propagation in the vocal tract cavity (Radolf, 2010):

$$\frac{\partial^2\varphi}{\partial x^2}+\frac{1}{A}\frac{\partial A}{\partial x}\frac{\partial\varphi}{\partial x}-\frac{1}{c_0^2}\left(\frac{\partial^2\varphi}{\partial t^2}+c_0\,r_N\frac{\partial\varphi}{\partial t}\right)=0 \tag{1}$$

where (φ is the flow velocity potential, x is longitudinal coordinate along the vocal tract measured from the vocal folds to the lips, t is time, r_N is specific acoustic resistance per a unite length, $A(x)$ is the cross-sectional area of the cavity and c_0 is speed of sound.

Relation between the acoustic pressure p and the volume velocity W at the input and output of each conical acoustic element can be described by the transfer matrix as

$$\begin{bmatrix} p_{OUT} \\ W_{OUT} \end{bmatrix}=\begin{bmatrix} a & b \\ c & d \end{bmatrix}\cdot\begin{bmatrix} p_{IN} \\ W_{IN} \end{bmatrix}, \tag{2}$$

where the elements of the transfer matrix are

$$a=\frac{\xi_0}{\xi_0+L}\cdot\left(\cosh(\gamma L)+\frac{1}{\gamma\,\xi_0}\cdot\sinh(\gamma L)\right),\quad b=-\frac{z_0(r_N+j\,k)\cdot\xi_0}{A_{IN}\cdot\gamma(\xi_0+L)}\cdot\sinh(\gamma L),$$

$$c=A_{OUT}\cdot\frac{\left(1-\gamma^2\xi_0(\xi_0+L)\right)\cdot\sinh(\gamma L)-\gamma L\cdot\cosh(\gamma L)}{\gamma(\xi_0+L)^2\cdot z_0(r_N+j\,k)},$$

$$d=\frac{A_{OUT}}{A_{IN}}\frac{\xi_0}{\xi_0+L}\cdot\left(\cosh(\gamma L)-\frac{1}{\gamma(\xi_0+L)}\cdot\sinh(\gamma L)\right),$$

L is length of the element, A_{IN} and A_{OUT} are the cross-sectional areas of the element input and output, respectively, γ is a complex exponent given by the formulas:

$$\gamma=\alpha+j\beta,\quad \alpha=\frac{r_N}{\sqrt{2+2\cdot\sqrt{1+(r_N/k)^2}}},\quad \beta=\frac{k}{2}\cdot\sqrt{2+2\cdot\sqrt{1+(r_N/k)^2}}, \tag{3}$$

$k=\omega/c_0$ is the wave number, ω is angular frequency of harmonic signal, j is imaginary unit: $j=\sqrt{-1}$. The coefficient ξ_0 is defined by input and output radius of the element R_{IN} and R_{OUT}, respectively,

$$\xi_0=\frac{R_{IN}}{R_{OUT}-R_{IN}}\cdot L. \tag{4}$$

Frequency dependent viscous losses were considered as

$$r_N=\frac{1}{R}\cdot\sqrt{2k\mu/c_0\rho_0}, \tag{5}$$

where μ is dynamic air viscosity.

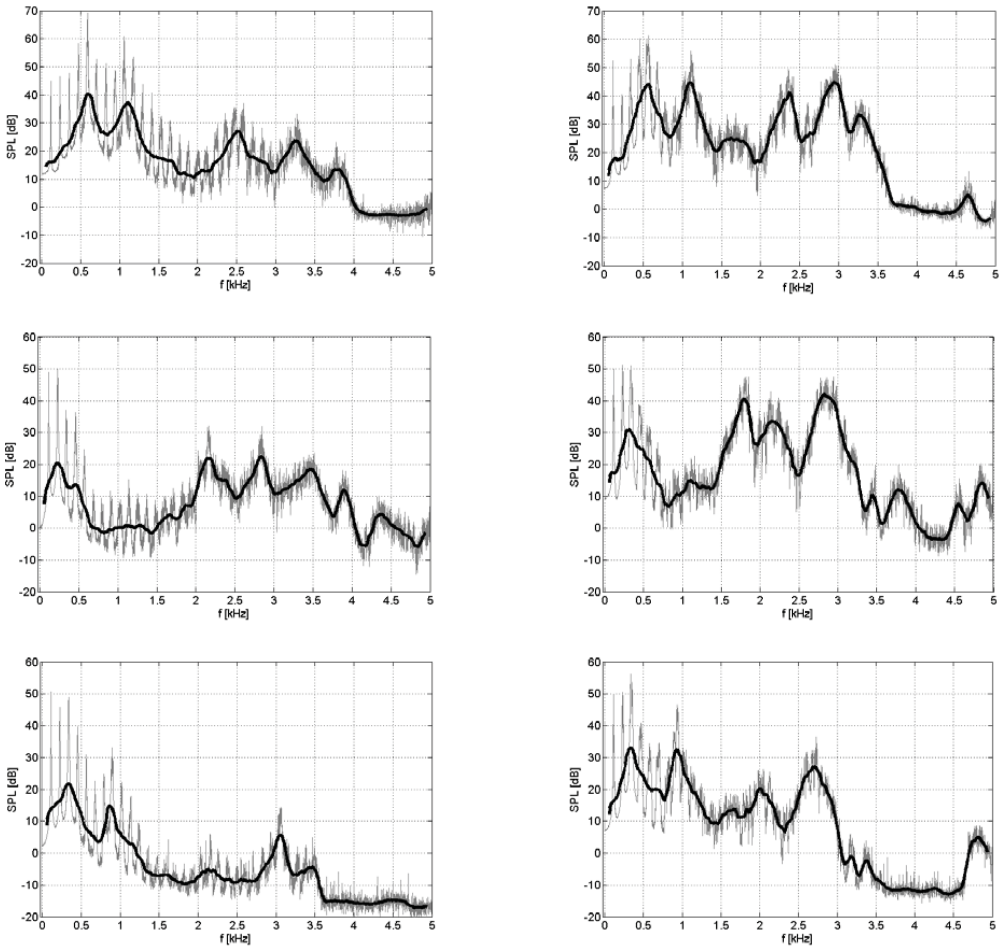

Fig. 4: Spectra (LTAS – Rectangular window) of the acoustic signals for the vowels [a:] (top panels) , [i:] (middle) and [u:] (bootom) before (left) and after (right) the vocal exercise.

Acoustic properties of the whole vocal tract can be described by matrix form

$$\begin{bmatrix} p_{LIP} \\ W_{LIP} \end{bmatrix} = \mathbf{T}_{VT} \cdot \begin{bmatrix} p_{GLOT} \\ W_{GLOT} \end{bmatrix}, \tag{6}$$

where $\mathbf{T}_{VT}$ is a transfer matrix obtained by multiplication of transfer matrices of all elements from the vocal folds to the lips

$$\mathbf{T}_{VT} = \begin{bmatrix} a_{VT} & b_{VT} \\ c_{VT} & d_{VT} \end{bmatrix} = \mathbf{T}_{N_e+1,N_e} \cdot \mathbf{T}_{N_e,N_e-1} \cdot \ldots \cdot \mathbf{T}_{3,2} \cdot \mathbf{T}_{2,1}, \tag{7}$$

and N_e is number of conical elements.

Both for the calculation of the eigenfrequency and for the numerical simulation of the acoustic pressure at the lips we assume the output at the lips loaded by the acoustic radiation impedance of vibrating circular plate with radius *R* placed in an infinite wall (see e.g. Vampola *et al*., 2008)

$$Z_{A\,rad} = \frac{c_0 \rho_0}{\pi R^2} \cdot \left[1 - \frac{J_1(2kR)}{kR} + j \frac{H_1(2kR)}{kR} \right], \tag{8}$$

where J_1 is the Bessel function of the first kind of order 1 and H_1 is the Struve function of order 1 and ρ_0 is fluid density.

Since the radiation impedance gives the ratio of acoustic pressure and volume velocity $Z_{A\,rad} = p_{LIP}/W_{LIP}$, we get from (6) and (7)

$$\begin{bmatrix} p_{LIP} \\ p_{LIP}/Z_{A\,rad} \end{bmatrix} = \begin{bmatrix} a_{VT} & b_{VT} \\ c_{VT} & d_{VT} \end{bmatrix} \cdot \begin{bmatrix} p_{GLOT} \\ W_{GLOT} \end{bmatrix}. \tag{9}$$

In the eigenfrequency calculations, the boundary condition: $W_{GLOT} = 0$ is assumed at the vocal folds, i.e. a closed input by a rigid wall, which gives the following frequency equation:

$$a_{VT} - Z_{A\,rad} \cdot c_{VT} = 0. \tag{10}$$

Directly from the system of equations (9), we obtain the acoustic pressure at the lips linearly dependent on the excitation velocity signal at the vocal folds:

$$p_{LIP} = \frac{a_{VT} \cdot d_{VT} - b_{VT} \cdot c_{VT}}{a_{VT} - Z_{A\,rad} \cdot c_{VT}} \cdot Z_{A\,rad} \cdot W_{GLOT}. \tag{11}$$

Tab. 3: Fundamental frequency (F0) and the formant frequencies (F1 - F5) evaluated from the acoustic recordings and obtained from the modeling for the vowels [a:], [i:] and [u:] before and after the vocal exercise.

[a:]	F_0 [Hz]	F_1 [Hz]	F_2 [Hz]	F_3 [Hz]	F_4 [Hz]	F_5 [Hz]
Acoustic signal – before exercising	118	600	1100	2510	3260	3780
Model – before exercising	random	600	1099	2507	3254	3787
Acoustic signal - after exercising	112	560	1100	2370	2940	3260
Model - after exercising	random	560	1099	2367	2935	3268
[i:]						
Acoustic signal – before exercising	114	230	2170	2840	3470	3890
Model – before exercising	random	230	2171	2831	3473	4543*
Acoustic signal-after exercising	114	310	1790	2160	2820	3770
Model - after exercising	random	310	1783	2162	2826	4166*
[u:]						
Acoustic signal – before exercising	114	340	860	2150	3060	-
Model – before exercising	random	343	856	2149	3052	4783*
Acoustic signal - after exercising	115	340	940	2010	2700	-
Model - after exercising	random	340	940	2003	2707	4160*

* Formants resulted from modeling, but were not prescribed for tuning where only F_1-F_4 were used.

The sensitivity of a particular eigenfrequency f_n to a change in cross-sectional area A_i in dimensionless form:

$$ {}^{A}S_{i,n} = \frac{\Delta f_n / f_n}{\Delta A_i / A_i} \tag{12} $$

can be substituted by the following relation (see Radolf (2010)):

$$ {}^{A}\tilde{S}_{i,n} = \frac{1}{2}\left\{ L_{i-1}\partial_i^{i-1} \cdot \left[\frac{\rho_0}{2A_{i-1\,red}^2}\left(W_{i-1,n}^{\,2} + W_{i,n}^{\,2} \right) - \frac{1}{\rho_0 c_0^2} p_{i-1,n}^2 \right] \right. $$

$$ \left. + L_i \partial_i^{i} \cdot \left[\frac{\rho_0}{2A_{i\,red}^2}\left(W_{i,n}^{\,2} + W_{i+1,n}^{\,2} \right) - \frac{1}{\rho_0 c_0^2} p_{i,n}^2 \right] \right\} \cdot \frac{A_i}{\sum_{e=2}^{N_e+1} m_e W_{e,n}^{\,2}}, \tag{13} $$

where $A_{i\,red}$ is a reduced cross-sectional area of an i-th conical element of length L_i

$$ A_{i\,red} = \frac{1}{3}\left(A_i + \sqrt{A_i A_{i+1}} + A_{i+1} \right), \tag{14} $$

m_i is an acoustic mass lumped into i-th cross-section:

$$ m_i = \frac{\rho_0}{2}\left(\frac{L_{i-1}}{A_{i-1\,red}} + \frac{L_i}{A_{i\,red}} \right), \tag{15} $$

∂_i^{i-1} and ∂_i^{i} are the partial derivatives of the reduced cross-section

$$ \partial_i^{i-1} = \frac{\partial A_{i-1\,red}}{\partial A_i} = \frac{1}{3} \cdot \left(1 + \frac{1}{2}\sqrt{\frac{A_{i-1}}{A_i}} \right), \qquad \partial_i^{i} = \frac{\partial A_{i\,red}}{\partial A_i} = \frac{1}{3} \cdot \left(1 + \frac{1}{2}\sqrt{\frac{A_{i+1}}{A_i}} \right), \tag{16} $$

N_e is number of conical elements, $p_{i,n}$ resp. $W_{i,n}$ is an amplitude of acoustic pressure resp. volume velocity in the *i*-th cross-section for the *n*-th eigenfrequency f_n.

Radolf (2010) derived that the dimensionless sensitivity of a particular eigenfrequency f_n to a change of the length L_i of the i-th element:

$$ {}^{L}S_{i,n} = \frac{\Delta f_n / f_n}{\Delta L_i / L_i}, \tag{17} $$

can be substituted by the following relation

$$ {}^{L}\tilde{S}_{i,n} = -\frac{1}{2}\left(\frac{A_{i\,red}}{\rho_0 c_0^2} p_{i,n}^2 + \frac{\rho_0}{2A_{i\,red}}\left(W_{i,n}^2 + W_{i+1,n}^2 \right) \right) \cdot \frac{L_i}{\sum_{e=2}^{N_e+1} m_e W_{e,n}^2}. \tag{18} $$

Based on the results of Story (2006) and using the sensitivity functions (13) and (18) an iterative process was developed for computation of *i*-th cross-sectional area by the formula:

$$ \left(A_i \right)_{k+1} = \left(A_i \right)_k \cdot \left(1 + \sum_{n=1}^{N_F} \left(z_n \cdot {}^{A}\tilde{S}_{i,n} \right)_k \right), \tag{19} $$

and similarly for computation of *i*-th element length the following formula was derived

$$ \left(L_i \right)_{k+1} = \left(L_i \right)_k \cdot \left(1 + \sum_{n=1}^{N_F} \left(z_n \cdot {}^{L}\tilde{S}_{i,n} \right)_k \right), \tag{20} $$

where N_F is number of the prescribed formant frequencies, z_n is a function of the difference between the desired eigenfrequency $f_{n,d}$ and the instantaneous *n*-th eigenfrequency $f_{n,k}$ in the *k*- th step

$$z_n = \alpha \cdot \frac{f_{n,d} - f_{n,k}}{f_{n,k}} \ , \tag{21}$$

α is an additional coefficient that can accelerate the iterative process and it was typically set to $\alpha = 10$.

The iteration procedure stopped when the root of the sum of the squared differences between desired and instantaneous eigenfrequencies

$$\delta = \sqrt{\sum \left(f_{nd} - f_{nk} \right)^2} \tag{22}$$

was less than a desired tolerance value. This value was set in the computations to 10 Hz in all cases.

First five formants F1 – F5 were used for modeling of the vowel [a:] and first four formants F1 – F4 for modeling the vowels [i:] and [u:]. The speed of sound, the density, and the dynamic viscosity of the air were considered as follows: c_o= 353 ms^{-1}; ρ_o = 1.2 kgm^{-3}, μ = 1.8·10^{-5} kgm^{-1}s^{-1}. The number of iteration steps needed for computation of the geometry of the vocal tract for the vowel [a:] was 65 for before and 187 for after the warm up, for the vowel [i:] 34 iterations for before and 35 for after, and for the vowel [u:] it was 24 iterations for before and 26 iterations for after warm up. The numerical simulation of the acoustic pressure at the lips was performed in the frequency domain by random excitation of the vocal tract at the level of the vocal folds. Computational time was from 12s to 31s on PC Intel Core i5-670, 3.47 GHz, 3.49 GB RAM.

Figures 5-7 show the computed vocal tract shapes, the cross-sectional areas and the spectra of the numerically simulated acoustic signals at the lips for all three vowels before and after the warm-up.

7. Comparison of the audio and MRI results with modeling

The formant frequencies resulting from the optimization procedure are compared with the prescribed formants obtained from the acoustic analyses in Table 3. All formant frequencies after the optimization procedures are within the prescribed limit of 10 Hz.

The SPL values resulted from modeling are compared with the measured acoustic data in Table 4. The SPL values in the total frequency region 0–5 kHz analyzed have the same tendency in the measurements and in modeling, in both cases the SPL_{total} values decreased slightly after the vocal exercising for vowel [a:] and increased for the vowels [i:] and [u:]. The SPL values ($SPL_{\Delta sf}$) measured within the singer´s formant clustering frequency range Δ_{sf} increased for vowel [a:] by 15.2 dB and for the vowels [i:] and [u:] by 18.0 dB and 21.5 dB, respectively. Corresponding computed $SPL_{\Delta sf}$ values increased after the warm up by 0.6 dB, 2.2 dB and 6.7 dB.

The singer's formant clustering in the intervals Δ_{SF} between the formants F3 and F5 for vowel [a:], between the formants F2 and F4 for vowel [i:] and between F3 and F4 for vowel [u:] corresponds well with the measured frequency bands (compare the measured acoustic spectra in Fig. 4 with the spectra in Figs. 5–7 for modeling). After the vocal exercising the formants F_1 and F_2 of [a:] remained nearly unchanged while the formants F_3–F_5 were clustering, thereby increasing the SPL level in the frequency band of 2-4 kHz. The distance between F_3 and F_5 in the acoustic measurement decreased from 1270 Hz down to 890 Hz, and in the modeling the distance between these formants decreased from 1280 Hz to 901 Hz (see Table 4). Similarly for vowel [i:] the distance between F_2 and F_4 decreased from 1300 Hz to 1030 Hz in the measurement and from 1303 Hz to 1041 Hz in modeling. For vowel [u:] the distance between F3 and F4 decreased from 910 Hz down to 690 Hz in the measurement and from 903 Hz to 703 Hz in modeling. Thus, the singer's formant clustering frequency bandwidths Δ_{SF} in modeling decreased substantially and in good agreement with the acoustic measurements, the decrease is about 380 Hz for the vowel [a:], 270 Hz for vowel [i:] and 220 Hz for vowel [u:] (see Table 4).

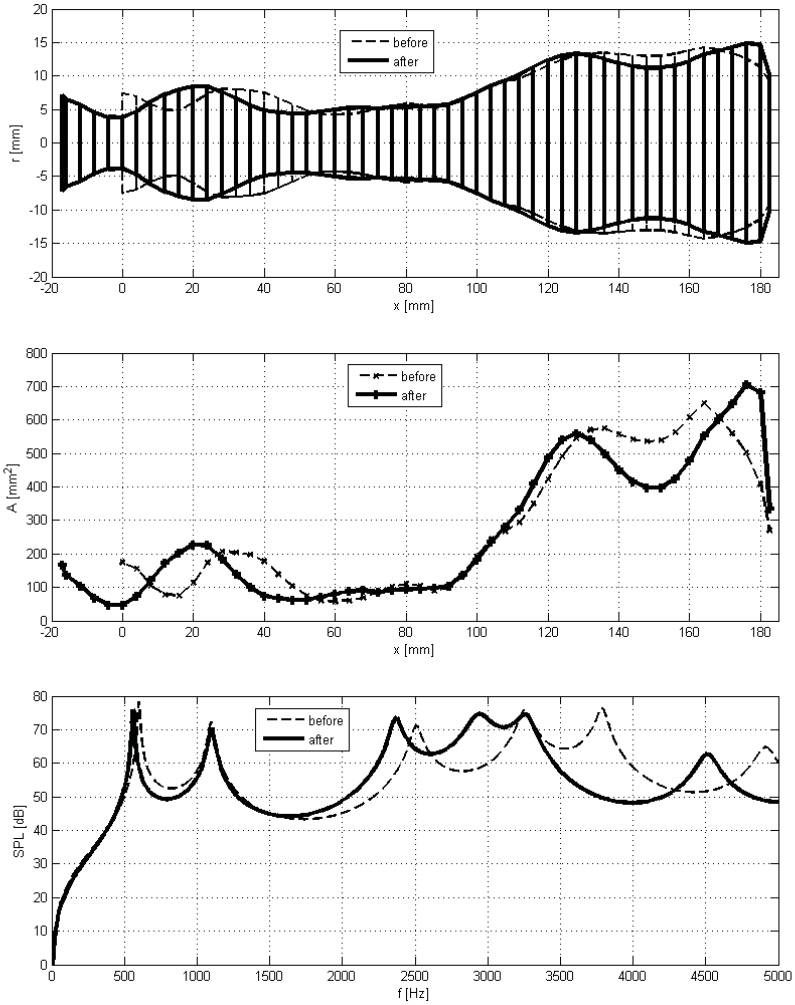

Fig. 5: Vocal tract geometry (top panel - from the vocal folds on the left to the lips on the right), cross-sectional areas along the vocal tract (middle panel) and acoustic pressure at the lips (lower panel) – results of modeling for vowel [a:] before and after the vocal exercise.

The geometrical changes resulting from modeling (see Figs. 5–7) can be compared with the MRI midsagittal slices shown in Fig. 1. The most important change in the vocal tract geometry for vowel [a:] was the prolongation of the vocal tract by lowering of the larynx. The changes in the oral cavity that can be realized by changes of the tongue position and/or by the lips opening are not well visible in the MR images, because the subject had some small metal piece in his lower jaw and therefore the images near the lower lip are of poor quality and the comparison between the modeling and MRI in this vocal tract region is problematic. For the vowels [i:] and [u:], the most important changes were also the prolongation of the vocal tract at the vocal folds end due to a downward shifting of the larynx and the lower pharynx. The main change in the vocal tract geometry for the vowel [i:] was the increase of the vocal tract volume in the upper pharynx (compare Figs. 1 and 6).

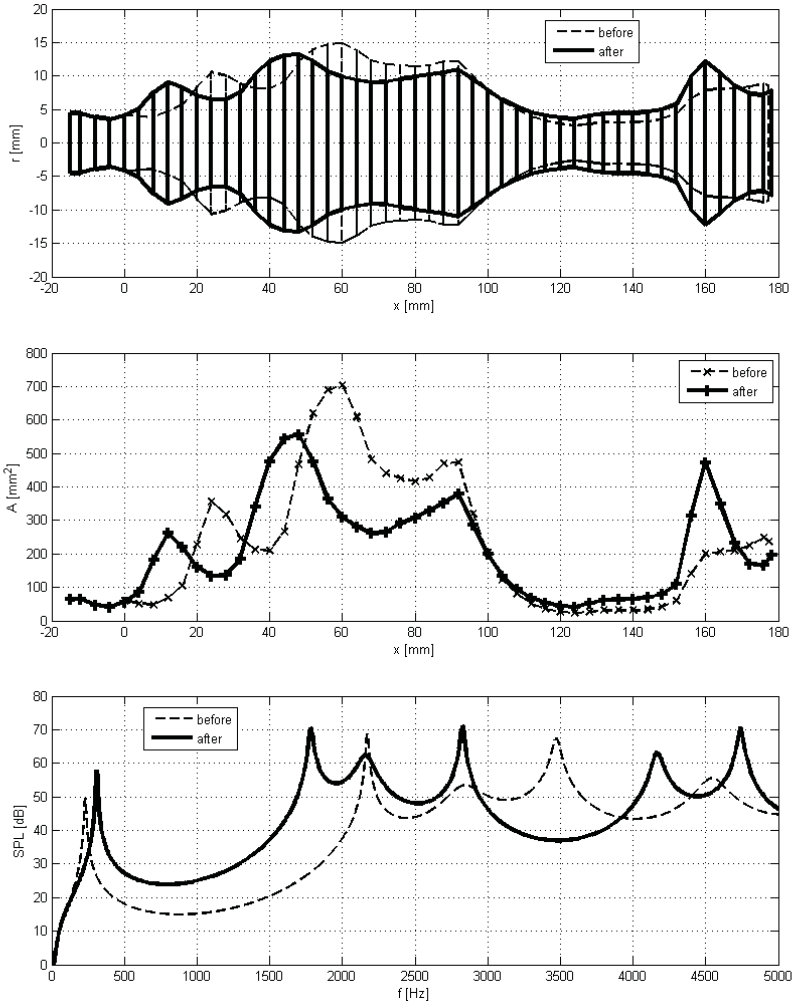

Fig. 6: Vocal tract geometry (top panel - from the vocal folds on the left to the lips on the right), cross-sectional areas along the vocal tract (middle panel) and acoustic pressure at the lips (lower panel) – results of modeling for vowel [i:] before and after the vocal exercise.

The area ratio $R=A_{ph}/A_{ep}$ of the vocal tract cross-sections (the inlet of the lower pharynx over the outlet of the epilarynx) for the model were measured from the computed areas shown in Figs. 5 – 7 taking into account the epilarynx length (EP) specified in Table 1. The area ratios are summarized in Table 5 for all three vowels and compared with the ratios obtained from the volume model of the vocal tract (see Fig. 2 and Table 2). Results from modeling were from 1.82 to 5.02 for phonation before and from 2.35 to 4.10 for phonation after the exercising. The area ratios measured from the MRI, where from 3.60 to 4.56 for phonation before and from 3.33 to 4.39 for phonation after exercising. It should be noted that an exact quantitative comparison of the area ratios measured from the MRI and modeling is problematic, because the ratio value is sensitive to the specifically chosen cross-sections. However, the tendency in the changes of the ratio before and after the vocal exercising is the same for modeling and MRI measurements, the increase of the area ratio for the vowel [a:] and the decrease for the vowels [i:] and [u:] – see R_{after}/R_{before} in Table 2. The area ratios measured and modeled for all vowels after exercising were found to be between 2.35 and 4.39 (see Table 5). These values are lower than the hypothetical ratio 6 considered being optimal for the establishment of a singer's formant cluster by

Sundberg and Fant (Sundberg, 2003), however the present results are in agreement with the results by Detweiler (1994), where the ratio was found between 2.9 and 3.7.

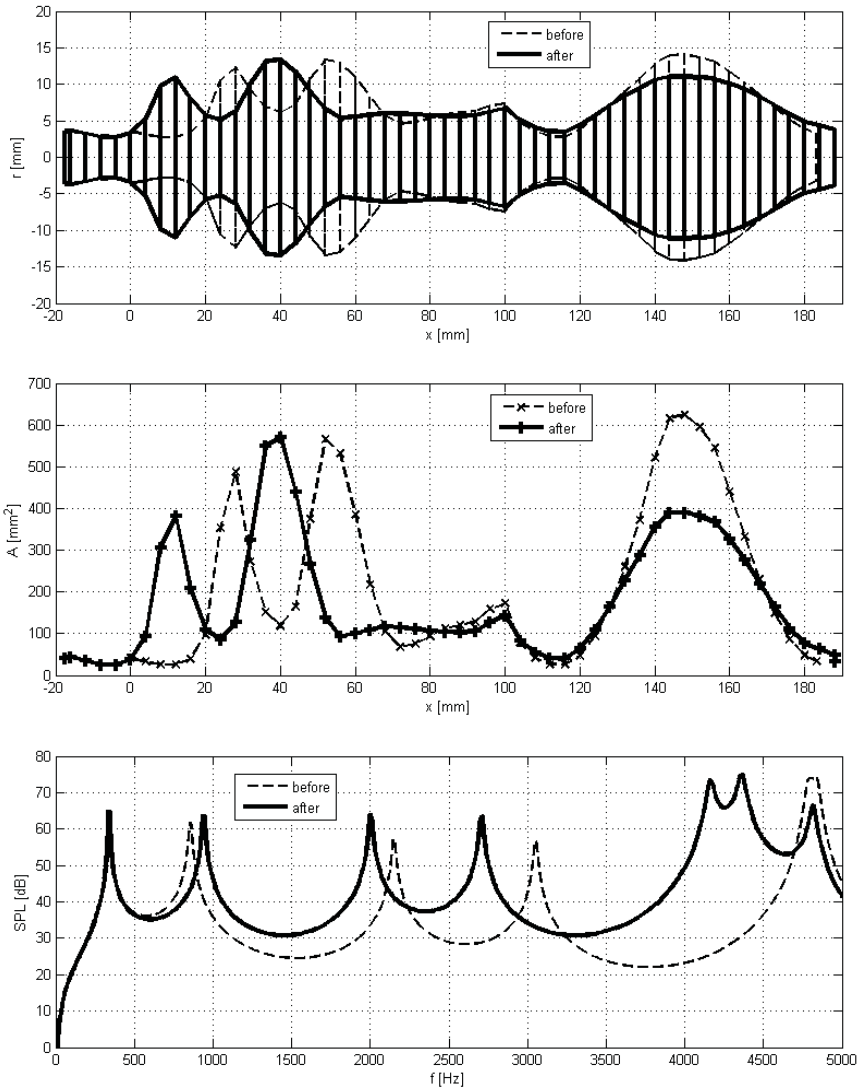

Fig. 7: Vocal tract geometry (top panel - from the vocal folds on the left to the lips on the right), cross-sectional areas along the vocal tract (middle panel) and acoustic pressure at the lips (lower panel) – results of modeling for vowel [u:] before and after the vocal exercise.

Table 4: Comparison of the measured and modeled results for the vowels [a:], [i:] and [u:] before and after the vocal exercise: (a) the frequency distance Δ_{SF} between the formants important for creation the singer's formant cluster, (b) the SPL computed in the frequency bandwidth Δ_{sf} of the singer's formant cluster ($SPL_{\Delta_{sf}}$) and (c) the SPL_{total} computed in the total frequency range considered.

[a:]		$\Delta_{SF} = F_5 - F_3$ [Hz]	$SPL_{\Delta_{sf}}$ [dB] Δ_{sf} = 2-4 kHz	SPL_{total} [dB] 0 – 5 kHz
before exercising	acoustic signal	1270	55	77.8
	modeling	1280	128.2	131.5
after exercising	acoustic signal	890	70.2	76.9
	modeling	901	128.8	131.4
differences	acoustic signal	-380	15.20	-0.90
after - before	modeling	-379	0.60	-0.10

[i:]		$\Delta_{SF} = F_4 - F_2$ [Hz]	$SPL_{\Delta_{sf}}$ [dB] Δ_{sf} = 1.4-4 kHz	SPL_{total} [dB] 0 – 5 kHz
before exercising	acoustic signal	1300	50.8	59.3
	modeling	1302	115.3	118.0
after exercising	acoustic signal	1030	68.8	70.2
	modeling	1043	117.5	122.0
differences	acoustic signal	-270	18.0	10.9
after - before	modeling	-259	2.2	4.0

[u:]		$\Delta_{SF} = F_4 - F_3$ [Hz]	$SPL_{\Delta_{sf}}$ [dB] Δ_{sf} = 1.8-3.5 kHz	SPL_{total} [dB] 0 – 5 kHz
before exercising	acoustic signal	910	31.3	60.3
	modeling	903	99.1	116.6
after exercising	acoustic signal	690	52.8	68.4
	modeling	704	105.8	122.7
differences	acoustic signal	-220	21.5	8.1
after - before	modeling	-199	6.7	6.1

Table 5: Comparison between the MRI measurement and the modeled cross-sectional area ratios measured inside the vocal tract at the lower pharynx (A_{ph}) and upper epilarynx (A_{ep}) for the vowels [a:], [i:] and [u:] before and after the vocal exercise.

Area ratios $R = A_{ph}$ [mm^2] / A_{ep} [mm^2]		**[a:]**	**[i:]**	**[u:]**
before exercising - R_{before}	modeling	207/114=1.82	356/104=3.42	487/97=5.02
	MRI	3.60	4.56	3.62
after exercising - R_{after}	modeling	228/97=2.35	262/86=3.05	381/93=4.10
	MRI	4.12	4.39	3.33
R_{after}/R_{before}	modeling	1.29	0.89	0.82
	MRI	1.14	0.96	0.92

8. Conclusions

The area ratios of the lower pharynx over the epilaryngeal tube were lower than earlier hypothesized for the male singers' voice. The results suggest that the origin of the singer's formant is not necessarily associated with an increase of the pharyngeal over the epilaryngeal cross-sectional area ratio but can also be obtained by other geometrical changes of the vocal tract cavity. The conclusions should be considered with caution because all results are only for one subject investigated.

Acknowledgement

The research was supported by the projects GAČR P101/12/P579 (modeling part) and GAČR P101/12/1306 (experimental part). The authors are also very grateful to Doc. MUDr. Petr Krupa from the Hospital U Svaté Anny in Brno for enabling the MRI measurements.

References

Detweiler, R.F. (1994) An investigation of the laryngeal system as the resonance source of the singer's formant. *Journal of Voice,* 8, 4, pp.303-313

Fant, G. (1960) *Acoustic theory of speech production*. Mouton, S'Gravenage, 2nd ed.

Laukkanen, A-M., Horáček, J., Krupa, P. & Švec, J.G. (2011) The effect of phonation into a straw on the vocal tract adjustments and formant frequencies. A preliminary MRI study on a single subject completed with acoustic results. *Biomedical Signal Processing and Control*. DOI 10.1016/j.bspc.2011.02.004.

Leino, T. (1994) Long-term average spectrum study on speaking voice quality in male actors, in: SMAC93, *Proceedings of the Stockholm Music Acoustics Conference*, (A. Friberg, J. Iwarsson, E. Jansson & J. Sundberg eds) The Royal Swedish Academy of Music, No 79, Stockholm, pp.206-210.

Leino, T., Laukkanen, A.M. & Radolf, V. (2011) Formation of the Actor's/Speaker's Formant: A Study Applying Spectrum Analysis and Computer Modeling. *Journal of Voice*, 25(2), pp. 150-158.

Radolf, V. (2010) Direct and inverse task in acoustics of the human vocal tract. *PhD . thesis*, Czech Technical University in Prague, 95 p.

Story, B.H. (2003) Using imaging and modeling techniques to understand the relation between vocal tract shape to acoustic characteristics, in: *Proc. of the Stockholm Music Acoustics Conf.* (SMAC 03), Stockholm, Sweden, pp. 435-438.

Story, B.H. (2006) Technique for "tuning" vocal tract area functions based on acoustic sensitivity functions, *Journal of the Acoustical Society of America,* 119(2), pp. 715-718.

Sundberg, J. (1974) Articulatory interpretation of the "singing formant". *Journal of the Acoustical Society of America,* 55 (4) pp. 838-844.

Sundberg, J. (2003) Research on the singing voice in retrospect. *Speech, Music and Hearing*, *TMH-QPSR,* Vol. 45, KTH Stockholm, pp. 11-22.

Titze, I.R. (2000) *Principles of voice production*. National Center for Voice and Speech, Iowa City, IA

Titze, I.R. & Story, B.H. (1997) Acoustic interactions of the voice source with the lower vocal tract, *Journal of the Acoustical Society of America,* 101, 4, pp. 2234–2243.

Vampola, T., Horáček, J. & Švec, J.G. (2008) FE modeling of human vocal tract acoustic. Part I: Production of Czech vowels. *Acta Acoustica united with Acoustica*, 94, pp. 433-447.

Vampola, T., Horáček, J., Vokřál, J. & Černý, L. (2008) FE modeling of human vocal tract acoustics. Part II. Influence of velopharyngeal insufficiency on phonation of vowels. *Acustica United with Acta Acustica*, 94, pp. 448-460.

18th International Conference
ENGINEERING MECHANICS 2012
Svratka, Czech Republic, May 14 – 17, 2012

pp. 1103–1107
Paper #33

MECHANICAL DESIGN OF THE ACTIVE ORTHOSIS

T. Ripel[*], J. Krejsa[**]

Abstract: *The paper proposes the design of mechanical components of the device for fully automated rehabilitation of elbow post intra-articular fractures further refered as the active orthosis. Motorized orthoses, which are at present used in physiotherapy, are mostly static and sturdy devices usually fixed with the chair. Active orthosis is (beside more efficient treatment) lighter, more comfortable and easier to handle with, which put specific requirements for its mechanical construction.*

Keywords: ***active, orthosis, rehabilitation, medical aid***

1. Introduction

Rehabilitation of human joints post intra-articular fractures is contemporary realized mostly with assistance of qualified physiotherapists providing full service during the whole process. Utilization of auxiliary electromechanical devices as motorized laths (Homma K., 1997) is ineffective primarily for their limited functions caused by the passive character of the joint movement realization and necessity of the professional personnel attendance. These devices are complex and robust, which makes them stationery therefore bonded to the medical area. The active orthosis is electromechanical device which main advantages are portability and more important active response on patient muscular activity providing assisted movement of the upper limb. Requirements for moderate dimensions, low weight and powerful technical solution make the mechanical design of the device complex task further described in this paper.

The main proposition while designing active orthosis is determination of the method of scanning action forces initiating the movement of the joint. There are several ways from direct sensing of the muscular activity using electromyographic (EMG) sensors (Mulas M., 1995) to indirect measuring of a physical quantity as for example reaction force in the body of the orthosis used in this solution. Requirement for the portability of the device significantly affects mechanical design of the body, especially the joint described in chapter 3. The body of the orthosis is subjected to ergonomic conditions necessary for all medical equipment. Indispensable parts of all devices utilized for health care are safety precautions. Active orthosis has multiple safety system where the mechanical section represents the final instance.

2. Analysis of action forces in the upper limb

Action forces in the upper limb were measured by unique device (Zezula M., 2009) which is able to record behavior of forces depending on actual angle of the elbow. Shape of the curve displaying acting force is flat, however the concept of mechanical solution is resistant to fluctuation of load. The table below shows results of maximal reaction force affecting the forearm 30cm from the elbow. According to figure 1 the fastening elements are similar to system of the active orthosis ensuring identical load.

[*] Ing. Tomáš Ripel.: Institute of Solid Mechanics, Mechatronics and Biomechanics, Brno University of technology, Technicka 2896/2; 616 69, Brno; CZ, e-mail: tripel@centrum.cz

[**] Ing. Jiří Krejsa, Ph.D.: Institute of Solid Mechanics, Mechatronics and Biomechanics, Brno University of technology, Technicka 2896/2; 616 69, Brno; CZ, e-mail: krejsa@fme.vutbr.cz

Tab. 1: Measured action forces

Force	Value	Torque
Direction up	70N	21Nm
Direction down	65N	19,5Nm

Measuring was executed to gain maximal torque which is possible to achieve in human elbow. These values have only informative character considering the various results from each measured person. Actual torque providing by the orthosis will be overdesigned to fit the biggest possible group of patients.

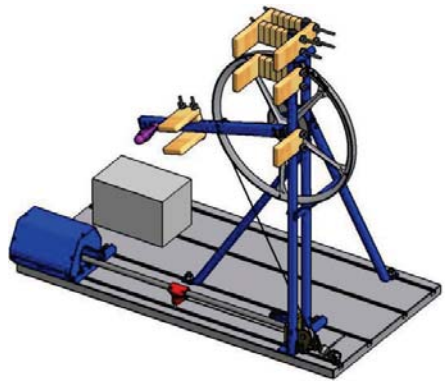

Fig. 1: Device for measuring of action forces in forearm (Zezula M., 2009)

3. Mechanical design

The final form of the mechanical design results especially from the requirement on portability which follows demands on low weight and moderate dimensions. The basic concept consist of the frame, mechanical rotational joint supporting the movement of the elbow, actuator and the fastening belts for fixing to the arm. The mechanical design overview is to be seen on figure 2.

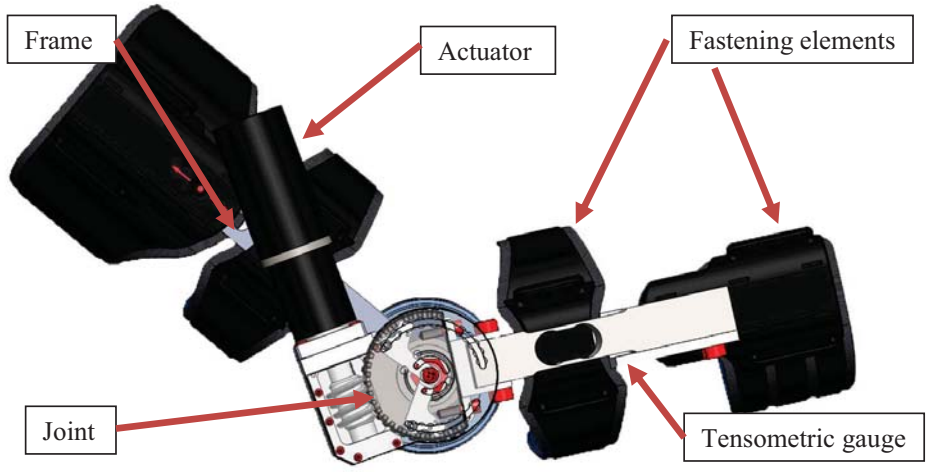

Fig. 2: Mechanical design overview

Before the detailed mechanical solution will be proposed, the function of the device is shortly described:

The active orthosis provides assisted movement of the upper limb fixed in the fastening elements. The device is able to react on patient muscular activity through tensometric gauge (see picture 2). This sensor is part of the frame and it measures patient's effort to move the injured elbow. Based on this information the actuator helps to move the orthosis through mechanical joint in desired direction and range with according sensitivity.

3.1. Frame

The frame of the active orthosis comes out of classical immovable orthosis frequently used to fix position of the joint. It consist of 2 aluminum splints, 4 steel sleeves and tensometric gauge (see chapter 4). Splints are connected through the mechanical joint realized by worm gear described in detail further in this chapter. Design of the frame needs to be adjusted to both requirements for low weight and rigidity. It has to provide full fixation of the arm in all positions.

3.2. Joint

The mechanical joint of the orthosis is realized by worm gear as shown on figure 3. This solution is utilized mainly for self-locking feature and sufficient gear ratio in spite of huge loss caused by friction. Self-locking mechanism allows fixing location of the arm in all position of the operation range. The joint ensures movement of the forearm splint which is bonded to the wheel. The worm embedded it the body of the joint is driven by DC actuator with planetary gearhead (see chapter 4).

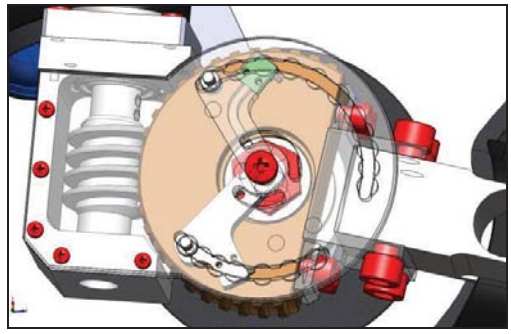

Fig. 3: Mechanical joint

Worm is embedded in radial ball and axial needle bearings as shown on figure 4a. Actuator is connected with the worm using setscrew bearing on the facet in the planetary gearhead shaft. Figure 4b shows bedding of the wheel which is centered on the body of the joint. The joint is equipped with mechanism for adjusting the operation range of the orthosis. The mechanism consists of two handles embedded in the main joint pivot. Each handle is possible to rotate separately around the joint axis and delimit maximal angle of the range. Definition of the proper position is realized by button in the end of the handle, which fits to the round canal on the periphery of the joint cover.

a.)

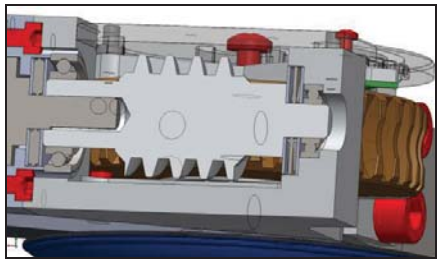

b.)

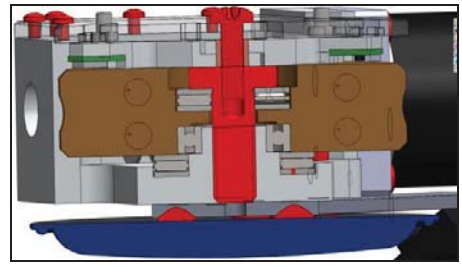

Fig. 4: Mechanical design of worm gear

4. Actuator and sensors

The active orthosis as the electromechanical consist of various electronic devices. The body of the orthosis comprehends also design of cable canals feeding all the electronic from the drive to small printed circuits for the micro switches (see figure 4). In this chapter are briefly described 2 main electronic parts, the actuator and the tensometric gauge.

4.3. Actuator

Design of the power system is difficult task considering there are strict demands on low weight and high power. Based on the calculation comprising all the physical influences the actuator Maxon RE 32 with DC motor of power 70W has been chosen. Actuator consist of planetary gear (66:1) and incremental sensor. The power supply voltage is 24V. Constant torque of the actuator is 2,25 Nm which gives total torque of the device about 50 Nm considering high loss of the worm gear. The value of the maximal torque is overdesigned on purpose. The orthosis is designated for wide spectrum of patients producing various values of load.

4.3. Sensor

For sensing the patients effort to move the arm the tensometric gauge is implemented as a part of the frame. It substitutes the forearm splint where the strain is most significant. Based on information about tension in the sensor is possible to determine the value and direction of the force affecting the forearm. Utilized sensor HBM PW6KRC3 is high sensitive device applicable for forces up to 400N.

5. Safety precautions

Movement of the orthosis out of desired range could harm the patient which is inadmissible. The range is adjustable by mechanism described in chapter 3. In addition to this function handles have also safety character. It serves as bedding for micro switches which stop the movement immediately as the forearm splint reach the boundary position. The mechanism described on figure 5 shows handles and also micro switches (green).

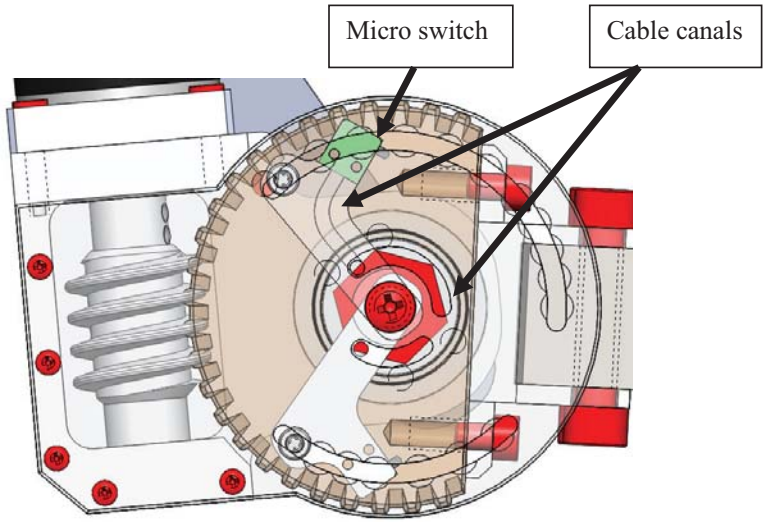

Fig. 5: Electromechanical safety mechanism

Mechanism showed on figure 3 is final instance of safety system, where the high level software represents the main control unit.

6. Conclusions

This paper describes mechanical design of unique medical equipment designated for rehabilitation purposes. Active orthosis is easily portable and compact device allowing fully assisted movement of the upper limb on qualitatively higher level than contemporary rehabilitation aids. Using tensometric gauge as the sensor of patients effort to move the arm it allows sensitive and effective treatment of intra-articular fractures.

The mechanical design fulfills requirement for low weight and moderate dimensions making the device easy to transfer and to manipulate with. The main parameters of the orthosis are in table 2.

Tab. 2: Basic parameters

Basic parameters	
Main dimensions	420x130x120mm
Weight	2,2
Voltage	24V
Actuator	DC motor Maxon RE 32 70W
Sensor	Tensometric gauge PW6KRC3
Maximal torque	50Nm
Operation range	100°
Rotation velocity	3rpm

Acknowledgement

Published results were acquired with the support of project FSI-S-11-15 "Design, testing and implementation of control algorithms with use of nonlinear models of mechatronics systems"

References

Homma, K.; Usuba, M.; Development of Ankle Dorsiflexion/Plantarflexion Exercise Device with Passive Mechanical Joint; Rehabilitation Robotics, 2007. ICORR 2007; p 292 – 297; ISBN 978-1-4244-1320-1

Zezula, M. *Design and realization of Measuring device for determination of human arm force depending on elbow.* Brno: University of technology, Faculty of mechanical engineering, 2009. 44 p

Mulas, M.; Folgheraiter, M.; Gini, G.; *An EMG-controlled Exoskeleton for Hand Rehabilitation;* 9th International Conference on Rehabilitation Robotics; Chicago 2005; p. 371 – 374; ISBN 0-7803-9003-2

Rocon, E.; Ruiz, A.F.; Pons, J.L.; Belda-Lois, J.M.; Sanchez-Lacuesta, J.J.; *Rehabilitation Robotics: a Wearable Exo-Skeleton for Tremor Assessment and Suppression*; IEEE International Conference on Robotics and automation, Barcelona 2005; p. 2271 – 2276; ISBN 0-7803-8914-X

18th International Conference
ENGINEERING MECHANICS 2012
Svratka, Czech Republic, May 14 – 17, 2012

pp. 1109–1117
Paper #79

HOMOGENIZED PHONONIC PLATES AND WAVE DISPERSION

E. Rohan* **R. Cimrman**** **B. Miara*****

Abstract: *We consider the problem of wave propagation in periodically heterogeneous composite plates with high contrasts in elastic coefficients. The unfolding method of homogenization is applied to obtain limit plate models. Due to the high contrast ansatz in scaling the elasticity coefficients of compliant inclusions, the dispersion properties are retained in the limit when the scale of the microstructure tends to zero. We study two plate models based on the Reissner-Mindlin theory and on the Kirchhoff-Love theory. We show that, when the size of the microstructures tends to zero, the limit homogeneous structure presents, for some wavelengths, a negative "mass density" tensor. This means that there exist intervals of frequencies in which there is no propagation of elastic waves, the so-called band-gaps.*

Keywords: ***phononic materials, plate models, homogenization, band gaps, wave dispersion***

1. Introduction

We consider problems of wave propagation in periodically heterogeneous plates with high contrasts in elastic coefficients. Following the approach of Ávila et al. (2008) and Rohan et al. (2009) we apply the unfolding method of homogenization Cioranescu et al. (2008) to obtain limit plate models. Two cases are studied: 1) according to the Reissner-Mindlin theory the plate deformation is described by the mid-plane deflections and by rotations of the plate cross-sections which account for the shear stress effects; 2) using the Kirchhoff-Love theory, the plate deflections are described by the bi-harmonic operator, thus neglecting the shear effects. In both cases we assume such heterogeneities which depend on the mid-plate coordinates only, but do not change with the transversal coordinate. As an example we can consider plates with soft cylindrical inclusions. Under such restrictions the homogenization is applied to the plate equations with the elastic coefficients defined as periodically fluctuating functions associated with the heterogeneities. Due to the high contrast ansatz in scaling the elasticity coefficients of inclusions, as employed in Ávila et al. (2008); Rohan and Miara (2011); Cimrman and Rohan (2009, 2010), dispersion properties are retained in the limit when the scale (the characteristic size) of the microstructure tends to zero.

We show that, when the size of the microstructures tends to zero, the limit homogeneous structure presents the phononic effect: for some wavelengths, a "mass density" tensor can be negative, see Rohan and Miara (2011). This means that there exist intervals of frequencies in which there is no propagation of elastic waves, the so-called band-gaps.

2. Heterogeneous plates

We consider heterogeneous structures associated with a given scale, say $\varepsilon_0 > 0$, which is the ratio between the characteristic lengths of the microscopic and the macroscopic description. There exist sequences of solutions of the plate problems characterized by scales $\varepsilon \to 0$. For any fixed $\varepsilon > 0$ we shall rely on the following essential material properties.

The fourth order, bi-dimensional elasticity tensor $\mathbb{C} = (C^{ijkl})$ is symmetric $C_{ijkl} = C_{klij} = C_{ikjl}$ and positive definite. In particular, for the sake of simplicity, we consider isotropic materials only, which

*Prof. Dr. Ing. Eduard Rohan: Faculty of Applied Sciences, University of West Bohemia in Pilsen, Univerzitní 22, 306 14 Plzeň; CZ, e-mail: rohan@kme.zcu.cz

**Ing. Robert Cimrman, Ph.D.: New Technologies Research Centre, University of West Bohemia in Pilsen, Univerzitní 22, 306 14 Plzeň; CZ, e-mail: cimrman3@ntc.zcu.cz

***Prof. Bernadette Miara: Université Paris-Est, ESIEE, Département de Modélisation et simulation numérique. Cité Descartes, 2 Boulevard Blaise Pascal, 93160 Noisy-le-Grand Cedex; France, e-mail: b.miara@esiee.fr

are characterized by two Lamé parameters. The plate model according the Reissner-Mindlin theory involves also the shear modulus, here denoted by $\gamma > 0$, which is associated with one of the Lamé parameters. The mass density ρ is positive.

We treat periodic composite materials, so that the material coefficients $\mathbb{C}$, γ and ρ are periodically oscillating functions in $\mathbb{R}^2$; it will be described in detail in Section 3.1.

2.1. The Reissner–Mindlin plate model

The plate model can be derived by an asymptotic analysis of the elasticity problem imposed in $\Omega\times]-h,h[$, where $\Omega \subset \mathbb{R}^2$ is an open bounded domain with regular boundary $\partial\Omega$ and h is the plate thickness. In the time interval $[0,T]$ the plate undergoes the following two modes of displacements: the in-plane "membrane modes" described by $\boldsymbol{U} = (U_1, U_2) : [0,T] \times \bar{\Omega} \longrightarrow \mathbb{R}^2$, and the "off-plane" transversal deflections $W : [0,T] \times \bar{\Omega} \longrightarrow \mathbb{R}$; moreover the cross-sections undergo rotations $\boldsymbol{\Theta} = (\Theta_1, \Theta_2) : [0,T] \times \bar{\Omega} \longrightarrow \mathbb{R}^2$.

The displacement and rotation $(\boldsymbol{U}, W, \boldsymbol{\Theta})$ of the plate satisfy the equilibrium equations

$$\left\{\begin{array}{rl} h\rho\dfrac{\mathrm{d}^2}{\mathrm{d}t^2}\boldsymbol{U} - h\mathrm{div}\boldsymbol{\sigma}(\boldsymbol{U}) = \boldsymbol{T} & \text{in } \Omega\,, \\ h\rho\dfrac{\mathrm{d}^2}{\mathrm{d}t^2}W - h\mathrm{div}\boldsymbol{\tau}(W,\boldsymbol{\Theta}) = F & \text{in } \Omega, \\ \dfrac{h^3}{3}\rho\dfrac{\mathrm{d}^2}{\mathrm{d}t^2}\boldsymbol{\Theta} - \dfrac{h^3}{3}\mathrm{div}\boldsymbol{\sigma}(\boldsymbol{\Theta}) + h\boldsymbol{\tau}(W,\boldsymbol{\Theta}) = \boldsymbol{M} & \text{in } \Omega, \\ \boldsymbol{U} = \boldsymbol{0}\,, \quad W = 0\,, \quad \boldsymbol{\Theta} = \boldsymbol{0} & \text{on } \partial\Omega\,. \end{array}\right. \tag{1}$$

with $\boldsymbol{\tau}$ and $\boldsymbol{\sigma}$ expressed by the following linear constitutive laws:

$$\left\{\begin{array}{lcll} \boldsymbol{\tau}(W,\boldsymbol{\Theta}) & := & \gamma(\nabla W - \boldsymbol{\Theta}), & \text{shear stress due to relative (to mid-plane) rotation of cross-s.} \\ \boldsymbol{\sigma}(\boldsymbol{\Theta}) & := & \mathbb{C}\boldsymbol{e}(\boldsymbol{\Theta})\,, & \text{normal stress due to bending induced by rotations} \\ \boldsymbol{\sigma}(\boldsymbol{U}) & := & \mathbb{C}\boldsymbol{e}(\boldsymbol{U})\,, & \text{normal stress due to the in-plane membrane modes.} \end{array}\right. \tag{2}$$

In general, we may consider a general decomposition of $\partial\Omega$ with respect tothe above displacements and rotations into the "Neumann" and "Dirichlet" parts of the boundary. However, for the sake of simplicity, we consider the fully supported and clamped plate.

The linearized deformation tensor $e(\boldsymbol{\Theta}) = (e_{ij}(\boldsymbol{\Theta}))$ is given by the symmetric gradient $\boldsymbol{e}(\boldsymbol{\Theta}) = 1/2\,(\partial_j\Theta_i + \partial_i\Theta_j)$, $i,j = 1,2$.

We shall consider solutions in the form of harmonic stationary waves induced by harmonic loading

$$\boldsymbol{T}(x,t) = \boldsymbol{t}(x)\exp\{\mathrm{i}\omega t\}\,, \qquad F(x,t) = f(x)\exp\{\mathrm{i}\omega t\}\,, \qquad \boldsymbol{M}(x,t) = \boldsymbol{m}(x)\exp\{\mathrm{i}\omega t\}\,, \tag{3}$$

where ω is a given frequency, so that

$$\boldsymbol{U}(x,t) = \boldsymbol{u}(x)\exp\{\mathrm{i}\omega t\}\,, \qquad W(x,t) = w(x)\exp\{\mathrm{i}\omega t\}\,, \qquad \boldsymbol{\Theta}(x,t) = \boldsymbol{\theta}(x)\exp\{\mathrm{i}\omega t\}\,. \tag{4}$$

On substituting (3) into (1), we get the following equations governing the amplitudes $(\boldsymbol{u}, w, \boldsymbol{\theta})$:

$$\left\{\begin{array}{rl} -\omega^2 h\rho\boldsymbol{u} - h\mathrm{div}\boldsymbol{\sigma}(\boldsymbol{u}) = \boldsymbol{t} & \text{in } \Omega\,, \\ -\omega^2 h\rho w - h\mathrm{div}\boldsymbol{\tau}(w,\boldsymbol{\theta}) = f & \text{in } \Omega, \\ -\omega^2\dfrac{h^3}{3}\rho\boldsymbol{\theta} - \dfrac{h^3}{3}\mathrm{div}\boldsymbol{\sigma}(\boldsymbol{\theta}) + h\boldsymbol{\tau}(w,\boldsymbol{\theta}) = \boldsymbol{m} & \text{in } \Omega, \\ \boldsymbol{u} = 0, \quad w = 0, \quad \boldsymbol{\theta} = 0 & \text{on } \partial\Omega. \end{array}\right. \tag{5}$$

2.2. The Kirchhoff–Love plate model

The motion of the plate is given by the out-off plate deflections W and by the in-plane (membrane modes) displacements $\boldsymbol{U}$. Let us recall that this kind of plate does not admit any relative rotation of the plate cross-sections w.r.t. the plate mean surface, therefore, it is convenient rather for thin plates.

We shall consider solutions in the form of harmonic stationary waves induced by harmonic loading, see (3). Thus, in analogy with (4), for a given fixed frequency ω, the amplitudes $(\boldsymbol{u}, w)$ satisfy

$$\begin{cases} -\omega^2 h\rho\boldsymbol{u} - h\mathrm{div}\boldsymbol{\sigma}(\boldsymbol{u}) = \boldsymbol{t} \quad \text{in } \Omega\,, \\ \dfrac{h^3}{3}\nabla\nabla : \boldsymbol{\Sigma}(w) - \omega^2\rho\left(hw - \dfrac{h^3}{3}\nabla\cdot\nabla w\right) = f - \nabla\cdot\boldsymbol{m} \quad \text{in } \Omega\,, \\ w = 0, \quad \boldsymbol{n}\cdot\nabla w = 0, \quad \boldsymbol{u} = 0 \quad \text{on } \partial\Omega\,, \end{cases} \tag{6}$$

where $\nabla\nabla v = (\partial^2 v/\partial x_i \partial x_j)$ is the 2nd order differential operator and stresses $\boldsymbol{\sigma}$ and $\boldsymbol{\Sigma}$ are given in terms of the elasticity tensor, as follows:

$$\begin{aligned} \boldsymbol{\sigma}(\boldsymbol{u}) &= \mathbb{C}\boldsymbol{e}(\boldsymbol{u})\,, \\ \boldsymbol{\Sigma}(w) &= \mathbb{C}\nabla\nabla w = \boldsymbol{\sigma}(\nabla w)\,. \end{aligned} \tag{7}$$

In the rest of the paper we consider just the out-of-plane "deflection" and "rotation" modes of plate deformation, since, in the linear theory used here, there is no coupling between these modes and the "membrane" modes described by displacements $\boldsymbol{u}$. The "membrane" modes are driven by the same type of equations as in the 3D elasticity which was discussed in papers Ávila et al. (2008); Rohan et al. (2009); Cimrman and Rohan (2009, 2010).

3. Homogenization

We consider a plate made of a heterogeneous material, whereby its periodic structure is defined in the reduced $2D$ configuration directly. As usually, we use small parameter ε describing the characteristic size of the microstructure. The solutions of (5) and (6) depend upon ε, which will be indicated by the superscript $\square^\varepsilon$. Using asymptotic analysis, the limit model for $\varepsilon \to 0$ can be obtained which describes behaviour of the homogenized material. Details on the homogenization procedure are out of the scope in this short paper, interested readers are refered to associated publications Ávila et al. (2008); Rohan and Miara (2011), (Cioranescu et al., 2008).

3.1. Strongly heterogeneous periodic composite

We assume the plate Ω is constituted by the matrix Ω_m and by periodically distributed inclusions; their collection forms domain Ω_c. Thus, we consider

1. $\Omega_m, \Omega_c \subset \Omega \subset \mathbb{R}^2$ and $\Omega_m \cap \Omega_c = \emptyset$,
2. $\Omega = \Omega_m^\varepsilon \cup \Omega_c^\varepsilon \cup \Gamma^\varepsilon$, where $\Gamma^\varepsilon = \overline{\Omega_m^\varepsilon} \cap \overline{\Omega_c^\varepsilon}$.
3. matrix: Ω_m^ε is connected. As the result, inclusions Ω_c^ε are disconnected.

The microstructure is generated as a periodic lattice using the representative periodic cell (RPC) denoted by Y. For simplicity, we consider a rectangular RPC with the following definition: $Y = \Pi_{i=1}^2]0, \bar{y}_i[\subset \mathbb{R}^2$ ($\mathbb{R}$ being the set of real numbers) where $\bar{y}_i > 0$ can be chosen so that $|Y| = 1$. The RPC is decomposed in coherence with Ω, i.e. $Y_m \subset Y$ and $Y_c = Y \setminus \overline{Y_m}$ are strictly contained in Y.

The coordinates of any point in Ω can be split into a "coarse" part $\xi = (\xi_i)$ and a "fine" part $y = (y_i)$, also called fast and slow evolving parts: For a given finite $\varepsilon > 0$ we have the unique decomposition

$$\begin{aligned} x &\equiv \varepsilon \left[\frac{x}{\varepsilon}\right]_Y + \varepsilon \left\{\frac{x}{\varepsilon}\right\}_Y \\ &= \xi + \varepsilon y\,, \quad \text{where } y = \left\{\frac{x}{\varepsilon}\right\}_Y \in Y \quad \text{and } \xi = \varepsilon \left[\frac{x}{\varepsilon}\right]_Y \in \Omega\,, \end{aligned} \tag{8}$$

where $\xi_i = \varepsilon k_i \bar{y}_i$, $i = 1, 2$, $k_i \in \mathbb{Z}$ is the lattice coordinate. Such a decomposition is unique, once $Y \in \mathbb{R}^2$ is defined. Note that $[z_i]_Y$ is the integer part of $z_i/\bar{y}_i$ and $\{z_i\}_Y$ is the remainder.

Material parameters $\mathbb{C}^\varepsilon = (C^\varepsilon_{ijkl})$ and γ^ε are periodically oscillating. For the sake of simplicity we shall consider only piecewise constant material. To retain the phononic effect in the homogenized plate, following the analogous approach employed in the case of phononic 3D periodic structures, we introduce the scaling of the material coefficients in the inclusions:

$$\begin{aligned} \mathbb{C}^\varepsilon(x) &= \chi^\varepsilon_c(x)\varepsilon^2\mathbb{C}^c + \chi^\varepsilon_m(x)\mathbb{C}^m \,, \\ \gamma^\varepsilon(x) &= \chi^\varepsilon_c(x)\varepsilon^2\gamma^c + \chi^\varepsilon_m(x)\gamma^m \,, \end{aligned} \tag{9}$$

We recall the standard properties of constant tensors $\mathbb{C}^c, \mathbb{C}^m$ and coefficients γ^c, γ^m which usually are considered: there exist constants $0 < \underline{m} < \overline{m} < \infty$ independent of ε such that (recall $|\boldsymbol{e}|^2 = e_{ij}e_{ij}$),

$$\begin{aligned} &C^m_{ijkl}e_{ij}e_{kl} \geq \underline{m}|\boldsymbol{e}|^2 \quad \forall \boldsymbol{e} = (e_{ij}) \in \mathbb{R}^{2\times 2}, \quad e_{ij} = e_{ji} \,, \quad \sup_{x\in\Omega}|C^m_{ijkl}| \leq \overline{m} \,, \\ &\underline{m} \leq \gamma^m \leq \overline{m} \,, \end{aligned} \tag{10}$$

and in analogy for $\mathbb{C}^c$ and γ^c. The rotation-deflection coupling coefficient $\gamma^\varepsilon(x)$, i.e. the shear stiffness, is only relevant for the Reissner-Mindlin plate model. It is worth noting that $\mathbb{C}^\varepsilon(x)$ and $\gamma^\varepsilon(x)$ are positive definite for $\varepsilon > 0$ only.

The density of the two materials is assumed to be of the same order of magnitude, therefore we shall consider

$$\begin{aligned} \rho^\varepsilon(x) &= \chi^\varepsilon_c(x)\rho^c + \chi^\varepsilon_m(x)\rho^m \,, \\ \underline{\rho} &\leq \rho^s \leq \overline{\rho} \,, \end{aligned} \tag{11}$$

where $\underline{\rho}, \overline{\rho}$ are given positive real numbers.

Some preliminaries The homogenized model was obtained using the periodic unfolding method which is based on the unfolding operator $\mathcal{T}_\varepsilon : v \in L^1(\Omega;\mathbb{R}) \to L^1(\Omega \times Y;\mathbb{R})$ defined, as follows, see Cioranescu et al. (2008),

$$\mathcal{T}_\varepsilon(v)(x,y) = \; v(\varepsilon\left[\tfrac{x}{\varepsilon}\right] + \varepsilon y) \,, \qquad x \in \Omega, y \in Y \,.$$

We shall use $H^1_\#(Y)$ and $H^2_\#(Y)$, the spaces of periodic (scalar) functions,

$$\begin{aligned} H^1_\#(Y) &= \{v \in H^1(Y) \,|\, v \text{ is Y-periodic } \} \,, \\ H^2_\#(Y) &= \{w \in H^2(Y) |\, w, \nabla_y w \;\text{ are Y-periodic}\} \,, \end{aligned} \tag{12}$$

and the associated space of vector-valued functions $\mathbf{H}^1_\#(Y) = (H^1_\#(Y))^2$.

3.2. Reissner-Mindlin phononic plate

We apply the unfolding method of homogenization to obtain a limit model of the R-M plate for $\varepsilon \to 0$. The elastic standing waves are described by the solution of the following problem with the oscillating material coefficients: For a given frequency, find triplet $(w^\varepsilon, \boldsymbol{\theta}^\varepsilon) \in \left(H^1_0(\Omega)\right)^3$ such that

$$\begin{aligned} &-h\omega^2\int_\Omega \rho^\varepsilon\left(w^\varepsilon z^\varepsilon + \frac{h^2}{3}\boldsymbol{\theta}^\varepsilon\cdot\boldsymbol{\psi}^\varepsilon\right) + h\int_\Omega [\gamma^\varepsilon(\nabla w^\varepsilon - \boldsymbol{\theta}^\varepsilon)]\cdot(\nabla z^\varepsilon - \boldsymbol{\psi}^\varepsilon) + \frac{h^3}{3}\int_\Omega [\mathbb{C}^\varepsilon e(\boldsymbol{\theta}^\varepsilon)] : e(\boldsymbol{\psi}^\varepsilon) \\ &= \int_\Omega (f z^\varepsilon + \boldsymbol{m}\cdot\boldsymbol{\psi}^\varepsilon) \,, \end{aligned} \tag{13}$$

for all $(z^\varepsilon, \boldsymbol{\psi}^\varepsilon) \in \left(H^1_0(\Omega)\right)^3$.

Here we present the homogenized "macroscopic" model which involves homogenized coefficients descibing the effective mass and elasticity coefficients.

The standing waves propagating in the homogenized plate are described in terms of amplitudes $(\boldsymbol{\theta}, w) \in \mathbf{H}_0^1(\Omega) \times \in H_0^1(\Omega)$ which satisfy the following equations:

$$\begin{aligned} &-\omega^2 \int_\Omega \left(\frac{h^3}{3} [\boldsymbol{\mathcal{M}}(\omega^2)\boldsymbol{\theta}] \cdot \boldsymbol{\psi} + h\mathcal{N}(\omega^2) w z \right) \\ &+ \frac{h^3}{3} \int_\Omega [\boldsymbol{\mathcal{D}} \boldsymbol{e}_x(\boldsymbol{\theta})] : \boldsymbol{e}_x(\boldsymbol{\psi}) + h \int_\Omega [\boldsymbol{\mathcal{G}}(\nabla_x w - \boldsymbol{\theta})] \cdot (\nabla_x z - \boldsymbol{\psi}) \\ &= \int_\Omega \left([\boldsymbol{R}(\omega^2)\boldsymbol{m}] \cdot \boldsymbol{\psi} + S(\omega^2) f z \right) \quad \forall \boldsymbol{\psi} \in \mathbf{H}_0^1(\Omega), z \in H_0^1(\Omega) \,, \end{aligned} \tag{14}$$

where $\boldsymbol{\mathcal{D}}$ is the 4th order tensor of homogenized elasticity coefficients see (21), $\boldsymbol{\mathcal{G}}$ is the 2nd order tensor given in (22) describing the shear stiffness of the plate, $\boldsymbol{\mathcal{M}}(\omega^2)$ and $\mathcal{N}(\omega^2)$ are homogenized mass coefficients. Below we explain how these coefficients are computed.

Characteristic microscopic responses. The homogenized coefficients are expressed in terms of the characteristic responses, the so-called corrector basis functions. We proceed in analogy with Ávila et al. (2008) where the 3D elasticity dynamic problems were considered. For the sake of brevity we employ the elasticity bilinear form

$$c_{Y_m}(\tilde{\boldsymbol{u}}, \tilde{\boldsymbol{v}}) = \int_{Y_m} (\mathbb{C}^m \boldsymbol{e}_y(\tilde{\boldsymbol{u}})) : \boldsymbol{e}_y(\tilde{\boldsymbol{v}}) \,. \tag{15}$$

The following characteristic responses depend exclusively on properties of the stiffer material in Y_m; two problems for the so-called corrector basis functions are to be solved:

- Find $\tilde{\boldsymbol{\theta}}^{rs} \in \mathbf{H}^1_{\#}(Y)/\mathbb{R}$ such that

$$c_{Y_m}\left(\tilde{\boldsymbol{\theta}}^{rs} + \boldsymbol{\Pi}^{rs}, \tilde{\boldsymbol{v}}\right) = 0 \quad \forall \tilde{\boldsymbol{v}} \in \mathbf{H}^1_{\#}(Y_m) \,. \tag{16}$$

- Find $\tilde{w}^k \in H^1_{\#}(Y_m)/\mathbb{R}$ such that

$$\int_{Y_m} \gamma^m \nabla_y (\tilde{w}^k + y_k) \cdot \nabla_y \tilde{z} = 0 \quad \forall \tilde{z} \in H^1_{\#}(Y_m) \,. \tag{17}$$

To express the homogenized mass coefficients, we need the eigenfrequencies and eigenfunctions which describe vibration of the inclusions clamped into the matrix. Two eigenvalue problems with discrete spectra are solved:

- Find $(\boldsymbol{\Theta}^r, \lambda^r) \in \mathbf{H}^1_{\#0}(Y) \times \mathbb{R}$ for $r = 1, 2, \ldots$ such that (note $\boldsymbol{\Theta}^r = (\Theta^r_i)$)

$$\fint_{Y_c} [\mathbb{C}^c \boldsymbol{e}_y(\boldsymbol{\Theta}^r)] : \boldsymbol{e}_y(\boldsymbol{\psi}) = \lambda^r \fint_{Y_c} \rho \boldsymbol{\Theta}^r \cdot \boldsymbol{\psi} \quad \forall \boldsymbol{\psi} \in \mathbf{H}^1_{\#0}(Y) \,, \tag{18}$$

- Find $(W^r, \mu^r) \in H^1_{\#0}(Y_c) \times \mathbb{R}$ for $r = 1, 2, \ldots$ such that

$$\fint_{Y_c} [\gamma^c \nabla_y W^r] \cdot \nabla_y \zeta = \mu^r \fint_{Y_c} \rho W^r \zeta \quad \forall \zeta \in H^1_{\#0}(Y_c) \,. \tag{19}$$

The eigenfunctions are normalized, so that

$$\fint_{Y_c} \rho \boldsymbol{\Theta}^r \cdot \boldsymbol{\Theta}^s = \delta_{rs} \,, \qquad \fint_{Y_c} \rho W^r W^s = \delta_{rs} \,. \tag{20}$$

Homogenized coefficients. The homogenized plate elasticity is represented by the following two tensors:

- *Homogenized "in-plane" elasticity* $\mathbb{D} = (\mathcal{D}_{ijkl})$:

$$\begin{aligned}\mathcal{D}_{ijkl} &= c_{Y_m}\left(\tilde{\boldsymbol{\theta}}^{kl} + \boldsymbol{\Pi}^{kl},\, \boldsymbol{\Pi}^{ij}\right) \\ &= c_{Y_m}\left(\tilde{\boldsymbol{\theta}}^{kl} + \boldsymbol{\Pi}^{kl},\, \tilde{\boldsymbol{\theta}}^{ij} + \boldsymbol{\Pi}^{ij}\right)\ .\end{aligned} \tag{21}$$

  The symmetric expression is obtained due to (16).

- *Homogenized shear elasticity* $\boldsymbol{\mathcal{G}} = (\mathcal{G}_{kl})$ introduced as

$$\begin{aligned}\mathcal{G}_{kl} &= \int_{Y_m} \gamma^m \partial_l^y(\tilde{w}^k + y_k) \\ &= \int_{Y_m} \gamma^m \nabla_y(\tilde{w}^k + y_k)\cdot\nabla_y(\tilde{w}^l + y_l)\ .\end{aligned} \tag{22}$$

  The symmetric expression is obtained due to (17).

Inertia of the homogenized plate is represented by the following two mass coefficients, see Ávila et al. (2008); Rohan et al. (2009) for derivation of the analogical mass coefficients in 3D elasticity problems:

$$\begin{aligned}\boldsymbol{\mathcal{M}}(\omega^2) &= \boldsymbol{I}\fint_Y \rho - \sum_r \frac{\omega^2}{\omega^2-\lambda^r}\fint_{Y_c}\rho\boldsymbol{\Theta}^r\otimes\fint_{Y_c}\rho\boldsymbol{\Theta}^r\ , \\ \mathcal{N}(\omega^2) &= \fint_Y \rho - \sum_r \frac{\omega^2}{\omega^2-\mu^r}\left|\fint_{Y_c}\rho W^r\right|^2\ .\end{aligned} \tag{23}$$

Influence of the load is weighted by the load coefficients which are computed by similar formulae

$$\begin{aligned}\boldsymbol{\mathcal{R}}(\omega^2) &= \boldsymbol{I} - \sum_r \frac{\omega^2}{\omega^2-\lambda^r}\fint_{Y_c}\rho\boldsymbol{\Theta}^r\otimes\fint_{Y_c}\boldsymbol{\Theta}^r\ , \\ \mathcal{S}(\omega^2) &= 1 - \sum_r \frac{\omega^2}{\omega^2-\mu^r}\fint_{Y_c}\rho W^r\fint_{Y_c} W^r\ .\end{aligned} \tag{24}$$

As the result of our homogenization procedure, we obtain Problem (14) where $(w, \boldsymbol{\theta})$ are the local amplitudes of harmonic waves excited by harmonic "homogenized" loads with frequency ω. Let us note that, when for some ω the tensor $\boldsymbol{\mathcal{M}}(\omega)$ is positive definite and the scalar $\mathcal{N}(\omega)$ is positive, then also free structure vibrations (i.e. stationary waves in domain Ω) can be excited. However, $\boldsymbol{\mathcal{M}}^*(\omega)$ or $\mathcal{N}(\omega)$ may not by positive (definite) for some ω; for the "membrane mode", cf. Ávila et al. (2008) and Rohan et al. (2009), we proved existence of whole frequency intervals – *the band gaps* – where the positivity of $\boldsymbol{\mathcal{M}}(\omega)$ fails. An analogical result can be proved for the coupled rotational and deflection modes: in each interval of frequencies $\omega^2 \in (\lambda^r, \lambda^{r+1})$ given by (18) there exists a sub-interval of frequencies for which $\boldsymbol{\mathcal{M}}(\omega)$ is not positive. In such intervals, free vibration "rotation modes" are restricted, or completely suppressed. Also for the shear modes associated with the deflection w and the corresponding mass $\mathcal{N}(\omega) < 0$, in each interval of frequencies $\omega^2 \in (\mu^r, \mu^{r+1})$ there exist subintervals with restricted or suppressed wave propagation.

Thus, the band gaps for stationary waves can be predicted just upon analyzing positive definiteness of $\boldsymbol{\mathcal{M}}(\omega)$ and $\mathcal{N}^*(\omega)$. Although for the membrane mode $\boldsymbol{u}$ such band gaps prediction holds also for guided plane waves in infinite plates, see Rohan et al. (2009), for the coupled modes $\boldsymbol{q} := (\boldsymbol{\theta}, w)$ the dispersion analysis is more complex. Interesting applications can be found Vasseur et al. (2008).

3.3. Kirchhoff-Love phononic plate

In analogy with the Reissner-Mindlin plate model (13), we consider the elastic standing waves, cf. Ghergu et al. (2007) for the plate homogenization. We find solutions to the following problem with the oscillating material coefficients: For a given frequency, find deflection $w^\varepsilon \in H^2_0(\Omega)$ such that

$$\begin{aligned} -\omega^2 h \int_{\Omega^\varepsilon_c} \rho^c w^\varepsilon v - \omega^2 h \int_{\Omega^\varepsilon_m} \rho^m w^\varepsilon v - \omega^2 \frac{h^3}{3} \int_{\Omega^\varepsilon_m} \rho^m \nabla w^\varepsilon \cdot \nabla v - \omega^2 \frac{h^3}{3} \int_{\Omega^\varepsilon_c} \rho^c \nabla w^\varepsilon \cdot \nabla v \\ + \frac{h^3}{3} \int_{\Omega^\varepsilon_m} \mathbb{C}^m \nabla\nabla w^\varepsilon : \nabla\nabla v + \varepsilon^2 \frac{h^3}{3} \int_{\Omega^\varepsilon_c} \mathbb{C}^c \nabla\nabla w^\varepsilon : \nabla\nabla v \\ = \int_\Omega (f v + \boldsymbol{m} \cdot \nabla v) \qquad \forall v \in H^2_0(\Omega) \,. \end{aligned} \tag{25}$$

To present the homogenization result for $\varepsilon \to 0$, we proceed in analogy with the case of the Reissner-Mindlin plates. Using the unfolding method of homogenization Cioranescu et al. (2008) and obtain the following equation for the transversal deflections $w \in H^2_0(\Omega)$ such that

$$\begin{aligned} -\omega^2 h \int_\Omega \bar\rho w v - \omega^2 \frac{h^3}{3} \int_\Omega (\boldsymbol{\mathcal{M}}(\omega^2) \nabla w) \cdot \nabla v + \frac{h^3}{3} \int_\Omega (\boldsymbol{\mathcal{D}} \nabla\nabla w) : \nabla\nabla v \\ = \int_\Omega \left([\boldsymbol{R}(\omega^2) \boldsymbol{m}] \cdot \nabla v + f v \right) \quad \forall v \in H^2_0(\Omega) \,, \end{aligned} \tag{26}$$

where $\bar\rho$ is the average density of both material components situated in Y. Above $\boldsymbol{\mathcal{D}}$ is the 4th order homogenized bending stiffness tensor defined below in (31) and $\boldsymbol{\mathcal{M}}(\omega^2)$ is the homogenized mass tensor computed using a similar expression to (23), see (32). The "effective material parameters" are defined in terms of the characteristic microscopic responses.

Characteristic microscopic responses. In contrast with the Reissner-Mindlin plates, the cross-section rotations in the Kirchhoff-Love theory are fully determined by the gradients of deflections; consequently only two instead of four microscopic problems must be solved. The corrector basis function $\tilde w^{kl} \in H^2_\#(Y_m)$ solves the following equation

$$\int_{Y_m} \left[\mathbb{C}^m \nabla\nabla_{yy} (\tilde w^{kl} + \Pi^{kl}) \right] : \nabla\nabla_{yy} \tilde v = 0 \quad \forall \tilde v \in H^2_\#(Y) \,, \tag{27}$$

where $\Pi^{kl} = y_k y_l$. To compute the homogenized mass tensor, one needs to solve the local problem: find $(\lambda^r, \boldsymbol{\varphi}^r) \in \mathbb{R} \times \boldsymbol{W}(Y_c)$ satisfying

$$\int_{Y_c} [\mathbb{C}^c \nabla_y \boldsymbol{\varphi}^r] : \nabla_y \boldsymbol{\vartheta} = \lambda^r \int_{Y_c} \rho \boldsymbol{\varphi}^r \cdot \boldsymbol{\vartheta} \qquad \forall \boldsymbol{\vartheta} \in \boldsymbol{W}(Y_c) \,, \tag{28}$$

where we employ the spaces of rotation-free vector fields:

$$\boldsymbol{W}(Y_c) = \{ \boldsymbol{w} \in \mathbf{H}^1_\#(Y_c) |\ \nabla_y \times \boldsymbol{w} = 0 \} \,. \tag{29}$$

Obviously, due to the ellipticity of the operator in (28), functions $\{\boldsymbol{\varphi}^r\}_r$ are orthogonal; we use the standard normalization

$$\int_{Y_c} \rho \boldsymbol{\varphi}^r \cdot \boldsymbol{\varphi}^s = \delta_{rs} \,. \tag{30}$$

Homogenized coefficients The homogenized Kirchhoff-Love plate model involves the following material coefficients defined in terms of the characteristic responses just introduced:

- *Homogenized elastic coefficients* $\boldsymbol{\mathcal{D}} = (\mathcal{D}_{ijkl})$

$$\begin{aligned} \mathcal{D}_{ijkl} &= \fint_{Y_m} [\mathbb{C}^m \nabla\nabla_{yy} (\tilde w^{kl} + \Pi^{kl})] : \nabla\nabla_{yy} \Pi^{ij} \\ &= \fint_{Y_m} [\mathbb{C}^m \nabla\nabla_{yy} (\tilde w^{kl} + \Pi^{kl})] : \nabla\nabla_{yy} (\pi^{ij} + \Pi^{ij}) \end{aligned} \tag{31}$$

  where the symmetric expression follows due to (27);

- *Homogenized mass tensor* $\boldsymbol{\mathcal{M}} = (\mathcal{M}_{ij})$

$$\boldsymbol{\mathcal{M}}(\omega^2) = \boldsymbol{I} \fint_Y \rho - \sum_{r\geq 1} \frac{\omega^2}{\omega^2 - \lambda^r} \fint_{Y_c} \rho \boldsymbol{\varphi}^r \otimes \fint_{Y_c} \rho \boldsymbol{\varphi}^r \ . \tag{32}$$

- *Homogenized load coefficient* $\boldsymbol{\mathcal{R}} = (\mathcal{R}_{ij})$

$$\boldsymbol{\mathcal{R}}(\omega^2) = \boldsymbol{I} - \sum_{r\geq 1} \frac{\omega^2}{\omega^2 - \lambda^r} \fint_{Y_c} \rho \boldsymbol{\varphi}^r \otimes \fint_{Y_c} \boldsymbol{\varphi}^r \ . \tag{33}$$

By virtue of the right-hand side expression in (32), $\boldsymbol{\mathcal{M}}(\omega^2)$ can be negative, or negative semi-definite for some frequencies ω. In such a case, wave propagation can be restricted or even suppressed for modes characterized by the deflection gradient $\boldsymbol{\psi} := \nabla w$ being the eigenvector associated with the non-positive eigenvalue of $\boldsymbol{\mathcal{M}}(\omega^2)$. However, the theory explained in Ávila et al. (2008) for the standard 3D elasticity must be adapted because the first left hand side term in (26) does not change its sign and contributes to the positive inertia even for negative $\boldsymbol{\mathcal{M}}(\omega^2)$.

4. Conclusions

We presented homogenized models of wave propagation in strongly heterogeneous plates, considering the Reissner-Mindlin (R-M) and the Kirchhoff-Love (K-L) theories; while the first one takes into account shear effects related to rotations of the plate cross-section with respect tothe mid-plane, the second theory neglects this phenomenon, thus, being convenient for thin plates only. The homogenization results reveal dispersion properties for the homogenized R-M plates: we claim that there exist bands of frequencies for which the wave equations admit evanescent solutions only, at least for certain polarizations. There is remarkable difference between the R-M and K-L models: while for R-M the wave polarization is determined by components of $(\boldsymbol{\theta}, w)$, i.e. the rotation and deflection, for K-L there is just a scalar wave associated with the deflection w. Existence of the band gap effect for the K-L plates is to be examined in a more detail.

The phononic effect, in general, is associated with vibration modes excited at the "microscopic" level. By virtue of definitions (23) and (32), these modes determine "positivity", or "negativity" of the homogenized masses; in Ávila et al. (2008) we described how this observation can be employed to predict band gaps. The classical method of the band gap identification is based on analysis of guided waves, thus, upon construction of dispersion curves; it is necessary to compute frequencies for selected wave numbers ranging the Brillouin zone, cf. Rohan et al. (2009).

In a forthcoming publication we will study dispersion properties and band gaps distributions for some basic microstructures. An important restriction of both presented models is related to the transversal isotropy: here only cylindrical inclusions are admissible, although their shapes can be arbitrary. To treat more general composite plates with e.g. spheroidal inclusions, the homogenization procedure must be applied to a 3D composite with thickness proportional to ε, i.e. to the microstructure scale.

Acknowledgments

The research of E.R. was supported by the European Regional Development Fund (ERDF), project "NTIS – New Technologies for Information Society", European Centre of Excellence,

CZ.1.05/1.1.00/02.0090, and in part by the Czech Scientific Foundation project GACR P101/12/2315.

References

Ávila, A., Griso, G., Miara, B., and Rohan, E. (2008). Multiscale modeling of elastic waves: Theoretical justification and numerical simulation of band gaps. *Multiscale Modeling & Simulation, SIAM*, 7:1–21.

Cimrman, R. and Rohan, E. (2009). Three-phase phononic materials. *Appl. Comp. Mech.*, 3:516.

Cimrman, R. and Rohan, E. (2010). On acoustic band gaps in homogenized piezoelectric phononic materials. *Appl. Comp. Mech.*, 4:89–100.

Cioranescu, D., Damlamian, A., and Griso, G. (2008). The periodic unfolding method in homogenization. *SIAM Journal on Mathematical Analysis*, 40(4):1585–1620.

Ghergu, M., Griso, G., Mechkour, H., and Miara, B. (2007). Homogenization of thin perforated plates. *ESAIM: Mathematical Modelling and Numerical Analysis*, 56:875–895.

Rohan, E. and Miara, B. (2011). Band gaps and vibration of strongly heterogeneous reissner-mindlin elastic plates. *Comptes Rendus Mathematique*, 349:777–781.

Rohan, E., Miara, B., and Seifrt, F. (2009). Numerical simulation of acoustic band gaps in homogenized elastic composites. *International Journal of Engineering Science*, 47:573–594.

Vasseur, J., Deymier, P., Djafari-Rouhani, B., and Pennec, Y. (2008). Absolute forbidden bands and waveguiding in two-dimensional phononic crystal plates. *Phys. Rev. B*, 77.

18th International Conference
ENGINEERING MECHANICS 2012
Svratka, Czech Republic, May 14 – 17, 2012

pp. 1119–1122
Paper #109

UNSTEADY MEASUREMENTS OF AERODYNAMIC CHARACTERISTICS OF THE AIRFOIL

D. Rozehnal*

Abstract: *This paper deals with unsteady measurements of aerodynamic characteristics of the symmetric airfoil for the angle of attack within the range from 0° to 360° with variable value of angular velocity. These results are processed for first and second revolution of airfoil NACA 0012 Mod. A special device was designed for these tests.*

Keywords: *Unsteady Aerodynamic, Dynamic Stall, Measurement, Wind Tunnel Tests.*

1. Introduction

Measurement is an integral part of the design, development and practical verification of real qualities of the proposed devices. Their use in aerodynamic applications is an integral part of development of aviation and rocket technology from the outset.

The article is a continuation of the topic presented by the author at the conference EM in the past. The new results were obtained in the Department of Aircraft and Rocket Techniques, Defense University in Brno in the period from 2006 until now.

Aerodynamic measurements are still irreplaceable in the development of new aviation techniques, although the current period is characterized by intensive development of numerical methods and computer simulations of all kinds.

Computational methods are still inconclusive in the areas of simulation blowing unconventional aircraft and do not provide sufficiently reliable results for engineers. Incorrect input aerodynamic data may cause either significant time lag in development of new aircraft, or may also lead to significant financial losses and problems associated with the late start of the new product to market. In the numerical calculations can be considered one of the main problems the absence of input and boundary conditions, which would properly characterize the real aerodynamic effects.

In the rapid and large changes of angle of attack are stationary values of aerodynamic coefficients exceeded. These values are generally used for calculations, although actual unsteady aerodynamic loads of blown airfoil reach higher loads than in stationary cases.

Differences between the courses of steady and unsteady aerodynamic coefficients are so significant that steady aerodynamic coefficients are not recommended even for approximate calculations in unsteady conditions.

2. Test stand

Implementation of the measurement of unsteady aerodynamic characteristics in the dynamic stall belongs to a particularly difficult area of experimental aerodynamics applications.

For unsteady aerodynamic measurements are normally used methods based on sensing the pressure distribution on the measured object. Integral piezometrical pressure modules are used for measurement of the unsteady pressure loads on the airfoil. This technique allows to record the actual pressure process on the airfoil without time delay.

*Doc. Ing. Dalibor Rozehnal, Ph.D.: University of Defence Brno, Department of Aircraft and Rocket Techniques, Kounicova 65, 612 00 Brno, Czech Republic, e-mail: dalibor.rozehnal@unob.cz

Another way for measuring aerodynamic forces is based on load measurements. This method was also used in the UO Brno, where a new test device was developed for implementation of this type of measuring system. This device has integrated strain-gauge load cells. These load cells transfer values of aerodynamic forces which act on the tested model.

Fig. 1: Sensing of pressure from the wall of the object, the left - IAG Stuttgart ,UO Brno - the right.

3. Types and results of measured tasks

These newly developed device furthermore permit measurements of aerodynamic characteristics of the airfoil within the range from 0° to 360°, and you can freely change starting value of the mean angle of attack, the oscillation amplitude and angular velocity.

One of the implemented variants of measurements of unsteady aerodynamic characteristics of the airfoil (the ACHP), included a set of measurements which changed the angle of attack within the range from 0° to 720 ° (2nd airfoil´s revolutions) with the default start-up angle of attack 0 ° or 90 ° or 180 ° or 270 °. Each set of measurements included 14 variations of the values of angular frequency of airfoil within the range from 7.2° s^{-1} to 360° s^{-1} (ratio 1:50) for inflow air velocity 24.m·s^{-1}, Re=10^5).

Fig. 3 shows the results obtained by measuring lift curve with the default start-up angle of attack 0°. From the process of lift curves there is clearly demonstrated the significant phase shift at which the airfoil is achieved zero lift. At the same time increasing the value of angular velocity lowers the maximum value of the coefficient of lift up to 40%. Results are plotted for the angle of attack within the range from 0° to 360° during the first and second airfoil´s revolution fig. 3 and fig. 4.

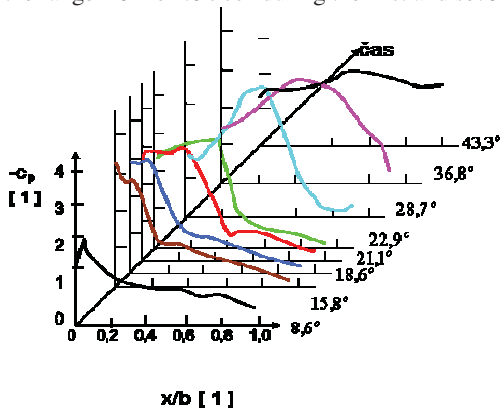

Fig. 2: Time history of pressure distribution on the NACA 0012 airfoil, a sudden change at pitching angle of attack (Francis, M. S., Keesee, J. E., 1985).

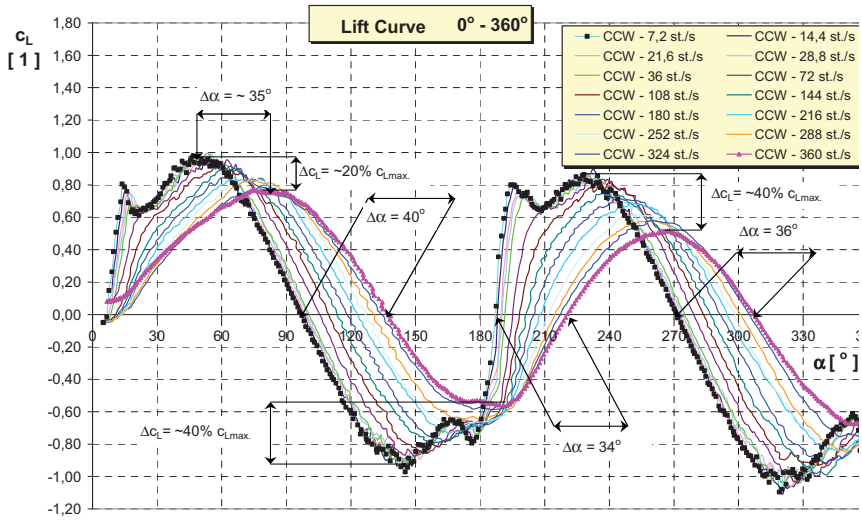

Fig. 3: Airfoil lift curve at pitching angular velocity from 7,2 deg./s to 360 deg./s, first rotation (Rozehnal, 2008).

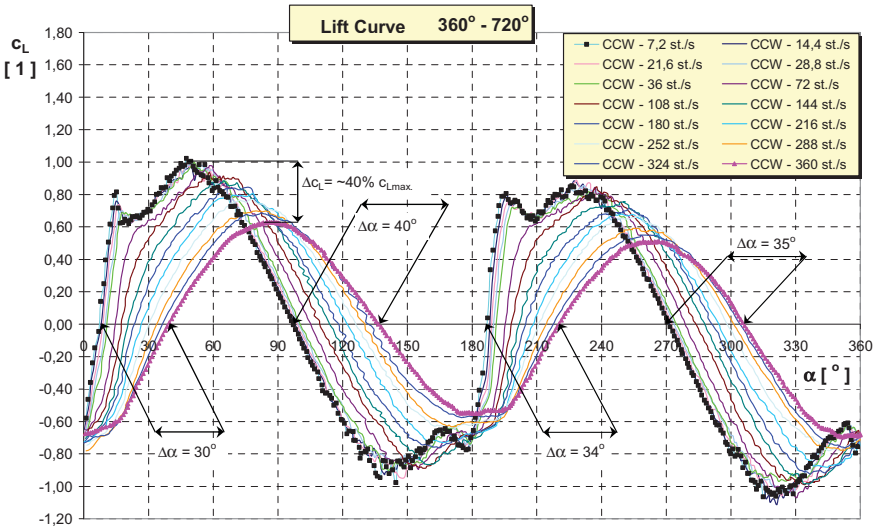

Fig. 4: Airfoil lift curve at pitching angular velocity from 7,2 deg./s to 360 deg./s, second rotation (Rozehnal, 2008).

4. Conclusion

From the experimental results it is clear that at increasing pitching angular velocity between 0^o and 360^o of angle of attack, the phase shift of angle of attack occurs at zero lift α_o (Fig.3 and Fig.4). The value of minimum drag coefficient increases and the maximum value of lift coefficient decreases. The aerodynamic ratio, "$K=c_L/c_D$" decreases from the approximate value of 55 in the stationary regime of flow to values k<1. This occurs at maximum pitching angular velocity α = 360 deg/s. Therefore, profile degradation of the lifting surface occurs. For calculating the bending load of the lifting surface effected by aerodynamic forces, it is necessary to take into consideration in addition to the lifting

component of aerodynamic resulting force its drag component as well. The drag component now attains higher values. Under such conditions, the normal component of the resulting aerodynamic force coefficient c_n reaches more than two times the value of the lift coefficient.

Under actual operating conditions, such situations may happen to high manoeuvring planes, to wind turbine rotors as a result of sudden wind direction changes, to helicopter lift rotors etc. It appears that using the classical method of calculating the load factor based upon statistical characteristics, results in significant errors when calculating maximum loads. The resulting aerodynamic loads during the whole period do not show great differences due to the relative symmetry of the hysteresis when compared to their static course. The oscillating character of these dynamic forces results in worsening ergonomic operation of this equipment (technology). Dynamic stall, which occurs under these conditions, has a dangerous effect on rotor blades and shortens their life time.

5. References

Francis, M. S., Keesee, J. E. (1985) Airfoil Dynamic Stall Performance with Large-Amplitude Motions. *AIAA Journal*, Vol. 23, November 1985, ISSN 0001-1452.

Carrl, W. (1988) Progress in Analysis and Prediction of Dynamic Stall. *Journal of Aircraft*, Vol.25, January 1988.

Ericsson, L. E., Reding, J. P. (1980) Dynamic Stall at High Frequency and Large Amplitude. *Journal of Aircraft*, Vol. 17, March 1980, ISSN 0021-8669.

Rozehnal, D. (2008) Unsteady Measurement of Aerodynamic Characteristics of a Profile During Dynamic Stall. *Internal Report,* K-204/A, UO Brno (in Czech).

Acknowledgements:

The work presented in this paper has been supported by the Czech Science Foundation project No. P101/10/0257.

18th International Conference
ENGINEERING MECHANICS 2012
Svratka, Czech Republic, May 14 – 17, 2012

pp. 1123–1124
Paper #145

INSTABILITY OF THE SWIRLING FLOWS WITH/WITHOUT CAVITATION

P. Rudolf[*], F. Pochylý[**], L. Čermák[***], D. Štefan[****]

Abstract: *Swirling flows are very susceptible to instabilities. Very often they are present in draft tubes of hydraulic turbines as so called vortex ropes resulting from spiral vortex breakdown. Moreover the situation can be complicated by cavitation within the core of the vortex. Paper presents various approaches, which were applied to enhance understanding of this problem. Numerical approach to study the linear stability including influence of cavitation is proposed and extensive nonlinear CFD simulations are described.*

Keywords: ***swirling flow, cavitation, stability, vortex breakdown***

1. Introduction

Swirling flow is very susceptible to instability (Lucca-Negro & O., O'Doherty, T., 2001). Rotating flow leaves the turbine runner for off design operating points, which is a result of the mismatch between angular momentum produced by guide vanes and angular momentum utilized by the runner. The instability is manifested as so called vortex breakdown, which can take either form of axisymmetric bubble or spiral vortex breakdown. The spiral form is typical for hydraulic turbine draft tubes, where the resulting spiral coherent structure is called vortex rope. Precessing vortex rope appears with frequency between 20 and 40% of the runner rotational frequency and its sense of rotation depends on the operational point with respect to the best efficiency point. Induced pressure pulsations deteriorate performance of the turbine.

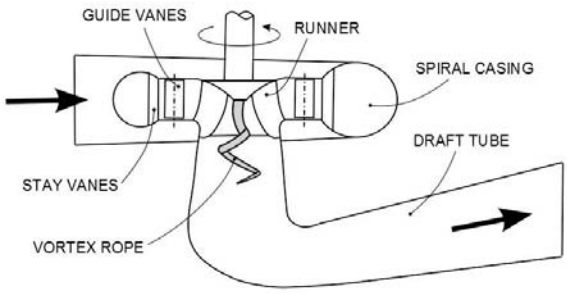

Fig. 1: Francis turbine during part load operation

[*] doc. Ing. Pavel Rudolf, Ph.D.: V. Kaplan Department of Fluid Engineering, Faculty of Mechanical Engineering, Brno University of Technology, Technická 2896/2; 616 69, Brno; CZ, e-mail: rudolf@fme.vutbr.cz

[**] prof. Ing. František Pochylý, CSc.: V. Kaplan Department of Fluid Engineering, Faculty of Mechanical Engineering, Brno University of Technology, Technická 2896/2; 616 69, Brno; CZ, e-mail: pochyly@fme.vutbr.cz

[***] doc. RNDr. Libor Čermák, CSc.: Institute of Mathematics, Faculty of Mechanical Engineering, Brno University of Technology, Technická 2896/2; 616 69, Brno; CZ, e-mail: cermak@fme.vutbr.cz

[****] Ing. David Štefan: V. Kaplan Department of Fluid Engineering, Faculty of Mechanical Engineering, Brno University of Technology, Technická 2896/2; 616 69, Brno; CZ, e-mail: y101274@stud.fme.vutbr.cz

2. Analytical approach

Analytical approaches were based on two concepts: study of vortex vector dynamics and investigation of linearized Euler equations (Pochylý et al, 2009). The first approach enables to reveal the role of vorticity vector components on evolution of the spiral vortex breakdown. The latter approach, which is based on perturbation theory also brings quantitative information concerning tendency of the flow towards instability and frequency of possible instabilities.

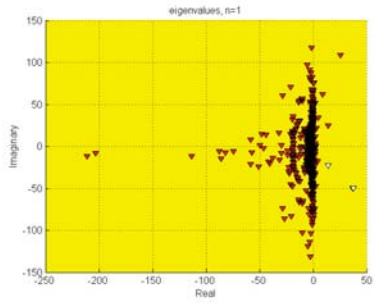

Fig. 2: Eigenvalues of the swirling flow in diffuser

3. Computational and experimental investigation

Experimental research includes measurements of pressure pulsations and flow visualizations. Both types of the vortex rope i.e. cavitating and non-cavitating were observed. Computational investigations combine complex turbulence models coupled with cavitation models (Rudolf et al, 2011).

Fig.3: Cavitating vortex rope (experiment)

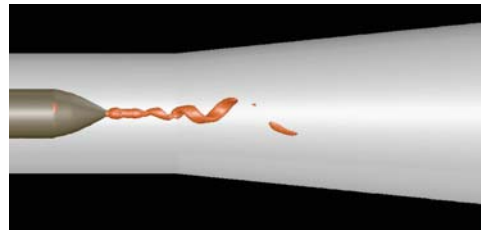

Fig.4: Cavitating vortex rope (simulation)

4. Conclusion

An extensive analytical, computational and experimental research was carried out at Kaplan Dept. of Fluid Engineering aiming on better understanding of the cavitating vortical structures in swirling flow. The main conclusions yet point to velocity gradients of the oncoming flow as the most important parameter in the onset of instability.

Acknowledgement
Czech Science Foundation is gratefully acknowledged for support of the research under project No. 101/09/1715 “Cavitating vortical structures induced by rotating liquid”.

References

Lucca-Negro & O., O'Doherty, T. (2001) Vortex breakdown - a review, *Progress in Energy and Combustion Science*, Vol. 27,pp. 431-481.

Pochylý, F., Čermák, L., Rudolf, P.; Habán, V.; Koutník, J. (2009) Assessment of the steady swirling flow stability using amplitude-frequency characteristic, *Proc. of the 3rd IAHR Int. Meeting of the Workgroup on Cavitation and Dynamic Problems in Hydr. Mach. and Systems - part I*, pp.25-34

Rudolf, P.; Hudec, M.; Zubík, P.; Štefan, D. (2011) Experimental measurement and numerical modeling of cavitating flow in converging-diverging nozzle, *Proc. of the Int. Conf. Exp. Fluid Mech. 2011*, pp.423-431

18th International Conference
ENGINEERING MECHANICS 2012
Svratka, Czech Republic, May 14 – 17, 2012

pp. 1125–1134
Paper #143

IDENTIFICATION OF PARAMETERS FOR MODELS OF DUCTILE DAMAGE

J. Růžička*, M. Španiel, M. Moravec, A. Prantl, J. Džugan, J. Kuželka

Abstract: *This paper introduces the description of effective method of calibration of a material plasticity. This problem is solved in the project „Identification parameters of ductile damage materials for nuclear facilities". The research focuses on the phenomenological material models and identification of their parameters. The calibration of the material parameter is based on the evaluation of the experimental samples series and FE simulations that are calculated in Abaqus 6.10 software.*

Keywords: ***Plasticity, calibration, FEM, Johnson-Cook, ductile damage***

1. Úvod

Vzhledem ke zvyšujícím se nárokům na bezpečnost, spolehlivost a prodlužování životnosti dílů jaderných zařízení je nutno zahrnout do výpočtových simulací vstupní materiálová data, která odpovídají možnostem stávajícího výpočtového systému používaného ve Škoda JS i současnému stavu poznání. Cílem je nalezení parametrů a způsobu jejich identifikace pro počítačové simulace umožňujících vyhodnocení odolnosti vůči tvárnému porušení. To umožní zpřesnění výpočtů při návrhu konstrukce sledovaných zařízení a současně umožní vyhodnocení aktuálního stavu sledovaných komponent, což může mít pozitivní dopad na jejich efektivnější využití za podmínky dodržení nejvyšších standardů pro bezpečný provoz jaderných zařízení .

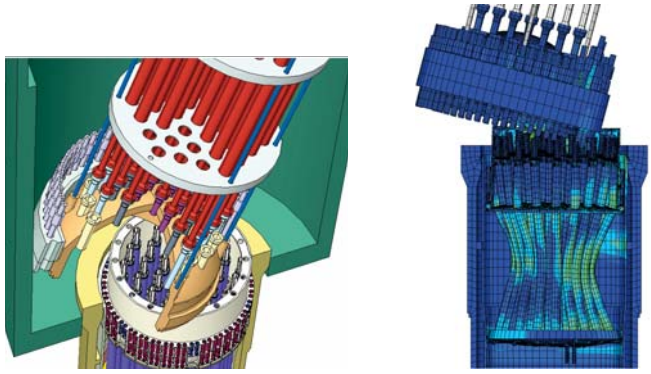

Obr.1: Studie hypotetického pádu horního bloku do šachty reaktoru.

K porušování strojních součástí dochází zpravidla ze dvou příčin. První příčinou bývá iniciace a šíření únavových trhlin u cyklicky namáhaných konstrukcí. Trhlina postupně prorůstá zatěžovanou součástí

* Ing. Jan Růžička : Ústav mechaniky/Odbor pružnosti a pevnosti, České vysoké učení technické v Praze;
e-mail: ruzicka.jan@seznam.cz

a zeslabuje tak její nosný průřez. Druhou příčinou bývá překročení pevnostní dispozice konstrukce. Vlastní proces lomu lze dále dělit na lom křehký a tvárný. V průběhu křehkého lomu zpravidla nevznikají makroskopicky významné plastické deformace. K lomu dochází, pokud v tělese vzniknou podmínky pro nestabilní šíření existující trhliny. Popisem této problematiky se detailně zabývá lomová mechanika. K tvárnému lomu dochází po vyčerpání plastické zásoby materiálu. Plastická deformace má v tomto případě veliký podíl na celkovém přetvoření tělesa, a proto je práce potřebná pro celkové porušení součásti významně větší než v případě křehkého lomu. Popis tvárného porušování je velice komplexní problém. Vlastní proces porušování materiálu je v mnoha případech silně závislý na lokální napjatosti materiálu, teplotě, rychlosti deformace atd. Z tohoto důvodu se nelze příliš spoléhat na jednoduché hypotézy, které zpravidla dávají uspokojivé výsledky pouze v úzké oblasti zatěžování. Pro komplexnější popis problematiky jsou v současné době vyvíjeny složitější fenomenologické modely tvárného porušování. Tyto modely zpravidla obsahují mnoho materiálových parametrů, které je třeba identifikovat. Proto je nutné experimentálně zmapovat chování materiálu na poměrně rozsáhlém souboru vhodných vzorků. Z tohoto důvodu je úspěšná kalibrace tvárného porušování poměrně nákladná záležitost.

2. Teoretické aspekty modelů tvárného porušování

Stávající fenomenologické modely tvárného porušení lze z hlediska zahrnutí poznatků o mikrostruktuře rozdělit do dvou skupin. První skupinou jsou mikromechanické kontinuální modely, které vycházejí z rozboru vlivu dutin na napjatost v mikroobjemech kontinua. Typickým představitelem mikromechanických modelů poškození kontinua je Gurson-Tvergaardův model. Ten definuje poškození jako objemový podíl dutin v materiálu. Druhou skupinou jsou modely poškození kontinua. Koncept mechaniky poškozování kontinua je založen na představě, že odezva poškozeného materiálu je odvozena z odezvy materiálu základního. Geometrické a fyzikální parametry poškození nejsou popisovány na úrovni mikrostruktury, ale vycházejí typicky ze skalárního fiktivního parametru poškození ω, které lze obecně vyjádřit kumulací v procesu plastické deformace.

$$\omega = \int_0^{\varepsilon_c} f\left(p, q, \xi, T, \varepsilon, \dot{\varepsilon}\right) \mathrm{d}\varepsilon^{pl} \tag{1}$$

Pokud poškození zpětně ovlivňuje plastické chování materiálu mluvíme o svázaném modelu poškození kontinua, pokud ne, jedná se o model nesvázaný. V MKP programu Abaqus, na který je tento projekt orientován, je implementován fenomenologický model poškození kontinua jako nadstavba klasických modelů plasticity kovů. Tyto modely nejsou svázané, což klade vyšší nároky na modely plasticity. Plastická deformace má v procesu tvárného porušování klíčový význam. Fenomenologické modely tvárného porušení jsou proto vesměs vázány ke stávajícím modelům plasticity. Klasické fenomenologické modely plastické odezvy pracují se stavovými veličinami: tenzor napětí $\boldsymbol{\sigma}$ a akumulovanou intenzitou plastické deformace ε^{pl}.

$$\bar{\varepsilon}^{pl} = \int_0^t \tilde{\varepsilon}^{pl} \mathrm{d}t, \quad \tilde{\varepsilon}^{pl} = \sqrt{\frac{2}{3}\boldsymbol{\varepsilon}^{pl} : \boldsymbol{\varepsilon}^{pl}} \tag{2}$$

Plastická deformace je definována jako proces. O tom, zda při změně zatížení dojde k nárůstu plastické deformace rozhoduje kritérium závislé na aktuálním stavu. Za předpokladu isotropie může být z hlediska samotného materiálu napjatost popsána hlavními napětími σ_1 σ_2 a σ_3. Budeme-li předpokládat nezávislost plastické odezvy na hydrostatickém napětí, jsou klasické plastické modely kovů formulovány pro deviátor tenzoru napjatosti. Formulace významné skupiny klasických modelů plasticity kovů je založena pouze na druhém invariantu tenzoru napjatosti.

$$J_2 = \frac{1}{6}\left[\left(\sigma_1 - \sigma_2\right)^2 + \left(\sigma_2 - \sigma_3\right)^2 + \left(\sigma_3 - \sigma_1\right)^2\right] = \frac{1}{2}\left(S_1^2 + S_2^2 + S_3^2\right) \tag{3}$$

Takový model plasticity byl použit při identifikaci parametrů tvárného porušení v rámci tohoto projektu. Jednalo se o model s misesovskou plochou plasticity, s asociovaným zákonem plastického tečení a bez posunu středu plochy plasticity (s izotropním zpevněním). Při předpokládaném

monotónním zatěžování do porušení je tento velmi jednoduchý model plasticity dostatečný. Principiálně je možno použít i komplikovanější plastické modely.

3. Metodika kalibrace modelu plasticity

Kalibrace materiálových parametrů je založena na porovnávání měřené odezvy experimentálních vzorků s výsledky simulace metodou konečných prvků. Měřenou odezvou se rozumí závislost mezi prodloužením a silou. Například pro tahový vzorek je to síla zkušebního stroje a prodloužení měřené buď na čelistech nebo extenzometrem. Cílem kalibrace je dosáhnout takových hodnot materiálových parametrů, aby výpočet vystihoval experiment co nejpřesněji. Pro uvedený model plasticity je nutno kalibrovat závislost okamžité meze kluzu na akumulované intenzitě plastické deformace $\sigma_Y^{True} = \sigma_Y^{True}(\varepsilon_{\ln}^{pl})$. Základním experimentálním podkladem pro určení této závislosti bývá standardně uniaxiální tahový test na hladkém tyčovém vzorku. Výstupem tahového testu je závislost smluvního napětí σ na poměrné deformaci ε.

$$\varepsilon = \frac{\Delta L}{L_0} \quad , \quad \sigma = \frac{F}{S_0} \tag{4}$$

Za předpokladu rovnoměrného rozložení deformace lze z podmínky konstantního objemu materiálu vypočítat skutečné hodnoty napětí a logaritmické deformace pomocí vztahů (5)

$$\varepsilon_{\ln} = \ln(1+\varepsilon) \quad , \quad \sigma^{True} = \sigma(1+\varepsilon) \tag{5}$$

Dalším krokem je odečtení elastické složky deformace. Z tahového diagramu je výhodnější tuto složku deformace stanovit na základě počáteční meze kluzu σ_y.

$$\varepsilon_{\ln}^{pl} = \varepsilon_{\ln} - \varepsilon_{\ln}^{el} = \varepsilon_{\ln} - \frac{\sigma_y}{E} \tag{6}$$

Tímto postupem lze stanovit plastickou část tahové křivky $\sigma_Y^{True}(\varepsilon_{\ln}^{pl})$ až do okamžiku lokálního zaškrcení vzorku, kdy vztahy (5) přestávají být platné. Napjatost v zaškrcené oblasti již není dále uniaxiální a plastickou část tahové křivky je pro větší plastické deformace nutné stanovit pomocí vhodné korekce (např. Bridgmanovy), nebo iterativně s využitím MKP simulace. K vlastnímu zaškrcování hladkého vzorku začíná zpravidla docházet v okamžiku maximální experimentálně dosažené síly, kterému odpovídá prodloužení vzorku ΔL_{neck}. Pomocí vztahů (4)-(6) lze v tomto bodě stanovit plastickou deformaci při zaškrcení $\varepsilon_{\ln.neck}^{pl}$ a odpovídající napětí $\sigma_{Y.neck}^{True}$.

Obecný tvar funkce $\sigma_Y^{True}(\varepsilon_{\ln}^{pl})$ je možné ve vhodně zvolených bodech interpolovat posloupností korespondujících bodů $\left[\left(\varepsilon_{\ln}^{pl}\right)_j, \left(\sigma_Y^{True}\right)_j\right]$. Plastická část tahové křivky je pak do výpočetních programů zadávána ve formě tabulky. Tento přístup s sebou nese výhodu možnosti popisu plastické části tahové křivky i v případě, kdy ji nelze s dostatečnou přesností aproximovat vhodnou analytickou funkcí. Nevýhodou je často značný rozsah dat (zvláště v případě definice dalších závislostí např. na teplotě, rychlosti deformace, atd.) a problematika regularizace dat (viz. níže).

Výsledná funkce $\sigma_Y^{True}(\varepsilon_{\ln}^{pl})$ je sestavena ze dvou částí. První část, která je platná až do vniku plastického zaškrcení $\varepsilon_{\ln}^{pl} < \varepsilon_{\ln.neck}^{pl}$ je tvořena hodnotami skutečného napětí a plastických deformací, které byly vypočítány pomocí vztahů (5),(6) přímo z experimentálních dat. V případě výraznějšího šumu, který v reálném měření nevyhnutelně vzniká, je vhodné experimentální data nejprve vyhladit. Druhá část závislosti $\sigma_Y^{True}(\varepsilon_{\ln}^{pl})$ je pro $\varepsilon_{\ln}^{pl} \geq \varepsilon_{\ln.neck}^{pl}$ nahrazena vhodnou aproximační funkcí, která je volena tak, aby splňovala podmínku tečného napojení v místě plastické deformace při zaškrcení $\varepsilon_{\ln.neck}^{pl}$. Vlivem šumu zpravidla nelze směrnici tečny v tomto místě stanovit přímo. Z tohoto důvodu je malá oblast kolem kritické plastické deformace aproximována kvadratickou funkcí a směrnice

$\frac{d\sigma_Y^{True}\left(\varepsilon_{\ln.neck}^{pl}\right)}{d\varepsilon_{\ln}^{pl}}$ je pomocí této funkce následně vypočítána analyticky. V této práci byla plastická část tahové křivky pro velké plastické deformace nahrazena mocninou funkcí. Tato funkce odpovídá prvnímu členu, který popisuje závislost okamžité meze kluzu na akumulované intenzitě plastické deformace Johnson Cookova plastického modelu (7).

$$\sigma_Y^{True} = \left(A + B\left(\varepsilon_{\ln}^{pl}\right)^n\right)\left(1 + c\ln\frac{\dot{\varepsilon}_{\ln}^{pl}}{\dot{\varepsilon}_{\ln}^{0}}\right)\left(1 - \widetilde{T}^m\right), \tag{7}$$

kde *A, B, n, c, m* jsou materiálové parametry. Aplikací podmínek tečného napojení dostaneme soustavu rovnic.

$$A + B\left(\varepsilon_{\ln.neck}^{pl}\right)^n = \sigma_{Y.neck}^{True} \tag{8}$$

$$Bn\left(\varepsilon_{\ln.neck}^{pl}\right)^{n-1} = \frac{d\sigma_Y^{True}\left(\varepsilon_{\ln.neck}^{pl}\right)}{d\varepsilon_{\ln}^{pl}} \tag{9}$$

Řešením soustavy lze parametry *A, B* vyjádřit jako funkci exponentu *n*, který je možné následně kalibrovat iterativně. Protože aproximační funkce je definována až od hodnoty $\varepsilon_{\ln.neck}^{pl} > 0$, lze definiční obor exponentu *n* rozšířit i do oblasti záporných čísel. Pro nenulovou směrnici plastické části tahové křivky v místě napojení však nelze aproximační funkci definovat pro *n=0*, protože tak nelze obecně splnit rovnici (9). V případě iterativní kalibrace je proto nutné hodnotu *n=0* vyloučit. Pro popis tvarově složitější plastické funkce je samozřejmě možné zvolit aproximační funkci, která je popsána více parametry.

Tab. 1: Vlastnosti plastického modelu navrženého podle (8),(9) pro různé hodnoty n

n>1	Rychlost plastického zpevnění po zaškrcení vzorku roste.
n=1	Rychlost plastického zpevnění je po zaškrcení vzorku konstantní.
n<1	Rychlost plastického zpevnění po zaškrcení vzorku klesá.
n=0	Model není v obecném případě definován.
$n \to -\infty$	Plastické zpevnění po zaškrcení se blíží ideálně plastickému materiálu

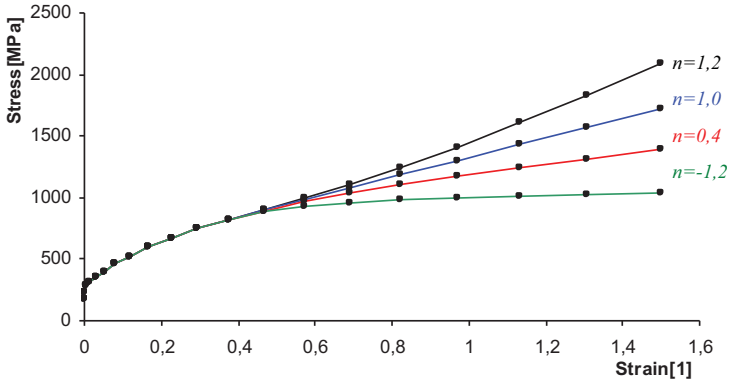

Obr.2: Výsledný tvar plastické části tahové křivky pro různá n

Závěrečným krokem kalibrace je interpolace obou částí závislosti $\sigma_Y^{True}(\varepsilon_{\ln}^{pl})$ do vhodně zvolených interpolačních bodů $\left[\left(\varepsilon_{\ln}^{pl}\right)_j, \left(\sigma_Y^{True}\right)_j\right]$. Rozvržení těchto bodů by mělo vystihovat tvar plastické části tahové křivky. V místě větších gradientů napětí je vhodné hustotu interpolačních bodů zvýšit. Dále je nutné si uvědomit, že pokud budeme definovat plastický model materiálu, který je závislý na dalších veličinách (teplota, rychlost plastické deformace, atd.), bude celkový počet interpolačních bodů prudce narůstat. V této práci bylo definováno polynomické rozvržení

$$\left(\varepsilon_{\ln}^{pl}\right)_j = a \cdot j^{\alpha} \quad , j = 0, 1, 2, ..., N \quad , \quad \alpha \geq 1 \quad , \tag{10}$$

kde N je počet interpolačních intervalů. V současné době bývá ve většině případů tvárné porušování simulováno v explicitním řešiči. Abaqus/Explicit z důvodu efektivity výpočtu nepoužívá materiálová data ve stejném tvaru, ve kterém jsou definována uživatelem. Veškerá data, která jsou zadána ve formě tabulky jsou automaticky regularizována. Materiálová data jsou interpolována stanoveným počtem bodů s konstantním krokem. Při použití $N \leq 50$ intervalů definovaných uživatelem, Abaqus použije pro regularizaci $100 \cdot N$ intervalů s konstantní velikostí. V případě, že v některé oblasti jsou uživatelem definované intervaly výrazně menší, než je velikost intervalu regularizovaného, dochází ke ztrátě informace o průběhu $\sigma_Y^{True}(\varepsilon_{\ln}^{pl})$. Tento efekt může mít zcela zásadní vliv na kvalitu výsledků dosažených MKP simulací. Vzniklou chybu lze do značné míry eliminovat vhodnou volbou maximální plastické deformace (ta by měla být jen tak veliká jak je bezpodmínečně nutné) a vhodným rozvržením interpolačních bodů (volba parametrů *a, α*). Aby nedocházelo ke ztrátě informace, o tvaru závislosti $\sigma_Y^{True}(\varepsilon_{\ln}^{pl})$, je vhodné požadovat, aby nejmenší uživatelem definovaný interval (pro případ $\alpha \geq 1$ se jedná o první interval definované posloupnosti) byl roven velikosti intervalu regularizovaného. Tuto podmínku lze zapsat následující rovnicí.

$$a \cdot 1^{\alpha} = \frac{\varepsilon_{\ln.\max}^{pl}}{100 \cdot N} = \frac{a \cdot N^{\alpha}}{100 \cdot N} \quad , \quad \alpha \geq 1 \quad , \tag{11}$$

kde $\varepsilon_{\ln.\max}^{pl}$ je maximální definovaná plastická deformace. Řešením rovnice je vztah pro výpočet exponentu α, který je závislí pouze na počtu zvolených interpolačních intervalů.

$$\alpha = \frac{\ln(100N)}{\ln N} \quad , \quad \mathrm{N} \leq 50 \tag{12}$$

Parametr *a* lze vypočítat z podmínky maximální požadované deformace.

$$a \cdot N^{\alpha} = \varepsilon_{\ln.\max}^{pl} \quad \rightarrow \quad a = \frac{\varepsilon_{\ln.\max}^{pl}}{N^{\alpha}} \tag{13}$$

Tímto způsobem lze efektivně rozvrhnout interpolační body v závislosti na předpokládaném rozsahu redukované plastické deformace a počtu interpolačních bodů.

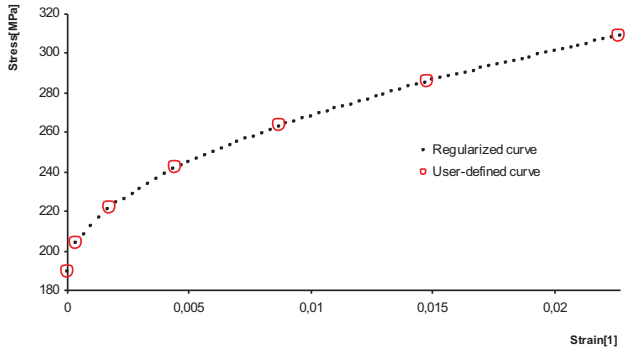

Obr.3: Začátek regularizované funkce plasticity s navrženou interpolací ($\varepsilon_{\ln.\max}^{pl}$=1, N=30)

4. Kalibrace plastického modelu Johnson-Cook

Plastická část tahové křivky je v inženýrské praxi často aproximována mocninou závislostí ve tvaru, který odpovídá prvnímu členu Johnson-Cookova modelu plasticity. Plastický model Johnson-Cook je v programu Abaqus přímo implementován. Použití této aproximace je v případě dobré shody s experimentem velice výhodné, protože celá funkce $\sigma_Y^{True}(\varepsilon_{\ln}^{pl})$ je popsána pouze třemi parametry *A, B, n*. Funkce je navíc spojitá a odpadají tak problémy s vhodnou volbou interpolačních bodů a problémům s regularizací dat v případě, kdy jsou materiálová data definována formou tabulky. Při aproximaci plastické části tahové křivky Johnson-Cookovým modelem, nelze v případě MKP simulace tahového testu očekávat dokonalou shodu s experimentem. Je však rozumné požadovat, aby korespondovala alespoň maximální dosažená zátěžná síla a prodloužení, při kterém dochází ke vzniku zaškrcení. Podmínka shody experimentu a materiálového modelu v bodě zaškrcení umožňuje vyjádřit parametry *A, B* v závislosti na volbě *n*. Podle článku Havner, K.S. (2004) k zaškrcování vzorku dochází pokud funkce $\sigma_Y^{True}(\varepsilon_{\ln}^{pl})$ pro dané $\varepsilon_{\ln}^{pl}$ splňuje následující podmínku.

$$\frac{d\sigma_Y^{True}\left(\varepsilon_{\ln}^{pl}\right)}{d\varepsilon_{\ln}^{pl}} < \sigma_Y^{True}\left(\varepsilon_{\ln}^{pl}\right) \tag{14}$$

Pomocí vztahů (5) lze jednoduše odvodit speciální případ funkce, která během zatěžování vzorku generuje konstantní silovou odezvu F_0.

$$\sigma_Y^{True}\left(\varepsilon_{\ln}^{pl}\right) = \sigma_Y e^{\varepsilon_{\ln}^{pl}} = \frac{F_0}{A_0} e^{\varepsilon_{\ln}^{pl}}, \tag{15}$$

kde A_0 je počáteční průřez testovaného vzorku. Tato funkce je podle rovnice (14) v celém rozsahu plastické deformace mezním případem vzniku plastického zaškrcení. Dosazením mocninné závislosti do (14) a aplikací podmínky dosažení síly při zaškrcení dostaneme následující soustavu rovnic.

$$A + B\left(\varepsilon_{\ln.neck}^{pl}\right)^n = Bn\left(\varepsilon_{\ln.neck}^{pl}\right)^{n-1} \tag{16}$$

$$A + B\left(\varepsilon_{\ln.neck}^{pl}\right)^n = \sigma_{Y.neck}^{True} \tag{17}$$

Řešením lze vyjádřit parametry mocninné plastické závislosti jako funkci exponentu *n*.

$$A(n) = \frac{\sigma_{Y.neck}^{True}\left(n - \varepsilon_{\ln.neck}^{pl}\right)}{n} \tag{18}$$

$$B(n) = \frac{\sigma_{Y.neck}^{True}\left(\varepsilon_{\ln.neck}^{pl}\right)^{1-n}}{n} \tag{19}$$

Zbylý parametr *n* lze následně vypočítat přidáním další podmínky, která definuje napětí experimentálně stanovené meze kluzu σ_y pro $\varepsilon_{\ln}^{pl} = 0$. Tento přístup ale zpravidla nevede k optimálnímu výsledku. Počáteční mez kluzu navíc nebývá ostře ohraničena. Proto je zbylý parametr *n* výhodnější identifikovat iterativně. Funkce $\sigma_Y^{True}(\varepsilon_{\ln}^{pl})$ musí být v celém svém rozsahu nezáporná. Z tohoto důvodu musí být nutně nezáporné i *A(n)*, které má v tomto případě fyzikální význam počáteční meze kluzu σ_y. Z rovnice (19) tedy plyne minimální možná hodnota parametru $n \geq \varepsilon_{\ln.neck}^{pl}$. Na *Obr. 4 (vlevo)* jsou zachyceny průběhy mocninných závislostí a jejich derivací (čárkovaně) pro různá *n*. Ty jsou podle vztahů (18), (19) navrženy tak, aby se protínaly v bodě plastické deformace a napětí při zaškrcení $\left[\varepsilon_{\ln.neck}^{pl}, \sigma_{Y.neck}^{True}\right]$. Výsledné silové odezvy modelovaného hladkého vzorku jsou zachyceny na *Obr. 4 (vpravo)*. K procesu kalibrace Johnson-Cookova modelu lze samozřejmě přistoupit obecněji pomocí nezávislé iterativní identifikace všech tří parametrů. Metodika popsaná v tomto článku však dává efektivním způsobem velice dobrou představu o možnosti aproximovat plastickou odezvu materiálu pomocí tohoto modelu.

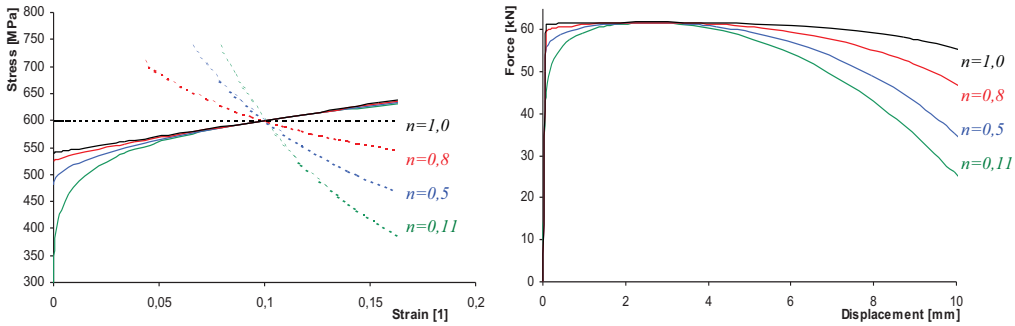

Obr.4: Vlevo - Průběhy navržených funkcí Johnson-Cooka a jejich derivací (čárkovaně). Vpravo - Odpovídající silové odezvy hladkého tyčového vzorku vypočtených pomocí MKP.

Iterativní kalibrace může být zvláště v případě identifikace více parametrů zdlouhavý proces. Z tohoto důvodu byl v rámci projektu vyvinut optimalizační skript v jazyce Python, který je spouštěn přímo pod programem Abaqus. Měřítkem přesnosti kalibrace je plocha mezi vypočítanou a experimentálně naměřenou křivkou síla-prodloužení. Čím menší je tato plocha, tím jsou kalibrované parametry přesnější (*Obr. 5 - vlevo*).

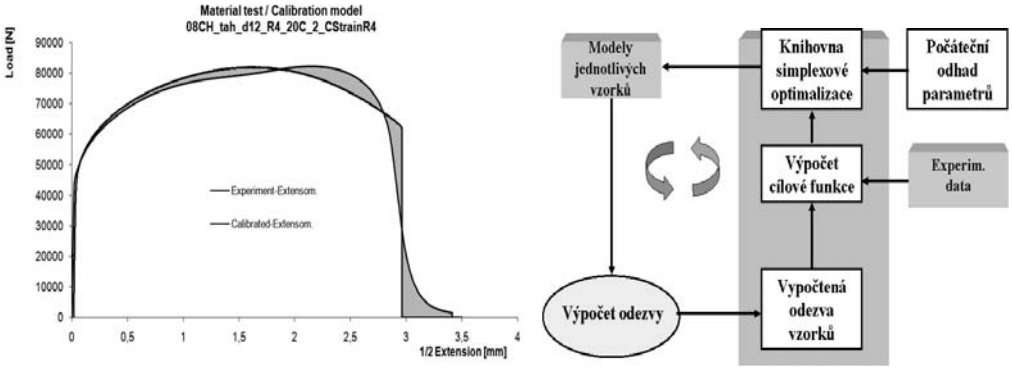

Obr.5: Vlevo - Plocha odchylky mezi MKP simulací a experimentem. Vpravo – Schéma optimalizačního skriptu pro lokální optimalizaci.

Kalibrační skript je založený na simplexovém algoritmu lokální optimalizace. Tento algoritmus umožňuje efektivně optimalizovat více parametrů současně. Náročnost a nejistota optimalizace však s počtem parametrů velice rychle roste. Proto je vždy snaha o popis modelu s co nejméně parametry, které je nutno identifikovat. Nevýhodou lokální optimalizace je vysoká náročnost na počáteční odhad řešení. Simplexový algoritmus zaručuje nalezení pouze lokálního minima cílové funkce. Vlastní procedura kalibrace je naznačena na *Obr. 5 – vpravo.*

1. Do optimalizačního bloku jsou načteny počáteční odhady parametrů a experimentálně stanovené odezvy síla-posuv pro jednotlivé vzorky. Je vytvořena databáze MKP modelů pro simulaci kalibračních experimentů na jednotlivých vzorcích.
2. MKP modely jednotlivých vzorků jsou modifikovány aktuálními hodnotami materiálových dat. Na počátku kalibrace jsou použity počáteční odhady.
3. Pro všechny vzorky je vypočtena odezva síla-posuv a načtena do optimalizačního bloku.

4. Z vypočtených a experimentálně stanovených odezev síla-posuv pro jednotlivé vzorky je vypočtena cílová funkce - míra jejich odchylky - jako plocha mezi jejich křivkami (viz. *Obr. 5*).
5. Optimalizační algoritmus navrhne potřebné změny materiálových dat a cyklus 2 – 5 probíhá, dokud není nalezeno lokální minimum cílové funkce.

5. Kalibrace teplotní závislosti plastického modelu

V technické praxi je často potřebné provádět výpočty konstrukcí pro různé teploty materiálu. Z tohoto hlediska je třeba kalibrovat plastické chování materiálů také v závislosti na teplotě. U některých materiálů lze v tomto případě využít proporcionality závislosti $\sigma_Y^{True}(\varepsilon_{\ln}^{pl})$ vzhledem k silové odezvě jednotlivých vzorků $F(\Delta l)$. Pokud lze naměřené závislosti síla-prodloužení při daných teplotách $F(\Delta l)_T$ úspěšně aproximovat závislostí síla-prodloužení téhož vzorku při referenční teplotě $F(\Delta l)_{T_0}$ ve tvaru $F(\Delta l)_T \approx \tau(T)\cdot F(\Delta l)_{T0}$, kde *τ(T)* je vhodná korekční funkce závislá pouze na teplotě, poté je možné vypočítat korigovanou plastickou křivku jako $\sigma_{Y.crit}^{True}\left(\varepsilon_{\ln}^{pl}\right)_T = \tau(T)\cdot\sigma_{Y.crit}^{True}\left(\varepsilon_{\ln}^{pl}\right)_{T0}$. Korekční teplotní funkci lze navrhnout např. ve tvaru, který je obsažen v Johnson-Cookově plastickém modelu.

$$\tau(T) = 1 - \left(\frac{T - T_0}{T_{melt} - T_0}\right)^m , \tag{20}$$

kde T_0 je teplota referenčního vzorku pro který byla identifikována plastická část tahové křivky, T_{melt} je teplota tavení daného materiálu a m je materiálový parametr, který popisuje teplotní odpevnění. Pokud je k dispozici větší soubor experimentálně naměřených dat pro různé teploty, lze T_{melt} chápat jako další materiálový parametr, který poté ovšem ztrácí přímý fyzikální význam. Vlastní proces kalibrace je možné rozdělit do dvou kroků. V prvním kroku je nutné stanovit hodnotu korekční funkce pro jednotlivé teploty. Vhodným nástrojem je v tomto případě metoda nejmenších čtverců. Její aplikací na danou problematiku lze vypočítat hodnotu korekční funkce pomocí vztahu:

$$\tau(T_j) = \frac{\int_0^{\Delta l} F(\Delta l)_{T_j}\, d\Delta l}{\int_0^{\Delta l} F(\Delta l)_{T_0}\, d\Delta l} \tag{21}$$

Druhým krokem je nalezení parametrů modelu m a T_{melt}. Parametry není možné explicitně vyjádřit a musí být proto vypočítány numericky. Úlohu lze převést na optimalizační problém. Parametry jsou hledány tak, aby minimalizovali následující cílový funkcionál.

$$F(m, T_{melt}) = \sum_j \left|\tau_j - \tau(T_j)\right| \tag{22}$$

V případě, že experimentální závislosti nelze uspokojivě korigovat vhodnou funkcí ve tvaru $F(u)_T \approx \tau(T)\cdot F(u)_{T0}$, je nutné kalibrovat závislost $\sigma_Y^{True}(\varepsilon_{\ln}^{pl})$ pro každou teplotu zvlášť.

6. Dosažené výsledky kalibrace

Výsledky kalibrace plasticity, které byly dosaženy metodikou popsanou v tomto článku jsou prezentovány na materiálech 08Ch18N10T a 15CH2NMFA. Model tvárného porušení v těchto simulacích nebyl použit. Plastická část tahové křivky materiálu 15CH2NMFA byla aproximována Johnson-Cookovým modelem plasticity. Výsledkem kalibrace bylo nalezení parametrů *A, B, n, T_{melt}, m*. *Obr. 6, 7* Zachycují srovnání MKP simulace tahových tyčových vzorků pro jednotlivé teploty s experimentálními daty.

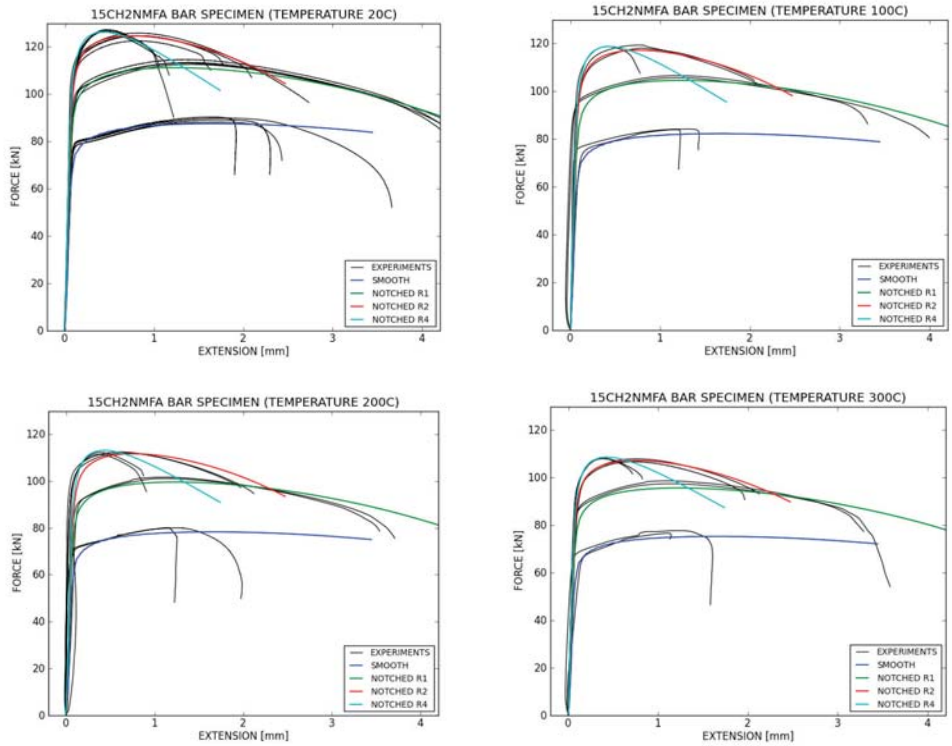

Obr.6: Porovnání experimentálních závislostí síla-prodloužení tahových tyčových vzorků pro různé teploty s MKP simulacemi (barevně) materiálu 15CH2NMFA.

Plastická část tahové křivky materiálu 08Ch18N10T byla interpolována tabulkou. Teplotní závislost v tomto případě nebylo možné s dostatečnou přesností aproximovat korekční funkcí $\tau(T)$. Plastická část tahové křivky byla proto identifikována pro jednotlivé teploty zvlášť.

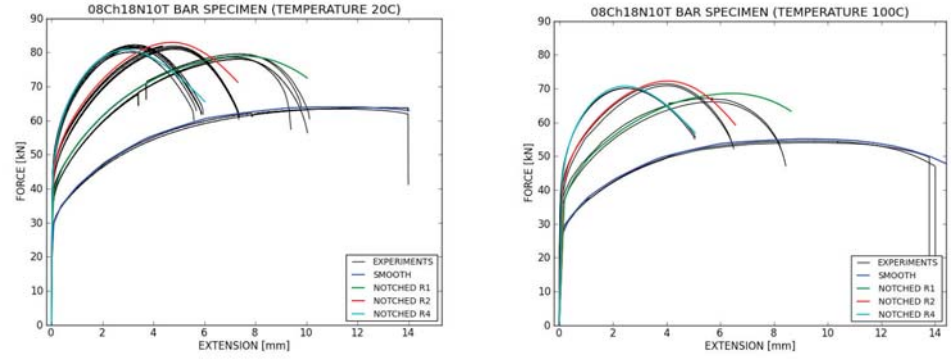

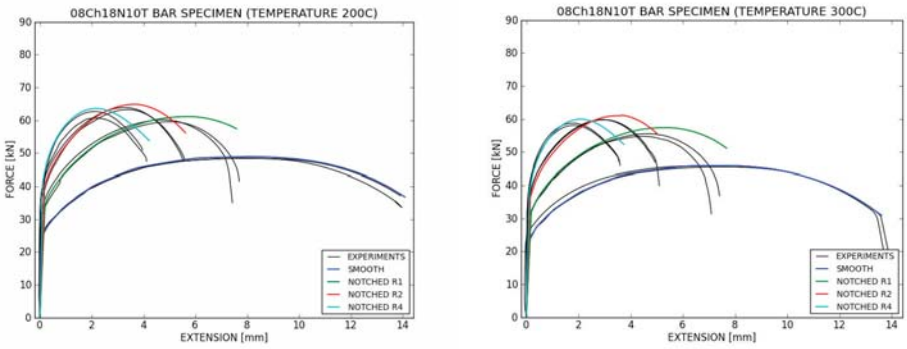

Obr.7: Porovnání experimentálních závislostí síla-prodloužení tahových tyčových vzorků pro různé teploty s MKP simulacemi (barevně) materiálu 08Ch18N10T.

7. Závěr

V příspěvku byla detailně popsána metodika kalibrace plastické části tahové křivky, která je důležitým aspektem modelů tvárného porušování. Byly zvoleny dva způsoby aproximace závislosti $\sigma_Y^{True}(\varepsilon_{\ln}^{pl})$ a navržen efektivní postup jejich identifikace. Tento postup se opírá o teoretické poznatky plastického chování materiálů, na základě kterých podstatně snižuje náročnost kalibrace. Identifikace nezávislých parametrů modelů probíhá iterativně pomocí optimalizačního skriptu, který byl v rámci projektu vyvinut. Kalibrace plasticity dává pro zkoumané materiály poměrně dobrou shodu s experimenty. V současné době probíhají práce na kalibraci plastických modelů v závislosti na rychlosti deformace. V následujícím období bude naše pozornost v oblasti plasticity zaměřena na plastické modely, které zohledňují i třetí invariant deviátoru napětí a hydrostatický tlak.

Použitá literatura

Ling, Y. (1996) Uniaxial True Stress-Strain after Necking. *AMP Journal of Technology Vol. 5*

Abaqus Online Documentation: Version 6.10

Havner, K.S. (2004) On the onset of necking in the tensile test. *International Journal of Plasticity 20 965-978*

Bridgman, P. W. Studies in Large Plastic Flow and Fracture. *Cambridge, Harvard University Press, 1956*

Gurson, A.L. Continuum theory of ductile rupture by void nucleation and growth. *Journal of Engineering Materials and Technology 1977, vol. 99*

Johnson, G. R., Cook, W. H. Fracture characteristics of three metals subjected to various strains, strain rates, temperatures and pressures. *Engineering Fracture Mechanics, 1985, vol. 21*

18th International Conference
ENGINEERING MECHANICS 2012
Svratka, Czech Republic, May 14 – 17, 2012

pp. 1135–1143
Paper #304

STUDY OF COMPUTATIONAL EFFICIENCY OF NUMERICAL QUADRATURE SCHEMES IN THE ISOGEOMETRIC ANALYSIS

D. Rypl*, B. Patzák**

Abstract: *Isogeometric analysis has been recently introduced as a viable alternative to the standard, polynomial-based finite element analysis. One of the fundamental performance issues of the isogeometric analysis is the quadrature of individual components of the discretized governing differential equation. The capability of the isogeometric analysis to easily adopt basis functions of high degree together with the (generally) rational form of those basis functions implies that high order numerical quadrature schemes must be employed. This may become computationally prohibitive because the evaluation of the high degree basis functions and/or their derivatives at individual integration points is quite demanding. The situation tends to be critical in three-dimensional space where the total number of integration points can increase dramatically. The aim of this paper is to compare computational efficiency of several numerical quadrature concepts which are nowadays available in the isogeometric analysis. Their performance is assessed on the assembly of stiffness matrix of B-spline based problems with special geometrical arrangement allowing to determine minimum number of integration points leading to exact results.*

Keywords: ***Isogeometric analysis, numerical quadrature, Gaussian quadrature, Bezier extraction, half-point rule.***

1. Introduction

The concept of the isogeometric analysis (IGA) (see papers Hughes (2005); Cottrell (2009)), initially motivated by the gap between the computer aided design (CAD) and the finite element analysis (FEA), builds upon the concept of isoparametric elements, in which the same shape functions are used to approximate the geometry and the solution on a single finite element. The IGA, as its name suggests, goes one step further because it employs the same functions for the description of the geometry and for the approximation of the solution space on that geometry. This implies that the isogeometric mesh (discretization for computational purposes) of the CAD geometry encapsulates the exact geometry no matter how coarse the mesh actually is. As a consequence, the need to have a separate representation for the original CAD model and another one for the actual computational geometry is completely eliminated.

The isogeometric approach has been originally developed (see paper Hughes (2005)) using the NURBS (non-uniform rational B-splines – Rogers (2000); Piegl (1997)) which are the basic building blocks in most CAD systems and which allow precise representation of wide class of objects (e.g. conics and quadrics). To overcome several drawbacks related to handling of NURBS patches (propagation of the refinement through the entire control grid, difficult merging of adjacent patches and handling of trimmed patches, etc.), this approach has been recently extended to so-called T-splines (see papers Sederberg (2003); Bazilevs (2010)) which are a generalization of NURBS. The advantage of T-splines consists in the fact that they allow truly local refinement, without propagating the entire row of control points, which enables efficient merging of several NURBS patches of different parameterization into a single gap free model of C^0 or higher order continuity (see papers Sederberg (2004); Bazilevs (2010)).

It has been shown (see papers Hughes (2005); Cottrell (2006, 2007); Auricchio (2007); Lipton (2010)) that the IGA outperforms the classical FEA in various aspects (accuracy, robustness, system condition number, etc.), which is the consequence of several important advantages of the IGA compared to the FEA. On the other hand, the computational effort of the IGA, especially when using higher

*Doc. Dr. Ing. Daniel Rypl: Department of Mechanics, Faculty of Civil Engineering, Czech Technical University in Prague, Thákurova 7; 166 29, Prague; CZ, e-mail: daniel.rypl@fsv.cvut.cz
**Prof. Dr. Ing. Bořek Patzák: Department of Mechanics, Faculty of Civil Engineering, Czech Technical University in Prague, Thákurova 7; 166 29, Prague; CZ, e-mail: borek.patzak@fsv.cvut.cz

order basis functions, seems to exceed that for the FEA. The significant source of the computational inefficiency has been identified to be related to the numerical quadrature of individual components of the discretized governing differential equation (for example in the context of structural mechanics, of stiffness matrix, mass matrix, load vector, etc.). The basic computational scheme of the IGA resembles very much that of the FEA with the only difference that instead of performing the numerical quadrature on individual finite elements the quadrature is accomplished over individual non-zero knot spans*** of the underlying B-spline based geometry. Due to the tensor product structure of the basis functions on individual knot spans of a two- and three-dimensional B-spline patch, the Gaussian quadrature schemes used for (so much popular) quadrilateral and hexahedral finite elements can be readily adopted in the IGA.

Analogical concept of Gaussian quadrature is also offered by the Bezier extraction approach (see papers Borden (2011); Scott (2011)) typically used when implementing the IGA into existing finite element computational codes. This approach utilizes the fact that the smooth B-spline basis can be constructed as a linear combination of a C^0 Bernstein polynomials which are the basis functions on the so-called Bezier element. Note that the coefficients of the linear combination are dependent only on the parameterization of the B-spline patch and are independent of the geometry (position of control points) itself. The beauty of this approach consists in the fact that the code does not have to implement the B-spline technology. It is enough to implement rather simple Bernstein polynomials in the interpolation engine (similarly as the standard Lagrange polynomials) and to apply appropriate linear operator (so-called the extraction operator) which hides the transformation between the C^0 Bernstein basis and smooth B-spline basis and which is typically part of the input data. Since the individual Bezier elements correspond to the individual non-zero knot-spans, the Gaussian integration over individual Bezier elements is equivalent to the Gaussian integration over the individual non-zero knot spans. There is, however, one important difference. Because the Bernstein polynomials are defined over the same parametric domain (typically from 0 to 1) and because the degree of Bernstein basis is the same for all Bezier elements within a single B-spline patch, the values of individual Bernstein basis functions and their derivatives are the same at individual Gauss integration points on all Bezier elements and can be therefore precomputed (only once) and stored (also only once) thus saving potentionally a huge number (depending on the number of integration points) of their evaluations.

Recently, there has been initiated a study (see paper Hughes (2010)) on efficient quadrature schemes for the NURBS-based IGA which profits from the continuity of higher degree B-spline basis functions between adjacent knot spans compared to the C^0 continuity of the basis functions between classical finite elements. While the Gaussian quadrature is optimal for the C^0 continuous finite elements, it is far from optimal for smooth B-spline basis functions spanning several consecutive knot spans. By taking into account the precise smoothness of the basis functions across boundaries of infinite number of uniform knot spans, a simple integration rule (so-called half-point rule) independent (in terms of the number of integrations points, not in terms of their location) of the degree of the polynomial basis and having (in 1D) just one integration point per two knot spans has been derived. For practical purposes, however, integration rules corresponding to open non-uniform finite knot vector are desirable. These rules can be obtained by numerical solution of a system of non-linear equations which is computationally demanding and which is worth only if the rules are applied repeatedly many times. Therefore only rules on 2, 3, 4, or 5 consecutive uniform knot spans for few cases of degree of practical interest have been derived. Although these rules only approach the best possible performance, the savings, especially in 3D, are significant.

The aim of this paper is to compare the efficiency of the above three approaches within the same software (Patzak (2012)) using the same programming techniques. The results of the comparison are given in the following Section. The discussion of the results together with the concluding remarks are given in Section 3.

*** In the context of the IGA, the non-zero knot spans are often called elements.

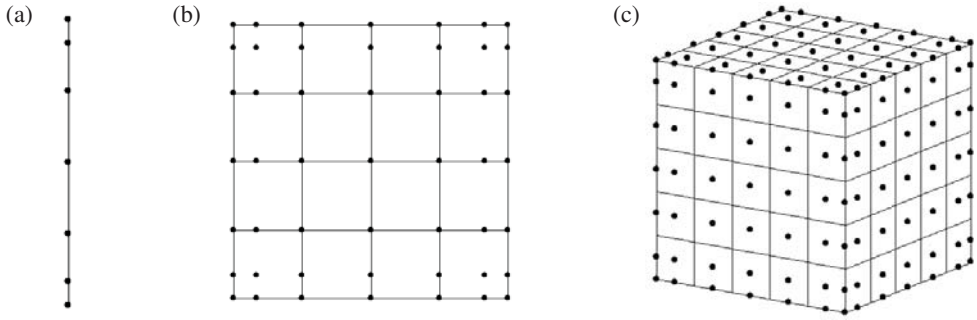

Fig. 1: Examples of geometry of investigated B-spline patches: (a) 1D:4-3, (b) 2D:3-4, (c) 3D:2-5

2. Quadrature schemes and comparison of their efficiency

Although the discussed quadrature schemes are used generally for (only approximate) integration of rational functions, they can handle precisely only polynomials. Therefore the examples on which the quadrature schemes have been tested are chosen to be B-spline patches with orthogonal system of isoparametric curves with control points defined by Graville's coordinates (see Fig. 1). This ensures that all components as well as the determinant of the Jacobian matrix are constant. In order to enable application of half-point rules (derived in paper Hughes (2010)), the (open) knot vectors describing the parameterization of the B-spline patch are always uniform having from 2 to 5 non-zero consecutive knot spans. Since the efficiency of these rules is dependent on the actual number of knot spans, the same number of knot spans is used for each spatial dimension. Furthermore, the available half-point rules limit the adopted uni-variate B-spline basis to degree 2, 3, and 4[†]. All the problems have been run in one-, two-, and three-dimensional space. The particular jobs are identified as xD:y-z where x $\in \{1, 2, 3\}$ stands for the spatial dimension of the problem, y $\in \{2, 3, 4\}$ denotes the degree of B-spline basis functions (common for all spatial dimensions), and z $\in \{2, 3, 4, 5\}$ indicates the number of uniform knot spans (also common for all spatial dimensions). For example, 2D:3-4 denotes two-dimensional analysis of degree 3×3 with 4×4 non-zero uniform knot spans (see Fig. 1).

The investigated quadrature schemes are the following

- GSR – Gauss Standard Rule,
- GBE – Gauss rule on Bezier Elements,
- GPS – Gauss rule with basis functions Precomputed for all knot Spans,
- HPR – Half-Point Rule.

Quadrature scheme GPS, considered only to assess the slow-down of GBE due the application of the extraction operator, is similar to GBE in that the values of B-spline basis functions and their derivatives are precomputed. However, since the concept of Bezier extraction is not adopted in GPS scheme, the precomputed values must be stored for all knot spans. Note that due to the tensor product structure of the Gauss rules, only the uni-variate B-spline functions and their derivatives are stored for individual spatial directions in GPS as well as in GBE.

The performance of individual quadrature schemes has been assessed by measuring the time needed for the assembly of complete stiffness matrix (in the symmetric skyline format). In order to make the time measurable, the stiffness matrix has been assembled repeatedly, namely 10^6 times for 1D problems, 10^4 for 2D problems, and 10^2 for 3D problems. Recalling that the Jacobian matrix is constant, the integrated terms of the stiffness matrix are uni-variate polynomials of order equal to $2p - 2$ in 1D case and multivariate (but of tensor product structure) polynomials of order $2p$ (in each variable) in 2D and 3D case, where p denotes the degree of B-spline basis functions. This allows to select the appropriate

[†]The case of degree 1 is not interesting, because then the IGA is identical with FEM and the Gaussian quadrature is optimal in such a case.

Tab. 1: Pseudo-code for the evaluation of the stiffness matrix

```
compute_stiffness_matrix {
   initialize K_global;
   loop over all B-spline patches (Bp) {
      loop over all integration rules (ir) of Bp {
         initialize K_local;
         loop over all integration points (ip) of ir {
            B = compute B_matrix at(ip);
            D = compute D_matrix at(ip);
            J = compute Jacobian at(ip);
            K_local += B^T.D.B.J;
         }
         assemble K_local to K_global;
      }
   }
   return K_global;
}
```

quadrature rule with minimum number of integration points which still leads to exact results. Note, however, that for HPR scheme, only the rules for the integration in spaces with C^0 continuity, namely in spaces $\varphi_{2,0}$, $\varphi_{4,0}$, $\varphi_{6,0}$, and $\varphi_{8,0}$[‡] (see paper Hughes (2010) for details) have been adopted.

A typical pseudo-code for the assembly of the stiffness matrix (on an abstract level) using the Gaussian quadrature is presented in Table 1. Each knot span is associated with an integration rule (see papers Rypl (2012a,b)) which stores individual integration points, position of which are defined within that single knot span. Note that at all integration points within the same integration rule, the same basis function attain non-zero value. Such an implementation can be easily adopted for the half-point quadrature schemes. It is just enough to localize the individual integration points, distribution of which is defined over several consecutive knot spans, into individual knot spans and create corresponding integration rules.

The results of individual analyses are summarized separately in Tables 2, 3, and 4 for spatial dimension 1, 2, and 3, respectively. Note that the elapsed time does not account neither for precomputing the values of B-spline basis functions and their derivatives (for schemes GBE and GPS) nor for the evaluation of the extraction operator (in GBE scheme) which is also precomputed and stored. Except the timing, also some additional quantities are provided to complete the information:

- Ctrl pnts - total number of control points describing the B-spline patch,
- G* tip - total number of integrations points for GSR/GBE/GPS schemes,
- G* ip/s - number of integrations points in a single direction on a single knot span for GSR/GBE/GPS schemes,
- HPR tip - total number of integrations points for HPR scheme,
- HPR ip - number of integration points in a single direction on the whole patch for HPR scheme.

The inspection of 1D results in Table 2 reveals that the times needed by GSR and HPR schemes are, not surprisingly, approximately in the ratio of the total number of integration points. It also shows that the application of GBE scheme leads to significant speedup which increases with the growing degree of B-spline basis functions (as the demands for their evaluation are growing). Therefore the GBE scheme outperforms the HPR scheme, which is obvious especially for degree 3 and 4. From the table it is also apparent, that the costs of GBE (compared to GPS) due to the application of the extraction operator are

[‡]See Appendix A for coordinates and weights of integration points for exact integration in $\varphi_{8,0}$.

Tab. 2: Summary of 1D jobs assembling 10^6 times stiffness matrix (timing in seconds)

Job id	Ctrl pnts	G* tip	G* ip/s	GSR time	GBE time	GPS time	HPR tip	HPR ip	HPR time
1D:2-2	4	4	2	6.7	4.6	4.0	3	3	5.7
1D:2-3	5	6	2	10.5	7.0	5.9	4	4	7.2
1D:2-4	6	8	2	13.4	9.3	7.6	5	5	9.8
1D:2-5	7	10	2	17.2	11.6	9.6	6	6	11.0
1D:3-2	5	6	3	12.2	7.3	6.1	5	5	10.3
1D:3-3	6	9	3	18.5	10.8	8.9	7	7	14.9
1D:3-4	7	12	3	24.8	14.0	11.9	9	9	19.2
1D:3-5	8	15	3	31.2	18.1	15.0	11	11	23.5
1D:4-2	6	8	4	19.1	10.9	8.6	7	7	17.0
1D:4-3	7	12	4	29.3	15.6	13.1	10	10	25.2
1D:4-4	8	16	4	38.8	23.3	17.3	13	13	33.0
1D:4-5	9	20	4	50.1	29.1	22.3	16	16	40.6

quickly growing with the increasing degree as the size of the extraction operator grows as well. In the case of results of 2D analyses (see Table 3), the situation changes quite considerably. While the ratio between the time consumed by GSR and HPR schemes is still in reasonable agreement (however not as good as for 1D case) with the ratio of total number of integration points used in these schemes, the profit from precomputing the values of basis functions and their derivatives is much less pronounced, which causes that HPR scheme is generally better than any of the Gauss based schemes. It is also worth to note that the cost of Bezier extraction for the 2D case is, compared to 1D, diminishing. This is, however, not caused by the improved efficiency of the Bezier extraction in 2D but by the decrease of its participation in the overall computational demands, which are enlarged by two facts. Firstly, the evaluation of the derivatives of basis functions with respect to Cartesian coordinates is more complex and secondly, the size of matrices B and K_{local} handled in the stiffness matrix assembly algorithm (see Table 1) is growing rapidly with the increasing degree. Assuming that the degree is the same in both spatial directions (which is the considered case), the number of basis functions which are non-zero at a particular integration point is growing with square of the degree. This effect becomes critical in 3D (see Table 4) where there is virtually no difference between individual Gauss based schemes. In this case the size of matrix K_{local} grows with the cube of the degree of the B-spline basis functions. Thus the costs related to the computation of the product B^TDBJ are dominating and the overall assembly time, for a given degree, is more or less linearly dependent on the total number of integration points. Since the total number of integrations points for HPR scheme is much smaller than the number used by the Gauss based schemes, HPR scheme in 3D is apparently superior to GSR, GBE as well as GPS scheme for all degrees and number of knot spans. It is interesting to see, however, that despite the fact that the costs of the numerical quadrature in 3D are driven predominantly by the evaluation of the product B^TDBJ (not of its components), the times for GSR and HPR schemes are only approximately in the ratio of the total number of integration points. A detailed inspection of the profiling information has uncovered that the time consumed by the function evaluating the product B^TDBJ per integration point is noticeably smaller for GSR scheme. This could be attributed to the effect of caching K_{local} because the number of processed integration points per integration rule is generally higher for GSR scheme compared to HPR scheme.

Tab. 3: Summary of 2D jobs assembling 10^4 times stiffness matrix (timing in seconds)

Job id	Ctrl pnts	G* tip	G* ip/s	GSR time	GBE time	GPS time	HPR tip	HPR ip	HPR time
2D:2-2	16	36	3	2.2	1.7	1.6	25	5	1.5
2D:2-3	25	81	3	4.8	3.8	3.6	49	7	3.0
2D:2-4	36	144	3	8.5	7.2	6.5	81	9	5.0
2D:2-5	49	225	3	13.6	10.7	10.1	121	11	8.0
2D:3-2	25	64	4	6.9	6.0	5.6	49	7	5.7
2D:3-3	36	144	4	15.4	13.3	13.1	100	10	11.9
2D:3-4	49	256	4	27.9	23.5	22.6	169	13	19.4
2D:3-5	64	400	4	43.3	37.7	35.3	256	16	30.1
2D:4-2	36	100	5	19.4	17.7	16.7	81	9	17.6
2D:4-3	49	225	5	44.1	39.5	38.2	169	13	36.8
2D:4-4	64	400	5	78.5	70.2	68.0	289	17	62.1
2D:4-5	81	625	5	121.1	109.7	105.8	441	21	94.8

3. Conclusions

In this paper, a study of computational efficiency of several numerical quadrature schemes available for the IGA has been performed. The performance of the schemes has been assessed on the assembly of the stiffness matrix on such a geometrical arrangement of a B-spline patch that the minimum number of integration points leading to exact results could have been safely determined. The investigation has revealed that the main source of the computational costs of the numerical quadrature is dependent on the spatial dimension qualitatively as well as quantitatively. While in 1D the prevailing costs are related to the expensive evaluation of basis functions and their derivatives and are increasing with the degree and consequently with the complexity of the B-spline basis functions, in 3D, the dominating costs are associated with the assembly of the contributions to the stiffness matrix at individual integration points, number of which as well as the size of the contributions is also growing with the degree. This implies that in 1D, faster algorithms are those which profit from the precomputed values of the basis functions and their derivatives (such as GBE scheme). In 3D, on the other hand, since the critical factor is the total number of integrations points, the quadrature rules that benefit from taking into account the continuity between the knot spans (such as HPR scheme) are the better ones. In 2D, both effects are combined. The numerical evidence shows, however, that the HPR scheme is more appropriate than GBE scheme.

In the current implementation of two- and three-dimensional GSR, GBE as well as HPR schemes, there is still some space for savings. For example, the evaluation of particular components of the stiffness matrix could be accelerated if they are computed on the level of integration rule rather than on the level of integration point, because the locally precomputed uni-variate quantities (on the level of integration rule) can be repeatedly reused (due to the tensor product structure) for all integration points within the same integration rule. The preliminary results reveal, however, that this effect is of only a little significance in 2D and completely negligible in 3D.

An important issue is related to the fact that in reality the integrated functions are only rarely polynomials. More commonly, the integrated terms are of rational character as the consequence of non-constant Jacobian (does not matter whether due to the location of control points[§] of a B-spline geometry or because

[§]Note that while in the FEA the Jacobian (more precisely, its variation) could be reasonably controlled by the quality of the finite element mesh, in the IGA, the analyst does not have usually such a possibility as he/she is stuck with the geometry.

Tab. 4: Summary of 3D jobs assembling 10^2 times stiffness matrix (timing in seconds)

Job id	Ctrl pnts	G* tip	G* ip/s	GSR time	GBE time	GPS time	HPR tip	HPR ip	HPR time
3D:2-2	64	216	3	1.3	1.3	1.3	125	5	0.8
3D:2-3	125	729	3	4.5	4.3	4.3	343	7	2.3
3D:2-4	216	1728	3	10.6	10.2	10.1	729	9	5.0
3D:2-5	343	3375	3	20.8	20.1	20.0	1331	11	9.1
3D:3-2	125	512	4	13.7	13.6	13.6	343	7	10.2
3D:3-3	216	1728	4	46.4	46.1	46.0	1000	10	30.1
3D:3-4	343	4096	4	110.2	109.5	108.8	2197	13	66.3
3D:3-5	512	8000	4	217.3	215.2	214.5	4096	16	125.1
3D:4-2	216	1000	5	93.0	92.9	92.6	729	9	75.8
3D:4-3	343	3375	5	315.6	314.2	314.0	2197	13	228.8
3D:4-4	512	8000	5	747.1	744.6	745.8	4913	17	512.6
3D:4-5	729	15625	5	1456.8	1458.5	1457.3	9261	21	967.7

of using non-uniform weights in a NURBS geometry). In such a case, the common practice to select the quadrature rule under the assumption that the Jacobian is constant may lead to significant error. Thus the over-integration when using Gaussian quadrature rule may play also a positive role. Moreover, taking into account the fact that the derivation of half-point rule for non-uniform knot spans is computationally prohibitive, especially if large number of spans and high degree of basis functions is considered, and that refining the knot vector to (at least piece-wise) uniform knot vector leads to increase of both the number of control points (and thus also problem unknowns) and the number of integration points, the use of standard Gaussian quadrature per non-zero knot span still remains competitive approach (in a general case). This, however, implies that the question of numerical quadrature in the IGA remains open and that there is a strong need to further search for efficient quadrature rules.

Acknowledgments

This work was supported by the Technology Agency of the Czech Republic - Project No. TA02011196. Its financial assistance is gratefully acknowledged.

Appendix A.

In this Appendix, the quadrature schemes (not presented in paper Hughes (2010)) for the exact integration in $\varphi_{8,0}$ on the interval $[0, 1]$ with 2, 3, 4, and 5 uniform knot spans are provided. Coordinates and weights of quadrature points, summarized in Tables 5 – 8, have been computed by the numerical procedure outlined in paper Hughes (2010) using the MATLAB *fsolve* tolerance 10^{-12}.

References

Auricchio, F., da Veiga, L.B., Buffa, A., Lovadina, C., Reali, A., Sangalli, G. (2007), A Fully "Locking-free" Isogeometric Approach for Plane Linear Elasticity Problems: A Stream Function Formulation, *Computer Methods in Applied Mechanics and Engineering*, Vol. 197, pp. 160–172.

Bazilevs, Y., Calo, V.M., Cottrell, J.A., Evans, J.A., Hughes, T.J.R., Lipton, S., Scott, M.A., Sederberg, T.W. (2010), Isogeometric Analysis Using T-splines, *Computer Methods in Applied Mechanics and Engineering*, Vol. 199, No. 5–8, pp. 229–263.

Tab. 5: Coordinates and weights of quadrature points for exact quadrature in $\varphi_{8,0}$ on the interval $[0, 1]$ with 2 uniform knot spans

#	Coordinate	Weight
1	0.028552098057259	0.071856780395612
2	0.138421506819060	0.140678007574721
3	0.291795216184451	0.155913261487865
4	0.430120067828107	0.111551950541791
5	0.500000000000000	0.040000000000000
6	0.569879932171893	0.111551950541791
7	0.708204783815549	0.155913261487865
8	0.861578493180940	0.140678007574721
9	0.971447901942741	0.071856780395612

Tab. 6: Coordinates and weights of quadrature points for exact quadrature in $\varphi_{8,0}$ on the interval $[0, 1]$ with 5 uniform knot spans

#	Coordinate	Weight
1	0.011420839222904	0.028742712158246
2	0.055368602727625	0.056271203029890
3	0.116718086473782	0.062365304595146
4	0.172048027131244	0.044620780216714
5	0.206831767683998	0.033121642297043
6	0.252360380590827	0.057525896479555
7	0.315009929291968	0.063655560553979
8	0.371476934778886	0.045533635363296
9	0.405222463773460	0.028872252516536
10	0.444079687961464	0.049762970461542
11	0.500000000000000	0.059056084656084
12	0.555920312038536	0.049762970461542
13	0.594777536226540	0.028872252516536
14	0.628523065221114	0.045533635363296
15	0.684990070708033	0.063655560553979
16	0.747639619409173	0.057525896479555
17	0.793168232316002	0.033121642297043
18	0.827951972868756	0.044620780216714
19	0.883281913526218	0.062365304595146
20	0.944631397272375	0.056271203029890
21	0.988579160777096	0.028742712158246

Tab. 7: Coordinates and weights of quadrature points for exact quadrature in $\varphi_{8,0}$ on the interval $[0, 1]$ with 3 uniform knot spans

#	Coordinate	Weight
1	0.019034732038173	0.047904520263742
2	0.092281004546041	0.093785338383150
3	0.194530144122971	0.103942174325245
4	0.286746711885407	0.074367967027856
5	0.342115696184178	0.047895861179092
6	0.406832256845926	0.082907772643406
7	0.500000000000000	0.098392732354997
8	0.593167743154074	0.082907772643406
9	0.657884303815822	0.047895861179092
10	0.713253288114593	0.074367967027856
11	0.805469855877029	0.103942174325245
12	0.907718995453959	0.093785338383150
13	0.980965267961827	0.047904520263742

Tab. 8: Coordinates and weights of quadrature points for exact quadrature in $\varphi_{8,0}$ on the interval $[0, 1]$ with 4 uniform knot spans

#	Coordinate	Weight
1	0.014276049028629	0.035928390197806
2	0.069210753409518	0.070339003787363
3	0.145897608092228	0.077956630743933
4	0.215060033914055	0.055775975270892
5	0.258539709605000	0.041402052871308
6	0.315450475738540	0.071907370599436
7	0.393762411614959	0.079569450692479
8	0.464346168473608	0.056917044204120
9	0.500000000000000	0.020408163265306
10	0.535653831526392	0.056917044204120
11	0.606237588385041	0.079569450692479
12	0.684549524261460	0.071907370599436
13	0.741460290395000	0.041402052871308
14	0.784939966085945	0.055775975270892
15	0.854102391907772	0.077956630743933
16	0.930789246590482	0.070339003787363
17	0.985723950971371	0.035928390197806

Borden, M.J., Scott, M.A., Evans, J.A., Hughes, T.J.R. (2011), Isogeometric Finite Element Data Structures Based on Bezier Extraction of NURBS, *International Journal for Numerical Methods in Engineering*, Vol. 87, No. 1–5, pp. 15–47.

Cottrell, J.A., Reali, A., Bazilevs, Y., Hughes, T.J.R. (2006), Isogeometric Analysis of Structural Vibrations, *Computer Methods in Applied Mechanics and Engineering*, Vol. 195, pp. 5257–5296.

Cottrell, J.A., Hughes, T.J.R., Reali, A. (2007), Studies of Refinement and Continuity in Isogeometric Structural Analysis, *Computer Methods in Applied Mechanics and Engineering*, Vol. 196, pp. 4160–4183.

Cottrell, J.A., Hughes, T.J.R., Bazilevs, Y. (2009), *Isogeometric Analysis: Toward Integration of CAD and FEA*, John Wiley & Sons.

Hughes, T.J.R., Cottrell, J.A., Bazilevs Y. (2005), Isogeometric Analysis: CAD, Finite Elements, NURBS, Exact Geometry and Mesh Refinement, *Computer Methods in Applied Mechanics and Engineering*, Vol. 194, pp. 4135–4195.

Hughes, T.J.R., Reali, A., Sangalli, G. (2010), Efficient Quadrature for NURBS-based Isogeometric Analysis, *Computer Methods in Applied Mechanics and Engineering*, Vol. 199, No. 5–8, pp. 301–313.

Lipton, S., Evans, J.A., Bazilevs, Y., Elguedj, T., Hughes, T.J.R. (2010), Robustness of Isogeometric Structural Discretizations under Severe Mesh Distortion, *Computer Methods in Applied Mechanics and Engineering*, Vol. 199, pp. 357–373.

Patzák, B. (2012), OOFEM project home page, http://www.oofem.org.

Piegl, L., Tiller, W. (1997), *The NURBS Book*, Springer-Verlag.

Rogers, D.F. (2000), *An Introduction to NURBS: With Historical Perspective*, Morgan Kaufmann.

Rypl, D., Patzák, B. (2012a), From the Finite Element Analysis to the Isogeometric Analysis in an Object Oriented Computing Environment, *Advances in Engineering Software*, Vol. 44, No. 1, pp. 116–125.

Rypl, D., Patzák, B. (2012b), Object Oriented Implementation of the T-spline Based Isogeometric Analysis, *Advances in Engineering Software*, in print.

Scott, M.A., Borden, M.J., Verhoosel, C.V., Sederberg, T.W., Hughes, T.J.R. (2011), Isogeometric Finite Element Data Structures Based on Bezier Extraction of T-splines, *International Journal for Numerical Methods in Engineering*, Vol. 88, No. 2, pp. 126–156.

Sederberg, T.W., Zheng, J., Bakenov, A., Nasri, A. (2003), T-splines and T-NURCCs, *ACM Transactions on Graphics (SIGGRAPH 2003)*, Vol. 22, No. 3, pp. 477–484.

Sederberg, T.W., Gardon, D., Finnigan, G., North, N., Zheng, J., Lyche, T. (2004), T-spline Simplification and Local Refinement, *ACM Transactions on Graphics (SIGGRAPH 2004)*, Vol. 23, No. 3, pp. 276–283.

18th International Conference
ENGINEERING MECHANICS 2012
Svratka, Czech Republic, May 14 – 17, 2012

pp. 1145–1156
Paper #45

LOCAL INTEGRAL FORMULATIONS FOR THIN PLATE BENDING PROBLEMS

L. Sator, V. Sladek, J. Sladek*

Abstract: *In this paper, we present that the decomposition of the biharmonic equation into two Poisson equations is applicable to general case of boundary conditions and any shape of the boundary edge of the plate, if we use the Local Integral Equation (LIE) formulation and a meshless approximation for primary field variables. Besides the standard advantages of mesh free formulations remember the new advantage consisting in decreasing the order of the derivatives of field variables. Instead of the third order derivatives of the deflection field in the weak formulation for the biharmonic equation the highest order of the derivatives in the present weak formulation does not exceed the first order. Mostly, it is decreased also the order of the derivativesof new field variables in the expressions of the boundary conditions. Several illustrative examples are presented for comparison of accuracy, convergence and computational efficiency achieved by using various approaches.*

Keywords: ***Local Integral Equation formulation, meshless approximation, decomposition, biharmonic equation, Poisson equations***

1. Introduction

It is well known that high order derivatives of field variables in the governing equations give rise to difficulties in solution of boundary value problems because of worse accuracy of numerically evaluated high order derivatives. The order of the differential operator can be decreased by decomposing this operator into two lower order differential operators with introducing new field variables. The relevant boundary densities in the decomposed problem are different from the boundary densities in the original boundary value problem. Therefore, sometime it can be problematic to express the original boundary conditions in terms of the new field variables and/or their derivatives. Especially, it is impossible in general in the boundary element formulations where the unknowns are localized and approximated on boundary alone.

In two recent decades, solution of many engineering problems as well as problems of mathematical physics have been reformulated by using various mesh free formulations with meshless approximations. Such approximations belong to domain type approximations and the restrictions of boundary elements can be eliminated.

In this paper, we present that the decomposition of the biharmonic equation into two Poisson equations is applicable to general case of boundary conditions and any shape of the boundary edge of the plate, if we use the weak formulation based on the Local Integral Equations (LIE) formulation and a meshless approximation for primary field variables. In the local weak formulation, the constant test function with the support on the sub-domain is utilized, what corresponds to integral satisfaction of physical balance principles (equilibrium of forces and force moments) on local sub-domains. To illustrate the robustness of the proposed formulation, we present also the weak formulation for the original biharmonic problem. The strong formulation is not considered because of the 4^{th} order derivatives of deflections. Owing to the decomposition, the order of the derivatives in the governing equations is decreased form four to two. The prescribed boundary conditions are considered in each formulation in

* Ing. Ladislav Sátor, Prof. RNDr. Vladimír Sládek, DrSc., Prof. Ing. Ján Sládek, DrSc., Institute of Construction and Architecture, Slovak Academy of Science, 845 03 Bratislava, Slovakia, e-mail: ladislav.sator@savba.sk

strong form by collocation at boundary nodes. Two kinds of the meshless approximations are employed in this paper, such as the Moving Least Square (MLS) approximation (Lancaster and Salkauskas, 1981) and the Point Interpolation Method (PIM) (Liu, 2003). Besides the standard advantages of mesh free formulations remember that the domain-type character of the approximation enables us to express all the boundary quantities in terms of the new field variables and/or their derivatives on the boundary. Numerical examples with exact benchmark solution are considered for comparisons of accuracy, convergence and computational efficiency of various approaches.

2. Physical decomposition of the governing equations

In Kirchoff's theory of bending of thin plates (Timoshenko and Woinowsky-Krieger, 1959) the all physical quantities are expressed in terms us the functions of deflection $w(x)$ and/or their derivatives. For the plate of thickness h and midplane Ω orthogonal to the axis x_3, the tensor of moments can be expressed in terms of the second order derivative of deflection as

$$M_{ij} = -D\left[(1-\nu)w_{,ij} + \nu\delta_{ij}\nabla^2 w\right], \qquad D = \frac{Eh^3}{12(1-\nu^2)} \tag{1}$$

where D is the bending stiffness, E and ν is the Young modulus and Poisson ratio, respectively.
The bending moment M and the twisting moment T on the boundary edge $\Gamma = \partial\Omega$ are given as

$$M = n_i n_j M_{ij} = -D\left[(1-\nu)n_i n_j w_{,ij} + \nu\nabla^2 w\right] \tag{2}$$

$$T = n_i t_j M_{ij} = -D(1-\nu)n_i t_j w_{,ij} = -D(1-\nu)t_i n_j w_{,ij} \tag{3}$$

where n_i and t_i are the Cartesian components of the unit normal and tangent vector on Γ, respectively. The transversal the shear force N and the equivalent shear force on the boundary edge are defined as

$$N := n_i M_{ij,j} = -n_i D\nabla^2 w_{,i}, \qquad V := N + \frac{\partial T}{\partial \mathbf{t}} \tag{4}$$

The governing equation for deflections of thin plane is given as

$$M_{ij,ij}(\mathbf{x}) = -q(\mathbf{x}), \tag{5}$$

hence after substituting (1_1) to (5) we can obtain governing equation in form

$$\left[D(1-\nu)w_{,ij}\right]_{,ij} + \nabla^2\left[\nu D\nabla^2 w\right] = q \tag{6}$$

with $q(\mathbf{x})$ being the density of transversal loading applied on the plate surface.

Usually, Poisson ratio is constant and the governing equation becomes

$$D\nabla^2\nabla^2 w + 2D_{,i}(\nabla^2 w)_{,i} + (1-\nu)D_{,ij}w_{,ij} + \nu(\nabla^2 D)(\nabla^2 w) = q\,. \tag{7}$$

If we shall consider the bending stiffness to be constant, then the governing equation is simplified as

$$D\nabla^2\nabla^2 w = q\,. \tag{8}$$

Three basic boundary conditions can be assumed on the boundary edge Γ:

(i) clamped edge: $w|_\Gamma = 0;\ \left.\frac{\partial w}{\partial n}\right|_\Gamma = 0$

(ii) simply supported edge: $w|_\Gamma = 0;\ M|_\Gamma = 0$ (9)

(iii) free edge: $M|_{\Gamma} = 0;\ V|_{\Gamma} = 0$

The fourth order derivatives of deflections in governing equations can give rise to serious difficulties not only in strong formulation for numerical solution, but also in weak formulation owing to inaccurate approximation of high order derivatives of deflections occurring in the integral equations as well as in boundary conditions.

Therefore, it is expedient to introduce the new field variable defined as

$$m(\mathbf{x}) := -D\nabla^2 w(\mathbf{x}) \quad \text{for} \quad \mathbf{x}\in\Omega \tag{10}$$

Then the governing equation (8) is split into two equations given by (10) and (11)

$$\nabla^2 m(\mathbf{x}) = q(\mathbf{x}) \quad \text{for..} \ \mathbf{x}\in\Omega \tag{11}$$

3. Weak formulation of governing equations

The weak formulations of governing equations (10) and (11) corresponding to two field variables with assuming the bending stiffness to be constant, can be written as

$$D\int_{\partial\Omega^s} n_i w_{,i} d\Gamma + \int_{\Omega^s} m d\Omega = 0 \tag{12}$$

$$\int_{\partial\Omega^s} n_i m_{,i} d\Gamma = -\int_{\Omega^s} q d\Omega \tag{13}$$

The relevant boundary quantities $\{w, \partial w/\partial\mathbf{n}, M, V\}$ are expressed in terms of two field variables and their derivatives on boundary edges.

4. Meshless approximation of fields variables

In general, a meshless approximation uses a local interpolation to represent trial function with the values of the unknown variables at some randomly distributed nodes. Now, we shortly describe two kinds of meshless approximations. For the sake of brevity, we shall use the common notation $u(\mathbf{x})$ for the scalar fields $w(\mathbf{x})$ and/or $m(\mathbf{x})$.

Moving Least Square (MLS) approximation

In the MLS-approximation, the polynomial basis $\{p_\mu(\mathbf{x})\}_{\mu=1}^m$ is employed and the expansion coefficients are found from minimization of weighted squares of residua at a finite number of nodal points (Lancaster and Salkauskas, 1981). The scalar field $u(\mathbf{x})$ can be approximated as

$$u(\mathbf{x}) \approx \sum_{a=1}^{N} \hat{u}^a \phi^a(\mathbf{x}) \tag{14}$$

where N is the total number of nodes, $\hat{u}^a$ is a nodal unknown different from the nodal value $u(\mathbf{x}^a)$, and $\phi^a(\mathbf{x})$ is the shape function associated with the nodal point $\mathbf{x}^a$. Instead of standard MLS-approximation, one can utilize the Central Approximation Node (CAN) concept of MLS-approximation (Sladek et al., 2008). Let $\mathbf{x}^q$ be the CAN for the approximation at a point $\mathbf{x}$. Then, the amount of nodes involved into the approximation at $\mathbf{x}$ is reduced a-priori from N to N^q, where N^q is the number of nodes supporting the approximation at the CAN $\mathbf{x}^q$, i.e. the amount of nodes in the set $M^q = \{\forall \mathbf{x}^a; w^a(\mathbf{x}^q) > 0\}_{a=1}^N$, where

$w^a(\mathbf{x})$ is the weight function associated with the node $\mathbf{x}^a$ at the field point $\mathbf{x}$. In this paper, we employ the Gaussian weights (Sladek et al., 2008). The MLS-CAN approximation is given as

$$u(\mathbf{x}) \approx \sum_{a=1}^{N^q} \hat{u}^{\bar{a}} \phi^{(q,a)}(\mathbf{x}) , \quad \bar{a} = n(q,a) \tag{15}$$

where $\bar{a}$ is the global number of the a-th node from the N^q nodal points $\mathbf{x}^{\bar{a}} \in M^{q}$. The CAN node can be selected as the nearest node to the field point $\mathbf{x}$.

The derivatives of the field variable $u(\mathbf{x})$ can be approximated by differentiating the approximation (15), i.e.

$$u_{,i}(\mathbf{x}) \approx \sum_{a=1}^{N^q} \hat{u}^{\bar{a}} \phi_{,i}^{(q,a)}(\mathbf{x}) , u_{,ij}(\mathbf{x}) \approx \sum_{a=1}^{N^q} \hat{u}^{\bar{a}} \phi_{,ij}^{(q,a)}(\mathbf{x}), u_{,ijk}(\mathbf{x}) \approx \sum_{a=1}^{N^q} \hat{u}^{\bar{a}} \phi_{,ijk}^{(q,a)}(\mathbf{x}) \tag{16}$$

The evaluation of the shape functions and their derivatives at each field point is a numerical procedure which prolongs the CPU time. The relationships required in such numerical evaluations can be found in (Sladek et al., 2012)where Gaussian weights are used in MLS-approximation.

It is worth of consideration the modification of shape functions and their derivatives. Making use the definitions

$$s(\mathbf{x}) := \sum_{a=1}^{N^q} \phi^{(q,a)}(\mathbf{x}), \; s_i(\mathbf{x}) := \sum_{a=1}^{N^q} \phi_{,i}^{(q,a)}(\mathbf{x}),$$

$$s_{ij}(\mathbf{x}) := \sum_{a=1}^{N^q} \phi_{,ij}^{(q,a)}(\mathbf{x}), \; s_{ijk}(\mathbf{x}) := \sum_{a=1}^{N^q} \phi_{,ijk}^{(q,a)}(\mathbf{x}) \tag{17}$$

and adopting the modifications

$$\begin{aligned}
&\phi^{(q,a)}(\mathbf{x}) \to \%\phi^{(q,a)}(\mathbf{x}) := \phi^{(q,a)}(\mathbf{x}) / s(\mathbf{x}),\\
&\phi_{,i}^{(q,a)}(\mathbf{x}) \to \%\phi_{,i}^{(q,a)}(\mathbf{x}) := \phi_{,i}^{(q,a)}(\mathbf{x}) - s_i(\mathbf{x})\%\phi^{(q,a)}(\mathbf{x}),\\
&\phi_{,ij}^{(q,a)}(\mathbf{x}) \to \%\phi_{,ij}^{(q,a)}(\mathbf{x}) := \phi_{,ij}^{(q,a)}(\mathbf{x}) - s_{ij}(\mathbf{x})\%\phi^{(q,a)}(\mathbf{x}),\\
&\phi_{,ijk}^{(q,a)}(\mathbf{x}) \to \%\phi_{,ijk}^{(q,a)}(\mathbf{x}) := \phi_{,ijk}^{(q,a)}(\mathbf{x}) - s_{ijk}(\mathbf{x})\%\phi^{(q,a)}(\mathbf{x})
\end{aligned} \tag{18}$$

one can guarantee satisfaction of the following equations

$$\begin{aligned}
&\sum_{a=1}^{N^q} \phi^{(q,a)}(\mathbf{x}) = 1 , \quad \sum_{a=1}^{N^q} \phi_{,i}^{(q,a)}(\mathbf{x}) = 0 ,\\
&\sum_{a=1}^{N^q} \phi_{,ij}^{(q,a)}(\mathbf{x}) = 0 , \quad \sum_{a=1}^{N^q} \phi_{,ijk}^{(q,a)}(\mathbf{x}) = 0
\end{aligned} \tag{19}$$

with the wave notation being omitted in Eq. (19) and in what follows.

Point interpolation method (RBF+P)

In this approximation the basis functions are taken as a combination of polynomials and radial basis functions (RBF) (Liu, 2003). Then, one can solve the problem of accuracy and numerical stability of the

approximation(Liu, 2003),(Sladek et al., 2008). We shall consider the same polynomial basis as in the MLS-approximation and the RBFs will be taken as multiquadrics

$$R^n(\mathbf{x}) = \left(\left| \mathbf{x} - \mathbf{x}^n \right|^2 + (c^n)^2 \right)^{p/2} \tag{20}$$

with c^n being the shape parameter.

The approximation of the field variable $u(\mathbf{x})$ can be expressed by

$$u(\mathbf{x}) \approx \sum_{a=1}^{N^q} u^{\bar{a}} \varphi^{(q,a)}(\mathbf{x}) \ , \bar{a} = n(q,a) \tag{21}$$

i.e. formally, it is the same as in the MLS-approximation, but now the nodal unknowns are directly the values of the approximated field variable, since the shape functions obey the Kronecker–delta property $\varphi^{(q,a)}(\mathbf{x}^{\bar{b}}) = \delta_{ab}$.
The derivatives of the field variable are approximated as

$$u_{,i}(\mathbf{x}) \approx \sum_{a=1}^{N^q} u^{\bar{a}} \varphi_{,i}^{(q,a)}(\mathbf{x}), \ u_{,ij}(\mathbf{x}) \approx \sum_{a=1}^{N^q} u^{\bar{a}} \varphi_{,ij}^{(q,a)}(\mathbf{x}), \ u_{,ijk}(\mathbf{x}) \approx \sum_{a=1}^{N^q} u^{\bar{a}} \varphi_{,ijk}^{(q,a)}(\mathbf{x}) \tag{22}$$

Again certain numerical procedures are required for evaluation of the shape functions and their derivatives at a field point. For more details, we refer the reader to(Sladek et al., 2012).

5. Rotationally symmetric bending of circular plates

Having regard to the symmetry, the problem simplified when instead of Cartesian coordinates we use polar coordinates (r,φ), where $(x_1, x_2) = (r\cos\varphi, r\sin\varphi)$ and $\partial(.)/\partial\varphi \equiv 0$. Then

$$\begin{aligned} w_{,i}(r) &= r_{,i} \frac{\partial w(r)}{\partial r}, \\ w_{,ij}(r) &= \frac{1}{r}\left(\delta_{ij} - r_{,i}r_{,j}\right)\frac{\partial w(r)}{\partial r} + r_{,i}r_{,j}\frac{\partial^2 w(r)}{\partial r^2}, \\ \nabla^2 w(r) &= \left(\frac{\partial^2}{\partial r^2} + \frac{1}{r}\frac{\partial}{\partial r}\right) w(r) \end{aligned} \tag{23}$$

Since the boundary edge Γ is a circle, the outer unit normal vector on Γ is $n_i = \pm r_{,i}$, where the lower sign is valid on the inner boundary edge in the case of the circular plate with central circular hole. The unit tangent vector on the boundary edge is $t_i = \varepsilon_{3ki} n_k = \pm \varepsilon_{3ki} r_{,k}$. Thus, we may write on the boundary edge

$$M = n_i n_j M_{ij}\big|_\Gamma = -D r_{,i} r_{,j} \left[(1-\nu) w_{,ij}(r) + \nu \delta_{ij} \nabla^2 w(r) \right]\Big|_\Gamma = -D \left[(1-\nu) \frac{\partial^2 w(r)}{\partial r^2} + \nu \nabla^2 w(r) \right]\Bigg|_\Gamma \tag{24}$$

$$\begin{aligned} T = n_i t_j M_{ij}\big|_\Gamma &= \mathrm{m} D \varepsilon_{3lj} r_{,i} r_{,l} \left[(1-\nu) w_{,ij}(r) + \nu \delta_{ij} \nabla^2 w(r) \right]\Big|_\Gamma = \\ &= \mathrm{m} D (1-\nu) \varepsilon_{3lj} r_{,i} r_{,l} \left[\frac{1}{r}\left(\delta_{ij} - r_{,i}r_{,j}\right)\frac{\partial w(r)}{\partial r} + r_{,i}r_{,j}\frac{\partial^2 w(r)}{\partial r^2} \right]\Bigg|_\Gamma \equiv 0 \end{aligned} \tag{25}$$

$$N = n_i M_{ij,j}\big|_\Gamma = -Dn_i\left(\nabla^2 w(r)\right)_{,i}\Big|_\Gamma = \mathrm{m}D\frac{\partial\nabla^2 w(r)}{\partial r}\Big|_\Gamma \tag{26}$$

where we have utilized the fact that

$$\frac{\partial f(r)}{\partial \mathbf{t}}\Big|_\Gamma = \pm\varepsilon_{3ik} r_{,i} f_{,k}(r)\big|_\Gamma = \pm\varepsilon_{3ik} r_{,i} r_{,k}\frac{\partial f(r)}{\partial r}\Big|_\Gamma \equiv 0\,. \tag{27}$$

Two field variable formulation

The governing equations (10) and (11) can be written now as

$$D\left(\frac{\partial^2}{\partial r^2}+\frac{1}{r}\frac{\partial}{\partial r}\right)w(r)+m(r)=0 \text{ or } D\frac{1}{r}\frac{\partial}{\partial r}\left(r\frac{\partial w(r)}{\partial r}\right)+m(r)=0 \tag{28}$$

$$\left(\frac{\partial^2}{\partial r^2}+\frac{1}{r}\frac{\partial}{\partial r}\right)m(r)=-q(r) \text{ or } \frac{1}{r}\frac{\partial}{\partial r}\left(r\frac{\partial m(r)}{\partial r}\right)=-q(r) \tag{29}$$

Thus, in view of (24)-(26) and (28), we may write

$$M = \left[m(r)+D(1-\nu)\frac{1}{r}\frac{\partial w(r)}{\partial r}\right]\Big|_\Gamma \tag{30}$$

$$T = 0 \tag{31}$$

$$N = \pm\frac{\partial m(r)}{\partial r}\Big|_\Gamma = V \tag{32}$$

The weak form of the governing equations (28) and (29) is given by

$$Dr\frac{\partial w(r)}{\partial r}\Big|_{r^c-r_o}^{r^c+r_o} + \int_{r^c-r_o}^{r^c+r_o} r\,m(r)dr = 0 \tag{33}$$

$$r\frac{\partial m(r)}{\partial r}\Big|_{r^c-r_o}^{r^c+r_o} = -\int_{r^c-r_o}^{r^c+r_o} r\,q(r)dr \text{ or } r\frac{\partial m(r)}{\partial r}\Big|_{r^c-r_o}^{r^c+r_o} = -2qr^c r_0, \text{ if } q=\text{const.} \tag{34}$$

From Eqs. (30)-(34), one can see that the weak formulation does not involves higher than first order derivatives of field variables. The numerical results corresponding to this formulation will be denoted by LIE(2xPoiss).

One field variable formulation

In order to see the effect of the proposed decomposition, we present also the standard formulation where all physical quantities are expressed in terms of deflections and their derivatives. The weak form of the governing equation

$$D\left(\frac{\partial^2}{\partial r^2}+\frac{1}{r}\frac{\partial}{\partial r}\right)^2 w(r)=q(r) \quad \text{or} \quad \frac{D}{r}\frac{\partial}{\partial r}\left(r\frac{\partial\nabla^2 w(r)}{\partial r}\right)=q(r) \tag{35}$$

is given by

$$Dr\frac{\partial\nabla^2 w(r)}{\partial r}\Bigg|_{r^c-r_o}^{r^c+r_o} = \int_{r^c-r_o}^{r^c+r_o} rq(r)dr, \tag{36}$$

Hence, with assuming a constant loading, one obtains

$$D\left(r\frac{\partial^3 w(r)}{\partial r^3}+\frac{\partial^2 w(r)}{\partial r^2}-\frac{1}{r}\frac{\partial w(r)}{\partial r}\right)\Bigg|_{r^c-r_o}^{r^c+r_o} = 2qr^c r_0 \ . \tag{37}$$

In the case of symmetric problem for bending of circular plate, the integration can be performed in closed form. One can see that the third order derivatives of the deflection occur in both the weak form of the governing equation and the boundary conditions (on free edge). The numerical results obtained by this formulation will be denoted as LIE(biharmonic).

Recall that exact solutions are available for some simple angular symmetric boundary value problems on circular plate (Sladek et al., 2012).

6. Numerical examples

Several numerical examples will be considered for angularly symmetric bending of circular plate for which exact solutions are available. Then, we can investigate the accuracy and convergence as well as computational efficiency of various presented formulations and techniques. The accuracy of numerical solutions of boundary value problems will be characterized by error norm defined as

$$\text{error norm} = 100\left(\sum_{a=1}^{N}\left[w(r^a)-w^{ex}(r^a)\right]^2\right)^{1/2}\left(\sum_{a=1}^{N}\left[w^{ex}(r^a)\right]^2\right)^{-1/2} \tag{37}$$

in the formulation for one field variable, while for two field variables we shall use the definition

$$\text{error norm} = 100\left(\sum_{a=1}^{N}\left\{\left[w(r^a)-w^{ex}(r^a)\right]^2+\left[m(r^a)-m^{ex}(r^a)\right]^2\right\}\right)^{1/2}\left(\sum_{a=1}^{N}\left\{\left[w^{ex}(r^a)\right]^2+\left[m^{ex}(r^a)\right]^2\right\}\right)^{-1/2} \tag{38}$$

where N is the total number of nodal points.

In all numerical computations, we have used a uniform distribution of nodal points and the radius of the sub-domain $r_o = 0.1h$ with h being the distance between two neighbour nodes. The other parameters in the MLS-approximation have been taken as: radius of the interpolation domain $r^a = 3.001h$, shape function parameter $c^a = h$, cubic polynomial basis $m = 4$. In the PIM(RBF+P)-approximation, we have chosen: type of RBF – inverse multiquadrics with $p = -1$, number of multiquadrics around each node $N^q = 16$, number of polynomials $M = 7$, shape parameter $c^a = 2h$. As regards the geometry, we shall consider either the circular plate without any hole $\Omega = \{\forall(r,\varphi); r\in[0,r_a],\ \varphi\in[0,2\pi]\}$ or the circular plate with central hole $\Omega = \{\forall(r,\varphi); r\in[r_b,r_a],\ \varphi\in[0,2\pi]\}$. Three kinds of the boundary value problems will be discussed: (A) $r\in[0,r_a]$, clamped edge (CE) $r = r_a$; (B) $r\in[0,r_a]$, simply supported edge (SSE) $r = r_a$; (C) $r\in[r_b,r_a]$, simply supported edge (SSE) $r = r_b$, free edge $r = r_a$.

Now, we present the results for accuracy and convergence of numerical solutions of three considered boundary value problems with using the MLS-approximations for field variables in two different formulations LIE(biharm) and LIE(2xPoiss). Each formulation is combined with two techniques for creation of shape functions and their derivatives (denoted by S0 and S1). Fig. 1 shows convergence of

accuracy of numerical solutions of all considered b.v.p. by LIE(2xPoiss) with increasing the density of nodes (decreasing the h parameter in uniformly distributed nodes). The results are insensitive to the choice of S0 or S1 technique. On the other hand, the LIE(biharm) formulation yields the numerical solutions with unacceptable accuracy and without any indication of convergence (lines with empty symbols in Fig.2). This collapse could be explained by insufficient accuracy of the approximation of $w_{,rrr}(r)$, especially at endpoints $r = r_b$, $r = r_a$. In order to verify this hypothesis, we have modified the LIE(biharm) formulation with replacement of the approximation of $w_{,rrr}(r)$ by exact values $w^{ex}_{,rrr}(r)$. The renewal of convergence of accuracy of numerical solutions (lines with solid symbols in Fig.2) confirms the explanation of the collapse, but there is no proposal how to eliminate this collapse within LIE(biharm).

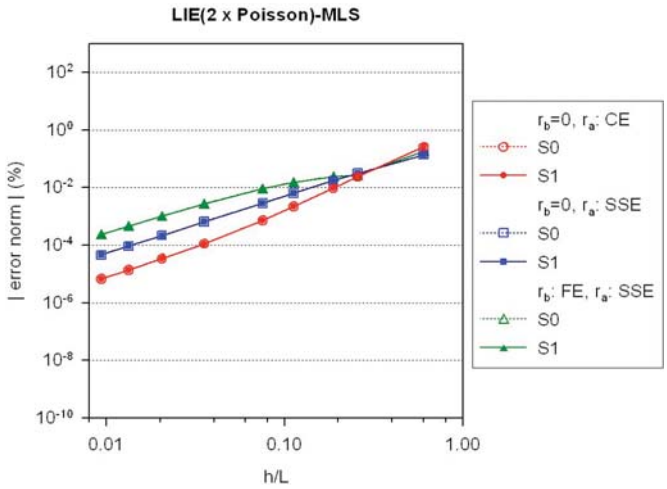

Fig.1 Accuracy and convergence of numerical solutions for three b.v.p. by LIE(2xPoiss) combined with MLS-approximations of field variables

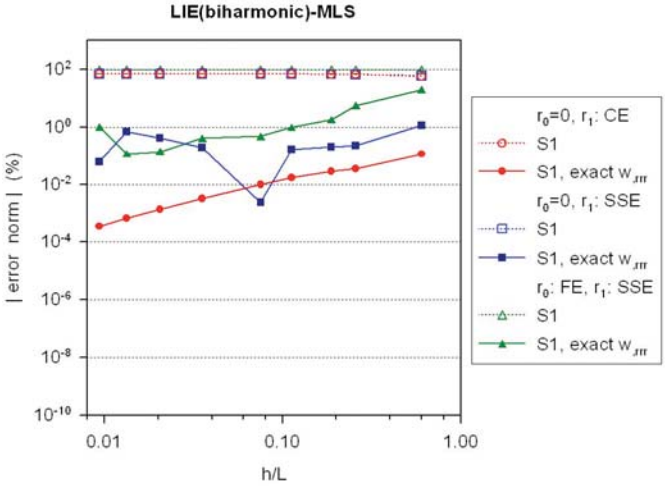

Fig.2 Accuracy and convergence of numerical solutions for three b.v.p. by LIE(biharm) combined with MLS-approximations of field variables

From the above study of the accuracy of numerical solutions by two formulations implemented with MLS-approximations of field variables, the following conclusions can be drawn:

(i) only the formulations for decomposed problem yield meaningful results; the LIE(biharm) formulation fails because of inaccurate approximation of the higher order derivatives of deflections

(ii) the influence of S1-modification for evaluation of shape functions and their derivatives on accuracy is negligible.

Finally, we present the results for numerical solutions of the considered boundary value problems by two discussed formulations but implemented by PIM-approximations of field variables.

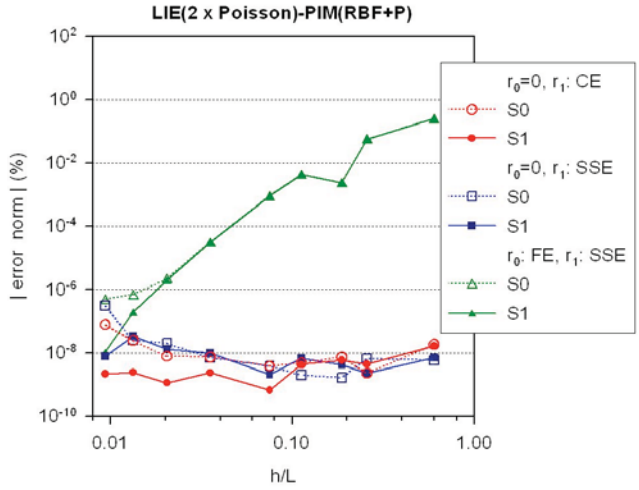

Fig.3 Accuracy and convergence of numerical solutions for three b.v.p. by LIE(2xPoiss) combined with PIM-approximations of field variables

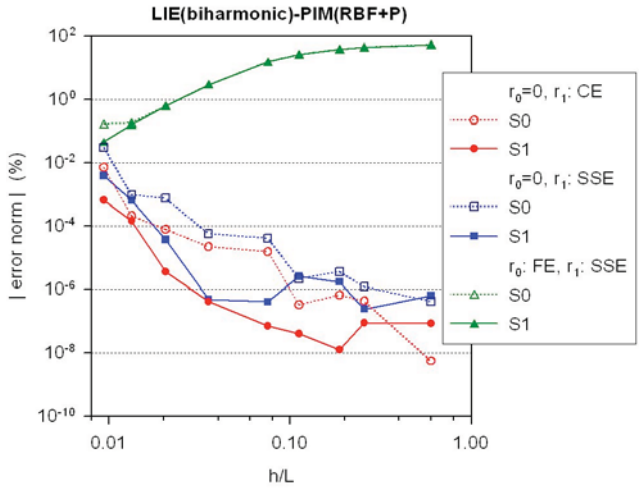

Fig.4 Accuracy and convergence of numerical solutions for three b.v.p. by LIE(biharm) combined with PIM-approximations of field variables

It can be seen from Fig. 3 that in the case of b.v.p. (A) and (B), the accuracy of numerical solutions by LIE(2xPoiss) is very high and more or less invariable with respect to the parameter h in contrast to the case of b.v.p. (C). This can be explained by the detailed study of accuracy of the first order derivatives of the field variables which are almost indifferent to increasing the amount of nodal points only in the case of b.v.p. (A) and (B). The very accurate results are sensitive also to the choice of S0 or S1 technique. Fig. 4 shows that qualitatively different results have been obtained by the LIE(biharm), where the accuracy of the numerical solution of a boundary value problem is affected also by the accuracy of approximations of the third order derivative $w_{,rrr}(r)$. It can be seen that the accuracies of the numerical solutions of b.v.p. (A) and (B) are divergent with respect to decreasing the parameter h, while the convergence of accuracy of the numerical solutions of the b.v.p. (C) is achieved. The detailed study shows that the accuracy of $w_{,rrr}(r)$ is divergent with respect to increasing the amount of nodal points in the b.v.p. (A) and (B) in contrast to improving accuracy of $w_{,rrr}(r)$ in the b.v.p. (C).

Summarizing the study of the accuracy of numerical solutions by two formulations implemented with PIM-approximations of field variables, we conclude:

(i) the LIE(biharm) formulation gives unreliable results (convergence is achieved only in the b.v.p. (C))
(ii) the LIE(2xPoiss) formulation gives stable and highly accurate numerical solutions of the b.v.p. (A) and (B); in the case of b.v.p. (C) the accuracy is good with excellent convergence rate
(iii) the influence of S1-modification for evaluation of shape functions and their derivatives on accuracy is observable as long as the accuracy is very good.

As regards the computational efficiency, the considered computational methods exhibit similar CPU-times (see Fig. 5) when implemented by the MLS- and/or PIM-approximations. Only the LIE(biharm)-MLS spends approximately 3 times shorted computational time than other methods. But this method is disqualified owing to unreliable accuracy.

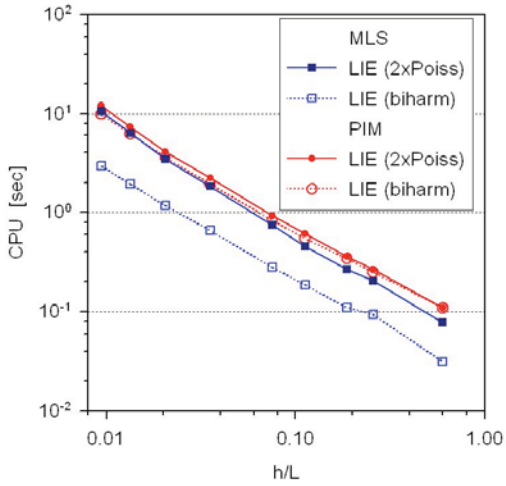

Fig. 5 Comparison of computational times spent by various formulations implemented either by MLS or PIM-approximations

In order to compare the accuracy of two powerful formulations, LIE(2xPoiss)-MLS and LIE(2xPoiss)-PIM, we present following figures with using standard differentiation and S1-technique for evaluation of the shape functions and their derivatives. From Fig. 6, we conclude that much better accuracy is achieved when the formulations are implemented by PIM-approximations of field variables.

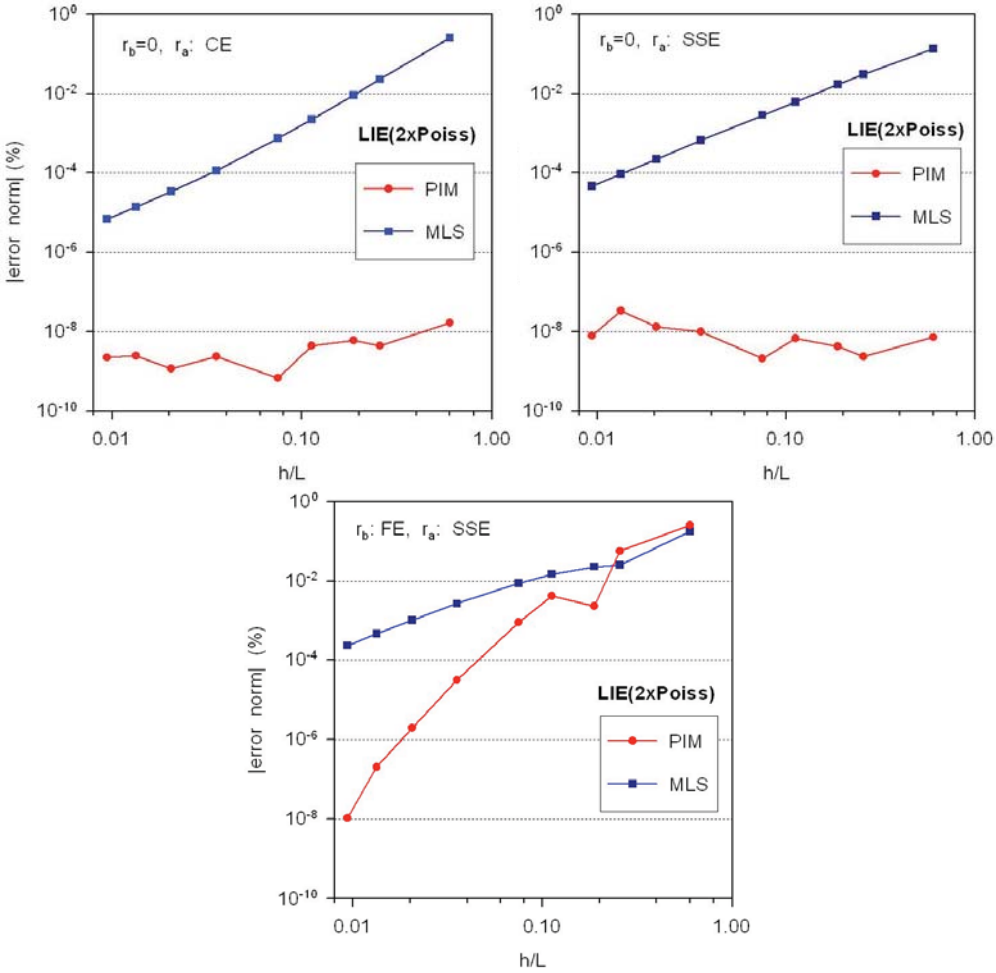

Fig. 6 Comparison of accuracy and convergence of numerical solutions for three kinds of b.v.p. by LIE for decomposed formulations implemented by both PIM- and MLS-approximations

7. Conclusions

The decomposition of the thin plate bending problems governed by the biharmonic operator into two coupled problems governed by Poisson equations is developed and discussed. Two kinds of meshless approximations of field variables are employed in each formulation for numerical solution of boundary value problems. The developed decomposed formulations are not restricted to certain class of boundary value problems. For solution of the decomposed problem, both the strong and local weak formulations have been developed. The accuracy, convergence of accuracy and computational efficiency have been studied for two formulations combined with two meshless approximation of field variables in simple boundary value problems for circular plate. The discussed methods give reasonable numerical results when applied to decomposed problem, while the methods applied to original biharmonic problem fail.

Acknowledgements

This work was partially supported by the Slovak Research and Development Agency under the contract No. APVV-0032-10. This article has been produced also with the financial assistance of the European Regional Development Fund (ERDF) under the Operational Programme Research and Development/Measure 4.1 Support of networks of excellence in research and development as the pillars of regional development and support to international cooperation in the Bratislava region/Project No. 26240120020 Building the centre of excellence for research and development of structural composite materials – 2nd stage**.**

References

Lancaster P., Salkauskas K. (1981) Surfaces generated by moving least square method. *Mathematics of Computations*; **3**7: 141-158.

Liu GR. (2003) Mesh Free Methods, Moving Beyond the Finite Element Method. CRC Press: Boca Raton.

Sladek V, Sladek J, Zhang Ch. (2008) Computation of stresses in non-homogeneous elastic solids by local integral equation method: a comparative study. *Computational Mechanics*, **41**: 827-845.

Sladek V, Sladek J, Tanaka M. (2005) Local integral equations and two meshelss interpolations with application to potential problems in non-homogeneous media. *CMES - Computer Modeling in Engineering & Sciences*; **7**: 69-83.

Sladek, V., Sladek, J., Sator, L. (2012) Physical decomposition of thin plate bending problems and their solution by mesh-free methods, submitted for publication

Timoshenko S.P., Woinowsky-Krieger S. (1959) *Theory of Plates and Shells*. McGraw-Hill: New York.

18th International Conference
ENGINEERING MECHANICS 2012
Svratka, Czech Republic, May 14 – 17, 2012

pp. 1157–1160
Paper #110

ON-LINE CORRECTION OF ROBOTS PATH BASED ON COMPUTER VISION

S. Selingerova[*], T. Kubela[**], A. Pochyly[***], V. Singule[****]

Abstract: *This paper presents the methodology for a real-time trajectory correction applied to industrial robots. The application is based on computer vision concerned with the line detection creating a trajectory for the robot motion. The algorithm for the line detection was developed in Matlab/Simulink computing software. The trajectory is corrected by a controller implemented in PLC Beckhoff that communicated with the robot controller via DeviceNet in real-time.*

Keywords: ***Computer vision, control, trajectory, PLC, real-time, industrial robot.***

1. Introduction

In industrial robotics there are applications where we need to correct a robot trajectory in real-time. It could be for example robotic welding. To connect two points by a seam, industrial robot interpolates the trajectory by a line. However many variables enter this process, such as the errors of pre-machining, in-process thermal distortions, which would cause changes of the seam position (Shen et al., 2010). Another variable is the accuracy of the robot movement. All of these variables will cause inaccurate placement of the seam and will affect the quality of the seam. That is why the robot path needs to be corrected by a sensory-based system.

Robots path is usually corrected by a controller. An important thing at any trajectory correction is to choose a controller and set it. A lot of previous researches have been done in the field of robot trajectory correction. Most of the previous works used the PID controller, for example Shen et al. (2010), Yilmaz & Sagiroglu (2009), Fang et al. (2010) or Xu et al. (2004). Fang et al. (2011) has done an experiment comparing the PID controller against a fuzzy controller which was improved by him (called self-tuning fuzzy controller). In this experiment he found out that the self-tuning fuzzy controller had better response to a large step disturbance than the PID controller. He described the self-tuning fuzzy controller to be more robust, steady and to have higher tracking accuracy than the PID controller in the case of trajectory correction.

2. Proposed solution

2.1. System description

The whole on-line trajectory correction system includes following parts: industrial camera Manta (Allied Vision Technologies), PLC Beckhoff, industrial robot KUKA and PC (Fig. 1 Photo of the workplace).

[*] Ing. Simona Selingerová: Institute of Production Machines, Systems and Robotics, Brno University of Technology, Faculty of Mechanical Engineering, Technicka 2896/2; 616 69, Brno; CZ, e-mail: yselin01@stud.fme.vutbr.cz

[**] Ing. Tomáš Kubela: Institute of Production Machines, Systems and Robotics, Brno University of Technology, Faculty of Mechanical Engineering; Technicka 2896/2; 616 69, Brno; CZ, e-mail: kubela@fme.vutbr.cz

[***] Ing. Aleš Pochylý: Institute of Production Machines, Systems and Robotics, Brno University of Technology, Faculty of Mechanical Engineering; Technicka 2896/2; 616 69, Brno; CZ, e-mail: pochyly.a@fme.vutbr.cz

[****] doc. Ing. Vladislav Singule, CSc.: Institute of Production Machines, Systems and Robotics, Brno University of Technology, Faculty of Mechanical Engineering; Technicka 2896/2; 616 69, Brno; CZ, e-mail: singule@fme.vutbr.cz

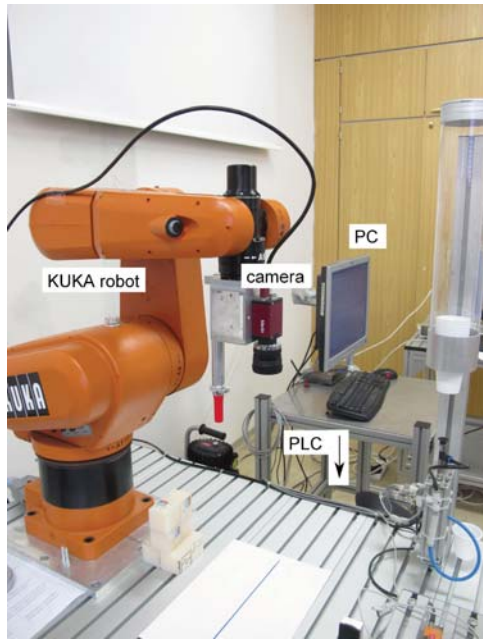

Fig. 1: Photo of the workplace

Processing starts in the industrial camera where an image is acquired. Then the image is processed in the Matlab software implemented in the PC. Processed data from the Matlab are then forwarded to the PLC where a PI controller is implemented influencing the robot´s movement (Fig. 2 Control loop, green arrows).

On the Fig. 2 there is also a communication loop (blue arrows). The industrial camera is connected to the PC by the FireWire. In the Matlab software there is implemented a TCP/IP client which instructs a TCP/IP server implemented in the PLC. PLC is connected with the robot controller via DeviceNet fieldbus in real-time. The PLC is also used as a main control of the whole task.

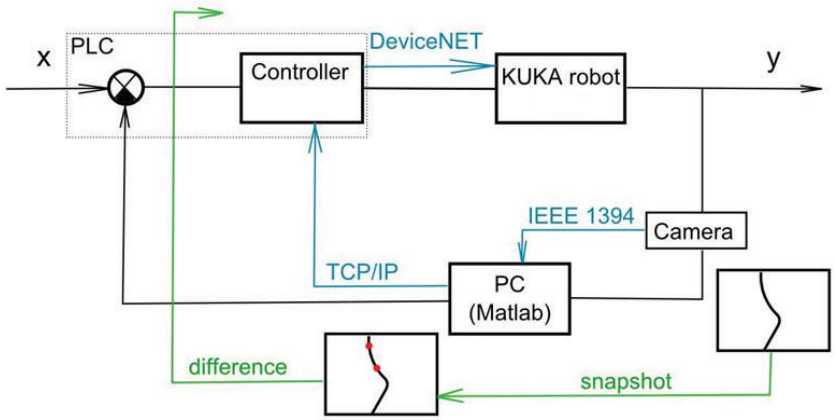

Fig. 2: Control loop

2.2. Detailed description

A simple image processing algorithm is programmed in the Matlab software. The algorithm is based on extraction a center of a line viewed through the camera. After the extraction the center is compared against the center of the camera´s field of view. The difference is then forwarded to the PI controller as the error.

2.3. Experiment result

An experiment was designed to test system accuracy to correct robot´s trajectory in an industrial application. The system accuracy could be tested by watching the difference by eyes between a certain drawn trajectory and the robot corrected trajectory. However watching the difference by eyes would not be accurate because we would not get exact information. For the purpose of extracting the number data, the experiment was designed as follows. First a sine curve trajectory was created by the robot. This trajectory was drawn by a fix mounted on the robot´s effector. During the drawing the trajectory points were recorded. Then the robot was moving along the created trajectory and tried to on-line correct the movement by the proposed system. Errors of proposed control system were recorded and both records were then compared against themselves (Fig. 3 Comparison of a drawn sine curve and the robot corrected trajectory).

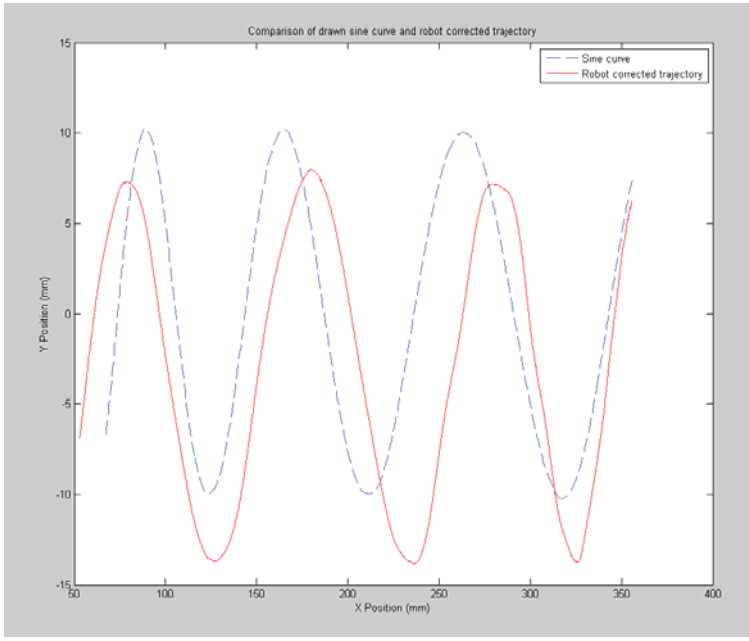

Fig. 3: Comparison of a drawn sine curve and the robot corrected trajectory

In this experiment the PI controller was implemented to influent the robot´s movement.

There has not been done any calibration of the camera in the sense of unification of the Cartesian coordinate system of the robot and the camera. For our testing purposes we needed only to recalculate the difference from pixel units to millimeters. To recalculate the difference from pixel units to millimeters we simply calculate the difference at a specific camera´s depth of focus in millimeters.

The cycle from acquiring image data to giving move instructions to the robot last about 20ms. The whole process could be faster but because of complex algorithm of TCP/IP communication we could not have a better processing time. Another thing is that we did not need better processing time in this pilot study.

3. Conclusions

An experiment has been done to correct the robot´s trajectory by a computer vision system. In the experiment a data from the image processing algorithm were send to the PI controller.

Most of image processing algorithms are light sensitive which cause low robustness of the algorithm and of course a lot of errors during the running application. Changes of light or creating shadows in the workplace caused a lot of errors in our experiment too. Problem of changing light conditions is still a developing area in computer vision. Therefore there will be an improvements concerning investigation of light influence on the image processing algorithm and there will be also some precautions leading to reduce the light influence. Another improvement of the image processing algorithm will be also focused on a correction of more complex-shaped trajectories, for example trajectories with step changes.

On the Fig. 3 is shown our experiment result. The robot trajectory was corrected only in the Y position. Errors between the drawn sine curve and the robot corrected movement along the sine curve are about 1 to 3 mm. Such a relatively high errors will be reduced towards zero in the next experiment prepared after this pilot study.

References

Shen Hongyuan, Lin Tao, Chen Shanben, Li Laiping (September 2010). Real-Time Seam Tracking Technology of Welding Robot with Visual Sensing. *Journal of Intelligent and Robotic Systems*. 59 (3-4) , 283-298.

Fang Zaojun, Xu De, Tan Min (June 2011). A Vision-Based Self-Tuning Fuzzy Controller for Fillet Weld Seam Tracking. *IEEE/ASME Transactions on Mechatronics*. 16(3), 540-550.

Yilmaz Nihat, Sagiroglu Seref (May 2009). Real-Time Line Tracking Based on Web Robot Vision. *Computer Applications in Engineering Education*. 19(4), 806-813.

Fang Zaojun, Xu De, Tan Min (January 2010). Visual seam tracking system for butt weld of thin plate. *The International Journal of Advanced Manufacturing Technology*. 49(5-8), 519-526.

Xu De, Tan Min, Zhao Xiaoguang, Tu Zhiguo (2004). Seam Tracking and Visual Control for Robotic Arc Welding Based on Structured Light Stereovision. *International Journal of Automation and Computing*. , 63-75.

18th International Conference
ENGINEERING MECHANICS 2012
Svratka, Czech Republic, May 14 – 17, 2012

pp. 1161–1171
Paper #122

MASS LUMPING METHODS FOR THE SEMI-LOOF SHELL ELEMENT

Vít Sháněl [*], **Radek Kolman** [**] **and Jiří Plešek** [***]

Abstract: *Mass matrix diagonalization in terms of a finite element method (FEM) is essential for an effective deployment of the explicit method as one of the direct integration methods of the motion equations of elastodynamics. A particular attention is focused on the mass matrix diagonalization of the semi-loof shell element. Its diagonalization requires a specially designed universal diagonalization scheme that is derived from the scaling HRZ method. Another analyzed aspect is the problem of preserving the moment of inertia for various types of finite elements. The proposed scheme is implemented in the finite element program and consequently tested on several problems.*

Keywords: ***FEM, mass matrix lumping, semi-loof finite shell element, impacts and waves in solids, elastodynamics.***

1. Introduction

The most suitable approach to numerically solving problems of elastodynamics turns out to be a finite element method (FEM) [Hughes (1987)] that seems to provide the most effective way of dealing with practical cases. A vast majority of those cannot be worked out using analytical closed-form solutions, or the solutions are just too difficult. FEM is a wonderfully versatile method that can be used even in the most complex constitutive equations and which enables the approximation of a wide range of boundary conditions [Zienkiewicz et al. (2005)]. After applying the FEM to elastodynamics problems you will obtain

$$\mathbf{M}\ddot{\mathbf{q}} + \mathbf{K}\mathbf{q} = \mathbf{F}_{ext} \tag{1}$$

where $\mathbf{q}$ is a nodal displacement, $\ddot{\mathbf{q}}$ nodal acceleration, $\mathbf{F}_{ext}$ represents external forces, $\mathbf{K}$ denotes the stiffness matrix, which is symmetric, and after applying boundaries conditions also positive semidefinite and $\mathbf{M}$ is a symmetric and positive definite mass matrix given by the integral

$$\mathbf{M} = \int_V \rho \mathbf{H}^T \mathbf{H} dV = [m_{ij}] \tag{2}$$

where ρ is mass density, $\mathbf{H}$ matrix of shape functions and V represents elements volume.

There is a large number of different numerical methods that are related to a FEM-based spatial discretization [Zienkiewicz et al. (2005)]. One of the most frequently implemented methods is a so called semidiscretization which initially performs a spatial discretization and then runs an independent time discretization. The time part of any problem is usually dealt with using methods of direct integration, which can be implicit or explicit [Hughes (1987)]. This work focuses especially on explicit methods, notably the central difference method [Dokainish (1989)] which deals with time derivations this way

$$\dot{\mathbf{q}}^t = \frac{1}{2\Delta t}\left(\mathbf{q}^{t+\Delta t} - \mathbf{q}^{t-\Delta t}\right) \quad \text{a} \quad \ddot{\mathbf{q}}^t = \frac{1}{\Delta t^2}\left(\mathbf{q}^{t+\Delta t} - 2\mathbf{q}^t + \mathbf{q}^{t-\Delta t}\right) \tag{3}$$

[*]Ing. Vít Sháněl: Institute of Thermomechanics AS CR, Impact and Waves in Solids, Dolejškova 1402/5, Prague, CZ, email: shanel@it.cas.cz
[**]Ing. Radek Kolman, Ph.D.: Institute of Thermomechanics AS CR, Impact and Waves in Solids, Dolejškova 1402/5, Prague, CZ, email: kolman@it.cas.cz
[***]Ing. Jiří Plešek, CSc.: Institute of Thermomechanics AS CR, Impact and Waves in Solids, Dolejškova 1402/5, Prague, CZ, email: plesek@it.cas.cz

where Δt denotes time step and $\mathbf{q}^{t-\Delta t}$, $\mathbf{q}^{t}$ and $\mathbf{q}^{t+\Delta t}$ are nodal displacements in previous, actual and next time step, respectively. In order to ensure effectivity of this method, explicit formulation of $\mathbf{q}^{t+\Delta t}$, it is vital to stress the importance of the mass matrix of the system which needs to be diagonal – as you can see in equation (4) which combines (2) and (3)

$$\frac{1}{\Delta t^2}\mathbf{M}\mathbf{q}^{t+\Delta t} = \mathbf{F}_{ext} - \left(\mathbf{K} - 2\mathbf{M}/\Delta t^2\right)\mathbf{q}^{t} - \left(\mathbf{M}/\Delta t^2\right)\mathbf{q}^{t-\Delta t} \tag{4}$$

Only then, with diagonal mass matrix $\mathbf{M}$, becomes the related inversion simple and the actual computation is elementary. However, a consistent mass matrix does not fulfill this requirement generally. Hence a great effort has been made to develop some diagonalization methods [Zienkiewicz et al. (2005)].

The mass matrix diagonalization may involve some changes in fundamental physical properties (e.g. mass, the moment of inertia) which could have a significant impact on the system behavior. It is therefore desirable to devise a method that preserves those system parameters to the highest possible degree and at the same time allows for a universal application on a wide range of finite elements.

1.1. Semi-loof Shell elements

A versatility of the isoparametric elements has been transferred to a semi-loof shell element during the years of the research conducted by Irons and his team, related to the study of semi-loof shell element [Hellen (1986)] such as sharp edges, curved sides and surfaces and multiply-connected regions. This element has been widely used for elastic analysis and later extended for material and geometric nonlinearities. The element is available in the 8-node quadrilateral and 6-node triangle form which significantly aids the meshing process. The topology of the semi-loof element is depicted in Figure 1 where

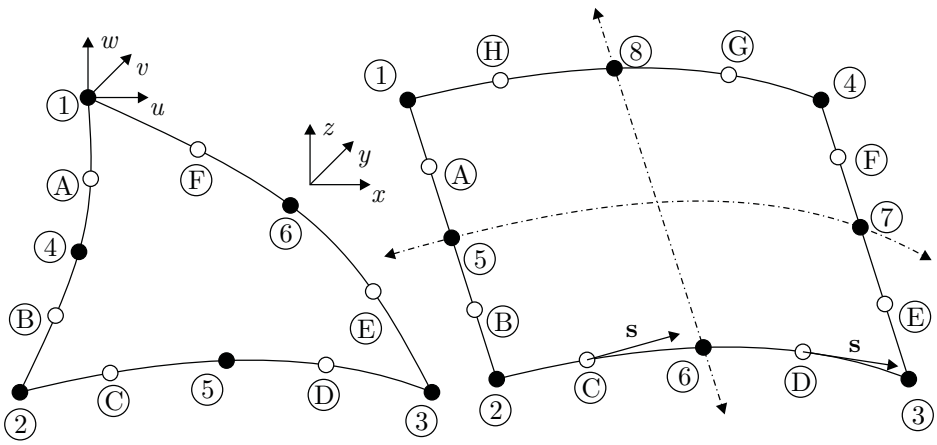

Fig. 1: Semi-loof element configuration [Irons (1976)]

1 to 6 or 8 (represented as a filled circle) are the classic nodes containing three translational DOFs u, v and w. The local normal rotation $\mathbf{s}$ acts at each loof node labeled A to F or H (empty circle). They are situated at side position ± 0.57735 from the midside nodes outwards. The normal is defined in each loof node, but they are identified to the adjacent midside node and therefore a user does not have to define a loof node geometry. Thus nodes A and B are coupled with the midside node 4 (or 5 in a quadrilateral geometry) so that the DOFs in midside node become u, v, w, $\mathbf{s}_1$ and $\mathbf{s}_2$. The element employs three different shape functions [Leština (1980)]. A membrane deformation is described using isoparametric biquadratic shape functions and a bending deformation is approximated by loof and bubble functions.

2. Diagonalization method analysis and design

2.1. HRZ scheme

Also called diagonal scaling method, the essential idea of which is contained in [Hinton et al. (1976)] where Hinton, Rock and Zienkiewicz says: *"The procedure of lumping recommended in view of the infinite possibilities offered by condition* (5) *is to compute the diagonal terms of the consistent mass matrix and then scale these terms so as to preserve the total mass of the element."*

$$\begin{aligned} \bar{H}_i &= 1 \quad \text{at} \quad i\text{th node} \\ \bar{H}_i &= 0 \quad \text{at} \quad j\text{th node} \\ \textstyle\sum \bar{H}_i &= 1 \end{aligned} \tag{5}$$

This scheme has a plenty of advantages compared to other lumping techniques. Mainly, the HRZ scheme is able to diagonalize mass matrices of the elements which include rotational as well as translational DOFs. A modification of the procedure which ensures rotational DOFs scaling is apparent from the algorithm description below. Another advantage of this scheme is that an assemblage of the whole consistent matrix is not necessary – only diagonal terms are required and the implementation is performed on an element level.

The HRZ procedure is as follows [Fellipa (2011)]:

1. Compute diagonal terms of the consistent mass matrix $\mathbf{M}_c$.
2. Determine the element mass m^e.
3. For each coordinate direction, select the DOFs – translational and rotational – which contribute to the motion in the respective direction.
4. Segment these selections into sub-selections of the rotational and translational DOFs.
5. Sum all the terms of the each translational sub-selections, call this sum S_i, where i is the problem dimension.
6. Multiply all the entries in the *i*th selection (step 3) by the m^e/S_i for all i coordinate directions.

2.2. Conservation of the moment of inertia

The HRZ lumping method conserves only the mass of the element but no moment of inertia [Fellipa (2011)]. This was a motivation for the modification of the HRZ algorithm to conserve the element rotational inertia as well.

The algorithm is based on the idea to calculate three rotational kinetic energies for the consistent mass matrix induced by a set of three orthogonal angular velocity vectors (Figure 2). What follows is the execution of the HRZ lumping process on the translational DOFs and a calculation of the kinetic energy induced by the same group of angular velocities. In the last step the angular kinetic energies are compared and correction coefficients for rotational DOFs are computed in order to preserve the total moment of inertia.

The basic input for the created algorithm is a consistent mass matrix of the element, coordinates of the nodes and also the information about DOFs in every node. In this example vectors describing translational and rotational DOF position were assembled manually. A definition of the three orthogonal angular velocities uses a Miller indices notation which describes a turn of the coordinate system of the three velocities. In general, the velocity orientation can be chosen arbitrarily but it is very useful for the algorithm testing of this approach which allows an easy change in orientation of the input velocities.

All the computations below are performed for all of the three input angular velocities in a vector $\boldsymbol{\omega}_i$ where $i = 1, 2, 3$ which are denoted in the source code with indices x, y and z.

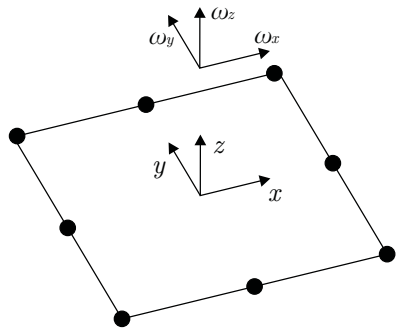

Fig. 2: Orientation of the three angular velocity vectors

Translational degrees of freedom

So as to translate the DOF scaling, it is necessary to have a consistent mass matrix. In result, the scaling coefficient α_{ti} for the translational DOFs is computed

$$\alpha_{ti} = \frac{\mathbf{v}_{t_i}^T \, \mathbf{M}_c \, \mathbf{v}_{ti}}{\mathbf{v}_{t_i}^T \, \mathrm{diag}\, \mathbf{M}_c \, \mathbf{v}_{ti}} \tag{6}$$

where $\mathbf{v}_{ti}$ consists of the nodal velocities corresponding to the translation rigid body motion in directions x, y and z. Then α_{ti} is used for the scaling of the terms on the $\mathbf{M}_c$ diagonal to preserve the element mass.

$$\mathbf{M}_t^l = \boldsymbol{\alpha}_t \mathbf{P}_t \, \mathrm{diag}\, \mathbf{M}_c \tag{7}$$

where $\mathbf{P}_t$ is a distribution matrix of the components of $\boldsymbol{\alpha}_t = (\alpha_{ti})$ to the corresponding terms in $\mathbf{M}_c$. This scaling method is an equivalent to the classic HRZ.

Rotational degrees of freedom

In order to compute rotational kinetic energy the projection of the angular velocity vectors to the nodes is necessary, thus the peripheral velocity in the nodes is a result of the vector product

$$\mathbf{v}_{\mathbf{p}ij} = \boldsymbol{\omega}_i \times \mathbf{p}_j \tag{8}$$

where $\mathbf{v}_{\mathbf{p}_{ij}}$ is peripheral velocity caused by one of the three induced angular velocities $\boldsymbol{\omega}_i$ and the position coordinates of the *j*th node in the global coordinate system $\mathbf{p}_j$. In that case, the velocities $\mathbf{v}_{p_{ij}}$ are arranged in the vector $\mathbf{v}_{g_i}$ which corresponds to the positions of the DOFs in the mass matrix.

The scalar product of the input angular velocities with the directions of the rotational DOFs is used here as an angular velocity projection to the rotational DOFs

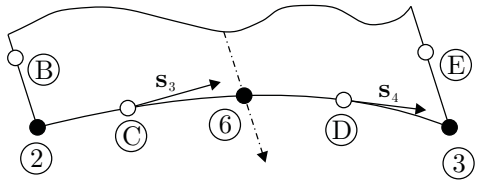

Fig. 3: The orientation of the rotational DOFs in the semi-loof shell element

$$\boldsymbol{\omega}_{p_{ij}} = (\boldsymbol{\omega}_i \cdot \mathbf{s}_j) \cdot \mathbf{s}_j \tag{9}$$

where $\mathbf{s}_j$ is the directional unit vector of the *j*th rotational loof node (Figure 3) oriented from the node with a lower number to the node with a higher one and they are tangential to the element border. Then the

Tab. 1: Conservation of the moment of inertia

	Kinetic energy [J]		
	$E_{k\,c}$ (consistent)	$E_{k\,l}$ (lumped)	$E_{k\,lm}$ (lumped + modified)
x	3.25416666×10^{-3}	5.55154715×10^{-3}	3.67418730×10^{-3}
y	3.25416666×10^{-3}	5.55154715×10^{-3}	3.67418730×10^{-3}
z	3.11666666×10^{-3}	4.98978214×10^{-3}	2.48663570×10^{-3}

Tab. 2: Conservation of the moment of inertia – error %

	Error of the kinetic energy [%]	
ε_r	lumped	lumped + modified
x	70.6	12.9
y	70.6	12.9
z	60.1	-20.2

vector $\mathbf{v}_g$ of all (translational and rotational) projected velocities (peripheral and angular) is assembled and the total kinetic energy $E_{k\,c}$ of the consistent mass matrix can be computed as

$$E_{k\,ci} = \frac{1}{2}\mathbf{v}_{g_i}{}^T\mathbf{M}_c\mathbf{v}_{g_i} \tag{10}$$

and equally for lumped mass matrix

$$E_{k\,li} = \frac{1}{2}\mathbf{v}_{g_i}{}^T\mathbf{M}_l\mathbf{v}_{g_i} \tag{11}$$

where the lumped mass matrix consist of two mass matrices

$$\mathbf{M}_l = \mathbf{M}_t^l + \mathbf{M}_r^l \tag{12}$$

The first one contains only terms corresponding to the translational DOFs where $\boldsymbol{\alpha}_t$ is computed in equation (6) and the second one $\mathbf{M}_r^l$ contains only terms corresponding to the rotational DOFs

$$\mathbf{M}_r^l = \boldsymbol{\alpha}_r\mathbf{P}_r\mathrm{diag}\mathbf{M}_c \tag{13}$$

where $\mathbf{P}_r$ is a distribution matrix of the components of $\boldsymbol{\alpha}_r = (\alpha_{r\,i})$ to the corresponding terms in $\mathbf{M}_c$. To conserve kinetic energy of the element during the lumping process, the energies in (10) and (11) must be equal $\mathbf{E}_{k\,c} = \mathbf{E}_{k\,l}$. The substitution of the equations (10) and (11) will result in

$$\mathbf{v}_{g_i}{}^T\mathbf{M}_c\mathbf{v}_{g_i} = \mathbf{v}_{g_i}{}^T\mathbf{M}_l\mathbf{v}_{g_i} \tag{14}$$

and after another substitution with equation (12), (7) and (13) we will get

$$\mathbf{v}_{g_i}{}^T\mathbf{M}_c\mathbf{v}_{g_i} = \mathbf{v}_{g_i}{}^T\boldsymbol{\alpha}_t\mathbf{P}_t\mathrm{diag}\mathbf{M}_c\mathbf{v}_{g_i} + \mathbf{v}_{g_i}{}^T\boldsymbol{\alpha}_r\mathbf{P}_r\mathrm{diag}\mathbf{M}_c\mathbf{v}_{g_i} \tag{15}$$

Equation (15) consist of three equations ($i = 1, 2, 3$) and only the vector $\boldsymbol{\alpha}_r$ is an unknown. In this case $\boldsymbol{\alpha}_r$ contains eight generally different terms and (15) just three equations which can be rewritten as

$$\mathbf{A}\boldsymbol{\alpha}_r = \mathbf{E}_{k\,c} - \mathbf{E}_{k\,t} \tag{16}$$

and for $\boldsymbol{\alpha}_r$

$$\boldsymbol{\alpha}_r = \mathbf{A}^+\left(\mathbf{E}_{k\,c} - \mathbf{E}_{k\,t}\right) \tag{17}$$

where $\mathbf{A}^+$ denotes Moore-Penrose pseudo-inverse. Then the lumped mass matrix can be easily assembled according to the equation (12).

The system of equations (17) is over-determined, therefore pseudo-inversion has to be employed. Then the solution of this system is accordance with the solution using the least squares method. This method does not provide an exact solution which is impossible due to the system over-determination but the final solution is an approximation as can be seen in Table 1. The final kinetic energies will not be exactly the same as the ones computed from the CMM. In Table 2 there is a relative error in percentage of the lumped and lumped + modified kinetic energy where ε_r is for kinetic energy of the lumped mass matrix computed as

$$\varepsilon_r = 100 \cdot \frac{E_{k\,c} - E_{k\,l}}{E_{k\,c}} \quad \text{and for lumped + modified} \quad \varepsilon_r = 100 \cdot \frac{E_{k\,c} - E_{k\,lm}}{E_{k\,c}} \tag{18}$$

It is clear that the first two kinetic energies computed from the modified DLMM are slightly larger then the ones from CMM but the third one is smaller – precisely in compliance with the approximation assumption mentioned above.

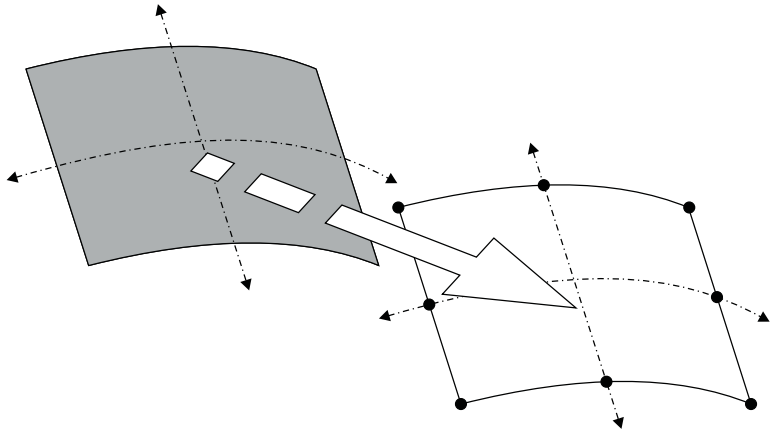

Fig. 4: The mass lumping process

The algorithm described above works well. The angular kinetic energy of the lumped and modified mass matrix is preserved – considering the feasibility of the last square method. On the other hand negative entries in the lumped mass matrix are detected. The reason for that is obvious provided that the lumping process has been performed and the element mass has been concentrated to the nodes. If the element mass is preserved and stored to the most outlying places – the nodes, the element moment of inertia has to increase together with the rotational kinetic energy when the angular velocity is introduced. In order to preserve the rotational kinetic energy, the rotational DOFs contained in the semi-loof element have to be negative to suppress the effect of the lumping process to the moment of inertia.

2.3. Rotational degrees of freedom

The fundamental question in mass matrix lumping is the importance of the rotational DOFs. How significant is their contribution to the kinetic energy when we work with a semi-loof shell element? In the previous section we investigated the rotational DOF contribution in order to produce a lumped mass matrix with the equal inertia characteristic and also described the production of negative entries. In the Section 2.1. we explained the HRZ algorithm with the modification to deal with rotational DOFs. To use this algorithm for a diagonalization semi-loof element, it is necessary to decide in which direction they contribute to the translational motion. It is not easy and clear-cut to determine, and when this decision is made the rotational DOFs are scaled without any physical reason. Therefore, let's examine and focus on the importance and the contribution of the rotational DOFs of the semi-loof element on the influence of the rotational kinetic energy during the diagonalization process.

The rotational DOF influence was tested on the plate (Figure 5) of the dimensions width w = 1 mm, height h = 1 mm, thickness t_1 = 0.1 mm and t_2 = 0.01 mm, mass density $\rho = 7800\ \mathrm{kg/m^3}$ and the angular

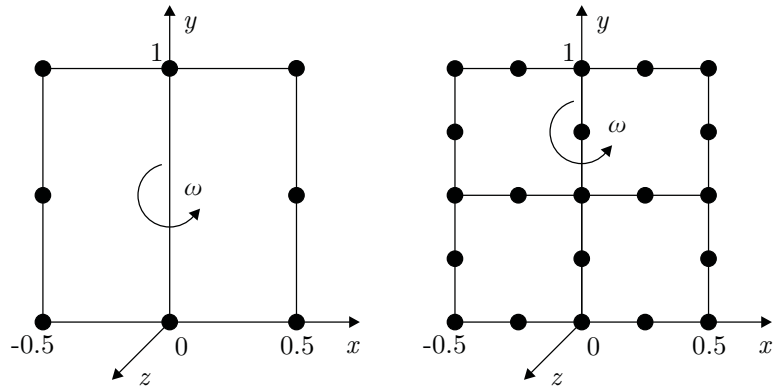

Fig. 5: Influence of the rotational DOFs ($n_{el} = 1$ and 2)

Tab. 3: Influence of the rotational DOF – semi-loof element, thickness = 0.1 mm

	Angular kinetic energy [J]	
n_{el}	with rotational DOFs	without rotational DOFs
1	$5.936942830255\times10^{-8}$	$5.93694266761\times10^{-8}$
2	$3.926416299426\times10^{-8}$	$3.926416251202\times10^{-8}$
4	$3.42309784091590\times10^{-8}$	$3.42309782178395\times10^{-8}$
8	$3.29567308352155\times10^{-8}$	$3.29567307279155\times10^{-8}$

velocity $\omega = 1$ rad/s. This plate was discretized into four meshes differing in density. All four discretized plates are displayed in Figures 5 and 6 where n_{el} denotes the number of elements along the plate side. In Table 3 you can see the kinetic energy of all four plates with and without considering the rotational DOFs obtained after applying angular velocity ω for thickness $t_1 = 0.1$ mm and in Table 4 for element thickness $t_1 = 0.01$ mm.

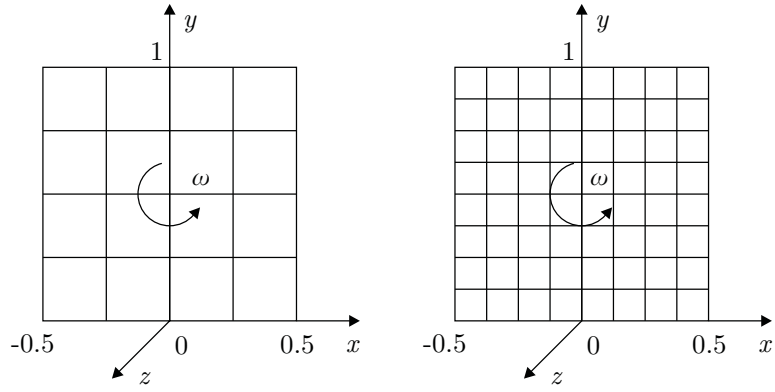

Fig. 6: Influence of the rotational DOFs ($n_{el} = 4$ and 8)

It is important to realize that whether we keep the original entries on the mass matrix diagonal corresponding to the rotational DOFs or reset the values to zero, the differences in results are almost identical. Further information about the influence of the rotational DOFs on a semi-loof element can be

Tab. 4: Influence of the rotational DOF – semi-loof element, thickness = 0.01 mm

	Angular kinetic energy [J]	
n_{el}	with rotational DOFs	without rotational DOFs
1	$5.930478568835\times10^{-9}$	$5.930478416375\times10^{-9}$
2	$3.920169155838\times10^{-9}$	$3.9201691176445\times10^{-9}$
4	$3.4175917166041\times10^{-9}$	$3.4175917069787\times10^{-9}$
8	$3.29194701535405\times10^{-9}$	$3.29194701287015\times10^{-9}$

found in Figure 7 where the error is computed as

$$\varepsilon_r = 100 \cdot \frac{|E_{k\,l} - E_{k\,lr}|}{E_{k\,l}} \tag{19}$$

where $E_{k\,l}$ is the kinetic energy of the plate with a lumped mass matrix while considering the rotational DOFs, and $E_{k\,lr}$ is the same energy without considering the rotational DOFs.

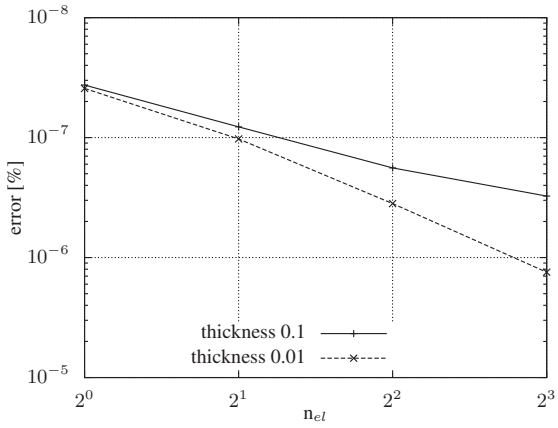

Fig. 7: The influence of rotational DOF on kinetic energy

The influence of the rotational DOFs on the kinetic energy of the rotating plate is almost negligible. If the plate consists of only one semi-loof element the contribution of the rotational DOFs to the kinetic energy is approximately 2.7×10^{-6} %, and the denser the mesh the smaller the contribution.

Having established these facts, we can now omit the rotational DOFs in the diagonalization process and keep only the original entries which come out from the consistent mass matrix, corresponding to the variational principles as only these values have a physical reason.

3. Results and Discussion

The previous sections of this paper dealt with the difference between consistent and lumped mass matrices and described the influence of this difference on the kinetic energy. It is now highly important to prove that the kinetic energy of the plate (Figures 5 and 6) converges to the analytical solution when the mesh contains more elements.

A technique which we already used for testing an algorithm convergence is similar to the one used in Section 2.3. to check the influence of the rotational DOFs on the kinetic energy – the same testing plates

with the induced angular velocity ω will also be used and those can be chosen arbitrarily. The angular velocity ω was projected to the loof nodes direction and the result was reassembled into vector $\mathbf{v}_g$ as described in Section 2.2.. The kinetic energy was calculated as

$$E_{k\,c} = \frac{1}{2}\mathbf{v}_g^T \mathbf{M}_c \mathbf{v}_g \tag{20}$$

Figure 9 shows the kinetic energy convergence of the numerical solution using the consistent mass matrix as well as the analytical one with the raising ratio of element width to element thickness. The error is computed as

$$\varepsilon_r = 100 \cdot \frac{|E_k - E_{k\,c}|}{E_k} \tag{21}$$

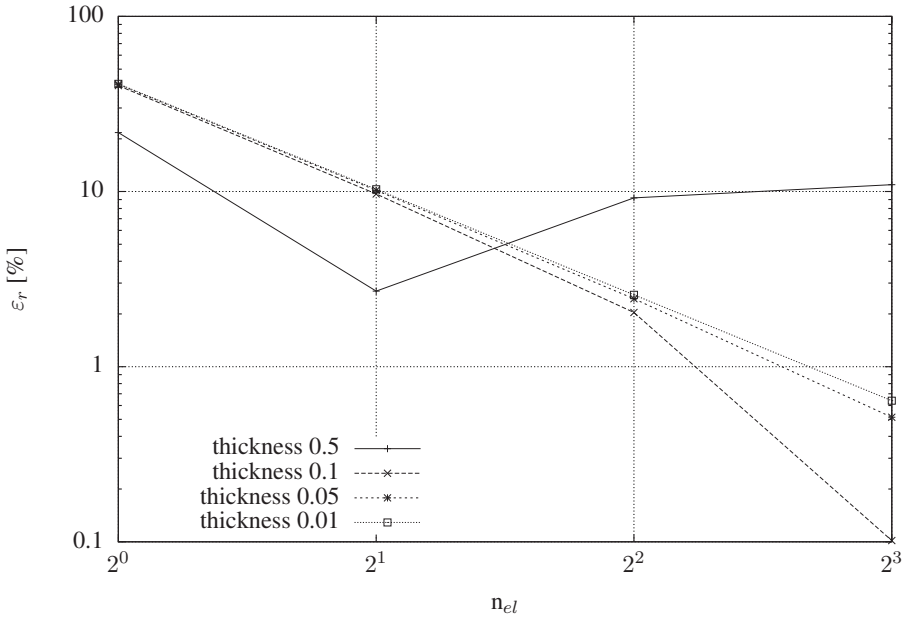

Fig. 8: Relative error in the kinetic energy corresponding to the numerical solution with CMM and DLMM – convergence test

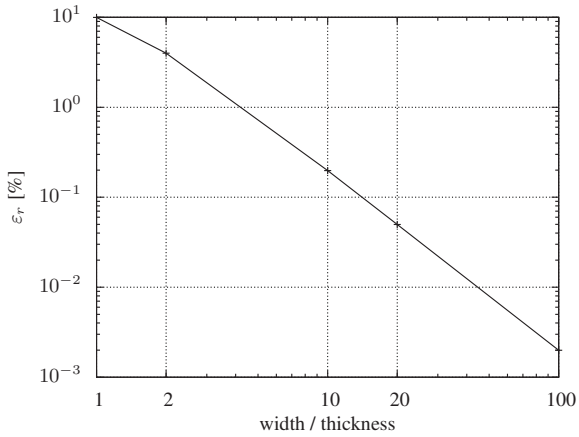

Fig. 9: Relative error in the kinetic energy corresponding to the analytical and numerical solution (CMM) – convergence test

where E_k is the analytical, exact, solution and $E_{k\,c}$ the numerical one with a consistent mass matrix. This test proved that the solution for kinetic energy of the plate modelled with semi-loof shell element converges to the analytical solution.

Figures 8 and 10 show a convergence rate of the solution with the lumped mass matrix to the solution with the consistent mass matrix (Figure 8) and to the analytical solution (Figure 10).

4. Conclusions

Due to the nature of the requirements related to the process of diagonalization (a universal algorithm, preserving the mass, an easy implementation), a method called HRZ was ultimately selected as a frequently-used approach that was the most suitable option for a consequent implementation. A special attention was paid to mass matrices of elements that contained rotational degrees of freedom – such as shells. Therefore a modification of this scaling method had to be devised not only in order to preserve the element mass, but also to preserve the moment of inertia. This method unfortunately returned negative terms in mass matrices. They lost their positive definiteness and consequently also became useless for an explicit solver implemented in the PMD program.

The standard HRZ method implementation involves a scaling of the rotational degrees of freedom in the same way which applies to the translational degrees of freedom, and it has no physical basis, thus it does not provide any solution for semi-loof shell elements in this form. This was the reason why the interest shifted entirely on the problem of a mass matrix diagonalization with rotational degrees of freedom in which we determined the influence of the rotational degrees of freedom on the total moment of inertia of the semi-loof element. The numerical test proved that the influence of the rotational degrees of freedom was negligible. And hence the implemented algorithm was designed to leave the original values belonging to the rotational degrees of freedom on the diagonal without any changes whatsoever.

Convergence tests were then carried out to observe the kinetic energy of the rotating element which would confirm a convergence to the consistent matrix as well as, most importantly, a convergence to the analytically calculated values. The implemented algorithm was tested on problems which involved natural frequencies and the shock wave propagation.

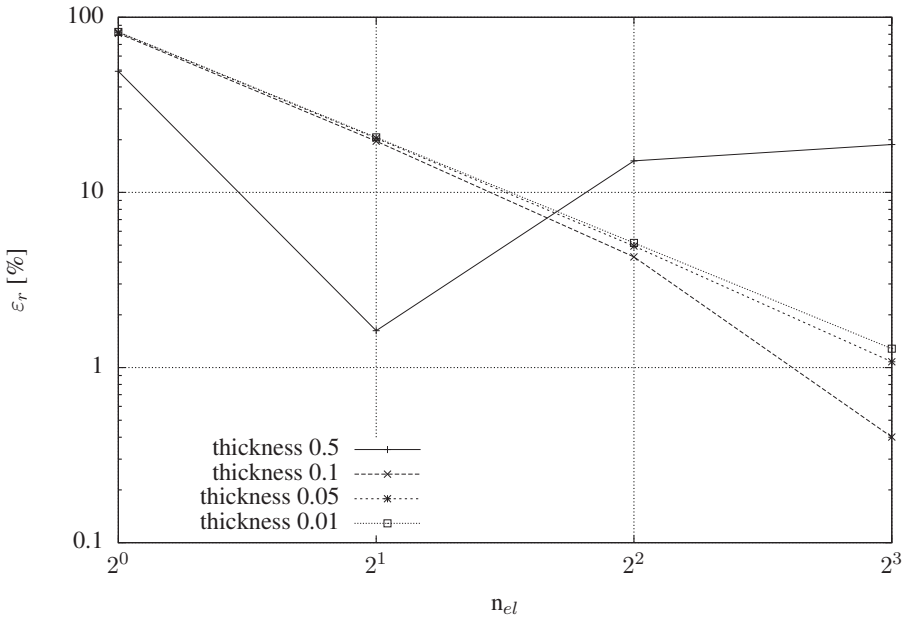

Fig. 10: Relative error in the kinetic energy corresponding to the analytical and numerical solution (DLMM) – convergence test

Acknowledgments

This work was supported by the grant projects GA CR 101/09/1630, ME10114, P101/10/P376 and P101/11/0288 under AV0Z20760514.

References

Cook, R. D., Malkus, D. S. & Plesha, M. E. (2002) *Concepts and applications of finite element analysis.* Wiley, New York.

Dokainish, M. A. & Subbaraj, K. (1989) A survey of direct time-integration methods in computational structural dynamics—I. explicit methods. *Computers & Structures*, 32, 6, pp. 1371–1386.

Fellipa, C. (2011) *Introduction to finite element methods (asen 5007) – fall 2010*, online (March 11, 2011). *http://www.colorado.edu/engineering/cas/courses.d/IFEM.d/*

Hellen, T. K. (1986) An assessment of the semiloof shell element, *International Journal for Numerical Methods in Engineering*, 22, 1, pp. 133–151.

Hinton, E., Rock, T. & Zienkiewicz, O. (1976) A note on mass lumping and related processes in the Finite element method. *Earthquake Engineering and Structural Dynamics*, 13, 9, p. A112.

Hughes, T. J. R. (1987) *The Finite Element Method*, Prentice-Hall Inc., New Jersey.

Irons, B. (1976) *Finite Elements for Thin Shells and Curved Membranes*, Wiley, London, Ch. The semi-loof shell elements.

Leština, J. (1980) Tenkoskořepinový konečný prvek semiloof, *Strojírenství*, 39, 12, pp. 714–719.

Sháněl, V. (2011) *On the Mass Lumping in the Finite Element Method.* Master Thesis, CTU in Prague, Faculty of Mechanical Engineering, Prague.

Zienkiewicz, O., Taylor, R. & Zhu, J. (2005) *Finite Element Method*, sixth Edition, Elsevier, Oxford.

18th International Conference
ENGINEERING MECHANICS 2012
Svratka, Czech Republic, May 14 – 17, 2012

pp. 1173–1181
Paper #229

PREDICTING SELF-COMPACTING CONCRETE SHRINKAGE BASED ON A MODIFIED FUZZY LOGIC MODEL

W. R. L. da Silva*, P. Štemberk**

Abstract: *The occurrence of shrinkage in concrete leads to development of internal tension stresses which can result in concrete cracking. The presence of cracks in concrete creates pathways that ease the access of aggressive agents reducing concrete structure durability and service life. Consequently, the correct reduction of shrinkage strain during the designing process is important to assure the structure's durability and long time serviceability. In light of this, the objective of this research was to develop an experimental based fuzzy logic model to predicting self-compacting concrete shrinkage. The fuzzy logic model decision-making is optimized though an evolutionary computing method, therefore enhancing computational effectiveness. The obtained results are compared to the B3 shrinkage prediction model and statistical analysis, indicating the reliability of the proposed model, are presented.*

Keywords: ***Fuzzy logics, shrinkage, self-compacting concrete, evolutionary computing***

1. Introduction

Concrete shrinkage is defined as decrease in concrete volume with time. This volume decrease does not depend on external stress and it is not completely reversible. The shrinkage in concrete is associated with a series of factors, such as chemical reaction, gradient in temperature, and movement and loss of water. Each one of these factors leads to different types of shrinkage, such as, autogenous, plastic, drying and thermal shrinkage, among others. For comprehensive review see Brooks, J., 2003, and Mehta & Monteiro, 2006, publications.

The occurrence of shrinkage leads to development of internal tension stresses, which may result in concrete cracking. The presence of cracks in concrete creates pathways that ease the access of aggressive agents into concrete and contributing to reduction in concrete structure durability. An example of concrete structure damaged by the occurrence of excessive shrinkage is illustrated in Fig. 1.

(a) (b)

Fig.1: Foundation block of a residential building in Prague, Czech Republic: (a) construction side overall view and (b) detail of 0.8mm crack width caused by concrete shrinkage.

* Ing. Wilson Ricardo Leal da Silva, MSc., Department of Concrete and Masonry Structures, Czech Technical University in Prague, Thakurova 7; 166 29, Prague; CZ, e-mail: wilsonecv@gmail.com

** Associate Professor Petr Štemberk, PhD.: Department of Concrete and Masonry Structures, Czech Technical University in Prague, Thakurova 7; 166 29, Prague; CZ, e-mail:stemberk@fsv.cvut.cz

Hence, it can be noticed that a trustworthy definition of concrete shrinkage strain is important in the designing process of structures, since it helps reducing maintenance costs and ensures that the specifications of expected service life and durability requirements will be fulfilled.

Self-compacting concrete, *SCC*, is a high-performance concrete that can flow under its own weight so as to completely fill the formwork and self-consolidate without any mechanical vibration (Erdem et al., 2009, Gaimster et al., 2003). *SCC* is specifically designed to achieve excellent deformability, a low risk of blockage, and good stability, ensuring a high formwork filling capacity. The use of *SCC* is rapidly developing in the construction industry, most likely due to the production process costs and the advantageous organizational nature of this material.

Nonetheless, it is important to consider that the production of *SCC* is more difficult than that of conventional concrete and many parameters have to be considered in order to obtain a final product that has an acceptable quality for the intended purpose. When compared to conventional concrete, *SCC* mixtures requires a higher volume of cement paste in the composition to achieve excellent deformability and high formwork filling capacity. Then, considering that shrinkage is a results of hydration reaction in the cement paste, *SCCs* are likely to present higher values of shrinkage strain. Hence, measuring shrinkage strain in *SCC* mixtures arises as a relevant issue.

Usually, experimental measurements are required to determine the concrete shrinkage strain. However, measurement of shrinkage strain is laborious, time consuming and expensive, therefore construction designers tend to use shrinkage prediction models. These models aim to determine concrete shrinkage strain in a faster and less expensive way when compared to experimental measurements.Amongst several existing prediction models, the *B3* model has been selected for comparison in this research. The *B3* model was developed in 1995 by Bažant, (Bažant, 1995), this model has been updated over time and its latest version dates back to 2000, (Bažant et al., 2000),

Though regularly used, shrinkage strains obtained from the prediction models do not necessarily match experimental measurements. The comparison of experimentally measured and predicted, shrinkage strain curves by the *B3* model are presented in Fig. 2. The experimental curves, shown in Fig. 2a and b, consist of a part of experimental data from published by Al-Attar, 2008 and Brook et al., 2001. for different types of concrete.

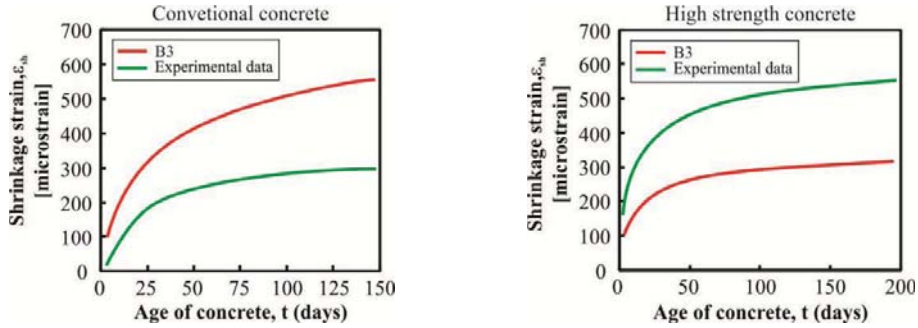

Fig. 2: Comparison of predicted and experimental shrinkage strain curves for (a) Conventional Concrete – input data from Al-Attar, 2008, and (b) High Strength Concrete – input data from Brooks et al., 2001.

From Fig. 2, a considerable difference from experimental and predicted shrinkage strain can be noticed, showing the relative error of *B3* model in predicting shrinkage strains. This way, it can be stated that the reliability of this prediction model is open to discussion, and improvements are required.

In light of this, the present work aims to develop a methodology for defining an experimental-based prediction model for *SCC* shrinkage. In this study, Soft-computing techniques, particularly fuzzy logic systems and evolutionary computing, were used to develop a modelling methodology, which was then applied to build a *SCC* shrinkage strain prediction model. Further, through statistical analysis, the results from the obtained model were compared to other published data.

2. Fuzzy logic and evolutionary computing

Fuzzy theory, first introduced by Zadeh in 1967, (Zadeh, 1967), correspond to a natural way of thinking where verbally expressed rules are applied to deal with vagueness, imprecision and ill-defined data. Basically, fuzzy logic control systems comprise three steps: fuzzification, decision-making and defuzzification. The fuzzification consists of converting the crisp input values into degrees of membership by means of input membership functions. This step is followed by the decision-making, where a degree of membership is assigned to the output variable based on the rule based and output fuzzy sets. Finally, the defuzzification is processed to convert the output fuzzy set in to a single value, in this case, the predicted shrinkage strain value.

The key factors to achieve an acceptable performance in a fuzzy logic system are connected to the definition of the number of fuzzy sets and the shape of the membership functions. Commonly, there are x^y fuzzy rules, where x and y are the number of sets and input variables, accordingly. In the classical fuzzy logic approach, the number of fuzzy rules can be reduced by the user's experience, and the shape of membership functions is usually adopted as linear to simplify calculations. This approach application has been used by Štemberk et al., 2011 to simulate heat evolution during hydration of typical Portland cement.

Nevertheless, when the classical approach is implemented to model non-linear materials behavior, the final results are a rather rough shaped piecewise curve as indicated in Fig.3. Note that, the use of the classical fuzzy logic approach is also feasible to model non-linear materials behavior. However, a considerable larger number of linear fuzzy sets is required to obtain smoothed curves, thus leading to a longer data collection time and high computational cost. In order to improve the entire modelling process a modified approach, which includes evolutionary computing methods, is proposed in this research.

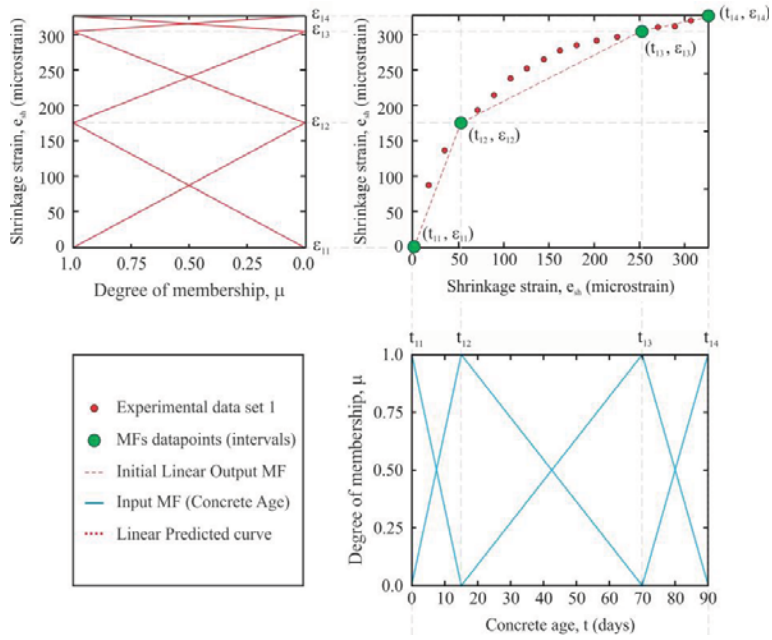

Fig. 3: Shrinkage strain curve predicted by the classical fuzzy logic approach

Evolutionary computing comprises robust optimization methods that can be generally applied without recourse to domain-specific heuristics. These methods operate on a population of potential solutions and apply the principle of survival of the fittest to produce successively better approximations to a solution, (Coley, 1999). Amongst several Evolutionary computing methods, Genetic Algorithms, *GA*, have been successfully applied for numerical optimization in civil

engineering, e.g., Rokonuzzaman et al., 2010 presents an application of *GA* for calibration of parameters for a hardening-softening constitutive model.

*GA*s consist of adaptive heuristic search algorithms based on the principles of Darwin's theory of natural selection. They represent an intelligent exploitation of a random search that uses historical information to guide the search into the region of better performance, within a defined search space. The basic form of a *GA* involves three operators to achieve evolution: selection, or reproduction, crossover and mutation, (Coley, 1999).

3. Proposed methodology for optimization of fuzzy decision-making

The proposed methodology combines fuzzy logics and genetic algorithms to optimize fuzzy decision making, which is achieved by optimizing the shape of the membership functions. Bearing in mind this idea, and focusing on *SCC* shrinkage, the following methodology is proposed:

Initially, the user has to define the number of representative intervals, N_{int}, of shrinkage strain, e_{sh}, and concrete age, t, for experimental shrinkage strain curves obtained from concrete mixtures with different volumes of cement paste. Note that, the more complex the shape of the curve the higher the number of intervals necessary to achieve optimal results. In the sequence, the user specifies the size of the population, S_{pop}, defined as *10*, which will be used in the genetic part of the algorithm. The optimization process is from this point on an automatic process. Based on the value set for N_{int}, the encoding of each individual, or chromosome, from the population is defined. The encoding comprises a string of $n_{enc} = 2 \times N_{int}$ real numbers, which correspond to the exponent values, E_L and E_R, from each membership function to be optimized, see Fig.4.

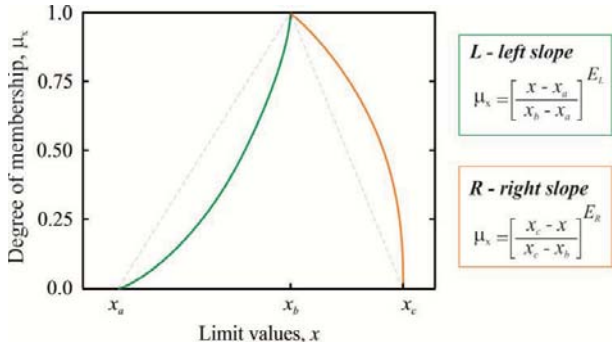

Fig. 4: General equation and shape of the membership functions to be optimized.

Subsequently, an initial random population is generated and the fitness function, *f(x)*, is evaluated. The fitness function corresponds to the *MSE* function described in Eq.(1).

$$f_j = \sqrt{\frac{1}{n-1} \cdot \sum_{j=1}^{n} d_j^2} \ , \tag{1}$$

where n is the number of data points considered in the analysis, d_j is the percent difference between each predicted and measured data point, f_j is the mean square error for data set j, and f_{all} is the overall mean square error, computed by means of Eq.(2).

$$f_{all} = \sqrt{\frac{1}{N} \cdot \sum_{j=1}^{n} f_j^2} \ , \tag{2}$$

with N as the total number of data sets.

Next, three genetic operators: selection, crossover and mutation, are applied to generate a new population. The selection operator chooses the chromosomes in the population for reproduction. In this case, the tournament selection scheme, which selects the best fitness from individuals chosen at

random from the population, was applied. The selected chromosomes, or parents, are then crossed over by one-point crossover scheme, with a probability, C_{prob} set as *90%*, to create a new individual to be included in the population. This scheme sets an independent randomized crossover point for couples of parents, whose data is swapped to create a new population. After that, a mutation operator is applied to maintain genetic diversity. The mutation is performed by disturbance with a probability, M_{prob}, set as of *10%*. The mutation operator randomly flips some of the values in a chromosome to create a mutated version of the individual to be incorporated in the population. After a new population has been generated, the fitness function re-evaluates all individuals from the new population. The obtained results, *f(x')*, are then compared with those from previous populations. Further, elitism is applied, i.e., the best overall solution is stored. In case none of individual from the new population shows better fitness than the stored solution, the individual with the worst solution from the new population is replaced by the best overall solution. The automatic process of generating a new population and evaluating the best fit is repeated until convergence occurs. Convergence was considered as achieved when more than *200* consecutive runs do not lead to any improvements in the fitness function result. The final result consists of a group of optimized fuzzy sets which will compose the fuzzy decision-making. Once the group of optimized fuzzy sets is defined, the decision making is then based on the rule base, R^{nr}, defined in (3), and the final predicted shrinkage strain, $\varepsilon_{sh,output}$, is computed by means of Eq.(4).

$$R^{nr}: IF\, V_{cp}\, is\, V_{cp,nr}\, THEN\, \varepsilon_{sh}\, is\, \varepsilon_{sh,nr}, \tag{3}$$

$$\varepsilon_{sh,output} = \sum_{nr=1}^{nr} \mu_n \cdot \varepsilon_{sh,n_r} \Big/ \sum_{nr=1}^{nr} \mu_{nr}\ , \tag{4}$$

where *nr* is the number of rules; V_{cp} is the cement paste volume input value, in l/m^3; $V_{cp,nr}$ and $e_{sh,nr}$ are the optimized group of fuzzy sets for cement paste volume and shrinkage strain, respectively; μ_{nr} is the degree of membership assigned to the group $e_{sh,nr}$ from each rule R^{nr}.

The methodology described in this section was applied for the experimental data presented by Leemann et al., 2011, and the results from Loser et al., 2009, were used to verify the optimized model.

4. Results and discussion

In the present analysis the volume of cement paste was chosen as input parameter and two experimental curves, illustrated in Fig.5, were considered as training data. The curves from Fig.5 were taken from the experimental database presented by Leemann et al., 2011.

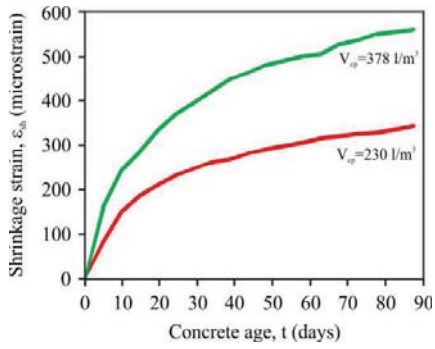

Fig. 5: Shrinkage strain curves of SCC mixtures from Leemann et al., 2011.

The proposed methodology was performed for this data and convergence was achieved after approximately *500* iterations. The fuzzy logic prediction model for *SCC*, named *FL-I* model, is then composed by the optimized fuzzy sets, the rule base, and the final output equation, presented in Eq.(4). The graphical representation of the *FL-I* model, illustrated in Fig.6, indicates the exponent values of the membership functions and the rule base use by the model to predict the *SCC* shrinkage strain curve.

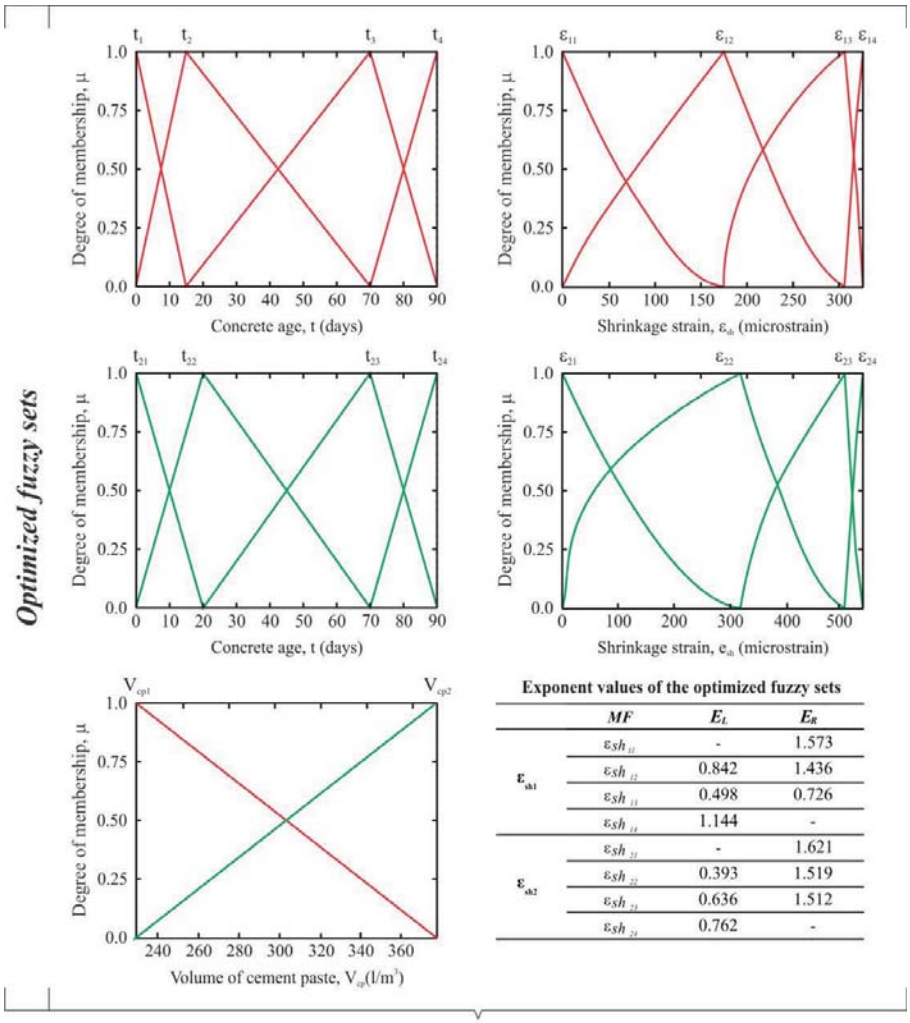

Exponent values of the optimized fuzzy sets

	MF	E_L	E_R
ε_{sh1}	εsh_{11}	-	1.573
	εsh_{12}	0.842	1.436
	εsh_{13}	0.498	0.726
	εsh_{14}	1.144	-
ε_{sh2}	εsh_{21}	-	1.621
	εsh_{22}	0.393	1.519
	εsh_{23}	0.636	1.512
	εsh_{24}	0.762	-

FL-I rule base matrix

	$t_{11} = 0$	$t_{12} = 15$	$t_{13} = 70$	$t_{14} = 90$
$V_{cp1} = 230$	$\varepsilon_{sh\,11} = 0$	$\varepsilon_{sh\,12} = 175$	$\varepsilon_{sh\,13} = 305$	$\varepsilon_{sh\,14} = 325$
	$t_{21} = 0$	$t_{22} = 20$	$t_{23} = 70$	$t_{24} = 90$
$V_{cp2} = 380$	$\varepsilon_{sh\,12} = 0$	$\varepsilon_{sh\,22} = 315$	$\varepsilon_{sh\,23} = 500$	$\varepsilon_{sh\,24} = 530$

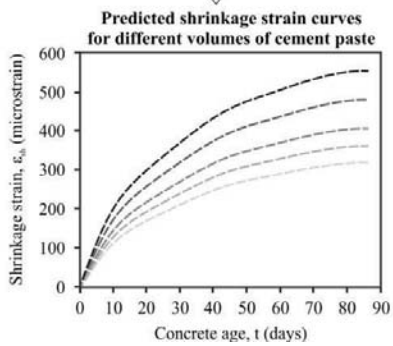

Fig. 6: Graphical representation of FL-I model.

Since only two curves were available for the optimization process, the fuzzy sets connected to the volume of cement paste had to be set as a linear functions, see Fig.6. It is also important to observe that the obtained model is suitable for predicting shrinkage strain up to *90* days and testing conditions defined by Leemann et al., 2011.

The experimental data published by Loser et al., 2009 was used to verify the quality of the *FL-I* model in predicting shrinkage strain. This data comprises shrinkage curves of five different *SCCs* with testing conditions compatible to the limits defined to the *FL-I* model. The volume of cement paste of each *SCC*, necessary as an input parameter, is listed in Table 1. Moreover, the shrinkage strain curves of each *SCC* mixture from Loser et al., 2009 were also compared to the strain curves obtained from the *B3* prediction model. For that, the input data shown in Table 1 was used.

Table 1. Input data used to predict shrinkage strain based on B3 and FL-I model, (Loser et al., 2009).

Input Parameters	**SCC**				
	I	**II**	**III**	**IV**	**V**
Cement paste volume, V_{cp} [l/m^3]*	329.0	349.0	316.0	342.0	332.0
Design compressive strength, f_c' [MPa]	53.3	63.1	51.0	49.4	66.0
Compressive strength at 28 days, f_{cm28} [MPa]	61.3	71.1	59.0	57.4	74.0
Curing time, t_c [days]	1				
Relative Humidity, RH [%]	70.0%				
Cement type	CEM I 42.5				
Specimen size [mm]	120 × 120 × 360 *(Shape: infinite prism)*				

** Considered as an input parameter of the FL-I model;*

The *MSE* values, computed by Eq.(1), for the *FL-I* and the *B3* model are presented in Table 2.

Table 2. Individual and overall MSE values for different shrinkage prediction models.

f_{model} *[%]*	**SCC**					$f_{overall}$*[%]*
	I	**II**	**III**	**IV**	**V**	
B3	31.3	27.4	29.0	17.2	32.9	28.1
FL-I	6.9	19.1	4.4	16.2	14.1	23.7

From Table 2, it can be seen that the *FL-I* model presented the lower *MSE* values than the *B3* model in all cases. By using the values from Table 2 in Eq.2 an overall *MSE* of *23.7%* is obtained for the *FL-I* model, against 28.*1%* for the *B3*. Therefore, it can be concluded that, once the limits *FL-I* model are respected, the results predicted by the *FL-I* model are more reliable than *B3*.

Nonetheless, though the overall *MSE* presented by the *FL-I* model was lower than the *B3*, its value is still considered high, around *20%*. The reason for that is probably because only two experimental curves were used as training data. If an intermediary curve was included in the training data set, the linear shape of the V_{cp} fuzzy set, see Fig.6, would be optimized. Consequently, the final *MSE* of *FL-I* model would be even lower than observed.

To verify this assumption, one of the experimental curves from Loser et al., 2009, more specifically *SCC IV*, see Table 1, was included in the training data. The optimization process was again performed and the exponent values, E_R and E_L, obtained for the optimized fuzzy sets are indicated in Fig.7. This leads to a new prediction model, called *FL-II* model. It is important to observe that the experimental data from *SCC IV* was only used as training data to optimize the shape of the fuzzy set of cement paste volume, therefore the optimized fuzzy sets connected to the shrinkage strain, e_{sh}, and the rule base, presented Fig.6, remained the same.

Once more, the experimental and predicted shrinkage strains, from *FL-II* model, were compared and the *MSE* values were computed by Eq.(1). The obtained results are presented in Table 3 together with the *MSE* values from *FL-I* model.

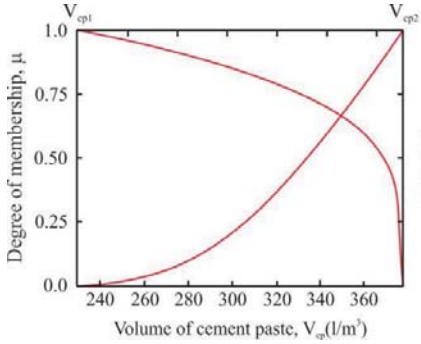

Fig. 7: Optimized group of fuzzy sets connected to the volume of cement paste for FL-II model.

Table 3. Individual and overall MSE values for different shrinkage prediction models.

f_{model} [%]	SCC					$f_{overall}$ [%]
	I	II	III	IV	V	
FL-I	6.9	19.1	4.4	16.2	14.1	23.7
FL-II	8.9	3.8	11.2	-	3.9	7.6

From Table 3, it can be seen that the overall *MSE* value for the *FL-II* are considerably lower than the *FL-I* model. Hence, the assumption that including additional training data would lead to a prediction model with lower error is verified. Although higher than the *FL-I* model in one case, the individual values of *MSE* for the *FL-II* were always below those obtained for the *B3* model.

Finally, the lower *MSE* values from *FL-I* and *FL-II* models, compared to the *B3* model, confirm their quality to simulate materials behaviour, and also the success in combining fuzzy logics and genetic algorithms to build optimized materials models. The obtained model are suitable to predict *SCC* shrinkage strain within the limits of the model, excluding the need of additional experimental analyses.

5. Final considerations

By defining a shrinkage strain prediction model for *SCC* the objective of this paper has been achieved. Based on the presented results the following conclusion can be drawn.

The use of the proposed methodology for optimization of fuzzy decision-making has shown satisfactory results. The optimized group of fuzzy sets led to a proper prediction of the shrinkage curves with a reduced number of rules, making the modelling process more effective.

The statistical analysis leads to overall mean square error around *30%* for the *B3* model, against 20% for the *FL-I* model, indicating that the *FL-I* model better represents the materials behaviour and can be used to predict *SCC* shrinkage once the limits of the model are respected. The further inclusion of additional training data in the optimization methodology contributed to reduce the overall error of the model from *~20%* to *~7%,* demonstrating the flexibility of the model in self-adjusting according to the training data. Such flexibility is a great advantage of fuzzy logic-based model when compared to the prediction models that are based on equations and its constants.

Acknoledgements

The authors wish to express their appreciation to the Czech Science Foundation project P105/10/2098, to the Erasmus Mundus External Cooperation Window EMEWC – EUBrazil Startup program for providing

funds for the first author's PhD study abroad, and also to Grant Agency of the Czech Technical University in Prague (grant n^{o} SGS11/107/OHK1/2T/11).

References

Al-Attar, T.S. (2008).Effect of coarse aggregate characteristics on drying shrinkage of concrete. *Eng. & Tech*, 26, 2.

Bažant, Z.P. (1995) Creep and Shrinkage Prediction Model for Analysis and Design of Concrete Structures – Model B3, *Materials and Structures*, 28, pp.357-365.

Bažant, P.Z., Baweja, S. (2000) Creep and shrinkage prediction model for analysis and design of concrete structures: Model B3, in.: *Adam Neville Symposium: Creep and Shrinkage – Structural Design Effects, ACI SP-194*, American Concrete Institute, Farmington Hills, MI, pp.1-83.

Brooks, J.J., Johari, M.A.M. (2001) Effect of metakaolin on creep and shrinkage of concrete. C*em. Concr. Comp.,* 23, pp.495-502.

Brook, J., Elasticity, shrinkage, creep and thermal movement. (2003) In: *Newman, J. & Choo, B. S. 3rd Ed. Advanced Concrete Technology – Testing and Quality*. Elsevier, London.

Coley, D.A. (1999) An introduction to genetic algorithms for scientists and engineers. *World Scientific*, Singapore 244p.

Erdem, T. K., Khayat, K. H., Yahia, H.. (2009) Correlating Rheology of Self-Consolidating Concrete to Corresponding Concrete-Equivalent Mortar, *ACI Materials Journal*, 106, 2, March-April.

Gaimster, R., Dixon, N. (2003) Self-Compacting Concrete, in: Newman, J. & Choo, B. S. 3rd Ed. *Advanced Concrete Technology – Processes*, London.

Leemann, A., Lura, P., Loser, R. (2011) Shrinkage and creep of SCC – The influence of paste volume and binder composition. *Cons. Build. Mat.,* 25, pp.2283-2289.

Loser, R., Leemann, A. (2009) Shrinkage and restrained shrinkage cracking of self-compacting concrete compared to conventionally vibrated concrete*. Materials and Structures*, 42, pp.71-82.

Mehta, P. K., Monteiro, P. J. M. (2006) Concrete: Microstructure, properties and materials, 3rd Ed, McGrawHill, New York.

Rokonuzzaman, Md., Sakai, T. (2010) Calibration of the parameters for a hardening-softening constitutive model using genetic algorithms. *Computers and Geotechnics*, 37, pp.573-579.

Štemberk, P., Rainová, A. (2011) Simulation of hydration and cracking propagation with temperature effect based on fuzzy logic theory. *Mechanika,* 17, 4, pp.358-362.

Zadeh, L.A. (1967) Fuzzy sets. *Information and Control*, 8, pp.38-53.

18th International Conference
ENGINEERING MECHANICS 2012
Svratka, Czech Republic, May 14 – 17, 2012

pp. 1183–1187
Paper #106

I

M

V. Skála , M. Matějka

Abstract: *The work deals with measurement of characteristics of the synthetic jet generator. Synthetic jet mean velocity in dependence of the parameters of actuating signal (type of signal, frequency, electrical current value) and the velocity profile in the wake behind the hump with controlled boundary layer was studied. A hot wire anemometry method (HWA) measurement technique was used. Profiles of the mean velocity and turbulence intensity behind hump was evaluated. Variants with and without the synthetic jet were measured and compared.*

Keywords: Boundary layer, flow control, HWA, synthetic jet, wake.

1. Introduction

For the purpose of investigation of the flow with controlled boundary layer behind the aerodynamic obstacle in the laboratories of the Department of Fluid Mechanics and Thermodynamics 12112, was rebuilt sucked open wind tunnel with a closed test section, including measuring equipment with traversing device and measuring software in LabVIEW. The scheme of the wind tunnel is on Fig. 1. Synthetic jet was chosen as method of active boundary layer control.

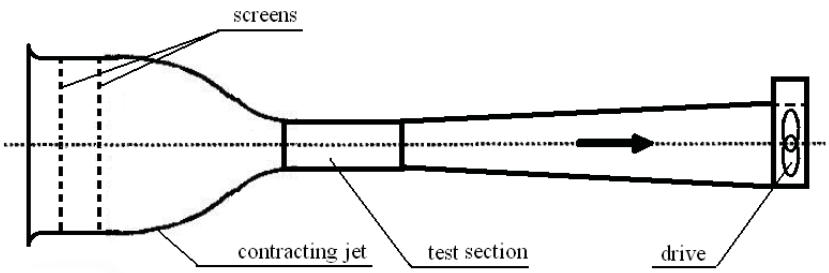

2. Model with synthetic jet generators

Block of nine synthetic jet generators driven by electrodynamics actuators was used. The block is instaled inside the model. The outcome of generators is connected smoothly to the top surface of the model, see Fig. 2 (the flow direction is being from left to right).

* Ing. Vladislav Skála: Department of Fluid Mechanics and Thermodynamics 12112; CTU Prague, Technická 4, 166 07, Prague; CZ, e-mail.: Vladislav.Skala@fs.cvut.cz

** Ing. Milan Matějka, Ph.D.: Department of Fluid Mechanics and Thermodynamics 12112; CTU Prague, Technická 4, 166 07, Prague; CZ, e-mail.: Milan.Matejka@fs.cvut.cz

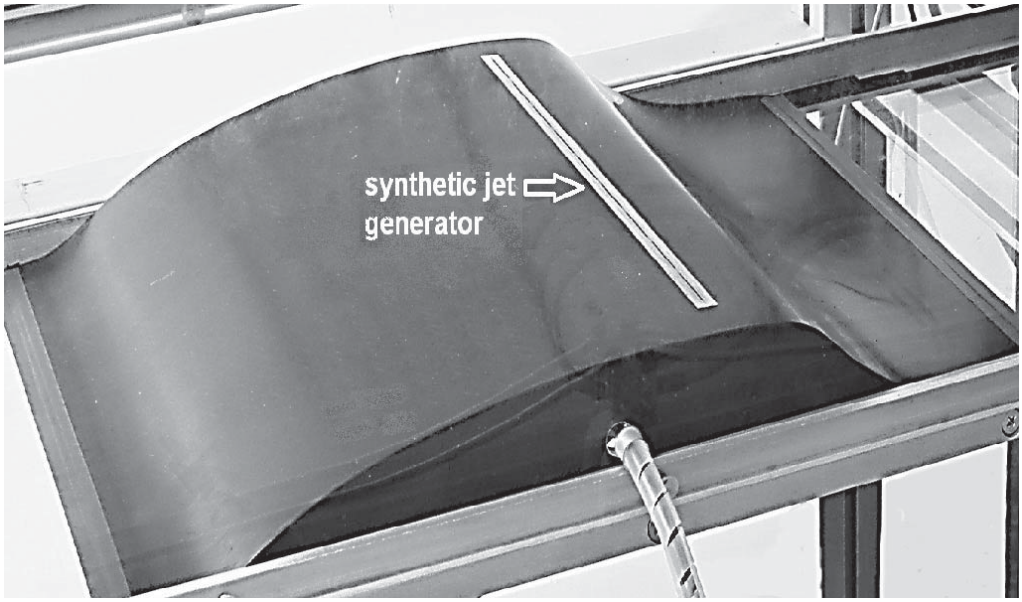

Fig. 2 Model with installed synthetic jet generators in the testing section of the wind tunnel

3. Synthetic jet generator calibration

The calibration of the synthetic jet generator is to determine dependence of the intensity/velocity u_0 of the synthetic jet on exciting frequency, type of signal and input electrical current value. Time average value of the velocity of the synthetic jet is defined:

$$u_0 = \frac{2}{T} \cdot \int_0^{\frac{T}{2}} u_0(t) \cdot dt \tag{1}$$

where $u_0(t)$ is the instantaneous velocity generated by the synthetic jet and T is positive period of the signal.

Measuring system with hot wire probe (HWA) was used. The measuring system was realized using computer (PC) with measuring card and software in LabVIEW, to generate the jet-excitation signal and to collect measured data from the HWA device 54T30 MiniCTA, Dantec Dynamic company, stabilized power supply and one wire HWA probe.

On Fig. 3 mean velovity u_0 dependence on frequency of sine type excitation signal is visible. Value of imput current of the excitation signal was constant in this case. Maximum mean velocity u_0 of generated synthetic jet was about 11,5 m/s. Maximum intensity of the synthetic jet for excitation frequency of 370 [Hz] was found. This corresponds to the value of cavity resonance.

On the next figure, Fig. 4, the dependence of mean velocity of the synthetic jet on input current value with sine type excitation signal for resonant frequency is shown. This characteristics is useful for wind tunnel measurements to define the input current value which corresponds to the required velocity u_0 of the synthetic jet.

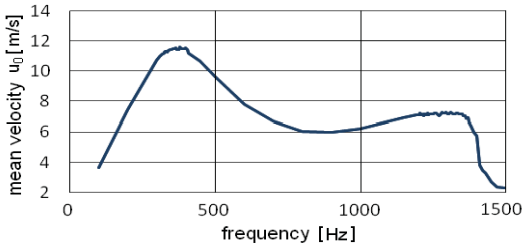

Fig. 3 Mean velocity dependence on frequency excitation signal

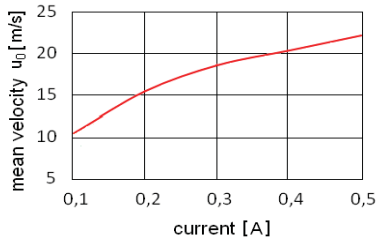

Fig. 4 Mean velocity dependence on input current for resonant frequency

4. Wind tunnel measurement

The excitation signal for measurement was sine type modulated by rectangular signal. The sine type signal – carrying was created on resonant frequency of the actuator – 370 [Hz]. The square type - modulation frequency corresponds to the natural vortex shedding frequency of the flow behind the aerodynamic obstacle. That frequency can be estimated from optimal value of Strouhal number – non-dimensional frequency. Strouhal number *St* is defined as:

$$St = \frac{f \cdot L}{v} \tag{2}$$

where f is frequency of vortex shedding, L characteristic dimension and v fluid velocity.

Evaluated was the mean velocity value $\bar{u}$:

$$\bar{u}_i = \frac{1}{T}\int_0^T u_i(t)dt \tag{3}$$

and turbulence intensity *Tu:*

$$Tu_i = \frac{\sqrt{\overline{u_i'^2}}}{|\bar{u}_i|} \tag{4}$$

where $\bar{u}_i$ is the mean velocity, $\sqrt{\overline{u_i'^2}}$ is the standard deviation of velocity in the i-thest point cross-section and T is positive period of the signal.

Measuerement area in cross-section is marked on Fig. 5. Measurements were made with and without the synthetic jet. Both cases was compared, see Fig. 6.

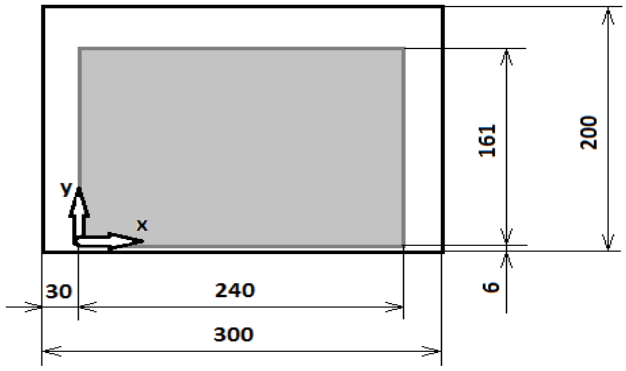

Fig. 5 Measuered area in cross-section

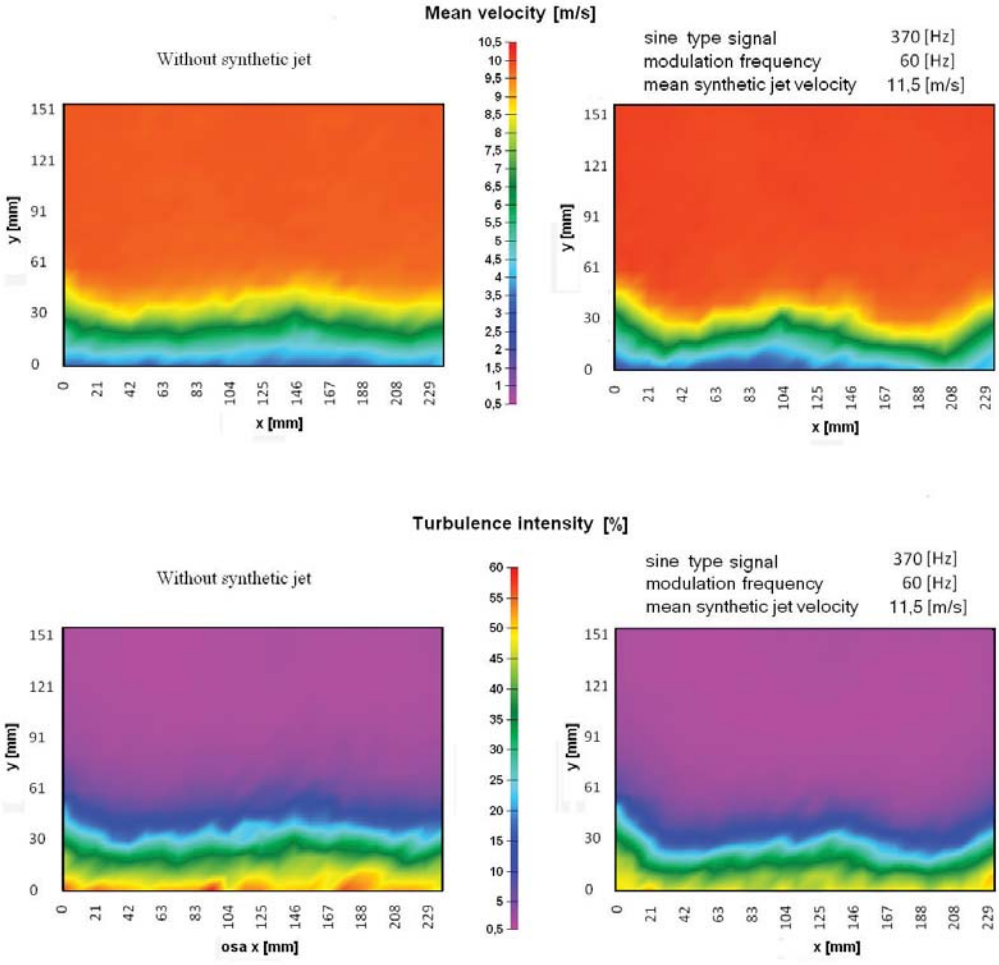

Fig. 6 Mean velocity and turbulence intensity, wind tunnel drive set on 1740 rpm

5. Conclusions

It was found, that the synthetic jet have positive influence on the flow. Dominant vortex structures can be observed probably in the wake behind the model. The mean velocity in non-influenced part of cross-section increased from 9,8 [m/s] in case without synthetic jet to 10,1 [m/s] i case with synthetic jet. The wake magnitude in cross-section was reduced. The maximum of turbulence intensity in the wake was decreased from 60% to 50%.

It was made introductory measurements. Following measurements in another cross-sections and advanced data processing give more interesting results. It seems, that synthetic jet is promissing technique of boundary layer control.

Acknowledgment

The work has been supported from GA of the Czech Republic 101/08/1112.

References

Glezer, A. (1998) *Shear flow control using fluidic actuator technology.* Georgia Institute of Technology, Georgia.

Kundys, J, Fabián, P., Kozubková, M. (2004) *Měření žárovým anemometrem.* VŠB – TU Ostrava.

Matějka, M. (2007) *Vliv aktivních metod řízení na smykovou vrstvu v lopatkové mříži*. Dissertacion thesis, CTU Prague.

Pick, P. (2007) *Software pro návrh generátoru syntetizovaného paprsku*. Thesis, CTU Prague.

Skála, V. (2011) *Vliv střední rychlosti proudu na charakter úplavu za překážkou*. Thesis, CTU Prague.

Uruba, V (2005) Flow control using synthetic jet actuators. *Engineering MECHANICS, 1, 12,* pp.41-62.

18th International Conference
ENGINEERING MECHANICS 2012
Svratka, Czech Republic, May 14 – 17, 2012

pp. 1189–1193
Paper #62

METHODOLOGY FOR DETERMINATION OF MOISTURE DISTRIBUTION

J. Skramlik[*], M. Novotny[**], K. Suhajda[***]

Abstract: *The aim of the research is to determine the capillary conductivity coefficient as a characteristic material moisture parameter of the building materials using a non-destructive method while using microwave radiation. A test specimen of ceramic is subjected to an isothermal moisture intake process. The transient moisture distribution in the specimen during the process is determined, at different stages of the process, using EMW-ray equipment. Boltzmann transformation of the experimental data results in a single moisture distribution curve, characteristic of the specimen.*

Keywords: ***Moisture, capillary conductivity, diffusion, water flow, EMWR microwave radiation***

1. Introduction

Into porous material of structures can penetrate moisture in liquid or gaseous form. To express the negative effects of moisture on building materials or building structures more accurately, it is needed to use the most accurate method of detecting moisture diffusion. The article deals with the issues related to moisture content in building materials and presents the results of experimental monitoring of one-dimensional water flow in inert porous materials and it's entrapping in non-stationary damping condition. The measuring device developed at the Institute of Civil Structures, University of Technology Brno, is used to verify the measurement method using samples of building materials.

2.Transfer of the moisture

As a quantity characteristic to define moisture transfer within materials consists from capillary porous matters is used the coefficient of capillary conductivity. It is characteristic parameter (by humidity gradient) for transfer of liquid moisture within porous substance. All methods explaining the coefficient of moisture conductivity used the one-dimensional diffusion equation (Kutilek 1992):

$$\frac{\partial u}{\partial t} = \frac{\partial}{\partial x}(\kappa \frac{\partial u}{\partial x}) \qquad (1)$$

The basis is set as definition of moisture distribution $u(x,t)$ for particular length of sample in the defined time scale (deliquescence curves). The higher is the moisture level of material the lower is amount of microwave radiation, which goes through the material. This is caused by the fact that hydrogen nuclei of water molecule absorb the microwave radiation. Based on the measurement applied by microwave way there can be specified moisture in the particular material part as well as deliquescence curves. These curves are necessary to define coefficient of capillary conductivity calculation.

To obtain deliquescence curves' coefficient of capillary conductivity calculation, is used the following Lykov formula covering the consistency of moisture flow (Kutilek 1992):

[*] Assoc. prof. Ing. Jan Skramlik, Ph.D..: Brno University of Technology, Faculty of Civil Engineering, Veveri 95; 60200, Brno; CZ, e-mail: skramlik.j@fce.vutbr.cz

[**] Assoc. prof. Ing. Miloslav Novotny, CSc.: Brno University of Technology, Faculty of Civil Engineering, Veveri 95; 60200, Brno; CZ, e-mail: novotny.m@fce.vutbr.cz

[***] Ing. Karel Suhajda,Ph.D.: Brno University of Technology, Faculty of Civil Engineering, Veveri 95; 60200, Brno; CZ, e-mail: suhajda.k@fce.vutbr.cz

$$\rho_S \frac{\partial u}{\partial t} = -\frac{\partial q}{\partial x} \tag{2}$$

and continuity formula (Mrlík 1986):

$$q = -\rho_S \kappa \frac{du}{dx} \tag{3}$$

and supposed mock-up moistening tracked exhibits material s. Fig. 1 and Fig. 2.

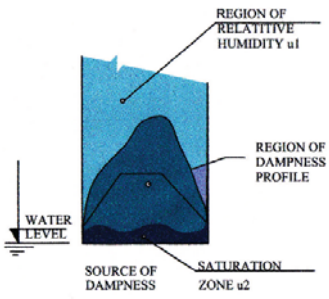

Fig. 1 Hypothetical progress of sample's deliquescence free of immurement

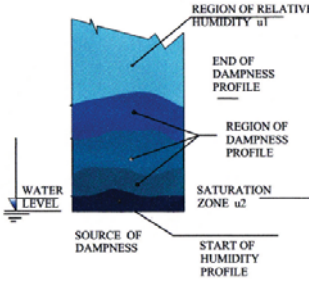

Fig. 2 Hypothetical progress of sample's deliquescence with immurement

3. Experimentally assembled apparatus

On the basis of the patens there has been experimentally assembled by the institute (US) the measurement apparatus s. Fig. 3 and detail Fig. 4.

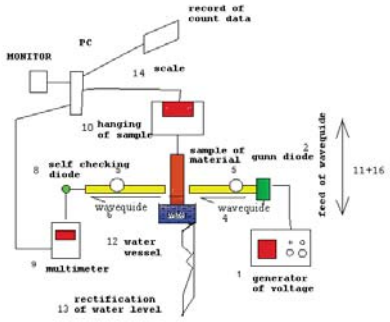

Fig. 3 Scheme of measurement apparatus

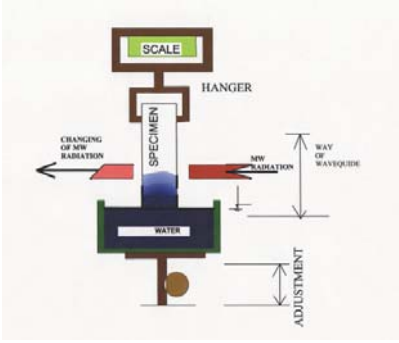

Fig. 4 Position of specimen - detail

4. Change in intensity of EMW radiation

By the aim of measurement apparatus constructed experimentally, has been defined functional dependence for each material – Fig. 5 and 6.

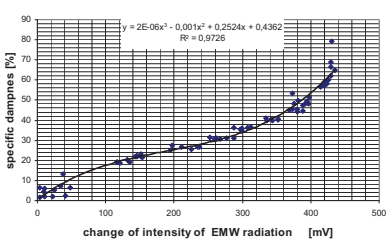

Fig. 5 Functional dependence formulation for gas concrete

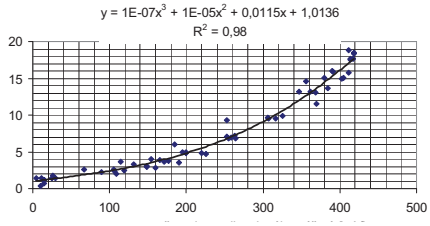

Fig. 6 Functional dependence formulation for material of ceramics

5. Primary measure

By the help of change of electromagnetic microwave radiation intensity depending on quantities of moisture in porous material is description of moisture transport, Fig. 7.

Such results can be used in Excel software for additional mathematic processing – profile of the moisture's front in the particular time line s. Fig. 8. In accordance with the speed waveguides was determined dependence of EMWR on moisture in specimen (in graphics software Excel) Fig. 8.

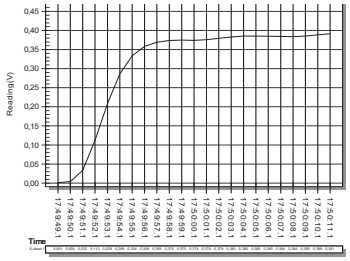

Fig. 7 Primary measure results within time interval 10 min

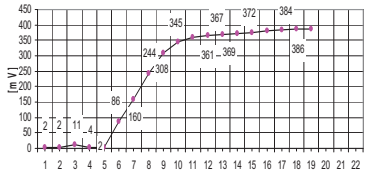

Fig. 8 Primary results measured into time interval 10 min in Excel processing

The Fig. 8 shows the spread of moisture in porous material, which is capture of liquid water within time interval after 10 min from beginning of deliquescence. One section on the axis x = 3 mm on the sample.

The Functional dependence formulation, s. Fig 5 (or 6), is defined by the Maple software s. Fig. 9

In the Fig. 10 is dependence formulation of EMW radiation change within time interval 10, 20 and 30 min. for length of specimen.

As well as in the Maple software – spread of the moisture through the whole sample in the particular time lines.

6. Procedure deliquescence curves assessment

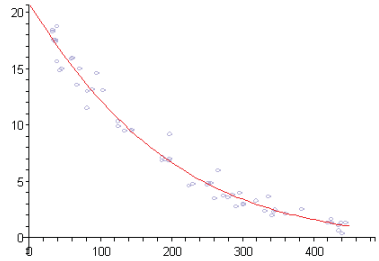

Fig. 9 Functional dependence of measured variable defined by the Maple software (y-axis = moisture by weight /%/; x-axis = dependence of EMWR on moisture /mV/

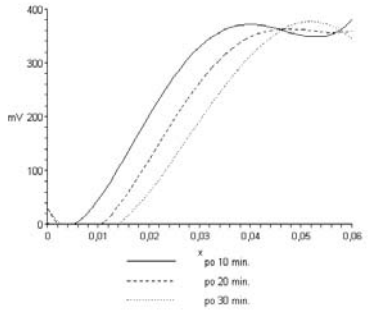

Fig.10 Curves of dependence of EMWR on moisture in the Maple software

a) Dependence between EMW radiation and content of moisture in material from regression formula, Fig. 3, 4 and 10

$u_m = -1{,}342033167.10\text{-}7\ .z^3 + 0{,}0001936510773\ .z^2 - 0{,}1038753765\ .z + 20{,}78641097$

b) Dependence between change of EMWR and moisture into distance from source of dampness,

c) Moisture distribution defined by the Maple software, Fig. 11

$u_{m,t} = f(z_t(x))$

u_m is specific moisture

z EMWR intensity which come through Specimen

x position data of moisture

t time interval of measurement

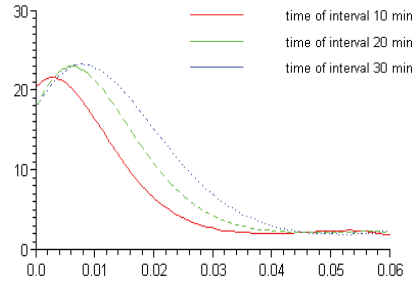

Fig. 11 The moisture distribution defined by the Maple software (y-axis = moisture by weight /%/; x-axis = length of sample /m/

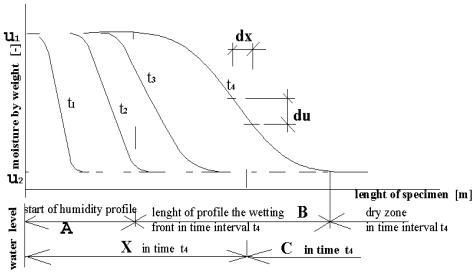

Fig.12 Assumption of the moisture distribution in porous material u (x) at the time intervals t_x (Mrlik 1986):

Figures measured by experimentally assembled measurement apparatus allow us to calculate coefficient of capillary conductivity. Moreover, there are several other possibilities how we can use these figures – for example mass moisture dependency in the particular time intervals.

7. Conclusions

Diffusion of moisture in porous material is currently adequately addressed. The problem remains the condensations of water vapor inside of the porous structures, for which there is no practical basis. In comparison with the destructive method, this methodology of calculating the capillary conductivity coefficient provides more data and more accurate information of the moisture content in detailed sections. The advantage is the relatively fast obtaining of the measurement results and the possibility of continuous measurement of more moisture curves on one sample of the material in any time interval without interrupting the measurement and handling the sample.

Acknowledgements

This research paper was created with the help of the P104/10/1390 grant "Analysis of microwave radiation influence by application of chemical grouting damp masonry“ and GACR P104/10/P388 “Experimental analysis of the effect of microwave radiation for destruction of biological agents causing corrosion of building materials” at the Brno University of Technology, Faculty of Civil Engineering.

References

Gertis, K., Kiessl, K. (1980) *Feuchtetransport in Baustoffen*, Berichte aus dem Fachbereich Bauwesen.

Künzel, H., (1986) Bestimmt der volumen- oder der Massebezogene Feuchtegehalt die Wärmeleitfähigkeit von Baustoffen, *Bauphysik* 8.

Mrlik, F. (1986) *Buildings materials and construction moisture problems*, SR, Alfa Bratislava.

Kutilek M. (1992) *Dampness porous material*, Czech Republic Prague SNTL.

Skramlik, J., Novotný, M. (2009) *Moisture transfer in building material*, PROHITECH 09, Italy, Taylor and Francis Group, UK.

18th International Conference
ENGINEERING MECHANICS 2012
Svratka, Czech Republic, May 14 – 17, 2012

pp. 1195–1200
Paper #26

ON APPLICATIONS OF DISTRIBUTIONS TO ANALYSIS OF CIRCULAR PLATE DESIGN ELEMENTS

J. Sobotka*

Abstract: *The mathematical model of a circular plate according to Kirchhoff's theory contains classical derivatives of internal forces, moments, slopes of a middle surface and deflection. However these derivatives are not defined at such internal points of middle plane where a line lateral loading, a line moment loading, a line support, or a rotational coupling between plate segments is situated. We have used the distributional derivatives for the unknown discontinuous functions, and developed a generalized mathematical model in the form of a system of ordinary differential equations in order that the mathematical model of the circular plate subjected to axisymmetric loading may be valid also along the lines of discontinuity mentioned, which are common in calculating experience. We have found a general solution to the generalized system of differential equations by means of a symbolic programming approach using Maple.*

Keywords: ***Circular plate, discontinuities, Dirac singular distribution, Heaviside step function.***

1. Introduction

Solving analytically a circular or annular plate subjected to an axisymmetric bending with discontinuous loading, support or geometry, we at first divide the plate into segments without discontinuities. Then, we find continuous solutions with integration constants for each plate segment separately. Finally, we determine integration constants using boundary conditions and continuity conditions among adjoining plate segments.

Applying distributional derivative (Schwartz, 1966) for the transverse shear force, the radial bending moment, and for the slope of a middle-surface in a meridian plane, we can derive a generalized mathematical model of the circular plate with discontinuities in loading, support and geometry that can be solved like only one differential problem without dividing plates into segments, and without using continuity conditions.

2. The classical mathematical model of an axisymmetric bending of the plate

According to the Kirchhoff's plate bending theory, a system of differential equations describing axisymmetric bending of circular plates may be composed of five ordinary differential equations of the first order (Reddy, 1999; Höschl, 1971; Timoshenko & Woinowsky-Krieger, 1959) as follows:

$$\frac{d}{dr}\left(r\, q_r(r)\right) = -r\, \mathrm{p}(r) \quad , \tag{1}$$

$$\frac{d}{dr}\left(r\, m_r(r)\right) = m_t(r) + r\, q_r(r)\,, \tag{2}$$

$$m_r(r) = B\left(\left(\frac{d}{dr}\,\phi(r)\right) + \frac{\mu\,\phi(r)}{r}\right) \quad , \tag{3}$$

$$m_t(r) = B\left(\mu\left(\frac{d}{dr}\,\phi(r)\right) + \frac{\phi(r)}{r}\right) \quad , \tag{4}$$

* Ing. Jiří Sobotka, Ph.D., ČEZ, a.s., 67550 Dukovany, tel. +420 561 10 5234, e-mail: jiri.sobotka@cez.cz

$$\frac{d}{dr}\mathrm{w}(r) = -\phi(r) \quad , \tag{5}$$

for

$$\left(\frac{d}{dx}\mathrm{w}(x)\right)^2 << 1 \tag{6}$$

and

$$B = \frac{E\,h^3}{12\,(1-\mu^2)} \quad . \tag{7}$$

where

$q_r(r)$	the transverse shear force per unit length,
$m_r(r)$	the radial bending moment per unit length,
$m_t(r)$	the circumferential bending moment per unit length,
$\phi(x)$	the slope of a middle-surface in a meridian plane,
w(x)	the deflection,
p(r)	the surface loading in normal direction to the middle plane,
r	the radial coordinate.
B	the plate bending stiffness,
E	Young's modulus,
μ	Poisson's ratio,
h	the thickness of the plate.

Equations (1), (2) are equilibrium conditions of a plate element cut out in the undeformed shape. Bending moments (3), (4) have been derived for curvatures supposing (6).

3. The normal form of the ordinary differential equations system

In order to be able to express discontinuities of unknown dependently variable quantities mathematically, we at first express the system of differential equations (1), (2), (3), (5) in the normal form as follows where the circumferential bending moment has been excluded using equation (4):

$$\frac{d}{dr}Q_{rc}(r) = -2\,\pi\,r\,\mathrm{p}(r) \quad , \tag{8}$$

$$\frac{d}{dr}M_{rc}(r) = \frac{\mu\,M_{rc}(r)}{r} + \frac{2\,\pi\,B\,(1-\mu^2)\,\phi(r)}{r} + Q_{rc}(r) \quad , \tag{9}$$

$$\frac{d}{dr}\phi(r) = \frac{1}{2}\frac{M_{rc}(r)}{\pi\,B\,r} - \frac{\mu\,\phi(r)}{r} \quad , \tag{10}$$

$$\frac{d}{dr}\mathrm{w}(r) = -\phi(r) \quad , \tag{11}$$

where the total transverse shear force is:

$$Q_{rc}(r) = 2\,\pi\,r\,q_r(r) \quad , \tag{12}$$

and the total radial bending moment is:

$$M_{rc}(r) = 2\,\pi\,r\,m_r(r) \quad . \tag{13}$$

4. Dividing discontinuities of loading, support and geometry into groups

All the given discontinuities can be divided into two groups according to their influence on discontinuities of unknown dependently variable quantities, i.e. generalized internal forces and generalized deformations.

The first group contains such discontinuities which do not cause another ones, so they can be expressed by means of Heaviside step function denoted further by Heaviside(x).

The second group contains such discontinuities which cause another ones, so they can be expressed by means of Dirac singular distribution denoted further by Dirac(x).

E.g., the discontinuous surface loading p(r) occurring in equation (1) or (8) belongs into the first group of given discontinuities. A line lateral loading, a line support or a line bending loading acting at internal points of the middle-plane or a line joint between plate segments belong into the second group of the given discontinuities.

The equation (8) is not valid at such internal points of the middle-plane of the plate where a line lateral loading is applied, or a line support is situated. Likewise, the equation (9) is not valid at such internal points of the middle-plane of the plate where a line bending loading is applied. Similarly, the equation (10) is not valid at such internal points of the middle-plane of the plate where a line joint along a circle is placed connecting plate segments. In order that the mathematical model of the axisymmetric bending of the circular or annular plate may be valid also at internal points of the middle-plane in which jump discontinuities of the lateral shear force or the bending moment or the slope of the middle-surface may occur, we have to extend the right-hand side of the equations (8), (9), (10) by adding appropriate distributional part according to the distributional derivative definition (Schwarz, 1966; Kanwal, 2004) that is as follows:

$$\frac{d}{dx}\,\mathrm{f}(x) = \{\frac{d}{dx}\,\mathrm{f}(x)\} + [f]_{x_0}\,\mathrm{Dirac}(x - x_0)\ , \tag{14}$$

where

$\{\frac{d}{dx}\,\mathrm{f}(x)\}$	the classical derivative,
$[f]_{x_0}$	the magnitude of the jump discontinuity of the quantity f(x) at point $x = x_0$; $[f]_{x_0} = \mathrm{f}(x_0 + 0) - \mathrm{f}(x_0 - 0)$
$\mathrm{f}(x_0 + 0)$	the right-hand limit of f(x) at point x_0,
$\mathrm{f}(x_0 - 0)$	the left-hand limit of f(x) at point x_0,
$\mathrm{Dirac}(x - x_0)$	Dirac distribution with its singularity at point $x = x_0$.

5. The generalized mathematical model of axisymmetric bending of the circular plate

Considering n_1 line lateral loadings, n_2 line support reactions, and applying the equation (14) along with the equation (8), we can generalize the force equilibrium equation of the plate element into the form of the equation (15), which is valid also for a discontinuous diagram of the transverse shear force. Likewise, considering n_3 line bending loadings, and applying the equation (14) along with the equation (9), we can generalize the moment equilibrium equation of the plate element into the form of the equation (16), which is valid also for a discontinuous diagram of the bending moment. Similarly, considering n_4 line joints connecting plate segments, and applying the equation (14) along with the equation (10), we can generalize the first derivative of the slope into the form of the equation (17), which is valid also for a discontinuous diagram of the slope of the middle-surface of the plate in a meridian plane:

$$\frac{d}{dr} Q_{rc}(r) = -2\,\pi\, r\, \mathrm{p}(r) - \left(\sum_{i=1}^{n_1} F_i\, \mathrm{Dirac}(x - a_i) \right) + \left(\sum_{i=1}^{n_2} R_i\, \mathrm{Dirac}(x - b_i) \right) \quad , \tag{15}$$

$$\frac{d}{dr} M_{rc}(r) = \frac{\mu\, M_{rc}(r)}{r} + \frac{2\,\pi\, B\,(1-\mu^2)\,\phi(r)}{r} + Q_{rc}(r) + \left(\sum_{i=1}^{n_3} C_i\, \mathrm{Dirac}(x - g_i) \right) \quad , \tag{16}$$

$$\frac{d}{dr} \phi(r) = \frac{1}{2} \frac{M_{rc}(r)}{\pi\, B\, r} - \frac{\mu\, \phi(r)}{r} + \left(\sum_{i=1}^{n_4} \Phi_i\, \mathrm{Dirac}(x - k_i) \right) \quad , \tag{17}$$

$$\frac{d}{dr} \mathrm{w}(r) = -\phi(r) \quad , \tag{18}$$

where

F_i	the i-th line lateral loading on a 360º basis,
R_i	the i-th line reaction force on a 360º basis,
C_i	the i-th line bending loading on a 360º basis,
Φ_i	the magnitude of a jump discontinuity of the slope, $\phi(x)$, at i-th line joint connection of plate segments,
a_i	the radius of the circle along which the line lateral loading F_i is applied,
b_i	the radius of the circle along which the plate is supported, and where a line reaction force R_i may occur,
g_i	the radius of the circle along which the line bending loading C_i is applied,
k_i	the radius of the circle along which two plate segments are joined, and where a jump discontinuity Φ_i of the slope may occur,
n_1	the number of line lateral loadings,
n_2	the number of line supports,
n_3	the number of line moment loadings,
n_4	the number of line joints connecting plate segments.

6. The general solution to the generalized system of differential equations (15) to (18)

Using equations (15) and (17), we can eliminate the shear force and the bending moment from the equation (16), receiving a final equation for only one unknown quantity, i.e. the slope of the middle-surface. We can integrate the final equation by using integrating factors.

In order that results gained may be easier to survey, we have computed the general solutions to the system of equations (15) to (18) for simple cases of discontinuous loading and geometry: i) a line lateral loading, ii) a line bending loading, iii) a line joint along a circle between plate segments.

A particular solution to the inhomogeneous system (15) to (18) for a combination of the line loadings, supports or joint couplings of the plate segments can be found as a sum of simple particular solutions presented further, where the particular solution for a line support is different from the particular solution for the line lateral loading by minus sign. Integration constants have been denoted by c_1, c_2, c_3, c_4. In order to determine the integration constants, we have to formulate boundary conditions. To determine support reactions at internal points of the middle-plane of the plate, we have to create deformation conditions of the line supports. Likewise, so as to be able to determine the magnitude of the jump discontinuity of the slope of the middle-surface at the line joint between plate segments, we have to put a deformation condition of the joint together.

6.1. The general solution to the system (15) to (18) for one line lateral loading

Let the line lateral loading be denoted by $F_1 = F$ acting along a circle of diameter $r=a_1=a$, i.e. $n_1=1$, $n_2=n_3=n_4=0$. In this case, the general solution can be expressed as follows:

$$Q_{rc}(r) = -F\,\text{Heaviside}(r-a) - 16\,B\,\pi\,c_4 \tag{19}$$

$$M_{rc}(r) = (-4\,\pi\,\mu - 4\,\pi)\,r\,B\,c_2 + \frac{(2\,\pi - 2\,\pi\,\mu)\,B\,c_3}{r} + ((-8\,\pi - 8\,\pi\,\mu)\ln(r) - 8\,\pi)\,r\,B\,c_4 + \left(\left(\left(-\frac{\mu}{2} - \frac{1}{2}\right)\ln(r) + \frac{1}{2}\,\mu\ln(a) + \frac{1}{2}\ln(a) - \frac{1}{4} + \frac{\mu}{4}\right)r + \frac{-\frac{1}{4}\,\mu\,a^2 + \frac{1}{4}\,a^2}{r}\right)F\,\text{Heaviside}(r-a) \tag{20}$$

$$\phi(r) = -2\,r\,c_2 - \frac{c_3}{r} - 4\,r\ln(r)\,c_4 + \frac{\left(\left(-\frac{1}{4}\frac{\ln(r)}{\pi} - \frac{1}{8}\frac{-2\ln(a)-1}{\pi}\right)r - \frac{a^2}{8\,\pi\,r}\right)\text{Heaviside}(r-a)\,F}{B} \tag{21}$$

$$w(r) = c_1 + r^2\,c_2 + \ln(r)\,c_3 + r^2\,(2\ln(r)-1)\,c_4 + \frac{\left(\left(\frac{1}{8}\frac{\ln(r)}{\pi} + \frac{1}{8}\frac{-\ln(a)-1}{\pi}\right)r^2 + \frac{1}{8}\frac{a^2\ln(r)}{\pi} + \frac{1}{8}\frac{-a^2\ln(a)+a^2}{\pi}\right)F\,\text{Heaviside}(r-a)}{B} \tag{22}$$

6.2. The general solution to the system (15) to (18) for one line bending loading

Let the line bending loading be denoted by $C_1 = C$ acting along a circle of diameter $r = g_1 = g$, i.e. $n_3=1$, $n_1=n_2=n_4=0$. In this case, the general solution can be expressed as follows:

$$Q_{rc}(r) = -16\,\pi\,B\,c_4 \quad , \tag{23}$$

$$M_{rc}(r) = (-4\,\pi - 4\,\pi\,\mu)\,r\,B\,c_2 + \frac{(-2\,\pi\,\mu + 2\,\pi)\,B\,c_3}{r} + ((-8\,\pi\,\mu - 8\,\pi)\ln(r) - 8\,\pi)\,r\,B\,c_4 + \left(\frac{\left(-\frac{\mu}{2} + \frac{1}{2}\right)g}{r} + \frac{\left(\frac{\mu}{2} + \frac{1}{2}\right)r}{g}\right)C\,\text{Heaviside}(r-g) \quad , \tag{24}$$

$$\phi(r) = -2\,r\,c_2 - \frac{c_3}{r} - 4\,r\ln(r)\,c_4 + \frac{\left(-\frac{g}{4\,r\,\pi} + \frac{r}{4\,\pi\,g}\right)\text{Heaviside}(r-g)\,C}{B} \quad , \tag{25}$$

$$w(r) = c_1 + r^2\,c_2 + \ln(r)\,c_3 + r^2\,(2\ln(r)-1)\,c_4 + \frac{\left(\left(\frac{1}{4}\frac{\ln(r)}{\pi} + \frac{1}{8}\frac{-2\ln(g)+1}{\pi}\right)g - \frac{r^2}{8\,\pi\,g}\right)C\,\text{Heaviside}(r-g)}{B} \quad . \tag{26}$$

6.3. The general solution to the system (15) to (18) for one line joint between plate segments

Let the magnitude of the jump discontinuity of the slope be denoted by $\Phi_1 = \Phi$ occurring along a circle of diameter $r = k_1 = k$, i.e. $n_4 = 1$, $n_1 = n_2 = n_3 = 0$. In this case, the general solution can be expressed as follows:

$$Q_{rc}(r) = -16\,\pi\,B\,c_4 \tag{27}$$

$$M_{rc}(r) = -\pi\,(4\,\mu + 4)\,r\,B\,c_2 - \frac{\pi\,(-2 + 2\,\mu)\,B\,c_3}{r} + (-\pi\,(8 + 8\,\mu)\ln(r) - 8\,\pi)\,r\,B\,c_4 + \left(-\frac{\pi\,(1 - \mu^2)\,k}{r} - \frac{\pi\,(\mu^2 - 1)\,r}{k}\right) B\,\Phi\,\text{Heaviside}(r - k) \tag{28}$$

$$\phi(r) = -2\,r\,c_2 - \frac{c_3}{r} - 4\,r\,c_4\ln(r) + \left(\frac{\left(\frac{\mu}{2} + \frac{1}{2}\right)k}{r} + \frac{\left(-\frac{\mu}{2} + \frac{1}{2}\right)r}{k}\right)\text{Heaviside}(r - k)\,\Phi \tag{29}$$

$$w(r) = c_1 + r^2\,c_2 + \ln(r)\,c_3 + r^2\,(2\ln(r) - 1)\,c_4 + \left(\left(\left(-\frac{\mu}{2} - \frac{1}{2}\right)\ln(r) + \frac{1}{2}\ln(k) + \frac{1}{4} - \frac{\mu}{4} + \frac{1}{2}\ln(k)\,\mu\right)k + \frac{\left(-\frac{1}{4} + \frac{\mu}{4}\right)r^2}{k}\right)\Phi\,\text{Heaviside}(r - k) \tag{30}$$

7. Conclusions

The contribution of this paper is that the generalized mathematical model of the plate, Eq. (15) to (18), is valid also for discontinuous graphs of the transverse shear force, the radial bending moment, and the slope of the middle-surface in a meridian plane caused by line lateral loadings or line supports, line moment loadings situated along the circles lying inside the middle-plane of the plate, and by line joints connecting plate segments, resp.. The jump discontinuities of the unknown dependently variable quantities have been expressed using Dirac singular distribution at the right side of Eq. (15) to (17).

In order to determine magnitudes of the unknown jump discontinuities owing to the internal along-circular supports or joints, we have to use deformation conditions at points of these geometric discontinuities.

The general solution to the system of ordinary differential equations (15) to (18) has been computed using symbolic programming approach, and has been partly presented in Eq. (19) to (30).

References

Höschl, C. (1971) *Pružnost a pevnost ve strojnictví*. SNTL, Praha.

Kanwal, R. P. (2004) *Generalized Functions*. Birkhäuser, Boston.

Němec, J., Dvořák, J. & Höschl, C. (1989) *Pružnost a pevnost ve strojírenství*. SNTL, Praha.

Reddy, J. N. (1999) *Theory and Analysis of Elastic Plates*. Taylor & Francis, Philadelphia.

Schwartz, L., (1966) *Théorie des distributions*. Hermann, Paris.

Štěpánek, J. (2001) *Distribuce a diferenciální rovnice*. Karolinum, Praha.

Timoshenko, S. & Woinowsky-Krieger, S. (1959) *Theory of plates and shells*. McGraw-Hill, N.Y.

18th International Conference
ENGINEERING MECHANICS 2012
Svratka, Czech Republic, May 14 – 17, 2012

pp. 1201–1205
Paper #213

ASSESSMENT OF FATIGUE OF RAILWAY BRIDGE

P. Stachová[*], P. Štemberk[**]

Abstract: *The aim of this paper is to investigate the change of stiffness of concrete railway bridge subjected to cyclic loading since cyclic loading affects several types of concrete structures during their service life. Its greatest impact can be seen on bridges, which are subjected to enormous loads from passenger of freight traffic in terms of weight as well as frequency. A railway bridge was chosen for application in order to simplify the task, as the trains are represented by uniformly distributed load at a specific location defined by the track. In this analysis, only the changes in concrete were considered. The reduced stiffness values were placed in to the calculation model following the standard staggered algorithm scheme. This application provided a base for drawing conclusions regarding the used cross-section of the bridge deck.*

Keywords: ***Cyclic loading, dynamic analysis, fatigue of concrete, stiffness of structures.***

1. Introduction

The civil engineering structures suffer from enormous static and cyclic loads and dynamics effects. For investigation of the effect of cyclic loading, the best example is a railway bridge. This structure has to sustain millions of loading cycles. With proper observation and scanning of the bridge, it is possible to recognize and study the fatigue development.

Fatigue is a permanent process, which is occurring under cycling loading. In concrete the change is connected with grow of the internal micro cracks. This effect is very progressive and may lead to increasing of the strain level. It is displayed as a change in material mechanical properties (Sýkorová, 2008; Stachová, 2010).

The change is unnoticeable at the beginning of cyclic loading. The cracks are appearing on the both sides in tensile reinforcement and in compressed concrete. The cracks developed at the present cycle do not have time to close before a new cycle. That leads to increasing of the crack grow until whole element fails.

Fig. 1: Örnsköldsvik Bridge (Elfgren et. al., 2007)

[*] Ing. Petra Stachová: Czech Technical University in Prague, Thakurova 7, 166 29 Prague 6, CZ, petra.stachova@fsv.cvut.cz

[**] doc. Ing. Petr Štemberk, Ph.D.: Czech Technical University in Prague, Thakurova 7, 166 29 Prague 6, CZ, stemberk@fsv.cvut.cz

2. Model of bridge

Before the calculation could take place, it was necessary to pick a structure in question. The model was inspired by a real structure in Sweden. This bridge stood in Örnsköldsvik (Fig. 1) and it was used for a fatigue field test. It was a two-span concrete railway bridge with a ballast bed.

The bridge has two spans of the length of 11.92 meters and 12.18 meters. The bridge deck is supported by a pier in the middle and two abutments on each side. The railway deck is 4.5 meters above the road level and has a width of 2.9 meters (filled with ballast to the level of the side beam of the deck). The total width of the bridge is 6.15 meters. The structure goes in horizontal curve with a very wide radius and with a slope of 1.75 %. The foundations consist of footing in the basis of the pier and two abutments. They are connected by two underground beams with width of 0.7 meters.

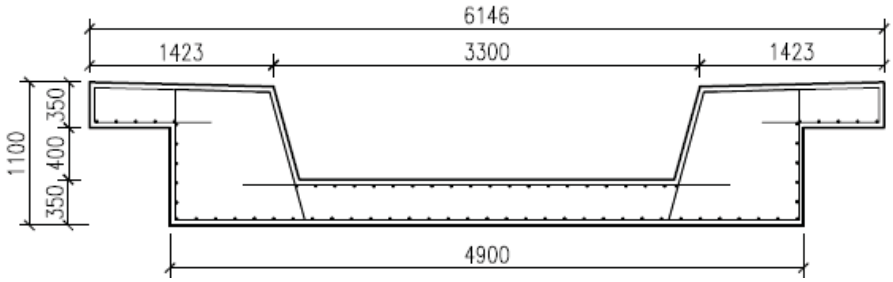

Fig. 2: Cross-section of the bridge deck (Elfgren et. al., 2007)

For further calculation, concrete class C 55/67 was used. This should correspond with the original design of the bridge. Of course the structure would be brand new without any defects from weather or chemical attacks. The original bridge, which had to be torn down, suffered damage from heavy traffic. There were minor cracking, spalling of concrete and wetting. The bottom of the south span had several damages from track collisions. The same was found on the bottom of the north span with addition of visible reinforcement with corrosion. The western and eastern faces have exhibiting a low concrete cover. The reinforcement bars were visible.

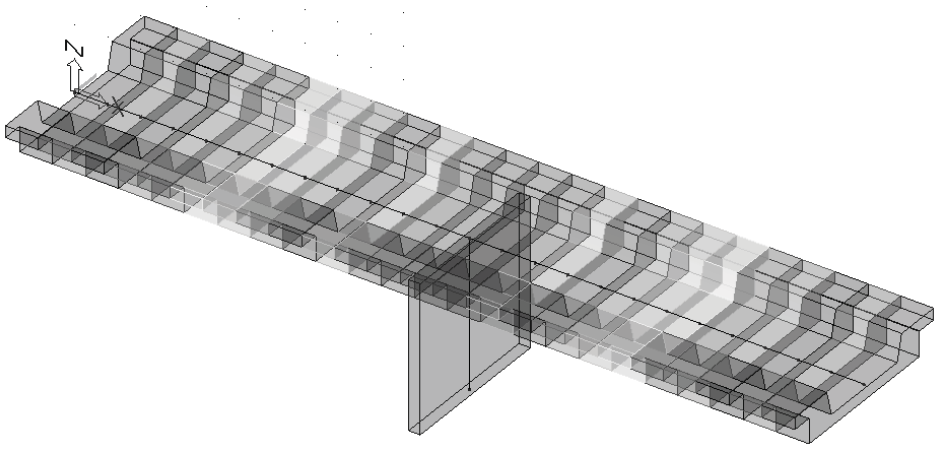

Fig. 3: Static scheme of bridge (SCIA Engineer)

The static system is with two simple beams connected above the swinging rod. The whole model is cut into 24 even pieces and created in SCIA Engineer. Each piece is 1 meter long and its characteristics could be changed accordingly to the calculation.

3. Analysis of bridge

For fatigue testing it is necessary to use a train loading scheme, in this case it was taken from Eurocode. The heaviest condition was considered by using a freight train shown in Fig. 4. The dynamic effect of the train moving across the bridge is represented by the dynamic ratio provided in Eurocode.

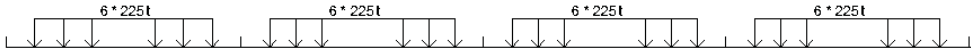

Fig. 4: Heavy train loading scheme.

For exact calculation of fatigue behavior, the structure is divided to smaller elements (see Fig. 3). These elements are 1 meter long and the values from the start and end is interpolated to get the approximate value from the middle. Every element is calculated separately. The bridge has two spans, but the results are the same on each span. Further in calculation it is assumed that both spans are behaving the same.

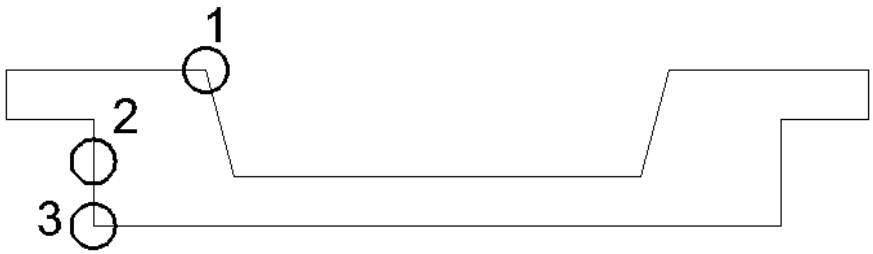

Fig. 5: Heavy train loading scheme.

For the calculation it is necessary to determine stresses acting on the structure. It can be seemed well in Fig. 5, where the checking points are indication in the cross section. One is on the top of the cross section right next to the ballast bed. The second one is in the middle of the cross section and the third is in the bottom of the bridge deck. These stresses have to be calculated for dead load of the structure and dead load and traffic load.

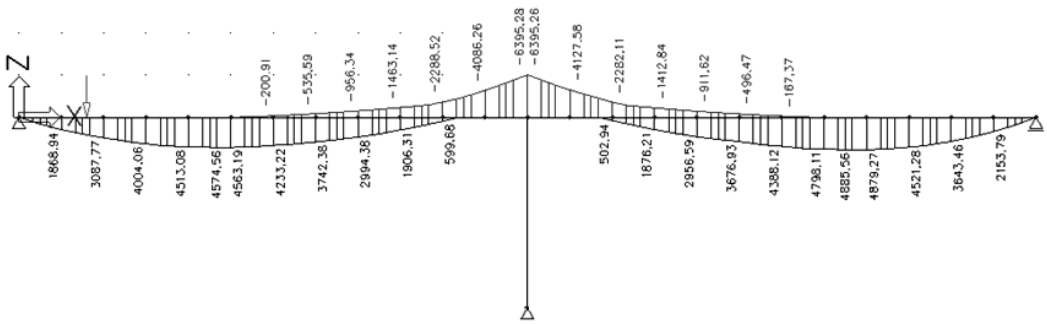

Fig. 6: Moments on structure at year 0

The calculation is run by static program and results from those points are placed into excel spread sheet. The minimum stress is from the period were there is just a dead load acting on the structure. If this value is in fact tensile stress, the calculation value is 0. The same point exhibits also different value such as the maximum stress, which is obtained from the train traffic and dead load of the bridge.

From Figs. 6 and 7 it possible to see that the bending moments are changing, but very slowly, over the 100 years of cyclic loading. The values in the mid-span are slowly decreasing. On the other hand, the values above the support increased gradually. It is explainable that in the mid-span a loss of stiffness started the process of softening. This change of concrete resulted in creation of a hinge while the rest of the beam is acting more as a cantilever.

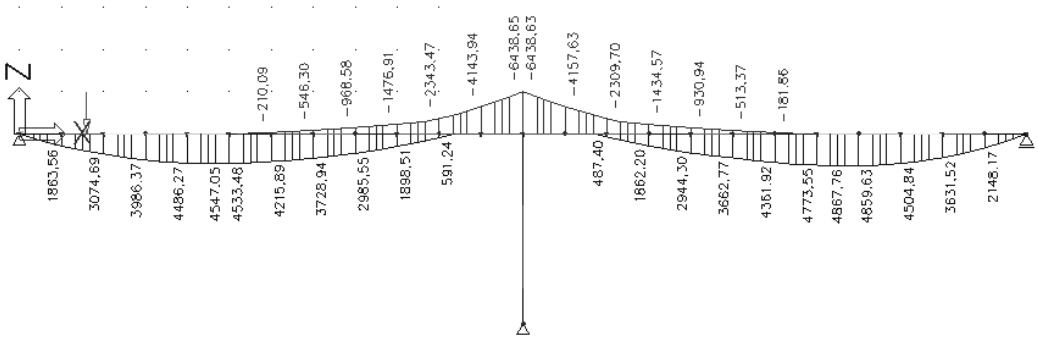

Fig. 7: Moments on a structure at year 100

From the previous calculations it was learned that the compressive stresses were very small along the structure. Then, S_{max} resulted in a small percentage. It is known that smaller stresses lead to faster reduction of stiffness in first interval (see Fig. 8). In this interval, the stiffness changed noticeably. In the second interval, the shape is almost flat with the almost same values of E_c after the first interval, see Tab. 1.

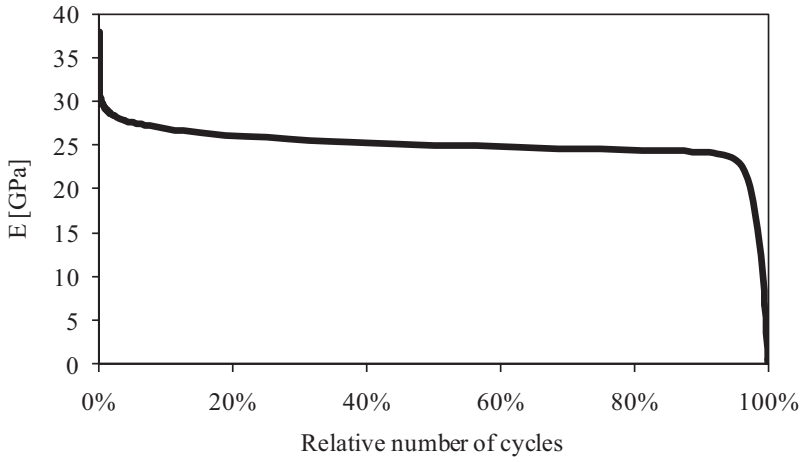

Fig. 8: Decrease of modulus of elasticity

The greatest value of S_{max} was 0.11. The total number of cycles lead to 10^{13}. The minimum number of cycles is 10^6 so this condition is fulfilled with sufficient margin. The initial modulus of elasticity E_c is 38 GPa, as can be seen in Fig. 8.

After this analysis it was concluded that the bridge cross section is very stiff even in extreme conditions when only fatigue of concrete is considered and that the fatigue of concrete does not influence the structure so much since the stresses on the structure are small. It is due to type of the cross section of the bridge. It is shown in Tab. 1 that the structure will not collapse from fatigue of concrete.

Tab. 1: Decrease of modulus of elasticity.

Cyclic loading (year)	E_c (MPa)
1	32.70
25	32.67
50	32.66
75	32.66
100	32.66
200	32.65
300	32.65
400	32.64
500	32.64
600	32.64
700	32.64
800	32.64
900	32.64
1000	32.63

4. Conclusions

A method for evaluation of stiffness decrease of concrete railway bridges due to cyclic loading was developed. The method combines the concept of the fatigue damage function and the commonly available finite element tools for structural dynamics analyses. The computation method represents a staggered algorithm when the actual stiffness of concrete at a given point is updated after a sufficiently small number of load cycles. Then the updated stiffness is used for the dynamic analysis at the following time step. It is believed that the proposed method can help to assess the residual service life of existing concrete structures subjected to cyclic loading or it can support design of new concrete structures and improve their long-term resistance to fatigue effects of concrete.

To prove the applicability of the proposed method, it was applied to an existing reinforced concrete railway bridge, which in turn helped the author to understand some of the dynamic aspects of bridge engineering. The data used in this application were taken from the relevant design documentation and from literature. The tested bridge responded to the cyclic loading by gradual redistribution of the bending moments and deflections. However, the magnitude of the tensile and compressive stresses remained almost constant during the entire tested period, even though an extreme load scenario in terms of the frequency of heavy trains was considered. Therefore, based on the obtained result, it can be concluded that the relatively stiffer bridges with U-shaped cross section decks do not tend to fail due to poor fatigue performance. Then, the actual failure is likely to happen due to exposure to weather and chemicals, which may accelerate the process of loss of stiffness.

Acknowledgement

The financial support by the Czech Science Foundation, project P105/10/2098, and the CTU in Prague, project SGS11/107/OHK1/2T/11, which is gratefully acknowledged.

References

Elfgren, L., Enochsson, O., Thun, H. (2007) *Field Test of a Concrete Bridge in Örnsköldsvik Bridge*, Sweden, WP7-07-T-070625-D-D7.3.

Stachová, P., Štemberk, P., Hejnic, F. (2010) The effect of cyclic load on Örnsköldsvik bridge, in: *Proc. of the International Conference on Modelling and Simulation 2010 in Prague*, Czech Technical University, Prague, pp. 455-459.

Sýkorová, J., Foglar, M., Štemberk, P. (2008) Fatigue of reinforced concrete bridges with influence of deterioration of concrete, in: *Microstructure Related Durability of Cementitious Composites*. Bagneux: Rilem Publications s.a.r.l., pp. 825-832.

18th International Conference
ENGINEERING MECHANICS 2012
Svratka, Czech Republic, May 14 – 17, 2012

pp. 1207–1217
Paper #48

BENDING OF FUNCTIONALLY GRADED CIRCULAR PLATES WITH PIEZOELECTRIC LAYER BY THE MLPG METHOD

P. Staňák[*], J. Sladek[*], V. Sladek[*], S. Krahulec[*]

Abstract: *A meshless local Petrov-Galerkin (MLPG) method is applied to solve bending of circular plate with piezoelectric layer attached at the top. Plate is analyzed as a 3D axisymmetric. Functionally graded material properties with continuous variation in the plate thickness direction are considered. Piezoelectric layer with applied nonzero voltage difference acts as a piezoelectric actuator, thus deflection of the plate can be controlled. Local integral equations are defined from the set of governing equations for mechanical and electric fields using appropriate test functions. Spatial variation of all physical fields is approximated by the moving least-squares (MLS) method only in terms of nodes. After performing all spatial integrations the system of ordinary differential equations is finally obtained and solved using Houbolt finite-difference scheme.*

Keywords: ***Meshless local Petrov-Galerkin method (MLPG), moving least-squares (MLS) approximation, piezoelectric actuation, functionally graded materials.***

1. Introduction

Advanced structural systems are required to be low-weight, high-strength and often to have also self-monitoring capabilities. Recent progress in engineering and material sciences offers new possibility in design of such structures; the multifunctional composites (Gibson, 2010) composed of so-called smart materials. Among many smart materials the piezoelectric materials are dominantly used for control and suppression of structural vibration (Adachi et al., 1994) because of their sensory/active capabilities. In the recent years also the functionally graded materials (FGMs) (Suresh and Mortensen, 1998) are widely applied in structural design because of their excellent properties. FGMs are multi-component composite materials in which the volume fraction of the material constituents is varying in a predominant direction. This feature can be used to tune the selected properties into desired value. For example structural element can be designed to have the strength of steel on one side combined with the heat resistance of ceramics on the other side.

Analysis of complex structural systems requires advanced numerical methods because of complex geometry or boundary conditions. Although the well established finite element method (FEM) is applicable to analysis of piezoelectric structures (Benjeddou, 2000), the analysis of materials with continuously nonhomogeneous properties such as FGMs can lead to certain difficulties. The material coefficients in commercial FEM codes are assumed to be constant within an element, thus leading to piecewise homogeneous idealization of FGMs. Boundary element method (BEM) is also not suitable since proper fundamental solution is not available. In the last decade, an increasing attention has been devoted to meshfree or meshless methods for numerical analyses. The motivation is clear from their name; to avoid difficulties associated with mesh of finite elements such as expensive mesh generation, shear locking or above mentioned difficulties in modeling of continuously nonhomogeneous media. The meshless local Petrov-Galerkin (MLPG) method (Atluri, 2004) is considered as a basis for many meshless techniquess. Meshless formulations based on the MLPG were recently applied to laminated plates (Sladek et al, 2010a) and also to piezoelectric plates (Sladek et al, 2010b). Analysis of FGM materials using MLPG was presented in (Sladek et al. 2005, Sladek et al. 2008).

In the present paper the analysis of functionally graded circular plate with homogeneous piezoelectric actuator is presented. Similar problem was analyzed by Tauchert and Ashida (1999)

[*] Ing. Peter Staňák, Prof. Ing. Ján Sládek, DrSc., Prof. RNDr. Vladimír Sládek, DrSc. and Ing. Slavomír Krahulec : Institute of Construction and Architecture, Slovak Academy of Sciences, Dúbravská cesta 9, 845 03, Bratislava; SK, e-mails: peter.stanak@savba.sk, jan.sladek@savba.sk, vladimir.sladek@savba.sk, slavomir.krahulec@savba.sk

using potential function method, although they considered only homogeneous material properties. Fig. 1a) shows proposed geometry with FGM layer labeled by index 1 and piezoelectric layer by index 2. A circular plate together with piezoelectric actuator can be considered as a 3-D axisymmetric body with axis of symmetry passing through the center of the plate. With use of cylindrical coordinates the original 3-D axisymmetric problem can be reduced to 2-D problem considered on the cross-section of the plate (see Fig. 1b). An exponential variation of material properties is assumed for the FGM plate. The coupled electro-mechanical fields are described by constitutive relations and governing partial differential equations (PDEs). Nodal points are spread on the analyzed domain without any restrictions. Small local circular subdomain is introduced around each nodal point. Local integral equations (LIEs) constructed from governing PDEs are defined over these circular subdomains. For a simple shape of subdomains- like circles used here, numerical integration of LIEs can be easily carried out. Moving Least-Squares (MLS) approximation scheme (Lancaster & Salkauskas, 1981) is used to approximate the spatial variations of electric and mechanical fields. MLS scheme ensures C^1 continuity in each layer, but not across the material interface of plate and piezoelectric actuator. Thus MLS approximation is carried out separately in each considered layer. Additional coupling equations are considered for nodes on the interface to ensure the continuity of primary variables, normal components of electric displacements (surface charges) and the equilibrium of the tractions. The essential boundary conditions are satisfied by the collocation of MLS approximation expressions for unknowns at boundary nodes. After performing the MLS approximation a system of ordinary differential equations (ODEs) for certain nodal unknowns is obtained. Houbolt finite difference scheme (Houbolt, 1950) is finally used to solve the system of ODEs.

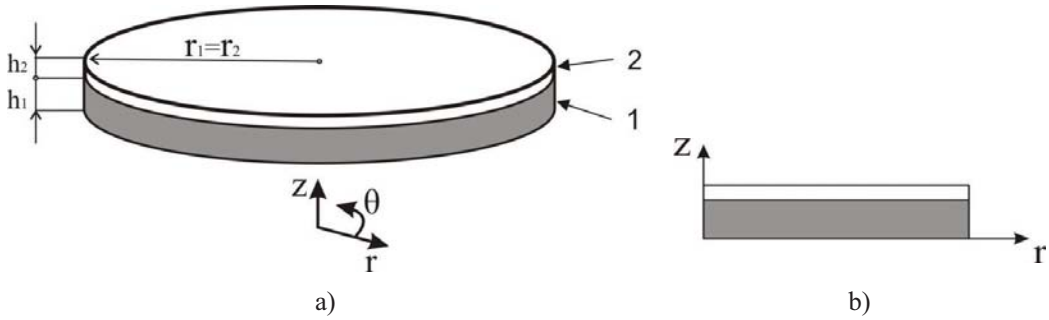

Fig. 1: Geometry of the circular plate: a) original 3-D problem, b) assumed 2-D geometry

2. Local integral equations

Governing equations for general piezoelectric body under quasi-electrostatic assumption is given by the equation of motion for displacements and the first Maxwell's equation for the vector of electric displacements as

$$\sigma_{ij,j}(\mathbf{x},t)+X_i(\mathbf{x},t)=\rho(\mathbf{x})\ddot{u}_i(\mathbf{x},t) \tag{1}$$

$$D_{i,i}(\mathbf{x},t)-R(\mathbf{x},t)=0 \tag{2}$$

where t, u_i, σ_{ij}, D_i, X_i, R, ρ are time, displacements, stresses, electric displacements, vector of body forces, volume density of free charges and material density, respectively. The dots over quantity indicate the time derivative. Omitting the acceleration term in Eq. (1) one can easily transform the dynamic problem to static one. The piezoelectric constitutive equations, representing the coupling of mechanical and electric fields, are given by

$$\sigma_{ij}(\mathbf{x},t)=C_{ijkl}\varepsilon_{kl}(\mathbf{x},t)-e_{kij}E_k(\mathbf{x},t) \tag{3}$$

$$D_i(\mathbf{x},t)=e_{ikl}\varepsilon_{kl}(\mathbf{x},t)+h_{ik}E_k(\mathbf{x},t) \tag{4}$$

where C_{ijkl}, e_{kij}, h_{ik} represents elastic, piezoelectric and dielectric material constants, respectively. The strain tensor ε_{ij} and electric field vector E_k are related to mechanical displacements u_i and electric potential ψ by

$$\varepsilon_{ij} = \frac{1}{2}\left(u_{i,j} + u_{j,i}\right) \tag{5}$$

$$E_k = -\psi_{,k} = -\frac{\partial \psi}{\partial x_k} \tag{6}$$

The following essential and natural boundary conditions are assumed for the mechanical field

$$u_i\left(\mathbf{x},t\right) = \tilde{u}_i\left(\mathbf{x},t\right) \text{ on } \Gamma_u,\ \sigma_{ij}n_j = \tilde{T}_i\left(\mathbf{x},t\right) \text{on } \Gamma_t, \tag{7}$$

and for the electrical field

$$\psi\left(\mathbf{x},t\right) = \tilde{\psi}\left(\mathbf{x},t\right) \text{ on } \Gamma_p,\ D_i n_i = \tilde{Q}\left(\mathbf{x},t\right) \text{on } \Gamma_q \tag{8}$$

where Γ_u, Γ_t, Γ_p, Γ_q are parts of the global boundary Γ with prescribed displacements, tractions, electric potential and surface density of electric field flux (surface charge density), respectively.

Consider now 2-layer circular plate as shown in Fig. 1a. Base layer, with index 1, has radius r_1 and height h_1, top layer, with index 2 and considered as piezoelectric, has the height h_2 but the same radius $r_2 = r_1$. Owing to the plate geometry, it is convenient to use polar (cylindrical) coordinates $\mathbf{x} = (r,\theta,z)$.

Coupled equations of piezoelectricity can be used for both layers, even if one is not made of piezoelectric material. This is done simply by decoupling the equations using all piezoelectric constants e_{ikl}=0, but keeping nonzero dielectric material constants for non-piezoelectric (base) material.

Since the problem is assumed to be axisymmetric, it can be reduced to 2-D, if cylindrical coordinates are used, as in Fig. 1.b. Thus all physical quantities are independent on angular coordinate θ. Then, for the axisymmetric piezoelectric body we can write the governing equations (1), (2) in the following form

$$\sigma_{rr,r}\left(r,z,t\right) + \sigma_{rz,z}\left(r,z,t\right) + \frac{\sigma_{rr}\left(r,z,t\right) - \sigma_{\theta\theta}\left(r,z,t\right)}{r} + X_r\left(r,z,t\right) = \rho\ddot{u}_r\left(r,z,t\right) \tag{9}$$

$$\sigma_{rz,r}\left(r,z,t\right) + \sigma_{zz,z}\left(r,z,t\right) + \frac{\sigma_{rz}\left(r,z,t\right)}{r} + X_z\left(r,z,t\right) = \rho\ddot{u}_z\left(r,z,t\right) \tag{10}$$

$$D_{r,r}\left(r,z,t\right) + D_{z,z}\left(r,z,t\right) + \frac{D_r\left(r,z,t\right)}{r} = 0 \tag{11}$$

Constitutive equation for mechanical fields (3) is then also rewritten into

$$\sigma_{rr} = c_{11}\varepsilon_{rr} + c_{12}\varepsilon_{\theta\theta} + c_{13}\varepsilon_{zz} - e_{31}E_z \tag{12}$$

$$\sigma_{\theta\theta} = c_{12}\varepsilon_{rr} + c_{11}\varepsilon_{\theta\theta} + c_{13}\varepsilon_{zz} - e_{31}E_z \tag{13}$$

$$\sigma_{zz} = c_{13}\varepsilon_{rr} + c_{13}\varepsilon_{\theta\theta} + c_{33}\varepsilon_{zz} - e_{33}E_z \tag{14}$$

$$\sigma_{rz} = c_{44}\varepsilon_{rz} - e_{15}E_r \tag{15}$$

with mechanical strains specified to be

$$\varepsilon_{rr} = u_{r,r}, \ \varepsilon_{\theta\theta} = \frac{1}{r}u_r, \ \varepsilon_{zz} = u_{z,z}, \ \varepsilon_{rz} = u_{r,z} + u_{z,r} \tag{16}$$

Finally, the constitutive relations for the electric fields are

$$D_r = e_{15}\varepsilon_{rz} + h_{11}E_r \tag{17}$$

$$D_z = e_{31}\varepsilon_{rr} + e_{31}\varepsilon_{\theta\theta} + e_{33}\varepsilon_{zz} + h_{33}E_z \tag{18}$$

The MLPG method is based on the local weak form of the governing equations (9-11) that is written over local subdomain Ω_s. Local subdomain is a small region taken for each node inside the global domain (Atluri, 2004). The local subdomains could be of any geometrical shape; in this paper they posses circular shape just for simplicity. Local weak forms can be written as

$$\begin{aligned}\int_{\Omega_s}\sigma_{rr,r}(r,z,t)\,p^*d\Omega + \int_{\Omega_s}\sigma_{rz,z}(r,z,t)\,p^*d\Omega + \int_{\Omega_s}\frac{1}{r}\left[\sigma_{rr}(r,z,t) - \sigma_{\theta\theta}(r,z,t)\right]p^*d\Omega + \\ + \int_{\Omega_s}X_r(r,z,t)\,p^*d\Omega = \int_{\Omega_s}\rho\ddot{u}_r(r,z,t)\,p^*d\Omega\end{aligned} \tag{19}$$

$$\begin{aligned}\int_{\Omega_s}\sigma_{rz,r}(r,z,t)q^*d\Omega + \int_{\Omega_s}\sigma_{zz,z}(r,z,t)q^*d\Omega + \int_{\Omega_s}\frac{1}{r}\sigma_{rz}(r,z,t)q^*d\Omega + \int_{\Omega_s}X_z(r,z,t)q^*d\Omega = \\ = \int_{\Omega_s}\rho\ddot{u}_z(r,z,t)q^*d\Omega\end{aligned} \tag{20}$$

$$\int_{\Omega_s}D_{r,r}(r,z,t)w^*d\Omega + \int_{\Omega_s}D_{z,z}(r,z,t)w^*d\Omega + \int_{\Omega_s}\frac{1}{r}D_r(r,z,t)w^*d\Omega = 0 \tag{21}$$

where $p^*(\mathbf{x})$, $q^*(\mathbf{x})$, $w^*(\mathbf{x})$ are the test functions.

Local weak forms (19-21) are then the starting point for deriving local integral equations with the use of Gauss divergence theorem and appropriate test functions. Heaviside unit step functions are chosen as test functions for the presented problem in the same way as in (Sladek et al., 2010a). Local integral equations take the form:

$$\begin{aligned}\int_{\partial\Omega_s}\sigma_{rr}(r,z,t)\,n_r d\Gamma + \int_{\partial\Omega_s}\sigma_{rz}(r,z,t)\,n_z d\Gamma + \int_{\Omega_s}\frac{1}{r}\left[\sigma_{rr}(r,z,t) - \sigma_{\theta\theta}(r,z,t)\right]d\Omega + \\ + \int_{\Omega_s}X_r(r,z,t)\,d\Omega = \int_{\Omega_s}\rho\ddot{u}_r(r,z,t)\,d\Omega\end{aligned} \tag{22}$$

$$\begin{aligned}\int_{\partial\Omega_s}\sigma_{rz}(r,z,t)\,n_r d\Gamma + \int_{\partial\Omega_s}\sigma_{zz}(r,z,t)\,n_z d\Gamma + \int_{\Omega_s}\frac{1}{r}\sigma_{rz}(r,z,t)\,d\Omega + \int_{\Omega_s}X_z(r,z,t)\,d\Omega = \\ = \int_{\Omega_s}\rho\ddot{u}_z(r,z,t)\,d\Omega\end{aligned} \tag{23}$$

$$\int_{\partial\Omega_s}D_r(r,z,t)\,n_r d\Gamma + \int_{\partial\Omega_s}D_z(r,z,t)\,n_z d\Gamma + \int_{\Omega_s}\frac{1}{r}D_r(r,z,t)\,d\Omega = 0 \tag{24}$$

where $\partial\Omega_s$ represents boundary of the local subdomain Ω_s and n_i is the unit outward normal vector.

A meshless approximation is convenient for numerical solution of local integral equations. The Moving least-squares (MLS) approximation can be used for the approximation of displacement and electric potential fields $u_r(\mathbf{x},t)$, $u_z(\mathbf{x},t)$, $\psi(\mathbf{x},t)$ by $u_r^h(\mathbf{x},t)$, $u_z^h(\mathbf{x},t)$, $\psi^h(\mathbf{x},t)$ in terms of nodal values as

$$u_r(\mathbf{x},t) \cong u_r^h(\mathbf{x},t) = \sum_{i=1}^{n} \phi^i(\mathbf{x}) \hat{u}_r^i(t) \tag{25}$$

$$u_z(\mathbf{x},t) \cong u_z^h(\mathbf{x},t) = \sum_{i=1}^{n} \phi^i(\mathbf{x}) \hat{u}_z^i(t) \tag{26}$$

$$\psi(\mathbf{x},t) \cong \psi^h(\mathbf{x},t) = \sum_{i=1}^{n} \phi^i(\mathbf{x}) \hat{\psi}^i(t) \tag{27}$$

where the nodal values $\hat{u}_r^i(t)$, $\hat{u}_z^i(t)$, $\hat{\psi}^i(t)$ are so called fictitious parameters for the displacements and electric potential, and $\phi^i(\mathbf{x})$ is called the MLS shape function defined over *n* nodes located in a support domain of MLS approximation. However, MLS support domain must contain only nodes from a single layer bounded by the two-material interface due to discontinuities of strains and electric vector on the interface of the plate and actuator (Sladek et al, 2009). The appropriate derivatives can be obtained with use of the shape function derivative as shown in (Atluri, 2004). Derivatives of displacements and electric potential are then given as

$$u_{k,l}^h(\mathbf{x},t) = \sum_{i=1}^{n} \phi_{,l}^i(\mathbf{x}) \hat{u}_k^i(t) \quad , \quad \psi_{,l}^h(\mathbf{x},t) = \sum_{i=1}^{n} \phi_{,l}^i(\mathbf{x}) \hat{\psi}^i(t) \tag{28}$$

with indices $k,l = (r,z)$.

C^1 continuity of the MLS approximation in each domain (layer) is ensured by the fourth-order spline type weight function used for the construction of the shape function $\phi^i(\mathbf{x})$ (Atluri, 2004).

Applying Eqs. (25-27) for approximation of trial functions $u_r(\mathbf{x},t)$, $u_z(\mathbf{x},t)$, $\psi(\mathbf{x},t)$ and their derivatives in constitutive relations (12-18) and their insertion into local integral equations (22-24) is leading to discretized local integral equations in the following form

$$\begin{aligned}
&\sum_{i=1}^{n} \hat{u}_r^i(t) \int_{\partial\Omega_s} \left[c_{11} n_r(\mathbf{x}) \phi_{,r}^i(\mathbf{x}) + \frac{c_{12}}{r} n_r(\mathbf{x}) \phi^i(\mathbf{x}) + c_{44} n_z(\mathbf{x}) \phi_{,z}^i(\mathbf{x}) \right] d\Gamma + \\
&+ \sum_{i=1}^{n} \hat{u}_r^i(t) \int_{\Omega_s} \left[\frac{c_{11}}{r} \phi_{,r}^i(\mathbf{x}) + \frac{c_{12}}{r^2} \phi^i(\mathbf{x}) - \frac{c_{11}}{r^2} \phi^i(\mathbf{x}) - \frac{c_{12}}{r} \phi_{,r}^i(\mathbf{x}) \right] d\Omega - \\
&- \sum_{i=1}^{n} \hat{\ddot{u}}_r^i(t) \int_{\Omega_s} \rho \phi^i(\mathbf{x}) d\Omega + \sum_{i=1}^{n} \hat{u}_z^i(t) \int_{\partial\Omega_s} \left[c_{13} n_r(\mathbf{x}) \phi_{,z}^i(\mathbf{x}) + c_{44} n_z(\mathbf{x}) \phi_{,r}^i(\mathbf{x}) \right] d\Gamma + \\
&+ \sum_{i=1}^{n} \hat{\psi}^i(t) \int_{\partial\Omega_s} \left[e_{31} n_r(\mathbf{x}) \phi_{,z}^i(\mathbf{x}) + e_{15} n_z(\mathbf{x}) \phi_{,r}^i(\mathbf{x}) \right] d\Gamma = - \int_{\Omega_s} X_r(r,z,t) d\Omega
\end{aligned} \tag{29}$$

$$\sum_{i=1}^{n}\hat{u}_r^i(t)\int_{\partial\Omega_s}\left[c_{44}n_r(\mathbf{x})\phi_{,z}^i(\mathbf{x})+\frac{c_{13}}{r}n_z(\mathbf{x})\phi^i(\mathbf{x})+c_{13}n_z(\mathbf{x})\phi_{,r}^i(\mathbf{x})\right]d\Gamma+$$
$$+\sum_{i=1}^{n}\hat{u}_r^i(t)\int_{\Omega_s}\frac{c_{44}}{r}\phi_{,z}^i(\mathbf{x})d\Omega+\sum_{i=1}^{n}\hat{u}_z^i(t)\int_{\partial\Omega_s}\left[c_{33}n_z(\mathbf{x})\phi_{,z}^i(\mathbf{x})+c_{44}n_r(\mathbf{x})\phi_{,r}^i(\mathbf{x})\right]d\Gamma+$$
$$+\sum_{i=1}^{n}\hat{u}_z^i(t)\int_{\Omega_s}\frac{c_{44}}{r}\phi_{,r}^i(\mathbf{x})d\Omega-\sum_{i=1}^{n}\hat{\ddot{u}}_z^i(t)\int_{\Omega_s}\rho\phi^i(\mathbf{x})d\Omega+ \tag{30}$$
$$+\sum_{i=1}^{n}\hat{\psi}^i(t)\int_{\partial\Omega_s}\left[e_{15}n_r(\mathbf{x})\phi_{,r}^i(\mathbf{x})+e_{33}n_z(\mathbf{x})\phi_{,z}^i(\mathbf{x})\right]d\Gamma+\sum_{i=1}^{n}\hat{\psi}^i(t)\int_{\Omega_s}\frac{e_{15}}{r}\phi_{,r}^i(\mathbf{x})d\Omega=$$
$$=-\int_{\Omega_s}X_z(r,z,t)d\Omega$$

$$\sum_{i=1}^{n}\hat{u}_r^i(t)\int_{\partial\Omega_s}\left[e_{15}n_r(\mathbf{x})\phi_{,z}^i(\mathbf{x})+\frac{e_{31}}{r}n_z(\mathbf{x})\phi^i(\mathbf{x})+e_{31}n_z(\mathbf{x})\phi_{,r}^i(\mathbf{x})\right]d\Gamma+$$
$$+\sum_{i=1}^{n}\hat{u}_r^i(t)\int_{\Omega_s}\frac{e_{15}}{r}\phi_{,z}^i(\mathbf{x})d\Omega+\sum_{i=1}^{n}\hat{u}_z^i(t)\int_{\partial\Omega_s}\left[e_{15}n_r(\mathbf{x})\phi_{,r}^i(\mathbf{x})+e_{33}n_z(\mathbf{x})\phi_{,z}^i(\mathbf{x})\right]d\Gamma+$$
$$+\sum_{i=1}^{n}\hat{u}_z^i(t)\int_{\Omega_s}\frac{e_{15}}{r}\phi_{,r}^i(\mathbf{x})d\Omega-\sum_{i=1}^{n}\hat{\psi}^i(t)\int_{\partial\Omega_s}\left[h_{11}n_r(\mathbf{x})\phi_{,r}^i(\mathbf{x})+h_{33}n_z(\mathbf{x})\phi_{,z}^i(\mathbf{x})\right]d\Gamma- \tag{31}$$
$$-\sum_{i=1}^{n}\hat{\psi}^i(t)\int_{\Omega_s}\frac{h_{11}}{r}\phi_{,r}^i(\mathbf{x})d\Omega=0$$

Collocation approach is used to impose essential boundary conditions directly, using MLS variable approximations (25-27). For natural boundary conditions local integral equations are written for the nodes on the global boundary.

Interface between two layers of the plate represents a discontinuity. The plate must be partitioned to two patches with different material properties for the presented numerical modeling approach. Patches or layers are discretized by meshfree nodes individually. Double nodes are defined on the interface. One node belongs to each layer. Except the condition of coincidence of interface nodes there is no restriction on the node location in the presented approach. For these interface nodes one has to specify coupling conditions in order to ensure the continuity of displacements, potentials, flux of electric displacements and the equilibrium of the tractions across the interface as

$$^1u_r(\mathbf{x}^l,t)=\,^2u_r(\mathbf{x}^l,t),\quad ^1T_r(\mathbf{x}^l,t)+\,^2T_r(\mathbf{x}^l,t)=0 \tag{32}$$

$$^1u_z(\mathbf{x}^l,t)=\,^2u_z(\mathbf{x}^l,t),\quad ^1T_z(\mathbf{x}^l,t)+\,^2T_z(\mathbf{x}^l,t)=0 \tag{33}$$

$$^1\psi(\mathbf{x}^l,t)=\,^2\psi(\mathbf{x}^l,t),\quad ^1Q(\mathbf{x}^l,t)+\,^2Q(\mathbf{x}^l,t)=0 \tag{34}$$

indices 1, 2 indicate the corresponding layer and $\mathbf{x}^l$ is an interface node.

Collocation approach is again used based on the MLS approximation (7). For example, the equilibrium of radial displacements (first part of Eq. 32) is specified as

$$\sum_{i=1}^{^1n}\phi^i(\mathbf{x}^l)\,^1\hat{u}_r^i=\sum_{j=1}^{^2n}\phi^j(\mathbf{x}^l)\,^2\hat{u}_r^j \tag{35}$$

In the same manner the equilibrium of tractions and electric charge can be specified, based on the second part of Eqs. (7, 8).

Collecting the discretized local integral equations together with the discretized boundary conditions and interface conditions, one obtains a complete system of ordinary differential equations (ODE) which can be rearranged in such a way that all known quantities are on the r.h.s. Thus, in the matrix form the system becomes

$$\mathbf{A}\ddot{\mathbf{x}} + \mathbf{C}\mathbf{x} = \mathbf{Y} \tag{36}$$

This system of ODE can be solved by the Houbolt finite-difference scheme (Houbolt, 1950; Sladek et al., 2010a). In this method "acceleration" term is defined as

$$\ddot{\mathbf{x}}_{t+\Delta t} = \frac{2\mathbf{x}_{t+\Delta t} - 5\mathbf{x}_t + 4\mathbf{x}_{t-\Delta t} - \mathbf{x}_{t-2\Delta t}}{\Delta t^2} \tag{37}$$

where Δt is the time step. The value of the time-step has to be appropriately selected with respect to material parameters (elastic wave velocities).

3. Numerical solution

For the numerical examples functionally graded graphite/epoxy circular plate is considered with radius $r_1 = 0.3\text{m}$ and thickness $h_1 = 0.02\text{m}$. For the top layer of the thickness $h_2 = 0.01\text{m}$ PZT-4 piezoelectric material is considered. The plate is loaded with uniform load of $\sigma_0 = 10000\text{Pa}$ and varying electric potential at the top. Potential at the interface is vanishing. For the approximation of unknown field quantities in FGM layer 847 nodes were used and 726 nodes were specified for the piezoelectric layer. Material properties of the graphite/epoxy layer are graded using exponential variations

$$f_{ij}(\mathbf{x}) = f_{ij0}\exp(\gamma_f z) \tag{38}$$

where the symbol f_{ij} is commonly used for particular material coefficients and f_{ij0} correspond to the material parameters at the bottom surface of the FG layer. It should be noted that various exponential coefficients γ_f can be used for the individual material parameters. In presented analysis two different values of the exponential coefficient $\gamma_f = 34.6575$ and 20.273 are used for each graded material coefficient. For the first coefficient $\gamma_f = 34.6575$ material parameters are doubled with respect to ones at the bottom surface. In other words, such a gradation will gradually increase material coefficients defined at the bottom $(z = 0)$ to twice that large coefficients at the top $(z = h_1)$ of the graphite/epoxy plate.

The material coefficients of the graphite/epoxy layer are:

$$c_{110} = 10.2\cdot 10^{10}\,Nm^{-2}\ ,\ c_{120} = 4.98\cdot 10^{10}\,Nm^{-2}\ ,\ c_{130} = c_{230} = 6.86\cdot 10^{9}\,Nm^{-2}\ ,$$
$$c_{330} = 1.09\cdot 10^{10}\,Nm^{-2}\ ,\ c_{440} = 2.87\cdot 10^{9}\,Nm^{-2}\ ,\ e_{150} = e_{310} = e_{330} = 0\,Cm^{-2}\ ,$$
$$h_{110} = 3.09\cdot 10^{-11}C(Vm)^{-1}\ ,\quad h_{330} = 2.65\cdot 10^{-11}C(Vm)^{-1}\ ,\ \rho = 1578\,\text{kg/m}^3$$

Piezoelectric PZT-4 layer posses these material properties:

$$c_{11} = 13.9\cdot 10^{10}\,Nm^{-2}\ ,\ c_{12} = 7.78\cdot 10^{10}\,Nm^{-2}\ ,\ c_{13} = c_{23} = 7.43\cdot 10^{10}\,Nm^{-2}\ ,$$
$$c_{33} = 11.5\cdot 10^{10}\,Nm^{-2}\ ,\ c_{44} = 2.56\cdot 10^{10}\,Nm^{-2}\ ,$$
$$e_{15} = 12.7\,Cm^{-2}\ ,\ e_{31} = -5.2\,Cm^{-2}\ ,\quad e_{33} = 15.1\,Cm^{-2}\ ,$$
$$h_{11} = 6.46\cdot 10^{-9}C(Vm)^{-1}\ ,\quad h_{33} = 5.62\cdot 10^{-9}C(Vm)^{-1}\ ,\ \rho = 7500\,\text{kg/m}^3\ .$$

In the first numerical example two different exponential variations are applied. Variation represented by Eq. (38) increases (grades) material properties from bottom to the top, while following variation

$$f_{ij}(\mathbf{x}) = f_{ij0}\left(d - \exp(\gamma_f z)\right) \tag{39}$$

grades material properties in opposite direction. Constant d depends on the coefficients γ_f, values d=3 and d=2.5 are used, respectively. Results are compared to FEM-ANSYS solution with the fine mesh. For FGM material modeling the piecewise homogeneous approach is adopted. Fig. 2 presents variation of deflection for simply supported plate with the radial coordinate under static mechanical loading and vanishing surface charge density. For both gradation schemes the coefficient $\gamma_f = 34.6575$. One can clearly observe that material gradation according to Eq. (39) gives lower deflection compared to Eq. (38). This must hold true since increase of material constants in direction towards the plate center has smaller effect on flexural stiffness compared to increase of material parameters out of the center, as in case of Eq. (39). Thus exponential variation (39) should be preferred in cases of 2-layer plates.

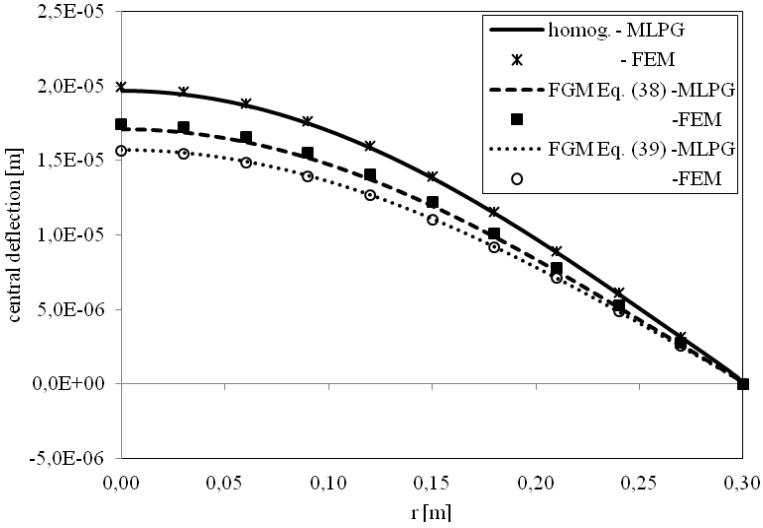

Fig. 2: Variation of central deflection with radial coordinate for simply supported plate with different material gradations

In the Fig. 3 the effect of exponential coefficient γ_f is observed. Pure mechanical load is applied again. Exponential variation (39) is assumed. One can observe that deflection of the plate with $\gamma_f = 20.273$ is very close to one obtained for variation (38) as shown in Fig. 2. Very good agreement between MLPG and FEM results can be observed. Effect of deflection suppression by active piezoelectric layer is well observed in Fig. 4. FGM exponential coefficient $\gamma_f = 34.6575$ is used. It is clearly observable that for FGM plate the deflection is almost totally suppressed. If electric potential is not specified, vanishing values of normal components of electric displacement must be specified.

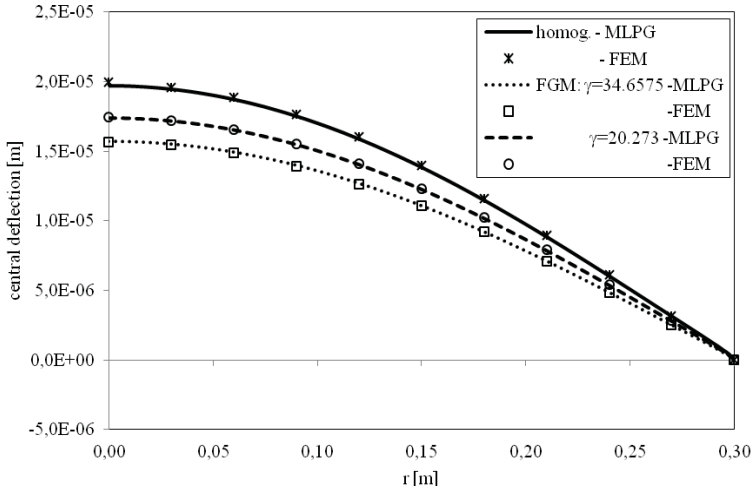

Fig. 3: Variation of central deflection with radial coordinate for simply supported plate with two different exponential coefficients

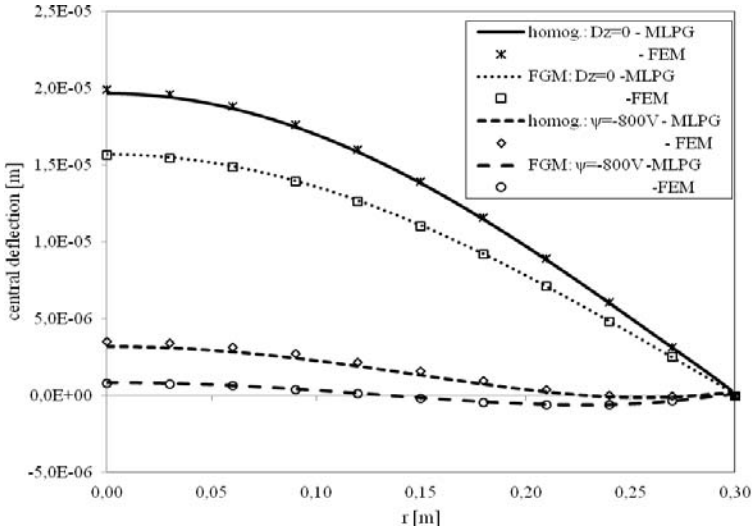

Fig. 4: Variation of central deflection with radial coordinate for simply supported plate under mechanical and electric load

Clamped circular plates are also analyzed. Both electric and mechanical loads are assumed. FGM exponential coefficient $\gamma_f = 34.6575$ is used again. Fig. 5 shows variation of deflection for clamped plates with homogeneous and FGM graphite/epoxy layer. Potential load $\psi = -800$ V is not sufficient to suppress the deflection completely as in case of simply supported plate, larger values have to be applied. Note that negative potential difference must be applied between the surfaces of piezoelectric layer. Positive values would act in opposite sense, thus increasing the deflection.

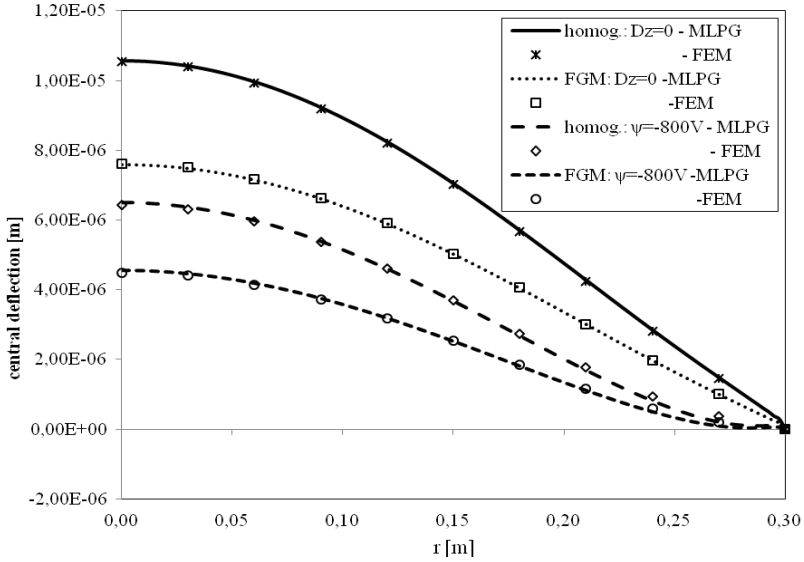

Fig. 5: Variation of central deflection with radial coordinate for clamped plate under mechanical and electric load

Response of simply supported 2-layer plate is also investigated under an impact mechanical load with Heaviside time variation. Numerical calculations are carried out for 100 time steps and a time-step size $\Delta\tau = 0.3\times10^{-4}\,s$. The time variation of the deflection at the plate center $(r=0; z=h_1/2)$ is given in Fig. 6. The value of the central deflection of the FGM plate is smaller than that of the homogeneous plate. It is due to the higher stiffness of the FGM plate. The peak deflection is shifted to shorter time instants for the FGM plate, where the flexural rigidity is higher and the mass density is the same for the FGM and homogeneous plates. Then, the wave velocities of the FGM plate are larger.

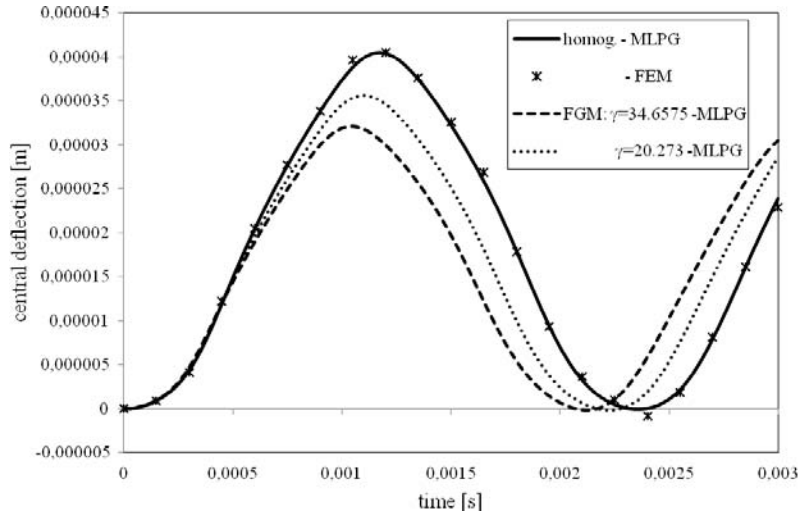

Fig. 6: Time variation of the central deflection for a simply supported plate under an impact mechanical load

4. Conclusion

A meshless local Petrov-Galerkin (MLPG) method was presented for the modeling and analysis of plate bending of 2-layer circular plate with functionally graded bottom layer and active piezoelectric layer. Special treatment of material interface was employed through coupling of interface variables. The MLS approximation was adopted for approximation of unknown physical quantities in each layer separately. Proposed method is a truly meshless method as no elements were used for approximation or for integration of unknowns. Numerical examples showed the effect of material grading and active piezoelectric layer on enhancement of the plate's flexural strength.

Acknowledgement

The authors gratefully acknowledge the support by the Slovak Science and Technology Assistance Agency registered under number APVV-0014-10.

References

Adachi, A., Kitamura, Y., Iwatsubo, T. (2004) Integrated design of piezoelectric damping system for flexible structure. *Applied Acoustics*, 65, pp. 293-310.

Atluri, S. N. (2004) *The meshless method (MLPG) for domain & BIE discretizations*. Tech Science Press, Forsyth, USA.

Benjeddou, A. (2000) Advances in piezoelectric finite element modeling of adaptive structural elements: a survey. *Computers and Structures*, 76, pp. 347-363.

Gibson, R. F. (2010) A review of recent research on mechanics of multifunctional composite materials and structures. *Composite structures*, 92, pp. 2793-2810.

Houbolt, J. C. (1950) A recurrence matrix solution for the dynamic response of elastic aircraft. *Journal of Aeronautical Sciences,* 17, pp. 371-376.

Lancaster, P., Salkauskas, T. (1981) Surfaces generatad by moving least-square methods. *Math. Comput*., 37, pp. 141-158.

Sladek, J., Sladek, V., Stanak, P., Zhang, Ch. (2010a) Meshless Local Petrov-Galerkin (MLPG) Method for Laminate Plates under Dynamic Loading. *CMC- Computers, Materials & Continua*, 15, pp. 1-26.

Sladek, J., Sladek, V., Stanak, P., Pan, E. (2010b) The MLPG for bending of electroelastic plates. *CMES- Computer Modeling in Engineering & Sciences*, 64, pp. 267-298.

Sladek, J., Sladek, V., Solek, P. & Saez, A. (2008) Dynamic 3D axisymmetric problems in continuously nonhomogeneous piezoelectric solids. *International Journal of Solids and Structures*, 45, pp. 4523-4542.

Sladek, J., Sladek, V., Wunsche, M. & Zhang , C. (2009) Interface crack problems in anisotropic solids analyzed by the MLPG. *CMES - Computer Modeling in Engineering & Sciences,* 54, pp. 223-252.

Sladek, V., Sladek, J. & Tanaka, M. (2005) Local Integral Equations and two Meshless Polynomial Interpolations with Application to Potential Problems in Non-homogeneous Media. *CMES- Computer Modeling in Engineering & Sciences*, 7, pp. 69-83.

Suresh, S., Mortensen, A. (1998) *Fundamentals of Functionally Graded Materials*. Institute of Materials, London

Tauchert, T. R., Ashida, F. (1999) Application of the potential function method in piezothermoelasticity: Solutions for composite circular plates. *Journal of Thermal Stresses*, 22, pp. 387-420.

18th International Conference
ENGINEERING MECHANICS 2012
Svratka, Czech Republic, May 14 – 17, 2012

pp. 1219–1228
Paper #63

USE OF ELECTRO-MAGNETIC DAMPING FOR VIBRATION CONTROL

G. J. Stein [*], R. Darula[**], S. Sorokin[**]

Abstract: *Vibration of machines is an unwanted phenomenon, and it is usually of interest to eliminate it. There are various means to be used in order to reach the goal, where the utilization of the electromagnet augmented by an external shunt circuit is analyzed in the paper. The magnetic force is used to introduce additional electromagnetic damping into vibrating mechanical system. The hysteretic losses and eddy currents are included in the model, to take into account more realistic dynamic behaviour of the system. The mathematical model of the controller is derived using lumped parameter approach. The parameters are assumed from an experimental set-up using and an industrial type of electromagnet. Considering the harmonic excitation of mechanical system, a steady-state response and performance of the controller is analyzed. Simulation results show the influence of introduced electromagnetic damping on the dynamical response of the system.*

Keywords: ***electromagnet, oscillatory system, damping, natural frequency detuning***

1. Introduction

In rotating machinery, the resonance phenomena can cause severe problems or even a failure of components. In order to avoid it, a vibration control need to be implemented, e.g.:

- Eliminating the coincidence of operation frequency with resonance;
- Introduction of mechanical damping.

Furthermore, active and semi-active methods of vibration control, i.e. capability to adjust the controller's properties, can be implemented in vibration reduction as well. Piezoelectric, electro-dynamic and electro-magnetic actuators are widely used for such a control strategy, as presented in (Bishop, 2002; Giurgiutiu & Lyshewski, 2009). Energy dissipation by a shunt circuit damper combined with piezoelectric elements is discussed in (Hagood & von Flotow, 1990; Giurgiutiu & Lyshewski, 2009; Preumont, 2011). In the vibration control of large machinery, utilization of piezoceramics is not an optimal choice, since the material is brittle and does not withstand large strains. Furthermore, the manufacturing costs and requirements on high voltage amplifiers are also drawbacks in large scale applications (Bishop, 2002; Giurgiutiu & Lyshewski, 2009).

On the other hand, electromagnetic and electrodynamic vibration controllers are capable to operate at larger amplitudes of vibration, too. Some applications of vibration control of cantilever beams using these elements are published by Gospodarič et al. (2007); Cheng & Oh (2009); Niu, Xie & Wang (2009); Brezina et al. (2011). The vibratory energy damping using an electromagnetic element connected to a shunt resistance is analyzed in Gospodarič et al. (2007), Niu et al. (2009), Brezina et al. (2011). Cheng & Oh (2009) use a set-up in which the current generated in a coil is dissipated by a shunt circuit, consisting of a battery of series RLC circuits. Utilization of the eddy currents damping in vibration control is explored in Sodano & Inman (2007).

This contribution, based on authors' previous work (Darula et al., 2011), analyses the electromagnetic actuation principle. It has been shown that the controller of interest is capable to

[*] Ing. George Juraj Stein, PhD.: Institute of Materials and Machine Mechancis, Slovak Academy of Sciences; Račianska 75; SK-83102 Bratislava 3; SR, e-mail: stein@savba.sk

[**] MSc. Radoslav Darula & Prof. Sergey Sorokin, DSc.: Department of Mechanical and Manufacturing Engineering, Aalborg University; Fibigerstraede 16; DK-9220 Aalborg East, DK, e-mail: dra@m-tech.aau.dk, svs@m-tech.aau.dk

introduce damping, as well as alter damped natural frequency of the oscillatory system. In order to model more realistic system, internal electrical losses are introduced, which were not considered in (Darula, *et al.*, 2011). It is shown that electrical losses significantly influence the system properties in respect to a loss-less system.

2. Concept of the vibration controller

The use of an industrial circular type electromagnet with a ferromagnetic yoke fixed by a spring-damper system, as shown in Fig. 1, is analyzed. A coil of N_w turns with a wire resistance R_W is energised by a direct current I_{DC} and it generates a static magnetic field. Exposing the yoke into vibration, described by a mechanical displacement $w(t)$, the air gap width $d(t)$ changes in time, which causes variation of an air gap reluctance.

According to Faraday's law (Fitzgerald et al., 2003), change in reluctance, i.e. a change of primary magnetic flux, is responsible for induction of alternating voltage $u_i(t)$ in the coil, where it forces a current $i_i(t)$ to flow in the electrical shunt circuit.

From the Lenz's law, the direction of $i_i(t)$ is opposite to I_{DC}, i.e. the magnetic field generated in the coil ($i_i(t)$ contribution) opposes the primary field generated by I_{DC}. Using the shunt resistance R_S, the current $i_i(t)$ is dissipated.

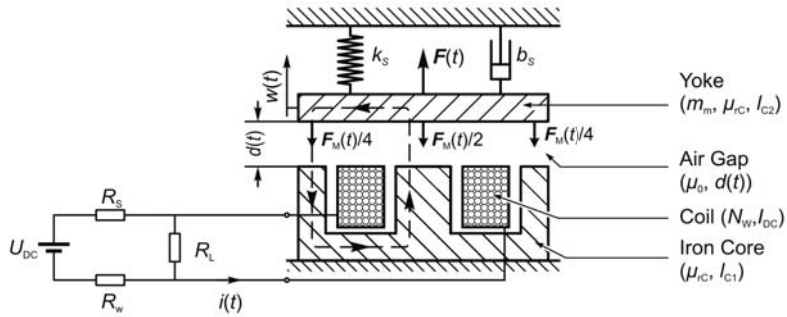

Fig. 1: Schematics of the analyzed electro-mechanical system (flux line is denoted dashed)

To extend the model derived in (Darula, et al., 2011), the material losses within the electrical circuit, which are supposed to influence the performance of the controller, are also taken into account:

1. *Hysteresis losses* in the core material,
2. *Eddy currents* in the core material.

As was shown in (Darula et al., 2012), the eddy current losses are frequency dependent.

The core loses can be modelled as a parallel loss resistance R_L to the electromagnet coil inductance (Fig. 1). Due to frequency dependence of losses, the resistance R_L is frequency dependent (Darula et al., 2012).

3. Simplified analysis of the electro-magnetic circuit

The magnetic system is modelled using a lamped parameter approach, where one can identify three elements (Fig. 2(a)):

- *Source of magnetic flux* – a coil of N_W turns energized with the current $i(t) = I_{DC} + i_i(t)$;
- *Air gap reluctance* ($\Re_{AG}$) – magnetic resistance caused by the air gap, where the width of air gap is $d(t)$ and the permeability of the free space μ_0;
- *Core reluctance* ($\Re_C$) – magnetic resistance of the iron core and armature with relative permeability μ_{rC}. From experimental results (Darula, 2008) a constant value of the permeability $\mu_{rC} \approx 500$ was estimated and used further. This is an acceptable simplification of the real situation.

From Ampere's law (e.g. in (Fitzgerald, et al, 2003)), assuming a constant core cross-section S_C, the magnetomotive force $F_\Phi(t)$:

$$F_\Phi(t) = \oint_C \vec{H} \cdot d\vec{l} = \left(\frac{l_C}{\mu_{rC}} + 2d(t) \right) \frac{B(t)}{\mu_0} = N_W \left[I_{DC} + i_i(t) \right] \tag{1}$$

where $\vec{H}$ is magnetic field intensity vector, $l = l_c + 2d(t)$ is total magnetic flux line path and $B(t)$ the magnetic field induction. Due to geometry of core and yoke of length l_C, the middle magnetic flux line is crossing twice the air gap of width $d(t)$, as seen from Fig. 1.

The source of DC voltage, U_{DC}, is assumed to be ideal, i.e. its internal resistance is neglected. The time variation of total magnetic flux $\Phi_T(w(t), i(t))$ in the coil is represented by the induced voltage $u_i(t)$. From Ohm's law we can write for the electric circuit (Fig. 2(b)):

$$U_{DC} + \frac{d\Phi_T(w(t), i(t))}{dt} = \left[\frac{(R_S + R_W)R_L}{R_S + R_W + R_L} \right] \left(I_{DC} + i_i(t) \right) \tag{2}$$

The total magnetic flux is in fact the induced voltage $u_i(t)$, as given by the Faraday's induction law (Bishop, 2002; Fitzgerald, et al, 2003; Giurgiutiu & Lyshewski, 2009):

$$u_i(t) = - \frac{d\Phi_T(w(t), i(t))}{dt} = - N_w S_w \frac{dB(t)}{dt} \tag{3}$$

where S_w is the coil winding cross-section and $B(t)$ is the time variable magnetic induction (magnetic field density) in the air gap.

From Eq. (2)-(3) can be concluded, that in the electric circuit of Fig. 2(b) two voltage sources are present acting in against each other. The circuit can be divided in respect to its behaviour into:

- the response to the DC voltage source: $U_{DC} = (R_s + R_w)I_{DC}$;
- the response to the induced AC voltage: $i_i(t) = u_i(t)/R_T(f)$, at given frequency f, where $R_T(f)$ is the bracketed term in Eq. (2), which is frequency dependent.

Since material losses are included in electrical circuit, the loss term in the magnetic model can be neglected, which simplifies derivations. Furthermore, neglecting also fringing effects (sufficiently small air gaps are assumed), the magnetic induction $B(t)$ can be derived from Eq. (1):

$$B(t) = \frac{\mu_0}{2d_0} \frac{N_w \left[I_{DC} + i_i(t) \right]}{\left[(1 + \delta) + \varepsilon(t) \right]} \tag{4}$$

using scaling coefficients $d_C = l_C/(2\mu_{rC})$, $\varepsilon = [d(t) - d_0]/d_0$, $\delta = d_C/d_0$. The parameter d_0 represents the static air gap width for a defined I_{DC}. To make the problem tractable, let us assume further $|w(t)| << d_0$, i.e. $|\varepsilon(t)| << 1$.

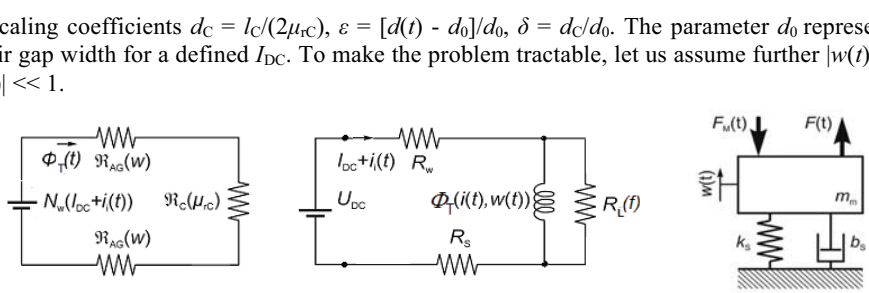

(a) *(b)* *(c)*

Fig. 2:(a) magnetic loop, (b) equivalent electric circuit, (c) mechanical system

In the static case, i.e. $i_i(t) = 0$ and $\varepsilon(t) = 0$, the static magnetic field in the air gap becomes:

$$B_0(I_{DC}, d_0) = \frac{\mu_0}{2d_0} \frac{N_w I_{DC}}{(1 + \delta)} \tag{5}$$

which is function of both the air gap width d_0, as well as the magnetising DC current I_{DC}.

Assuming a harmonic excitation of mechanical system, a steady state response of the system is of interest. The analysis of a transition phase is beyond the scope of this article. The steady-state is governed by two time variables:

- the air gap width $\varepsilon(t)$, which influences reluctance in the magnetic circuit;
- induced current $i_i(t)$, due to magnetic field variation.

As was derived for a similar electromagnetic system in (Darula et al., 2011), assuming $|i_i(t)| << I_{DC}$ and $|\varepsilon(t)| << 1$, the dynamical response of the electro-magnetic system can be expressed combining Eqs. (2) to (4) as:

$$\frac{d^2B(t)}{dt^2}\left[\frac{\mu_0 N_w^2 S_w}{2d_0(1+\delta)}\right]\frac{1}{R_T}+\frac{dB(t)}{dt}=-\frac{B_0}{(1+\delta)}\dot{\varepsilon} \tag{6}$$

where the term in the square bracket is inductance L_0 of the electromagnet coil with the ferromagnetic core at air gap of width d_0.

4. Calculation of the acting magnetic force

The electromagnetic force, called the Maxwell's pulling force, is given (Bishop, 2002; Fitzgerald, et. al., 2003; Giurgiutiu & Lyshewski, 2009; Meyer & Ulrych, 2009):

$$F_M(t)=2\cdot\frac{1}{\mu_0}B^2(t)S_C \tag{7}$$

The magnetic pulling force is acting through the central part of the core of cross-section S_C, as well as through the torus of the pot-type core, assumed to have the same cross-section. Substituting the expression for $B(t)$ from Eq. (4) and introducing the inductance L_0 from Eq. (6), following holds:

$$F_M(d(t),I_{DC},i_i(t)) = \frac{(1+\delta)L_0}{N_w^2 d_0}\frac{F_\Phi(t)^2}{\left[(1+\delta)+\varepsilon(t)\right]^2} \tag{8}$$

From Eq. (8), the quadratic dependence of the electromagnetic force on the magnetomotive force $F_\Phi(t)$ (Eq. (1)), i.e. on the total current flowing in the electrical circuit, $i_T(t) = I_{DC} + i_i(t)$, can be noticed. It is also inversely proportional to the square of the dynamic relative air gap $\varepsilon(t)$. As pointed out in Stein, et al (2011), there is a limit in the magnetic pulling force extent. If the total current $i_T(t)$ exceeds a critical value I_C, dependent on mechanical configuration, the magnetic pulling force would dominate over the elastic force. This would result in full attraction of the yoke to the electromagnet and the oscillatory motion would hence cease. Further, despite the difference in the areas S_w (cross-section of coil) and S_c (cross-section of core), it can be stated that the most of the magnetic flux is flowing through the ferromagnetic core because the magnetic resistance of the air, $2\times\Re_{AG}$ is μ_{rC}, i.e. 500–times larger than that one of the core, $\Re_C$. Hence, the ratio $\sigma = S_C/S_w \approx 1$.

In order to solve Eq. (8) analytically, it is advantageous to apply linearization in the vicinity of the operation point using first two terms of a power series. Hence:

$$F_M(\varepsilon(t),I_{DC},i_i(t))\approx\frac{L_0}{N_w^2 d_0(1+\delta)}F_\Phi(t)^2-\frac{2L_0}{N_w^2 d_0(1+\delta)^2}F_\Phi(t)^2\varepsilon(t) \tag{9}$$

The magnetomotive force is given by applying fundamental electromagnetic laws of Eqs. (1) and (3):

$$F_\Phi(t)=N_W\left[I_{DC}+i_i(t)\right]=N_W\left[I_{DC}-\frac{N_w S_w}{R_T}\frac{dB(t)}{dt}\right] \tag{10}$$

where for the magnetic induction, a total time derivative of Eq. (6) has to be substituted.

In further analysis, let us focus to the frequency domain, which can provide more information about dynamic response then time domain can. Therefore, let us introduce the respective phasor representation in respect to a supposed harmonic excitation force $\widetilde{F}=F_0 e^{j\omega_a t}$, where ω_a represents angular frequency. Then:

$$\widetilde{F}_{\Phi} = N_{\mathrm{W}}\left[I_{\mathrm{DC}} - \frac{\mathrm{j}\omega N_{\mathrm{w}} S_{\mathrm{w}}}{R_{\mathrm{T}}(\omega)}\widetilde{B}\right] \tag{11}$$

Substituting the dynamic magnetic induction phasor $\widetilde{B} = B_D e^{j\varphi_B}$ and the relative air gap width phasor $\widetilde{E}e^{\mathrm{j}\omega t} = \varepsilon_0 e^{\mathrm{j}\varphi_\varepsilon} e^{\mathrm{j}\omega t}$ into Eq. (6) and some re-arrangement following is valid:

$$\widetilde{B} = -\frac{B_0}{(1+\delta)}\frac{R_{\mathrm{T}}(\omega)}{\left[R_{\mathrm{T}}(\omega) + \mathrm{j}\omega L_0\right]}\widetilde{E} \tag{12}$$

which is the relationship between $\varepsilon(t)$ (the relative air gap) and the $B(t)$ (the induced magnetic field in the air gap due to yoke vibrations), expressed in the complex (phasor) form.

Substituting Eq. (12) into Eq. (11) the magnetomotive force becomes:

$$\widetilde{F}_{\Phi} = N_{\mathrm{W}} I_{\mathrm{DC}}\left[1 + \frac{\mathrm{j}\omega L_0}{(1+\delta)\left(R_{\mathrm{T}}(\omega) + \mathrm{j}\omega L_0\right)}\widetilde{E}\right] \tag{13}$$

Having expressed the magnetomotive force in the complex form, Eq. (13) can be inserted into Eq. (9) transformed into the complex plane. This allows to introduce a complex magnetic force phasor $\widetilde{F}_{\mathrm{MT}}$. According to Eqs. (8) and (9), the magnetic force is proportional to square of the magnetomotive force F_Φ. Therefore, the magnetic force phasor will contain also higher harmonics of ω_a. This is a well known phenomenon in electrical engineering (Bishop, 2002; Fitzgerald, et al., 2003; Giurgiutiu & Lyshewski, 2009; Mayer & Ulrych, 2009). Hence:

$$\widetilde{F}_{\mathrm{MT}} = \sum_{n=0}^{\infty}\widetilde{F}_{\mathrm{M}n}e^{jn\omega_a t} = \frac{L_0}{N_{\mathrm{w}}^2 d_0(1+\delta)}\widetilde{F}_{\Phi}{}^2 - \frac{2L_0}{N_{\mathrm{w}}^2 d_0(1+\delta)^2}\widetilde{F}_{\Phi}^2\cdot\widetilde{E}e^{j\omega_a t} \tag{14}$$

with:

$$\left(\widetilde{F}_{\Phi}\right)^2 = \left(N_{\mathrm{w}}^2 I_{\mathrm{DC}}^2\right)\cdot\left[1 + \frac{2\mathrm{j}\omega_{\mathrm{a}} L_0}{R_{\mathrm{T}}(\omega) + \mathrm{j}\omega_{\mathrm{a}} L_0}\widetilde{E}e^{\mathrm{j}\omega_{\mathrm{a}} t} - \frac{\omega_{\mathrm{a}}^2 L_0^2}{\left(R_{\mathrm{T}}(\omega) + \mathrm{j}\omega_{\mathrm{a}} L_0\right)^2}\left(\widetilde{E}\right)^2 e^{2\mathrm{j}\omega_{\mathrm{a}} t}\right] \tag{15}$$

The components of the total magnetic force under harmonic excitation emerge by explicitly expressing the particular low order components:

- *A static component* for $n = 0$:

$$F_{\mathrm{M0}} = \frac{L_0}{d_0(1+\delta)}I_{\mathrm{DC}}^2 \tag{16}$$

- *A component at the angular frequency* ω_a ($n = 1$):

$$\widetilde{F}_{\mathrm{M1}} = -\frac{2L_0 I_{\mathrm{DC}}^2}{d_0(1+\delta)^2}\left[1 - \frac{\mathrm{j}\omega_{\mathrm{a}} L_0}{R_{\mathrm{T}}(\omega) + \mathrm{j}\omega_{\mathrm{a}} L_0}\right]\cdot\widetilde{E} \tag{17}$$

- *A second harmonic component* at the angular frequency $2\times\omega_a$ ($n = 2$):

$$\widetilde{F}_{\mathrm{M2}} = -\frac{L_0 I_{\mathrm{DC}}^2}{(1+\delta)^3}\left\{\frac{5\omega_{\mathrm{a}}^2 L_0^2 R_{\mathrm{T}}^2 + 3\omega_{\mathrm{a}}^4 L_0^4}{\left(R_{\mathrm{T}}^2(\omega_{\mathrm{a}}) + \omega_{\mathrm{a}}^2 L_0^2\right)^2} - 2\mathrm{j}\frac{R_{\mathrm{T}}(\omega_{\mathrm{a}})\omega_{\mathrm{a}} L_0}{\left(R_{\mathrm{T}}^2(\omega_{\mathrm{a}}) + \omega_{\mathrm{a}}^2 L_0^2\right)}\right\}\cdot\left|\widetilde{E}\right|^2 \tag{18}$$

which is coupled to mechanical motion by excitation amplitude $\varepsilon_0{}^2$.

- *Higher order harmonic components* being of the order of $|\varepsilon|^{\mathrm{n}}$, where $n \geq 3$. Because of $|\varepsilon| < 1$, these can be neglected.

5. Simplified analysis of the coupled system in the complex plane

Let us analyse the static deflection of the analysed SDOF oscillatory system loaded by the mass of the yoke of mass m_m (Fig. 1). The yoke is at a distance d_0* from the upper plane of the de-energised electromagnet core. Energizing the electromagnet by the DC current I_{DC}, the exerted static magnetic force F_{M0} elongates the spring further and a static equilibrium position in the distance d_0 is attained. Equilibrium is described as (Bishop, 2002; Rao, 2004):

$$(d_0^* - d_0)k_s = F_{M0}(I_{DC}, d_0) = \frac{L_0}{d_0(1+\delta)} I_{DC}^2 \tag{19}$$

If an external excitation force $F_E(t)$ of harmonic course, described as $F_E(t) = F_{E0}\sin(\omega_a t)$, is acting onto the mass m_m additional dynamic components of the Maxwell's pulling force F_{Mi} come into action. Then the equation of motion of the SDOF oscillatory system (Fig. 2(c)) is (Darula, et al., 2011):

$$m_m \frac{d^2 w(t)}{dt^2} + b_S \frac{dw(t)}{dt} + k_S w(t) = F_E(t) - F_{Mi}(t) \tag{20}$$

Lets turn into the complex domain, i.e. let us describe the external harmonic excitation $F_E(t)$ by the complex force phasor $\widetilde{F} = F_0 e^{j\omega_a t}$. The steady state response is of interest, i.e. all transient phenomena (electric and mechanic) are extinct. The response is assumed to be harmonic with the same angular frequency ω_a, i.e. the complex relative air gap width in the form $\widetilde{E}e^{j\omega_a t} = \varepsilon_0 e^{j\varphi_E} e^{j\omega_a t}$. Then, Eq. (20) in non-dimensional form becomes:

$$\left[1 - \Omega^2 + 2j\xi_S\Omega\right]\widetilde{E}e^{j\omega_a t} = \frac{\widetilde{F}e^{j\omega_a t}}{k_s d_0} - \sum_{i=1}^{2} \frac{\widetilde{F}_{Mi} e^{j\omega_a i t}}{k_s d_0} \tag{21}$$

where:

- $\Omega = \omega_a / \omega_0$ is the non-dimensional frequency scaled with respect to natural frequency of the mechanical system;
- $\omega_0^2 = k_S / m$ is the square of the natural frequency of the SDOF mechanical system;
- $\xi_S = b_S / b_C$ is the damping ratio, where $b_C = 2\sqrt{k_s m}$ is the critical damping coefficient,
- $\widetilde{F}_{M1}$ and $\widetilde{F}_{M2}$ are the above derived first and second harmonics of the magnetic force.

The left hand side of Eq. (21) represents the oscillation of a general SDOF system, i.e. without action of any external forces. The external forces (excitation and magnetic force components) are on the right hand side of the equation.

Let analyze just the influence of the first harmonics of magnetic force (Eq. (17)) on the dynamics of the coupled system. The influence of the first harmonics is by far the largest and the most important. The influence of the higher harmonics is acknowledged; however will not be analysed. By introducing the formula into Eq. (21) and re-arranging, following is obtained:

$$\left[1 - \Omega^2 + 2j\xi_S\Omega\right]\widetilde{E}e^{j\omega_a t} = \frac{\widetilde{F}e^{j\omega_a t}}{k_s d_0} + \frac{1}{k_s}\left(\frac{2L_0 I_{DC}^2}{d_0^2(1+\delta)^2}\right)\left[1 - \frac{j\omega_a L_0}{R_T(\omega_a) + j\omega_a L_0}\right]\cdot \widetilde{E}e^{j\omega_a t} \tag{22}$$

The term in round parenthesis on the right-hand-side has a physical dimension of N/m, i.e. from mechanical point of view it represents a 'stiffness' associated with the static magnetic field, k_M:

$$k_M = \frac{2L_0}{d_0^2(1+\delta)^2} I_{DC}^2 = \frac{\mu_0 S_c N_w^2 I_{DC}^2}{d_0^3(1+\delta)^3} = \frac{F_{M0}(I_{DC}, d_0)}{d_0(1+\delta)} \tag{23}$$

Taking a dimension-less ratio of the magnetic field stiffness k_M to the mechanical stiffness k_s, $\kappa = k_M/k_s$, Eq. (22) is modified to become:

$$\left[1-\Omega^2+2\mathrm{j}\Omega\xi_\mathrm{S}-\kappa\frac{R_\mathrm{T}(\omega_\mathrm{a})}{R_\mathrm{T}(\omega_\mathrm{a})+\mathrm{j}\omega_\mathrm{a}L_0}\right]\widetilde{E}=\frac{\widetilde{F}}{k_\mathrm{s}d_0} \tag{24}$$

The left hand-side of Eq. (24) resembles the linear second order operator of Eq. (21), albeit with the addition of the last term, containing all the electrical parameters. After further re-formulation:

$$\left[\left(1-\kappa\frac{R_\mathrm{T}^2(\omega_\mathrm{a})}{R_\mathrm{T}^2(\omega_\mathrm{a})+\omega_\mathrm{a}^2L_0^2}\right)-\Omega^2+2\mathrm{j}\Omega\left(\xi_\mathrm{S}+\frac{\kappa}{2}\frac{R_\mathrm{T}(\omega_\mathrm{a})\cdot\omega_0L_0}{R_\mathrm{T}^2(\omega_\mathrm{a})+\omega_\mathrm{a}^2L_0^2}\right)\right]\widetilde{E}=\frac{\widetilde{F}}{k_\mathrm{s}d_0} \tag{25}$$

with:

$$\kappa=\frac{k_\mathrm{M}}{k_\mathrm{s}}=\frac{1}{k_\mathrm{s}}\cdot\frac{F_{M0}(I_\mathrm{DC},d_0)}{d_0(1+\delta)}=\frac{1}{k_\mathrm{s}}\cdot\frac{2L_0}{d_0^2(1+\delta)^2}I_\mathrm{DC}^2 \tag{26}$$

The derived equations are valid for any excitation angular frequency ω_a in the working range of the vibration controller. Further the coil reactance at angular frequency ω_0, $X_0=\omega_0\cdot L_0$ can be introduced and related to the total circuit ohmic resistance R_T in the following way:

$$\left\{\left[1-\kappa\cdot\frac{1}{1+\Omega^2\left(\frac{X_0}{R_\mathrm{T}}\right)^2}\right]-\Omega^2+2\mathrm{j}\Omega\left[\xi_\mathrm{S}+\frac{\kappa}{2}\cdot\frac{\left(\frac{X_0}{R_\mathrm{T}}\right)}{1+\Omega^2\left(\frac{X_0}{R_\mathrm{T}}\right)^2}\right]\right\}\widetilde{E}=\frac{\widetilde{F}}{k_\mathrm{s}d_0} \tag{27}$$

The complicated formula on the left hand side of Eq. (27) is the complex displacement transmissibility of the coupled system, $\widetilde{G}(\Omega)$, which has to be compared with the displacement transmissibility of the original, purely mechanical system, which is described by the left hand side of Eq. (21).

Comparing Eq. (27) with the left hand side of Eq. (21) we may conclude:

- The natural frequency of the modified oscillatory system (first left-hand-term term of Eq. (27)) is influenced by the electrical parameters of the electric circuit – total circuit resistance R_T and coil reactance X_0; by the static air gap width d_0 and by the magnetising DC current I_DC. The equivalent natural angular frequency of the coupled system is lower than the natural angular frequency ω_0 of the original (purely mechanical) one system. Hence de-tuning occurs, whose extent is controlled by the I_DC magnitude, entering the dimension-less variable κ, and by shunt resistance R_S, embedded in the total circuit resistance R_T;
- Additional damping is introduced to the mechanical system damping ξ_s, described by the last term in the left-hand-side of Eq. (27), which is controlled by the I_DC, R_S and X_0, too. The last term consists of the original system damping ratio ξ_s and an additional damping ratio, which can be termed additional 'electro-magnetic damping ratio' ξ_EM:

It is seen that the properties of the electrical components of the system markedly influence its vibration control performance. The total circuit resistance $R_\mathrm{T}(f)$ has already been introduced in Eq. (2), after Fig. 2(c):

$$R_\mathrm{T}(f)=\frac{(R_\mathrm{S}+R_\mathrm{W})R_\mathrm{L}(f)}{R_\mathrm{S}+R_\mathrm{W}+R_\mathrm{L}(f)}, \tag{28}$$

where the coil losses resistance R_L is assumed, following the results presented in Darula et al. (2012):

$$\frac{1}{R_\mathrm{L}(I_\mathrm{DC},d_0,f)}=\frac{1}{R_\mathrm{E}}+\frac{1}{R_\mathrm{H}(f)}, \tag{29}$$

where parameters R_E, representing the eddy current loses and R_H the hysteretic losses, which are linearly frequency dependent ($R_\mathrm{H}(f)=\gamma f$). The parameters were estimated from experiments (Darula, 2008). Estimation of numerical values of the parameters is presented in Darula et al. (2012). Then:

$$\frac{1}{R_{\mathrm{T}}(R_{\mathrm{S}},f)}=\frac{1}{R_{\mathrm{w}}+R_{\mathrm{S}}}+\frac{1}{R_{\mathrm{E}}}+\frac{1}{R_{\mathrm{H}}(f)} \tag{30}$$

In formula (30) just the shunt resistance R_S is available for control.

After substitution of expression (30) into Eq. (27), the extent of de-tuning and additional electro-magnetic damping can be quantified. The above obtained formulas can be illustrated in graphical form using the Matlab® simulation environment. The simulation is done for a particular case, addressed in Darula (2008): inductance $L_0 = 4.95$ H for air gap width $d_0 = 0.75$ mm. The loss properties of the electromagnet coil were identified in Darula et al. (2012). Following values were used: DC winding resistance $R_w = 34.9$ Ω; eddy current losses $R_{eE} = 1000$ Ω; hysteresis losses constant $\gamma = 90$ Ω/Hz. The equivalent mechanical system properties were assessed as $m_m = 51.7$ kg (load + joke mass); $k_s = 3.25\times10^6$ N/m and damping ratio $\xi = 0.025$. This leads to the natural frequency $f_0 = 39.9$ Hz ($\omega_0 = 250.7$ rad/s, $\Omega = 1.00$). The excitation force amplitude is set at 20 N and the excitation frequency is varied by ± 20 % from the mechanical system natural frequency to visualise the variation in the resonance peak position on the frequency axis due to the electro-magnetic influence. The shunt resistance R_S was varied from the value $R_S = 0$ Ω (short circuited coil), up to $R_S = 1\times10^6$ Ω (1 MΩ). A three-dimensional map of the FRF modulus dependence $\left|\widetilde{G}(\Omega)\right|$ on the R_S value is depicted in Fig. 3.

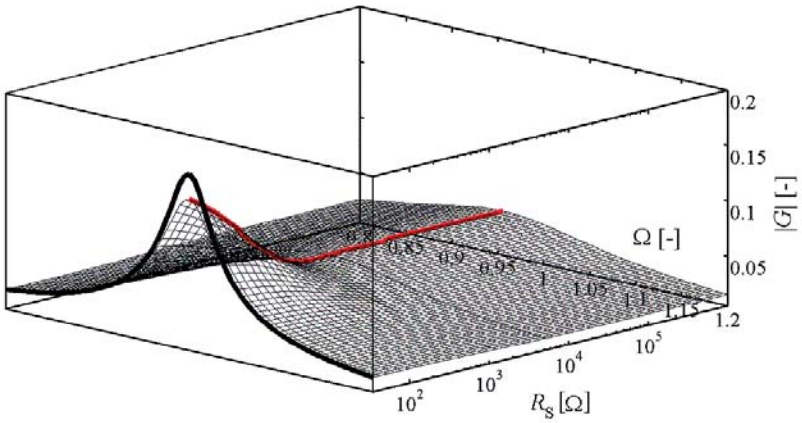

Fig. 3: Three-dimensional surface map of the FRF displacement modulus in respect to Ω and R. In bold the FRF of the sole mechanical part; in red the course of the FRF maximum, corresponding to the de-tuned natural frequency of the coupled system as a function of R_s

The bold black curve is the displacement FRF of the oscillatory system without the electromagnet, while the red curve indicates the variation of the FRF peak maximum, corresponding to the de-tuned frequency ratio Ω in respect to changing R_S in the range (0 Ω, 1 MΩ) (on a logarithmic scale).

It is interesting to assess the extent of de-tuning and displacement FRF attenuation in respect to the variation of the shunt resistance R_S. In Fig. 4(a) the dependence of the frequency ratio Ω is depicted; while in Fig. 4(b) the modulus of the coupled system $\left|\widetilde{G}\right|$ is presented. From both figures it is seen, that the extent of de-tuning is not large, attaining at most $\Omega = 0.955$ ($f_{D0} = 38.1$ Hz) for $R = 1$ MΩ ~ infinity, while for a more realistic value of $R_S = 5$ kΩ the de-tuning is to $\Omega = 0.965$ ($f_{D0} = 38.5$ Hz). The attenuation of displacement transmissibility for this particular case is from $G_0 = 0.1641$ (for the solely mechanical system) to $G_{inf} = 0.0447$ for $R = 1$ MΩ, or $G_R = 0.0470$ for the shunt resistance $R_S = 5$ kΩ. This is a 3.49–fold attenuation at the damped natural frequency of the original system, or by some 10.9 dB. The utmost attenuation for $R = 1$ MΩ would be 3.67–times, i.e. by 11.3 dB. From Fig. 4 it is seen, that the influence of the shunt resistance above some value to the vibration attenuation, as well as to the extent of the de-tuning is limited. This is due to the fact, that the resistance R_S is connected in parallel to the coil internal loss resistance R_e (see Eq. (30)) and so cannot

influence much the total resistance R_T by increasing the value of R_S to infinity. The obtained results are quite different from those for a system with neglected electromagnet losses, as presented, e.g. by Darula et al. (2011).

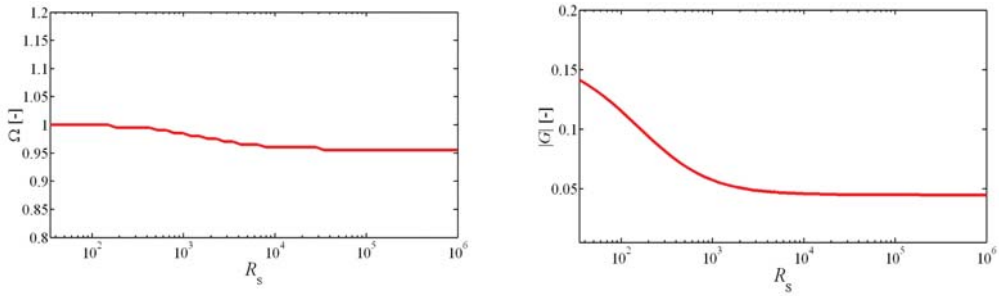

(a) (b)

Fig. 4: Dependence of: (a) detuned frequency ratio Ω and (b) FRF displacement modulus $|G|$ on R_S

6. Conclusion

An electro-magneto-mechanical system for vibration control of an SDOF oscillatory system, subject to external harmonic excitation, was analysed in a simplified, linearised form. The fundamental equation of motion (Eq. (25)) was derived, which includes the non-linear magnetic force (Maxwell's pulling force), described by Eqs. (9) and (10). The extra magnetic force causes:

- Generation of higher harmonics,
- Change (decrease) in oscillatory system natural frequency, i.e. de-tuning of the system,
- Inclusion of additional electro-magnetic damping, so decreasing the vibration transmissibility. The attainable extent of the de-tuning and of the additional electro-magnetic damping was illustrated for a particular case using parameters determined experimentally for an industrial electromagnet. It is markedly limited by the electrical parameters (coil inductance, and equivalent loss resistance) of the electromagnet.

Acknowledgement

This contribution is a result of the project No. 2/0075/10 of the Slovak VEGA Grant Agency for Science and InterReg IV A – 'Silent Spaces' Project, whose one Partner is Aalborg University.

References

Bishop, R.H., ed. (2002) *The Mechatronics Handbook*. CRC Press, Boca Raton.

Brezina, T., Vetiska, J., Hadas, Z. & Brezina, L. (2011) Simulation Modelling and Control of Mechatronic Systems with Flexible Parts, in: *Proc. 9th Int.Conf. Mechatronics 2011* (R. Jablonski & T.Brezina eds), Springer Verlag, Berlin, pp. 569-578.

Darula, R. (2008). *Multidisciplinary Analysis and Experimental Verification of Electromagnetic SAVC*. Masters Thesis. IME, Aalborg University, Aalborg.

Darula, R., Stein, G.J., Kallesøe, C.S. & Sorokin, S. (2012) Identification and Mathematical Modelling of the Electromechanical Vibration Controller, in: *Proc. 11th Int.Conf. ESDA 2012*, submitted.

Darula, R., Stein, G.J. & Sorokin, S. (2011) An Application of Electromagnetic Induction in Vibration Control, in: *Proc.10th Int.Conf. ICoVP 2011* (J. Naprstek, et al. eds), TU Liberec, Liberec, pp. 447-453.

Fitzgerald, A.E., Kingsley. Ch. & Umans, S.D. (2003) *Electric Machinery*, 6th ed. McGraw-Hill, Boston.

Giurgiutiu, V. & Lyshewski, S.E. (2009) *Micromechatronics: Modeling, Analysis and Design*, 2nd ed. CRC Press, Boca Raton.

Gospodarič, B., Vončina, D. & Bučar, B. (2007) Active electromagnetic damping of laterally vibrating ferromagnetic cantilever beam. *Mechatronics* 17, 6, pp. 291-298.

Hagood, N. & von Flotow, A. (1991) Damping of structural vibration with piezoelectric materials and passive electrical networks. *Journal of Sound and Vibration*, 146, 2, pp. 243-268.

Cheng, T.-H. & Oh, I.-K. (2009) A current-flowing electromagnetic shunt damper for multi-mode vibration control of cantilever beams. *Smart Materials and Structures*, 18, 9, art.no. 095036 (10pp).

Mayer, D. & Ulrych, B. (2009) *Elektromagneticke aktuatory (Electromagnetic actuators - in Czech).* BEN, Prague.

Niu, H. X., Xie, S. & Wang, P. (2009) A new electromagnetic shunt damping treatment and vibration control of beam structures. *Smart Materials and Structures*, 18, 4, art.no. 045009 (15pp).

Preumont, A. (2011) *Vibration Control of Active Structures,* 3rd ed. Springer, Berlin.

Rao, S.S. (2004) *Mechanical Vibrations*, 4th ed. Pearson, Upper Saddle River.

Sodano, H.A. & Inman, D.J. (2007) Non-contact vibration control system employing an active eddy current damper. *Journal of Sound and Vibration*, 305, 4-5, pp.596-613.

Stein, G.J., Darula, R. & Chmúrny, R. (2011) A clamped-clamped beam static sag limits under perpendicular magnetic force, in: *Proc.17th Int.Conf. Engineering Mechanics 2011*, (V. Fuis ed), IT ASCR, pp.567-571.

18th International Conference
ENGINEERING MECHANICS 2012
Svratka, Czech Republic, May 14 – 17, 2012

pp. 1229–1235
Paper #146

HYDRAULIC DESIGN OF INDUCER

J. Stejskal*

Abstract: *The paper deals with hydraulic design of an inducer. The mathematical model based on the Lagrange coordinates is presented. It is based on a choice of trajectory of a fluid particle in accordance with the continuity equation. Given the trajectory shape, it is possible to determine the specific energy of an inducer. The inducer blade is then determined by the family of these trajectories.*

Key words: ***Inducer, Euler equations, Continuity equation, Lagrange coordinates***

1 Introduction

When designing an inducer, the main criteria are high suction performance, high head rise and a positive pressure gradient. Currently, the design methods to avoid cavitation in inducers are becoming a major concern. This article provides relatively quick and easy methodology to do the preliminary blade design satisfying demanded parameters, while focus is put on suitable specific energy and pressure gradient. Cavitation in inducers is studied in papers (Rebattet et al 2001; Acosta et al 2001; Wegner et al 2003). No attempts to improve the cavitation performance have been made here.

2 Liquid Motion on a Helical Surface

Let us consider the helical surface in the coordinate system $\mathbf{x} = [x_1, x_2, x_3]$, as shown in Fig. 1.

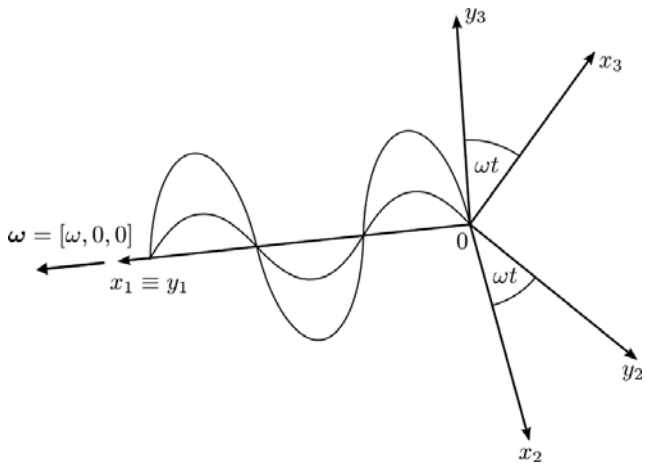

Fig. 1

This surface rotates around axis x_1 with angular velocity ω. We connect the rotating coordinate system $\mathbf{y} = [y_1, y_2, y_3]$ with the helix. In the system y_i we may write down the general parametric helical surface as

* Ing. Jiří Stejskal: Energy Institute, Brno University of Technology, Faculty of Mechanical Engineering, Technická 2896/2; 616 69, Brno; CZ, e-mail: jstejskal@gmail.com

$$y_2 = F(a_1, a_3)\cos A(a_1, a_2, a_3)\ ,$$
$$y_3 = F(a_1, a_3)\sin A(a_1, a_2, a_3)\ , \tag{1}$$
$$y_1 = G(a_3)\ ,$$

where $a_1 \in \langle a_{1\mathrm{i}}, a_{1\mathrm{f}}\rangle$, $a_3 \in \langle 0, a_{3\mathrm{f}}\rangle$ and a_2 is fixed in the interval $\langle 0, 2\pi\rangle$. The relation between coordinates x_i and y_i is easily seen from Fig. 1. It holds that

$$x_2 = \cos(\omega t)\, y_2 - \sin(\omega t)\, y_3\ ,$$
$$x_3 = \sin(\omega t)\, y_2 + \cos(\omega t)\, y_3\ ,$$
$$x_1 = y_1\ .$$

Substituting from (1), we have:

$$x_2 = F\cos(\omega t)\cos A - F\sin(\omega t)\sin A = F\cos(A + \omega t)\ ,$$
$$x_3 = F\sin(\omega t)\cos A - F\cos(\omega t)\sin A = F\sin(A + \omega t)\ , \tag{2}$$
$$x_1 = y_1\ .$$

Equations (1) define the shape of helix. To describe the motion of a fluid particle on this helix we choose the Lagrange coordinates, while this particle will be moving in the opposite direction of axis y_1, see Fig. 2. We will follow the motion of the fluid in time t from a certain point of the helix given by coordinates a_1, a_3. In general, this motion is described by

$$y_2 = F(a_1, a_3, t)\cos A(a_1, a_2, a_3, t)\ ,$$
$$y_3 = F(a_1, a_3, t)\sin A(a_1, a_2, a_3, t)\ ,$$
$$y_1 = G(a_3, t)\ .$$

To ensure that the particle follows the shape of the helix against the direction of axis y_1, we choose

$$y_2 = F(a_1, a_3 - \Omega t)\cos A(a_1, a_2, a_3 - \Omega t)\ ,$$
$$y_3 = F(a_1, a_3 - \Omega t)\sin A(a_1, a_2, a_3 - \Omega t)\ , \tag{3}$$
$$y_1 = G(a_3 - \Omega t)\ ,$$

Where $t \in \langle 0, t_{\mathrm{f}}\rangle$ and Ω is the angular velocity of the fluid.

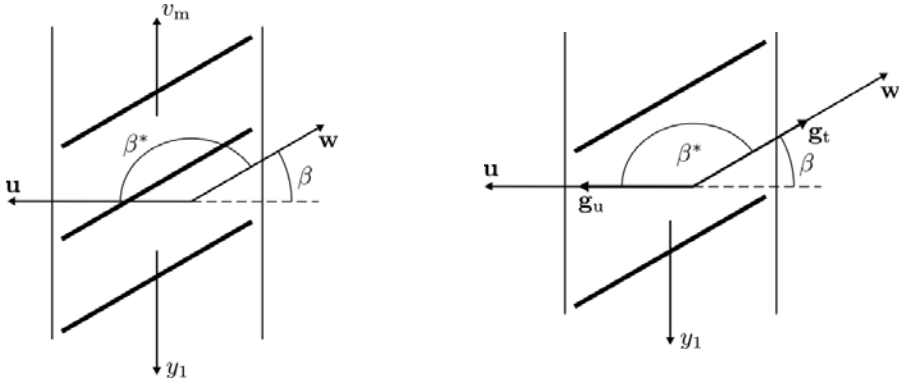

*Fig. 2: Velocities and angles between them (**u** is the moving frame velocity, **w** is the relative velocity and v_m is the meridional velocity).*

In system x_i, the fluid motion must satisfy the Continuity Equation (Brdička et al 2005), which in Lagrange coordinates takes the form $J(0) = J(t)$, where

$$J = \det\begin{bmatrix} \frac{\partial x_1}{\partial a_1} & \frac{\partial x_1}{\partial a_2} & \frac{\partial x_1}{\partial a_3} \\ \frac{\partial x_2}{\partial a_1} & \frac{\partial x_2}{\partial a_2} & \frac{\partial x_2}{\partial a_3} \\ \frac{\partial x_3}{\partial a_1} & \frac{\partial x_3}{\partial a_2} & \frac{\partial x_3}{\partial a_3} \end{bmatrix}.$$

Substituting from (2) and solving the determinant, we get

$$J(t) = F\frac{\partial F}{\partial a_1}\frac{\partial A}{\partial a_2}\frac{\partial G}{\partial a_3} = J(0)\,. \tag{4}$$

2.1 Important Relations for the Inducer Design

To determine the specific energy we need to know the circumferential velocity component v_u. To set it down, let us do the time derivative of equations (2). Hence

$$\dot{x}_2 = \dot{F}\cos(A+\omega t) - F\left(\dot{A}+\omega\right)\sin(A+\omega t)\,,$$

$$\dot{x}_3 = \dot{F}\sin(A+\omega t) - F\left(\dot{A}+\omega\right)\cos(A+\omega t)\,,$$

where dot denotes the time derivative. Therefore, we have

$$v_\mathrm{u} = F\left(\dot{A}+\omega\right), \tag{5}$$

$$v_\mathrm{r} = \dot{F}\,. \tag{6}$$

Now we determine the blade angle β. According to Fig. 2, we get

$$\cos\beta^* = \frac{\mathbf{g}_\mathrm{u}\cdot\mathbf{g}_\mathrm{t}}{\|\mathbf{g}_\mathrm{u}\|\|\mathbf{g}_\mathrm{t}\|}\,, \qquad \cos\beta = -\frac{\mathbf{g}_\mathrm{u}\cdot\mathbf{g}_\mathrm{t}}{\|\mathbf{g}_\mathrm{u}\|\|\mathbf{g}_\mathrm{t}\|}\,, \tag{7}$$

where $\mathbf{g}_\mathrm{u}$ is a vector in the direction of the moving frame velocity and $\mathbf{g}_\mathrm{t}$ is a vector tangential to the fluid particle trajectory. Obviously,

$$\mathbf{g}_\mathrm{u} = \begin{bmatrix} 0 \\ -F\sin A \\ F\cos A \end{bmatrix}, \qquad \mathbf{g}_\mathrm{t} = \begin{bmatrix} \dot{G} \\ \dot{F}\cos A - F\dot{A}\sin A \\ \dot{F}\sin A + F\dot{A}\cos A \end{bmatrix}.$$

Substituting these into (7), we obtain

$$\cos\beta = -\frac{F\dot{A}}{\sqrt{\dot{G}^2+\dot{F}^2+\left(F\dot{A}\right)^2}}, \tag{8}$$

from where

$$\sin^2\beta = 1-\cos^2\beta = \frac{\dot{G}^2+\dot{F}^2}{\dot{G}^2+\dot{F}^2+\left(F\dot{A}\right)^2},$$

which implies

$$\mathrm{tg}\,\beta = -\frac{\sqrt{\dot{G}^2+\dot{F}^2}}{F\dot{A}}. \tag{9}$$

2.2 Pressure

The pressure field can be determined from the Euler equations, which in Lagrange coordinates take the form (Brdička et al 2005)

$$\rho\frac{\partial^2 x_1}{\partial t^2}\frac{\partial x_1}{\partial a_k}+\rho\frac{\partial^2 x_2}{\partial t^2}\frac{\partial x_2}{\partial a_k}+\rho\frac{\partial^2 x_3}{\partial t^2}\frac{\partial x_3}{\partial a_k}=-\frac{\partial p}{\partial a_k}\,,\qquad k=1,2,3\,. \tag{10}$$

Using equations (2) in (10), we obtain equations describing the pressure field as

$$-\frac{\partial p}{\partial a_k}=\rho\left[\frac{\partial G}{\partial a_k}\ddot{G}+\frac{\partial F}{\partial a_k}\left(\ddot{F}-F\left(\dot{A}+\omega\right)^2\right)+\frac{\partial A}{\partial a_k}\left(2F\dot{F}\left(\dot{A}+\omega\right)+F^2\ddot{A}\right)\right]. \tag{11}$$

3 Results

The inducer blade for the following parameters was designed:

$$L=0{,}06\ \text{m},\quad Q=6{,}94\,\frac{\text{l}}{\text{s}},\quad n=1450\ \text{min}^{-1},\quad D_1=0{,}08\ \text{m}\,,\quad D_2=0{,}04\ \text{m}\,,$$

where D_1 and D_2 are inner and outer diameters, respectively. Other quantites are as follows:

$$S=\frac{\pi}{4}(D_1^2-D_2^2)=0{,}00377\ \text{m}^2\,,\quad v_\text{m}=\frac{Q}{S}=1{,}84\ \frac{\text{m}}{\text{s}}\,,\quad \omega=\frac{2\pi n}{60}=151{,}84\ \frac{\text{rad}}{s}.$$

Resulting blade surface is in Fig. 3.

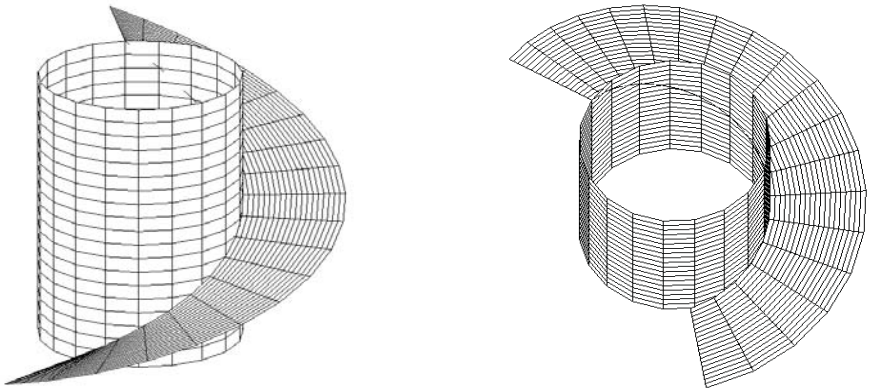

Fig. 3

Blade parameters in the mean region are:

$$v_{\text{u}1}=0\,\frac{\text{m}}{\text{s}},\quad v_{\text{u}2}=1{,}7\,\frac{\text{m}}{\text{s}},\quad Y=7{,}84\,\frac{\text{J}}{\text{kg}}\,,\quad H_{75\%}=0{,}5994\ \text{m}\,,$$

where $H_{75\%}$ is the head at efficiency of 75%. To compare these results, numerical computations by the singularity method were performed. Results were obtained for 20 blades of zero thickness as an approximation to the infinite number of blades. It gives

$$r_\text{min}\text{:}\quad \Delta p=2770\ \text{Pa},\ H_{75\%}=0{,}2614\ \text{m},$$
$$r_\text{mean}\text{:}\quad \Delta p=6202\ \text{Pa},\ H_{75\%}=0{,}5851\ \text{m},$$
$$r_\text{max}\text{:}\quad \Delta p=10996\ \text{Pa},\ H_{75\%}=1{,}0368\ \text{m},$$

This is a good approximation to the theoretical result.

As another example, the following inducer was designed (see Fig. 4):

$$L_{\max} = 0{,}14 \text{ m}, \quad L_{\min} = 0{,}111 \text{ m}, \quad Q = 616 \frac{\text{l}}{\text{s}}, \quad n = 2980 \text{ min}^{-1},$$

$$D_1 = 0{,}306 \text{ m}, \quad D_2 = 0{,}150 \text{ m}.$$

Resulting blade surface is in Fig. 5. Assuming the infinite number of blades, the head is

$$H_{75\%} = 38 \text{ m}.$$

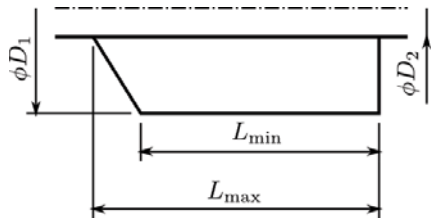

Fig. 4: Meridional section.

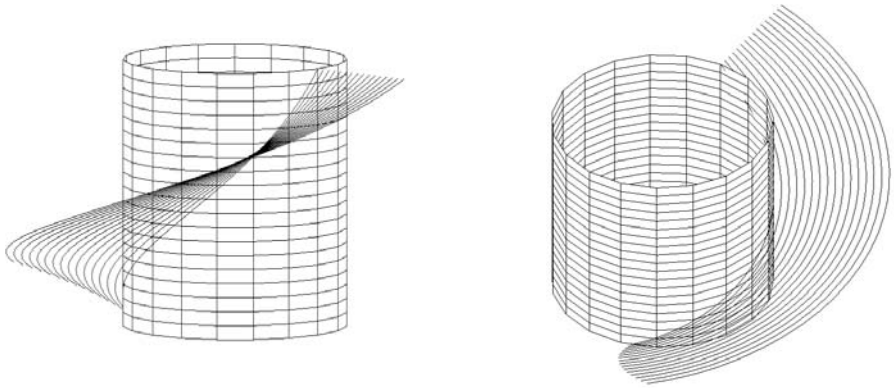

Fig. 5

This inducer was proceeded to a CFD computation. Its three dimensional model is in Fig. 6.

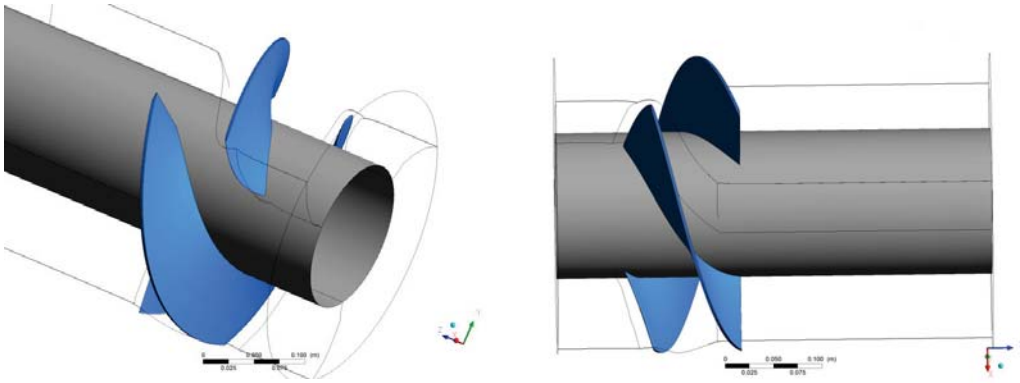

Fig. 6

From Fig. 7 we see that this inducer was designed with zero angle of incidence along the leading edge (Pochylý et al 2011). Head $H = 23{,}18$ m. The blade loading is in Fig. 8, from where the pressure

difference between pressure and suction side of the blade can be seen. A value of the pressure in a point has no meaning, only differences are meaningful.

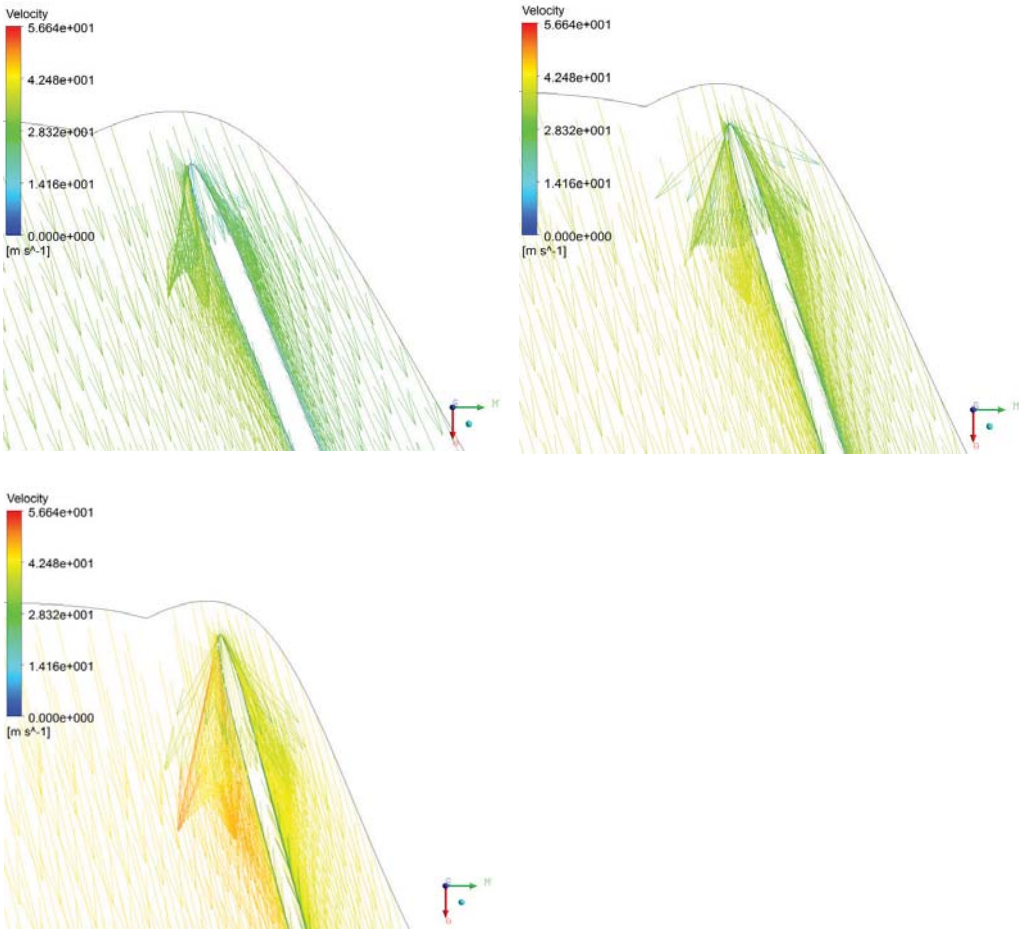

Fig. 7: Relative velocities at 20%, 50% *and* 80% *span between hub and tip.*

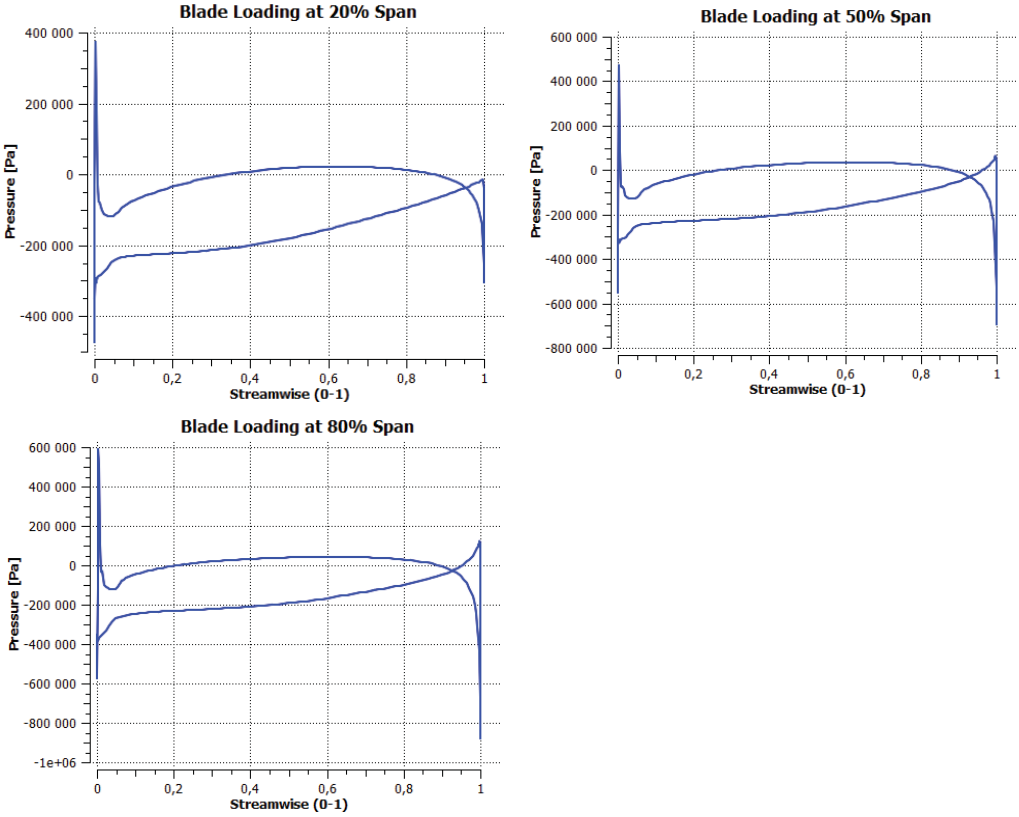

Fig. 8

4 Conclusions

This paper presents the methodology to design an inducer blade. It is based on Euler equations together with the continuity equation in Lagrange coordinates. It can be used to perform the preliminary blade design and to predict its parameters (specific energy, pressure gradient, etc.). Several inducers were designed and compared to numerical computations. It was shown that these numerical results are in good agreement with the presented theory.

Acknowledgement

The financial support of the Specified Research Grants No. FSI-J-12-21/1698, No. FSI-S-12-2 and NETME Centre project - New technologies for Mechanical Engineering CZ.1.05/2.1.00/01.0002 is gratefully acknowledged.

References

Rebattet, C., Wegner, M., Morel, P. & Bonhomme, Ch. (2001) *Inducer design that avoids rotating cavitation.* CREMHyG's research report.

Acosta, A. J., Tsujimoto, Y., Yoshida, Y., Azuma, S. & Cooper, P. (2001) Effects of Leading Edge Sweep on the Cavitating Characteristics of Inducer Pumps. *International Journal of Rotating Machinery*, 7(6), pp.397-404.

Wegner, M., Acosta, A. J. & Tsujimoto, Y. (2003) Panel Discussions on Inducer Design Criteria. *International Journal of Rotating Machinery*, 9, pp.229-237.

Pochylý, F., Stejskal, J., Haluza, M. & Rudolf, P. (2011) *Hydraulický návrh induceru.* Brno University of Technology research report No. VUT-EU 13303-QR-20-11.

Brdička, M., Samek, L. & Sopko, B. (2005) *Mechanika kontinua.* Academia, Praha.

18th International Conference
ENGINEERING MECHANICS 2012
Svratka, Czech Republic, May 14 – 17, 2012

pp. 1237–1251
Paper #18

OPEN SOURCE FEM-DEM COUPLING

J. Stránský [*], M. Jirásek [**]

Abstract: *Finite element method (FEM) and discrete element method (DEM) are leading strategies for numerical solution of engineering problems of solid phase. Both are applicable in different situations and sometimes can be beneficially coupled. Coupling of two free open source programs (finite element code OOFEM and discrete element code YADE, both with C++ core and Python user interface) is presented. Some of the basic coupling strategies (surface coupling, volume coupling, multi-scale approach and contact analysis) are explained on patch tests and simple simulations.*

Keywords: ***FEM, DEM, coupling, Python scripting, open source***

1. Introduction

Numerical simulations are an indispensible part of the current engineering and science development. For different engineering areas there are different numerical methods used. In solid phase mechanics, the leading methods are the finite element method (FEM) and the discrete (distinct) element method (DEM). FEM is rigorously derived from the continuum theory and is being used for the description of deformable continuous bodies, while DEM describes particulate materials, usually modeled by perfectly rigid particles and their interactions determined from fictitious overlaps of these rigid particles.

Often an engineering problem can be modeled using only one of the aforementioned methods. A steel beam would be simulated by FEM, a small assembly of gravel particles by DEM. But what if we wanted to simulate an impact of the steel bar on the gravel? One possible approach would be to split the problem into two domains (the steel part modeled by FEM and the gravel part modeled by DEM) and appropriately *couple* them.

There are countless software programs for both FEM and DEM. Some of them are commercial (usually) without possibility to change the code and adjust the behavior to our requirements (combination with another software for instance). However, there exist programs with open source code, which the user can modify, possibly for coupling with another programs. In the present article, coupling of FEM code OOFEM (Patzák & Bittnar, 2001) and DEM code YADE (Šmilauer et al., 2010) is presented. Both programs have the core written in C++ (providing efficient execution of time consuming routines), user interface written in Python (modern dynamic object oriented scripting language, providing easy to use scripting while preserving the C++ efficiency) and extensible object oriented architecture allowing independent implementation of new features - new material model or new particle shapes for instance.

Basic principles of different coupling strategies (surface, volume, multiscale and contact coupling) are explained in section 2, implementation issues are covered in section 3 and specific examples for each coupling strategy are presented in section 4. Python scripts controlling these examples are for illustration placed in Appendix A.

2. Theory

In this section, firstly the two numerical methods are quickly reviewed for the simplest case of small strain/displacement linear elasticity (to establish consistent notation and to help readers familiar with

[*]Ing. Jan Stránský: Czech Technical University in Prague, Faculty of Civil Engineering, Department of Mechanics, Thákurova 7; 166 29, Prague; CZ, email: jan.stransky@fsv.cvut.cz
[**]Prof. Ing. Milan Jirásek, DrSc.: Czech Technical University in Prague, Faculty of Civil Engineering, Department of Mechanics, Thákurova 7; 166 29, Prague; CZ, email: milan.jirasek@fsv.cvut.cz

one method to understand the other one). Then the basic principles of the chosen coupling strategies are explained.

2.1. Finite element method

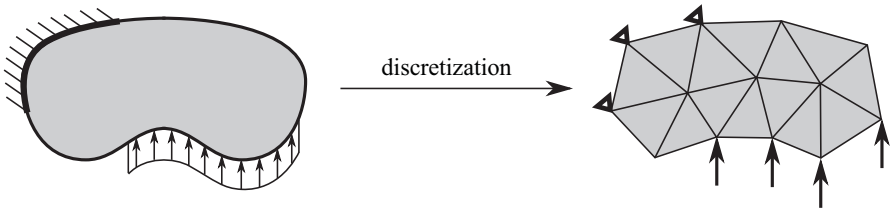

Fig. 1: Simplified illustration of FEM discretization

The continuous (static) linear elasticity solves the boundary value problem

$$\boldsymbol{\varepsilon} = \boldsymbol{\nabla}^{\mathrm{sym}}\mathbf{u} \qquad \mathbf{x} \in \Omega \tag{1}$$

$$\boldsymbol{\sigma} = {}^4\mathbf{D} : \boldsymbol{\varepsilon} \qquad \mathbf{x} \in \Omega \tag{2}$$

$$\boldsymbol{\nabla} \cdot \boldsymbol{\sigma} + \mathbf{b} = \mathbf{0} \qquad \mathbf{x} \in \Omega \tag{3}$$

$$\mathbf{u} = \overline{\mathbf{u}} \qquad \mathbf{x} \in \Gamma_u \tag{4}$$

$$\mathbf{n} \cdot \boldsymbol{\sigma} = \overline{\mathbf{t}} \qquad \mathbf{x} \in \Gamma_t \tag{5}$$

where $\mathbf{x}$ = vector of Cartesian coordinates, $\mathbf{u} = \mathbf{u}(\mathbf{x})$ = displacement vector, $\boldsymbol{\varepsilon} = \boldsymbol{\varepsilon}(\mathbf{x})$ = strain tensor, $\boldsymbol{\sigma} = \boldsymbol{\sigma}(\mathbf{x})$ = stress tensor, ${}^4\mathbf{D} = {}^4\mathbf{D}(\mathbf{x})$ = fourth-order stiffness tensor, $\mathbf{b} = \mathbf{b}(\mathbf{x})$ = body forces, $\mathbf{t} = \mathbf{t}(\mathbf{x})$ = surface tractions, Ω = domain of the problem, Γ_u = boundary of the domain with prescribed displacements, Γ_t = boundary of the domain with prescribed tractions and $\mathbf{n} = \mathbf{n}(\mathbf{x})$ = outer unit normal vector of the boundary. $\boldsymbol{\nabla}$ is the vector of spatial partial derivatives, $\cdot$ is contraction and : is double contraction (tensor operations). Overbars indicate prescribed values.

Combining geometric equations (1), constitutive equations (2) and equilibrium (Cauchy) equations (3) yields Lamé equations

$$\boldsymbol{\nabla} \cdot \left[{}^4\mathbf{D} : (\boldsymbol{\nabla}\mathbf{u}) \right] + \mathbf{b} = \mathbf{0}, \tag{6}$$

which describe the elasticity problem in the strong sense.

The basic idea of FEM is to discretize the domain Ω into finite elements. On each element e, the displacement field $\mathbf{u}^e(\mathbf{x})$ is approximated as a combination of nodal displacement values $\{\mathbf{d}\}^e$. From the element geometry and material parameters, the element stiffness matrix $[\mathbf{K}]^e$ can be constructed, providing the relationship between the nodal displacements $\{\mathbf{d}\}^e$ and nodal internal forces $\{\mathbf{f}\}^e$ (7). Approximating the load by nodal forces, the global system of equations

$$[\mathbf{K}]^e\{\mathbf{d}\}^e = \{\mathbf{f}\}^e \quad \rightarrow \quad [\mathbf{K}]^g\{\mathbf{d}\}^g = \{\mathbf{f}\}^g \tag{7}$$

is assembled and unknown nodal displacements are solved for defined boundary conditions. Equation (7) can be derived from the virtual work principle and describes the elasticity problem in the weak sense.

2.2. Discrete element method

Consider an assembly of rigid particles. The contact (bond, interaction etc.) c between particles is created either initially in the beginning of the simulation or when the particles overlap. The contact (see equations (8-9) and figure 2) can be described by a branch vector $\mathbf{l}^c$ (connecting the centers of linked particles) with normal $\mathbf{n}^c = \mathbf{l}^c / \|\mathbf{l}^c\|$. The (linearized) relative contact displacement $\mathbf{u}^c$ can be expressed in terms of particle displacement $\mathbf{x}^p$ and rotation $\boldsymbol{\varphi}^p$ and decomposed into the normal component u_N^c and the shear component $\mathbf{u}_T^c$. Constitutive (linear elastic) contact law is also expressed (independently) in the normal and shear directions in terms of the normal and shear forces f_N^c and $\mathbf{f}_T^c$ and normal and shear contact stiffnesses k_N^c and k_T^c. The total contact force $\mathbf{f}^c$ is composed from normal and shear

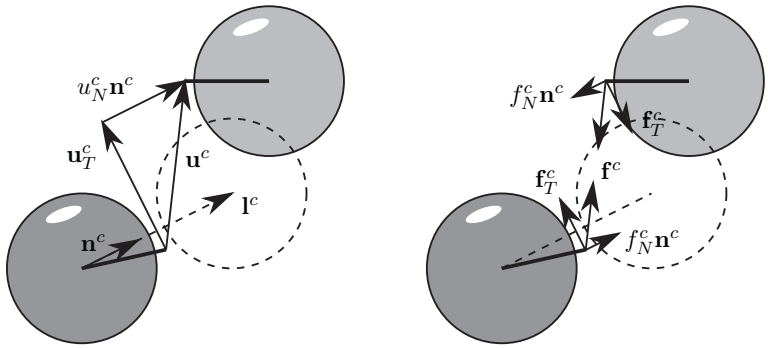

Fig. 2: Simplified illustration of the contact displacement and contact forces and their decompositions

components. The contact force is considered to act at the contact point (in the middle between particle centers for example), and so its shear component also causes a moment on both particles.

$$u_N^c = \mathbf{u}^c \cdot \mathbf{n}^c, \qquad \mathbf{u}^c = u_N^c \mathbf{n}^c + \mathbf{u}_T^c \tag{8}$$

$$f_N^c = k_N^c u_N^c, \qquad \mathbf{f}_T^c = k_T^c \mathbf{u}_T^c, \qquad \mathbf{f}^c = f_N^c \mathbf{n}^c + \mathbf{f}_T^c \tag{9}$$

For each particle p, the forces are then summed from all particles contacts and the Newton's equations of motion

$$\mathbf{f}^p = \sum_{c \in p} \mathbf{f}^c, \quad \ddot{\mathbf{u}}^p = \frac{\mathbf{f}^p}{m^p} \tag{10}$$

are solved using Verlet explicit time integration scheme. m^p is the mass of particle p and $\ddot{\mathbf{u}}^p$ its acceleration. The summation and integration of the equation of motion is also defined for moments and angular accelerations. For more details about time integration as well as DEM in general see (Šmilauer et al., 2010) or (Kuhl et. al, 2001).

2.3. Surface coupling

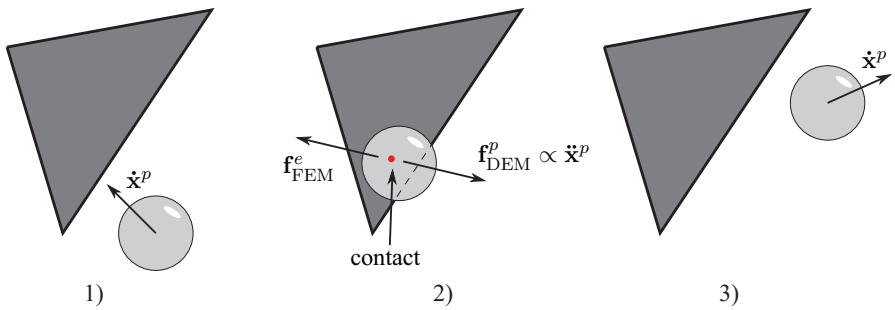

Fig. 3: Illustration of FEM/DEM surface coupling

The so-called surface coupling (Fakhimi, 2009; Nakashima & Oida, 2004; Oñate & Rojek, 2004; Villard et al., 2009) is probably the most straightforward coupling method. The principle is to split the whole problem into two non-overlapping domains, one modeled by FEM and the other by DEM (as already illustrated on the steel beam – gravel example in the introduction). As long as there is no overlap between the two domains, nothing special happens - both methods are applied independently.

If a contact between a finite element and a DEM particle is detected, the new force becomes acting on the DEM particle (causing its acceleration). The same force (with the same magnitude and the opposite direction) of course acts also on the FEM element and is processed as a load boundary condition, see figure 3.

In the current OOFEM/YADE implementation, the FEM boundary (surface) elements are copied into DEM part as special particles. This approach allows us to exploit efficient YADE contact detection algorithms. The resulting DEM force and moment acting on surface element are in FEM part transfered into nodal forces and further assumed as external load.

2.4. Volume coupling

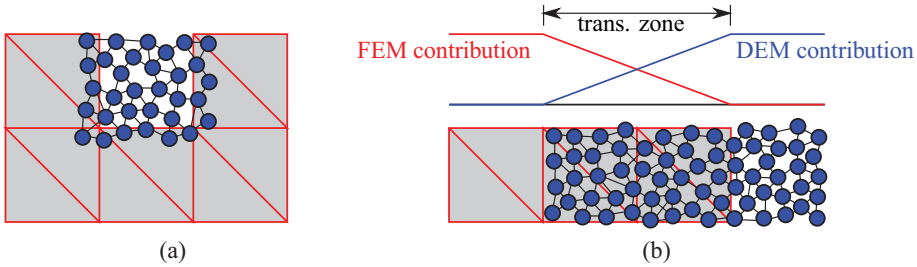

Fig. 4: Illustration of "master/slave" (a) and "Arlequin" (b) FEM/DEM volume coupling

Volume coupling is similar to the surface coupling. The difference is that the two subdomains overlap each other. The possible usage of this approach could be a model of concrete beam subjected to an impact load (blast for example). The whole beam would be modeled by FEM and only a small volume of the concrete (the volume to be fragmented and crushed) would be modeled by DEM.

There are two basic strategies how to model transition between FEM and DEM domains. The first one, "direct" or "master/slave" method, (Azvedo & Lemos, 2004) considers DEM particles overlapping with FEM as direct slaves of the FEM mesh (using standard "master/slave" or "hanging nodes" approach). The second one, the "Arlequin" method (Rousseau et al., 2009; Wellmann & Wriggers, 2012), considers a transition bridging zone, where the total response is superposed from contributions of the two models and is interpolated between both domains.

2.5. Multiscale coupling

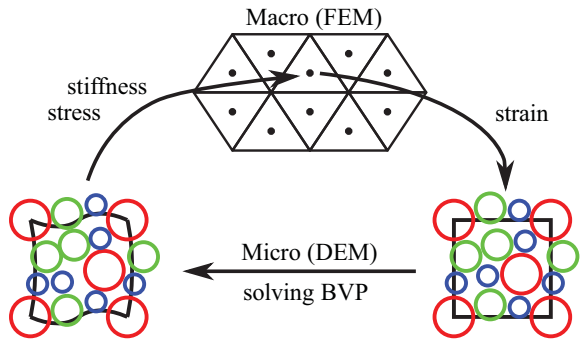

Fig. 5: Illustration of multiscale coupling according to (Geers et. al, 2010) applied to FEM/DEM

The idea of multiscale simulations is to model the problem on the large (macro) scale using information from a lower (micro) scale. In the current context, the (first order) homogenization (Geers et. al, 2010) is presented. Geometric information (strain) from macro scale (Gauss points of FEM mesh) is transfered to the micro scale (representative volume element - RVE - modeled by DEM), see figure 5. On the micro scale, the boundary value problem (BVP) governed by the transfered prescribed strain is solved using periodic boundary conditions (Stránský & Jirásek, 2010). The output of the micro-scale problem are the stress tensor and the constitutive characteristics (stiffness tensor), which are transfered back to the macro-scale problem.

As an example of this approach, consider a model of a large sample of sand. On macro scale, sand is usually considered as a continuous material. DEM modeling of a large sand sample with individual grains modeled by individual particles would not be feasible. According to these two facts, the macro scale problem is modeled by FEM. However, the particular nature of sand is preserved in the microscale RVE simulations, which provides the FEM part with stress and stiffness. Thus we do not need any explicit expression of the material law on the FEM scale (it is determined from the actual micro RVE response).

The stress and stiffness can be evaluated either analytically or numerically. The analytical formulas (Kuhl et. al, 2001) are inspired by the microplane theory and are derived from Voigt's hypothesis. It assumes that the strain $\boldsymbol{\varepsilon}$ is distributed uniformly in the RVE and, consequently, the relative displacement $\mathbf{u}^c$ of each contact c can be expressed and decomposed in the form (see (Kuhl et. al, 2001) and equations (8-9) for more details):

$$\mathbf{u}^c = \boldsymbol{\varepsilon} \cdot \mathbf{l}^c = \|\mathbf{l}^c\| \, \boldsymbol{\varepsilon} \cdot \mathbf{n}^c = u_N^c \mathbf{n}^c + \mathbf{u}_T^c \tag{11}$$

$$u_N^c = \mathbf{u}^c \cdot \mathbf{n}^c = (\|\mathbf{l}^c\| \, \boldsymbol{\varepsilon} \cdot \mathbf{n}^c) \cdot \mathbf{n}^c = \|\mathbf{l}^c\| \, (\mathbf{n}^c \otimes \mathbf{n}^c) : \boldsymbol{\varepsilon} = \|\mathbf{l}^c\| \, \mathbf{N}^c : \boldsymbol{\varepsilon} \tag{12}$$

$$\mathbf{u}_T^c = \mathbf{u}^c - u_N^c \mathbf{n}^c = \|\mathbf{l}^c\| \, \boldsymbol{\varepsilon} \cdot \mathbf{n}^c - \|\mathbf{l}^c\| \, \boldsymbol{\varepsilon} : (\mathbf{n}^c \otimes \mathbf{n}^c)\mathbf{n}^c = \|\mathbf{l}^c\| \, \boldsymbol{\varepsilon} : (\mathbf{I}^{\mathrm{sym}} \cdot \mathbf{n} - \mathbf{n} \otimes \mathbf{n} \otimes \mathbf{n}) = \|\mathbf{l}^c\| \, \mathbf{T}^c : \boldsymbol{\varepsilon} \tag{13}$$

$\mathbf{N}^c = \mathbf{n}^c \otimes \mathbf{n}^c$ and $\mathbf{T}^c = \mathbf{I}^{\mathrm{sym}} \cdot \mathbf{n}^c - \mathbf{n}^c \otimes \mathbf{n}^c \otimes \mathbf{n}^c$ are auxiliary projection tensors and $\mathbf{I}^{\mathrm{sym}} = \frac{1}{2}[\delta_{il}\delta_{jk} + \delta_{ik}\delta_{jl}]$ is the fourth order symmetric identity tensor. The equivalence of macroscopic (M) and microscopic (m) virtual work

$$\boldsymbol{\sigma} : \delta\boldsymbol{\varepsilon} = \delta W^M \quad = \quad \delta W^m = \frac{1}{V} \sum_{c \in V} \mathbf{f}^c \cdot \delta \mathbf{u}^c = \frac{1}{V} \sum_{c \in V} \mathbf{f}^c \cdot \delta\boldsymbol{\varepsilon} \cdot \mathbf{l}^c = \frac{1}{V} \sum_{c \in V} [\mathbf{f}^c \otimes \mathbf{l}^c] : \delta\boldsymbol{\varepsilon} \tag{14}$$

yields the expression for the stress tensor (with substitution of equations (8) and (9))

$$\boldsymbol{\sigma} = \frac{1}{V} \sum_{c \in V} [\mathbf{f}^c \otimes \mathbf{l}^c]^{\mathrm{sym}} = \frac{1}{V} \sum_{c \in V} \|\mathbf{l}^c\| \, (\mathbf{N}^c f_N^c + [\mathbf{f}_T^c \otimes \mathbf{n}^c]^{\mathrm{sym}}). \tag{15}$$

Substituting equations (9), (12) and (13) into (15)

$$\begin{aligned} \boldsymbol{\sigma} &= \frac{1}{V} \sum_{c \in V} \|\mathbf{l}^c\| \, (\mathbf{N}^c k_N^c u_N^c + [\mathbf{n}^c \otimes k_T^c \mathbf{u}_T^c]^{\mathrm{sym}}) = \\ &= \frac{1}{V} \sum_{c \in V} \|\mathbf{l}^c\| \, (\mathbf{N}^c k_N^c \|\mathbf{l}^c\| \, \mathbf{N}^c : \boldsymbol{\varepsilon} + [\mathbf{n}^c \otimes k_T^c \|\mathbf{l}^c\| \, \mathbf{T}^c : \boldsymbol{\varepsilon}]^{\mathrm{sym}}) = \\ &= \frac{1}{V} \sum_{c \in V} \|\mathbf{l}^c\|^2 (k_N^c \mathbf{N}^c \otimes \mathbf{N}^c + k_T^c [\mathbf{n}^c \otimes \mathbf{T}^c]^{\mathrm{sym}}) : \boldsymbol{\varepsilon} \end{aligned} \tag{16}$$

and comparing (16) with (2) yields the expression for the stiffness tensor

$$\begin{aligned} {}^4\mathbf{D} &= \frac{1}{V} \sum_{c \in V} \|\mathbf{l}^c\|^2 (k_N^c \mathbf{N}^c \otimes \mathbf{N}^c + k_T^c [\mathbf{n}^c \otimes \mathbf{T}^c]^{\mathrm{sym}}) \\ D_{ijkl} &= \frac{1}{V} \sum_{c \in V} \|\mathbf{l}^c\|^2 \left[(k_N^c - k_T^c) n_i^c n_j^c n_k^c n_l^c + k_T^c \frac{1}{4} \left(n_i^c n_l^c \delta_{jk} + n_i^c n_k^c \delta_{jl} + n_j^c n_l^c \delta_{ik} + n_j^c n_k^c \delta_{il} \right) \right]. \end{aligned} \tag{17}$$

This estimation of the stiffness tensor is derived from the kinematic constraint, thus it is an upper bound of the real one. If the real strain state differs too much from the assumed uniform state (strain localization for instance), the analytical stiffness estimation is no more valid and the stiffness has to be computed numerically. The aspect of strain localization can be in same cases captured by the implemented periodic boundary conditions, see (Šmilauer et al., 2010) and (Stránský & Jirásek, 2010), but it will be among other aspects (second order homogenization for instance) subjected to further analysis and development.

2.6. Contact analysis

The idea of contact analysis (Frenning, 2009) is very simple and opposite to the multiscale approach. The material on the large scale is considered to be of a particulate nature and is modeled by particles using DEM. Each such particle is further modeled by FEM.

There is no strict border between the cases when the solution can be considered as contact FEM analysis and when it is already DEM. For only a few particles we would probably use the former one, but when the number of particles is large, the DEM modeling (with its efficient contact detection algorithms) would be more convenient. This strategy can be actually considered as full FEM, only the contact detection is ”borrowed” from the DEM program.

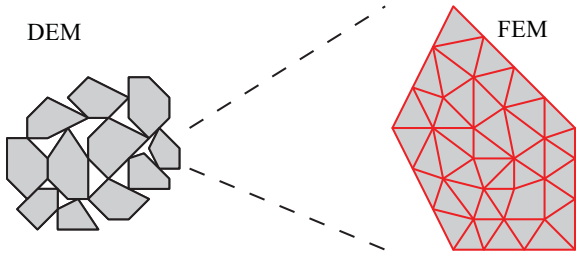

Fig. 6: Illustration of multimethod FEM/DEM contact analysis

3. Implementation

The current implementation serves only for testing of the methods and functionality, therefore not all features are in public versions of OOFEM and YADE yet. Since this paper is about open source coupling, the changes will be (after further testing and bug-fixing) of course merged to public versions and will be available for any potential user/developer.

From the point of view of Python, all important functionality is concentrated into the **`fakemupif`** module, which provides several classes derived from the base **`FemDemCoupler`** class. Each such class has its **`step`** method, which is the only needed additional command in comparison with non-coupled simulations (see the example scripts in the following sections). When the testing is finished, the functionality (probably with some syntax and internal code modifications, but with same high-level simplicity) will be implemented into the **`MuPIF`** project (Patzák, 2011) to enable coupling with other programs or other physical models (heat transfer for instance).

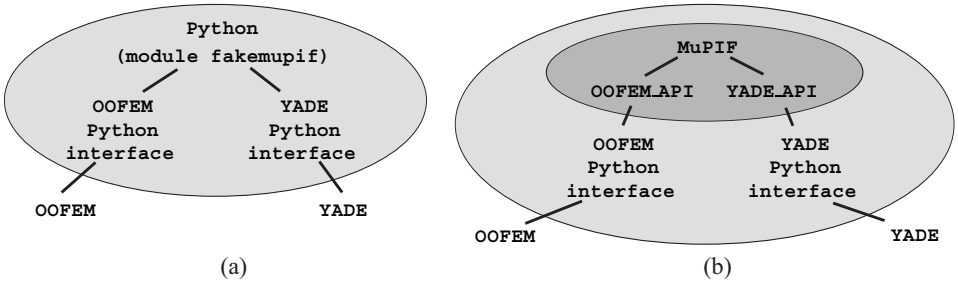

Fig. 7: Current (testing) (a) and planned (b) implementation

4. Examples

In this section, one specific simple example for each discussed coupling strategy is presented.

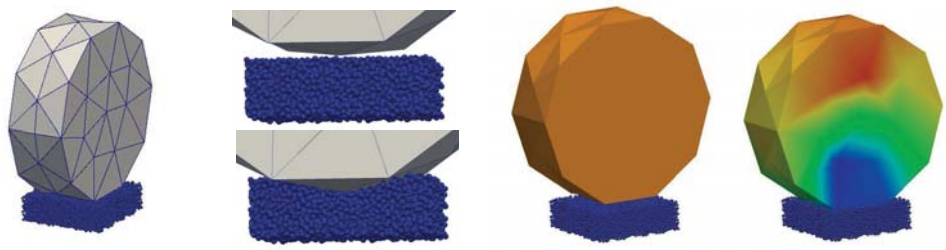

(a) (b) (c)

Fig. 8: Results of surface coupling - soil-tire contact:
simulation setup (a), detail of contact (b) and resulting vertical normal stress in FEM domain (c)

4.1. Surface coupling: soil-tire contact

Simulation of the soil-tire contact, inspired by (Nakashima & Oida, 2004), is presented here. The tire is modeled by FEM as a linear elastic material, the soil is modeled by DEM as spherical particles. Of course, in a real simulation we could use a more complicated soil grain geometry, a more advanced (than just linear elastic) material model for the tire and so on, but for an illustrating and testing example the present assumptions are sufficient. See figure 8 and codes 1 and 5.

4.2. Volume coupling: three point bending

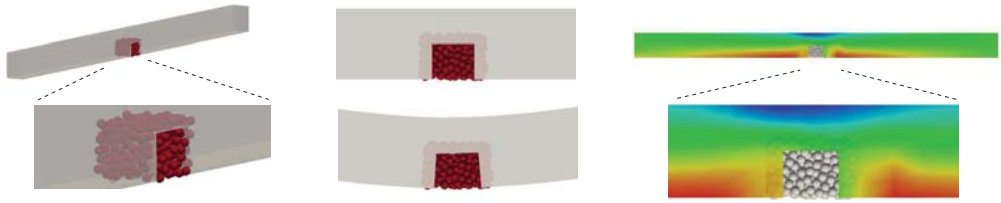

Fig. 9: Results of three point bending:
initial state (a), undeformed and deformed final state (b) and normal stress (c)

In this example, a simply supported beam was simulated. The whole beam body was simulated by FEM, only the part with maximal tensile normal stress was simulated by DEM. The vertical displacement of the middle cross section was prescribed.

Again, the elastic solution is nothing special here, but instead of linear elastic particles we could use a kind of material model for fracture description (Azvedo & Lemos, 2004), thus the expected crack initiation and propagation in the middle cross section would be modeled with the help of discrete models. See figure 9 and codes 2 and 6.

4.3. Multiscale coupling: uniaxial strain

Uniaxial strain (oedometric test) of a sample consisting of two different (linear elastic) materials (with stiffness ratio $1/2$) is simulated in this example. The macro-scale problem is modeled by two brick elements. Each FEM element has eight integration points. For each integration point, a DEM micro-scale RVE simulation is performed, in which the FEM prescribed strain is imposed. The resulting stress and stiffness are transfered back to the macro-scale FEM simulation.

In figure 10, magnified results are plotted. In each material, one micro RVE result is displayed (all RVEs in the same material, due to the simulation setup, correspond to each other). The results of linear elastic behavior are not extremely spectacular indeed, but using nonlinear behavior of RVEs (resulting

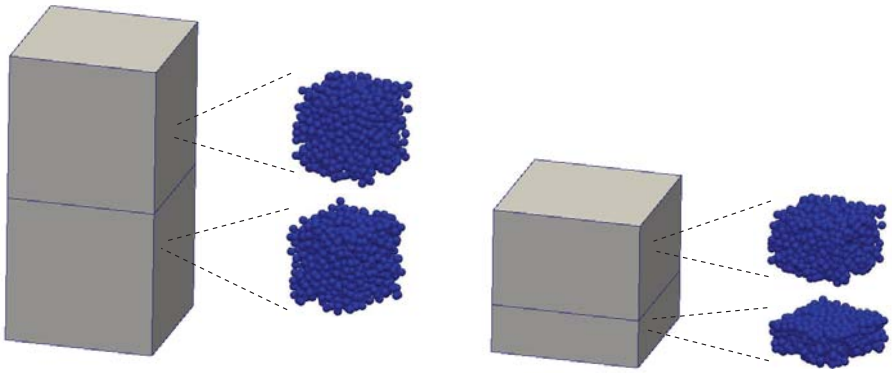

Fig. 10: Results of multiscale uniaxial strain test

in higher stiffness when more inter-particle contact occur for instance) could be very useful for certain applications.

See figure 10 and codes 3 and 7.

4.4. Contact analysis: cantilever shock analysis

In this example, the simulation of a cantilever shock is presented. The shock is caused by the fall of an impactor – another beam in our example – on the end of the cantilever. Both cantilever and the falling beam are modeled by FEM, only a detection algorithm is borrowed from DEM. This contact detection between particles of FEM elements shapes (tetrahedra or bricks) is a typical example of the code, which is not public yet and needs more testing to be committed to public version. See figure 11 and codes 4 and 8.

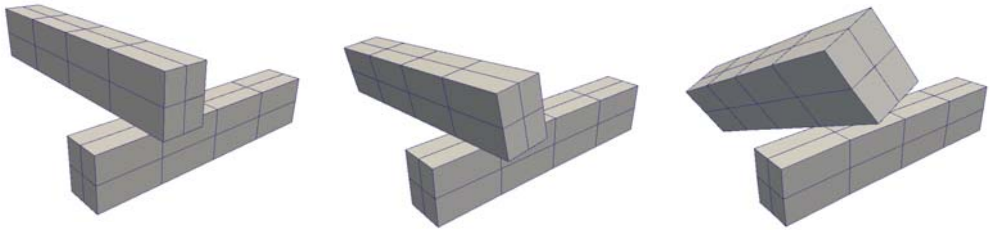

Fig. 11: Results of cantilever shock analysis – different stages of impact

5. Conclusions

The basic principles of the most popular FEM/DEM coupling strategies (surface, volume, multiscale and contact coupling) were presented, together with specific examples and corresponding Python scripts. All methods can be arbitrarily combined with each other or with different methods/programs (which uses Python user interface).

As an example, consider a dynamic soil compaction. The compacted soil would be definitely modeled by DEM, the compactor by FEM (here we have surface coupling) and the rest of the soil domain by FEM. The soil DEM / soil FEM interface would probably be of a volume coupling kind. Of course, the FEM soil could be modeled using the multiscale approach, and we could go in coupling further and further.

This example was just to show the variety of possible coupling combinations and that there are a lot of real world problems, where such coupled methods could be useful. Together with the simplicity of creating, modifying and running such simulations and extensibility of the used programs (due to the open source character of the code) it makes this approach attractive for a variety of engineering problems.

Future work on this topic will address (among others) second order DEM homogenization, adjustment of DEM periodic boundary conditions for arbitrary localization analysis, implementation and testing of Arlequin volume coupling method, implementation of contact detection algorithms of FEM element shaped particles and implementation of testing **`fakemupif`** interface into **`MuPIF`** framework.

Acknowledgments

Financial support of the Czech Technical University in Prague under project SGS12/027/OHK1/1T/11 is gratefully acknowledged.

References

Azvedo, N. M. & Lemos, L. V. (2006) Hybrid discrete element/finite element method for fracture analysis. *Computer Methods in Applied Mechanics and Engineering*, 195, pp. 4579–4593.

Fakhimi, A. (2009) A hybrid discretefinite element model for numerical simulation of geomaterials. *Computers and Geotechnics*, 36, pp. 386–395.

Frenning, D. (2008) An efficient finite/discrete element procedure for simulating compression of 3D particle assemblies. *Computer Methods in Applied Mechanics and Engineering*, 197, pp. 4266–4272.

Geers, M. G. D., Kouznetsova, Brekelmans, W. A. M. (2010) Multi-scale computational homogenization: Trends and challenges. *Journal of Computational and Applied Mathematics*, 234, pp. 2175–2182.

Kuhl, E., DAddetta, G. A., Leukart, M. and Ramm, E. (2001) Microplane modelling and particle modelling of cohesive-frictional materials. In: *Continuous and Discontinuous Modelling of Cohesive-Frictional Materials* (P. A. Veemer et al. eds). Springer, Berlin, pp. 31–46

Nakashima, H. & Oida, A. (2004) Algorithm and implementation of soiltire contact analysis code based on dynamic FEDE method. *Journal of Terramechanics*, 41, pp. 127–137.

Oñate, E. & Rojek, J. (2004) Combination of discrete element and finite element methods for dynamic analysis of geomechanics problems. *Computer Methods in Applied Mechanics and Engineering*, 193, pp. 3087–3128.

Patzák, B. & Bittnar, Z. (2001) Design of object oriented finite element code. *Advances in Engineering Software*, 32, pp. 759–767.

Patzák, B. (2011) MuPIF: A Distributed Multi-Physics Integration Tool. In: *Proceedings of the Second International Conference on Parallel, Distributed, Grid and Cloud Computing for Engineering* (P. Ivnyi & B. H. V. Topping eds.). Stirlingshire, United Kingdom, paper 15.

Rousseau, J., Frangin, E., Marin, P. & Daudeville, L. (2009) Multidomain finite and discrete elements method for impact analysis of a concrete structure. *Engineering Structures*, 31, pp. 2735–2743.

Stránský, J. & Jirásek, M. (2010) Calibration of particle-based models using cells with periodic boundary conditions. In: *Proc. II International Conference on Particle-based Methods - Fundamentals and Applications* (E. Oñate and D.R.J. Owen eds.), CIMNE, Barcelona, pp. 274–285.

Šmilauer, V., Catalano, E., Chareyre, B., Dorofeenko, S., Duriez, J., Gladky, A., Kozicki, J., Modenese, C., Scholtès, L., Sibille, L., Stránský, J. & Thoeni, K. (2010) *Yade Documentation* (V. Šmilauer ed.), The Yade Project, 1st ed. http://yade-dem.org/doc/.

Villard, P., Chevalier, B., Le Hello, B. & Combe, G. (2009) Coupling between finite and discrete element methods for the modelling of earth structures reinforced by geosynthetic. *Computers and Geotechnics*, 36, pp. 709–717.

Wellmann, C. & Wriggers, P. (2012) A two-scale model of granular materials. *Computer Methods in Applied Mechanics and Engineering*, 205–208, pp. 46–58.

Xu, M., Gracie, R. & Belytschko, T. (2002) Multiscale Modeling with Extended Bridging Domain Method. In: *Bridging the Scales in Science and Engineering* (J. Fish ed.). Oxford University Press.

Appendix A. Example scripts and input files

Python scripts controlling examples in section 4 are presented in this section.

Currently, OOFEM simulations use input text files, while YADE constructs the simulation directly in a Python script. Therefore the OOFEM input files (or a significant parts of them) are followed by the actual Python scripts.

Since the **`fakemupif`** module will be changed and adjusted to **`MuPIF`** requirements, the actual code **`fakemupif`** is not presented. However, the simplicity of **`coupler.step()`** line (from the user point of view representing the entire coupling process) should be preserved.

```
test_surface.oofem.out
surface coupling test - tire-soil contact
LinearStatic nsteps 1000 nmodules 1
vtk 1 tstep_step 20 domain_all vars 2 1 4 primvars 1 1
domain 3d
OutputManager tstep_all dofman_all element_all
ndofman 64 nelem 192 ncrosssect 1 nmat 1 nbc 2 nic 0 nltf 2
node 1 coords 3 -3.000000e-01 0.000000e+00 -1.000000e-01 bc 3 0 0 0
...
node 34 coords 3 0.000000e+00 0.000000e+00 -1.000000e-01 bc 3 1 2 1
...
node 64 coords 3 -1.307587e-01 1.822355e-01 -4.467372e-02 bc 3 0 0 0
ltrspace 1 nodes 4 32 40 42 45 crosssect 1 mat 1
...
ltrspace 192 nodes 4 38 32 55 46 crosssect 1 mat 1
SimpleCS 1 thick 1.0 width 1.0
IsoLE 1 d 0. E 100e9 n 0.4 talpha 0.0
BoundaryCondition 1 loadTimeFunction 1 prescribedvalue 0.0
BoundaryCondition 2 loadTimeFunction 2 prescribedvalue 1.0
ConstantFunction 1 f(t) 1.0
PiecewiseLinFunction 2 npoints 3 t 3 0 500 1000 f(t) 3 0 0.01 0
```

Code 1: test_surface.oofem.in

```
test_volume.oofem.out
volume coupling test - hanging nodes - three point bending
NonLinearStatic nsteps 50 nmodules 1
vtk 1 tstep_step 1 domain_all vars 2 1 4 primvars 1 1
domain 3d
OutputManager tstep_all dofman_all element_all
ndofman 2478 nelem 1764 ncrosssect 1 nmat 1 nbc 2 nic 0 nltf 1
node 1 coords 3 0.000000e+00 0.000000e+00 0.000000e+00 bc 3 0 1 0
...
node 2478 coords 3 6.000000e+00 3.000000e-01 4.000000e-01 bc 3 0 1 1
lspace 1 nodes 8 2 9 58 51 1 8 57 50 crosssect 1 mat 1
...
lspace 1800 nodes 8 2422 ... 2470 crosssect 1 mat 1
SimpleCS 1 thick 1.0 width 1.0
IsoLE 1 d 0. E 40e9 n 0.2 talpha 0.0
BoundaryCondition 1 loadTimeFunction 1 prescribedvalue 0.0
BoundaryCondition 2 loadTimeFunction 1 prescribedvalue 1e-2
PiecewiseLinFunction 1 npoints 2 t 2 0 50 f(t) 2 0. 1.
```

Code 2: test_volume.oofem.in

```
test_multi.oofem.out
multiscale coupling test
NonLinearStatic nsteps 50 nmodules 1
vtk 1 tstep_step 1 domain_all vars 2 1 4 primvars 1 1
domain 3d
OutputManager tstep_all dofman_all element_all
ndofman 12 nelem 2 ncrosssect 1 nmat 2 nbc 2 nic 0 nltf 2
node 1  coords 3 0.0 0.0 0.1 bc 3 1 1 1
...
lspace 1 nodes 8 1 2 3 4  5 6 7  8  crosssect 1 mat 1
lspace 2 nodes 8 4 3 9 10 8 7 11 12 crosssect 1 mat 2
SimpleCS 1 thick 1.0 width 1.0
MultiScaleSMMat 1 d 0. E 40e6 n 0.2 talpha 0.0
MultiScaleSMMat 2 d 0. E 80e6 n 0.2 talpha 0.0
BoundaryCondition 1 loadTimeFunction 2 prescribedvalue 0.0
BoundaryCondition 2 loadTimeFunction 2 prescribedvalue -1e-2
PiecewiseLinFunction 1 npoints 2 t 2 0 50 f(t) 2 0. 1.
ConstantFunction 2 f(t) 1.
```

Code 3: test_multi.oofem.in

```
test_contact.oofem.out
contact coupling test - cantilever inpact
DEIDynamic nsteps 12000 nmodules 1 dumpcoef 0 deltaT 1e-4
vtk 1 tstep_step 30 domain_all vars 2 1 4 primvars 1 1
domain 3d
OutputManager tstep_all dofman_all element_all
ndofman 90 nelem 32 ncrosssect 1 nmat 1 nbc 2 nic 0 nltf 1
node 1 coords 3 0.000000e+00 0.000000e+00 0.000000e+00  bc 3 1 1 1
...
node 90 coords 3 1.723500e+00 1.744000e+00 -1.000000e-01
lspace 1 nodes 8 2 5 14 11 1 4 13 10 crosssect 1 mat 1 bodyloads 1 2
...
lspace 32 nodes 8 72 75 90 87 71 74 89 86 crosssect 1 mat 1 bodyloads 1 2
SimpleCS 1 thick 1.0 width 1
IsoLE 1 d 1000. E 1e8 n 0.2 talpha 0.0
BoundaryCondition 1 loadTimeFunction 1 prescribedvalue 0.0
deadweight 2 loadTimeFunction 1 components 3 0 0 10
ConstantFunction 1 f(t) 1.
```

Code 4: test_contact.oofem.in

```
# example script for surface coupling - soil-tire contact
# first import required modules
import fakemupif
from fakemupif import oofem,yade

nSteps = 1000
output = 50
# then instanciate FEM ...
oofemFile = 'test_surface.oofem.in'
fem = fakemupif.instanciateOofemProblem(oofemFile)
dem = yade.Omega()

# ... as well as DEM problem
dem.materials.append(fakemupif.defaultMat)
c1,c2 = (0,-.015,-.008), (.03,-.004,.017)
c1,c2 = (-.15,-.4,-.15), (.15,-.3,.15)
rect = yade.pack.inAlignedBox(c1,c2)
rad = .005
sphs = yade.pack.randomDensePack(rect,rad,spheresInCell=1000)
dem.bodies.append([sph for sph in sphs])

# DEM BCs
bcw = 3*rad
for b in dem.bodies:
   p = b.state.pos
   if not (p[0]<c1[0]+bcw or p[0]>c2[0]-bcw): continue
   if not (p[1]<c1[1]+bcw or p[2]<c1[2]+bcw or p[2]>c2[2]-bcw): continue
   b.state.blockedDOFs = 'xyzXYZ'

#
coupler = fakemupif.SurfaceFemDemCoupler(fem,dem,oofemFile)
dem.bodies.append([facet for facet in coupler.facets])
#

dem.engines=[
   yade.ForceResetter(),
   yade.InsertionSortCollider([
      yade.Bo1_Sphere_Aabb(),
      yade.Bo1_Facet_Aabb()]),
   yade.InteractionLoop(
      [yade.Ig2_Sphere_Sphere_Dem3DofGeom(),
         yade.Ig2_Facet_Sphere_Dem3DofGeom()],
      [yade.Ip2_CpmMat_CpmMat_CpmPhys()],
      [yade.Law2_Dem3DofGeom_CpmPhys_Cpm()]
   ),
   yade.NewtonIntegrator(),
   yade.PyRunner(command='vtk.exportSpheres(); vtk.exportFacets()',\
      iterPeriod=max(1,nSteps/output)),
]
dem.dt = yade.utils.PWaveTimeStep()/2.

# Yade vtk export
import yade.export
vtk = yade.export.VTKExporter('test_surface.yade',startSnap=1)

# run
for i in xrange(nSteps):
   coupler.step()

# exit
print 'Finished!'
fem.terminateAnalysis()
dem.exitNoBacktrace()
```

Code 5: controlling script for soil-tire contact simulation

```
# example script for volume coupling - three point ending
# first import required modules
import fakemupif
from fakemupif import oofem,yade

# then instanciate FEM ...
oofemFile = 'test_volume.oofem.in'
fem = fakemupif.instanciateOofemProblem(oofemFile)

# ... as well as DEM problem
dem = yade.Omega()
dem.materials.append(fakemupif.defaultMat)
rect = yade.pack.inAlignedBox((2.8,0.0,0.12),(3.2,0.3,0.4))
sphs = yade.pack.randomDensePack(rect,0.02,spheresInCell=1000)
dem.bodies.append(sphs)

#
coupler = fakemupif.VolumeFemDemCoupler(fem,dem,oofemFile)
#

dem.dt = .5*yade.utils.SpherePWaveTimeStep(.02,1000,25e9)
dem.engines=[
   yade.ForceResetter(),
   yade.InsertionSortCollider([
      yade.Bo1_Sphere_Aabb(aabbEnlargeFactor=1.5,label='is2aabb')
      ]),
   yade.InteractionLoop(
      [yade.Ig2_Sphere_Sphere_Dem3DofGeom(distFactor=1.5,label='ss2d3dg')],
      [yade.Ip2_CpmMat_CpmMat_CpmPhys()],
      [yade.Law2_Dem3DofGeom_CpmPhys_Cpm()]),
   yade.NewtonIntegrator(damping=.3),
]
dem.step()
is2aabb.aabbEnlargeFactor = ss2d3dg.distFactor = -1.

# Yade vtk export
import yade.export
vtk = yade.export.VTKExporter('test_volume.yade',startSnap=1)

# run 50 steps of simulation and save results
for i in xrange(50):
   coupler.step()
   vtk.exportSpheres(what=[('dspl','b.state.displ()')])

# exit
print 'Finished!'
fem.terminateAnalysis()
dem.exitNoBacktrace()
```

Code 6: controlling script for three point bending volume coupling example

```
# example script for multiscale coupling - uniaxial strain
# first import required modules
import fakemupif
from fakemupif import oofem,yade

# then instanciate FEM ...
oofemFile = 'test_multi.oofem.in'
fem = fakemupif.instanciateOofemProblem(oofemFile)

# ... as well as DEM problem
dem = yade.Omega()
demMat1 = dem.materials.append(fakemupif.defaultMat)
demMat2 = dem.materials.append(fakemupif.defaultMat2)

#
coupler = fakemupif.MultiScaleFemDemCoupler(fem,dem,oofemFile)
#

# Yade vtk export
import yade.export
vtks = {}
for gp in coupler.gps:
   newScene = dem.addScene()
   coupler.scenes.append(newScene)
   dem.switchToScene(newScene)
   dem.dt = .5*yade.utils.SpherePWaveTimeStep(.001,1000,25e9)
   dem.bodies.append(yade.pack.randomPeriPack(.001,.02))
   dem.engines=[
      yade.ForceResetter(),
      yade.InsertionSortCollider([
         yade.Bo1_Sphere_Aabb(aabbEnlargeFactor=1.5,label='is2aabb')
         ]),
      yade.InteractionLoop(
         [yade.Ig2_Sphere_Sphere_Dem3DofGeom(distFactor=1.5,label='ss2d3dg')],
         [yade.Ip2_CpmMat_CpmMat_CpmPhys()],
         [yade.Law2_Dem3DofGeom_CpmPhys_Cpm()]),
      yade.NewtonIntegrator(damping=.3),
   ]
   dem.step()
   is2aabb.aabbEnlargeFactor = ss2d3dg.distFactor = -1.
   vtks[newScene] = yade.export.VTKExporter('test_multi.yade%d'%newScene)

# run 50 steps of simulation and save results
for i in xrange(50):
   coupler.step()
   for scene in coupler.scenes:
      vtks[scene].exportSpheres(what=[('dspl','b.state.displ()')])

# exit
print 'Finished!'
fem.terminateAnalysis()
dem.exitNoBacktrace()
```

Code 7: controlling script for multiscale uniaxial strain simulation

```
# example script for contact coupling - cantilever impact
# first import required modules
import fakemupif
from fakemupif import oofem,yade

nSteps = 12000
# then instanciate FEM ...
oofemFile = 'test_contact.oofem.in'
fem = fakemupif.instanciateOofemProblem(oofemFile)

# ... as well as DEM problem
dem = yade.Omega()
dem.materials.append(fakemupif.defaultMat)

#
coupler = fakemupif.ContactFemDemCoupler(fem,dem,oofemFile)
#

dem.bodies.append(coupler.demImages)
dem.engines=[
   yade.ForceResetter(),
   yade.InsertionSortCollider([
      yade.Bo1_Facet_Aabb()
      ]),
   yade.InteractionLoop(
      [yade.Ig2_Facet_Facet_Dem3DofGeom()],
      [yade.Ip2_CpmMat_CpmMat_CpmPhys()],
      [yade.Law2_Dem3DofGeom_CpmPhys_Cpm()]),
]

# run
for i in xrange(nSteps):
   coupler.step()

# exit
print 'Finished!'
fem.terminateAnalysis()
dem.exitNoBacktrace()
```

Code 8: controlling script for cantilever shock analysis

18th International Conference
ENGINEERING MECHANICS 2012
Svratka, Czech Republic, May 14 – 17, 2012

pp. 1253–1258
Paper #108

MODELLING OF DUCTILE FRACTURE FOR SUB-SIZED THREE-POINT-BEND GEOMETRY

L. Stratil[*], H. Hadraba[**], V. Kozák[***], I. Dlouhý[****]

Abstract: *The contribution deals with the simulation of R-curve using complete Gurson model of ductile fracture. The R-curve was experimentally determined for a Eurofer97 steel on sub-sized three-point-bend geometry in previous study. To apply complete Gurson model the parameters describing the voids´ behaviour and characteristic length parameter need to be determined. The nucleation parameters were identified by single specimen method of smooth tensile test specimen and from metallographic examination of fracture micro-mechanism. The characteristic length parameter was derived by fitting load versus deflection curves of sub-sized specimens. The simulations of the tests were carried out by FEM software ABAQUS 6.11 in Standard and Explicit modules. The identification was supported by parametric studies. Comparing experimental and simulated R-curve the ductile tearing was not successfully achieved. Insufficient calibrated parameters as a result non-uniqueness problem of single specimen method were found.*

Keywords: ***complete Gurson model, single specimen approach, Eurofer97, R-curve***

1. Introduction

Generally, the macroscopic parameters for ductile fracture for example ductility or crack resistance curve cannot be directly transferred from one geometry to another. Because of this one if the important tasks is to separate parameters describing the ductile fracture from the parameters which describe geometry and size effect. Ductile fracture is for the most engineering materials driven by nucleation of microvoids, their growth and subsequently in certain cases by their coalescence. From that point of view is convenient to obtain the parameters describing the micro-ductile fracture. The failure will be then connected with the material behaviour and that could be used for separation of geometry and size effect. It is not that case when ductile fracture is connected with macroscopic pseudo fracture parameters, because those parameters are evidently influenced by above mentioned effects.

In the paper (Ødegård et al., 2000) the authors propose a method for determining void nucleation parameter. They pursue an idea that for the same material, complete Gurson model should work both at low stress triaxiality case (tensile specimens) and high triaxiality case (cracked specimens). The void nucleation parameter can therefore be determined from tensile specimens where the mesh size has no significant effect. There are two different approaches for application of introduced method namely single specimen approach and multispecimen approach. Within these approaches smooth and both smooth and notched tensile specimens are used, respectively. Once the void nucleation parameters are determined, the remaining characteristic length parameter which describes the strain gradient effect can be fitted from fracture mechanics tests. If these parameters are known and verified, they can be used as transferable parameters between different components.

[*] Ing. Luděk Stratil: Institute of Physics of Materials, ASCR, Žižkova 22; 616 62, Brno; CZ, e-mail: stratil@ipm.cz

[**] Ing. Hynek Hadraba, Ph.D.: Institute of Physics of Materials, ASCR, Žižkova 22; 616 62, Brno; CZ, e-mail: hadraba@ipm.cz

[***] Ing. Vladislav Kozák, CSc.: Institute of Physics of Materials, ASCR, Žižkova 22; 616 62, Brno; CZ, e-mail: kozak@ipm.cz

[****] Prof. Ing. Ivo Dlouhý, CSc.: Institute of Physics of Materials, ASCR, Žižkova 22; 616 62, Brno; CZ, e-mail: idlouhy@ipm.cz and Institute of Material Science and Engineering, Faculty of Mechanical Engineering, Brno University of Technology, Technická 2896/2; 616 69, Brno; CZ, email: dlouhy@fme.vutbr.cz

The contribution deals with determination of ductile fracture parameters for advanced Eurofer97 steel developed for fusion/fission power generation using complete Gurson model. Apart from getting be familiar with Gurson model, the possibility to derive the Gurson parameters from smooth tensile specimens was verified. The identified parameters were used for simulation of R-curves which were measured by single and multispecimen method using sub-sized three-point-bend specimen type of KLST by Dlouhý et al. (2011) in previous study.

In the following, the complete Gurson model is described first. Next the applied procedure of parameters identification from tensile test is introduced. Then the results of R-curve simulation are compared and discussed with experimentally determined ones. At the end the conclusion of the study is presented.

2. Complete Gurson model

The Gurson model describes the plasticity of material via behaviour of void in ideal-plastic Mises material (Ødegård et al., 2000). The material described by Gurson model behaves like continuum within it is the void effect averaged. That connects the microscopic and macroscopic behaviour of the material. The yield function of the Gurson model has the following form:

$$\phi(q,\overline{\sigma},f,\sigma_m)=\frac{q^2}{\overline{\sigma}^2}+2q_1f^*\cosh\left(\frac{3q_2\sigma_m}{2\overline{\varsigma}}\right)-1-\left(q_1f^*\right)^2=0 \tag{1}$$

where f is the void volume fraction, σ_m is the mean normal stress, q is conventional von Mises equivalent stress, $\overline{\sigma}$ is the flow stress of the matrix material, q_1, q_2 are constants introduced by Tvergaard (1981, 1982). The function $f^*(f)$ was applied by Needleman & Tvergaard (1984) to model rapid loss of the material stress-carrying capacity after the occurrence of void coalescence as observed during the test. This function is expressed as follows:

$$f^*=f \text{ for } f<f_c \tag{2}$$

$$f^*=f_c+\frac{f_u^*-f_c}{f_f-f_c} \text{ for } f\geq f_c, \tag{3}$$

where $f_u^*=1/q_1$. The complete loss of load-carrying capacity occurs at $f=f_F$ i.e. ultimate void volume fraction.

The function becomes more predominant once the void volume fraction f exceeds a critical value f_c.

The increase in void volume fraction consists of two terms: the nucleation of new voids and growth of existing voids. It can be written as:

$$\Delta f=\Delta f_{nucl}+\Delta f_{gr}. \tag{4}$$

The symbol Δ represents the increment in the quantity.

The complete Gurson model can simulate microvoid nucleation, growth and by introducing empirical void coalescence criterion the void coalescence. For existing voids the model can describe the softening effect caused by the voids on material behaviour and at the same time can predict the void growth rate during plastic deformation. Void nucleation can be stress controlled or strain controlled. In the literature, strain controlled nucleation has been preferred, because it is easier to handle in the finite element implementation. Different materials may have different nucleation laws. For many engineering materials which contain large inclusion voids can be nucleated during the early stage of plastic deformation. For such a materials, a cluster mode may be used to simulate the void nucleation (parameter f_0). For materials where voids are nucleated from carbides or intermetallic phases a continuous or statistical void nucleation model (parameter f_n) may be applied. For material, where neither one of models is suitable, complex model consisting of their combination should be used. Because the laws describing voids growth and nucleation cannot itself treat void coalescence, the complete Gurson models contains one empirical treatment of it called critical volume fraction (f_c). The

coalescence occurs via faster growth rate when a critical void volume fraction has been reached. The void coalescence will be finished (material load carrying capacity becomes zero) when the void volume fraction reaches another value – the volume fraction at final failure (f_F).

When the Gurson model is applied to the ductile fracture problem, the void nucleation parameter and crack tip mesh size need to be determined. The void nucleation parameters can therefore be determined from tensile specimen, where the mesh size has no significant effect. The crack tip mesh size, which is described by the characteristic length l_c, can be then determined from fracture mechanics tests, where the effect of mesh size is significant (Ødegård et al., 2000).

The ductile behaviour of the material is described by its stress-strain curve and ductile fracture behaviour is in the case of complete Gurson model characterized by eight parameters: q_1, q_2, f_0, ε_n, s_n, f_n, f_c, f_F. Parameters q_1 and q_2 describe growth of voids, ε_n and s_n together with f_n describe the statistical nucleation model.

Abaqus explicit module can be used for simulation of damage of material. Its benefit is also lower computational cost comparing with standard module. But certain issues should be resolved before its application i.e. the effect of applied velocity and its comparison with solution of standard module.

2.1. Derivation of Gurson parameters

To derive the Gurson parameters the single specimen approach was applied. This methodology involves the description of ductility of the material from smooth tensile test (trace load-elongation or load-diameter reduction). When ductility of the material is known, the optimal nucleation parameters (f_0, f_n), which give the best fit to the experimental results, can be obtained. The results of tensile tests were used from study (Dlouhý et al., 2011). Only smooth tensile specimen results as a load vs. elongation were available.

To choose which nucleation model, if cluster or continuous nucleation, should be applied, metallographic study of micro-void nucleation mechanism was performed. The broken parts of tensile specimens were longitudinally cut and specimens were prepared by standard metallographic processes. The voids were revealed by mechanical-chemical polishing with OPS suspension (colloidal solution with fine particles of silicon carbide). The specimens were then studied using scanning electron microscopy (JSM 6460, Jeol) and quantification of voids fraction was performed by image analysis. The images from the corresponding sites of specimens were acquired at different magnification. The examination revealed that voids nucleate just in the neck region and no voids were observed in uniformly deformed part of specimen. This fact exclude the cluster nucleation model as a possible description of void nucleation mechanism and leaving its value f_0=0. The value of void volume fraction from region near to the fracture surface 0.011 was chosen as f_c. It is important to note that the values of void volume fraction were magnification dependent. With higher magnification, the void volume fraction was higher. The void volume fraction was determined at value of magnification which was the most relevant also for observation of precipitates in studied steel thus 2500 times. The value of void volume fraction f_F and the values of parameters describing void growth q_1 and q_2 were chosen as recommended in literature (Ødegård et al., 2000; Dutta et al., 2008) thus 0.15, 1.5 and 1.0, respectively. The statistical nucleation model was applied by choosing recommended values of ε_n=0.3, s_n=0.1 (Ødegård et al., 2000) and parameter f_n was fitted to experimentally determined trace load-elongation. The axisymmetric model of tensile specimen was created consisted from 1160 elements type of CAX4 (4 nodes, reduced integration) using ABAQUS 6.11 software. The loading was displacement driven. The stress-strain curve of the steel prior to necking was given by the true strain and true stress computed from experiments. In order to obtain true response in the post-necking regime up to final failure the relevant part of true stress-true strain curve was fitted by iterations, until the response load vs. elongation from finite element simulation was comparable with experimental results. It was found that f_n=0.001 gives good fit to the experimental data Fig. 1. By obtaining parameter f_n the process of their identification has finished.

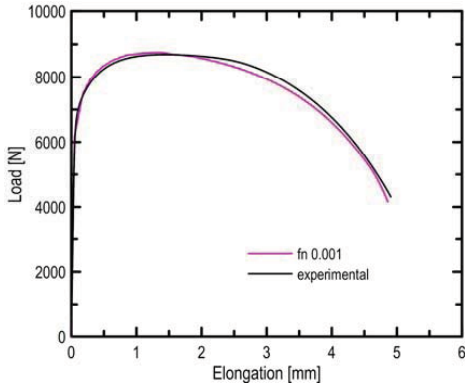

Fig. 1: Experimental and computed tensile curves.

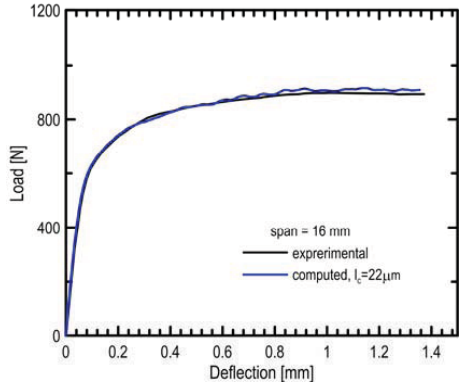

Fig. 2: Experimental and computed three-point-bend traces load-deflection.

2.2. Determination of characteristic length parameter

The 3D models of the tested KLST specimens were built according to (Dlouhý et al., 2011). Using symmetry only one quarter of specimen was modelled. The meshes with various elements´ size in process zone, where the crack propagation was prescribed, were created using the elements with square cross-section and with size ranging from 10 μm to 100 μm. In dependence on the specimen mesh the models consisted from 20.10^3 to 45.10^3 elements of C3D8R (8 nodes, reduced integration). From comparison of experimental and simulated curves the mesh with element size 22 μm fits the best to the results Fig. 2. Based on that element size characteristic length parameter l_c=22 μm was obtained.

3. Comparison of computed and experimental R-curves

The explicit module in ABAQUS naturally does not allow determination of the J-integral. Its values were determined from load-displacement curve according to the standard determination like for fracture mechanics test (ISO 12135:2002). The ductile tearing at different deflection was determined by counting the elements, where void volume fraction reached value of f_F. Comparison of experimental and computed R-curves is shown in Fig. 3.

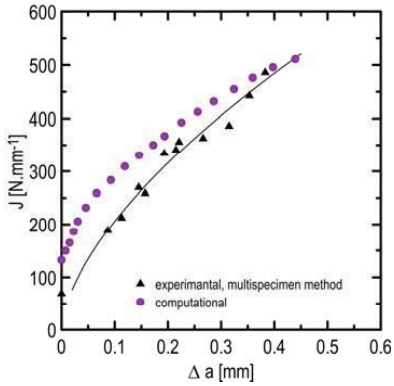

Fig. 3: Computed and experimentally determined R-curves.

4. Discussion of results

The simulated R-curve fits with experimental one within its upper parts. However, the J-initiation values and values of J-integral up to about 0.2 mm of crack extension are considerably overestimated. That is not problem of values of J-integral counted from load-displacement curve but of crack extension. The crack propagation up to 0.2 mm is slow because model behaviour is too stiff. The slope of R-curve seems to be right, but the curve should be turned or shaped. It could be changed just by parameters of Gurson model. Thus it seems to be that the parameters were not successfully identified. In fact it is disadvantage of single specimen approach of nucleation parameter identification, which is non-uniqueness problem. The same fit to the tensile test data can be obtained by fitting parameter of nucleation model and at the same time by fitting parameter of cluster model (Dutta et al., 2008). But the latter was reliably excluded on the basis of metallographic examination. However, this above mentioned non-uniqueness problem can be resolved by using multispecimen approach. Both smooth and notched tensile specimens are used. The results from those tests serve for construction of a ductility diagram (fracture strain vs. a representative stress triaxility from specimen center). Within that approach various geometries of specimens cover a wide range of stress triaxiality. If two nucleation models yield same results at smooth specimen (low triaxiality), they will certainly give different results at notched specimens (high triaxiality), vice versa.

The shape of R-curve predicted by using the nucleation parameter from tensile tests may be different to the experimentally one. There are several factors which may contribute to this discrepancy (Ødegård et al., 2000). Also appropriate choice of Gurson model parameter values, which were treated as fixed in present study, is questionable. In this contribution, fixed values of Tvergaard parameters q_1 and q_2 are applied. In general, q_1 and q_2 are also dependent on the hardening exponent n. In the study (Faleskog et al., 1998) values of $q_1$and q_2 was tabulated as a function of n. The question is if the Gurson model is suitable for Eurofer97 steel. The problem could be also Gurson model itself. It is known that this model works well for many engineering material but certainly not for all.

5. Conclusion

In this study the process of identification of complete Gurson model parameters was carried out. The parameters describing the voids´ behaviour and characteristic length parameter need to be determined. In first, the identification process of nucleation parameters was applied using single specimen approach from results of smooth tensile specimen. The identification procedure was supported by examination of fracture mechanism via micro-void nucleation. Next, the characteristic length parameter was derived by fitting load versus deflection curves of sub-sized three-point-bend geometry. Difficulty was encountered while computing R-curve of fracture specimens using identified parameters in agreement with the experimental data. Insufficient calibrated parameters as a result non-uniqueness problem of single specimen method were found. The possibility of multispecimen approach of nucleation parameters identification and also performance of Gurson model for Eurofer97 steel will be studied further.

Acknowledgement

The authors gratefully thank for the financial support of projects of the Czech Science Foundation No. 106/09/H035 and 107/10/0361.

References

Dlouhý, I., Hadraba, H. & Stratil, L. (2011) Určování J-Δa křivek pomocí miniaturních těles pro tříbodový ohyb, in: *Proc. Multiscale modelling of advanced materials* (I. Dlouhý), Inst. of Physics of Mater. ASCR, Brno, pp.145-154.

Dutta, B.K. et al. (2008) A phenomenological form of the q_2 parameter in the Gurson model. *Int J Press Vessels Piping*, 85, pp.1599-210.

Faleskog, J., Gao, X. & Shih, C.F. (1998) Cell model for nonlinear fracture mechanics-I micromechanics calibration. Int J Fract, 89, pp. 355-373.

ISO 12135:2002(E) – Metallic materials – Unified method of test for the determination of quasistatic fracture toughness.

Needleman, A. & Tvergaard, V. (1984) Analysis of the cup–cone fracture in a round tensile bar. Acta Metall, 32, pp. 157–169.

Ødegård, J., Taulow, C. & Zhang, Z.L. (2000) A complete Gurson model approach for ductile fracture. *Eng Fract Mech*, 64, pp.155-168.

Tvergaard, V. (1981) Influence of voids on shear band instabilities under plane strain conditions. Int J Fract, 17, pp. 389-407.

Tvergaard, V. (1982) On localization in ductile materials containing spherical voids. Int J Fract, 18, pp.237-252.

18th International Conference
ENGINEERING MECHANICS 2012
Svratka, Czech Republic, May 14 – 17, 2012

pp. 1259–1262
Paper #94

VERIFICATION OF RAPID METHOD FOR DETERMINING THE S-N CURVE IN LIMITED LIFE REGION

P. Strzelecki[*], J. Sempruch[**]

Abstract: *The paper presents the method for determining the S-N curve in limited life region. To verify the method, C45material was tested to estimate fatigue characteristics. The load was applied by rotating bending and the testing equipment used had been designed by us. The data analysis confirms a good functioning of the testing machine. The verification of the method proposed and the results are presented.*

Keywords: ***fatigue design, S-N curve, high-cycle fatigue, accelerated method***

1. Introduction

To estimate the life or fatigue strength of the component, we use, depending on the assumed load conditions, the corresponding computational models. By using any of the calculation models, we need to know the fatigue characteristics of this component. To acquire such characteristics, experimental, analytical and experimental-analytical methods can be used. The method of determining the fatigue characteristics for high-cycle material fatigue can be found e.g. in PN H 04325:1976. Analytical characteristics determination methods have been presented, among others, by Neimitz A. et al. (2008), Lee Yung-Li et al. (2005) and Strzelecki & Sempruch (2011).

The above accelerated and approximated fatigue curve plotting methods need defining the fatigue properties determining accuracy. To do so, the use of a specially planned experiment is most applicable. An attempt at determining the error made applying the methods presented has been given in Strzelecki & Sempruch (2011) and Sempruch & Strzelecki (2011).

2. Experimental procedures

In order to determine the reference curve, own-design research testing equipment was applied. The research involved the use of C45 + C material (Rm = 826 MPa Rp0.2 = 647 MPa) supplied in a form of the rod 10 mm in diameter the sample shown in Figure 1a was made of.

Figure 1b presents C45 + C material fatigue plot. In its upper right corner regression equation and the coefficient of determination (0.952) are found.

3. Method of verification

Based on the experimental results, it was possible to perform statistical calculations verifying the null hypothesis which assumes that the slope and the absolute term of the regression line determined based on the experimental data are equal to the coefficients of the line obtained by applying the analytical method.

[*] M.Sc. Ing. Przemysław Strzelecki, a Ph. D. student, Institute of Mechanical Engineering, University of Technology and Life Sciences, 85-789 Bydgoszcz , Poland; PL, e-mail:p.strzelecki@utp.edu.pl

[**] Prof. Ing. Janusz Sempruch, Institute of Mechanical Engineering, University of Technology and Life Sciences, , 85-789 Bydgoszcz , Poland; PL, e-mail: semjan@utp.edu.pl

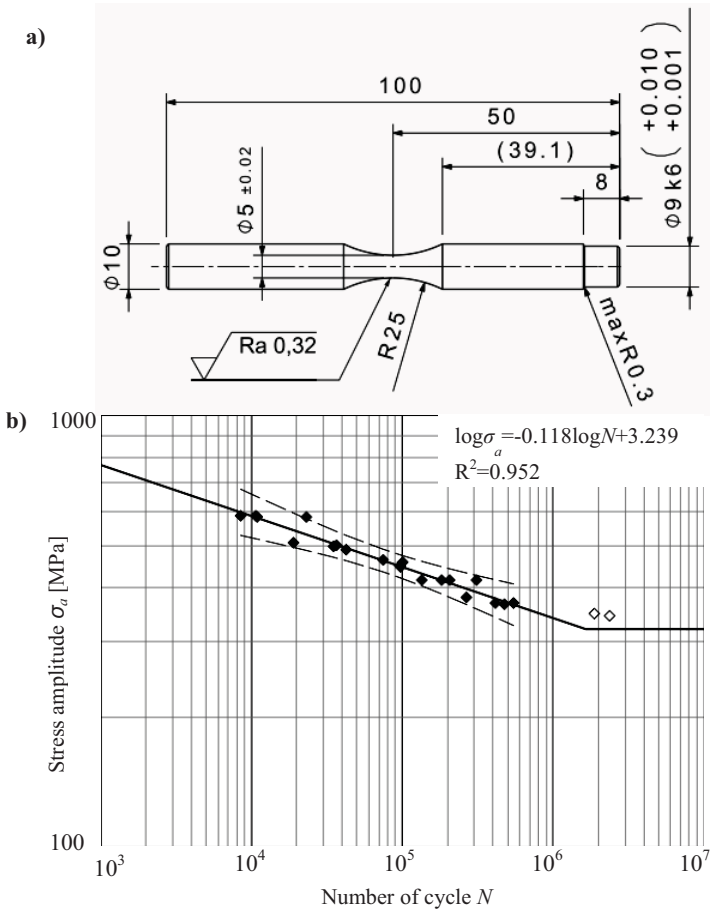

Fig. 1. a) Figure of the sample b) S-N curve for C45+C

For the statistical value calculations, the following equations were used:

$$S_a = \sqrt{\frac{\sum_{i=1}^{n}(Y_i - \hat{Y}_i)^2}{(n-1)\left[\sum_{i=1}^{n} X_i^2 - \frac{1}{n}\left(\sum_{i=1}^{n} X_i\right)^2\right]}}, \tag{1}$$

$$t_a = \frac{a - a_0}{S_a}, \tag{2}$$

$$S_b = \sqrt{\frac{\sum_{i=1}^{n}(Y_i - \hat{Y}_i)^2 \cdot \sum_{i=1}^{n} X_i^2}{(n-2)\left[n\sum_{i=1}^{n} X_i^2 - \left(\sum_{i=1}^{n} X_i\right)^2\right]}}, \tag{3}$$

$$t_b = \frac{b - b_0}{S_b}, \tag{4}$$

where: $X=\log N$, $Y=\log\sigma$, n – number of data, $\hat{Y}=a_0X+b_0$ – equation derived using the analytical method, $Y=aX+b$ – equation derived using the experimental data.

4. Results of verification

It is assumed that there is no reason to reject the null hypothesis when the following is met:

$$|t_a| < t(p,n-2) \text{ or } |t_b| < t(p,n-2) \tag{5}$$

Examples of calculations results are presented in Table 1.

Tab. 1: Results of statistical calculations

Statistics type	*Method given in the paper Strzelecki & Sempruch (2011)*	*FITNET method*	*Method by Lee Yung-Li et al. (2005)*
t_a	-1.063	2.163	-3.099
t_b	1.435	-2.506	3.242
p_{value} (97.5%,t_a)	22.1%	4.36%	0.66%
p_{value} (97.5%,t_b)	14.1%	2.27%	0.48%
t(97.5%,19)		2.093	

For a qualitative comparison, the curve estimated applying each of the methods was plotted (see Fig. 2.). In the upper right corner the equations for every curve are given. With a black line the figure demonstrates the experimental curve, with the blue line – the method proposed by Strzelecki & Sempruch (2011), with the green line – the FITNET method and with the violet line – the method by Lee Yung-Li et al. (2005).

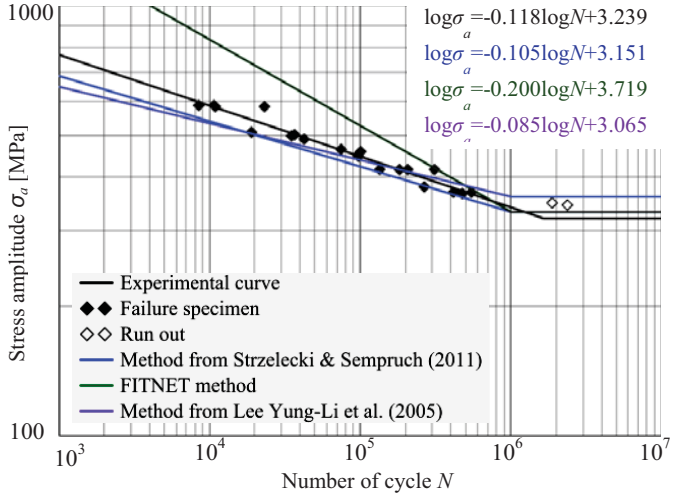

Fig. 2. Diagrams of fatigue curves according to experimental (black line) and analytical methods by Strzelecki & Sempruch (2011) (blue line), FITNET (green line) and Lee Yung-Li et al. (2005) (violet line)

5. Conclusions

Based on the statistical calculations made, one can note that the method provided by Strzelecki & Sempruch (2011) is the only one which facilitates assuming the hypothesis of the equality of slope and

the absolute term of the equation determined and the equation of the regression curve defined drawing on the experimental data.

The conclusion is reflected in Figure 2. The diagram shows that the curve plotted with the method suggested by Strzelecki & Sempruch (2011) matches the experimental line better than the other methods.

Acknowledgement

The work has been co-financed by the European Union Social Fund, the state budget of Poland and the budget of the Kujawsko-Pomorskie Province as part of the project '*Krok w przyszłość – stypendia dla doktorantów'* the 4th edition.

References

Lee Yung-Li, Pan Jwo, Hathaway R. B., Barkey M. E. (2005) *Fatigue testing and analysis*, University of Alabama, Elsevier.

Neimitz A., Dzioba I., Graba M.& Okrajni J. (2008) *Evaluation of strength, life and safety of structural components contain defects*. Politechnika Świętokrzyska, Kielce.

PN-H-04325:1976, *Test of metal fatigue - Basic terms and general guidelines for preparing of samples and carry out tests.*

Sempruch J., Strzelecki P. (2011) Error of fatigue life determination according to the FITNET method. *17th International Conference Engineering Mechanics*, pp. 531-534.

Strzelecki P., Sempruch J. (2011) Modification of selected methods of rapid determination of fatigue characteristics in the range of limited fatigue life*, Journal of Polish Cimac Selected problems of designing and operating technical systems* Vol. 6 No 3; pp. 289

18th International Conference
ENGINEERING MECHANICS 2012
Svratka, Czech Republic, May 14 – 17, 2012

pp. 1263–1272
Paper #200

ASSESSMENT OF MODEL UNCERTAINTIES IN THE ANALYSIS OF REINFORCED CONCRETE STRUCTURES

M. Sýkora[*], V. Červenka[**], M. Holický[***]

Abstract: *Numerical methods of structural analysis enable consideration of material and geometrical non-linearity of reinforced concrete structures. While the effect of variability of materials and geometry can be relatively well described, the model uncertainty is not yet well understood. The present contribution is, therefore, focused on resistance model uncertainties in the analysis of reinforced concrete structures. Available definitions of the model uncertainties are critically reviewed. Statistical characteristics of the model uncertainties are obtained from previous studies. Simple engineering formulas (beam models, section-oriented approaches) as well as complex numerical solutions are considered. To facilitate practical applications the partial factors for the model uncertainties related to various types of the analysis are derived using the design value method.*

Keywords: ***Model uncertainties, reinforced concrete structures, partial factors.***

1. Introduction

Recent development in structural design of concrete structures reflects advances in the fields of material engineering, reliability theory, structural mechanics and numerical methods of structural analysis. These advances provide exact tools for the reliability assessment of structural resistance in engineering practice.

Safety formats for the analysis of reinforced concrete structures were investigated in previous studies by Bertagnoli et al. (2004), Červenka (2008), Schlune et al. (2011) and Sýkora & Holický (2011). Some of these studies were used as background materials for the new Model Code of fib (2010). Different approaches for resistance modelling and safety were compared and suggestions for design applications proposed. These studies covered resistance models based on both the finite element technique as well as section-oriented engineering models. Safety formats were based on probabilistic analyses and estimates of resistance variability.

It has been indicated that structural resistances can be predicted by appropriate modelling of material properties, geometry variables and uncertainties associated with an applied model. The effect of variability of materials and geometry is relatively well understood and has been extensively addressed by the aforementioned studies. However, better description of model uncertainties seems to be desired as concluded by Vrouwenvelder (2010).

The submitted study is, therefore, aimed at the model uncertainties with a particular focus on the analysis of reinforced concrete structures. Statistical characteristics of the model uncertainties are summarized from data available in scientific literature considering simple engineering formulas (beam models, section-oriented approaches) as well as complex numerical solutions based on FE methods. To facilitate practical applications based on the partial factor method, the partial factors for model uncertainties related to various types of the analysis are derived using the design value method.

The study is an initial step of the research project of the authors' team in which the model uncertainties related to resistance models of reinforced concrete structures are to be systematically

[*] Ing. Miroslav Sýkora, Ph.D.: Klokner Institute, Czech Technical University in Prague, Solinova 7; 166 08 Prague; CZ, e-mail: miroslav.sykora@klok.cvut.cz

[**] Ing. Vladimír Červenka, Ph.D., Feng: Cervenka Consulting s.r.o., Na Hrebenkach 55, 15000 Prague; CZ; e-mail: vladimir.cervenka@cervenka.cz

[***] Prof. Ing. Milan Holický, PhD., DrSc.: Klokner Institute, Czech Technical University in Prague, Solinova 7; 166 08 Prague; CZ; e-mail: milan.holicky@klok.cvut.cz

investigated. Outcomes of the project are also foreseen to provide background materials for the Joint Committee on Structural Safety (JCSS) that is currently updating the models for uncertainties provided in the Probabilistic Model Code, JCSS (2006).

2. Definitions of the model uncertainties

According to JCSS (2006) the model uncertainty is generally a random variable accounting for effects neglected in the models and simplifications in the mathematical relations. The model uncertainties can be related to:

- Resistance models (based on structural mechanics, constitutive laws),
- Models for action effects (assessment of load effects and their combinations).

This study is fully focused on the uncertainties related to resistance models of reinforced concrete structures. It is assumed that the uncertainty of actions can be treated separately.

The uncertainty of a resistance model should cover the following aspects (if relevant):

- Simplifications of known physical principles in an applied model,
- Approximations inherent to numerical methods,
- Influence of different interpretations of complex software tools and related errors by users.

Commonly variability of material properties and possibly related statistical uncertainty are included in relevant models for material properties.

In general the model uncertainty can be obtained from comparisons of physical tests and model results. A great care should be taken to define correctly test conditions and evaluate test results. It should be always assured that a specimen fails in an investigated failure mode. For instance when the model uncertainty in shear is investigated, beams failed in bending should be excluded from the assessment. Accuracy of tests (related to the test method and execution of an individual test) should be considered in the assessment of model uncertainties.

JCSS (2006) proposed the following definitions of the model uncertainty θ based on different relationships between the response of a structure (actual resistance) R and a model resistance $\mathrm{R}_{\mathrm{model}}$ (estimate of the resistance based on a numerical model or analytical expression) as follows:

$$R = \theta\, \mathrm{R}_{\mathrm{model}}(\mathbf{X}) \tag{1}$$

or

$$R = \theta + \mathrm{R}_{\mathrm{model}}(\mathbf{X}) \tag{2}$$

or a combination of both; $\mathbf{X}^{\mathrm{T}} = (X_1,\ldots, X_m)$ is the vector of basic variables X_i. In this paper the model uncertainty is assumed to be a random variable θ. However, in more advanced analyses it may be represented by functions of several auxiliary random variables $\boldsymbol{\theta}$ and variables $\mathbf{X}$ involved in the model resistance.

It is difficult to specify general conditions under which Eq. (1) or (2) becomes more preferable than the other since the choice always depends on task-specific conditions. Current practice indicates that the multiplicative definition in Eq. (1) is widely applied to the model uncertainties while the additive relationship in Eq. (2) is used to account for systematic measurement errors.

From a purely statistical point of view the multiplicative relationship is more appropriate when the structural resistance R and the model resistance $\mathrm{R}_{\mathrm{model}}(\cdot)$ are described by lognormal distributions since the model uncertainty θ is likewise lognormally distributed and its statistical characteristics can be readily derived. Similarly, the additive formula becomes preferable when normal distributions are relevant.

It is worth noting that Eq. (1) can be transformed to Eq. (2) using the logarithmic transformation:

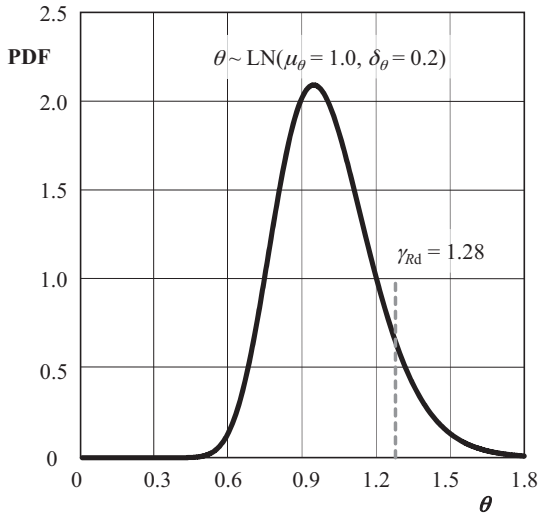

Fig. 1: Probability density function of θ and the model uncertainty factor γ_{Rd}

$$\ln R = \ln \theta + \ln[\mathrm{R}_{\mathrm{model}}(X_1,\ldots, X_m)] \tag{3}$$

The model uncertainty θ in general depends on basic variables $(X_1,\ldots,X_m)$. Influence of individual variables on θ can be assessed by a regression analysis as described e.g. by Ditlevsen & Madsen (1996). It is also indicated that the model describes well the essential dependency between R and $(X_1,\ldots, X_m)$ only if the model uncertainty:

- Has either a suitably small coefficient of variation (how small is the question of the practical importance of the accuracy of the model) or

- Is statistically independent of the basic variables $(X_1,\ldots, X_m)$.

For deterministic reliability verifications EN 1990 (2002) introduces the partial factor γ_{Rd} to describe the uncertainty associated with the resistance model ("design value of the model uncertainty"). Fig. 2 illustrates the relationship between the probabilistic distribution of θ and factor γ_{Rd}. As an example the lognormal distribution (mean $\mu_\theta = 1$ and coefficient of variation $\delta_\theta = 0.2$) and the relevant model uncertainty factor $\gamma_{Rd} = 1.28$ are shown (more details are provided in Section 5).

3. Uncertainties related to the models provided in EN 1992

The model uncertainty should be always clearly associated with an assumed resistance model. In this section uncertainties related to basic resistance models provided in EN 1992-1-1 (2004) are considered. Model resistances of structural members exposed to compression, bending, shear without and with stirrups are assumed to be given as follows, respectively:

$$\mathrm{R}_{\mathrm{model}}(\mathbf{X}) = b^2(\alpha_{\mathrm{cc}} f_{\mathrm{c}} + \rho_{\mathrm{l}} f_{\mathrm{y}}) \tag{4a}$$

$$\mathrm{R}_{\mathrm{model}}(\mathbf{X}) = \rho_{\mathrm{l}} b\, d f_{\mathrm{y}}[d - 0.5\rho_{\mathrm{l}}\, d\, f_{\mathrm{y}} / (\alpha_{\mathrm{cc}} f_{\mathrm{c}})] \tag{4b}$$

$$\mathrm{R}_{\mathrm{model}}(\mathbf{X}) = \max[0.18k \min(\rho_{\mathrm{l}}; 0.02)(100\rho_{\mathrm{l}} f_{\mathrm{c}})^{1/3} b_{\mathrm{w}} d; \quad 0.035k^{3/2} f_{\mathrm{c}}^{1/2} b_{\mathrm{w}} d] \tag{4c}$$

$$\mathrm{R}_{\mathrm{model}}(\mathbf{X}) = \max_{1 \le \cot\theta \le 2.5}\{\min[\rho_{\mathrm{w}} b_{\mathrm{w}} z f_{\mathrm{yw}} \cot\theta,\ \alpha_{\mathrm{cw}} b_{\mathrm{w}} z \nu f_{\mathrm{c}} / (\cot\theta + \tan\theta)]\} \tag{4d}$$

where:

b denotes width

$b_{\mathrm{w}} = b$ minimum width between tension and compression chords

d effective depth

f_c concrete compressive strength

f_y, f_{yw} yield strength of reinforcement (longitudinal, shear)

$k = \min[1 + \sqrt{(200 \text{ mm} / d)}; 2.0]$

$z \approx 0.9d$ inner lever arm

$\alpha_{cc} = 1$ coefficient accounting for long-term effects on concrete strength

$\alpha_{cw} = 1$ coefficient taking account of the state of the stress in the compression chord

θ angle between concrete compression struts and the main tension chord

$\nu = 0.6(1 - f_{ck} / 250 \text{ MPa})$ strength reduction factor for concrete cracked in shear

ρ_l, ρ_w longitudinal/shear reinforcement ratio.

Note that coefficients α_c are assumed to be one and thus not included in Eqs. (4). For shear without stirrups no axial compressive force is considered and the partial factor γ_C is not applied in the assessment of the coefficient $C_{Rd,c}$ and thus $C_{Rd,c} = 0.18$.

Statistical characteristics of the uncertainties related to the resistance models in Eqs. (4) obtained in previous studies are provided in Tab. 1. These characteristics were derived using the definition of the model uncertainty given in Eq. (1). The reported values seem to be in a broad agreement for the failure modes where several results are available. It should be noted that some of the studies are based on overlapping experimental results and thus are partly dependent.

The previous studies also provided a valuable insight into factors influencing the model uncertainties for bending and shear. As a background information for the paper by Holický et al. (2007), the analysis of experimental data revealed no significant statistical correlation between the model uncertainty and any of the basic variables influencing flexural resistance (including reinforcement ratio $0.25\ \% < \rho_l < 3.5\ \%$ and concrete compressive strength $17 \text{ MPa} < f_c < 45 \text{ MPa}$).

For shear without stirrups, researchers at the University of Stellenbosch concluded that the model uncertainty is significantly decreasing with the ratio of the shear span to the effective depth a/d and the effective depth d while it is not subject to trends with the other shear parameters, Retief (2007). The results were limited to the range of $2.9 < a/d$ as deep beam and shear bond failures are expected for lower values of a/d in accordance with O'Brien & Dixon (1995). For lower a/d the shear resistance is likely to be underestimated since the positive contribution of an arch action is neglected in the Eurocode model. Cladera & Marí (2004a) reported decrease of the model uncertainty with d and also with ρ_l. The discrepancy with results by Retief (2007) should be further investigated. It is important to emphasise that the failure of members without shear reinforcement is sudden and brittle and adequate reliability should be assured.

For shear with stirrups, Cladera & Marí (2007) and Mensah (2012) indicated that the model uncertainty significantly decreases with an increasing strength of shear reinforcement $\rho_w f_y$. Influences of the other basic variables are much lower. In addition Cladera & Marí (2004b) noted that influence of the amount of shear reinforcement is not linearly proportional to the shear strength and the truss model in EN 1992-1-1 (2004) may be unconservative for highly reinforced concrete members ($\rho_w f_y > 2$ MPa).

Based on the results given in Tab. 1 and neglecting trends with the basic variables, the following stochastic characteristics of θ may be applied as a first approximation:

- Axial compression without effects of buckling: $\mu_\theta \approx 1$; $V_\theta \approx 0.05$,
- Bending: $\mu_\theta \approx 1.1$; $V_\theta \approx 0.1$,
- Shear of the members without shear reinforcement: $\mu_\theta \approx 1$; $V_\theta \approx 0.2$,
- Shear of the members with shear reinforcement: $\mu_\theta \approx 1.7$; $V_\theta \approx 0.35$.

When different failure modes are combined, less favourable model uncertainty may be considered.

Tab. 1: Statistical characteristics of the model uncertainties related to the resistance models provided in EN 1992-1-1

Failure type	Note	μ_θ	V_θ	Source
Axial compression	Validated to comply with the model uncertainty factors used in ENs	1	0.05	Working draft of the bulletin on semi-probabilistic methods for verifications of reinforced concrete structures by *fib* SAG7
Bending	Number of tests $n = 109$	1.08	0.093	Holický et al. (2007)
Shear without stirrups	$n = 718$	1.75**	0.33	Hawkins et al. (2005)
	$n = 193$	1.02	0.22	Cladera & Marí (2004a)
	$n = 184$, $2.9 < a/d < 8.03$*	0.94	0.13	Retief (2007)
Shear with stirrups	$n = 160$	1.7	0.37	Hawkins et al. (2005)
	$n = 123$	1.83	0.40	Cladera & Marí (2004b)
	$n = 122$	1.64	0.32	Cladera & Marí (2007)

*a/d denotes the ratio of the shear span to the effective depth; **discrepancy with the other sources needs to be further clarified.

4. Uncertainties related to FE models

In general well validated advanced FE models should perform much better than the standardised formulas, with mean model uncertainty approaching unity. However, Vrouwenvelder (2010) indicated that variability of the uncertainty of FE models might be greater than that of the standardised formulas since:

- There may be lower experience with applications of FE models,

- Additional input data (material properties) and decisions in set-up of a FE model (discretization) may significantly influence predicted results.

JCSS (2006) recommends probabilistic models for the model uncertainties associated with "a more or less standard structural FE model", see Tab. 2.

Schlune et al. (2011) provided an overview of the model uncertainties related to FE analyses of different failure modes. The study was based on an extensive review of round robin exercises and modelling competitions published in scientific literature as well as on engineering judgement. The proposed models (accepted here in Tab. 2) were intended to be used as a first approximation of quantification of the model uncertainty.

Schlune et al. (2011) noted that the round robin exercises and modelling competitions dealt mainly with statically determinate structures for which the resistance in one critical section is decisive. However, for statically indeterminate structures the deformation capacity allowing for redistribution often becomes important. Since modelling of the deformation capacity is usually more difficult than of the ultimate strength, the coefficients of variation given in Tab. 2 may need to be increased. It was also emphasised that values in Tab. 2 are not affected by gross human errors.

For shear authors' experience from previous round robin exercises and competitions (see e.g. Jaeger & Marti (2009)) indicates the mean value of the model uncertainty of about 1.15 and the coefficient of variation ranging from 0.05 to 0.3 (exceptionally up to 0.6).

Tab. 2: Indicative probabilistic models for the model uncertainties associated with FE models.

Failure type	Note	μ_θ	V_θ	Source
Compression	Normal strength concrete	0.9 - 1.0	0.1 – 0.2	Schlune et al. (2011)
	High strength concrete	1.0	0.2 – 0.3	Schlune et al. (2011)
Bending	Including the effects of normal and shear forces, standard structural FE models	1.2	0.15	JCSS (2006)
	Under-reinforced	1.0 - 1.2	0.05 – 0.15	Schlune et al. (2011)
	Under-reinforced, bending reinforcement not aligned in principal moment direction	0.9	0.05 – 0.15	Schlune et al. (2011)
	Over-reinforced, normal strength concrete	0.9 - 1.0	0.1 – 0.15	Schlune et al. (2011)
	Over-reinforced, high strength concrete	1.0	0.2 – 0.3	Schlune et al. (2011)
Shear	-	1.4	0.25	JCSS (2006)
	Failure due to yielding of the reinforcement	0.9 - 1.0	0.1 – 0.25	Schlune et al. (2011)
	Failure due to crushing of concrete, combination of compression and shear loading, large members, bending reinforcement not aligned in principal moment direction	0.7 - 1.0	0.2 – 0.4	Schlune et al. (2011)
	Resistance of slabs with inclined main reinforcement and stirrups, compressive failure of inclined concrete struts	1.15	0.05-0.3	Jaeger & Marti (2009)

Tab. 2 indicates that the available experimental data are insufficient and inconclusive for establishing the model uncertainties for FE calculations. The information provided by JCSS (2006) and Jaeger & Marti (2009) reveals considerably higher mean values of the model uncertainties than that given by Schlune et al. (2011). In addition note that for the compression, Tab. 2 provides higher coefficients of variation than those in Tab. 1 which is rather surprising. These discrepancies should be clarified by further research.

It seems to be very difficult to propose a generally applicable model for the uncertainties related to FE models. Careful consideration of the data in Tab. 2 in conjunction with other available information is advised when an appropriate model for θ needs to be selected. As a very rough approximation $\mu_\theta \approx 1$ and $V_\theta \approx 0.2$ might be considered.

Reduction of variability of the model uncertainty and perhaps convergence of the mean to unity can be achieved by introduction of the guidelines for FE analysis of concrete structures. The foreseen guidelines should provide recommendations concerning assumptions, model choices and validation, and reporting results of analysis.

Differentiation of the model uncertainties with respect to complexity of the model and experience of user seems to be needed. Based on engineering judgement, a failure mode (ductile, steel, concrete in compression and tension, etc.) is an obvious additional factor for the differentiation of model uncertainty. However, the authors feel that these effects are already well covered in advanced numerical models and material uncertainties and need not to be included in the model uncertainty. Therefore, they might be considered only in simplified engineering formulas where various approximations are applied.

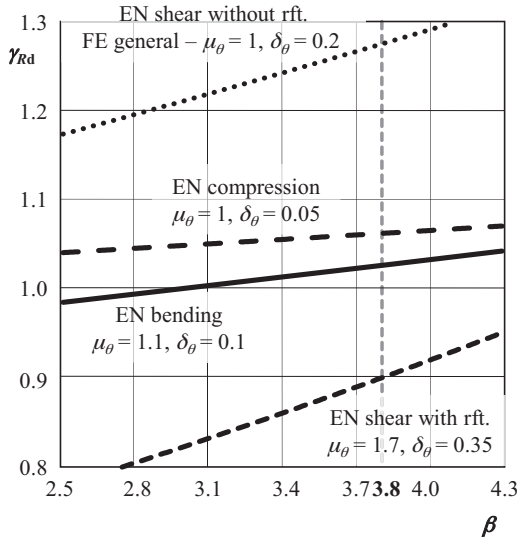

Fig. 2: Variation of the partial factor γ_{Rd} with β for $\alpha_R = 0.32$ (rft. denoting shear reinforcement)

5. Model uncertainty factor for deterministic reliability verifications

In accordance with fib SAG 9 (2010) the model uncertainty factor γ_{Rd} for reinforced concrete structures can be obtained as a product of:

$$\gamma_{Rd} = \gamma_{Rd1}\ \gamma_{Rd2} \tag{5}$$

where γ_{Rd1} denotes the partial factor accounting for model uncertainty and γ_{Rd2} is the partial factor accounting for geometrical uncertainties.

EN 1992-1-1 (2004) provides no specific recommendations concerning model uncertainties. EN 1992-2 (2005) introduces the global safety format for a nonlinear analysis with the recommended model uncertainty factor of 1.06. However, it was shown by Sýkora & Holický (2011) that such a factor is rather low and should be increased in most cases depending on relevant failure mode (bending, shear, compression).

In accordance with fib SAG 9 (2010) $\gamma_{Rd1} = 1.05$ for concrete strength and $\gamma_{Rd1} = 1.025$ for reinforcement may be assumed in common cases. However, larger model uncertainty needs to be considered for punching shear in the case when concrete crushing is governing. A value of $\gamma_{Rd2} = 1.05$ may be assumed for geometrical uncertainties of the concrete section size or reinforcement position. When relevant measurements of an existing structure indicate insignificant variability of geometrical properties, $\gamma_{Rd2} = 1.0$ may be considered.

Alternatively, the partial factor γ_{Rd} can be obtained from the following relationship based on a lognormal distribution:

$$\gamma_{Rd} = 1 / [\mu_e \exp(-\alpha_R \beta V_e)] \tag{6}$$

where α_R denotes the FORM sensitivity factor and β is the target reliability index according to EN 1990 (2002). Assuming the probabilistic models for the model uncertainty given in previous sections, variation of the partial factor γ_{Rd} obtained from Eq. (6) with the target reliability β for $\alpha_R = 0.4 \times 0.8 = 0.32$ ("non-dominant resistance variable") is indicated in Fig. 2.

It follows from Fig. 2 that the model uncertainty factor γ_{Rd} is close to unity for well-established models of flexural and axial compression resistances given in EN 1992-1-1 (2004). The partial factor decreases below unity for the EN shear model for the members with shear reinforcement due to the high value of μ_e. For $\beta = 3.8$ the model uncertainty factor of about 1.3 is obtained for the EN shear model for the members without shear reinforcement and also for FE models (see also Fig. 1). The

value for FE models shall, however, be considered indicative; further refinements with regard to different failure modes are foreseen (cf. Tab. 2).

It is interesting to observe that the results in Fig. 2 are in agreement with the findings by Taerwe (1993) who concluded (with regard to derivation of the global resistance factor, EN 1992-2 (2005) and fib (2010)) that:

- special calibration of the model uncertainty as part of the global resistance factor is warranted for coefficients of variation of 0.2 and above,

- for smaller coefficients of variation it could be tentatively suggested that the model uncertainties do not require an additional safety factor if conservative models are used.

The selection of $\alpha_R = 0.32$ deserves additional comments. Leading and accompanying actions (with associated factors $\alpha_E = -0.7$ and $\alpha_E = -0.4 \times 0.7 = -0.28$, respectively) are distinguished in Annex C of EN 1990 (2002) while $\alpha_R = 0.8$ is recommended for resistance variables under conditions specified in the Eurocode. When the model uncertainty factor γ_{Rd} and material factor γ_m are assessed separately considering $\alpha_R = 0.8$, overly conservative designs may be obtained. Therefore, working draft of the bulletin on semi-probabilistic methods for verifications of reinforced concrete structures by *fib* SAG7 assumes that the model uncertainty is not a leading resistance variable and the sensitivity factor is thus reduced to $\alpha_R = 0.4 \times 0.8 = 0.32$. This assumption is accepted in this study.

It is worth noting that for $\alpha_R = 0.8$ the partial factor γ_{Rd} increases:

- significantly for shear without shear reinforcement and FE models ($\gamma_{Rd} \approx 1.85$ for $\beta = 3.8$) and for shear with shear reinforcement ($\gamma_{Rd} \approx 1.7$ for $\beta = 3.8$),

- less significantly for axial compression and flexural resistance ($\gamma_{Rd} \approx 1.2$ for $\beta = 3.8$).

6. Outlook of further research

The study indicates that the uncertainties related to the resistance models for reinforced concrete structures should be further investigated. Basically two classes of models should be distinguished:

- Engineering models with strictly defined assumptions (beam and sectional approaches),

- Complex models based on general principles of structural mechanics with much wider options and potentially higher uncertainties.

In particular for FE applications outcomes of the further research should facilitate implementation of sophisticated resistance models with the full exploitation of the present know-how while limiting the model uncertainty by controlling model and user errors.

Note that the terms “modelling uncertainty” or “modelling factor” are more appropriate than “model uncertainty” when human factors are included.

The research framework is proposed as follows:

1. For structural members, reference values of the resistance will be obtained from available experimental tests. When experimental data is little or missing (large and complex structures, continuous members, members supporting distributed loads, members that fail in regions other than adjacent to a support), test values are to be found by interpretation of test results in different conditions (simpler structural members), using different software tools and verification methods. Yet, this will introduce an additional uncertainty.
2. The classes with different uncertainty levels originating from complexity of the task, underlying structural models and experience of users will be proposed. The differences between model and actual resistances will be analysed and evaluated for common types of reinforced concrete structures. The resistance at ultimate limit states will be investigated for ductile and brittle failure modes. The errors due to numerical approximations will be assessed.
3. Appropriate probabilistic description of resistance represented by models with various levels of sophistication and users’ experience will be proposed. For practical applications the partial factors for model uncertainties will be derived.

4. In models based on numerical simulations, the variability of the model uncertainty can be reduced by appropriate model validation. Such validation should cover sources of uncertainties related to numerical methods and constitutive models. Rules for such improvements will be formulated and adjusted model uncertainties will be proposed.

For deteriorating structures the resistance model should inevitably incorporate degradation effects that may be a source of additional uncertainties and should be also quantified within the further research. The study by Tanner et al. (2011) provides the first insight into the model uncertainties of deteriorating concrete structures.

7. Concluding remarks

Previous reliability studies indicate that description of model uncertainties is a crucial problem of the design of reinforced concrete structures. Therefore, the present paper is focused on the model uncertainties; the following concluding remarks can be drawn:

1. The model uncertainty should be always clearly associated with an assumed resistance model.
2. The model uncertainty should cover the following aspects (if relevant): simplifications of known physical principles, approximations inherent to numerical methods, influence of different interpretations of users of complex software tools and related errors.
3. Relationship between the model uncertainty and resistance obtained by the model can be multiplicative or additive or combination thereof; in common cases the multiplicative form is acceptable.
4. Uncertainties related to sectional-oriented models provided in EN 1992-1-1 (2004) can be described by the following statistical characteristics and partial factors:

   - Axial compression without effects of buckling: mean $\mu_\theta \approx 1$; coefficient of variation $V_\theta \approx 0.05$; model uncertainty factor $\gamma_{Rd} \approx 1.05$,

   - Bending: $\mu_\theta \approx 1.1$; $V_\theta \approx 0.1$ and $\gamma_{Rd} \approx 1.05$,

   - Shear of the members without shear reinforcement: $\mu_\theta \approx 1$; $V_\theta \approx 0.2$ and $\gamma_{Rd} \approx 1.3$,

   - Shear of the members with shear reinforcement: $\mu_\theta \approx 1.7$; $V_\theta \approx 0.35$ and $\gamma_{Rd} \approx 0.9$.

5. The present experimental data are insufficient and inconclusive for establishing the model uncertainties for FE calculations. As a first approximation $\mu_\theta \approx 1$; $V_\theta \approx 0.2$ and $\gamma_{Rd} \approx 1.3$ might be considered.

Further research activities should focus on differentiation of the model uncertainties with respect to the level of the model and complexity of the task. For existing structures uncertainties of degradation models should be specified.

Acknowledgements

This study is an outcome of the research project P105/12/2051, supported by the Czech Science Foundation. Results of the projects TA01031314 and LG11043 have been utilised.

References

Bertagnoli, G., Giordano, L. & Mancini, G. (2004) Safety format for the nonlinear analysis of concrete structures. *Studi e ricerche - Politecnico di Milano. Scuola di specializzazione in costruzioni in cemento armato,* 2004, 25. pp. 31-56.

Červenka, V. (2008) Global Safety Format for Nonlinear Calculation of Reinforced Concrete. *Beton- und Stahlbetonbau,* 103, 2008. pp. 37-42.

Cladera, A. & Marí, A.R. (2004a) Shear design procedure for reinforced normal and high-strength concrete beams using artificial neural networks. Part I: beams without stirrups. *Engineering Structures,* 26, 7. pp. 917-926.

Cladera, A. & Marí, A.R. (2004b) Shear design procedure for reinforced normal and high-strength concrete beams using artificial neural networks. Part II: beams with stirrups. *Engineering Structures,* 26, 7. pp. 927-936.

Cladera, A. & Marí, A.R. (2007) Shear strength in the new Eurocode 2. A step forward? *Structural Concrete,* 26, 7. pp. 917-66.

Ditlevsen, O. & Madsen, H.O. (1996) *Structural Reliability Methods.* Chichester (England), John Wiley & Sons.

EN 1990 (2002) *Eurocode - Basis of structural design.* Brussels, CEN.

EN 1992-1-1 (2004) *Design of concrete structures - Part 1-1: General rules and rules for buildings.* Brussels, CEN.

EN 1992-2 (2005) *Eurocode 2 - Design of concrete structures - Part 2: Concrete bridges - Design and detailing rules.* Brussels, CEN.

fib (2010) *Model Code 2010 (First complete draft March-April 2010).* Lausanne, fib.

fib SAG 9 (2010) *Revision of partial safety factors (report),* December 2010.

Hawkins, N.M., Kuchma, D.A., Mast, R.F., Marsh, M.L. & Reineck, K. (2005) *Simplified Shear Design of Structural Concrete Members,* NCHRP Report 549. Transportation Research Board.

Holický, M., Retief, J.V. & Dunaiski, P.E. (2007) The reliability basis of design for structural resistance, In: *Proc. SEMC 2007* , University of Cape Town, Millpress.

Jaeger, T. & Marti, P. (2009) Reinforced Concrete Slab Shear Prediction Competition: Experiments. *ACI Structural Journal,* 33, 3. pp. 2350-308.

JCSS (2006) *JCSS Probabilistic Model Code.* Zurich, Joint Committee on Structural Safety. <http://www.jcss.ethz.ch/>.

Mensah, K.K. (2012) *Reliability Assessment of Structural Concrete with Special Reference to Shear Resistance (MSc thesis).* Stellenbosch, South Africa, University of Stellenbosch.

O'Brien, E.J. & Dixon, A.S. (1995) *Reinforced and prestressed concrete design: the complete process.* Longman Scientific & Technical.

Retief, J.V. (2007) Personal communication.

Schlune, H., Plos, M. & Gylltoft, K. (2011) Safety formats for nonlinear analysis tested on concrete beams subjected to shear forces and bending moments. *Engineering Structures,* 33, 8. pp. 2350-2356.

Sýkora, M. & Holický, M. (2011) Safety format for non-linear analysis in the model code - verification of reliability level, In: *Proceedings of the fib Symposium PRAGUE 2011 Concrete engineering for excellence and efficiency* (V. Sruma ed.), Prague, Czech Concrete Society.

Taerwe, L. (1993) *Towards a consistent treatment of model uncertainties in reliability formats for concrete sfuctures,* CEB Bulletin d'Information n° 219 'Safety and Performance Concepts'. Lausanne: CEB.

Tanner, P., Lara, C. & Prieto, M. (2011) Semi-probabilistic models for the assessment of existing concrete structures, In: *Proc. ICASP11* (M.H. Faber, J. Köhler & K. Nishijima eds.), ETH Zurich, CRC Press/Balkema.

Vrouwenvelder, A.C.W.M. (2010) *Conclusions of the JCSS Workshop on Semi-probabilistic FEM calculations, Delft, 1-2 December 2009,* 18/02/2010. Delft: TNO.

18th International Conference
ENGINEERING MECHANICS 2012
Svratka, Czech Republic, May 14 – 17, 2012

pp. 1273–1280
Paper #100

RELIABILITY ASSESSMENT OF INDUSTRIAL HERITAGE BUILDINGS

M. Sykora, M. Holicky *

Abstract: *A number of factories, warehouses, power plants and other industrial buildings have been recognised as industrial culture heritage. At present considerable effort of architects and civil engineers is aimed at re-use of these structures in order to preserve their cultural and heritage value and to avoid wasting energy. However, heritage structures usually do not fulfil requirements of present codes of practice. Simplified conservative procedures of design of new structures given in present codes may lead to expensive repairs and losses of the cultural and heritage value when applied to existing structures. In accordance with EN 1990 (2002) and ISO 13822 (2003), probabilistic procedure is proposed to improve the reliability assessment of industrial heritage buildings. The procedure is applied in the reliability assessment of a steel member.*

Keywords: ***Industrial heritage, reliability assessment, probabilistic methods.***

1. Introduction

1.1. General motivation

A number of factories, warehouses, power plants and other industrial buildings has been worldwide registered as industrial cultural heritage. According to the International Committee on the Conservation of the Industrial Heritage TICCIH (2003), such structures are mostly of significant architectural, historic, technological or social value. An example of such a structure under reconversion, the former factory for boiler production built in 1900's in Prague – Karlin, is shown in Fig. 1.

It is indicated that protection (including adaptations and re-use) of the industrial heritage structures is an important issue since it often positively contributes to the sustainable development of urban areas by the following:

- Preservation of cultural values (the industrial heritage often forms a part of the urban landscape and provide the cityscape with a visual historical landmark),
- Recycling of potential resources and avoiding wasting energy,
- Facilitating the economic regeneration of regions in decline.

However, insufficient attention seems to be paid to systematic recognizing, declaring and protecting the industrial heritage in most countries. This is an alarming situation as the lack of attention and awareness of the industrial structures may gradually lead to their extinction.

When out of use, the industrial heritage buildings are degrading and often turning into ruins. Re-use and adaptation of such structures allow for integration of the industrial heritage into a modern urban lifestyle and help protect cities' cultural heritage, Läuferts & Mavunganidze (2009) and Sýkora et al. (2010b). These structures are often adapted to become hotels, museums, residential parks, commercial centres etc.

Decisions about adequate construction interventions should be based on the complex assessment of a structure. It has been recognised that many heritage structures do not fulfil requirements of present codes of practice. Minimisation of construction interventions is required in rehabilitation and upgrades, but sufficient reliability should also be guaranteed. Application of simplified procedures

* Ing. Miroslav Sýkora, Ph.D., Prof. Ing. Milan Holický, PhD., DrSc.: Klokner Institute, Czech Technical University in Prague, Solinova 7; 166 08, Prague; CZ, e-mail: miroslav.sykora@klok.cvut.cz, milan.holicky@klok.cvut.cz

Fig. 1: Former factory for boiler production in Prague – Karlin under reconversion

used for design of new structures may lead to expensive repairs and losses of the cultural and heritage value. In the paper a general probabilistic procedure is thus proposed to improve the reliability assessment of industrial heritage buildings particularly with respect to:

- Better description of uncertainties related to the assessment and

- Facilitating inclusion of results of inspections and tests and the satisfactory past performance of a structure.

1.2. Initiatives concerning protection of the industrial heritage

The protection of the industrial heritage is a multidisciplinary topic including historical, architectonic, civil engineering and ecological aspects. In 1978 the International Committee on the Conservation of the Industrial Heritage (TICCIH) was founded to study, protect, conserve and explain remains of industrialisation. Its recent efforts have resulted in registration of more than 40 industrial sites in the World Heritage List, Zhang (2007).

In the Czech Republic numerous industrial heritage structures were built from 1870 to 1930. Fragner (2010) indicates that views of Czech architects and civil engineers on protection of the industrial heritage are often considerably different and an important issue may be to achieve consensus on significance of the heritage value. Desired coordinating platform is provided by the Research Centre for Industrial Heritage that maintains a database of the Czech industrial monuments (containing more then 10 000 monuments) and seeks for new uses of the industrial heritage structures.

In addition the Czech Technical University in Prague and the University of Applied Sciences in Ås (Norway) in 2009-2010 participated in the research project focused on the structural assessment of historical immovables, mainly focused on the industrial heritage buildings. Main results of the project are summarised by Sýkora et al. (2010). General findings of this project are presently improved in a national project of the applied research aimed at development of the operational guidelines for structural assessment of the industrial heritage buildings. The guidelines shall be primarily focused on reinforced concrete and steel (iron) structures.

2. General aspects of the assessment

As a rule re-use and adaptation of the industrial structures require assessment of structural reliability. However, it appears that insufficient attention has been paid by experts to specific issues of the reliability assessment of such structures so far. The following differences between the assessment and design of new structures should be carefully considered:

- Social and cultural aspects - loss of cultural and heritage values,

- Economic aspects - additional costs of measures to increase reliability of a heritage building in comparison with a new structure (at a design stage cost of such measures is normally minor while cost of strengthening is much higher),

- Principles of the sustainable development - waste reduction and recycling of materials (these aspects may be more significant in case of the assessment),

- Lack of information for the assessment - commonly, testing of the mechanical properties of materials is difficult, expensive, but also very important due to variability of mechanical properties and changes that may have occurred during the working life of a structure (influence of deterioration and damage).

It has been recognised that many heritage buildings do not fulfil requirements of present codes of practice. Minimisation of construction interventions is required in rehabilitation and upgrades, but sufficient reliability should also be guaranteed. Decisions about adequate construction interventions should be based on the complex assessment of a structure considering actual material properties, use and environmental conditions.

Significant uncertainties related to actual material properties and structural conditions usually need to be considered in the reliability assessment of the industrial heritage buildings. In design codes a limited number of safety factors is intended to cover all possible design situations. Therefore, verifications based on deterministic design procedures may be too conservative. Application of commonly used design procedures may thus lead to expensive repairs and losses of the cultural and heritage value. It follows that use of deterministic design procedures may not be an appropriate approach.

It has been recognised that assessment of existing structures is a structure-specific task that is difficult to codify. In accordance with EN 1990 (2002) and ISO 13822 (2003), a general probabilistic procedure is thus proposed to improve the reliability assessment of the industrial heritage buildings and allow for inclusion of results of inspections, testing and consideration of the satisfactory past performance of a structure.

3. Principles of probabilistic analysis

In accordance with Diamantidis (2001) and Holický & Sýkora (2012) probabilistic methods may be useful for the assessment of existing structures where appropriate data can be obtained. Ellingwood (1996) indicates that uncertainties that can be greater than in structural design (such as uncertainties related to inaccessible members and connections where construction details cannot be inspected and verified) can be adequately described by such methods. On the contrary, some of the uncertainties reflected (often implicitly) in the load and resistance factors (modelling approximations, deviations from specified dimensions and strengths) may be less than in new construction, particularly when in-situ measurements are taken.

3.1. Specification of models for basic variables

Models for basic variables should be adjusted to the actual situation and state of a structure and verified by inspection and testing. The following principles should be taken into account:

- Material properties should be considered according to the actual state of a structure verified by destructive or non-destructive testing. It may often be appropriate to combine limited new information with prior information. Bayesian techniques, described e.g. in ISO 12491 (1997), Diamantidis (2001) or JCSS (2006), provide a consistent basis for this updating. Prior information may be found in normative documents (for example in the Czech National Annex to ISO 13822 (2003) where characteristics of different historical materials are provided), scientific literature, reports of producers etc.

- When significant deterioration is observed, an appropriate deterioration model should be used to predict changes in structural parameters due to foreseen environmental conditions, structural loading, maintenance practices and past exposures, based on theoretical or experimental investigation, inspection and experience.

- Dimensions of structural members should be determined by measurements. When the original design documentation is available and no changes in dimensions exist, nominal dimensions given in the documentation may be used.

- Load characteristics should be introduced considering the values corresponding to the actual situation. For structures with significant permanent actions, the actual geometry should be verified by measurements and weight densities should be obtained from tests.

- Model uncertainties should be considered in the same way as at a design stage unless previous structural behaviour (especially damage) indicates otherwise. In some cases model factors, coefficients and other design assumptions may be established from measurements.

It follows that reliability verification of a heritage building should be backed up by inspection including collection of appropriate data. Evaluation of prior information and its updating using newly obtained measurements may be a crucial step of the assessment.

3.2. Probabilistic updating

The failure probability, related to the period from the assessment to the end of a working life t_D, can be obtained from a general probabilistic relationship:

$$p_f(t_D) = P\{\min Z[\mathbf{X}(\tau)] < 0 \text{ for } 0 < \tau < t_D\} = P\{F(t_D)\} \quad (1)$$

where $Z(\cdot)$ = limit state function; $\mathbf{X}(\cdot)$ = vector of basic variables including model uncertainties, resistance, permanent and variable actions; and $F(t_D)$ = failure in the interval $(0,t_D)$.

When additional new information I related to structural conditions is available, the failure probability may be updated according to ISO 13822 (2003) as follows:

$$p_f''(t_D|I) = P\{F(t_D) \cap I\} / P(I) \quad (2)$$

The information should be selected to maximise correlation between the events $\{F\}$ and $\{I\}$. Strong correlation improves the posterior estimate of failure probability while weak correlation yields nearly the same estimates as based on Eq. (1), Ellingwood (1996). The new information may be based on:

1. Inspections that can for instance provide data for the updating of a deterioration model,
2. Material tests and in-situ measurements that can be taken to improve models of concrete compressive strength, steel yield strength, geometry etc.,
3. Consideration of the satisfactory past performance.

In the first two cases the new information is usually applied in the direct updating of (prior) distributions of relevant basic variables that are commonly based on experience from assessments of similar structures, long-term material production, findings reported in literature or engineering judgement. The last case may be very important for the industrial heritage buildings. For instance a structure, originally used as a factory, might have likely survived loads much greater than those expected for future use as e.g. a museum or gallery.

The satisfactory past performance of a structure during a period t_A till the time of assessment may be included in the reliability analysis considering the conditional failure probability $p_f''(t_D|t_A)$ that a structure will fail during a working life t_D given that it has survived the period t_A. This probability may be estimated in several ways. When the load to which the structure has been exposed during the period t_A is known with negligible uncertainties, the resistance or a joint distribution of time-invariant variables may be truncated (a lower bound is set to the value of load). Using the bounded distribution, the conditional (updated) probability $p_f''(t_D|t_A)$ can be estimated. This approach, similar to the updating for proof load testing described by Diamantidis (2001), is illustrated elsewhere, Sýkora et al. (2010a). More generally, the updated failure probability may be determined using the following relationship:

$$p_f''(t_D|t_A) = P\{F(t_D) \cap \overline{F}(t_A)\} / P\{\overline{F}(t_A)\} \quad (3)$$

where $\overline{F}$ = complementary event to the failure. The updated probability can be determined by standard techniques for reliability analysis such as the FORM/SORM methods or importance sampling. Updating based on Eq. (3) is applied in a numerical example.

4. Target reliability levels

Reliability verification may be based on the following (equivalent) relationships:

$$p_f^{"}(t_D|I) < p_t, \quad \beta^{"}(t_D|I) = -\Phi^{-1}[p_f^{"}(t_D|I)] \geq \beta_t \tag{4}$$

where p_t = target failure probability; Φ^{-1} = inverse cumulative distribution function of the standardised normal variable; and β_t = target reliability index.

The target reliability level can be taken as the level of reliability implied by acceptance criteria defined in proved and accepted design codes. The target level should be stated together with clearly defined limit state functions and specific models of basic variables. ISO 2394 (1998) provides examples of the target reliability indices for the anticipated life-time period, related to different relative costs of safety measures and failure consequences, see Tab. 1.

Tab. 1: Target reliability index (life-time, examples) in accordance with ISO 2394 (1998)

Relative costs of safety measures	**Consequences of failure small**	**some**	**moderate**	**great**
High	0	1.5	2.3	3.1
Moderate	1.3	2.3	3.1	3.8
Low	2.3	3.1	3.8	4.3

For the industrial heritage buildings, moderate consequences of failure and moderate costs of safety measures can often be assumed. In this case ISO 2394 (1998) indicates $\beta_t = 3.1$. It is worth noting that other standards such as EN 1990 (2002) and ISO 13822 (2003) provide different target reliability levels. EN 1990 (2002) and ISO 13822 (2003) differentiate reliability levels with respect to the failure consequences only. However, the costs of safety measures may become an important aspect in case of the industrial heritage structures.

Yet none of aforementioned standards explicitly takes into account the cultural heritage value of a structure. To the best knowledge of the authors, the only model accounting for the cultural heritage value is a simple empirical relationship proposed by Schueremans & Van Gemert (2004):

$$p_t = S_c \, t_D \, A_c \, C_f / (n_p \, W) \times 10^{-4} \tag{5}$$

where

- S_c = social criterion factor (recommended value for listed historical buildings 0.05),
- t_D = remaining working life (considered as 50 years); A_c = activity factor (recommended value for buildings 3),
- C_f = economical factor (5 for a moderate consequences, recommended values: 10 for not serious and 1 for serious consequences of failure),
- n_p = number of endangered persons (in accordance with Trbojevic (2009) the most favourable and unfavourable estimates $n_{p,min} = 1$ and $n_{p,max} = 10$, respectively, are considered for significant risk of injury or fatalities - a middle class of consequences), and
- W = warning factor (1 - sudden failure without previous warning).

Considering these indicative data, lower and upper estimates of the target reliability level are obtained from Eq. (5):

$$\begin{aligned} p_{t,max} &= 0.05\times50\times3\times5/(1\times0.3) \times 10^{-4} \approx 3.8 \times 10^{-3}; \; \beta_{t,min} = 2.7 \\ p_{t,min} &= 0.05\times50\times3\times5/(10\times0.3) \times 10^{-4} \approx 3.8 \times 10^{-4}; \; \beta_{t,max} = 3.4 \end{aligned} \tag{6}$$

It appears that the target reliability is within the broad range from 2.7 to 3.4. The value recommended in ISO 2394 (1998) is approximately in the middle of this range.

It is interesting to indicate the target reliability levels for a structure with the same characteristics entering Eq. (6), but the social criterion factor S_c. For a structure not listed as the historical building, the factor $S_c = 1$ might be assumed. Then, Eq. (5) yields:

$$p_{t,max} = 1\times50\times3\times5/(1\times0.3) \times 10^{-4} \approx 7.6 \times 10^{-2};\ \beta_{t,min} = 1.4 \qquad (7)$$
$$p_{t,min} = 1\times50\times3\times5/(10\times0.3) \times 10^{-4} \approx 7.6 \times 10^{-3};\ \beta_{t,max} = 2.4$$

It follows from Eqs. (6) and (7) that the target reliability index for the heritage building should be greater (by about 1) than that for a similar structure not listed as a historical building. Whether this is an adequate increase of reliability is a complex question that should be investigated individually by a supplementary investigation. In such an investigation it should be taken into account that an increase in the target reliability may potentially result in losses of the cultural heritage values.

More detailed information on the procedures for assessment of the target reliabilities for existing structures is provided by Steenbergen & Vrouwenvelder (2010) and Sykora & Holicky (2012).

5. Design of construction interventions

If the structure does not satisfy reliability requirements, construction interventions may become necessary. When dealing with preservation of the industrial heritage buildings, it may be difficult to propose construction interventions that respect all requirements for preservation of the cultural heritage value. According to Lourenco (2002) modern principles of interventions seem to include the following aspects:

- Removability,
- Unobtrusiveness and respect of the original conception,
- Safety of the construction,
- Durability and compatibility of materials,
- Balance between cost and available financial resources.

6. Numerical example

The proposed procedure is applied in the example of reliability assessment of a steel member of a 100-year old building registered as the industrial heritage. The building, originally built as a part of a textile mill, will be used as an office building. The selected structural member is exposed to bending moment due to permanent and imposed loads. An anticipated working life is 50 years. Note that the reliability assessment is considerably simplified to illustrate general steps of the probabilistic verification rather than to describe case-specific details.

Initially, reliability of the member is verified by the partial factor method. Characteristic values of the resistance and permanent action, given in Tab. 2, are specified considering results of on-site surveys and original design documentation. During the previous use of the structure, degradation has resulted in loss of the steel section. In the following assessment the actual steel section characteristics are considered and no further degradation is expected during the remaining working life. Characteristic value of the imposed load is determined in accordance with EN 1991-1-1 (2002).

The deterministic verification reveals that reliability of the member is insufficient as the actual resistance is approximately by 40 % lower than required by Eurocodes.

Probabilistic reliability analysis is based on the limit state function for the member exposed to bending:

$$Z(\mathbf{X},t) = K_R R - K_E [G + Q] \qquad (8)$$

where K_R = model uncertainty of resistance; R = flexural resistance; K_E = model uncertainty of load effects; G = permanent action; and Q = maxima of the imposed load related to a reference period. The considered characteristic values and probabilistic models of the basic variables, based on recommendations of JCSS (2006) and findings published by Holický & Sýkora (2011), are given in Tab. 2. The model uncertainty for a flexural resistance of the steel beam is accepted from the report by the Eurocode 3 Editorial Group (1989). For convenience all the basic variables in Tab. 2 are normalised by $L^2 / 8$ (L is a span of the member).

The reliability verification is firstly based on Eq. (1) (no new information). Using the FORM method, the reliability index is rather low, $\beta \approx 2.0$. Considering the target reliability levels indicated in Section 4, the reliability of the member seems to be insufficient.

Tab. 2: Models for basic variables

Variable	Sym.	Unit	Dist.	x_k	μ_X / x_k	V_X
Bending resistance	R	kN/m	lognormal	5.21	1.19	0.08
Permanent load effect	G	kN/m	normal	3.06	1	0.05
Imposed load effect (50 y.)	Q	kN/m	Gumbel	3	0.6	0.35
Effect of the load that the structure has survived	S	kN/m	normal	3.6	1	0.05
Resistance uncertainty	K_R	-	lognormal	1	1.15	0.05
Load effect uncertainty	K_E	-	lognormal	1	1	0.1

x_k = characteristic value; μ_X = mean; V_X = coefficient of variation.

Secondly, the reliability is updated considering the satisfactory past performance to improve this estimate. It is known from previous performance of the structure that the member has survived the load S equal to 1.2-times the characteristic value of the imposed load. Uncertainties in the survived load effect are described by the normal distribution with the mean equal to the observed value and coefficient of variation 0.05. Given the survival of the load S, the updated reliability index $\beta^{"}(t_D|S) \approx 2.45$ follows from the conditional failure probability based on Eq. (3):

$$p_f^{"}(t_D|S) = \langle P\{[K_R R - K_E(G+Q) < 0] \cap [K_R R - K_E(G+S) > 0]\} / P\{K_R R - K_E(G+S) > 0\} \quad (9)$$

It appears that the predicted reliability is still rather low. In general four options can now be discussed with a client:

1. to upgrade the member,
2. to propose an adequate limit on the imposed action,
3. to accept a shorter remaining working (such as 15 years) and after that re-assess the beam,
4. to derive optimum target reliability following the principles provided by ISO 2394 (1998).

Note that the second option may be applicable for industrial plants rather than office buildings. When the third option is accepted the updated reliability index $\beta^{"}(15\text{ y.}|S) \approx 2.9$ is obtained from Eq. (9) using 15-year maxima of the imposed load. This reliability level might be acceptable (see Section 4). The fourth option is thoroughly discussed by Sykora & Holicky (2012) where optimisation of the total costs related to a structure including potential failure consequences and human safety criteria are considered.

7. Conclusions

Protection of the industrial heritage buildings helps preserve cultural values, avoids wasting energy and facilitates economic regeneration of regions in decline. Present insufficient attention to systematic recognizing, declaring and protecting the industrial heritage may, however, lead to their extinction.

Reliability verifications of the industrial heritage buildings should be backed up by inspection including collection of appropriate data. Assessments based on simplified conservative procedures used for structural design may lead to expensive repairs and losses of the cultural and heritage value.

Probabilistic methods can thus be applied to better describe uncertainties and take into account results of inspections and tests as well as satisfactory past performance. Target reliability levels are primarily dependent on the costs of safety measures and consequences of failure including loss of the cultural heritage value.

Acknowledgements

This study is an outcome of the research project DF12P01OVV040 "Assessment of safety and working life of industrial heritage buildings", supported by the Ministry of Culture of the Czech Republic.

References

Diamantidis, D. (2001) *Probabilistic Assessment of Existing Structures.* Joint Committee on Structural Safety, RILEM Publications S.A.R.L.

Ellingwood, B.R. (1996) Reliability-based condition assessment and LRFD for existing structures. *Structural Safety,* 18, 2-3. pp. 67-80.

EN 1990 (2002) *Eurocode - Basis of structural design.* Brussels, CEN.

EN 1991-1-1 (2002) *Eurocode 1: Actions on structures - Part 1-1: General actions; Densities, self-weight, imposed loads for buildings.* Brussels, CEN.

Eurocode 3 Editorial Group (1989) *Background Documentation to Eurocode No. 3 Design of Steel Structures Part 1 – General Rules and Rules for Buildings, Background Document for Chapter 5 of Eurocode 3, Document 5.01.*

Fragner, B. (2010) Přístupy k záchraně průmyslového dědictví v České republice. *Stavebnictví,* IV, 01/2010. pp. 16-18.

Holický, M. & Sýkora, M. (2011) Conventional probabilistic models for calibration of codes, *in: Proc. ICASP11* (M.H. Faber, J. Köhler & K. Nishijima eds.), ETH Zurich, CRC Press/Balkema.

Holický, M. & Sýkora, M. (2012) Structural assessment of heritage buildings (accepted for publication), *in: Proceedings of the 1st International Conference on Defence Sites: Heritage and Future 2012*, Portsmouth, WIT Press.

ISO 12491 (1997) *Statistical methods for quality control of building materials and components.* Geneve, Switzerland, ISO.

ISO 13822 (2003) *Bases for design of structures - Assessment of existing structures.* Geneve, Switzerland, ISO TC98/SC2.

ISO 2394 (1998) *General principles on reliability for structures.* Geneve, Switzerland, ISO.

JCSS (2006) *JCSS Probabilistic Model Code.* Zurich, Joint Committee on Structural Safety. http://www.jcss.ethz.ch/.

Läuferts, M. & Mavunganidze, J. (2009) Ruins of the past: Industrial heritage in Johannesburg, *in: Proc. STREMAH XI* (C.A. Brebbia ed.), Tallin, Estonia, WIT Press.

Lourenco, P.B. (2002) Computations on historic masonry structures. *Progress in Structural Engineering and Materials,* 4, 3. pp. 301-319.

Schueremans, L. & Van Gemert, D. (2004) Assessing the safety of existing structures: reliability based assessment framework, examples and application. *Journal of Civil Engineering and Management,* X, 2. pp. 131-141.

Steenbergen, R.D.J.M. & Vrouwenvelder, A.C.W.M. (2010) Safety philosophy for existing structures and partial factors for traffic loads on bridges. *Heron,* 55, 2. pp. 123-139.

Sýkora, M., Holický, M., Jung, K., Marková, J., Kvaal, K. & Thiis, T. (2010a) Reliability Assessment of Industrial Heritage Structures and Application to a Light-Weight Steel Roof, *in: Proc. ICSA2010* (P.J.S. Cruz ed.), Guimaraes, Portugal, CRC Press/Balkema.

Sýkora, M., Holický, M. & Marková, J. (2010b) Advanced assessment of industrial heritage buildings for sustainable cities' development, *in: Proc. CESB10* (P. Hájek, J. Tywoniak, A. Lupíšek, J. Růžička & K. Sojková eds.), Prague, Grada Publishing.

Sykora, M. & Holicky, M. (2012) Target reliability levels for the assessment of existing structures - case study (submitted for publication), *in: Proc. IALCCE 2012* (A. Strauss, K. Bergmeister & D.M. Frangopol eds.), Vienna, CRC Press/Balkema.

Sýkora, M., Holický, M., Jung, K., Marková, J., Thiis, T., Kvaal, K. et al. (2010) *Structural assessment of industrial heritage buildings.* Prague, CTU in Prague, Klokner Institute.

TICCIH (2003) *The Nizhny Tagil Charter for the Industrial Heritage.* Nizhny Tagil, The International Committee for the Conservation of the Industrial Heritage. <http://www.mnactec.cat/ticcih/>.

Trbojevic, V.M. (2009) Another look at risk and structural reliability criteria. *Structural Safety,* 31, 3. pp. 245-250.

Zhang, S. (2007) Conservation and adaptive reuse of industrial heritage in Shanghai. *Frontiers of Architecture and Civil Engineering in China,* 1, 4. pp. 481-490.

18th International Conference
ENGINEERING MECHANICS 2012
Svratka, Czech Republic, May 14 – 17, 2012

pp. 1281–1286
Paper #222

PRESTRESSED CONCRETE SLEEPER UNDER EXTREME LOADING CONDITIONS

J. Sýkorová[*], J. Bártová[**], P. Štemberk[***]

Abstract: *Prestressed concrete sleepers are among the most common structural components of the railway tracks. Nowadays, the majority of railway sleepers are made of prestressed concrete. During their service life, the sleepers are subjected to extreme loading conditions, which may drastically reduce the span of their service life. This paper focuses on the optimized design of prestressed railway sleeper subjected to extreme loading conditions, which represented here by the impact of a flat wheel and by the cyclic loading.*

Keywords: ***Extreme loading, prestressed concrete sleeper, optimization, cyclic loading, fatigue.***

1. Introduction

The classical railway track consists of the rails, fasteners, sleepers, ballast and underlying subgrade (Fig. 1). The railway sleepers lie on the ballast transversally to the rails, which supports and holds them in place, and provides drainage and flexibility. The sleepers transfer the loads from rails to the ballast and subgrade, hold the rails to the correct gauge, restrain longitudinal and lateral rail movements, and provide strength and stability to whole track structure. That is why the concrete sleepers are the essential components of the track structure. It is obvious that the sleepers are subjected to extreme loading conditions and their design should be provided with high attention.

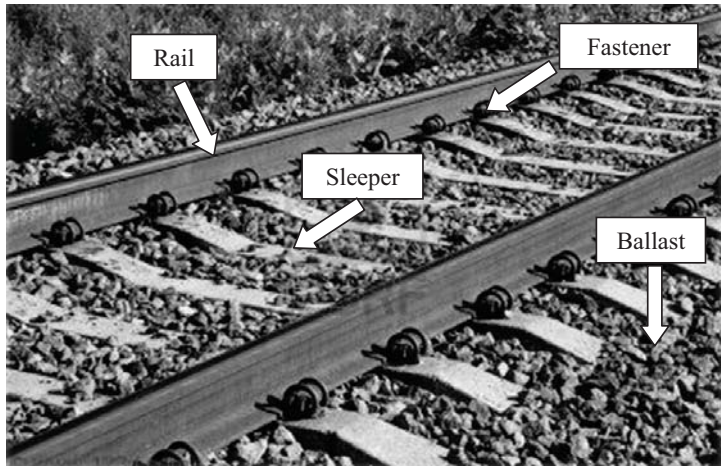

Fig. 1: Components of classical railway ballast track

[*] Ing. Jana Sýkorová: Czech Technical University in Prague, Faculty of Civil Engineering, Thákurova 7, 166 29, Prague 6; CZ, e-mail: jana.sykorova.1@fsv.cvut.cz

[**] Ing. Jana Bártová: Czech Technical University in Prague, Faculty of Civil Engineering, Thákurova 7, 166 29, Prague 6; CZ, e-mail: jana.bartova@fsv.cvut.cz

[***] doc. Ing. Petr Štemberk, Ph.D.: Czech Technical University in Prague, Faculty of Civil Engineering, Thákurova 7, 166 29, Prague 6; CZ, e-mail: stemberk@fsv.cvut.cz

This paper focuses on explanation of the design of prestressed concrete sleeper when the emphasis is put on optimization of the shape of the sleeper and position of prestressing wires with respect to the load distribution and extreme loading conditions caused by impact of flat wheel and cyclic loading.

2. Loading of railway sleepers

The whole railway track is subjected to static and dynamic load, which is caused by train transportation. The magnitude of this load depends on many factors. The main factors are the geometry of the railway track (straight or curved), type of the train, travelling speed of the train, maintenance of the railway vehicles and also the ballast reaction on the sleeper.

The design static wheel load per rail seat for standard railway tracks is 125 kN, which roughly corresponds to the maximum speed of 160 km/hour. But it should be also noted that the railway tracks often suffer from extreme loading conditions. The extreme loading is attributed to the wheel and rail abnormalities or missing subgrade under parts of the sleeper. The rail and wheel abnormalities are, for example, the flat wheels (Fig. 2), wheel corrugation, out-of-round wheels, dipped rails, etc.

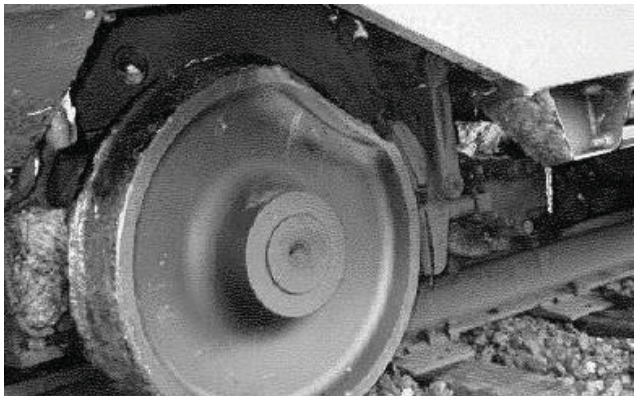

Fig. 2: Illustrative example of extremely flat wheel

These defects can cause loading of a very high magnitude but short duration and the occurrence of such loading is of low probability during the design life of the railway sleeper (Kaewunruen & Remennikov, 2009). The magnitude of the dynamic impact loads per rail seat varies from 200 kN up to 750 kN (Remennikov & Kaewunruen, 2008). These forces may cause cracking and failure of the sleeper (Sýkorová, et al., 2011).

Railway sleeper is a structural element which is subjected to cyclic loading during its entire service life. The cyclic loading causes fatigue of concrete, which results in permanent progressive changes in the structure of the material. These changes can cause crack, or micro-crack, propagation which consequently reduces stiffness of the structure, which in the extreme case can lead to fatigue failure. The fatigue damage of concrete can be assessed by using the fatigue damage function. This function expresses the decreasing of stiffness of the structure by decreasing the value of the modulus of elasticity during the cyclic loading (Foglar, 2008; Sýkorová et al., 2008).

3. Numerical analysis of railway sleeper

The resulting shape of the sleeper was obtained by the optimization of the shape of the standard B70 prestressed concrete mono-block sleeper. The prestressing force and the position of prestressing wires are then determined accordingly for the optimized shape of the sleeper.

3.1. Optimized design of the concrete sleeper for the standard load and the impact of flat wheel

In the following, the problem is divided into two cases. The first case is related to the design of the sleeper to withstand the standard load of 125 kN per rail seat. The second case deals with the design of the same prestressed concrete sleeper to withstand the load of 400 kN per rail seat, which represents the impact of the flat wheel. In general, the resulting shape of the sleepers resembles that of the standard B70 when the height and the width of the sleeper are slightly increased. Also, the prestressing forces are induced by a similar distribution of the prestressing wires, whose arrangement reflects the increased loading conditions. The resulting shape and the distribution of prestressing wires are shown in Fig. 3 and Fig. 4.

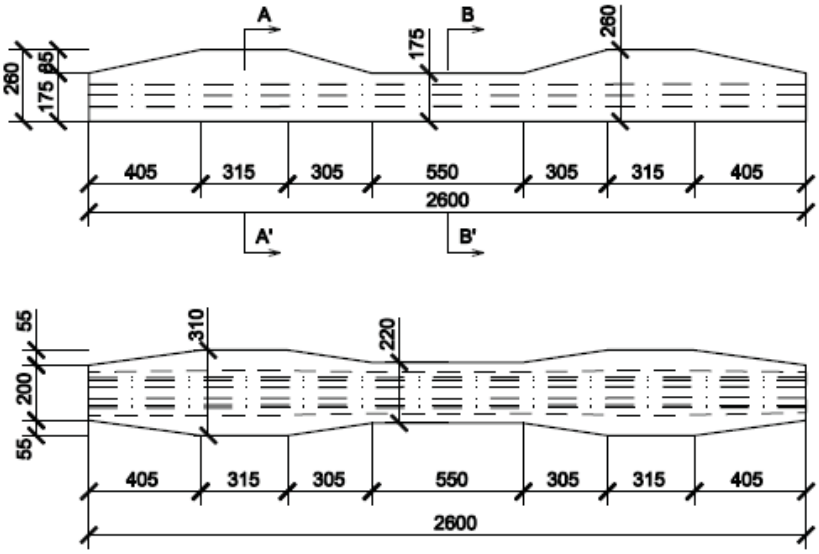

Fig. 3: Shape of optimized railway sleeper

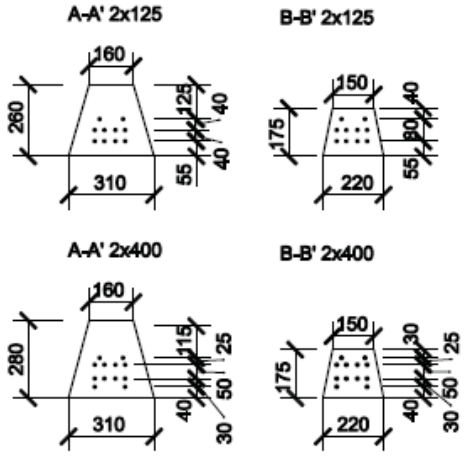

Fig. 4: Cross-sections of analysed sleepers: rail seat (left), mid-span (right)

The necessary prestressing reinforcement is provided with the identical prestressing wires with the proof test of 1860 MPa. The sleeper with standard load of 125 kN on both rail seats is prestressed with 10 wires with the diameter of 6 mm. The sleeper designed for impact load of 400 kN on both rail seats is prestressed with 12 wires with the diameter of 8 mm. The 28-day compressive strength of concrete used in the analysed sleeper must be greater than 50 MPa, which is a common value for prestressed concrete sleepers, such as the B70.

The distribution of the contact stresses under the analysed sleeper, which corresponds to the stiffness of the ballast and the underlying subgrade layers, is schematically depicted in Fig. 5.

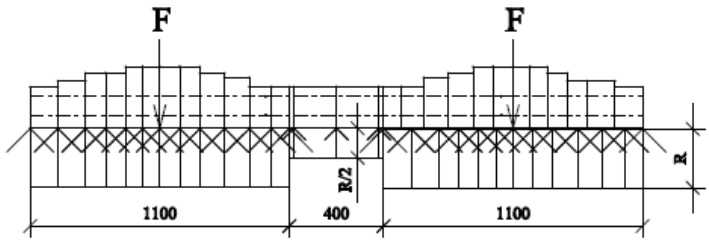

Fig. 5: Distribution of contact stresses under analysed railway sleeper

The numerical analysis was performed with the commercial software ESA Engineer 2008, which is based on the finite element method. The load configuration shown in Fig. 5 was considered in the analysis and the resulting distributions of the bending moment for both the load cases (F=125 kN and F=400 kN) are shown in Fig. 6. This identical bending moment distribution was considered in the optimization of the shape and the peak positive and the peak negative bending moments were considered in determination of the presstressing force.

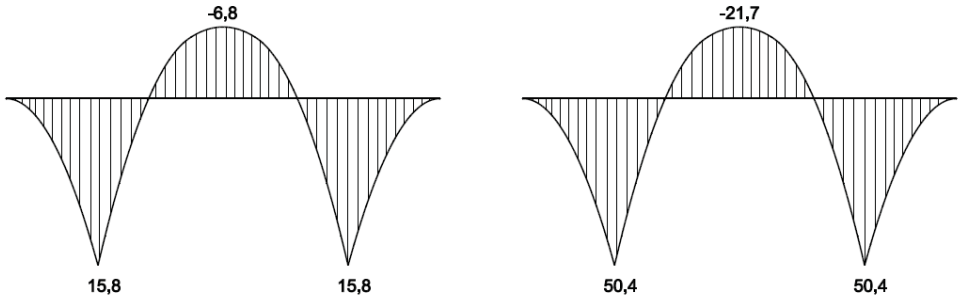

Fig. 6: Bending moment distribution (in kNm) for load: 2 x 125 kN (left), 2 x 400 kN (right)

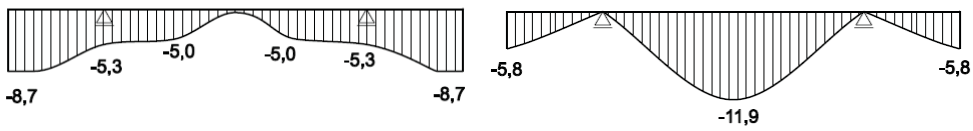

Fig. 7: Normal stress distribution (in MPa) from combination of prestressing and forces of 125 kN per rail seat: upper surface (left), lower surface (right)

The normal stresses at the upper and lower surfaces of the sleeper under the standard load of 125 kN per rail seat, corresponding to the bending moment distributions shown in Fig. 6, are shown in Fig. 7 and the maximum and minimum values at the mid-span and the rail seat cross sections are summarized in Tab. 1.

Tab. 1: Maximum and minimum normal stresses.

Load	Stress (MPa)			
	Upper surface		Lower surface	
	Mid-span	Rail seat	Mid-span	Rail seat
2 x 125 kN	7.7	-6.8	-6.8	5.5
2 x 400 kN	27.3	-18.7	-24.3	14.9
Prestressing and 2 x 125 kN	-1.7	-5.3	-11.9	-0.7
Prestressing and 2 x 125 kN	-27.1	-1.1	-11.2	-14.5

3.2. Cyclic loading

The railway sleeper is subjected to cyclic loading which causes fatigue of concrete. The analysis of the prestressed concrete sleeper under fatigue load is done for the sleeper with standard load of 125 kN on both rail seats.

The most important characteristic when analysing the fatigue behaviour of concrete is the decrease of stiffness, which is calculated here by using fatigue damage function (Foglar, 2008; Sýkorová et al., 2008). This function depends on the total number of load cycles and the load level. The total number of load cycles which the prestressed concrete railway sleeper can resist during its service life, was determined by formulae in Eurocode 2 (CEN, 2005) as 80 millions. With respect to the maximum and minimum compressive stresses in the cross section under the rail seat, the load level is determined as 0.44. The initial average secant modulus of elasticity for concrete C50/60 is 37 GPa. Based on the fatigue damage function defined using the above values, the decrease of stiffness, which is expressed in terms of the modulus of elasticity, is shown in Fig. 8.

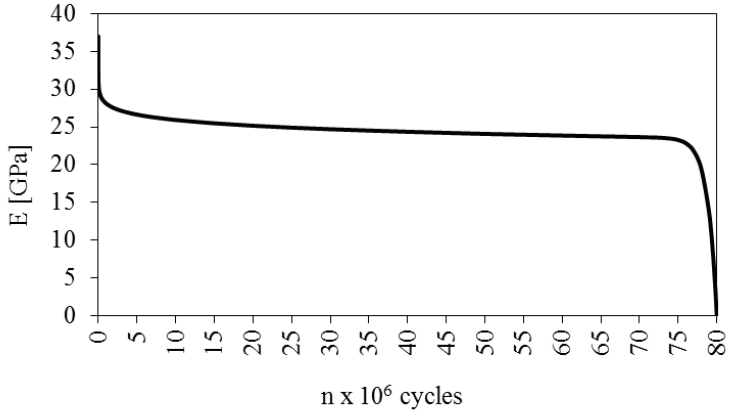

Fig. 8: Decrease of modulus of elasticity of the sleeper during entire service life

From Fig. 8, it is obvious that the modulus of elasticity decreases rapidly during the first few hundred thousands of load cycles and then again at the end of its service life. During the first 10 per cent of all load cycles the mean value of the modulus of elasticity decreases from the initial value of 37 GPa to 26.2 GPa. Such reduction of stiffness results in greater deformations and even in cracking and thus in reduction of the expected service life.

4. Conclusions

This paper presented an analysis of prestressed concrete railway sleeper subjected to two types of extreme loading conditions.

Railway sleeper can suffer during its service life from impact load caused by flat wheels. The occurrence of this impact load is of low probability during the design life of the railway sleeper, but once it happens the sleeper sustains ultimate damage, which requires replacement of the sleeper. Therefore, the standard shape of the sleeper known as B70 was optimized and the prestressing force designed so that it can withstand the impact load of 400 kN instead of the ordinary 125 kN per rail seat.

Railway sleeper is also structure which is subjected to cyclic loading. Cyclic loading of the railway sleepers commonly exceeds 80 millions of cycles during their service life which is commonly more than 40 years. Therefore, the optimized railway sleeper was analysed for the effect of cyclic loading which causes fatigue of structural elements. For the analysis of reduction of stiffness during the cyclic loading was used cyclic damage function.

Acknowledgement

The financial support by the Czech Science Foundation, project P105/10/2098, and the CTU in Prague, project SGS11/107/OHK1/2T/11, which is gratefully acknowledged.

References

Eurocode 2 - Design of Concrete Structures - Concrete Bridges - Design and detailing Rules (2005) CEN.

Foglar, M. (2008) *Strain development under cyclic loading*. Ph. D. Thesis, CTU in Prague, Prague.

Kaewunruen, S. & Remennikov, A. M. (2009) Progressive failure of prestressed concrete sleepers under multiple high-intensity impact loads. *Engineering Structures*, 31, pp.2460-2473.

Remennikov, A. M. & Kaewunruen, S. (2008) A review on loading conditions for railway track structures due to wheel and rail vertical interactions. *Progress in Structural Engineering and Materials*, 15, pp.207-234.

Sýkorová, J., Bártová, J. & Štemberk, P. (2011) Analysis of Prestressed Concrete Sleeper under Extreme Loading Conditions, in: *Mechanika 2011 - Proceedings of the 16th International Conference*, Kauno technologijos universitetas, Kaunas, pp.282-286.

Sýkorová, J., Foglar, M. & Štemberk, P. (2008) Fatigue of reinforced concrete bridges with influence of deterioration of concrete, in: *Microstructure Related Durability of Cementitious Composites – Proceedings of the First International Conference*, Bagneux: Rilem Publications s.a.r.l., pp.825-832.

18th International Conference
ENGINEERING MECHANICS 2012
Svratka, Czech Republic, May 14 – 17, 2012

pp. 1287–1292
Paper #234

MATERIAL PARAMETERS OF CEMENT AND ALKALI ACTIVATED FLY ASH CONCRETE MIXTURES LABORATORY MEASUREMENTS AND NUMERICAL SIMULATION

M. Šejnoha, [*] **M. Brouček,** [**] **E. Novotná,** [***] **D. Lehký,** [†] **P. Frantík,** [‡] **Z. Keršner** [†‡]

Abstract: *The paper reports on the determination of basic mechanical material parameters of several concrete and alkali activated concrete and fly ash mixtures intended for the construction of segmental lining used in TBM tunneling. The results of an extensive experimental program are discussed first. The principal attention is accorded to the experimental determination of specific fracture energy, which, when compared to numerical simulations, shows certain inconsistency with the measurements of other material data. This is supported by the derivation of the data from inverse analysis employing the elements of soft computing. Dynamic simulation of crack propagation experiments is suggested to reconcile the essential differences and to identify the most important impacts affecting the results of experimental measurements.*

Keywords: ***Alkali activated fly ash, Concrete, Fracture energy, Finite element simulation, Soft computing.***

1. Introduction

Massive increase of CO_2 emission in recent years has supported a considerable effort towards substitution of ordinary Portland cement by alkali-activated aluminosilicate materials such as fly ash in the production of concrete. Using fly ash as admixture in cements is now common in many applications. Full substitution for large scale structural units, however, is still at its infancy and to foster its progress beyond laboratory samples will require fundamental understanding of what is occurring already on the level of paste during alkali-activation process. Starting with recent accomplishments by Smilauer et al. (2011) we expect considerable activity in this field in the coming decade.

This topic, however, goes beyond the present scope. Instead we focus our attention on the macroscopic evaluation of the response of various mixtures of concrete and alkali-activated materials with emphases on the influence of fly ash replacing either a certain portion or an entire amount of cement. We report on both experimental and numerical part of this research effort as these should be considered on the same footing to mutually corroborate the obtained results.

Motivated by possible applications of these mixtures in the production of the segments of lining often used in hostile environment we set up an extensive experimental program that includes on the one hand small scale laboratory measurements of basic material parameters, material degradation due to activity of acid solutions, and on the other hand full scale measurements of resistance of lining segments to fire.

The present contribution is limited to the first part of this program aiming at quantification of individual mixtures with regard to their mechanical material data in the light of the required strength corre-

[*]Prof. Ing. Michal Šejnoha, Ph.D., DSc.: Czech Technical University in Prague, Faculty of Civil Engineering, Thákurova 7; 166 29, Prague; CZ, e-mail:sejnom@fsv.cvut.cz
[**]Ing. Miroslav Brouček, : Czech Technical University in Prague, Faculty of Civil Engineering, Thákurova 7; 166 29, Prague; CZ, e-mail:miroslav.broucek@fsv.cvut.cz
[***]Ing. Eva Novotná, Ph.D.: Czech Technical University in Prague, Faculty of Civil Engineering, Thákurova 7; 166 29, Prague; CZ, e-mail:novotnae@fsv.cvut.cz
[†]Ing. David Lehký, Ph.D.: Brno University of Technology Faculty of Civil Engineering Veveří 331/95 602 00 Brno;CZ, e-mail:lehky.d@fce.vutbr.cz
[‡]Ing. Petr Frantík, Ph.D.: Brno University of Technology Faculty of Civil Engineering Veveří 331/95 602 00 Brno;CZ, e-mail:kitnarf@centrum.cz
[†‡]Doc. Ing. Zbyně Keršner, CSc.: Brno University of Technology Faculty of Civil Engineering Veveří 331/95 602 00 Brno;CZ, e-mail:kersner.z@fce.vutbr.cz

sponding to concrete C$50/60$. The results of numerical simulations of selected tests are also present to warn engineers against blindly accepting the provided laboratory data which might not be suitable for intended numerical analysis on a structural level.

The remainder of this paper is organized as follows. Section 2. provides the list of examined mixtures. The results of experimental investigation are summarized in Section 3. Numerical part embracing also the identification of material parameters based on fracture energy measurements is described in Section 4. Brief summary is finally provided in Section 5.

2. Concrete and alkali activated mixtures

We begin by providing the list of examined concrete and alkali activated mixtures. Eight mixtures in overall were proposed. Two mixtures in particular assumed total replacement of concrete by fly ash activated by strong alkaline liquids such as a mixture of NaOH pellets dissolved in tap water and sodium silicate in the form of water glass. Low-calcium fly ash coming from the Mělník (FAM) and Opatovice (FAO) thermal electric power plants, the Czech Republic was used. Half the mixtures were further modified by adding 0.5% of volume of synthetic fibers Forta-Ferro. This amounted to 4.5 kg of fibers per 1 m^3 of the mixture.

The following notation is introduced to distinguish individual mixtures: C - Cement based concrete (reference mixture), POP - Alkali-activate fly ash, Fi - mixture containing fibers, FAC-1(2) - mixtures with partial replacement of concrete by fly-ash. All the mixtures considered the same grading curve. Specific fractions of stone grains are listed in Table 1. Individual mixtures are stored in Table 2.

Tab. 1: Fraction of grains

Fraction	Amount per 1 m^3 of mixture in [kg]
0/4	705
3/8	130
8/16	865

Tab. 2: List of selected mixtures

Material	Amount per 1 m^3 of mixture in [kg]			
Mixture →	C	FAC-1	FAC-2	POP
CEM I 52,5 R	460	322	322	-
limestone powder	40	40	40	-
Water	150	150	187	51
Fly ash		138 (FAM)	276 (FAM)	400 (FAO)
NAOH	-	-	-	29,4
Water glass 34%	-	-	-	127,5
Slaked lime	-	-	-	12
Glenium ACE	4.2	4.2	4.2	12

It will be seen in the next section that all cement based mixtures exceeded the required compressive strength of 50 MPa. Inability of alkali-activated mixtures (POP, FiPOP) to reach this value can be attributed to the insufficient curing temperature of about $40 - 45$°C which was chosen to meet the massive production feasibility.

3. Experimental program

Standard laboratory measurements were carried out at the Klokner Institute in Prague to obtain elastic moduli, cubic compressive strength and strength in transverse tension. While cubic specimens having edge length of 150 mm were used to measure strength properties ($f_{c,cube}$, f_t), $300 \times 150 \times 150$ mm prisms

were manufactured to acquire the values of Young's moduli. These specimens were further utilized to provide the uniaxial compressive strength $f_{c,prism}$. All measurements were performed 28 days since the time of their production. The results appear in Table 3.

Tab. 3: Material properties

Notation	Elastic modulus	Compressive strength	Transverse tension strength	Fracture energy
	E [GPa]	$f_{c,cube}/f_{c,prism}$ [MPa]	f_t [MPa]	G_f [N/m]
C	38.5	84.7 / 72	4.4	207.4 220.3, 190.3
FiC	39.5	78.0 / 65	3.7	-
FAC-1	40.1	66.3 / 59	3.1	190.9
FiFAC-1	39.7	61.3 / 63	3.1	-
FAC-2	-	54.0* (71.0**)	-	-
FiFAC-2	-	48.2* (69.9**)	-	-
POP	18.9	36.2 / 28	2.9	112.3
FiPOP	20	39.5 / 30	2.9	-

To address the expected pozzolanic reaction the samples corresponding to mixtures FAC-2 and FiFAC-2 with increased amount of fly ash were tested after 60 $(*)$ and 180 $(**)$ days of curing. The measured values of cubic strength confirm the ongoing pozzolanic reaction even without alkaline activators. Unfortunately, the applicability of structural elements made from these mixtures might be limited by low strength at early time of curing.

3.1. Specific fracture energy

A particular attention was dedicated to the determination of fracture energy from a three-point bending test displayed in Fig. 1(a). Three notched specimens for each mixture having dimensions $150 \times 150 \times 700$ mm with a notch depth of 25 mm were tested in a displacement-controlled loading regime at the rate of 0.05 mm/min up to 0.2 mm of crack mouth opening displacement (CMOD) and at the rate of 0.2 mm/min until failure. Averages calculated for individual mixtures are available in the last column of Table 3. Although specimens containing fibers were also tested, the corresponding values are not provided owing to the uncertainty in the calculation of this value from associated loading diagrams. Some representatives are plotted in Fig. 1(c) showing relatively large residual strength up to 30% of the peak value.

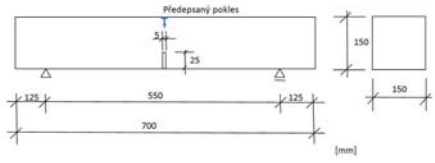

(a)

(b)

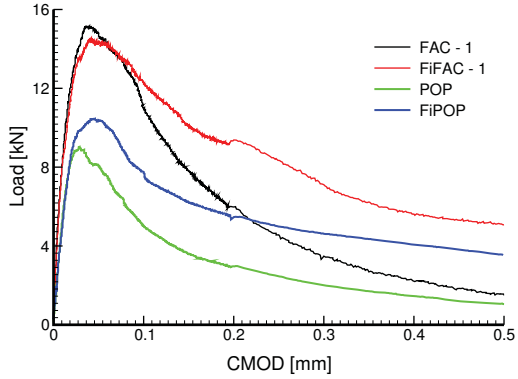

(c)

Fig. 1: Three-point bending test: (a) Computational scheme, (b) Experimental set-up, (c) Selected loading diagrams

4. Numerical simulation

This section offers the possibility of estimating the material parameters from fracture-mechanics tests by matching the experimentally measured and numerically derived loading curves. At the same, it raises a number of questions regarding the reliability of the results provided by either of the two methods if these are not mutually corroborated. The macroscopic loading curves of two selected concrete specimens denoted as C1 and C2 plotted in Fig. 3 as black solid lines were selected as our point of departure.

4.1. Static simulation of fracture energy test

To begin with, we adopted a simple trial and error method. The associated results stored in Table 4 are labeled as IDTE Mesh-TE where Mesh-TE denotes the finite element mesh seen in Fig. 2(a).

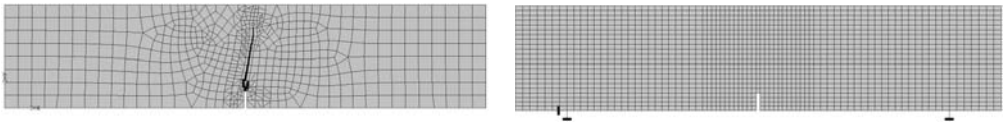

(a) (b)

Fig. 2: Finite element meshes adopted in numerical simulations: (a) Mesh-TE, (b) Mesh-NN

The ATENA finite element code (Červenka et al. (2007)) was used to simulate the three-point bending test numerically. A 3D Non Linear Cementitious 2 material model was selected to govern the gradual evolution of localized damage. The model is formulated in the total format assuming small strains and initial isotropy of a material. The tensile behavior is governed by the Rankine-type criterion with exponential softening while in compression, the Menétrey-Willam yield surface with hardening and softening phases is used. The fracture model employs the orthotropic smeared crack formulation and the fixed crack model with the mesh adjusted softening modulus. This model is defined on the basis of characteristic element dimensions in tension and compression to ensure the objectivity in the strain-softening regime. The required material parameters are presented in Table 4

Tab. 4: Material data of 3D Non Linear Cementitious 2 model for two specimens C1/C2

Parameter	IDTE Mesh-TE	IDNN Mesh-NN	IDNN Mesh-TE
Elastic modulus [GPa]	48 / 55	82* / 96*	82 / 96
Poisson's number [-]	0.2	0.2	0.2
Tensile strength [MPa]	3.8 / 4.5	2.7* / 2.9*	2.7 / 2.9
Compressive strength [MPa]	72	72	72
Specific fracture energy [N/m]	70 / 60	228* / 206*	228 / 206
Specific weight [kN/m^3]	24.7	24.7	24.7

The material parameters employed in this case study are introduced in the first column of Table 4 (IDTE Mesh-TE). The objective was to use the experimentally obtained data if possible while attempting to match the available loading curves. While the Young's moduli and tensile strengths received only minor adjustment if compared with the measured values in Table 3, the specific fracture energy required a significant reduction to match measured and simulated loading curves reasonably close; compare the black and red solid lines in Fig. 3. Compare also model fracture energies in the 1st column of Table 4 and the corresponding ones available in the 2nd row of Table 3. These results are the first indication as to the inadequacy of the measured fracture energy to be used as a geometry independent material parameter in full scale structural simulations.

4.2. Numerical derivation of material data from inverse analysis

Quite severe deviations between measured and numerically estimated specific fracture energies provided by a simple direct approach promoted the application of a more rigorous type of inverse analysis adopting

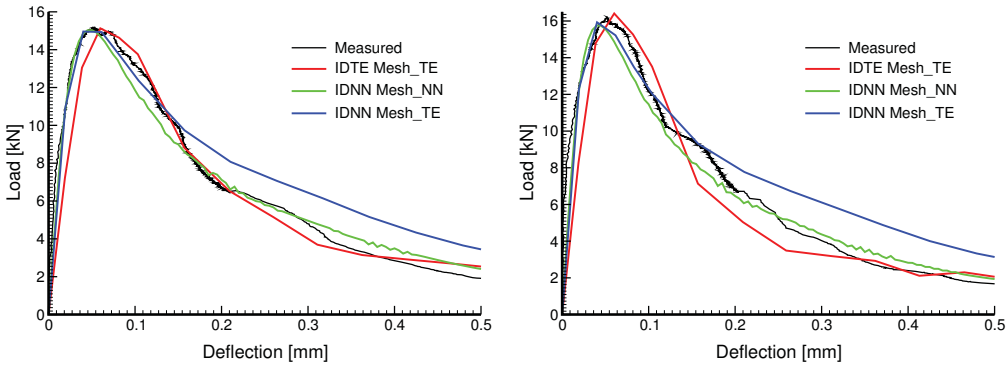

Fig. 3: Measured and numerically derived loading curves for two concrete specimens: (a) C1, (b) C2

the elements of soft computing (Novák and Lehký (2006); Lehký and Novák (2009)). Herein, we report on the approach combining artificial neural network (ANN) and finite element method.

Again the ATENA code was used to perform numerical simulations. The corresponding finite element mesh appears in Fig. 2(b). Based on sensitivity analysis (Novák et al. (1993)) we considered Young's modulus E, tensile strength f_t and specific fracture energy G_f be subject to identification. These are labeled with (*) in Table 4. Other material data were assumed fixed either provided by experiment such as the compressive strength $f_{c,prism}$ or assigned default values offered by the program for the selected material model.

As for the searching strategy, the implemented artificial neural network is of a feed-forward multilayer type. The network consisted of 3 inputs, one hidden layer having 5 neurons with non-linear transfer function (hyperbolic tangent) and output layer having 3 neurons with a linear transfer function. Each of the output neurons corresponds to one of the identified parameter. The size of training set was set to 50 samples generated using the Latin Hypercube Sampling method (McKay et al. (1979)). To train ANN Levenberg-Marquardt optimization method (Singh et al. (2007)) and genetic algorithms (Haupt and Haupt (2004)) were used. Once ANN was trained the experimental response was used to obtain identified parameters. With this set of parameters numerical analysis was carried out and resulting response was compared with the experimental one. The resulting loading curves corresponding to identified parameters in Table 4 are plotted as solid green lines (IDNN Mesh-NN) in Fig. 3.

Note that while the identified values of G_f are in a very good agreement with those provided by experiment, recall the 2nd row in Table 2, the identified values of Young's moduli are unrealistically high especially when compared to the measured ones. Further indication suggesting that the measured values of fracture energy can hardly be accepted as material parameters for structural analysis is a strong dependence of the results on finite element mesh evident from plots in Fig. 3, blue solid lines labeled as IDNN Mesh-TE. These were found after running the numerical analysis with identified data but adopting the unstructured coarse mesh in Fig. 2(a). It is reasonable to expect that for large scale structural analysis the adopted finite element mesh would be even coarser.

4.3. Dynamic simulation of fracture energy test

Learning from experience (Keršner et al. (2011)) a number of issues might be examined to provide solid explanation for inconsistency between experimental results and numerical simulations. The principal impact factor affecting the experimental results can be attributed to the relatively fast rate of loading which should be reflected in numerical simulations by accounting for inertia properties of the components of loading test setup. Dynamic simulation of the crack propagation test discussed already by Frantik (2008) can provide explanation to a high initial stiffness, recall the results of identification analysis, by incorporating the viscous damping of the specimen. This causes a slower stress distribution inside of the specimen and consequently leads to higher forces during fast loading. Other issues worth of future inves-

tigation include significant oscillations of time series of vertical displacements, unsymmetrical bending, etc.

5. Conclusions

The present contribution summarizes the experimental part of the project concerned with the modeling of TBM based tunneling in densely populated areas. Emphases were given to the experimental investigation of several cement and alkali activated fly ash based concrete mixtures. With principal attention paid to the specific fracture energy we attempted to confirm the experimental measurements by an independent numerical simulation of a three-point bending test employing the ATENA finite element code. Both simple trial and error method as well as more rigorous ANN based identification method were exercised. Both approaches revealed unreliability in the direct use of experimentally measured values of fracture energy as a material parameter. Most probably, this could be attributed to the applied rate of loading, which should be at least $10\times$ smaller to comply with the assumption of static analysis generally neglecting the viscous effects. This issues will be the subject of further research. Attention also deserves a considerable dependence of the results of simulations on the finite element mesh promoting similar mesh coarseness used in lab experiments and structural simulations at least in areas prone to damage evolution.

Acknowledgments

The financial support of the project No. TA01030245 provided by the Czech Technology Agency is gratefully acknowledged. We extend our personal thanks to Doc. Petr Bouška and Doc. Jiří Kolísko from the Klokner Institute in Prague for executing the experimental program.

References

Šmilauer, V. and Hlaváček, P. and Škvára F. and Kopecký, L. and Němeček, J., (2011), Micromechanical multiscale model for alkali activation of fly ash and metakaolin, *Journal of Material Sciece*, Vol 46, No.20, pp 6545–6555.

Červenka, V., Jendele, L. and Červenka, J. (2007), ATENA Program Documentation - Part 1: Theory, *Cervenka Consulting*, Prague, Czech Republic.

Novák, D. and Lehký, D. (2006), ANN Inverse Analysis Based on Stochastic Small-Sample Training Set Simulation. *Engineering Application of Artificial Intelligence*, Vol 19, pp 731–740.

Lehký, D. and Novák, D. (2009), ANN Inverse Analysis in Stochastic Computational Mechanics. In: *Artificial Intelligence: New Research, Berstein*, (R.B., Curtis, W.N. eds). Nova Science Publishers, Hauppauge NY, USA, 323–350.

Novák, D., Teplý, B. and Shiraishi, N. (1993), Sensitivity analysis of structures: a review. In: *5th International Conference on Civil and Structural Engineering Computing, Edinburgh*, Scotland, pp 201–207.

Haupt, R.L. and Haupt, S.E. (2004), *Practical Genetic Algorithms*, John Wiley Sons, Inc., Hoboken, New Jersey. USA.

McKay, M.D., Conover, W.J. and Beckman, R.J. (1979). A comparison of three methods for selecting values of input variables in the analysis of output from a computer code. *Technometrics*, Vol 21, pp 239–245.

Singh, V., Gupta, I. and Gupta, H.O. (2007), ANN-based estimator for distillation using Levenberg-Marquardt approach. *Engineering Applications of Artificial Intelligence*, Vol 20, pp 249–259.

Frantík, P. (2008), Czech Dynamic simulation of crack propagation experiments, In: *Engineering Mechanics 2008*, May 12-15, Svratka, Czech Republic.

Zbyněk Keršner, David Lehký, Drahomír Novák, Barbara Kucharczyková, Petr Frantík, Jan Bedáň (2011), Fracture Energy Tests: Specimens (C30/37 H), II (C25/30 B3), III (C25/30 XC1 GK16), IV (C20/25 XC1 GK16), *Internal Report*, Brno University of Technology, Faculty of Civil Engineering, Institute of Structural Mechanics and Institute of Building Testing.

18th International Conference
ENGINEERING MECHANICS 2012
Svratka, Czech Republic, May 14 – 17, 2012

pp. 1293–1300
Paper #232

RESISTANCE OF CONCRETE WITH FLY ASH CONTENT UNDER THE RWS CURVE FIRE LOADING

M. Šejnoha[*], M. Brouček[**], E. Novotná[***], J. Sýkora[****]

Abstract: *The first part of the paper presents the results obtained from large scale fire experiments on reinforced concrete panels 1.5 x 3.0 meters and small scale high temperature experiments on cubes with a side length equal to 0.15 meters. Concrete mixtures with large content of fly ash as a binder were selected for large scale experiments whereas cubes were made of cement based mixtures as well as of alkali activated fly ash mixtures. The influence on polypropylene fibres, added into half of the specimens, on the fire resistance is also described. Second part of the paper is focused on the numerical modelling of the effect of fire using a simplified numerical approach. Experimental data are used for calibration of the models as well as for the comparison of results. The loading is governed by RWS Curve which assumes 50 cubic meters of petrol or oil fire in the tunnel.*

Keywords: ***Fire resistance, Heat transfer, Spalling, Fly ash, PP fibres***

1. Introduction

Increased effort in use of waste material as well as in decrease of CO_2 emissions powered by international agreements, increased taxation and subsidy from national and international agencies, and new challenges and improved standards on structural safety enable incorporation of materials which so far have been used only under specific circumstances. The idea of substituting fly ash for cement and thus reducing the heat from hydration has been successfully used in the past (e.g. Keil J., 1966) for massive concrete structures with low requirements on strength or strength increase rate.

Presented results are part of an extensive experimental program aimed at possible application of cement free (alkali activated) or cement reduced (fly ash replaced) concrete in the production of precast segmental linings for tunnels created by TBM. In particular, this topic is focused on fire resistance of enhanced mixtures including large and small scale experiments as well as numerical simulations of large scale tests. Requirements applied on mechanical parameters of tested mixtures correspond with concrete C50/60 with improved resistance against fire and hostile environment (mainly aggressive sulphate).

Fire outbreaks in tunnels differ from others especially in terms of peak temperature and rate of temperature increase. In recent years a great deal of research has taken place internationally to ascertain the types of fire which could occur in tunnel and underground spaces. Such research has taken place in laboratory conditions as well as in disused tunnels. In the presented experiments, RWS curve, which assumes 50 m^3 fuel tanker fire which last for 120 minutes, is considered.

The results from the physical experiments including spalling, overall damage of the surface and deformations of the tested panels are presented. The possibility of numerically approximate the deformations and time dependent temperature distribution throughout the specimens is evaluated.

[*] Prof. Ing. Michal Šejnoha, Ph.D., DSc.: Czech Technical University in Prague, Faculty of Civil Engineering, Thákurova 7; 166 29, Prague; CZ, e-mail:sejnom@fsv.cvut.cz

[**] Ing. Miroslav Brouček: Czech Technical University in Prague, Faculty of Civil Engineering, Thákurova 7; 166 29, Prague; CZ, e-mail:miroslav.broucek@fsv.cvut.cz

[***] Ing. Eva Novotná, Ph.D.: Czech Technical University in Prague, Faculty of Civil Engineering, Thákurova 7; 166 29, Prague; CZ, e-mail:novotnae@fsv.cvut.cz

[****] Ing. Jan Sýkora, Ph.D.: Czech Technical University in Prague, Faculty of Civil Engineering, Thákurova 7; 166 29, Prague; CZ, e-mail:jan.sykora.1@fsv.cvut.cz

2. Full scale physical experiments

In order to fairly describe the impact of the heavy fire load on tunnel linings full scale experiments have been set up. Two specimens having dimensions and other properties, e.g. reinforcement, very similar to the linings used in tunnels (except for the shape) have been installed in the fire chamber. In fact they present one of the sides of fire chamber as shown in Fig. 1 (a). The fire chamber is cube shaped with a side length 3.4 m. Four computer controlled gas burners are responsible for keeping the temperature inside the chamber at the designed level. The temperature inside the chamber is measured by 7 plate and 2 shell thermometers.

The temperature inside the specimen is measured in 3 points (upper third, middle, lower third) located on the middle vertical line. Each point contains again 3 thermocouples positioned 50 mm, 125 mm (centre) and 200 mm from the inner surface. Another seven thermocouples are measuring the temperature of the outer surface of each specimen.

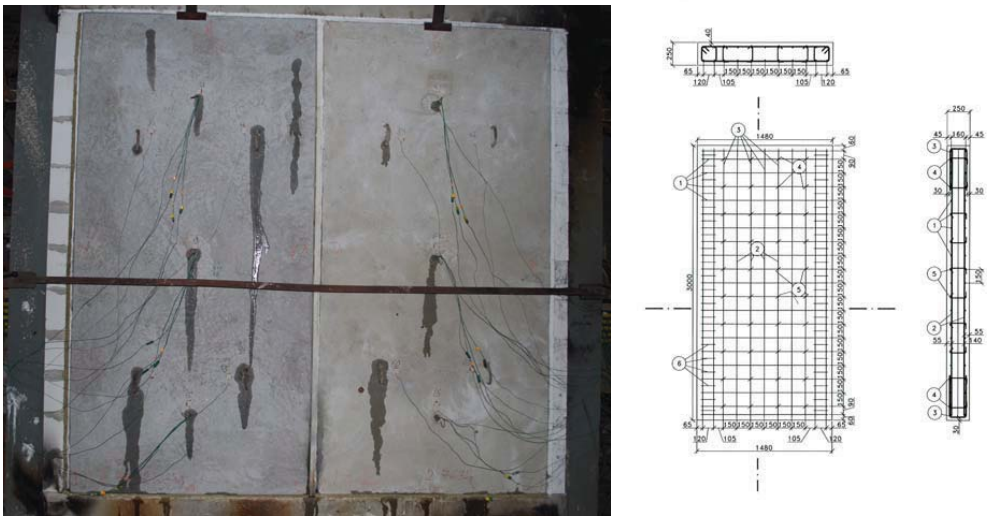

(a) (b)

Fig. 1: Full scale experiments: (a) Specimens built-in the fire chamber, (b) Reinforcement of the panels

The deflection of the specimen is measured in nine points located by three in three horizontal lines (top, middle and bottom) against parallel vertical plane created by rotational laser beam. All measured values are plotted against time, counting from the start of the experiment.

2.1. Specimen description

The specimens intended for large scale experiments are panels with dimensions 3000x1500x250 mm. Major reinforcement present steel bars 10 mm in diameter at 150 mm distance in both directions and surfaces. The cover thickness is 40 mm. Shear reinforcement bars are 6 or 8 mm in diameter. Position of the reinforcement is evident from Fig. 1 (b). Both the specimen geometry and reinforcement were selected as close to the ones used in tunnels as possible. Thus only the concrete mixtures were alternated.

Four different mixtures were tested in order to describe the effect of increased amount of fly ash in the mixture and the possible enhancement by plastic fibres. The grain distribution remains the same for all the mixtures and is presented in Tab. 1.

Tab. 1: Grain distribution in mixtures

Grain fraction (mm)	**Amount** (kg/m^3 of mixture)
0 / 4	705
4 / 8	130
8 / 16	865

The principal aim of the experimental program was to substitute cement by brown coal fly ash. Therefore, all the mixtures were based on the replacement of 30% of the cement. In order to improve the long term behaviour more fly ash (30% of the original cement weight) was added into two of the mixtures increasing the total amount of binding material. The improvement is expected due to Pozzolanic reaction of the fly ash that runs more slowly but for longer time than in the case of pure clinker cement as described by (e.g. Helmuth, 1987 or Fraay, Bijen and de Haan, 1989). Half the mixtures were further modified by adding 0.5% of volume of polypropylene monofilament 54 mm long fibres Forta-Ferro. Table 2 shows the amounts of materials used for mixtures in specimens for full scale experiments except for grains.

Tab. 2: Mixtures for full scale experiments

Mixture	**FAC1**	**FiFAC1**	**FAC2**	**FiFAC2**
Material	Amount (kg/m^3 of mixture)			
CEM I 52.5 R	322	322	322	322
Fly ash (Melnik I)	138	138	276	276
Water	150	150	187	187
Limestone powder	40	40	40	40
Gleanium ACE	4.2	4.2	4.2	4.2
FORTA-FERRO fibres	0	4.5	0	4.5

2.2. Results

The obtained results include temperatrure distribution along the specimens as is shown in Figure 2 (a) and (b), surface spalling of the specimens as discribed in Figure 3 and Figure 4 and Table 4. Measured deflection of the specimens is plotted in Figure 8 together with the results obtained from numericall analyses.

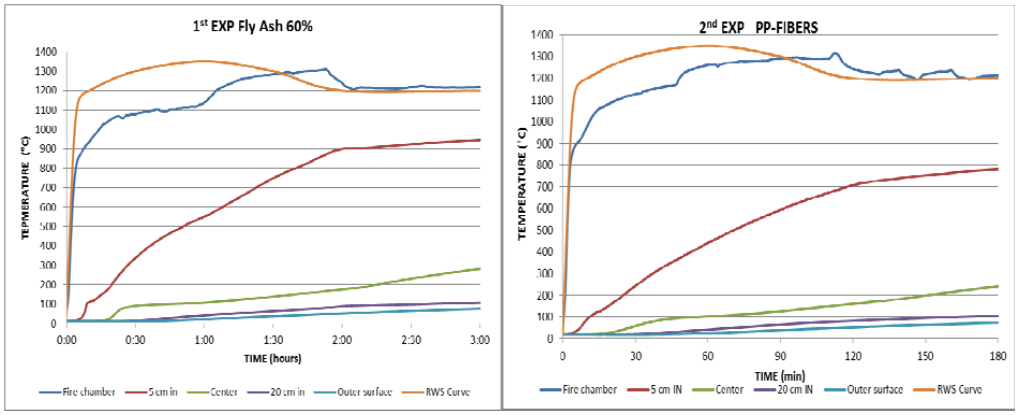

(a) (b)

Fig. 2: Measured temperatures: (a) FAC2 specimen, (b) FiFAC2 specimen (PP fibres included)

Mixtures enhanced by plastic fibres experienced significantly lower temperatures in the surface areas during the entire experiment and also during cooling. This fact also influences the spalling of the surface areas. Differences in the amount of fly ash content did not prove any significant influence on the results.

Tab. 3: Temperatures in °C inside specimens

Mixture	**FAC1**	**FiFAC1**	**FAC2**	**FiFAC2**
Location	End of fire loading (T = 180 min)			
50 mm from inner surface	929	781	945	862
Centre of the specimen	312	241	282	242
Location	Peak temperature (time differs)			
50 mm from inner surface	930	789	946	869
Centre of the specimen	348*	297	322*	277

* The logging was stopped after 210 minutes although the peak temperature in the centre of the specimen is reached after app. 250 minutes.

The fast increase of pore pressure due to evaporation is typically indentified as the main cause of spalling of concrete mixtures during the fire load. It seems, however, that is mainly influenced by the temperature rate increase and by the peak temperature in the exposed zones. Positive effect of the polypropylene fibres that burn out and therefore create additional "space", due to which the pore pressure increase is smaller and spalling is also less likely to occur or be of less magnitude, was experimentally proved several times in the past (e.g. Kodur, Cheng, Wang and Sultan, 2003). The mixtures with added fibres shown better behaviour during fire loading indeed but as the fibres also influence other mechanical parameters of the specimens it was necessary to include these mixtures in the program.

The effect of fibres can be observed in the temperatures measured during the experiment (Tab. 3) and is also visible in the following figure which clearly states the extent of damage. Figure 3 (a) shows a specimen without fibres. Although the surface is not scoured by 40 mm, which is the cover thickness, and only on average by 10.5 mm as shown in Figure 4 and Table 4, the reinforcement bars are exposed. On the other hand, Figure 3 (b) shows a specimen with added fibres, which surface was also scoured on average by 10.5 mm and yet the reinforcement bars were not exposed.

(a) (b)

Fig. 3: Specimens after an experiment: (a) FAC2 mixture, (b) FiFAC2 mixture (PP fibres included)

The following figure shows surfaces of the same specimens created by plotting measured points. For the measuring purpose rectangular mesh was created and measurement was done at each node against selected parallel plane on specimens without any further treatment. That is important mainly due to the presence of large "bubbles" with very thin shell cover on the surfaces. Even though in

average the surface is scoured by 10.5 mm some areas are actually higher than the original surface due to these bubbles.

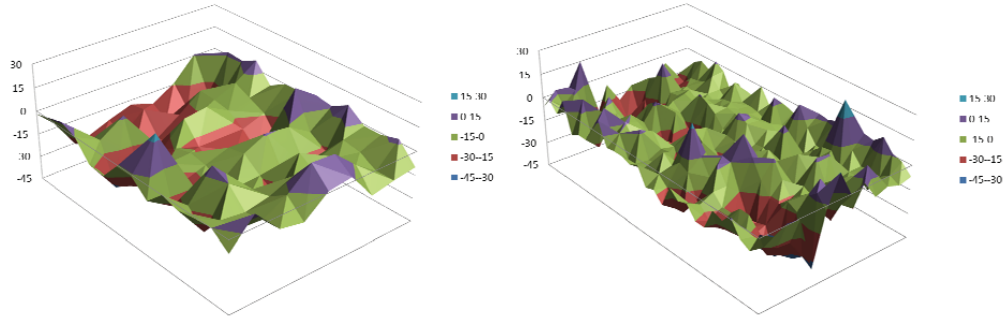

(a) (b)

Fig. 4: Measured surface after an experiment: (a) FAC2 mixture, (b) FiFAC2 mixture

Tab. 4: Spalling

Mixture / Value	FAC1	FiFAC1	FAC2	FiFAC2
Weight before experiment (kg)	2775	2763	9633	2637
Weight after experiment (kg)	2443	2511	2325	2360
Weight of the scrap (kg)	172	96	146	116
Scrap in % of weight	6.4	3.6	5.8	4.6
Average scour depth (mm)	10.5	4.4	9.5	10.5
Exposed reinforcement	large zones	not at all	large zones	locally

Missing weight i.e. the difference between weight before the experiment and weight after the experiment plus the weight of the scrap is vapored water. From the measured values it is clear that the amount of evaporated water is in overall the same for all tested specimens and nearly equals the total amount of water included in the mixture. Therefore, it can be stated that even chemically bonded water vaporize during the fire loading with RWS curve.

3. Small scale physical experiment

The original governing idea of small scale experiments was to provide faster and cheaper way to experimentally compare the fire resistance of different mixtures. For this purpose cubes with 150 mm side length were prepared from the same mixtures. The limits of available equipment i.e. fire or electric heated chambers respectively which would be large enough to accommodate cubes of this size did not, however, allow for precisely copying the required loading curve. Nevertheless after comparing several small scale experiments with full scale results it would be possible to find correlation sufficient to further utilize the small scale experiments for original purpose. The size of the cubes was originally influenced by the expected range of spalling and should prevent the entire specimen to collapse.

The limits of the used chamber are as follows. Maximum temperature the specimen can be exposed to is lowered to 1100°C and the temperature increase rate is limited to 20°C per minute.

3.1. Results

Despite the claimed parameters of the chamber which were actually tested on smaller samples, the temperature increase was even smaller, see Fig. 5 (b). Although the small temperature increase rate in fact prevent the surface spalling to occur, the concrete specimens could not sustained temperature above 750°C and burst as shown in Fig. 5 (a). The above thus moved the small scale experiments to the reassessment stage.

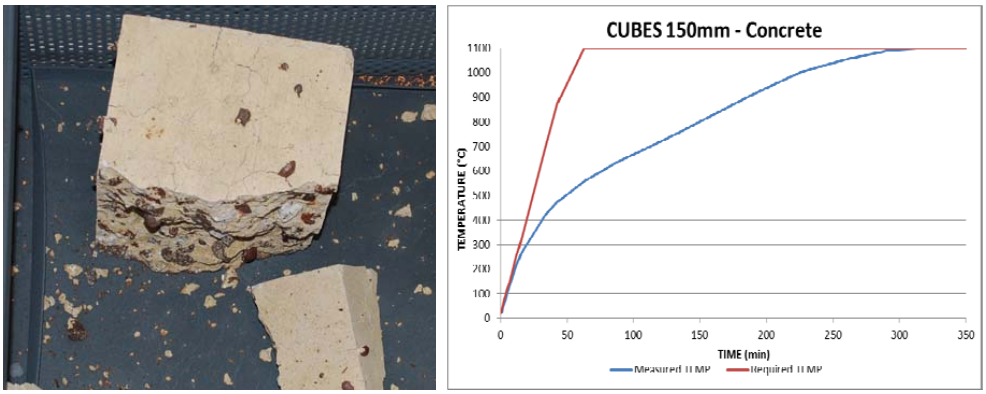

(a) (b)

Fig. 5: Small scale experiment: (a) Concrete specimen after experiment, (b) Temperature inside the chamber during the experiment

4. Numerical modelling

The possibility of using fully coupled modelling in order to faithfully represent the entire experiment was refused due to the rapid temperature increase in surface areas of the specimen and other difficulties. Instead we concentrate on staggered approach using the heat transport modelling in order to gain appropriate loading conditions for static analysis at different times.

4.1. Heat transfer

Due to lack of the measured data on the side of specimen exposed to fire, we utilize the numerical model for thermal behaviour of concrete at high temperatures. The heat transport is governed by energy conservation law proposed by (Beneš and Mayer, 2007). Two heat sinks representing the energy exchange of vaporation process and hydration / dehydration process are added to the balance equation.

To address this issue we consider two-dimensional rectangular domain discretized by FE mesh. One side of the domain was submitted to the convection and radiation boundary conditions while the opposite side was subjected to the prescribed boundary temperature. The evolutions of λ (thermal conductivity) and c (specific heat capacity) as functions of temperature were found also in (Beneš and Mayer, 2007). The resulting temperatures are plotted in Fig. 6 (a) for FAC2 mixture and (b) for FiFAC2 mixture.

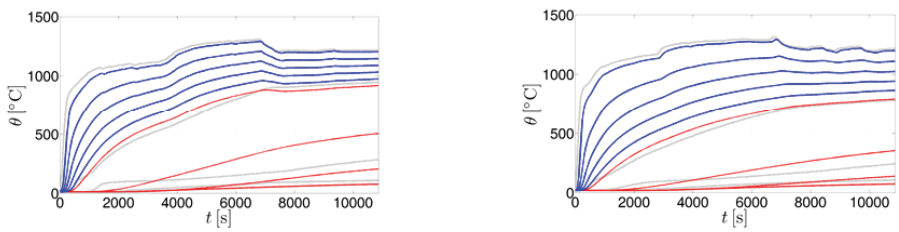

(a) (b)

Fig. 6: Calculated temperature distribution – blue lines 0,1,2,3,4 cm from inner surface; calibration lines in red: (a) FAC2 mixture, (b) FiFAC2 mixture

4.2. Static simulation of thermal load

For the static simulations we begun with ATENA code and simple elastic isotropic material for both concrete (3D brick elements – 0.2 m side length) and steel, using parameters provided by other laboratory experiments of tested mixtures. Table 5 summarizes all the material characteristic that have been used.

Tab. 5: Material characteristic for numerical simulations

Characteristic	Concrete	Steel
Elastic modulus (GPa)	40	210
Poisson`s ratio (-)	0.2	0.3
Specific weight (kN.m^{-3})	23	78.5
Coefficient of thermal expansion (K^{-1})	1.2e^{-5}	1.2e^{-5}

The load was applied on vertical layers with different thickness. As the inner surface areas are affected most the layers there were only 10 mm thick while the thicknesses of other five layers were increasing from 37.5 to 50 mm. The finite element mesh used is clear from Fig. 7 (a) while constrains and reinforcement bars incorporated into model can be seen in Fig. 7 (b).

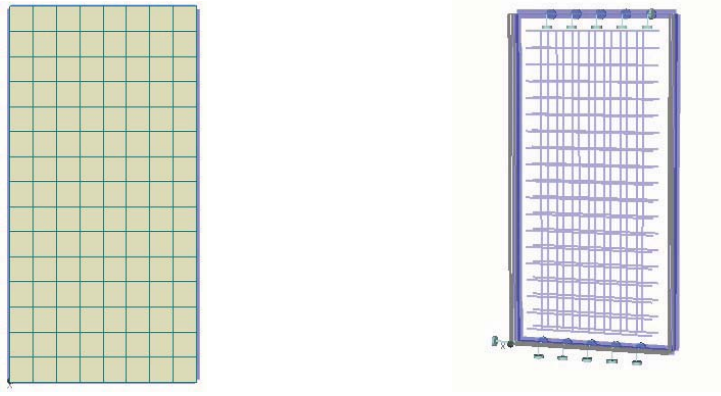

(a) (b)

Fig. 7: Finite element model: (a) mesh – front view, (b) constrains and reinforcements

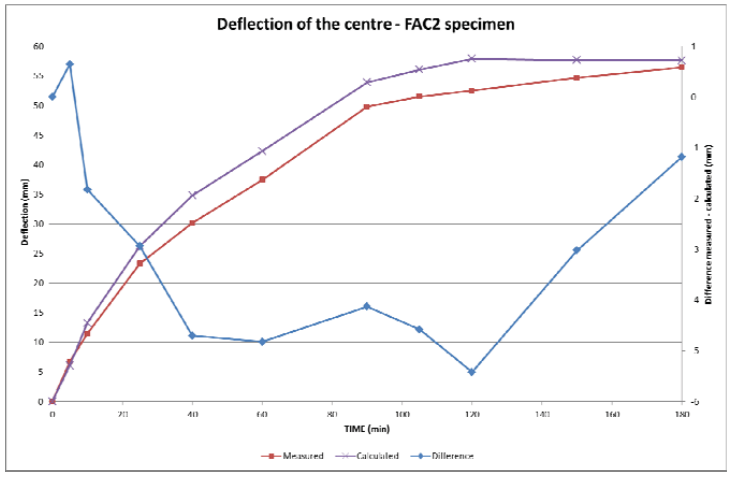

Fig. 8: Measured and calculated deflection of specimen FAC2 – centre of the outer surface

It can be observed in Fig. 8 that the calculated data acquire about 10% difference in the total deflection for most of the time, however, at the end of the experiment the difference is less than 2.5%. These results were obtained by careful estimation of the temperature distribution in the most exposed 50 mm. The effect of heat transfer between the surface and first thermometer plays crucial role as it is heavily time dependent. Using the values gained by numerical model described in section 4.1. larger values of deflection can be observed at the beginning of the experiment.

5. Conclusions

The paper summarizes the results obtained from experiments and numerical simulations of fire loading applied on TBM segment linings made of enhanced concrete mixtures. However, the full scale experiments proved to be irreplaceable when it comes to proper evaluation of the fire resistance of reinforced concrete panels, simple static simulations with appropriate loading distribution can give good results when it comes to total deflection of the panels. Valuable experience obtained due to the issues with small scale specimens will allow for improvement of the method for testing the enhanced mixtures.

Mixtures with increased amount of fly ash did not show significantly different behaviour unlike the mixtures with added plastic fibres. Even though the temperature in the 50 mm distance from the inner surface in all specimens have risen above 500°C, the specimen with the plastic fibres experienced smaller spalling and their reinforcement was not exposed after the experiment.

Numerical approximation of the impact of fire loading will be subjected to further research activities concentrating specifically on the heat transfer problem and spalling.

Acknowledgement

The financial support of the project No. TA01030245 provided by the Czech Technology Agency is gratefully acknowledged.

References

Beneš, M. and Mayer, P. (2007), Coupled model of hygro-thermal behavior of concrete during fire. *International Journal for Numerical Methods in Engineering*, (218):12–20.

Červenka, V., Jendele, L. and Červenka, J. (2007), ATENA Program Documentation - Part 1: Theory, *Cervenka Consulting*, Prague, Czech Republic.

Fraay, A.L.A., Bijen, J.M. and de Haan Y.M. (1989) The reaction of fly ash in concrete a critical examination, *Cement and Concrete Research*, 19(2): 235-246

Helmuth, R. (1987), Fly Ash in Cement and Concrete. *Portland Cement Association*, Illinois

Keil J. (1966), *Construction of the Orlik dam* - collection of essays, the national water company, (in Czech).

Kodur, V.K.R., Cheng, F-P., Wang, T-C., Sultan, M.A. (2003), Effect of strength and fiber reinforcement on fire resistance of high-strength concrete columns, *Journal of Structural Engineering*, 129(2):253-259

18th International Conference
ENGINEERING MECHANICS 2012
Svratka, Czech Republic, May 14 – 17, 2012

pp. 1301–1307
Paper #344

MIXED-MODE HIGHER-ORDER TERMS COEFFICIENTS ESTIMATED USING THE OVER-DETERMINISTIC METHOD

L. Šestáková*

Abstract: *The so-called 'over-deterministic' method (ODM) is applied on a mixed-mode configuration in order to determine higher-order terms coefficients of the Williams expansion approximating the stress and displacement fields in a cracked body. Results obtained agree very well to data found in literature (calculated by means of hybrid crack elements and boundary collocation method) and therefore further convergence studies are made in order to find some restrictions and recommendations corresponding to use of the ODM. Note, that more than five terms of the Williams expansions are considered and investigated in this contribution.*

Keywords: ***Crack, Williams expansion, higher-order terms coefficients, FE analysis, over-deterministic method.***

1. Introduction

It has been shown in recent years that conventional linear elastic fracture mechanics using a single controlling parameter, *i.e.* the stress intensity factor, for assessment of the initiaiton and propagation of a crack is not suitable in the case of quasi-brittle materials (such as ceramics or concrete). Therefore, not only the first (singular) term of the Williams series approximation of the crack tip asymptotic field (represented through the stress intensity factor), but also the other (higher-order) terms of the asymptotic field should be taken into account. It has been documented that the higher-order terms are of great relevance because they can predict the constraint of crack tip fields (Chao & Zhang, 1997; Berto & Lazzarin, 2010) and interpret the size/geometry/boundary effect, which both correspond to the extent of the zone around the crack tip with the nonlinear material behaviour, that is (in size) comparable to the typical structural dimensions (Karihaloo, 1999; Karihaloo et al., 2003; Veselý & Frantík, 2010).

The use of numerical techniques (such as finite element method) for higher-order terms determination is unavoidable for more complicated crack problems. The coefficients of the third and higher-order terms of the crack tip asymptotic field are very difficult to obtain. So far, there have been very few FE methods with the ability of calculating the coefficients of the higher-order terms, *e.g.* hybrid crack element method (HCE), boundary collocation method (BCM), etc. (Karihaloo & Xiao, 2001; Tong et al., 1997; Su & Fok, 2007; Xiao et al., 2004). However, all of these methods require special elements or complicated FE formulations. In this paper, the over-deterministic approach (ODM) based on the formulation of linear least-squares is introduced and tested on calculations of mixed-mode higher-order terms coefficients in Williams expansion (Williams, 1957). The main advantage of this method is that conventional finite elements (FE) can be used.

2. Problem description

Because only mode I configurations (three-point bend single edge notched beam and wedge splitting test) have been modelled in autor's previous work (Šestáková, 2011), a mixed-mode cracked specimen configuration has been chosen for testing of the ODM in this paper, see Fig. 1. Higher-order terms have been estimated on a plate with an angled edge-crack under uniaxial tension (AECT), whereas the crack angle was chosen as $\beta = 30°$, see Fig. 1 and (Ayatollahi & Nejati, 2010) for detailed geometry.

* Ing. Lucie Šestáková, Ph.D.: Institute of Structural Mechanics, Faculty of Civil Engineering, Brno University of Technology; Veveří 331/95; 60200, Brno; CZ, e-mail: sestakova.l@fce.vutbr.cz

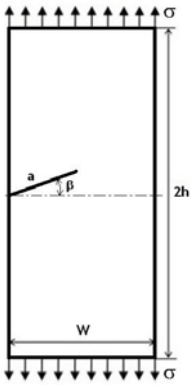

Fig 1: A plate with an angled edge-crack under uniaxial tension, $\beta = 30°$.

Results determined by means of the ODM (using displacement fields obtained from conventional FE analysis) have been compared to data found in literature. Moreover, more than five first higher-order terms have been investigated and a study on the displacement field influence on the data convergence has been carried out.

2.1. Displacement field around the crack tip

Williams (1957) derived that the linear elastic stress field in a cracked plate subjected to an arbitrary in-plane load can be expressed in the so-called Williams series expansion. Because the ODM is based on the numerically calculated displacements field around the crack tip (due to its better accuracy in comparison to the stress field), it is necessary to introduce the relations for displacements u and v:

$$u = \sum_{n=0}^{\infty} \frac{r^{n/2}}{2\mu} a_n \left[\left(\kappa + \frac{n}{2} + (-1)^n \right) \cos\frac{n}{2}\theta - \frac{n}{2}\cos\left(\frac{n}{2} - 2\right)\theta \right] + \\ + \sum_{n=0}^{\infty} \frac{r^{n/2}}{2\mu} b_n \left[\left(-\kappa - \frac{n}{2} + (-1)^n \right) \sin\frac{n}{2}\theta + \frac{n}{2}\sin\left(\frac{n}{2} - 2\right)\theta \right] \tag{1}$$

$$v = \sum_{n=0}^{\infty} \frac{r^{n/2}}{2\mu} a_n \left[\left(\kappa - \frac{n}{2} - (-1)^n \right) \sin\frac{n}{2}\theta + \frac{n}{2}\sin\left(\frac{n}{2} - 2\right)\theta \right] + \\ + \sum_{n=0}^{\infty} \frac{r^{n/2}}{2\mu} b_n \left[\left(\kappa - \frac{n}{2} + (-1)^n \right) \cos\frac{n}{2}\theta + \frac{n}{2}\cos\left(\frac{n}{2} - 2\right)\theta \right] \tag{2}$$

In Eq. (1) and (2), r and θ correspond to the polar coordinates centred at the crack tip (considering the crack with traction-free faces lying on the negative x-axis), μ is the shear modulus ($\mu = E/2(1 + \nu)$) and $\kappa = (3 - \nu)/(1 + \nu)$ for plane stress or $\kappa = 3 - 4\nu$ for plane strain; E and ν are Young's modulus and Poisson's ratio. First two terms coefficients in Eq. (1) and (2) are related to the well-known mode I stress intensity factor K_I ($a_1 = K_I/\sqrt{2\pi}$) and to the in-plane T-stress ($a_2 = T/4$), respectively. Third and higher-order terms were in the past rather ignored and are not connected to any conventional fracture parameters.

2.2. Principle of the over-deterministic method (ODM)

It has been mentioned that there exist several methods for determination of the higher-order terms. The so-called over-deterministic method has been chosen for the analysis presented in this work. This method has a really big advantage – there is no need to use complicated crack elements, which ensures only minimal requirements on the FE software. The ODM is well explained for example in (Ayatollahi & Nejati, 2010) and for the sake of brevity only the basic strategy is described further.

The ODM is based on the knowledge of the displacements field near the crack tip, see Eqs. (1) and (2). Important inputs for the method are therefore nodes displacements u and v obtained from numerical calculation for the particular geometry. Higher-order terms coefficients a_n and b_n are then calculated from a system of $2k$ equations, where k is the number of nodes selected around the crack tip. The number of higher-order terms can be chosen arbitrarily, but there are some restrictions: in order to obtain an over-determined set of equations, a relation between the number of nodes k and the number of the higher-order terms coefficients calculated should be satisfied:

$$2k > N + M + 2 \ , \tag{3}$$

where N corresponds to the number of mode I terms, a_n, of the Williams series expansion and M to the number of mode II terms, b_n (see Eqs. (1) and (2)).

There are also other recommendations introduced in (Ayatollahi & Nejati, 2010) connected to the number of nodes selected for the calculations or their distance from the crack tip, etc.; convergence criteria are discussed in the referred paper as well. Some suggestions published in (Ayatollahi & Nejati, 2010) are taken into consideration during this study and further investigations in this field are made and discussed.

2.3. Numerical model

In order to obtain the displacement field near the crack tip, a numerical model corresponding to the geometric and loading configuration introduced in Fig. 1 was created. The dimensions of the specimens were taken from (Ayatollahi & Nejati, 2010): $W = 1$, $h = 1$, $a = 0.6$, $\beta = 30°$ and the thickness was assumed to be unity and the units were self-consistent (therefore no units are presented). 8-node isoparametric elements (PLANE82) with plane stress conditions were used to model the cracked specimen. An FE mesh used for the whole analysis can be seen in Fig. 2, including corresponding boundary and loading conditions ($\sigma = 1$).

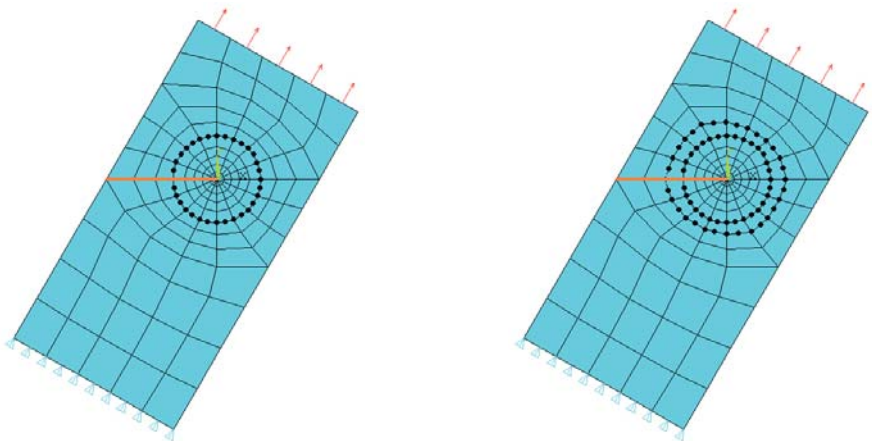

a) b)

Fig. 2: FE mesh of the plate with an angled edge-crack under uniaxial tension (AECT) used for the analysis; displacements of the highlighted nodes were used for application of the ODM.

The crack singularity was modelled through the first row of elements that is made of the so-called crack elements with shifted mid-side nodes. Because the coefficients of the Williams expansion do not depend on material properties, arbitrary values can be considered for Young's modulus and Poisson's ratio; $E = 1$ and $\nu = 0.25$ in the study presented.

In the first step of the analysis, displacements u, v of the fifth ring nodes around the crack tip, see Fig. 2a, were used for determination of the higher-order terms coefficients $a_1 \ldots a_{10}$ and $b_1 \ldots b_{10}$ by means of the ODM. Then the study was extended to determination of the coefficients a_n and b_n up to order $N = M = 20$, and therefore more nodes had to be used for evaluation, see Fig. 2b.

3. Results and discussion

An elementary goal of this work was to validate the ODM procedure on a mixed-mode configuration in order to obtain a reliable tool for further analysis of the stress field in quasi-brittle materials. Therefore, a plate with an angled edge-crack under uniaxial tension (AECT) has been investigated and higher-order terms coefficients estimated from the displacement field of the fifth ring nodes, see Fig. 2a. Data comparison can be found in Tab. 1; calculations were made under consideration of $N = M = 14$. Note that only first five terms are mostly available in literature. It can be seen in Tab. 1 that the coefficients calculated by means of the ODM correspond very well with the data published in the literature.

Tab. 1: Higher-order terms coefficients determined by means of the ODM (3. column) in comparison to data published in literature obtained by means of: HCE (1. column), see (Xiao et al., 2004); and BCM (2. column), see (Xiao et al., 2004)

	HCE	BCM	ODM		HCE	BCM	ODM
a_1	1.3867	1.3918	1.3938	b_1	-0.3762	-0.3777	-0.3784
a_2	0.1463	0.1485	0.1493	b_2			-1.6653
a_3	-1.2416	-1.2681	-1.2724	b_3	-0.2141	-0.2213	-0.2210
a_4	0.2400	0.2468	0.2472	b_4	-0.1954	-0.1906	-0.1928
a_5	-0.5226	-0.5422	-0.5433	b_5	0.1888	0.1792	0.1807

It has been shown that the higher-order terms up to fifth order fit to data published in literature and thus, more detailed analyses could be done. For the basic analysis the displacement field of 31 nodes of the fifth ring around the crack tip, see Fig. 2a, were used for investigation of higher-order terms convergence with increasing number of the Williams series expansion terms N and M. The dependences studied are introduced as 3D plots in Fig. 3 for the a_3-term and b_2-term.

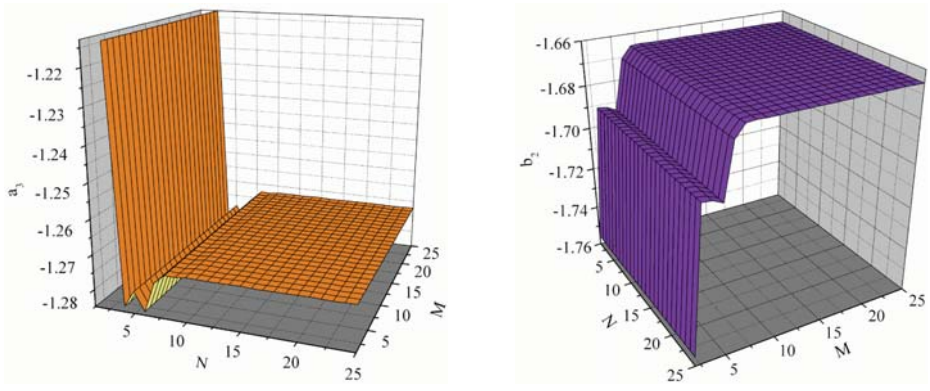

a) b)

Fig. 3: Higher-order terms a_3 and b_2 convergence in dependence on the number of Williams expansion coefficients N, M considered during calculations.

It can be seen in Fig. 3a that for mode I higher-order terms convergence is obviously more important the number of corresponding mode I terms N whereas the number of mode II terms M is rather irrelevant and vice versa for mode II higher-order terms b_n, see Fig. 3b. A detailed view on the dependences in Fig. 3 brings even harder conclusion, namely that there is no influence of the number

of mode I terms N on the b_n-values and similarly M is not important for a_n-values, see Fig. 4a. Thus, it seems that as a consequence, only 2D plots can be considered for a_n and b_n convergence analysis. However, it has been found out that it is not so easy. This independence was observed only if the displacements data set was perfectly symmetrical. If only one node displacements were left out from the analysis, a non-constant dependence on the both values (N, M) developed, see Fig. 4b.

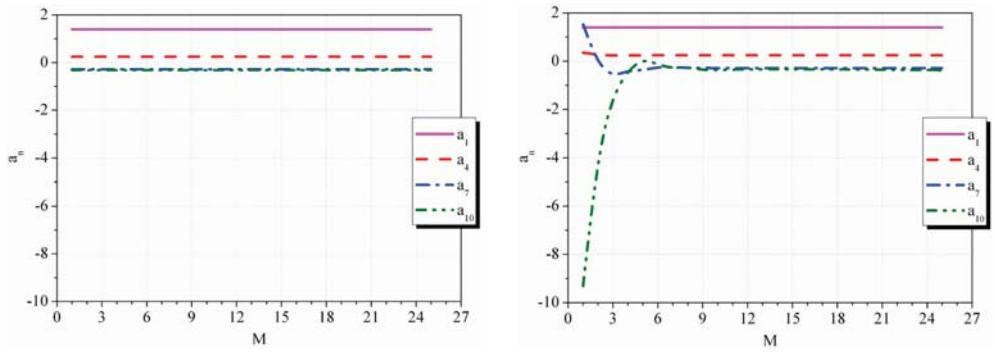

a) b)

Fig. 4: Higher-order terms coefficients a_n dependence on the number of Williams expansion mode II coefficients considered during calculations; a) perfectly symmetrical set of the displacements field; b) non-symmetrical set of the displacements field (one node missing).

Fig. 4 shows that a non-symmetrical displacement field around the crack tip used for evaluation of higher-order terms causes a purposeless dependence that can be easily avoided. Therefore, it should be recommended to use a symmetrical mesh around the crack tip in order to eliminate this kind of dependence.

When the previous conclusion is known, the two-dimensional dependences of the higher-order terms (a_n and b_n) on the corresponding number of coefficients considered during calculations (N for a_n and M for b_n) can be studied instead of the more complicated 3D plots. For the sake of better comparison and data manipulation, a dependence of the normalized higher-order terms coefficients ($a_{n,norm} = a_n/a_{n,N=14}$ and $b_{n,norm} = b_n/b_{n,M=14}$) on the number of coefficients was investigated, see Fig. 5.

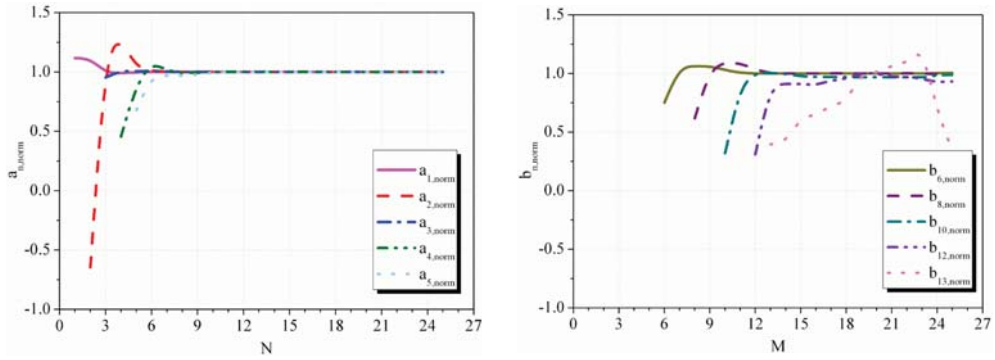

a) b)

Fig. 5: Normalized higher-order terms coefficients convergence in dependence on the number of Williams expansion coefficients considered during calculations; a) mode I terms $a_{1,norm} - a_{5,norm}$; b) mode II terms $b_{6,norm}$, $b_{8,norm}$, $b_{10,norm}$, $b_{12,norm}$, $b_{13,norm}$.

Fig. 5a shows that the coefficients a_n up to fifth order converge relatively fast; $N = M = 11$ seems to be enough (the same conclusion can be derived in the case of b_n coefficients). The dependences presented show that it holds, the higher n, the higher number of higher-order terms has to be considered in order to obtain reliable a_n and b_n values. It has been observed that it is possible to determine relatively accurately 12 higher-order terms coefficients under consideration of $k = 31$, see Fig. 5b. Then the uncertainty increases.

Further study was made on the same numerical model, the only difference was the number of nodes used for displacement field evaluation. The main effort was to find out if it is possible to calculate the Williams expansion term a_{14} and higher ones, which was not possible (with sufficient accuracy) with the data set of 31 nodes. Therefore, additional set of nodes was used with $k = 62$, see Fig. 2b. Several results are presented in Fig. 6.

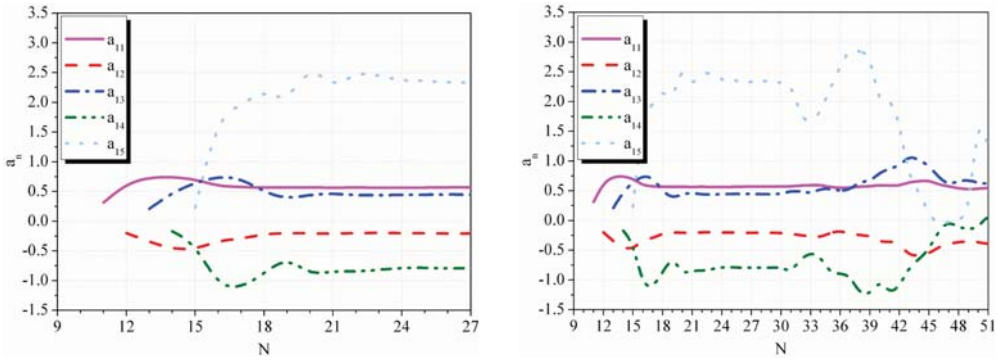

Fig. 6: Higher-order terms coefficients convergence in dependence on the number of Williams expansion coefficients considered during calculations in the case of 62 nodes investigated around the crack tip; note that only the x-axis scale differs.

As it can be seen in Fig. 6a, the higher-order terms $a_{11} - a_{15}$ seem to converge with number of terms $N = 22$ (similar dependences exist for $b_{11} - b_{15}$ as well), but a more complex view on the whole curve in Fig. 6b provides an ambiguous dependence. The curve really looks like it converges between $N = 20$ and $N = 30$ but then it exhibits nearly random behaviour again. Thus, it is not sure if the a_n (and b_n) values are correct and more studies should be done in this direction.

4. Conclusion

A numerical study has been carried out in order to test and validate the so-called over-deterministic method suggested for determination of higher-order terms coefficients in Williams expansion describing the stress field near a crack tip. A very good agreement has been found between the mixed-mode coefficients calculated and data published in literature for a plate with an angled edge-crack under uniaxial tension. On the basis of a convergence study performed, a recommendation on a symmetrical mesh around the crack tip (and symmetrical displacements field, respectively) can be expressed in order to avoid the general 3-dimensional dependence of higher-order terms on the number of terms considered during calculations N, M. Further, it has been observed that only first several terms (let's say up to $n = 12$) converge clearly with the increasing number of terms considered during calculations; the higher ones are not sure and thus, additional studies should be done in this direction because these terms can be important for better understanding of fracture in quasi-brittle materials as well.

Acknowledgement

This work was supported by the Czech Science Foundation, project No. P105/12/P417.

References

Ayatollahi, M.R., Nejati, M. (2010) An over-deterministic method for calculation of coefficients of crack tip asymptotic field from finite element analysis. *Fatigue & Fracture of Engineering Materials & Structures*, 34(3) , pp. 159-176

Berto, F., Lazzarin, P. (2010) On higher order terms in the crack tip stress field. *International Journal of Fracture*, 161(2), pp. 221-226.

Chao, Y.J., Zhang, X. (1997) Constraint effect in brittle fracture, in: *Proceedings of 27th National Symposium on Fatigue and Fracture* (Piacik, R.S., Newman, J.C., Dowling, D.E. Eds.), ASTM STP 1296, pp. 41-60, Philadelphia.

Karihaloo, B.L. (1999) Size effect in shallow and deep notched quasi-brittle structures. *International Journal of Fracture*, 95, pp. 379-390.

Karihaloo, B.L., Abdalla, H.M., Xiao, Q.Z. (2003) Size effect in concrete beams. *Engineering Fracture Mechanics*, 70, pp. 979-993.

Karihaloo, B.L., Xiao, Q.Z. (2001) Accurate determination of the coefficients of elastic crack tip asymptotic field by a hybrid crack element with p-adaptivity. *Engineering Fracture Mechanics*, 68, pp. 1609-1630.

Su, R.K.L., Fok, S.L. (2007) Determination of coefficients of the crack tip asymptotic field by fractal hybrid finite elements. *Engineering Fracture Mechanics*, 74, pp. 1649-1664.

Šestáková, L. (2011) Tuning of an over-deterministic method for calculation of higher-order terms coefficients of the Williams expansion for basic cracked specimen configurations, in: *Sborník konference Applied Mechanics 2011* (Náhlík, L., Zouhar, M., Ševčík, M., Seitl, S., Majer, Z. Eds.), IPM ASCR Brno, pp. 211-214, Velké Bílovice.

Tong, P., Pian, T.H.H., Lasry, S.J. (1997) A hybrid element approach to crack problems in plane elasticity. *International Journal for Numerical Methods in Engineering*, 7, pp. 297-308.

Veselý, V., Frantík, P. (2010) Reconstruction of a fracture process zone during tensile failure of quasi-brittle materials. *Applied and Computational Mechanics*, 4, pp. 237-250.

Williams, M.L. (1957) On the stress distribution at the base of a stationary crack. *Journal of Applied Mechanics*, 24, pp.109-114.

Xiao, Q.Z., Karihaloo, B.L., Liu, X.Y. (2004) Direct determination of SIF and higher order terms of mixed mode cracks by a hybrid crack element. *International Journal of Fracture*, 125, pp. 207-225.

18th International Conference
ENGINEERING MECHANICS 2012
Svratka, Czech Republic, May 14 – 17, 2012

pp. 1309–1310
Paper #321

MODELLING OF FATIGUE FAILURE OF GEARS WITH THIN RIM

M. Ševčík[*], L. Náhlík[**], P. Hutař[***], M. Zouhar[****], B. Máša[*****]

Abstract: *This work is focused on a fracture mechanics analysis of a spur gear with thin rim. The fatigue crack propagation is numerically studied using special routine implemented in the numerical model. Two criteria for crack kinking are considered: MTS criterion and modified MTS criterion which takes constraint effect into account. Sensitivity analysis of the crack increment size is present. It was found that for the same crack path obtained numerically the MTS criterion requires smaller crack increment in comparison with modified MTS criterion.*

Keywords: ***crack, fatigue fracture, gear, thin-rim,***

Crack propagation in a non-homogenous stress field generally displays a complicated trajectory. Accurate estimation of the crack path can aid the prediction of unexpected failures in engineering structures. The usual assessment of the crack trajectory and crack propagation rates is based on a phenomenological approach. According to classical linear elastic fracture mechanics two cracks display similar behaviour if the stress intensity factors are equivalent (Anderson, 1995). Recently it has been shown that in some cases two-parameter fracture mechanics, which take into account the constraint effect, can describe the crack tip stress field more accurately. Consequently, the criteria used for estimation of the fatigue crack trajectory were also modified (Ayatollahi & Aliha, 2008).

For the work presented the commonly known (Maximum Tangential Stress) MTS criterion was used for an estimation of the crack path. As a practical application, the numerical estimation of the gear with a thin rim failure is shown. An advantage of this kind of gear is important weight reduction in comparison to classical gear designs. The disadvantage of this type of gear is higher susceptibility to fracture failure originating from the tooth foot. The crack propagating below the tooth causes only fracture of the tooth. The aim of this research is attempt at clarification of discrepancies found in the current literature (Lewicki & Ballarini, 1997) and to introduce a constraint based methodology for estimation of the crack behaviour.

Minimal gear rim thickness refers to the thickness in which the crack is still growing below the tooth. From a practical perspective, this represents the state where the function of the gear is endangered but a degree of survival probability remains. For this reason knowledge of the minimal gear rim thickness is necessary in many engineering applications. The crack growth is modeled by an incremental method similar to the one published by (Španiel, Jurenka & Kuželka, 2009). All cracks start in the tooth root with an initial length of 0.25mm. The position of the initial defect was found using numerical analysis of the gear without the crack where highest tensile stresses occurred and corresponds with the location of the initial defect based on experience with gear failure (Kramberger et al., 2004a; Kramberger et al., 2004b). The gear studied was a spur gear with 25 teeth and involute tooth profile. Parameters of the gear studied were: normal modulus $m = 4$ and tooth width $b_w = 30$ mm.

[*] Ing. Martin Ševčík, Ph.D.: Institute of Physics of Materials Academy of Science of the Czech Republic, v. v. i., Žižkova 22, 616 62 Brno; Czech Republic, sevcik@ipm.cz

[**] doc. Ing. Luboš Náhlík, Ph.D.: Institute of Physics of Materials Academy of Science of the Czech Republic, v. v. i., Žižkova 22, 616 62 Brno; Czech Republic, nahlik@ipm.cz

[***] doc. Ing. Pavel Hutař, Ph.D.: Institute of Physics of Materials Academy of Science of the Czech Republic, v. v. i., Žižkova 22, 616 62 Brno; Czech Republic, nahlik@ipm.cz

[****] Ing. Michal Zouhar: Institute of Solid Mechanics, Mechatronics and Biomechanice, Faculty of Mechanical Engineering, Brno University of Technology, Technická 2896/2, 616 69 Brno; Czech Republic, zouhar@ipm.cz

[*****] Ing. Bohuslav Máša: Institute of Solid Mechanics, Mechatronics and Biomechanice, Faculty of Mechanical Engineering, Brno University of Technology, Technická 2896/2, 616 69 Brno; Czech Republic, masa@ipm.cz

All simulations were performed as a 2D model under plane strain condition. The contact between the gears was substituted by a contact force which acts at the highest point of the active tooth flank. The numerical model is shown in Fig. 1.

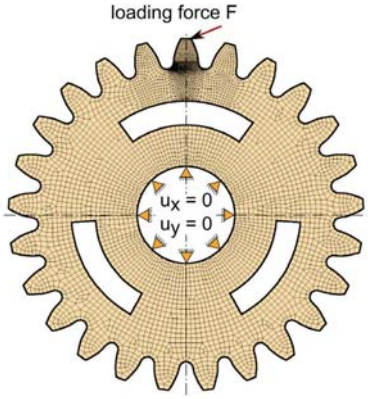

Fig. 1: Finite element model of the gear studied with boundary conditions and applied load

LEFM approach used in (Lewicki & Ballarini, 1997) was not able to predict correctly the crack path for a gear of this kind. In the present work two-parameter linear elastic fracture mechanics is used for simulation of the crack propagation in the same gear as in paper (Lewicki & Ballarini, 1997). The two-parameter LEFM estimated well the type of the gear failure in the case studied in comparison to classical LEFM where the prediction led to a non-conservative estimation of the crack path.

To support the obtained conclusions, a fracture mechanics analysis of a special specimen with high level of constraint (modified CT specimen) was used to prove experimentally numerical predictions for the crack path calculated on the basis of classical and modified MTS criterion (two-parameter crack description). The accuracy of the numerical estimations was dependent more on the crack increment size than on the criteria used. Smaller crack increment leads to better accuracy of prediction for both. It can be concluded that the use of two-parameter description for numerical predictions of crack path approximates experimental results more sufficiently with less crack increments than the crack path predicted on the base of stress intensity factor only.

Acknowledgement

This work was supported by the Specific academic research grant of the Ministry of Education, Youth and Sports of the Czech Republic provided to Brno University of Technology, Faculty of Mechanical Engineering No. FSI-J-12-21/1693.

References

Anderson, T.L., 1995, Fracture Mechanics - Fundamentals and Applications, CRC Press, Boca Raton, Florida.

Ayatollahi M & Aliha M. (2008) Cracked Brazilian disc specimen subjected to mode II deformation. Engineering Fracture Mechanics, 72, p. 493-503.

Kramberger, J., et al. (2004a) Numerical calculation of bending fatigue life of thin-rim spur gears. Engineering Fracture Mechanics, 71, pp. 647-656.

Kramberger J., et al. (2004b) Computational model for the analysis of bending fatigue in gears, Computers & Structures, 82, pp. 2261-2269.

Lewicki, D. G. & Ballarini, R. (1996) Effect of rim thickness on gear crack propagation path. NASA TM-107229.

Španiel M., Jurenka J. & Kuželka J. (2009) Verification of FE model of fatigue crack propagation under mixed mode conditions, *Meccanica* , 44, 2, pp. 189-196.

18th International Conference
ENGINEERING MECHANICS 2012
Svratka, Czech Republic, May 14 – 17, 2012

pp. 1311–1317
Paper #311

APPLICATION OF DYNAMIC RELAXATION METHOD IN ANALYSIS OF CABLE MEMBRANE STRUCTURES

K. Šobra[*], M. Hüttner[**], J. Máca[***]

Abstract: *The article is focused on analysis of the cable membrane structure mainly the dynamic relaxation method and parameters which influence the stability and the speed of computation.*

Keywords: ***Dynamic relaxation method, cable membrane structures, iteration parameters.***

1. Motivation

Light cable membrane construction founds its utilization mainly on the structures where it is necessary to cover large areas like warehouses, exhibition areas and stadiums. Thanks to the modern design, many cable membrane structures were built in the last twenty years.

There are many causes for their permanently higher utilization. They can be transported with very low costs because they are very light. Their lightness also causes that large areas should be covered under good costs for area unit. They can be prefabricated which leads to effective build considering usage of material. One of the most noticeable aspects is design. Cable membrane structures are highly visible. In case of design they are significant architectonical elements. The examples of cable membrane structures are shown in Figure 1 and Figure 2.

Fig. 1: Tram station K Barrandovu, Prague

Fig. 2: Munich Olympic Stadium

2. Design of cable membrane structures

By Topping and Iványi (2007) there are several steps which are necessary for design cable membrane structure. At the beginning shape definition, discussion about general shape of structure between client and architect is necessary. After the shape definition the engineering model can be created and the main parameters for *form finding* are defined. During the form finding process the equilibrium state of

[*] Ing. Karel Šobra: Department of Mechanics, Czech Technical University in Prague - Faculty of Civil Engineering, Thákurova 7; 166 29, Prague 6 - Dejvice; CZ, e-mail: karel.sobra@fsv.cvut.cz

[**] Ing. Miloš Hüttner.: Department of Mechanics, Czech Technical University in Prague - Faculty of Civil Engineering, Thákurova 7; 166 29, Prague 6 - Dejvice; CZ, e-mail: milos.hüttner@fsv.cvut.cz

[***] Prof. Ing. Jiří Máca, CSc.: Department of Mechanics, Czech Technical University in Prague - Faculty of Civil Engineering, Thákurova 7; 166 29, Prague 6 - Dejvice; CZ, e-mail: maca@fsv.cvut.cz

cable membrane structure is found and the specific boundary conditions are obtained from this process. The final equilibrium state is found by optimizations methods. Using geometrical optimization the surface is described by a mathematical surface equation. In the second type of optimization, equilibrium form finding methods, the equilibrium state is numerically computed. Equilibrium form finding methods may be employed to analyse greater and more complicated constructions and structures with unconventional shapes. In the next step, the response of construction to loading is *analysed*. Now, the appropriate shape of structure is known and it is necessary to make the *cutting pattern generation* and *design the details*. This minimizes the wastage of material during the production plan parts of construction from roll of material.

The aim of this article is to introduce the main methods which can be used for the cable membrane structure analysis.

3. Cable membrane structures analysis

Various methods are used for cable membrane structure analysis. One of the simplest methods is *grid method*. When the horizontal forces are in equilibrium, the height of grid points can be calculated from the equilibrium of vertical forces. System of linear equations is a set considering all nodes of grid.

Further, there are simply numerical methods, *finite difference method* and *finite element method*. Nowadays it is possible to solve constructions with arbitrary irregular shape and prestressed construction using these methods.

From many various methods there are two others suitable. *Force density method* which is based on the constant ratio between the force in the element and the length of the element. At last the *dynamic relaxation method* which is highly used for the form finding and analysis of construction.

4. Dynamic relaxation

Dynamic relaxation is not used for finding dynamic response of construction but it is used for static problems using a fictitious dynamic analysis. In this method the motion of construction from the time of loading to the state of equilibrium is traced step by step. From the motion it is possible to determine the curve of the construction without compile the matrix of stiffness. This characteristic leads to the conclusion that the dynamic relaxation is a method, which is suitable for highly nonlinear problems.

The method is a direct application of Newton's second law of motion ($F = M.a$). During the static analysis of construction the fictitious damping is used. The proportional, frequently critical damping factor is mostly applied. Iteration to the static solution is relatively fast when critically damped or overdamped construction is used. The influence of various damping factors is shown in Figure 3. Speed of iteration also depends on the fictitious masses. Because the masses are fictitious, their appropriate distribution between joints can accelerate the speed of calculation.

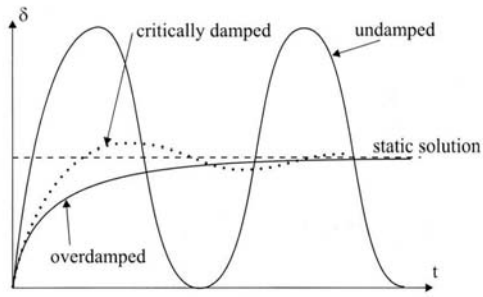

Fig. 3: One degree of freedom time – displacement trace

4.1. Numerical procedure

The Newton's second law of motion is presented in the equation which describes residual forces in time *t* and joint *i*. To the calculation of residual forces it is necessary to add the effect of prestress. The Equation (1) describes the calculation of residual forces in *x* direction:

$$R_{ix}^{t} = M_{ix}.\ddot{v}_{ix}^{t} + C_{ix}.v_{ix}^{t} \tag{1}$$

where:

R_{ix}^{t} is the residual force at joint *i* at time *t*

M_{ix} is the fictitious mass at joint *i*

C_{ix} is the viscous damping factor for joint *i*

$\ddot{v}_{ix}, v_{ix}^{t}$ are the acceleration and velocity at the time *t* at joint *i*.

By calculating the response of construction to the loading it is necessary to determine the acceleration and velocity at joint at the demanded time. The result of substituting the average velocity and the acceleration over the time step Δt into the Equation (1) is:

$$R_{ix}^{t} = \frac{M_{ix}}{\Delta t}.\left(v_{ix}^{(t+\Delta t/2)} - v_{ix}^{(t-\Delta t/2)}\right) + \frac{C_{ix}}{2}.\left(v_{ix}^{(t+\Delta t/2)} - v_{ix}^{(t-\Delta t/2)}\right) \tag{2}$$

The rearrangement of the Equation (2) enables to calculate the velocity at the new time step $(t+\Delta t)$:

$$v_{ix}^{(t+\Delta t/2)} = v_{ix}^{(t-\Delta t/2)}\left(\frac{M_{ix}/\Delta t - C_{ix}/2}{M_{ix}/\Delta t + C_{ix}/2}\right) + R_{ix}^{t}\left(\frac{1}{M_{ix}/\Delta t + C_{ix}/2}\right) \tag{3}$$

In the next step the Equation (3) is used to calculate the current coordinates of joint *i*:

$$x_{i}^{(t+\Delta t)} = x_{i}^{t} + \Delta t.v_{ix}^{(t+\Delta t/2)} \tag{4}$$

The residual forces are calculated from the Equation (5), where T_{ix} represents the internal forces and F_{ix} represents the applied loading including prestress. The internal forces are calculated at the joints where the residuals are determined – Equation (6).

$$R_{ix}^{(t+\Delta t)} = F_{ix} + T_{ix}^{(t+\Delta t)} \tag{5}$$

$$T_{m}^{(t+\Delta t)} = \frac{EA_{m}}{l_{m}^{0}}\left(l_{m}^{(t+\Delta t)} - l_{m}^{0}\right) + T_{m}^{0} \tag{6}$$

where:

l_{m}^{0} is the internal initial length of link

$l_{m}^{(t+\Delta t)}$ is the current length of link at time $(t+\Delta t)$

EA_{m} is the elastic modulus multiplied by the cross sectional area of the link *m*

T_{m}^{0} is the internal prestress in link

For calculating the current coordinates of joint *i* at the end of the first time step ($x_{i}^{(t+\Delta t)}$) it is necessary to set the initial conditions for time *t=0*: $v_{ix}^{0} = 0$. Substituting initial conditions to the Equation (3) enables to calculate the initial velocity at time $t = \Delta t/2$:

$$v_{ix}^{(\Delta t/2)} = \frac{R_{ix}^{0}}{2M_{ix}} \tag{7}$$

4.2. Dynamic relaxation method stability and convergence

The stability and convergence of the dynamic relaxation is influenced by the distribution of fictitious nodal mass, the damping factor and the time interval of the step. During the calculation fixed time step is often used and other factors are tuned until the required accuracy and stability of calculation is reached. When the time step Δt exceeds a critical value or fictitious masses are too low, numerical instability of the calculations will occur and the equilibrium state cannot be reached. This shortage can be eliminated by decreasing the time step or increasing the fictitious masses. Speed of convergence is partially affected by the damping factor. Critically damped or overdamped constructions have good speed of convergence.

From the previously stated it is obvious that the tuning of the calculation parameters (time step, fictitious masses and damping factor) is really an attractive area of interest since these parameters have a large influence on the speed of calculation. Beside these factors are specific for each construction.

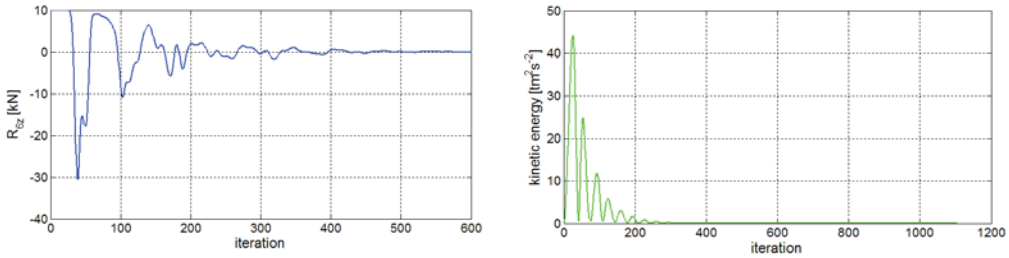

Fig. 4: Residual force and kinetic energy in the middle of span - damping factor 10 t.s^{-1}

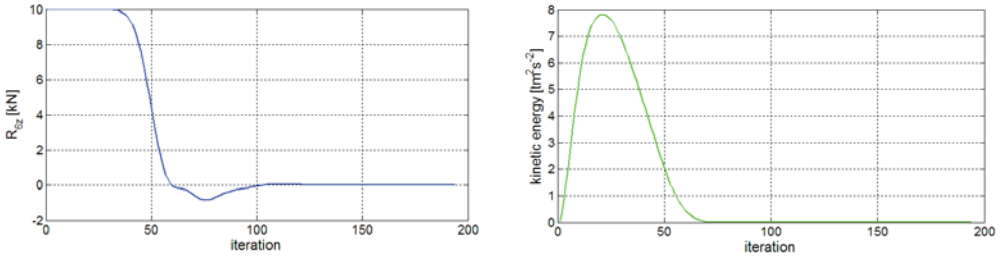

Fig. 5: Residual force and kinetic energy in the middle of span - damping factor 65 t.s^{-1}

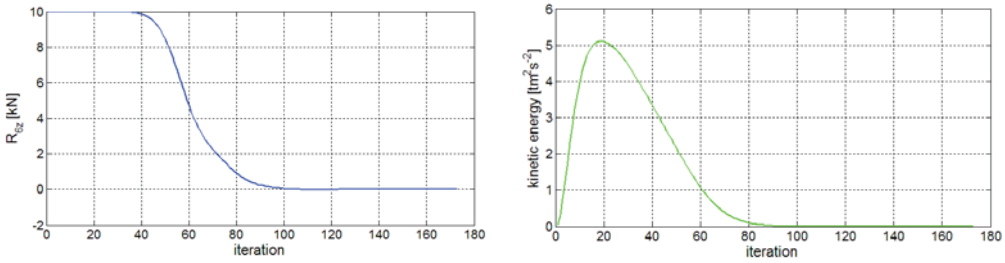

Fig. 6: Residual force and kinetic energy in the middle of span - damping factor 85 t.s^{-1}

The influence of the various damping factor on the iteration speed is shown in the Figure 4, Figure 5 and Figure 6. In Table 1 fixed parameters, which were used for the calculation of simple supported bar are shown. External distributed loading was equally spread between all joints.

Tab. 1: Basic construction characteristics

Span	l = 20 [m]
Yong's modulus of elasticity	$E = 210.10^6$ [kPa]
External load	$f_z = 5$ [kN/m]
Time step	$\Delta t = 0{,}01$ [s]
Cross section area	$A = 5.10^{-4}$ [m^2]

In Table 2 z coordinates in the middle of span there are shown. Influence of various calculation parameters on the speed of iteration is also obvious from Table 2. For comparison results calculated by deformation method are shown in Table 3.

Tab. 2: Z coordinate – dynamic relaxation method

n	M_{ix} [t]	M_{iz} [t]	Δt [s]	C_{iz} [$t.s^{-1}$]	Accuracy R_{zi}	Count of iteration	z coordinate [m]
10	5000	50	0,1	0,5	0,001	22374	0,7128
10	5000	50	0,1	10	0,001	1114	0,7128
10	5000	50	0,1	85	0,001	173	0,7128
10	5000	50	0,25	10	0,001	Unstable	-
10	5000	50	0,01	10	0,001	10679	0,7128
10	500	5	0,01	10	0,001	1101	0,7128
10	5000	5000	0,1	1000	0,001	1786	0,7128
10	5000	50	0,1	10	0,1	559	0,7122
10	5000	50	0,1	10	0,0001	1370	0,7128
50	5000	50	0,1	10	0,001	Unstable	-
50	5000	50	0,05	10	0,001	2095	0,7105
50	5000	50	0,05	40	0,001	1110	0,7105

where:

n is the number of elements on the bar

M_i is the fictitious mass in various directions (in x and y direction the same mass was considered)

Δt is the length of the time step

C_{iz} is the damping factor for joint i in z direction

Tab. 3: Z coordinate – deformation method

n	Count of iteration	z coordinate [m]
10	59	0,7128
50	17	0,7121
50	65	0,7105

5. Application and conclusion

The iteration speed and the accuracy of the method with various parameters were shown on the simple supported bar. For more illustrative functionality of the dynamic relaxation method the cable net was calculated. Figure 7 shows the shape of the construction. The construction is composed from 12 cable elements and 12 joints (joints 4, 5, 8 and 9 are unsupported). All cables have the same cross section area ($A = 1{,}4645.10^{-4}$ m^2) and the same Young's modulus of elasticity ($E = 8{,}2737.10^{7}$ kPa). Unsupported length of the elements 3, 4, 8, 11 is 30,419 m, unsupported length of other elements is 31,76 m. The distributed load was equally spread between the unsupported joints. The concentrated load at all unsupported joints is F = 35,56 kN. For the calculation of this example the deformation method and the dynamic relaxation was used. In both cases truss element was used. From Deng, Jiang and Kwan (2005) specification of this example was implemented.

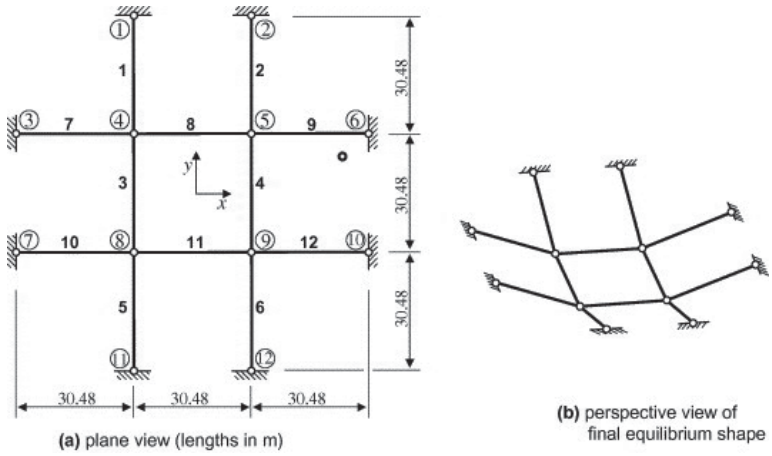

Fig. 7: Schema of cable net

After the calculation, some conclusions were set. First of all, both methods iterates to almost the same results (in Table 4 and Table 5 results from dynamic relaxation and deformation method are shown). However, the iteration speed is influenced by various factors which were assumed. Deformation method is faster than the dynamic relaxation one in case that the initial shape of construction is similar to equilibrium shape. Moreover, this behavior leads to another simple analysis of construction before deformation method is initiated. In opposite to the deformation method the dynamic relaxation one is faster in general. Almost arbitrary initial shape can be used and the dynamic relaxation converges to equilibrium shape. As it was mentioned, in dynamic relaxation method it is not necessary to compile the matrix of stiffness what leads to higher speed of iteration. In case of larger and more complicated construction this advantage should be more visible. On the other hand in dynamic relaxation the appropriate set up of the calculation parameters is difficult and nowadays the general approach to their set up is not known. Comparison of results in case of various calculating parameters is shown in Figure 8.

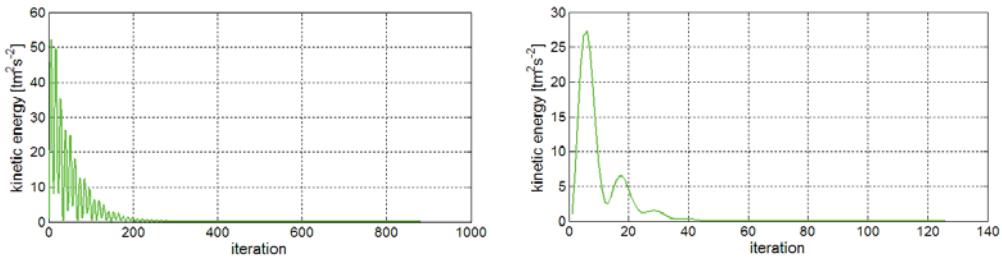

Fig. 8: Kinetic energy in joint 5 - damping factor 10 t.s^{-1} (left) and 75 t.s^{-1}

Tab. 4: Coordinates of joint 5 – dynamic relaxation method

M_{ix} [t]	M_{iy} [t]	M_{iz} [t]	Δt [s]	C_{iz} [$t.s^{-1}$]	Accuracy R_{zi}	Count of iteration	x coordinate [m]	z coordinate [m]
1000	1000	10	0,1	2	0,001	882	15,2804	9,5930
1000	1000	10	0,1	10	0,001	203	15,2804	9,5930
1000	1000	10	0,1	15	0,001	126	15,2804	9,5930
5000	5000	50	0,1	10	0,001	937	15,2804	9,5930
5000	5000	50	0,1	30	0,001	328	15,2804	9,5930
5000	5000	50	0,1	75	0,001	948	15,2804	9,5930

Tab. 5: Coordinates of joint 5 – deformation method

Count of iteration	x coordinate [m]	z coordinate [m]
13	15,2802	9,5917
20	15,2804	9,5930

Acknowledgement

The results presented in this paper are outputs of the research project "P105/11/1529 - Cable - membrane structures analyses" supported by Czech Science Foundation and project "SGS12/027/OHK1/1T/11 - Numerical modeling in mechanics of structures and materials" supported by CTU in Prague.

References

Barnes, M.R. (1999) Form Finding and Analysis of Tension Structures by Dynamic Relaxation. *International Journal of Space Structures*. Vol. 14, No. 2, pp. 89 - 104.

Barnes, M.R. (1975) Applications of dynamic relaxation to the design and analysis of cable, membrane and pneumatic structures. International Conference on Space Structures, pp. 211 - 219.

Deng, H., Q.F. Jiang a A.S.K. Kwan. Shape finding of incomplete cable-strut assemblies containing slack and prestressed elements. *Computers & Structures.* 2005, Vol. 83, No. 21-22, pp. 1767-1779.

Hüttner, Miloš. (2012) *Cable membrane analysis: Static analysis.* Prague. Diploma thesis. Czech Technical University in Prague. Advisor Doc. Ing. Petr Fajman, CSc.

Topping, B.H.V. and Iványi, P. (2007) *Computer Aided Design of Cable Membrane Structures*. Kippen (Stirlingshire, Scotland): Saxe-Coburg Publications.

18th International Conference
ENGINEERING MECHANICS 2012
Svratka, Czech Republic, May 14 – 17, 2012

pp. 1319–1329
Paper #288

FATIGUE UNDER FRETTING CONDITIONS

M. Španiel, M. Nesládek, J. Jurenka, J. Kuželka, J. Růžička*

Abstract: *Presented paper deals with application of phenomenological fatigue criteria on fatigue under fretting conditions. The objective is evaluation of fretting fatigue based on phenomenological criteria calibrated with relatively small set of experiments. Numerical stress analysis using finite element method was used (as usual in engineering applications) to determine stress fields and relative slips in contact interface of specimen in experimental set up. These quantities serve as input to several fatigue criteria that are to be compared each to other and evaluated. Optical measuring system DANTEC DYNAMICS Q-450 employing digital image correlation method for displacement field evaluation was used to calibrate and verify numerical model of friction. Basic results of experiments and computations are presented to be discussed.*

Keywords: ***Fatigue, fretting.***

1. Introduction

By definition, fretting fatigue is characterized as fatigue damage caused by stress peak concentrated near contact interface accelerated due to small relative tangential movements of contacting surfaces. Fretting fatigue occurs particularly in pressed joints, turbine blades lock joints, slot couplings and other typical machines parts. Stress field at the vicinity of contact interface, friction and partial slipping of contact surfaces are commonly considered as significant parameters affecting fretting fatigue.

1.1. Assumptions and classification of fretting

The values of relative slips of the contacting surfaces are widely used for description of the contact regimes under the fretting conditions Hoeppner (2006). Regarding the slip range, those regimes are: the *stick regime* with the slip magnitude up to $3\,\mu\mathrm{m}$, the partial slip regime with the slips from 3 to $50\,\mu\mathrm{m}$, and the gross sliding where the slips are more than $50\,\mu\mathrm{m}$.

It should be noted that the relation between the slip magnitudes and the fatigue life is not monotonic. One can observe a dramatic decrease in the partial slip regime. This state is specific for sticking in the centre of the interface and for slipping of both surfaces around the contact edges – see figure 1. This is the area of the most severe material damage which can, together with high stresses, act as "the weakest link" accelerating fatigue crack nucleation.

Decrease of the fatigue life in the partial-slip regime is followed by a rapid increase in the phase of transition to the gross sliding. This is due to intensive material erosion removing initial cracks. Note, that from practical point of view the exposed component will be damaged with abrasion instead of fatigue in such a case.

All the three above mentioned factors – stress, friction and contact slips – are closely dependent and in the real structures they change during their life-time.

1.2. Fretting fatigue evaluation approaches

Due to the multi-axial stress state in the fretted contact, conventional multi-axial fatigue criteria based on the critical plane estimation are widely used to predict the place of the initiation and the direction of the initial crack growth. Relations for conversion of some of these criteria to the number of cycles can be found e.g. in Navarro (2008). The target of presented research is to evaluate fatigue damage under

*Associate Prof. Ing. Miroslav Španiel, CSc., Ing. Martin Nesládek, Ing. Josef Jurenka, Ing. Jiří Kuželka, Ing. Jan Růžička Faculty of Mechanical Engineerig, Czech Technical University in Prague, Technická 4; 166 07, Prague; CZ, e-mail: miroslav.spaniel@fs.cvut.cz

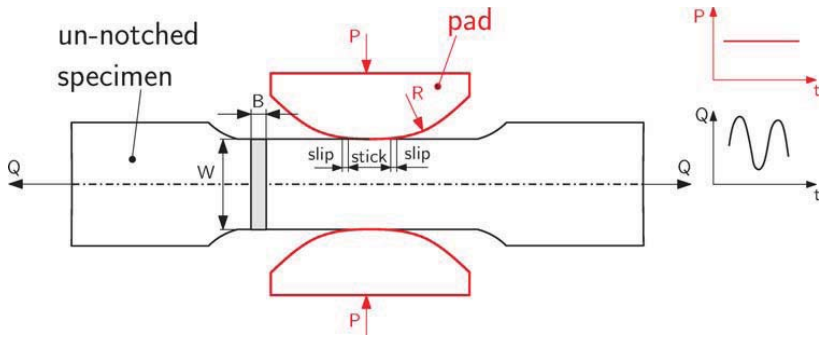

Fig. 1: A typical laboratory configuration for simulation of partial-slip fretting conditions (cylinder on a flat contact geometry)

fretting conditions. Evaluation is based on phenomenological criteria the verification of which should be based on reliable experimental and computational results. As mentioned, fretting is understood as fatigue process, therefore fatigue criteria are common base of fretting evaluation. Some authors have been trying to include surface wear simulation (based on the Archard's formula Madge (2007) or the dissipated energy concept Mary (2007)). Nevertheless, incremental estimation of wear together with damage cumulating is still infeasible for practical application on real structures.

Another possibility how to improve the results of conventional fatigue criteria is to incorporate certain correction with respect to the fretting wear. Ideally, it should reflect the values that cause surface damage, i.e. relative slips and surface shear stress. Ding et al. introduced a simple parameter correcting the multi-axial SWT criterion. According to the authors, the main contribution of it is that SWT can now handle the increase in the fatigue life in the transition domain between the partial and gross slips.

Evaluation of fatigue damage under fretting conditions based on phenomenological criteria is target of presented research. Verification of fretting fatigue criteria have to be based on reliable experimental and computational results. Quantities describing local material loading as stress field, contact slips etc., the measurement of which is very difficult, are in practice often calculated using finite element method. It is dependent on phenomenological description of friction. That is why we decided to verify and identify numerical model of experimental set up from the point of view of friction.

Material loading parameters as stress field, contact slips etc., the measurement of which is very difficult, are in practice usually calculated using finite element method. It is dependent on phenomenological description of friction. That is why we decided to verify and identify numerical model of experimental set up from the point of view of friction.

2. The experiments

Phenomenological modelling always requires experiments for both calibration and verification purposes. Therefore, experimental research represents important part of presented project. We have designed, manufactured and tuned up experimental set up utilizing electromagnetic pulsator AMSLER. Series of fatigue experiments under fretting conditions was carried out on the set up. Moreover the measurement of contact slips using digital image correlation optical method was implemented.

2.1. The experimental set up description

Original set up for testing of fatigue under fretting conditions developed in the scope of an acknowledged project was designed as a single dog-bone specimen in contact with two cylindrical pads causing fretting (see fig. 2). The main advantage of the cylinder on flat contact geometry is the possibility of its use in standard fatigue testing machines. The specimen is clamped in the jaws of the testing machine and loaded by a time-varying force in axial (vertical) direction. The loading frequency (as follows from the testing machine principles) corresponds to the natural frequency of the system which reflects the mass

Tab. 1: Loading conditions and number of cycles to crack initiation in the fretting experiments.

Experiment no.	Q_{amp} [kN]	Q_{mean} [kN]	P [kN]	N [cycles]
1	14	15	15	2 849 000
2	14	15	5	1 577 000
3	14	15	15	1 676 000

of the machine and the stiffness of additional experimental equipment and the specimen and reaches approximately 100 Hz. The normal contact force is kept approximately constant during a single test and acts in the horizontal direction which is perpendicular to the axial cyclic loading.

The material of the specimens was Cr-Ni-Mo-V martensitic steel with the plain fatigue strength in reversed tension $f_{-1} = 485\,\mathrm{Nmm}^{-2}$. The cross-sectional dimensions were thickness $B = 6\,\mathrm{mm}$ and width $W = 20\,\mathrm{mm}$ (see figure 1). Fretting pads with the radius $R = 200\,\mathrm{mm}$ were used.

After preliminary tests some modifications of experimental set up had to be done to eliminate weaknesses of experimental setup that manifested themselves through relatively high scatter of measured lifetime under assumed the same conditions (lading conditions and measured lifetimes estimation of which is based on the stiffness decrease in the experimental set up, can be found in table 1). Especially the difference between tests no. 1 and 3 reflects certain auxiliary influence. Fatigue crack initiation always took place on the top contact edge–see figures 3 that is vertically oriented according to the position of the specimen in the testing rig (figure 2). This fact is in agreement with the general observations. According to them crack occurs in the slipping area of a partial-slip regime contact. This is also the place of the most severe damage of the exterior faces as can be visually evaluated from the pictures of the surface relief. By contrast, mild damage of the central contact area where sticking occurs can be seen. Relief

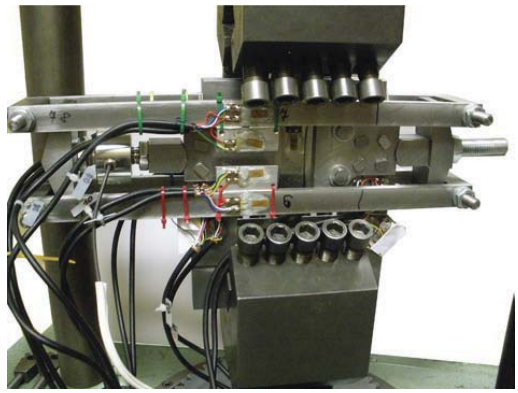

Fig. 2: The setup for the fretting fatigue testing. The equipment is clamped in the electromagnetic pulsator AMSLER.

of both contact surfaces of each specimen was scanned by a digital microscopic camera with 2Mpix resolution. Panoramic pictures, like those in figure2, were then obtained by merging more than 100 single scans. In some cases, the contact area was shifted from the centre of thickness towards the edge of the specimen, as shown at figure 3. This violates the uniform load distribution between both specimen edges assumption. Revision of the testing apparatus was done in order to reveal sources of this problem. Severe inaccuracy in the surface finish of the fretting pads was detected by roughness tester. In the thickness direction, the measured surface contour was curved, so more precise finishing was performed on a CNC machine. A detail of original pad installation is shown in figure 4. Rigidity of this design did not allow rotation of the fretting pads which could eliminate the initial non-parallel set up of the contact surfaces. That is the reason why additional chamfers were manufactured. Together with lateral gaps as shown in figure 5 this arrangement is capable of compensating the initial inaccuracies given by manufacturing.

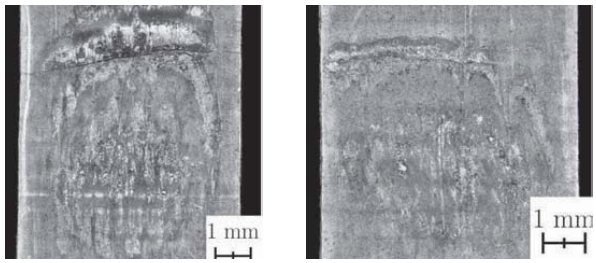

Fig. 3: Detail of worn contact surfaces of the specimen after fretting test no. 1

Fig. 4: Detail of the fretting pad installation in the experimental equipment – the original configuration without chamfers.

Usually no fatigue cracks occur on the pads after the experiment termination. The contact surfaces can then be renovated by grinding and after that the pads can be reused. Since this is a costly operation, the following simple modification of the fretting pad installation was introduced. Both pads are now fixed in a moderately rotated position (compare figure 5 and figure 6). Due to this, the contact area is shifted horizontally on the fretting pads which enable their one-off reuse when they are installed upside down. The beneficial effect is that it will halve the time losses and expenses for their renovation.

3. Experimental results

31 relevant experiments with specimens made of creep-resistant chromium steel were carried out at the Czech Technical University in Prague.

The loading conditions–axial prestress Q_{mean} and amplitude Q_{amp} as well as pressing force P, numbers of cycles to detected crack N and number of cycles N_{corr} renormalized to $1\,\mathrm{mm}$ crack[**] for the experiments are presented in Table 2. Note that experimental observations proved that the initiation phase represents the major part of specimen lifetime. Long crack growth period is negligible. Thus the achievement of $1\,\mathrm{mm}$ crack length can be satisfactorily considered as the initiation.

Four levels of periodical axial load Q and two levels of constant pressure force P were tested. Axial loading frequency was about $120\,\mathrm{Hz}$.

Averaged Wohler curve under fretting conditions in comparison with plain fatigue one is plotted in figure 6. All measured data were used together to determine linear dependency of axial stress amplitude

[**] Renormalized lifetime was computed by extrapolation of subsequenly measured crack growth data for most of specimens.

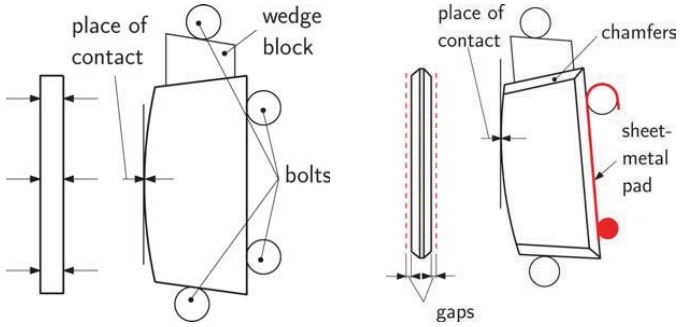

Fig. 5: The original (left) and modified (right) fretting pad geometry with flat side faces. The rotated position enables reusing of the same pad.

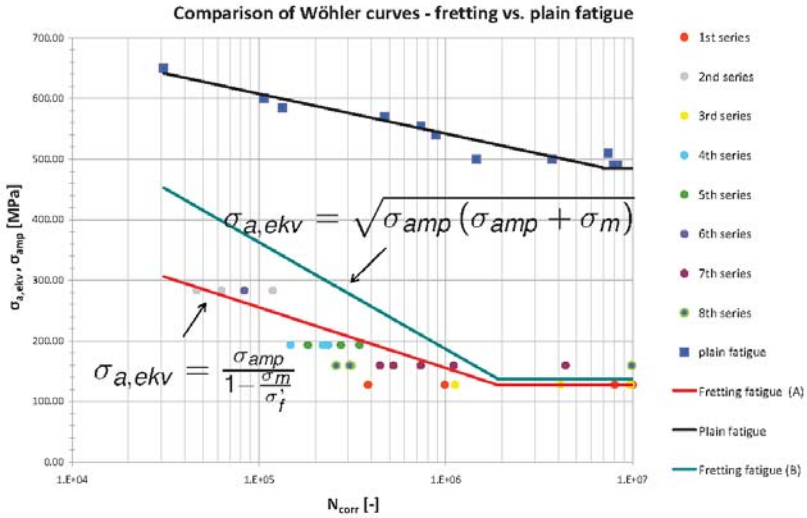

Fig. 6: Comparison of plain fatigue and fretting fatigue Wohler curves. The colours correspond with table 2.

σ_{amp} (of real loading cycle) on number of cycles N_{corr} causing crack initiation. Then the curve was recomputed with respect to amplitude $\sigma_{a,ekv}$ of equivalent alternating loading cycle (according to two commonly used formulas shown directly in figure 6) and plotted together with plain fatigue curve.

Tab. 2: Complete list of fretting fatigue tests.

Spec.	Q_{amp} [kN]	Q_{mean} [kN]	P [kN]	N [-]	l_0 [mm]	N_{corr} [mm]
1	14	15	5	500000	1.5	-
2	14	15	5	-	-	-
3	14	15	5	10 000 000	No init	10 000 000
17	14	15	5	1 160 000	2.40	987 700
23	14	15	5	260 000	0.33	383 600
25	14	15	5	8 180 000	2.20	8 024 000
26	14	15	5	10 000 000	No init	10 000 000
27	14	15	5	10 000 000	No init	10 000 000
4	28.1	30.1	5	126 500	4.10	118 300
5	28.1	30.1	5	70 000	3.20	63 100
6	28.1	30.1	5	40 000	0.40	46 430
7	14	15	15	9 800 000	1.10	9 784 000
20	14	15	15	9 875 000	4.30	9 635 000
21	14	15	15	9 730 000	1.55	9 648 000
22	14	15	15	1 250 000	1.95	1 122 000
24	14	15	15	4 030 000	0.50	4 118 000
8	20.3	21.7	5	174 000	2.50	147 700
9	20.3	21.7	5	210 000	0.70	219 900
10	20.3	21.7	5	235 000	1.00	235 000
11	20.3	21.7	15	190 000	1.30	182 600
12	20.3	21.7	15	370 000	2.40	344 700
13	20.3	21.7	15	265 000	0.70	274 400
14	28.1	30.1	15	80 000	0.60	83 530
15	17.1	18.4	15	260 000	1.00	260 0000
16	17.1	18.4	15	4 447 000	2.80	4 380 000
18	17.1	18.4	15	450 000	1.10	444 200
19	17.	18.4	15	810 000	2.93/3.60	735 300
32	17.1	18.4	15	1 180 000	3.60	1 102 000
33	17.1	18.4	15	535 000	1.20	523 700
28	17.1	18.4	5	310 000	1,00	310 000
29	17.1	18.4	5	285 000	0.70	306 000
30	17.1	18.4	5	9 980 000	3.60	9 900 000
31	17.1	18.4	5	225 000	0.53	259 000

4. Calibration of friction model

The calibration is based on measurements of relative contact slips and their comparison with slips obtained from FE simulation. Simple Coulomb's friction model with the only parameter–friction coefficient μ– has recently been calibrated. Calibration itself is based on comparison between measured and calculated relative slip Δ along appropriate path near contact surface (see dot lines in figure 7). Calculations were done for various values of friction coefficient ($\mu \in \langle 0.1;\ 0.8 \rangle$) and the $\mu = 0.6$ representing the best agreement between measured and computed curve $\Delta\,(y)$ was determined as correct value for subsequent (fretting fatigue) calculations. To calibrate friction coefficient on the base of agreement of measured and

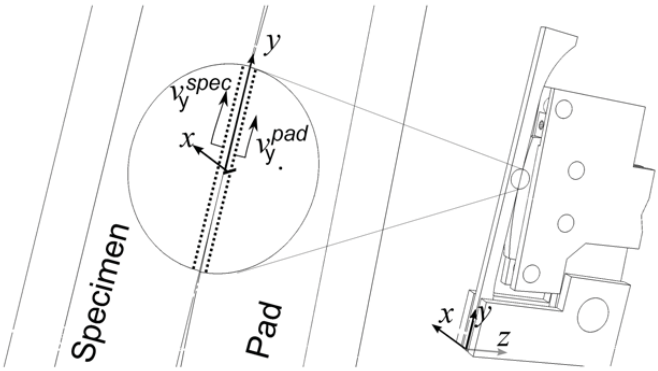

Fig. 7: Accumulated contact slips.

calculated response proper quantity for comparison of the experimental and numerical results must be chosen. The choice of the slip amplitudes along the contact area was found misleading for this purpose. According to the experimental results, this quantity is not convenient since approaching the bottom edge of the contact the slipping process becomes more stochasti (see figure 8). When using more averaged quantity better conformity can be expected. Accumulated slip per period of exciting axial load Q

$$\Delta\,(y) = \frac{1}{n}\int_{t_0}^{t_0+nT} \left| v_y^{spec}\,(y) - v_y^{pad}\,(y) \right| \mathrm{d}t\ , \tag{1}$$

seems to be a more suitable measure. This quantity has more understandable physical meaning than the slip amplitudes (in sense of dissipated work) and can be evaluated from both experimentally and computationally determined motion of surface points in the vicinity of contact. In equation (1) $T\,[\mathrm{s}]$ is the period of exciting force Q, n means number of periods of integration, $v_y^{spec}\,(y)$, resp. $v_y^{pad}\,(y)\ \left[\mathrm{mms}^{-1}\right]$ represents $y-\mathrm{component}$ of velocity of point with coordinate y along the contact edge[***]. Experimentally and computationally determined accumulated contact slips in dependence on the position in contact area after calibration procedure are plotted in graph on figure 9.

4.1. The measurements of relative slips

Dantec Dynamics Q-450 optical system was used for relative displacements measurements. Since displacements in order of $\mu\mathrm{m}$ had been measured at high frame rate, the demands on pattern quality and lighting were quite high. Regarding $1\,\mathrm{Mpix}$ resolution of CCD chip the objective and extension tubes were used to achieve spatial resolution of approximately $8\,\mu\mathrm{m/pix}$ with the field of view of about $\times 8\,\mathrm{mm}$. The viewed surfaces were clothed in a very fine contrast stochastic speckle pattern considering the recommendations in Kuželka (2010). Two special high frequency $1\,\mathrm{kW}$ lamps were used for sufficient lighting. The images of the vicinity of the contact interface between the specimen and pad were recorded by a high speed NanoSense Mk III camera with the frequency of 2 kHz (corresponds to

[***]The intersection of (common) contact surface with front surface of specimen (parallel with yz plane)laying on specimen, resp. pad in the vicinity of contact.

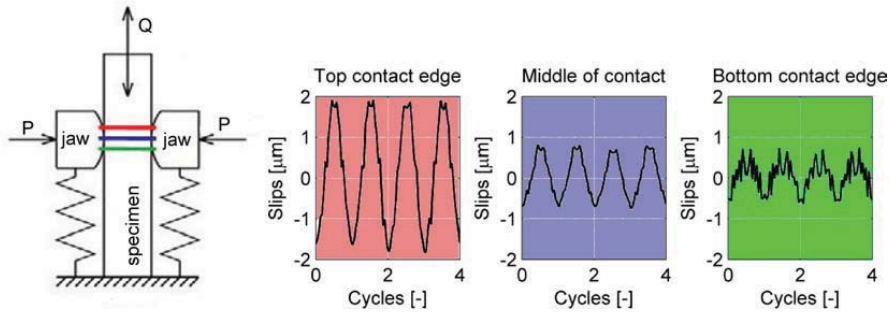

Fig. 8: Experimentally measured time history of relative slips in different locations in the contact interface for 10 kN *pressure loading.*

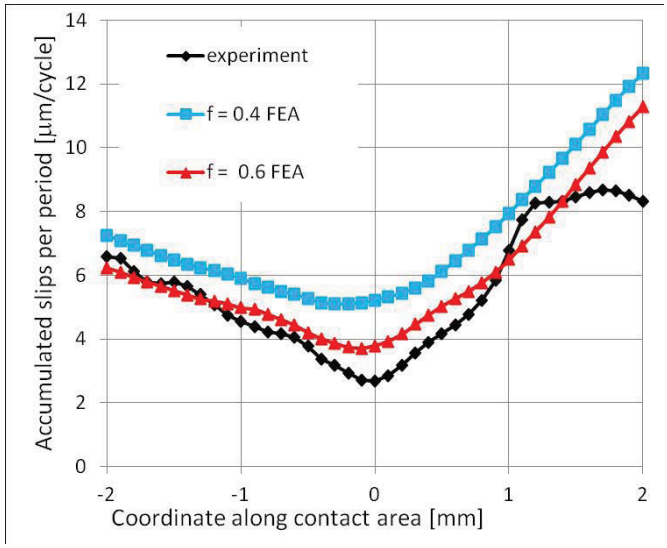

Fig. 9: Accumulated relative slips per single cycle period along the contact interface for 10 kN *pressure force* P*. Comparison of experimental and numerical results.*

20 images per loading cycle).Data were acquired during a relatively short period (about 50 cycles) after every 200 000 cycles. The acquired sets of image sequences were processed in the commercial image correlation software Istra 4-D. The displacements were evaluated in a $0.1\,\mathrm{mm}$ $(12\,\mathrm{pix})$ equally spaced grid. Each grid point corresponds to a subset $0.2 \times 0.2\,\mathrm{mm}$ $(25 \times 25\,\mathrm{pix})$. The obtained results were further post-processed by Matlab scripts. The centre point of contact area was approximately located on the basis of horizontal displacement field in case of pure pressure loading of $P = 10\,\mathrm{kN}$. At this point, a coordinate system for relative slip evaluation was introduced (figure 10).

4.2. Calibrating of friction coefficient

To obtain required input data for the fatigue criteria, a 3D FE model of the testing apparatus was assembled – see figure 9 – and analysed. FE solver Abaqus was used for the numerical simulation which was divided into several computation steps reflecting pressure and axial pre load (static) and application of axial cyclic loading.(explicit dynamics). Plasticity of material was included as well. Geometry was discretized with linear hexahedron continuum elements. Smallest element edge in the contact area was approximately $85\,\mu\mathrm{m}$–see figure 11. A proper modelling of the contact friction has a significant effect on relative slips determination. Contact slips is the significant parameter of fretting fatigue evaluation.

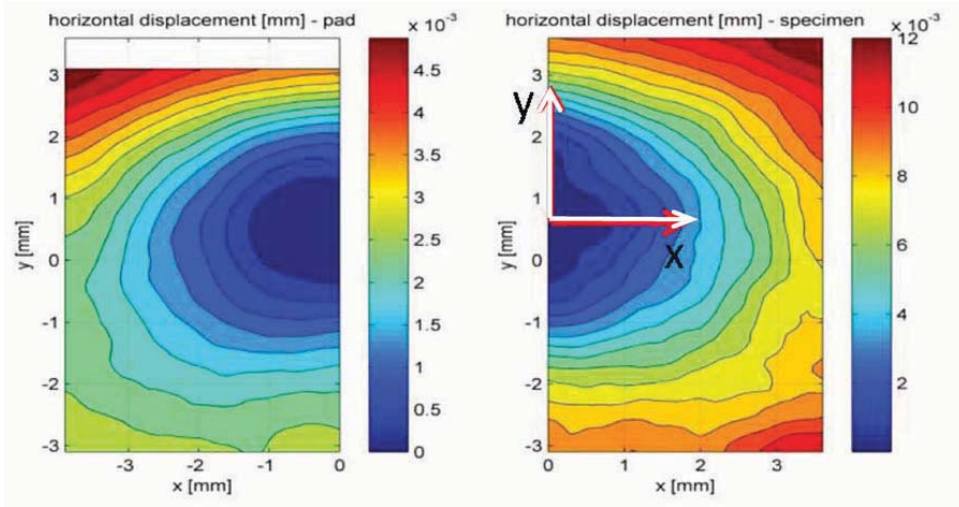

Fig. 10: Determining of contact center based on horizontal displacemet.

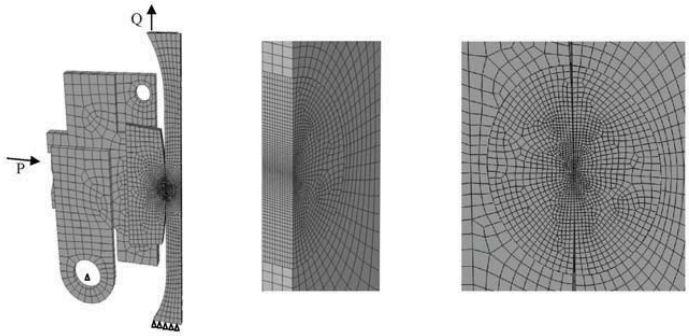

Fig. 11: FE model utilized for friction calibration. Detail of specimen mesh. Detail of contact area.

The friction coefficient used in the fretting simulations is usually higher than in a conventional contact and should reflect its change during the life-time. FE solver Abaqus contact algorithms adopt several computation techniques. In our model, surface-to-surface discretization, finite-sliding tracking approach and hard contact with the Coulomb friction was applied.

5. First results of fatigue analysis

Various multi-axial fatigue criteria were employed to evaluate experimentally measured fretting fatigue based on plain fatigue parameters of specimen material. Fatigue index approach has been utilized so far. Most of known multi-axial criteria used to evaluate high-cycle fatigue (HCF) can be written in form

$$\mathrm{L.H.S} = af\left(C\right) + bg\left(N\right) \leq \mathrm{R.H.S}\,, \tag{2}$$

where $f\left(C\right)$, resp. $g\left(N\right)$ are functions of shear C, resp. normal N stress amplitude, expressed from stress/strain invariants or from stress/strain components in some plane. These invariants or components were as usual calculated using finite element method. FE model was similar as model used for friction coefficient calibration. Constants a and b as well as right hand side R.H.S. of equation 2 representing

fatigue limit are material parameters. *Fatigue index* is defined as coefficient

$$\mathrm{FI} = \left(\frac{\mathrm{L.H.S.}}{\mathrm{R.H.S.}} \right) , \tag{3}$$

expressing material loading with respect to fatigue limit. To compare various criteria, fatigue index error

$$\Delta\mathrm{FI} = \left(\frac{\mathrm{L.H.S.} - \mathrm{R.H.S.}}{\mathrm{R.H.S.}} \right) \cdot 100\% = (\mathrm{FI} - 1) \cdot 100\% \tag{4}$$

was evaluated in small domains in vicinity of contact for loading representing experimentally determined

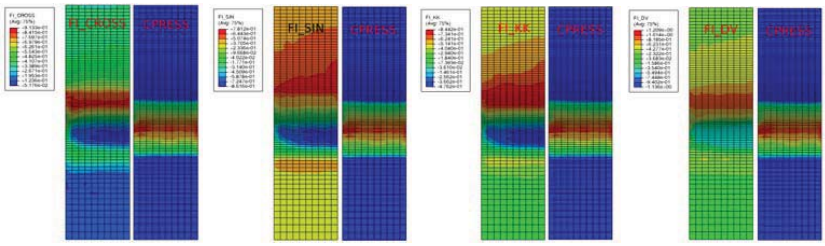

Fig. 12: Fatigue index FI *(left) and contact pressure* p *(right figure in pair) distribution at the vicinity of contacting surface. Four pairs from left to right represent Crossland, Sines, Kakun-Kawada and Dang Van criteria.*

fatigue limit (according to the graph on figure 9 $Q_{mean} = 15\,\mathrm{kN}$, $Q_{amp} = 14\,\mathrm{kN}$, and $P = 5\,\mathrm{kN}$ or $P = 15\,\mathrm{kN}$) for set of criteria including Crossland (Cross), Sines (Sin), Kakun-Kawada (KK), Dang Van (DV), Gonçalves, Araújo, Mamiya (GAM), Mamiya (Mam), Papuga (PCr). These criteria are well described in Papuga (2011). Fatigue index errors for these criteria are printed in table 3, examples of fatigue index along contact surface can be found in figure 12.

Tab. 3: Fatigue index error values for the selected multiaxial criteria.

	Fatigue index error ΔFI [%]						
P [kN]	Cross	Sin	DV	KK	GAM	Mam	PCr
5	2.1	-35.4	6.8	-6.8	14.9	12.7	14.8
15	25.1	-8.3	21.8	19.4	57.7	54.0	27.2

6. Conclusions

Series of 31 test simulating fretting fatigue conditions was done using flat dog bone samples from heat resisting chromium steel. Based on S-N curves of fretting tests and plain fatigue tests comparison (see figure 9) significant negative effect of fretting on lifetime of samples can be observed. Compared to the fatigue of smooth specimens in tension-compression alternating load fatigue limit decreased to the quarter of original value, i.e. $125\,\mathrm{MPa}$ for 3×10^6 cycles. No significant influence of various transversal pressure load of contact pads by values of $5\,\mathrm{kN}$ and $15\,\mathrm{kN}$ on life of samples could be seen. According to the nature of contact surfaces damage under different pressure loads different damaging micro mechanisms can be supposed as discussed bellow.

Significant variance of number of cycles to crack initiation for different specimens with the same loading probably follows from

- Non uniformly distributed contact pressure

- Initial surface roughness with possible surface defects from machining
- Other factors, especially boundary conditions

The closer the load approaches fatigue limit, the more significant variance appear. The higher load the lower variances. In all cases the location of crack initiation was the domain in upper part of contact.

Measured S-N curves served as base of verification of the ability of various HCF multi-axial criteria to predict fatigue failure under fretting conditions. Stress fields analysed by FEM were used as input into these fatigue criteria. Fatigue index error was used as measure of criteria quality. This research resulted into some hints and hypotheses:

1. Elastic-plastic material model in FE calculations provides us with much better fretting fatigue predictions, however elastic material model in FE analysis has negligible influence onto predicted crack placement
2. The best correspondence can be seen for Crossland and Dang Van criteria. For pressing force $P = 5\,\mathrm{kN}$ fatigue index error approaches almost zero. For $15\,\mathrm{kN}$ it is conservative. This tendency have shown all tested criteria.
3. All tested criteria except the Sines one are conservative. That is why the Sines criterion cannot be recommended.
4. Tested criteria do not evaluate the influence of pressing force correctly. While the experiments have not shown any difference in the life of flat dog bone specimens under pressing force $P = 5\,\mathrm{kN}$ and $P = 15\,\mathrm{kN}$, the criteria have. According to fractographic analysis, pressing load $P = 5\,\mathrm{kN}$ leads to more uniform damage of entire contact area. Probably some micro-nothes with high stress are formed. Conventional numerical models are not able to calculate these stresses. Surface areal damage under $P = 15\,\mathrm{kN}$ is much less, contact interface rather acts as a notch increasing the stress concentration at a point. It would be appropriate to consider some correction of criteria based on correlation of life and contact slips. Establish a reliable correction would require a further series of experiments with different pressing forces.

Acknowledgments

This project is kindly supported by GAČR grant no. 101/09/1709.

References

Hoeppner, D.W. (2006), Fretting fatigue case studies of engineering components. *Tribology Int.*, Vol. 39(10), pp. 1271–1276.

Papuga J. (2011), A survey on evaluating the fatigue limit under multiaxial loading. *Int J Fatigue*, Vol.33(2), pp. 153–165.

Vingsbo O., Soderberg, S. (1988), On fretting wears, *Wear*, Vol. 126, pp. 131-147.

Navarro, C., Mun?oz, S., Domínguez, J. (2008), On the use of multiaxial fatigue citeria for fretting fatigue life assesment, *Int. J. of Fatigue*, Vol. 30, pp. 32-44 .

Madge, J.J., Leen, S.B., McColl, I.R., Shipway, P.H. (2007), Contact-evolution based prediction of fretting fatigue life: Effect of slip amplitude,*Wear*, Vol. 262, pp. 1159-1170.

Mary, C., Fouvry, S. (2007), Numerical prediction of fretting contact durability using energy wear approach: Optimisation of finite-element model,*Wear*, Vol. 263, pp. 444-450

Ding, J., Houghton, D., Williams, E.J., Leen, S.B. (2011), Simple parameters to predict effect of surface damage on fretting fatigue,*Int. J. of Fatigue*, Vol. 33, pp. 332-342.

Kuželka, J., Chlup, H., Jurenka, J., Španiel, M. (2010), Fatigue degradation in the vicinity of contact interface under fretting conditions. In: *Proc. of Experimental Stress Analysis*, pp. 201-208. ISBN 978-80-244-2533-7.

Sutton A.M., Orteu J. and Schreier W.H. (2009), *Image Correlation for Shape, Motion and Deformation Measurements*Springer, New York.

18th International Conference
ENGINEERING MECHANICS 2012
Svratka, Czech Republic, May 14 – 17, 2012

pp. 1331–1342
Paper #57

STRUCTURE OF FLOW FIELDS DOWNSTREAM OF TWO DIFFERENT SWIRL GENERATORS

D. Štefan[*], P. Rudolf[**], S. Muntean[***], R. F. Susan-Resiga[****]

Abstract: *This paper discusses the comparison of the flow fields downstream of two different swirl generators. Both swirl generators are used to imitate the flow at the exit of the hydraulic turbine runner and study spatio-temporal behaviour of the swirling flow in the draft tube (i.e. outlet diffuser part of the hydraulic turbine), which undergoes breakdown into vortex rope. Unsteady CFD computations are carried out for identical Reynolds number. Resulting velocity and vorticity profiles are correlated with the structure of the vortex rope. Difference in excited pressure pulsations is illustrated on amplitude-frequency spectra of static wall pressure.*

Keywords: ***swirl generator, vortex rope, velocity profile, vorticity, pressure fluctuations.***

1. Introduction

Control of energy distribution and electricity production are in last several years considerably influenced by electricity produced from renewable sources highly depending on changes in weather conditions i.e. solar power plants and wind power plants. Pump storage hydro power plants (PSHPP) are proved to be effective to reduce voltage fluctuations in whole distribution power grid. Control ability of PSHPP is connected with operation of turbine in extended area quite far from the best efficiency point (BEP). Unfortunately, operation of Francis turbine with constant pitch of turbine runner (mainly used for PSHPP) at partial discharge, where flow rate $Q < Q_{BEP}$, is connected with occurrence of high swirling flow at the inlet of the draft tube with formation of so called vortex rope. The vortex rope evolution correlates with the vortex breakdown and leads to the high pressure fluctuation in the draft tube. This draft tube surge propagates pressure pulsations into whole machinery system. Moreover, when the frequency of pressure pulsations generated by the vortex rope rotation corresponds with natural frequency of machine unit, it can lead to restriction of turbine operation.

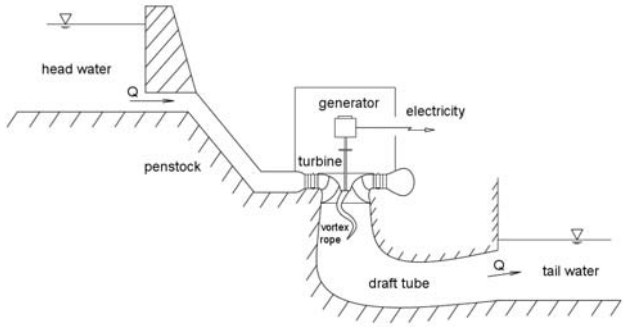

Fig. 1: Cross-sectional schema of hydraulic power plant.

[*] Ing. David Štefan: V. Kaplan Dept. of Fluid Engineering, Faculty of Mechanical Engineering, Brno University of Technology, Technická 2896/2; 61669, Brno; CZ, e-mail: y101274@stud.fme.vutbr.cz

[**] doc. Ing. Pavel Rudolf, Ph.D.: V. Kaplan Dept. of Fluid Engineering, Faculty of Mechanical Engineering, Brno University of Technology, Technická 2896/2; 61669, Brno; CZ, e-mail: rudolf@fme.vutbr.cz

[***] Ing. Sebastian Muntean, Ph.D.: Centre for Advanced Research in Engineering Sciences, Romanian Academy-Timisoara Branch; Bvd. Mihai Viteazu 24; RO-300223, Timisoara; RO, e-mail:seby@acad-tim.tm.edu.ro

[****] prof. Romeo F. Susan-Resiga, Ph.D.: Departmen of Hydraulic Machinery, "Politehnica" University of Timisoara; Bvd. Mihai Viteazu 1; RO-300222, Timisoara; RO, e-mail:resiga@mh.mec.upt.ro

In the last decade, these conclusions lead to large investigation of the swirling flow occurred in the Francis turbine draft tube. As a result, FLINDT (Flow Investigation in Draft Tubes) research project was established with relatively large amount of experimental measured data base describing a wide range of operating points (Avellan 2000, Susan-Resiga 2006). At last time the experimental data base of FLINDT project was employed for various theoretical (Susan-Resiga et al., 2006, Susan-Resiga et al., 2010, Susan-Resiga et al., 2011), experimental (Iliescu et al., 2008) and computational (Ciocan et al., 2007) investigations of swirling flow. Difficulty of the swirling flow investigation in scaled model of hydraulic turbine draft tube leads to idea of building up a simplified apparatus that best imitates flow at the exit of the hydraulic turbine operated at partial discharge.

2. Swirl generators

Swirl generators have been developed at "Politehnica" University of Timisoara as well as at V. Kaplan Dept. of Fluid Engineering, Brno University of Technology. The swirl generators are used to study compactness of generated vortex rope and decay of the vortex rope downstream in the diffuser. Those attributes are farther evaluated with aspect to spectral properties and decrease of the static pressure in vortex rope with respect to the dynamic pressure at the outlet section of swirl generator. Particular design of each referred swirl generator is completely different than the other one.

2.1. Swirl generator RO (SG-RO)

The swirl generator SG-RO has been developed by team at Politehnica University of Timisoara (UPT) and National Center for Engineering Systems with Complex Fluids (NCESCF) as a simplified device to further study the precessing vortex rope (Susan-Resiga et al., 2008a , Petit et al., 2011). The present swirling flow apparatus consists of four leaned strouts, 13 guide vanes, free runner with 10 blades, convergent divergent draft tube (Susan-Resiga et al., 2008a, Bosioc et al., 2008) and is mounted into test rig in hydraulic laboratory at UPT (Bosioc et al., 2009). The stay vanes and runner vanes were designed using inverse design technology in order to create precessing vortex rope (Susan-Resiga et al., 2008b). The swirl flow apparatus is also designed to investigate reduction of the pressure fluctuations of precessing vortex rope by water injection from the nozzle. For this purpose the water supply is provided by auxiliary circuit to leaned strouts.

Design of SG-RO (Susan-Resiga et al., 2008a) is such, that the swirl (i.e. axial and circumferential velocity profiles) in section at the outlet of the runner blades and downstream in convergent divergent section is similar to the Francis turbine investigated in Ciocan et al., 2007.

Numerical simulation of convergent divergent section was carried out by Muntean et al., 2009 and Petit et al., 2011. Both commercial software ANSYS Fluent and open source software OpenFOAM were employed to compute unsteady swirling flow with precessing vortex rope in order to compare the numerical results provided by software codes and experimental results. Due to lower computational requirements the realizable k-ε turbulence model was applied.

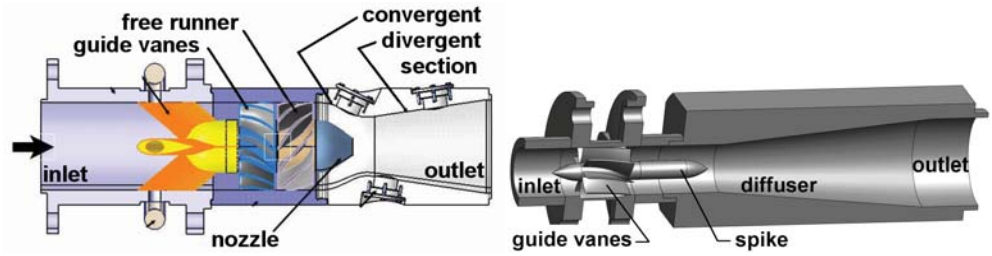

Fig. 2: Experimental setup of swirl generators SG-RO on the left and SG-CZ on the right.

2.2. Swirl generator CZ (SG-CZ)

Differently designed swirl generator has been developed at V. Kaplan Dept. of Fluid Engineering, Faculty of Mechanical Engineering, Brno University of Technology.

The swirl generator consists of 10 fixed blades with relatively long narrow channels to prevent flow separations along the blade surface for a broad range of operating regimes. CFD simulation

proved that almost identical velocity angles are provided by the generator for flow rates between 4 and 13 l/s (Rudolf et al., 2011). The swirl generator is part of test rig placed in hydraulic laboratory of V.K. Dept. of Fluid Engineering. The test rig is supplied from tank by centrifugal pump and swirl generator is situated approximately in the middle of pipeline system. Control of the discharge is enabled via frequency convertor coupled to centrifugal pump.

3. Swirling flow

Swirling flow in diffusers is subject of investigation because of the phenomena (e.g. vortex breakdown, vortex rope), which are not still completely described and understood. Summary of vortex breakdown research can be found in Luca-Negro et al. 2001, where significant influences on vortex rope formation are described.

Experimental and numerical results show, that circumferential velocity profile shape, namely location of the velocity maximum and magnitude of the maximum velocity are decisive for the shape of the cavitating vortical structure (Rudolf et al., 2011). It has to be pointed out, that the two structurally diverse swirl generators produce completely different structure of vortex ropes.

4. CFD calculation

In order to compare swirling flows generated by each swirl generator and resulting vortex rope developing in downstream parts, the unsteady computational study is carried out by commercial software ANSYS Fluent R13 using Reynolds Averaged Navier-Stokes equations (RANS) and Reynolds stress turbulence model (RSM) for turbulence modeling. Considered computational domains are downstream parts of swirl generator apparatuses and diffusers. For better comparison of computed results, we employed RSM turbulence model with higher computational requirements but better performance for highly swirling flow (Jawarneh et al., 2006). The effect of strong turbulence anisotropy can by modeled rigorously only by the second-moment closure adopted in the RSM (Susan-Resiga et al., 2010)

Both computational domains include mesh with approximately 2 million hexahedral cells. The velocity components, turbulence kinetic energy k and dissipation of turbulence kinetic energy ε, obtained from the separate computation of swirl generator part, are defined as the inlet boundary conditions. At the outlet boundary condition is defined constant value of static gauge pressure (0 Pa) with radial equilibrium distribution, where the pressure gradient is governed by the radial component of Euler equation (1).

$$\frac{\partial p}{\partial r} = \frac{\rho v_\theta^2}{r} \tag{1}$$

Where r is distance from the axis of rotation and v_θ is circumferential velocity.

4.1. Computational domain of downstream part of SG-RO

In case of SG-RO the computational domain CD-RO is convergent divergent section with inlet diameter 150 mm, throat diameter D = 100 mm and outlet diameter 160 mm. Survey section S_0 is situated in the throat as a boundary between convergent and divergent section. Survey sections S1, S2 and S3 are in distances 0.5D, D and 1.5D from S_0. Longitudinal cross section of CD-RO with position of survey sections is shown in fig. 3.

4.2. Computational domain of downstream part of SG-CZ

Computational domain CD-CZ as a downstream part of SG-CZ is a diffuser with inlet diameter 53.6 mm, outlet diameter 98 mm and opening angle 12°. Survey section S_0 is placed at the end of cylindrical part with same diameter as the inlet diameter D =53.6 mm. Survey sections S1, S2 and S3 are in distances 0.5D, D and 1.5D from S_0. Longitudinal cross section of CD-RO with position of survey sections is shown in fig. 4.

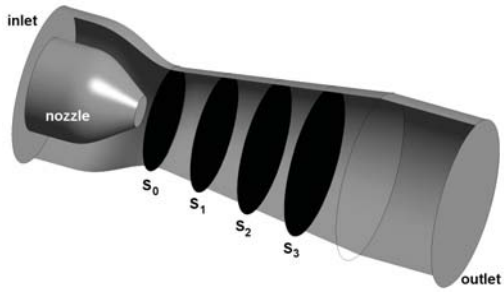

Fig. 3: Computational domain (CD-RO) in case of SG-RO.

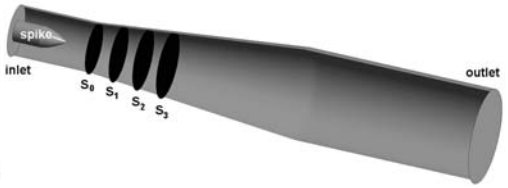

Fig. 4: Computational domain (CD-CZ) in case of SG-CZ.

4.3. Computational set-up

The numerical computations were carried out for flow regimes with identical Reynolds number (2) defined in survey section S_0. The value of Reynolds number is Re = 380143 and corresponds with flow rate Q = 30 l/s for SG-RO and Q = 15.9 l/s for SG-CZ.

$$Re = \frac{\bar{v} \cdot D}{\nu} \tag{2}$$

In fig. 5 are shown velocity profiles generated by SG-RO and in fig. 6 profiles generated by SG-CZ. Those profiles were used as the inlet boundary conditions for numerical computations. Only axial and circumferential components are shown because of very small magnitude of radial velocity component. But in the boundary condition the radial component is included. Velocity components are circumferentially averaged and made dimensionless with respect to the bulk velocity at the outlet of the swirl generator.

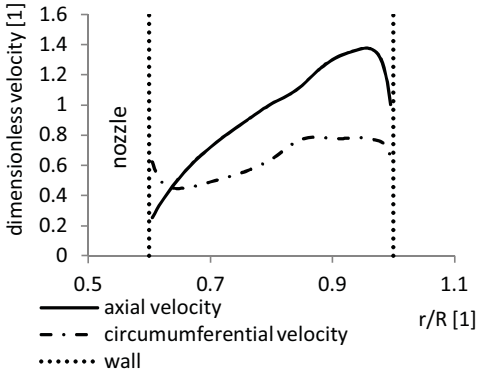

Fig. 5: Velocity components generated by SG-RO.

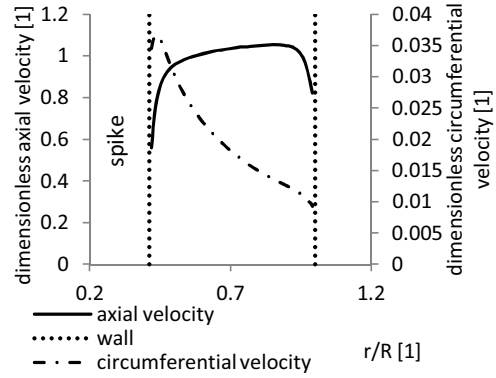

Fig. 6: Velocity components generated by SG-CZ.

5. Evaluation and results

For global quantitative description of the swirling flow we used swirl number (3) defined as the axial flux of swirl momentum divided by the axial flux of axial momentum (Susan-Resiga et al., 2006, Susan-Resiga et al., 2009)

$$S_n = \frac{\int v_{ax} v_{tan} r dS}{R \int v_{ax}^2 dS} \tag{3}$$

Computed value of swirl number generated by SG-RO is $S_{n\text{-}RO}$ = 0,581 and is substantially larger than swirl number computed in case of SG-CZ where $S_{n\text{-}CZ}$ = 0,122. This difference is also noticeable in dimensionless circumferential velocity components, see fig. 5 and fig. 6. Comparison for identical swirl number is not carried out due to different design of swirl generators (blade design of SG- CZ produces much smaller circumferential velocity component than SG-RO).

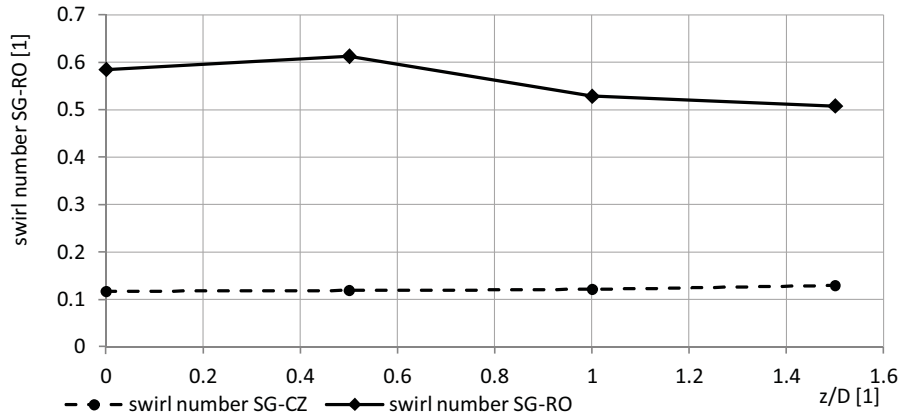

Fig. 7: Swirl number streamwise development in case of CD-RO (solid line) and CD-CZ (dashed line).

5.1. Velocity profiles computed in survey section S_0

Velocity profiles computed in survey sections S_0 are time averaged and made dimensionless with respect to equation (4).

$$v_{dim-less} = \frac{v}{\frac{Q}{S}} = \frac{v}{\bar{v}} \tag{4}$$

Where v is corresponding velocity component and $\bar{v}$ is bulk velocity defined as a flow rate Q divided by cross-sectional area S.

In figure are plotted dimensionless axial velocity components and in fig. 9 circumferential velocity components computed in survey section of the corresponding swirl generator.

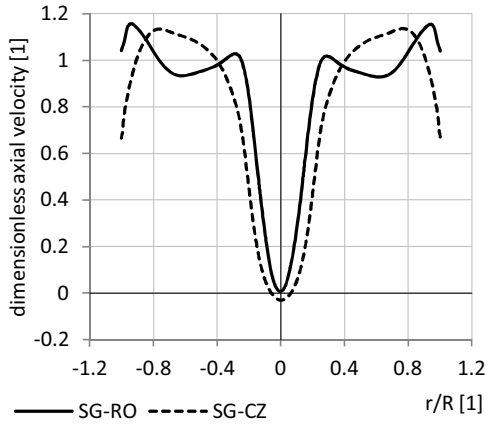

Fig. 8: Dimensionless axial velocity components computed in survey section S0.

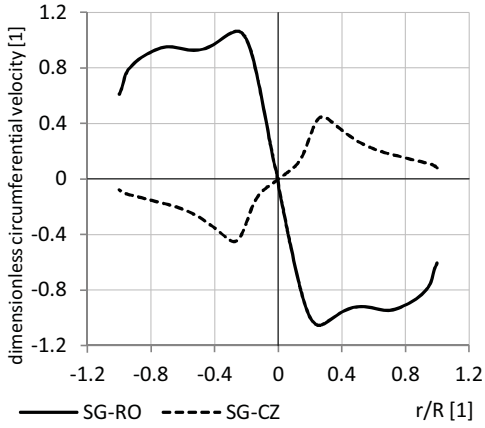

Fig. 9: Dimensionless circumferential velocity components computed in survey section S0.

5.2. Streamwise evolution of axial velocity, circumferential velocity and vorticity magnitude

Evolution of axial velocity components along the diffuser axis are shown in figs. 10 and 13. Enlargement of stagnant region is evident and related with extending of vortex rope helix in streamwise direction. Axial velocity component is much larger in case of SG-CZ than in case of SG-RO. On the other hand circumferential velocity component is much smaller in case of SG-CZ than in case of SG-RO. Different sense of flow rotation, caused by different design of swirl generators, is noticeable in circumferential velocity profiles (see fig. 11 versus fig. 14 or fig. 9). Magnitudes of corresponding profiles (axial, circumferential or vorticity) are plotted in equal dimensional scale.

Important fact is, that boundary of stagnant region (apparent by the large gradient of velocity profile curve), is in appropriate distance from the diffuser axis for both, axial and circumferential velocity component. This fact shows strong coupling between corresponding axial and circumferential velocities (Batchelor, 1964).

Vorticity magnitude profiles evolution (fig. 12 versus fig. 15) shows higher compactness of vortex core in streamwise direction (significant peaks of vorticity) for case of SG-CZ. This conclusion is evident in fig. 18, where streamlines in combination with vortex core are shown. Abrupt vortex decay, approximately situated near survey section S1, is apparent in case of SG-RO. This abrupt vortex decay is also probably related with formation of huge backflow region (visualized in fig. 17 (left) as a time averaged) and linked with significant longitudinal vortex rope pulsation with computed frequency around 2.5Hz (see figs. 23 and 24).

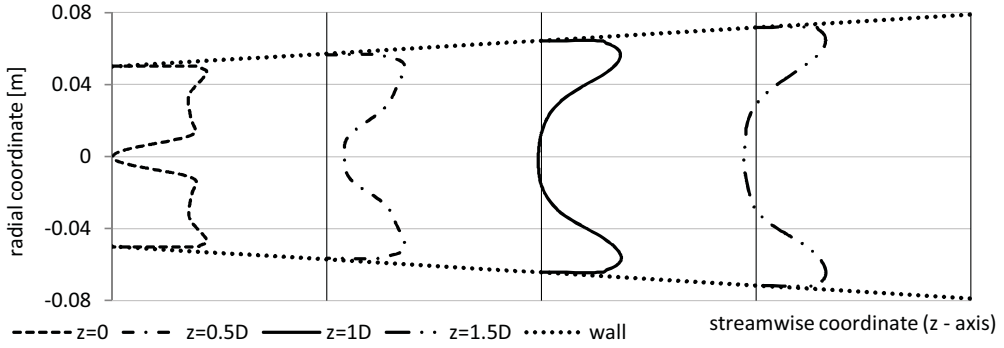

Fig. 10: Time averaged axial velocity profile development downstream in diffuser of CD-RO.

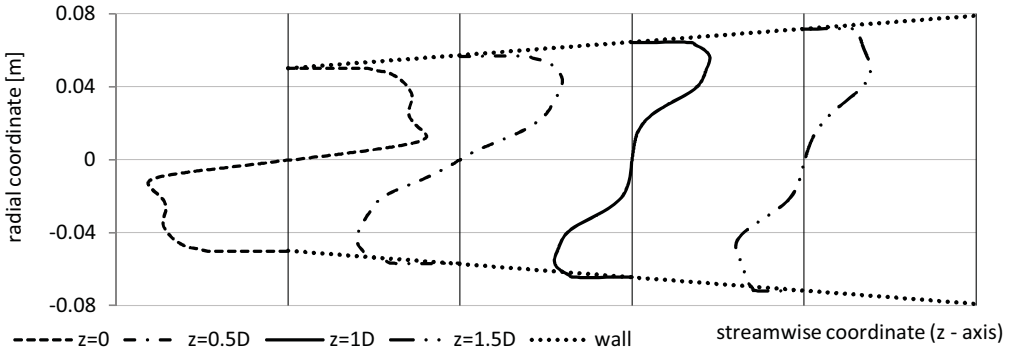

Fig. 11: Time averaged circumferential velocity profile development downstream in diffuser of CD-RO.

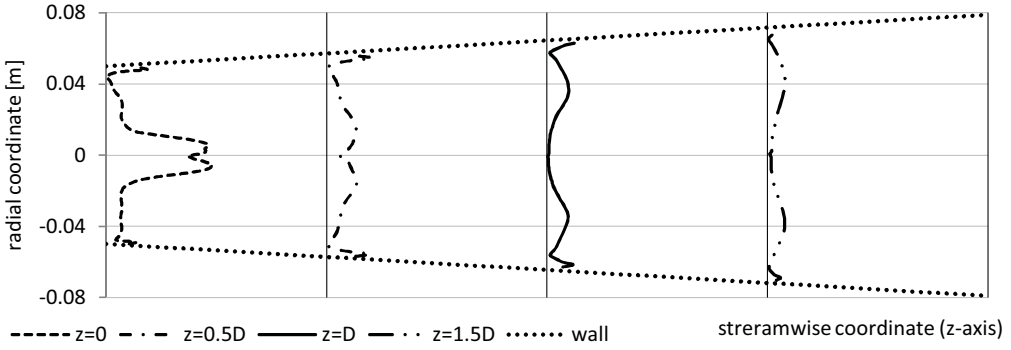

Fig. 12: Time averaged vorticity magnitude profile development downstream in diffuser of CD-RO.

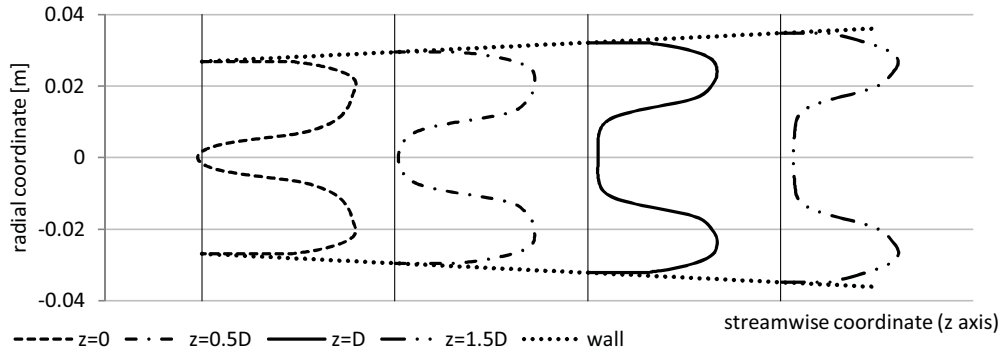

Fig. 13: Time averaged axial velocity profile development downstream in diffuser of CD-CZ.

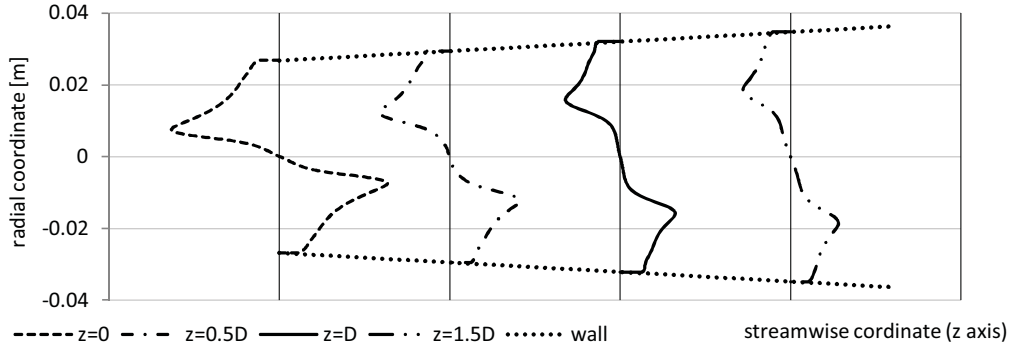

Fig. 14: Time averaged circumferential velocity profile development downstream in diffuser of CD-CZ.

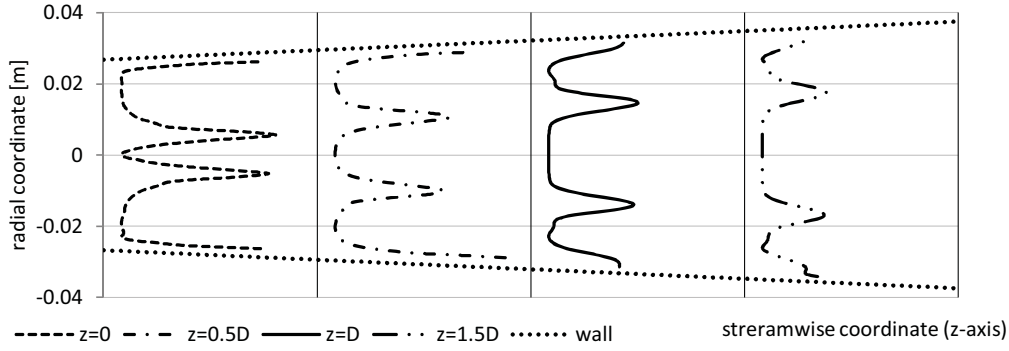

Fig. 15: Time averaged vorticity magnitude profile development downstream in diffuser of CD-CZ.

5.3. Flow field analysis

Calculation is based on one phase model, thus for the vortex rope visualization is applied isosurface of very low pressure. Significant difference between pressure drop generated by each swirl generator is noticeable. Vortex ropes are visualized for ratio $^{p_{stat}}/_{p_{dyn\_inlet}}$ = -1.95 in case of SG-RO and -1.08 in case of SG-CZ, where p_{stat} is value of static pressure isosurface and p_{dyn_inlet} is dynamic pressure at the inlet of computational domain. Time snapshot of vortex ropes with corresponding backflow regions are shown in fig. 16. On the other hand time averaged backflow regions are visualized in fig. 17. In fig. 19 is shown longitudinal development of SG-RO vortex rope in time. Time period is around 0.4 s and corresponds with frequency around 2.5 Hz extracted from pressure signal evaluated in section 5.4. Noticeable is transition from one long vortex rope (t = 0s) to one longer and one very short intertwined vortex ropes (t = 0.1s or 0.2s).

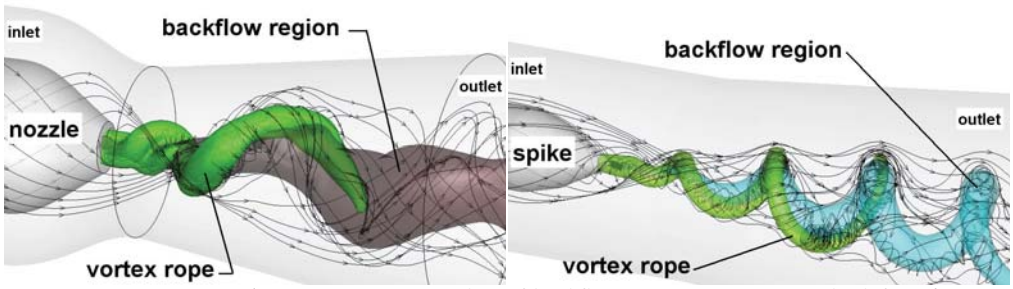

Fig. 16: Vortex rope and instantaneous snapshot of backflow region, CD-RO on the left and CD-CZ on the right.

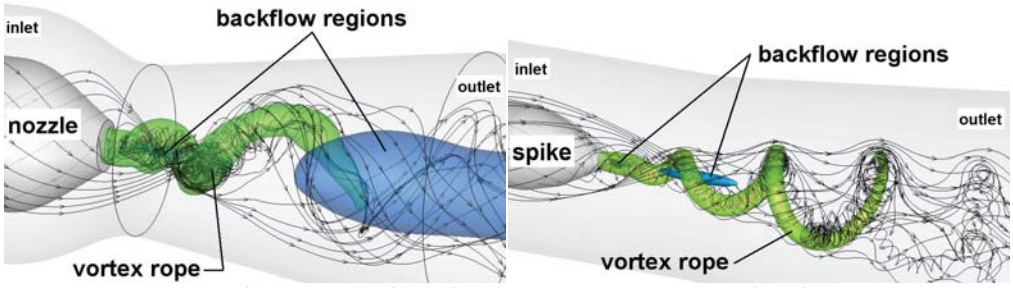

Fig. 17: Vortex rope and time averaged backflow regions, CD-RO on the left and CD-CZ on the right.

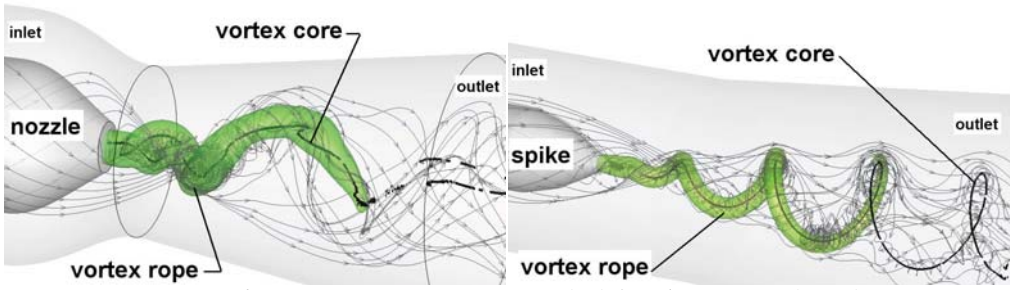

Fig. 18: Vortex rope and vortex core region, CD-RO on the left and CD-CZ on the right.

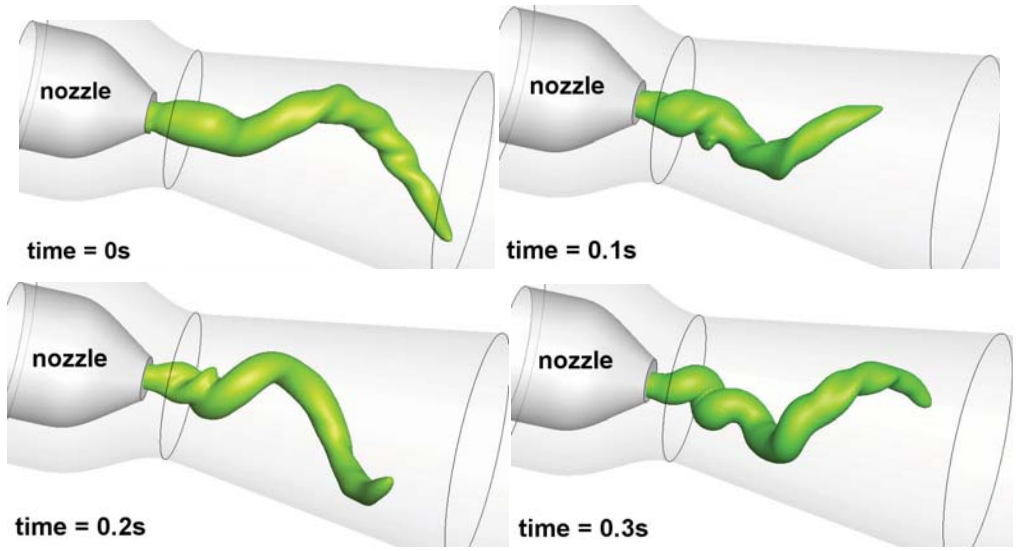

Fig. 19: Longitudinal development of SG-RO vortex rope in time

5.3.1. Comparison with experimental measurement

In this section axial and circumferential velocity components extracted from CFD computation are compared with experimentally measured velocity components carried out by 2D LDV measurement in case of SG-RO (Bosioc et al., 2009), see fig. 20. Comparison is carried out for two survey sections corresponding with window W1 (plotted in fig. 21) and window W2 (plotted in fig. 22). One can see good fitting of numerical curves with experimentally measured axial velocity. Higher discrepancy appears in circumferential velocity component outside of the diffuser axis. Computed circumferential velocity profiles are flatter than the measured ones.

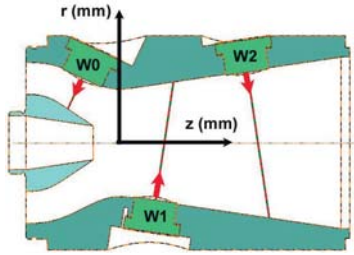

Fig. 20: Survey axis for LDV measurement in convergent divergent part of SG-RO (Bosioc et al., 2009).

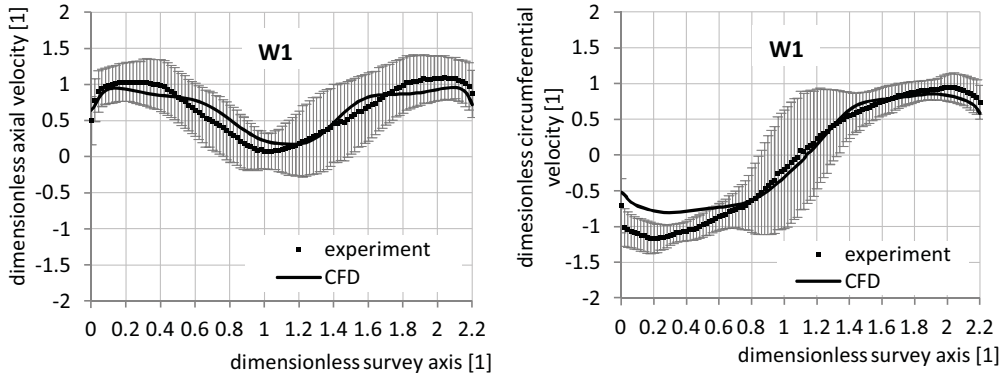

Fig. 21: Velocity components from 2D LDV measurement compared with CFD results (window W1).

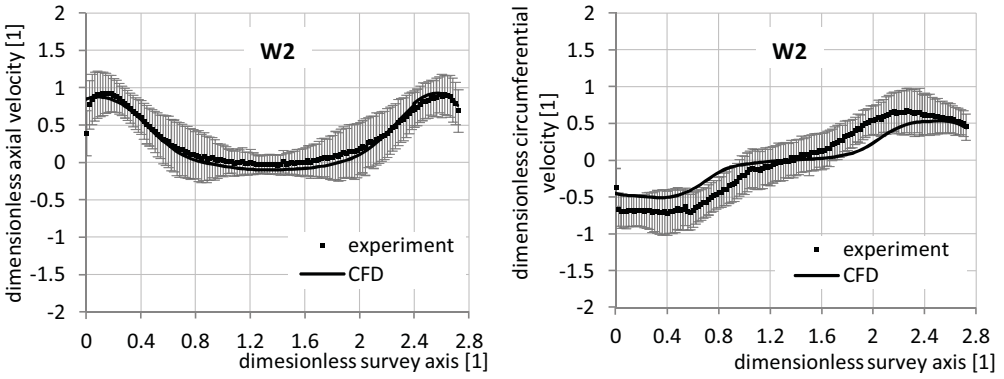

Fig. 22: Velocity components from 2D LDV measurement compared with CFD results (window W2).

5.4. Fourier analysis of the pressure fluctuations

As a results of vortex breakdown high pressure fluctuations are generated in downstream part of swirl generator. Time record of numerically computed static pressure was set in four monitoring points to perform Fast Fourier Analysis. The monitoring points are situated near the wall of the computational domain in downstream distances in order 0, 0.5D, D and 1.5D from S_0, where D is diameter of survey

section S_0. Simply script written in MATLAB software was employed to extract spectral information of the numerical pressure record. Frequencies with dominant amplitude are shown in tab. 1 for CD-RO and in tab. 2 for CD-CZ. In fourth column are amplitudes related to the inlet dynamic pressure p_{dyn}.

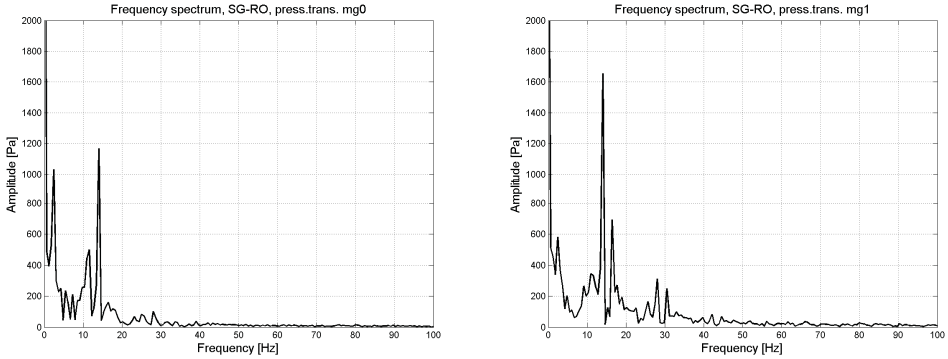

Fig. 23: Amplitude-frequency spectrum of pressure pulsations in case of CD-RO (MG0 on the left, MG1 on the right).

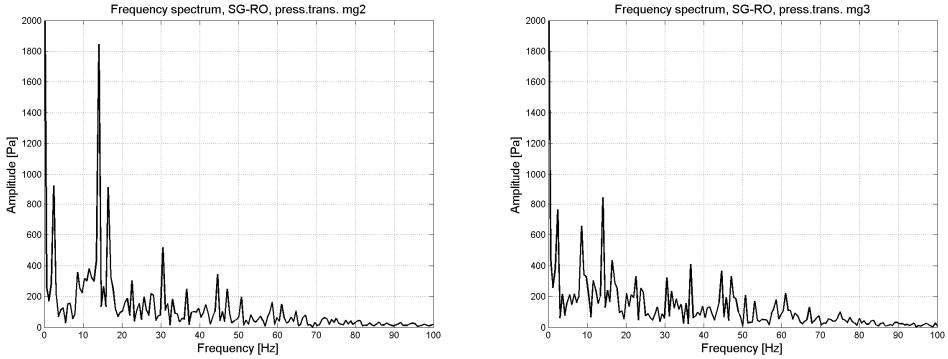

Fig. 24: Amplitude-frequency spectrum of pressure pulsations in case of CD-RO (MG2 on the left, MG3 on the right).

Tab. 1: Spectral analysis of CD- RO

Monitoring point	Dominant frequency [Hz]	Amplitude [Pa]	Amplitude/p_{dyn} [1]
MG0	14.04	1166	0.189
MG1	14.04	1655	0.268
MG2	14.04	1847	0.299
MG3	14.04	843	0.137

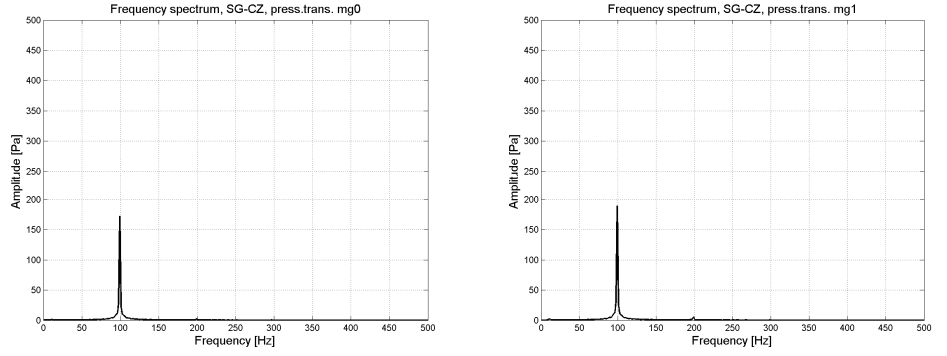

Fig. 25: Amplitude-frequency spectrum of pressure pulsations in case of CD-CZ (MG0 on the left, MG1 on the right).

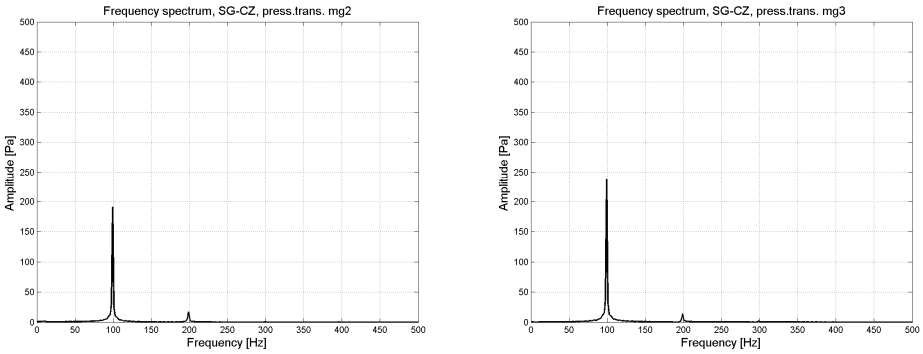

Fig. 26 Amplitude-frequency spectrum of pressure pulsations in case of CD-RO (MG2 on the left, MG3 on the right).

Tab. 2: Spectral analysis of CD- CZ

Monitoring point	Dominant frequency [Hz]	Amplitude [Pa]	Amplitude/p_{dyn} [1]
MG0	99.46	172.5	$3.37 \cdot 10^{-3}$
MG1	99.46	189.9	$5.02 \cdot 10^{-3}$
MG2	99.46	191	$5.04 \cdot 10^{-3}$
MG3	99.46	237.4	$6.28 \cdot 10^{-3}$

5.4.1. Comparison with experimental measurement

Experimentally measured frequency of vortex rope rotation in case of SG-RO is found around 14.95Hz. One can see only small difference (6%) between experimentally measured and numerically computed frequency and good agreement with previous computational results (Muntean et al., 2009, Petit et al., 2011). Lower value of numerical frequency confirms that numerical model is more dissipative than experiment. Suitable agreement in comparison of numerical and experimental (Muntean et al., 2009) amplitude magnitude is obtained only for pressure transducers MG0, while computed amplitudes for MG1, MG2 and MG3 overestimate experimental results. Comparison for case of SG-CZ is not carried out because of high interference in experimental data. This problem is being further investigated.

6. Conclusions

Different shape of vortex rope, generated by each swirl generator, corresponds with different value of swirl number. SG-RO with higher swirl number than SG-CZ composes swirling flow with more massive vortex rope. Vortex rope has larger width and forms into shape with higher ascend of helix. This shape is similar to the vortex rope appearing in Francis turbine draft tube (FLINDT project) during operation on 70% Q_{BEP} and was main designed parameter of SG-RO.

On the other hand, vortex rope generated by SG-CZ is thinner and forms into shape with lower ascend of the helix. In comparison with the vortex ropes computed in paper Rudolf 2009 for inlet boundary conditions derived by Susan-Resiga et al., 2006, the vortex rope generated by SG-CZ is very similar one to the vortex rope corresponding with the turbine operation on 90%Q_{BEP}.

During calculation it has been observed, that shape of vortex rope generated by SG-RO is in time more unstable than vortex rope generated by SG-CZ. Moreover for calculation with employing of RSM turbulence, the vortex rope changes its structure periodically from one long compact vortex rope into two (long and one very short) vortex ropes which are intertwined close to the nozzle. This change is realized in longitudinal direction with frequency around 2.5Hz and amplitudes around 800Pa.

Results confirmed strong coupling between circumferential and axial velocity components and this coupling is full maintained in streamwise direction.

Acknowledgement

Czech Science Foundation is gratefully acknowledged for support of the research under project No. 101/09/1715 "Cavitating vortical structures induced by rotating liquid". This project is supported by junior research grant number FSI-J-12-21/1698 provided by Brno University of Technology. The Timisoara swirl generator test case and associated experimental data was supported by the Romanian Agency CNCSIS – UEFISCSU, Exploratory Research Project PN II - IDEI 799/2008.

References

Avellan, F. (2000) Flow Investigation in a Francis Draft Tube: The FLINDT Project, in: *Proceedings of the 20th IAHR Symposium on Hydraulic Machinery and Systems*, Charlotte, USA, Paper DES-11.

Batchelor, G. K., (1964) Axial Flow in Trailing Line Vortices, *J. Fluid Mech*., 20 (4), pp. 645–658.

Bosioc, A., Susan-Resiga, R. F., and Muntean, S. (2008) Design and Manufacturing of a Convergent-Divergent Test Section for Swirling Flow Apparatus, in: *Proceedings of the 4th German – Romanian Workshop on Turbomachinery Hydrodynamics* (GRoWTH), June 12-15, 2008, Stuttgart, Germany.

Bosioc, A., Tanasa, C., Muntean, S., Susan-Resiga, R.F. (2009) 2D LDV Measurements of Swirling Flow in a Simplified Draft Tube, in: Proceedings of the CMFF09, Vol. II, Budapest, Hungary. p.p. 833-838

Ciocan, G. D., Iliescu, M. S., Vu, T. C., Nennemann, B., Avellan, F. (2007) Experimental study and numerical simulation of the FLINDT draft tube rotating vortex, *Journal of Fluids Engineering*, Vol. 129, pp.146–158.

Hydrodynamics, Stuttgart, Germany, June 12-15.

Iliescu, M. S., Ciocan, G. D., Avellan, F. (2008) Analysis of the Cavitating Draft Tube Vortex in a Francis Turbine Using Particle Image Velocimetry Measurements in Two-Phase Flow. *Journal of Fluid Engineering.* Vol. 130.

Jawarneh, A. M., Vatistas, G. H. (2006) Reynolds Stress Model in the Prediction of Confined Turbulent Swirling Flows, in: *ASME Journal of Fluid Engineering,* Vol. 128, p.p.1377-1382.

Lucca-Negro, O., O'Doherty, T. (2001) Vortex breakdown: a review, in: Annual Review of Fluid Mechanics, 10, 221-246, 1978.

Muntean, S., Nilsson, H., and Susan-Resiga, R. (2009) 3D Numerical Analysis of the Unsteady Turbulent Swirling Flow in a Conical Diffuser Using Fluent and OpenFOAM, in: *Proceedings of the 3rd IAHR International Meeting of the Workgroup on Cavitation and Dynamic Problem in Hydraulic Machinery and Systems*, Brno, Czech Republic.

Petit, O., Bosioc, A. I., Nilsson, H., Muntean, S., Susan-Resiga, R. F. (2011) Unsteady Simulations of the Flow in a Swirl Generator, Using OpenFOAM, *International Journal of Fluid Machinery and Sytsems,* Vol. 4, No. 1.

Rudolf, P. (2009) Connection between inlet velocity field and diffuser flow instability, in: *Applied and Computational Mechanics,* Vol. 3, No. 1, pp. 177 - 184

Rudolf, P., Hudec, M., Zubík, P., Štefan, D. (2011) Experimental measurement and numerical modeling of cavitating flow in converging-diverging nozzle, in: *Proceedings of the International Conference Experimental Fluid Mechanics 2011*, pp.423-431, Jíčín, Czech Republic.

Susan-Resiga, R. F., Ciocan, G. D., Anton, I., Avellan, F. (2006) Analysis of the swirling flow downstream of a Francis turbine runner. *Journal of Fluid Engineering,* Vol. 128, pp.177-189.

Susan-Resiga, R. F., Muntean, S., and Bosioc, A. (2008b) Blade Design for Swirling Flow Generator, in: *Proceedings of the 4th German – Romanian Workshop on Turbomachinery Hydrodynamics* (GRoWTH), June 12-15, Stuttgart, Germany.

Susan-Resiga, R. F., Muntean, S., Avellan, F., Anton, I. (2011) Mathematical modelling of swirling flow in hydraulic turbines for the full operating range, *Appl. Math. Modell.* doi:10.1016/j.apm.2011.03.052

Susan-Resiga, R. F., Muntean, S., Hasmatuchi, V., Anton, I., Avellan, F. (2010) Analysis and prevention of vortex breakdown in the simplified discharge cone of a Francis turbine, *Journal of Fluid Engineering*, Vol. 132, 15 pages.

Susan-Resiga, R. F., Muntean, S., Stein, P., Avellan, F. (2009) Axisymmetric swirling flow simulation of the draft tube vortex in Francis turbines at partial discharge, in: *Int. J. Fluid Mach. Sys.* 2, pp.295–302.

Susan-Resiga, R. F., Muntean, S., Tanasa, C., Bosioc, A. (2008a) Hydrodynamic Design and Analysis of a Swirling Flow Generator, in: *Proceedings of the 4th German – Romanian Workshop on Turbomachinery Hydrodynamics* (GRoWTH), June 12-15, 2008, Stuttgart, Germany.

18th International Conference
ENGINEERING MECHANICS 2012
Svratka, Czech Republic, May 14 – 17, 2012

pp. 1343–1352
Paper #148

INTRODUCTION OF THE ANALYTICAL TURBULENT VELOCITY PROFILE BETWEEN TWO PARALLEL PLATES

J. Štigler*

Abstract: *A new analytical velocity profile between two parallel plates is introduced in this article. It is possible to use this velocity profile for both laminar and turbulent flow. All necessary parameters can be obtained from the unit flow rate and the pressure drop. We can also use this model in case when the material of the upper and lower wall is different.*

Keywords: ***velocity profile, laminar flow, turbulent flow, flow between parallel plates.***

1. Introduction

The laminar velocity profile between two laminar plates is very well known from the fundamental lectures of the hydromechanics. The velocity profile, in case of Poiseuille flow means the laminar flow governed by the pressure gradient, can be then expressed by the quadratic function.

$$v_{(x)} = \frac{\Delta p}{L.\mu}.\frac{h^2}{2}\left[1-\left(\frac{x_2}{h}\right)^2\right] \tag{1}$$

Where Δp/L is a pressure gradient, μ is dynamic viscosity, h is a half of distance between the parallel plates.

Maximal velocity is in the middle of the channel where y=0.

$$v_{(x\max)} = \frac{\Delta p}{L.\mu}.\frac{h^2}{2} \tag{2}$$

Then the velocity profile could be expressed as

$$v_{(x)} = v_{(x\max)}\left[1-\left(\frac{y}{h}\right)^2\right] \tag{3}$$

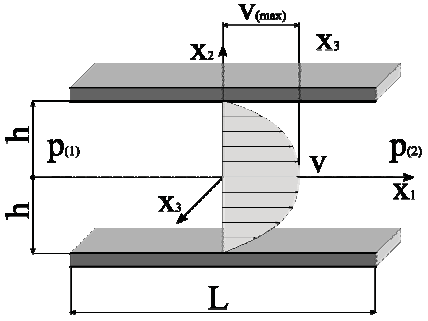

Fig. 1.Velocity profile between two parallel plates

* doc Ing. Jaroslav Štigler, Ph.D.: Department of Fluid Engineering, Energy Institute, Faculty of Mechanical Engineering, Brno University of Technology, Technická 2; 140 00, Brno; CZ, e-mail: stigler@fme.vutbr.cz

It is more complicated to find any analytical solution in the case of turbulent flow. There is some expression which was found on the basis of experimental data. It is known as the *power law*. Unfortunately it was derived only for the flow in a pipe with radius R.

$$v_{(x)} = v_{(x\max)}\left[1-\left(\frac{r}{R}\right)^2\right]^{n_0} \tag{4}$$

Where r is a radius within interval <0,R>, R is the pipe radius, n_0 is the exponent which is a function of the Reynolds number. This exponent can be evaluated from the expression

$$\frac{1}{n_0} = 1+\sqrt[6]{\frac{Re}{50}} \tag{5}$$

There is some discrepancy in this power law definition. It cannot be used near the wall, for r=R, because the derivative has an infinite value there. The wall shear stress τ_w is then infinite, which does not correspond with the reality.

There is also another power law definition by Munson (2006).

$$v_{(x)} = v_{(x\max)}\left(1-\frac{r}{R}\right)^{1/n_0} \tag{6}$$

Where n_0 is a function of the Reynolds number, see Munson (2006). This turbulent velocity profile has problems in two locations. The first one is the same as in the previous formulation. The wall shear stress goes to infinity. The second problematic location is in the middle of the channel, the derivative for r=0 is not zero.

From the above examples it is clear that these models have problems near the wall. Therefore it is necessary to focus on the near wall region – boundary shear layer. The boundary shear layer in the case of turbulent flow can be divided into three regions.

The first region is called viscous sub-layer. This region is close to the wall and the viscosity plays a dominant role in this region. The velocity profile is linear within this region.

The second region is the transition area – this is the region of smooth transition into the logarithmic velocity profile.

The third one is the region where the turbulent viscosity plays a dominant role.

$$\frac{v_{(x)}}{v^*} = \frac{1}{\kappa}.\log\frac{v^*.y}{\nu}+B \tag{7}$$

We can define dimensionless velocity v^+ and dimensionless distance from the wall y^+.

$$v^+ = \frac{v_{(x)}}{v^*} \tag{8}$$

$$y^+ = \frac{v^*.y}{\nu} \tag{9}$$

Where shear velocity v* is expressed by the formula

$$v^* = \sqrt{\frac{\tau_w}{\rho}} \tag{10}$$

Many different authors use different values of constants κ and B. For example Janalík (2008) uses the κ=0,174 and B=5,5 or Munson (2006) uses κ=0,4 and B=5 or Pope (2008) uses κ=0,41 and B 5,2.

2. Derivation of a new velocity profile

The new velocity profile is derived on the basis of the vorticity distribution over the space between two parallel plates. This velocity profile can be used for all, laminar, turbulent and constant velocity profile. The derivation of this type of velocity profile is based on a Biott-Savart law, the derivation of it is made in Brdička 2000, applied on a straight vortex filament with circulation Γ.

$$v_i = \frac{\Gamma}{2.\pi}.\frac{1}{r^2}.\varepsilon_{i3k}.(x'_k - x_k) \tag{11}$$

This expression is valid for a special situation when the straight vortex filament is parallel to the x_3 axis. This is also an expression of the velocity induced by a single potential vortex in case of 2D flow (Lewis 1991). Einstein summation convection is used in the expression (11). The v_i is the velocity induced by the single vortex, the Γ is a circulation around the single vortex, x_k – are coordinates of vortex location, x'_k are coordinates of induced velocity location, ε_{ijk} is an Levi-Civita tensor of 3rd order, r is a distance between vortex and point of induced velocity.

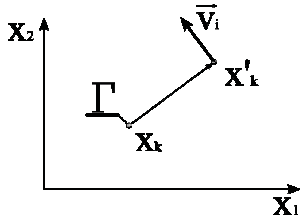

Fig. 2.Velocity induced by a single 2D vortex.

Velocity induced by a plain vortex sheet

There is another well known example of the velocity induced by an infinite plain vortex sheet Lewis (1991). This sheet consists of the vortex filaments, with constant circulation Γ which are parallel to the x_3 axis. The situation is depicted in the Fig. 3. It is necessary to define linear vorticity density γ in this case. The circulation dΓ around the infinitesimal length of sheet ds can be expressed this way

$$d\Gamma = \gamma.ds \Rightarrow \gamma = \frac{d\Gamma}{ds} \tag{12}$$

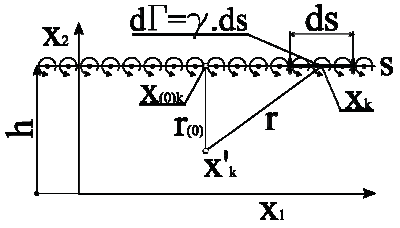

Fig. 3.Velocity induced by the plain vortex sheet parallel to the x_1,x_3 plain.

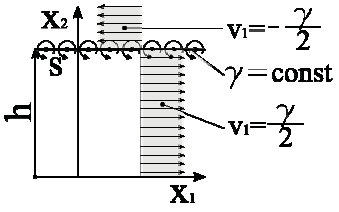

Fig.4. Velocity profile induced by a plain vortex sheet parallel to the x_1,x_3 plain.

In case that the vorticity density is constant, over the whole sheet, the velocity induced by a vortex sheet can be expressed this way.

$$v_i = \frac{\gamma}{2}.\varepsilon_{i3k}.\frac{\left(x'_k - x_{(0)k}\right)}{r_{(0)}} \tag{13}$$

Where γ is the vorticity density, x'_k are the coordinates of location where the velocity is induced, $x_{(0)k}$ are the coordinates of x'_k point projection on the vortex sheet, $r_{(0)}$ is a distance of point x'_k from the vortex sheet. For the case depicted in a fig. 3, when the vortex sheet is collinear with plane $x_1\, x_3$, the velocity components are:

$$v_1 = -\frac{\gamma}{2};\ \ v_2 = 0 \quad \text{within the interval } x'_2 \in \left(h,\ \ +\infty\right) \tag{14}$$

$$v_1 = \frac{\gamma}{2};\ \ v_2 = 0 \quad \text{within the interval } x'_2 \in \left(h,\ \ -\infty\right) \tag{15}$$

This type of flow is depicted in the fig 4. It means that velocity within half-plane above vortex sheet is constant, parallel to the vortex sheet and with the orientation to the left. Velocity within the half-plane below vortex sheet is also parallel to the vortex sheet but with the orientation to the right.

Velocity induced by two vortex sheets with the opposite vorticity density orientation

Now it is possible to study fluid flow with two parallel vortex sheet $s_{(1)}$, and $s_{(2)}$. The magnitude of the vorticity density of both vortex sheets is equal but the orientation is opposite. It means that $\gamma_{(1)}=\gamma$ and $\gamma_{(2)}=-\gamma$. The vortex sheet $s_{(1)}$ position is $x_2=h_1$. The vortex sheet $s_{(2)}$ position is $x_2=-h_2$. This situation is depicted in the fig. 5.

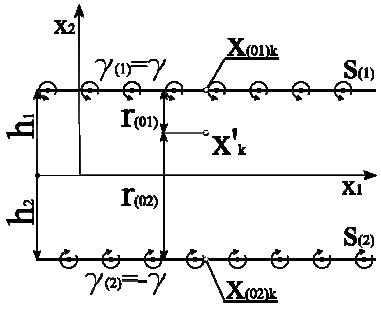

Fig. 5. Velocity induced by the two plain vortex sheets parallel to the x_1,x_3 plain.

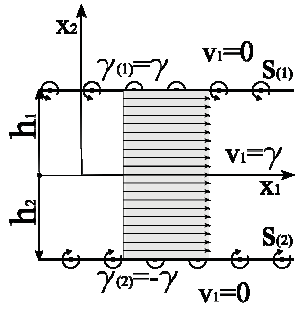

Fig.6. Velocity profile induced by a plain vortex sheet parallel to the x_1,x_3 plain.

The induced velocity for this case should be expressed by this formula

$$v_i = \sum_{j=1}^{n} \frac{\gamma_{(j)}}{2}.\varepsilon_{i3k}\frac{\left(x'_k - x_{(0j)k}\right)}{r_{(0j)}} \tag{16}$$

This formula is general for an arbitrary number n of vortex sheets. It is possible, for case of two vortex sheets with respect to the (16), to write

$$v_i = \frac{\gamma}{2}.\varepsilon_{i3k}\frac{\left(x'_k - x_{(01)k}\right)}{r_{(01)}} - \frac{\gamma}{2}.\varepsilon_{i3k}\frac{\left(x'_k - x_{(02)k}\right)}{r_{(02)}} \tag{17}$$

Explanation all parameter in above equation are clear from the fig. 5.

It is possible to have three different solutions now.

$$v_1 = 0;\ \ v_2 = 0 \ \text{ within the interval } x'_2 \in (h, \ \ +\infty) \tag{18}$$

$$\mathrm{v}_1 = \gamma;\ \ v_2 = 0 \ \text{ within the interval } \mathrm{x}'_2 \in (-\mathrm{h}, \ \ +\mathrm{h}) \tag{19}$$

$$\mathrm{v}_1 = 0;\ \ \mathrm{v}_2 = 0 \ \text{ within the interval } \mathrm{x}'_2 \in (-\infty, \ \ -\mathrm{h}) \tag{20}$$

This solution is very nice and reasonable. It is kind of the fluid flow between two parallel plates for infinite Reynolds number Re=∞.

Now it is only a small step to find the expression of the velocity profile for the finite Reynolds number.

Velocity profile for the continuous vorticity distribution over the cross-section

It has to be assumed, for this case, that the vorticity density is not the linear density but it is the planar vorticity density. It will be function of the x_2 coordinate between the plates. Vorticity density for the fixed coordinate x_2 is constant. The situation is depicted in a fig 7. It is necessary to define the coordinate system. The axis x_1 is parallel to the plates and it is located in the maximal velocity position.

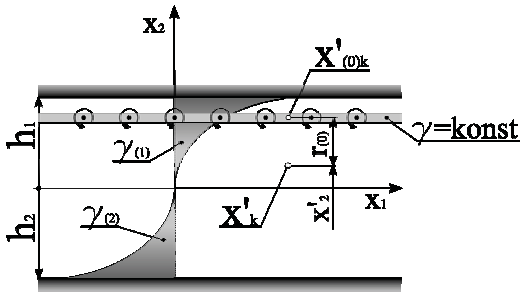

Fig. 7.The distribution of the planar vorticity density between two plates

The velocity profile is derived under these assumptions:

- It is the fluid flow between two parallel infinite plane plates.
- The vorticity density distribution is continuous between plates. It will be described by two polynomial functions $\gamma_{(1)}$ and $\gamma_{(2)}$ of the N^{th} order.
- The unit flow rate Q and the pressure drop Δp are known parameters.

The continuous vorticity density distribution can be expressed by the next formulas.

$$\gamma_{(1)} = \sum_{n=0}^{N} A_{(n)}.|x_2|^n \tag{21}$$

$$\gamma_{(2)} = -\sum_{n=0}^{N} B_{(n)}.|x_2|^n \tag{22}$$

Now the velocity can be expressed this way

$$v_{(+)1} = \sum_{n=0}^{N} \frac{1}{2.(n+1)} \left(B_{(n)}.h_2^{n+1} + A_{(n)}.h_1^{n+1} - 2.A_{(n)}.|x_2|^{n+1} \right) \text{ within the interval } x_2 = \langle 0, \ \ h_1 \rangle \tag{23}$$

$$\mathrm{v}_{(-)1} = \sum_{\mathrm{n}=0}^{\mathrm{N}} \frac{1}{2.(\mathrm{n}+1)} \left(\mathrm{B}_{(\mathrm{n})}.\mathrm{h}_2^{\mathrm{n}+1} + \mathrm{A}_{(\mathrm{n})}.\mathrm{h}_1^{\mathrm{n}+1} - 2.\mathrm{B}_{(\mathrm{n})}.|\mathrm{x}_2|^{\mathrm{n}+1} \right) \text{ within the interval } x_2 = \langle -h_2, \ \ 0 \rangle \tag{24}$$

It is necessary to determine the coefficients $A_{(n)}$ and $B_{(n)}$ for n=1-N. These coefficients can be determined on the basis of the following conditions.

- Slip condition on the walls
  $v_{(+)} = 0$, for $x_2 = h_1$
  $v_{(-)} = 0$, for $x_2 = -h_2$
- The unit flow rate is known.
- Circulation around element $dx_1.(h_{(1)}+h_{(2)})$ is zero.
- The necessary number of derivative at point $x_2 = 0$ is zero.

On the basis of these conditions it is possible to express velocity profile

$$v_{(+)1} = \frac{(N+2)}{(N+1)}.\frac{Q}{(h_1+h_2)}.\left[1-\left(\frac{|x_2|}{h_1}\right)^{N+1}\right] \text{ within the interval } x_2 = \langle 0, \quad h_1 \rangle \tag{25}$$

$$v_{(-)1} = \frac{(N+2)}{(N+1)}.\frac{Q}{(h_1+h_2)}.\left[1-\left(\frac{|x_2|}{h_2}\right)^{N+1}\right] \text{ within the interval } x_2 = \langle -h_2, \quad 0 \rangle \tag{26}$$

The maximal and average velocity can be expressed this way

$$v_{(max)1} = \frac{(N+2)}{(N+1)}.\frac{Q}{(h_1+h_2)} \tag{27}$$

$$v_{(av)1} = \frac{Q}{(h_1+h_2)} \tag{28}$$

The expression for the number N has to be found now. It is possible to do this from the known pressure drop.

$$N = \frac{h_1.h_2}{\mu.v_{(av)}}.\frac{(p_1-p_2)}{L} - 2 \tag{29}$$

Where μ is the dynamic viscosity. All above expressions are derived for a case that the plate 1 and plate 2 were made from different materials. So it means that there could be different conditions on the walls. If the conditions on the plates are identical then the velocity profile will be symmetrical ($h_1=h_2$ = h) and it is possible to write

$$v_1 = \frac{(N+2)}{(N+1)}.\frac{Q}{2.h}.\left[1-\left(\frac{|x_2|}{h}\right)^{N+1}\right] \text{ within the interval } x_2 = \langle -h, \quad h \rangle \tag{30}$$

$$N = \frac{h^2}{\mu.v_{(av)}}.\frac{(p_1-p_2)}{L} - 2 \tag{31}$$

This expression can be used for all types velocity profiles from laminar velocity profile (N=1), for turbulent velocity profiles and also for a piston velocity profiles $N\to\infty$. There is no problem with the derivatives near the wall and with the zero value of the first derivative in the centre of channel.

3. Discussion

The formal comparison of different velocity profiles will be presented in this chapter. The only problem of it is that the power law velocity profiles are derived for a turbulent flow in pipes. But it is

possible to compare the velocity profiles normalized by v_{max} velocity. Comparison of velocity profiles is in the fig. 8. It is only formal comparison because the pressure drop or the friction factor for the fluid flow between the parallel plates is not known. Therefore the three new velocity profiles for different values of power N are compared with Munson (2006) power law velocity profile and with Janalík (2008) power law velocity profile in the fig 8. It is apparent that the character all kind of velocity profiles are different. The Janalik's velocity profile is rather rounded even for very high Reynolds number. The Munson velocity profile has no continuous first derivative in the center of channel. The new velocity profiles have also a problem that there is a zero second derivative in the centre of channel. It means that there is an infinite radius there. But this problem should be solved during derivation its derivation. It means that the velocity profile can be modified in way to ensure non zero second derivative. But it has not been done yet.

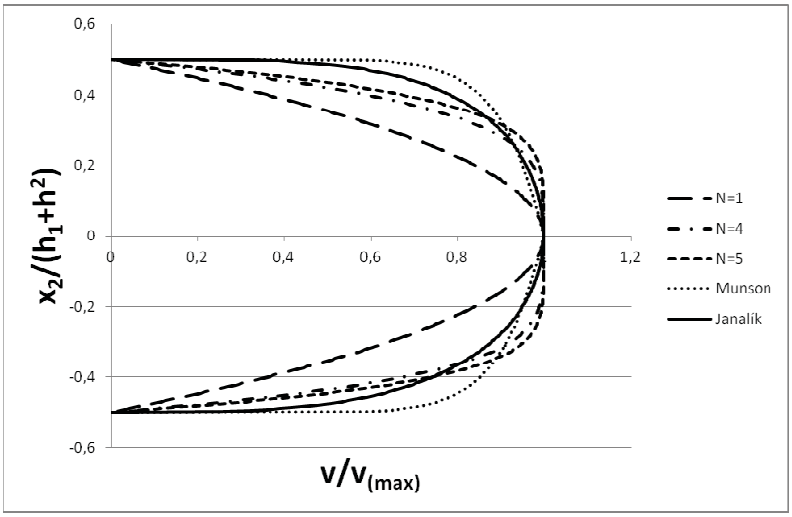

Fig. 8.New velocity profiles in comparison with power law velocity profiles.

It is possible also compare the velocity profile near the wall with a logarithm wall law. This comparison is depicted in a fig. 9.

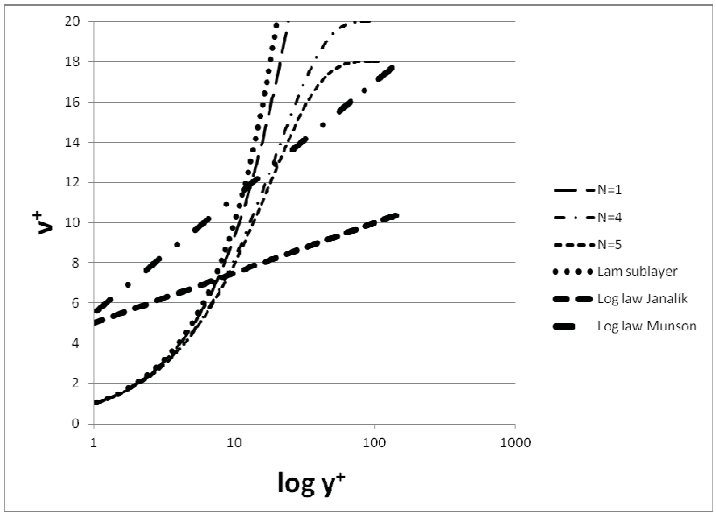

Fig. 9.The new velocity profiles comparison with log wall law.

The comparison is not so good because the exponent N is not evaluated, because there is no a measuring of pressure drop and flow rate. Therefore there are depicted several velocity profiles for different exponent N. It is apparent that the boundary shear layer in case of the new velocity profile is thinner than in the case of real velocity profile. This is probably consequence of the zero value of the second derivative of the velocity profile in the channel centre. There is no comparison for the power law profiles because there is no possible to express y^+ and v^+ because infinite shear stress at the wall.

At the end it would be interesting to draw the shear stress over channel. It is known that the total shear stress is linear. Total shear stress is a sum of the viscous shear stress τ_μ and the turbulent or (Reynolds) shear stress τ_t.

$$\tau = \tau_\mu + \tau_t \tag{32}$$

Viscous shear stress should be expressed from a velocity profile formula (29).

$$\tau_\mu = \mu.v_{(max)} \cdot \frac{(N+1)}{h} \cdot \left(\frac{|x_2|}{h} \right)^N \text{ within the interval } x_2 = \langle -h, \quad 0 \rangle \tag{33}$$

$$\tau_\mu = -\mu.v_{(max)} \cdot \frac{(N+1)}{h} \cdot \left(\frac{|x_2|}{h} \right)^N \text{ within the interval } x_2 = \langle 0, \quad h \rangle \tag{34}$$

This stress can be expressed in a dimensionless form

$$\frac{\tau_\mu.h}{\mu.v_{(max)}} = (N+1) \cdot \left(\frac{|x_2|}{h} \right)^N \text{ within the interval } x_2 = \langle -h, \quad 0 \rangle \tag{35}$$

$$\frac{\tau_\mu.h}{\mu.v_{(max)}} = -(N+1) \cdot \left(\frac{|x_2|}{h} \right)^N \text{ within the interval } x_2 = \langle 0, \quad h \rangle \tag{36}$$

The viscous stress together with the Reynolds stress for three different exponents N are depicted in the fig. 10. This also can't be compared with the power law velocity profiles because its shear stress at the wall is infinite.

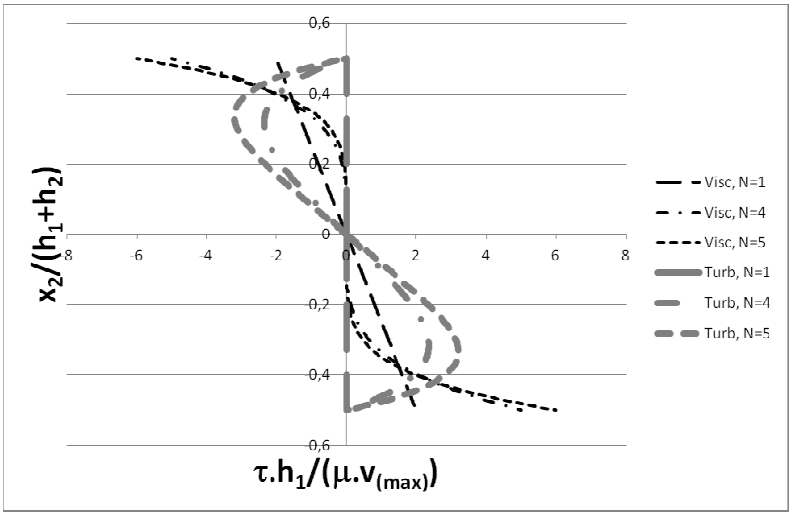

Fig. 10.The Reynolds and viscous stresses derived from a new velocity profile..

4. Conclusion

The new velocity profile based on a vorticity distribution between two parallel plates has been presented in this paper. This velocity profile is better than the power law velocity profiles because it has not infinite shear stress at the wall. It means that it is possible to express the Reynolds stresses and it is possible to compare this profile with the logarithmic law near the wall. This is not possible in case of the power law velocity profiles because they have infinite derivative near the wall. The new velocity profile has only one problem which can be removed. The problem is that this profile has zero second derivative in the centre of channel. It means that there is an infinite radius of curvature. It is also necessary to compare this velocity profile directly with an experimental velocity profiles. This work can help in understanding or even in modeling of boundary shear layers in CFD software.

List of Symbols

Symbol	Units	Description
$A_{(n)}$	Varies	Polynom coefficients
$B_{(n)}$	Varies	Polynom coefficients
h	[m]	Half distance between two parallel plates
h_1, h_2	[m]	Distance of plate s_1/s_2 from a coordinate system origin
L	[m]	Length. Distance between the pressure location measuring.
n_0	-	Exponent
Δp	[Pa]	Pressure difference
$p_{(1)}$, $p_{(2)}$	[Pa]	Pressure at location 1 or 2 respectively
Q	[m]	Unit flow rate. Flow rate between two parallel plates with 1m width.
r, R	[m]	Radius
Re	[-]	Reynolds number
$r_{(0)}$	[m]	Distance of point x'_k from vortex sheet
$v_{(av)}$	$[m.s^{-1}]$	Average velocity between two parallel plates
$v_{(x)}$	$[m.s^{-1}]$	Component of velocity in x direction
$v_{(x\ max)}$	$[m.s^{-1}]$	Maximal velocity component in x direction
v*	$[m.s^{-1}]$	Shear velocity
v^+	[-]	Dimensionless velocity near the wall
v_i	$[m.s^{-1}]$	Velocity vector
v_2, v_2, v_3	$[m.s^{-1}]$	Components of velocity vector
x_1, x_2, x_3	[m]	Coordinates of location
x'_k	[m]	Coordinates of the induced velocity point
$x_{(0)k}$	[m]	Coordinates of point x'_k projected onto the vortex sheet
y	[m]	Coordinate y, or distance from wall
y^+	[-]	Dimensionless distance from the wall
Γ	$[m^2.s^{-1}]$	Circulation
γ	$[m.s^{-1}]/[s^{-1}]$	Linear /planar vorticity density
μ	[Pa.s]	Dynamic viscosity
ν	$[m^2.s^{-1}]$	Kinematic viscosity
ε_{ijk}	[-]	Levi-Civita tensor
τ_μ	[Pa]	Viscous shear stress
τ_t	[Pa]	Turbulent (Reynolds) shear stress

Acknowledgement

This research was funded by Brno University of Technology, Faculty of Mechanical Engineering through project with number FSI-S-12-2.

References

Pope, S.B. (2008) Turbulent Flows. Fifth printing, Cambridge University Press, ISBN 978-0-521-59889-6.

Janalík, J. (2008) Vybrané kapitoly z mechaniky tekutin. VŠB – Technická univerzita Ostrava, ISBN 978-80-248-1910-5

Munson, B.R. & Young, D. F. & Okiishi, T.H. (2006) Fundamentals of Fluid Mechanics, Fifth Edition, John Wiley & Sons, Inc., ISBN 978-0-471-67582-2.

Brdička, M. & Samek, L. & Sopko, B. (2000) *Mechanika kontinua*. Akademie věd České republiky, ACADEMIA, ISBN 80-200-0772-5.

Lewis, R.I. (1991) *Vortex Element Mehods for Fluid Dynamics Analysis of Engineering Systems.* Cambridge Engine Technology Series, Cambridge University Press, ISBN 0-521-36010-2.

18th International Conference
ENGINEERING MECHANICS 2012
Svratka, Czech Republic, May 14 – 17, 2012

pp. 1353–1361
Paper #31

FLOW CONDITIONS IN THE LAST STAGE DURING IDLING OPERATION AND LOW OUTPUT OF 1000MW TURBINE

L. Tajč[*], L. Bednář[**], M. Hoznedl[***]

Abstract: *Measurement of temperatures at the tip of the last stage during startup and idle operation of the turbine with nominal output of 1000 MW is described. Monitoring of liquid phase coarse dispersion occurrence, the direction of drops movement and investigating whether the origin of the drops comes from the natural expansion of steam in the stage or from an additional cooling system is presented. The flow of the steam phase behind the last stage is determined.*

Keywords: ***Experimental measurement, steam turbine, low output***

1. Introduction

At low output levels of the turbine and during idling, the last stages are run in a ventilation mode. Due to the effect of centrifugal power, steam is transported to the tip of the rotor blade. Separation of the flow from the hub end wall occurs together with the suction of steam to the blading root section from the area of the output diffuser after the last stage. Backflow area is formed here. A part of the turbine stages performs the work, while another part partially or completely consumes it. An enclosed eddy area may be formed at the tip of the last stage during idling operation and very low turbine outputs. There is a certain risk of local overheating. The ventilation mode is accompanied by heat production. To prevent the overheating of last sections of low-pressure parts during operation of the turbine at a low output due to ventilation losses, additional cooling is installed on the internal side of the exhaust hood. Cooling water is injected into the area after the last stage. If the non-evaporated drops are caught by return flow, they may be sucked into the last stage and erode the blades near the root section radius. This phenomenon was first noticed on the trailing edges of the last stage of the 200 MW turbine Tajč & Bednář (2001). Therefore, there is an effort to place and direct the cooling system nozzles in such a way as to minimise the risk of damaging the blades. The objective of the performed experiments was to verify whether or not the last stage overheats at the tip of the blading, and whether the water droplets from the nozzles reach the rotor blades.

2. Arrangement of the experiment

Various types of probes may be placed in the area after the last stage during operation. The arrangement of measuring places is shown in fig. 1.

A comb ball probe is shown here for identification of liquid phase. The balls are covered with coating of suitable consistency. The droplets of water with the greatest erosion effect remove a part of the coating upon impact. A colour divide between the coated and the original surface is created. Using a simple jig, the impact direction of drops may then be determined.

A pair of thermocouples is used for measuring temperature. One thermocouple is placed in the well in the slot between the L-1 rotor blades and the last stage stator blades. The second well with the thermocouple is placed at the tip between the stator and the rotor of the last stage.

[*] Ing. Ladislav Tajč, CSc.: ŠKODA POWER s.r.o., Tylova 1/57; 301 28, Plzeň; CZ, e-mail: ladislav.tajc@doosan.com
[**] Ing. Lukáš Bednář.: ŠKODA POWER s.r.o., Tylova 1/57; 301 28, Plzeň; CZ, e-mail: lukas.bednar@doosan.com
[***] Ing.Michal Hoznedl, Ph.D..: ŠKODA POWER s.r.o.,Tylova 1/57; 301 28, Plzeň; CZ,
e-mail: michal.hoznedl@doosan.com

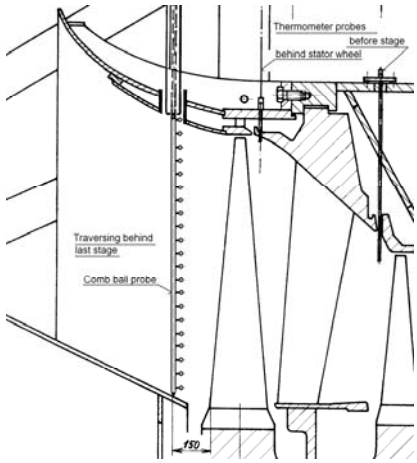

Fig. 1: Arrangement of measuring places in the last stage of the steam turbine

The movement of the steam phase may be verified using a multi-hole pneumatic probe behind the last stage. Suitable technical conditions were not created for measuring before the stage and between the diaphragm and rotor blading to determine velocity field. The flow character may only be estimated from the analysis of the velocity field behind the stage and then based on the findings from measuring similar output parameters of a 200 MW turbine with the last stage including a rotor blade 840 mm long (Tajč,1995; Šťastný & Tajč, 1977).

From the velocity before and behind the stage, a flow field model was arranged which is shown in fig. 2. Characteristic eddy structures are created at the tip and root section, whose existence may be assumed even in a stage with another rotor blade.

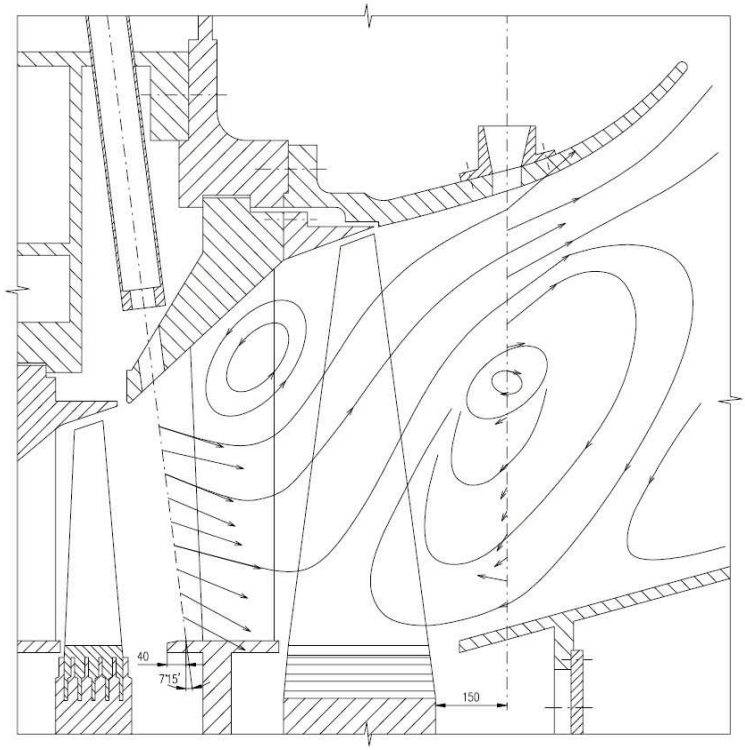

Fig. 2: Characteristic flow field in the last stage during idling operation

3. Measurement results

3.1. Measuring of temperature in the last stage

As the turbine output is lowered, the inlet pressure to the LP parts drops. Steam temperature after superheating changes in a substantial manner. During idling operation and low turbine output, superheated steam may occur in the last stage. Velocity is gradually increased during startup. Ventilation losses correspond to a third power of the speed. The temperature of any superheated stream in the last stage will increased with the velocity. In a wet steam, only the steam wetness and not the temperature would change. The temperature in the last stage at the tip during startup is shown in fig. 3 and fig. 4.

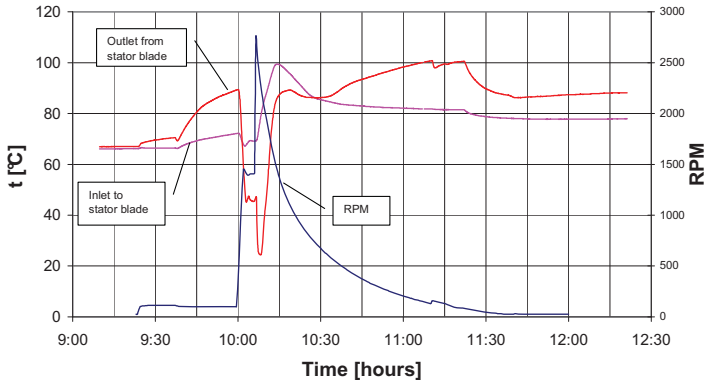

Fig. 3: Temperatures in last stage

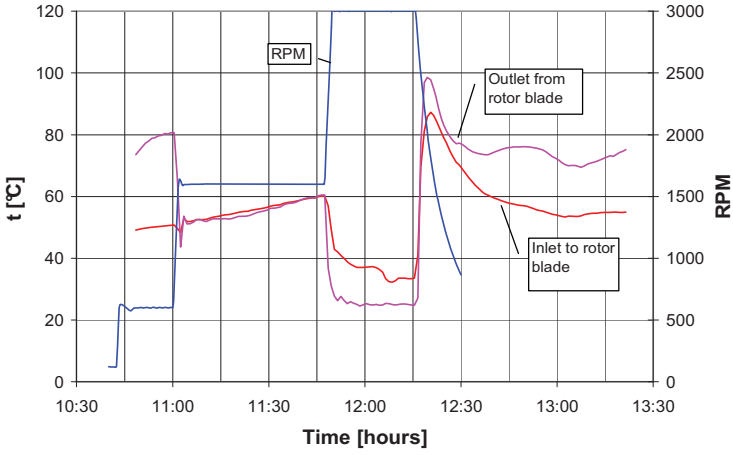

Fig. 4: Temperatures in last stage

Both cases show conditions during a step speed change - speed increase and shut down. If the turbine is on the turning gear, the temperature behind the stator blade is higher than behind the inlet to the stator blade. This is a ventilation loss effect. The temperature in both wells gradually grows. According to the condition of temperature values it is obvious that it is a mildly superheated steam. As the velocity increases so does the mass flow rate of the stage through the last stage. Steam parameters change when the temperature behind the diaphragm rapidly drops to the level of the saturation temperature at the given pressure. Superheated steam occurs again at the tip of the last stage during shutdown and a drop of speed when the temperature of the steam after the diaphragm cascade is higher than before it. If turbine operation passes from a warming-up speed (ca 1600/min) to full speed as confirmed by fig. 4 and fig. 5, a step change of temperatures occurs. The temperature behind the stator cascade is now smaller than the temperature at the inlet to the last stage. During long-term ventilation mode, temperatures in the last stage increase. The growth of temperature is also probably caused by the ventilation loss from the L-1 stage. Temperatures may be comparable here to the temperatures at

the inlet to the LP part. Additional cooling of steam at the exhaust hood does not affect the temperatures at the inlet to the last stage.

The course of temperature and pressure values in the turbine during idling operation is shown in fig. 6. A substantial drop of pressure occurs at the control valve and the trapping flap. A part of the HP and LP stages participates in overcoming bearing loss and ventilation loss in other stages. The temperatures at the inlet and outlet from the diaphragm with turbine output at ca 200 MW, i.e. at 20% of loading are recorded in fig. 7. During this operation mode, temperatures are already stable. These are saturation temperatures for the given pressure in the stator cascade. The inlet temperature is higher because the pressure is higher as well. Similar conditions even apply for a higher turbine output. The pressure values recorded during turbine operation at 450 MW are shown in fig. 8. Higher temperatures before and behind the diaphragm document the changes in pressure distribution in the stage after transition to another output level.

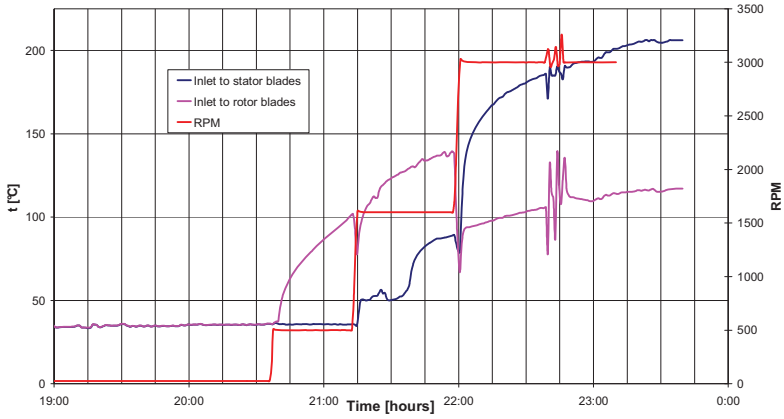

Fig. 5: Temperature in the last stage when starting up the turbine to speed

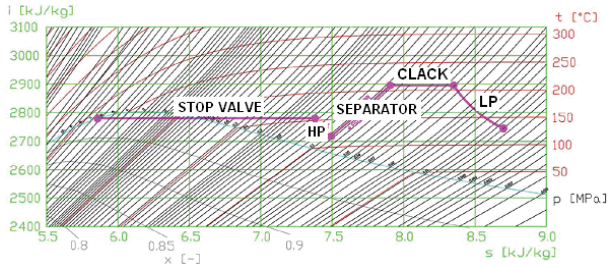

Fig. 6: Expansion of steam during idling operation

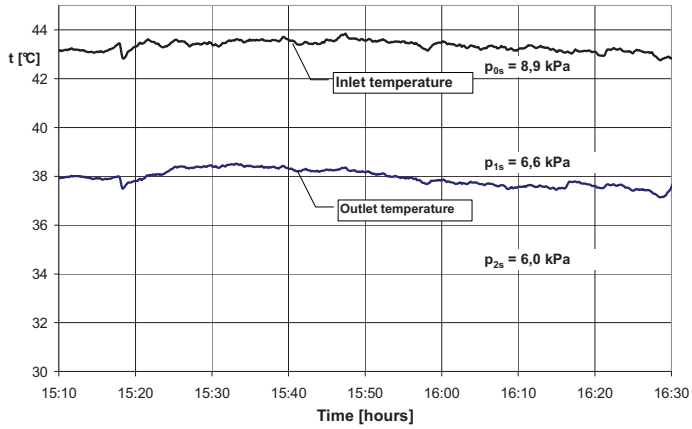

Fig. 7: Temperatures on the stator blade wih turbine output at 200MW

It is shown that there is no risk of a closed zone with substantial overheating in the last stage. Local heating of steam due to the existence of ventilation loss occurs only with limited rotor speed and during the long-term ventilation mode. However, it is not a long-term operational mode of the turbine. A transition in the last stage from wet steam to superheated steam, whose temperature depends on the time of ventilation operation, occurs at nominal speed. It is impossible to prove whether the additional cooling in the outlet part of the turbine affects the temperatures in the last stage. An experiment without additional turbine cooling and idling was not conducted. It may only be assumed that the artificially cooled steam may not reach the monitored place.

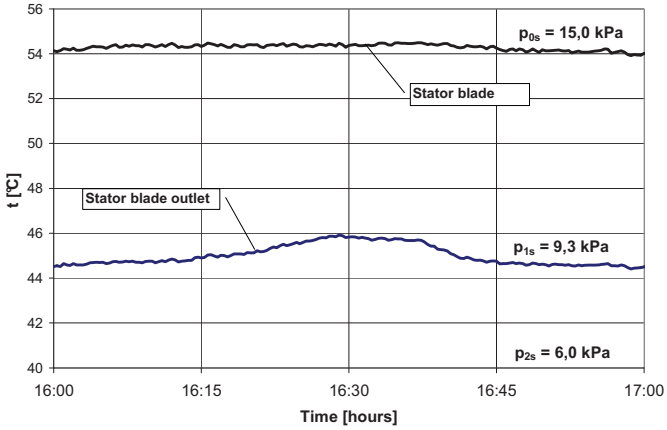

Fig. 8: Temperature on the stator blade with turbine output at 450 MW

The temperatures present on the external casing of LP body are shown in fig. 10. Fig. 9 shows the places where the temperature is measured. Three characteristic surfaces are distinguished. The internal and external front face and casing of the body are considered. The hottest place is on the cover of the seal at 0, where the temperature may reach as high as 100°C. It is affected by the heat of the steam flooding the seal. The temperature evenly decreases along the radial line towards the external casing and levels off at the saturation temperature for the given temperature at the exhaust hood. An even distribution of temperature values was apparent in all operational modes including idling. A lower temperature on the external casing is only found in the securing diaphragm areas. During idling operation, a lower temperature is present on the surface of the external body than that which would correspond to the saturation temperature. It means that cooler water from the cooling system reaches the internal surface of the external casing.

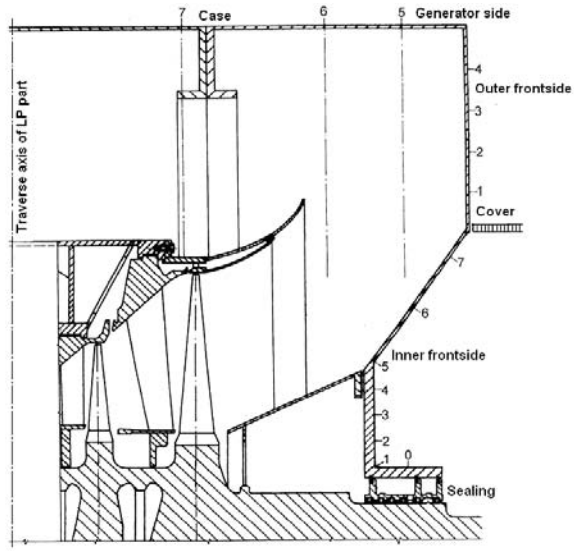

Fig. 9: Temperature measuring places

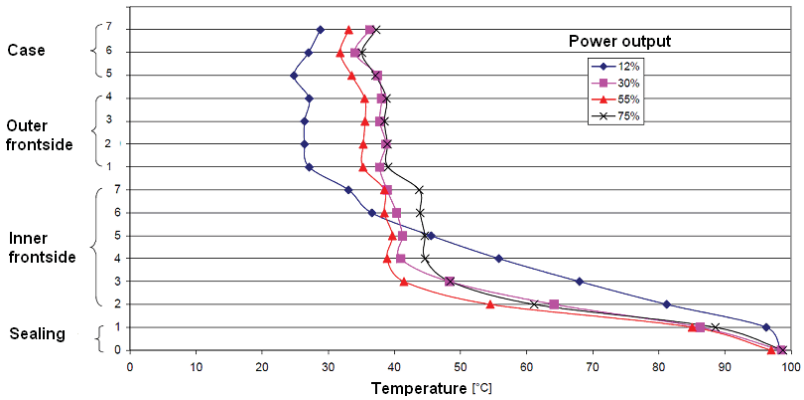

Fig. 10: Temperature on external casing of LP part

3.2. Identification of liquid phase

The occurrence and movement direction of coarse dispersion liquid phase using an erosion probe is monitored behind the last stage on the right and left side of the turbine. The erosion effect of drops differs according to the distance from the blading root section. The highest effect tends to occur at the tip of the rotor blade. As the experiment was to verify the origin of droplets at the root of the blading, the exposition time was governed by the need to capture the effect of droplets near the hub radius. It is always necessary to take various differences in 3D flow along the perimeter of a stage into account. This is the main reason for measuring and recording of data on the right and left side of the turbine.

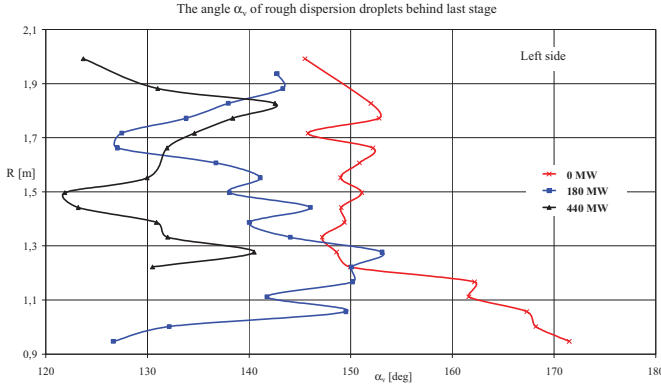

Fig. 11: Movement of droplets behind last stage

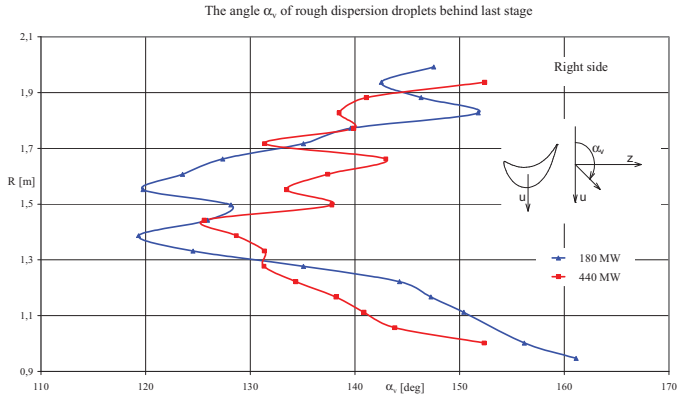

Fig. 12: Movement of droplets behind last stage

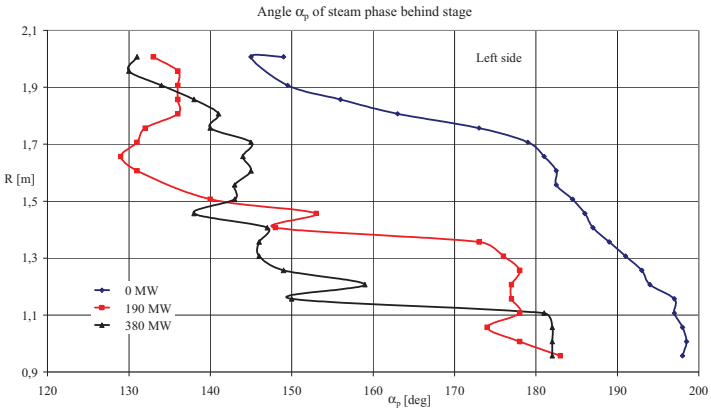

Fig. 13: Direction of movement of steam

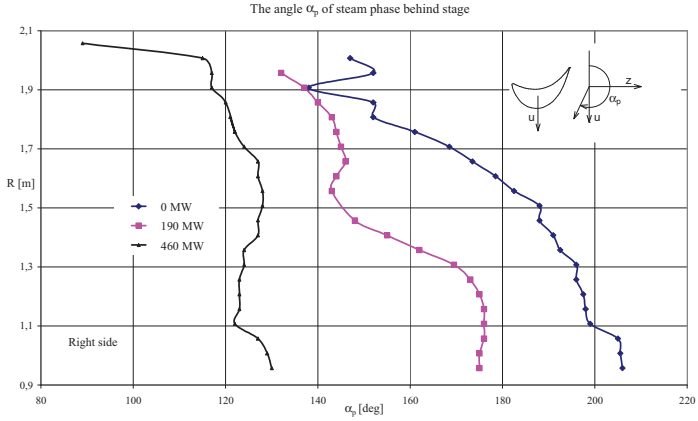

Fig. 14: Direction of movement of steam

The water drops are not monodisperse. Their size differs and the direction of movement is more or less affected by the movement of the steam phase. To which the erosion displayed on the surface of the balls of the erosion probe corresponds. An estimate of the direction of droplets movement is therefore always subject to the subjective effect of the experimenter. Therefore information about the direction of droplets movement needs to be taken for guidance only. However, it is certainly possible to see whether the droplets are moving to the blades or away from them.

Droplets movement in the circumferential direction is shown in fig. 11 and fig. 12. It was revealed that during idling operation (output 0 MW) droplets occur only on the left side of the low pressure part. Angle α_v is a projection angle of the vector of droplets speed in the plane defined by circumferential and axial direction. If $\alpha_v > 180°$, then the droplets move towards the rotor blade. It shows that this instance does not occur even during idling operation. At the root, the angle α_v is greater than in the central part of the stage. The movement of the steam phase in the area behind the stage is shown in fig. 13 and fig. 14. The backflow of steam was established during idling operation and low output. The direction of droplets movement did not correspond to the direction of flow of the steam phase. Water droplets of coarse dispersion are not carried by steam at the root section. Therefore, these are not droplets from the additional cooling system but droplets from the flow-through part of the turbine. Provided droplets are moving mainly due to inertia and are removed from the trailing edges of blades and the rotor disc, it is possible to determine the original place of drops using directional angles.

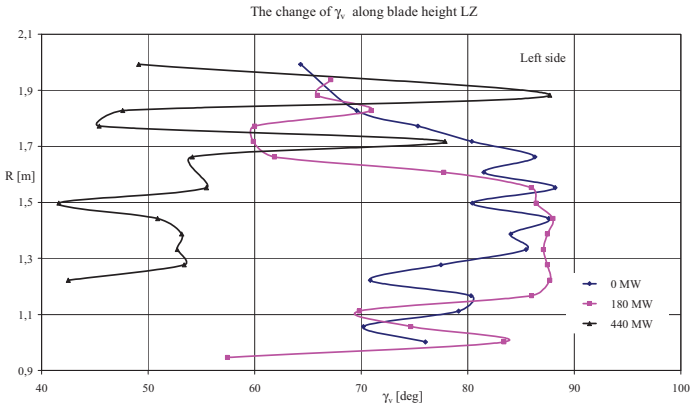

Fig. 15: Direction of droplets movement

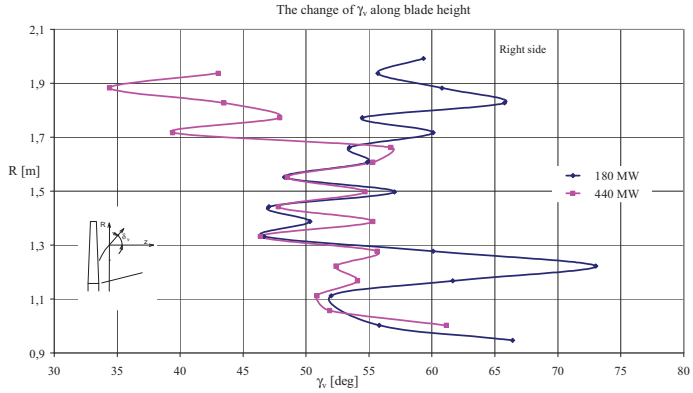

Fig. 16: Direction of droplets movement

The angle of the droplets movement γ_v perpendicular to the rotor for the right and left side is shown in fig. 15 and fig. 16. The measured angles are rather unbalanced. It applies in particular to the left side of the turbine. There is a possibility that there are places on the blade from which more water is removed than from others. It is also shown on the quality of the eroded coating on the balls of a comb probe. The final idea of the radius on trailing edges R_{oh} from which water droplets are dragged is stated in fig. 17 and fig. 18. The droplets, which are caught on the erosion probe placed 150 mm behind the rotor blade near the root section, come from the rotor disc. The origin of droplets is usually from the wider section of the blade. It depends on their size and the degree of impact of steam flow on the direction of droplets movement.

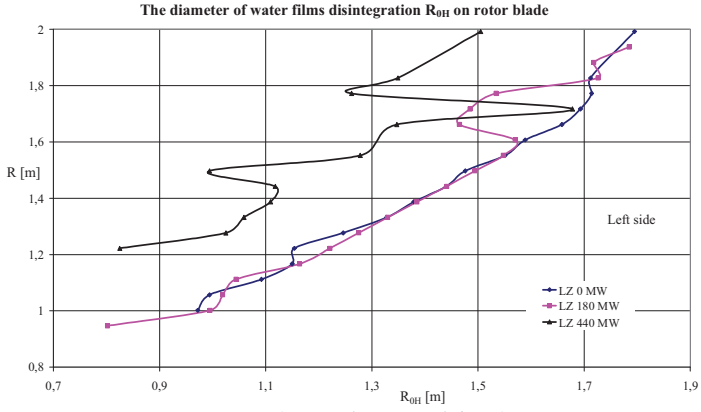

Fig. 17: Places of origin of droplets

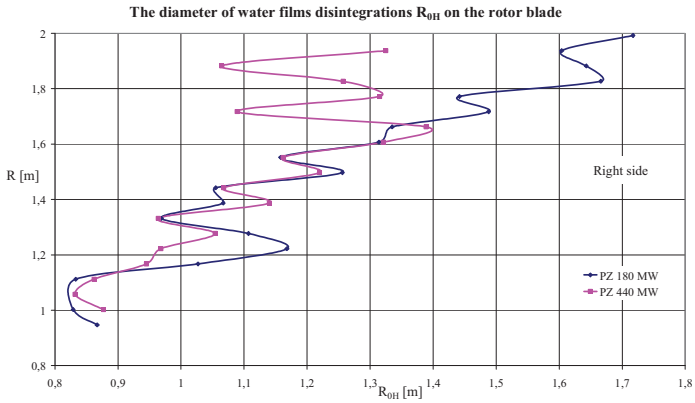

Fig. 18: Places of origin of droplets

4. Conclusions

Areas with backflow are formed in the last stage during idling and under decreased turbine output. A closed eddy zone is formed near the tip at the stator blades.

Due to ventilation losses, heat is produced in the blading part and the steam is heated. A part of the stages work on balancing the bearing losses and covering the ventilation losses during idling operation.

Operation temperatures in the last stage may be comparable to temperatures at the inlet to the LP part due to ventilation losses during turbine idling.

Flow conditions are modified at the tip of the last stage during a gradual growth of speed. A lower temperature may be seen in the inlet to the diaphragm than at the outlet.

The cooling system of the exhaust hood probably does not affect the flow and temperatures in the last stage.

Water droplets from the cooling system do not reach as far as the root of the rotor blade in the last stage.

Coarse dispersion droplets after the last stage move in the direction away from the blades in all operation modes. This also applies to the conditions when return flow occurs at the root section in the last stage. The origin of the droplets comes from the disc of the stage and from trailing edges of rotor blades.

References

Tajč, L. & Bednář, L. (2001) Modulový stupeň č. 4 při sníženém zatížení. *Research work ŠKODA*, Plzeň, TZTP 741.

Tajč, L. (1995) Koncový stupeň turbíny 200MW při chodu naprázdno a při sníženém zatížení. *Research work* ŠKODA, Plzeň, TZTP 0656.

Šťastný, M & Tajč, L. (1977) Experimentální výzkum kapalné fáze s hrubou disperzí v posledním stupni s délkou lopatky 840 mm, *Research work ŠKODA*, Plzeň, Tp VZ 9/77, 1977.

18th International Conference
ENGINEERING MECHANICS 2012
Svratka, Czech Republic, May 14 – 17, 2012

pp. 1363–1367
Paper #99

LIMIT STATES OF CONCRETE STRUCTURES SUBJECTED TO ENVIRONMENTAL ACTIONS

B. Teplý[*], D. Novák[**]

Abstract: *In the context of performance requirements, whole life costing and sustainability, the concrete structure durability issue has recently gained considerable attention. The present paper deals with service life assessment utilizing durability limit states specially defined for concrete structures, i.e. focusing on degradation due to environmental effects. Both the initiation and propagation periods of reinforcement corrosion are considered and a comprehensive choice of limit states is provided. The approach is based on degradation modelling together with probabilistic assessment, enabling the evaluation of service life and the relevant reliability level. A suitable software tool is introduced which makes use of a variety of degradation models and is thus able to facilitate the effective decision making of designers and clients.*

Keywords: ***Concrete structures, Limit states, Durability, Reliability, Environmental effects, Modelling.***

1. Introduction

Structures must be designed to have adequate structural resistance, serviceability and durability. This is achieved by quality management measures including (among other things) reliability requirements, which are usually assessed by the use of limit states as stipulated by ISO 2394 (1998) and EN 1990 (2001). In general, a distinction between ultimate limit states (ULS) and serviceability limit states (SLS) should be made together with the associated levels of reliability described by the probability of failure or by the index of reliability. The relevant design situation should be taken into account with consideration also given to time dependent effects related to the specified period, i.e. the specified design working life (or the service life). Inevitably, the mathematical modelling of degradation phenomena and the utilization of probabilistic simulation methods are needed for both newly designed structures (in the design phase) and existing structures (during assessment, redesign and refurbishment). Thus, not only the mechanical load/actions (permanent, variable and accidental actions) but also the environmental influences/actions that could affect durability should be taken into account. Due to such environmental actions structural materials can be degraded and so both the ULS and SLS can be affected.

The formulation and assessment of relevant limit states for environmental actions differs from those commonly considered by engineers while solving mechanical action effects; therefore, "durability" limit states are discussed in the following section in more detail. Moreover, the present paper concentrates on concrete structures where a variety of degradation processes due to environmental actions may be encountered.

2. Concrete structures

2.1. Limit states in the context of durability - DLS

The *level of reliability* in the context of durability should be left to the client's decision as well as the appropriate serviceability criteria - as indicated e.g. in *fib* Draft Model Code (2010). It should be noted that reliability level, limit state definition, target service life and financial savings are mutually related

[*] Prof. Ing. Břetislav Teplý, CSc.: Faculty of Civil Engineering, Brno University of Technology, Veveří 95; 602 00, Brno; CZ, e-mail: teply.b@fce.vutbr.cz

[**] Prof. Ing. Drahomír Novák, DrSc.: Faculty of Civil Engineering, Brno University of Technology, Veveří 95; 602 00, Brno; CZ, e-mail: novak.d@fce.vutbr.cz

- some elements of whole life costs are service-life dependent. The joint impact of these values, as well as their effect on the cost of the project, can be considerable.

Durability and its reliability implications need to be addressed during the design process; the agreement or decision of the client should be a basic part of that process - which is not yet common. While assessing the reliability level, an appropriate LS has to be defined and assessed. Within this context, limit states associated with durability (for the purpose of this paper they are termed Durability Limit States - DLS) are recognized – also see ISO 13823 (2008) and the *fib* Bulletin (2006). They can fall into either the ULS or the SLS category, according to the type of degradation effect, its extent and location.

Basically, the reliability level is described by the probability of failure P_f, which may be converted into the reliability index β. For SLS (and hence DLS) the values $0.8 \leq \beta \leq 1.8$ are currently being discussed/considered. The "older" codes (still currently utilized) generally do not provide sufficient reliability support in this respect – they do not allow for a design which is subject to a specific (target) service life and/or to a specific reliability level. Note that the serviceability requirements are agreed for each individual project by a relevant authority.

The service life of a building, structure and/or structural member is determined by its design, construction, ageing and maintenance during use. The combined effect of structural performance and ageing should be considered. When assessing the degradation of reinforced concrete structures, the corrosion of reinforcement is the dominant effect. Usually the initiation and propagation periods are considered – Tuutti (1982). The first period is the time from concrete casting to the moment when the reinforcement is no longer passivated, while the latter also includes the period after corrosion initiation. Generally, the DLS condition may be written as:

$$P_f(t_D) = P\left\{B(t_D) - A(t_D) \leq 0\right\} \leq P_d \quad , \tag{1}$$

where P_f is the probability of failure, A is the action effect, B is the barrier at time t_D = design service life and P_d is the design (acceptable, target) probability value. P_d refers to an acceptable failure probability required to assure the performance of the structure and corresponding to a specified reference period.

In the following section let us summarize the possible basic actions and barriers usable for the DLS of concrete structures noting that the corrosion of reinforcement is the dominating effect.

2.2 Initiation period - depassivation of reinforcement

Generally, the dominant factors causing depassivation of reinforcement in concrete are carbonation and chloride ingress:

(i) *Carbonation*: the carbonation process is driven by the diffusivity of ambient CO_2 in concrete and the reactivity of CO_2 with concrete. The CO_2 penetrating from the surface decreases pH to a value of 8.3. When the carbonation depth equals the concrete cover, the steel is depassivated and corrosion may start (when oxygen and moisture are present). The rate of carbonation progress from the concrete surface to the reinforcement depends on many parameters, e.g. concrete cover thickness and permeability, the ambient temperature, relative humidity and carbon dioxide content, while the concrete cover permeability itself depends on the concrete mix type and composition, the aggregate gradation and the processing and curing of the concrete mix. All these variables are uncertain in reality and should be represented by random variables (or random fields). In the case of carbonation the B in condition (1) is represented by concrete cover a while A is represented by x_c – the depth of carbonation at time t_D. So, Eq. (1) specializes into

$$P_f(t_D) = P\left\{a - x_c(t_D) \leq 0\right\} \leq P_d \quad . \tag{2}$$

Analytical models of the effect of this action are based on the diffusion of CO_2 in the concrete pore system and have been discussed elsewhere, e.g. in *fib* Bulletin (2006) and Teplý et al. (2010). Note that the carbonation processes in concretes fabricated from Portland Cement (OPC) and from blended cements should be distinguished from each other; more details about the latter case can be found e.g. in (Chromá et al. 2007), including a discussion of the *k*-value concept.

(ii) *Chloride ingress*: In order to consider chloride ingress (e.g. due to de-icing salts) Eq. (1) may be transformed into the formula:

$$P_f(t_D) = P\left\{C_{cr} - C_a\left(t_D\right) \le 0\right\} \le P_d \ . \tag{3}$$

So, in this case $B = C_{cr}$ represents the critical concentration of dissolved Cl^- (a prerequisite of steel depassivation) and $A = C_a$, which is the concentration of Cl^- at the reinforcement at time t_D.
Note that the depassivation of reinforcement in concrete can also be caused by other chemical influences, e.g. sulphate attack; a suitable model for the prognosis of such an effect is not yet known (to the present authors´ knowledge).

2.3 Propagation period - corrosion of reinforcement

When reinforcing steel is depassivated then corrosion is initiated in the presence of sufficient oxygen and moisture. Damage to the structure can proceed via one or more of the following processes:

(iii) *Concrete cracking due to corrosion*: $B = \sigma_{cr}$ is a critical tensile stress that initiates a crack in the concrete at the interface with the reinforcing bars; $A = \sigma_t$ is the tensile strength of the concrete. Eq. (1) specializes into

$$P_f(t_D) = P\left\{\sigma_{cr} - \sigma_t\left(t_D\right) \le 0\right\} \le P_d . \tag{4}$$

Also, a consecutive stage may be assessed where $B = w_{cr}$ is the critical crack width on the concrete surface and $A = w_a$ is the current crack width on the concrete surface at time t_D. The condition reads

$$P_f(t_D) = P\left\{w_{cr} - w_a\left(t_D\right) \le 0\right\} \le P_d \ . \tag{5}$$

(iv) *A decrease in the effective reinforcement cross-section* due to corrosion: $B = A_t$ is the effective reinforcement cross-sectional area at time t_D and $A = A_{min}$ is the minimum acceptable reinforcement cross-sectional area with regard to the relevant SLS or ULS:

$$P_f(t_D) = P\left\{A\left(t_D\right) - A_{\min} \le 0\right\} \le P_d \ . \tag{6}$$

Note that an alternative formulation to the general Eq. (1) may be used, this being Eq. (7):

$$P_f(t_D) = P\left\{t_{PS}\left(X_i, t\right) \le t_D\right\} \le P_d \quad , \tag{7}$$

where t_{PS} is a predicted time value modelled as a function of basic variables $\boldsymbol{X}_i$ (i = 1, 2,..., n), n is the number of input parameters involved in the model in question, and time is t.

The values and characteristics of the variables presented in Eqs. (2) to (7) have to be gained via utilization of the stochastic approach together with a suitable model. Evidently, some efficient tools are needed – two such codes developed under the supervision of the authors are briefly described in the next section and have been referred to previously, e.g. Teplý et al. (2007), (2010) and Vořechovská et al. (2009).

3. Software

- The ***RC LifeTime*** programme has been specially developed for carbonation process modelling and uses three models – two for concretes made from Portland cement and one for concretes made from blended cements; it is freely accessible at http://rc-lifetime.stm.fce.vutbr.cz and offers two options:

(i) "Service Life Assessment", which provides the evaluation of service life and its statistical characteristics based on Eq. (2). The input data are model variables (optionally deterministic or random). The statistical characteristics of the relevant service life are output data automatically generated for a series of cover values or for a specific concrete cover. Optionally, the reliability index may be an additional input value associated with the given cover value; the corresponding service life then becomes an output value.

(ii) "Concrete Cover Assessment", providing the statistical evaluation of concrete cover. Apart from model variables the specified/target service life can also be inputted. The statistical characteristics of the carbonation depth vs. time are output data automatically calculated for a series of time

values. Optionally, the value of the required concrete cover may be an input value and the relevant reliability index β then becomes an output value, again along the time axis.

Thus, structural members may be designed for a given service life or given reliability level during the initiation period due to the carbonation effect while considering the statistical characteristics of concrete mix, concrete cover and environmental conditions.

• The software package **FReET-D** represents a specialized professional code for the assessment of the potential degradation of newly designed as well as existing concrete structures. For more details see www.freet.cz, Teplý et. al. 2012, Novák et al. 2011. Altogether, 35 models for different reinforced concrete degradation types are implemented as pre-defined dynamic-link library functions. Models were selected from the literature; some of them were originally developed as deterministic models and have been converted into probabilistic form for the purposes of the presented software:

(i) models for concrete carbonation – 13 models or variants for the assessment of Eqs. (2) or (7);

(ii) chloride ingress effect – 7 models or variants, Eqs. (3) or (7);

(iii) reinforcement corrosion – 9 models or variants, Eqs. (4) to (7);

(iv) frost attack – 4 models. A condition in the form of Eq. (1) can be constructed;

(v) acid attack – 2 models. A condition in the form of Eq. (1) can be constructed.

The uncertainties associated with parameters involved in deterioration processes are modeled by random variables, and several simulation techniques may be optionally used (Crude Monte Carlo, Latin Hypercube Sampling or FORM). Statistical, sensitivity as well as reliability analyses are provided. The implemented models may serve directly in the durability assessment of concrete structures in the form of a DLS, i.e. the assessment of service life and the safety level of the relevant reliability measure. Several features are offered, including automatic parametric studies and Bayesian updating. Statistical correlation of input variables is efficiently imposed by a stochastic optimization technique termed simulated annealing (Vořechovský & Novák, 2009). Sensitivity analysis is based on nonparametric rank-order correlation coefficients. The models included in the new international document *fib* Model Code (2010) are also inserted within model groups (i) and (ii).

The software has already been used in several practical tasks, e.g. the analysis of a cooling tower, bridges, a TV tower, and other structures. Some illustrative examples created while using the above-mentioned software will be presented at the conference.

5. Conclusions

The usefulness of effective degradation modelling and hence reliable design or assessment for durability may bring positive financial and sustainability impacts - the probabilistic approach often results in a safer and more realistic design than the frequently used deemed-to-satisfy approach encompassed in current codes. Moreover, the availability of a variety of models seems to be beneficial in some situations, bearing in mind that a more sophisticated computational model requires a larger amount of input data, which are not always available.

The probabilistic approach provides quantitative information about the safety level of reliability measures and, together with degradation modelling, enables service life prognosis. It is a useful methodology with regard to the fact that the required level of reliability and the target service life should be left to the client's decision.

Acknowledgement

This outcome has been achieved with the financial support of the Czech Ministry of Education, project MSM 0021630519, and Czech Technology Agency, grant No. TA01011019.

References

EN 1990 (2001) Eurocode – Bases of structural design, CEN.

ISO 2394 (1998) General principles on reliability for structures, ISO.

ISO 13823 (2008) General principles on the Design of Structures for Durability, ISO.

fib Model Code for Service Life Design (2006), *fib Bulletin* No. 34, Federation for Structural Concrete, Lausanne.

fib Draft Model Code (2010), *fib Bulletins* No. 55 and 56, Federation for Structural Concrete, Lausanne.

Novák, D., Vořechovský, M. & Rusina, R. 2011. FReET v.1.5 – program documentation. User´s and Theory Guides. Brno/Červenka Consulting, Czech Republic, http://www.freet.cz.

Tuutti, K. (1982) Corrosion of steel in concrete. Swedish Cement and Concrete research Institute. Stockholm, p. 468.

Teplý, B., Chromá, M. and Rovnaník, P. (2010), Durability assessment of concrete structures: Reinforcement depassivation due to carbonation, *Structure and Infrastructure Engineering*, 6, 3, pp.317 – 327.

Teplý, B, Chromá, M, Vořechovská, D. & Rovnaník, P. 2010 FReET-D. Program documentation, Part 1: Theory, Brno/Červenka Consulting, Czech Republic, http://www.freet.cz.

Chromá, M., Rovnaník, P. a Teplý, B. (2006) Carbonation Modelling and reliability analysis of RC structures made from blended cements. *International RILEM Workshop on Performance Based Evaluation and Indicators for Concrete Durability,* (V.Baroghel-Bouny,et al.), Madrid, Spain, pp. 319-325.

Vořechovský, M., Novák, D. (2009) Correlation control in small-sample Monte Carlo type simulations I: A simulated annealing approach. *Probabilistic Engineering Mechanics* 24: 452-462.

Teplý, B., Chromá, M., Rovnaník, P. (2010) Durability assessment of concrete structures: reinforcement depassivation due to carbonation. *Structure and Infrastructure Engineering* 6(3): 317–327.

Teplý, B., Matesová, D., Chromá, M. and Rovnaník, P. (2007) Stochastic degradation models for durability limit state evaluation, *Proceedings of 3rd International Conference on Structural Health Monitoring of Intelligent Infrastructure*, Vancouver, British Columbia, Canada.

Vořechovská, D., Chromá, M., Podroužek, J., Rovnaníková, P., Teplý, B. (2009) Modelling of Chloride Concentration Effect on Reinforcement Corrosion. *Computer-Aided Civil and Infrastructure Engineering* 24: 446-458.

18th International Conference
ENGINEERING MECHANICS 2012
Svratka, Czech Republic, May 14 – 17, 2012

pp. 1369–1379
Paper #35

TURBULENCES IN ARTIFICIAL BOUNDARY LAYER OF FOTOVOLTAIC POWER PLANTS

A.Tesar*

Abstract: *The aeroelastic assessment of turbulences appearing in artificial boundary layer of fotovoltaic power plants is treated in present paper. The approach suggested takes into account multiple functions in the analysis of skew flat plates of solar panels subjected to laminar and turbulent wind forcing. Analysis and experimental assessments in aerodynamic tunnel are presented. Some results obtained are discussed.*

Keywords: ***Aerodynamic tunnel, aeroelasticity, artificial boundary layer, fotovoltaic power plant, mechanics of turbulent wind motion.***

1. Introduction

The modeling of the turbulent air flow in aerodynamic tunnels is a research domain based on advanced scientific technologies. They are imposed, for example, by the necessity of studying the turbulent air movement in the proximity of fotovoltaic power plants treated in this paper. Due to the testing of models in aerodynamic tunnels the modern codes for design of structures exposed to wind turbulences are able to assess in a highly accurate degree the effect of such actions. The models of turbulent air flow are used in the assessments being validated by tunnel testing measurements of the parameters integrated in the calculation.

The topic of present paper is the assessment of ultimate aeroelastic behaviour of skew plates of solar panels in fotovoltaic power plants subjected to laminar and turbulent forcing of wind (see Fig. 1). The skew flat plates of solar panels are supported by metal structures anchored into terrain. The panels create the active fields of the power plants studied. The fotovoltaic power plants are located in territories where the wind loads represent the dominant environmental forcing. The forcing is to be unified into maximal design values for given territory. All structural elements are to be designed in accordance with valid standards and their aeroelastic assessments are required, for example, due to the recommendations of the EUROCODE 1, Loads on Structures, Part 1.4, General Loads, Wind Loads.

Active fields of fotovoltaic power plants with a multitude of flat plates with solar panels create artificial boundary layer with laminar and turbulent wind forcing. The aeroelastic response depends on following options:

- wind speed,
- wind direction,
- wind flow (laminar or turbulent),
- wind temperature and humidity,
- snow and ice loads,
- gaps between panels,
- geometry and configuration of active fields of panels,
- dynamic properties of all structural elements.

Because of the small height of solar panels above the terrain there occur the cataract air flows on edges of the flat plates, which increase the wind speeds and pressures. Regarding the variability of configurations of fotovoltaic power plants with artificial boundary layer in small heights, there appear the turbulent wind flows. The measurements in aerodynamic tunnels submit the data required for the analysis of the problem.

* Alexander Tesár, Civ.Eng., PhD, DrSc, doc., visiting prof.: Institute of Construction and Architectuire, Slovak Academy of Sciences, Dúbravská cesta 9, 845 03 Bratislava 45, Slovak Republic, e-mail: alexander.tesar@gmail.com

2. Analysis

The idea of application of the flat plate aerodynamics in the field of preliminary structural design was introduced by Bleich (1950). Selberg and Hjorth-Hansen (1961 and 1966) carried out an experimental investigation of a number of cross-sections presented an approximate expression for the flutter velocity of a plate acted upon by Theodorsen´s forces (1935). In their contribution Klöppel and Weber (1963) employed the flat plate stability limit as a reference quantity in the same way as Selberg. A general solution of the flat plate equations for a linear model was given by Frandsen (1966). He showed that a simplified expression by Rocard (1965) for the limit state stability of bridges turned out to be a good approximation for the flat plate flutter velocity. Scruton in (1965) pointed to apparent similarities of the behaviour of realistic models and flat plate computational model. Buffeting appearing by some forcing conditions was the topic of research by Davenport (1962). Bridge deck flutter derivatives and their action in general aeroelasticity were treated by Scanlan and coworkers (1971, 1974, 1971 and 1996). Some aspects of non-stationary airfoil theory were dealt with by Sears in (1941). Significant research results concerning the problem are contained also in works of Curami, A. and Zasso, A. (1993), Diana, G., Bruni, S., Cigada, A. and Collina, A. (1993), Diana, G., Chelli, Zasso and Bocciolone (1999), Diana, Chelli, Collina, Zasso and Bruni (1998), Larose, Davenport, and King (1992), Miyata, Yamada, Kanazaki, and Iijima (1992) as well as Tanaka (1992).

Slender structures of skew flat plates of fotovoltaic power plants are prone to wind-induced vibrations for various reasons. Some issues considered in their wind resistant design are mentioned by:

1. Wind turbulences force the plate with a considerable power and the forced movements owing to turbulence and associated mechanisms are stochastic in nature.
2. There can be produced a strong vortex wake associated with aerodynamic drag force experienced by the plate. Depending on wind speed and cross-section's shape, the shedding of vortices is regular with shedding periods inversely proportional to the wind speed. In resonance conditions the structure's oscillation can control the rhythm of the vortex shedding.
3. Aside the known vortex trail type loads the more general types of forcing appear there. The possible re-attachement of separated flow, the vortices generated by the local geometry and movement of the plate contribute to such periodic forcing.
4. Aeroelastic forces proportional to the movement of the plate can produce self-induced divergent vibrations at some wind speeds.
5. In the design of plate is to be avoided that the absolute value of negative aerodynamic damping exceeds the positive mechanical damping producing across-wind flexural mode instability. Associated critical wind speed is the flutter velocity while corresponding circular frequency is the flutter frequency.
6. At the onset of divergence the aerodynamic instability of the plate is initiated.

In this paper the wind induced structural phenomena are treated by transient dynamics (see Tesar (1978 and 1988)). Laminar and turbulent wind forcing is studied adopting the wave propagation approach as given by Tesar and Svolik (1993). The goal is to develop the approach based on transient dynamics combined with wave propagation forcing and adopted for the analysis of aeroelastic response of skew flat plates of fotovoltaic power plants on the basis of results obtained in scope of experimental testing in the wind tunnel (see Juhasova, Motlik and Vrabec (1998)) as well as in standards STN EN (1991).

The skew plates of fotovoltaic power plants are exposed to low frequency vibrations initiated by wind. Such forcing causes vibrations due to the von Kármán vortices possibly occurring with frequencies close to resonance behaviour. The fotovoltaic power plants are created by active fields of fotovoltaic panels positioned close together. There is created the artificial boundary layer having variable parameters due to direction and velocity of the wind. The aeroelastic assessment is made by the analysis of turbulences modeled by waves in the air flow. For the analysis is suggested the FETM-approach as combination of finite element and transfer matrix techniques as developed by Tesar and Tvrda (2006 and 2007).

The models of turbulent air flow are adopted in assessments being validated by tunnel testing measurements of parameters integrated in the analysis. The nonlinear time response is studied by the energy approach suggested by Tesar and Tvrda (2006 and 2007).

3. Mechanics of turbulent motion

All turbulences in the wind forcing are considered as a special family of motions from one space region into another one. Their updated configuration is specified by location of air displacements in space and time. The variations of configurations are continuous and during deformation there appear no new boundary conditions. Each new configuration is related to the reference position stated.

When taking into account the Cartesian coordinates *x, y, z* and corresponding displacements *u, v, w*, the Green strain tensor is given by

$$E_{xx} = \partial u_x/\partial x + [(\partial u_x/\partial x)^2 + (\partial u_y/\partial y)^2 + (\partial u_z/\partial z)^2]/2 \quad , \tag{1}$$

$$E_{xy} = [(\partial u_y/\partial x) + (\partial u_x/\partial y) + (\partial u_x/\partial x)(\partial u_x/\partial u_y) + (\partial u_y/\partial x)(\partial u_y/\partial y) + (\partial u_z/\partial x)(\partial u_z/\partial y)]/2 \quad , \tag{2}$$

.... , etc.

In order to set up the constitutive equations, the stress tensor with the same reference is needed. The second Piola-Kirchhoff stress tensor S_{ij} has the properties required and the generalized equation of motion for the air flow is given by

$$S_{ij} = g(E_{ij}) \quad , \tag{3}$$

with g as function of the Green strain tensor E_{ij}.

When analysing the air flow with volume, surface area and density, B, S and ρ_o, respectively, the volume forces of the mass unit are given by $F_{o,i}$ and the strains by T_i. The system in equilibrium is submitted to a virtual displacement δu_i being kinematically consistent with initial conditions assumed. The equilibrium of virtual work is given by

$$\int S_{ij}\, \delta E_{ij}\, dB - \int T_i\, \delta u_i\, dS - \int P_i\, \delta u_i\, dB = 0 \quad , \tag{4}$$

with substitution

$$P_i = \rho_o\, F_{o,i} \quad . \tag{5}$$

Equation (4) specifies the stationary value of the potential energy in all deformations u_i. The incremental equivalent of corresponding variation principle is given by

$$\int S_{ij}^{(1)}\, \delta E_{ij}^{(1)}\, dB - \int T_i^{(1)}\, du_i^{(1)}\, dS - \int P_i^{(1)}\, \delta u_i^{(1)}\, dB = 0 \quad , \tag{6}$$

$$\int S_{ij}^{(2)}\, \delta E_{ij}^{(2)}\, dB - \int T_i^{(2)}\, du_i^{(2)}\, dS - \int P_i^{(2)}\, \delta u_i^{(2)}\, dB = 0 \quad , \tag{7}$$

with superscripts (1) and (2) for neighbouring configurations studied. The strains and volume forces have the same reference configuration and there holds

$$\Delta T_i = T_i^{(2)} - T_i^{(1)} \quad , \tag{8}$$

$$\Delta P_i = P_i^{(2)} - P_i^{(1)} \quad , \tag{9}$$

The variations of both deformation fields are the same

$$\delta u_i = \delta u_i^{(1)} = \delta u_i^{(2)} \quad . \tag{10}$$

The incremental virtual work equation is given by Eqs. (6) and (7) as

$$\int (S_{ij}^{(2)}\, \delta E_{ij}^{(2)} - S_{ij}^{(1)}\, \delta E_{ij}^{(1)})\, dB - \int \Delta T_i\, \delta u_i\, dS - \int \Delta P_i\, \delta u_i\, dB = 0 \quad , \tag{11}$$

when taking into account the virtual variations of both configurations studied. Equation (11) specifies the configuration (2) from known configuration (1) and known load increments. When the work made by mass and damping forces on virtual displacements δu_i is added to Eq. (4), the principle of virtual works for the problem studied is given by

$$\int S_{ij}\, \delta E_{ij}\, dB + \int \rho\, u_i\, \delta u_i\, dB + \int C_i\, u_i\, \delta u_i\, dB - \int T_i\, \delta u_i\, dS - \int P_i\, \delta u_i\, dB = 0 \quad , \tag{12}$$

where ρ and C are mass and damping terms.

The turbulence in the air flow is described by instantaneous wind speed as a function of space and time with mean and fluctuation components given by

$$u(x, y, z, t) = U(x, y, z) + u'(x, y, z) \quad , \tag{13}$$

$$v(x, y, z, t) = V(x, y, z) + v'(x, y, z) \quad , \tag{14}$$

$$w(x, y, z, t) = W(x, y, z) + w'(x, y, z) \quad . \tag{15}$$

The mean values of projections *U, V, W* are the result of averaging in a certain interval of time the wind speed and the fluctuating components.

The turbulence scales of the instantaneous wind speed are the measure of the representative dimensions of vortices induced by turbulences inside the air flow. Their importance lies in the fact that they describe the turbulences which „wrap" the plate in a certain time.

The assessment of turbulence motion starts with the specification of the correlation functions of fluctuating components which may be longitudinal, transversal and vertical. In general, the characteristics of the air flow are well defined if the correlation functions are specified for the mean streamwise components longitudinally and transversally. The correlation in time is specified by formulae

$$\rho_{u(i)u(j)}(\tau) = R_{u(i)u(j)}(\tau)/[(\sqrt{(u')^2(t)}).(\sqrt{(u')^2(t+\tau)})] \quad , \tag{16}$$

$$R_{u(i)u(j)}(\tau) = u_i(t).u_j(t+\tau) = lim_{T\to\infty}\, 1/T \int [u_i(t).u_j(t+\tau)]dt \quad . \tag{17}$$

Eq. (17) represents the covariance function of the process *u(t)* being determined by measuring in two different points in space at the difference of time τ (see Hautoy (1990), Moonen, Blocken, and Carmeliet (2007) as well as Teleman, Silion, Axinte and Pescaru (2008).

According to Taylor´s hypothesis (see Hautoy (1990)) the inter-correlation between any of the fluctuating parts, discarding the wind instantaneous speed measured in two points being separated by distance Δx in the direction of the wind flow, is equal with the auto-covariance determined for the period studied. The inter-correlation functions give information concerning the dimensions of the turbulences in direction of the wind action. The existence of the mean values of the wind speed inside of turbulent flow is given by the reality that in a certain point i the turbulence has a certain periodicity in time. After a certain period the phenomenon repeats itself in space. These two idioms specify the turbulence scales in time and space. The turbulence scales define frequency of gusts in the wind action. The integral length scales correspond to spatial nature of the wind action specifying the longitudinal, lateral and vertical scales given by

$$L_x = \int \rho_{u'(i)u'(j)}(\Delta x,0,0)\, d(\Delta x) \quad , \tag{18}$$

$$L_y = \int \rho_{u'(i)u'(j)}(0,\Delta y,0)\, d(\Delta y) \quad , \tag{19}$$

$$L_z = \int \rho_{u'(i)u'(j)}(0,0,\Delta z)\, d(\Delta z) \quad , \tag{20}$$

with integration from *0* until ∞. The most important of these three is the longitudinal scale, the other two being practically its derivatives. The integral time scale of the turbulence is defined by

$$\Lambda_T = \int \rho_{u'(i)u'(j)}(\tau)\, d\tau \quad . \tag{21}$$

According to above Taylor´s hypothesis, the longitudinal scale of a turbulence may be specified by the integral time scale and by the mean wind speed value *V* in streamwise direction by

$$L_x = V.\Lambda_T \quad , \tag{22}$$

The studies for determination of the turbulence scale, both at natural scale and in laboratory, have produced the empirical Davenport´s formula

$$\Lambda_T = 0.084\, L/V \quad , \tag{23}$$

given in sec, where *L* is the longitudinal scale of the in-wind speed and *V* is the mean wind speed.

The incorporation of above forcing into behaviour of the flat plate is specified by wave propagation with corresponding interactions and reflexions of laminar and turbulent air flows. The waves initiated are specified by the spectral evolution describing the occurrence of wind turbulences. The spectral evolution is based on following definitions:

1. Each stationary function *x(t)* is given in integral form

$$x(t) = \int e^{i.t}\, dA(\omega) \quad , \tag{24}$$

with symbol *A(ω)* for orthogonal complex process studied.

2. Linear transformation $y(t)$ of the function $x(t)$ in Eq. (24) is given by

$$y(t) = \int H(i\omega)\, e^{i_\omega t}\, dA(\omega) \quad , \tag{25}$$

with $H(\omega)$ as corresponding admittance function.

3. Spectral densities of functions $x(t)$ and $y(t)$ are connected by

$$S_y(\omega)/S_x(\omega) = |\, H(i\omega)|^2 \quad . \tag{26}$$

Turbulent air flow is defined by a wave number $r_i(\omega)$, with longitudinal and shear waves. Stationary waves are emitted with complex amplitude $F(\omega,z_o)$, e.g., $z=z_o$. The wave superposition is given by

$$w_i(t,z) = \int e^{-i_\omega t}\, e^{ir(_\omega z)}\, dF(\omega,z_o) \quad . \tag{27}$$

For wave interactions in the turbulences the forcing spectrum is given by

$$S(\omega,0) = S(\omega,z_o)\, |H(\omega,0)|^2\, e^{-2\, Im r(_{\omega j})} \quad , \tag{28}$$

with $H(\omega,0)$ as response due to the wind action.

4. Dynamic analysis

The analysis of ultimate behaviour of skew plates subjected to above forcing is based on the adoption of the Lagrange formulation of motion. The reference state of plate is incrementally updated during deformation process. The new reference configuration is established at each degree of updated deformation curve of ultimate response of plate. Incremental form of the equation of motion is given by the analysis of aeroelastic equilibrium of two configurations at time step Δt apart. The increments of laminar and turbulent forcing balance the aeroelastic equilibrium in time $t+\Delta t$ by

$$M_t\, \Delta a_t + C_t\, \Delta v_t + K_t\, \Delta u_t = R_{t+\Delta t} - (V_t^I + V_t^D + V_t^S) \quad , \tag{29}$$

with inertia forces $V_t^I = M_t\, a_t$, damping forces $V_t^D = C_t\, v_t$, stiffness forces $V_t^S = K_t\, u_t$ and with accelerations, velocities and displacements a_t, v_t, u_t , respectively. The vectors of accelerations and velocities are given by time derivatives of the vector of deformations u_t . The mass, damping and stiffness matrices M_t, C_t *and* K_t , respectively, are constructed of the element matrices of the plate model studied. The subscript t denotes the actual time and R is the vector of laminar and turbulent forcing. If the system is in equilibrium in time t, then right side of Eq. (29) is identical with the increments of forcing in time step Δt. The increments in displacements, velocities and accelerations are given by increments of forcing and by the matrices of physical properties of the plate studied. If such matrices are variable in time then the validity of Eq. (29) is satisfied only approximately. The approximation error is given by

$$\Delta V_{t+\Delta t} = R_{t+\Delta t} - (V_{t+\Delta t}^I + V_{t+\Delta t} + V_{t+\Delta t}) \quad , \tag{30}$$

as measure of the solution accuracy when adopting Eq. (29). Governing incremental equation of motion is then given by modification of Eq. (29) as

$$M_t\, \Delta a_t + C_t\, \Delta v_t + P_t\, \Delta u_t = \Delta R_t \quad , \tag{31}$$

where $P_t\, \Delta u_t$ is the vector of nonlinear forces. The pseudo-force method ([23]), adopted for the solution of the problem, is given by

$$P_t\, \Delta u_t = K_t\, \Delta u_t + N_t\, \Delta u_t - \Delta V_{t+\Delta t} \quad , \tag{32}$$

where $N_t\, \Delta u_t$ is the vector of aerodynamic nonlinear forces (pseudo-forces) and $\Delta V_{t+\Delta t}$ is above approximation error. When adopting the pseudo-force technique, the member $P_t\, \Delta u_t$ is located on the right side of Eq. (31) and the vector of nonlinear forces is applied as the vector of pseudo-forces. In each time step the approximation $N_t\, \Delta u_t$ is calculated and the iterations run until the term $\Delta V_{t+\Delta t}$ is comparable with the tolerance norm adopted. The approximation of $N_t\, \Delta u_t$ in first iteration step is given by

$$N_t\, \Delta u_t = (1 + \beta)\, N_{t-\Delta t}\, \Delta u_{t-\Delta t} - \beta\, N_{t-2\Delta t}\, \Delta u_{t-2\Delta t} \quad , \tag{33}$$

with β as extrapolation parameter in scope from 0 until 1.

5. Experiments in aerodynamic tunnel

The testing was made with the model set-up of typical skew flat plate in scale 1:10, developed on the basis of the model similarity with actual structure in fotovoltaic power plant. Aerodynamic testing was made in the wind tunnel of the Institute of Construction and Architecture of Slovak Academy of Sciences in Bratislava, Slovakia.

For testing was used the modul section with cross-sectional dimensions 1200 x 1200 mm and length 6000 mm. Maximal wind velocity obtained was 51 m/sec. The model of the skew flat plate was made of aluminium with dimensions 1000 x 300 mm and width 4 mm. The plate was supported by steel supports Jäckl 20/20/2 and anchored into the floor of the tunnel. The view of the experimental set-up in the tunnel is in Fig. 1.

In case of the wind forcing there appear the turbulences on upper and lower edges of the plate accompanied by wind gusts and local changes of the wind velocity.

The wind velocity influences the standard wind pressure being used in the design of the plate. Required was therefore the specification of actual wind velocities appearing on all edges of the skew plate at various speeds in wind tunnel.

Fig. 1. Side view of the skew plate studied in aerodynamic tunnel

The speed variations in the wind flow were given by aerodynamic coefficient α

$$\alpha = v_{loc}/v_{ave} \quad , \tag{34}$$

with v_{loc} as local velocity of turbulent wind flow measured on the edge of the plate and with v_{ave} as averaged velocity of laminar wind flow in aerodynamic tunnel. The value v_{ave} corresponds to the standard wind velocity in given territory and was used for the design of all structural elements of the skew flat plates studied. The coefficient α specifies the increase of the wind velocity on the edges of the plate. The first goal of experimental testing was therefore the specification of the aerodynamic coefficient α on all edges of the skew plate. The values of coefficient α were adopted for specification of resulting stress and deformation states in the plate. With the data measured was made the virtual modeling of typical active fields of fotovoltaic power plant, consisting of a number of skew plates and subjected to wind forcing. For the measurement of the wind velocities were used the anemometers positioned in the axis of the tunnel (measurement of velocities v_{ave}) as well as on the edges of the skew plate (measurement of velocities v_{loc}). The anemometers for the measurement of velocities v_{loc} were adopted in various positions in order to find the variability of wind velocities on all edges of the plate

studied. The time records were made on channels measuring three accelerations A1, A2, A3, four strains T1, T2, T3, T4 in the centres of all four edges of the skew plate as well as the wind velocities in the tunnel. The accelerations A1, A2 a A3 were measured on upper (A1), lower (A2) and side edges (A3) of the plate. The testing was made for:

a) Model in horizontal attitude 0° and located perpendicularly to the direction of the wind flow – the assessment of the shear wind along the plate (Fig. 2).
b) Model in horizontal attitude and turned -180° compared with the wind flow – the assessment of the air sucking on the plate (Fig. 3).
c) Model in horizontal attitude and turned +90° compared with the wind flow - the assessment of the wind pressure on the plate (Fig. 4).

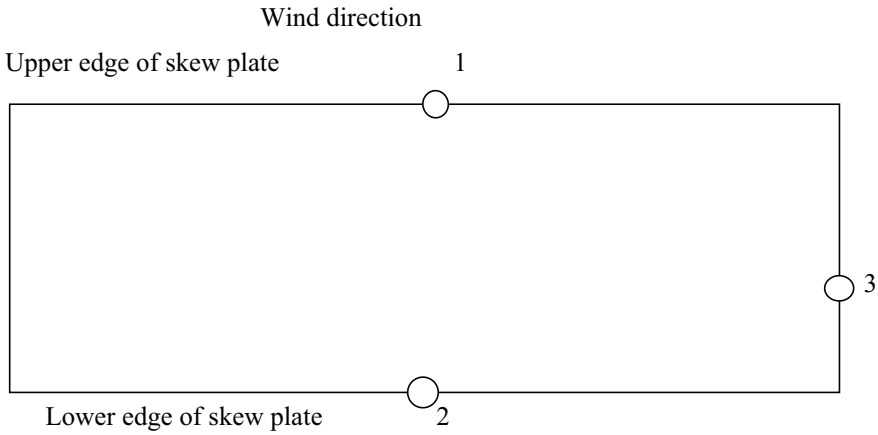

Fig. 2. Numbering of measurements in model position 0°

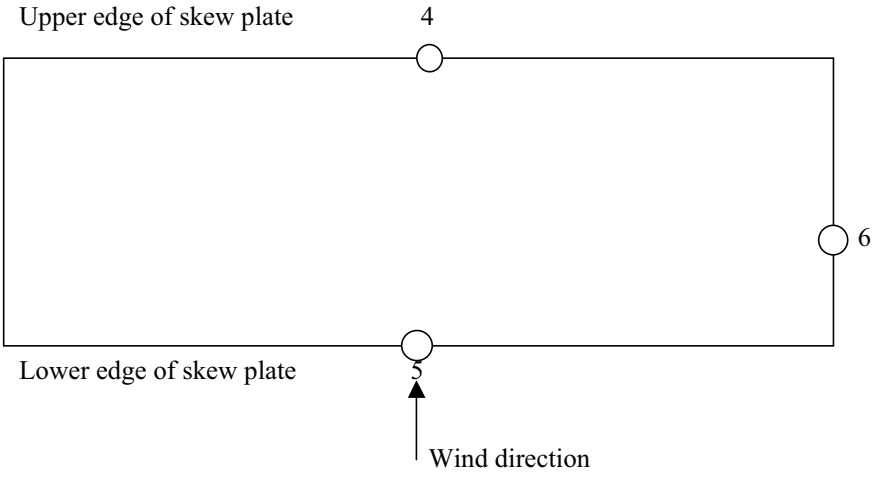

Fig. 3. Numbering of measurements in model position -180°

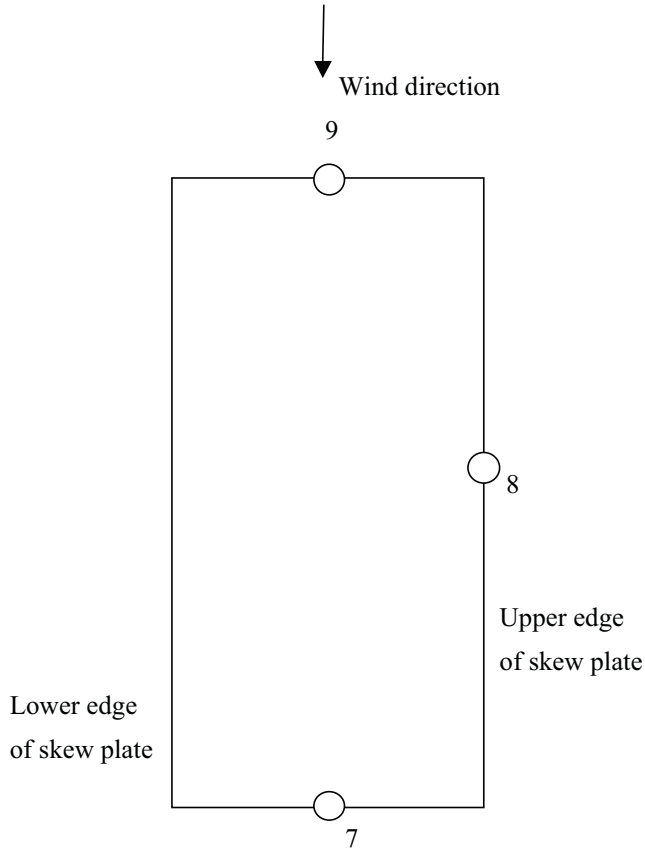

Fig. 4. Numbering of measurements in model position +90°

In accordance with the measurements made in critical points (see Figs. 2, 3 and 4) and summed up in Tables 1 - 3 was stated, that response of the plate is dominated by deformations with turbulent components of pressure and sucking of wind which are irregularly distributed along the surface of plate. Turbulent wind flows initiated the ultimate aeroelastic response of plate.

The values of aerodynamic coefficient α, obtained in aerodynamic tunnel, are summed up in Tables 1, 2 and 3. The tables contain the wind speeds on the edges of skew plate, specified in scope of measurements 1 until 9 at various wind speeds. In tables are summed up the automatically established wind speeds 10 - 50 m/sec in the aerodynamic tunnel, averaged actual wind speeds v_{ave} in the wind tunnel as well as the local wind speeds v_{loc} on all edges of the plate. In tables are also corresponding aerodynamic coefficients α on all edges of the plate.

The averaged increase of speeds and pressures of wind flows on the upper, lower and side edges of the plate are given by aerodynamic coefficients α = 1.4255, 1.6532 and 1.4080, respectively. The averaged increase of the wind pressure on the plate due to change of wind direction and due to turbulences appearing is given for wind sucking by multiplicator –1.65 and for the wind pressure by multiplicator 1.43 of the standard values valid for the face action of the wind on the model. Due to appearance of the wind gusts was initiated ultimate response of the model. There appeared combined axial and shear amplitudes of vibration parallel with the plane of the skew plate.

Tab. 1: Results of measurements Nr. 1, 2 and 3

Wind speed [m/sec]	Measurement Nr. 1 v_{loc} [m/sec]	Measurement Nr. 1 v_{ave} [m/sec]	Measurement Nr. 1 $\alpha=v_{loc}/v_{ave}$	Measurement Nr. 2 v_{loc} [m/sec]	Measurement Nr. 2 v_{ave} [m/sec]	Measurement Nr. 2 $\alpha=v_{loc}/v_{ave}$	Measurement Nr. 3 v_{loc} [m/sec]	Measurement Nr. 3 v_{ave} [m/sec]	Measurement Nr. 3 $\alpha=v_{loc}/v_{ave}$
10	14.5	10.1	1.4356	18.8	10.1	1.8614	15.8	10.1	1.5643
20	28.8	20.2	1.4257	35.6	20.2	1.7624	30.6	20.2	1.5148
30	39.9	30.1	1.3256	48.9	30.1	1.6249	42.9	30.1	1.4252
40	51.4	40.1	1.2817	59.7	40.1	1.4888	55.7	40.1	1.3890
50	65.2	50.2	1.2988	74.8	50.2	1.4900	69.8	50.2	1.3904

Tab. 2: Results of measurements Nr. 4, 5 and 6

Wind speed [m/sec]	Measurement Nr. 4 v_{loc} [m/sec]	Measurement Nr. 4 v_{ave} [m/sec]	Measurement Nr. 4 $\alpha=v_{loc}/v_{ave}$	Measurement Nr. 5 v_{loc} [m/sec]	Measurement Nr. 5 v_{ave} [m/sec]	Measurement Nr. 5 $\alpha=v_{loc}/v_{ave}$	Measurement Nr. 6 v_{loc} [m/sec]	Measurement Nr. 6 v_{ave} [m/sec]	Measurement Nr. 6 $\alpha=v_{loc}/v_{ave}$
10	13.5	10.1	1.3366	18.8	10.1	1.9603	14.0	10.1	1.7129
20	26.8	20.2	1.3267	34.6	20.2	1.8119	27.5	20.2	1.5742
30	36.9	30.1	1.2259	47.9	30.1	1.6578	40.9	30.1	1.3588
40	49.4	40.1	1.2319	56.7	40.1	1.4638	52.7	40.1	1.4389
50	61.2	50.2	1.2191	66.8	50.2	1.4103	63.8	50.2	1.3506

Tab. 3: Resuls of measurements Nr. 7, 8 and 9

Wind speed [m/sec]	Measurement Nr. 7 v_{loc} [m/sec]	Measurement Nr. 7 v_{ave} [m/sec]	Measurement Nr. 7 $\alpha=v_{loc}/v_{ave}$	Measurement Nr. 8 v_{loc} [m/sec]	Measurement Nr. 8 v_{ave} [m/sec]	Measurement Nr. 8 $\alpha=v_{loc}/v_{ave}$	Measurement Nr. 9 v_{loc} [m/sec]	Measurement Nr. 9 v_{ave} [m/sec]	Measurement Nr. 9 $\alpha=v_{loc}/v_{ave}$
10	13.7	10.1	1.3564	17.8	10.1	1.7623	14.3	10.1	1.4158
20	26.8	20.2	1.3267	36.6	20.2	1.8119	28.7	20.2	1.4208
30	38.9	30.1	1.2923	49.9	30.1	1.6578	40.4	30.1	1.3422
40	52.4	40.1	1.3067	60.7	40.1	1.5137	52.6	40.1	1.3117
50	66.2	50.2	1.3187	76.8	50.2	1.5299	67.7	50.2	1.3488

6. Conclusions

On the basis of evaluation of virtual results obtained in active fields of fotovoltaic power plants has been found that ultimate displacements and stress states appear in boundary regions of fields where the wind flows have distinctly turbulent character. In real structures such regions are created by boundary strips having width 3 m along the periphery of the field studied.

Acknowledgement

Author appreciates a kind sponsorship of Slovak Grant Agency APVV, which granted the research reported.

References

Bleich, F. (1950) *The Flutter Theory*. Ch. 7 of Bleich, F, McCullough, C.B., Rosencrans, R. and Vincent, G.S.: The mathematical theory of vibration in suspension bridges. United States Government Printing Office, Washington, pp. 241-281.

Selberg, A. (1961) Oscillation and aerodynamic stability of suspension bridges. *Acta P*. 308, Ci. 13, pp. 43-54.

Selberg, A. & Hjorth-Hansen, E. (1966) Aerodynamic stability and related aspects of suspension bridges. *Proceedings of International Symposium on Suspension Bridges*, , Laboratório Nacional de Engenharia Civil, Lisboa, paper 20, pp. 361-366.

Theodorsen, T. (1935) *General Theory of Aerodynamic Instability and the Mechanism of Flutter.* 496 U.S. Advisory Committee for Aeronautics, Langley, VA, U.S.A.

Klöppel, K. & Weber, G. (1963) Teilmodellversuche zur Beurteilung des aerodynamischen Verhaltens von Brücken. *Der Stahlbau* 4, pp. 113-121.

Frandsen, A.G. (1966) Wind stability of suspension bridges. Paper 43 of *International Symposium on Suspension Bridges,* Proceedings. Laboratório Nacional de Engenharia Civil, Lisboa, , pp. 609-627.

Rocard, . (1965) Instabilité des ponts suspendus dand le vent – expériences sur modéle réduit. Paper 10 of *Wind Effects on Buildings and Structures.* H.M.S.O., London, Vol. II, pp. 434-459.

Scruton, C. (1965) Discussion. *Wind Effects on Buildings and Structures*. H.M.S.O., London, Vol. II, , pp. 555-556.

Davenport, A.G. (1962) Buffeting of a suspension bridge by storm winds. *ASCE Journal of Structures Division* 88, pp. 233-264.

Scanlan, R.H. & Tomko, J.J. (1971) Airfoil and bridge deck fluttyer derivatives. *ASCE Journal of Engineering Mechanics*. 97, pp. 1717-1737.

Scanlan, R.H. Béliveau, J.G. & Budlong, G. (1974) Indicial aerodynamics functions for bridge decks. *ASCE Journal of Engineering Mechanics*, 100, pp. 657-672.

Scanlan, R.H., Jones, N.P. & Singh, L. (1971) Inter-relations among flutter derivatives. *Journal of Wind Engineering and Industrial Aerodynamics,* 69-71, pp. 829-837.

Sears, R.W. (1941) Some aspects of non-stationary airfoil theory and its practical application. *Journal of Aeronautical Sciences*, 8, pp. 104-108.

Simiu, E. & Scanlan, R.H. (1996) *Wind Effects on Structuresd*. Wiley Interscience, New York.

Curami, A. & Zasso, A. (1993) *Extensive identification of bridge deck aeroelastic coefficients, average angle of attack, Reynolds number and other parameter effects*. ProWE III, Hong Kong.

Diana, G., Bruni, S.,. Cigada, A. & Collina, A. (1993) Turbulence effect on flutter velocity in long span suspended bridges. Journal of Wind Engineering and Industrial Aerodynamics, 48, pp. 329-342.

Diana, G., Chelli, F., Zasso, A. & Bocciolone, M. (1999) Suspension bridge response to turbulent wind. Comparison of new numerical simulation method results with full scale data. Proc. of *10-th International Conference on Wind Engineering*, Copenhagen.

Diana, G., Chelli, F., Collina, A., Zasso, A. & Bruni, S. (1998) Aerodynamic design of long span suspension bridges. *IABSE Symposium*, Kobe,.

Larose, G.L., Davenport, A.G. & King, J.P.C. (1992) Wind effects on long span bridges. Consistency of wind tunnel tests. *Journal of Wind Engineering and Industrial Aerodynamics*, 41-44, pp. 1191-1202.

Miyata, T., Yamada, K., Kanazaki, T. & Iijima, T. (1992) Constructionm of boundary layer wind tunnel for long-span bridges. *Journal for Wind Engineering and Industrial Aerodynamics*, 41-44, , pp. 885-896.

Tanaka, H. (1992) Similitude and modeling in bridge aerodynamics. In: A. Larsen (ed.): *Aerodynamics of Large Bridges,* Balkema, Rotterdam,.

Tesar, A. (1978) *Aeroelastic Response of Transporter Shell Bridges in Smooth Air Flow.* The Norwegian Institute of Technology, Tapir, Trondheim.

Tesar, A. (1988) *Transfer Matrix Method.* KLUWER Academic Publishers, Dordrecht, Boston, London.

Tesar, A. & Svolik, J. (1993) Wave distribution in fibre members subjected to kinematic forcing. *International Journal for Communication in Numerical Mechanics*, 9.

Juhasova, E., Motlik, I. & Vrabec, M. (1998) Some experiences with calibration and modeling in wind tunnel of ICA SAS. *Building Research Journbal*, 46, pp. 47-69.

STN EN 1991-1-4 Eurocode 1, Structural Loads, Part 1.4, General Loads, Wind Loads.

Tesar, A. & Tvrda, K. (2006) Energy approach for analysis of nonlinear time response. *Building Research Journal*, Vol. 54, Nr. 2, pp. 101-122.

Tesar, A. & Tvrda, K. (2007) Energy approach for solution of nonlinear natural vibration. *Building Research Journal*, Vol. 55, Nr. 1-2, pp. 71-84.

Hautoy, C. (1990) *Simulation des proprietes dynamiques du vent.* Souflerie a couche limite du C.S.T.B., Nantes, France,

Moonen, P., Blocken, B. & Carmeliet, J. (2007) Indicators for the evaluation of wind tunnel test section flow quality and application to a numerical closed circuit wind tunnel. *J.W.E.I.A.*, (95), pp. 1289-1314.

Teleman, E.C., Silion, R., Axinte, E. & Pescaru, R. (2008) *Turbulence scale simulations in atmospheric boundary layer wind tunnels*. Bulletinul Institutului Polytehnic din Iasi, Publicat de Universitatea Tehnice "Gheorghe Asachi" din Iasi, Tomul LIV (LVIII), Fasc. 2, pp. 7-14.

18th International Conference
ENGINEERING MECHANICS 2012
Svratka, Czech Republic, May 14 – 17, 2012

pp. 1381–1394
Paper #73

ENIGMA OF SUBMERGED FENCE SKIN FRICTION SENSOR

V. Tesař*

Abstract: *The problem with "sublayer fence" skin friction sensor is the disturbance caused by the fence protruding above the surface, however small it is. In an application to the Coanda effect attachment to a curved wall it is known to cause premature transition into turbulence or even flow separation. from the. Author eliminated, already quite a long time ago, these adverse influences in his original version of the sensor with the fence submerged slightly below the surface. Recent detailed investigations revealed the pressure difference output to be dependent on creation of miniature recirculation regions. An attempt to facilitate the recirculation, quite surprisingly, has led to total disappearance of a useful output signal.*

Keywords: ***Skin friction, surface shear stress,***

1. Introduction

Measurement of wall shear stress has been an important – but difficult to perform – part of experimental turbulence research, since the value of this quantity is an indispensable characterisation parameter for description of turbulence. The sudden local increase of the shear stress value taking place in transition from laminar into turbulent character of the flow makes skin friction sensors useful determining the transition position, Tesař (1974). Characteristic feature of contemporary Fluid Mechanics is the progress from mere understanding of fluid flows to controlling them. One of the challenge for the control action is the high turbulent friction. If it were possible to suppress turbulence, efficiency in many fields of activities – from aircraft flight to pipeline transport – would be increased substantially. In principle (although at present neither easy nor economical) it is possible as shown in Ikeda 2007, or Kasagi, Suzuki, and Fukagata 2009 to reduce the friction drag by manipulating the hairpin shaped coherent structures that dominate the near-wall turbulence. The precondition is, of course, detecting the presence of the hairpins. Sensors of local shear stress can perform this task (Grosse and Schröder, 2009). There are two essential requirements the sensor for such application has to meet:

a) its size has to be very small, and

b) must not disturb the flow by its presence.

Other properties, in particular sensitivity, dynamic range of response, and certain robustness are also of importance, but these may be improved upon by development. Most currently used and known methods, however, fail to meet the two basic requirements above, **a** and **b**.

Known methods (their classical but still useful survey is in Rechenberg, 1963) may be sorted into five groups:

1) direct force measurement
2) evaluations from measured velocity profile
3) deformation of inserted second phase (e.g. a liquid on wall in gas flow)
4) piezometric principles generating pressure output signal
5) heat or mass transfer analogy

The ***direct*** method (one of the earliest sources: Dhawan 1953), measuring the extremely small) force acting on a „floating" element of the surface, is generally difficult to use. It is not easy to

* Prof. Ing. Václav Tesař, Institute of Thermomechanics v.v.v.i., Academy of Sciences of the Czech Republic, Dolejškova 5; 182 00, Prague 8; CZ, e-mail: tesar@it.cas.cz

suppress the influence of the pressure forces acting on the element walls in the gaps surrounding the element. It is also extremely difficult to adjust the sensitive alignment of the element surface with the surrounding wall. Solutions of some of these problems is being sought in microfabricated versions, e.g. Shaji, Ng, and Schmidt, 1992).

Measurement of velocity in several points above the surface and use the ***velocity profile*** data is, of course, a typical laboratory technique not suitable for engineering sensors.

Equally limited to the laboratory environment are the methods evaluating the ***deformation*** changes of the geometry of a liquid film applied on the surface exposed to an air flow (Tanner and Blows, 1976, modern version: Desse 2003) - or conversely changes of geometry of a gas bubble in liquid flow.

The ***piezometric*** sensors generate a pressure difference in their output terminals, usually derived from the dynamic pressure on a small body protruding above the surface. These used to be the standard choice for several decades. Typical are Stanton tube (Stanton, Marhall, and Bryant 1920), Preston tube (1053), or sub-layer fence (Konstantinov 1953). The difference is measured by a manometer. Of course, the disturbance to the investigated flow is inevitably significant – especially on a wall of small curvature radius the probe is known to cause premature transition into turbulence or even flow separation.

Considering the disadvantages of the above methods, the interest in a few recent decades has concentrated on the methods based on the analogy between the momentum transfer and the transfer of heat and/or mass. Use of the mass transfer remains somewhat exceptional — the naphtalene sublimation method of Trávníček (Trávníček and Tesař, 2003) can measure the shear stress in principle, but is practically always used to evaluate a different quantity: the total convective transfer rate. This specifically shear stress measurements are now made solely by electrodiffusion method in liquid flows (e.g., Sobolík et al., 1990). In flows of air and other gasses, several practical reasons has led to the current dominance of the ***heat transfer*** principle (Liepman and Skinner G. , 1954, Laghrouche M., et al., 2011). Majority of its users believe the heat transfer method does not disturb the investigated flow. This is a grave mistake: the heating of the wall even by a few degrees can demonstrably influence transition into turbulence and cause flow separation from the wall – as was convincingly manifested by the experiment described by Tesař in 1998.

2. Author's "split-cylinder" sensor

Present author has encountered the problem of the skin friction measurement devices influencing the measured flowfield as long as 40 years ago – Tesař, 1973. The particular flow in question was the Coanda-effect attachment to a strongly curved wall – in the configuration presented in Fig. 1.In this case the influence is particularly strong: even a very small object placed on the surface can change the character of the flowfield completely. The Coanda attachment is also exactly the very case in which the strong sensitivity to even small wall heating was demonstrated by Tesař, 1998. The heating was shown to cause a separation of the attached wall-jet from its attachment wall.

The solution was found in the "split-cylinder" sensor, Tesař 1974 — with no component above the surface (there is no object there - like, e.g., the Stanton tube or the conventional sublayer fence) and no heating. The reason why this approach is now discussed is the fact that it was recently found to be a promising potential component - combined with the high-frequency small-scale fluidic oscillators, described by Tesař, 2012 - of the microfluidic devices that may be used for the suppression of turbulent drag by blowing away from the wall individual hairpin vortices.

The absence of any disturbance in this sensor is possible due to the surprising discovery in 1973 of the fence (like the one at the left-hand side of Fig. 2) generating a useful output pressure signal even if its top edge is submerged to $h < 0$, i.e. under the surrounding surface, as shown at right in Fig. 2.

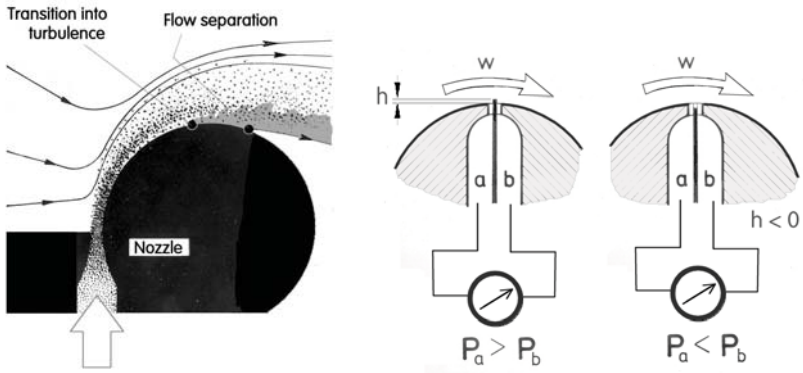

Fig. 1 (Left) The problem that inspired developing the new surface shear stress sensor: Coanda attachment to a curved wall. The sensor is used to detect transition to turbulence and/or separation of the jet from the attachment wall.

Fig. 2 (Right) The disturbance caused by the standard sub-layer fence sensor (at left) can give rise to earlier separation and/or transition. Quite surprisingly (at right), is was found possible to obtain a useful pressure difference signal (of opposite sign) with the fence top submerged below the surrounding surface.

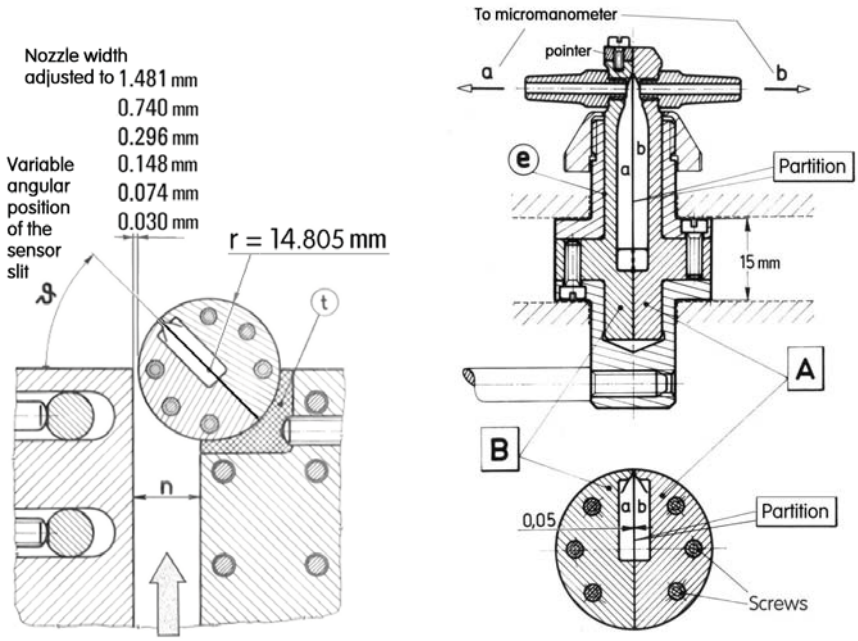

Fig. 3 (Left) Drawing of the central part of the set-up for skin friction measurements under the attached wall-jet. Because of the constant curvature of the attachment wall, the sensor could be positioned to different distances downstream from the nozzle by rotation of the "split cylinder".

Fig. 4 Design of the "split cylinder" component (the attachment wall with the "submerged fence" sensor). The basic part of the cylindrical body consists of two mirror-image parts A and B, separated by 0.05 mm thin metal partition.

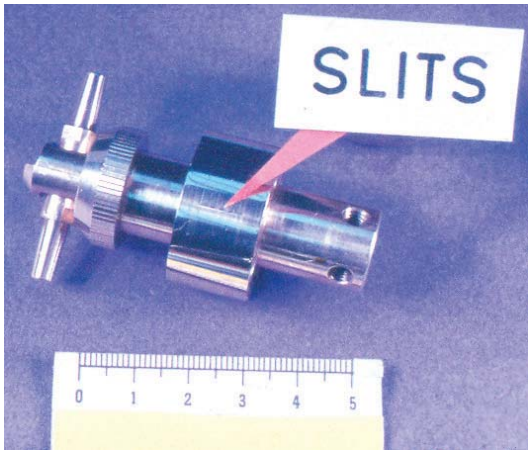

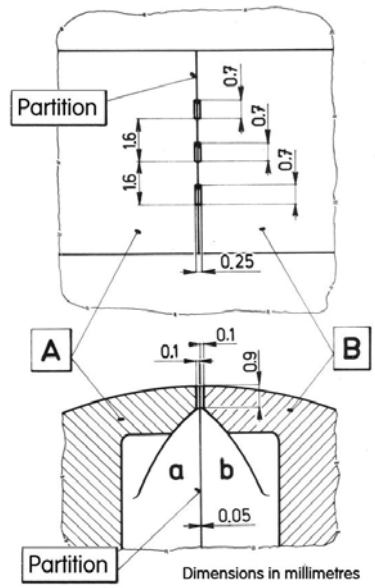

Fig. 5 (Left) Photograph of the "split cylinder" component made according to the drawing in Fig. 4.
Fig. 6 (Right) Detail of the sensing slits geometry.

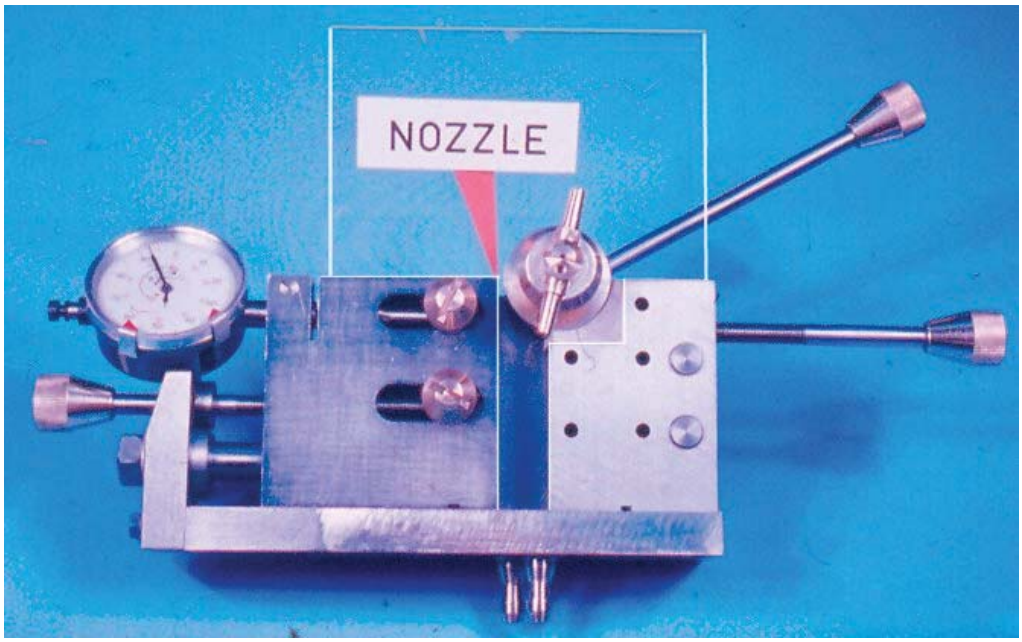

Fig. 7 Photograph of the partly disassembled experimental set-up for investigation of the Coanda-effect attachment. The "split cylinder" component, to which the jet attaches upon leaving the nozzle, is in the centre of the photograph. The curved wall-jet flow takes place between two polymethylemeatcrylate end places, of which only one is in its position here.

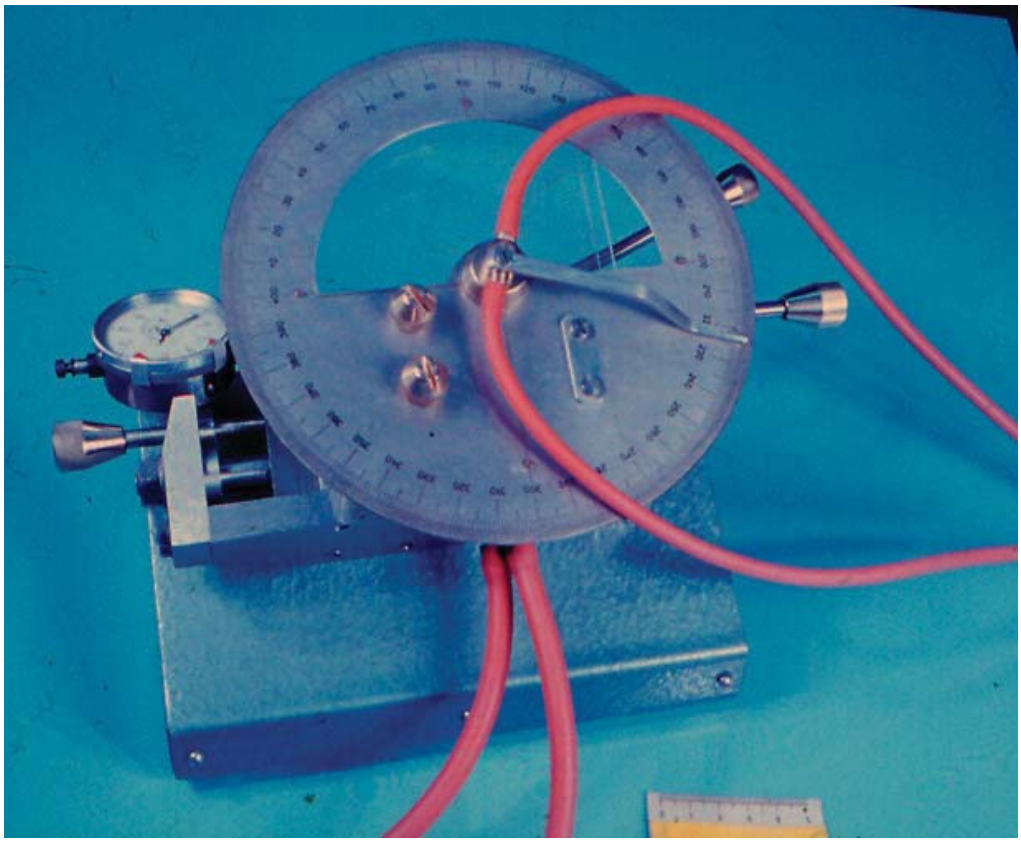

Fig. 8 The experimental set-up assembled. The two bottom rubber tubes supply air into the nozzle, two upper ones carry the pressure-difference signal to the manometer. The angular position of the rotated „split-cylinder" is indicated on the round scale.

The experiment in which this phenomenon was investigated was the Coanda attachment in the set-up shown in Figs. 1, 3, and 7. The flow is a nominally two-dimensional configuration – i.e. with the wall jet bounded on both sides by flat end walls. The important parameter of the attachment, the curvature radius r of the attachment wall, is characterised by its ratio to the nozzle exit width b. As shown in Fig. 3, the radius r in the course of these experiments was 14.805 mm (the decrease from the originally planned 15 mm was due to additional machining of the cylindrical surface necessary to achieve the very high quality) while the width b was adjustable by movement of the left-hand nozzle lip. The values b presented in Fig. 3 indicate that the ratio of the width to the radius r could be set from 0.1 to 0.002. Smaller values mean the nozzle width is so small it is not possible to adjust it with sufficient reproducible precision. On the other hand, larger nozzle width to radius ratios than 0.1 would mean too small nozzle aspect ratio, less than 10, which is not acceptable for the nominal two-dimensionality with the test space bounded by the 15 mm distance between the end walls (Figs. 4, 7).

The fence in the sensor was made from a thin, 0.05 mm foil of phosphor bronze. The foil also served for separation of the cavities through which the pressure difference signals were carried to the manometer. The sensing slits on both sides of the fence - upstream and downstream – were very narrow, of 0.1 mm width (Fig. 6). This small size made possible high spatial resolution of the investigated transition positions. The sensor did not span the full 15 mm height of the cylindrical attachment wall between the plexiglass end plates; its length perpendicular to the flow direction was only 0.7 mm (Fig. 6) to avoid possible bending of the very thin fence by the acting pressure difference in some extreme regimes. To increase sensitivity, there were actually three sensors side by side, operating in parallel: apart from the central one in the middle of the cylindrical attachment wall height there was another sensor on its both sides, separated by the 0.9 mm wide flat surfaces, well

seen in Fig. 10. In the initial verification tests, it was quite surprisingly possible to receive a useful output pressure difference signal from the sensor with the fence machined flush with the surrounding cylindrical surface. However, the measured pressure difference ΔP in these tests with the nominally zero fence height h was of the opposite sign to the standard output signal of the sublayer fence method. Visual inspection at a very large magnification made this sign reversal comprehensible: the machining on a lathe caused the top of the fence – exposed in the 0.7 mm wide sensing slits unsupported to the machining tool - to be cut away more than the surrounding surface. Obviously, the machining made unintentionally the configuration to become actually the one with the " submerged", negative height h fence (right-hand part of Fig. 2).

The accompanying drawings (Figs. 3, 4, and 6) and the photographs (Figs. 6, 7, 8, 9, 10, and 11) provide all the information about the design of the shear stress sensor, used for measurement of the skin friction on the surface of the "split cylinder" . The cylinder actually consisted of two separately made symmetric halves, A and B, with the thin 0.05 mm phosphor bronze partition between them. The three sensors arranged in parallel (Fig. 6, 10, 11) were on both sides connected to the common outlet channels (a and b) indicated in the drawing Fig. 4 and well visible in the photograph Fig. 9.

The cylindrical core body with the three sensors was used in the experimental set-up the design of which is apparent from Figs. 3, 7, and 8. The cylinder was adjusted to different angular positions, read on the large circular scale in Fig. 8.

The " split-cylinder" sensing method, being indirect, necessitated performing a calibration prior to the actual measurements. Because of the cylindrical geometry, the calibration could use the Blasius solution of laminar boundary layer on a cylindrical surface. Again, the output pressure difference measurements were made at various angular positions relative to the parallel flow in a wind tunnel. To get nearer to the assumed infinite length of the cylinder, the sensor part was provided with extensions (Figs. 12, 13, and 14). The assembly is seen tin the test section of the wind tunnel in Fig. 15.

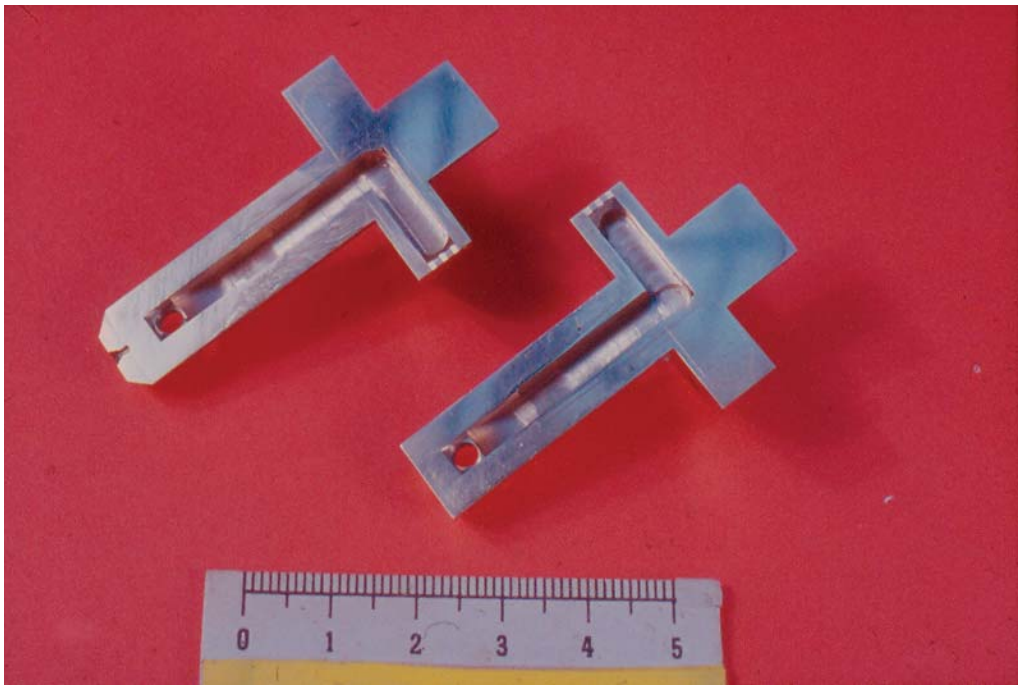

Fig. 9 The key parts A and B (cf. Fig. 4, 6) of the "split cylinder". The two components are mutual mirror images; the milled cavities for transfer of the pressure difference signal to micro-manometer are in the assembled state separated by the phosphor-bronze partition (not shown here).

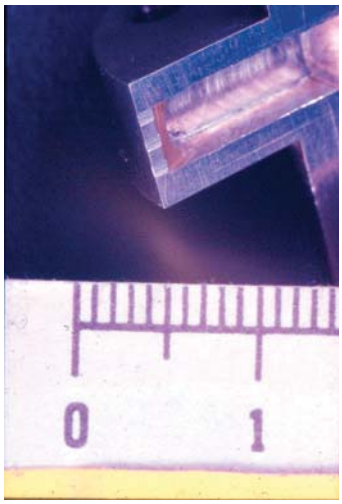

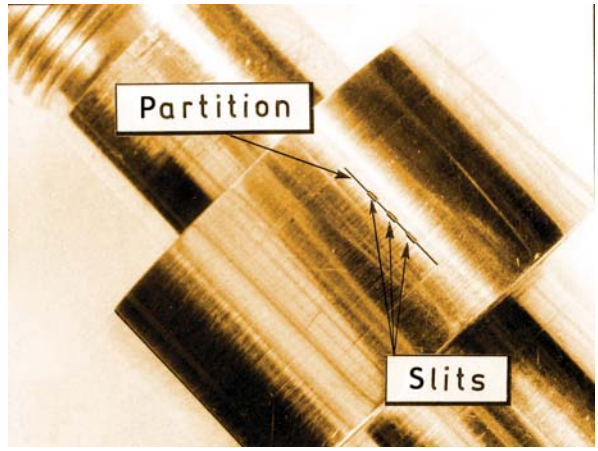

Fig. 10 (Left) Detail photograph of the grooves that form sensing slits.

Fig. 11 (Right) The sensing slits as they were actually used in subsequent measurement: the external edge of the partition was machined to be nominally flush with the surface of the surrounding parts A and B, but lack of support during the machining operation resulted in this edge being slightly lower inside the slits.

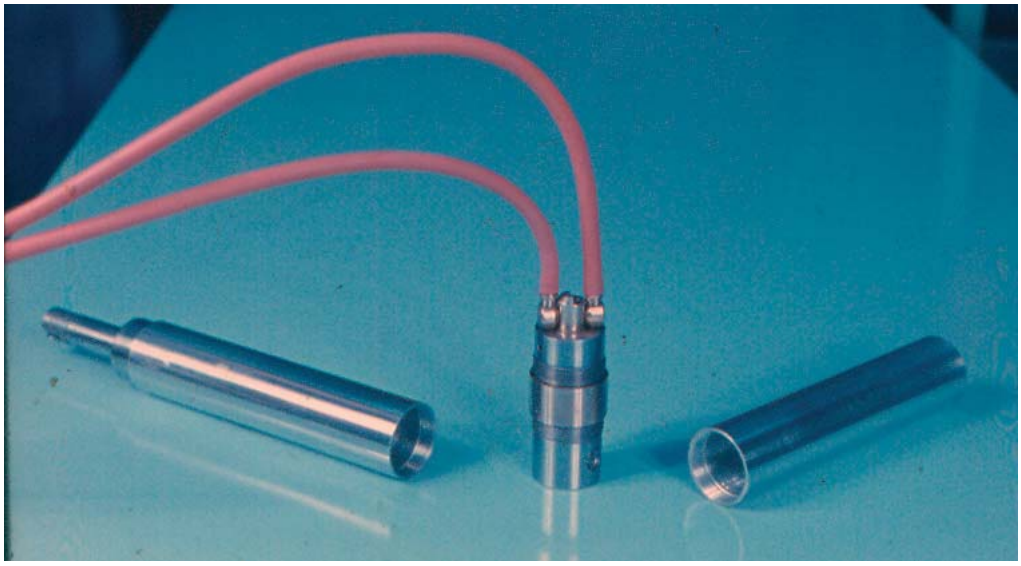

Fig. 12 For calibration in the wind tunnel, the „split cylinder“ component was provided with extensions that converted the assembly into a constant-diameter cylinder body spanning the tunnel test section.

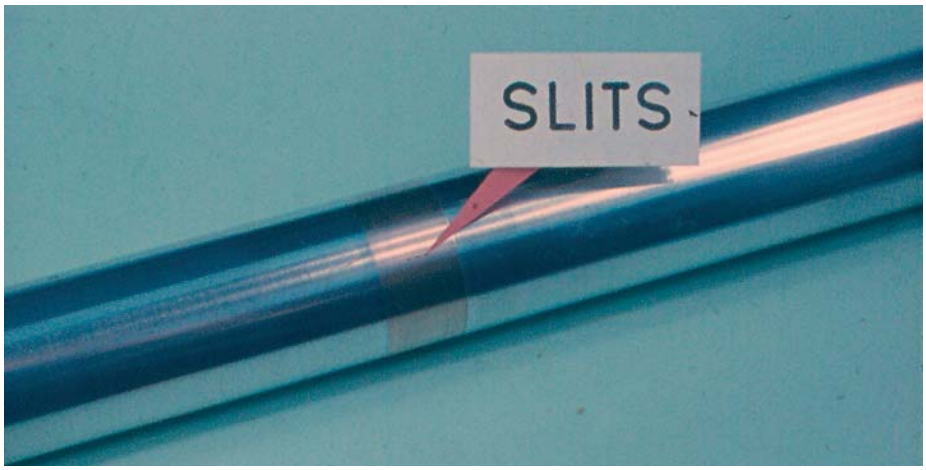

Fig. 13 (Right) Detailed photograph of the surface of the component M (see the next Fig. 14) and the flush fitting extensions. The diameter to length ratio of the complete assembly was satisfactory d / l = 0.1057 so that the local surface shear stress may be calculated from the known Blasius boundary layer solution for infinitely long round cylinder.

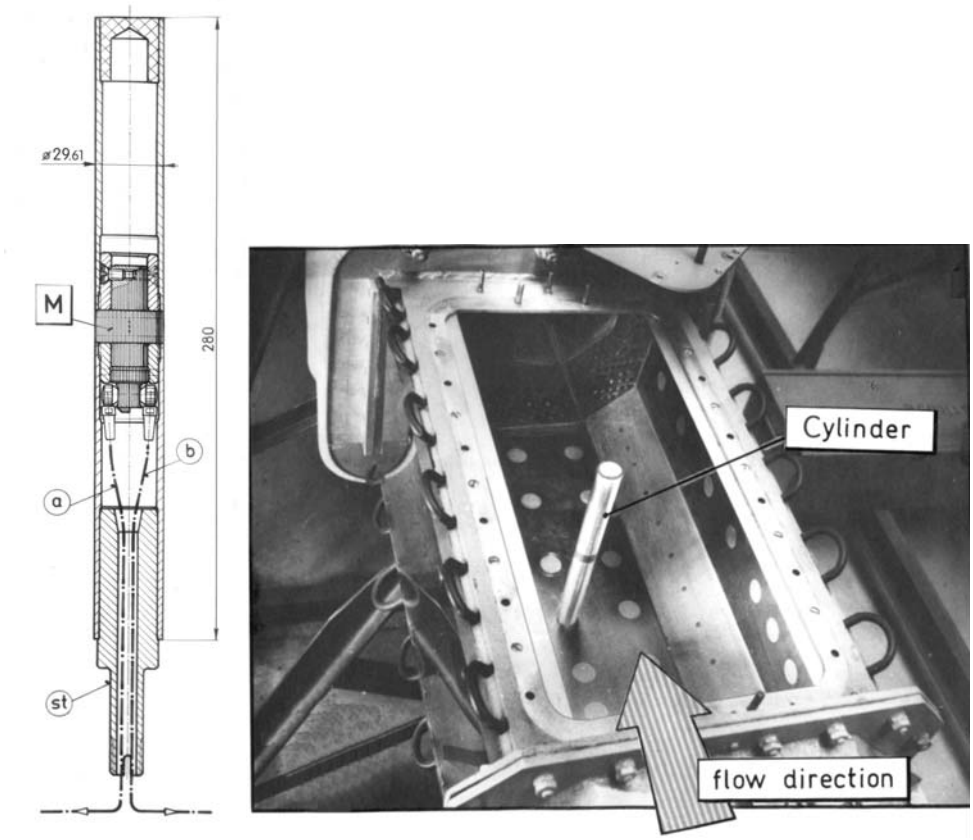

Fig. 14 (Left) Drawing presenting the internal layout of the cylinder with the central component M and the fitting extensions.

Fig. 15 (Right) Photograph of the cylinder body as shown in Fig. 14 positioned in the wind tunnel test section. The blockage ratio of the cylinder diameter to the test section width was 0.075, small enough for neglecting any blockage corrections.

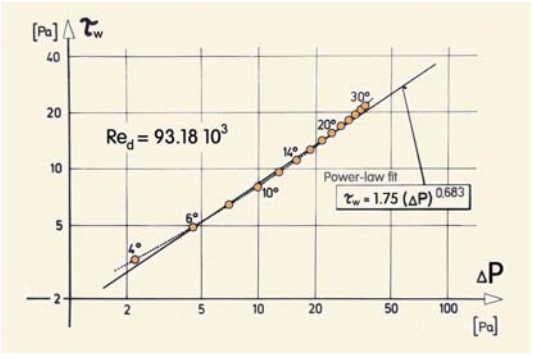

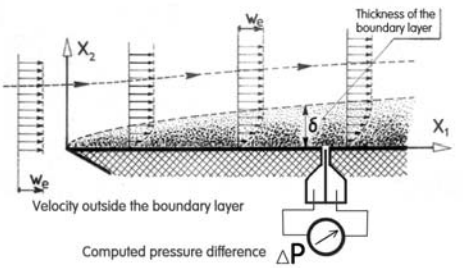

Fig. 16 (Left) An example of the dependence obtained in one of the calibration runs. The wall shear stress τ_w is calculated from the Blasius solution, the pressure difference ΔP in the sensor output was measured by a 1:50 inclined tube Rosenmüller alcohol micromanometer.

Fig. 17 (Right) Configuration of the numerical flowfield solutions: the sensor is positioned at several downstream locations X_1 from the leading edge of a flat plate laminar boundary layer.

Calibration runs in the wind tunnel were made at six different Reynolds numbers (i. e. six wind tunnel flow velocities). An example of the typical measurement run (with a polynomial fit) is presented in Fig. 16. The computed wall shear stress τ_w was in the range from 1 Pa to 50 Pa, the corresponding measured output pressure differences ΔP were within the range from 0.5 Pa to 100 Pa. The results of all six calibration measurement runs could be fitted reasonably by a single calibration dependence.

It seemed obvious that the mechanism of the sensing is associated with the standing vortical structures one can imagine to form in the entrances of the sensing slits. The details of the mechanism, however, remained unexplained. This was a grave hindrance in a way towards obtaining desirable higher sensitivity.

What seemed to be a plausible proposition was that an improvement in the output signal levels should be possible by providing more space for the standing vortical structures so that the air there could recirculate more freely. The simplest way how to provide this space was retracting the fence somewhat more (i.e. to get a higher absolute value of the negative height h, Fig. 2). Unfortunately, contrary to the expectation, instead of an improvement the measured pressure difference after such adaptation was found practically independent of the acting skin friction, making the sensor useless. This fact has shown that the basic concept of the sensor followed so far was obviously incorrect.

3. Numerical flowfield computations as a way towards understanding the flow

Obtaining more insight into the sensor working mechanism experimentally, by observations and direct tests, was not possible because of the sensor inaccessibility during operation and its extremely small size. It was therefore decided to get more information by performing numerical computations of the flowfield inside the sensor inlet space. It should be emphasised that there was no intention to perform the computations in a way simulating the conditions in the "split-cylinder" sensor — even though the size of the sensor duplicated the $b = 0.25$ mm dimension with the 0.05 mm thick fence. The aim was to demonstrate the reality of generating of the output pressure difference with the submerged fence $h < 0$ and possibly to find the ways towards a performance improvement, using as the guide the computed internal conditions in the sensor entrance and its vicinity. For this purpose, it was considered preferable leave aside the somewhat special case of the Coanda attachment as well as the effects of wall curvature and to perform the computations in the flat-plate boundary layer flow, as shown in Fig. 17. This, of course, was likely to provide more general conclusions.

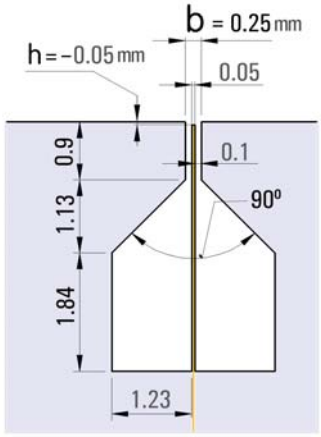

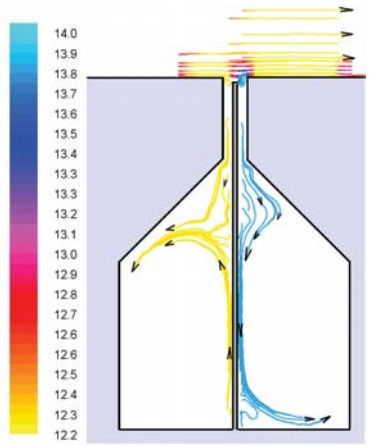

Fig. 18 (Left) Geometry of the sensor used in the computations. The negative height h *of the top of the fence was varied; the results presented here were obtained with* $h = -0.2\ b$ *(shown in this illustration) and* $-0.4\ b$. *The output pressure values were read at the bottom of the two cavities.*

Fig. 19 (Right) Computed pathlines inside the sensor cavities show the induced vortical motions with opposed directions at the partition surface. The velocities of these motions, however, are too slow for this phenomenon having any practical significance.

The computation domain was two-dimensional, with flow in rectangular space 580 mm long and 80 mm high, the boundary layer formed on the domain bottom. The geometry of the sensor as used in the first computation series (later series were made with slightly varied geometry) is presented in detail in Fig. 18: the top of the fence was chosen to be 0.05 mm below the top of the wall – the wall at which was generated the laminar boundary layer. The used solver operated with pressure-based implicit formulation, and assumed laminar flow (because even if used in turbulent flows, the sensor works in the viscous "laminar" sublayer). Initially, the sensor was placed at the streamwise distance $X_1 = 500$ mm from the leading edge. — i.e. sufficiently far on all sides from the boundaries of the computation domain. In some later computations, the sensor entrance was also positioned at streamwise distances 400, 300 and 200 mm. The working fluid was air with specific volume $v = 0.8163\ m^3/kg$ and kinematic viscosity $\nu = 14.6073\ 10^{-6}\ m^2/s$. The boundary conditions were the constant velocity w_e everywhere along the entrance at left, which was 80 mm high. The same also constant velocity w_e was demanded to prevail over the whole top of the domain (80 mm above the bottom solid wall). These velocities were varied to be different in different computation runs, in the range from 3 m/s to 15 m/s (rather small values in agreement with the assumed laminar flow character). In the exit from the domain, at 580 mm horizontal distance from the leading edge, the condition was an everywhere constant, atmospheric pressure.

The domain discretisation was by unstructured triangular elements, the number of which was gradually increased in the course of the computation by refinement in the regions with static pressure gradient above a gradually decreased limit value. Typical final number of the discretisation cells in the final, converged state of the solution was ~ 200 000 cells and ~ 300 000 triangle sides, the typical limiting (highest) value of the gradient was 0.0028 Pa/mm. The computation was considered converged if the solved relative residua of all equations were below 10^{-6}. The 80 mm height of the domain was more than sufficient to accommodate the test shear flows, since typical boundary layer thickness above the sensor was $\delta = 13.6$ mm (the highest value encountered in the course of the whole computation series was $\delta = 19.95$ mm).

The geometry of the sensor cavities, simulating the chambers of the pressure transducer, did not have practically any influence on the computed output pressure difference $\triangle P$ (with the higher pressure in the downstream cavity). The computations actually revealed, as shown in Fig. 19, that there was an upwards flow past the downstream face of the partition and an opposite downwards flow

past the upstream face of the fence. These directions correspond to the character of the generated pressure difference $\triangle P$ in the output terminals - nevertheless the velocities involved were extremely slow and unlikely to result in a practically significant pressure effect. Of more importance are the pressure minimum an maximum that were found in the performed computations — Fig. 20 — at the entrance and exit corners, respectively, of the sensor entry . The pressure values correspond to the colourbar at left in Fig. 20.

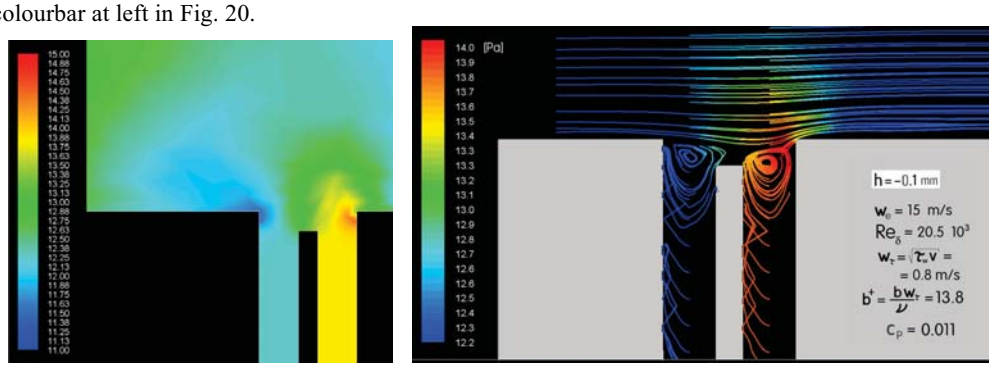

Fig. 20 (Left) An example of computed pressure field near the sensor entrance. The computations suggest the pressure differences measured by the sensor are generated in the flows past the entrance corner at left and the exit corner at right, respectively. The colourbar shows values of pressure relative to the domain exit.

Fig. 21 (Right) Typically for the configurations generating the reasonable pressure signal, also in the $h = -0.2\ b$ case presented here, the computed pathlines show existence of two separate vortices in the two sensor entrances.

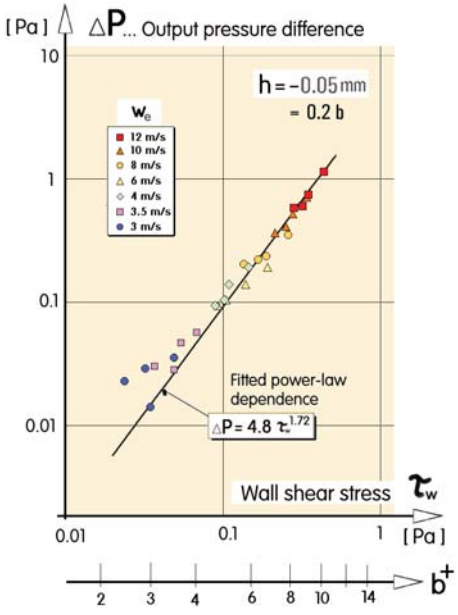

Fig. 22 Results of the large number of performed computations: dependence of the sensor output pressure difference $\triangle P$ on the shear stress τ_w, the latter evaluated from the slope of the velocity profile at the wall. The auxiliary scale below indicates very small magnitude of the sensor entrance width b when evaluated in the friction co-ordinates.

What was the most important phenomenon shown by these computations is the character of fluid motion inside the entrance, as shown in Fig. 21. As expected, it is a motion of vortical character. What was perhaps not expected is there are two, co-rotating mutually non-communicating standing vortices.

As the numerical results of performed computations is presented in Fig. 22 the dependence between the generated output pressure difference $\triangle P$ and the wall shear stress τ_w. The latter was evaluated from the slope of the computed velocity profile one wall in the vicinity of the sensor entrances. Perhaps more important than the evaluated overall dependence (power-law expression fitted to the data — which is valid for the simplified case chosen for obtaining the insight into the mechanism rather than to model any particular real sensor) are the values of the corresponding sensor entrance width b converted into the friction co-ordinates:

$$b^+ = \frac{b w_\tau}{\nu} = \frac{b}{l_\tau} \qquad ...(1)$$

These values may be read on the auxiliary scale at the bottom of Fig. 22.

Conditions on a solid surface influenced by prevailing shear stress τ_w [N/m^2 = Pa] are characterised by *friction velocity* w_τ [m/s] — a quantity evaluated as

$$w_\tau = \sqrt{\tau_w v} \qquad ...(2)$$

where v [m3/kg] is the specific volume of the fluid. The scales of the coherent structures in turbulence - and consequently also the devices used for their detection - are characterised by the friction length, evaluated as

$$l_\tau = \nu / w_\tau \qquad ...(3)$$

where ν [m^2/s] is the fluid kinematic viscosity.

A typical hairpin vortex has its two arms of diameter $30\text{-}40\ l_\tau$ and length $\sim 10^3\ l_\tau$. It is commonly estimated that the sensor capable to detect these vortices should be smaller than about $30\ l_\tau$. The auxiliary scale at the bottom of Fig. 22 shows that in spite of the size of the investigated sensor example chosen as being manufacturable by standard large-scale machine tools, this condition of the sensor smaller than $30\ l_\tau$ is more than sufficiently fulfilled (in fact leaving actually ample reserve for further miniaturisation).

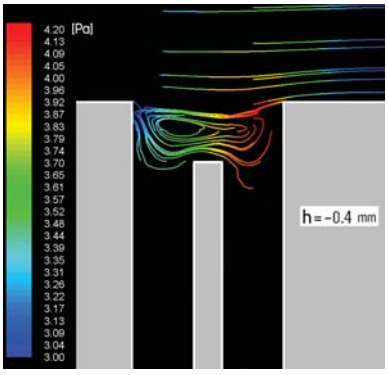

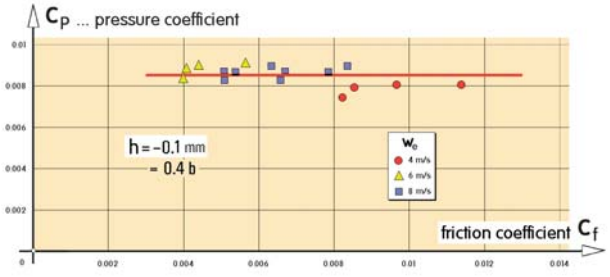

Fig. 23 (Left) Typical computed pathlines for the larger cavity - increased over the previous geometry from Figs. 18 and 21 by moving the fence downwards to $h = -0.4\ b$. This makes easier the vortical motions in the sensor entrance – but makes it possible for the two vortical motions (Fig. 21) to unite and form just a single larger vortex.

Fig. 24 (Right) Contrary to the expectations, the results show practically constant output pressure (here presented in terms of pressure coefficient c_P) irrespective of the variations of the wall shear stress (characterised by the friction coefficient)..

4. The enigma of single vortex

Early thoughts about the operation mechanism of the submerged fence sensor led to the conviction that the fluidic output signal could be increased by giving more free unconstrained space to the generation of the standing vortices in the sensor entrance. The simplest way how to do it is obviously further retraction of the fence, making larger the unobstructed space above the fence top. However, as mentioned already above, the simple tests made with the sensor model failed to bring the expected improvement: on the contrary, the measured pressure difference after moving the fence slightly down have shown the output pressure difference $\triangle P$ independent of the acting shear stress τ_w.

In an attempt at getting an insight into the reason fro this surprising behaviour, the computations were extended to the configuration differing only in the height h in Fig. 18 changed to $h = -0.4$ mm. The resultant dependence of the generated output pressure difference $\triangle P$ on the wall shear stress τ_w is presented in Fig. 24 – in terms of the corresponding pressure coefficient

$$C_p = \frac{2\,v\,\triangle P}{w_e^2} \qquad ...(4)$$

and friction coefficient

$$C_f = \frac{2\,v\,\tau_w}{w_e^2} \qquad ...(5).$$

It is obvious that, as in the laboratory tests with the sensor, this adaptation of the fence height resulted in loss of the capability to measure the shear stress τ_w.

Because the computations were made by the same procedures with the identical boundary conditions and other parameter values as those described in the previous section it is quite probable that this surprising result is not due to some mistake made in the numerical solutions and reflects some real change in the character of the flowfield past the sensor entrance.

A detail of the computed flowfield displayed again by means of the calculated pathlines presented in Fig. 23 shows that the only – but substantial - change when compared with the previous results is the two vortices from the analogous Fig. 21 have here coalesced into a single flat vortex. This, however, does not seem to be a reason for the apparent equalisation of the pressure values in the two pressure-reading cavities.

5. Conclusions

Experiments as well as performed numerical flowfield computations have demonstrated that the submerged fence skin friction sensor, having the exceptional property of causing a minimal disturbance to the investigated flow, can operate and generate a useful measurable output fluidic signal at extremely small dimensions – less than those discussed in literature as being capable of discriminating the dissipative vortical structures in turbulent boundary layers. The computations made with the intention to understand the mechanism of generating the output pressure difference by the vortical motion in the sensor entrance did provide some answers, but failed to explain the enigma of the pressure difference loss with the more submerged fence.

Acknowledgement

Author expresses his gratitude for the support by the grant 101/11/J019 donated by GAČR, and by grant TA02020795 received from the Technological Agency of the Czech Republic, programme ALPHA.

References

Desse J. M. (2003) Oil-Film Interferometry Skin-Friction Measurements under White Light, *AIAA Journal*, Vol. 41, p. 2468

Dhawan S. (1953) *Direct Measurements of Skin Friction*, NACA Report 1121, p. 281

Grosse S., Schröder W. (2009) Wall-Shear Stress Patterns of Coherent Structures in Turbulent Duct Flow, Journal of Fluid Mechanics, Vol. 633, p. 147, 2009

Ikeda K. (2007) Trends in Research on Turbulence Control Aiming at Reducing Friction Drag, *Science and Technology Trends Quarterly Review*, No. 22, p. 98

Kasagi N., Suzuki Y., Fukagata K.. (2009) Microelectromachnical Systems-Based Control of Turbulence for Skin Friction Reduction, *Annual Review of Fluid Mechanics*, Vol. 41, p. 231

Konstantinov N. I (1953) Comparative Investigation of the Friction Stress on the Surface of a Body (original in Russian, Translated 1960 DSIR RTS 1499), *Energomashinostroenie*, Vol. 176, p. 201

Laghrouche M., et al. (2011) In Situ Calibration of Wall Shear Stress Sensor for Micro Fluidic Application, *Proc. of Conf. „Eurosensors XXV"*, Athens, Greece, 2011

Liepman H., Skinner G. (1954) Shearing Stress Measurement by Use of a Heated Element, *NACA TM 3268,* 1954

Preston J. H. (1953) The Determination of a Turbulent Skin Friction by means of Pitot Tubes, *Journal of the Royal Aeronautical Society*, Vol. 58, p. 109

Rechenberg I. (1963) Messung der turbulenten Wandschubspannung (Measurement of wall shear stress — in German), *Zeitschrift für Flugwissenschaften*, Vol. 11, p. 429

Shaji J., Ng K.-Y., Schmidt M. A. (1992) A Microfabricated Floating-Element Shear-Styress Semsor Using Wafer-Bondong Technology, *Journ. of Microelectromechanical Systems*, Vol. 1, p. 89

Sobolík V., Wein O., Gil O., Tribollet B. (1990) Three-Segment Electrodiffusion Probes for Measuring Velocity Fields Close to a Wall, *Experiments in Fluids*, Vol. 9, p. 43

Stanton T. E., Marshall D., Bryant C. N. (1920) On the Conditions at the Boundary of a Fluid in Turbulent Motion, *Proc. of the Royal Soc. (A)*, Vol. 97, p. 413

Tanner L. H., Blows L. G. (1976) A Study of the Motion of Oil Films on the Surfaces in Air Flow, with Application to the Measurement of Skin Friction", *Journal of Physics E: Scientific Instruments*, Vol. 9, p. 194

Tesař V. (1973) Experimentální vyšetřování přilnutí proudu tekutiny k zakřivenému povrchu (Experimental Investigations of fluid jet attachment to a curved surface – in Czech), *ACTA POLYTECHNICA - Práce ČVUT v Praze* II, 5

Tesař V. (1974) The 'Split-Cylinder' Sensor for Skin Friction Measurement in Curved Wall-Jet Flows, *Proc. of the Vth 'Jablonna' Fluidics Conference*, p. 17, Budapest, Hungary

Tesař V. (1998) Control of Flow Separation by Temperature Gradient, *Proc. of Euromech Colloquium 377 "Stability and Control of Shear Flows with Strong Temperature or Density Gradients"*, p. 54 , ISBN 80-85918-43-9, Prague

Tesař V. (2012) High-Frequency, Small-Scale Fluidic Oscillators for Boundary Layer Control, *Proc. of Conf. 'Topical problem of Fluid Mechanics 2012*', Inst. of Thermomechanicvs AS CR, Prague

Trávníček Z., Tesař V. (2003) Annular synthetic jet used for impinging flow mass transfer, *International Journal of Heat and Mass Transfer*, Vol. 46, p. 3291

18th International Conference
ENGINEERING MECHANICS 2012
Svratka, Czech Republic, May 14 – 17, 2012

pp. 1395–1405
Paper #278

TRAPPED VORTEX RING

V. Tesař*

Abstract: *Paper discusses an almost unknown and yet interesting operating principle of fluidic no-moving-part devices for flow control. The principle is based on the properties of vortex rings. A standing vortex ring is kept in a semi-toroidal recession positioned opposite to an annular nozzle from which issues an annular fluid jet. The ring can exist in the recession with two alternative senses of rotation so that the annular jet is led to either the central exit through the centre of the vortex, or to the outer space past the outer vortex circumference.*

Keywords: ***Fluidics, vortex ring, fluid flow control.***

1. Introduction

Fluid flow control valves are indispensable components in innumerable systems working with fluids. Their standard layouts with mechanical moving components are produced in large quantities. There are, however, situations in which the mechanical motions bring problems or disadvantages so that it is desirable to control the flow by phenomena taking place inside solid, constant-geometry cavities.

A typical situation is control of hot gas flows: the high temperature makes questionable the operation of bearings and sealing gaskets. A solution brings the little-known branch of fluidics, called "power fluidics" (Tesař 1983, 1998). A typical large-scale fluidic diverter is based on idea of deflection of a jet formed in a nozzle. The nozzle is usually of rectangular cross section and the generated jet is diverted by the action of small control flows acting on the main jet form one or other of its sides. A particular branch of these diverter valves operates in switching regime, with bistability (or monostability) achieved by the Coanda-

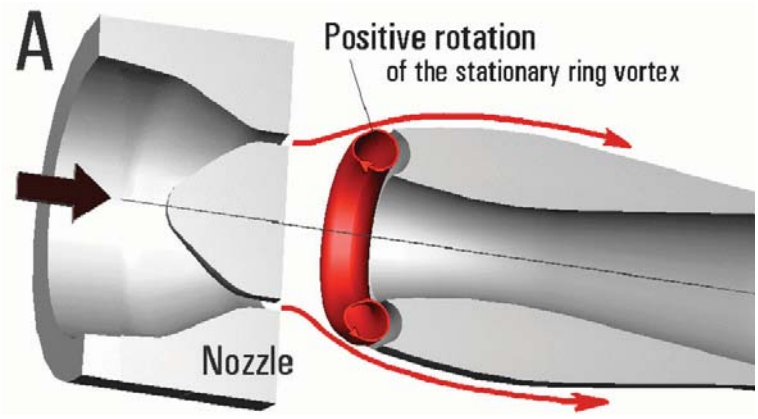

Fig. 1 The idea of flow control by the vortex ring trapped in the semi-toroidal recession. The annular jet impinges on the vortex which deflects is depending on the sense of the vortex ring poloidal rotation. Shown here is the positive rotation which causes the jet to move outside the annular body.

* Prof. Ing. Václav Tesař, Institute of Thermomechanics v.v.v.i., Academy of Sciences of the Czech Republic, Dolejškova 5; 182 00, Prague 8; CZ, e-mail: tesar@it.cas.cz

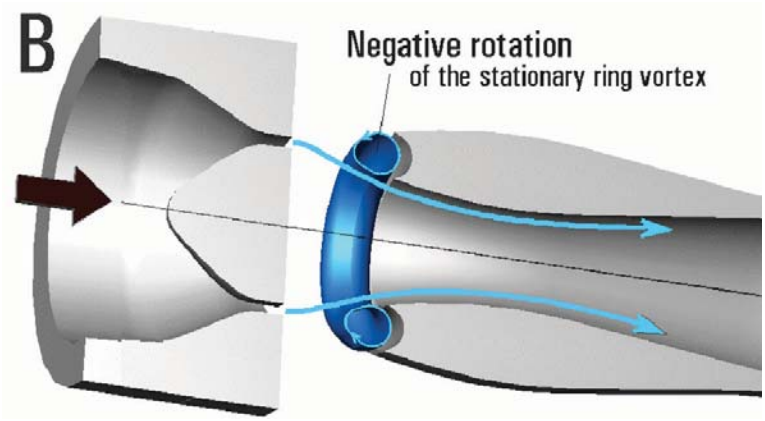

Fig. 2 The action of the negative poloidal rotation, which causes the impinging annular jet to move through the central hole inside the annular body. At the same time, the jet keeps the vortex ring in the rotation.

effect attachment of the jet to attachment walls. This approach was, e.g., applied to their high-temperature gas flow control valves by Pereira and Syred, 1983. The deflected gas flow is captured by a pair of collectors downstream from the deflection section. The collectors are shaped as diffusers in which the kinetic energy of the gas accelerated in the nozzle is re-converted back into the pressure rise (Tesař, 2009). The main disadvantage is the nozzle and even much more the small divergence angle diffusers occupy a considerable streamwise length and make the control valve difficult to stow in the often limited available space.

The fluidic flow control principle described here is an even less known idea. It is based on the special properties of vortex rings (Maxworthy, 1972) – particularly stable structures formed spontaneously in fluid flows. They are well known since antiquity since they can be easily blown from the mouth – and became well visible after the introduction of tobacco smoking.

In the fluidic flow control valves discussed here, a vortex ring is used in a role similar to that of the Coanda effect: it secures bistability — alternative existence of two different flow

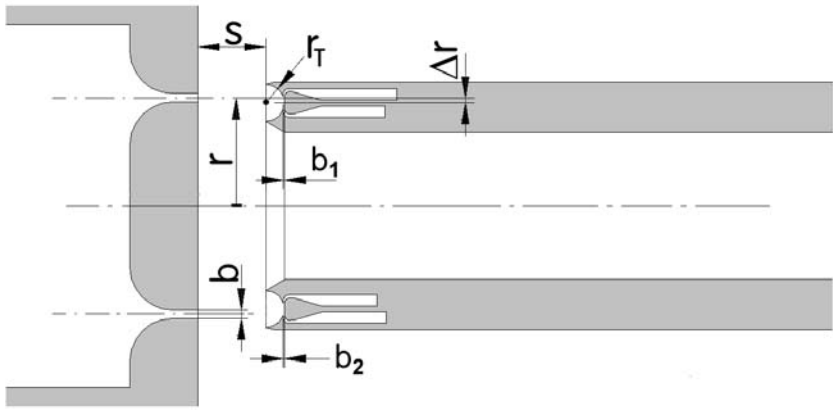

Fig. 3 The basic parameters of the model used in the feasibility tests. Note the difference Δr between the central radius r of the nozzle and the radial position of the centre C of the smallest circle on the torus that defines the geometry of the semi-toroidal recession.

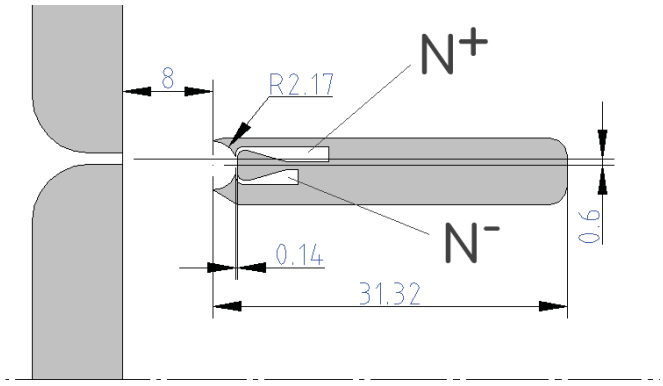

Fig. 4 Detail of the control nozzles and several dimensions (in millimetres) of the annular body used in the feasibility testing numerical flowfield computations. Bringing the control flow into one of the control nozzles N^+ or N^- decides the sense of the poloidal rotation of the vortex ring. For example, a small control flow into N^+ produces the positive rotation as shown in Fig. 1.

regimes in spite of the same set of boundary conditions. The vortex ring is "trapped" - held stationary inside a semi-toroidal cavity. This idea of keeping a vortex in a semi-open cavity follows to a degree the unsuccessful Ringleb's idea (1961) of using stationary vortices (but not a vortex ring !) in a diffuser. This keeping in a semi-open recession prevents the ring from escaping by being shed and carried way with the flow. The two different stable regimes differ in the sense of the poloidal rotation of the vortex ring in its cavity. The incoming flow is in the form of an annular jet, produced by an annular nozzle. The nozzle is designed and positioned so that the jet it generated is directed against the semi-toroidal cavity, made in an annular body coaxial with the nozzle. When the jet leaves the annular nozzle, it collides with the vortex ring. Unable to continue in its original flow direction, the jet is deformed by the interaction with the ring and forced to divert as shown in the cases A and B presented in Figs. 1 and 2.

The sense of the poloidal rotation of the vortex ring presented in Fig. 1 is here described as ***positive***. Upon the interaction with the vortex ring the jet is directed outwards and flows past the outer surface of the annular body. It should be noted that when flowing tangentially around the vortex ring (and acting on it by the shear stress between them) the jet provides the energy that keeps the vortex ring in rotation.

On the other hand, the other sense of poloidal rotation of the vortex ring presented in Fig. 2 is described as ***negative*** (this naming is arbitrary). In this case the interaction of the annular jet with the vortex ring forces the jet to move inwards so that it flows into the central hole in the annular body. As in the case A, also in this case the jet when moving tangentially around the vortex ring keeps it in its rotation.

2. Flow control by stationary vortex ring

In flow control applications, of course, the space outside the annular body and its central hole lead to different locations in which the presence of the fluid flow is desirable. The setup will be provided with means for controlling the rotation direction of the vortex ring. There are several alternative possibilities achieving this control action. Perhaps the most obvious arrangement of this ring vortex control is the use of an auxiliary small control flow entering the semi-toroidal recession through nozzles directed tangentially to the poloidal motion. An

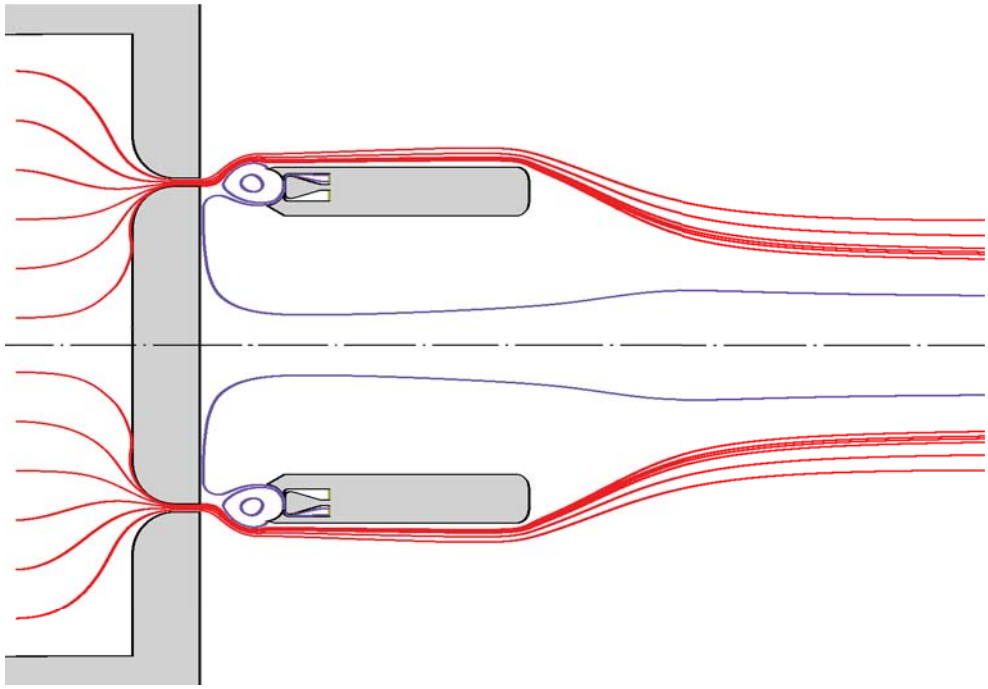

Fig. 5 Computed pathlines of the of the flow responding to a very small control flow fed into the positive control nozzle N^+. All the flow coming from the annular nozzle at left continues past the outer surface of the annular body . Only a very small percentage of the flow leaving the control nozzle (pathline coloured blue) here escapes through the central hole.

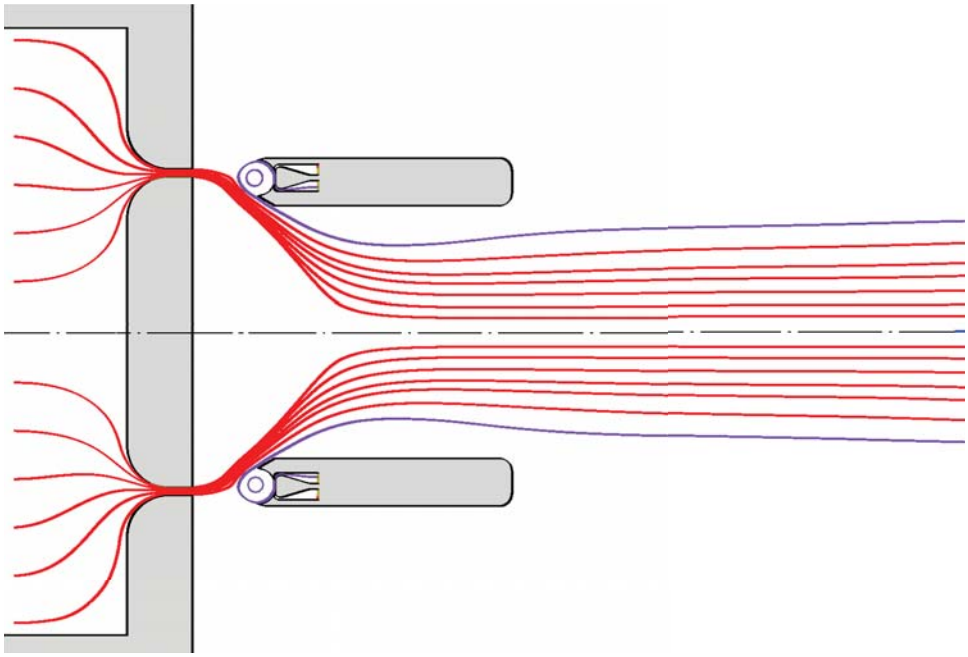

Fig. 6 Computed pathlines in the investigated device as it is formed in response to a very small control flow from the negative control nozzle N^- . All fluid flow passes through the central hole in the annular body.

example of such control nozzles — the positive nozzle N^+ and oppositely directed negative nozzle N^- is presented in Fig. 3 and Fig. 4.

The character of the two alternative flows described above may be considered an unsupported conjecture. To demonstrate the reality if the idea, the two alternative flows were evaluated in a series of extensive numerical flowfield computations. They were performed for the mathematical model the geometry of which is shown in the illustrations Fig. 3 and Fig. 4. The computational results are presented by means of evaluated pathlines in the following two illustration Figs. 5 and 6. The pathlines coloured red are those coming through the annular nozzle at left. There are also pathlines coloured blue – these are released alternatively through either one of the two control nozzles. Well discernible in these illustrations are the closed pathlines of the section through the vortex ring. The parameters (dimensions and velocity) correspond to a typical application considered: central radius r of the nozzle was 19.5 mm, the nozzle slit width was b = 1 mm, the distance s = 8 mm of the annular body from the nozzle body (Fig. 4). The radius of the semi-toroidal cavity in the annular body was r_T = 2.17 mm. Both control nozzles were of the same exit widths b_1 = b_2 = 0.14 mm.

It should be kept in mind that the entrainment into the annular jet decreases the internal pressure in the space inside the flow – so that even without the interaction with the vortex ring the annular jet flow has a tendency to approach the configuration shown in Fig. 6. As a result, if the radial position of the centre C (Fig. 3) of the poloidal motion were flush with the central radius r of the nozzle, the annular jet would be at the distance s at a smaller diameter than r and the outwards and inwards deflection of the jet would not be hydraulically symmetric. This is why the illustration in Fig. 3 emphasises the difference Δr = 0.6 mm.

The outer diameter of the annular body was 43.6 mm, its overall axial length 31.3 mm, and diameter of the central hole in this body was 31.8 mm. The computations presented in Figs. 5 and 6 were performed with the velocity of the flow from the annular nozzle w = 19 m/s. The fluid was air of kinematic viscosity $\nu = 14.61 \cdot 10^{-5}$ m^2/s, so that the Reynolds number of the flow in the annular nozzle exit was Re = 1 300.

3. An example of the valve

The following Figs. 7 and 8 present an example of the use of the discussed principle in a no-moving-part fluidic diverter valve. All that is necessary is providing an outer shell around the

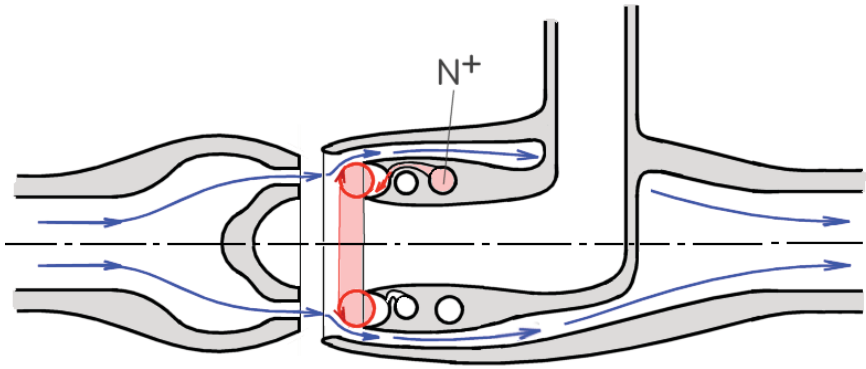

Fig. 7 Practical use of the controlled vortex ring mechanism in a no-moving-part fluidic diverter valve. This is a situation occurring in response to the a very small control flow from the positive control nozzle N^+. The fluid flow coming from left continues in the axial direction.

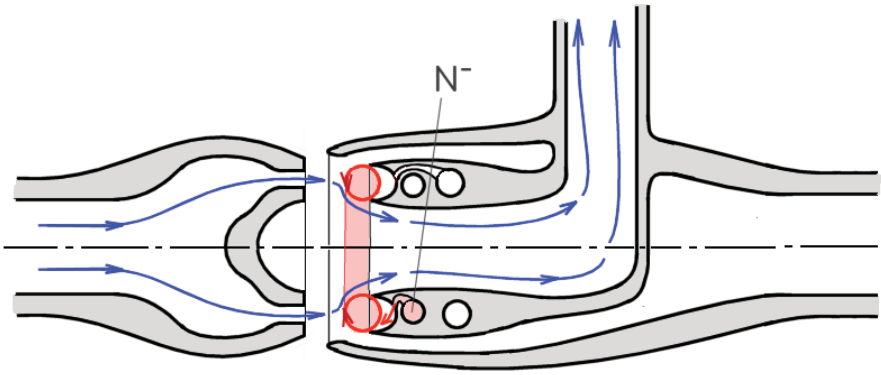

Fig. 8 The same no-moving-part fluidic diverter valve as above (in Fig. 9) in the situation that occurs in response to the a very small control flow from the negative control nozzle N⁻. The flow coming from left is diverted upwards. The control nozzles are not extended over the full 360 deg circumference of the semi-toroidal cavity, but each of them is divided into six parts mutually alternating with the nozzle slits of opposed polarity.

annular body to capture the jet flow moving across this region in its positive flow configuration (Fig. 1). Then there is to be also a different outlet as a continuation of the central hole in the annular body. In Fig. 7 there is an illustration of such a valve in the regime responding to a control flow issuing from the positive control nozzle N^+. The generated trapped vortex ring is coloured red. The fluid (lines coloured blue) supplied into the annular nozzle at the left-hand side of the picture leaves the valve on the right-hand side and continues in the original axial flow direction. The next Fig. 8 presents the flowfield in the case of the fluidic signal brought into the oppositely directed negative nozzle N^- . The oppositely rotating vortex ring forces the annular jet to enter the central hole in the body on the right-hand side. The hole is connected to the outlet that in this version leaves the valve vertically, at a right angle to the initial flow direction.

4. Alternative control by suction

In all configurations above discussed so far, the control of the vortex ring rotation was performed by a fluid outflow from the control nozzles. The two next illustrations, Figs. 9 and 10, demonstrate a different possibility: control by signals of the suction character. The basic principle is presented in Fig. 9. It shows the left-hand part of the annular body, with its semi-toroidal cavity for keeping in position the trapped vortex ring. The suction action is not so strong as the action of outflow from a nozzle, even at the same input power levels. It is therefore necessary for this control mode to arrange for the trapped vortex ring a considerably deeper, more closed cavity. This ensures the motion in the cavity is more influenced by the suction channels. These channels, as show in Fig. 9, are ended by orifices located near the rim of the semi-toroidal cavity. Suction applied into these orifices generates in the ring cavity a tangentially directed flow, indicated in the picture by a part of an air flowpath. This again acts on the fluid inside the cavity in a manner causing it to rotate. The next Fig. 10 demonstrates a result of a numerical flowfield computation, very similar to those examples presented above in Figs. 5 and 6, as a demonstration of feasibility of this control mode. The configuration differs from Fig. 6 only in the layout of the semi-toroidal recession and the suction orifices. The flowfield is in Fig. 10 also (as in Gig. 6) characterised by the computed pathlines. The consequences of the negative rotation of the vortex ring in Fig. 10 also has some resemblance

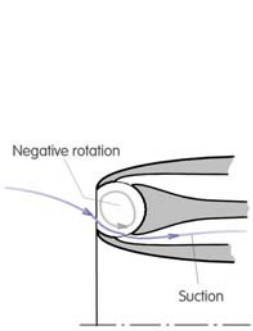

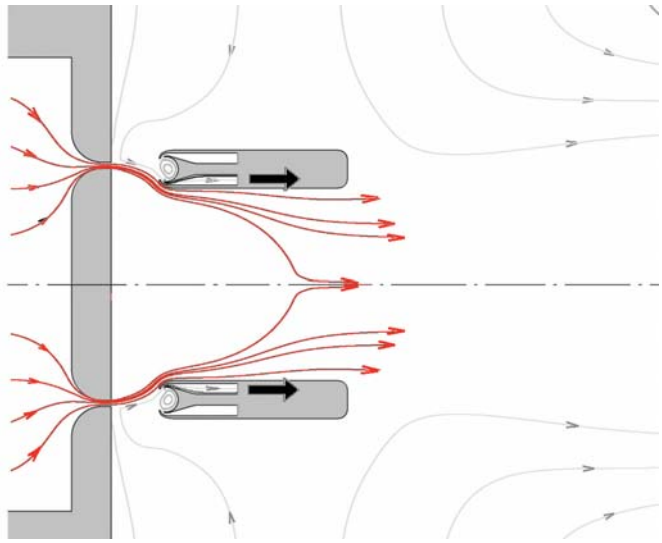

Fig. 9 (Left) In principle, it is possible to generate rotation in the toroidal cavity by a suction signal – here producing a vortex ring with negative rotation.

Fig. 10 (Right) A computed example of the flowfield generated in response to the suction signal, as shown in Fig. 9. All the flow coming through the annular nozzle leaves through the central hole in the annular body.

of the flow into the central hole in the annular body shown above in Fig. 6: the annular jet leaves the annular nozzle and by the interaction with the vortex ring is forced to pass through the central hole. Compared with acting on the vortex ring by flows issuing out from a nozzle, the suction is not very efficient mode of control, which is an obvious disadvantage. On the other hand, there may be situations where there is vacuum available for this control purpose and the efficiency question of the control action is not of primary importance.

5. An example of use

In the example of practical application of the discussed principle which is presented in the next Fig. 11, the trapped vortex ring secures an alternative cold or hot air flow resultant in the proper temperature and ventilation of a crew cabin. The heating is electrical: the air passes through the narrow channels between the coils of an electric heater. The configuration as shown in Fig. 11 closely resembles the geometry presented above in Fig. 3 and 4 . The main difference is the presence of the electric heating coil. This is positioned inside the central hole in the annular body.

In the regime of there being a (very small) control flow of air issuing from the positive control nozzle N^+, the air jet coming from the annular nozzle at left does not enter the central hole and thus by-passes the heating coil – as shown above in Fig. 5. The flow thus enters the cabin as a cold ventilation air. If, however, there is a control flow leaving the negative control nozzle N^- , then all supplied air is forced into the central hole in the annular body and is heated there. The temperature control was designed to operate in the pulse width modulation mode. The flow is permanently switched between the cold and hot regimes by the two flows generated in a fluidic oscillator (not shown here) with two output terminals. The oscillator is governed by a thermostat that causes an asymmetry of the switching: if it is necessary to heat

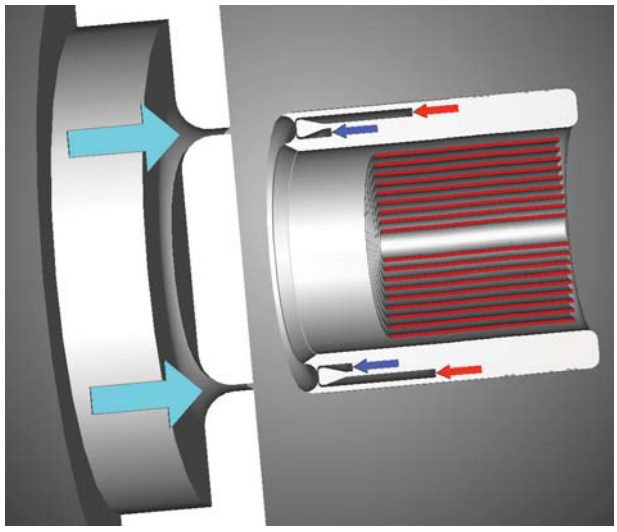

Fig. 11 An example of application of the flow control principle with the trapped ring vortex. The electric heating coil inside the central hole of the annular body heats the air if the control flow is fed into the negative nozzle (blue colour). If the control flow is fed into the positive control nozzle (red colour), the air by-passes the heating.

the cabin, the pulses into the negative control nozzle N^- last longer. Contrary to this, if the heating is needed less, then the flow pulses from the positive control nozzle N^+ are longer – they may dominate so that as a result most of the time the heater coil is by-passed.

5. Combined vortex ring and Coanda bistability (and monostability)

In his another practical use of the trapped vortex principle in a switched fluidic valve, the author combined the action on the annular jet by the vortex ring with another mechanism: the Coanda-effect attachment of the jet to adjacent walls. The geometry of the attachment was unusual: the annular jet was switched radially between two conical attachment walls (Tesař,

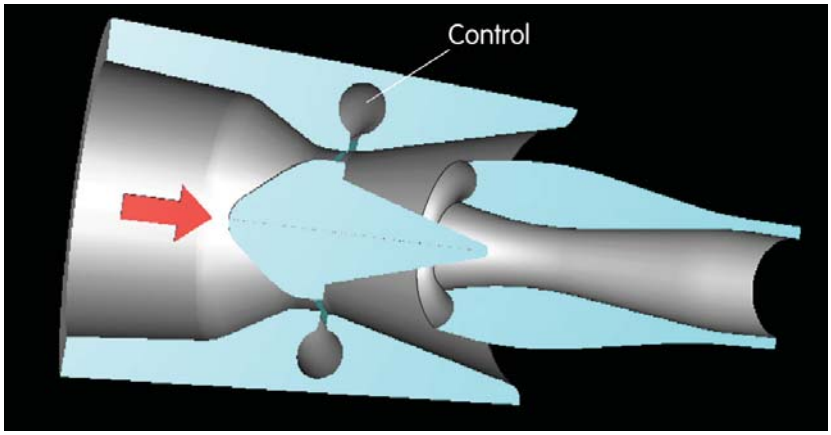

Fig. 12 A flow control valve in which the trapped vortex ring principle is combined with the radial switching of an annular jet (Tesař, 1995) between the conical attachment walls, inner and outer one.

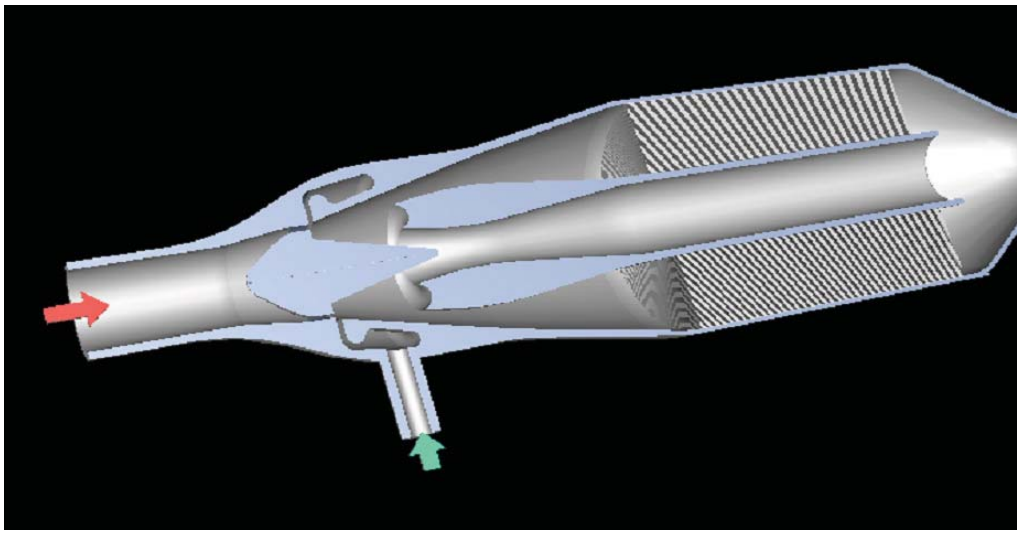

Fig. 13 The monostable flow control valve applied to the variable-configuration exhaust gas aftertreatment system developed by the author for Volkswagen A.G. (Tesař et al., 1996).

1995). The crucial parts of the valve are presented in Fig. 12. The layout was monostable: the valve remained in one of its two regimes as long as there was no control air flow signal. This regime was present for most of the time. Only exceptionally the regime was changed into the other one by an incoming signal.

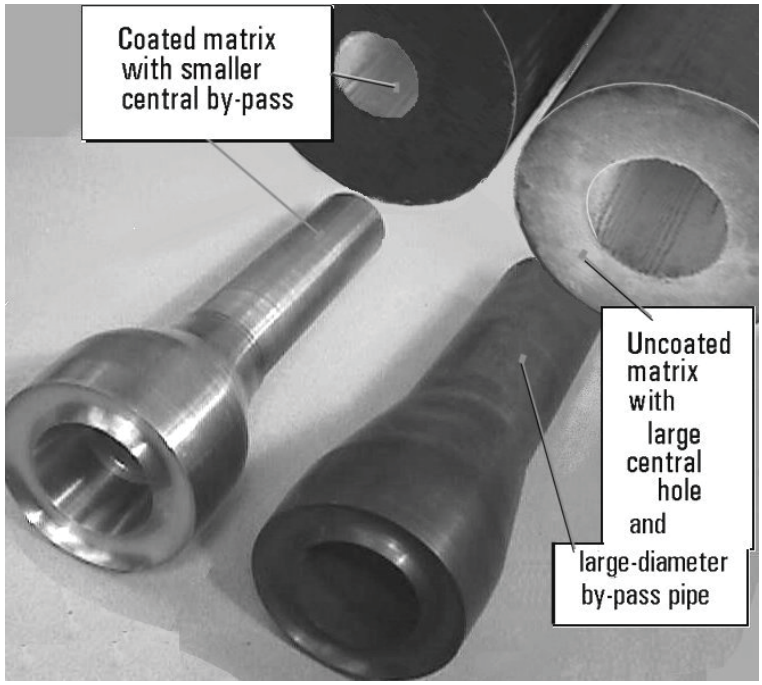

Fig. 14 Photograph of parts of disassembled test models used in laboratory investigations of the system shown in Fig. 13. The two alternative annular bodies have different size of the smallest circle on the torus that defines the geometry of the semi-toroidal recession.

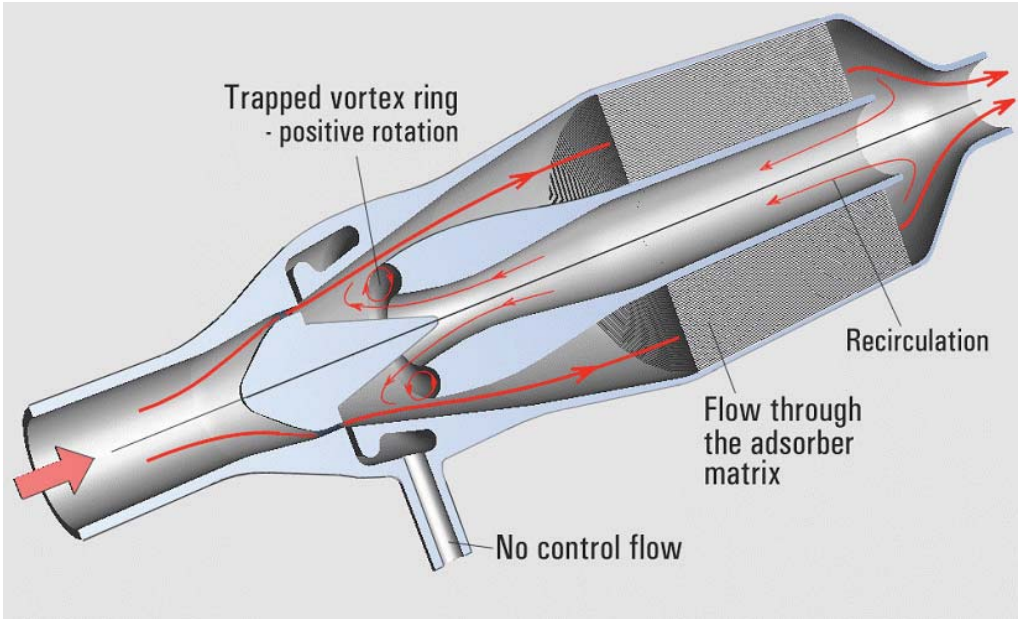

Fig. 15 The aftertreatment system in the basic flow regime without control flow signal: exhaust gas passes through the catalytic reactor matrix.

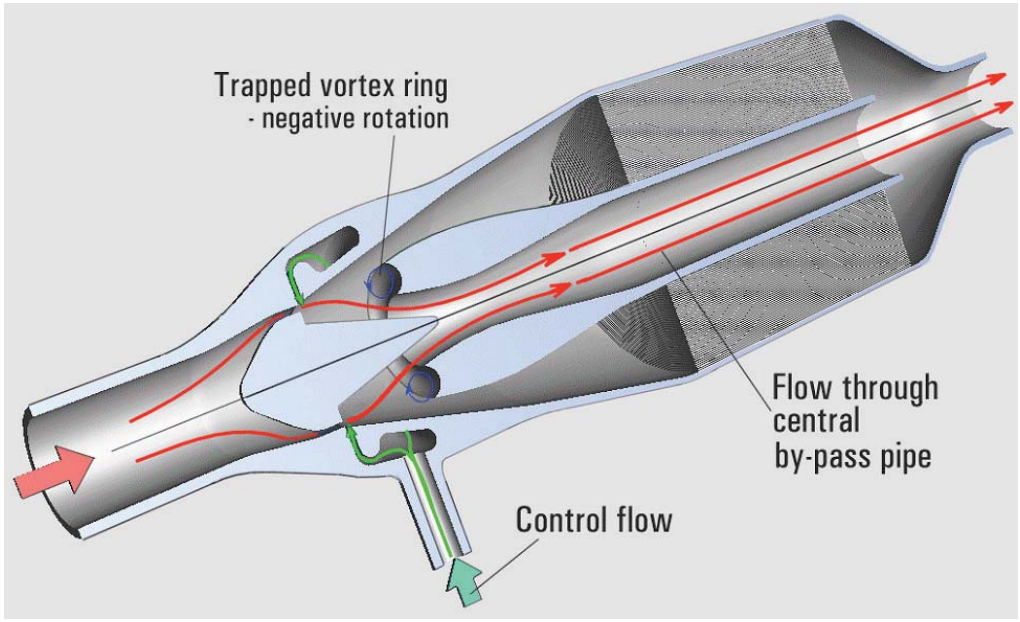

Fig. 16 The same aftertreatment system as in previous Fig. 16: in response to the small air control flow the exhaust gas flow is switched into the by-pass pipe.

It is apparent from Fig. 12 that the outer, hollow conical attachment wall dominates. The attachment to the small central cone is much less stable – and this was accentuated by the outer large concave cone wall being a flush continuation of the outer lip of the annular nozzle — while the surface of the inner small cone was separated from the nozzle inner lip by a large setback. This asymmetry of attachment was used in securing the monostable character of the valve. The valve was

built – Fig. 13 — as an integral part in the upstream end of the body of an automobile catalytic converter for an aftertreatment processing of engine exhaust gas. The catalyst requested temporary by-passing of the gas flow in a layout the important requirement of which was spatial compactness. The photograph in Fig. 14 is here included as a demonstration that the valve was actually built and tested (for a car manufacturer customer in Germany). The last two illustrations – Figs. 15 and 15 provide an explanation of the operation in the two regimes.

The main factor in this application was the spatial compactness (available space in an engine compartment of contemporary car is scarce), resistance to extremely high temperatures (the valve can operate while actually glowing hot above 700 °C), and robustness securing long-time life without maintenance.

6. Conclusions

This contribution aims at spreading the knowledge of an interesting flow control principle that may find application in fluid flow control by fluidic valves without moving components. It is practically unknown despite its offering several interesting application opportunities.

Acknowledgement

Author expresses his gratitude for the support by the grant 101/11/J019 donated by GAČR, and by grant TA02020795 received from the Technological Agency of the Czech Republic, programme ALPHA.

References

Maxworthy, T. J. (1972) The structure and stability of vortex ring, *Journal of Fluid Mechanics*, Vol. 51, p. 15

Perera P.C., Syred N. (1983) A Coanda Switch for High Temperature Gas Control, Paper 83-WA/DSC-26, *Proc. of American Society of Mechanical Engineers Winter Annual Meeting,* Boston

Ringleb F.O. (1961) Separation control by trapped vortices. In: *Boundary Layer and Flow Control*, Ed. Lachmann G.V., Pergamon Press

Tesař V. (1983) Großmaßstäbliche fluidische Ventile für die Durchflußsteuerung“(Large-Scale Fluidic Valves for Flow Control – in German), *Messen-steuern-regeln*, Bd. 26

Tesař V. (1995), Use of Radially Switched Jet Attachment in an Exhaust Gas Flow Control Valve*, Proc of Workshop 95*, CTU Prague, p.265

Tesař V., Jílek M., Reisenberger E., Randa Z. (1999) Bistabilní proudění se stojatým virovým prstencem (Bistable flow with stationary vortex ring – in Czech), *Proceedings of XVIIIth International Conf. of Departments of Fluid Mechanics and Thermomechanics*, p..141, Prague

Tesař V., Baumruk P., Macek J., König A., Decker G., Donnerstag A. (1996) Fluidic Valves for Variable-Configuration Exhaust Gas Aftertreatment System, *Proc. of XXVIth Congress FISITA (Féderation Internationale des Sociétés d'Ingénieurs des Techniques de l'Automobile)*, section A ("Engine Emissions, Regulations and Treatment Methods", Prague

Tesař V. (1998) Valvole fluidiche senza parti mobili (Fluidic valves without moving parts – in Italian) *Oleodinamica – pneumatica, revista delle applicazioni fluidodinamiche e controllo del sistemi,* p. 216, Numero 3, Anno 39

Tesař V. (2009) Mechanism of Pressure Recovery in Jet-Type Actuators, *Sensors and Actuators A – Physical*, Vol. 152, p. 182

Tesař V., Reisenberger E. (1999), Trapped Vortex Ring Bistability, *Proc. of Cololoq. "Topical problems of Fluid Mechanics '99"*, p. 51, ISBN 8085918-47-1 , publ. by IT AS CR

Tesař V., Reisenberger E. (1999) Aerodynamic Investigations of Trapped Vortex Rings, p.244, *CTU Reports, Special Issue, Proc. of 8th WORKSHOP 99*, Vol. 3

18th International Conference
ENGINEERING MECHANICS 2012
Svratka, Czech Republic, May 14 – 17, 2012

pp. 1407–1411
Paper #302

LOW CYCLE FATIGUE AND ANALYSIS OF THE CYCLIC STRESS-STRAIN RESPONSE IN SUPERALLOY INCONEL 738LC

J. Tobiáš[*], A. Chlupová[**], M. Petrenec[***], J. Polák[****]

Abstract: *The paper describes the results of fatigue behavior study on cast polycrystalline nickel based superalloy tested at 23 and 800 °C. Cylindrical specimens of Inconel 738LC were cyclically strained under total strain control to fracture and multiple step tests were performed to study the effect of temperature on the internal and effective cyclic stress components. Fatigue life curves were approximated by the Manson-Coffin and Basquin laws. The resulting curves were shifted to lower fatigue lives with increasing temperature. The evolution of the effective and internal stress components and effective elastic modules were derived from the hysteresis loops which were analyzed according to the statistical theory of hysteresis loop. Cyclic stress-strain response at both temperatures and the changes of internal and effective stress components were discussed in relation to microstructural parameters of the superalloy.*

Keywords: ***Low cycle fatigue, Inconel 738LC, hardening/softening curves, cyclic stress-strain curve, fatigue life curve.***

1. Introduction

Nickel based superalloy Inconel 738 LC is cast polycrystalline material precipitation strengthened to achieve excellent high temperature strength and hot corrosion resistance. Designers widely use this material for production of structural parts such as blades and disks for gas turbine engines subjected to repeated elastic-plastic straining in a wide range of temperatures (Donachie, 2002).

In a design of components for high temperature applications the thorough knowledge of fatigue behaviour of IN 738 LC is crucial. The hardening and softening behaviour as well as the cyclic stress-strain curves were studied at temperatures 23 and 900°C (Jianting, 1983, Jianting et al. 1983, Wahi et al. 1997). Nevertheless a more detailed study of the sources of cyclic stress which can be obtained from the analysis of the shape of the hysteresis loops in this type of material has not been performed. Analysis of the loop shape allows determining and splitting total cyclic stress in two components: effective and internal stress (Polák 1991). According to statistical theory of hysteresis loop used already for the study of cyclic plasticity in stainless steels the second derivative of the hysteresis half-loop contains information about the effective stress and the probability density distribution of the critical internal stresses (2x Polák et al. 2001).

The aim of the present work is to describe results obtained in the study of low cycle fatigue behaviour of this material. Effect of temperature on the internal and effective cyclic stress components in repeated loading performed in total strain control was studied at room temperature and at 800 °C.

2. Experimental

Material IN 738 LC in the form of conventionally cast rods having chemical composition 16.22 Cr, 8.78 Co, 2.63 W, 1.71 Mo, 1.77 Ta, 3.37 Ti, 3.35 Al, 0.84 Nb, 0.2 Fe, 0.1 C, 0.04 Zr, 0.008 B, the rest Ni (all in wt. %) was provided by PSB Turbo, Velká Bíteš a.s. Microstructure of the material is dendritic and consists of large γ grains having average size about 3 mm and containing 59% volume fraction of γ′ precipitates with near-cuboidal shape having average diameter of 670 nm (see *Fig. 1*).

[*] Ing. Jiří Tobiáš: IPM, AS CR, Žižkova 22; 616 62, Brno; CZ, e-mail: tobias@ipm.cz

[**] Ing. Alice Chlupová, Ph.D.: IPM, AS CR, Žižkova 22; 616 62, Brno; CZ, e-mail: prasil@ipm.cz

[***] Ing. Martin Petrenec, Ph.D.: CEITEC IPM, AS CR, Žižkova 22; 616 62, Brno; CZ, e-mail: petrenec@ipm.cz

[****] Prof. RNDr. Jaroslav Polák, DrSc., dr.h.c.: CEITEC IPM, AS CR, Žižkova 22; 616 62, Brno; CZ, e-mail: polak@ipm.cz

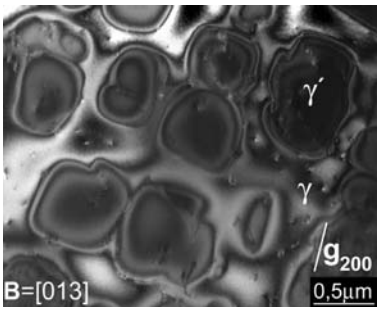

Fig. 1: TEM image of microstructure with 59% volume fraction of the γ´ precipitates.

Cylindrical button-end specimens with diameter 15mm and gauge length 6mm were fatigued in electrohydraulic testing machine MTS 880 in regime of strain control. The total strain amplitude was kept constant, strain rate was $2x10^{-3}s^{-1}$ and loading was fully reversed, i.e. symmetrical push-pull cycle was applied. The strain was measured and controlled using a sensitive extensometer with a 12 mm base. The loading was performed in air at two temperatures: 23°C and 800°C.

The stress-strain history at each temperature was recorded with the sampling rate 1 ms, i.e. each hysteresis loop contained more than 2000 data points. Relative strain and relative stress from the tensile and compression parts of hysteresis loops were calculated using maximum and minimum strains in a cycle and the first and the second derivatives of the hysteresis half-loops were determined (Polák 1991). The numerical smoothing procedures were used and the number of neighbour points involved in evaluation of derivatives was optimized.

3. Results and discussion

Cyclic hardening/softening curves i.e. the dependences of the stress amplitude σ_a on the number of cycles N are plotted in *Fig. 2*. At room temperature and for low levels of strain amplitude (see *Fig. 2a*) the saturation until failure is observed. For middle amplitudes the initial hardening is followed by the slow softening which changes into the secondary hardening. For high amplitudes the continuous hardening becomes more pronounced. At elevated temperature (800°C) the material exhibits different behaviour. In cycling with high strain amplitudes superalloy initially cyclically hardens and later slowly softens up to the end of the fatigue life. For low levels of applied strain amplitude the saturated behaviour can be seen (*Fig. 2b*).

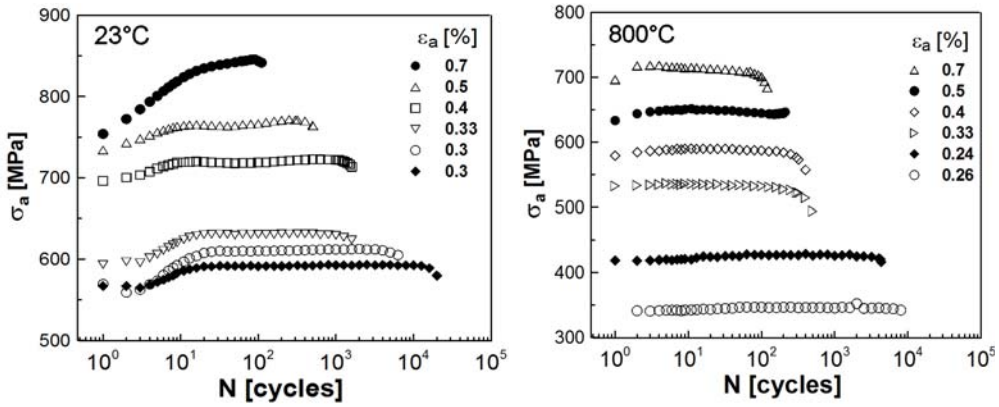

Fig. 2. Cyclic hardening/softening curves at room and at elevated temperatures.

In the *Fig. 3a* the cyclic stress-strain curves (CSSCs), i.e. dependences of the stress amplitude on plastic strain amplitude at half-life for both temperatures are plotted together with the lines representing the approximation of the data by the power law:

$$\log \sigma_a = \log K' + n' \log \varepsilon_{ap}. \quad (1)$$

Fatigue life curves in the representation of the stress amplitude σ_a at half life vs. the number of cycles to fracture N_f are shown in *Fig. 3b*. Experimental data can be fitted by the Basquin law:

$$\log 2N_f = (1/b)(\log \sigma_a - \log \sigma'_f). \quad (2)$$

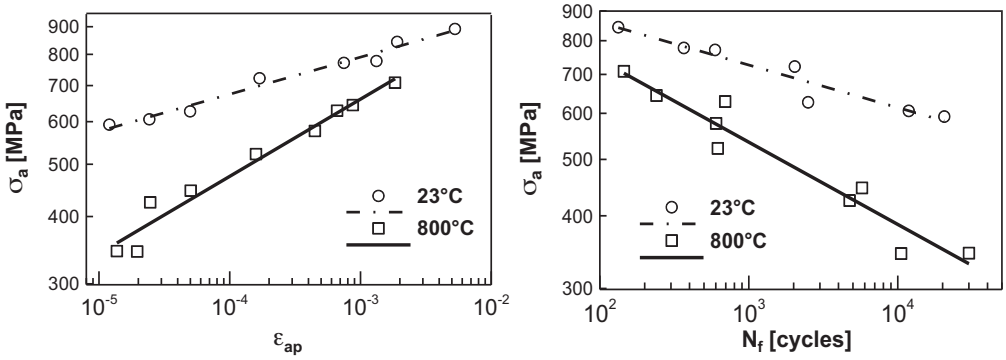

(a) (b)

Fig. 3. (a) Cyclic stress-strain curves, (b) Fatigue endurance curves.

Parameters of CSSC and Basquin curves, i.e. fatigue hardening coefficient, K′, fatigue hardening exponent n′, fatigue strength coefficient σ'_f and fatigue strength exponent b were evaluated using regression analysis and are shown in Table 1.

Table 1. Parameters of CSSC and Basquin curves of IN 738 LC.

Temperature	K′	n′	σ'_f	b
23°C	1 270 MPa	0.068	1 330MPa	- 0.079
800°C	1 780 MPa	0.140	1 700 MPa	- 0.152

Two saturated hysteresis loops recorded at both temperatures of cycling with approximately the same amplitude of plastic strain ~1.4×10^{-3} are shown in *Fig. 4*. The shape of respective half-loops was then analyzed and the first and the second derivatives of tensile parts of hysteresis loops (divided by effective modulus E_{eff} or by the half of the square of effective modulus) were plotted vs. relative strain ε_r (lower axis) and/or vs. fictive/effective stress $\varepsilon_r E_{eff}/2$ (upper axis) in *Fig. 5*.

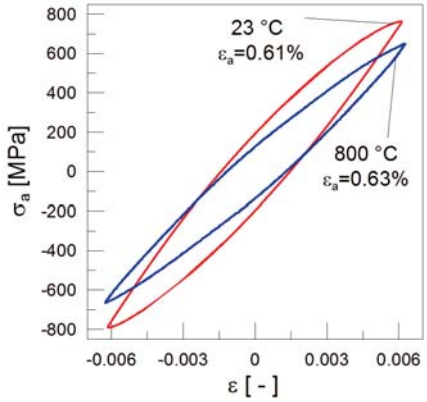

Fig. 4: The saturated hysteresis loops at 23 °C cycled with ε_a = 0.61%, and at 800 °C with ε_a = 0.63%.

Fig. 5 shows the first and the second derivatives for two temperatures (23°C and 800°C) and their evolution with the number of cycles. The initial drop of the second derivative corresponds to the

relaxation of the plastic strain under decreasing effective stress. At relative strain where the second derivative reaches its first minimum the effective modulus E_{eff} and the effective stress can be evaluated.

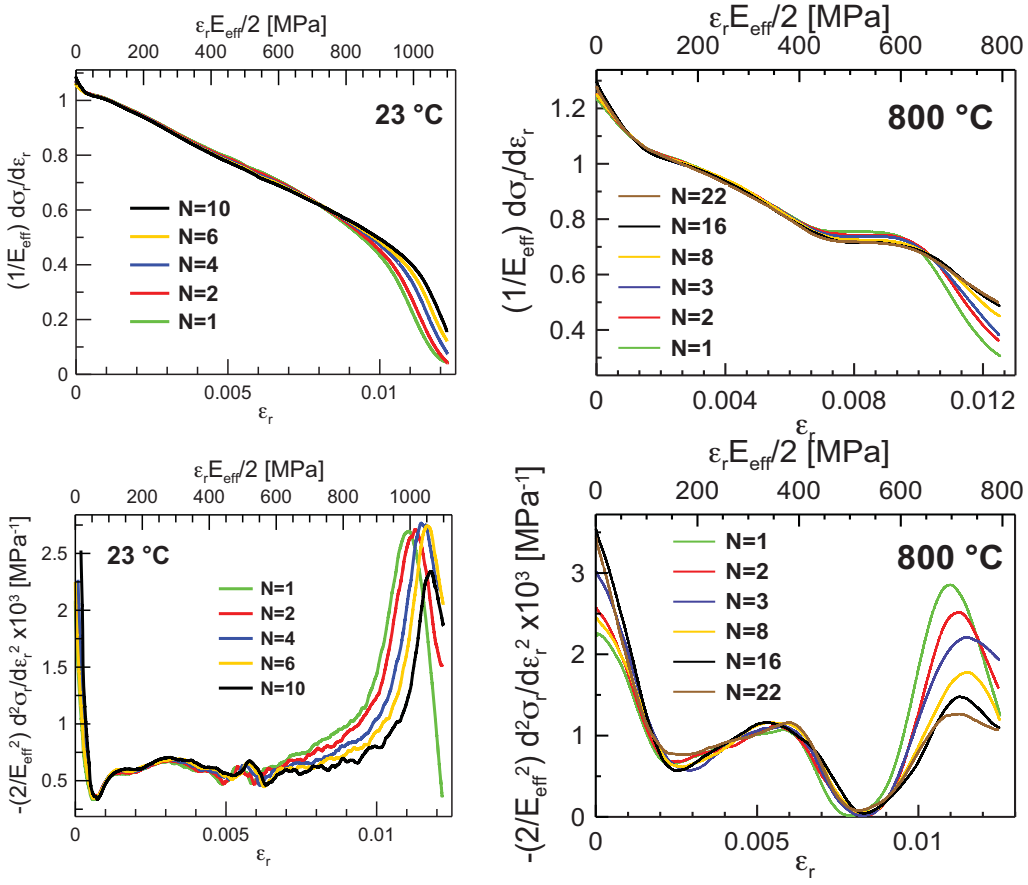

Fig. 5. The first and the second derivatives of the tensile half-loops (from Fig. 4) in relative coordinates cycled at 23°C (E_{eff} =180 GPa) and 800°C (E_{eff} = 127 GPa).

Two peaks of the second derivative are characteristic for a two-phase alloy. They correspond to the subsequent plastic deformation of γ and γ´ phases within a cycle and approximate the probability density function of the critical internal stresses of both components.

The analysis of the hysteresis loop shape obtained in room temperature cyclic straining reveals only poorly defined first maximum. This first peak is more pronounced for elevated temperature. The second peak is well developed for both temperatures and its position at room temperature changes with increasing number of applied cycles, i.e. it is moving to higher fictive stresses, which corresponds to the cyclic hardening. It is in agreement with cyclic hardening/softening curves (see *Fig. 2*)

The effective stresses of γ and γ´ phases at different temperatures can be estimated only approximately and the resulting values are displayed in *Table 2*.

Tab. 2. Effective stresses for both phases (γ and γ´) of In 738 LC tested at two temperatures.

Temperature	23°C	800°C
σ_{eff} (γ)	≈ 100 MPa	170 MPa
σ_{eff} (γ´)	≈ 550 MPa	540 MPa

The effective stress in γ and γ′ phases was found precisely enough only in cycling at 800°C. The effective stress in γ′ phase is high which is in agreement with the difficult movement of dislocations in an ordered structure.

The effective stress of the γ phase is low but increased when the cycling temperature increased to 800 °C. This can be the result of continuous annihilation of dislocations in soft γ phase at elevated temperature and resulting in a drop of dislocation density. In order to achieve the same strain rate the dislocation velocity is high and thus the effective stress increases.

The effective stress of the γ′ phase could be precisely found only at temperature 800 °C but approximate estimate at the room temperature shows that this quantity is nearly temperature independent.

The cyclic hardening observed at room temperature is connected with the continuous increase of the dislocation density in the channels and results in the shift of the second peak of the probability density distribution of the internal critical stresses. In high temperature straining the continuous recovery of the γ phase leads to stabilized stress response.

4. Conclusions

The results of fatigue tests performed on cast Inconel 738LC in regime of controlled total strain in symmetrical strain cycling at temperatures 23°C and 800 °C can be summarized as follows:

High amplitude cyclic straining at 23°C is characterized by hardening that is followed by saturation, at 800 °C a weak softening is shown. Low amplitude cycling at temperature 800°C results in nearly stabilized stress response.

The cyclic stress-strain curve and fatigue life curve in the form of Basquin curve exhibits strong temperature dependence.

Analysis of hysteresis half-loops according to the statistical theory of hysteresis loop allows the estimation of contribution of effective stress and of the distribution of the critical internal stresses.

High stress response of the Inconel 738LC superalloy at high temperature is due to high effective stress in the γ′ phase.

Acknowledgement

The research was supported by the project RVO: 68081723 and grant of Grant Agency of the Czech Republic No.: P204/11/1453.

References

Donachie M.J. & Donachie S.J. (2002): *Superalloys: A Technical Guide*. (ASM International, Materials Park).

Jianting G. & Ranucci D. (1983): *Int. J. Fatigue*, Vol. 5, p. 95.

Jianting G., Ranucci D. & Picco E. (1983): *Mater. Sci. Eng.*, Vol. 58, p. 127

Polák J. (1991): *Cyclic Plasticity and Low Cycle Fatigue Life of Metals*. Elsevier, Amsterdam

Wahi R.P., Auerswald J., Mukherji D., Dudka A., Fecht H.-J. & Chen W. (1997): *Int. J. Fatigue* Vol. 19, p. 89

Polák J., Fardoun F. & Degallaix S.: *Mater. Sci. Engng* Vol. A297 (2001), p. 144.

Polák J., Fardoun F. & Degallaix S.: *Mater. Sci. Engng* Vol. A297 (2001), p. 154.

18th International Conference
ENGINEERING MECHANICS 2012
Svratka, Czech Republic, May 14 – 17, 2012

pp. 1413–1418
Paper #23

DESIGN OF UNIVERSAL CONTROL UNIT FOR BRUSHLESS DC MOTORS

J. Toman[*], J. Hrbacek[**], V. Singule[***]

Abstract: *The paper presents the design of both power and control electronics used to develop a universal BLDC (brushless DC) motor control unit intended for an aircraft fuel metering pump. The controller allows employing various methods for sensor and sensor-less control including frequency, trapezoidal, sinusoidal and fielding oriented control. The power subsystem provides three power totem-pole switches as well as a wide range of input and auxiliary circuitry. As needed by the target aircraft industry standards, conclusions of a thorough FMECA analysis of the resulting device are given.*

Keywords: ***BLDC motor, control unit, model based design***

1. Introduction

The Brushless Direct Current (BLDC) motors have recently gained substantial popularity among applications that require increased mechanical reliability, operation in explosive or otherwise harsh environments and accept slightly higher demands on the control unit. It has been proven that BLDC motors are suitable for use in critical control applications in aerospace due to their architecture, performance and characteristics. One of such applications is a fuel metering pump drive that is being developed as a part of the CESAR (Cost Effective Small Aircraft) EU project.

The operation of any aerospace actuator based on a BLDC motor (e.g. the fuel metering pump) is safety-critical and its safe operation requires a reliable control algorithm that ensures safe start-up and running of the BLDC motor in the whole operation range. Several applicable control algorithms and methods which have been evaluated within the CESAR project are described hereinafter as well as the controller itself that host these algorithms.

2. BLDC motor control theory

Brushless DC motor (BLDC, also known as electronically commutated motor) is from the construction point of view very similar to the synchronous motor with permanent magnets in the rotor. The main difference is usually different shape of the developed EMF waveform – trapezoidal for BLDC (simple block commutation optimization) and sinusoidal for synchronous motors (complex sinusoidal control).

From the modeling perspective, the trapezoidally wound BLDC motor can be perceived as a DC motor whose mechanical commutator is replaced by electronic means, i.e. by sequential switching of the windings to the power. This similarity implies that the quantities current-torque and voltage-speed are linearly dependent.

2.1. Frequency control

The basic control principle of the BLDC motors is frequency control. In its simplest form, called trapezoidal control or six-step commutation, it provides a winding power switching sequence as a replacement of the mechanical commutating device. As Fig. 1a depicts, the commutation law defines six succeeding states with only two windings powered simultaneously (the third one is left floating).

[*] Ing. Jiří Toman: UNIS, a.s., Department of Mechatronics, Jundrovska 33, Brno, Czech Republic, e-mail: jtoman@unis.cz

[**] Ing. Jan Hrbáček: Faculty of Mechanical Engineering, Brno Univesity of Technology, Technická 2, Brno, Czech Republic, e-mail: jan@hrbacek.info. Brno Ph.D. Talent Scholarship Holder

[***] doc. Ing. Vladislav Singule, CSc.: Faculty of Mechanical Engineering, Brno Univesity of Technology, Technická 2, Brno, Czech Republic, e-mail: singule@fme.vutbr.cz

The biggest strength of this method is its simplicity; on the other side, the moment control at lower speeds is rather worse which leads to moment and speed pulsations.

The other technique – sinusoidal control – overcomes this ripple by harmonic driving of all three windings at the same time. Smoothly rotating current space vector has a constant magnitude and is always in the quadrature direction to the rotor, as shown in Fig. 1b. However, the complexity of this control method is much higher compared to the trapezoidal commutation. A precise position of the rotor has to be known; moreover, the sinusoidal commutation is prone to be suboptimal in the area of higher angular speeds. The reason is that the winding current magnitude controllers are limited in their bandwidth and are not able to precisely follow fast harmonic signals.

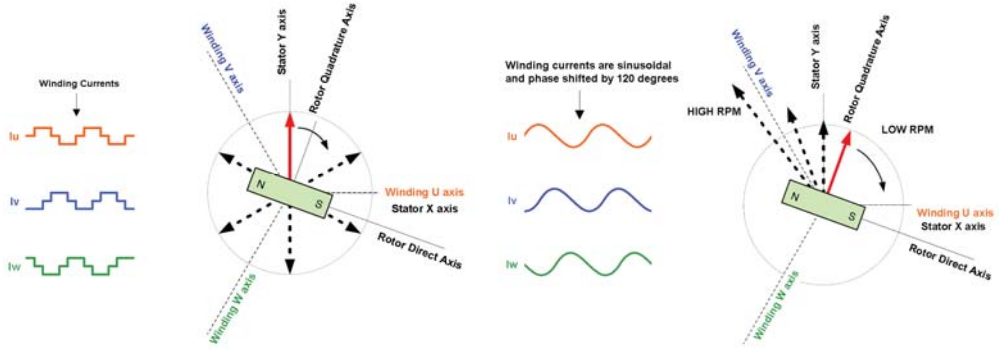

Fig. 1: Commutation law of a) trapezoidal control b) sinusoidal control (Microchip, 2011)

2.2. Field oriented control (FOC)

FOC overcomes the problem mentioned in the previous paragraph by direct control of the current space vector in the rotor coordinates. This vector should have a fixed size and its direction should be perpendicular to the rotor (quadrature axis). The current control is then provided also in the rotor coordinates which means that the control problem transforms from exact tracking of a sinusoidal signal to much simpler regulation of steady quantities. This ensures that the quality of current control is independent on rotor angular velocity. The technique that allows such a control method is the Park's forward and inverse transformation between the three-phase stator coordinate system and the rotor d-q coordinate system. Because the frequency of these transformations calculation has to be the same as the needed working frequency of the current control loop, the FOC is quite heavy on computational power of the host system.

2.3. Sensor and sensor-less control

Each control principle has different demands on sensory inputs needed for its successful operation. The simplest case is the block commutation that only needs to know three angular positions where the commutation should occur; this is usually accomplished using Hall or optical sensors. Basically, there are two types of sensor-less control techniques (Leonhard, 2001). The first type is position sensing using back EMF of the motor, and the second one is computational position estimation that uses motor parameters, terminal voltages and currents.

In the case of the sinusoidal-based control methods high-resolution measurements of rotor position are required. Hall/optical sensors produce only discrete information about rotor angular position and do not fulfill the demands; a quadrature encoder or a resolver seems to fit well.

3. Control system architecture

The control system can be divided into two main parts – the control unit itself and a software tool for diagnostic/control purposes. The control unit is further comprised of its hardware platform (providing power electronics, sensory, computations means and auxiliary circuits) and firmware equipment (implementing described control algorithms).

3.1. Hardware subsystem

The hardware development has been conducted in order to comply with aerospace quality standards, including RTCA/DO-254 – "Design Assurance Guidance for Airborne Electronic Hardware" (FAA Advisory Circulars, 2005) and RTCA/DO-160F – "Environmental Conditions and Test Procedures for Airborne Equipment" (RTCA, Inc., 2007).

Three milestone hardware versions (and several more development versions) have been developed within the CESAR project. Each new version of the control and power electronics meant progress and new possibilities in the control methods, such as sensor-less or FOC methods. The newest, 3rd, generation is shown in Fig. 2 and consists of a power electronic board to which the control board is connected using a 50-pin connector.

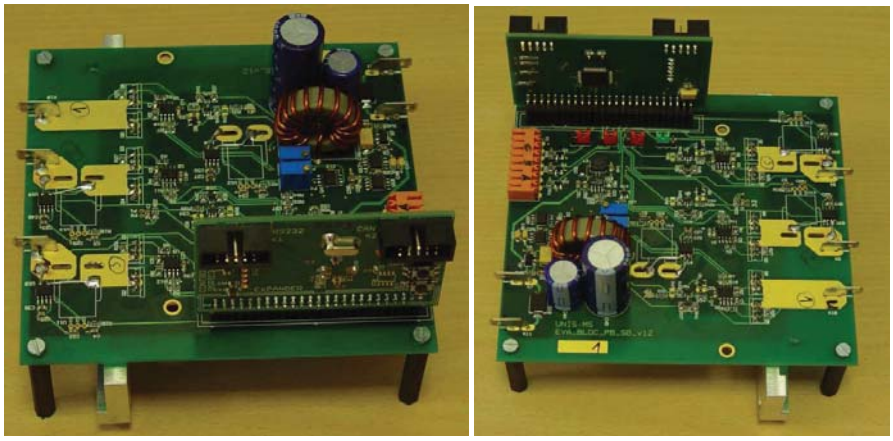

Fig. 2: The 3rd generation hardware

The control board features the Microchip dsPIC30F6015 16-bit DSP that disposes of UART and CAN bus communication lines usable for communication with superior systems. This DSP fully supports motor control applications and has 4 independent PWM channels – 3 for the three-phase power unit and 1 for the electrical brake and PFC of the main DC bus.

The power electronics are composed of three power MOSFET totem-pole switches with appropriate drivers, fast over-current and over-voltage protection circuits and 3 Hall-effect current sensors. Both current shapes – trapezoidal or sinusoidal – are feasible. The analog part of the board allows measuring of back EMF voltages needed for sensor-less control also during the start-up phase, when the angular speed is low.

An extra MOSFET with driver is added onto the main DC bus on this board. If necessary it allows active breaking of connected electrical drive. Performance of this electrical brake depends on the amount of returning energy and recuperation possibilities of main DC power supply.

3.1.1 Firmware

The firmware acts in the following three main roles:

- motor control itself – robust operation of the BLDC motor in all regimes
- safety provision – proper reaction to failure events/states
- communication with master/diagnostic systems – parameter setup, logging etc.

The control principles described in the theoretical section of the paper have been algorithmized and implemented as a part of the control system's firmware. A MATLAB/Simulink blockset capable of generating C code for the chosen DSP family is available – it can be advantageously utilized for fast functional evaluation of the control algorithms developed using simulations. A benchmarking study of this approach is provided in (Lambersky & Vejlupek, 2011). However, use of the generated code in the final product would not be suitable because of significant demands on code efficiency and reliability originating from the aerospace application area (RTCA, Inc., 1992).

The architecture of the used dsPIC30F6015 DSP is fully optimized for the use of C as programming language. The Microchip-supplied C compiler can also be used in conjunction with the MATLAB/Simulink environment during the Hardware-in-the-Loop development phase.

3.2. Software control tool

Developed control software Graphical User Interface (GUI) is shown in Fig. 3. It depicts a simplified electrical schematic of three MOSFET half-bridge switches and a three-phase BLDC motor. The software communicates via a serial RS-232 line or a CAN bus with the control electronics and displays the main values from the power electronics.

This SW tool works with the presented 3rd version of the control hardware. Operation with the 2nd generation has minor limitations due to its less complex design. The designer can monitor immediate conditions in the circuit; all monitored data can be stored for further analysis.

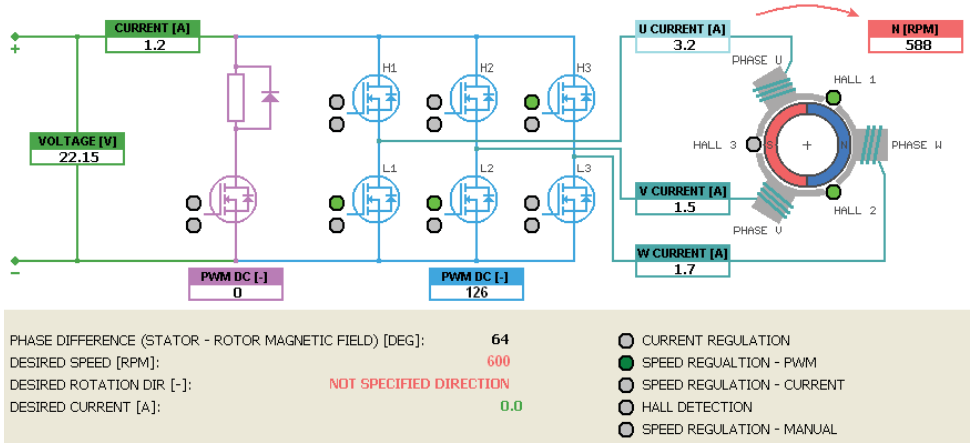

Fig. 3: GUI of the control software tool

4. Control algorithm test results

To evaluate the performance of the control system and the designed electronics, two types of the evaluation test were used. Firstly, the start sequence of the fuel pump was performed. The start sequence of the fuel pump, shown in Fig. 4 left, was verified for a step change request from 50 percent of the fuel flow. This means that the starting flow level was 43 l/h (3250 rpm of the BLDC motor) at 2 MPa of back pressure. The required flow after step change should be 92 l/h (7300 rpm of the BLDC motor) at 3.9 MPa of back pressure. The start time of 174 ms was achieved which is acceptable.

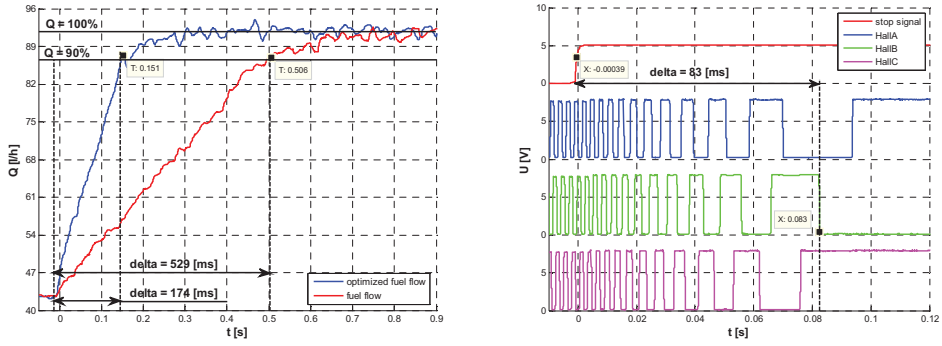

Fig. 4: Start and stop sequence with optimized controller

The next important feature of the fuel pump is the stop time performance. The stop time characteristic was much more difficult to measure. The directly connected speed or flow sensor to the fuel pump influences the stop time characteristic. The only way was to measure the speed from the motor's internal Hall sensors.

Stop time characteristic is shown in Fig. 4 right. The fuel pump should stop in this case from the nominal fuel flow of 92 l/h (7300 rpm of the BLDC motor) at 3.9 MPa of back pressure. The stop time value of 83 ms was achieved which is acceptable.

5. Failure mode analysis – FMECA

Failure Mode, Effects, and Criticality Analysis is a mandatory part of the development of any electrical application in the aerospace industry. FMECA is also a part of the certification process and there is no possibility to operate any device without the approval of relevant authorities. A preliminary FMECA study of the 3rd generation of electronics was carried out within the CESAR project. The main aim is to find the most critical components in the electrical design and provide a feedback to innovate or supersede critical components. Next to the FMECA analysis, a set of DO-178B, DO-160 (Environmental Conditions and Test Procedures for Airborne Equipment), MIL-STD-810 and other standards have to be followed during the whole development cycle.

5.1. Reliability and safety requirements

The technical life of any actuator and especially a fuel pump should be at least 20 000 hours or 20 years (the earlier applies). In aerospace the probability of failure in a flight hour is usually defined as follows:

- Failure S1 – "Unsolicited FMP running on maximal speed" **10^{-6}**
- Failure S2 – "Lost of regulation" **10^{-5}**
- Failure S3 – "False indication of the FMP failure" **10^{-7}**
- Failure S4 – "Impossibility to stop the FMP" **10^{-6}**

The failure analysis should be evaluated with reference to the outside environmental conditions in one year of operation.

5.2. FMECA conclusions

During the preliminary FMECA evaluation about 859 possible failure states on about 386 failure positions have been analyzed. The most significant failures have been located along a short-circuit path through the semiconductor switching components of the device. Its risk factor RN is higher than 600.

Reliability and safety analysis has found 9 possible failures of the electronic control unit, which can be critical. The most critical devices are semiconductor diodes. The probability of their failure is possible to decrease by usage the special types with higher reliability (devices with the M category dedicated for special purposes).

The overloaded components are usually source of failures and decrease the whole failure probability. According to the FMECA calculations it is not recommended to overload any active or passive components more then 50 % of their maximal values to keep high reliability.

In the conclusion of the FMECA document there is usually a summary of the components that built the whole reliability number. The main rule is not to use complicated integration circuits (such as ASIC circuits), under-designed power semiconductors (diodes, MOSFETs), under-designed electrolytic capacitors and to use as little mechanical connections, connectors, relays etc. as possible (especially no-name low cost devices).

The following Tab. 1 captures the FMECA preliminary results in numbers. F(t) means the probability of failure in one flight hour.

Resulting value	F(t)	Requirement
Failure S1	$1{,}250 \cdot 10^{-8}$	$1 \cdot 10^{-6}$
Failure S2	$1{,}565 \cdot 10^{-6}$	$1 \cdot 10^{-5}$
Failure S3	$1{,}500 \cdot 10^{-8}$	$1 \cdot 10^{-7}$
Failure S4	$3{,}138 \cdot 10^{-8}$	$1 \cdot 10^{-6}$

Tab. 1: The failure probability of FMP system control unit

6. Conclusion

Three evaluation versions of the BLDC motor control hardware have been developed within the CESAR project. With all three generations of electronics we have been able to verify the sensor and sensor-less control algorithms described hereinabove. The optimal control method for the fuel metering pump actuator system has been found: a combination of the sinusoidal frequency start-up phase with operational trapezoidal sensor mode control seems to best fit the needs. The requirements for a fluid metering pump control system have been fulfilled and requested dynamic behavior has been achieved.

In addition it has also been possible to apply and evaluate modern trends in the aerospace industry development. Using appropriate software environment we have been able to prepare a mathematical model of the system and determine suitable settings of the controller during simulation and modeling. This approach, called Model Based Design, is rapidly gaining popularity and its principles have been applied and tested within the CESAR project.

Acknowledgement

Published results were acquired within the EU project No. 30888 “Cost-Effective Small Aircraft” (CESAR). Hardware and software development and physical modules were realized at and the project was supported by UNIS, a.s.

The work was also supported by project No. MSM 0021630518 “Simulation modeling of mechatronic systems” solved at the Faculty of Mechanical Engineering, Institute of Production Machines, Systems and Robotics, Brno Technical University.

References

FAA Advisory Circulars. (2005) *RTCA/DO-254 ”Design Assurance Guidance for Airborne Electronic Hardware”*.

Lambersky, V. & Vejlupek, J. (2011) Performance of dsPIC controller programmed with code generated from Simulink, in: *Mechatronics, Recent Technological and Scientific Advances* (R. Jablonski & T. Brezina eds), Warsaw, pp. 105-113.

Leonhard, W. (2001) *Control of Electrical Drives* (3rd ed.). Springer Verlag, Berlin.

Microchip (2011) URL: http://www.microchip.com.

RTCA Inc. (1992). *RTCA/DO-178B ”Software Considerations in Airborne systems and Equipment Certification”*. USA.

RTCA, Inc. (2007). *RTCA/DO-160F ”Environmental Conditions and Test Procedures for Airborne Equipment”*. USA.

18th International Conference
ENGINEERING MECHANICS 2012
Svratka, Czech Republic, May 14 – 17, 2012

pp. 1419–1423
Paper #340

RELATIONSHIP BETWEEN FATIGUE LIFE AND STRUCTURE OF HUMAN TRABECULAR BONE

T. Topoliński*, A. Mazurkiewicz**

Abstract: *In the work results of investigation of fatigue behaviour of human trabecular bone are presented. In total, 61 samples were collected from human trabecular bone after hip arthroplasty. Samples were examined on microCT device. As the result, values of four structural indices (BV/TV, Tb.Th, Tb.N and BS/BV) describing the structure of trabecular bone were obtained. The fatigue tests of the samples were carried out with stepwise increasing amplitude. From the test obtained fatigue life N_s was found between $3{,}75 \cdot 10^3$ cycles and $5{,}02 \cdot 10^4$ cycles. Relations between fatigue life and structure indices were described by determination coefficient R^2. Values of the coefficient were found in range 0,49-0,69. On the base of the obtained results we ascertained existing relation between selected structure indices and fatigue life obtained from test with stepwise increasing amplitude.*

Keywords: ***Trabecular bone, Fatigue life, Structure indices of trabecular bone***

1. Introduction

A typical loading for bone, eg. during gait is the cyclic loading variable in time, and thus behaviors under such loading are fatigue behaviors (Taylor & Tanner, 1997; Martin, 2003). Thus, apart experiments with bone samples subjected to static compression, bending or torsion, research is carried out under cyclic variable loadings. These investigations include the cortical bone parts (Evens & Riolo, 1970) and the trabecular bone parts (Bewill et. al., 2009; Ding et. al., 2003).

The aim of the work is to determine relationship between fatigue life N_s under cyclic loadings with stepwise increasing amplitude and structural indices of human trabecular bone.

2. Material and Method

Investigated material were 61 samples of human trabecular bone. Samples were collected from osteoporotic and coxarthrotic femoral heads gained in result of hip arthroplasty. Diameter of the samples was 10 mm and height 8,5 mm. The age of the patients ranged from 46 to 88 years with an average of 73 years. The samples were obtained from 40 women and 21 men and were stored in 10% formalin solution at the room temperature. Position and direction of the sample in the femoral head is schematically shown in. Fig. 1

Samples were examined using a microCT device (μCT80) with resolution 36 microns (parameters: 70 kV, 114 μA, 500 projections/180°, 300 ms integration time). As a result, values of four structural indices of samples were obtained. Description the indices (Parfitt & Drezner, 1987) are included in Table 1.

* Prof. dr eng. Tomasz Topoliński: Department of Mechanical Engineering, University of Technology and Life Sciences, Kaliskiego 7 Street; 85-789 Bydgoszcz; PL, e-mail: topol@utp.edu.pl

** Dr eng. Adam Mazurkiewicz: Department of Mechanical Engineering, University of Technology and Life Sciences, Kaliskiego 7 Street; 85-789 Bydgoszcz; PL, e-mail: adam.mazurkiewicz@utp.edu.pl

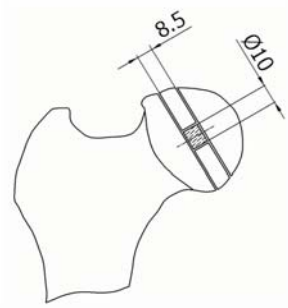

Fig. 1: Trabecular bone sampling method. The sample axis coincided with the axis of the head and neck of the femur.

Tab. 1: Description structure indices investigated on microCT system.

Indicator	Name	Description
BV/TV	Bone volume fraction	Volume of bone tissue inside sample BV /volume of sample TV
Tb.Th	Trabecular thickness	Mean thickness single trabeculae in sample
Tb.N	Trabecular number	Mean number continuous trabecular inside sample
BS/BV	Bone surface ratio	Surface of bone tissue inside sample BS/volume of bone tissue inside sample BV

The bone sample fatigue tests were carried out under compression with stepwise increasing loading using the testing machine INSTRON 8874. The frequency of sinusoidal loading was 1 Hz, the minimum loading for all the loading levels was 5-7 N. The maximum loading started from 20 N with a gain every 10 N at successive steps. Each level of load maintained 500 cycles realized under constant amplitude loadings. Program of the fatigue test is presented in Fig. 2.

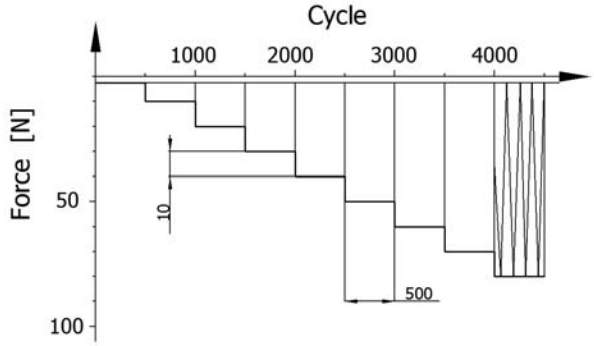

Fig. 2: Program of the fatigue test.

Fatigue life N_s was determined by estimation of the median of the values of deformation increment and then considering the value of the first loop for which the deformation gain exceeded the value of the median by 10% (to be the fatigue life).

The temperature plays an important role in fatigue tests because it influences the obtained fatigue life. Therefore the tests were conducted in 0,7% NaCl water solution in constant temperature 37±2 ^{0}C, which corresponds to the normal human body temperature.

3. Results

Structural indices of trabecular bone obtained from microCT investigation are presented in Tab. 2. For investigated indices relation between the fatigue life N_s described value determination coefficient R^2 was minimum 0,49 (it corresponds value of correlation coefficient R=0,7).

Fatigue tests with stepwise increasing loading demonstrated the fatigue life of the trabecular bone samples between $3{,}75 \cdot 10^3$ cycles and $5{,}02 \cdot 10^4$ cycles (time of test between 1,04 h and 13,95 h).

Tab. 2: Values of selected indices structure of trabecular bone obtained from microCT investigation.

Indicator	**Value**				
	Min	**Max**	**Mean**	**SD**	**RSD**
BV/TV,-	0,0759	0,4595	0,2049	0,0759	37 %
Tb.Th, mm	0,1053	0,2677	0,1714	0,0354	21 %
Tb.N, 1/mm	0,511	1,544	1,133	0,222	20%
BS/BV, 1/mm	5,206	18,995	11,998	2,747	23%

Min - minimum value, Max - maximum value, Mean - mean value, SD - standard deviation, RSD - relative standard deviation

Relationship between fatigue life and BV/TV and Tb.Th is presented in Fig. 3 and 4. Relationship between fatigue life and Tb.N. and BS/BV is presented in Fig. 5 and 6.

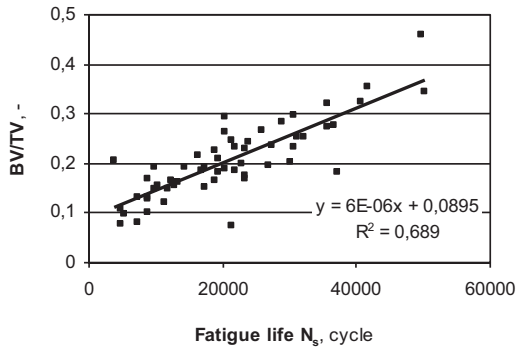

Fig. 3: Relationship between bone volume fraction BV/TV and fatigue life N_s.

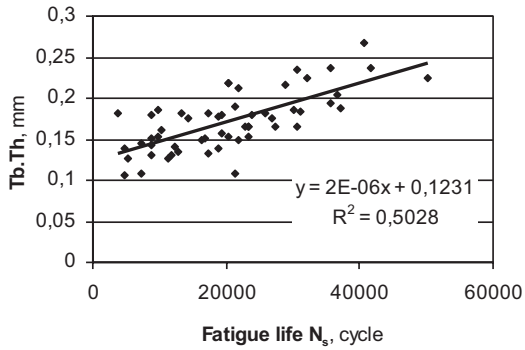

Fig. 4: Relationship between trabecular thickness Tb.Th and fatigue life N_s.

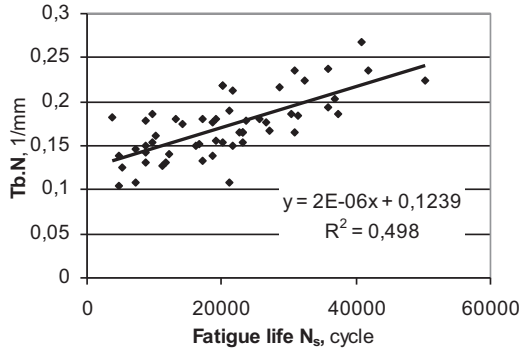

Fig. 5: Relationship between trabecular number Tb.N and fatigue life N_s.

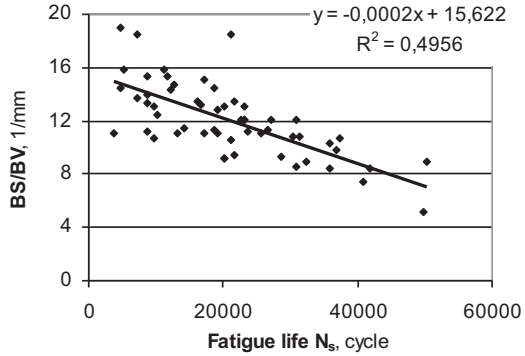

Fig. 6: Relationship between bone surface ratio BS/BV and fatigue life N_s.

4. Conclusions

Indices BV/TV and Tb.Th are often use for description of the trabecular bone. For the investigated samples value of indices varying in wide range (0,08-0,46 and 0,11-0,27 for BV/TV and Tb.Th respectively) and significant values SD or RSD.

From the comparison of obtained relation between fatigue life and structure indices with results other investigators was impossible, because majority fatigue tests trabecular bone was carried out with constant load amplitude. Therefore it is possible comparison ours results with the similar relations obtained during this kind of test.

Haddock et. al. (2004) presented results fatigue test trabecular bone carried out constant load amplitude. The scatter of BV/TV values for 35 samples (9 donors RSD=38,5%) was comparable with the scatter obtained in our experiment (61 donors and RSD=37%). Obtained fatigue curve was described by the value of coefficient of determination R^2=0,54.

Rapillard et. al. (2006) obtained for 29 samples from 4 donors scatter higher than in our experiment (RSD=42,5%), however they introduced the stress modification, included in fatigue equation volume fraction and the fabric eigenvalue. It resulted in a higher correlation between the stress and the fatigue life R^2=0,95 (fatigue test was also carried out under constant load amplitude).

Concluded, the relationship between the fatigue life results and structure indices, does exist. The highest value coefficient of determination R^2=0,69 obtained for bone volume fraction. In opinion of authors these relations cover not only the bone properties (structure characteristics, damage and the effects of remodeling) but also the specificity of the fatigue damage process for stepwise loading with the dynamics, also associated with the bone properties.

References

Bevill, G., Eswaran, S.K., Farahmand, F. & Keaveny, T.M. (2009) The influence of boundary conditions and loading mode on high-resolution finite element-computed trabecular tissue properties. *Bone*, Vol. 44, pp. 573-578.

Ding, M., Odgaard, A. & Hvid, I. (2003) Changes in the three-dimensional microstructure of human tibial cancellous bone in early osteoarthritis. *J Bone Joint Surg.*, Vol. 85-B, pp. 906-912.

Evens, F.G. & Riolo, M.L. (1970) Relations between the fatigue life and histology of adult human cortical bone. *J Bone Joint Surg.*, Vol. 52-A, pp. 1579-86.

Haddock, S.M., Yeh, O.C., Mummaneni, P.V., Rosenberg, W.S. & Keaveny, T.M. (2004) Similarity in the fatigue behavior of trabecular bone across site and species. *Journal of Biomechanics*, Vol. 37, pp. 181-187.

Martin, R.B. (2003) Fatigue microdamage as an essential element of bone mechanics and biology. *Calcif Tissue Int.*, Vol. 73, pp. 101-107.

Parfitt, A.M. & Drezner, M.K. (1987) Bone histomorphometry: Standarization of nomenclature, symbols and units. *J. Bone Miner. Res.*, Vol. 2, pp. 595-610.

Taylor, M. & Tanner, K.E. (1997) Fatigue failure of cancellous bone: a possible cause of implant migration and loosening. *J Bone Joint Surg.*, Vol. 79-B, pp. 181-182.

Rapillard, L., Charlebois, M. & Zysset, P.K. (2006) Compressive fatigue behavior of human vertebral trabecular bone. *Journal of Biomechanics*, Vol. 39, pp. 2133-2139.

18th International Conference
ENGINEERING MECHANICS 2012
Svratka, Czech Republic, May 14 – 17, 2012

pp. 1425–1428
Paper #331

PROBLEMS OF PRODUCING TEST SAMPLES FROM CALLUS DENTAL

T. Topoliński*, M. Wirwicki**

Abstract: *Human Teeth under the influence of food constant attacks by bacteria, which cause degradation of the enamel, and thus the formation of cavities. Dentists thanks to modern methods can remove the defect and fill the resulting hole with a composite, by gluing the two surfaces. The article presents three ways to append to the tooth composite and zircon crowns. It also presents problems in obtaining samples of a particular size due multilayer glue connections and anatomical structure of the tooth. The solution to this problem is to define sets of each group of materials comprising the laminated multi-layer connection.*

Keywords: ***dentin, zirconium, composite, bonding, samples,***

1. Introduction

The main problem of today's bonded connections tooth - filler (composite), tooth - zircon is limited vivo stability. During clinical trials, it appears that the efficacy of the combination of the two surfaces is very low, although usually the manufacturer confirms the very high adhesion strength. The basic mechanism of complement fixation or zirconium is the process of turning minerals from the hard tissue of the resin monomers, which are micro - mechanically locked in the created porous surfaces. Based on this system of dental fillings and crowns assembling, we can distinguish two systems, the mechanisms of adhesion:

a) **etch and rinse** – tooth bonds operate in three steps way: preparation step, etching the surface and then applying foundation, so that we could attach the bond to a porous surface, and the last stage which is putting the bond which binds the extender with tooth blade.

b) **self – etch adhesive** – the most promising binding system, which dentist applies just in two steps. The base is also the etching surface. The treatment reduces the possibility of error and reduces the time of doing the treatment.

The primary function of the assumed composite fillings and crowns are:

– **replacement** - hard tissue replenishment and chewing surfaces that have been damaged or broken,

– **protection** - protect the health of the tooth from the bad effects of external factors and disease (eg. caries),

– **empowerment** (Supporting) - are used as support for partial dentures and bridges,

– **aesthetic** (cosmetic) - give the correct shape of the teeth, cover discolorations.

Aim of this study is to present the configuration of materials for fitting crowns and fillings with natural tooth.

* Prof. Ing. Tomasz Topoliński, Institute of Mechanic and Machine Design, University of Technology and Life Sciences in Bydgoszcz, Al. Prof. Kaliskiego 7; 85-796, Bydgoszcz; PL, e-mail: tomasz.topolinski@utp.edu.pl

** Ing. Mateusz Wirwicki, Institute of Mechanic and Machine Design, University of Technology and Life Sciences in Bydgoszcz; Al. Prof. Kaliskiego 7; 85-796, Bydgoszcz; PL, e-mail: wirwicki@utp.edu.pl

2. Preferred set of samples to analyze the strength of teeth filled and reconstructed

Review of literature shows that each type of clinical research is conducted on specially selected healthy molars. The dental practice is a very small percentage, when the dentist for healthy teeth will build a crown or bridge. Mostly there are treatments that take place on the teeth of dead in endodontic (root canal treatment) Fig. 1.

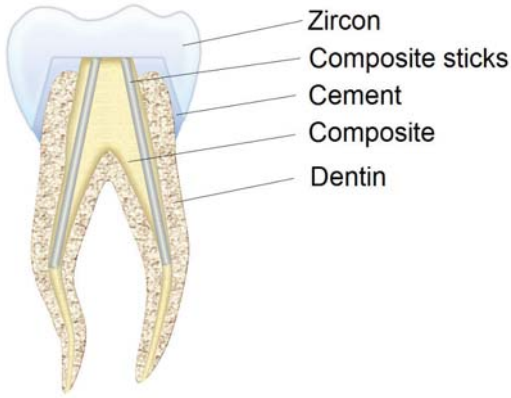

Fig 1. Schematic representation of the cross section of the tooth after root canal treatment and crown sticking zircon.

Analysis of the figure shows that after drilling and cleaning the canals of the tooth, composite sticks are being applied to meet them and to maintain the crown. This treatment is widely used to reduce the risk of separating themselves from the crown of the tooth root. At a later stage the hole is flooded with composite filler and zirconium crown is appended.

Another case is that the teeth have earlier fillings, as for example those shown in Fig 2.

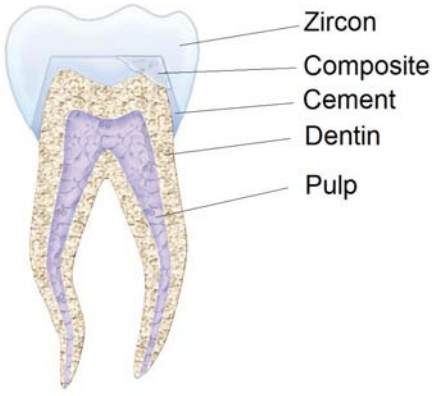

Fig 2. Schematic representation of the tooth in cross section with composite filler

Figure 2 shows the tooth, where the partial filling defect caused by the break off a part of the tooth. On such a prepared tooth crown zirconium is appended.

Sometimes, the dentist during root canal treatment or disposal of the loss of Class IV, V loses the layer above the gum of the tooth, thus the need for a composite material to rebuild the tooth crown. Cavities of Class IV, V arise as a result of the development of caries in the contact surface, usually these are very large cavities occupying half of the tooth. The loss may also come as a result of trauma to the tooth fractures. With this size of the defect must be considered an indirect method of reconstruction of the tooth (veneer, crown piece) or direct (filling). Sporadic case of attachment of zirconium in healthy teeth are hard to remove stains while whitening your teeth, as shown in Fig 3.

Fig 3. Schematic presentation of the tooth in cross section with appended crown zircon.

By modeling the in vivo environment, where patients previously treated for a tooth crown is appended zircon, you will find that there comes to be bonded multilayer which could be schematically represented as in Fig 4.

Such join may be the problem in evaluating the connection strength, adhesion strength, which is why a study should be made in different groups that make up the whole system shown in Figure 4: zircon - cement - composite, composite - bond - dentine, zircon - cement - dentine . The above-mentioned components of the connection will be tested in fatigue. The research is to demonstrate which of the components you need to pay special attention when preparing the surface and connecting the same procedure to connect the two. Designated durability and strength of such a facility will be used to further analyze whether the product (glue) meets the expectations of dentists and patients, and that you will not need replacement binding agent. The biggest problem is to produce a micro sample study because each sample must be cut along the axis of the tooth and needs to be maintained parallel and perpendicularity of the walls. Literature review points to the conclusion that the tested sample, due to their shape must be placed either in a block of plaster, latex or acrylic completely flooded.

Placement of the tooth in the block cannot be accidental, you need to keep the axis of the tooth, which is not easy, because each tooth from an anatomical point of view is different. Analyzing the structure of the tooth (Fig. 5) can be seen that in the midst of a solid tooth is little hole, which is filled with pulp - unripe connective tissue, heavily innervated and vascularized, which when cutting with the saw Isomet 4000 will break off the entire length of the tooth two pieces.

3. Summary

There were shown three offers of tested samples, in which is a multi-layer adhesion. For the study of sustainability and strength of connections must be extracted three options glued connections. The article presents the problems associated with obtaining samples of a particular size. Is related toz anatomy of molars. The above article is to present the problems that have to face taking a materials testing included in biomechanics. Literature review has allowed to conclude that the research shall be used only on and off healthy teeth after orthodontic extractions. Authors of articles trying to realize

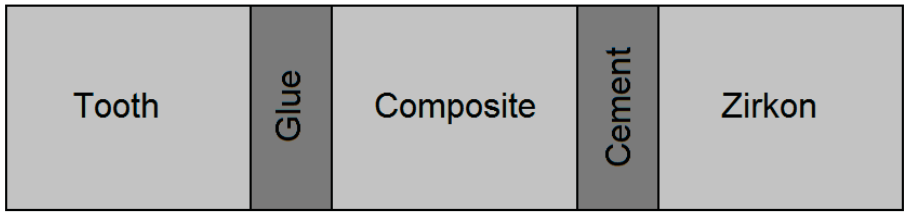

Fig 4. Schematic presentation of multilayer laminated connections

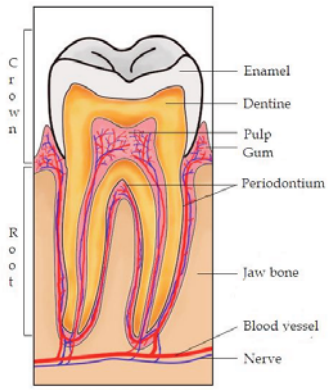

Fig 5. Schematic presentation of the structure of the tooth.

that such cases is very small even for purely economic. Do not be moved by the problem of research on the teeth that are already dead teeth (root canal treated teeth) or teeth that have been filling the cavities.

References

Braem, M. (2007) Microshear Fatigue Testing of Tooth/Adhesive Interfaces, *J Adhes Dent*., Vol. 9, Supplement 2, ss. 249 – 253

Drummond, J.L. (2008) Degradation, fatigue and failure of resin dental composite materials, *J Dent Res.,* Vol. 087, No. 8, ss. 710-719

Herion, T., Ferracane, J.L., Covell, D.A.Jr. (2007) Three Cements Used for Orthodontic Banding of Porcelain Molars, *Angle Orthod.,* Vol. 77, No.l, ss. 94-99

http://www.portaldentystyczny.pl/pacjent/korony/art7.html [Online] Access 1.03.2012

http://www.implanty-dentystyczne.pl/?page=periodontologia [Online] Access: 1.03.2012

Inoue, T., Nishimura, F., Debari, K., Kou, K., Miyazaki, T. (2011) Fatigue and tensile properties of radicular dentin substrate, *Journal of Biomechanics*, Vol 44(4) ss. 586 – 592

Karatasil, Ö., Kursoglu, P., Çapa, N., Kazazoglu, E. (2011) Comparison of the marginal fit of different coping materials and designs produced by computer aided manufacturing systems, *Dental Materials Journal,* 30(1), pp. 97 – 102

Kokubo, Y., Tsumita, M., Kano, T., Fukushima, S. (2011) The influence of zirconia doping design on the fracture load of all-ceramic molar crowns, *Dental Materials Journal*, 30(3) pp. 281 -285

Loher, H., Behr M., Hintereder, M., Rosentritt, M., Handel, G. (2009) The impact of cement mixing and storage errors on the risk of failure of glass-ceramic crowns, *Clin Oral Invest*, Vol. 13, No. 2, ss. 217-222

Ozkurt, Z., Iseri, U., Kazazoglu, E. (2010) Zirconia ceramic post systems a literature review and a case report, *Dental Materials Journal*, pp. 233 – 245

Piątowska, D., Cynkier, J., Paul-Stalmaszczyk, M. (2009) Stomatologia Zachowawcza, współczesne metody opracowania i wypełniania ubytków próchnicowych. *Bestom DENTOnet.pl*, Łódz.

Poitevin, A., De Munck, J., Cardoso, M., Mine, A., Peumans, M., Lambrechts, P., Van Meerbeek, B. (2010) Dynamic versus static bond-strength testing of adhesive interfaces, *Dental Matherials* Vol. 26 ss. 1068–1076

Staninec, M., Kim, P., Marshall, G., Ritchie, R., Marshall, S. (2008) Fatigue of dentin–composite interfaces with four-point bend, *Dental Materials*, Vol. 24 ss. 799 – 803

Tartaglia, G., Sidoti, E., Sforza, C. (2011) A 3-year follow-up study of all-ceramic single and multiple crowns performer in a private practice: a perospective case series, *Clinical Science* 66(12) pp. 2063 – 2070

Topoliński, T., Wirwicki, M. (2011) Metodology of fatigue tests for glued dental samples. *Journal of Polish CIMAC,* Vol.6 No.3 pp. 355 – 364

Topoliśnki T. (2009) Problemy wytrzymałości i trwałości zmęczeniowej w materiałach i konstrukcjach inżynierii biomedycznej, *WNITiE*, Bydgoszcz

18th International Conference
ENGINEERING MECHANICS 2012
Svratka, Czech Republic, May 14 – 17, 2012

pp. 1429–1434
Paper #34

NEW APPROACHES TO ASSESSMENT OF STRESS AND STRAIN FIELDS WITH APPLICATION OF PHOTOSTRESS METHOD

F. Trebuňa[*], P. Frankovský[*], J. Jadlovský[**]

Abstract: *Isoclinic and isochromatic fringes provide qualitative and quantitative information in experimental method PhotoStress. They are the source of data on directions and magnitudes of principal strain and principal normal stress on the surface of analysed objects with photoelastic coating. The article reviews methodology of autonomous assessment of magnitudes and directions of stress fields and strains as carried out by the authors of the article by means of PhotoStress method.*

Keywords: ***Linear and circular polarization, isoclinics, isostatics, singular points, isochromatics.***

1. Introduction

Experimental method PhotoStress is based on temporary birefringence that appears in photoelastic coating applied to a tested object subjected to loads. When photoelastic coating applied to the tested object under load is illuminated with polarized light, two types of photoelastic entities can be observed: isoclinic and isochromatic fringes. These photoelastic entities allow us to perform qualitative (visual) and quantitative analysis of principal strain and principal normal stress directions and magnitudes on the surface of the object subjected to load. Quantitative analysis of principal strain and stress directions and magnitudes is performed manually at a point and hence is time-consuming when it comes to strain and stress determination at more points on the analysed surface. For the above-mentioned reasons, the authors of the article developed a PhotoStress software application that enables automatic determination of parameters of isoclinics and isochromatics from their images. From these parameters we can determine directions and magnitudes of principal strains and principal normal stresses at all points of tested surfaces.

2. Photoelastic entities

Isoclinic fringes are used in PhotoStress method in order to determine parameters of principal strains and principal normal stresses. They are dark lines or areas which are defined as geometrical points in which directions of principal stresses are parallel to intersected polarization planes of the polarizer and analyzer. Isoclinic fringes appear in a plane-polarized beam of light (Fig.1).

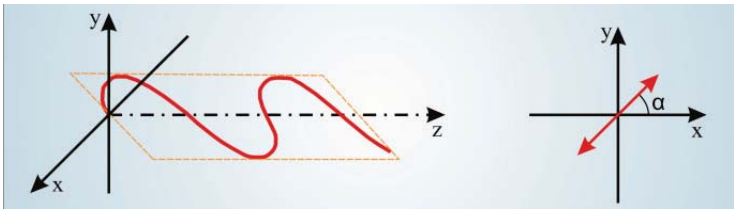

Fig. 1: Linear polarization.

[*] Dr.h.c. mult. prof. Ing. František Trebuňa, CSc.: Technical Univerzity of Košice, Faculty of Mechanical Engineering, Department of applied mechanics and mechatronics, Letná 9, 042 00, Košice, SK, e-mail: frantisek.trebuna@tuke.sk

[*] Ing. Peter Frankovský, PhD.: Technical Univerzity of Košice, Faculty of Mechanical Engineering, Department of applied mechanics and mechatronics, Letná 9, 042 00, Košice, SK, e-mail: peter.frankovsky@tuke.sk

[**] Doc. Ing. Ján Jadlovský, CSc.: Technical Univerzity of Košice, Faculty of Electrical Engineering and Informatics, Department of Cybernetics and Artificial Intelligence, Letná 9, 042 00, Košice, SK, e-mail: jan.jadlovsky@tuke.sk

When examining isoclinic fringes, the axes of polarizer and analyzer are perpendicular to one another. When intersected polaroids rotate synchronically, the isoclinics viewed under reflection polariscope are continuously changing from the isoclinics with parameter 0° up to the isoclinics with parameter 90°. Isoclinics are distributed through the whole tested surface of an object under minimum load with respect to the changing directions of principal strains or stresses. Only one isoclinic with a particular parameter can intersect a particular point of a photoelastically coated test surface since in that point there is only one principal stress direction, i.e. α or α+π/2.

However, isoclinics of all parameters intersect points in which both principal stresses have the same magnitude and in which these stresses are principal in all directions. Such points are called singular points.

Singular points are points where both principal stresses are equal and hence

$$\sigma_1 = \sigma_2, \text{ or } \sigma_1 - \sigma_2 = 0.$$

Singular points have qualitative value for the behaviour analysis of isostatics and isochromatics. If $\sigma_1 = \sigma_2$, then the fringe order is expressed as $N = 0$. As a result, singular point is a zero-order isochromatic point. The material is at this point in the state of hydrostatic pressure ($\sigma_1 < 0$), tension ($\sigma_1 > 0$) or is in a stress-free state ($\sigma_1 = 0$) (Frocht, 1949).

Singular points can be classified as the points of the first, second and higher orders. They can be further classified according to the behavior of isoclinics when the polariscope is being rotated (either positive or negative singular point). With respect to the nature of mathematical expressions for stress components, points of the second and higher order are not stable in the sense that even a slight change in the shape of the part, load or position causes a break-up into singular points of lower orders (for instance a point of the second order would break up into two points of the second order). Fig. 2 depicts a few examples of singular points of different orders that occur in the net system of isostatic curves.

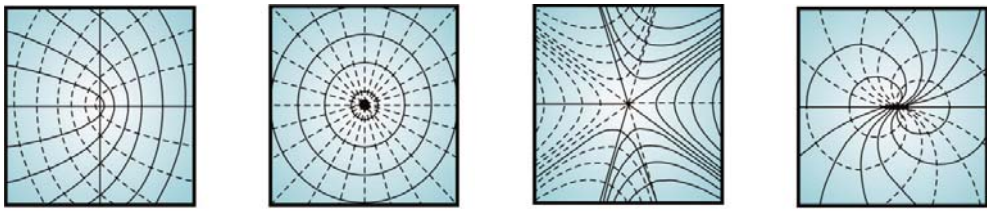

Fig. 2: Singular points of the a) first order, b) second order, c) third order, d) forth order.

The set of isostatic lines is displayed on the basis of the set of isoclinic fringes which were obtained at the angles from 0° to 90° with 5- or 10-degree increments and on the basis of classifications of singular points. Isostatic lines can be defined as stress trajectories. These are the sources of information about the directions of principal normal stresses σ_1 and σ_2 along the whole tested surface. Fig.3 depicts isoclinic fringes on an eccentrically loaded split ring obtained at 0°, 20°, 60°, 80° and 90° angle parameter. From the Fig.3 is evident that the isoclinics with 0° and 90° angle parameter are identical.

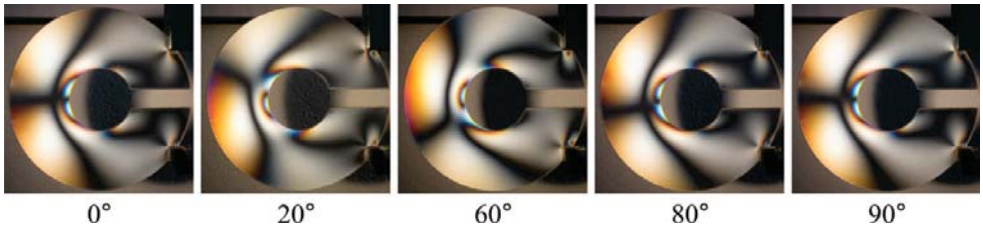

Fig. 3: Isoclinic fringes on the eccentrically loaded split ring.

Traditional projections of a set of isoclinic fringes and isostatic lines are relatively time-consuming. The authors of the article hence developed a PhotoStress software application that enables a quick and simple projection of a set of isoclinic fringes and isostatic lines from the shot set of isoclinic lines

taken at 0° up to 90° angle with 5- or 10-degree increments. In the application are isoclinic lines projected by means of quadratic Bézier curves which are determined by three control points. Fig.4 illustrates the projection of isoclinic lines in PhotoStress application.

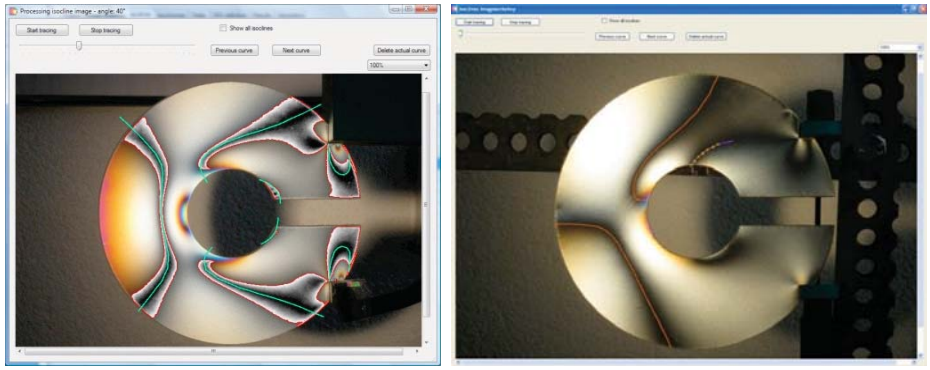

Fig. 4: Projection of isoclinics in PhotoStress application.

The approximation of principal strain or principal normal stress directions is performed in PhotoStress application on the basis of manually projected isoclinics with direction parameter α. The calculation of direction parameter for pixels, which are not included in the area of defined lines, is done on the basis of weighted average of direction parameter of the two closest pixels which belong to drawn isolcinics with a different direction parameter. Important is in this case the distance between the pixel being calculated and the pixel that belongs to some isoclinics.

Fig.5a depicts the set of isoclinics of a split ring subjected to diametrical pressure with the angle increment 5° as being projected in PhotoStress application. The set of isoclinic fringes of the first and second type is shown in the fig.5b. Blue curves represent isostatic lines of the first type and red curves represent isostatic lines of the second type.

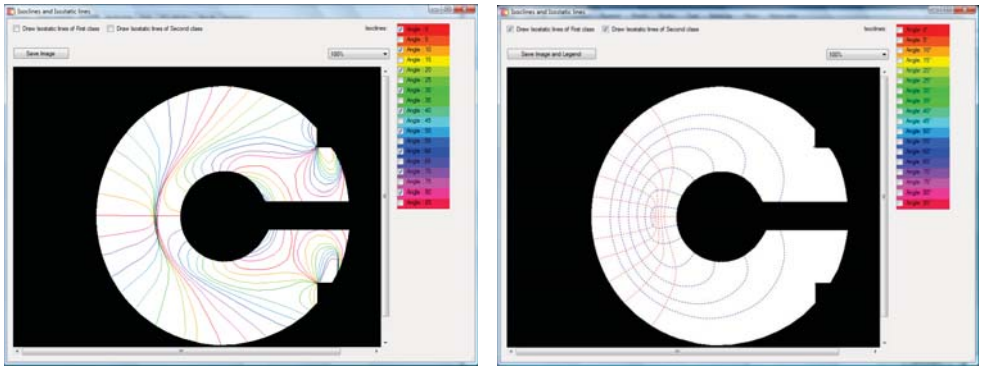

a) **b)**

Fig. 5: a) the set of isoclinic fringes, b) projection of the set of isostatic lines.

The above-mentioned isoclinic and isostatic curves are the source of information about the behaviour of principal strains or principal normal stresses. Quantitative information about strain and stress magnitudes at particular points of the photoelastically coated surface of a tested object can be derived from another type of photoelastic lines, i.e. isochromatic fringes. Isochromatics are connection lines of points along which the difference between principal normal stresses $\sigma_1 - \sigma_2$ is constant. They occur in a circle-polarized light (Fig.6). Deformations of some photoelastically coated object under load are transformed to the photoelastic coating. When illuminated with polarized light from reflection polariscope, surface deformations appear as colourful isochromatic fringes or the areas of the same (iso) colour (chromos).

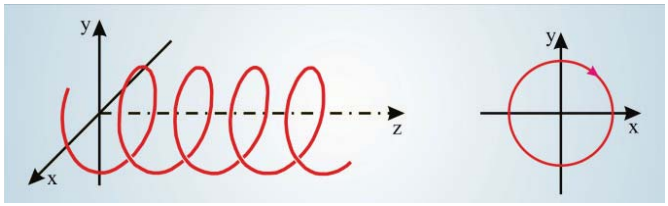

Fig. 6: Circular polarization.

When the load is applied to the tested object in increments, isochromatic fringes will appear first at the most highly stressed points. As the load is increased and new fringes appear, the earlier fringes are pushed toward areas of lower stresses. The appearance of isochromatic fringes is dependent upon optical sensitivity of applied photoelastic coating and load applied to the object. A specific number of isochromatic fringes can appear on the photoelastic coating. These are numbered as n-order isochromatics. The colour of each fringe represents specific birefringence or fringe order *N*. Full colour order, relative lags and numerical fringe order for each colour can be found in Trebuňa (2006). In the full-field strain and stress analysis of isochromatic fringes it is required to know the relationship between colourful isochromatic fringes obtained through PhotoStress method and strain or stress.

The basic relation for PhotoStress method is expressed as follows:

relative elongation (ε) = calibration constant (f) x fringe order value (N)

where f is fringe value of photoelastic coating,

N - fringe order value read from the compensator during manual determination of photoelastic fringe order at particular point.

There is a linear relationship between the fringe order value N and strain ε, i.e. with the increase of fringe order value N at given fringe value f strain or stress value increases as well.

Fig.7 illustrates isochromatic fringes that occur when the split ring is subjected to incremental loading by diametrical pressure.

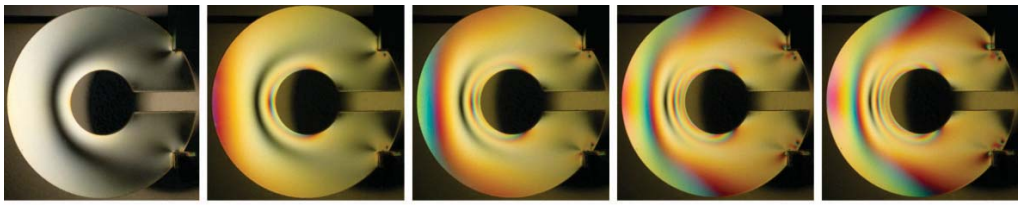

Fig. 7: Isochromatic fringes during incremental loading of a split ring by diametrical pressure.

Null-Balance Compensator (Fig.8) is used in PhotoStress method for manual determination of fringe order value at analysed point. The compensator can determine fringe order value only at one point. However, this process is time-consuming in the analysis at more points of tested surface.

Fig. 8: Null-Balance Compensator model 832.

Nevertheless, with PhotoStress application full-field automatic analysis of colourful isochromatic fringes can be done. It allows us to determine principal strains and principal normal stresses not only at a point, but also along line and surface.

In PhotoStress application, the area of colourful isochromatic fringes is divided into two sub-areas (Fig.9):

- area with the order of isochromatic fringes *N* from *0* to *0,35*,
- area with the order of isochromatic fringes *N* from *0,36* to *3,00*.

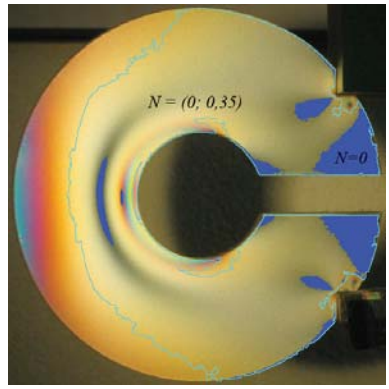

Fig. 9: The area of colourful isochromatic fringes.

In the areas with the values of fringe orders lower than *0,35,* colours are faint and gradient method is applied in order to calculate isochromatic fringe order. At the beginning, the darkest area (the area of zero point) should be marked. Then, on the surface that arose when blue and green luminance components merged together, the shortest trajectories between zero point area and isochromatic fringe with 0,35 fringe order should be found by means of gradient method. Each point in that area will be assigned fringe order value with respect to the relation of its distance from the zero point and the isochromatic fringe with fringe order 0,35 within given trajectory.

For determination of isochromatic fringe order in the area with *N* from *0,36* to *3,00* is the algorithm of PhotoStress application based on determination of colour of a given pixel in HSV colour space and its index, which represents the order in which six photoelastic colours re-occur from the order $N = 0$. Each pixel from the picture of a colourful photoelastic pattern surrounded by logical mask is assigned specific value of RGB colour. The value of RGB colour specifies relative intensity of red, green and blue. However, this does not suffice in PhotoStress method. For this reason, HSV colour space is more useful when using PhotoStress method. PhotoStress application thus includes algorithm for transformation of colour components from RGB colour space into HSV colour space.

Fig.10 shows determination of zero points and colourful isochromatic fringes of tested split ring by PhotoStress application.

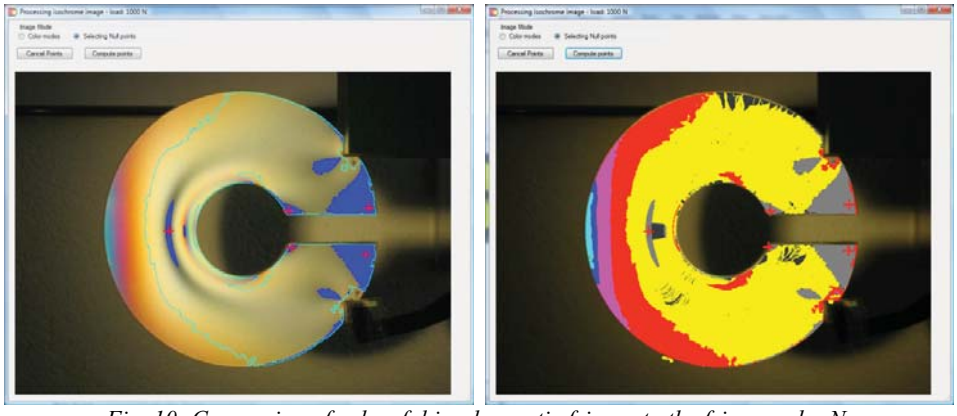

Fig. 10: Conversion of colourful isochromatic fringes to the fringe order N.

3. Conclusions

As it is evident from the article, software application PhotoStress makes the analysis of principal strain and principal normal stress directions and magnitudes on photoelastically coated objects faster. The foundations of this improvement lie in automatic processing of photoelastic entities such as isoclinic fringes, singular points and isochromatic fringes. The application is currently subjected to some improvements regarding little imperfections that arise during automatic projection of isostatic curves and recognition of colourful isochromatic fringes or surfaces. Amendments and other additions to the software application will be discussed in future articles.

Acknowledgement

This contribution is the result of the project implementation „Center for research of control of technical, environmental and human risks for permanent development of production and products in mechanical engineering“ ITMS:26220120060, supported by the Research & Development Operational Programme funded by the ERDF and grant project VEGA no. 1/0937/12.

References

Bocko, J. et al. (2009) Design and experimental verification of landing gear for ultralight aircraft, In Proceedings: *EAN 2009: 47th International Scientific Conference*, Liberec, TU. 7 p.

Frocht, M.M. (1949) *Photoelasticity I.*, New York: John Wiley, 1949.

Frocht, M.M. (1957) *Photoelasticity II.*, New York: John Wiley, 1957.

Kobayashi, A.S. (1993) *Handbook on Experimental Mechanics.* Seattle: Society for Experimental Mechanics.

Macura, P. (2002) Úloha a postavení experimentálních metod při řešení současných problémů praxe. In: *Aplikovaná mechanika 2002*. Ostrava: VŠB-Technická univerzita Ostrava, vol. 4 , pp. 3-10.

Macura, P. (2010) Experimental Stress Analysis of Transducers by Means of PhotoStress Method. In: *Acta Mechanica Slovaca*. Roč. 14, č. 4, s. 52-57.

Milbauer, M., Perla, M. (1959) *Fotoelasticimetrické přístroje a měřicí metody.* ČSAV, Praha.

Ostertag, O., Ostertagová, E. (2996) Automatizácia merania a vyhodnotenia napätosti programovým systémom photoelast. *Bulletin of Applied Mechanics,* roč. 2, č. 6, s. 105 – 119. Faculty of Mechanical Engineering, Czech Technical University in Prague.

Ramesh, K. (2000) *Digital Photoelasticity - Advanced Techniques and Applications*, Springer-Verlag, Berlin.

Trebuňa, F. (2006) *Princípy, postupy, prístroje v metóde PhotoStress.* TypoPress, Košice.

Trebuňa, F., Frankovský, P., Huňady R. (2011) Optical methods and their application in experimental analysis of mechanical and mechatronic systems. *Hutnické listy*. Vol. 64, no. 7 pp. 173-178.

Trebuňa, F. et al. (2010) Abilities of New Software for PhotoStress Method. In Proceedings: *EAN 2010, 48th International Scientific Conference,* Palacky University Olomouc,.

Trebuňa, F., Šimčák, F. (2007) *Príručka experimentálnej mechaniky.* TypoPress, Košice.

18th International Conference
ENGINEERING MECHANICS 2012
Svratka, Czech Republic, May 14 – 17, 2012

pp. 1435–1440
Paper #299

DETERMINATION OF MECHANICAL PROPERTIES FROM MICROCOMPRESSION TEST

M. Truhlář[1], T. Kruml[2], I. Kuběna[3], K. Petráčková[3], L. Náhlík[3]

Abstract: *This paper describes a microcompression test of Al - 1.5 wt. % Cu thin film deposited on Si substrate. Microcompression combines the sample preparation with the use of ion focused beam (FIB) with a compression test carried out using nanoindenter. Cylindrical specimens (pillars) were prepared using FIB. The diameter of pillars was about 1.3 μm and their height was about 2 μm (equal to the film thickness). Stress-strain curves of the thin film were obtained. The results depend on crystallographic orientation of pillar. The paper is focused to an attempt to determine as precisely as possible Young modulus of the film using experimental data and finite element modelling.*

Keywords: ***microcompression, thin film properties, focused ion beam, Young modulus, FEM modelling***

1. Introduction

Measurements of mechanical properties of thin film are not generally easy to be done. There are few methods for measuring of plastic and elastic properties of materials. Each of them has some weaknesses (Nix, 1989). This paper is aimed on recently developed microcompression experiments (Uchic & Dimiduk, 2005; Kruml et al., 2009; Kuběna et al., 2009; Kuběna & Kruml, 2009). This method combines preparation of specimen using focused ion beam (FIB) and compressive test using nanoindentation device. Combination of the two techniques enables one to fabricate micrometric cylindrical specimens with the axis normal to film plane, attached by bottom to the surface. Such specimens are referred in the literature as pillars.

In previous experiments it was found that pillars with diameter under 1 μm show a significant increase in yield strength. This can be explained by the fact that in such small volumes no longer any mobile dislocations are present and the stress required for plastic deformation is determined by stress which is required for activation of dislocation sources and not by stress needed for dislocation movement (Nix et al., 2007). Nowadays such experiments are rather popular. The majority of the effort is focused on effect of specimen size to the mechanical behaviour of material. Generally, it is found that "smaller is stronger".

Microcompression experiments on pillars made from Al thin films have already been performed in our laboratory several times (Kruml et al. 2009; Kuběna et al., 2008; Kuběna et al., 2009; Kuběna & Kruml, 2009). The main goal is to use the technique for determining mechanical properties of thin films. In this paper, we tried to improve calculation method for determining Young modulus with higher precision from the microcompression data.

[1] Mgr. Michal Truhlář; Institute of Physics of Materials AS CR, Žižkova 22, 61662 Brno, Czech Republic and Masaryk University, Faculty of Science, Kotlářská 2, 61137 Brno, Czech Republic, truhlar@ipm.cz

[2] Prof. Mgr. Tomáš Kruml, CSc.; Institute of Physics of Materials AS CR, Žižkova 22, 61662 Brno, Czech Republic, kruml@imp.cz

[3] Bc. Klára Petráčková; Ing. Ivo Kuběna; doc. Ing. Luboš Náhlík, Ph.D.; Institute of Physics of Materials AS CR, Žižkova 22, 61662 Brno, Czech Republic and Brno University of Technology, Faculty of Material Engineering, Technická 2, 61669 Brno, Czech Republic, klara.petrackova@seznam.cz, kubena@ipm.cz, nahlik@ipm.cz

2. Experiment

The studied material was a thin film of Al – 1.5 wt. % Cu of chemical composition and 2.06±0.05 μm of thickness, prepared by Physical vapour deposition (PVD) method in the ON Semiconductors company. The Al film was composed of relatively large grains with the average diameter in the plane parallel to the film surface of 3.8±0.3 μm. Such large grains are a consequence of a relatively high substrate temperature during deposition (340°C). Substrate for the chemical deposition was <100> Si monocrystalline wafer. The EBSD analysis showed a very strong preferential <111> orientation of the normal to the film surface. In between Al layer and Si substrate there was an intermediate thin film of W – 10 wt. % Ti and thickness about 0.14±0.04 μm. This embedded layer improves the adhesion of Al layer and is used also as a diffusion barrier. The sandwich was prepared on Varian 3190 sputtering system at the ON Semiconductor company.

The aim of experiment was prepare perfect cylindrical specimens with a diameter of about 1.3 μm with height determined by film thickness. Pillars were prepared in the FEI Quanta 3D FEG DualBeam™ system and Tescan Lyra 3 FEG microscopes. To ensure that the whole pillar is single crystalline were pillars produced in centres of large grains. The FIB milling procedure was optimized (Kuběna et al., 2009) so that the final shape of Al part of the pillar is as close to the perfect cylinder as possible.

The FIB milling was performed in several steps. First, faster milling by higher ion currents (~5 nA) was used for removing the majority of material in outer diameters, whereas the fine final milling of the central circular zone of about 3 μm in diameter was performed at low ion current (50 pA).

Loading of the pillars was carried out in compression using the MTS Nanoindenter XP machine equipped with a diamond flat punch of 20 μm in diameter. The diameter of the removed zone by FIB was chosen to be 25 μm, to ensure that the punch will not touch any other object except the pillar. During the deformation, it was ensured that the face of the flat punch was parallel to the upper face of pillars. The tests were carried out at nominal constant loading rate of 0.001 mNs^{-1}. At the onset of the deformation, pillars were therefore loaded in pure compression. Several unloading cycles were done with the purpose to measure elastic slope of the curve and to calculate Young modulus from these data.

Continuous stiffness measurement technique was used for measuring of indentation modulus and hardness as function of indentation depth. The indentation depth was chosen as 2 μm. It is know, that indentation modulus and hardness depend on indentation depth especially in case of thin film deposited on surface. A representative value of Al thin film was determined from plateau witch was found in dependences of indentation modulus and hardness on indentation depth.

From the microcompression experiments an equivalent of macroscopic compression curve is obtained. Such stress-strain curve provides information about yield stress, stress at chosen strain level or work hardening rate. For calculation of Young modulus, finite elements modelling must be used.

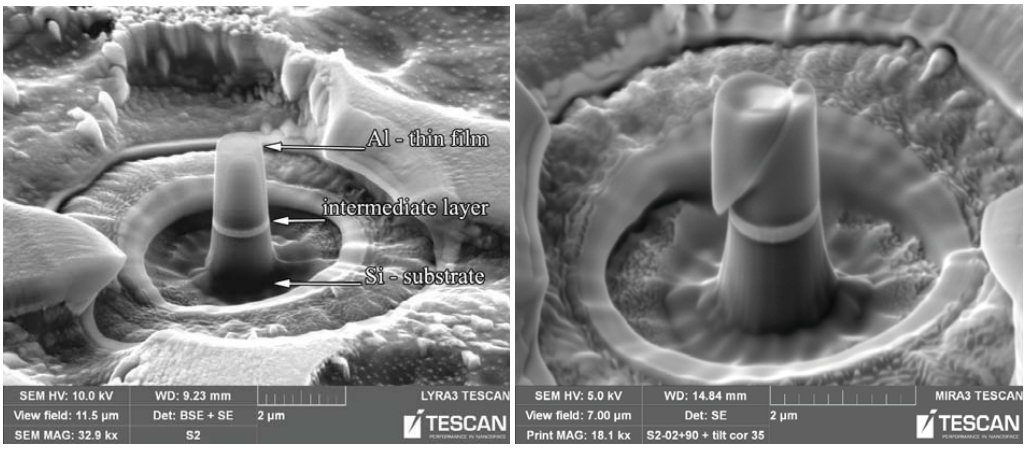

Fig. 1: The microcompression pillar S2 (a) before deformation; (b) after deformation

3. Results

3.1. Microcompression test

Prepared pillar from previous experiment is shown in Figure 1a. It was prepared using optimized process, (Kuběna et al., 2009). It is obvious that its geometry is close to the ideal shape, the minimum possible taper angle, smooth transition of the sample into the surrounding substrate and optimum depth of removed zone. These parameters have the greatest impact on homogeneous stress distribution in the sample. In this case the tapper angle is only 4 degree, substrate surface around pillar is also partially removed and substrate around pillar is not too rough. Pillar after microcompression test is show in Figure 1b. The obvious slip bands are likely produced during plastic bursts during deformation.

During microcompression test force and displacement of flat punch and time was continuously recorder. This data were recalculated on values of engineering stress and engineering deformation according to equations

$$\sigma = \frac{F}{S_0} \tag{1}$$

$$\varepsilon = \frac{\Delta l}{l_0} \tag{2}$$

where S_0 is the initial cross-section of the pillar, l_0 is initial height of pillar.

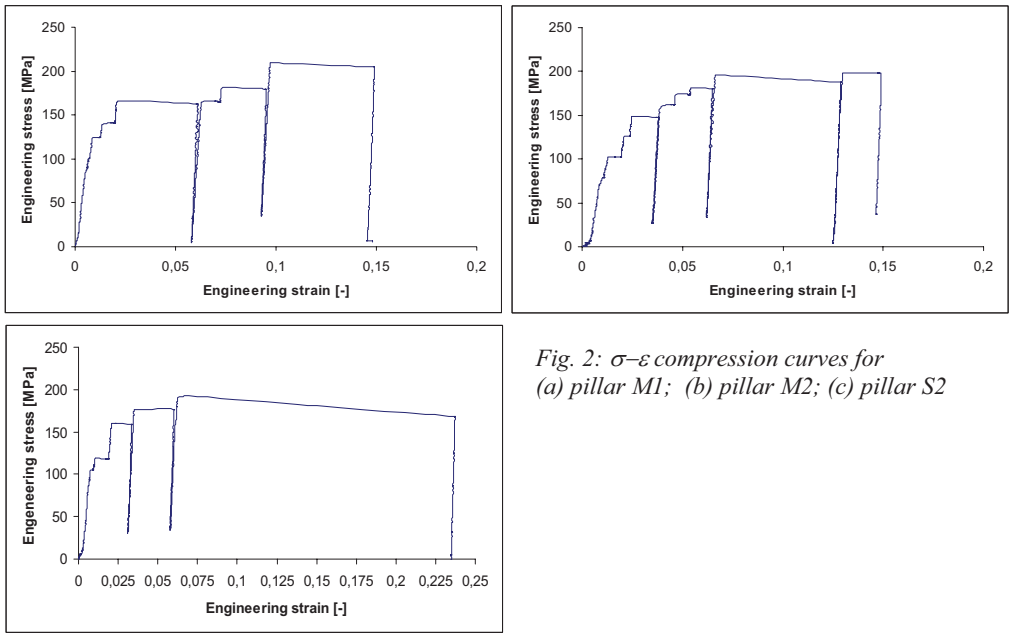

Fig. 2: σ–ε compression curves for (a) pillar M1; (b) pillar M2; (c) pillar S2

Actually, compression tests were carried out on monocrystalline pillars, therefore results strongly depend on crystallographic orientation of pillars. The crystallographic orientation was measured by EBSD followed by Schimd factor m determination. Subsequently, it was possible to recalculate σ–ε coordinates to τ–γ coordinates by equations $\tau = \sigma.m$ and $\gamma = \varepsilon / m$. Example of σ–ε compression curves for three different pillars are shown in Figure 2.

Obviously, the shapes of compression curves in Figure 2 are completely different from typical curve of the bulk materials. The deformation behaviour of pillars consisted of sudden jumps of fast plastic deformation called plastic bursts in the literature. Firstly, stress increases and pillars are deformed only elastically. After reaching of stress necessary for activation of a dislocation source, tens or hundreds

dislocations loops propagate through pillar and disappear on free surface of pillars. It results in plastic bursts and in fast deformation of pillars as long as the dislocation source is active. When the dislocation source is exhausted, pillars are deformed again only elastically until other dislocation source is activated. The strain hardening was not observed.

3.2. Determination of elastic slope from experimental measurements

A methodology for evaluation of experimental data for given type of testing (Petráčková et al., 2012) has not been fully established yet. Since dependence of loading force on deformation of pillar is measured, following procedure was adopted:

- To determine a strain $\varepsilon(z)$ in direction of loading we consider height h of Al film (see Fig. 3). Then $\varepsilon(z) = u(z)/h$, where $u(z)$ is experimentally measured displacement applied on the top surface of the pillar.
- As a stress σ we consider force applied on top of pillar (loading force of nanoindenter) divided by mean value of area cut perpendicular to pillar axis through Al layer. The typical dependence of σ - $\varepsilon(z)$ is shown in Fig. 2

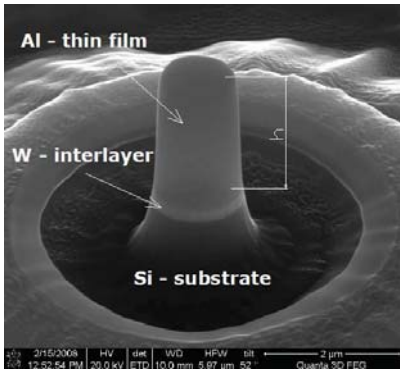

Fig. 3: Example of tested pillar. Geometry of the substrate part of the pillar, the tapper angle and the intermediate layer are taken into account for the Young modulus determination.

We assume that the elastic deformation of σ - $\varepsilon(z)$ curve is described by the unloading parts. From the first unloading, the elastic slope was determined. The elastic slope reflects the elastic deformation of the Al specimen, W – intermediate layer and Si substrate.

During the next loading cycle the sample is already partially deformed and has already a different shape than that used for numerical calculation. For this reason, data from first unloading are considered as the most reliable (see $E_{exp,1}$ value in Table 1). The parameters of second unloading are presented for the comparison (see $E_{exp,2}$ values in Table 1).

Three different pillars were measured and the resulting values of measured elastic slopes E_{exp} are shown in Table 1 for each tested pillar.

3.3 Numerical simulation for determination of Young modulus

Finite element method (FEM) was used for numerical simulation of microcompressive test and theoretical values of elastic slope were found (see E_p values in Table 1).

The data determined from experimental measurements (E_{exp1}) are slightly but systematically smaller than the values calculated with FEM. It is caused by the fact that the mechanical properties of all simulated components were taken from literature for the pure, bulk Al which may differ from the properties of thin film prepared by the PVD process.

Geometric factors of tested pillars such as conical shape of pillar, tungsten interlayer between studied Al layer and Si substrate, silicon substrate, etc. influence the measured elastic slopes. The influence of the three mentioned factors was numerically evaluated. Due to the linear elasticity, the influence of the individual factors on experimental data is proportional.

The most influencing geometric factor is the presence of Si substrate. It was estimated that it reduces the measured elastic slope during the microcompressive testing by almost 30%. That can be expected because the substrate creates a significant part of pillar and is also deformed during the testing. Quantitatively, influence of the substrate is described by coefficient C_1. Its values are presented in Table 1.

Tab. 1: Measured and calculated data.

Sample	pillar axis	$E_{exp,1}$ [GPa]	$E_{exp,2}$ [GPa]	E_p [GPa]	C_1	C_2	C_3	$E_{p,cor}$ [GPa]
M1	[3 5 9]	48.0	56.1	52.35	1.36	1.03	0.99	**66.6**
M2	[2 4 5]	45.6	52.3	56.30	1.22	1.07	0.99	**58.9**
S2	[1 2 3]	48.7	55.5	52.22	1.33	1.04	0.99	**66.7**

$E_{exp,1}$ – elastic slope obtained by experimental measurements (first unloading),

$E_{exp,2}$ – elastic slope obtained by experimental measurements (second unloading),

E_p – theoretical elastic slope obtained by numerical simulation of microcompressive test. As the input, elastic constants found in the literature for pure Al were used,

C_1, C_2, C_3 – correcting coefficients describing influence of substrate, conical geometry, and interlayer,

$E_{p,cor} = E_{exp,1} \cdot C_1 \cdot C_2 \cdot C_3$, i.e. the values of Young modulus for given orientation of Al crystal lattice

Second geometric factor which has influence on the elastic slope is conical shape of pillars. The FIB procedure used for preparation of testing pillars does not allow producing the pillar as a prefect cylinder. With the optimized procedure (Kuběna et al., 2009), it can be ensuring that pillar shape is close to cylindrical one with the taper angle of 4°. Numerical expression of the influence on elastic slope is shown in table 1 as coefficient C_2. In this case the conical geometry of pillar influences data obtained by experiment of about 5%. This factor does not depend on material parameters of the pillar but only on the geometry. It means that multiplying experimental data by $C_2 = 1.05$ eliminates the influence of conical geometry with taper angle of 4 degree for any type of material tested.

Finally, it was estimated that existence of tungsten interlayer affects the elastic slope by about 1%. If the interlayer has the same thickness, negligible in comparison with the studied thin film, its influence is small and can be neglected. This holds for any combination of materials. Numerical expression of this effect is shown in Table 1 as C_3 coefficient.

The last column in Table 1 is the Young modulus of the Al film, for the given crystallographic orientation. It was calculated from the first elastic unloading and corrected for the three geometrical effects:

$$E_{p,cor} = E_{exp,1} \cdot C_1 \cdot C_2 \cdot C_3 \quad (3)$$

It is visible that the E values are in a good agreement with the values for bulk Al, which varies from 64.1 GPa for <100> direction to 77.4 GPa for <111> direction. On the other hand, the E values of Al thin films prepared by PVD process reported in the literature varies significantly, from about 47 to 74 GPa (Chinmulgund et al., 1995). It can be explained by the fact that the deposited materials contain porosities and other defects. The high values of E found in this work shows that the tested film is of a very good quality.

4. Conclusions

In this paper, the methodology for evaluation of Young modulus of thin film from data obtained by microcompressive test was suggested. The influence of specific pillar geometry and presence of other phases (W – interlayer, Si – substrate) within the tested specimen can be calculated by finite element method and elastic slope obtained directly from experimental stress–strain curve can be corrected for these factors. The measured value of elastic slope was taken from the first unloading part of the curve. It was found that the elastic constants of the tested film are close to the ones reported for bulk Al which means that the film is of a good quality and did not contain significant amount of porosity.

Acknowledgement

This work was supported by Specific academic research grant of the Ministry of Education, Young and Sports of the Czech Republic provided to Brno University of Technology, Faculty of Mechanical Engineering FSI-S-11-11/1190

References

Chinmulgund, M., Inturi, R.B., Barnard, J.A.: Effect of Ar gas pressure on growth structure, and mechanical properties of sputtered Ti, Al, TiAl, and Ti_3Al film. *Thin Solid Films* 270, 260, (1995)

Kruml, T., Stranyanek, M., Ctvrtlik, R., Bohac, P., Vystavel, T. and Panek, P.: A new method for mechanical testing of thin films: application on Aluminum. *Journal of Material Research 24* (2009), 1353

Kuběna, I., Kruml, T.: Optimalizace přípravy mikrokomresních vzorků z tenkých vrstev pomocí fokusovaného iontovéhosvazku. In: *Víceúrovňový design pokrokových materiálů '09*,

Kubena, I., Kruml, T., Hutar, P., Bohac, P., Stranyanek, M., Ctvrtlik, R., Panek P. and Vystavel, T.: Measurement of mechanical properties of thin films by nanocompresion. In: *Vrstvy a povlaky 2008*, Liss, Roznov p R., 103, (2008)

Kuběna, I., Kruml. T., Vystavěl, T.: Příprava mikrokompresních vzorků z tenkých vrstev po-mocí fokusovaných iontových svazků. *SEMDOK 2009 Conference proceedings*, Súlov, 73, (2009)

Nix, W.D.: Mechanical properties of thin films. *Metallurgical Transactions A* 20 A (1989), 2217

Nix, W.D., Greer, J.R., Feng, G., Lilleodden, E.T.: Deformation at the nanometer an microme-ter length scales: Effect of strain gradients an dislocation starvation. *Thin Solid Films* 515 (2007), 3152

Petráčková, K., Kuběna, I., Truhlář, M., Náhlík, L., Kruml, T.: Estimation of mechanical properties of thin Al surface layer. *Applied Mechanics 2012*

Uchic, M.D., Dimiduk, D.M.: A methodology to investigate size scale effects in crystalline plasticity using uniaxial compression testing. *Materials Science and Engineering A* 400-401 (2005), 268

18th International Conference
ENGINEERING MECHANICS 2012
Svratka, Czech Republic, May 14 – 17, 2012

pp. 1441–1448
Paper #55

ACTIVE VIBRATION CONTROL OF A CANTILEVER BEAM

J. Tůma*

Abstract: *The paper deals with analysis of a cantilever beam equipped by the active vibration control system. The cantilever beam as a continuum is approximated by a lumped-parameter system. The lumped-parameter model enables to derive the transfer functions relating forces to displacements, to determine the appropriate controller type and to determine under what conditions the system will work.*

Keywords: ***cantilever beam, lumped-parameter model, active vibration control, controller type.***

1. Introduction

Control theory is based on the models with one (single) input and one output (SISO) or models with multiple inputs and multiple outputs (MIMO). These models are described by systems of ordinary differential equations. The description of a continuum on the contrary uses partial differential equations. For the analysis of the continuum, suitable approximation of systems with a lumped parameter model must be used (Preumont, & Seto, 2008).

The computed transfer functions of the lumped-parameter system allow to determine the appropriate controller type and to determine under what conditions the system will work (Genta, 2009).

2. Lumped parameter model

A cantilever beam of the length L as a continuum can be divided into discrete elements of the same length ΔL that are modeled using rigid-body dynamics. How to create the lumped parameter model of the cantilever beam of the rectangular cross section and to associate this multibody system with the Cartesians coordinates x, y, z is shown in Fig. 1. The cantilever beam is clamped at the xy-plane and its centerline is parallel to the z-axis. It is assumed only planar motion of the cantilever beam in the yz-plane. Let N be the number of flexible links in the model. Linking of a pair of adjacent beam elements is considered in the mentioned plane as free with a torsion spring. The coordinates of the multibody systems are usually associated with the gravity centers. Such coordinate system requires the additional set of constrains for linking of the individual beam elements in one point. Additional equations are not needed if the coordinate system is chosen in such a way that describes motion of the meeting points of two adjacent elementary beams. The vertical coordinates of these points are marked by $y_1, y_2, \ldots, y_N$. The angle of rotation with respect to the horizontal axis can be marked by $_1$ $_2$ $_N$.

The deflection of the beam may be expressed as a function of the beam length and the difference $\Delta\delta$ of the adjacent elements $\Delta y = \Delta\delta\,\Delta L$. The bending stiffness K_δ of the elementary cantilever beam relates the applied bending moment M to the resulting relative rotation δ of the elementary beam

$$K_\delta = \frac{M}{\Delta\delta} = \frac{3EI_x}{\Delta L} \tag{1}$$

where E is oung s modulus of the beam material [N/m^2], $I_x = bh^3/12$ is the area moment of inertia of the beam cross-section [m^4] about the horizontal x-axis, b is the beam width and h is the beam height.

Prof. Ing. Jiří Tůma, CSc.: VSB – Technical University of Ostrava, Faculty of Mechanical Engineering, 17. listopadu 15, 703 88 Ostrava, Czech Republic, e-mail: jiri.tuma@vsb.cz

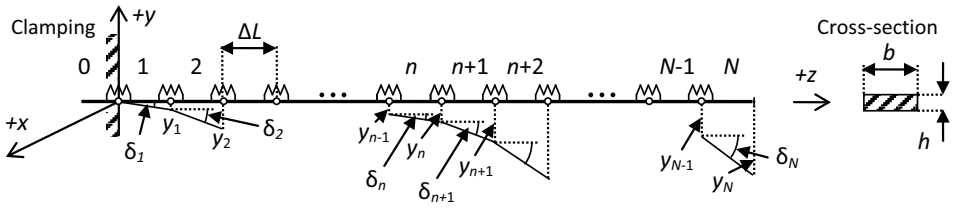

Fig. 1: Coordinates and elements of a cantilever beam.

The coordinates of the beam equidistant points in the Cartesian coordinates and the independent generalized coordinates for Lagrangian equations of motion are identical. For further derivation it makes sense only motion in the direction of the *y*-axis. Because they are assumed small deformations, the shifts of the meeting points in the direction of the *z*-axis are neglected. If all angles are small enough, then their measure in radians is given by the formula

$$\begin{aligned} &\delta_n = \left(y_n - y_{n-1}\right)/\Delta L, \\ &\Delta\delta_n = \delta_{n+1} - \delta_n. \end{aligned} \tag{2}$$

The coordinates of the gravity centre of the elementary beams are as follows

$$Y_1 = y_1/2, \quad Y_n = \left(y_n + y_{n-1}\right)/2 \tag{3}$$

The potential V and kinetic T energy of the cantilever beam in the horizontal position as a continuum replaced by its lumped parameter model is as follows

$$\begin{aligned} V &= \sum_{n=0}^{N-1} \frac{1}{2} K_\delta \left(\Delta\delta_n\right)^2 + \sum_{n=1}^{N} \Delta m g Y_n, \\ T &= \sum_{n=1}^{N} \left(\frac{1}{2} \Delta m \left(\frac{\mathrm{d}\, Y_n}{\mathrm{d}\, t} \right)^2 + \frac{1}{2} J_x \left(\frac{\mathrm{d}\, \delta_n}{\mathrm{d}\, t} \right)^2 \right), \end{aligned} \tag{4}$$

where J_x is the moment of inertia [kgm^2] about the horizontal x-axis and perpendicular to the centerline of the elementary beam. For a solid cuboid of height h, and length ΔL it is $J_x = \Delta m\left(\Delta L^2 + h^2\right)/12$. The cantilever beam is considered as a conservative system. Lagrange s equations of motion of such a system are as follows

$$\frac{\mathrm{d}}{\mathrm{d}\, t}\left(\frac{\partial T}{\partial \dot{y}_n}\right) - \frac{\partial T}{\partial y_n} + \frac{\partial V}{\partial y_n} = 0, \quad n = 1,\, 2, \ldots, N \tag{5}$$

After introduction symbols **M** for a mass square matrix and **K** for a stiffness square matrix and **G** for a gravity force column vector and **y** for a coordinate column vector into the matrix equation of motion we obtain

$$\mathbf{M}\ddot{\mathbf{y}} + \mathbf{K}\mathbf{y} + \mathbf{G} = \mathbf{0} \tag{6}$$

where

$$\mathbf{M} = \begin{bmatrix} B & A & & & \\ \vdots & \vdots & \vdots & \vdots & \vdots \\ & A & B & A & \\ & \vdots & \vdots & \vdots & \vdots \\ & & & A & B/2 \end{bmatrix}, \quad \mathbf{K} = \frac{K_\delta}{\Delta L^2} \begin{bmatrix} 6 & \cdots & & & & & \\ \vdots & \vdots & \vdots & \vdots & \vdots & \vdots & \vdots \\ & 1 & -4 & 6 & -4 & 1 & \\ & \vdots & \vdots & \vdots & \vdots & \vdots & \vdots \\ & & & & & \cdots & 1 \end{bmatrix}, \quad \mathbf{G} = mg \begin{bmatrix} 1 \\ \vdots \\ 1 \\ \vdots \\ \frac{1}{2} \end{bmatrix}, \quad \mathbf{y} = \begin{bmatrix} y_1 \\ \vdots \\ y_n \\ \vdots \\ y_N \end{bmatrix}, \tag{7}$$

$$A = \frac{\Delta m}{4}\left(1 - \frac{1}{3}\left(1 + \left(\frac{h}{\Delta L}\right)^2\right)\right), \; B = \frac{\Delta m}{2}\left(1 + \frac{1}{3}\left(1 + \left(\frac{h}{\Delta L}\right)^2\right)\right) \tag{8}$$

2.1 Steady state deformation shape of the cantilever beam

Steady state deformation of the beam in the horizontal position due to the gravity force is resulting from solution of the equation $\mathbf{Ky}+\mathbf{G}=\mathbf{0}$. If the cantilever beam is in vertical position then $\mathbf{y}_0=\mathbf{0}$. For testing a beam with the following parameters is prepared: L = 0.5 [m], b = 0.04 [m], h = 0.005 [m]. The beam is divided into N = 10 elements. Deflection of the beam s own self-weight is shown in Fig. 2A.

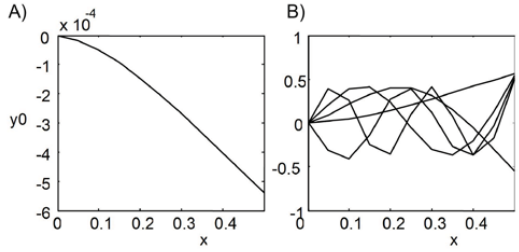

Fig. 2: A) Deflection of the cantilever beam's own self-weight, B) The first 5 of 10 modal shapes of the cantilever beam.

2.2 Free vibration

For vertical position of the cantilever beam the governing equation of free vibration is as follows

$$\mathbf{M}\ddot{\mathbf{y}}+\mathbf{Ky}=\mathbf{0} \tag{9}$$

The solution of this equation of the homogenous type is assumed to be in the form of $\mathbf{y}=\mathbf{u}\exp(j\omega t)$, where $\mathbf{u}$ is an n-dimensional vector of the oscillation amplitudes and ω is an angular frequency. After substitution into (9) we obtain

$$\left(\mathbf{K}-\omega^2\mathbf{M}\right)\mathbf{u}=\mathbf{0} \tag{10}$$

Given that the mass matrix is symmetric and positive definite then substitution $\lambda=\omega^2$ and multiplication of the previous equation by the inverse mass matrix on the left side results in

$$\left(\mathbf{A}-\lambda\mathbf{I}\right)\mathbf{u}=\mathbf{0},\quad \mathbf{A}=\mathbf{M}^{-1}\mathbf{K} \tag{11}$$

where $\mathbf{I}$ is a unit matrix. Given that the mass and stiffness matrices are symmetric then the matrix $\mathbf{A}$ is symmetric as well. For the nonzero vector u the determinant of the matrix $(\mathbf{A}-\lambda\mathbf{I})$ has to be zero. Because the determinant $\det(\mathbf{A}-\lambda\mathbf{I})$ is an n-degree characteristic polynomial of λ, the number of roots λ_n, called the eigenvalues, is equal to the degree of polynomial. The corresponding nonzero solution of the homogenous equation is called an eigenvector. It is proved in the linear algebra theory that all the eigenvalues of the symmetric matrix are real and an arbitrary pair of the eigenvectors, corresponding to different eigenvalues, is orthogonal. We form a spectral matrix $\mathbf{\Lambda}=\mathrm{diag}(\lambda_1,\lambda_2,...,\lambda_N)$ and an eigenvector matrix $\mathbf{U}=[\mathbf{u}_1,\mathbf{u}_2,...,\mathbf{u}_N]$.

Because the beam is divided into 10 elements, it is possible to calculate 10 modal frequencies and 10 modal shapes of vibration. Only 5 out of the modal shapes, identifiable by the number of nodes, are shown in Fig. 2B. The modal frequencies are summarized in Tab. 1.

Tab. 1: Modal frequencies for N = 10.

Mode	1	2	3	4	5	6	7	8	9	10
Freq in Hz	26.6	167	470	922	1522	2256	3093	3965	4755	5309

2.3 Excited vibration

The excited vibration of the cantilever beam in the vertical position describes the equation of motion with the external forces p_1, p_2, , p_N assembled into a vector $\mathbf{p}$ on the right side and acting at the gravity centers of the beam elements

$$\mathbf{M}\ddot{\mathbf{y}} + \mathbf{K}\mathbf{y} = \mathbf{p} \tag{12}$$

The presence of viscous damping, such as a dissipative force, extends the left side of the equation of motion by an additional term which is proportional to velocity

$$\mathbf{M}\ddot{\mathbf{y}} + \mathbf{C}\dot{\mathbf{y}} + \mathbf{K}\mathbf{y} = \mathbf{p}, \quad \mathbf{C} = \alpha\mathbf{M} + \beta\mathbf{K}, \tag{13}$$

where the matrix of proportionality **C** for Rayleigh damping is a linear combination of the mass and stiffness matrices, and α, β are constants of proportionality. The relationship to the damping ratio ξ can be seen using the formula $\xi = \pi(\alpha/f_0 + \beta f)$, where f_0 is the frequency in hertz

3. Transfer Function

Vibration of mechanical structures is dampened very slightly. It s only a few percent of critical damping. The purpose of active vibration control is increase ability of structures to absorb vibration by adding an artificial electronic feedback. To analyze the effect of active vibration damping it is firstly assumed that the system is not damped at all.

It is assumed that **y** and **p** are complex harmonic functions of time ($\exp(\omega t)$) and **Y** and **P** are complex amplitudes, respectively. The transfer function in the form of a squared matrix **H**, relating the displacement $y_r, r = 1,...,N$ of the lumped masses to the force $p_q, q = 1,...,N$ acting at these masses, is defined by the following formula (Hi & Fu, 2001)

$$\mathbf{Y} = (\mathbf{K} - \lambda\mathbf{M})^{-1}\mathbf{P} = \mathbf{H}\,\mathbf{P} \tag{13}$$

A modal transform $\mathbf{y} = \mathbf{V}\,\mathbf{q}$ is the basis for the derivation of the transfer function. The coordinates y are transformed into generalized coordinates q by using the matrix **V**. The relationship of the transfer function to the modal properties of the structure can be defined if the modal transformation matrix V has the following property $\mathbf{V}^T\mathbf{M}\,\mathbf{V} = \mathbf{I}$. It can be proved that the orthonormal eigenvectors vn arranged in the matrix V are given by

$$\mathbf{v}_n = \mathbf{u}_n \Big/ \sqrt{\mathbf{u}_n^T\mathbf{M}\mathbf{u}_n}, \quad n = 1,...,N \tag{14}$$

The transfer function matrix **H**, called the receptance, as a function of $\lambda = \omega^2$ depends on the eigenvectors and eigenvalues according to the formulas

$$\begin{aligned} &\mathbf{H} = (\mathbf{K} - \lambda\mathbf{M})^{-1} = \mathbf{V}\mathbf{D}\mathbf{V}^T, \\ &\mathbf{D} = \mathrm{diag}(1/(\lambda_1 - \lambda), 1/(\lambda_2 - \lambda), ..., 1/(\lambda_N - \lambda)), \end{aligned} \tag{15}$$

where **D** is a diagonal matrix. The matrix **H** relates the force acting at the *q*-th lumped mass, to the displacement y_r of the *r*-th lumped mass, where is measured. The Laplace transform of the individual elements of the matrix **H** is as follows

$$H_{r,q}(s) = \sum_{n=1}^{N} \frac{v_{nr}v_{qn}}{\omega_n^2 + s^2}, \quad r, q = 1, 2, ..., N, \tag{16}$$

where $v_{q,r}$ *q, r* =1,...,N is the *r*-th element of the *q*-th normalized eigenvector. The poles of the transfer function lie on the imaginary axis of the complex plane. The system is on the stability margin, not stable and simultaneously not unstable.

Tab. 2: Values of the product $v_{nN}v_{1n}$ for N=10.

n	1	2	3	4	5	6	7	8	9	10
$v_{nN}v_{1n}$	0.146	0.669	1.339	-1.775	1.866	1.628	1.176	0.670	-0.264	0.049

The product $v_{nN}v_{1n}$ of the elements of the matrix **V** is given in Tab. 2.

The assumption (16) about the stability margin of the cantilever beam as a dynamic system is the worst one, because the amplitude of vibration always decays after some time.

4. Active vibration control

The purpose of the system for the active vibration control (AVC) is to compensate the effect of a disturbing external force on the vibration of the beam. It is desirable to relocate the poles of the transfer function of the controlled system from the imaginary axis in the left half-plane of the complex plane. The cantilever beam is considered as an MIMO system composed of the lumped masses whose count is equal to N. Vibration of all these masses can be controlled by forces acting at all of them as it is shown in Fig. 3.

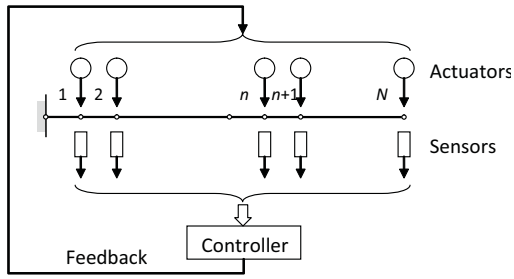

Fig. 3: Active vibration control.

We assume that the system is of the SISO type with a controller with a transfer function $R(s)$. There are two possible solutions, the collocated and non-collocated active vibration control. For the collocated system the correcting force p_n acts and the response Y_n is measured in the same centre gravity of the beam element. For the non-collocated system it is assumed that the correcting force p_q acts at the lumped mass indexed by q and the vibrations are sensed at the lumped mass indexed by r. An example of the non-collocated system is shown in Fig. 4. Vibration of the free end element of this cantilever beam is sensed at $r = N$ and the correcting force acts at the element just next to the clamped end, therefore $q = 1$. A block diagram of the closed loop system is shown in Fig. 5.

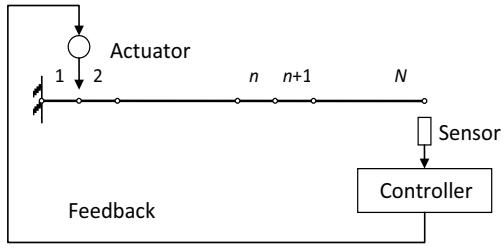

Fig. 4: Non-collocated system of active vibration control.

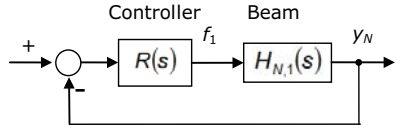

Fig. 5: Closed loop system of AVC

There is a transfer function of the closed-loop system $H_{r,SP}$, relating the displacement y_r of r-th lumped mass to the set point x_{SP}, and the function $H_{r,q}$, relating the displacement y_r to the feedback force p_q acting at q-th lumped mass

$$H_{r,SP}(s)=\frac{X_r(s)}{X_{SP}(s)}=\frac{R(s)H_{r,q}(s)}{1+R(s)H_{r,q}(s)}=\frac{R(s)\sum_{n=1}^{N}\frac{v_{mr}v_{qn}}{\omega_n^2+s^2}}{1+R(s)\sum_{n=1}^{N}\frac{v_{mr}v_{qn}}{\omega_n^2+s^2}}=\frac{R(s)\sum_{n=1}^{N}v_{mr}v_{qn}\prod_{\substack{k=1\\k\neq n}}^{N}\left(\omega_k^2+s^2\right)}{\prod_{n=1}^{N}\left(\omega_n^2+s^2\right)+R(s)\sum_{n=1}^{N}v_{mr}v_{qn}\prod_{\substack{k=1\\k\neq n}}^{N}\left(\omega_k^2+s^2\right)} \quad (17)$$

The term in the denominator of (2) is a polynomial of the squared variable *s*, the coefficients of the odd power are equal to zero. For a stable system, the variable *s* raised to odd powers must be added

$$R(s)\sum_{n=1}^{N}v_{mr}v_{qn}\prod_{\substack{k=1\\k\neq n}}^{N}\left(\omega_k^2+s^2\right)=\sum_{n=1}^{N}T_{D,n}s^{2n-1} \quad \Rightarrow \quad R(s)=\frac{\sum_{n=1}^{N}T_{D,n}s^{2n-1}}{\sum_{n=1}^{N}v_{mr}v_{qn}\prod_{\substack{k=1\\k\neq n}}^{N}\left(\omega_k^2+s^2\right)} \quad (18)$$

where $T_{D,n}$, n = 1,...,N are the mentioned positive coefficients. The degree of the polynomial in the numerator of the transfer function $R(s)$ is greater than the degree of the polynomial in the denominator. The feedback controller of the derivative type is on the stability margin by itself due to lack of terms with variable *s* raised to an odd power. The additional proportional part of the controller ensures stability (Tůma, 2012).

$$R(s)=F+Ts \quad (19)$$

where F is a gain and T is a time constant.

The disturbance force can be of the broad or narrow frequency spectrum. Suppose that the frequency spectrum of disturbance affects only the *d*-th mode of vibration.

$$H_{r,q}(s)=\frac{v_{dr}v_{qd}}{\omega_d^2+s^2}=\frac{K_d}{\omega_d^2+s^2} \quad (20)$$

The transfer function of the close loop with the controller described by the transfer function (19) is as follows

$$H_{r,SP}(s)=\frac{X_r(s)}{X_{SP}(s)}=\frac{(F+Ts)\frac{K_d}{\omega_d^2+s^2}}{1+(F+Ts)\frac{K_d}{\omega_d^2+s^2}}=\frac{K_d(F+Ts)}{s^2+K_dTs+\left(\omega_d^2+K_dF\right)} \quad (21)$$

where a gain factor $K_d=v_{dr}v_{qd}$ is called a residuum. As it is shown in Tab. 2 some of the gain factors are negative. The damping ratio ξ and the decay constant σ of the system described by (21) is equal to

$$\xi=\frac{1}{2}\frac{K_dT}{\sqrt{\omega_d^2+K_dF}}, \quad \sigma=\xi\sqrt{\omega_d^2+K_dF}=\frac{K_dT}{2} \quad (22)$$

The decay constant σ for $0<\xi<1$ and $\omega_d^2+K_dF>0$ determines an envelope of decaying vibration $\exp(-\sigma t)$. Strictly speaking if the decay constant is negative since $K_d<0$, then the vibration of the corresponding frequency does not decay and the system is unstable. Only natural damping of the cantilever beam can compensate this instability caused by active vibration control. Design of the controller parameters requires taking into account a number of external influences and mainly the natural material damping of the beam vibration.

The effect of active vibration control is often demonstrates on the vibration decay of the beam which is bended into a deflected position and suddenly released. In this case, only the lowest modes of vibration are excited.

Both the controller parameters can be calculated using the partial pole placement (Mottershead & Tehrani & Ram, 2009) as well. The pair of the complex conjugate poles $j\omega_k$, and $-j\omega_k$ of the transfer

function $H_{r,q}(s)$ will be placed in the complex conjugate poles $\mu_k = -\sigma_k + j\Omega_k$, and $\mu_k = -\sigma_k - j\Omega_k$ of the closed loop transfer function $H_{r,SP}(s)$. For both the replaced poles the denominator of $H_{r,SP}(s)$ have to be zero. We obtain two equations with unknown parameters T and F

$$\begin{aligned} 1 + (F + T\mu_k) H_{r,q}(\mu_k) &= 0, \\ 1 + (F + T\mu_k) H_{r,q}(\mu_k) &= 0. \end{aligned} \tag{23}$$

After rearranging the equations (19) we get

$$\begin{aligned} H_{r,q}(\mu_k) F + H_{r,q}(\mu_k)\,\mu_k T &= -1, \\ H_{r,q}(\mu_k) F + H_{r,q}(\mu_k)\,\mu_k T &= -1. \end{aligned} \tag{24}$$

The solution of these two equations is as follows

$$\begin{aligned} F &= -\frac{H_{r,q}(\mu_k)\,\mu_k - H_{r,q}(\mu_k)\,\mu_k}{H_{r,q}(\mu_k) H_{r,q}(\mu_k)\,\mu_k - H_{r,q}(\mu_k) H_{r,q}(\mu_k)\,\mu_k} \\ T &= +\frac{H_{r,q}(\mu_k) - H_{r,q}(\mu_k)}{H_{r,q}(\mu_k) H_{r,q}(\mu_k)\,\mu_k - H_{r,q}(\mu_k) H_{r,q}(\mu_k)\,\mu_k} \end{aligned} \tag{25}$$

Using the controller of the proportional-derivative type only one pair of poles can be placed into the stable part of the complex plane.

5. Simulation of active vibration control

Equations of motion of a mechanical system with an electronic feedback can be written in the form

$$(\mathbf{M}s^2 + \mathbf{C}s + \mathbf{K})\mathbf{y} = \mathbf{b}u + \mathbf{p}, \quad u = -(\mathbf{F} + \mathbf{T}s)^T \mathbf{y}, \tag{26}$$

where **b, F** and **T** are column vectors defined as follows

$$b_i = \begin{cases} 1, & i = q \\ 0, & i \neq q \end{cases}, \quad F_i = \begin{cases} F, & i = r \\ 0, & i \neq r \end{cases}, \quad T_i = \begin{cases} T, & i = r \\ 0, & i \neq r \end{cases}. \tag{27}$$

Then, by combining equations (25), we obtain the corrected damping and stiffness matrices

$$(\mathbf{M}s^2 + (\mathbf{C} + \mathbf{b}\mathbf{T}^T)s + (\mathbf{K} + \mathbf{b}\mathbf{F}^T))\mathbf{y} = \mathbf{p}. \tag{28}$$

For the cantilever beam described above we assume now that $N = 5$. Vibration of the free end element of this cantilever beam is sensed at $r = 5$ and the correcting force acts at the element just next to the clamped end, therefore $q = 1$. The damping **C** and stiffness **K** matrices are influenced by the feedback in the following way

$$\mathbf{K} + \mathbf{b}\mathbf{F}^T = \mathbf{K} + \begin{bmatrix} 0 & \cdots & F \\ \vdots & \ddots & \vdots \\ 0 & \cdots & 0 \end{bmatrix} \quad \mathbf{C} + \mathbf{b}\mathbf{T}^T = \mathbf{C} + \begin{bmatrix} 0 & \cdots & T \\ \vdots & \ddots & \vdots \\ 0 & \cdots & 0 \end{bmatrix} \tag{29}$$

Both the matrices **C** and **K** become asymmetric.

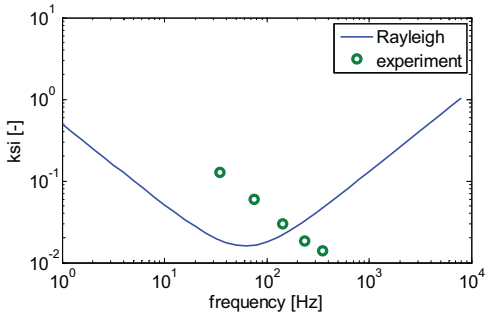

Fig. 6: The dependence of the damping ration ξ on frequency

It is assumed the viscous damping force (13), defined by the matrix $\mathbf{C} = \alpha\mathbf{M} + \beta\mathbf{K}$, where $\alpha = 0.159$, $\beta = 0.0000411$. The damping ratio "ksi" (ξ) for the first two modes of vibration is about 0.004 and the corresponding damping constant (σ) is about 0.6. The dependence of the damping ration ξ on frequency is shown in Fig. 6. Small circles indicate the damping ratio from the experimental modal analysis.

A force of 9.81 [N] is acting at the free end of the cantilever beam which is on the opposite side of the clamped end. The force is suddenly released at t = 0. A weak damping is added to avoid instability of the undamped response. The result of simulation of free vibration is shown in the left panel of Fig. 7 (AVC OFF).

The effect of the active vibration control in operation is shown in the right panel of Fig. 7 (AVC ON) as well. The gain F = 66.8 and the time constant T = 20.7 [s] were designed for the undamped cantilever beam. The damping constant of the first vibration mode was increased 10 times by using a simulated feedback. All the responses were calculated using Newmark s method for integrating differential equations.

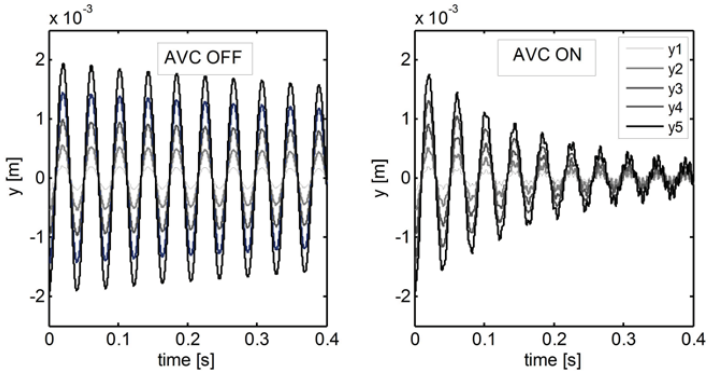

Fig. 7: Free vibration of the cantilever beam with AVC OFF and ON

6. Conclusions

The lumped-parameters model of the cantilever beam was designed using the method based on the modal analysis. It was proved that the cantilever beam can be actively damped only by a force which is controlled by the PD controller. The feedback of the D type is not sufficient for damping undamped systems. This paper is focused on the computation of the PD controller parameters using the pole placement method. The formulas for calculation the controller gain and time constant are derived.

Acknowledgement

This research has been supported by the Czech Grant Agency project No. P101/12/2520 "Active vibration damping of rotor with the use of parametric excitation of journal bearings".

References

Preumont, A. & Seto, K. (2008) Active Control of Structures, Wiley.

Genta, G. (2009) Vibration Dynamics and Control, Springer.

Hi, J. & Fu, -F. (2001) Modal Analysis, Butterworth Heinemann, Oxford.

Tůma, J. (2012) Analysis of active vibration control for a cantilever beam with the use of the lumped parameter model. In Dynamic of machines 2012. February 7-8, 2012, Prague, Cyech Republic, pp. 157-164.

Mottershead, J. E. & Tehrani, M. G. & . M. Ram, . M. (2009) An Introduction to the Receptance Method in Active Vibration Control. In Proceedings of the IMAC-XXVII, February 9-12, 2009 Orlando, Florida USA.

18th International Conference
ENGINEERING MECHANICS 2012
Svratka, Czech Republic, May 14 – 17, 2012

pp. 1449–1455
Paper #16

INVESTIGATIONS OF ORTHOTROPIC DECKS

Sh. Urushadze [*], L. Frýba [**], M. Pirner [***]

Abstract: *The partial investigations of orthotropic decks carried out in the Institute of Theoretical and Applied Mechanics, v.v.i., in Prague for a project of the European Union „BRIFAG" is described. The performance of orthotropic decks is studied under dynamic loads including the crack propagation, estimation of fatigue life of the bridge elements, etc. It was found that the most vulnerable detail appeared at the spatial connection of the deck with cross and longitudinal beams. The results are concentrated in a figure of stress ranges as a function of the number of stress cycles.*

Keywords: ***Orthotropic decks, fatigue, stress, Wöhler line.***

1. Introduction

The European Union approved the research of fatigue behaviour of orthotropic decks that are applied to highway as well as railway bridges and formed an international team see Fig. 1 whose main task is to study the fatigue of orthotropic decks on both the highway and railway bridges. The impact on economy and research is the most important.

Each of the participant team has its own research programme and, here, only the results achieved in ITAM (and not all) are shortly mentioned. The team can be seen in the Fig. 1 during its meeting in the laboratory of ITAM in Prague, (Lukić et al., 2009), (Akhlaghi et al., 2009).

ITAM tested the elements of orthotropic decks on fatigue in the testing machine up to the cracks. The evaluation of tests presented the relationship of stress ranges on the number of absorbed stress cycles (Wöhler line). It is supposed that the stress ranges are the main factor of fatigue cracks in structures. This function enables also to estimate the fatigue life of the investigated structural element.

Fig. 1: The BRIFAG meeting in the laboratory of ITAM, Prague, 2010.

[*] Ing. Shota Urushadze, CSc.: Institute of Theoretical and Applied Mechanics Academy of Sciences of the Czech Republic, v.v.i; Prosecká 76, 190 00 Praha 9. Tel.: +420.286882121, Fax.: +420.222363071; E-mail: urushadze@itam.cas.cz.

[**] Prof. Ing. dr.h.c. Ladislav Frýba, DrSc.: Institute of Theoretical and Applied Mechanics Academy of Sciences of the Czech Republic, v.v.i; Prosecká 76, 190 00 Praha 9. Tel.: +420.283881646, Fax.: +420.286884634; E-mail: fryba@itam.cas.cz

[***] Prof. Ing. dr.h.c. Miroš Pirner, DrSc.: Institute of Theoretical and Applied Mechanics Academy of Sciences of the Czech Republic, v.v.i; Prosecká 76, 190 00 Praha 9. Tel.: +420.286882121, Fax.: +420.286884634; E-mail: pirner@itam.cas.cz.

The orthotropic decks represent a popular structural element since the Second World War and it is counted now several thousands in structural engineering (civil, industrial, ship and space structures) all over the world. Their advantages are: light weight, low height and low first natural frequencies. On the other hand, as they are fully welded, they suffer from the secondary stresses that cause cracks and the initiation of fatigue cracks. Therefore, the orthotropic decks should be carefully studied and tested.

2. Specimens

The investigated model (see Fig. 2) represents a part (a cutout) of a railway bridge in the approximate scale 1 : 1. The strait ribs are preferred on railway bridges because they provide several advantages: no closed spaces, no corrosion, simple welding, easy maintenance and painting.

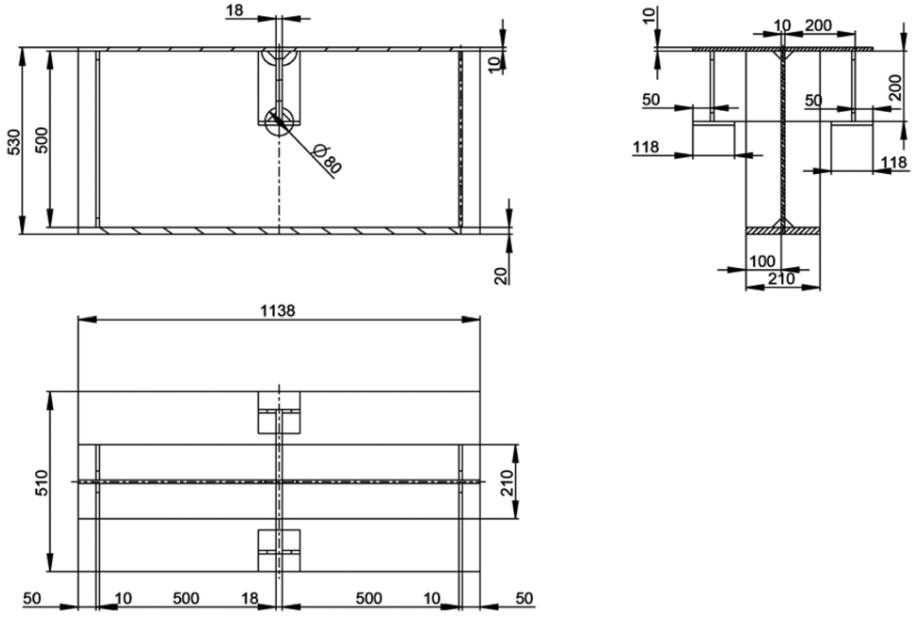

Fig. 2: The tested model of the orthotropic deck.

A series of 16 specimens was tested under the harmonic load in the laboratory of ITAM. The applied forces with various minimum $F_{\min}$ and the maximum $F_{\max}$ forces as well as the number of stress cycles up to the fracture were recorded. All tested specimens results are summarized in the Table 1.

Tab. 1: A survey of static and dynamic tests.

N. of specimens	type of testing machines	Fmin [kN]	Fmax [kN]	Number of cycles
A1 static force	ITAM GTM 500 kN	0	477	
	TZUS RK MFL PRUFSYSTEME	0	780	
A2 dynamic force	test machine MTS 250 kN, frequency 3 Hz	10	210	5 527 812
	test machine GTM 500 kN, frequency 2 Hz	10	410	1 543 930

A3 dynamic force	test machine GTM 500 kN, frequency 2 Hz	10	360	5 000 000
A4 static force	test machine GTM 500 kN,	0	200	
A4 dynamic force	test machine GTM 500 kN, frequency 2 Hz	10	380	2 236 037
A5 static force	test machine GTM 500 kN,	0	200	
A5 dynamic force	test machine GTM 500 kN, frequency 2 Hz	10	390	547 400
A6 dynamic force	test machine GTM 500 kN, frequency 2 Hz	10	390	576 000
A7 with CFRC	test machine GTM 500 kN, frequency 2 Hz	10	390	3 210 000
A8 with CFRC	test machine GTM 500 kN, frequency 2 Hz	10	390	2 320 000
A9 dynamic force	test machine GTM 500 kN, frequency 2 Hz	10	390	596 453
A10 dynamic force	test machine GTM 500 kN, frequency 2 Hz	10	400	371 000
A11 dynamic force	test machine GTM 500 kN, frequency 2 Hz	10	400	716 000
A12 dynamic force	test machine GTM 500 kN, frequency 2 Hz	20	380	1 350 000
A13 dynamic force	test machine GTM 500 kN, frequency 2 Hz	20	400	820 000
A14 dynamic force	test machine GTM 500 kN, frequency 2 Hz	10	370	2 600 000
A15 dynamic force	test machine GTM 500 kN, frequency 2 Hz	20	390	682 500
A16 dynamic force	test machine GTM 500 kN, frequency 2 Hz	20	370	1207000

It has approved that the stress range is the most important parameter affecting the fatigue of structures. The stress range is defined as the difference of the local maximum and minimum of stresses in the investigated point:

$$\Delta\sigma = \sigma_{\max} - \sigma_{\min} \tag{1}$$

It enables also to estimate the fatigue life of the investigated structural element.

The key results were concentrated in the Fig. 3 and evaluated by the last square method. It presented the mean value

$$\Delta\sigma = -10^{-6} N + 81{,}126 \tag{2}$$

where is $\Delta\sigma$ in N/mm^2 and N is the number of absorbed stress cycles

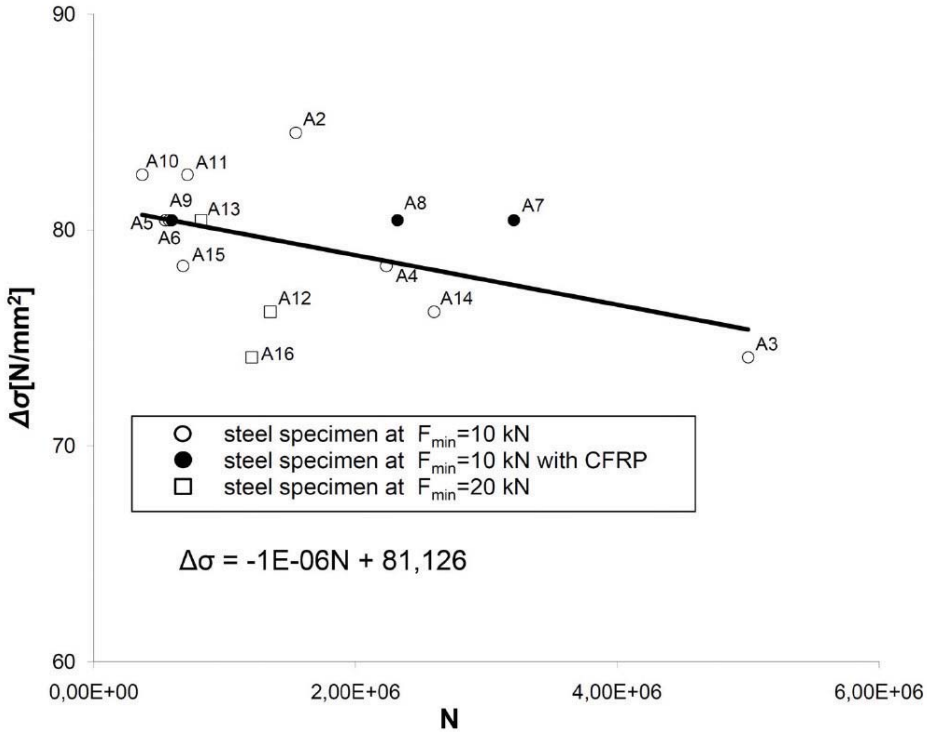

Fig. 3: Stress ranges as a function of absorbed cycles.

The other involved teams tried to raise the fatigue life with the glued carbon fibre elements (Prof. Pirner et al.) and to study the breathing of webs (Prof. Škaloud et al.). Together with the other international teams, the programme has presented a picture on the problem from various sites.

3. Arising of cracks

The arised cracks have at the beginning an unimportant significance. The traffic can continue in most cases. However, the regular (or irregular) inspections signalize that the inspections should be more often. In the mean time, the bridge authorities may prepare the suitable precautions: design a new structure or its repair, etc.

The typical cracs in the cross girder web can be seen in the on the Fig. 4 (specimen A 2) and on the Fig. 5 (specimen A 3).

Fig. 4: Fatigue cracks on the specimen A2.

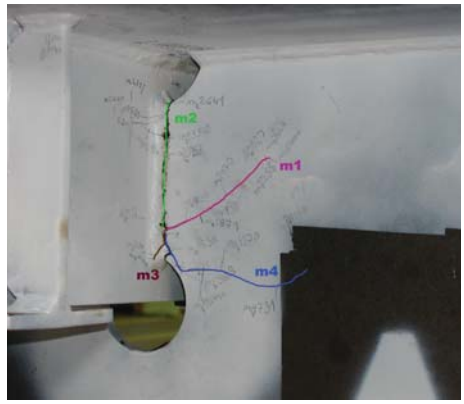

Fig. 5: The fatigue cracks of the element A 3.

The propagation of fatigue cracks on the element A 3 can be seen in the Fig. 6.

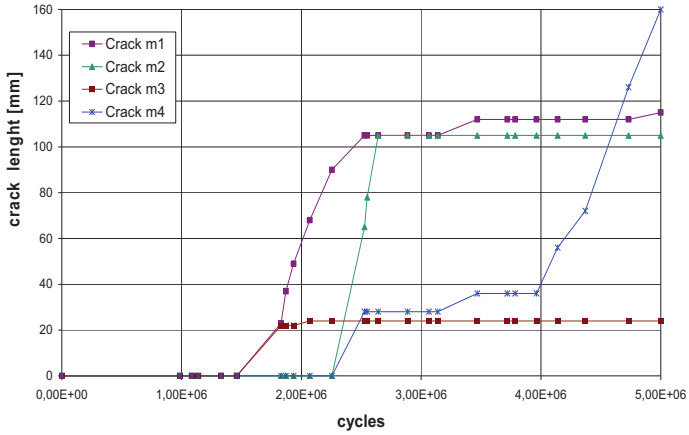

Fig. 6: Propagation of fatigue cracks on the specimen A 3.

The specimen A 4 was statically tested for the hot spot method. The static forces were: 20, 40, ..., 200 kN with steps 20 kN. The static stresses were measured and the results delivered to the Chalmers University for further evaluation using the hot spot method, see the Figs. 7 and 8.

The dynamic forces subjected to the specimen A 4 were 10 kN and 380 kN, respectively, and absorbed 2 236 037 times. The cracks can be seen in the Fig. 8 and their propagation on the Fig. 9.

Fig. 7: The static tests on the specimen A 4 (arrangement for the hot spot method).

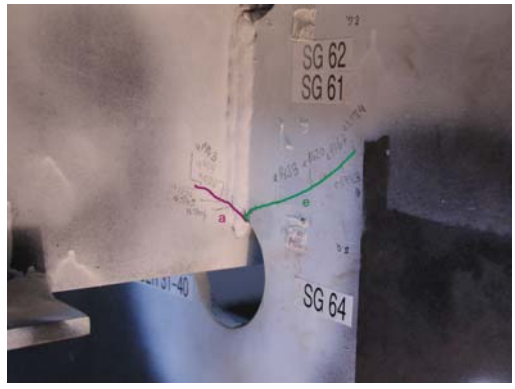

Fig. 8: The cracks on the specimen A4.

The specimen A 5 absorbed first of all the static forces 0 to 200 kN and then the dynamic forces 10 to 390 kN repeated 547 400 times. Analogous results were obtained on the specimen A6. with the forces 10 to 390 and with 576 00 repetitions.

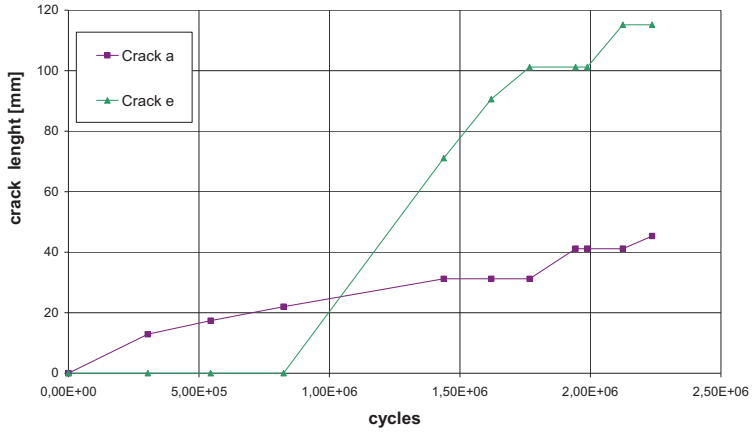

Fig. 9: Propagation of the fatigue cracks on the specimen A4.

The critical places on the specimen A7 were covered with the Carbon Fibre Reinforcement Composites (CFRC) whose statical properties were investigated in details earlier (see the report BRIFAG.ITAM.2009.1). The view of the specimen together with the CFRC is in the Fig. 10. The specimen was loaded by the same forces as that ones on the specimens A 5 and A6 (10 and 390 kN, respectively). To our surprise, the number of cycles was N = 3 500 000. Therefore, the investigation will be repeated on the specimen A 8.

Fig. 10: The specimen A7 covered by the CFRC.

4. Conclusions

The international project "BRIFAG" has presented the fatigue data of orthotropic decks on both the railway and highway bridges. The fatigue cracks appear in the places (in most cases) where the stress concentration arise and form the initiation of fatigue cracks. It happens usually in spatial crossing the deck with cross and longitudinal beams.

The function on N enables to estimate the fatigue life of structural elements. It is the most important result of investigations, Frýba, & Urushadze (2011), Urushadze et al., (2011).

Acknowledgement

The authors express their gratitude to the project "BRIFAG", the Czech Science Foundation for the financial support of their research carried out within the project 105/10/2159, and the ITAM AS CR, v.v.i. for the support RVO: 68378297.

References

Lukič, M. Righiniotis, T. & Frýba L. (2009) BRIFAG – bridge fatigue guidance : An European Research Project, In: *Proc. conference "Fatigue Design"*, Senlis, France, 2009, 10 pp.

Akhlaghi, Z. Al-Emrani, M. Frýba, L. Urushadze Sh. (2009) Fatigue testing and analysis of an orthotropic bridge welded detail using structural hot spot stress method, In: *Proc. of the conference "Fatigue Design"*, 25-26 November 2009, CETIM, Senlis, France. 10 pp.

Frýba, L. & Urushadze Sh. (2011) Improvement of fatigue properties of orthotropic decks. *Engineering Structures*, 33 (2011), vol. 3, issue 4, pp. 1166-1169.

Urushadze, Sh. Frýba, L. & Pirner, M. (2011) Improvement of fatigue life of steel orthotropic decks with carbon fibre reinforcement composites, in: Proc. *Experimental Stress Analysis* 2011, pp. 403-410.

18th International Conference
ENGINEERING MECHANICS 2012
Svratka, Czech Republic, May 14 – 17, 2012

pp. 1457–1464
Paper #22

EXPERIMENTAL AND NUMERICAL VERIFICATION OF VORTEX-INDUCED VIBRATION OF HANGERS ON THE FOOTBRIDGE

Sh. Urushadze [*], M. Pirner [**], S. Pospíšil [***], R. Král [****]

Abstract: *The paper deals with vortex-induced oscillations of footbridge hangers at a very low wind speed. The two-spans (2x50m) reinforced concrete structure with the central pylon (25m height) is designed as the harp system of hangers with circular cross-section. The oscillations were observed at the low wind speed and the high double amplitudes has been measured. The wind-excited deformation shape corresponded to the 6th, 7th and 8th natural modes of a hanger. The individual hanger as well as their group were analysed to estimate the dynamic response, possible aeroelastic vibration and special interference or coupling effects. It also includes proposal for the elimination of the extensive vibration. The analysis is complemented by numerical investigation using Computational Fluid Dynamics methods.*

Keywords: ***Footbridge, vortex-induced oscillations, Kármán vortex, fluid dynamics.***

1. Introduction

Long-span footbridges rank among engineering structures with a high social significance. Their architecture design must in general satisfy matters such as attractive look, reliability and weight. These requirements determine the bridge to be sensitive to the wind effects and the assessment against the wind becomes crucial. One of the several wind phenomena occurring on such a type of structures is termed the vortex shedding with consequent vortex induced vibration. This flow-induced excitation originating from the periodic separation of the vortices may arise even at a low wind velocity. According to the character and the intensity of an excitations, the adequate treatment to reduce or avoid the oscillations should be carried out also in cases when the vibration amplitudes could lead to the pedestrian discomfort or panic.

In this paper, the unacceptable vibrations of the bridge hangers were measured and investigated with respect to the pedestrian comfort. The examination includes a frequency analysis of the hangers accompanied by the analysis of the origin of the unstable behaviour. Moreover the numerical simulation of such an aero-elastic system, which provides addition information to discover the problem, was carried out.

2. Bridge description

The suspended three-section bridge with the almost straight deck, see Fig.1 was examined. The bearing structure consists of pre-fabricated and pre-stressed concrete sections. An A-shaped steel pylon supports the first two sections. The bridge deck core is composed from the steal beams of 800 mm height with the distance between their axes d=3.3 m. The bridge deck is 3.9 m wide. The pre-fabricated section material is made from C55/67 concrete.

The supports are V-shaped, made of steel tubes and are founded on the drilled piles. The supporting structure rest upon the roller bearings. The bearing structure is hanging on pairs of hangers

[*] Ing. Shota Urushadze, CSc.: Institute of Theor. and App. Mechanics Academy of Sciences of the Czech Republic, v.v.i; Prosecká 76, 190 00 Praha 9. Tel.: +420.222363071, Fax.: +420.286884634; E-mail: urushadze@itam.cas.cz.

[**] Prof. Ing. dr.h.c. Miroš Pirner, DrSc.: Institute of Theor. and App. Mechanics Academy of Sciences of the Czech Republic, v.v.i; Prosecká 76, 190 00 Praha 9. Tel.: +420.286882121, Fax.: +420.286884634; E-mail: pirner@itam.cas.cz.

[***] Doc. Ing. Stanislav Pospíšil, PhD.: Institute of Theor. and App. Mechanics Academy of Sciences of the Czech Republic, v.v.i; Prosecká 76, 190 00 Praha 9. Tel.: +420.283880854, Fax.: +420.286884634; E-mail: pospisil@itam.cas.cz.

[****] Ing. Radomil Král, PhD.: Institute of Theor. and App. Mechanics Academy of Sciences of the Czech Republic, v.v.i; Prosecká 76, 190 00 Praha 9. Tel.: +420.286882121, Fax.: +420.286884634; E-mail: kral@itam.cas.cz.

formed by three cables; the cables are placed in a polyethylene tube. The hangers are strained up to 45 pct of their strength at maximum and 10 pct at minimum. Maximum amplitude of tension is 80 MPa at 1200 MPa. The hangers are semi harp-type, exchangeable and rectifiable.

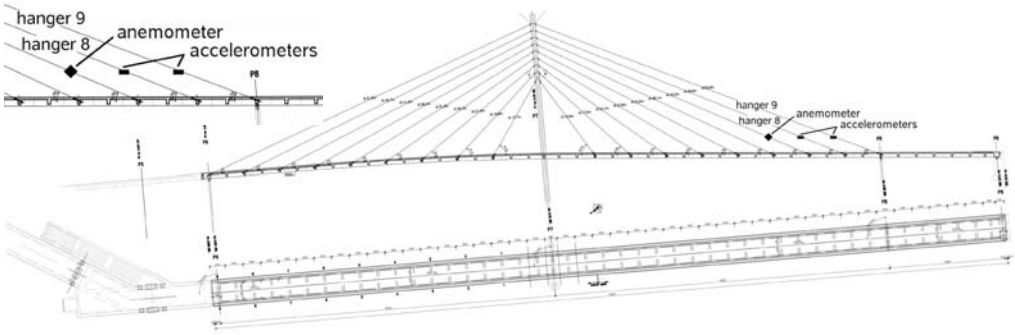

Fig. 1: Side and ground view of the footbridge.

3. Vibration measurement of hangers

The vibrations of the 9th and 8th left hangers (see Fig. 1) appeared at the relatively low wind speed (up to 3 m/s) when the wind direction was perpendicular to the footbridge axis.

Two pairs of ENDEVCO accelerometers type 86 measured dynamic response of the 9th and 8th hangers. The sensor distance from the hanger anchorage into the deck, projected onto the horizontal level, was 5 m. Tab. 1 shows the results of 60 s records for 9th and 8th hangers during the wind excitation.

Tab. 1: Forced frequency of hangers [Hz] and expected shapes of vibrations.

excitation	frequency [Hz]/ mode No. 9th hanger vertical	frequency [Hz]/ mode No. 9th hanger horizontal	frequency [Hz]/ mode No. 8th hanger vertical	frequency [Hz] / mode No. 8th hanger horizontal
wind	12.8/6	10.01/5; 12.08/6; 14.10/7	9.70/4; 12.26/5; 17.29/7	9.68/4; 10.13/4; 12.19/5; 17.29/7
wind	12.08/6; 16.26/8	10.01/5; 12.08/6; 16.26/8	9.70/4; 12.30/5; 14.80/6; 17.29/7	9.70/4; 12.30/5; 14.80/6; 17.29/7

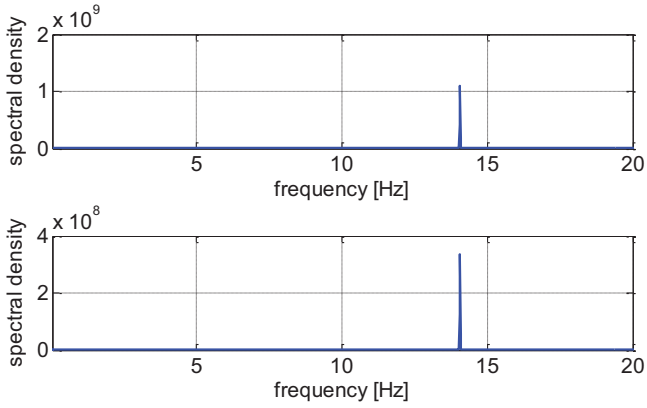

Fig. 2: Power spectral densities in vertical and horizontal directions of 9th hangers.

Fig. 2 shows frequency analysis corresponding to the measurement recorded during the excessive vibrations (see Tab. 2),while Fig. 3 shows the time history of acceleration.

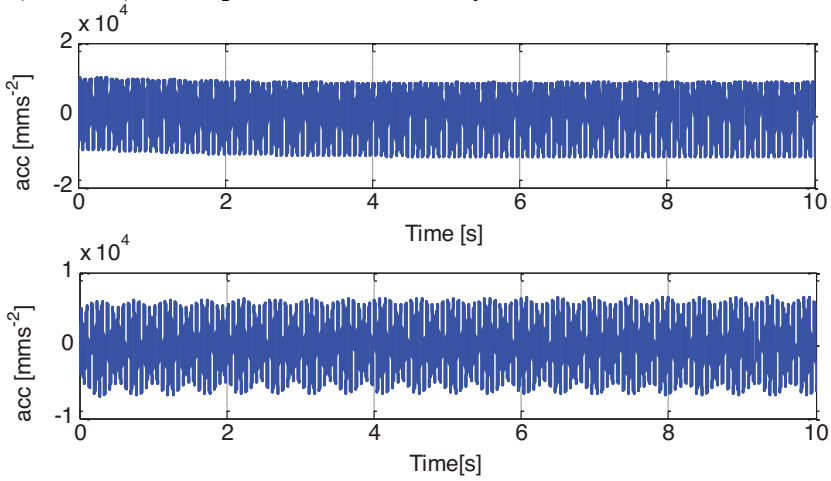

Fig. 3: Time history of the displacement of hanger 9 in the vertical and the horizontal directions.

Dynamic vertical response of the deck from the cable vibration was measured by the same accelerometer as the hanger, placed at the deck edge. In the still air periods, the 9th and 8th hangers were forced to vibrate in the vertical plane; thus, the effects of possible vandals activities were simulated. The measured signals were recorded using a DEWETRON computer type 2010 and analysed by the MATLAB software.

Tab. 2: Amplitudes v [mm] in sensor location for left and right hangers.

excitation	9th hangers		8th hangers	
	vertical	horizontal	vertical	horizontal
wind 1.75 ms^{-1}	4.6E-2	2.9E-2	2.3E-2	1.7E-2
wind 2.2 ms^{-1}	7.9E-2	2.5E-2	3.2E-2	1.6E-2
*wind 2.0 ms^{-1}	left: 1.9E-1 right: 1.36	left: 3.8E-2 right: 7.4E-1	–	–
wind 1.8 ms^{-1}	left: 8.8E-2 right: 1.45E-1	left: 3.3E-2 right: 6.6E-2	–	–
wind 1.75 ms^{-1}	left: 7.2E-2 right: 3.0E-1	left: 2.5E-2 right: 1.8E-1	–	–

Note: * The measurement with observed excessive vibrations.

Tab. 3: Frequencies of vertical vibrations of the footbridge deck.

excitation	frequency [Hz]	amplitude v_0 vibration [mm]
wind	10.01	≈9.2E-4
wind	1.75; 2.90; 10.01; 12.60; 14.26	≈6.8E-4
wind	12.60; 14.00; 14.26; 14.91	≈2.9E-3
wind	12.30; 12.60; 14.00	≈9.4E-4
wind	1.75; 12.60	1.5E-1

On Tab. 2, there are amplitudes (in mm) of vertical and horizontal movements of hangers in the sensor locations. Vertical means perpendicular to the catenary tangent, in the sensor location.

Tab. 3, there are frequencies of vertical vibrations of the deck edge near anchorage of the 7th left hanger, and sizes of deviations. Dominant frequency is underlined.

4. Forced vibration of hangers

The 9th and 8th hangers were forced to the rhythmical oscillations in the vertical plane. The excitation frequency was selected to correspond the frequency of the 1st modal shape of the hanger; in case of 9th hanger the frequency was $f_{(1)}$=2.03 Hz, in the case of 8th hanger the frequency was $f_{(1)}$=2.45 Hz.

Amplitude of the vertical vibration of the midpoint of the 9th hanger in the sensor location and in the vertical plane movement in the middle of the hanger end points is v_0= 62.15 mm. Similarly, in the horizontal direction, the amplitude was v_0= 23.8 mm. During the rhythmic forcing of the hanger, it was not possible to eliminate the horizontal component of the motion. Amplitude of the vertical vibration of the 8th hanger in the sensor location was v_{0exp}= 13.55 mm. Then, the amplitude of vertical movement in the middle of the hanger end points is v_0= 38.34 mm. Similarly, in the horizontal direction v_0= 13.72 mm

From the analysis of response of the 9th and 8th hangers, footbridge section above the trackage, from the testimony of local citizens and from the video recording it is certain that the excitation is caused by the wind, the direction of which is perpendicular, or close to perpendicular, to the footbridge axis.

5. Selected aeroelastic effects

It has been concluded, from the analysis of the motion, that excessive vibration is not a wake galloping, since the hangers distance is too large, ($L > 3$ m, $d = 0.054$ m). This phenomenon would happen when the wind sped exceed 15 m/s. Parameter L is the distance between the cables. Also, the geometric configuration excludes the so-called jet-switch mechanism (Dye, 1965).

We can also exclude the rivulets from the analysis, because the above mentioned vibration was observed also in dry conditions and the relation between the frequency of vibration of this type and wind speed is dramatically different from the frequency of separated vortices corresponding to the Strouhal effect.

Hence, the effect under examination is caused by a periodical vortices separation behind a smooth cylinder with the circular cross-section. The influence of the surface smoothness is testimonied by the by the fact that for example hanger no. 9 vibrated with almost as double amplitude in the vertical direction as that one in the horizontal direction.

This is a typical effect of a periodical vortices shedding. In principle, the frequency of the separation is given by the Strouhal frequency:

$$f_{Sr} = S_r \cdot \frac{\bar{V}}{d} \tag{1}$$

where V is the mean value of speed of the wind, the direction of which is perpendicular to the roller axis, d is the roller diameter and 0.28 is Strouhal number S_r, (Anagnostopoulos, (2002), Pirner & Fischer, 2003) for the given Re number and intensity of turbulence. No higher frequencies have been considered for S_r = 0.4, 0.6.

Note: Reynolds numbers, characterising the circumfluence mode, are:

$$\mathrm{Re}_{12,08} \doteq 0{,}13 \cdot 10^5 \ , \ \mathrm{Re}_{14,10} \doteq 0{,}14 \cdot 10^5 \ , \ \mathrm{Re}_{16,26} \doteq 0{,}16 \cdot 10^5 \ .$$

Hence, this mode is called "critical"; some authors call it "transitional" (Pirner & Fischer, 2003). For this mode, the specified Reynolds numbers and turbulence intensity was I_m = 9.1 % and S_r = 0.28.

The 9th hanger vibrated perpendicular to the wind direction with frequencies (see Table 1): 12.08; 14.10; 16.26 Hz.

$\bar{V}_{12.08} = 2.31$ m/s , $\bar{V}_{14.10} = 2.72$ m/s , $\bar{V}_{16.26} = 3.13$ m/s .

Mean wind speeds correspond to those frequencies.

6. Examination of excessive vibrations using numerical simulation

To identify an origin of the unstable behaviour of the selected hanger and to investigate the possibilities to suppress excessive vibrations, two-dimensional numerical model adapted for solving the fluid-structure interaction has been defined. This method employs three boundary value problems respecting the Newton's fluid, elastodynamic equations and equations of the Lagrangian-Eulerian description of motion. A circular cross-section with adequate dimensions $d = 0.054$ m is free oscillating in vertical and horizontal direction *x* and *y*, respectively, with specific frequencies. Each of the degrees of freedom is proportionally damped with respect to the velocity. Furthermore, it is assumed that the hanger is subjected to the wind action with a constant velocity profile. Due to the primitive variable formulation of the Navier-Stokes equations, no turbulence is given on the inlet boundary. This does not correspond to the experiment, wherein turbulence components are always presented, and therefore certain discrepancy in the results may be expected.
Simulations have been performed with COMSOL^R software. This partly-open computation package solves an arbitrary weak-form of integral-differential equations with boundary conditions (Pospíšil et al., 2006). It makes a possible to define the modified Navier-Stokes equations for incompressible fluid, see Tezduyar et al., (1992).

6.1. Strouhal number determination on stationary hanger

The Aerodynamic effects of the vortex separation on a structure are studied when the body is considered immovable (Simiu & Scanlan, 1996). This analysis provides fundamental data about aerodynamic forces acting on the body, which are, in general, function of the time. Drag, lift or moment coefficients can be established as well as their periodic character.

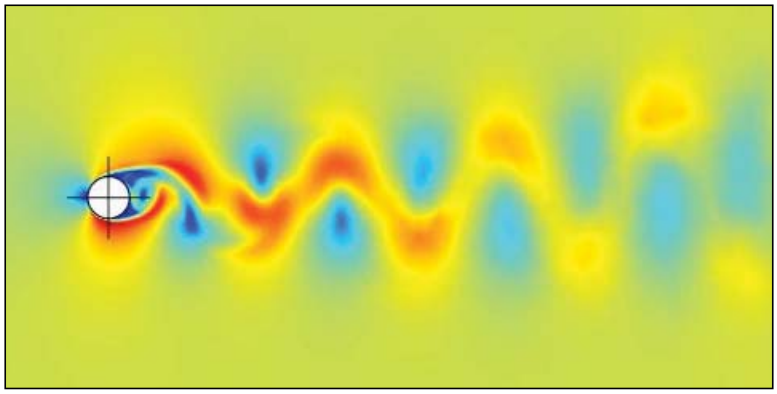

Fig. 4: Instantaneous velocity field around the hanger in the smooth flow regime at 2 m/s.

In Fig. 4 the velocity field in the immediate neighbourhood of the section is illustrated. The Kármán vortex street behind the hanger is evident. The wind velocity is $V = 2$ m/s and the fluid characteristics correspond to the air at 20 degrees of Celsius. Periodic flow pattern around the stationary section generates a loading in the vertical and horizontal plane, as demonstrated by the time histories diagrams in Fig. 5. Both force components are noticeable periodic with dominant frequencies. They are predicted by a spectral analysis as displayed in Fig. 6. For the vortex shedding type of instability, the Strouhal number S_r related to the vertical component is crucial. The right hand side figure shows one dominant normalised frequency $fd/V = 0.2265$ corresponding to S_r.

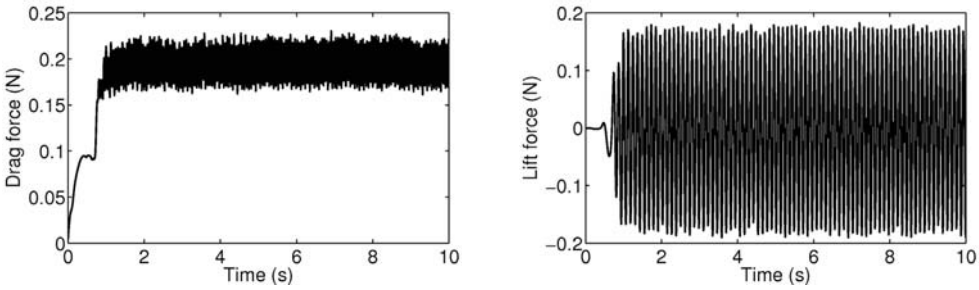

Fig. 5: Time histories of drag (left) and lift (right) force component.

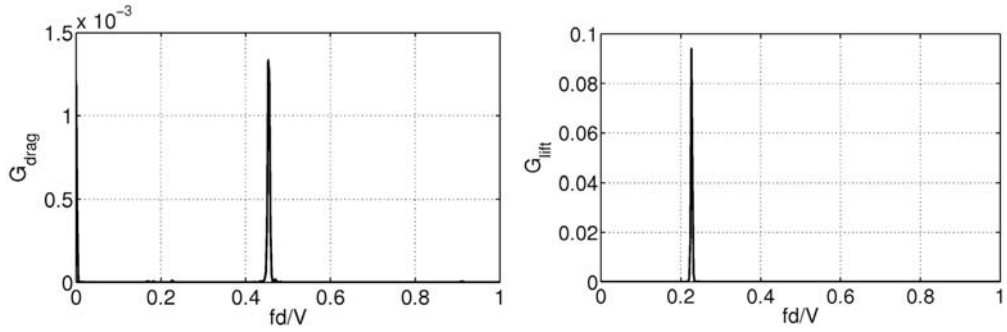

Fig. 6: Normalised power spectral density of drag (left) and lift (right) force component.

6.2. Figures and tables (subsection)

Elastic mounting of the circular section is modelled by fictitious supports. For the both degrees of freedom reaction force F is established in its centre representing a spring-mounting with the linear characteristic. This force depends on the body displacement and the spring stiffness k. Analogously; the net damping effect is applied being a function of hanger response velocity and the damping parameter δ.

The vertical and horizontal frequencies of the hanger are identical and they correspond to the seventh natural frequency $f_{(7)}$=14.10 Hz, see Tab. 1. This is achieved by the appropriate combination of the mass of the section and the spring stiffness k. Damping parameter is selected equally for both degrees of freedom as empirical value for steel structures; $\delta = 0.02$.

When the air is passing the circular section, the vortex development in the wind is generated acting as a powerful force on the section surface and the loading of the body itself. Provided the vortices separation frequency is relatively close to one of the natural frequencies of the hangers, harmonic fluid-induced oscillations with high amplitudes may occur. In terms of the geometric, modal and fluid characteristics, the critical wind velocity associated with the vortex-induced instability onset can be determined. Considering S_r obtained in the previous section and the natural frequency of the hanger $f_{(7)}$, an estimation of the instability onset can be stated as:

$$V = f_{(7)} \cdot d / S_r = 14.10 \cdot 0.054 / 0.226 = 3.37 \,\mathrm{m}/s$$

Dynamic response of the circular section at this wind velocity is presented in Fig. 7. It is evident that for t > 0.5 s, (after vanishing fluid transient behaviour), the vibrations in the cross-wind direction increased up to the value of almost 2 mm in the steady state.

The horizontal response component is shown in Fig. 8. It is of several orders lower than the amplitude for the vertical oscillations. According to its oscillation character it can be concluded that a force vibration regime occurred however, no frequency correlation between the oscillating mass and aerodynamic forces was observed.

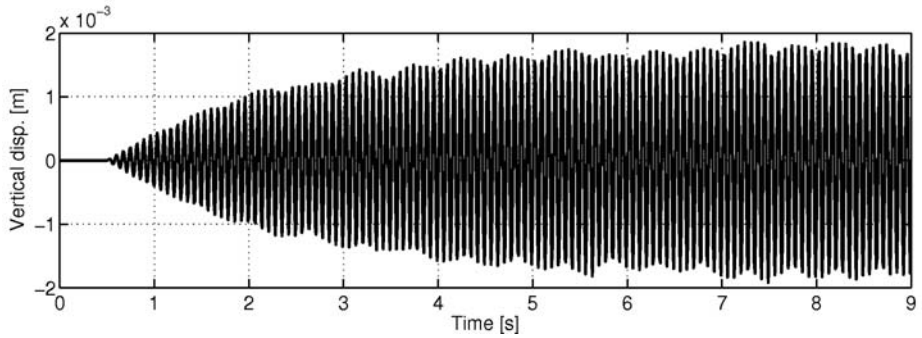

Fig. 7: Cross-wind response time-histories of the hanger 9 at $V = 3.37$ m/s.

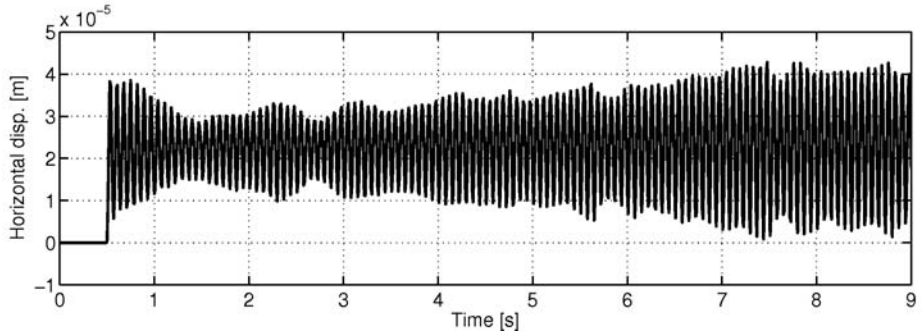

Fig. 8: Along-wind response time-histories of the hanger 9 at $V = 3.37$ m/s.

Comparing the experimentally obtained responses with the numerical ones, a good agreement is reached only for the vertical amplitudes. The numerical simulation does not cover well the spatial behaviour of the hanger along the elliptic path as it has been observed in the experiment.

Analogous simulation has been performed supposing a lower wind velocity $V = 2.70$ m/s. This value agrees with the experimental wind measurement in the anemometer location. In addition to that an initial excitation is applied to the hanger which establishes favourable conditions to start oscillating. This procedure simulates the case of lock-in mechanism when a part of the hanger (at the top of the pylon, e.g.) is subjected to the vortex shedding instability while the remaining part is placed in the wind with lower velocity. The dynamic behaviour of the hanger under such conditions is depicted in Fig. 9. From the figure it follows that the system does not maintain the stable vibrations and the amplitudes are decaying. In fact, it proves that even though the effective length of a hanger with generation of the flow-induced oscillations is limited, excessive vibrations of the whole hanger may arise and sustain for relatively wide range of the wind speeds.

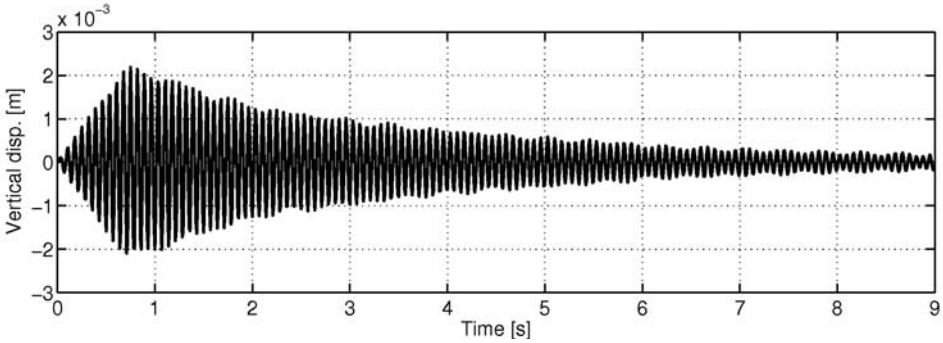

Fig. 9: Cross-wind response time-histories of the hanger 9 at $V = 2.70$ m/s *under an initial excitation.*

7. Conclusion: proposal on elimination (or reduction) of the hanger vibrations

Hangers 9 and 8 in the footbridge section above the bridge deck vibrate with higher shapes and clearly visible amplitudes under the load of the wind as slow as 1.75 to 2 m/s, if its direction is perpendicular to the footbridge axis.

Vibrations of the cables under the wind load are results from the periodical separation of vortices behind the hanger with circular cross-section (Strouhal vibrations, Kármán vortex path). Theoretical calculation has indicated that:

Vibrations of the cables caused by wind load on the deck can be neglected.

The main cause of the unacceptable effect is the smoothness of the PE pipe surface affecting the flow regime.

The vibrations of the 9^{th} and 8^{th} hangers caused by wind do not pose a threat to the footbridge structure (or cables, deck or pylon), so it would be possible to keep it in the original state.

However, the motion of the cables could lead to the discomfort or fear of some pedestrians and, in the case of a larger amount of people on the footbridge, even panic. Therefore it is necessary to reduce the vibrations to the indistinctive level, or eliminate them.

In this case, there are three possibilities:

- To equip the 9^{th} and 8^{th} hangers with Stockbridge dampers (see Anagnostopoulos, (2002), the dampers there are doubled; in our case, single ones will do).
- Interlocking, by means of an additional cable, the 9^{th} and 8^{th}, perhaps also the 7^{th}, hangers and anchor them into an anchorage "block".
- Changing the flow regime by coarsening the hanger surface through covering with (sticking) grains with diameter up to 5 mm onto the upper half of the circular cross-section.

The first possibility affects negatively the footbridge architecture. Despite that, the necessary masses of the dampers for the 9^{th} hanger are as follows: Total mass of 3 cables is 171.27 kg. The recommended ballast mass is 1/10 to 1/20 of the total cable mass, i.e., in the more efficient case, $m_{abs,tot}$ B~ 17 kg.

The 9^{th} hanger vibrates in the 6^{th}, 7^{th} and 8^{th} shape when subjected to the wind. The number of the vibration mode is identical with the number of antinodes and hence with the number of Stockbridge dampers.

The ballast mass, providing they are made of steel, would not exceed the hanger diameter in order to maintain the visual aspects of the footbridge.

Acknowledgement

The support of the grants GA CR 103/09/0094, MPO TIP FR-TI3/654 and GA CR P105/10/2159 are gratefully acknowledged. Identification code of research project of the Institute of Theoretical and Applied mechanics is RVO: 68378297.

References

Anagnostopoulos P. (2002), Flow induced vibrations in engineering practice, *WIT press, Southampton*, Boston.

Dye, R.C.F. (1965), Flow-Induced Vibration and Noise with Particular Reference to Heat Exchanger Tube Systems, in: Proc. *Proceedings of the Institution of Mechanical Engineers*, Conference Proceedings June 1965 180: 260-267.

Pirner, M., Fischer, O. (2003), *Wind loads of buildings*, ČKAIT, ISBN 80-86769-10-0, Prague 2003 (in Czech)

Pospíšil S., Král R., Náprstek J. (2006), Numerical model of nonlinear wind-structure interaction. *In proceedings of CWE2006: JAWE*, 307-311, 2006.

Simiu E., Scanlan R.H., (1996), *Wind Effects on Structures*. John Wiley & Sons, New York, 1996.

Tezduyar T.E., Mittal S., Ray S.E., Shih R. (1992), Incompressible flow computations with stabilised bilinear and linear equal-order-interpolation velocity-pressure elements. *Computer Methods in Applied Mechanics and Engineering*, 95, 221-242.

18th International Conference
ENGINEERING MECHANICS 2012
Svratka, Czech Republic, May 14 – 17, 2012

pp. 1465–1471
Paper #231

THE METHODOLOGY OF FATIGUE TEST SIMPLIFICATION

J. Vágner[*], B. Culek jr.[**], B. Culek[***]

Abstract: *The contribution is focused on the issues of experimental determination of fatigue characteristics of structural nodes of rail vehicle parts on a dynamic test stand. The aim of the contribution is to describe a methodology allowing simplifying the experiments. The proposed methodology uses FEM computation, correlation analysis and estimation based on specific stress response. In order to validate the methodology, an experiment with a physical specimen was performed.*

Keywords: ***Rail vehicle, structural node, fatigue testing, FEM analysis, dynamic test stand.***

1. Introduction

The aim of this contribution is to describe a methodology which allowing simplify experimental testing of fatigue strength of structural nodes of rail vehicle bogie frames. The purpose of the proposed methodology is to reduce the number of cylinders (and thus also other equipment) necessary for fatigue testing for determining the fatigue properties of structural nodes, especially structural nodes of rail vehicle constructions.

The methodology contains particular points listed below:

1. Finding a suitable set of criteria for assessment of the equivalence of two modes of loading of the structural node.
2. Finding the relation between the evaluated component of the material response and the loading mode.
3. Defining the procedure leading to simplification of the loading mode (reduction of number of the loading cylinders).
4. Verifying the above points at theoretical models with use of FEM analysis.
5. Experimental validating (demonstrating) the methodology at a physical specimen.

Although the work is focused at the simplification of experimental testing of fatigue strength, many theoretical techniques and methods also had to be used to reach the aim. In order to prove the theoretical methods (and thus also their result) acceptable, the methods were to be validated by experiments in each step. For this purpose, a specimen representing a characteristic structural node used with bogie frames of rail vehicles was designed. The methodology was validating by FEM analysis and testing on real specimens at an electrohydraulic stand.

2. The proposed methodology

The method assumes that the loaded assembly is linear. Further assumption is that the sample, subjected to the applied loading, has one critical point. Fig. 1 shows a block diagram of the theoretical model of the original and the simplified loading sets including three levels of checking of equivalence

[*] Ing. Jakub Vágner, Ph.D.: University of Pardubice, Jan Perner Transport Faculty, Department of Transport Means and Diagnostics, Studentská 95, 532 10 Pardubice, Czech Republic, e-mail: Jakub.Vagner@upce.cz

[**] doc. Ing. Bohumil Culek, Ph.D.: University of Pardubice, Jan Perner Transport Faculty, Department of Transport Infrastructure, Studentská 95, 532 10 Pardubice, Czech Republic, e-mail: Culek@upce.cz

[***] Prof. Ing. Bohumil Culek, CSc.: University of Pardubice, Jan Perner Transport Faculty, Department of Transport Means and Diagnostics, Studentská 95, 532 10 Pardubice, Czech Republic, e-mail: Bohumil.Culek@upce.cz

of both sets. Both models are identical as to the included modules; however the transfer functions between the modules are different.

In order to enable utilising of the method, not only that the simplification system itself had to be designed, but also a way of assessment of the equivalence of the simplified loading mode had to be found. It was necessary to find a hypothesis which would not be much conservative and allowed to compare the effects of two loading sets, with regards to the material fatigue, as precisely and simply as possible.

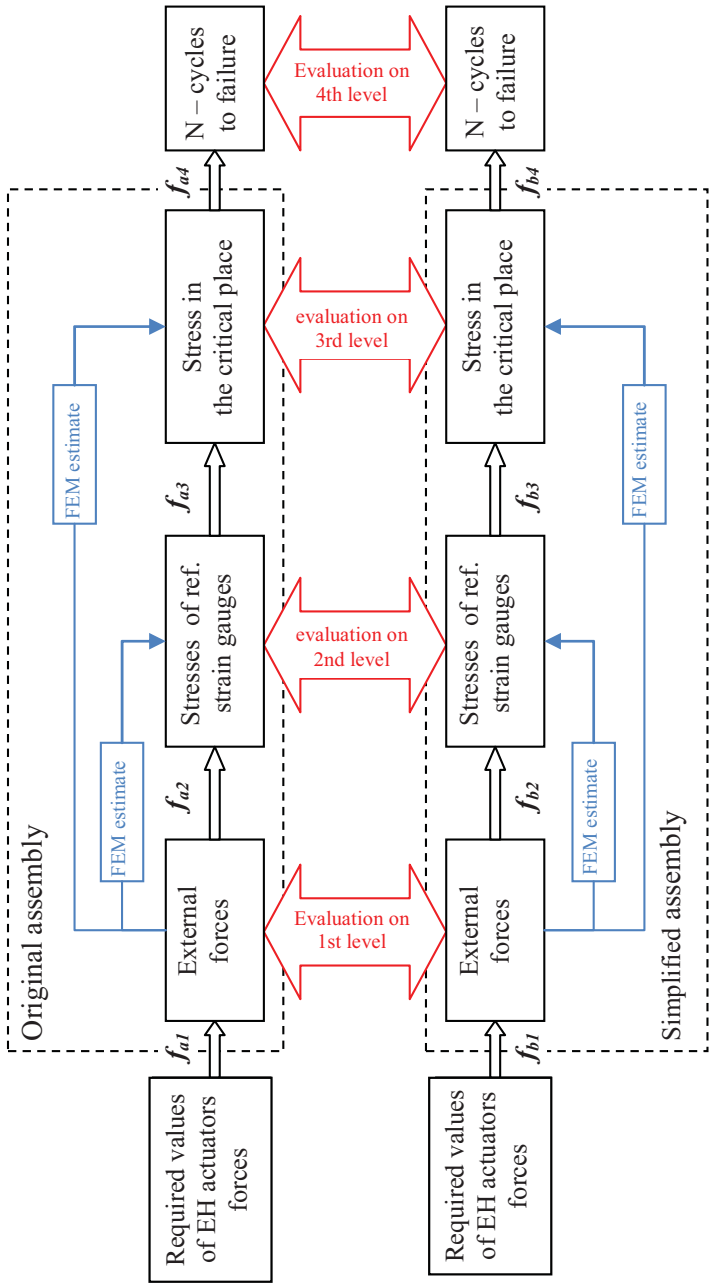

Fig. 1: Block diagram of the theoretical model of the assembly.

3. The criteria for assessment of the equivalence of two modes of loading

The aim is to reach the same number of cycles to failure (the 4th level on Fig.1), but another requirement has still to be fulfilled, that the same mode of failure occurs at the same point as with the original loading set. In an extreme case it may also happen that the specimen is loaded in a completely different way but the failure occurs at the same (almost the same) number of cycles. Based on the aforementioned information, several assessment methods were proposed (which does not exclude other methods):

One-parameter methods

a) The value of σ_1 – only the magnitude of the principal stress is evaluated, its direction is not taken into account!

b) The value of τ_{max} - only the magnitude of the maximum tangential stress is evaluated, its direction is not taken into account!

c) The value of σ_{HMH} – the directions and relation of the shear and tensile components are not taken into account; negative values of stress are not taken into account either.

d) Reference stress σ – one or more strain gauges are positioned at a suitable place of the construction. The assumption may be made that there is a relationship between this stress and the maximum stress in the notch. The value of the stress in the direction of the strain gauge is evaluated and subsequently transformed to the stress in the notch (critical point).

Two-parameter methods

e) The values of σ_1 and τ_{max} – Magnitudes of both stresses are evaluated, with regard to the fatigue limit ellipse in the σ–τ diagram. The direction in relation to the critical point is not taken into account.

f) The values of σ and τ – The values of tensile stress and shear stress in a selected reference direction are evaluated. The direction must be chosen with regards to the supposed direction of the crack. The direction in relation to the critical point is thus taken into account.

The loading modes are equivalent if the points of both compared situations are located on a common ellipse of constant fatigue strength in the σ–τ diagram.

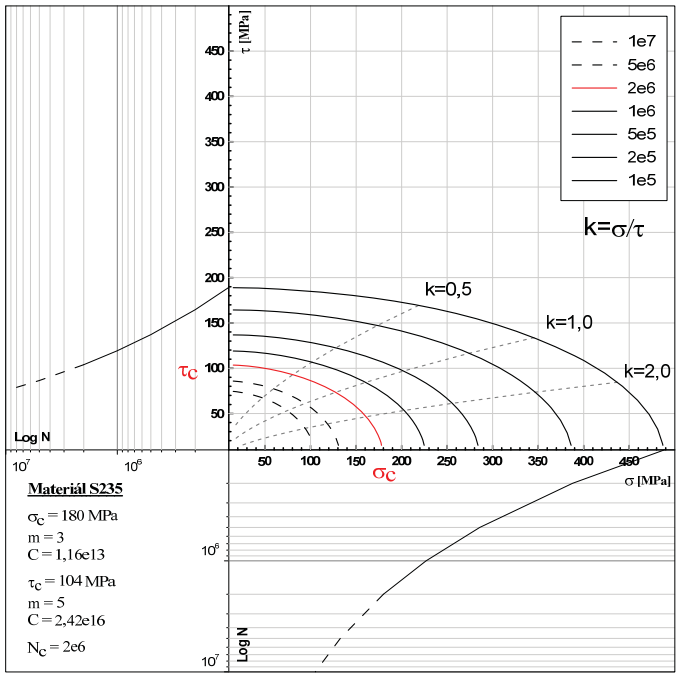

Fig. 2: Extended σ–τ diagram.

4. The specific stress response metho

As the stress in the critical point may not be experimentally verified, a method for estimating the stress on the basis of specific stress response was created. It comprises the following steps:

1) An appropriate FEM model is created.

2) All load components are applied with the magnitude of 1.

3) All variants for only one component at a time are computed.

4) All components of stress in the nodes are exported for further processing.

The stress in a selected point (FEM node) is then:

$$\begin{bmatrix} k_{\sigma x\,1} & \dots & k_{\sigma x\,n} \\ k_{\sigma y\,1} & \dots & k_{\sigma y\,n} \\ k_{\sigma z\,1} & \dots & k_{\sigma z\,n} \\ k_{\tau xy\,1} & \dots & k_{\tau xy\,n} \\ k_{\tau yz\,1} & \dots & k_{\tau yz\,n} \\ k_{\tau zx\,1} & \dots & k_{\tau zx\,n} \end{bmatrix} \cdot \begin{bmatrix} F_1 \\ \cdot \\ \cdot \\ \cdot \\ F_n \end{bmatrix} = \begin{bmatrix} \sigma_x \\ \sigma_y \\ \sigma_z \\ \tau_{xy} \\ \tau_{yz} \\ \tau_{zx} \end{bmatrix} \quad (1),$$

where the coefficients k represent values of the specific stress response. These values may also be obtained experimentally.

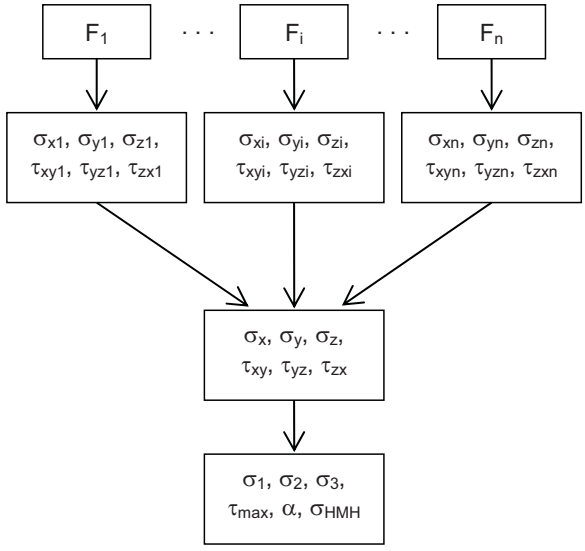

Fig. 3: Schema of application of the specific stress response method.

5. Typical process of simplification

Typical process of simplification is as follows:

1) The time histories of external forces assumed in operation (experiment) serve as input.

2) Another input is constituted by the data necessary for assessment of equivalence of the loading – stresses from the FEM analysis calculated under the loading specified in the previous point.

3) The experiment loading set is designed. It is required that the dominant component(s) of the original loading be preserved. This loading set will be henceforth referred to as „simplified".

4) Design of the assembly with the structural node (specimen), fastening equipment and system of applying the loading forces.

5) FEM analysis of the sample loaded in the designed assembly with unit loading from external forces (specific stress response).
6) Finding the suitable location for reference strain gauges so that the measured values correlate sufficiently with the stress in the critical point.
7) Based on the original loading, the stress response to the dominant force is calculated.
8) The difference between the original stress and the stress resulting from the dominant force will be compensated for by other forces remaining in the loading set.
9) The values of other forces are calculated using the superposition principle so that required effect is achieved.
10) After the calculation of the new loading, new stress histories in the critical point are calculated.
11) The original and the new histories are compared following a selected criterion for assessment of load equivalence. If the agreement is not sufficient, the proposition must be modified.
12) Before the experiment is started, a check is made whether the responses from the reference strain gauges, with respect to the loading forces, are accurate enough compared with the FEM calculation.

The process may be slightly different with regard to the purpose of simplification and with regard to the character of the test specimen. In particular, the range of input parameters may differ.

6. Achieved results

The methodology was applied on an actual specimen. A steel weldment was constructed, representing the structural node of connection of a sideframe and a transom. It was loaded by three EH cylinders; the simplified assembly was loaded by two EH cylinders. There are two potential critical places on the specimen (CP1, CP2) but with regard to load system only one of them is critical.

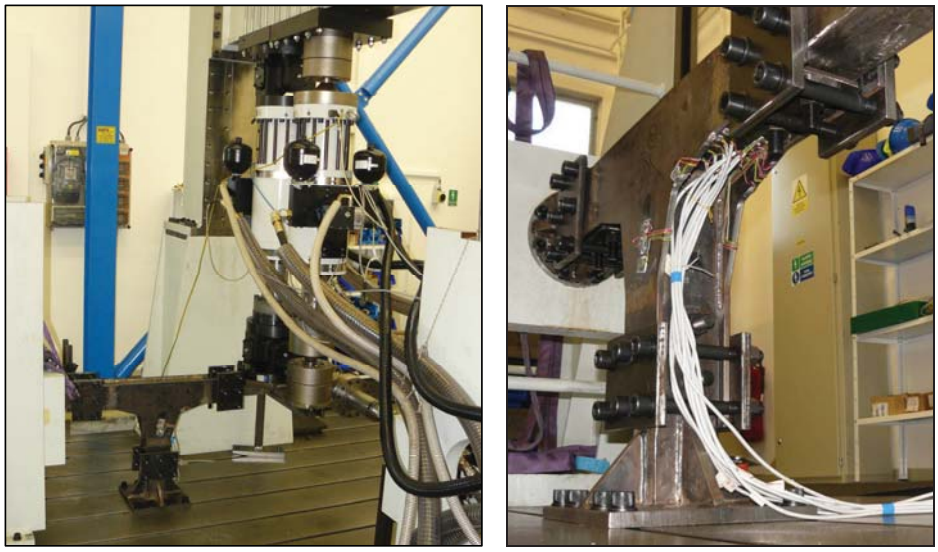

Fig. 4: The experimental assembly and the specimen with strain.

Results of comparison between theoretical and experimental determination of specific stress response are listed in Tab. 1. The presented results were obtained under one cylinder loading conditions.

Tab. 1: Comparison between theoretical and experimental determination.

Strain gages	FEM [MPa/kN]	Experiment [MPa/kN]	Difference
T3	4.97	5.07	2%
T4	4.97	4.97	0%
T5	4.85	4.85	0%
T6	4.85	4.58	-6%
R1A	1.23	1.26	3%
R1B	4.44	4.57	3%
R1C	2.16	2.21	2%
R2A	2.16	2.15	0%
R2B	4.44	4.50	1%
R2C	1.24	1.25	1%

Following variants of load have been proposed for verification of the methodology (Tab. 2):

a) **Original version**: This is the basic version for comparison.

b) **Version A**: In this version, the force *F2* was omitted and compensated by other forces. The resulting tensile component for the secondary critical point decreased; the shear component remained without significant change for all values.

c) **Version B**: In this version, the force *F2* was omitted and compensated by remaining cylinders. The resulting tensile component for the secondary critical point was lower again; the shear component remained similar for all values.

d) **Version C**: In this version, the forces *F1* and *F2* were both omitted and compensated only by the force *F3*. The tensile component was maintained, the ratio of the tensile and shear components was not (difference 7.5 %).

e) **Version C1**: This version differs from the version C solely by the fact that, besides varying the loading intensity, the ratio of amplitude and mean value of the force also varied in order to attain the appropriate loading. The ratio was changed from original 1:0,25 to 1:0,6.

f) **Version D**: In this version, the forces of the cylinders *F*2 and *F*3 were omitted and compensated only by the force *F*1. The tensile component was maintained, the ratio of the tensile and shear components was satisfactory. In this case it was observed that the stress state in the in the secondary critical point (CP2) was the same as in the primary critical point (CP2). Although this loading is apparently suitable according to the comparison of numbers of cycles to failure, the failure might occur in another place than in the assumed primary critical point (CP1)!

Tab. 2 – Load forces (two-parameter simplification).

Version	F1 [kN]	F2 [kN]	F3 [kN]
Original	+/- 4.3	-/+ 1.3	8.5 +/- 2.10
Version A	+/- 3.5	0	7.1 +/- 1.75
Version B	+/- 2.9	0	5.8 +/- 2.90
Version C	0	0	19.3 +/- 4.80
Version C1	0	0	10.6 +/- 6.40
Version D	+/- 5.5	0	0

Results of stress responses obtained by proposed variants of load are listed in tab. 3. Results of the **σ/τ** ratio are listed in tab. 4.

Tab. 3: Stress response (two-parameter simplification).

Version	CP1		CP2	
	σ	**τ**	**σ**	**τ**
Original	64.9	28.4	49.7	28.6
Version A	64.8	30.7	40.8	30.9
Version B	65.0	31.0	33.5	31.1
Version C	64.7	28.3	-1.0	28.3
Version C1	64.4	30.0	-1.3	30.0
Version D	64.9	31.6	64.9	31.9

Tab. 4: The σ/τ ratio (two-parameter simplification).

Version	CP1	CP2
	σ/τ	**σ/τ**
Original	2.12 (0%)	1.61 (0%)
Version A	2.11 (-0.65%)	1.32 (-18.22%)
Version B	2.1 (-1.17%)	1.08 (-33.29%)
Version C	2.28 (7.52%)	-0.03 (-102.09%)
Version C1	2.15 (1.17%)	-0.04 (-102.61%)
Version D	2.05 (-3.35%)	2.03 (26.05%)

7. Conclusions

The described methodology allows simplifying the loading of a structural node of a rail vehicle for the purpose of simulation of its operational loading at a dynamical test stand. However, the methodology should be taken only as a starting point of further research, since it still has many limitations in the present stage. For simple structural nodes loaded by external loading components with the same phase it is applicable, though. It is also difficult to use for tests, which are conclusively defined by standards.

Acknowledgements

This work has been supported by the project of Research Centre of Rail vehicles No. 1M0519 and Competence Center of Railway Vehicles No. TE01010038.

References

Vágner, J. (2012) *Simulace provozního namáhání částí kolejových vozidel na zatěžovacích standech*. Pardubice. Disertační práce. Univerzita Pardubice, Dopravní fakulta Jana Pernera.

Vágner, J., Culek ml., B., Culek, B. (2011) *Simulace rozhodujících složek provozního namáhání částí kolejových vozidel na multiaxiálních zatěžovacích standech.* Přehledová zpráva VCKV č. B8-01-2011-UPa. Pardubice.

Vágner, J., Culek ml., B., Culek, B. (2010) *Simulace rozhodujících složek provozního namáhání částí kolejových vozidel na multiaxiálních zatěžovacích standech*. Přehledová zpráva VCKV č. B8-01-2010-UPa. Pardubice.

18th International Conference
ENGINEERING MECHANICS 2012
Svratka, Czech Republic, May 14 – 17, 2012

pp. 1473–1474
Paper #309

MONDIS: KNOWLEDGE-BASED SYSTEM OF FAILURE OF HISTORICAL CONSTRUCTIONS

J. Valach, R. Cacciotti, M. Čerňanský, P. Kuneš*

Abstract: *Preservation of built cultural heritage, although constituting a well-documented branch in the field of conservation, presents a considerable knowledge gap in the systematic understanding of its common failures, physical, chemical or other mechanism of their occurrence and corresponding mitigation measures. The lack of available data coupled with the complex heterogeneity of their sources raises issues concerning the establishment of a framework able to process the information sensibly. The main aim of introducing and developing a knowledge-based system of failure of historical constructions called MONDIS is to address this demand. MONDIS proposes a methodology capable of reproducing the logical relationship between the manifestation of damage, its diagnosis and the possible interventions. Based on novel information sciences tools, like semantic technologies, the system will be able to assist users in finding similar failures cases, in analyzing the causes of damage and also suggesting suitable restoration techniques accordingly to conservation principles of intervention.*

Keywords: ***Historical structures, knowledge-based systems, defects of cultural heritage objects, risk assessment.***

1. Introduction

With certain delay information technologies are entering the field of protection of cultural heritage. This delay can be partially explained by the multi-disciplinary nature of the subject. Currently there exist databases which serve primarily as archives for storage of general data but that unfortunately provide little scientific insight and technical support to users in understanding the actual cause-effect relationship in the evolution of damages. MONDIS proposes a comprehensive knowledge-based system with innovative perspective to decision-making processes. This system is the result of an evolution of previous efforts spanning more than ten years (e.g. Strufail see Drdácký et al., 2011).

2. Historical immovable objects

Historical objects present valuable peculiarities of technical and cultural interest. It is indubitable that remarkable efforts should be made to preserve for future generations historical objects as witnesses of a prolonged experience in building adaptation and optimization. The accessibility to exact information relevant for the assessment of such value is however often limited or impossible. The lengthy sequence of events suffered in the course of time by the object, the absence of original designs and constructive details makes difficult for individuals to clearly distinguish the context in which artifacts developed. Further the complexity of the agents impacting the objects´ fabric generates multiple unknowns in the determination of causes of degradation.

3. System description

Understanding cultural heritage pathologies requires exploring basic methodological phases: the identification of the object and its damage (presentation of the problem), the diagnosis (its understanding of decay mechanism involved) and finally the selection of adequate intervention (its solution). In order to match such sequence of phases MONDIS system introduces a structured

* Ing. Jaroslav Valach, PhD, Riccardo Cacciotti MSc, Ing. Martin Čerňanský, PhD., Ing. Petr Kuneš: Institute of Theoretical and Applied Mechanics AS CR, v.v.i., Prosecka 76; 190 00 Prague 9; CZ. Corresponding author: valach@itam.cas.cz

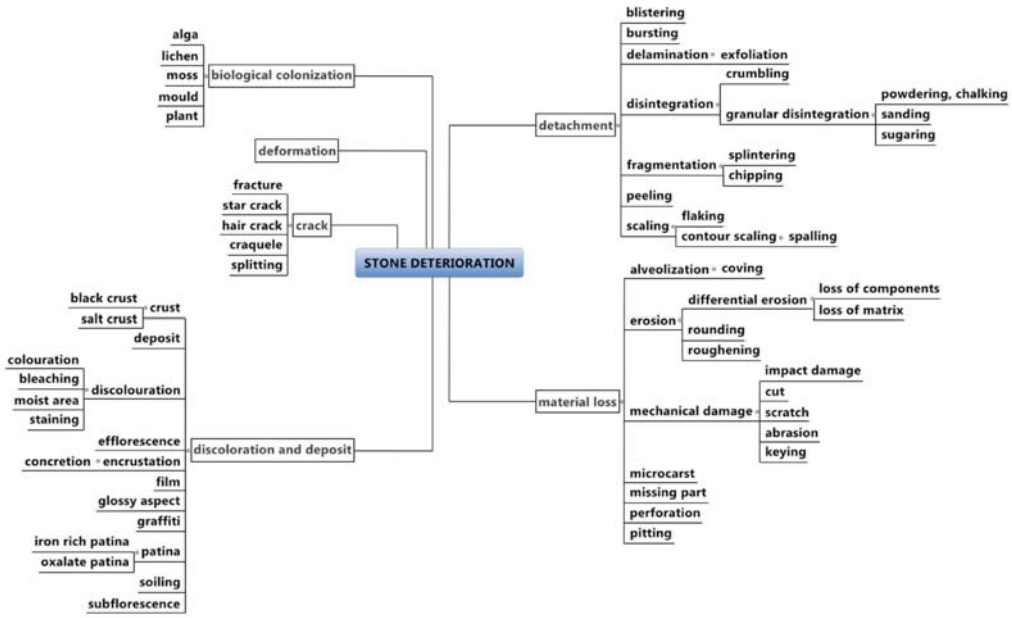

Fig.1 Example of knowledge map for stone damage

framework able to logically relate different concepts (component, material, damage, cause and intervention) and allowing for integration of users' knowledge by the implementation and improvement of built-in mapping of factors (fig.1).

MONDIS serves two main functions: input of knowledge (complete analysis and diagnosis of failures) and searching of stored solutions. Each entry can include a full description of a damage manifestation to which acting damaging mechanisms, primary and secondary causes can be assigned. For this purpose the system presents a layering in the modeling of cases´ entry dependent on the depth of information provided by the user. The option to either qualitatively or quantitatively assess damages, risk and a component condition is supported. The user interface is backed by a pictographic vocabulary for improved precision in entering or retrieving records.

MONDIS is composed of several parts: dedicated server for storing data, semantic web engine, user interface for entering/retrieving data, and a tool for in situ damage surveying. It is designed to accommodate a diverse community of users, being able to adapt to their different perspectives: experts in the field of restoration and conservation, owners and property managers, researchers, students and general public. It can be accessed on-line on the Internet: http://www.mondis.cz.

4. Conclusions

The paper presents a project aiming to develop a knowledge-based system for documentation and analysis of defects of cultural heritage objects. The MONDIS information system covers mainly damage of immovable structures due to various causes, and preventive/remedial actions. Its main goal is to create an artificial intelligence able to reproduce the interplay between relevant factors which govern damaging mechanisms in historical constructions.

Acknowledgement

This research and paper was supported by the project DF11P01OVV002

References

Drdácký M., Valach J., Křemen P. & Abrahamčík J. (2011) Damage database. *In Cultural Heritage Protection Against Flooding.* Prague: Institute of Theoretical and Applied Mechanics AS CR, p. 185-195. ISBN 978-80-86246-37-6.

18th International Conference
ENGINEERING MECHANICS 2012
Svratka, Czech Republic, May 14 – 17, 2012

pp. 1475–1483
Paper #89

INFLUENCE OF THE GEOMETRIC CONFIGURATIONS OF THE HUMAN VOCAL TRACT ON THE VOICE PRODUCTION

T. Vampola*, J. Horáček**

Abstract: *The three-dimensional (3D) finite element (FE) model of the human vocal tract was constructed, based on CT measurements of a subject phonating on [a:]. A special attention is given to the higher frequency range (above 3.5 Hz) where transversal modes exist between piriform sinuses (PS) and valleculae (VA) and where the higher formants can create a formant cluster known as the speaker's or singer's formant. Since the human ear is most sensitive to frequencies between 2 and 4 kHz concentration of sound energy in this frequency region (F4-F5) is effective for communication.*

Keywords: *Boimechanics of voice, 3D FE model, acoustics characteristics, singer's formant*

1. Introduction

At present, a considerable attention is given to the computer simulation of voice production in relation to the sound pressure field inside the human vocal tract during phonation. Main effort is focused on understanding the generation of the articulated audio signal and all the factors influencing this process and the voice quality. The mathematical models of the human vocal tract allow much easier and detailed computer analysis of the acoustic pressure in the vocal tract than it can be obtained by acoustic measurements *in vivo*. A number of simplified 1D models of the vocal tract cavities can be found in literature - see e.g. Titze at al. (1997) or Laukkanen at al. (2009). The advantage of these approaches lie in the relatively simple mathematical description of the behaviour of such derived models. However, it is necessary to accept, that these models were derived under the assumption of planar acoustic waves travelling in the vocal tract and don t accept the 3D geometric configuration of the real human vocal tract (Vampola at al., 2008). For lower values of frequencies of the vocal cavities, for which are not excited the transversal shapes of vibrations, are computed pressure fields of these models in a good relationship with measured data. For a precise evaluation of the voice quality due to geometric modification of the vocal tract for which must be taken into account the hire frequency spectrum are these models inadequate. However, for the evaluation of the impact of individual factors that need to be taken into consideration in the preparation of the real 3D model of the vocal tract are these simplified models very useful computation tool.

2. Simplified model of the human vocal tract

The influence of geometric configuration of the human vocal tract on the generated acoustic pressure was in the first step simulated by the simplified model shown in *Fig 1*. The method of direct physical discretization was used for derivation of the physical parameters of this model. This method is sufficient for a quantitative assessment of the influence of geometric modification of the vocal tract on the acoustic characteristics. The mass and damping matrixes of the simplified model were derived by the direct physical discretization according to *Fig.1*. The stiffness matrix was derived by the inverse procedure. In the first step was accepted the simplified model without parallel chains (the masses m_8 and m_9 were neglected).

Doc. Dr. Ing. Tomáš Vampola: Department of Mechanics, Biomechanics and Mechatronics, Faculty of Mechanical Engineering,CTU, Technická 4 166 07, Prague 6 C , e-mail: tomas.vampola@fs.cvut.cz

Ing. Jaromír Horáček, DrSc.: Institute of Thermomechanics, Academy of Science of the Czech Republic Dolejškova 5, 182 00 Praha 8 C , e-mail:jaromirh@it.cas.cz

In the position defined by the coordinate x_0 was assumed the inhomogeneous pressure boundary condition $p(x_0,t)=p_0(t)$. In the position of mouth was used the homogeneous pressure boundary condition $p(x_{10},t)=0$.

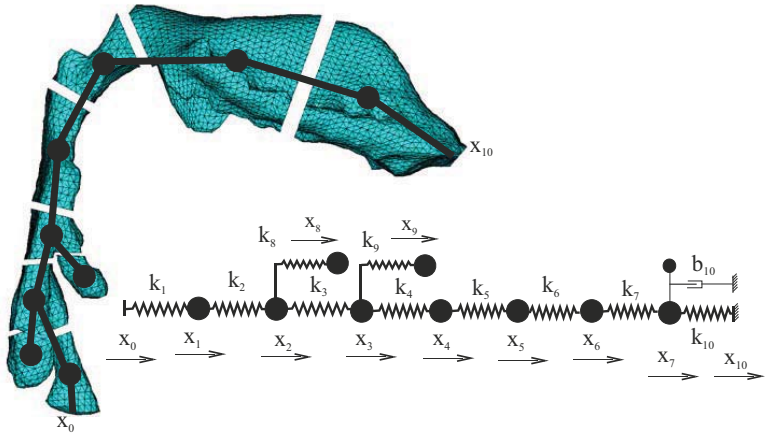

Fig.1 Simplified model of the human vocal tract

The condition of the static pressure equilibrium can be reformulated as

$$\begin{bmatrix} k_{12} & -k_2 & 0 & 0 & 0 & 0 & 0 \\ & k_{23} & -k_3 & 0 & 0 & 0 & 0 \\ & & k_{34} & -k_4 & 0 & 0 & 0 \\ & & & k_{45} & -k_5 & 0 & 0 \\ & sym. & & & k_{56} & -k_6 & 0 \\ & & & & & k_{67} & -k_7 \\ & & & & & & k_{710} \end{bmatrix} \begin{bmatrix} p_1 \\ p_2 \\ p_3 \\ p_4 \\ p_5 \\ p_6 \\ p_7 \end{bmatrix} = \begin{bmatrix} k_0 p_0 \\ 0 \\ 0 \\ 0 \\ 0 \\ 0 \\ 0 \end{bmatrix} \tag{1}$$

where, the symbols $k_{ij}=k_i+k_j$ were used for simplification of notation. By using the global stiffness matrixes of the separate flexible members of the model according to *Fig.1* can be the equation of the pressure static equilibrium (1) rewritten to:

$$\left(k_1\mathrm{K}_{1\mathrm{g}} + k_2\mathrm{K}_{2\mathrm{g}} + \cdots + k_{10}\mathrm{K}_{10\mathrm{g}}\right)\mathrm{p} = \mathrm{f} \tag{2}$$

where k_i $i=1,\ldots10$ are the unknown stiffness parameters of the simplified model and vector **p** was assembled from the known values of the pressure field computed by the FE analysis of the 3D volume model in positions defined by coordinates x_i $i=1,\ldots10$. Vector **f** contains the kinematic excitation of the simplified model. In the following analyses was used the harmonic excitation in position of vocal folds - position x_0. The form of the matrixes $\mathbf{K}_{\mathrm{ig}}$ can be derived from (1). For example the matrix $\mathbf{K}_{\mathbf{2g}}$ can be defined in the form:

$$\mathrm{K}_{2g} = \begin{bmatrix} 1 & -1 & 0 & 0 & 0 & 0 & 0 \\ & 1 & 0 & 0 & 0 & 0 & 0 \\ & & 0 & 0 & 0 & 0 & 0 \\ & & & 0 & 0 & 0 & 0 \\ & \textit{sym.} & & & 0 & 0 & 0 \\ & & & & & 0 & 0 \\ & & & & & & 0 \end{bmatrix} \tag{3}$$

Equation (2) can be reformulated to the final form:

$$\left(\mathrm{K}_{1g}\mathrm{p}, \mathrm{K}_{2g}\mathrm{p}, \cdots, \mathrm{K}_{10g}\mathrm{p}\right)\mathrm{k} = \mathrm{f} \tag{4}$$

The order of the stiffness matrix in the equation (4) is *n*(n+1),* where *n* is the number of discrete masses in the linear chain. Choosing the value of stiffness $k_1=\xi$ can be the equation (4) rewritten to the final form:

$$\mathrm{K}(\mathrm{p})\,\mathrm{k} = \mathrm{f} \tag{5}$$

where **K(p)** is the stiffness matrix whose elements are functions of the pressure obtained from the analysis of 3D FE model. The vector **k** contains unknown stiffness parameters of the linear chain (*Fig.1)* and the vector **f** results from the inhomogeneous boundary condition $p(x_0,t)=p_0(t)$ at the position of the vocal folds. The stiffness parameters of the simplified model are computed by using the additional condition on the first eigen-frequency that is identical with the 3D model. The similar procedure can be used for determination of the stiffness parameters of the PS and the VA, where the shortened chain between the vocal folds and the PA or VA was used. The volumes of the PS and the VA are connected with the basic frame by the very soft stiffness. The matrixes derived in this way are only approximate but maintain the proportionality of the stiffness parameters of the 3D volume model. The dominant mechanism of the energy dissipation from the human vocal tract is due to emitting the acoustic energy from the mouth to the open space. In the simplified model was this mechanism of energy dissipation modeled by the acoustic impedance Z_a. The model of the circular plate vibrating in the infinite wall was used (Vampola at al., 2008)

$$_{a} = \frac{c_0\rho_0}{S}\left(A + iB\right), \quad A = 1 - \frac{J_1(2kR)}{kR},\ B = \frac{H_1(2kR)}{1+kR}, \tag{6}$$

where functions J_1 and H_1 can be expressed by means of the infinite series

$$J_1(2kR) = \left(\frac{2kR}{2}\right)\sum_{m=0}^{\infty}\frac{(-1)^m}{m(m+1)}\left(\frac{2kR}{2}\right)^{2m}, \tag{7}$$

$$H_1(2kR) = \sum_{m=0}^{\infty}\frac{(-1)^m}{\Gamma\left(m+3/2\right)\Gamma\left(m+3/2+1\right)}\left(\frac{2kR}{2}\right)^{2m+2}.$$

In the equation (6) is $k = \omega/c_0$ wave number. *R,S* are the radius and area of the vibrating circular plate simulating the mouth area, c_0 is speed of the sound in the air cavity of the vocal tract and ρ_0 is density of the air for the defined conditions. The expression (6) can be normalized due to standardized wave resistance $\rho_0 c_0$ and area of the vibrating circular plate:

$$z_{nv} = A + iB\,, \tag{8}$$

where the real part describes the emitting resistance and the imaginary part is the fictional mass air-column vibrating with the human vocal tract. Using the validity of the relations between the acoustic and mechanical impedance can be parameters used in the model of the vocal tract in *Fig. 1*, defined by the expressions:

$$b_{10}(\omega) = S^2 r_a(\omega), \quad m_{10}(\omega) = S^2 m_a(\omega) \quad , \tag{9}$$

where $r_a(\omega)$, $m_a(\omega)$ are the frequency dependent values of the acoustic resistance and the acoustic mass following from (8). The character of the acoustic radiation impedance for the area of the mouse approximately 7e-3 m^2 is presented in the *Fig.2*.

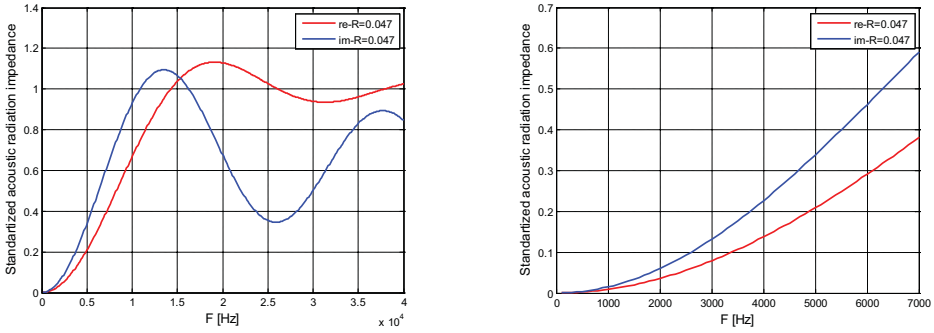

Fig.2 Standartized acoustic radiation impedance

It is necessary to keep in mind that the using of the simplified model of the human vocal tract is limited to the lower frequency span. The model acts as a frequency filter, which removes from the frequency spectrum the frequencies of the transversal vibrating modes, which the simplified model is not able properly modeled. With regard to this fact, it is evident that for the lower values of the frequency range, can be the standard radiation impedance approximated with sufficient precision by the polygon line.

3. Influence of geometric configuration of the model to the position of the resonant peaks

The influence of the shape modification of PS and VA to the generated pressure characteristics of the human vocal tract was in the first step used the simplified model according to *Fig.1*. This model is sufficient for the quantitative assessment influence of the geometric modification to the predicted pressure fields of the human vocal tract. The character of the pressure field in the position defined by the coordinate x_7 was simulated. In the first step can be this value accepted as the output pressure from the human vocal tract. The pressure fields were calculated using the method of harmonic analysis. The vector of unknown pressures amplitudes is considered in the form

$$\mathrm{p}(t) = \mathrm{r}e^{j\omega t}\,. \tag{10}$$

The amplitudes of excited vibration ***r*** can be derived from the equation of motion:

$$\mathrm{r} = (\mathrm{K} - \omega^2\mathrm{M} + i\omega\mathrm{B})^{-1}\mathrm{h}(\omega) = \mathrm{A}^{-1}\mathrm{h}(\omega)\,. \tag{11}$$

where h(ω) is vector of the kinematic excitation of the system. The complex amplitudes of the excited vibration can be derived from the expression (11):

$$\mathrm{r}_i = \frac{\mathrm{q}_i}{\det(\mathrm{A})}\mathrm{h}(\omega)\,. \tag{12}$$

From equation (12) results

$$q_7 = k_2 k_3 k_4 k_5 k_6 k_7 \,. \tag{13}$$

for the model, when were not used the masses m_8 and m_9 in the linear chain. In case, that the mass m_9 is not used, we got:

$$q_7 = k_2 k_3 k_4 k_5 k_6 k_7 \left(k_8 - m_8 \omega^2\right). \tag{14}$$

For the full model according to *Fig.1* was

$$q_7 = k_2 k_3 k_4 k_5 k_6 k_7 \left(k_8 k_9 - \omega^2 \left(k_8 m_9 + k_9 m_8\right) + \omega^4 m_8 m_9\right). \tag{15}$$

From the equations (14 and 15) it is apparent that by adding a "parallel" branch to a serial chain the state of antirezonance can occurs, when the output pressure amplitude of the forced vibrations on the output from the model are zero. The equations (14 and 15) from the equation (11) differ by the modifier

$$mo_1 = \left(k_8 - m_8 \omega^2\right) \tag{16}$$

$$mo_2 = \left(k_8 k_9 - \omega^2 \left(k_8 m_9 + k_9 m_8\right) + \omega^4 m_8 m_9\right)$$

In the *Fig.3* is presented the dependence of the amplitude of the output pressure at the point defined by the coordinate x_7 due to the excitation frequency for the nominal size of the volume of the PA and VA

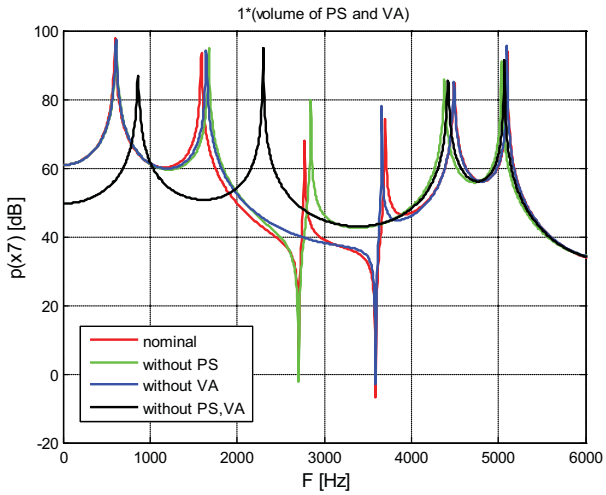

Fig.3 The dependence of the amplitude of the output pressure in position x_7 on the excitation frequency

It is evident that, in accordance with the (13) that for the model without the "parallel" branches is not in the output signal presented the antirezonance frequency. On the contrary, by adding one or two parallel branches arise in the output pressure signal one or two antirezonance frequency. The dependence of the relationship (16) on the excitation frequency is presented in *Fig.4*.

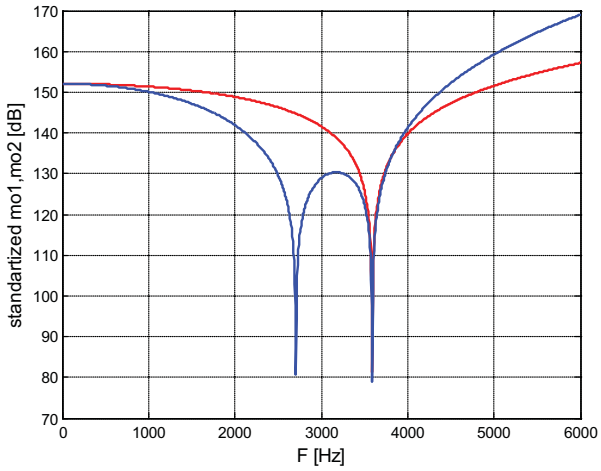

Fig.4 The dependence of "modifiers" on the output pressure in position x_7 on the excitation frequency

In the *Fig. 5* is introduced the dependence of the resonant and antirezonant peaks for the simplified model, where the volumes of PA and VA were changed.

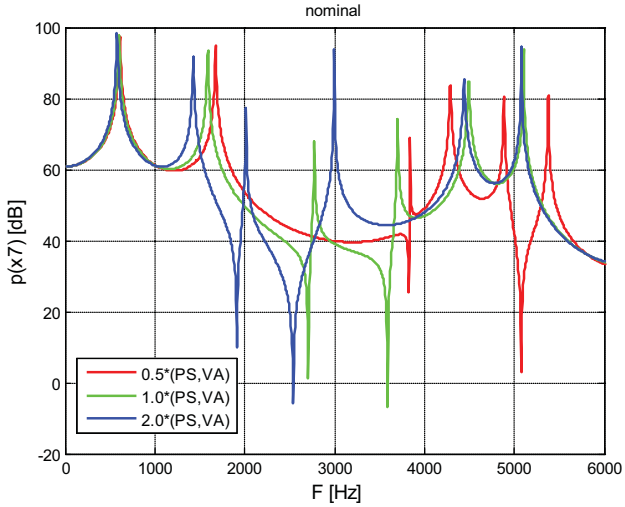

Fig.5 The dependence of the position of the resonant peaks for the modified volume of PS and VA

It is apparent that for increasing volume of the "parallel" branches the frequency range between antirezonance frequencies decreases and shift to the lower frequency values. The position of the antirezonance peaks can therefore be used to evaluating the size of the volume of the "parallel" branches of the human vocal tract. In the *Fig. 6* can be seen that if in the output signal is presented the antiresonance frequency then the energy coming into the system is "consumed" by the relatively heavy vibration of the parallel branches. It is to be noted that in these considerations do not take into account the influence of transversal shapes of vibrations.

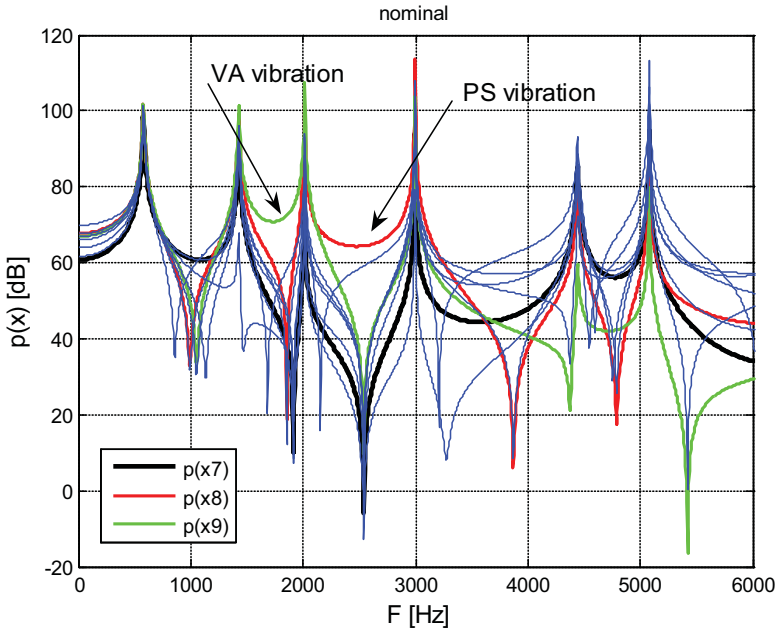

Fig.6 Pressure field of the simplified model of the human focal tract

Therefore these findings were proved on the 3D volume models.

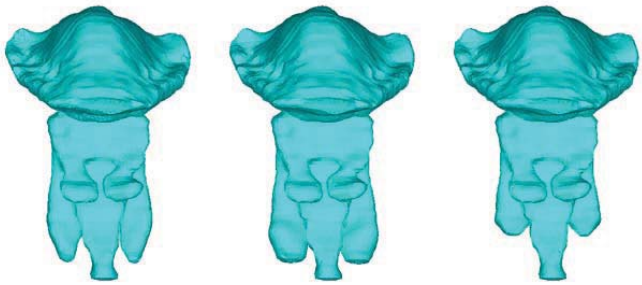

Fig.7 Volume modification of PS

The geometric modification of the PS is presented on the *Fig.8* in more detail

	Volume [mm^3]
smaller	304
nominal	1317
bigger	2437

Fig.8 Volume modification of the PS

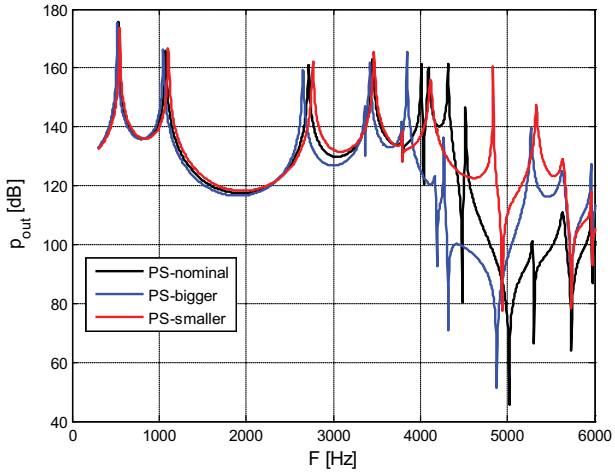

Fig.9 The output pressure field of the 3D model

In the *Figs. 10* and *11* are introduced the characters of the vibration of the 3D volume model of the human vocal tract during the antiresonace frequencies.

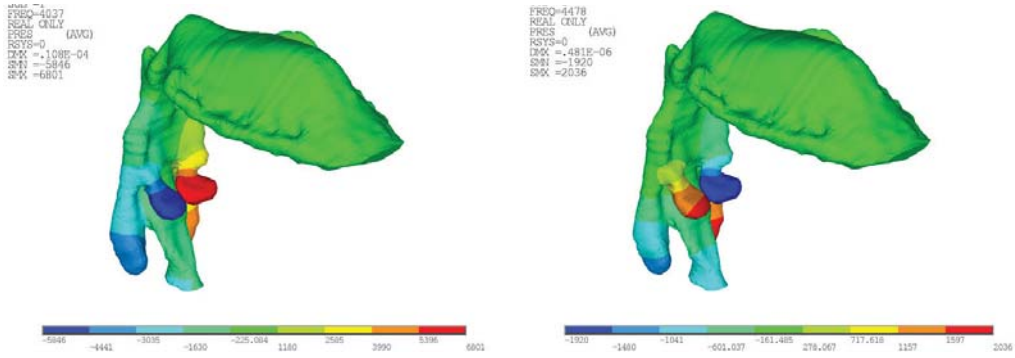

Fig.10 The first and the second significant antiresonance frequencies for the nominal volume PS

In accordance with the *Fig.9* it can be seen the significant (rarely damped) vibration of the „parallel branches“ of the vocal tract.

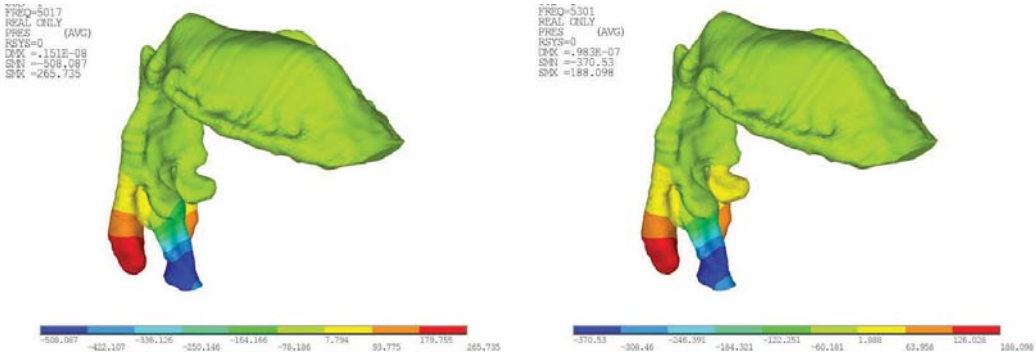

Fig.11 The third and fourth significant antiresonance frequency for the nominal volume PS

From the above it is apparent that in the frequency region about 4kHz the accumulation of the energy occurs by increasing of the volume of parallel branches. So called the singer s formant is formed. For frequencies values about 4kHz are the human ears the most sensitive. The accumulation of energy in this frequency span contributes to the clarity of communication. On the contrary, when is disproportionately enlarged PS the shift in the frequency spectrum occurs and the level of the emitted energy is lower. It can be seen that for optimal phonation it is necessary to reach the appropriate "optimal" volume configuration of the parallel branches of the vocal tract. For too small PA and VA is voice energy concentrated in other frequency ranges than would be appropriate for the sensitivity of the ear. For very large volumes of PS and VA occurs in the required frequency range decreasing of the energy level. In the frequency spectrum (*Fig.9*) is interesting the frequency peek about 3.8kHz. It is the first excited transversal mode of vibration, when the energy emitted from the vocal tract is decreased.

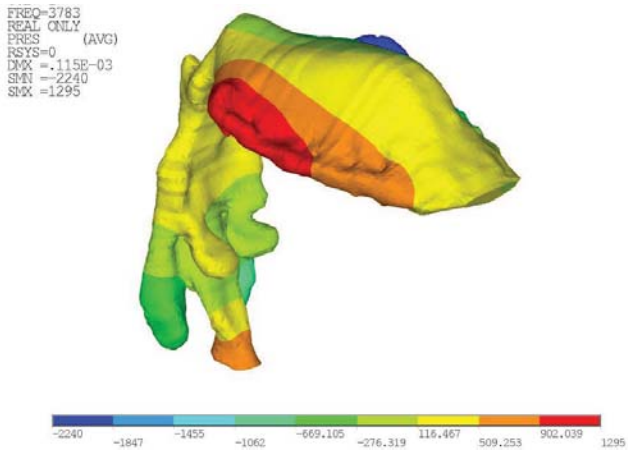

Fig.12 The first transversal shape of vibration

4. Conclusions

The simplified, computationally efficient 1D model of the vocal tract was assembled and used for prediction of the pressure fields for a more clear explanation of effects of geometrically changed configurations of the human vocal tract resulted from the size of piriform sinuses and valleculae. The findings were compared with the results acquired from the 3D FE models with the good correlation.

Acknowledgement

The research was supported by the grant GACR No. P101/12/1306 *Biomechanical modeling of human voice production – way to artificial vocal folds*.

References

Titze, I.R. and Story, B.H. (1997). "Acoustic interactions of the voice source with the lower vocal tract", *J. Acoust. Soc. Am.,* 101, 2234-2243.

Vampola, T., Horáček, J. and Švec, J.G. (2008). "FE modeling of human vocal tract acoustic. Part I: Production of Czech vowels", *Acta Acust. United Acust.*, 94, 433-447.

Laukkanen, A.M., Radolf, V., Horáček, J., Leino, T. (2009). "Estimation of the origin of a speaker's and singer's formant cluster using an optimization of 1D vocal tract model", *Proceedings of 3rd Advanced Voice Function Assessment*. Madrid: EUIT Telecomunicación, 2009, pp. 1-4. ISBN 84-95227-64-9.

18th International Conference
ENGINEERING MECHANICS 2012
Svratka, Czech Republic, May 14 – 17, 2012

pp. 1485–1491
Paper #282

X-RAY OBSERVATION OF THE LOADED SILICATE COMPOSITE

D. Vavřík[1], T. Fíla[2], I. Jandejsek[3], V. Veselý[4],

Abstract: *An intensive internal material damage evolution precedes a failure in quasi-brittle materials. Not only the existence of damage but also its quantification and the geometry of the Fracture Process Zone have to be identified in order to validate approaches on both numerical modelling of quasi-brittle behaviour and experimental determination of fracture properties. Radiographic techniques and Digital Image Correlation method are very appropriate for analysing of the Fracture Process Zone evolution during specimen loading.*

Keywords: ***Quasi-brittle fracture, Cementitious composite, Digital radiography, Computed tomography, Digital Image Correlation***

1. Introduction

The area of determination of characteristics of quasi-brittle building materials (most commonly cementitious composites) which should describe their ability to resist the fracture propagation has been thoroughly researched for several decades (van Mier, 1997, Bažant & Planas, 1998). However, some aspects that can be referred to as crucial are still among the topics of intensive research. Effects of the size and geometry of the test specimen (Yu et al., 2010) regarded also as the effect of the specimen free boundaries (Hu & Duan, 2007) seems to be the most relevant. An approach incorporating the parameters of the zone of material failure developing at the propagating macroscopic crack tip (fracture process zone, FPZ) has been proposed and (partially) employed recently (Veselý et al., 2009). The development of this approach is motivated by capturing of the above-mentioned effects in order to provide values of the fracture-mechanical parameters of the tested material independent of these effects. This methodology works with the reconstruction of the current size and shape of the FPZ (and perhaps also the intensity of the cohesive behaviour over the FPZ volume) (Veselý & Frantík, 2010) to which the amount of energy dissipated during the current step of fracture process should be related.

The development of the methodology is in a stage of testing, verification by numerical simulations (Frantík et al., 2011) and experimental validation (Vesely et al., 2010) at present. It has to be emphasized that sound experimental evidence the FPZ size and shape (and possibly other characteristics) is published rather rarely. Techniques based on acoustic emission (Otsuka & Date, 2000, Mihashi & Nomura, 1996, Muralidhara et al. 2010), holographic interferometry, X-ray imaging (in combination with digital image analysis − Jandejsek et. al. 2011) and infrared thermography were reported to be used to determine the FPZ in quasi-brittle materials (summarized e.g. in van Mier, 1997).

Investigation of the material failure employing X-ray imaging is presented in this paper. Notched specimen prepared from cementitious composite was loaded in three point bending in a specially designed loading device. Crack and FPZ shape was analysed using digital transmission radiography

[1] Ing. Daniel Vavřík, Ph.D.: Institute of Theoretical and Applied Mechanics AS CR v. v. i., Prosecka 76, Prague 9, Czech Republic, vavrik@itam.cas.cz, Institute of Experimental and Applied Physics, Czech Technical University in Prague, Horska 3a/22, Prague 2, Czech Republic

[2] Bc. Tomáš Fíla: Institute of Theoretical and Applied Mechanics AS CR v. v. i., Prosecka 76, Prague 9, Czech Republic, fila@itam.cas.cz

[3] Ing. Ivan Jandejsek: Institute of Theoretical and Applied Mechanics AS CR v. v. i., Prosecka 76, Prague 9, Czech Republic, jandejs@itam.cas.cz

[4] Ing. Václav Veselý, Ph.D.: Brno University of Technology, Faculty of Civil Engineering, Institute of Structural Mechanics, Veveří 331/95; 602 00, Brno; Czech Republic, vesely.v1@fce.vutbr.cz,

and X-ray Computed Tomography (XCT). Visualization of the FPZ was emphasized using tools of the Digital Image Correlation method (DIC).

2. Investigated material, specimen dimensions

The radiographic investigations of the material failure have limits in the dimensions of the test specimens. In our case, the length of the beam subjected to three point bending is limited by the chamber diameter of the loading device in which the specimen was placed.

As a material for the specimen preparation, a fine-grained cementitious composite was chosen to simulate the failure process of normal-sized building structures/structural members made of concrete. Commercial dry plaster mix with maximum aggregate size equal to 1.2 mm (limestone debris) was selected. The bonding agent of this mix consists of both cement and calcium hydroxide. Minimal value of modulus of rupture quoted by the producer is 0.7 MPa. The mix was prepared according to the producer's instructions.

The presented experiment was made as a pilot test to develop appropriate methodology of the FPZ and crack analysis intended for future experimental campaign. Series of 9 specimens were casted into the mould for this campaign. Three specimens' breadths B (15, 25 and 30 mm) were selected; three different notch lengths a (4, 10 and 16 mm) were taken into account for each specimen breadth B. The notches were cut using diamond saw. It provides the relative notch length α equal to 0.1, 0.25 and 0.4. Specimen height W and length L are equal to 40 and 150 mm, respectively. From this specimen series the specimen with 25 mm breadth and 10 mm notch length was selected for the developing of the methodology for macroscopic crack and FPZ analysis. The loading span of the specimen was set as equal to 120 mm. Schematic picture of the specimen and related bending test is depicted in Figure 1.

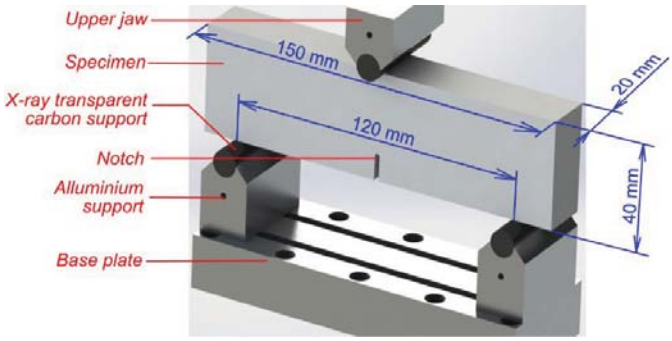

Figure 1: Three point bending of the specimen.

3. Instrumentation

The modular tomographic system (Jakůbek et. al., 2006) provides an experimental setup allowing positioning adjustment of the X-ray tube, motorized positioning of the detector and the operational movement of the observed object fixed on a motorized stage. The linear axis of this stage enables to set the projective magnification of the object. The rotation axis is used for tomographic data acquisition. The setup is equipped by the motorized revolver holder of the filters used for the fully automated acquisition of data needed for beam hardening correction, using the Signal to Equivalent Thickness (SET) method (Vavřík 2011).

Hamamatsu microspot tube is employed as X-ray source in the tomographic system. This tube has a 5 μm spot size and cone beam. The pixelated Hamamatsu flat panel was utilized as X-ray imager in our work. This detector has active area 120x120 mm with 50 μm pixel size. Binning of 2×2 pixels was used in our work, so effective pixel pitch was equal to 0.1 mm.

Highly stiff loading compressive device was used for the specimen loading. This device allows very low loading velocity while it's relatively low weight and dimensions enable X-ray observation of the specimen in the radiographic cabin. Loading device generally consists of the actuating part and of

the chamber in which specimen is placed. This chamber was manufactured from two parts. Top one is from the aluminium alloy and bottom one from the 0.6 mm thick carbon epoxy laminate, which is practically transparent for X-rays. These parts are connected using bayonet mechanism. Support pins of the bending mechanism were also prepared from the carbon material. This solution enables radiographic observation of the analysed specimen without any influence of the loading device for X-ray measurement. Whole setup is depicted in Figure 2 left. Disassembled chamber with the specimen is in Figure 2 right.

Figure 2: Radiographic setup with loading device left. Disassembled chamber with the specimen right.

4. Experimental details

Specimen was loaded with velocity 6 μm/min. Exposure time of one X-ray radiograms was 5×0.48 seconds (it corresponds to the 0.5 μm displacement increment due to read out time). These radiograms were recorded continuously during loading while CT measurement was done in two loading levels. For the CT measurement, 240 snapshots (180° rotation) were taken. Total time of one CT measurement was 50 minutes. The specimen rotation axis was at a distance 188 mm from the X-ray tube spot and flat panel was at distance 429 mm X-ray from the tube spot. The projected magnification was 2.3 from this reason. The X-ray tube was operated at 80 kV and 125 μA. CT reconstruction was done considering divergent X-ray beam (Vavřík & Soukup, 2011).

5. Results

A load−displacement diagram (LD diagram) is plotted in Figure 3. It is clearly visible that loading device enables to study processes with very high loading precision. The radiogram of the specimen taken 1.5 μm after reaching maximal loading force (point *A* in LD diagram: 108 N at 134 μm) is in Figure 4 left. Significant structure corresponds to the material inhomogeneity. It is almost impossible to observe FPZ directly in the investigated specimen thanks to this structure.

DIC tools were used to avoid this difficulty, where actual and initial radiograms were subtracted (subtraction image) to find changes of the specimen density considering specimen movement during its loading. Such image is shown in Figure 4 right (three blue diamond shape spots occurred thanks to flat panel local noise). It is visible that FPZ has significant role for the fracture mechanics description, where crack is much shorter (0.7 mm) than FPZ (6.5 mm) as visible in Figure 4 right.

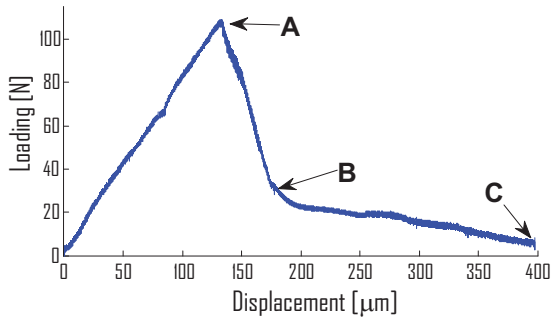

Figure 3: LD diagram. Loading levels in which FPZ zone was detailed studied are labelled by letters.

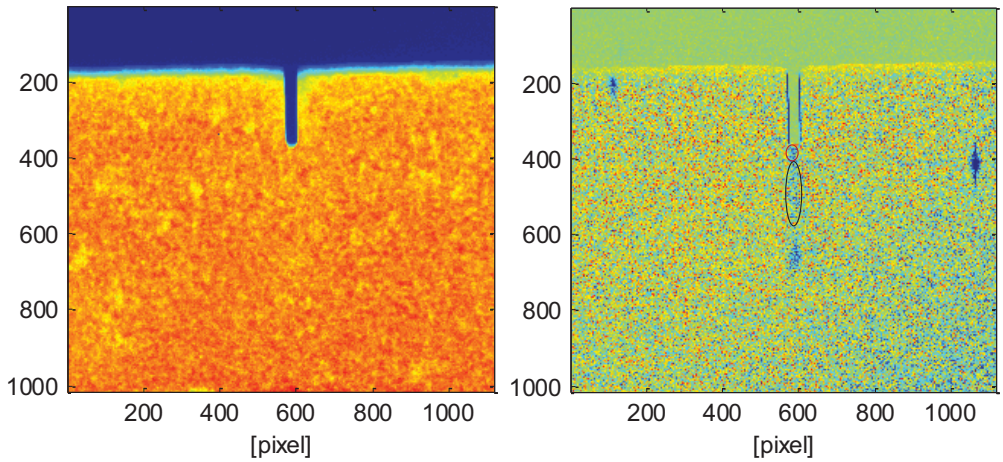

Figure 4: Radiogram of the specimen taken at the maximal loading force is left. Note, that FPZ is not visible due to significant variation of the material density. Colours correspond to the material effective density (averaged through the specimen thickness). The crack (surrounded by red ellipse) and FPZ (surrounded by black ellipse) are visible in subtraction image right. The radiogram pixel size is 44 μm.

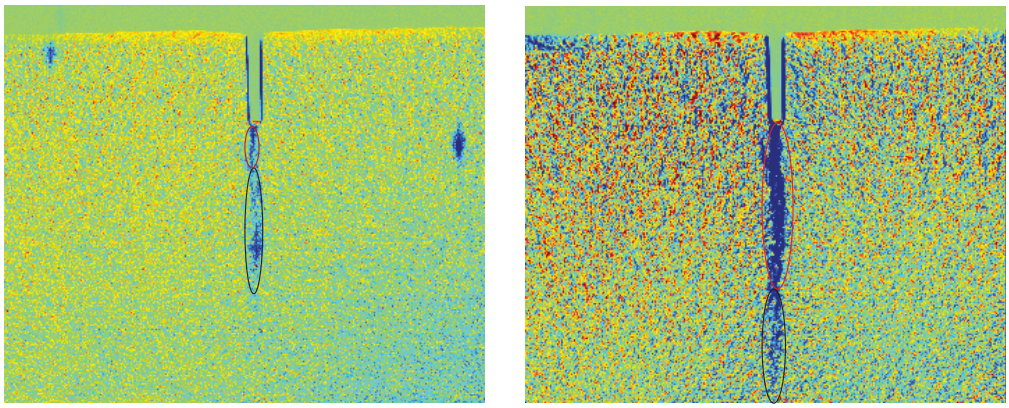

Figure 5: Subtraction image at the loading level B left. Image of the specimen at the end of the experiment is right.

The subtraction image in the moment where loading force dropped down is depicted in Figure 5 left (point *B* in LD diagram: 28 N at 160 μm). The CT measurement was done at the same loading level. It was proven that subtraction image (comparing with CT measurement) can describe crack front

position and FPZ shape thanks to the significant change of the specimen density, although boundary between crack tip and FPZ is quite blurred. Crack and FPZ were 2.7 and 16 mm long respectively at the loading level *B*. The subtraction image from the end of the loading experiment is depicted in Figure 5 right (point 3 in LD diagram: 5 N at 380 μm). The crack was 17 mm long and practically whole remaining ligament was weakened by the FPZ.

As was mentioned above, CT measurement was done in two loading levels (*B* and *C* at LD diagram). Vertical cross-section of the CT reconstruction at loading level *B* is depicted in Figure 6 left. This cross-section lies in the centre of the notch. It is visible, that specimen is damaged preferentially in the specimen centre. Virtual hole in the middle came from the flat panel local noise. Tip of transversal crack is imaged in Figure 7 right (slice number 73 at cross-section left, crack is surrounded by blue ellipse). This crack tip is in the same position as in subtraction image, Figure 5 left.

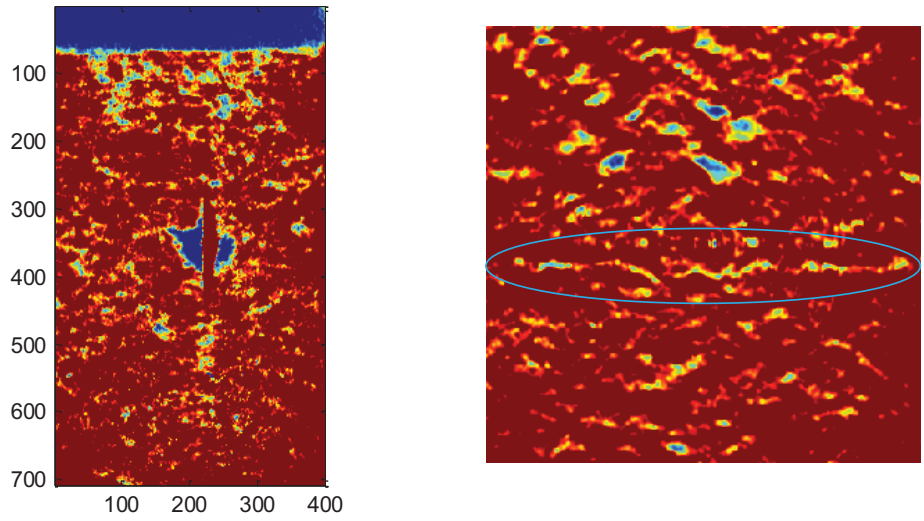

Figure 6: CT reconstruction of the specimen at loading level B. Vertical CT cross-section which corresponds to the notch central plane is imaged left. Tip of transversal crack surrounded by blue ellipse right.

Similarly, vertical cross-section at loading level *C* is imaged in Figure 7 left. Squiggly macroscopic crack from slice number 270 is in Figure 7 right.

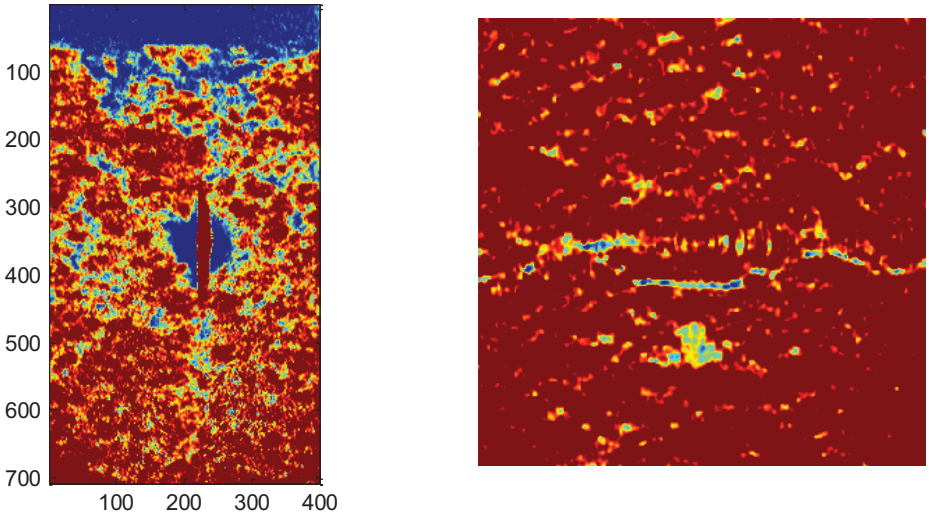

Figure 7: CT reconstruction of the specimen at loading level C. Vertical CT cross-section left. Squiggly macroscopic crack right.

Generally, crack does not follow straight direction and its front is not sharp as it is possible to document using CT reconstruction. It is hard to distinguish which individual voids were born during loading and which were presented from the beginning. However it can be shown, that void density is significantly increasing during loading as presented in Figure 8 using 3D visualization. Situation at loading *B* is left and at loading *C* right. Only central part of the specimen containing crack was selected for this visualisation.

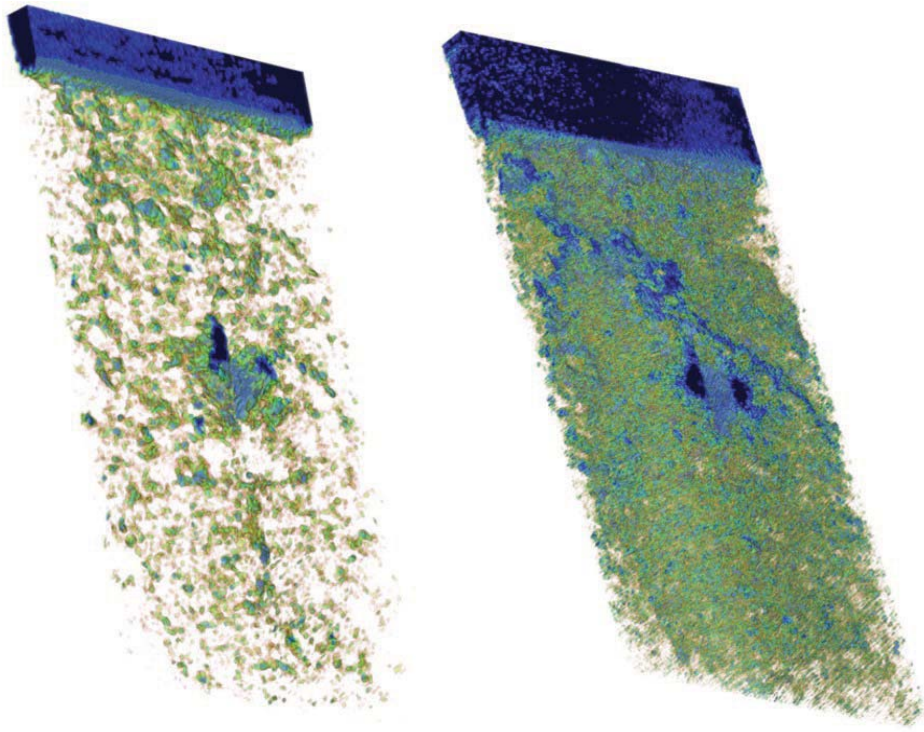

Figure 8: 3D visualisation of the voids at loading level B left and C right. It is visible that these voids and consequent macroscopic crack are preferentially occurring in the middle of the specimen.

6. Conclusions

It was proven that X-ray radiography in conjunction with Digital Image Correlation and CT reconstruction are powerful tools for analysing of the crack and FPZ evolution during quasi brittle specimen loading.

Experimental results showed that fracture process zone is generally significantly larger than macroscopic crack. Moreover, crack does not follow straight direction and its front is not sharp. It can be concluded from these reasons that linear fracture mechanics based on assumption of the continuum material can't describe such crack behaviour.

Acknowledgement

Financial support from the Czech Science Foundation, project No. P105/11/1551, and RVO 68378297 are gratefully acknowledged. Material for the specimen preparation was granted by PROFI am BAU CM, spol. s r.o.

References

Bažant, Z.P., Planas, J. (1998) Fracture and size effect in concrete and other quasi-brittle materials, CRC Press, Boca Raton.

Frantík, P., Veselý, V., Keršner, Z. (2011) Efficient lattice modelling of fracture process zone extent in cementitious composites. Proc. of the 2nd Int. Conf. on Parallel, Distributed, Grid and Cloud Computing for Engineering, P. Iványi and B.H.V. Topping (eds), Civil-Comp Press, Stirlingshire, UK, paper 62, 2011. doi:10.4203/ccp.95.62.

Hu, X-Z, Duan, K. (2007) Size effect: Influence of proximity of fracture process zone to specimen boundary. Engng. Fract. Mech. 74, 1093-1100.

Mihashi, H., Nomura, N. (1996) Correlation between characteristics of fracture process zone and tension-softening properties of concrete. Nuclear Engineering and Design 165, 359-376.

Muralidhara, S., Raghu Prasad, B.K., Eskadri, H., Karihaloo, B.L. (2010) Fracture process zone size and true fracture energy of concrete using acoustic emission. Construction and Building Materials 24, 479-486.

Otsuka, K., Date, H. (2000) Fracture process zone in concrete tension specimen. Engrg. Fract. Mech. 65, 111-131.

van Mier, J.G.M. (2007) Fracture processes of concrete: Assessment of material parameters for fracture models, CRC Press, Inc., Boca Raton.

Veselý, V, Frantík, P. (2010) Reconstruction of a fracture process zone during tensile failure of quasi-brittle materials. Applied and Computational Mechanics 4, 237-250.

Veselý, V., Frantík, P., Keršner, Z. (2009) Cracked volume specified work of fracture. Proc. of conf. CC 2009, Funchal, Portugal. B.H.V. Topping, L.F. Costa Neves, R.C. Barros (eds.), Civil-Comp Press, Stirlingshire, UK, paper 194 (16 p.), 2009. doi:10.4203/ccp.91.194.

Veselý, V., Keršner, Z., Němeček, J., Frantík, P., Řoutil, L., Kucharczyková, B. (2010) Estimation of fracture process zone extent in cementitious composites, Chem. Listy 104, 382-385.

Yu, Q., Le, J.-L., Hoover, C.G., Bažant, Z.P. (2010) Problems with Hu-Duan Boundary effect model and its comparison to size-shape effect law for quasi-brittle fracture. Journal of Engineering Mechanics (ASCE), 136(1).

Jandejsek, I., Nachtrab, F., Uhlmann, N., Vavřík, D. (2011) X-ray dynamic defectoscopy utilizing digital image correlation. Nuclear Instruments & Methods in Physics Research Section A, Vol. 6, 185-186. doi:10.1016/j.nima.2010.06.162,

Jakůbek, J., Vavřík, D., Holý, T., Jakúbek, M., Vykydal, Z., (2006), Experimental system for high resolution X-ray transmission radiography, NIM A, Vol. 563, Issue 1, p. 278-281, doi:10.1016/j.nima.2006.01.033

Vavřík, D. (2011), CT Artefact Reduction by Signal to Thickness Calibration Function Shaping, NIM A, Volume 633, Supplement 1, May 2011, Pages S152-S155, doi: 10.1016/j.nima.2010.06.160

Vavřík, D., Soukup, P. (2011) Metal Grain Structure Resolved with Table-top micro-Tomographic System, JINST_007P_1011, doi:10.1088/1748-0221/6/11/C11034

18th International Conference
ENGINEERING MECHANICS 2012
Svratka, Czech Republic, May 14 – 17, 2012

pp. 1493–1496
Paper #245

ARTIFICIAL ANT COLONY METHOD FOR STATE-SPACE EXPLORATION

S. Vechet[*], J. Krejsa[**], J. Hrbacek[+]

Abstract: *Finding a way through an unexplored environment belongs to actual problems in many artificial agent systems. Common algorithms as state-space searching or rapidly exploring random trees are used when the map of given environment is known. In this paper we present a simulation experiments with multi agent system which is represented as artificial ant colony.*

Keywords: ***artificial ant colony, path planning, state space exploration.***

1. Introduction

Finding a way through an unexplored environment belongs to actual problems in many artificial agent systems. Common algorithms as state-space searching or rapidly exploring random trees are used when the map of given environment is known. In many real-world applications the agent is faced to problem find path in partially mapped or unknown environment (Krejsa,2011).

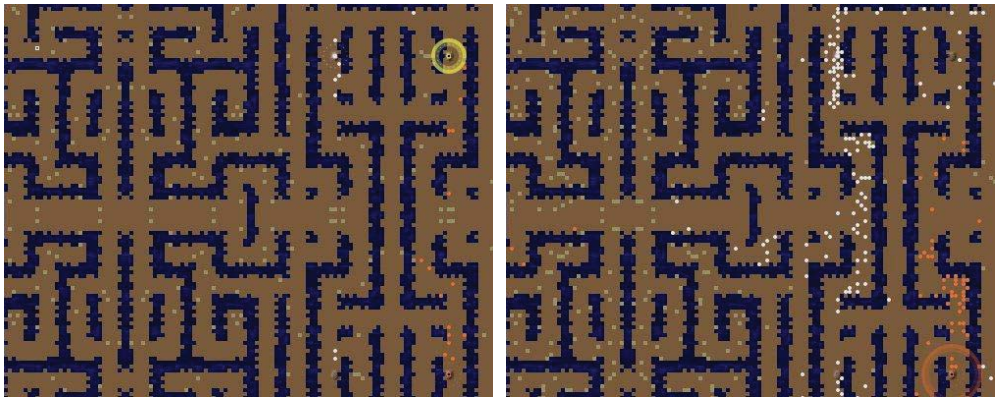

Fig. 1. Simulation framework

Presented algorithm of artificial ant colony is used to finding a path through unexplored environment. The main issue is to explore the biggest space in shortest time. Each ant is represented as simple agent with its own searching strategy (Krejsa,Ondrousek,2011). As each agent is a part of the ant colony, this local strategy can be very simple, but the exploring efficiency of the whole colony can be huge. Each agent has local information only, about near environment based on visible range of agents sensors.

[*+] Ing. Stanislav Vechet, Ph.D., Ing. Jan Hrbacek: Brno University of Technology, Faculty of Mechanical Engineering, Faculty of Mechanical Engineering, Brno University of Technology, Technicka 2896/2, Brno, Czech Rep, e-mail: vechet.s@fme.vutbr.cz, yhrbac03@stud.fme.vutbr.cz

[**] Ing. Jiří Krejsa, PhD.: Institute of Thermomechanics ASCR, v.i.i, Brno department, Technická 2, 616 69, Brno, CZ, email: krejsa@fme.vutbr. cz

2. State-space exploration

Path planning using artificial ant colony method is based on state space searching algorithms. Each artificial ant/agent implements simple local behavior which can results in complex global solution. Each agent is represented by simple rules described in high level programming language. In our case the Python is used. The main advantage of Python is the simple and powerful syntax. In some cases when pseudo-code is needed the *pythonic* syntax is used. In next step, there is no conversion needed for writing a runnable simulation code.

The state space for searching is represented by static environment in two dimensional rectangular grid G. Each cell C in the grid can represents one of possible states S. For better understanding of simulation results each state is also represented by different color. All used states and its colors are described as follows:

S_{free} – Free unoccupied space (brown),

S_{water} – Water represents an obstacle (blue),

S_{food} – Food represents free cell for movement but with food placed on it (light brown),

S_{ant} – Ant represents single agent (another colors), each ant colony has its own color,

$S_{anthill}$ – Anthill is the place where the new ants are born and also the anthill of opponent colony is the goal G for path planning.

Each agent can perform one of four possible actions A:

A_{north} – move to the north,

A_{south} – move to the south,

A_{east} – move to the east,

A_{west} – move to the west,

The simulation starts with single agent in each ant colony. Each food founded by the agent results in new agent in the colony. The colony has to grow rapidly to explore as much space as possible in shortest time which results in quick finding of goal for the path planning.

The need of finding food is in opposite to space exploration, because of those agents which are searching for food cannot perform the space exploration task. There are two main tasks for agents: exploration or searching, each agent has to decide what task to choose in single simulation step. The simulation is discrete, in one simulation step the agent can change its position, gathering food or explore some unexplored space. The space is explored when is in small given range from agent which represents the visible neighborhood.

Tab. 1: Algorithm SRCH1 of simple Agent

```
1.  GetClosestFood()
2.  GoStraight4Food()
3.  if Obstacle(x,y):
4.      Avoid()
5.  if AnotherAntHill(x,y):
6.      GoalReached()
```

However, the algorithm SRCH1 (the main task for agent is searching) looks very simple its very powerful. The main task of this algorithm is just searching nearest food and avoiding obstacles, if necessary. This kind of algorithm has also big ability for state space exploration because of the near food is quickly harvested and is necessary to find a new food in higher distances. On the other hand

the goal is founded accidentally in case that the agent in visible distance to the goal, this make in some cases the algorithm very slow.

Tab. 1: Algorithm of modified Agent, SRCH2

```
1.  Get4OneAntOneFood()
2.  GoStraight4Food()
3.  if Obstacle(x,y):
4.      Avoid()
5.  if AnotherAntHill(x,y):
6.      GoalReached()
7.  if AnotherAntHillLocationIsKnown():
8.      SendAllAnt2AntHill(x,y)
```

The algorithm of smarter agent SRCH2 is similar to the simple algorithm but with one small difference. In this method each agent goes for one different food, in such a case there are lot of agents without task. If the position of goal is known, but the path to goal is still unknown, all remains agent are searching the way to the goal. This simple change makes this algorithm much more efficient.

3. Simulation environment

For simulations the AI challenge framework was used. The native language of AI challenge framework (figure 1) is Python for running the simulation code and Java for showing simulation results. This framework is freeware and open source so anyone can used it for own experiments.

For comparing the efficiency of our algorithms there are number of different environments. Each environment can run simulation at least two artificial ant colonies in duel. The maximum number of colonies in one environment is ten. The main reason for using more colonies in one simulation is the possibility to straight comparison of colonies in performed simulation.

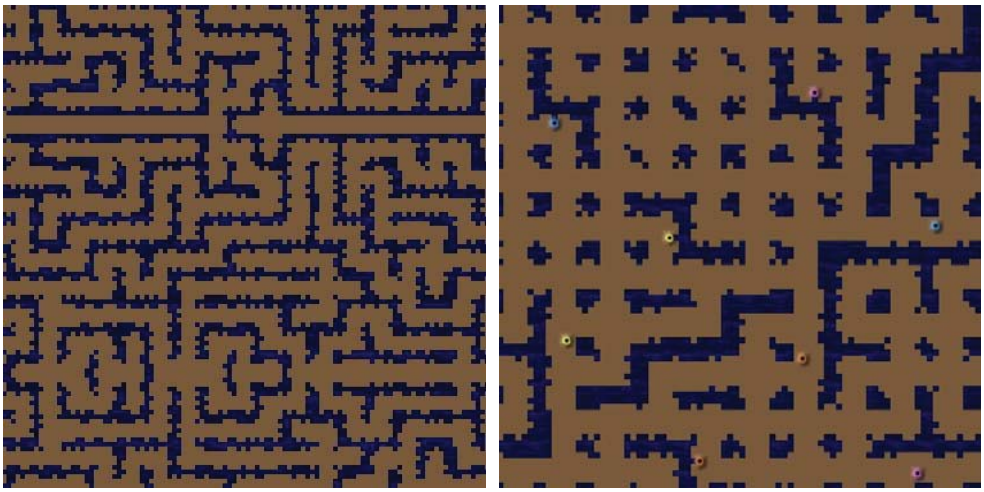

Fig. 2.Typical rectangular mazes with open cycles

Typical rectangular mazes for two artificial ant colonies are shown on fig. 2. The main issue on this kind of environment are the open cycles around the obstacles, which usually results in infinite loops so the ant colony cannot efficiently explore other parts of given map.

4. Simulation results

This chapter presents the simulation results from performed experiments. We prepare number of simulations with two artificial ant colonies for direct comparison and also some experiments with more, usually six, ant colonies (see figure 3). Each colony used in single simulation has different strategy. As the main criterion for the classification of the efficiency of the method, the number of ants in one colony, was used. The exploration strategy is based on efficient algorithm for path planning and also on effective food searching policy. Thus, the final number of ants in one colony, after the maximal number of simulation steps, was used as the main criterion for the classification.

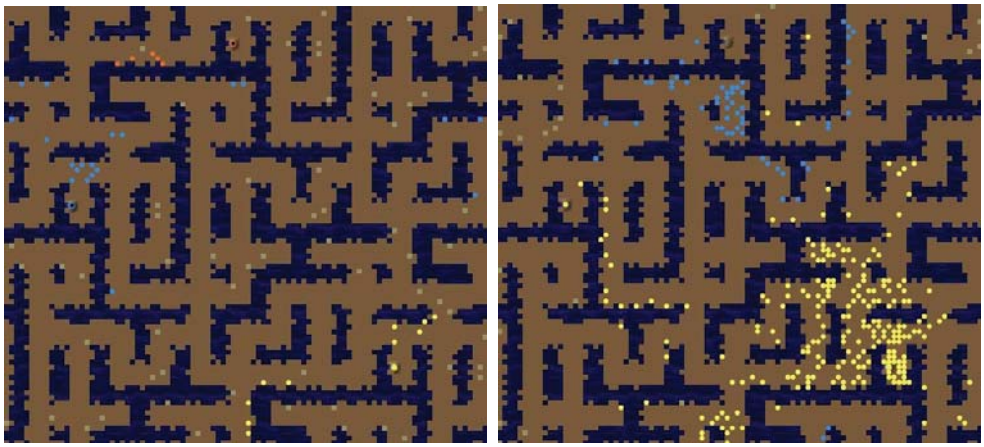

Fig. 3.Comparison of algorithms SRCH1 and SRCH2

5. Summary

Methods for finding path through unknown environment via artificial ant colony algorithms were presented in this paper. In simulation experiments were successfully tested two main approaches to artificial ant colony behavior: searching and exploration. The searching method is very easily implemented and is computationally fast, on the other hand the exploration method is more complicated for implementation, more time consuming but very efficient.

6. Acknowledgement

Presented results were obtained with the support of the Academy of Sciences of the Czech Republic under the research plan AV0Z20760514 and Brno University of Technology under project FSI-S-11-15.

References

Krejsa, J., Reduction of face detection false positives in mobile robot interaction using proximity sensors, in *Proceedings of Mendel 2011, 17th International Conference on Soft Computing*, pp. 540-545, 2011

Krejsa, J., Ondrousek, V.: The design of human-machine interface module of presentation robot Advee, in *Mechatronics, recent technological and scientific advances*, Springer, pp. 423-428, 2011

18th International Conference
ENGINEERING MECHANICS 2012
Svratka, Czech Republic, May 14 – 17, 2012

pp. 1497–1504
Paper #186

NUMERICAL PREDICTION OF PARASITIC ENERGY DISSIPATION IN WEDGE SPLITTING TESTS ON CONCRETE SPECIMENS

V. Veselý[*], T. Holušová[**], S. Seitl[***]

Abstract: *Undesirable energy dissipation taking place during wedge-splitting tests on cementitious composites and resulting in overestimation of the values of the determined fracture-mechanical characteristics of the tested materials is investigated in this paper via numerical simulations performed using a commercial finite element method tool with an implemented cohesive crack model. The rather broad range of cohesive behaviour of the studied materials was simulated through adjustments made to the corresponding characteristic length of the composite. The parasitic amount of energy is dissipated in fracture processes around the corners of the groove for the insertion of the loading platens, as these corners introduce rather strong stress concentrators to the specimen. This amount was extracted from simulated load-displacement curves and it was discovered that the amount considerably depends on the specimen proportions but its dependence on the level of material brittleness is not so significant.*

Keywords: ***wedge-splitting test, concrete fracture, specimen proportions, energy dissipation, numerical simulation***

1. Introduction

The wedge splitting test can be conveniently used for measuring the fracture-mechanical parameters of quasi-brittle building materials, particularly cement-based composites. The desirable failure propagation in the area of the ligament of the test specimen, i.e. starting at the specimen's notch tip and propagating towards the opposite surface of the specimen, can be accompanied by parasitic failure around the other considerable stress concentrator(s) – the corner(s) of the groove for inserting the loading platens. The amount of energy released in such failures is not being separated from the energy consumed in the desired fracture process within ordinary testing and evaluation procedures. Therefore, noticeable errors in the values of fracture parameters may arise in some cases depending on the specimen's proportions and the test configuration. The paper presents the results of a numerical study conducted in order to develop and propose a solution applicable in the evaluation of classical fracture-mechanical parameters via the wedge-splitting test, which in this case was carried out on cylinder-shaped specimens prepared either as standard test specimens cast into cylinder moulds or as cores drilled from existing structures by a hollow drill. This numerical study will be accompanied by experimental validation; however, the experimental campaign is not finished yet, so only the results of the numerical part of the study are presented in the paper. The experimental data from a rather broad test series (under preparation) will be evaluated using the proposed procedure stemming from the results of the numerical simulations.

2. Wedge-splitting test configuration

The test referred to as the wedge-splitting test is considered in this paper. A variety of notched specimen shapes can be used with it; see Fig. 1 or (Linsbauer & Tschegg, 1986, Brühwiler & Wittmann, 1990). This work is exclusively focused on cylinder-shaped specimens with a diameter of 150 mm and a width of 100 mm. The paper presents selected results from work by Holušová (2012). A similar analysis was also carried out by the authors for cube-shaped (or square-prism-

[·] Ing. Václav Veselý, Ph.D.: Brno University of Technology, Faculty of Civil Engineering, Institute of Structural Mechanics, Veveří 331/95; 602 00, Brno; CZ, e-mail: vesely.v1@fce.vutbr.cz

[*] Ing. Táňa Holušová: ditto, e-mail:holusova.t@ fce.vutbr.cz

[**] Ing. Stanislav Seitl, Ph.D.: Academy of Sciences of the Czech Republic, v. v. i., Institute of Physics of Materials; Žižkova 22; 616 62, Brno; CZ, e-mail: seitl@ipm.cz

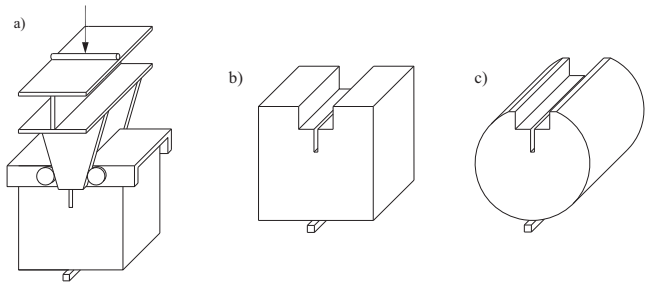

Fig. 1: Wedge splitting test configuration: schematic diagrams of the loading mechanism (a) and typical specimen shapes (b, c) (adapted from Brühwiler & Wittmann, 1990)

shaped) WST specimens (Řoutil et al., 2010, 2011a,b, 2012, Veselý et al., 2011). The wedge-splitting test configuration is becoming frequently used in the area of quasi-brittle materials and related fields connected with numerical modelling, inverse analysis, material research, etc.

3. Problem description

The studied problematic aspect of the WST concerns the area in the upper part of the specimen where the load is imposed. Apart from the main stress concentrator – the notch tip – the specimen includes other two stress concentrators – the corners of the groove for inserting the loading platens. For the correct evaluation of the fracture experiment, the failure should only take place between the initial notch tip and the specimen's back face (Fig. 2 left). In the case of quasi-brittle materials, which are characterized by the formation of what is referred to as a fracture process zone (FPZ) around the stress concentrator before the macro-crack starts to propagate, the failure can take place at several points in the specimen simultaneously (Fig. 2 middle). A major crack can finally localize in the ligament area, but substantial (undesirable) damage may also occur elsewhere. The occurrence of this failure mode is here considered as the most undesirable during a real test because an unknown amount of energy is released in the failure around the groove corners. If the major crack localizes from the corner (Fig. 2 right), the results of such a test are useless; however, it doesn't lead to an overestimation of the fracture parameters at least, because such a record is not used in the evaluation procedure.

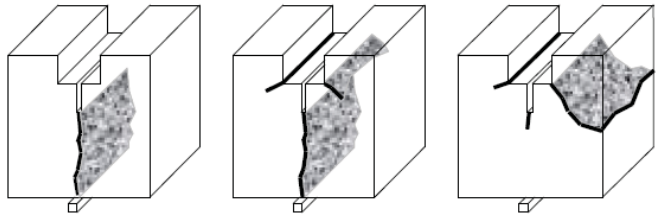

Figure 2: Desirable (left) and undesirable (middle, right) types of failure of the WST specimen (Veselý et al. 2011)

The amount of mechanical energy dissipated in the undesirable failure processes around the groove corners (including potential crushing around the support and loading platens) can be quantified based on the difference between the work of fracture (RILEM, 1985) in the desirable and undesirable failure mode cases. Therefore, two variants of the model for each studied specimen of different proportions were prepared: *i)* a reference variant with the constitutive model for quasi-brittle material used throughout the entire specimen volume (marked as *V1*), and *ii)* an artificial variant with elastic material around the groove corners (marked as *V2*). The differences between the two models are indicated in Fig. 3 left.

The subtraction of the areas under the load–displacement curves corresponding to the reference and alternative model gives an estimation of the amount of energy dissipated in the failure around the groove corners. The loading curve corresponding to the original model typically differs from the

alternative one by the rather wide hump around and after its peak indicating the extra energy release taking place around the corners of the groove for the insertion of the loading platens.

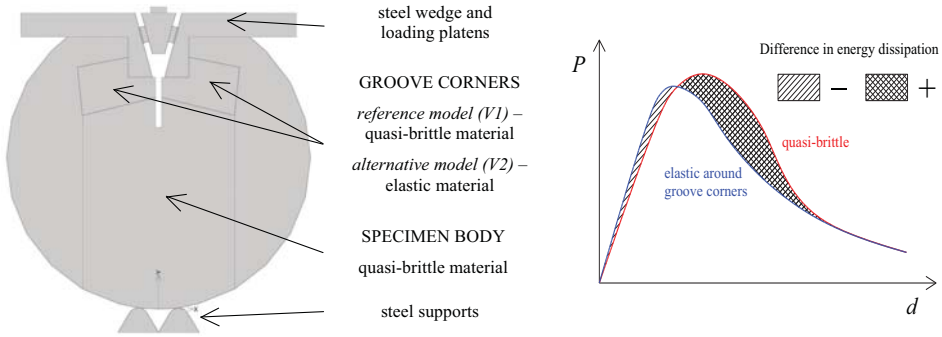

Fig. 3: Illustration of both the reference and alternative geometric model (left); sketch of the evaluation of energy dissipated in failure around the groove corners (right) (Řoutil et al. 2011b)

4. Numerical simulations

The numerical study was conducted using a commercial finite element (FE) tool with an implemented cohesive crack model governing the tensile failure – ATENA 2D software (Červenka et al., 2005).

4.1. Geometrical model, FE mesh

The 2D model used for the study is depicted in Fig. 3 left, where its macroelement structure is outlined, and Fig. 4 right, where the FE mesh and boundary conditions are indicated. The specimen is supported by two closely placed steel supports and loaded via steel angular platens which are being split by a wedge (in 3D reality with the use of roller bearings, in the used 2D model via sliding pads). In the loading groove a no-tension interface is assumed between the concrete specimen and the steel loading platens. The model reflects the boundary condition details of real tests which are currently in preparation (test configuration sketched in Fig. 4 left).

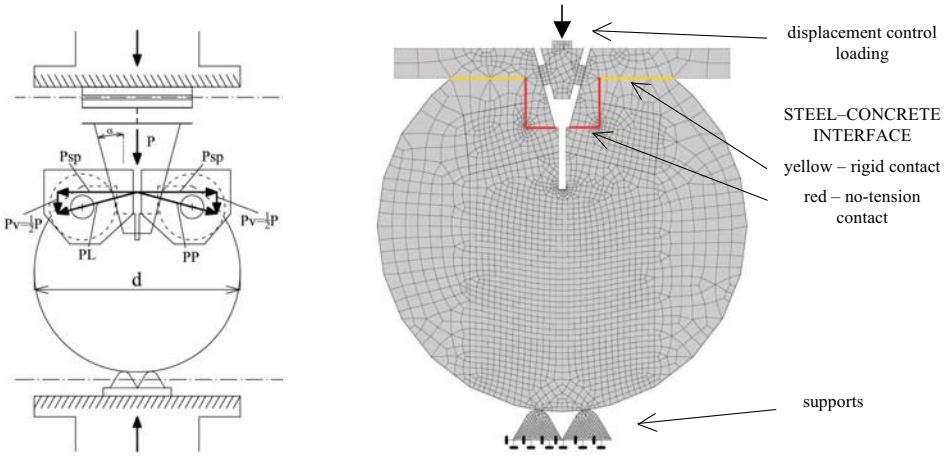

Fig. 4: Considered test configuration with indication of load transfer (left) (Holušová, 2012), FE model with indication of boundary conditions

The model was created in variants with different relative notch lengths α defined as the absolute notch length a (measured as the vertical distance between the roller bearing axis and the notch tip) divided by the specimen width W (measured as the vertical distance between the roller bearing axis and the opposite surface of the specimen). Note that the diameter d of the cylinder-shaped specimen was equal to 150 mm, the height of the segment cut from the top of the specimen was equal to 15 mm, and the distance of the roller bearing axis from the top (flat) surface was 15 mm, so that the specimen

Tab. 1: Modelled notch length variants

a [mm]	7.2	9.6	12	15	18	24	30
α [-]	0.06	0.08	0.1	0.125	0.15	0.2	0.25

width W = 120 mm. The values of the notch length a and corresponding relative notch length α are summarized in Tab. 1. The width and depth of the groove for inserting the loading platens is 30 and 20 mm, respectively.

4.2. Material model description

For modelling of the cementitious composite material of the specimen a fracture-plastic material model was used (Červenka et al., 2005); within the employed ATENA software the material model is referred to as the 3D Non Linear Cementitious 2 model. Several material sets were created in order to simulate cementitious composites of a relative wide range of material (quasi-)brittleness, i.e. ranging from rather ductile softening composites (for instance those reinforced with fibres) to nearly brittle ones (for instance cement pastes). For the reference material set (marked *C0*) the default setting of the software for cubic compressive strength f_{cu} = 35 MPa was used. The fracture behaviour of the model is governed by the cohesive crack model, which is based on following characteristics: the value of the tensile strength f_t, the shape of the traction–separation law $\sigma(w)$ and the value of fracture energy G_f. The f_t and G_f values of the reference material set were equal to 2.568 MPa and 64.2 Jm^{-2}, respectively. These characteristics, together with a Young's modulus value of E = 32.29 GPa, can be linked to a measure of material brittleness via what is referred to as the characteristic length l_{ch}, defined as

$$l_{ch} = \frac{EG_f}{f_t^2}. \tag{1}$$

Hordijk's exponential softening function (Červenka et al., 2005) was used as the traction–separation law. The other material sets used differed from the reference set marked as *C0* in their f_t and G_f values, which were changed in such a way that the reference characteristic length value ${}^0l_{ch}$ was multiplied by the factor 2^{2j}, where $j \in \langle -4,-3,-2,-1,0,1,2 \rangle$. This was obtained by multiplying the ${}^0f_t$ value by $\sqrt{2^j}$ and dividing the value of ${}^0G_f$ by 2^j. The material sets were then marked with the symbol *C*, the value of the multiplying factor $2^{2|j|}$ and a positive or negative sign indicating the increasing or decreasing of the characteristic length value. The corresponding values of the fracture-mechanical parameters entering the computations are shown in Tab. 2; however, only for the non-negative values of j, which mean the increasing of the characteristic length of the reference concrete, i.e. the decreasing of its brittleness. The reason is that for characteristic length values lower than ${}^0l_{ch}$ the results of the present study were found to be of a low significance (Holušová, 2012). On the other hand, the material sets $C2^{2|j|}-$ were used for an analysis leading to the determination of the minimal notch length for major failure propagation from its tip, not the groove corner (details in Holušová, 2012).

Note that the described types of analyses were invented, developed and successively presented in Řoutil et al. (2010a,b), Řoutil et al. (2011a,b), Veselý et al. (2011) and Řoutil et al. (2012).

4.3. Results − load−displacement curves

Two types of results from the conducted simulations are utilized in the subsequent analysis. One group is represented by the load−displacement diagrams that shall simulate the corresponding experimental

Tab. 2: Selected variants of the material model parameters

Concrete	E	f_t	G_f	l_{ch}	Note
	GPa	MPa	Jm^{-2}	m	
C0	32.29	2.56800	64.2	0.31435	${}^0l_{ch}$
C4+	32.29	1.81585	128.4	1.25740	$4\times{}^0l_{ch}$
C16+	32.29	1.28400	256.8	5.02960	$16\times{}^0l_{ch}$

records. Due to the wedge mechanism in the area where the load was imposed, special treatment of the recorded quantities must be taken into account. As is obvious from Fig. 4 left, the imposed load P is transferred from the loading wedge to the roller bearings as forces P^{P} and P^{L} on the interface between the wedge and the bearings on the right and left side, respectively. These forces are perpendicular to the side edge of the loading wedge (of angle α_w) and can be decomposed into horizontal splitting force P_{sp} and vertical force $P_v = P/2$.

The dependences of the forces on the displacements of their points of action are necessary for the determination of mechanical work, an energetic quantity, in the following analysis. Two alternatives of the dependences were considered: *i)* the load−displacement diagrams were drawn as functions of both the right and left reaction on the wedge−bearing interface, these being P^{P} and P^{L}, respectively, and the corresponding displacement of the roller bearings' axis on either side (determined as the vector composition of the horizontal and vertical displacement), *ii)* and as functions of both the horizontal splitting force P_{sp} on the mutual horizontal displacements of the roller bearings' axis and the vertical force P_v on the vertical roller bearings' axis displacement (in both the force and the vertical displacement case, the mean value from the right and left side was considered). The former and latter alternative is shown for selected relative notch length simulations in the top and bottom row of Fig. 5, respectively. Simulated responses for both the reference (*V1*) and alternative (*V2*) variants of the geometric model and the reference (*C0*) and two adjusted (*C4+* and *C16+*) material sets are compared there. Results for the other relative notch lengths can be found in Holušová (2012).

4.4. Results − crack patterns

The other results relevant to the study are represented by the crack patterns from which the extent of the material failure is apparent. As is evident from Fig. 6, the failure around the groove corners does not develop in the case of the alternative model and so none of the energy flux from the external loading is aimed at the corner areas. Contrariwise, in the case of the reference model, significant failure takes place at these locations in direct relation to the size of the notch and characteristic length. The crack patterns correspond to a stage in the fracture process at peak load. Figs. 5 and 6 correspond

i) dependences of the right and left reactions on the wedge−roller bearing interface P^{P} and P^{L}, resp., on the resulting displacement of the roller bearing's axis on either side

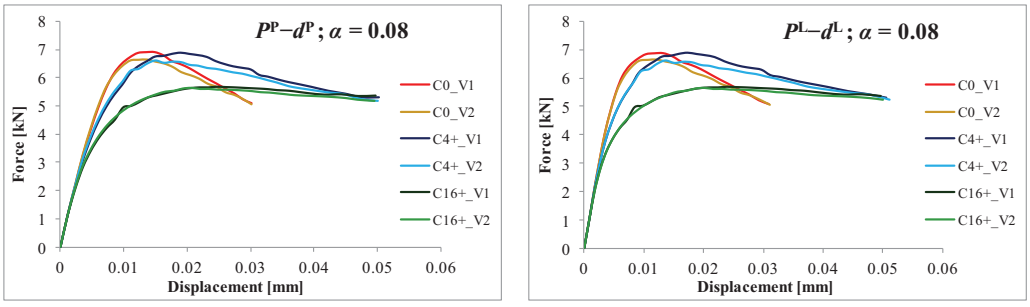

ii) dependences of the splitting and vertical force P_{sp} and P_v, resp., on the mutual horizontal and mean value of vertical displacement, resp., of the roller bearing's axis on either side

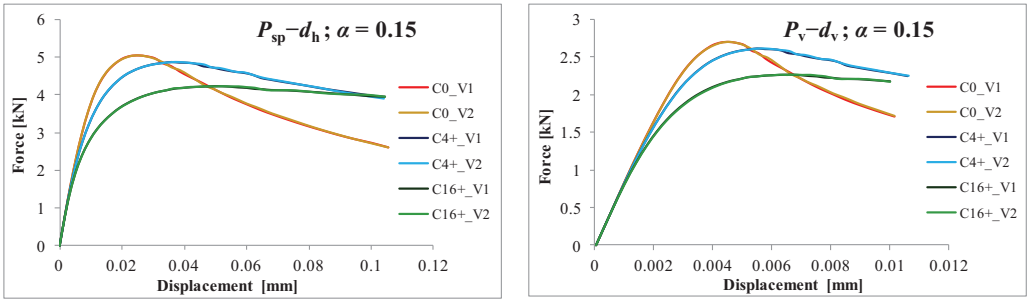

Fig. 5: Simulated load−displacement diagrams for selected relative notch lengths and selected material parameters sets

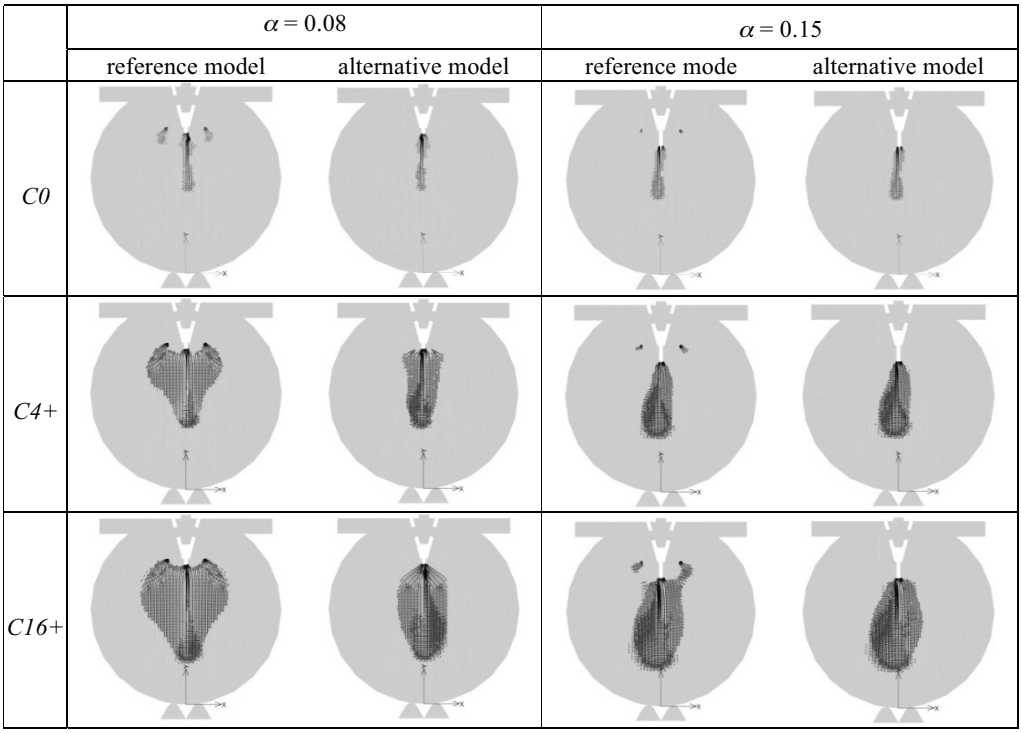

Fig. 6: Simulated crack patterns representing the extent of the material failure zone at the peak load stage of the load−displacement diagrams; the figures correspond to the loading curves in Fig. 5

well in showing the trend in the amount of energy needed for the fracture propagation around the groove corners; it is obvious from the differences (between model variants *V1* and *V2*) between the failure zone extents in Fig. 6 and between the areas under the loading curves in Fig. 5. Again, complete results for the whole of the study described here are presented in Holušová (2012).

4.5. Evaluation of the energy release for failures around the groove corners

As was discussed above, a difference exists in the extent of the zone of failure between the reference model (the real test) and the alternative model (the artificial variant). The difference corresponds to the difference in the load−displacement curves, which is particularly apparent near peak load and in a relatively short part after it. Therefore, in order to quantify the difference, work of fracture values were calculated from the load−displacement diagrams simulated for the *V1* and *V2* model variants.

The work of fracture W_f is calculated as

$$W_\mathrm{f} = W - U, \quad \text{where} \quad W = \int P \mathrm{d}d \quad \text{and} \quad U = \frac{1}{2} P d. \tag{2}$$

The integration was performed numerically using the trapezoidal rule. Actually, the value of work of fracture was not calculated from the whole load−displacement diagram but only from the portion up to the point where the curves for the *V1* and *V2* variants start to match. Considerable computational error accumulates at the tail of the simulated loading curve. Therefore, processing of the tail part of the curve was avoided. The absolute value of the amount of energy dissipated around the groove corners can then be estimated as

$$\Delta W_\mathrm{f} = {}^{V1}W_\mathrm{f} - {}^{V2}W_\mathrm{f}. \tag{3}$$

In order to relate the absolute amount of energy dissipation at the groove corners to the entire work of fracture value corresponding to the fracture propagated through the whole specimen ligament, the quantity $\overline{W_\mathrm{f}}$ was introduced. Due to the above-mentioned error at the load−displacement curve tail

$\overline{W_f}$ is estimated as a product of the area of the specimen ligament $A = (D - a_0)B$, where D is the specimen width, a_0 is the notch length and B is the specimen breadth, and the value of fracture energy G_f serving as the input to the FE calculations (see Tab. 2), i.e. $\overline{W_f} = G_f A$. Then, the relative amount of parasitic energy dissipation is calculated as

$$\omega_f = \Delta W_f / \overline{W_f} . \tag{4}$$

The quantities ΔW_f and ω_f were calculated for both types of load−displacement curve representation, i.e. the P^P–d^P, P^L–d^L and P_{sp}–d_h, P_v–d_v curves, respectively.

5. Discussion of results

The absolute and relative quantities representing the energy release around the corners of the groove for inserting the loading platens into the WST specimen for the three material sets (*C0*, *C4+* and *C16+*) and several considered notch lengths are shown in graphs in Fig. 7. The trends of the curves obviously correspond to the graphical representations of the failure depicted in Fig. 6.

The amount of parasitic energy dissipation decreases with increasing notch length, and for relative notch lengths around 0.25 it can be neglected. Facts resulting from the comparison of the absolute and relative energy dissipation are worth noticing. Whilst the absolute dissipation is higher for larger characteristic lengths (and visually agrees with the failure extents given by crack patterns), its relative value slightly decreases with increasing brittleness (i.e. decreasing l_{ch}). This fact is not obvious from a basic comparison of the load−displacement curves and crack patterns.

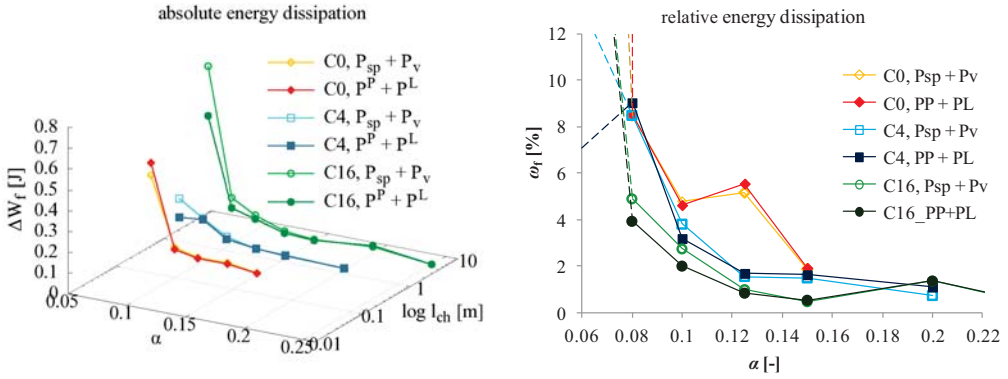

Fig. 7: The amount of absolute and relative energy dissipation around groove corners as a function of the relative notch length for three levels of brittleness of cementitious composite

This analysis is supplemented by an estimation of the minimal length of the notch in Holušová (2012). This is the minimal notch length that must be cut in the test specimen in order to obtain the major fracture propagation from the notch tip and not the groove corner. It is intended that this study will be supplemented with more potential variants of specimen shapes, sizes and boundary conditions/testing fixtures to provide a tool (recommendation) for experimental testing resulting in more accurate estimates of the fracture-mechanical parameters of tested materials.

6. Conclusions

This paper focuses on the analysis of failure in the cylinder-shaped WST specimens used for determination of the fracture-mechanical parameters of quasi-brittle materials. The amount of parasitic energy dissipated outside of the desired volume of the specimen is evaluated based on the numerically simulated responses of fracture tests. This amount of energy causes overestimation of the determined fracture-mechanical parameters, particularly fracture energy. The main conclusions from this study on the particular case of the size and shape of the specimen can be summarized in the following points:

- The amount of energy dissipated additionally around the groove corners decreases with increasing notch length; for short notches (α less than 0.1) it can take a proportion of the entire dissipated energy ranging from 3 to 10 %. For notches with a relative length greater than approx. 0.25 the effect becomes negligible.
- An increase in the absolute amount and a slight decrease in the relative amount of parasitic energy dissipation with increasing characteristic length are observed; an extension of this study in this respect is worth considering. However, it seems that for a common range of (quasi-)brittleness of cementitious composites the previous item holds true.

Verification of these results via another simulation method as well as experimental validation of the basic conclusions of this study is planned for future research.

Acknowledgement

This outcome has been achieved with the financial support of the Czech Scientific Foundation, project No. GA CR P105/11/1551.

References

Brühwiler, E. & Wittmann, F.H. (1990) The wedge splitting test, a new method of performing stable fracture mechanics test, *Engineering Fracture Mechanics*, 35, pp. 117-125.

Červenka, V. et al. (2005) *ATENA Program Documentation, Theory and User manual*. Prague: Cervenka Consulting.

Holušová, T. (2012) *Analýza napjatosti a porušení ve zkušebních tělesech používaných pro určování lomově-mechanických parametrů kvazikřehkých materiálů. Diploma Thesise.* Brno: BUT Brno, Faculty of Civil Engineering, Institute of Structural Mechanics, 74 p., 20 p. appendix (in Czech).

Holušová, T. & Veselý, V. (2011) Numerické simulace porušení v betonových válcových tělesech při zkoušce štípáním klínem. In: Proc. of *Víceúrovňový design pokrokových materiálů 2011* (I. Dlouhý, J. Švejcar & M. Šob eds.), Brno, 1st–2nd December 2011. Institute of Physics of Materials AV CR, v. v. i., pp. 185-192 (in Czech).

Linsbauer, H.N. & Tschegg, E.K. (1986) Fracture energy determination of concrete with cube-shaped specimens, *Zement und Beton*, 31, pp. 38-40.

RILEM Report 5 (1991) *Fracture Mechanics Test Methods for Concrete*, S.P. Shah, A. Carpinteri (Eds.), Hall, London.

Řoutil, L., Veselý, V. & Seitl, S. (2010a) Numerical study of wedge-splitting test on concrete specimens, In: *Proc. of Applied mechanics 2010* (J. Blekta ed.), Jablonec nad Nisou, 19th–22nd April 2010. Technical University of Liberec, pp. 107-110.

Řoutil, L., Veselý, V., Seitl, S. & Klusák, J. (2010b) Posouzení geometrie zkušebního tělesa pro WST kvazikřehkých kompozitů: Numerická studie. In: Proc. of *Křehký lom 2010, (Design a porušování material)* (I. Dlouhý ed.), Brno, 4th November 2010. Institute of Physics of Materials AS CR, v. v. i., pp. 201-212 (in Czech).

Řoutil, L., Veselý, V. & Seitl, S. (2011a) Wedge splitting test of quasi-brittle cylinder-shaped specimen: Numerical study on minimal notch length. In: *Proc. of Applied Mechanics 2011* (L. Náhlík, M. Zouhar, M. Ševčík, S. Seitl & Z. Majer eds.)., Velké Bílovice, 18th–20th April 2011 IPM AS CR, v. v. i., pp. 179-182.

Řoutil, L., Veselý, V., Seitl, S. & Klusák, J. (2011b) Optimal proportions of wedge splitting test specimen for testing of various cement based composites. In: Proc. of *1st Interquadrennial ICF Conference in Middle East and Africa* (CD) (A.-M. El-Batahgy & M. Waly eds.), Luxor, Egypt, November 14–17, 2011, pp. 457-465.

Řoutil, L., Veselý, V. & Seitl, S. (2012) Fracture analysis of cube- and cylinder-shaped WST specimens made of cementitious composites with various characteristic length. *Key Engineering Materials*, Vols. 488–489, pp. 533-536.

Seitl, S., Veselý, V. & Řoutil, L. (2011) Two-parameter fracture mechanical analysis of a near-crack-tip stress field in wedge splitting test specimens. *Computers and Structures*, 89, pp. 1852-1858.

Veselý, V., Řoutil, L. & Seitl, S. (2011) Wedge-splitting test – determination of minimal starting notch length for various cement based composites. Part I: Cohesive crack modelling. *Key Engineering Materials*, Vols. 452-453, pp. 77-80.

Veselý, V., Šestáková, L. & Seitl, S. (2012) Influence of boundary conditions on higher order terms of near-crack-tip stress field in a WST specimen. *Key Engineering Materials*, Vols. 488–489, pp. 399-402.

18th International Conference
ENGINEERING MECHANICS 2012
Svratka, Czech Republic, May 14 – 17, 2012

pp. 1505–1516
Paper #38

NON-NEWTONIAN EFFECTS OF PULSATILE BLOOD FLOW IN A REALISTIC BYPASS GRAFT GEOMETRY

J. Vimmr[*], A. Jonášová [**] O. Bublík [***]

Abstract: *The study is focused on mathematical modelling of pulsatile blood flow in a patient-specific aorto-coronary bypass model with individual graft. Blood is considered to be an incompressible non-Newtonian fluid, whose behaviour is described by the macroscopic Carreau-Yasuda model. The numerical solution of the non-linear system of incompressible Navier-Stokes equations is based on the three-stage fractional step method and the cell-centred finite volume method formulated for hybrid unstructured tetrahedral grids. Since patency and long-term performance of all implanted bypass grafts is closely related to hemodynamics, all obtained results are analysed and discussed with the help of several significant hemodynamical wall parameters such as cycle-averaged wall shear stress and oscillatory shear index.*

Keywords: ***aorto-coronary bypass, non-Newtonian fluid, fractional step method, finite volume method.***

1. Introduction

Nowadays it is generally accepted that the performance and patency of implanted bypass grafts is significantly affected by local hemodynamics, Loth et al. (2008). Beside thrombogenesis, usually originating in low flow rates or technical mistakes, Vural et al. (2001), the majority of recorded bypass failures is often caused by intimal hyperplasia, Haruguchi and Teraoka (2003). This type of intimal thickening represents a form of abnormal healing process observed at the distal anastomosis of the implanted graft, Fig. 1. The morphological and metabolic changes observed in vessel walls are hypothesised to be triggered by disturbed blood flow and low and oscillating shear stress, Bassiouny et al. (1992). In this regard, the investigation of hemodynamics in the form of numerical simulations represents a valuable contribution to the understanding of graft disease formation.

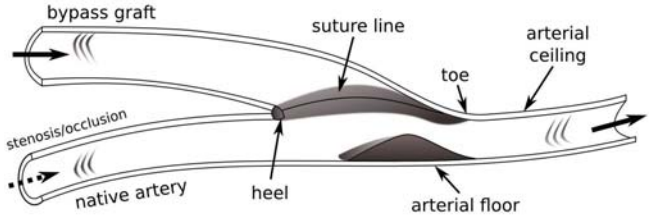

Fig. 1: Localisation of intimal thickening at the distal end-to-side anastomosis with relevant terminology, modified from Bassiouny et al. (1992).

In relation to previous modelling of steady non-Newtonian blood flow performed in an idealized complete bypass model with two end-to-side anastomoses, Vimmr and Jonášová (2010), present study tries to contribute to this investigation by modelling pulsatile non-Newtonian blood flow in a realistic aorto-coronary bypass model. The analysis and discussion of obtained numerical results is carried out with the help of two hemodynamically significant wall parameters – cycle-averaged wall shear stress (WSS) and oscillatory shear index (OSI).

[*]Doc. Ing. Jan Vimmr, Ph.D.: Department of Mechanics, University of West Bohemia, Univerzitní 22; 306 14, Pilsen; CZ, e-mail: jvimmr@kme.zcu.cz
[**]Ing. Alena Jonášová: Department of Mechanics, University of West Bohemia, Univerzitní 22; 306 14, Pilsen; CZ, e-mail: jonasova@kme.zcu.cz
[***]Ing. Ondřej Bublík: Department of Mechanics, University of West Bohemia, Univerzitní 22; 306 14, Pilsen; CZ, e-mail: obublik@kme.zcu.cz

2. Problem formulation

The main objective of this study is the analysis of hemodynamics in an individual aorto-coronary bypass graft. In cardiovascular surgery, the term individual denotes a vascular graft with one distal end-to-side anastomosis, i.e., the graft provides a direct connection between the aorta and the stenosed or occluded coronary artery. The bypass model considered in this study is reconstructed from CT data provided by the courtesy of the University Hospital in Pilsen, Czech Republic. The reconstruction process and computational mesh generation are carried out in software packages Amira and Altair Hypermesh, respectively. An example of primary reconstruction of the chest region and of the individual bypass graft is shown in Fig. 2. The final shape of the bypass model after smoothing is displayed in Fig. 3. The unstructured computational mesh used for all numerical simulations consists of 362,437 tetrahedral cells.

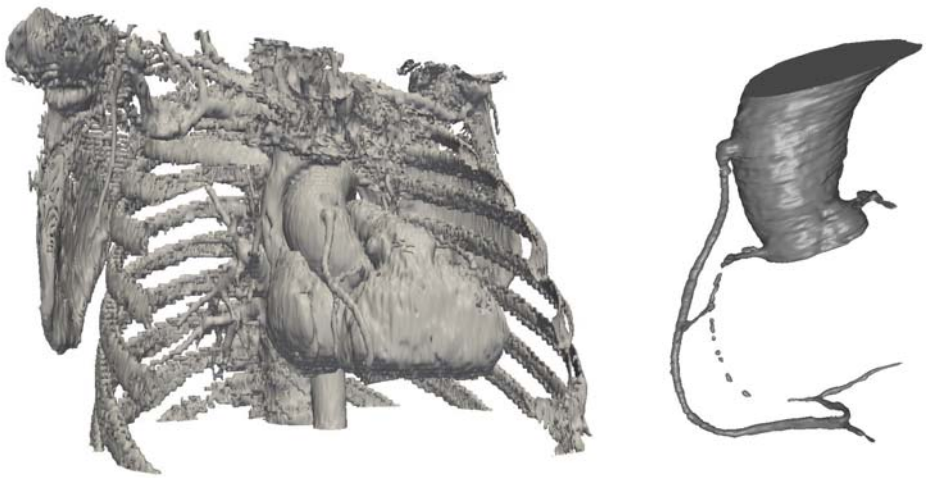

Fig. 2: CT reconstruction of the chest region (left) and of the aorto-coronary bypass graft (right)

For the purpose of blood flow simulations in the prepared individual graft, we choose an approach similar to that found in other studies published to the theme of bypass hemodynamics, see the review paper Loth et al. (2008). Firstly, taking into account the fact that at the end of the arterialisation process, venous grafts lose their compliance, all the bypass walls are, in this study, modelled as impermeable and rigid, including the wall of the aorta. In the light of this simplification, we are aware that the neglected aortic elasticity represents a considerable limitation of the present study. We hope to rectify it in one of our future projects by solving the fluid-structure interaction problem. In this study, we further assume a static aorto-coronary bypass model, i.e., the impact of heart beating is not considered. This assumption is based on the findings published in Zeng et al. (2003), where it was shown that the arterial motion does not significantly affect blood flow in the case of flow pulsatility. In order to model blood's complex rheological properties, we introduce the macroscopic non-Newtonian Carreau-Yasuda model, which we have successfully applied in our previous simulations, Vimmr and Jonášová (2010),

$$\eta(\dot{\gamma}) = \eta_\infty + (\eta_0 - \eta_\infty)\Big[1 + \big(\lambda\dot{\gamma}\big)^a\Big]^{\frac{n-1}{a}}, \tag{1}$$

where η_0 and η_∞ are the zero and infinite shear viscosities, respectively, λ is the characteristic relaxation time and n is the flow index. The five parameters occurring in the Carreau-Yasuda model (1) may be determined by numerical fitting of experimental data. In this study, we adopt data mentioned in Cho and Kensey (1991): $\eta_\infty = 3.45 \cdot 10^{-3}\,\mathrm{Pa}\cdot\mathrm{s}$, $\eta_0 = 56 \cdot 10^{-3}\,\mathrm{Pa}\cdot\mathrm{s}$, $\lambda = 1.902\,\mathrm{s}$, $a = 1.25$, $n = 0.22$. The shear rate is given as $\dot{\gamma} = 2\sqrt{D_{II}}$, where D_{II} denotes the second invariant of the rate of deformation tensor $\mathbf{D} = \frac{1}{2}\left(\nabla\boldsymbol{v} + (\nabla\boldsymbol{v})^T\right)$. For the incompressible fluid, the second invariant is defined as $D_{II} = \frac{1}{2}\,d_{ij}d_{ij}$, $i,j = 1,2,3$, where d_{ij} are the components of the rate of deformation tensor $\mathbf{D}$. For the Newtonian flow, the molecular viscosity is kept constant and equal to infinite shear viscosity η_∞. Finally, note that the coronary arteries shown in Fig. 3 are considered to be occluded (with no inflow) so that the only relevant incoming flow will be that of the bypass graft.

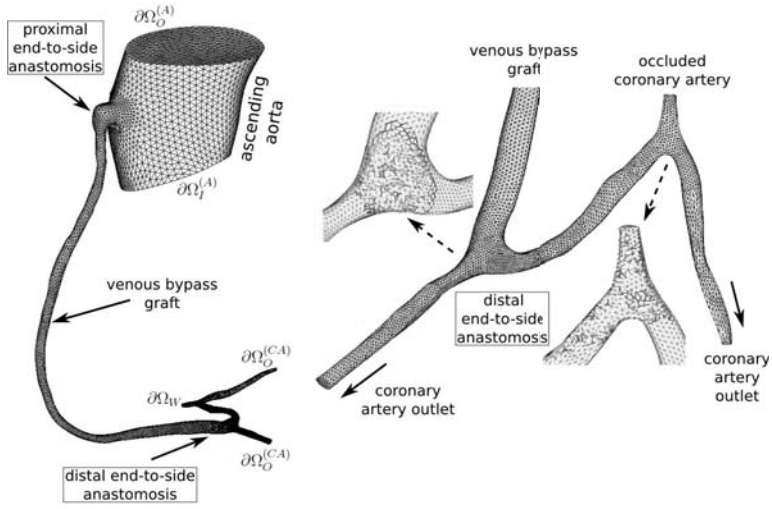

Fig. 3: Individual graft – unstructured computational mesh and relevant terminology

3. Mathematical model

Let us consider a time interval $(0, \mathcal{T})$, $\mathcal{T} > 0$ and a bounded three-dimensional computational domain $\Omega \subset \mathbf{R}^3$ with boundary $\partial\Omega = \partial\Omega_I \cup \partial\Omega_O \cup \partial\Omega_W$, where $\partial\Omega_I$, $\partial\Omega_O$ and $\partial\Omega_W$ denote the inlet, the outlet and the walls of the computational domain, respectively. In this study, coronary blood flow is modelled as unsteady laminar isothermal flow of incompressible generalised Newtonian fluid that in the space-time cylinder $\Omega_T = \Omega \times (0, \mathcal{T})$ is mathematically described by the non-linear system of incompressible Navier-Stokes (NS) equations written in the non-dimensional form

$$\frac{\partial v_i}{\partial x_i} = 0\,, \tag{2}$$

$$\frac{\partial v_i}{\partial t} + \frac{\partial}{\partial x_j}(v_i v_j) + \frac{\partial p}{\partial x_i} = \frac{1}{\mathrm{Re}}\frac{\partial}{\partial x_j}\left[\eta(\dot\gamma)\,\left(\frac{\partial v_i}{\partial x_j} + \frac{\partial v_j}{\partial x_i}\right)\right] \quad \text{for } i,j = 1,2,3\,, \tag{3}$$

where $t \in (0, \mathcal{T})$ is the time, v_i is the i-th component of the velocity vector $\boldsymbol{v} = [v_1, v_2, v_3]^T$ corresponding to the Cartesian component x_i of the space variables vector $\boldsymbol{x} = [x_1, x_2, x_3]^T \in \Omega$, p is the pressure, Re is the reference Reynolds number and $\eta(\dot\gamma)$ is the shear-dependent viscosity given by Eq. (1).

All variables appearing in Eqs. (2) – (3) are non-dimensionalized by the reference velocity $U_{ref} > 0$ and characteristic length $D_{ref} > 0$. For the bypass model considered in this study, the characteristic length value was chosen to be equal to the aorta diameter $D_{ref} \equiv D_{(A)} = 0.036\,\mathrm{m}$ and the reference velocity is stated as $U_{ref} = 4Q_0/(\pi\, D_{ref}^2) = 0.1592\,\mathrm{m}\cdot\mathrm{s}^{-1}$, where average aortic inlet flow rate is $Q_0 = 112.56 \cdot 10^{-6}\,\mathrm{m}^3\cdot\mathrm{s}^{-1}$, see Fig. 6 (left). As for the reference Reynolds number, it is determined as $\mathrm{Re} = U_{ref} D_{ref} \varrho/\eta_{ref} = 1\,744.3$, where $\varrho = 1050\,\mathrm{kg}\cdot\mathrm{m}^{-3}$ and $\eta_{ref} \equiv \eta_\infty = 3.45 \cdot 10^{-3}\,\mathrm{Pa}\cdot\mathrm{s}$. For the sake of completeness, reference pressure and reference time are computed as $p_{ref} = \varrho\, U_{ref}^2$ and $t_{ref} = D_{ref}/U_{ref}$, respectively.

4. Numerical method

The numerical solution of the non-linear time-dependent system of incompressible NS equations (2) – (3) is based on the projection method. In this study, the computation of velocity components v_i^{n+1}, which satisfy the divergence-free condition (2), employs the three-stage fractional step scheme, Ferziger and Perić (1999). In the first stage, intermediate velocity components v_i^* are explicitly computed from the convective part of the NS equation (3) as

$$\frac{v_i^* - v_i^n}{\Delta t} + \frac{\partial}{\partial x_j}(v_i^n v_j^n) = 0\,, \quad i,j = 1,2,3\,. \tag{4}$$

For the second stage of the fractional step scheme, the intermediate velocity components $\hat{v}_i$ are computed applying the unconditionally stable implicit Crank-Nicolson scheme to the viscous term of Eq. (3)

$$\frac{\hat{v}_i - v_i^*}{\Delta t} = \frac{1}{2\mathrm{Re}} \frac{\partial}{\partial x_j} \left[\eta(\dot{\gamma}) \left(\frac{\partial(\hat{v}_i + v_i^*)}{\partial x_j} + \frac{\partial(\hat{v}_j + v_j^*)}{\partial x_i} \right) \right] , \quad i,j = 1,2,3. \tag{5}$$

Let us linearise the shear-dependent dynamic viscosity $\eta(\dot{\gamma})$ as $\overline{\eta}(\dot{\gamma}) = \eta(\dot{\gamma}(v^*))$ and introduce an auxiliary variable $d_{ij} = \frac{1}{2}\left(\frac{\partial v_i}{\partial x_j} + \frac{\partial v_j}{\partial x_i}\right)$, which in this case is equal to the components of the rate of deformation tensor **D** mentioned in section 2. Then Eq. (5) can be rewritten as a system of two linear equations

$$\frac{\hat{v}_i - v_i^*}{\Delta t} = \frac{1}{\mathrm{Re}} \frac{\partial}{\partial x_j} \left[\overline{\eta}(\dot{\gamma}) \left(\hat{d}_{ij} + d_{ij}^* \right) \right] , \tag{6}$$

$$\hat{d}_{ij} = \frac{1}{2} \left(\frac{\partial \hat{v}_i}{\partial x_j} + \frac{\partial \hat{v}_j}{\partial x_i} \right) . \tag{7}$$

In the third stage, pressure is used for the projection of the intermediate velocity vector $\hat{\boldsymbol{v}}$ onto a space of divergence-free velocity field to get the values of velocity and pressure at the next time level $(n+1)$. Hence, the velocity components v_i^{n+1} are computed from

$$\frac{v_i^{n+1} - \hat{v}_i}{\Delta t} + \frac{\partial p^{n+1}}{\partial x_i} = 0 , \quad i = 1,2,3, \tag{8}$$

where p^{n+1} is computed from the Poisson equation for pressure

$$\frac{\partial^2 p^{n+1}}{\partial x_i \partial x_i} = \frac{1}{\Delta t} \frac{\partial \hat{v}_i}{\partial x_i} . \tag{9}$$

It can be easily shown that sum of Eqs. (4), (5) and (8) yields the approximation of NS equations of first order time accuracy. Finally, the whole algorithm of the fractional step method may be written for $i,j = 1,2,3$ as follows

$$v_i^* = v_i^n - \Delta t \frac{\partial}{\partial x_j} \left(v_i^n v_j^n \right) , \tag{10}$$

$$\frac{\hat{v}_i}{\Delta t} - \frac{1}{\mathrm{Re}} \frac{\partial}{\partial x_j} \left(\overline{\eta}(\dot{\gamma})\, \hat{d}_{ij} \right) = \frac{v_i^*}{\Delta t} + \frac{1}{\mathrm{Re}} \frac{\partial}{\partial x_j} \left(\overline{\eta}(\dot{\gamma})\, d_{ij}^* \right) , \tag{11}$$

$$\hat{d}_{ij} - \frac{1}{2} \left(\frac{\partial \hat{v}_i}{\partial x_j} + \frac{\partial \hat{v}_j}{\partial x_i} \right) = 0 , \tag{12}$$

$$\frac{\partial^2 p^{n+1}}{\partial x_i \partial x_i} = \frac{1}{\Delta t} \frac{\partial \hat{v}_i}{\partial x_i} , \tag{13}$$

$$v_i^{n+1} = \hat{v}_i - \Delta t \frac{\partial p^{n+1}}{\partial x_i} . \tag{14}$$

The space discretization of the system of Eqs. (10) – (14) is performed using the cell-centred finite volume method for hybrid unstructured tetrahedral grids. The idea of applying the hybrid unstructured grid for the numerical solution of time-dependent incompressible NS equations in 2D was introduced in Kim and Choi (2000). The principle of this grid system lies in the coupling between an interpolation method, which will be described later, and the non-staggered grid system. Being inspired with this idea, we consider in this study a control volume Ω_k in the form of tetrahedron, Fig. 4. The hybrid grid system defines the values of pressure and Cartesian velocity components in the centre of the control volume Ω_k and the values of face-normal velocity V_m, which has the direction of outward unit vector $\boldsymbol{n}_k^m$ normal to the m-th face Γ_k^m of the control volume Ω_k, is defined in the middle of the face Γ_k^m.

After the integration of Eqs. (10) – (14) over each control volume Ω_k, Fig. 4, $k = 1,2,\ldots,N_{CV}$, where N_{CV} is the number of control volumes within the hybrid unstructured tetrahedral computational mesh, after the introduction of integral average for an arbitrary flow quantity Φ over the control volume Ω_k

$$(\Phi)_k = \frac{1}{|\Omega_k|} \int_{\Omega_k} \Phi \mathrm{d}\Omega, \tag{15}$$

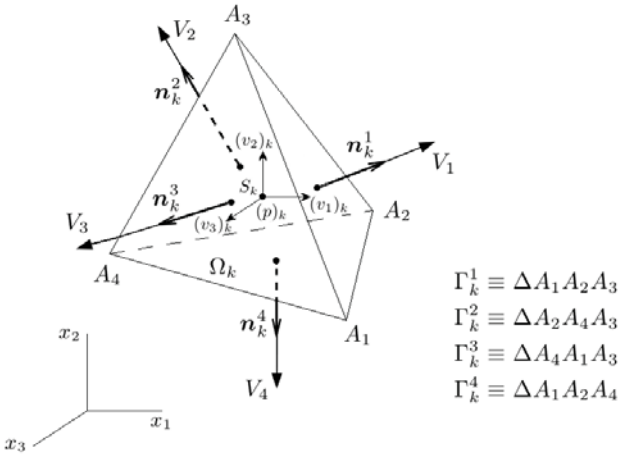

Fig. 4: A tetrahedral control volume $\Omega_k = A_1A_2A_3A_4$ with boundary $\partial\Omega_k = \bigcup_{m=1}^{4} \Gamma_k^m$ belonging to the hybrid unstructured computational mesh.

where $|\Omega_k|$ is the volume of the tetrahedral control volume Ω_k, and finally, after the application of the Gauss-Ostrogradsky theorem, which converts the volume integrals to surface integrals, we get

$$(v_i^*)_k = (v_i^n)_k - \frac{\Delta t}{|\Omega_k|} \oint\limits_{\partial\Omega_k} \left(v_j^n \cdot {}^j n_k\right) \cdot v_i^n \, \mathrm{d}\Gamma, \tag{16}$$

$$\frac{1}{\Delta t}(\hat{v}_i)_k - \frac{1}{\mathrm{Re}|\Omega_k|} \oint\limits_{\partial\Omega_k} \overline{\eta}(\dot{\gamma})\, \hat{d}_{ij} \cdot {}^j n_k \, \mathrm{d}\Gamma = \frac{1}{\Delta t}(v_i^*)_k + \frac{1}{\mathrm{Re}|\Omega_k|} \oint\limits_{\partial\Omega_k} \overline{\eta}(\dot{\gamma})\, d_{ij}^* \cdot {}^j n_k \, \mathrm{d}\Gamma, \tag{17}$$

$$\left(\hat{d}_{ij}\right)_k - \frac{1}{2}\left(\oint\limits_{\partial\Omega_k} \hat{v}_i \cdot {}^j n_k \, \mathrm{d}\Gamma + \oint\limits_{\partial\Omega_k} \hat{v}_j \cdot {}^i n_k \, \mathrm{d}\Gamma \right) = 0\,, \tag{18}$$

$$\oint\limits_{\partial\Omega_k} \frac{\partial p^{n+1}}{\partial \boldsymbol{n}_k} \, \mathrm{d}\Gamma = \frac{1}{\Delta t} \oint\limits_{\partial\Omega_k} \hat{v}_i \cdot {}^i n_k \, \mathrm{d}\Gamma, \tag{19}$$

$$(v_i^{n+1})_k = (\hat{v}_i)_k - \frac{\Delta t}{|\Omega_k|} \oint\limits_{\partial\Omega_k} p^{n+1} \cdot {}^i n_k \, \mathrm{d}\Gamma, \tag{20}$$

where ${}^i n_k$ is the i-th component of the outward unit vector $\boldsymbol{n}_k = [{}^1 n_k, {}^2 n_k, {}^3 n_k]^T$ normal to the boundary $\partial\Omega_k$ of the tetrahedral control volume Ω_k, Fig. 4. In order to achieve the satisfaction of the continuity equation for the normal velocity $V = v_i \cdot {}^i n_k$, the system of Eqs. (16) – (20) is completed with following equation

$$V^{n+1} = \hat{V} - \Delta t \, \frac{\partial p^{n+1}}{\partial \boldsymbol{n}_k}\,. \tag{21}$$

This equation defines the normal velocity V^{n+1} at the time level $(n+1)$ having the direction of the outward unit vector $\boldsymbol{n}_k$ normal to the boundary $\partial\Omega_k$ of the control volume Ω_k. For the intermediate normal velocity $\hat{V}$, it is valid that $\hat{V} = \hat{v}_i \cdot {}^i n_k$.

Further, we perform the approximation of surface integrals in the system of Eqs. (16) – (20). Firstly, each integral is replaced by the sum of integrals over each face Γ_k^m of the control volume Ω_k, Fig. 4, and

then approximated by the midpoint rule

$$\oint_{\partial\Omega_k} \Phi \, \mathrm{d}\Gamma = \sum_{m=1}^{4} \int_{\Gamma_k^m} \Phi \, \mathrm{d}\Gamma \approx \sum_{m=1}^{4} \Phi_m |\Gamma_k^m|, \tag{22}$$

where $|\Gamma_k^m|$, $m = 1, \ldots, 4$ is the area of the m-th face Γ_k^m of the control volume Ω_k and Φ_m is the value of an arbitrary flow quantity at the integration point at the same face. The interpolation process needed for the determination of Φ_m at the m-th face Γ_k^m of the control volume Ω_k will be described later. Using Eq. (22), the system of Eqs. (16) – (21) is modified as follows

$$(v_i^*)_k = (v_i^n)_k - \frac{\Delta t}{|\Omega_k|} \sum_{m=1}^{4} \left(V_m^n \cdot v_{i\,m}^n|_{\text{upwind}} \right) |\Gamma_k^m| \,, \tag{23}$$

$$\frac{(\hat{v}_i)_k}{\Delta t} - \frac{1}{\mathrm{Re}\,|\Omega_k|} \sum_{m=1}^{4} \overline{\eta}(\dot{\gamma})^m \, \hat{d}_{ij}^m \cdot {}^j n_k^m \, |\Gamma_k^m| = \frac{(v_i^*)_k}{\Delta t} + \frac{1}{\mathrm{Re}\,|\Omega_k|} \sum_{m=1}^{4} \overline{\eta}(\dot{\gamma})^m \, d_{ij}^{*m} \cdot {}^j n_k^m \, |\Gamma_k^m|, \tag{24}$$

$$\left(\hat{d}_{ij}\right)_k - \frac{1}{2} \left(\sum_{m=1}^{4} \hat{v}_{i\,m} \cdot {}^j n_k^m |\, \Gamma_k^m| \; + \; \sum_{m=1}^{4} \hat{v}_{j\,m} \cdot {}^i n_k^m |\, \Gamma_k^m| \right) = 0 \,, \tag{25}$$

$$\sum_{m=1}^{4} \frac{\partial p^{n+1}}{\partial \boldsymbol{n}_k^m} |\Gamma_k^m| = \frac{1}{\Delta t} \sum_{m=1}^{4} \hat{v}_{i\,m} \cdot {}^i n_k^m |\, \Gamma_k^m| \equiv \frac{1}{\Delta t} \sum_{m=1}^{4} \hat{V}_m \, |\Gamma_k^m|, \tag{26}$$

$$(v_i^{n+1})_k = (\hat{v}_i)_k - \frac{\Delta t}{|\Omega_k|} \sum_{m=1}^{4} p_m^{n+1} \cdot {}^i n_k^m \, |\Gamma_k^m| \,, \tag{27}$$

$$V_m^{n+1} = \hat{V}_m - \Delta t \, \frac{\partial p^{n+1}}{\partial \boldsymbol{n}_k^m} \,, \tag{28}$$

where ${}^i n_k^m$ is the i-th component of the outward unit vector $\boldsymbol{n}_k^m = [{}^1 n_k^m, \, {}^2 n_k^m, \, {}^3 n_k^m]^T$ normal to the m-th face Γ_k^m of the control volume Ω_k and for the intermediate face-normal velocity $\hat{V}_m$ at the m-th face Γ_k^m of the control volume Ω_k, it is valid that $\hat{V}_m = \hat{v}_{im} \cdot {}^i n_k^m$. Note that the values of face-normal velocity V_m^{n+1} computed with the help of Eq. (28) are used as values of face-normal velocity V_m^n in Eq. (23) at the next time level.

Explicit schemes are known for their disadvantage in the form of restricted time steps. The CFL stability condition imposed on the time step size becomes essential when it is applied for grids with large differences in cell size, e.g., in complex geometries. In this case, the efficiency of explicit schemes is lost, since the cell with the most restrictive local time step determines the size of the global time step for all grid cells. One of possible solutions to this problem lies in the application of the well-known local time-stepping method. This method, whose approach is also employed in our developed solver, enables each cell of the computational grid to run with its own time step in a time-consistent manner.

Interpolation method

To perform numerical computations according to Eqs. (23) – (28), it is necessary to determine values of $v_{i\,m}^n|_{\text{upwind}}$, $\hat{v}_{i\,m}$, p_m^{n+1} and derivatives $\frac{\partial \hat{v}_i}{\partial \boldsymbol{n}_k^m}$, $\frac{\partial v_i^*}{\partial \boldsymbol{n}_k^m}$, $\frac{\partial p^{n+1}}{\partial \boldsymbol{n}_k^m}$ at the m-th face Γ_k^m of the control volume Ω_k. The value of $v_{i\,m}^n|_{\text{upwind}}$ is computed by the upwind scheme, whose first order accuracy is increased by linear reconstruction with Barth's limiter,

$$v_{i\,m}^n|_{\text{upwind}} = \begin{cases} (v_i^n)_L + \sigma_L^{Barth} \cdot \frac{\partial (v_i^n)_L}{\partial x_j} \cdot r_{jL} \,, & V_m^n > 0 \,, \\ (v_i^n)_R + \sigma_R^{Barth} \cdot \frac{\partial (v_i^n)_R}{\partial x_j} \cdot r_{jR} \,, & V_m^n \leq 0 \,, \end{cases} \tag{29}$$

where $\sigma^{Barth} \in [0, 1]$ is the Barth's limiter, Barth and Jesperson (1989), and vectors $\boldsymbol{r}_L$, $\boldsymbol{r}_R$ are denoted in Fig. 5 (*left*). Further, the value Φ_m of an arbitrary flow quantity Φ at the mid-point O of the m-th face Γ_k^m, Fig. 5 (*right*), can be stated with the help of second order accurate linear interpolation from

values $(\Phi)_k$ and $(\Phi)_{l_m}$ defined in cell-centres S_k and S_{l_m} of two adjacent control volumes Ω_k and Ω_{l_m}, respectively,

$$\Phi_m = (\Phi)_k + \frac{(\Phi)_{l_m} - (\Phi)_k}{\gamma_k + \gamma_{l_m}} \cdot \gamma_k = \frac{\gamma_{l_m}(\Phi)_k + \gamma_k(\Phi)_{l_m}}{\gamma_k + \gamma_{l_m}}\,, \tag{30}$$

where γ_k and γ_{l_m} are the minimal distances to the cell-face Γ_k^m from cell-centres S_k and S_{l_m} of the adjacent control volumes Ω_k and Ω_{l_m}, respectively, Fig. 5 (*right*). The derivative of flow quantity Φ in the direction of the outward unit vector $\boldsymbol{n}_k^m$ normal to the m-th face Γ_k^m of the control volume Ω_k, is approximated at the mid-point O of the face Γ_k^m, Fig. 5 (*right*), as

$$\left.\frac{\partial \Phi}{\partial \boldsymbol{n}_k^m}\right|_{\Gamma_k^m} \approx \frac{(\Phi)_{l_m} - (\Phi)_k}{\gamma_k + \gamma_{l_m}}. \tag{31}$$

A crucial part of the interpolation method is the application of Eq. (31) to the normal derivative in Eqs. (26) and (28). In this way, it is ensured that the face-normal velocity V_m^{n+1} satisfies the continuity equation at the time level $(n+1)$ exactly, see Eq. (37). However, in general velocities $(v_i^{n+1})_k$ in cell-centres of control volumes Ω_k do not satisfy the continuity equation.

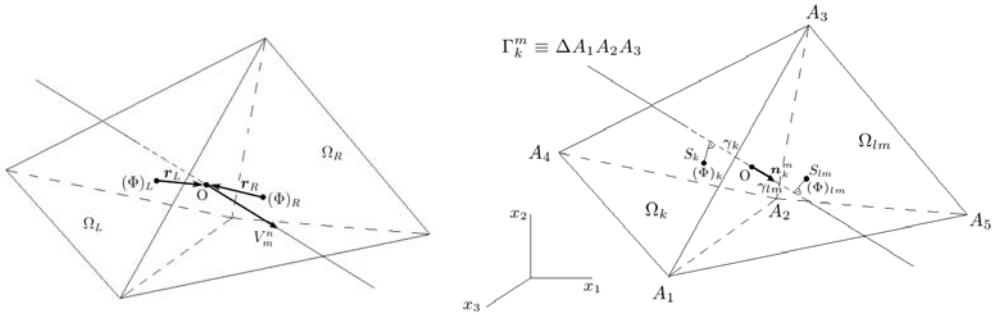

Fig. 5: Definition of the vectors $\boldsymbol{r}_L$ and $\boldsymbol{r}_R$ for two adjacent tetrahedral control volumes Ω_L and Ω_R (left). Two adjacent tetrahedral control volumes $\Omega_k = A_1A_2A_3A_4$ and $\Omega_{l_m} = A_1A_2A_3A_5$ with their contact face $\Gamma_k^m = \Delta A_1A_2A_3$ (right).

Regarding the implementation of non-dimensional *boundary conditions* at the boundary $\partial\Omega$ of the computational domain $\Omega \subset \mathbf{R}^3$, three boundary types are considered in this study:

- **inlet** $\Gamma_k^m \subset \partial\Omega_I$ – In this case, Dirichlet boundary conditions for the velocity components $v_{i\,m}$ and the auxiliary variable d_{ij}^m are prescribed

$$v_{i\,m} = v_{i\,I}\,, \qquad d_{ij}^m \cdot {}^j n = 0. \tag{32}$$

  The value of face-normal velocity V_m^I at the face Γ_k^m is computed as $V_m^I = v_{i\,I} \cdot {}^i n_k^m$, where values $v_{i\,I}$ are given according to section 5. For the normal derivative of the pressure p^{n+1} at the face Γ_k^m, we prescribe

$$\left.\frac{\partial p^{n+1}}{\partial \boldsymbol{n}_k^m}\right|_{\Gamma_k^m} = 0. \tag{33}$$

- **rigid and impermeable wall** $\Gamma_k^m \subset \partial\Omega_W$ – Velocity components $v_{i\,m}$ at the face Γ_k^m are set equal to zero

$$v_{i\,m} = 0\,, \tag{34}$$

  leading to zero value of the face-normal velocity $V_m^W = v_{i\,m} \cdot {}^i n_k^m = 0$ at the face Γ_k^m. For the auxiliary variable d_{ij}^m, we apply the Dirichlet boundary condition in the following form

$$d_{ij}^m \cdot {}^j n = 0\,. \tag{35}$$

  Further, zero normal derivative of the pressure p^{n+1} (33) is prescribed at the wall.

- **outlet** $\Gamma_k^m \subset \partial\Omega_O$ – Following type of boundary condition is stated

$$p_m \boldsymbol{n}_k^m - \frac{1}{\mathrm{Re}} 2\,\overline{\eta}(\dot{\gamma})^m\, d_{ij}^m \cdot {}^j n_k^m = p_O \boldsymbol{n}_k^m, \tag{36}$$

  where p_O is the given value of the outlet pressure, for details see section 5.

Substituting the derivative $\frac{\partial p^{n+1}}{\partial \boldsymbol{n}_k^m}$ in Eq. (26) with Eq. (28), we get

$$\begin{aligned} \sum_{m=1}^{4} \frac{\partial p^{n+1}}{\partial \boldsymbol{n}_k^m} |\Gamma_k^m| &= \frac{1}{\Delta t} \sum_{m=1}^{4} \left(\hat{V}_m - V_m^{n+1} \right) |\Gamma_k^m| = \frac{1}{\Delta t} \sum_{m=1}^{4} \hat{V}_m\, |\Gamma_k^m| \\ &\Longrightarrow \sum_{m=1}^{4} V_m^{n+1} |\Gamma_k^m| = 0, \end{aligned} \tag{37}$$

i.e., face-normal velocities V_m^{n+1} satisfy the continuity equation exactly. At this point, let us mention that at the outlet boundary $\partial\Omega_O$, i.e., at the face Γ_k^m of the control volume Ω_k, where $\Gamma_k^m \subset \partial\Omega_O$, values $\frac{\partial p^{n+1}}{\partial \boldsymbol{n}_k^m}$ are unknown. In order to ensure the satisfaction of the continuity equation (37) for this control volume Ω_k, it is necessary to compute the face-normal velocity V_m^{n+1} at the face $\Gamma_k^m \subset \partial\Omega_O$ as

$$V_{m_O}^{n+1} = -\frac{1}{|\Gamma_k^{m_O}|} \sum_{\substack{m=1 \\ m \neq m_O}}^{4} V_m^{n+1} |\Gamma_k^m|, \tag{38}$$

where m_O is the index of the outlet face $\Gamma_k^{m_O}$ of the control volume Ω_k. For the whole computational domain $\Omega \subset \mathbf{R}^3$ at the time $t = 0$, following *initial conditions* are used

$$(v_i^0)_k = \frac{1}{|\Omega_k|} \int_{\Omega_k} v_i(\boldsymbol{x}, 0) \mathrm{d}\Omega = 0, \qquad (p^0)_k = \frac{1}{|\Omega_k|} \int_{\Omega_k} p(\boldsymbol{x}, 0) \mathrm{d}\Omega = p_{initial},\ k = 1, 2, \ldots, N_{CV},$$

where $p_{initial}$ is a non-dimensional value of static pressure.

5. Numerical results

In accordance with the boundaries of the computational domain denoted in Fig. 3 for the model of the individual aorto-coronary bypass, the numerical simulations of pulsatile Newtonian and non-Newtonian blood flow are carried out with following values of the time-dependent boundary conditions:

- aortic inlet $\partial\Omega_I^{(A)}$ – constant time-dependent velocity profile $|\boldsymbol{v}_I|$ according to the flow rate waveform $Q(t)$ shown in Fig. 6 (left);
- aortic outlet $\partial\Omega_O^{(A)}$ – time-dependent pressure $p(t)$ shown in Fig. 6 (right), where the aortic pressure is plotted in the medical units of millimeters of mercury ($1\,\mathrm{mmHg} = 133.333\,\mathrm{Pa}$);
- coronary outlets $\partial\Omega_O^{(CA)}$ – constant pressure related to average arterial pressure of $12\,000\,\mathrm{Pa}$;
- rigid and impermeable walls $\partial\Omega_W$ – non-slip boundary condition.

Note that the boundary values mentioned above are, for the computation, non-dimensionalized using the reference values mentioned in section 3. The implementation of the boundary conditions in the numerical code is described in detail in section 4.

For the analysis of computed numerical results, we introduce two significant hemodynamical wall parameters – the cycle-averaged wall shear stress (WSS) and the oscillatory shear index (OSI) that are evaluated according to formulas mentioned in Xiong and Chong (2008) and He and Ku (1996), respectively,

$$\overline{|\boldsymbol{\tau}_W|} = \frac{1}{T} \int_0^T |\boldsymbol{\tau}_W| \mathrm{d}t\,, \qquad \mathrm{OSI} = \frac{1}{2} \left[1 - \left| \int_0^T \boldsymbol{\tau}_W \mathrm{d}t \right| \cdot \left(\int_0^T |\boldsymbol{\tau}_W| \mathrm{d}t \right)^{-1} \right], \tag{39}$$

where $|\boldsymbol{\tau}_W|$ is the WSS magnitude and $T = 1\,\mathrm{s}$ is the duration of one cardiac cycle, Fig. 6.

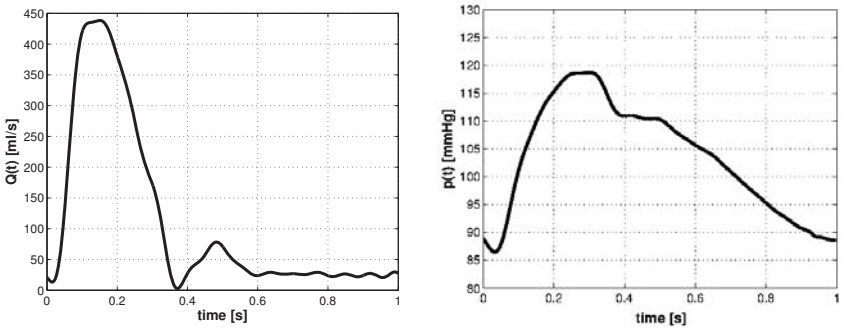

Fig. 6: Time-dependent boundary conditions for the aorta – inlet flow rate $Q(t)$ (left) and outlet pressure $p(t)$ (right), data taken from Olufsen et al. (2000)

Firstly, let us analyse the velocity profiles of the non-Newtonian blood flow in Fig. 7 for three selected time instants, corresponding to systole, diastole and late diastole, respectively. During the systolic phase ($t_1 = 0.16\,\mathrm{s}$), Fig. 7 (left), the graft's proximal anastomosis becomes exposed to the increased flow rate in the aorta. Although the skewed velocity profiles at the graft entrance may indicate incoming blood flow, the real graft filling occurs later. By comparing the pictures in Fig. 7, it becomes quite apparent that the systolic phase of the cardiac cycle is represented by decreased blood flow through the individual bypass graft, whereas an opposite effect is observed during most of the diastolic phase ($t_2 = 0.47\,\mathrm{s}$ and $t_3 = 0.98\,\mathrm{s}$). In this case, the velocity increase observed along the individual graft is also accompanied by skewed or otherwise shaped velocity profiles that are a result of the out-of-plane geometry and the graft's winding around the heart, see Fig. 2. At the distal end-to-side anastomosis, Fig. 7c, the incoming blood flow seems to prefer the closer branch of the coronary artery more than the second one. Moreover, the closer coronary artery shows a tendency to considerably increase velocity magnitude downstream from the anastomosis. The reason for this phenomenon is a partly stenosed coronary artery.

The comparison between the Newtonian and non-Newtonian blood flow is illustrated by the distributions of the cycle-averaged WSS and OSI in Figs. 8 and 9, respectively. At this point, note the lowered value range in Fig. 8, which is chosen according to conclusions mentioned in Haruguchi and Teraoka (2003) and He and Ku (1996). Namely, that low WSS, as compared to the normal range between $1 - 2\,\mathrm{Pa}$ in healthy arteries, is one of the confirmed triggers of vessel remodelling, plaque growth and intimal thickening. In light of this fact, we will further assess the resulting shear distribution, which regardless of the viscosity model (Newtonian or non-Newtonian), seems to be non-uniform at both anastomoses, Fig. 8. One of the distinct areas with extremely low shear is situated at the entrance of the graft, where it is caused by a large recirculation zone that is present there most of the cardiac cycle. This negative stimulation of the proximal suture line is also confirmed by the high OSI shown in Fig. 9. At the distal anastomosis, shear values below $1\,\mathrm{Pa}$ are observed at the heel and the arterial floor in accordance with the sites of intimal hyperplasia displayed in Fig. 1. In this case, the critical shear stress also shows a oscillatory tendency as is apparent from the OSI distribution in Fig. 9.

The objective of our previous study, Vimmr and Jonášová (2010), was the investigation of blood's non-Newtonian behaviour in complete bypass models with coronary or femoral native arteries. The numerical simulations were carried out under steady flow conditions and for an idealized bypass geometry. In the present study, we want to extend our previous conclusions about the importance of blood's non-Newtonian modelling in coronary bypasses by considering pulsatile blood flow and a realistic and more complex bypass geometry. As is illustrated by Figs. 8 – 9, the influence of non-Newtonian flow conditions is very small or rather negligible (as is the case of the velocity profiles). On the basis of these observations, we can draw a conclusion similar to that mentioned in Vimmr and Jonášová (2010). Namely, that blood's non-Newtonian behaviour does not have any significant impact on the hemodynamics in coronary bypasses. In light of this observation and our present experience with the modelling of non-Newtonian blood flow, it may be said that an hemodynamic study in patient-specific femoral bypasses would be more promising in regard to the occurrence of non-Newtonian effects as was concluded in our previous study Vimmr and Jonášová (2010). This problem will be addressed in the future.

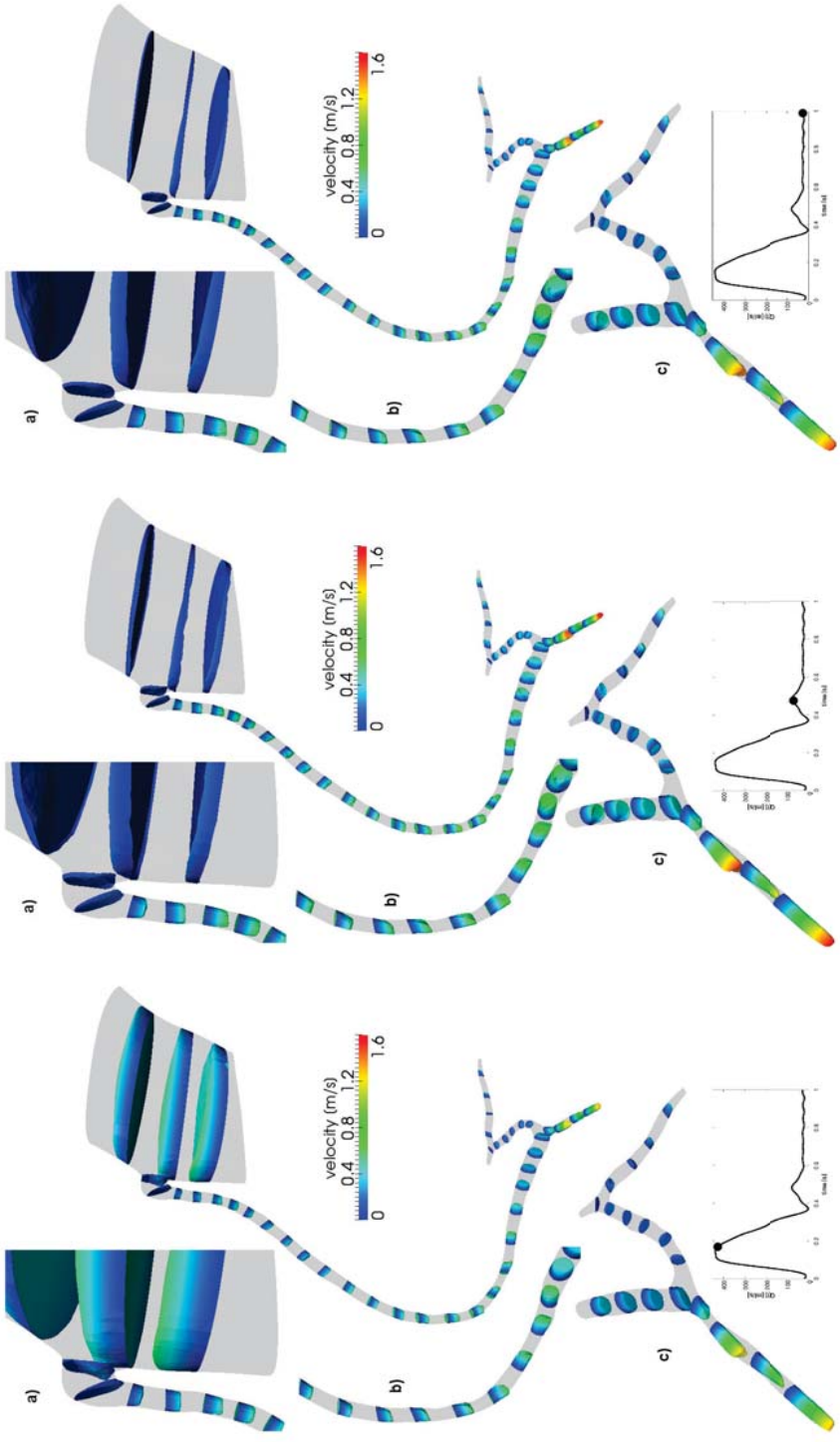

Fig. 7: Non-Newtonian blood flow – velocity profiles at selected cross-sections of the aorto-coronary bypass at the time instants $t_1 = 0.16\,s$, $t_2 = 0.47\,s$ and $t_3 = 0.98\,s$ (from left to right); detailed views at (a) the proximal anastomosis, (b) individual graft, (c) coronary arteries with the distal anastomosis

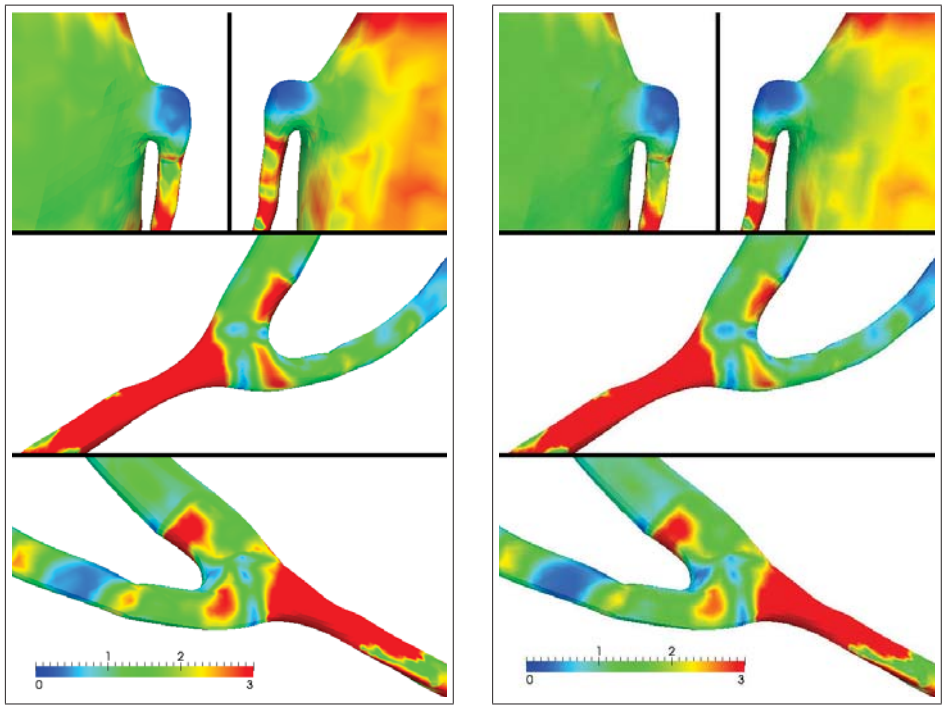

Fig. 8: Distribution of cycle-averaged WSS for the Newtonian (left) and non-Newtonian flow (right)

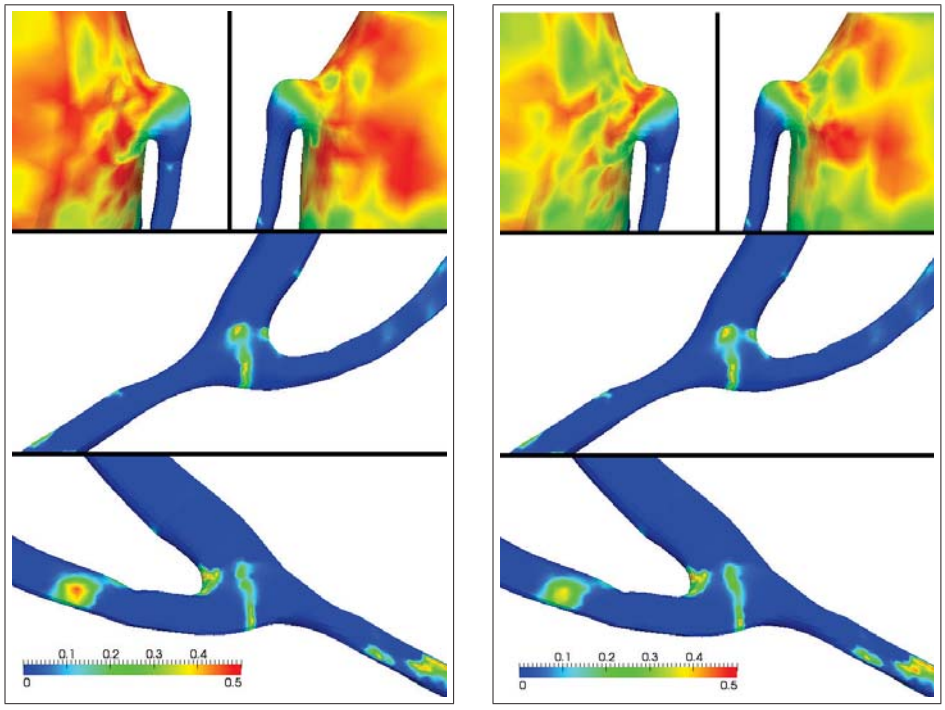

Fig. 9: Distribution of OSI for the Newtonian (left) and non-Newtonian flow (right)

Acknowledgments

This study was supported by the European Regional Development Fund (ERDF), project NTIS - New Technologies for Information Society, European Centre of Excellence, CZ.1.05/1.1.00/02.0090 and by the internal student grant project SGS-2010-046 of the University of West Bohemia.

References

Bassiouny, H.S., White, S., Glagov, S., Choi, E., Giddens, D.P., Zarins, C.K. (1992), Anastomotic intimal hyperplasia: Mechanical injury or flow induced. *Journal of Vascular Surgery*, Vol 15, No.4, pp 708-717.

Barth, T.J., Jesperson, D.C. (1989), The design and application of upwind schemes on unstructured meshes. In: *Proceedings of the 27th AIAA Aerospace Sciences Meeting*. AIAA Paper 89-0366.

Cho, Y.I., Kensey, K.R. (1991), Effects of the non-Newtonian viscosity of blood on flows in diseased arterial vessels. Part I: Steady flows. *Biorheology*, Vol 28, No.3-4, pp 241-262.

Ferziger, J.H., Perić M. (1999), *Computational methods for fluid dynamics*, Springer, Heidelberg.

Haruguchi, H., Teraoka, S. (2003), Intimal hyperplasia and hemodynamic factors in arterial bypass and arteriovenous grafts: A review. *Journal of Artificial Organs*, Vol 6, No.4, pp 227-235.

He, X., Ku, D.N. (1996), Pulsatile flow in the human left coronary artery bifurcation: Average conditions. *Journal of Biomechanical Engineering*, Vol 118, No.1, pp 74-82.

Kim, D., Choi, H. (2000) A second-order time accurate finite volume method for unsteady incompressible flow on hybrid unstructured grids. *Journal of Computational Physics*, Vol 162, No.2, pp 411-428.

Loth, F., Fischer, P.F., Bassiouny, H.S. (2008) Blood flow in end-to-side anastomoses. *Annual Review of Fluid Mechanics*, Vol 40, pp 367-393.

Olufsen, M.S., Peskin, C.S., Kim, W.Y., Pedersen, E.M., Nadim, A., Larsen, J. (2000) Numerical simulation and experimental validation of blood flow in arteries with structured-tree outflow conditions. *Annals of Biomedical Engineering*, Vol 28, No.11, pp 1281-1299.

Vimmr, J., Jonášová, A. (2010), Non-Newtonian effects of blood flow in complete coronary and femoral bypasses. *Mathematics and Computers in Simulation*, Vol 80, No.6, pp 1324-1336.

Vural, K.M., Şener, E., Taşdemir, O. (2001) Long-term patency of sequential and individual saphenous vein coronary bypass grafts. *European Journal of Cardio-thoracic Surgery*, Vol 19, No.2, pp 140-144.

Xiong, F.L., Chong, C.K. (2008), A parametric numerical investigation on haemodynamics in distal coronary anastomoses. *Medical Engineering & Physics*, Vol 30, No.3, pp 311-320.

Zeng, D., Ding, Z., Friedman, M.H., Ethier, C.R. (2003), Effects of cardiac motion on right coronary artery hemodynamics. *Annals of Biomedical Engineering*, Vol 31, No.4, pp 420-429.

18th International Conference
ENGINEERING MECHANICS 2012
Svratka, Czech Republic, May 14 – 17, 2012

pp. 1517–1524
Paper #64

SEDIMENTATION OF DILUTE SUSPENSION IN INTERMEDIATE REGION

P. Vlasak[*], Z. Chara[**]

Abstract: *The present paper describes the results of experimental investigation of the continuous sedimentation of a dilute model of fine-grained suspension in the intermediate region of settlement. The effects of particle size (glass beads of average diameter 150–850 μm), concentration, and inclination of the vessel axis on particle fall velocity were evaluated. It was confirmed that the local relative particle-liquid velocity has a practically constant value across the vessel cross-section. The settling pattern is strongly affected even by a very gentle slope of the vessel axis, which causes an asymmetrical absolute velocity profile and significant increase of the local concentration and absolute fall velocity of particles near the upward-facing wall of the vessel.*

Keywords: ***sedimentation, intermediate settlement, particle size, concentration, vessel inclination.***

1. Introduction

The particle fall velocity is one of the main hydrodynamic parameters of solid-liquid mixture flow in natural conditions, for example sediment transport in rivers and channels, as well as in technical applications for water or waste – water treatment, chemical and civil engineering, pipeline hydraulic transport, or dredging. The fall velocity is a common integral parameter describing the mutual interaction between the particles and the carrier fluid. However, a reliable method of determining the fall velocity of particles of general shape is still not available, and in fact there is still a significant lack of experimental data and theoretical solutions for the sedimentation of clouds of solid particles in the intermediate region of sedimentation.

The paper describes the experimental results of dilute model suspension sedimentation in the intermediate region of sedimentation, for particle Reynolds number Re_p varying from 3 to 140 in a vertical and slightly inclined sedimentation vessel.

The fall velocity of a particle moving in suspension in a container is generally determined by the particle diameter d, shape b, and density ρ_p, the volumetric concentration of the suspension C_v, the distance from the container wall y, and the density ρ_o and viscosity μ_o of the carrier liquid. It is also dependent on the dimension D of the horizontal cross-section and shape B of the container, and, as will be shown below, on the inclination of the container walls α. The particle fall velocity (Ah Chin et al., 1986) can be generally described by Eq. (1)

$$w_c = (d,\ b,\ \rho_p,\ C_v,\ y,\ \rho_o,\ \mu_o,\ D,\ \alpha). \tag{1}$$

The effect of the selected parameters of Eq. (1) on particle fall velocity will be discussed in the following paragraphs. The absolute local velocity of the settling particles and carrier liquid were measured for different volumetric concentrations and sedimentation vessel inclinations, and thus relative particle-water velocities were also determined. The effects of the particle concentration of the suspension and the vessel inclination on the particle velocity and the internal structure of sedimentation will be described.

[*] Prof. Ing. Pavel Vlasák, DrSc.: Institute of Hydrodynamics AS CR, v. v. i., Pod Paťankou 30/5, 166 12 Prague 6; CZ, e-mail: vlasak@ih.cas.cz

[**] Ing. Zdeněk Chára, CSc.: Institute of Hydrodynamics AS CR, v. v. i., Pod Paťankou 30/5, 166 12 Prague 6; CZ, e-mail: chara@ih.cas.cz

2. Experimental equipment and procedure

Several experimental methods are suitable for measuring continuous sedimentation, for example the radiometric tracer method, PIV (Particle Image Velocimetry), and LDA (Laser Doppler Anemometry). The LDA or PIV methods are suitable for very dilute transparent suspensions and make it possible to determine both local particle and liquid velocities. The radiometric tracer method allows the absolute particle velocity of different species of suspended solids to be measured, but for higher concentrations of relatively fine particles, problems with accuracy can arise (Vlasak et al., 1994). For this reason, we used LDA for measuring the local velocities, but for higher particle concentrations a method based on the increment of hydrostatic pressure due to the increase in suspension density was developed. This method makes it possible to measure the mean fall velocity in suspensions with a relatively wide range of concentrations.

The volumetric concentration is generally given as

$$C_v = (\rho_s - \rho_o)/(\rho_p - \rho_o), \tag{2}$$

where ρ_s is the density of suspension. Because the particles which enter the elementary volume V_C at time $t_o = 0$ and fall in the suspension with velocity w_c reach, during the time interval t the distance $l = w_c\, t$, the elementary volume is given as

$$V_C = w_c \,.\, t.\, S_D = l.\, S_D, \tag{3}$$

and the volumetric concentration of the suspension can be determined as the ratio of the volume of the particles V_p and of the suspension V_s in the elementary volume V_C

$$C_v = V_p / V_C = (q_p \,.\, t) / (w_c \,.\, t.\, S_D), \tag{4}$$

where q_p is the flow rate of solid particles, and S_D is the cross-sectional area of the sedimentation vessel.

The increase in hydrostatic pressure in the column of the suspension compared to the hydrostatic pressure of the carrier liquid alone is

$$\Delta p = h.\,(\rho_s - \rho_o).\, g, \tag{5}$$

where h is the height of the column. From Eqs. (2 – 5) the mean fall velocity w_c of suspended particles can be expressed as

$$w_c = 4\, g.\rho_p \,.\, h \,.\, (\rho_p - \rho_o) / (\pi \,.\, \Delta p.D^2), \tag{6}$$

To determine the local absolute particle velocity w_p of the individual particles and also the local velocity of displaced water, v_o, the LDA technique was used (Vlasak et al., 1991). The LDA apparatus consists of a laser and optical parts from a DISA system (beam divider, Bragg-cell, optics, photomultiplier working in the lateral forward diffraction regime). The Doppler signal detected in the photomultiplier was processed by a frequency synthesizer and evaluated by a counter. The primary experimental data, Doppler frequencies in the form of 12 bit words, were statistically processed and as a result pairs of velocity data distributions on the velocity histogram were obtained. One group of bins of the velocity distribution in the higher velocity range represents the absolute particle fall velocities in suspension, w_c, and the second one, close to the zero velocity values, represents the local velocities of the displaced waver, v_o. To investigate the effect of concentration and sedimentation vessel axis inclination on the inner structure of the suspension during the settlement process, visualization was also used.

To measure the particle fall velocity in the model suspensions, equipment consisting of a sedimentation vessel (a glass tube of inner diameter D = 0.05 m and length L = 2.3 m), a particle dosing device, and measuring devices were used. The particle dosing device maintained the continuous uniform supply of particles and ensured a constant concentration of the measured suspension.

Water was used as the carrier liquid, and narrow sized glass beads of different mean diameters (average particle diameter varied in range d_{50} = 150, 280, 350 and 850 μm) were used as model particles. The temperature of the suspensions was in range $T = 20 \pm 2$°C. It was possible to operate the equipment continuously over a sufficiently long time period to obtain a stationary regime. A schematic diagram of the equipment is presented in Fig. 1.

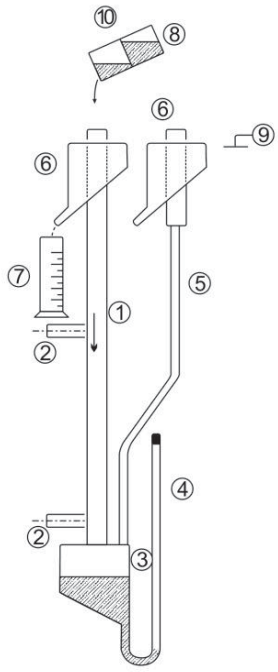

Fig. 1. Experimental equipment (1 – sedimentation vessel, 2 – γ-detector, 3 – sedimentation tank, 4 – let out hose, 5 – coupling hose, 6 – control and out-let set-up, 7 – calibrated vessel, 8 – particle dosing device, 9 – level of suspension, 10 – particles)

3. Results and discussion

The absolute local particle fall velocities and local water velocities were measured for different volumetric concentrations C_v of the suspension and three values of the sedimentation vessel axis inclination α. The effects of concentration and vessel inclination on the particle fall velocity and particles distribution in the vessel cross-section were evaluated.

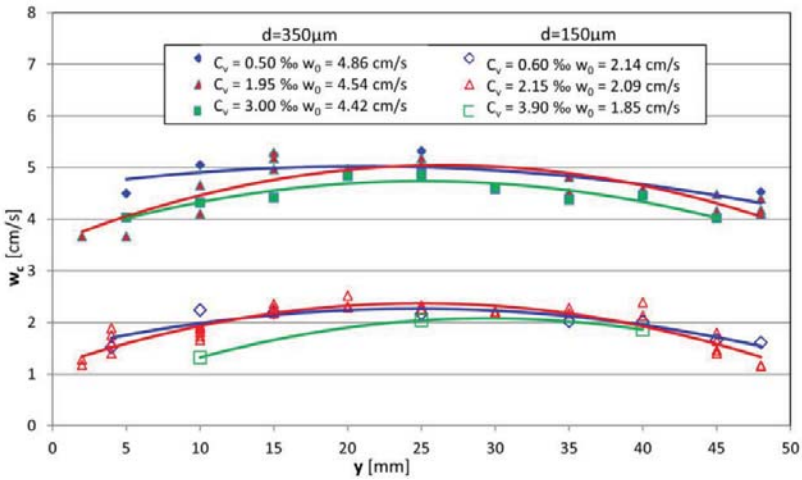

Fig. 2. Absolute fall velocity profiles in the vertical sedimentation vessel

The absolute particle fall velocities in a vertical vessel are shown in Fig. 2. For the smaller particles (mean diameter d_{50} = 150 μm) the velocity profiles are relatively flat and symmetrical. Velocity profiles are slightly asymmetrical, more so for particles with mean diameter d_{50} = 350 μm. The curvature of the velocity profiles is steeper in the area near the vessel walls, while a relatively flat plateau can be seen in the central part of the vessel cross-section. The maximum local velocity values are located 5 to 10 mm from the column axis; the profile asymmetry increases with decreasing concentration. The reason for the velocity profile distortion is probably an imperfect circular shape or imperfect verticality of the vessel.

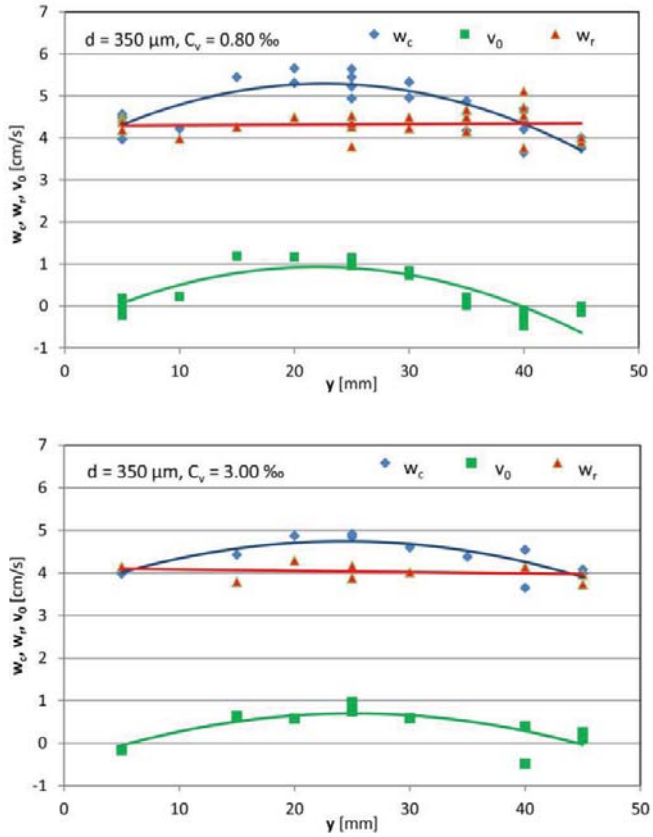

Fig. 3. Relative and absolute particle velocities and water velocity profiles in the vertical sedimentation vessel

The measured profiles of displaced water show very similar shapes to absolute particle fall velocity profiles, with the opposite direction, of course. This indicates, that it may be useful to introduce the relative particle fall velocity:

$$w_r = w_c - v_o, \tag{7}$$

where w_r is the relative particle fall velocity and v_o is the local velocity of displaced water with respect to the sedimentation vessel.

While the absolute fall velocity profiles are arch-shaped, the relative particle-water velocity values are nearly constant, independently of the position in the vessel (see Fig. 3). This indicates that the difference in the absolute fall velocities is due to the different velocities of displaced water. In the vertical sedimentation vessel, upward flow of the displaced water was observed near the wall, while downward flow of the displaced water was observed in the central area. This explains why the local absolute fall velocity of particle w_c is observed to be even higher than the fall velocity $w_{p,\infty}$ of the same

single particle in the unbounded liquid medium. This inner flow structure in the sedimentation vessel was also confirmed by visualization of the sedimentation process. In the central area and in the vicinity of vessel walls the flow lines are smooth and straight; at the boundary of these areas, with opposite flow directions, wavy trajectories and even swirls can be observed (see Fig. 4).

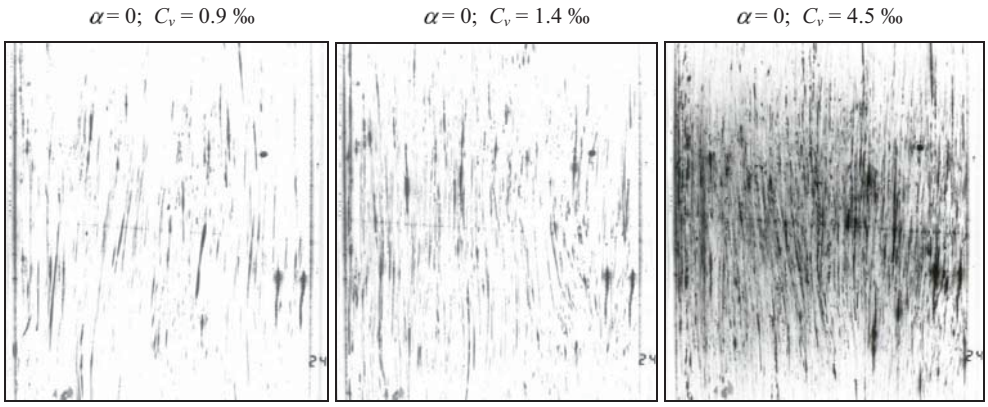

Fig. 4. Structure of sedimentation in vertical sedimentation vessel.

In the sedimentation vessel, during continuous sedimentation the suspension divides into channels in which the velocities of the particles and water can be in the same direction (the so-called co-current regime) and the particles apparently move faster than a single particle in unbounded calm liquid. On the other hand, other channels exist where a counter-current regime of the particles and liquid occurs and the absolute fall velocity of the particles is lower than that of a single particle.

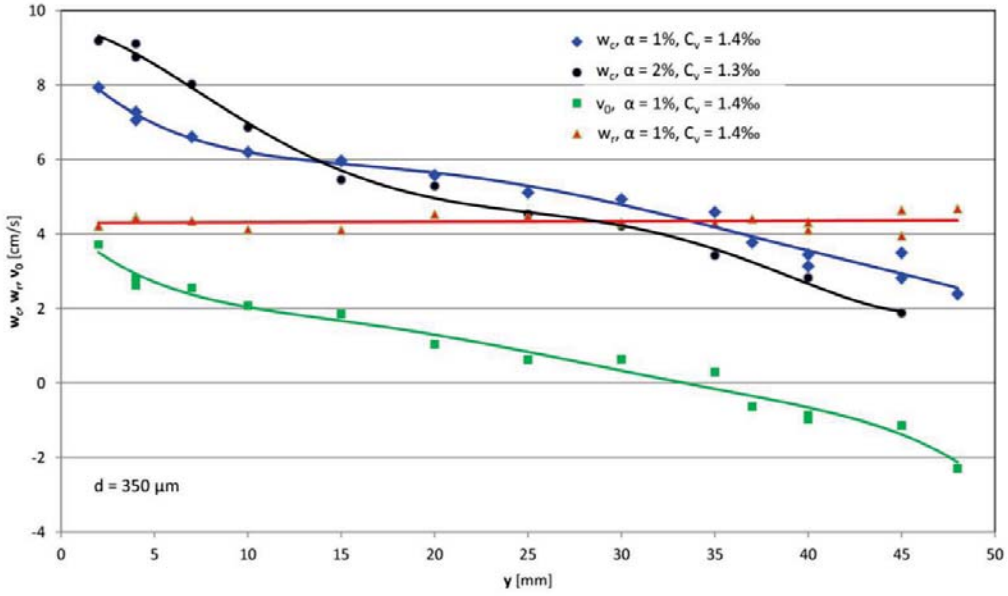

Fig. 5. Relative and absolute particle velocities and water velocity profiles in the inclined sedimentation vessel

The sedimentation process is highly sensitive to the inclination of the sedimentation vessel; even very small inclination causes a considerable change in the inner structure of the sedimentation process. If the axis of the sedimentation vessel is slightly inclined, the absolute particle velocity profiles

become significantly asymmetric (see Fig. 5). Higher particle fall velocities are attained near the upward-facing wall, which is located at co-ordinate $y = 0$. In the vicinity of the upward-facing wall the co-current regime of the particles and carrier liquid was observed in combination with a significant increase in the local particle concentration. In contrast, near the downward-facing wall of the vessel a counter-current flow regime of the particles and water and lower particle concentration were observed. Nevertheless, the relative particle-water velocity reached an almost constant value over the whole cross-section. In the central part of the vessel between the co-current and counter-current flow regimes, wavy trajectories and even local swirls were observed (see Fig. 6). If the inclination of the vessel axis increases the transverse migration of the particles in the direction of the upward-facing wall becomes significant, while near the downward-facing wall the occurrence of particles is entirely random.

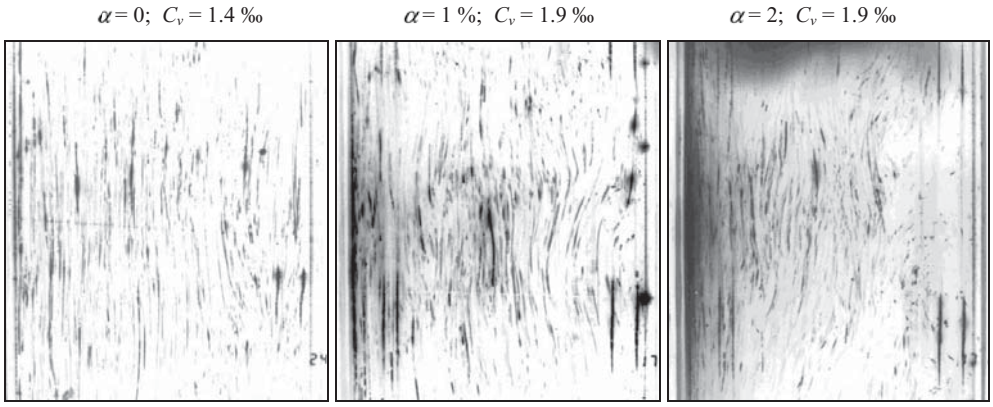

Fig. 6. Structure of sedimentation in inclined sedimentation vessel.

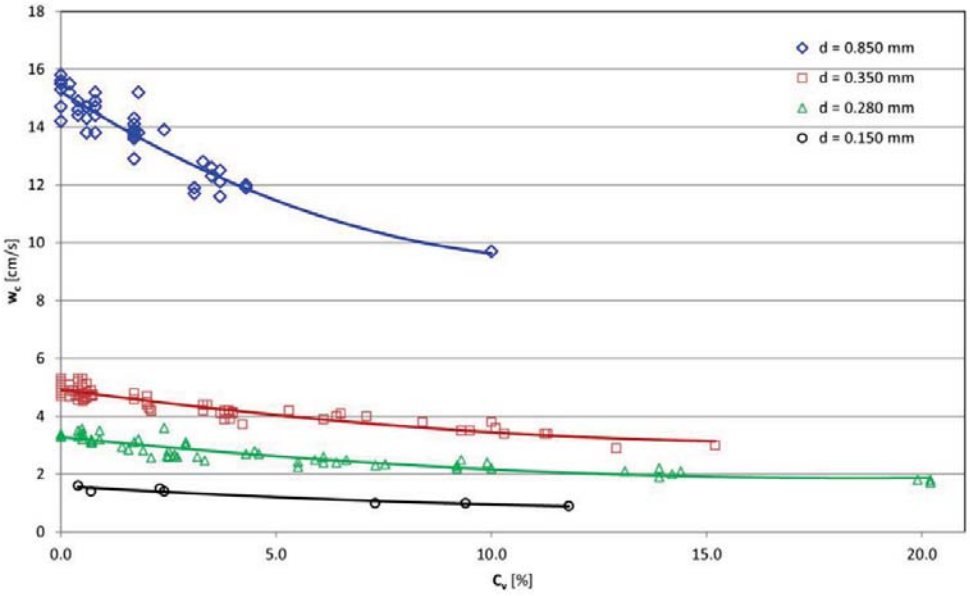

Fig. 7. Effect of concentration on particle fall velocity in a vertical sedimentation vessel

It is generally known that the value of absolute particle fall velocity decreases with increasing concentration. Many relations have been proposed to solve this effect, but unfortunately their validity

is limited by certain conditions. They are usually suitable for small concentrations or concentration above 10%. If we compare our experimental data with the proposed relations, rather wide scattering can be observed. Based on our experimental data obtained by the hydrostatic pressure method and the radiometric tracer method measurement (Vlasak et al., 1994; Vlasak & Chara, 1995), the relation

$$w/w_c = (1 + 4.92\ C_v)^{-1}, \tag{8}$$

similarly to the model of Burgers (1942), is proposed (see Fig. 7).

4. Conclusions

The results of an experimental investigation of continuous sedimentation of a suspension of glass beads in water in a vertical or inclined sedimentation vessel confirm the significant impact of sedimentation-induced flow of the displaced liquid on the absolute particle fall velocity. The absolute particle velocity is affected by the particle diameter and concentration, the inclination of the sedimentation vessel axis, and the distance of the particle from the vessel wall.

The value of particle fall velocity decreases with increasing concentration.

The distribution of the local absolute particle fall velocity exhibits arch-shaped profiles; however the values of local particle-liquid relative velocity are nearly constant across the cross-section of the sedimentation vessel.

The sedimentation process is highly sensitive to the inclination of the sedimentation vessel axis. Even an inclination in the range 1% causes considerable change in the structure of the sedimentation process, with a tendency to form an asymmetric absolute particle fall velocity distribution. An upward flow of displaced liquid took place near the downward-facing surface of the vessel, and significantly more concentrated down ward flow was observed near the upward-facing wall.

If the inclination of the sedimentation vessel axis exceeds 1%, a significant transversal migration of the suspended particles combined with an increase in the local concentration is observed near the upward-facing wall, as well as wavy trajectories and swirl areas in regions where the downward flow of the suspension and upward flow of the displaced liquid are in contact.

Acknowledgements

Support under the project P105/10/1574 of the Grant Agency of the Czech Republic and Institutional Research Plan No. AV0Z20600510 of the Academy of Sciences of the Czech Republic is gratefully acknowledged.

References

Ah Chin, A.D., Portz, J. Ward, M., Beddow, J.K. & Vetter, A.F. (1986) A shape-modified size correction for terminal settling velocity in the intermediate region. *Powder Technology*, 48, pp. 59–65.

Barnea, E. & Mizrahi, J. (1973) A generalized approach to the fluid dynamics of particulate systems. Chem. Eng. J., 5, pp. 171-189.

Burgers, J.M. (1942) On the influence of the concentration of a suspension upon the sedimentation velocity (in particular for a suspension of spherical particles) *Proc. Koninklijke Nederlandse Akademie van Wetenschappen* (Amsterdam), 45, pp. 9-16.

Vlasak, P. & Chara, Z. (1995) Contribution to the effect of concentration on settling velocity of model suspensions, in: Proc. 8th Int. Conf. on Transport and Sedimentation of Solid Particles, CTU & Inst. of Hydrodynamics ASCR (Z. Chara, V. Havlik & P. Vlasak, eds.), Prague, pp. F3-1–F3-6.

Vlasak, P., Chara, Z. & Severa, M. (1994) Experimental investigation of settlement by means of radiometric tracer method. Vodohosp. Cas., 42, 2-3, pp. 122–130.

Vlasak, P., Chara, Z., Gardavsky, J. & Severa, M. (1991) LDA measurement of the settling velocity in a solid-liquid mixture. Vodohosp. Cas., 39, 2, pp. 18–153.

Symbols

b shape of particle
B shape of sedimentation vessel
C concentration
d particle diameter
D diameter of sedimentation vessel
h height
l distance
L length
p pressure
q flow rate
Re Reynolds number
S area
S_D sedimentation vessel cross-sectional area
t time
T temperature
v liquid velocity
V volume
V_C elementary volume
w particle fall velocity
y coordinate
α angle, slope of sedimentation vessel axis
μ viscosity
ρ density
Δ increment

Subscripts
c cloud of particles
o liquid
p particle
r relative
s suspension
v volumetric
50 mean diameter
∞ unbounded

18th International Conference
ENGINEERING MECHANICS 2012
Svratka, Czech Republic, May 14 – 17, 2012

pp. 1525–1533
Paper #279

THE SELF-EXCITED VIBRATION OF THE NACA0015 PROFILE

V. Vlček, I. Zolotarev, J. Kozánek*

Abstract: *The two-dimensional flow patterns around the profile NACA0015 vibrating in self-excitation modes were measured in the wind tunnel by optical methods. The profile with two-degree-of-freedom moved in the vertical direction and rotated around the elastic axis in 1/3 of the profile chord. The Mach numbers for the self-excited vibrations were in the interval 0.2 – 0.45. Results of the interferometric measurement and the profile kinematic movements during the self-oscillations are presented.*

Keywords: ***self-excited vibrations, aeroelastic experiment, wind tunnel, flutter .***

1. Introduction

Aeroelastic experiments were realized in the subsonic aerodynamic tunnel of the Institute of Thermomechanics AS CR in Nový Knín with a modified NACA0015 profile. The Mach numbers corresponding to the self-excited vibrations were in the range M = 0.2 – 0.45 and the Reynolds number range was $(0.25 – 0.54)\cdot 10^6$. The detail description of the experimental setup is in Vlček (2009) and a schematic arrangement is in Fig. 1. The flow field was measured by interferometric and pneumatic methods, the profile vertical position was indicated by a mechanical sensor.

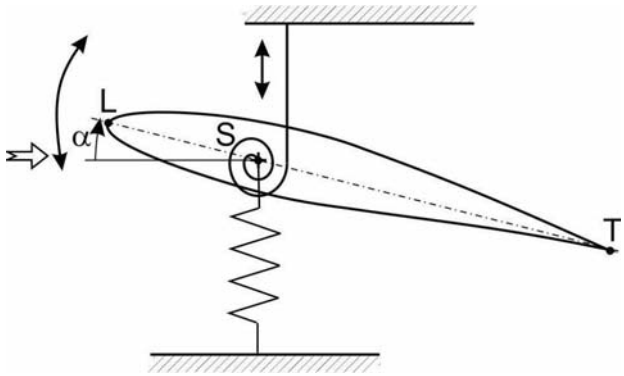

Fig. 1: Schematic arrangement of the experiment.

Eigenfrequencies for M = 0 were 19.0 Hz with 9.3 % damping in translation mode and 21.5 Hz with 11.9 % damping in rotation mode. Measured eigenfrequencies for M = 0 were 16.4 Hz with 2.0 % damping, 19.3 Hz with 9.3 % damping in translation mode, and 24.5 Hz with 1.5 % damping, 21.5 Hz with 11.9 % damping in rotation mode, respectively.

The Table 1 presents a list of data, setting for various experimental trials in the measurements and evaluated flutter frequencies.

* Ing. Václav Vlček, CSc., Ing. Igor Zolotarev, CSc., Ing. Jan Kozánek, CSc.: Institute of Thermomechanics AS CR, v.v.i., Dolejškova 1402/5, 182 00 Praha 8, Czech Republic; e-mail: vlcek@it.cas.cz, igor@it.cas.cz, kozanek@it.cas.cz .

profile (meas. No.)	M [1]	Re [1]	mode	f_o [Hz]	damping [%]	f [Hz] evaluated	film pict/sec
NACA0015	0	0	translat	16.4	2.0		
(for 2510)	0	0	rotation	24.5	1.5		
NACA0015_2510-06	0.43	$0.52 \cdot 10^6$				19.5	1000
NACA0015	0	0	translat	19.0	9.3		
(for 2662,2663)	0	0	rotation	21.5	11.9		
NACA0015_2662-14	0.33	$0.40 \cdot 10^6$				31.2	500
NACA0015_2662-15	0.30	$0.36 \cdot 10^6$				28.5	1000
NACA0015_2662-16	0.28	$0.34 \cdot 10^6$				27.8	1000
NACA0015_2662-17	0.22	$0.27 \cdot 10^6$				21.2	500
NACA0015_2663-01	0.26	$0.31 \cdot 10^6$				22.7	500
NACA0015_2663-02	0.21	$0.25 \cdot 10^6$				21.7	1000
NACA0015_2663-03	0.38	$0.46 \cdot 10^6$				31.8	1000
NACA0015_2663-04	0.40	$0.48 \cdot 10^6$				32.2	1000
NACA0015_2663-05	0.45	$0.54 \cdot 10^6$				32.2	1000

Tab. 1: Experimental value sets.

2. Experimental results

Šafařík, Vlček (1985).The example of measured interferogram is depicted on Fig. 2, where it is possible to see flow separation beside the whole the upper profile surface.

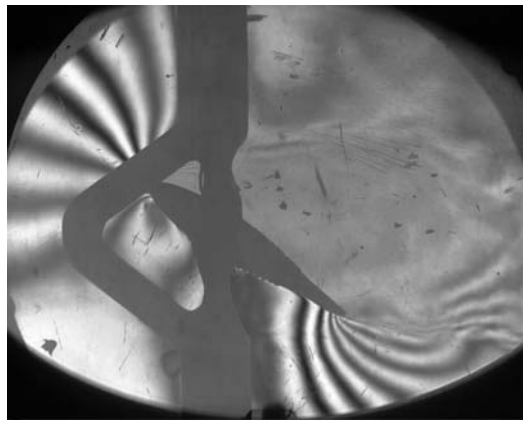

Fig. 2: Interferogram of a studied profile.

The arrangement of the system with different eigenfrequencies (corresponding to the translation and rotation motion of the profile) influenced the properties of the flow-field and the mechanical structure interaction. As it is depicted in Fig. 3 by increasing the inflow velocity higher than M = 0.26, the separation area is larger and the vibration frequency rises above the both eigenfrequencies identified for M = 0. The couple mode flutter found between M = 0.21 and M = 0.26 is changed to the stall flutter for the bigger Mach numbers. The increase of the vibration level was so high, that at M = 0.45 the experiment had to be finished due to the danger of system destruction. The flutter frequency of the vibration in this process increased 1.6 times and the optical measurements showed that the area-wide separation appears during 25% to 50% of the vibration period. In this case we can observe so-called stall flutter Dowell (1995). The evaluation of interferograms is described in Vlček (2010).

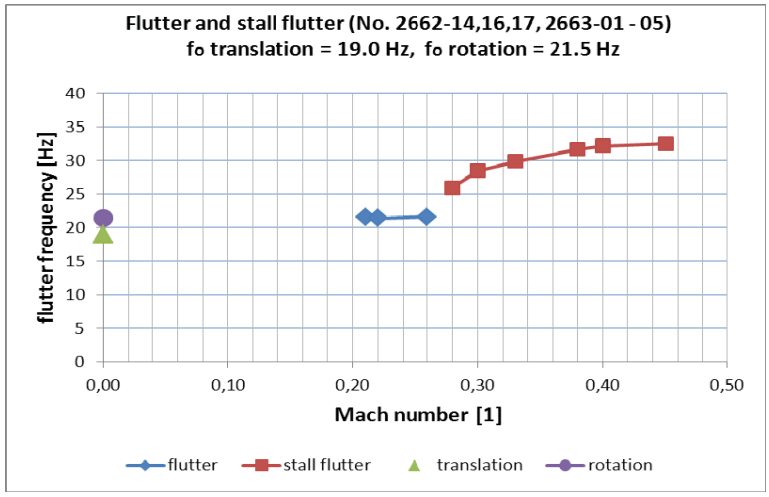

Fig. 3: The eigenfrequency changes of the self-excited vibration as a function of the Mach number.

In case of the bigger difference between the eigenfrequencies for translation and rotation modes for M = 0 no stall flutter was observed. Fig. 4 illustrates this result: original translation frequency was 16.4 Hz and the rotational frequency was 24.5 Hz, i.e. the difference in this case was 8.1 Hz (about four times more than in previous case shown in Fig. 3). The flutter frequency 19.9 Hz (M = 0.44) lies between original profile fequencies measured for M = 0. It means that the origin of the aeroelastic instability was in the classic coupled mode flutter with two-degrees of freedom.

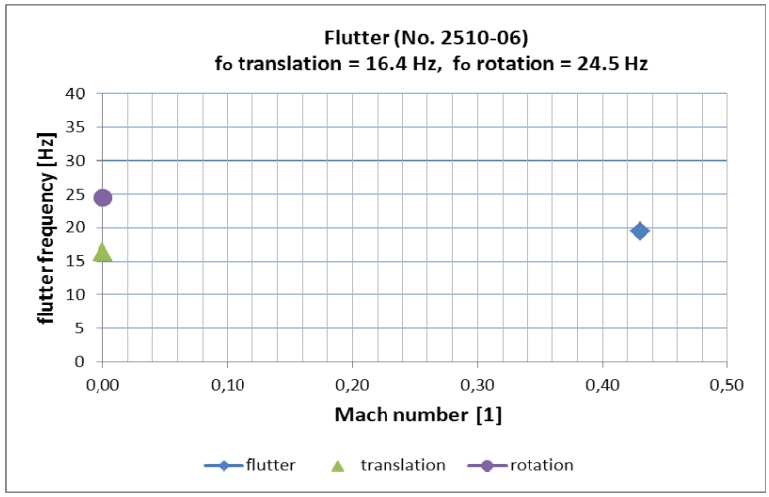

Fig. 4: The eigenfrequency changes of the self-excited vibration as a function of the Mach number for the case of bigger difference between the profile eigenfrequencies.

The kinematics of the airfoil motion during one period of the self-excitation is presented in the next Figures 5a) – 5e) for several Mach numbers in increasing order. There is interesting that in Figure 5c), 5d) and 5e) zero angle of attack was achieved at the value 80-85% of the maximal amplitude of the rotation center motion. This was found in the case of the profile with the eigenfrequencies 19,0 Hz without flow (M = 0) for translation mode, and 21,5 Hz for rotation mode. On the all figures, the red points inside denote the trajectory of motion of the profile rotation center.

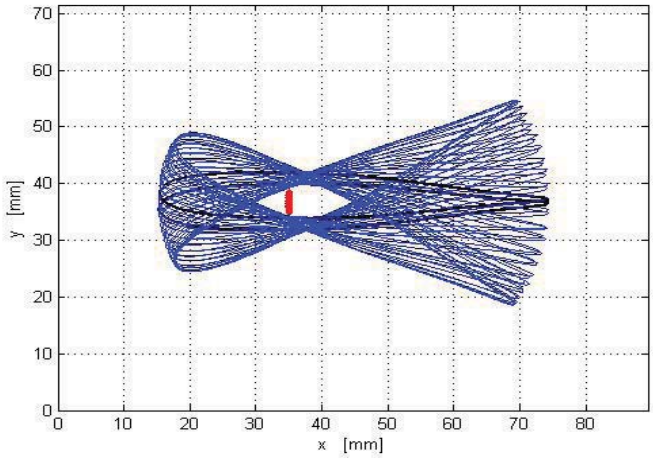

Fig. 5a): Profile motion during one period of its self-excited vibration by flutter for M = 0.21 (2663-02).

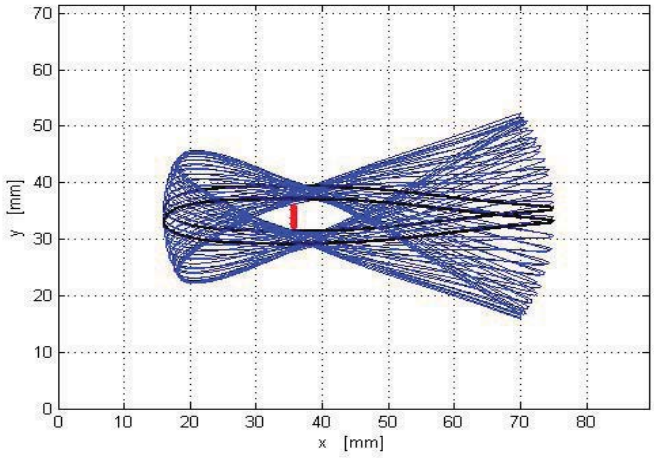

Fig. 5b): M = 0.22 (2662-17).

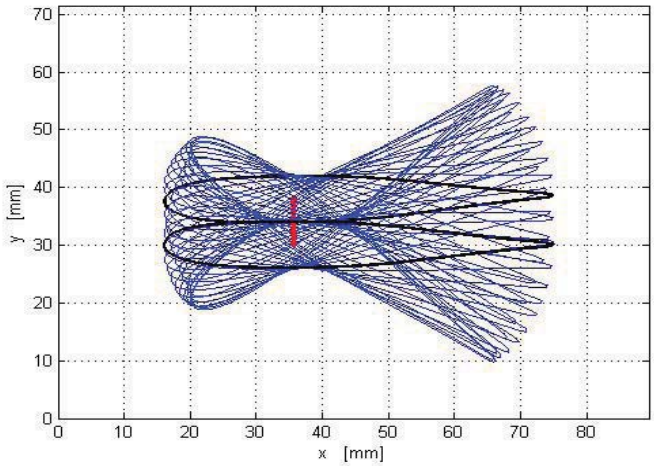

Fig. 5c): M = 0.28 (2662-16).

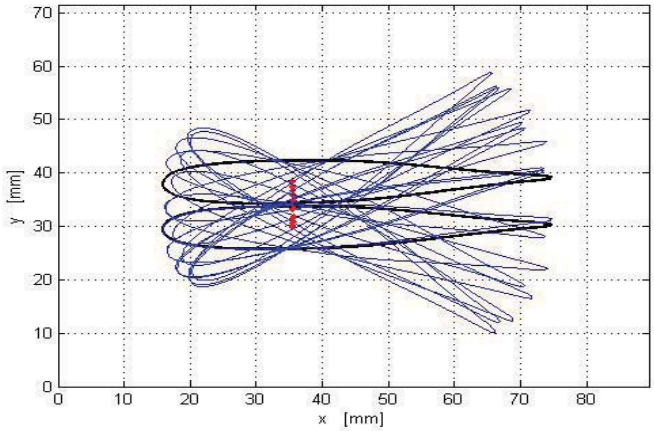

Fig. 5d): M = 0.33 (2662-14).

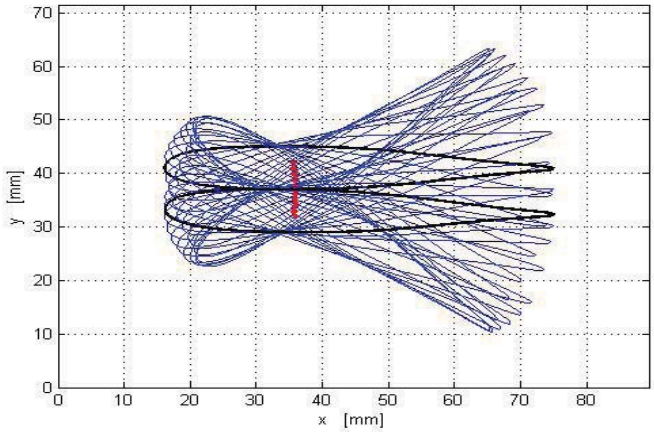

Fig. 5e): M = 0.45 (2663-05).

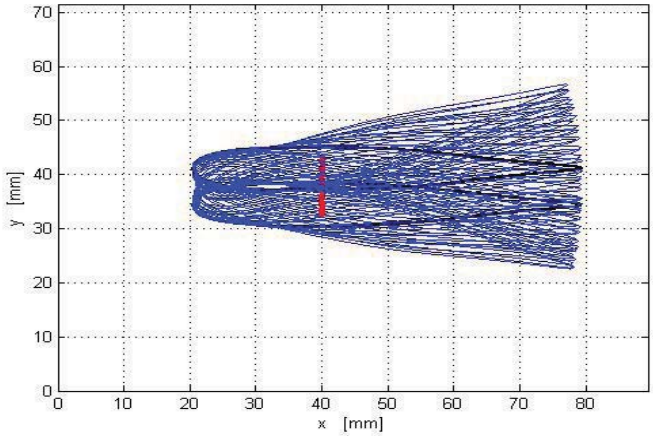

Fig. 6: The profile NACA0015, M = 0.43.

Figure 6 shows the kinematics of the airfoil motion of the profile for the case bigger difference between profile eigenfrequencies: translation mode – 16.4 Hz (damping 2.0 %), rotation mode 24.5 Hz (damping 1.5 %).

Figures 7a) – 7c) explain the stall flutter arise during the flow velocity increase. On the presented results it is possible to see the jumping between the flutter frequencies with increasing the flow velocity in the interval of Mach numbers 0.25 – 0.35. Outside of this velocity interval the system has properties as follows: unstable by coupled mode flutter is for M < 0.25 and by stall flutter for M > 0.35.

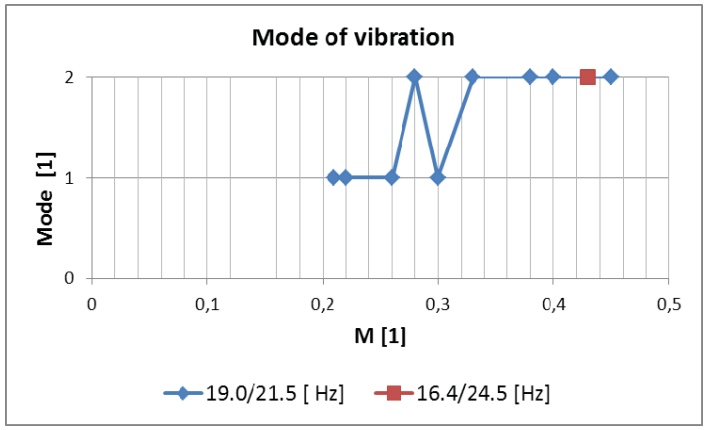

Fig. 7a): Mode of vibration.

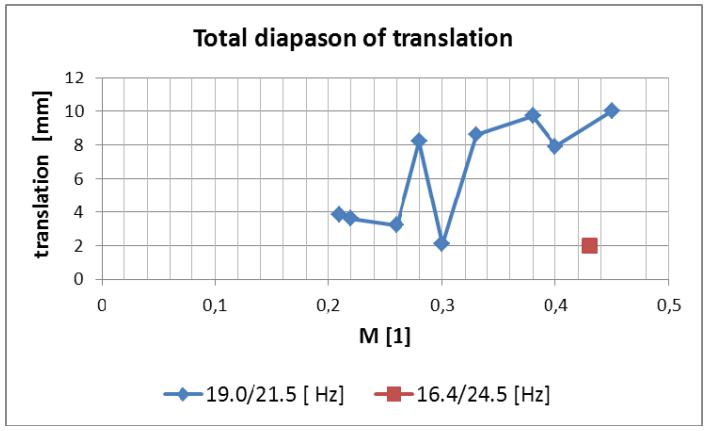

Fig. 7b): Total diapason of translation.

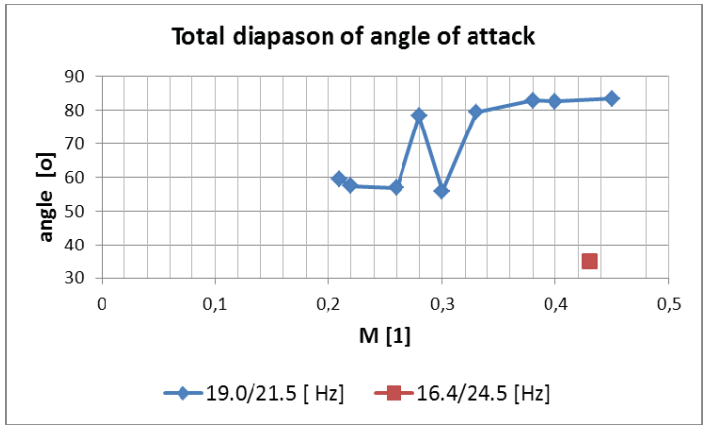

Fig. 7c): Total diapason of angle of attack.

The relations between axis rotation center shift of the profile and approach angle are presented on the Fig. 8a) – i) for Mach number from interval 0.21 – 0.45.

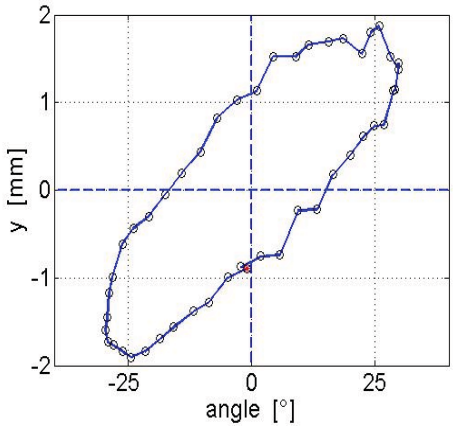

Fig. 8a): M=0.21 for measure No. 2663-02.

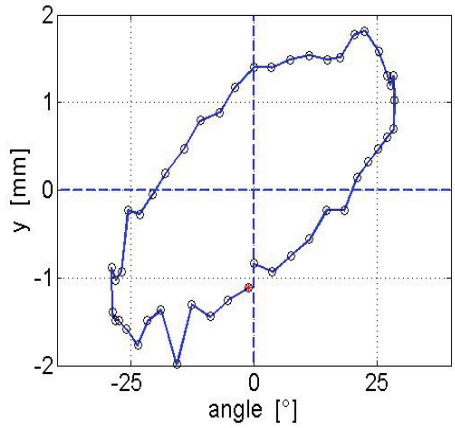

Fig. 8b): M=0.22 for measure No. 2662-17.

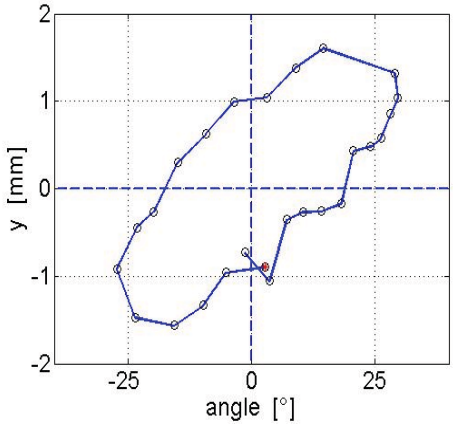

Fig. 8c): M=0.26 for measure No. 2663-01.

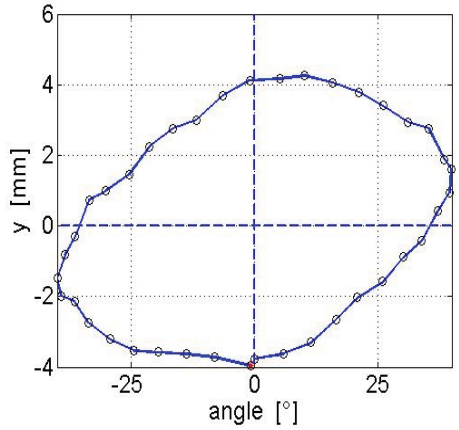

Fig. 8d): M=0.28 for measure No. 2662-16.

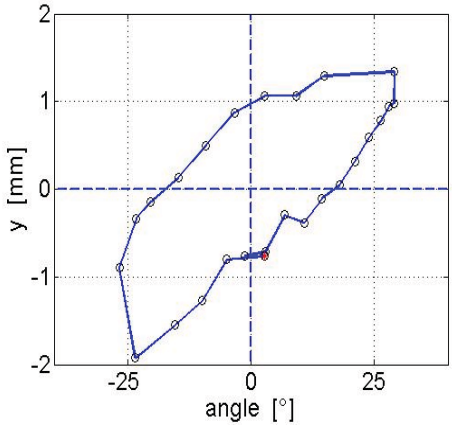

Fig. 8e): M=0.30 for measure No. 2662-15.

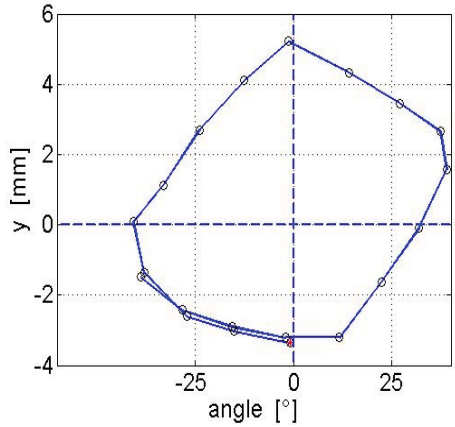

Fig. 8f): M=0.33 for measure No. 2662-14.

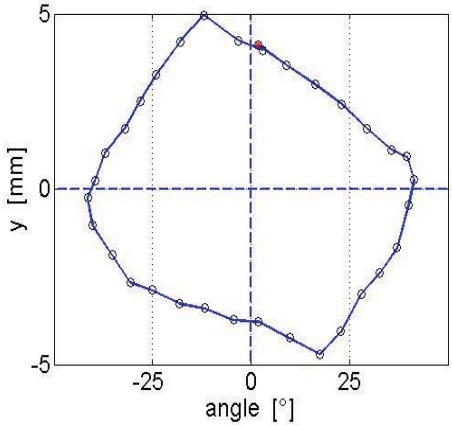

Fig. 8g): M=0.38 for measure No. 2663-03.

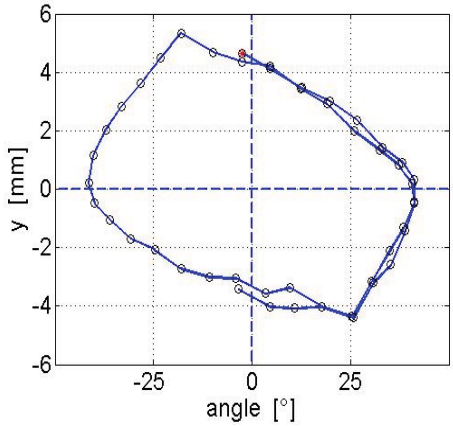

Fig. 8h): M=0.40 for measure No. 2663-04.

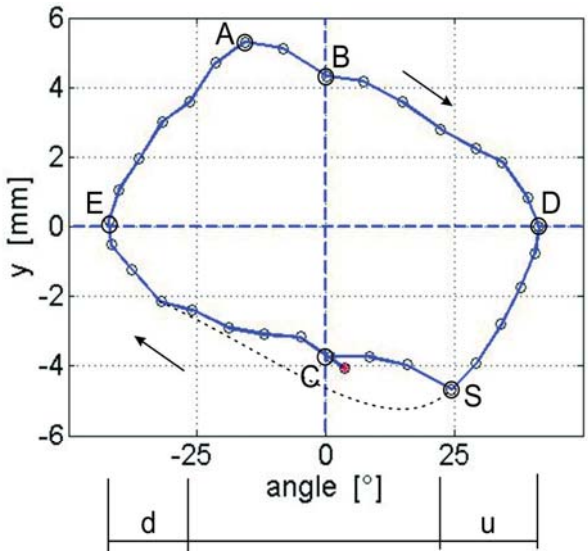

Fig. 8i): Relation between axis rotation center shift of the profile (vertical, [mm]) and approach angle (horizontal, [°]) for measure No. 2663-05, M=0.45, translation frequency for M = 0 is 19.0 Hz and rotation frequency is 21.5 Hz.

The motion of the profile during the stall flutter is shown in more detail on Fig. 8i) for the highest Mach number M = 0.45. The point B in the diagram denotes zero angle of attack, the point A denotes the maximal translation and precedes the point B in time. In the point S the profile impacts to some artificial mechanical barrier; a point-line represents the profile trajectory that could be realised in the system without impacts. The points A and C correspond to the maximal translation deplacement in positive and negative direction, respectively. The intervals denoted by letters **u** and **d** correspond to the regimes when the whole break of the flow appears on the upper (**u**) and lower (**d**) profile surface, respectively. The maximal positive (point D) and negative (point E) angles of attack correspond to zero profile translation.

An example of the phase shift between the translation and rotation of the profile demonstrated in Figure 9.

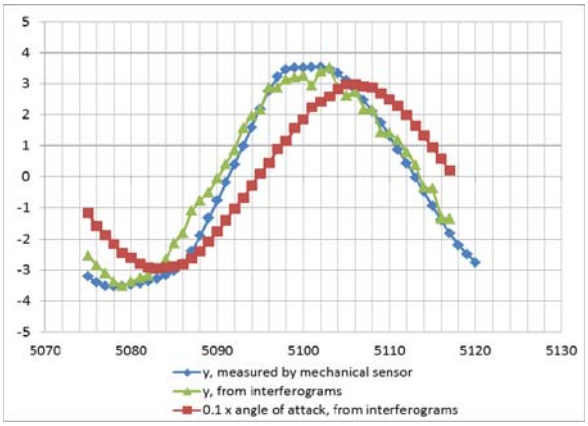

Fig. 9: The angle of attack (in [°]) and vertical translation (in 10 time scale, [mm]) on the vertical axis versus the time (horizontal, [ms]) during one period of the self-excited vibrations, for measurement No. 2663-02, M=0.21.

3. Conclusion

Several combinations of experimental parameters were realized during aeroelastic measurements of the self-excited profile vibrations in the Mach number range M=0.21 – 0.45. The influence of Mach number on the coupled mode flutter and stall flutter in relation to the difference between the eigenfrequencies corresponding to the translation and rotation motion of the profile was determined.

Acknowledgement

The authors gratefully acknowledge the Grant Agency of the Czech Republic for supporting this work under Grant No. 101/09/1522 and our colleagues Prof. P. Šafařík, Dr. M. Luxa, Mr. V. Bula, Dr. F. Vaněk, Mr. J. Cibulka, Mr. J. Česal for their kind collaboration.

References

Dowell, Earl H. (Editor) (1995): A Modern Course in Aeroelasticity. Kluwer Academic Publishers, Dordrecht/Boston / London, 3rd edition.

Vlček, V., Horáček, J., Luxa, M., Veselý, J., Bulla, V. (2009) Visualization of unsteady flow around a vibrating profile: experimental set-up and preliminary tests. *Interaction and Feedbacks Proceedings, 2009,* ed. Zolotarev I., Praha, IT AS CR, v.v.i., pp. 75-83, ISBN 978-80-87012-23-9.

Vlček, V., Kozánek, J. (2010) Preliminary interferometry measurements of flow field around a fluttering NACA0015 profile. *Engineering Mechanics 2010*, ed. Zolotarev I., Svratka, May 10 – 13, 2010, pp. 167-168 (full paper on the CD, ISBN 978-80-87012-26-0).

Šafařík, P., Vlček, V. (1985): Using interferometric measurements in calculation of aerodynamic forces, pp. 301-305. In : *Optical Methods in Dynamics of Fluid and Solids* (editor Píchal M.), Springer Verlag, Berlin.

18th International Conference
ENGINEERING MECHANICS 2012
Svratka, Czech Republic, May 14 – 17, 2012

pp. 1535–1542
Paper #203

WIRE GLASS IN BUILDING CONSTRUCTION

M. Vokáč[*], M. Špaček[**], M. Sýkora[***], P. Bouška[****]

Abstract: *Wire glass is frequently used in present-day building projects, not only as a filling material, but also for load-bearing members. Thus, there are the special requirements for glass, and it is necessary to assess the reliability of glass structures. In the framework of European standardization, there is not yet sufficient documentation for implementing standards for glass structures. However, a standardisation committee for structural glass has recently been established, and work is being done in this field. The present paper discusses use of the wire patterned glass and assessment of its design characteristics.*

Keywords: ***Wire glass, failure, strength.***

1. Introduction

Wire patterned glass is applied in a number of existing and new building structures. The wire mesh should prevent brittle failure and subsequent collapse of structural members. The design of a load-bearing member made of wire patterned glass should take into account actual properties of the material. Unrealistic design strengths have recently been published in the Czech Republic for wire patterned glass structures. This paper discusses the use of wire patterned glass, and proposes partial factors for glass strength based on previous experience and a limited amount of experimental data.

2. Wire glass

In this paper, wire glass refers to a normal glass which has a steel mesh inserted during the manufacturing process. This type of glass was often used in the past, when present-day requirements for the so-called safe glass were unattainable. Manufacturers formerly used the only available technology, which involved rolling the wire in the glass. When a glass panel is broken the mesh holds parts of the material together. However, this type of product cannot be considered as a safety glass, because the fragments are very sharp and dangerous.

Wire glass may fracture due to local non-homogeneities such as notches created when the glass is cut, and air cavities in the material formed when the wire mesh is embedded into the molten glass before rolling, initial corrosion of wires at edges of panels, etc. The strength of glass is also affected by climate effects. The effects of ageing reduce the critical stress intensity factor, and thus it is difficult to cut old glass even by diamonds.

Glass deforms proportionally to the load, and it breaks suddenly. It is a brittle material, and the failure occurs suddenly when the limit stress in tension is reached. The strength is usually determined as the flexural strength of glass, and is significantly variable. The coefficient of variation ranges from 15 to 30 %. The strength of glass depends significantly on its surface, defects, impurities and ambient moisture, Mencik (1990) and Volf (1984).

* Ing. Miroslav Vokáč, Ph.D.: CTU in Prague, Klokner Institute, Šolínova 7; 166 08 Prague 6, CZ; e-mail: miroslav.vokac@klok.cvut.cz

** Ing. Miroslav Špaček: Habena s.r.o., Korunní 1440/60; 120 00 Prague 2; CZ; e-mail: m.spacek@habena.cz

*** Ing. Miroslav Sýkora, Ph.D.: CTU in Prague, Klokner Institute, Šolínova 7; 166 08 Prague 6, CZ; e-mail: miroslav.sykora@klok.cvut.cz

**** Doc. Ing. Petr Bouška, CSc.: CTU in Prague, Klokner Institute, Šolínova 7; 166 08 Prague 6, CZ; e-mail: petr.bouska@klok.cvut.cz

The following standards are valid for the production of the wire glass:

- CSN EN 572-1 (2004) – determines the basic physical and mechanical properties of soda lime silicate glass (characteristic value of strength of glass without the embedded wire declared as 45 MPa),

- CSN EN 572-3 (2004) – specifies requirements for quality polished glass in terms of size and optical defects,

- CSN EN 572-6 (2004) – specifies the requirements for dimensions, including tolerances and permissible defects in wire patterned glass.

Traditional wire glass has been frequently used in building construction not only as a filling material, but often as a structural member that should meet safety requirements. In this case, it is necessary to supplement architectural design by reliability verification. The design of glass structures has often been based on long experience. With modern trends in architecture, the demands related to glass structures have been rising, but a design standard for structural glass is still missing.

Designers have access to some values of strengths given in available sources, but these values are not sufficiently specified, or may be completely unrealistic. Some sources provide values for the flexural strength of wire glass that corresponds to the strength of glass produced using modern technologies (up to 52 MPa). However, these values could have been hardly achieved using a traditional production technology.

A designer with insufficient experience and without detailed knowledge may then take these unverified material properties and design an unsafe structure (Fig. 1). Recently there has been an increasing number of problems associated with cracking or collapses of traditional wire glass. Accidents are very dangerous and not only pose a threat to life and health, but also lead to major financial losses. In most cases, structural members made from the wire glass are not properly statically assessed. Construction companies often employ craftsmen who have insufficient experience with the wire glass and poor assembly increases the frequency of failures.

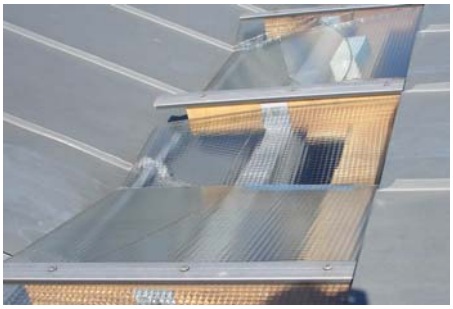

Fig. 1: Failure of wire glass caused by snow

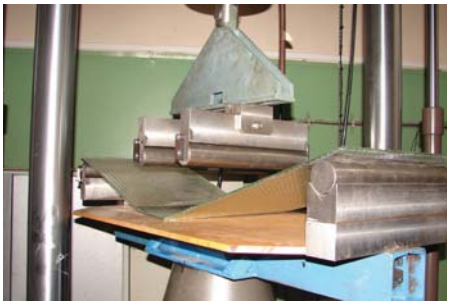

Fig. 2: Four point bending test on wire glass

3. Experimental determination of strength characteristics

The use of tests is an important aspect of ensuring the reliability of building structures, particularly when there are significant uncertainties about the material properties, as in the case of wire glass. No special standard is available for determining the tensile strength of this material.

Therefore, the standards for determining the flexural strength of monolithic glass for use in the construction industry have been applied for experimental determination of the flexural strength of wire glass. These standards can be used for establishing the equivalent strength, i.e. the apparent flexural strength of a glass in which irregularities in thickness do not permit a precise calculation of the normal stress.

The tensile strength of glass is influenced by the state of the surface, the rate of loading, the surrounding environment, the age of the glass, and temperature. According to CSN EN 1288-3 (2001), the dimensions of the glass specimen are 1100x360 mm, and the test is conducted as a four-pointed bending test for a span of 1000 mm. Three samples of wire glass specimens were tested in the CPU controlled hydraulic test machine. Before the test, specimens were weighed and their dimensions

measured. Flexural tests must be carried out at a test facility that enables the specimen to be loaded with proportional loading with a limit error of ±2 % of the measurement range. The test (Fig. 2) has to be carried out in laboratory conditions.

4. Evaluation of the tests

Tests are usually evaluated using statistical methods. For conventional structural materials such as concrete and steel, the characteristic value of the material property is determined on the basis of tests, and the design value is determined using the partial safety factor. In the case of wire glass, however, there is no long-term experience and there are no recommended values for the partial factor. In this paper, the characteristic and design values of the wire glass strength are thus derived.

Three samples of the glass were tested in the laboratory of the Klokner Institute at the Czech Technical University in Prague.

A total of 31 tests were performed:

- 9 specimens provided by a manufacturer (*sample 1*),
- 10 specimens taken from a roof structure exposed to climatic effects (*sample 2*),
- 12 specimens stored in reserve for this roof structure (*sample 3*).

5. Strength of the wire glass

Sample 1 consists of specimens delivered directly from a manufacturer, so they do not include the effects of variability in strength among different batches nor climatic exposure. Specimens of nominal thickness of 6 mm fulfil the requirements according to the standard CSN EN 572-6 (2004). For *samples 2 and 3*, sufficiently large specimens were not available for the tests to be in full accordance with CSN EN 1288-1 (2001) and CSN EN 1288-3 (2001). The tests were performed on specimens with dimensions 150 x 800 mm supported in a span of 600 mm. The results of the tests may therefore be slightly affected by the smaller size of the specimens. However, this influence is assumed to be negligible.

The actual thickness shall be within a range of ±10 % (table 1 in CSN EN 572-3 (2004)) in the case of nominal thickness of 6 mm (*sample 1*) and 7 mm (*sample 2 and 3*). It is recommended to take the lower limit of tolerance into account when designing a structure.

Tab. 1 shows the statistical characteristics of *samples 1 to 3*. Apparently the mean value varies in a wide range from 31 to 40 MPa, and the coefficient of variation is in the interval 0.14 to 0.22. Fig. 3 presents a histogram and the probability density function of a lognormal distribution with the sample characteristics according to Tab. 1. Using standard statistical tests described e.g. by Vorlicek et al. (1982), no outliers were identified for all the *samples*.

Tab. 1: Statistical characteristics of samples 1 to 3

Sample characteristics	**Unit**	**Sample 1**	**Sample 2**	**Sample 3**
Number of samples n	-	9	10	12
Mean $m = \frac{1}{n}\sum_n f_i$	MPa	40.0	31.1	34.5
Coefficient of variation $V = s/m = \sqrt{\frac{1}{n\text{-}1}\sum_n (f_i - m)^2}\,/\,m$	-	0.22	0.22	0.14
Skewness $w = \frac{n}{(n-1)(n-2)s^3}\sum_n (f_i - m)^3$	-	0.77	0.95	0.75

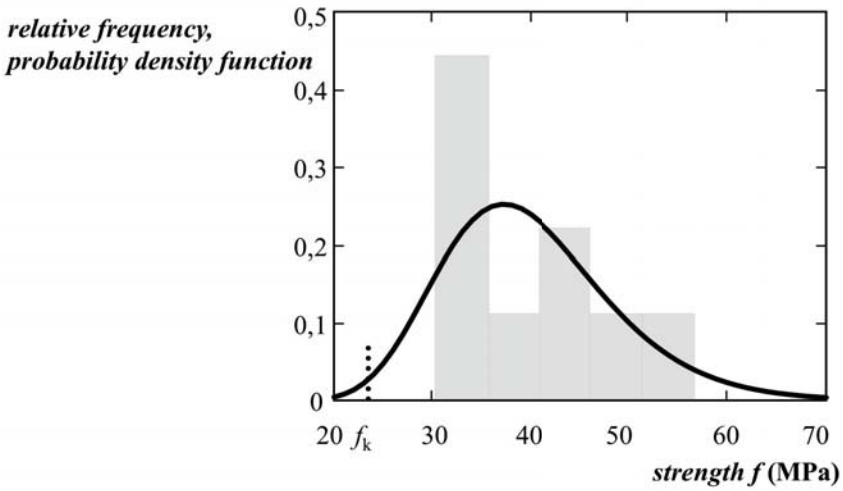

Fig. 3: Histogram and the probability density function of a lognormal distribution according to Tab. 1 for sample 1

6. Assessment of the characteristic value

Assessment of characteristic and design values of the strength of the wire glass is based on the method provided in Annex D to CSN EN 1990 (2011). This procedure assumes either normal or lognormal distribution of a construction material. In the following analysis the assumption of a lognormal distribution is accepted due to the following reasons:

- long-term experience with strengths of construction materials suggests a lognormal distribution,

- due to higher coefficients of variation of the glass strength (in comparison to steel and concrete) a normal distribution yields small or even negative values, which are unrealistic from the physical point of view,

- the skewness w of the *samples 1 to 3* (Tab. 4) is positive and relatively high, better corresponding to the skewness of a lognormal distribution ($w = 3V+V^3$) rather than to that of a symmetric normal distribution ($w = 0$).

CSN EN 1990 (2011) distinguishes between the two fundamental cases: the coefficient of variation of the strength population is "unknown" or "known". Due to the small sizes of all the *samples* taken from single production batches, the sample coefficient of variation is considered spurious. The long-term experience from a large number of tests in industrial production indicates that the coefficient of variation of glass commonly varies in the range of 0.15 to 0.3, Mencik (1990). Taking into account also experience from previous tests carried out in the Klokner Institute, a conservative coefficient of variation $V = 0.3$ is hereafter assumed to be “known”.

For a lognormal distribution, the characteristic value can be estimated as follows:

$$f_k = \exp[m_Y(1-k_n V_Y)] \tag{1}$$

where m_Y and V_Y are characteristics of the normally distributed variable $Y = \ln f$:

$$m_Y = (\Sigma_n \ln f_i) / n; \quad V_Y = \sqrt{[\ln(1 + V^2)]} / m_Y \tag{2}$$

The coefficient k_n can be either obtained from table D.1 in CSN EN 1990 (2011) or estimated by the following expression:

$$k_n(p) = -u_p\sqrt{(1 + 1 / n)} \tag{3}$$

where u_p is the fractile of the standardized normal variable corresponding to probability p. As an example $k_n(p = 0.05) = 1{,}73$ is obtained for $n = 9$ (*sample 1*). Estimated characteristic values are shown in Tab. 5. When a producer does not specify the characteristic value, it is highly recommended to determine f_k on the basis of tests.

7. Assessment of the design value and partial factor

According to relationships (6.6a,b) in CSN EN 1990 (2011), the design resistance R_d of a structural member can be determined from a general expression:

$$R_d = R(\eta_d f_k / \gamma_M, a_d) \quad (4)$$

where R(·) denotes the resistance function (e.g. the product of section modulus and the strength of the material), η_d is the design value of the conversion factor, and a_d is the design value of a geometrical property (e.g. the nominal width and thickness of the member reduced by the tolerance limit). The partial factor of material property γ_M, which takes into account model uncertainty and variability of dimensions, is determined from expression (6.6b) in CSN EN 1990 (2011):

$$\gamma_M = \gamma_{Rd}\ \gamma_m \quad (5)$$

where γ_{Rd} is the partial factor accounting for the uncertainty of the resistance model and the variability of dimensions, and γ_m is the partial factor for the material.

According to article 4.2(4)P in CSN EN 1990 (2011), it may be necessary to convert the test results to values representing the real behaviour of the material in a structure. The conversion factor η should then be used. For the wire glass, the conversion factor may account for the following influences that may affect structural members and are not included in laboratory tests:

- ageing,
- damage of a surface due to transport and assembly,
- size effects, etc.

A comparison of the mean values of *samples 2 and 3* (wire glass exposed to climatic effects, and wire glass without the exposure) shows decrease by about 10 %. In the absence of additional information the conversion factor $\eta_d = 0{,}9$ is considered taking into account a long-term experience with structural glass design. However, this assumption should be verified by further research.

For the wire glass, the model uncertainty factor γ_{Rd} should take into account the following:

- glass fracture usually occurs in places of local non-homogeneities (i.e. notches caused by glass cutting, air cavities due to a production process, wire corrosion at edges of a member progressing inward, see Figs. 4 to 6).
- actual thickness of the glass member is often lower than the nominal value.

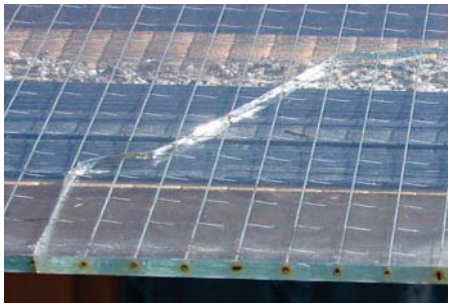

Fig. 4: Fracture due to corrosion of wires

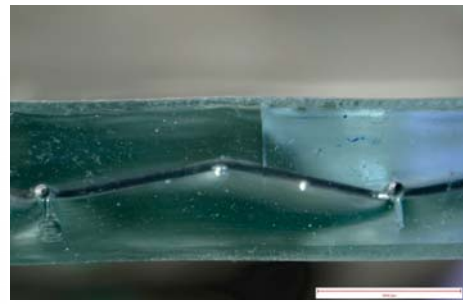

Fig.5: Notches caused by the cutting

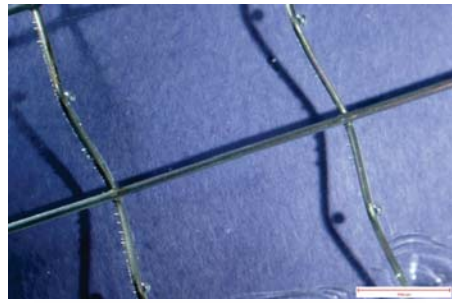

Fig. 6:Air cavities in glass

Report by fib SAG 9 (2010) indicates the model uncertainty factor for reinforced concrete members be usually γ_{Rd} ~ 1,1 to 1,15. For the wire glass, a larger model uncertainty is expected and γ_{Rd} = 1,2 is thus accepted. This assumption also needs to be further justified.

The partial factor for material property γ_m can be determined as follows:

$$\gamma_m = f_k / f_{pd} \tag{6}$$

where f_{pd} is the fractile of the strength corresponding to probability p_d (see relationship (C.6b) in CSN EN 1990 (2011)):

$$p_d = \Phi(-\alpha_R \beta) \tag{7}$$

where $\Phi(\cdot)$ denotes the cumulative distribution function of the standardised normal variable, α_R = 0,8 is the sensitivity factor of the FORM method (CSN EN 1990 (2011)), and β is the target reliability index.

CSN EN 1990 (2011) gives minimum values of the reliability index β for the Ultimate Limit States (Tab. 2). Appropriate reliability class RC should be selected for a wire glass structure considering potential consequences of failure. Brittle failure of the wire glass is immediately followed by large deformations and displacements in mounting may lead to a sudden downfall of the wire glass panels. The collapse is not preceded by any warning such as development of cracks, sound effects or delaminating of surface layers. Therefore, it is recommended to consider RC3 for the wire glass structures where people gather, β = 4,3. Further information on selection of the target reliability index is provided e.g. by Holicky and Sykora (2012).

Tab. 2: Recommended minimum values of the reliability index β according to EN 1990 (Ultimate Limit States, reference period of 50 years)

Reliability class	**Consequence of failure**	β	**Examples of building or engineering structures**
RC3	High consequence for loss of human life, or economic, social or environmental consequences very great	4,3	Grandstands, public buildings where consequences of failure are high (e.g. a concert hall)
RC2	Medium consequence for loss of human life, economic, social or environmental consequences considerable	3,8	Residential and office buildings, public buildings where consequences of failure are medium (e.g. an office building)
RC1	Low consequence for loss of human life, and economic, social or environmental consequences small or negligible	3,3	Agricultural buildings where people do not normally enter (e.g. storage buildings), greenhouses

Tab. 3: Characteristic and design values and partial factors of the wire glass strength (samples 1 to 3)

	Unit	**Sample 1**	**Sample 2**	**Sample 3**
Characteristic value f_k	MPa	23,5	18,4	20,7
Partial factor γ_m				
RC1	-	1,36	1,36	1,36
RC2		1,54	1,54	1,53
RC3		1,74	1,74	1,73
Partial factor $\gamma_M = \gamma_{Rd}\ \gamma_m$				
RC1	-	1,63	1,63	1,63
RC2		1,85	1,84	1,84
RC3		2,09	2,09	2,08
Design value $f_d = \eta_d f_k / \gamma_M$				
RC1	MPa	13,0	11,3*	11,5
RC2		11,5	10,0*	10,1
RC3		10,1	8,8*	9,0

* η_d = 1,0 (panels tested after exposure to climatic effects)

Taking into account the target reliabilities according to Tab. 2, the probability p_d can be determined from Eq. (7):

$$p_d(\text{RC1}) = 0{,}0041;\ p_d(\text{RC2}) = 0{,}0012;\ p_d(\text{RC3}) = 0{,}00029 \quad (8)$$

These values can be substituted into Eq. (3), and for instance the coefficient $k_n(p = 0{,}00029) = 3{,}63$ is obtained for $n = 9$ (*sample 1*) and RC3. Then, the design value f_{pd} is determined from Eq. (1) and the partial factor γ_m from Eq. (6), see Tab. 3.

Partial factors γ_m obtained for *samples 1 to 3* and various reliability classes are given in Tab. 3. It appears that the partial factors γ_m for *samples 1 to 3* differ insignificantly which is attributed to the choice of the "known" coefficient of variation $V = 0{,}3$. As a first approximation partial factors γ_m can be estimated by the following values:

- $\gamma_m \approx 1{,}4$ for RC1,
- $\gamma_m \approx 1{,}6$ for RC2,
- $\gamma_m \approx 1{,}8$ for RC3.

Partial factors γ_M are determined using Eq. (5) and the design strength f_d is then obtained as follows:

$$f_d = \eta_d f_k / \gamma_M \quad (9)$$

For instance the design strength f_d varies from 9 up to 10 MPa for different samples and RC3.

8. Recommendations for practical applications

On the basis of long-term experience with the design of structural glass and evaluations of a limited number of tests, careful consideration of the following aspects is recommended in practical design of the wire glass:

1. tolerance of panel thickness (use of the lower limit of the tolerance interval is advised in common cases),
2. assessment of the characteristic value on the basis of tests unless specified by a producer,
3. account for influences likely affecting structural glass and hardly covered by laboratory tests (for example ageing, surface damage due to transport and assembly and size effect), using the conversion factor η,
4. application of the model uncertainty factor γ_{Rd} that if relevant, shall describe inaccuracy of the resistance models due to insufficient regard of the following factors:
   - fracture of the glass due to local non-homogeneities (notches, air cavities, wire corrosion).
   - thickness of the glass lower than the nominal value reduced by a tolerance limit, etc.
5. assessment of potential consequences of failure, and selection of an appropriate reliability class; when samples of the glass comply with the assumptions made in this paper (in particular $V < 0{,}3$), the following partial factors might be used:
   - $\gamma_m \approx 1{,}4$ for RC1,
   - $\gamma_m \approx 1{,}6$ for RC2,
   - $\gamma_m \approx 1{,}8$ for RC3,
6. when RC1 or RC3 is selected, the relevant partial factors γ_m given above should be applied in conjunction with the partial factors for permanent and variable actions γ_G and γ_Q adjusted for the relevant target reliability level. The adjustment should be, however, made in collaboration with qualified experts.
   Alternatively, it is possible to differentiate reliability in accordance with Annex B of CSN EN 1990 (2011) (clause B.3.3(1)) and modify partial factors γ_F only. In this case γ_m for RC2 is accepted and partial factors of unfavourable actions are multiplied by the factor K_{FI} (for instance $1{,}1\gamma_G$ and $1{,}1\gamma_Q$ are applied for unfavourable actions and RC3).

9. Materials alternative to the wire glass

Use of the wire glass in new building structures should be prevented since:

- strength of the wire glass is significantly lower than that of a safety glass,
- unlike safety glass the wire glass breaks into sharp fragments that may cause additional injuries.

Various types of the safety glass that may be used instead of the wire glass include a multi-layered laminated glass made from various films (for example polyvinylbutyral) or a single-layered glass.

10. Conclusions

Due to a production process a characteristic strength of the wire glass is significantly lower than the characteristic strength of the soda-lime-silicate glass declared in CSN EN 572-1 (2004) as 45 MPa. The design of structural wire glass should take into account local non-homogeneities and degradation effects. For structural members exposed to climatic effects use of modern safety glass is preferable.

Acknowledgement

This study has been conducted at the Klokner Institute, CTU in Prague, with the financial support of the research projects MPO FR-TI3/776 and GACR P105/12/0589.

References

CSN EN 1288-3 (2001) *Determination of the bending strength of glass - Part 3: Test with the specimen supported at two points (four point bending)*, Prague, ČNI.

CSN EN 572-1 (2004) *Basic soda lime silicate glass products – Part 1: Definitions and general physical and mechanical properties,* Prague, ČNI.

CSN EN 572-3 (2004) *Basic soda lime silicate glass products – Part 3. Polished wire glass*, Prague, ČNI.

CSN EN 572-6 (2004) *Basic soda lime silicate glass products – Part 6: Wired patterned glass*, Prague, ČNI.

fib SAG 9 (2010). *Revision of partial safety factors* (report).

Holický, M., Marková, J. (2005) *Základy teorie spolehlivost a hodnocení rizik* (Fundamentals of the reliability theory and risk assessment – in Czech). CTU in Prague.

Holický, M., Sýkora, M. (2012) *Stanovení směrných úrovní spolehlivosti pro stavební konstrukce* (Assessment of the target reliabilities for civil engineering structures – in Czech); In: Stavební obzor, ročník 2012, číslo 2, pp. 36-39, ISSN 1210-4027.

Menčík J.(1990) *Pevnost a lom skla a keramiky* (Strength and fracture of glass and ceramics – in Czech), Prague, SNTL.

Volf M. B.(1984) *Sklo ve výpočtech* (Design of structural glass – in Czech), Prague, SNTL.

Vorlíček M., Holický M. & Špačková M. (1982) *Pravděpodobnost a matematická statistika pro inženýry* (Probability and mathematical statistics for engineers – in Czech). CTU in Prague.

18th International Conference
ENGINEERING MECHANICS 2012
Svratka, Czech Republic, May 14 – 17, 2012

pp. 1543–1553
Paper #181

MEASURING OF WHEEL–RAIL ADHESION CHARACTERISTICS AT A TEST STAND

P. Voltr[*], M. Lata[**], O. Černý[***]

Abstract: *The properties of the adhesion contact of wheel and rail, expressed by the adhesion characteristic (non-linear dependence of tangential force on creepage), are of great importance for rail vehicle dynamics and drive regulation systems. The paper deals with the results of measurements of adhesion characteristics on a tram wheel test stand which was equipped with a new measurement chain in 2011 and provided a great volume of data. The measured characteristics are described, special attention being paid to the transitions which show influence of changes of friction conditions during the sliding.*

Keywords: ***adhesion, adhesion characteristic, experimental measurement, wheel–rail contact, sliding***

1. Introduction

The wheel–rail contact is a key element of the mechanical system of a rail vehicle moving along the track. The wheel and the rail, being flexible bodies, are deformed by the action of the vehicle gravitational force and a contact area is formed. The ability of transmission of tangential forces through this area under normal loading is, in the field of vehicle dynamics, referred to as adhesion.

The transmission of tangential forces is, also due to the flexibility of the bodies, inseparably connected with creep: there is a difference between peripheral and translational velocities of a powered or braking wheel rolling over the rail, even if apparent sliding does not take place. A significant property of the contact is a dependence of the transmitted forces upon kinematics of the bodies in contact. The dependence is expressed by adhesion (or, creep) characteristics – see e.g. Čáp (1999), Polách (2005). This paper is focused on the characteristic that has the greatest importance in drive dynamics: the longitudinal adhesion characteristic – dependence of the longitudinal tangential force (T) between the wheel and the rail on the longitudinal creep velocity ($w = \omega r - v$) or dimensionless creepage ($s = w / v$).

Several theories with various degree of simplification are available for description of the adhesion characteristic. Even the most accurate ones cannot, however, do without parameters, the values of which cannot be calculated but have to be measured. Therefore, experiments play an important role in this field of research. They are performed on test stands of various arrangement and size or on actual vehicles. The following sections describe the course and results of experiments conducted at the tram wheel test stand of the Jan Perner Transport Faculty in Pardubice.

2. The experiments

2.1. The test stand

The test stand on which the experiments were performed (see *Fig. 1*) was built by VÚKV (Výzkumný ústav kolejových vozidel – Rail Vehicle Research Institute) and underwent an extensive reconstruction at the Jan Perner Transport Faculty. The test stand has a main frame bearing a tram vehicle wheel (⌀ 700 mm) and a rotating rail (⌀ 905 mm) rolling over each other. The wheel is powered by

[*] Ing. Petr Voltr: Dopravní fakulta Jana Pernera, Univerzita Pardubice, Studentská 95, 532 10 Pardubice; CZ, e-mail: petr.voltr@student.upce.cz

[**] doc. Ing. Michael Lata, PhD.: dtto, e-mail: michael.lata@upce.cz

[***] Ing. Ondřej Černý, PhD.: dtto, e-mail: ondrej.cerny@upce.cz

a permanent-magnet synchronous motor (PMSM), and the rotating rail is connected with an asynchronous motor. The wheel is mounted in a swinging arm and may be pressed to the rail by air pressure in a bellow. The rotating rail is mounted on a swivel base plate which enables adjusting the wheel–rail attack angle.

The test stand serves not only for adhesion experiments but also for development of PMSM regulation systems. The regulation of both motors is provided by frequency converters and a control computer. Originally, the measured signals were obtained directly from the memory of the control system. In 2011, however, a separate measurement chain was introduced, which enabled recording of data with higher sample frequency and, in particular, without limitation of the length of the recorded signal. The measurement chain contains incremental rotation sensors (IRC) at both wheels and a strain gauge torque transducer for measuring the torque at the rotating rail shaft.

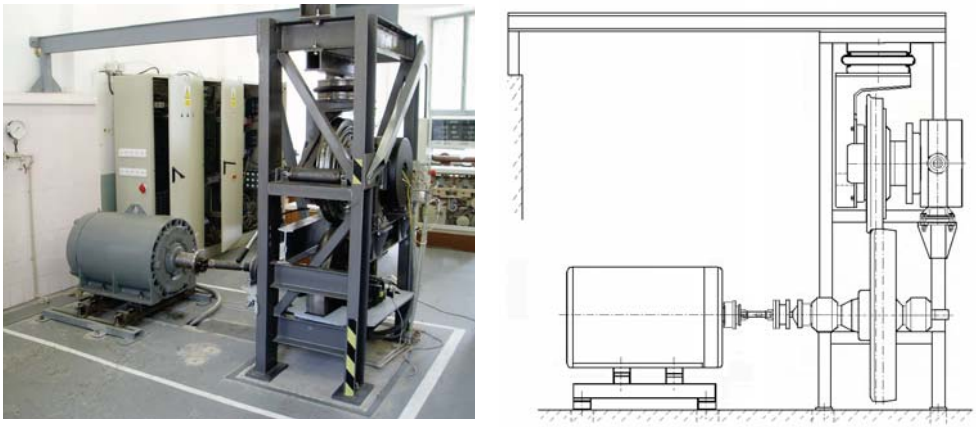

Fig. 1: The tram wheel test stand at which the experiments were performed

2.2. The course of the experiments

The aim of the experiments is to measure the dependence of the longitudinal tangential force acting between the wheels on the creepage or creep velocity not only during the effective slip (micro-slip), but also in the mode of full sliding. During the experiment, the torque of the tractive synchronous motor connected with the wheel is adjusted; it starts at zero and progressively increases until the adhesion capabilities of the contact are exhausted and the wheel starts sliding. After a short time, the torque is reduced until gross sliding terminates and the state of adhesion is restored. A direct transition into the mode of dynamic brake may also be made and sliding in opposite direction may be induced. The torque of the asynchronous motor which brakes the rail is automatically regulated so that the rail rotates with constant speed.

Magnitude of the force that may be transmitted depends significantly on the conditions of the surfaces in contact. In order to deteriorate the adhesion conditions in experiments (decrease the friction coefficient), lubricating oil was applied to the running surfaces. As the test stand is not equipped for continuous supply of oil, the surfaces are gradually cleaned by repeated sliding and the adhesion conditions get somewhat better during the experiments. Really good adhesion conditions are not, however, attained unless the surfaces are degreased by a solvent.

Experiments with non-zero attack angle were performed, too. In this situation, the wheel axis is not parallel to the rotating rail axis, which simulates the passage of a vehicle through a curve. Increased wear of the running surfaces occurs, since lateral slip is always present.

Each measurement record contains about ten measured adhesion characteristics for a constant rotational speed of the rail (corresponding to running speed of a vehicle of 10.3, 20.6 or 41.2 km/h). After each recording, the test stand was brought to a standstill and usually some of the conditions were changed; and a new output file was initialized on the PC's hard disk. In 2011, over 200 adhesion characteristics were measured during three days.

2.3. Data processing

The signals from the IRC sensors and the torque sensor are acquired by a personal computer equipped with an interface card. The data are recorded and saved as a text file by a program developed in the LabView environment. The files contain signals of time and values obtained from the three sensors with a sample rate of 200 Hz.

The values from the counters at both wheels are converted to angular position in radians and differentiated in order to obtain angular and peripheral velocities of the wheels. The difference of the peripheral velocities is the creep velocity w which, divided by the (almost constant) peripheral velocity v of the rotating rail yields the dimensionless creepage s.

The recorded voltage signal from the torque transducer is converted to the torque M_2 in Nm on the basis of a calibration measurement preceding the experiments. Further, the tangential force T and adhesion coefficient μ, defined as the ratio of the tangential and normal forces, is calculated. The signal is affected by both periodic and random parasitic components. The periodic component is brought about by mechanical imperfections of the test stand; it contains a fundamental frequency equal to the frequency of rotation of the rail and three or four harmonics. This parasitic effect is eliminated by a suitable filter – moving average with a window length precisely adjusted to the period of the rail rotation.

By plotting of the measured adhesion coefficient against the creepage, the adhesion characteristic is obtained (see *Fig. 4, 6, 7*). The measured characteristics have, as expected, a steep ascending effective branch, a peak at several percent creepage, and a slowly descending ineffective branch. In some cases, however, different shapes are observed, which is described and commented upon in the Section 4.

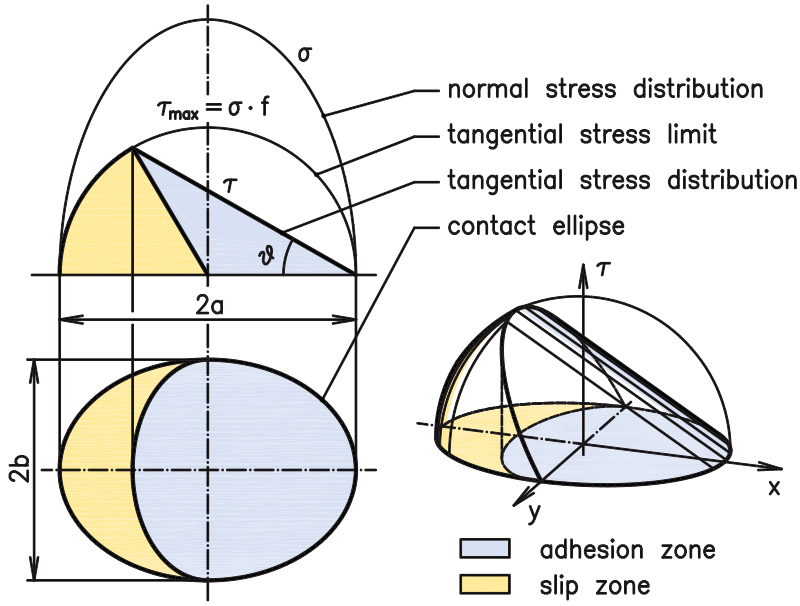

Fig. 2 Tangential stress distribution in the contact area in steady rolling with creep and the division of the area into zones of adhesion and slip according to Freibauer

3. Evaluation of the measured characteristics

3.1. The method used

Quantitative description of the measured characteristics may be made e.g. on the basis of the coordinates of the adhesion characteristic peak, or the tangent to the curve in the origin. In earlier

times, researchers approximated the characteristics by polynomials, see Čejka (1970) or by piecewise linear functions. A more complex and useful description may be obtained if the Freibauer adhesion theory is employed – Freibauer (1983). The theory yields a function expressing the dependence of adhesion coefficient on creepage; the function is obtained as an analytical integration of the distribution of tangential stress in the contact area (see *Fig. 2*) in steady state rolling under certain simplifying assumptions on elastic properties of the material.

The measured adhesion characteristic is approximated by the function prescribed by the Freibauer theory; the quantitative description is then constituted by the set of parameters appearing in the function. Adjustment of the parameter values and assessment of accuracy of the approximation is performed by a human factor – no mathematical method is used, since the attempts to do so led to fair results in a limited number of cases only.

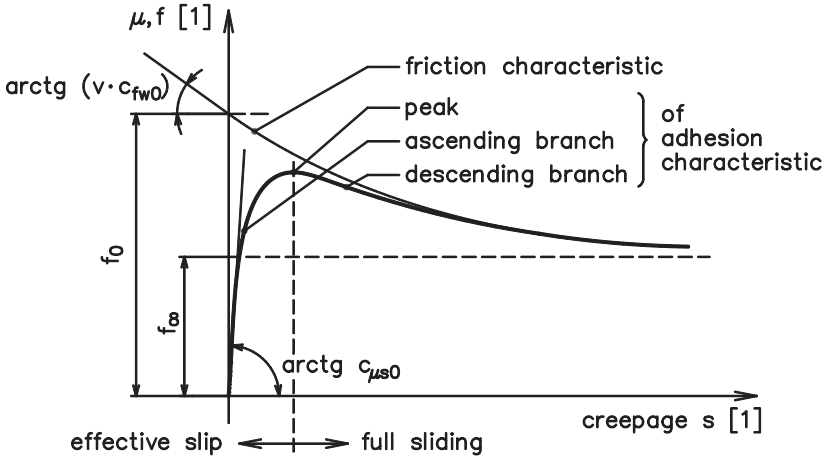

Fig. 3: A sketch of the theoretical friction and adhesion characteristics

3.2. The adhesion characteristic parameters

The Freibauer adhesion characteristic (see a sketch in *Fig. 3*) unites

- the dry friction force characteristic describing the dependence of friction coefficient f on the velocity of relative motion which is the creep velocity w,
- the saturation function describing the expansion of the slip zone in the contact area with increasing creepage s.

In our work, the extension of Freibauer theory developed by Polách (2005) is used. It includes an additional parameter which may be physically justified and which, according to the author, enables to achieve a closer agreement of theoretical and measured curves. Further explanation may be found in the cited article. In this paper, let us confine to the statement that the used formula is

$$\mu = \frac{2}{\pi} \cdot f \cdot \left(\arctan k_{\mathrm{S}} \varepsilon + \frac{k_{\mathrm{A}} \varepsilon}{1 + \left(k_{\mathrm{A}} \varepsilon \right)^2} \right) \tag{1}$$

where

$$k_{\mathrm{S}} \varepsilon = \frac{\pi}{2f} \cdot \frac{c_{\mu s0}}{1 + 1/\lambda} \cdot s \tag{2}$$

$$k_{\mathrm{A}} \varepsilon = \frac{\pi}{2f} \cdot \frac{c_{\mu s0}}{1 + \lambda} \cdot s \tag{3}$$

and the dry friction characteristic $f = \mathrm{f}(w)$ is exponential,

$$f = f_0 \cdot \left((1 - A) \cdot \mathrm{e}^{-Bw} + A \right) \tag{4}$$

$$B = -\frac{f_0 \cdot c_{fw0}}{A} \tag{5}$$

Five parameters, the values of which are to be found, appear in the above formulae. These are:

1. $c_{\mu s0} > 0$ [1] – initial steepness of the ascending branch of the adhesion characteristic,
2. $c_{fw0} > 0$ [s/m] – negative initial steepness of the friction characteristic,
3. $f_0 > 0$ [1] – static friction coefficient,
4. $A \in \langle 0, 1 \rangle$ [1] – ratio of friction coefficient at $w \to \infty$ to the static friction coefficient,
5. $\lambda \in (0, 1\rangle$ [1] – ratio of the surface stiffness reduction coefficient in the area of slip k_S to that in the area of adhesion k_A (sharpness of the adhesion characteristic peak).

These formulae and parameters describe the same function as in Polách (2005), the difference consisting only in different expression of some parameters. The inclusion of the parameter λ in our work corresponds to the distinction of two reduction coefficients k_A and k_S in Polách's extension. The difference between these two formulations is as follows:

- Utilization of the parameters k_A and k_S requires the dimensions of the contact area and Kalker's creep coefficient c_{11} to be known. In return, values of two parameters presumably independent on contact geometry are obtained.
- Thanks to the expression of the same by the parameters $c_{\mu s0}$ and λ, the measured characteristic may be approximated even if the geometry of the contact area is not known. The parameter $c_{\mu s0}$ is, however, valid only for the present contact conditions.

The original Freibauer's function without this extension is equivalent to the extended function with $k_A = k_S$, thus $\lambda = k_S / k_A = 1$. The arithmetic mean $k = (k_A + k_S)/2$ equals to the reduction of Kalker's creep coefficient c_{11}. For the creep coefficients, see e.g. Kalker (1973).

An example of a measured characteristic approximated by a function with these parameters is shown in *Fig. 4*. The agreement of the measured and theoretical curves in their ascending branches and near their peaks is good and the inclusion of the parameter λ contributes to it (especially under degraded adhesion conditions). Our experiments thus confirm the suitability of Polách's extension to the Freibauer theory.

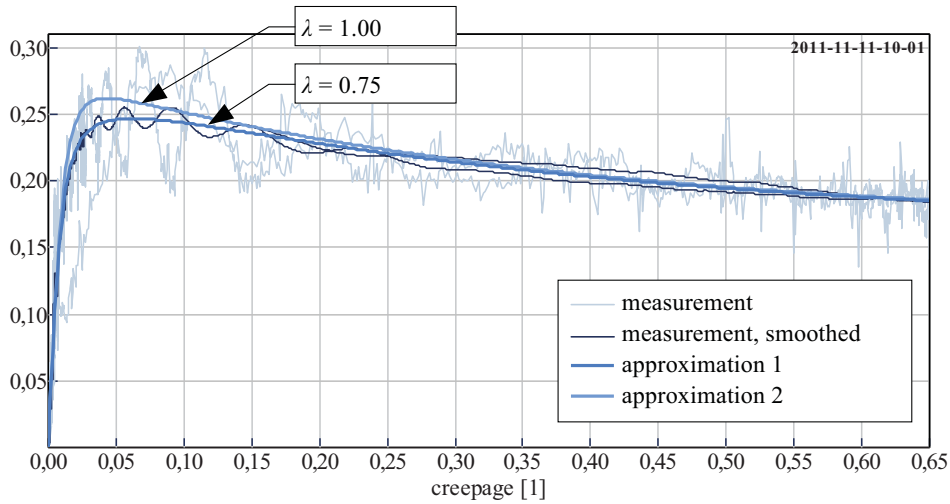

Fig. 4: Example of a measured and approximated adhesion characteristic showing the influence of the parameter λ. The function with λ = 0.75 is a better fit.

4. Changes of friction conditions during the measurement

4.1. Overview

Some measured characteristics may be well approximated by the theoretical function; a majority of them, however, has different shapes. The approximation may be used, but it is suitable only for a certain part of the characteristic. For instance, a characteristic may be approximated in the region of low slip (s < 0.3–0.5) and the agreement would be very good, but the same approximating function would not be appropriate for high-slip regions of the same measured curve. The measured characteristics include those with a peak at as far as s = 1–2 or those with multiple peaks.

In our opinion, these observations do not disprove the adhesion theory but document the variability of adhesion conditions during a single measurement. The plotting of a measured characteristic as a dependence of the adhesion coefficient on creepage should be regarded as a simplification, because it eliminates time. A correct graphical representation of measured data would have to use three coordinates: adhesion coefficient, creepage and time. In case the surface conditions change during the measurement, the plotted characteristic $\mu = f(s)$ may not be expected to agree with a theoretical function with constant parameters. And it is obvious that the change of the conditions can occur – owing to the sliding, the running surfaces may be cleaned, worn and warmed, which changes the friction conditions.

Therefore, the measured adhesion characteristics are not approximated by a function with one set of parameters but by a zone defined by ranges in which the parameters vary, the formula itself remaining unchanged. Over a measured characteristic, two theoretical ones are plotted which delimit the zone; one of them is referred to as initial and the other as final.

4.2. Degraded adhesion conditions

In the case of experiments with degraded adhesion conditions where the running surfaces were contaminated with lubricating oil, the ascending branch of the measured characteristic is as expected; its peak is not very sharp and is located usually at s = 0.05 or higher. With the inception of gross sliding, the cleaning influence of sliding emerges: the contaminants are being forced out of the contact region or entirely removed from the wheels. The friction coefficient increases and the descending branch of the adhesion characteristic thus turns into a second increase. Further course depends on the operation of the traction motor (see *Fig. 5*):

1. if the sliding is terminated shortly, the surfaces do not get cleaned much and the adhesion characteristic returns through almost the same course when creepage is reduced;
2. if the increase in creepage continues above approx. 0.5, the return course then lies significantly higher and makes a closed loop;
3. if the creepage alternately increases and decreases several times, a waved curve or several loops appear in the plot;
4. if the wheel is allowed to slide on, at the creepage of s = 1–2 the increase in the tangential force ceases and a customary decreasing exponential dependence takes place; the return course more or less follows the same exponential function but usually lies somewhat lower.

The effect described in the last point (see *Fig. 6* left) shows that there is a stage at which a certain maximum possible cleaning occurs and a near-steady state is reached. It appears that varying one parameter of the theoretical adhesion characteristic is sufficient to express the observed change in friction conditions; it is the parameter f_0 – static friction coefficient. Whereas its initial value is usually 0.7–0.11, its final value – in case the mentioned near-steady state is reached – may be higher than 0.3.

In some cases of strong contamination by lubricating oil, adhesion characteristics have been recorded where there was no decrease in adhesion coefficient after full sliding began but an almost linear increase was observed (*Fig. 6* right). This increase was accompanied by strong torsional vibration and continued up to the creepage of s = 1–2 where it eventually turned into an expected dry friction exponential. Effects of hydrodynamic lubrication could have been taking place in the phase of linear increase. These effects, being dependent on the normal loading, presumably would not occur at a real vehicle whose vertical wheel load is considerably higher than at the test stand.

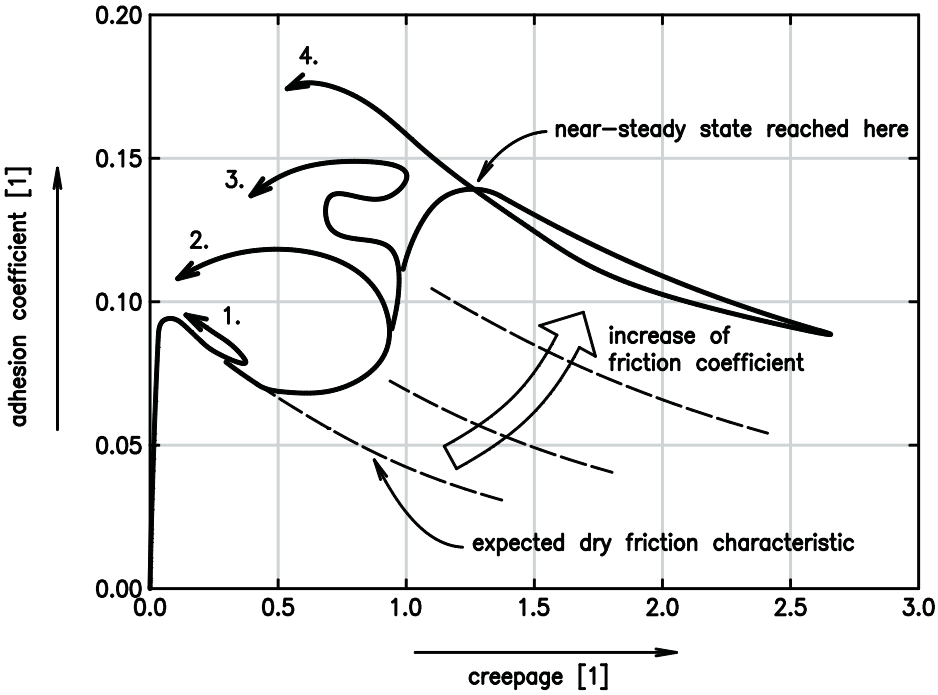

Fig. 5 A sketch of recorded adhesion characteristics showing influence of change of friction conditions during the sliding

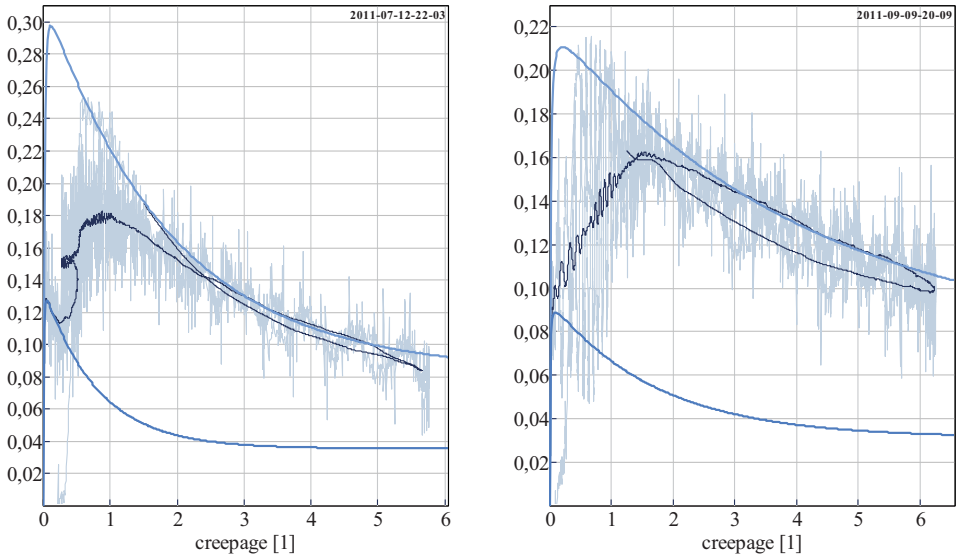

Fig. 6: Lubricated contact – adhesion characteristics: a curve with multiple peaks (left) and with a peak at s = 1.5 but no peak where it would be expected (right)

4.3. Good adhesion conditions

In general, it may be stated that the changes occurring under good adhesion conditions are less significant than the changes under bad conditions, which is comprehensible as in this case there is less contaminating material to remove from the contact. The steepness of the ascending branch is higher,

as expected. The peak is sharper, and in case that the surfaces are degreased by a solvent, static friction coefficient f_0 of 0.40–0.45 is reached.

In the experiments where the traction motor torque was increased very slowly and rolling with effective slip was taking place for a long time (up to 50 s), the measured characteristics show a continual change at the ascending branch, too. The change may be modelled as an increase of the parameters $c_{\mu s0}$ and λ, and sometimes also f_0. This is illustrated in *Fig. 7* to the left, where the measured data are overlaid by the initial and final theoretical curves which differ in the values of $c_{\mu s0}$ and λ. If we tried to express the measured curve with one theoretical function with constant parameters, the agreement would never be close around the sharp peak.

Results of the measurements where creep velocity was not restrained from rising to high values show transitions at the descending branch. As opposed to the transitions under bad adhesion conditions, varying the parameter f_0 is not sufficient for expressing this transition. In the first place, the value of c_{fw0} has to be changed: transition to a less steep friction curve takes place. The theoretical curves plotted in *Fig. 7* to the right have slightly different values of f_0 (0.343 vs. 0.350) but more important is the difference of c_{fw0} (0.056 vs. 0.041). The two functions together can express a recorded one which has a higher steepness immediately after the peak ($s < 0.5$) than what corresponds to the rest (s = 2–6). The question is suggested whether there is any relation of the described shapes to the characteristics measured by Barwell (1957) and Čejka (1970), at which the peak is followed by a decrease so significant that it is denoted as a discontinuity.

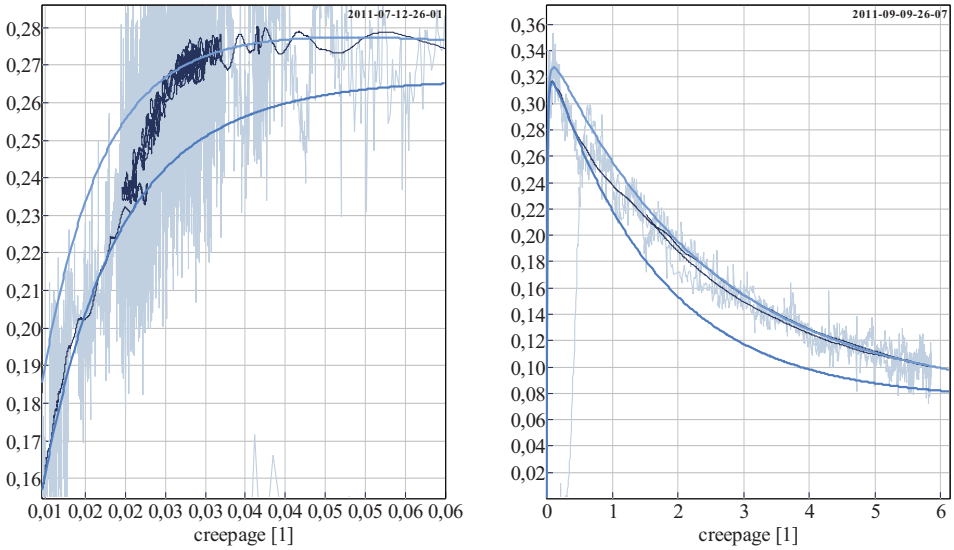

Fig. 7: Some measurement results under good adhesion conditions. Left: detail view of a peak exhibiting a transition at the ascending branch; right: a characteristic which clearly shows a transition at the descending branch.

5. Quantitative results

The static friction coefficient f_0 may serve for characterisation of the adhesion conditions. The lowest values – cca 0.07 – were naturally observed in the experiments before which the running surfaces were lubricated. During each occurrence of sliding that continued to high relative velocities, f_0 increased up to the values of 0.2–0.3. When adhesion was restored and afterwards sliding was induced anew, the friction coefficient did not start at 0.2–0.3, but at its lower values again: the phenomenon of cleaning was in effect during the sliding only.

As a consequence of repeated sliding, however, the initial friction coefficient value increased, too – up to approx. 0.28. A more substantial increase was reached by degreasing the surfaces: then, the friction coefficient would exceed 0.4.

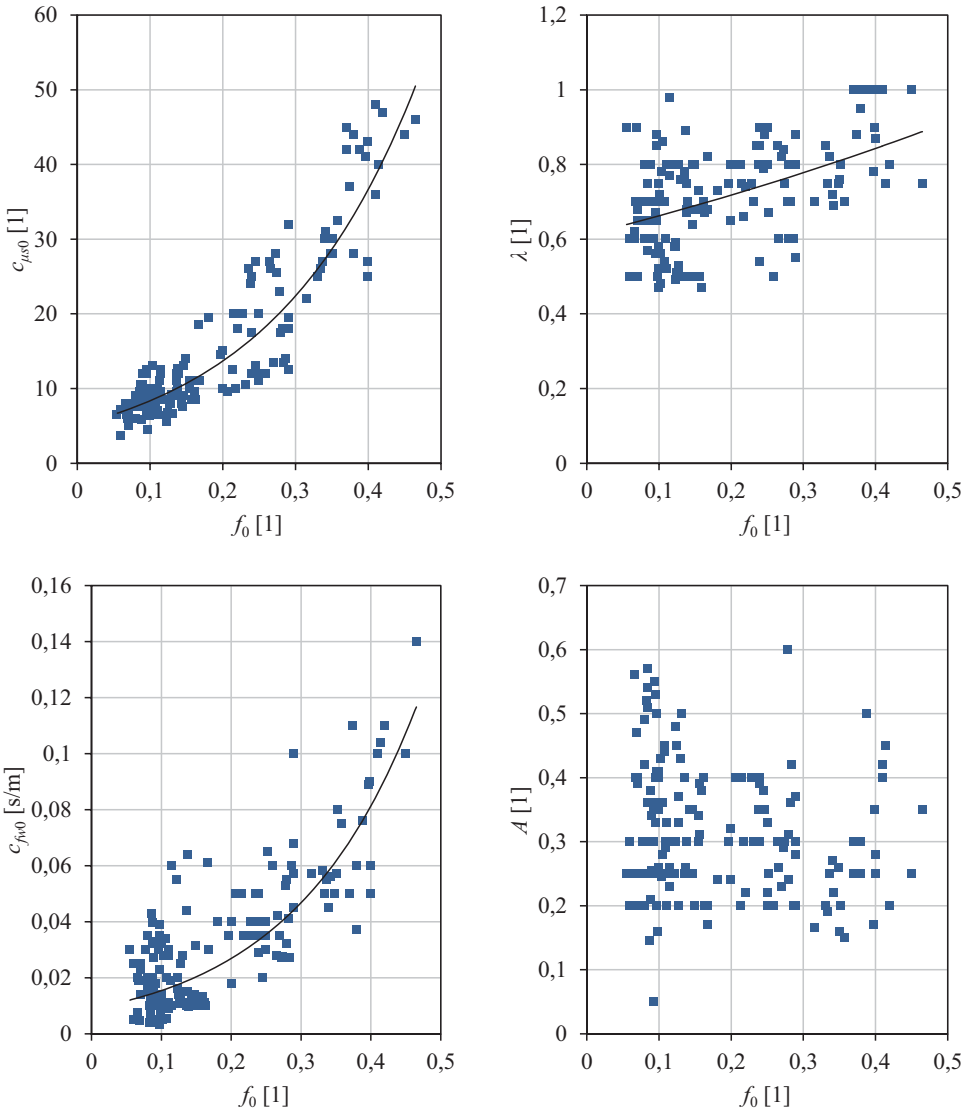

Fig. 8: Graphical representation of quantitative results. The static friction coefficient f_0 (horizontal axes) was chosen as a parameter describing the adhesion conditions; other four parameters are plotted against it. Each point corresponds to one measured characteristic. Measurements with non-zero angle of attack are not included.

It must be noted that the maximum reached adhesion coefficient $\mu_{\max}$ is, due to the decreasing nature of friction characteristic, lower than the static friction coefficient f_0, as seen in Fig. 3.

The initial adhesion characteristic steepness $c_{\mu s0}$ also depends on adhesion conditions. This parameter of the adhesion model depends on the tangential stiffness of the surface layers of the bodies in contact which is lower if there is contaminant between them. Values of $c_{\mu s0}$ = 5–10 were observed with strongly lubricated surfaces; with increasing friction coefficient f_0 the stiffness clearly increases and reaches maximum values of about 50.

It should be emphasized that the initial steepness depends also on contact geometry and that in the case of a real vehicle running on real not rotating rails the value may differ – its values are higher, see Lata and Čáp (2010). The reduction coefficient k of Kalker's creep coefficient c_{11} has a similar

meaning but is independent of the contact geometry. We cannot determine its value from the measurements but it may be supposed that the maximum steepness values which were reached under the best adhesion conditions correspond to an almost ideal state where Kalker's coefficient are not reduced ($k = 1$). Thus under the worst adhesion conditions in the experiments, the reduction would be $k = c_{\mu s0,\,\min}/c_{\mu s0,\,\max} = 5/50 = 0{,}1$.

The parameter λ has, according to our measurements, the value in a wide range of 0.45–0.95 under bad adhesion conditions; under good conditions, it is higher, up to 1.0 with degreased surfaces. That is the state which may be apparently regarded as almost ideal where the reduction coefficients k_S and k_A both approach to 1 whence their ratio λ approaches to the same number.

The initial steepness of the friction characteristic c_{fw0} is in a wide range of 0.002–0.04 s/m under bad adhesion conditions; with an increase of f_0 it increases, too, and under very good adhesion conditions it can exceed 0.1 s/m. Our measurements thus indicate that if the friction coefficient at zero relative speed w is higher, it decreases more rapidly with increasing speed.

The parameter A has a value about 0.2–0.55 under bad adhesion conditions. Under good conditions (dry surfaces) it tends to fall in a narrower range of 0.2–0.4. The parameter does not influence the shape of the adhesion characteristic until higher creep velocities; in the zone of $s < 0.5$, its value (within the mentioned range) is almost immaterial.

6. Conclusions

The paper deals with the course and results of adhesion measurements at a tram wheel test stand at the Jan Perner Transport Faculty in Pardubice. The test stands simulates rolling of a powered and braked wheel over a rail; the rail has a form of rotating rail, i.e. a wheel with a railhead profile. The processed measurement output gives dependences of the adhesion coefficient μ (ratio of the tangential and normal forces in the contact) on the creep velocity w or dimensionless creepage s. Evaluation of the output involves approximation of the measured adhesion characteristics by theoretical ones given by the Freibauer theory. Values of their parameters then quantitatively characterise the measured dependences and serve as input parameters in rail vehicle dynamics modelling – see Lata (2008), Voltr and Lata (2011).

Most of the measured characteristics may be approximated in this way in a certain range only. During the experiments, namely during gross sliding of the wheel, changes of surface conditions occur, wherefore the values of the parameters change even during the recording of a single adhesion characteristic. Thus each measured dependence is approximated not by a single theoretical function but by two of them (initial and final) between which there is a transition, which is left without description in this work. The approximation is often not unequivocal because it is difficult to decide in which region the measured course is near-steady and in which region it should be regarded as the transition. This fact affects the results with a subjective influence.

The conclusion is that the change of friction conditions during sliding should not be neglected if high sliding velocities are concerned. The influence is more significant under bad adhesion conditions – the contaminant is being removed during the sliding. The change may then be expressed by an increase of the parameter f_0 in the model. The consequence is that the descending branch of the adhesion characteristic falls more slowly or even may rise and form another peak. Its occurrence is not a property of the μ–s dependence but a consequence of change of friction conditions in time; the peak does not occur at the upper boundary of an effective slip mode but far higher in full sliding mode. Thus it appears not to be convenient to utilise the peak in slip regulation.

Even under good adhesion conditions, however, certain changes are encountered which may be modelled by increasing the parameters $c_{\mu s0}$ and λ, or decreasing the steepness c_{fw0}, respectively.

In the application of the results one should consider the following differences between the test stand and a real vehicle on a track:

- The substitution of a straight rail by a rotating one results in shortening the contact area in longitudinal direction and slight widening in lateral direction. The contact conditions are thus different.

- In our opinion, however, the difference of normal loading is more substantial – the vertical wheel force of a modern tram vehicle is 25–40 kN whereas at the test stand it is 4 kN.
- As another consequence of the use of rotating rail is that in rolling with sliding, the parts of the rail which have been cleaned by sliding come into the contact each time again; a real vehicle, on the contrary, moves continually over a new, contaminated sections of rails.

The observed changes of friction conditions during sliding imply suggestions for further work: it might be possible to express the changes mathematically e.g. in dependence on friction force work/power, see Blau (2009), Pugi et al. (2011). For validation of such a model it could be useful to perform experiments under the same conditions but with different speed of increasing and decreasing of creepage.

Acknowledgement

This work was supported by the University of Pardubice, project No.51030/20/SG520001.

References

Barwell, F. T. (1957) Několik výsledků o tření a opotřebení se zvláštním zřetelem na koeficient tření mezi kolem a kolejnicí. Transl. from German: Einige Ergebnisse über Reibung und Verschleiß unter besonderer Bezugnahme auf die Reibzahl zwischen Rad und Schiene. *Glasers Analen*, Hf. 2, 1957, pp. 231–261.

Blau, P. J. (2009) Embedding Wear Models into Friction Models. *Tribol Lett* 34, pp. 75–79.

Čáp, J. (1995) Teoretický rozbor tečných a interaktivních sil ve styku kolo–kolejnice. *Scientific Papers of the University of Pardubice*, Ser. B., 5 (1999), pp. 29–47.

Čejka, J. (1970) *Adhesní vlastnosti elektrických lokomotiv na střídavý proud.* Dissertation thesis, Vysoká škola dopravní v Žilině, Fakulta strojní a elektrotechnická.

Freibauer, L. (1983) Adheze kola vozidla na dráze, in: *7. vedecká konferencia Vysokej školy dopravy a spojov v Žiline – Zborník referátov*, VŠDS Žilina, pp. 214–219.

Kalker, J. J. (1973) Simplified theory of rolling contact. *Delft Progress Report*, Ser. C, 1 (1973), pp. 1–10.

Lata, M. (2008) The modern wheelset drive system and possibilities of modelling the torsion dynamics. *Transport*, 23(2), pp. 172–181.

Lata, M. & Čáp, J. (2010) The steepness of the rising branch of adhesive characteristics between wheel and rail. *Transport*, 25(1), pp. 17–21.

Polách, O. (2005) Creep forces in simulations of traction vehicles running on adhesion limit. *Wear* 258, pp. 998–1000.

Pugi, L. et al. (2011) Three-dimensional modelling of wheel–rail degraded adhesion conditions, in: *22nd International Symposium on Dynamics of Vehicles on Roads and Tracks – Proceedings* [CD]. Manchester Metropolitan University, Manchester.

Voltr, P. & Lata, M. (2011) Dynamical behaviour of a locomotive drive system at the adhesion limit – experiment and simulation, in: *22nd International Symposium on Dynamics of Vehicles on Roads and Tracks – Proceedings* [CD]. Manchester Metropolitan University, Manchester.

18th International Conference
ENGINEERING MECHANICS 2012
Svratka, Czech Republic, May 14 – 17, 2012

pp. 1555–1564
Paper #28

NUMERICAL MODELLING OF ENGINEERED CEMENT-BASED COMPOSITES

J. Vorel [*], **W.P. Boshoff** [**]

Abstract: *Strain Hardening Cement-based Composite (SHCC) is a type of High Performance Concrete (HPC) that was developed to overcome the brittleness of conventional concrete. Even though there is no significant compressive strength increase compared to conventional concrete, it exhibits superior behavior in tension. The primary objective of the presented research is to develop a constitutive model that can be used to simulate structural components with SHCC under different types of loading conditions.*

Keywords: ***Strain Hardening Cement-based Composite (SHCC), rotating crack model, damage, cyclic loading, nonlinear unloading***

1. Introduction

Strain Hardening Cement-based Composite (SHCC) is a type of High Performance Concrete (HPC) that was developed to overcome the brittleness of conventional concrete. Even though there is no significant compressive strength increase compared to conventional concrete, it exhibits superior behavior in tension. It has been shown to reach a tensile strain capacity of more than 4% during a pseudo strain hardening phase (Li and Wang, 2001; Boshoff and van Zijl, 2007). This pseudo strain hardening is achieved by the formation of fine, closely spaced multiple cracks with crack widths normally not exceeding $100\mu m$ (Li and Wang, 2001). These fine cracks, compared to large (larger than $100\mu m$) localized cracks found in conventional concrete, have the advantage of increased durability. For a further discussion of the mechanical properties of SHCC, the reader is referred to (Boshoff *et al.*, 2009*a*,*b*).

Several scholars have simulated SHCC mechanical behavior with the Finite Element Method (FEM). Kabele (2000) formulated a model to simulate the mechanical behavior of SHCC using a smeared cracking approach. Despite acknowledging that a discrete cracking model would be best for the final localizing crack, Kabele decided to use a smeared cracking approach for the localization. This is due to the uncertainty of the position of the final localizing crack. Another model was proposed by Han *et al.* (2003). This model was created to simulate the behavior of SHCC under cyclic loading to test the improvement of structural response if SHCC elements are used to dissipate energy during earth-quake loadings. Computational modeling of SHCC was also performed by Simone *et al.* (2003) who used an embedded discontinuity approach for the final material softening. This method would have the same kinematic characterization as one obtained with interface elements for discrete cracking, but does not require remeshing procedures. Their conclusion was that it did not simulate the experimental results of SHCC satisfactorily due to the simplicity of the model.

Boshoff (2007) created a simple damage mechanics based model for the tensile behavior of SHCC. This was implemented numerically using the FEM. Even though numerous shortcomings still exist, the model showed relatively good results. Remaining issues include an unresolved mesh dependence and the under prediction of the deformation when analyzing a structure with a strain gradient.

The primary objective of the presented research is to develop a constitutive model that can be used to simulate structural components with SHCC under different types of loading conditions. In particular, the constitutive model must be efficient and robust for large-scale simulations while restricted number

[*]Ing. Jan Vorel, Ph.D.: Department of Mechanics, Faculty of Civil Engineering, Czech Technical University in Prague, Thákurova 7; 166 29, Prague; CZ, e-mail: jan.vorel@fsv.cvut.cz
[**]Dr William Peter Boshoff: Stellenbosch University, Department of Civil Engineering; Private Bag X1 Matieland 7602; South Africa, e-mail: bboshoff@sun.ac.za

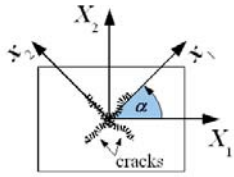

Fig. 1: Coordinates and transformation angle

of material parameters is needed. The proposed model for plane stress is outlined and the results of the preliminary implementation are shown.

2. Model definition

For the modeling of specific behavior of SHCC in tension, the application of classical constitutive material models used for quasi-brittle materials is not straightforward. The proposed numerical model is based on a rotating crack assumption to capture specific characteristics of SHCC, i.e. the strain hardening and softening, the multiple cracking and the crack localization. Multiple orthogonal crack patterns are allowed which is in accordance with the observations presented by Suryanto *et al.* (2008). A schematic representation of orthogonal cracking using the rotating crack model is shown using global and local axes in Fig. 1. A complete description of the rotating crack model can be found in (Rots, 1998).

The presented model is implemented in a commercially available software package, **DIANA** (BV., 2008), for a plane stress elements using a coaxial rotating crack model (RCM) with two orthogonal cracks as described in (Han *et al.*, 2003). This numerical approach is classified as the smeared cracking approach. When implementing the model into a nonlinear fine element code, the incremental-iterative procedure based on a strain increment is assumed. Therefore, the strain vector $\boldsymbol{\varepsilon} = \{\varepsilon_{11}, \varepsilon_{22}, \gamma_{12}\}^{\mathsf{T}}$ reads

$$\boldsymbol{\varepsilon}^{(i)} = \boldsymbol{\varepsilon}^{(i-1)} + \Delta\boldsymbol{\varepsilon}, \tag{1}$$

where i stands for an increment number and $\Delta\boldsymbol{\varepsilon}$ is a strain increment vector. The rotating crack model evaluates a given strain state and generates the inelastic strain in the principal directions of the strain. Therefore, it is inevitably required to introduce a transformation tensor $([\mathsf{T}]_{\varepsilon}, [\mathsf{T}]_{\sigma})$ interconnecting global and a principal strain $\mathbf{e} = \{e_1, e_2, 0\}^{\mathsf{T}}$ or stress $\mathbf{s} = \{s_1, s_2, 0\}^{\mathsf{T}}$, respectively

$$\mathbf{e} = [\mathsf{T}]_{\varepsilon}\,\boldsymbol{\varepsilon}, \quad \mathbf{s} = [\mathsf{T}]_{\sigma}\,\boldsymbol{\sigma}. \tag{2}$$

Using the standard transformation rule the tensors are

$$[\mathsf{T}]_{\varepsilon} = \begin{bmatrix} n_{11}^2 & n_{12}^2 & n_{11}n_{12} \\ n_{21}^2 & n_{22}^2 & n_{21}n_{22} \\ 2n_{11}n_{21} & 2n_{12}n_{22} & n_{11}n_{22} + n_{12}n_{21} \end{bmatrix}, \tag{3}$$

$$\boldsymbol{n} = \begin{bmatrix} \cos\alpha & \sin\alpha \\ -\sin\alpha & \cos\alpha \end{bmatrix}, \tag{4}$$

with the relations between $[\mathsf{T}_{\varepsilon}]$ and $[\mathsf{T}_{\sigma}]$

$$[\mathsf{T}]_{\sigma}{}^{\mathsf{T}} = [\mathsf{T}]_{\varepsilon}{}^{-1} \quad \text{and} \quad [\mathsf{T}]_{\varepsilon}{}^{\mathsf{T}} = [\mathsf{T}]_{\sigma}{}^{-1}. \tag{5}$$

The rotation angle α can be obtained by means of a standard relation

$$\alpha = 1/2 \arctan\left[\gamma_{12}/\left(\varepsilon_{11} - \varepsilon_{22}\right)\right]. \tag{6}$$

The incremental stress-strain law (in the crack orientation) reads

$$\Delta \mathbf{s} = [\tilde{\mathsf{D}}]\Delta \mathbf{e}, \tag{7}$$

$$[\tilde{\mathsf{D}}] = \begin{bmatrix} \frac{\mathrm{d}s_1}{\mathrm{d}e_1} & \frac{\mathrm{d}s_1}{\mathrm{d}e_2} & 0 \\ \frac{\mathrm{d}s_2}{\mathrm{d}e_1} & \frac{\mathrm{d}s_2}{\mathrm{d}e_2} & 0 \\ 0 & 0 & \frac{s_1 - s_2}{2(e_1 - e_2)} \end{bmatrix}, \tag{8}$$

where $[\tilde{\mathsf{D}}]$ is the tangent material stiffness matrix. The derivation can be found in (Jirásek and Zimmermann, 1998). The stiffness matrix is transformed to the global coordinates using the standard transformation rule

$$[\mathsf{D}] = [\mathsf{T}_\varepsilon]^{\mathsf{T}} [\tilde{\mathsf{D}}] [\mathsf{T}_\varepsilon]. \tag{9}$$

2.1. Poisson's ratio effect and equivalent principal stresses

It has to be mentioned that the rotating crack approach does not automatically include the effect of Poisson's ratio as the stress is evaluated on the basis of individual principal strains. In (Han *et al.*, 2003) the definition of equivalent strain is used to take this effect into account. This approach is reliable when a model formulation does not permit residual deformations by cyclic loading, i.e. by changing state (tension to compression and vice versa). However, in the model presented in this study permanent (residual) deformations are allowed. Therefore, a new approach was employed to treat the effect of Poisson's ratio. The effective principal strain $(\hat{\mathbf{e}})$ is used to determine the equivalent stress $(\hat{\mathbf{s}})$ from the simplified uniaxial stress-strain diagram (see Sec. 2.2.). The effective principal strain is based on the principal strain $(\mathbf{e})$ which is free of inelastic deformations caused during the stress state change. The final stresses are consequently evaluated as

$$\begin{Bmatrix} s_1 \\ s_2 \end{Bmatrix} = \frac{1}{1 - \nu_{12}\nu_{21}} \begin{bmatrix} 1 & \nu_{12} \\ \nu_{21} & 1 \end{bmatrix} \begin{Bmatrix} \hat{s}_1 \\ \hat{s}_2 \end{Bmatrix}, \tag{10}$$

$$\nu_{12} = \nu_0 E_1 / E_0, \quad \nu_{21} = \nu_0 E_2 / E_0, \tag{11}$$

where E_0 and ν_0 stand for Young's modulus and Poisson's ratio of the undamaged material respectively. The parameters E_1, E_2, ν_{12} and ν_{21} represent the characteristics of the damaged material in a given direction and are defined in Sec. 2.2.. The isotropic elastic material is represented in the state without cracks ($E_1 = E_2 = E_0$, $\nu_{12} = \nu_{21} = \nu_0$) and the orthotropic when the crushing or cracking starts

$$\{\hat{s}_1, \hat{s}_2\}^{\mathsf{T}} = \left\{E_1 e_1^{\mathsf{el}}, E_2 e_2^{\mathsf{el}}\right\}^{\mathsf{T}}. \tag{12}$$

Stiffness matrix introduced with this approach satisfies the condition of symmetry for orthotropic materials. Combining Eqs. (10,12) further gives

$$\begin{Bmatrix} s_1 \\ s_2 \end{Bmatrix} = \frac{1}{1 - \nu_{12}\nu_{21}} \begin{bmatrix} E_1 & \nu_{12}E_2 \\ \nu_{21}E_1 & E_2 \end{bmatrix} \begin{Bmatrix} e_1^{\mathsf{el}} \\ e_2^{\mathsf{el}} \end{Bmatrix}, \tag{13}$$

where $\nu_{12}E_2 = \nu_{21}E_1$ and superscript $\cdot^{\mathsf{el}}$ represents the elastic part.

2.2. Equivalent stress

The equivalent stress state in principal direction is determined by the stress function $\hat{s}_{t(c)}$ as a function of the current principal strain and associated history parameters.

The stress function is based on the uniaxial strain-stress diagrams in compression and tension. The experimental data are idealized to obtain a suitable mathematical representation of this constitutive model.

Tension

The material response for virgin loading in tension (Fig. 2(a)) is described for each individual part by

$$\hat{s}_t\left(\hat{e} \geq \varepsilon_{tmax}\right) = \begin{cases} E_0 \hat{e} & 0 \leq \hat{e} \leq \varepsilon_{t0} \\ \sigma_{t0} + \left(\sigma_{tp} - \sigma_{t0}\right)\left[-2\left(\frac{\hat{e}-\varepsilon_{t0}}{\varepsilon_{tp}-\varepsilon_{t0}}\right)^3 + 3\left(\frac{\hat{e}-\varepsilon_{t0}}{\varepsilon_{tp}-\varepsilon_{t0}}\right)^2\right] & \varepsilon_{t0} < \hat{e} \leq \varepsilon_{tp} \\ \sigma_{tp}\left[2\left(\frac{\hat{e}-\varepsilon_{tp}}{\varepsilon_{tu}-\varepsilon_{tp}}\right)^3 - 3\left(\frac{\hat{e}-\varepsilon_{tp}}{\varepsilon_{tu}-\varepsilon_{tp}}\right)^2 + 1\right] & \varepsilon_{tp} < \hat{e} < \varepsilon_{tu} \\ 0 & \varepsilon_{tu} \leq \hat{e}. \end{cases} \tag{14}$$

The model parameters are depicted in Fig. 2(a). The elastic part is assumed to be linear whereas the hardening and the softening sections are defined by means of the Hermit functions.

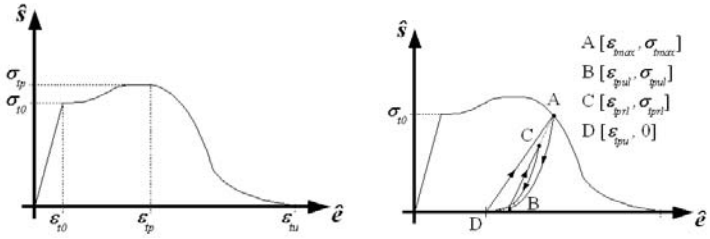

(a) (b)

Fig. 2: Tensile response: (a) Virgin loading, (b) loading/unloading

The unloading and reloading scheme shown in Fig. 2(b) is based on the experiments presented by Mechtcherine and Jůn (2007).

$$\hat{s}_t\left(\hat{e} < \varepsilon_{tmax}\right) = \begin{cases} E_0 \hat{e} & 0 \leq \varepsilon_{tmax} \leq \varepsilon_{t0} \\ \sigma^*_{tmax}\left(\frac{\hat{e}-\varepsilon_{tul}}{\varepsilon^*_{tmax}-\varepsilon_{tul}}\right)^{a_t} & \varepsilon_{t0} < \varepsilon_{tmax} < \varepsilon_{tu}, \dot{\varepsilon} < 0 \\ \sigma^*_{tul} + \left(\sigma_{tmax} - \sigma^*_{tul}\right)\frac{\hat{e}-\varepsilon^*_{tul}}{\varepsilon_{tmax}-\varepsilon^*_{tul}} & \varepsilon_{t0} < \varepsilon_{tmax} < \varepsilon_{tu}, \dot{\varepsilon} \geq 0 \\ 0 & \varepsilon_{tu} \leq \varepsilon_{tmax}. \end{cases} \tag{15}$$

The unloading curve is based on the polynomial function and the reloading is assumed to be linear. The partial unloading and reloading is incorporated using

$$\begin{aligned} \varepsilon^*_{tmax} &= \min\left(\varepsilon_{tmax}, \varepsilon_{tprl}\right), \\ \varepsilon^*_{tul} &= \max\left(\varepsilon_{tul}, \varepsilon_{tpul}\right), \end{aligned} \tag{16}$$

where $\sigma^*_{tmax}, \sigma^*_{tul}$ are associated stresses and ε_{tmax} is the maximum strain experienced in previous steps with stress σ_{tmax}. The evolution of inelastic strain ε_{tul} is assumed to be linearly dependent on ε_{tmax} for the elastic and hardening part and linearly dependent on the crack opening for the softening branch (Eq. (17)). This simplification correlates well with recent, unpublished cyclic tensile results done at Stellenbosch University, see Fig. 3(a).

$$\varepsilon_{tul} = \begin{cases} 0 & 0 \leq \varepsilon_{tmax} \leq \varepsilon_{t0} \\ b_t\left(\varepsilon_{tmax} - \varepsilon_{t0}\right) & \varepsilon_{t0} < \varepsilon_{tmax} \leq \varepsilon_{tp} \\ \min\left\{b_t\left(\varepsilon_{tp} - \varepsilon_{t0}\right) + b_t\left[\varepsilon_{tmax} - b_t\left(\varepsilon_{tp} - \varepsilon_{t0}\right) - \sigma_{tmax}/E_{tp}\right], \right. & \\ \left. b_t\left(\varepsilon_{tp} - \varepsilon_{t0} + w_t/h\right)\right\} & \varepsilon_{tp} < \varepsilon_{tmax}, \end{cases} \tag{17}$$

where $E_{tp} = \sigma_{tp}/\left[\varepsilon_{tp} - b_t(\varepsilon_{tp} - \varepsilon_{t0})\right]$. The parameter a_t governs the unloading trajectory and must be determined from the experimental tests as well as the material characteristic b_t.

To ensure proper energy dissipation during localizing, the crack band approach is used which relates the strain ε_{tu} to the crack opening for the complete force transfer loss (w_t) and element size (h), see

Eq. (18). The crack opening can be considered as a half of the fiber length (Boshoff, 2007). In the present study the equivalent crack band width is evaluated by projecting the element into the direction normal to the crack at its initiation (h). This is done for each cracking direction separately. The last term in Eq. (18) describes the influence of the unloading where more energy is dissipated when the non-linear law is employed (Fig. 3(b)).

$$\varepsilon_{tu} = \varepsilon_{tp} + \frac{w_t}{h} - 2\frac{\varepsilon_{tp} - b_t\left(\varepsilon_{tp} - \varepsilon_{t0}\right)}{a_t + 1}. \tag{18}$$

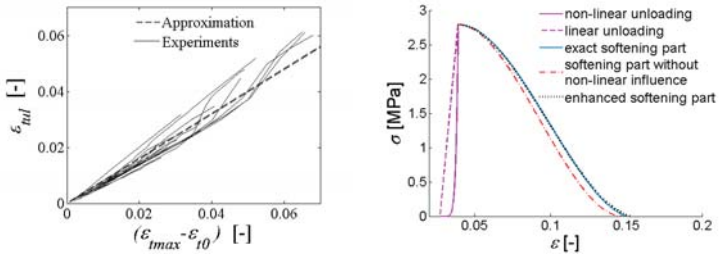

(a) (b)

Fig. 3: Tension: (a) Evolution of inelastic strain, (b) comparison of softening branches

As seen in Eq. (17), the damage and cracking strains are mainly driven by a single material parameter, namely b_t. By considering the standard definition of the damage parameter ω

$$E_t = (1 - \omega_t)E_0, \tag{19}$$

where E_t denotes the actual elastic modulus, the damage variable can be determined by introducing Eq. (17) into Eq. (19) as

$$\omega_t = 1 - \frac{E_t}{E_0} = 1 - \frac{\sigma_{tmax}}{\left(\varepsilon_{tmax} - \varepsilon_{tul}\right)E_0}. \tag{20}$$

The transverse strain ratio in Eq. (11) can be then evaluated as

$$\nu_{ij} = -\nu_0\left(1 - \omega_t\right). \tag{21}$$

This definition assures the decreasing influence of Poisson's ratio while the material cracks.

Compression

The virgin compression loading response is shown in Fig. 4(a) and is defined mathematically as

$$\hat{s}_c\left(\hat{e} \le \varepsilon_{min}\right) = \begin{cases} E_0\hat{e} & 0 > \hat{e} \ge \varepsilon_{c0} \\ \sigma_{cp} - \left(\sigma_{cp} - \sigma_{c0}\right)\left(\frac{\varepsilon_{cp}-\hat{e}}{\varepsilon_{cp}-\varepsilon_{c0}}\right)^{E_0\frac{\varepsilon_{cp}-\varepsilon_{c0}}{\sigma_{cp}-\sigma_{c0}}} & \varepsilon_{c0} > \hat{e} \ge \varepsilon_{cp} \\ \sigma_{cp}\left[2\left(\frac{\hat{e}-\varepsilon_{cp}}{\varepsilon_{cu}-\varepsilon_{cp}}\right)^3 - 3\left(\frac{\hat{e}-\varepsilon_{cp}}{\varepsilon_{cu}-\varepsilon_{cp}}\right)^2 + 1\right] & \varepsilon_{cp} > \hat{e} > \varepsilon_{cu} \\ 0 & \varepsilon_{cu} \ge \hat{e}. \end{cases} \tag{22}$$

The unloading and reloading scheme is depicted in Fig. 4(b) and is based on a similar assumptions as for tension

$$\hat{s}_c\left(\hat{e} > \varepsilon_{cmin}\right) = \begin{cases} E_0\hat{e} & 0 > \varepsilon_{cmin} \ge \varepsilon_{t0} \\ \sigma^*_{cmin}\left(\frac{\hat{e}-\varepsilon_{cul}}{\varepsilon^*_{cmin}-\varepsilon_{cul}}\right)^{a_c} & \varepsilon_{c0} > \varepsilon_{cmin} > \varepsilon_{cu}, \dot{e} > 0 \\ \sigma^*_{cul} + \left(\sigma_{cmin} - \sigma^*_{cul}\right)\frac{\hat{e}-\varepsilon^*_{cul}}{\varepsilon_{cmin}-\varepsilon^*_{cul}} & \varepsilon_{c0} > \varepsilon_{cmin} > \varepsilon_{cu}, \dot{e} \le 0 \\ 0 & \varepsilon_{cu} \ge \varepsilon_{cmin}, \end{cases} \tag{23}$$

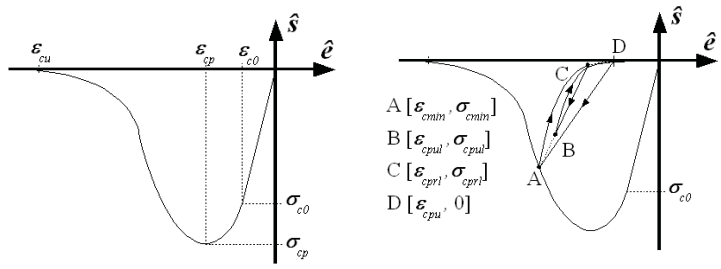

Fig. 4: Compressive response: (a) Virgin loading, (b) loading/unloading

where

$$\begin{aligned} \varepsilon^*_{cmin} &= \max\left(\varepsilon_{cmin}, \varepsilon_{cprl}\right), \\ \varepsilon^*_{cul} &= \min\left(\varepsilon_{cul}, \varepsilon_{cpul}\right). \end{aligned} \tag{24}$$

where $\sigma^*_{cmin}, \sigma^*_{cul}$ are associated stresses and ε_{cmin} is the minimum strain reached in previous steps with stress σ_{cmin}. The evolution of inelastic strain is again assumed to be linearly dependent on ε_{cmin} and crushing (Eq. (25)). Suppose that the strain $\left(\varepsilon^{test}_{cu}\right)$ for which the force is totally released is determined from the experimental test and the corresponding localisation band in real material is denoted d_c. Next, with the knowledge of the remaining material parameters, we can define the displacement needed for releasing correct energy during material softening as $w_c = \left[\varepsilon^{test}_{cu} - b_c\left(\varepsilon_{cp} - \varepsilon_{c0}\right)\right] d_c$. The inelastic strain then takes the form

$$\varepsilon_{cul} = \begin{cases} 0 & 0 > \varepsilon_{cmin} \geq \varepsilon_{c0} \\ b_c\left(\varepsilon_{cmin} - \varepsilon_{c0}\right) & \varepsilon_{c0} > \varepsilon_{cmin} \geq \varepsilon_{cp} \\ \min\left\{b_c\left(\varepsilon_{cp} - \varepsilon_{c0}\right) + b_c\left[\varepsilon_{cmin} - b_c\left(\varepsilon_{cp} - \varepsilon_{c0}\right) - \sigma_{cmin}/E_{cp}\right], \right. & \\ \left. b_c\left(\varepsilon_{cp} - \varepsilon_{c0} + w_c/h\right)\right\} & \varepsilon_{cp} > \varepsilon_{cmin}. \end{cases} \tag{25}$$

The material parameters a_c and b_c have to be determined from experimental test results.

The dissipated energy during the crushing should also be mesh-independent as for tensile cracking. Therefore, the strain ε_{cu} is defined with respect to the mesh size as

$$\varepsilon_{cu} = \varepsilon_{cp} + \frac{w_c}{h} - 2\frac{\varepsilon_{cp} - b_c\left(\varepsilon_{cp} - \varepsilon_{c0}\right)}{a_c + 1}, \tag{26}$$

where h represents the equivalent band (element size) where the crushing occurs and is determined at its initiation. The damage parameter is determined in a similar fashion as for tension (Eq. (20)) and reads

$$\omega_c = 1 - \frac{E_c}{E_0} = 1 - \frac{\sigma_{cmin}}{\left(\varepsilon_{cmin} - \varepsilon_{cul}\right) E_0}. \tag{27}$$

2.3. Biaxial behavior

To demonstrate the complex behavior of the proposed approach the failure envelope in space of principal stresses is shown in Fig. 5. The boundaries are influenced by the transverse strain ratio of cracked and crushed material which is expected when the failure criterion is based on principal strains. This disadvantage of the presented model can be solved by defining the dependence between tensile and compressive strength. Nevertheless, the real shape of failure envelope for SHCC will only be included at a later stage as the biaxial behavior is currently under investigation at Stellenbosch University.

2.4. Cyclic loading

The above described model is adjusted for cyclic loading when the orientation of principle stresses changes. The residual deformations are assumed to be dependant on the inelastic strain. Therefore,

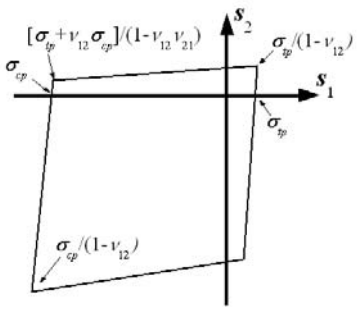

Fig. 5: Failure envelope in the principal stress space

a simple linear definition is employed and the permissible closing (opening) strain is evaluated as

$$\varepsilon_{t(c)}^{cl} = b_{t(c)}^{cl} \varepsilon_{tul(cul)}, \tag{28}$$

where b_t^{cl} and b_c^{cl} are material parameters and can therefore be calculated from reverse cyclic loading tests. The trajectories of reloading after the stress state change are in a good agreement with experimental results presented in (Billington, 2004).

For the space limitation only tension behavior after stress state change is introduced (Eqs. (29,30)). The stress evolution for compression can be obtain by substitution of tensile driving parameters for compressive variables and replacement of the maximum (max) with the minimum (min) value and vice versa. Note that during the loading after stress state change the old cracks are reopened and the tangent modulus increases to reach the value of the previously experienced modulus E_t.

$$\sigma\left(\dot{e} \geq 0\right) = \sigma_{tul}^{*} + \left(\sigma_{tmax}^{**} - \sigma_{tul}^{*}\right)\left(\frac{\hat{e} - \varepsilon_{tul}^{*}}{\varepsilon_{tmax}^{**} - \varepsilon_{tul}^{*}}\right)^{E_t \frac{\varepsilon_{tmax}^{**} - \varepsilon_{tul}^{*}}{\sigma_{tmax}^{**} - \sigma_{tul}^{*}}}, \tag{29}$$

$$\sigma\left(\dot{e} < 0\right) = \sigma_{tmax}^{*}\left[\frac{\hat{e} - \varepsilon_{tul}^{**}}{\sigma_{tmax}^{*}/E_t}\right]^{a_t}, \tag{30}$$

where the driving parameter $\hat{e}$ is again shifted to correspond with the diagram for a virgin loading and $\varepsilon_{tmax}^{**} = \max\left(\varepsilon_{t0}, \varepsilon_{tmax}\right)$ with associated stress σ_{tmax}^{**}. The experienced modulus is determined as

$$E_t = \begin{cases} E_0 & \varepsilon_{tmax} \leq \varepsilon_{t0} \quad (31) \\ \dfrac{\sigma_{tmax}}{\varepsilon_{tmax} - b_t\left(\varepsilon_{tmax} - \varepsilon_{t0}\right)} & \varepsilon_{tmax} > \varepsilon_{t0}, \quad (32) \end{cases}$$

and inelastic strain ε_{tul}^{**} is assumed to be

$$\varepsilon_{tul}^{**} = \min\left[\varepsilon_{tmax}^{*} - \sigma_{tmax}^{*}/E_t, b_t\left(\varepsilon_{tmax} - \varepsilon_{t0}\right)\right]. \tag{33}$$

To demonstrate the model response, a loading change from tension to compression to tension (A-G) is shown in Fig. 6(a):

- A-B: initial virgin loading (Eq. (14)),
- B-C: unloading (Eq. (15)),
- C-D: cracks closing and compressive loading,
- D-E: virgin loading (Eq. (22)),

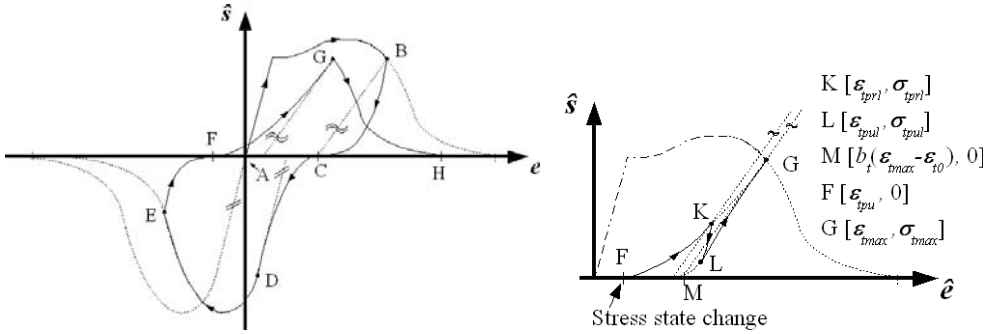

(a) (b)

Fig. 6: Schematic cyclic behavior

- E-F: unloading (Eq. (23)),
- F-G: cracks reopening and tensile loading (Eq. (29)),
- G-H: virgin loading (Eq. (14)).

Note that if the loading follows the stress state change, the loading path has the tangent equal to the actual modulus (Eq. (29)), intervals F-K and L-G in Fig. 6(b). The unloading from this stage is defined in Eq. (30), see interval K-L in Fig. 6(b).

3. Implementation and application

As mentioned in the previous section, the constitutive model is implemented in the commercial available finite element code **DIANA** version 9.3 using the "User supplied subroutine" option to demonstrate its suitability for SHCC. Note that this section is brief demonstration. Therefore, a more wide and deep study is preparing by the authors and will be presented separately. The Newton-Raphson iterative procedure is used for the solution of nonlinear equations.

Finite element analyses of the flexural tests is performed to verify the constitutive model analyses. The three-point bending test is introduced using parameters based on the tensile tests and data presented by Boshoff (2007). The obtained results are compared with experimental data.

3.1. Model description

The numerical model is based on experimental data obtained over the past 5 years by the Institute of Structural Engineering based at the Department of Civil Engineering, Stellenbosch University. Due to the lack of a reverse cyclic loading some parameters are set up using the engineering judgement of the authors as this will not have a significant influence on the presented results. The available tensile tests for the same mixture as beams are used to set up the parameters describing tension, see Fig. 7(a). All the model parameters are listed in Tab. 1. To examine the feasibility of the proposed numerical approach, two different meshes are used. The flexural test is modelled using four node quadrilateral isoparametric plane stress element Q8MEM which are based on linear interpolation and Gauss integration. Two by two integration scheme is set up.

The finite element mesh is refined towards the middle of the beam with the size of the elements in the expected softening and localization zone 1.33 mm x 1.33 mm and 4.0 x 4.0 mm. The former dimension of elements in the middle of the beam is chosen in accordance with the theory introduced in (Boshoff, 2007) to deal with the crack spacing. The boundary conditions of the model are shown in Fig. 7(b) as well as the beam dimensions. The other mesh size is chosen to study the mesh sensitivity.

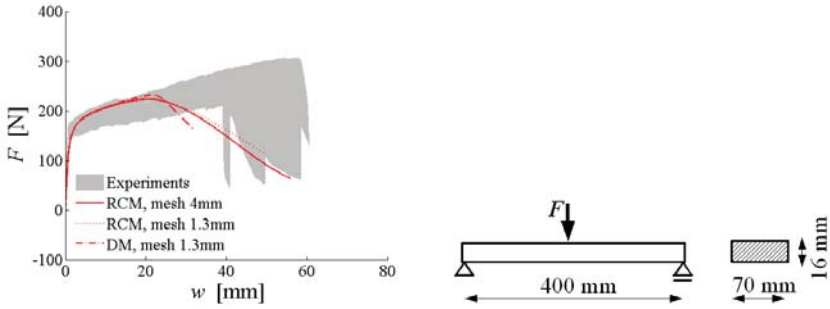

(a) (b)

Fig. 7: Three-point bending test: (a) Comparison, (b) setup setup

Tab. 1: Model parameters

General			Tension			Compression		
Param.	Value		Param.	Value		Param.	Value	
E	9200	MPa	ε_{t0}	$2.42 \cdot 10^{-4}$		ε_{c0}	$-4.89 \cdot 10^{-3}$	
ν	0.35		ε_{tp}	$3.92 \cdot 10^{-2}$		ε_{cp}	$-5.89 \cdot 10^{-3}$	
			σ_{tp}	2.79	MPa	σ_{cp}	-50.0	MPa
			w_t	6.0	mm	ε_{cu}	$-2.00 \cdot 10^{-1}$	
			a_t	3.0		d_c	50	mm
			b_t	0.8		a_c	3.0	
			b_t^{cl}	0.6		b_c	0.8	
						b_c^{cl}	0.8	

3.2. Results

The presented crack rotating model (RCM) is used to obtain the force-deflection diagrams. These results are plotted in Fig. 7(a) together with the experimental data and response produced by the model based on a damage mechanics formulation (DM) by Boshoff (2007). As can be seen, the numerical models demonstrate good agreement with experimental data in the elastic as well as hardening part. The discrepancy is detected for the softening part. This is probably caused by the fibers alignment close to the surface which is not taken into account for generally used numerical models and the interested readers are referred to (Boshoff, 2007). The mesh dependency is observed by comparison of the two different mesh sizes.

4. Conclusion and future work

In this paper a two-dimensional numerical model for Strain Hardening Cement-based Composites was introduced. This approach is based on a rotating crack model implemented in the commercially available software package **DIANA**. The presented model takes into account:

- strain hardening and softening in tension as well as in compression,
- nonlinear unloading,
- nonlinear loading after stress state change - crack closing,
- the effect of Poisson's ratio.

The accuracy of the introduced approach was demonstrated by means of a three-point flexural test. Nevertheless, the model must be further verified before the proposed approach will be used for larger structural components under different loading conditions.

Acknowledgment

The financial support provided by the GAČR grant No. 105/12/P353 is gratefully acknowledged.

References

Billington S (2004). Damage-tolerant cement-based materials for performence-based erthquake engineering design: Research needs, *in Fracture Mechanics of Concrete Structures*, pp. 53–60.

Boshoff W (2007), Time-Dependant Behaviour of Engineered Cement-Based Composites, PhD thesis, University of Stellenbosch. Ph.D. thesis.

Boshoff W, Mechtcherine V and van Zijl G (2009*a*). Characterising the time-dependant behaviour on the single fibre level of SHCC: Part 1: Mechanism of fibre pull-out creep, *Cement and Concrete Research* **39**, 779–786.

Boshoff W, Mechtcherine V and van Zijl G (2009*b*). Characterising the time-dependant behaviour on the single fibre level of SHCC: Part 2: The rate effects on fibre pull-out tests, *Cement and Concrete Research* **39**, 787–797.

Boshoff W and van Zijl G (2007). Time-dependant response of ECC: Characterisation of creep and rate dependence, *Cement and Concrete Research* **37**, 725–734.

BV. T D (2008). *DIANA Finite Element Analysis*.

Han T S, Feenstra P and Billington S (2003). Simulation of Highly Ductile Fiber-Reinforced Cement-Based Composite Components Under Cyclic Loading, *ACI Structural Journal* **100**(6), 749–757.

Jirásek M and Zimmermann Z (1998). Analysis of Rotating Crack Model, *Journal of Engineering Mechanics* **124**(8), 842–851.

Kabele P (2000), Assessment of Structural Performance of Engineered Cemetitious Composites by Computer Simulation, PhD thesis, Czech Technical University in Prague. A habilitation thesis.

Li V and Wang S (2001). Tensile Strain-hardening Behavior of PVA-ECC, *ACI Materials Journal* **98**(6), 483–492.

Mechtcherine V and Jůn P (2007). Stress-strain behaviour of strain-hardening cement-based composites (SHCC) under repeated tensile loading, *in Fracture Mechanics of Concrete Structures*, pp. 1441–1448.

Rots J (1998), Computational modeling of concrete fracture, PhD thesis, Delft University of Technology. Ph.D. thesis.

Simone A, Sluys L and Kabele P (2003). Combined continuous/discontinuous failure of cementitious composites, *in Proceedings for EURO-C 2003: Computational Modelling of Concrete Structures*, pp. 133–137.

Suryanto B, Nagai K and Maekawa K (2008). Influence of damage on cracking behavior of ductile fibre-reinforced cementitious composite, *in Proceedings of 8th International Conference on Creep, Shrinkage and Durability of Concrete and Concrete Structures*, pp. 495–500.

18th International Conference
ENGINEERING MECHANICS 2012
Svratka, Czech Republic, May 14 – 17, 2012

pp. 1565–1572
Paper #75

CYCLIC LOADING OF MASONRY WALLS AND ITS ANTI SEISMIC REINFORCING

M. Wünsche, S. Hračov, S. Pospíšil, S. Urushadze*

Abstract: *The damage of structural masonry walls is one of the most widespread harming injuries and cause of loss of serviceability and seismic capacity for a building. Therefore a research into possibilities which would improve these characteristics have been carried out within the 7th EC Framework programme project NIKER. The retrofitting approach is constrained by conservation requirements of minimum interventions which should not severely change the structural behavior and the structural appearance, and should prefer solutions without a necessity of total structural disassembling. This article provides an overview about the research that led to applications of the steel wire ropes and geo-nets onto adobe brick walls.*

Keywords: ***Seismic retrofitting, Adobe, Brick wall.***

1. Introduction

In the laboratory of ITAM were tested total 5 samples. Onto every the sample was applied various reinforcing except the first sample which was unreinforced. Overview of the tests shows Table 1.

Tab. 1: Overview of the test.

Title	Description
ABW_1	Unreinforced sample
ABW_2	Reinforced sample by wire ropes
ABW_3	Reinforced sample by PET geo-nets
ABW_4	Retrofitting ABW_1 by PET geo-nets
ABW_5	Reinforced sample by PP geo-nets

The specifications of the material and physical properties of the geo-nets and the wire steel ropes, which were used for the reinforcement of the walls, are summarized in Table 2.

The overall dimensions of the tested walls were 240 mm in thickness, 1050 mm in width and 1295 mm in height. The specimens have been walled up on steel-supported channels with fixtures that enabled the specimens to be lifted by a crane and positioned into the testing rig. The three types of unreinforced masonry considered in tests are depicted in Figure 1.

For the reinforced specimens a polyethylene TENCATE geo-nets and polypropylene TENAX geo-nets externally applied onto the wall surfaces have been used. After they have been mechanically fastened, the walls were rendered with about 2 cm thick plaster made with lime mortar.

The second reinforcement method is represented by means of steel wire ropes placed diagonally and in two directions on the wall surfaces. The wire ropes were installed in three grooves per direction previously produced on the surface of the wall and adequately anchored at their extremities by means of mechanics fasteners.

* Ing. Martin Wünsche, Ing. Stanislav Hračov, Ph.D., doc. Ing. Stanislav Pospíšil, Ph.D., Ing. Shota Urushadze, Ph.D.: Institute of Theory and Applied Mechanics AS CR, v.v.i, Prosecká 709/76; 190 00, Prague 9; CZ, e-mail: wunsche@itam.cas.cz

Tab. 2: Material specifications.

Title	ρ [kgm3]	Tension strength [MPa]	μ [/]	E [GPa]	Compression strength [MPa]
Adobe brick (CLAYTEC)	2000	0	0,35	3,5	5,5
Mortar – adobe (CLAYTEC)	1900	0,2	-	0,023	1,5

Title	E [GPa]	Ø [mm]	Tensile strength	Mesh sizes [mm]
Wire ropes	210	4	1770 MPa	-
Geo-nets – polypropylene (PP) (TENAX)	-	-	9,3/17 kN/m	30 x 45
Geo-nets – polyester (PET) Miragrid GX 35/35(TENCATE)	-	-	35 kN/m (both directions)	25 x 25

For the experimental program was prepared an adobe specimen severely damaged in a previous test, which has been repaired using the same system of geo-nets and tested again. The cracks have been only plastered with a thin cement mortar in order to smooth the surface for fixation of geo-nets.

In Figures 2 – 3 the tested walls are showed onto which the reinforcement nets were applied. Figure 4 shows a detail of the anchoring (reinforcement with wire ropes).

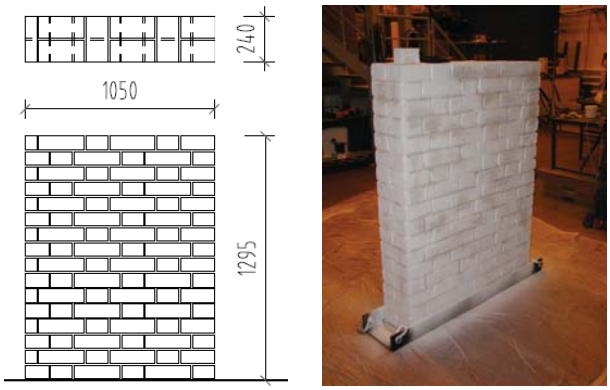

Fig. 1: Test sample

Fig. 2: Adobe brick wall with geo-nets (ABW_3)

Fig. 3: Adobe brick wall with a steel wire ropes (ABW_2)

Fig. 4: Connection detail (ABW_2)

The test specimens were mounted into a special testing rig that enabled simultaneous uniform compression and cyclic horizontal loading on the top of the tested specimen. The outline of the experimental equipment is illustrated in Figure 5 including the location of the sample into the test facility.

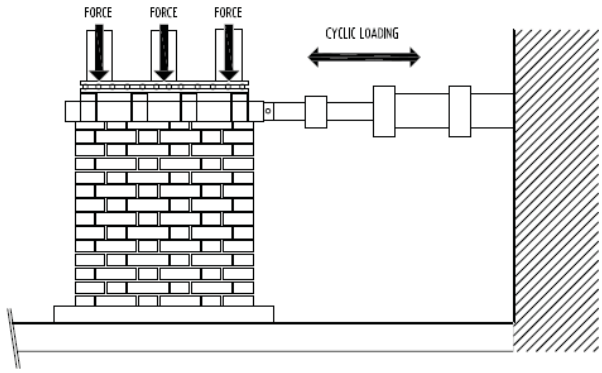

Fig. 5: Scheme of the testing system

Three hydraulic jacks generated the vertical load, which was transmitted to the wall by a steel 'hat' on the top of the wall. A horizontal displacement (force) on the top of the wall was introduced using a servo-hydraulic MTS actuator of 250 kN capacity. During the first loading combination, with static vertical loading only, the deformation characteristics of the wall were obtained. The horizontal displacement on the top of the wall and the deformations perpendicular to the shear diagonals of the panels were measured during combined vertical and horizontal loading. In the experimental testing the following loading condition has been considered. First, the above-mentioned compressive loading only was applied, and was increased continually up to a value of 80 kN, evenly distributed across the cross-section. Then, the vertical compressive pre-stress was combined with cyclic horizontal loading mode with a stepwise increase in the maximum cycling limits. The application of the horizontal load follows the pattern illustrated in Figure 6. In particular, for each step of loading defined by a maximum value of the amplitude (step = 2,5mm) of the displacement imposed by the actuator, three cycles were performed. For each step of loading, the frequency of application of the horizontal force was kept constant and equal to 0.1 Hz.

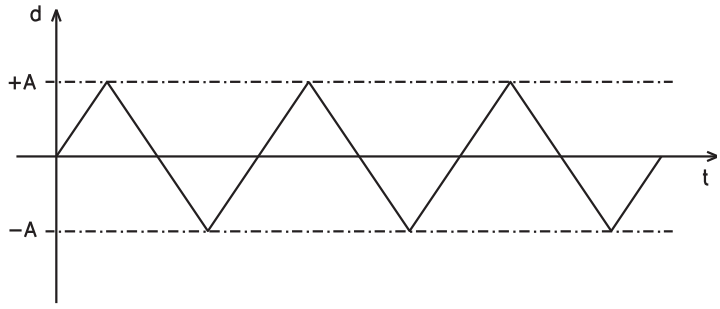

Fig. 6: Loading pattern for each step of application of the horizontal force.

During the test the forces on the vertical hydraulic jacks as well as on the horizontal actuator were recorded. Further, horizontal displacements at the bottom and top of the wall and diagonal deformations of four lines on both surfaces were measured. The sequence of initiation and development of cracks on both surfaces were recorded in all loading steps. Loading was terminated in a moment when the force started to decrease at the controlled deformation.

2. Results on wall segments

2.1. ABW_1 Adobe brick wall - unreinforced

The tests on all walls have been carried out considering fixed the frequency of the load and equal to 0,1 Hz, and incrementing the maximum displacement imposed in the actuator, starting from 2,5 mm and with increment of 2,5 mm.

Typical failure cracking of a plain masonry wall without plaster loaded by combined uniformly distributed vertical static stress and a horizontal cyclic load is shown in Figure 7. The development is highlighted by means of colouring of the cracks.

The envelope curve of the maximum horizontal force and the correspondent displacement obtained from the cyclic curves for each step of loading are plotted in Figure 8. In particular both the tension and the compression side of the cyclic curves are presented.

Fig. 7: Crack pattern at failure of the plain masonry control wall under a combination of vertical compression and cyclic shear.

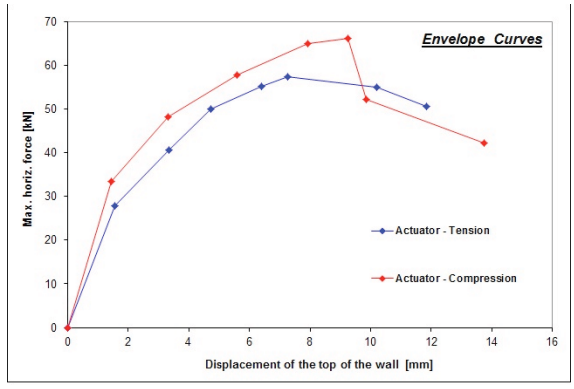

Fig. 8 - Envelope curves for unreinforced adobe wall (ABW_1).

2.2. ABW_2 – Adobe brick wall with reinforced by the wire ropes

The adobe brick wall reinforced by means of steel wire ropes also has been tested. In Figure 9 the crack pattern upon failure of the specimen is shown. In case this kind of reinforcement is adopted an important improvement in terms of resistance can be attained. The wall reinforced by means of this technique behaves in a quite compact manner since the wire ropes play a very effective role in sewing up the cracks and keeping the masonry blocks together. Some cracks can appear along the mortar joints in the surroundings of the reinforcement and, in general, there is a good redistribution of the stresses and a more widespread crack pattern compared to the unreinforced wall.

Fig. 9: Crack pattern at failure of the plain masonry control wall under a combination of vertical compression and cyclic shear.

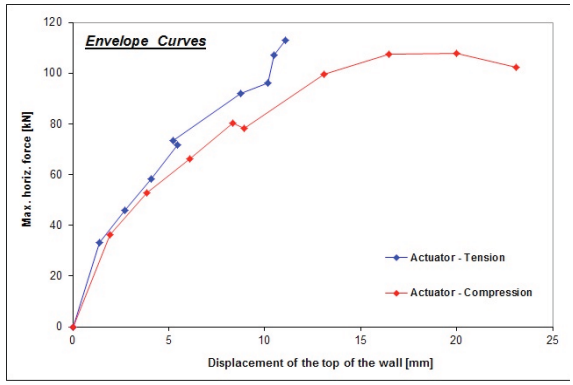

Fig. 10: Envelope curves for reinforced adobe wall by wire ropes (ABW_2).

Another important aspect brought to light by the experiments is related to the damage due to the possible out-of-plane of the reinforcement. In particular, the wire ropes are places quite superficially in grooves made on the wall faces and just plastered with mortar. Since during the application of cyclic horizontal loading both direction of reinforcement can be subjected alternatively to compression, causing the tendency to the ropes to go out of the grooves. However, since the reinforcement is made by steel wire, during tension phase they can easily be able to continue to be effective, involving only superficial damage of the wall. The envelope curves for the wall reinforced by the wire ropes is depicted obtained from the cyclic curves are plotted in Figure 10.

2.3. ABW_3 – Adobe brick wall reinforced by the geo-nets (PET)

The tested reinforcement of adobe walls was the reinforcement by PET geo-nets. The nets were attached to the both surface of the wall by means of steel staples shooted by pneumatic pistol.

It is, thus, evidenced the typical behaviour of walls reinforced by means of this technique. It is noticed that the cracks visible on the surface represent a combination of two sets of damages: masonry cracks and cracks which occur in the plaster only and originate from the differential movement of the geo-nets mesh. It is observed that compared to the typical crack pattern usually found in plane masonry walls, the case of the wall strengthened with reinforced mortar layer present a more widespread and diffused crack pattern. In fact, when unreinforced masonry wall is subjected to a combination of vertical pre-stress and horizontal cyclic load cracks are localized in the two diagonal lines of the walls evidencing the typical X-shaped pattern. The application of the reinforced mortar with geo-nets to the surfaces of the wall has also the effect to redistribute the stresses originated upon loading along the two diagonal lines of the wall and, thus, to spread the pattern over a wider area of the wall surface. An important aspect to be taken into account in the evaluation of the effectiveness of this kind of reinforcement is the interface behaviour between the external reinforcement and the masonry substrate to which it is applied represented by the wall. Since the reinforced mortar layer applied on the wall surfaces is slightly thin (1.5 ÷ 2.0 cm), and due to the different stiffness compared to the substrate, the out-of-plane forces can detach it. The experimental evidence of the detachment of this layer is much more evident when the difference in stiffness is larger. This happens particularly in the cases of application to this kind of reinforcement to clay bricks walls, while in case of adobe walls it is not so evident since the plaster has been made of the same material of the bricks. In Figure 11 it is shown a detail of the detachment of the plaster from the surface of the masonry wall.

Fig. 11 - Evidence of the detachment of the plaster from the wall surface.

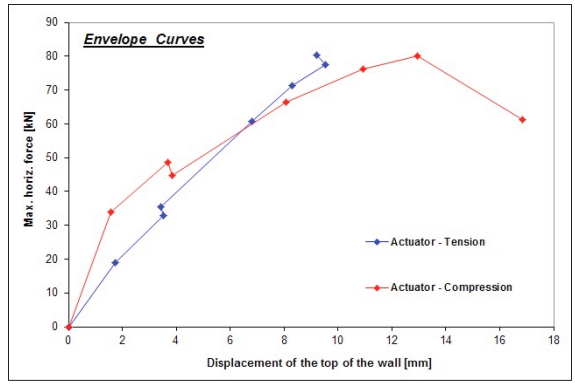

Fig. 12 - Envelope curves for reinforced adobe wall by the geo-nets PET (ABW_3).

2.4. ABW_4 - Reinforced adobe brick wall by the geo-nets PET (retrofitted ABW_1)

The experimental campaign carried out also a test on a retrofitted wall. It is the case of an adobe brick wall (ABW_1) severely damaged under cyclic loading conditions in a test carried out in a previous study at the ITAM. The damaged specimen has been repaired employing the same strengthening technique of the other walls, using geo-nets and plastering the surface with about 2 cm thick layer of mortar. The retrofitted wall has been, thus, tested again under combination of vertical pre-stressing load and cyclic horizontal load. During the loading steps the development of cracking in the central

area of the panel with detachment of mortar plaster and a concentration of damage at the base corners of the specimen were observed. Also in this case, as already observed in the case of the undamaged wall strengthened with reinforced mortar layers, the wall experienced the detachment of the mortar. However, in this case the major detachment is in the central area of the specimen. For higher values of the driven displacement, the out-of-plane detachment of the plaster in the lower part of the wall close to the corners was also observed. Moreover, due to a very high stress concentration in that area, a significant crack appeared and spread in the wall thickness, as reported in Figure 13.

In the Figure 14 the global envelope curve of the maximum force and corresponding displacement at the top of the wall cyclic for particular loading are showed.

Fig. 13: Vertical crack in the wall thickness

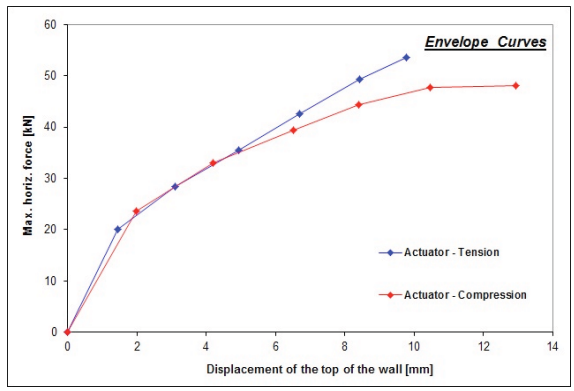

Fig. 14: Envelope curves for retrofitted adobe wall by the geo-nets PET (ABW_4).

2.5. ABW_5 – Adobe brick wall reinforced by the geo-nets (PP)

The further tested reinforcement of adobe walls was the reinforcement by PP geo-nets. The nets were attached to the both surface of the wall by means of steel staples shooted by pneumatic pistol. Figure 15 presents the crack pattern at failure registered for the wall with reinforced plaster by PP geo-nets after test. The behaviour of this reinforced wall is the same as the behaviour of the wall ABW_3. It is, thus, evidenced the typical behaviour of walls strengthened by means of this technique. Also in this case the wall experienced the detachment of the mortar. However, in this case the major detachment is in the central area of the specimen. For higher values of the driven displacement, the out-of-plane detachment of the plaster in the lower part of the wall close to the corners was also observed. Moreover, due to a very high stress concentration in that area, a significant crack appeared and spread in the wall thickness. The cracks in the case ABW_3 and ABW_5 are similar. The envelope curve of the maximum horizontal force and the correspondent displacement obtained from the cyclic curves for each step of loading are plotted in Figure 16.

Fig. 15: Vertical crack in the wall thickness

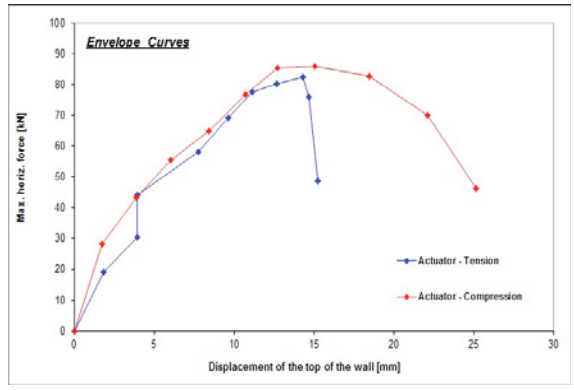

Fig. 16: Envelope curves for retrofitted adobe wall with geo-nets PP (ABW_5).

3. Evaluation and interpretation of results

In the following paragraphs, the results and the interpretation of the experimental tests on adobe brick walls are presented in terms of deformation capacity. In particular, attention is paid to the resulting ductility ratio μ_u (equal to ratio between ultimate displacement δ_u and elastic displacement δ_e). Clearly, the results in terms of deformation capacity are influenced by several factors such as the geometry of the specimen, the level of compression and the boundary conditions. Still, it is difficult from the results analyzed herein to find a clear trend regarding the influence of the vertical stress on deformation capacity. Another issue that seem to affect the results is represented by the dimensions of the specimens which are in turn determined by the available experimental facilities. The confinement provided by the top and bottom restrains in these small specimens can affect the results especially as regards the cracking initiation and propagation with respect to specimens having larger dimensions.

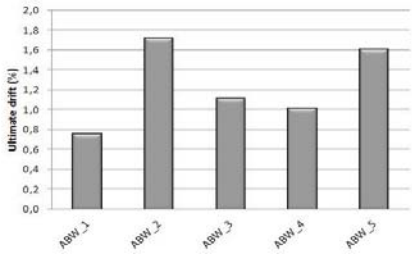

Fig. 17: Ultimate drift

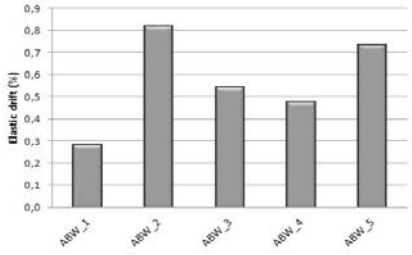

Fig. 18: Elastic drift

In conclusion, the values of ultimate drift are extremely dispersed. The minimum value is related to the specimen ABW_1 and it is equal to 0,76%. The mean value of the ultimate drift of all the tests is equal to 1,24%, see Figure 17. The elastic drift is depends on the reinforcement technique. The greatest value have the specimens ABW_2 and ABW_5, see Figure 18. The values of ultimate displacement ductility of the specimens are very low but quite homogenous, see Figure 19.

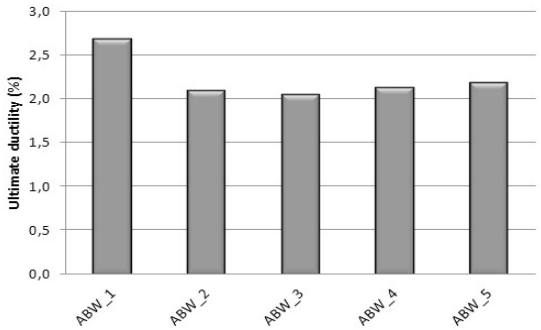

Fig. 19: Ductility

The next comparison is by the energy dissipation. Energy dissipation was calculated from the area of a hysteresis loop. The area was determined from one cycle in a given step. The tests carried out here provide several important results for adobe brick walls. It has been shown that steel wire ropes on an adobe wall surface increase significantly the energy dissipation of the wall. The effectiveness of the system is evident also in terms of increment of the displacement capacity of the wall. This type of reinforcement is very cheap in costs and the most efficient from the point of view of the strengthening from the all used method. It was observed that the application of the reinforced mortar layers onto the wall's surfaces allows the specimen to reach a higher value of energy dissipation. Moreover, an increment in terms of ductility is also registered. Geo-nets have also a better ratio of strength to the strength of brick and, therefore, it is favourable to apply them. Unlike in the case of steel wire ropes, there is not such a danger of pulling out the reinforcement in the out-of plane. Comparing the energy dissipation of the retrofitted wall by means of geo-nets (PET) with the unreinforced adobe brick wall it can be observed that the stiffness of the retrofitted wall is lower than the stiffness of the control wall, even after the intervention. Comparing the energy dissipation of the retrofitted wall by means of geo-

nets (PET) with the unreinforced adobe brick wall it can be observed that the stiffness of the retrofitted wall is lower than the stiffness of the control wall, even after the intervention. Comparing the force-displacement curve of the reinforced wall by means of geo-nets (PET) with the reinforced wall by means of geo-nets (PP) it can be observed that the strengthening with mortar reinforced with both geo-net is similar. However, energy dissipation is greater in the use of geo-nets (PP), see Figure 20.

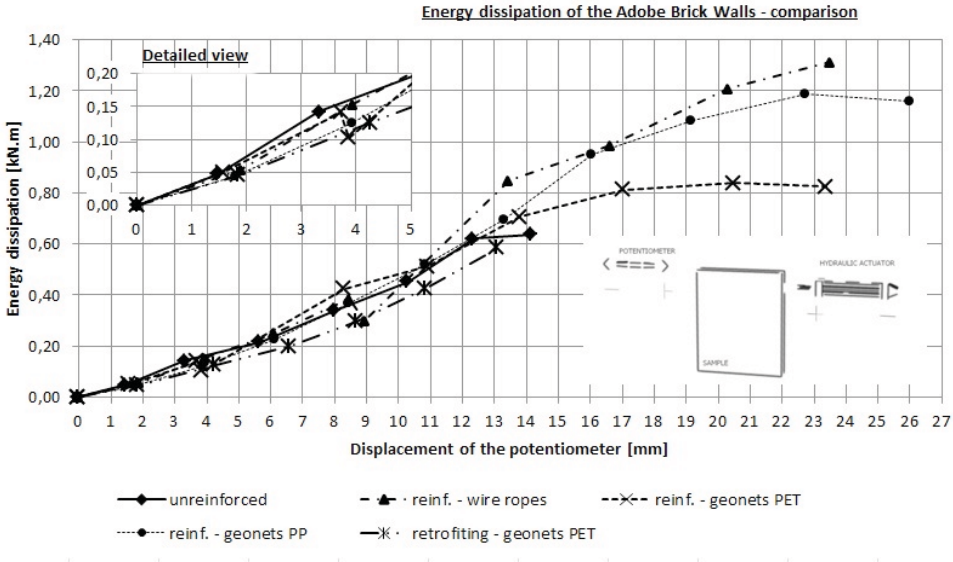

Fig. 20: Comparison of the energy dissipation

Acknowledgement
This work was supported by NIKER project (New integrated knowledge based approaches to the protection of cultural heritage from earthquake-induced risk), Grand Agreement no. 244123.

References

D3.1 2010*:* Inventory of earthquake-induced failure mechanisms related to construction types, structural elements, and materials; *Deliverable 3.1, Project NIKER (Grand Agreement No.: 244123)*

D4.1 2010: Specification for laboratory specimens and testing strategies on walls; *Deliverable 4.1, Project NIKER (Grand Agreement No.: 244123)*

D4.3 2010: Technical report with the experimental results on vertical elements; *Deliverable 4.3, Project NIKER (Grand Agreement No.: 244123).*

Magenes G., Morandi P., (2008a), Proposal for the evaluation of the q-factor from cyclic test results of masonry walls, *ESECMaSE project*, University of Pavia and Eucentre unpublished report

18th International Conference
ENGINEERING MECHANICS 2012
Svratka, Czech Republic, May 14 – 17, 2012

pp. 1573–1579
Paper #46

EXPERIMENTAL INVESTIGATION OF PEDESTRIAN LEVEL WINDS USING MULTIPLE MEASURING METHODS

D. Zacho*, P. Michálek*

Abstract: *In the project, methods for the pedestrian wind comfort determination were investigated. Few methods can be used for the qualitative and quantitative measurement of the wind condition at the pedestrian level. Pressure difference measurement by the omnidirectional Irwin probes, the Particle Image Velocimetry, the Hot wire anemometry, flow visualization by a little flags, sand spreading on surface around the building model, were used during solving this project. The Irwin probes are most frequently used for the pedestrian wind comfort measurement. The velocity calibration of the Irwin probe isn't trivial so other methods were used for its verification. In this contribution the comparison of all mentioned methods was described.*

Keywords: ***Pedestrian, pedestrian wind comfort, boundary layer wind tunnel, particle image velocimetry, environment, physical modeling.***

1 Introduction

The monitoring of the wind conditions at pedestrian level is very interesting topic for Central Europe. The criteria of the pedestrian wind comfort were set in countries with strong wind exposition (Nederland, Denmark, Great Britain, France, USA, Japan, …) first.

The expansion of the high-rise building development in Czech city centers needs the prediction of the pedestrian wind condition and it could be interesting for the Civil service of the Czech Republic. The High rise building can greatly affect the wind condition at the pedestrian level. Windy quiet rest area could be affected by the wind generated by new High-rise building. Such area would be good just for kiteflying.

The forecast of the wind condition at the pedestrian level can be done by the methods of physical or mathematical modeling of the atmospheric boundary layer. The physical modeling includes quantitative and qualitative methods. The qualitative method is for example visualization by the sand, small paper flags, cotton fibers, oil coating etc. The quantitative methods are the hot wire anemometry at the position, Particle image velocimetry (time resolved PIV), pressure measurement with the Irwin probes, measurement with the thermistors at the positions etc.

In case of the complicated topographic model, using few methods for the prediction of the pedestrian wind comfort is suitable. For example, visualization by sending or small paper flags, hot wire anemometry, and PIV in the area of interest.

The results of the pedestrian wind comfort prediction can use for the planning authority when they have to approve new project of high-rise building in the city centre for example.

2 Methods of the pedestrian wind conditions monitoring

The qualitative methods give information about the wind direction in the parter of the complex of building and the quantitative methods can give information about the wind speed and the wind speed fluctuation at the monitored positions. The pedestrian wind comfort is assessed in accordance with the criteria which were developed for the specific locality (Nederland, Denmark, USA, ...). The criteria

* Mgr. David Zacho: Výzkumný a zkušební letecký ústav, a.s., Beranových 130; 199 05, Prague; CZ, e-mail: zacho@vzlu.cz

* Ing. Petr Michálek, Ph.D.: Výzkumný a zkušební letecký ústav, a.s., Beranových 130; 199 05, Prague; CZ, e-mail: michalek@vzlu.cz

were made on base of subjective feelings of people which were surveyed by questionnaires. Unfortunately the criteria of the pedestrian wind comfort are absent for Central Europe.

2.1 Visualization by cotton fiber or small paper flags

This method is focused on the wind direction determination and depiction of the uniformity of the flow at the monitored positions. The cotton or the flags are put in surrounding of the high-rise building models. The cotton or the flags can rotate around its vertical axes. Into the model with cotton or flags the atmospheric boundary layer comes and the cotton or flags follow the wind with its gusts. The cotton or flags can be photographed with different shooter speed or with high speed camera. The resulting image of the flow field around the buildings model can be seen immediately after capturing of the photos or videos.

2.2 Visualization by sanding

The Vicinity of the building model or of the complex of buildings is filled with the sanding (pollen, small-grained sand ...) in uniform and thin layer. Then the modeled situation is exposed to the wind with the atmospheric boundary layer conditions with constant wind speed above the boundary layer. The building or complex of buildings forms the wind at the pedestrian level and the sending is swept from areas with the intensifying wind speed. If the wind speeds above the boundary layers increase the sanding will be swept over largest areas then before. If the photos will be taken there the maps of the sanding in different increasing wind speed there could make the sum of all pictures and there the map of the wind situation at pedestrian level in vicinity of the observe building or complex of building can be obtained.

2.3 The Hot Wire Anemometry

This method makes determining the field of the wind speed around the building model possible. It is standard method of anemometry which determining the mean velocity and the fluctuation part of the turbulent wind speed enables. The hot wire probes have high sensitivity to the wind direction. The building or complex of buildings is able to generate wind which direction can be each of 360 degrees with the same probability. There is need to determine the wind direction before the measurement with the hot wire. It could be disadvantage of using this method for the pedestrian level wind assessment.

2.4 Irwin probes

The Irwin probes (IP) and their physics are described in article H. P. A. H. Irwin, 1981. The IP is the omnidirectional pressure probe which consists from two small tubes with same longitudinal axis. The outer tube is mounted as at the same level as surrounding surface of the model and inner tube is placed at the pedestrian height (the body height or the centre of human body height). The pressure signal is connected with the wind speed by the hot wire anemometry. The mean value and the standard deviation of the wind speed signal as wrote Irwin can be reconstructed. This probe works good if the wind comes perpendicular with the axis of the IP tubes. General situation around building includes also vertical movement of the air mass. It could be the disadvantage of this method.

2.5 Particle Image Velocimetry measurement

The PIV system makes possible showing the field of wind speed. If Time resolved PIV system is used, the mean value and standard deviation of the wind speed signal at all position in the shot can be determined. The clear and concise description of the PIV principle can be found at the Dantec dynamics web page for example. Extensive description of the PIV is in the Raffel, M. & Hansen, S. (2007). The wind flow is filled with particles with diameter about two micrometers and the light sheet is placed at the monitored area. The pictures of the particles in the light sheet in exactly time distance are taken. The correlation between two images gives information about shift of particles in subsection parts of full shot. The known time and the known shift of the particles between two pictures give information about size and direction of the wind velocity vector.

This method depends on quantity of particles in the monitored area and on the light sheet position. If there is complicated geometry of the building model or the complex of buildings model there could

be problem with the light sheet setting. It could be disadvantage of the use of the PIV method for the pedestrian wind comfort assessment.

3 Results

This article describes the result of few experiments and measurement which were performed in Boundary Layer Wind Tunnel (BLWT) in Výzkumný a zkušební letecký ústav, s.s. (VZLU). Simulation of the atmospheric boundary layer in BLWT VZLU is correct and its similarity with real atmospheric boundary layer is in scale approximately 1:350. Simulation of the III. category of terrain as it is prescribed in codes (EUROCOD, Czech standard, ...) was used. The models of building were made in 1:350 scale and it guarantees the geometric similarity of this physical modeling.

The typical problem of the high rise building and its influence to the pedestrian wind comfort was chosen. It is the DownWash (DW) effect. It means that the high-rise building give a direction to the wind from higher part of the atmosphere and the wind blow down along the building envelope. The higher mean wind speed and strong wind gust is coming into the pedestrian level around the high-rise building. It is strongly unfavorable influence of the high-rise building on the pedestrian wind comfort.

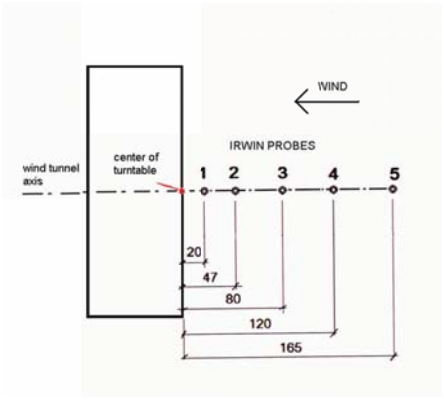

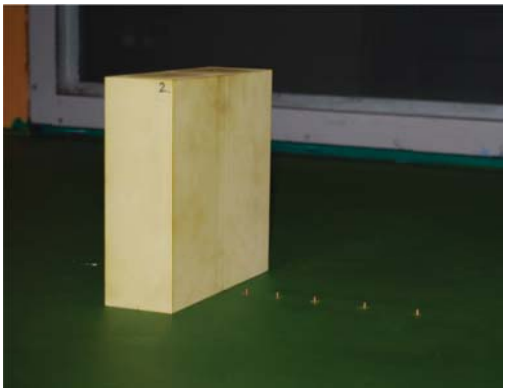

Fig. 1 & Fig 2: Experimental settings, downwash measurement.

The building of Faculty of civil engineering CVUT in Prague was chosen as the common building. Just high-rise part of the building was modeled. The model had dimensions 175 mm high, 175 wide and 55 mm depth. The position of the measurement point is labeled as ratio between distance of the point from the foot of the building and the height of the building (Fig. 1 & Fig. 2).

All tasks which were made during this work were focused on the comparison of various methods of the pedestrian wind condition determination. Specifying methodology for the pedestrian comfort assessment was the aim. It is very complex problem and using just one method isn't possible. It needs combination of visualization and measurement methods.

Literature shows the IP as good tool for this measurement so it was chosen as main probe for the pedestrian wind measurement. The calibration of the IP is realized on base of HWA. The Hot wire probe has strong sensitivity to the wind direction so the visualization with small paper flags at the IP positions was performed. Fig 3 shows position with clear wind direction and without it.

The calibration constants as it is required in the Irwin article were calculate from the pressure signal on IP 5 and the flow speed signal from HWA which was measured above the IP 5 position.

The wind speeds from IP measurement and from the HWA measurement at all points are compared in Fig. 7.

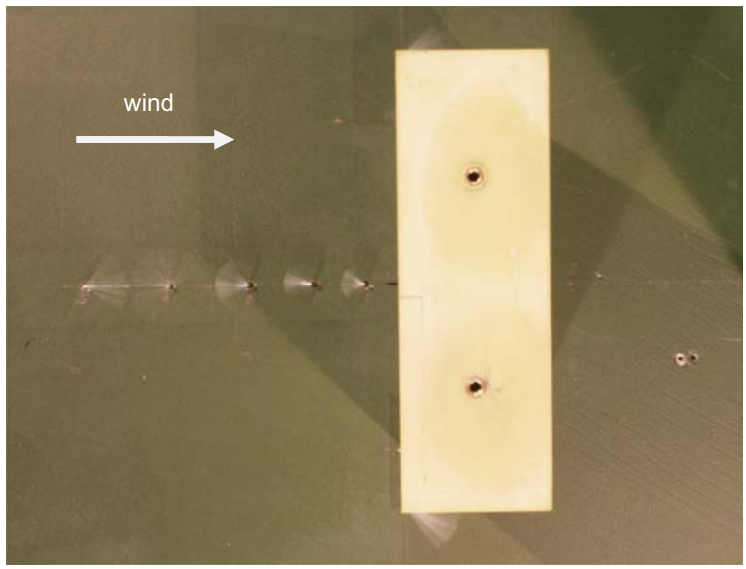

Fig. 3: Visualization of the wind flow by the paper flags.

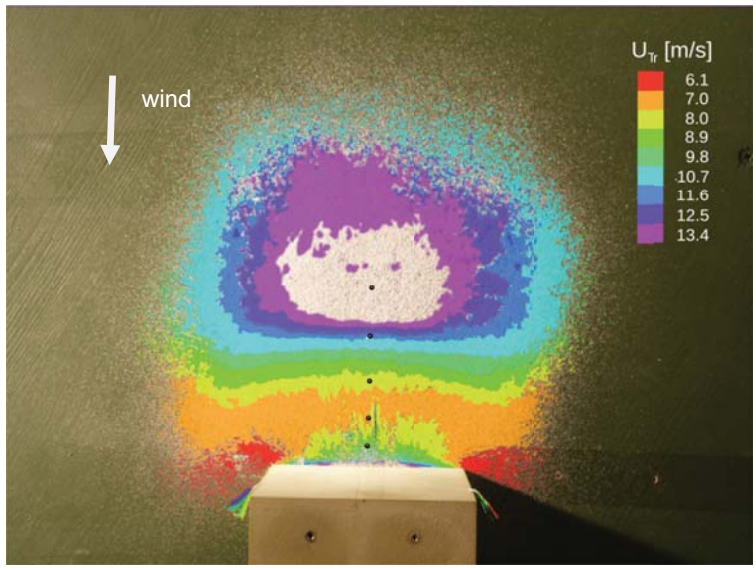

Fig. 4: Suma of nine digital pictures of the sending visualization method.

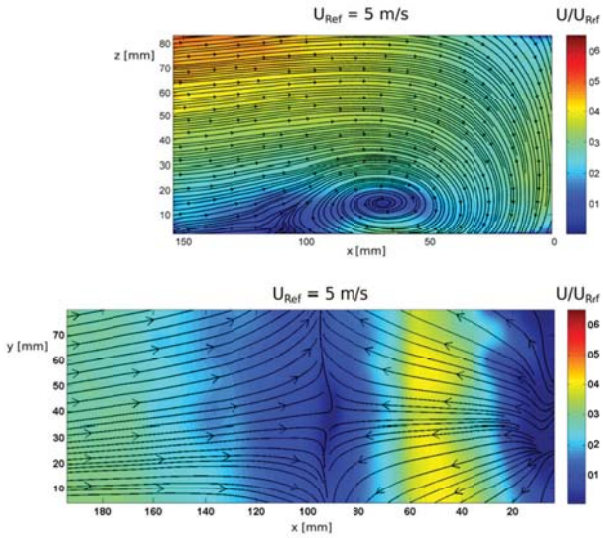

Fig. 5: Flow field in downwash effect in front of the building.

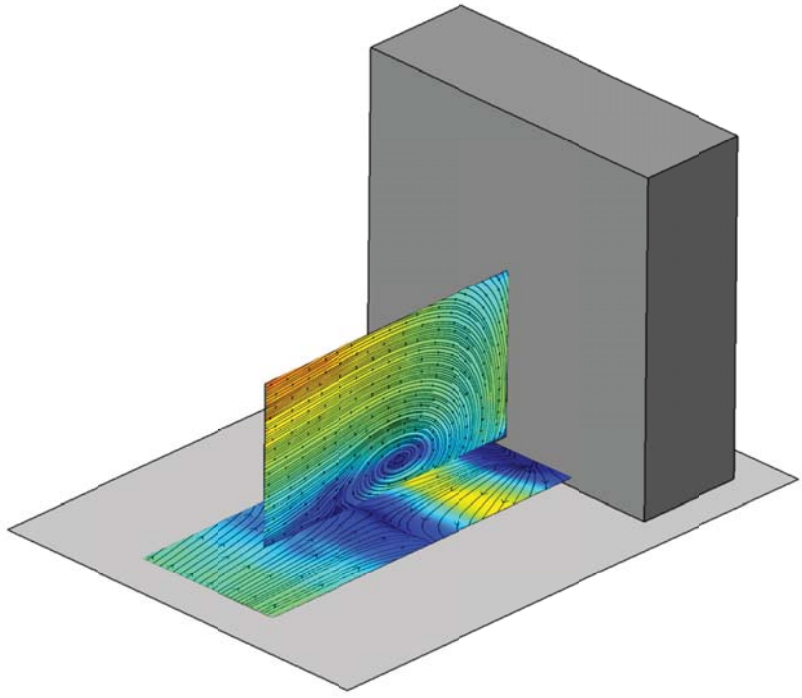

Fig. 6: The PIV results at the sagittal and the transversal plane.

The visualization by sanding method was used for the estimation of the flow field around the building. It is effective method, but the results depend on the weight of the sanding material and on the thickness of the sanding layer. The IP, HWA or PIV measurement are performed at the height of pedestrian but the sending is much smaller. But this method can show the areas around the building with strong wind exposure. The digital photography of the sequential swept of the sanding could be processed and the result of the digital image processing is on Fig. 4. The colors of the Fig. 4 represent bare areas which were bared at constant wind speed above the boundary layer. White color is the color of the sanding (the silica sand was used). The stagnation area is visible around the IP 5.

The PIV method is very effective visualization and measurement method for showing of the flow field in the monitored area. The Time Resolved PIV method was used with the 150 frames per second of the shooting frequency. Three thousand double frames were taken. It is enough long signal for the statistical analysis of the wind speed signal.

The comparison of the results from quantitative measurement methods is shown in Fig. 7. On horizontal axis is the ratio between the distance of the IP from foot of the building and the height of the modelled building. On vertical axis, there is the ratio between the wind speed which was measured at the monitored measurement point and the reference wind speed which was measured at the level which corresponds 10 m level in full scale. The relevant are: compressions of the IP and PIV measurement (methods which show the length of the velocity vector) and the HWA and PIV-U measurement (methods which show longitudinal part of the velocity vector).

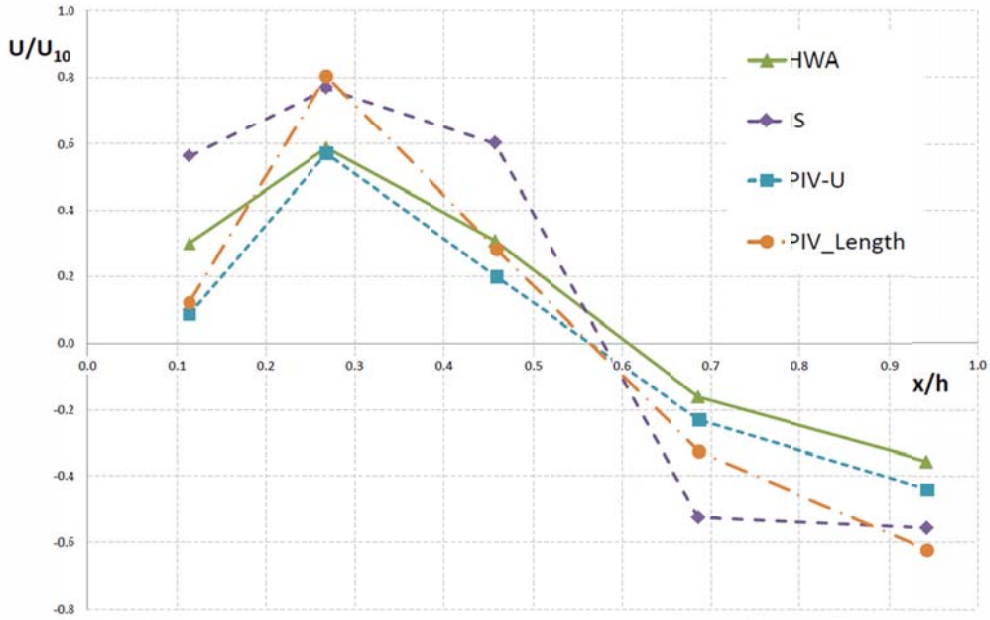

Fig. 7: Graph of the pedestrian wind measurement.

4 Conclusions

Correct prediction of the wind conditions at the pedestrian level around the new high-rise building can be created on base of combination of few methods of measurement and visualization.

Combination of the visualization with small paper flags and IP is the simplest one and this combination can be used in many positions in the model irrespective complexity of geometry modeled built-up area.

Time resolved PIV system could be very effective for the pedestrian wind comfort assessment. The setting of the PIV measurement (positioning of the light sheet) could be very expensive at the complicate geometry of the model.

The suitable solution of the pedestrian wind comfort assessment is the using of combination of methods mentioned above. The visualization can show areas with strong wind exposition and there measurements with the HWA or PIV can be performed. These case studies of the pedestrian wind comfort have to be carry out with consideration to effective employment of means.

Acknowledgement

These works have been supported from Institutional funding, which were provided by Ministry of Industry and Trade of Czech Republic.

References

Irwin, H. P. A. H. (1981) A simple omnidirectional sensor for wind-tunnel studies of pedestrian-level wind, . *Journal of wind engineering and industrial aerodynamics*, 7, pp 219-239;

Wu, H. & Stathopoulos, T. (1994) Further experiments on Irwin's surface wind sensor, *Journal of wind engineering and industrial aerodynamics*, 53, pp 441-452;

Stathopoulos, T. (2006) Pedestrian level winds and outdoor human comfort, *Journal of wind engineering and industrial aerodynamics*, 94, pp 769-780;

Raffel, M. & Hansen, S. (2007) *Particle Image Velocimetry: a practical guide.* Springer, Berlin.

18th International Conference
ENGINEERING MECHANICS 2012
Svratka, Czech Republic, May 14 – 17, 2012

pp. 1581–1588
Paper #29

MATHEMATICAL MODELLING OF A DAMPING ELEMENT WORKING ON THE PRINCIPLE OF SQUEEZING TWO LAYERS OF NORMAL AND MAGNETORHEOLOGICAL OILS ARRANGED IN SERIES AND ITS APPLICATION FOR VIBRATION ATTENUATION OF A RIGID ROTOR

J. Zapoměl[*], P. Ferfecki[*], J. Kozánek[*]

Abstract: *The oscillations amplitude and the forces transmitted between the rotor and the stationary part can be considerably reduced if damping devices are added to the coupling elements placed between the rotor and its casing. To achieve their optimum performance the damping effect must be controllable. In this paper there is proposed a new concept of a damping element working on the principle of squeezing two lubricating layers that are formed by normal and magnetorheological oils and that are mutually separated by a movable thin ring. Unlike to previous solutions, the magnetorheological layer always decreases the amount of damping. This decrease can be controlled and is required by certain operating conditions. In the developed mathematical model the normal and magnetorheological oils are represented by Newtonian and Bingham materials respectively and the pressure distribution in the lubricating layers is governed by the Reynolds' equations. The examination of the properties and efficiency of the proposed damping element was carried out by means of its application for vibration attenuation of a rigid unbalanced rotor. Results of the performed computational simulations proved that a suitable control of the damping effect made it possible to reach an optimum compromise between reduction of the oscillation amplitude and minimizing magnitude of the force transmitted into the rotor casing. A big advantage of the proposed damping element is that it does not need a complicated and expensive control system for its operation.*

Keywords: ***Controlled damping, new semiactive damping element, magnetorheological oil layer, Bingham fluid, modified Reynolds equation.***

1. Introduction

Unbalance of the rotating parts is one of the main sources of time variable forces that are transmitted between the rotor and its stationary part. Their magnitude can be significantly reduced if the rotor is flexibly supported and if the damping devices are added to the coupling elements. The theoretical analyses, confirmed by practical experience, show that to achieve the optimum performance of the rotating machines during their steady state running, the damping devices must be controllable.

One of the first reported works dealing with controllable dampers was published by Burrows et al., (1984). The damper was of a squeeze film kind and the authors examined the effect of controlling the oil-supply pressure on the change of the system damping coefficients. Another design of a controllable squeeze film damper was reported by Mu et al., (1991). In their solution, the gap between the damper inner and outer rings is conical filled with classical oil. Moving of the outer ring in the axial direction changes the damper radial clearance and land length, which changes the damping force. A new concept of controlling the damping devices is represented by magnetorheological dampers. Much work has been already done in this field. Wang et al., (2003) studied experimentally the vibration characteristics and the control method of a flexible rotor equipped with a magnetorheological squeeze

[*] Prof. Ing. Jaroslav Zapoměl, DrSc.: Institute of Thermomechanics, Dolejškova 1402/5; 182 00, Prague 8; CZ, e-mail: jaroslav.zapomel@vsb.cz

[*] Ing. Petr Ferfecki, PhD.: Institute of Thermomechanics, Dolejškova 1402/5; 182 00, Prague 8; CZ, e-mail: petr.ferfecki@vsb.cz

[*] Ing. Jan Kozánek, CSc.: Institute of Thermomechanics, Dolejškova 1402/5; 182 00, Prague 8; CZ, e-mail: kozanek@it.cas.cz

film damper. Zapoměl & Ferfecki (2009a) developed a mathematical model of a short magnetorheological damper of a squeeze film kind and utilized it for computational simulations of a transient response of a rigid rotor passing the critical speeds (Zapoměl & Ferfecki, 2009b). The same authors (Zapoměl & Ferfecki, 2011) proposed a combined damper formed by two lubricating layers of normal and magnetorheological oils arranged in parallel. Their investigations done by means of computational simulations were focused on its contribution to attenuation of the steady state vibration of a flexibly supported rigid rotor and on its stability.

In this paper there is investigated a new semiactive damping element generating the damping force by squeezing two mutually separated layers of normal and magnetorheological oils. The damping effect is controlled by changing the magnetic flux passing through the magnetorheological film. Results of the performed simulations show that a suitable setting of magnitude of the damping effect enables to reach the optimum compromise between attenuation of the rotor vibration amplitude and reduction of the forces transmitted into the rotor casing and its foundation plate.

2. Mathematical model of the new damping element

The principal parts of the proposed damping element (Figure 1) are the inner and outer rings between which there are two mutually separated layers of lubricating liquids. The inner ring is movable. It is coupled with the damper's body by a flexible element (squirrel spring) and supports the rolling element bearing, in which the rotor journal is mounted. The outer ring is stationary, fixed to the damper housing. The lubricating films are formed by normal (inner) and magnetorheological (outer) oils and their mutual separation is accomplished by a thin ring flexibly coupled with the damper's body. The damping device is equipped with an electric coil generating magnetic field. The magnetic flux passes through the layer of magnetorheological liquid and because its resistance against the flow depends on magnetic induction the change of the electric current can be used to control the damping effect.

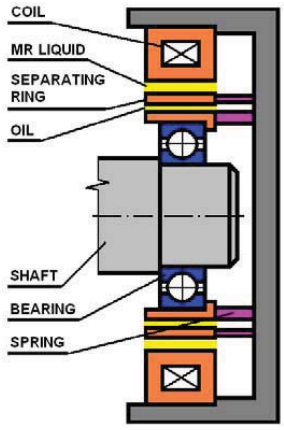

Fig. 1: Scheme of the proposed damping element

The developed mathematical model of the proposed constraint element is based on assumptions of the classical theory of lubrication but with some modifications. The normal and magnetorheological oils are represented by Newtonian and Bingham materials with the yield shear stress depending on magnetic induction. A further attention is focused only on the dampers whose geometric and design parameters make it possible to treat them as short (Krämer, 1993).

The thickness of the oil films depends on positions of the centres of the damper rings relative to the damper body (Krämer, 1993)

$$h_{CO} = c_{CO} - e_H \cos(\varphi - \gamma), \tag{1}$$

$$h_{MR} = c_{MR} - e_H \cos(\varphi - \gamma). \tag{2}$$

h_{CO}, h_{MR} denote the thickness of the films of classical and magnetorheological oils, c_{CO}, c_{MR} are the widths of the gaps between the rings filled with classical and magnetorheological oils, e_H denotes the rotor journal eccentricity, φ is the circumferential coordinate and γ denotes the position angle of the line of centres.

The pressure distribution in the layer of classical oil is governed by a Reynolds equation modified for short squeeze film dampers (Krämer, 1993)

$$\frac{\partial^2 p_{CO}}{\partial Z^2} = \frac{12\eta}{h_{CO}^3}\dot{h}_{CO}. \tag{3}$$

p_{CO} denotes the pressure in the layer of classical oil, η is the normal oil dynamic viscosity, Z is the axial coordinate and $\dot{(\cdot)}$ denotes the first derivative with respect to time.

To describe the pressure field in the layer of the magnetorheological fluid, the Reynolds equation has been modified for Bingham material (Zapoměl & Ferfecki, 2009a)

$$h_{MR}^3 p_{MR}'^3 + 3\left(h_{MR}^2\,\tau_y - 4\eta_B\,\dot{h}_{MR}\,Z\right)p_{MR}'^2 - 4\tau_y^3 = 0\,, \qquad \text{for} \qquad p_{MR}' < 0\,, \tag{4}$$

$$h_{MR}^3 p_{MR}'^3 - 3\left(h_{MR}^2\,\tau_y + 4\eta_B\,\dot{h}_{MR}\,Z\right)p_{MR}'^2 + 4\tau_y^3 = 0 \qquad \text{for} \qquad p_{MR}' > 0\,. \tag{5}$$

Both these equations are valid for $Z > 0$. p_{MR}, p_{MR}' denote the pressure and the pressure gradient in the axial direction in the layer of magnetorheological liquid, η_B is the Bingham viscosity and τ_y represents the yield shear stress.

Equations (3), (4) and (5) are solved for the boundary conditions expressing that the pressure at the damper's ends is equal to the pressure in the ambient space. Relationships (4) and (5) represent polynomial algebraic equations of the third order. The sought root must fulfil the conditions that the pressure gradient p_{MR}' is real (not complex), is negative (for equation (4)) or positive (for equation (5)) and satisfies the relation

$$\left|p_{MR}'\right| > \frac{2\tau_y}{h_{MR}}\,. \tag{6}$$

After calculation of the pressure gradient from equations (4) or (5) the pressure distribution in the axial direction is obtained by the integration

$$p_{MR} = \int p_{MR}'\,\mathrm{d}Z\,. \tag{7}$$

In the damper simplest design arrangement the rings, between which there is a layer of magnetorheological liquid, can be considered as a divided core of an electromagnet. Then the dependence of the yielding shear stress on magnetic induction can be approximately expressed

$$\tau_y = k_y\left(\frac{N_C\,I}{2\,h_{MR}}\right)^{n_y}. \tag{8}$$

k_y and n_y are material constants of the magnetorheological liquid, N_C is the number of the coil turns and I is the electric current.

In the areas where the thickness of the lubricating films rises with time ($\dot{h}_{CO} > 0\,, \dot{h}_{MR} > 0$) a cavitation is assumed. Pressure of the medium in these regions remains constant and equal to the pressure in the ambient space. In noncavitated areas the magnitude of the pressure is governed by solutions of the Reynolds equation (3) and integral (7).

Components of the damping forces are calculated by integration of the pressure distributions around the circumference and along the length of the damping element taking into account a cavitation in the oil films.

$$F_{MRy} = -2\,R_{MR}\int_0^{2\pi}\int_0^{\frac{L}{2}} p_{DMR}\cos\varphi\,\mathrm{d}Z\,\mathrm{d}\varphi\,, \tag{9}$$

$$F_{MRz} = -2\,R_{MR}\int_0^{2\pi}\int_0^{\frac{L}{2}} p_{DMR}\sin\varphi\,\mathrm{d}Z\,\mathrm{d}\varphi\,, \tag{10}$$

$$F_{COy} = -2\,R_{CO}\int_0^{2\pi}\int_0^{\frac{L}{2}} p_{DCO}\cos\varphi\,\mathrm{d}Z\,\mathrm{d}\varphi\,, \tag{11}$$

$$F_{COz} = -2\,R_{CO}\int_0^{2\pi}\int_0^{\frac{L}{2}} p_{DCO}\sin\varphi\,\mathrm{d}Z\,\mathrm{d}\varphi\,. \tag{12}$$

F_{COy}, F_{COz}, F_{MRy}, F_{MRz} are the y and z components of the hydraulic forces produced by the layers of normal and magnetorheological oils respectively, R_{CO}, R_{MR} are the mean radii of the layers of normal and magnetorheological oils, L is the axial length of the damping element and p_{DCO}, p_{DMR} denote the pressure distributions (taking into account different pressures in cavitated and noncavitated regions) in the layers of normal and magnetorheological oils.

3. The equation of motion of a rigid rotor damped by the new damping elements

The investigated rotor (Figure 2) consists of a shaft and of one disc and with the stationary part it is flexibly coupled by the proposed damping elements at both its ends. The rotor is considered to be absolutely rigid, it is unbalanced, turns at constant angular speed and is loaded by its weight. The system is symmetric relative to the plane perpendicular to the shaft axis. The squirrel springs are prestressed to be eliminated their deflection caused by the rotor weight.

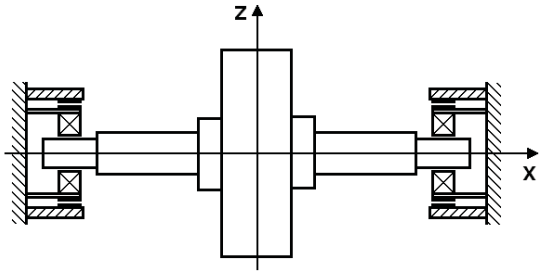

Fig. 2: Scheme of the investigated rotor system

The rotor vibration is governed by a set of four equations of motion

$$m_R\ddot{y}_1 + b_P\dot{y}_1 + 2\,k_{DA}y_1 = m_R e_T\omega^2\cos(\omega t+\psi_o) + 2\,F_{COy}\left(y_1,z_1,y_2,z_2,\dot{y}_1,\dot{z}_1,\dot{y}_2,\dot{z}_2\right), \tag{13}$$

$$m_R\ddot{z}_1 + b_P\dot{z}_1 + 2\,k_{DA}z_1 = m_R e_T\omega^2\sin(\omega t+\psi_o) + 2\,F_{COz}\left(y_1,z_1,y_2,z_2,\dot{y}_1,\dot{z}_1,\dot{y}_2,\dot{z}_2\right), \tag{14}$$

$$m_{SR}\ddot{y}_2 + 2\,k_{SR}y_2 = -2\,F_{COy}\left(y_1,z_1,y_2,z_2,\dot{y}_1,\dot{z}_1,\dot{y}_2,\dot{z}_2\right) + 2\,F_{MRy}\left(y_2,z_2,\dot{y}_2,\dot{z}_2\right), \tag{15}$$

$$m_{SR}\ddot{z}_2 + 2\,k_{SR}z_2 = -2\,F_{COz}\left(y_1,z_1,y_2,z_2,\dot{y}_1,\dot{z}_1,\dot{y}_2,\dot{z}_2\right) + 2\,F_{MRz}\left(y_2,z_2,\dot{y}_2,\dot{z}_2\right). \tag{16}$$

m_R is the rotor mass, b_P is the coefficient of the rotor external damping, k_{DA} is stiffness of the squirrel spring, m_{SR}, k_{SR} are the mass of the ring separating the lubricating layers and the stiffness of its support respectively, ω is angular speed of the rotor rotation, e_T is eccentricity of the rotor unbalance, t is the time, ψ_o is the phase shift, y_1, z_1, y_2, z_2 are displacements of the rotor centre (centre of the rotor journal) and of the centre of the ring separating the lubricating layers and $\dot{()}$, $\ddot{()}$ denote the first and second derivatives with respect to time.

The steady state solution of the equations of motion is obtained by a trigonometric collocation method. As the system is symmetric and the squirrel springs are prestressed, it can be assumed that trajectories of the rotor and the rings centres are circular. Then it holds for the displacements

$$y_1 = r_{C1}\cos\omega t - r_{S1}\sin\omega t\,, \tag{17}$$

$$z_1 = r_{C1}\sin\omega t + r_{S1}\cos\omega t\,, \tag{18}$$

$$y_2 = r_{C2}\cos\omega t - r_{S2}\sin\omega t\,, \tag{19}$$

$$z_2 = r_{C2}\sin\omega t + r_{S2}\cos\omega t\,. \tag{20}$$

Substitution of (17) - (20) and of their first and second derivatives with respect to time in (13) - (16) gives a set of four nonlinear algebraic equations. As the number of resulting equations is equal to the number of unknown parameters (r_{C1}, r_{S1}, r_{C2}, r_{S2}), only one collocation point of time is needed for their determination. For the moment of time $t = 0$ they read

$$\left(2k_{DA} - \omega^2 m_R\right) r_{C1} - \omega b_P r_{S1} = m_R e_T \omega^2 \cos\psi_o + 2F_{COy}\,, \tag{21}$$

$$\omega b_P r_{C1} + \left(2k_{DA} - \omega^2 m_R\right) r_{S1} = m_R e_T \omega^2 \sin\psi_o + 2F_{COz}\,, \tag{22}$$

$$\left(2k_{SR} - \omega^2 m_{SR}\right) r_{C2} = -2F_{COy} + 2F_{MRy}\,, \tag{23}$$

$$\left(2k_{SR} - \omega^2 m_{SR}\right) r_{S2} = -2F_{COz} + 2F_{MRz}\,. \tag{24}$$

Solution of the set of equations (21) - (24) makes it possible to determine amplitudes of the rotor steady state vibration and of the forces transmitted into the stationary part for the specified angular speeds.

4. Results of the computational simulations

The basic data of the investigated system are : mass of the rotor 450 kg, stiffness of the squirrel spring 2 MN/m, linear coefficient of the rotor external damping 1000 Ns/m, mass of the separating ring 2 kg, eccentricity of the rotor centre of gravity 100 μm, viscosity of the normal oil 0.002 Pas, Bingham viscosity of the magnetorheological liquid 0.3 Pas, length of the damping element 60 mm, mean diameters of the lubricating layers 110 mm (normal oil), 150 mm (magnetorheological oil) and the damper gap width 0.2 mm (normal oil), 1 mm (magnetorheological oil). The task was to analyse dependences of amplitude of the rotor vibration and of the force transmitted through the coupling elements into the stationary part on the rotor angular speed and magnitude of the applied current and to compare them with the allowed values (maximum vibration amplitude 140 μm, maximum transmitted force 800 N).

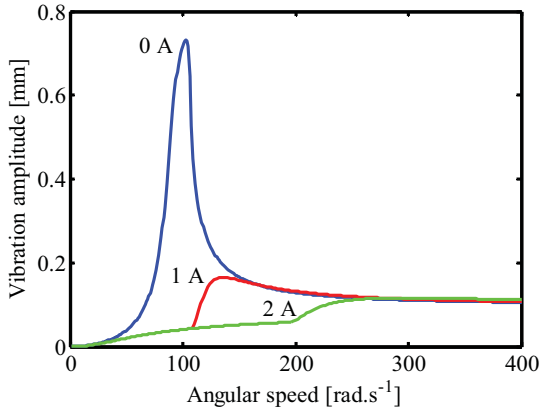

Fig. 3: Frequency response characteristic (centre of the rotor)

Figures 3 and 4 depict the frequency response characteristics of the centres of the rotor (rotor journal) and of the separating ring for several magnitudes of the applied electric current. It is evident

that the increasing current has only little influence on amplitude of the rotor vibration in the region of high velocities. But in the area of low angular speeds the system behaves in a different way. Only large applied current makes it possible to attenuate the vibration sufficiently. The vibration amplitude of the centre of the ring separating the layers of normal and magnetorheological oils approaches to zero if magnitude of the current rises and angular velocity of the rotor decreases. If magnitude of the current is sufficiently high (depending on the speed of rotation), the layer of magnetorheological liquid becomes almost absolutely rigid and the rotor behaves as it would be damped only by normal squeeze film dampers.

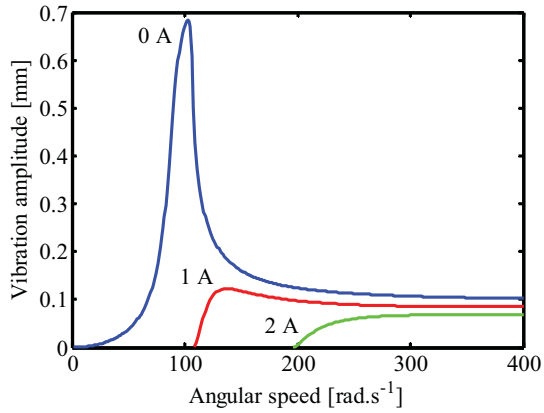

Fig. 4: Frequency response characteristic (centre of the separating ring)

The force is transmitted between the rotor and its casing through the squirrel springs and the damping layers. Figure 5 shows that to minimize magnitude of the total transmitted force in the area of low angular speeds the applied current must be large, in the area of higher angular velocities its magnitude must be zero or very low.

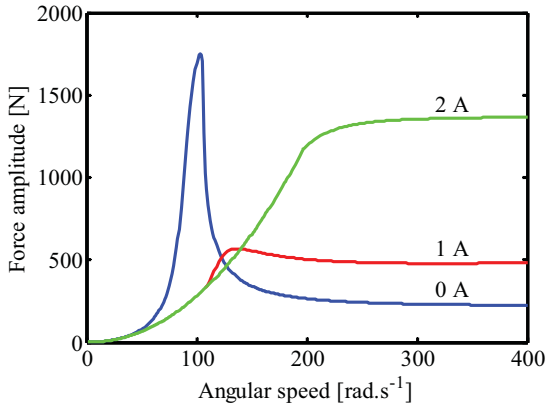

Fig. 5: Transmitted force amplitude – angular velocity relationship

Figures 6 and 7 show the admissible magnitudes of the electric current, for which the requirements put on the maximum allowable vibration amplitude and magnitude of the force transmitted into the stationary part are satisfied, in dependence on the speed of the rotor rotation. The combination of these results is depicted in Figure 8. It is evident that the condition for allowed values of parameters of the rotor steady state vibration can be satisfied in the whole extent of the operating speeds except for the

ones from a small velocity range approximately between 150 and 180 rad/s. In this speed interval amplitude of the vibration cannot be reduced without exceeding the allowed value of the transmitted force.

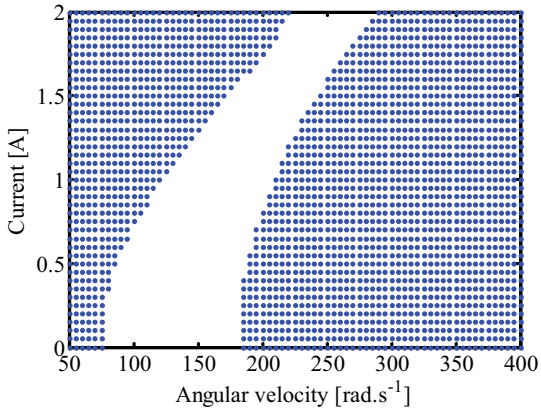

Fig. 6: Current - angular velocity relationship from the point of view of allowed vibration

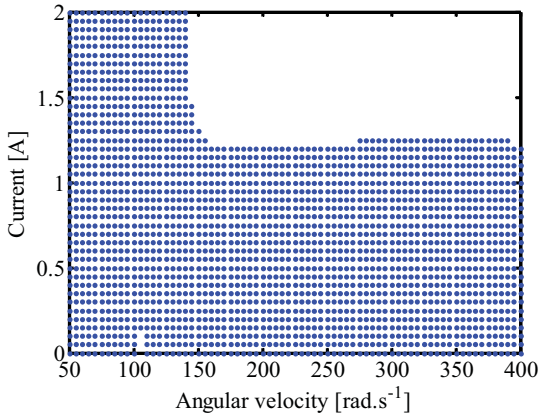

Fig. 7: Current - angular velocity relationship from the point of view of allowed force

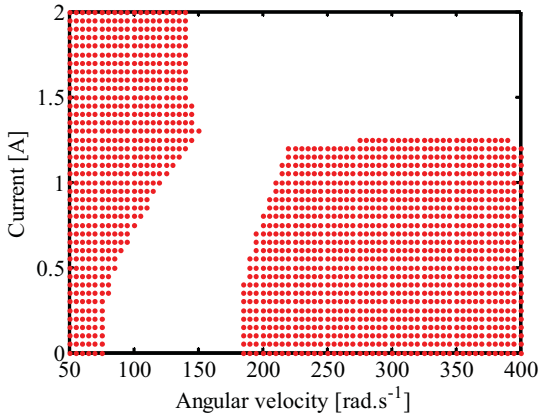

Fig. 8: Current - angular velocity relationship for allowed vibration and force

A detailed analysis of the frequency response characteristics given in Figures 3, 4 and 5 shows that to achieve the optimum performance of the damping device in the velocity interval above approximately 200 rad/s the electric current should be switched off. The decrease of the damping arrives at considerable reduction of the force transmitted into the rotor casing and increase of the rotor vibration amplitude is only negligible.

5. Conclusions

The damping effect of the new proposed damping element is produced by squeezing two layers of lubricating liquids, which are mutually separated by a ring. The layers are formed by normal and magnetorheological oils. The control of the damping force is accomplished by means of the change of magnetic flux passing through the film of magnetorheological liquid. Results of the carried out computational simulations show that a suitable setting of magnitude of the applied current makes it possible to reach the optimum compromise between attenuation of the rotor vibration and reduction of the force transmitted into the stationary part and into the foundation plate. It is evident that at lower angular velocities a higher damping effect is needed to suppress both the vibration and the transmitted force. In the interval of higher velocities large damping arrives at a strong increase of the transmitted force but only at little attenuation of the rotor oscillations. This implies that for these operating conditions it is desirable to switch off the auxiliary magnetorheological damping or to apply only a very small electric current.

Acknowledgement

The work reported here has been supported by research projects AVO Z20760514 and P101/10/0209. This help is gratefully acknowledged.

References

Burrows, C.R., Sahinkaya, M.N. & Turkay, O.S. (1984) An adaptive squeeze-film bearing. *ASME Journal of Tribology*, 106, 1, pp. 145-151.

Krämer, E. (1993) *Dynamics of Rotors and Foundations*. Springer-Verlag, Berlin-Heidelberg-New York.

Mu, C., Darling, J. & Burrows, C.R. (1991) An appraisal of a proposed active squeeze film damper. *ASME Journal of Tribology*, 113, 4, pp. 750-754.

Wang, J., Meng, G. & Hahn E.-J. (2003) Experimental study on vibration properties and control of squeeze mode MR fluid damper-flexible rotor system, in: *Proceedings of the 2003 ASME Design Engineering Technical Conference & Computers and Information in Engineering Conference*, ASME, Chicago, pp. 955-959.

Zapoměl, J. & Ferfecki, P. (2009a) Mathematical modelling of a short magnetorheological damper. *Transactions of the VŠB – Technical University of Ostrava, Mechanical Series*, LV, 1, pp. 289-294.

Zapoměl, J. & Ferfecki, P. (2009b) A computational investigation of vibration attenuation of a rigid rotor turning at a variable speed by means of short magnetorheological dampers. *Applied and Computational Mechanics*, 3, 2, pp. 411-422.

Zapoměl, J. & Ferfecki, P. (2011) Stability investigation of the steady state response of flexibly supported rigid rotors, in: *Vibration Problems ICOVP 2011: The 10th International Conference on Vibration Problems* (J. Náprstek et al. eds), Springer Proceedings in Physics 139, Prague, pp. 521-527.

18th International Conference
ENGINEERING MECHANICS 2012
Svratka, Czech Republic, May 14 – 17, 2012

pp. 1589–1595
Paper #197

APPLICATION OF SENSITIVITY ANALYSIS IN DESIGN OF CHARACTERISTICS OF DAMPING JOINTS IN LOCOMOTIVE RUNNING GEAR

J. Zelenka*, M. Kohout**

Abstract: *Operation of railway vehicles at higher speeds is conditioned by assurance of a stable run of the vehicle in straight track with a high level of geometric parameters. This property is usually reached by retrofitting of a joint between the vehicle body and the bogies with an efficient damping with suitable characteristics. Because the relative motion between the vehicle body and the bogies in the straight track shows low amplitudes and high velocities, special longitudinal dampers – so-called yaw dampers – are used for these purposes. The aim of this paper is a theoretical analysis of the yaw damper characteristics on the stability limit of a locomotive performed by means of sensitivity analysis.*

Keywords: ***Sensitivity analysis, stability of vehicle run, critical speed, yaw dampers, simulations.***

1. Introduction

Nowadays, computer simulations of running and guiding behaviour create an integral part of development of new or modernized rail vehicles. The simulations are practically the only possible way for verification of dynamic properties of the vehicle in the design stage. It is possible to use them for optimization of suspension and damping parameters, as well.

Jan Perner Transport Faculty of the University of Pardubice co-operates with the company CZ LOKO, a.s. on solving of R&D project "TIP" of the Ministry of Industry and Trade of the Czech Republic; the aim of this project is manufacturing of a prototype of a locomotive Class 744.0 as well as preparation of a broad-gauged version of this locomotive according to the GOST standards. The computer simulations of dynamic behaviour of the new locomotive create one of the main parts at the project solving.

2. Locomotive Class 744.0 CZ LOKO

The locomotive Class 744.0 CZ LOKO (see fig. 1) is a four-axled diesel-electric locomotive with AC/AC or AC/DC power transmission which is intended for track as well as shunting service. The maximum speed is 120 km/h. The modular conception of the locomotive allows manufacturing of various versions with a maximum power of combustion engine of 800 up to 1500 kW. Traction drive is assured by means of four asynchronous or serial direct-current axle-mounted nose-suspended traction motors with roller bearing. Each of these motors belongs to one wheelset and has a maximum power of 360 kW.

The main frame of the locomotive is mounted on two two-axled bogies (see fig. 2 and Kopal, 2009) by means of flexi-coil springs. The longitudinal force transmission between the bogie and the locomotive body is performed with a central pivot. The wheelset guiding in the bogie frame is performed by means of connection rods; the primary suspension is created by two flexi-coil springs at each journal box. The vertical (primary as well as secondary) suspension is supplemented by hydraulic dampers; damping of lateral oscillations between the vehicle body and the bogies is performed by two lateral hydraulic dampers per bogie.

* doc. Ing. Jaromír Zelenka, CSc.: University of Pardubice, Jan Perner Transport Faculty, Department of Rail Vehicles, Detached Branch Česká Třebová, Slovanská 452; 560 02, Česká Třebová; CZ, e-mail: jaromir.zelenka@upce.cz

** Ing. Martin Kohout, Ph.D.: University of Pardubice, Jan Perner Transport Faculty, Department of Rail Vehicles, Detached Branch Česká Třebová, Slovanská 452; 560 02, Česká Třebová; CZ, e-mail: martin.kohout@upce.cz

Besides the locomotive for European track gauge 1435 mm, a broad-gauged version of the locomotive for eastern market is developed parallelly. This locomotive, which comes out from the standard-gauged locomotive to a maximum degree, is intended for the "Russian" track gauge 1520 mm and is designed according to the GOST standards. Besides indispensable modifications of the bogie frames and usage of new wheelsets it is necessary to perform a modification of parameters of the suspension (because of the intended total weight of the locomotive from the range of 80 up to 90 t) and to verify the influence of these modifications on the dynamic behaviour of the locomotive.

Fig. 1 Visualization of the Class 744.0.

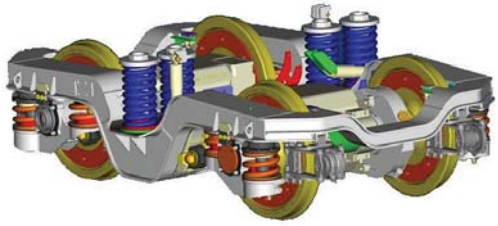

Fig. 2 A bogie of the Class 744.0.

3. Simulations of dynamic behaviour of the locomotive

The computer simulations of dynamic behaviour of the new locomotive are performed by means of an original multi-body simulation software (Zelenka, 2009). The first simulation results of the broad-gauged version of the locomotive Class 744.0 CZ LOKO are shown in paper (Zelenka & Michálek, 2011). On the basis of current documentation and measurement of real parameters of the locomotive suspension (Zelenka et al., 2011), simulation input data were specified. Investigation of the influence of change of relevant parameters, which is related with the modification of the locomotive for the broad track gauge, was also performed and its results are shown in paper (Kohout et al., 2011).

The main input parameters of the dynamic model of the locomotive (i.e. the mass and geometric parameters, characteristics of elastic and damping joints etc.) were determined with the project documentation and they are gradually specified during the development and subsequent manufacturing of the locomotive by the project manager. A substantial influence on the dynamic behaviour also has the characteristics of wheel/rail contact geometry which characterize the joint between the wheelset and the track. In this stage, simulations were performed for two different sets of characteristics of wheel/rail contact geometry – $\lambda_{ekv} = 0.207$ (theoretical wheel profiles and rail profiles 60E1/1:40) and $\lambda_{ekv} = 0.403$ (operationally worn wheel and rail profiles). In fig. 3, there are shown curves of delta-*r* function and equivalent conicity. In the next, the relevant wheel/rail contact geometry will always be named by means of value of the equivalent conicity for the wheelset amplitude $y_0 = 3$ mm.

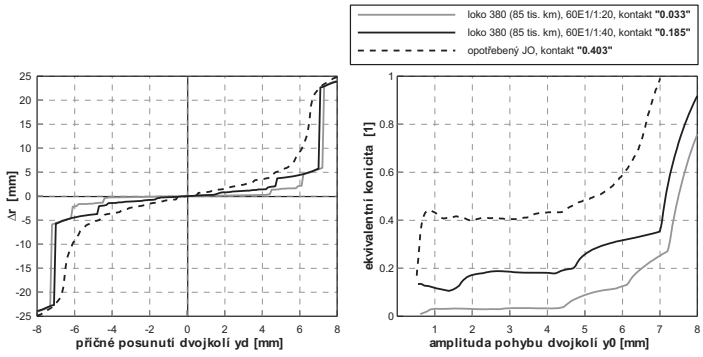

Fig. 3 Characteristics of wheel/rail contact geometry.

From the point of view of the vehicle dynamics, the locomotive comprises complicated non-linear dynamic system. Therefore, for purposes of determination of influence of different input parameters on dynamic behaviour of the whole locomotive a sensitivity analysis can be used. The sensitivity

analysis allows acquisition of an image describing a qualitative behaviour of such complicated system (locomotive) with respect to variable input parameters. One of the most important parameter of the rail vehicle is its critical speed. The critical speed represents the maximum speed at which the rail vehicle shows so-called stable run, i.e. running behaviour without lateral oscillations of wheelsets, bogies and the vehicle body. Value of the critical speed is influenced by many parameters and exceeding of this speed can lead to exceeding of the safety limits of the vehicle run (see the EN 14363) and degradation of the ride comfort. For purposes of sensitivity analysis of the locomotive Class 744.0, four weight variants (with a total weight of 80, 84, 86 and 90 t) were considered. Besides to that, influence of some other parameters was observed, above all the equivalent conicity (i.e. the wheel/rail contact geometry), friction coefficient in the wheel/rail contact and the influence of yaw dampers.

4. Assessment of stability of run of the locomotive

For purposes of assessment of the stability of vehicle run (i.e. determination of the critical speed of the vehicle), several methods are usually used – see paper (Polách, 2010), for example. In case of the locomotive Class 744.0, the sensitivity analysis was performed by means of non-linear method on theoretical straight track; the excitation of the dynamic model of the locomotive was carried out with isolated lateral track unevenness. For purposes of the stability assessment, lateral motion of the wheelsets (lateral oscillations) was observed at the decreasing vehicle speed.

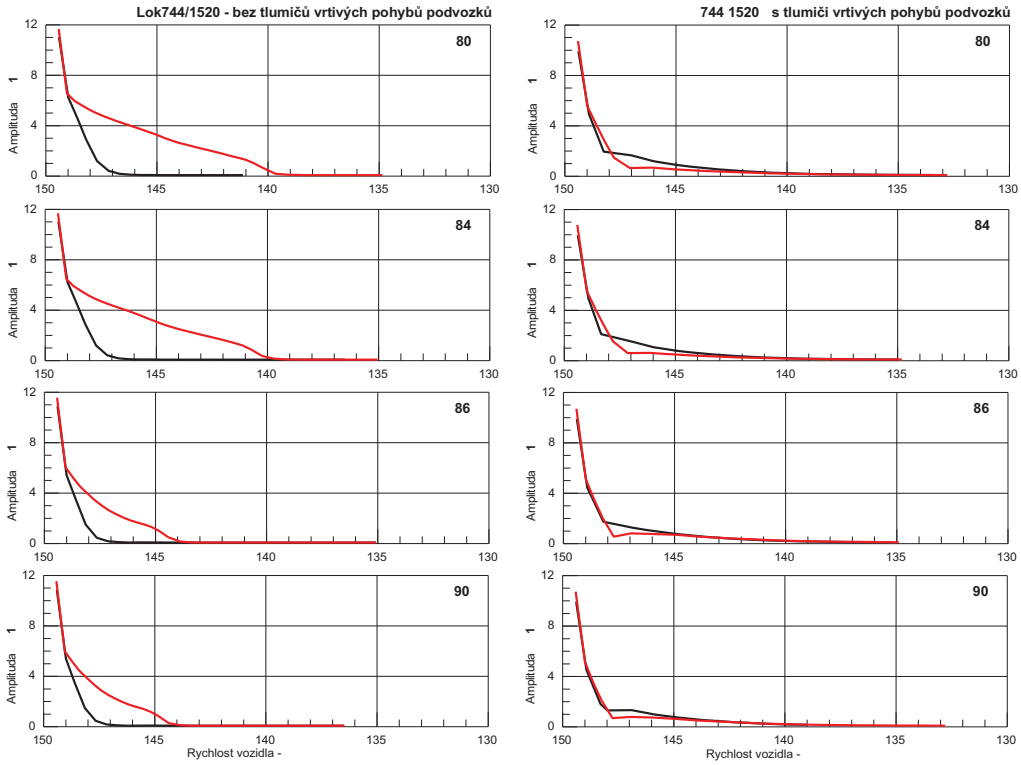

Fig. 4 Amplitude of the lateral motion of the 1st wheelset after the excitation on the ideal straight track for various total weight of locomotive and various contact conditions (decreasing speed; value of a friction coefficient in the wheel/rail contact: 0.40; red – λ_{ekv} = 0.403, black – λ_{ekv} = 0.207).

In the graphs in fig. 4 there are shown curves of the amplitudes of lateral motion of the 1st wheelset of the broad-gauged version of the locomotive. These curves were obtained by means of simulations of response of the locomotive on lateral unevenness at the speed 150 km/h. Four weight variants (with a total weight of 80, 84, 86 and 90 t), two different conditions of the wheel/rail contact geometry (red lines – λ_{ekv} = 0.403, black lines – λ_{ekv} = 0.207) and a value of friction coefficient in the wheel/rail contact of 0.4 were considered here. On the left side there are shown the results of the locomotive

without yaw dampers, the results on the right side represent the locomotive equipped with yaw dampers (two pieces per bogie). As it is evident from the graphs in fig. 4, the critical speed is higher than ca. 140 km/h in all considered cases. Especially in case of locomotive with yaw dampers, the wheelset oscillations disappear immediately after the excitation. From this reason, analogous assessment of the stability was performed at higher initial speed (200 km/h); relevant results for locomotives with total weight 80 and 90 t are shown in fig. 5. It is apparent that the yaw dampers can shift the critical speed to higher values; however, the wheel/rail contact geometry influences the stability very significantly, as well.

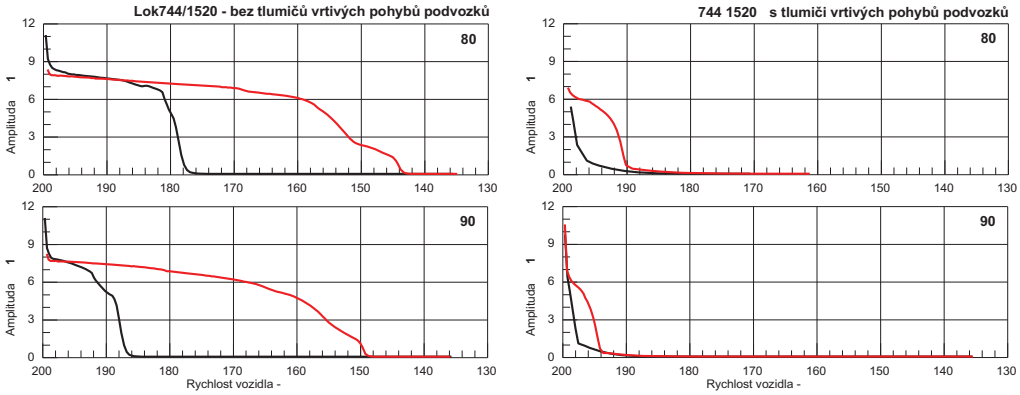

Fig. 5 Amplitude of the lateral motion of the 1st wheelset after the excitation on the ideal straight track for various total weight of locomotive and various contact conditions (decreasing speed; value of a friction coefficient in the wheel/rail contact: 0.35; red – λ_{ekv} = 0.403, black – λ_{ekv} = 0.207).

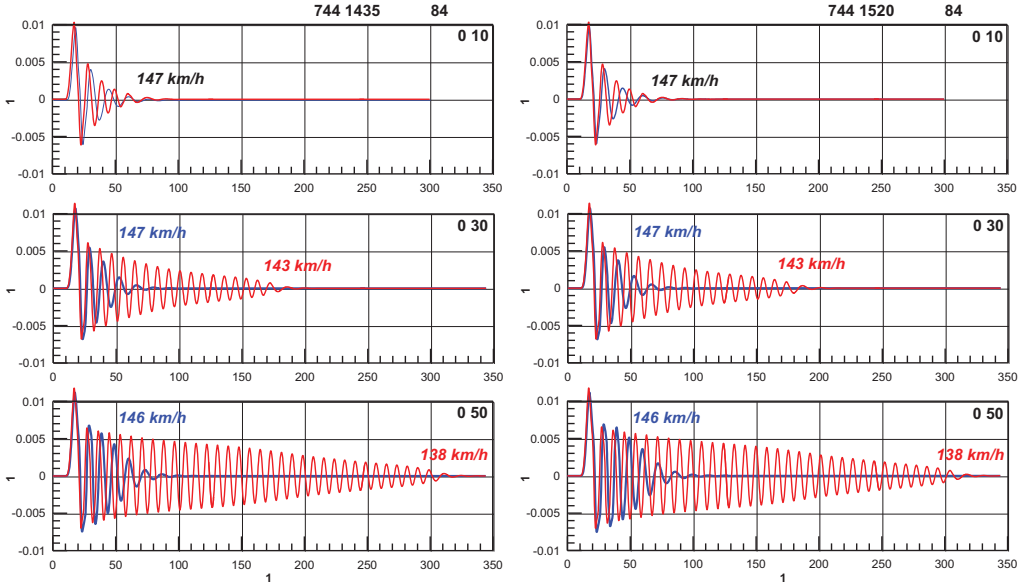

Fig. 6 Lateral motion of the 1st wheelset after the excitation on the ideal straight track for the standard- (left) as well as broad-gauged (right) version of the locomotive with total weight 84 t without yaw dampers, for various friction coefficient and various contact conditions (decreasing speed; red – λ_{ekv} = 0.403, blue – λ_{ekv} = 0.207).

In the graphs in fig. 6 there is demonstrated influence of the friction coefficient in wheel/rail contact on the critical speed. The simulations were performed in the same way as in case of results in fig. 4. However, the broad-gauged version as well as the standard gauged version of the locomotive

with a total weight of 84 and without the yaw dampers was considered in this case. The friction coefficient in wheel/rail contact ranged from 0.10 up to 0.50. It is apparent that increasing value of the friction coefficient in wheel/rail contact shifts the critical speed to lower values. The graphs in fig. 6 also show that a difference between the standard-gauged and broad-gauged version of the locomotive is negligible from the point of view of the stability of run.

The second way, how to investigate the stability of run of a rail vehicle, is usage of simulations of the run on the ideal straight track at constant speed; see (Polách, 2010 or Zelenka & Kohout, 2011), for example. After the excitation of the vehicle by means of isolated lateral track unevenness, the lateral wheelset motion stabilizes in a steady state which is characterized with its amplitude. Then, the qualitative change of the dynamic behaviour at the parameter change can be presented by means of bifurcation diagrams. In case of stability assessment, the bifurcation diagrams usually represent dependency of the amplitude of lateral wheelset motion on the vehicle speed. For better clearness, this method is demonstrated on example of an electric locomotive – see also the paper (Zelenka & Kohout, 2011). In fig. 7 there are shown the simulation results (i.e. histories of lateral motion of the 1st and 3rd wheelset of the locomotive) at different speeds for concrete conditions given by wheel/rail contact geometry (λ_{ekv} = 0.033) and characteristics of yaw dampers (named as "Os4", in this case).

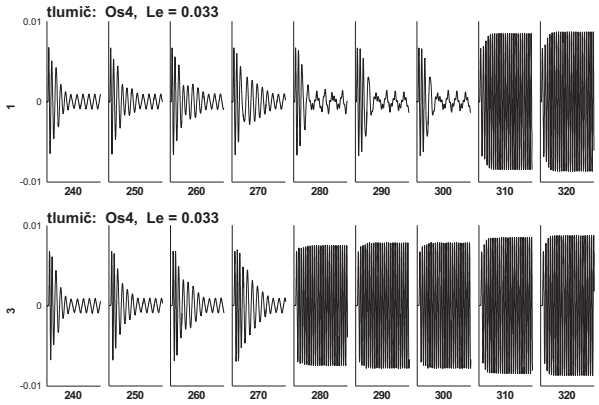

Fig. 7 Lateral motion of the 1st (top) and 3rd (bottom) wheelset of investigated locomotive for concrete conditions given by wheel/rail contact geometry and characteristics of yaw dampers at various speeds.

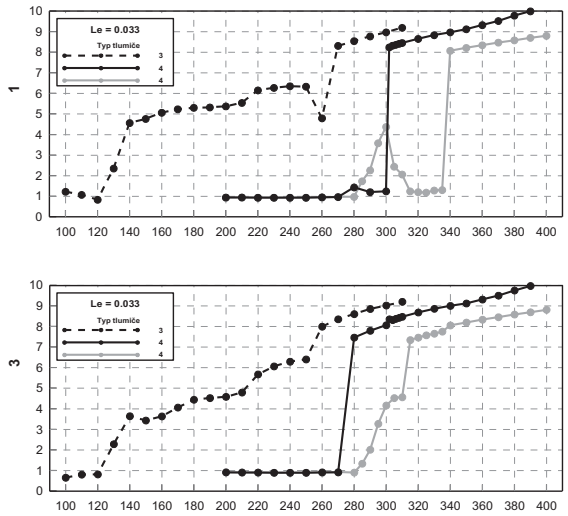

Fig. 8 Bifurcation diagrams – amplitudes of the 1st (top) and 3rd (bottom) wheelset of investigated locomotive for concrete wheel/rail contact geometry and various characteristics of yaw dampers.

In fig. 8 there are presented relevant bifurcation diagrams (i.e. dependencies of amplitudes of the lateral motion of the 1st and 3rd wheelset on the vehicle speed) for the concrete wheel/rail contact geometry (λ_{ekv} = 0.033) and for various characteristics of yaw dampers. It is evident that the characteristics of the yaw dampers can influence dynamic behaviour of the whole locomotive very significantly; even it can change the type of Hopf's bifurcation. Besides yaw dampers, characteristics of the wheel/rail contact geometry can influence the stability of the run very significantly, as well. In fig. 9 there are shown examples of bifurcation diagrams of the lateral motion of the 1st wheelset of the electric locomotive for various condition of the wheel/rail contact geometry (left – λ_{ekv} = 0.185, right – λ_{ekv} = 0.403; see also fig. 3) and for various characteristics of used yaw dampers.

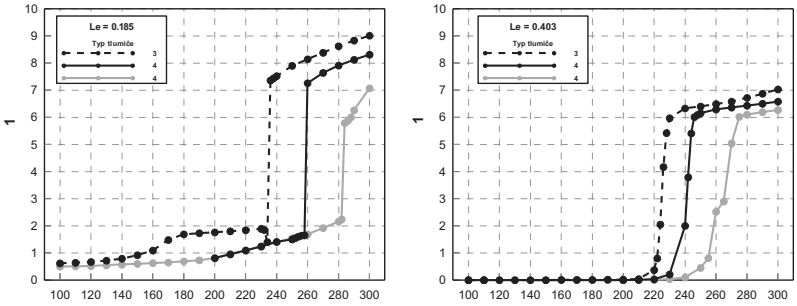

Fig. 9 Bifurcation diagrams – amplitudes of the 1st wheelset of investigated locomotive for various conditions of wheel/rail contact geometry and various characteristics of yaw dampers.

The results of this method are more exact and allow more detailed assessment of the dynamic behaviour of the rail vehicle at the stability limit, but they are equivalent to the usage of the above described method of the stability assessment using the decreasing vehicle speed at the simulations (see fig. 4 and 5), practically. Especially in case of the locomotive Class 744.0 CZ LOKO without the yaw dampers (see fig. 5), the wheel/rail contact geometry also has a significant influence on the dynamic behaviour of the whole locomotive. The contact with equivalent conicity λ_{ekv} = 0.207 seems to lead to the subcritical Hopf's bifurcation; the other one (λ_{ekv} = 0.403) leads to the supercritical Hopf's bifurcation evidently. Application of the considered yaw dampers shifts the critical speed to higher values in both cases. More detailed description of methods of determination of the bifurcation diagrams is presented in the paper (Polách, 2010).

5. Conclusions

This paper deals with application of sensitivity analysis at the assessment of dynamic behaviour of railway vehicles by means of computer simulations. By means of the sensitivity analysis, many different parameters and above all an influence of their changes on the dynamic behaviour of the vehicles can be observed in the design stage of these vehicles. In this way, the computer simulations of running and guiding behaviour allow the optimization of design and properties of some important constructional parts of newly developed vehicles.

In chapter 4, an analysis of stability of the run of the new diesel-electric locomotive Class 744.0 CZ LOKO for the "Russian" track gauge 1520 mm is performed. By means of sensitivity analysis, influences of the total weight of locomotive (from the range of 80 up to 90 t), application of the yaw dampers into the running gear, various conditions of the wheel/rail contact geometry and various values of the friction coefficient in the wheel/rail contact on the critical speed were observed. In all cases the critical speed seems to be higher than the intended maximum speed of this locomotive. At this assessment, the stability analysis performed on an ideal straight track with isolated lateral unevenness at decreasing vehicle speed was used.

Besides to this, another method of the stability analysis, which serves for determination of so-called bifurcation diagrams is described and presented on example of en electric locomotive in chapter 4, as well. This method is used for purposes of assessment of influence of characteristics of yaw dampers and wheel/rail contact geometry on dynamic behaviour of the vehicle at the stability limit.

In the next stage, authors will deal with analysis of influence of other simulation input parameters on dynamic behaviour of the new locomotive. Areas of sudden increase of amplitudes of lateral oscillations of the wheelsets in bifurcation diagrams – i.e. the dynamic behaviour of the vehicle at the stability limit – will be observed for purposes of acquisition of a more detailed image of dynamic properties of the whole non-linear dynamic system of the rail vehicle. Knowledge, which will be obtained in this way, will be used for verification of dynamic behaviour of other types of rail vehicles, subsequently.

Acknowledgement

This work was supported by R&D project No. FR-TI2/562 "Research and Development of a Modular Four-axled Locomotive" of the Ministry of Industry and Trade of the Czech Republic.

References

ČSN EN 14363:2006 *Railway applications – Testing for the acceptance of running characteristics of railway vehicles – Testing of running behaviour and stationary tests*, (in Czech). Czech Institute for Normalization, Prague.

Kopal, J. (2009) Running gear of CZ LOKO locomotives, (in Czech), in: *Proceedings of the 19th conference with international participation "Current Problems in Rail Vehicles"*, University of Pardubice, pp. 1-6.

Kohout, M., Zelenka, J. & Michálek, T. (2011) Influence of parameter's change of locomotive CZ LOKO series 744.0 modified for track gauge 1520 mm on dynamic behaviour, (in Czech), in: *Proceedings of the 20th international conference "Current Problems in Rail Vehicles – PRORAIL 2011", Volume II.*, University of Žilina, pp. 131-137.

Polách, O. (2010) Application of nonlinear stability analysis in railway vehicle industry, in: *Non-smooth Problems in Vehicle System Dynamics*, pp. 15-27.

Zelenka, J. (2009) Running and guiding behaviour of two-axled diesel-electric locomotives CZ LOKO, (in Czech), *New Railway Technique*, 2009, 6, pp. 15-23.

Zelenka, J. & Kohout, M. (2011) Sensitivity analysis of yaw damper's characteristics on ride stability of the locomotive, (in Czech), in: *Proceedings of the 20th international conference "Current Problems in Rail Vehicles – PRORAIL 2011", Volume III.*, University of Žilina, pp. 247-258.

Zelenka, J. & Michálek, T. (2011) Running and guiding behaviour of the locomotive class 744.0 CZ LOKO for the track gauge 1520 mm. *Транспорт Урала*, 2011, 28, pp. 59-63. URL: http://www.usurt.ru/transporturala/arxiv/028_1_20_2_1.pdf [cit. 2012-03-19].

Zelenka, J., Vágner, J. & Hába, A. (2011) Experimental verification of possibilities of determination of lateral stiffness of flexi-coil springs, (in Czech), *Vědeckotechnický sborník ČD*, 2011, 31, pp. 1-9. URL: http://vts.cd.cz/VTS/CLANKY/vts31/3114.pdf [cit. 2012-04-01].

18th International Conference
ENGINEERING MECHANICS 2012
Svratka, Czech Republic, May 14 – 17, 2012

pp. 1597–1602
Paper #19

KINEMATICAL EXCITED VIBRATION OF THE NUCLEAR FUEL ASSEMBLY

V. Zeman, Z. Hlaváč *

Abstract: *The paper deals with modelling of the hexagonal type nuclear fuel assembly vibration caused by kinematical excitation determined by motion of the support plates in the reactor core. The support plate motion is excited by pressure pulsations generated by circulation pumps in the main circulation loops. The cyclic and central symmetry of the system is advantageous for the fuel assembly decomposition into six identical revolved fuel rod segments, central tube and skeleton linked by several spacer grids in horizontal planes. The modal synthesis method with condensation of the fuel rod segments is used for determination of steady vibration.*

Keywords: ***Vibrations, nuclear fuel assembly, kinematic excitation, modal synthesis method, DOF number reduction.***

1. Introduction

The hexagonal nuclear fuel assembly TVSA/T (further FA) (Fig.1) is in term of mechanics very complicated system of beam type (Sýkora (2009)). Because of the cyclic and central symmetry of the whole system (Fig.2) the FA decomposition into six rod segments (S), centre tube (CT) and load-bearing skeleton (LS) shall be applied (Zeman & Hlaváč (2011b)). Each rod segment (on Fig.2 circumscribed by triangles) is composed of 52 fuel rods with fixed bottom ends in the lower support plate and 3 guide thimbles fully restrained in the lower and upper support plates in reactor core. The centre tube is fully restrained. The skeleton is created of 6 angle pieces (AP) coupled by divided grid rims (GR) at all levels

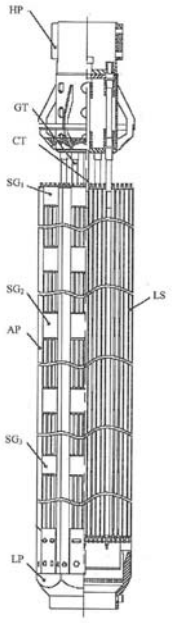

Fig. 1: Scheme of the fuel assembly

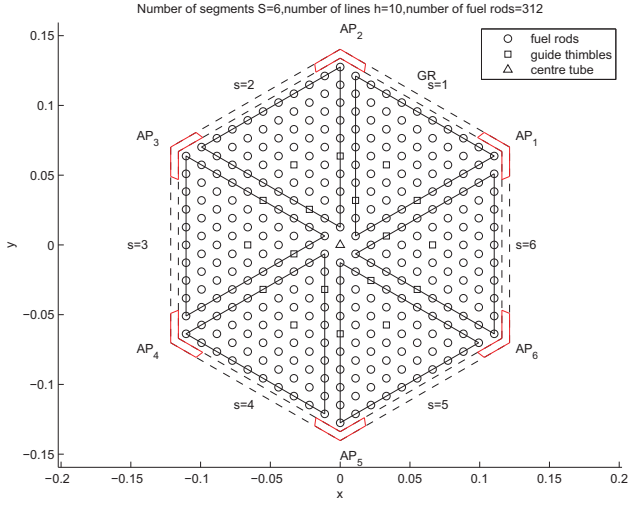

Fig. 2: The FA cross-section

*Prof. Ing Vladimír Zeman, DrSc., Doc. RNDr. Zdeněk Hlaváč, CSc.: University of West Bohemia, Univerzitní 22, 306 14 Plzeň, tel. 420 377 63 23 32, e-mail zemanv@kme.zcu.cz

of spacer grigs (SG). All FA components are linked by transverse spacer grids which elastic properties are expressed by linear springs with stiffness k_g placed on 8 different horizontal planes $g = 1, \ldots, 8$.

2. Mathematical model of the system

The vectors of generalized coordinates of the fully restrained subsystems (rod segments and centre tube) loosed in kinematical excited nodes can be partitioned in the form

$$\boldsymbol{q}_s = [(\boldsymbol{q}_L^{(s)})^T, (\boldsymbol{q}_F^{(s)})^T, (\boldsymbol{q}_U^{(s)})^T]^T,\ s = 1, \ldots, 6, CT\,, \tag{1}$$

and the skeleton s =LS fixed only in bottom ends in the form

$$\boldsymbol{q}_{LS} = [(\boldsymbol{q}_L^{(LS)})^T, (\boldsymbol{q}_F^{(LS)})^T]^T\,. \tag{2}$$

The coordinates of subvectors $\boldsymbol{q}_L^{(s)}$ and $\boldsymbol{q}_U^{(s)}$ are displacements of end-nods of fuel assembly components coupled with moving rigid support plates and displacements of free system nodes are integrated in vectors $\boldsymbol{q}_F^{(s)} \in R^{n_s}$. The conservative mathematical models of the loosed subsystems in the decomposed block form corresponding to partitioned vectors can be written as

$$\begin{bmatrix} \boldsymbol{M}_L^{(s)} & \boldsymbol{M}_{L,F}^{(s)} & \boldsymbol{0} \\ \boldsymbol{M}_{F,L}^{(s)} & \boldsymbol{M}_F^{(s)} & \boldsymbol{M}_{F,U}^{(s)} \\ \boldsymbol{0} & \boldsymbol{M}_{U,F}^{(s)} & \boldsymbol{M}_U^{(s)} \end{bmatrix} \begin{bmatrix} \ddot{\boldsymbol{q}}_L^{(s)} \\ \ddot{\boldsymbol{q}}_F^{(s)} \\ \ddot{\boldsymbol{q}}_U^{(s)} \end{bmatrix} + \begin{bmatrix} \boldsymbol{K}_L^{(s)} & \boldsymbol{K}_{L,F}^{(s)} & \boldsymbol{0} \\ \boldsymbol{K}_{F,L}^{(s)} & \boldsymbol{K}_F^{(s)} & \boldsymbol{K}_{F,U}^{(s)} \\ \boldsymbol{0} & \boldsymbol{K}_{U,F}^{(s)} & \boldsymbol{K}_U^{(s)} \end{bmatrix} \begin{bmatrix} \boldsymbol{q}_L^{(s)} \\ \boldsymbol{q}_F^{(s)} \\ \boldsymbol{q}_U^{(s)} \end{bmatrix} = \begin{bmatrix} \boldsymbol{f}_L^{(s)} \\ \boldsymbol{f}_C^{(s)} \\ \boldsymbol{f}_U^{(s)} \end{bmatrix} \tag{3}$$

for the $s = 1, \ldots, 6, CT$ and for the skeleton as

$$\begin{bmatrix} \boldsymbol{M}_L^{(LS)} & \boldsymbol{M}_{L,F}^{(LS)} \\ \boldsymbol{M}_{F,L}^{(LS)} & \boldsymbol{M}_F^{(LS)} \end{bmatrix} \begin{bmatrix} \ddot{\boldsymbol{q}}_L^{(LS)} \\ \ddot{\boldsymbol{q}}_F^{(LS)} \end{bmatrix} + \begin{bmatrix} \boldsymbol{K}_L^{(LS)} & \boldsymbol{K}_{L,F}^{(LS)} \\ \boldsymbol{K}_{F,L}^{(LS)} & \boldsymbol{K}_F^{(LS)} \end{bmatrix} \begin{bmatrix} \boldsymbol{q}_L^{(LS)} \\ \boldsymbol{q}_F^{(LS)} \end{bmatrix} = \begin{bmatrix} \boldsymbol{f}_L^{(LS)} \\ \boldsymbol{f}_C^{(LS)} \end{bmatrix}. \tag{4}$$

The force subvectors $\boldsymbol{f}_C^{(s)}$ express the coupling forces between subsystem s and adjacent subsystems transmitted by spacer grids. The displacements of the end-nodes of the subsystem components coupled with support plates can be expressed by the displacements of the lower and upper plates in the form

$$\boldsymbol{q}_L^{(s)} = \boldsymbol{T}_L^{(s)} \boldsymbol{q}_L,\ s = 1, \ldots, 6, CT, NS\,;\ \boldsymbol{q}_U^{(s)} = \boldsymbol{T}_U^{(s)} \boldsymbol{q}_U,\ s = 1, \ldots, 6, CT\,. \tag{5}$$

The second set of equations extracted from (3) and (4) for each subsystem is

$$\boldsymbol{M}_F^{(s)} \ddot{\boldsymbol{q}}_F^{(s)} + \boldsymbol{K}_F^{(s)} \boldsymbol{q}_F^{(s)} = -\boldsymbol{M}_{F,L}^{(s)} \boldsymbol{T}_L^{(s)} \ddot{\boldsymbol{q}}_L - \boldsymbol{M}_{F,U}^{(s)} \boldsymbol{T}_U^{(s)} \ddot{\boldsymbol{q}}_U - \boldsymbol{K}_{F,L}^{(s)} \boldsymbol{T}_L^{(s)} \boldsymbol{q}_L - \boldsymbol{K}_{F,U}^{(s)} \boldsymbol{T}_U^{(s)} \boldsymbol{q}_U + \boldsymbol{f}_C^{(s)}\,, \tag{6}$$

where $\boldsymbol{M}_{F,U}^{(LS)} = \boldsymbol{0}$, $\boldsymbol{K}_{F,U}^{(LS)} = \boldsymbol{0}$. The global model of the FA has to large DOF number for calculation of dynamic response excited by support plate motion. Therefore we assemble the condensed model using the modal synthesis method presented in the paper Zeman & Hlaváč (2011a). Let the modal properties of the conservative models of the mutually uncoupled subsystems with the strengthened end-nodes coupled with immovable support plates be characterized by spectral $\boldsymbol{\Lambda}_s$ and modal $\boldsymbol{V}_s$ matrices of order n_s, suitable to orthonormality conditions

$$\boldsymbol{V}_s^T \boldsymbol{M}_F^{(s)} \boldsymbol{V}_s = \boldsymbol{E}\,,\ \boldsymbol{V}_s^T \boldsymbol{K}_F^{(s)} \boldsymbol{V}_s = \boldsymbol{\Lambda}_s,\ s = 1, \ldots, 6, CT, LS\,. \tag{7}$$

The vectors $\boldsymbol{q}_F^{(s)}$ of dimension n_s, corresponding to free nodes of subsystems, can be approximately transformed in the form

$$\boldsymbol{q}_F^{(s)} = {}^m\boldsymbol{V}_s \boldsymbol{x}_s\,,\ \boldsymbol{x}_s \in R^{m_s}\,,\ s = 1, \ldots, 6, CT, LS\,, \tag{8}$$

where ${}^m\boldsymbol{V}_s \in R^{n_s, m_s}$ are modal submatrices of chosen m_s master eigenvectors of fixed subsystems. The equations (6) can be rewritten using (7) and (8) in the form

$$\ddot{\boldsymbol{x}}_s + {}^m\boldsymbol{\Lambda}_s \boldsymbol{x}_s = -{}^m\boldsymbol{V}_s^T (\boldsymbol{M}_{F,L}^{(s)} \boldsymbol{T}_L^{(s)} \ddot{\boldsymbol{q}}_L + \boldsymbol{M}_{F,U}^{(s)} \boldsymbol{T}_U^{(s)} \ddot{\boldsymbol{q}}_U + \boldsymbol{K}_{F,L}^{(s)} \boldsymbol{T}_L^{(s)} \boldsymbol{q}_L + \boldsymbol{K}_{F,U}^{(s)} \boldsymbol{T}_U^{(s)} \boldsymbol{q}_U) + {}^m\boldsymbol{V}_s^T \boldsymbol{f}_C^{(s)}, \tag{9}$$

$$s = 1, \ldots, 6, CT, LS\,,$$

where spectral submatrices ${}^m\boldsymbol{\Lambda}_s \in R^{m_s,m_s}$ correspond to chosen master eigenvectors in ${}^m\boldsymbol{V}_s$. The models (9) of all subsystems can be written in the configuration space $\boldsymbol{x} = [\boldsymbol{x}_s]$, $s = 1, \ldots, 6, CT, LS$ of dimension $m = \sum_s m_s$ as

$$\ddot{\boldsymbol{x}}(t) + \boldsymbol{\Lambda}\boldsymbol{x}(t) = -\boldsymbol{V}^T(\boldsymbol{M}_L\ddot{\boldsymbol{Q}}_L + \boldsymbol{M}_U\ddot{\boldsymbol{Q}}_U + \boldsymbol{K}_L\boldsymbol{Q}_L + \boldsymbol{K}_U\boldsymbol{Q}_U) + \boldsymbol{V}^T\boldsymbol{f}_C\,, \tag{10}$$

where $\boldsymbol{f}_C = [\boldsymbol{f}_C^{(s)}] \in R^n$, $n = \sum_s n_s$ is global vector of coupling forces between subsystems and matrices

$$\boldsymbol{\Lambda} = \mathrm{diag}[{}^m\boldsymbol{\Lambda}_s] \in R^{m,m};\ \boldsymbol{V} = \mathrm{diag}[{}^m\boldsymbol{V}_s] \in R^{n,m};\ \boldsymbol{X}_X = \mathrm{diag}[\boldsymbol{X}_{F,X}^{(s)}\boldsymbol{T}_X^{(s)}] \in R^{n,48};$$

$$\boldsymbol{Q}_X = [\boldsymbol{q}_X^T, \ldots, \boldsymbol{q}_X^T]^T \in R^{48};\ \boldsymbol{X} = \boldsymbol{M}, \boldsymbol{K};\ X = L, U;\ s = 1, \ldots, 6, CT, LS$$

are block diagonal, composed from corresponding matrices of subsystems. The global vector of coupling forces between subsystems can be calculated from identity

$$\boldsymbol{f}_C = -\frac{\partial E_p}{\partial \boldsymbol{q}_F} = -\boldsymbol{K}_C\boldsymbol{q}_F,\ \boldsymbol{q}_F = [\boldsymbol{q}_F^{(s)}]\,, \tag{11}$$

where E_p is potential (deformation) energy of the all spacer grids (springs) between subsystems. The expressions (11) can be substituted in (10) and then we get the condensed model of the nuclear fuel assembly of order m

$$\ddot{\boldsymbol{x}}(t) + (\boldsymbol{\Lambda} + \boldsymbol{V}^T\boldsymbol{K}_C\boldsymbol{V})\boldsymbol{x}(t) = -\boldsymbol{V}^T(\boldsymbol{M}_L\ddot{\boldsymbol{Q}}_L(t) + \boldsymbol{M}_U\ddot{\boldsymbol{Q}}_U(t) + \boldsymbol{K}_L\boldsymbol{Q}_L(t) + \boldsymbol{K}_U\boldsymbol{Q}_U(t))\,. \tag{12}$$

3. Application

The VVER 1000 reactor core is formed from 163 nuclear fuel assemblies. Each fuel assembly is placed in the core basket between core support plate and lower supporting plate of the block of protection tubes by means of lower support tailpiece (LP) and headpiece (HP) (see Fig.1). These support plates and pieces can be considered in transverse direction as rigid bodies.

Let us consider the steady vibration of both mentioned support plates excited by pressure pulsations generated by circulation pumps in the main circulation loops (Pečínka - Krupa & Klátil (1997)). The force effect of pressure pulsations in the gap between core barrel and pressure vessel walls can be expressed in the global model of the reactor by excitation vector in the complex form (Zeman & Hlaváč (2008))

$$\boldsymbol{f}(t) = \sum_j \sum_k \boldsymbol{f}_j^{(k)} \mathrm{e}^{\mathrm{i}k\omega_j\, t}\,, \tag{13}$$

where $\boldsymbol{f}_j^{(k)}$ is vector of complex amplitudes of $k-$th excitation harmonic component caused by hydrodynamic forces generated in one $j-$th circulation pump. Corresponding angular rotational frequency of the $j-$th pump $\omega_j = 2\pi f_j$ is defined by pump revolutions per minute n_j [rpm], where can be for particular pumps slightly different. Steady dynamic response of the reactor in generalized coordinates is given by identical form

$$\boldsymbol{q}(t) = \sum_j \sum_k \boldsymbol{q}_j^{(k)} \mathrm{e}^{\mathrm{i}k\omega_j\, t}\,. \tag{14}$$

The vectors of complex amplitudes $\boldsymbol{q}_j^{(k)}$ must be transformed into vectors of $\boldsymbol{Q}_{X,j}^{(k)}\,(X = L, U)$ describing steady vibration of the support plates caused by $k-$th harmonic of $j-$th pump.

In consequence of lightly damped fuel assembly components we consider modal damping of the subsystems characterized in the space of modal coordinates $\boldsymbol{x}_s$ by diagonal matrices $\boldsymbol{D}_s = \mathrm{diag}[2D_\nu^{(s)}\Omega_\nu^{(s)}]$, where $D_\nu^{(s)}$ are damping factors of natural modes and $\Omega_\nu^{(s)}$ are eigenfrequencies of the mutually uncoupled subsystems. The damping of spacer grids can be approximative expressed by damping matrix $\boldsymbol{B}_C = \beta\boldsymbol{K}_C$ proportional to stiffness matrix $\boldsymbol{K}_C$ by coefficient β.

That being simplifying supposed and the polyharmonic excitation (13) the conservative condensed model (12) will be completed in the complex form

$$\ddot{\boldsymbol{x}}(t) + (\boldsymbol{D} + \beta \boldsymbol{V}^T \boldsymbol{K}_C \boldsymbol{V})\dot{\boldsymbol{x}}(t) + (\boldsymbol{\Lambda} + \boldsymbol{V}^T \boldsymbol{K}_C \boldsymbol{V})\boldsymbol{x}(t) =$$

$$= -\boldsymbol{V}^T \sum_j \sum_k \left[(\boldsymbol{K}_L - k^2\omega_j^2 \boldsymbol{M}_L)\boldsymbol{Q}_{L,j}^{(k)} + (\boldsymbol{K}_U - k^2\omega_j^2 \boldsymbol{M}_U)\boldsymbol{Q}_{U,j}^{(k)} \right] \mathrm{e}^{\mathrm{i}k\omega_j t} . \tag{15}$$

Steady response of the fuel assembly subsystems according to (8) is

$$\boldsymbol{q}_F^{(s)}(t) = \sum_j \sum_k {}^m\boldsymbol{V}_s \boldsymbol{x}_{s,j}^{(k)} \mathrm{e}^{\mathrm{i}k\omega_j t} , \ s = 1, \ldots, 6, CT, LS , \tag{16}$$

where $\boldsymbol{x}_{s,j}^{(k)}$ are subvectors of the global vector $\boldsymbol{x}_j^{(k)}$ of the complex amplitudes

$$\boldsymbol{x}_j^{(k)} = -[\boldsymbol{\Lambda} + (1 + \mathrm{i}\beta k\omega_j)\boldsymbol{V}^T \boldsymbol{K}_C \boldsymbol{V} + \mathrm{i}k\omega_j \boldsymbol{D}]^{-1} \cdot$$

$$\cdot \boldsymbol{V}^T \sum_j \sum_k \left[(\boldsymbol{K}_L - k^2\omega_j^2 \boldsymbol{M}_L)\boldsymbol{Q}_{L,j}^{(k)} + (\boldsymbol{K}_U - k^2\omega_j^2 \boldsymbol{M}_U)\boldsymbol{Q}_{U,j}^{(k)} \right] \tag{17}$$

corresponding to subsystem s. Subscript $j \in \{1, 2, 3, 4\}$ is assigned to the operating circulation pump and subscript k to the harmonic component of pressure pulsations.

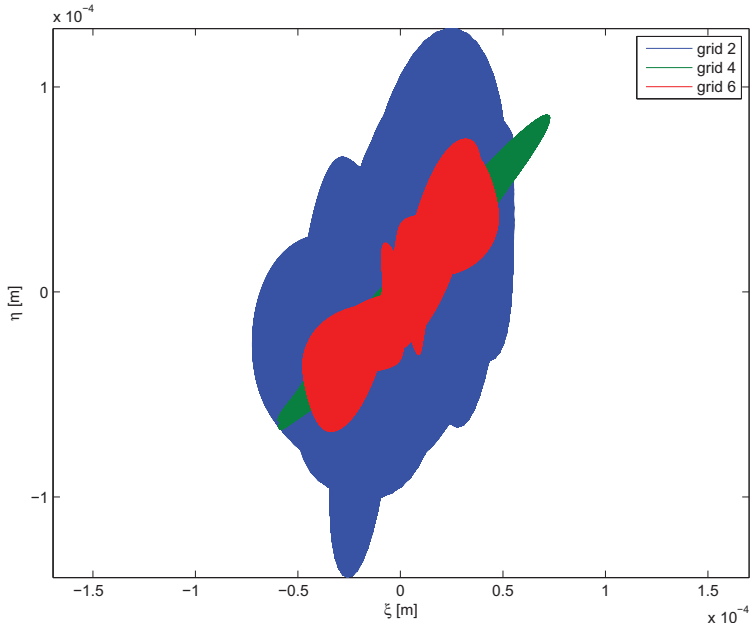

Fig. 3: Orbits of the fuel rod centre r =14 in the first fuel rod segment on the level spacer grids 2,4,6

The methodology was applied for steady polyharmonic response of the Russian TVSA-T fuel assembly in the VVER 1000 reactor core in NPP Temelín. As an illustration, the orbits in transverse planes of the random selected (r =14) fuel rod centre in the first fuel rod segment ($s = 1$) on the level spacer grids g =2,4,6 caused by pressure pulsations generated by all circulation pumps (Zeman & Hlaváč (2008)) are shown in Fig.3 and separately in Fig.4. The rotational frequencies of the particular pumps were $f_1 = f_2$ =16,635 Hz and $f_3 = f_4 = 16,645$ Hz. The condensed model (15) with 3272 DOF ($m_s = 500$, $m_{CT} = n_{CT} = 32$, $m_{LS} = n_{LS} = 240$) was used for the calculation of the orbits. The accuracy of condensed model was tested in terms of relative errors of 125 lowest fuel assembly eigenfrequencies defined in the form

$$\varepsilon_\nu = \frac{|f_\nu(m_s) - f_\nu|}{f_\nu}, \ \nu = 1, \ldots, 125 , \tag{18}$$

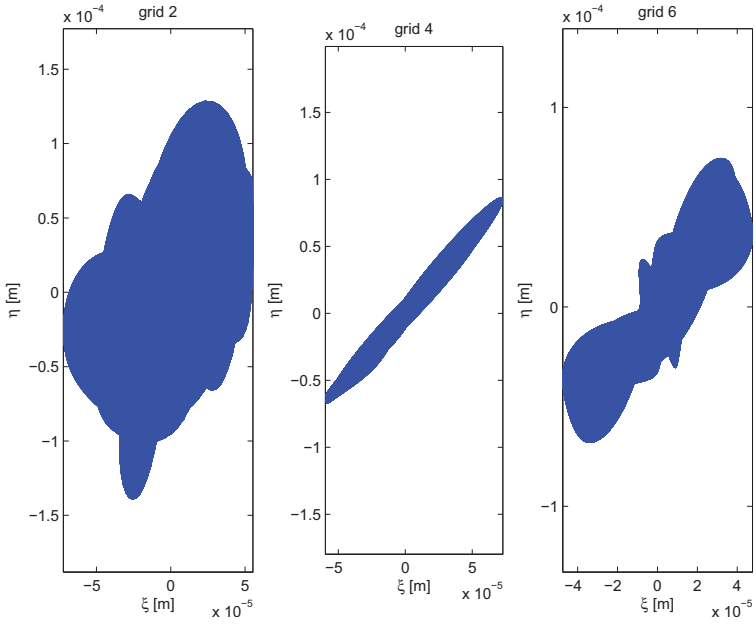

Fig. 4: Orbits from the figure 3 depicted separately

where f_ν are eigenfrequencies of the full (noncondensed) model with 10832 DOF. The relative errors ε_ν for different condensation level of the rod segments expressed by number of the rod segment master eigenvectors m_s =100,300,500 is shown in Fig.5. Relative errors decrease with decreasing condensation level (m_s increases) in all FA eigenfrequencies. The orbits of these particular models distinguish only little.

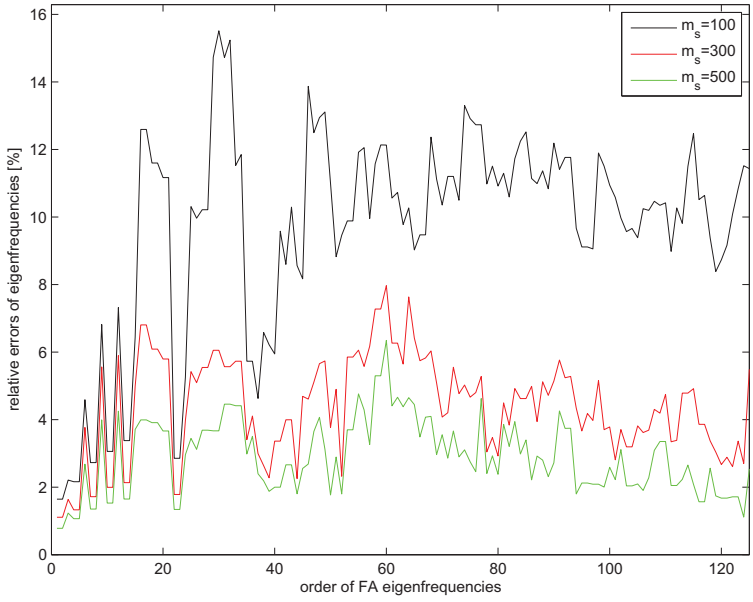

Fig. 5: Relative errors of the fuel assembly eigenfrequencies for different number m_s of rod segment master eigenvectors

4. Conclusion

The described method enables to investigate effectively the combined flexural and torsional kinematic excited vibrations of the nuclear fuel assembly. The fuel assembly vibrations are caused by motion of the two support horizontal plates in the reactor core. The special coordinate system of radial and orthogonal lateral axes for each fuel rod and guide thimbles on the all spacer grid levels makes possible to separate the central symmetrical fuel assembly into several identical revolved rod segments characterized by identical mass, damping and stiffness matrices.

The presented new approach based on the system decomposition into subsystems linked by spacer grids and modal synthesis method with reduction of DOF number was applied to hexagonal type nuclear fuel assembly vibration. The developed methodology, mathematical model and software in MATLAB was used for modelling and dynamic deformation analysis of the Russian type nuclear fuel assembly components caused by motion of the support plates excited by pressure pulsations generated by circulation pumps in the main reactor circulation loops.

Acknowledgement

This work was supported by the research project ”Fuel cycle of NPP” of the NRI Řež plc.

References

Pečínka, L., Krupa, V., Klátil, J., (1997), Mathematical modelling of the propagation of the pressure pulsations in the piping systems of NPPs. In: *Proceedings of the Conf. Computational Mechanics*, UWB Plzeň, pp. 203-210 (in Czech).

Sýkora, M., (2009), *Reactor TVSA-T fuel assembly insertion, part 4.* Research report PpBZ 1,2, ČEZ-ETE (in Czech).

Zeman, V., Hlaváč, Z., (2008), Dynamic response of VVER 1000 type reactor excited by pressure pulsations. *Engineering Mechanics*, 15, pp. 435-446.

Zeman, V., Hlaváč, Z., (2011a), Vibration of the Package of Rods Linked by Spacer Grids. In: *Vibration Problem ICOVP 2011*, Springer, pp. 227-233.

Zeman, V., Hlaváč, Z., (2011b), Modelling and modal properties of the nuclear fuel assembly. *Applied and Computational Mechanics*, 5, pp. 253-266.

18th International Conference
ENGINEERING MECHANICS 2012
Svratka, Czech Republic, May 14 – 17, 2012

pp. 1603–1610
Paper #291

LONG-TERM MONITORING OF MECHANICAL DAMAGE ON THE HISTORICAL STRUCTURES

P. Zíma*

Abstract: *Important information for the risk assessment of some damages on the historical structures represents data of failure development. Cracks in the load-bearing walls are one of the observed failures. This article focuses on remarkable method of damage measurement, their long-term monitoring and devices used for measurement.*

Keywords: ***Long-term monitoring, linear variable differential transformer, crack on the wall***

1. Introduction

Long-term monitoring of crack movement in load-bearing walls and arches is one of the methods for a diagnosis of historical structures. Decision about reconstruction or structural adjustment of walls, ceilings or even bases is based on the results from the monitoring of the damage development. Changes that have to be monitored are very slow and relatively small. So that the long-term crack monitoring and data recording is necessary for determination of the crack development.

The automatic measurement by the linear variable differential transformer has emerged as the most suitable method. High resolution, accuracy and measurement stability are the most important advantages of the method. The sensors requirements such as operation difficulty and price come from the fact that the measurement often goes on while the historical structure is in common use, e.g. sightseeing tours, cultural actions or restoration works take place there. There are several examples of testing and evaluation of the measurement that have been made on the historical structures in the Czech Republic in last years in the paper.

2. Analysis of requirements and choice of the method

A used device has to be able to measure the displacement in units of micrometers, because the change of the crack dimension in the walls is generally tens or hundreds of micrometers for a period of several months. Sensor has to be mechanically connectable to the measured structure in an easy way, so that the historical building is not damaged. It has to survive adverse effects of local climate such as wind or rain and also the presence of dust or vibration has to be taken into account. The measurements itself and data recording has to be in a motion unattended for a long time; potential power cuts can't stop them. Data have to be saved continuously throughout the monitoring of the structure without risk of loss. The monitoring device is placed on the historical building for a long time (up to several years), often in a hardly accessible location. In spite of that its price can't be extremely high. The chosen method can also allow measuring the temperature in an area of the crack, temperature outside and relative humidity of the air altogether because all the information is relevant while evaluating the damage development.

3. Reasons for use of LVDT

The linear variable differential transformers (LVDT) have certain significant features and benefits, most of which derive from their fundamental physical principles of operation or from the materials and techniques used in its construction. Following characteristics are decisive for choosing of the sensor for our objective.

* Ing. Pavel Zíma: Institute of Theoretical and Applied Mechanics AS CR, v. v. i., Prosecká 809/76, 190 00, Prague; CZ, e-mail: zima@itam.cas.cz

Fig. 1: *LVDT sensors*

Friction-Free Operation

Usually there is no mechanical contact between the LVDT's core and coil assembly therefore no rubbing, dragging or the other source of friction is there. This feature is particularly useful in displacement measurements and high resolution dimensional gaging systems.

Infinite Resolution

Since LVDT operates on electromagnetic coupling principles in a friction-free structure, it can measure infinitesimally small changes in the core position. This infinite resolution capability is limited only by the noise in LVDT signal conditioner and the output display's resolution. These same factors also give LVDT its outstanding repeatability.

Unlimited Mechanical Life

Because there is normally no contact between the LVDT's core and coil structure, no parts can rub together or wear out. This means that LVDT features unlimited mechanical life. This factor is especially important in high reliability in operation on places without longstanding supervision as in the case of monitoring of the historical objects.

Single Axis Sensitivity

LVDT responds to motion of the core along the coil's axis, but is generally insensitive to cross-axis motion of the core or to its radial position. Thus, LVDT can usually operate without adverse effect in applications involving misaligned or floating moving members and in cases where the core doesn't travel in a precisely straight line.

Environmentally Robust

The materials and construction techniques used in assembling LVDT result in a rugged, durable sensor that is robust to a variety of environmental conditions. Bonding of winding is followed by epoxy encapsulation into the case, resulting in superior moisture and humidity resistance, as well as the capability to take substantial shock loads and high vibration levels in all axes. And the internal high-permeability magnetic shield minimizes the effects of external AC fields.

Both the case and the core are made of corrosion resistant metals, with the case also acting as a supplemental magnetic shield. For those applications where the sensor must withstand exposure to flammable or corrosive vapours and liquids or operate in pressurized fluid, the case and coil assembly can be hermetically sealed using a variety of welding processes. Ordinary LVDTs can operate over a very wide temperature range, but if required, they can be produced to operate down to cryogenic temperatures.

Null Point Repeatability

The location of LVDT's intrinsic null point is extremely stable and repeatable, even over its very wide operating temperature range. This makes LVDT performing well as a null position sensor in closed-loop control systems and in high performance servo-balance instruments.

Absolute Output

LVDT is an absolute output device, as opposed to an incremental output device. This means that in the event of loss of power, the position data sent from LVDT will not be lost. When the measuring system is restarted, LVDT's output value will be the same as it was before the power failure occurred.

4. Working principle

The linear variable differential transformer (LVDT) is an excellent device for converting mechanical displacement into an electrical signal. It can be employed in a large variety of transducers, including strain, displacement, pressure, acceleration, force and temperature. In **Fig. 2** is shown a schematic illustration of a linear variable differential transformer employed as a displacement sensor suitable for our demand of a long time monitoring.

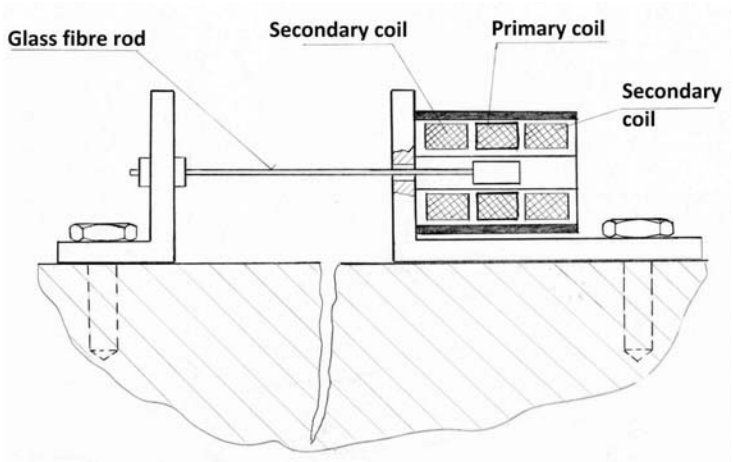

Fig. 2: Schematic illustration of linear variable differential transformer employed as a displacement sensor for monitoring of crack

In the figure we can see crack of the wall, whose movement we want to measure. The body of LVDT with coils is closely fixed to wall on one hand of the crack and glass fibre rod with ferrite core on the other hand. A linear differential transformer has three coils. Every position of the core in coils gives different electrical output. As the core moves within the coils, it varies the mutual inductance between the primary and each secondary winding, with one secondary becoming more tightly coupled to the primary and the other secondary becoming more loosely coupled. The two secondary coils are wired in series opposition, and consequently the output voltage E_{out} is the difference between the voltages developed in each secondary (that is, $E_{out}=E_1-E_2$, see **Fig. 3**). In a symmetrically constructed transformer a null output should occur when the core is at the center point between the two secondary coils.

The output low level voltage E0 is in special electronic integrated circuit (demodulator) transferred to high level DC voltage EDC. The output voltage EDC of the demodulator for typical linear variable differential transformer as a function of core position is given in **Fig. 4**.

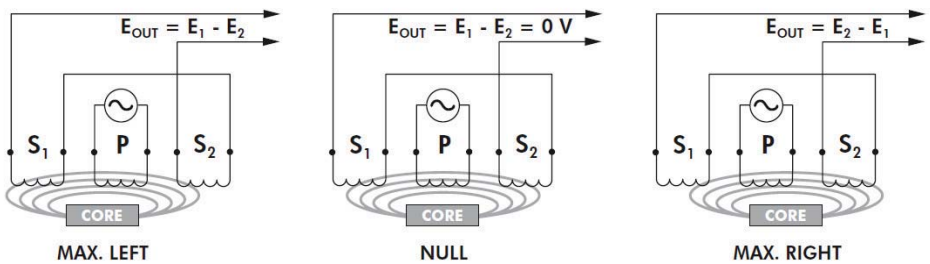

Fig. 3: Schematic diagram of the linear variable differential transformer circuit

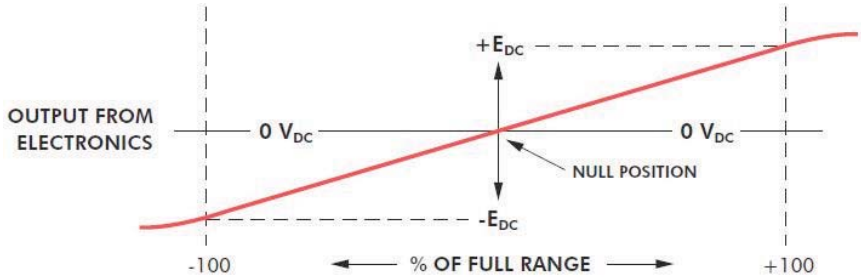

Fig. 4: DC output from electronics as a function of core position

5. Data acquisition system

Most of the data loggers available on the market fulfilling the requirements of the long-therm monitoring exceeds with its price level of 100 000 CZK. It would be uneconomic to use them for capturing date at hourly intervals, because they are designed for demanding measurements in laboratories or in situ. Therefore the DAM logger of price about 30 000 CZK was chosen. It was developed as a "low-cost" option of data logger for requirements of building geology workers. It is used for many years in situ for monitoring various physical parameters (temperature, relative humidity, pressure, displacements, etc.). It can be equipped with up to 6 modules for measuring those variables and it measures in 18-bit resolution. Resulting price of the system is determined by the number of channels required and therefore by the number of used modules.

This system was in recent years retrofitted with other optional auxiliary units, such as remote connection to computer via GSM module sending simple SMS messages to selected phone numbers, or charging system using solar cells. SMS messages send to mobile phones are used for reporting emergency situation on the monitored object (exceeding the limits of specified displacement or speed of increase of measuring variable, etc.). We can build sophisticated monitoring system that will withstand even in severe conditions.

6. Practical applications of LVDT in monitoring

The above mentioned system was already used in many projects related to reconstruction and preservation of historical monuments.

Examples of use:

- monitoring of cracks in Telč Castle during works on the sewer drain in the neighbourhood of the castle
- monitoring of Holy Trinity Column – Olomouc during its reconstruction
- monitoring of cracks in the walls of the pilgrimage church in Stříbrná Skalice during its reconstruction
- monitoring of cracks in the walls of the Pragues New Town Hall
- monitoring of failures in the vaults in the Franciscan monastery in Kadaň
- monitoring of the movement of the roof balustrade corner pillars of the southern façade of the National Museum in Prague
- study loading test of the arch above ground floor in Hvězda Summer Pavilion
- monitoring and warning system on the rock tower in Dolní Žleb u Děčína close to the railway line Děčín – Dresden
- monitoring in Hřensko

Two last examples do not belong among historical structures, but they are natural rocks whose erosion threatens objects in their neighborhood. Currently the monitoring of cracks takes place at two historical monuments, St. Jacob's Church in Kutná Hora and Viceroy's Summerhouse in Stromovka Park in Prague.

7. Examples of monitoring results

7.1 Monitoring of failures in the vaults in the Franciscan monastery in Kadaň

Monitoring of the structure was going on from 2006 to 2008. The vaults in monastery chapter hall has been disrupted by a net of cracks, see **Fig. 5.** The positions of LVDT sensors 1, 2 and 3 are also marked in the picture. Diagrams were made using measured data and the movements of the cracks have been evaluated for the entire measurement, see **Fig. 6**, **Fig. 7** and **Fig. 8** where the crack opening and closing are shown. The temperature in the LVDT positions was measured, see **Fig. 9**.

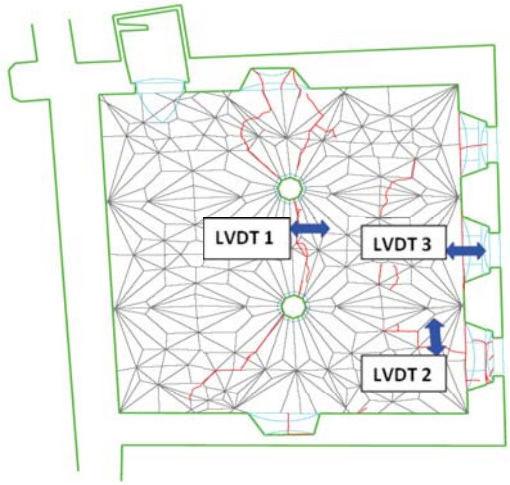

Fig. 5: Crack net and positioning of the sensors in the vaults

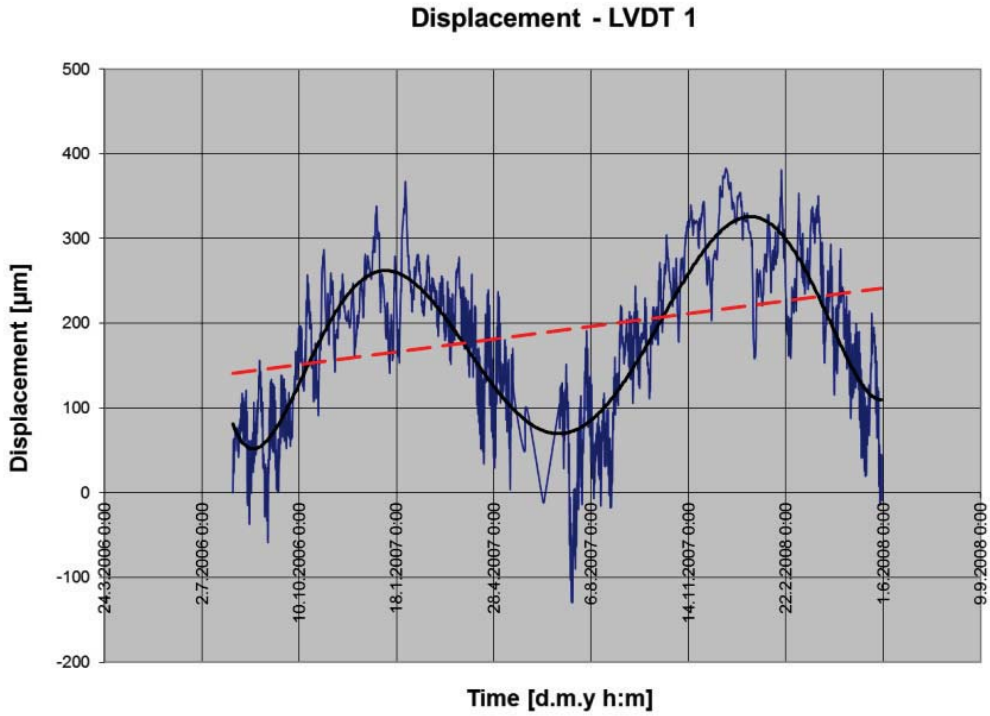

Fig. 6: Movements of the (LVDT 1)

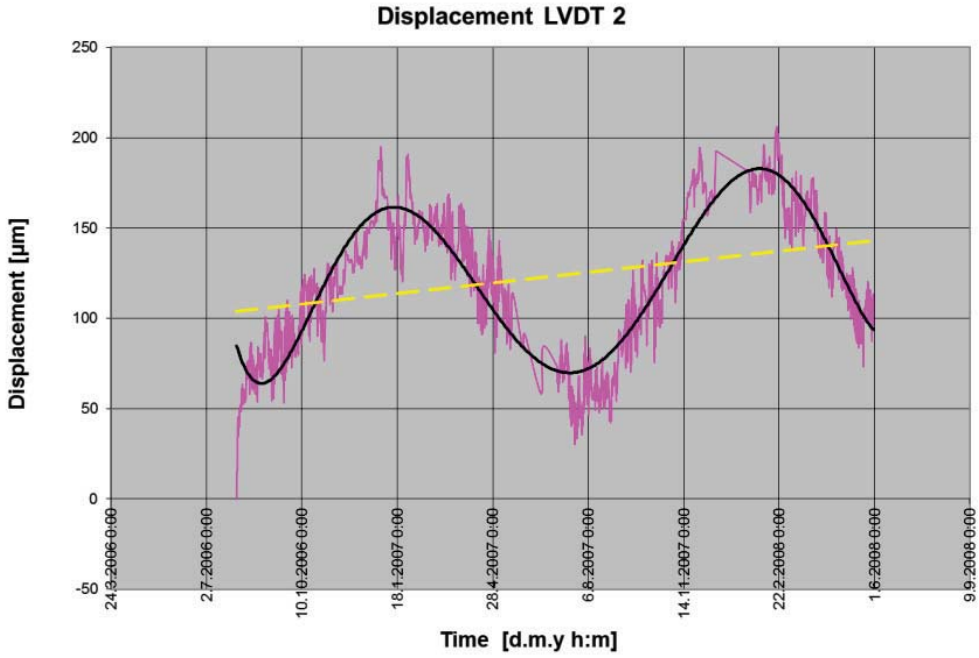

Fig. 7: Movements of crack (LVDT 2)

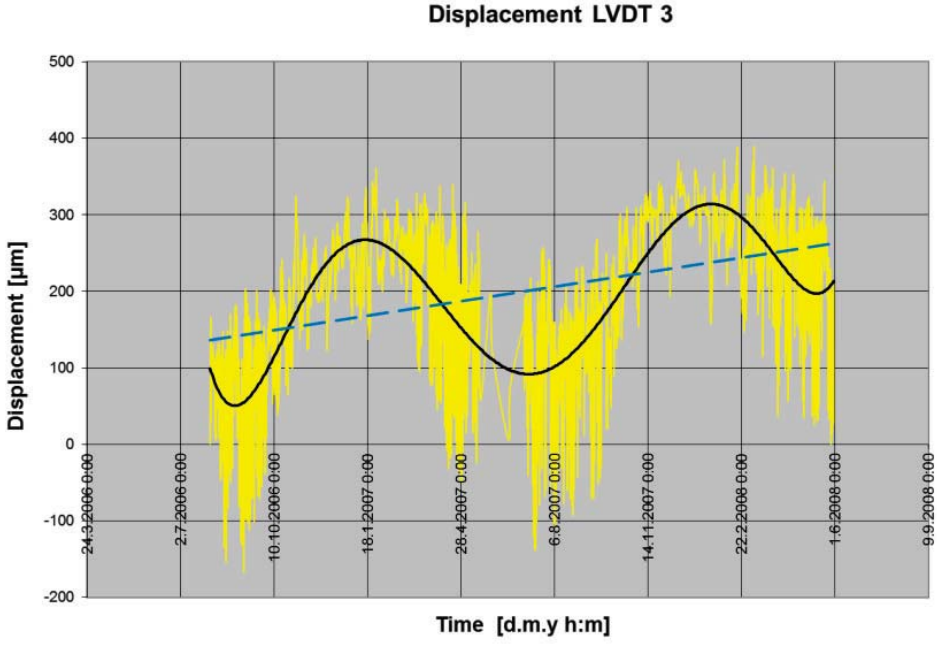

Fig. 8: Movements of crack (LVDT 3)

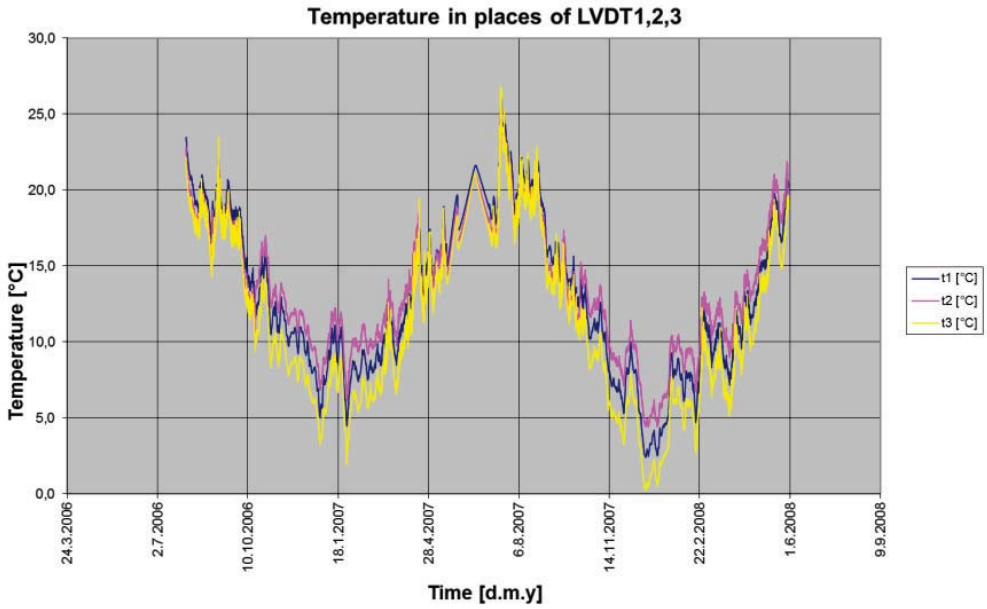

Fig. 9: Temperature in the positions of LVDT

7.2 Monitoring of cracks in the south wall of St. Jacob's Church in Kutná Hora

Monitoring in the structure is going on nowadays simultaneously with the reconstruction of the roof that started in 2011. There are large cracks in the south wall of the object, therefore monitoring of their development during the reconstruction has been suggested. Two positions for LVDT sensors at inner side of the wall, where the cables do not hinder works, were chosen in the first phase. As the next step the other place for sensors will be chosen. The sensor set up is shown in the **Fig. 10**.

The significant crack's movement was observed from the record of LVDT 2 when the roof was removed and the reconstruction started, see **Fig. 11** below. However, there is no obvious change on the record of LVDT 1 from this time. The following development of the cracks will be monitored to control condition of the wall.

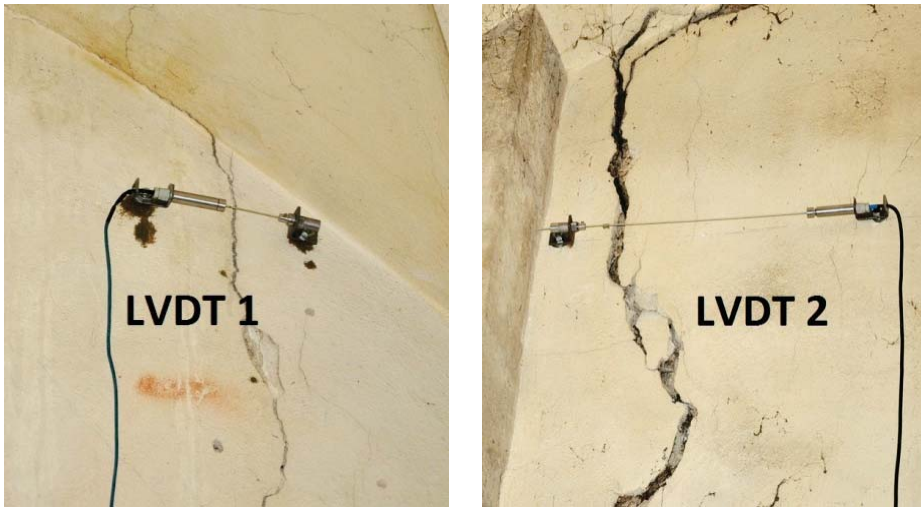

Fig. 10: LVDT set up, a) an inner side of the wall, b)an exterior side of the load-bearing wall

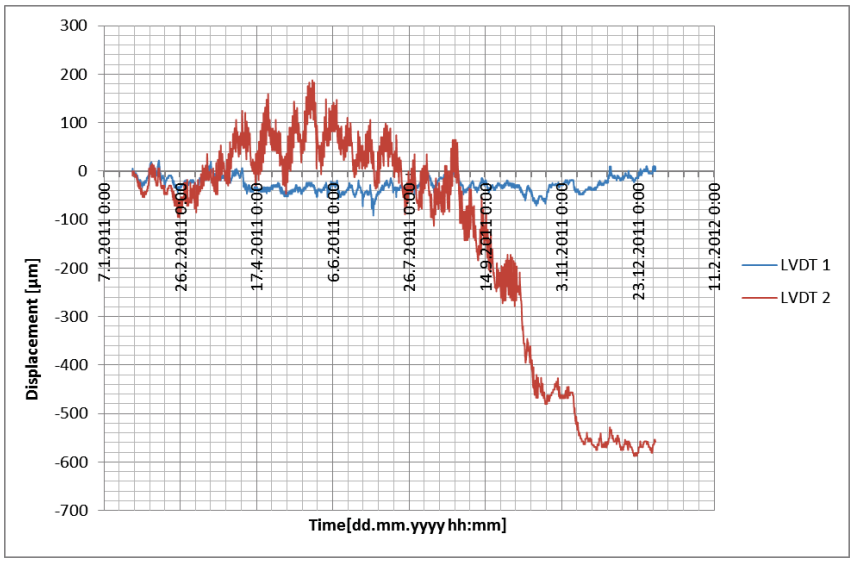

Fig. 11: Movements of cracks in St. Jacob's Church

References

Drdácký, M., Zíma, P. (2008) *Monitorování poruch sklípkové klenby v klášteře Františkánů v Kadani*, Zpráva ÚTAM AV ČR, 15 str., ÚTAM AV ČR, Praha.

Drdácký, M. (2004) *Vybrané metody diagnostiky, monitorování a analýzy poruch historických konstrukcí a materiálů*, Vědecké spisy VUT v Brně, Edice Habilitační a inaugurační spisy, sv.141, 31 p., ISBN 80-214-2723-X, VUTIUM Brno, 2004

Macro Sensors: *Position Sensing Solutions*, Capability Brochure

18th International Conference
ENGINEERING MECHANICS 2012
Svratka, Czech Republic, May 14 – 17, 2012

pp. 1611–1620
Paper #194

INDIRECT DETERMINATION OF MATERIAL MODEL PARAMETERS FOR SINGLE TRABECULA BASED ON NANOINDENTATION AND THREE-POINT BENDING TEST

P. Zlámal [*], O. Jiroušek, D. Kytýř, T. Doktor [**]

Abstract: *The aim of the paper is to develop a procedure for determination of elasto-visco-plastic constitutive model with damage for human single trabecula. The procedure is suited for indirect establishing of material model based on nanoindentation and three-point bending test. Constants of the material model are identified by Finite Element (FE) simulations and curve fitting using an algorithm based pn least squares fitting of the experimental curves. In the case of nanoindentation, the penetration depth of tip during the FE analyses (FEA) is fitted to experimental nanoindentation curves. In the case of three-point bending, displacements of nodes are compared with displacements of markers observed during the experiment using digital image correlation.*

Keywords: ***elasto-visco-plastic-damage model, FEM, trabecular bone, three-point bending***

1. Introduction

A single trabecula is the basic beam-shaped element of bone structure and knowledge of mechanical properties at this level is important for understanding of overall deformation behaviour of bone tissue as well as for simulation of osteoporotic changes. Recently, one of the powerful methods used to measure the elastic properties of samples at microscale level is nanoindentation. Nanoindentation is usually used for determination of elastic properties of material, whereas yield properties as well as softening behaviour can not be directly measured. On the other hand, mechanical testing (tension test, three-point bending test etc.) is often carried out to describe nonelastic deformation behaviour. In this study an elasto-visco-plastic constitutive model with damage for human single trabecula was developed using two different procedures including experimental tests and FEA. First procedure is based on nanoindentation and inverse FE modelling. During the procedure the numerical results were fitted to experimental indentation curves to obtain nonelastic constants of material model. In the second procedure a three-point bending is performed and the constants are identified from displacement of nodes in FEA. Displacements of nodes of numerical model are compared with displacements of markers observed experimentally using digital image correlation (DIC) technique.

2. Materials and Methods

2.1. Nanoindentation test

For nanoindentation test a 3mm thick sample was cutted from human (72-year male) femoral head using precision saw (Isomet 1000, Buehler GmbH, Germany). The sample was delipidated in 1% Alconox (Alconox detergent, Alconox Inc., USA) detergent lotion in ultrasonic bath (Sonic 3, Polsonic, Poland) for 15 minutes and then rinsed with distilled water. The temperature of the bath has not exceeded 40°C. In our test an indentation depth during nanoindentation was approximately 1 μm, therefore it was necessary reduce the surface roughness of the sample to a minimal possible value. For this reason the

[*]Ing. Petr Zlámal: Czech Technical University in Prague, Faculty of Transportation Sciences; Konviktská 20;110 00; Prague; CZ; e-mail: xzlamal@fd.cvut.cz
[**]Doc. Ing. Ondřej Jiroušek, PhD., Ing. Daniel Kytýř PhD., Ing. Tomáš Doktor: Institute of Theoretical and Applied Mechanics, v.v.i., Academy of Sciences of the Czech Republic; Prosecká 76; 190 00; Prague; CZ; e-mail: {jirousek, kytyr, doktor}@itam.cas.cz

cleaned sample was embedded into a low shrinkage epoxy resin (EpoxyCure, Buehler GmbH, Germany) and grinded using polishing machine (LaboPol-4, Struers, Denmark) with diamond grinding discs (grain sizes: 35 μm and 15 μm) and monocrystalline diamond suspensions (9 μm, 3 μm, 1 μm). Final polishing was performed by aluminium-oxide suspension (Al_2O_3) with grain size 0.05 μm. Average surface roughness achieved using the procedure was 25 nm [Kytyr (2011)].

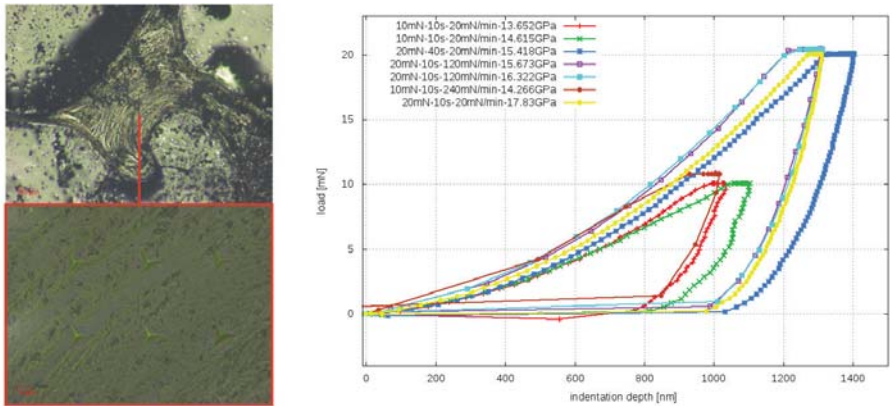

Fig. 1: Trabecular bone indentation area with grid of indents (left), selected indentation curves for FEA (description of legend: peak force - holding time - loading rate - Young's modulus) (right)

During the nanoindentation the applied force and penetration depth of diamond indenter (Berkovich tip) were measured. For statistically significant FEM fitting procedure of nanoindentation test multiple indents (approximately 300) with two peak forces ($10, 20$ mN), three holding times ($10, 20, 40$ s) and loading rates ($20, 120, 240$ mN/min) were performed. The indents were made with 10 μm grid size (Fig. 1-left). Young's modulus was determined directly from nanoindentation curves (Fig. 1-right) by Oliver-Pharr method [Oliver and Pharr (1992)]:

$$\frac{1}{E_r} = \frac{1-\nu^2}{E} + \frac{1-\nu_i^2}{E_i} \tag{1}$$

where E_i, ν_i is Young's modulus and Poisson's ratio of the diamond tip; E, ν is Young's modulus and Poisson's ratio of the specimen (ν is expertly estimated). Reduced modulus E_r can be calculated:

$$E_r = \frac{\sqrt{\pi}}{2}\frac{S}{\sqrt{A}}, \qquad S = \frac{dP}{dh} \tag{2}$$

where A is the projected area of elastic contact , S is stiffness of the upper portion of the unloading data, P is applied load and h is penetration depth. Obtained values of Young's modulus for selected indentation curves for FEA are shown in the legend of Fig. 1-right.

2.2. Numerical simulation of nanoindentation test

For FE simulations of the nanoindentation test a rotationally axisymmetric plane model was used. The Berkovich indenter (three sided pyramid) was replaced with a cone with equivalent contact surface [Lucchini (2011)]. For better numerical convergence the sharp tip of the cone is usually rounded $100 \div 300$ nm. Radius 200 nm was chosen based on the study of Chen (2009). The FE model (see Fig. 2) was composed from 13,806 2-D structural solid elements (6,997 nodes) with linear shape function and contact elements inserted between the model of indenter and the specimen. For the indenter a pure elastic material model with Young's modulus E_i =1140 GPa and Poisson's ratio $\mu_i = 0.07$ was applied. For the model of trabecular bone elasto-visco-plastic material model with damage was used. From experimental indentation curves, especially from the shape during the unloading phase, the necessity to use damage model was apparent. Usage of the damage model was a logical step to extend the elasto-plastic material model previously published in Jirousek (2011). For the considered model it is necessary to identify 10 material constants:

- two elastic constants: Young's modulus ($\mathbf{E}$) and Poisson's ratio ($\boldsymbol{\nu}$)
- two constants for plasticity with von Mises yield criterion and bilinear isotropic hardening: yield point ($\boldsymbol{\sigma_y}$) and tangent modulus ($\mathbf{E_{tan}}$)
- four constants ($\mathbf{C_1}$, $\mathbf{C_2}$, $\mathbf{C_3}$, $\mathbf{C_3}$) for implicit creep with time hardening according to the equation:

$$\dot{\varepsilon}_{cr} = C_1 \sigma^{C_2} t^{C_3} e^{-C_4/T} \tag{3}$$

where $\dot{\varepsilon}_{cr}$ is the change in equivalent creep strain with respect to time, σ is the equivalent stress, t is the time at end of substep and T is the temperature

- constants ($\mathbf{D_1}$,$\mathbf{D_2}$) for damage model published in Zhang (2010):

$$E_{new} = (1 - d_c) E_0 \tag{4}$$

$$d_c = D_1 (1 - e^{-D_2 \cdot \varepsilon_{eqa}^{pl}}) \tag{5}$$

where E_{new} is the degradated Young's modulus of the element which is calculated at the end of each loadstep, E_0 is the initial Young's modulus of the element and ε_{eqa}^{pl} is the accumulated equivalent plastic strain in the element at the end of loadstep according to:

$$\varepsilon_{eqa}^{pl} = \sum \Delta\varepsilon_{eq}^{pl} \tag{6}$$

$$\begin{aligned} \Delta\varepsilon_{eq}^{pl} = \frac{\sqrt{2}}{3}[(\Delta\varepsilon_x^{pl} - \Delta\varepsilon_y^{pl})^2 + (\Delta\varepsilon_y^{pl} - \Delta\varepsilon_z^{pl})^2 + (\Delta\varepsilon_z^{pl} - \Delta\varepsilon_x^{pl})^2 \\ + \frac{3}{2}(\Delta\gamma_{xy}^{pl^2} + \Delta\gamma_{yz}^{pl^2} + \Delta\gamma_{xz}^{pl^2})]^{\frac{1}{2}} \end{aligned} \tag{7}$$

where $\varepsilon_x, \varepsilon_y, \cdots$ are appropriate strain components. Equation 7 is derived from von Mises equation:

$$\varepsilon_{eq} = \frac{1}{\sqrt{2}(1+\nu')}[(\varepsilon_x - \varepsilon_y)^2 + (\varepsilon_y - \varepsilon_z)^2 + (\varepsilon_z - \varepsilon_x)^2 + \frac{3}{2}(\gamma_{xy}^2 + \gamma_{yz}^2 + \gamma_{xz}^2)]^{\frac{1}{2}} \tag{8}$$

where ν' is the effective Poison's ratio and in case of plastic deformation it is $\nu' = 0.5$.

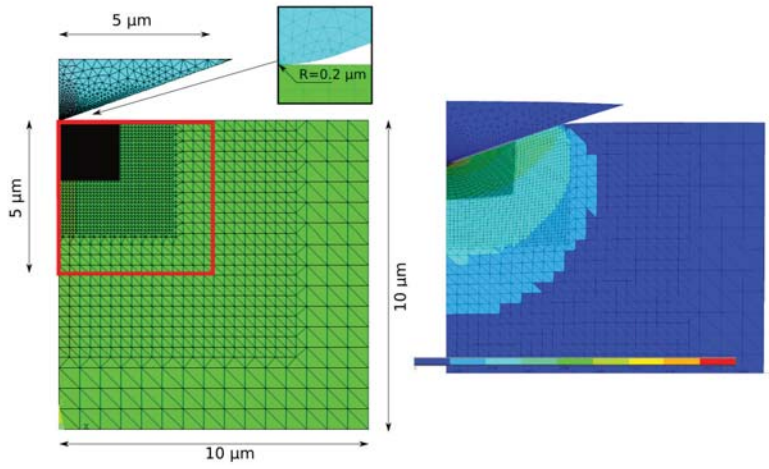

Fig. 2: FE model of nanoindentation with damage model application zone (red box)(left), equivalent plastic strain distribution (right)

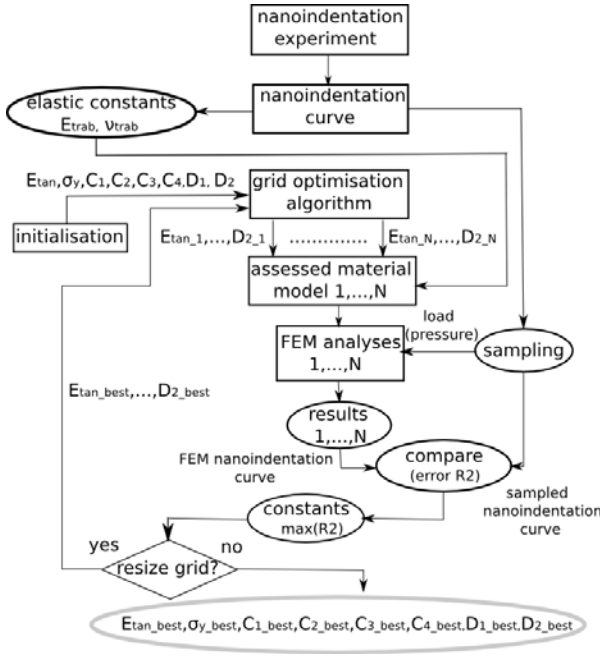

Fig. 3: Flowchart of the algorithm for material constants optimization

The size of the damage model application zone was determined according to nonzero equivalent plastic strain values obtained during the analyses. Equivalent plastic strain distribution caused by $20\ \mathrm{mN}$ peak force and the size of damage zone are shown in Fig 2.

Material constants (except the elastic constants which were determined directly from experiment) were identified using FEA of the nanoindentation test. Nanoindentation curves were sampled and load values were applied to model of the indenter in each loadstep. Resulting penetration depths were compared to experimentally obtained ones by least squares method and R^2 error was calculated. Initial values of material constants were modified in each simulation using custom grid optimisation algorithm (described in the flowchart in Fig. 3) to minimalize R^2.

2.3. Three-point bending test

Samples of trabeculae were extracted under magnifying glass (4 x magnification) from the same proximal human femur (Fig. 4) as in the case of the nanoindentation using a sharp-tip scalpel and pair of tweezers. Trabeculae were cleaned off marrow and grease in a detergent in an ultrasonic bath.

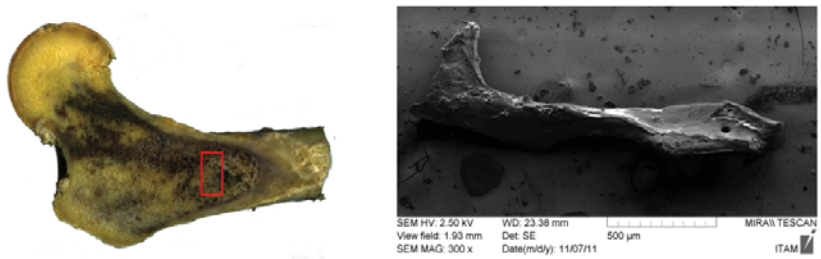

Fig. 4: Cross-section of human femur with harvesting area (left), single trabecula captured by SEM (right)

For three-point bending test an experimental setup (Fig. 5) composed from translation stages (Standa Ltd., Lithuania) was developed. Loading is controlled by steeper motor (SX16, Microcon, Czech Republic) and the load is applied using a precision linear stage (M-UMR3.5, Newport Corp., USA) with differential micrometer (DM11-5, Newport Corp., USA) with $0.1\ \mu\mathrm{m}$ sensitivity and $5\ \mathrm{mm}$ travel range. Applied force is measured using $2.2\ \mathrm{N}$ load sensor (FBB350, FUTEK Advanced Sensor Technology Inc., USA). For optical measurement of deformations the setup is equipped with a CCD camera (CCD 1300-F, VDS Vosskuhler GmbH, Germany) with 1280x1024 px resolution attached to an optical microscope (Navitar Inc., USA). This configuration enables to acquire images of deformation behaviour of

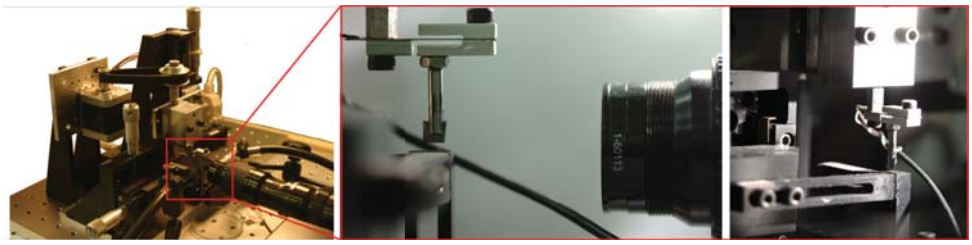

Fig. 5: Experimental setup (left), CCD camera capturing (middle), detail of the loading area (right)

the single trabecula during the bending test. Groups of markers were selected in the captured image data (Fig. 6-left) and their position were tracked using DIC toolkit [Jandejsek (2010)] based on Lucas-Kanade algorithm. During the tracking it is possible that correlation is lost in some of the markers (significant change in the brightness of the pixel in an image due to reflections, blur, large movement etc.). The markers with lost correlation are automatically identified and eliminated from further strain calculation. Loss of the correlation for one marker is shown in Fig. 6-bottom left and marked by a green circle. From the identified vertical displacements (Fig. 6-right) of middle span markers (6,7,8), strain values were determined according to equation for flexural strain of simply supported beam:

$$\varepsilon_f = \frac{6uh}{l^2} \tag{9}$$

where u is the average deflection of mid-span markers, h is the trabecula height in place of the applied load and l is the length between the supports.

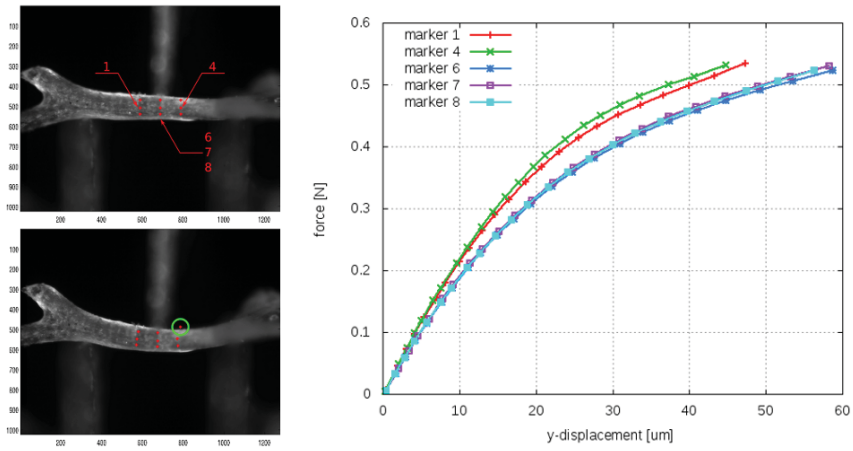

Fig. 6: Deflection of the single trabecula with group of markers (left), displacements of markers during the bending test (right)

For stress calculation, moment of inertia of the sample in the mid-span and the measured force were used. Young's modulus and the yield stress were established from stress-strain curve by the 0.2%

offset method [McNamara (2006)]. For estimation of measurement errors a precision of the setup was evaluated for materials with known properties, namely for BoPET film (Biaxially-oriented polyethylene terephthalate, DuPont, USA) and for Co-Ni wire. Overall precision of measurement was determined as upper limit of all measurement: Young's modulus 5% and yield stress 7% [Zlamal (2011)].

2.4. Numerical simulation of three-point bending test

For numerical simulation of the three-point bending test it is necessary to develop accurate geometrical model of the single trabecula. To facilitate this, each trabecular sample was mounted on a rotational stage and 360 images (with 1° step size) were captured using the CCD camera. The shape-from-silhouette method based on inverse Radon transform [Pintavirooj (2002)] was employed for geometrical model development. The volumetric model was created from the reconstructed data based on marching cubes algorithm [Lorensen (1987)] and segmentation techniques using our in-house segmentation and modelling software [Vavrik (2010)]. Volumetric model was meshed and exported to general purpose FE software Ansys (v12.1, Ansys Inc., USA). Example of the developed FE model of trabecula is shown in Fig. 7. The FE model of trabecula was composed from 3-D 10-nodes tetrahedral elements with quadratic

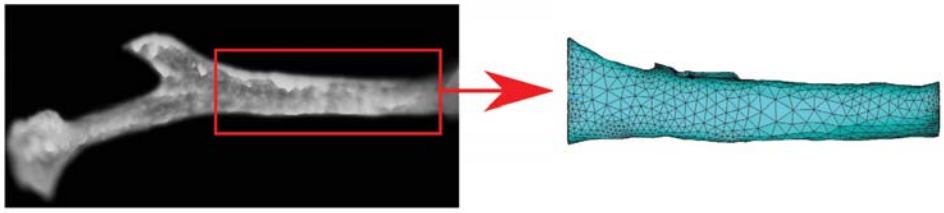

Fig. 7: The FE model development: captured image (left), final FE model (right)

shape functions. Nodes corresponding with position of correlation markers were selected on the surface of the model and the same boundary conditions as in the experiment were applied. To simulate the bending test, the same material model for the single trabecula as in case of the nanoindentation was used. In contrast to identification from the nanoindentation test, elastic constants (Young's modulus and Poisson's ration) were also identified. All ten constants were varied using the modified algorithm (described in Fig. 3) and resulting displacements of nodes were compared with displacements of the markers. The best set of material constants was determined based on R^2 error calculation.

3. Results and discussions

From the nanoindentation experiment, only the elastic constants were directly identified. Remaining constants for the elasto-visco-plastic material model with damage were identified using FEA of the nanoindentation test. For the statistically significant results, the emphasis was given to variety of control parameters (peak forces, holding times, loading rates) in the set (n=6) of curves for the FEA. Resulting constants were found using minimizing error based on least squares method in the optimization procedure and are shown in Tab. 1. A comparison of nanoindentation curves for the experiment and the FEA for the resulting constants are shown in Fig. 8-left. From the results it is evident that some constants have standard deviations larger than 20%, namely σ_y, C_1, C_3, D_2. This deviation may be due to several aspects, e.g: (i) the trabecular bone is biological material and its material properties are site-dependent. The indentation curves used in FEA were obtained from various indentation matrix, consequently, on various trabeculae; (ii) different material model sensitivity on identified constants. The second assumption was tested by sensitivity study.

The sensitivity study was performed for one indent and resulting curves are shown in Fig. 9. From the curves we can make following assumptions: (i) from graph for yield point it is obvious that the sensitivity is decreases with increasing σ_y value and for values above $100\,\mathrm{MPa}$ the changes between the curves are minimal. Small changes of curves in observed range $100 \div 300\,\mathrm{MPa}$ are the reason for relatively large deviation (24.3%) for the resulting mean value σ_y =180 MPa; (ii) values of C_1 should

Tab. 1: Resulting constants from the nanoindentation of human trabecular bone

	mean value	standard deviation
Young's modulus [GPa]	15.39	1.4 (9.1%)
Poisson's ratio [-]	0.2[1]	-
σ_y [MPa]	180	43 (24.3%)
E_{tan} [MPa]	1854	336 (18.1%)
C_1 [-]	3.1e-18	4.08e-18 (135%)
C_2 [-]	6.1	0.42 (6.9%)
C_3 [-]	0.88	0.71 (80.7%)
C_4 [-]	0	-[2]
D_1 [-]	0.73	0.037 (5.1%)
D_2 [-]	25.3	7.48 (29.4%)

[1] expertly determined

[2] not varied

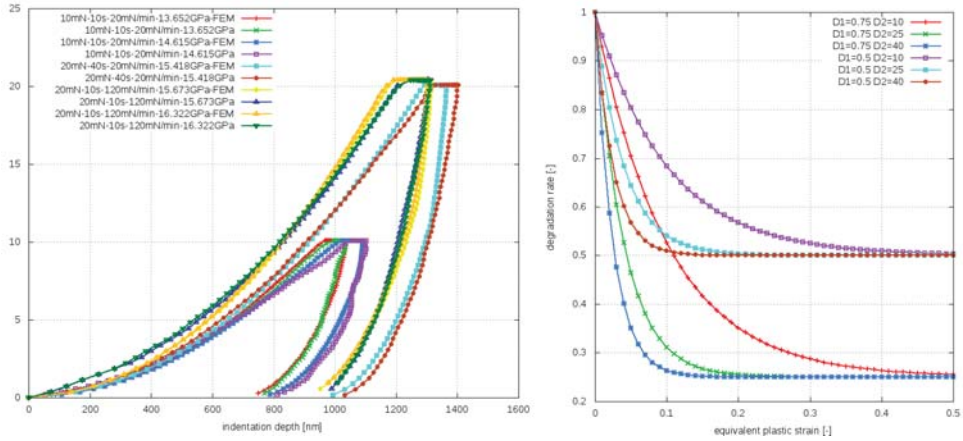

Fig. 8: Resulting nanoindentation curves for the best set of constants (left), damage variable as a function of the equivalent strain for variable values of D_1 and D_2

be varied in range up to order e-18. Lower values have no effect on the FEM curves. After exclusion of the low values (lower than $1 \cdot$ e-18), standard deviation was decreased to 2.06e-18$\pm$9.72e-19 (48%); (iii) constant C_2 is useful varied up to 6.5, higher values produced large creep which was not observed during the experiment; (iv) from equation 3 and graph in Fig. 9 (row 3, column 1) it is evident that constant C_3 has significant effect only for values larger than 1.9. Identified resulting value 0.88$\pm$0.71 is lower than this threshold and its influence for the material model is insignificant; (v) insensitivity to constant C_4 in varied range confirms zero effect of temperature creep during the FEA and C_4 constant can not be varied; (vi) the damage model as a function of the equivalent strain depends on variables D_1 and D_2 and this dependency is shown in Fig. 8-right. Constant D_1 determines the maximum degradation rate and constant D_2 governs the rate which degradation approaches this limiting value. The influence of these constants on the nanoindentation curve is predictable and shown in Fig. 9 (row 4, column 1 and 2). For increasing values of D_1 and D_2 increased penetration depth for the same value of load was observed.

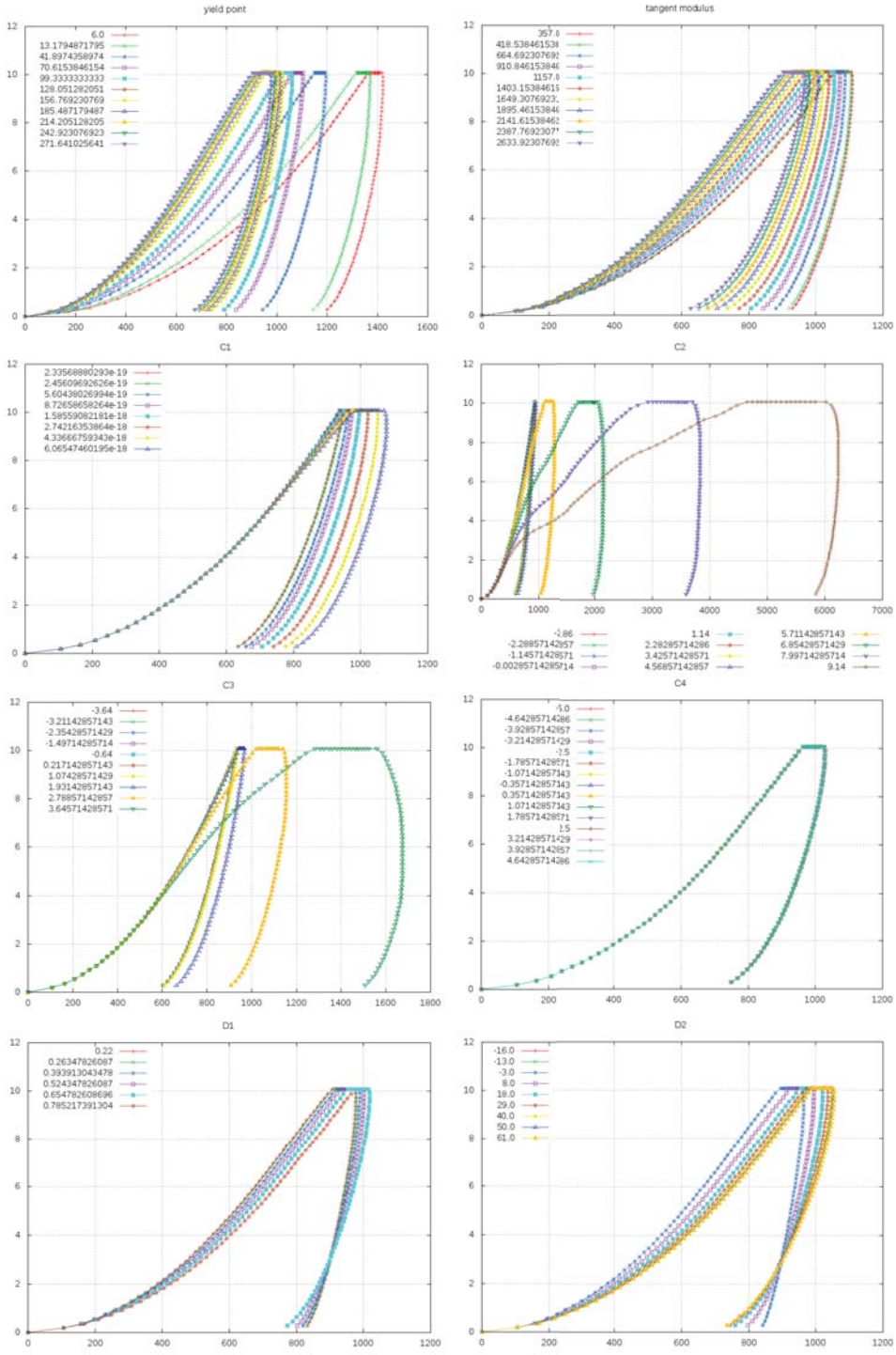

Fig. 9: Sensitivity study

Tab. 2: Resulting constants from the three-point bending test of human trabecular bone

	exp:mean value	exp:STD	FEM:mean value	FEM:STD
Young's modulus [GPa]	9.34	1.36 (14.5%)	12.093	0.727 (6%)
Poisson's ratio [-]	-	-	0.2	0.05 (24%)
σ_y [MPa]	185.6	42 (22.6%)	170	4.96 (2.9%)
E_{tan} [MPa]	-	-	1924	263 (13%)
C_1 [-]	-	-	8.6e-18	5.1e-18 (59.4%)
C_2 [-]	-	-	4.7	0.88 (18.6%)
C_3 [-]	-	-	2.1	0.67 (32.7%)
C_4 [-]	-	-	0	-
D_1 [-]	-	-	0.52	0.08 (16%)
D_2 [-]	-	-	30.1	1.4 (4.6%)

From the three-point bending test of the single trabecula Young's modulus and yield stress were directly determined. The experimental results, namely displacements of correlation markers and the applied force were used for FEA with goal to identify the constants for a material model same as in case of the nanoindentation. Resulting constants is shown in Tab. 2 and the comparison of displacements of the markers for the experiment and FEA are shown in Fig. 10-left, final distribution of vertical displacements is shown in Fig. 10-right. Experimentally measured values of Young's modulus for the single trabecula in the case of the nanoindentation and three-point bending were 15.3 ± 1.4 GPa and 9.34 ± 1.36 GPa, respectively. Difference in values can be explained by the nature of experiments, the nanoindentation measurement of elastic properties is very localised and depend on place of indent. Usual procedure is to indent a polished sample not necessarily taken perpendicularly to the longitudinal axis of trabecula and thus measured elastic constants can be significantly different. It was shown by Brennan (2009) that Young's modulus measured by nanoindentation can vary in the cross-section of a trabecula in 5 GPa range. On the other hand, Young's modulus measured by three-point bending is expected to the average of values measured by nanoindentation in the cross-section. Second aspect is related to place of harvesting that was not the exactly same.

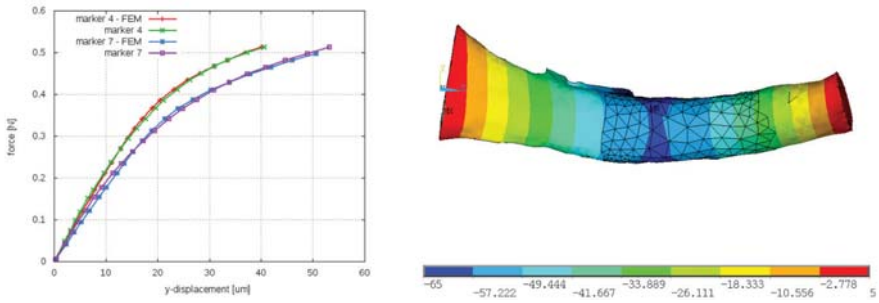

Fig. 10: Comparison of displacements of markers (left), distribution of vertical displacements

4. Conclusions

In this study elasto-visco-plastic material model with damage for the human single trabecula based on the nanoindentation test and three-bending test using the very similar procedure was established. Results

from FE simulation of experiments were fitted to experimentally measured values. Measured dependencies during the nanoindentation and three-point bending were force-penetration depth and force-displacements of the markers, respectively. From the numerical fitting procedure, the constants of material model were identified. Some of the constants can be directly determined from experiments. In the case of the nanoindentation the Young's modulus was 15.39 ± 1.4 GPa and in the case of the three-point bending test the Young's modulus and the yield stress were 9.34 ± 1.36 GPa and 185.64 ± 42 MPa, respectively. The visco-plastic constants and constants for the damage model were assessed from inverse FE modelling in both experiments. Young's modulus (E=12.093 ± 0.72 GPa) and yield stress (170 ± 4.96 MPa) were also determined by numerical analyses but only for the three-bending test. Influence of individual constants were investigated using sensitivity analysis of the nanoindentation test. The study confirms the possibility of using the indirect determination of the numerical material model for single trabecula based on FEM and experimental methods (nanoindentation and the micromechanical testing).

Acknowledgments

The research has been supported by the Grant Agency of the Czech Republic (grant no. P105/10/2305), Czech Technical University (grant no. SGS11/140/OHK2/2T/16), RVO: 68378297 and research plan of Ministry of Education and Sports (MSM 6840770043).

References

Kytyr, D., Doktor, T., Valach, J., et al. (2011), Evaluation of sample preparation procedures for micro-mechanical testing of trabecular bone. In: *10th Youth Symposium on Experimental Solid Mechanics* (M. Stockmann et al). Chemnitz University of Technology, Chemnitz, pp 71-72.

Oliver, W. C. and Pharr, G. M. (1992), An improved technique for determining hardness and elastic modulus using load and displacement sensing indentation experiments. *Journal of Materials Research, Cambridge Univ Press*, Vol 7, No.6, pp 1564-1583.

Jirousek, O., Nemecek, J., Kytyr, D., et al. (2011), Nanoindentation of Trabecular Bone – Comparison with Uniaxial Testing of Single Trabecula, *Chemicke listy, Ceska spolecnost chemicka*, Vol. 105, No.17, pp 668-671.

Lucchini, R., Carnelli, D., Ponzoni M., et al. (2011), Role of damage mechanics in nanoindentation of lamellar bone at multiple sizes: Experiments and numerical modeling. *Journal of the Mechanical Behavior of Biomedical Materials, Elsevier Ltd.*, Vol 4, No.8, pp 1852-1863.

Chen, Ch. (2009), 2-D finite element modeling for nanoindentation and fracture stress analysis. *PhD Thesis, University of South Florida*

Zhang, J., Michalenko, M. M., Kuhl, E., et al. (2010), Characterization of indentation response and stiffness reduction of bone using a continuum damage model. *Journal of the mechanical behavior of biomedical materials, Elsevier Ltd*, Vol 3, No.2, pp 189-202.

Zlamal, P., Jirousek, O. (2011), Parameter estimation of material model for single trabecula from micromechanical testing. *Chemicke listy, Ceska spolecnost chemicka*, article in press.

Jandejsek, I., Valach, J., Vavrik, D. (2010), Optimization and Calibration of Digital Image Correlation Method. *Experimentalni analyza napeti 2010* (Smid, P.). Univerzita Palackeho v Olomouci, Olomouc, pp 121-126.

McNamara L.M., Ederveen, A.G.H., Lyons C.G., et al. (2006), Strength of cancellous bone trabecular tissue from normal, ovariectomized and drug-treated rats over the course of ageing. *Bone, Elsevier Ltd*, Vol 39, No.2, pp 392-400.

Pintavirooj, C., Sangworasil, M. (2002), 3d-shape reconstruction based on radon transform with application in volume measurment. *The 10-th International Conference in Central Europe on Computer Graphics, Visualization and Computer Vision'2002*, Pilsen, Czech Republic.

Lorensen, W. E., Cline, H. E. (1987), Marching Cubes: A high resolution 3D surface construction algorithm. *Computer Graphics*, Vol. 21, No. 4, pp 163-169.

Vavrik, D., Dammer J., Jakubek, J., et. al. (2010), Advanced X-ray radiography and tomography in several engineering applications. *Nuclear Instruments and Methods in Physics Research Section A: Accelerators, Spectrometers, Detectors and Associated Equipment, Elsevier Ltd*, Vol 633, Supplement 1, pp 152-155.

Brennan, O., Kennedy, O.D., Lee, T.C., et al. (2009), Biomechanical properties across trabeculae from the proximal femur of normal and ovariectomised sheep. *Journal of Biomechanics, Elsevier Ltd*,Vol 42, No.4, pp 498-503. 42(4):498-503.

18th International Conference
ENGINEERING MECHANICS 2012
Svratka, Czech Republic, May 14 – 17, 2012

pp. 1621–1624
Paper #259

MECHANICAL PROPERTIES OF CEMENT PASTE WITH VARIOUS CONTENT OF FLY ASH AFTER 6 MONTHS

O. Zobal[*], P. Padevět[**]

Abstract: *Nowadays there is a heated discussion about using fly ash as an important concrete binder. It is therefore essential to define properties of this material. This paper presents results of an experiment which deals with mechanical and material properties of cement paste with different proportion of fly ash. More specifically, the compressive strength and tensile strength in bending of individual mixtures after 6 months will be presented.*

Keywords: ***Cement, fly ash, compressive strength, tensile strength in bending.***

1. Introduction

Worldwide and in the Czech Republic building industry is currently affected by several aspects. Among the most important ones there are economic and ecological aspects of construction. This means saving money while protecting the environment. Concrete and reinforced concrete are still the most widely used construction materials. Regarding concrete, money can be saved on the binder, the cement. There is an opportunity to use fly ash to a greater extend. This would positively influence the environment because of efficient waste disposal. It is widely known that the Czech Republic is among the greatest fly ash producers (Fečko, 2003).

Fly ash has already been used as an essential part of concrete for several decades. This fact is demonstrated by construction of one of the most significant structures in the Czech Republic, which is a water reservoir Orlík built and opened in 1961. The concrete used for construction of the massive dam body contains almost 30% of fly ash. One of the most important properties of fly ash was made use of. This property is the fact that larger quantity of fly ash in a concrete mixture reduces heat of hydration. In the graph, Fig. 1 summary of measurement during construction and measurement after 50 years, excellent durability of this concrete is shown. (Bittnar at al., 2011).

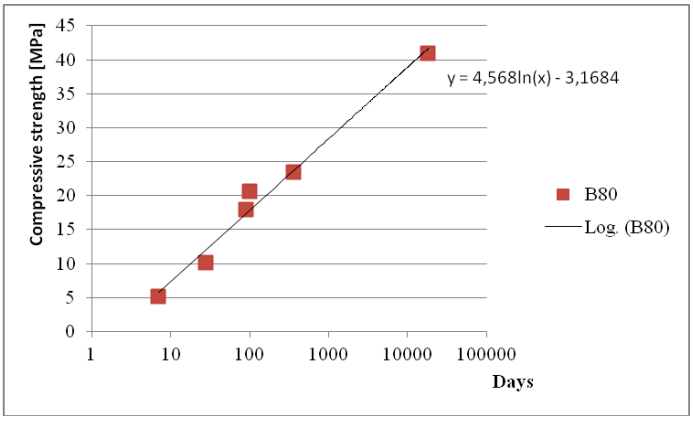

Fig. 1: The increase in compressive strength of concrete B80 dam Orlik (Bittnar at al., 2011)

[*] Ing. Ondřej Zobal: Faculty of Civil Ingineering, CTU in Prague, Thakurova 7, 166 29, Prague; CZ, e-mail: ondrej.zobal@fsv.cvut.cz

[**] Ing. Pavel Padevět, Ph.D.: Faculty of Civil Ingineering, CTU in Prague, Thakurova 7, 166 29, Prague; CZ, e-mail: pavel.padevet@fsv.cvut.cz

This secondary energy product is currently used when constructing significant structures such as Washington Dept. of Transportation, USA, in 2006 and Liu Center U.B.C, Canada, in 2000 (Schmidt & Fast, 2000). It is possible to produce alkali-activated fly ash and make it part of the concrete hydration process (Němeček at al., 2010). Fly ash has been used in construction industry for many years but there is still a considerable number of issues and problems to be dealt with. The paper deals with mixtures of concrete, water and fly ash free of alkaline agents and development of material properties over time.

2. Types of mixtures for production of test specimens

Water ratio of all mixtures - cement – fly ash – water - reaches up to 0.4. Cement was acquired from Radotín locality and it is Portland cement labelled CEM I 42,5R. Fly ash was acquired from Mělník and is commonly added in blended cements. Several types of mixtures with different ratio of fly ash in comparison to cement content were produced. Individual sets are described in Table 1 which shows density development of individual sets of mixtures. The larger content of fly ash, the sparser the density.

Tab. 1: Types of mixtures and their density

Type of mixture [-]	Cement [%]	Fly Ash [%]	Density [kg/m^š]
I	100	0	2059 ± 89
II	60	40	1820 ± 22
III	50	50	1844 ± 19
IV	40	60	1749 ± 32
V	30	70	1650 ± 29

3. Test specimens and testing methods

There were two groups of specimens designed for the purposes of the experiment. Planned measurements could thus be carried out:

- cylinders – diameter of 10 mm, length of 100 mm
  → produced for the compressive strength test
- beams – dimensions of 20 × 20 × 100 mm
  → produced for the tensile strength in bending test

Cylinder specimens were made in special plastic moulds. Beam specimens were made in classic steel moulds. After 48 hours they finally became hard and were placed in water for long-term storage at 20°C.

There were two mechanical tests carried out – determination of compressive strength and tensile strength in bending. Electromechanical testing machine, MTS Aliance RT-30, was used to perform both tests. Maximum loading force of the machine is 30 kN in compression and tension. The compressive strength test was carried out on adjusted cylinders. Cylinders were shortened at 40 mm of length. Diameter of the specimens remained the same; thus, the load area covered 78,5 mm^2. During performing the test, a strain gauge which recorded figures of transformation was fixed to each specimen. A three-point ending test to obtain tensile strength in bending figures was performed on beams. The beams were not adjusted before the test was initiated. Load affected the middle of the span, supports were placed 10 mm from the specimen edges and the span between individual supports (effective length) was 80 mm.

4. Experiment results

Graphic summary of measured figures is shown in Fig. 2 where development of compressive strength over time is shown. Fig. 3 displays tensile strength in bending over time. Description of trends resulting from the experiment is listed in the conclusion.

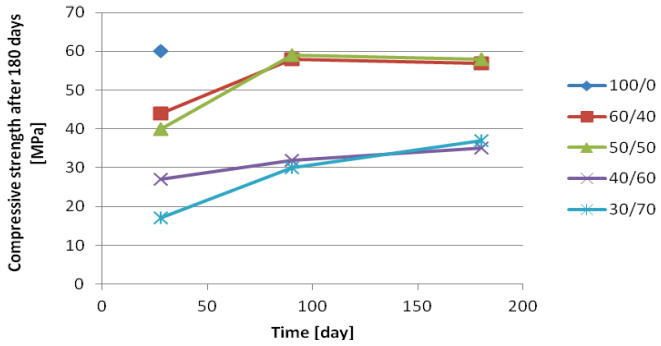

Fig. 2: Average compressive strength of cement pastes after 180 days

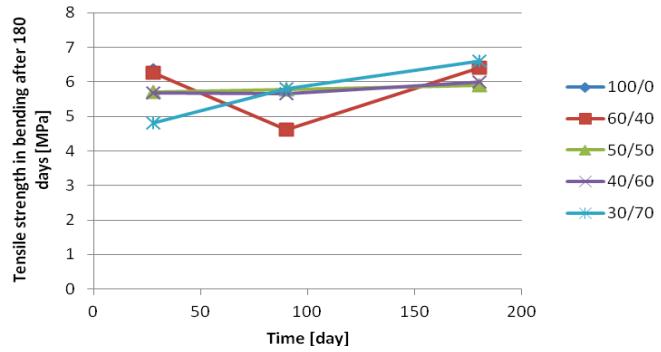

Fig. 3: Average tensile strength in bending of cement pastes after 180 days

5. Conclusions

Thanks to measurement results of observed mechanical properties of cement and fly ash mixtures blended in different proportion with water coefficient of 0,4 without any other additives we attained the knowledge as follows (all measurement results were statistically evaluated and a standard deviation ranging up to 10% was determined).

The density of mixture with higher ratio of fly ash in it decreased. Compressive strength with higher content of fly ash in it decreased as well after the period of 28 days. After the period of 90 days, the figures increased evenly and after the period of 180 days, the increase in strength was observed only in mixtures with higher ratio of fly ash. The figures of pure cement paste measured after several days were unfortunately not available at the time of completing this paper. Compressive strength of pure cement measured after 28 days was about 60 MPa. When there was only 30% of cement and 70% of fly ash in the mixture, the compressive strength figure rose to its third. After the period of 180 days the compressive strength figure regarding mixtures with higher fly ash content reached 60% of those mixtures with lower fly ash content; at the beginning it was only 50%. Increasing fly ash content in the mixture had no significant effect on tensile strength in bending under bend after 28 days. The figures ranged between 5 and 6 MPa. After 90 as well as 180 days there was only a slight increase of this strength (value of pure cement paste was unfortunately not available at the time of completing the paper). As far as the set II was concerned, a decrease in value occurred, which might have been associated with an error made during measuring.

Another aim of our work is to further observe the development of material properties over time and focus on other properties such as statistical flexibility module, heat of hydration, fracture energy etc. We would like to pay attention to material structure at micro level as well.

Acknowledgement

The financial support of this experiment by the Faculty of Civil Engineering, Czech Technical University in Prague (SGS project No. 12/117/OHK1/2T/11) is gratefully acknowledged.

References

Fečko, P. (2003) *Fly Ash*, VSB - Technical Univerzity of Ostrava.

Bittnar, Z., Padevět, P., Zobal, O. (2011) Dam Orlik - concrete with addition fly ash after 50 years, In: *18. Concreting Days 2011*. Prague: CBS in Czech.

Schmidt, R., Fast, P. A. (2000) *High volume fly ash concrete usage for skytrain stations*, Technical report.

Němeček, J., Šmilauer, V., Němečková, J., Kopecký, L. (2010) Nanoindentation of alkali-activated Fly Ash. In: *Nanotechnology in Cement and Concrete*. Washington: Transportation Research Board.

18th International Conference
ENGINEERING MECHANICS 2012
Svratka, Czech Republic, May 14 – 17, 2012

pp. 1625–1630
Paper #310

ENERGY SENSITIVE X–RAY IMAGING WITH PIXEL STACK DETECTOR

J. Zemlicka[*], J. Jakubek[**], P. Soukup[***]

Abstract: *Material decomposition based on dual energy X–ray radiography which was primarily developed for tissue differentiation in medical imaging can be favorably used for composite material examination. The principle of this method is obtaining several absorption images of the sample with different energy spectra which allows for the identification of main material components. The need of measurement at several X–ray spectra can be achieved either by alternation of the tube voltage and/or by the use of additional filters. The single photon counting pixel detector Medipix allows direct energy discrimination of registered radiation enabling spectrum selection at the detector side without the need to first modify the X–ray source spectrum. Our approach provides moreover low noise images with broad dynamic range and thus high sensitivity and enhanced contrast. Utilization of a 3D voxel detector with two or more sensor layers allows obtaining all required images simultaneously in a single exposure. The results of the material decomposition obtained with the Medipix detector are presented and discussed in this contribution.*

Keywords: ***energy sensitive X–ray radiography, Medipix, signal to thickness calibration, material decomposition***

1. Introduction

Transmission X–ray radiography is a well-established method for the inspection of the inner structure of objects. The method as such is non-destructive and can be used for a wide variety of sample materials with low and intermediate atomic number (other methods are preferable for materials with high atomic number). The radiograph registers the changes in the intensity of the transmitted beam. These changes are caused by the differences in the inner composition of the sample.

For the registration of the transmitted X–ray radiation we utilize in our work the single particle counting 3D voxel detector based on the Medipix chip (details can be found on the **Medipix Collaboration website)**.

To evaluate material differences it is necessary to measure the same sample in several energy ranges (the differences in material attenuations are then pronounced). One of the ways how to achieve this is to use the 3D voxel detector structure. Individual detector layers then work as spectrum filters – only the first layer is illuminated by the original spectrum while the others are illuminated by the spectra filtered by previous layers. This filtering effect can be further enhanced by the change of the individual sensitivity of the detector layers (by threshold shifting). Intensity data measured with the 3D voxel detector are measured on all layers at the same time. Then it is necessary to convert them to the equivalent thicknesses of the reference material (described in ref. Jakubek, 2007). The material separation is done by the decomposition of the measured material vector to the chosen (base) material vectors (see ref. Soukup, 2011b).

[*] Ing. Jan Žemlička: Institute of Experimental and Applied Physics, Czech Technical University in Prague, Horská 3a/22; 128 00, Prague; Czech Republic, e-mail: jan.zemlicka@utef.cvut.cz

[**] Ing. Jan Jakůbek, Ph.D.: Institute of Experimental and Applied Physics, Czech Technical University in Prague, Horská 3a/22; 128 00, Prague; Czech Republic, e-mail: jan.jakubek@utef.cvut.cz

[***] Ing. Pavel Soukup, Ph.D. : Institute of Experimental and Applied Physics, Czech Technical University in Prague, Horská 3a/22; 128 00, Prague; Czech Republic, e-mail: pavel.soukup@utef.cvut.cz

2. Materials and Methods

2.1. Medipix Family Detectors

The Medipix and Timepix chips are hybrid semiconductor pixelated detectors developed in the framework of the Medipix collaboration. These devices are composed of a standard semiconductor sensor which can be fabricated of different materials (Si, CdTe, GaAs) and thickness (e.g. 300 μm, 700 μm, 1 mm) coupled to a pixelated electrode and a readout chip with integrated micro-electronics for signal processing chain for each pixel. The Medipix2 detector used in this work consists of a 256 × 256 pixels chip (each pixel of 55 × 55 μm^2 size) bump-bonded to a silicon sensor of 300 μm thickness.

Direct per pixel digitalization of the measured signal together with the possibility to set threshold in each pixel above the noise level allows single photon counting with no dark current and practically unlimited dynamic range (see ref. Jakubek, 2005). These features cannot be provided by charge integrating devices (such as CCD and CMOS). No sensitivity to dark current and readout noise allows obtaining high sensitivity and very high contrast in radiographic images even under low illumination intensity which is very desirable, for example, in medical applications (e.g. Master Thesis Dammer, 2005)

Visualization and high portability of the detectors are provided by the possibility to operate them from a standard PC via the Pixelman software (see ref. Holy, 2007, Turecek, 2011). Detector data acquisition, power and control are provided by the USB readout interface FITPix (see ref. Kraus, 2011).

2.2. 3D Voxel Detector Based on Medipix Chip

The 3D Voxel detector is a modular device consisting of several layers of Medipix chips (each layer can be considered as a 2D detector), interconnected in a daisy-chain structure (see figure 1, details can be found in ref. Soukup, 2011a). The readout chips used for this device were thinned to 120 μm (from their manufactured standard thickness of 740 μm) to decrease the thickness of the insensitive material between the individual detector layers.

Originally planned applications for this type of device are particle tracking and X–ray imaging with increased efficiency (ref. Soukup, 2011b).When used for imaging one limitation of this geometry lies in the fact that the first layer works as a spectrum filter for the second layer and so on. Nevertheless this situation can be advantage for material sensitive imaging which is the main reason why such device was selected for this work.

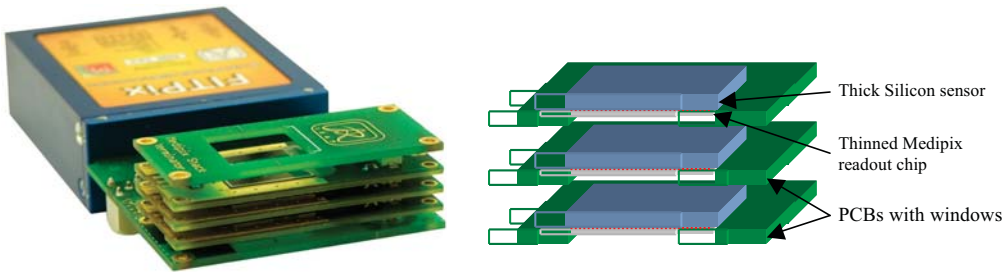

Fig. 1: 3D voxel detector consisting of 3 layers of Medipix chips on a single board attached to a FITPix readout interface (left). Schematic illustration of the stacked architecture (right)(Soukup, 2011b).

2.3. Signal to Thickness Calibration (STC)

For the purpose of imaging with the pixel detector it is necessary to correct the registered raw images for the individual pixel sensitivity (flat field correction) or to directly calibrate the detector response to a reference material thickness (signal-to-thickness calibration (STC)). The STC provides linearization of the detector signal taken with a polychromatic X–ray beam (transformation of intensity to

equivalent thickness of the reference material). This linearization is very useful for 3D object reconstructions such as computed tomography and laminography.

In case of the 3D voxel detector the STC is measured for all its layers at the same time. The equivalent thicknesses obtained from the detector layers are identical only for the reference material (measured material response in equivalent thicknesses on the first and second detector layers is illustrated in figure 2). Other materials will show different thickness in different layers. The alteration between equivalent thicknesses obtained from detector layers can be used as a measure of the differences between the sample and reference materials. The obtained difference between materials can be pronounced by threshold (THL) shift of the second layer (the low energies are cut off) as illustrated in figure 4.

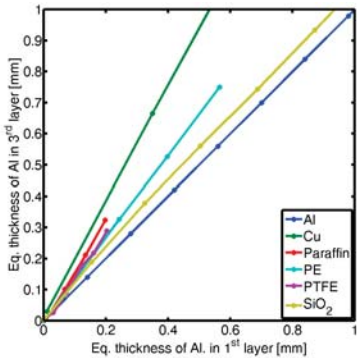

Measured points correspond to thicknesses of:

Al – 140, 280, 420, 560, 700, 840, 980 µm

Cu – 17 µm, (35 µm)

Paraffin – 2.5, 5.2, 7.5 mm

PE – 2.5, 5, 7.5 mm

PTFE – 1, 2, 3, 4 mm

SiO_2 – 150, 300, 450, 600, 750, (900 µm)

Fig. 2: Response vectors obtained by STC technique (reference material was Al). The differences in equivalent thicknesses in the first and second detector layers are shown for several materials (taken from Soukup, 2011b)

Two equivalent thicknesses are calculated for each point in the sample when two stacked layers are used. By the decomposition of the obtained data to base material vectors (real or chosen) it is possible to visualize the distribution of base materials inside the sample (for details about decomposition see article Soukup, 2011b).

3. Results

3.1. Decomposition into Two Base Materials

The basic test for the estimation of reliability of this method can be measured on an overlaying segmented phantom. The chosen phantom was composed of perpendicular aluminium and paraffin segments which is shown in figure 3 (left) together with equivalent thickness images reconstructed on the first and second layers (figure 3 right). Each combination of thicknesses can be used as one validation point (the mean values from each thickness combination were taken). Individual acquisitions took 5 seconds, the distance between the X–ray tube and detector was 10 cm and the Xray tube was configured to 60 kV and 350 µA.

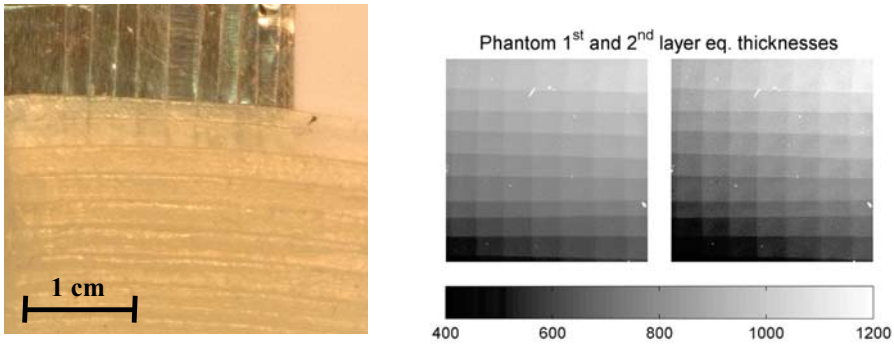

Fig. 3: Photograph (left) and equivalent thickness images obtained for first and second detector layer after the signal-to-thickness calibration (right). The scale is in μm equivalent of Al.

A shift of the energy threshold on the second detector layer cuts off the low energy spectrum and enhances the differences in materials. Figure 4 shows the obtained equivalent thicknesses at the validation points (line colours are noted above) for standard settings of the energy threshold and for energy threshold shifted by 50 THL points (about 20 keV). The slope of blue (aluminium) lines is close to 45 degrees because the aluminium was used as a reference material for STC.

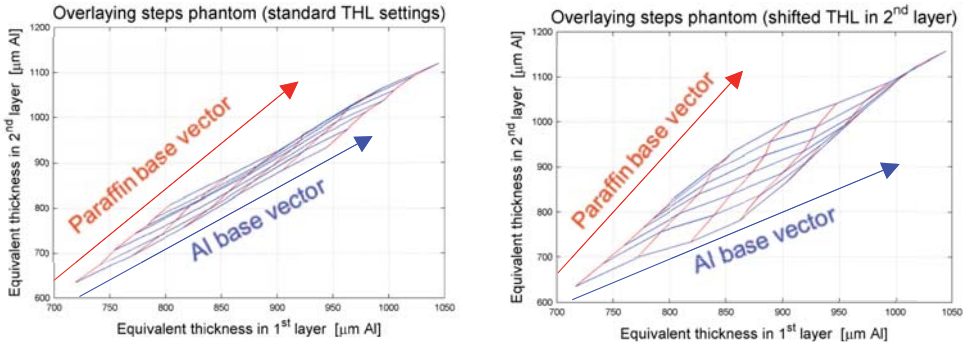

Fig. 4: Equivalent thicknesses for the overlaying segmented phantom: standard THL settings (left) and THL shifted by 50 points - about 20 keV (right). Red lines represent paraffin steps (constant aluminium thickness) and blue lines represent aluminium steps (constant paraffin thickness). Equivalent thicknesses obtained with

It can be seen that material vectors (colour lines in image 4 above) are not perfectly linear over the entire thickness range – linear approximation was used for the decomposition. The irregularities are caused mainly by the presence of moiré pattern on the second detector layer (created by first detectors metal bump-bonding balls beneath each pixel). This side effect of the use of 3D voxel detector can be strongly suppressed by increasing the distance between X–ray tube and the detector.

The result of equivalent thickness decomposition to two base vectors (aluminium and paraffin) is shown in figure 5 below together with the decomposed aluminium thickness in the phantom.

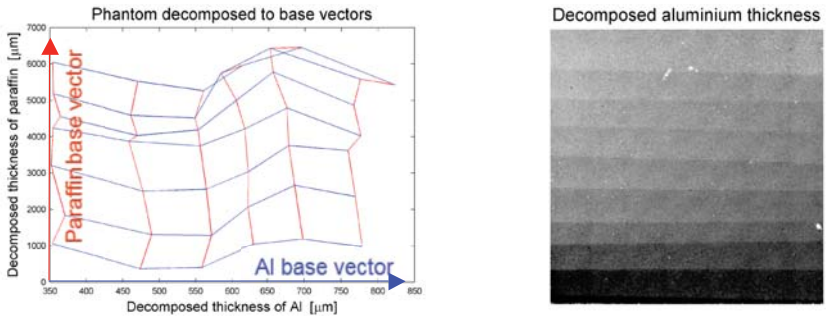

Fig. 5: Decomposed thicknesses for overlaying segmented phantom (left). Red lines represent paraffin steps (constant aluminium thickness) and blue lines represent aluminium steps (constant paraffin thickness) (left). Area distribution of aluminium in the sample (right).

3.2. Practical application of the method – composite sample

This method can be used for composite samples where the exact composition is not known or when it would be very hard to create reference samples of pure materials contained in the inspected object. The idea then is to do the decomposition to pseudo-materials (simply soft and hard components in this article but it can be as well a characteristic mixture of materials (colour pigment etc.))

As a testing object for the pseudo-material decomposition, the replica of a painting was used (painted with metallic pigments). The distance between the X–ray tube and the detector was increased to 100 cm to avoid moiré pattern on the second detector layer (the period of the pattern increases with distance). It was necessary to scan the sample in two positions to capture the image of the larger segment (area with the eye) of the painting. The radiography of the selected area is shown in figure 6 together with the result of the material decomposition into two components (soft and hard). Similar results were initially obtained with a less complex dual energy method (see ref. Zemlicka, 2010), the measurement with the 3D voxel detector composed of N-layers brings the possibility to measure the sample directly with N different energy filters at once.

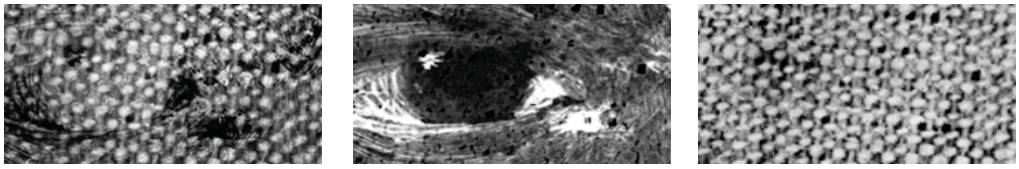

Fig. 6: Radiography of the eye area in the painting (left) and the result of the material decomposition into two components. The hard component group (middle) and soft component group (right) were separated. Two acquisitions were needed for this decomposition – the sample was shifted after the first acquisition to double the inspected area.

4. Summary

It has been demonstrated that material decomposition method can evaluate the radiographic data obtained with the 3D voxel detector assembled from Medipix family detectors. The advantage of this device lies in the possibility to take pictures in all subsequent detector layers at once. Moreover the front layers themself work as an energy filter for the layers behind. When the material composition of the sample is known it is possible to directly calibrate the method and to carry out the material decomposition into the chosen components. In other cases when the sample composition is too complex it is still possible to group all materials with similar properties into pseudo-materials and use them for the decomposition.

Acknowledgement

This work was supported by the Ministry of Education, Youth and Sports of the Czech Republic under Research Center No. LC06041 and by Grant No. P105/11/1551 of the Grant Agency of the Czech Republic. Research carried out in frame of the Medipix Collaboration.

References

Dammer, J. (2005) Application of Medipix2 imaging detectors in X–ray mammography (in Czech), First faculty of medicine, Charles University in Prague, Master Thesis

Holy, T., Jakubek,J., Pospisil, S., Uher, J., Vavrik, D. & Vykydal, Z. (2006) Data acquisition and processing software package for Medipix-2 device, *Nuclear Instruments and Methods A*, Vol. 563, pp. 254-258

Jakubek, D. Vavrik, S. Pospisil, J. Uher, (2005) Quality of X–ray transmission radiography based on single photon counting pixel device, *Nuclear Instruments and Methods A,* Vol. 546, pp. 113-117

Jakubek, J. (2007) Data processing and image reconstruction methods for pixel detectors*, Nuclear Instruments and Methods A,* Vol. 576, pp. 223-234

Kraus, V., Holik, M., Jakubek, J., Kroupa, M., Soukup, P. & Vykydal, Z. (2011) FITPix – Fast Interface for Timepix Pixel Detectors, *Journal of Instrumentation*, Vol. 6, C01079

Medipix Collaboration, website: http://medipix.web.cern.ch/MEDIPIX/

Soukup, P., Jakubek, J. & Vykydal, Z. (2011a) 3D sensitive voxel detector of ionizing radiation based on Timepix device, *Journal of Instrumentation*, Vol. 6, C01060

Soukup, P., Jakubek, J., Jandejsek, I. & Zemlicka, J. (2011b) X–ray color imaging with 3D sensitive voxel detector, *Journal of Instrumentation*, Vol. 6, C12014

Turecek D., Holy, T., Jakubek, J., Pospisil, S. & Vykydal, Z. (2011) Pixelman: a multi-platform data acquisition and processing software package for Medipix2, Timepix and Medipix3 detectors, *Journal of Instrumentation*, Vol. 6, C01046

Zemlicka, J., Jakubek J., Kroupa, M., Hradil, D., Hradilova, J. & Mislerova, H. (2010) Energy sensitive X–ray radiography for the non-destructive inspection of historical paintings, *Acta Artis Academica: Příběh umění - Proměny výtvarného díla v čase*, s. 339-350

18th International Conference
ENGINEERING MECHANICS 2012
Svratka, Czech Republic, May 14 – 17, 2012

pp. 1631–1642
Paper #319

FEM SIMULATION OF HIGH VELOCITY SHOCK WAVES IN FIBER REINFORCED COMPOSITES

M. Žmindák[*], Z.Pelagič[*]

Abstract: *Fiber reinforced composites are very efficient in damping shock waves. Computational simulations enable to evaluate the damping properties and to design the structure of the fiber reinforced materials (FRM) and response of the whole structure to explosion and impact load. Especially important is the case when fibers are much stiffer than the matrix. The shock waves reflect, refract and interact in such material and the shock wave is damped and attenuated in this way. Material properties of fibers, matrix and volume content of both components are material design parameters, which define the structural response to explosion and impact load in computational simulations by multi-level modeling. We will present computational models for elastic material. The modulus of elasticity of fibres is 100 times larger than that of the matrix. .*

Keywords: ***Computational simulation, high velocity impact, fiber reinforced composite.***

1. Introduction

Composite materials have been used more extensively in the recent years in many fields of industry. Composite materials reinforced by stiff particles or fibers are important materials possessing excellent mechanical and also thermal and electro-magnetic properties. The main advantages of such materials are high strength and stiffness together with low weight, and possibility of designing desired mechanical properties of the structure in different locations and directions. This fact involves higher demands on the computational analysis, especially when compared to corresponding analysis of conventional materials. One of the important tasks is to assess the critical stress state for static or dynamic loadings. There are many criteria which are used to predict the failure of composite materials. The accuracy of prediction of failure strongly depends on the criterion (Kormaníková, et al., 2011).

Properties of fiber composites reinforced by long fibers significantly depend on the selection of fiber and matrix and on the way of how they are combined, fiber volume fraction, fiber length, fiber orientation, laminate thickness and presence of bond medium for improvement of fiber-matrix bond. Glass fibers have high strength at low costs; carbon fibers have very high strength, stiffness and low density. Kevlar fibers have high strength and low density, they prevent the spread of fire and are penetrable by transparent to radio waves. Polyesters are most often used matrices, because they offer good properties at relatively low costs. The best properties of epoxies and application of polyamides at temperatures predestinate them to special use, but they are expensive. Strength of composites increases by fiber volume fraction and fiber orientation parallel to load direction. By increasing length of fibers, the reinforcement is more effective at load carrying. Shorter fibers are better for manufacturing and less expensive.

In present time creating new scientific discipline „ Simulation-Based Engineering Science (SBES)“, which on basis of mathematical methods and computer simulated engineering system behavior. Computer simulation represents an extension of theoretical science in that it is based on mathematical models. Simulation also provides a powerful alternative to the techniques of experimental science and the observation when phenomena are not observable or when measurements are impractical or too expensive.

[*] Prof. Ing. Milan Žmindák, CSc.: University of Žilina, Faculty of Mechanical Engineering, Department of Applied Mechanics, Univerzitná 8215/1; 010 26, Žilina; SK, e-mail: milan.zmindak@fstroj.uniza.sk

[*] Zoran Pelagič, Bc. University of Žilina, Faculty of Mechanical Engineering, Department of Applied Mechanics, Univerzitná 8215/1; 010 26, Žilina; SK, e-mail: ropfly@gmail.com

Wave propagation in heterogeneous material is a very old and complex problem (Brepta, 1997; Okrouhlik, 2001). The phenomenon of material and geometric dispersion are so far very little studied. It is a complex problem with regard to interaction of pressure and tension phase waves generated on the boundary of an inhomogeneous material. The smaller the particles, the greater the number of material interfaces, which interact with each other and wave progresses, the greater the reduction and dispersion. Interaction of the bow shock wave with the secondary pressure waves resulting dissipation, shock-wave attenuation.

Currently, for wave propagation modeling in composite structures at high speeds are mainly used the Finite Element Method (FEM) (Bathe, 2011), Boundary Element Method (BEM) (Sládek, 2002), Fast Multipole BEM (Liu, 2009), respectively, Finite Volume Method (FVM), mesh free formulations and recently connection of FEM and element free based formulations, used in commercial program systems LS-DYNA (LS-DYNA ,2006), AUTODYN and PAM CRASH etc.. However very effective methods appear to be spectral FEM (SFEM) and wavelet methods. The SFEM is a numerical method evolved from the Fourier Transform based method. More details about the solution is given in (Tsai, 2006; Gopalakrishnan, 2008).

Shock wave propagation in heterogeneous materials is a complex matter (Datta, 2009). Phenomenon of material and geometric dispersion is yet poorly understood as complex pattern is generated by a continuous interaction of compression and rarefaction waves generated by inter-face in non-homogeneous material. The smaller is the particle size, the greater is the number of interfaces that interact with propagating stress waves and the higher is attenuation and dispersion. Interaction of leading shock front with secondary compression waves results in dissipation of the shock wave. The behaviour of materials by shock wave loading can be simulated and studied by commercial softwares like LS DYNA, AUTODYN, DYTRAN, ABAQUS, PAM-SHOCK, etc., but the models require large number of equations that have to be solved and resolved during propagation of the shock waves and so, very efficient computers/supercomputers are necessary for modelling of complicated problems.

The aim of this paper is to contribute better understanding and modelling of scattering and dispersion of shock waves using commercial software. It is supposed that readers are familiar with basics of continuum mechanics and basic methods of simulation classical problems of statics and dynamics using FEM. Some special methods and corresponding governing equations used especially in simulations of shock propagation in solids are introduced.

2. Wave propagation in elastic solids

In this section we first present the basic considerations about physical problems and then we mentioned about most important wave forms in solids. We note that we consider only an elastic, isotropic homogeneous isotropic medium.

2.1 Governing equations

We will not present here all governing equations for shock wave propagation as it would contain basic relations of continuum mechanics, which can the reader find in textbook of continuum mechanics (Malvern, 2007, Meyres, 1999 & Wu, 2005). These equations are used to describe:

- the kinematics of solid continuum, the equations which present relation between displacements and corresponding displacement gradient for finite displacements in material and spatial description, strain tensors for finite strain formulation, strain measures and strain rate tensors,
- material and spatial time derivatives of deformations, velocity and velocity gradients,
- corresponding stress measures,
- formulation of equilibrium,
- conservation equations (conservation of mass, momentum and energy),

Thermodynamic laws give:

- the first law – the conservation of total energy,
- the second law – change in entropy,
- thermodynamic potentials – internal energy, enthalpy, Helmholtz and Gibbs free energy.

Further, the constitutive equations, which have to be thermodynamically consistent, give the relation between stress and strain measures. Dynamic deformation processes, especially when shock wave formation is involved, are usually modelled by decomposed stress tensor. The decomposition splits the stress tensor into a deviatoric tensor S_{ij}

$$\sigma_{ij} = S_{ij} - p\,\delta_{ij} \tag{1}$$

The usefulness of the decomposition results from the needed nonlinear character of equations of state (EOS) to describe shock waves. In general, a pure material can be solid, fluid and gas.

We will deal further with solids and only with special problems concerning shock waves propagation. More general problems can be found in textbooks, e.g. (Hiermaier, 2008; Malvern 1969; Meyers at al., 1999; Wu, 2005). Dynamic compressive behaviour of materials at strain rates in the regime of 10^6 [s^{-1}] is typical for shock loading resulting elastic-plastic characteristic.

For most engineering applications involving equations of states, empirical relations with experimentally derived data are used. It is most simple representation is the so called *linear equation of state* which assumes isothermal processes and a linear pressure-volume or pressure-density relation. Via the bulk modulus K the linear equation of state is formulated as:

$$p = K_{\varepsilon kk} = K(\rho/\rho_0 - 1) = K\mu \tag{2}$$

with the compression term μ describing the ratio of change in volume and density ρ from its initial state, ρ_0.

For isotropic materials, the bulk modulus K is linked to the Young's modulus E and the shear modulus G via the Poisson ratio ν by:

$$K = E/(3-6\nu) = 2G(1+\nu)/(3-6\nu) \tag{3}$$

meaning that the knowledge of any two other elastic constants provides the needed material dependent input for the linear equation of state.

Whenever the linear elastic region described in equation (2) is left, which is for example the case when a wide spectrum of pressure and energy shall be covered by the EOS, nonlinear relations are needed. A polynomial description of an equation of state can for instance be written as:

$$p = K_1\mu_1 + K_2\mu_2 + K_3\mu_3 + (B_0 + B_1\mu)\rho_0 \tag{4}$$

where K_i and B_i are material constants usually defined separately for compression and expansion, respectively. An important difference to the linear equation (2) is marked by the energy dependency, e, of the last term in (4). Whereas the linear equation is only a compression curve along an isotherm, the latter can really be called equation of state in the sense of (4).

The observation of shock wave propagation can provide information to identify the material parameters in (4). The underlying theory is composed of the thermomechanics of shock waves, i.e. essentially the Rankine-Hugoniot equations providing a line of reference configurations on the state surface, used to identify the parameters K_i and an assumption on the pressure change of the Hugoniot-line along isochores, defining the constants B_i.

In the case of quasi-static loads, wave effects are not investigated since the loading duration is long compared to the duration of multiple reflections throughout the structure. In addition, the resulting structural deformation and material state is not influenced in a comparable way by single wave transition. However, if the induced waves take the shape and amplitude of shock waves or the load speed is in the order of magnitude of the local sound speed, then wave effects and their propagation through the structure needs to be resolved in time and space.

2.2 Wave forms

Waves in solids are basically perturbations in the velocity field propagating through the continuum in different forms and at related different velocities. The propagating perturbation leads to wave form specific motion of the particles. The most important wave forms in solids are:

- *Longitudinal waves* of compressive or tensile type which cause particle deflections along propagating direction. They are the fastest wave forms in solids and are also called *primary waves* and the velocity is given by

$$c_L = \sqrt{\frac{E}{\rho}} \tag{5}$$

  The next fastest waves are the *shear* or *secondary waves* causing particle motion perpendicular to the wave propagation. The speed is given by

$$c_S = \sqrt{\frac{G}{\rho}} \tag{6}$$

  where G is shear modulus of material.
- Along the surface of solids propagate so called *Rayleigh waves* setting surface particles into elliptic motion and decaying in direction perpendicular to the surface.
- In structures of finite bending stiffness *flexural wave* propagate upon dynamic loading. In structures of complicated form a complicated combination of all basic wave forms can be observed.

Characteristic properties of all shock waves are extremely short rise times as well as high pressure, density and temperature amplitudes. Basically, shock waves can arise as a sequence of both wave superposition and dispersion effects:

- If the source of a pressure disturbance is moving at a speed of sound of the surrounding medium or faster, superposition of the propagated disturbance and thus pressure waves leads to increased amplitudes and pressure gradients.
- In case of nonlinear pressure-density relations the corresponding dispersion effects lead to the formation of shock waves if faster wave components overtake earlier induced waves of lower propagation speed.

External dynamic compressive loads, initiated e.g. by impact or detonation, can possibly cause very strong waves with extremely short rise times inside structure. Superposition of different wave components is responsible for the steepening of the wave front. Superposition takes place as a consequence of dispersion, an effect that arises with nonlinear compressive behaviour.

In the initial elastic regime (p_0, V_0) compressive waves are propagated at the elastic wave speed (see Fig.1)

$$c_{elastic} = c_0 = -\frac{1}{V^2}\sqrt{\left.\frac{\partial p}{\partial V}\right|_0} \tag{7}$$

As the load rises to higher pressures beyond the plastic threshold, the gradient and thus the propagation speed decreases drastically. Enhancement of pressure beyond the state of (p_1, V_1) leads to a gradual increase of the modulus. From that turn around point onwards, pressure waves are initiated that propagate faster than others before. Consequently, a superposition of slower wave packages by faster ones with higher amplitude occurs.

In the light of these observations and with a mathematical description for the slopes in the $p-V$ diagram of **Chyba! Nenašiel sa žiaden zdroj odkazov.**, conditions for the formation of shock waves can be formulated as:

$$\frac{\partial p}{\partial V} < 0 \tag{8}$$

$$\frac{\partial^2 p}{\partial V^2} > 0 \tag{9}$$

In materials with an elastic-plastic compressive behaviour according **Chyba! Nenašiel sa žiaden zdroj odkazov.**, only loading conditions achieving pressures of $p1$ or more can lead to shock waves. In gases and fluids, however, compression shocks can arise from ambient pressures onwards since no regions with $\left(\partial^2 p/\partial V^2\right) \leq 0$ exist.

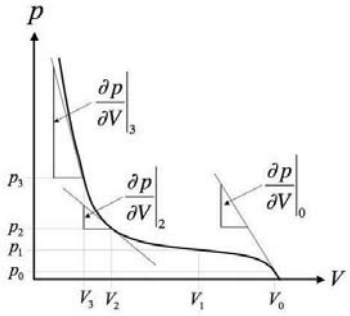

Fig. 1 Nonlinear compression curve of a solid elastic-plastic material allowing for dispersion driven shock waves.

Another necessary precondition for the shock formation is the rapid loading. Imagine a quasi-static load application to a pressure level indicated by p_1 in **Chyba! Nenašiel sa žiaden zdroj odkazov.**. Still, information about the applied load would be transported by waves at the sound speed defined by dispersion effects, i.e. depending on $\partial p/\partial V$. But time delay for each pressure increment along a certain equilibrium path would avoid the formation of a shock wave.

Only if the load application is fast enough, the wave fronts of the faster packages keep up with the earlier wave fronts. The result is a steepened wave front and shorter rise times to higher pressures. Often, the wave components from the elastic regime are fast enough that a so called *elastic precursor* is formed. It is, however, also possible that even the elastic precursor is overtaken by very fast plastic waves. Whether or not this happens is only a matter of the load application speed and the achieved maximum pressure level.

3. Computational simulations

As it was shown in the previous section the shock wave velocity is influenced by material properties, modulus of elasticity, material density, temperature, etc. Modern composite materials are reinforced by particles, fibres or layers from materials of much higher stiffness than that of the matrix. Such materials are important for many applications, as its stiffness and strength is often much higher than that of the homogeneous material (Harper, 1971; Kompiš et al., 2010; Kompiš et al., 2011). Also the dynamical properties of such materials differ from homogeneous materials by much higher damping which is important for impact by low and high velocities, but also by other loading conditions. Computational simulations described below document great importance of the damping in materials reinforced by fibres.

In following example the composite material with modulus of elasticity and density equal to 210 GPa and 7830 kg m^{-3}, respectively, is reinforced by straight fibres regularly distributed parallel to the upper surface (see Fig. 2). The modulus of elasticity of fibres is 100 times larger than that of the matrix. The loading of the material is perpendicular to the surface and it is increasing from zero to 0.0315 GPa in 0.05 μs and decreasing back to zero in same time.

In order to describe the stress behaviour of a FRM, the material is modelled as a Representative Volume Element (RVE). This element describes the homogenous behaviour of the two phases, matrix and fiber, inside the RVE. Simulations are carried out with fibers with different diameters and volume fraction of fibers. We assume perfect adhesion between the fibers and matrix.

It is a 2D problem (plain stress, t =1) and computational simulations were performed in FE software ABAQUS. The geometric parameters of the RVE are given in fig. 2. The regular FE mesh of the model consist CPS4R, 4-noded, bilinear plane stress quadrilateral element with linear base functions with hourglass control. Most number of elements (27 348) and nodes (27856) has variant 3. The problem was solved in 2000 cycles with time step 2.5 x 10^{-10} s in the model.

Boundary conditions, FE mesh are described in fig 2a and in fig. 2b is described the mesh of 14 fibers. Dimensions are the same as for RVE with 6 fibers. The pressure load is applied on the upper side of RVE. The bottom side of RVE is fixed in the Y-direction and axis symmetry was applied on the both vertical sides. Calculations were made for following 4 variants:

Variant 0 - model without fibers.

Variant 1 - model with fiber radius r_f= 1 mm and volume fraction of fiber v_f= 35%.
Variant 2 - model with r_f= 0.5 mm and v_f = 17,5%.
Variant 3 - model with r_f= 0.5mm and v_f= 35%.

In fig. 3a are described coordinates of investigated point for all four variants and in tab. 1 are their numerical values.

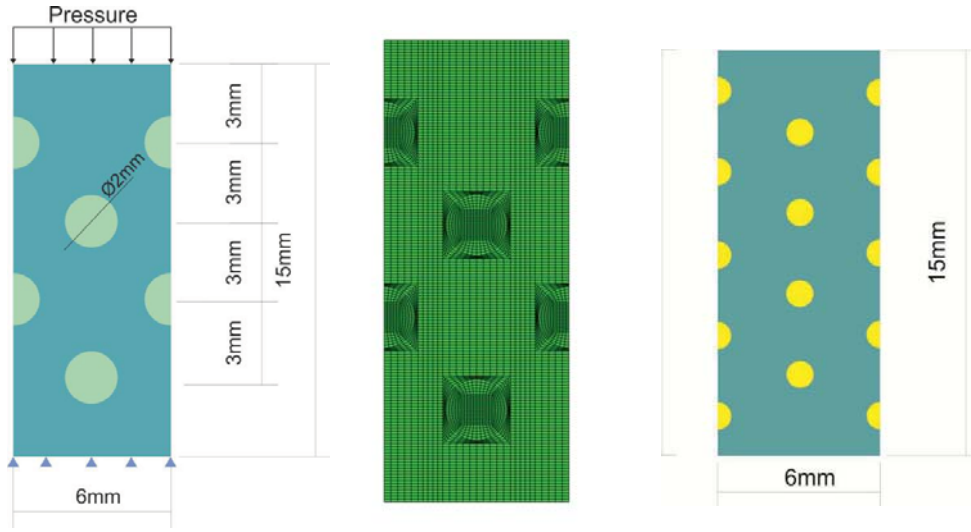

a) Boundary conditions and FEM mesh *b) Mesh of 14 fibers*

Fig. 2 Problem definition and boundary conditions

Tab. 1: Coordinates of investigated points

Point:	1	2	3	4	5	6	7	8	9	10	11	12	13	14	15
X[mm]	0	0	0	0	0	1.5	1.5	1.5	1.5	1.5	3	3	3	3	3
Y[mm]	6	3	0	-3	-6	6	3	0	-3	-6	6	3	0	-3	-6

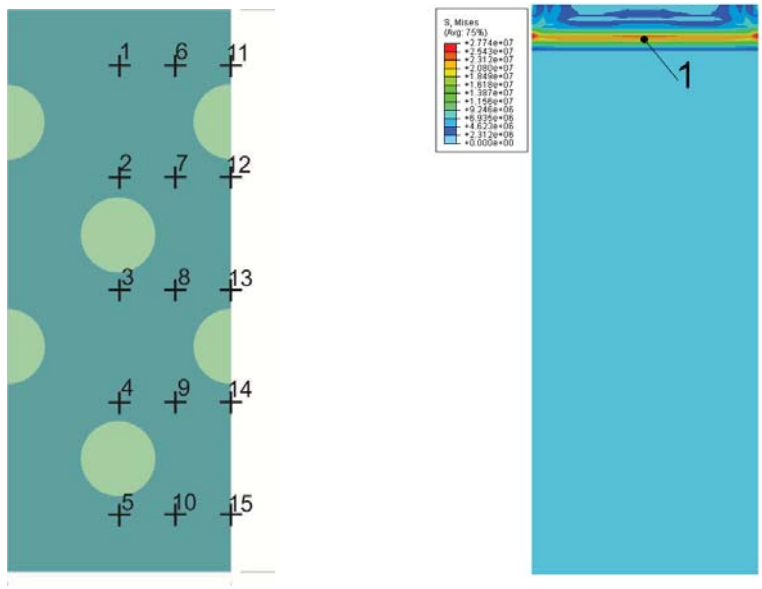

a) evaluated points

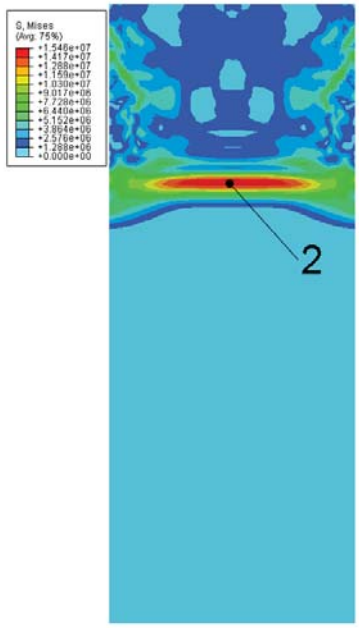

b) Point 1, t = 2.3275 E-07 s

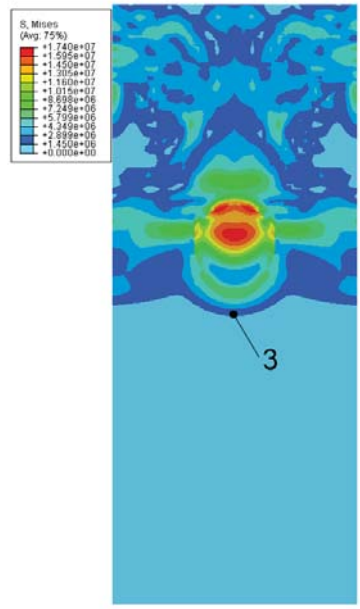

c) Point 2, t =8.4774 E-07 s

d) Point 3, t = 1.1477 E-06 s

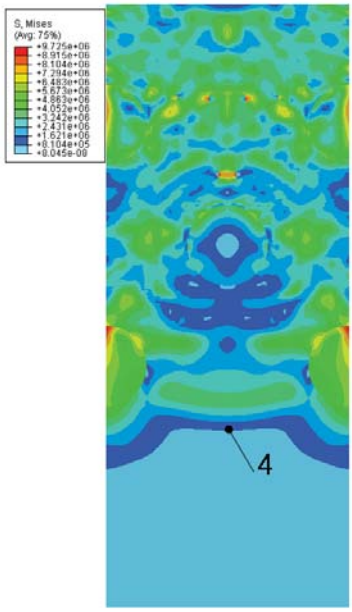

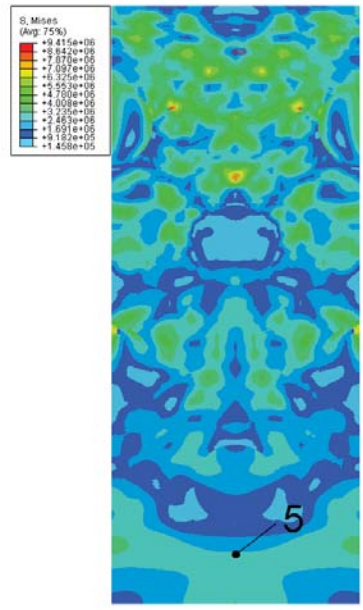

e) Point 4, t = 2.6301 E-06 s

f) Point 5, t = 2.81165 E-06

Fig. 3 Von Mises stress in investigate points 1 to 5 for variant 1

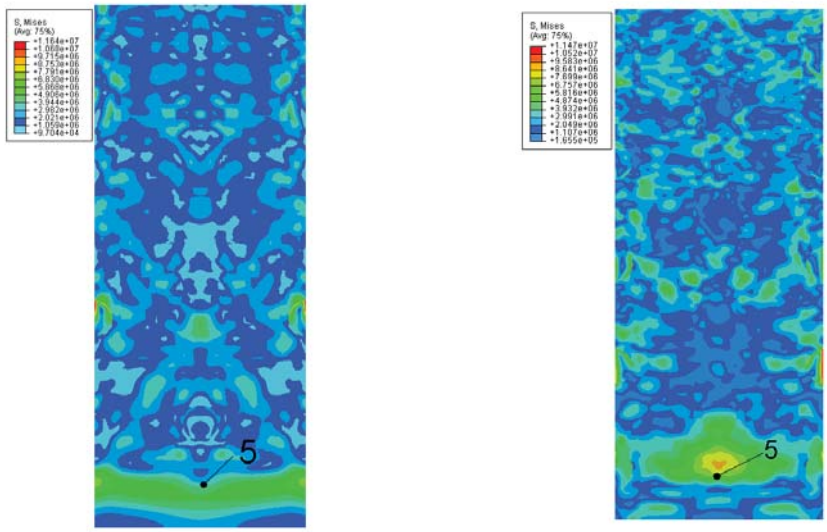

a) Variant 2, t = 3.0227 E-06 b) Variant 3, t =3.005 E-06

Fig. 4 Von Mises stress in point 5

At beginning the wave propagates parallel to the surface without any interaction (Fig.3b). After reaching first fibres the wave reflects from the fibre and interact with reflected part, however, the front of the wave is still expressive (Fig.3c). After the front of wave continues to propagate to lower part under the surface, the maximum in corresponding point is not as high as in many other points closer to the surface. Fig. 3e and fig.3f corresponds to the moment when the effective stress is maximal in point 5, but the stresses in points closer to the upper surface are larger because of complicated interactions of the waves.

Fig. 4a and fig. 4b shows the same situation for variant 2 and variant 3. Fig.5 to fig.6 shows time course of the von Misses stresses after the shock achieving the surface of the material all in points 1 to 5. The red colour corresponds to the point 1 close to the surface and other colours to the other points below the first one. From the figures we can find the movement of the front as well the maximum of the stress in time. In fig.7 and fig.8 are described time courses of the von Mises stress for variant 2 and variant 3.

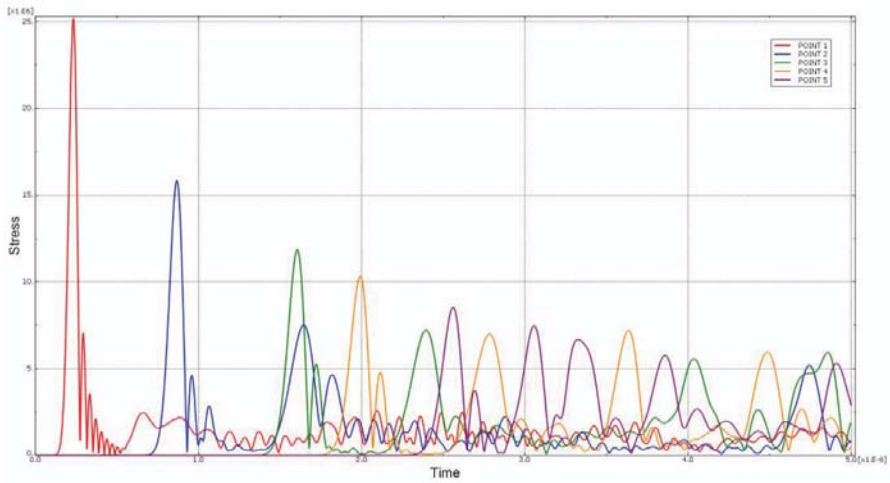

Fig. 5 Time course of the von Mises stress for variant 0

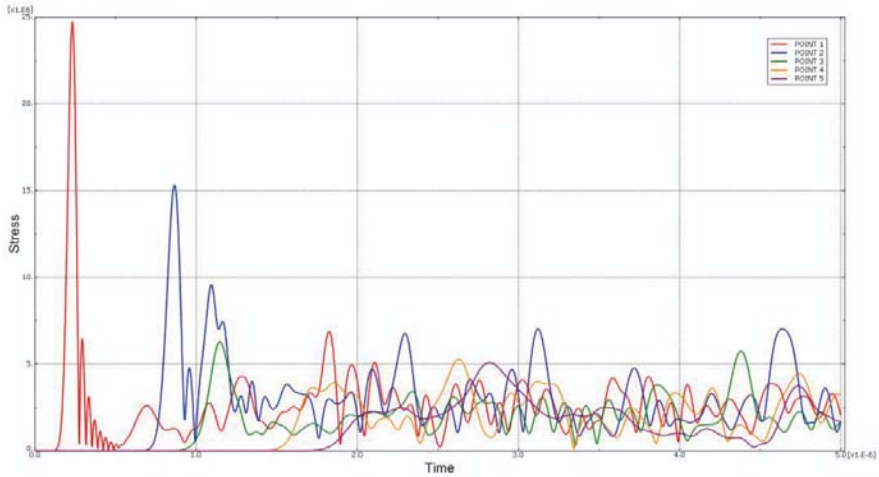

Fig. 6 Time course of the von Mises stress for variant 1

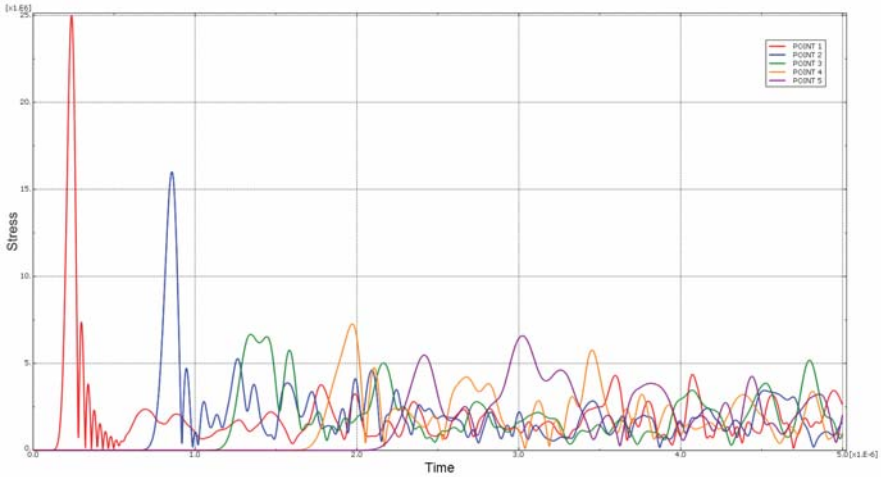

Fig. 7 Time course of the von Mises stress for variant 2

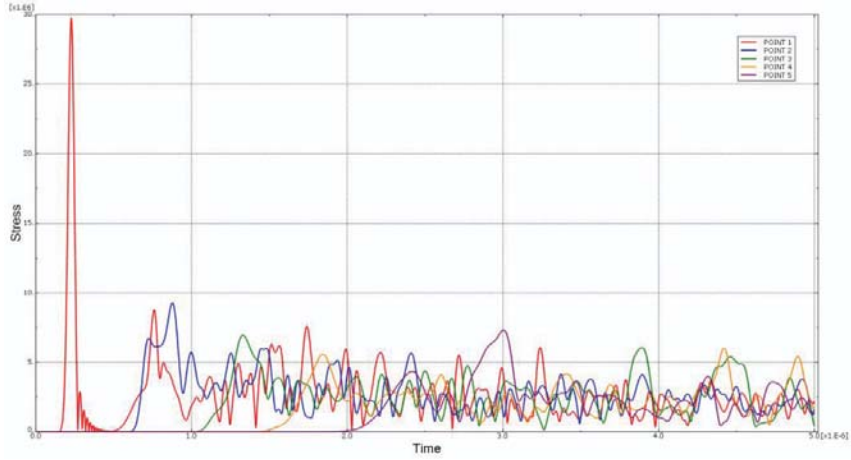

Fig. 8 Time course of the von Mises stress for variant 3

Finally, all results are summarised in tab.1, which gives maximum von Mises stress for all 4 variants in 15 investigated points throughout the period of time. In fig.9 is course of maximum von Mises stress for all variants and all investigated points. The sharp drop in maximum von Mises stress from point 1 to point 2 and 11 to 12 for variant 3 is due to passing stress wave through the fiber. The von Mises stress drop is modest from point 6 to 11 because the plane defined by points 6-10 is between fibers.

Tab. 1: maximum von Mises stresses (Pa) in points for different variants

Point	Variant 0	Variant 1	Variant 2	Variant 3
1	2.51873E+007	2.46752E+007	2.50021E+007	2.97331E+007
2	1.58461E+007	1.53314E+007	1.60142E+007	9.27268E+006
3	1.18519E+007	6.27792E+006	6.53354E+006	6.94687E+006
4	1.03242E+007	5.28174E+006	7.27257E+006	6.0145E+006
5	8.54604E+006	5.08785E+006	6.58414E+006	7.32889E+006
6	2.51873E+007	2.47847E+007	2.43585E+007	2.96361E+007
7	1.52088E+007	1.25627E+007	1.47267E+007	1.94574E+007
8	1.08391E+007	6.52019E+006	1.05614E+007	1.1574E+007
9	9.49899E+006	3.99877E+006	7.04418E+006	7.59478E+006
10	9.75734E+006	5.03414E+006	7.21751E+006	5.78076E+006
11	2.80318E+007	2.44781E+007	2.80414E+007	7.74334E+007
12	1.7466E+007	6.97456E+006	1.01383E+007	1.98204E+007
13	1.3209E+007	6.71266E+006	8.95498E+006	1.49838E+007
14	1.18789E+007	5.92797E+006	7.30872E+006	1.07567E+007
15	1.04222E+007	3.62426E+006	1.02094E+007	1.09097E+007

If we define damping ratio as von Mises stress drop in 3 planes vertical to the upper surface defined by investigated points 1-5, 6-10 and 11-15 as

$$Dampingratio = \frac{(\sigma_{von})_i - (\sigma_{von})_{i-4}}{(\sigma_{von})_i}, \; i = 5,\ 10,\ 15, \tag{10}$$

then damping ratios of stress waves for going through indicated planes are given in tab. 2. As expected, the largest value of damping ratio is for variant 3 in plane 11-15 and is 0.8591. This means that the drop of maximum von Mises stress is almost 86 percentage.

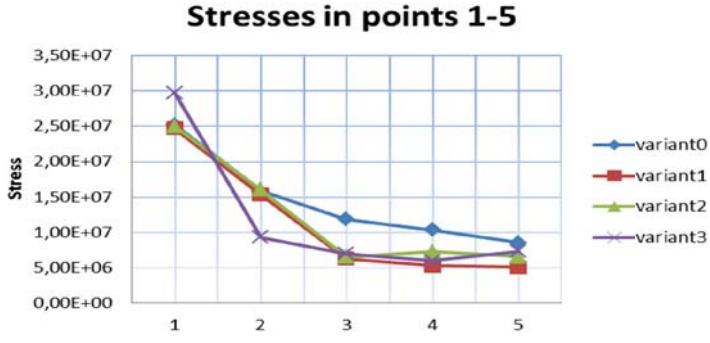

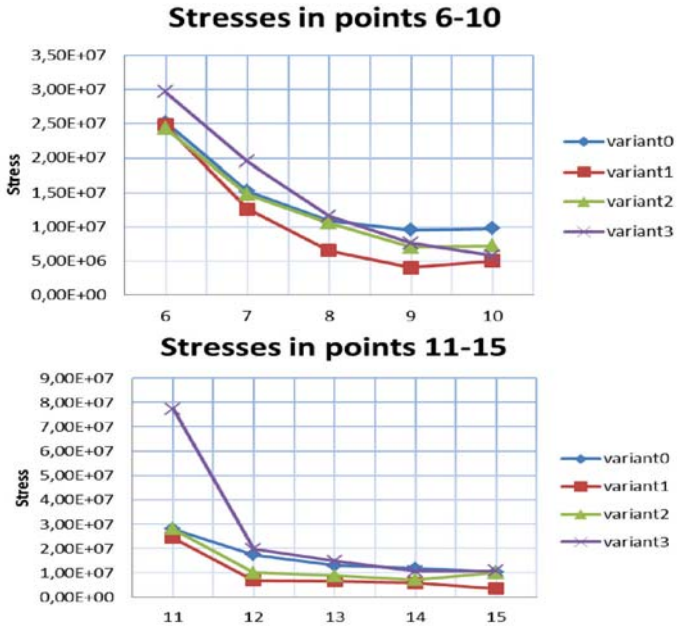

Fig. 9 Course of von Mises stress in investigated points

Tab: 2 Damping ratios of stress waves

Plane	Variant 0	Variant 1	Variant 2	Variant3
1 - 5	0.6607	0.7938	0.7367	0.7535
6-10	0.6126	0.7969	0.7037	0.8049
11-15	0.6282	0.8519	0.6359	0.8591

We note that computational models do not contain any other damping except of the interaction of the shock wave with fibres (each material contains some imperfections in the structure and in material properties and so, there is some material damping also in homogeneous material) and shows as the reinforcing fibres because of very different material properties of both material components result in very efficient damping of shock waves and thus such composite can be very efficient in defence against explosion.

The shock wave in homogeneous material is not influenced by propagation through material and only when it is reflected on the boundaries there is an interaction with propagated wave [Hermaier, (2008); Kompiš, at al. (2010)]. On the other side there is very complicated interaction of the wave by reflection, and refraction on the interface between softer matrix and stiffer fibres leading to strong damping of the shock wave.

4. Conclusions

The problem of shock wave propagation was studied in this work. Computational simulations were performed in FE software ABAQUS. The FEM simulation was based on the RVE model. Simulations are carried out with fibers with different diameters and volume fraction of fiber. The proposed procedure allow very effectively without expensive experiments to study the behaviour of composite materials from all points of view, the material structure topology, material properties of components, percentage of reinforcement, etc. That the longest calculation time was for variant 3 and used CPU time was only 1:47:17 on Pentium desktop computer with Intel core i5 with 2,6 GHz frequency and 8 GB RAM.

Acknowledgement

The authors gratefully acknowledge the support by the Slovak Grant Agency VEGA 1/1226/12 and Slovak Science and Technology Assistance Agency registered under number APVV-0169-07.

References

ABAQUS 6.11 (2011), *Theory-manual*, DS Simulia, Providence, RI.

Barker, L. M. & Barker, Z. B. (2006) *The VALYN multi-beam VISAR*, Valyn Press, Albuquerque, New Mexico.

Bathe, K.J., (2011) A finite element method enriched for wave propagation problems, Int. J. of Computers and Structures (to be published).

Brepta, R (1997) *Shocks and stress waves in solid elastic bodies*. CVUT publisher, (in Czech)

Datta, K.S., Shah, A.H. (2009) *Elastic Waves in Composite Media and Structures wit Applications to ultrasonic Nondestructive Evaluation*, CRC Press, Taylor & Francis Group , LLC.

Gopalakrishnan, S., Chakraborty, A., Mahapatra D.R. (2008) *Spectral Finite element Method, Wave Propagation, diagnostics and Control in Anisotropic and Inhomogeneous Structures*. Springer –Verlag London Limited.

Harper, E. Y. (1971) *Method and means for attenuating shock waves propagating within a solid*, US Patent 3592147.

Hiermaier, S. J. (2008) *Structures under crash and impact, Continuum mechanics, discretization and experimental characterization*, Springer, New York.

Kompiš, V., Vančo, M. & Ferencey, V. (2010) Shock waves in composite materials, *Mechanical Engineering Journal*, pp 73-87.

Kompiš, V., Qin, Q.H., Fu, Z., Chen, C.S., Droppa, P., Kelemen & M., Chen, W. (2011) Parallel computational models for composites reinforced by short fibres, *Engineering Analysis with Boundary Elements*, 36, pp. 47-52.

Kormaníková, E., Riecky, D., Žmindák, M. (2011): Strength of Composites with Short Fibers. In: Eds, J. Murín: *Computational Modelling and Advanced Simulations*, Springer Series: Computational Methods in Applied Sciences, Vol. 24.

Liu, Y. (2009) Fast Multipole Boundary Element Method, Theory and Applications in Engineering, Cambridge University Press.

LS DYNA theory-manual, Livermore Software Technology Corporation, Livermore, California, 2006.

Malvern, L.E. (1969) *Introduction to mechanics of a continuous medium*, Prentice Hall, Englewood Cliffs, New Jersey.

Mader, C.R. (2008) *Numerical modeling of explosives and propellants*, CRC Press Taylor & Francis, Boca Raton.

Meyers, M.A., Armstrong, R.W. & Kirchner, H.O.K. (1999) *Mechanics and materials. Fundamentals and linkages*, John Wiley & Sons, New York.

Meyers, M. A. (1994) *Dynamic behaviour of materials*, John Wiley, New York.

Okrouhlik M. (2001) Computational Aspects of Stress Waves Problems in Solids . *2nd European Conference on Computational Mechanics*, Abstracts Vol. 1, Cracow, Poland, pp. 1- 30.

Sládek, J, Sládek, V, Jakubovičová, J., (2002) *Application of Boundary Element Methods in Fracture Mechanics*. University of Žilina, Faculty of Mechanical Engineering, Žilina.

Tsai, L. (2006) *Shock wave structure and spall strength of layered heterogeneous glass polymer composite*, PhD Thesis, Case Western Reserve University.

Wu, H.C. (2005) *Continuum mechanics and plasticity*, Chapman and Hall/CRC London.

Author index

Items are referred in the form: SECTION-page number, #paper number

G

H

Ch

I

J

K

L

M

N

O

P

R

S

T

U

V

W

Y

Z

ISBN 978-80-86246-39-0
ISSN 1805-8256